PROCEEDINGS

ismab2026.ksam76.or.kr

The 12th International Symposium on Machinery and Mechatronics for Agricultural and Biosystems Engineering

ISMAB2026

October 20 (Tue) - 24 (Sat)

BEXCO Exhibition Center 2

Busan, Republic of Korea

Organized by

Korean Society for Agricultural Machinery (KSAM)

Japanese Society of Agricultural Machinery and Food Engineers (JSAM)

Chinese Institute of Agricultural Machinery (CIAM)





Host and Organizer (사)한국농업기계학회 KSAM Korean Society for Agricultural Machinery

Co-organizer 밭농업기계개발연구센터 UPLAND-FIELD MACHINERY RESEARCH CENTER · 전남대학교 디지털농업 전문인력양성 및 기술 개발 사업단 · PIONEER 부산대학교 국립대학육성사업 · 부산대학교 PUSAN NATIONAL UNIVERSITY 생명산업융합연구원 · 부산관광공사

Sponsor KAMICO 한국농기계공업협동조합 · daedong · LS Tractor · TYM · (주)볼스 · 그린제어시스템 Green Control System · ALPHA ON · NPG · HMC 희망 · (주)대신에이씨엔 대신종합농기계

PROCEEDINGS

ismab2026.ksam76.or.kr

The 12th International Symposium on Machinery and Mechatronics for Agricultural and Biosystems Engineering

ISMAB2026

October 20 (Tue) - 24 (Sat)

BEXCO Exhibition Center 2

Busan, Republic of Korea

Organized by

Korean Society for Agricultural Machinery (KSAM)

Japanese Society of Agricultural Machinery and Food Engineers (JSAM)

Chinese Institute of Agricultural Machinery (CIAM)



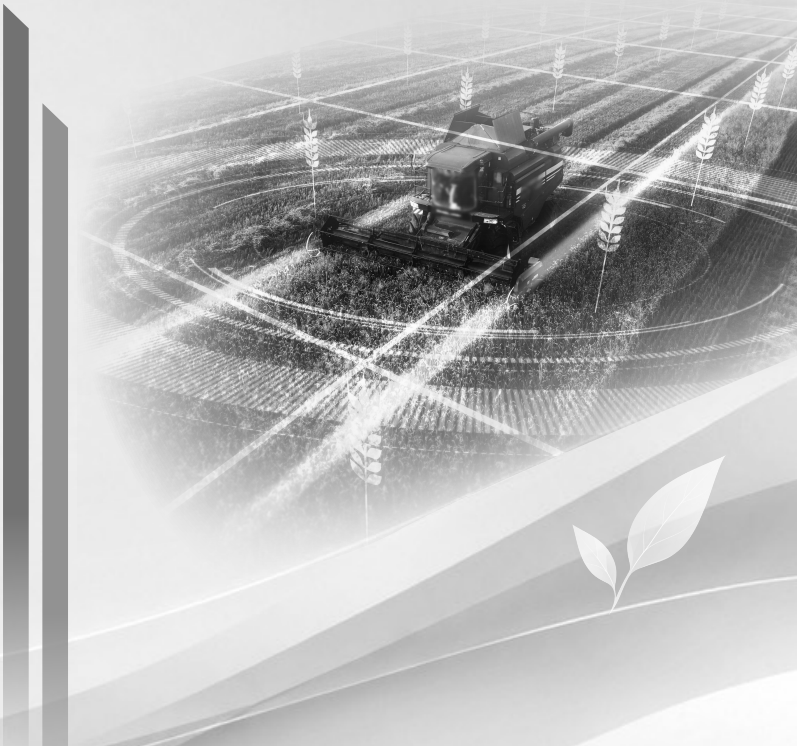

Host and Organizer (사)한국농업기계학회 KSAM Korean Society for Agricultural Machinery

Co-organizer 밭농업기계개발연구센터 UPLAND-FIELD MACHINERY RESEARCH CENTER · 전남대학교 디지털농업 전문인력양성 및 기술 개발 사업단 · PIONEER 부산대학교 국립대학육성사업 · 부산대학교 생명산업융합연구원 PUSAN NATIONAL UNIVERSITY · 부산관광공사

Sponsor KAMICO 한국농기계공업협동조합 · daedong · LS Tractor · TYM · (주)볼스 · 그린제어시스템 Green Control System · ALPHA ON · NPG · HMC 희망 · (주)대신에이씨엠 대신종합농기계

TABLE OF CONTENTS

- Welcome and Opening Address ····· 2
- Congratulatory Remarks ····· 3
- ISMAB2026 Committee ····· 4
- Program Overview ····· 6
- Floor Plan ····· 7
- Plenary Session: Invited Speakers ····· 9
- Keynote Speakers ····· 10
- ISMAB2026 Oral Presentation ····· 11
- ISMAB2026 Poster Presentation ····· 40
- KSAM Special Session ····· 55

Welcome and Opening Address

Good morning, ladies and gentlemen, respected invited speakers, distinguished professors and students, and honored guests, welcome to Korea and welcome to Busan.

On behalf of the Korean Society for Agricultural Machinery (KSAM), we welcome all of you to the 12th ISMAB conference, 20th ~ 24th October 2026, here at BEXCO, Busan, Republic of Korea. AABEA (Asian Agricultural and Biological Engineering Association), is for members of CIAM (The Chinese Institute of Agricultural Machinery), JSAM (The Japanese Society of Agricultural Machinery), and KSAM. AABEA continues the tradition to hold the biennial ISMAB (International Symposium on Machinery and Mechatronics for Agriculture and Biosystems Engineering). We would like to express our deep appreciation to Dr. Je-Hoon Sung for congratulatory remarks, to invited speakers for valuable presentations, and AABEA members and all the participants for grateful contribution. Special thanks also should go to the ISMAB committee members and staffs for their tremendous efforts.

Agriculture and Biosystems Engineering field has made dramatic and meaningful achievement to provide necessary engineering technologies for food security. However, recent backgrounds of world population increase, climate change, agricultural labor reduction, global market competitiveness assign us various problems and challenges. Quick mega trends of 4th revolution technologies such as AI and robot enable to overcome these issues and develop better opportunities.

This conference will bring together leading researchers, engineers, scientists from various disciplines of agriculture and biosystems engineering around the world. We have about 450 pre-registrations, and including on-site registration, we expect to have a total of about 550 attendants. Total 317 abstracts, including 166 for oral and 151 for poster presentations, were submitted. The symposium will provide a unified communication platform for researchers and engineers in the topics of Machinery and Mechatronics for Agriculture and Biosystems Engineering. During the conference, there will be substantial time for presentation and discussion. Attendants will find various activities useful in bringing together a diverse group of engineers and technologists across the disciplines for the generation of new ideas, collaboration potential, and business opportunities.

We also hope all attendees spend an enjoyable time in Busan, one of the beautiful cities in Korea. Welcome to the conference again and thank you very much.

Hyuck Joo Kim
ISMAB Conference Chair, AABEA

Sun-Ok Chung
President, Korean Society for Agricultural Machinery

Congratulatory Remarks

Good morning, distinguished scholars, researchers, industry experts, and honored guests. It is a great pleasure and honor to be with you today. My name is Sung Je-hoon, and I am the Director General of the National Institute of Agricultural Sciences under the Rural Development Administration of the Republic of Korea.

On behalf of the National Institute of Agricultural Sciences, I would like to extend my warmest congratulations on the opening of the 12th International Symposium on Machinery and Mechatronics for Agriculture and Biosystems Engineering, ISMAB, here in Busan. The 12th ISMAB comes at a particularly important time for agriculture and biosystems engineering. Today, agriculture is facing increasingly complex challenges, including climate change, resource constraints, and the growing need for more sustainable and resilient production systems. Against this backdrop, the 12th ISMAB provides a timely and valuable forum for researchers and professionals from around the world to exchange ideas, share the latest research findings, and explore new possibilities in machinery and mechatronics for agriculture and biosystems engineering.

As a researcher with a background in precision agriculture, I am particularly interested in how agricultural machinery and intelligent technologies are evolving to enable more precise, efficient, and sustainable farming systems. In particular, the convergence of AI, information processing, sensing technologies, and agricultural machinery is opening new possibilities for smart and autonomous agriculture. The diverse perspectives offered by our distinguished keynote speakers, covering agricultural mechanization, smart and precision agriculture, and future research directions across Asia, will provide valuable insights into the future of agricultural engineering. I look forward to the insightful discussions and exchanges that this symposium will bring, and to seeing how advances in agricultural engineering can contribute to a more sustainable and resilient future for agriculture. Finally, I would like to sincerely thank the ISMAB organizers for inviting me to this meaningful gathering and for bringing together distinguished experts from around the world. I hope this symposium will foster lasting international networks, meaningful collaborations, and new opportunities for innovation.

I also hope that, after the scientific sessions, you will enjoy a pleasant evening together and have the opportunity to experience Busan's beautiful coastline, vibrant culture, and unique local attractions. Thank you once again, and I wish you all a successful symposium and a memorable stay in Busan. Thank you very much.

Je-hoon Sung

Director General
National Institute of Agricultural Sciences
Rural Development Administration, Republic of Korea

ISMAB2026 Committee

KSAM President and Conference Chair

- Prof. Sun-Ok Chung, Chungnam National University (KSAM President, Korea)
- Prof. Hyuck Joo Kim, Sunchon National University (Conference Chair, Korea)

Advisory Committee

- Prof. Choong Ho Lee, Jeonju University (Korea)
- Dr. Jong Hoon Kim, Korea Food Research Institute (Korea)
- Dr. Je Hoon Sung, National Institute of Agricultural Sciences (Korea)
- Mr. Ho-Jong Choi, Korea Agricultural Machinery Industry Cooperative (Korea)
- Mr. Dae Sik Kang, GreenMax Corporation (Korea)
- Prof. (Emeritus) Naoshi Kondo, Kyoto University (Japan)
- Prof. (Emeritus) Kenshi Sakai, Tokyo University of Agriculture and Technology (Japan)
- Prof. Michihisa Iida, Kyoto University (Japan)
- Prof. Huaang-Youh Hurng, National Chiayi University (Taiwan)
- Prof. Suming Chen, National Taiwan University (Taiwan)
- Prof. Yi-Chich Chiu, National Ilan University (Taiwan)

Organizing Committee

- Dr. Kyu-Chul Nam, Korea Agricultural Machinery Industry Cooperative (Korea)
- Mr. Youngjo Nam, Bulls Corporation (Korea)
- Dr. Young-Joo Kim, Korea Institute of Industrial Technology (Korea)
- Dr. Sunghwan Jeong, Korea Electronics Technology Institute (Korea)
- Dr. Young-Tae Kim, Korea Agriculture Technology Promotion Agency (Korea)
- Dr. Kyungran Kim, National Institute of Agricultural Sciences (Korea)
- Prof. Dong Eok Kim, Korea National University of Agriculture and Fisheries (Korea)
- Prof. Woong Kim, Kongju National University (Korea)
- Prof. Ghiseok Kim, Seoul National University (Korea)
- Prof. Dae Hyun Kim, Kangwon National University (Korea)
- Prof. Dong-Hoon Lee, Chungbuk National University (Korea)
- Prof. Jongsoon Kim, Pusan National University (Korea)
- Prof. Chanseok Ryu, Gyeongsang National University (Korea)
- Prof. Kyeong-Hwan Lee, Chonnam National University (Korea)
- Prof. Dae-Cheol Kim, Jeonbuk National University (Korea)
- Prof. Byoung-Kwan Cho, Chungnam National University (Korea)

- Prof. Michihisa Iida, Kyoto University (Japan)
- Prof. Tadashi Chosa, Tokyo University of Agriculture and Technology (Japan)
- Prof. Yukiharu Ogawa, Chiba University (Japan)
- Prof. Eiji Morimoto, Kobe University (Japan)
- Prof. Takashi Okayasu, Kyushu University (Japan)
- Prof. Kohei Nakano, Gifu University (Japan)
- Prof. Chien-Yu Chen, National Taiwan University (Taiwan)
- Prof. Ping-Lang Yen, National Taiwan University (Taiwan)
- Prof. Yao-Chuan Tsai, National Chung Hsing University (Taiwan)
- Prof. Yung-Chuan Chiou, National Chiayi University (Taiwan)
- Prof. Chung-Liang Chang, National Pingtung University of Science and Technology (Taiwan)
- Prof. Meng Li Tsai, National Ilan University (Taiwan)

Program Committee

- Prof. Yu Shin Ha, Kyungpook National University (Korea)
- Prof. Taehwan Kang, Kongju National University (Korea)
- Prof. Ju-Seok Nam, Kangwon National University (Korea)
- Prof. Yongjin Cho, Jeonbuk National University (Korea)
- Dr. Minyoung Kim, Rural Development Administration (Korea)
- Prof. Sangbae Park, Seoul National University (Korea)
- Prof. Sung Bo Shim, Kyungpook National University (Korea)
- Dr. Young-ki Hong, National Institute of Agricultural Sciences (Korea)
- Prof. Jae-Woong Han, Kongju National University (Korea)
- Prof. Meong Hun Lee, Sunchon National University (Korea)
- Prof. Hoon Seonwoo, Sunchon National University (Korea)
- Prof. Hyun Kwon Suh, Sejong University (Korea)
- Prof. Jaesung Park, Pusan National University (Korea)
- Prof. Xiongzhe Han, Seoul National University (Korea)
- Prof. Rackwoo Kim, Seoul National University (Korea)
- Prof. Woo Jae Cho, Gyeongsang National University (Korea)

Program Overview

Title	12th International Symposium on Machinery and Mechatronics for Agriculture and Biosystems Engineering (ISMAB2026)
Venue	Exhibition Center 2, BEXCO (https://www.bexco.co.kr/eng), Busan, Republic of Korea
Theme	Strengthening Global Competitiveness and Exploring Market Opportunity
Date	October 20 (Tue), afternoon – 24 (Sat), morning (*subject to change depending on circumstances)

Program			
Date	Event and Schedule		Venue
20th (Tue)	▪ 13:00~18:00 ▪ 13:00~17:00 ▪ 18:00~21:00	Registration Open Technical Special Lectures for KSAM students, 4 Lectures Welcome Reception for invited VIPs and ISMAB committee members	▪ 3rd Floor ▪ Rooms 321~324 ▪ Unloading parking → restaurant
21st (Wed)	▪ 09:30~10:00 ▪ 10:00~12:30 ▪ 12:30~14:00 ▪ 14:00~17:30 ▪ 18:00~21:00	ISMAB Opening Ceremony, Group Photo Plenary Session (5 speakers, 25 min each) Lunch (Exhibition Center 1, B1) Technical Sessions, Oral, coffee break KSAM Special Sessions Conference Banquet	▪ Hall 5A ▪ Hall 5A ▪ The Party Buffet ▪ Rooms 321~326, 121~122 ▪ Rooms 123~126, 320 ▪ Hall 5A
22nd (Thu)	▪ 09:00~10:00 ▪ 10:00~12:00 ▪ 12:00~13:30 ▪ 13:30~16:30 ▪ 17:00~18:00 ▪ 18:00~21:00	KSAM General Assembly Poster Session, 1 coffee any time Lunch (Exhibition Center 1, B1) Technical Sessions, Oral, coffee break KSAM Special Sessions AABEA, ISMAB, EAEF Meetings ISMAB Closing Ceremony AABEA, ISMAB, EAEF Dinner	▪ Hall 5A ▪ Hall 5A ▪ The Party Buffet ▪ Rooms 321~326, 121~122 ▪ Rooms 124~126 ▪ Room 320 ▪ Hall 5A ▪ Unloading parking → restaurant
23rd (Fri)	▪ 09:00~17:00 – 09:00~10:00 – 10:00~12:00 – 12:00~13:00 – 13:00~14:00 – 14:00~16:00 – 16:00~17:00	Technical Tour BEXCO to “Department of Upland Crop Science, RDA” (Miryang) Tour of “Department of Upland Crop Science, RDA” Lunch Move to “Protected Horticulture Research Institute” (Haman) Tour of “Protected Horticulture Research Institute” Return to BEXCO	▪ Meet at “Unloading parking” at 09:00
24th (Sat)	▪ 09:00~18:00	Committee Meetings	▪ To be assigned

Floor Plan

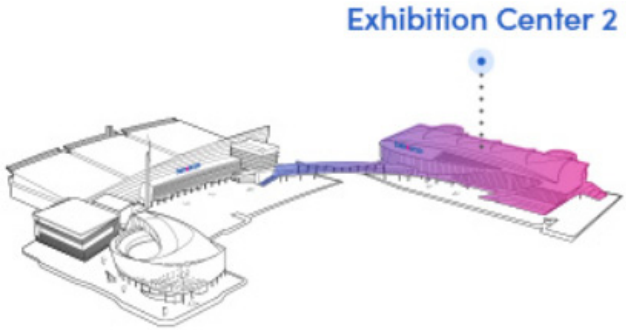

Exhibition Center 2
F3

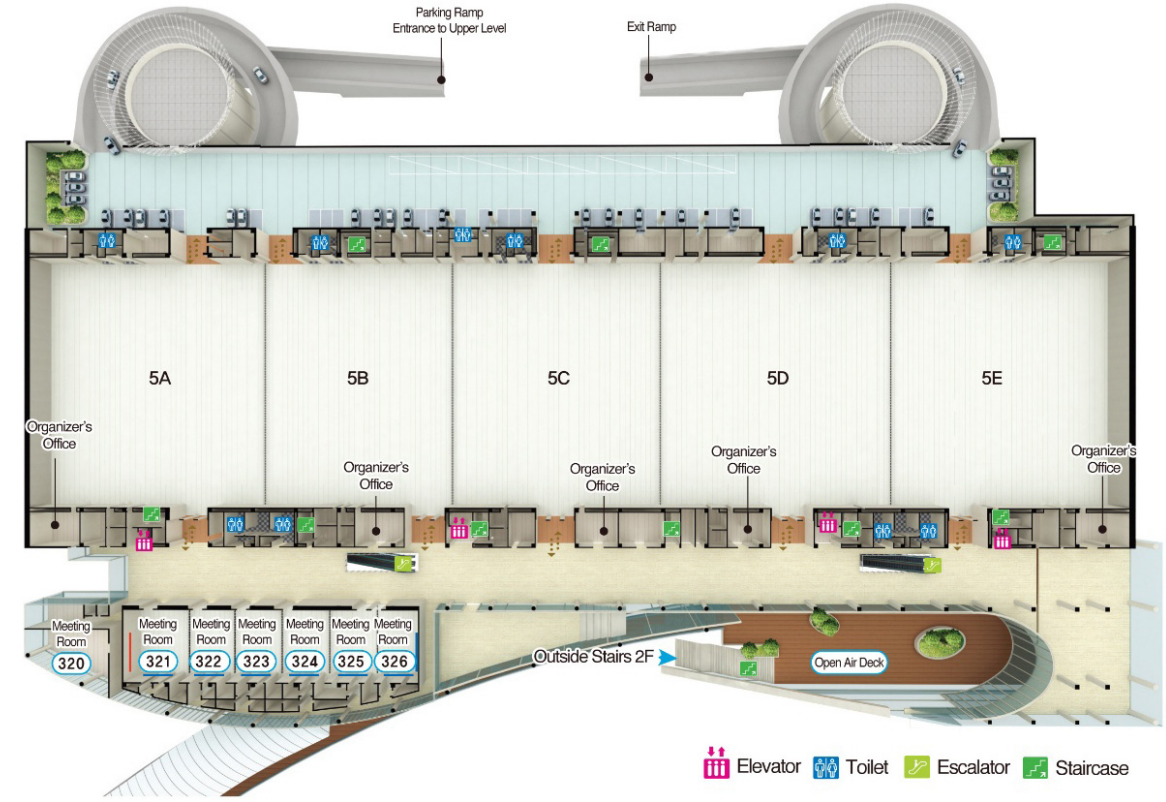

Exhibition Center 2

F1



Exhibition Center 1

B1

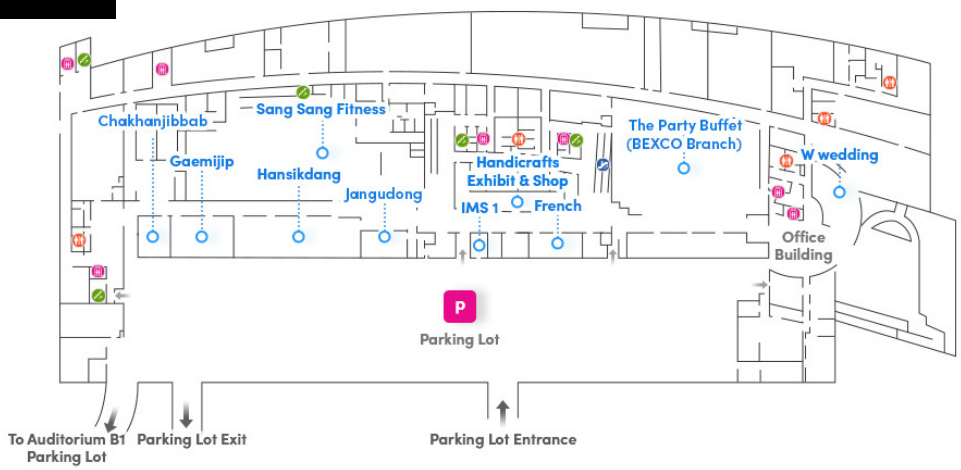

Plenary Session: Invited Speakers

■ | 10/21 (Wed) | 10:00~12:30, Hall 5A

	Name	Nation	Affiliation	Presentation Title
				Chair: Xiongzhe Han (Seoul National University)
	**Engr. Eleonor Fausto Santiago**	Philippines	DA–PHilMech	The PHilMech Green Blueprint: Transforming Philippine Agriculture through Mechanization
	**Dr. Rosnah Shamsudin**	Malaysia	Universiti Putra Malaysia / Malaysian Society of Agricultural and Food Engineers	Agricultural and food Mechanization in Malaysian SMEs: Industry Status, Market Trends, and Future Research Directions
	**Dr. Yi-Chich Chiu**	Taiwan	National Ilan University	Agricultural machinery market trends, industry status, and current research landscapes in Taiwan
	**Dr. Michihisa Iida**	Japan	Kyoto University	Agricultural machinery market trends, industry status, and current research landscapes in Japan
	**Dr. Sun-Ok Chung**	Republic of Korea	Chungnam National University	Trends of Smart Precision Agriculture in Korea

Keynote Speakers

■ | 10/21 (Wed) | 14:00~14:30, Room 323

	Name	Nation	Affiliation	Presentation Title
				Chair: Prof. Eiji Morimoto (Kobe University)
	Dr. Eiji Morimoto	Japan	Kobe University	AI-Driven Innovation for Sustainable and Intelligent Agricultural Systems

■ | 10/21 (Wed) | 14:00~14:30, Room 326

	Name	Nation	Affiliation	Presentation Title
				Chair: Prof. Rack-woo Kim (Seoul National University)
	Dr. Yao-Chuan Tsai	Taiwan	National Chung Hsing University	Smart poultry farming: Integrating AI for next-generation management

ISMAB2026 Oral Presentation

| 10/21 (Wed) |

Room 321 **Precision Agriculture Machinery and Systems 1 (PA-1)**

Chair: Prof. Xiongzhe Han (Seoul National University)

PA-01	14:00~14:15	CORN SILK MATURITY RECOGNITION FROM UAV IMAGERY USING YOLO SEGMENTATION AND FUZZY C-MEANS CLUSTERING Sheng-Wei Chen*, Wu-Yang Sean
PA-02	14:15~14:30	SIMULATION-TO-FIELD DEVELOPMENT OF AN AUTONOMOUS GREENHOUSE NAVIGATION AND SENSING ROBOT Sutan Muhamad Sadam Awal*, Yamato Sakurai, Dong Thanh Pham, Koichi Nomura, Masaharu Kitano, Daisuke Yasutake, Muneshi Mitsuoka, Takashi Okayasu
PA-03	14:30~14:45	ARUCO-BASED INDOOR LOCALIZATION AND HOVERING CONTROL FOR A QUADROTOR UAV Yu-Tse Lee, Chung-Liang Chang*
PA-04	14:45~15:00	PERFORMANCE EVALUATION AND IMPROVEMENT POTENTIAL OF A TOMATO DE-LEAFING ROBOT USING A MAIN STEM-BASED APPROACH Tokihiro FUKATSU*, Masakazu KASHINO, Hideto KUROSAKI
PA-05	15:00~15:15	DEVELOPMENT OF AN ELECTRONIC NOSE WITH PI-CONTROLLED TEMPERATURE REGULATION FOR MONITORING POULTRY LITTER FERMENTATION Jing-Xiang Lu, Chin-Cheng Wu *, Chung-Yen Chuang
PA-06	15:15~15:30	ACCURACY EVALUATION OF LIDAR-INERTIAL SLAM-BASED AUTONOMOUS NAVIGATION IN GREENHOUSE ENVIRONMENTS Nang Nguyen Van*, Hayato Seki, Oyetayo Olukorede Oyebode
PA-07	15:30~15:45	DESIGN OF AN INTEGRATED THREE-AXIS MAGNETIC FIELD SENSOR Shu-Yi Wen, Zhi-Xuan Dai*

Room 321 Precision Agriculture Machinery and Systems 2 (PA-2)

Chair: Prof. Xiongzhe Han (Seoul National University)

PA-08	16:00~16:15	ON-TREE PEAR SIZE ESTIMATION USING UPWARD-FACING RGB-D IMAGING IN HORIZONTAL TRELLIS ORCHARDS Meguna OHATA, Jaehwan LEE, Tomoko HORIE, Hiromichil TOH, Eiji MORIMOTO*
PA-09	16:15~16:30	DEVELOPMENT OF ROBUST 3D PEAR FRUIT COUNTING SYSTEM USING LIDAR-CAMERA FUSION Jaehwan LEE, Meguna OHATA, Tomoko HORIE, Hiromichi ITOH, Eiji MORIMOTO*
PA-10	16:30~16:45	GROUND-BASED LIDAR FOR CROP STRUCTURAL ASSESSMENT: FIELD ACQUISITION AND WIND-EFFECT EVALUATION Eldon DE PADUA, Jaehwan LEE, Eiji MORIMOTO*
PA-11	16:45~17:00	FIELD PERFORMANCE OF THE SELF-PROPELLED CABBAGE HARVESTERS UNDER SINGLE AND DOUBLE-ROW FIELD CONDITIONS Cholet Nyangoma Atulinda, Md Nasim Reza, Ezatullah Zakir, Md Razob Ali, Jose Pocholo Dorongon, Sun-Ok Chung*
PA-12	17:00~17:15	DEVELOPMENT AND EVALUATION OF A TRANSFER PLATFORM FOR RAIL-TO-RAIL MOVEMENT IN GREENHOUSE HORTICULTURE Sota Yoshida*, Kota Shimomoto, Nozomu Ohta, Tokihiro Fukatsu

Room 322 Precision Agriculture Machinery and Systems 3 (PA–3)

Chair: Prof. Woo–Jae Cho (Gyeongsang National University)

PA–13	14:00~14:15	DEVELOPMENT OF A CFD–BASED GREENHOUSE SURROGATE MODEL FOR DIGITAL TWIN ENVIRONMENTAL CONTROL Hsuan–Yu Chen, Cheng–Wei Fu, Chen–Kang Huang*
PA–14	14:15~14:30	RESEARCH ON A VISION–GUIDED MULTI–TASK ROBOTIC SYSTEM FOR AUTONOMOUS *PHALAENOPSIS* ORCHID MANAGEMENT IN GREENHOUSES Duc Tai Nguyen, Doan Dang Khoa Nguyen, Wei–Chih Lin*
PA–15	14:30~14:45	A CLUSTER–BASED THINNING RECOMMENDATION FRAMEWORK FOR INTELLIGENT PEACH FRUITLET SELECTION Nilda Navarette Dela Cruz, Hao–Ting Lin*
PA–16	14:45~15:00	A HYBRID WHEELED–LEGGED QUADRUPED PLATFORM WITH ACTIVE BALANCING FOR MULTI–TASK AGRICULTURAL APPLICATIONS Doan Dang Khoa Nguyen, Nam Khanh Nguyen, Dang Khanh Linh Le, Wei–Chih Lin*
PA–17	15:00~15:15	3D SLAM AND RELOCALIZATION TOWARDS AUTONOMOUS NAVIGATION IN PAPAYA GREENHOUSE USING NANO–GICP REGISTRATION Chi Cuong Nguyen, Dang Khanh Linh Le, Wei–Chih Lin*
PA–18	15:15~15:30	EARLY DETECTION OF BARLEY WATERLOGGING USING UAV–BASED HYPERSPECTRAL IMAGERY Ji An Kim, Do Hyun An, Hyo Jeong Lee, Ye Seong Kang*, Yeong Son Jo, Seung Ga Oh, Hui Su Bae, Woo Jin Im
PA–19	15:30~15:45	PRE–HARVEST PREDICTION OF APPLE SOLUBLE SOLIDS CONTENT USING UAV BASED MULTISPECTRAL IMAGERY Chang Hyeok Park, Chan Seok Ryu*, Gangln Je, HoJun Kwon, Gang–Jin Lee

Room 322 Precision Agriculture Machinery and Systems 4 (PA-4)

Chair: Prof. Woo-Jae Cho (Gyeongsang National University)

PA-20	16:00~16:15	STUDY ON THE ESTIMATION OF LOCAL HORIZONTAL WIND ABOVE FIELD FROM UAV-MOUNTED ULTRASONIC ANEMOMETER Hiroto Zushi, Atsuru Fujimoto*
PA-21	16:15~16:30	PRELIMINARY EVALUATION OF ULTRASONIC-BASED LATERAL OFFSET SENSING FOR A SELF-PROPELLED SEEDER Miaomiao Tu, Md Nasim Reza, Dae-Hyun Lee, Sun-Ok Chung*
PA-22	16:30~16:45	DEVELOPMENT OF AN AIOT-BASED MONITORING SYSTEM FOR EARLY WARNING OF RED IMPORTED FIRE ANT (*SOLENOPSIS INVICTA*) NUPTIAL FLIGHTS Jui-Lin Hsu, Pei-Tzu O, Po-Cheng Shih, Cheng-Wei Fu, Scotty Yang, Chen-Kang Huang*
PA-23	16:45~17:00	LED-BASED FREQUENCY-DOMAIN FLIM FOR CELLULAR-SCALE CHLOROPHYLL A FLUORESCENCE CHARACTERIZATION IN *ELODEA DENSA* Cheng-Hao Lin, Hsiao-Mei Wu*
PA-24	17:00~17:15	BRIDGING UAV AND SATELLITE OBSERVATIONS FOR SOYBEAN LAI MAPPING Gyujin Jang, Jaeyoung Lee, Haneul Kim, Seung Hwan Jeong, Hak-Jin Kim*

Room 323 AI and Information Processing 1 (AI-1)

Chair: Prof. Eiji Morimoto (Kobe University)

Keynote	14:00~14:30	AI-DRIVEN INNOVATION FOR SUSTAINABLE AND INTELLIGENT AGRICULTURAL SYSTEMS Dr. Eiji Morimoto
AI-01	14:30~14:45	INTERACTIVE WHAT-IF DASHBOARD FOR SIX-HOUR VENTILATION PLANNING IN COMMERCIAL BROILER HOUSES Suhendra, Hao-Ting Lin*
AI-02	14:45~15:00	INTELLIGENT-ASSISTED REAL-TIME SPECTRAL SENSING PLATFORM FOR POINT-OF-CARE *SALMONELLA* TYPHIMURIUM DNA DETECTION Hong Zhi Zhang, Jyh Jian Chen*
AI-03	15:00~15:15	POULTRY LITTER CONDITION CLASSIFICATION USING AN ELECTRONIC NOSE WITH RFECV-BASED FEATURE SELECTION Kai-Feng Cheng, Yu-Hsuan Shen, Chin-Cheng Wu*
AI-04	15:15~15:30	MULTI-SCALE PHENOTYPING OF GREENHOUSE CUCUMBER CANOPIES: INTEGRATING AI VISION WITH 3D GAUSSIAN SPLATTING Dong Thanh Pham, *, Muneshi Mitsuoka, Daisuke Yasutake, Takenori Ozaki, Masaharu Koga, Takashi Okayasu
AI-05	15:30~15:45	DOMAIN ADAPTATION BASED ON INTERPOLATION IMAGES GENERATION IMPROVE DEER DETECTION PERFORMANCE Yu Tanaka, Ryohei Masuda*, Michihisa Iida*, Masahiko Suguri

Room 323 AI and Information Processing 2 (AI-2)

Chair: Prof. Eiji Morimoto (Kobe University)

AI-06	16:00~16:15	TIME-OF-DAY VARIATION IN UAS-DERIVED CANOPY TEMPERATURE ACROSS IRRIGATION LEVELS IN SOYBEAN Anjin Chang*, Caden Wade, Angie Gradiz, Kristine Lee, Younsuk Dong
AI-07	16:15~16:30	DRL-BASED FRUIT-APPROACH CONTROL IN A DIGITAL TWIN SIMULATION ENVIRONMENT FOR TOMATO-HARVESTING ROBOTS Hiroto Nakakubo, Hiroshi Fukuoka, Masahiro Ohtani, Kenichi Iida*
AI-08	16:30~16:45	PREDICTION OF LIGNIN CONTENT IN RICE STRAW USING EXCITATION-EMISSION MATRIX FLUORESCENCE SPECTROSCOPY AND CHEMOMETRIC MODELING Pornpimol Moolkaew, Yoshito Saito*, Takuji Miyamoto
AI-09	16:45~17:00	ONE BACKBONE IS ENOUGH: UNIFYING RGB-NIR SEMANTIC AND INSTANCE SEGMENTATION FOR EFFICIENT POTATO DEFECT INSPECTION Aulia Rizkiana, Byoung-Kwan Cho*
AI-10	17:00~17:15	LLM-ASSISTED WEB DATA INTEGRATION FOR CABBAGE SEEDLING SUPPLY, AGROMETEOROLOGICAL LAGS, AND WHOLESALE PRICE-RISK WARNING Po-Cheng Shih, Po-Yu Ho, Yi-Chih Chiu*

Room 324 AI and Information Processing 3 (AI-3)

Chair: Dae-Hyun Jung (Kyung Hee University)

AI-11	14:00~14:15	BERRYCOMP: JOINT GEOMETRY AND APPEARANCE RECONSTRUCTION OF OCCLUDED STRAWBERRIES Minhyeok Jang, Su-Min Chin, Dae-Hyun Jung*
AI-12	14:15~14:30	MULTISPECTRAL IMAGING AND AI-BASED DEFECT SEGMENTATION FOR AUTOMATED NON-DESTRUCTIVE QUALITY INSPECTION AND SORTING OF TOMATOES Umuhoza Aline*, Yena Kim, Aulia Rizkiana, Byoung-Kwan Cho*
AI-13	14:30~14:45	TOPOSKEL-GNN: TOPOLOGY-AWARE SKELETON GRAPH LEARNING FOR APPLE TREE PRUNING POINT DETECTION Anqi Liu, Woo-Young Kim, Kyeong-Hwan Lee*
AI-14	14:45~15:00	MULTI-VIEW FUSION OF UAV IMAGE MASKS FOR 3D FLOWER INSTANCE SEGMENTATION AND COUNTING Phanith Chea, Kyeong-Hwan Lee*
AI-15	15:00~15:15	DEEP LEARNING-BASED MONITORING AND EARLY WARNING OF EXTERNAL ABNORMALITIES IN MULTI-TIER AVIARY LAYING HENS Jia-En Lin*, Yu-Chieh Chen, Ming-Kun Hsieh, Yao-Chuan Tsai
AI-16	15:15~15:30	DEVELOPMENT OF A HYBRID RAG ADVISORY SYSTEM FOR PHALAENOPSIS CULTIVATION BASED ON A LOCAL LLM Shao-Yang Wu, Wen-Lin Chu*, Wei-Ling Chen[2], Hsi-Chun Hung
AI-17	15:30~15:45	INTEGRATING CFD, ENVIRONMENTAL SENSING, AND COMPUTER VISION TO CHARACTERIZE SPATIAL ASSOCIATIONS BETWEEN AIRFLOW AND BROILER DISTRIBUTION Jin-Yeong Lee, Min-Young Hwang, Ryu-Gap Lim*

Room 324 AI and Information Processing 4 (AI-4)

Chair: Dae-Hyun Jung (Kyung Hee University)

AI-18	16:00~16:15	ANATOMY-AWARE COMPOSITIONAL GENERATION OF 3D TOMATO PLANTS: COUPLING A MEASURED L-SYSTEM GRAMMAR WITH PER-ORGAN DIFFUSION MODELS Omia Emmanuel, Byoung-Kwan Cho*
AI-19	16:15~16:30	SELECTION OF DIFFUSION-GENERATED IMAGES FOR PEST INSTANCE SEGMENTATION ON STICKY TRAPS Jung-sang Yoo, Soo Been Cho, Ji Won Choi, Seung-Hwan Yang*
AI-20	16:30~16:45	SEQUENTIAL 3D SHAPE COMPLETION OF ON-PLANT KOREAN MELONS TOWARD AUTO MATED SELECTIVE HARVESTING Sungjay Kim, Gyumin Kim, Xianghui Xin, Yeongjun Go, Ghiseok Kim*
AI-21	16:45~17:00	PHYSICS-GUIDED HYPERSPECTRAL CLASSIFICATION OF MICRO- AND NANOPLASTICS IN HYDROPONIC NUTRIENT SOLUTIONS Yea-Jin Park, Youngho Jeon, Suji Lee, Jungmok You*, Dae-Hyun Jung
AI-22	17:00~17:15	REFERENCE-GUIDED INSTANCE SEGMENTATION OF APPLE FLOWERS AND BUDS USING VISION FOUNDATION MODELS Jintack Jeon, Baek-Gyeom Sung, Man-Jung Kim, Dae-Hyun Lee*
AI-23	17:15~17:30	BAND-COMBINATION CHANNELS FOR NON-DESTRUCTIVE RICE PROTEIN PREDICTION USING NIR HYPER SPECTRAL IMAGING Jeong-Yong Shin, Hong Gu Lee, Seung Woo Chun, Woo Hyeong Yu, Jeong Woo Han, Woon Tak Han, Giyoung Kim, Wan-Gyu Sang, Changju Yang, Changyeun Mo*

Room 325 Field Machinery and Systems 1 (FM-1)

Chair: Prof. Young-Jun Park (Seoul National University)

FM-01	14:00~14:15	A RETROFIT SYSTEM FOR AUTOMATIC TILLAGE DEPTH CONTROL ON CONVENTIONAL TRACTORS Phuoc Bao Long Do, Dang Khanh Linh Le, Wei-Chih Lin*
FM-02	14:15~14:30	TILLAGE ELECTRIFICATION: EFFECTS OF A REDUCED-TILLAGE IMPLEMENT ON ENERGY USE AND GREENHOUSE SPINACH PERFORMANCE Oyetayo Olukorede Oyebode, Ryota Sakata, Naoki Tsunekawa, Nang Nguyen Van
FM-03	14:30~14:45	TEMPORAL OBSERVATION FOR REINFORCEMENT LEARNING OBSTACLE AVOIDANCE IN A TRACKED AGRICULTURAL ROBOT Yu-Hsien Lee*, Wu-Huan Hsu
FM-04	14:45~15:00	DEVELOPMENT OF STICK-SLIP STEERING MODEL FOR AGRICULTURAL VEHICLES Masahisa Watanabe*
FM-05	15:00~15:15	DEVELOPMENT OF SENSOR FUSION FRAMEWORK FOR OBSTACLE DETECTION AND COLLISION AVOIDANCE IN AN ELECTRIC MOWER Runa Kato, Jia Qin, Michihisa Iida*
FM-06	15:15~15:30	TREND ANALYSIS OF FACTORS AFFECTING LATERAL OVERTURNING SAFETY IN WHEELED AND TRACKED FORESTRY TRACTORS Moon-Kyeong Jang, Jeong-Hun Kim, Chan-Young Lee, Ju-Seok Nam*
FM-07	15:30~15:45	STRUCTURAL SAFETY EVALUATION OF AN AGRICULTURAL TRACTOR FRONT-END LOADER Jeong-Hun Kim, Joon-Hyung Park, Moon-Kyeong Jang, Ju-Seok Nam*

Room 325 Field Machinery and Systems 2 (FM-2)

Chair: Prof. Young-Jun Park (Seoul National University)

FM-08	16:00~16:15	OPERATOR COMFORT EVALUATION BY VIBRATION AND INCLINATION OF A 36.8-kW ONE-ROW CABBAGE HARVESTER UNDER KOREAN FIELD CONDITIONS Md Razob Ali, Md Nasim Reza, Ezatullah Zakir, Cholet Nyangoma Atulinda, Sun-Ok Chung*
FM-09	16:15~16:30	PHYSICS-GUIDED NEURAL NETWORK FOR CONE INDEX PREDICTION FROM SOIL PHYSICAL PROPERTIES Joon-Seo Kim, Sang-Wook Park, Seung-Yeon Lee, Ji-Tae Kim*
FM-10	16:30~16:45	AN ADAPTIVE NMPC FRAMEWORK FOR ACCURATE AND EFFICIENT PATH TRACKING OF ORCHARD ROBOTS Andong Huang, Woo-Young Kim, Kyeong-Hwan Lee*
FM-11	16:45~17:00	ANALYSIS OF SLOPE DRIVING CHARACTERISTICS OF A SMALL TRACKED VEHICLE THROUGH SOIL BIN TESTS Chan-Young Lee, Jeong-Hun Kim, Joon-Hyung Park, Ju-Seok Nam*
FM-12	17:00~17:15	STRUCTURAL AND DYNAMIC ASSESSMENT OF A BROILER-CATCHING ROBOT UNDER VARIABLE LOADS WITH EXPERIMENTAL VALIDATION Md Faruk Hossain, Md Rayhan Mahmud, Jeong-Chan Lee, Ryu-Gap Lim*
FM-13	17:15~17:30	HISTORY-DEPENDENT ELASTO-PLASTIC CONTACT MODEL FOR DEM SIMULATION OF CYCLIC SOIL COMPACTION Toyohiro KATO, Taiki ARAO, Dong Thanh PHAM, Takashi OKAYASU, Muneshi MITSUOKA*

Room 326 Smart Farm Systems and Renewable Energy 1 (SF-1)

Chair: Prof. Rack-woo Kim (Seoul National University)

Keynote	14:00~14:30	SMART POULTRY FARMING: INTEGRATING AI FOR NEXT-GENERATION MANAGEMENT Dr. Yao-Chuan Tsai
SF-01	14:30~14:45	SPATIAL DYNAMICS OF AMMONIA GRADIENTS AND DIRECTIONAL SENSING EFFECTS IN LAYER HOUSES USING INSPECTION ROBOT Chin-Kai Kuo, Xiang-Sheng Huang, Chen-Wei Liang*
SF-02	14:45~15:00	CAPACITY AND INTERNAL RESISTANCE VARIATION OF NCM BATTERIES UNDER DIFFERENT CHARGE-DISCHARGE STRATEGIES AND TEMPERATURE CONTROL Li-Ya Hsiao, Chen-Kang Huang*
SF-03	15:00~15:15	DEVELOPMENT OF A DEEP LEARNING-BASED IMAGE EARLY WARNING SYSTEM FOR BROILER CHICKENS Yu-Jen Shih*, Ming-Kun Hsieh, Yao-Chuan Tsai
SF-04	15:15~15:30	STRATEGY VALIDATION AND ENERGY INTEGRATION OF AN AI LASER WILD BIRD DETERRENT IN AGRICULTURAL FIELDS Chang-Chi Huang*, Wei-Lun Hsu, Kuang-Wen Hsieh, Yao-Chuan Tsai
SF-05	15:30~15:45	AN EDGE-COMPUTING SYSTEM INTEGRATING ACOUSTIC RECOGNITION AND GAS SENSING FOR COW RUMINATION MONITORING Chin-Cheng Wu*, Chung-Yen Chuang, Yi-Chich Chiu

Room 326 Smart Farm Systems and Renewable Energy 2 (SF-2)

Chair: Prof. Rack-woo Kim (Seoul National University)

SF-06	16:00~16:15	DEVELOPMENT OF A VISION-BASED EARLY WARNING STRATEGY FOR FLOCK DISTRIBUTION IN BROILER HOUSES Yu-Chi Liu, Ming-Yih Chang*
SF-07	16:15~16:30	EFFECTS OF SEEDLING IMAGE GRADING ON MARKETABLE WEIGHT-BASED STAGGERED HARVESTING FOR PLANT FACTORY GROWN LETTUCE Chen I-I, Ming-Yih Chang*
SF-08	16:30~16:45	CWSI MAPPING USING POINT MEASUREMENT AND THERMAL IMAGING FOR CABBAGE FIELDS AND APPLE ORCHARDS Md Mamunur Rashid, Jin Hongbin, Md Ashikur Rahman, Md Nasim Reza, Se Yong Lee, Sun-Ok Chung*
SF-09	16:45~17:00	VARIABILITY CHARACTERIZATION OF AMBIENT ENVIRONMENTAL CONDITIONS FOR SMART GREENHOUSE NUTRIENT MANAGEMENT Sakib Robin, Cholet Nyangoma Atulinda, Md Nasim Reza, Hyeunseok Choi, Sun-Ok Chung*
SF-10	17:00~17:15	REAL-TIME SENSOR DATA QUALITY MONITORING AND FAULT DETECTION IN A VERTICAL FARM Md Ashikur Rahman, Ezatullah Zakir, Md Mamunur Rashid, Su Young Lee, MdNasim Reza, Sun-Ok Chung*

Room 121 Post-harvest and Food Processing 1 (PH-1)

Chair: Prof. Changyeun Mo (Kangwon National University)

PH-01	14:00~14:15	DEM SIMULATION OF APPLE MECHANICAL IMPACT RESPONSE Jui-Chun Wang, Wei-Lun Hsu*
PH-02	14:15~14:30	COLOR-UV IMAGE FUSION FOR NONDESTRUCTIVE PREDICTION OF EDAMAME WATER AND FRUCTOSE CONTENT Takumi Murai, Gao Tianqi, Mayume Adachi, Yoshito Saito*
PH-03	14:30~14:45	EFFECTS OF HYDROSTATIC PRESSURE TREATMENT ON THE FUNCTIONAL PROPERTIES OF BLACK GARLIC Sayaka Nishi, Chandan Das, Takahisa Nishizu, Teppei Imaizumi*
PH-04	14:45~15:00	DEEP LEARNING-BASED ESTIMATION OF INTERNAL GARLIC CLOVE TRAITS FROM EXTERNAL BULB IMAGES Jinho Son, Seoeun Lee, Daewook Kwon, Juhee Lee, Wonyeol Choi, Bumseok Park, Youngjune An, Hyunggyu Park, Yushin Ha*
PH-05	15:00~15:15	VISION-BASED SWEET CORN MATURITY IDENTIFICATION FOR AUTOMATED POST-HARVEST GRADING YI-SIANG WANG*, PO-CHUN WANG, BING-YUAN HSIEH, Wu-Yang Sean
PH-06	15:15~15:30	INTERNAL STRUCTURAL ANALYSIS UNCOVERS MICROSCALE WATER MOLECULAR DIFFUSION IN POSTHARVEST SPINACH Kohaku Kawase, Shinichiro Kuroki*
PH-07	15:30~15:45	FROM CONTACT TO NEAR-CONTACTLESS ULTRASOUND: COUPLING EFFECTS ON APPLE FIRMNESS PREDICTION Yudha Putra Arisandy, Chang-Hyup Lee, Jiwon Ryu, Sang-Yeon Kim, Dong-Heun Sung, Sun Seongmi, Ghiseok Kim*

Room 121 Post-harvest and Food Processing 2 (PH-2)

Chair: Prof. Changyeun Mo (Kangwon National University)

PH-08	16:00~16:15	FOREIGN OBJECT DETECTION IN POTATO CHUNKS USING RGB IMAGING AND DEEP LEARNING: PERFORMANCE AND LIMITATIONS Trinh Thanh Duy, Minhyun Kim, Dong-Heun Sung, Seokha Hwang, Harin Jang, Ghiseok Kim*
PH-09	16:15~16:30	SPECTRAL ANALYSIS OF POTATO SLICES AND FOREIGN MATERIALS USING SWIR HYPERSPECTRAL IMAGING Harin Jang, Minhyun Kim, Seokha Hwang, Dong-Heun Sung, Trinh Thanh Duy, Ghiseok Kim*
PH-10	16:30~16:45	DEVELOPMENT OF A PORTABLE NEAR-INFRARED SPECTROSCOPY SYSTEM FOR MONITORING GOCHUJANG FERMENTATION Dong Heun Sung, Jiwon Ryu, Min hyun Kim, Lee Jae-Eun, Trinh Thanh Duy, Ghiseok Kim*
PH-11	16:45~17:00	AUTOMATED QUALITY INSPECTION OF VANILLA BEANS USING COMPUTER VISION AND HYPERSPECTRAL IMAGING Tzu-Yen Weng, Chih-Hsin Yeh, Yi-Hua Lin, Shih-Fang Chen*
PH-12	17:00~17:15	EXPLAINABLE DEEP LEARNING FOR ANALYSIS OF ONION STORAGE ENVIRONMENTAL DATA Jaeeun Lee, Sang-Yeon Kim, Uik Lee, Ghiseok Kim*
PH-13	17:15~17:30	DEVELOPMENT AND OPERATIONAL PARAMETER OPTIMIZATION OF AN AUTOMATED SHELLING SYSTEM FOR DRIED LONGAN Xin-Liang Lai*, Ching-Wei Cheng, Wu-Yang Sean, Ping-Kun Tsai

Room 122 Post-harvest and Food Processing 3 (PH-3)

Chair: Prof. Gun-Woo Kim (Gyeongsang National University)

PH-14	14:00~14:15	TRANSFERABLE WEIGHT LOSS FORECASTING IN COLD-STORED ONIONS USING PHYSICS-CONSTRAINED DEEP LEARNING AND SHORT-TERM CALIBRATION Sang-Yeon Kim, Jaeeun Lee, Uik Lee, Ghiseok Kim*
PH-15	14:15~14:30	BENCHMARKING AND DEPLOYING REAL-TIME DEFECT SEGMENTATION MODELS ON A FRUIT SORTING LINE Huynh Cao The Cuong, Seokha Hwang, Arisandy Yudha Putra, Ghiseok Kim*
PH-16	14:30~14:45	EFFECT OF $CACL_2$-ASSISTED VACUUM IMPREGNATION ON THE ELECTRICAL PROPERTIES OF CARROT TISSUE Kumari Sapna, Takahisa Nishizu, Teppei Imaizumi*
PH-17	14:45~15:00	DEVELOPMENT OF AN ELECTRONIC NOSE FOR MONITORING GOCHUJANG FERMENTATION: GC-MS VOLATILE ANALYSIS AND SENSOR RESPONSE EVALUATION Minhyun Kim, Jiwon Ryu, Dong-Heun Sung, Trinh Thanh Duy, Lee Uik, Ghiseok Kim*
PH-18	15:00~15:15	EARLY DETECTION OF FUTURE BROWNING SITES IN BASIL LEAVES USING HYPERSPECTRAL IMAGING Ayumu Yamada, Shinichiro Kuroki*
PH-19	15:15~15:30	DEEP SPECTRAL-SPATIAL LEARNING FOR APPLE BRUISE DETECTION AND INTERNAL DAMAGE ESTIMATION USING HYPERSPECTRAL IMAGING Jiwon Ryu, Chang-Hyup Lee, Sang-Yeon Kim, Sungjay Kim, Minhyun Kim, Dong Heun Sung, Ghiseok Kim*
PH-20	15:30~15:45	STARCH DIGESTIBILITY OF COOKED RICE WITH DIFFERENT POLISHING DEGREES Yukiharu Ogawa*, Masatsugu Tamura

Room 122 Post-harvest and Food Processing 4 (PH-4)

Chair: Prof. Gun-Woo Kim (Gyeongsang National University)

PH-21	16:00~16:15	MILLIMATER-WAVE TRANSMISSION IMAGING FOR DETECTION OF FOREIGN MATERIAL IN POWDERED PARSLEY AND "AJINOMOTO" Ayano Tamaoki, Kensuke Nakasuka, Tetsuhito Suzuki*
PH-22	16:15~16:30	WIRELESS SENSING SYSTEM WITH AN ONION MIMIC FOR AMBIENT TEMPERATURE, HUMIDITY, AND INTERNAL TEMPERATURE Uik Lee, Jaeeun Lee, Sang-Yeon Kim, Ghiseok Kim*
PH-23	16:30~16:45	NON-DESTRUCTIVE ESTIMATION OF THEANINE CONTENT IN FRESH SHADE-GROWN TEA LEAVES USING MULTI-EXCITATION FLUORESCENCE IMAGING Mao Ito, Tsutomu Niwa, Tomoko Matsuda, Tetsuhito Suzuki*
PH-24	16:45~17:00	NON-DESTRUCTIVE DETECTION OF INTERNAL FLESH ABNORMALITIES IN TILAPIA USING HYPERSPECTRAL IMAGING AND DEEP LEARNING Pin-Wei Chen, Pi-Chung Wu, Kuo-Chi Liao, Shih-Fang Chen*
PH-25	17:00~17:15	REAL-TIME MONITORING FOR ENDPOINT DETERMINATION IN COMMERCIAL-SCALE TWIN-SCREW FRUIT JUICE EXTRACTION Dong-Hyeon Kim, Jae-Min Jung, Do-Hyeok Choi, Wang-Hee Lee*
PH-26	17:15~17:30	POST-HARVEST METABOLIC DYNAMICS IN LETTUCE AND THEIR ASSOCIATION WITH HYPERSPECTRAL RESPONSES K.R.T. Amani Kahandawa, Yuzu Shiota, Shinichiro Kuroki*

ISMAB2026 Oral Presentation

| 10/22 (Thu) |

Room 321	Precision Agriculture Machinery and Systems 5 (PA-5)	
		Chair: Prof. Tadashi Chosa (Tokyo University of Agriculture and Technology)
PA-25	13:30~13:45	KEYPOINT-DRIVEN GEOMETIC POSE ESTIMATION FOR AUTONOMOUS SEEDBED LIFTING WITH NONHOLONOMIC MOBILE ROBOTS Rattana Seng, Woo-Young Kim, Kyeong-Hwan Lee*
PA-26	13:45~14:00	PERSISTENT TARGET RE-IDENTIFICATION FOR HUMAN-FOLLOWING ROBOTS IN ORCHARD ENVIRONMENTS Sanjay Tamang, Woo-Young Kim², Kyeong-Hwan Lee*
PA-27	14:00~14:15	EVALUATION OF SEED METERING AND IN-SOIL PLACEMENT CHARACTERISTICS OF A VACUUM TYPE POINT SEEDER USING SOYBEAN Juhee Lee, Jinho Son, Wonyeol Choi, Bumseok Park, Hyunggyu Park, Yushin Ha*
PA-28	14:15~14:30	RECONSTRUCTION-FREE SOIL PULVERISATION-RATIO ASSESSMENT FRAMEWORK: PIXEL-WISE PHYSICAL-SCALE RECOVERY FROM HETEROGENEOUS RGB-D Zhewang Zhang, Kyeong-Hwan Lee*
PA-29	14:30~14:45	TRACKING ACCURACY EVALUATION OF AUTONOMOUS TRACTORS USING A HYBRID EKF-TRANSFORMER MODEL FOR REAR 3-POINT ESTIMATION Md Rayhan Mahmud, Md Faruk Hossain, Ki-Dong Park, Ryu-Gap Lim*
PA-30	14:45~15:00	PREDICTION OF BARLEY SPIKE COUNT UNDER WATERLOGGING STRESS USING UAV-BASED MULTISPECTRAL IMAGERY Do Hyun An, Ji An Kim, Hyo Jeong Lee, Ye Seong Kang*, Yeong Son Jo, Seung Ga Oh, Hui Su Bae, WooJin Im

Room 321 Precision Agriculture Machinery and Systems 6 (PA-6)

Chair: Prof. Tadashi Chosa (Tokyo University of Agriculture and Technology)

PA-31	15:15~15:30	NON-DESTRUCTIVE PREDICTION OF INTERNAL QUALITY IN ON-VINE MELONS USING HYPERSPECTRAL IMAGING AND MACHINE LEARNING Gyumin Kim, Sungjay Kim, Xianghui Xin, Yeongjun Go, Jaeeun Lee, Donghyeon Seong, Ghiseok Kim*
PA-32	15:30~15:45	PRELIMINARY EVALUATION OF GLASS COATING EFFECTS ON HOPPER DISCHARGE AND FERTILIZER SPREADING DISTRIBUTION Atsuru Fujimoto*
PA-33	15:45~16:00	COMPARISON OF MANUAL AND MECHANIZED TRANSPLANTING OF CABBAGE PRODUCTION IN GREENHOUSE CONDITIONS Ezatullah Zakir, Md Nasim Reza, Cholet Nyangoma Atulinda, Sun-Ok Chung*
PA-34	16:00~16:15	BLOB SELECTION EVALUATION FOR VISION-BASED OUTDOOR ROBOT LOCALIZATION USING MOG2 SUBTRACTION Nguyen Van Dieu, Tadashi Chosa*
PA-35	16:15~16:30	MEASUREMENT BIAS OF AN FDR SOIL MOISTURE SENSOR UNDER DRYING-REWETTING CONDITIONS Minjoo Kim, Jaesung Park*, Seokyung Park

Room 322 Precision Agriculture Machinery and Systems 7 (PA-7)

Chair: Prof. Wen-Lin Chu (National Chung Hsing University)

PA-36	13:30~13:45	DEVELOPMENT OF A GENERAL GUIDELINE FOR DATA-BASED INTEGRATED PEST MANAGEMENT UNDER ISO/TC 347 Seongmin Park, Soo Chung*
PA-37	13:45~14:00	STEM FOLLOWING AND CONTINUOUS CUTTING OF TOMATO LOWER LEAVES USING A FORCE CONTROLLED HEDGE TRIMMER-TYPE DE-LEAFING ROBOT Masakazu Kashino*, Hideto Kurosaki, Tokihiro Fukatsu
PA-38	14:00~14:15	LiDAR-BASED HITCH CONTROL OF SOWING DEPTH FOR A GARLIC PLANTER UNDER LABORATORY CONDITIONS Jumyeong Lee, Yong-Hyun Kim, Chankeun Lee, Seokhyun Ahn, Hak-Jin Kim*
PA-39	14:15~14:30	SIMULATION STUDY OF REINFORCEMENT LEARNING-BASED STEERING CONTROL FOR AUTONOMOUS TRACTOR AT HEADLAND TURNS Chankeun Lee, Hak-Jin Kim*, Yong-Hyun Kim, Jumyeong Lee, Seokhyun Ahn
PA-40	14:30~14:45	EVALUATION OF AN ROI-BASED MODEL AND TWO-STAGE PIPELINE FOR TOMATO SURFACE DEFECT LOCALIZATION Hojun Kwon, Chanseok Ryu*, Changhyeok Park, Gangin Je, Hakchan Kim, Yeseong Kang, Dohyun An, Jian Kim
PA-41	14:45~15:00	MORPHOLOGY-INFORMED SPECTRAL-SPATIAL FUSION FOR LEAF WATER CONTENT ESTIMATION FROM HYPERSPECTRAL IMAGES Chi-Won Choi, Dae-Hyun Jung*

Room 322 Precision Agriculture Machinery and Systems 8 (PA-8)

Chair: Prof. Wen-Lin Chu (National Chung Hsing University)

PA-42	15:15~15:30	RAIL ENTRY TRAJECTORY ALGORITHM BASED ON FORWARD AND BACKWARD MOVEMENTS, CONSIDERING THE NAVIGATION SPACE OF A GREENHOUSE MOBILE ROBOT Ji Won Choi, Soo Been Cho, Jung-sang Yoo, Seung-Hwan Yang*
PA-43	15:30~15:45	DEVELOPMENT OF AN UNKNOWN OBJECT DETECTION ALGORITHM FOR ORCHARD ROBOTS USING A MONOCULAR RGB CAMERA Seokhyun Ahn, Yong-Hyun Kim, Jumyeong Lee, Chankeun Lee, Hak-Jin Kim*
PA-44	15:45~16:00	DEEP REINFORCEMENT LEARNING-BASED ACTIVE SUSPENSION CONTROL FOR BODY LEVELING OF AN AGRICULTURAL MOBILE PLATFORM Heonsoo Choi, Hyunggil Hong, Haeyong Yun, Yongjun Cho*
PA-45	16:00~16:15	FEASIBILITY OF BURIED CROP DETECTION USING PROXIMAL GAMMA-RAY SPECTROSCOPY Bum-Seok Park, Jin-Ho Son, Ju-Hee Lee, Won-Yeol Choi, Young-June An, Seo-Eun Lee, Dae-Wook Kwon, Hyung-Gyu Park, Yu-Shin Ha*
PA-46	16:15~16:30	DEVELOPMENT OF AN INDOOR-OUTDOOR AUTONOMOUS PATROL ROBOT FOR LIVESTOCK FACILITIES Ayumu NAKASHIMA*, Yamato Sakurai, Sutan Muhamad Sadam Awal, Dong Thanh PHAM, Takashi OKAYASU, Muneshi MITUOKA

Room 323 Precision Agriculture Machinery and Systems 9 (PA-9)

Chair: Prof. Chen-Kang Huang (National Taiwan University)

PA-47	13:30~13:45	NATIONAL-SCALE PARCEL GEOMETRY AND FIDELITY EVALUATION OF ISOXML PRESCRIPTION MAPS FOR KOREAN FIELDS Yi-Seo Min, Du-Han Kim, Wan-Soo Kim*
PA-48	13:45~14:00	EFFECTS OF ANALYSIS REGION AND CANOPY HEIGHT ON LEAF AREA ESTIMATION IN PLANAR-CANOPY APPLE TREES Je-Min Park, Yeong Hyeon Shin, Muhammad Amjad, Hyeon-Soo Kim, Woo-Jae Cho*
PA-49	14:00~14:15	ISO 11783 PRESCRIPTION MAP GENERATION FROM WEED DISTRIBUTION AND VIRTUAL VERIFICATION FOR SPRAYING Nayoung Kim, Changho Yun, Yeseong Kang, Deokheung Kim, Xiongzhe Han*
PA-50	14:15~14:30	AN RGB-D VISION AND DIGITAL-TWIN FRAMEWORK FOR DUAL-ARM COOPERATIVE HARVESTING OF OCCLUDED STRAWBERRIES Chen-En Lee, Chung-Liang Chang*
PA-51	14:30~14:45	RICE HILL DETECTION AND INDIVIDUAL RICE GROWTH MAPPING USING UAV IMAGERY Doan Le Cong, Gyujin Jang, Hak-Jin Kim*
PA-52	14:45~15:00	UAV-BASED ESTIMATION OF SOIL WATER CONTENT UNDER DIFFERENT SURFACE ROUGHNESS CONDITIONS USING RGB AND NIR IMAGERY Jaehun Lee, Jaesung Park*, Minjoo Kim, Seokyung Park, Hyeonjun Hwang

Room 324 AI and Information Processing 5 (AI-5)

Chair: Prof. Chang-Seop Shin (Chungbuk National University)

AI-24	13:30~13:45	CONTEXTUALIZING CNN ATTRIBUTION MAPS WITH IMAGE-DERIVED DESCRIPTORS IN MEDICINAL PLANT SEED CLASSIFICATION Su-Min Chin, Yea-Jin Park, Dae-Hyun Jung*
AI-25	13:45~14:00	DEEP LEARNING-BASED WAVELENGTH SELECTION FOR MULTISPECTRAL SENSING OF FOREST FUEL MOISTURE CONTENT Seung Woo Chun, Hong Gu Lee, Woo Hyeong Yu, Jeong Yong Shin, Jeong Woo Han, Woon Tak Han, Giyoung Kim, Sujung Ahn, Changyeun Mo*
AI-26	14:00~14:15	DEVELOPMENT OF A YOLO-SAM-BASED PIPELINE FOR STRAWBERRY LEAF EXTRACTION AND DISEASE SYMPTOM SYNTHESIS Soo Been Cho, Ji Won Choi, Jung-sang Yoo, Jung Hyun Lee, Seung-Hwan Yang*
AI-27	14:15~14:30	REAL-TIME OPEN-VOCABULARY 3D OCCUPANCY PREDICTION FOR AUTONOMOUS AGRICULTURAL MACHINERY Minwoo Kim, Sanghyeok Choi, Taehyun Jung, Gyeongmin Kang, Woosang Jeon, Taehyeong Kim*
AI-28	14:30~14:45	AUTOMATIC GENERATION OF THREE-DIMENSIONAL CUCUMBER CANOPY SCENES WITH HETEROGENEOUS LEAF SHAPES Tatsuki Nishimura, Dong Thanh Pham, Muneshi Mitsuoka, Daisuke Yasutake, Takenori Ozaki, Seji Koga, Yasumaru Hirai, Takashi Okayasu*
AI-29	14:45~15:00	RANKING-BASED LOSS FUNCTIONS FOR DEEP LEARNING PREDICTION OF POST-BLENDING COFFEE SENSORY ATTRIBUTES Chih-Yun Tsai, Yu-Tang Chang, Shu-Ping Hung, Chia-Hung Peng, Chun-Ming Lu, Shih-Fang Chen*

Room 324 AI and Information Processing 6 (AI-6)

Chair: Prof. Chang-Seop Shin (Chungbuk National University)

AI-30	15:15~15:30	AI-BASED EARLY DETECTION OF VISUALLY SIMILAR TOMATO DISEASES AND DROUGHT: COMPARISON OF BIOIMPEDANCE SENSING AND RGB IMAGING Yejin Kim, Daesik Son, Kyuseok Yang, Yulim Park, Dhayanti Makyorukty, Junseung Bae, Chanwoo Park, Soo Chung*
AI-31	15:30~15:45	IMPROVED KEYPOINT ESTIMATION USING A MULTI-TASK YOLO MODEL FOR WEED RECOGNITION IN GARLIC FIELDS Sohyeon Kang, Junghwa Park, Seokyung Park, Minjoo Kim, Yeonsoo Kim, Jaesung Park*
AI-32	15:45~16:00	DEVELOPMENT OF INTELLIGENT ROSE GROWTH MONITORING SYSTEM USING DEEP LEARNING AND BUD TRACKING Yu-Shan Wang, Wei-Ling Chen, Hsing-Ying Chung, Shih-Fang Chen*
AI-33	16:00~16:15	EVALUATION OF STRATEGIES TO IMPROVE INTERANNUAL TRANSFERABILITY OF UAV-BASED MULTISPECTRAL PEPPER PLANT HEIGHT MODELS Gangin Je, Chanseok Ryu*, Changhyeok Park, Hojun Kwon, Hakchan Kim, Yeseong Kang, Dohyun An, Jian Kim
AI-34	16:15~16:30	INTEGRATED DEEP LEARNING SYSTEM FOR ORAL CANCER SCREENING, RISK STRATIFICATION, AND IMAGE QUALITY ASSURANCE Jing-Han Jang, Cheng-Ying Chou*, Shyh-Jye Chen, Jang-Jaer Lee, Ling-Ying Wei, Ting-Yi Chen

Room 325 Field Machinery and Systems 3 (FM-3)

Chair: Prof. Jooseon Oh (Chonnam National University)

FM-14	13:30~13:45	MULTIVARIATE MOBILITY ANALYSIS OF LUNAR ROVER WHEELS USING NUMERICAL METHOD UNDER LUNAR GRAVITY Moo-Young Oh, Ju-Hyeon Ahn, Dan-A Kim, Se-Hee Park, Ji-Tae Kim*
FM-15	13:45~14:00	DEVELOPMENT OF AN EEPA-BASED DEM MODEL FOR PREDICTING CULTIVATOR-SWEEP FORCES UNDER DIFFERENT SOIL WATER CONTENTS Dae-Wi Jeong, Min-Seung Kim, Se-O Choi, Shin-Young Noh, Ye-Na Lee, Yeon-Soo Kim*, Jae-Sung Park, Yong-Joo Kim
FM-16	14:00~14:15	TRACTOR OVERTURNING-PREVENTION CONTROL USING MACHINE LEARNING TO ESTIMATE THE CENTRE OF MASS Hideo Tamashiro, Yuya Aoyagi*, Takeshi Shikanai, Masami Matsui, Shuto Ohara
FM-17	14:15~14:30	EVALUATION OF A NEW TWO-ROW CULTIVATION SYSTEM AND MECHANIZATION FOR SPRING POTATO PRODUCTION Kilkyu Oh, Seungmin Lee, Ki Yong Lee*
FM-18	14:30~14:45	A CONTINUOUS MULTI-TARGET TOMATO HARVESTING STRATEGY WITH COARSE-TO-FINE PEDICEL-GUIDED MANIPULATION Hao-Cheng Zuo, Bo-Jhih Chang, Ping-Lang Yen*
FM-19	14:45~15:00	VIBRATION ANALYSIS OF A MECANUM WHEEL AGRICULTURAL TRANSPORT PLATFORM Yeonsong Lee, Minkyo Kong, Sung-Bo Shim*

Room 325 Field Machinery and Systems 4 (FM-4)

Chair: Jooseon Oh (Chonnam National University)

FM-20	15:15~15:30	DEVELOPMENT OF A DEM-MBD CO-SIMULATION MODEL FOR PREDICTION PICKUP UNIT LOAD IN A 103KW-CLASS ROUND BALER Min-Seung Kim, Dae-Wi Jeong, Se-O Choi, Shin-Young Noh, Ye-Na Lee, Yeon-Soo Kim*, Yong-Joo Kim
FM-21	15:30~15:45	EXPERIMENTAL AND THEORETICAL ANALYSIS OF SINGLE TIRE SOIL THRUST UNDER DIFFERENT NORMAL LOADS Se-O Choi, Min-Seung Kim, Dae-Wi Jeong, Shin-Young Noh, Ye-NaLee, Yeon-Soo Kim*, Yong-Joo Kim
FM-22	15:45~16:00	DEM-BASED PERFORMANCE EVALUATION OF A GARLIC CLOVE SORTER FOR MACHINE PLANTING Won-Yeol Choi, Hyung-Gyu Park, Jinho Son, Ju-Hee Lee, Bum-seok Park, Young-June An, Seo-Eun Lee, Dae-Wook Kwon, Yushin Ha*
FM-23	16:00~16:15	HIERARCHICAL GREENHOUSE NAVIGATION USING POINT-LIO LOCALIZATION AND SEMANTIC AISLE FOLLOWING Hao-Cheng Zuo, Bo-Jhih Chang, Ping-Lang Yen*
FM-24	16:15~16:30	FIELD RELIABILITY EVALUATION OF A SELF-BUILT IOT MONITORING DEVICE FOR APPLE COLD STORAGE Joon-Mo Kang, Hyuck-Joo Kim*

Room 326 Smart Farm Systems and Renewable Energy 3 (SF-3)

Chair: Prof. Soo Chung (Seoul National University)

SF-11	13:30~13:45	SENSOR PLACEMENT STRATEGY FOR ENVIRONMENTAL MONITORING IN VERTICAL FARMS BASED ON SPATIAL, VERTICAL, AND TEMPORAL VARIABILITY Arnab Majumder, Md Razob Ali, Gusti Ayu Putri Mei Ulianti, Md Nasim Reza, Choa Mun Yun, Sun-Ok Chung*
SF-12	13:45~14:00	WATER STRESS VARIABILITY MAPPING BY GROWTH STAGE USING THERMAL VIDEO PROCESSING FOR CABBAGE GROWN IN GREENHOUSE Md Nasim Reza, Ezatullah Zakir, Miao MiaoTu, Cholet Nyangoma Atulinda, Su Young Lee, Sun-Ok Chung*
SF-13	14:00~14:15	USER-DEFINED MODEL COMPONENT DEVELOPMENT IN TRNSYS 18 FOR A DYNAMIC ENERGY SIMULATION: CASE STUDY OF A PCM-IN-CONTAINER Qazeem Opeyemi Ogunlowo, Seung-hun Lee, Chan-min Kim, Hee-Woong Seok, Sun-hyoung Lee, Su-been Ahn, Han Kim, Jin-seo Choi, Yun-Jeong Lee, Yoon-Kyu Hur, Jun-seop Mun, Hyeon-chae Kim, Rack-woo Kim*
SF-14	14:15~14:30	ROBOTIC MULTI-VIEW RGB PHENOTYPING OF STRAWBERRY PETIOLE LENGTH WITHOUT DEPTH SENSING Min-Woo Kim, Dae-Hyun Jung*
SF-15	14:30~14:45	3D RECONSTRUCTION OF GREENHOUSE CROPS: FROM SINGLE-CAMERA RGB-D MAPPING TO LIDAR-CAMERA INTEGRATION Xianghui Xin, Sungjay Kim, Gyumin Kim, Yeongjun Go, Yudha Putra Arisandy, Seongmi Sun, Ghiseok Kim*
SF-16	14:45~15:00	FEASIBILITY EVALUATION OF A LABORATORY-DEVELOPED EMBEDDED EC AND PH ANALYZER FOR HYDROPONIC NUTRIENT SOLUTIONS Minki Kang, Hak-Jin Kim*, Yuna Kwon, Joonhwan Kim

Room 326 Smart Farm Systems and Renewable Energy 4 (SF–4)

Chair: Prof. Soo Chung (Seoul National University)

SF–17	15:15~15:30	THERMAL PERFORMANCE OF A TRACKING LINEAR FRESNEL LENS SYSTEM WITH AN EVACUATED TUBE COLLECTOR Seung–Hyeon Cheon, Byeong–Eun Moon*
SF–18	15:30~15:45	DEVELOPMENT OF A 3D CLINOSTAT PLATFORM FOR GROUND–BASED SIMULATED MICROGRAVITY RESEARCH IN AGRICULTURAL BIOSCIENCES Uik Lee, Yeongjun Go, Jiwon Ryu, Ghiseok Kim*
SF–19	15:45~16:00	OPTIMAL BASELINE DETERMINATION FOR STEREO VISION–BASED PLANT HEIGHT MEASUREMENT OF PEPPER SEEDLING TRAYS AT A FIXED CAMERA HEIGHT Gunhui Park, Junghwa Park, Sohyeon Kang, Minjoo Kim, Jaesung Park*

Room 121 Bio-processing Engineering 1 (BP-1)

Chair: Prof. Kyoung-Je Jang (Gyeongsang National University)

BP-01	13:30~13:45	HOLLOW FIBER MEMBRANE BASED VACUUM MEMBRANE DISTILLATION FOR AMMONIA NITROGEN REMOVAL Megha Pramod, Bo-Sheng Wu, Wu-Yang Sean*
BP-02	13:45~14:00	GRAVITY-ASSISTED TWO-STEP CRISPR-CAS12A SYSTEM FOR RAPID MOLECULAR DETECTION Shauqi Abda'i Lubis, Jyh Jian Chen*
BP-03	14:00~14:15	EFFECTS OF HIGH-VOLTAGE PULSE PRETREATMENT ON THE SURFACE AND STRUCTURAL CHARACTERISTICS OF RICE STRAW Wu-Huan Hsu*, Tsung-Chun Lin, Yun-Sheng Lu
BP-04	14:15~14:30	SELF-OXYGENATING SCAFFOLDS MODULATE HYPOXIC RESILIENCE AND EPIGENETICALLY GUIDE MUSCLE DEVELOPMENT Woobin Choi, Yuseung Choi, Wooseok Jung, Kanghee Han, Daeun Jung, Sangbae Park*
BP-05	14:30~14:45	REUSABLE AGAR HYDROGEL BEADS FOR CONTROLLED NUTRIENT DELIVERY IN HYDROPONIC SYSTEMS Yeonseo Kim, Seyeong Heo, Hojin Wang, Sunho Park*
BP-06	14:45~15:00	ALGINATE-ZEIN CORE-SHELL MICROCAPSULES FOR SUSTAINED BACTERIA DELIVERY IN WILDFIRE-AFFECTED SOIL Yeonseo Kim, Seyeong Heo, Hojin Wang, Sunho Park*

Room 121 Bio-processing Engineering 2 (BP-2)

Chair: Prof. Kyoung-Je Jang (Gyeongsang National University)

BP-07	15:15~15:30	DEVELOPMENT AND VALIDATION OF A STRAWBERRY-SHAPED SENSOR FOR MEASURING FRUIT VIBRATION CHARACTERISTICS Taiki Arao, Toyohiro Kato, Muneshi Mitsuoka, Masahiro Misumi, Takeshi Kuroyanagi, Takashi Okayasu*
BP-08	15:30~15:45	EFFECTS OF GELATIN NANOPARTICLES AND UREA, APPLIED INDIVIDUALLY OR IN COMBINATION, ON SEEDLING GROWTH OF ARABIDOPSIS THALIANA AND LETTUCE Donggyu Du, Hyojin Moon, Shinyull Lee, Woochan Kim, Dream Kim, Jangho Kim*
BP-09	15:45~16:00	EXTRUSION-BASED 3D BIOPRINTING OF SOFT CARROT CALLUS USING AN ALGINATE-LAPONITE-METHYLCELLULOSE HYDROGEL AND QUANTIFICATION OF SECONDARY METABOLITES Susmita Ghosh, Yeong-Jin Choi*, Hee-Gyeong Yi*

ISMAB2026 Poster Presentation (10/22 (Thu) 10:00~12:00, Hall 5A)

Poster 1 AI and Information Processing

AI-P01 ESTIMATION OF RICE ABOVEGROUND WEIGHT FROM OVERHEAD 2D IMAGES
Byeonghan Lee*, Sangyeob Lee, Su-jin Jeong, Deok-Gyeong Seong, Jeong-Ho Shin, Gil-Seok Park

AI-P02 AN INTELLIGENT PASSION FRUIT DISEASE DIAGNOSIS SYSTEM USING ADVANCED YOLO ARCHITECTURES AND TRANSFER LEARNING
Chuan-Yi Chang, Chao-Wang Young*

AI-P03 A METHOD FOR GROUND ELEVATION MEASUREMENT USING MOVING BASE RTK AND TILT COMPENSATION FOR PADDY FIELD LEVELING
Shanon Yamaguchi, Tatsuro Taniyama, Kyosuke Nishizawa, Hiroshi Iwata*, Ken'ichi Yamaguchi, Yuki Ashihara

AI-P04 DECOUPLING SUBSTRATE AND SAMPLING DIRECTION IN NON-SPHERICAL COMPOUND EYES
You-Rong Zheng, Shang-Jui Fu, En-Cheng Yang, Cheng-Ying Chou*

AI-P05 EVALUATION OF eDNA ANALYSIS PIPELINES TO IDENTIFY FRESHWATER FISH SPECIES
Chao-You Sung, Zong-Yan Liu, Sheng-Kai Hsu, Jose A. Andres, Chien-Yu Chen*

AI-P06 PRELIMINARY STUDY ON IMPROVING THE COMPUTATIONAL EFFICIENCY OF A VIEWPOINT PROPOSAL SYSTEM FOR BUD DETECTION USING A REDUNDANT ROBOT ARM
Hiroyuki Terai*, Shinsuke Yasukawa

AI-P07 COMPARATIVE ANALYSIS OF INSTANCE SEGMENTATION MODELS FOR NET SEGMENTATION IN MELONS
Dong-Han Lee, Seongmin Lee, Jeong Gyun Kang, Jun-Woo Park, Ho-seung Jang, Jayeong Paek*

AI-P08 IMPROVING ROBUSTNESS OF YOLO11-BASED MELON DETECTION USING OCCLUSION AND ILLUMINATION DATA AUGMENTATION
Seongho Lee, Donghan Lee, Jayeong Paek, Jeong Gyun Kang, Jun-Woo Park, Ho-seung Jang, Manjung Kim*

AI-P09 DEVELOPMENT OF AN OPEN-SOURCE AUTOMATIC TRACKING SYSTEM FOR STYLET-BEARING NEMATODES UNDER A MICROSCOPE
Atsuru Fujimoto*, Taisuke Ekino

AI-P10 ESTIMATING ANIMAL MOVEMENT PATHS USING MULTI-NODE INFRARED PYROELECTRIC SENSORS FOR WILDLIFE DAMAGE PREVENTION
Shota Sawada, Hiroshi Iwata*, Ken'ichi Yamaguchi

AI-P11 GENERALIZATION PERFORMANCE OF HYPERSPECTRAL IMAGING-BASED MODEL FOR MELON HARVEST-TIME PREDICTION
Seongmin Lee, Seongho Lee, Jeong Gyun Kang, Jun-Woo Park, Ho-seung Jang, Jayeong Paek*

AI-P12 LESION DETECTION AND DISEASE STAGE CLASSIFICATION IN STRAWBERRY AND TOMATO USING DEEP LEARNING
Tae-Hwi Lee, Yu-Jin Jeon, Dae-Hyun Jung*

AI-P13 WHY THE BEST MODEL CHANGES: IMAGE-BASED FRESH-WEIGHT ESTIMATION OF LETTUCE UNDER TRAINING–DEPLOYMENT SHIFTS
Ki-Su Park, Woo-Joo Choi, Myongkyoon Yang*

AI-P14 DATA-DRIVEN IDENTIFICATION OF THI THRESHOLDS FOR PRODUCTIVITY AND EGG GRADE DISTRIBUTION IN LAYING HENS
Leecheon Kim, Darae Kang*

AI-P15 DEEP LEARNING-BASED MODEL FOR OPTIMAL HARVEST STAGE IDENTIFICATION AND SIZE GRADING OF SHIITAKE MUSHROOM
Che-Wei Liu*, Chien-Ying Lee, Syuan-You Lin, Chi-Wei Liu, Yao-Chuan Tsai

AI-P16 COMPARING REAL-TIME INFERENCE PERFORMENCE AND ENERGY EFFICIENCY OF EDGE DEVICES FOR WEED DETECTION
Jae-Min Lee, Seung-Jin Jeong, Ryu-Gap Lim*

AI-P17 COMPARISON OF ENSEMBLE METHODS FOR GREENHOUSE TOMATO YIELD PREDICTION USING HETEROGENEOUS CROP MODELS
Woo Hyeok Jeong, Seung A Kim, Meoung Hun Lee*

AI-P18 A STUDY ON THE FEASIBILITY OF A STAND-ALONE SAP-FLOW SENSOR FOR PRECISION IRRIGATION
Muhammad Amjad, Yeong-Hyeon Shin, Je-Min Park, JinWoo Nam, Mi Young Lim, Ji Woong Bang, Myeongsuk Kim, Junyoung Park, Soo Chung, Woo-Jae Cho*

AI-P19 CANDIDATE-LEVEL RESCORING DETERMINES DETECTION PERFORMANCE UNDER SCARCE LESION ANNOTATION
Peng-Yuan Wu, Shyh-Jye Chen, Cheng-Ying Chou*

AI-P20 INTERPRETABLE HERBAL MEDICINE IMAGE CLASSIFICATION USING A CONCEPT BOTTLENECK MODEL
JIN-SEOK OH, Dae-Hyun Jung*

AI-P21 FORECASTING AFTERNOON GREENHOUSE SOLAR RADIATION WITH GK2A CLOUD OPTICAL THICKNESS AND DAY-AHEAD WEATHER FORECASTS
Hyein Lee, Su Yeon Lee, Joo Eun Lee, Joon Yong Kim*

AI-P22 ZERO-SHOT OPEN-VOCABULARY DETECTION WITH TRANSFER LEARNING FOR BLOSSOM-END ROT IDENTIFICATION IN A COMMERCIAL TOMATO GREENHOUSE
Hyein Lee, Young-Kyun Jang, Joon Yong Kim*

AI-P23 DEVELOPMENT OF AN ALGORITHM FOR PEPPER FRUIT AND FLOWER DETECTION AND COUNTING USING TWO-SIDED OBLIQUE UAV IMAGERY
Hyeonjun Lee, Taeyoung Woo, Dohyeon Jeong, Junyeong Kim, Dong-Wook Kim*

AI-P24 DEVELOPMENT OF A DEEP LEARNING-BASED METHOD FOR DETECTING SOYBEAN PLANTING GROUPS AND COUNTING PLANTS FROM UAV IMAGERY
Taeyoung Woo, Hyeonjun Lee, Junyeong Kim, Dohyeon Jeong, Dong-Wook Kim*

AI-P25 INDIVIDUAL-PLANT SPAD ESTIMATION IN FIELD-GROWN PEPPER USING UAV-DERIVED SPECTRAL, TEXTURAL, AND STRUCTURAL INFORMATION
Dohyeon Jeong, Hyeonjun Lee, Junyeong Kim, Taeyoung Woo, Dong-Wook Kim*

AI-P26 REGRESSION-BASED PREDICTION OF HUMAN AFFECTIVE CHANGES FROM INSECT SOUND MEL-SPECTROGRAMS
Junyeong Kim, Su Ji Jang, Hyeonjun Lee, Dohyeon Jeong, Taeyoung Woo, Dong-Wook Kim*

AI-P27 EFFECTS OF MARKER-HEIGHT VARIATION ON TRACTOR-IMPLEMENT RELATIVE POSE IN SIMULATED EXTERNAL AERIAL MEASUREMENT
Jaewoo Kim, Eun-Kuk Kim, Tae-Ho Han, Hyunggun Kim*

AI-P28 DEVELOPMENT OF POULTRY VOCAL MONITIORING SYSTEM FOR CHICKEN RESPIRATORY DISEASE DETECTION
Li-Yun Huang, Jun-Qian Zhu, Yao-Chuan Tsai*

AI-P29 INVESTIGATION OF PLANT STEM CELL REGENERATION USING DEEP LEARNING-BASED IMAGE PROCESSING
Kai-lun Liu*, Han Tang, Yao-Chuan Tsai

AI-P30 LLM AGENT-BASED CITRUS DISEASE AND PEST DIAGNOSIS USING FIELD IMAGING AND MICROFLUIDIC PCR
Yin-Hao Lai, I-Huai Lu, Li Chang[2], Ming-Chung Chiu[3], Ting-Hsuan Hung[2], Shiuh-Feng Shiao[3], Joe-Air Jiang*

AI-P31 COMPUTER VISION FOR BAT DETECTION AND TRACKING IN INFRARED-ILLUMINATED CAVE VIDEOS
Yu-Wei Chang*, Chen-Wei Liang

AI-P32 ANGULAR-MARGIN LEARNING FOR SPARSE-ENROLMENT CATTLE FACE RE-IDENTIFICATION: WITHIN-BREED REPLICATION AND BIDIRECTIONAL CROSS-DATASET EVALUATION
Jongho Park, Youngjun Na, Imjoung Choi, Sumin Seo, Joungho Lee, Youngjun Choi*, Jung Eek Son*

AI-P33 COMPARATIVE EVALUATION OF MACHINE LEARNING ALGORITHMS FOR PREDICTING WEEKLY YIELD OF HYDROPONIC CUCUMBER IN A SMART FARM
JongWon Park, kyeonghee Choi, Kyongeun Jeon, Heekyoung Lee, Soosang Hahm, Tae Hwan Kang*

AI-P34 BUILDING A MULTIMODAL HYPERSPECTRAL IMAGE DATASET FOR CHARACTERIZING PHYSIOLOGICAL DISORDERS IN SMART FARM-GROWN TOMATOES
JongWon Park, kyeonghee Choi, Kyongeun Jeon, Heekyoung Lee, Soosang Hahm, TaeHwan Kang*

AI-P35 FLOW MATCHING ENABLES HIGH-RESOLUTION TREE SKELETONIZATION FROM OCCLUDED POINT CLOUDS
Dayeon Yang, Chanyoung Ju*, Pyojin Kim

Poster 2 Bio-processing Engineering

BP-P01 GROWTH AND MORPHOLOGICAL RESPONSES OF *PYTHIUM ULTIMUM* UNDER SIMULATED MICROGRAVITY
Hyeon Tae Kim*, Jeong-In Choi, Si-joong Lee

BP-P02 A REPLACEABLE COMPOSITE DIELECTRIC FILM FORLOW-COSTPCB-BASED DIGITAL MICROFLUIDICS
Hung Pin Pan, Yen-Wen Lu*

BP-P03 ECO-FRIENDLY SUPERCRITICAL CO_2 EXTRACTION FOR VALUE-ADDED FUNCTIONAL INGREDIENTS FROM AHNFELTIOPSIS FLABELLIFORMIS
Yo Seph Lee, Jae Hyeok Choi, Sung Wan Park, Hoon Seonwoo*

BP-P04 SUSTAINABLE HIGH-THROUGHPUT 3D FOOD PRINTING VIA UPCYCLED SESAME MEAL ISOLATED PROTEIN INKS FOR PLANT BASED MEAT ANALOGUES
Yuseung Choi, Hyun-Su Choi, Hyunjin Lee, Woobin Choi, Kanghee Han, Sungchul Shin, Yong-Ro Kim, Sangbae Park*

BP-P05 EFFECT OF UREA LOADING METHOD AND DRYING CONDITION ON ALGINATE-BASED SLOW-RELEASEING FERTILIZER BEADS
Jaehyeok Choi, Yoseph Lee, Sungwan Park, Jae Woon Lim, Hoon Seonwoo*

BP-P06 EFFECTS OF STARCH RETROGRADATION ON REHYDRATABLE, EDIBLE SCAFFOLD FOR CULTURED MEAT
Yeonggeol Hong, Agatha Harta Muliani, Kyoung-Je Jang*

BP-P07 MITIGATING EXPERIMENTAL DATA LIMITATIONS IN MICROBIAL CELL FACTORY RESEARCH VIA PHYSICS-INFORMED MACHINE LEARNING
Woo Kyung Lee, Dohyeok Choi, Kwang Young Park, Hee Taek Kim, Wang-Hee Lee*

BP-P08 PHOTOSYNTHETIC SELF-OXYGENATING CULTURED MEAT VIA COAXIAL BIOPRINTING OF CHLORELLA-MUSCLE CELL BIOINK
Kanghee Han, Yuseung Choi, Daeun Jung, Woobin Choi, Woo Seok Jung, Sangbae Park*

Poster 3 Field Machinery and Systems

FM-P01 FABRICATION AND FACTORIAL TESTING OF A PULLING TEST RIG FOR A SELF-PROPELLED RADISH HARVESTER
Seok-Jun Hong, Il-Su Choi*, Young-Hwa Kim, Jea-Keun Woo, Chun-Gu Lee, Kyu-Ho Lee, Yun-Jeong Yang, Si-Yun Kim, Myeong-Hee Lee, Kyung-Sik Choi

FM-P02 COMPARATIVE EVALUATION OF THE TORSIONAL PERFORMANCE OF STEEL WIRE CLAMPS AND STEEL PLATE CLAMPS FOR GALVANIZED STEEL TUBE CONNECTIONS IN GREENHOUSE STRUCTURES
Cheng-Chang Lien, Yu-Min Wang*, Zong-Xian Xie, Jun-Han Mei

FM-P03 EFFECTS OF SHORT-TERM NATURAL AGING ON THE MECHANICAL PROPERTIES OF GREENHOUSE PLASTIC FILMS
Cheng-Chang Lien, Po-Yu Zeng*, Zong-Xian Xie, Jun-Han Mei

FM-P04 DEVELOPMENT OF VIRTUAL UPLAND FIELD ENVIRONMENTS WITH SPATIALLY VARYING FRICTION FOR TRACTOR DRIVING SIMULATION
Eun-Chae Roh, Kyung-Do Kwon, Chang-Ho Yun, Chang-Ju Yang*

FM-P05 A SURVEY-BASED ANALYSIS ON HEAT-ILLNESS PREVENTION COMPLIANCE AMONG FLORICULTURE FARMERS
Joon-Hyung Park, Moon-Kyeong Jang, Chan-Young Lee, Ju-Seok Nam*

FM-P06 DEVELOPMENT AND PERFORMANCE EVALUATION OF AN ELECTRIC AGRICULTURAL TRANSPORTER
Cheng-Chang Lien*, Min-Jie Li, Zong-Xian Xie, Jun-Han Mei

FM-P07 DEVELOPMENT OF A SMART SPRINKLER WITH VARIABLE WATER FLOW DEPENDING ON THE WATER SUPPLY LOCATION(1) (WATER VOLUME CONTROL USING AN ELECTRONIC VALVE)
Jin Hyun Kim, Seol Ha Kim, Jeong Hun Kim, Won Hyeong Lee, Seok Hyun Seo, Dong Seok Kim, Sang Hun Lee*

FM-P08 DEVELOPMENT OF A SMART SPRINKLER WITH VARIABLE WATER FLOW DEPENDING ON THE WATER SUPPLY LOCATION(2) (WATER VOLUME CONTROL USING AN INVERTER)
Jin Hyun Kim, Seol Ha Kim, Jeong Hun Kim, Won Hyeong Lee, Seok Hyun Seo, Dong Seok Kim, Sang Hun Lee*

FM-P09 PRELIMINARY FIELD EVALUATION OF A MODEL PREDICTIVE CONTROL SYSTEM FOR ROTARY TILLAGE BASED ON SOIL PULVERIZATION RATIO
Hirotaka Tsuchikawa*, Shintaro Noda, Keita Kurashiki, Hidefumi Saito, Yuka Nakano

FM-P10 KINEMATIC ACCELERATION FOR BONDED-PARTICLE DISCRETE ELEMENT SIMULATION OF ROTARY CORE DRILLING
Joon-Seo Kim, Sang-Wook Park, Seung-Yeon Lee, Tae-Kyeong Yeu, Ji-Tae Kim*

FM-P11 EFFECT OF UNDERCARRIAGE CONFIGURATION ON THE MOBILITY OF DEEP-SEA TRACKED VEHICLES OVER HYDROTHERMAL VENT-FIELD TERRAIN
Moo-Young Oh, Ju-Hyeon An, Dan-A Kim, Se-Hee Park, Tae-Kyeong Yeu*, Ji-Tae Kim

FM-P12 GROWTH CHARACTERISTICS OF LEAFY VEGETABLE SEEDLINGS FOR ESTABLISHING SUITABLE SIZE CRITERIA FOR MECHANICAL TRANSPLANTING
Inseok Hwang, Changseop Shin*, Donggyu Kim, Dohyun Ahn

FM-P13 DEM SOIL PARAMETER CALIBRATION USING ANGLE OF REPOSE AND CONE PENETRATION TEST
Donggyu Kim, Sebin Jeong, Changseop Shin*

FM-P14 ENGINE SAFETY CONTROL MODULE FOR BACKPACK BRUSH CUTTERS USING PPE WEAR AND TILT SIGNALS
Young-Tae Yun*, Jeong-Min Lee, Seok-Cheol Yu, Jae-Seung Noh

FM-P15 ANALYSIS OF ISO 18497 SAFETY REQUIREMENTS FOR OPEN-FIELD AGRICULTURAL ENVIRONMENTS IN THE REPUBLIC OF KOREA
Seung-hun Lee, Qazeem Opeyemi Ogunlowo, Chan-min Kim, Hee-Woong Seok, Sun-hyoung Lee, Su-been Ahn, Han Kim, Jin-seo Choi, Yun-Jeong Lee, Yoon-Kyu Hur, Jun-seop Mun, Hyeon-chae Kim, Rack-woo Kim*

FM-P16 DESIGN AND PRELIMINARY EVALUATION OF A MULTI-CHANNEL PNEUMATIC STRIKER FOR GARLIC HARVESTER DISCHARGE
Kyu-Ho Lee, Chun-Gu Lee*, Il-Su Choi, Seok-Jun Hong, Yeong-Hwa Kim, Jea-Keun Woo, Yun-Jeong Yang

FM-P17 CHARACTERIZATION OF THE DASHING BEHAVIOUR OF A WALKING TRACTOR CONSIDERING OPERATOR RESPONSE
Shuto Ohara, Yuya Aoyagi*, Takeshi Shikanai, Masami Matsui, HideoTamashiro

FM-P18 A STUDY ON THE PREDICTION OF DRAFT AND VERTICAL FORCES DURING MOULDBOARD PLOUGHING USING MACHINE LEARNING
Shin-Young Noh, Dae-Wi Jeong, Min-Seung Kim, Se-O Choi, Ye-Na Lee, Yeon-Soo Kim*, Jae-Sung Park, Yong-Joo Kim, Sang-Dae Lee, Jeong-Gil Kim, Seung-Je Cho

FM-P19 FATIGUE BEHAVIOR ANALYSIS AND LIFE ASSESSMENT OF A SCALED HOLLOW CYLINDICAL RUBBER FENDER UNDER FULLY COMPRESSIVE LOADING
Yung-Chuan Chiou*, Po-Yu Weng, Bo-Jyun Lin

FM-P20 COMPARATIVE ANALYSIS OF SWEET POTATO ESTABLISHMENT RATES IN CONVERTED PADDY AND UPLAND FIELDS FOR THE DEVELOPMENT OF A STANDARD CULTIVATION MODEL
Jinho Won, Sun-Bin Min, Jeongju Chae, Yongjin Cho, Dae Cheol Kim*

FM-P21 MAPPING SOIL HARDNESS USING UNMANNED PLOUGHING WORKINGDATA
Adeer Maluk Jacob Ajak, Atsuru Fujimoto*

FM-P22 ANALYSIS OF SPRAY CHARACTERISTICS OF A SPEED SPRAYER ACCORDING TO NOZZLE TYPE AND AIRFLOW RATE

Yun-Jeong Yang, Il-Su Choi, Young-Hwa Kim, Jea-Keun Woo, Seok-Jun Hong, Hyun-Ho Noh, Chun-Gu Lee*

FM-P23 EFFECT OF GARLIC CLOVE PLANTING ANGLE ON GROWTH AND YIELD UNDER MECHANICAL PLANTING

Hye-Min Oh*, Woo-Young Cho, Young-Jun You, Hye-Jeong Jeong, Yu-Shin Ha, Mun-Jung Lee

FM-P24 DESIGN AND DEVELOPMENT OF AN ELECTRIC PLATFORM-BASED INTELLIGENT GARLIC SCAPE REMOVAL SYSTEM

Tae Wook Kang*, Chang Shoo Kim, Seung Heon Cho, Jungsil Kim

FM-P25 THEORETICAL STRESS ANALYSIS OF A 55-KW SELF-PROPELLED SWEET POTATO HARVESTER

Sakib Robin, Md Nasim Reza, Ezatullah Zakir, Karma Osama Sayedlsmaail, Jong Won Lee, Il-Su Choi, Sun-Ok Chung*

FM-P26 DESIGN OF A FULL-BOOM SHIELD AND SPRAY RECOVERY SYSTEM FOR DRIFT REDUCTION

Chun-Gu Lee, Ilsu Choi, Younghwa Kim, Jea-keun Woo, Kyu-ho Lee, Siyun Kim, Seokjoon Hong, Jeekeun Lee, Dong Hyeon Kang

Poster 4 Post-harvest and Food Processing

PH-P01 EFFECTS OF PRE-FREEZING ON POLYPHENOL CONTENT AND DPPH RADICAL SCAVENGING ACTIVITY IN MICROWAVE-VACUUM DRIED APPLE
Akari Saito, Takahiro Orikasa*, Shoji Koide, Yasumasa Ando

PH-P02 ROOM-TEMPERATURE ETHYLENE GAS SENSOR BASED ON GRAPHENE OXIDE AND ZINC OXIDE
Kuan-Ju Chen*, Yao-Chuan Tsai

PH-P03 EFFECTS OF MICROWAVE-VACUUM DRYING PROCESSING ON THE PHYSICAL PROPERTIES OF BANANA CHIPS
Jan Jeng Huang, Jia FangLi*

PH-P04 DEVELOPMENT OF AN IMPELLER FOR BROWN RICE MACHINE SPECIFICALLY FOR MEDIUM GRAIN RICE
Seok-Jin Lee, Sun-young Lee Jong-seung Cho, Ji-Ae Lee, Kyung-Soo Kim, Sung-Ha Hong, Hwang-Gye Lee, Jin-Hyun Kim, Tae-Wook Kim*

PH-P05 ESTIMATION OF ADDED SORBITOL CONCENTRATION IN CARROT USING RAMAN SPECTROSCOPY
Shiori Furukawa, Takahisa Nishizu, Teppei Imaizumi*

PH-P06 EFFECT OF SUB-ZERO TEMPERATURE STORAGE ON PHYSICOCHEMICAL PROPERTIES AND MICROBIOLOGICAL QUALITY OF FRESH-CUT YELLOW BELL PEPPERS
Shuri Takahashi, Takahiro Orikasa, Shoji Koide*

PH-P07 INFLUENCE OF BOTTLE-DERIVED SIGNALS ON RAMAN SPECTROSCOPIC AUTHENTICATION OF JAPANESE WHISKY
Masato Yoshisako, Mihir Kumar Purkait, Takahisa Nishizu, Teppei Imaizumi*

PH-P08 ANTIOXIDANT PROPERTIES OF COFFEE SUBSTITUTES MADE FROM GERMINATED LEGUMES AND CEREALS
Reina Tanaka, Takahisa Nishizu, Nijolė Vaitkevičienė, Teppei Imaizumi*

PH-P09 METABOLITE PROFILES AT HARVEST AS POTENTIAL INDICATORS OF POSTHARVEST SHELF LIFE IN BROCCOLI SPROUTS UNDER DIFFERENT CULTIVATION TEMPERATURES
Ayana Kawabata, Kohei Nakano*

PH-P10 DEVELOPMENT AND COMPARATIVE EVALUATION OF SEGMENTATION MODELS FOR SURFACE DEFECT DETECTION IN MULTIPLE FRUIT TYPES
Seokha Hwang, Harin Jang, Kim Min hyun, Huynh Cao The Cuong, Donghyeon Seong, Ghiseok Kim*

PH-P11 EFFECTS OF HIGH-PRESSURE PRETREATMENT ON CHEMICAL COMPOSITION OF ARABICA COFFEE BEANS
Nisa Vinka Nurul Hayati, Manami Yamada, Teppeilmaizumi*, Takahisa Nishizu

PH-P12 FUNDAMENTAL STUDY ON NON-DESTRUCTIVE DETECTION FOR CRYSTALLIZED SYMPTOMS OF TARO WITH X-RAY IMAGE

Noriko Takahashi*, Keiji Konagaya, Takumi Tachibana, Kazunori Ninomiya, Yuri Shimamoto, Nina Alissa Favergeat, Ziwei Zheng, Naoshi Kondo

PH-P13 EFFECTS OF FRUIT CANOPY POSITION IN THE TREE ON WATER LOSS AND CUTICLE STRUCTURE OF 'KAWACHI BANKAN' FRUIT DURING STORAGE

Tomoka Ida, Keiji Konagaya, Nanako Saito, Noriko Takahashi*

PH-P14 DEVELOPMENT OF A DEEP LEARNING MODEL FOR AUTOMATIC FIVE-GRADE QUALITY CLASSIFICATION OF PEELED GARLIC USING MULTI-VIEW IMAGES

Hyeon-Chae Yu, Saet-Byeol Park, Ji-Hee Han, Seong Min Kim*

PH-P15 CLASSIFICATION AND SEGMENTATION OF EXTERNAL DEFECTS IN ORIENTAL MELON USING RGB IMAGIN AND DEEP LEARNING

Saet-Byeol Park, Hyeon-Chae Yu*, Ji-Hee Han

PH-P16 IMPACT ON ELECTRICAL AND PHYSICOCHEMICAL PROPERTIES OF Ag/TiO_2 NANOCOMPOSITE-ASSISTED VACUUM-IMPREGNATED CARROT

Sourav Kumar Singha, Takahisa Nishizu, Teppei Imaizumi*

PH-P17 STUDY ON KEY FACTORS BY MOISTURE CONTENT TO IMPROVE CLEANING EFFICIENCY OF DOMESTIC WHEAT

Eun-Jin Kwak, Dong-Gwan Shin, Hoon Kim, Jae-Woong Han*

PH-P18 ANALYSIS OF DRYING CHARACTERISTICS OF A CIRCULATING CROSS-FLOW GRAIN DRYER FOR DOMESTIC WHEAT USING SIMULATION

Woo-Jin Choi, Dong-Gwan Shin, Hoon Kim, Jae-Woong Han*

PH-P19 DEVELOPMENT OF AN OPERATION SCHEDULING PROGRAM FOR DOMESTIC WHEAT DRYING AND STORAGE FACILITIES

Jun-Yeong Kim, Dong-Gwan Shin, Hoon Kim, Jae-Woong Han*

PH-P20 DEVELOPMENT OF EMBEDDED DYNAMIC QR SCANNER AND IOT SENSOR NODES FOR AGRICULTURAL PRODUCT TRACEABILITY

Sung-Min Han, Hyo-Eun Lee, Su-Hyeon Lim, Dong-Soo Ryu, Seong-Min Kim*

PH-P21 EFFECTS OF POST-HARVEST DRYING DELAY ON QUALITY CHANGES IN DOMESTIC WHEAT

Soo-In Kim, Dong-Gwan Shin, Hoon Kim, Jae-Woong Han*

PH-P22 DEEP LEARNING-BASED JUICE EXTRACTION RATE PREDICTION AND SPEED OPTIMIZATION FOR A TWIN-SCREW JUICER USING SENSOR TIME-SERIES DATA

Jae-Min Jung, Dong-Hyeon Kim*, Tae-Hyeon Kim, Wang-Hee Lee*

Poster 5 Precision Agriculture Machinery and Systems

PA-P01 A STEREO VISION AND 3D POINT CLOUD-BASED BREEDING ASSISTIVE SYSTEM FOR SWEET POTATO SHOOT PHENOTYPING
Ting-Han Lin*, Shang-Yu Hsieh, Chin-Ying Yang, Shu-Yun Chen, Chung-Feng Kao, Po-Hsien Lu, Tsai-Wen Yang, Yao-Chuan Tsai

PA-P02 COMMUNICATION AND DRIVE INTEGRATION OF GANTRY-TYPE ROBOT
Zhen-Fan Lin, Chao-Wang Young*

PA-P03 BASED ON DEEP LEARNING AND IMAGE PROCESSING AN AUTOMATED FIELD-BASED PHENOTYPIC TRAIT MEASUREMENT AND BREEDING SUPPORT SYSTEM FOR SWEET POTATOES
Shang-Yu Hsieh*, Ting-Han Lin, Chin-Ying Yang, Po-Hsien Lu, Yao-ChuanTsai

PA-P04 DEEP LEARNING-BASED LOW-ACTIVITY STANDING ABNORMALITY DETECTION AND EAR-TAG TRACKING IN DAIRY COWS
Yu-Lun Tseng*, Yao-Chuan Tsai

PA-P05 CONSTRUCTION AND TASK-LEVEL VALIDATION OF A VIRTUAL PLATFORM FOR A SPONGE-SEEDLING TRANSPLANTING ROBOT UNDER VARIABLE TRAY POSES
Tianle Shen, Phanith Chea, Dong-Hoo Shin, Young-Min Kim, Lim-Du Hee, Woo-Young Kim, Kyeong-Hwan Lee*

PA-P06 EFFECTS OF FIELD SIZE AND SHAPE ON THE OPERATIONAL FEASIBILITY AND COVERAGE PERFORMANCE OF AUTONOMOUS AGRICULTURAL MACHINERY
Yong-Hyun Kim, Jumyeong Lee, Chankeun Lee, Seokhyun Ahn, Hak-Jin Kim*

PA-P07 INTERFERENCE-GUIDED BRANCH MANIPULATION FOR DUAL-ARM ROBOTIC PRUNING
Chao Teng, Woo-Young Kim, Kyeong-Hwan Lee*

PA-P08 RGB-BASED 3D RECONSTRUCTION AND PHENOTYPING WORKFLOW FOR TOMATO PLANTS
Yi Chen, Kyeong-Hwan Lee*

PA-P09 SIMULATION OF PESTCIDE TRANSPORT IN A SOYBEAN-GROWING FIELD: A CASE STUDY OF DINOTEFURAN
Uk Heo, Jongsoon Kim*

PA-P10 BIAS-AUGMENTED IEKF-BASED GNSS/INS INTEGRATION ALGORITHM FOR AUTONOMOUS AGRICULTURAL TRACTORS
Choongmin Lee, Wonhee Lee, Kwanjin Kim*

PA-P11 DEVELOPMENT OF A MACHINE LEARNING MODEL FOR PREDICTING SOIL MOISTURE IN CROP FIELDS USING WEATHER AND IRRIGATION DATA
Gyeong-Tae Kim, Hyung-Min Kim, Jun-Ha Choi, Hwang Gyu Lee, Tae-Wook Kim, Jin-Hyun Kim, Dong Suk Kim, Sang-Hun Lee, Suk-Ju Hong*

PA-P12 A REVIEW ON METAL BINDER JETTING PROCESSES APPLYING ACTIVE POWDER FEEDING-RECOATING MODULES

Do Hyun Ahn, Ye Jin Park, Pil Ho Lee, Chang Seop Shin*

PA-P13 THEORETICAL POWER REQUIREMENT OF A SPRAYER MODULE FOR A MULTIPURPOSE ELECTRIC PEPPER CULTIVATION PLATFORM

Md Nasim Reza, Hongbin Jin, Miao Miao Tu, Md Mamunur Rashid, Sujeong Jeong, Jong-Su Lee, Sun-Ok Chung*

PA-P14 SELF-CALIBRATING VIDEO MEASUREMENT OF CORRIDOR CROWDING AND ITS ASSOCIATION WITH DAIRY COW LAMENESS SCORING

Jia-Ming Zhou, Wen-Lin Chu*, Hsin-I Chiang

PA-P15 A PLANT GROWTH MONITORING SYSTEM BASED ON A PORTABLE LASER-INDUCED GRAPHENE SENSOR

I-Yin Chang*, Yao-Chuan Tsai

PA-P16 MOISTURE GRADING OF SPHAGNUM MOSS MEDIA USING MULTI-SOURCE FEATURE FUSION AND NEAR-INFRARED IMAGING

Xue-Ru Huang, Wei-Ling Chen, Hsi-Chun Hung, Wen-Lin Chu*

PA-P17 AUTOMATED PIPELINE FOR CONSTRUCTING AND BENCHMARKING A TOP-VIEW DAIRY COW IMAGE DATASET USING RFID INTEGRATION

Yu-Min Lee, Wen-Lin Chu*, Chien-Kai Wang

PA-P18 RELATING MACRONUTRIENT RATIOS IN THE TISSUE CULTURE MEDIUM TO PHALAENOPSIS GROWTH

Yi-Wei Lin, Wen-Lin Chu*, Chan-Yi Lin

PA-P19 NON-DESTRUCTIVE PREDICTION OF SUBSTRATE MOISTURE CONTENT IN *PHALAENOPSIS* ORCHIDS USING HYPERSPECTRAL IMAGING

Wei-Chun Lin, Wen-Lin Chu*, Wei-Ling Chen, Hsi-Chun Hung

PA-P20 DISTANCE-ADAPTIVE DEPTH CAMERA-LIDAR FUSION FOR PROXIMITY WARNING ON AGRICULTURAL MACHINERY

Seung-Yong Seo, Jin-Yeong Lee, Jae-Min Lee, Ryu-Gap Lim*

PA-P21 END-SENSING SYSTEM FOR IRRIGATION MONITORING IN BUILDING-INTEGRATED VERTICAL FARMS

Joo won Jeong, Meong Hun Lee*

PA-P22 PHYSICAL AI-BASED ARCHITECTURE FOR AUTONOMOUS AGRICULTURAL ROBOT OPERATIONS

Kiwoong Song, Myeong Hun Lee*

PA-P23 A DATA ACQUISITION STABILITY EVALUATION FRAMEWORK FOR MULTISENSING DEVICES IN SMART PIG BARNS
Hyun Jun Kim, Ik Tae Choi, Lee Meoung Hun*

PA-P24 DEVELOPMENT OF A VISION-GUIDED ROBOTIC ARM FOR AUTOMATED TOMATO POLLINATION
Li-Yun Wen*, Yi-Rou Hung, Wei-Lun Hsu, Yao-Chuan Tsai

PA-P25 DEEP LEARNING-BASED TOMATO AXILLARY SHOOT RECOGNITION WITH ROBOTIC ARM POSITIONING
Yi-Rou Hung*, Li-Yun Wen, Syuan-You Lin, Yao-Chuan Tsai

PA-P26 DEVELOPMENT OF A DISCRETE ELEMENT MODEL FOR DEHISCED KOREAN GINSENG SEEDS
Jin-Woo Park, Ju-Hyun Kim, Seung-Gwi Kwon, Wan-Soo Kim*

PA-P27 REQUIRED POWER OF AN AIR-DRILL SEEDER BY MUTIBODY DYNAMICS SIMULATION
Kang Uk Lee, Choong Ho Lee*

PA-P28 ANALYSIS OF SEED DISCHARGE CHARACTERISTICS ACCORDING TO THE CHANGES IN THE GEOMETRY OF AN AIR SEEDER SEED DELIVERY TUBE
Dae Seong Lee, Choong Ho Lee*

PA-P29 STITCH-BASED STRAIN SENSOR FOR REAL-TIME MONITORING OF STEM CIRCUMFERENCE VARIATION
Jongho Baek, Junyoung Park, Soo Chung*

PA-P30 UAV RGB IMAGE-BASED ANALYSIS OF CROP ROWS AND MISSING PLANTS IN PADDY-FIELD SOYBEAN FOR PRECISION WEEDING
In Seop Jang, June-Young Han, Sun-Bin Min, Dae-Cheol Kim, Yongjin Cho*

PA-P31 SPATIAL ESTIMATION OF PADDY SOIL PROPERTIES BY INTEGRATING MULTI-TEMPORAL UAV SPECTRAL FEATURES AND BLOCK KRIGING
June-Young Han, In-Seop Jang, Jeongju Chae, Seong-Won Lim, Dae-Cheol Kim, Yongjin Cho*

PA-P32 EVALUATION OF SATELLITE IMAGERY FOR PREDICTING ELECTRICAL CONDUCTIVITY IN PADDY SOILS
Sun-Bin Min, In Seop Jang, Jeong Ju Chae, Dae-Cheol Kim, Yongjin Cho*

PA-P33 DEVELOPMENT OF A SPATIAL OVERLAY FRAMEWORK FOR UAV-DERIVED NDVI AND PADDY SOIL PROPERTY MAPS
Seong-won Lim, Jin-ho Won, June-Young Han, Dae-Cheol Kim, Yong-jin Cho*

PA-P34 FIELD-SPECIFIC RELATIONSHIPS OF PROXIMAL SOIL SENSOR MEASUREMENTS WITH ORGANIC MATTER AND TOTAL NITROGEN IN PADDY SOILS
JeongJu Chae, Jinho Won, Seongwon Lim, Dae-Cheol Kim, Yongjin Cho*

PA-P35 GENETIC ALGORITHM-BASED FEATURE EXTRACTION FROM VISIBLE TRANSMISSION SPECTRA AND IMAGES FORCHICKENEMBRYOSEX PREDICTION

Akito Arimura, Hitomi Shibagaki, Tetsuhito Suzuki*

PA-P36 MULTI-VIEW CHICKEN FLOCK UNIFORMITY ESTIMATION COMBINING PERSPECTIVE TRANSFORMATION AND IMAGE ANALYSIS

Ting-Shao Chen*, Ming-Kun Hsieh, Kuang-Fu Chang, Yao-Chuan Tsai

PA-P37 WORK PATH OPTIMIZATION ALGORITHM FOR AUTONOMOUS BOOM SPRAYING IN RIDGE CULTIVATION ENVIRONMENTS

Deok-Keun Kim, Ji Won Choi, Soo Been Cho, Jung-sang Yoo, Seung-Hwan Yang*

PA-P38 DESIGN AND ADSORPTION CHARACTERISTIC ANALYSIS OF A SEED FEEDING DEVICE FOR NON-DESTRUCTIVE FOREST SEED SORTING

Hwang-Gyu Lee, Chung-Kwan Lee, Chan-Eun Kim, Tae-Wook Kim*

PA-P39 DISCUSSION OF STRUCTURAL SAFETY OF AN AUTONOMOUS AGRICULTURAL MOBILITY VEHICLE

Sang Min Lee, Kang Uk Lee, Jung Min Bae, Dae Seong Lee, Choong Ho Lee*

PA-P40 DEVELOPMENT AND DEMONSTRATION OF A MODULAR SMART FARM ROBOT FOR WHOLE-CYCLE STRAWBERRY CULTIVATION

Lae-Kyoung Lee*, Su-Yong An

PA-P41 PREDICTION OF SOYBEAN PLANT HEIGHT AND STEM DIAMETER USING UAV MULTISPECTRAL IMAGERY AND GROWTH RESPONSES TO SMART CULTIVATION TREATMENTS

ChangHyeok Park, ChanSeok Ryu*, GangIn Je, HoJun Kwon, Gang-Jin Lee

Poster 6 Smart Farm Systems and Renewable Energy

SF-P01 DEVELOPMENT OF A MULTIMODAL AI-BASED POULTRY HEALTH MONITORING SYSTEM INTEGRATING EDGE COMPUTING AND TRANSFER LEARNING FOR LAYING HEN PRODUCTION
Fu-Kai Chang*, Tsui-Lan Chou, Ming-Kun Hsieh, Yao-Chuan Tsai

SF-P02 A TWO-STAGE DEEP LEARNING-BASED MULTI-TYPE ABNORMAL COMB RECOGNITION SYSTEM
Yun-I Chu*, Yu-Jen Shih, Fu-Kai Chang, Ming-Kun Hsieh, Yao-Chuan Tsai

SF-P03 PERFORMANCE AND FIELD APPLICABILITY OF A SIMPLIFIED DRINKING-WATER TEMPERATURE CONTROL SYSTEM FOR BROILER HOUSES
La-Hoon Cho, Jin Kyung Kwon, Chung-Geon Lee, Jae Kyung Jang, Sung-Wook Yun, Jong-Pil Moon, Seong-Heon Kim*

SF-P04 CFD-BASED AIRFLOW ANALYSIS AND OPTIMIZATION OF HVAC AND DUST COLLECTION SYSTEMS IN BROILER HOUSES
Sun-hyoung Lee, Rack-woo Kim*, Su-been Ahn, Seung-hun Lee, Chan-min Kim, Hee-woong Seok, han Kim, Yun-jeong Lee, Yoon-kyu Hur, Hyeon-Chae Kim

SF-P05 PREDICTION OF METHANE EMISSIONS IN SWINE HOUSING BY MACHINE LEARNING APPLIED TO CONTINUOUS SENSOR DATA
Su-Been Ahn, Rack-Woo Kim*, Hang-Ju Cho, Yoo-Kyoung Seo, Da-Yeon Song

SF-P06 INTERNATIONAL STANDARDIZATION TRENDS FOR DATA INTEROPERABILITY IN AGRICULTURAL ELECTRONICS AND DATA-DRIVEN AGRIFOOD SYSTEMS
Hyuk Ki*, Hyunseok Lee, Sanghyuk Lee, Jihyeong Kim

SF-P07 IMPACT OF INITIAL MOISTURE ON FUEL QUALITY AND ENERGY RECOVERY DURING TORREFACTION
Sunyong Park*

SF-P08 DEVELOPMENT OF A TRACKED GREENHOUSE MOBILE MAPPING SYSTEM USING 3D LIDAR AND 2D SLAM
Ping-Chun Chen*, Fu-Kai Chang, Li-Yun Wen, Wu-Yang Shih, Yao-Chuan Tsai

SF-P09 RESISTIVE AMMONIA SENSOR BASED ON POLYPYRROLE, ZINC OXIDE, AND REDUCED GRAPHENE OXIDE COMPOSITES
Chih-Chieh Liu*, Yao-Chuan Tsai

SF-P10 RELATIONSHIP BETWEEN MUSHROOM FRUITING INITIATION RATEAND ENVIRONMENTAL FACTORS USING IMAGE RECOGNITIONAND DATA ANALYSIS
Chien-Ying Lee*, Yu-Jen Shih, Wu-Yang Sean, Chi-Wei Liu, Yao-Chuan Tsai

SF-P11 COMPARATIVE LIFE CYCLE ASSESSMENT OF SMART AND CONVENTIONAL SEEDLING NURSERY SYSTEMS

Kyungjae Song, Changseop Shin*

SF-P12 ELECTRODE STATUS DIAGNOSIS FOR REAL-TIME IN-SITU MONITORING OF HYDROPONIC NUTRIENT SOLUTIONS USING ION-SELECTIVE ELECTRODES

Yuna Kwon, Hak-Jin Kim*, Minki Kang, Joonhwan Kim

SF-P13 COOLING PERFORMANCE AND AI-BASED PREDICTION OF GREENHOUSE ACTUATOR CONTROL SIGNALS AND VALIDATION

Min Hwan Yu, Kyeong Sik Kang, Seon Yeop Kim, Dae Hyun Kim*

SF-P14 ENVIRONMENTAL AND ENERGY ANALYSIS OF A MINI-GREENHOUSE USING LED PWM AND CFD

Ga Eun Kim, Soo min Lim, Kyeong Sik Kang, Seon Yeop Kim, Dae Hyun Kim*

SF-P15 FUEL PROPERTY EVALUATION AND MACHINE LEARNING PREDICTION FOR CATALYTIC TORREFACTION OF *QUERCUS VARIABILIS*

Chae Young Jang, Su Jeong Lee, Kyeong Sik Kang, Seon Yeop Kim, Sunyong Park, Dae Hyun Kim*

SF-P16 ANALYSIS OF NUTRIENT UPTAKE PATTERNS IN FOGPONICS-CULTIVATED SEED POTATOES ACROSS GROWTH STAGES

Yeong Hyeon Shin, Je-Min Park, Muhammad Amjad, Uk-Hyeon Yeo*, Woo-Jae Cho*

SF-P17 VERIFYING A DRAFT STANDARD BEFORE ENACTMENT: IMPLEMENTATION AND MEASUREMENT OF SMART GREENHOUSE NODE DISCOVERY

Dae-Hyun Jung, Inchan Choi, Joon Yong Kim*

SF-P18 ADMITTING INSTALLED EQUIPMENT TO AN OPEN-FIELD STANDARD UNDER DEVELOPMENT: WHAT THE GATEWAY BOUNDARY COSTS

Hyein Lee, Jae-Seok Seo, Joon Yong Kim*

SF-P19 THREE-DIMENSIONAL SHAPE AND VOLUME ANALYSIS OF A PIG MODEL USING MULTI-VIEW DEPTH IMAGES

Seung Hyeon Cheon, Byeong Eun Moon*

KSAM Special Session

특별세션 1

○ **세션명: 애그테크 산학연 기술교류회**

○ **일　시: 2026. 10. 21.(수) 오후**

○ **장　소: 부산 BEXCO 제2전시장 320호**

○ **세션 일정**

시간	분	내용	발표자
13:30~14:00	30	▪ 등록	
14:00~14:10	10	▪ 개회 및 내빈소개	박학순 (경북대학교 밭농업기계개발연구센터)
14:10~14:20	10	▪ 개회사	하유신 (경북대학교 밭농업기계개발연구센터)
14:20~16:20	120	▪ 초청강연: 노지농업 분야 Physical AI 기술 – 이론 및 적용사례	권오준 대표이사 (JS FLUX)
16:20~16:30	10	Coffee Break	
16:30~17:00	30	▪ 질의응답	홍동혁 (경북대학교 밭농업기계개발연구센터)

※ 강연자 및 내용은 진행상황에 따라 변경 가능.

특별세션 2

○ **세션명: 신뢰할 수 있는 농업AI, 원칙에서 현장까지**

○ **일　시: 2026. 10. 21.(수) 오후**

○ **장　소: 부산 BEXCO 제2전시장 124호**

○ **세션 일정**

시간	분	내용	발표자
13:00~13:20	20	▪ 등록	
13:20~13:30	10	▪ 개회 및 세션 소개	강윤임 연구관 (농촌진흥청)
13:30~13:50	20	▪ 신뢰할 수 있는 AI 생태계와 농업분야 정책 방향 – 인증 · 자율규제 동향, 법적 가이드라인, 거버넌스 등	전창배 이사장 (국제인공지능윤리협회)
13:50~14:10	20	▪ 스마트팜 현장에서 마주하는 AI, 기대와 우려 – 자동화 · 데이터 도입 경험, 편익, 오작동 리스크 등	정병두 대표 (로즈벨리)
14:10~14:30	20	▪ 농업 특화 AI 서비스 개발과 윤리적 책임 – 데이터 활용과 설명 가능성 확보 등	박흔동 대표 ((주)지농)
14:30~14:50	20	▪ 신뢰할 수 있는 농업AI를 위한 가이드라인 검토 방향 – 기본원칙, 핵심요건, 자율점검체계(안) 등	양승엽 연구위원 (한국노동연구원)
14:50~15:00	10	Coffee Break	
15:00~15:30	30	▪ 종합토론: 선언에서 이행으로, 신뢰할 수 있는 농업 AI 현장의 과제 – 전창배 이사장(국제인공지능윤리협회) – 양승엽 연구위원(한국노동연구원) – 박흔동 대표((주)지농) – 정병두 대표(로즈벨리) – 문광진 교수(국립목포대) – 정휘웅 소장(42MARU) 등	좌장: 김민영 과장 (농촌진흥청)

※ 강연자 및 내용은 진행상황에 따라 변경 가능.

특별세션 3

○ **세션명: AgTech 기업의 Physical AI 기술 개발과 상용화 전략**

○ **일　시: 2026. 10. 21.(수) 오후**

○ **장　소: 부산 BEXCO 제2전시장 125호**

○ **세션 일정**

시간	분	내용	발표자
13:00~13:20	20	▪ 등록, 개회 및 세션 소개	전찬우 ((주)아그모)
13:20~13:50	30	▪ Safety for Full Autonomy: build AI safely, prove safety beyond AI	이창주 ((주)아그모)
13:50~14:20	30	▪ Physical AI 기반 농업 AX와 성공 생태계	최준기 ((주)대동 에이아이랩)
14:20~14:50	30	▪ Robot learning for greenhouse task automation: field practice and challenges	조진형 (아이오크롭스)
14:50~15:00	10	Coffee Break	
15:00~15:30	30	▪ Physical AI, 이상과 현실. 실타래를 풀어나가는 방법	정남형 (LS엠트론)
15:30~16:00	30	▪ 농업/건설기계 AI를 위한 센서 시스템 사례	김정원 (보쉬코리아)
16:00~16:30	30	▪ 농업 physical AI의 현재와 미래	이규화 ((주)메타파머스)
16:30~17:00	30	▪ 필드 환경에서의 Physical AI 시스템 신뢰성: 농업용 자율주행 Level 4 개발 사례를 중심으로	서민열 ((주)티와이엠 아이씨티)

※ 강연자 및 내용은 진행 상황에 따라 변경 가능.

특별세션 4

○ **세션명: 농업기계 현장기술 확산 및 전문인력 양성 방안**

○ **일　시: 2026. 10. 21.(수) 오후**

○ **장　소: 부산 BEXCO 제2전시장 126호**

○ **세션 일정**

시간	분	내용	발표자
13:00~13:20	20	▪ 등록	
13:20~13:30	10	▪ 개회 및 세션 소개	홍순중 (한국농수산대학교)
13:30~13:45	15	▪ 첨단농업기계 기술동향	임류갑 (순천대학교)
13:45~14:00	15	▪ 농업기계 교육 • 자격 • 채용 연계 전문인력 양성 현황	강진석 (용인시농업기술센터)
14:00~14:15	15	▪ 시군 농업기술센터 임대사업소 운영실태 현황	이정민 (국립농업과학원)
14:15~14:30	15	▪ 농업기계 사후관리 시군 전문인력 양성 현황	서일환 (강화군농업기술센터)
14:30~14:45	15	▪ 농업기계 현장기술 확산 실태	정해동 (한국농수산대학교)
14:45~15:00	15	Coffee Break	
15:00~16:30	90	▪ 종합토론: 농업기계 현장기술 확산 및 전문인력 양성 방안 – 정명갑(농촌진흥청 농촌인적자원개발센터 센터장) – 안상화(한국농기계공업협동조합 정책지원팀 팀장) – 황민호(강원도 원주영서고등학교 산업기계과 부장) – 이영환(한국농업기계학회 농기계교관분과 위원장) – 유정영(홍천군농업기술센터, 농기계전문지도연구회 회장)	좌장 김병갑 (국립농업과학원 농업공학부)

※ 발표자, 토론자 등 추진일정은 상황에 따라 변경될 수 있음.

특별세션 5

○ **세션명: 농축산 수확후공정 시스템과 최적화 전략 및 연구동향**

○ **일　시: 2026. 10. 21.(수) 오후**

○ **장　소: 부산 BEXCO 제2전시장 123호**

○ **세션 일정**

시간	분	내용	발표자
14:00~14:10	10	▪ 개회 및 세션 소개	이현동 (농과원)
14:10~14:30	20	▪ 식품 가공 시스템 설계 및 공정 최적화 접근법	이승현 (충남대)
14:30~14:50	20	▪ 김치 가공 부산물 전처리 시스템 기술	천호현 (김치연)
14:50~15:10	20	▪ 농산물 벌크 단위 예건 및 저장 일관화 기술	지형용 (생기연)
15:10~15:30	20	▪ 냉동식품 포장 자동화 시스템 기술	조세운 (전자연)
15:30~15:40	10	Coffee Break	
15:40~16:00	20	▪ 농산물 수확후 선별과 저장 · 유통 중 품질평가 기술	김기석 (서울대)
16:00~16:20	20	▪ 스마트 APC 적용을 위한 Physical A.I 솔루션	이상호 (KT)
16:20~16:40	20	▪ 스마트 도축장 기술의 현재와 미래 : 지능형 도체 평가와 자동화 기술 현황	김준태 (충남대)
16:40~17:00	20	▪ 곡류 수확후처리 기술의 연구 동향과 미래 전망 : 쌀과 밀을 중심으로	한재웅 (공주대)

※ 강연자 및 내용은 진행상황에 따라 변경 가능.

특별세션 6

○ **세션명: 스마트시설원예 현황 및 국제경쟁력확보 전략**

○ **일　시: 2026. 10. 22.(목) 오후**

○ **장　소: 부산 BEXCO 제2전시장 124호**

○ **세션 일정**

시간	분	내용	발표자
13:00~13:20	30	▪ 등록	
13:20~13:30	10	▪ 개회 및 세션 소개	장영균 (그린씨에스(주))
13:30~13:50	20	▪ 첨단온실 구조 · 기자재 기술 현황과 국산화 전략 – 수입의존 기자재의 국산화와 해외진출 방향	정순목 ((주)그린플러스)
13:50~14:10	20	▪ 한국형 스마트팜 제어기술 현황 및 경쟁력 – 복합환경 · 양액 통합제어 기술의 현장적용기술	장영균 (그린씨에스(주))
14:10~14:30	20	▪ 스마트팜 데이터 활용 현황과 AI기술 적용 전략 – 통합관제시스템 데이터 컨설팅 및 AI 도입 사례	장익훈 ((주)지농)
14:30~14:50	20	▪ 개방형 스마트팜 플랫폼과 민관협력 산업화 전략 – 스마트팜표준 연계를 통한 상호운용성 확보	방지웅 (농촌진흥청 시설원예연구소)
14:50~15:10	20	▪ 한국형 스마트온실의 에너지절감 측면 경쟁력 – 에너지절감기술로 본 한국형 온실의 기술 진단	김락우 (서울대학교)
15:10~15:30	20	Coffee Break	
15:30~16:00	30	▪ 종합토론: 시설원예 스마트팜의 국제경쟁력확보 전략 – 정순목((주)그린플러스 수석연구원): – 장영균(그린씨에스(주) 연구소장): – 양명균(전북대학교 생물산업기계공학과 교수): – 김준용(서울대학교 농업생명과학연구원 팀장): – 최인찬(국립농업과학원 스마트팜개발과 연구관): – 장유섭(팜패스 대표이사):	좌장 이시영 (농촌진흥청 국립농업과학원)

※ 강연자 및 내용은 진행상황에 따라 변경 가능.

Special Session 7

○ Title : Latest Research Trends in Agricultural Robots

○ Date : 2026. 10. 22. (Thu)

○ Venue : Room 125, Exhibition Center 2, BEXCO

○ Session Schedule

Time	min.	Presentation Title	Presenter
14:00~14:10	10	▪ Opening and Session Introduction	Seung-Hwan Yang (KITECH)
14:10~14:30	20	▪ Characteristics of Tactile Sensors in Grasping Operations for Fruit and Vegetables using Five-Fingered Robot Hand	Seung-Hwan Yang (KITECH)
14:30~14:50	20	▪ Perception and Autonomy in Agricultural Robotics: Crop Perception, SLAM, and Multi-Robot Control	Chanyoung Ju (KITECH)
14:50~15:10	20	▪ Development of an Imitation Learning Algorithm for Strawberry Harvesting in Irregular Environments	Byeong-gil Han (KIMM)
15:10~15:30	20	▪ Development of a Robotic tool for Stemless Strawberry Harvesting	Taeyong Choi (KIMM)
15:30~15:40	10	Coffee Break	
15:40~16:00	20	▪ Load distribution control of a Deep-RL-based variable driving platform considering eccentric loads	Heon Soo Choi (KIRO)
16:00~16:20	20	▪ Application and Performance Evaluation of Offset Driving Paths for Orchard Weeding Robots	Jae Wan Koo (KIRO)
16:20~16:40	20	▪ Method for Heterogeneous Sensor Data Fusion and Crop 3D Data Generation for AI Robot Demonstration in Facility Agriculture	Sunghwan Jeong (KETI)
16:40~17:00	20	▪ Development and Demonstration of a Modular Smart Farm Robot System for Whole-Cycle Strawberry Cultivation	Laekyoung Lee (ETRI)

Plenary Session
: Invited Speakers

Plenary 1

Department of Agriculture
Philippine Center for Postharvest Development and Mechanization
www.philmech.gov.ph

International Symposium on Machinery and Mechatronics for Agricultural and Biosystems Engineering (ISMAB2026)
20 to 24 October 2026 in Busan, Republic of Korea

The PHilMech green blueprint: Transforming Philippine agriculture through mechanization

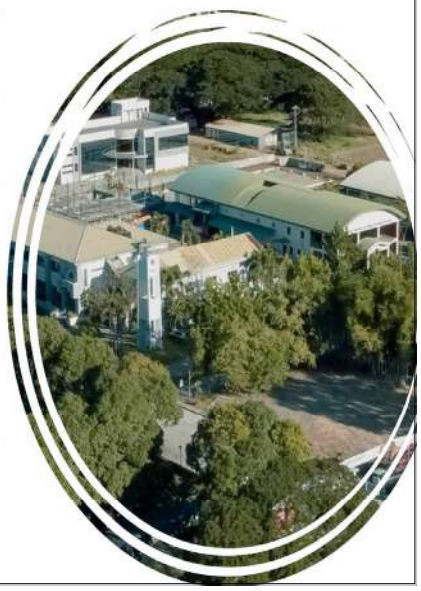

Engr. Eleonor Fausto Santiago
Supervising Science Research Specialist
Laboratory Services Division
21 October 2026

PHilMech highlights

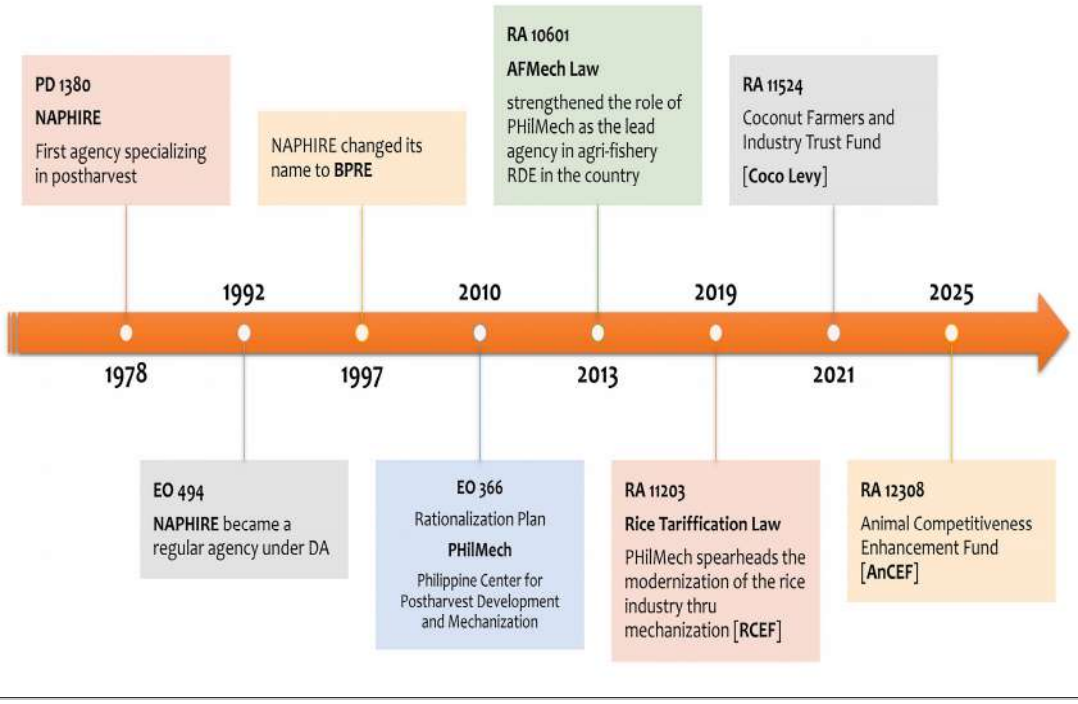

Vision, Mission, and Mandate

Vision

The premiere center for postharvest and mechanization development for a gender-responsive, globally competitive and food secure Philippines with empowered and prosperous farmers and fisherfolks.

Mission

Modernize the agriculture and fisheries sector by increasing resource-use efficiency and productivity, reducing losses and adding value to the produce through a partnership-based R&D, extension, commercialization, and deployment of appropriate postharvest and mechanization technologies.

Mandate

To generate, extend, commercialize and deploy appropriate and solution-focused agriculture and fishery postharvest and mechanization technologies

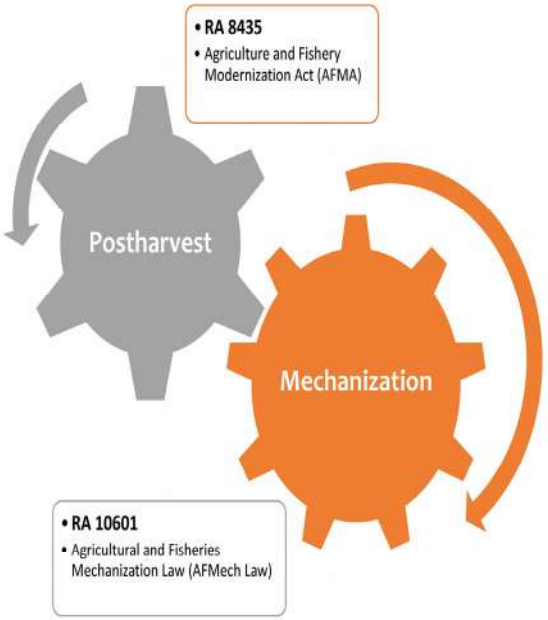

PHilMech mechanization programs priority commodities

Rice

14.51% losses 2016
From 16.47% 2008-2009
Loss reduction to 13.81% 2028

Mango

26.47% losses
Loss reduction to 22.47-24.47%

Banana (Cavendish/Latundan/Lacatan)

14.33% losses
Loss reduction to 12.89%

6.43 % losses (2020)[2]
From 7.18 % (2005-2006)[1]
Loss reduction to 5.98%

Corn

17.07% losses
Loss reduction to 10.25-14.57%

Calamansi

31.61% losses
Loss reduction to 27.61-29.61%

Bulb Onion

Cabbage	Carrots	Eggplant	Garlic	Papaya	Pineapple	Roses/Mums
20.80%	20.30%	4.78-8.05%	20-40% (www.apcaem.org)	42% (PHTRC, 1996)	30-40% (Kader, 1998)	1-40% (Agravante, 2001)

Philippine level of mechanization

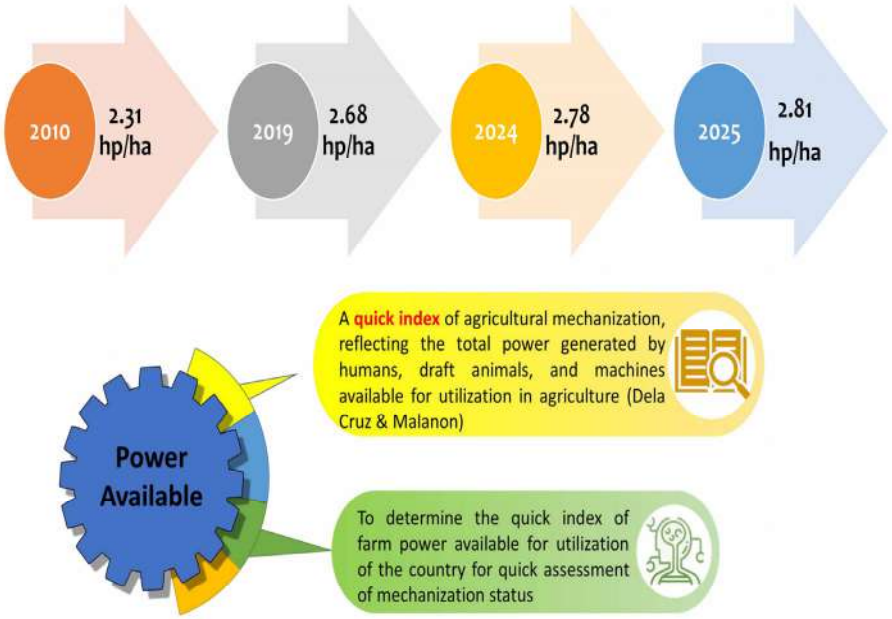

PHilMech roadmap to modernization

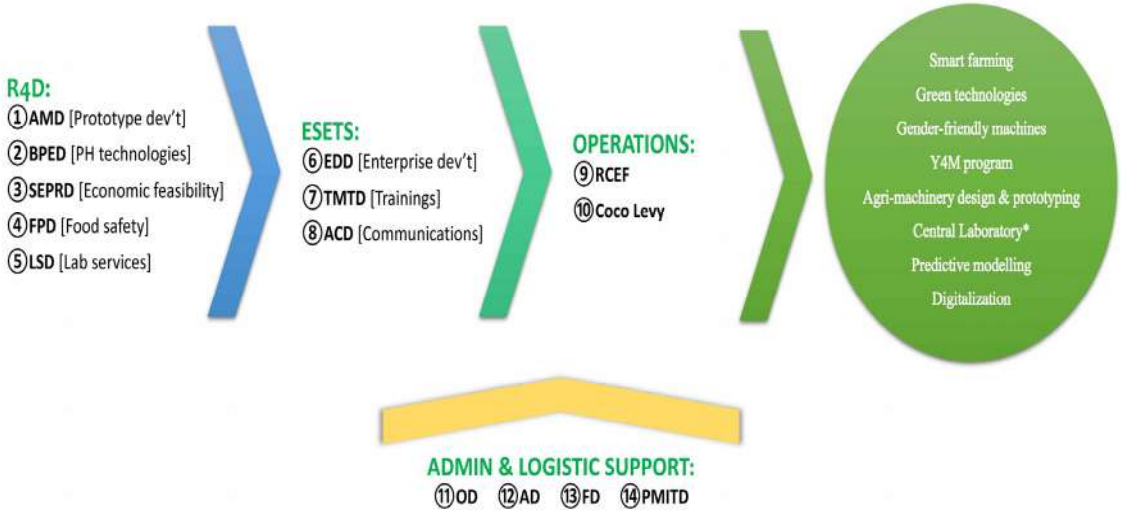

Technical cooperation on agricultural mechanization development with the Republic of Korea

Research and Development

- **Design and Development of a Village Level Corn Milling Machine** *[in collaboration with Lee·Hwa]*
- **Mechanized Onion Production System:** ①Technology Performance ②Verification and Adaptation *[PHilMech-Kamico collaborative program]*
- **Adaptability Testing of Self-propelled Mechanical Elevating Work Platform for Harvesting and other Farm Production Operations of Mango** *[in collaboration with Sungboo Co., Ltd.]*
- **Design and Development of Sugarcane Whole Stalk Harvester** *[pipeline project to be collaborated with Sambu]*

Expert Exchange

- **Korea technology immersion** *[sharing of expertise and provision of technical support]*

Training

- **Training for the personnel involve in the project implementation conducted by Kamico** *[workshops, training courses, and study tours on relevant topics]*

Stakeholder Involvement

- **Technology Advice and Solutions from Korea (TASK)** *[encouraging participation from relevant agencies, academic institutions, business communities, and NGOs in both countries to foster interest and support for cooperative activities]*

Development Assistance

- **Establishment of the Agricultural Mechanization Design and Prototyping Center (AMDPC)** *[funded by KOICA]*

[Kamico assists PHilMech in strengthening agriculture-related initiatives]







Smart Farming: Precision Rice Processing

- **Combine Harvesters:** Replaces 15-20 manual labor days per hectare into a single-day 2-in-1 harvest and thresh operation.
- **Precision Mechanical Transplanters:** Optimizes seed density and seedling distance for higher yield productivity.
- **Recirculating Mechanical Dryers:** Eliminates road drying hazards, preserving kernel head rice quality.
- **Integrated Rice Processing System Units:** Empowers farmer cooperatives (FCAs) to become commercial rice mill operators. Improved postharvest and rice milling recovery.





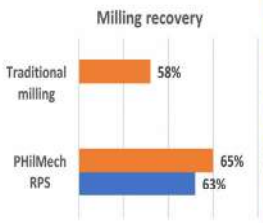



Green Mechanization Strategy

Low-Carbon Agricultural Fleet

- Tier 3 low-emission engines under the RCEF initiative
- Tractor auxiliaries for tilling drylands requiring less water





Green Postharvest Innovations

Solar Tunnel Dryers

Multi-Commodity Solar Tunnel Dryers (MCSTD) utilize natural solar heat to hygienically dry crops like cacao, coffee, cassava, fruits, and fishery products without weather contamination.



Biomass Furnaces

Greenhouse-type Solar Dryers fitted with biomass furnaces utilize agricultural waste (rice husks, coconut shells, cacao pods) for uninterrupted thermal drying during rain.



Biological Controls

Formulations DGA02/DGA14 offer eco-friendly biocontrol solutions to protect bananas and mangoes, reducing chemical pesticide reliance.

DGA02 and DGA14 protect crops against *Colletotrichum gloeosporioides* (anthracnose) and *Lasiodiplodia theobromae* (stem-end rot)

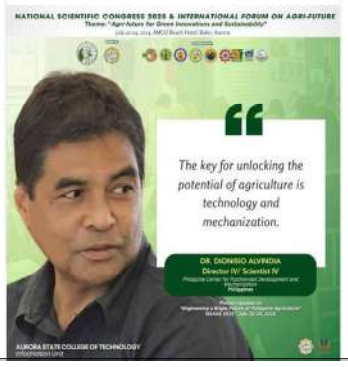

Green Postharvest Innovations

Biological Controls

LS12 project under Laboratory Services Division screens atoxigenic *Aspergillus flavus* strains as BCA for economically important crops (corn, copra, ...)





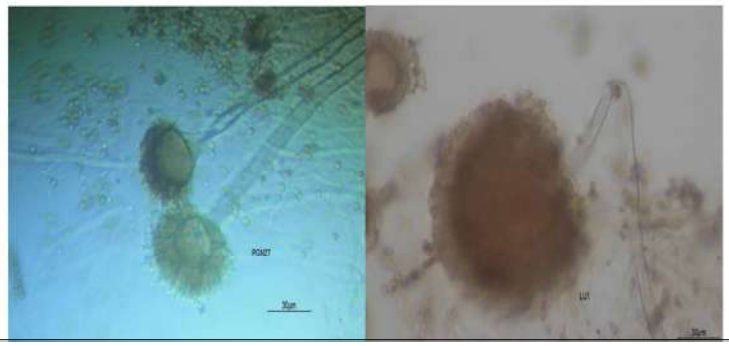

Next-Gen Innovations, Y4M & Digitalization



AMDPC Prototyping Hub

Established with KOICA to locally design, test, and manufacture agricultural machinery tailored to PH soil conditions.



Youth 4 Mechanization

Rebranding farming into a tech-driven, lucrative venture to attract the next generation of agri-entrepreneurs.



GeoKlik

Web and mobile application for geotagging, field data collection, and monitoring of infrastructure projects and field activities.

Legislated mechanization programs for various commodities

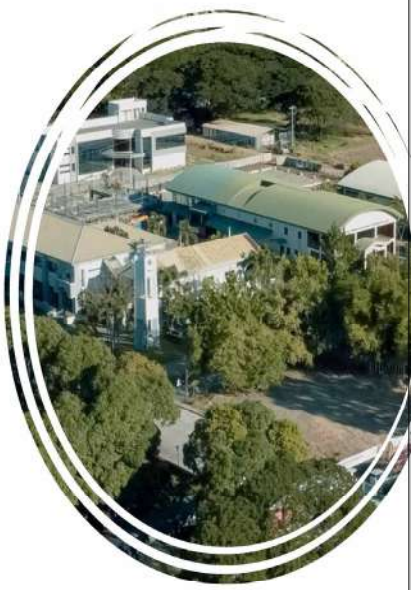

Republic Act 11203 (RCEF)

RCEF aims to **raise rice farmers' productivity, profitability and global competitiveness…**

Specifically:

- Accessible **appropriate rice production and postharvest** machinery and equipment
- Promote **use of efficient and cost reducing** rice mechanization interventions
- Strengthen **local agricultural machinery manufacturing** industry

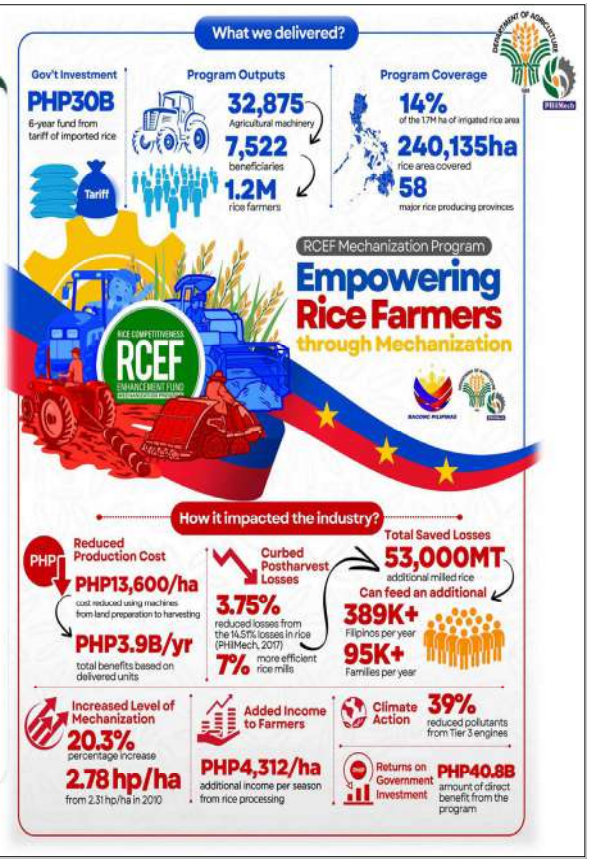

RCEF 1.0 Technology Interventions

LAND PREPARATION



Four Wheel Drive Tractor



Walking Type Agricultural Tractor



Float-Assisted Walking Type Agricultural Tractor

CROP ESTABLISHMENT



Rice Precision Seeder



Walk Behind Transplanter



Riding Type Transplanter

HARVESTING AND THRESHING



Rice Reaper



Rice Thresher



Rice Combine Harvester

DRYING AND MILLING



Recirculating Dryer



Single Pass and Multi-Stage Rice Mill

Republic Act 11524 (Coco Levy)

Establish **community and coconut-based shared processing facilities** nationwide for coconut FCAs or LGUs.

3 Components:

- Construction of buildings or plants
- Provision of processing technologies
- Transportation equipment

Some value chains to address:

- Copra-crude coconut oil, refined, bleached and deodorized coconut oil-oleochemicals
- Desiccated coconut
- Virgin coconut oil
- Coconut coir, shell, sap
- Young coconut

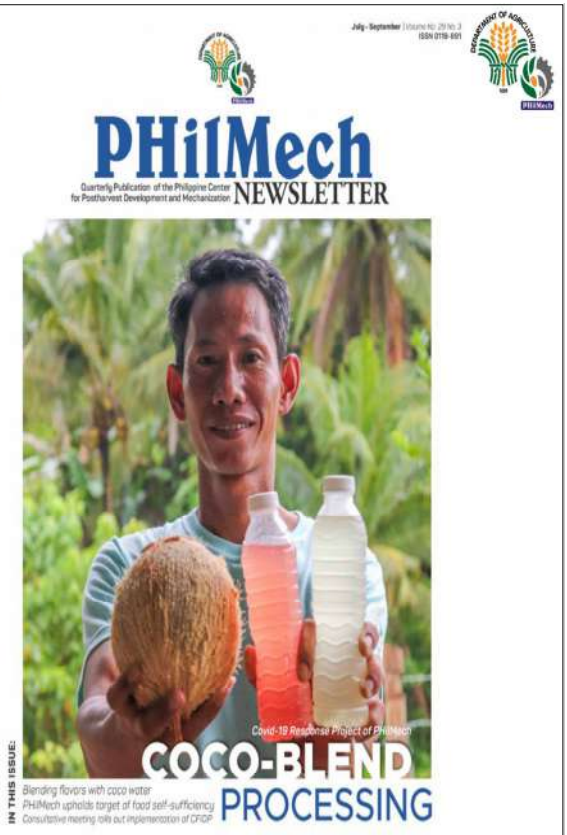

Republic Act 12308 (AnCEF)

The livestock, poultry, and dairy mechanization program operates under the National Livestock Program of the Department of Agriculture

3 Components:

- **Modernization**. Upgrading facilities with automatic feeding, modern housing, and climate-resilient farm structures
- **Postharvest infrastructure**. Funding slaughterhouses, cold storage facilities, and processing equipment
- **Disease control**. Improving biosecurity and mechanizing sanitation to fight threats like African Swine Fever (ASF) and Avian Influenza





Corn Mechanization Program*

is a government initiative by the DA and PHilMech to boost farm productivity and lower production cost through modern machinery.

3 Components:

- **Technology and equipment**. Distribution of heavy equipment [4-wheel tractors, mechanical corn seed planters, fertilizer applicators, and high-capacity corn shellers]
- **Farm clustering**. Land consolidation to share resources and maximize efficiency of large machines
- **Training**. Field demonstrations and technical training for operators and agricultural extension workers





Thank You

Philippine Center for Postharvest Development and Mechanization
CLSU Compound, Science City of Muñoz, Nueva Ecija 3120 Philippines

Office of the Director IV

Tel.nos. +63 917 8004526 local 101

Email: od@philmech.gov.ph / lsd@philmech.gov.ph

Website: www.philmech.gov.ph

Plenary 2


MSAE
MALAYSIAN SOCIETY OF AGRICULTURAL AND FOOD ENGINEERS
AGRICULTURAL AND FOOD MECHANIZATION IN MALAYSIAN SMEs: INDUSTRY STATUS, MARKET TRENDS, AND FUTURE DIRECTIONS
PROF. DR. ROSNAH SHAMSUDIN
DEPARTMENT OF PROCESS AND FOOD ENGINEERING
FACULTY OF ENGINEERING, UNIVERSITI PUTRA MALAYSIA
PRESIDENT
MALAYSIAN SOCIETY OF AGRICULTURAL AND FOOD ENGINEERS (MSAE)
With Knowledge We Serve Agriculture • Innovation • Life
EXPERTISE :
AGRICULTURAL PROCESS ENGINEERING
FOOD ENGINEERING
FOOD MACHINERY DESIGN
rosnahs@upm.edu.my
upm.edu.my

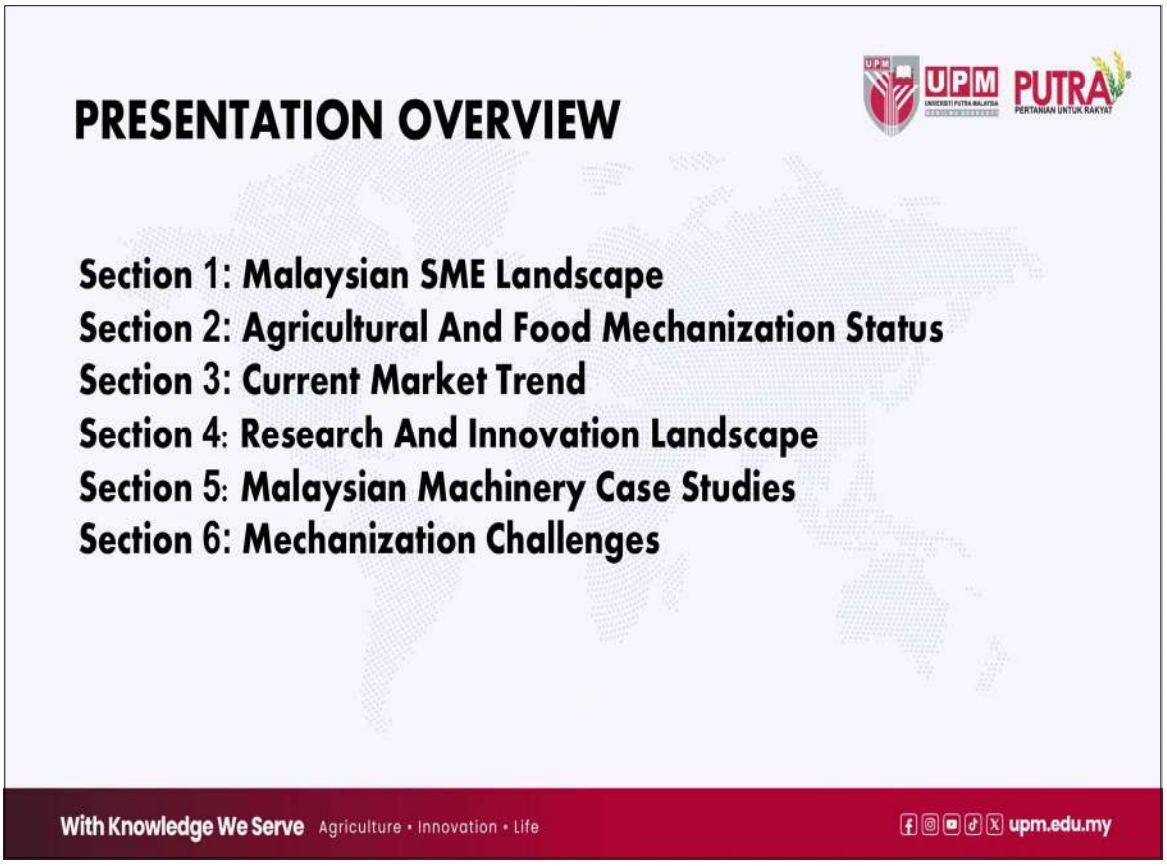
PRESENTATION OVERVIEW
Section 1: Malaysian SME Landscape
Section 2: Agricultural And Food Mechanization Status
Section 3: Current Market Trend
Section 4: Research And Innovation Landscape
Section 5: Malaysian Machinery Case Studies
Section 6: Mechanization Challenges
With Knowledge We Serve Agriculture • Innovation • Life
upm.edu.my

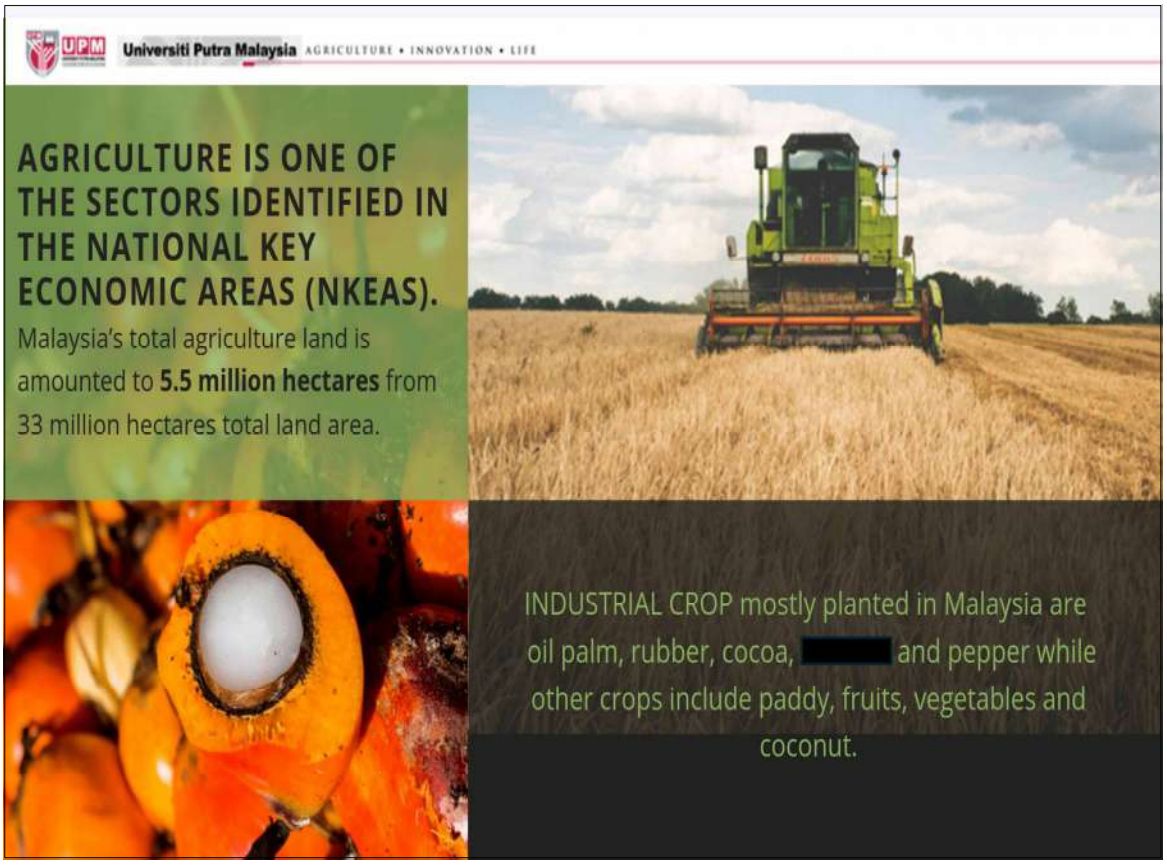
Universiti Putra Malaysia AGRICULTURE • INNOVATION • LIFE
AGRICULTURE IS ONE OF THE SECTORS IDENTIFIED IN THE NATIONAL KEY ECONOMIC AREAS (NKEAS).
Malaysia's total agriculture land is amounted to 5.5 million hectares from 33 million hectares total land area.
INDUSTRIAL CROP mostly planted in Malaysia are oil palm, rubber, cocoa, [redacted] and pepper while other crops include paddy, fruits, vegetables and coconut.

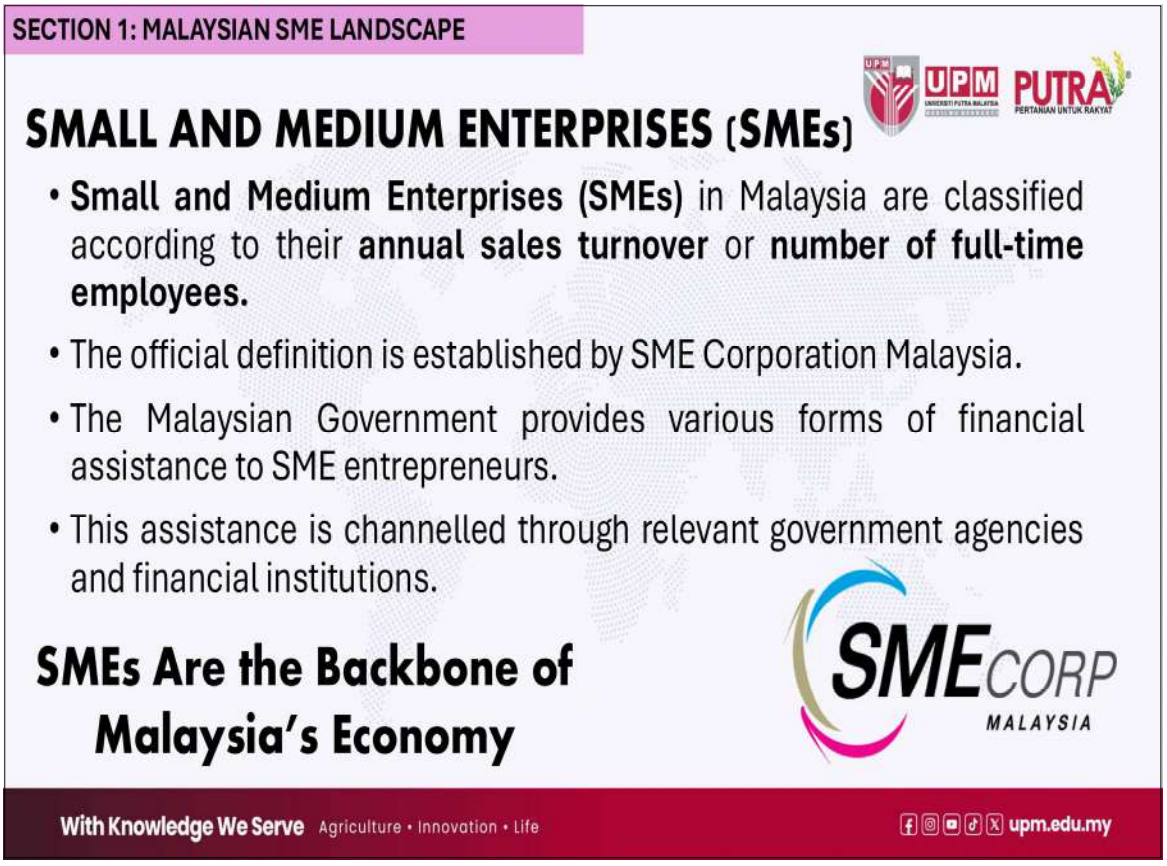
SECTION 1: MALAYSIAN SME LANDSCAPE
SMALL AND MEDIUM ENTERPRISES (SMEs)
• Small and Medium Enterprises (SMEs) in Malaysia are classified according to their annual sales turnover or number of full-time employees.
• The official definition is established by SME Corporation Malaysia.
• The Malaysian Government provides various forms of financial assistance to SME entrepreneurs.
• This assistance is channelled through relevant government agencies and financial institutions.
SMEs Are the Backbone of Malaysia's Economy
SMECORP MALAYSIA
With Knowledge We Serve Agriculture • Innovation • Life
upm.edu.my

DEFINITION OF MALAYSIAN SMEs

SMEs Are Classified by Sales Turnover or Number of Employees

SECTOR	SMALL ENTERPRISE	MEDIUM ENTERPRISE
Manufacturing	RM300,000 to < RM15 million OR 5 to <75 full-time employees	RM15 million to ≤ RM50 million OR 75 to ≤200 full-time employees
Services and Other Sectors	RM300,000 to < RM3 million OR 5 to <30 full-time employees	RM3 million to ≤ RM20 million OR 30 to ≤75 full-time employees

Microenterprise – all sectors

- < RM300,000 annual sales turnover OR
- <5 full-time employees

Official SME Definition – SME Corp. Malaysia

Malaysia's SMEs in 2024

- **96.1% of Malaysian business establishments** (1.09 million SMEs)
- **39.5% contribution to national GDP** (RM652.4 billion)
- **48.7% of total national employment** (8.10 million persons)
- **RM196.8 billion in exports** (14.3% of national exports)
- **1.31 million workers in SME manufacturing**

Department of Statistics Malaysia (DOSM).

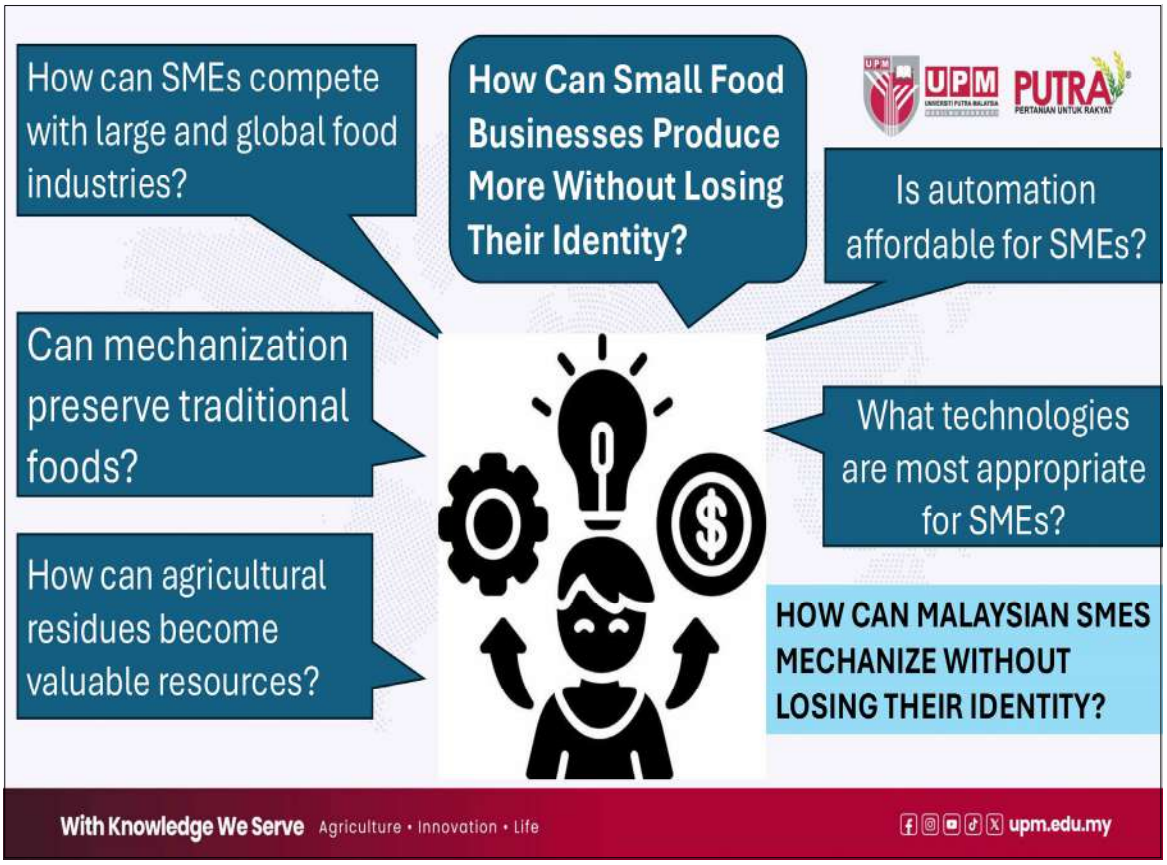
How can SMEs compete with large and global food industries?
How Can Small Food Businesses Produce More Without Losing Their Identity?
Is automation affordable for SMEs?
Can mechanization preserve traditional foods?
What technologies are most appropriate for SMEs?
How can agricultural residues become valuable resources?
HOW CAN MALAYSIAN SMES MECHANIZE WITHOUT LOSING THEIR IDENTITY?
With Knowledge We Serve Agriculture • Innovation • Life
upm.edu.my

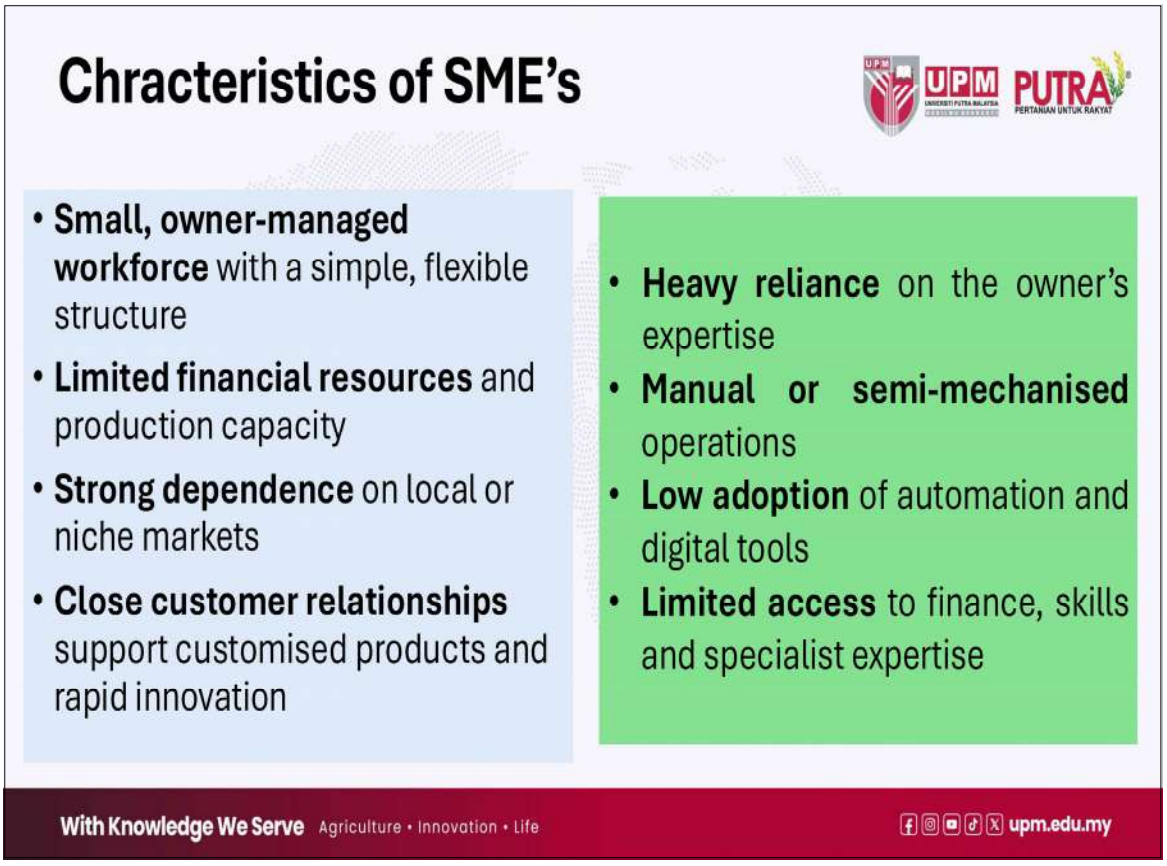
Chracteristics of SME's
• Small, owner-managed workforce with a simple, flexible structure
• Limited financial resources and production capacity
• Strong dependence on local or niche markets
• Close customer relationships support customised products and rapid innovation
• Heavy reliance on the owner's expertise
• Manual or semi-mechanised operations
• Low adoption of automation and digital tools
• Limited access to finance, skills and specialist expertise
With Knowledge We Serve Agriculture • Innovation • Life
upm.edu.my

Contributions of SMEs

- **Generate employment, income and entrepreneurship**
- Contribute to **GDP and local economic development**
- **Support local and global supply chains**
- Supply products and services to **larger industries**
- **Promote innovation, customisation and market diversity**
- Use local resources to develop **value-added agricultural products**

GDP = Gross Domestic Product)

PROBLEMS FACED BY SMEs

- **Limited financing** and high machinery costs
- **Rising operating costs** for labour, materials and utilities
- **Skilled-worker shortages** and reliance on manual operations
- **Low productivity** and limited production capacity
- **Inconsistent quality** and limited digital automation
- **Maintenance challenges** and limited after-sales support



With Knowledge We Serve Agriculture • Innovation • Life upm.edu.my

Agricultural SMEs vs Food SMEs in Malaysia

ASPECT	AGRICULTURAL SMES	FOOD SMES
Main position	• Primary production and farm-level activities • Produce agricultural raw materials	• Postharvest transformation and food manufacturing • Convert raw materials into food products
Typical activities	Cultivation, livestock, aquaculture, harvesting and farm services	Cleaning, grading, extraction, mixing, cooking, drying, forming and packaging
Examples	Fruit farms, vegetable growers, livestock farms, aquaculture operators, contract machinery providers and nurseries	Bakeries, snack manufacturers, beverage processors, fruit processors, coconut-product companies and traditional food producers
Typical machinery	Tractors, planters, sprayers, harvesters, shredders, choppers and irrigation systems	Washers, peelers, grinders, mixers, extractors, dryers, fryers and packaging machines
Operating environment	Mainly field, farm or collection centre	Mainly processing facility or food factory
Major challenges	Seasonal production, weather, labour shortages and biological variability	Food safety, product consistency, hygiene, shelf life and market compliance
Output	Fresh produce or agricultural raw material	Processed, packaged or value-added food

With Knowledge We Serve Agriculture • Innovation • Life upm.edu.my

"Agri or Food mechanization is not simply replacing human labour with machines. It is about empowering SMEs to become more productive, competitive, resilient, and sustainable."



APPROPRIATELY DESIGNED MECHANIZATION CAN HELP CLOSE THE PRODUCTIVITY GAP

With Knowledge We Serve Agriculture • Innovation • Life upm.edu.my


Universiti Putra Malaysia AGRICULTURE • INNOVATION • LIFE
Malaysian Agencies & their Roles
RESEARCH & DEVELOPMENT
Malaysian Agricultural Research and Development Institute (MARDI)
Malaysian Palm Oil Board (MPOB)
Pepper Board (MPB)
Malaysian Cocoa Board (MCB)
Forest Research Institute Malaysia (FRIM)
Malaysian Rubber Research And Development Board (MRB)


Universiti Putra Malaysia AGRICULTURE • INNOVATION • LIFE
Malaysian Agencies & their Roles
ORGANIZATIONS
Department of Agriculture (DOA)
Federal Agricultural Marketing Authority (FAMA)
Farmer's Organization Authority (LPP)


Universiti Putra Malaysia AGRICULTURE • INNOVATION • LIFE
Malaysian Agencies & their Roles
FUNDING
midf
SMECORP MALAYSIA
MIDA
TEKUN NASIONAL
MARA
AGRO BANK
Malaysian Industrial Development Finance Berhad
SME Corporation Berhad
Malaysian Investment Development Authority (MIDA)
TEKUN National
Majlis Amanah Rakyat (MARA)
AGRO Bank


UPM PUTRA
The Most Important Agency for Food SMEs
SME Corp Malaysia
MARDI
FAMA
TEKUN Nasional
MARA
SIRIM
JAKIM
MATRADE
These agencies are highly relevant for Agricultural and Food Entrepreneurs because they provide assistance in aspects of technology, financing, certification, packaging, marketing, and export.
SMECORP MALAYSIA
MARDI
FAMA
TEKUN NASIONAL
SIRIM
JAKIM
MATRADE
With Knowledge We Serve Agriculture • Innovation • Life
upm.edu.my

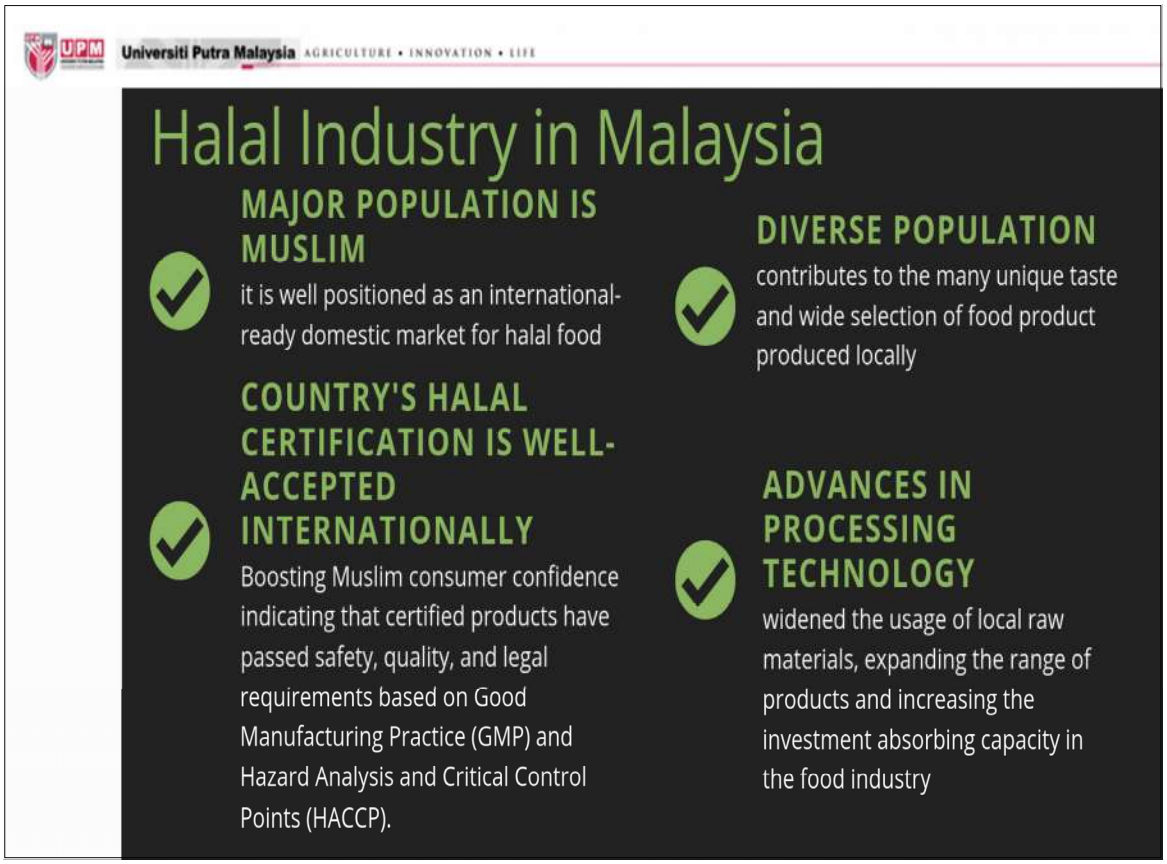
Universiti Putra Malaysia AGRICULTURE • INNOVATION • LIFE
Halal Industry in Malaysia
MAJOR POPULATION IS MUSLIM
it is well positioned as an international-ready domestic market for halal food
DIVERSE POPULATION
contributes to the many unique taste and wide selection of food product produced locally
COUNTRY'S HALAL CERTIFICATION IS WELL-ACCEPTED INTERNATIONALLY
Boosting Muslim consumer confidence indicating that certified products have passed safety, quality, and legal requirements based on Good Manufacturing Practice (GMP) and Hazard Analysis and Critical Control Points (HACCP).
ADVANCES IN PROCESSING TECHNOLOGY
widened the usage of local raw materials, expanding the range of products and increasing the investment absorbing capacity in the food industry

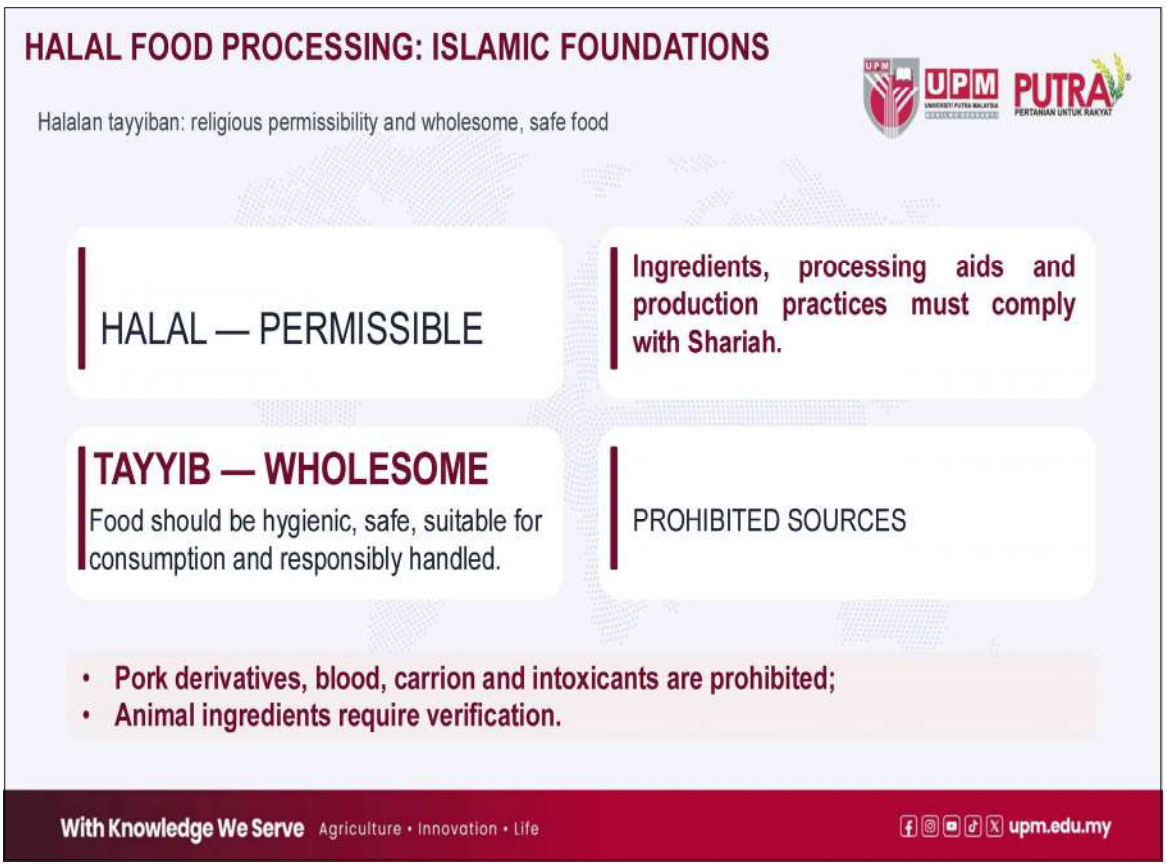
HALAL FOOD PROCESSING: ISLAMIC FOUNDATIONS
Halalan tayyiban: religious permissibility and wholesome, safe food
HALAL — PERMISSIBLE
Ingredients, processing aids and production practices must comply with Shariah.
TAYYIB — WHOLESOME
Food should be hygienic, safe, suitable for consumption and responsibly handled.
PROHIBITED SOURCES
• Pork derivatives, blood, carrion and intoxicants are prohibited;
• Animal ingredients require verification.
With Knowledge We Serve Agriculture • Innovation • Life
upm.edu.my

ISLAMIC REQUIREMENTS FROM FARM TO FORK

Every processing stage must preserve halal status

ANIMAL SOURCING & SLAUGHTER

Permissible species; Shariah-compliant slaughter and applicable stunning controls for meat/poultry.

RECEIVING & STORAGE

Approved suppliers, supporting documents, lot identity and separation from non-halal materials.

PROCESSING & PACKAGING

Verified formulations, clean equipment, controlled handling, hygienic packaging and batch records.

With Knowledge We Serve Agriculture • Innovation • Life upm.edu.my

PREVENTING NON-HALAL CONTAMINATION

Facility design and daily operating controls are essential

LAYOUT & SEGREGATION

Separate incompatible materials, utensils, personnel flows and waste; use dedicated lines when required.

EQUIPMENT & CLEANING

Use cleanable food-contact surfaces, documented cleaning and controlled production changeovers.

IMPURITY & RITUAL CLEANSING (SERTU)

SERTU (ritual cleansing) is a Shariah-compliant purification method prescribed for cleansing contamination by dogs, pigs, or their derivatives. The procedure consists of seven washings, including one wash with water mixed with clean soil and six subsequent washes with clean water.

With Knowledge We Serve Agriculture • Innovation • Life upm.edu.my

MALAYSIAN HALAL CERTIFICATION & ASSURANCE

JAKIM and relevant state Islamic authorities oversee certification

KEY REFERENCES

MS 1500:2019; Malaysia Halal Certification Procedure (Domestic) 2020; MHMS 2020.

CERTIFICATION PROCESS

Submit application and evidence; undergo document review and on-site assessment.

INTERNAL HALAL MANAGEMENT

Assign responsible personnel, train staff, verify suppliers and manage ingredient or process changes.

With Knowledge We Serve Agriculture • Innovation • Life upm.edu.my

MECHANIZATION FOR HALAL FOOD SMEs

An engineering pathway to integrity, consistency and scale

HYGIENIC MACHINERY DESIGN

Accessible equipment, effective cleaning and reduced contamination opportunities.

CONTROLLED PROCESSING

Automated mixing, heating and filling can improve repeatability and reduce unnecessary manual handling.

DIGITAL TRACEABILITY

Use barcode/QR batch identification, ingredient verification and electronic cleaning records.

With Knowledge We Serve Agriculture • Innovation • Life upm.edu.my

SECTION 2: SCOPE AND INDUSTRY STATUS

Connecting Agriculture and Food Processing

Agricultural Mechanization
- Land preparation
- Planting and crop establishment
- Crop maintenance
- Harvesting
- Biomass handling

Postharvest Mechanization
- Cleaning and grading
- Sorting
- Drying
- Storage
- Transportation

Food Mechanization
- Size reduction
- Extraction and separation
- Mixing and forming
- Thermal processing
- Packaging and waste valorisation







With Knowledge We Serve Agriculture • Innovation • Life upm.edu.my

WHY MECHANIZATION IS URGENTLY NEEDED?

- Labour shortages & ageing workforce
- Rising production costs
- Variable inputs & inconsistent quality
- Food-safety & traceability demands
- Growing demand & large-scale competition
- Reduce waste, energy & water use



FARMER

With Knowledge We Serve Agriculture • Innovation • Life upm.edu.my

CURRENT MECHANIZATION STATUS IN MALAYSIA

Advanced Mechanization
- Large-scale plantations
- Export-oriented food manufacturers
- Integrated processing facilities
- Standardised commodity production

Moderate Mechanization
- Established food-processing SMEs
- Contract farming and machinery services
- Semi-automated production systems

Limited Mechanization
- Smallholders
- Microenterprises
- Traditional food producers
- Seasonal and rural processors

MECHANIZATION CAPACITY VARIES CONSIDERABLY ACROSS COMMODITIES, LOCATIONS AND ENTERPRISE SIZES.

With Knowledge We Serve Agriculture • Innovation • Life upm.edu.my

THE MECHANIZATION ECOSYSTEM

- Farmers, smallholders and agro-food entrepreneurs
- Machinery manufacturers and fabricators
- Universities, research and technology-transfer organisations
- Government agencies and financial institutions
- Standards and certification bodies
- Service providers and industry associations

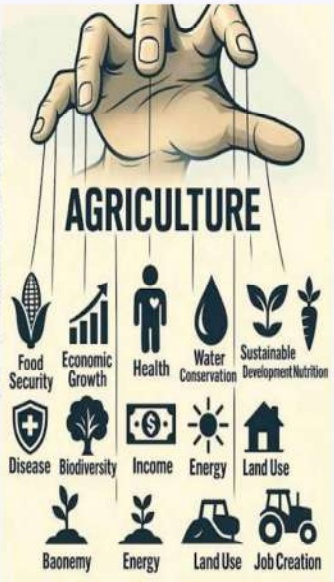

With Knowledge We Serve Agriculture • Innovation • Life upm.edu.my

MECHANIZATION IS A PROGRESSION...

- Manual operation
- Improved hand tools and workstations
- Single-purpose machines
- Semi-automated processing
- Integrated production lines
- Sensor-assisted automation
- AI-enabled and autonomous systems



SMEs should enter the progression at the level that matches their needs and resources



Mechanization Does Not Always Mean Robotics

With Knowledge We Serve Agriculture • Innovation • Life upm.edu.my

SECTION 3: MARKET TRENDS

What Is Driving Machinery Demand?

- Labour-saving technology
- Modular and scalable machines
- Multi-purpose processing equipment
- Hygienic and easy-to-clean design
- Energy- and water-efficient processing
- Sensors and real-time process monitoring



With Knowledge We Serve Agriculture • Innovation • Life upm.edu.my

Market Trend 1: Affordable and Modular Machines

Characteristics of SME-friendly machines:

- Lower initial investment
- Compact, modular design
- Adjustable production capacity
- Interchangeable processing components
- Simple operation, cleaning and maintenance
- Local spare parts and future automation readiness

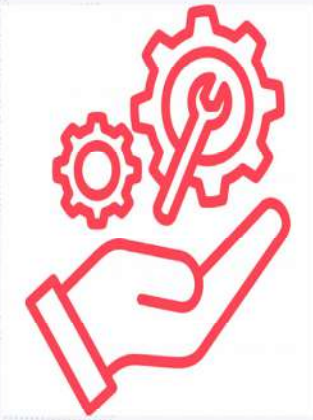

SMEs DO NOT NECESSARILY NEED CHEAPER MACHINES; THEY NEED MACHINES THAT PROVIDE MEASURABLE VALUE.

With Knowledge We Serve Agriculture • Innovation • Life upm.edu.my

Market Trend 2: Digital and Smart Processing
The Transition from Machines to Connected Systems

Emerging applications:

- Temperature and moisture sensors
- Automated process control
- Machine-vision inspection
- Digital records and traceability
- Remote monitoring and dashboards
- Predictive maintenance and AI

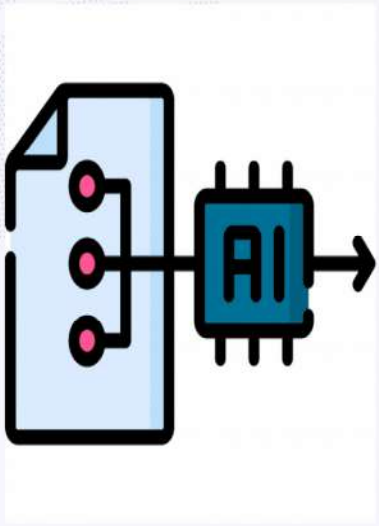

With Knowledge We Serve Agriculture • Innovation • Life upm.edu.my

Market Trend 3: Sustainable Mechanization
Future Machinery Must Deliver Environmental Value

- Lower energy and water consumption
- Improved raw-material recovery
- Reduced product rejection and wastewater
- By-product separation and reuse
- Agricultural residue processing
- Waste conversion into food, feed, biomaterials or compost

Circular pathway

Agricultural production
↓
Food processing
↓
By-products
↓
Value-added products
↓
Reduced disposal

SECTION 4: Research and Innovation Landscape

Agricultural Mechanization Research

- Precision agriculture
- Smart irrigation
- Crop monitoring
- Autonomous field machinery
- Robotics for harvesting
- Drone-based agricultural operations



Food Mechanization Research

- Machinery for tropical commodities
- Hygienic equipment design
- Smart drying and thermal processing
- Machine vision for quality inspection
- Intelligent process control
- Waste-to-wealth processing
- SME-scale modular machinery

DESIGN PHILOSOPHY

START WITH THE FOOD PRODUCER

1. Understand the traditional process
2. Identify the critical bottleneck
3. Measure product & raw-material properties
4. Translate manual skills into engineering functions
5. Design for hygiene, safety & maintainability
6. Test with actual users
7. Improve using producer feedback
8. Prepare for scale-up & commercialisation

A TECHNICALLY ADVANCED MACHINE IS UNSUCCESSFUL IF THE FOOD PRODUCER CANNOT AFFORD, OPERATE OR MAINTAIN IT.

With Knowledge We Serve Agriculture • Innovation • Life upm.edu.my

SECTION 3: MACHINERY CASE STUDIES

Case Study 1: Pineapple Residue Mechanization Turning Field Residues into Valuable Resources

The Problem

- Pineapple leaves and plants remain after harvesting.
- The residues are bulky and fibrous.
- Collection and size reduction require substantial labour.
- Unmanaged residues may create environmental problems



Engineering Solutions

- Pineapple Plant Shredder (PI2023006981)
- Pineapple Leaf Pellet (LY2021E02135)

Potential Benefits

- Easier handling and transportation
- Faster residue decomposition
- Production of pellets and biomaterial
- New revenue streams for producers
- Reduced field-waste disposal

With Knowledge We Serve Agriculture • Innovation • Life upm.edu.my

Case Study 2: Machines Designed Around Local Needs

Versmap Azolla System

- Space-efficient Azolla Pinnata cultivation
- Production capacity of approximately 900 kg per month
- Supports feed and sustainable farming applications

AR2018001497





With Knowledge We Serve Agriculture • Innovation • Life upm.edu.my

CASE STUDY 3:
D'PALPA – MECHANISING DABAI PULP SEPARATION

MY-206391-A

TRADITIONAL CHALLENGE

- Separation of mesocarp from the nut is slow and labour-intensive.
- Dabai fruit presents variability in size, ripeness and softness.
- Manual processing limits commercial production.



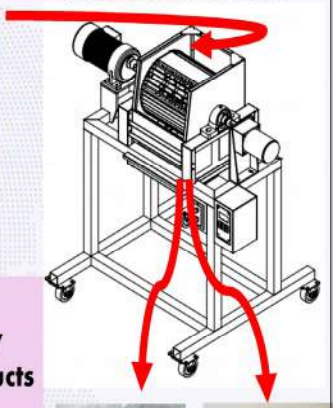

ENGINEERING SOLUTION

- Mechanised separation of dabai mesocarp and nut
- Reported separation efficiency of approximately 90%
- Reduced manual handling
- Improved processing capacity and product recovery

IMPACT

- Commercialisation opportunity for indigenous Sarawak products
- Greater potential for dabai paste, sauce and value-added ingredients
- Preservation of a culturally significant local fruit





With Knowledge We Serve Agriculture • Innovation • Life upm.edu.my

CASE STUDY 4: M'SRED
TURNING DURIAN RIND FROM WASTE INTO A RESOURCE

PI2021006005

PROBLEM : Durian rind is bulky, fibrous and difficult to reduce in size

SOLUTION

- Specially designed durian-rind shredding machine
- Size reduction before drying and further processing
- Application for flour, pectin, fibre and compost production

CONTRIBUTION

- Lower waste volume
- Easier material handling
- Supports downstream value-added processing
- Creates a link between mechanization and the circular economy

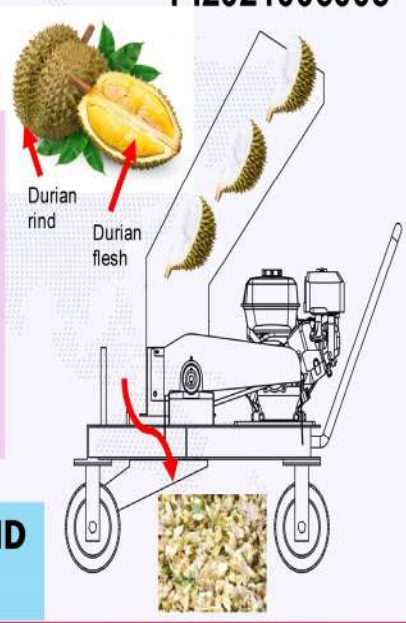

MECHANIZATION CAN CREATE VALUE BEYOND THE PRIMARY FOOD PRODUCT

With Knowledge We Serve Agriculture • Innovation • Life upm.edu.my

COMPOSTING OF AGRICULTURAL WASTE



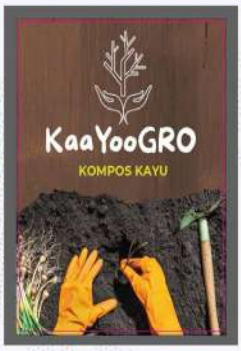









With Knowledge We Serve Agriculture • Innovation • Life upm.edu.my

CASE STUDY 5: FRUIT-PROCESSING MACHINERY ENGINEERING FOR MALAYSIA'S DIVERSE TROPICAL FRUITS

Examples include:
- Pomelo juice extractor
- Pineapple multi-peeler
- Corn Miner machine
- Krisphy Chip (Fruit slicing) and size-reduction systems



MY-151701-A



PI2014702241



AR2018000938



DESIGN CHALLENGES
- Biological variability
- Irregular geometry
- Delicate tissues
- High moisture and stickiness
- Seasonal availability
- Need to minimise product damage and loss

FOOD MACHINES MUST BE DESIGNED AROUND BIOLOGICAL PROPERTIES, NOT ONLY MECHANICAL PRINCIPLES.

With Knowledge We Serve Agriculture • Innovation • Life upm.edu.my

CASE STUDY 6: MECHANISING TRADITIONAL FOODS PRESERVING TRADITIONAL FOODS THROUGH ENGINEERING

Examples:
- Curry-puff Maker
- Sesame cracker processing
- Neu'dol Maker
- Coconut milk extraction
- Pineapple Tart Rolled
- Traditional snack forming

MY-142132



MY-168812-A





PI2015702780







14-00445-0101





What must be preserved?
- Characteristic shape
- Texture and mouthfeel
- Recipe identity
- Sensory quality
- Cultural recognition

GOOD MECHANIZATION REPRODUCES THE ARTISAN'S CRITICAL ACTIONS CONSISTENTLY

With Knowledge We Serve Agriculture • Innovation • Life upm.edu.my

SECTION 6: CURRENT ADOPTION CHALLENGES

What Has Mechanization Achieved?

- Faster processing
- Longer operating hours
- Less repetitive labour
- Improved worker safety
- Consistent, standardised production
- Better hygiene and certification readiness
- Lower material loss and higher product recovery
- Greater commercialisation and export potential



PEPPER PEEL-O-MATIC
MY168003A

Major Challenges to SME Adoption

Economic Challenges
- High initial investment
- Limited access to financing
- Uncertain return on investment
- Seasonal production

Technical Challenges
- Variable biological materials
- Limited local spare parts
- Difficult machine cleaning
- Inadequate technical support

Human-Capacity Challenges
- Shortage of skilled operators
- Limited maintenance knowledge
- Resistance to changing traditional practices
- Weak digital readiness

Commercialisation Challenges
- Prototype-to-market gap
- Low-volume machinery production
- Limited after-sales service
- Weak university–industry linkage

Challenge 1: Affordability and Return on Investment

Why SMEs Delay Investment?

- High initial equipment cost
- Uncertain production demand
- Seasonal raw-material supply
- Limited access to financing
- Lack of reliable cost–benefit data
- Fear of machine breakdown and production interruption
- Additional costs for utilities, maintenance and training



With Knowledge We Serve Agriculture • Innovation • Life upm.edu.my

Challenge 2: Food Is Naturally Variable

#One Machine Must Handle Many Variations

- **Size**
- **Shape**
- **Ripeness**
- **Moisture content**
- **Firmness**
- **Fibre orientation**
- **Stickiness**
- **Ingredient composition**

Engineering implication:

- Machines require adjustable settings
- Interchangeable components
- and robust operating ranges.

A MACHINE DESIGNED ONLY FOR THE "AVERAGE PRODUCT" MAY FAIL IN REAL PRODUCTION

With Knowledge We Serve Agriculture • Innovation • Life upm.edu.my

Challenge 3: The Technology–User Gap

Why Technically Successful Machines May Not Be Adopted:

- Design ignores operator workflow and input
- Equipment is too large or complex
- Cleaning and sanitation are difficult
- Spare parts are not locally available
- User guidance and technical support are limited
- Machine capacity exceeds market demand



CO-DESIGN WITH SMES IS ESSENTIAL

With Knowledge We Serve Agriculture • Innovation • Life upm.edu.my

Challenge 4: Skills, Maintenance and Compliance

SMEs also need:

- **Trained operators**
- **Preventive maintenance** practices
- **Hygienic equipment**-design knowledge
- **Standard operating procedures**
- **Food safety** and traceability systems
- Access to **technicians and spare parts**
- **Production and cost data**
- **Digital and automation skills**

Mechanization Requires More Than Equipment

BUYING A MACHINE IS AN EVENT. BUILDING MECHANIZATION CAPABILITY IS A CONTINUOUS PROCESS

With Knowledge We Serve Agriculture • Innovation • Life upm.edu.my

Questions:

1. **Can SMEs compete globally?**

   Yes—through product specialisation, consistent quality, certification and appropriate mechanization.

2. **Can mechanization preserve traditional foods?**

   Yes—when the machine preserves the product's defining sensory and cultural characteristics.

3. **Is automation affordable?**

   Yes—when introduced incrementally, beginning with the highest-cost or highest-risk bottleneck.

SECTION 5: AN AFFORDABLE MECHANIZATION PATHWAY

IMPORTANT! Choose Technology According to the Production Problem

Production situation	→	Appropriate response
High physical workload	→	Handling aid or ergonomic workstation
One repetitive bottleneck	→	Single-purpose machine
Inconsistent product quality	→	Controlled operating parameters
Labour-intensive production line	→	Semi-automated system
Frequent process variation	→	Sensors and real-time monitoring
High-volume standardised production	→	Integrated automation
Large, reliable datasets	→	AI-assisted optimisation

AUTOMATE ONLY WHERE AUTOMATION CREATES MEASURABLE VALUE

THE MODULAR MECHANIZATION STRATEGY

Phase 1: Mechanise the critical bottleneck
Phase 2: Standardise product and operating parameters
Phase 3: Add safety and quality-control features
Phase 4: Connect upstream and downstream operations
Phase 5: Introduce sensors and data collection
Phase 6: Apply intelligent control when sufficient data exist

Start Small, Design for Expansion

Benefits

- Lower initial investment
- Reduced adoption risk
- Easier operator training
- Expansion according to market demand
- Faster return on investment

With Knowledge We Serve Agriculture • Innovation • Life upm.edu.my

DATA BEFORE ARTIFICIAL INTELLIGENCE

A Practical Digitalisation Path for SMEs

1. Record production time, yield and rejection rates
2. Monitor critical temperature, moisture and processing parameters
3. Establish digital batch records
4. Analyse downtime and maintenance frequency
5. Use dashboards for operational decisions
6. Introduce machine vision or predictive models
7. Apply AI only when reliable data and clear decisions exist



AI CANNOT IMPROVE A PROCESS THAT HAS NOT YET BEEN MEASURED OR STANDARDISED

With Knowledge We Serve Agriculture • Innovation • Life upm.edu.my

SUSTAINABLE MECHANIZATION

Food machinery should be designed to:

- Reduce raw-material loss
- Use water and energy efficiently
- Recover valuable by-products
- Minimise wastewater
- Support cleaner production
- Enable recycling and reuse
- Convert agricultural residues into food ingredients, feed, biomaterials

Future Machines Must Improve More Than Productivity

CIRCULAR PATHWAY:
RAW MATERIAL → FOOD PRODUCT → BY-PRODUCT RECOVERY → VALUE-ADDED PRODUCT → REDUCED DISPOSAL

With Knowledge We Serve Agriculture • Innovation • Life upm.edu.my

SECTION 6 : FUTURE DIRECTIONS

Malaysia's Policy Direction Supports Transformation

National Agrofood Policy 2021–2030
- Sustainable and resilient agrofood systems
- Greater application of technology
- Improved productivity and food security

New Industrial Master Plan 2030
- Advance economic complexity
- Create a digitally vibrant nation
- Accelerate the transition towards net zero
- Strengthen economic security and inclusivity
- Build strong local SMEs

Malaysia has also used support instruments such as automation incentives, readiness assessments and intervention programmes to encourage technology adoption.
National Agrofood Policy 2021–2030, NIMP 2030, MIDA

With Knowledge We Serve Agriculture • Innovation • Life upm.edu.my

OPPORTUNITIES FOR MALAYSIA–KOREA COLLABORATION

Malaysia contributes:
- Tropical agricultural commodities
- Multicultural traditional foods
- Halal food-processing expertise
- SME machinery-testing environments
- Biomass and waste-valorisation opportunities

Potential Joint Initiatives
- Modular machinery for tropical commodities
- Smart postharvest systems
- Automated halal food processing
- AI-assisted quality inspection
- Energy-efficient drying
- Joint SME pilot plants

Korea contributes:
- Advanced robotics
- Smart manufacturing
- Sensors and machine vision
- Precision fabrication
- Intelligent control systems
- Technology commercialisation

With Knowledge We Serve Agriculture • Innovation • Life upm.edu.my

FUTURE VISION

The Future of Food Mechanization Is:

Affordable enough for SMEs
Adaptable to biological variability
Modular for gradual investment
Hygienic and easy to maintain
Connected through meaningful data
Sustainable in its use of resources
Human-centred in design
Culturally sensitive to traditional foods

THE GOAL IS NOT TO BUILD THE MOST SOPHISTICATED MACHINE. THE GOAL IS TO BUILD THE RIGHT MACHINE—ONE THAT SMES CAN AFFORD, OPERATE, MAINTAIN AND USE TO GROW

With Knowledge We Serve Agriculture • Innovation • Life upm.edu.my

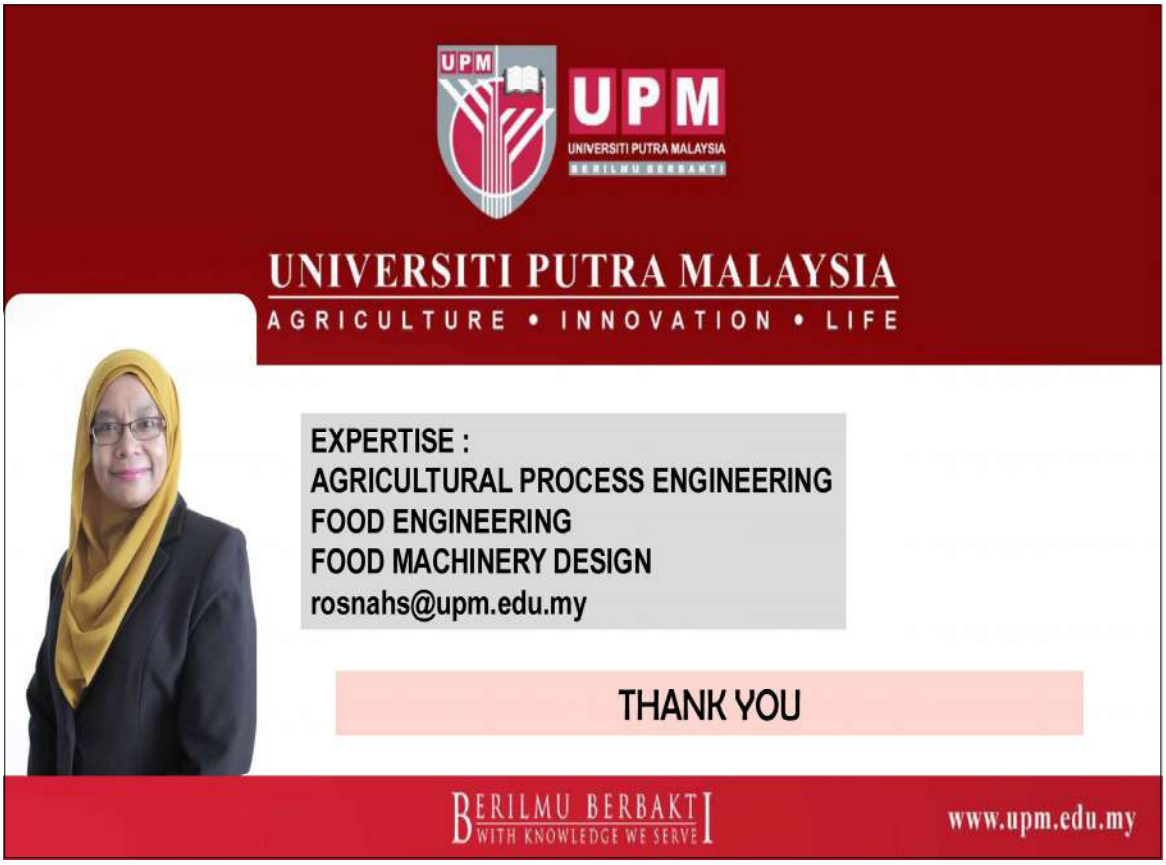
UPM
UNIVERSITI PUTRA MALAYSIA
BERILMU BERBAKTI
UNIVERSITI PUTRA MALAYSIA
AGRICULTURE • INNOVATION • LIFE
EXPERTISE :
AGRICULTURAL PROCESS ENGINEERING
FOOD ENGINEERING
FOOD MACHINERY DESIGN
rosnahs@upm.edu.my
THANK YOU
BERILMU BERBAKTI
WITH KNOWLEDGE WE SERVE
www.upm.edu.my

Plenary 3

Agricultural Machinery Market Trends, Industry Status, and Current Research Landscapes in Taiwan



Prof. Yi-Chich Chiu

Vice President, National Ilan University

President, Taiwan Institute of Biological Mechatronics

Director, Taiwan Agricultural Mechanization Research and Development Center

2026.10.21

Agricultural Machinery Exhibition in Taiwan (1/2)







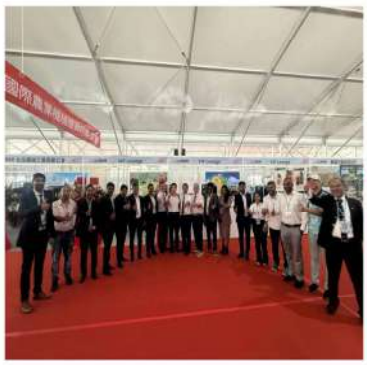



Date: 2026.05.30~06.01
Venue: Chiayi County
Scale: 250 Exhibitors;
Profits: 420,000 Visitors,
16 Million USD

2

Agricultural Machinery Exhibition in Taiwan (2/2)








Date: 2026.10.17~10.19
Venue: Yunlin County
Scale: 400 Exhibitors;
Profits: 800,000 Visitors,
23.4 Million USD

3

Taiwan Smart Agriweek









Date: 2026.09.08~09.10
Venue: Taipei
Scale: 250 Exhibitors;
23 Forums
Profits: 18,188 Visitors,
20 Countries

4

The 19th 2026 Agricultural Robot Competition











Funding Support: SUNCUE Co.
High School Students: 14 Teams
University: 26 Teams
1ST Place Award: $1000 USD

5

Agriculture Challenges and Machinery Development

Challenges Facing Taiwan's Agriculture

Climate Change
Extreme weather events are becoming more frequent, crop yields are unstable, and the risk of food shortages is increasing, leading to disruptions in production and sales.

Safety Awareness
The rate of fatal accidents among agricultural workers is twice that of other industries, while safety training and awareness remain insufficient.

Labor Shortage and an Aging Workforce
The agricultural workforce is aging, with 50–65-year-olds accounting for 65.38% of agricultural workers, making labor shortages an increasingly serious issue.

Net-Zero Emissions
In response to the global trend toward net-zero emissions by 2050, traditional fuel-powered agricultural machinery is facing increasing pressure to phase out.

Sharing Economy
Small-scale farmers face high costs for large agricultural machinery and high equipment utilization rates, making shared access to machinery an alternative to individual ownership.

Smart Agriculture and Farming Strategies

Low-Carbon and Smart Farming
Use AI and sensing technologies to achieve net-zero emissions and transition toward 2040 net-zero goals.

Public-Private Partnerships
Build agricultural service networks and promote the use of machinery through "use rights" models to reduce purchasing costs and increase utilization rates.

Enhanced Safety and Training
Build comprehensive training programs and strengthen safety awareness to reduce the risk of occupational accidents and injuries.

Mechanize labor, decarbonize energy, and automatic operations toward a smart, net-zero agricultural future.

6

Agricultural Machinery Industry Development Framework

MOA

Policy Research

- International trend analysis
- Domestic R&D assessment
- Regulatory analysis
- Resource assessment

Functional Groups

Mechanization	Electrification	Next-Generation Technologies	Agricultural Machinery Workforce
Functional development (cutting, harvesting, conveying, etc.)	Electric motor systems	AI computing	Academic and research talent assessment
Field demonstration	Batteries and charging	Autonomous operation	Workforce demand assessment
Extension and promotion	Communication and control	Chip modules	Talent recruitment and training
	Mechanical structures	Systems engineering	

Industry Support

Industry visits	Education and training	Expert support	Carbon emissions

7

Subsidies Policies of Agricultural Machinery Purchase

Subsidy Programs

- Labor-saving Agri. Mach. Electric Agri. Mach.
- Replacement of Old Mach. with Electric Models
- Newly Developed Agri. Mach.
- Custom Farming Service Mach.
- Imported Labor-saving Mach.
- Agri. Drones
- Carbon-reducing Agri. Mach.

Eligibility (Applicants meeting any one of the following criteria):

- Farmers with relevant certification
- Producers using traceability QR codes
- Registered eco-friendly farmers
- Registered young farmers
- Floriculture production and marketing groups
- Participants in approved green farming programs

Newly Developed Mach.: 1/2 Price Subsidy in Purchase





Subsidy priority → Eligible applicants are prioritized according to established criteria.

Subsidy rates

- **Conventional agri. machinery:** 1/3 of cost; NT$4,000–300,000/unit
- **Electric agri. machinery:** 1/2 of cost; NT$4,000–200,000/unit
- **Newly developed machinery**: generally 1/2; up to 3 units for demonstration programs
- Up to NT$2,000,000/unit

***Indigenous farmers: 10% additional subsidy**



8

Newly Developed – Green Onion Transplanter









9

Newly Developed – Automated Orchid Repotting System





Two-line operation with sphagnum moss: repotting from 3.5-inch to 5-inch pots.
(Contract service model)





10

Integrated Labor-Saving Mechanized System for Tea Processing

Tea and Beverage Research Station

Planting, Spraying, Harvesting → Transport → Collection & Grading → Withering → Tumbling











Automated storage system

Conveyor-type Hot-air Automatic Withering Machine




Continuous tumbling system




11

Integrated Labor-Saving Mechanized System for Onion Production

Integrated Mechanized Operations for Onion Production

Kaohsiung District Agricultural Research and Extension Station

Seedling Production → Land Preparation → Transplanting → Field Management → Harvesting → Transport → Collection & Grading

Direct seeder for plug trays (import)
448-cell plug tray
Plug tray washer
Seedling leaf trimmer
Dibbling machine

Tractor (import)
Laser land Leveler (import)
Bed former (import)
Rotary tiller (import)
Disc harrow (import)
Cultivator

Onion transplanter

Multipurpose field Management machine (import)
Broadcast fertilizer applicator
High-pressure sprayer
Mounted boom sprayer
Rice transplanter (import)

Tractor (import)
Onion digger
Ridge maker
Tractor-mounted leaf trimmer
Onion topping machine
Onion harvester

Farm transporter



Onion grader
Root trimmer














12

Integrated Labor-Saving System for Papaya Seedling Production

Seed Improvement and Propagation Station

Tissue Culture, Seed Production & Sowing → Growing-Medium Disinfection & Tray Filling → Seedling Acclimatization → Transplanting & Repotting → Transport



Aseptic workstation
Seed sowing machine





Growing-medium disinfection system
Plug-tray filling machine





Tissue-cultured seedling acclimatization system



Automatic Transplanter / repotting machine





Automated transport vehicle



13

Electric Agri. Mach. - Root-Cutting Vegetable Harvester



Water Spinach harvesting



Amaranth harvesting



Taoyuan District Agricultural Research and Extension Station

14

Electric Agri. Mach. – Small Scale Tractor

Initial performance tests were conducted on the developed electric tractor prototype, including PTO output torque, travel speed, braking distance, minimum turning radius, energy consumption, and vehicle weight.



15 kW electric tractor: PTO output power, speed, and torque testing



Kulin Co.

15

Green Energy Agricultural Machinery – Seeders

Taitung District Agricultural Research and Extension Station



Solar-powered electric seeder



Wheeled unmanned ground seeder



Tracked unmanned ground seeder

16

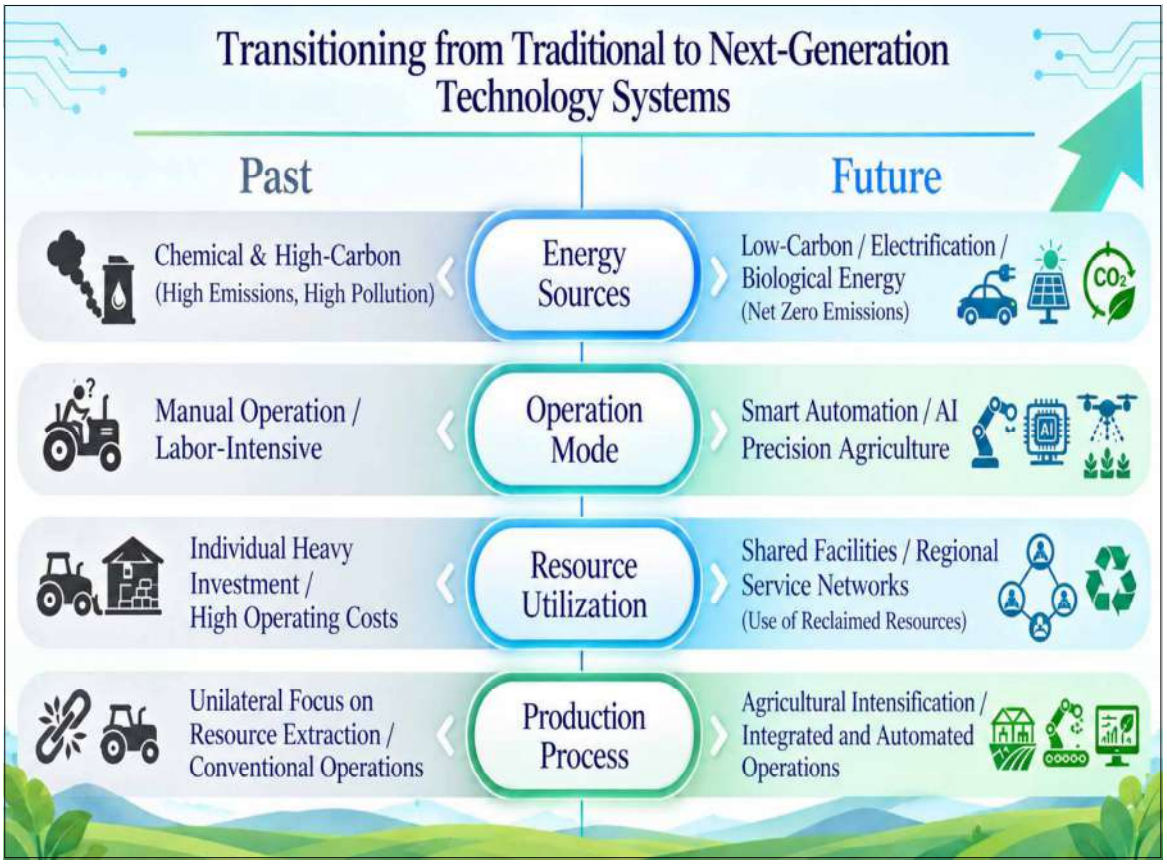
Transitioning from Traditional to Next-Generation Technology Systems
Past
Future
Energy Sources
Chemical & High-Carbon (High Emissions, High Pollution)
Low-Carbon / Electrification / Biological Energy (Net Zero Emissions)
Operation Mode
Manual Operation / Labor-Intensive
Smart Automation / AI Precision Agriculture
Resource Utilization
Individual Heavy Investment / High Operating Costs
Shared Facilities / Regional Service Networks (Use of Reclaimed Resources)
Production Process
Unilateral Focus on Resource Extraction / Conventional Operations
Agricultural Intensification / Integrated and Automated Operations

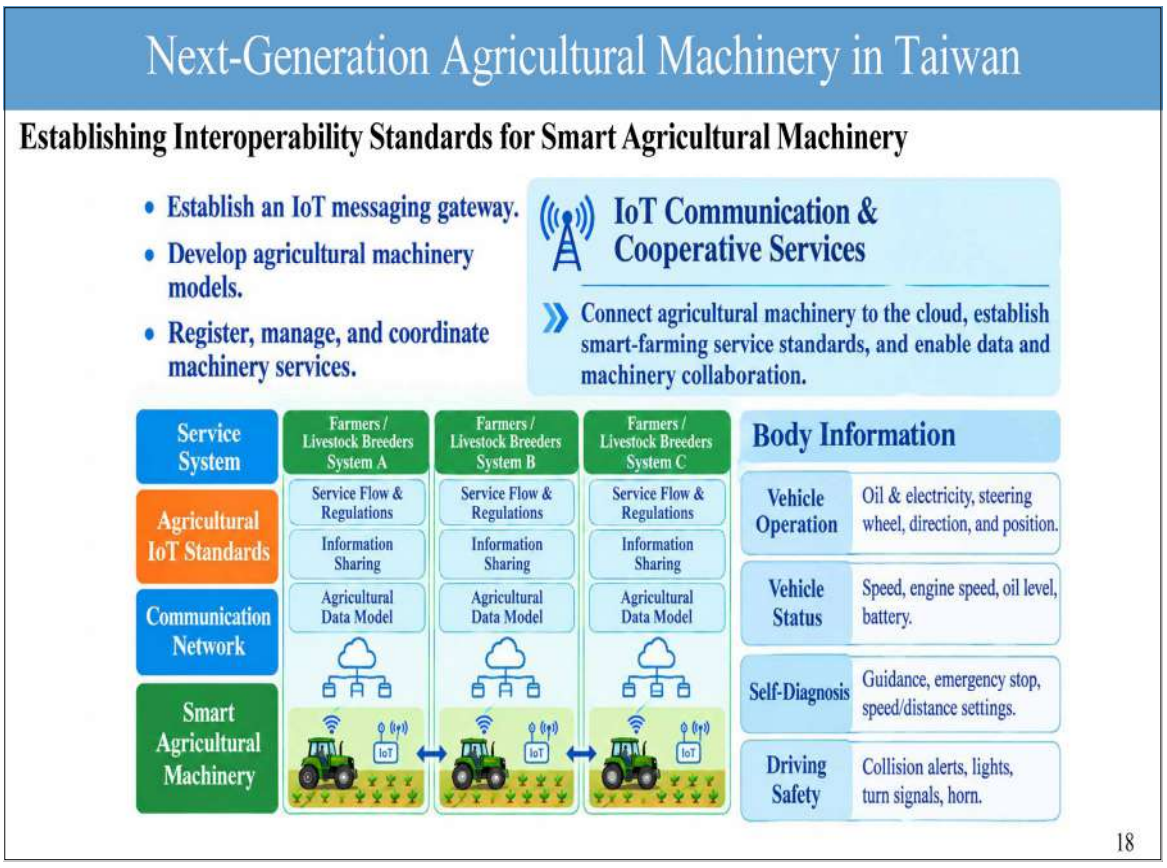
Next-Generation Agricultural Machinery in Taiwan
Establishing Interoperability Standards for Smart Agricultural Machinery
Establish an IoT messaging gateway.
Develop agricultural machinery models.
Register, manage, and coordinate machinery services.
IoT Communication & Cooperative Services
Connect agricultural machinery to the cloud, establish smart-farming service standards, and enable data and machinery collaboration.
Service System
Agricultural IoT Standards
Communication Network
Smart Agricultural Machinery
Farmers / Livestock Breeders System A
Farmers / Livestock Breeders System B
Farmers / Livestock Breeders System C
Service Flow & Regulations
Information Sharing
Agricultural Data Model
IoT
Body Information
Vehicle Operation
Oil & electricity, steering wheel, direction, and position.
Vehicle Status
Speed, engine speed, oil level, battery.
Self-Diagnosis
Guidance, emergency stop, speed/distance settings.
Driving Safety
Collision alerts, lights, turn signals, horn.
18

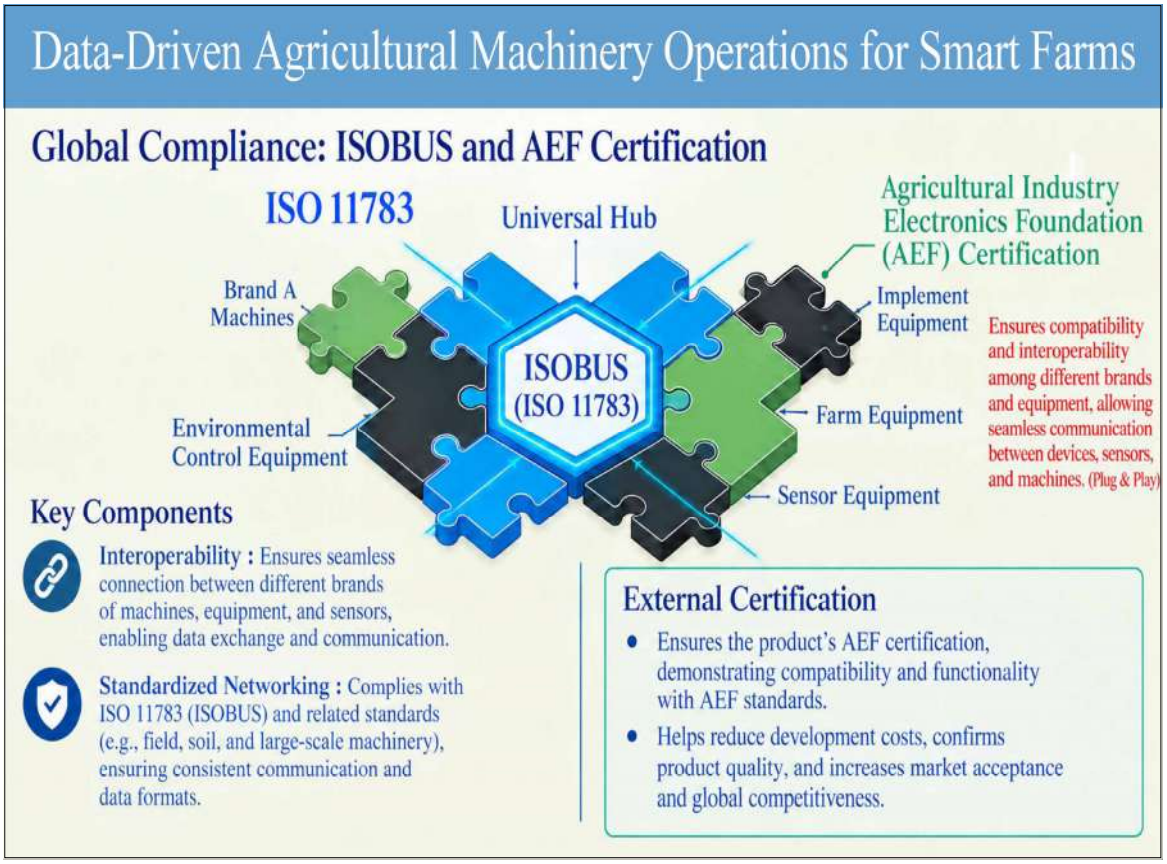
Data-Driven Agricultural Machinery Operations for Smart Farms
Global Compliance: ISOBUS and AEF Certification
ISO 11783
Universal Hub
Agricultural Industry Electronics Foundation (AEF) Certification
Brand A Machines
Implement Equipment
ISOBUS (ISO 11783)
Ensures compatibility and interoperability among different brands and equipment, allowing seamless communication between devices, sensors, and machines. (Plug & Play)
Environmental Control Equipment
Farm Equipment
Sensor Equipment
Key Components
Interoperability : Ensures seamless connection between different brands of machines, equipment, and sensors, enabling data exchange and communication.
Standardized Networking : Complies with ISO 11783 (ISOBUS) and related standards (e.g., field, soil, and large-scale machinery), ensuring consistent communication and data formats.
External Certification
Ensures the product's AEF certification, demonstrating compatibility and functionality with AEF standards.
Helps reduce development costs, confirms product quality, and increases market acceptance and global competitiveness.

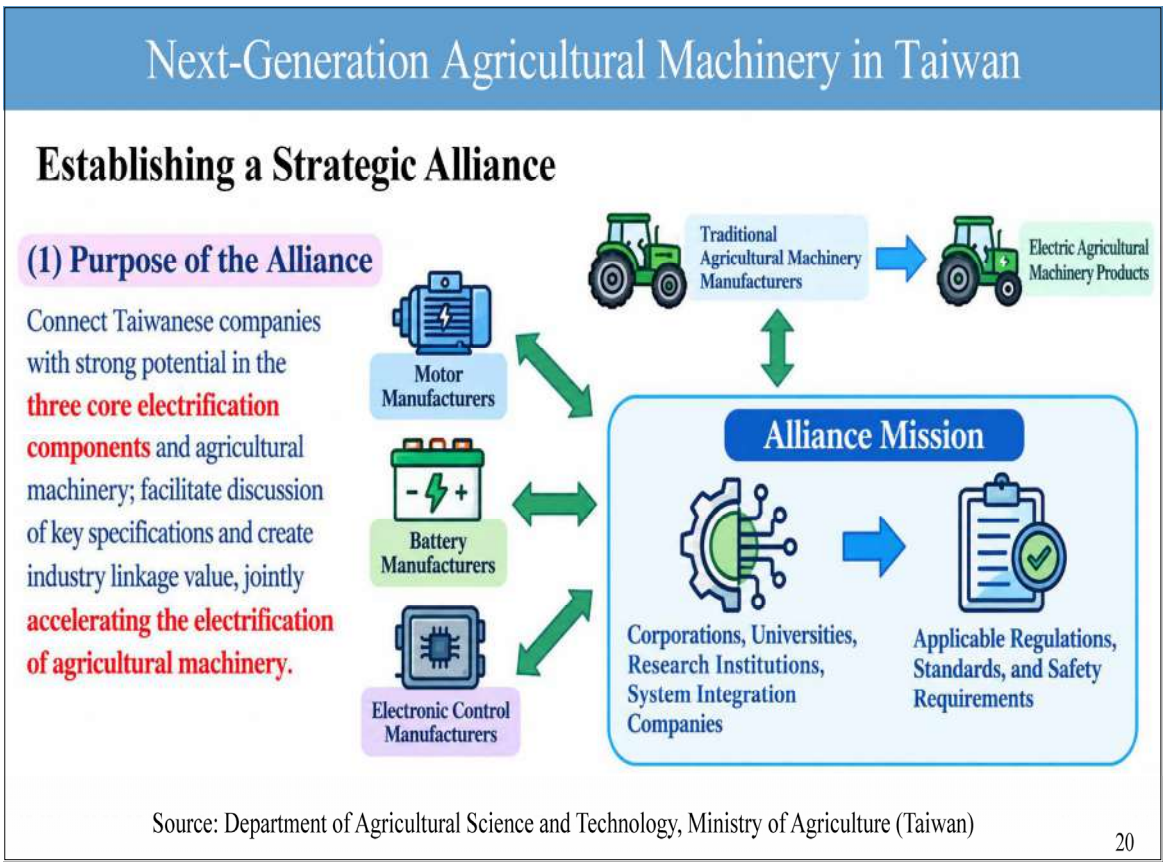
Next-Generation Agricultural Machinery in Taiwan
Establishing a Strategic Alliance
(1) Purpose of the Alliance
Connect Taiwanese companies with strong potential in the three core electrification components and agricultural machinery; facilitate discussion of key specifications and create industry linkage value, jointly accelerating the electrification of agricultural machinery.
Traditional Agricultural Machinery Manufacturers
Electric Agricultural Machinery Products
Motor Manufacturers
Battery Manufacturers
Electronic Control Manufacturers
Alliance Mission
Corporations, Universities, Research Institutions, System Integration Companies
Applicable Regulations, Standards, and Safety Requirements
Source: Department of Agricultural Science and Technology, Ministry of Agriculture (Taiwan)
20

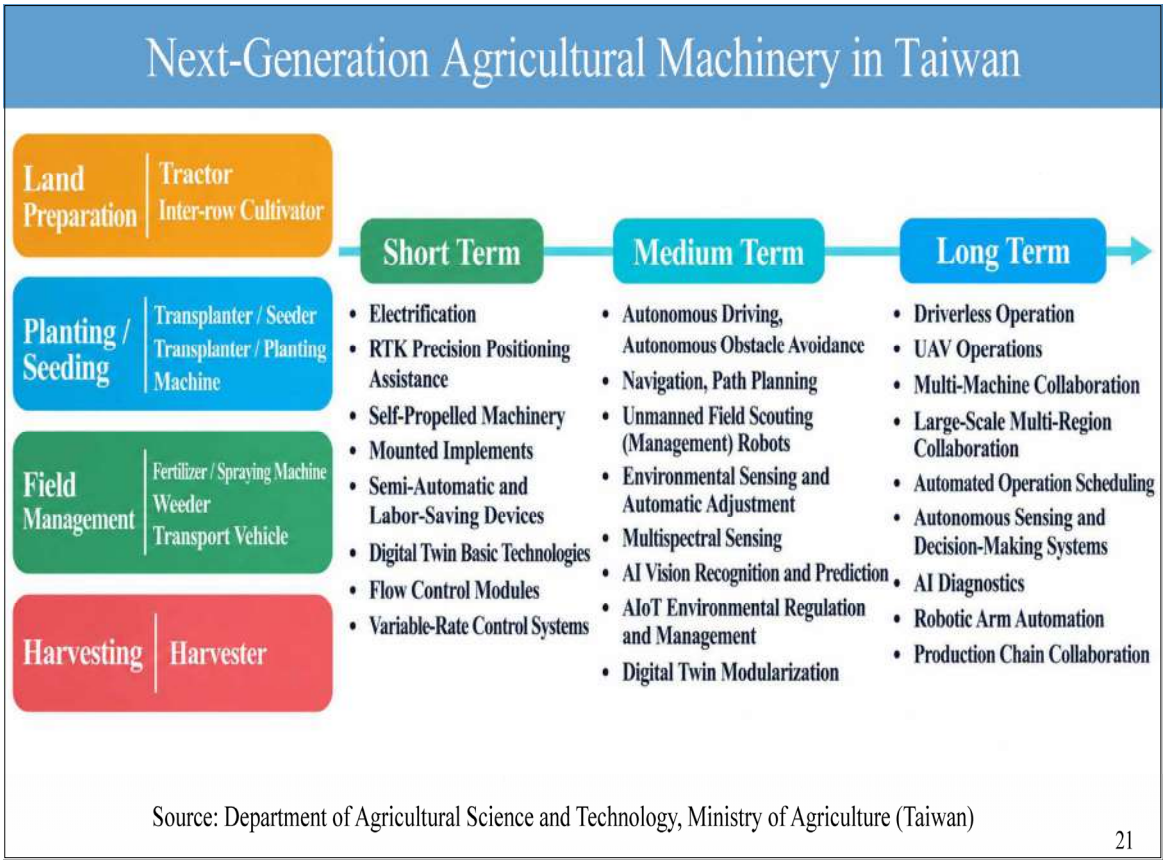

Source: Department of Agricultural Science and Technology, Ministry of Agriculture (Taiwan)

21

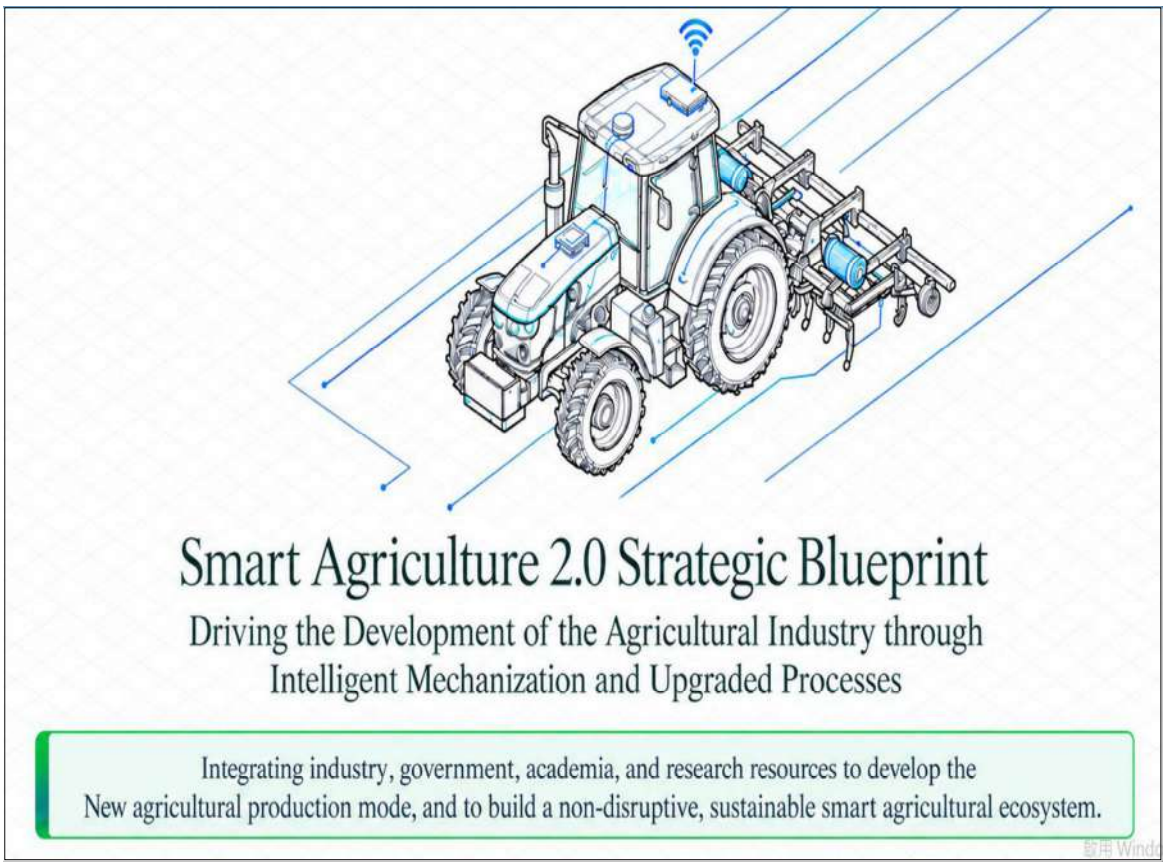

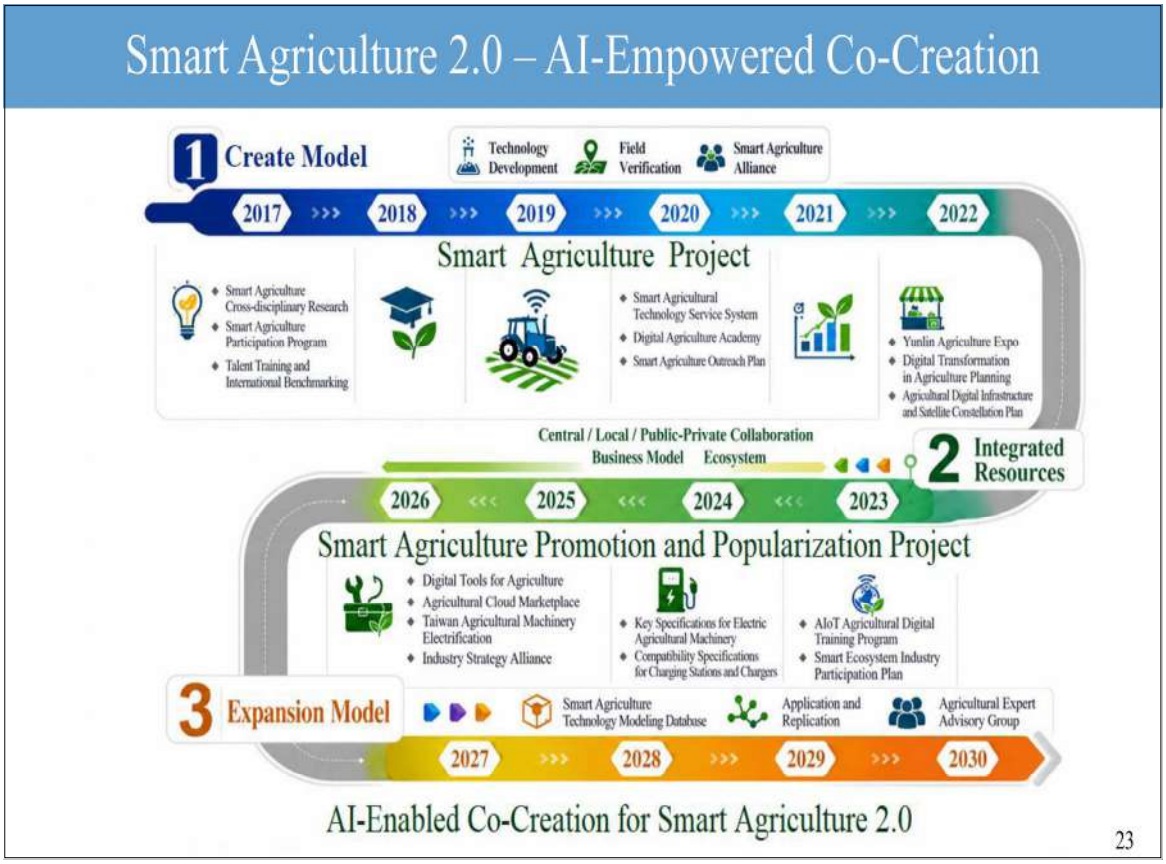
Smart Agriculture 2.0 – AI-Empowered Co-Creation
1 Create Model
Technology Development
Field Verification
Smart Agriculture Alliance
2017
2018
2019
2020
2021
2022
Smart Agriculture Project
Smart Agriculture Cross-disciplinary Research
Smart Agriculture Participation Program
Talent Training and International Benchmarking
Smart Agricultural Technology Service System
Digital Agriculture Academy
Smart Agriculture Outreach Plan
Yunlin Agriculture Expo
Digital Transformation in Agriculture Planning
Agricultural Digital Infrastructure and Satellite Constellation Plan
Central / Local / Public-Private Collaboration
Business Model
Ecosystem
2 Integrated Resources
2026
2025
2024
2023
Smart Agriculture Promotion and Popularization Project
Digital Tools for Agriculture
Agricultural Cloud Marketplace
Taiwan Agricultural Machinery Electrification
Industry Strategy Alliance
Key Specifications for Electric Agricultural Machinery
Compatibility Specifications for Charging Stations and Chargers
AIoT Agricultural Digital Training Program
Smart Ecosystem Industry Participation Plan
3 Expansion Model
Smart Agriculture Technology Modeling Database
Application and Replication
Agricultural Expert Advisory Group
2027
2028
2029
2030
AI-Enabled Co-Creation for Smart Agriculture 2.0
23

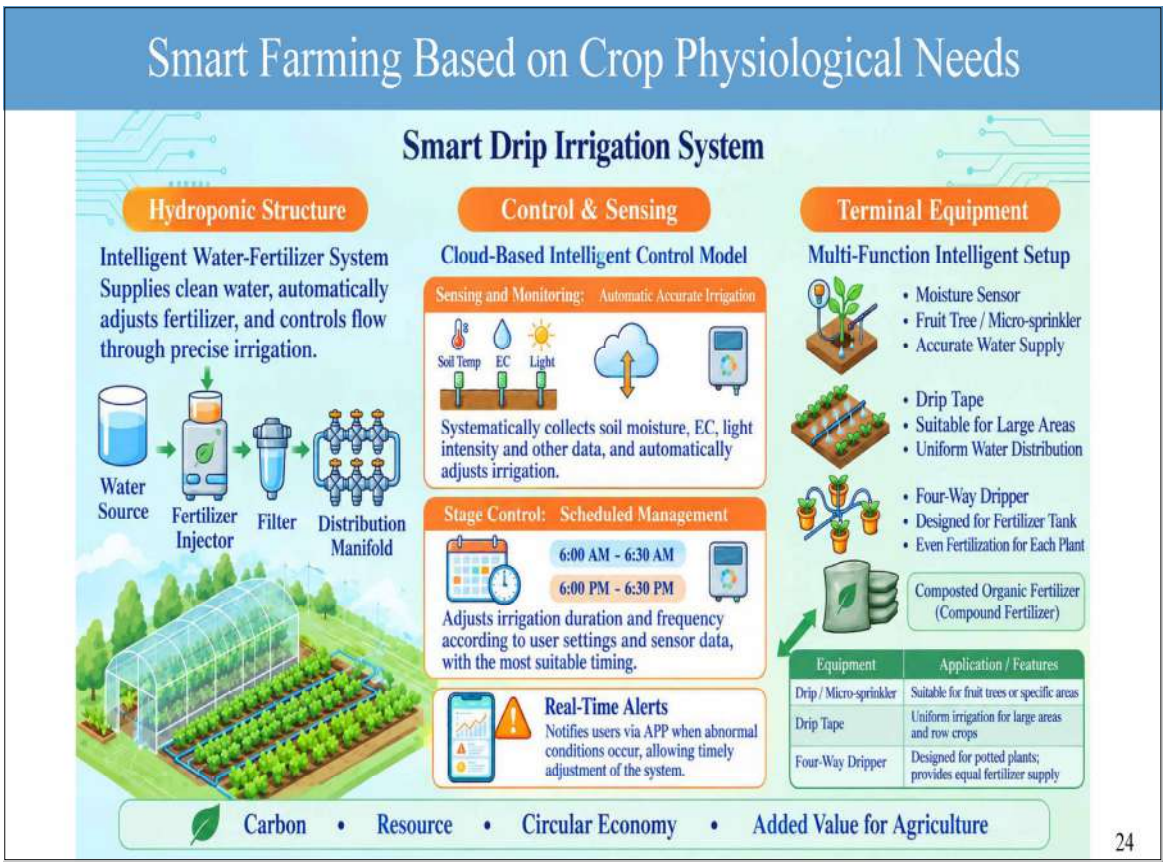
Smart Farming Based on Crop Physiological Needs
Smart Drip Irrigation System
Hydroponic Structure
Intelligent Water-Fertilizer System
Supplies clean water, automatically adjusts fertilizer, and controls flow through precise irrigation.
Water Source
Fertilizer Injector
Filter
Distribution Manifold
Control & Sensing
Cloud-Based Intelligent Control Model
Sensing and Monitoring: Automatic Accurate Irrigation
Soil Temp
EC
Light
Systematically collects soil moisture, EC, light intensity and other data, and automatically adjusts irrigation.
Stage Control: Scheduled Management
6:00 AM - 6:30 AM
6:00 PM - 6:30 PM
Adjusts irrigation duration and frequency according to user settings and sensor data, with the most suitable timing.
Real-Time Alerts
Notifies users via APP when abnormal conditions occur, allowing timely adjustment of the system.
Terminal Equipment
Multi-Function Intelligent Setup
Moisture Sensor
Fruit Tree / Micro-sprinkler
Accurate Water Supply
Drip Tape
Suitable for Large Areas
Uniform Water Distribution
Four-Way Dripper
Designed for Fertilizer Tank
Even Fertilization for Each Plant
Composted Organic Fertilizer (Compound Fertilizer)
Equipment
Application / Features
Drip / Micro-sprinkler
Suitable for fruit trees or specific areas
Drip Tape
Uniform irrigation for large areas and row crops
Four-Way Dripper
Designed for potted plants; provides equal fertilizer supply
Carbon • Resource • Circular Economy • Added Value for Agriculture
24

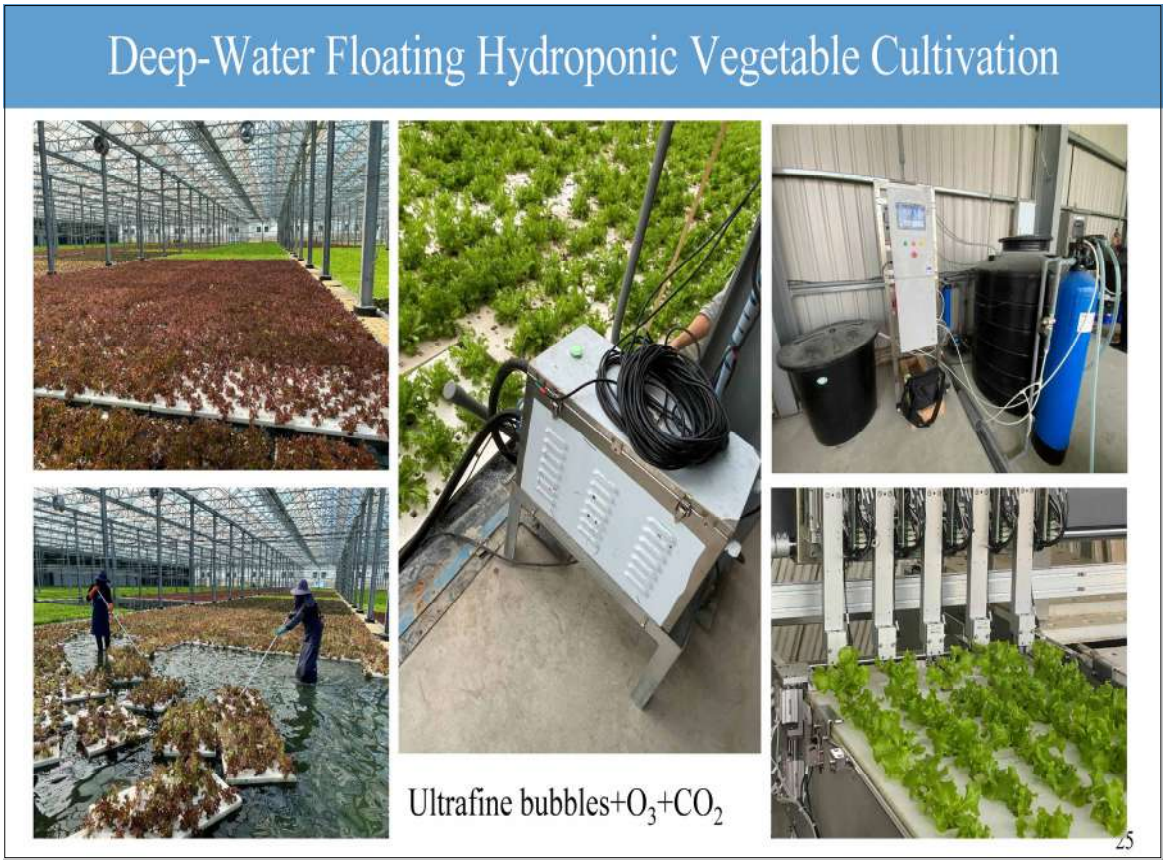
Deep-Water Floating Hydroponic Vegetable Cultivation
Ultrafine bubbles+O_3+CO_2
25

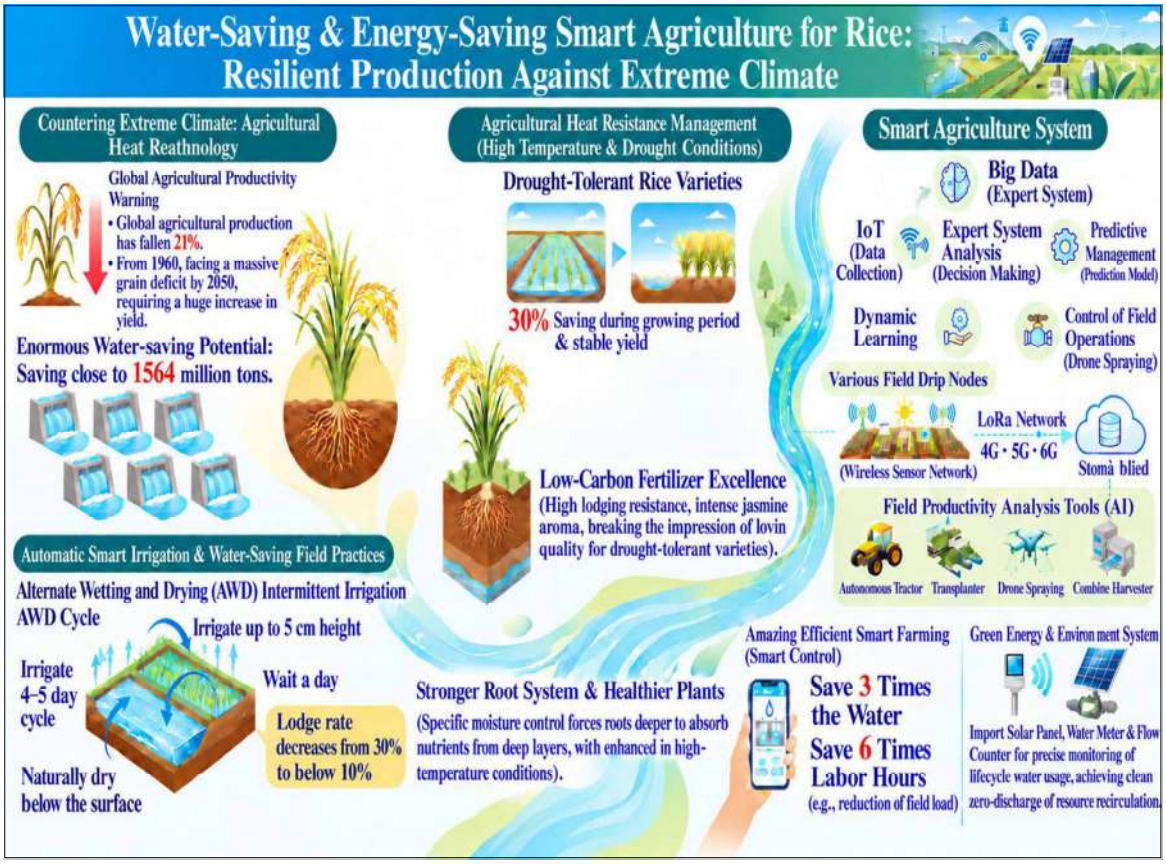
Water-Saving & Energy-Saving Smart Agriculture for Rice:
Resilient Production Against Extreme Climate
Countering Extreme Climate: Agricultural Heat Reathnology
Global Agricultural Productivity Warning
• Global agricultural production has fallen 21%.
• From 1960, facing a massive grain deficit by 2050, requiring a huge increase in yield.
Enormous Water-saving Potential: Saving close to 1564 million tons.
Agricultural Heat Resistance Management (High Temperature & Drought Conditions)
Drought-Tolerant Rice Varieties
30% Saving during growing period & stable yield
Low-Carbon Fertilizer Excellence
(High lodging resistance, intense jasmine aroma, breaking the impression of lovin quality for drought-tolerant varieties).
Smart Agriculture System
Big Data (Expert System)
IoT (Data Collection)
Expert System Analysis (Decision Making)
Predictive Management (Prediction Model)
Dynamic Learning
Control of Field Operations (Drone Spraying)
Various Field Drip Nodes
LoRa Network
4G • 5G • 6G
(Wireless Sensor Network)
Stomà blied
Field Productivity Analysis Tools (AI)
Autonomous Tractor
Transplanter
Drone Spraying
Combine Harvester
Automatic Smart Irrigation & Water-Saving Field Practices
Alternate Wetting and Drying (AWD) Intermittent Irrigation
AWD Cycle
Irrigate up to 5 cm height
Irrigate 4–5 day cycle
Wait a day
Naturally dry below the surface
Lodge rate decreases from 30% to below 10%
Stronger Root System & Healthier Plants
(Specific moisture control forces roots deeper to absorb nutrients from deep layers, with enhanced in high-temperature conditions).
Amazing Efficient Smart Farming (Smart Control)
Save 3 Times the Water
Save 6 Times Labor Hours
(e.g., reduction of field load)
Green Energy & Environ ment System
Import Solar Panel, Water Meter & Flow Counter for precise monitoring of lifecycle water usage, achieving clean zero-discharge of resource recirculation.

Water-Saving Rice Cultivation



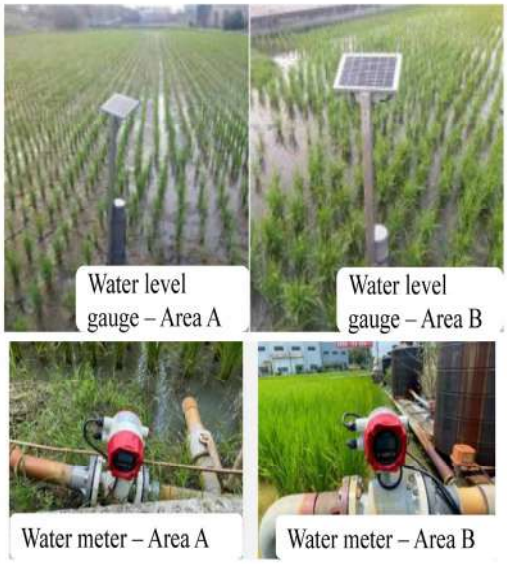

Image source: Prof. Chung Ay

Image source: Demeter Technology Inc.

Smart Irrigation for Rice Fields

27

UAV-Based Smart Rice Management







Rice Disease Early Warning

UAVs equipped with multispectral cameras are used to capture images in five spectral bands: red (R), green (G), blue (B), red-edge (RGE), and near-infrared (NIR). Vegetation indices are calculated to assess the extent of pathogen infection. Red pixels indicate infected plants, while transparent areas indicate little or no infection.

Plant Nitrogen Status Monitoring

UAVs equipped with multispectral cameras are used to estimate crop nitrogen status based on the normalized difference vegetation index (NDVI). Differences between the current and optimal nitrogen levels are then used to determine the amount of supplemental nitrogen fertilizer required.

Source: Dr. Ming-Hsin Lai

28

AIoT-Based Rice Cultivation

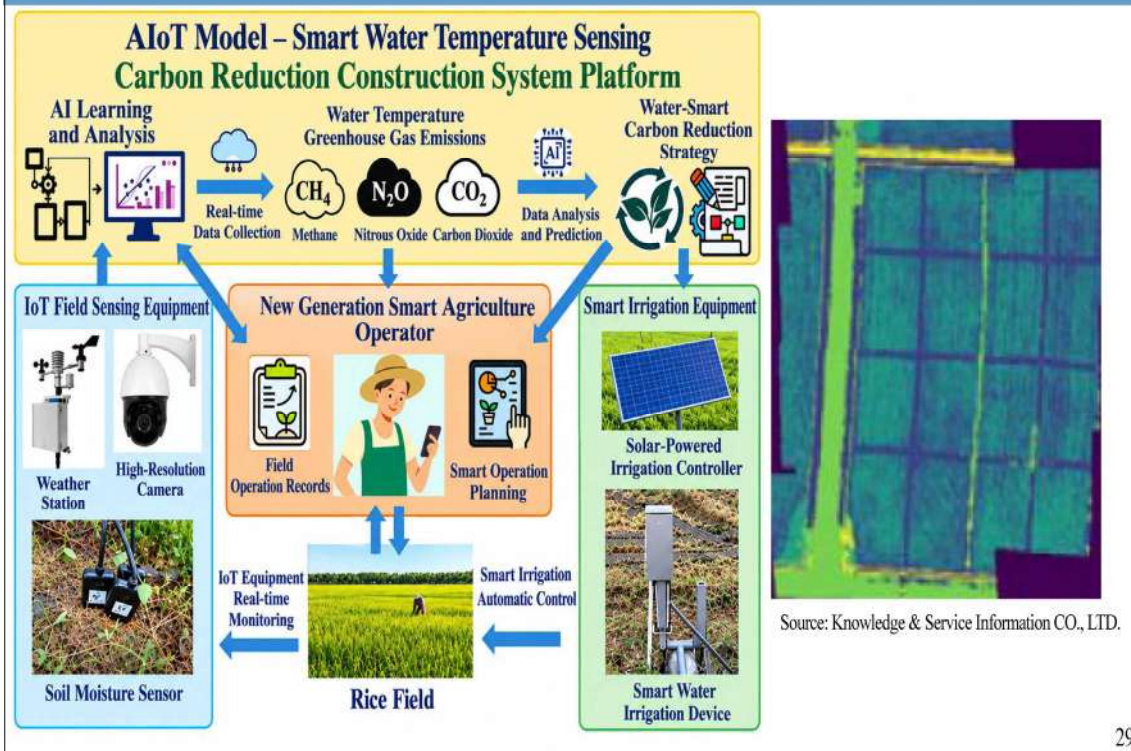

Source: Knowledge & Service Information CO., LTD.

29

AI Low-Carbon Rice Product

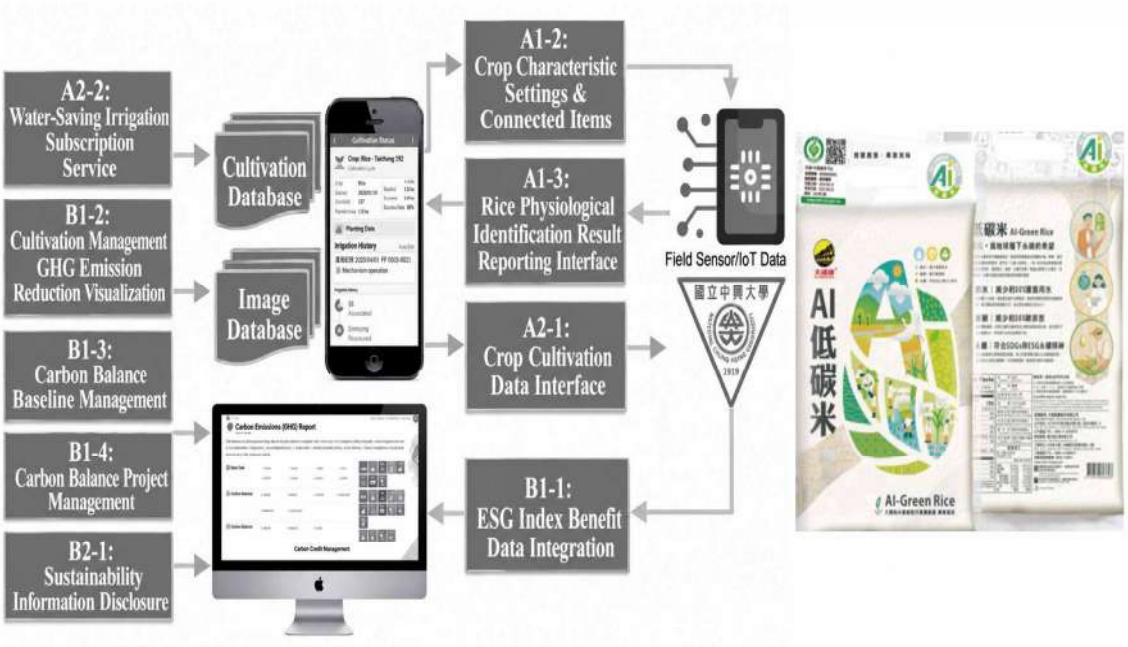

Source: RICE HOUSE SMART AGRI CO., LTD.

30

Dry Land Direct-Seeded Rice Cultivation



Rice Cultivation During Irrigation Water Suspension

31

Drip Irrigation for Rice Cultivation

Google and Netafim launched a precision drip irrigation trial for rice in Changhua, Taiwan, An alternative to conventional flooded paddy irrigation. The system uses gravity-fed drip irrigation to address water scarcity and reduce water consumption. Preliminary results showed significant water-saving potential.

According to Netafim, drip-irrigated rice can reduce water use by up to 70%. Rice cultivation accounts for approximately 30%–40% of global freshwater use and an estimated 10% of anthropogenic methane emissions. Drip irrigation can reduce methane emissions by avoiding prolonged flooding.



https://www.nchu.edu.tw/news-detail.php?id=60507

32

Tomato Pollination and Harvesting Robotic Systems



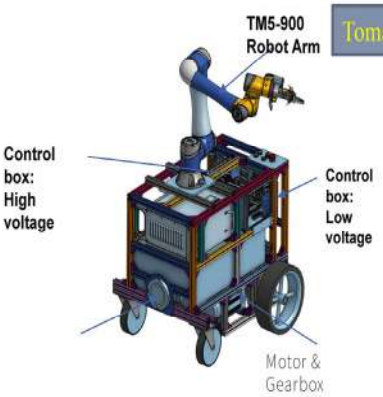

Tomato harvesting robot-National Taiwan University











Tomato pollination robot – Kaohsiung District Agricultural Research and Extension Station

33

AI-Based Image Recognition for Plant Health Assessment

National Yang Ming Chiao Tung University



Disease model developing process

1 Development of pathology site
- IoT farming sensors
  - Real-time microenvironment data collecting
  - Total 11 sensors (above and below the ground)
- Camera
  - High resolution
  - Capture photos of disease spot on leaves
- Plant
  - Strawberry in pot cultivation



• Greenhouse



2 Training data collection
- Micro-env. data
  - Barometric pressure, humidity, temperature,
  - light intensity, carbon dioxide, soil moisture,
  - soil temp, pH, EC, etc.
- Photos focusing on plant leaves
  - Infected plants
  - Healthy plants



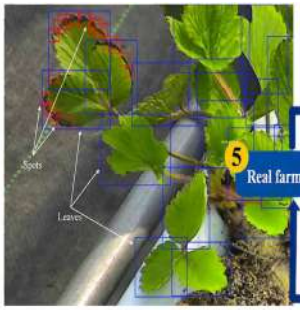

3 Data characteristic extraction and identifying
- 11 micro-env. data
- Infected plants
- Healthy plants

Average, the minimum, the maximum, the range measure in a day, the daily difference measure, the accumulated amount measure

Object detection with YOLO method

Build-up the DataBank

(Domain knowledge of fungus life-cycle)

Spore germination function



5 Real farm validation

IoT talk Engine

4 Machine learning with Neural Network Method

Online adjustment and fitting

Final Output

Disease prediction with alert ⚠

34

Smart and Autonomous Agricultural Machinery



35

Smart Agricultural Machinery – Heavy-Duty Transport Vehicle

Developed under the leadership of the Central Taiwan Innovation Campus and the Mechanical and Mechatronics Systems Research Laboratories of the Industrial Technology Research Institute (ITRI), this electric unmanned heavy-duty transport vehicle features a chassis designed to accommodate diverse agricultural terrain. It is intended for heavy-load agricultural transport and has a maximum payload capacity of 400 kg.



36

Promotion of Smart Agriculture Policies in Changhua County













qualified seedling rate: up to 95%

GREENBELT

37

Promotion of Smart Agriculture Policies in Local Govern.

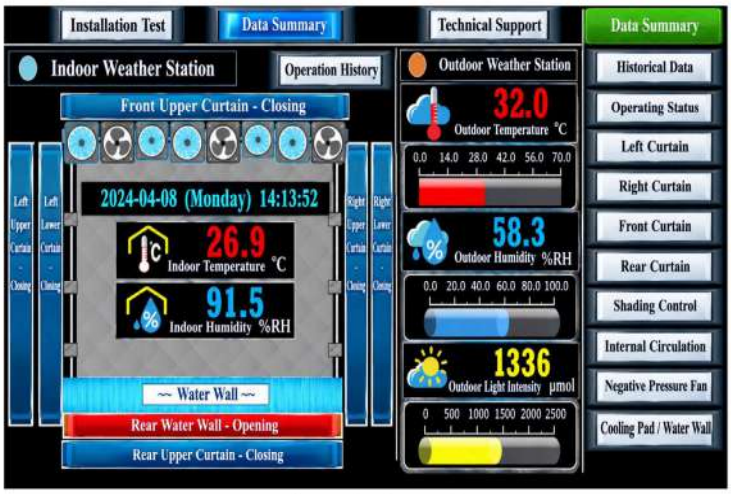

Remote App-Based Monitoring and Control System



Negative-Pressure Ventilation Fans



Evaporative Cooling Pad System

Passion Fruit Seedling Nursery

38

Promotion of Smart Agriculture Policies in Local Govern.

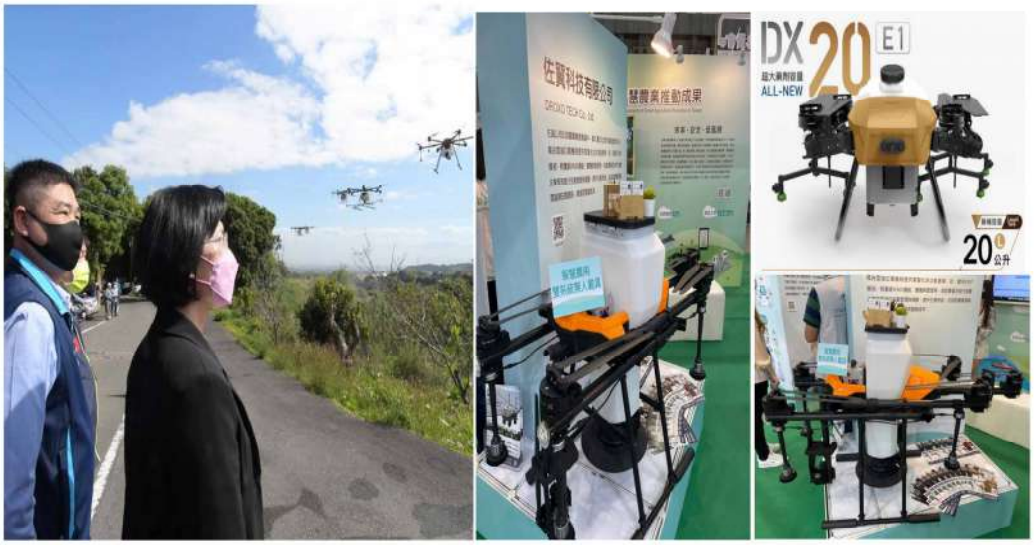

Drone for Pest and Disease Management

39

Taiwan Smart Farm Blueprint: AI-Driven, Net-Zero Sustainable Agricultural Transformation Path

Smart
Accelerate technology diffusion: Provide digital integration services, perfect the agricultural industry chain, and build a precise, high-efficiency, low-risk business environment.

Resilient
Strengthen disaster resilience: Build agricultural infrastructure, promote climate change adaptation disaster and disease tolerance, and ensure food security.

Sustainable
Establish a net-zero ecological blueprint: Expand group management models, promote energy transition and green energy, and pursue resource circulation and reuse.

Safe
Perfect guarantee system: Build agricultural service support networks, reduce labor burdens, and promote safe, traceable, and high-quality agricultural products.

System Closed-Loop Flow: From Sensing to Execution

Data Sensing: Full-time, All-domain Environmental Monitoring

Apply 33 technologies (GIS Geographical Information, RS Remote Sensing, GPS Global Positioning) and multi-modal sensors. Precisely collect farm soil information, weather environment, and crop growth data.



AI Decision-Making Brain: Generative Intelligent Analysis

Combine Gen-AI (Generative Artificial Intelligence) and RAG (Retrieval-Augmented Generation) knowledge base. Integrate expert experience and historical data to provide real-time management suggestions with scientific basis.

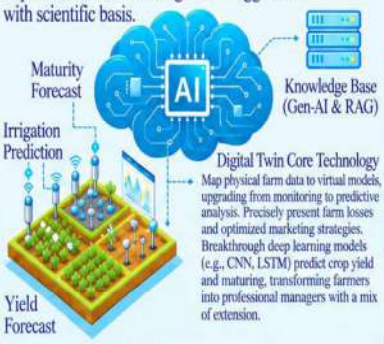

Digital Twin Core Technology
Map physical farm data to virtual models, upgrading from monitoring to predictive analysis. Precisely present farm losses and optimized marketing strategies. Breakthrough deep learning models (e.g., CNN, LSTM) predict crop yield and maturing, transforming farmers into professional managers with a mix of extension.

Intelligent Execution: Precision Agriculture Realization

Implement decision-making on next-generation smart farm machinery (electrification, automation) & environmental facilities. Realize automated precision spraying, irrigation, and harvesting.

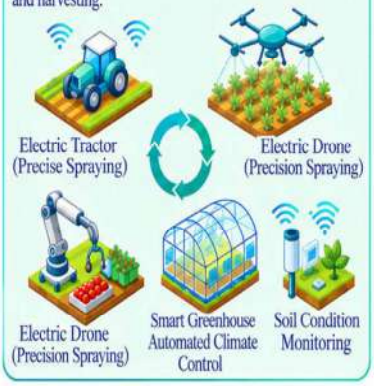

AI Five-layer Cake of Smart Farm



41

Accelerate Smart Farm Agriculture and Livestock Chain, Improving Resilience and Quality for All Sectors



Agriculture & Grains (Climate-Resilient Storage)

- Expand capabilities for drying and low-temperature storage of wet grains, for emergency harvesting in extreme climate events.
- Introduce large-scale grain harvesting machinery, optimizing storage automation to improve domestic self-sufficiency rate.



Forestry (High-Efficiency Circularity)

- Adopt new, resource-saving logging machinery and methods, improving silviculture and harvesting efficiency.
- Strengthen circular utilization of forestry residues, creating new value from under-forest resources.



Fisheries (Smart Adaptation to Environment)

- Research and develop intelligent aquaculture and automated product processing equipment to overcome high-salinity and high-humidity limits.
- Transition from labor-intensive models, ensuring aquatic product freshness and increasing processing capacity.



Livestock (Pre-Biosecurity)

- Promote environmental-control, closed water-curtain poultry and livestock housing to increase biosecurity protection.
- Introduce automatic feeding/ watering and intelligent manure treatment equipment to implement environmental sustainability.

Two Circular Economy Acts







Agricultural Resource Circularity

Branches → Biofuel & Power

Digestate → Irrigation & Biogas Power

Black Soldier Fly Bioeconomy

Rice Straw Recycling

Passed the Third Reading by the Legislative Yuan on June 2, 2026

43

Branch Shredding and Circular Utilization



Crawler-type shredder



Typical green bamboo plantation



Self-propelled shredder



Large-scale shredding test



Crawler-type shredder

Pruned Branches → Shredding → Biomass Fuel → Resource Circulation





Taoyuan District Agricultural Research and Extension Station

44

Circular Utilization of Shredded Branches for Biochar Production



45

Circular Utilization of Livestock Manure and Wastewater

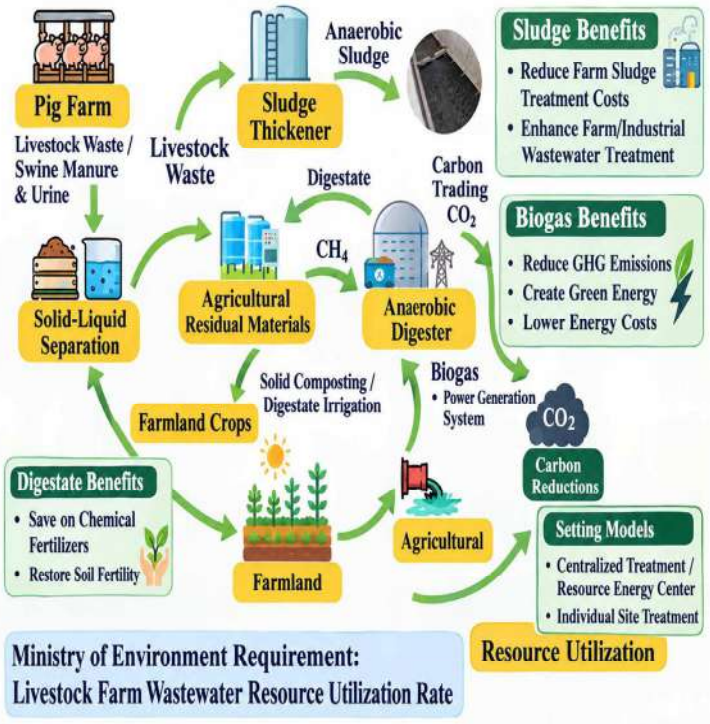





46

Challenges Facing Smart Farms

Economic Benefit

- **Long-term growth:** Increase agricultural output and stabilize farmers' income.

Research & Development

- Develop long-term soil and crop models.
- Monitor crop growth.
- Optimize environmental control.

Service Support

- AI tools for farmland.
- Build AI software infrastructure.
- Enable AI Agent capabilities.

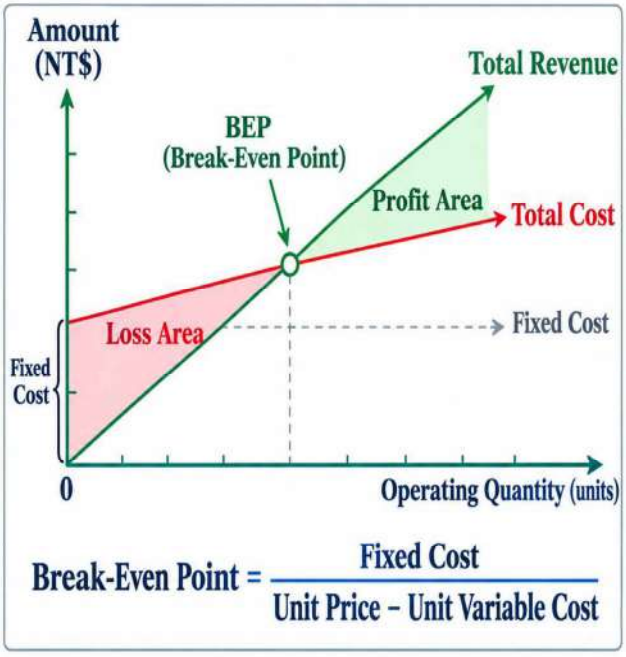

$$\text{Break-Even Point} = \frac{\text{Fixed Cost}}{\text{Unit Price} - \text{Unit Variable Cost}}$$

47



Thank You

Plenary 4

ISMAB2026, Plenary Speech, 10:00-12:00, Hall 5A, Oct.21, 2026.

一般社団法人
農業食料工学会
The Japanese Society of Agricultural Machinery and Food Engineers (JSAM)

Agricultural machinery market trends, industry status, and current research landscapes in Japan

Michihisa IIDA, Prof., Dr.
President of JSAM
Laboratory of Field Robotics,
Graduate School of Agriculture,
Kyoto University, Japan

Agenda

1. Market Trend of Agricultural Machinery in Japan
2. Industrial Status of Agricultural Machinery in Japan
3. Current Research Landscapes

Market Trends of Agricultural Machinery

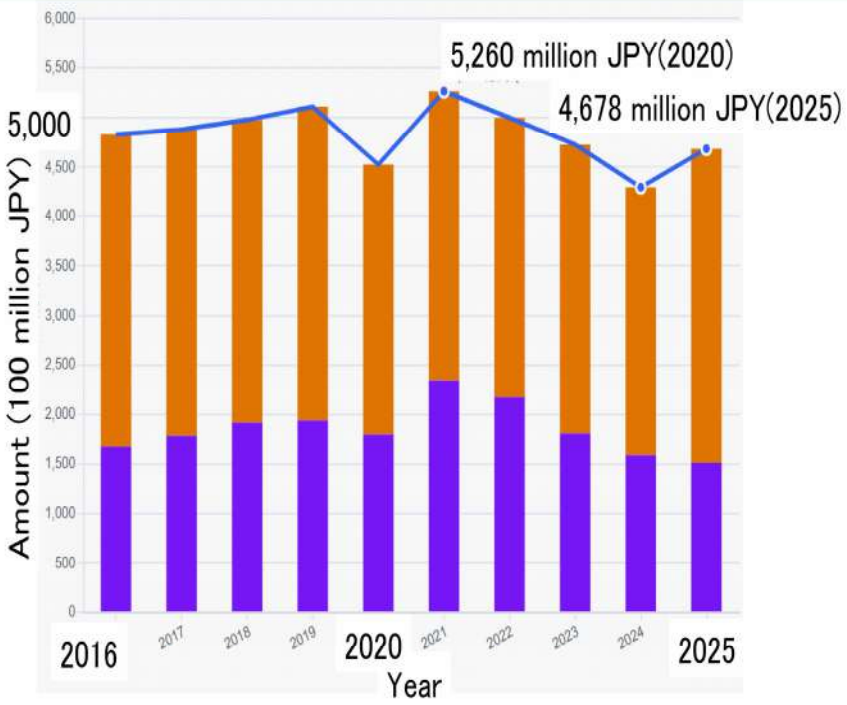

Market Trends of Agricultural Machinery in 2025

Total domestic shipments and production scale of agricultural machinery in Japan is approximately 467.8 billion JPY (2.958 billion USD) as of 2025.

Shipment amount by major model (2025)

- Tractor: 215.6 billion JPY (46.1%)
- Combine harvester: 85.4 billion JPY (18.3%)
- Implements (rotaries, etc.): 48.2 billion JPY (10.3%)
- Rice transplanters: 33.4 billion JPY (7.1%)
- Brush cutter: 21.2 billion JPY (4.5%)
- Pest control machine: 15.8 billion JPY (3.4%)
- Others: 48.2 billion JPY (10.3%)



Robotic Agricultural Machinery Compatible with Smart Agriculture

In Japan, robotic agricultural machines classified as Level 1 and Level 2 are commercially available. Among these, Level 1 models are the most common.



https://www.iseki.co.jp/ https://agriculture.kubota.co.jp/product/ https://www.yanmar.com/jp/agri/products/

Autonomous Operation Guidelines of Agricultural Robot

There are no specific laws governing robotic agricultural machinery; instead, regulations such as the Road Traffic Act must be observed. The "Guidelines for Ensuring Safety in the Autonomous Operation of Agricultural Machinery" (March 2017) provide standards for safe operation.

Leverl 0: Manual operation of agricultural machinery

Level 1: Human-operated with partial automation



Auto-pilot system

Level 2: Autonomous driving under human supervision

"Simultaneous operations by manned and unmanned machines"



Level 3: Automated operations under remote monitoring



Autonomous Driving Level 3 Compatible, Robotic Combine Harvester

World's first autonomous combine harvester (KUBOTA DHR1200A-A) capable of unmanned harvesting operations in 2024.

(1) Autonomous driving
(2) Automatic harvesting
+
(3) AI camera
(4) Header control for lodging rice
(5) Ridge detection for corner harvesting



https://www.youtube.com/watch?v=4ydLDmIldSU

Industrial Status of Agricultural Machinery in Japan

Until September of this year, there were four agricultural machinery manufacturers in Japan that developed and produced tractors, rice transplanters, and combines.

Mitsubishi Mahindra Agricultural Machinery Co., Ltd. completely withdrew from the agricultural machinery business as of **September 30, 2026**, and proceeded to dissolve and undergo ordinary liquidation.

MAM Co., Ltd.
Establishment of a company to take over the provision of repair parts and compensation obligations.

Current Research Landscapes

1. Small Agricultural Robots
   (1) Control and navigation
   (2) SLAM and object detection
2. Harvesting Robots
   (1) End-effectors and hands
   (2) Sensing and AI for quality evaluation and position detection
3. Digital Twin in Agriculture
   (1) AI for Sensing and diagnosis of plants growth
   (2) Reconstruction of 3D plant model
4. Evaluation and AI in Post-harvesting
5. Smart Agriculture in Livestock and Aquaculture
6. Utilization of Biological Resources for a Decarbonized Society
7. Safety in Agricultural Works

1. Small Agricultural Robots

(1) Control and navigation



Weed mowing on steep slope (35°)

GNSS-based autonomous driving

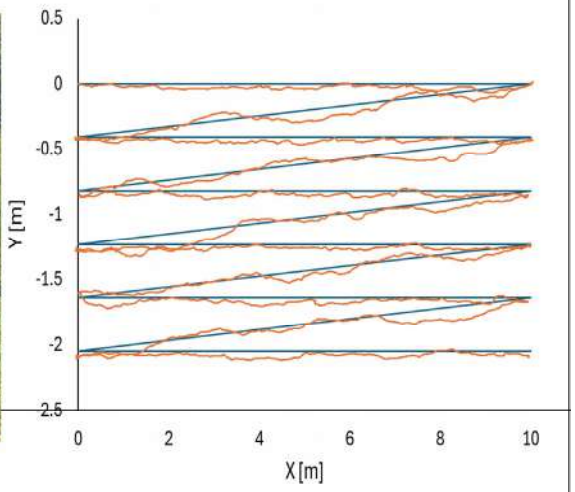

Woking trajectory

1. Small Agricultural Robots

(1) Control and navigation



Spaying in sweet pepper field

Vision-based autonomous driving

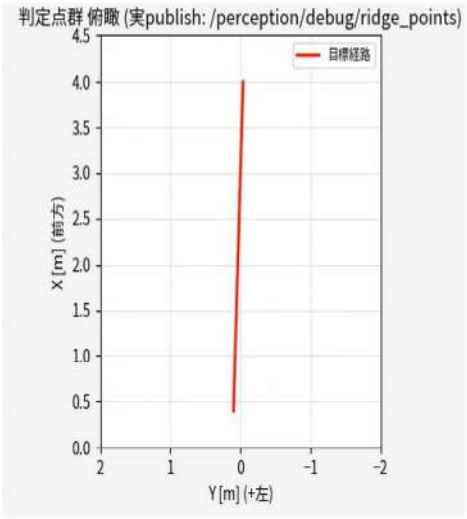

Detection of furrow centerline by stereo camera images

1. Small Agricultural Robots

(2) SLAM and object detection



Real-world environment

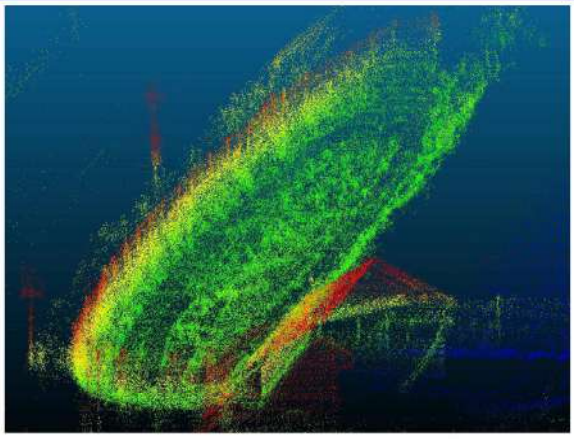

3D PCD map by LIO-SAM

2. Harvesting Robots

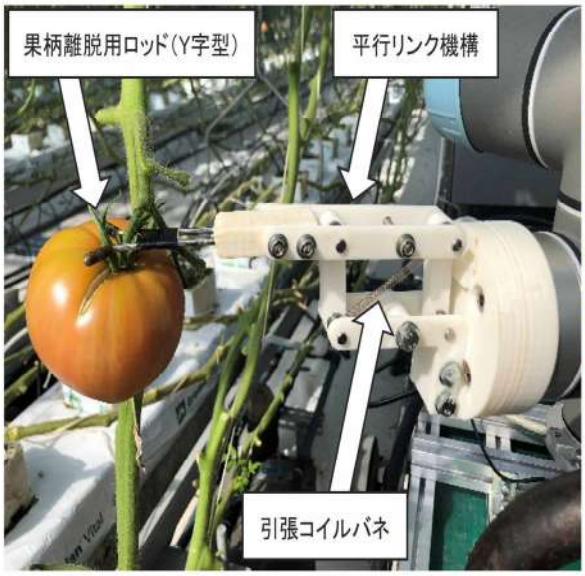

End-effector for harvesting tomatos



Detection of tomato plant by removing background

Courtesy of Prof. Shuhei Ohata, Ehime University

https://www.agr.ehime-u.ac.jp/education/view/ohata-shuhei.html

3. Digital Twin in Agriculture

(1) AI for Sensing and diagnosis of plants growth
(2) Reconstruction of 3D plant model

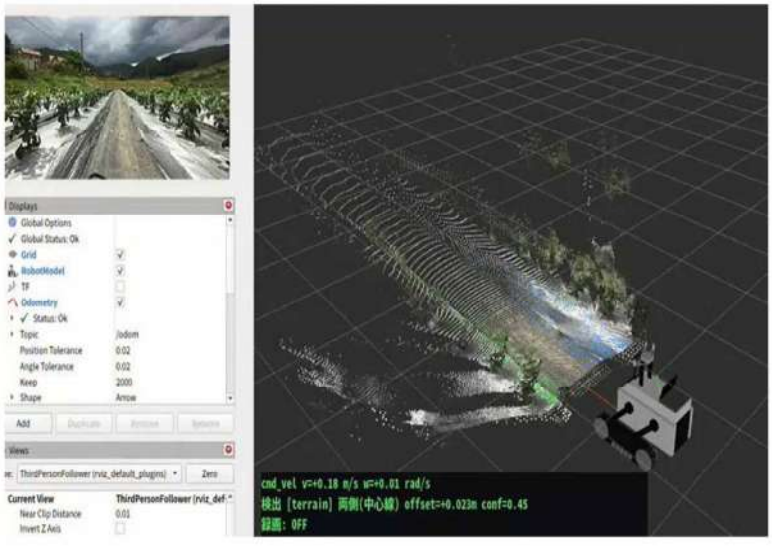

4. Evaluation and AI in Post-harvesting

1. Fluorescence analysis and fluorescence imaging for quality evaluation
2. Grading and sorting of quality
3. Maintaining freshness during transportation and distribution

5. Smart Agriculture in Livestock and Aquaculture

1. Pupillary imaging for the estimation of blood vitamin A levels in cattle
2. Analysis of Feeding Behavior in Japanese Black Cattle Using 3D Measurement and Deep Learning
3. Prediction of Chicken Egg Sex Using Transmission Spectra
4. Measurement of fish body size using images and sound waves

etc.

6. Utilization of Biological Resources for a Decarbonized Society

1. Utilization of Methane Fermentation Digestate
2. Soil carbon sequestration via biochar
3. Pelletization of livestock manure-derived biochar
4. Reduction of Kerosene Consumption and Utilization of Combustion Ash of a Rice Husk

etc.



Combustion ash of rice husk

7. Safety in Agricultural Works

Driving simulator



Courtesy of Prof. Kenshi Sakai,
Tokyo University of Technology and Agriculture

7. Safety in Agricultural Works

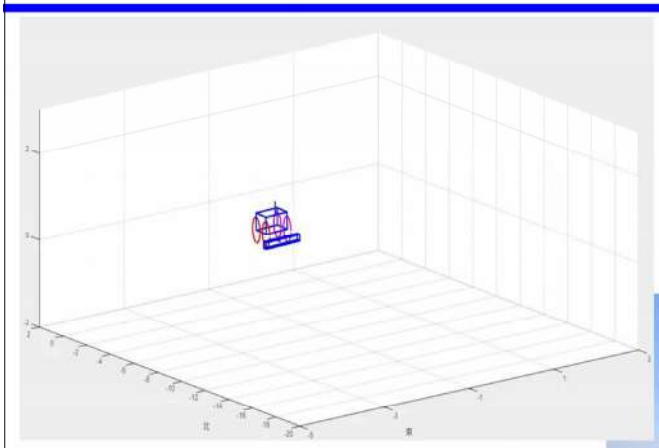

Simulation to prevent the rollover during weed mowing on slope



Weed mowing on slope

Conclusions

1. Market Trend of Agricultural Machinery in Japan
2. Industrial Status of Agricultural Machinery in Japan
3. Current Research Landscapes

Thank you for your kind listening!

Plenary 5



Contents

- Background and concept
- Research stage (Late 1990s~Early 2010s): focus on rice production
  - Variability, Sensors
  - Variable rate technologies, Autonomous field machinery
- Implement stage (Early 2010s~ Present): strong government drive
  - R&D&B: multi-disciplinary + feasibility tests + commercialization
  - Protected facilities (horticultural crop and animal production), dryland fields, orchards
  - Pilot complex, feasibility test complex, innovation valley, …
  - Technology transfer, standardization, performance test
  - Education (master degree), consulting expert fostering
- Summary and remarks

Background

Increasing world population, climate change ▶ Food crisis

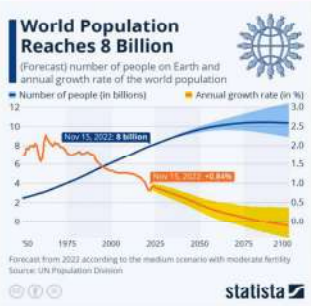

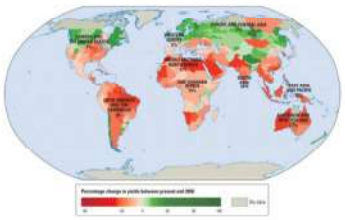

Predicted global crop production in 2050 (50% of the current production)

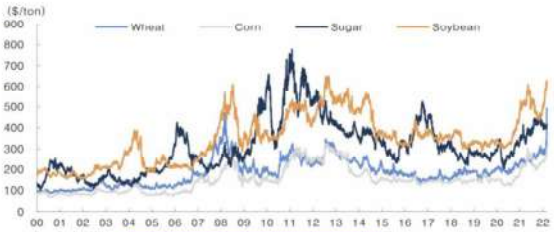

Crop price change since 2000

Farming population and aging ▶ Ag. crisis

- Farm population: 4.3% of the total population
- 46.8% > 65 yrs → highly aged society

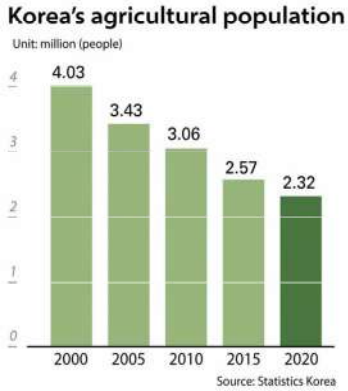

Background

Advancement of Available Technologies

- 4th revolution (Davosforum, 2016): adoption of new technology determines advancement of countries
  - Improvement of potential for human and machine: "cyber-physical system"
  - Keywords: block chain, 3D printing, gene-editing, sensor, ICT (Information and Communication Technology) robot, big data, AI (Artificial Intelligence)
- Paradigm is changing in agriculture: Future agriculture?
  - Farmer experience → data-based farming
  - Operated by human → by computer and robot

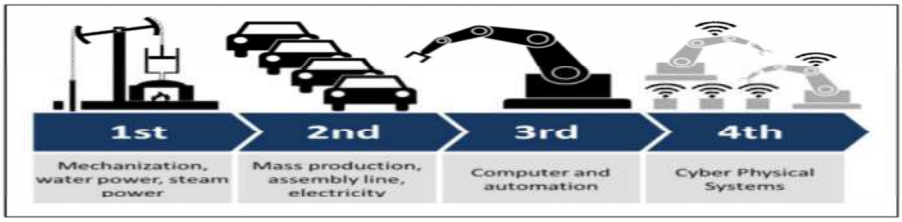

Concept

Precision Agriculture (Spatial variability) → **Smart Agriculture (ICT → big data → AI)** → Digital Agriculture (Models → cyber-physical world)











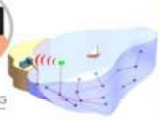





History of Korean PA (Smart agriculture)

- Establishment of a department of environment-friendly agriculture by Korean Ministry of Agriculture and Forestry in the middle of 1990s: has been focused on "LISA" and "Organic farming" → recently PA
- Introduction of PA concept in a Korean journal (Chang and Chung, 1998)
- International symposiums on PA on April 9, 1999 by Korean Society for Agricultural Machinery, and on May 27, 1999 by Rural Development Administration (RDA): initiation of Korean PA
- Korean Society of Precision Agriculture on December 24, 2013
- 2010 ~ present: mega trends of ICT agriculture, Smart Agriculture, Digital Agriculture for protected crop and animal production
- 2020 ~ present: strong promotion of open field smart agriculture, for rice paddy fields, orchards, and dryland fields

Memory of International Symposium (1999)

Visit to Hyundai Farm (10,000 ha)



Initiation of ACPA (2003)



Research Stage (Late 1990 ~ Early 2010s)
Focus on Rice Production

- Standard rice field size: 100 m x 30 m (1.6 ha / household)
- Small, flat, paddy field → base fertilization based on soil sampling in spring

  additional fertilization based on remote sensing in summer





Research Stage (Late 1990 ~ Early 2010s)
Focus on Rice Production

Variability Assessment

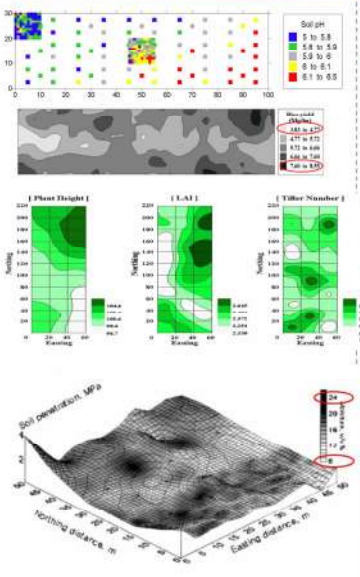

Soil and Crop Sensors

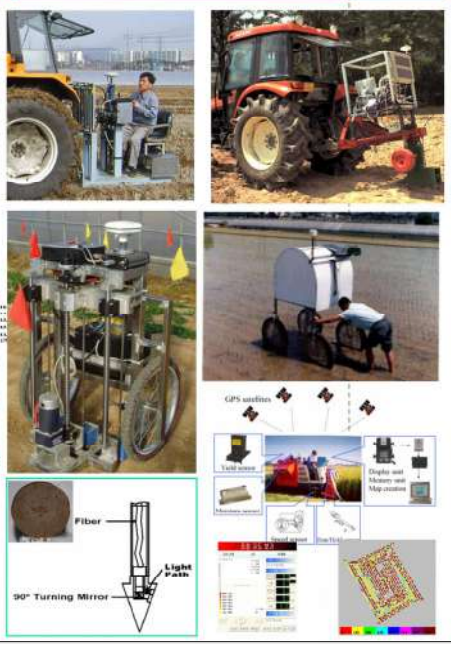

Variable Liquid and Granule Applicator



Research Stage (Late 1990 ~ Early 2010s)

Focus on Rice Production

Field Robots

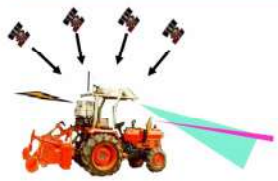

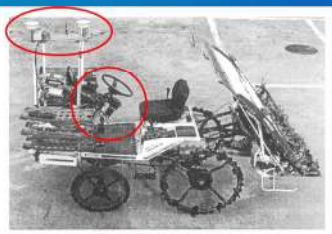







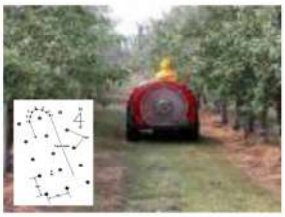


Implement Stage (Early 2010s ~ present)

Strong Government Drive

As-is (Initial supply stage)	To-be (Intelligent agriculture)	Target: open field (USA), protected facility (Netherlands) Gap: technology 70%, 10 years










- Field 1.7 M ha (Rice 60%, Other 40%)
- Greenhouse 52 thousand-ha
- Short-term Goal: 30% smart ag-tech

Implement Stage (Early 2010s ~ present)
Selected Policy

Year	Contents
2014	▪ Long- term plan to foster science and technology for agriculture, forestry, and foods (Fusion of ICT technology)
2016	▪ Counter-measure to accelerate smart-farm expansion and infra-structure preparation
2017	▪ Plan of intelligent information and ICT technology
2017	▪ Plan of medium- and long-term smart farm promotion
2018	▪ Development plan for agriculture, rural area, and food industry (smart agriculture promotion, bigdata infra-structure revision)
2022	▪ Plan of agriculture innovation through smart agriculture expansion
2023	▪ Legislation of Smart Agriculture Promotion Law → Implementation in July 2024
2025	▪ 1st Policy Plan for Smart Agriculture Promotion
On-going	▪ ICT-fusion and expansion support for protected horticulture and animal production, and orchards ▪ Modernization of greenhouse and animal production facilities ▪ Mechanization of dryland crop production + open field smart agriculture ▪ Community-based pilot complex: smart farm innovation valley, pilot complex for open field smart agriculture, unmanned agriculture production pilot complex ▪ Intelligent agriculture machinery feasibility test complex on reclaimed lands
Target	- World-leading Korean Smart Agriculture - ▪ Smartification of 30% of protected crop and animal production facilities by 2027 ▪ Promotion of smart agriculture for open field production (community based)

Implement Stage (Early 2010s ~ present)
Strong Government Drive: www.smartfarmkorea.net

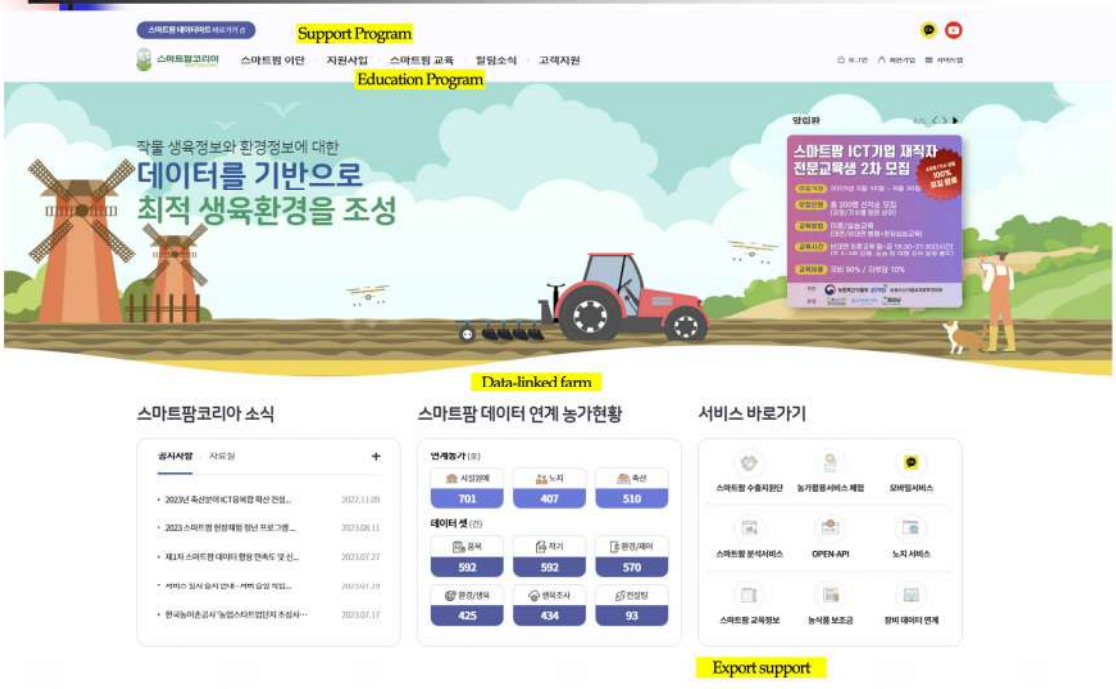

- Sensors and actuators are defined
- Data to be collected are defined
- Need to be better defined

Smart Farm Models
Greenhouse

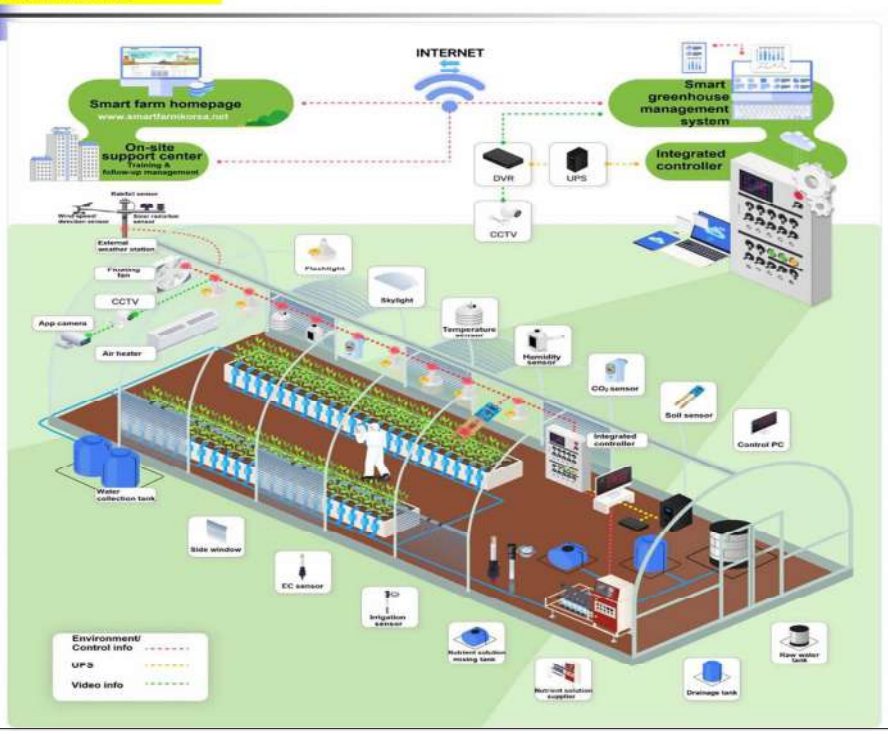

Cow: meat, dairy
Pig: piglet, pig
Chicken: meat, egg

Smart Farm Models
Animal Production

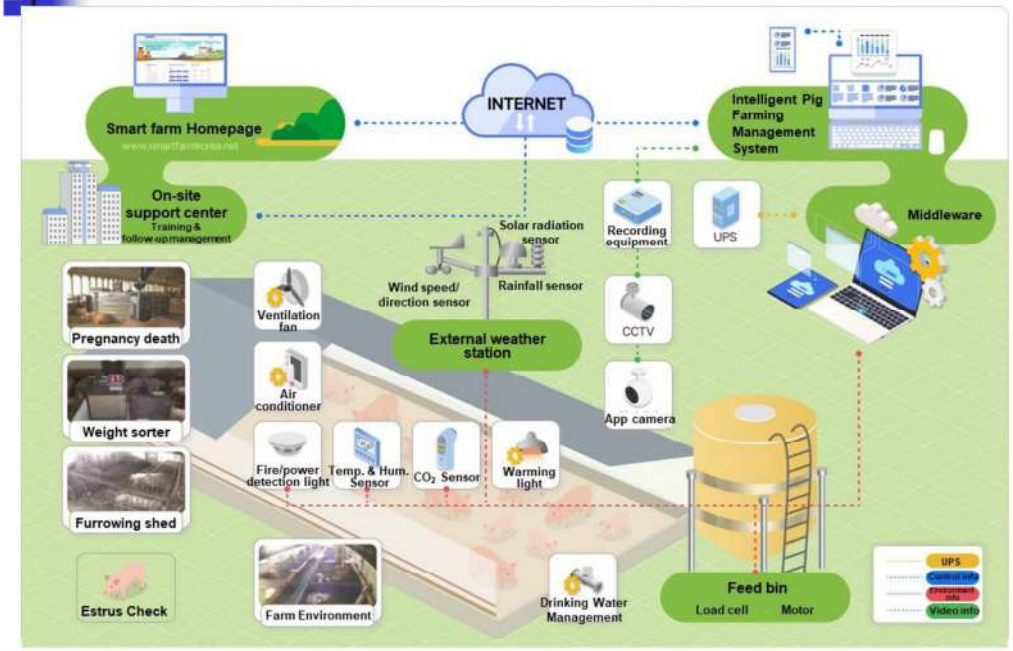

Smart Farm Models
Fruit Production: Orchards

Apple
Pear
Peach
Grape
Citrus

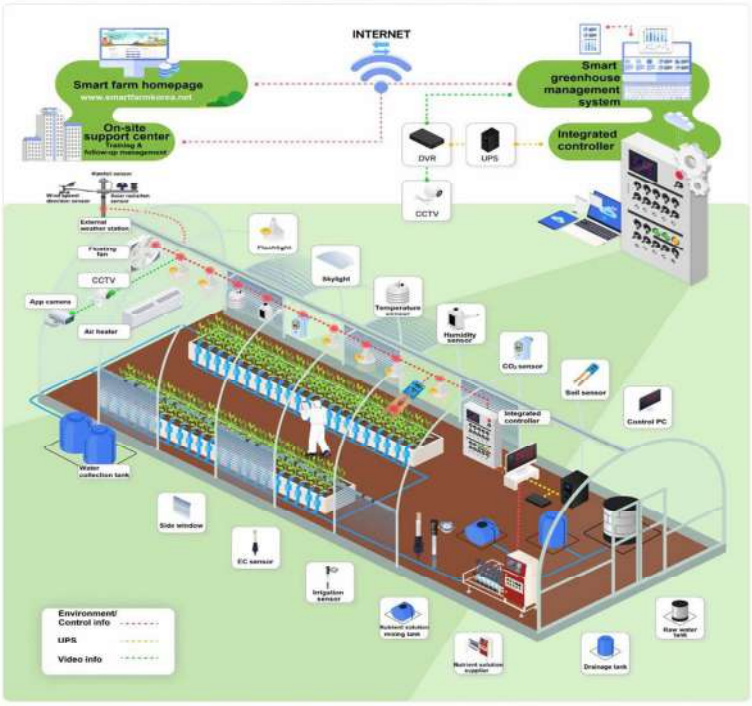

Smart Farm Models
Grain and Vegetable Production: Open Fields

Cabbage
Radish
Pepper
Onion
Garlic
Potato
Sweet potato
Soybean
Barley
Small grain crops

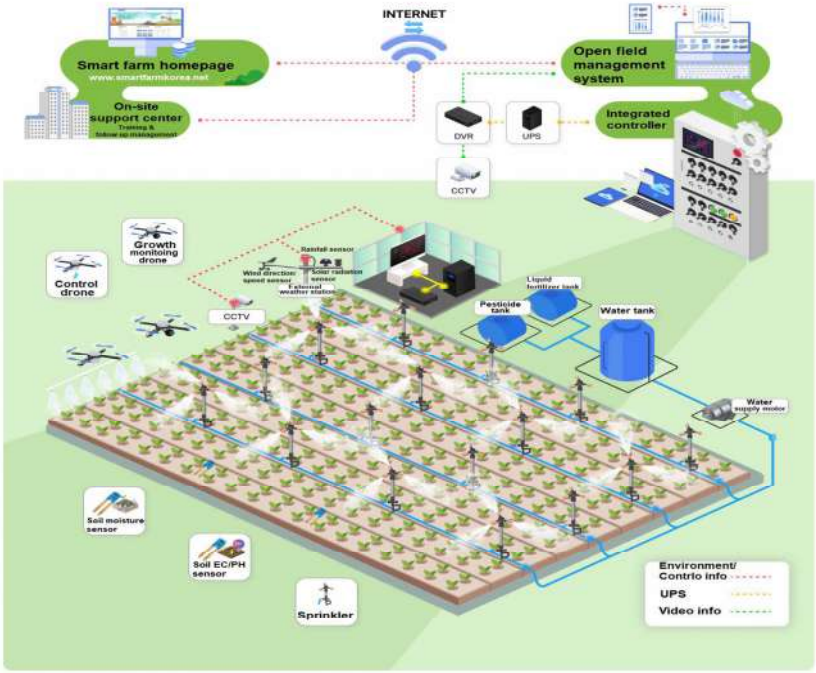

Multi-ministry Special R&D Fund (2021 ~ present)

Smartfarm R&D Foundation



- Fund: Ministry of Agriculture, Forestry, Food, and Rural Affairs, Ministry of Science and Technology, Rural Development Administration
- Project requirements: technology development + prototype + feasibility test + commercialization (+ export)

Multi-ministry Special R&D Fund (2021 ~ present)

Smartfarm R&D Foundation

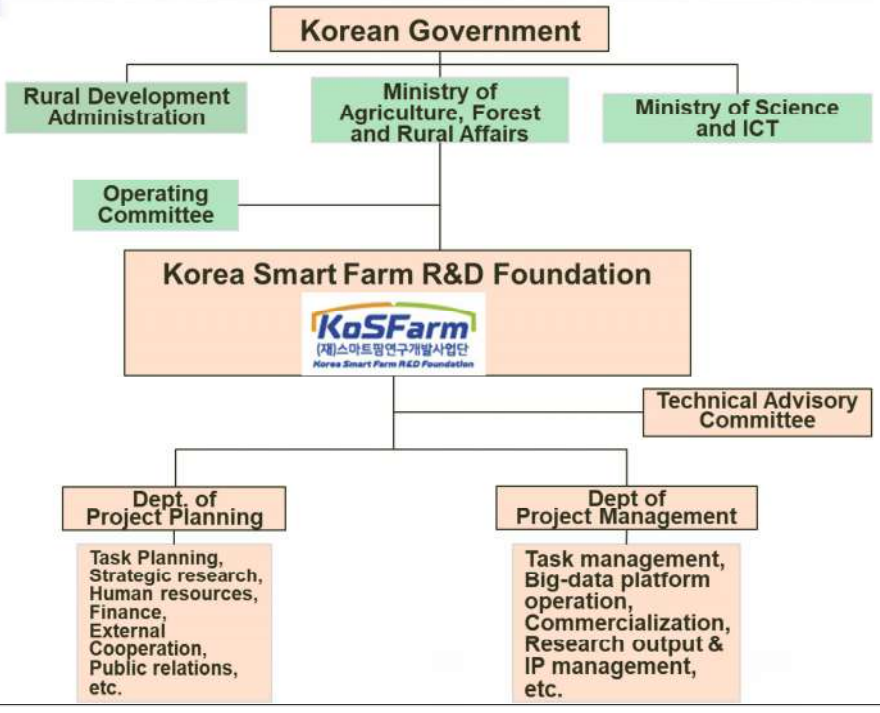

Multi-ministry Special R&D Fund (2021 ~ present)

Smartfarm R&D Foundation

❑ Goal of R&D is Commercialization !

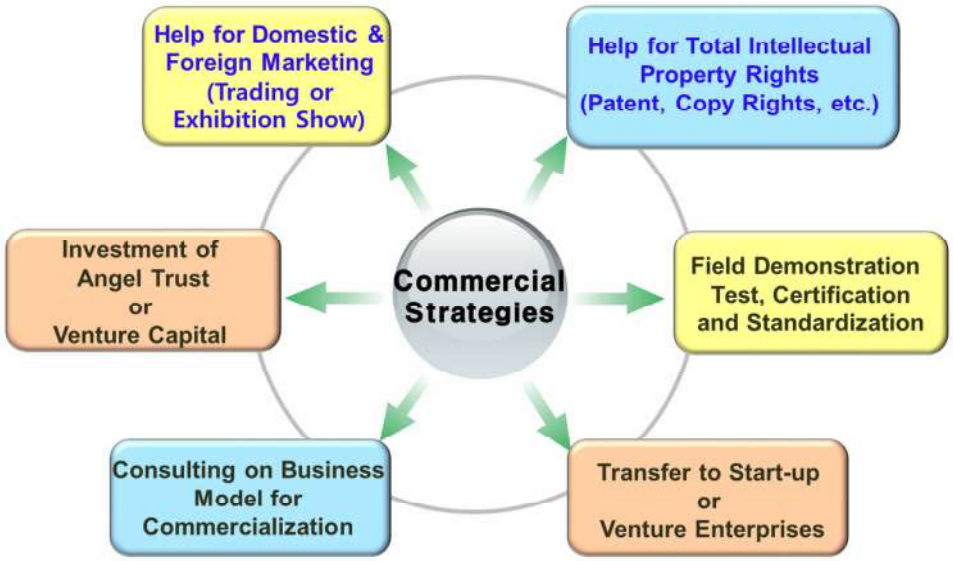

Trend 1: Mechanization

Dryland and Orchard Farming

❑ Dryland: mechanized ratio 63.3%, strong and urgent demand of seeding/transplanting and harvesting

❑ Orchard

- > 90%: tillage, pest control, weed control
- 10~20%: pollination, pruning, bagging, harvesting

Crop	Avg.	Mechanization ratio(%)				
		Tillage·preparation	Seeding·transplanting	Mulching	Spraing	Harvesting
Potato	72.4	99.5	4.6	83.6	97.3	77.2
Soybean	71.1	99.9	37.2	76.5	95.8	46.1
Sweet potato	70.2	99.9	0	92.2	98.9	60.1
Onion	66.3	100	16.1	90.6	99.0	25.8
Garlic	61.8	99.9	14.8	54.8	95.7	43.8
Radish	60.0	99.9	0.8	90.7	98.3	10.4
Cabbage	55.3	99.8	0	86.6	90.0	0
Pepper	48.3	99.6	0	54.0	87.8	0
Avg.	63.3	99.8	12.6	76.9	94.8	32.4

❑ Issues

- Cultivation pattern for better mechanization
- Seedling production for mechanized transplanting
- Harvesting operation, considering post-harvest handling and processing
- Community-based feasibility test and improvement
- Criteria establishment: irrigation flow during transplanting by seedling quality, soil condition, and crop variety

Trend 1: Mechanization
Dryland and Orchard Farming

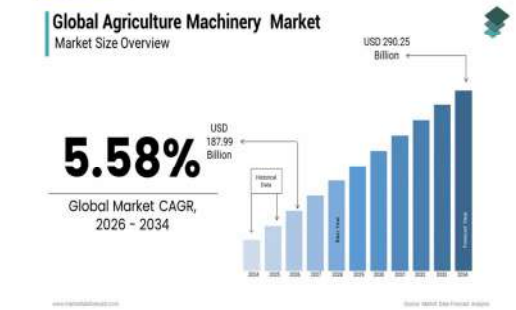



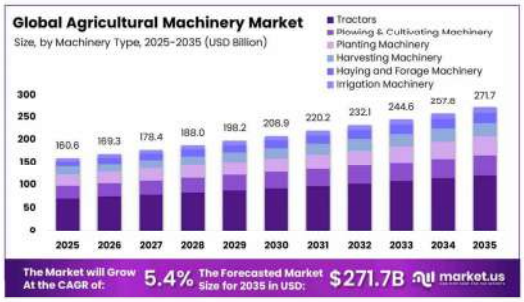

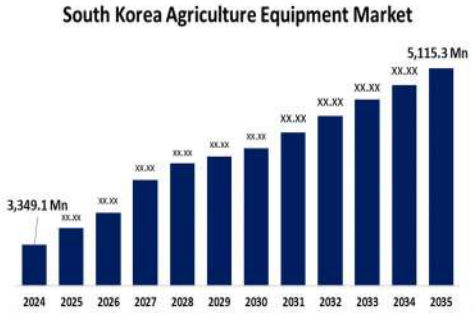

Local Adaptability Improvement and Performance Advancement of Integrated Cabbage Collector

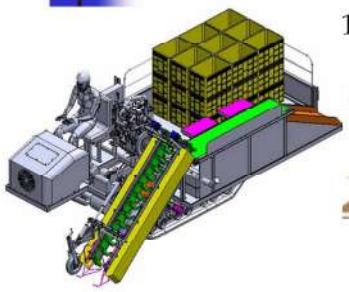

<Cabbage harvester machine >

1. Site selection

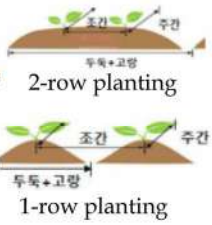

<Field preparation>

2. Field performance



3. Data collection

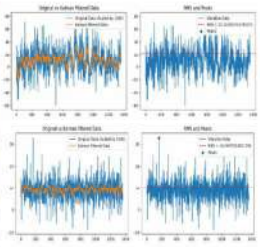

<Cabbage collector performance and data collection>

4. Cabbage collector stability test

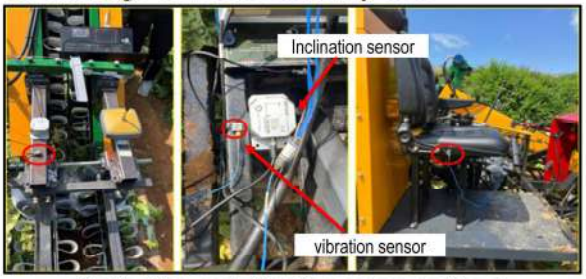

<Inclination and vibration sensor positions>

5. Identification of improvement issues



<Performance improvement issues (stability, safety)>

Fostering Expert Manpower and Advancing Technologies in Digital Agriculture

❑ Test bench for seeding, spraying, and yield monitoring module

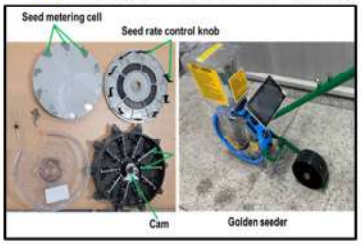

<Seed monitoring module>

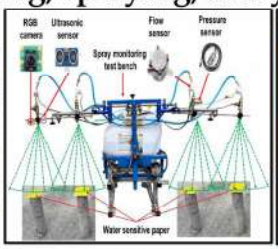

<Spray monitoring module>



<Yield monitoring test bench>



<Filed test of spray and seed monitoring module>



<Filed test of the yield monitoring module>

Trend 2: Automation & Robot

Dryland and Orchard Farming

❑ Global: 20.2 billion USD ('26) → 71.4 billion USD('32) (CAGR 19.8%)
- Drone, UAV, harvesting, weeding, autonomous travelling

❑ Korea: 0.3 billion USD('26) (CAGR 14%)
- Drone, spraying, weeding, transportation

❑ Issues
- Farm infrastructure: farmland structure, communication
- Cultivation pattern suitable for robot operation
- Safety measure, laws & regulations
- Feasible robot system models: big robots vs. small robots

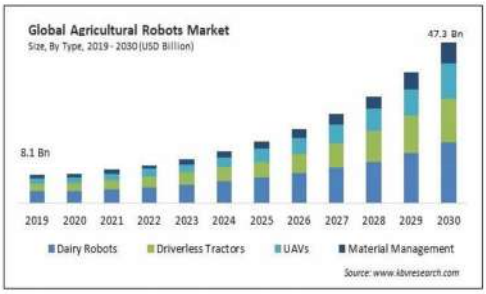



Trend 2: Automation & Robot

daedong









Trend 2: Automation & Robot

TYM

Autonomous operation





Telematics



Trend 2: Automation & Robot

LS Mtron



Autonomous operation



Telematics

Trend 2: Automation & Robot

AGMO





농지 전영역
자율주행 경로 생성

Path Planning

농작업기
제어 기술

Tractor Implement
Automation (TIA)

DANGER

농작업
환경 인식

Perception
System

90%

농장경영
정보시스템

Farm Management
Information System

Trend 2: Automation & Robot
Dryland, Orchard



Trend 2: Automation & Robot
Smart Robots with New Concept



EV Autonomous Driving Platform and Multipurpose Modules for Smart Mechanized Cultivation of Pepper

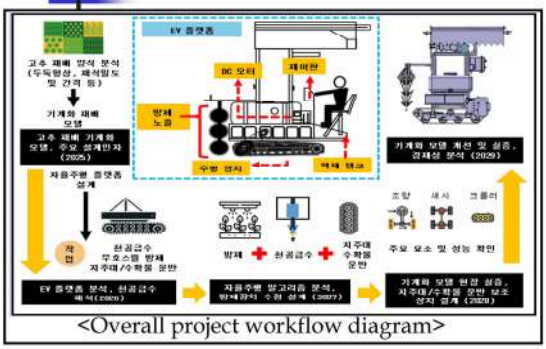

<Overall project workflow diagram>

Step 1. Analysis of autonomous driving platforms based on pepper cultivation patterns and design factors according to work processes

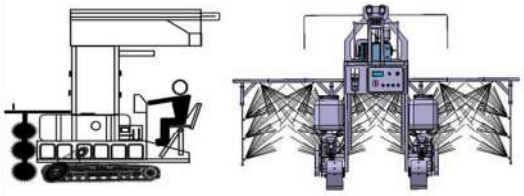

<Self-propelled EV platform concept considering pepper cultivation style and smart mechanized cultivation goals>

Step 2. Analysis of autonomous driving algorithm, Verification of model for mechanization of pepper cultivation, Modification and supplementation design and economic feasibility

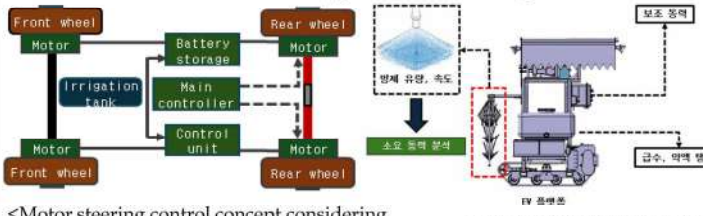

<Motor steering control concept considering power transmission for the EV platform>

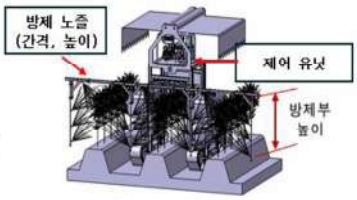

<Flow rate and pressure control concept of sprayer control device>

Trend 3: Satellite & Drone

- Global market: CAGR 17%~20%, spraying, land and crop monitoring
- Agri-forestry satellite (launched on July 7th) 5-m spatial resolution + drone + proximal sensing → land use monitoring, demand and supply regulation, disaster detection
- Issues
  - Correlation and calibration for crop growth, disease vs. input requirement
  - Automated image processing
  - Ground-truthing and validation, feasibility tests

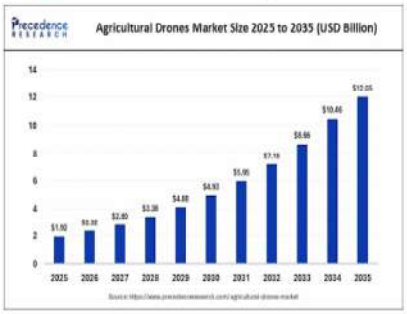

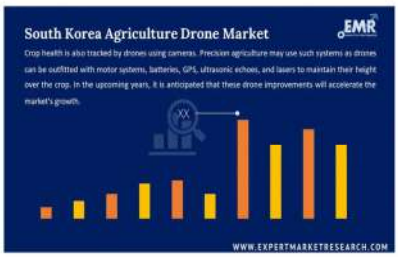





Memory of 1999

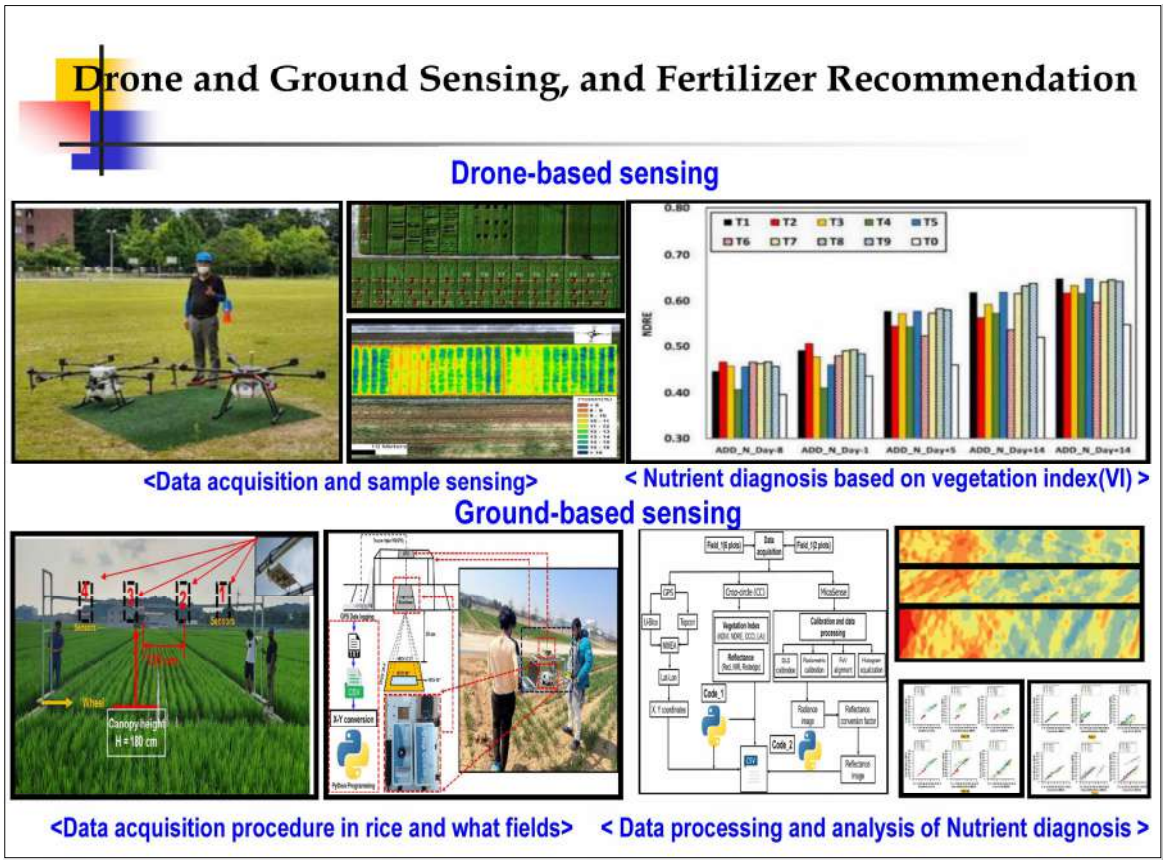
Drone and Ground Sensing, and Fertilizer Recommendation
Drone-based sensing
T1 T2 T3 T4 T5
T6 T7 T8 T9 T0
NDRE
ADD_N_Day-8
ADD_N_Day-1
ADD_N_Day+5
ADD_N_Day+14
ADD_N_Day+14
<Data acquisition and sample sensing>
< Nutrient diagnosis based on vegetation index(VI) >
Ground-based sensing
Canopy height
H = 180 cm
<Data acquisition procedure in rice and what fields>
< Data processing and analysis of Nutrient diagnosis >

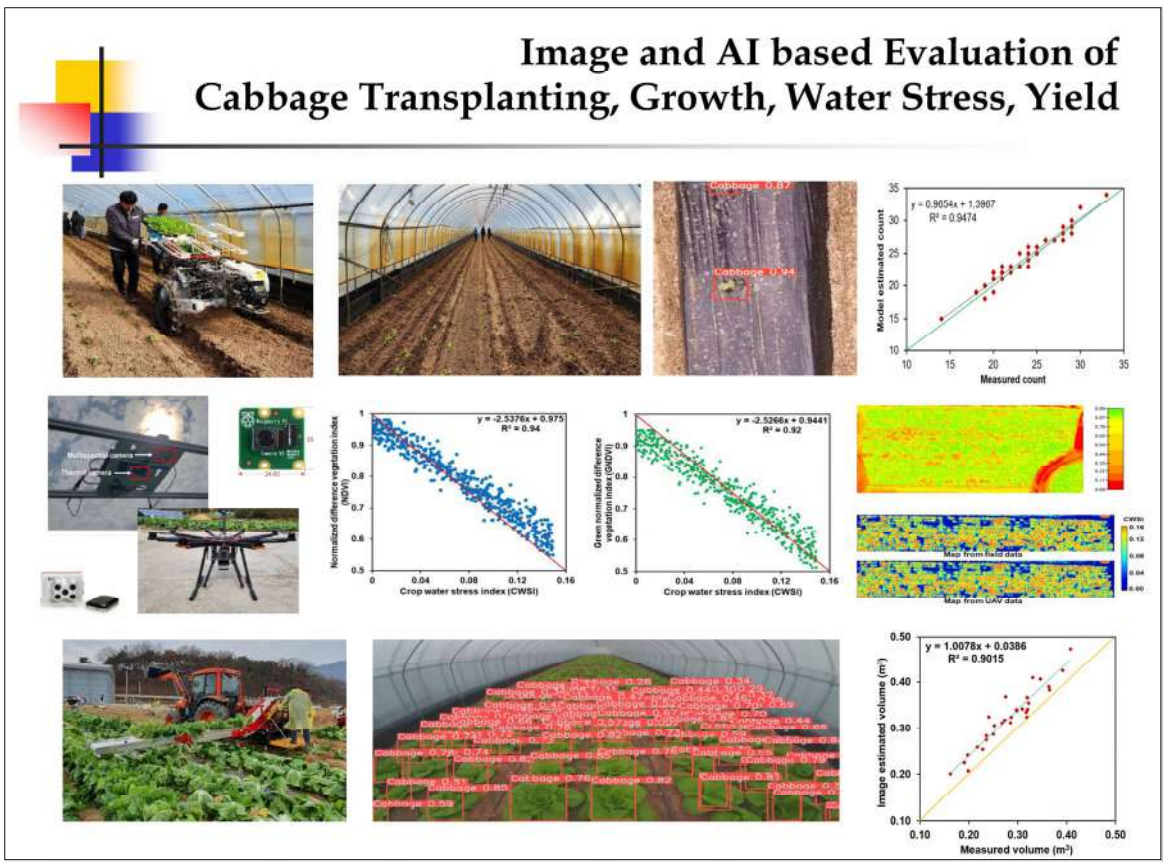
Image and AI based Evaluation of
Cabbage Transplanting, Growth, Water Stress, Yield
y = 0.9654x + 1.3867
R² = 0.9474
Model estimated count
Measured count
y = -2.5376x + 0.975
R² = 0.94
Normalized difference vegetation index (NDVI)
Crop water stress index (CWSI)
y = -2.5266x + 0.9441
R² = 0.92
Green normalized difference vegetation index (GNDVI)
Crop water stress index (CWSI)
Map from field data
Map from UAV data
y = 1.0078x + 0.0386
R² = 0.9015
Image estimated volume (m³)
Measured volume (m³)

Trend 4: ICT, AI, Digital Twin

- ICT → Big data → AI + Modelling → Digital twin
- ICT for improved number of sensors and actuators
- Issues
  - Data collection with target problems and issues
  - Location, time, resolution, and sampling frequency of data communication?
  - Robust and adaptive models: crop growth, energy balance, AI

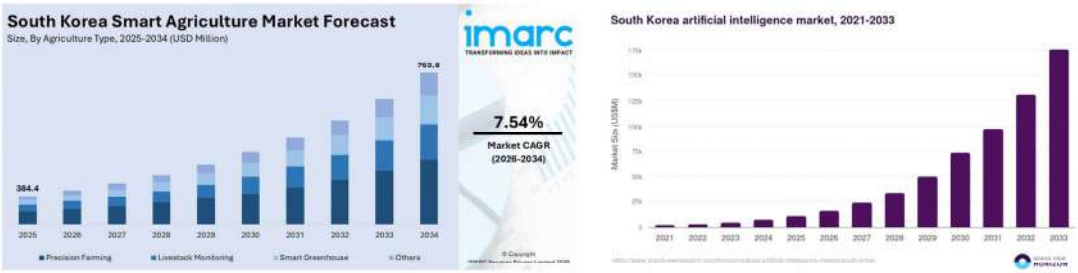

CWSI-based Variable Irrigation for Drylands and Orchards

Step 1. Advanced automatic irrigation system considering spatial variation by zone

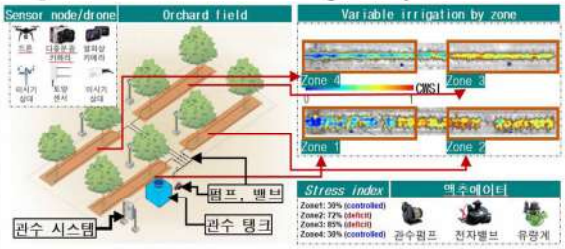

<Advancement of irrigation system considering spatial variation of crop water stress>

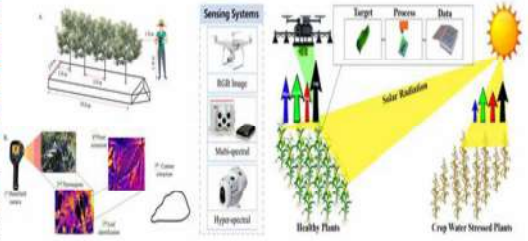

<Crop moisture stress detection using thermal imaging cameras, drones, etc.>

Step 2. Field demonstration and industrialization of integrated automatic irrigation system by zone



<<Irrigation system integrated with moisture stress spatial variation detection module>

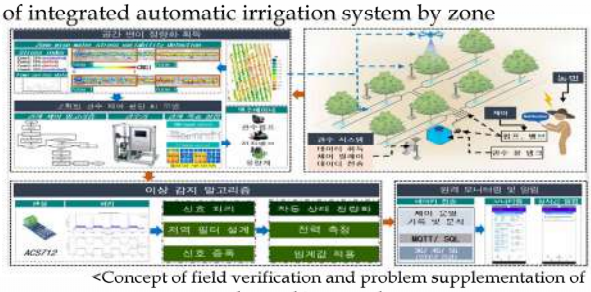

<Concept of field verification and problem supplementation of advanced integrated system>

Variable Nutrient Supply based on Spatial Variability of Environmental Conditions

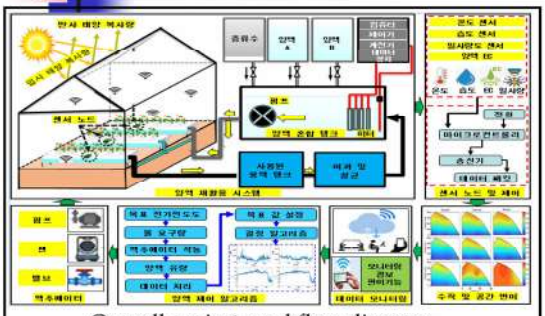

Overall project workflow diagram

Step 1. Development of environmental variation monitoring and intelligent nutrient solution control model and field application



<Sensor node design and nutrient supply and drainage recycling algorithm development>

Step 2. Environmental variation monitoring and intelligent nutrient solution control model field evaluation



<<Improved intelligent integrated system field performance evaluation concept diagram>

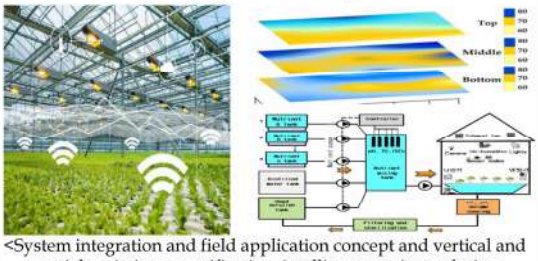

<System integration and field application concept and vertical and spatial variation quantification, intelligent nutrient solution control concept>

Vertical Farm Model Development and Feasibility Tests for Leafy and Medicinal Plants

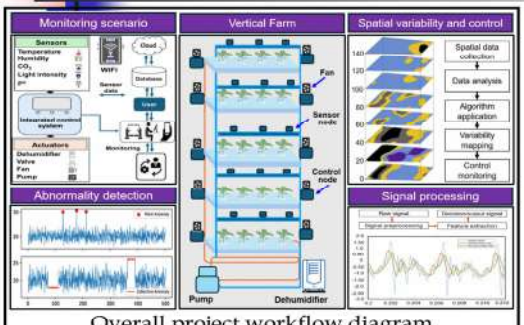

Overall project workflow diagram

Step 1. Implementation of element technology and integrated operational performance testing in domestic test beds

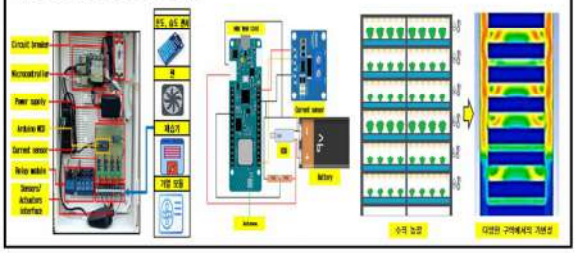

Step 2. Installation and advancement in North American testbed

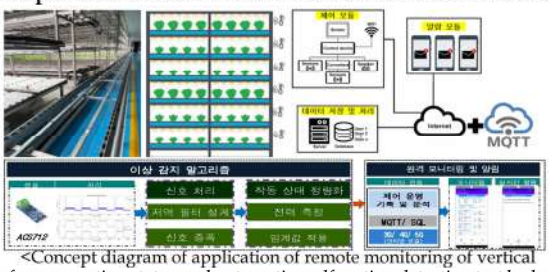

<Concept diagram of application of remote monitoring of vertical farm operation status and automatic malfunction detection test bed>

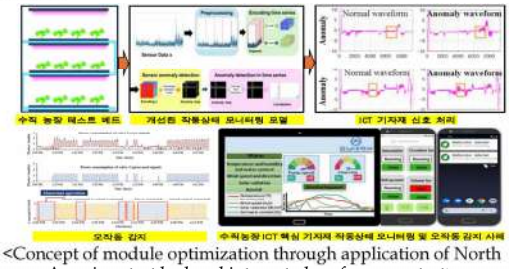

<Concept of module optimization through application of North American test bed and integrated performance test>

Plant Factory in CNU



Pig Disease Symptom Detection

Demonstration of AI Models

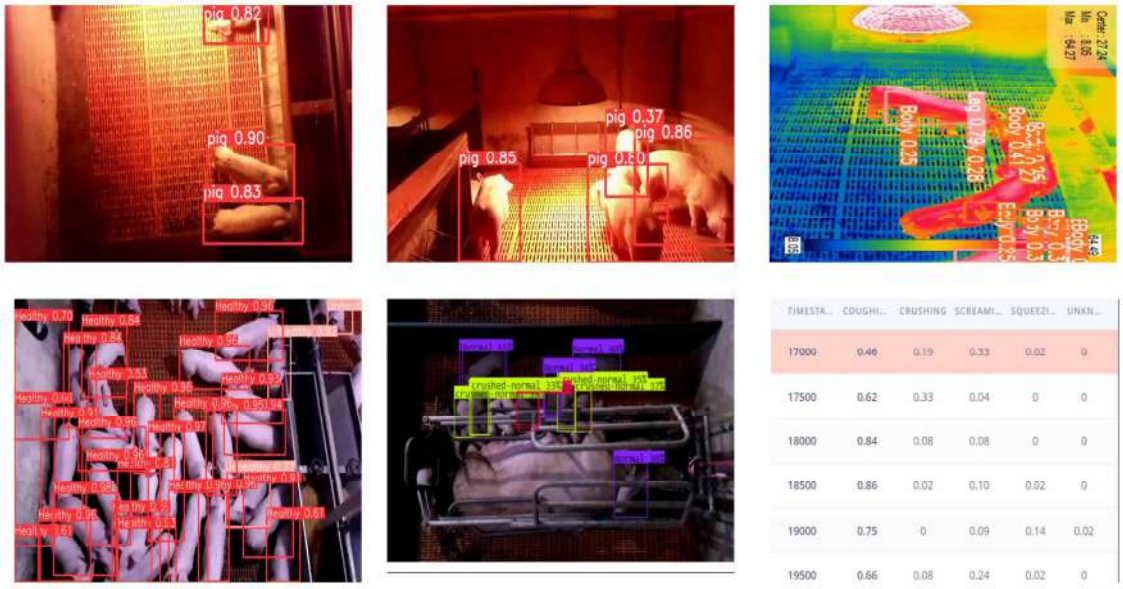

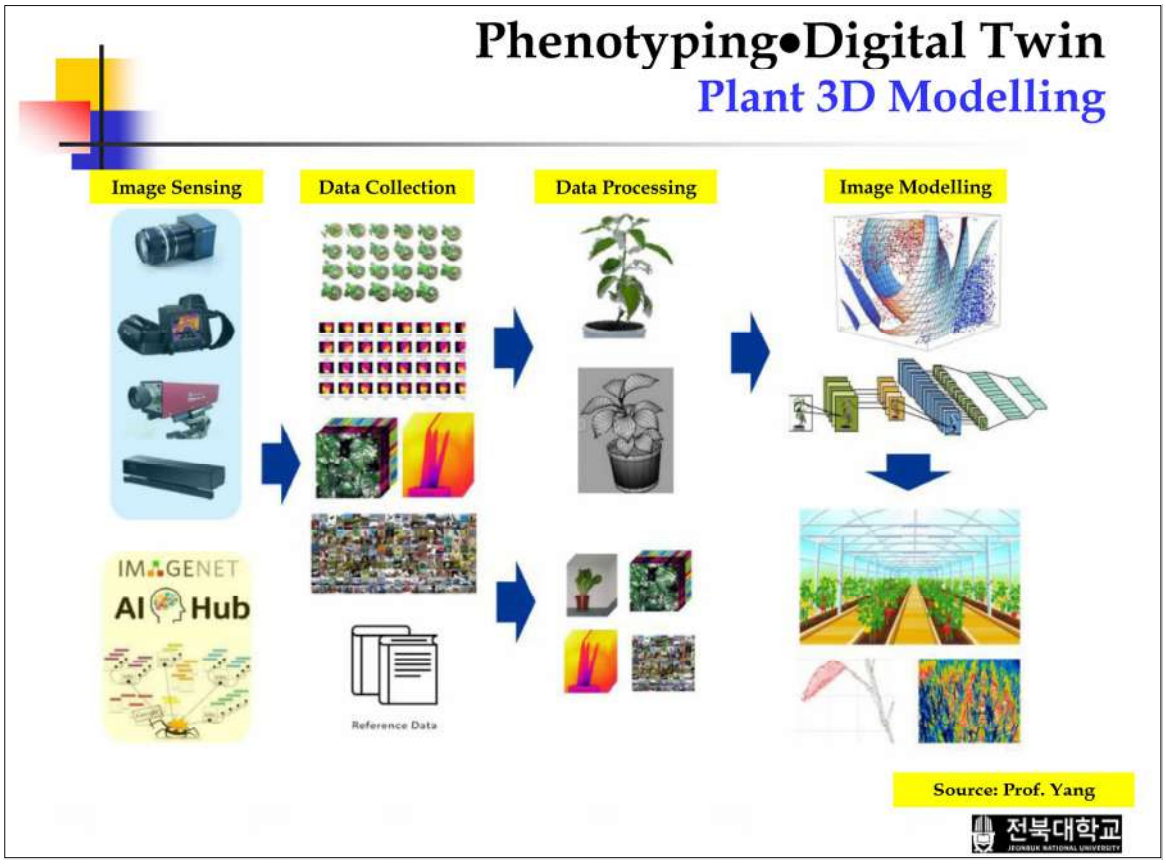
Phenotyping•Digital Twin
Plant 3D Modelling
Image Sensing
Data Collection
Data Processing
Image Modelling
IMAGENET
AI Hub
Reference Data
Source: Prof. Yang
전북대학교

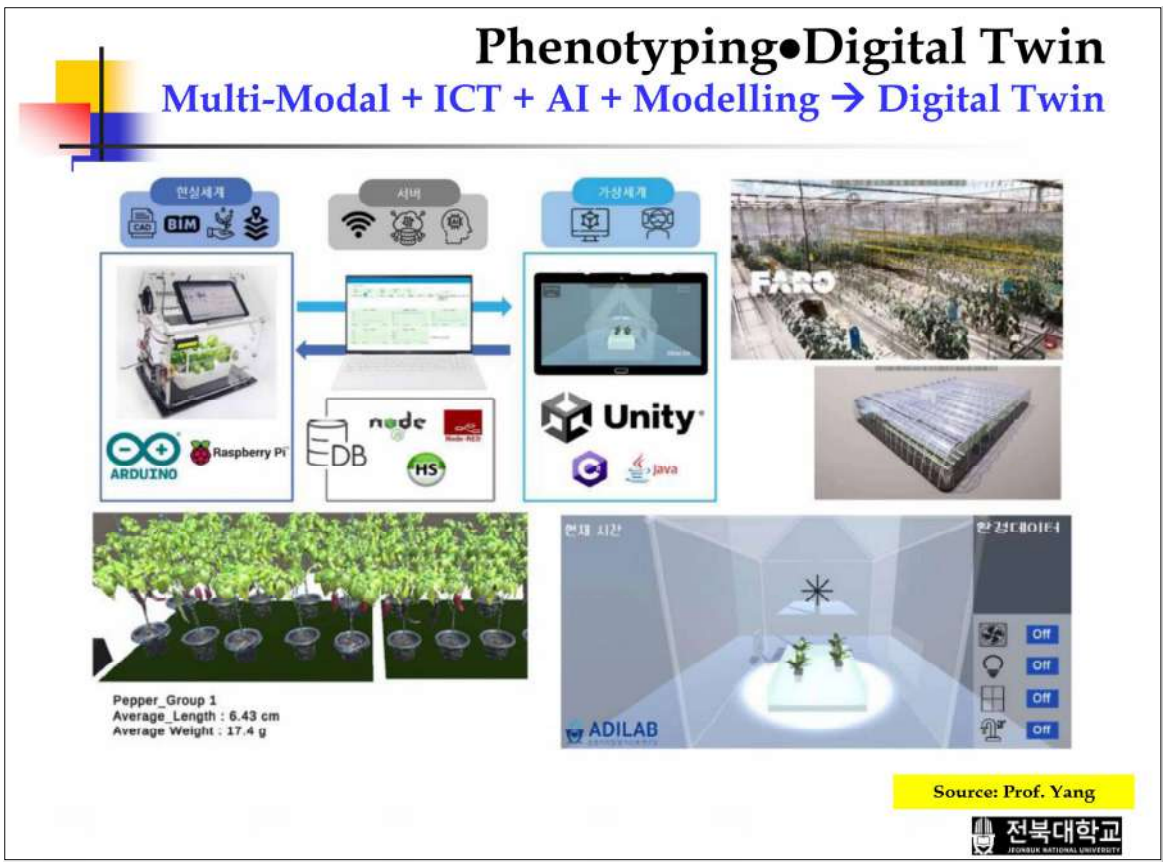
Phenotyping•Digital Twin
Multi-Modal + ICT + AI + Modelling → Digital Twin
현실세계
서버
가상세계
BIM
ARDUINO
Raspberry Pi
node
DB
HS
Unity
java
FARO
Pepper_Group 1
Average_Length : 6.43 cm
Average Weight : 17.4 g
현재 시간
환경데이터
Off
ADILAB
Source: Prof. Yang
전북대학교

Community-based Pilot Complex

Smart Farm Innovation Valley: 4 Cities and Counties



Rental-type smart farm	Farming complex
Feasibility test bed	Smart distribution center
Venture fostering center	Energy facility





Community-based Pilot Complex

Smart Agriculture Promotion Complex, Pilot Farm

- MAFRA: > 30 sites by 2030
  - Open field: 5 sites(~'25) + new 5 sites('26)
  - Protected horticulture: 5 sites(~'25) + new 5 sites('26)
- RDA: 9 sites ('24~'26)









Community-based Pilot Complex

Robot Agriculture Pilot Complex: 1 City



Intelligent Ag. Machinery Feasibility Test Complex

Reclaimed Land: 1 Province



Movie: 50-year History of KSAM



Summary and Remarks

- Site-specific field operation
  - → Acquisition and utilization of information + robotics
- Paddy rice → high-value crops, livestock, orchard fruits, dry lands
- Strong government policies to promote smart agriculture
- Community-based pilot complex(2018~): "Smart-farm Innovation Valley", "Unmanned Agricultural Production Pilot Complex", farmer-oriented, combined production-business, technology test bed, …
- Multi-ministry R&D fund: 2021~2027 for protected horticulture and livestock production (smart ag.), *in preparation for open fields (precision ag.)*
  - Focus on AI and Bigdata
- Technology transfer, standardization, performance test
- Education support program: for undergraduate and graduate school, funded by Ministry of Agriculture, Food, and Rural Affairs
  - Special Graduate School of Smart Agriculture: related workers, MS degree, tuition support

Keynote Speakers

Keynote 1


The 12th International Symposium on
Machinery and Mechatronics for
Agricultural and Biosystems Engineering
ISMAB2026
Sponsor
AI-Driven Innovation for Sustainable and Intelligent Agricultural Systems
Eiji Morimoto Ph.D.
Kobe University

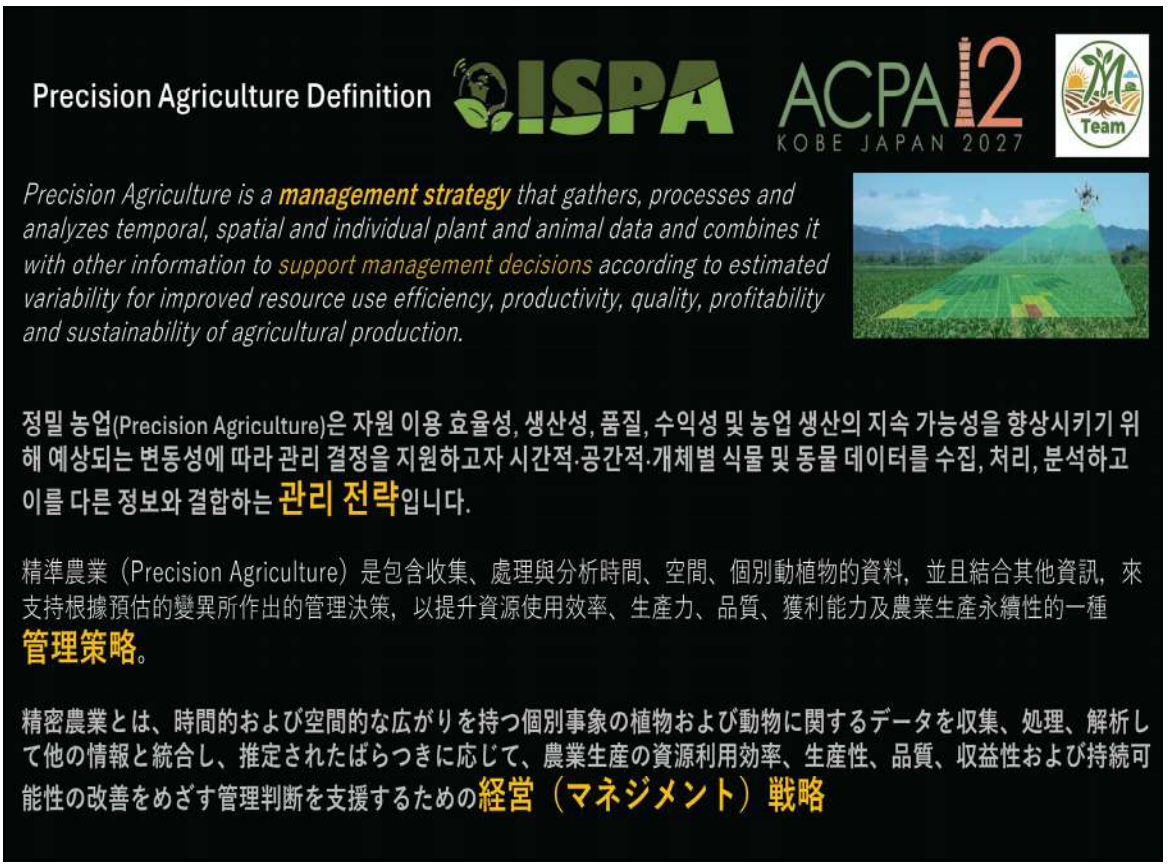
Precision Agriculture Definition
ISPA
ACPA 12
KOBE JAPAN 2027
Team
Precision Agriculture is a management strategy that gathers, processes and analyzes temporal, spatial and individual plant and animal data and combines it with other information to support management decisions according to estimated variability for improved resource use efficiency, productivity, quality, profitability and sustainability of agricultural production.
정밀 농업(Precision Agriculture)은 자원 이용 효율성, 생산성, 품질, 수익성 및 농업 생산의 지속 가능성을 향상시키기 위해 예상되는 변동성에 따라 관리 결정을 지원하고자 시간적·공간적·개체별 식물 및 동물 데이터를 수집, 처리, 분석하고 이를 다른 정보와 결합하는 관리 전략입니다.
精準農業（Precision Agriculture）是包含收集、處理與分析時間、空間、個別動植物的資料，並且結合其他資訊，來支持根據預估的變異所作出的管理決策，以提升資源使用效率、生產力、品質、獲利能力及農業生產永續性的一種管理策略。
精密農業とは、時間的および空間的な広がりを持つ個別事象の植物および動物に関するデータを収集、処理、解析して他の情報と統合し、推定されたばらつきに応じて、農業生産の資源利用効率、生産性、品質、収益性および持続可能性の改善をめざす管理判断を支援するための経営（マネジメント）戦略

Key factors of Precision Agriculture are

Sensing: Measurement of Variability

Modeling: Calculation of Variable-Rate Prescription

Action: Localized Machinery Control

Thanks to technological innovation..

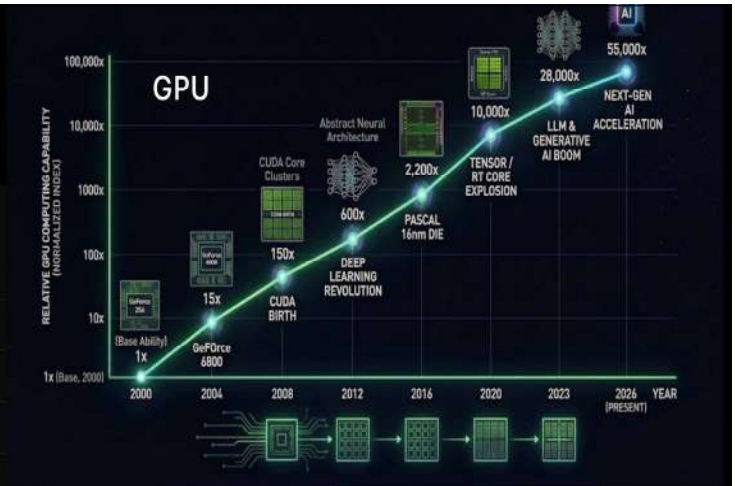

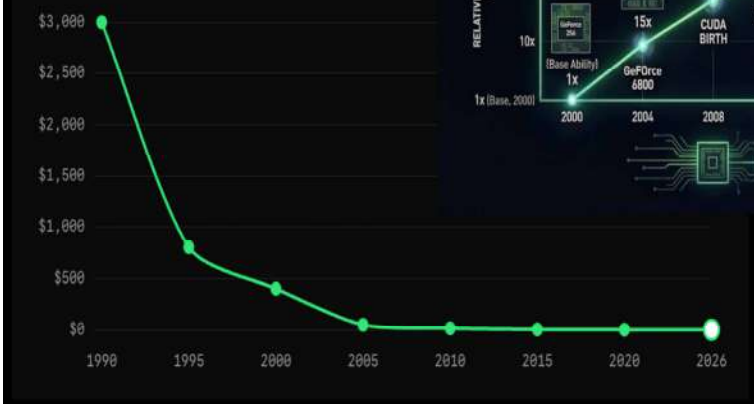



Lightweight deep learning models and edge GPUs (e.g., NVIDIA Jetson) for robot combines enable real-time, high-resolution field analysis.
@Michihisa IIDA



Paradigm Shift:
From "Post-Analysis" to "On-Site Real-Time Processing"

Conventional Batch Processing (Post-Processing)
Drone capturing
→Data export & PC analysis
→Prescription map creation
→Loading into machinery at a later date. Time lag introduces the risk of missing optimal timing.

Modern Edge AI (Real-Time Integration)
The moment the front-mounted camera detects a target, variable-rate commands are sent to nozzles or seeding units within milliseconds. Diagnosis and operation are **completed in a single pass.**

The Paradox of LLM-Driven Optimization



Even When LLM-Driven Optimization Yields Correct Answers, Sometimes Farmers Refuse to Adopt Them, Especially the answer was different from their intuition.

Farmers know the nuances of their own fields best. When model parameters conflict with a farmer's tacit knowledge and years of field experience, they will pass on adopting the technology.

Sustainable and Intelligent Agricultural Systems require trust, not just statistical accuracy.


Question:
Which monitor should I look at?
RAM
RAVEN


Data consistency that farmers can truly grasp may be limited to what is right in front of them.
freereft = algoth()
data_input = { 80...)
Team

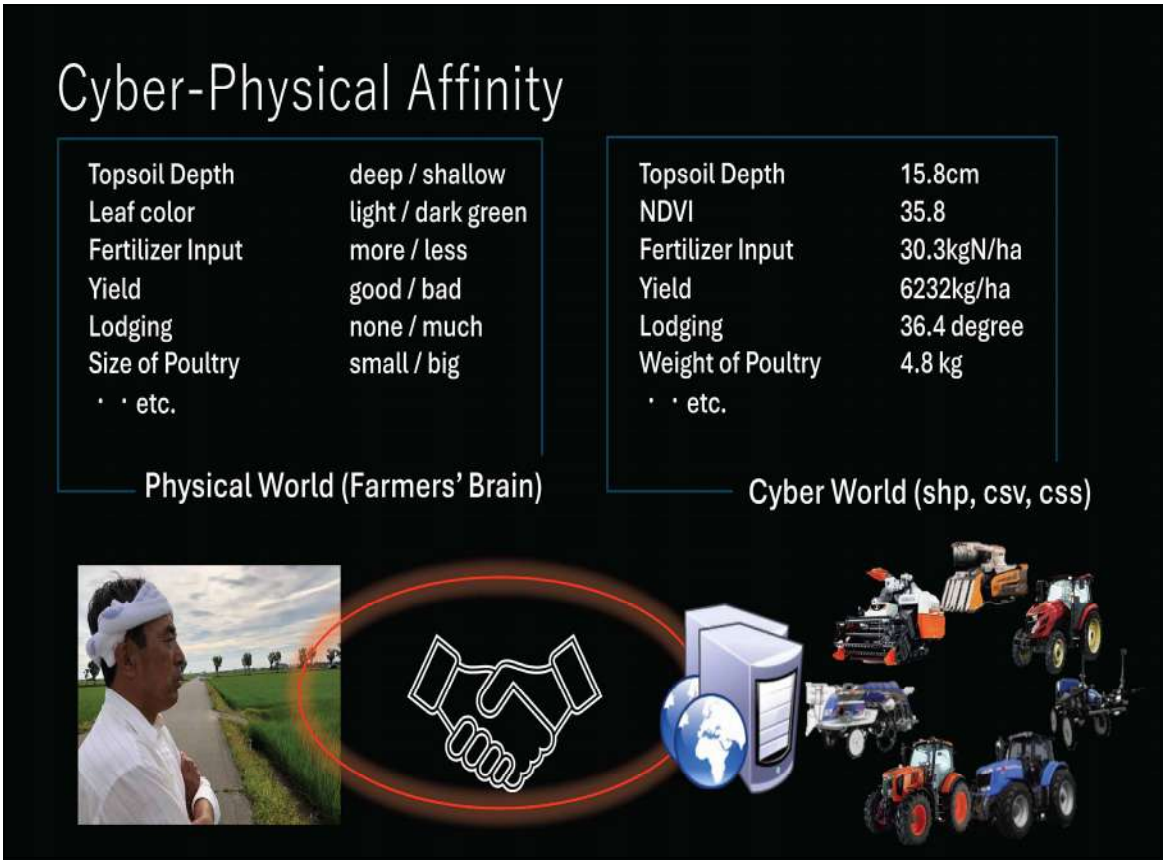
Cyber-Physical Affinity
Topsoil Depth deep / shallow
Leaf color light / dark green
Fertilizer Input more / less
Yield good / bad
Lodging none / much
Size of Poultry small / big
・・etc.
Physical World (Farmers' Brain)
Topsoil Depth 15.8cm
NDVI 35.8
Fertilizer Input 30.3kgN/ha
Yield 6232kg/ha
Lodging 36.4 degree
Weight of Poultry 4.8 kg
・・etc.
Cyber World (shp, csv, css)


7 research activities are undergoing with farmer by team M.
Team

AI-Based Pear Scouting (2016-)



@Jaehwan LEE

Flower Bud Count Map

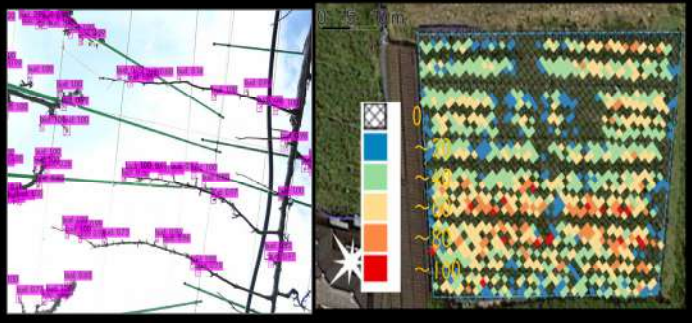

Potential limit of fruit production

Measuring Pre-Harvest Fruit Count

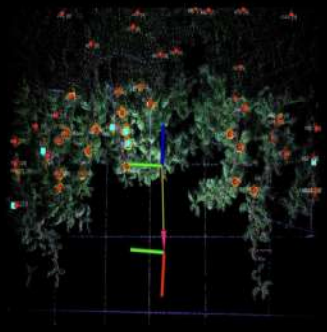

Estimating Fruit Size and Quantity
→ Estimated Income

Smart Rice Transplanter (2008-)



Topsoil Depth map





Identifying Rice Transplanting Difficulty →Variable-Rate Field Management

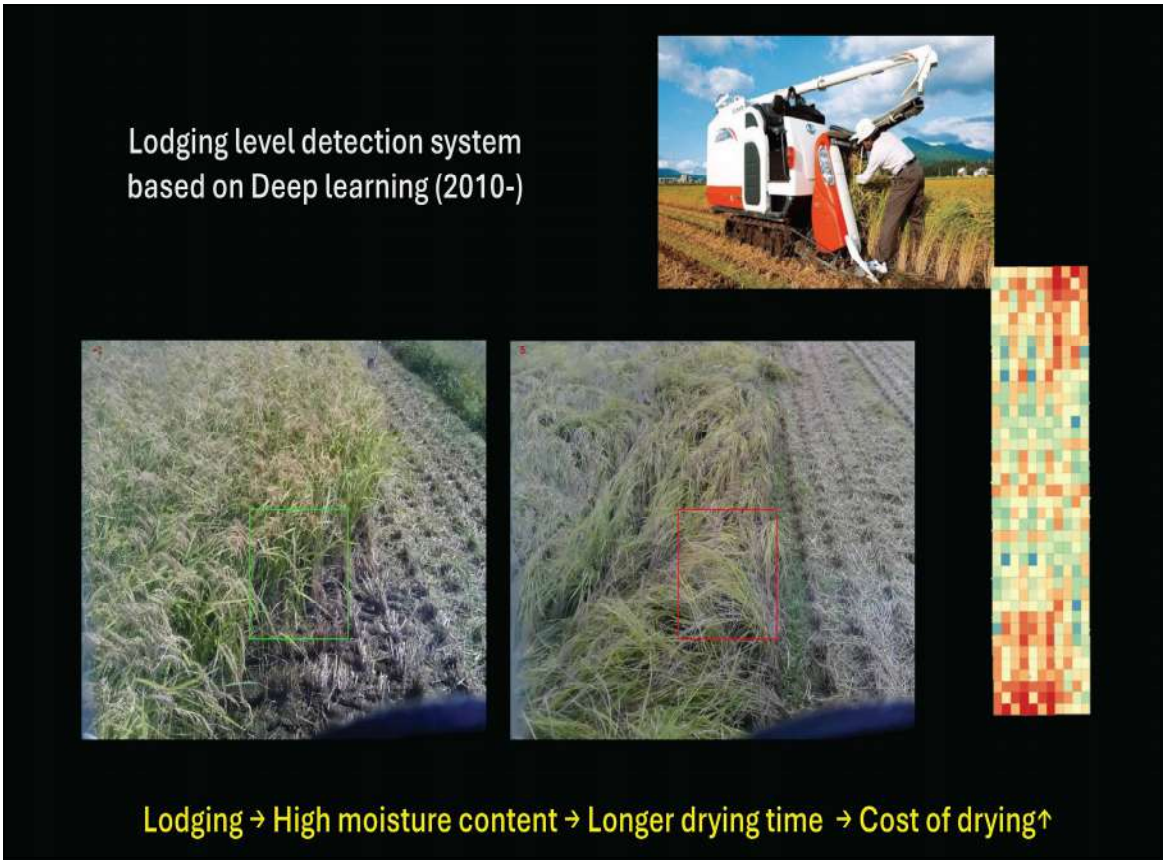
Lodging level detection system
based on Deep learning (2010-)
Lodging → High moisture content → Longer drying time → Cost of drying↑

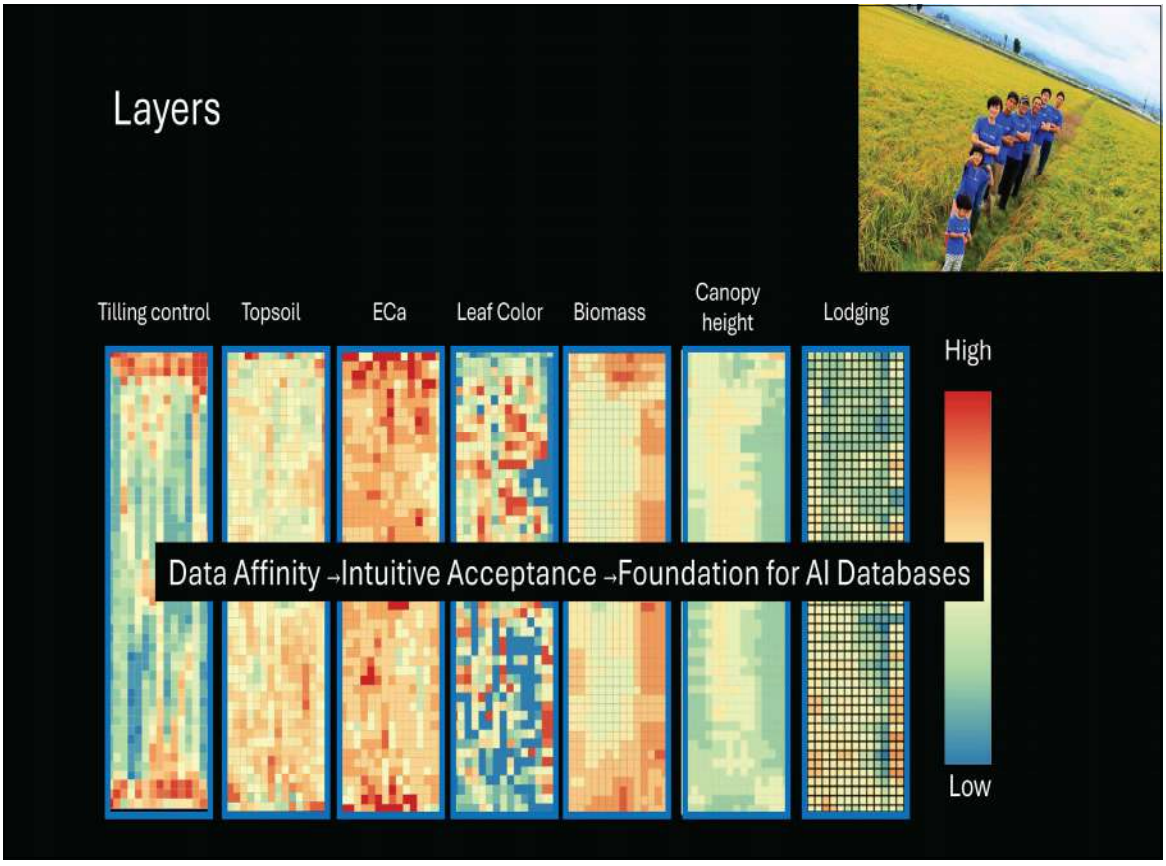
Layers
Tilling control
Topsoil
ECa
Leaf Color
Biomass
Canopy height
Lodging
High
Low
Data Affinity →Intuitive Acceptance →Foundation for AI Databases

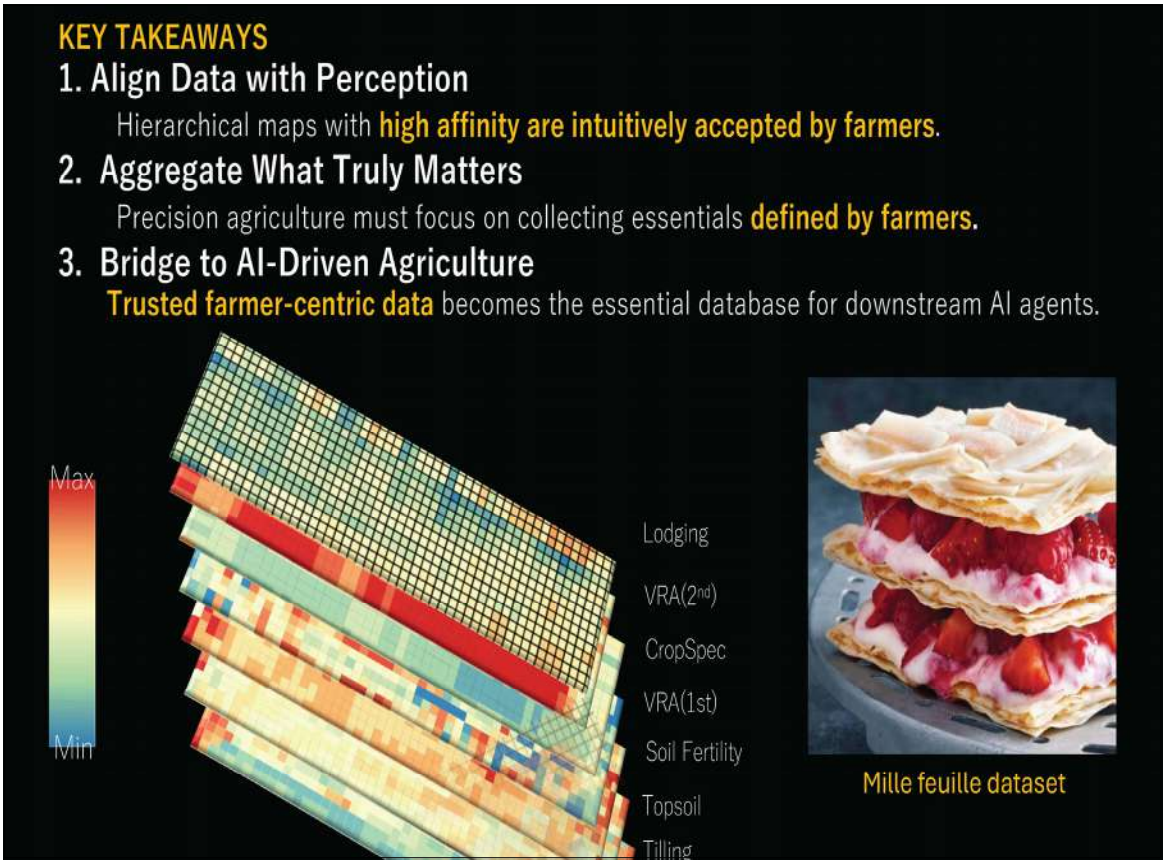
KEY TAKEAWAYS
1. Align Data with Perception
Hierarchical maps with high affinity are intuitively accepted by farmers.
2. Aggregate What Truly Matters
Precision agriculture must focus on collecting essentials defined by farmers.
3. Bridge to AI-Driven Agriculture
Trusted farmer-centric data becomes the essential database for downstream AI agents.
Max
Min
Lodging
VRA(2nd)
CropSpec
VRA(1st)
Soil Fertility
Topsoil
Tilling
Mille feuille dataset


ACPA 12
KOBE JAPAN 2027
The 12th Asian-Australasian Conference on Precision Agriculture (ACPA 12)
If you want to know more about us…
SAVE THE DATE
September 15-18, 2027
Abstract submission deadline 28th Feb

Keynote 2

The 12th International Symposium on
Machinery and Mechatronics for
Agricultural and Biosystems Engineering (ISMAB 2026)

國立中興大學
NATIONAL CHUNG HSING UNIVERSITY

Smart poultry farming: Integrating AI for next-generation management

Yao-Chuan Tsai (蔡燿全)
Associate Professor and Director
Department of Bio-Industrial Mechatronics Engineering,
National Chung Hsing University, Taiwan

1

Outline

- Introduction to Taiwan's Poultry Farms
- AI Laser Wild Bird Repellent System
- AI Poultry Weight Scale
- Chicken Activity and Laser Response Assessment System
- AI Chicken's Comb and Eyes Identification Technologies
- Conclusion and Future Works






2

Introduction to Taiwan's Poultry

- For Taiwan **poultry meat**, two important types are **broiler** and **Taiwanese native chicken**.
- For the **broiler**, the feeding duration is shorter and about 5-7 weeks.
- For the **Taiwanese native chicken**, the feeding duration is longer and about 13-24 weeks.
- The selling weights are around **2.0-3.0 kg for broiler** and **2.5-3.5 kg for Taiwanese native chicken**.
- Due to the animal's behaviors, the **feeding density** for Taiwanese native chicken is lower than it for broiler.
- Besides, the **laying hens** is another important poultry industrial.

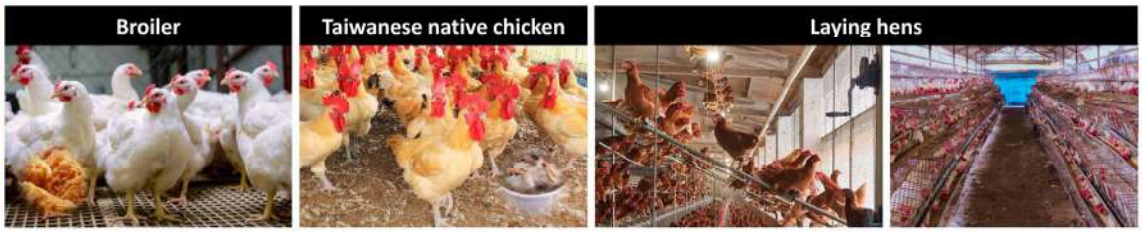

3

Introduction to Taiwan's Poultry Farm Development

- The Taiwanese poultry houses are gradually changed from **outdoor farming** to **indoor house**. To provide poultry with suitable growth conditions, many **environmental control systems** have been installed within poultry houses.
- To save farmer labor, many poultry houses have adopted **automatic feeding and watering systems**. In recent years, **environmental sensing and automatic control systems** have been applied for achieving automated control of the poultry house environment.

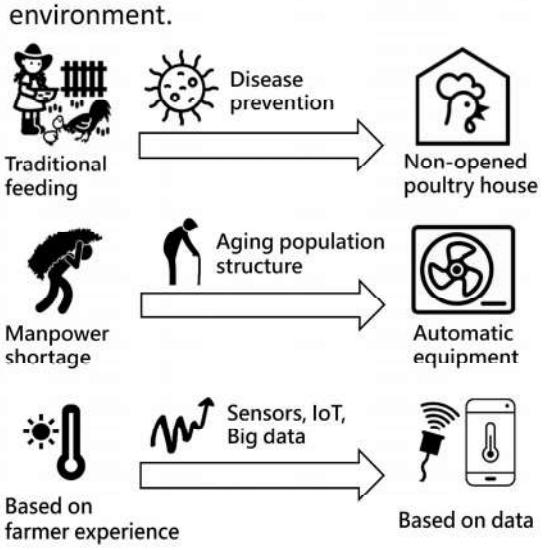



4

Issues for the Taiwanese Poultry Industry

- In today's automated poultry houses, there are still **some challenges** that need to be addressed. These challenges include:
  - **The risk of avian influenza from wild birds**: When wild birds are closed with poultry, the risk of the transmit diseases such like avian influenza would be increased.
  - Currently, **poultry farm managers still need to enter and exit poultry houses to observe the growth and health of the poultry**. This frequent entry and exit not only increase the labor intensity for farmers but also increase a risk of pathogen transmission.
  - **Observation criteria depended on the farmer's experience**. The absence of scientific data-driven support may lead to inaccurate management and low efficiency.

▼ The issue of wild birds in poultry houses

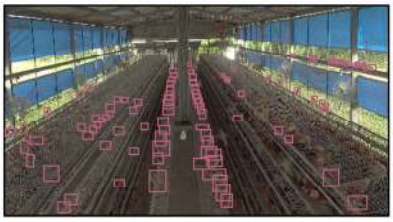

▼ Farmers still need to enter the poultry houses to observe the condition of the chickens



5

Development of the Taiwanese poultry house

- In order to improve the poultry house from **traditional and automatic** types to **smart poultry house**, the **wild birds issue** and **poultry health condition assessment system** is necessary.

Development of the poultry house			
	Traditional	Automatic	Smart
House type	Opened and non-opened	Non-opened (wild birds) and closed	
Environmental control equipment	Fans	Automatic fans, water curtain and ...	
Sensor and feedback control	No	Temperature and humidity sensor	+Wind and Gas sensors
Feed and water	By manpower	Automatic	
Feed and water monitoring	No	No	Yes
Management records	No	Pen and paper	Digitization
Poultry weight measurement	Only the average weight of the final chickens are known or the human weight measurement		Automatic measure everyday
Poultry health assessment and warming	By manager or farmers		By video, image and sound

6

AI Laser Wild Bird Repellent System

- In the world, the **wild bird** is an important and difficult issue in the poultry farm.
- The wild bird made not only the **feed loss** but also the **spread of avian influenza**.
- Therefore, how to decrease and avoid the wild birds to appear in the poultry farm and to contact with poultry is a necessary work.



Wild birds appear in the poultry house and farm.

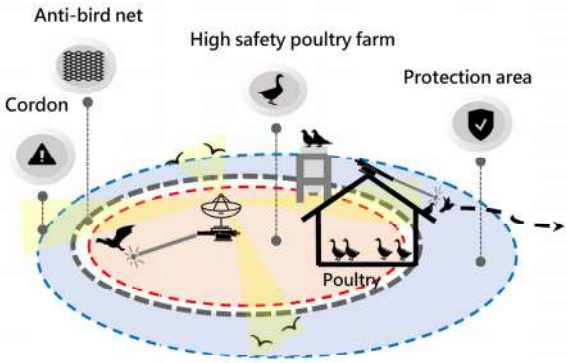

High safety poultry farm is necessary to the poultry health and the farmer.

7

AI Laser Wild Bird Repellent System

- According to the experiment result, the wild birds were repelled when they see the laser spot light around them.
- The wild birds feel the laser spot light as the **physical attack** and flied away from the laser.



8

AI Laser Wild Bird Repellent System

- The poultry are interesting on the laser spot. The laser would not make the stress on the feeding poultry.



Fields	Poultry	0.5 mW	2 mW	5 mW	100 mW	200 mW	250 mW
Indoor	Chicken	Interesting	Interesting	Interesting	Interesting	Interesting	Interesting
Semi-outdoor	Duck	×	×	×	Interesting	Interesting	Interesting
Semi-outdoor	Goose	×	×	×	Interesting	Interesting	Interesting
Outdoor	**Wild bird**	×	×	×	**Repellent**	**Repellent**	**Repellent**

9

AI Laser Wild Bird Repellent System

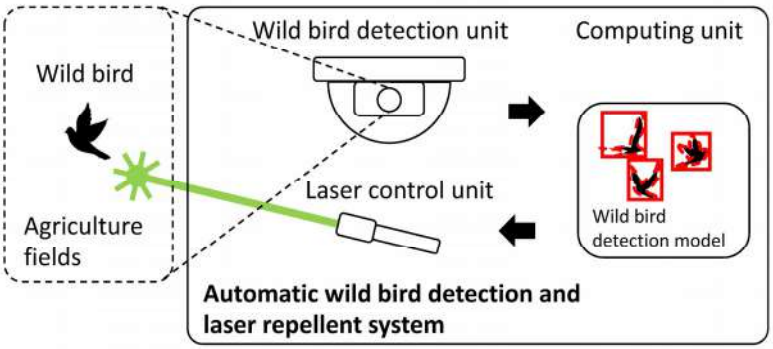

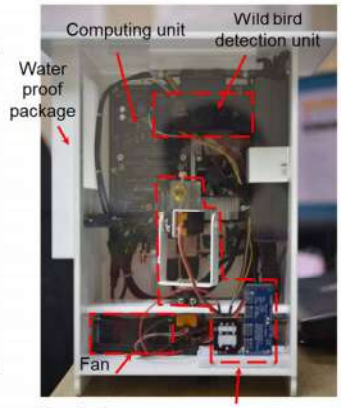

Prototype



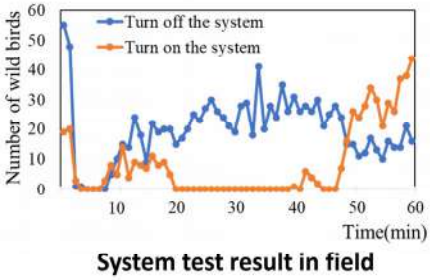

System test result in field

10

AI Laser Bird Repeller – AI Bird Detection and Automated Laser Repellent

Commercialization completed



Operational workflow

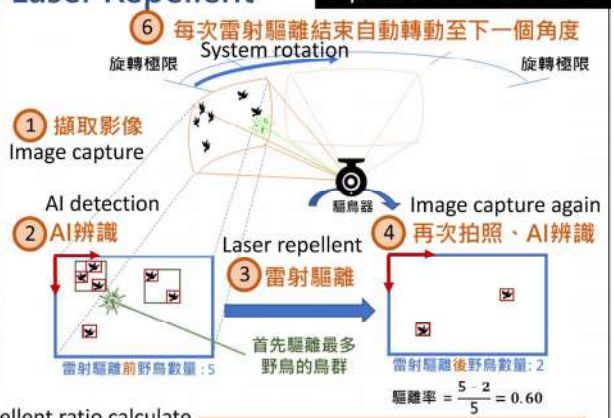



Repellent ratio calculate

5 計算驅離率

$$驅離率 = \frac{雷射驅離前野鳥數量 - 雷射驅離後野鳥數量}{雷射驅離前野鳥數量}$$

Test result



- According to the test results, the wild birds could decreased 50%-70%.

11

AI Poultry Weight Scale - Important of poultry weight

- The increase of **poultry weight** is one of the important index for the **poultry growth and health condition** and **farmer's income**.
- The poultry production performance such as growth rate, feed meat exchange rate is related to the poultry weight.
- If the poultry weight could not be known, it is difficult to understand the feeding situation.

Floor scale



Hanging type



Floor type



Plate type

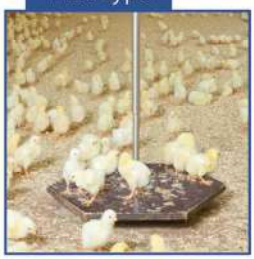

- The **floor scale measurement** is only done **once when the chickens are released**. The disadvantage is that **the feeding situation is not known until the end**, and it is difficult to adjust the feeding strategy in time.
- The scales currently used in poultry houses all have their **shortcomings**, such as **labor consumption, durability, safety, and accuracy**.

12

AI Poultry Weight Scale

- Integrating the **camera** into the weighing machine, the AI algorithm could be used to know **how many poultry are on the weighing platform** to further obtain accurate poultry average weight.
- Collect poultry images for machine learning and train a poultry identification model.
- Mechatronic integration technology integrates weight sensors, cameras, and computing units.
- Integrated wireless communication function, the measured data can be automatically uploaded to the cloud. This system equipped with automatic zero correction function.

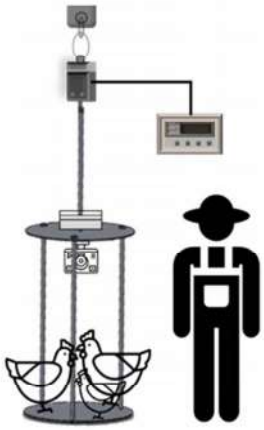

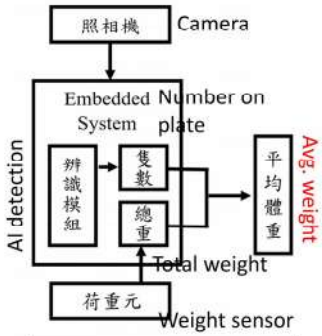

System structure

Average weight =

$$\frac{\text{Total weight}}{\text{Number of chickens on the platform}}$$

13

AI Poultry Weight Scale – AI poultry detection model

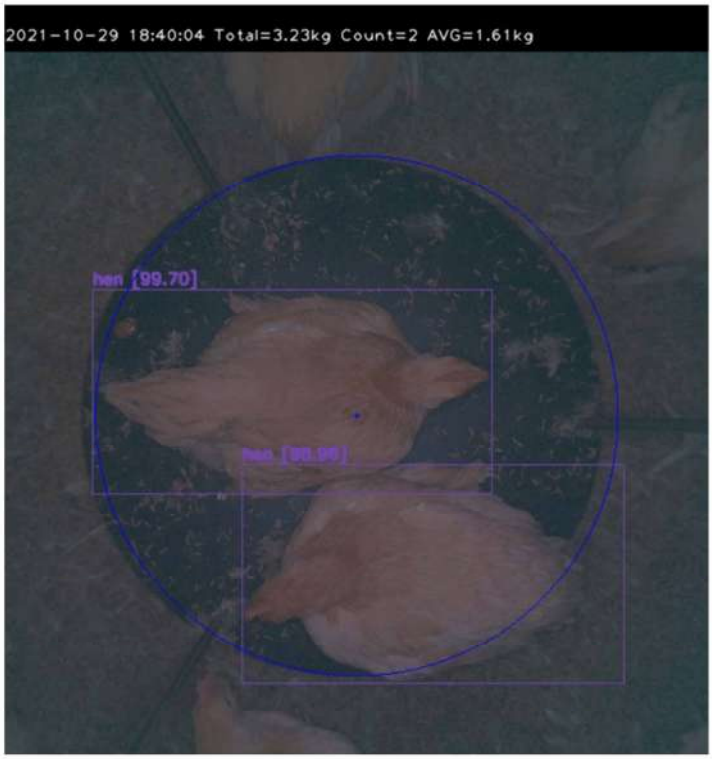

- YOLO was used as the poultry detection train model.
- So far, the labelled images are Taiwanese native chicken, broiler, turkey, goose, duck for 5000, respectively.

IoU = 0.5	Predict-Yes	Predict-No
Actual-Yes	TP = 426	FN = 32
Actual-No	FP = 8	TN

- The accuracy of Taiwanese native chicken detection by AI is over than 95%.

14

AI Poultry Weight Scale – Automated Chicken Weight Measurement and Daily Weight Monitoring

Commercialization completed



Equipment installed in field





Power, Wi-Fi, internet are necessary for installation

15

Chicken Activity and Laser Response Assessment System

- **Chicken activity** is one of important index that the farmer need to observe everyday.
- The **activity algorithm based on density change** was used to quantify the **chicken activity** in the continuous images in real time.
- However, there are **too many factors would effect the chicken activity** such like environmental conditions, chicken age, event (feeding time..), daily routine behaviors, health condition and …
- Therefore, if we want to **make the warning based on chicken activity**, the **big data about activity** should be collected firstly.



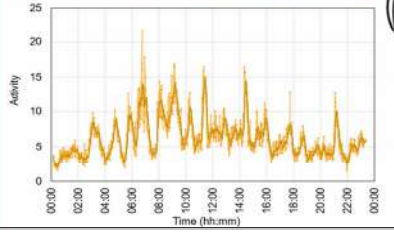

AI algorithm for calculating chicken activity in real time

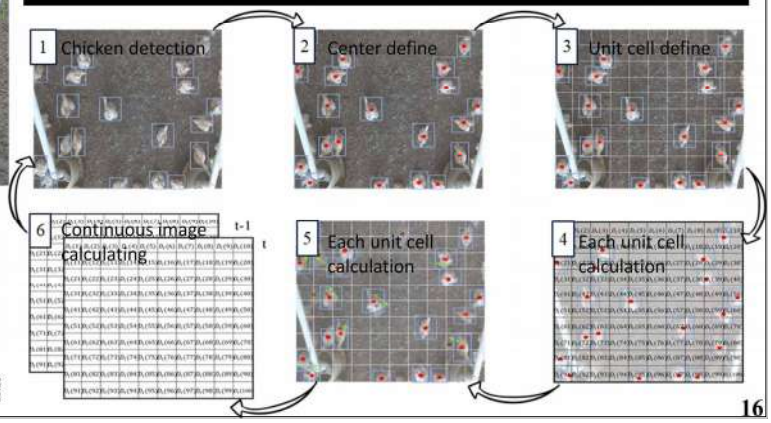

16

Chicken Activity and Laser Response Assessment System

- The **response** means the **chicken activity condition during the stimulation process.**
- **Laser** was used as the **stimulation** for replacing the farmer stimulation.
- Using laser as a stimulation and integrating AI image processing technology to develop a chicken laser response assessment system.



Farmer as a stimulation to poultry

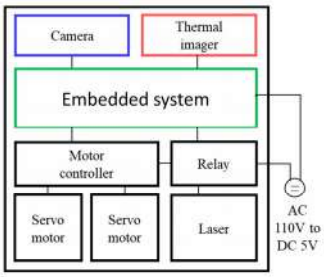

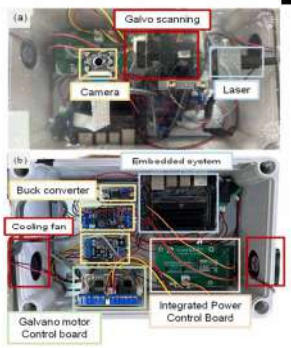

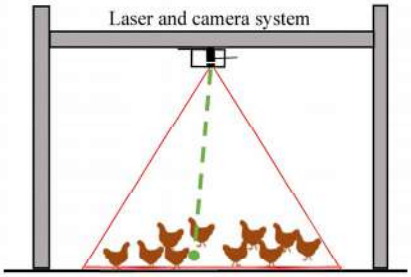

17

Chicken Activity and Laser Response Assessment System

- Laser response tests were carried out up to 3 times a day, with at least 3 hours between each tests.
- For health chicken, the chicken have **RESPONSE to the laser stimulation**. The **activity were increased** at or after laser stimulation process.

Health chicken at 4-6 weeks age



Health chicken at 7-10 weeks age



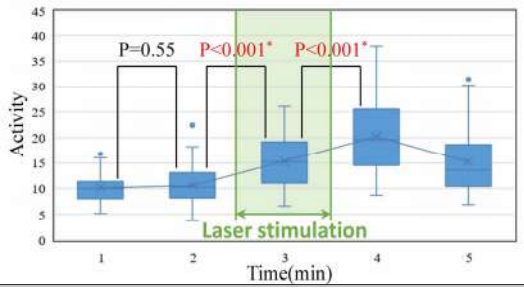

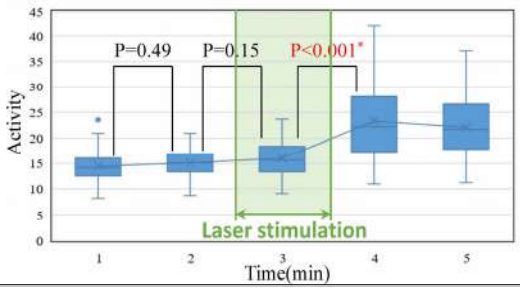

18

Chicken Activity and Laser Response Assessment System

- For **unhealthy chicken** or chicken **on heat stress condition**, these chicken were **not have RESPONSE** to the laser stimulation.
- So far, we have test for **3 months** for health Taiwanese native chicken. With **laser stimulation 3 times a day**, the chickens still have interest to the laser and will **not become habituated**.





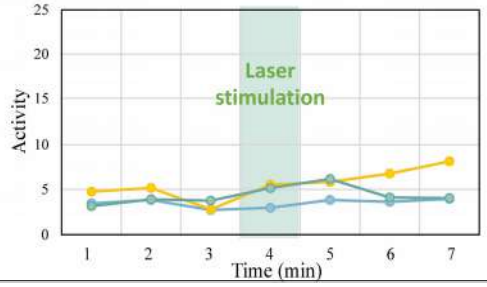

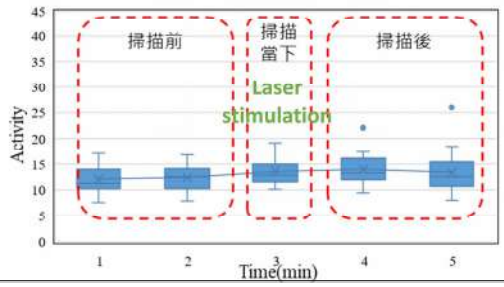

19

Chicken Activity and Laser Response Assessment System

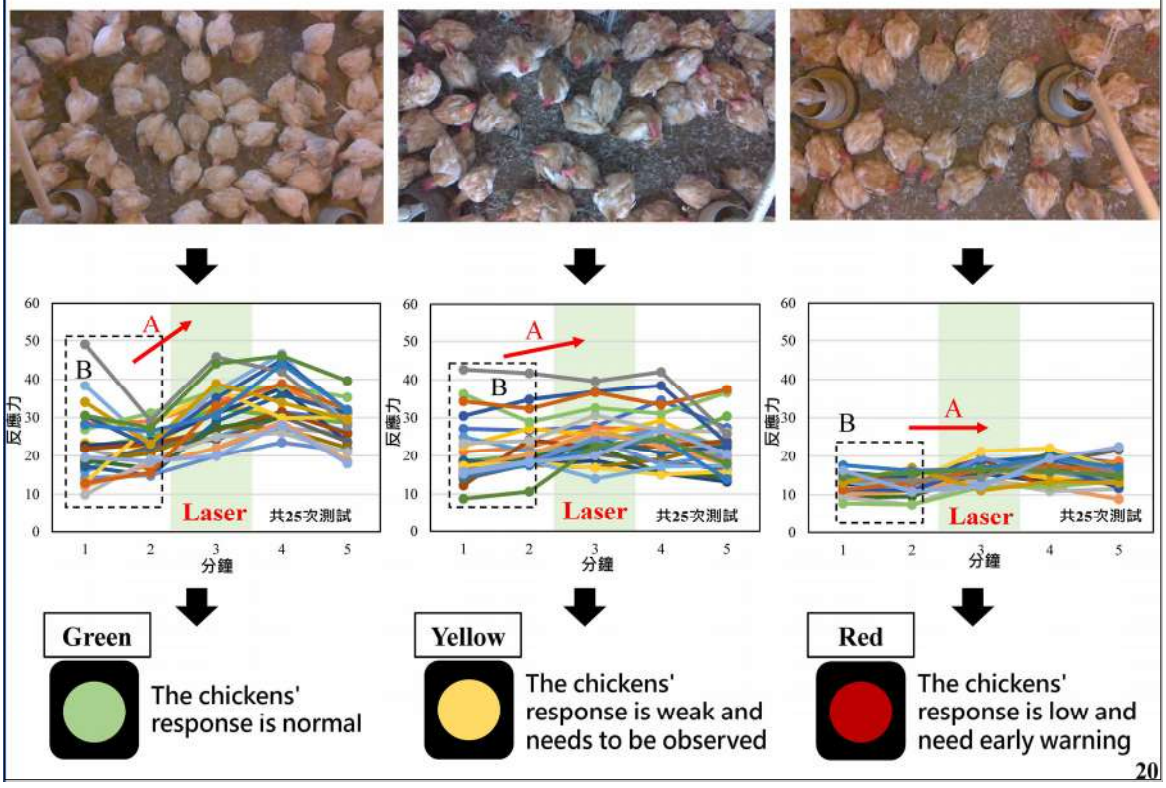

20

Chicken Activity and Laser Response Assessment System

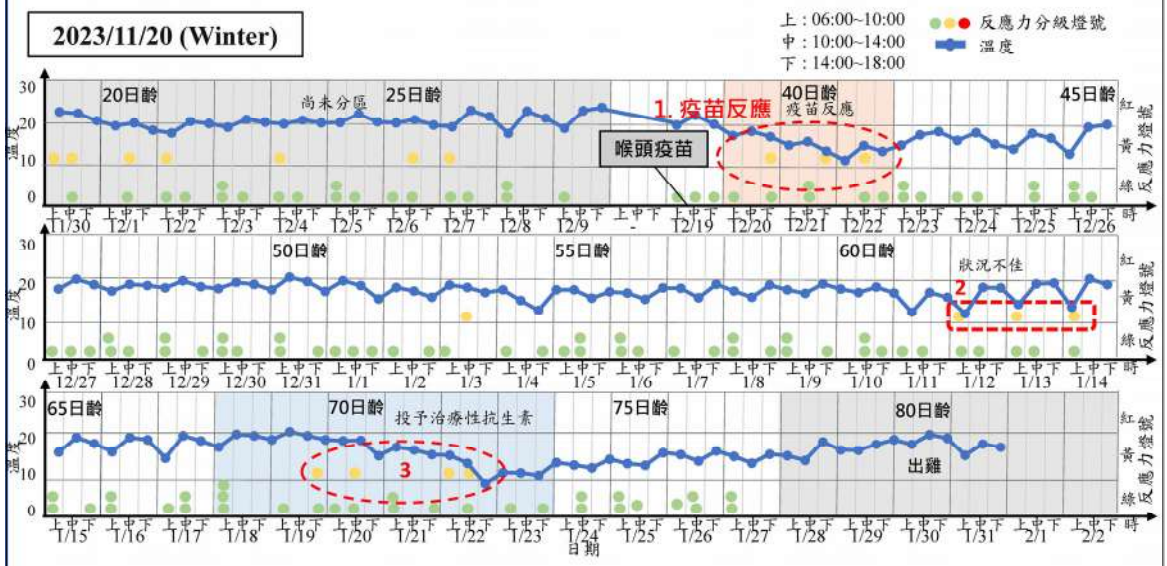

- Long-term testing in commercial poultry houses was consistent with farmers' observations of chicken response.
- This system could effectively and **long-term monitor the chicken's response** and **provide the early warming**.

21

Chicken's comb and eyes identification technologies

- For farmers' daily work, in addition to observing the response of poultry, the **appearance of poultry** is also an important observation indicator.
- Among the appearance of poultry, **combs** and **eyes** are two important points.





- For chicken combs, **uniformity** is an important quantitative indicator.
- If there are some combs that are too dark or too white often means the feeding management problem or the risk of disease.
- For chicken eyes, **abnormal eyes** need to be attended.
- Diseased chickens often have abnormalities in the eyes, and the disease spreads very quickly.
- Due to the **comb and eyes are much smaller objective**, the **high resolution and zoom controllable camera** should be used in the poultry house.

22

Chicken's comb and eyes identification technologies

- In order to achieve the **automatic chicken's comb and eyes monitoring**, the high resolution camera was used to routinely capture the images in the poultry house.
- The deep learning was used to establish the chicken's comb and eyes detection models.

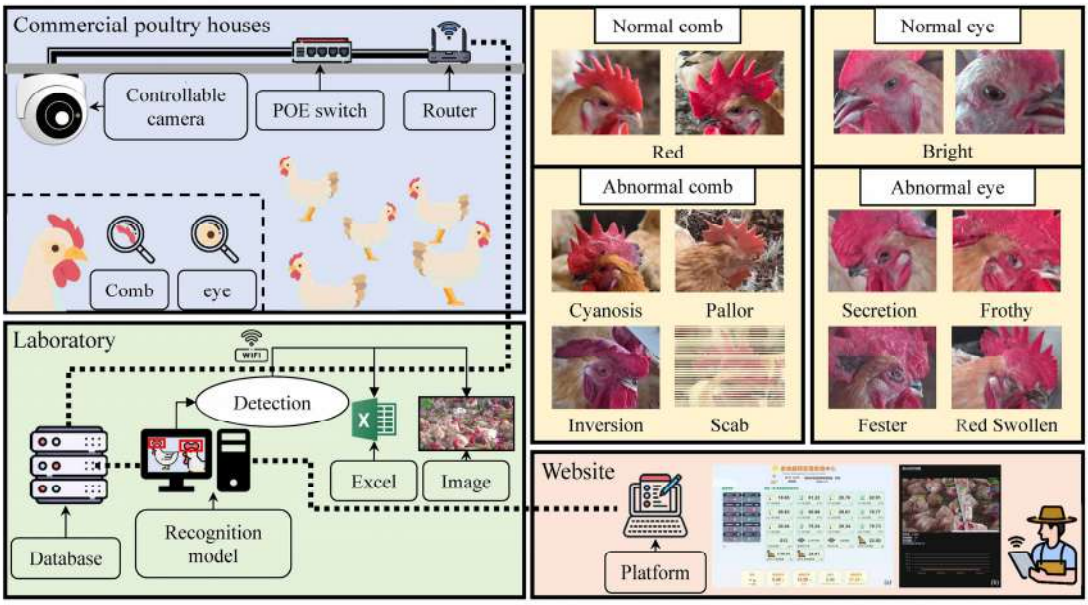

23

Chicken's comb and eyes identification technologies

- Yolo.v7 object detection model was used for the chicken's comb and eyes identification.
- The number of labelled images are 1000 images for both combs and eyes.

Comb AI detection results

	Precision		Recall		F1-score	
	Normal	Ab-normal	Normal	Ab-normal	Normal	Ab-normal
Dataset	0.70		0.69		0.68	
	0.84	0.55	0.75	0.62	0.79	0.57

Eyes AI detection results

	Precision		Recall		F1-score	
	Normal	Ab-normal	Normal	Ab-normal	Normal	Ab-normal
Dataset	0.95		0.83		0.88	
	0.94	0.95	0.83	0.8	0.88	0.88

Comb AI detection results



Eyes AI detection results

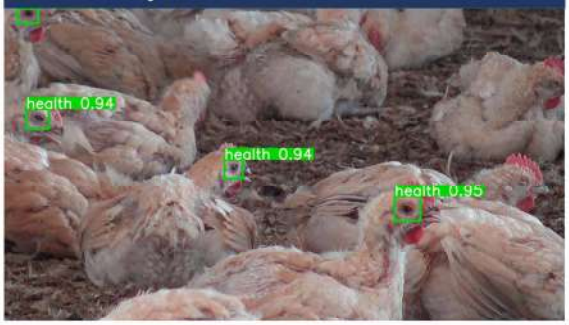

24

Chicken's comb and eyes identification technologies

- The proportions of chickens with comb and eye abnormalities can be monitored over the long term using cameras and deep learning models.

Video: High-Resolution Imaging + AI Comb Recognition



Video: High-Resolution Imaging + AI Eyes Recognition



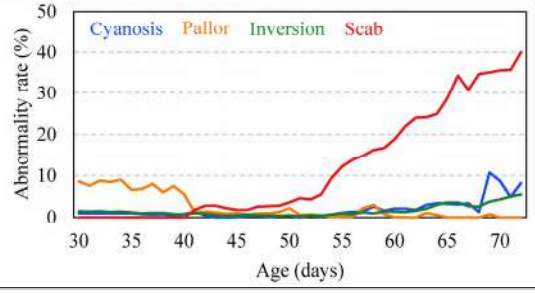

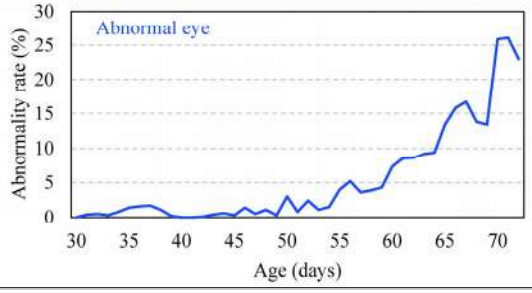

25

Chicken's comb and eyes for early warning

- **Eye abnormalities**: May increase 1–2 days before mortality rises, providing potential early warning.
- **Comb abnormalities**: Follow mortality trends more closely, supporting assessment of current flock health.
- **Field action**: Inspect the house early when abnormality rates rise; check water intake, feed intake, and flock condition.
- **Interpretation**: Consider bird age, disease status, medication, and environmental conditions.

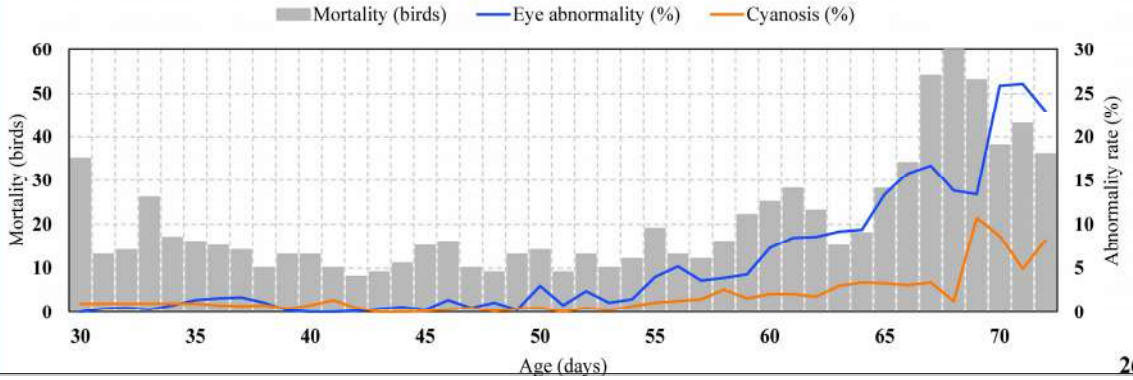

26

Poultry Management and Command Center



Integration with environmental sensing and control system

27

Conclusions and Future works

- With the technology development, **artificial intelligence and automation technology were introduced and applied into the poultry farms.**
- The application of artificial intelligence and automation technology could effectively **save manpower** and **improve poultry production efficiency.**
- The **AI laser bird repellent system** and **AI poultry weight scale** have been **commercialized**, with **160 AI laser bird repellent system** and **150 AI poultry weight scale** sold across **15 countries** worldwide.



Thank you for your attention

28

Oral

Precision Agriculture Machinery and Systems 1 (PA-1)



PA-01

Proceedings of The 12th International Symposium on Machinery and Mechatronics for Agriculture and Biosystems Engineering (ISMAB 2026)
20-24 October 2026, Busan, Republic of Korea

CORN SILK MATURITY RECOGNITION FROM UAV IMAGERY USING YOLO SEGMENTATION AND FUZZY C-MEANS CLUSTERING

Sheng-Wei Chen[1]*, Wu-Yang Sean[1]

[1] Dept. of Bio-industrial Mechatronics Engineering, National Chung Hsing University, Taiwan
*Corresponding Author-- Voice: +886-937-357-175, Email: billchen93825@gmail.com

Abstract: The color of corn silk is an important visual indicator of ear maturity. Traditionally, growers judge the transition from green to brown by inspecting individual plants, which is subjective, labor-intensive, and impractical for large fields, leaving no quantitative record. This study proposes an automated method that recognizes and quantifies corn-silk maturity from unmanned aerial vehicle (UAV) imagery by combining YOLO instance segmentation with fuzzy clustering. 4K aerial images captured over a field with a complex background were sliced into 640 × 640 tiles to preserve small-object detail. A model-assisted, human-in-the-loop annotation strategy was used: 50 polygon-labeled images trained a bootstrap model, after which the CVAT platform pre-annotated subsequent batches for manual correction, iteratively expanding the dataset over successive generations to more than 2,300 annotated tiles. Five training settings and architectures were compared under the same dataset and train/validation partition: YOLOv11m-seg without and with early stopping, YOLOv26m-seg, YOLO v26n-seg, and an RT-DETR Transformer detector. The no-early-stop model reached mAP50 of about 0.80 but overfitted as its validation loss rose in late training; the early-stopping model converged stably at about 140 epochs with box and mask mAP50 near 0.78 and mAP50-95 of about 0.50 and 0.44, without overfitting. The YOLOv26 variants gave comparable metrics but slightly lower recall or stability, and RT-DETR provided only bounding boxes, unsuitable for the downstream color analysis. Considering generalization and the downstream requirement, the early-stopping YOLOv11m-seg model was selected. To determine maturity scores, an interquartile range (IQR) filter was first applied to eliminate illumination outliers caused by highlights and shadows. A 2D hue–saturation (HS) histogram was then extracted as the feature representation and clustered using a fuzzy C-means (FCM) algorithm. The resulting cluster centroids were sorted by hue to establish a linear 0–100% maturity scale. Qualitative field inspection indicated plausible detection and a spatially coherent maturity trend. Nonetheless, the requirement for site-specific tuning of the confidence threshold and score-gain factor motivates the development of an automated retraining pipeline in future work.

Key Words: Smart Agriculture, Corn Silk Maturity, UAV Imagery, Instance Segmentation, Fuzzy C-Means (FCM)

INTRODUCTION

Fresh-market corn is an important economic crop whose market value depends strongly on harvest timing. In waxy corn, which is harvested at the milk-to-dough stage for fresh consumption, delayed harvest causes the kernel pericarp to toughen and the moisture content to decline, degrading the tender, glutinous texture on which eating quality depends. Among the available maturity indicators, the color of corn silk is the most readily observed from RGB imagery. Shortly after pollination, the silk is bright green or pale yellow-green, and it gradually turns brown as the ear fills.

Conventionally, growers judge maturity by inspecting silk color, squeezing the ear tip, and peeling back the husk to check kernel color. This process is subjective, time-consuming, difficult to apply across large fields, and leaves no quantitative record. In recent years, UAV aerial photography combined with deep-learning image recognition has matured and is now widely used for crop phenotyping and growth monitoring (Alzadjali et al., 2021; Du et al., 2024). A UAV carrying a high-resolution camera can survey a field far more rapidly than plant-by-plant inspection; if corn silk can be automatically recognized and its maturity quantified, growers could map the field-wide maturity distribution, plan harvest scheduling, and reduce labor cost; if corn silk can be automatically recognized and its maturity quantified, growers could map the field-wide maturity distribution, plan harvest scheduling, and reduce labor cost.

The objectives of this study are: (1) to build a corn-silk dataset from UAV 4K imagery with a complex field background while reducing annotation cost through model-assisted labeling; (2) to train YOLO instance-segmentation models that segment corn-silk contours under occlusion and uneven illumination, and to compare them against a Transformer-based detector (Zhao et al., 2024) ; (3) to convert the color of segmented regions into a continuous 0–100% maturity score by combining IQR brightness filtering with FCM clustering; and (4) to integrate the pipeline into a system validated in the field.

MATERIALS AND METHODS

Overall Workflow

The overall workflow (Fig. 1) consists of three primary stages: data acquisition, iterative model training, and maturity inference. First, 4K aerial images captured by the UAV are sliced into standardized tiles during data acquisition. Second, an iterative training loop expands the dataset across successive generations using model-assisted annotation, retraining the network to obtain optimal model weights. Finally, the inference and scoring pipeline applies brightness filtering, color feature extraction, and fuzzy clustering to each segmented corn-silk mask, yielding an interpretable 0–100% maturity score.

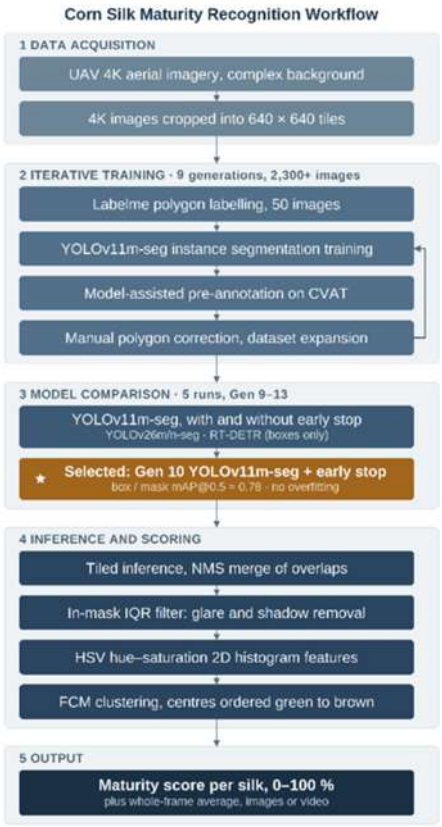

Fig. 1. Overall workflow of the corn-silk maturity recognition pipeline.

Image Acquisition and Slicing Preprocessing

Ultra-high-resolution 4K aerial images (4,000 × 2,250 pixels) were acquired over a field of black waxy corn (Zea mays L. var. ceratina) in central Taiwan during August 2025, using a DJI Mini 3 quadrotor UAV flown at an altitude of 3–5 m above ground level (Fig. 2). The target scenes featured complex agricultural conditions, characterized by overlapping foliage, weed interference, bare soil, and harsh illumination artifacts (e.g., solar specular highlights and deep shadows). Since corn-silk instances constitute small-scale visual targets within a full 4K frame, direct downscaling degrades essential textural details. Conversely, native-resolution processing incurs prohibitive computational costs. To address this trade-off, a slicing-aided inference framework (Akyon et al., 2022; Telceken et al., 2024) was implemented: full-scale 4K images were divided into uniform 640 × 640 tiles during both model training and inference, with redundant detections across tile boundaries resolved via non-maximum suppression (NMS).



Fig. 2. Example UAV 4K image of the field with a complex background.

Model-Assisted Iterative Annotation and Training Pipeline

Because instance segmentation requires dense polygonal boundary annotations, purely manual labeling across extensive agricultural datasets is prohibitively labor-intensive. To overcome this bottleneck, a model-assisted, human-in-the-loop annotation strategy was implemented. Initially, 50 images were manually polygon-labeled using Labelme (Wada, 2018) to train a first-generation bootstrap YOLOv11m-seg model (Khanam and Hussain, 2024; Jocher and Qiu, 2024) at a resolution of 640 × 640 pixels. The resulting weights were deployed onto the CVAT platform (CVAT.ai Corporation, 2018) to automatically pre-annotate subsequent image batches (50–200 tiles), requiring human annotators to only adjust and verify boundary vertices. The refined annotations were progressively merged into the training corpus to retrain subsequent model generations with expanded batch capacities. This iterative loop was executed over nine generations, ultimately yielding a benchmark dataset of over 2,300 verified tiles while drastically reducing labeling overhead. The annotated tiles were split into training and validation subsets at a ratio of approximately 88:12, and the identical split was reused across all five benchmark runs. No independent test set was withheld; the metrics reported in Table 1 are therefore validation metrics.

Training protocols integrated comprehensive spatial and photometric augmentations, including random rotation (±25°), translation (0.1), scaling (0.5), shearing (±5°), perspective distortion (0.0005), horizontal/vertical flips, Mosaic (1.0), MixUp (0.2), Copy-Paste (0.3), and HSV color jitter, utilizing a dropout rate of 0.2 and a batch size of 16. Upon completing dataset expansion at the ninth generation, the dataset was frozen and five training configurations were evaluated on the identical dataset and train/validation partition: (1) Gen-9: YOLOv11m-seg without early stopping, serving as the baseline; (2) Gen-10: YOLOv11m-seg with early stopping (patience = 20 epochs); (3) Gen-11: YOLOv26m-seg (Sapkota et al., 2025); (4) Gen-12: YOLOv26n-seg; and (5) Gen-13: an RT-DETR Transformer-based detector (Zhao et al., 2024). Generation indices run sequentially across the entire training history: generations 1–9 correspond to the model-assisted annotation loop, whereas generations 10–13 introduce no additional data and differ from Gen-9 only in training setting or architecture. Gen-9 and Gen-10 therefore constitute a controlled single-variable comparison of the early-stopping criterion.

Feature Extraction and Maturity Quantification

Although silk color serves as the core determinant of ear maturity, raw in-field RGB pixels are

susceptible to radiometric distortions caused by specular sun glints and ambient leaf shadows. To mitigate these artifacts, segmented silk instances were transformed into the HSV color space. An interquartile-range (IQR) filter was applied along the Value ($\mathbf{V}$) channel: pixels outside the valid luminance interval [Q_1 - 0.30×IQR, Q_3 + 0.33×IQR] (where IQR = Q_3 - Q_1) were discarded as illumination outliers (Fig. 3). From the filtered pixel subset, a joint 2D Hue–Saturation (HS) histogram was extracted using 16 hue bins and 8 saturation bins, each histogram was min–max normalized to [0, 1] and flattened into a 128-dimensional feature vector for downstream clustering. Instances containing fewer than 10 pixels within the mask were excluded from scoring. When fewer than 5 pixels remained after IQR filtering, as may occur for instances lying entirely in deep shadow, the unfiltered pixel set was retained rather than discarding the instance.

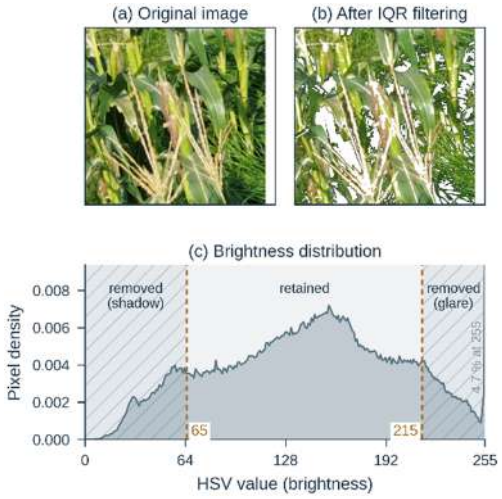

Fig. 3. Illumination outlier removal via IQR filtering: (a) original segmented corn silk, (b) filtered pixel mask with specular reflections and shadows eliminated, and (c) corresponding Value (**V**) channel histogram showing the upper and lower outlier thresholds.

Fuzzy Clustering and Maturity Scoring

The extracted 128-D color feature vectors were grouped using the Fuzzy C-Means (FCM) algorithm (Bezdek, 1981) configured with c = 5 clusters, a weighting exponent m = 2.0, and a fixed random seed for reproducibility. To eliminate the permutation ambiguity of unsupervised clustering, cluster centroids were sorted in descending order of their mean hue value (i.e., from green to brown). Consequently, Cluster 0 represents the earliest vegetative/unripe stage, while Cluster 4 corresponds to fully mature, desiccated silk. The final maturity score $\boldsymbol{S} \in [0, 100]$ for any queried instance is calculated via a fuzzy weighted sum:

$$S = \min(\ 100,\ \alpha \sum_{i=0}^{4} wi\mu i) \tag{1}$$

where μi denotes the fuzzy membership degree for cluster i , **w** = [0, 25, 50, 75, 100] represents the discrete maturity baseline weights, and α is an empirical gain factor. In this study α was set to 1.2, chosen so that the resulting scores were visually consistent with expert field assessment during preliminary trials.

The gain factor was determined by visual agreement rather than quantitative calibration, and was established under a specific field and illumination condition. A systematic calibration of the score scale

against rated field samples, and its generalization across sites, remain future work.

Field-Scale Inference and Deployment Framework

During operational inference, whole-field aerial images are partitioned into 640 × 640 tiles with a 25% overlap to ensure boundary continuity. Predicted instance masks are reprojected onto global image coordinates and consolidated via non-maximum suppression (NMS, **IoU** = 0.5). Each resolved ear instance is rendered with color-coded boundary contours and percentage annotations, yielding spatial distribution maps and aggregate field-wide maturity averages. The current implementation runs on a GPU-accelerated workstation (NVIDIA RTX GPU under WSL2 Linux), sustaining inference latencies of a few tens of milliseconds per tile.

RESULTS & DISCUSSION

Iterative Dataset Expansion and Detection Results

Throughout the nine-generation human-in-the-loop training pipeline, the dataset expanded from an initial 50 images to over 2,300 verified tiles, steadily enhancing the model's feature representation and detection robustness against cluttered field backgrounds. As demonstrated in Fig. 4, the trained segmentation network reliably delineates individual corn-silk contours under severe foliage occlusion, assigning each detected instance a continuous maturity index represented by a color-coded spectrum from green (unripe) to red (fully ripe).



Fig. 4. Corn-silk instance segmentation and maturity scoring on 640 × 640 tiles.

Performance Benchmarking and Convergence Analysis

A comprehensive benchmarking of five training configurations was conducted on the curated dataset of >2,300 annotated tiles (Table 1). As depicted in the convergence profiles (Fig. 5), the selected configuration, Gen-10 (YOLOv11m-seg with early stopping), demonstrated steady learning dynamics, with validation losses stabilizing around epoch 140. Gen-10 yielded balanced performance across both tasks, achieving a box mAP50 and mask mAP50 of approximately 0.78, with corresponding mAP50-95 scores of 0.50 and 0.44. These metrics confirm high boundary delineation precision and strong generalization under complex field conditions.

Table 1. Quantitative evaluation of candidate models on the corn-silk dataset (640 × 640 resolution).

Model	Architecture & training setting	mAP50 (B / M)	mAP50-95 (B / M)	Suitability for FCM color analysis
Gen-9	YOLOv11m-seg (no early stop)	≈ 0.80 / 0.80	≈ 0.50 / 0.45	Yes, but overfits in late training
Gen-10 *	YOLOv11m-seg(early stop, patience=20)	≈ 0.78 / 0.78	≈ 0.50 / 0.44	Yes; stable convergence, selected
Gen-11	YOLOv26m-seg	≈ 0.79 / 0.78	≈ 0.47 / 0.46	Yes; more detections, possible false positives
Gen-12	YOLOv26n-seg (nano)	≈ 0.78 / 0.78	≈ 0.45 / 0.42	Yes; lower recall, suited to edge devices
Gen-13	RT-DETR Transformer (detection)	—	—	No; bounding box only, no mask

* Selected model. Gen-13 (RT-DETR) produces bounding boxes only and was excluded from the segmentation-based comparison; mAP values are therefore not reported.

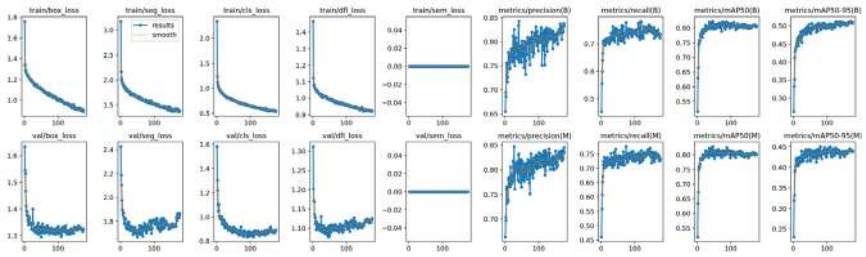

Fig. 5. Training and validation curves of Gen-10 (best, YOLOv11m-seg with early stopping).

In contrast, Gen-9 (the baseline configuration without early stopping) yielded lower training losses, yet its validation loss diverged and exhibited an upward trajectory during later epochs—a distinct manifestation of overfitting (Fig. 6). This divergence illustrates that extending training epochs does not guarantee monotonic performance gains. Since Gen-9 and Gen-10 shared identical data, partitions, dropout (0.2), and augmentation settings, and differed solely in the early-stopping criterion, this comparison isolates early stopping as the decisive factor in preserving generalizability. Model checkpoint selection must therefore be governed by validation convergence rather than by training loss.

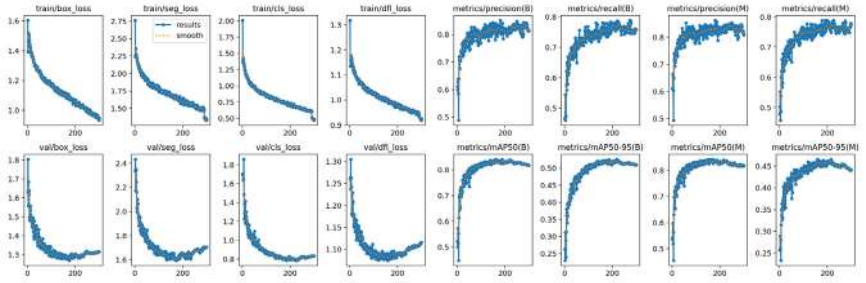

Fig. 6. Training and validation curves of Gen-9 (YOLOv11m-seg without early stopping); validation loss rises in late training, indicating overfitting.

Comparative Trade-offs and Model Selection

Analysis across the YOLO26 variants reveals distinct operational trade-offs. While YOLOv26m-seg (Gen-11) demonstrated competitive detection metrics (mAP50 ≈ 0.78-0.79) alongside higher raw detection counts (~190 vs. ~100 instances per frame), qualitative inspection indicated a noticeable propensity toward false-positive oversegmentation. Conversely, the lightweight YOLOv26n-seg (Gen-12) maximized inference throughput at the cost of sensitivity, yielding a lower recall of 0.65 (~ 0.07 deficit relative to larger variants), rendering it suitable primarily for compute-restricted edge scenarios. RT-DETR (Gen-13) was additionally trained as a Transformer-based reference, but is inherently constrained to bounding-box predictions and was therefore excluded from the quantitative comparison. In the context of downstream maturity quantification, bounding boxes inevitably capture extraneous background noise (e.g., green leaves, soil matrix, and solar glints), thereby corrupting the extracted HSV histograms and distorting FCM maturity assignments. Consequently, synthesizing the quantitative metrics and architectural constraints (Table 1), Gen-10 (YOLOv11m-seg with early stopping) was selected as the optimal deployment backbone: it prevents late-stage overfitting, exhibits stable convergence comparable to YOLOv26m-seg, and outputs high-fidelity polygon masks essential for the integrated IQR–FCM phenotyping pipeline.

Colorimetric Validation and Continuous Ripeness Mapping

By trimming extreme luminance tails along the Value ($\mathbf{V}$) channel, the IQR filtering framework suppresses high-frequency specular glints and deep cast shadows, thereby preserving the genuine chromatic fidelity of corn silk across variable solar angles. Fig. 7 illustrates the resulting color feature topology projected onto the 2D Hue–Saturation ($\mathbf{H}$–$\mathbf{S}$) space, partitioned according to FCM cluster assignments. The scatter distribution exhibits a coherent directional gradient transitioning smoothly from high hue (representing unripe, vegetative green silk) to low hue (representing fully senesced, mature brown silk). Sorting the five cluster centroids along this trajectory establishes an agronomically meaningful baseline, allowing fuzzy membership interpolation to map arbitrary segmented instances into an objective, continuous 0–100% maturity score.

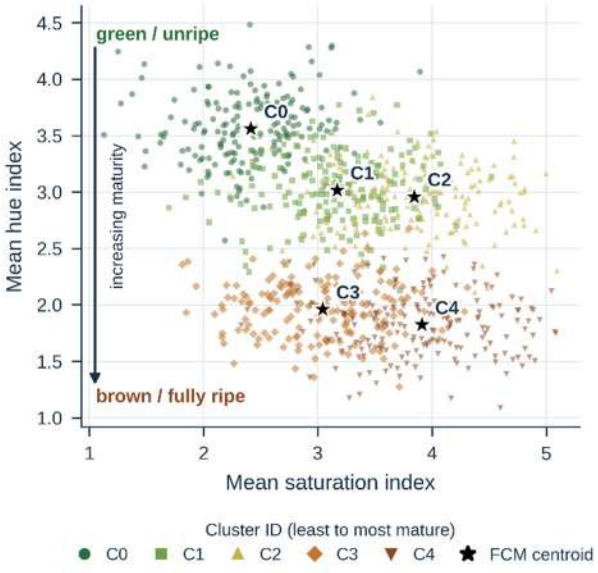

Fig. 7. FCM clustering of corn-silk color features on the hue-saturation plane.

Field-scale validation indicated that the integrated pipeline robustly delineates corn-silk contours amidst severe background clutter, generating spatial maturity progressions visually consistent with growers' assessment of the same plots. However, practical deployment revealed two primary constraints: (1) ambient illumination dynamics (driven by diurnal solar angles and cloud cover) necessitate empirical fine-tuning of the instance confidence threshold, and (2) the colorimetric score-gain factor (α) is expected to require site-specific calibration. Sustaining generalization across multi-temporal and multi-regional deployments therefore demands continual data ingestion and automated model retraining pipelines—the manual overhead of which remains the foremost bottleneck for turnkey agricultural automation.

CONCLUSIONS

In this study, an integrated end-to-end framework was developed for automated corn-silk maturity phenotyping using high-resolution UAV remote sensing. By implementing a human-in-the-loop annotation loop, an extensive agricultural instance-segmentation dataset exceeding 2,300 tiles was curated across nine iterative generations, cutting labeling overhead substantially. Systematic benchmarking demonstrated that YOLOv11m-seg regularized with early stopping (Gen-10) achieved optimal generalized performance (box and mask mAP50 ≈ 0.78), effectively preventing the late-stage overfitting observed in unconstrained training. Bounding-box detectors such as RT-DETR, by contrast, lack the pixel masks required by the downstream colorimetric analysis. Downstream, the combination of IQR Value-channel filtering, 2D HS histogram modeling, and centroid-ordered Fuzzy C-Means (FCM) clustering provided a continuous, illumination-robust 0–100% maturity metric qualitatively examined against field observations. Future research will advance this framework across five key dimensions:

1. **Active Learning Automation**: Transitioning the iterative annotation loop into a fully automated active-learning pipeline to minimize human intervention during domain shifts.
2. **Multi-Environment Benchmarking:** Expanding dataset coverage across diverse geographical sites, diurnal illumination conditions, and commercial maize varieties.
3. **Physiological Calibration:** Correlating the visual 0–100% maturity index with internal quality parameters relevant to waxy corn, such as kernel moisture content, pericarp thickness, and textural firmness.
4. **Edge Deployment:** Quantizing lightweight models (e.g., YOLOv26n-seg) via ONNX-to-TensorRT (FP16/INT8) for real-time, on-drone edge inference on NVIDIA Jetson embedded platforms.
5. **Altitude scaling:** Extending acquisition from the present close-range, low-altitude configuration to survey-altitude flight, and quantifying the resulting trade-off between ground coverage rate and silk-level detectability.

ACKNOWLEDGEMENTS (optional)

The authors thank the Department of Bio-Industrial Mechatronics Engineering, National Chung Hsing University, for support of this research.

The dataset, trained weights, and calibration data are not publicly released as they form part of an ongoing research programme; enquiries may be directed to the corresponding author.

REFERENCES

Akyon, F. C., S. O. Altinuc, and A. Temizel. 2022. Slicing aided hyper inference and fine-tuning for small object detection. In 2022 IEEE Int. Conf. on Image Processing (ICIP), 966-970. Bordeaux, France: IEEE.

Alzadjali, A., M. H. Alali, A. N. Veeranampalayam Sivakumar, J. S. Deogun, S. Scott, J. C. Schnable, and Y. Shi. 2021. Maize tassel detection from UAV imagery using deep learning. Frontiers in Robotics and AI 8: 600410.

Bezdek, J. C. 1981. Pattern Recognition with Fuzzy Objective Function Algorithms. New York, N.Y.: Plenum Press.

CVAT.ai Corporation. 2018. Computer Vision Annotation Tool (CVAT) [Computer software]. Available at: https://github.com/cvat-ai/cvat. Accessed 12 June 2026.

Du, J., J. Li, J. Fan, S. Gu, X. Guo, and C. Zhao. 2024. Detection and identification of tassel states at different maize tasseling stages using UAV imagery and deep learning. Plant Phenomics 6: 0188.

Jocher, G., and J. Qiu. 2024. Ultralytics YOLO11 [Computer software]. Available at: https://github.com/ultralytics/ultralytics. Accessed 12 June 2026.

Khanam, R., and M. Hussain. 2024. YOLOv11: an overview of the key architectural enhancements. arXiv preprint arXiv:2410.17725.

Sapkota, R., R. H. Cheppally, A. Sharda, and M. Karkee. 2025. YOLO26: key architectural enhancements and performance benchmarking for real-time object detection. arXiv preprint arXiv:2509.25164.

Telceken, M., D. Akgun, and S. Kacar. 2024. An evaluation of image slicing and YOLO architectures for object detection in UAV images. Applied Sciences 14(23): 11293.

Wada, K. 2018. labelme: image polygonal annotation with Python [Computer software]. Available at: https://github.com/wkentaro/labelme. Accessed 12 June 2026.

Zhao, Y., W. Lv, S. Xu, J. Wei, G. Wang, Q. Dang, Y. Liu, and J. Chen. 2024. DETRs beat YOLOs on real-time object detection. In 2024 IEEE/CVF Conf. on Computer Vision and Pattern Recognition (CVPR), 16965-16974. Seattle, Wash.: IEEE.

PA-02

Proceedings of The 12th International Symposium on Machinery and Mechatronics for Agriculture and Biosystems Engineering (ISMAB 2026)
20-24 October 2026, Busan, Republic of Korea

SIMULATION-TO-FIELD DEVELOPMENT OF AN AUTONOMOUS GREENHOUSE NAVIGATION AND SENSING ROBOT

Sutan Muhamad Sadam Awal[1,2*], Yamato Sakurai[1], Dong Thanh Pham[3], Koichi Nomura[2], Masaharu Kitano[2], Daisuke Yasutake[3], Muneshi Mitsuoka[3], and Takashi Okayasu[3]

[1] Graduate School of Bioresources and Bioenvironmental Sciences, Kyushu University, Fukuoka, Japan

[2] IoP Collaborative Creation Center, Kochi University, Kochi, Japan

[3] Faculty of Agriculture, Kyushu University, Fukuoka, Japan

*Corresponding Author — Voice: +81-8048727503, Email: sutanmsadoc@gmail.com

Abstract: Autonomous mobile robots for greenhouse crop monitoring must navigate irregular row structures, cope with canopy occlusion and lighting variation, and perform reliable fruit sensing, yet moving such systems directly from concept to field deployment carries a high risk of costly trial-and-error. This study presents a two-stage research program that first validated an autonomous greenhouse sensing robot in a virtual environment and then extended the resulting navigation strategy to a physical robot operating in real greenhouses. In the first stage, a simulation-driven ROS2–Gazebo workflow was developed for an omnidirectional mobile robot integrating LiDAR-based crop-row centering, AprilTag-guided multi-row mission control, and ripeness-specific cherry-tomato counting using PTZ-RGB and front RGB cameras with YOLO instance segmentation, ByteTrack, and canonical-identity-based counting. The workflow was evaluated in a procedurally generated greenhouse with known plant-level fruit distributions across a range of robot speeds (0.2–1.0 m/s). In the second stage, the navigation concept validated in simulation was carried over to a physical four-wheel mecanum-drive robot, but the visual AprilTag mission logic was replaced with RFID-tag-triggered state-transition control, since radio-based tag detection is inherently more robust than a printed visual fiducial marker, which is prone to soiling, dust, and moisture on its surface under real greenhouse conditions. This RFID-triggered method was integrated with LiDAR–IMU fusion SLAM (LIO-SAM) and Pure-Pursuit path following, yielding a lightweight, map-free, event-driven control scheme suited to real, dynamically changing greenhouse rows. Field trials were conducted in commercial vinyl greenhouses under both non-cultivation and cultivation conditions. In simulation, the AprilTag-guided mission reproduced the intended multi-row route with mean cross-track errors of 0.045–0.056 m and RMSE below 0.10 m, and fruit counting recovered 90.1% of the ground-truth count (F1 = 0.898) at 0.2 m/s, with accuracy declining at higher speeds because of reduced observation time and canopy occlusion. In the physical implementation, the RFID-triggered system achieved a 100% travel success rate over repeated in-row and inter-row trials, a mean cross-track error of a few centimeters to 10 cm, and a return-to-start RMSE of 3.4 cm, confirming that the localization strategy identified as most robust in simulation-scale testing also performed reliably under real greenhouse conditions. Together, these two stages demonstrate the value of a simulation-first approach: the virtual environment enabled early, low-

cost validation of the row-centering and multi-row navigation logic and systematic characterization of the speed–accuracy trade-off in fruit sensing, before any physical hardware or crops were put at risk. When field conditions later required replacing the vision-based AprilTag trigger with a more robust RFID-based one — since visual fiducials are prone to soiling and moisture in real greenhouses — the navigation strategy and operating parameters validated in simulation carried over directly, allowing the physical system to achieve a 100% travel success rate and centimeter-level accuracy while substantially shortening the path from concept to reliable field deployment. Future work will integrate the vision-based fruit-sensing pipeline validated in simulation with the field-proven RFID-SLAM navigation system and extend field trials to greenhouses during active cultivation.

Key Words: Autonomous greenhouse robot; Simulation-to-field validation; RFID-triggered navigation; SLAM (LIO-SAM); Fruit sensing and counting

INTRODUCTION

Japan's rapidly aging, shrinking farming population and rising input costs have pushed policy and industry toward agricultural robotics, accelerated by Japan's 2024 Act on Promotion of Smart Agriculture Technology Utilization. Robots that can navigate and monitor crops autonomously inside enclosed, structured environments such as greenhouses are especially attractive for reducing labor while supporting higher-value production. Existing greenhouse navigation approaches, however, either assume a static, pre-built map that is repeatedly violated as plants grow — e.g., Cartographer/DWA (Jiang et al., 2022) or Gmapping/AMCL/A* (Liu et al., 2024) — or rely on visual landmarks and markers, such as stereo-camera segmentation of structural landmarks (Tsiakas et al., 2023) or fiducial tags like AprilTag, that are themselves vulnerable to soiling, dust, and condensation in a working greenhouse.

Physically iterating on navigation and perception strategies in a working greenhouse is costly and slow, so this study used a ROS 2–Gazebo simulation platform to develop and diagnose a navigation-and-sensing framework before field deployment, then carried the validated concept over to a physical robot. In the first stage, an integrated workflow combining LiDAR-based row-centering, AprilTag-guided multi-row mission control, and YOLO/ByteTrack-based fruit counting were developed and evaluated in a procedurally generated virtual greenhouse (Awal et al., 2026). In the second stage, this navigation concept — including the core Jetson-based, LiDAR-equipped, four-wheel Mecanum-drive platform — was carried over to a physical robot and field-tested in commercial greenhouses, with the AprilTag mission trigger replaced by RFID tags for robustness against real-world marker soiling; at this stage, field trials evaluated navigation performance only, since integration of the PTZ-camera-based plant-sensing system validated in simulation onto the physical robot remains ongoing. The objectives were to (1) identify, in simulation, a practical operating-speed range balancing navigation accuracy and fruit-counting reliability, (2) select, through controlled comparison, the self-localization method best suited to a real, dynamically changing greenhouse, and (3) verify that the resulting RFID-triggered navigation system reproduces, in the field, the accuracy established in simulation.

MATERIALS AND METHODS

Stage 1: Simulation-Based Navigation and Sensing Framework

Robot Platform and Simulation Environment

The simulation was implemented in ROS 2 Humble and Gazebo Classic 11.10.2, executed on an Ubuntu 22.04 desktop workstation, which sustained a simulation update rate of 25–30 FPS throughout the trials. An omnidirectional mobile robot was modeled in Fusion 360 and converted to URDF, comprising a Jetson Orin Nano control computer — specified as the intended onboard compute platform for physical deployment — a 3D LiDAR, a pan-tilt-zoom (PTZ) RGB camera on a height-adjustable slider, and a fixed front RGB camera. Four Mecanum wheels were included for mechanical fidelity, while base motion was implemented through a planar-motion Gazebo plugin. A procedurally generated greenhouse, built using a tomato-farm simulation framework, produced six 10-m crop rows containing 126 cherry-tomato plants with known, plant-level ripeness and fruit-count ground truth (1320 fruits: 62.7% red, 25.5% orange, 11.8% green), providing a heterogeneous but reproducible benchmark for evaluating navigation and perception.

Navigation and Mission Control

A LiDAR-based lateral controller kept the robot centered within each crop-row aisle during forward and backward traversal, while odometry-based heading control stabilized orientation. AprilTags placed at predefined in-row and row-transition positions triggered the mission state machine — forward traversal, PTZ reorientation, backward traversal, lateral row transition, and mission termination — allowing a complete multi-row mission to be executed without a pre-built occupancy map.

Fruit Perception and Counting

Fruit sensing built on the YOLO family of real-time object detectors, using the latest YOLOv11 instance-segmentation variant on the PTZ and front-camera streams to classify green, orange, and red cherry tomatoes, with ByteTrack maintaining fruit identity across frames and a canonical-identity layer preventing duplicate counts after temporary tracking loss.

Simulation Evaluation

Two evaluations were performed. (1) The full AprilTag-guided multi-row mission was executed at five commanded speeds (0.2, 0.4, 0.6, 0.8, and 1.0 m/s), each repeated three times, and compared against a manually driven ground-truth trajectory using cross-track MAE, RMSE, and 95th-percentile error. (2) Class-wise fruit counting was evaluated at the same five speeds against manual plant-level ground truth, using recovery rate and count-level precision, recall, and F1-score.

Stage 2: Physical Robot Field Validation

Robot Platform and Sensor Configuration

The physical robot inherited the core platform architecture validated in simulation — a Jetson (NVIDIA) control computer and a four-wheel independent-drive Mecanum base (A4WD3, Lynxmotion) providing the same omnidirectional maneuverability in narrow aisles (Fig. 1) — and

added a Teensy 4.0 motor-control microcontroller, a 3D LiDAR with built-in IMU (Livox Mid-360), and a UHF-band passive RFID reader and tag set (TOPPAN Edge TF-AMI2450N-AT09/RS; ~10–20 cm read range) in place of the AprilTag markers used in simulation. RFID was adopted for the field system specifically because a passive radio tag is not subject to the soiling, dust, and moisture that would progressively degrade a printed visual marker under continuous greenhouse operation, while remaining low-cost and simple to install along a crop row. At this stage, the physical platform was configured for navigation only, without an onboard PTZ camera; integrating the PTZ-camera-based plant-sensing system validated in simulation onto the physical robot is an ongoing part of this research program. All processing ran onboard the Jetson under ROS 2, with LiDAR processing, state-transition control, and path-following control coupled through asynchronous communication.

Self-Localization: Method Selection

Because greenhouse SLAM must tolerate frequent appearance change from plant growth and lighting, two LiDAR-IMU fusion methods were compared using identical recorded sensor data (rosbag2 playback): LIO-SAM, which uses factor-graph optimization (Shan et al., 2020), and FAST-LIO, based on a computationally lighter iterated Extended Kalman Filter (Xu and Zhang, 2021). The comparison, conducted in two greenhouses (cultivated and non-cultivated) at a commercial farm, evaluated straight-line accuracy, long-distance (40 m loop) cumulative error, speed-dependent accuracy, CPU/memory load, and sensitivity to sunlight condition.

Path Generation and Following Control

The current position (from the selected SLAM method) and the coordinate of the detected RFID tag were used to generate a straight-line path via ROS 2's tf2 library, followed using Pure-Pursuit control (Coulter, 1992). The controller computes the required curvature κ toward a look-ahead point at distance Ld and angle θ:

$$\kappa = \frac{2 \sin \theta}{L_d} \tag{1}$$

and the resulting angular-velocity command is

$$\omega = v\kappa \tag{2}$$

where v is the commanded travel speed. State transitions between path generation, travel, posture correction (PID-controlled row alignment), and row-completion judgment were managed with ROS 2's SMACH state-machine library, and RFID tag metadata (row ID, tag type, coordinates) were served from a local MongoDB instance on the Jetson.

Field Experiments

Three field evaluations were conducted. (1) An indoor 20-m straight-path Pure-Pursuit test (Kyushu University, Ito campus) at 1.0 m/s and a fixed look-ahead distance of 0.8 m, over 10 trials, evaluated cross-track error (XTE). (2) The LIO-SAM/FAST-LIO comparison described above. (3) A full RFID-triggered navigation test in a non-cultivation greenhouse (Welzo Co., Imazu farm), with

10 trials, evaluated XTE, mission success rate, and return-to-start accuracy against a fixed reference marker.

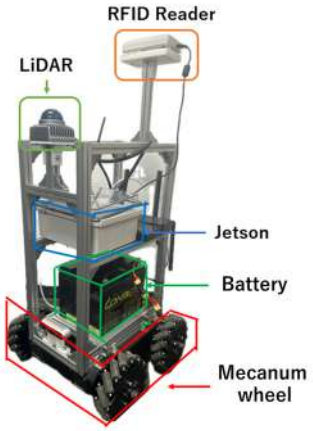

Fig. 1 The physical robot used in Stage 2, built on the Jetson-controlled, four-wheel Mecanum-drive platform first validated in the Stage 1 simulation model.

RESULTS & DISCUSSION

Simulation Results

In the AprilTag-guided multi-row mission, mean cross-track error remained narrow across all tested speeds (0.045–0.056 m; RMSE below 0.10 m), showing that increasing commanded speed did not substantially alter the geometric path followed. Fruit counting was far more speed-sensitive: at 0.2 m/s the system recovered 90.1% of the ground-truth fruit count with a count-level F1-score of 0.898, but performance declined markedly above 0.4 m/s because of reduced per-fruit observation time, canopy occlusion, and less stable temporal association. This asymmetry — stable navigation but speed-limited perception — indicated that 0.2–0.4 m/s was the practical operating range for combined navigation-and-sensing missions, a constraint that directly informed the operating speeds used in field testing.

Self-Localization Method Selection

LIO-SAM maintained stable localization accuracy in both cultivated and non-cultivated greenhouse conditions, with long-distance (40 m) return error of about 3–4 cm, whereas FAST-LIO's error grew to more than 10 cm in the non-cultivated field and at high travel speed, although FAST-LIO used less CPU and memory. LIO-SAM was therefore selected for the field system, prioritizing accuracy and robustness to canopy change over computational cost — consistent with the simulation-stage finding that navigation stability, not raw processing speed, was the limiting factor for reliable operation.

Field Validation

The indoor Pure-Pursuit test achieved a mean XTE of 3.5 cm (maximum 14.5 cm, RMSE below 0.10 m), confirming stable straight-line tracking on the Mecanum-wheel base. In the full RFID-triggered greenhouse test, all 10 trials completed successfully (100% success rate), mean XTE across rows ranged from 3.2–9.8 cm, and the robot returned to its starting position with an RMSE of 3.4 cm (Fig. 2). These field results are consistent in magnitude with the sub-decimeter accuracy obtained in simulation, directly supporting the central premise of the two-stage approach: a navigation strategy diagnosed and tuned virtually — including the choice to prioritize a robust, factor-graph SLAM method and a simple, map-free event trigger — transferred successfully to a physical greenhouse without a large increase in tracking error. The one deliberate departure from the simulated design, replacing AprilTag with RFID as the mission trigger, was supported by the field results: RFID detection was unaffected by the greenhouse's dust and humidity, whereas a printed AprilTag under the same conditions would be expected to degrade.

Continuity and Limitations

The field trials reported here were conducted in a non-cultivation greenhouse to isolate control-logic behavior from visual and structural disturbance, while the simulation stage already showed that the selected localization method (LIO-SAM) remains accurate under dense-canopy conditions (cultivated greenhouse). Because RFID-based state transition is not a vision-based process, it is expected to be similarly unaffected by canopy presence, so combining these two results supports feasibility for full-cultivation operation, which remains to be directly verified. Likewise, the PTZ-camera-based, vision-based fruit-counting pipeline validated in simulation has not yet been mounted on the physical robot or integrated with the field-proven RFID-SLAM navigation system; doing so, and re-measuring counting accuracy under real illumination, plant motion, and marker-free navigation, is the immediate next step in this research program.

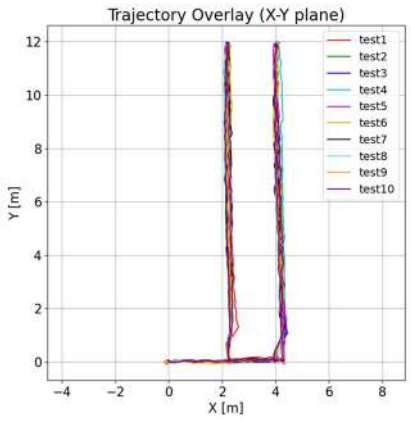

Fig. 2 Recorded field trajectory from the RFID-triggered navigation test, showing the robot's realized path relative to the target crop rows.

CONCLUSIONS

This study developed and field-validated an autonomous greenhouse sensing and navigation robot through a two-stage, simulation-to-real research program. (1) In simulation, an integrated ROS 2–Gazebo workflow combining LiDAR row-centering, AprilTag-guided mission control, and YOLO/ByteTrack fruit counting achieved sub-decimeter navigation accuracy across all tested speeds and identified 0.2–0.4 m/s as the practical operating range for reliable fruit counting. (2) A controlled comparison showed LIO-SAM to be the more robust self-localization method for a real, dynamically changing greenhouse, and this choice, carried over from the simulation-informed design process, enabled a physical, RFID-tag-triggered, map-free navigation system to achieve a 100% mission success rate, cross-track error of a few centimeters to 10 cm, and 3.4 cm return-to-start accuracy in field trials. (3) Replacing the simulated AprilTag trigger with RFID tags — motivated by RFID's robustness to the soiling and moisture that degrade a printed visual marker in a working greenhouse — preserved the accuracy established in simulation while removing a known failure mode of vision-based triggering. Together, these results demonstrate that a simulation-first development approach can shorten the path from concept to reliable field deployment for greenhouse robots. Future work will extend field trials to active cultivation periods and integrate the vision-based fruit-sensing pipeline validated in simulation with the field-proven RFID-SLAM navigation system to realize a single, combined navigation-and-sensing platform.

ACKNOWLEDGEMENTS

This work was supported by Cabinet Office grant in aid “Evolution to Society 5.0 Agriculture Driven by IoP (Internet of Plants),” and the joint-research project with welzo Co. Ltd. Japan.

REFERENCES

Awal, S.M.S., Sakurai, Y., Pham, D.T., Nomura, K., Kitano, M., Yasutake, D., Mitsuoka, M., Okayasu, T., 2026. Development of a plant sensing robot using virtual space and evaluation of its accuracy. Smart Agricultural Technology 15, 102429. https://doi.org/10.1016/j.atech.2026.102429

Coulter, R. C. 1992. Implementation of the Pure Pursuit path tracking algorithm. Tech. Rep. CMU-RI-TR-92-01. Pittsburgh, Pa.: Carnegie Mellon University, The Robotics Institute.

Jiang, S., S. Wang, Z. Yi, M. Zhang, and X. Lv. 2022. Autonomous navigation system of greenhouse mobile robot based on 3D Lidar and 2D Lidar SLAM. Frontiers in Plant Science 13: 815218.

Liu, K., J. Yu, Z. Huang, L. Liu, and Y. Shi. 2024. Autonomous navigation system for greenhouse tomato picking robots based on laser SLAM. Alexandria Engineering Journal 100: 208-219.

Shan, T., B. Englot, D. Meyers, W. Wang, C. Ratti, and D. Rus. 2020. LIO-SAM: Tightly-coupled lidar inertial odometry via smoothing and mapping. In Proc. 2020 IEEE/RSJ Int. Conf. on Intelligent Robots and Systems (IROS), 5135-5142.

Tsiakas, K., A. Papadimitriou, E. M. Pechlivani, D. Giakoumis, N. Frangakis, A. Gasteratos, and D. Tzovaras. 2023. An autonomous navigation framework for holonomic mobile robots in confined agricultural environments. Robotics 12(6): 146.

Xu, W., and F. Zhang. 2021. FAST-LIO: A fast, robust LiDAR-inertial odometry package by tightly-coupled iterated Kalman filter. IEEE Robotics and Automation Letters 6(2): 3317-3324.

PA-03

Proceedings of The 12th International Symposium on Machinery and Mechatronics for Agriculture and Biosystems Engineering (ISMAB 2026)
20-24 October 2026, Busan, Republic of Korea

ARUCO-BASED INDOOR LOCALIZATION AND HOVERING CONTROL FOR A QUADROTOR UAV

Yu-Tse Lee, Chung-Liang Chang*

Biomechatronics Engineering Department,
National Pingtung University of Science and Technology
*Corresponding Author-- Voice: +886-8-7703202 ext. 7586,
Email: chungliang@mail.npust.edu.tw

Abstract: Indoor flight environments often suffer from degraded or unavailable Global Navigation Satellite System (GNSS) signals, which can result in progressive horizontal position drift during prolonged unmanned aerial vehicle (UAV) hovering. To address this issue, this study proposes an indoor position-holding method that integrates ArUco-based visual localization with flight control for a quadrotor UAV operating in GNSS-denied environments. The experimental platform consists of a quadrotor equipped with a Cube Orange flight controller running the PX4 autopilot. A baseline hovering framework is first established by integrating inertial measurements, downward-facing optical flow, and range measurements to provide state estimation and flight stabilization without GNSS. To further compensate for horizontal position drift, a downward-facing camera is used to detect an ArUco marker placed at the target hovering location. Marker detection and relative pose estimation are performed in real time on an NVIDIA Jetson AGX, enabling the horizontal displacement of the UAV relative to the target position to be estimated. Based on the error between the desired and estimated positions, the Jetson AGX computes corrective motion commands and transmits them to the PX4 flight controller. The flight controller then executes the corresponding attitude and motion control commands to compensate for accumulated horizontal drift. Experimental evaluations compare hovering performance with and without ArUco-based visual position correction. Horizontal position error, root-mean-square error (RMSE), maximum drift, and final position deviation are used as quantitative performance metrics to evaluate the effectiveness of the proposed visual feedback correction mechanism. The proposed framework provides a practical vision-aided position correction approach for improving the stability and hovering accuracy of UAVs in GNSS-denied indoor environments.

Key Words: Unmanned aerial vehicle (UAV), ArUco, Indoor Localization, Optical flow, Hovering control, Visual localization.

PA-04

Proceedings of The 12th International Symposium on Machinery and Mechatronics for Agriculture and Biosystems Engineering (ISMAB 2026)
20-24 October 2026, Busan, Republic of Korea

PERFORMANCE EVALUATION AND IMPROVEMENT POTENTIAL OF A TOMATO DE-LEAFING ROBOT USING A MAIN STEM-BASED APPROACH

Tokihiro FUKATSU[1*], Masakazu KASHINO[1], Hideto KUROSAKI[1]

[1]Institute of Agricultural Machinery, National Agriculture and Food Research Organization, 1-31-1 Kannondai, Tsukuba, Ibaraki 305-0856, Japan
*Corresponding Author-- Voice: +81-29-838-8966, Email: fukatsu.tokihiro604@naro.go.jp

Abstract:
We previously proposed a main stem-based approach for robotic crop management and have since developed a tomato de-leafing robot based on this concept. In this approach, the robot does not need to precisely detect and directly approach each target petiole. Instead, the robot first approaches the main stem, which is relatively easy to detect. The end-effector then moves along the stem and continuously removes multiple lower leaves. This approach is expected to simplify the de-leafing operation under dense foliage conditions. The developed robot was tested under practical greenhouse conditions. The average processing time was approximately 66 s per plant, and the average removal rate of the target lower leaves was approximately 72%. Although these results demonstrated the feasibility of the system, the current performance is still insufficient for practical use, and further improvement is required.
In this study, we analyzed the practical potential of the main stem-based approach from several viewpoints. First, image data collected during the greenhouse tests were used to evaluate the visibility and accessibility of the main stem and petiole bases. The analysis showed that the main stem was more visible and accessible than the target petiole bases, indicating an advantage of the proposed main stem-based approach. Second, the processing time of the prototype robot was analyzed for each robot motion, and the major factors limiting the processing speed were identified. Finally, we examined possible ways to improve the performance, such as faster robot motion, shorter approach paths, and selection of a suitable approach direction based on the positions of the target leaves.
These analyses indicated that the main stem-based approach has practical advantages under conditions where individual petiole bases are difficult to observe or access directly. They also showed that a substantial part of the current processing time is spent on approach, repositioning, and retreat motions rather than on the actual cutting operation. Therefore, the processing time may be reduced without greatly decreasing the leaf-removal performance by improving the robot motion and selecting a suitable approach direction based on the positions of the target leaves. Based on these results, we discuss the technical challenges and future developments required for practical tomato de-leafing.

Key Words: Tomato, De-leafing Robot, Main Stem-based Approach, Greenhouse Horticulture, Agricultural Robotics

INTRODUCTION

Large-scale greenhouse tomato production is highly labor-intensive. Some production systems require more than 2,000 h of labor per 10 a, much higher than for rice production (Fig. 1, Aichi, 1995; MAFF, 2012). Harvesting accounts for the largest proportion of labor time, typically about 30–40%, followed by de-leafing at approximately 10–15% (Kurosaki et al., 2014). Many cultivation management tasks are still performed manually, and robotic technologies are therefore needed to reduce labor requirements and improve production efficiency.

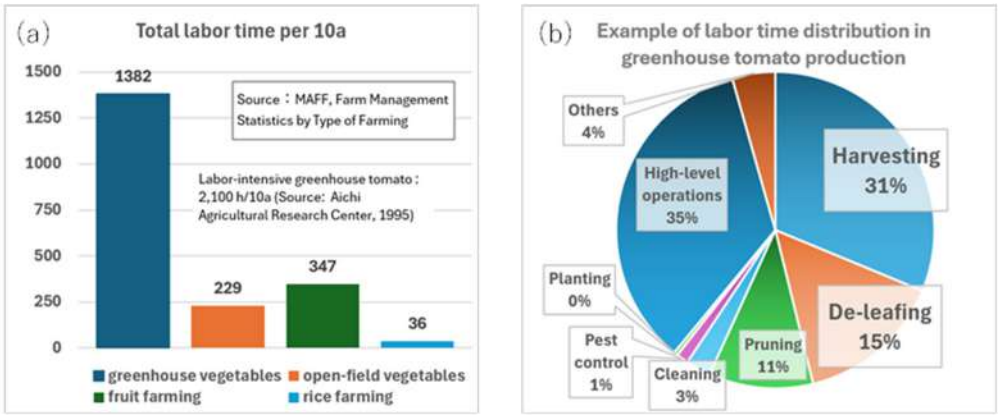

Fig.1 Labor requirements: (a) total labor time for different types of crop production and (b) breakdown of labor time in greenhouse tomato production.

Agricultural robot research has mainly focused on harvesting, one of the most labor-intensive operations (Zhou et al., 2022). De-leafing is also an important target for automation, but relatively few robotic systems have been developed for this task. Robotic de-leafing can directly reduce the labor requirement for crop management. In addition, removing lower leaves improves the visibility of fruits and the accessibility of robot arms. Therefore, de-leafing may also support other robotic operations, such as harvesting.

Many conventional crop-management robots use a direct-approach method, in which the robot detects individual targets, such as petioles, and moves the end-effector directly to each target. However, this method has several limitations under practical greenhouse conditions. In dense foliage, the base of a target petiole may be hidden by surrounding leaves or fruits. Even when the target can be detected, nearby plant parts may block end-effector access.

To address these limitations, we previously proposed a main stem-based approach (Fukatsu et al., 2023), which uses the main stem of a tomato plant as a reference for robotic operations (Fig. 2). In this approach, the robot first detects and approaches the main stem instead of

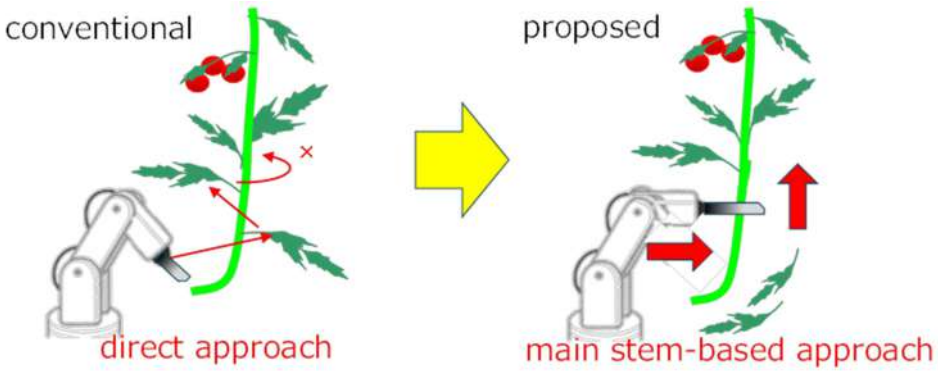

Fig.2 Concept of the main stem-based approach.

directly approaching each target petiole. The end-effector then moves along the main stem and continuously removes multiple lower leaves. To realize this approach, we developed a main-stem recognition method, a hedge-trimmer-based end-effector for continuously cutting multiple lower leaves, and a robot control method for following the main stem. These components were integrated into a prototype tomato de-leafing robot.
In this study, we investigate whether the main stem-based approach can be a practical method for robotic tomato de-leafing. First, we present the current performance of the prototype. We then analyze practical greenhouse conditions and robot motions to assess the practical advantages of the main stem-based approach compared with the conventional direct-approach method. Finally, we examine the potential for further performance improvement and discuss the technical challenges required for practical application.

MAIN STEM-BASED APPROACH AND DEVELOPED SYSTEM

MAIN STEM-BASED APPROACH

In the conventional direct-approach method, the robot first detects a target petiole and estimates its cutting position. The end-effector then moves to the position and cuts the petiole. Therefore, detection, position estimation, approach, and cutting must be performed for each target petiole. In contrast, in the main stem-based approach (Fukatsu et al., 2023), the robot first detects the main stem of the target plant and moves the end-effector toward it. The end-effector then moves along the main stem, using the stem as a guide, and continuously cuts multiple petioles along its path.
This approach has three main features. First, unlike the conventional direct-approach method, it does not require detection of each individual petiole or estimation of its cutting position. Second, multiple lower leaves can be continuously removed during a single stem-following motion. Third, the system is less affected by position errors in image-based recognition and deformation of the plant caused by physical contact. This is because the plant's own main stem is used as a reference for the robot operation.

DEVELOPED TOMATO DE-LEAFING ROBOT

To evaluate the proposed main stem-based approach, we developed the prototype robot shown in Fig. 3. The robot consists of a mobile platform, a 6-DOF robot arm, a depth camera,

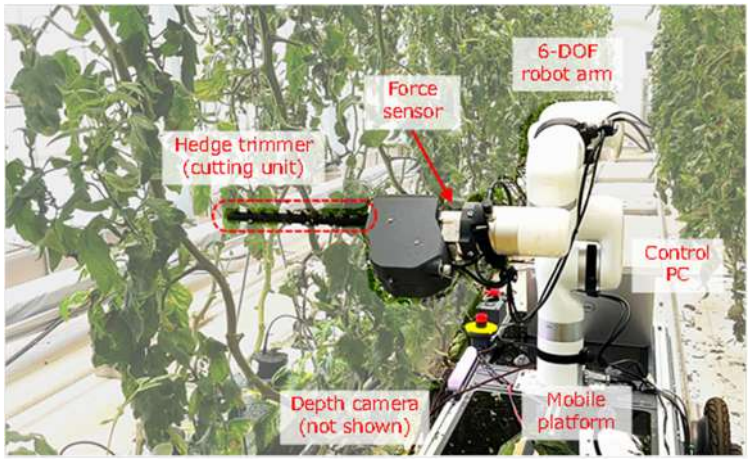

Fig.3 Prototype tomato de-leafing robot.

a force sensor, a hedge-trimmer-based end-effector, and a control computer. The prototype incorporates three key technologies for realizing the proposed approach. First, a main-stem recognition method was developed using depth information and deep-learning-based image processing. The position and shape of the main stem are estimated by combining the recognition results with geometric processing. This method can estimate the complete shape of the main stem even when it is partially occluded by leaves and is detected as separate segments. Second, a hedge-trimmer-based end-effector was developed to continuously cut multiple petioles while preventing accidental cutting of the main stem. The slit width is designed so that only the petioles can reach the reciprocating blades, while the main stem is kept away from the blades. Third, force-feedback control was developed to make the end-effector follow the main stem according to the reaction force from the stem. This allows stable tracking even when the stem deforms during operation or is naturally curved. For details of the force-feedback control method, see the paper by Kashino et al. in these proceedings.

CURRENT PERFORMANCE OF THE PROTOTYPE

TEST CONDITIONS

A continuous de-leafing test was conducted under practical greenhouse conditions using the developed prototype robot. The test was carried out from May to June 2025 in a high-roof greenhouse at our research institute in Tsukuba, Ibaraki, Japan. The experiments were conducted using the large-fruited tomato cultivar ‘Momotaro Hope’ grown under a long-term high-wire cultivation system. The plants were grown in rows on rockwool slabs and trained by wrapping the main stems around support strings. The spacing between plants processed by the robot was approximately 50 cm.

The robot operated in the following sequence: (1) moving the mobile platform to the target plant, (2) image acquisition, (3) main-stem recognition, (4) approaching the main stem with the end-effector, (5) de-leafing on one side of the stem, (6) moving to the opposite side, (7) de-leafing on the opposite side, and (8) retracting the end-effector. The test was conducted in four separate trials with a total of 98 plants.

TEST RESULTS

Figure 4 shows an example of the continuous de-leafing test. The robot successfully identified an average of 62% of the plants as targets for de-leafing. For the plants identified as targets,

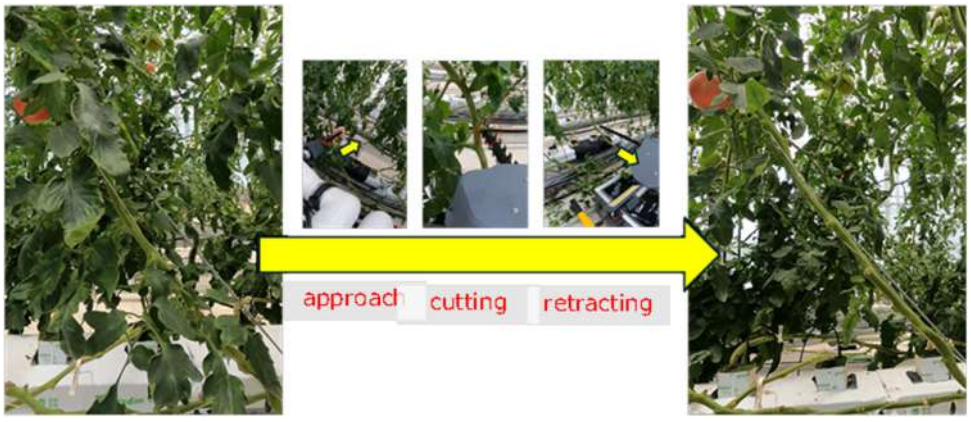

Fig.4 Example of a continuous de-leafing test (before / after).

the average weight-based lower-leaf removal rate was 72%. The average processing time was approximately 66 s per plant. No accidental cutting of the main stem was observed during the test.
In February 2026, an additional test was conducted at a commercial tomato greenhouse in Kuki, Saitama, Japan. This greenhouse had a denser planting arrangement than the previous test greenhouse, with a mean distance between main stems of approximately 230 mm and a standard deviation of approximately 110 mm. Even under these conditions, no accidental cutting of the main stem was observed. The average processing time was approximately 66 s per plant, and the average weight-based lower-leaf removal rate was 56%.

EFFECTIVENESS AND IMPROVEMENT POTENTIAL

VISIBILITY AND ACCESSIBILITY

To examine the effectiveness of the main stem-based approach, crop images acquired under practical greenhouse conditions were analyzed. The prototype robot was moved along a crop row at a constant speed, and images of 18 consecutive tomato plants were captured at 1-s intervals using a camera mounted on the mobile platform. For each plant, six frames around the central part of the image sequence, corresponding approximately to the robot working area, were selected for analysis.
We examined whether the bases of the target petioles and the lower part of the main stem were visible in the images. For visible targets, we also examined whether sufficient space was available for the end-effector to approach without interference from surrounding leaves or fruits (Fig. 5).



Fig.5 Example of visibility and accessibility assessment.

The bases of the target petioles were visible in approximately 55% of the evaluated images, whereas the lower part of the main stem was visible in approximately 89%. When accessibility was also considered, approximately 29% of the images provided sufficient visibility and access to the petiole bases, whereas approximately 74% provided sufficient visibility and access to the main stem.
Thus, the combined visibility and accessibility requirements were satisfied in approximately 29% of the images for the direct-approach method and 74% for the main stem-based approach. This result indicates that the main stem was more likely than the petiole base to satisfy both visibility and accessibility requirements under these greenhouse conditions.
These proportions may vary depending on camera position and field of view, plant spacing, growth stage, and foliage density. However, the results suggest that using the main stem as a reference is advantageous under practical greenhouse conditions in which individual petiole bases can be occluded by dense foliage. In the prototype tests described above, each target

plant was identified using only a single frame captured after the robot stopped. Therefore, using information from multiple frames may further improve the proportion of plants that can be identified as targets for de-leafing.

ANALYSIS OF THE CURRENT PROCESSING TIME

The current average processing time of approximately 66 s per plant was analyzed in detail. The mobile-platform movement in step (1) required approximately 7 s, while image acquisition and recognition in steps (2) and (3) required less than 1 s. Approaching the cutting start position and preparing the end-effector in step (4) required approximately 12 s. Cutting on one side of the stem in step (5) required approximately 10 s, switching to the opposite side in step (6) approximately 16 s, cutting on the opposite side in step (7) approximately 10 s, and retracting the robot arm after de-leafing in step (8) approximately 10 s (Fig. 6).

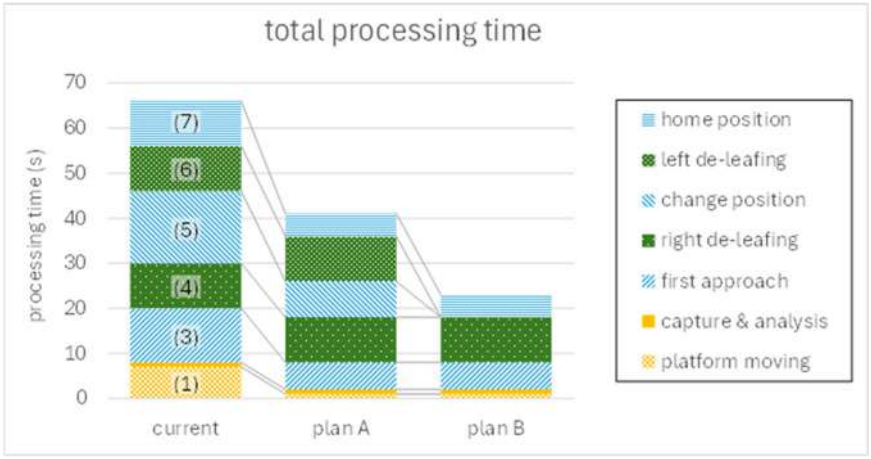

Fig.6 Breakdown of de-leafing processing time.

These results show that actual cutting accounts for only part of the total processing time. A substantial amount of time is spent on non-cutting motions, such as approaching the plant, switching the processing side, and retracting the arm. In the current system, these motions are intentionally performed conservatively to avoid unexpected contact with and damage to the plant. For example, after moving the end-effector near the main stem, the robot adjusts its orientation to align the end-effector with the stem axis, approaches the stem at low speed, confirms contact, and then starts cutting. These safety-oriented motions contribute to the current processing time.

POTENTIAL IMPROVEMENT THROUGH FASTER ROBOT MOTIONS

The analysis in the previous section indicates that a considerable part of the current processing time could be reduced by increasing the motion speed and improving the motion paths. At present, the mobile platform moves at a relatively low speed of approximately 0.05–0.1 m/s to ensure safety and reduce positioning errors. If the control performance and safety functions of the platform are improved, the travel time of approximately 7 s could be substantially reduced if the platform speed were increased.

The end-effector speed of the robot arm is also currently limited to approximately 0.1 m/s, well below its maximum speed of about 1 m/s, because safety is prioritized. Non-cutting arm motions, including approach, side switching, and retraction, currently require approximately 38

s in total. By improving collision-free motion planning and increasing the end-effector speed, these motions could be shortened substantially. For example, even increasing the end-effector speed to approximately 0.2 m/s may considerably reduce the non-cutting motion time.

POTENTIAL IMPROVEMENT THROUGH CUTTING STRATEGY

Increasing the cutting speed requires careful consideration because it may affect cutting performance. However, several improvements are possible without simply increasing the cutting speed. In the current main stem-based approach, stem-following starts from a lower part of the main stem where recognition is relatively easy. As a result, the end-effector also moves along sections of the stem where no target lower leaves are present. If the positions of the main stem and target leaves can be estimated more accurately, stem-following could start just below the target leaves, reducing unnecessary travel distance.

Another possible way to reduce the processing time is to decrease the number of cutting motions per plant. The current prototype performs cutting from two predetermined directions on either side of the main stem. Previous experiments showed that one cutting motion can cover an angular range of approximately 120° around the main stem (Kashino et al., 2026). These directions are selected without considering the actual directions of the target leaves. If the directions of the target leaves around the main stem are recognized before cutting, the robot could select an approach direction that includes more target leaves within the cutting range. For example, if two of three target leaves can be covered by a single cutting motion, one-sided processing may maintain a useful removal rate while eliminating both the side-switching motion and the second cutting motion. Alternatively, if two cutting motions are retained, selecting the cutting directions according to the actual leaf arrangement may improve the removal rate without increasing the processing time.

Tomato leaves generally have a regular arrangement around the main stem. However, under practical greenhouse conditions, the actual directions of the petioles can deviate from this regular pattern because of plant training, stem lowering, and plant development. Therefore, the cutting directions should not be determined only from a fixed leaf-arrangement pattern. Instead, it would be more practical to recognize the actual directions of the target leaves at the time of operation and select an appropriate approach direction for each plant. Combining the main stem-based approach with recognition of the actual target-leaf arrangement may therefore improve both processing time and leaf-removal performance.

DISCUSSION AND FUTURE WORK

ADAPTATION TO CROP AND CULTIVATION CONDITIONS

For practical application of the main stem-based approach, it is important not only to adapt the robot to existing cultivation conditions but also to establish cultivation conditions that are suitable for robotic operation. In this approach, for example, large training clips around the main stem may interfere with the stem-following motion of the end-effector. Therefore, training methods that reduce obstacles around the main stem, such as stem wrapping used in the present test, and training materials that minimize interference with the robot may be desirable. Narrow spacing between adjacent main stems may increase the risk of misidentifying a neighboring stem as the target stem. It may also increase the risk of interference between the end-effector and adjacent plants. Stem lowering can cause main stems to become curved or overlap with one another. Therefore, cultivation management methods that allow stable stem

recognition and stem-following control are important.
The current system is basically designed to remove lower leaves located below the fruit clusters. If leaves located higher on the plant are also targeted, the risk of interference with fruits and fruit clusters will increase. In such cases, the robot will need not only to recognize the target leaves, fruits and fruit clusters, but also to plan a cutting path that avoids damaging them. More detailed recognition of the spatial relationships among the main stem, target leaves, and fruits will therefore be important for extending the operating range of the robot.

PROSPECTS FOR PRACTICAL ROBOTIC OPERATION

For practical use of robotic systems in greenhouse production, not only the de-leafing function itself but also a mobile system for operating throughout the greenhouse will be required. The current prototype moves along a crop row, but greenhouse-wide operation will also require movement between crop rows. We are also developing a two-stage mobile platform consisting of an in-row unit that travels within crop rows and an inter-row carrier unit that transports it between rows (Shimomoto et al., 2024). Although this platform is being developed mainly for transporting crop-monitoring equipment, it is also designed to carry the de-leafing robot and may enable operation across multiple crop rows.
At present, the developed robot operates more slowly than a skilled worker. Therefore, practical operation will likely involve the robot working alongside human workers. In such a system, it may be more efficient to assign the robot to crop rows containing plants that are well suited to robotic operation, such as those that have many target lower leaves, are easy for the robot to access, or can be processed relatively quickly, rather than assigning the work uniformly. In the future, task-planning methods that consider factors such as battery level, travel time, workload, and task difficulty will be important for selecting suitable work areas and targets for the robot.
Another important issue for practical deployment is the cost of major components such as the robot arm and mobile platform. If these components are used only for de-leafing, their utilization may remain low. Using the same hardware for multiple crop-management tasks by exchanging the end-effector could improve equipment utilization. We are therefore extending the de-leafing robot toward a multi-use platform that can support other tasks, such as harvesting.

CONCLUSIONS

In this study, we evaluated the current performance of a tomato de-leafing robot using the main stem-based approach, and examined its effectiveness and potential for improvement under practical greenhouse conditions. The current prototype removed approximately 72% of the target lower leaves in approximately 66 s per plant. No accidental cutting of the main stem was observed during the tests. However, improvements in recognition performance and processing speed are still required for practical use.
Analysis of data collected under practical greenhouse conditions showed that only a limited proportion of the target petiole bases satisfied the visibility and accessibility requirements for direct approach. In contrast, the main stem satisfied these requirements in a much higher proportion of the images. This result suggests that the main stem-based approach, which does not depend on recognizing and directly approaching individual petioles, may be suitable for practical conditions with frequent occlusion.
Analysis of the current processing time also showed that a substantial amount of time was

spent on approach, side switching, and retraction motions rather than on cutting itself. Increasing the speed and shortening the paths of these motions could substantially reduce the processing time. Selecting suitable cutting directions based on the actual arrangement of the target leaves could further improve efficiency while maintaining the current leaf-removal performance.

Future work will focus on improving recognition and motion control, developing cultivation methods suitable for robotic operation, integrating the robot with an inter-row mobile system, and developing a multi-use robotic platform. These developments will be important for practical robotic systems for greenhouse crop management.

ACKNOWLEDGEMENTS

This work was supported in part by JSPS KAKENHI Grant Number 25K02135 and by a donation from Tokai Pickling Co., Ltd.

REFERENCES

Aichi Agricultural Research Center. 1995. Tomato hydroponic long-term cultivation and its economic effects. Available at: agresearcher.maff.go.jp/seika/show/214971. Accessed 5 Sep. 2026. (in Japanese).

Fukatsu, T., M. Kashino, N. Nakayama, and H. Kurosaki. 2023. A main stem-based operation method for a cultivation management robot system in greenhouse horticulture. In Proc. GreenSys 2023, 243.

Kashino, M., H. Kurosaki, and T. Fukatsu. 2026. Development of a tomato de-leafing robot with a hedge trimmer-typed end-effector: Effect of hedge trimmer position and orientation on lower leaf removal performance. J. Japanese Soc. Agric. Machinery Food Eng. 88(3): 169–177. (in Japanese).

Kurosaki, H., H. Ohmori, H. Hamamoto, and Y. Iwasaki. 2014. Work hours and yield for large-scale tomato production in Japan. Acta Hortic. 1037: 753-758.

Shimomoto, K., M. Shimazu, H. Naito, T. Ota, and T. Fukatsu. 2024. Development of a rail-guided vehicle and platform for monitoring multiple planting rows in greenhouses. In Proc. 11th International Symposium on Machinery and Mechatronics for Agriculture and Biosystems Engineering (ISMAB 2024), BR-R20.

MAFF. 2012. Farm management statistics by type of farming: Labor time by operation for major greenhouse vegetables and rice. Tokyo, Japan: Ministry of Agriculture, Forestry and Fisheries. (in Japanese).

Zhou, H., X. Wang, W. Au, H. Kang, and C. Chen. 2022. Intelligent robots for fruit harvesting: Recent developments and future challenges. Precision Agric. 23: 1856-1907.

PA-05

Proceedings of The 12th International Symposium on Machinery and Mechatronics for Agriculture and Biosystems Engineering (ISMAB 2026)
20-24 October 2026, Busan, Republic of Korea

DEVELOPMENT OF AN ELECTRONIC NOSE WITH PI-CONTROLLED TEMPERATURE REGULATION FOR MONITORING POULTRY LITTER FERMENTATION

Jing-Xiang Lu[1], Chin-Cheng Wu[2] *,Chung-Yen Chuang[3]

[1,2,3]Department of Biomechatronic Engineering, National Ilan University Taiwan
*Corresponding Author, Email: chincheng@niu.edu.tw

Abstract: Enclosed floor-raised poultry house typically use litter on the floor, utilizing microbial fermentation to generate high temperatures for the purpose of eliminating pathogens and parasite eggs. However, traditional litter management relies heavily on experience, visual observation, or destructive sampling to measure the quality of litter content, making it difficult to accurately assess the overall fermentation maturity of the litter without disturbing the site. To address this, this study proposes an electronic nose (E-Nose) detection system equipped with temperature control. By measuring the concentration of volatile organic compounds (VOCs) in the poultry house environment, the system aims to determine the fermentation stage of the litter and establish a standardized fermentation process. This study conducted an experiment in May 2026. The May results showed that 12 hours after litter tilling, the concentrations of ammonia, sulfides, carbon monoxide, methane, alcohol, and various organic volatiles reached their peaks and then gradually declined, with an average relative change rate of -16.66% across all sensors. The experimental results confirm that this detection method possesses good reproducibility and can serve as an effective tool for the non-destructive monitoring of litter fermentation maturity. It also shows potential for combining with machine learning to predict the degree of litter fermentation.

Key Words: Electronic Nose, PI-Controlled Temperature Regulation, Poultry Litter Fermentation

INTRODUCTION

The broiler industry in Taiwan predominantly adopts an enclosed floor-rearing system, in which litter is placed on the floor to absorb poultry excreta and prevent footpad dermatitis. However, the increasing cost of litter has necessitated its reuse across successive broiler production cycles. After completing a production cycle, farmers typically subject the used litter to a fermentation process. Common litter treatment procedures include first removing the surface layer of caked litter and manure, followed by using a cultivator to turn over and break up the remaining litter. Commercially available probiotics are then evenly sprayed onto the litter to initiate fermentation. The poultry house is subsequently sealed to create a relatively anaerobic environment and increase the internal temperature. This process promotes ammonia volatilization and utilizes the elevated temperature to eliminate pathogens and parasite eggs

before the placement of the next batch of chicks (Hsu et al., 2020). However, the chemical reactions occurring during microbial fermentation produce a complex mixture of volatile organic compounds (VOCs), making it difficult to accurately characterize the fermentation process using a single sensor. Therefore, metal-oxide-semiconductor (MOS) sensor arrays are commonly used to monitor environmental conditions in modern poultry production systems. Analysis of environmental VOCs can facilitate the early detection of potential poultry health problems, thereby improving animal welfare and sustainability (Abbas & Comini, 2025).
The primary objective of this study is to utilize the high sensitivity and reliability of MOS sensors for continuous monitoring of the litter fermentation process. In addition, to minimize the influence of ambient temperature fluctuations on measurement results, this study introduces a pulse-width modulation (PWM) heater controlled by a proportional-integral (PI) controller to regulate the temperature of the inlet air. Previous studies have shown that this temperature-control method can significantly improve experimental reproducibility (Iswanto et al., 2025).

MATERIALS AND METHODS

The architecture of the E-Nose system developed in this study is mainly divided into two core parts: the frontend hardware layer (Data Acquisition Unit) responsible for collecting the analog signals of VOCs, and the backend software and storage layer (Application & Storage Layer) responsible for receiving, processing, and storing the detection data. The frontend hardware layer is centered on a microcontroller unit (MCU, ATmega2560) and integrates a Gas Sensor Array, a Temperature Control Module (PI controlled), and a Flow Control Module. This hardware layer precisely controls the sampling environment and airflow, converting the analog gas signals captured by the sensors into digital data. The backend software layer consists of a Host PC that receives data, provides real-time data visualization through a graphical user interface (GUI), and utilizes an SQL database for structured data storage and archiving. The complete system architecture is shown in Fig. 1:

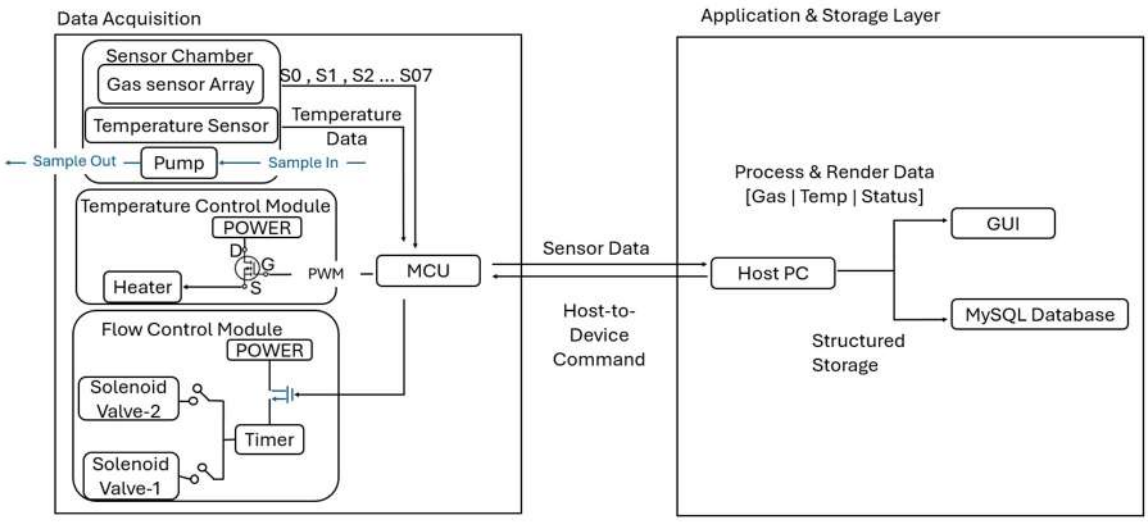

Fig. 1 System Architecture.

GAS DATA ACQUISITION

Gas sensor array module

This module utilizes a custom-designed PCB to drive all sensors (Fig. 2). The PCB supplies power to the sensors and receives the analog signals representing gas concentrations.

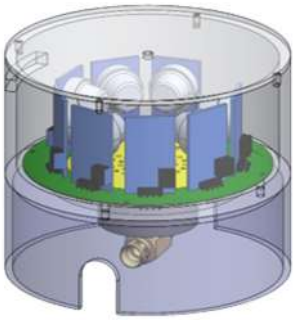

Fig. 2 Gas Sensor Array Module

For the gas sensors, the MQ-series metal-oxide-semiconductor gas sensors were selected. This series of sensors has demonstrated good performance and reliability in numerous previous studies. These sensors operate based on the principle that gas molecules in the poultry house contact the sensor surface, causing a change in the sensor's resistance (R_s), which is then used to estimate the environmental VOC concentration.

Temperature Control Module

The primary function of this module is to control the temperature of the gas as it enters the Gas Sensor Array Module, preventing signal drift in the gas sensors caused by temperature and humidity fluctuations. Using the MCU paired with a temperature sensor, real-time temperature data is acquired. The temperature control algorithm employs proportional-integral (PI) control, where the MCU outputs a PWM signal to a MOSFET, thereby regulating the driving power of the heater and accurately maintaining the chamber temperature at the target setpoint. The continuous-time output equation of the PI controller is as follows:

$$u(t) = K_p e(t) + K_i \int_0^t e(\tau) d\tau \quad (1)$$

Where:

$u(t)$: output signal of the controller (PWM)

$e(t)$= Error value between the set temperature and the actual temperature(℃)
K_p= Proportional gain
K_i= Integral gain

The proportional and integral parameters (K_p, K_i) of the controller were set based on the Ziegler-Nichols frequency response method. By setting an ultimate gain $K_u = 1800$, the system was induced into sustained temperature oscillation, and the time interval between adjacent temperature peaks was measured (as shown in the figure) to derive the average ultimate oscillation period of the system, $T_u \approx 836.2$ s. The standard Ziegler-Nichols calculation formulas are as follows:

$$Kp = 0.45 \times K_u = 0.45 \times 1800 = 810 \quad (2)$$

$$K_i = \frac{1.2K_p}{T_u} \approx 1.17 \quad (3)$$

Where:

K_p= Proportional gain derived from the Ziegler-Nichols method

K_u= Ultimate gain input when the system reaches sustained oscillation

K_i = Integral gain derived from the Ziegler-Nichols method

T_u= Oscillation period during system oscillation

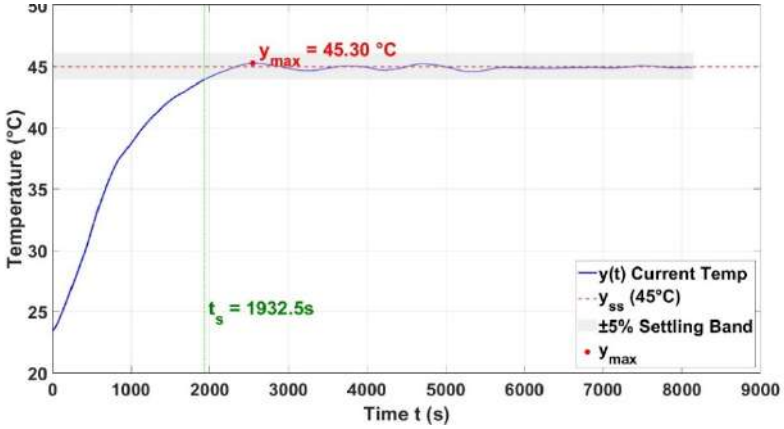

Fig. 3 Actual Temperature Control Performance

This figure displays the step response and time-domain analysis results of the system's PI temperature control module. The blue solid line $y(t)$ represents the actual measured temperature inside the sensing chamber, while the red dashed line y_{ss} represents the target steady-state temperature (45°C) set by the system. From the dynamic response curve, it can be observed that after the system initiates heating from the initial room temperature, the temperature rises smoothly. The green vertical dashed line indicates the settling time required for the system to stabilize and remain within the ±5% tolerance band (gray shaded area) of the target temperature. The temperature when the system crosses the target temperature (overshoot) is 45.30°C, occurring at 2500 seconds. This indicates that the system's maximum overshoot is extremely small, exceeding the set value by only 0.30°C. This demonstrates that the PI control parameters tuned via the Ziegler-Nichols method effectively suppress excessive temperature rise during the initial heating phase.



Fig 4 On-site Experimental Setup. (Left) The electronic nose system and real-time data monitoring interface; (Right) The PVC hose deployed inside the poultry house for gas sampling.

RESULTS & DISCUSSION

This study conducted experiments from May 3 to May 5, 2026. The experimental site was a negative-pressure pad-and-fan floor-raised broiler house located in Xidi Village, Shengang Township, Changhua County. The experimental method measured the concentrations of volatile organic compounds (VOCs) in the poultry house at least once in the morning and once in the afternoon. The procedure for a single measurement session involved drawing clean air through an activated carbon filter for the first 6 minutes to establish the baseline for the experiment, drawing the target gas from inside the poultry house from minutes 6 to 9, and then drawing clean air again from minutes 9 to 15 to desorb the VOCs from the sensor array. This measurement procedure was repeated 3 times per session.

In this study, the initial measurement was conducted prior to litter tilling, and post-tilling measurements were taken at least twice daily to continuously observe the dynamic changes in VOC concentrations. Fig. 5 shows radar charts of the VOC gases measured inside the poultry house from May 3 to May 5. The plotted data represent the normalized average of the maximum response increases from the three replicate measurements in each session.

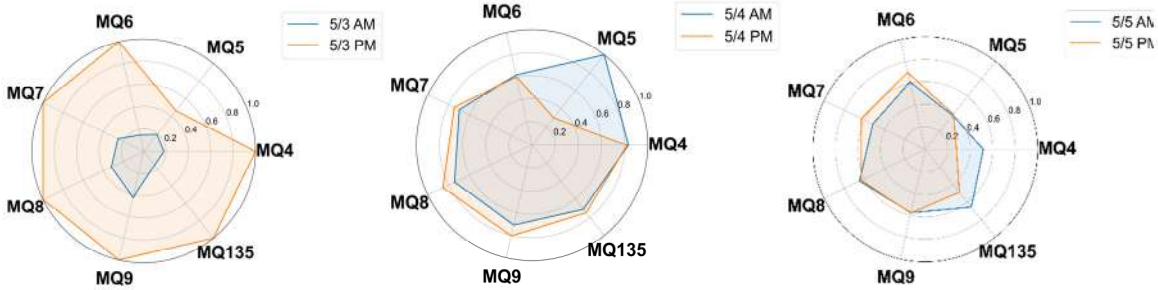

Fig. 5 E-Nose Sensor Response Radar Charts - May Trial

From the overlaid comparison charts of the same time periods across different days, the trend in gas concentration changes throughout the litter fermentation process can be clearly observed. During the initial stage of litter tilling, the odor fingerprint area was relatively small in the morning of May 3 (May 3 AM), but expanded significantly by the afternoon (May 3 PM). Except for the MQ5 sensor, all other gas sensors reached their maximum responses approximately 12 hours after litter tilling (May 3 PM) and subsequently exhibited a decreasing trend over the following days. In contrast, the MQ5 sensor reached its maximum response approximately 24 hours after litter tilling, during the morning session of May 4 (May 4 AM), after which its response also began to decrease. By the third day of the experiment (May 5), the overall odor fingerprint area had significantly contracted during both the morning and afternoon sessions, returning to a low-response state similar to that observed during the initial stage of fermentation.

CONCLUSIONS

This study successfully developed a smart electronic nose (E-Nose) system equipped with a PI temperature control function. The temperature control system, utilizing PI parameters tuned via the Ziegler-Nichols method, demonstrated excellent dynamic response. When the system heated from room temperature to the target steady-state temperature of 45°C, the overshoot was extremely minimal (exceeding the setpoint by only 0.30°C), and it quickly and smoothly entered and maintained within the ±5% tolerance band. Through the design of a constant-

temperature sensing chamber, this system effectively minimized the influence of external temperature fluctuations on the gas sensors, ensuring high stability and reproducibility of the gas signals during continuous measurement. A notable observation was that in the May experiment, after the VOC concentration peaked (May 3 PM), the sensor variation measured the next day remained around 80% (May 4 AM, May 4 PM), and the concentration only began to decrease after a certain period.

The E-Nose system proposed in this study possesses excellent potential as a non-destructive tool for evaluating litter fermentation maturity, addressing the lack of scientific monitoring methods in litter management within Taiwan's poultry industry. This system can objectively and quantitatively reflect the fermentation status, thereby overcoming the limitations of traditional management that relies on farmers' experience and visual observation. Future research will further integrate machine learning technologies, utilizing the continuous odor fingerprint database established by this system for model training, with the goal of achieving automated prediction of the litter fermentation completion time. This will provide standardized management solutions for modern precision poultry farming and promote the sustainable development of the industry and animal welfare.

ACKNOWLEDGEMENTS

This study was financially supported by the Ministry of Agriculture, Taiwan, under Grant No. 115AS-10.2.3-AD-01. The authors gratefully acknowledge this support.

REFERENCES

Abbas, I. E., and E. Comini. 2025. Gas Sensing for Poultry Farm Air Quality Monitoring to Enhance Welfare and Sustainability. Chemosensors 13(9): 347. https://www.mdpi.com/2227-9040/13/9/347

Hsu, W. H., M. C. Tsai, M. P. Cheng, and T. H. Hsiao. 2020. The effect of litter reuse on the production efficiency of broilers and the quantity of the litter. Journal of Taiwan Livestock Research 53(4): 229-236. https://doi.org/10.6991/jtlr.202012_53(4).0004

Iswanto, B. H., M. Suseno, F. Hardoyono, and M. Delina. 2025. Development of an Integrated E-Nose System with Controlled Sample Heating Chamber for Coffee Aroma Discrimination. Journal of Physics: Conference Series 3139.

PA-06

Proceedings of The 12th International Symposium on Machinery and Mechatronics for Agriculture and Biosystems Engineering (ISMAB 2026)
20-24 October 2026, Busan, Republic of Korea

ACCURACY EVALUATION OF LIDAR–INERTIAL SLAM-BASED AUTONOMOUS NAVIGATION IN GREENHOUSE ENVIRONMENTS

Nang Nguyen Van[1*], Hayato Seki[1], Oyetayo Olukorede Oyebode[1]

[1]Department of Agricultural Mechanization and Smart Farming Research Institute of Agricultural Machinery, NARO, 1-40-2 Nisshin, Kita-ku, Saitama City, Saitama 331-8537, Japan
*Corresponding Author-- Voice: +81-48-654-7074,
Email: nguyen.van.nang937@naro.go.jp

Abstract: Accurate mapping, localization, and path tracking are essential for auto nomous greenhouse machinery, where repetitive structures, narrow spaces, and vinyl surfaces can challenge onboard perception. This study evaluated a LiDAR–inertial SLAM-based navigation system for a small electric crawler intended for greenhouse soil preparation and seeding. The system used a Livox MID-360, FAST-LIO for LiDAR–inertial odometry, RTAB-Map for map optimization and database-based localization, and a pure-pursuit controller. Experiments were conducted in a real greenhouse with measured inner dimensions of 26.748 × 8.758 m and a 12 × 7.5 m roofless vinyl-wall greenhouse model. FAST-LIO horizontal RMSE was 0.042 m relative to a total station in the real greenhouse and 0.040 m relative to RTK-GNSS in the roofless model. Dimensions estimated from RTAB-Map-derived occupancy maps were 26.740 × 8.760 m and 12.000 × 7.524 m, respectively. Preliminary navigation used manual initial map alignment. In the real greenhouse, ROS and total-station cross-track RMSEs were 0.031 and 0.055 m over a 15-m straight path. In the roofless model, ROS and RTK-GNSS cross-track RMSEs were 0.027 and 0.021 m over the first 6 m. These results demon strate centimeter-level mapping and preliminary straight-path tracking performance.

Key Words: Greenhouse Robot, LiDAR–inertial SLAM, Total Station, RTK-GNSS, Path Tracking.

INTRODUCTION

Reliable localization and path tracking are required for autonomous agricultural operations such as tillage, seeding, spraying, and crop management. RTK-GNSS provides centimeter-level positioning under favorable satellite visibility, but greenhouse structures can block or degrade GNSS signals. Consequently, onboard perception and simultaneous localization and mapping (SLAM) have become important alternatives or complements for agricultural robot navigation when GNSS is unavailable or unreliable (Wang et al., 2022).

Greenhouses are particularly challenging because long parallel walls and repetitive structural members can produce similar geometric observations, while crops and vinyl surfaces may degrade perception. LiDAR–inertial odometry is therefore attractive because inertial

measurements complement three-dimensional geometric observations. FAST-LIO2 tightly couples LiDAR and IMU data for real-time odometry (Xu et al., 2022), whereas RTAB-Map provides graph-based mapping, map management, and localization (Labbé and Michaud, 2019).

LiDAR-based navigation has recently been applied to agricultural environments. Wang et al. (2024) integrated LiDAR, IMU, and GNSS for orchard robot navigation, while Huang et al. (2025) demonstrated FAST-LIO2-based autonomous navigation in greenhouse environments. For path tracking, pure pursuit remains a practical geometric controller for low-speed mobile robots because of its simplicity and low computational requirements (Coulter, 1992).

This study evaluates three components of a LiDAR–inertial navigation system developed for greenhouse tillage and seeding: (1) FAST-LIO trajectory accuracy during mapping, (2) geometric accuracy of greenhouse dimensions obtained from RTAB-Map occupancy maps, and (3) preliminary straight-path tracking accuracy. Initial map alignment was performed manually, and turning and multi-segment navigation were outside the scope of the present study.

MATERIALS AND METHODS

Robotic System and Experimental Environments

The experimental platform was a small electric crawler equipped with a Livox MID-360 LiDAR and a Jetson AGX Orin computer (Fig. 1a). FAST-LIO2, implemented using the FAST-LIO ROS package, was used to estimate LiDAR–inertial odometry from the Livox MID-360 LiDAR and IMU data. FAST-LIO2 provided odometry at approximately 10 Hz, whereas RTAB-Map updated the optimized map/localization pose at approximately 5 Hz. RTAB-Map used the odometry and point clouds to construct and optimize the map, maintain the mapping database, and generate the two-dimensional occupancy map. During navigation, RTAB-Map performed database-based localization, and a pure-pursuit controller generated velocity commands at 20 Hz to follow the predefined paths.

Two experimental environments were used (Fig. 1b, c). The first was a nominal 30 × 10 m greenhouse with measured inner dimensions of 26.748 × 8.758 m. A total-station prism was mounted above the center of the MID-360 and provided the independent reference trajectory. The second was a 12 × 7.5 m roofless greenhouse model with grass-covered ground and 1.6-m-high vinyl-sheet walls. An RTK-GNSS antenna and ground plane were mounted above the center of the MID-360, and only RTK-fixed positions were used for evaluation.

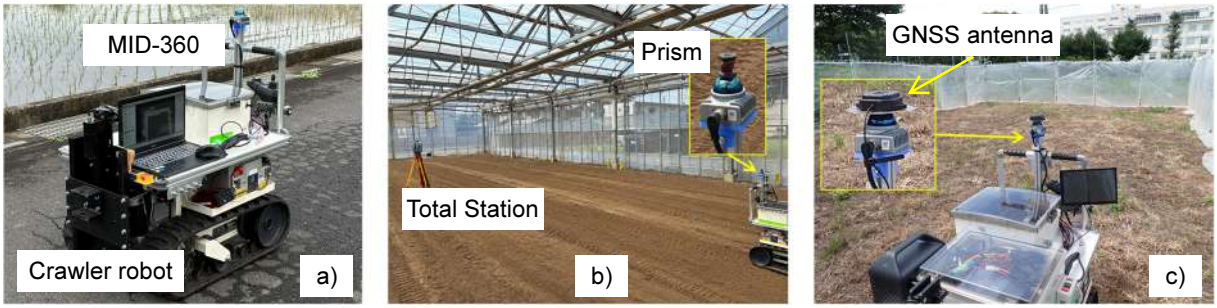

Fig.1 Experimental electric crawler robot and test environments: (a) sensor arrangement, (b) real greenhouse, and (c) roofless greenhouse model.

Mapping and Map-Dimension Evaluation

During mapping, FAST-LIO odometry (Fig. 2a, b) and independent reference trajectories were recorded simultaneously. The trajectories were synchronized in time and aligned using a two-dimensional rigid transformation consisting of translation and rotation, because their coordinate systems had different origins and orientations. Horizontal position error for synchronized sample *i* was calculated using Eq. (1), and horizontal RMSE was calculated from all synchronized samples.

$$e_i = \sqrt{\left(x_i - x_{r,i}\right)^2 + \left(y_i - y_{r,i}\right)^2} \qquad (1)$$

where e_i is the horizontal position error at synchronized sample i; x_i and y_i are the spatially aligned coordinates estimated by FAST-LIO; and $x_{r,i}$ and $y_{r,i}$ are the corresponding coordinates from the independent reference system.

RTAB-Map was subsequently used to generate two-dimensional PGM occupancy maps. For the real greenhouse, the reference boundary was defined by the inner edges of the structural pole bases. A rectangle was fitted to the corresponding map boundaries, and pixel dimensions were converted to metric dimensions using the map resolution. The same procedure was applied to the roofless model using its known 12 × 7.5 m dimensions (Fig. 2c, d).

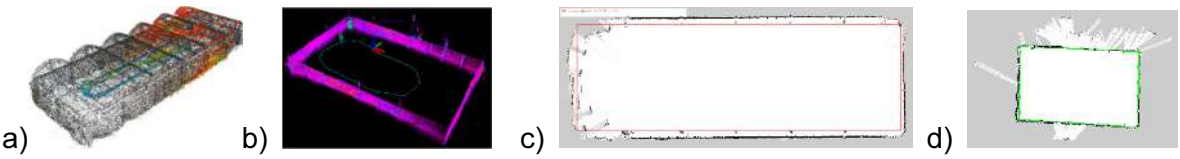

Fig. 2 Samples of FAST-LIO point-cloud maps and odometry trajectories, and inner-boundary estimation from RTAB-Map-derived occupancy maps: (a, c) real greenhouse and (b, d) roofless greenhouse model.

Localization and Straight-Path Tracking

For navigation, the saved RTAB-Map database and occupancy map were loaded. The crawler was manually returned near the mapping start position and heading. After restarting FAST-LIO, RViz 2D Pose Estimate was used to provide the initial robot pose in the map frame, after which RTAB-Map performed scan-to-map localization.

Straight paths were followed at approximately 0.1 m/s using pure pursuit. A 15 m path was evaluated in the real greenhouse using ROS localization and total-station trajectories. In the roofless model, the first 6 m of a straight path were evaluated using ROS localization and RTK-GNSS (Fig. 3).

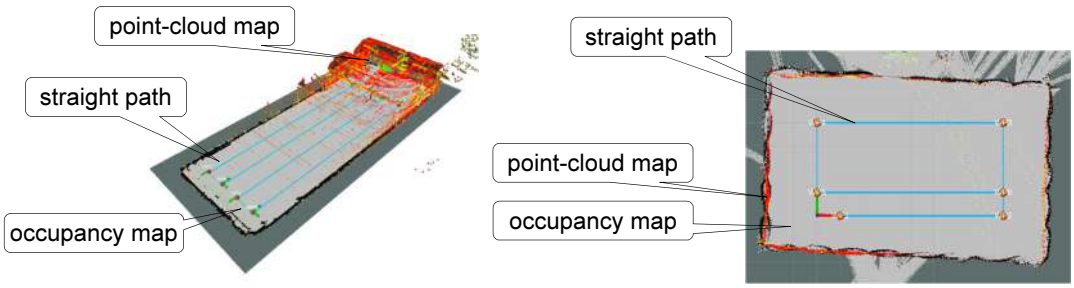

Fig. 3 RViz visualizations of manual initial pose estimation and planned straight paths for tracking tests in the real greenhouse (left) and roofless greenhouse model (right).

Signed cross-track error was defined as the perpendicular distance from each trajectory position to the planned path. Cross-track RMSE was calculated for both ROS localization and the independent physical reference. Synchronized ROS and external-reference coordinates were also directly compared to obtain two-dimensional localization RMSE.

RESULTS & DISCUSSION

Mapping Accuracy and Greenhouse Geometry

Figure 4 shows the MID-360 trajectories estimated by FAST-LIO odometry and those measured by total station and RTK-GNSS for different environments. FAST-LIO achieved centimeter-level horizontal trajectory accuracy in both environments. Horizontal RMSE was 0.042 m relative to the total station in the real greenhouse and 0.040 m relative to RTK-GNSS in the roofless model (Table 1).

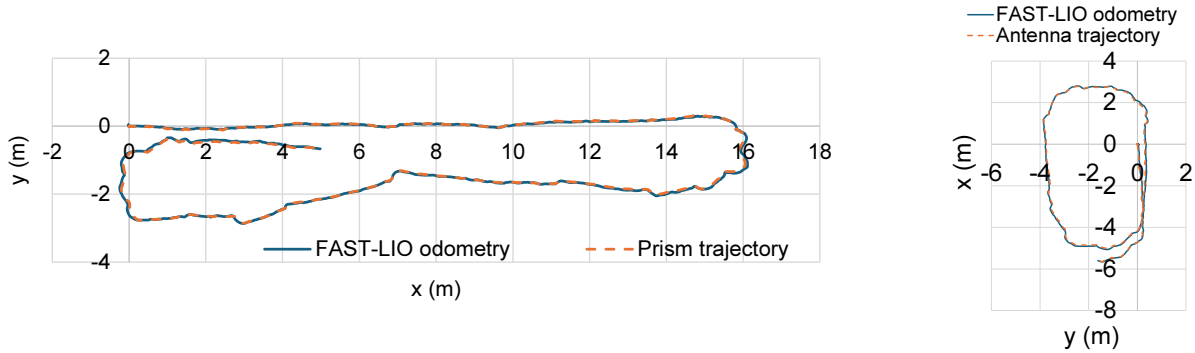

Fig. 4 FAST-LIO odometry relative to independent references in the real greenhouse (left) and roofless model (right).

Table 1 Mapping and greenhouse-dimension accuracy

Environment	Mapping reference	FAST-LIO RMSE (m)	Reference dimensions (m)	PGM-estimated dimensions (m)
Real greenhouse	Total station	0.042	26.748 × 8.758	26.740 × 8.760
Roofless model	RTK-GNSS	0.040	12.000 × 7.500	12.000 × 7.524

The similar mapping RMSE values obtained in the two environments indicate that FAST-LIO maintained consistent local trajectory estimation despite the different greenhouse structures and reference systems. The approximately 4-cm RMSE values are of the same order as centimeter-level performance reported for recent greenhouse LiDAR–inertial navigation systems, although direct comparison is limited by differences in trajectories and evaluation metrics (Huang et al., 2025).

The occupancy maps also preserved the greenhouse geometry. For the real greenhouse, the estimated dimensions differed from the total-station dimensions by −0.008 m in length and +0.002 m in width. For the roofless model, the estimated length matched the nominal 12.000 m value, while the width differed by +0.024 m (Table 1).

These very small dimension differences should not be interpreted as sub-centimeter LiDAR positioning accuracy because the boundary location is affected by occupancy-grid resolution and boundary selection. Rather, they indicate that RTAB-Map optimization retained the overall scale and rectangular geometry of the greenhouse.

Mapping trajectory error and map-dimension error describe different properties. FAST-LIO RMSE evaluates instantaneous position accuracy along the mapping trajectory, whereas the estimated greenhouse dimensions evaluate the global geometric consistency of the optimized occupancy map. Consequently, a map may accurately preserve overall dimensions even when individual trajectory positions contain several centimeters of error.

Preliminary Straight-Path Tracking

Figure 5 and Table 2 summarize the preliminary navigation results. In the real greenhouse, the ROS localization trajectory had a cross-track RMSE of 0.031 m, whereas the total-station trajectory produced a physical cross-track RMSE of 0.055 m. The synchronized ROS-to-total-station two-dimensional RMSE was 0.048 m.

In the roofless model, cross-track RMSE was 0.027 m for ROS localization and 0.021 m for RTK-GNSS. The corresponding ROS-to-RTK-GNSS two-dimensional RMSE was 0.055 m.

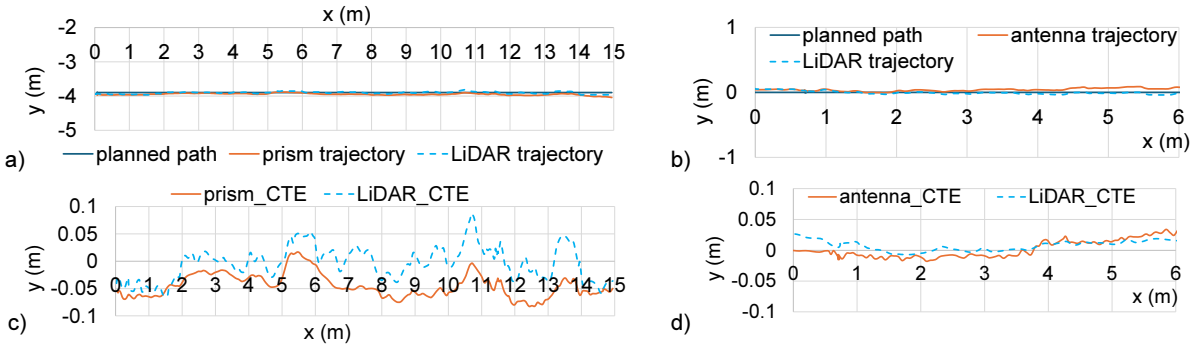

Fig. 5 Planned, ROS-localized, and reference trajectories and signed cross-track errors during straight-path tracking: (a, c) real greenhouse and (b, d) roofless greenhouse model.

Table 2 Preliminary straight-path tracking accuracy

Environment	Distance	ROS CTE RMSE (m)	Reference CTE RMSE (m)	ROS-reference 2D RMSE (m)
Real greenhouse	15 m	0.031	0.055	0.048
Roofless model	6 m	0.027	0.021	0.055

The ROS cross-track error represents tracking performance within the map coordinate frame and therefore should not be interpreted alone as physical navigation accuracy. Errors in manual map alignment or localization can shift the relationship between the planned map path and the physical greenhouse. Total-station and RTK-GNSS trajectories provide the direct physical path-following evaluation.

This explains why the internal ROS cross-track RMSE can be smaller than the direct two-dimensional ROS-to-reference disagreement. Cross-track error contains only the component perpendicular to the planned line, whereas two-dimensional error also includes along-track differences.

The total-station cross-track RMSE of 0.055 m over the 15-m real-greenhouse path and the RTK-GNSS RMSE of 0.021 m over the evaluated 6-m roofless-model section demonstrate promising preliminary straight-path performance. However, these experiments were pre-tests and did not include repeated trials, turning, headland maneuvers, row transitions, or full multi-segment trajectories. In addition, the initial map pose was manually established using RViz; therefore, autonomous global map alignment was not evaluated.

CONCLUSIONS

A MID-360-based LiDAR–inertial navigation system using FAST-LIO, RTAB-Map, and pure-pursuit control was evaluated in a real greenhouse and a roofless vinyl-wall greenhouse model.

FAST-LIO horizontal mapping RMSE was 0.042 m relative to a total station in the real greenhouse and 0.040 m relative to RTK-GNSS in the roofless model. RTAB-Map-derived occupancy maps accurately preserved the overall greenhouse geometry, giving 26.740 × 8.760 m compared with the measured 26.748 × 8.758 m in the real greenhouse and 12.000 × 7.524 m compared with the nominal 12.000 × 7.500 m roofless model.

Preliminary straight-path tracking produced physical cross-track RMSE values of 0.055 m over 15 m in the real greenhouse and 0.021 m over the first 6 m in the roofless model. The results indicate that the system provides a practical basis for autonomous greenhouse navigation. Future work will evaluate repeated trials, map-alignment repeatability, turns, row transitions, and complete tillage and seeding trajectories.

REFERENCES

Coulter, R. C. 1992. Implementation of the Pure Pursuit Path Tracking Algorithm. Technical Report CMU-RI-TR-92-01. Pittsburgh, Pa.: Robotics Institute, Carnegie Mellon University.

Huang, Z., N. Yang, R. Cao, Z. Li, Y. He, and X. Feng. 2025. Autonomous navigation system in various greenhouse scenarios based on improved FAST-LIO2. Computers and Electronics in Agriculture 234: 110279. https://doi.org/10.1016/j.compag.2025.110279.

Labbé, M., and F. Michaud. 2019. RTAB-Map as an open-source lidar and visual simultaneous localization and mapping library for large-scale and long-term online operation. Journal of Field Robotics 36(2): 416–446. https://doi.org/10.1002/rob.21831.

Wang, T., B. Chen, Z. Zhang, H. Li, and M. Zhang. 2022. Applications of machine vision in agricultural robot navigation: A review. Computers and Electronics in Agriculture 198: 107085. https://doi.org/10.1016/j.compag.2022.107085.

Wang, W., J. Qin, D. Huang, F. Zhang, Z. Liu, Z. Wang, and F. Yang. 2024. Integrated navigation method for orchard-dosing robot based on LiDAR/IMU/GNSS. Agronomy 14(11): 2541. https://doi.org/10.3390/agronomy14112541.

Xu, W., Y. Cai, D. He, J. Lin, and F. Zhang. 2022. FAST-LIO2: Fast direct LiDAR-inertial odometry. IEEE Transactions on Robotics 38(4): 2053–2073. https://doi.org/10.1109/TRO.2022.3141876.

PA-07

Proceedings of The 12th International Symposium on Machinery and Mechatronics for Agriculture and Biosystems Engineering (ISMAB 2026)
20-24 October 2026, Busan, Republic of Korea

DESIGN OF AN INTEGRATED THREE-AXIS MAGNETIC FIELD SENSOR

Shu-Yi Wen[1] and Zhi-Xuan Dai[1]*
[1]Department of Bio-Industrial Mechatronics Engineering, National Chung Hsing University, Taiwan
*Corresponding Author-- Email: zxdai@nchu.edu.tw

Abstract: This study presents a high-sensitivity three-axis magnetic field sensor fabricated using the UMC 0.18-μm CMOS process. The proposed sensor is developed by modifying a conventional Hall sensor through different doping profiles to form a magnetotransistor structure. In addition, post-process etching of the silicon substrate is employed to further enhance the magnetic sensitivity. For the Z-axis sensing structure, a current-splitting configuration is adopted, in which the current injection electrode (CIE) is divided into left and right sections. The resulting sensing voltages are superimposed, thereby increasing the overall sensitivity. Simulation results show that the sensitivities of the proposed sensor are 373 mV/T for the X- and Y-axes and 456 mV/T for the Z-axis.

Key Words: Magnetic Field Sensor, MEMS

INTRODUCTION

With the continuous advancement of intelligent systems and precision sensing technologies, magnetic field sensors have played an increasingly important role in industrial monitoring, vehicle control, biomedical detection, and agricultural applications. In vehicle control systems, the integration of Internet of Things (IoT) technology enables measurement data from onboard magnetic sensors to be transmitted to cloud-based or Internet of Vehicles platforms in real time for remote monitoring and large-scale data analysis. This approach can further support vehicle condition diagnosis, predictive maintenance, and driving safety. For example, abnormal trends in sensing data can provide early warnings of component wear or positional deviation, thereby reducing the risk of system failure and improving overall reliability. Similarly, in agricultural applications, IoT-enabled smart farming systems can use various sensors to continuously monitor air conditions, soil properties, and environmental humidity. Based on the collected data, irrigation, ventilation, and shading systems can be adjusted accordingly, thereby improving crop quality and production stability. (Leepattarapongpan et al., 2008; Crescentini et al., 2017)

In recent years, the continuous development of magnetic field sensing technologies has enabled magnetic signals to be converted into measurable electrical signals more effectively, while also providing new possibilities for the design of advanced magnetic sensing devices. Among the various types of magnetic field sensors, Hall sensors are commonly used sensing elements that generate a sensing voltage through the deflection of charge carriers under an applied magnetic field. (Paun et al., 2012; Skucha et al., 2013; Tseng et al., 2017; Ruggeri et al., 2025) However, conventional Hall sensors generally produce relatively small output signals and are susceptible to offset voltage, temperature drift, and other nonideal effects. To address these limitations, magnetotransistor sensors employ multi-electrode structures and specially

designed carrier transport paths to convert magnetic-field-induced carrier deflection into current or voltage differences between electrodes. Therefore, this study adopts a magnetotransistor-based sensing architecture and optimizes the device geometry, electrode positions, and electrode configuration to improve carrier transport and current distribution, thereby enhancing magnetic field sensitivity.

MATERIALS AND METHODS

Structure and Operating Principle

X- and Y-Axis Magnetic Field Sensors

Figure 1 illustrates an isometric view of the X- and Y-axis magnetic field sensor structure. In this design, the shallow trench isolation (STI) region is reduced in size to prevent it from obstructing the current path and to facilitate carrier transport along the intended direction. When an external magnetic field is applied, the moving charge carriers are deflected laterally by the Lorentz force, resulting in a potential difference between the two sensing electrodes. This potential difference serves as the output signal corresponding to the magnitude of the magnetic field along the X- or Y-axis.

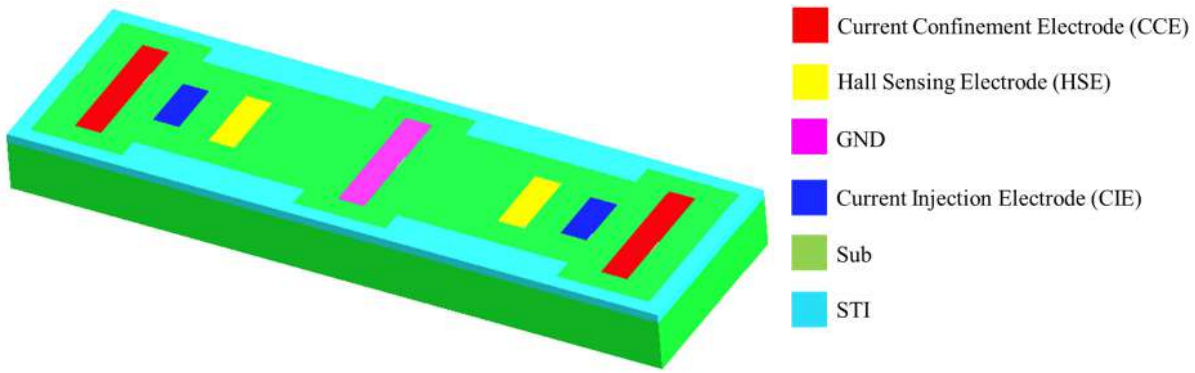

Figure 1 Structural Design of the X- and Y-Axis Magnetic Field Sensor

Figure 2(a) shows the simulated current-density distribution under a zero magnetic field, whereas Figure 2(b) shows the simulated current-density distribution under an applied magnetic field of 300 mT.

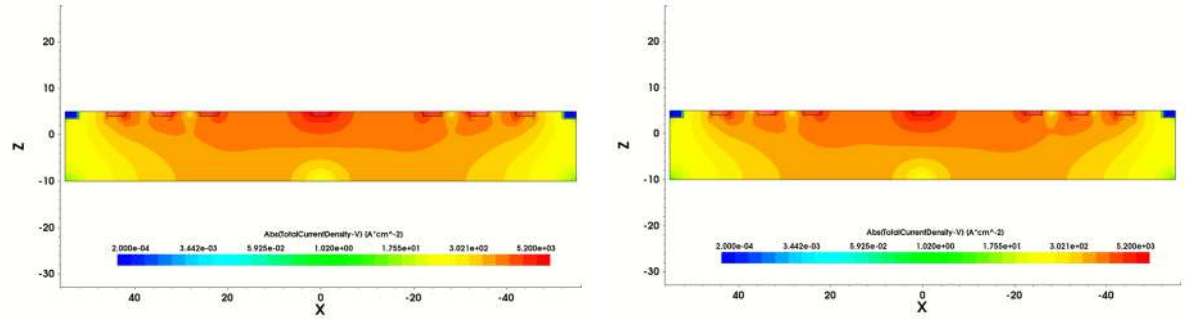

Figure 2(a) Carrier Deflection in the X- and Y-Axis Magnetic Sensor at 0 mT (b) Carrier Deflection in the X- and Y-Axis Magnetic Sensor at 300 mT

Z-Axis Magnetic Field Sensor

Figure 3 presents an isometric view of the structural design of the Z-axis magnetic field sensor. In this structure, the primary conduction current within the active region is injected from the current injection electrode (CIE), flows toward the lower-potential secondary current injection electrode (SCIE), and is subsequently directed from the SCIE region toward the Hall sensing electrode (HSE) or ground (GND) to complete the current loop. Therefore, the overall current path can be regarded as a two-stage transport channel consisting of CIE-to-SCIE and SCIE-to-HSE conduction paths.

When an external magnetic field is applied along the Z-axis, the electrons traveling through these channels are laterally deflected by the Lorentz force, resulting in an asymmetric carrier distribution between the left and right sides. Because the carriers undergo magnetic-field-induced lateral deflection in both the CIE-to-SCIE and SCIE-to-HSE transport channels, the structure effectively produces two successive deflections. This double-deflection mechanism enhances the sensor sensitivity and further increases the asymmetry between the two sides. Consequently, a difference is generated between the currents collected by the left and right base electrodes. This differential current serves as the sensing signal for the Z-axis magnetic field.

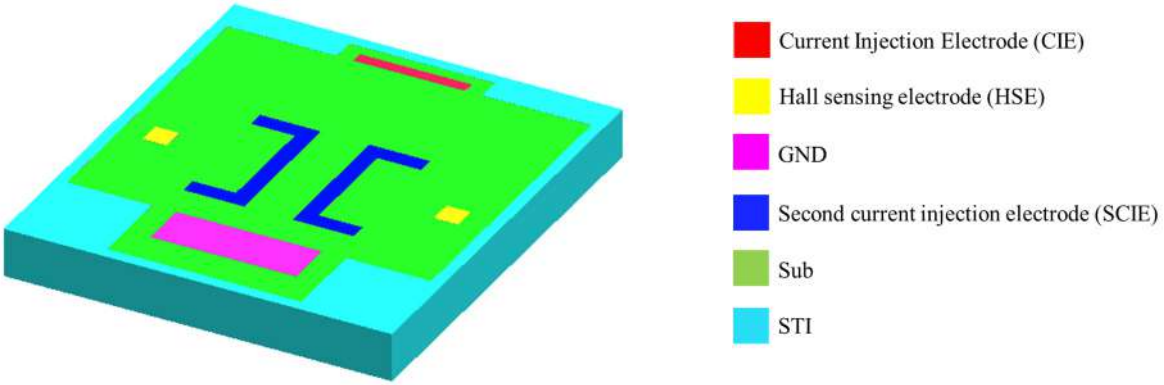

Figure 3 Structural Design of the Z-Axis Magnetic Field Sensor

Figure 4(a) shows the simulated current-density distribution under a zero magnetic field, whereas Figure 4(b) shows the simulated current-density distribution under an applied magnetic field of 300 mT.

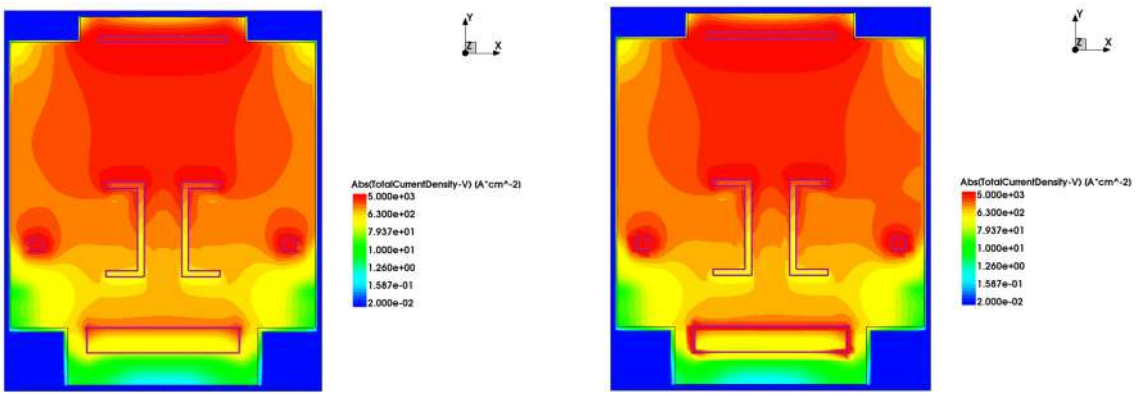

Figure 4 (a) Carrier Deflection in the Z-Axis Magnetic Sensor at 0 mT (b) Carrier Deflection in the Z-Axis Magnetic Sensor at 300 mT

RESULTS & DISCUSSION

Figure 5(a) also shows that the simulated response of the X- and Y-axis magnetic field sensor exhibits good linearity, with a linearity of 99.9%, indicating that it is a stable magnetic field sensor. For magnetotransistor-based sensors, cross-sensitivity must also be taken into consideration. As shown in Figure 5(b), when a magnetic field is applied to the Y-axis magnetic field sensor along non-sensing directions, the responses to the X- and Z-axis magnetic fields are close to zero, indicating that almost no output signal is generated.

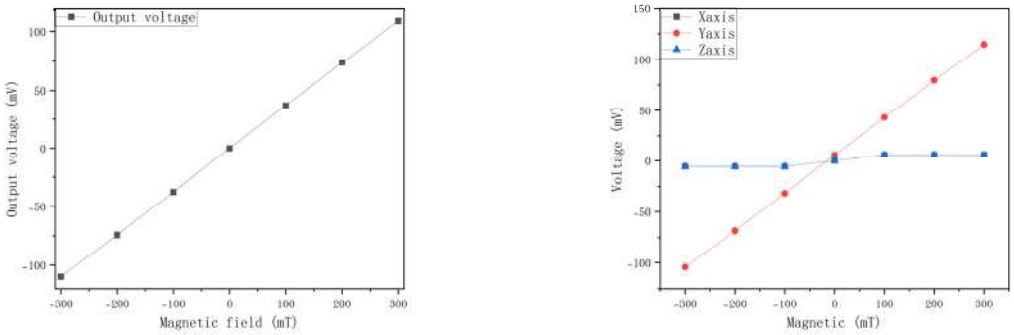

Figure 5 (a) Output Voltage versus Magnetic Field for the X- and Y-Axis Magnetic Field Sensor (b) Rotational Sensitivity of the Y-Axis Magnetic Field Sensor

Figure 6(a) also shows that the simulated response of the Z-axis magnetic field sensor exhibits good linearity, with a linearity of 99.9%, indicating that it is a stable magnetic field sensor. Figure 6(b) shows the response of the Z-axis magnetic field sensor when magnetic fields are applied along non-sensing directions. It can be observed that the responses to the X- and Y-axis magnetic fields are close to zero, indicating that almost no output signal is generated.

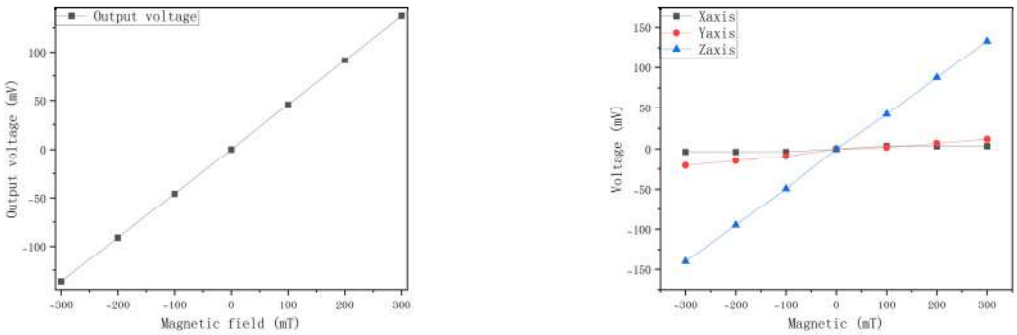

Figure 6 (a) Output Voltage versus Magnetic Field for the Z-Axis Magnetic Field (b) Rotational Sensitivity of the Z-Axis Magnetic Field Sensor

CONCLUSIONS

This study presents a three-axis magnetic field sensor fabricated using the UMC 0.18 μm CMOS process. Simulation results show sensitivities of 373 mV/T and 456 mV/T for the XY- and Z-axis sensors, respectively, with linearity reaching 99.9%. The near-zero outputs under non-sensing magnetic fields demonstrate good sensitivity, linearity, and directional selectivity.

ACKNOWLEDGEMENTS

The authors would like to thank the National Science and Technology Council of R.O.C. for financial support under the Grant NSTC-114-2221-E-005-069, and NSTC-115-2221-E-005 - 106.

REFERENCES

Crescentini, M., M. Biondi, A. Romani, M. Tartagni, and E. Sangiorgi. 2017. Optimum design rules for CMOS Hall sensors. Sensors 17(4): 765.

Leepattarapongpan, C., N. Penpondee, T. Phetchakul, W. Phengan, E. Chaowicharat, C. Hruanun, and A. Poyai. 2008. Merged three-terminal magnetotransistor based on the carrier recombination-deflection effect. In Proc. IEEE Sensors 2008, 399-402. Piscataway, N.J.: IEEE.

Paun, M. A., J. M. Sallese, and M. Kayal. 2012. Offset and drift analysis of Hall effect sensors: The influence of geometrical parameters. Digest Journal of Nanomaterials and Biostructures 7(3): 883-891.

Ruggeri, J., U. Ausserlechner, H. Köck, and K. M. Dowling. 2025. Inverted pyramid 3-axis silicon Hall-effect magnetic sensor with offset cancellation. Microsystems & Nanoengineering 11(1): 26.

Skucha, K., S. Gambini, P. Liu, M. Megens, J. Kim, and B. E. Boser. 2013. Design considerations for CMOS-integrated Hall-effect magnetic bead detectors for biosensor applications. Journal of Microelectromechanical Systems 22(6): 1327-1338.

Tseng, J. Z., P. J. Shih, C. C. Hsu, and C. L. Dai. 2017. A three-axis magnetic field microsensor fabricated utilizing a CMOS process. Applied Sciences 7(12): 1289.

Precision Agriculture Machinery and Systems 2 (PA-2)



PA-08

Proceedings of The 12th International Symposium on Machinery and Mechatronics for Agriculture and Biosystems Engineering (ISMAB 2026)
20-24 October 2026, Busan, Republic of Korea

ON-TREE PEAR SIZE ESTIMATION USING UPWARD-FACING RGB-D IMAGING IN HORIZONTAL TRELLIS ORCHARDS

Meguna OHATA [1], Jaehwan LEE [1], Tomoko HORIE [2], Hiromichi ITOH [1], Eiji MORIMOTO [1*]

[1]Graduate School of Agricultural Science, Kobe University, Kobe, Hyogo 657-8501, Japan
[2]Department of Agriculture, Kobe University, Rokkodai 1-1, Nada-ku, Kobe 657-8501, Japan
* Corresponding Author-- Email: morimoto@gold.kobe-u.ac.jp

Abstract: Non-destructive pre-harvest fruit sizing is essential for optimizing harvest logistics, market grading, and yield valuation. This study presents an automated, non-contact on-tree fruit sizing pipeline for horizontal trellis pear orchards using an upward-facing RGB-D camera. After localizing 2D fruit bounding boxes via YOLOv11s, depth data from the central 50% of each bounding box are extracted to isolate fruit surfaces from canopy clutter. Surface point clusters are segmented using DBSCAN clustering, and transverse equatorial diameters are estimated through RANSAC sphere fitting. In field validation across 56 mature 'Kousui' pears (reference diameters: 79.7–100.1 mm), the system achieved a mean absolute error (MAE) of 5.4 mm and a maximum absolute error of 14.5 mm, with 85.7% of the estimated diameters within ±10.0 mm of the reference measurements. These results demonstrate the potential of upward-facing geometric fitting for non-contact pre-harvest fruit size estimation under dense orchard canopies.

Key Words: Fruit size estimation, RGB-D camera, Sphere fitting, DBSCAN, Horizontal trellis.

INTRODUCTION

In commercial deciduous fruit production, pre-harvest quantification of fruit dimensions is important for predicting size-grade distributions, planning selective harvesting, and estimating potential economic returns. In Japanese pear (*Pyrus pyrifolia* Nakai) cultivation, horizontal trellis systems are widely used to improve light interception and promote uniform fruit development. However, conventional fruit size assessment typically relies on manual caliper measurements, which require direct contact with the fruit, are labor-intensive, and are generally limited to relatively small sample sizes.

Deep-learning-based two-dimensional (2D) vision models can provide reliable fruit detection; however, 2D bounding boxes alone cannot provide direct metric measurements because of depth ambiguity and perspective effects. RGB-D sensors overcome this limitation by providing depth information that enables three-dimensional (3D) reconstruction of fruit surfaces. Nevertheless, estimating fruit dimensions beneath horizontal trellis systems presents several challenges. Fruits are observed from a bottom-up perspective, foliage and branches may

partially obscure or border the fruit surface, and the non-spherical morphology of Japanese pears can produce perspective-dependent variations in the observed surface geometry.

To address these challenges, this study proposes and evaluates an automated, non-contact fruit sizing framework that integrates upward-facing RGB-D sensing, foreground point cloud extraction, and RANSAC-based sphere fitting for on-tree estimation of fruit equatorial diameter under nocturnal field conditions.

MATERIALS AND METHODS

Sensor Configuration and Data Acquisition

Field trials were conducted in a mature Japanese pear orchard ('Kousui') at the Food Resources Education and Research Center, Kobe University. A tracked mobile platform (Hunter SE, AgileX Robotics) traversed beneath the horizontal wire trellises. An RGB-D camera (Femto Bolt, Orbbec) was mounted in an upward-facing orientation to record overhead fruits. To minimize the effects of direct sunlight and dynamic canopy shadows, data acquisition was conducted at night using four diffused LED floodlights providing an illuminance of approximately 220 lux. Color images were logged at 3840 × 2160 pixels (15 fps), and depth maps were acquired at 1024 × 1024 pixels (15 fps) through a unified ROS 2 Humble node.

2D Detection and Region-of-Interest Extraction

A pretrained YOLOv11s model developed in our previous orchard study (Lee et al., 2026) was employed to generate 2D bounding boxes for fruit localization. A confidence threshold of 0.70 was applied. To prevent depth bleeding from background leaves positioned at higher canopy elevations, depth extraction was strictly confined to the central 50% spatial region of each detected bounding box.

Point Cloud Processing and Geometric Fitting

To ensure comprehensive depth data acquisition across the entire field of view (FOV) of the RGB camera, the depth sensor was operated in Wide FOV mode. Because the raw depth images acquired under this configuration present a circular FOV (Fig. 1a), geometric registration was performed to compensate for baseline displacement and FOV discrepancies, establishing a one-to-one pixel correspondence (u, v) between the RGB image and the depth coordinates. Furthermore, a morphological closing operation was applied to fill minor dropouts within the aligned depth map (Fig. 1b). Through this preprocessing pipeline, the RGB images (Fig. 1c) and depth information were integrated to enable downstream geometric analysis. Next, RGB and depth image pairs were extracted using synchronized timestamps. Based on the 2D bounding boxes, depth patches corresponding to each detected fruit were extracted and projected into 3D camera coordinates. To eliminate edge noise and disjointed leaf fragments, the DBSCAN algorithm was applied to segment the densest contiguous surface cluster corresponding to the fruit surface. Because the equatorial cross-section of the fruit closely approximates a circle despite its overall oblate profile, RANSAC sphere fitting was applied to the segmented point cluster. Fruit diameter was estimated as twice the fitted sphere radius.



Fig.1 Depth image alignment: (a) Raw data of the acquired depth image, (b) Depth image after alignment, (c) RGB image acquired simultaneously with the depth image.

Field Verification Protocol

System performance was evaluated on August 10, 2026, across 56 individual pears under stop-and-go robotic traversal. Reference ground truth was established by manually measuring the maximum transverse equatorial diameter of each target fruit using a digital vernier caliper immediately following sensor logging (Figure 2). Performance was quantified using the mean absolute error (MAE) and maximum absolute error.

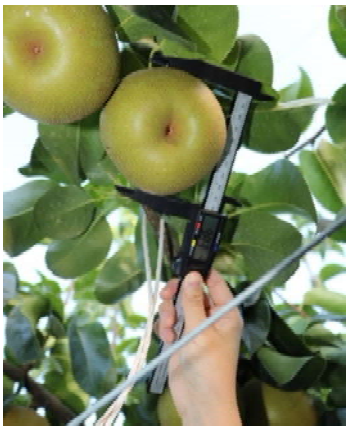

Fig. 2 Manual measurement of pear equatorial diameter using a digital caliper.

RESULTS & DISCUSSION

The reference equatorial diameters of the 56 evaluated pears ranged from 79.7 to 100.1 mm. The automated sizing pipeline achieved an overall mean absolute error (MAE) of 5.4 mm and a maximum absolute error of 14.5 mm. Furthermore, 85.7% of the tested fruits (48 of 56) had absolute estimation errors within 10.0 mm, indicating generally consistent sizing performance across the evaluated fruit-size range.

The interaction between fruit shape and viewing angle appears to be an important contributor to estimation error. Because Japanese pears exhibit a non-spherical, oblate morphology, variations in fruit orientation and camera position can alter the observed surface geometry and may consequently affect sphere-fitting accuracy. The maximum absolute error of 14.5 mm was observed for a fruit positioned near the outer region of the camera field of view, where the relatively oblique viewing angle may have contributed to distortion of the observed depth profile and overestimation of the fitted sphere radius. In contrast, fruits observed from near-nadir viewing angles exhibited a mean absolute error below 4.0 mm.

These findings suggest that single-frame sphere fitting can provide relatively accurate fruit-size estimates under near-nadir viewing conditions, whereas performance may deteriorate at more oblique viewing angles. Incorporating multi-view temporal surface reconstruction may therefore help reduce viewing-angle-related errors and improve the robustness of fruit size estimation across the orchard canopy.

The equatorial diameters of the 56 evaluated pear fruits ranged from 79.7 to 100.1 mm. The automated sizing pipeline achieved an overall MAE of 5.4 mm and a maximum absolute error of 14.5 mm. Furthermore, 85.7% of the tested fruits (48 of 56) exhibited absolute estimation errors within ±10.0 mm, indicating consistent sizing performance across the tested fruit-size range.

CONCLUSIONS

This study presented a non-contact fruit sizing framework that integrates upward-facing RGB-D sensing, DBSCAN-based surface segmentation, and RANSAC-based sphere fitting for Japanese pears grown under horizontal trellis systems. Field validation using 56 pears resulted in a mean absolute error (MAE) of 5.4 mm, with 85.7% of the estimated diameters exhibiting absolute errors within 10.0 mm of the manual caliper measurements. These results indicate the potential of the proposed approach for pre-harvest on-tree fruit size estimation. Future work will focus on multi-view spatial registration to reduce viewing-angle-related errors and improve the robustness of real-time fruit size estimation.

ACKNOWLEDGEMENTS

This work was supported by JSPS KAKENHI Grant-in-Aid for Early-Career Scientists Grant Number 25K18327.

REFERENCES

Khanam, R., and M. Hussain. 2024. YOLOV11: An overview of the key architectural enhancements. arXiv preprint arXiv:2410.17725.

Lee, J., M. Ohata, H. Itoh, and E. Morimoto. 2026. LiDAR-camera fusion for 3D fruit counting and density mapping in horizontal trellis orchards. Journal of Robotics and Mechatronics 38(2): 449–459. https://doi.org/10.20965/jrm.2026.p0449

PA-09

Proceedings of The 12th International Symposium on Machinery and Mechatronics for Agriculture and Biosystems Engineering (ISMAB 2026)
20-24 October 2026, Busan, Republic of Korea

DEVELOPMENT OF ROBUST 3D PEAR FRUIT COUNTING SYSTEM USING LIDAR-CAMERA FUSION

Jaehwan LEE [1], Meguna OHATA [1], Tomoko HORIE [2], Hiromichi ITOH [1], Eiji MORIMOTO [1*]

[1]Graduate School of Agricultural Science, Kobe University, Kobe, Hyogo 657-8501, Japan
[2]Department of Agriculture, Kobe University, Rokkodai 1-1, Nada-ku, Kobe 657-8501, Japan
* Corresponding Author-- Email: morimoto@gold.kobe-u.ac.jp

Abstract: This study presents a 3D fruit counting and spatial mapping system based on LiDAR–camera sensor fusion for horizontal trellis orchards. To prevent duplicate counting during repeated and overlapping observations, the proposed framework projects 2D fruit detections from a YOLOv11s detector into a dense global 3D coordinate frame constructed using Super-LIO simultaneous localization and mapping (SLAM). Individual fruits are then associated in the global coordinate frame and assigned persistent spatial IDs. Field validation on target trees showed that the system estimated 415 fruits compared with 390 ground-truth fruits, corresponding to a relative counting error of 6.4%. At the instance level, the system achieved a Precision of 0.93, a Recall of 0.99, and an F1-score of 0.96. These results demonstrate the effectiveness of the proposed framework for reducing duplicate counts across overlapping multi-pass observations and enabling accurate tree-level fruit enumeration.

Key Words: 3D fruit counting, Sensor fusion, Duplicate-count reduction, Super-LIO, YOLO.

INTRODUCTION

Accurate quantification of fruit load is essential for optimizing orchard management practices, including flower and fruit thinning, yield forecasting, and harvest logistics. In Japanese pear (*Pyrus pyrifolia* Nakai) production, horizontal trellis training systems are widely used to improve light interception and promote uniform fruit growth. However, managing crop load across expansive planar canopies requires considerable manual effort. Conventional orchard monitoring relies primarily on visual counting, which is subjective, labor-intensive, and unable to provide georeferenced spatial information.

Recent advances in agricultural robotics and deep learning have enabled automated fruit detection using image-based object detection models such as YOLO. However, 2D image-based fruit counting is vulnerable to duplicate counts when the same fruit is observed repeatedly from overlapping fields of view during multi-pass traversal. In contrast, 3D LiDAR sensors can accurately capture orchard geometry but lack the semantic information required

to reliably distinguish fruits from surrounding canopy structures. Therefore, integrating image-based semantic detection with spatial information from LiDAR and simultaneous localization and mapping (SLAM) offers an effective approach for robust fruit counting.

Our previous work demonstrated the feasibility of orchard-scale fruit mapping using FAST-LIO2 and stereo cameras (Lee et al., 2026). However, robust tree-level fruit enumeration under repeated observations remains challenging, particularly in dense horizontal trellis environments. Therefore, this study proposes and evaluates an integrated 3D fruit counting and spatial mapping framework combining an upward-facing RGB camera and a 3D LiDAR sensor on a mobile robot. The proposed pipeline projects 2D fruit detections into a global coordinate frame generated by Super-LIO SLAM, associating repeated observations to maintain spatial consistency and prevent duplicate counts during multi-pass traversal.

MATERIALS AND METHODS

System Configuration and Data Acquisition

Field experiments were conducted in a pear orchard at the Food Resources Education and Research Center, Kobe University. An unmanned ground vehicle (Hunter SE, AgileX Robotics) was used as the mobile platform. The perception system consisted of an upward-facing RGB camera (Femto Bolt, Orbbec) and a solid-state 3D LiDAR sensor (Mid-360s, Livox). The upward-facing sensor configuration enabled observation of fruits located above the vehicle beneath the horizontal trellis canopy.

To minimize illumination variability caused by direct sunlight and shadows, data acquisition was conducted at night under four LED floodlights providing approximately 220 lux. RGB images were acquired at a resolution of 3840 × 2160 pixels and a frame rate of 15 fps. Multi-sensor data logging and synchronization were managed using ROS 2 Humble.

3D Mapping and Instance-Level Sensor Fusion

A Super-LIO SLAM algorithm (Wang et al., 2025) was used to construct a consistent global 3D point cloud map of the orchard environment. The rigid-body transformation between the LiDAR and camera coordinate systems was estimated using an automatic LiDAR–camera extrinsic calibration toolbox (Koide et al., 2023).

For each 2D fruit detection, the corresponding 3D points within the camera viewing frustum were extracted from the global point cloud map. To suppress background canopy clutter, only points projected into the central region of each bounding box were used for fruit localization. The 3D centroid of the selected point cluster was then calculated as the estimated spatial position of the detected fruit.

Fruit instances were associated in the global SLAM coordinate frame using nearest-neighbor matching. Persistent spatial IDs were assigned to associated detections, enabling repeated observations of the same fruit to be identified and preventing duplicate counts across overlapping views and repeated traversals.

Fruit Detection Model

YOLOv11s (Khanam and Hussain, 2024) was used as the 2D fruit detector. The model was trained using a pear dataset containing 9,000 images and 451,051 annotated fruit instances established in our previous work (Lee et al., 2026). Training was conducted for 500 epochs with a batch size of 40.

For evaluation, inference was performed on 100 test images containing 4,077 annotated fruit instances. A confidence threshold of 0.70 was applied to balance detection accuracy and computational efficiency. The trained model was subsequently used to detect fruits in RGB images acquired by the upward-facing Femto Bolt camera.

Field Verification Protocol

Field validation was conducted on August 10, 2025, using two mature Japanese pear trees ('Kousui'). The mobile platform traversed the inter-row paths using a stop-and-go acquisition protocol to ensure dense LiDAR point accumulation and minimize motion blur in the RGB images.

Ground truth was established through exhaustive manual counting of all fruits on the target trees. The estimated number of unique fruit instances in the global coordinate frame was compared with the ground-truth count. Detection and association performance were evaluated using Precision, Recall, and F1-score.

RESULTS & DISCUSSION

Figure 1 illustrates the qualitative results of fruit localization and spatial mapping. The proposed framework reconstructed a coherent global 3D point cloud map and registered individual fruit instances in the SLAM coordinate frame (Fig. 1a). The resulting spatial distribution was consistent with the fruit arrangement observed in the upward-facing RGB images (Fig. 1b). By associating repeated observations in the global coordinate frame, the proposed framework successfully reduced duplicate counts across overlapping observations during multi-pass traversal.



Fig.1 Quantitative and qualitative results of the fruit counting algorithm: (a) Individual fruits registered in the SLAM coordinate system on the 3D point cloud, (b) Fruit arrangement observed in the RGB image.

In the quantitative evaluation of the target trees, the system estimated 415 fruits compared with 390 ground-truth fruits, corresponding to a relative counting error of 6.4%. At the instance level, the system achieved a Precision of 0.93, a Recall of 0.99, and an F1-score of 0.96.

The overestimation of 25 fruits was primarily caused by false-positive detections in which senescent yellow leaves and artificial branch-training tapes exhibited visual characteristics similar to those of pear fruits. In addition, minor SLAM drift during turning maneuvers occasionally caused the spatial displacement between repeated observations to exceed the association threshold, resulting in duplicate registrations. False negatives were mainly associated with severe physical occlusion by primary scaffold limbs.

These results indicate that the proposed LiDAR–camera fusion framework can effectively maintain spatial consistency among repeated fruit observations and reduce duplicate counts during multi-pass acquisition. Further improvements in 3D geometric filtering and hard-negative mining during model fine-tuning are expected to reduce false-positive detections and improve counting accuracy.

CONCLUSIONS

This study developed a 3D pear fruit counting and spatial mapping framework combining an upward-facing RGB camera, a solid-state 3D LiDAR sensor, and Super-LIO SLAM. By projecting 2D visual detections into a global 3D point cloud frame and tracking instances via persistent spatial IDs, the system demonstrated robust tree-level enumeration (F1-score: 0.96, counting error: 6.4%) and effectively suppressed multi-view redundancies beneath dense horizontal trellises. Future work will focus on incorporating 3D geometric filtering and hard-negative sample learning to further suppress false positives arising from orchard structures and training materials.

ACKNOWLEDGEMENTS

This work was supported by JSPS KAKENHI Grant-in-Aid for Early-Career Scientists Grant Number 25K18327.

REFERENCES

Khanam, R., and M. Hussain. 2024. YOLOV11: An overview of the key architectural enhancements. arXiv preprint arXiv:2410.17725.

Koide, K., S. Oishi, M. Yokozuka, and A. Banno. 2023. General, single-shot, target-less, and automatic LiDAR-camera extrinsic calibration toolbox. arXiv preprint arXiv:2302.05094.

Lee, J., M. Ohata, H. Itoh, and E. Morimoto. 2026. LiDAR-camera fusion for 3D fruit counting and density mapping in horizontal trellis orchards. Journal of Robotics and Mechatronics 38(2): 449–459. https://doi.org/10.20965/jrm.2026.p0449

Wang, L., X. Zhang, C. Li, D. He, Y. Pan, and J. Yi. 2025. Super-LIO: A robust and efficient LiDAR-inertial odometry system with a compact mapping strategy. arXiv preprint arXiv:2509.05723.

PA-10

Proceedings of The 12th International Symposium on Machinery and Mechatronics for Agriculture and Biosystems Engineering (ISMAB 2026)
20-24 October 2026, Busan, Republic of Korea

GROUND-BASED LIDAR FOR CROP STRUCTURAL ASSESSMENT: FIELD ACQUISITION AND WIND-EFFECT EVALUATION

Eldon DE PADUA[1], Jaehwan LEE[1], Eiji MORIMOTO[1]*

[1]Graduate School of Agricultural Science, Kobe University, Kobe, Hyogo, Japan
*Corresponding Author: morimoto@gold.kobe-u.ac.jp

Abstract: Structural information is needed to complement spectral indicators for more comprehensive crop assessment. This study experimentally evaluated a ground-based LiDAR approach for crop structural measurement using canopy height (CH) as the main indicator. The work consisted of three parts: evaluation of solid-state 3D LiDAR dimensional measurement performance, field-scale point-cloud acquisition, and controlled evaluation of wind-induced canopy effects. Reference targets of known dimensions were manually measured and scanned with LiDAR, and the extracted dimensions were evaluated using R^2 and RMSE. Field surveys were conducted in rice fields at Awaji, Kasai, and Tsuruga, Japan. A controlled indoor experiment was also conducted using *Makomo* grass under wind speeds of 0, 8.1, 9.8, and 12.2 ms^{-1}. LiDAR-derived dimensions showed strong agreement with reference measurements, with $R^2 \approx 1.0$ and RMSE=0.04 m. The field surveys covered eight fields, 344 are, and 12 visits, generating approximately 866.6 million LiDAR points for ongoing structural evaluation. The acquired datasets are currently under further evaluation for canopy-height mapping. Meanwhile, LiDAR-derived CH decreased with increasing wind speed, and a quadratic wind-response model fitted the tested conditions with R^2=0.9975. These results support the use of ground-based LiDAR for crop structural assessment while highlighting wind-induced canopy motion as an important source of uncertainty requiring crop-specific validation.

Key Words: Ground-based LiDAR, canopy height, point cloud, wind response

INTRODUCTION

Crop growth is commonly assessed using spectral indicators such as NDVI, EVI, NDRE, and OSAVI. These indices are derived from canopy reflectance and are related to optical responses associated with greenness, chlorophyll, leaf area index (LAI), and biomass. However, spectral indicators do not directly quantify three-dimensional crop structure such as canopy height, architecture, or volume. Structural information therefore provides a complementary description of crop physical form and development. This complementarity is important for comprehensive crop assessment: Gong et al. (2021) reported that adding canopy height to vegetation-index models reduced whole-season rice LAI estimation error by more than 20%, while Lu et al. (2019) showed improved wheat biomass estimation when image and point-cloud information were combined.

LiDAR is suitable for structural sensing because laser-based ranging generates three-dimensional point clouds that represent canopy geometry and vertical structure. Ground-based LiDAR enables non-destructive canopy-height measurement and related crop structural assessment (Jimenez-Berni et al., 2018). Accordingly, this study experimentally evaluated a ground-based LiDAR approach for crop structural assessment using as the main structural indicator, with emphasis on sensor measurement performance, field-scale point-cloud acquisition, and wind-induced measurement effects.

The objectives were to: (1) evaluate the dimensional measurement performance of the solid-state 3D LiDAR sensor; (2) conduct field-scale LiDAR surveys and establish point-cloud datasets for subsequent canopy-height mapping and evaluation; and (3) quantify wind-induced canopy effects on LiDAR-derived CH and develop a preliminary wind-response correction model.

MATERIALS AND METHODS

LiDAR Sensor and measurement evaluation

A solid-state 3D LiDAR sensor (MID-360, Livox) was used as the ground-based LiDAR sensor. Key specifications include range accuracy of ≤2 cm at 10 m and ≤3 cm at 0.2 m, angular accuracy <0.15°, and maximum detection ranges of 40 m at 10% reflectivity and 70 m at 80% reflectivity. For measurement evaluation, reference targets of known dimensions were measured manually, scanned with LiDAR, and extracted from the resulting point clouds. LiDAR-derived dimensions were compared with the reference measurements using R^2 and RMSE.



Fig.1 Livox MID-360 LiDAR device used for ground-based structural sensing.

Field-scale LiDAR data acquisition and georeferencing

Ground-based LiDAR surveys were conducted in rice fields at Awaji, Kasai, and Tsuruga, Japan. Data were acquired mainly by walking along the field boundaries using the LiDAR. Super-LIO (Wang et al., 2025) was used for simultaneous localization and mapping (SLAM) to generate three-dimensional point clouds in a local coordinate system. For georeferencing, at least four field markers with known RTK-GNSS coordinates were placed or identified within each survey area. The corresponding marker positions in the LiDAR point cloud were used to transform the local point-cloud coordinates into real-world coordinate system. The resulting georeferenced point-cloud datasets were then prepared for subsequent canopy-height mapping and evaluation.

Controlled wind experiment

Field observations indicated that wind could bend and move the crop canopy and alter the canopy position captured by LiDAR. A controlled indoor experiment was therefore conducted using *Makomo* grass (Manchurian wild rice). The Livox MID-360 LiDAR and Intel RealSense D435 camera were fixed at defined positions and viewing angles, while an axial fan inclined at 30° generated four wind conditions: 0, 8.1, 9.8, and 12.2 m/s. This fixed geometry was used to isolate and quantify the wind response of LiDAR-derived CH.

RESULTS & DISCUSSION

LiDAR measurement performance

In Fig. 2, LiDAR-derived dimensions showed strong agreement with the manual reference measurements ($R^2 \approx 1.0$; RMSE= 0.04 m). The regression relationship was close to 1:1 line, indicating that the Livox MID-360 LiDAR reproduced the dimensions of the reference targets consistently over the tested measurement range. The relatively low RMSE further indicates limited dimensional error. These results supported the use of the Livox MID-360 LiDAR for subsequent field data acquisition; however, they represent sensor dimensional performance on reference targets rather than direct validation of crop canopy-height accuracy.

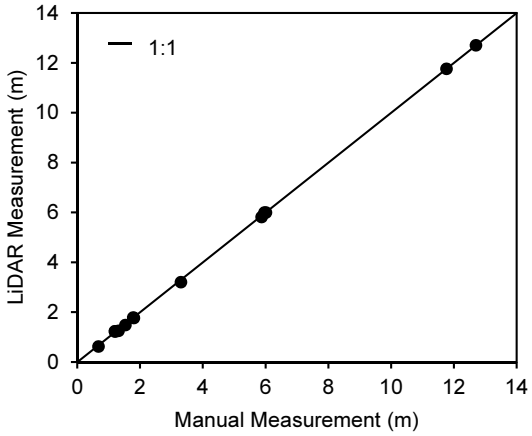

Fig.2 Livox MID-360 LiDAR dimensional measurement performance.

Field experiment inventory and preliminary mapping

Field surveys covered eight fields with a combined area of 344 are across 12 visits. Approximately 866.6 million LiDAR points were acquired: 434.6 million in Awaji; 16.8 million in Kasai; and 415.2 million in Tsuruga. The Awaji and Tsuruga rice fields contributed most of the total point-cloud volume. The resulting georeferenced point-cloud datasets provide the basis for subsequent canopy-height mapping and structural evaluation, which are still under further analysis.

Wind response and preliminary correction model

In Fig. 3, LiDAR-derived CH decreased as wind speed increased. The percent change in CH was described by a quadratic wind-response relationship, $y = -0.0004x^2 + 0.0007x - 7\times10^{-5}$,

with $R^2 = 0.9975$ across the tested wind settings. This relationship provides a preliminary basis for adjusting wind-affected CH toward the no-wind condition. Because it was derived from one controlled *Makomo* experiment and four wind settings, it is interpreted as a preliminary model requiring crop-specific testing and validation.

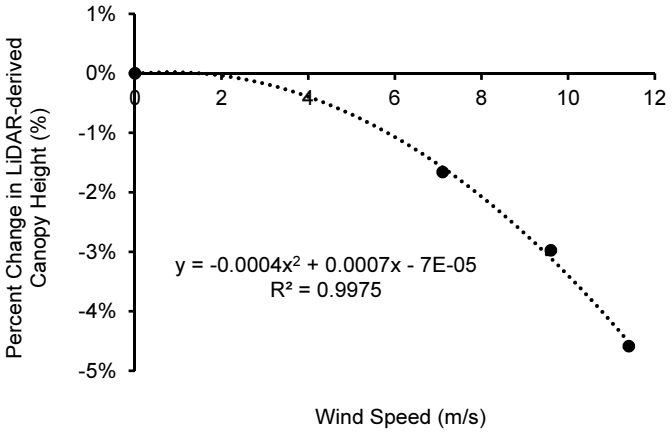

Fig.3 Wind-response relationship.

CONCLUSIONS

The Livox MID-360 showed strong agreement with reference target measurements. The ground-based LiDAR workflow enabled field-scale acquisition of crop structural point-cloud data, although reliable CH mapping still requires further evaluation. Wind reduced LiDAR-derived CH, and the preliminary wind-response model provides a basis for correction toward the no-wind condition. Future work will extend the controlled wind experiment to different crop species and growth stages, develop and validate crop-specific wind-correction models, apply the models to field LiDAR data for improved CH and broader three-dimensional structural estimation, and integrate spectral information from a spectral device and structural information from LiDAR for more comprehensive crop growth and condition assessment.

REFERENCES

Gong, Y., Yang, K., Lin, Z., Fang, S., Wu, X., Zhu, R., & Peng, Y. 2021. Remote estimation of leaf area index (LAI) with unmanned aerial vehicle (UAV) imaging for different rice cultivars throughout the entire growing season. Plant Methods, 17, 88. https://doi.org/10.1186/s13007-021-00789-4

Jimenez-Berni, J. A., Deery, D. M., Rozas-Larraondo, P., Condon, A. G., Rebetzke, G. J., James, R. A., Bovill, W. D., Furbank, R. T., & Sirault, X. R. R. 2018. High throughput determination of plant height, ground cover, and above-ground biomass in wheat with LiDAR. Frontiers in Plant Science, 9, 237. https://doi.org/10.3389/fpls.2018.00237

Lu, N., Zhou, J., Han, Z., Li, D., Cao, Q., Yao, X., Tian, Y., Zhu, Y., Cao, W., & Cheng, T. 2019. Improved estimation of aboveground biomass in wheat from RGB imagery and point cloud data acquired with a low-cost unmanned aerial vehicle system. Plant Methods, 15, 17. https://doi.org/10.1186/s13007-019-0402-3

Wang, L., X. Zhang, C. Li, D. He, Y. Pan, and J. Yi. 2025. Super-LIO: A robust and efficient LiDAR-inertial odometry system with a compact mapping strategy. arXiv preprint arXiv:2509.05723.

PA-11

Proceedings of The 12th International Symposium on Machinery and Mechatronics for Agriculture and Biosystems Engineering (ISMAB 2026)
20-24 October 2026, Busan, Republic of Korea

FIELD PERFORMANCE OF THE SELF-PROPELLED CABBAGE HARVESTERS UNDER SINGLE AND DOUBLE-ROW FIELD CONDITIONS

Cholet Nyangoma Atulinda[1], Md Nasim Reza[1,2], Ezatullah Zakir[1], Md Razob Ali[1], Jose Pocholo Dorongon[2], Sun-Ok Chung[1,2*]

[1]Department of Agricultural Machinery Engineering, Graduate School, Chungnam National University, Daejeon 34134, Republic of Korea
[2]Department of Smart Agricultural Systems, Graduate School, Chungnam National University, Daejeon 34134, Republic of Korea
*Corresponding Author- - Voice: +82-42-821-6712, Email: sochung@cnu.ac.kr

Abstract: This study compared the field performance and collection quality of self-propelled single-row and double-row cabbage harvesters under different cultivation conditions. Field performance was evaluated using working speed, theoretical field capacity, effective field capacity, field efficiency, and operational interruptions, while collection quality was assessed from collection outcomes and cabbage damage. The single-row harvester was tested in Mungyeong-si on rounded ridges under wet-soil conditions. The average ridge width, furrow width, row spacing, and plant spacing were 38.17, 36.17, 70.00, and 37.58 cm, respectively. The mean cabbage mass and uprooting force were 2.07 kg and 104.7 N. The double-row harvester was tested in Haenam-gun on flat, plastic-mulched ridges in dry sandy-loam soil with a moisture content of 22% and soil hardness of 3.1 MPa. The mean cabbage mass and uprooting force were 4.968 kg and 266.9 N, respectively. The average operating speeds of the single- and double-row harvesters were 0.333 and 0.350 km/h, respectively. Their theoretical field capacities were 0.0233 and 0.0301 ha/h, while their effective field capacities were 0.0221 and 0.0284 ha/h, corresponding to field efficiencies of 96.7% and 94.4%, respectively. The single-row harvester completed five of six trials without collection failure, with one clogging event. The double-row harvester experienced two normal runs, two clogging events, and one delay. Among 233 cabbage heads evaluated in the double-row field, 209 were normally collected and 24 were damaged, corresponding to a damage rate of 10.3%. The double-row system provided greater field capacity because of its wider working width, whereas both harvesters showed similar field efficiency. The results indicate that feeding and conveying mechanisms should be adjusted according to cultivation pattern, cabbage properties, and soil conditions to improve collection reliability and reduce crop damage.

Key Words: Cabbage harvester, field capacity, field efficiency, collection quality, crop damage, cultivation pattern

INTRODUCTION

Field adaptability is a central requirement for self-propelled cabbage collection because cabbage is cultivated under markedly different ridge layouts and field conditions. In the present project, the harvesters were evaluated at two representative sites: a rounded single-row field and a flat double-row field. These sites differed not only in row arrangement, but also in working width, soil condition, mulch, crop mass, and uprooting force. Such differences can alter crop feeding, conveying demand, machine throughput, and the likelihood of operational interruptions.

A meaningful comparison therefore requires more than operating speed alone. Field capacity indicates the area that can be covered per unit time, whereas field efficiency reflects how closely effective operation approaches theoretical capacity after accounting for field operation. Collection reliability and crop damage are also important because a machine can achieve high area capacity while still experiencing clogging, delays, or unacceptable crop damage. The project consequently evaluated both field performance and collection quality under the two cultivation patterns.

The objective of this study was to compare the field performance and collection quality of self-propelled single-row and double-row cabbage harvesters under their respective field conditions, with emphasis on operating speed, field capacity, field efficiency, operational interruptions, and cabbage damage. A further objective was to identify practical machine-improvement needs associated with differences in cultivation pattern and crop characteristics

MATERIALS AND METHODS

Experimental sites and cultivation conditions

The single-row field test was conducted in Mungyeong-si on 21 May 2026. The field used rounded single-row ridges and had wet-soil conditions. Twelve measurements were used to characterize the cultivation pattern. Average ridge width, furrow width, row spacing, and plant spacing were 38.17, 36.17, 70.00, and 37.58 cm, respectively. The machine working width used for the performance test was 0.70 m.
The double-row test was conducted in Haenam-gun on 16 June 2026. The field was an upland field with flat, two-row, plastic-mulched ridges. The soil was dry sandy loam with a moisture content of 22% and hardness of 3.1 MPa, and no weeds were reported. The machine working width was 0.86 m. The field geometry and crop conditions therefore represented a distinctly different operating environment from the single-row site. Table 1 shows field and crop conditions used for the single-row and double-row harvester tests.

Table 1 Field and crop conditions used for the single-row and double-row harvester tests.

Parameter	Single-row field	Double-row field
Location	Mungyeong-si	Haenam-gun
Cultivation pattern	Rounded ridge, single row	Flat ridge, double row

Parameter	Single-row field	Double-row field
Soil / surface condition	Wet soil	Dry sandy loam; plastic mulch
Soil moisture / hardness	Not reported	22% / 3.1 MPa
Working width (m)	0.70	0.86
Ridge width (cm)	38.17 (mean)	Approximately 87.8 (mean)
Row spacing (cm)	70.00 (mean)	Approximately 42.3 (mean)
Plant spacing (cm)	37.58 (mean)	Approximately 43.0 (mean)
Mean cabbage mass (kg)	2.07	4.968
Mean uprooting force (N)	104.7	266.9

Cabbage physical-property measurements

Before, and during the field tests, cabbage physical properties were measured to describe the crop presented to each harvester. At the single-row site, the measured parameters included uprooting force, mass, vertical height, head width, base size, root length and mass, and leaf dimensions. The mean uprooting force and mass were 104.7 N and 2.07 kg respectively. At the double-row site, the corresponding mean uprooting force and mass were 266.9 N and 4.968 kg. These values show that the double-row test involved substantially heavier cabbages and higher removal force.

Field-performance evaluation

Six 10-m runs were conducted for the single-row harvester and five 10-m runs for the double-row harvester. For each run, travel time and operating speed were recorded together with operational observations such as normal collection, clogging, or delay. Theoretical field capacity (TFC) was determined from operating speed and working width. Effective field capacity (EFC) was determined from harvested area and actual field working time, and field efficiency (FE) was calculated as EFC/TFC x 100. Operational interruptions were retained in the performance interpretation because they directly affect practical collection reliability.

Collection quality was evaluated from the observed collection outcome. For the double-row field, 233 cabbage heads from five rows were classified as normally collected or damaged. The crop-damage rate was calculated as the number of damaged heads divided by the total number of evaluated heads multiplied by 100.

RESULTS & DISCUSSION

Field and crop differences

The two test sites presented clearly different crop and field conditions (Table 1). The mean cabbage mass in the double-row field was about 2.4 times that in the single-row field, while the mean uprooting force was about 2.5 times higher. The double-row site also used plastic mulch and dry sandy-loam soil, whereas the single-row site was characterized by wet soil. Consequently, the comparison represents field performance under two practical cultivation systems rather than a controlled experiment in which row number was the only changing factor. This distinction is important when interpreting differences in clogging, damage, and collection

behavior. Table 2 shows field performance outcomes of the single-row and double-row harvesters.

Table 2 Field performance and collection outcomes of the single-row and double-row harvesters.

Performance indicator	Single-row harvester	Double-row harvester	Comparison / interpretation
Average operating speed (km/h)	0.333	0.350	Similar practical travel speed
Theoretical field capacity (ha/h)	0.0233	0.0301	Double-row: about 29% higher
Effective field capacity (ha/h)	0.0221	0.0284	Double-row: about 28.5% higher
Field efficiency (%)	96.7	94.4	Difference: 2.3 percentage points
Run outcome	5 normal, 1 clog	2 normal, 2 clogs, 1 delay	More interruptions in double-row test
Collection quality	Run-level collection outcome	209 normal, 24 damaged of 233	Double-row damage rate: 10.3%

Field capacity and efficiency

Average operating speed differed only slightly between the single-row and double-row harvesters, at 0.333 and 0.350 km/h, respectively. In contrast, theoretical field capacity increased from 0.0233 ha/h for the single-row harvester to 0.0301 ha/h for the double-row, an increase of approximately 29%. Effective field capacity similarly increased from 0.0221 to 0.0284 ha/h. The main practical reason for this increase was the wider working width of the double-row system (0.86 m versus 0.70 m), rather than a large difference in travel speed.

Field efficiency was a bit different: 96.7% for the single-row harvester and 94.4% for the double-row harvester. The difference of only 2.3% indicating that both systems converted theoretical capacity into effective field capacity at a comparable overall level. However, close field efficiency does not imply similar collection reliability, because the type and frequency of interruptions differed between the two tests.

$$\mathrm{FE} = \frac{E_{fc}}{T_{fc}} X\ 100\% \quad (1)$$

Where:

FE = Field efficiency

$E_{fc} = \text{Effective field capacity}$

$T_{fc} = \text{Theoretical field capacity}$

Operational interruptions and collection quality

The single-row harvester completed five of six test runs with all cabbages collected and recorded one clogging event. The double-row harvester recorded two normal runs, two

clogging events, and one delay. In the double-row field, 209 of 233 evaluated heads were normally collected and 24 were damaged, corresponding to a crop-damage rate of 10.3%. Thus, the double-row system provided higher area capacity but also showed more frequent interruptions and measurable crop damage under the tested conditions.

The observed difference should not be attributed to row arrangement alone. The double-row test also involved larger cabbages, approximately 2.5 times greater uprooting force, plastic mulch, and different soil conditions. These factors change the loading and feeding environment presented to the machine. The results therefore support practical improvement of the feeding and conveying mechanisms, including better synchronization of conveyor motion and greater tolerance to crop-size variation, misalignment, and clogging. Machine settings and intake geometry should be adjusted to the cultivation pattern and crop condition rather than applying one fixed configuration across sites. Figure 1 shows operational interruptions during field performance.

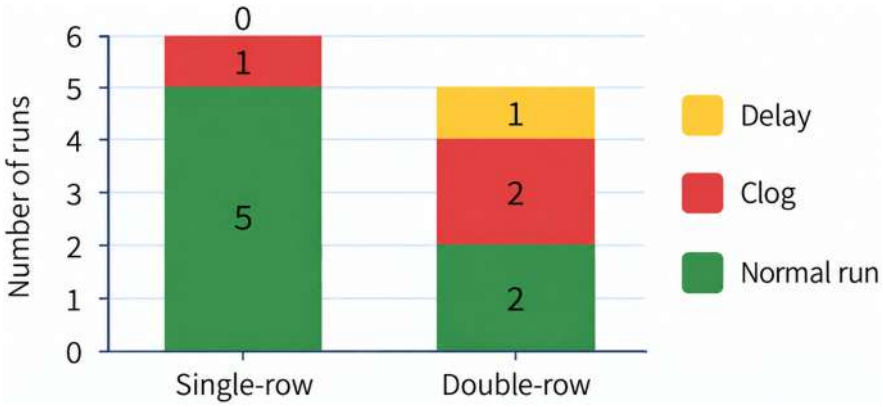

Fig. 1 operational interruptions

CONCLUSIONS

The self-propelled single-row and double-row cabbage harvesters showed similar operating speeds and field efficiencies but different field capacities and collection behavior. The double-row harvester achieved a theoretical field capacity of 0.0301 ha/h and an effective field capacity of 0.0284 ha/h, compared with 0.0233 and 0.0221 ha/h for the single-row harvester. Field efficiencies were 96.7% and 94.4%, respectively. The higher capacity of the double-row system was mainly associated with its wider working width.

Collection reliability differed more clearly than field efficiency. The single-row harvester had one clogging event in six trials, whereas the double-row harvester had two clogging events and one delay in five trials. The double-row test also produced a 10.3% damage rate among 233 evaluated heads. These findings indicate that future machine improvement should focus on crop feeding, conveyor synchronization, and adjustment to ridge pattern, cabbage size, uprooting resistance, mulch, and soil conditions. Because the two sites differed in several factors simultaneously, future comparative tests under matched field conditions are recommended to isolate the effect of row configuration and to quantify crop damage for both harvester types.

REFERENCES

Chung, S.-O., & Reza, M. N. 2024. *Development and performance evaluation of a self-propelled cabbage harvester under Korean field conditions*. Journal of Biosystems Engineering, 49(2), 85–96.

Sarkar, P., H. Raheman, and A. U. Sahoo. 2025. Field performance evaluation and economic analysis of an electric cabbage harvester suitable for small farms. *Discover Agriculture* 3: 15.

Shibusawa, S., & Sato, K. 2019. *Mechanization of vegetable harvesting in East Asia: Current status and prospects*. Agricultural Mechanization in Asia, Africa and Latin America, 50(4), 23–30.

Zhang, Q., & Peterson, D. E. 1999. *Field capacity and efficiency of agricultural machinery under varying soil conditions*. Transactions of the ASAE, 42(4), 927–934.

Kim, J. H., Park, S. H., & Chung, S.-O. 2022. *Performance analysis of conveyor mechanisms in vegetable harvesters*. Journal of the Korean Society for Agricultural Machinery, 27(1), 15–24.

Griepentrog, H. W., & Nielsen, J. 2018. *Crop damage assessment in mechanized vegetable harvesting*. Precision Agriculture, 19(5), 765–781.

Reza, M. N., Ali, M. R., & Chung, S.-O. 2025. *Design optimization of feeding mechanisms for cabbage harvesters*. Biosystems Engineering, 210, 45–57.

Kataoka, T., & Okamoto, H. 2017. *Evaluation of uprooting forces and mechanical properties of cabbage roots for harvesting machine design*. Journal of Agricultural Engineering, 54(3), 112–120.

PA-12

Proceedings of The 12th International Symposium on Machinery and Mechatronics for Agriculture and Biosystems Engineering (ISMAB 2026)
20-24 October 2026, Busan, Republic of Korea

DEVELOPMENT AND EVALUATION OF A TRANSFER PLATFORM FOR RAIL-TO-RAIL MOVEMENT IN GREENHOUSE HORTICULTURE

Sota Yoshida[1]*, Kota Shimomoto[1], Nozomu Ohta[1], Tokihiro Fukatsu[1]

[1]Institute of Agricultural Machinery, National Agriculture and Food Research Organization, 1-31-1 Kannondai, Tsukuba-shi, Ibaraki, 305-0856, Japan
*Corresponding Author-- Voice: +81-29-838-8909, Email: yoshida.sota012@naro.go.jp

Abstract: This study aimed to equip commercial automated guided vehicles (AGVs) with the capability to transport rail-guided vehicles (RGVs) traveling on heating pipe rails in greenhouses. A transfer platform unit was developed using pipes with the same profile as the heating pipe rails used in greenhouse facilities. The transfer platform unit was installed on both custom-built vehicles incorporating a commercially available AGV unit (Vehicle A), and a commercial AGV (Vehicle B). Transfer experiments were conducted to evaluate the adaptability of the platform unit to Vehicle A and Vehicle B. In these experiments, the RGV was transferred from the platform unit to the rail installed between crop rows and vice versa. The relative position between the rail end and platform unit was varied in both the longitudinal and lateral directions. Transfer success rates were evaluated under each condition. The results indicate that both vehicles achieved stable rail-to-rail transfer even under positional misalignment conditions.

Key Words: Automated guided vehicle, Greenhouse horticulture, Multi-row operations, Robotics, Transportation

INTRODUCTION

Various robotic and monitoring systems are being developed to reduce labor requirements for harvesting and crop management in greenhouse horticulture. Several large-scale greenhouse facilities consist of cultivation areas equipped with heating pipe rails and concrete floors. Therefore, mobile systems designed to perform tasks on plants throughout the facility are required to travel on both rails and concrete floors.

Shimomoto et al. (2024) developed a system comprising a rail-guided vehicle (RGV) that moves on heating pipe rails and a row-transfer platform that carries the RGV and shifts it to the target rail. In the row-transfer platform, wheel derailment caused by misalignment between the rail and the transfer platform was a major issue. To address this limitation, we previously developed an improved row-transfer platform equipped with a transfer section using the profile of the heating pipe rails and fitted the RGV with flanged wheels (Yoshida et al., 2025). The improved system was shown to tolerate a certain range of longitudinal and lateral positional offsets. However, the row-transfer platform could only transfer RGVs between rails. Therefore, despite its simple and cost-effective structure, its practical applicability has remained limited.

In this study, we developed a transfer platform unit based on the profile of the heating pipe rails to extend the previously developed rail-shifting mechanism for RGVs to commercial automated guided vehicles (AGVs). The unit was installed on two distinct commercial AGVs, and transfer experiments were conducted to evaluate the transfer stability and versatility of the proposed mechanism.

MATERIALS AND METHODS

Materials

A transfer platform unit was developed using pipes with the same profile as the heating pipe rails and mounted on two types of commercial AGVs. Vehicle A was a custom-built AGV based on a commercially available AGV unit (FH-B50066 MJ2, Yazaki Kako Co., Ltd.) that follows magnetic tape installed on the ground (Fig. 1(a)). Vehicle B was a commercial AGV (M2, Ricoh Co., Ltd.) that follows black tape detected by an onboard camera (Fig. 1(b)).

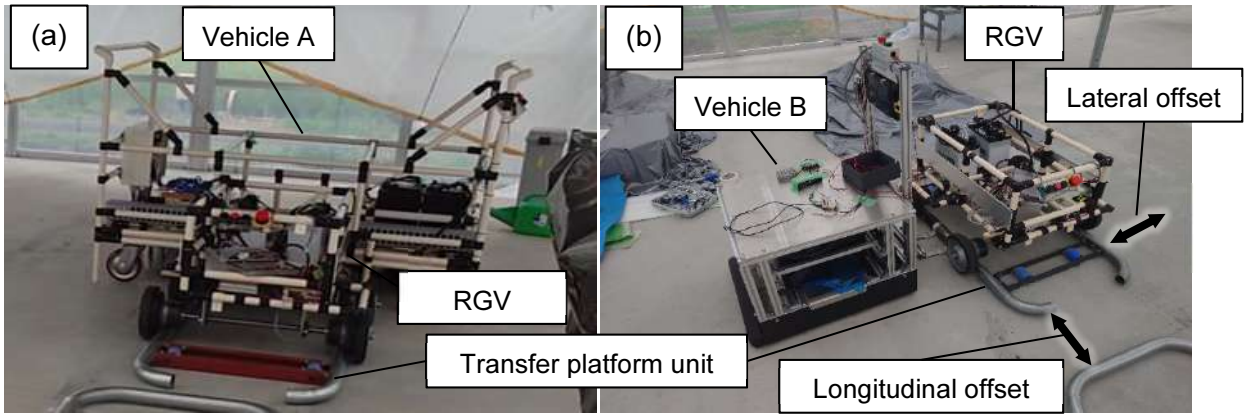

Fig. 1 Two types of commercial AGVs equipped with a transfer platform unit, (a): Vehicle A (custom-built AGV based on an AGV unit (FH-B50066 MJ2, Yazaki Kako Co., Ltd.), (b): Vehicle B (commercial AGV (M2, Ricoh Co., Ltd.))

The RGV consisted of a pipe-frame structure (28-mm-diameter Creform, Yazaki Kako Co., Ltd.), wheels (drive wheels: K-676-1 and K-673-200-A; driven wheels: K-677-1 and K-673-200, Takigen MFG Co., Ltd.), DC brushless motors (BLHM51000KC-GFS, Oriental Motor Co., Ltd.), and two 12 V batteries (EB35, GS Yuasa Co., Ltd.).

RGV transfer experiments

The reference position was defined as the position where the end of the greenhouse rail coincided with the end of the platform unit, and positional offsets were introduced in both the longitudinal and lateral directions (Yoshida et al., 2025). One trial consisted of a round-trip transfer in which the RGV moved from the unit to the greenhouse rail and then returned to the unit. Five trials were conducted under each condition, and the transfer success rate was recorded.

RESULTS & DISCUSSION

Table 1 presents the results for Vehicle A under different longitudinal and lateral offsets. The

RGV was able to transfer at a lateral offset of 12 cm when the longitudinal offset was 8 cm or greater. In addition, the RGV was able to transfer at a lateral offset of 8 cm under all longitudinal offset conditions. Table 2 presents the results for Vehicle B under different longitudinal and lateral offsets. The RGV was able to transfer at a lateral offset of 12 cm when the longitudinal offset was 0, 8, or 20 cm. Furthermore, the RGV was able to transfer at a lateral offset of 8 cm under all longitudinal offset conditions.

Table 1 Transfer success rates (%) of Vehicle A under different longitudinal and lateral offset conditions.

Longitudinal offset(cm)	Lateral offset(cm)			
	0	4	8	12
0	100	100	100	0
4	100	100	100	20
8	100	100	100	100
12	100	100	100	100
16	100	100	100	100
20	100	100	100	100

Table 2 Transfer success rates (%) of Vehicle B under different longitudinal and lateral offset conditions.

Longitudinal offset(cm)	Lateral offset(cm)			
	0	4	8	12
0	100	100	100	100
4	100	100	100	20
8	100	100	100	100
12	100	100	100	60
16	100	100	100	20
20	100	100	100	100

The improved row-transfer platform developed by Yoshida et al. (2025) enabled the RGV to transfer at a lateral offset of 8 cm when the longitudinal offset was 12 cm or greater.

These results suggest that the present transfer platform provides misalignment tolerance comparable to or greater than that of the previously developed dedicated platform, even when mounted on different AGVs. This misalignment tolerance can reduce the risk of derailment during transfer and expand the range of transport options available for rail-to-rail transfer systems.

CONCLUSIONS

Transfer performance equivalent to or greater than that of the previously developed row-transfer platform using pipes was confirmed. Stable transfer was demonstrated at lateral offsets of up to 8 cm under all tested longitudinal offset conditions for both vehicles. These results suggest that the present transfer platform unit is effective for stable rail-to-rail transfer even when mounted on commercially available AGVs. In addition, the consistent transfer performance obtained across different AGV models suggests that the proposed rail-shifting mechanism may be applicable to multiple AGV platforms. This may enable the use of the same AGV platform for both rail shifting and existing transport operations in greenhouse horticulture,

thereby reducing barriers to adoption and wider dissemination. Integration with our rail-recognition and stopping system (Ohta et al., 2026) may also provide a basis for automated row-to-row transfer.

ACKNOWLEDGEMENTS

This work was supported by Nurturing development of Agricultural Robotics by Offering of Base Output

REFERENCES

Ohta, N., K. Shimomoto, S. Yoshida, and T. Fukatsu. 2026. Onshitsu nai jidou soukou daisha no une utsuri no tame no paipu reru kenshutsu (Pipe-rail detection for row-to-row transfer of automated vehicles in greenhouses). Proceedings of the 2026 Annual Meeting of the Japanese Society of Agricultural Informatics (JSAI). [in Japanese]

Shimomoto, K., M. Shimazu, H. Naito, T. Ota, and T. Fukatsu. 2024. Development of a rail-guided vehicle and platform for monitoring multiple planting rows in greenhouses. Proceedings of the 11th International Symposium on Machinery and Mechatronics for Agriculture and Biosystems Engineering, BR-R20.

Yoshida, S., M. Shimazu, K. Shimomoto, N. Ohta, and T. Fukatsu. 2025. Shisetsu engei yo jidou soukou daisha no reru kan idou gijutsu no kaihatsu(Development of rail-to-rail transfer technology for automated vehicles in greenhouse horticulture). Proceedings of the 83rd Annual Meeting of the Japanese Society of Agricultural Machinery and Food Engineers (JSAM), G-11, 1-9. [in Japanese]

Precision Agriculture Machinery and Systems 3 (PA-3)



PA-13

Proceedings of The 12th International Symposium on Machinery and Mechatronics for Agriculture and Biosystems Engineering (ISMAB 2026)
20-24 October 2026, Busan, Republic of Korea

DEVELOPMENT OF A CFD-BASED GREENHOUSE SURROGATE MODEL FOR DIGITAL TWIN ENVIRONMENTAL CONTROL

Hsuan-Yu Chen[1], Cheng-Wei Fu[2], Chen-Kang Huang[1*]

[1]Department of Biomechatronics Engineering, National Taiwan University,
1 Sec. 4, Roosevelt Rd., Taipei 106, Taiwan
[2]Advantech Co., Ltd.,
1 Aly. 20, Ln. 26, Rueiguang Rd., Taipei 114, Taiwan
*Corresponding Author-- Voice: +886-2-3366-5351, Email: ckhuang94530@ntu.edu.tw

Abstract: In modern Controlled Environment Agriculture (CEA), precise environmental control is essential for promoting crop growth and ensuring product quality. Next-generation greenhouse control aims not only to maintain target temperature, but also to optimize plant development, reduce energy use, and minimize carbon emissions. To achieve these goals, digital twin system plays a key role by enabling real-time virtual simulation and smart control strategies. However, traditional Computational Fluid Dynamics (CFD) simulations require substantial computational resources, making real-time implementation challenging. Therefore, this study develops fast surrogate models based on CFD data to support real-time environmental prediction. This research framework has two main stages. First, CFD simulations were conducted for a smart greenhouse under four fan operating conditions to generate temperature and airflow datasets for model training. Second, surrogate models were developed using a Multilayer Perceptron (MLP) and a Convolutional Neural Network (CNN). For the MLP model, physical constraints were added during training to keep the predictions consistent with basic physical laws. The two models showed clear differences in performance. In the crop bed area, the MLP model achieved an average prediction error of less than 0.8°C for temperature and less than 0.09 m/s for wind speed compared to the CFD data, while achieving inference speeds approximately twenty-four times faster than the CFD simulations. In contrast, although the CNN model preserved physical boundaries, it failed to accurately capture airflow distribution patterns, resulting in large differences from the CFD data. This study demonstrates that the physics-constrained MLP surrogate model offers both high speed and reliable accuracy. With these advantages, the proposed model can serve as the core engine for greenhouse digital twin, supporting efficient, energy-saving, and low-carbon greenhouse management.

Key Words: Controlled Environment Agriculture (CEA), Computational Fluid Dynamics (CFD), Surrogate Model, Multilayer Perceptron (MLP), Digital Twin

INTRODUCTION

Greenhouses are a controlled way of agricultural production. They can effectively block unstable outdoor climate conditions, so crops grow in an environment that is less affected by nature. Compared with open-field farming, greenhouses not only extend the growing season, but also help maintain stable production even under extreme weather conditions and pest

damage. Through unified management of greenhouse facilities, growers can also gain better control over crop quality and yield. Therefore, greenhouse environmental control is regarded as an important strategy for mitigating the impacts of climate change on agricultural production and ensuring food security.

However, as greenhouse cultivation technology advances, the new generation of environmental control systems no longer aim only at a single goal, such as keeping environmental variables at a fixed setpoint, as traditional Proportional-Integral-Derivative Control (PID) control does. In recent years, as the world pays more attention to sustainable development, greenhouse control systems are also required to consider energy saving, carbon reduction, and production cost at the same time (Howard et al., 2021). In other words, an ideal control strategy must not only maintain the best growth environment for crops, but also reduce energy use, equipment wear, and carbon emissions (Bhat et al., 2021). This makes the design of control systems and automated decisions more complex.

To meet these complex, multi-objective control needs, digital twin technology has been widely used in smart greenhouse research and applications in recent years. By building a virtual model that closely matches the real greenhouse, a digital twin system can reflect changes in the greenhouse environment in real time, and test different control strategies in a virtual environment, without the risk of crop loss or energy waste caused by wrong decisions in real greenhouses. In addition, a digital twin can also serve as the core for predictive control and automated decisions, helping managers adjust equipment before the environment changes quickly, and achieving more precise environmental management (Hindi et al., 2026).

Although digital twin offers these advantages, building a virtual model that can reflect airflow and temperature distribution inside a greenhouse in real time still faces some technical challenges. Traditionally, CFD has been regarded as a method that can simulate velocity and temperature fields inside a greenhouse with relatively high accuracy, but this simulation process often requires substantial computational resources, making it hard to meet the real-time computing needs of a digital twin system. Therefore, developing an accurate and computationally efficient surrogate model is a key technical challenge for practical greenhouse digital twin system. Based on this need, this study proposes a greenhouse surrogate model trained on CFD data.

MATERIALS AND METHODS

This experiment consists of two main stages. The first stage involves CFD simulation, in which SolidWorks Flow Simulation is used to simulate the airflow inside the greenhouse under four different fan operation conditions. The resulting temperature and wind speed data from these simulations serve as the training data for the surrogate models. In the second stage, surrogate models are developed using a Multilayer Perceptron (MLP) and a Convolutional Neural Network (CNN)(X. Guo et al., 2016; Van Quang et al., 2024), based on the CFD simulation results. The predictions of both models are then compared with the CFD simulation data to evaluate their accuracy and applicability.

CFD simulation

This study used the smart greenhouse in National Taiwan University (NTU) as the simulation

site. The greenhouse was about 33.44 (m) in length, 8.52 (m) in width, and 6.02 (m) in height, and the overall structure is shown in Figure 1. The water curtains were placed at the front of the greenhouse, andthe exhaust fans were placed at the back, which kept the inside of the greenhouse under negative pressure. In addition, 12 hydroponic crop beds were placed inside the greenhouse. This study used SolidWorks Flow Simulation to run the CFD simulation. The simulation time for solar radiation was set to the winter solstice, December 22, at 12:00 noon. The four fan operation conditions were: no fan is on, only the left fan is on, only the right fan is on, and both fans are on.

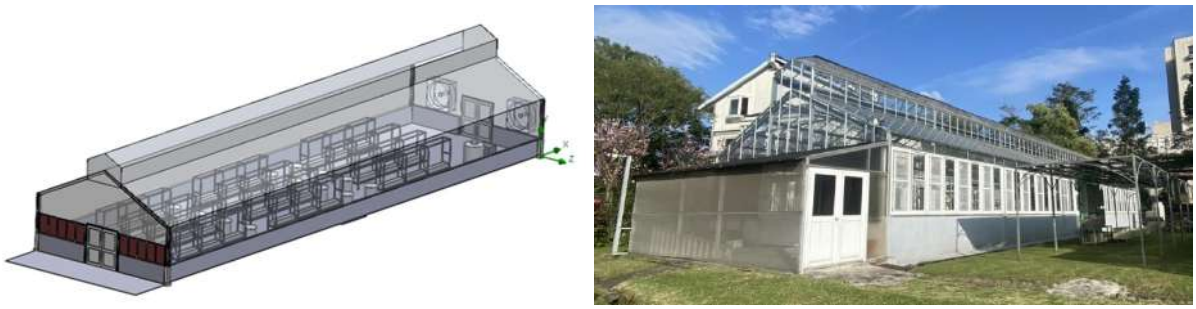

(a) (b)

Fig. 1 (a) 3D model and (b) photo of the NTU smart greenhouse

Surrogate Models

This study compared two types of neural networks, MLP and CNN, as surrogate models, and evaluated their prediction error against the real CFD simulation results. For each model, the CFD data from four fan operation conditions were used to train four separate sub-networks, so each sub-network learned the flow field under one fan combination. A loss penalty was added to reduce outputs that broke physical rules, to keep the model outputs physically reasonable. Finally, bilinear interpolation was used to combine the predictions, and the combined result was compared with the CFD result at 80% efficiency for both fans. The hyperparameters of the MLP were listed in Table 1, and the hyperparameters of the CNN were listed in Table 2.

Table 1 MLP Hyperparameters

Hyperparameter	Value
Number of hidden layers	3
Batch Size	4096
Learning Rate	0.03
Activation Function	ReLU
Epochs	50

Table 2 CNN Hyperparameters

Hyperparameter	Value
Kernel Size	3×3
Batch Size	4
Learning Rate	0.003
Activation Function	LeakyReLU
Epochs	300

RESULTS & DISCUSSION

The results showed that, for the MLP model, the maximum temperature error across the whole domain was 23.71°C, and the average error was 1.76°C. The maximum wind speed error was 3.29 m/s, and the average error was 0.20 m/s. However, the errors in the crop bed area were much smaller: the maximum temperature error was 6.14°C, with an average error of 0.75°C, and the maximum wind speed error was 1.22 m/s, with an average error of 0.09 m/s. As shown in the error map in Figure 2, most of the large errors were located near the solid boundaries of the greenhouse.

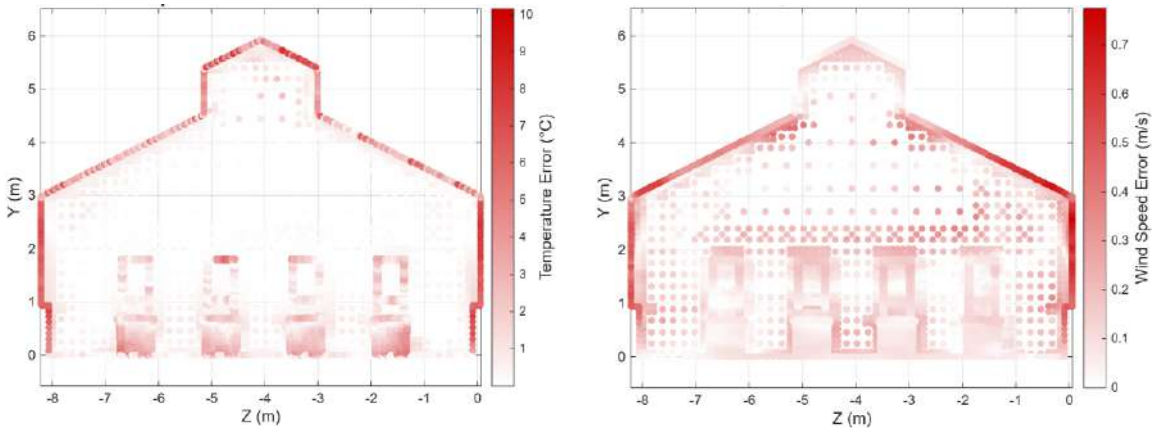

Fig. 2 Absolute error of (a) temperature and (b) wind speed from the MLP surrogate model

The prediction results of the CNN model are shown in Figure 3. Although the CNN model performed well in following physical rules and keeping the flow field continuous, its predictions in the crop bed area were very different from the CFD results. This showed the different strengths and weaknesses of the two models.

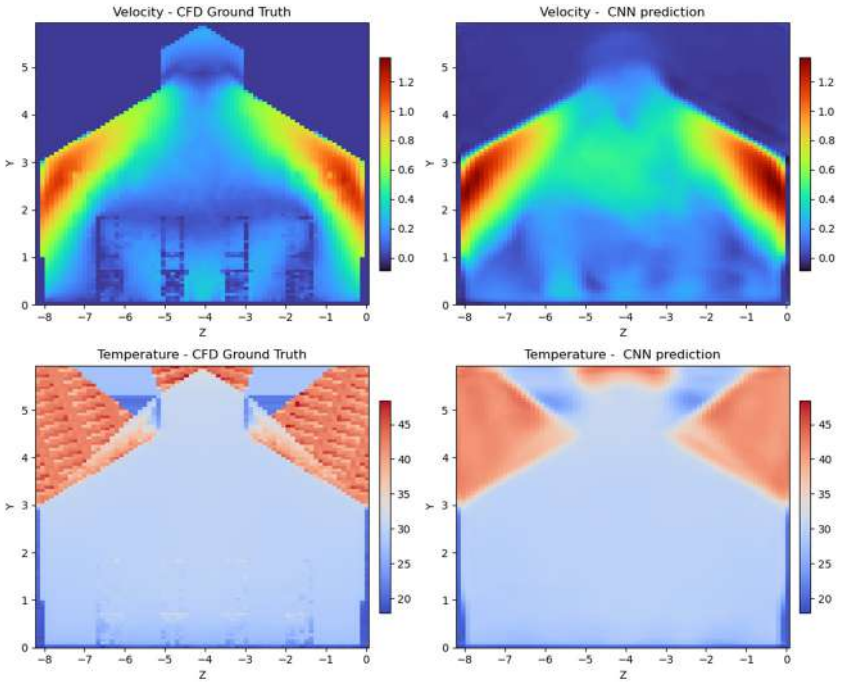

Fig. 3 Results from the CNN surrogate model

In terms of computational speed, the traditional CFD simulation required approximately 12 hours to compute four fan operating conditions, whereas the MLP model required approximately 30 minutes for training, and the CNN model required approximately 10 minutes for training. Compared with CFD, the MLP model was approximately 24 times faster, and the CNN model was approximately 72 times faster, clearly demonstrating the computational speed advantage of the surrogate models.

CONCLUSIONS

This study investigated the indoor microclimate of the smart greenhouse at National Taiwan University. Computational fluid dynamics (CFD) was used to simulate temperature and air velocity distributions under four fan operating conditions. Based on the CFD results, multilayer perceptron (MLP) and convolutional neural network (CNN) surrogate models were developed to reduce the high computational cost of numerical simulations and to serve as the computing core for a future greenhouse digital twin system.

The results showed that the MLP surrogate model achieved high accuracy in the crop bed area, with a mean absolute error (MAE) below 0.8°C for temperature and below 0.09 m/s for air velocity. In addition, the inference speed of the MLP model was approximately 24 times faster than traditional CFD simulations. However, the prediction errors of the MLP model increased significantly near the solid wall boundaries, likely because high gradients and strong non-linearity in the boundary layer made regression difficult. In contrast, the CNN model captured physical constraints and flow continuity well, but its predictions inside the greenhouse deviated notably from the CFD baseline.

Overall, this work demonstrates the feasibility of data-driven surrogate models for greenhouse microclimate prediction. Future work will focus on improving the boundary prediction of the MLP model and the local resolution of the CNN model. In addition, developing a hybrid architecture that combines CNN for global airflow modeling with MLP for local microclimate prediction offers a promising direction for improving model accuracy and supporting the development of sustainable smart agriculture.

ACKNOWLEDGEMENTS (optional)

The authors gratefully acknowledge the financial support provided by the National Science and Technology Council (NSTC), Taiwan, under Grant No. NSTC 115-2313-B-002-027-MY3.

REFERENCES

Bhat, S. A., Huang, N.-F., Hussain, I., Bibi, F., Sajjad, U., Sultan, M., … Mahmoud, K. H. (2021). On the Classification of a Greenhouse Environment for a Rose Crop Based on AI-Based Surrogate Models. *Sustainability*, *13*(21), 12166.

Guo, X., Li, W., Iorio, F. (2016). Convolutional Neural Networks for Steady Flow Approximation. In *Proceedings of the 22nd ACM SIGKDD International Conference on Knowledge Discovery and Data Mining* (pp. 481–490). New York, NY, USA: Association for

Hindi, I., Alsharkawi, A., Al-Ajlouni, M., Qarallah, B. (2026). Enhancing autonomous agriculture control systems in greenhouses for sustainable resource usage using deep learning

techniques. *PLOS ONE*, *21*(3), e0344946.

Howard, D. A., Ma, Z., Veje, C., Clausen, A., Aaslyng, J. M., Jørgensen, B. N. (2021). Greenhouse industry 4.0 – digital twin technology for commercial greenhouses.

Van Quang, T., N. L. Phuong, and D. T. Doan. 2024. Efficient prediction of indoor airflow in naturally ventilated residential buildings using a CFD-DNN model approach. In Proc. 2023 International Conference on Green Building, Civil Engineering and Smart City, 759-770. W. Guo, K. Qian, H. Tang, and L. Gong, eds. Singapore: Springer.

PA-14

Proceedings of The 12th International Symposium on Machinery and Mechatronics for Agriculture and Biosystems Engineering (ISMAB 2026)
20-24 October 2026, Busan, Republic of Korea

RESEARCH ON A VISION-GUIDED MULTI-TASK ROBOTIC SYSTEM FOR AUTONOMOUS *PHALAENOPSIS* ORCHID MANAGEMENT IN GREENHOUSES

Duc Tai Nguyen[1], Doan Dang Khoa Nguyen[1], and Wei-Chih Lin[1*]

[1]Department of Mechanical and Electro-Mechanical Engineering,
National Sun Yat-sen University, Taiwan
*Corresponding Author: wc.lin@mail.nsysu.edu.tw.

Abstract: *Phalaenopsis* orchid cultivation requires intensive manual operations for plant inspection, arrangement, and removal of defective plants. To improve automation in greenhouse management, this paper proposes a vision-guided multi-task robotic system capable of performing both orchid orientation adjustment and defective pot removal within a unified framework. The system integrates RGB-D perception, deep-learning-based defective orchid detection, leaf orientation estimation, and robotic manipulation. Based on the perception results, healthy orchids with undesired orientations are automatically grasped and rotated to the desired direction, whereas defective orchids are identified, picked, and transferred to a designated collection area. A customized gripper and disinfection procedure are further incorporated to support reliable manipulation and reduce potential cross-contamination. Experimental evaluations under greenhouse conditions demonstrate the feasibility of the proposed system in perception and autonomous task execution. These results demonstrate the potential of the proposed multi-task robotic framework for reducing manual labor and improving the efficiency of automated *Phalaenopsis* greenhouse management.

Key Words: *Phalaenopsis* orchid, greenhouse automation, agricultural robotics, multi-task robotic system, deep learning-based perception.

INTRODUCTION

Phalaenopsis orchids are high-value ornamental crops widely cultivated under controlled greenhouse conditions. Their commercial production requires intensive management throughout the cultivation cycle. In particular, orchid leaf development is closely related to greenhouse management, while the timely identification of diseased plants is important for maintaining crop quality and limiting potential disease spread (Chen et al., 2023). However, these operations still rely considerably on manual inspection and handling, making large-scale greenhouse management labor-intensive and time-consuming.

Recent advances in computer vision and deep learning have promoted the automation of several *Phalaenopsis*-related tasks. (Tsai et al., 2022) developed an image-based system for orchid disease recognition, while (Yang et al., 2024) employed deep learning and multi-view imaging for automatic flower detection and counting of potted *Phalaenopsis*. From the robotic

perspective, (Huang et al., 2010) introduced a machine-vision-guided system for locating and grasping *Phalaenopsis* tissue-culture plantlets. Similar progress has also been reported for automated handling of potted plants (Tanabata et al., 2022) and robotic disease monitoring in greenhouse environments (Ouyang et al., 2022). These systems focus on a single perception or manipulation task, such as disease detection, grading, monitoring, or grasping. However, *Phalaenopsis* management requires different actions depending on plant condition. Therefore, an autonomous system should not only identify and localize individual pots but also determine and execute the appropriate management task. To address this gap, we propose a vision-guided multi-task robotic system integrating RGB-D perception, defective orchid detection, leaf orientation estimation, and the robotic manipulation. Healthy orchids with undesirable orientations are automatically rotated, whereas defective orchids are picked and transferred to a collection area. The proposed framework therefore extends the single-task orchid automation toward an integrated robotic system capable of performing multiple management operations using a shared perception and manipulation platform.

MATERIALS AND METHODS

OVERALL SYSTEM ARCHITECTURE

The proposed robotic system is designed to automate two greenhouse management tasks: identifying and removing defective orchid pots, and correcting the orientation of orchid pots to achieve a uniform leaf arrangement. As illustrated in Fig. 1, the overall system consists of three functional layers: perception, computation, and actuation. In the perception layer, an RGB-D camera mounted on the gantry robot continuously acquires color and depth images of the orchid cultivation bench. These images provide the visual information required for monitoring the greenhouse environment and identifying individual orchid pots.The computation layer processes the acquired images using computer vision and artificial intelligence algorithms. The system extracts the required information, including orchid detection, defect identification, and leaf orientation estimation, before generating the corresponding robotic commands for either pot picking or orientation correction. Finally, the actuation layer executes the planned operations through a 3-axis Cartesian gantry robot equipped with a customized robotic gripper. According to the perception results, the robot autonomously performs either defective pot collection or pot rotation. The integration of perception, decision-making framework, and robotic manipulation enables efficient and autonomous orchid management in the commercial greenhouse environments.

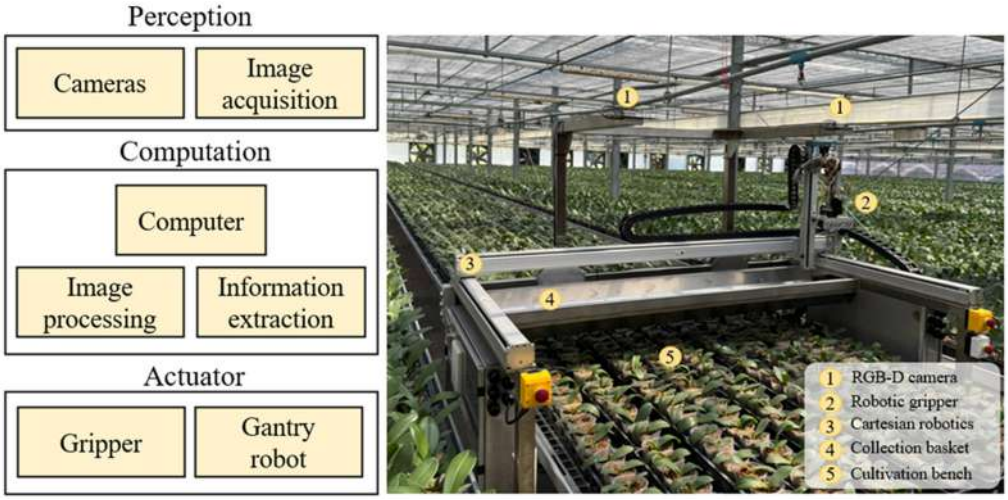

Fig. 1. Overall architecture of the proposed intelligent orchid management system.

SYSTEM OPERATIONAL WORKFLOW

The proposed robotic system performs autonomous orchid management by integrating visual perception, and robotic manipulation, as illustrated in Fig. 2. After initializing the RGB-D cameras, gantry robot, and gripper, RGB and depth images of the cultivation bench are acquired. Deep learning models simultaneously perform defective orchid detection and leaf orientation estimation to obtain each pot position and orientation angle. RGB information is then mapped to depth data, and the detected targets are transformed from image coordinates to the robot coordinate system. Based on these results, appropriate motion commands are generated and transmitted to the gantry robot and gripper controllers.The robot subsequently executes two manipulation tasks. In stage 1, healthy orchid pots are grasped and rotated to the desired orientation. In stage 2, defective pots are picked and transferred to a designated collection basket. After each picking operation, the gripper is sterilized at the alcohol-based disinfection station to reduce disease transmission. Once all targets are processed, the robot returns to its home position, completing the operation cycle.

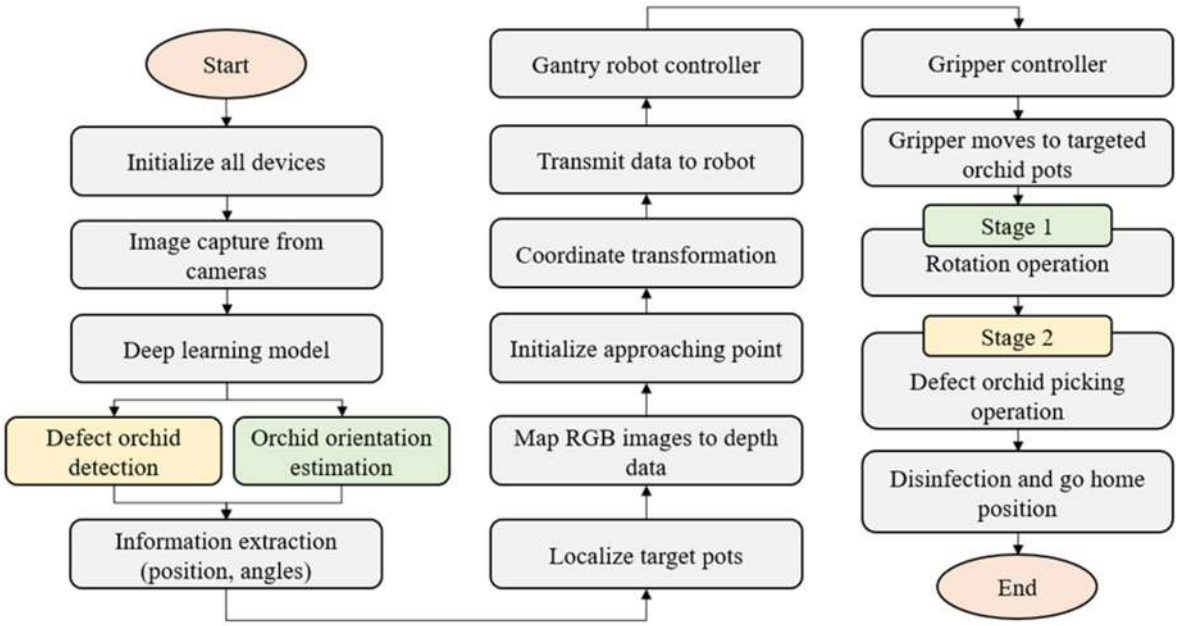

Fig. 2. Operational workflow of the proposed robotic orchid management system.

The computer vision module provides the perception capability required for autonomous orchid management. As illustrated in Fig. 3, the workflow begins with RGB image acquisition from the overhead camera mounted on the gantry robot. The captured images are first pre-processed to improve image quality and provide consistent visual information for subsequent analysis. The processed images are then analyzed through two parallel perception branches. The first branch detects defective orchid pots and estimates their target locations for robotic collection. The second branch identifies healthy orchid pots and extracts their leaf geometry to estimate the dominant leaf orientation. The outputs from both branches are subsequently integrated through a fusion module, which combines the perception results into a unified representation of the greenhouse scene. Based on the fused information, the decision-making framework determines the appropriate robotic operation for each detected orchid pot. Defective orchid pots are assigned to the collection task, whereas healthy orchid pots are assigned to the orientation correction task. The generated operation commands are then transmitted to the robotic perception and control modules, enabling the gantry robot to execute autonomous picking or pot rotation according to the identified management objective

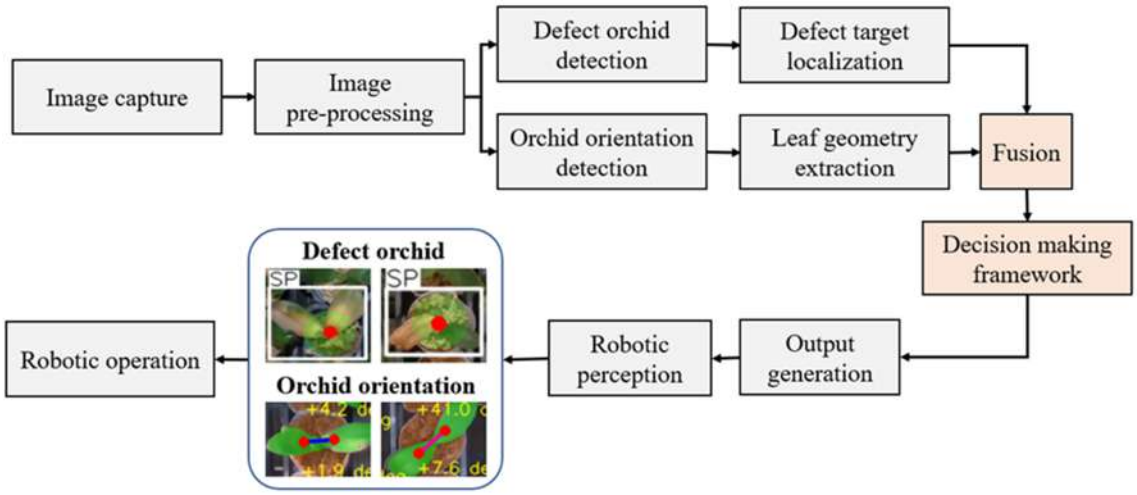

Fig. 3. Workflow of the proposed perception framework for autonomous orchid management.

RESULTS & DISCUSSION

Successful robotic manipulation relies on accurate perception of the greenhouse environment. Before executing any physical operation, the robot must first identify the target orchid pots and extract the information required for autonomous decision making. Fig. 4 presents representative perception results obtained by the proposed vision system in a commercial orchid greenhouse. The upper row (A) shows the original RGB images captured by the overhead camera, while the lower row (B) illustrates the corresponding robotic perception results. The proposed system successfully detects individual orchid pots and estimates the dominant leaf orientation of healthy orchids. For each detected pot, the perception module determines its location and calculates the corresponding leaf orientation angle, providing the essential information required for robotic manipulation. These perception results serve as the basis for the subsequent robotic operations. Based on the extracted position and orientation information, the robot determines the appropriate management task and generates the corresponding control commands for autonomous orchid pot rotation or defective orchid collection.

Following the perception and decision-making process, the gantry robot autonomously executes the assigned greenhouse management tasks. Fig. 5 presents representative operation sequences of the proposed robotic system, including both healthy orchid orientation correction and defective orchid collection. The operation begins with the robot approaching the selected orchid pot (A). For healthy orchids requiring orientation correction, the customized gripper securely grasps the target pot through the drainage holes and rotates it according to the estimated correction angle, as illustrated in (B) and (C). Once the orientation correction is completed, the robot proceeds to the next assigned task. For defective orchids, the robot approaches and grasps the identified pot before lifting it from the cultivation bench (D). The defective orchid is then transported to the designated collection basket and automatically released using the gripper mechanism (E). After releasing the defective pot, the robot moves the gripper to the disinfection station for sterilization, reducing the risk of disease transmission before continuing with the next operation (F). Through the integration of intelligent perception, precise localization, and coordinated robotic manipulation, the proposed system is capable of autonomously performing both orchid orientation correction and defective orchid collection in a commercial greenhouse environment.

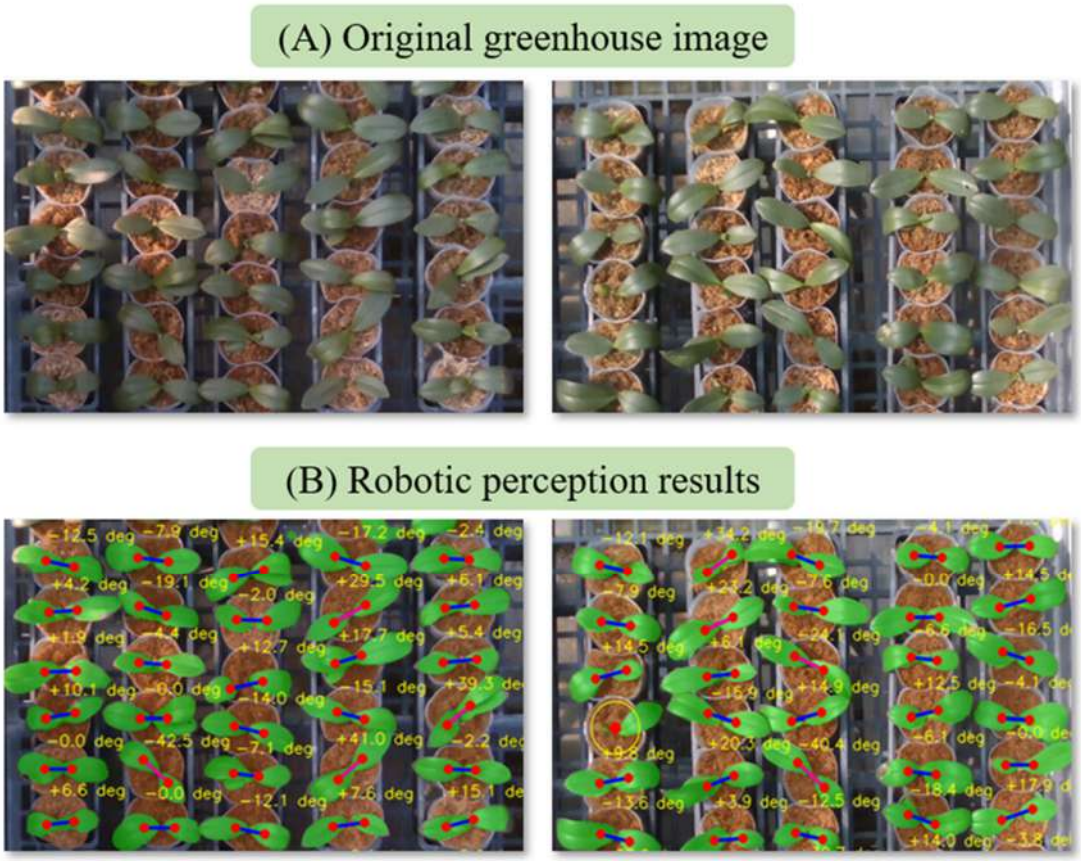

Fig. 4. Robotic perception results in a orchid greenhouse. (A) Original RGB images captured by the overhead camera. (B) Perception results showing orchid detection and leaf orientation estimation for robotic manipulation. Perception results, where blue lines denote orchids requiring no adjustment, red lines denote orchids selected for orientation correction, and yellow circles identify defective orchid pots for robotic collection.

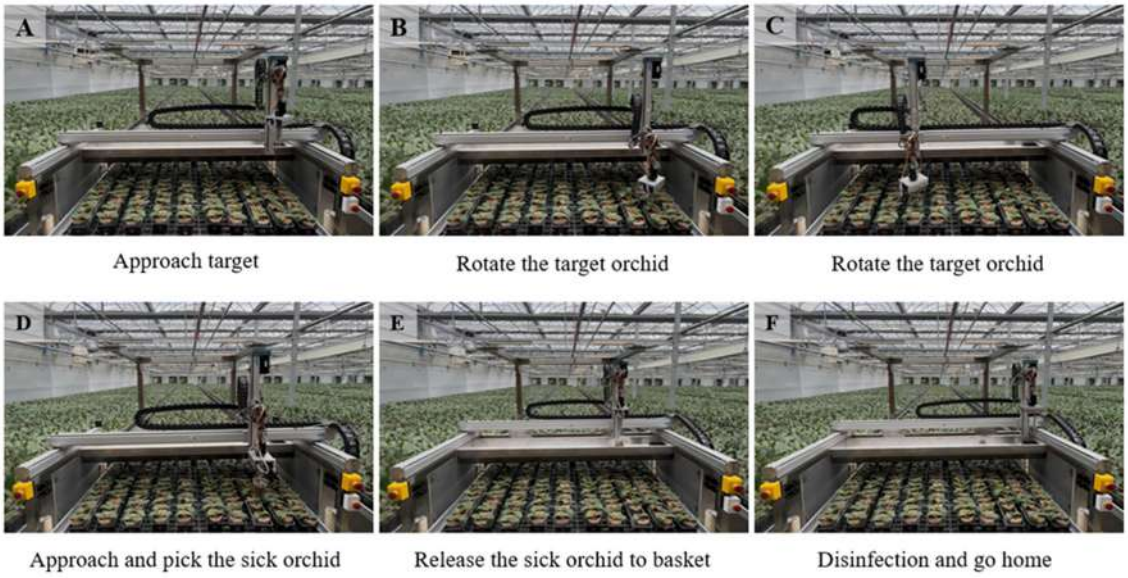

Fig. 5. Robotic operation sequences in a commercial orchid greenhouse. (A) Robot approaching the target orchid. (B-C) Autonomous orientation correction of healthy orchid pots. (D) Picking a defective orchid pot. (E) Placing the defective orchid pot into the designated collection basket. (F) Disinfection and robot returning to continue the next operation.

CONCLUSIONS

This study demonstrated the feasibility of integrating multiple orchid management tasks into a single autonomous robotic platform. The experimental results confirmed that the proposed system can reliably identify defective orchids, estimate leaf orientation, localize target pots in 3D space, and execute the corresponding manipulation tasks. More importantly, combining orchid rotation and defective-pot removal within the unified robotic framework improves operational flexibility and reduces the need for separate manual interventions. The proposed system therefore provides a practical foundation for intelligent and autonomous orchid management in greenhouse environments.

ACKNOWLEDGEMENTS

This work was supported by the Ministry of Agriculture (MOA), Taiwan, under Grant No. 115AS-12.2.2-AS-02, and the National Science and Technology Council (NSTC), Taiwan, under Grant No. 114-2313-B-110-004-MY3. The authors would also like to thank the Biomimicking & Engineering Lab at National Sun Yat-sen University, Taiwan, for providing valuable support and research resources. In addition, the authors gratefully acknowledge Star Orchids for providing the experimental site for conducting the field tests.

REFERENCES

Chen, J., & Chen, C. (2023). Study on the shape characteristics and the allometry of Phalaenopsis leaves for greenhouse management. Plants, 12(10), 2031.

Tsai, C. F., Huang, C. H., Wu, F. H., Lin, C. H., Lee, C. H., Yu, S. S., ... & Jan, F. J. (2022). Intelligent image analysis recognizes important orchid viral diseases. Frontiers in Plant Science, 13, 1051348.

Yang, Y., Zhang, G., Ma, S., Wang, Z., Liu, H., & Gu, S. (2024). Potted phalaenopsis grading: Precise bloom and bud counting with the PA-YOLO algorithm and multiviewpoint imaging. Agronomy, 14(1), 115.

Huang, Y. J., & Lee, F. F. (2010). An automatic machine vision-guided grasping system for Phalaenopsis tissue culture plantlets. Computers and Electronics in Agriculture, 70(1), 42-51.

Tanabata, T., Kodama, K., Hashiguchi, T., Inomata, D., Tanaka, H., & Isobe, S. (2022). Development of a plant conveyance system using an AGV and a self-designed plant-handling device: A case study of DIY plant phenotyping. Breeding science, 72(1), 85-95.

Ouyang, C., Hatsugai, E., & Shimizu, I. (2022). Tomato disease monitoring system using modular extendable mobile robot for greenhouses: Automatically reporting locations of diseased tomatoes. Agronomy, 12(12), 3160.

PA-15

Proceedings of The 12th International Symposium on Machinery and Mechatronics for Agriculture and Biosystems Engineering (ISMAB 2026)
20-24 October 2026, Busan, Republic of Korea

A CLUSTER-BASED THINNING RECOMMENDATION FRAMEWORK FOR INTELLIGENT PEACH FRUITLET SELECTION

Nilda Navarette Dela Cruz[1], Hao-Ting Lin[2*]

[12] Department of Bio-industrial Mechatronics Engineering
National Chung Hsing University
Taichung, Taiwan
*Corresponding Author: haotlin@dragon.nchu.edu.tw

Abstract: Peach thinning is a critical orchard management practice for improving fruit size and quality, yet it remains labor-intensive and highly dependent on grower experience. This study proposes a cluster-based thinning recommendation framework for intelligent peach fruitlet selection. A YOLOv11 object detection model was employed to detect and localize young peach fruitlets, followed by normalized relative-size estimation, adaptive pairwise distance evaluation, spatial clustering, and size-based ranking to generate RETAIN or REMOVE recommendations. The trained YOLOv11 model achieved a precision of 0.9448, recall of 0.9610, F1-score of 0.9528, and mAP@0.5 of 0.9888 on the test dataset. Experimental results demonstrated that the proposed framework successfully identified thinning candidates by integrating fruit size and spatial relationships into an interpretable decision-making process. The proposed approach provides a practical foundation for precision thinning and future vision-guided robotic orchard operations.

Key Words: Peach thinning, YOLOv11, Fruitlet detection, Spatial clustering, Decision support

INTRODUCTION

Peach thinning is an essential orchard management practice that improves fruit size, quality, and market value by removing excess fruitlets during early fruit development. However, the process remains labor-intensive, time-consuming, and highly dependent on human expertise. Conventional manual, mechanical, and chemical thinning methods also face limitations in labor efficiency, cost, and consistency (Costa and Botton, 2022; Dutta et al., 2025; Lămureanu and Gavat, 2025; Sutton et al., 2020). Recent advances in artificial intelligence and computer vision have enabled accurate detection and localization of young peach fruitlets under complex orchard conditions. Nevertheless, most existing studies focus primarily on fruit detection, with limited attention to translating detection results into practical thinning decision support (Fan et al., 2024; Zhou et al., 2023).

This study proposes a cluster-based thinning recommendation framework for intelligent peach fruitlet selection. The framework combines YOLOv11-based fruitlet detection with relative size estimation, spatial cluster identification, and rule-based decision-making to generate interpretable retain/remove recommendations for precision orchard management.

MATERIALS AND METHODS

The proposed methodology consists of three stages: data preparation, YOLOv11-based fruitlet detection, and cluster-based thinning recommendation.

A. Dataset and YOLOv11 Detection

The NinePeach dataset (Zhao et al., 2023) was used to develop the model. A total of 150 images of young peach fruitlets were selected and divided into training (70%), validation (15%), and test (15%) sets. All visible fruitlets were manually annotated with bounding boxes using MATLAB Image Labeler. A YOLOv11n object detection model was trained using the Ultralytics framework on Google Colab to detect and localize young peach fruitlets.

B. Cluster-Based Thinning Recommendation Framework

Following YOLOv11 detection, the proposed framework estimates the relative size of each detected fruitlet using its normalized bounding-box area. The framework then computes pairwise Euclidean distances between neighboring fruitlets to identify spatial clusters for thinning recommendations.

$$R_i = \frac{A_i}{\max(A)}, \tag{1}$$

where R_i is the normalized relative size of a fruitlet i.

$$T_{ij} = 1.20 \times \frac{D_i + D_j}{2} \tag{2}$$

where neighboring fruitlets are assigned to the same cluster when $d_{ij} < T_{ij}$.

The threshold multiplier of 1.20 was empirically selected to balance over-clustering and under-clustering, consistent with prior work noting that overly strict thresholds risk irreversible over-thinning, while looser thresholds permit correction in later thinning passes (Hussain et al., 2025).

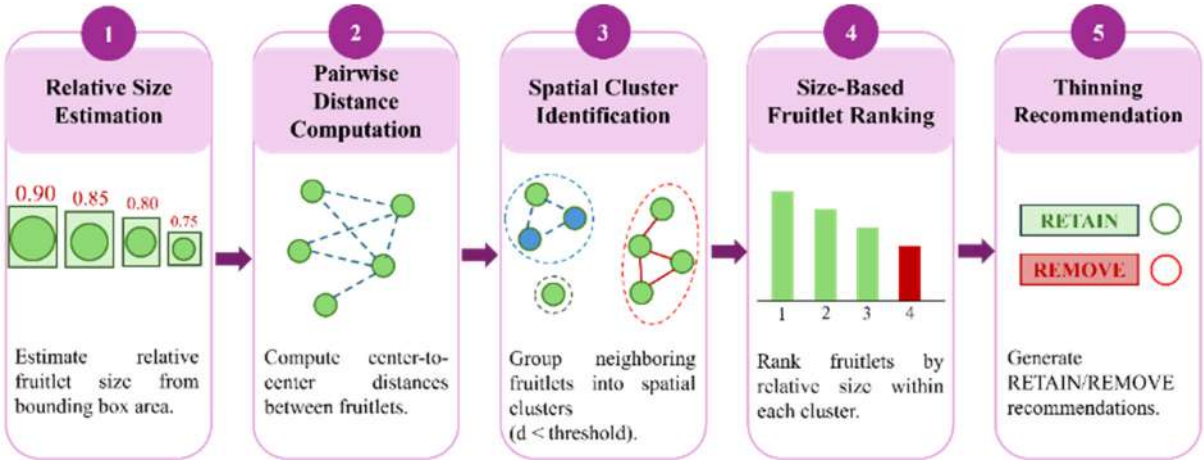

Fig. 1. Proposed cluster-based thinning framework

Within each cluster, fruitlets are ranked by normalized relative size. The largest fruitlet is retained, whereas smaller neighboring fruitlets are recommended for removal. This hierarchical decision-making strategy combines relative fruit size and spatial relationships to generate interpretable thinning recommendations.

RESULTS & DISCUSSION

Table I summarizes the detection performance of the trained YOLOv11 model on the test dataset.

TABLE 1 YOLOv11 Peach Fruitlet Detection Performance

Model	Precision	Recall	F1	mAP@0.5
YOLOv11	0.9448	0.9610	0.9528	0.9888

The model achieved a precision of 0.9448, meaning that of all fruitlets the model predicted, roughly 94.5% were correctly identified as true fruitlets, with a low false-positive rate. The recall of 0.9610 indicates that the model successfully detected about 96.1% of all actual fruitlets present in the test images, reflecting a low rate of missed detections. The F1-score of 0.9528, which balances precision and recall into a single metric, confirms that the model maintains a strong and consistent trade-off between correctly identifying true fruitlets and avoiding false detections. Finally, the mAP@0.5 of 0.9888 (mean Average Precision at an IoU threshold of 0.5) demonstrates that the model localizes fruitlets accurately.

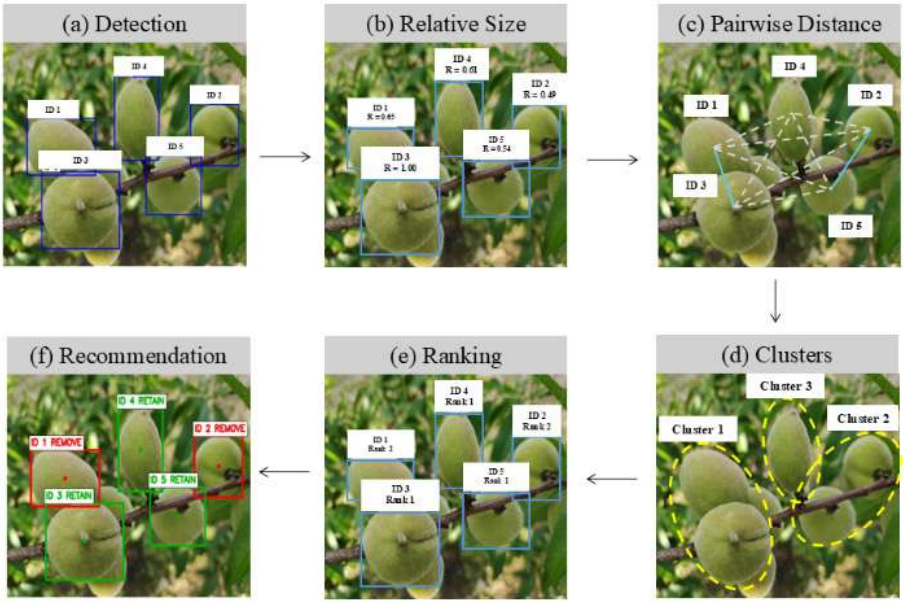

Fig. 2. Representative example of the thinning recommendation results.

Fig. 2 presents a representative example illustrating the intermediate processing stages and final thinning recommendation generated by the proposed framework. Five detected fruitlets, each localized with detection confidence above 0.90, were grouped into three spatial clusters based on pairwise distance thresholds. Within Cluster 1, Fruitlet 3 (relative size 1.00) was retained as the highest-ranked fruitlet, while the smaller, closely spaced Fruitlet 1 (relative size 0.65) was recommended for removal. Similarly, in Cluster 2, Fruitlet 5 (relative size 0.54) was

retained over the smaller Fruitlet 2 (relative size 0.49) due to their proximity. Fruitlet 4, forming a singleton cluster with adequate spacing from its neighbors, was retained independently. These results demonstrate the framework's ability to combine relative fruit size and spatial proximity into a structured, interpretable decision-making process for fruitlet thinning.

CONCLUSIONS

This paper presented a cluster-based thinning framework for intelligent peach fruitlet selection using computer vision. By combining YOLOv11-based fruitlet detection with relative size estimation and spatial clustering, the framework generated interpretable RETAIN/REMOVE recommendations based on fruitlet size and proximity. Experimental results confirmed that accurate fruitlet detection is essential to reliable downstream thinning decisions, and the proposed rule-based clustering approach offers a transparent alternative to end-to-end black-box decision models. This study did not include manual validation of thinning decisions against expert-selected ground truth; future work will compare decisions with grower-determined thinning outcomes to quantitatively assess accuracy, consistent with agronomic guidance recommending fruit spacing of approximately 6–8 inches in peach orchards [9]. Future work will validate the framework on larger, more diverse orchard datasets and extend it to real-time, vision-guided robotic thinning applications.

REFERENCES

Costa, G., Botton, A. (2022). Thinning in peach: Past, present and future of an indispensable practice. Scientia Horticulturae, 296, 110895. https://doi.org/10.1016/j.scienta.2022.110895

Dutta, S. K., Bhutia, B., Misra, T., Mishra, V. K., Singh, S. K., Patel, V. B. (2025). Application and Prospects of Artificial Intelligence (AI)-Based Technologies in Fruit Production Systems. Applied Fruit Science, 67(1), 16. https://doi.org/10.1007/s10341-024-01223-4

Fan, J., Salam, Md. S. B. H., Rong, X., Han, Y., Yang, J., Zhang, J. (2024). Peach fruit thinning image detection based on improved YOLOv8 and data enhancement techniques. IEEE Access, 1–1. https://doi.org/10.1109/ACCESS.2024.3516484

Hussain, M., He, L., Schupp, J., Lyons, D., Heinemann, P. (2025). Green Fruit-Stem Pairing and Clustering for Machine Vision System in Robotic Thinning of Apples. Journal of Field Robotics, 42(4), 1463–1490. https://doi.org/10.1002/rob.22465

Lămureanu, G., Gavat, C. (2025). THE EFFECT OF THINNING OF PEACH IN SOUTH-EASTERN ROMANIA. ANNALS OF THE UNIVERSITY OF CRAIOVA, Biology, Horticulture, Food Products Processing Technology, Environmental Engineering, 30(66). https://doi.org/10.52846/bihpt.v30i66.250

Sutton, M., Doyle, J., Chavez, D., Malladi, A. (2020). Optimizing Fruit-Thinning Strategies in Peach (Prunus persica) Production. Horticulturae, 6(3), 41. https://doi.org/10.3390/horticulturae6030041

Zhao, Z., Hicks, Y., Sun, X., Luo, C. (2023). Peach ripeness classification based on a new one-stage instance segmentation model. Computers and Electronics in Agriculture, 214, 108369. https://doi.org/10.1016/j.compag.2023.108369

Zhou, Z., Zahid, U., Majeed, Y., Nisha, Mustafa, S., Sajjad, M. M., … Fu, L. (2023). Advancement in artificial intelligence for on-farm fruit sorting and transportation. Frontiers in Plant Science, 14, 1082860. https://doi.org/10.3389/fpls.2023.1082860

PA-16

Proceedings of The 12th International Symposium on Machinery and Mechatronics for Agriculture and Biosystems Engineering (ISMAB 2026)
20-24 October 2026, Busan, Republic of Korea

A HYBRID WHEELED–LEGGED QUADRUPED PLATFORM WITH ACTIVE BALANCING FOR MULTI-TASK AGRICULTURAL APPLICATIONS

Doan Dang Khoa Nguyen[1], Nam Khanh Nguyen[1], Dang Khanh Linh Le[1], Wei-Chih Lin[1*]

[1]National Sun Yat-sen University, Department of Mechanical and Electro-Mechanical Engineering, Taiwan
*Corresponding Author-- Voice: + 886-922-272-615, Email: wc.lin@mail.nsysu.edu.tw

Abstract: Agricultural robots operating in greenhouses must maintain stability when moving across rough and uneven terrain. Conventional wheeled platforms offer high mobility and payload capacity, but their ability to adapt to body tilt caused by terrain is limited. This research aims to develop a hybrid wheel-legged four-legged robotic platform with an active balancing system for multi-functional agricultural applications. The platform is designed to combine wheeled movement for efficient ground transport with leg-based posture adjustment for operation on uneven terrain. The design payload for various robot tasks is 100 kg with a speed of 1 km/h. Kinematic analysis and force calculations were performed to determine the robot configuration and actuator requirements. Finite element analysis was used to evaluate the structural strength of the main components. A Sliding Mode Control (SMC)-based active balancing controller has been developed to compensate for terrain-induced rolling and tilt disturbances using inertial measurement data. The proposed balance control strategy involves adjusting the height of the legs in response to changes in wheel height caused by terrain, thereby maintaining the desired vehicle posture. A prototype was constructed and experimentally evaluated under uneven terrain conditions set up in the laboratory. Experimental results showed that the proposed balancing system maintained the robot's rolling and tilt errors within ±0.4° and ±0.6°, respectively. These results demonstrate that the developed wheel-foot hybrid platform can actively compensate for terrain-induced tilt and maintain a stable posture during operation on uneven terrain, providing a potential robotic platform for multi-functional agricultural applications.

Key Words: quadruped robot, wheel-legged robot, unstructured terrain, balanced platform, multifunctional robot

INTRODUCTION

Population decline and aging are pressing issues in developed countries. Due to the manual nature of agricultural labour, achieving a high level of automation is extremely urgent (Wei et al., 2024). Advances in science have boosted agricultural automation (Mucchiani, Zaccaria, & Karydis, 2024). However, dynamic conditions significantly affect the operational efficiency of equipment and vehicles (Yang et al., 2026). Terrain is a crucial issue that needs to be addressed for the successful deployment of agricultural automation. The diversity of terrain in

hilly areas, valleys, and plateaus poses significant challenges for mobile platforms.
In agriculture, four-wheeled or tracked mobile platforms have long been developed. They demonstrate advantages due to their flexibility and small turning radius, efficient energy consumption, and cost savings in agricultural production (Baek, Jeon, Kim, Kim, & Kim, 2026). However, four-wheeled chassis significantly reduce performance when operating on hilly and steep terrain. Conversely, biomimetic four-legged platforms demonstrate superior obstacle avoidance and terrain mobility (Bellicoso et al., 2018). The development of biomimetic multi-legged robots combined with active wheels is a potential option for unstructured farming terrains. The load-carrying capacity of current legged robots is limited, with research largely focused on motion control algorithms. Meanwhile, agriculture requires a multi-tasking platform with multi-tasking capabilities.
This study presents the development of a multifunctional hybrid four-legged robotic platform with wheels and legs for agricultural applications. The proposed platform combines wheeled locomotion for efficient ground transport with leg-based posture adjustment to enhance adaptability to terrain and maintain stability on uneven greenhouse surfaces. The robot was designed through kinematic and force analysis, while a SMC-based active balance controller was developed to compensate for roll and pitch disturbances caused by the terrain. A prototype was built and tested under laboratory setup conditions. Experiments evaluated the performance of the developed platform and its active balance capabilities under uneven terrain conditions.

MATERIALS AND METHODS

DESIGN OF THE ACTIVE LEVELLING SYSTEM

The active balancing system primarily consists of four 3-degree-of-freedom leg mechanisms installed at four suspension points of the robot body, along with a coordinated operating controller. An embedded computer extracts tilt data from the platform using an Inertial Measurement Unit (IMU) via RS485. An HWT901B IMU was mounted on the robot body to measure the roll and pitch angles. The sensor provides an inclination accuracy of 0.1° and a maximum output rate of 200 Hz. The measured attitude data were used as feedback signals for the SMC-based active balancing controller. The tilt data are converted into control signals for the four legs to simultaneously operate and return the body to a balanced position. Each leg integrates an independent control system to create the wheel trajectory and communicates with the central computer via the CAN Bus. The forward and inverse kinematic equations for each leg are shown in Fig. 1. The study proposes a SMC controller to adapt to terrain tilt. The controller uses the roll and pitch angle deviations to estimate the velocity of height change of the four legs. From the velocity change, the displacement distance of each leg is calculated. The displacement distance of each leg is calculated to compensate for the nominal height. The synchronized movement of all four legs maintains the robot posture.

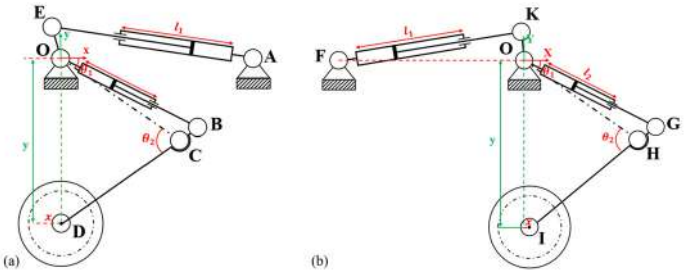

Fig. 1 Robot leg kinematics: (a) Front leg kinematics and (b) Rear Leg kinematics

DESIGN OF KEY COMPONENTS

Based on the system architecture shown in Fig. 1, the detailed configuration of the hybrid quadruped wheel-legged platform is shown in Fig. 2. The platform is designed to handle multiple agricultural tasks, including transport, harvesting assistance, robotic arm stabilization, and pesticide spraying. Transporting is a heavy task requiring significant energy. Therefore, the robot is designed with a payload capacity of 100 kg. Each leg has two degrees of freedom and is driven by electric cylinders. The electric cylinders drive the thigh joint, providing a pulling force of approximately 8700 N. With a 100 mm lever arm, the translational movement of the cylinder is converted into rotational movement of the joint. The peak torque of the thigh joint is approximately 870 Nm. Similarly, the knee joint is also driven by electric cylinders with a pulling force of approximately 7830 N. With a 70 mm lever arm, the peak torque of the knee joint reaches 548 Nm. The four-wheel differential steering system is designed with a peak torque of approximately 150 Nm per wheel. The wheel diameter is 10 inches. The mass of the platform is approximately 160 kg without load. The passive suspension system consists of four air suspension wheels.

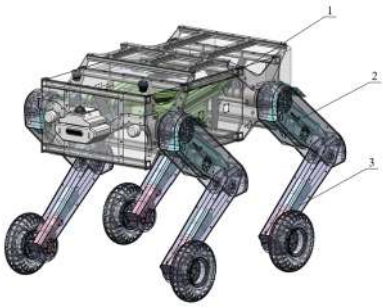

Fig. 2 Drive system of the platform: (1) Thigh joint drive cylinder, (2) Knee joint drive cylinder, and (3) Four-wheel differential steering system

SYSTEM STRUCTURE AND DESIGN PRINCIPLES

The hybrid wheeled quadruped robot consists of seven components: the working base, the robot body, the thigh mechanism, the calf mechanism, the drive wheels, the perception system, and the safety system. The robot body includes four electric cylinders that drive the thigh joints of each leg. Each leg is a two-degree-of-freedom mechanism. The calf is driven by cylinders located within the thigh. Each leg is equipped with drive wheels. The four-wheel drive system provides translational movement for the robot. The robot's steering method is a four-wheel differential system. The platform width must not exceed 2000 mm. In compliance with industry standardization, the robot's width is 940 mm. The differential drive system requires a short chassis length. The four legs are spaced apart to avoid collisions during operation. The length of the chassis is determined to be 1200 mm. The distance between the centres of the two drive wheels when the robot is in a balanced state is 700 mm. Due to operating on terrain with a horizontal slope of 8 degrees and a vertical slope of 10 degrees, each leg can adjust its height within a range of 300 mm. This results in a height range of the robot from 860 mm to 1160 mm.

VELOCITY-LEVEL ATTITUDE MODEL-BASED SLIDING-MODE BALANCE CONTROL

The control algorithm is designed based on the idea that each leg of the robot acts as an active component that changes height at corresponding angles of the robot's torso. Thus, based on the inclination of the target ground surface to be moved, a certain height is automatically

adjusted to each corresponding leg. Fig. 3 illustrates the operation of the controller. Based on the nominal height $z_{i,nom}$, which is considered the height of the robot, the leg heights are adjusted in response to terrain-induced wheel height variations to maintain the desired body posture.

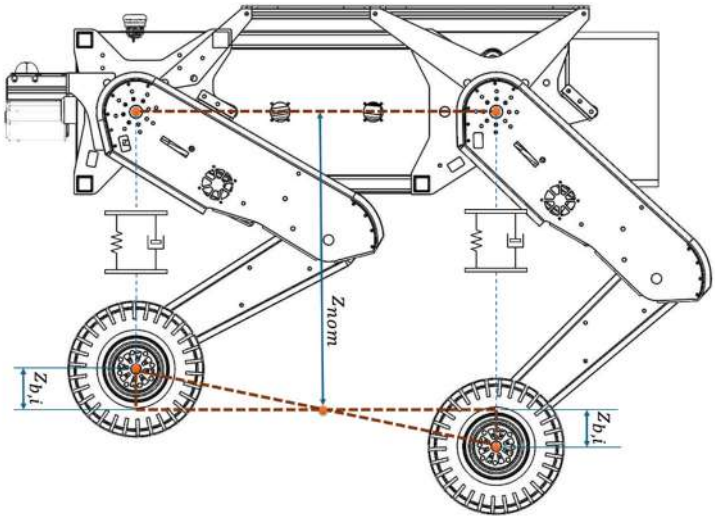

Fig. 3 The proposed body-balance control concept on uneven terrain.

Let $\mathbf{q} = \begin{bmatrix} \phi & \theta \end{bmatrix}^T$ and $\mathbf{q}_d = \begin{bmatrix} \phi_d & \theta_d \end{bmatrix}^T$ be the measured and desired body roll–pitch attitudes. The persistent balance correction is $\mathbf{u} = \begin{bmatrix} u_\phi & u_\theta \end{bmatrix}^T$, and $\mathbf{v} = \dot{\mathbf{u}}$ is its correction velocity. The four leg-height balance offsets, ordered as FL, RL, RR, and FR, are:

$$\Delta \mathbf{z}_b = M\mathbf{u}, \quad M = \begin{bmatrix} 1 & -1 \\ 1 & 1 \\ -1 & 1 \\ -1 & -1 \end{bmatrix} \tag{1}$$

Based on (Tran et al., 2026), modeling a leg as a variable-length link and relating the two leg heights to body roll is also used in wheel-legged posture kinematics. For support half-width h_y and half-length h_x, the support-plane geometry gives:

$$\tan\phi = \frac{u_\phi}{h_y}, \quad \tan\theta = \frac{u_\theta}{h_x}, \quad \mathbf{q}_{rad} = \begin{bmatrix} \arctan\left(u_\phi / h_y\right) \\ \arctan\left(u_\theta / h_x\right) \end{bmatrix} \tag{2}$$

The model constructed below utilizes the Jacobian principle (Grand et al., 2010) in a forward direction: from the virtual vertical leg correction velocity to the pitch and roll velocity of the robot's torso. Differentiating (2) yields the exact geometric Jacobian:

$$\dot{\mathbf{q}}_{rad} = J_g(\mathbf{u})\mathbf{v}, \quad J_g(\mathbf{u}) = \begin{bmatrix} \dfrac{h_y}{h_y^2 + u_\phi^2} & 0 \\ 0 & \dfrac{h_x}{h_x^2 + u_\theta^2} \end{bmatrix} \tag{3}$$

Near the balanced posture, $J_g(\mathbf{u})$ is linearized at $\mathbf{u} = 0$. After converting radians to degrees,

$$G = \frac{180}{\pi} J_g(\mathbf{0}) = \frac{180}{\pi} \begin{bmatrix} h_y^{-1} & 0 \\ 0 & h_x^{-1} \end{bmatrix} \tag{4}$$

$$\Rightarrow \dot{\mathbf{q}} = G\mathbf{v} + \mathbf{d}$$

Here $\mathbf{d}$ collects geometric linearization error, actuator and tracking error, compliance, roll–

pitch coupling, load transfer, and external disturbances.

Define the attitude error and first-order sliding variable as $\mathbf{e} = \mathbf{q}_d - \mathbf{q}$ and $\mathbf{s} = \mathbf{e}$. To reduce chattering, the discontinuous sign function is replaced by the componentwise saturation:

$$sat(\mathrm{x}) = \begin{cases} -1, & x < -1 \\ x, & |x| \le 1 \\ 1, & x > 1 \end{cases} \tag{5}$$

At sample n, with measured interval Δt_n, desired-rate limit $r_{d,\max}$, and low-pass cutoff f_c, the desired attitude velocity is estimated by

$$\begin{aligned} \dot{\mathbf{q}}_{d,raw}[n] &= r_{d,\max} sat\left(\frac{\mathbf{q}_d[n] - \mathbf{q}_d[n-1]}{\Delta t_n r_{d,\max}}\right), \\ \dot{\mathbf{q}}_d[n] &= \alpha_n \dot{\mathbf{q}}_d[n-1] + (1-\alpha_n)\dot{\mathbf{q}}_{d,raw}[n], \\ \alpha_n &= e^{-2\pi f_c \Delta t_n} \end{aligned} \tag{6}$$

Let $\Lambda = diag(\lambda_\phi, \lambda_\theta), \mathrm{K} = diag(k_\phi, \mathrm{k}_\theta)$, and $\Phi = diag(\Phi_\phi, \Phi_\theta)$ are positive diagonal matrices. The virtual attitude-rate command and unconstrained correction velocity are:

$$\mathbf{r} = \hat{\dot{\mathbf{q}}}_d + \Lambda \mathbf{e} + K sat\left(\Phi^{-1}\mathbf{e}\right), \quad \mathbf{v}^* = G^{-1}\mathbf{r} \tag{7}$$

The implemented correction velocity is limited componentwise: $v_a = v_{\max} sat\left(\frac{v_a^*}{v_{\max}}\right), a \in \{\phi, \theta\}$.

A hysteretic hold sets $v_a = 0$ when the error, measured attitude and desired attitude velocity are all small, while retaining the accumulated correction u_a:

$$\begin{aligned} H_{a,entry} &:= \left(|e_a| \le \varepsilon_{a,in}\right) \wedge \left(|\dot{q}_a| \le \rho_{a,in}\right) \wedge \left(|\hat{\dot{q}}_{d,a}| \le \rho_{\mathrm{d},in}\right), \\ H_{a,keep} &:= \left(|e_a| \le \varepsilon_{a,\mathrm{out}}\right) \wedge \left(|\dot{q}_a| \le \rho_{a,\mathrm{out}}\right) \wedge \left(|\hat{\dot{q}}_{d,a}| \le \rho_{\mathrm{d,out}}\right) \end{aligned} \tag{8}$$

where every “out” threshold is larger than its corresponding “in” threshold. The symbols $\varepsilon, \rho,$ and ρ_d denote error, measured-rate, and desired-rate thresholds, respectively.

With $\bar{\Delta}t_n = sat_{[0,0.05]}(\Delta t_n)$, persistent correction and the L_1 bound are implemented as:

$$\begin{aligned} \mathbf{u}^-[n] &= \mathbf{u}[n-1] + \mathbf{v}[n]\bar{\Delta}t_n, \\ \mathbf{u}[n] &= \begin{cases} \mathbf{u}^-[n], & \|\mathbf{u}^-[n]\|_1 \le u_{\max}, \\ \dfrac{u_{\max}}{\|\mathbf{u}^-[n]\|_1}\mathbf{u}^-[n], & \|\mathbf{u}^-[n]\|_1 > u_{\max} \end{cases} \end{aligned} \tag{9}$$

Then, the balance correction is superimposed on the nominal command:

$$z_i = z_{i,nom} + (M\mathbf{u})_i, \quad i \in \{FL, RL, \mathrm{RR}, \mathrm{FR}\} \tag{10}$$

With $z_{i,nom}$ is nominal leg height.

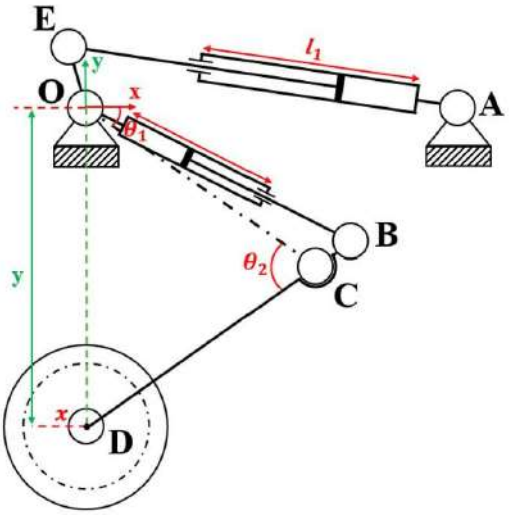

Fig. 4 Geometric structure of one of the robot's legs.

Finally, this height is used to derive the robot's joint angle from the leg kinematic equation. This equation is precisely calculated based on the leg's geometric structure as shown in Fig. 4 and has been verified experimentally:

$$\begin{cases} \theta_1 = \dfrac{\pi}{2} - \tan^{-1}\left(\dfrac{x}{z}\right) - \cos^{-1}\left(\dfrac{x^2 + z^2 + l_1^2 - l_2^2}{2l_1\sqrt{x^2 + z^2}}\right) \\ \theta_2 = \cos^{-1}\left(\dfrac{-x^2 - z^2 + l_1^2 + l_2^2}{2l_1 l_2}\right) \end{cases} \tag{11}$$

RESULTS & DISCUSSION

MECHANICAL SIMULATION RESULTS

The four-legged system is the bearing foundation of the robot. The mechanical strength of the legs and joints connecting to the body directly affects the stability of the entire robot. The study conducted static simulations using SolidWorks Simulation software. The material parameters of the thigh and calf are a yield strength of 325 MPa and a density of 7870 kg/m³. The model uses constraints at the upper part. The radial and axial forces acting on the entire lower part of the component are 1000 N and 500 N, respectively. The safety factor compared to the actual load is 2. The material parameters of the joints are a yield strength of 530 MPa and a density of 7850 kg/m³. The model uses fixed constraints at the axis. The force acting on the lever arm simulates the thrust force of an electric cylinder. Compared to the actual thrust force of 8700 N of the electric cylinder, the safety factor is 1.14. The global mesh size is 7 mm. The simulation results are shown in Table 1. The simulation verification results show that the maximum stresses of the thigh and calf are 116.57 MPa and 247.05 MPa, respectively. The safety factors are 3 and 1.3, respectively. The maximum strain of the thigh is 0.578 mm. The maximum strain of the calf is 0.32 mm. The maximum stress of the front joint is 394.07 MPa, and of the rear joint is 407.74 MPa. The safety factor for both joints is 1.3. The maximum strain of the front and rear joints is 0.18 mm.

Component	Static simulation results	
	Von Mises	Displacement
Thigh	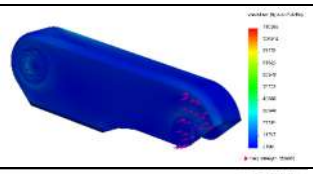	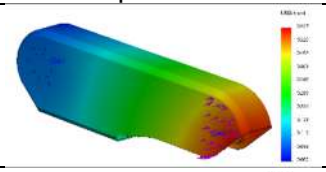
Calf	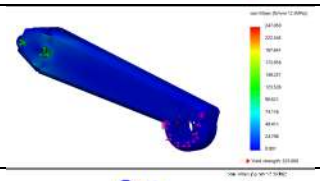	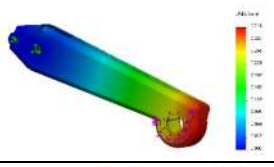
Front joint	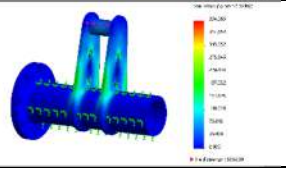	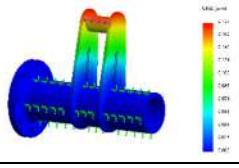
Rear joint	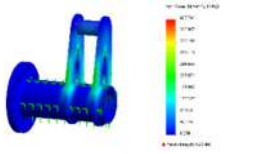	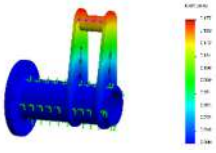

Table 1 Static simulation results of components

RESULTS OF THE BALANCE TEST IN THE LABORATORY

The experiment was conducted on a practical wheel-legged quadruped robot model as shown in Fig. 5. The overall dimensions, configuration, and technical specifications of the system were ensured to be accurate according to the previously presented design.

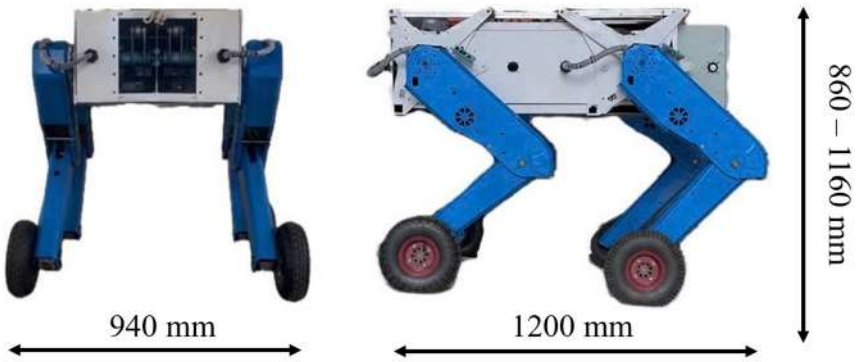

Fig. 5 The components of the hybrid quadruped wheel-legged platform

An experiment with unstructured terrain was performed to evaluate the drive system and the effectiveness of the controller in maintaining the robot's body stability. The obstacle height was 20 mm. Obstacles are randomly placed on both sides of the robot as shown in Fig. 6. The payload 30kg was placed in the centre of the body. The speed of the robot is 0.2 km/h. The balance controller maintained a reference height of 650 mm, and the data was collected as shown in Fig. 7.



Fig. 6 Unstructured experiment setup

The roll angle and pitch angle are maintained within the ranges of ±0.4° and ±0.6°, respectively. The roll and pitch angle graphs show the controller's response when the wheels approach an obstacle. This demonstrates the effectiveness of the SMC algorithm in maintaining the robot's balance on unstructured terrain. The roll angle error is maintained within ±0.4°. The pitch angle error range is larger, cantered at ±0.6°. The error represents the real-time posture correction of the robot on unstructured terrain. The control signal changes accordingly with the posture error. The displacement is in the range of -4 to 8 mm. The balance speed feedback fluctuates around 0° when the robot reaches a stable state. At some points when contacting an obstacle, the peak changes by approximately 2°. This peak dropped to approximately 0° in 2 seconds., demonstrating the ability to restore the balance in real time. Overall, the experimental results in an unstructured environment demonstrate the effectiveness of the balance control strategy. The robot's posture is always maintained in stable balance with an angle of inclination of less than 1 degree by the proposed balance control method.

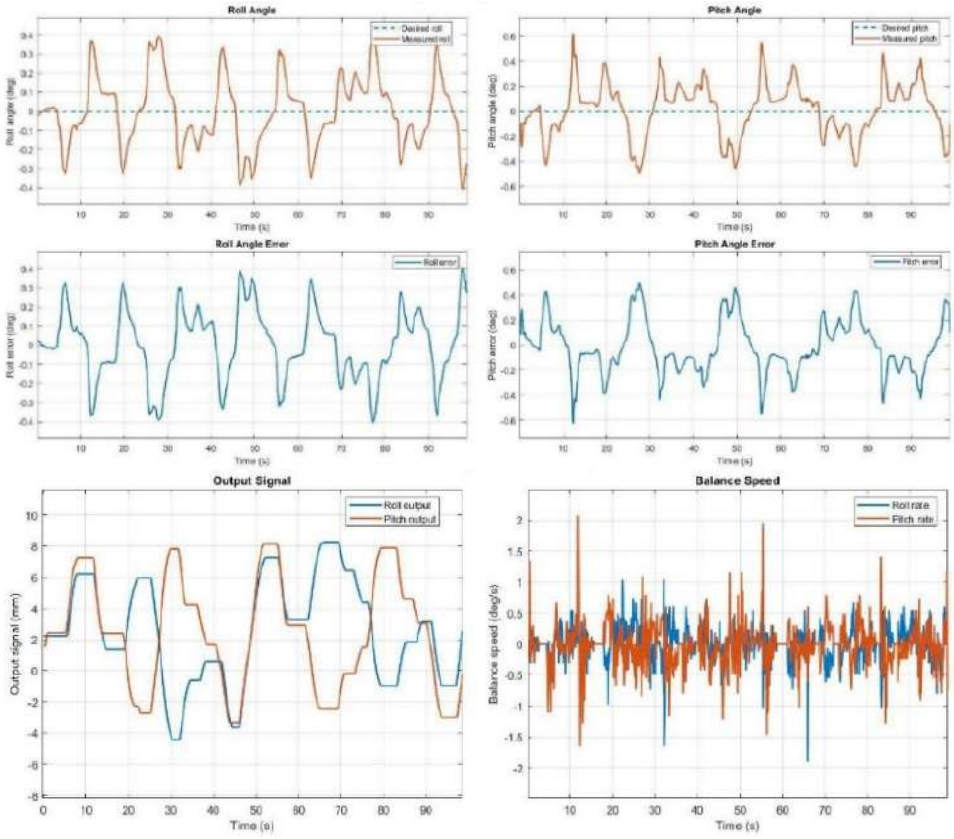

Fig. 7 Data acquisition in unstructured terrain

CONCLUSIONS

In this study, a wheel-legged robot configuration is proposed. The core components are statically simulated using software. In addition, a controller to maintain body stability was developed. A proposed sliding mode method maintained the body's equilibrium on unstructured terrain. Simulation results demonstrated the safety of the robot's components. Field experiments of the robot on unstructured terrain were conducted. The results demonstrate the effectiveness of the robot's drive system. The balance controller demonstrated reliable performance. The roll angle and pitch angle errors were $\pm 0.4°$ and $\pm 0.6°$, respectively. The described robot is still in development, and autonomous driving on unstructured terrain is being considered.

ACKNOWLEDGEMENTS

This study received funding from grants National Science and Technology Council (NSTC), Taiwan 114-2313-B-110-004-MY3. The authors are grateful for the support and resources provided by the Biomimicking and Engineering Lab (Being2 Lab) at National Sun Yat-sen University, Taiwan.

REFERENCES

Baek, S. Y., Jeon, H. H., Kim, W. S., Kim, Y. S., & Kim, Y. J. (2026). Slip control model for an electric tractor with four-wheel independent driving E-axle systems. Computers and Electronics in Agriculture, 244, 111452.

Bellicoso, C. D., Bjelonic, M., Wellhausen, L., Holtmann, K., Günther, F., Tranzatto, M., ... & Hutter, M. (2018). Advances in real-world applications for legged robots. Journal of Field Robotics, 35(8), 1311-1326.

Mucchiani, C., Zaccaria, D., & Karydis, K. (2024). Assessing the potential of integrating automation and artificial intelligence across sample-destructive methods to determine plant water status: A review and score-based evaluation. Computers and Electronics in Agriculture, 224, 108992.

Wei, W., Xiao, M., Wang, H., Zhu, Y., Xie, C., & Geng, G. (2024). Research progress of multiple agricultural machines for cooperative operations: A review. Computers and Electronics in Agriculture, 227, 109628.

Yang, C., Zheng, D., Mansurova, M., Belgibaev, B., Amirkhanova, G., & Zhao, B. (2026). Robust multimodal fusion for terrain perception and autonomous robot navigation in unstructured agricultural environments. Computers and Electronics in Agriculture, 252, 112142.

Grand, C., Benamar, F., & Plumet, F. (2010). Motion kinematics analysis of wheeled–legged rover over 3D surface with posture adaptation. Mechanism and Machine Theory, 45(3), 477-495.

Tran, D. T., Tran, M. H., Nguyen, N. H., & Truong, Q. T. (2026). Adaptive Fuzzy-LQR for Stability Control of Bipedal Wheel-Legged Robots on Variable Terrain. Journal of Robotics, 2026(1), 7752149.

PA-17

Proceedings of The 12th International Symposium on Machinery and Mechatronics for Agriculture and Biosystems Engineering (ISMAB 2026)
20-24 October 2026, Busan, Republic of Korea

3D SLAM AND RELOCALIZATION TOWARDS AUTONOMOUS NAVIGATION IN PAPAYA GREENHOUSE USING NANO-GICP REGISTRATION

Chi Cuong Nguyen[1], Dang Khanh Linh Le[2], Wei-Chih Lin[3*]

[1]Department of Mechanical and Electro-Mechanical Engineering, National Sun Yat-sen University, Kaohsiung City, Taiwan
*Corresponding Author-- Voice: +886-922-272-615, Email: wc.lin@mail.nsysu.edu.tw

Abstract: Autonomous mobile robots can reduce labor requirements and improve the efficiency of monitoring, spraying, and transportation in greenhouse operation. However, reliable localization in papaya greenhouses remains challenging because dense canopies, repetitive crop rows, and uneven terrain provide limited geometric information. This study presents a 3D LiDAR–inertial SLAM and prior-map relocalization framework for autonomous mobile robots working in papaya greenhouse. The system first constructs a 3D greenhouse map by integrating FAST-LIO2 odometry with loop-closure detection and backend graph optimization. A global relocalization module subsequently combines continuous odometry estimates with point-cloud registration algorithm to localize the robot within the previously constructed map. To improve point-cloud matching under challenging greenhouse conditions, Nano-GICP registration is incorporated into the framework to accurately align current point-cloud observation to the prior-map. Field experiments demonstrated the successful reconstruction of the greenhouse boundaries, crop rows, and connecting paths. For global localization evaluation, point-cloud registration methods including ICP, GICP, NDT, and Nano-GICP were evaluated and compared in greenhouse environment. Nano-GICP achieved the lowest mean translational error of approximately 0.23 m and a mean registration time of 5.49 ms. Although NDT provided more stable rotational estimates, its mean translational error and registration time were higher, at 0.42 m and 12.80 ms, respectively. Both positional alignment and computational efficiency of Nano-GICP provides an competitive approach, supporting robust 3D prior-map relocalization for future autonomous operation in papaya greenhouses.

Key Words: 3D LiDAR–inertial SLAM, map-based localization, Nano-GICP, agricultural robot, papaya greenhouse.

INTRODUCTION

Papaya cultivation in greenhouses reduces the adverse effects of environmental conditions and maintains more stable yields than open-field cultivation. However, repetitive operations, such as monitoring, spraying, transportation, and harvesting, remain labor-intensive. In the context of labor shortages and rising labor costs, autonomous mobile robots (AMRs) are considered a promising solution for improving production efficiency. Papaya greenhouses present considerable challenges to AMRs' localization system due to their long, narrow, and repetitive crop rows as well as dense and overlapping foliage. The limitation and similarity of

sensor observations at different locations weakens the geometric constraints required for pose estimation. GNSS performance degrades inside greenhouse structures, while vision-based localization is sensitive to lighting and repetitive vegetation. These limitations motivate the use of 3D LiDAR–IMU localization as a promising approach for pose estimation in papaya greenhouse environments. To achieve accurate localization, recent studies commonly combine local pose estimation with 3D-map alignment. Tightly coupled LiDAR–inertial odometry methods, such as FAST-LIO2 (Xu et al., 2022) and LIO-SAM (Shan et al., 2020), provide locally consistent motion estimates but remain susceptible to accumulated drift. Therefore, point-cloud registration, which registers with the corresponding region of a prior map to determine the global pose, plays a crucial role in correcting accumulated errors and optimizing global localization.

(Jiang et al., 2024) employed NDT for coarse registration to reduce the initial pose discrepancy between two point clouds, thereby enabling ICP to establish more reliable correspondences and improve mapping accuracy in orchards. (Segal et al., 2009) introduced GICP to improve registration accuracy and robustness relative to conventional ICP (Besl and Mckay, 1992) by exploiting the local geometric structure of point clouds. However, covariance estimation and correspondence search substantially increase its computational cost. Recently, The studies (Liang et al., 2026) and (Liu et al., 2026) have used NDT to reduce the cost of correspondence searching and improve localization stability in orchard environments. Nevertheless, its performance depends considerably on voxel resolution and may deteriorate in environments lacking distinctive geometric features. Although various registration methods have been investigated in agricultural contexts, most existing studies have focused on outdoor orchards. Papaya greenhouses are differently characterized by denser foliage, more repetitive structures, and severe occlusion. These conditions require a registration method capable of efficiently exploiting detailed local geometric information while maintaining robust alignment in structurally repetitive environments.

To address these challenges, this study proposes a robust 3D mapping and map-based localization framework incorporating loop closure and backend optimization for an autonomous robot operating in a papaya greenhouse. FAST-LIO2 is integrated with LIO-SAM-based backend optimization to enable accurate and globally consistent mapping. To improve global localization accuracy within the constructed 3D prior map, Nano-GICP (Chen et al., 2022) is employed in the relocalization module to accurately align point clouds while improving computational efficiency through the NanoFLANN k-d tree structure and efficient reuse of registration data. In addition, ICP, GICP, NDT, and Nano-GICP are experimentally compared under identical operating conditions to assess their suitability for localization in papaya greenhouse environment.

MATERIALS AND METHODS

DESIGN OF ROBOTIC PLATFORM

The robotic platform used a differential-drive tracked chassis for stable mobility on uneven greenhouse terrain. It supports speeds above 1 m/s and high payloads for spraying and transportation. A Livox MID-360 3D LiDAR with a built-in IMU provided mapping and navigation data at 200,000 points/s and 10 Hz. Motor encoders enabled track-motion measurement and closed-loop velocity control. An ASUS NUC 14 Pro with 16 GB RAM,

running Ubuntu 24.04 and ROS 2 Kilted, executed all autonomous functions. An onboard rechargeable battery powered the integrated platform (Fig. 1).



Fig.1 Hardware overview.

SYSTEM OVERVIEW

The proposed system (Fig. 2) consisted of an mapping module and a prior-map-based relocalization module. During the mapping stage, FAST-LIO2 estimated the local LiDAR–inertial odometry, while keyframe management, loop-closure detection, and factor-graph optimization were used to reduce accumulated drift and construct a globally consistent 3D point-cloud map.

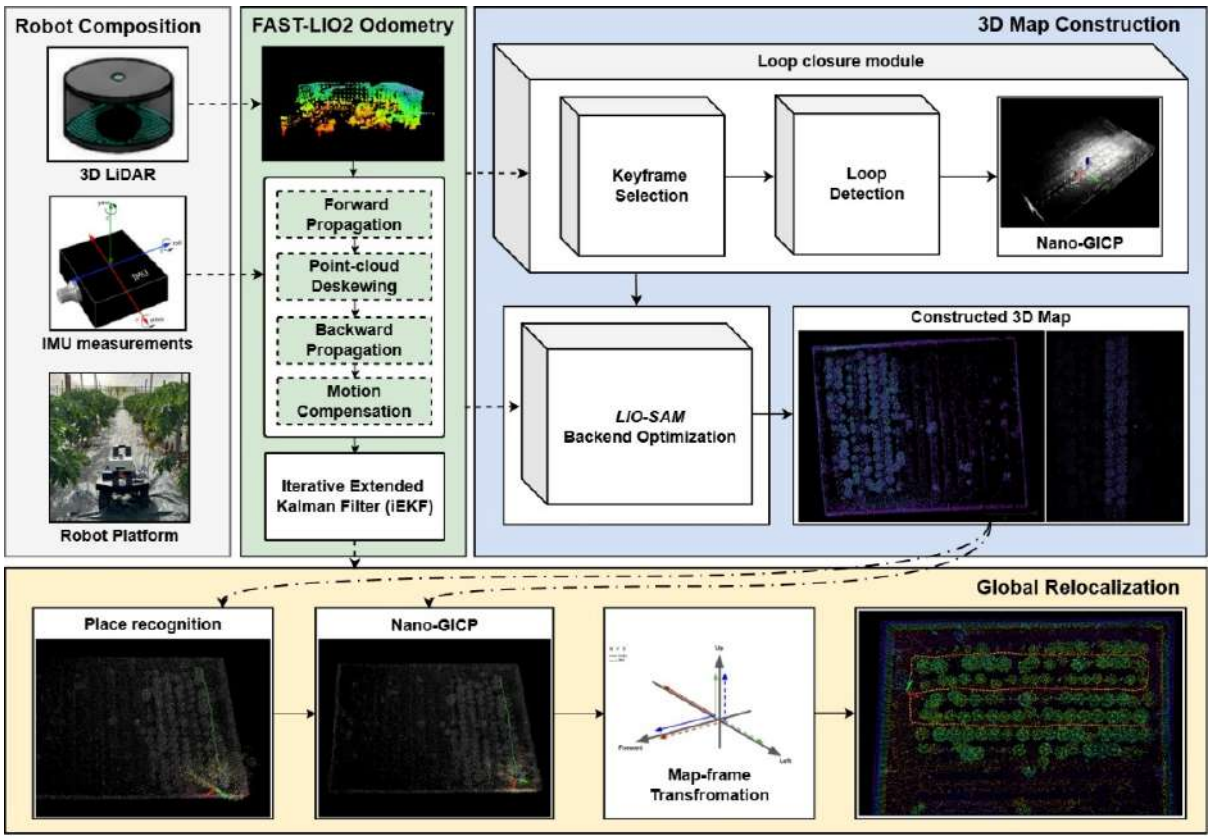

Fig.2 3D SLAM and relocalization framework for autonomous agricultural robot.

During the relocalization stage, the current LiDAR scan was registered against the prior map to estimate the robot pose transformation in the global map frame. The resulting global pose correction was combined with the locally continuous FAST-LIO2 odometry to enable reliable positioning with constructed map.

3D MAP CONSTRUCTION

FAST-LIO2 was employed as the LiDAR–inertial odometry frontend for SLAM system. Selected poses and their corresponding point clouds were stored as keyframes when the translational distance from the most recent keyframe exceeded 0.15 m. Scan Context (Kim and Kim, 2018) was used to detect loop-closure candidates based on global point-cloud descriptors. For each detected candidate, Nano-GICP registered the current submap P_k with the historical submap Q_j by estimating the relative transformation $T_{j \leftarrow k} \in SE(3)$. The optimal transformation was obtained by minimizing the covariance-weighted alignment error. A loop-closure constraint was accepted only when the registration converged and its fitness score was lower than 0.4. The accepted constraint was subsequently added to the factor graph, and the keyframe poses were globally optimized. The final 3D map was generated by transforming and accumulating the keyframe point clouds using their optimized poses.

RELOCALIZATION ON PRIOR MAP

The current LiDAR scan is aligned with the corresponding region of the prior map to estimate the robot's global pose. This study employed Nano-GICP to determine the global transformation that minimizes the alignment error between the current scan and local map submap. NanoFLANN k-d trees accelerate nearest-neighbor searches, while k-d trees and point covariances are reused to reduce redundant computation. Because the source scan at time (k-1) becomes the target at time (k), its k-d tree and covariances are transferred to the next registration cycle. Similarly, the local-submap k-d tree and covariances are recomputed only when the keyframes forming the submap change. Thus, the existing submap data are reused under the following condition:

$$T_{S_k} = \begin{cases} T_{S_{k-1}}, & if \;\; P_k = P_{k-1} \\ Build \;\; KdTree(P_k), & otherwise, \end{cases} \tag{3}$$

denote the source and target k-d trees at time k, respectively. Per-point covariances are computed once for each incoming scan and reused when it later serves as a source or target. Submap covariances are assembled from those of their constituent keyframes and updated only when the submap changes. Nano-GICP then applies the GICP objective to estimate the rigid transformation $T = (R, t)$ between the source and target point clouds. The estimated pose is accepted when Nano-GICP converges and its fitness score is below a predefined acceptance threshold. After successful registration, the transformation between the global map frame M and the local odometry frame O is calculated as:

$$T_{M,O} = T^*_{M,L_k} \left(T_{O,L_k}\right)^{-1} \tag{4}$$

where L_k denotes the current LiDAR frame. The continuous global pose at a subsequent

time n can then be obtained as:

$$T_{M,L_n} = T_{M,O} T_{O,L_n} \quad (5)$$

During autonomous navigation, the resulting global pose is used by the navigation stack for global path planning, trajectory tracking, and traversability-aware navigation. Therefore, the accuracy of the transformation estimated by the relocalization module directly influences the robot's localization consistency, path-tracking performance, and overall operational reliability.

GREENHOUSE EXPERIMENTAL ENVIRONMENT

The experiments were conducted in a papaya greenhouse at the Fengshan Tropical Horticultural Experiment Branch in Kaohsiung, Taiwan. The greenhouse comprised long, narrow papaya rows, each approximately 35 m long and 2.5 m wide. Three rows with different canopy densities were selected for evaluation. Unlike conventional orchards with relatively wide tree spacing, the greenhouse featured dense cultivation and restricted LiDAR visibility within the rows. Papaya canopies extended approximately 0.4-0.7 m into the aisle from each side, and mature plants covered much of the row width in several sections, causing substantial environmental occlusion. Moreover, the rough and stony ground induced vertical and rotational disturbances in the mobile platform, unlike the relatively level surfaces of modern greenhouses. Combined with the repetitive geometry of the crop rows, these conditions provided a challenging environment for evaluating 3D mapping, prior-map localization, and autonomous navigation.

RESULTS & DISCUSSION

POSITIONING ACCURACY TEST

To evaluate localization accuracy, four manually measured targets representing different perceptual conditions were selected. In each trial, the robot followed a predefined 150-m route through all targets and returned to its initial pose. Targets 1 and 4 were located at the ends of dense crop rows, Target 2 within a more uniform row, and Target 3 on a connecting path providing additional geometric features from the greenhouse walls. The robot stopped at each target to record its estimated pose. Five trials were conducted at each operating speed of 0.2, 0.4, and 0.6 m/s. Figure 3 shows that positioning accuracy depended on environmental geometry, traveled distance, and speed. At Targets 1-4, deviations were 47.4-55.4, 29.6-35.1, 20.6-30.3, and 38.2-52.4 cm, respectively. Target 3 achieved the lowest errors because the connecting path provided wider observations and stronger geometric constraints from the greenhouse walls. In contrast, dense, repetitive vegetation increased errors at Targets 1 and 4. Deviations generally increased at 0.6 m/s, although the trend was not monotonic, demonstrating the influence of local geometry. After returning to the initial region, errors decreased to 8.1, 9.7, and 11.2 cm at 0.2, 0.4, and 0.6 m/s, respectively. Overall, the localization framework performed better in geometrically distinctive areas but remained sensitive to canopy density, speed, and accumulated drift.

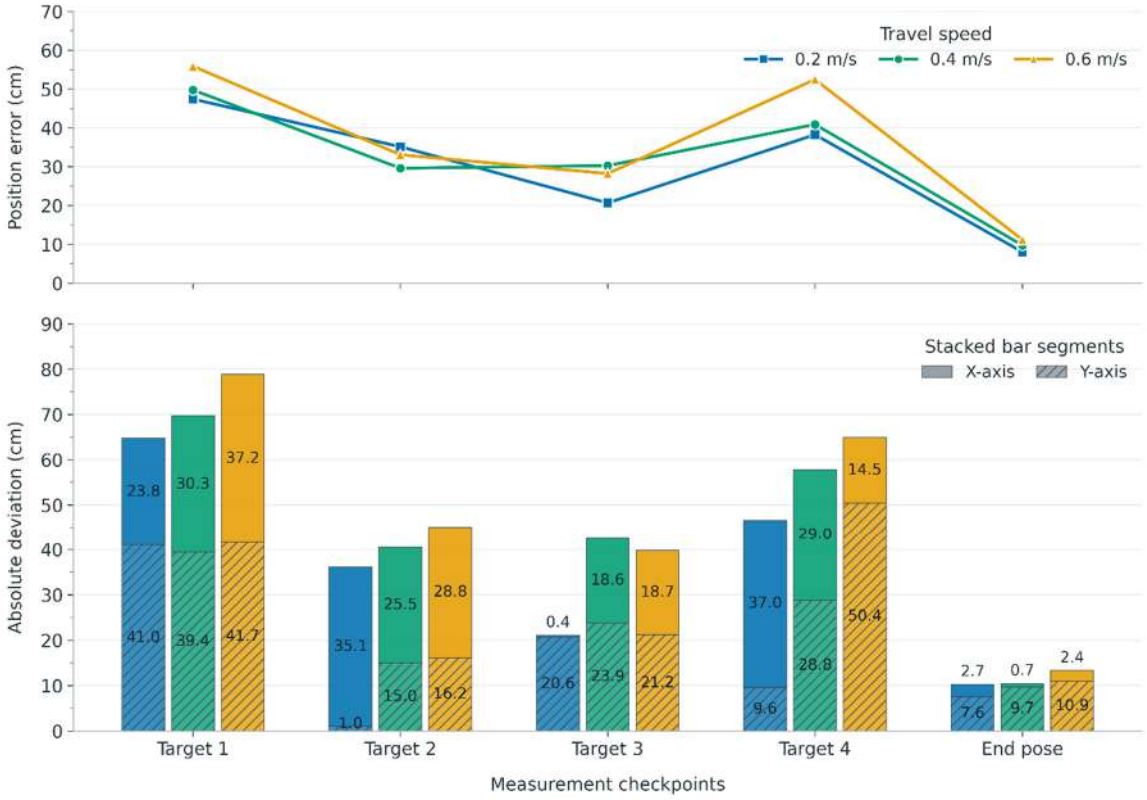

Fig.3 Robot positioning accuracy.

CONSTRUCTION OF 3D GREENHOUSE MAP

To construct the prior 3D map, the robot was manually driven through all crop rows and connecting paths at approximately 0.4 m/s. Each area was revisited twice from different directions to provide sufficient scan overlap for loop-closure detection. The resulting map (Fig. 4d-f) clearly reconstructed the greenhouse boundaries, walls, crop rows, and ground corridors. The top and oblique views show consistent, straight, and continuous row structures suitable for map-based localization and navigation. However, repetitive vegetation may still cause localization ambiguity in dense areas.

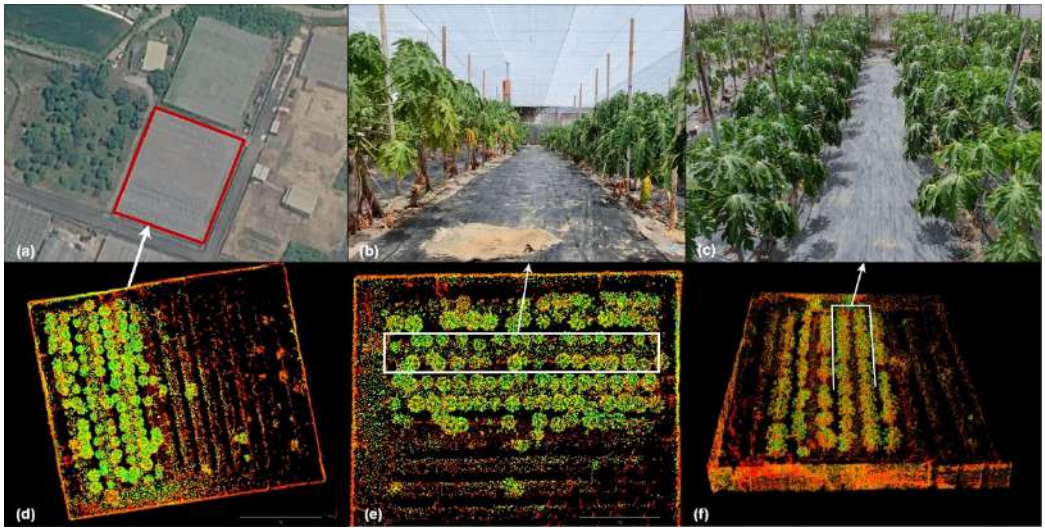

Fig.4 Experimental papaya greenhouse scenarios with different views are shown in (a)–(c). Mapping results in papaya greenhouse are presented in (d)–(f).

COMPARISON OF PRIOR MAP RELOCALIZATION TRAJECTORIES

The positioning evaluation revealed substantial errors and accumulated drift in long, densely vegetated crop rows, highlighting the need for prior-map-based relocalization. Accordingly, ICP, GICP, NDT, and Nano-GICP were evaluated using five sensor datasets recorded along the experimental trajectory shown in Fig. 5(b), with the 3D point-cloud map in Fig. 4d-f used as the prior map. Figure 6 presents the distributions of translational and rotational relocalization errors aggregated across the five experimental trials with a clear reduction in translational error from ICP to GICP, NDT, and Nano-GICP. The mean error decreased from 2.18 m for ICP to 1.35 m for GICP, 0.42 m for NDT, and 0.23 m for Nano-GICP. This trend agrees with the trajectory alignment in Fig. 5, where ICP exhibited substantial displacement, GICP improved row alignment, and NDT and Nano-GICP more closely followed the reference trajectory. Among the evaluated methods, Nano-GICP produced the lowest median translational error and the narrowest interquartile range, indicating lower and less dispersed errors for most trajectory samples. The differences in rotational performance were less consistent. GICP reduced the mean rotational error from approximately 4.87° for ICP to about 2.19°, while NDT and Nano-GICP both achieved 1.20° and 1.9° with compact interquartile ranges, respectively. Through experiments, NDT provided the most robust rotational performance, whereas Nano-GICP achieved the best translational accuracy and trajectory alignment.

Table 1 Computational-time comparison between NDT and Nano-GICP registration.

Method	Median (ms)	Mean (ms)
NDT	11.46	12.80
Nano-GICP	4.30	5.49

Both NDT and Nano-GICP provided effective point-cloud registration under challenging greenhouse conditions. NDT achieved more stable rotational estimation, but its voxel-based representation showed greater sensitivity in cluttered, low-canopy rows and required careful parameter tuning. Nano-GICP combined lower translational errors with better computational efficiency, requiring a mean of 5.49 ms per registration compared with 12.80 ms for NDT. This represents a 57.1% reduction in mean computation time. These results indicate that Nano-GICP offers a promised balance between localization performance and computational efficiency for prior-map relocalization in papaya greenhouses.

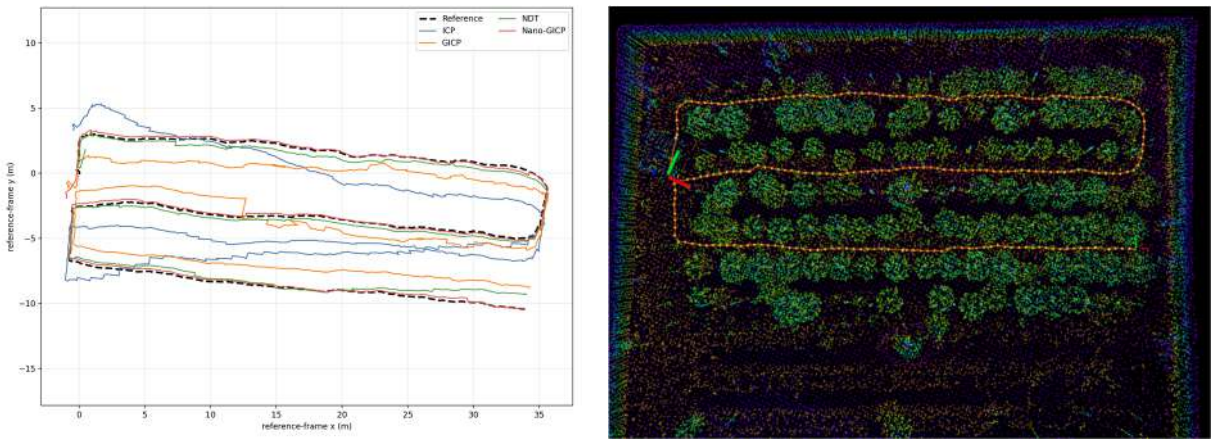

Fig.5 The comparison of relocalization trajectories on prior map using different point cloud registration methods (a) and experimental trajectory in greenhouse map (b).

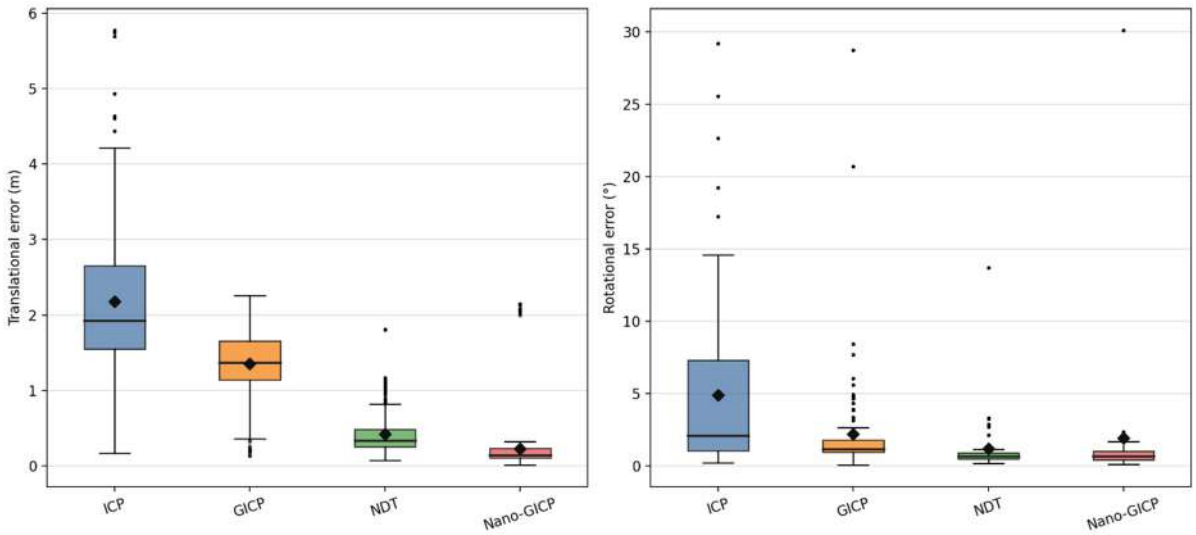

Fig.6 Translational and rotational relocalization errors of the point-cloud registration methods.

CONCLUSIONS

This study developed a 3D SLAM and map-based localization framework for papaya greenhouse robots. FAST-LIO2 odometry, loop-closure detection, and graph optimization produced a structurally consistent prior 3D map. Field experiments indicated reliable odometry and global localization in the environment of repetitive rows and dense canopies. Among the evaluated registration methods, Nano-GICP achieved the balance between localization accuracy and computational efficiency, offering competitive global localization approach in papaya greenhouse environment with mulitple environmental challenges. The framework provides a practical foundation for integration with path planning, obstacle avoidance, and motion control toward fully autonomous greenhouse operation.

ACKNOWLEDGEMENTS

This study received funding from grants National Science and Technology Council (NSTC), Taiwan 114-2313-B-110-004-MY3. The authors are grateful for the support and resources provided by the Biomimicking and Engineering Lab (Being2 Lab) at National Sun Yat-sen University, Taiwan.

REFERENCES

Besl, P. J., and N. D. Mckay. 1992. A Method for Registration of 3-D Shapes. *Ieee Transactions on Pattern Analysis and Machine Intelligence* 14(2):239–256.

Chen, K., B. T. Lopez, A. A. Agha-mohammadi, and A. Mehta. 2022. Direct LiDAR Odometry: Fast Localization With Dense Point Clouds. *Ieee Robotics and Automation Letters* 7(2):2000–2007.

Jiang, S. K., P. Qi, L. Han, L. M. Liu, Y. F. Li, Z. Huang, Y. J. Liu, and X. K. He. 2024. Navigation system for orchard spraying robot based on 3D LiDAR SLAM with NDT_ICP point cloud registration. *Computers and Electronics in Agriculture* 220.

Kim, G., and A. Kim. 2018. Scan Context: Egocentric Spatial Descriptor for Place Recognition Within 3D Point Cloud Map.

Liang, Z. Y., L. H. Wang, H. X. Wang, B. H. Zhang, and C. L. Liu. 2026. Autonomous obstacle avoidance and path planning for mobile robots in orchard environments combining with map construction and positioning methods. *Computers and Electronics in Agriculture* 244.

Liu, T., Y. F. Bian, B. H. Zhang, L. J. Bai, G. X. Wang, and G. Z. Tian. 2026. Robust autonomous navigation in unstructured orchards: Integrated LIO-SAM with NDT-based relocalization and Bayesian traversability mapping. *Computers and Electronics in Agriculture* 253.

Segal, A., D. Haehnel, and S. Thrun. 2009. Generalized-ICP.

Shan, T., B. Englot, D. Meyers, W. Wang, C. Ratti, and D. Rus. 2020. LIO-SAM: Tightly-coupled Lidar Inertial Odometry via Smoothing and Mapping.

Xu, W., Y. X. Cai, D. J. He, J. R. Lin, and F. Zhang. 2022. FAST-LIO2: Fast Direct LiDAD-Inertial Odometry. *Ieee Transactions on Robotics* 38(4):2053–2073.

PA-18

Proceedings of The 12th International Symposium on Machinery and Mechatronics for Agriculture and Biosystems Engineering (ISMAB 2026)
20-24 October 2026, Busan, Republic of Korea

EARLY DETECTION OF BARLEY WATERLOGGING USING UAV-BASED HYPERSPECTRAL IMAGERY

Ji An Kim[1], Do Hyun An[1], Hyo Jeong Lee[1], Ye Seong Kang[1*], Yeong Son Jo[1], Seung Ga Oh[2], Hui Su Bae[3], Woo Jin Im[3]

[1]Department of Smart Agro-industry, Gyeongsang National University, Jinju 52725, Republic of Korea
[2]Agri-Food Bio Convergence Institute, Gyeongsang National University, Jinju 52725, Republic of Korea
[3]National Institute of Crop Science, Rural Development Administration, Wanju 55365, Republic of Korea
*Corresponding Author -- Voice: +82-55-772-3222, Email: slow321@gnu.ac.kr

Abstract: Barley (Hordeum vulgare L.) is highly susceptible to waterlogging, and because the chance of recovery falls as the stress persists, detecting the damage before visible symptoms appear is critical for minimizing yield loss. Contact-based diagnosis such as SPAD chlorophyll measurement responds only after the stress has reached the individual-plant level. This study developed machine learning classification models that diagnose waterlogging in barley from UAV-based hyperspectral imagery and compared their detectable timing with that of SPAD measurement. A field experiment on the barley cultivar 'Nurichal' was conducted at the National Institute of Crop Science, Wanju, Republic of Korea, with waterlogged and well-watered plots in a split-plot design of three replicates treated from 19 March to 3 April 2026. Hyperspectral images were acquired seven times at two-day intervals with a 150-band sensor on a UAV flown 25 m above ground. Representative wavelengths were selected in the Blue, Green, Red, Red-edge and NIR regions by two-sample t-tests on canopy reflectance, and vegetation indices computed from these bands were reduced from five to oneby SHAP importance while machine learning classifiers were trained for each combination. In the whole time-series model, mean F1-score was almost unchanged from five to four indices but fell clearly below three, and the K-nearest neighbor (KNN) model with four indices performed best (F1-score 0.962, accuracy 0.949) with the fewest missed waterlogged samples. In the date-specific models, KNN scored 0.920 or higher from 23 March using only two indices and classified without error from 27 March to 1 April, whereas SPAD values did not differ significantly between treatments until 27 March. The proposed approach therefore detected waterlogging earlier than the contact-based method while requiring only a few indices, indicating practical potential for rapid field diagnosis.

Key Words: Barley, Early detection, Hyperspectral imagery, Machine learning, Waterlogging

INTRODUCTION

Barley (Hordeum vulgare L.) is a major winter cereal in the Republic of Korea and is frequently exposed to waterlogging when spring rainfall is concentrated after sowing; among winter

cereals it is particularly vulnerable to excess soil water (De Castro et al., 2022). The resulting hypoxia impairs root function, reduces chlorophyll content and delays growth, all of which translate into yield loss, and because recovery is more likely at an earlier stage, rapid diagnosis followed by prompt drainage is essential (Ploschuk et al., 2018). In practice, crop stress is still diagnosed mainly by visual inspection or by contact-based instruments such as the SPAD chlorophyll meter, which detect damage only after it has advanced far enough to be visible at the individual-plant level (Jin et al., 2025).

Unmanned aerial vehicles (UAVs) carrying hyperspectral sensors allow large fields to be observed repeatedly at high spatial resolution without contact (Ram et al., 2024). Hyperspectral indices have been reported to capture waterlogging-induced changes in leaf water content in wheat at an early stage (Yang et al., 2021). Vegetation indices are the indicator most commonly shared by such studies because they indirectly represent physiological and structural states such as chlorophyll content and canopy density. Visible-range indices reflect canopy greenness and density, whereas red-edge indices respond sensitively to chlorophyll change and are advantageous for detecting stress before symptoms become visible (Dash and Curran, 2004). Which index family and which classification algorithm are better suited at each stage of stress progression, however, has not been sufficiently compared.

The objectives of this study were (1) to develop machine learning classification models that discriminate waterlogged from well-watered barley using vegetation indices derived from UAV hyperspectral imagery, (2) to identify the model and the minimum number of indices giving stable discrimination, and (3) to compare the timing at which waterlogging becomes detectable by this non-contact approach with that of conventional SPAD measurement.

MATERIALS AND METHODS

Experimental Design and Image Acquisition

The experiment was carried out in 2026 at the experimental field of the National Institute of Crop Science, Wanju-gun, Republic of Korea (35°50'35.19"N, 127°02'52.93"E). The barley cultivar 'Nurichal' was broadcast-sown on raised beds on 5 November 2025. A waterlogged plot (W) and a well-watered control plot (N) were arranged in a split-plot design with three replicates over 20 m by 31.8 m, each replicate measuring 2.5 m by 4.8 m. In the W plots, drip hoses supplied water for 30 min at 09:00, 13:00 and 17:00 daily so that volumetric water content (VWC) stayed above 40 %, exceeding field capacity; the N plots received only natural rainfall and were maintained at 25-30 % VWC. The treatment ran from 19 March to 3 April 2026. SPAD values were measured with a portable chlorophyll meter (SPAD-502, Minolta, Osaka, Japan) on the first fully expanded upper leaf of the five central rows of each replicate.

Hyperspectral images were acquired with a sensor (MicroHSI 410 SHARK, Corning Incorporated, USA) mounted on a UAV (Matrice 300 RTK, DJI, China) seven times at two-day intervals between 21 March and 3 April 2026. The flight altitude was 25 m and the speed 2 m/s, and all flights were made between 11:00 and 14:00 to minimize illumination effects. The sensor

covers 400-1000 nm in 150 bands with a ground sample distance of 1.83 cm. Radiometric, geometric and orthorectification corrections were applied in ENVI Classic 5.6 (Exelis Visual Information Solutions, USA) following Kang et al. (2023). To isolate the barley canopy, corrected images were converted to NDVI using Equation (1) and thresholded to exclude soil and shadow; mean reflectance was then extracted from the vegetation pixels of a region of interest defined for each plot and averaged over the five rows.

$$NDVI = (NIR - Red) / (NIR + Red) \quad (1)$$

Band Selection, Vegetation Indices and Classification

Two-sample t-tests were performed in Python 3.11 to identify wavelengths that discriminate the treatments. Within each of the Blue (410-499 nm), Green (500-599 nm), Red (600-680 nm), Red-edge (680-740 nm) and NIR (740-990 nm) regions, the wavelength with the lowest p-value was selected as the representative band. Missing values and outliers were removed with the interquartile range (IQR) method (An et al., 2025), discarding samples below Q1 − 1.5 × IQR or above Q3 + 1.5 × IQR. A total of 58 vegetation indices covering visible, red-edge and chlorophyll-related families were then calculated from the representative bands.

Indices were standardized and split into 60 % training and 40 % test sets. Seven classifiers were applied to the binary discrimination: Logistic Regression (LR), K-Nearest Neighbors (KNN), Support Vector Classifier (SVC), Gaussian Process (GP), Gradient Boosting (GB), Random Forest (RF) and Extreme Gradient Boosting (XGB). Hyperparameters of LR, KNN, SVC and GP were optimized by grid search with cross-validation, while GB, RF and XGB were fixed at conservative values to suppress overfitting. Performance was evaluated on the test set with accuracy, precision, recall and F1-score from the confusion matrix, and minimizing false negatives (FN) — waterlogged canopies classified as well-watered — was treated as an important criterion because such cases let the stress go unnoticed. The contribution of each index was quantified with SHapley Additive exPlanations (SHAP; Lundberg and Lee, 2017); indices were ranked by mean absolute SHAP value on the training data, the top N were reselected as inputs, and models were retrained with N reduced from five to one. Models were built both for the pooled whole time-series dataset and separately for each imaging date. A fuller description of the procedure is given in Kim et al. (2026).

RESULTS & DISCUSSION

SPAD Response and Representative Bands

Changes in SPAD value are shown in Figure 1. From 21 to 25 March no clear difference appeared between the two plots, and on 21 March the waterlogged plot was even slightly higher, indicating that a certain period is required before waterlogging is expressed as a reduction in chlorophyll content. A significant difference ($p < 0.05$) emerged from 27 March, and the gap was largest on 30 March (51.2 in the control against 44.9 in the waterlogged plot). The temporary decline in both plots on 1 April coincided with rainfall on 30-31 March recorded in the

field log, and by 3 April both plots had recovered, with the difference widening again (50.7 against 43.6).

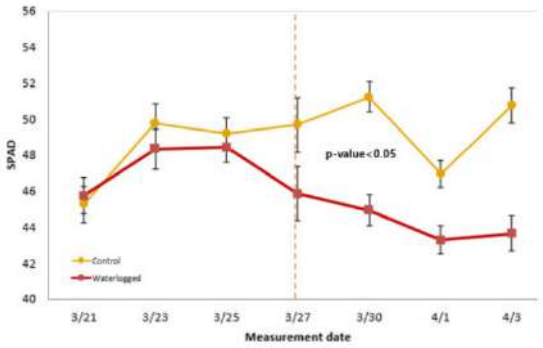

Fig. 1 SPAD values of control and waterlogged barley at each imaging date.

Two-sample t-tests on canopy reflectance showed that the treatments differed more in the NIR region than in the visible region, and NIR reflectance of the waterlogged plot was generally lower. The treatments differed more in the NIR region than in the visible region, and NIR reflectance of the waterlogged plot was generally lower. Of the 150 bands, 121 differed significantly between treatments ($p < 0.05$). The representative bands were 489.33 nm (Blue), 569.55 nm (Green), 609.66 nm (Red), 701.92 nm (Red-edge) and 826.27 nm (NIR); the lowest p-values occurred in the NIR region, suggesting that the spectral response to waterlogging is most sensitive in the near-infrared. After IQR-based outlier removal, 295 samples (100 control and 195 waterlogged) remained. All NIR outliers originated from the waterlogged plot, indicating that waterlogging-induced changes in NIR reflectance varied considerably among individual plants.

Whole Time-Series Model

Changes in performance with the number of input indices are shown in Figure 3. Mean F1-score of the seven models was 0.928 with five indices and 0.922 with four, then decreased clearly to 0.885, 0.874 and 0.757 with three, two and one index; mean accuracy followed the same pattern (0.906, 0.897, 0.850, 0.837 and 0.717). KNN retained the highest values across the whole range, so four indices were taken as the condition that minimizes inputs without loss of performance.

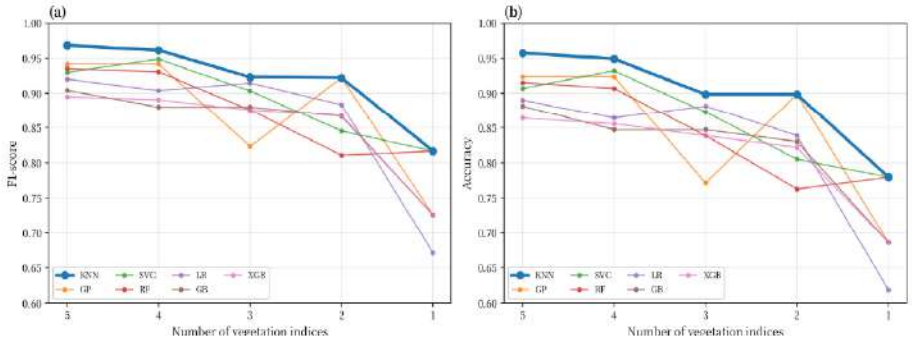

Fig. 3 Changes in (a) F1-score and (b) accuracy with the number of input vegetation indices in the whole time-series model.

Table 1 Classification performance of seven models using the top four vegetation indices in the whole time-series model (6:4 train-test split).

Model	KNN	SVC	GP	RF	LR	XGB	GB
Selected variables	GDVI, GLI, TVI, RGR	GDVI, TVI, GLI, RGR	GLI, GDVI, RGR, NGRDI	GDVI, TVI, GLI, CVI	RGR, CCCI, RRI2, CVI	GLI, TVI, CCCI, NGBDI	GLI, TVI, NGBDI, GDVI
Accuracy	0.949	0.932	0.924	0.907	0.864	0.856	0.848
Precision	0.962	0.949	0.948	0.914	0.852	0.896	0.917
Recall	0.962	0.949	0.936	0.949	0.962	0.885	0.846
F1-score	0.962	0.949	0.942	0.931	0.904	0.890	0.880
AUC	0.958	0.952	0.961	0.963	0.913	0.947	0.938
TP	75	74	73	74	75	69	66
TN	37	36	36	33	27	32	34
FP	3	4	4	7	13	8	6
FN	3	4	5	4	3	9	12

Table 1 gives the performance of the seven models under the four-index condition. KNN was best (F1-score 0.962, accuracy 0.949), followed by SVC, GP, RF, LR, XGB and GB. LR and RF combined high recall with low precision, wrongly flagging well-watered samples (FP = 13 and 7), while GB, XGB and GP missed the most waterlogged samples (FN = 12, 9 and 5). Since minimizing FN is critical, KNN, with three missed samples and balanced precision and recall, was the most appropriate model; its strength is attributed to the two treatments occupying clearly separated regions in the vegetation-index space, whereas the boosting-based models suffered from a sample size (295) insufficient for sequential learning. GDVI and GLI complement each other by representing the spectral change in the near-infrared and visible regions respectively, so two indices are the minimum workable combination, but total misclassification doubled when inputs were cut from four to three, making four indices the appropriate choice.

Date-Specific Models and Comparison with SPAD

Independent models were also built for each imaging date. Mean F1-score decreased only gradually as inputs were reduced, from 0.941 with five indices to 0.936, 0.933 and 0.917 with four, three and two, but with a single index it varied between 0.250 and 1.000 depending on date and model. Two indices therefore again represented the minimum stable combination, and the performance of LR and KNN under this condition is summarized in Table 2.

Table 2 Date-specific classification performance of the LR and KNN models with two vegetation indices.

Model	Date	Selected variables	Accuracy	F1-score	Precision	Recall	TP	TN	FP	FN
LR	21 Mar.	GCI, CVI	0.933	0.952	0.909	1.000	10	4	1	0
	23 Mar.	MTCI, CCCI	0.944	0.963	0.929	1.000	13	4	1	0
	25 Mar.	GDVI, TVI	0.944	0.960	0.923	1.000	12	5	1	0
	27 Mar.	GLI, RI	0.778	0.857	0.750	1.000	12	2	4	0
	30 Mar.	RGR, CCCI	0.833	0.880	0.846	0.917	11	4	2	1
	1 Apr.	MCARI, CCCI	1.000	1.000	1.000	1.000	8	6	0	0

	3 Apr.	GLI, NGBDI	1.000	1.000	1.000	1.000	12	6	0	0
KNN	21 Mar.	BRI, ARI	0.800	0.857	0.818	0.900	9	3	2	1
	23 Mar.	MTCI, CCCI	0.889	0.923	0.923	0.923	12	4	1	1
	25 Mar.	GDVI, TVI	0.889	0.923	0.857	1.000	12	4	2	0
	27 Mar.	GLI, TVI	1.000	1.000	1.000	1.000	12	6	0	0
	30 Mar.	TVI, GDVI	1.000	1.000	1.000	1.000	12	6	0	0
	1 Apr.	MCARI, CCCI	1.000	1.000	1.000	1.000	8	6	0	0
	3 Apr.	MCARI, GLI	0.944	0.960	0.923	1.000	12	5	1	0

LR was best in the early and late stages but fell behind in the middle stage (F1-score 0.857 on 27 March and 0.880 on 30 March against 1.000 for KNN), so KNN was the more consistent choice. KNN was weakest on 21 March (F1-score 0.857), reached 0.923 on 23 and 25 March, classified without error from 27 March to 1 April and scored 0.960 on 3 April, with no waterlogged sample missed from 25 March onward. The lower performance in the earliest stage reflects insufficient accumulation of stress, so that index values of the two treatments overlapped. The indices selected by SHAP also shifted with stress progression: red-edge and chlorophyll-related indices (ARI, CCCI, MTCI) dominated on 21 and 23 March, when subtle chlorophyll changes preceded visible symptoms, whereas visible and near-infrared indices (TVI, GDVI, GLI) dominated from the middle stage as leaf yellowing became clearer. Because each date-specific model used approximately 45 samples, several reached an F1-score of 1.000, so this analysis is best read as supporting evidence for the change in spectral response over time.

Whereas SPAD values differed significantly only from 27 March, the index-based models discriminated waterlogged canopies from the earliest imaging date, 21 March, two days after the treatment began, so the proposed approach offers a clear advantage in early detection while removing the labour and time constraints of contact-based measurement.

CONCLUSIONS

Machine learning classification models were developed for the early detection of waterlogging in barley using vegetation indices derived from UAV-based hyperspectral imagery. The near-infrared region was the most sensitive to waterlogging, and waterlogged canopies were distinguished before visible symptoms appeared: KNN with four indices was optimal for the whole time-series model, and KNN with two indices allowed early diagnosis at every imaging date. Whereas SPAD measurement revealed a difference only in the middle stage of treatment, the proposed approach discriminated waterlogging from the start of the treatment period. Since the results come from a single cultivar in a single field, generalization requires caution; extending the sample across cultivars and environments would allow them to serve as basic data for early warning and precision water management in barley.

ACKNOWLEDGEMENTS

This work was carried out with the support of the “Development of image interpretation and

quantification technology for weather stress damage in barley and red beans" project (Project No. RS-2026-25519310), National Institute of Crop Science, Rural Development Administration, Republic of Korea.

REFERENCES

An, D. H., Y. S. Kang, C. H. Park, G. I. Je, and C. S. Ryu. 2025. Development of prediction models for apple fruit diameter and length using unmanned aerial vehicle-based multispectral imagery. AgriEngineering 7(11): 361.

Dash, J., and P. J. Curran. 2004. The MERIS terrestrial chlorophyll index. Intl. J. Remote Sensing 25(23): 5403-5413.

De Castro, J., R. D. Hill, C. Stasolla, and A. Badea. 2022. Waterlogging stress physiology in barley. Agronomy 12(4): 780.

Jin, Y., Y. Peng, H. Song, Y. Jin, L. Jiang, Y. Ji, and M. Ding. 2025. Combining hyperspectral imaging with ensemble learning for estimating rapeseed chlorophyll content under different waterlogging durations. Plants 14(24): 3713.

Kang, Y. S., K. S. Park, E. L. Kim, J. C. Jeong, C. S. Ryu, and J. G. Cho. 2023. Estimation of chlorophyll contents in pear tree using unmanned aerial vehicle-based hyperspectral imagery. Korean J. Remote Sensing 39(5-1): 669-681.

Kim, J. A., D. H. An, H. J. Lee, Y. S. Kang, Y. S. Jo, S. G. Oh, H. S. Bae, and W. J. Im. 2026. Early detection of barley waterlogging using unmanned aerial vehicle-based hyperspectral imagery. J. Agric. Life Sci. 60(4): 1-13.

Lundberg, S. M., and S. I. Lee. 2017. A unified approach to interpreting model predictions. Advances in Neural Information Processing Systems 30: 4765-4774.

Ploschuk, R. A., D. J. Miralles, T. D. Colmer, E. L. Ploschuk, and G. G. Striker. 2018. Waterlogging of winter crops at early and late stages: Impacts on leaf physiology, growth and yield. Frontiers in Plant Sci. 9: 1863.

Ram, B. G., P. Oduor, C. Igathinathane, K. Howatt, and X. Sun. 2024. A systematic review of hyperspectral imaging in precision agriculture: Analysis of its current state and future prospects. Computers and Electronics in Agric. 222: 109037.

Yang, F. F., T. Liu, Q. Y. Wang, M. Z. Du, T. L. Yang, D. Z. Liu, S. J. Li, and S. P. Liu. 2021. Rapid determination of leaf water content for monitoring waterlogging in winter wheat based on hyperspectral parameters. J. Integrative Agric. 20(10): 2613-2626.

PA-19

Proceedings of The 12th International Symposium on Machinery and Mechatronics for Agriculture and Biosystems Engineering (ISMAB 2026)
20-24 October 2026, Busan, Republic of Korea

PRE-HARVEST PREDICTION OF APPLE SOLUBLE SOLIDS CONTENT USING UAV BASED MULTISPECTRAL IMAGERY

Chang Hyeok Park[1], ChanSeok Ryu[1*], GangIn Je[1], HoJun Kwon[1], Gang-Jin Lee[2]

[1] Department of Bio-System Engineering, Institute of Agriculture & Life Science, GyeongSang National University, Jinju-si 52828, Korea
[2] Institute of Agriculture & Life Science, GyeongSang National University, Jinju-si 52828, Korea
*Corresponding Author-- Voice: +82-55-772-1897, Email: ryucs@gnu.ac.kr

Abstract: This study developed and validated machine learning models for predicting the pre-harvest soluble solids content (SSC) of apples using only vegetation indices (VIs) derived from unmanned aerial vehicle (UAV) based multispectral imagery. Thirty-nine 'Fuji' apple trees distributed across ten orchards in Andong, Gyeongsangbuk-do, Republic of Korea, were surveyed over two growing seasons (2024–2025), with thirteen trees repeatedly measured in both years. Imagery was acquired at noon on 17 September 2024 and 16 September 2025 using a Trinity F90+ fixed-wing UAV equipped with an Altum-PT multispectral sensor, flown at an altitude of 150 m with 75% overlap, yielding a ground sample distance of 3.17 cm/pixel. After radiometric calibration, mosaicking, and pansharpening, canopy and background were separated using NDVI thresholding, and the anthocyanin reflectance index (ARI), green leaf index (GLI), and rededge normalized difference vegetation index (NDVI_rededge) were extracted at the individual-tree level. Using SSC measured with a handheld refractometer as the dependent variable, multiple linear regression (MLR) and k-nearest neighbor regression (KNR) models were constructed and evaluated by leave-one-out cross-validation (LOOCV) in terms of R^2, RMSE, and MAPE. At the validation stage, MLR yielded an R^2 of 0.55, a MAPE of 9.21%, and an RMSE of 1.34 °Brix, outperforming KNR (R^2 = 0.47, MAPE = 9.65%, RMSE = 1.45 °Brix). SHAP analysis indicated that NDVI_rededge contributed consistently across both models, whereas the relative contributions of GLI and ARI were reversed depending on the learning scheme. These results confirm that individual-tree SSC can be estimated non-destructively and without contact from canopy-level spectral information alone, supporting the use of this approach for orchard-scale maturity assessment and harvest timing decisions in precision agriculture.

Key Words: Apple, Unmanned aerial vehicle, Vegetation index, Soluble solids content, Machine learning

INTRODUCTION

Apple (*Malus* × *domestica* Borkh.) is one of the most widely cultivated fruit crops worldwide, and in the Republic of Korea it occupies approximately 33,313 ha, accounting for about 23.2% of the total fruit cultivation area (KOSTAT, 2024). Sweetness, expressed as soluble solids content (SSC), directly influences consumer purchasing decisions (Giovanelli et al., 2014) and serves as a key indicator for evaluating fruit maturity and determining the optimal harvest date

(Peng and Lu, 2008). Conventional SSC assessment requires destructive sampling of developing fruit, which is labor-intensive and time-consuming (Magwaza and Opara, 2015).

Numerous non-destructive approaches have therefore been investigated (Lu et al., 2020; Walsh et al., 2020). However, most of these methods require an optical instrument to be placed in contact with, or in close proximity to, individual fruits (Zude et al., 2006; Fan et al., 2020; Li et al., 2022), so the labor and time constraints remain when an entire orchard must be assessed. Unmanned aerial vehicles (UAVs) can acquire canopy spectral information over large areas within a short time (Deng et al., 2018), and the resulting vegetation indices (VIs) have been used to quantify and predict crop growth status (Xue and Su, 2017). Recent studies have combined UAV-derived VIs with machine learning to estimate apple canopy chlorophyll content (Wang et al., 2025) and individual-tree yield (Chen et al., 2022), demonstrating the effectiveness of this approach for orchard monitoring.

The objective of this study was to develop and validate machine learning models that predict the pre-harvest SSC of individual apple trees using only VIs obtained from a five-band multispectral camera mounted on a UAV, thereby enabling rapid, non-destructive quality assessment prior to harvest.

MATERIALS AND METHODS

STUDY SITE AND PLANT MATERIALS

The study was conducted over two years (2024 and 2025) on 39 'Fuji' apple trees located in ten orchards in Imha-myeon, Andong-si, Gyeongsangbuk-do, Republic of Korea (36.4717° N, 128.8937° E). Thirteen trees were repeatedly surveyed in both years (n = 26). Training systems included slender spindle, bi-axis, and multi-axis forms. To characterize inter-annual differences in the growing environment, meteorological data were obtained from Agricultural Weather 365 (Rural Development Administration), and growing degree days (GDD) were calculated for the growing season (April–October) with a base temperature of 5 °C (Stanley et al., 2000), setting daily values below the base temperature to zero (McMaster and Wilhelm, 1997)

MULTISPECTRAL IMAGE ACQUISITION

Images were acquired at noon on 17 September 2024 and 16 September 2025 using a Trinity F90+ fixed-wing UAV (Quantum Systems, Germany) equipped with an Altum-PT multispectral sensor (MicaSense Inc., USA). Radiometric calibration was performed before each flight using an RP-06 reflectance panel. Flights were conducted at an altitude of 150 m with 75% overlap, giving a ground sample distance of 3.17 cm/pixel. Band images were mosaicked in Pix4D mapper (Pix4D S.A., Switzerland), pansharpened and co-registered in QGIS, and vegetation was separated from background using NDVI in ENVI 5.3 (Exelis Visual Information Solutions Inc., USA) before extracting reflectance for each individual tree. Three VIs were then computed. ARI estimates leaf anthocyanin content from the difference between the inverse reflectances in the green and red-edge regions and reflects pigment change and stress response (Gitelson et al., 2001). GLI combines green, red, and blue reflectance in the visible region and is used to assess chlorophyll content and canopy vigor (Eng et al., 2019). NDVI_rededge substitutes the red-edge band for the near-infrared band of conventional NDVI and is sensitive to chlorophyll variation in dense canopies where NDVI saturates (Ehammer et al., 2010).

SSC MEASUREMENT

For each target tree, fruits were randomly sampled from every main scaffold branch, harvested, and juiced. SSC was measured with a handheld refractometer (AL-BX|ACID5 Master Kit,

ATAGO, Japan).

MODEL DEVELOPMENT AND EVALUATION

Multiple linear regression (MLR), which captures linear relationships between variables, and k-nearest neighbor regression (KNR), which can learn non-linear relationships between VIs and SSC, were used to predict measured SSC. Optimal KNR hyperparameters were determined by grid search cross-validation. Because the number of surveyed trees was limited, leave-one-out cross-validation (LOOCV) was applied to secure generalization performance; predictions from all iterations were pooled to evaluate model accuracy using the coefficient of determination (R^2), root mean square error (RMSE), and mean absolute percentage error (MAPE). SHapley Additive exPlanations (SHAP) was applied to quantify the contribution of each VI to model predictions (Lundberg and Lee, 2017).

RESULTS & DISCUSSION

DESCRIPTIVE STATISTICS

ARI increased significantly from 16.80 ± 2.60 in 2024 to 21.31 ± 2.90 in 2025 ($p < 0.001$). GLI and NDVI_rededge were both lower in 2025 than in 2024; the difference was not significant for GLI ($p = 0.137$) but was significant for NDVI_rededge ($p = 0.001$). SSC increased significantly from 11.24 ± 1.18 °Brix in 2024 to 14.35 ± 1.39 °Brix in 2025 ($p < 0.001$).

Accumulated GDD over the growing season was comparable between years (3,487.93 ± 7.95 °C in 2024 and 3,515.65 ± 89.6 °C in 2025), whereas the frequency of high-temperature exposure differed clearly: the number of days with a maximum temperature above 35 °C was 20 in 2024 and 13 in 2025. Prolonged high temperature during fruit development suppresses the expression of anthocyanin biosynthesis genes, promotes degradation of accumulated anthocyanin, and increases respiratory consumption of assimilates, thereby limiting sugar translocation into fruit (Sagong et al., 2013; Do et al., 2024). The inter-annual difference in SSC is therefore attributed primarily to the difference in high-temperature exposure between the two seasons.

SSC PREDICTION MODELS

Variance inflation factors for ARI, GLI, and NDVI_rededge were 1.142, 3.706, and 3.916, respectively, all below the conventional threshold of 10, indicating no severe multicollinearity. The regression results of each model are presented in Table 1 and Fig. 1. MLR achieved R^2 = 0.66, MAPE = 8.13%, and RMSE = 1.16 °Brix in calibration, and R^2 = 0.55, MAPE = 9.21%, and RMSE = 1.34 °Brix in validation. For KNR, grid search selected uniform weights, n_neighbors = 9, and p = 2; the model achieved R^2 = 0.55, MAPE = 8.93%, and RMSE = 1.34 °Brix in calibration, and R^2 = 0.47, MAPE = 9.65%, and RMSE = 1.45 °Brix in validation.

KNR thus showed larger errors and lower R^2 than MLR. This is attributed to the instance-based, non-parametric nature of the KNN algorithm: unlike MLR, which produces continuous predictions from a regression equation, KNR averages the observed values of the selected k neighbors, so predictions shrink toward the sample mean (Györfi et al., 2002). Because SSC in this dataset was clearly separated between the two years, and ARI and NDVI_rededge showed the same inter-annual separation, KNR tended to predict values close to each year's mean and was limited in explaining tree-to-tree variation.

Table 1. Comparison of prediction performance for Soluble Solids Content (SSC) using different regression models

	Calibration			Validation		
Model	R^2C	MAPEC (%)	RMSEC (Brix)	R^2V	MAPEV (%)	RMSEV (Brix)
MLR	0.66	8.13	1.16	0.55	9.21	1.34
KNR	0.55	8.93	1.34	0.47	9.65	1.45

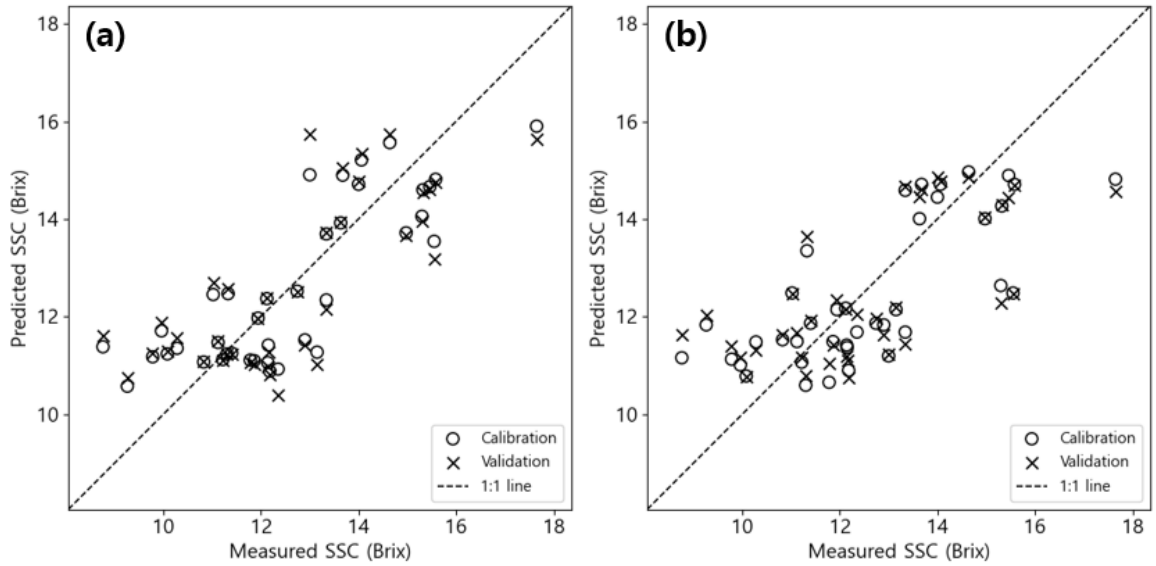

Fig. 1 Comparison of predicted and measured Soluble Solids Content (SSC) values for each regression model: (a) MLR scatter plot; (b) KNR scatter plot.

VARIABLE IMPORTANCE

In MLR, NDVI_rededge showed the highest mean absolute SHAP value (1.62), followed by GLI (1.37) and ARI (0.90). In KNR the ranking was reversed, with ARI highest (0.93), followed by NDVI_rededge (0.63) and GLI (0.10). Since SHAP values decompose deviations from the model mean prediction, the smaller total SHAP magnitude in KNR reflects the same shrinkage toward the sample mean that produced its lower R^2. Contributions were therefore compared as relative shares of each model's total SHAP magnitude. NDVI_rededge remained similar between models (41.6% in MLR, 37.9% in KNR), whereas ARI increased from 23.1% to 56.0% and GLI decreased from 35.2% to 6.0%. Because the absolute contribution of ARI was nearly identical in both models (0.90 and 0.93) while that of GLI fell sharply (1.37 to 0.10), the reversal in ranking is attributable to the decline in GLI rather than to a genuine increase in ARI. NDVI_rededge sensitively reflects chlorophyll and nitrogen status and thus indirectly represents canopy photosynthetic capacity and the resulting translocation of photosynthates into fruit (Ehammer et al., 2010); its consistent share across both models indicates a stable contribution to SSC prediction regardless of the learning scheme. GLI, also derived from chlorophyll-related visible reflectance (Eng et al., 2019), contributed strongly in MLR but marginally in KNR, suggesting that its independent explanatory power is limited. ARI, related to anthocyanin content (Gitelson et al., 2001), reflects the progress of coloration and ripening;

during maturation starch is converted to soluble sugars while anthocyanin accumulates, so ARI can be directly associated with SSC and appears to provide information independent of the other two indices.

SIGNIFICANCE AND LIMITATIONS

This study demonstrated that pre-harvest SSC can be estimated non-destructively from VIs alone, allowing a large orchard area to be evaluated in a short time by remote measurement at the individual-tree level. However, the dataset was limited to 39 samples over two seasons, which restricts validation of generalization performance across diverse cultivation conditions. In addition, only multispectral VIs were used; cultivation factors such as pruning intensity, crop load, tree vigor, and canopy architecture, as well as environmental variables other than accumulated temperature, were not considered, and these may have affected prediction accuracy through their influence on photosynthesis and assimilate partitioning.

CONCLUSIONS

Models for predicting pre-harvest apple SSC were developed and compared using ARI, GLI, and NDVI_rededge obtained from a UAV-mounted multispectral camera. MLR (validation R^2 = 0.55, MAPE = 9.21%, RMSE = 1.34 °Brix) outperformed KNR (R^2 = 0.47, MAPE = 9.65%, RMSE = 1.45 °Brix), indicating that a linear model was more advantageous than an instance-based model under conditions of limited sample size and year-separated data structure. These results demonstrate the potential of non-contact, non-destructive individual-tree measurement for orchard-scale quality assessment. Future work should expand the number of orchards and trees surveyed, incorporate multi-temporal UAV imagery acquired at successive growth stages within a single season, and integrate environmental data such as temperature, precipitation, GDD, and soil moisture with VIs to improve generalization and prediction accuracy, thereby supporting quality management and harvest timing decisions in precision agriculture.

ACKNOWLEDGEMENTS

This work was supported by the Technology Innovation Program (RS-2022-KT218635, Development of smart farm management system and growth monitoring) funded by the Ministry of Trade, Industry and Resources (MOTIR, Korea).

REFERENCES

Chen, R., C. Zhang, B. Xu, Y. Zhu, F. Zhao, S. Han, G. Yang, and H. Yang. 2022. Predicting individual apple tree yield using UAV multi-source remote sensing data and ensemble learning. *Computers and Electronics in Agric.* 201: 107275.

Deng, L., Z. Mao, X. Li, Z. Hu, F. Duan, and Y. Yan. 2018. UAV-based multispectral remote sensing for precision agriculture: A comparison between different cameras. *ISPRS J. Photogrammetry and Remote Sensing* 146: 124-136.

Do, V. G., Y. Lee, J. Park, N. M. Win, S.-I. Kwon, S. Yang, and S. Kim. 2024. Heat stress and water irrigation management effects on the fruit color and quality of 'Hongro' apples. *Agriculture* 14(5): 761.

Ehammer, A., S. Fritsch, C. Conrad, J. Lamers, and S. Dech. 2010. Statistical derivation of fPAR and LAI for irrigated cotton and rice in arid Uzbekistan by combining multi-temporal RapidEye data and ground measurements. In *Proc. SPIE 7824, Remote Sensing for*

Agriculture, Ecosystems, and Hydrology XII, 782409. Bellingham, Wash.: SPIE.
Eng, L. S., R. Ismail, W. Hashim, and A. Baharum. 2019. The use of VARI, GLI, and VIgreen formulas in detecting vegetation in aerial images. *Int. J. Technol.* 10(7): 1385-1394.
Fan, S., Q. Wang, X. Tian, G. Yang, Y. Xia, J. Li, and W. Huang. 2020. Non-destructive evaluation of soluble solids content of apples using a developed portable Vis/NIR device. *Biosystems Eng.* 193: 138-148.
Giovanelli, G., N. Sinelli, R. Beghi, R. Guidetti, and E. Casiraghi. 2014. NIR spectroscopy for the optimization of postharvest apple management. *Postharvest Biol. and Technol.* 87: 13-20.
Gitelson, A. A., M. N. Merzlyak, and O. B. Chivkunova. 2001. Optical properties and nondestructive estimation of anthocyanin content in plant leaves. *Photochemistry and Photobiol.* 74(1): 38-45.
Györfi, L., M. Kohler, A. Krzyżak, and H. Walk. 2002. *A Distribution-Free Theory of Nonparametric Regression*. New York, N.Y.: Springer.
KOSTAT. 2024. *Results of the 2024 Autumn Production Survey for Cabbage, Radish, Soybean, Apple, and Pear*. Daejeon, Republic of Korea: Statistics Korea. (in Korean)
Li, L., W. Huang, Z. Wang, S. Liu, X. He, and S. Fan. 2022. Calibration transfer between developed portable Vis/NIR devices for detection of soluble solids contents in apple. *Postharvest Biol. and Technol.* 183: 111720.
Lu, R., R. Van Beers, W. Saeys, C. Li, and H. Cen. 2020. Measurement of optical properties of fruits and vegetables: A review. *Postharvest Biol. and Technol.* 159: 111003.
Lundberg, S. M., and S.-I. Lee. 2017. A unified approach to interpreting model predictions. In *Advances in Neural Information Processing Systems 30*, 4765-4774. Long Beach, Cal.: Curran Associates.
Magwaza, L. S., and U. L. Opara. 2015. Analytical methods for determination of sugars and sweetness of horticultural products: A review. *Scientia Horticulturae* 184: 179-192.
McMaster, G. S., and W. W. Wilhelm. 1997. Growing degree-days: One equation, two interpretations. *Agric. and Forest Meteorology* 87(4): 291-300.
Peng, Y., and R. Lu. 2008. Analysis of spatially resolved hyperspectral scattering images for assessing apple fruit firmness and soluble solids content. *Postharvest Biol. and Technol.* 48(1): 52-62.
Sagong, D. H., H. J. Kweon, M. Y. Park, Y. Y. Song, S. H. Ryu, M. J. Kim, K. H. Choi, and T. M. Yoon. 2013. Impacts of urban high temperature events on physiology of apple trees: A case study of 'Fuji'/M.9 apple trees in Daegu, Korea. *Korean J. Agric. and Forest Meteorology* 15(3): 128-136.
Stanley, C. J., D. S. Tustin, G. B. Lupton, S. McArtney, W. M. Cashmore, and H. N. De Silva. 2000. Towards understanding the role of temperature in apple fruit growth responses in three geographical regions within New Zealand. *J. Hort. Sci. and Biotechnol.* 75(4): 413-422.
Walsh, K. B., V. A. McGlone, and D. H. Han. 2020. The uses of near infra-red spectroscopy in postharvest decision support: A review. *Postharvest Biol. and Technol.* 163: 111139.
Wang, J., Y. Zhang, F. Han, Z. Shi, F. Zhao, F. Zhang, W. Pan, Z. Zhang, and Q. Cui. 2025. Estimation of canopy chlorophyll content of apple trees based on UAV multispectral remote sensing images. *Agriculture* 15(12): 1308.
Xue, J., and B. Su. 2017. Significant remote sensing vegetation indices: A review of developments and applications. *J. Sensors* 2017: 1353691.
Zude, M., B. Herold, J.-M. Roger, V. Bellon-Maurel, and S. Landahl. 2006. Non-destructive tests on the prediction of apple fruit flesh firmness and soluble solids content on tree and in shelf life. *J. Food Eng.* 77(2): 254-260.

Precision Agriculture Machinery and Systems 4 (PA-4)



PA-20

Proceedings of The 12th International Symposium on Machinery and Mechatronics for Agriculture and Biosystems Engineering (ISMAB 2026)
20-24 October 2026, Busan, Republic of Korea

STUDY ON THE ESTIMATION OF LOCAL HORIZONTAL WIND ABOVE FIELD FROM UAV-MOUNTED ULTRASONIC ANEMOMETER

Hiroto Zushi[1], Atsuru Fujimoto[2*]

[1] Graduate School of Animal and Veterinary Sciences and Agriculture, Obihiro University of Agriculture and Veterinary Medicine, 2-11 Nishi, Inada, Obihiro, 080-8555, Japan
[2] Department of Agro-environmental Science, Obihiro University of Agriculture and Veterinary Medicine, 2-11 Nishi, Inada, Obihiro, 080-8555, Japan
*Corresponding Author-- Voice: +81-155-49-5526, Email: fujimoto@obihiro.ac.jp

Abstract: Agricultural UAV spraying is susceptible to spray drift caused by ambient wind, making wind information important for estimating spray distribution. This study investigated the feasibility of estimating ambient horizontal wind during hovering using a two-dimensional ultrasonic anemometer mounted on an agricultural UAV. An onboard data-logging system consisting of an ultrasonic anemometer and RTK-GNSS receiver was mounted on a DJI Agras T25, and simultaneous measurements were obtained using a stationary reference anemometer. Five flight experiments were conducted, and a correction method accounting for directional offset and additive wind-speed bias was evaluated. The onboard anemometer consistently overestimated wind speed relative to the reference anemometer, with mean wind speeds of 2.410 and 0.874 m/s, respectively. The mean additive wind-speed bias across the five flights was 1.542 m/s. Applying this value as a common correction substantially reduced the systematic overestimation, resulting in a wind-speed RMSE of 0.518 m/s. These results suggest that ambient horizontal wind during hovering can be estimated using an onboard anemometer by accounting for systematic measurement bias. Further validation under a wider range of wind conditions is required to establish the applicability of the proposed method.

Key Words: Agricultural UAV, Horizontal wind, Ultrasonic anemometer, Wind estimation, Spray drift

INTRODUCTION

Pesticide application is essential for protecting crops and ensuring stable agricultural production. Meanwhile, reducing pesticide use and improving application accuracy are increasingly important to minimize crop damage and environmental impacts caused by spray drift. Agricultural unmanned aerial vehicles (UAVs) have therefore attracted attention in Japan as an alternative means of pesticide application.

UAV spraying is generally conducted at greater heights than ground-based spraying, raising concerns about spray drift. Previous studies have investigated droplet behavior under windless conditions (Liu et al., 2024) and analyzed droplet drift using wind-tunnel experiments and computational fluid dynamics (CFD) simulations (Zhou et al., 2026). In actual fields, however,

spray droplets are advected by ambient horizontal wind, making wind information essential for estimating spray distribution. Fujimoto et al. (2016) demonstrated the feasibility of estimating spray distribution in ground-based spraying using measured horizontal winds and predetermined drift patterns. A similar approach may be applicable to agricultural UAVs if ambient horizontal wind can be measured during spraying.

Ultrasonic anemometers mounted on multirotor UAVs have been investigated for wind measurement. Thielicke et al. (2021) demonstrated that accurate wind measurement can be achieved by appropriately accounting for rotor-induced airflow, while Scicluna et al. (2023) reported systematic wind-speed bias attributable partly to rotor-induced airflow. Thus, aircraft-induced airflow must be considered when estimating ambient wind using onboard anemometers. However, this approach has not been sufficiently investigated for agricultural UAVs, which generate strong rotor-induced airflow.

In this study, we investigated a method for estimating ambient horizontal wind during hovering using a two-dimensional ultrasonic anemometer mounted on an agricultural UAV. Onboard measurements were compared with reference measurements from a stationary anemometer to evaluate the feasibility of estimating ambient horizontal wind while accounting for aircraft-induced airflow.

MATERIALS AND METHODS

Hardware Overview

As shown in Fig. 1, an onboard data-logging system was developed, consisting of a two-dimensional ultrasonic anemometer (CMI1018, CALYPSO Instruments), a microcomputer (Raspberry Pi 5, Raspberry Pi Ltd.), and an RTK-GNSS receiver (DG-PRO1RWS, BizStation Corp.), and was mounted on an agricultural drone (Agras T25, DJI). The anemometer was installed 0.50 m vertically above the rotor plane using a gimbal mechanism to maintain its horizontal orientation and thereby reduce the influence of changes in the drone attitude on wind measurements. Data acquisition was initiated by connecting a laptop computer to the microcomputer via SSH and executing a dedicated logging program. The recorded data consisted of timestamps, wind speed, wind direction, latitude, longitude, ground speed, and direction of travel. These data were recorded at 10 Hz and stored on the microcomputer in CSV format.

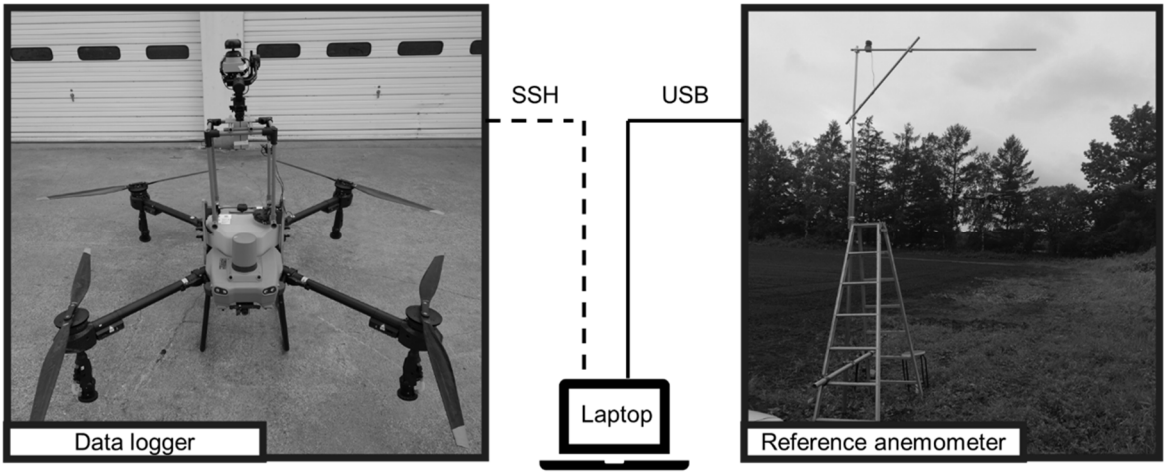

Fig. 1 Hardware configuration of the wind measurement system.

A reference anemometer station was also constructed to provide reference measurements for comparison with the onboard anemometer. The station used the same model of two-dimensional ultrasonic anemometer as that mounted on the drone and was installed at a height of 3 m above ground level. Timestamps, wind speed, and wind direction were recorded at 10 Hz and stored on the laptop computer in CSV format.

Wind Estimation and Field Experiment

As shown in Fig. 2, the UAV was hovered within the same observation area as the reference anemometer, while wind speed and direction were simultaneously measured by the onboard and reference anemometers. To estimate the ambient horizontal wind from the onboard measurements, a directional offset and an additive wind-speed bias were assumed to exist between the horizontal wind velocity vectors measured by the two anemometers, and these effects were corrected.

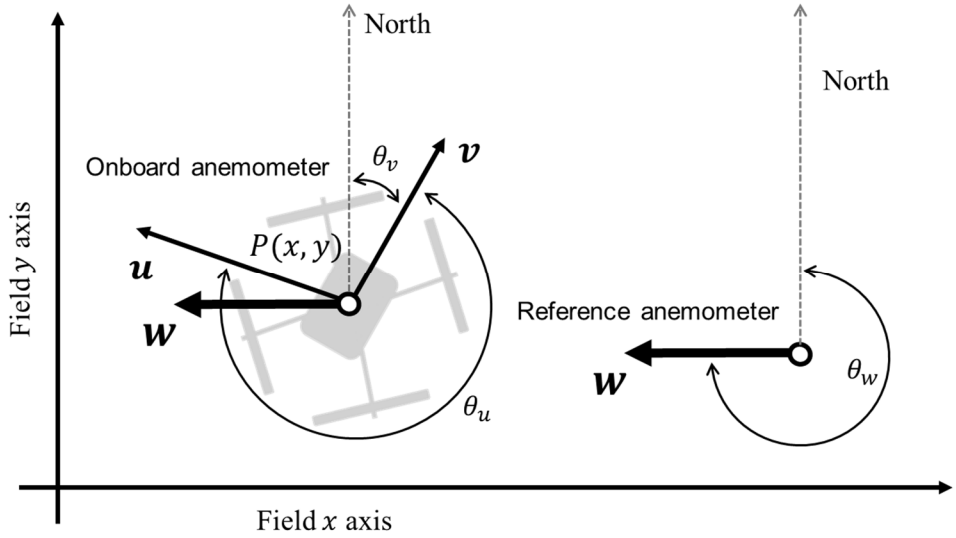

Fig. 2 Vector diagram of the wind around the reference and the onboard anemometer.

First, the wind speed and direction measured by each anemometer were converted into horizontal wind velocity vectors consisting of eastward and northward components. Wind direction was defined according to the meteorological convention (wind-from direction). Under this convention, the apparent wind induced by UAV motion is oriented in the same direction as the UAV ground-velocity vector. Therefore, to account for the relative wind induced by UAV motion, the motion-corrected horizontal wind velocity vector was defined as

$$\boldsymbol{x_i} = \boldsymbol{u_i} - \boldsymbol{v_i} \tag{1}$$

where:

$\boldsymbol{x_i}$ = motion-corrected horizontal wind velocity vector at time i (m/s)
$\boldsymbol{u_i}$ = horizontal wind velocity vector measured by the onboard anemometer at time i (m/s)
$\boldsymbol{v_i}$ = horizontal ground-velocity vector of the UAV obtained from RTK-GNSS at time i (m/s)

For the hovering conditions examined in this study, the horizontal velocity of the UAV was assumed to be sufficiently small relative to the measured wind velocity and was therefore

approximated as $\boldsymbol{v}_i = 0$ in the wind estimation.

A rotation angle θ was introduced to correct the relative directional offset between the onboard and reference anemometers. In addition, a constant additive wind-speed bias b, representing the influence of UAV-induced airflow and other systematic effects, was assumed. The estimated horizontal wind velocity vector was calculated as

$$\widehat{\boldsymbol{w}}_{\boldsymbol{i}} = \max\left(0, \left|\left|\boldsymbol{x}_{\boldsymbol{i}}\right|\right|_2 - b\right) \frac{\mathbf{R}(\theta)\boldsymbol{x}_{\boldsymbol{i}}}{\left|\left|\boldsymbol{x}_{\boldsymbol{i}}\right|\right|_2} \tag{2}$$

where:

$\widehat{\boldsymbol{w}}_{\boldsymbol{i}} =$ estimated horizontal wind velocity vector at time i (m/s)

$\left|\left|\boldsymbol{x}_{\boldsymbol{i}}\right|\right|_2 =$ magnitude of the motion-corrected horizontal wind velocity vector (m/s)

$b =$ additive wind-speed bias (m/s)

$\mathbf{R}(\theta) =$ two-dimensional rotation matrix

$\theta =$ rotation angle for correcting the relative directional offset (rad)

The term $\max(0, \cdot)$ constrains the corrected wind speed to non-negative values.

The onboard and reference measurements were synchronized using timestamps. Residual time offsets were corrected by selecting the time shift that minimized the difference between the two measurements. After synchronization, the eastward and northward components were averaged over 1 s intervals. The first and last 30 s of each experiment and measurements more than 0.3 m from the representative hovering position were excluded.

For each experiment, θ and b were determined by least-squares fitting to the reference wind velocity vectors. Estimation accuracy was evaluated using vector RMSE, wind-speed error, and wind-direction error.

RESULTS & DISCUSSION

A total of five flight experiments were conducted at the experimental field of Obihiro University of Agriculture and Veterinary Medicine from early to late August 2026. During each experiment, the UAV was hovered at a height of 3 m above ground level. The horizontal distance between the UAV and the reference wind station was set to 6 m, which was the minimum distance at which the UAV obstacle detection system was not activated. After excluding data that did not meet the criteria described above, 3,338 sets of one-second averaged onboard and reference measurements remained for analysis. The mean wind speeds measured by the onboard and reference anemometers across all flights were 2.410 and 0.874 m/s, respectively, indicating a consistent positive bias in the onboard measurements.

As shown in Table 1, the additive wind-speed bias was relatively consistent among the five flights, with a mean of 1.542 m/s and an inter-flight standard deviation of 0.077 m/s. Applying the mean bias as a common correction substantially reduced the systematic overestimation of wind speed, as shown in Fig. 3, resulting in an RMSE of 0.518 m/s. The directional correction angles were small and showed no clear trend among flights. These small directional

differences may reflect relative orientation errors caused by manual installation of the onboard and reference anemometers.

Table 1 Directional corrections and additive wind-speed biases for each flight.

Flight	Number of data sets	Directional correction (deg)	Wind bias (m/s)
Aug. 6, Run1	477	-7.0	1.59
Aug. 19, Run1	687	+15.1	1.63
Aug. 19, Run2	773	+14.9	1.43
Aug. 20, Run1	716	-16.2	1.56
Aug. 20, Run2	685	-15.7	1.51

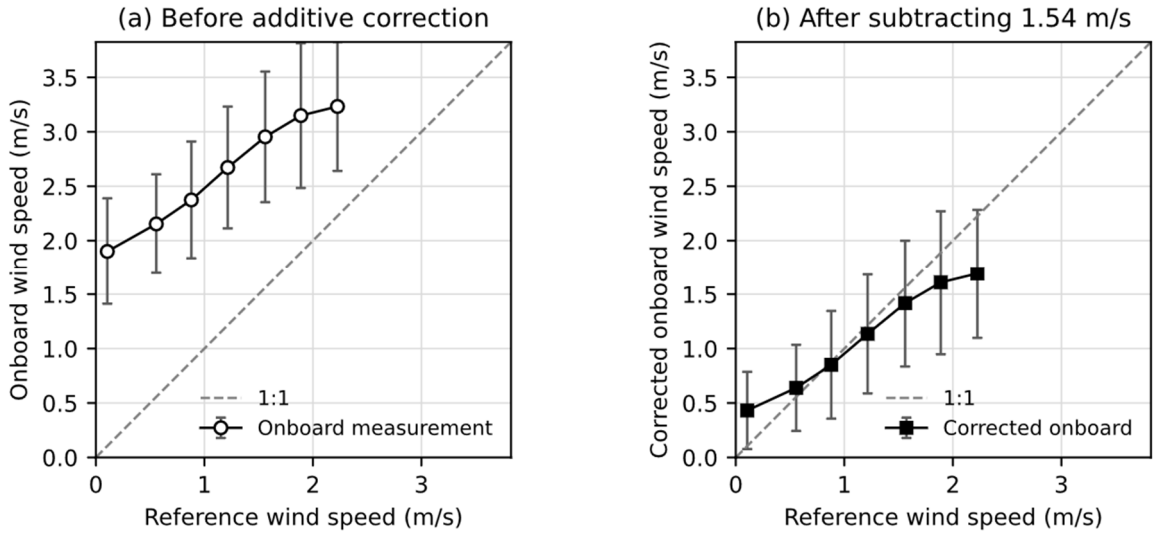

Fig. 3 Wind-speed measurements before and after additive bias correction.

The positive wind-speed bias may have been influenced by rotor-induced airflow and the local flow field around the UAV. Thielicke et al. (2021) similarly reported that rotor-induced airflow, aircraft motion and attitude, and sensor placement should be considered in UAV-based wind measurements. However, because rotor-induced airflow was not directly measured, its contribution to the observed bias could not be determined. Furthermore, the experiments were limited to five flights over three days under relatively low wind speeds. Therefore, the correction value of 1.542 m/s should be regarded as specific to the UAV, sensor configuration, and hovering conditions examined in this study. Further validation under a wider range of wind conditions is required.

CONCLUSIONS

This study investigated the feasibility of estimating ambient horizontal wind during hovering using a two-dimensional ultrasonic anemometer mounted on an agricultural UAV. Onboard wind measurements were compared with measurements from a stationary reference anemometer, and a correction method accounting for directional offset and additive wind-speed bias was evaluated. The main conclusions are summarized as follows:

1. The onboard anemometer consistently measured higher wind speeds than the reference anemometer, indicating a systematic positive wind-speed bias during hovering.

2. Applying a common additive wind-speed bias correction substantially reduced the systematic difference between the onboard and reference measurements. This result suggests the feasibility of estimating ambient horizontal wind using an anemometer mounted on an agricultural UAV.
3. The experiments were limited to relatively low wind conditions, and the cause of the observed bias was not directly identified. Further experiments under a wider range of wind conditions are required to validate the correction method and investigate the effects of rotor-induced airflow and sensor placement.

ACKNOWLEDGEMENTS

This work was supported by JSPS KAKENHI Grant Number JP25K09337.

REFERENCES

Fujimoto, A., T. Satow, and T. Kishimoto. 2016. Simulation of spray distribution with boom sprayer considering effect of wind for agricultural cloud computing analysis. Engineering in Agriculture, Environment and Food 9(4): 305-310.

Liu, Z., R. Gao, Y. Zhao, H. Wu, Y. Liang, K. Liang, D. Liu, T. Huang, S. Xie, J. Lv, and J. Li. 2024. Study on the characteristics of downwash field range and consistency of spray deposition of agricultural UAVs. Agriculture 14(6): 931.

Scicluna, L., T. Sant, and R. N. Farrugia. 2023. Validation of wind measurements from a multirotor RPAS-mounted ultrasonic wind sensor using a ground-based LiDAR system. Drone Systems and Applications 11: 1-17.

Thielicke, W., W. Hübert, U. Müller, M. Eggert, and P. Wilhelm. 2021. Towards accurate and practical drone-based wind measurements with an ultrasonic anemometer. Atmospheric Measurement Techniques 14: 1303-1318.

Zhou, Q., S. Zhang, M. Huang, C. Cai, H. Zhang, Y. Jiao, and X. Xue. 2026. Construction of a CFD simulation and prediction model for pesticide droplet drift in agricultural UAV spraying. Agronomy 16(1): 129.

PA-21

Proceedings of The 12th International Symposium on Machinery and Mechatronics for Agriculture and Biosystems Engineering (ISMAB 2026)
20-24 October 2026, Busan, Republic of Korea

PRELIMINARY EVALUATION OF ULTRASONIC-BASED LATERAL OFFSET SENSING FOR A SELF-PROPELLED SEEDER

Miaomiao Tu[1], Md Nasim Reza[1,2], Dae-Hyun Lee[1,2], Sun-Ok Chung[1,2*]

[1] Department of Agricultural Machinery Engineering, Graduate School, Chungnam National University, Daejeon 34134, Republic of Korea
[2] Department of Smart Agricultural Systems, Graduate School, Chungnam National University, Daejeon 34134, Republic of Korea
* Corresponding Author-- Voice: +82-(0)42-821-6712, Email: sochung@cnu.ac.kr

Abstract: Small self-propelled walk-behind seeders reduce the physical effort required for forward propulsion, but operators must still manually correct the travel direction. This study evaluated ultrasonic sensing as a preliminary perception method for lateral guidance of a self-propelled seeder before integration of an automatic steering actuator. Three ultrasonic sensors (HC-SR04, Grove V2.0, and A0221AU) were first compared under static reference distances from 10 to 40 cm using mean absolute error (MAE), root mean square error (RMSE), standard deviation (SD), maximum absolute error, and coefficient of determination (R^2). The best-performing sensor was then evaluated at a 35 cm reference distance under engine-off stationary, engine-on stationary, and moving conditions. Finally, a preliminary dual-sensor lateral-offset test was conducted at a fixed travel speed using actual offsets of −10, −5, and 0 cm, and steering decisions were classified as LEFT, STRAIGHT, or RIGHT using a ±3 cm dead band. A0221AU showed the best static performance, with an MAE of 1.896 cm, RMSE of 1.916 cm, mean SD of 0.060 cm, maximum absolute error of 2.30 cm, and R^2 of 0.9994. Under moving conditions, RMSE increased to 3.564 cm and SD to 0.813 cm, indicating reduced measurement stability during machine motion. In the preliminary lateral-offset test, estimation and steering-decision performance varied substantially among the tested offsets, indicating limited reliability under the current dynamic test conditions. These results suggest that ultrasonic sensing can provide useful lateral-position information for a self-propelled seeder; however, improved reference-boundary geometry, sensor placement, and further dynamic validation are required before closed-loop automatic steering is implemented.

Key Words: Ultrasonic sensor, lateral offset, self-propelled seeder, steering decision, autonomous guidance

INTRODUCTION

Small self-propelled seeders can reduce manual pushing effort because engine power provides forward propulsion; however, the operator must still hold the handles and continuously correct the travel direction. This limits the degree of automation and can increase operator workload during long field operations.

A practical first step toward automatic steering is to determine whether the machine can reliably perceive its position relative to a target path. Ultrasonic sensors provide a simple and low-cost means of measuring distance to nearby boundaries. When left and right distances are measured simultaneously, the difference between the measurements can be used to estimate the lateral position of the machine.

The objective of this study was to preliminarily evaluate ultrasonic sensing for lateral-offset estimation on a self-propelled seeder before physical steering actuation. The specific objectives were to: (1) compare the static performance of three ultrasonic sensors, (2) quantify the effect of engine operation and machine movement on the selected sensor, and (3) evaluate lateral-offset estimation at a fixed travel speed.

MATERIALS AND METHODS

EXPERIMENTAL MACHINE AND SENSING CONCEPT

The experimental platform was a self-propelled walk-behind seeder with engine-powered forward propulsion and manual directional correction. HC-SR04, Grove V2.0, and A0221AU sensors were first evaluated under static laboratory conditions. A0221AU was then selected for the machine operating-condition test, and two A0221AU sensors were mounted on the left and right sides for the preliminary lateral-offset test using controlled parallel boundaries.



Fig.1 Self-propelled walk-behind seeder used as the experimental platform.

EXPERIMENTAL DESIGN

The three experiments were conducted sequentially as summarized in Table 1. Static sensor performance was assessed using MAE, RMSE, mean SD, maximum absolute error, and R^2; the selected A0221AU sensor was then evaluated under three machine operating conditions using mean distance, MAE, RMSE, SD, and maximum absolute error. For the preliminary dual-sensor test, lateral offset was estimated from one-half of the difference between the measured left- and right-boundary distances, and performance was summarized using mean estimated offset, MAE, and RMSE. Because the reference boundary was short, only samples collected while both sensors faced the controlled boundary were retained (n = 10, 15, and 4 for −10, −5, and 0 cm, respectively).

Table 1. Experimental conditions used in the ultrasonic guidance tests.

Test item	Levels / conditions	Main output
Static sensor comparison	HC-SR04, Grove V2.0, A0221AU; 10–40 cm at 5 cm intervals; 30 measurements per distance	MAE, RMSE, mean SD, maximum absolute error, R^2
Machine operating condition	A0221AU; 35 cm reference; engine OFF–stationary, engine ON–stationary, engine ON–moving; 50 measurements per condition	Mean distance, MAE, RMSE, SD, maximum absolute error
Preliminary lateral-offset test	Two A0221AU sensors; actual offsets −10, −5, and 0 cm; fixed travel speed	Mean estimated offset, MAE, RMSE

RESULTS & DISCUSSION

INTEGRATED ULTRASONIC SENSING PERFORMANCE

Across the three experimental stages, A0221AU showed the best static performance among the tested sensors, with MAE 1.896 cm, RMSE 1.916 cm, mean SD 0.060 cm, maximum absolute error 2.30 cm, and R^2 0.9994; it was therefore used in the subsequent tests.

Table 2. Static performance of the three ultrasonic sensors.

Sensor	MAE (cm)	RMSE (cm)	Mean SD (cm)
HC-SR04	2.956	2.988	0.064
Grove V2.0	2.879	2.936	0.238
A0221AU	1.896	1.916	0.060
Sensor	MAE (cm)	RMSE (cm)	Mean SD (cm)
HC-SR04	2.956	2.988	0.064

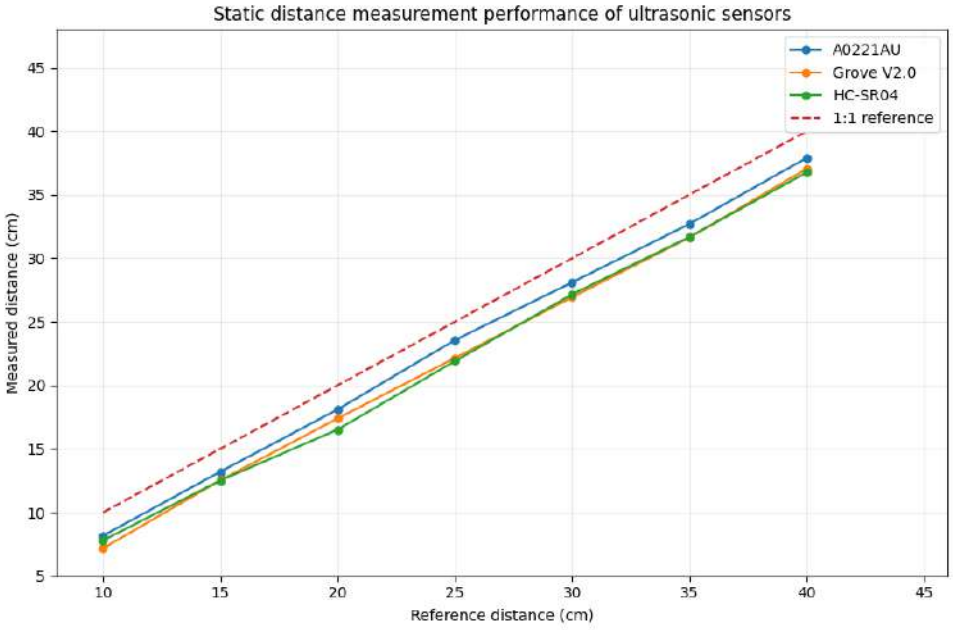

Fig. 2 Static distance response of the three ultrasonic sensors.

At the 35 cm reference distance, stationary measurements remained relatively stable (RMSE 1.712 cm with engine OFF and 1.494 cm with engine ON), whereas machine movement increased RMSE to 3.564 cm, SD to 0.813 cm, and maximum absolute error to 5.40 cm, indicating that movement was the dominant source of instability.

Table 3. A0221AU performance under machine operating conditions.

Operating condition	Mean distance (cm)	MAE (cm)	RMSE (cm)	SD (cm)	Maximum absolute error (cm)
Engine OFF – Stationary	36.672	1.672	1.712	0.371	3.10
Engine ON – Stationary	36.486	1.486	1.494	0.159	1.60
Engine ON – Moving	38.472	3.472	3.564	0.813	5.40

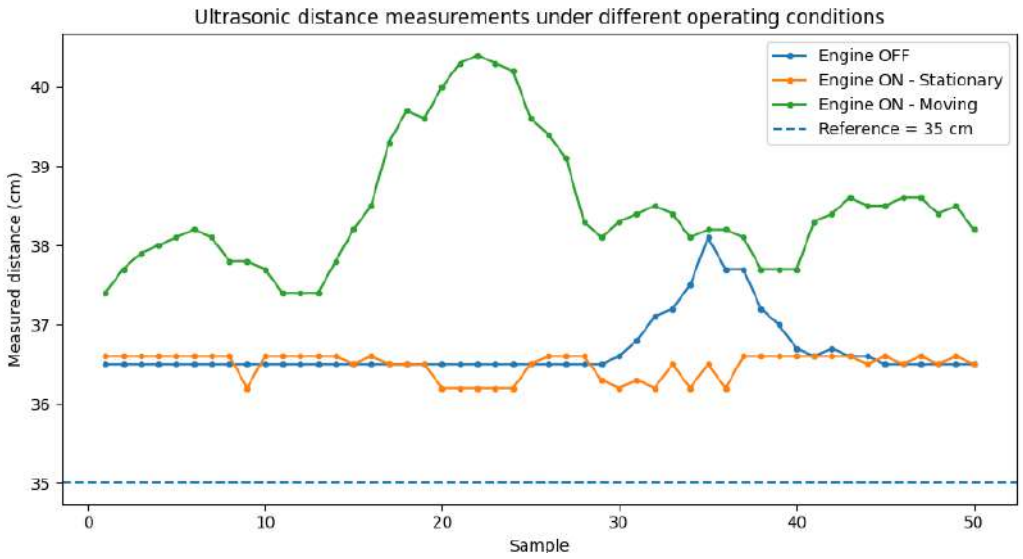

Fig. 3 Distance measurements under the three machine operating conditions.

In the preliminary lateral-offset test, the −10 cm condition showed the closest agreement (mean estimated offset −12.49 cm; MAE 2.49 cm; RMSE 2.60 cm). Larger errors occurred at −5 cm (mean +6.93 cm; RMSE 12.79 cm) and 0 cm (mean +3.21 cm; RMSE 3.25 cm), showing limited reliability near the target path.

The lateral-offset results are preliminary because the controlled reference boundary was shorter than the travel path; measurements obtained after the sensors left the boundary were excluded. A longer continuous boundary, improved sensor mounting, and a larger balanced dataset are required for further validation.

Table 4. Preliminary lateral-offset estimation performance.

Actual offset	Valid samples (n)	Mean estimated offset	MAE	RMSE
−10 cm	10	−12.49 cm	2.49 cm	2.60 cm
−5 cm	15	+6.93 cm	11.93 cm	12.79 cm
0 cm	4	+3.21 cm	3.21 cm	3.25 cm

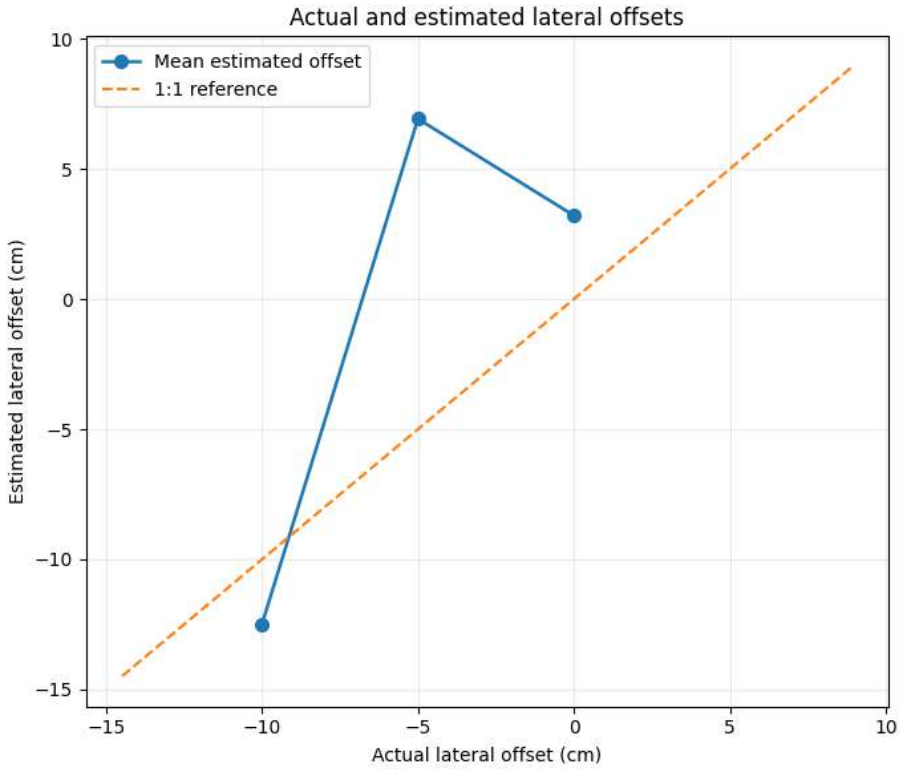

Figure 4. Actual and mean estimated lateral offsets in the preliminary dynamic test.

CONCLUSIONS

This study preliminarily evaluated ultrasonic sensing for lateral guidance of a self-propelled walk-behind seeder. A0221AU provided the best static performance (MAE 1.896 cm, RMSE 1.916 cm, mean SD 0.060 cm, maximum absolute error 2.30 cm, R^2 0.9994). Engine operation alone caused little degradation at a 35 cm reference distance, whereas machine movement increased RMSE to 3.564 cm and SD to 0.813 cm. In the preliminary lateral-offset test, the −10 cm condition was estimated reasonably well, but substantial errors occurred at −5 and 0 cm. The current configuration is therefore useful for detecting relatively large deviations but requires a longer continuous reference boundary, improved sensor mounting, and further dynamic validation before closed-loop steering integration.

ACKNOWLEDGEMENTS

This work was supported by Korea Institute of Planning and Evaluation for Technology in Food, Agriculture and Forestry (IPET) through the Agriculture and Food Convergence Technologies Program for Research Manpower Development, funded by Ministry of Agriculture, Food and Rural Affairs (MAFRA) (RS-2024-00397026), Republic of Korea

REFERENCES

Ahmadi, A., M. Halstead, and C. McCool. 2022. Towards autonomous visual navigation in arable fields. In 2022 IEEE/RSJ International Conference on Intelligent Robots and Systems (IROS), 6585-6592. IEEE.

Alagbo, O., M. Spaeth, M. Saile, M. Schumacher, and R. Gerhards. 2022. Weed management in ridge tillage systems—A review. Agronomy 12(4): 910.

An, G., Z. Zhong, S. Yang, L. Yang, C. Jin, J. Du, and X. Yin. 2024. EASS: An automatic steering system for agricultural wheeled vehicles using fuzzy control.

Åstrand, B., and A. J. Baerveldt. 2005. A vision based row-following system for agricultural field machinery. Mechatronics 15(2): 251-269.
Bah, M. D., A. Hafiane, and R. Canals. 2019. CRowNet: Deep network for crop row detection in UAV images. IEEE Access 8: 5189-5200.
Bakker, T., K. van Asselt, J. Bontsema, J. Müller, and G. van Straten. 2011. Autonomous navigation using a robot platform in a sugar beet field. Biosystems Engineering 109(4): 357-368.
Bakker, T., H. Wouters, K. van Asselt, J. Bontsema, L. Tang, J. Müller, and G. van Straten. 2008. A vision-based row detection system for sugar beet. Computers and Electronics in Agriculture 60(1): 87-95.
Bechar, A., and C. Vigneault. 2016. Agricultural robots for field operations: Concepts and components. Biosystems Engineering 149: 94-111.

PA-22

Proceedings of The 12th International Symposium on Machinery and Mechatronics for Agriculture and Biosystems Engineering (ISMAB 2026)
20-24 October 2026, Busan, Republic of Korea

DEVELOPMENT OF AN AIOT-BASED MONITORING SYSTEM FOR EARLY WARNING OF RED IMPORTED FIRE ANT (*SOLENOPSIS INVICTA*) NUPTIAL FLIGHTS

Jui-Lin Hsu[1], Pei-Tzu O[1], Po-Cheng Shih[1], Cheng-Wei Fu[2], Scotty Yang[3], Chen-Kang Huang[1*]

[1]Department of Biomechatronics Engineering, National Taiwan University,
1 Sec. 4, Roosevelt Rd., Taipei 106, Taiwan
[2]Advantech Co., Ltd.,
1 Aly. 20, Lin. 26, Rueiguang Rd., Taipei 114, Taiwan
[3]Department of Entomology, Texas A&M University,
370 Olsen Blvd., TAMU 2475, College Station, TX 77843, USA
*Corresponding Author-- Voice: +886-2-3366-5351, Email: ckhuang94530@ntu.edu.tw

Abstract: The red imported fire ant (*Solenopsis invicta*) is one of the most invasive alien species worldwide, causing significant ecological, agricultural, and public health impacts. Effective monitoring of colony activities, particularly nuptial flights, is critical for understanding population dynamics and supporting early intervention strategies. However, conventional field inspections are labor-intensive, time-consuming, and often unable to provide continuous observations of colony behavior.

This study presents the development of an Artificial Intelligence of Things (AIoT)-based monitoring system for automated observation of red imported fire ant colonies and early warning of impending nuptial flights. The proposed system integrates environmental sensors, image acquisition devices, edge computing, and wireless communication technologies to continuously collect colony activity and microclimatic data in real time. Computer vision algorithms are employed to detect and quantify behavioral indicators associated with pre-flight colony conditions, including worker traffic intensity, mound surface activity, and the emergence of alates. Simultaneously, environmental parameters such as temperature, relative humidity, atmospheric pressure, rainfall, and illumination are recorded to identify conditions favorable for flight initiation.

The collected data are transmitted to a cloud-based platform, where machine learning models can be developed to characterize behavioral patterns and predict the likelihood of nuptial flight events. When predefined thresholds or predictive criteria are satisfied, the system automatically generates warning notifications for pest management personnel and researchers. The proposed AIoT framework aims to provide continuous, non-invasive, and autonomous monitoring of fire ant colonies while improving the efficiency and timeliness of surveillance activities.

This work demonstrates the feasibility of combining AI, IoT, and ecological sensing technologies for intelligent monitoring of invasive insect behavior and establishes a foundation for future forecasting and management of red imported fire ant dispersal.

Keywords: Red Imported Fire Ant (Solenopsis invicta); AIoT; Computer Vision; Nuptial Flight Prediction; Smart Pest Monitoring

INTRODUCTION

The red imported fire ant (*Solenopsis invicta* Buren) is a highly invasive species causing ecological and economic threats worldwide. By aggressively outcompeting native fauna, *S. invicta* can substantially reduce native ant diversity and disrupt ecosystem functions and agricultural productivity (Khan et al., 2025). The natural dispersal of *S. invicta* relies predominantly on nuptial flights, where alates mate and establish new colonies (Lu et al., 2007). Although the survival rate of newly founded queens is estimated to be approximately 1%, newly established colonies may require several months to develop visually detectable mounds (Lu et al., 2007), making early detection exceptionally difficult. Traditional reactive management approaches, which often rely on large-scale pesticide applications after widespread establishment, are frequently insufficient, costly, and environmentally restricted (Shafiq et al., 2024). Consequently, proactive Early Detection and Rapid Response (EDRR) strategies supported by long-term automated monitoring are essential for detecting early-stage dispersal and limiting subsequent population expansion (Liu et al., 2020; Shafiq et al., 2024).

Nuptial flights of *S. invicta* are associated with specific environmental conditions and characteristic pre-flight behaviors, providing potential indicators for automated monitoring (Milio et al., 1988). However, conventional manual inspections are labor-intensive and intermittent, making it difficult to continuously monitor these short-duration events (Shafiq et al., 2024). AIoT-based automated monitoring provides a potential approach for integrating continuous environmental sensing with image-based observation. In particular, combining visual information with environmental context can provide a more comprehensive basis for ecological monitoring and subsequent analysis (Kumaresan et al., 2025).

The deployment of AIoT-based monitoring systems in remote and off-grid environments is constrained by limited power availability and communication bandwidth. While LoRaWAN is suitable for low-bandwidth sensor data, it is generally unsuitable for high-resolution image transmission due to its limited payload capacity and data rate (Xiongfei et al., 2020; Tabatowski-Bush, 2024). Cellular technologies such as 4G LTE provide higher data transmission capability but can substantially increase power consumption in solar-powered systems (Khan et al., 2025). Therefore, an event-driven, low-power architecture is needed to balance continuous monitoring, image transmission, and energy consumption.

The primary objective of this study is to develop the Fire Ant Smart Surveillance (FASS) system, an AIoT-based early warning system for detecting *S. invicta* nuptial flights. Specifically, this research aims to: (1) design a hierarchical, ultra-low-power hardware architecture that utilizes microclimatic sensors to monitor environmental conditions associated with nuptial flights and trigger a high-performance Edge computing module via a MOSFET switch, ensuring independent off-grid operation; (2) implement time-lapse, high-resolution image acquisition targeting the aerial space above prominent fire ant mounds to capture images of airborne alates during nuptial flights and establish a foundational image dataset for future AI-based detection and classification; and (3) establish a flexible, direct-to-cloud communication framework via 4G LTE/Wi-Fi, synchronizing multimodal data to predict dispersal pathways and optimize the timing of EDRR interventions.

MATERIALS AND METHODS

Environmental Conditions and System Operation

Previous studies have reported that *S. invicta* nuptial flights are associated with specific environmental conditions and pre-flight behaviors. Based on these findings, air temperature, relative humidity, soil temperature, wind speed, and time of day are selected as key environmental variables for the proposed FASS system. Reported flight conditions include air temperatures of approximately 24–32°C, with optimal conditions around 27–29°C, soil

temperatures above 18°C, relative humidity above 80%, and ground-level wind speeds below approximately 5 mph (2.2 m/s) (Milio et al., 1988). Increased worker activity on the mound and the movement of alates onto surrounding vegetation are also reported as potential pre-flight indicators (Milio et al., 1988; Obin and Vander Meer, 1994). Based on these indicators, the FASS system continuously monitors environmental conditions and activates the high-power imaging and edge computing modules when predefined potential nuptial flight conditions are reached. The camera then acquires images of the aerial region above the ant mound for remote monitoring, while the event-driven operation keeps high-power components inactive during low-probability periods, reducing unnecessary energy consumption and supporting long-term field deployment.

Wiring Diagram and Hardware Architecture

Two alternative system architectures are illustrated in Fig. 1, including the non-AI architecture and the AI-enabled architecture. As shown in Fig. 1(a), the non-AI architecture integrates environmental sensors, a camera, and wireless communication through the MCU for basic monitoring and data transmission. In contrast, Fig. 1(b) introduces the MIC-710AIX for image processing and AI inference. The AI-enabled architecture further adopts a MOSFET-based power control scheme and separate low- and high-power buck converters, allowing the high-power computing and imaging modules to be activated only when potential nuptial flight conditions are detected. LoRaWAN is used for low-bandwidth environmental data transmission, while 4G LTE provides higher-bandwidth communication for image data.

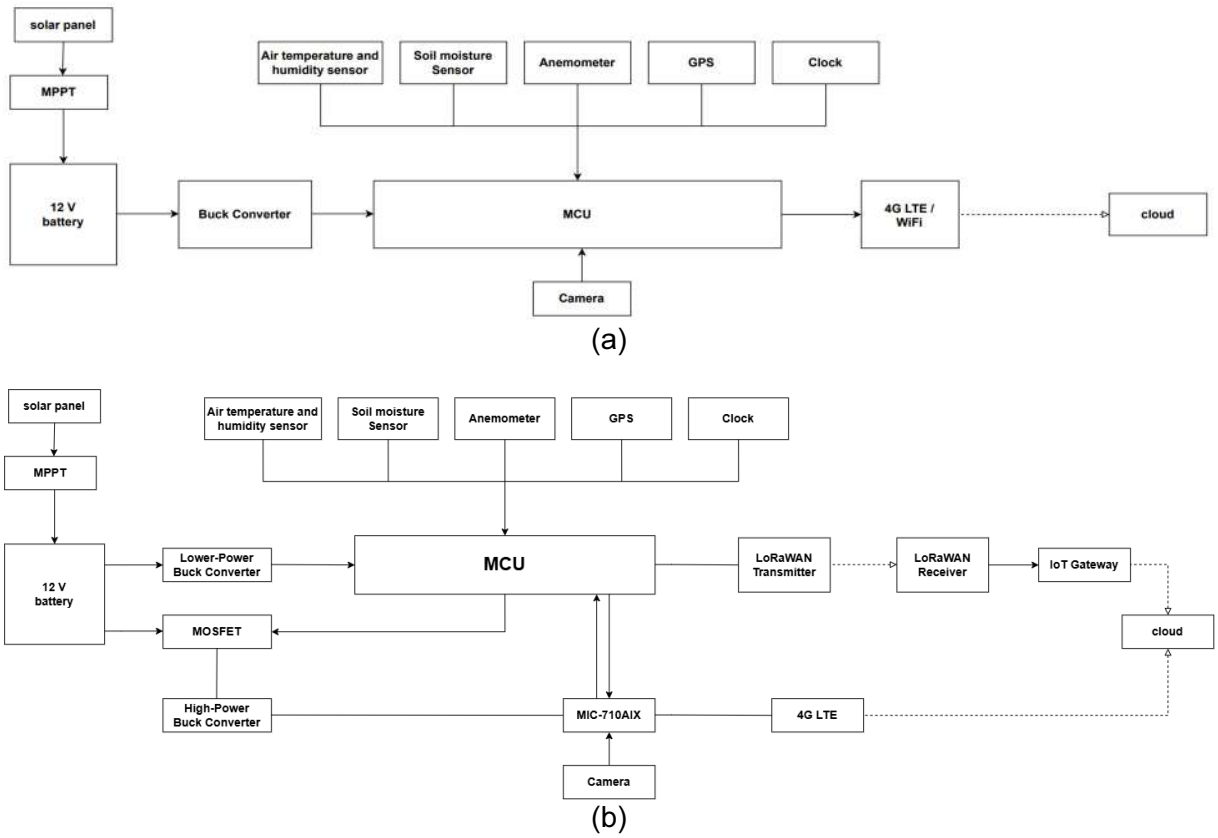

Fig.1 (a) Non-AI architecture and (b) AI-enabled architecture.

The wiring diagram and detailed hardware architecture of the proposed FASS system are shown in Fig. 2. The entire system is powered by an off-grid 12-V solar battery, utilizing a bifurcated power management strategy to meet the distinct voltage requirements of the sensing and computing modules. A buck converter is used to step down the voltage, providing

a continuous, low-power supply to the ESP32 microcontroller, which remains in an always-on standby state to monitor the environmental sensors. Simultaneously, a boost converter steps up the battery voltage to 19 V to supply the high-performance Advantech MIC-710AIX edge computer (DC IN 19-24V). To eliminate idle power consumption, this 19-V power line is gated by a MOSFET-based switching circuit. When the ESP32 detects that the predefined environmental thresholds for a nuptial flight are met, it outputs a 3.3-V control signal to the MOSFET, smoothly activating the edge computing module.

Once activated, the Advantech MIC-710AIX manages high-bandwidth tasks, directly interfacing with the camera and 4G LTE/GPS module via its USB ports for image acquisition and cloud transmission. Crucially, a bi-directional USB link connects the ESP32 and the edge computer, enabling the continuous upload of synchronized environmental data. After completing data transmission, the edge computer uses this same link to issue a software shutdown command to the ESP32. This prompts the MCU to deactivate the MOSFET, securely returning the system to its ultra-low-power standby state. The hardware specifications are summarized in Table 1.

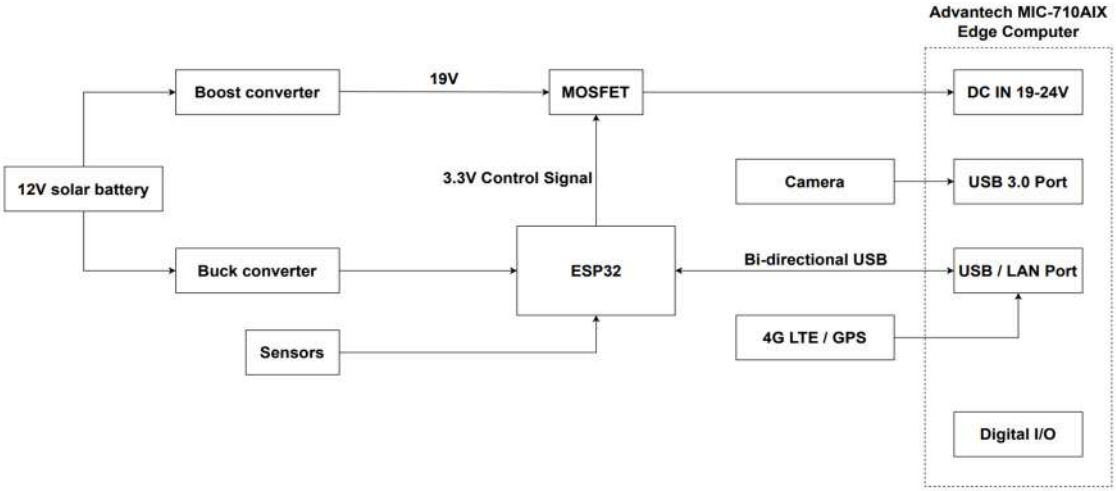

Fig.2 Wiring diagram of the proposed FASS system.

The hardware architecture integrates sensing, computing, communication, and power management functions to support autonomous field deployment. The hardware components and their corresponding models are summarized in Table 1.

Table 1 Hardware components and models of the proposed FASS system.

Purpose	Model
Major controller	MIC-710AIX
Minor controller	ESP32
4G LTE/WiFi	SIM7600G-H 4G LTE Module Expansion Board
Air Temperature and Humidity Sensor	SHT20 I2C Waterproof Temperature and Humidity Sensor Probe
Soil Moisture Sensor	DFRobot Gravity: Analogue Waterproof Capacitive Soil Moisture Sensor
Anemometer	Ultra-Low-Power Ultrasonic wind meter(ULP Standard)
GPS	U-blox NEO-M8N
12V Battery	Battle Born 12V 20Ah LiFePO4
Solar panel	Renogy 50 Watt 12 Volt Monocrystalline Solar Panel
MPPT	Victron SmartSolar MPPT 100/20

MOSFET	IRF3708
Buck Converter	PC817 optocoupler isolation module
Boost Converter	Daygreen H10-12-19

RESULTS & DISCUSSION

The proposed FASS station is conceptually designed to integrate environmental sensing, image acquisition, edge computing, wireless communication, and solar power management into a field-deployable configuration, as illustrated in Fig. 3. The conceptual configuration includes sensors for air temperature, relative humidity, soil moisture, and wind speed, together with GPS and a camera for monitoring the aerial region above the fire ant mound. The proposed MIC-710AIX edge computing system, 4G LTE module, and MOSFET-based power control circuit are intended to be housed within the control and power enclosure. Solar power and battery storage are also incorporated into the proposed design to support autonomous operation. Based on this architecture, environmental, image, and location data are expected to be integrated into a unified cloud-based monitoring interface, as shown in Fig. 4, providing a basis for remote observation of environmental conditions and fire ant activity.

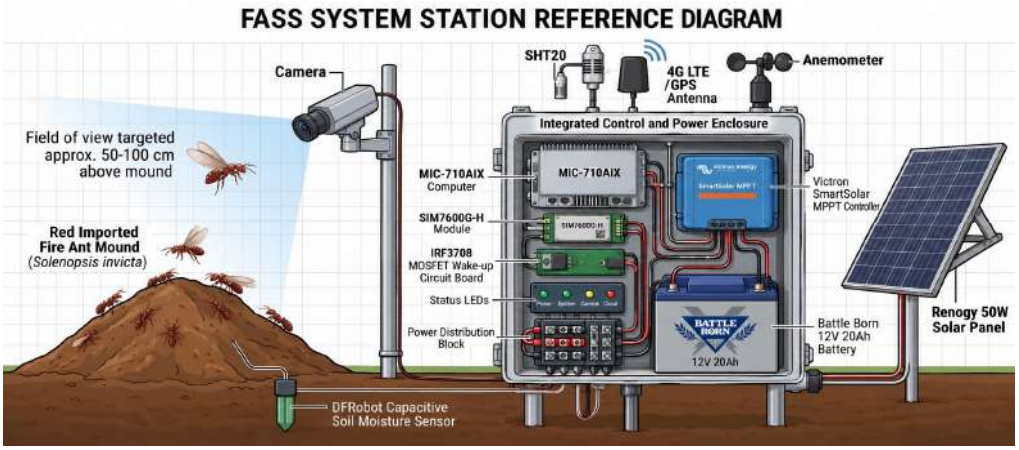

Fig.3 Proposed FASS station configuration.

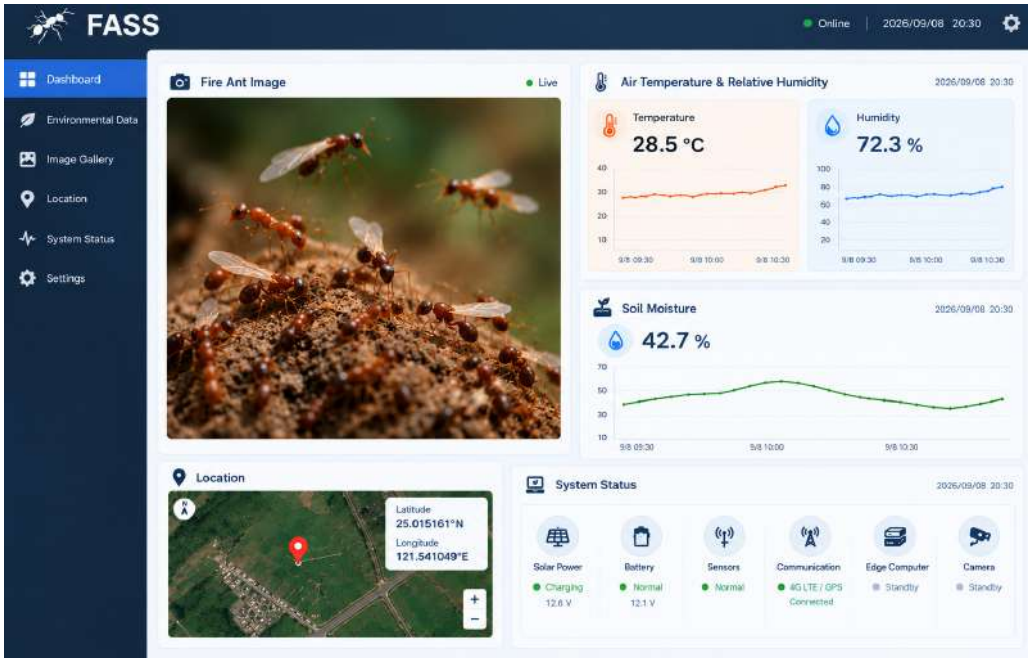

Fig.4 Conceptual interface of the proposed FASS system.

The proposed architecture is designed to adopt an event-driven monitoring strategy in which environmental measurements are continuously evaluated for conditions associated with potential *S. invicta* nuptial flight activity. When predefined conditions are reached, the high-power imaging and edge computing modules are intended to be activated through the MOSFET-based power control circuit, allowing images of the aerial region above the mound to be acquired while reducing unnecessary energy consumption during low-probability periods. The collected environmental and image data are expected to form a multimodal dataset for future AI-based detection of airborne alates and development of automated nuptial flight prediction and early warning. As the AI detection and prediction functions remain under development, the proposed architecture is intended to provide a foundation for future automated monitoring and EDRR applications.

CONCLUSIONS

This study proposes the Fire Ant Smart Surveillance (FASS) system, an AIoT-based framework for automated monitoring and early warning of *Solenopsis invicta* nuptial flights. The proposed system integrates environmental sensing, event-driven power management, image acquisition, edge computing, wireless communication, and solar power to support autonomous field monitoring. Environmental conditions associated with potential nuptial flight activity are used as the basis for triggering high-power imaging and computing modules, while the proposed hardware architecture enables the integration of sensing and communication functions. A conceptual station configuration and monitoring interface were also developed to illustrate the integration of environmental, image, and location information. Overall, the proposed FASS architecture provides a foundation for continuous and energy-efficient monitoring of *S. invicta* activity and future development of automated early warning.

Future work will focus on system implementation and field deployment to collect environmental and image data during *S. invicta* activity and nuptial flight events. Fire ant counts obtained from the proposed monitoring station will be compared with those obtained through manual observations with previously recorded counts obtained through manual observations to evaluate the consistency and reliability of the automated monitoring approach. The collected data will also support the development of AI-based image detection for airborne alates and environmental prediction models for automated nuptial flight forecasting. Ultimately, the system is expected to provide a more continuous and efficient monitoring approach and support timely Early Detection and Rapid Response (EDRR) interventions for red imported fire ant management.

ACKNOWLEDGEMENTS

This research was supported by the "Climate-Resilient Smart Agriculture & One Health International Collaboration Platform" under the University Academic Alliance in Taiwan (UAAT), funded by the Ministry of Education (MoE), Taiwan.

REFERENCES

Ajagekar, A., Jiang, Y., You, F. 2026. Computer vision and IoT based plant phenotyping and growth monitoring with 3D point clouds. Biosystems Engineering, 264, 104398.

Khan, T. 2025. LoRaWAN-enabled IoT Solution for Smart Farming. MS thesis. South Dakota State University. Available at: https://openprairie.sdstate.edu/etd2/1899/. Accessed 18 August 2026.

Tabatowski-Bush, B. A. 2024. Optimization of LoRaWAN based IoT when applied to warehouse battery monitoring system through time serial forecasting. PhD diss. Dearborn, Mich.: University of Michigan-Dearborn.

Xiongfei, L., Yunyi, Z., Liao, B. 2020. LoRaWAN Anti-collision Algorithm Based on Dynamic Frame-slotted ALOHA. Journal of Physics: Conference Series, 1486(3), 032045.

Kumaresan, M., Abhishek, N., Yokesh, R. 2025. Smart pest guardian: IoT and AI-driven insect detection with IoT. International Journal of Engineering Research and Sustainable Technologies (IJERST), 3(2), 32–41.

Su, X., Shi, G., Zhong, J., Li, Y., Dai, W., Xu, G., … Yan, Z. 2023. Use of Artificial Intelligence for Automated Detection and Surveillance of Red Imported Fire Ants Nests. BioRxiv (Cold Spring Harbor Laboratory). Cold Spring Harbor Laboratory.

Lu Yong-yue, Li Ning-dong, Liang Guang-wen, Zeng Ling. Spatial Distribution of *Solenopsis invicta* New Founded Mounds by Nuptial Flight[J]. Journal of South China Agricultural University, 2007, 28(4): 1-5.

Obin, M. S., Vander Meer, R. K. 1994. Alate Semiochemicals Release Worker Behavior During Fire Ant Nuptial Flights. Journal of Entomological Science, 29(1), 143–151.

Milio, J., Lofgren, C. S., Williams, D. F. (1988). Nuptial Flight Studies of Field-Collected Colonies of *Solenopsis invicta* Buren (pp. 419–431). brill.

Liu, H. K., Lin, C.-C., Huang, L.-H., Huang, S.-A., Huang, R.-N. 2020. Eradication and Control Strategies for Red Imported Fire Ants (*Solenopsis invicta*) in Taiwan. *Sustainability*, *12*(10), 3951.

Khan, S. A., A. I. Weemaels, M. Liang, and B. Guénard. 2025. Ecological and environmental impacts of the red imported fire ants (*Solenopsis invicta*) in Mainland China, Hong Kong and Macau. Global Environ. Res. Available at: https://www.researchgate.net/publication/390671684_Ecological_and_Environmental_Impacts_of_the_Red_Imported_Fire_Ants_*Solenopsis_invicta*_in_Mainland_China_Hong_Kong_and_Macau. Accessed 7 September 2026.

Shafiq, A., M. Aftab, and M. M. Ali. 2024. Artificial intelligence in invasive species management: Transforming detection and response. *Trends in Animal and Plant Sciences* 4: 82–96.

PA-23

Proceedings of The 12th International Symposium on Machinery and Mechatronics for Agriculture and Biosystems Engineering (ISMAB 2026)
20-24 October 2026, Busan, Republic of Korea

LED-BASED FREQUENCY-DOMAIN FLIM FOR CELLULAR-SCALE CHLOROPHYLL A FLUORESCENCE CHARACTERIZATION IN *ELODEA DENSA*

Cheng-Hao Lin[1], Hsiao-Mei Wu[1,2*]

[1] Department of Biomechatronics Engineering, National Taiwan University, No. 1, Sec. 4, Roosevelt Rd., Taipei 10617, Taiwan (R.O.C.)
[2] Global Agriculture Technology and Genomic Science, National Taiwan University, No. 1, Sec. 4, Roosevelt Rd., Taipei 10617, Taiwan (R.O.C.)
*Corresponding Author-- Voice: +886-2-33665350, Email: hsmwu@ntu.edu.tw

Abstract: Plant phenotyping relies on quantitative measurements of plant physiological responses. Chlorophyll a fluorescence (ChlF) is widely used to assess photosynthetic performance. However, ChlF intensity measurements can b e easily influenced by sample and imaging conditions. Fluorescence lifetime imaging microscopy (FLIM) provides an alternative approach based on fluorescence decay, while LED excitation reduces speckle artifacts associated with spatially coherent laser illumination. In this study, an LED-based frequency-domain FLIM (FD-FLIM) system was developed for cellular-scale ChlF imaging in *E. densa*. Samples treated with 0.1–0.3 M NaCl were examined under dark-adapted and non-dark-adapted conditions. Fluorescence intensity images showed no significant differences between the two adaptation conditions, whereas fluorescence lifetime varied with NaCl concentration. At 0.3 M NaCl, reduced intracellular movement resulted in more stable ChlF images, accompanied by a shift in the lifetime distribution toward shorter lifetimes. Moreover, dark-adapted and non-dark-adapted samples exhibited only minor lifetime differences at 0.3 M NaCl, and both followed similar NaCl-dependent trends. These results demonstrate the feasibility of LED-based FD-FLIM for cellular-scale ChlF characterization and suggest that dark adaptation may not be essential for detecting salt-induced changes in ChlF lifetime under the conditions examined.

Key Words: Frequency-domain FLIM, Chlorophyll a fluorescence, Dark adaptation, Elodea densa, Phasor analysis

INTRODUCTION

Plant phenotyping provides quantitative information on plant structure, function, and environmental responses (Fiorani and Schurr, 2013). Chlorophyll *a* fluorescence (ChlF) is widely used to assess photosynthetic performance (Baker, 2008), but fluorescence intensity is easily influenced by fluorophore concentration, tissue morphology, and excitation conditions. Fluorescence lifetime imaging microscopy (FLIM) provides intrinsic information, which is independent of fluorophore concentration and excitation intensity (Berezin and Achilefu, 2010). In frequency-domain FLIM (FD-FLIM), lifetime is derived from the phase shift

and demodulation relative to intensity-modulated excitation. Modulated LEDs provide excitation source while reducing the speckle associated with spatially coherent laser illumination (Gayathri et al., 2022; Redding et al., 2012). Meanwhile, phasor analysis enables pixel-wise evaluation of lifetime distributions (Digman et al., 2008).

Elodea densa was selected for system validation because its leaf structure allows chloroplast movement to be readily observed (Hara et al., 2015). However, this intracellular movement could reduce image stability during FD-FLIM acquisition, affecting the spatial correspondence among phase images. To limit this movement and maintain image stability during acquisition, samples were treated with 0.1–0.3 M NaCl based on the reported inhibition of cytoplasmic streaming by hypertonic treatment in aquatic plant cells (Hayashi and Takagi, 2003).

Dark adaptation is commonly performed before ChlF measurements to establish a defined photosynthetic state (Kalaji et al., 2014; Murchie and Lawson, 2013). However, the required adaptation period is time-consuming and limits measurement throughput, making it less practical for rapid phenotyping applications. Whether dark adaptation is necessary for cellular-scale ChlF lifetime measurements using FD-FLIM remains unclear. Therefore, this study developed an LED-based FD-FLIM system for cellular-scale ChlF imaging in *E. densa* and evaluated the effects of NaCl treatments and adaptation on lifetime measurements. Fluorescence intensity, phase and modulation lifetimes, and phasor distributions were compared across 0.1–0.3 M NaCl treatments under dark-adapted and non-dark-adapted conditions.

MATERIALS AND METHODS

Frequency-Domain Fluorescence Lifetime Imaging Microscopy (FD-FLIM) System

FD-FLIM system was integrated with an inverted microscope platform, as shown in Figure 1. A 458 nm LED was used as the excitation source. The modulation signal generated by the dual-tap CMOS camera was amplified by a power amplifier to drive the LED. The excitation light was directed to the sample through a dichroic mirror. Then the camera captured ChlF for lifetime measurements. Image acquisition and hardware synchronization were controlled using Micro-Manager (Edelstein et al., 2014).

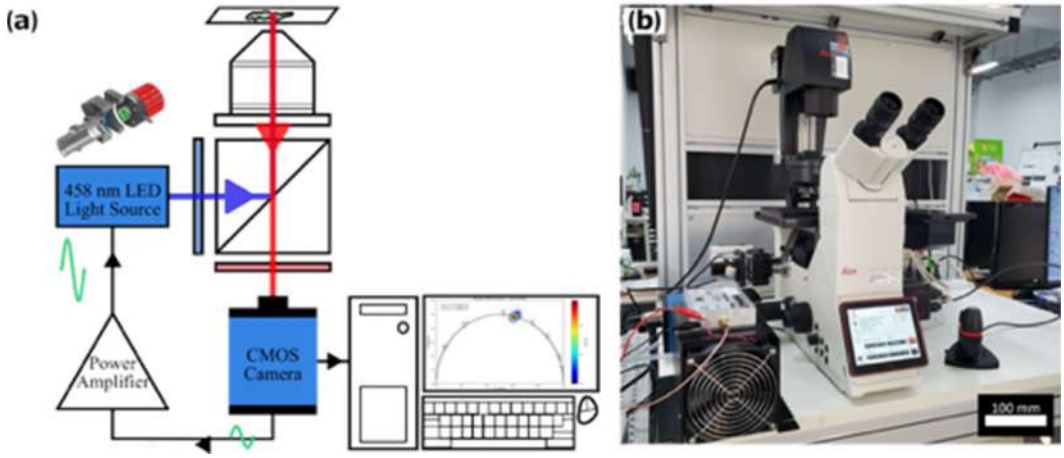

Fig.1 (a) Schematic and (b) assembled LED-based FD-FLIM system.

Sample Preparation

Elodea densa (*E. densa*) leaves were excised using forceps and immersed in 0.1, 0.2, or 0.3 M NaCl solutions to reduce intracellular movement during image acquisition. Samples were maintained under ambient light for approximately 20 min before being transferred onto microscope slides for FD-FLIM measurements.

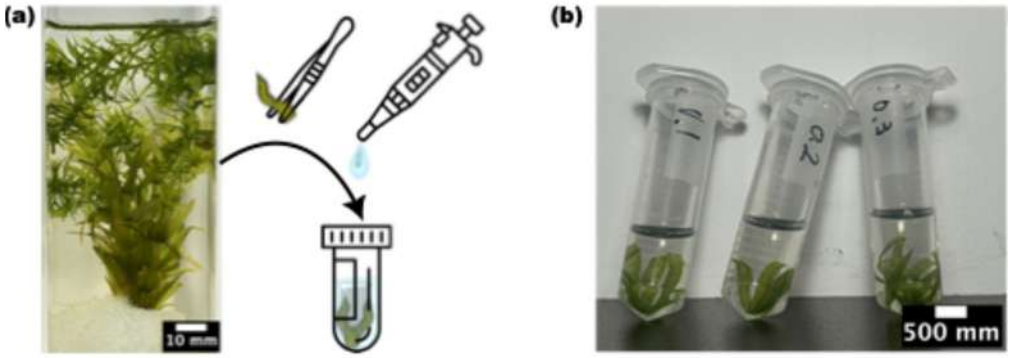

Fig.2 (a) Sample preparation and (b) prepared leaf sample.

Experimental Design

FD-FLIM measurements were performed under dark-adapted and non-dark-adapted conditions at three randomly selected positions per sample (Figure 3). Samples were dark-adapted for 15 min before the first acquisition, followed by 5 min of transmitted-light (TL) illumination and the second acquisition. We used 5 g/L fluorescein solution as a reference and operated the system at 30 MHz with a 500 ms exposure time.

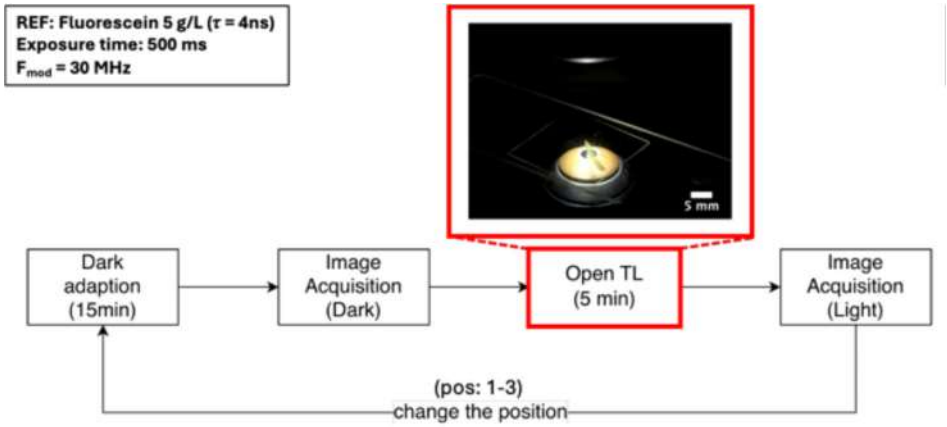

Fig.3 Experimental workflow. “Dark” means “dark adaptation”; “Light” means “non-dark adaptation”.

Image Processing and Lifetime Analysis

Acquired image stacks were preprocessed to filter out the noise (Figure 4). Lifetimes were calculated pixel-wise from the phase shift and modulation index. Then, the lifetime was transformed into phasor coordinates.

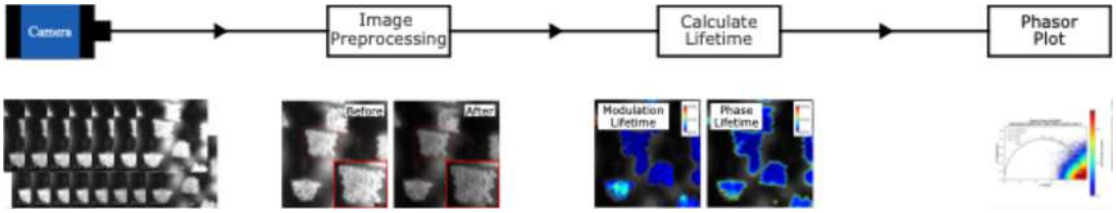

Fig.4 Image processing and fluorescence lifetime analysis workflow from preprocessing to pixel-wise lifetime calculation and phasor transformation.

RESULTS & DISCUSSION

Fluorescence Intensity and Sample Stability

Fluorescence intensity images showed no apparant NaCl-dependent changes across 0.1–0.3 M NaCl treatments (Figure 5), and no clear differences in ChlF intensity were observed between dark-adapted and non-dark-adapted conditions. In contrast, intracellular movement decreased with increasing NaCl concentration. Movement and occasional focus variations remained apparent at 0.1 and 0.2 M NaCl, whereas little intracellular movement was observed at 0.3 M NaCl, resulting in more stable images. This observation is consistent with the reported inhibition of cytoplasmic streaming by hypertonic treatment in aquatic plant cells (Hayashi and Takagi, 2003).

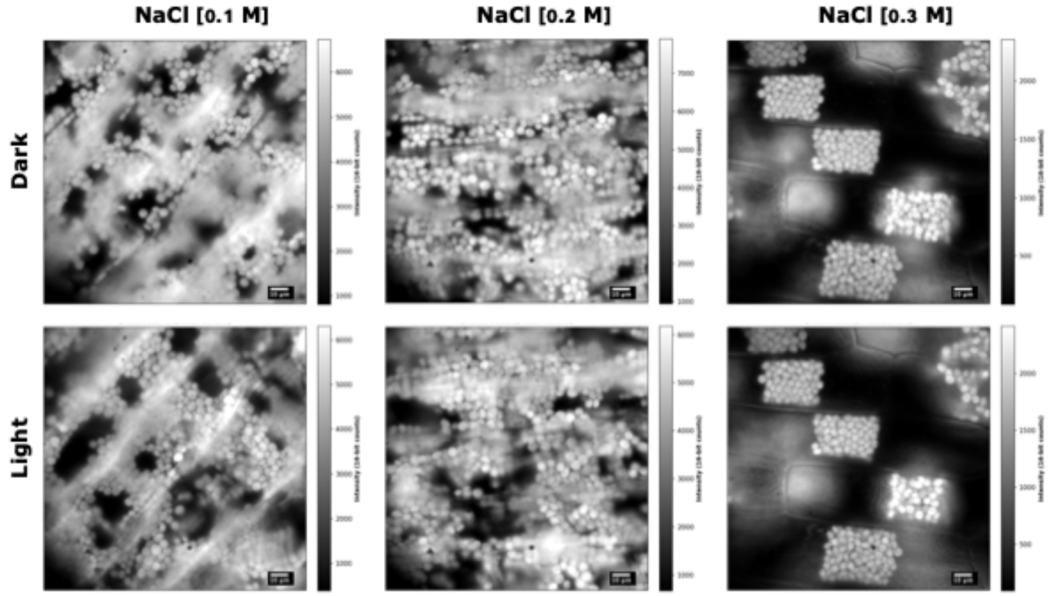

Fig.5 Mean fluorescence intensity images at 0.1–0.3 M NaCl.

Fluorescence Lifetime and Dark Adaptation

In contrast to fluorescence intensity, lifetime and phasor analyses revealed clear NaCl-dependent changes (Figures 6 and 7). The 0.1 and 0.2 M NaCl treatments showed similar phasor distributions, whereas 0.3 M shifted toward shorter lifetimes. Phase and modulation lifetimes showed the same overall trend, indicating that fluorescence lifetime distinguished treatment-associated changes that were not readily apparent from intensity images alone.

Dark-adapted measurements exhibited longer lifetimes at 0.1 and 0.2 M NaCl, whereas only minor differences between adaptation conditions were observed at 0.3 M NaCl. Nevertheless, both adaptation conditions retained a similar NaCl-dependent lifetime trend. These results suggest that dark adaptation may not be essential for detecting NaCl-induced ChlF lifetime changes using FD-FLIM, potentially reducing sample preparation time for rapid plant phenotyping.

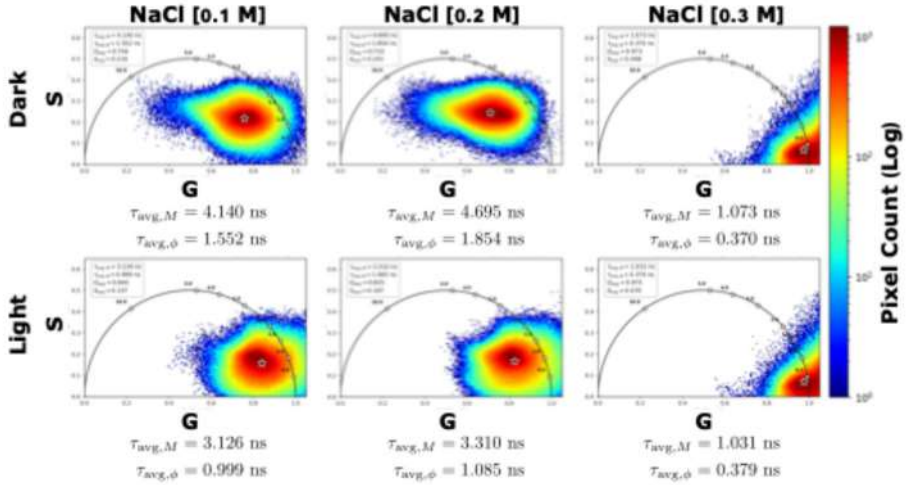

Fig.6 Pixel-wise phasor distributions at 0.1–0.3 M NaCl.

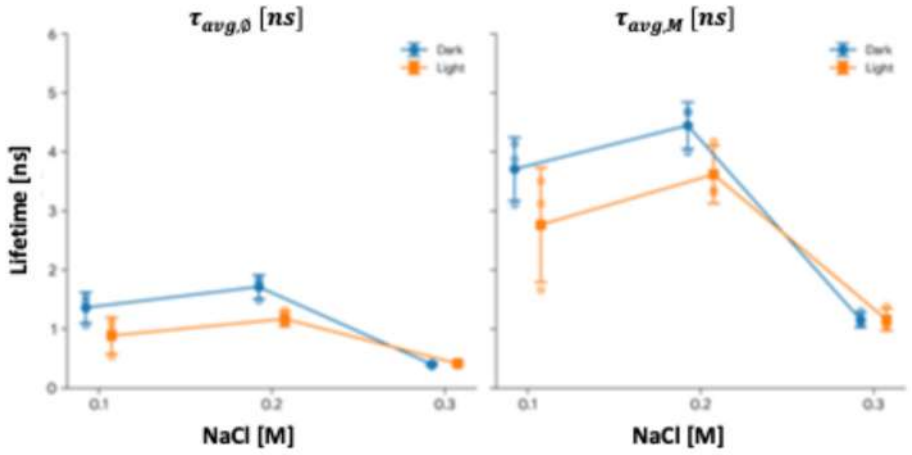

Fig.7 Mean phase and modulation lifetimes at 0.1–0.3 M NaCl.

CONCLUSIONS

This study demonstrated the feasibility of an LED-based FD-FLIM system for cellular-scale ChlF characterization in *E. densa* under different NaCl treatments and adaptation conditions. While ChlF intensity showed no clear differences between dark-adapted and non-dark-adapted conditions, fluorescence lifetime exhibited distinct NaCl-dependent changes. At 0.3 M NaCl, reduced intracellular movement improved images stability, while the lifetime distribution shifted toward shorter lifetimes. Under this more stable condition, only minor lifetime differences were observed between dark-adapted and non-dark-adapted conditions, with both showing similar NaCl-dependent trends. These findings demonstrate that the LED-

based FD-FLIM can detect cellular-scale ChlF changes that are not readily apparent from fluorescence intensity alone and suggest that dark adaptation may not be necessary for FD-FLIM measurements.

ACKNOWLEDGEMENTS

We gratefully acknowledge the financial support provided by the National Science and Technology Council, Taiwan (grant numbers 112-2313-B-002-008-MY2 and 113-2313-B-002-046-MY3), the Ministry of Agriculture, Taiwan (grant numbers 112 農再-2.4.1-1.1-糧-015, 113 農再-2.4.1-1.1-糧-015, 114 農科-16.1.1-科-04(1), and 115 農科-16.1.1-科-04), and the Ministry of Education, Taiwan (grant number 111L7455).

REFERENCES

Baker, N. R. (2008). Chlorophyll Fluorescence: A Probe of Photosynthesis In Vivo. Annual Review of Plant Biology, 59(1), 89–113. https://doi.org/10.1146/annurev.arplant.59.032607.092759

Berezin, M. Y., Achilefu, S. (2010). Fluorescence Lifetime Measurements and Biological Imaging. Chemical Reviews, 110(5), 2641–2684. https://doi.org/10.1021/cr900343z

Digman, M. A., Caiolfa, V. R., Zamai, M., Gratton, E. (2008). The Phasor Approach to Fluorescence Lifetime Imaging Analysis. Biophysical Journal, 94(2), L14–L16. https://doi.org/10.1529/biophysj.107.120154

Fiorani, F., Schurr, U. (2013). Future Scenarios for Plant Phenotyping. Annual Review of Plant Biology, 64(Volume 64, 2013), 267–291. https://doi.org/10.1146/annurev-arplant-050312-120137

Gayathri, R., Suchand Sandeep, C. S., Gummaluri, V. S., Asik, R. M., Padmanabhan, P., Gulyás, B., … Murukeshan, V. M. (2022). Plasmonic random laser enabled artefact-free wide-field fluorescence bioimaging: uncovering finer cellular features. Nanoscale Advances, 4(10), 2278–2287. https://doi.org/10.1039/d1na00866h

Hara, T., Kobayashi, E., Ohtsubo, K., Kumada, S., Kanazawa, M., Abe, T., … Fujiwara, M. T. (2015). Organ-Level Analysis of Idioblast Patterning in Egeria densa Planch. Leaves. PLOS ONE, 10(3), e0118965. https://doi.org/10.1371/journal.pone.0118965

Hayashi, T., Takagi, S. (2003). Ca2+-Dependent Cessation of Cytoplasmic Streaming Induced by Hypertonic Treatment in Vallisneria Mesophyll Cells: Possible Role of Cell Wall–Plasma Membrane Adhesion. Plant and Cell Physiology, 44(10), 1027–1036. https://doi.org/10.1093/pcp/pcg123

Kalaji, H. M., Schansker, G., Ladle, R. J., Goltsev, V., Bosa, K., Allakhverdiev, S. I., … Zivcak, M. (2014). Frequently asked questions about in vivo chlorophyll fluorescence: practical issues. Photosynthesis Research, 122(2), 121–158. https://doi.org/10.1007/s11120-014-0024-6

Murchie, E. H., Lawson, T. (2013). Chlorophyll fluorescence analysis: a guide to good practice and understanding some new applications. Journal of Experimental Botany, 64(13), 3983–3998. https://doi.org/10.1093/jxb/ert208

Redding, B., Choma, M. A., Cao, H. (2012). Speckle-free laser imaging using random laser illumination. Nature Photonics, 6, 355–359. https://doi.org/10.1038/nphoton.2012.90

PA-24

Proceedings of The 12th International Symposium on Machinery and Mechatronics for Agriculture and Biosystems Engineering (ISMAB 2026)
20-24 October 2026, Busan, Republic of Korea

BRIDGING UAV AND SATELLITE OBSERVATIONS FOR SOYBEAN LAI MAPPING

Gyujin Jang[1,2], Jaeyoung Lee[3], Haneul Kim[3], SeungHwan Jeong[4], Hak-Jin Kim[1,2,5*]

[1]Department of Biosystems Engineering, College of Agriculture and Life Sciences, Seoul National University, Seoul 08826 Republic Korea
[2]Integrated Major in Global Smart Farm, College of Agriculture and Life Sciences, Seoul National University, Seoul 08826 Republic Korea
[3]Satellite Team, R&D Department, SaeFarm Inc., Seoul 08506 Republic of Korea
[4]SaeFarm Inc., Seoul 08506 Republic of Korea
[5]Research Institute of Agriculture and Life Sciences, Sciences, Seoul National University, Seoul 08826 Republic Korea
* Corresponding author email: kimhj69@snu.ac.kr

Abstract: Leaf area index (LAI) is a key indicator of crop growth status and photo synthetic capacity in soybean (*Glycine max*), and spatially continuous LAI mapping is increasingly needed for precision agriculture. UAV-based remote sensing provides high prediction accuracy but limited coverage, whereas satellite imagery offers broad, cost-effective coverage better suited to farm-scale application. However, satellite-based LAI models remain difficult to develop because acquiring ground-truth data at a density matching the satellite's pixel resolution is labor-intensive and largely infeasible; conventional point-based sampling, which averages a few measurements within a much larger pixel footprint, suffers from spatial support mismatch and cannot capture within-pixel canopy heterogeneity. To address this, we propose a framework in which UAVs are used to produce model-based LAI estimates at every individual soybean plants within the field, rather than relying on sparse manual sampling. Individual plant-level LAI measurements and UAV-based spectral and RGB imagery were collected from soybean fields at the Suwon Experiment Farm of Seoul National University during the 2024–2025 growing seasons to develop a machine learning-based UAV LAI estimation model. This model was applied to adjacent, unsampled fields to generate spatially continuous synthetic LAI maps, which were matched to individual PlanetScope satellite pixels (3 m resolution) to train a machine learning-based satellite LAI prediction model. The resulting model achieved high prediction performance on the test dataset, showing that UAV-derived, model-based LAI estimates can serve as effective training labels for satellite-based, large-scale LAI mapping. Future work will extend the model to additional fields to evaluate its spatial scalability and generalizability.

Key Words: Soybean, Leaf Area Index, UAV, Satellite Remote Sensing, PlanetScope, Machine Learning
Acknowledgement: This work was supported by SaeFarm Inc. under the project "Advancement of Soybean Leaf Area Index (LAI) Prediction Using Drone Aerial Imagery" (Grant No. 500-20260258).

AI and Information Processing 1 (AI-1)



AI-01

Proceedings of The 12th International Symposium on Machinery and Mechatronics for Agriculture and Biosystems Engineering (ISMAB 2026)
20-24 October 2026, Busan, Republic of Korea

INTERACTIVE WHAT-IF DASHBOARD FOR SIX-HOUR VENTILATION PLANNING IN COMMERCIAL BROILER HOUSES

Suhendra[1], Hao-Ting Lin[2*]

[1]International Doctoral Program in Agriculture, National Chung Hsing University, Taichung 402, Taiwan
[2]Department of Bio-Industrial Mechatronics Engineering, National Chung Hsing University, Taichung 402, Taiwan
*Corresponding Author - Email: haotlin@nchu.edu.tw

Abstract: Commercial broiler-house ventilation is a multi-objective decision problem in which ammonia mitigation, thermal stability, and operational efficiency must be considered simultaneously. This study developed an operator-facing what-if dashboard that converts six-hour forecasts into transparent, scenario-based ventilation planning. The dataset comprised 7,344 hourly observations collected over 306 days and four consecutive flock cycles in one commercial broiler house. After quality control and temporal aggregation, 1,224 six-hour decision windows were obtained. A multi-output neural surrogate, evaluated through leave-one-cycle-out testing, forecast next-window ammonia concentration (NH3), indoor-outdoor temperature gradient (dT), and the Adaptive Agro-Environmental Efficiency Index (AAEEI). The dashboard enables users to select a flock-cycle context, initialize the rollout from a high-ammonia state using P90 or P95 criteria, define a 6-72 h planning horizon, compare two constant inlet perturbations with a no-change baseline, select single or composite decision objectives, and export the complete scenario trajectory. Two contrasting cases were evaluated. In Cycle 1 at P90 over 24 h, moderate and stronger inlet increments increased mean NH3 by 0.194 and 0.497 ppm and increased mean dT by 0.649 and 1.255 °C, respectively. The composite objective therefore retained the baseline despite small AAEEI gains. In Cycle 3 at P95 over 54 h, the two interventions reduced mean NH3 by 1.820 and 1.508 ppm, but imposed mean dT penalties of 4.887 and 4.151 °C and slightly reduced AAEEI. The baseline was again retained because the air-quality gains were outweighed by thermal and efficiency penalties. These results show that identical recommendations can arise from different physical trade-offs and that stronger ventilation cannot be assumed to be universally beneficial. By displaying synchronized trajectories, objective-dependent rankings, and exportable stepwise records, the dashboard provides an auditable bridge between predictive modeling and human-supervised environmental management. The system is intended as a comparative decision-support tool; further development should incorporate hardware-calibrated control actions, uncertainty-aware rollouts, safety constraints, and multi-site validation.

Key Words: Precision livestock farming, Decision support, Ammonia, Scenario rollout, Broiler ventilation

AI-02

Proceedings of The 12th International Symposium on Machinery and Mechatronics for Agriculture and Biosystems Engineering (ISMAB 2026)
20-24 October 2026, Busan, Republic of Korea

INTELLIGENT-ASSISTED REAL-TIME SPECTRAL SENSING PLATFORM FOR POINT-OF-CARE *SALMONELLA* TYPHIMURIUM DNA DETECTION

Hong Zhi Zhang[1], Jyh Jian Chen[1*]

[1]Department of Biomechatronics Engineering, National Pingtung University of Science and Technology, Taiwan
*Corresponding Author-- Voice: +88687703202#7839
Email: chaucer@mail.npust.edu.tw

Abstract: *Salmonella enterica* serovar Typhimurium is a primary causative agent of acute gastroenteritis in humans and animals, frequently manifesting as fever, vomiting, and severe diarrhea following exposure to contaminated meat, unpasteurized dairy, or animal feces. To mitigate food safety risks and enable early disease prevention, this study presents a compact, portable nucleic acid isothermal amplification device integrated with real-time artificial intelligence (AI) inference. Constructed via 3D printing and laser cutting, the platform incorporates an Arduino microcontroller for precise reaction temperature control and a Raspberry Pi for real-time edge AI processing. The system utilizes loop-mediated isothermal amplification (LAMP) coupled with a pH-sensitive colorimetric indicator; successful DNA amplification triggers a distinct color transition from pink (negative) to yellow (positive). The integrated AI model processes real-time optical signals to deliver automated, rapid, and objective result interpretation, overcoming the subjectivity of visual inspection. Experimental validation demonstrates a limit of detection (LOD) below 10^{-3} ng/μL for *S.* Typhimurium DNA, along with high specificity against non-target species. Combining high portability, low detection limits, and automated AI analysis, this platform exhibits high potential for on-site food safety monitoring, agricultural disease control, and resource-limited point-of-care diagnostics.

Key Words: *Salmonella* Typhimurium, LAMP, Colorimetric Detection, AI-Assisted Interpretation.

AI-03

Proceedings of The 12th International Symposium on Machinery and Mechatronics for Agriculture and Biosystems Engineering (ISMAB 2026)
20-24 October 2026, Busan, Republic of Korea

POULTRY LITTER CONDITION CLASSIFICATION USING AN ELECTRONIC NOSE WITH RFECV-BASED FEATURE SELECTION

Kai-Feng Cheng[1], Yu-Hsuan Shen[1], Chin-Cheng Wu[1*]

[1]Department of Biomechatronic Engineering, National Ilan University,
No. 1, Sec. 1, Shennong Rd., Yilan City, Yilan County 260007, Taiwan
*Corresponding Author-- Voice: +886-3-9357400 #7825, Email: chincheng@niu.edu.tw

Abstract: Multi-dimensional gas sensor arrays in electronic noses often capture redundant information, thereby leading to the curse of dimensionality and model overfitting. To address this, this study developed a machine learning-based E-nose system for the non-destructive odor profiling of poultry litter across different reuse stages. After extracting five features from each of the seven sensors (totaling 35 features) from the litter samples, four machine learning algorithms (KNN, Linear SVM, RBF SVM, and LDA) were evaluated. However, direct classification using all 35 features resulted in poor performance, with LDA yielding an accuracy of merely 44.4%. Therefore, an RFECV-based feature selection pipeline was integrated to enhance recognition performance. As the first step, Recursive Feature Elimination with Cross-Validation (RFECV) was applied to eliminate redundant features, reducing the dimensionality from 35 to an intermediate set of 11. Next, the second step (evaluated by Leave-One-Out Cross-Validation, LOO-CV) was conducted to determine the final optimal six-feature set for multi-model comparison. The results showed that under a strict six-feature constraint, a traditional Pearson Correlation-based selection yielded an accuracy of only 63.0% when applied to Linear Discriminant Analysis (LDA). However, by narrowing down to a complementary six-feature set through the proposed RFECV-based feature selection pipeline, the LDA accuracy substantially improved to 88.9% (F1 score: 0.888), achieving classification performance comparable to Linear SVM. These optimized features were associated with sensor response patterns potentially related to changes in the gaseous environment of poultry litter. This study demonstrates that appropriate feature engineering significantly enhances system discrimination, supporting the development of data-driven tools for monitoring litter reuse conditions in the poultry industry.

Key Words: Poultry litter, Electronic nose, Feature Selection engineering, Linear discriminant analysis

INTRODUCTION

In floor-rearing broiler systems, litter is commonly laid on the ground to maintain animal welfare and absorb excrement and spilled moisture. According to statistics from the Ministry of Agriculture in Taiwan, each broiler produces approximately 1.1 to 1.4 kg of manure during its rearing period. With a domestic standing flock size of around 55 million birds, the estimated annual cost for bedding materials in Taiwan exceeds 6.3 million USD. Due to this massive

scale of intensive farming and persistently high costs of litter procurement and disposal, farms frequently reuse poultry litter across multiple flocks. However, consecutive litter reuse leads to severe accumulation of feces and gaseous pollutants, including ammonia (NH_3), hydrogen sulfide (H_2S), and various volatile organic compounds (VOCs) within the poultry house (Xin et al., 2009). This deteriorates the rearing environment, decreases the survival rate, and compromises animal welfare. Accurately evaluating litter reuse stages assists managers in tracking litter conditions to achieve sustainable agriculture.

Traditional litter evaluation heavily relies on subjective human olfaction or time-consuming gas chromatography-mass spectrometry (GC-MS). As a biomimetic olfactory system, the electronic nose (E-nose) has emerged as a promising non-destructive tool for agricultural odor monitoring (Gutierrez-Osuna, 2002; Capelli et al., 2014). While E-noses have been applied to broad environmental monitoring, their application to discriminating poultry litter reuse stages remains limited. Furthermore, multi-dimensional gas sensor arrays easily capture redundant information and environmental noise, leading to model overfitting and degraded classification performance (Laref et al., 2019).

To address these issues, this study proposed an optimized feature selected method to enhance the system's discrimination capability through Recursive Feature Elimination with Cross-Validation (RFECV). The specific objectives are: (1) to investigate whether E-nose response patterns can effectively discriminate poultry litter at different reuse stages; and (2) to evaluate whether an RFECV-based feature selection pipeline can improve classification performance compared with a traditional Pearson Correlation-based approach (Tu et al., 2023).

MATERIALS AND METHODS

Data Collection and Litter Stages

This E-nose system was equipped with a commercial metal-oxide-semiconductor (MOS) gas sensor array. The hardware configuration and experimental setup are shown in Fig. 1. The system comprises seven MOS sensors (MQ-4 to MQ-9 and MQ-135), which respond to various VOCs, combustible gases, and ammonia. To reflect the real-world industry practice, a long-term tracking study was conducted on the same batch of litter within a single poultry house. Consequently, three reuse stages were defined: "Stage 1" represents the condition after the first flock was harvested (after approximately 35 to 37 days of rearing). Subsequently, the conditions before litter turning following each successive flock harvest (each cycle taking approximately 35 to 37 days) were defined as "Stage 2" and "Stage 3," respectively. The experimental procedure yielded a total of 27 sample measurements (9 per stage) for analysis.

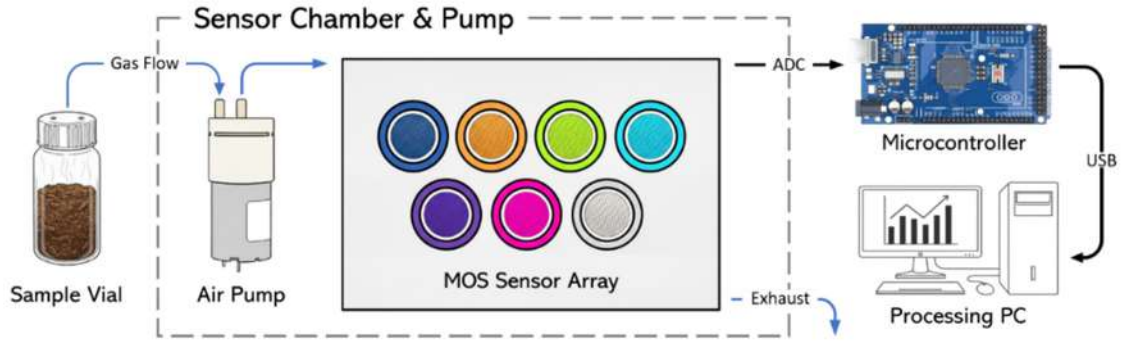

Fig.1 Schematic diagram of the E-nose hardware architecture and experimental setup.

Signal Preprocessing and Feature Engineering

To mitigate high-frequency noise and baseline fluctuations, the raw sensor response curves were processed using filtering, noise reduction, and baseline correction, as illustrated in Fig. 2. To comprehensively characterize volatile-gas dynamics and sensor responses, a set of multidimensional static and dynamic features was extracted. Five features were derived from each sensor: response ratio, log ratio, maximum slope, skewness, and area under the response curve. With seven sensors, a total of 35 features were obtained. After extraction, Z-score standardization was applied independently to each feature. This ensures that sensors with larger output voltages do not dominate the model weights, while preserving the relative variability within each individual sensor.

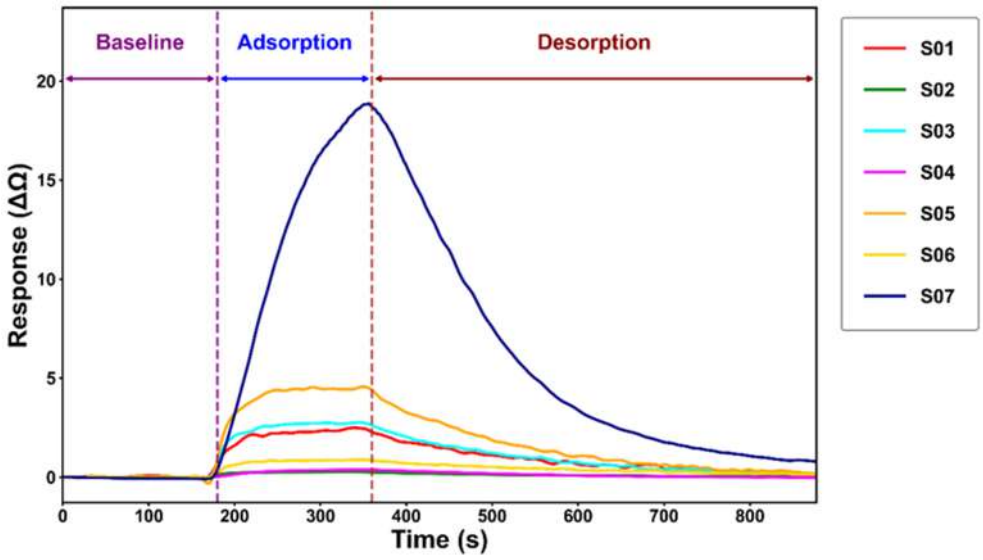

Fig.2 Sensor dynamic response curves after signal preprocessing.

Model Construction, Feature Selection, and Performance Comparison

To avoid overfitting in a high-dimensional, small-sample-size scenario, a machine learning pipeline was implemented, as detailed in Fig. 3. The proposed workflow integrates initial feature dimension reduction via RFECV (using a linear SVM estimator), reducing the dimensionality from 35 to an intermediate set of 11. Next, feature selection by LOO-CV was conducted to determine the optimal final feature set of 6.

To rigorously evaluate the selection effectiveness of the proposed pipeline, a traditional univariate filter method using Pearson Correlation was implemented for comparison by selecting the top 6 features. Both the optimized 6-feature subset and the Pearson Correlation subset were then applied to KNN, Linear SVM, RBF SVM, and LDA using 5-fold Stratified K-Fold cross-validation. Ultimately, the optimal classifier and feature subset were determined based on the best overall classification performance, evaluated by accuracy and F1-score.

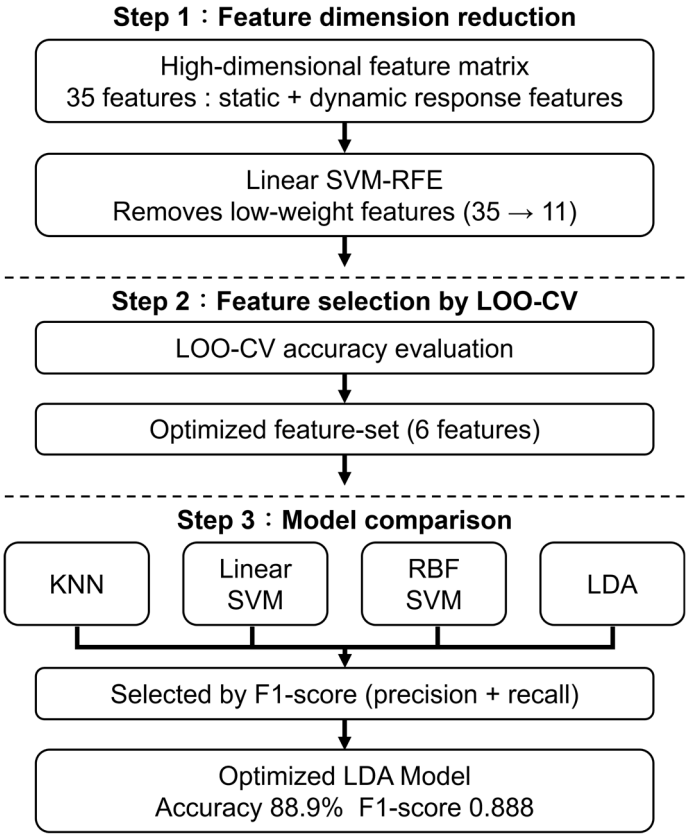

Fig.3 Flowchart of the feature selection and machine learning classification algorithm.

RESULTS & DISCUSSION

Classification Performance

Although extracting multi-dimensional features captures dynamic responses comprehensively, it inevitably introduces redundancy. When utilizing a total of 35 features, the classification performance was significantly hindered by the high-dimensional space, yielding an LDA accuracy of merely 44.4%. As shown in Table 1, employing a traditional Pearson Correlation approach to select the top six features provided limited improvement, with the LDA accuracy reaching only 63.0%. This indicates that while Pearson Correlation successfully ranks individually correlated features, it ignores the complementary effects and potential multicollinearity between features, thereby failing to form optimal decision boundaries for complex odor mixtures (Guyon and Elisseeff, 2003).

In contrast, the first-step RFECV systematically pruned variables with low discriminative power, narrowing the original 35 features down to 11. Next, feature selection by LOO-CV was

conducted to lock in an optimal feature set consisting of exactly 6 features. Under the exact same dimensional constraints (6D), the optimized feature-set improved LDA accuracy substantially by 25.9%. The confusion matrices are shown in Fig. 4. The final cross-validation results showed that the optimized feature set improved the performance of both classifiers, with LDA and linear SVM each achieving an accuracy of 88.9%.

Table 1 Performance comparison of classification models under different feature selection strategies

Method	Classifier	Accuracy	F1-score
Pearson Correlation	KNN	0.630	0.583
	SVM (linear)	0.852	0.818
	SVM (rbf)	0.741	0.713
	LDA	0.630	0.616
RFECV-based feature selection	KNN	0.778	0.780
	SVM (linear)	0.889	0.888
	SVM (rbf)	0.815	0.812
	LDA	0.889	0.888

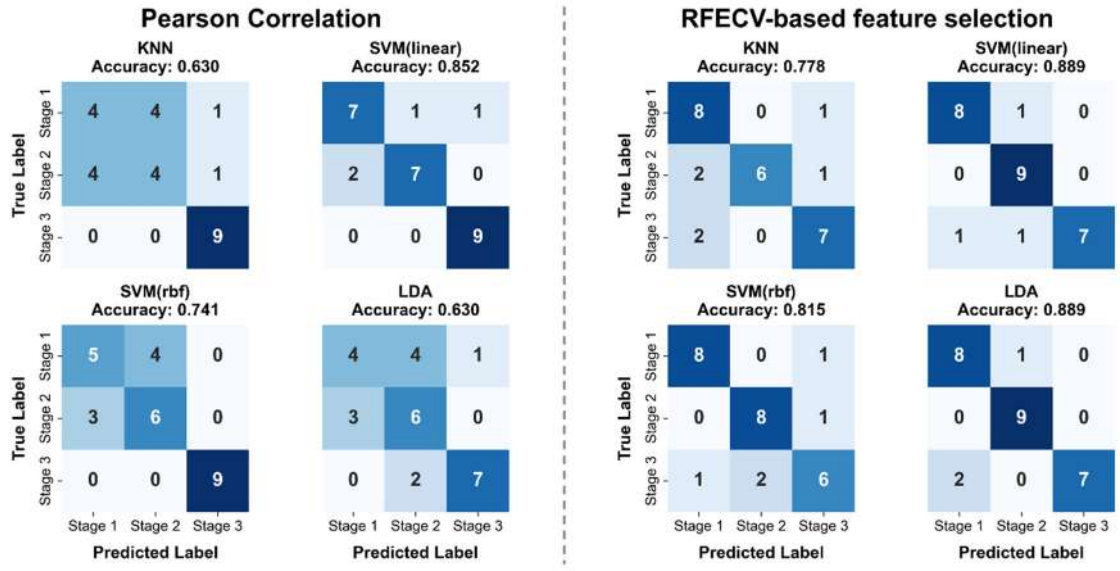

Fig.4 Confusion matrices of Pearson Correlation and RFECV-based feature selection

Discussion

The optimized feature set derived from four sensors (MQ-5, MQ-6, MQ-9, and MQ-135), exhibits response patterns potentially related to litter decomposition chemistry. Specifically, MQ-135 is known to be sensitive to ammonia and sulfides—the dominant emissions from feces

fermentation (Dunlop et al., 2016). MQ-9 responds to combustible gases, while MQ-5 and MQ-6 effectively capture general changes in VOC gas mixtures released during anaerobic decomposition.

While the algorithm mitigates environmental drift by proactively selecting relative indicators (log ratio) and dynamic shape features (area), it is important to note that MOS sensors possess cross-sensitivity. The selected features reflect overall gas-response patterns rather than exact chemical concentrations. Future studies should validate these sensor response patterns against reference gas measurements, such as precise NH_3, H_2S, or VOC analyses, using appropriate analytical instruments.

CONCLUSIONS

This study developed an optimized machine learning classification framework applied to evaluate the reuse stages of poultry litter. Through signal preprocessing and an RFECV-based feature selection pipeline, the dimensionality of the feature space was effectively reduced from 35 down to 6. By selecting an optimized six-feature subset, the classification accuracy of the LDA model was significantly improved from 63.0% (obtained via Pearson Correlation) to 88.9%, with an F1-score of 0.888, comparable to Linear SVM for the best overall classification performance. These selected features capture complementary sensor-response characteristics associated with changes in the gaseous environment of poultry litter, indicating that feature selection is a critical factor for substantially improving the performance of models. This approach provides a non-destructive and cost-effective evaluation tool, supporting the development of data-driven methods to track litter reuse conditions and assist future litter management decisions.

ACKNOWLEDGEMENTS

This study was financially supported by the Ministry of Agriculture, Taiwan, under Grant No. 115AS-10.2.3-AD-01. The authors gratefully acknowledge this support.

REFERENCES

Capelli, L., S. Sironi, and R. Del Rosso. 2014. Electronic noses for environmental monitoring applications. Sensors 14(11): 19979-20007.

Dunlop, M. W., P. J. Blackall, and R. M. Stuetz. 2016. Odour emissions from poultry litter—A review litter properties, odour formation and odorant emissions from porous materials. Journal of Environmental Management 177: 306-319.

Gutierrez-Osuna, R. 2002. Pattern analysis for machine olfaction: a review. IEEE Sensors Journal 2(3): 189-202.

Guyon, I., and A. Elisseeff. 2003. An introduction to variable and feature selection. Journal of Machine Learning Research 3: 1157-1182.

Laref, R., E. Losson, A. Sava, and M. Siadat. 2019. On the study of feature extraction and classification methods for electronic nose. Sensors 19(2): 274.

Tu, T., Y. Su, Y. Tang, W. Tan, and S. Ren. 2023. A More Flexible and Robust Feature Selection Algorithm. IEEE Access 11: 141512-141522.

Xin, H., R. T. Burns, and H. Li. 2009. Ammonia (NH3) and hydrogen sulfide (H2S) emission rates for poultry operations. National Air Emissions Monitoring Study. West Lafayette, Ind.: Purdue University.

AI-04

Proceedings of The 12th International Symposium on Machinery and Mechatronics for Agriculture and Biosystems Engineering (ISMAB 2026)
20-24 October 2026, Busan, Republic of Korea

MULTI-SCALE PHENOTYPING OF GREENHOUSE CUCUMBER CANOPIES: INTEGRATING AI VISION WITH 3D GAUSSIAN SPLATTING

Dong Thanh Pham[1,*], Muneshi Mitsuoka[1], Daisuke Yasutake[1,2], Takenori Ozaki[3], Masaharu Koga[3], and Takashi Okayasu[1,2]

[1]Faculty of Agriculture, Kyushu University, Fukuoka, Japan
[2]IoP Collaborative Creation Center, Kochi University, Kochi, Japan
[3]welzo Co. Ltd., Fukuoka, Japan
*Corresponding Author: pham.thanh.dong.660@m.kyushu-u.ac.jp

Abstract: Traditional 3D reconstruction limitations and computational bottlenecks fundamentally restrict the structural monitoring of complex agricultural canopies. The principal objective of this study is to develop an automated, multi-scale 3D phenotyping pipeline to quantify axial stem traits alongside volumetric canopy architecture in dense greenhouse cucumbers. The methodology integrates dual robotic and orbital scanning trajectories with 3D Gaussian Splatting (3DGS) and zero-shot semantic segmentation. Prior to whole-canopy segmentation, an automated rail-mounted overhead PTZ robotic system was utilized to acquire multi-angle individual plant scans for axial framework analysis. Structural internode coordinates were extracted via a 2D projection, machine vision detection, and 3D reprojection framework, achieving high metric accuracy within a 1%–4% relative error margin compared to physical ground truth. For whole-canopy foliage isolation, custom-trained CNNs (YOLO11) were benchmarked against a zero-shot foundation model (SAM3), where SAM3 provided superior boundary precision (mIoU = 0.96). Following 3DGS optimization, spatial means were normalized onto a uniform 0.01 m voxel grid, neutralizing algorithmic densification bias and achieving an RMSE of 0.56–0.59 cm against physical leaf dimensions. Real-time rendering speeds of 48 fps were maintained while explicitly mapping structural congestion zones and dynamic pruning interventions. In conclusion, integrating overhead robotic stem quantification with canopy-scale semantic 3DGS provides an accurate, multi-scale phenotyping tool for precision agriculture.

Key Words: Plant Phenotyping, 3D Gaussian Splatting, Semantic Segmentation, Voxelization, SAM.

INTRODUCTION

Precise characterization of plant canopy architecture is essential for optimizing crop yields and driving precision agriculture. While 2D computer vision networks allow high-throughput monitoring, flat images inherently compress depth and mask vital structural traits such as volumetric canopy spread, leaf orientation, and 3D axial growth. Conversely, traditional 3D sensing methods (e.g., LiDAR, Structure-from-Motion, and Multi-View Stereo) struggle with dense greenhouse crops characterized by severe self-occlusion, thin non-Lambertian foliage, and variable light, often producing incomplete point clouds.

In our previous work, we explored high-throughput 3D plant reconstruction and feature segmentation using automated overhead robotic systems and 2D post-rendering analysis (Pham et al., 2024; Pham et al., 2025). While these approaches established automated data collection, applying segmentation after rendering lacks inherent 3D spatial semantics prior to optimization. To overcome these challenges in complex greenhouse canopies, our recent study introduced semantic-aware Gaussian splatting for architectural analysis (Pham et al., 2026). Building upon this, comprehensive digital phenotyping requires bridging axial framework traits (such as internode elongation) with full canopy-scale volumetric properties across temporal crop management cycles.

To address these gaps, this study presents an integrated multi-scale phenotyping framework optimized for dense greenhouse crops (cucumber). The primary objectives are: (1) to automate the non-destructive measurement of internode lengths using an overhead PTZ imaging robot coupled with a 2D projection and 3D reprojection pipeline; (2) to benchmark 2D semantic mask extraction between custom CNNs (YOLO11) and zero-shot foundation models (SAM3) prior to 3DGS for organ-level leaf isolation; and (3) to voxelize the continuous canopy space to quantify architectural phenotypic traits across temporal management events.

MATERIALS AND METHODS

Experimental Setup and Data Acquisition

Data collection was conducted across two distinct controlled greenhouse environments featuring mature cucumber crops with complex canopy structures

For axial internode trait characterization, an automated overhead robotic system mounted on an aluminum rail suspended above the crop bed was employed (Pham et al., 2025). The platform integrated an ArUco navigation camera for positioning, reed switches, and a Sunba PTZ camera (5MP, 20x optical zoom) mounted on a vertical sliding mechanism (60–210 cm above ground level, positioned 0.7 m horizontally from the cultivation bed). The robot traversed horizontally to acquire multi-angle imagery of individual plants while mitigating manual scanning variance. Spherical physical calibration markers (diameter: 4.0 cm) were installed within the scanning zone for absolute metric scaling (Fig. 1).

For continuous canopy-level and dynamic agronomic evaluation, video data across single-bed (0.5 m height, 0.45 m width, 13 m length) and parallel-bed layouts (0.25 m height, 1.05 m width, 8.5 m length; Pre- and Post-Pruning) were collected using a DJI Osmo Action 6 camera (3840$¥times$2880, 30 fps, locked shutter at 1/800 s). The operator traversed the 0.5

m wide walking path in an orbital scanning trajectory at heights of 1.4 m, 1.6 m, and 1.8 m, maintaining $>80¥%$ forward frame overlap (Fig. 1).

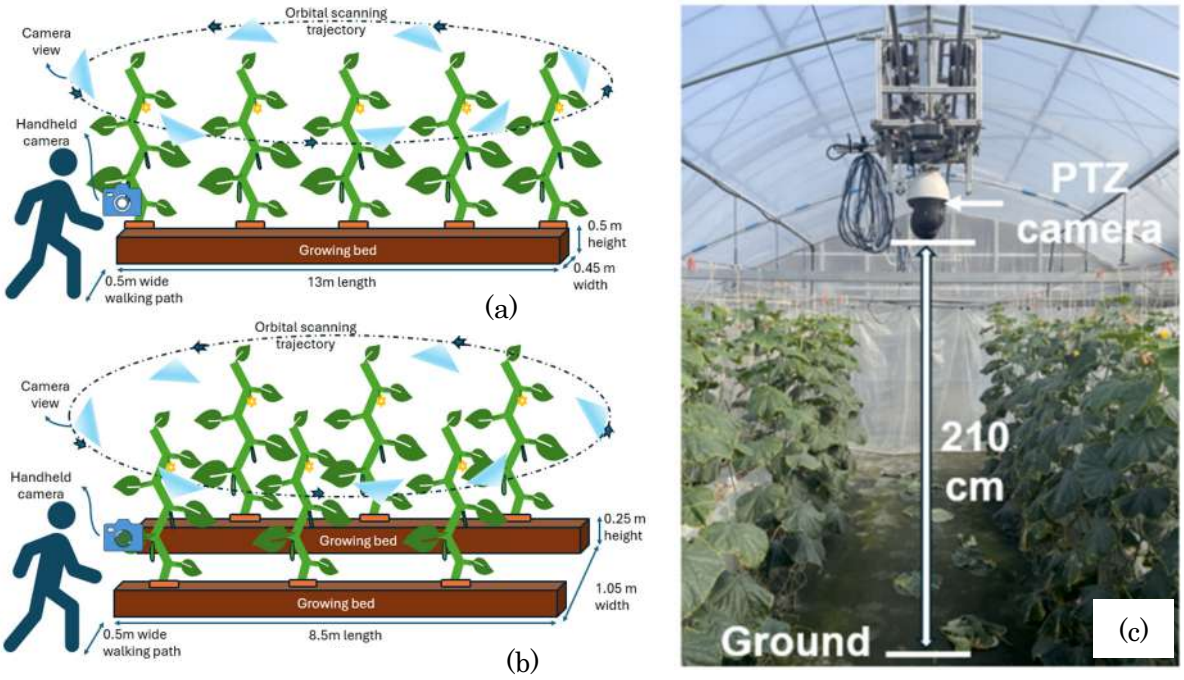

Fig. 1 Experimental setup and data acquisition platforms in the greenhouse: (a) single-bed canopy layout and orbital handheld scanning trajectory; (b) parallel-bed layout with pre- and post-pruning scanning paths; and (c) overhead rail-mounted robotic system equipped with a vertically mobile PTZ camera for automated multi-angle scanning of individual plants..

Robotic 3D Plant Feature Analysis: Internode Length Extraction

For individual plants scanned by the overhead robot, multi-view image sets and camera poses were resolved using Structure-from-Motion (SfM) in COLMAP to generate an initial 3D point cloud. To isolate axial skeletal traits without manual point selection in complex 3D space:

1. The metric scaling factor was defined using the detected diameter of the reference calibration sphere (4.0 cm ground truth vs. 0.098 units in point cloud space).
2. The 3D point cloud was flattened along primary viewing planes via planar 2D projection to clearly expose the stem axis and junction points.
3. 2D machine vision keypoint detection was applied to localize consecutive node junctions along the vine
4. The detected 2D node coordinates were reprojected back into the calibrated 3D point cloud coordinate system.
5. Spatial Euclidean vectors between adjacent nodes (AB, BC, CD, and DE) were computed to quantify individual internode lengths

2D Mask Generation and 3DGS Optimization

For canopy-scale reconstruction, camera poses and sparse points were estimated using SfM in COLMAP. To generate semantic masks isolating target foliage, custom YOLO11-seg models were benchmarked against the foundation Segment Anything Model 3 (SAM3) deployed in zero-shot configuration guided by the prompt "leaf". RGB frames were pre-masked by nullifying non-target background pixels and passed to the 3DGS optimization

pipeline (splatfacto in Nerfstudio) for 30,000 iterations. This pre-masking constrained Gaussian initialization and adaptive densification to active plant tissue, eliminating background infrastructure artifacts.

Voxelization and Canopy Trait Extraction

Following 3DGS optimization, the spatial means of the Gaussians were exported as a point cloud and scaled into metric units. To eliminate algorithmic densification bias—wherein high-contrast leaf edges generate disproportionate Gaussian clustering—the cloud was discretized into a uniform 0.01 m voxel grid, ensuring one occupied voxel represented approximately 1 cm^2 of physical foliage. The normalized voxel cloud was partitioned into vertical strata (0.4 m intervals) along the Z-axis to extract Point Density, Canopy Length, Lateral Spread, Projected Area, and Layer Porosity.

RESULTS & DISCUSSION

Internode Geometric Accuracy Analysis

Axial stem traits extracted via the robotic scanning, 2D projection, and 3D reprojection pipeline demonstrated high dimensional fidelity when compared directly against physical ground truth. Using the 4.0 cm reference sphere, metric scaling was established across the point cloud. As detailed in Table 1, the calibrated lengths for segments AB (8.00 cm), BC (11.92 cm), CD (12.20 cm), and DE (12.04 cm) closely matched physical ruler measurements (8.2 cm, 11.5 cm, 12.0 cm, and 12.2 cm, respectively). Relative errors remained between -4% and 2%. This confirms that the overhead robotic system and 2D-to-3D reprojection pipeline accurately capture axial stem elongation non-destructively, overcoming occlusion challenges common in dense crop beds.

Table 1 Geometric accuracy validation comparing physical ground truth (Ruler) to the extracted 3DGS Voxel Model (Mean ± Standard Deviation).

Feature / Node Segment	Ground Truth Length (cm)	Length in Point Cloud (units)	Calibrated Length (cm)	Relative Error (%)
Calibration Ball	4.0	0.098	4.0	
Segment AB	8.2	0.196	8.0	2
Segment BC	11.5	0.292	11.92	4
Segment CD	12.0	0.299	12.2	2
Segment DE	12.2	0.295	12.04	1

3DGS Reconstruction and Semantic Leaf Model Generation

The optimized 3DGS model outperformed NeRF baselines (Nerfacto, Instant-NGP), achieving superior rendering quality (PSNR: 22.53–24.08) and real-time rendering speeds of 48 fps. As shown in Fig. 2, 3DGS reconstructed full cucumber canopies across single-bed and parallel-bed configurations.

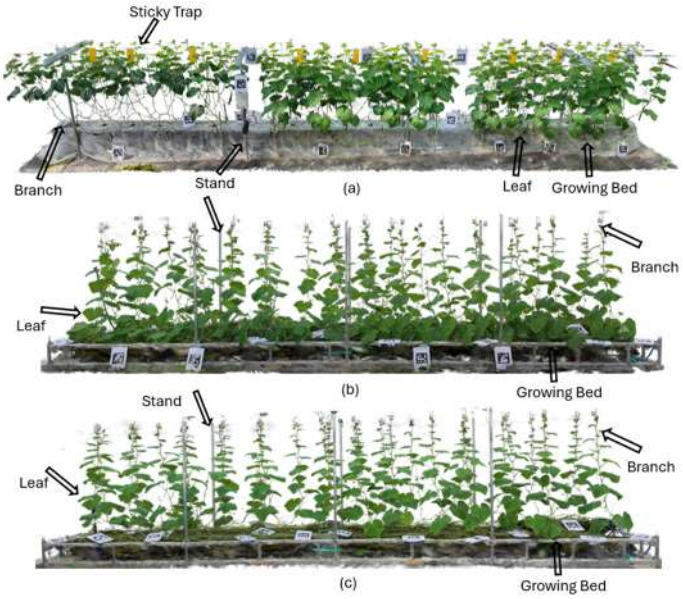

Fig.2 Rendered views from 3DGS models of full cucumber canopy: (a) Dataset 1 (Single-Bed); (b) Dataset 2 (Parallel-Bed, Pre-Pruning); and (c) Dataset 3 (Parallel-Bed, Post-Pruning).

Explicit optimization of anisotropic Gaussians prevented over-smoothing of delicate vegetative structures, resolving sharp leaf boundaries and petioles. Pre-filtering images using SAM3 zero-shot segmentation (mIoU = 0.9667) excluded background trellis wires, growing beds, and walking paths. Discretizing these filtered Gaussians onto a uniform 0.01 m voxel grid successfully neutralized densification bias (Fig. 3), converting arbitrary point clusters into physical representations of leaf surface area.

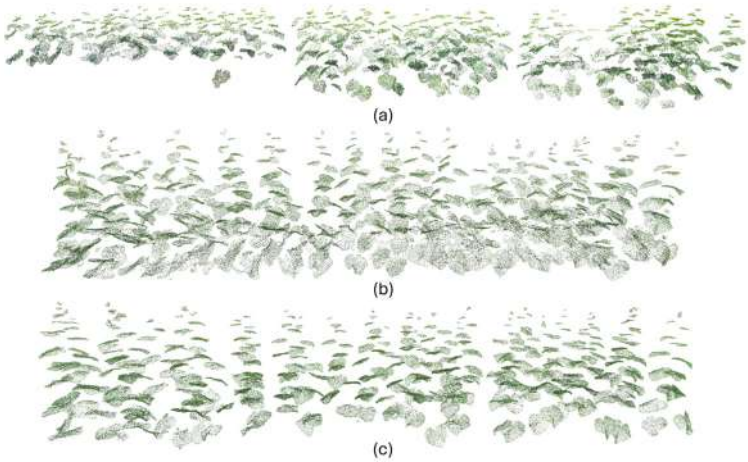

Fig.3 Semantic leaf voxel models extracted from the 3DGS reconstructions: (a) Dataset 1 (Single-Bed); (b) Dataset 2 (Parallel-Bed, Pre-Pruning); and (c) Dataset 3 (Parallel-Bed, Post-Pruning).

Leaf Dimensional Accuracy and Dynamic Canopy Profiling

At the organ level, 3DGS-derived voxel measurements were validated against in situ physical ruler measurements ($n=15$). As detailed in Table 2, the model achieved low RMSE values of 0.56 cm for leaf length and 0.59 cm for leaf width, maintaining millimeter-scale accuracy across complex foliage

Table 2 Geometric accuracy validation comparing physical ground truth (Ruler) to the extracted 3DGS Voxel Model (Mean ± Standard Deviation).

Phenotypic Metric	Physical Ground Truth (cm)	3DGS Voxel Model (cm)	RMSE (cm)
Leaf Length (n=15)	18.2 ± 1.0	17.9 ± 1.0	0.56
Leaf Width (n=15)	16.4 ± 1.2	16.1 ± 1.1	0.59

Vertical multi-metric canopy profiling successfully quantified the physical impacts of pruning interventions (Dataset 2 vs. Dataset 3). Lower foliage removal (0.2–0.6 m strata) significantly increased layer porosity, validating enhanced ventilation and light penetration zones. Concurrently, upper strata (1.0–2.2 m) documented the upward vertical translation of hoisted vines through localized increases in biomass density and lateral spread.

CONCLUSIONS

This study established an integrated multi-scale phenotyping pipeline combining automated overhead robotics, 2D-to-3D node reprojection, and semantic 3D Gaussian Splatting. Axial internode lengths were quantified non-destructively within a 1%–4% error margin, while organ-level leaf dimensions achieved an RMSE under 0.60 cm. Furthermore, uniform voxelization effectively eliminated densification bias, enabling objective volumetric quantification of dynamic canopy pruning. This framework provides a scalable, non-destructive solution for both plant-level morphological research and greenhouse canopy management.

ACKNOWLEDGEMENTS (optional)

This research was conducted as collaborative research with welzo Co. Ltd., and supported by the Cabinet Office grant-in-aid, Advanced Next-Generation Greenhouse Horticulture by IoP (Internet of Plants), Japan.

REFERENCES

Pham, D. T., N. A. Amin, D. Yasutake, Y. Hirai, T. Ozaki, M. Koga, K. Hidaka, M. Kitano, H. B. Vo, and T. Okayasu. 2024. Development of plant phenotyping system using Pan Tilt Zoom camera and verification of its validity. Computers and Electronics in Agriculture 227: 109579.

Pham, D. T., T. Iwakuma, Z. Jiang, S. Sar, D. Yasutake, T. Ozaki, M. Koga, Y. Hirai, M. Mitsuoka, M. R. Al Mamun, K. Nomura, H. B. Vo, and T. Okayasu. 2025. High-throughput 3D reconstruction of plants and its application to plant feature segmentation. Smart Agricultural Technology 12: 101063.

Pham, D. T., Z. Jiang, M. Mitsuoka, D. Yasutake, T. Ozaki, M. Koga, K. Nomura, and T. Okayasu. 2026. Cucumber3DGaussians: Plant architecture analysis using semantic-aware Gaussian splatting. Smart Agricultural Technology 15: 102456.

AI-05

Proceedings of The 12th International Symposium on Machinery and Mechatronics for Agriculture and Biosystems Engineering (ISMAB 2026)
20-24 October 2026, Busan, Republic of Korea

DOMAIN ADAPTATION BASED ON INTERPOLATION IMAGES GENERATION IMPROVE DEER DETECTION PERFORMANCE

Yu Tanaka[1], Ryohei Masuda[1*], Michihisa Iida[1*], Masahiko Suguri[1*]

[1]Graduate School of Agriculture, Kyoto University, Japan
*Corresponding Author-- Voice: +81-75-753-6167,
Email: iida.michihisa.4v@kyoto-u.ac.jp

Abstract: In recent years, damage to crops caused by wildlife, particularly deer, has become a serious problem in Japan. To mitigate damage caused by deer, identifying areas for prioritized culling is crucial. This requires an automated presence survey using camera imagery and deep-learning-based object detection models. However, deep learning relies on vast amounts of image data in the deployment environment, and collecting such data demands significant time and effort. To address this challenge, this study investigated a domain adaptation method generating deer images in forest environments using deer image data from public parks, which is relatively easy to collect. Since deer data from public parks have a different data distribution from that of forests, using such data directly as training data could lead to a decline in model performance because object detection models are trained on the assumption that the data distributions of the training and test datasets are consistent. Hence, this study introduces a method to compensate for data shortages using such different distribution data. First, image-to-image translation network is used to translate the style of public park deer images into the style of forests. This strategy alleviates the distribution gap in visual attributes across the two scenes. Then generated images are paired with the original public park deer images and imputed into detection model which is added a loss function called consistency loss. This loss enables the detection model to train to generate bounding boxes at the same position in paired images which have the same label. This study conducted performance comparison experiments between original training, data augmentation methods and the proposed method. Compared with large model and data augmentation methods, the proposed method was able to improve the detection performance of our test dataset of deer. The results confirm that the proposed method has the potential to become an effective training method to detect not only deer but also other wildlife with limited data.

Key Words: Deer Damage, Domain Adaptation, Image-to-image Translation, YOLO

INTRODUCTION

In recent years, economic losses from damage to crops caused by wildlife have become a

serious problem in Japan. According to the Ministry of Agriculture, Forestry and Fisheries in Japan, the total damage exceeded 18.7 billion yen in fiscal year 2024 (MAFF, 2026). To address wildlife damage, it is important to assess the population status of wildlife in forests surrounding farmland and to conduct wide-area culling based on that assessment (MAFF, 2026). With this background, there is a growing need for an automated presence survey system using camera imagery and deep-learning-based object detection models to pinpoint high-priority culling locations by continuously gathering occurrence data. Therefore, this study aims to improve the performance of detection technology targeting wild deer, which cause the most damage to crops in Japan.

High-performance detection models require large and diverse training data. However, a conventional data collection method using fixed-point trail cameras in forests often yields limited images lacking diversity of background (left and middle column of Fig.1), leading to overfitting and reduced generalization performance. Moreover, gathering and labeling diverse field data manually are extremely time-consuming and labor-intensive. To overcome these challenges, this study proposes the domain adaptation method. We focused on deer detection models for forests and utilized deer data from another environment where it is easy to collect diverse data. In this study, we used deer data from Nara Park, a public park on open land in Nara, Japan (right column of Fig.1), as training data for a deer detection model for forests.

The primary objective of this study is to develop a robust wild deer detection model by utilizing data with a different distribution from test data for training. The principal contributions are as follows: (1) Utilizing unpaired image translator CUT (Park et al., 2020) to generate interpolation samples to alleviate the distribution gap in visual attributes between the public park and the forest; and (2) Incorporating consistency loss, designed as domain adaptation penalty function, to YOLO11, a representative CNN-based detection model.

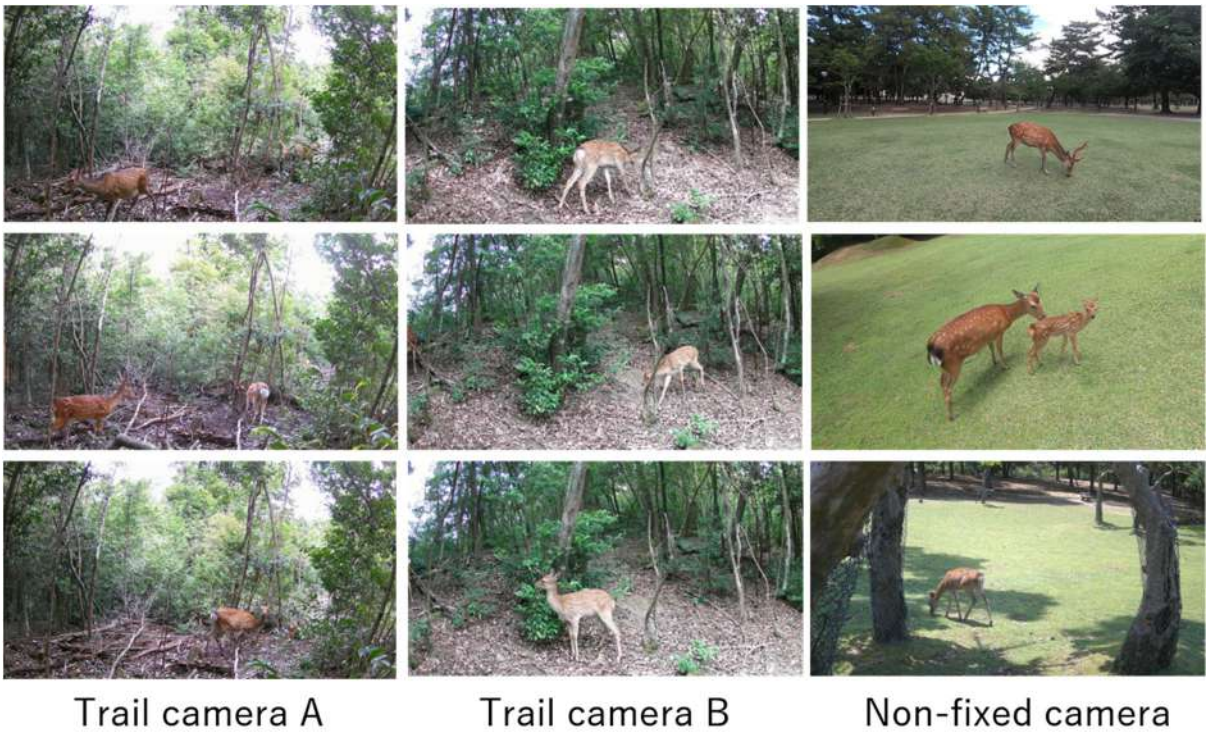

Fig. 1 Example images of deer collected by
(left and middle column): trail cameras installed at Takaragaike Park (Kyoto, Japan).
(right column): a non-fixed camera in Nara Park (Nara, Japan).

MATERIALS AND METHODS

PROPOSED METHOD

Hereinafter, deer data from the forest is called “target domain data” and that from the public park is called “source domain data”. In this study, we used these data only taken during the day.

Interpolation images generation

As the scene layout across domains differ significantly, simply adding source domain data to the training dataset consisting of target domain data yields limited performance gains since object detection models rely on the assumption that the data distributions of the training and test datasets are consistent. Therefore, we introduce interpolation images to alleviate the distribution gap in visual attributes (e.g., color, lighting and texture) across domains and utilize abundant source domain data’s information for detection tasks in target domain environment. Interpolation images are synthetic samples generated by unpaired image translator CUT (Park et al., 2020). Since CUT translates artificial scenes into forested ones without changing location, skeleton and pose of deer, the images share the same label, before and after translation (Fig.2). We trained CUT with 800 images per domain to generate 800 interpolation images.

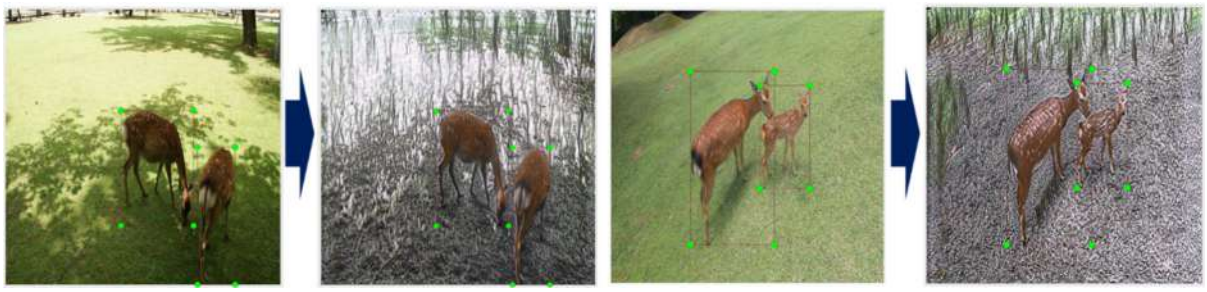

Fig.2 Examples of Interpolated Image Generation.

The additional loss function designed as domain adaptation penalty function

Although the source and interpolated paired images ($\mathbf{I}^S, \mathbf{I}_i^S$) have different scene-level appearances, they have the same label. Ideally, the prediction results of each image of the pair should be consistent. Therefore, to ensure that model’s predictions to each image are as close as possible, this study incorporated the additional loss function into the training of YOLO11. We call it consistency loss $\mathcal{L}_{con}$ designed as follows:

$$\mathcal{L}_{con} = \left|\mathcal{L}_{box}\left(\mathbf{I}_i^S, \mathcal{B}^S\right) - \mathcal{L}_{box}\left(\mathbf{I}^S, \mathcal{B}^S\right)\right| \quad (1)$$

where:

$\mathcal{L}_{box}\left(\mathbf{I}_i^S, \mathcal{B}^S\right)$, $\mathcal{L}_{box}\left(\mathbf{I}^S, \mathcal{B}^S\right)$: Bounding box regression loss computed on $\mathbf{I}_i^S$ / $\mathbf{I}^S$.

$\mathcal{B}^S$ = Ground-truth bounding box coordinates (x, y, w, h) shared across the paired images.

Here, $\mathcal{L}_{box}$ refers to one of the components of the detection loss used in YOLO11’s backpropagation. Based on another domain adaptation study (Zhou et al., 2023), we designed

this loss function. The consistency loss seemingly can allow the detection model to achieve real-world-consistent detection on generated fake images.

Framework of proposed method

The framework of proposed method is shown in Fig.3. First, Interpolation images $\mathbf{I}_i^S$ are generated by CUT and we added them to our dataset consisting of target domain images $\mathbf{I}^T$ and source domain images $\mathbf{I}^S$. Then, we started training of our customized YOLO11 including two forward passes. In a single training step, a regular batch consisting of $\mathbf{I}^T$ and $\mathbf{I}^S$ is inputted into the main forward pass which is the default pass of YOLO11 and calculates default detection loss, while paired images $(\mathbf{I}^S, \mathbf{I}_i^S)$ are inputted into the customized sub forward pass which calculates detection loss of $\mathbf{I}_i^S$ and consistency loss. At the end of a single step, respective losses are combined and the overall loss function is written as:

$$\mathcal{L}_{total} = \mathcal{L}_{det}(\mathbf{I}^T) + \mathcal{L}_{det}(\mathbf{I}^S) + \mathcal{L}_{det}(\mathbf{I}_i^S) + \alpha \cdot \mathcal{L}_{con}$$

Where:

$\mathcal{L}_{det}(\mathbf{I}^T)$, $\mathcal{L}_{det}(\mathbf{I}^S)$, $\mathcal{L}_{det}(\mathbf{I}_i^S)$ = Detection loss of $\mathbf{I}^T$, $\mathbf{I}^S$, $\mathbf{I}_i^S$.

$\alpha =$ A hyper-parameter determined by experience.

The computing environment of this study was conducted on Windows 11 Education version 24H2 with NVIDIA GeForce RTX 4060 Ti GPU and NVIDIA CUDA 13.1.

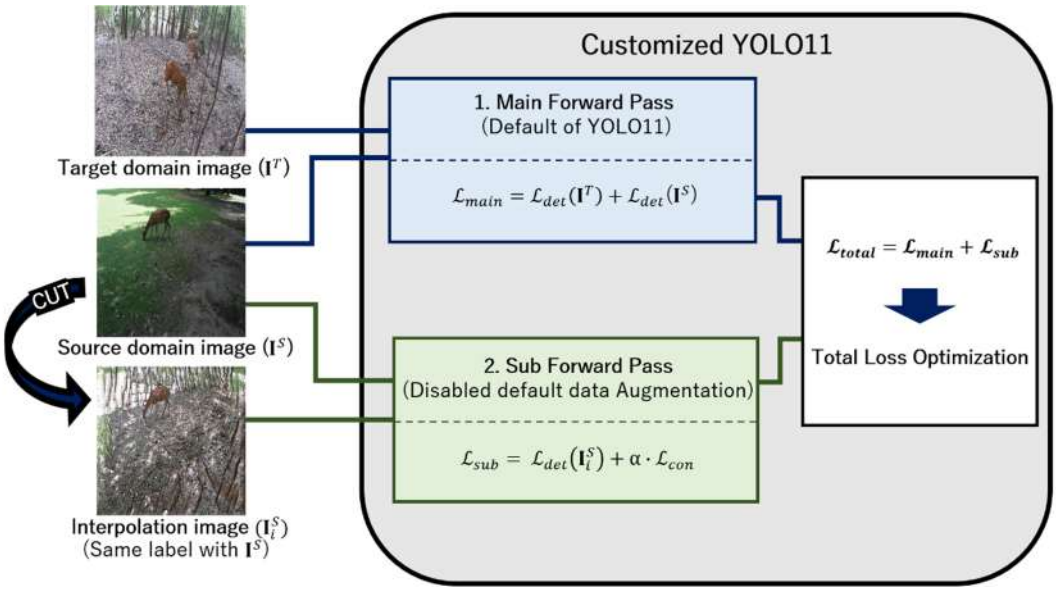

Fig.3 The overview of the proposed method.

RESULTS & DISCUSSION

DETECTION PERFORMANCE

We validated the proposed method by evaluating its detection performance on our test dataset and the results are summarized in Table 1 and 2. Table 1 shows that the proposed method outperforms the baseline and simple data augmentation methods, and Table 2 shows that our

framework, using lightweight model YOLO11s (small), outperforms large models of YOLO11 and Transformer-based RT-DETR (Zhao et al., 2024). These results revealed that proposed method effectively trained the model and offers a robust, cost-effective solution.

Table 1 Comparison of detection experiment results with the baseline and data augmentation methods. Columns $\mathbf{I}^T$, $\mathbf{I}^S$ and $\mathbf{I}_i^S$ contain the number of each domain image. In addition to these training datasets, we used 200 validation data which was not used to train CUT. This table shows the results obtained using YOLO11s trained on each dataset.

Augmentation	$\mathbf{I}^T$	$\mathbf{I}^S$	$\mathbf{I}_i^S$	AP_{50}	AP_{75}	$AP_{50:95}$
Baseline (Target domain data only)	800	0	0	0.910	0.734	0.657
Baseline + Source domain images	800	800	0	0.929	0.763	0.690
Baseline + Interpolation images	800	0	800	0.917	0.744	0.656
Baseline + Both images	800	800	800	0.914	0.723	0.670
Proposed method ($\alpha = 0.32$)	800	800	800	**0.939**	**0.774**	**0.699**

Table 2 Comparison of detection experiment results with large models of YOLO11 and a Transformer-based detection model. Proposed method used YOLO11s. The comparison model was trained on the baseline dataset and validation data shown in Table 1. The smaller the values in columns “Params” and “GFLOPs (Giga Floating-point Operations)”, the lighter the model.

Model	Params (M)	GFLOPs	AP_{50}	AP_{75}	$AP_{50:95}$
YOLO11m (medium)	20.05	68.2	0.925	0.704	0.644
YOLO11l (large)	25.31	87.3	0.915	0.733	0.651
RT-DETR Large	32.81	108.0	0.918	0.758	0.683
Proposed method ($\alpha = 0.32$)	**9.43**	**21.5**	**0.939**	**0.774**	**0.699**

VISUALIZATION OF DETECTION RESULTS

To intuitively show the effectiveness of the proposed method, Fig.4 compares some model’s detection results with the IoU threshold of 0.5. We picked up some results where the baseline model YOLO11s generated a false negative (FN) or a false positive (FP) in leftmost column of Fig.4. RT-DETR tended to produce more FPs in forested backgrounds. On the other hand, the proposed method reduced both the FN and the FP and achieved more accurate detection.

These improvements can be attributed to the synergistic effect of interpolation images and consistency loss. First, generating interpolation images not only alleviates the distribution gap in visual attributes across domains, but also serves as an effective approach to diversifying target domain representations. Since source domain naturally has diverse deer postures, viewing angles and varied lighting conditions, applying image translation using random noise to source domain can generate many kinds of target-domain-like images. As a result, this process enriches the training dataset with comprehensive variations of background environment, illumination conditions and deer’s orientation within target domain style. Second, consistency loss guides the network to leverage these diversified representations effectively. By forcing the detection model to generate bounding boxes at the same position in pseudo interpolation images and real source domain images pairs, the model not only produces prediction that reflect reality, but also learn domain-invariant deer features effectively. Consequently, consistency loss ensures robust detection in unlearned target scenes without data collection or manual labeling.

On the other hand, proposed method also produced FPs and FNs which were not present in baseline models. It is hypothesized that the detector occasionally learned irrelevant noise

patterns in interpolation images as important features to detect deer during training, which adversely affected model optimization. Therefore, analyzing the detector focus during detection and enhancing the quality of image translation remain key priorities for future study.

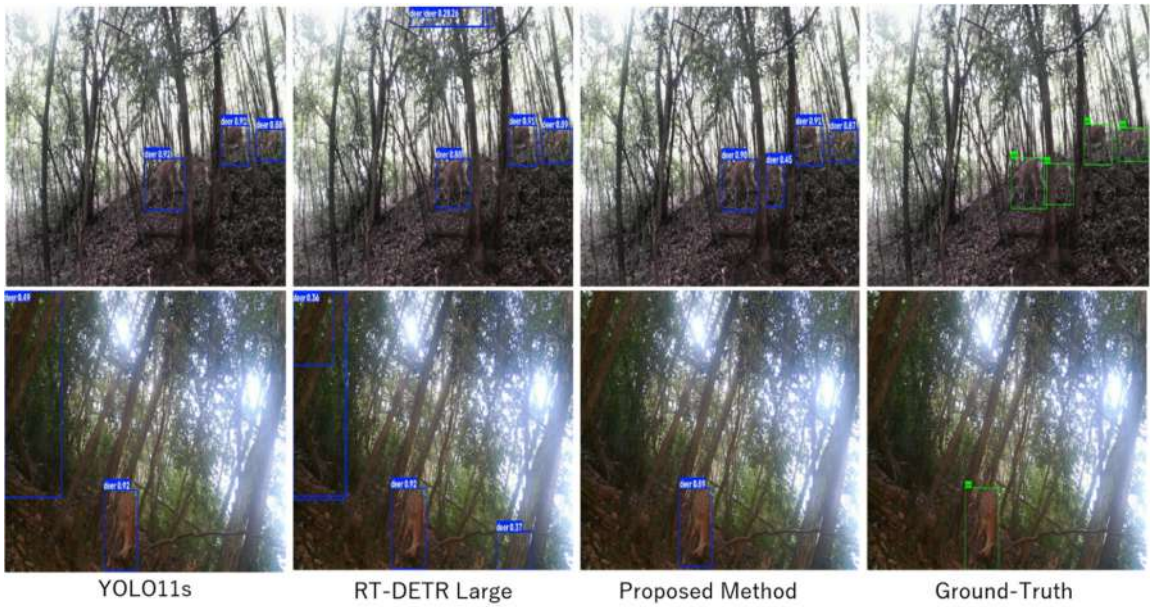

Fig.4 Examples of detection results of some model. The baseline model YOLO11s generated a FN (the first row) or a FP (the second row) in leftmost column.

CONCLUSIONS

In this study, we proposed domain adaptive wild deer detection method using abundant deer images from the public park. Based on the model YOLO11, interpolation images generation and consistency loss function have been introduced to alleviate the distribution gap in visual attributes across domains and correct the prediction shifts of images from different domains but with same labels. The detection experiment's results showed that proposed method using the lightweight model YOLO11s is superior to simple data augmentation method, large models of YOLO and Transformer-based model RT-DETR Large. These results confirm that the proposed method has the potential to become an effective approach to detect not only wild deer but also other wildlife with limited data for reducing wildlife damage to crops in the future.

REFERENCES

MAFF. 2026. Current status and measures for wildlife damage (July 2026 edition). Tokyo, Japan: Ministry of Agriculture, Forestry and Fisheries. Available at: https://www.maff.go.jp/ j/seisan/tyozyu/higai/attach/pdf/240605-117.pdf. Accessed 30 August 2026.

Park, T., A.A. Efros, R. Zhang, and J.-Y Zhu. 2020. Contrastive learning for unpaired image-to-image translation. In: ECCV. Springer, 319–345.

Zhao, Y., W. Lv, S. Xu, J. Wei and G. Wang. 2024. DETRs Beat YOLOs on Real-time Object Detection. In *Proc. IEEE/CVF Conf. on Computer Vision and Pattern Recognition (CVPR)*, 16965-16974. Piscataway, N.J.: IEEE.

Zhou, H., F. Jiang, and H. Lu. 2023. SSDA-YOLO: Semi-supervised domain adaptive YOLO for cross-domain object detection. *Comput. Vis. Image Understand.* 229: 103649.

AI and Information Processing 2 (AI-2)



AI-06

Proceedings of The 12th International Symposium on Machinery and Mechatronics for Agriculture and Biosystems Engineering (ISMAB 2026)
20-24 October 2026, Busan, Republic of Korea

TIME-OF-DAY VARIATION IN UAS-DERIVED CANOPY TEMPERATURE ACROSS IRRIGATION LEVELS IN SOYBEAN

Anjin Chang[1*], Caden Wade[1], Angie Gradiz[1], Kristine Lee[2], Younsuk Dong[1]

[1]Michigan State University, 524 S. Shaw Lane, East Lansing, MI 48824, USA
[2]Mt. Juliet High School, 1875 Golden Bear Gateway, Mt. Juliet, TN 37122
*Corresponding Author-- Email: changanj@msu.edu

Abstract: Timely assessment of crop water status is essential for improving irrigation management and water-use efficiency. UAS-based thermal imaging provides spatially continuous temperature measurements, but its sensitivity to irrigation treatments may vary with observation time and crop type. This study evaluated time-of-day variation in UAS-derived canopy temperature across irrigation levels in soybean and examined its relationship with leaf water potential (LWP).
The study was conducted in soybean and corn fields equipped with a smart sprinkler irrigation system. Treatments included non-irrigated, 50%, 100%, and 150% irrigation levels. Thermal imagery was collected on multiple dates approximately 24–48 hours after irrigation. Four or five UAS missions were conducted between 8:00 AM and 4:00 PM, with concurrent ground-based LWP measurements at three different times. Radiometric thermal images were converted to temperature and processed into georeferenced orthomosaics. Plot boundaries were delineated, and the mean and standard deviation of canopy temperature were extracted for each plot. Treatment differences were evaluated by observation time, and thermal metrics were compared with corresponding LWP measurements.
The analysis investigated when irrigation-level differences were most distinguishable, when canopy temperature was most strongly associated with LWP, and whether within-plot temperature variability provided additional information about crop water status. This study highlights the importance of observation timing in UAS thermal monitoring and provides a basis for selecting crop-specific data acquisition windows for irrigation assessment in soybean.

Key Words: UAS, thermal imaging, canopy temperature, precision irrigation.

AI-07

Proceedings of The 12th International Symposium on Machinery and Mechatronics for Agriculture and Biosystems Engineering (ISMAB 2026)
20-24 October 2026, Busan, Republic of Korea

DRL-BASED FRUIT-APPROACH CONTROL IN A DIGITAL TWIN SIMULATION ENVIRONMENT FOR TOMATO-HARVESTING ROBOTS

Hiroto Nakakubo[1], Hiroshi Fukuoka[1], Masahiro Ohtani[1], Kenichi Iida[1*]

[1]National Institute of Technology (KOSEN), Nara College, 22 Yata-cho, Yamatokoriyama, Nara, 639-1080, Japan
*Corresponding Author-- Voice: +81-743-55-6115, Email: iida@ctrl.nara-k.ac.jp

Abstract: The shortage of agricultural labor caused by a declining and aging workforce has increased the demand for automated harvesting operations. To address this issue, our laboratory has been developing an autonomous tomato-harvesting robot. However, a conventional fixed-path controller often follow predetermined trajectories, which may result in unintended contact with surrounding fruits. This study aims to acquire fruit-approach motions using deep reinforcement learning (DRL) to achieve collision-free and time-efficient trajectory generation. We trained single-fruit approach behavior in a digital twin simulation environment. The proposed DRL controller reduced the average execution time by approximately 46% compared to the conventional controller. These results demonstrate the effectiveness of DRL in generating flexible, time-efficient approach trajectories.

Key Words: Agricultural Robot, Deep Reinforcement Learning, Digital Twin, Simulation, Tomato

INTRODUCTION

The shortage of agricultural labor caused by a declining and aging workforce has become a critical challenge in the agricultural sector (MAFF, 2026). Crop harvesting remains highly dependent on manual labor (MAFF, 2019), resulting in a growing demand for harvesting automation. To address this issue, our laboratory has been developing an autonomous tomato-harvesting robot. However, conventional fruit-approach controllers typically rely on fixed motion trajectories and cannot flexibly adapt to varying fruit distribution. Consequently, the risk of damaging adjacent fruits increases. For obstacle-avoiding harvesting approaches, visual feedback control (Hayashi et al., 2013) and inverse-kinematics-based methods (Van Henten et al., 2010) have been investigated. However, the former struggles to adapt to unstructured fruit-cluster geometries, while the latter lacks real-time performance due to high computational overhead. Conversely, DRL can adapt to diverse environments via trial-and-error (Tang et al., 2025) and ensures high real-time performance, as execution relies only on inference of the trained model. Therefore, this study aims to generate fruit- approach motions using DRL that achieve efficient target-reaching behavior while minimizing contact with surrounding fruits. This paper reports on the learning of single-fruit approach behavior within a digital twin simulation environment and presents the obtained results.

MATERIALS AND METHODS

DRL FORMULATION AND LEARNING SETUP

The robot model used for training was constructed to replicate the degree-of-freedom configuration, link dimensions, and joint range constraints of the physical robot. An overview of the robot model is shown in Fig. 1. In this study, we employed Soft Actor-Critic (SAC) as the DRL algorithm to train the robot for the task of moving the end-effector (EE) to a harvestable position. The system configuration and data flow are shown in Fig. 2. The state space is defined as $\mathcal{S} \subset \mathbb{R}^{14}$, where the state s_t consists of the positions $q \in \mathbb{R}^3$ and velocities $q_v \in \mathbb{R}^3$ of the three prismatic joints, the angles $\theta \in \mathbb{R}^2$ of the two revolute joints, the EE coordinates $p_e \in \mathbb{R}^3$, and the distance vector to the target fruit $d \in \mathbb{R}^3$. The action space is defined as $\mathcal{A} \subset \mathbb{R}^5$, where the action a_t consists of velocity commands for the three prismatic joints $q_{cmd} \in \mathbb{R}^3$ and angular displacement commands for the two revolute joints $\theta_{cmd} \in \mathbb{R}^2$. The reward function r_t was designed to encourage a rapid approach toward the target fruit while avoiding collisions. The distance reward promotes convergence of the EE toward the target fruit. Furthermore, penalties on orientation errors and abrupt control variations encourage the generation of safe and smooth trajectories. The reward function is given in Eq. (1), and the details of each term are described below.

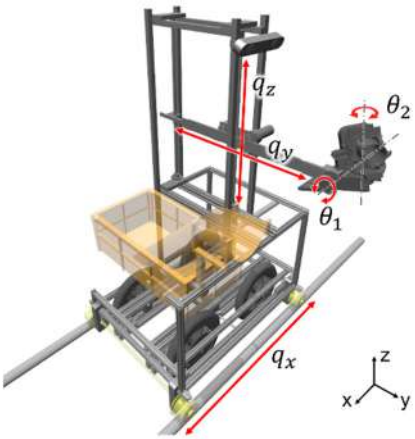

Fig.1 Overview of the robot model

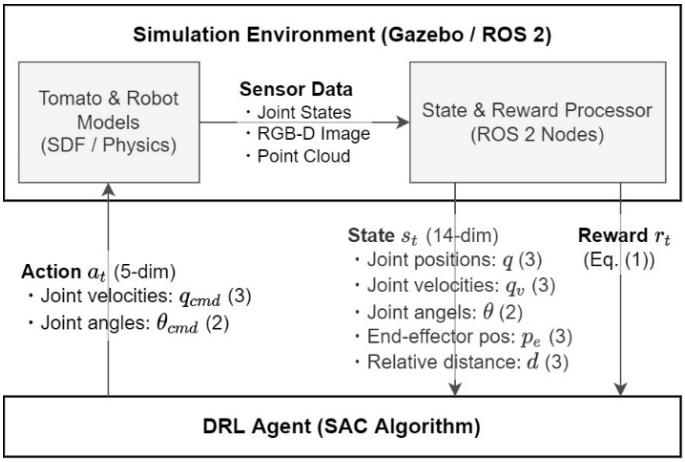

Fig.2 DRL training framework

$$r_t = w_1 r_{dist} + w_2 r_{ang} + w_3 r_{act} + r_{succ} + r_{coll} + r_{step} \quad (1)$$

where:

r_t= Reward at time step t (-)
r_{dist} = Reward for the distance between the EE and the fruit (-)
r_{ang} = Penalty for the angle between the EE orientation vector and the vector to the fruit (-)
r_{act} = Penalty for action changes (-)
r_{succ} = Reward for task success (-)
r_{coll} = Penalty for collisions between the EE and the fruit (-)
r_{step} = Step penalty (-)
w_1, w_2, w_3 = Weight coefficients (-)

COMPARATIVE EVALUATION METHOD

To evaluate the effectiveness of the trained DRL controller, comparative experiments were conducted against a conventional controller in 90 simulation environments with varying fruit

positions. The conventional controller employed a fixed-path strategy in which the EE is sequentially aligned along the x-, z-, and y-axes. In both methods, the approach motion was controlled via ROS 2 Actions. Execution time was defined as the elapsed time between transmission of an action request and the receipt of the corresponding completion response.

RESULTS AND DISCUSSION

DRL RESULT

Figure 3 shows the episode reward as a function of the total number of training steps. During the early stages of training, the reward exhibited considerable fluctuations due to exploratory actions. As training progressed, the reward steadily increased and converged to a stable level after approximately 740,000 training steps, corresponding to approximately 18 h of training. These results indicate that the proposed DRL model successfully learned effective fruit-approach behavior.

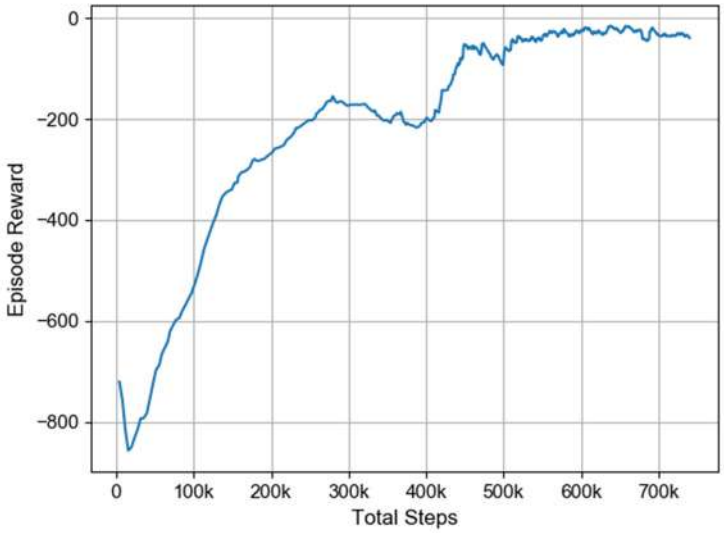

Fig.3 Learning curve of the episode reward as a function of training steps

COMPARATIVE EVALUATION RESULT

Table 1 summarizes the mean, maximum, minimum, and standard deviation of execution time for both methods. Furthermore, both methods achieved a task success rate of 100%. The proposed controller reduced the average execution time from 7.87 s to 4.22 s, corresponding to a 46.4% reduction relative to improvement over the conventional controller. In addition, the standard deviation was reduced from 2.11 s to 1.10 s, indicating more consistent performance. This performance improvement can be attributed to the controller's ability to generate direct and efficient trajectories depending on the target fruit position rather than following a predefined path.

Table 1 Execution time comparison for each method

Method	Mean [s]	Max. [s]	Min. [s]	S.D. [s]
Conventional	7.87	12.3	3.97	2.11
Proposed (DRL)	4.22	6.12	1.94	1.10

CONCLUSIONS

In this study, a DRL-based motion-learning framework was developed within a digital twin simulation environment to realize efficient fruit-approach motions for an autonomous tomato-harvesting robot. Experimental results demonstrated that the proposed controller reduced the average execution time by 46.4% compared with the conventional fixed-path controller while maintaining a 100% task success rate. These findings indicate the effectiveness of DRL in generating flexible and time-efficient fruit-approach trajectories. Future work will focus on incorporating obstacle-avoidance capabilities in cluttered environments and conducting sim-to-real transfer experiments using a physical harvesting robot.

REFERENCES

Hayashi, S., Takeshita, D., Yamamoto, S., Saito, S., Saga, K., and Imou, K. 2013. Obstacle avoidance control of strawberry harvesting robot based on recognition of immature fruits. Shokubutsu Kankyo Kogaku, 25(1), 29-37. https://doi.org/10.2525/shita.25.29

MAFF. 2019. Statistics by Vegetable and Fruit Crop Category (Management Statistics by Commodity). Available at: https://www.maff.go.jp/j/tokei/kouhyou/noukei/hinmoku/#l. Accessed 24 August 2026.

MAFF. 2026. Summary of the Annual Report on Food, Agriculture and Rural Areas in Japan. Available at: https://www.maff.go.jp/j/wpaper/w_maff/r7/pdf/zentaiban.pdf. p. 93. Accessed 24 August 2026.

Tang, C., Abbatematteo, B., Hu, J., Chandra, R., Martín-Martín, R., and Stone, P. 2025. DDp reinforcement learning for robotics: A survey of real-world successes. Proc. AAAI Conf. Artif. Intell., 39(27), 28694-28698. https://doi.org/10.1609/aaai.v39i27.35095

Van Henten, E. J., Schenk, E. J., van Willigenburg, L. G., Meuleman, J., and Barreiro, P. 2010. Collision-free inverse kinematics of the redundant seven-link manipulator used in a cucumber picking robot. Biosystems Engineering, 106(2), 112-124. https://doi.org/10.1016/j.biosystemseng.2010.01.007

AI-08

Proceedings of The 12th International Symposium on Machinery and Mechatronics for Agriculture and Biosystems Engineering (ISMAB 2026)
20-24 October 2026, Busan, Republic of Korea

PREDICTION OF LIGNIN CONTENT IN RICE STRAW USING EXCITATION–EMISSION MATRIX FLUORESCENCE SPECTROSCOPY AND CHEMOMETRIC MODELING

Pornpimol Moolkaew[1], Yoshito Saito[1*], Takuji Miyamoto[2]

[1]Graduate School of Science and Technology, Niigata University, Japan
[2]Sakeology Center, Niigata University, Japan
*Corresponding Author-- Voice: +81-25-262-6343, Email: mailto:ysaito@agr.niigata-u.ac.jp

Abstract: Rice straw is an abundant lignocellulosic residue with considerable potential for biorefinery applications. Its conversion to biofuels depends on the enzymatic hydrolysis of cellulose and hemicellulose into fermentable sugars, whereas lignin restricts enzyme accessibility and can reduce hydrolysis efficiency. Lignin content is therefore an important quality trait for both straw valorization and the evaluation of rice cultivars in breeding and lodging-resistance studies. Conventional lignin analysis is destructive, labor-intensive, and unsuitable for rapid screening. This study evaluated the feasibility of excitation–emission matrix (EEM) fluorescence spectroscopy combined with chemometric regression for predicting lignin content in rice straw. A total of 180 rice plants grown at Niigata University, Japan, were evaluated over two harvest years. In 2024, one cultivar, Koshitanrei, was grown under four fertilizer treatments and sampled at four stages after flowering (0, 10, 20, and 40 days), resulting in 80 samples from 16 growing-condition groups. In 2025, three cultivars (Koshitanrei, Nipponbare, and Tsukisuzuka) were grown under eight fertilizer treatments and sampled at 40 days after flowering, resulting in 100 samples from 24 growing-condition groups. Excised stem segments were measured using an FP-8350 spectrophotometer (JASCO, Japan) over excitation wavelengths of 270–735 nm and emission wavelengths of 280–750 nm at 5.0 nm intervals. Two measurement positions per plant were averaged to obtain one EEM matrix per sample. Lignin content was determined using the thioglycolic acid assay as the reference method. After denoising and unfolding the EEM data into row vectors, lignin prediction was performed using partial least-squares regression (PLSR), principal component analysis coupled with support vector regression (PCA–SVR), and Elastic Net regression. Model performance was assessed using repeated, group-aware nested cross-validation. Plants from the same growing-condition group were kept within the same fold to reduce information leakage, and model performance was summarized using the prediction coefficient of determination (R^2p), root mean square error of prediction (RMSEP), and residual prediction deviation (RPD).
Elastic Net provided the best predictive performance, with an R^2p of 0.709 ± 0.022, RMSEP of 1.730 ± 0.065, and RPD of 1.860 ± 0.070. PLSR yielded an R^2p of 0.659 ± 0.029, RMSEP of 1.872 ± 0.079, and RPD of 1.724 ± 0.071, whereas PCA–SVR yielded an R^2p of 0.641 ± 0.042, RMSEP of 1.920 ± 0.112, and RPD of 1.681 ± 0.097. These results indicate that EEM fluorescence spectroscopy, particularly when combined with Elastic Net regression, has potential for rapid estimation of lignin content in rice straw. However, the prediction performance was moderate, indicating that additional samples, independent external validation, and further optimization of EEM preprocessing may be needed before routine application.

Key Words: rice straw; lignin; excitation–emission matrix fluorescence; chemometrics; Elastic Net

AI-09

Proceedings of The 12th International Symposium on Machinery and Mechatronics for Agriculture and Biosystems Engineering (ISMAB 2026)
20-24 October 2026, Busan, Republic of Korea

ONE BACKBONE IS ENOUGH: UNIFYING RGB–NIR SEMANTIC AND INSTANCE SEGMENTATION FOR EFFICIENT POTATO DEFECT INSPECTION

Aulia Rizkiana[1], Byoung-Kwan Cho[1,2*]

[1]Department of Smart Agricultural System, Chungnam National University, Daejeon, Korea
[2]Department of Biosystems Machinery Engineering, Chungnam National University, Daejeon, Korea
*Corresponding Author-- Voice: +82-42-821-6715, Email: chobk@cnu.ac.kr

Abstract: Automated potato inspection must identify defects with different appearances while processing samples quickly enough for practical grading systems. This study examines whether one unified model can replace three defect-specific models for detecting surface blemishes, greening, and holes. The unified model receives aligned RGB, NIR1, and NIR2 images as a five-channel input. A shared EfficientNet-B2 feature pyramid backbone supports semantic segmentation of surface blemishes and greening and instance segmentation of holes. We compared this design with three dedicated models trained separately for the same tasks. The experiments used a selected subset of 6,000 potato images drawn from a larger collection acquired over 21 capture sessions. Five-fold cross-validation was grouped by capture session to prevent closely related images from appearing in both training and validation data. All models used the same data partitions, image resolution, augmentation, initialization, and number of parameter updates.

The dedicated pipeline achieved Dice scores of 0.906 for surface blemishes and 0.841 for greening, with a hole mask AP of 0.519. The best unified configuration achieved corresponding scores of 0.889, 0.809, and 0.491, retaining 96.3% of the dedicated pipeline's combined task performance. However, the unified model required only 28.45 million parameters, compared with 49.48 million for the three dedicated models. It reduced median inference time from 70.01 to 30.60 ms per image and increased throughput from 14.28 to 32.68 images/s. An RGB-only version produced a lower overall multi-task score, showing that the near-infrared channels contributed useful information. These results show that a shared RGB–NIR model can substantially improve processing efficiency while preserving most of the task performance achieved by separate models.

Key Words: Potato defect inspection; RGB–NIR imaging; multi-task learning; shared-backbone network; agricultural machine vision.

Acknowledgement: This work was supported by Korea Institute of Planning and Evaluation for Technology in Food, Agriculture, Forestry (IPET) through (Smart Agri Products Flow Storage Technology Development Program), funded by Ministry of Agriculture, Food and Rural Affairs (MAFRA) (No.322051052HD020).

AI-10

Proceedings of The 12th International Symposium on Machinery and Mechatronics for Agriculture and Biosystems Engineering (ISMAB 2026)
20-24 October 2026, Busan, Republic of Korea

LLM-ASSISTED WEB DATA INTEGRATION FOR CABBAGE SEEDLING SUPPLY, AGROMETEOROLOGICAL LAGS, AND WHOLESALE PRICE-RISK WARNING

Po-Cheng Shih[1], Po-Yu Ho[2], Yi-Chih Chiu[3*]

[1]Department of Biomechatronics Engineering, National Taiwan University, Taiwan
[2]BigObject Inc., Taiwan
[3] Department of Biomechatronic Engineering, National Ilan University, Taiwan
* Corresponding author. Tel.: +886 3 9317804. E-mail: yichiu@niu.edu.tw

Abstract: This study developed a time-series framework linking cabbage seedling supply, agrometeorological conditions, wholesale volume, and price risk in Taiwan, while evaluating an LLM-supported interface for cross-source data retrieval. Data for cabbage (*Brassica oleracea* var. *capitata*) cv. Early Autumn during 2021-2024 combined ten-day seedling-supply and production-warning records, daily temperature and solar radiation, and transactions from the Xiluo, Taipei First, and Taipei Second wholesale markets. The BigObject database and Aralia platform organized the data and supported natural-language queries and CSV or Excel export. Market volumes were summed and prices were volume-weighted. Annual January-April price distributions defined low-price days below Q25 and extreme events below Q10. Production-weighted weather observations from Yunlin and Changhua were used to calculate growing degree days with a 5 °C base temperature. Seedling supply, accumulated GDD, and accumulated solar radiation were evaluated at daily lags of 65-100 days, followed by principal component analysis and standardized multiple regression. The three markets showed strong price synchronization ($r = 0.899$-0.963). Red and purple warnings captured 89.8% of Q25 low-price days and 91.7% of Q10 extreme events, although precision was 44.5% and 18.5%, respectively. Seedling supply had its strongest association with later integrated market volume at an 84-day lag ($r = 0.496$, $p < 0.001$), with a stable interval of 83-87 days. At lag 84, PC1 explained 60.2% of variance and correlated with market volume ($r = 0.626$, $p < 0.001$). Integrated volume and weighted price were strongly negatively correlated ($r = -0.865$, $p < 0.001$). The results support a practical warning pathway from increased seedling supply to greater wholesale supply approximately 12 weeks later and a higher risk of price decline.

Key Words: Cabbage, Seedling Supply, Lag Analysis, Price Warning, Large Language Model

INTRODUCTION

Taiwan has accumulated substantial agricultural data through the joint efforts of agricultural producers, academic institutions, and government agencies. These data provide opportunities for researchers to identify meaningful patterns and address practical agricultural problems.

Before the data can be analyzed, however, several challenges must be addressed, including differences in measurement units, temporal resolution, geographic coverage, and data formats. For example, cabbage seedling supply is reported on a ten-day basis, whereas meteorological observations and wholesale market transactions are generally recorded daily. Although many government datasets are publicly accessible, identifying, retrieving, and integrating data from different platforms remain time-consuming tasks.

This study was conducted in collaboration with BigObject Inc. and the National Center for High-Performance Computing (NCHC). Within this collaborative framework, the BigObject® time-series database and the Aralia® data platform were used for data organization, integration, and cross-source exploration (Aralia, 2026). Aralia also integrates large language models (LLMs), allowing users to query databases through a question-and-answer interface and export the requested data in downloadable formats. This function can reduce the time required for data retrieval and help users identify relevant datasets and variables. In this study, the LLM-based interface was used to assist data querying and retrieval, while variable definitions, statistical calculations, and interpretation of the results were verified by the researchers.

In Taiwan, winter–spring lowland production of cabbage (*Brassica oleracea* var. *capitata*) is concentrated in areas such as Yunlin and Changhua. Similar planting schedules may result in synchronized harvests, excessive market supply, and substantial price declines. To support growers' planting decisions, the Agriculture and Food Agency (AFA) publishes ten-day information on cabbage seedling supply, expected harvest periods, and production and marketing warning signals(AFA, 2026). However, the relationships among these official indicators, subsequent wholesale supply, and low-price events require further quantitative evaluation.

Therefore, this study aimed to: (1) construct representative price and trading-volume indicators by integrating data from three major wholesale markets; (2) evaluate the relationship between official warning signals and subsequent low-price and extreme-low-price events; and (3) identify the time lag at which seedling supply, cumulative growing degree days, and cumulative solar radiation best correspond to subsequent wholesale trading volume. Through this framework, the study examined whether integrated open data and an LLM-assisted data interface could provide a quantitative basis for cabbage supply monitoring and price-risk warning..

MATERIALS AND METHODS

Data acquisition and platform integration

The Aralia® data platform was used for cross-source agricultural data integration, retrieval, and downloading. Through its web interface, users selected data sources, time ranges, and variables for cabbage seedling supply, meteorological observations, and wholesale transactions. An LLM-based question-and-answer interface allowed the researchers to describe data requirements in natural language and locate relevant datasets. After the datasets and temporal ranges were confirmed, records were exported in CSV or Excel format for data cleaning, temporal synchronization, lag analysis, and statistical analysis. Figure 1 shows the query and data-export interfaces.

(a)

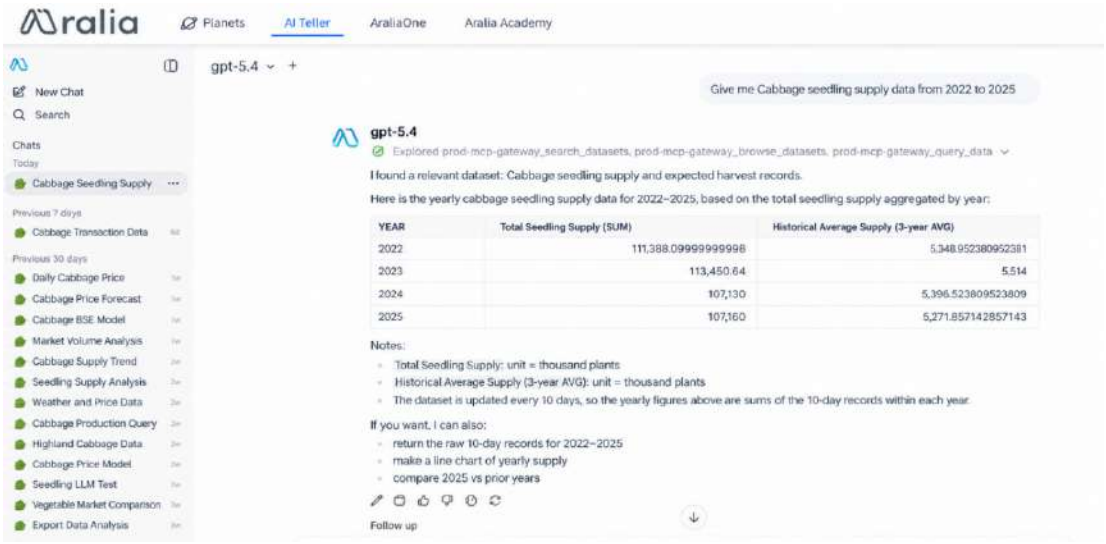

(b)



Fig. 1. Web-based data access in Aralia®: (a) LLM-based question-and-answer interface for dataset exploration and retrieval; (b) data-selection and export interface.

Data integration and market indicators

Data from 2021-2024 included ten-day seedling-supply and expected-harvest records, daily weather observations, and transactions from the Xiluo, Taipei First, and Taipei Second Fruit and Vegetable Wholesale Markets, which are among Taiwan's highest-volume markets for cabbage. A day without a market record was treated as a non-trading day rather than as zero volume. For each common trading day t, integrated market volume (Q_t^*) and volume-weighted price (P_t^W) were calculated as follows:

$$Q_t^* = \sum_{i=1}^{3} Q_{i,t} \tag{1}$$

$$P_t^W = \frac{\sum_{i=1}^{3} P_{i,t} Q_{i,t}}{\sum_{i=1}^{3} Q_{i,t}} \tag{2}$$

where:

Q_t^* = integrated trading volume of the three wholesale markets on trading day t (kg);
P_t^w = volume-weighted average price of the three wholesale markets on day t (NTD kg^{-1});
$P_{i,t}$ = average price in market i on day t (NTD kg^{-1});
$Q_{i,t}$ = trading volume in market i on day t (kg);
i = market index, where 1 is Xiluo, 2 is Taipei First, and 3 is Taipei Second; and
t = trading day.

Warning validation and low-price definition

The formal warning validation used January-April 2022-2024, when both warning coverage and market data were complete. Each trading day inherited the official warning color of its expected-harvest ten-day period. Feuz et al. (2025) classified the bottom 25th percentile of an average-price series as a depressed-price period. Following this percentile-based concept while retaining annual spring price levels, low-price events were defined as $P_t^w < Q25$ and extreme price-crash events as $P_t^w < Q10$. Red and purple signals were treated as positive risk warnings. Precision, recall, F1-score, accuracy, and specificity were calculated daily.

Weather accumulation and lag analysis

Lowland weather was represented by the NTU Yunlin Campus station and the Central Weather Administration Tianzhong station in Changhua. Based on the two-county production totals used in this study, Yunlin and Changhua were weighted 69.7% and 30.3%, respectively. Cross-station correlations were r = 0.997 for mean temperature and r = 0.949 for solar radiation. Ten-day seedling totals were distributed evenly across the actual number of calendar days in each period.Moon and Ku (2022) studied *B. oleracea* var. *capitata* and calculated accumulated GDD using a 5 °C base temperature. Accumulated daily GDD was computed as follows:

$$CGDD_t = \sum_{i=0}^{t-1} (T_{avg,t-i} - T_b) \quad (3)$$

where:

$CGDD_t$ = accumulated growing degree days over t days (°C·day);
T_b = base temperature (°C);
$T_{avg,t-i}$ = average temperature on the i-th day before harvest (°C).

For each market day n and lag L = 65, 66, ..., 100 days, the possible seedling date was n-L. GDD and global solar radiation were accumulated from the possible seedling date through the day before market trading. Pearson correlations were calculated for seedling supply, accumulated GDD, accumulated solar radiation, and Q_t^*. Standardized multiple regression compared partial effects. The representative lag maximized the absolute seedling-supply correlation with later Q_t^*; the core stable interval comprised consecutive lags retaining at least 95% of the peak correlation. For PCA, seedling supply, accumulated GDD, and accumulated solar radiation were Z-standardized; Q_t^* was retained as an external response and correlated with PC scores.

RESULTS & DISCUSSION

Market integration and warning performance

Across 964 common trading days, price correlations among the three markets were 0.899-

0.963 (all $p < 0.001$), while volume correlations were 0.651-0.929 (all $p < 0.001$). Price synchronization was stronger than volume synchronization, supporting a summed-volume indicator and a volume-weighted price rather than a simple market average. Mean integrated volume was approximately 339,646 kg d^{-1}, and mean integrated price was NT$23.10 kg^{-1}.
Within 234 formal spring validation days, Q25 low-price rates were 0.0%, 5.6%, 44.2%, and 46.7% for green, yellow, red, and purple signals, respectively; Q10 extreme-event rates were 0.0%, 1.9%, 15.4%, and 40.0%. Combining red and purple yielded recall of 89.8% for Q25 and 91.7% for Q10, but precision was 44.5% and 18.5%. The official warning system therefore functioned as a high-sensitivity risk-screening tool rather than a deterministic price forecast.

Lag identification and environmental structure

The seedling-supply correlation with later Q_t^* increased from r = 0.342 at 65 days to a maximum of r = 0.496 at 84 days (n = 511, $p < 0.001$), then declined to r = 0.328 at 100 days. The 95%-of-peak criterion defined 83-87 days as the core stable interval. Annual best lags were 81, 78, 86, and 97 days for 2021-2024, respectively, and Fisher-z aggregation across years again selected 84 days. The lag profile is shown in Fig. 2.

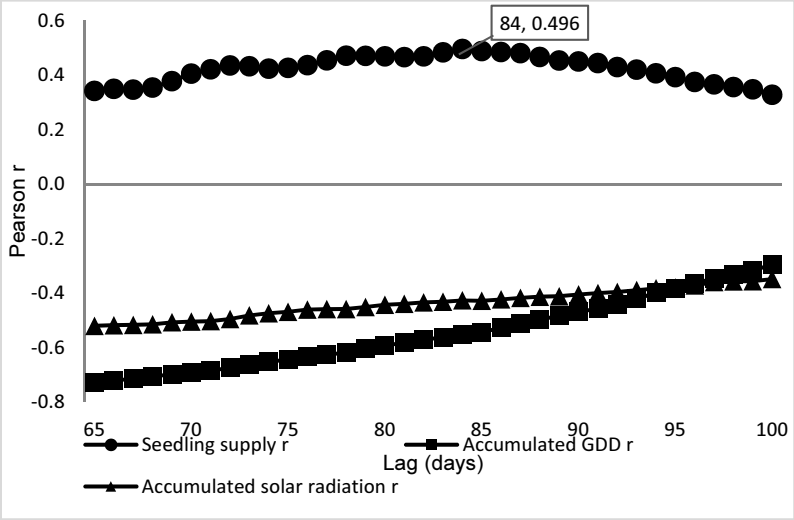

Fig. 2. Pearson correlations of seedling supply, accumulated GDD, and accumulated solar radiation with integrated market volume across lag periods.

Accumulated GDD and solar radiation were negatively correlated with Q_t^*, particularly at shorter lags (at 65 days: rGDD = -0.726 and rSolar = -0.520). These signs should not be interpreted as direct negative physiological effects on individual yield; instead, they mainly represent the strong seasonality of lowland cabbage, for which larger market supply occurs during the cooler winter-spring production season.
At lag 84, PC1 and PC2 explained 60.2% and 26.2% of total variance, respectively (86.3% cumulative). PC1 loadings were +0.500 for seedling supply, -0.574 for GDD, and -0.648 for accumulated solar radiation, and PC1 scores correlated with Q_t^* ($r = 0.626$, $p < 0.001$). However, loading magnitude did not represent an independent market effect. Standardized multiple-regression coefficients at lag 84 were +0.387 for seedling supply ($p < 0.001$), -0.457 for GDD ($p < 0.001$), and -0.015 for solar radiation ($p = 0.714$), with adjusted $R^2 = 0.447$. Solar radiation therefore contributed to the common seasonal structure captured by PCA but added little independent information after seedling supply and accumulated heat were controlled.

Linking seedling supply to price risk

Across 964 days, volume and price were negatively correlated ($r = -0.865$, $p < 0.001$), including the spring period ($r = -0.614$, $p < 0.001$). Q25 and Q10 days averaged 499,664 and 501,708 kg d^{-1}, versus 438,422 and 448,396 kg d^{-1} for comparison days (both $p < 0.001$). Lag-84 seedling supply correlated negatively with price ($r = -0.433$, $p < 0.001$). Thus, greater seedling supply preceded greater volume and lower prices by about 84 days.

CONCLUSIONS

This study established a time-series framework linking cabbage seedling supply, weather conditions, wholesale volume, and price risk in Taiwan. The BigObject® database and Aralia® platform provided an integrated environment for agricultural data from different sources. The LLM-based question-and-answer interface made dataset searching more direct, while CSV and Excel export reduced the time required for data preparation and analysis.

Seedling supply was most strongly associated with wholesale volume after about 84 days, with a stable interval of 83-87 days. PCA identified a clear seasonal structure among seedling supply, GDD, and solar radiation, while regression showed that seedling supply and GDD provided more independent information. The practical warning pathway was increased seedling supply, followed by increased market supply about 12 weeks later, then lower prices and higher price risk.

Future accuracy could be improved by adding detailed production-origin information, classifying market transactions by production area, and incorporating official regional data on refrigerated or frozen storage, imports, and exports. High-elevation summer-autumn production, rainfall, extreme weather, and time-series cross-validation should also be included.

ACKNOWLEDGEMENTS

The authors sincerely thank Dr. Wenwey Hseush, Co-Founder of BigObject Inc., for supporting data integration and the application of the Aralia® platform. We also thank Mr. Hsieh, owner of Bohua Vegetable Nursery, and Handsome Farmer Agricultural Produce for sharing practical knowledge of cabbage seedling production, cultivation, and agricultural operations. Their field experience provided valuable practical perspectives for this study.

REFERENCES

Agriculture and Food Agency (AFA). 2026. Bulk vegetable seedling-supply and production-warning information. Taipei, Taiwan: Ministry of Agriculture. Available at: https://www.afa.gov.tw/cht/index.php?article_id=25545&code=list&flag=detail&ids=3551.

Aralia. 2026. Aralia AI-ready data ecosystem and data services. Available at: https://one.araliadata.io/.

Feuz, R., C. Wilkins, R. Larsen, and R. Bosworth. 2025. Analyzing US alfalfa hay market dynamics: Effects of quality grade on premiums and discounts. Journal of Agricultural and Applied Economics 57: 276-291.

Moon, H.-W., and K.-M. Ku. 2022. Impact of an agriphotovoltaic system on metabolites and the sensorial quality of cabbage (Brassica oleracea var. capitata) and its high-temperature-extracted juice. Foods 11: 498.

AI and Information Processing 3 (AI-3)



AI-11

Proceedings of The 12th International Symposium on Machinery and Mechatronics for Agriculture and Biosystems Engineering (ISMAB 2026)
20-24 October 2026, Busan, Republic of Korea

BERRYCOMP: JOINT GEOMETRY AND APPEARANCE RECONSTRUCTION OF OCCLUDED STRAWBERRIES

Minhyeok Jang[1,2], Su-Min Chin[1,2], Dae-Hyun Jung[1,2*]

[1]Department of Smart Farm Science, Kyung Hee University, Yongin 17104, Republic of Korea
[2]BK21 Interdisciplinary Program in IT-Bio Convergence System, Kyung Hee University, Yongin 17104, Republic of Korea
*Corresponding Author-- Voice: +82-31-201-2657, Email: daehyun@khu.ac.kr

Abstract: Occlusion limits the reconstruction of strawberry geometry and surface appearance from visual observations. This study proposes BerryComp, a neural architecture that reconstructs missing geometry and appearance while preserving observed details. Depth Anything 3 was used to estimate depth maps from RGB images, which were combined with instance segmentation masks to generate colored three-dimensional representations of individual strawberries. Synthetic concavity was introduced at deformation ratios of 3%, 4%, and 5% relative to a reference object extent, and six occlusion patterns were applied to generate paired incomplete and reference samples. The dataset comprised 2,571 strawberry instances, divided into 1,912 training, 244 validation, and 415 test instances. BerryComp integrates local feature extraction, global attention, and a learnable query decoder to predict missing coordinates and RGB values. Whole-shape evaluation compared BerryComp with PCN, TopNet, PoinTr, and AdaPoinTr on 2,490 test pairs using the same 8,192-point references. For evaluation, BerryComp combined 6,144 sampled observed points with 2,048 generated points. It achieved a density-aware Chamfer distance of 0.3697, a symmetric mean nearest-neighbor Chamfer distance of 0.006062, and F-scores of 76.44% and 95.04% at normalized distance thresholds of 0.01 and 0.02, respectively, outperforming all four comparison models on these geometric metrics. Whole-shape appearance evaluation of BerryComp yielded an RGB peak signal-to-noise ratio of 22.41 dB and a CIEDE2000 color difference of 3.10 using nearest-neighbor geometric correspondence. These results support selective reconstruction as an effective approach to recovering occluded strawberry geometry and appearance while retaining observed details under the evaluated synthetic conditions.

Key Words: Strawberry, Geometry and Appearance, 3D Reconstruction, Occlusion Completion, Deep learning

INTRODUCTION

Three-dimensional information on fruit geometry and surface appearance can support agricultural applications such as phenotyping, external quality assessment, and robotic harvesting (He et al., 2017; Ge et al., 2020; Xiong et al., 2020). For strawberries, shape and

color provide complementary descriptors of external fruit traits (He et al., 2017). However, leaves, stems, neighboring fruits, and limited viewing angles can obscure portions of the fruit surface, resulting in incomplete observations that complicate fruit localization and reconstruction (Ge et al., 2020).

Recent depth estimation methods, including Depth Anything 3, enable image-based estimation of scene geometry (Lin et al., 2026). When combined with instance masks and RGB images, predicted depth maps can be back-projected to produce object-specific colored point clouds containing XYZ coordinates and RGB values. However, back-projecting a single depth map represents the visible surfaces and does not itself provide a complete reconstruction of hidden regions. Point cloud completion methods, including PCN (Yuan et al., 2018), TopNet (Tchapmi et al., 2019), PoinTr (Yu et al., 2021), and AdaPoinTr (Yu et al., 2023), address incomplete geometry through learned shape reconstruction. These methods provide relevant geometric baselines, while joint reconstruction of missing coordinates and RGB values remains an additional requirement for the colored strawberry representations considered here.

For this application, the reconstruction task therefore includes both geometry and appearance. Preserving reliable observations is also desirable because their coordinates and colors are already available. This motivates a selective reconstruction strategy that retains observed data while predicting the missing geometric and color information.

To address this problem, we propose BerryComp, a neural architecture for joint geometry and appearance reconstruction of occluded strawberries. BerryComp combines local feature extraction, global attention, and a learnable query decoder to predict missing XYZ coordinates and RGB values, which are integrated with the observed point cloud. To examine reconstruction under controlled geometric and occlusion variation, the dataset incorporated synthetic concavity deformation ratios of 3%, 4%, and 5% and six occlusion patterns. BerryComp was compared with PCN, TopNet, PoinTr, and AdaPoinTr using density-aware Chamfer distance (Wu et al., 2021), Chamfer distance, and F-score. Appearance reconstruction was evaluated using RGB peak signal-to-noise ratio (PSNR) and CIEDE2000 color difference, ΔE_{00} (Sharma et al., 2005).

The objective of this study was to develop and evaluate a framework for reconstructing missing geometry and appearance in image-derived strawberry representations while preserving observed details.

MATERIALS AND METHODS

Dataset Preparation and Occlusion Simulation

RGB images and strawberry instance masks from the StrawDI dataset were used to construct individual three-dimensional fruit representations. Depth maps were estimated from the RGB images using the DA3METRIC-LARGE variant of Depth Anything 3 and subsequently back-projected into three-dimensional coordinates. Instance segmentation masks were applied to isolate individual strawberries, and each three-dimensional point retained the RGB values of its corresponding image pixel. The fruit representations generated before synthetic

occlusion were used as reference data for reconstruction.

Before synthetic occlusion, depth maps and point clouds were preprocessed using mask erosion, local median filtering, robust depth rejection, and statistical outlier removal to reduce boundary artifacts and isolated noise.

Only intact and fully visible strawberry instances were selected from the StrawDI dataset and used as pseudo-ground-truth references for reconstruction. The dataset consisted of 2,571 strawberry instances, including 1,912 instances for training, 244 for validation, and 415 for testing. Six synthetic occlusion patterns were then applied to each intact fruit: line, ellipse, combined line and ellipse, triangle, double triangle, and vertical ellipse, as illustrated in Fig. 1.

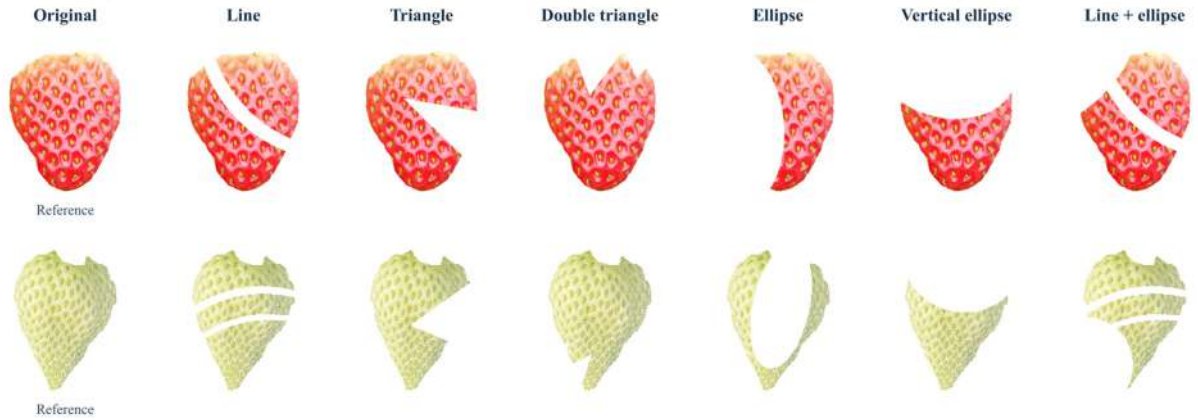

Fig. 1 Examples of synthetic occlusion patterns applied to intact strawberry instances.

Consequently, 11,472 training pairs, 1,464 validation pairs, and 2,490 test pairs were generated, with the intact fruit representation serving as the reconstruction reference and its synthetically occluded counterpart serving as the model input. All occlusion variants derived from the same strawberry instance were retained within the same data split to prevent information leakage between the training, validation, and test sets.

To introduce controlled variation in fruit surface geometry, each strawberry instance was assigned a deformation. The deformation was applied to the depth coordinate using a quadratic function of vertical position. The deformation magnitude was scaled according to the diagonal length of the fruit XY extent. The same deformation was applied to both the pseudo-ground-truth reference point cloud and its occluded variants.

Analysis of Concavity of Dataset

The geometric characteristics of the dataset were assessed using YZ profiles extracted from all 2,571 reference strawberry instances. Occluded variants were excluded, and each reference instance was analyzed once. The YZ plane was used to characterize longitudinal depth variation, where Y represents the vertical image direction and Z represents depth relative to the camera.

For each instance, a camera-facing depth profile was extracted along the vertical direction and normalized by the robust XY extent of the fruit. A quadratic function was fitted to the normalized profile, and the coefficient of determination R^2 was used to quantify agreement

with the overall quadratic shape. Relative roughness was additionally calculated from the residual variation between the extracted and smoothed profiles, normalized by the profile depth range. Both descriptors were calculated independently for each instance and summarized using medians and interquartile ranges. Higher R^2 indicated greater consistency with a quadratic longitudinal profile, whereas lower relative roughness indicated smaller local surface fluctuations.

Input Representation and Normalization

Each input point was represented by three-dimensional XYZ coordinates and corresponding RGB values. The coordinate system was normalized using the centroid of the observed points. The maximum input capacity was set to 12,288 points. For point clouds containing fewer points, padding was applied while retaining the valid point length for masking during network processing. During training, 2,048 points were sampled from the removed region and used as reconstruction targets. Data augmentation included random rotations, reflections, geometric scaling, coordinate perturbation, and RGB perturbation of the input points.

BerryComp Architecture

BerryComp was designed to reconstruct missing geometry and color information from occluded strawberry point clouds while preserving the observed regions. As illustrated in Fig. 2, the architecture consists of anchor sampling and local feature aggregation, global Transformer encoding, and query-based shape completion decoding. Farthest point sampling (FPS) selects 256 anchor points from the input XYZ–RGB point cloud, and local neighborhoods are constructed around each anchor.

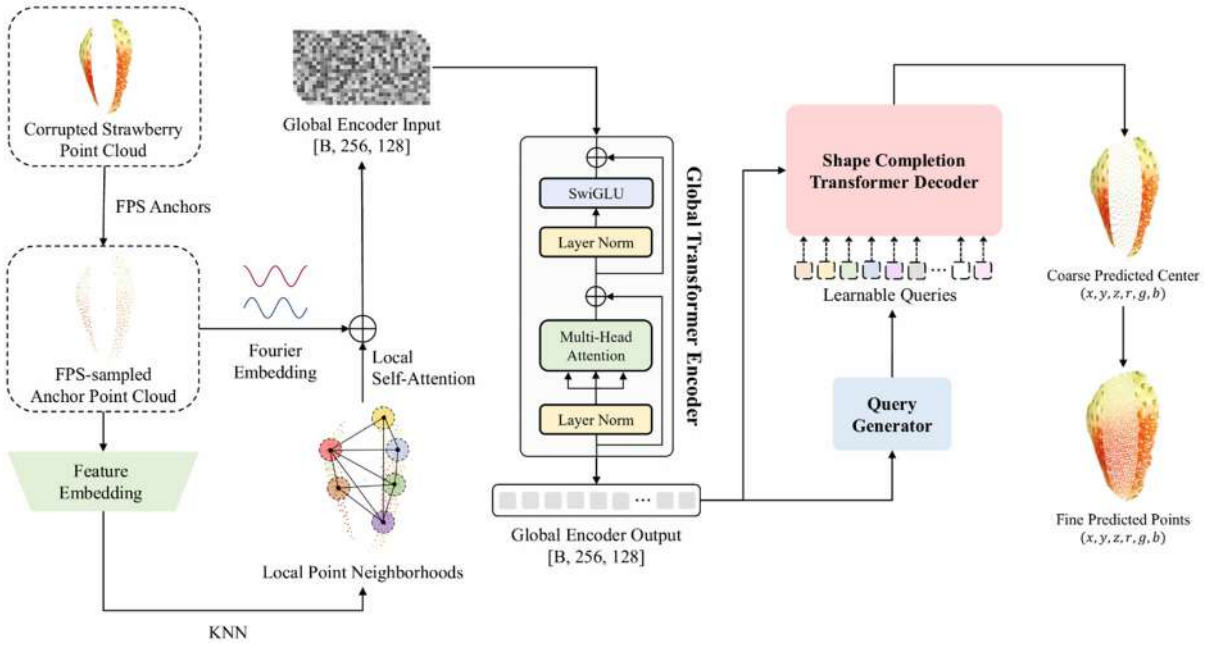

Fig. 2 Overview of the BerryComp architecture for joint geometry and appearance reconstruction of occluded strawberries.

The XYZ coordinates and RGB values are projected into 128-dimensional features, and local self-attention aggregates geometric and appearance information from up to 32 nearest neighbors. Fourier positional encoding is used to represent local and spatial relationships.

The resulting 256 anchor tokens are then processed by six Global Transformer Encoder blocks to capture long-range dependencies across the fruit surface. The decoder uses 256 learnable queries and four Transformer decoder blocks with self-attention and cross-attention.

Each query predicts a coarse XYZ–RGB representation of a missing region, which is subsequently expanded into eight fine points using learned geometric and color offsets. This produces a total of 2,048 reconstructed points with associated RGB values. The reconstructed points are combined with the original observed point cloud so that the measured coordinates and colors of visible regions are preserved. An auxiliary head estimates the missing-point fraction during training, although all 2,048 generated points were retained for the reported evaluation. BerryComp contains 2,199,379 trainable parameters.

Loss Function and Training

Supervision was applied specifically to the missing regions of the point cloud. The training objective combined density-aware Chamfer distance (DCD), bidirectional geometric reconstruction losses, RGB reconstruction loss, voxel occupancy loss, and missing-fraction regression loss. The respective loss weights for DCD, coverage, prediction, RGB, voxel occupancy, and missing-fraction estimation were 0.1, 1.0, 1.0, 0.2, 0.2, and 2.0. DCD was calculated using a distance sensitivity parameter of 100 and a density exponent of 1, while voxel occupancy was evaluated at a resolution of 128^3. BerryComp was trained for 300 epochs using AdamW with a batch size of 128 and an initial learning rate of 0.001.

Whole-Shape and Color Reconstruction Evaluation

Geometric performance was compared with PCN, TopNet, PoinTr, and AdaPoinTr using the same 2,490 test pairs and an identical 8,192-point reference. BerryComp combined 6,144 observed points with 2,048 generated points, while each baseline also produced an 8,192-point output. Geometry was evaluated using DCD, symmetric Chamfer distance (CD), and F-score at thresholds of 0.01 and 0.02. Appearance reconstruction was compared with a nearest-neighbor color-copy baseline using the same BerryComp output geometry. For the baseline, each generated point received the RGB value of its nearest observed input point, while retained observed points preserved their original colors. RGB PSNR and CIEDE2000 color difference ΔE_{00} were calculated after nearest-neighbor matching between the 8,192-point output and reference point clouds.

RESULTS & DISCUSSION

Geometric Characteristics of the Dataset

The YZ profile distributions of the 2,571 concavity-augmented strawberry references are presented in Fig. 3. The quadratic-fit R^2 values were concentrated near 1, with a median of 0.98612 and an interquartile range of 0.94603–0.99366. Relative profile roughness had a median of 0.00538 and an interquartile range of 0.00371–0.00763. The median corresponds to a local smoothing residual of approximately 0.54% of the profile depth range. Most instances therefore exhibited small local fluctuations relative to their overall longitudinal depth variation, although the right-hand tail indicates the presence of rougher profiles. These

measurements describe the final references after preprocessing and synthetic concavity deformation. Because the deformation itself contains a quadratic component, high R^2 values do not independently establish the accuracy of the DA3 depth predictions. Instead, the analysis characterizes the geometric distribution of the reference data used in the reconstruction experiments.

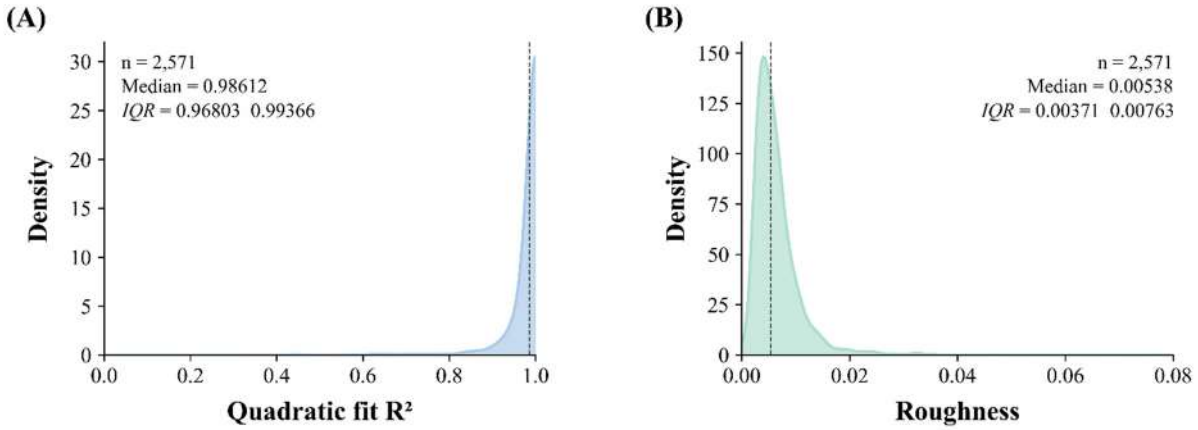

Fig. 3 Distributions of (A) quadratic-fit R^2 and (B) relative YZ profile roughness in the dataset. Shaded curves represent kernel density estimates, and dashed lines indicate medians.

Comparison of Geometric Reconstruction Performance

The geometric reconstruction results are summarized in Table 1. BerryComp achieved the lowest DCD of 0.3697 and the highest F-scores of 76.44% and 95.04% at normalized distance thresholds of 0.01 and 0.02, respectively. Its CD was 0.006062, compared with 0.010557 for AdaPoinTr, 0.010720 for PoinTr, 0.018291 for PCN, and 0.019852 for TopNet. These results indicate closer geometric agreement with the reference shapes under the evaluated conditions.

Table 1 Whole-point-cloud reconstruction performance on 2,490 test pairs from the concavity-augmented strawberry dataset.

Method	Parameters (M)	DCD	CD	F-score@0.01	F-score@0.02
TopNet	6.037	0.5769	0.020	26.97	67.84
PCN	5.290	0.4718	0.018	31.14	72.62
PoinTr	42.104	0.4167	0.011	60.54	90.42
AdaPoinTr	32.470	0.3735	0.011	66.87	93.17
Ours	2.199	0.3697	0.001	76.44	95.04

BerryComp also had the fewest trainable parameters, with 2.199 million compared with 5.290–42.104 million for the comparison models. Its strong reconstruction scores are consistent with a design that preserves observed geometry and concentrates prediction on missing regions. However, parameter count alone does not establish computational efficiency, which would require inference-time and memory measurements. Although all models were evaluated using the same reference samples and output size, their input configurations differed. BerryComp used up to 12,288 observed points, whereas the comparison models used 2,048. Therefore, the results demonstrate the performance of the configured reconstruction systems, while further experiments with matched input sampling would help

isolate the contribution of the proposed architecture.

Color Reconstruction Evaluation

As shown in Table 2, BerryComp's learned color predictions achieved a whole-output RGB PSNR of 22.41 dB and a mean CIEDE2000 color difference of 3.10, compared with 20.84 dB and 3.54 for nearest-neighbor color copying. This corresponds to a PSNR gain of 1.57 dB and a 12.40% reduction in mean CIEDE2000. Since output geometry and evaluation correspondence were held fixed, these differences reflect the choice of color assignment for generated points. The results indicate that the learned predictions provided better average color agreement than direct copying from the nearest observed point under this evaluation protocol.

Table 2 Comparison of color reconstruction performance using RGB PSNR and CIEDE2000 on 2,490 test pairs.

RGB assignment method	RGB PSNR (dB)	Mean CIEDE2000 (ΔE_{00})
Nearest-neighbor color	20.84	3.54
BerryComp predicted colors	22.41	3.10

These scores include retained observed regions and therefore describe the final-colored representation rather than the generated region alone. The comparison demonstrates an advantage over the evaluated nearest-neighbor baseline; it does not establish superiority over other interpolation methods or performance under real occlusions and varying illumination.

CONCLUSIONS

This study presented BerryComp for joint geometry and appearance reconstruction of occluded strawberries using depth representations generated by DA3METRIC-LARGE. By predicting missing regions and retaining observed coordinates and colors, BerryComp preserved available details in the reconstructed output. On 2,490 test pairs from the concavity-augmented dataset, the model achieved a whole-shape DCD of 0.3697, CD of 0.006062, and F-scores of 76.44% and 95.04% at normalized distance thresholds of 0.01 and 0.02, respectively. Under the shared output-size and reference-sampling protocol, BerryComp achieved better geometric scores than PCN, TopNet, PoinTr, and AdaPoinTr. Whole-shape appearance evaluation yielded an RGB PSNR of 22.41 dB and a mean CIEDE2000 color difference of 3.10. Analysis of the 2,571 reference instances yielded a median YZ quadratic-fit R^2 of 0.98612 and median relative profile roughness of 0.00538, characterizing the longitudinal shape distribution of the constructed dataset. Together, these findings support the feasibility of selective geometry and appearance reconstruction under the evaluated synthetic occlusion conditions. Future work should validate the approach using real occlusions and independently measured depth, and examine its performance in practical agricultural applications.

ACKNOWLEDGEMENTS

This research was supported by a grant (23192MFDS106).

REFERENCES

Ge, Y., Y. Xiong, and P. J. From. 2020. Symmetry-based 3D shape completion for fruit localisation for harvesting robots. Biosyst. Eng. 197: 188–202. https://doi.org/10.1016/j.biosystemseng.2020.07.003

He, J. Q., R. J. Harrison, and B. Li. 2017. A novel 3D imaging system for strawberry phenotyping. Plant Methods 13: 93. https://doi.org/10.1186/s13007-017-0243-x

Lin, H., S. Chen, J. H. Liew, D. Y. Chen, Z. Li, Y. Zhao, S. Peng, H. Guo, X. Zhou, G. Shi, J. Feng, and B. Kang. 2026. Depth Anything 3: Recovering the visual space from any views. In Proc. International Conference on Learning Representations (ICLR). https://proceedings.iclr.cc/paper_files/paper/2026/hash/e4cd50120b6d7e8daff1749d6bbaa889-Abstract-Conference.html

Sharma, G., W. Wu, and E. N. Dalal. 2005. The CIEDE2000 color-difference formula: Implementation notes, supplementary test data, and mathematical observations. Color Res. Appl. 30(1): 21–30. https://doi.org/10.1002/col.20070

Tchapmi, L. P., V. Kosaraju, H. Rezatofighi, I. Reid, and S. Savarese. 2019. TopNet: Structural point cloud decoder. In Proc. IEEE/CVF Conference on Computer Vision and Pattern Recognition (CVPR), 383–392. IEEE. https://doi.org/10.1109/CVPR.2019.00047

Wu, T., L. Pan, J. Zhang, T. Wang, Z. Liu, and D. Lin. 2021. Balanced Chamfer distance as a comprehensive metric for point cloud completion. In Advances in Neural Information Processing Systems 34, 29088–29100. Curran Associates, Inc. https://proceedings.neurips.cc/paper_files/paper/2021/hash/f3bd5ad57c8389a8a1a541a76be463bf-Abstract.html

Xiong, Y., Y. Ge, L. Grimstad, and P. J. From. 2020. An autonomous strawberry-harvesting robot: Design, development, integration, and field evaluation. J. Field Robot. 37(2): 202–224. https://doi.org/10.1002/rob.21889

Yu, X., Y. Rao, Z. Wang, Z. Liu, J. Lu, and J. Zhou. 2021. PoinTr: Diverse point cloud completion with geometry-aware transformers. In Proc. IEEE/CVF International Conference on Computer Vision (ICCV), 12498–12507. IEEE. https://openaccess.thecvf.com/content/ICCV2021/html/Yu_PoinTr_Diverse_Point_Cloud_Completion_With_Geometry-Aware_Transformers_ICCV_2021_paper.html

Yu, X., Y. Rao, Z. Wang, J. Lu, and J. Zhou. 2023. AdaPoinTr: Diverse point cloud completion with adaptive geometry-aware transformers. IEEE Trans. Pattern Anal. Mach. Intell. 45(12): 14114–14130. https://doi.org/10.1109/TPAMI.2023.3309253

Yuan, W., T. Khot, D. Held, C. Mertz, and M. Hebert. 2018. PCN: Point completion network. In Proc. International Conference on 3D Vision (3DV), 728–737. IEEE. https://doi.org/10.1109/3DV.2018.00088

AI-12

Proceedings of The 12th International Symposium on Machinery and Mechatronics for Agriculture and Biosystems Engineering (ISMAB 2026)
20-24 October 2026, Busan, Republic of Korea

MULTISPECTRAL IMAGING AND AI-BASED DEFECT SEGMENTATION FOR AUTOMATED NON-DESTRUCTIVE QUALITY INSPECTION AND SORTING OF TOMATOES

Umuhoza Aline[1*], Yena Kim[1], Aulia Rizkiana[2], Byoung-Kwan Cho[1,2*]

[1]Department of Smart Agricultural Systems, Chungnam National University, Daejeon, Korea

[2]Department of Biosystems Machinery Engineering, Chungnam National University, Daejeon, Korea

[*]Corresponding author: Byoung-Kwan Cho (chobk@cnu.ac.kr)

Abstract: Rapid and reliable quality assessment is critical for improving the competitiveness and market value of fresh agricultural products. Automated tomato quality assessment has advanced at the image-classification level, however localizing individual surface defects remains challenging due to variations in size and appearance. The objective of this study was to develop a segmentation model for non-destructive detection and localization of tomato surface defects including scar, zippering, crack, and catfacing. A total of 1349 tomato images were taken using multispectral imaging system. A YOLO11n-seg model was developed, and its overall performance was particularly strong with a 94.6% average accuracy at mAP@50. Scar, crack and catfacing defects segmentation achieved the highest accuracy of over 99% while zippering defect segmentation performance was slightly lower with accuracy above 80% due to smaller class sample count compared to other defects. These results provide a promising method for automated tomato sorting systems, potentially reducing manual inspection effort, and improving grading consistency. This approach could help identify factors contributing to fruit quality, benefiting the food industry for quality control and sorting purposes.

Key Words: **Multispectral imaging, AI, Defect, Segmentation, Tomato quality.**

AI-13

Proceedings of The 12th International Symposium on Machinery and Mechatronics for Agriculture and Biosystems Engineering (ISMAB 2026)
20–24 October 2026, Busan, Republic of Korea

TOPOSKEL-GNN: TOPOLOGY-AWARE SKELETON GRAPH LEARNING FOR APPLE TREE PRUNING POINT DETECTION

Anqi Liu[1,3], Woo-Young Kim[2], Kyeong-Hwan Lee[1,2,3*]

[1]Department of Convergence Biosystems Engineering, Chonnam National University, Gwangju, Republic of Korea
[2]AI Agri-Tech Research Center, Chonnam National University, Gwangju, Republic of Korea
[3]BK21 Interdisciplinary Program in IT-Bio Convergence System, Chonnam National University, Gwangju, Republic of Korea
*Corresponding Author — Email: khlee@jnu.ac.kr

Abstract: Accurate localization of pruning targets in dormant fruit trees requires a representation that preserves the connectivity and hierarchy of complex branching structures while remaining computationally efficient. This paper presents TopoSkel-GNN, a two-stage framework that converts dense three-dimensional orchard point clouds into compact topology-preserving skeleton graphs and then performs node-level pruning-point classification with a lightweight GraphSAGE network. The pipeline combines point-cloud downsampling, Laplacian-based contraction, graph construction with a minimum-spanning-tree topology backbone, and neighborhood aggregation for semantic prediction. Experiments on real apple-tree point clouds show an accuracy of 0.86 and an average intersection-over-union of 0.66, while the GraphSAGE classifier contains only 4,514 parameters (approximately 0.02 MB). Compared with DGCNN and Superpoint Graph baselines, the proposed representation provides a substantially smaller model while maintaining competitive pruning-point detection performance. Additional coordinate-wise evaluation gives an average RMSE of 0.062 m. The results indicate that explicit topological abstraction is a promising strategy for efficient structural perception in robotic pruning, although future work should evaluate inference latency, cross-orchard generalization, and end-to-end cutting success.

Key Words: 3D point cloud, graph neural network, skeletonization, robotic pruning, precision agriculture

ACKNOWLEDGEMENTS

This work was supported by Korea Institute of Planning and Evaluation for Technology in Food, Agriculture and Forestry (IPET) through the Technology Commercialization Support Program, funded by Ministry of Agriculture, Food and Rural Affairs (MAFRA) (RS-2024-00395265), and was conducted with support of the Cooperative Research Program for Agricultural Science & Technology Development (Project No. RS-2025-04092968), National Institute of Horticultural and Herbal Science, Rural Development Administration, Republic of Korea.

AI-14

Proceedings of The 12th International Symposium on Machinery and Mechatronics for Agriculture and Biosystems Engineering (ISMAB 2026)
20-24 October 2026, Busan, Republic of Korea

MULTI-VIEW FUSION OF UAV IMAGE MASKS FOR 3D FLOWER INSTANCE SEGMENTATION AND COUNTING

Phanith Chea[1,3], Kyeong-Hwan Lee[1,2,3,*]

[1]Department of Convergence Biosystems Engineering, Chonnam National University, Gwangju, Republic of Korea
[2]AI Agri-Tech Research Center, Chonnam National University, Gwangju, Republic of Korea
[3]BK21 Interdisciplinary Program in IT-Bio Convergence System, Chonnam National University, Gwangju, Republic of Korea
*Corresponding Author — Email: khlee@jnu.ac.kr

Abstract: Flower counts at bloom guide thinning and yield forecasting, but single-photograph counting is unreliable on a trellised fruiting wall: the same flower appears in many overlapping photos, flowers hide behind leaves and touch in clusters, and a photo gives no position along the row. This study fuses 2D flower masks from many side-view UAV photos into 3D flower instances on a photogrammetric point cloud. A row of 'Fuji' apple trees was photographed at full bloom with an RTK-positioned UAV from both sides at three heights, 1.5–3 m from the wall, and reconstructed by structure-from-motion into a dense point cloud. Flowers were segmented on full-resolution photos by a Mask2Former model trained on image tiles; a training-side truncation filter and an inference-side border rule kept border-cut flowers from appearing twice. Masks were projected onto the cloud with a depth-buffer occlusion test and combined by cross-view voting; the per-photo instance identity grouped detections of one flower across photos and separated touching flowers that distance-based clustering merges. Tiled segmentation with cleaned annotations and a truncation filter raised mask AP from 21.7 to 69.4 and reduced seam duplicates from 16.4% to 0.6% of detected flowers. On a five-tree test section (7.0 m of row, 63.6 M points, 802 photos) the pipeline produced 219 flower instances (median size 7.7 cm, 99.3% of flower points assigned), whereas geometry-only clustering of the same points gave 190 clumps. Counting accuracy against manual counts of the five trees is being measured and reported as work in progress.

Key Words: Flower counting, Instance segmentation, Multi-view fusion, Point cloud, UAV

ACKNOWLEDGEMENTS

This work was supported by Korea Institute of Planning and Evaluation for Technology in Food, Agriculture and Forestry(IPET) through the Technology Commercialization Support Program, funded by Ministry of Agriculture, Food and Rural Affairs (MAFRA)(RS-2024-00395265) and Korea Institute of Planning and Evaluation for Technology in Food, Agriculture and Forestry(IPET) through the Open Field Smart Agriculture Technology Short-term Advancement Program, funded by Ministry of Agriculture, Food and Rural Affairs(MAFRA)(32204003).

AI-15

Proceedings of The 12th International Symposium on Machinery and Mechatronics for Agriculture and Biosystems Engineering (ISMAB 2026)
20-24 October 2026, Busan, Republic of Korea

DEEP LEARNING-BASED MONITORING AND EARLY WARNING OF EXTERNAL ABNORMALITIES IN MULTI-TIER AVIARY LAYING HENS

Jia-En Lin[1*], Yu-Chieh Chen[1], Ming-Kun Hsieh[2], and Yao-Chuan Tsai[1]

[1]Department of Bio-Industrial Mechatronics Engineering, National Chung Hsing University, Taichung, Taiwan
[2]Graduate Institute of Microbiology and Public Health, College of Veterinary Medicine, National Chung Hsing University, Taichung, Taiwan
*Corresponding Author-- Voice: +886-903-335-994, Email: geniusdog123@gmail.com

Abstract: Non-cage housing complicates timely and objective manual inspection because of spatial complexity and flock movement. This study developed a non-contact vision system to quantify ocular and external cloacal (vent) abnormalities in commercial ISA Brown laying hens and assessed their relationships with mortality/culling and egg production. A pan-tilt-zoom (PTZ) camera conducted scheduled multi-view patrols in a commercial multi-tier aviary in Changhua County, Taiwan. Images of both regions were labeled as normal or abnormal. Ocular detection used YOLOv7 with transfer learning from a pretrained chicken-eye model, whereas cloacal detection used YOLOv11 with an expanded and rebalanced training set. Daily abnormality ratios were compared with flock records from April 1 to May 8, 2026. The ocular model achieved 62.8% precision, 64.9% recall, and an F1 score of 0.62. After dataset expansion and rebalancing, the cloacal model achieved 93.0% precision, 81.0% recall, 92.8% mAP@0.5, and an F1 score of 0.85. The daily mortality/culling rate exceeded 0.14% for at least two consecutive days during April 14-17. The ocular abnormality ratio exceeded 0.40 one to two days earlier, indicating early-warning potential. The cloacal abnormality ratio reached its minimum during peak egg production on April 3-5 and increased as egg production declined, indicating an inverse temporal association. The PTZ-YOLO system enabled repeatable, non-contact quantification of visible abnormalities in a commercial multi-tier aviary. These preliminary findings suggest that ocular and cloacal indicators may support early warning of flock health risks and production monitoring. Further validation across additional flocks and production cycles is required.

Key Words: laying hens; multi-tier aviary; computer vision; deep learning; health monitoring

AI-16

Proceedings of The 12th International Symposium on Machinery and Mechatronics for Agriculture and Biosystems Engineering (ISMAB 2026)
20-24 October 2026, Busan, Republic of Korea

DEVELOPMENT OF A HYBRID RAG ADVISORY SYSTEM FOR PHALAENOPSIS CULTIVATION BASED ON A LOCAL LLM

Shao-Yang Wu[1], Wen-Lin Chu[1*], Wei-Ling Chen[2], Hsi-Chun Hung[2]

[1]Department of bio-Industrial Mechatronics Engineering, National Chung Hsing University, Taiwan
[2] Floral Industry Innovation Center, Ministry of Agriculture, Taiwan
*Corresponding Author-- Voice: +886-4-2284-0377#509, Email: wlchu@nchu.edu.tw

Abstract: This study aims to develop a *Phalaenopsis* cultivation advisory system based on an on-premises Large Language Model (LLM) and Retrieval-Augmented Generation (RAG) technology. In the RAG retrieval phase, keyword retrieval and semantic retrieval are concurrently executed to obtain candidate documents. Subsequently, the retrieval results are integrated via weighted Reciprocal Rank Fusion (RRF), and a re-ranking model is applied to select the most relevant chunks, supplying the LLM with context for response generation. Experimental results demonstrate that the RAG system, augmented with external *Phalaenopsis* domain knowledge, comprehensively outper forms the large language model without RAG in response quality. Analysis of hybrid retrieval parameters indicates that optimal retrieval performance is achieved when the BM25 weight is set between 0.0 and 0.4. This study confirms that a Hybrid RAG architecture integrating sparse retrieval, dense retrieval, RRF, and re-ranking can effectively support specialized consultations in the *Phalaenopsis* domain, providing a localized, controllable, and scalable foundation for intelligent agricultural question-answering systems.

Key Words: *Phalaenopsis*, Large Language Models, Retrieval-Augmented Generation, Hybrid Retrieval, Reciprocal Rank Fusion.

INTRODUCTION

Phalaenopsis is a crucial floricultural crop with substantial export value in Taiwan. However, its cultivation cycle is lengthy, and its physiological characteristics as well as pest and disease management are highly sensitive to environmental fluctuations such as temperature, humidity, and illumination. Given its high economic significance and heavy reliance on empirical expertise, developing an advisory system powered by Large Language Models (LLM) holds tremendous potential. In recent years, LLM have frequently been utilized as development tools for intelligent advisory systems. Without requiring parameter updates or task-specific fine-tuning, these models can perform diverse downstream tasks via in-context learning guided by few-shot demonstrations, representing an optimal pathway to transition agricultural information systems from passive keyword querying to proactive intelligent consultation (Brown, Mann et al., 2020). However, when addressing in-depth agricultural knowledge,

general-purpose LLM frequently produce hallucinations, which may inflict substantial economic losses on growers. To mitigate this issue, this study introduces Retrieval-Augmented Generation (RAG) technology. RAG enables the LLM to retrieve and integrate relevant, up-to-date information from external data sources prior to answer generation, subsequently utilizing this retrieved information as the factual basis for generation (Lewis, Perez et al., 2020). In agricultural applications, RAG can bridge cultivation management documentation, pest and disease records, and agricultural expert knowledge, thereby enhancing the credibility and traceability of model responses while mitigating the risk of erroneous recommendations (Kandamali, Porter et al., 2025).
Given that *Phalaenopsis* is characterized by dense specialized nomenclature and domain-specific terminology, and that the Chinese language exhibits high sensitivity to semantic variations, this system implements a parallel Hybrid RAG strategy combining two retrieval paradigms. It initially employs both keyword and semantic matching to expand recall, followed by re-ranking models to enhance precision, thereby enabling the LLM to generate responses grounded in highly relevant evidence and mitigating the risks of hallucination and misleading guidance.

MATERIALS AND METHODS

LLM and RAG Architecture

This study employs LangChain as the development framework for large language model applications. The system utilizes " ministral-3-8b-instruct-2512-gguf " (an 8-billion parameter language model developed by Mistral AI) and the embedding model "jina-embeddings-v5-text-small-retrieval". It is deployed within a local closed-network environment to prevent data leakage and ensure high deployment flexibility. The RAG framework of this system is bifurcated into two stages: data preparation and retrieval. In the data preparation stage, imported documents are segmented into character chunks (chunk size = 300, chunk overlap = 50) using a text retriever, subsequently transformed into a 714-dimensional high-dimensional vector via the embedding model, and ingested into a vector database. In the retrieval stage, the system first utilizes the LLM to determine whether the user query is relevant to *Phalaenopsis*. If deemed relevant, the query is converted into a vector and matched against the database for similarity; the RAG pipeline is triggered only if the similarity exceeds a predefined threshold.

Regarding the retrieval strategy, this study employs a parallel hybrid retrieval approach (Hybrid RAG). User queries concurrently undergo keyword retrieval (BM25) and dense vector retrieval (cosine similarity). After each method independently retrieves the top 10 documents, the Reciprocal Rank Fusion (RRF) algorithm (Cormack, Clarke et al., 2009) is applied to compute a composite score based on assigned weights, filtering out the top 10 highest-scoring document chunks. Ultimately, these chunks are fed into a re-ranking model to select the top 3 candidates, which are packaged as the input context for the LLM to generate recommendations. Studies indicate that the optimal RRF weights for RAG systems vary depending on the domain and data sources (Bruch, Gai et al., 2023). To identify the optimal parameters for an LLM applied to Chinese *Phalaenopsis* corpora, an ablation study was designed to explore the optimal fusion weights between sparse and dense retrievers post-RRF, thereby defining the optimal RRF weighting configuration tailored to this system architecture.

Evaluation Metrics

To evaluate the quality of the generated answers, this study adopts the F1 score, Semantic Similarity, and Answer Relevancy as evaluation metrics. Since the F1 score primarily measures word-level overlap and exhibits high sensitivity to paraphrasing and stylistic variations in Chinese expression, this study concurrently incorporates semantic similarity and RAG-specific metrics for supplementary evaluation. Regarding the quantification of RAG retrieval quality, the retrieved reference documents are integrated as ground truth for assessment. This study employs Context Precision, Context Recall, and Faithfulness as evaluation metrics. All of the aforementioned metrics follow a "higher is better" principle, collectively characterizing the system's performance in terms of ranking efficiency, factual faithfulness to evidence, and semantic consistency.

F1 score, as shown in Eq. (1), defined as the harmonic mean of Precision and Recall; a higher F1 score indicates a more comprehensive and accurate response, which is widely utilized in machine reading comprehension and QA benchmarks (Rajpurkar, Zhang et al., 2016).

Studies have noted that long-text answers encompass diverse valid forms of expression; thus, when evaluating answers via the F1 score, the metric should generally not be equated directly with human judgments of quality. Given that long-form answers permit multiple legitimate phrasings, the F1 score serves as a relative comparative indicator rather than an absolute scale of quality (Fan, Jernite et al., 2019).

$$\text{Precision} = \frac{|G_i \cap R_i|}{|G_i|}, \text{Recall} = \frac{|G_i \cap R_i|}{|R_i|}, F1 = \frac{2\ \text{Precision}\ \text{Recall}}{\text{Precision} + \text{Recall}} \quad (1)$$

Where:

G_i = generated answer's token

R_i = reference answer's token.

Semantic similarity between the generated answer and the reference answer is evaluated via embedding vector cosine similarity, where higher values indicate greater semantic consistency.(Zhang, Kishore et al., 2019)

Answer Relevancy ,as shown in Eq. (2), is utilized to evaluate whether the generated answer is relevant to the user query specifically, whether the answer directly addresses the intent of the question and whether it contains excessive irrelevant content (Fan, Jernite et al., 2019).

$$\text{Answer Revealancy} = \frac{1}{N}\sum_{i=1}^{N} sim(q, \tilde{q}_i) \quad (2)$$

Where:

q = the user query

$\tilde{q}_i$ = the question reverse-generated based on answer,

N = the number of questions reverse-generated for each generated answer,
sim is the semantic similarity function between two question embedding vectors.

Faithfulness, as shown in Eq. (3), measures whether the generated answer is faithful to the

retrieved context specifically, whether the claims within the answer can be inferred from the provided evidence. A higher score signifies less reliance on internal model speculation, serving as a core metric for RAG credibility (Es, James et al., 2024).

$$\text{Faithfulness} = \frac{|V|}{|S|} \tag{3}$$

Where:

$|V|$ = the number of statements supported by the context

$|S|$ = the total number statements in the answer

Context Recall, as shown in Eq. (4), is used to evaluate whether the retrieved results cover the essential information required by the reference answer. The score ranges from 0 to 1, where a higher score indicates fewer omissions of critical information in the retrieved results (Es, James et al., 2024).

$$\text{ContextRecall} = \frac{\sum_{i=1}^{m} S_i}{m} \tag{4}$$

Where:

m = the total number of claims contained in the reference answer.

S_i = Binary indicator of whether the i-th claim is supported by the retrieved context; 1 if supported, 0 if unsupported.

Context Precision, as shown in Eq. (5), evaluates whether the retrieved context ranks relevant evidence at higher positions, typically accounting for the rank order of relevant passages through a weighted scheme. A higher value indicates that the retrieval results are more concentrated on key evidence, which helps mitigate interference and hallucinations in the LLM (Es, James et al., 2024).

$$\text{Context Precison} = \frac{\sum_{k=1}^{k} (\text{Precision@}k \times v_k)}{\text{total number of relevant items}} \tag{5}$$

Where:

k = Total number of retrieved context chunks.

v_k = Relevance indicator for the k-th chunk; 1 if relevant, 0 if irrelevant.

$\text{Precision@}k \times v_k$ = is the proportion of relevant chunks among the retrieval results up to rank k

RESULTS & DISCUSSION

In the experiments with and without the use of RAG, the results show (Fig. 1). that for domain-specific questions in *Phalaenopsis* cultivation, the response quality generated via the RAG architecture across all metrics significantly outperforms the baseline LLM system relying solely on pre-trained parametric memory. This underscores the critical necessity of coupling LLM with RAG for retrieving vital domain knowledge in *Phalaenopsis* applications.

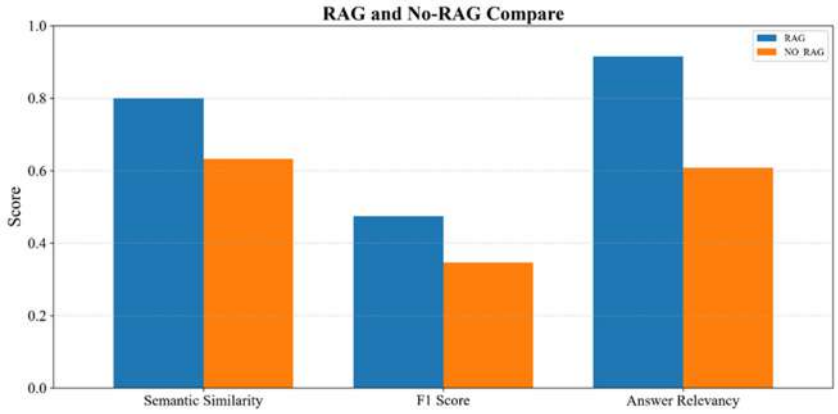

Fig. 1 Comparison Chart of RAG-Generated Answers

Furthermore, to determine the optimal RRF weights for the RAG system, an ablation study on hybrid retrieval parameters was conducted (Fig. 2). In the BM25 weight interval from 0.0 to 0.4, all evaluation metrics achieve an optimal balance. However, relying exclusively on dense vector retrieval risks omitting documents containing specific domain keywords that are vulnerability corroborated by the fact that the peak values across metrics do not uniformly occur at BM25 = 0.0. Thus, integrating sparse keyword retrieval is indispensable. Conversely, once the BM25 weight exceeds 0.5, both Context Recall and Context Precision experience a precipitous decline. This phenomenon empirically confirms that in *Phalaenopsis* pathology a substantial semantic gap often exists between Chinese user inquiries and the terminology documented in expert repositories. Over-reliance on exact keyword matching leads to severe false negatives, highlighting the irreplaceable role of dense vector retrieval in agricultural domains. These results demonstrate that neither pure vector retrieval nor pure keyword retrieval represents an optimal solution. Through empirical validation, this study identifies the optimal parameter range tailored to the *Phalaenopsis* corpus.

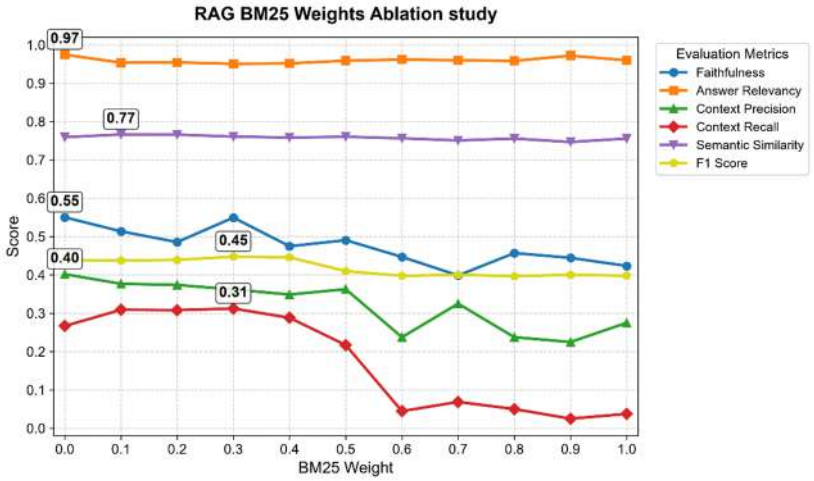

Fig. 2 Line Chart of BM25 Weight Ablation Study Results

CONCLUSIONS

This study couples an on-premises large language model with Retrieval-Augmented Generation (RAG) technology to construct a *Phalaenopsis* cultivation advisory system. Candidate data are retrieved via parallel BM25 keyword retrieval and dense vector similarity

retrieval, followed by weighted Reciprocal Rank Fusion (RRF) and a re-ranking model to filter the most query-relevant context for answer generation. Experimental results demonstrate that the RAG system integrating external domain-specific data comprehensively outperforms the baseline large language model relying solely on pre-trained parametric knowledge in response quality. Furthermore, an optimal overall balance across evaluation metrics is achieved when the BM25 weight is set between 0.0 and 0.4; when the BM25 weight exceeds 0.5, retrieval efficiency declines markedly, indicating that excessive reliance on superficial keyword matching fails to adequately resolve semantic discrepancies in *Phalaenopsis* descriptions. Consequently, combining semantic retrieval with keyword retrieval—supplemented by result fusion and re-ranking for candidate document filtering—constitutes the superior retrieval strategy for this study. This study confirms that an on-premises LLM coupled with Hybrid RAG provides a viable architecture for intelligent *Phalaenopsis* cultivation consultation, offering key advantages including closed-network deployment, data privacy preservation, flexible knowledge base updates, and traceable response grounding. Future work may further incorporate *Phalaenopsis* pest and disease imagery, environmental sensor data, and expert-annotated agronomic datasets to establish a multimodal RAG system unifying textual, visual, and temporal environmental information.

REFERENCES

Brown, T., B. Mann, N. Ryder, M. Subbiah, J. D. Kaplan, P. Dhariwal, A. Neelakantan, P. Shyam, G. Sastry and A. Askell 2020. "Language models are few-shot learners." Advances in neural information processing systems **33**: 1877–1901.

Bruch, S., S. Gai and A. Ingber 2023. "An Analysis of Fusion Functions for Hybrid Retrieval." ACM Trans. Inf. Syst. **42**(1): Article 20.

Cormack, G. V., C. L. Clarke and S. Buettcher 2009. Reciprocal rank fusion outperforms condorcet and individual rank learning methods. Proceedings of the 32nd international ACM SIGIR conference on Research and development in information retrieval.

Es, S., J. James, L. E. Anke and S. Schockaert 2024. Ragas: Automated evaluation of retrieval augmented generation. Proceedings of the 18th conference of the european chapter of the association for computational linguistics: system demonstrations.

Fan, A., Y. Jernite, E. Perez, D. Grangier, J. Weston and M. Auli 2019. ELI5: Long form question answering. Proceedings of the 57th annual meeting of the association for computational linguistics.

Kandamali, D. F., W. M. Porter, E. Porter, A. McLemore and G. C. Rains 2025. "CottonBot: An AI-driven cotton farming assistant and irrigation advisor using LLM-RAG and agentic AI tools." Smart Agricultural Technology: 101640.

Lewis, P., E. Perez, A. Piktus, F. Petroni, V. Karpukhin, N. Goyal, H. Küttler, M. Lewis, W.-t. Yih and T. Rocktäschel 2020. "Retrieval-augmented generation for knowledge-intensive nlp tasks." Advances in neural information processing systems **33**: 9459–9474.

Rajpurkar, P., J. Zhang, K. Lopyrev and P. Liang 2016. Squad: 100,000+ questions for machine comprehension of text. Proceedings of the 2016 conference on empirical methods in natural language processing.

Zhang, T., V. Kishore, F. Wu, K. Q. Weinberger and Y. Artzi 2019. "Bertscore: Evaluating text generation with bert." arXiv preprint arXiv:1904.09675.

AI-17

Proceedings of The 12th International Symposium on Machinery and Mechatronics for Agriculture and Biosystems Engineering (ISMAB 2026)
20-24 October 2026, Busan, Republic of Korea

INTEGRATING CFD, ENVIRONMENTAL SENSING, AND COMPUTER VISION TO CHARACTERIZE SPATIAL ASSOCIATIONS BETWEEN AIRFLOW AND BROILER DISTRIBUTION

Jin-Yeong Lee[1], Min-Young Hwang[2], Ryu-Gap Lim[1]*

[1]Department of Convergence Biosystem Mechanical Engineering, Sunchon National University, Sunchon, Korea
[2]Department of Smart Agricultural Engineering, Sunchon National University, Sunchon, Korea

*Corresponding Author-- Voice: +82-61-750-3264, Email: limrg11@scnu.ac.kr

Abstract: Airflow, temperature and humidity inside broiler houses can vary depending on location and ventilation conditions, making it necessary to understand these spatial environmental characteristics together with the spatial distribution of broiler flocks. This study aims to explore the relationship between the indoor air environment and broiler clustering distribution using environmental sensor data, computational fluid dynamics (CFD) and ceiling-mounted video footage. Real-time data collected from 12 tempe rature sensors and 3 humidity sensors installed on the ceiling of the broiler house are used to characterize temperature and humidity at each measurement point. An ANSYS-based CFD model reflecting the three-dimensional geometry of the broiler house, fan airflow rate, and inlet conditions are constructed. The air flow distribution and flow patterns at broiler living height are analyzed to identify major air circulation pathways and potential air stagnation zones. The validity of the airflow analysis results is examined by comparing them with indoor wind speed measurement data. An environmental distribution map is constructed by overlaying the CFD analysis results with the planar location and installation height of the ceiling sensors, along with the measured temperature and humidity data at each corresponding point. For the broiler distribution map, footage from five fixed ceiling-mounted cameras is used, and YOLO-based object detection is employed to estimate the location and number of broilers. Unobserved areas at both ends of the camera footage and areas obscured by equipment are excluded to define a valid analysis zone, which is then mapped onto the floor plan of the broiler house. The number of detected individuals in each zone is corrected by an effective observation area to calculate relative density, which is visualized using heatmaps and graphs. Subsequently, the two maps are matched by time based on the common valid observation area to analyze the relationship between zones of potential air stagnation and broiler clustering locations, as well as the relationship between temperature, humidity changes in sensor measurement zones and broiler distribution. This study aims to provide foundational data for understanding both the environmental characteristics of broiler houses and the clustering distribution of broilers through spatial analysis linking CFD airflow analysis with sensor and video data.

Key Words: Heatmap, CFD, Sensor, YOLO, Air Stagnation

ACKNOWLEDGEMENTS

This work was supported by Korea Institute of Planning and Evaluation for Technology in Food, Agriculture and Forestry (IPET) and Korea Smart Farm R&D Foundation (KosFarm) through Smart Farm Innovation Technology Development Program, funded by Ministry of Agriculture, Food and Rural Affairs (MAFRA) and Ministry of Science and ICT(MSIT), Rural Development Administration (RDA) (RS-2025-02316456)

AI and Information Processing 4 (AI-4)



AI-18

Proceedings of The 12th International Symposium on Machinery and Mechatronics for Agriculture and Biosystems Engineering (ISMAB 2026)
20-24 October 2026, Busan, Republic of Korea

ANATOMY-AWARE COMPOSITIONAL GENERATION OF 3D TOMATO PLANTS: COUPLING A MEASURED L-SYSTEM GRAMMAR WITH PER-ORGAN DIFFUSION MODELS

Omia Emmanuel[1], Byoung-Kwan Cho[1,*]

1Department of Biosystems Machinery Engineering, Chungnam National University, Daejeon 34134, Republic of Korea

*Corresponding Author-- Voice: +82-42-821-6715, Email: chobk@cnu.ac.kr

Abstract: Three-dimensional phenotyping models are data-hungry, yet measuring and labelling real 3D plant scans is slow and costly. Synthetic plants can close the gap only if they are botanically real. Existing routes each fail on a different axis: general 3D generative models are trained on rigid man-made objects and have never seen plant anatomy; hand-made assets do not scale; and procedural L-system models get topology right but represent organs as analytic tubes and blades. This study therefore seeks to ask whether organ surface geometry learned from real scans can supply what procedural primitives cannot.

We treat a plant not as a monolithic shape but as a hierarchical graph of connected organs, generated one phytomer at a time. Thirteen tomato plants were scanned and fully labelled at organ-instance level (2.5-3.5 million labelled points per plant) and decomposed into a curved stem centreline, recovered nodes, and per-organ clouds in a canonical frame. An L-system grammar fitted to these plants supplies topology, including node counts, internode spacing and a measured phyllotaxis near 132°. Three conditional denoising diffusion probabilistic models, stem internode, petiole with rachis, and leaflet, supply organ geometry, each steered by a conditioning vector encoding developmental position. A socket-based composition engine assembles organs using overlapping context windows so that each module continues from geometry it can already see.

The contribution of learned geometry was isolated by a twin-set ablation in which a primitive twin and a learned twin share the same grammar and composition engine and differ only in organ geometry. Surface roughness was 0.189 in real plants, 0.043 for primitives (about four times too smooth) and 0.202 for learned organs; cross-section eccentricity was 1.181, 1.047 and 1.211 respectively. Learned organ geometry therefore reproduces surface realism that primitives cannot. Stem taper stability and the insertion-angle gradient remain unreliable due to low training data volume. This indicates that the mechanism is validated and the remaining bottleneck is data volume and targeted developmental conditioning.

Because every generated plant carries organ-level labels by construction, the manual annotation step that dominates the cost of building 3D phenotyping datasets is removed rather than accelerated. The botanically grounded synthetic plants offer a route to deploying 3D phenotyping at commercial scale, where data scarcity and labelling cost has been the practical barrier to adoption.

Key Words: 3D plant phenotyping, denoising diffusion probabilistic model, L-system, compositional generation, tomato

AI-19

Proceedings of The 12th International Symposium on Machinery and Mechatronics for Agriculture and Biosystems Engineering (ISMAB 2026)
20-24 October 2026, Busan, Republic of Korea

SELECTION OF DIFFUSION-GENERATED IMAGES FOR PEST INSTANCE SEGMENTATION ON STICKY TRAPS

Jung-sang Yoo[1], Soo Been Cho[1], Ji Won Choi[1], Seung-Hwan Yang[1*]

[1]Specialized Machinery and Robotics Group, Korea Institute of Industrial Technology
Gimje-si, Jeonbuk-do 54325, Republic of Korea
*Corresponding Author: Email: yangsh@kitech.re.kr

Abstract: Reusing pest polygons in synthetic images can reduce the labeling burden for instance segmentation, but the fraction of generated data to retain remains a practical training decision. This decision was examined using *Ricania sublimata* and *Metcalfa pruinosa* in sticky trap imagery. Polygon-guided diffusion with species-specific low-rank adaptation generated image-label pairs, which were screened using features from a segmentation model trained on real images. Five image retention fractions were compared using YOLOv26s-seg and a location-based data split. Retaining 70% of the ranked images gave the highest overall scores among the evaluated settings: mAP50 increased from 75.3% to 88.0%, and mAP50-95 from 63.9% to 66.3%, relative to default augmentation. Retaining all images yielded 86.2% and 62.9%, respectively. Strict mask accuracy remained species-dependent. These observations support evaluating synthetic data selection alongside data volume when expanding small polygon-annotated pest datasets.

Key Words: Sticky traps, Pest segmentation, Diffusion augmentation, Synthetic data selection, Polygon labels

INTRODUCTION

Automated trap inspection requires training examples that represent the insects encountered during monitoring. For infrequent species, collecting images and tracing individual boundaries can limit the available segmentation data. Copy-Paste augmentation expands training scenes by relocating annotated objects (Ghiasi et al., 2021), while controllable diffusion offers a way to vary appearance within a specified layout (Fang et al., 2024). For polygon labels, the usefulness of these generated samples depends on whether the synthesized insect remains compatible with its assigned region.

This study was conducted to examine how the fraction of synthetic images admitted to training affects pest segmentation. It focuses on image selection and the distinction between recognition gains at a permissive overlap threshold and accuracy under stricter mask overlap requirements.

MATERIALS AND METHODS

This study used polygon-annotated sticky trap images from AI Hub for *R. sublimata* and *M. pruinosa*. Data obtained from different locations were used for the training and testing datasets, respectively. Training data from Gunsan comprised 55 images with 55 instances of *R. sublimata* and 509 images with 592 instances of *M. pruinosa*. Validation data were separated by collection session at the same location, giving 145 images. The test set from Iksan contained 64 images with 64 instances of *R. sublimata* and 48 images with 61 instances of *M. pruinosa*.

Synthetic images were produced from annotated original images using Qwen-Image-2512 with ControlNet inpainting and a separate low-rank adaptation (LoRA) adapter for each species. Polygon contours specified the regions to synthesize, including rotated and translated copies accepted only at non-overlapping positions within the image. Their transformed coordinates supplied the corresponding labels. Inpainting covered the polygon interiors and a dilated boundary margin. Generation used 1,328 × 1,328 pixels and 30 denoising steps, producing 1,947 candidate images. No additional manual polygon drawing was required for the generated images.

Synthetic images were selected using features extracted by the backbone of a baseline segmentation model trained on real data. Features pooled within each real polygon were averaged to obtain a reference vector for its species. Each synthetic annotation received a cosine similarity score against this reference. Labels scoring below 0.3 were removed, and images without remaining labels were discarded. The mean score of the remaining annotations determined each image's rank within its species. This study retained the highest-ranked fraction γ, testing 0.1, 0.3, 0.5, 0.7 and 1.0. The γ = 1.0 setting still included annotation-level screening; it omitted only image-level selection.

YOLOv26s-seg was trained with default augmentation at 640 × 640 pixels, with validation used for early stopping and a patience of 80 epochs. Synthetic pairs supplemented the original training data. We report mask mAP50, evaluated at intersection over union (IoU) 0.50, and mAP50-95, averaged over IoU thresholds from 0.50 to 0.95 in steps of 0.05. Overall scores average the two species.

RESULTS AND DISCUSSION

Segmentation performance was compared across different synthetic image retention fractions (Table 1). Overall mAP50 exceeded the baseline at every retention fraction, whereas mAP50-95 did not follow a consistent trend. The 70% setting used 1,362 synthetic images and exceeded the baseline by 12.7 percentage points in mAP50 and 2.4 percentage points in mAP50-95. Using all 1,947 images lowered both scores relative to this setting. However, the highest-ranked 10% also improved both metrics, while the 30% and 50% settings reduced mAP50-95. The observations therefore do not establish a simple relationship between synthetic sample count and boundary accuracy.

The species-level results further qualify the overall gain. At γ = 0.7, *R. sublimata* improved from 77.2% to 89.8% in mAP50, but its mAP50-95 decreased from 69.8% to 64.2%. *M. pruinosa* improved from 73.5% to 86.3% and from 58.0% to 68.5%, respectively. A higher score at IoU 0.50 consequently should not be interpreted as uniformly more accurate masks for both species.

These results support using task-specific screening when adding generated images to a small training set. Because adjusting γ changes both sample composition and sample count, this comparison does not isolate the contribution of the ranking rule. The evidence is also limited to two species and one location-based split. In order to find the general optimal retention fraction, additional experiments will be needed with more sites and implements and independent validation of the retention setting

Table 1 Synthetic image retention and overall mask performance of YOLOv26s-seg

Retention fraction γ	Synthetic images	mAP50 (%)	mAP50-95 (%)
Baseline	0	75.3	63.9
0.1	194	83.1	65.4
0.3	583	85.4	57.6
0.5	973	85.8	56.9
0.7	**1,362**	**88.0**	**66.3**
1.0	1,947	86.2	62.9

Baseline uses default augmentation without synthetic images. All synthetic settings apply the annotation threshold of 0.3. Bold values identify the highest overall scores among the tested settings.

CONCLUSIONS

The observed overall segmentation scores were improved without drawing new manual labels through selecting a subset of polygon-guided synthetic images. The best performance was found at the 70% retention setting among the tested fractions, but stricter mask accuracy remained uneven across species. For practical monitoring, both image selection and species-level mask quality should be considered when using synthetic training data.

ACKNOWLEDGEMENTS

This research was supported by the Korea Institute of Planning and Evaluation for Technology in Food, Agriculture and Forestry (IPET) and Korea Smart Farm R&D Foundation (KosFarm) through the Smart Farm Innovation Technology Development Program, funded by the Ministry of Agriculture, Food and Rural Affairs (MAFRA), Ministry of Science and ICT (MSIT), and Rural Development Administration (RDA) (RS-2025-02307287).

REFERENCES

Fang, H., B. Han, S. Zhang, S. Zhou, C. Hu, and W.-M. Ye. 2024. Data augmentation for object detection via controllable diffusion models. In Proc. IEEE/CVF Winter Conf. on Applications of Computer Vision, 1257-1266.

Ghiasi, G., Y. Cui, A. Srinivas, R. Qian, T.-Y. Lin, E. D. Cubuk, Q. V. Le, and B. Zoph. 2021. Simple copy-paste is a strong data augmentation method for instance segmentation. In Proc. IEEE/CVF Conf. on Computer Vision and Pattern Recognition, 2918-2928.

AI-20

Proceedings of The 12th International Symposium on Machinery and Mechatronics for Agriculture and Biosystems Engineering (ISMAB 2026)
20-24 October 2026, Busan, Republic of Korea

SEQUENTIAL 3D SHAPE COMPLETION OF ON-PLANT KOREAN MELONS TOWARD AUTOMATED SELECTIVE HARVESTING

Sungjay Kim[1,3], Gyumin Kim[1,2], Xianghui Xin[1,2], Yeongjun Go[1,2], Ghiseok Kim[1,2,3*]

[1] Department of Biosystems Engineering, Seoul National University, Seoul, Republic of Korea
[2] Global Smart Farm Convergence Major, Seoul National University, Seoul, Korea
[3] Research Institute of Agriculture and Life Sciences, Seoul National University, Seoul, Korea
* Corresponding Author– Voice: +82-2-880-4603, Email: ghiseok@snu.ac.kr

Abstract: Korean melon (*Cucumis melo* L. var. *makuwa*) requires per-fruit harvest decisions, but occlusion limits on-plant volume estimation, and single-frame 3D shape completion ignores temporal continuity. We present SCoRe (Sequential CoRe), which adds inference-time temporal latent fusion to a DeepSDF-based encoder without additional learned parameters. A time-aware exponential moving average integrates observations across visits, while a constraint prevents backward movement along growth axes identified by principal component analysis of within-fruit latent changes. Evaluation used 2,513 RGB-D frames of 210 fruits acquired at 2–3 day intervals by a rail-mounted platform across two seasons and three greenhouses, with post-harvest photogrammetric meshes as ground truth. Compared with an identical single-frame encoder, SCoRe reduced last-frame volume root mean squared error (RMSE) from 87.4 to 50.6 mL (42 %) and increased F1 at 5 mm from 66.1 % to 83.0 %, with the largest gains under heavy occlusion and robustness to irregular revisit intervals. The recovered volume trajectories supported harvest-date prediction through causally fitted logistic growth curves. A compact regressor combined growth-curve features, accumulated radiation and temperature, and visual ripeness to estimate days to harvest, issuing recommendations at three days or less. Trained on 2025 ripeness annotations and evaluated against 2026 expert-recommended dates, the predictor achieved a mean absolute error of 2.15 days, issuing recommendations for 34 of 37 fruits (91.9 %); removing the growth-curve structure increased error to 4.38 days. Fruit harvested 0–5 days after model recommendations (n = 15) and on expert-recommended dates (n = 14) showed equivalent soluble solids content within ±1.5 °Brix and no significant differences in seven other quality attributes. These results demonstrate the potential of sequential RGB-D shape completion to support per-fruit harvest scheduling.

Key Words: Korean melon; Selective harvesting; 3D shape completion; Temporal latent fusion; Harvest-date prediction

ACKNOWLEDGEMENTS

This work was supported by the Korea Institute of Planning and Evaluation for Technology in Food, Agriculture and Forestry (IPET) through the Smart Farm Innovation Technology Development Program, funded by the Ministry of Agriculture, Food and Rural Affairs (MAFRA), Republic of Korea (grant number RS-2025-02219360).

AI-21

Proceedings of The 12th International Symposium on Machinery and Mechatronics for Agriculture and Biosystems Engineering (ISMAB 2026)
20-24 October 2026, Busan, Republic of Korea

PHYSICS-GUIDED HYPERSPECTRAL CLASSIFICATION OF MICRO- AND NANOPLASTICS IN HYDROPONIC NUTRIENT SOLUTIONS

Yea-Jin Park[1,2,†], Youngho Jeon[3,†], Suji Lee[3], Jungmok You[3*], Dae-Hyun Jung[1,2,]**

[1] Department of Smart Farm Science, Kyung Hee University, Yongin 17104, Republic of Korea
[2]Interdisciplinary Program in IT-Bio Convergence System, Kyung Hee University, Yongin 17104, Republic of Korea
[3]Department of Convergent Biotechnology & Advanced Materials Science, BK21 Interdisciplinary Program in IT-Bio Convergence System, Kyung Hee University, Yongin 17104, Republic of Korea
* Correspondence author, e-mail address: jmyou@khu.ac.kr (J. You)
** Correspondence author, e-mail address: daehyun@khu.ac.kr (D.-H. Jung)

Abstract: The expansion of hydroponic cultivation has increased the need for direct monitoring of particulate contaminants in nutrient solutions. Microplastics can enter these systems through source water and cultivation infrastructure, yet their rapid and nondestructive detection in aqueous environments remains challenging without filtration or drying. Here, we combined visible and near-infrared hyperspectral imaging (VNIR HSI; 400–1000 nm) with physics-guided learning to classify polystyrene (PS), poly(methyl methacrylate) (PMMA), and polyethylene (PE) particles directly in tap water and nutrient solutions collected from strawberry and tomato hydroponic systems. Raw spectral analysis revealed that the measured responses were dominated by the surrounding aqueous matrix, while polymer type, concentration, and particle size introduced additional variations in spectral magnitude and shape. Rather than treating wavelength-dependent scattering as background noise, we represented its physical characteristics using 13 scattering-derived features (phys13), including spectral slope, curvature, continuum, residual, and spatial heterogeneity descriptors, and integrated them into neural spectral encoders through feature-wise linear modulation (FiLM). Using standard normal variate (SNV)-preprocessed spectra, phys13 improved ResNet1D accuracy from 0.898 to 0.938 for polymer type and from 0.695 to 0.839 for concentration classification. Particle-size classification further revealed the task-specific nature of physics-guided information. Although the full phys13 set did not improve performance under concentration-shift conditions, selecting size-relevant scattering features increased XGBoost accuracy from 0.630 to 0.806 and improved generalization to unseen con centrations. These findings demonstrate that task-specific integration of scattering-derived physical features can help extract particle-related information from matrix-dominated VNIR spectra, providing a promising framework for nondestructive classi fication of suspended micro- and nanoplastics in complex hydroponic nutrient solutions.

Key Words: Microplastics, Hyperspectral imaging, Deep learning, Hydroponics, Light scattering

ACKNOWLEDGEMENTS

This research was supported by a grant (23192MFDS106) from Ministry of Food and Drug Safety in 202

AI-22

Proceedings of The 12th International Symposium on Machinery and Mechatronics for Agriculture and Biosystems Engineering (ISMAB 2026)
20-24 October 2026, Busan, Republic of Korea

REFERENCE-GUIDED INSTANCE SEGMENTATION OF APPLE FLOWERS AND BUDS USING VISION FOUNDATION MODELS

Jintack Jeon[1], Baek-Gyeom Sung[1], Man-Jung Kim[2], Dae-Hyun Lee[1, 3*]

[1]Department of Agricultural Machinery Engineering, Chungnam National University, Daejeon, 34134, Republic of Korea
[2]National Academy of Agricultural Science, Rural Development Administration, Jeonju, 54875, Republic of Korea
[3]Department of Smart Agricultural Systems Engineering, Chungnam National University, Daejeon, 34134, Republic of Korea
*Corresponding Author-- Email: leedh7@cnu.ac.kr

Abstract: Target selection for artificial apple pollination requires identifying individual flowers within clusters and distinguishing open flowers from buds. However, dense clusters, occlusion, and morphological variation complicate instance delineation and classification. We developed a reference-guided instance segmentation method that uses a small set of annotated reference images to filter and classify predictions from vision foundation models. The detection, depth estimation, and segmentation models remained frozen, while separate classifiers and estimators were trained using features and annotations from reference images. These trained modules filtered and rescored detection candidates, classified masks as Flower or Bud, and selected the final masks. Instance masks and class labels were manually annotated for 1,267 images from the YO-AFD dataset. Thirty images were used for reference-based training, and the remaining 1,237 images were used for evaluation. The method achieved a mean mask average precision of 0.71 across the two classes at an intersection-over-union threshold of 0.50, an overall F1 score of 0.56, and an overall recall of 0.83. Final mask filtering reduced Flower false positives per image by 36.00% relative to the unfiltered predictions. These results indicate that filtering criteria learned from limited reference annotations reduced false-positive Flower predictions under the evaluated conditions. The method provides instance-level regions and class labels to support pollination target selection. Practical application requires further false-positive reduction and evaluation under other orchard conditions.

Key Words: Apple flowers, Artificial pollination, Instance segmentation, Reference images, Vision foundation models

INTRODUCTION

Supporting target selection for artificial pollination of apple trees requires distinguishing open flowers from buds in images and identifying the location and extent of each instance (Mu et al., 2023). Dense flower clusters, occlusion, complex orchard environments, and morphological changes across flowering stages make instance-level recognition difficult (Wang et al., 2025).

To reduce the manual annotation burden associated with training instance-level recognition models, pretrained vision foundation models have been applied to plant instance segmentation (Roggiolani et al., 2026). However, directly applying general-purpose vision foundation models to agricultural images may result in duplicate detections and inaccurate instance segmentation (Bao et al., 2025). This study proposes a reference-guided instance segmentation method that uses annotations from a few reference images and features from frozen vision foundation models to distinguish apple flowers from buds.

MATERIALS AND METHODS

Overview of the Proposed Method

The proposed method combines pretrained detection and segmentation models with decision criteria learned from annotated reference images to produce instance masks, class labels, and ranking scores for apple flowers and buds. The pretrained weights of CountGD-Box (Amini-Naieni and Zisserman, 2026), Depth Anything V1 with a ViT-B backbone (Yang et al., 2024), and the SAM 2.1-based HQ-SAM 2 implementation (Ke et al., 2023) were kept frozen. Features extracted from the reference images and their instance annotations were used to train foreground classifiers, a box-IoU estimator, Flower/Bud classifiers, and a binary classifier for mask filtering (Fig. 1a).

During inference, CountGD-Box generates candidate boxes, which are filtered using foreground predictions based on CountGD-Box and Depth Anything features. The retained candidates are rescored using predicted box IoU. Their boxes are provided to HQ-SAM 2 as prompts to generate instance masks, and features from the three models are used to assign Flower or Bud labels. Finally, masks are filtered according to the binary classifier scores, and the retained masks are output with their class labels and ranking scores (Fig. 1b).

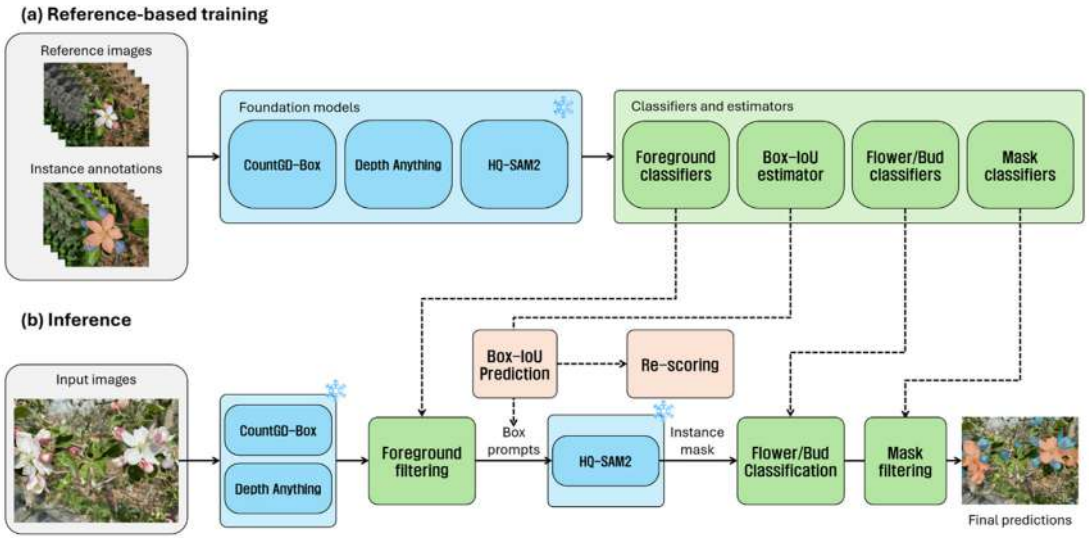

Fig.1 Overview of the proposed reference-guided instance segmentation method.

Reference-Guided Instance Segmentation

Separate linear foreground classifiers were fitted to CountGD-Box and Depth Anything features using the union of Flower and Bud masks as foreground labels. Candidates classified as foreground by both classifiers were retained. Duplicate boxes were suppressed using non-maximum suppression (NMS). A box-IoU estimator used pooled box features from both models

to predict the maximum IoU with ground-truth boxes in the same reference image. The ranking score was calculated using Eq. (1) by multiplying the original CountGD-Box detection score by the predicted box IoU, without changing the box coordinates.

$$s_i = D_i \, \hat{q}_{\mathrm{CD},i} \tag{1}$$

where:

s_i = Ranking score for candidate i

D_i = Original CountGD-Box detection score for candidate i

$\hat{q}_{\mathrm{CD},i}$ = Box IoU predicted from CountGD-Box and Depth Anything features

Three linear discriminant analysis (LDA) classifiers used CountGD-Box mask-region features, Depth Anything mask-region features, and SAM token features, respectively. They were trained using features extracted from predicted masks with unambiguous ground-truth correspondence in the reference images. Class probabilities were combined using an equally weighted product of experts (PoE; Hinton, 2002), and the class with the largest probability product was selected using Eq. (2).

$$\hat{c}_i = \underset{c \in \{\mathrm{Flower},\, \mathrm{Bud}\}}{\arg\max} \prod_{e \in \varepsilon} p_{e,i}(c) \tag{2}$$

where:

$\hat{c}_i$ = Predicted class of instance i (Flower or Bud)

ε = Set of three LDA classifiers

$p_{e,i}(c)$ = Probability of class c for instance i from classifier e

A binary logistic regression classifier was trained for mask filtering using detection information, predicted IoU, shape information, and model features. Empty masks and predictions with ambiguous ground-truth correspondences were excluded from training. Predictions were labeled positive (valid masks) when their maximum IoU with an individual ground-truth mask in the same reference image was at least 0.50, and negative otherwise. The filtering threshold was selected to maximize class-agnostic mask F1 using the classifier's out-of-fold (OOF) scores from four-fold cross-validation on the reference images. At least one valid mask had to be retained for each ground-truth Flower instance in the reference images that had at least one valid mask before filtering. Evaluation used models refitted on all reference images and the fixed threshold.

Experimental Data and Evaluation Methods

We used 1,267 images from the YO-AFD training set (Wang et al., 2025) and manually annotated instance masks and Flower/Bud classes. Open flowers were labeled Flower and closed buds as Bud; identifiable occluded or truncated instances were annotated over their visible regions. Thirty images were used for reference-based fitting and 1,237 for evaluation. Only reference annotations were used for model fitting and threshold selection. The evaluation set contained 28,584 ground-truth instances, comprising 8,736 Flower and 19,848 Bud instances.

Foreground filtering was evaluated using box precision, recall, and F1 under the same NMS settings. Re-scoring was compared using Bbox AP50 and AP75 on 70,001 boxes with fixed coordinates and NMS-selected boxes. The original CountGD-Box score was compared with scores multiplied by box IoU predicted from CountGD-Box features alone or together with Depth Anything features. Final segmentation was evaluated using class-wise precision, recall, F1, Mask AP50, and Mask AP75. Precision, recall, and F1 used score-ordered one-to-one

matching at IoU 0.50, ignoring classes for boxes but requiring class agreement for masks. Prediction counts and Flower false positives per image (FPPI) were compared before and after mask filtering.

RESULTS & DISCUSSION

Instance Segmentation Performance

Figure 2 presents three examples progressing from individual flower details to multiple instances and complex orchard backgrounds. Each row compares the input image, selected bounding boxes, final predictions, and ground truth for the same image region. Example 1 presents a close-up of one or two flowers for examining mask boundaries, correspondence with ground-truth instances, and any partial or duplicate masks. Example 2 illustrates Flower/Bud classification and segmentation in a scene containing multiple crowded flowers and buds. Example 3 allows predictions and remaining errors to be examined for nearer and more distant instances in a scene with the next orchard row visible in the background.

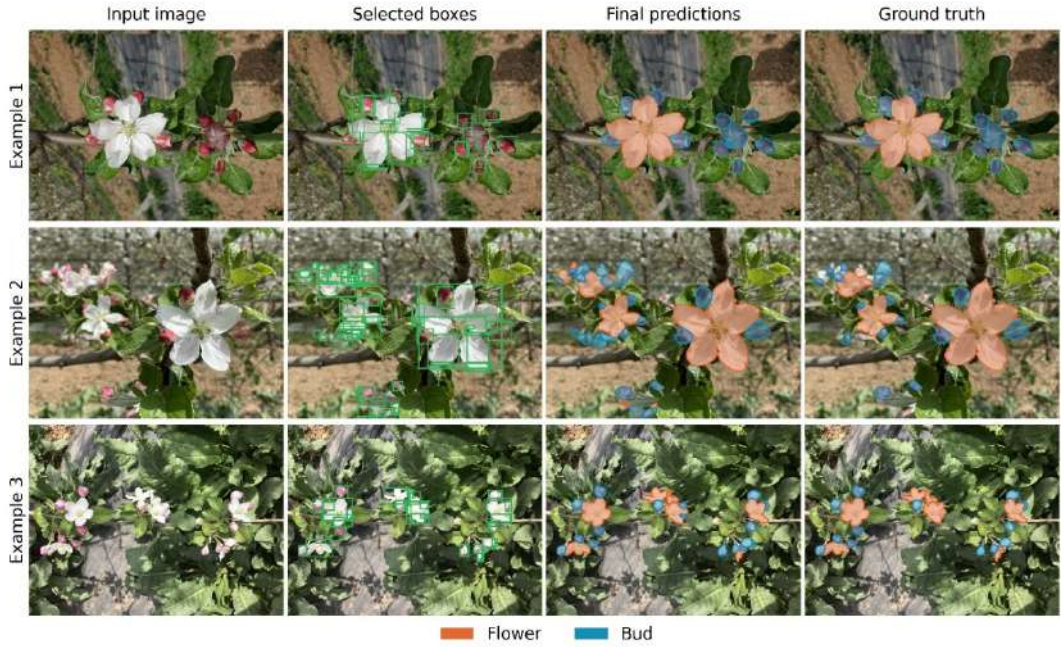

Fig.2 Qualitative results of apple flower and bud instance segmentation.

Final predictions showed higher recall but lower precision for Flower than for Bud (Table 1). Flower and Bud recall were 0.85 and 0.82, while precision was 0.33 and 0.48, respectively. Overall F1 and mean class-wise Mask AP50 were 0.56 and 0.71. Thus, the final masks corresponded to many ground-truth instances, but Flower false positives remained.

Table 1 Class-Wise Instance Segmentation Performance of the Proposed Method.

Class	Precision	Recall	F1	Mask AP50	Mask AP75
Flower	0.33	0.85	0.47	0.75	0.58
Bud	0.48	0.82	0.61	0.66	0.46
Overall	0.42	0.83	0.56	0.71	0.52

Note: Overall precision, recall, and F1 use pooled counts; AP is the unweighted mean across classes.

Component Analysis

The effects of foreground filtering, detection re-scoring, and mask filtering were compared separately to assess their contributions to the final recognition results. Foreground filtering reduced the number of candidates passed to the mask-generation model and improved precision and F1, but increased missed detections (Table 2). Precision and F1 increased by 14.88 and 16.84 percentage points, while recall decreased by 5.46 percentage points. The candidate count fell by 47.51%, from 133,366 to 70,001.

Table 2 Effect of Foreground Filtering on Bounding-Box Detection Performance.

Foreground filtering	Precision	Recall	F1
-	0.19	0.88	0.31
✓	**0.34**	**0.83**	**0.48**

Note: ✓: applied; –: not applied. Both conditions use the same NMS settings.

IoU-based re-scoring improved bounding-box AP over the original-score baseline (Table 3). Using CountGD-Box features alone yielded AP50 and AP75 of 0.65 and 0.34, respectively. Combining CountGD-Box and Depth Anything features increased these values to 0.68 and 0.36, corresponding to gains of 6.40 and 4.49 percentage points over the baseline. These gains reflect improved prediction ranking rather than box refinement.

Table 3 Effect of IoU-Based Re-Scoring on Bounding-Box AP.

CountGD-Box	Depth Anything	Bbox AP50	Bbox AP75
-	-	0.61	0.31
✓	-	0.65	0.34
✓	✓	**0.68**	**0.36**

Note: Checks indicate features used for IoU prediction. All rows use the same CountGD-Box detections.

Mask filtering reduced Flower false positives with only a small decrease in overall recall (Table 4). The prediction count decreased from 70,001 to 56,510, and Flower FPPI decreased by 36.00%, from 19.39 to 12.41. Overall recall decreased by 0.06 percentage points, and 12 previously correctly recognized Flower instances were additionally missed. Changes in Mask AP50 and AP75 were small, at −0.03 and +0.04 percentage points. Thus, the selected criterion removed some Flower false positives while nearly preserving recall, but did not eliminate all false positives.

Table 4 Effect of Mask Filtering on Predictions.

Mask filtering	Number of predictions	Flower FPPI
-	70,001	19.39
✓	**56,510**	**12.41**

Note: ✓ indicates that mask filtering was applied; – indicates that it was not applied. FPPI denotes false positives per image for Flower.

CONCLUSIONS

This study proposed a reference-guided instance segmentation method for apple flowers and buds using annotated reference images and features from frozen vision foundation models. Classifiers and estimators trained on annotated reference images were used to filter detection

candidates, rescore detections, classify masks, and select the final predictions. With 30 reference images, the final method achieved a mean class-wise Mask AP50 of 0.71 and an overall F1 of 0.56. Under the selected mask-filtering criterion, Flower false positives per image decreased by 36.00% with overall recall nearly preserved. These findings show that the trained classifiers and estimators can improve recognition results on the evaluated images without updating the foundation-model weights. However, false positives remained, and performance requires further evaluation under imaging conditions and flowering stages in other orchards. The method provides instance-level visual information to support target selection for artificial apple pollination.

ACKNOWLEDGEMENTS

This study was supported by a grant from the Rural Development Administration (No. RS-2026-25524139, Core Technology Development Program for Intelligent Agricultural Robots).

REFERENCES

Amini-Naieni, N., and A. Zisserman. 2026. Open-world object counting in videos. Proceedings of the AAAI Conference on Artificial Intelligence 40(4): 2300–2308. DOI: 10.1609/aaai.v40i4.37214.

Bao, Q. Z., Y. X. Yang, Q. Li, and H. C. Yang. 2025. Zero-shot instance segmentation for plant phenotyping in vertical farming with foundation models and VC-NMS. *Frontiers in Plant Science* 16: 1536226. DOI: 10.3389/fpls.2025.1536226.

Hinton, G. E. 2002. Training products of experts by minimizing contrastive divergence. *Neural Computation* 14(8): 1771–1800. DOI: 10.1162/089976602760128018.

Ke, L., M. Ye, M. Danelljan, Y. Liu, Y. W. Tai, C. K. Tang, and F. Yu. 2023. Segment anything in high quality. *Advances in Neural Information Processing Systems* 36. DOI: 10.52202/075280-1303.

Mu, X., L. He, P. Heinemann, J. Schupp, and M. Karkee. 2023. Mask R-CNN based apple flower detection and king flower identification for precision pollination. *Smart Agricultural Technology* 4: 100151. DOI: 10.1016/j.atech.2022.100151.

Roggiolani, G., C. Stachniss, and J. Behley. 2026. Tailored refinement of vision-language models for plant instance segmentation. *Information Processing in Agriculture*, in press. DOI: 10.1016/j.inpa.2026.01.015.

Wang, D., H. Song, and B. Wang. 2025. YO-AFD: An improved YOLOv8-based deep learning approach for rapid and accurate apple flower detection. *Frontiers in Plant Science* 16: 1541266. DOI: 10.3389/fpls.2025.1541266.

Yang, L., B. Kang, Z. Huang, X. Xu, J. Feng, and H. Zhao. 2024. Depth anything: Unleashing the power of large-scale unlabeled data. In *Proceedings of the IEEE/CVF Conference on Computer Vision and Pattern Recognition*, 10371–10381. DOI: 10.1109/CVPR52733.2024.00987.

AI-23

Proceedings of The 12th International Symposium on Machinery and Mechatronics for Agriculture and Biosystems Engineering (ISMAB 2026)
20-24 October 2026, Busan, Republic of Korea

BAND-COMBINATION CHANNELS FOR NON-DESTRUCTIVE RICE PROTEIN PREDICTION USING NIR HYPERSPECTRAL IMAGING

Jeong-Yong Shin[1], Hong Gu Lee[1], Seung Woo Chun[1], Woo Hyeong Yu[1], Jeong Woo Han[1], Woon Tak Han[1], Giyoung Kim[2], Wan-Gyu Sang[3], Changju Yang[4], Changyeun Mo[1,5*]

[1]Department of Interdisciplinary Program in Smart Agriculture, Kangwon National University, Chuncheon, Republic of Korea
[2]Agriculture and Life Sciences Research Institute, Kangwon National University, Chuncheon, Korea
[3]Department of Crop production and physiology, National Institute of Crop Science, Rural Development Administration, Wanju, Republic of Korea
[4]Department of Agricultural Engineering, National Institute of Agricultural Science, Rural Development Administration, Wanju, Republic of Korea
[5]Department of Biosystems Engineering, Kangwon National University, Chuncheon, Republic of Korea
*Corresponding Author-- Voice: +82-33-250-6494, Email: cymoh100@kangwon.ac.kr

Abstract: Protein content governs the eating quality and grading of rice. Measuring protein content in rice is combersome, because the reference Kjeldahl procedure is destructive and slow. Near-infrared hyperspectral imaging can be ais non-destructive alternative for measuring protein contein. Selecting meaningful wavelengths from hyperspectral imagery is critical for estimating protein content. However, conventional wavelength selection methods have lacked a systematic rationale. This study compared wavelength selection algorithms on paddy-rice dataset under an identical protocol, and tested whether recombining the selected bands into ratio and difference channels improves regression by a 2D convolutional neural network. Paddy rice (Oryza sativa L. cv. Gangdaechan) from thirteen fields in Korea gave 130 samples whose Kjeldahl protein content (AOAC 979.09) ranged from 5.3 to 7.1 g per 100 g. Each sample was imaged nine times over 895-1721 nm in 336 bands, giving 1,170 images. Partitions were sample-level to prevent leakage, with 26 samples held out. Nine selection groups each provided ten wavelengths, from which five input configurations were built and regressed with a 2D ResNet-34 over three seeds. The best configuration, ten wavelengths from a univariate correlation criterion with pairwise ratio and difference channels, gave a sample-level root mean square error of 0.116 g per 100 g and a coefficient of determination of 0.97 on the external test set, comparable to the reproducibility of the Kjeldahl reference. Ten near-infrared wavelengths, recombined into pairwise derived channels, therefore suffice for non-destructive paddy-rice protein prediction, a requirement met by a fixed-filter multispectral device for field application rather than a hyperspectral camera.

Key Words: hyperspectral imaging, wavelength selection, band combination, convolutional neural network, rice protein

Field Machinery and Systems 1 (FM-1)



FM-01

Proceedings of The 12th International Symposium on Machinery and Mechatronics for Agriculture and Biosystems Engineering (ISMAB 2026)
20-24 October 2026, Busan, Republic of Korea

A RETROFIT SYSTEM FOR AUTOMATIC TILLAGE DEPTH CONTROL ON CONVENTIONAL TRACTORS

Phuoc Bao Long Do[1], Dang Khanh Linh Le [1], Wei-Chih Lin[1,*]

[1]Department of Mechanical and Electro-Mechanical Engineering, National Sun Yat-sen University, Kaohsiung City, Taiwan
*Corresponding Author-- Voice: +886-922-272-615, Email: wc.lin@mail.nsysu.edu.tw

Abstract: Maintaining tillage depth stability is crucial for effective soil preparation, but conventional manual control mechanisms frequently result in inaccurate and inconsistent tillage depths. Meanwhile, upgrading to fully automated machinery requires substantial capital investment. To address these challenges, this study proposes a retrofit system for conventional tractors to achieve automatic tillage depth control. The system integrates a Linkage-Tailboard Kinematic Fusion (LTKF) model to estimate tillage depth and a retrofit control system for automatic depth regulation. The LTKF model utilizes the kinematic relationship between the lifting arm angle and the tailboard angle to accurately estimate tillage depth. Meanwhile, the retrofit control system uses a linear actuator to operate the original hydraulic mechanism without modifying the existing tractor structure. For performance validation, field experiments were conducted under various tillage depths and forward speeds to evaluate the proposed system. At forward speeds of 0.2–0.5 m/s, the system achieved RMSE values of 2.45–10.68 mm, with mean absolute errors ranging from 1.94 to 9.29 mm. Consequently, these results demonstrate the feasibility of retrofitting conventional tractors for precise automatic tillage depth control.

Key Words: Precision agriculture; Tillage machine; Tillage depth; Monitoring system; Adaptable measurement

INTRODUCTION

Maintaining a uniform tillage depth is a key factor in optimal soil preparation, ensuring uniform seed germination and minimising energy consumption. However, regulating the tillage depth remains a major challenge when the tiller operates on uneven terrain, as fluctuations in the tractor's pitch angle and continuous geometric changes in the three-point linkage constantly disrupt the position of the implement. On traditional tractor models, depth adjustment relies primarily on manual lever operation and the operator's experience, leading to fatigue, inconsistent tillage depth and a deterioration in soil quality. To overcome these manual limitations, several studies have focused on developing automated depth measurement methods, including surface contact mechanism(Ni et al., 2021; Wang et al., 2018), non-contact distance sensors (Lou et al., 2021; Tsuchikawa et al., 2026), and multi-sensor spatial reconstruction systems combining an IMU with RTK-GNSS positionin(Chen et al., 2025). Although certain advances have been made, existing methods still suffer from

significant research gaps: contact-based mechanisms are prone to soil adhesion and mechanical wear; non-contact sensors are heavily affected by soil dust, plant residues and surface scattering; whilst GNSS–attitude fusion systems require complex coordinate transformation algorithms and entail high hardware costs. Furthermore, the implementation of current automation solutions often requires significant intervention in the mechanical structure or the installation of specialised electro-hydraulic proportional valves, making both retrofitting and replacing machinery beyond the financial means of the majority of farmers. Consequently, research into an automated depth measurement and control system that is highly accurate, low-cost and non-invasive to the machine's structure, specifically designed for traditional tractors, is an urgent priority.

To address these limitations, this study proposes a retrofit system for automatic tillage depth control of conventional tractors. The system combines a Linkage-Tailboard Kinematic Fusion (LTKF) model for depth estimation with a non-invasive retrofit control system for depth regulation. The LTKF model estimates tillage depth from the lifting-arm and tailboard angles. Meanwhile, a linear actuator operates the original hydraulic control mechanism without modifying the existing tractor structure. The proposed system was evaluated through static and field experiments under different operating conditions to assess its feasibility for automatic tillage depth control.

MATERIALS AND METHODS

The proposed system was developed by retrofitting a conventional tractor equipped with a rotary tiller, as illustrated in Fig. 1. Two angular sensors were installed to measure the lifting-arm angle and tailboard angle. A linear electric actuator was coupled to the original hydraulic control lever to enable automatic operation without modifying the existing mechanical-hydraulic structure. The measured angles were processed by the LTKF model to estimate the actual tillage depth, which was used as feedback for automatic depth regulation.

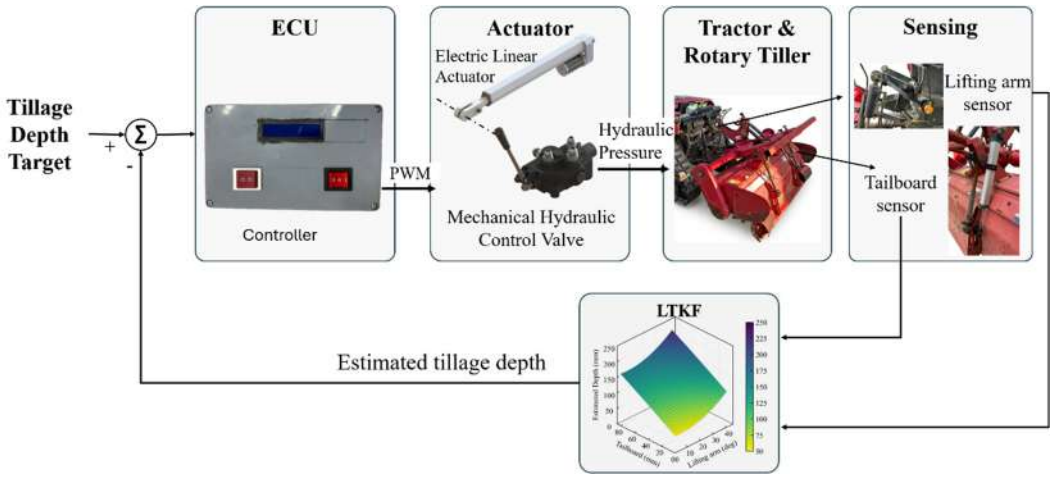

Fig. 1 Overall architecture of the retrofit automatic tillage depth control system.

LTKF DEPTH ESTIMATION

The LTKF model estimates the tillage depth from the geometric relationship of the three-point hitch and the tailboard without requiring external GNSS or IMU sensors. As illustrated in Fig. 2, two coordinate frames are established: the undisturbed soil surface frame $\{S\}$ (X_S horizontal,

Z_S vertical upward) and the vehicle body frame $\{V\}$ fixed at the rear-wheel axle.
From the lifting-arm angle (α) measured by a rotary sensor, the spatial position and orientation of the tiller frame are determined via planar linkage kinematics. During operation, the lower edge of the tailboard maintains continuous sliding contact with the tilled soil surface. Given the measured tailboard angle (β) relative to the tiller frame, the absolute vertical position of the tailboard contact point $I(x_I^V, z_I^V)$ transformed into $\{S\}$ is constrained by the soil bulking height δ_h:

$$z_I^S = R + z_I^V \cos(\theta_p) + x_I^V \sin(\theta_p) = \delta_h \tag{1}$$

where R is the rear-wheel radius. Transforming Eq. (1) into the standard form $x_I^V \sin(\theta_p) + z_I^V \cos(\theta_p) = \delta_h - R$ yields the analytical solution for the tractor pitch angle θ_p:

$$\theta_p = \text{atan2}(x_I^V, z_I^V) - \arccos\left(\frac{\delta_h - R}{\sqrt{(x_I^V)^2 + (z_I^V)^2}}\right) \tag{2}$$

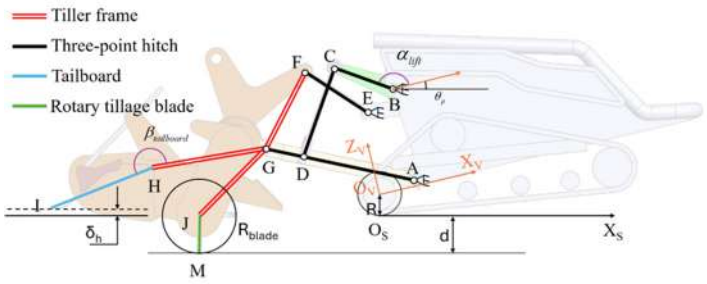

Fig. 2 Physical configuration and coordinate definition used by the LTKF measurement model.

Using the inferred pitch angle θ_p, the true tillage depth d—defined as the vertical distance from the undisturbed soil surface to the lowest cutting trajectory of the blades with rotational radius R_{blade}—is expressed analytically as:

$$d(\alpha, \beta, \delta_h) = R_{blade} - \left(R + z_J^V(\alpha)\cos(\theta_p) + x_J^V(\alpha)\sin(\theta_p)\right) \tag{3}$$

Although Eq. (3) provides an exact kinematic solution, executing nested trigonometric transformations and intermediate pitch calculations online imposes an excessive computational burden on real-time embedded microcontrollers. To simplify computation, a kinematic dataset of 15847 points spanning the operational ranges of α, β, and δ_h was generated using the analytical model. Fitting a response surface confirmed that a second-order multivariate polynomial can accurately approximate the theoretical depth mapping ($R^2 > 0.99$). Polynomial is used to get the expression of fitting surface:

$$\begin{aligned} d(\alpha, \beta, \delta_h) &= 53.7651 - 0.4259\alpha + 1.4838\beta - 0.4017\delta_h + 0.0484\alpha^2 \\ &-0.0007\alpha\beta - 0.0010\beta^2 - 0.0004\beta\delta_h - 0.0008\delta_h^2 \end{aligned} \tag{4}$$

RETROFIT DEPTH CONTROL

The retrofit depth-control architecture is illustrated in Fig. 3. The system begins with the acquisition of the lifting-arm and tailboard angles from two rotary sensors. These

measurements are processed by the LTKF model to estimate the actual tillage depth in real time. The estimated depth is compared with the target depth, and the resulting error is supplied to the hierarchical PID-SMC controller. The controller generates a command for a linear electric actuator, which directly operates the tractor's original hydraulic control lever. The existing mechanical feedback mechanism and hydraulic three-point hitch are retained, so the implement position is adjusted through the original tractor system without structural modification. This architecture enables automatic tillage depth regulation while preserving the conventional tractor's original mechanical-hydraulic design.

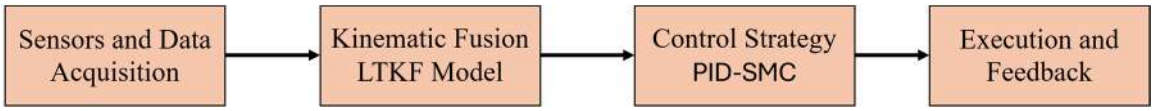

Fig. 3 Architecture of the retrofit automatic tillage depth control system.

RESULTS & DISCUSSION

Field tests were then conducted at different target depths and forward speeds to evaluate the proposed system. As shown in Fig. 4, the uncontrolled tillage depth fluctuated considerably, whereas the proposed system maintained the depth close to the target values at 0.2 m/s. At 0.2–0.5 m/s and target depths of 100–150 mm, the RMSE ranged from 2.45 to 10.68 mm across target depths of 100–150 mm. The best performance was obtained at a target depth of 150 mm and a speed of 0.2 m/s, with a mean absolute error of 1.94 mm and an RMSE of 2.45 mm. The detailed tracking errors are summarized in Table 1.

At 0.8 m/s, the tracking error generally increased, with the maximum RMSE reaching 11.59 mm at the 120 mm target depth. This degradation was mainly attributed to the limited response and soil-penetration capability of the original tractor-tiller mechanism at higher forward speeds. Overall, the results indicate that the proposed retrofit system can provide reliable automatic depth regulation while retaining the original mechanical-hydraulic architecture of the conventional tractor.

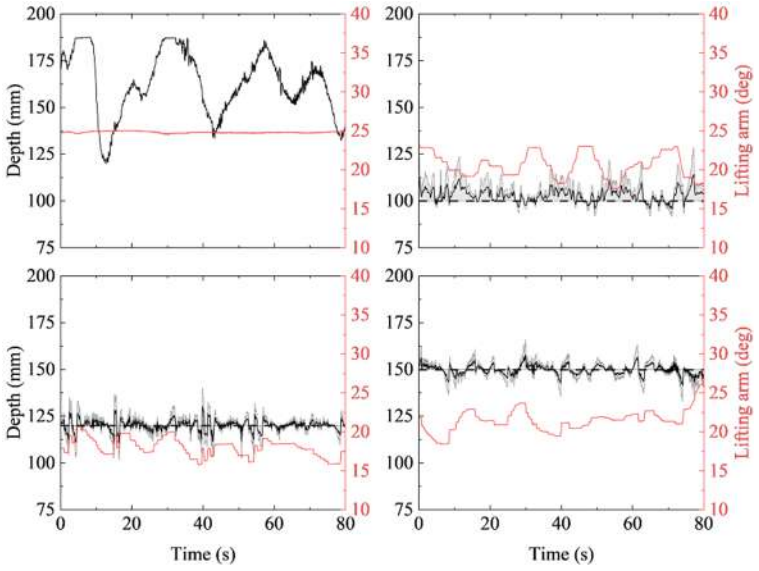

Fig. 4 Field tillage depth responses at 0.2 m/s: (a) manual/unregulated operation; (b) 100 mm target depth; (c) 120 mm target depth; and (d) 150 mm target depth.

Table1 Field measurement error

Target tillage depth (mm)	Speed(m/s)	Max AEV (mm)	Mean AEV (mm)	RMSE (mm)
100	0.2	14.26	3.67	4.51
	0.5	24.58	9.29	10.68
	0.8	27.13	6.94	8.74
120	0.2	10.07	1.99	2.68
	0.5	16.43	4.5	5.59
	0.8	36.09	8.87	11.59
150	0.2	8.65	1.94	2.45
	0.5	16.41	4.69	5.8
	0.8	23.09	4.99	6.18

CONCLUSIONS

This study developed a retrofit system for automatic tillage depth control of conventional tractors. The LTKF model enabled tillage depth estimation using only the lifting arm and tailboard angles, while the retrofitted actuator enabled automatic operation of the original hydraulic mechanism without structural modification. Static and field tests confirmed reliable depth regulation, particularly at forward speeds of 0.2–0.5 m/s, with mean absolute errors of 1.94–9.29 mm and RMSE values of 2.45–10.68 mm. The results demonstrate that the proposed approach provides a practical solution for upgrading conventional tractors with automatic tillage depth control.

ACKNOWLEDGEMENTS

This research was supported by funding from the Ministry of Agriculture, Taiwan (115 農科-11.2.2-科-02). The authors are grateful for the support and resources provided by the Biomimicking and Engineering Lab (Being2 Lab) at National Sun Yat-sen University, Taiwan.

REFERENCES

Chen, G., Y. Chen, Z. Huang, J. Wang, Y. Deng, P. Wang, R. Zhao, and L. Hu. 2025. Integrated measurement method for field surface topography and tillage depth in rotary tillage operations. *Computers and Electronics in Agriculture* 239.

Lou, S., J. He, C. Lu, P. Liu, H. Li, and Z. Zhang. 2021. A Tillage Depth Monitoring and Control System for the Independent Adjustment of Each Subsoiling Shovel. *Actuators* 10(10).

Ni, Y., C. Jin, M. Chen, W. Yuan, Z. Qian, T. Yang, and Z. Cai. 2021. Computational model and adjustment system of header height of soybean harvesters based on soil-machine system. *Computers and Electronics in Agriculture* 183.

Tsuchikawa, H., S. Noda, H. Saito, K. Kurashiki, and W. Iijima. 2026. Development and evaluation of an interoperable sensor-driven tractor control system for rotary tillage. *Smart Agricultural Technology* 14.

Wang, Y., H. Jing, D. Zhang, T. Cui, X. Zhong, and L. Yang. 2018. Development and performance evaluation of an electric-hydraulic control system for subsoiler with flexible tines. *Computers and Electronics in Agriculture* 151:249-257.

FM-02

Proceedings of The 12th International Symposium on Machinery and Mechatronics for Agriculture and Biosystems Engineering (ISMAB 2026)
20-24 October 2026, Busan, Republic of Korea

TILLAGE ELECTRIFICATION: EFFECTS OF A REDUCED-TILLAGE IMPLEMENT ON ENERGY USE AND GREENHOUSE SPINACH PERFORMANCE

Oyetayo Olukorede Oyebode[1*], Ryota Sakata[1], Naoki Tsunekawa[1], Nang Nguyen Van[1]

[1]Department of Agricultural Mechanization and Smart Farming Research, Institute of Agricultural Machinery, National Agriculture and Food Research Organization.
1-40-2 Nisshincho, Kita-ku, Saitama City, Saitama, 331-8537 Japan.

*Corresponding Author-- Voice: +81-654-7081, Email: oyebode.oyetayo.olukorede459@naro.go.jp

Abstract: Tillage is among the most energy-intensive operations in crop production and is commonly associated with substantial greenhouse gas emissions. Although electrification offers a promising pathway to reduce these emissions, its application to tillage remains challenging because conventional tillage implements consume considerable energy. Reducing the energy demand of the tillage process itself may therefore be an important first step toward practical tillage electrification. To this end, a low-energy tillage implement was developed to achieve sufficient soil pulverization without intensive disturbance of the entire soil. The implement was mounted on a commercially available small electric crawler robot for agricultural use. The energy requirement of the developed electric tillage system was measured and compared with that of a commercially available electric rotary tiller operating at a similar tilling width and depth and mounted on a similar electric transport vehicle. The rotary tiller required nearly twice as much energy as the developed partial tiller, demonstrating the potential of reduced tillage to lower the energy required for electrified tillage operations. A cultivation experiment was also conducted in a greenhouse to evaluate the effects of the two tillage methods on spinach germination, growth, and yield. Preliminary results from the first of three planned cultivation trials showed no significant differences between the partial-tillage and rotary-tillage treatments. Further trials are being conducted to confirm the consistency of these findings. Although the developed tiller substantially reduced energy consumption without adversely affecting spinach performance in the first trial, it produced a rougher soil surface than the rotary tiller. Methods to improve surface appearance are therefore being investigated to increase the practical acceptance of the proposed tillage system. These findings suggest that redesigning tillage operations to reduce soil disturbance and energy demand could facilitate near-term electrification. As battery energy density and related technologies continue to improve, the electrification of more energy-intensive conventional tillage methods may become increasingly feasible.

Key Words: Partial Tillage, Energy Consumption, Tillage Method, Spinach Cultivation, Crop Yield.

FM-03

Proceedings of The 12th International Symposium on Machinery and Mechatronics for Agriculture and Biosystems Engineering (ISMAB 2026)
20-24 October 2026, Busan, Republic of Korea

TEMPORAL OBSERVATION FOR REINFORCEMENT LEARNING OBSTACLE AVOIDANCE IN A TRACKED AGRICULTURAL ROBOT

Yu-Hsien Lee*, Wu-Huan Hsu

Taiwan Agricultural Research Institute, Ministry of Agriculture, Republic of China
*Corresponding Author-- Voice: +886-4-2331-7704, Email: yhlee@tari.gov.tw

Abstract: Dynamic obstacle avoidance in protected crop production requires an agricultural robot to respond not only to obstacle position but also to obstacle motion. This study evaluated whether temporal observation improves obstacle avoidance for a tracked agricultural robot and whether the same information can be incorporated into both learned and geometric navigation methods. Mobility tests on a 405 kg tracked platform showed angular-velocity saturation. A two-stage kinematic model reproduced the measured mobility within 3.2% and identified a saturation onset at approximately 0.52 m/s. A two-dimensional simulator constrained by this model was used to compare four navigation configurations: Vector Field Histogram Plus (VFH+) with a single LiDAR frame, VFH+ with temporal sector extrapolation, proximal policy optimization (PPO) with a single observation frame, and PPO with four stacked frames. Performance was evaluated in static wide-gap, dynamic wide-gap, and dynamic narrow-gap scenarios under domain randomization. For PPO, frame stacking produced no significant improvement in the static scenarios but increased success by 0.043 and 0.061 in the two dynamic groups. For VFH+, temporal extrapolation could also improve dynamic avoidance, but its effect depended strongly on the other planner parameters. The PPO-based policy did not consistently outperform the tuned geometric planner. However, temporal observation could be incorporated into PPO without retuning the remaining hyperparameters, whereas the geometric planner required joint adjustment with its heuristic parameters. These results support temporal observation as a practical input for dynamic obstacle avoidance in tracked agricultural robots.

Key Words: reinforcement learning, temporal observation, dynamic obstacle avoidance, tracked agricultural robot

INTRODUCTION

Autonomous agricultural robots are increasingly being developed to reduce labor demand in protected crop production. For precision weeding, a mobile platform must travel through confined working spaces while safely avoiding workers, carts, and other obstacles. Reactive geometric planners are commonly used because they are simple, predictable, and do not require training data. Reinforcement learning (RL) has also been applied to navigation among moving pedestrians and to agricultural path planning (Chen et al., 2017; Yang et al., 2022). A key issue in dynamic obstacle avoidance is whether a single sensor frame provides enough information for decision making. A single LiDAR scan can describe the current position of an obstacle, but it cannot directly indicate whether the obstacle is stationary or moving across the vehicle path. Navigation based on a single frame is therefore partially observable in dynamic environments (Ni et al., 2022). However, many comparisons change both the navigation method and the available observation history at the same time. As a result, the effect of

temporal observation may be difficult to separate from the effect of the navigation algorithm.

Vehicle motion also limits the avoidance maneuvers that can be performed. Tracked vehicles are often modeled using a constant steering-efficiency coefficient (Martínez et al., 2005). For a heavy tracked platform with a high-reduction-ratio drive system, however, steering performance may vary with operating speed. These kinematic limits should therefore be considered when navigation policies are trained and evaluated. The effect of temporal observation on obstacle avoidance for a tracked agricultural robot was investigated in this study. A kinematic model was first developed from measured vehicle mobility data. A geometric planner and a PPO-based learned policy were then evaluated with and without temporal observation under the same simulated scenario distribution. The study focused on whether temporal observation improves avoidance of moving obstacles and whether it can be added to each navigation method without retuning other control parameters.

MATERIALS AND METHODS

TRACKED PLATFORM AND KINEMATIC MODEL

The reference machine was a high-clearance tracked platform developed for precision weeding in protected crop production (Fig. 1a). The platform was 2.00 m long and 1.08 m high, with an adjustable overall width of 1.44–2.00 m and a mass of 405 kg. Each track was driven by a brushless DC motor through a 30:1 worm reduction. The track gauge, B, was 1.16 m. Vehicle mobility was measured on level concrete at 40%, 60%, and 80% throttle settings, with three repetitions in each turning direction. An additional test was conducted at 60% throttle with a 50 kg payload representing the planned weeding module. Steering efficiency was defined as $\eta = \omega/(2v/B)$, where v is the straight-line speed and ω is the pivot angular velocity. Because the measured angular velocity showed saturation, the following two-stage kinematic model was used:

$$\omega(v) = min\left(\eta_0 \frac{2v}{B}, \omega_{max}\right) \quad (1)$$

with η_0 = 0.48 and ω_{max} = 0.43 rad/s. The saturation onset was v^* = 0.52 m/s, giving a minimum turning radius of 1.21 m below this speed. The simulation speed limit was therefore set to 0.484 m/s, which was the highest measured speed below the saturation onset.

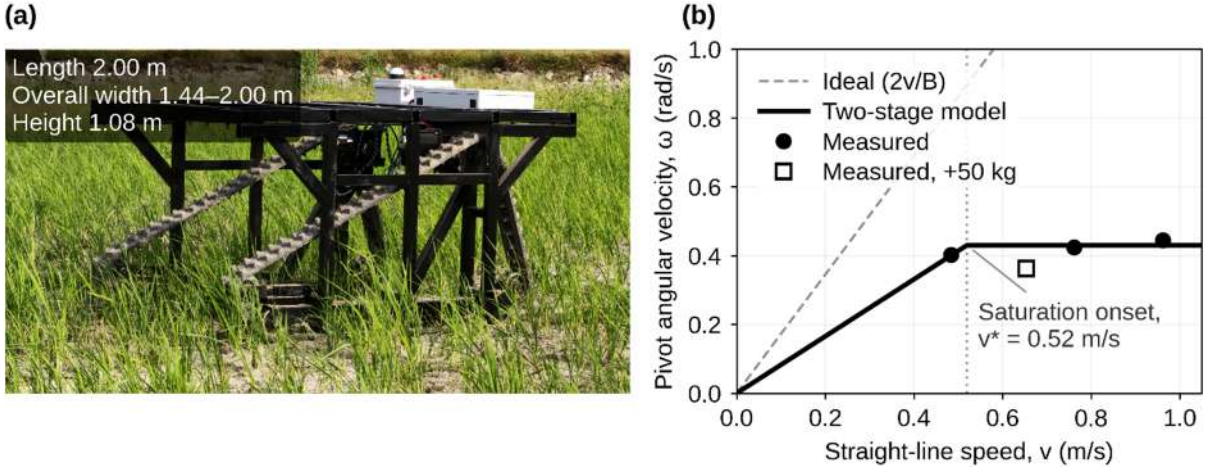

Figure 1. Reference platform and kinematic characterization. (a) Tracked agricultural platform. (b) Measured pivot angular velocity and the two-stage kinematic model.

SIMULATION ENVIRONMENT AND CONTROL

A purpose-built two-dimensional kinematic simulator was used for training and evaluation. The simulator implemented Eq. (1) with a control interval of 0.2 s and operated at approximately 6,400 steps/s on a single CPU thread. Open-loop consistency with Gazebo (Koenig and Howard, 2004) was checked by replaying five identical action sequences. Endpoint differences were 0.57–0.75% of the traveled distance, and pivot angular velocity differed by 3.3%. The simulated workspace was a 20.0 m × 6.0 m corridor representing a net house working area (Fig. 2). The start and goal were placed at opposite ends of the corridor with randomized lateral positions and initial headings. Static obstacles were rectangular boxes of 0.4–1.0 m. Dynamic scenarios included one or two moving obstacles represented as pedestrians or carts. Pedestrian speed ranged from 0.5 to 1.2 m/s, and cart speed ranged from 0.3 to 0.8 m/s. All generated scenarios were checked against the vehicle footprint and the minimum turning radius to ensure kinematic feasibility.

A single-frame observation contained 54 variables. These included 48 LiDAR sectors covering a 240° field of view, normalized goal distance, sine and cosine of the goal-bearing error, previous linear and angular velocities, and normalized track width. The simulated LiDAR range was 0.15–10.0 m. Range noise and beam dropout were randomized during training and evaluation. Six discrete actions were available, including an explicit stop action. The reward function included a goal-progress term, an obstacle-proximity penalty, and an action-change penalty, with weights of 5.0, 0.02, and 0.005, respectively. A reward of +10 was assigned for reaching the goal within 0.5 m, and a penalty of −10 was assigned for collision. No terminal reward was assigned at timeout. The episode time limit was scaled to four times the nominal straight-line travel time to the goal.

NAVIGATION METHODS AND TRAINING

Four navigation arms were arranged in a 2 × 2 design that compared navigation method and access to temporal observation (Table 1). Arm A used VFH+ (Ulrich and Borenstein, 1998) with the current LiDAR frame. Arm A′ used the same geometric planner with per-sector temporal extrapolation. The effective distance for each LiDAR sector was calculated as

$$d_{eff}[i] = clip(\ d_t[i] + h(d_t[i] - \ d_{t-1}[i]), 0\ , d_{max}) \quad (2)$$

where $d_t[i]$ is the current range in sector i, d_{max} is the LiDAR range limit, and h = 4 control steps. VFH+ was selected because its sector-based representation allowed temporal extrapolation to be added without changing the basic planner structure.

Arm B used a PPO policy (Schulman et al., 2017) with the 54-dimensional single-frame observation. Arm C used the same PPO architecture with four stacked frames, giving a 216-dimensional observation. All other PPO settings were kept identical between Arms B and C. All four arms were tuned or trained using the same mixed scenario distribution. It contained 40% static wide-gap scenarios with gaps of 2.6–3.5 m, 30% static narrow-gap scenarios with gaps of 2.1–2.5 m, and 30% dynamic wide-gap scenarios. Arms A and A′ were tuned independently using a two-stage grid search. The ten best parameter sets from the first stage were reevaluated using five independent seed bases to reduce selection bias. To separate the effect of temporal extrapolation from parameter tuning, a crossover analysis was conducted after tuning. Temporal extrapolation was switched on and off at the parameter settings selected for Arms A and A′, and the comparison was also repeated across all 64 non-temporal VFH+

parameter combinations.

PPO was implemented using Stable-Baselines3 (Raffin et al., 2021). The policy and value networks each contained two hidden layers with 256 units. Training used 16 parallel environments, 512-step rollouts, a learning rate of 3×10^{-4}, a clip range of 0.2, an entropy coefficient of 0.008, γ = 0.995, and λ = 0.95. Each policy was trained for 6×10^{6} steps using 40 independent training seeds. Arms A and A′ included an emergency-stop rule, while Arms B and C were provided only with the stop action.

EVALUATION AND STATISTICAL ANALYSIS

Three fixed evaluation groups were used with increasing demand for motion prediction. The Static-wide group contained static obstacles with wide gaps. The Dynamic-wide group added crossing traffic while retaining wide gaps. The Dynamic-narrow group combined crossing traffic with gaps of 2.1–2.5 m. Dynamic evaluation focused on crossing traffic because head-on encounters could not be safely avoided within the simulated sensing range given the vehicle's turning limits. Each group contained 100 fixed scenarios. All scenarios were evaluated under five independent domain-randomization seed bases. This produced 500 episodes per group for Arms A and A′. Each of the 40 independently trained PPO policies was evaluated on the same scenarios and randomization seeds, giving 20,000 episodes per group for Arms B and C. All training seeds were retained in the analysis. The primary performance measure was success rate. Median values across seeds were reported because PPO performance showed a skewed distribution in some training runs. Within-family differences between A and A′ and between B and C were evaluated using the Mann–Whitney U test.

Table 1. Navigation methods and temporal observations.

Arm	Navigation method	Observation
A	VFH+	Single LiDAR frame
A′	VFH+	Temporal sector extrapolation, h = 4
B	PPO	Single frame, 54 dimensions
C	PPO	Four stacked frames, 216 dimensions

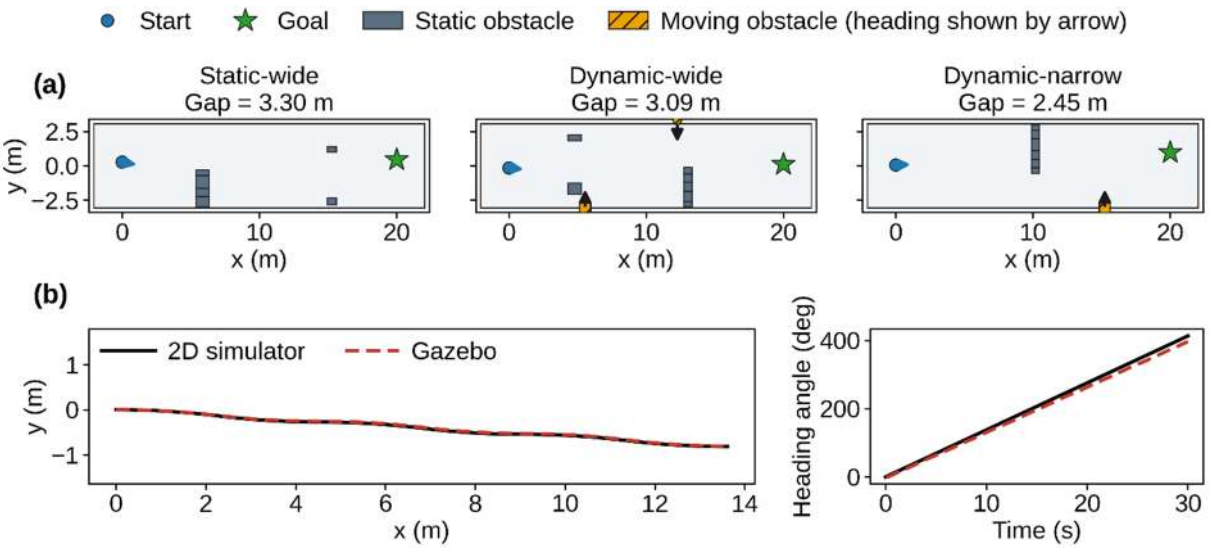

Figure 2. Simulation environment and Gazebo consistency check. (a) Representative Static-wide, Dynamic-wide, and Dynamic-narrow scenarios. (b) Representative open-loop comparisons between the 2D simulator and Gazebo.

RESULTS & DISCUSSION

KINEMATIC CHARACTERISTICS OF THE TRACKED PLATFORM

Straight-line speed increased from 0.484 to 0.962 m/s between the 40% and 80% throttle settings, an increase of approximately 99%. In contrast, pivot angular velocity increased only from 0.402 to 0.445 rad/s, or approximately 10.5% (Fig. 1b). As a result, steering efficiency decreased from 0.482 to 0.268 as speed increased. The two-stage kinematic model reproduced all measured settings within 3.2%. At the 60% throttle setting, adding the 50 kg payload reduced pivot angular velocity from 0.425 to 0.363 rad/s, or approximately 14%. These results indicate that the turning capability of the tracked platform was limited by angular-velocity saturation rather than increasing proportionally with forward speed. The speed limit of 0.484 m/s used in the navigation simulations therefore provided the highest measured operating speed below the identified saturation onset.

TEMPORAL OBSERVATION IN THE PPO POLICY

Navigation performance decreased as the scenarios became more demanding (Table 2 and Fig. 3a). All four arms achieved success rates above 0.89 in Static-wide. Greater differences appeared when moving obstacles and narrow passages were introduced. For the PPO-based learned policy, the only difference between Arms B and C was that Arm C used four stacked observation frames. Temporal observation produced no significant improvement in Static-wide, where the success rate increased only from 0.895 to 0.907 (p = 0.570). In contrast, significant improvements were obtained in both dynamic groups. Success increased from 0.588 to 0.631 in Dynamic-wide (+0.043, p < 0.001) and from 0.445 to 0.506 in Dynamic-narrow (+0.061, p = 0.002). The increasing benefit from Static-wide to Dynamic-narrow indicates that observation history became more useful as motion prediction became more important. A single LiDAR frame describes obstacle position but provides limited information about obstacle motion. Stacked observations allowed the policy to use short-term changes in range when responding to crossing traffic. Frame stacking also increased the network input size. Therefore, network capacity cannot be completely separated from the temporal effect. However, the absence of improvement in the static group suggests that increased network size alone was not the main source of the observed gains.

TEMPORAL OBSERVATION IN THE GEOMETRIC PLANNER

In the geometric planner, the effect of temporal observation depended more strongly on parameter settings. After independent tuning, Arm A′ achieved a higher success rate than Arm A in Dynamic-narrow, increasing from 0.320 to 0.450 (p = 0.011). However, its performance in Static-wide decreased from 0.970 to 0.930 (p = 0.020). Because Arms A and A′ were tuned separately, these differences included both the effect of temporal extrapolation and changes in other planner parameters. The crossover analysis showed a clear interaction between temporal extrapolation and the clearance threshold (Fig. 3b). When extrapolation was added to the parameter setting selected for Arm A, which used a 1.8 m clearance threshold, Dynamic-narrow success decreased from 0.320 to 0.110. In contrast, at the parameter setting selected for Arm A′ with a 1.2 m clearance threshold, temporal extrapolation improved success by 0.080, 0.120, and 0.060 in Static-wide, Dynamic-wide, and Dynamic-narrow, respectively.

Across the 64 non-temporal parameter combinations, the effect of adding temporal

extrapolation ranged from −0.18 to +0.30, with a median improvement of +0.09. At a clearance threshold of 1.2 m, the median improvement was +0.23 and 28 of 32 settings improved. At 1.8 m, the median effect was approximately zero. Temporal extrapolation shortens the effective obstacle distance when an obstacle approaches. When combined with an already conservative clearance threshold, this can cause traversable gaps to be rejected. With a smaller clearance threshold, the same temporal observation can provide useful anticipation without excessive blocking.

These results show an important difference between the two navigation approaches. Temporal observation was added to the PPO policy through the observation input without retuning other control parameters, and significant improvements were obtained in dynamic environments. For the geometric planner, temporal observation was also useful, but its benefit depended strongly on the other heuristic parameters. Effective use of temporal observation therefore required joint retuning of the planner. The learned policy did not significantly outperform the tuned geometric planner in Dynamic-narrow (0.506 versus 0.450, p = 0.159), and the geometric planner performed better in Dynamic-wide (p = 0.038). The main contribution is therefore not that PPO universally outperformed VFH+, but that temporal observation could be incorporated into the learned policy without manually adjusting the other heuristic rules. Physical validation of this behavior will be addressed in future work.

Table 2. Median success rates and effects of temporal observation.

Scenario	Arm A	Arm A′	Arm B	Arm C	A′ − A (p-value)	C − B (p-value)
Static-wide	0.970	0.930	0.895	0.907	−0.040 (0.020)	+0.012 (0.570)
Dynamic-wide	0.660	0.680	0.588	0.631	+0.020 (0.209)	+0.043 (<0.001)
Dynamic-narrow	0.320	0.450	0.445	0.506	+0.130 (0.011)	+0.061 (0.002)

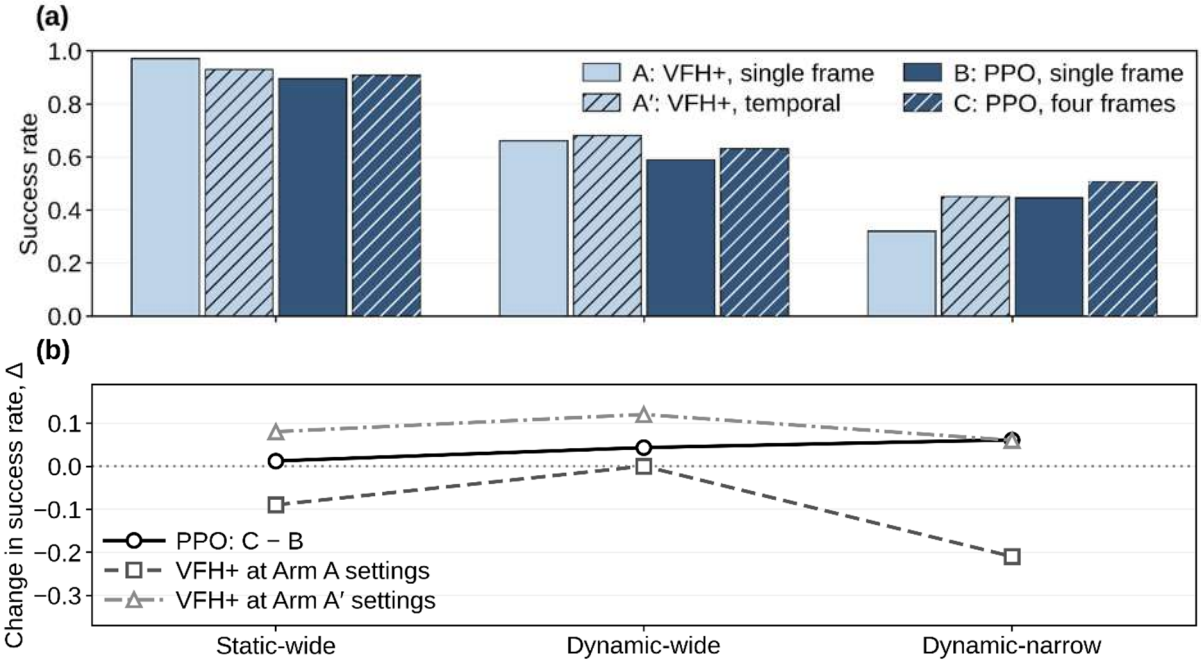

Figure 3. Effects of temporal observation on navigation performance. (a) Median success rates of the four navigation arms. (b) Change in success rate after adding temporal observation to the PPO policy and to two VFH+ parameter settings. Positive values indicate improved performance.

CONCLUSIONS

The tracked agricultural platform showed clear angular-velocity saturation at higher operating speeds. A two-stage kinematic model reproduced the measured mobility within 3.2% and identified a saturation onset of approximately 0.52 m/s. These results provided realistic motion constraints for the navigation simulations. Temporal observation had little effect on the PPO-based learned policy in the Static-wide scenarios, but significantly improved success in both dynamic groups. The improvement increased from +0.043 in Dynamic-wide to +0.061 in Dynamic-narrow, indicating that recent observation history became more useful as motion prediction became more important. For the geometric planner, temporal extrapolation was also useful, but its effect depended strongly on the other parameter settings. Across the evaluated settings, the change in success rate ranged from negative to positive values, with the clearance threshold having a major influence. Temporal observation therefore required joint adjustment with the planner heuristics.

Overall, the PPO-based policy was not found to universally outperform the tuned geometric planner. Its practical advantage was that temporal observation could be added through frame stacking without retuning the remaining PPO hyperparameters. The results support the use of temporal observation for dynamic obstacle avoidance on tracked agricultural robots. Future work will focus on validation with the physical platform and measured LiDAR data.

ACKNOWLEDGEMENTS

This work was supported by the Ministry of Agriculture, Taiwan, under grant 115AS-4.5.1-CI-02.

REFERENCES

Chen, Y. F., M. Everett, M. Liu, and J. P. How. 2017. Socially aware motion planning with deep reinforcement learning. In *Proc. IEEE/RSJ Int. Conf. on Intelligent Robots and Systems (IROS)*, 1343-1350.

Koenig, N., and A. Howard. 2004. Design and use paradigms for Gazebo, an open-source multi-robot simulator. In *Proc. IEEE/RSJ Int. Conf. on Intelligent Robots and Systems (IROS)*, 2149-2154. Sendai, Japan.

Martínez, J. L., A. Mandow, J. Morales, S. Pedraza, and A. García-Cerezo. 2005. Approximating kinematics for tracked mobile robots. Int. J. Robotics Research, 24(10): 867-878.

Ni, T., B. Eysenbach, and R. Salakhutdinov. 2022. Recurrent model-free RL can be a strong baseline for many POMDPs. In Proc. 39th Int. Conf. on Machine Learning, PMLR 162: 16691-16723.

Raffin, A., A. Hill, A. Gleave, A. Kanervisto, M. Ernestus, and N. Dormann. 2021. Stable-Baselines3: Reliable reinforcement learning implementations. J. Machine Learning Research, 22(268): 1-8.

Schulman, J., F. Wolski, P. Dhariwal, A. Radford, and O. Klimov. 2017. Proximal policy optimization algorithms. arXiv preprint arXiv:1707.06347.

Ulrich, I., and J. Borenstein. 1998. VFH+: Reliable obstacle avoidance for fast mobile robots. In Proc. IEEE Int. Conf. on Robotics and Automation (ICRA), 1572-1577. Leuven, Belgium.

Yang, J., J. Ni, Y. Li, J. Wen, and D. Chen. 2022. The intelligent path planning system of agricultural robot via reinforcement learning. Sensors 22(12): 4316.

FM-04

Proceedings of The 12th International Symposium on Machinery and Mechatronics for Agriculture and Biosystems Engineering (ISMAB 2026)
20-24 October 2026, Busan, Republic of Korea

DEVELOPMENT OF STICK-SLIP STEERING MODEL FOR AGRICULTURAL VEHICLES

Masahisa Watanabe[1]

[1] Division of Environmental and Agricultural Engineering, Institute of Agriculture, Tokyo University of Agriculture and Technology, Saiwai-cho, Fuchu, 3-5-8, Tokyo, 183-8509, Japan
*Corresponding Author-- Voice: +81-042-367-5626, Email: masahisa-watanabe@go.tuat.ac.jp

Abstract: The dynamics of agricultural vehicles play an important role in farm operational efficiency and safety. In particular, agricultural vehicles are typically operated in off-road terrain conditions, such as muddy farm roads. This can cause unstable nonlinear phenomena, which can increase the risk of accidents and reduce operational efficiency. Accurate descriptions of vehicle behavior are important to improve vehicle stability. In this study, nonlinear stick-slip phenomena in the vehicle steering system are modelled, and their responses are investigated numerically. The sinusoidal disturbance is input to the developed model. As the amplitude of disturbances increases, the responses change qualitatively. Especially, aperiodic behavior is observed at larger disturbance amplitudes. This random-like response can be a source of instability while vehicle driving on slippery farm roads.

Key Words: Agricultural vehicle, Stick-slip, Steering model, Bicycle model, Nonlinear dynamics

INTRODUCTION

Agricultural vehicles are operated in severe terrain environments, such as undulating roads, inclined side paths, and muddy farm roads with lower friction. In these operational situations, nonlinear phenomena, i.e., impact/stick-slip oscillations, are commonly observed in agricultural vehicle dynamics (Watanabe & Sakai, 2019, 2020). These nonlinear dynamics can induce unstable behavior of the vehicle, such as steering instability, excessive vibrations, and overturning. It is, therefore, essential to analyze and control the nonlinear dynamics of agricultural vehicles to enhance farm safety and automation. The first step to understanding nonlinear dynamics is to develop mathematical models of the phenomena. The objective of the current study is to develop a mathematical model of the stick-slip vehicle steering model and to analyze the developed model from a nonlinear dynamics perspective.

MATERIALS AND METHODS

In this study, a stick-slip vehicle steering model is developed in a bicycle model. Figure 1

shows the schematic diagram of the nonlinear bicycle model. The developed model has two degrees of freedom, that is, yaw rate r and slip angle β. This model assumes that the left and right wheels are equivalent.

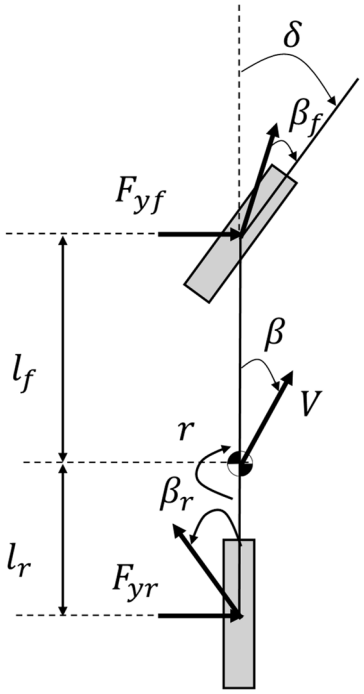

Fig.1 Nonlinear bicycle model for steering behavior.

The equations of motion for the nonlinear bicycle model are as follows:

$$\dot{\beta} = -r + \frac{F_{yf}}{mV} + \frac{F_{yr}}{mV}, \tag{1}$$

$$\dot{r} = \frac{l_f F_f}{J} - \frac{l_r F_r}{J}, \tag{2}$$

where l_f, l_r, m, and J are the distance from the center of gravity to the front wheel, distance from the center of gravity to the rear wheel, mass of the vehicle, and yawing inertia of the vehicle, respectively. The above bicycle model is combined with a driver model. The driver model is used to represent driver steering behavior (McRuer & Jex, 1967). In this study, a driver model is assumed to be a simple model with reaction time t_d as follows,

$$\dot{\delta} = -\frac{\delta}{t_d} + \frac{\delta_c}{t_d}, \tag{3}$$

where δ, δ_c, and δ_d are the steering angle, driver feedback angle, and disturbance for steering, respectively. Driver feedback is calculated based on a forward first-order preview model as follows (Kazama et al., 2017).

$$\delta_c = -k_p\left(y + l_p\theta\right), \tag{4}$$

where k_p, y, l_p, and θ are the drive feedback gain, current lateral position of the vehicle, forward preview distance, and yawing angle, respectively. The disturbance angle is assumed to be sinusoidal, which can be caused by farm roads or vehicle vibrations, as follows,

$$\delta_d = d_0 \cos(2\pi f_d t), \tag{5}$$

where d_0 and f_d are the disturbance amplitude and frequency, respectively. The disturbance angle is used for noise of driver input steering angle. To introduce nonlinearity caused by stick-slip, switching expressions of the cornering forces are employed as follows.

$$F_{yf} = \begin{cases} -C_f\beta_f, & |C_f\beta_f| < \mu_s F_{zf} \\ \mu_d F_{zf}\,\mathrm{sgn}(-\beta_f), & |C_f\beta_f| < \mu_s F_{zf}' \end{cases} \tag{6}$$

$$F_{yr} = \begin{cases} -C_r\beta_r, & |C_r\beta_r| < \mu_s F_{zr} \\ \mu_d F_{zr}\,\mathrm{sgn}(-\beta_r), & |C_r\beta_r| < \mu_s F_{zr}' \end{cases} \tag{7}$$

where F_{yf}, F_{yr}, C_f, C_r are the cornering force for the front wheel, cornering force for the rear wheel, cornering stiffness of the front wheel, and cornering stiffness of the rear wheel, respectively. The front and rear slip angles β_f and β_r are calculated as follows.

$$\beta_f = \beta + \frac{l_f r}{V} - \delta, \tag{8}$$

$$\beta_r = \beta - \frac{l_r r}{V}, \tag{9}$$

When cornering force exceeds the static friction limitation which is the product of friction coefficients and vertical tire forces, friction between tire and ground becomes dynamic. This is a typical switching of stick-slip dynamics, which is widely known as classical Columb friction theory.

RESULTS & DISCUSSION

In this study, the periodic disturbance shown in equation (5) is input to the developed nonlinear system to investigate the typical response of the system. The disturbance frequency f_d is fixed to 1, while disturbance amplitudes d_0 are varied from small (0.015), middle (0.032), to high (0.05). Figure 2 (a), (b), and (c) show corresponding responses of yaw rate r.

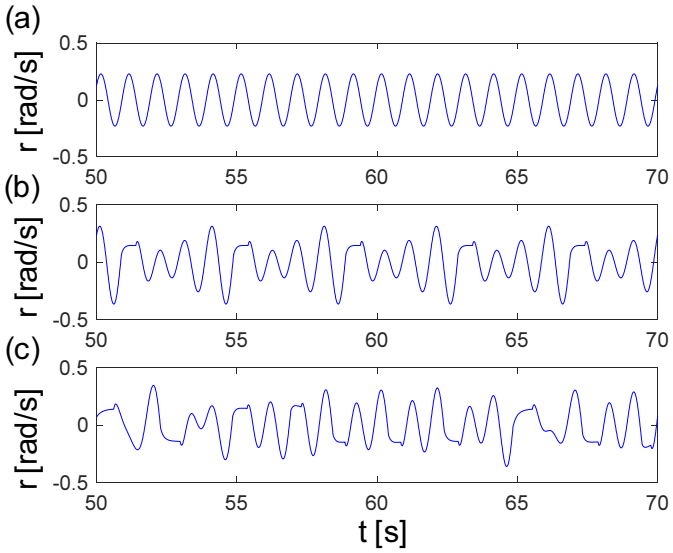

Fig.2 Yaw rate response at (a) d_0=0.02, (b) d_0=0.032, and (c) d_0=0.05.

As disturbance amplitude increases, responses become larger. In small disturbances, vibration is sinusoidal. On the other hand, the shapes of vibrations become more complex in middle and high disturbances. This is basically because nonlinear responses are caused by larger disturbances, which is typical in stick-slip dynamics. The finding in this study is that stick-slip vibrations can also be observed in a theoretical vehicle steering model.

CONCLUSIONS

In this study, nonlinear stick-slip vehicle steering models were developed, and their responses were investigated by numerical simulations. The sinusoidal disturbance can induce stick-slip vibrations in the developed steering model. Further theoretical investigations in terms of nonlinear dynamics and chaos would be conducted in future studies.

ACKNOWLEDGEMENTS (optional)

This work was supported by JSPS Grant-in-Aid (No.26K18165).

REFERENCES

Kazama, K., Nishizaki, K., Shirayama, Y., Furusho, H., & Mouri, H. (2017). Reduction of preview distance in lane-keeping control. International Journal of Automotive Technology, 18(4), 743-750.

McRuer, D. T., & Jex, H. R. (1967). A review of quasi-linear pilot models. IEEE transactions on human factors in electronics, (3), 231-249.

Watanabe, M., & Sakai, K. (2019). Impact dynamics model for a nonlinear bouncing tractor during inclined passage. Biosystems engineering, 182, 84-94.

Watanabe, M., & Sakai, K. (2020). Numerical analysis of steering instability in an agricultural tractor induced by bouncing and sliding. Biosystems engineering, 192, 108-116.

FM-05

Proceedings of The 12th International Symposium on Machinery and Mechatronics for Agriculture and Biosystems Engineering (ISMAB 2026)
20-24 October 2026, Busan, Republic of Korea

DEVELOPMENT OF SENSOR FUSION FRAMEWORK FOR OBSTACLE DETECTION AND COLLISION AVOIDANCE IN AN ELECTRIC MOWER

Runa Kato[1], Jia Qin[1], Michihisa Iida[1*]

[1]Graduate School of Agriculture, Kyoto University, Japan
*Corresponding Author-- Voice: +81-75-753-6167,
Email: iida.michihisa.4v@kyoto-u.ac.jp

Abstract: Autonomous navigation of an electric mower is essential for reducing agricultural labor demands and promoting carbon neutrality. However, reliable operation in complex, GNSS-denied fields require both robust dynamic obstacle detection and accurate self-localization, where single-sensor approaches often fail due to vibration during driving, dynamic occlusion, and changing illumination. This study proposes an integrated ROS2-based framework combining 3D-LiDAR and RGB-D camera data to achieve 360-degree obstacle tracking, robust SLAM, and adaptive collision avoidance for an electric mower. The framework comprises three core modules: (1) 3D object detection combining YOLOv8-seg instance segmentation with 3D-LiDAR point-cloud spatial projection via top 10% nearest-point averaging, complemented by Euclidean clustering and multi object tracking outside the camera field-of-view; (2) a sensor fusion SLAM model integrated into RTAB-Map for self-localization under vibration and geometric degeneration; and (3) a 20 Hz real-time control loop executing a 3-state velocity model (0.5 m/s cruise, 0.2 m/s slowdown at 5.0 m, and 0.0 m/s emergency stop at 3.0 m). Field evaluations at Kizu Experimental Farm of Kyoto University demonstrated stable human detection up to 10 m at ~30 FPS, preserving a 2.96 m safe physical stopping margin. Against RTK-GNSS ground truth, while LiDAR-only SLAM achieved the lowest average Absolute Trajectory Error (ATE 0.31 m), the proposed sensor fusion SLAM maintained comparable accuracy (ATE 0.30-0.49 m) across most runs, despite occasional visual mismatching under severe illumination changes (average ATE 1.13 m). These results confirm that the proposed framework provides a practical foundation for highly autonomous field operations.

Key Words: Sensor Fusion, Autonomous Driving, YOLO, SLAM, Collision Avoidance

INTRODUCTION

Autonomous electric mowers are essential for mitigating rural labor shortages and promoting carbon neutrality. However, fully autonomous field operations face severe challenges, including dynamic obstacles, vibration during driving, and frequent GNSS signal loss. While automated navigation performs reliably on structured urban roads, navigating complex agricultural landscapes presents fundamental challenges (Chen et al., 2026). Consequently, an autonomous vehicle must simultaneously achieve robust dynamic object detection, precise self-localization, and instantaneous collision avoidance to ensure operational safety.

Despite advancements in deep-learning, unimodal sensors remain insufficient in unstructured fields. Visual sensors offer rich semantic context (e.g., color and texture) for rapid target recognition via models like YOLO; however, camera-based perception suffers from spatial estimation errors and degradation under fluctuating illumination. Conversely, 3D-LiDAR captures precise spatial geometry regardless of lighting, but lacks semantic context, leading to point cloud sparsity, geometric degeneration in featureless terrain, and false positives from reflective vegetation (Wei et al., 2018; Jiang et al., 2026).

Furthermore, single-sensor SLAM introduces severe operational risks. Robust SLAM is essential for full autonomy, enabling machinery to construct maps and position itself without prior topological knowledge. Conventional systems struggle to reconstruct dynamic crop structures, particularly when dense canopies block GNSS signals or lighting variations disrupt Visual SLAM. Thus, multi-sensor fusion SLAM—integrating LiDAR, cameras, IMUs, wheel odometry, and GNSS—is vital to complement individual sensor limitations (Ding et al., 2022). Integrating visual semantic masks with high-precision 3D point cloud projections overcomes both visual localization ambiguities and LiDAR's semantic blindness, providing the precise spatial boundaries required for adaptive velocity control (Wei et al., 2018).

To address these challenges, this study proposes an integrated ROS2-based framework combining 3D-LiDAR and RGB-D camera data for an autonomous electric mower. The principal contributions are threefold: (1) integrating deep-learning instance segmentation with 3D point cloud projection and tracking for robust semantic-spatial object detection; (2) implementing a multi-sensor fusion SLAM pipeline to balance geometric accuracy with visual awareness in GNSS-denied environments; and (3) incorporating a real-time multi-state velocity control model to execute dynamic collision avoidance and guarantee safety margins during field operations.

MATERIALS AND METHODS

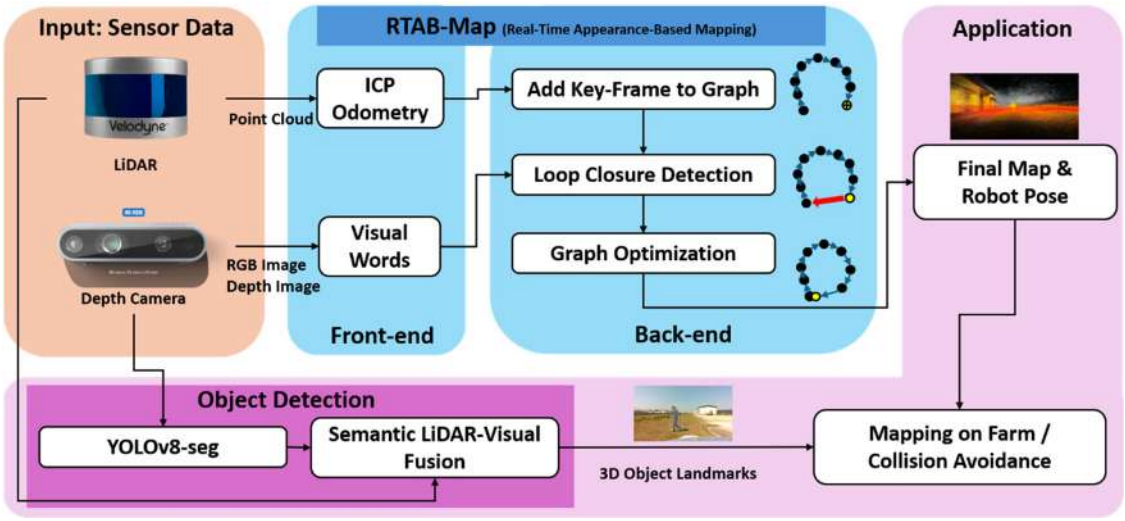

Fig.1 Overview of the proposed sensor fusion framework for autonomous mowers, integrating 3D object detection, RTAB-Map-based SLAM, and adaptive collision avoidance.

EXPERIMENTAL SETUP

An electric mower was utilized as an autonomous experimental machine. The mower was equipped with a 3D-LiDAR (VLP-16, Velodyne; 16 channels, 10 Hz) and an RGB-D camera

(Intel RealSense D435i; 30 fps) to collect environmental perception data. For ground truth evaluation of self-localization, a high-precision RTK-GNSS (Vision-RTK2, Fixposition) was mounted. System processing and vehicle control were executed on a laptop computer (Intel Core i7-13700H, NVIDIA GeForce RTX 4050) running Ubuntu 2022.04 LTS and ROS2 Humble. The spatial relationship (extrinsic parameters) between the 3D-LiDAR and the RGB-D camera was calibrated using the MATLAB LiDAR Camera Calibrator with a standard checkerboard.

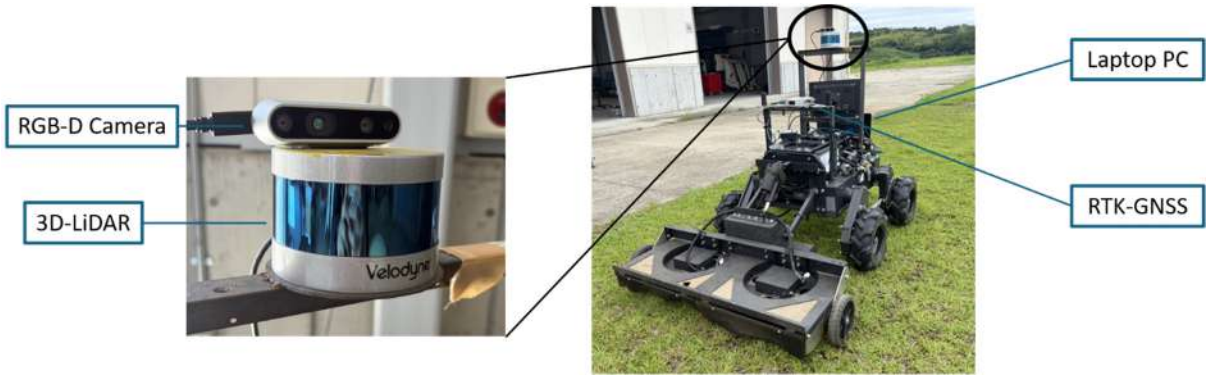

Fig. 2 Experimental electric mower equipped with 3D-LiDAR, RGB-D camera, and RTK-GNSS for field evaluation.

3D OBJECT DETECTION AND TRACKING

YOLOv8-seg and Spatial Projection

To eliminate background noise from agricultural fields, an instance segmentation model (YOLOv8-seg) was adopted to extract pixel-level object masks from camera images. The 3D-LiDAR point cloud was spatially projected onto the 2D image plane using camera intrinsic and extrinsic parameters calibrated in advance. Points falling inside the YOLOv8-seg mask were isolated. To prevent distance misestimation caused by partial occlusions or outliers, a top 10% nearest-point averaging method within the mask region was implemented to measure the true physical distance.

Out-of-FOV Tracking and Semantic Persistence

For regions outside the camera field-of-view (FOV), Euclidean clustering (0.4 m neighbor threshold) was performed on point clouds within a 3.0 m radius. A multi object tracking framework based on nearest-neighbor association assigned unique IDs to detected objects. When a person tracked inside the camera FOV moved out of view, the multi object tracking logic dynamically preserved the semantic class ("person") and passed it to downstream vehicle control.

SENSOR FUSION SLAM

To ensure robust self-localization in GNSS-denied or geometrically featureless paths, a hybrid registration model was integrated into the RTAB-Map (Real-Time Appearance-Based Mapping) framework. The overall optimization cost function E_{Total} combines geometric point-cloud matching error (E_{ICP}) and visual feature reprojection error (E_{Visual}):

$$E_{Total} = w_{ICP}E_{ICP} + w_{Visual}E_{Visual} \quad (1)$$

where w_{ICP} and w_{Visual} represent weighting factors based on sensor measurement covariances.

ADAPTIVE COLLISION AVOIDANCE AND VEHICLE CONTROL

To prevent velocity command oscillation (chattering) caused by vehicle pitch and sensor noise, a 3-state transition model with hysteresis was designed for the 20 Hz real-time control loop. In this framework, the vehicle maintains Cruise Mode (0.5 m/s) when no obstacle is detected within 5.0 m. Slow Down Mode (0.2 m/s) is triggered either when an identified object is detected within 5.0 m (returning to Cruise Mode when the distance exceeds 5.1 m) or when an unknown obstacle is detected by LiDAR alone. Emergency Stop Mode (0.0 m/s) is activated immediately whenever an identified object comes within 3.0 m, reverting to Slow Down Mode once the distance increases beyond 3.1 m. Target linear and angular velocities generated by this state machine were converted into motor RPM commands and transmitted via SocketCAN at 500 kbps.

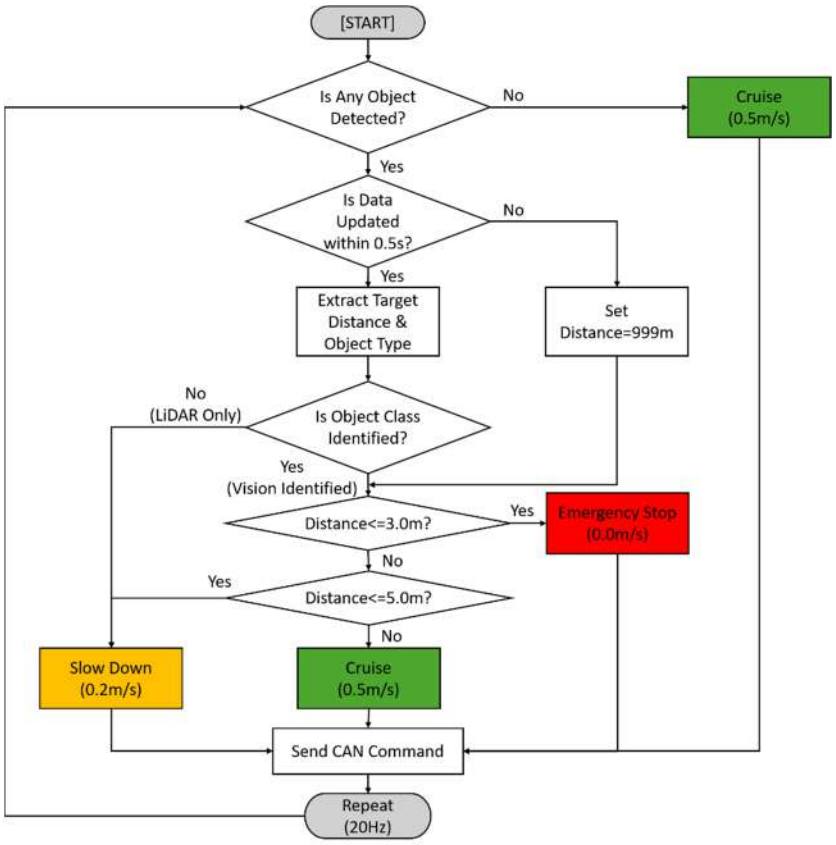

Fig.3 Flowchart of the 3-state real-time velocity control algorithm for adaptive collision avoidance at 20 Hz.

RESULTS & DISCUSSION

3D OBJECT DETECTION PERFORMANCE

The proposed YOLOv8-seg and 3D-LiDAR spatial projection framework was evaluated in field tests across four human postures up to 20 m. The system achieved stable human detection up to 10 m, except Side Facing T-Pose which was up to 7 m. The average pipeline execution

time was 25-35 ms (up to 30 FPS), satisfying real-time operation requirements.

Table1 Distance estimation errors (cm) and detection limits across different human postures.

Distance（m）	3	5	7	10	13	15	17	20
Standing	-14.8	-15.9	-11.4	-7.1	-6.2	△	△	×
Squatting	-24.2	-37.3	-28.9	-24.7	△	△	×	×
Front-Facing T-Pose	-14.8	-15.8	-7.3	-9.7	△	+6.2	+4.4	×
Side Facing T-Pose	-64.1	-71.4	-42.3	△	△	△	△	×

Self-Localization Accuracy (SLAM)

An ablation study compared Camera-only, LiDAR-only, and proposed Fusion SLAM against RTK-GNSS ground truth (Table 2). Camera-only SLAM failed due to severe drift from vibration during driving and lighting changes (average ATE: 8.81 m), whereas LiDAR-only SLAM achieved the highest accuracy (0.31 m). The proposed fusion SLAM maintained comparable sub-meter accuracy (0.30–0.49 m) across most runs, despite temporary visual mismatching under shadows (average ATE: 1.13 m). Despite higher LiDAR-only accuracy, camera integration is essential for real-time semantic perception. The proposed sensor fusion framework thus provides a practical balance between semantic perception and reliable self-localization (< 0.5 m ATE in normal conditions) for field operations.

Table 2 Quantitative comparison of ATE for Camera-only, LiDAR-only, and Proposed Fusion SLAM against RTK-GNSS ground truth.

	LiDAR+Camera		LiDAR Only		Camera Only	
Exp. No.	ATE (m)	Max ATE (m)	ATE (m)	Max ATE (m)	ATE (m)	Max ATE (m)
1	0.34	0.72	0.30	0.80	3.28	6.25
2	4.16	8.35	0.24	0.64	9.95	17.18
3	0.49	0.97	0.41	0.79	11.34	24.29
4	0.35	0.87	0.29	0.69	10.98	17.87
5	0.30	0.72	0.32	0.78	8.48	13.93
Average	1.13	2.33	0.31	0.74	8.81	15.90

Collision Avoidance

When approaching a stationary human obstacle, the system triggered the Emergency Stop mode (0.0 m/s CAN command) immediately upon detecting the target within 3.0 m. Due to mechanical inertia and motor driver response latency, the vehicle exhibited a minor braking deceleration delay. However, the final physical stopping distance measured manually was 2.96 m (system estimated distance: 2.99 m). The estimation error was only 0.03 m, proving that the system successfully preserved a 2.96m safety margin to guarantee operator safety in field operations.

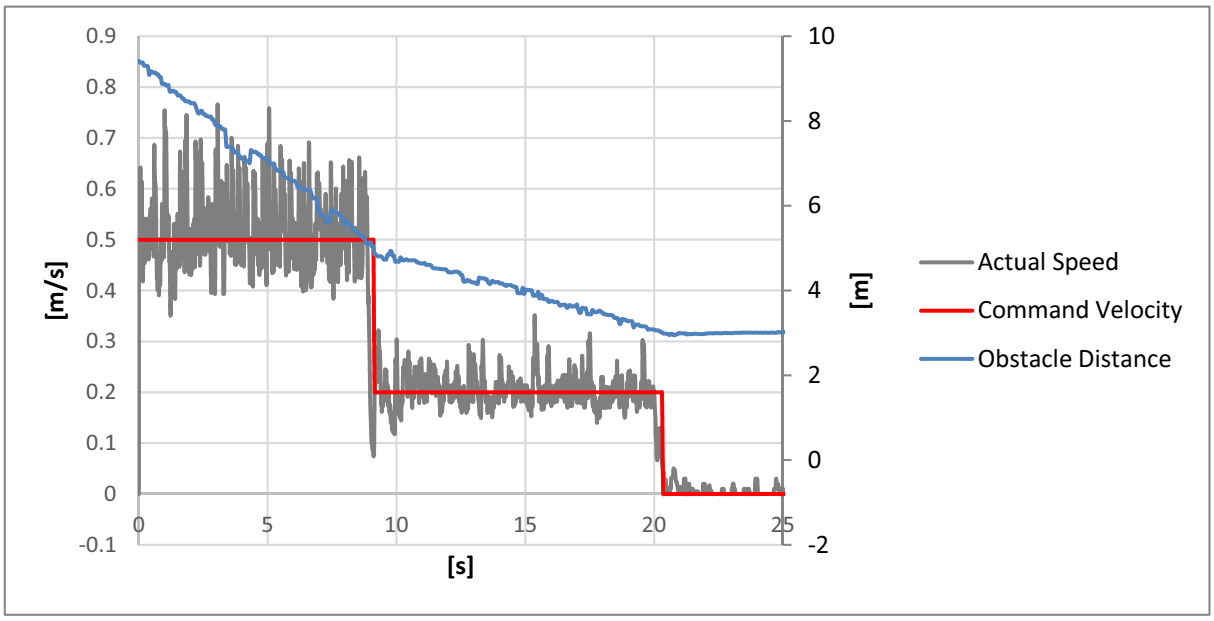

Fig. 4 Real-time dynamic response of vehicle velocity and target distance during a stationary obstacle approach test.

CONCLUSIONS

This study proposed and evaluated an integrated ROS2-based sensor fusion framework combining 3D-LiDAR and RGB-D camera data to achieve reliable 3D object detection, self-localization, and dynamic collision avoidance for autonomous electric mowers in complex agricultural environments. The integration of YOLOv8-seg instance segmentation and 3D-LiDAR spatial projection achieved robust human detection up to 10 m with real-time processing speeds (up to 30 FPS), while the Euclidean clustering and multi object tracking logic successfully preserved semantic class persistence for targets moving outside the camera field-of-view. In SLAM evaluations against RTK-GNSS ground truth, the proposed sensor fusion model maintained sub-meter self-localization accuracy (ATE 0.30–0.49 m across typical runs), demonstrating an effective balance between visual semantic awareness and geometric mapping stability in GNSS-denied field settings. Furthermore, the real-time control loop executing a 3-state velocity model provided smooth deceleration and immediate emergency stopping, maintaining a safe physical stopping distance of approximately 2.96 m. Overall, these experimental results confirm that the proposed framework provides a robust and practical foundation for enhancing field safety and operational autonomy in agricultural machinery.

ACKNOWLEDGEMENT

This research was supported by the development and supply program of smart agricultural technology grants (JPJ013136) from the Project of the Bio-oriented Technology Research Advancement Institution (BRAIN).

REFERENCES

Chen, Z., J. Yin, S. M. Farhan, L. Liu, D. Zhang, M. Zhou, and J. Cheng. 2026. A comprehensive review of obstacle avoidance for autonomous agricultural machinery in multi-operational environment. Artificial Intelligence in Agriculture 16(1): 139-163.

Ding, H., B. Zhang, J. Zhou, Y. Yan, G. Tian, and B. Gu. 2022. Recent developments and applications of simultaneous localization and mapping in agriculture. Journal of Field Robotics 39(6): 956-983.

Jiang, M., Z. Chu, Y. Pan, H. Yuan, Q. Han, J. Zou, Y. Zhang, X. Zhu, C. Zhang, X. Zhou, W. Lou, and Z. Wang. 2026. Multi-sensor fusion on autonomous driving perception: A comprehensive survey. Multimodal Transportation 5(4): 100325.

Wei, P., L. Cagle, T. Reza, J. Ball, and J. Gafford. 2018. LiDAR and camera detection fusion in a real-time industrial multi-sensor collision avoidance system. Electronics 7(6): 84.

FM-06

Proceedings of The 12th International Symposium on Machinery and Mechatronics for Agriculture and Biosystems Engineering (ISMAB 2026)
20-24 October 2026, Busan, Republic of Korea

TREND ANALYSIS OF FACTORS AFFECTING LATERAL OVERTURNING SAFETY IN WHEELED AND TRACKED FORESTRY TRACTORS

Moon-Kyeong Jang[1,2], Jeong-Hun Kim[1,2], Chan-Young Lee[1,2], Ju-Seok Nam[1,2*]

[1] Dept. of Biosystems Engineering, College of Agriculture and Life Sciences, Kangwon National University, Chuncheon, 24341, Korea
[2] Interdisciplinary Program in Smart Agriculture, Kangwon National University, Chuncheon, 24341, Korea
*Corresponding Author-- Voice: +82-33-250-6497, Email: njsg1218@kangwon.ac.kr

Abstract: This study synthesized five recent studies on the lateral overturning safety of agricultural and forestry tractors to identify common trends and underlying causes. Previous studies examined wheeled tractors and tracked forestry tractor separately, according to ground slope angle, obstacle height, and driving speed, but no comprehensive comparison across drivetrain types had been conducted. This study compared lateral overturning tendencies between wheeled and tracked tractors, safety differences between a wheeled tractor with an attached implement and a tracked tractor loaded with logs at the rear, and safety differences among both types according to implement attachment and loading conditions. All underlying studies used three-dimensional dynamic simulation models, validated against certified test results or scaled-model measurements, with ground slope angle, obstacle height, and driving speed as common variables. Critical conditions for lateral overturning and the resulting changes in center of gravity (COG) were derived for each case. As ground slope angle exceeded approximately 30°, the lateral overturning risk of wheeled tractors rose sharply, whereas tracked tractors remained safe up to higher slope angles because of their wide support base. Both a wheeled tractor with an attached implement and a tracked tractor loaded with logs showed reduced safety as their COG shifted upward and rearward, through a three-point hitch and a loading bed, respectively. Ground slope angle was confirmed as the most dominant factor in every study, and obstacle height amplified impact force and increased dynamic instability. Overall, ground slope angle, obstacles, COG, and driving speed interact to induce lateral overturning in both drivetrain types, but their sensitivity differed by drivetrain structure. Future safety standards and implement/loading limits for tractors should therefore be established according to drivetrain type.

Key Words: Lateral overturning; Tracked tractor; Wheeled tractor; Center of gravity; Dynamic simulation

ACKNOWLEDGEMENTS

This study was carried out with the support of the R&D Program for Forest Science Technology (Project No. RS-2026-2552326) provided by the Korea Forest Service (Korea Forestry Promotion Institute).

FM-07

Proceedings of The 12th International Symposium on Machinery and Mechatronics for Agriculture and Biosystems Engineering (ISMAB 2026)
20-24 October 2026, Busan, Republic of Korea

STRUCTURAL SAFETY EVALUATION OF AN AGRICULTURAL TRACTOR FRONT-END LOADER

Jeong-Hun Kim[1,2], Joon-Hyung Park[1], Moon-Kyeong Jang[3], Ju-Seok Nam[1,2*]

[1]Department of Biosystems Engineering, Kangwon National University, Chuncheon, Republic of Korea
[2]Interdisciplinary Program in Smart Agriculture, Kangwon National University, Chuncheon, Republic of Korea
*Corresponding Author-- Voice: +82-33-250-6497, Email: njsg1218@kangwon.ac.kr

Abstract: The front-end loader, attached to the front of agricultural tractors to transport soil and other materials, is subjected to complex loads during operation, yet no standardized test code reflecting actual working conditions currently exists. In this study, stress concentration spots of the front-end loader were derived through multibody dynamic simulation, and its structural safety was evaluated based on field measurements at these locations. A three-dimensional model was constructed using commercial multibody dynamic analysis software (Recurdyn V9R5, Functionbay, Korea) and validated by comparing its weight with the actual product. Dynamic simulations for the drop, impact, and pulling tests, which were expected to generate large instantaneous loads, yielded a total of 34 stress concentration spots (12 on the boom, 6 on the post, 8 on the mount, and 8 on the rear frame) and their principal stress directions. Uniaxial strain gauges were attached at these locations, and fluctuating stresses were measured for 1 h across five test conditions according to their duty percentages. The pulling and dumping tests produced the highest stresses, and maximum stresses exceeding the material's yield strength (331 MPa)—581.5 MPa and 3015 MPa—were measured at two locations on the mount, resulting in static yielding, attributed to large bending loads arising from the fixed conditions at the post–mount and mount–tractor body joints. Excluding these locations, the static safety factor exceeded 1.93 at all points, and the fatigue life, calculated using rain-flow counting, Goodman's equation, and the Palmgren–Miner rule, also satisfied the required lifespan everywhere (with the dumping test accounting for 72.5–99.9% of total fatigue damage). These results identify the mount as the structurally weakest component, indicating that a robust design—combining thickness/geometry modification with partial use of a higher-strength material—is needed.

Key Words: Fatigue life, Front-end loader, Multibody dynamic simulation, Static safety factor, Strain gauge

ACKNOWLEDGEMENTS

This work was supported by Korea Institute of Planning and Evaluation for Technology in Food, Agriculture and Forestry(IPET) through Machinery Mechanization Technology Development Program for Field Farming Program, funded by Ministry of Agriculture, Food and Rural Affairs(MAFRA)(RS-2023-00236201).

Field Machinery and Systems 2 (FM-2)



FM-08

Proceedings of The 12th International Symposium on Machinery and Mechatronics for Agriculture and Biosystems Engineering (ISMAB 2026)
20-24 October 2026, Busan, Republic of Korea

OPERATOR COMFORT EVALUATION BY VIBRATION AND INCLINATION OF A 36.8-kW ONE-ROW CABBAGE HARVESTER UNDER KOREAN FIELD CONDITIONS

Md Razob Ali[1], Md Nasim Reza[1,2], Ezatullah Zakir[1], Cholet Nyangoma Atulinda[1], Sun-Ok Chung[1,2*]

[1]Department of Agricultural Machinery Engineering, Graduate School, Chungnam National University, Daejeon 34134, Republic of Korea
[2]Department of Smart Agricultural Systems, Graduate School, Chungnam National University, Daejeon 34134, Republic of Korea
*Corresponding Author-- Voice: +82-42-821-6712, Email: sochung@cnu.ac.kr

Abstract: Operator comfort and operational stability in self-propelled cabbage harvesters can be adversely affected by irregular field surfaces, impulsive cutting loads, and repeated turning maneuvers. Field-based evaluations of vibration transmission from the power transmission unit to the operator station remain limited. Therefore, vibration transmission and machine inclination were evaluated in a 36.8-kW one-row self-propelled cabbage harvester under Korean field conditions. Triaxial accelerometers were installed at the power transmission unit, harvesting unit, and operator station. Pitch and roll were measured using a dual-axis inclinometer, while machine position and travel speed were recorded using an RTK-GNSS receiver. Measurements were conducted during engine idling, active harvesting, and turning. Vibration was characterized using resultant root mean square acceleration, peak acceleration, crest factor, kurtosis, power spectral density, and transmissibility. During idling, a resultant root mean square acceleration of approximately 0.030 m/s² and a 60 Hz engine-related harmonic were observed. During harvesting, 1-2 Hz impulsive excitation was strongly amplified at the harvesting unit, where vibration was approximately 9.9 times the power transmission unit level. Vibration at the operator station was approximately three times the power transmission unit level. During turning, a dominant resonance was observed at 13.7 Hz and harvesting-unit transmissibility increased to 27.0, whereas operator-station transmission was reduced. Kurtosis values exceeding 100 indicated repeated shocks and impulsive vibration. A mean travel speed of 0.14 km/h was recorded, and stable RTK-GNSS positioning was maintained. Major vibration sources and transmission paths affecting operator comfort and machine stability were identified. Additional field conditions, longer measurements, and standardized whole-body vibration assessment were recommended.

Key Words: Cabbage harvester, operator comfort, vibration transmissibility, machine inclination.

INTRODUCTION

Mechanized harvesting of upland crops necessitates the use of self-propelled machinery capable of operating on irregular soil while simultaneously engaging cutting, conveying, and propulsion systems. In field conditions, vibration arises from powertrain excitation, terrain irregularities, crop-machine interactions, and intermittent shocks, all of which can negatively impact operator comfort and musculoskeletal health (Ji et al., 2026). Field measurements conducted on tractors, combines, utility vehicles, and all-terrain vehicles have demonstrated substantial whole-body vibration and high crest factors, confirming the combined effects of continuous vibration and mechanical shocks in agricultural work (Fethke et al., 2018).

In small and medium-sized upland-crop machinery, vibration can influence both the performance of working mechanisms and overall operational quality. In a 12-kW self-propelled onion transplanter, vibration exposure varied with operating state and load condition, with elevated vibration levels recorded at the seedling conveyor, suggesting potential impacts on operator comfort and transplanting performance (Chowdhury et al., 2023). Similarly, in a tractor-mounted Chinese cabbage collector, vibration increased with conveyor speed, and high levels were detected at multiple structural locations during field operation (Jang et al., 2021). These findings indicate that multi-point measurements are necessary for crop-specific machinery.

The transmission of vibration from the chassis and working units to the operator station is influenced by structural load paths and seat suspension systems. Whole-body vibration has been evaluated using ISO 2631-1 frequency weighting and seat transmissibility, while both structural modeling and experimental measurements have been employed to assess the impact of suspension parameters on vibration levels at the operator seat (ISO, 1997). Despite these efforts, vibration, machine inclination, and travel motion are frequently assessed in isolation, and there is a lack of synchronized, condition-resolved field data for self-propelled cabbage harvesters.

Therefore, the objective of this study was to evaluate vibration transmission and inclination stability of a 36.8-kW one-row self-propelled cabbage harvester during engine idling, active harvesting, and turning conditions.

MATERIALS AND METHODS

Harvester and operating conditions

A one-row self-propelled cabbage harvester, equipped with a 36.8-kW diesel engine and a crawler-type driving unit, was evaluated under field conditions. This harvester was specifically designed for single-row cabbage harvesting and operated at a rated engine speed of 2400 rpm. The driving speed ranged from 0.3 to 0.9 m/s. The machine's overall dimensions were 4500 × 2200 × 2600 mm, and its total mass was 2000 kg. The main technical specifications are summarized in Table 1.

The harvester consisted of a harvesting header, cutting unit, conveying system, power transmission unit, crawler driving unit, and rear storage section. The harvesting header and cutting unit were located at the front of the machine to facilitate crop collection and cutting. The

conveying system transported harvested cabbages to the rear storage section. Power produced by the diesel engine was delivered to both the driving and harvesting mechanisms via the power transmission system. The configuration and arrangement of the primary machine components are shown in Fig. 1.

Table 1. Main specifications of the one-row self-propelled cabbage harvester.

Item	Specification	Value
Engine	Diesel engine	36.8 kW
Rated speed	Engine speed	2400 rpm
Driving unit	Type	Crawler
Driving speed	Available range	0.3-0.9 m/s
Main body size	L x W x H	Within 4500 x 2200 x 2600 mm
Weight	Machine mass	Within 2000 kg

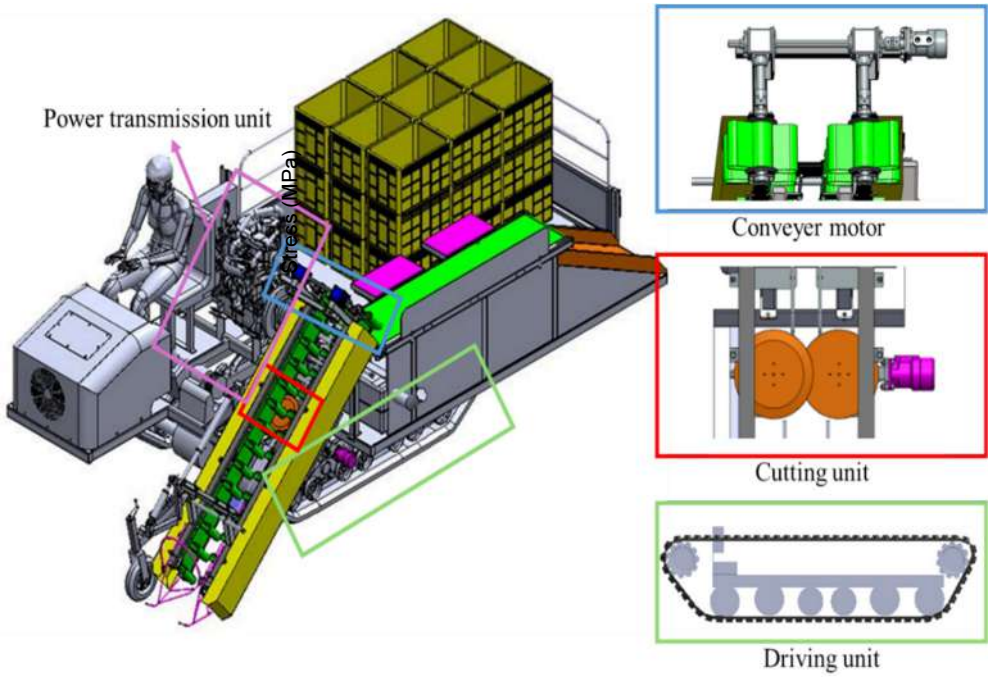

Fig.1. Three-dimensional model of the self-propelled cabbage harvester and major machine units.

Field test and measurement system

Measurements were conducted under three distinct operating conditions. Engine idling served as the baseline, with the harvester stationary and all working mechanisms disengaged. Active harvesting was assessed while crop rows were processed with both cutting and conveying mechanisms engaged. Turning was evaluated during row-end maneuvers required to align the machine with subsequent crop rows. These three states were chosen to differentiate the powertrain baseline, continuous harvesting loads, and transient maneuvering loads. The locations of the vibration sensors used during field testing are illustrated in Fig. 2.

Triaxial vibration sensors were installed at the power transmission unit, harvesting unit, and operator station. The vibration measurement system consisted of 356A15 triaxial adhesive-type accelerometers, an NI cDAQ-9178 chassis with an NI 9234 module, and LabVIEW 2020 software. Pitch and roll were measured using an STT400 dual-axis inclinometer connected via

an NI USB-6234 data acquisition device. Position and travel speed were recorded with an RTK-GNSS receiver. The specifications of the measurement system are summarized in Table 2.

Table 1. Measurement variables and acquisition system.

Measurement	Sensor or device	Measured quantity
Vibration	356A15 triaxial accelerometer	X, Y, and Z acceleration
Inclination	STT400 dual-axis inclinometer	Pitch and roll
Position and speed	RTK-GNSS receiver	Machine position Signal
Software	LabVIEW 2020	visualization



Fig.2. Positions of the triaxial vibration sensors on the cabbage harvester.

Signal processing and evaluation

Raw data from accelerometers, inclinometers, and RTK-GNSS were synchronized using timestamps. Vibration signals were sampled at 1000 Hz. Data points unrelated to machine operation were excluded, sensor sensitivity corrections were applied, and acceleration measurements were converted to physical units. Continuous datasets were segmented based on operator logs into engine idling, active harvesting, and turning phases.

Root mean square acceleration, peak acceleration, crest factor, kurtosis, resultant acceleration, power spectral density, and vibration transmissibility were computed. Frequency-weighted vibration assessments were performed in accordance with ISO 2631-1 (ISO, 1997). Pitch and roll variability quantified inclination stability, and chassis-to-seat coupling was analyzed using Pearson correlation and linear regression.

RESULTS & DISCUSSION

Condition-dependent vibration response

Engine idling served as the baseline condition for comparison with dynamic operating states. Comparable vibration magnitudes were recorded at the monitored locations, with a resultant root mean square acceleration of approximately 0.030 m/s² and a distinct harmonic component

at 60 Hz. At the chassis frame, the resultant vibration level was approximately 0.029 m/s², indicating a low-amplitude powertrain response during stationary operation.

During active harvesting, vibration levels increased substantially compared to engine idling. The resultant chassis vibration rose to approximately 0.302 m/s². Vibration at the harvesting unit was approximately 9.9 times higher than at the power transmission unit, while the operator station level was about three times higher. These findings suggest that crop interaction and the operation of cutting and conveying mechanisms generated additional excitation and increased vibration transmission toward the operator area.
During turning, the dynamic response increased further, resulting in the highest measured chassis vibration level. The resultant chassis vibration reached approximately 0.758 m/s², and the harvesting-unit transmissibility ratio increased to 27.0. Operator seat vibration corresponded to approximately 30% of the chassis level during harvesting and 5.7% during turning, representing about 70% and 94.3% attenuation, respectively. Table 3 summarizes the overall comparison of the three operating conditions.

Table 3. Overall vibration response under different operating conditions.

Operating condition	Chassis RMS (m/s²)	Dominant frequency (Hz)	Seat transmissibility
Engine idling	0.029	60	1.06
Active harvesting	0.302	1-2	0.30
Turning	0.758	13.7	0.057

Spectral and impulsive characteristics

Three distinct spectral regimes were identified across the operating states. Engine idling generated narrow frequency components corresponding to the powertrain baseline. During active harvesting, spectral energy was concentrated within a broad 1-2 Hz band, reflecting repeated machine-body excitation resulting from crop loading, cutting, conveying, and terrain interaction. Turning operations exhibited a pronounced resonance at 13.7 Hz, which suggests a structural response to transient chassis loading. The condition-resolved power spectral density characteristics are presented in Fig. 3.

Elevated crest factors and kurtosis values were recorded during dynamic operation. In certain raw data segments, kurtosis values exceeded 100, indicating that the field response was dominated by repeated shocks rather than by smooth random vibration. This impulsive behavior underscores the necessity for condition-specific evaluation, as short-duration peaks may be obscured when relying solely on overall average vibration metrics.

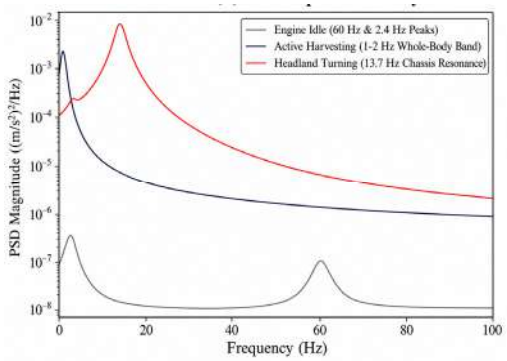

Fig.3. Representative acceleration power spectral density under engine idling, active harvesting, and turning.

Inclination stability, vibration coupling, and design implications

Machine inclination exhibited substantial variation across different operating conditions. Chassis roll fluctuation increased from approximately 0.0285° during idling to 0.7585° during turning. In contrast, harvesting-unit roll fluctuation remained stable at approximately 0.028–0.031° across all tested states. The consistent harvesting-unit inclination suggests significant mechanical isolation from chassis and terrain-induced roll disturbances.

The strongest chassis-to-seat coupling occurred in the vertical direction, with a Pearson correlation coefficient of 0.84, R^2 of 0.71, and a regression slope of 0.36. Regression slopes for all axes remained below 1.0, ranging from 0.27 to 0.36, which confirms attenuation of vibration toward the operator seat. These findings demonstrate that the seat and machine structure effectively reduce the proportion of transmitted vibration.

The combined results demonstrate that machine dynamics are highly dependent on operating conditions. Active harvesting is characterized by low-frequency excitation, while turning produces the highest chassis vibration, roll fluctuation, and a dominant resonance at 13.7 Hz. Therefore, structural vibration control should prioritize the chassis and turning-related load paths, and the 1–2 Hz harvesting range should be considered for whole-body vibration exposure. Stable RTK-GNSS positioning was maintained at a mean travel speed of 0.14 km/h. However, broader validation under additional field and operating conditions remains necessary.

Discussion

The increased vibration observed during active harvesting and turning was consistent with previous findings for agricultural machinery, where vibration exposure was strongly affected by field surface conditions, forward speed, and operating state. Scarlett et al. (2007) reported that vibration generated by agricultural tractors varied considerably with operating and terrain conditions, while Kabir et al. (2017) found that whole-body vibration exposure increased on rough farm roads and at higher travel speeds. Therefore, the higher chassis response measured during harvesting and turning was considered to result from the combined effects of terrain interaction, working-mechanism excitation, and transient maneuvering loads.

The attenuation observed between the chassis and operator seat was also consistent with previous investigations of agricultural-machine suspension systems. Marsili et al. (2002) reported that suspension systems could substantially reduce acceleration transmitted through

the driving seat, while Deboli et al. (2012) emphasized the importance of field-based vibration measurements for representative evaluation of operator exposure. The strong vertical coupling and the 1–2 Hz vibration range observed during harvesting indicated that low-frequency whole-body vibration remained important for operator comfort assessment. Evaluation according to ISO 2631-1 should therefore be considered in further field tests with longer exposure durations and additional operating conditions.

CONCLUSIONS

Vibration transmission and machine inclination were evaluated for a 36.8-kW one-row self-propelled cabbage harvester under engine idling, active harvesting, and turning. Active harvesting produced strong 1-2 Hz excitation and substantial amplification at the harvesting unit, while turning generated the most severe chassis response and a dominant 13.7 Hz resonance. Vibration transmitted to the operator seat was strongly attenuated under dynamic operation. Chassis roll increased markedly during turning, whereas the harvesting unit remained comparatively stable. Future mitigation should prioritize chassis structural damping and low-frequency whole-body vibration control while maintaining harvesting-unit and operator-seat isolation. Additional field conditions, longer measurements, and standardized whole-body vibration assessment are recommended.

ACKNOWLEDGEMENTS (optional)

This work was carried out with the support of "Advanced Field
Customized Upland Agricultural Machinery (R&D) program (Project No. RS-202625466765)", Rural Development Administration, Republic of Korea.

REFERENCES

Chowdhury, M., M. N. Reza, M. Ali, M. S. N. Kabir, S. Kiraga, S.J. Lim, I.S. Choi, and S.O. Chung. 2023. Vibration assessment of a 12-kW self-propelled riding-type automatic onion transplanter for transplanting performance and operator comfort. Applied Sciences 13(3): 1927.

Deboli, R., A. Calvo, and C. Preti. 2012. Comparison between ISO 5008 and field WBV tractor values. Journal of Agricultural Engineering 43(2): 49-54.

Fethke, N. B., M. C. Schall, L. A. Merlino, H. Chen, C. A. Branch, and M. Ramaswamy. 2018. Whole-body vibration and trunk posture during operation of agricultural machinery. Annals of Work Exposures and Health 62(9): 1123-1133.

ISO. 1997. ISO 2631-1:1997. Mechanical vibration and shock - Evaluation of human exposure to whole-body vibration - Part 1: General requirements. Geneva, Switzerland: International Organization for Standardization.

Jang, B. E., M. Chowdhury, M. Ali, M. N. Islam, K. M. Swe, D. U. Jung, S. H. Lee, and S. O. Chung. 2021. Stability and vibration analysis of a tractor-mounted Chinese cabbage collector. IOP Conference Series: Earth and Environmental Science 733: 012021.

Ji, K., Z. Zhou, and Y. Li. 2026. Vibration-based fault diagnosis of agricultural machinery: A review of field excitation, signal processing, intelligent models and engineering deployment. Machines 14(7): 795.

Kabir, M. S. N., S.O. Chung, Y.J. Kim, N.S. Sung, and S.J. Hong. 2017. Measurement and evaluation of whole body vibration of agricultural tractor operator. International Journal of Agricultural and Biological Engineering 10(1): 248-255.

Marsili, A., L. Ragni, G. Santoro, P. Servadio, and G. Vassalini. 2002. Innovative systems to reduce vibrations on agricultural tractors: Comparative analysis of acceleration transmitted through the driving seat. Biosystems Engineering 81(1): 35-47.

FM-09

Proceedings of The 12th International Symposium on Machinery and Mechatronics for Agriculture and Biosystems Engineering (ISMAB 2026)
20-24 October 2026, Busan, Republic of Korea

PHYSICS-GUIDED NEURAL NETWORK FOR CONE INDEX PREDICTION FROM SOIL PHYSICAL PROPERTIES

Joon-Seo Kim[1], Sang-Wook Park[1], Seung-Yeon Lee[1], Ji-Tae Kim[1,2*]

[1]Department of Convergence Biosystems Engineering, Chonnam National University, 77 Yongbong-ro, Buk-gu, Gwangju 61186, Republic of Korea
[2]Institute of Agricultural Science & Technology, Chonnam National University, 77 Yongbong-ro, Buk-gu, Gwangju 61186, Republic of Korea
*Corresponding Author-- Voice: +82-62-530-5188, Email: jtkim@jnu.ac.kr

Abstract: Assessing the mobility of agricultural tractors and other off-road vehicles requires quantification of soil strength, but measuring the cone index over a wide range of soil conditions demands considerable time and effort. Artificial neural networks can learn the nonlinear relationship between soil state variables and cone index without prescribing a functional form. However, because training and model selection are generally based on the error between observed and predicted values, a small overall prediction error does not guarantee that the local response direction agrees with prior engineering knowledge where measured data are sparse. The objective of this study was to develop a physics-guided neural network that predicts cone index from sand ratio, water content and condition-specific relative bulk density while maintaining the expected response directions to changes in the input variables. Reconstituted soils were prepared from a single parent soil separated into a sand fraction and a combined silt-clay fraction, and cone penetration tests were performed on specimens for which particle-size composition, moisture state and state of compaction were controlled. The measured records were divided into a development dataset and a held-out original test set by clustering in the standardized condition-response space, and directional information between the soil physical properties and cone index was introduced as soft training constraints. Compared with a baseline network that differed only in the absence of the directional constraints, the proposed model showed a lower prediction error at the held-out test conditions and a higher rate of agreement with the expected response directions, whereas the baseline network gave the higher fit to the development-side validation data. The results indicate that partially known directional knowledge can be used in soil-strength prediction problems for which governing equations are not established.

Key Words: Physics-guided neural network, Cone index, Terramechanics, Soil strength, Relative bulk density

INTRODUCTION

The mobility of off-road vehicles including agricultural tractors is affected by the interaction between the running gear and deformable soil, and under weak soil conditions the sinkage and slip of the running gear increase so that tractive performance is reduced (Wong, 2009).

The cone index (CI), obtained by dividing the penetration force of a standard cone by its base area, expresses soil strength as a single quantity (ASABE, 2023) and has been used as the soil parameter in empirical models that predict off-road vehicle mobility and wheel tractive performance (Wismer and Luth, 1973). CI is not a material constant, however, but a condition-dependent index that varies with particle-size composition, moisture state, bulk density and test conditions (Mulqueen et al., 1977; Kumar et al., 2012). Measuring CI over a wide range of soil conditions requires considerable time and effort, so indirect estimation from soil physical properties is of practical interest.

Artificial neural networks (ANN) have been used to predict penetration resistance from soil state variables (Ünal et al., 2024) and can learn nonlinear input-response relationships without prescribing a functional form in advance. In such studies, training and model selection were based mainly on the error between observed and predicted values, and the response direction to changes in the input variables was not treated as an explicit training constraint. Consequently, even when the overall prediction error is small, the local response direction in regions where measured data are sparse is not guaranteed to agree with the trends reported in previous work. Physics-informed neural networks incorporate the residual of governing equations into the loss function (Raissi et al., 2019), but no governing equation applicable over the whole experimental range links the soil physical properties considered here to CI. Physics-guided neural networks (PGNN), which introduce partially known physical and engineering knowledge into training, are better suited to this situation (Daw et al., 2022).

The objective of this study was to develop a PGNN, referred to as the soil cone index physics-guided neural network (SC-PGNN), that predicts CI from sand ratio (SR), water content (WC) and condition-specific relative bulk density (RBD), and to compare its prediction error at the held-out test conditions and its response-direction consistency with those of a baseline ANN trained without the directional constraints. This paper reports the experimental design and the main comparison outcomes; the detailed formulation of the physics-guided loss terms, the weight calibration and the model-selection criterion are reported separately.

MATERIALS AND METHODS

RECONSTITUTED SOIL SPECIMENS AND CONE PENETRATION TESTING

Specimen Preparation

All test soils were prepared from a single parent soil so that the effect of particle-size composition would not be confounded with material-specific properties such as particle shape and mineral composition. Gravel was removed and the remaining soil was separated at 0.05 mm into a sand fraction and a combined silt-clay fraction, following the USDA particle-size boundaries and standard sieving procedures (ASTM, 2009; Soil Science Division Staff, 2017). The two fractions were mixed on a dry-mass basis, and SR was defined as in Eq. (1).

$$SR = \frac{m_s}{m_s + m_{sc}} \times 100 \quad (1)$$

where:

m_s = dry mass of the sand fraction (kg)

m_{sc} = dry mass of the combined silt-clay fraction (kg)

Because the moisture characteristics of a soil vary with its composition, the same WC does not necessarily represent the same moisture state at different SR levels (Keller and Dexter, 2012). WC levels were therefore established for each SR relative to an estimated plastic limit derived from literature regression relationships between sand content and the Atterberg limits. Prepared mixtures were sealed and equilibrated for 24 h before specimen preparation.

The bulk density attainable under a given compaction procedure also differs among SR-WC conditions, so the same bulk density can represent a different state of compaction. Following the bulk-density normalization concept reviewed by Håkansson and Lipiec (2000), the state of compaction was expressed as RBD as in Eq. (2).

$$RBD = \frac{\rho_b}{\rho_{b,max}} \quad (2)$$

where:

ρ_b = bulk density of the prepared specimen (kg m^{-3})

$\rho_{b,max}$ = reference maximum bulk density for the same SR-WC condition (kg m^{-3})

For each SR-WC condition, the loose-fill bulk density and the reference maximum bulk density were determined in a cylindrical container, the latter by repeated drop-weight compaction until no further reduction in specimen height occurred. Three nominal density levels were placed between these two limits, and the reference maximum bulk density was used only as the upper reference for setting the target densities and calculating RBD. Combining the factor levels gave the test conditions summarized in Table 1.

Table 1 Experimental factors and nominal levels used for cone penetration testing.

Factor	Levels	Nominal levels
Sand ratio, SR (%)	5	0, 25, 50, 75, 100
Water content, WC (%)	5	Fractions of an estimated plastic limit
Relative bulk density, RBD (-)	3	Low, Mid, High
Total conditions	75	5 × 5 × 3

Cone Penetration Testing and Data Processing

Three specimens were prepared independently for each test condition to reflect within-condition variability arising from mixing, filling and compaction, and one cone penetration test was performed per specimen so that local disturbance from a preceding penetration would not affect subsequent measurements, giving 225 independent tests in total. CI was measured with an electronic cone penetrometer using the large standard cone, and testing and data recording followed ASAE S313.3 and ASAE EP542.1 (ASABE, 2023, 2024). CI was recorded at 10 mm intervals over the 0-150 mm depth range, averaged within each independent test, and then averaged over the three replicates to give one representative CI per condition, so that the original measured dataset consisted of 75 condition-level records.

MODEL DEVELOPMENT AND EVALUATION

The original measured dataset was divided into a development dataset and a held-out original test set. To avoid similar test conditions being shared between the two sets, the split was made on clusters formed in the standardized condition-response space rather than on individual

records. The measured CI over the input domain defined by SR, WC and RBD and the resulting partition are shown in Fig. 1. Data augmentation based on Latin hypercube sampling and Gaussian process regression was applied to the development dataset only, and the held-out original test set was fixed at the partitioning stage and excluded from model fitting, hyperparameter optimization and model selection. Network inputs were standardized, and CI was modeled in a log-transformed and standardized output space.

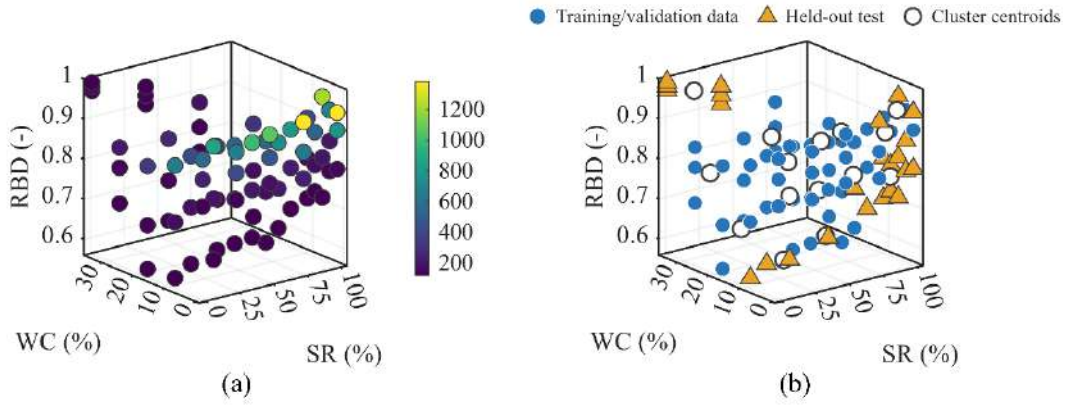

Fig. 1 Measured test conditions in the input domain: (a) mean cone index in kPa and (b) the cluster-based partition.

The baseline ANN and the SC-PGNN used the same input data, the same fully connected multilayer perceptron structure and the same training configuration, determined in advance using the data-fitting objective only; the two models differed solely in whether the physics-guided loss terms were applied. Two directional relationships were introduced as soft constraints: a decrease in CI with increasing WC and an increase in CI with increasing RBD, consistent with the moisture and density effects on CI reported previously (Ayers and Perumpral, 1982). A condition-dependent auxiliary constraint was applied to SR, for which no single monotonic relationship held over the whole input domain. The constraints were evaluated at collocation points distributed over the input domain occupied by the development dataset rather than at the training samples, and the partial derivatives of the network output with respect to each input variable were obtained by automatic differentiation. The specific form of the penalty terms, the calibration of their relative weights and the criterion used to select the final model are not presented here.

Predictive performance was evaluated using the coefficient of determination (R^2) and the root mean squared error (RMSE) after back-transformation to kPa. Response-direction consistency was evaluated at a separate set of evaluation points as the weighted proportion of points at which an expected response direction was satisfied, with points closer to the original input conditions of the development dataset given greater weight. The core response-direction agreement rate counted only those points at which the WC and RBD directions were satisfied simultaneously.

RESULTS & DISCUSSION

On the held-out original test set, the SC-PGNN gave a lower prediction error than the baseline ANN, and its weighted core response-direction agreement rate was substantially higher (Table 2). On the augmented validation data used during model development, however, the baseline

ANN gave the higher fit, with R^2 of approximately 0.97 compared with approximately 0.90 for the SC-PGNN, so the ranking of the two models reversed between the development-side data and the held-out test conditions. In this dataset, a higher fit to the development data did not by itself carry over to the held-out test conditions.

Table 2 Prediction performance on the held-out original test set and weighted core response-direction agreement on the evaluation point set.

Model	R^2	RMSE (kPa)	Core response-direction agreement (%)
Baseline ANN	0.44	310	43.1
SC-PGNN	0.94	101	97.2

For the baseline ANN, the individual agreement rates for the WC and RBD response directions both exceeded 60%, yet the core agreement rate was considerably lower. An appropriate response direction for one input variable therefore does not ensure that the direction for another input variable is also maintained at the same point, and the region in which both core directions held simultaneously was more limited than either individual rate suggests. For the SC-PGNN, agreement for the WC direction was complete, so all points at which the core condition was not met arose from violations of the RBD direction; local responses opposite to the expected direction remained for RBD, although to a limited extent.

Two limitations should be noted. The agreement rates were calculated on the evaluation point set that was also used in selecting the final model, so they cannot be interpreted as an independent physical validation, and they indicate satisfaction of the directional conditions set in this study rather than relationships that hold universally across soils. In addition, the dataset consists of laboratory reconstituted soils, and the comparison rests on a single cluster-based partition, so soil structure, organic matter, particle shape and time-dependent moisture changes are not represented, and the reported values should not be generalized directly to other soil types or to field conditions.

CONCLUSIONS

A physics-guided neural network was developed to predict cone index from sand ratio, water content and condition-specific relative bulk density using reconstituted soil specimens, with directional information between the soil physical properties and cone index introduced as soft training constraints. Relative to an otherwise identical network trained without them, the directional constraints reduced the prediction error at the held-out test conditions and raised the agreement with the expected response directions, at the cost of a poorer fit to the development-side validation data. Partially known directional knowledge can therefore be used as a soft training constraint in soil-strength prediction problems for which governing equations are not established. Future work will separate the evaluation points used for model selection from those used for final physical evaluation, examine the contributions of data augmentation and of the directional constraints separately, and extend the dataset toward natural soils and field conditions so that linkage with vehicle responses such as slip, sinkage and drawbar pull can be examined.

ACKNOWLEDGEMENTS

This work was supported by Korea Institute of Planning and Evaluation for Technology in Food, Agriculture and Forestry (IPET) through Open-field Smart Agriculture Utilization Model Development Program, funded by Ministry of Agriculture, Food and Rural Affairs (MAFRA) (RS-2025-02220331).

REFERENCES

ASABE. 2023. Soil cone penetrometer. ASAE S313.3 FEB1999 (R2023). St. Joseph, Mich.: ASABE.

ASABE. 2024. Procedures for using and reporting data obtained with the soil cone penetrometer. ASAE EP542.1 NOV2019 (R2024ED). St. Joseph, Mich.: ASABE.

ASTM. 2009. Standard test methods for particle-size distribution (gradation) of soils using sieve analysis. ASTM D6913-04(2009). West Conshohocken, Pa.: ASTM International.

Ayers, P. D., and J. V. Perumpral. 1982. Moisture and density effect on cone index. Trans. ASAE 25(5): 1169-1172.

Daw, A., A. Karpatne, W. Watkins, J. Read, and V. Kumar. 2022. Physics-guided neural networks (PGNN): An application in lake temperature modeling. In *Knowledge Guided Machine Learning*, 353-372. A. Karpatne, R. Kannan, and V. Kumar, eds. Boca Raton, Fla.: CRC Press.

Håkansson, I., and J. Lipiec. 2000. A review of the usefulness of relative bulk density values in studies of soil structure and compaction. Soil Tillage Res. 53(2): 71-85.

Keller, T., and A. R. Dexter. 2012. Plastic limits of agricultural soils as functions of soil texture and organic matter content. Soil Res. 50(1): 7-17.

Kumar, A., Y. Chen, A. Sadek, and S. Rahman. 2012. Soil cone index in relation to soil texture, moisture content, and bulk density for no-tillage and conventional tillage. Agric. Eng. Int.: CIGR J. 14(1): 26-37.

Mulqueen, J., J. V. Stafford, and D. W. Tanner. 1977. Evaluation of penetrometers for measuring soil strength. J. Terramech. 14(3): 137-151.

Raissi, M., P. Perdikaris, and G. E. Karniadakis. 2019. Physics-informed neural networks: A deep learning framework for solving forward and inverse problems involving nonlinear partial differential equations. J. Comput. Phys. 378: 686-707.

Soil Science Division Staff. 2017. *Soil Survey Manual*. USDA Handbook 18. Washington, D.C.: U.S. Department of Agriculture.

Ünal, İ., Ö. Kabaş, and S. Sözer. 2024. Comparison of two different artificial neural network models for prediction of soil penetration resistance. J. Agric. Eng. 55(2): 1550.

Wismer, R. D., and H. J. Luth. 1973. Off-road traction prediction for wheeled vehicles. J. Terramech. 10(2): 49-61.

Wong, J. Y. 2009. *Terramechanics and Off-Road Vehicle Engineering*. 2nd ed. Oxford, U.K.: Butterworth-Heinemann.

FM-10

Proceedings of The 12th International Symposium on Machinery and Mechatronics for Agriculture and Biosystems Engineering (ISMAB 2026)
20-24 October 2026, Busan, Republic of Korea

AN ADAPTIVE NMPC FRAMEWORK FOR ACCURATE AND EFFICIENT PATH TRACKING OF ORCHARD ROBOTS

Andong Huang[1,3] Woo-Young Kim[2] Kyeong-Hwan Lee[1,2,3*]

[1]*Department of Convergence Biosystems Engineering, Chonnam National University, Gwangju, Korea*

[2]*AI Agri-Tech Research Center, Chonnam National University, Gwangju, Korea*

[3]*BK21 Interdisciplinary Program in IT-Bio Convergence System, Chonnam National University, Gwangju, Korea*

*Corresponding author: Kyeong-Hwan Lee (khlee@jnu.ac.kr)

Abstract: Reliable path tracking is essential for autonomous orchard robots because field routes combine long inter-row travel with constrained headland turning and row-switching maneuvers that impose substantially different control demands. In addition, uneven terrain, wheel slip, steering asymmetry, and actuator calibration errors can create a persistent mismatch between the nominal steering command used by the controller and the effective steering response of the vehicle. This study presents an adaptive nonlinear model predictive control (NMPC) framework that addresses route-dependent control demand and steering-model inconsistency within a unified closed-loop architecture. The controller uses a low-speed Ackermann kinematic model and evaluates trajectory difficulty stage by stage over the prediction horizon. Difficulty is constructed from two complementary components: a tracking-recovery term derived from predicted lateral and heading errors and a path-maneuvering term derived from reference curvature, curvature-rate variation, and the corresponding steering demand. The resulting difficulty sequence jointly adapts the reference speed and the cross-cycle command-consistency weight. Difficult segments are therefore traversed more conservatively while allowing larger changes in the optimized command sequence when rapid correction is required, whereas low-difficulty segments retain higher speed and stronger command continuity. To compensate for steering-response mismatch, an extended Kalman filter (EKF) estimates steering gain together with direction-dependent left- and right-turn bias terms from pose innovations. The resulting effective steering angle is embedded directly in both the NMPC prediction model and steering constraints, so candidate control actions are evaluated using an online-updated actuator response rather than the nominal command alone. The NMPC objective combines path-tracking error, control effort, input-rate variation, and cross-cycle command inconsistency, and the constrained optimization is solved online using an Acados real-time iteration sequential quadratic programming solver. Field experiments were conducted with a front-wheel-steering orchard shuttle robot in a structured apple orchard in Geochang-gun, Korea. The test route combined long low-curvature inter-row segments with high-demand headland row-switching maneuvers, and the nominal reference speed was 1.0 m/s. Four controllers were

evaluated over three complete runs: Pure Pursuit, fixed-parameter NMPC, trajectory-speed-scheduled NMPC (TS-NMPC), and the proposed adaptive NMPC. The proposed controller achieved lateral RMS errors of 0.030, 0.032, and 0.034 m in the three runs, with lateral P95 errors of 0.064-0.067 m and mean vehicle speeds of 0.92-0.93 m/s. By comparison, the lateral RMS ranges were 0.050-0.056 m for Pure Pursuit, 0.042-0.047 m for fixed-parameter NMPC, and 0.039-0.044 m for TS-NMPC. Averaged over the three runs, the proposed method reduced lateral RMS error by approximately 39.2%, 26.7%, and 23.8% relative to these baselines, respectively, while operating faster on average than TS-NMPC. Yaw RMS error remained within 2.69-3.16 degrees and was not uniformly lower than that of the baselines, indicating that the principal demonstrated benefit is improved lateral path fidelity at a practical operating speed rather than simultaneous minimization of every orientation-error statistic. Overall, the results support combining trajectory-difficulty-driven motion adaptation with predictive steering compensation for accurate and efficient orchard robot path tracking under heterogeneous route conditions.

ACKNOWLEDGEMENTS

This work was supported by Korea Institute of Planning and Evaluation for Technology in Food, Agriculture and Forestry(IPET) through the Agriculture and Food Convergence Technologies Program for Research Manpower development, funded by Ministry of Agriculture, Food and Rural Affairs(MAFRA) (RS-2024-00397026) and through the Technology Commercialization Support Program, funded by Ministry of Agriculture, Food and Rural Affairs(MAFRA)(RS-2024-00395265).

FM-11

Proceedings of The 12th International Symposium on Machinery and Mechatronics for Agriculture and Biosystems Engineering (ISMAB 2026)
20-24 October 2026, Busan, Republic of Korea

ANALYSIS OF SLOPE DRIVING CHARACTERISTICS OF A SMALL TRACKED VEHICLE THROUGH SOIL BIN TESTS

Chan-Young Lee[1,2], Jeong-Hun Kim[1,2], Joon-Hyung Park[1,2], Ju-Seok Nam[1,2,*]

[1]Department of Biosystems Engineering, Kangwon National University, Chuncheon, South Korea
[2]Interdisciplinary Program in Smart Agriculture, Kangwon National University, Chuncheon, South Korea
*Corresponding Author-- Voice: +82-33-250-6497, Email: njsg1218@kangwon.ac.kr

Abstract: Tracked vehicles operating on slopes experience both soil deformation and sideslip. Therefore, a simulation model capable of reproducing actual driving behavior is required to analyze lateral overturning safety during slope driving. For this purpose, a slope driving test platform is needed to establish soil and slope conditions and measure vehicle driving behavior. In this study, the driving characteristics, angular velocity, and track sinkage of a small tracked vehicle were analyzed according to slope angle to provide basic data for simulation model validation. A soil bin measuring 4.0 × 0.5 × 0.2 m was prepared with two soil layers. Slope angle was set at seven levels from 0° to 30° at 5° intervals, and three repeated tests were conducted under each condition over a target driving distance of 3.4 m. The distance traveled and time elapsed until the small tracked vehicle contacted the soil-bin wall, three-axis angular velocity, and uphill and downhill track sinkage were measured. The time of contact with the soil-bin wall was identified from footage recorded by a stationary high-speed camera positioned behind the vehicle starting point. Mean angular velocity and root mean square (RMS) were calculated using data from the start of driving until immediately before wall contact. The results showed that the mean driving distance to wall contact decreased from 2.54 to 0.62 m as slope angle increased from 10° to 30°. Roll angular-velocity RMS did not increase monotonically with slope angle, whereas the magnitude of mean yaw angular velocity increased across slope-group means. In particular, yaw angular-velocity RMS exceeded roll angular-velocity RMS in every trial at 25° and 30°. Therefore, sideslip characteristics were considered more pronounced than lateral overturning tendencies under the present test conditions. These results can be used as basic data for validating EDEM-based driving simulation models and analyzing the lateral overturning safety of small tracked vehicles during slope driving. Further studies are needed to examine the effects of vehicle mass distribution and center-of-gravity location on changes in vehicle heading during slope driving.

Key Words: Small tracked vehicle, Slope angle, Angular velocity, Track sinkage, Sideslip

ACKNOWLEDGEMENTS (optional)

This work was supported by Korea Institute of Planning and Evaluation for Technology in Food, Agriculture and Forestry(IPET) through Machinery Mechanization Technology Development Program for Field Farming Program, funded by Ministry of Agriculture, Food and Rural Affairs(MAFRA)(RS-2023-00235957).

FM-12

Proceedings of The 12th International Symposium on Machinery and Mechatronics for Agriculture and Biosystems Engineering (ISMAB 2026)
20-24 October 2026, Busan, Republic of Korea

STRUCTURAL AND DYNAMIC ASSESSMENT OF A BROILER-CATCHING ROBOT UNDER VARIABLE LOADS WITH EXPERIMENTAL VALIDATION

Md Faruk Hossain[1], Md Rayhan Mahmud[1], Jeong-Chan Lee[2], Ryu-Gap Lim[2]*

[1]Department of Smart Agricultural Engineering, Sunchon National University, Sunchon 57922, Korea
[2]Department of Convergence Biosystem Mechanical Engineering, Sunchon National University, Sunchon 57922, Korea
*Corresponding Author-- Voice: 061-750-3264, Email: limrg11@scnu.ac.kr

Abstract: Broilers catching is labor-intensive work and it has impact on workers' ergonomics and welfare of broilers. Which motivate the Design and development of reliable automated broilers catching robot. The study aims to evaluate the structural integrity and dynamic stability of a four-wheeled broiler-catching robot under various loads. 3D model of the robot was created in SolidWorks software and was used for creating finite-element and multibody dynamic models. ANSYS was used for a structural analysis to determine von Mises stress, total deformation and factor of safety of the chassis, wheel rim-hub assemblies, suspension brackets and payload-supporting components for the specified payload conditions. The critical structural loading case resulted in a maximum von Mises stress of 85 MPa, a maximum deflection of 2.0 mm, and a minimum factor of safety of 2.5, which is acceptable. A RecurDyn multibody dynamic model was developed for analyzing robot mobility and dynamic stability for operating speeds of 0.30–0.70m s^{-1}. The three load levels were tested on flat ground, slopes, side slopes, rough ground, loose surfaces and obstacle crossing conditions. The maximum load was used to examine the worst-case dynamic response. In the simulated operating cases, the robot's pitch angle was the maximum 6.0°, the wheel-slip ratio was the maximum 8.0%, the minimum normal force was 280N, the maximum roll angle was 4.5°, and the maximum suspension travel was 30mm. The results show that the investigations maintained positive wheel ground contact and suspension travel was kept within the modeled operating range. Physical straight-line tests were performed to give reference data for the flat ground dynamic model. Six test passes covered 12.94–14.98m at mean speeds of 0.56–0.70ms^{-1}, with lateral root mean square trajectory deviations of 0.011–0.088m. The recorded coordinate units represent meters, the 200kg load at 0.60 ms^{-1} was selected as the principal flat-ground validation case. The proposed integrated framework of combined SolidWorks, ANSYS, RecurDyn and experimental method used to identify critical structural components and operating conditions of robot safety and dynamic stability. The results give a foundation for better design of the chassis, suspension, wheel assemblies, and load configuration to ensure a reliable broiler-catching operation in poultry-house conditions.

Key Words: Broiler-catching robot, Agricultural robotics, Structural analysis, Multibody dynamic.

ACKNOWLEDGEMENTS

This work was supported by Korea Institute of Planning and Evaluation for Technology in Food, Agriculture and Forestry (IPET) and Korea Smart Farm R&D Foundation (KosFarm) through Smart Farm Innovation Technology Development Program, funded by Ministry of Agriculture, Food and Rural Affairs (MAFRA) and Ministry of Science and ICT(MSIT), Rural Development Administration (RDA) (RS-2025-02316456)

FM-13

Proceedings of The 12th International Symposium on Machinery and Mechatronics for Agriculture and Biosystems Engineering (ISMAB 2026)
20-24 October 2026, Busan, Republic of Korea

HISTORY-DEPENDENT ELASTO-PLASTIC CONTACT MODEL FOR DEM SIMULATION OF CYCLIC SOIL COMPACTION

Toyohiro KATO[1], Taiki ARAO[1], Dong Thanh PHAM[2], Takashi OKAYASU[2], Muneshi MITSUOKA[2*]

[1]Graduate School of Bioresource and Bioenvironmental Sciences, Kyushu University, Japan
[2]Faculty of Agriculture, Kyushu University, Japan
*Corresponding Author-- Email: mitsuoka.muneshi.583@m.kyushu-u.ac.jp

Abstract: Repeated passes of heavy agricultural machinery causes progressive soil compaction, reducing porosity and impairing drainage and root elongation; cyclic loading is therefore a routine rather than exceptional field condition. Existing Discrete Element Method (DEM) contact models, including the Edinburgh Elasto-Plastic Adhesion (EEPA) model, assume identical unloading and reloading paths and thus cannot represent the load-history dependency governing cumulative plastic deformation under repeated compaction. The objective of this study was to develop and validate a DEM contact model in which each micro-scale contact retains a memory of its loading history, to reproduce cumulative plastic deformation of soil under repeated compressive loading.

The proposed model separates the unloading and reloading branches ($k2 \neq k3$), whereas EEPA treats them as identical ($k2 = k3$). The reloading stiffness evolves with an internal state variable, Ξ, defined as the plastic strain energy accumulated at the contact, which increases during loading/reloading and decreases during unloading/adhesion, and a hardening scale, Hr, which controls how quickly the reloading stiffness saturates toward the unloading stiffness. An elasto-plastic ratio, λp, scales the unloading stiffness relative to the Hertzian loading stiffness, and similar history-dependent effects were added to the tangential stiffness and friction coefficient. The model was implemented as a custom EDEM 2025 (Siemens) contact-model plugin via the EDEM API, and evaluated through a simulated 1D oedometer test matching a specimen geometry and load level used for comparison with published repeated-loading data: a cylindrical specimen 100 mm in diameter and 30 mm high, filled with 3 mm particles, under 100 cycles of load-controlled compression between 314 N and about 3-6 N, for Hr = 10-4, 10-5, and 10-10.

The fastest-saturating hardening condition (Hr = 10-10) produced less cumulative settlement after 100 cycles (2.33 mm, 7.8% of specimen height) than the more slowly saturating conditions (2.71 mm and 2.42 mm, 9.0% and 8.1%, for Hr = 10-4 and 10-5), with the curves separating clearly from around the 15th cycle. This indicates that contacts whose reloading stiffness hardens quickly resist further plastic deformation and stabilize the particle packing sooner, whereas more slowly saturating contacts keep accumulating settlement over more cycles—a saturating, cycle-count-dependent behaviour with no counterpart in EEPA. The results confirm that the proposed model reproduces cyclic-plasticity phenomena that cannot be captured by EEPA, and identify the hardening scale, Hr, as an important parameter for long-cycle, field-relevant predictions of cumulative soil compaction, providing a basis for a unified DEM framework to simulate both soil compaction and tillage.

Key Words: Discrete Element Method; EEPA; cyclic loading; soil compaction; history-dependent contact model

INTRODUCTION

The modernization and enlargement of agricultural machinery has led to physical degradation of field soil: heavier machines combined with repeated field traffic promote soil over-compaction (Mileusnić et al., 2022), and the resulting decrease in porosity worsens drainage and restricts root elongation (Hamza and Anderson, 2005). Repeated loading is routine rather than exceptional in the field—a given wheel track may be trafficked more than 50 times over five years, and permanent traffic lanes can reach on the order of 100 passes (Peth and Horn, 2006)—therefore clarifying and quantifying the mechanism of cumulative compaction is a prerequisite for predicting soil compaction under non-uniform, repeated traffic stress.

The Finite Element Method (FEM) has described cyclic plasticity of soil through subloading-surface-type constitutive models (Hashiguchi, 1989), but being continuum-based, it is inherently unsuited to the large deformation and discontinuous phenomena, such as soil fracture and separation, that occur during tillage. The Discrete Element Method (DEM) resolves soil as discrete particles and has been applied extensively to such problems; thus, a DEM contact model that also captures cyclic plasticity could treat compaction and tillage within one consistent framework. However, existing contact models—Hertz-Mindlin, Hertz-Mindlin with JKR, the Hysteretic Spring model, and the Edinburgh Elasto-Plastic Adhesion (EEPA) model, which already accounts for elasto-plastic and adhesive behaviour (Thakur et al., 2014)—all assume a single, path-independent unloading-reloading relationship, so none can represent the load-history dependency, i.e., cyclic plasticity, underlying cumulative deformation under repeated loading. The objective of this study was therefore to develop a DEM contact model in which each micro-scale contact retains a memory of its loading history, and to verify its effectiveness in reproducing the cumulative plastic deformation of soil under repeated compressive loading.

MATERIALS AND METHODS

MODEL FORMULATION

The proposed contact model represents each particle-particle contact with a spring (normal and tangential stiffnesses), a dashpot (viscous damping), and a slider (friction), following the standard DEM contact framework, and consists of four branches: loading, unloading, reloading, and adhesion. The loading branch follows Hertzian contact theory and the adhesion branch follows the existing surface-energy-based formulation used in EEPA, both as in Thakur et al. (2014); the loading force is

$$f_n^L(\delta) = f_0 + k_1\delta^n \tag{1}$$

where FL is the normal contact force, δ is the normal overlap, and $k1$ is the Hertzian loading stiffness. As in EEPA, the unloading stiffness, $k2$, is obtained from $k1$ through an elasto-plastic ratio, λp ($0 \le \lambda p < 1$):

$$k_2 = \frac{k_1}{1-\lambda_p} \quad (0 \le \lambda_p < 1) \tag{2}$$

The key extension of the proposed model is the reloading branch. As illustrated in Fig. 1, EEPA treats the unloading and reloading stiffnesses as identical ($k2 = k3$), so the path is fully reversible and no residual deformation accumulates over a closed cycle. The proposed model instead lets the reloading stiffness, $k3$, differ from $k2$ and evolve with accumulated deformation, producing a hysteresis loop, and therefore a residual deformation, at every cycle. The reloading force is

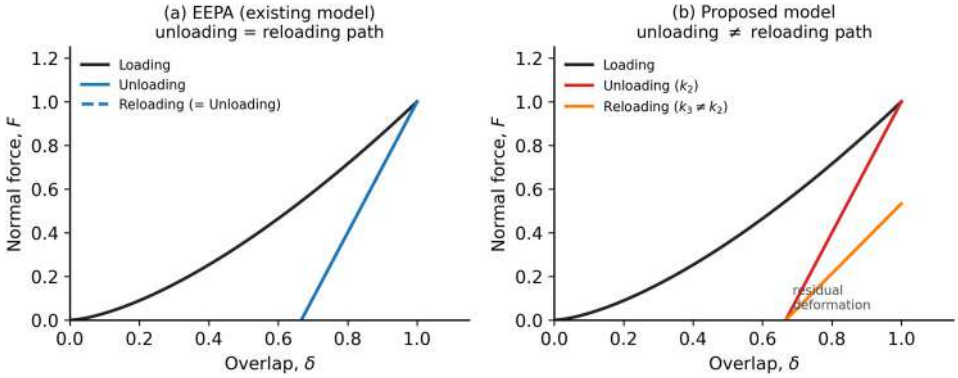

Fig. 1 Normal force-overlap relationship: (a) EEPA, where the unloading and reloading paths coincide; (b) proposed model, where k3 differs from k2, producing a residual deformation per cycle.

$$f_n^R(\delta) = f_{rev} + k_3(\Xi)\left(\delta^n - \delta_{rev}^n\right) \tag{3}$$

where k3 is governed by an internal state variable, Ξ, defined as the plastic strain energy accumulated at the contact:

$$k_3(\Xi) = k_1 + \left(k_2 - k_1\right)\left(1 - exp\left(-\frac{\Xi}{H_r}\right)\right) \tag{4}$$

where Hr is a hardening scale controlling how quickly k3 approaches k2 as Ξ increases: at Ξ = 0, k3 = k1 (no hardening); as Ξ increases, k3 approaches k2 (fully hardened). Because Ξ accumulates strain energy rather than counting cycles, the history dependency reflects the physical amount of accumulated deformation regardless of load amplitude or path. Ξ increases during loading/reloading and decreases during unloading/adhesion, at rates set by hardening/softening coefficients:

$$\Delta\Xi = \lambda_{hardening}\,\Delta W_p \quad (\text{loading, reloading}) \tag{5}$$

$$\Delta\Xi = -\lambda_{softening}\,\Delta W_e \quad (\text{unloading, adhesion}) \tag{6}$$

Two further history-dependent effects were added in the tangential direction: a reloading-only reduction of tangential stiffness coupled to Ξ, and a degradation of the friction coefficient from a peak to a residual value with accumulated sliding. The model was implemented as a custom contact-model plugin for EDEM 2025 (Siemens) via the EDEM API (C++/CUDA C++), since this hardening behaviour is not available in the standard EEPA model. Table 1 summarizes the model parameters.

Table 1 Contact-model parameters: inherited from EEPA and unique to the proposed model.

Parameters inherited from EEPA	
Young's modulus, E	material property
Poisson's ratio, ν	material property
Static friction coefficient, μs (peak value)	surface property
Rolling friction coefficient, μr	surface property
Coefficient of restitution, e	damping property
Surface energy, s	adhesion

Tangential stiffness multiplier, ksf	tangential stiffness, kt0
Elasto-plastic ratio, λp	sets k2 from k1 (Eq. 2)
Parameters unique to the proposed model	
Hardening scale, Hr	rate of reloading-stiffness hardening (Eq. 4)
Hardening coefficient, λhardening	rate of Ξ accumulation (Eq. 5)
Softening coefficient, λsoftening	rate of Ξ release (Eq. 6)

VALIDATION ANALYSIS

The proposed model was examined through a simulated oedometer test, following the specimen geometry and load level used for comparison with the repeated-loading data of Peth and Horn (2006). A cylindrical specimen 100 mm in diameter and 30 mm high was filled with 3 mm particles, and load-controlled cyclic compression was applied for 100 cycles between a peak of 314 N and a trough of about 3-6 N, with a period of about 3 s per cycle (Table 2). Three values of Hr (10-4, 10-5, and 10-10) were compared with all other parameters fixed, to isolate the effect of the rate at which k3 saturates toward k2 as Ξ accumulates.

Table 2 Specimen and loading parameters for the 100-cycle oedometer configuration (Peth and Horn, 2006 comparison geometry).

Item	Value
Specimen diameter	100 mm
Specimen height	30 mm
Particle diameter	3 mm (normal distribution, SD 10%)
Peak load	314 N
Trough load	≈ 3-6 N
Cycle period	≈ 3 s
Number of cycles	100
Hardening scale, Hr (compared)	10-4, 10-5, 10-10

RESULTS AND DISCUSSION

Table 3 summarizes the cumulative settlement at cycle 100, measured at the peak-load position of each cycle relative to the peak position of cycle 1, and expressed both as a displacement and, assuming a nominal specimen height of 30 mm, as a settlement ratio, for Hr = 10-4, 10-5, and 10-10. Hr = 10-4 produced the greatest settlement (2.71 mm, 9.0%), Hr = 10-5 an intermediate settlement (2.42 mm, 8.1%), and Hr = 10-10 the least settlement (2.33 mm, 7.8%), with the curves in Fig. 2 (below) separating clearly from approximately the 15th cycle onward.

Table 3 Cumulative settlement at cycle 100 for Hr = 10-4, 10-5, and 10-10 (peak-load position, cycle 1 = 0 mm; ratio assumes a 30 mm specimen height).

Condition	Cumulative settlement (mm) / ratio
Hr = 10-4	2.71 mm (9.0%)
Hr = 10-5	2.42 mm (8.1%)
Hr = 10-10	2.33 mm (7.8%)

Cumulative settlement decreased monotonically as Hr decreased across the three conditions (Hr = 10-4, 10-5, and 10-10), consistent with faster-saturating hardening (smaller Hr, for which k3 approaches k2 within fewer cycles) producing less residual

deformation. A plausible interpretation is that once a contact's reloading stiffness has hardened close to k2, it resists further plastic deformation, so a rapidly saturating population of contacts stabilizes the particle packing sooner and suppresses further rearrangement-driven settlement; with a slower-saturating Hr, more cycles are spent with a softer reloading stiffness, allowing settlement to continue accumulating for longer. This saturating, cycle-count-dependent transition has no counterpart in EEPA, and illustrates why Hr plays an important role in long-cycle (field-relevant) predictions of cumulative soil compaction.

To further characterize the settlement behaviour in a form comparable with the log-time secondary-compression relationship of Peth and Horn (2006), e(N) = cn·log(N) + eu1, the peak-cycle height was converted to an axial strain, ε(N) = (H1 − HN)/H1 × 100, where H1 is the peak-load height at cycle 1. Fig. 2 plots ε(N) against cycle number on a logarithmic axis for the three conditions, and Table 4 reports the coefficients of a least-squares fit of ε(N) = cn·log10(N) + eu1 over the steady logarithmic range (N = 10-100), which excludes the initial fast-transient cycles associated with contact establishment.

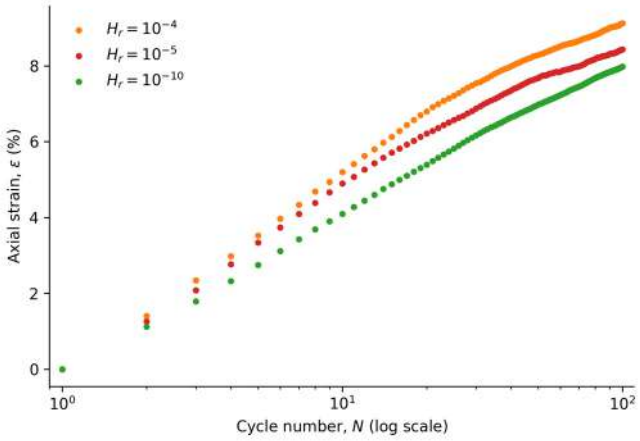

Fig. 2 Axial strain, ε(N), versus cycle number (logarithmic axis) for Hr = 10-4, 10-5, and 10-10.

Table 4 Least-squares fit of ε(N) = cn·log10(N) + eu1 over N = 10-100, and the final strain at N = 100, for Hr = 10-4, 10-5, and 10-10.

Condition	cn (%/decade)	eu1 (%)	R^2	ε at N=100 (%)
Hr = 10-4	3.58	2.11	0.979	9.12
Hr = 10-5	3.34	1.87	0.987	8.43
Hr = 10-10	3.78	0.50	0.996	7.98

The fitted slope, cn, varied only modestly across the three conditions (3.34-3.78 %/decade, $R^2 \geq 0.98$) and showed no monotonic trend with Hr; the smallest Hr (10-10) in fact produced the largest cn despite giving the smallest final strain. In contrast, the intercept, eu1, decreased systematically with decreasing Hr (2.11, 1.87, and 0.50% for Hr = 10-4, 10-5, and 10-10, respectively). This indicates that Hr primarily governs the magnitude of early, fast-transient deformation captured by eu1, rather than the sustained logarithmic creep rate cn, so that the differences in cumulative settlement reported in Table 3 arise mainly from how much plastic deformation occurs before the logarithmic regime is established, and not from a change in its subsequent rate.

CONCLUSIONS

A novel DEM contact model was developed via the EDEM API to reproduce cumulative residual deformation under repeated loading (cyclic plasticity), which EEPA cannot represent, by separating the unloading and reloading stiffnesses ($k2 \neq k3$) and governing $k3$ through an internal state variable, Ξ, and a hardening scale, Hr. Over 100 cycles, Hr governed a cycle-count-dependent effect: quickly saturating hardening (small Hr) ultimately gave less cumulative settlement (2.33 mm) than more slowly saturating conditions (2.42-2.71 mm for Hr = 10-5 and 10-4), consistent with rapidly hardening contacts stabilizing the particle packing sooner. These results show that a history-dependent contact model can reproduce soil compaction and cumulative deformation under repeated traffic, with effects absent from EEPA, marking a step toward a unified vehicle-terrain interaction simulator.

Future work will include calibrating the model parameters ($k2$, $k3$, λp, Hr) against real soil data, extending it to multiaxial stress states and actual vehicle traffic, separating particle-arrangement variability from the model's history dependency, and integrating it into vehicle-terrain simulations for traffic-path and tyre-pressure management.

ACKNOWLEDGMENT

This work was supported by JST SPRING, Japan Grant Number JPMJSP2136.

REFERENCES

Hamza, M. A., and W. K. Anderson. 2005. Soil compaction in cropping systems: A review of the nature, causes and possible solutions. Soil & Tillage Research 82(2): 121-145.

Hashiguchi, K. 1989. Subloading surface model in unconventional plasticity. International Journal of Solids and Structures 25(8): 917-945.

Mileusnić, Z. I., E. Saljnikov, R. L. Radojević, and D. V. Petrović. 2022. Soil compaction due to agricultural machinery impact. Journal of Terramechanics 100: 51-60.

Peth, S., and R. Horn. 2006. The mechanical behavior of structured and homogenized soil under repeated loading. Journal of Plant Nutrition and Soil Science 169(3): 401-410.

Thakur, S. C., J. P. Morrissey, J. Sun, J. F. Chen, and J. Y. Ooi. 2014. Micromechanical analysis of cohesive granular materials using discrete element method with an adhesive elasto-plastic contact model. Granular Matter 16(3): 383-400.

Tumonis, L., R. Kačianauskas, A. Norkus, and D. Žilionienė. 2012. Comparison study of spherical and multi-spherical particles under cyclic uniaxial compression. Journal of Civil Engineering and Management 18(4): 537-545.

Smart Farm Systems and Renewable Energy 1 (SF-1)



SF-01

Proceedings of The 12th International Symposium on Machinery and Mechatronics for Agriculture and Biosystems Engineering (ISMAB 2026)
20-24 October 2026, Busan, Republic of Korea

SPATIAL DYNAMICS OF AMMONIA GRADIENTS AND DIRECTIONAL SENSING EFFECTS IN LAYER HOUSES USING INSPECTION ROBOT

Chin-Kai Kuo[1], Xiang-Sheng Huang[1], Chen-Wei Liang[1]

[1]Department of Biomechatronic Engineering, National Ilan University, Yilan, Taiwan
*Corresponding Author-- Voice: +886-3-931-7805, Email: cwliang@niu.edu.tw

Abstract:

This study uses a multi-sensor mobile inspection robot to investigate the spatial dynamics of harmful gas emissions, vertical accumulation gradients, and directional sensing interferences in a commercial closed-system water curtain laying hen house. Experiments were conducted in a three-story, three-tier battery cage closed-system water curtain laying hen house in Yunlin, Taiwan. A tracked mobile robot equipped with an embedded sensor payload recorded temperature, relative humidity, three-axis wind velocity, carbon dioxide (CO_2), and ammonia (NH_3) at a constant speed of 0.2 m/s across multiple floor levels (1F and 2F), sensing heights (0.6 m and 1.2 m), and movement directions (downwind north to south and upwind south to north). Two-dimensional spatial distribution heatmaps were generated to map environmental variations. The results indicated a highly uniform thermal environment (31.0--33.0°C, 74%--88% RH). The absence of hydrogen sulfide (0 ppb) can be attributed to the automated removal of manure belts in cage systems. In contrast, NH_3 exhibited a prominent spatial accumulation gradient along the ventilation path, increasing from near 0 ppb at the north inlet to 1000 ppb (≈ 1.0 ppm) near the south exhaust fans on 1F and up to 800 ppb on 2F. Hotspot locations varied by floor level, accumulating on the outer rear aisles on the first floor and in the central rear aisle on the second floor. Importantly, upwind robot movement (S $\rightarrow$ N, against the primary airflow) led to a consistent underestimation of gas concentrations (NH_3 and CO_2) due to dilution by fresh air at the sensor intake. This study demonstrates that mobile sensing can effectively identify localized gas accumulation hotspots, establishing downwind inspection paths as a necessity for accurate environmental monitoring in closed-system water curtain laying hen houses.

Key Words: Closed-system water curtain laying hen house, Inspection robot, Ammonia gradient, Directional sensing, Spatial heatmap

INTRODUCTION

Modern layer egg production in tropical and subtropical regions is becoming increasingly dependent on high-density, multi-tier battery cage systems within closed-system water curtain laying hen houses (Lin et al., 2018; Yang et al., 2022). While these automated facilities optimize land use, stocking density, and evaporative cooling efficiency, they also generate substantial amounts of noxious gas emissions, primarily ammonia (NH_3) and carbon dioxide (CO_2) (Ni et al., 2012). Prolonged exposure to elevated NH_3 concentrations impairs respiratory health, suppresses immune function, and significantly reduces egg production and animal welfare in laying hens (Ni et al., 2012).

Traditional environmental monitoring in commercial poultry facilities relies on stationary sensors mounted on walls or structural pillars (Lin et al., 2018; Yang et al., 2022). However, single-point measurements cannot capture spatial gas accumulation gradients, localized ventilation dead zones, or vertical floor-level variations along 45-m-long cage rows (Yang et al., 2022). Mobile robotic inspection offers high spatial resolution for microclimate mapping; however, airflow dynamics created by negative-pressure ventilation and robot motion may introduce direction-dependent measurement biases during real-time sensing (Yang et al., 2022).

The primary objectives of this study were to: (1) quantify the spatial accumulation dynamics of NH_3 and CO_2 along the longitudinal ventilation path in a commercial, three-story, closed-system water curtain laying hen house; (2) evaluate variations in vertical and floor-level gas accumulation hotspots; and (3) analyze the effect of the direction of robot travel (downwind vs. upwind) on the accuracy of mobile environmental sensing to establish a standardized inspection protocol.

MATERIALS AND METHODS

Field Site and House Layout

Field experiments were conducted in Building B of a commercial livestock farm in Yunlin County, Taiwan. The three-story, closed-system, commercial water curtain laying hen house measures 45 m in length and 14 m in width and is oriented along a north-south axis. Each floor has four rows of double-sided, three-tier battery cages, which create five longitudinal aisles (each approximately 1 m wide and 40 m long). The building houses approximately 38,304 Hendrix White laying hens per story. Evaporative cooling water curtain pads are installed at the north entrance (air inlet), and negative-pressure exhaust fans are mounted on the south end wall (air outlet). A simple elevator (2 m x 1 m) at the north entrance facilitates the transportation of robots between floors.

Mobile Robot and Embedded Sensor Assembly

A tracked mobile robot platform manufactured by Hengrui International Co., Ltd., was deployed for autonomous inspection (Fig. 1b). The robot chassis (less than 0.8 m wide) employs a rubber track drive system designed for low maintenance, high traction, and stable navigation across wet or slippery poultry house floors and elevator gaps.

An embedded sensor payload, developed by National Ilan University, was secured to the top of the robot frame via an aluminum profile mount (Fig. 1a).

1. Core Compute and Touch HMI: A Raspberry Pi 4B served as the core edge computing and data aggregation unit. It was paired with a touchscreen display featuring a custom graphical user interface (GUI) for real-time visualization of environmental parameters. The unit also had an active cooling fan for thermal management.
2. Three-Axis Micro-Airflow Array: Three Renesas FS3000 thermal-wire anemometer sensors were mounted orthogonally on a 3D-printed fixture facing the front, vertical, and left directions. This setup enables high-sensitivity detection of micro-wind velocities (0–7.23 m/s).
3. Environmental and Gas Sensor Module: This module contains integrated sensors provided by Hengrui Technology Co., Ltd. that measure temperature, relative humidity, electrochemical H_2S (0–100 ppb), NDIR CO_2 (0–5,000 ppm), and electrochemical NH_3 (0–100 ppm).
4. Data Acquisition: The Raspberry Pi 4B aggregated all georeferenced sensor data at 1–10 Hz and logged it directly to local storage.



Fig. 1. (a) An embedded sensor assembly with three-axis FS3000 wind sensors and a touch HMI.



(b) A mobile inspection robot during a field operation in a layer house.

Experimental Design and Spatial Data Interpolation

Field inspections were performed with the robot traveling at a constant speed of 0.2 m/s along the aisles. Six experimental runs were conducted to analyze environmental spatial variations across floor levels (1F vs. 2F), sensing heights (0.6 m vs. 1.2 m), and travel directions (downwind: north to south vs. upwind: south to north), as summarized in Table 1. The collected time-series records were timestamped and georeferenced to spatial coordinates. Then, they were interpolated into two-dimensional (2D) spatial distribution heatmaps (e.g., the NH_3 heatmap shown in Fig. 2) for quantitative analysis.

Table 1: Experimental Design for Mobile Poultry House Inspection

Run	Floor Level	Aisles	Travel Direction	Sensing Height	Primary Objective
Run 1	1F	4, 3, 2, 1	Downwind (N -> S)	1.2 m	1F mid-level baseline survey
Run 2	1F	4, 3, 2	Upwind (S -> N)	1.2 m	Directional sensing interference evaluation
Run 3	1F	4, 3, 2, 1	Downwind (N -> S)	0.6 m	1F lower-level survey

Run 4	1F	4, 3, 2	Upwind (S -> N)	0.6 m	1F lower-level direction comparison
Run 5	2F	4, 3, 2, 1	Downwind (N -> S)	0.6 m	2F lower-level survey
Run 6	2F	4, 3, 2	Upwind (S -> N)	0.6 m	2F lower-level direction comparison

RESULTS & DISCUSSION

Spatial Dynamics of Ammonia (NH_3) and Carbon Dioxide (CO_2)

Gas measurements revealed significant accumulation gradient variations along the longitudinal ventilation path. During downwind sampling (Run 1), the concentration of NH_3 started near 0 ppb at the north cooling pad inlet and progressively accumulated toward the south exhaust fans. It reached a maximum concentration of 1,000 ppb (~1.0 ppm) in the rear zone (Table 2). On the second floor (Run 5), NH_3 reached a maximum of 800 ppb.

Interestingly, the distribution patterns of hotspots differed between floors. On 1F, NH_3 accumulated along the outer lateral aisles of the rear zone. On 2F, NH_3 concentrated in the central aisle of the rear zone. This variation is attributed to 3D airflow distribution and cage structure obstruction in multi-tier systems. CO_2 exhibited a similar accumulation trend, rising from 400–450 ppm at the inlet to 500–600 ppm at the exhaust end. H_2S was 0 ppb across all runs, confirming that automated manure belt removal prevents the anaerobic decomposition of manure typical of deep-litter floor systems.

Table 2. Summary of Environmental and Gas Sensing Analysis in Building B.

Parameter	**1F Range**	**2F Range**	**Spatial Distribution & Emission Characteristics**
Temperature (°C)	32.0–33.0	31.0–32.0	Highly uniform thermal environment without localized hot spots.
Relative Humidity (%)	74.0–82.0	80.0–88.0	Slightly higher in central and eastern aisles; smooth gradient.
Front Wind Speed (m/s)	2.0–4.0	2.0–3.0	Agrees with negative-pressure tunnel ventilation airflow.
H2S (ppb)	0	0	Not detected; excellent manure belt management.
CO2 (ppm)	400–600	400–550	Progressive accumulation from north inlet (400) to south fan (600).

NH3 (ppb)	0–1000	0–800	Strong spatial gradient; peak 1 ppm at rear fan zone (limit: 25 ppm).

Directional Interference Effect (Downwind vs. Upwind)

A key finding of this study is that the direction in which the robot travels has a significant impact on gas and wind speed readings. When travelling upwind (south to north, facing incoming fresh air in Runs 2 and 4), the measured concentrations of NH_3 and CO_2 were consistently lower than during downwind travel (north to south in Runs 1 and 3).

When moving upwind, the sensor head directly encounters clean air entering from the inlet. This creates a localised boundary-layer dilution effect around the sensor intake, resulting in an underestimation of the actual accumulated gas concentration in the aisle. Furthermore, upwind travel offsets the relative wind speed, altering thermal anemometer readings. Therefore, mobile robotic inspections in closed-system water curtain laying hen houses should use a standardised downwind trajectory in order to accurately identify hotspots.

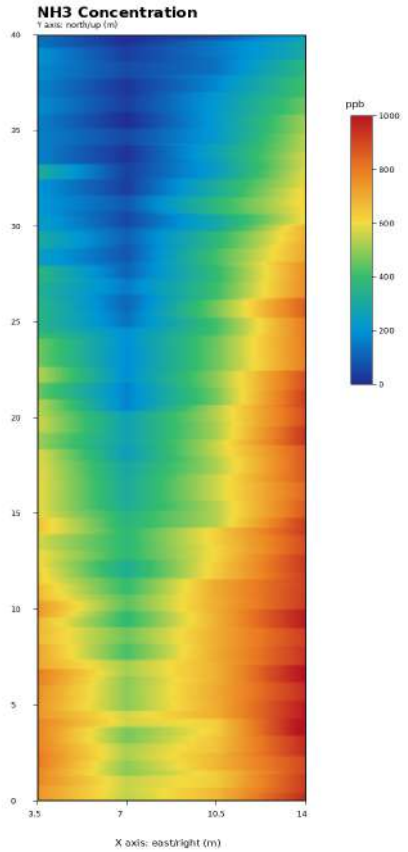

Fig. 2. 2D spatial distribution heatmap of ammonia (NH_3) concentration along the aisle on 1F.

CONCLUSIONS

1. A mobile inspection robot equipped with an embedded sensor assembly successfully mapped the two-dimensional distributions of microclimate and gas emissions within a three-storey commercial water curtain laying hen house operating as a closed system.
2. NH_3 (0–1,000 ppb) and CO_2 (400–600 ppm) exhibited distinct, floor-dependent hotspot

patterns (1F rear sides versus 2F rear centre) and demonstrated strong longitudinal accumulation gradients towards the exhaust fans.

3. Upwind movement of the robot causes localised air dilution, which underestimates gas accumulation. Standardised downwind travel paths are recommended for mobile sensing protocols.

ACKNOWLEDGEMENTS

This study was financially supported by the Ministry of Agriculture, Taiwan (Grant No. 115 MOA-10.2.3-Livestock-01(5)), The authors thank the commercial livestock farm in Yunlin for providing the field site and Hengrui International Co., Ltd. for technical support.

REFERENCES

Anderson, G. T., C. V. Renard, L. M. Strein, and E. C. Cayo. 1998. A new technique for rapid deployment of rollover protective structures. Applied Eng. in Agric. 23(2): 34-42.

Lin, T. T., C. C. Chen, and W. S. Chang. 2018. Application and prospects of smart agriculture in poultry environment control. Agric. Policy Newsl. (312): 88-93. (In Chinese).

Ni, J. Q., W. P. Robarge, C. Xiao, and A. J. Heber. 2012. Carbon dioxide emission from pig and poultry houses: A review. Biosystems Eng. 112(1): 1-15.

Yang, A. X., C. Chen, and Y. Wang. 2022. Mobile sensing and robotic inspection systems in poultry houses: A review. Computers and Electronics in Agric. 198: 107051.

SF-02

Proceedings of The 12th International Symposium on Machinery and Mechatronics for Agriculture and Biosystems Engineering (ISMAB 2026)
20-24 October 2026, Busan, Republic of Korea

CAPACITY AND INTERNAL RESISTANCE VARIATION OF NCM BATTERIES UNDER DIFFERENT CHARGE–DISCHARGE STRATEGIES AND TEMPERATURE CONTROL

Li-Ya Hsiao, Chen-Kang Huang*

Department of Biomechatronics Engineering, National Taiwan University, Taiwan
*Corresponding Author: ckhuang94530@ntu.edu.tw

Abstract: Lithium-ion batteries are increasingly used in electric agricultural machinery and autonomous mobile platforms, where capacity retention, internal resistance, and thermal response directly affect operating time, performance, and safety. Lithium nickel cobalt manganese oxide (NCM) batteries offer high energy density but are sensitive to charge–discharge strategies and operating temperature. Therefore, this study investigates the capacity, internal resistance, and temperature characteristics of lithium-ion batteries under different operating and temperature-control conditions. Initial short-term tests were conducted to explore pulse-width-modulation (PWM)-based intermittent pulse charging. A 21700 NCM cell showed an internal-resistance decrease of approximately 1.1% after 10 cycles of PWM-based intermittent pulse charging without active temperature control. For a TK18650 lithium titanate (LTO) cell maintained under temperature-controlled conditions, internal resistance increased by approximately 2.0% under conventional charge–discharge cycling and by approximately 1.2% after 10 cycles of PWM-based intermittent pulse charging. These exploratory results motivated further investigation of operating strategy and temperature control. The subsequent study focused on LG INR18650 M26 NCM cells and compared the response under uncontrolled and temperature-controlled conditions during conventional charge–discharge cycling. A specially designed aluminum-block temperature-control platform was developed to provide a more stable local thermal condition, maintaining the recorded temperature adjacent to the cell at approximately 23–25 °C. One cell was tested under each thermal condition, and a 1C full charge–discharge reference cycle was performed every 10 conventional cycles. At the matched cycle 70, capacity retention was 74.6% under the uncontrolled condition and 77.8% under the temperature-controlled condition, while internal-resistance change was +9.4% and +10.1%, respectively. These preliminary findings indicate that temperature control was associated with slightly higher capacity retention over the matched cycling interval, whereas a clear reduction in internal-resistance growth was not observed. The results provide a preliminary reference for battery operating-condition selection, temperature-control design, and charge–discharge strategy development in electric agricultural machinery.

Key Words: Lithium nickel cobalt manganese oxide (NCM), Pulse-width modulation (PWM), Temperature control, Internal resistance, Capacity retention

INTRODUCTION

The electrification of agricultural machinery has received increasing attention because electric

drive systems can improve energy efficiency, torque and speed control, noise reduction, and system-design flexibility (Moreda et al., 2016). In battery-powered agricultural machinery and autonomous mobile platforms, the usable energy and power available from the battery directly constrain operating time, payload capability, and mission reliability. Therefore, battery thermal conditions during charge–discharge operation are an important engineering concern.

Temperature strongly affects lithium-ion battery performance and ageing. It influences reaction kinetics, ionic transport, polarization, internal resistance, and degradation pathways (Ma et al., 2018). Previous studies have shown that cycling temperature can change both capacity retention and dominant ageing mechanisms in commercial 18650-type and NMC-based lithium-ion cells (Waldmann et al., 2014; Friesen et al., 2017; Li et al., 2018). Thus, thermal management should not be interpreted simply as making the cell colder; rather, the actual cell-temperature history must be measured and reported.

This preliminary study investigates the thermal and electrochemical response of a commercial 18650 NCM cell under uncontrolled and temperature-controlled conditions. The objectives were to compare the thermal response, capacity retention, and internal-resistance change of the tested NCM cells under uncontrolled and temperature-controlled conditions, and to examine whether a simple aluminum-block temperature-control platform could provide a more stable local thermal boundary during 1C charge–discharge operation. The results provide an initial experimental basis for future replicated testing of battery thermal management in electric agricultural machinery.

MATERIALS AND METHODS

Battery Samples

Three cylindrical lithium-ion cells were used in this study. Preliminary tests were performed using an NCM INR21700-50E cell and an LTO TK18650-NT35 cell to evaluate changes in internal resistance under different charging conditions. The main cycling experiment was conducted using an LG18650-M26 NCM cell to investigate the effect of temperature control on capacity retention, internal resistance, and thermal response.

Experimental Equipment

Table 1 Main instruments and specifications.

Instrument	Model	Specification
DC power supply	PSW 80-27, GW Instek	Charging; 0–80 V, 0–27 A, 720 W
DC electronic load	PEL-3041, GW Instek	Discharging/capacity measurement; 150 V, 70 A, 350 W
Battery meter	GBM-3300, GW Instek	Internal-resistance measurement; 1-kHz AC, four-wire measurement
Data logger	GL220, GRAPHTEC	Temperature recording; 10 channels, Type J,K,T,R,S,B,E,N,W T/C's
Temperature controller	SM5-LCD	ON/OFF temperature control; 0.1 °C resolution

Table 2 Summarizes the specifications of the tested cells.

Cell chemistry	Model	Size	Nominal voltage (V)	Nominal capacity (Ah)
NCM	INR21700-50E	21700	3.6	4.9
LTO	TK18650-NT35	18650	2.2	1.35
NCM	LG18650-M26	18650	3.7	2.6

Aluminum-Block Temperature-Control Platform

The temperature-controlled condition used a specially designed aluminum-block platform consisting of a machined aluminum block (approximately 100 × 60 × 130 mm), a thermoelectric cooling (TEC) module, a forced-air heat sink with cooling fans, an auxiliary DC power supply, and the SM5-LCD temperature controller. The 18650 cell was inserted into the block to provide thermal contact. A control sensor in the lower block supplied feedback to the controller; cooling was activated at 24.2 °C and deactivated at 24.0 °C. A separate T-type thermocouple connected to a GRAPHTEC GL220 was attached to the aluminum-block surface adjacent to the cell for temperature recording. In the uncontrolled condition, a T-type thermocouple was attached directly to the cell surface and no active cooling was applied. Fig. 1 shows the schematic diagram of the self-made aluminum-block temperature-controlled charge–discharge platform.

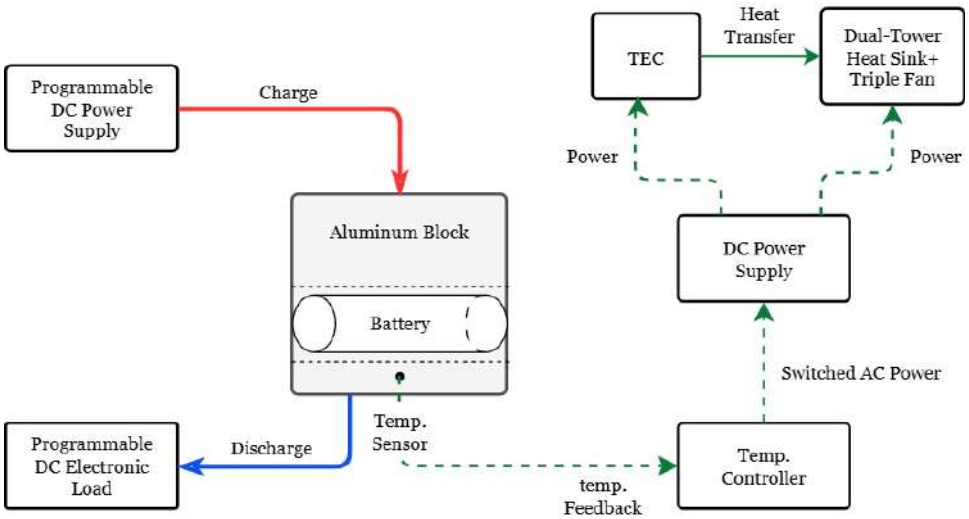

Fig. 1 Schematic of the temperature-controlled platform.

Preliminary Exploratory Tests

Preliminary experiments were conducted to compare conventional and PWM-based charging strategies prior to the main temperature-control experiment. A PWM-based intermittent pulse-charging protocol was applied using repeated 5-min charging and 1-min rest intervals. Before each pulse-charging sequence, the cell was discharged to 20% state of charge (SOC).

A 21700 NCM cell was tested for 10 cycles without active temperature control, during which the recorded temperature ranged from approximately 25 to 32 °C. In addition, a TK18650 LTO cell was evaluated for 10 cycles at approximately 20 °C under both conventional charge–discharge cycling and PWM-based pulse charging. Internal resistance was measured before and after the short-term cycling tests to evaluate the change associated with each charging strategy. These preliminary experiments were used to support the design of the subsequent NCM temperature-control experiment.

Main Battery Cell and Cycling Protocol

The main experiment used two commercial LG INR18650 M26 NCM cells, with one cell assigned to each thermal condition: an uncontrolled cell (NC) and a temperature-controlled cell (TC). Because only one cell was tested per condition, the results were treated as a preliminary comparison. The 1C current was based on the initial measured capacity: 2.3 A for the NC cell and 2.1 A for the TC cell. Cells were charged by CC–CV to 4.2 V with a 0.05C cutoff, rested for 30 min, discharged to 2.75 V at the cell-specific 1C current, and rested again for 30 min.

Reference cycles were performed before cycling and after every 10 conventional cycles. The NC cell was cycled for 100 cycles, whereas the TC cell has currently completed 70 cycles. Reference points were therefore obtained at 10-cycle intervals from cycles 0–100 for NC and cycles 0–70 for TC. Discharge capacity was recorded by the electronic load, and internal resistance was measured at approximately 100% SOC after the post-charge rest.

Charge–Discharge Protocols

The preliminary NCM INR21700-50E test was conducted under PWM charge–discharge operation without temperature control to observe the change in internal resistance. The LTO TK18650 tests were conducted under constant-temperature cycling and constant-temperature cycling with PWM operation to compare the effect of PWM operation on internal resistance variation.

For the main NCM LG18650-M26 test, two cycling conditions were compared: natural cycling without temperature-controlled and cycling with the aluminum-block temperature-controlled platform. The natural cycling test was used as the reference condition. The temperature-controlled test was used to evaluate whether reducing temperature accumulation could affect capacity retention and internal resistance growth.

Data Analysis

Capacity retention was calculated using Eq.(1):

$$Capacity\ retention = \frac{Q_n}{Q_0} \times 100\% \quad (1)$$

where Q_n is the discharge capacity after cycling (Ah), and Q_0 is the initial discharge capacity (Ah).

Internal resistance change was calculated using Eq.(2):

$$Internal\ resistance\ change = \frac{R_n - R_0}{R_0} \times 100\% \quad (2)$$

where R_n is the internal resistance after cycling (mΩ), and R_0 is the initial internal resistance (mΩ).

The capacity retention and internal resistance change were used as the main indicators to compare the effects of natural cycling, temperature-controlled cycling, and PWM charge–discharge operation on NCM lithium-ion battery performance.

RESULTS & DISCUSSION

Exploratory Internal-Resistance Response

The short-term tests produced different internal-resistance responses. The 21700 NCM cell showed an approximately 1.1% decrease after 10 cycles of PWM-based pulse charging without active temperature control. For the TK18650 LTO cell maintained at approximately 20 °C, internal resistance increased from 14.96 to 15.26 mΩ (+2.0%) during conventional cycling and from 15.19 to 15.38 mΩ (+1.2%) during PWM-based pulse charging. Because chemistry, initial condition, and thermal boundary differed among these tests, they are presented only as exploratory motivation rather than a controlled quantitative comparison.

Thermal Response, Capacity Retention, and Internal Resistance

Under the uncontrolled condition, cell-surface temperature began near 25 °C and rose progressively to approximately 32 °C during discharge. Under active temperature control, the temperature recorded on the aluminum block adjacent to the cell remained comparatively stable at approximately 23–25 °C. Because the sensing locations differed, the absolute values should not be treated as identical physical-point measurements; however, the profiles clearly show different thermal boundary behavior.

(a) (b)

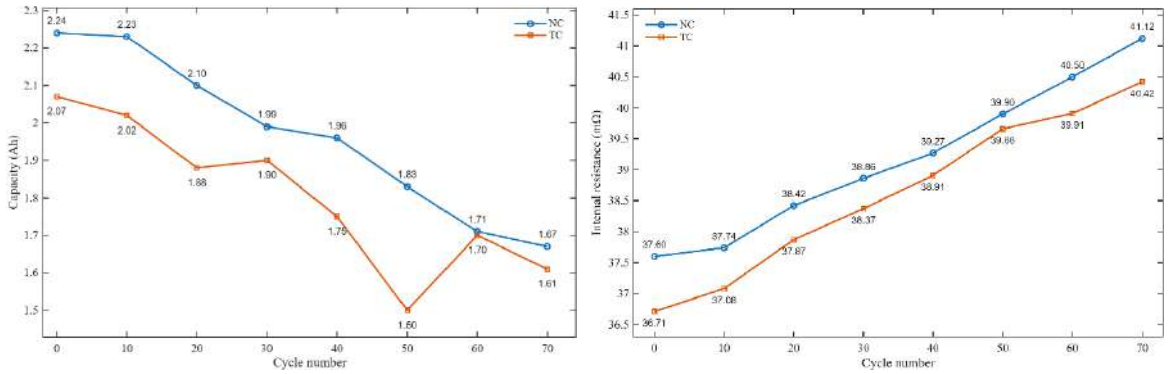

Fig. 2 Experimental results: (a) (b) internal resistance.

Under the uncontrolled condition, capacity decreased from 2.24 to 1.67 Ah after 70 conventional charge–discharge cycles, corresponding to a capacity retention of 74.6%. Internal resistance increased from 37.60 to 41.12 mΩ, corresponding to an increase of 9.4%. Under the temperature-controlled condition, capacity decreased from 2.07 to 1.61 Ah after 70 cycles, corresponding to a capacity retention of 77.8%, while internal resistance increased from 36.71 to 40.42 mΩ, corresponding to an increase of 10.1%. At the matched cycle 70, the temperature-controlled cell therefore showed a slightly higher capacity retention than the uncontrolled cell by 3.2 percentage points. However, the internal-resistance increase was slightly greater under the temperature-controlled condition. These results indicate that the aluminum-block temperature-control platform was associated with slightly higher capacity retention over the matched 70-cycle interval, whereas a reduction in internal-resistance growth was not observed.

CONCLUSIONS

This preliminary study evaluated short-term charging-strategy effects and temperature-controlled cycling of LG INR18650 M26 NCM cells. The exploratory tests showed internal-resistance changes of −1.1% for a 21700 NCM cell under PWM-based pulse charging, +2.0% for a temperature-controlled TK18650 LTO cell under conventional cycling, and +1.2% for the LTO cell under PWM-based pulse charging. In the main experiment, the aluminum-block temperature-control platform maintained a more stable local thermal condition. At the matched cycle 70, capacity retention was 74.6% for the uncontrolled condition (NC) and 77.8% for the temperature-controlled condition (TC), while internal-resistance change was +9.4% and +10.1%, respectively.

These results indicate that temperature control was associated with slightly higher capacity retention over the matched 70-cycle interval, whereas a clear reduction in internal-resistance growth was not observed. Because only one cell was tested per condition, further replicated experiments using multiple cells and matched reference temperatures are required before the results can be generalized. Nevertheless, the present findings provide a preliminary reference for battery operating-condition selection, temperature-control system design, and future charge–discharge strategy development for electric agricultural machinery and autonomous mobile platforms.

ACKNOWLEDGEMENTS

The authors gratefully acknowledge the financial support provided by the Ministry of Agriculture, Taiwan, under Grant No. 115AS-11.2.2-AS-01.

REFERENCES

Friesen, A., X. Mönnighoff, M. Börner, J. Haetge, F. Schappacher, and M. Winter. 2017. Influence of temperature on the aging behavior of 18650-type lithium ion cells: A comprehensive approach combining electrochemical characterization and post-mortem analysis.Journal of Power Sources 342: 88–97.

Li, D., H. Li, D. Danilov, L. Gao, J. Zhou, R.-A. Eichel, Y. Yang, and P. H. L. Notten. 2018. Temperature-dependent cycling performance and ageing mechanisms of C6/LiNi1/3Mn1/3Co1/3O2 batteries. Journal of Power Sources 396: 444–452.

Ma, S., M. Jiang, P. Tao, C. Song, J. Wu, J. Wang, T. Deng, and W. Shang. 2018. Temperature effect and thermal impact in lithium-ion batteries: A review. Progress in Natural Science: Materials International 28(6): 653–666.

Moreda, G. P., M. A. Muñoz-García, and P. Barreiro. 2016. High voltage electrification of tractor and agricultural machinery—A review. Energy Conversion and Management 115: 117–131.

Waldmann, T., M. Wilka, M. Kasper, M. Fleischhammer, and M. Wohlfahrt-Mehrens. 2014. Temperature dependent ageing mechanisms in lithium-ion batteries—A post-mortem study. Journal of Power Sources 262: 129–135.

SF-03

Proceedings of The 12th International Symposium on Machinery and Mechatronics for Agriculture and Biosystems Engineering (ISMAB 2026)
20-24 October 2026, Busan, Republic of Korea

DEVELOPMENT OF A DEEP LEARNING-BASED IMAGE EARLY WARNING SYSTEM FOR BROILER CHICKENS

Yu-Jen Shih[1*], Ming-Kun Hsieh[2], and Yao-Chuan Tsai[1]

[1]Dept. of Bio-Industrial Mechatronic Engineering, National Chung Hsing University, Taichung, Taiwan
[2]Graduate Institute of Microbiology and Public Health, National Chung Hsing University, Taichung, Taiwan
*Corresponding Author-- Email: kb3789@gmail.com

Abstract:
Broiler chickens are characterized by rapid growth and short production cycles. They are therefore susceptible to environmental stressors and diseases in poultry houses. These problems may reduce growth performance, increase mortality and culling rates, and cause economic losses. Conventional flock health monitoring mainly relies on routine visual inspections by farm personnel. However, this approach is labor-intensive and depends heavily on individual experience. Therefore, this study developed a deep learning-based image monitoring system for broiler chickens using controllable high-resolution cameras installed in a commercial poultry house. The proposed system first employs a YOLO11s object detection model to locate chicken heads in poultry-house images. The detected head images are then separately processed by two MobileNetV3-based classification models to determine whether the eyes are open or closed and whether the beak is open or closed. Eye-opening and eye-closing conditions can serve as reference indicators for assessing chicken activity and behavioral status, whereas beak-opening behavior can be used to monitor panting and assist in evaluating heat stress and potential respiratory symptoms. The system automatically calculates the proportions of chickens with closed eyes and open beaks, thereby transforming conventional visual observations into quantitative data that can be continuously monitored over time. Model performance evaluation showed that the chicken head detection model achieved an mAP@50 of 0.947, while both the eye-status and beak-status classification models achieved an F1-score of 0.93. The proposed system enables automated observation and quantification of eye and beak conditions in broiler chickens and has the potential to support the early detection of abnormal flock conditions and reduce associated economic losses.

Key Words: Broiler chickens; Deep learning; Image monitoring; Poultry health monitoring

INTRODUCTION

Broiler chickens are characterized by rapid growth and short production cycles, making their health and welfare highly sensitive to environmental stress and disease. In commercial poultry production, flock conditions are commonly assessed through manual observation by farm personnel. However, this approach is labor-intensive, subjective, and difficult to perform continuously, particularly in large-scale poultry houses. Recent advances in deep learning and computer vision provide opportunities for automated and non-invasive monitoring of animal conditions. Behavioral and external indicators, such as eye closure and beak opening, may provide useful information related to activity, thermal stress, and potential health abnormalities. Therefore, this study developed a deep learning-based image monitoring system for broiler chickens. The system integrates chicken head detection with eye- and beak-status classification to automatically quantify the proportions of closed eyes and open beaks, providing objective and continuous information for flock monitoring and supporting more efficient poultry management.

MATERIALS AND METHODS

2.1 Image Acquisition and Experimental Environment

Image data were collected in a commercial broiler poultry house at Yixin Poultry Farm in Erlin Township, Changhua County, Taiwan, where approximately 20,000 broiler chickens were raised. A high-resolution camera (OY-T441 X36RPE, Only, Taiwan) with a resolution of 2688 × 1520 pixels was installed at approximately 1.8 m above the ground. Image collection covered the entire broiler production cycle to obtain chicken images across different ages, body sizes, and environmental conditions for subsequent model training and validation.

2.2 Chicken Head Detection and Status Classification

A YOLO11s object detection model was first used to detect chicken heads, and the head regions were manually annotated using bounding boxes. As shown in Figure 1(a). A total of 1,000 images were divided into training, validation, and test sets containing 800, 100, and 100 images, respectively. The input image size was set to 1280 × 1280 pixels, with 150 training epochs and a batch size of 8. After head detection, the detected head regions were cropped and resized to 160 × 160 pixels for status classification using MobileNetV3-based models. Eye status was classified into three categories: open, closed, and unrecognizable, with 4,794 and 1,075 images used for training and validation, respectively. Beak status was also classified into three categories: open, closed, and unrecognizable, with 859 training images and 185 validation images. Both classification models were trained for 30 epochs with a batch size of 32.

(a) (b)

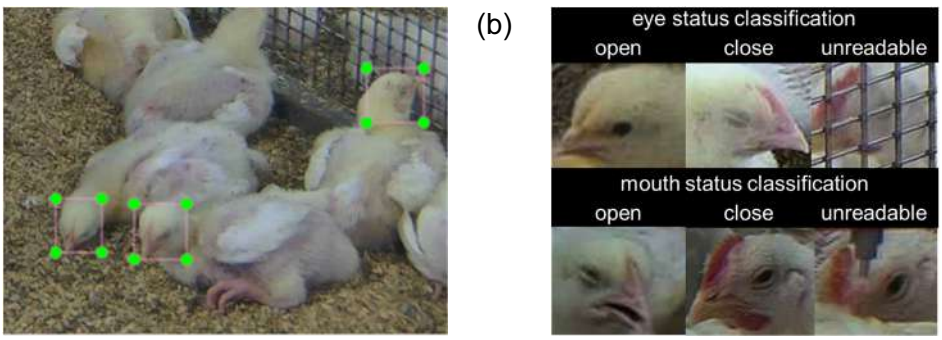

Figure 1. (a) Annotated image. (b) Examples of eye and beak status classification in broiler chickens.

2.3 Image Monitoring System

The proposed image monitoring system integrates chicken head detection and status classification into a complete analysis workflow. Poultry-house images were first processed by the YOLO11s model to detect and crop individual chicken heads. The cropped images were then resized to 160 × 160 pixels and separately analyzed using MobileNetV3-based models to classify eye and beak status. Based on the classification results, the system calculates the proportions of chickens with closed eyes and open beaks, generating quantitative indicators such as the closed-eye rate and open-beak rate for continuous monitoring and further analysis of flock conditions.

RESULTS & DISCUSSION

3.1 Image Monitoring System

The training set for the chicken head detection model contained 12,692 manually annotated chicken head objects. The test results showed that the YOLO11s model achieved a Precision of 0.867, a Recall of 0.897, and an mAP@50 of 0.947, indicating good performance in detecting and localizing chicken heads. The model was able to effectively identify chicken heads even under commercial poultry-house conditions with high stocking density and partial occlusion. However, some background regions or objects with appearances similar to chicken heads were incorrectly detected, resulting in a lower Precision than Recall. Examples of false detections in the poultry-house environment are shown in Fig. 3. Overall, the YOLO11s model demonstrated good detection performance and was capable of effectively extracting chicken head regions from poultry-house images for subsequent eye- and beak-status classification.

(a)  (b) 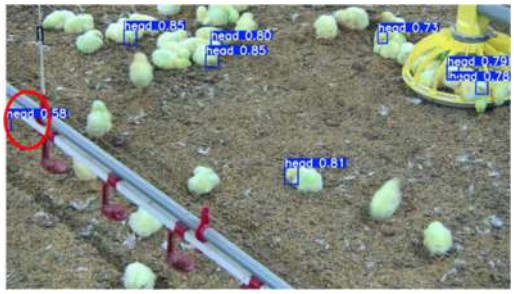

Figure 2. Examples of incorrect chicken head detection: (a) a severely occluded chicken head excluded from annotation but detected by the model; (b) a background region incorrectly detected as a chicken head.

3.2 Eye and Beak Status Classification Performance

Both the eye- and beak-status classification models achieved an average F1-score of 0.93, indicating good overall classification performance. The eye-status model effectively distinguished open and closed eyes, although some unclear or occluded images were misclassified. Similarly, the beak-status model showed stable performance, with most errors occurring when the beak opening was small or image details were insufficient. Overall, both models were suitable for automated quantification of closed-eye and open-beak conditions in broiler chickens.

Table 1. Performance of the status classification models: (a) eye-status classification and (b) beak-status classification.

(a)

	Precision	Recall
Open	0.96	0.97
Close	0.90	0.92
Unreadable	0.92	0.79
Average	0.93	0.93

(b)

	Precision	Recall
Open	0.90	0.84
Close	0.91	0.98
Unreadable	1	0.92
Average	0.94	0.94

3.3 Whole period result analysis

A batch of broiler image-monitoring data was analyzed over a 33-day period from March 26 to April 27, 2026. As shown in Fig. 4(a), during the middle and later stages of the production cycle, the daily duration of THI > 78 showed a trend similar to the daily average open-beak rate, suggesting that open-beak behavior may serve as a potential image-based indicator of heat-related environmental stress. As shown in Fig. 4(b), the daily maximum closed-eye rate tended to be higher on the days of ND-IB and IBD vaccination, possibly reflecting short-term physiological responses or changes in activity. However, as the results were obtained from only one production cycle, further validation using additional production cycles and health records is required. Overall, these results indicate the potential of open-beak and closed-eye rates as image-based indicators for monitoring environmental stress and short-term changes in flock condition.

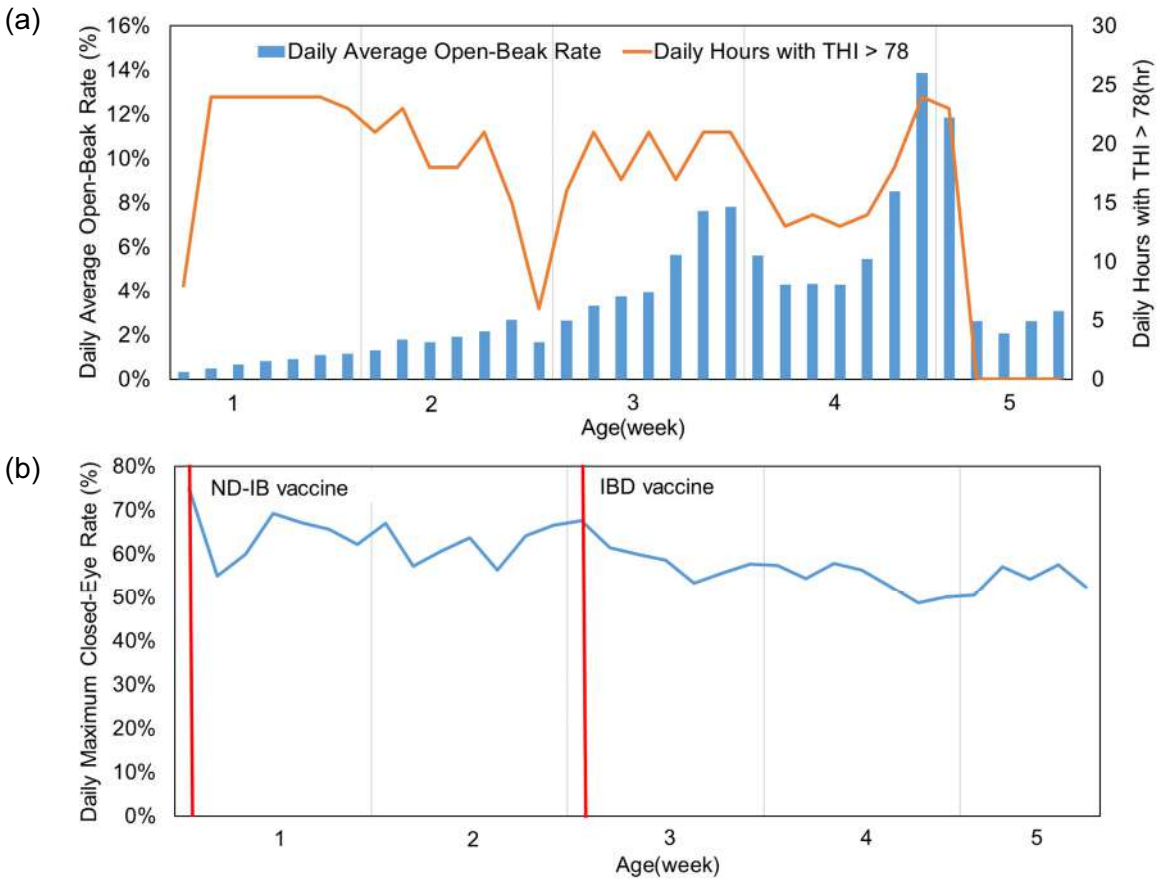

Figure 3. Changes in image-based indicators and environmental conditions throughout the broiler production cycle: (a) daily average open-beak rate and daily duration of THI > 78; (b) daily maximum closed-eye rate, with the timing of ND-IB and IBD vaccinations indicated by red vertical lines.

CONCLUSIONS

Overall, the proposed image monitoring workflow successfully integrated chicken head detection, head image cropping, and eye- and beak-status classification, allowing individual classification results to be further converted into flock-level indicators such as closed-eye rate and open-beak rate. The chicken head detection model achieved an mAP@50 of 0.947, while both the eye- and beak-status classification models achieved an average F1-score of 0.93. These results demonstrate the feasibility of applying the proposed workflow to automated image monitoring in commercial broiler houses. However, the present study mainly focused on the establishment and evaluation of the image recognition workflow and camera settings. The relationships between closed-eye rate, open-beak rate, flock health status, environmental stress, and production performance still require further validation. Future studies may integrate environmental and production data to further evaluate the potential of these image-based indicators for abnormal condition monitoring and early warning in broiler production.

ACKNOWLEDGEMENTS

Thanks to Mr. Hsueh Zhi-Sheng from Erlin, Changhua, Taiwan Livestock Farm. Provide an experimental or commercial site for this research and assist in system installation and troubleshooting. Experiments conducted to facilitate this study.

REFERENCES

Gregory, N. G., S. R. Payne, C. D. Devine, and C. J. Cook. 2009. Effect of lipopolysaccharide on sickness behaviour in hens kept in cage and free range environments. Res. Vet. Sci. 87(1): 167-170.

Cartoni Mancinelli, A., G. Baldi, F. Soglia, S. Mattioli, F. Sirri, M. Petracci, C. Castellini, and M. Zampiga. 2023. Impact of chronic heat stress on behavior, oxidative status and meat quality traits of fast-growing broiler chickens. Front. Physiol. 14: 1242094.

Schlegel, L., A. S. Kleine, M. G. Doherr, and C. Fischer-Tenhagen. 2024. How to see stress in chickens: On the way to a Stressed Chicken Scale. Poult. Sci. 103(8): 103875.

Cakic, S., T. Popovic, S. Krco, D. Nedic, D. Babic, and I. Jovovic. 2023. Developing Edge AI computer vision for smart poultry farms using deep learning and HPC. Sensors 23(6): 3002.

Wang, Y., K. Cuan, W. Pei, X. Yan, W. Lin, W. Shi, and K. Wang. 2025. A two-stage deep learning approach for identifying low-yield hens in stacked cage systems. Comput. Electron. Agric. 231: 109958.

SF-04

Proceedings of The 12th International Symposium on Machinery and Mechatronics for Agriculture and Biosystems Engineering (ISMAB 2026)
20-24 October 2026, Busan, Republic of Korea

STRATEGY VALIDATION AND ENERGY INTEGRATION OF AN AI LASER WILD BIRD DETERRENT IN AGRICULTURAL FIELDS

Chang-Chi Huang*, Wei-Lun Hsu, Kuang-Wen Hsieh, and Yao-Chuan Tsai

Dept. of Bio-industrial Mechatronics Engineering, National Chung Hsing University, Taichung, Taiwan

*Corresponding Author Email: kikihuang1997@gmail.com

Abstract: Rice crops are highly susceptible to feeding damage by wild birds during the ripening stage. Conventional bird-deterrent methods often lose effectiveness as birds become habituated, while limited access to electricity in agricultural fields restricts the long-term operation of smart deterrent devices. This study integrated artificial intelligence (AI)-based image recognition, laser bird deterrence, solar power, and energy storage systems to investigate the effects of different deterrent strategies on rice yield and evaluate the feasibility of off-grid power supply. Field experiments were conducted in a rice field in Pitou Township, Changhua County, Taiwan. Three treatment zones were established: an AI-triggered laser treatment, a scheduled laser treatment, and a no-laser control. Field images of birds were collected to develop a YOLOv11 detection model. The model achieved a precision of 0.900, recall of 0.629, F1-score of 0.740, and mAP@0.5 of 0.676. Rice yield was measured using individual rice hills as sampling units, with 90 hills randomly collected across the three treatments. The mean yields of the AI-triggered laser, scheduled laser, and no-laser treatments were 68.40, 91.57, and 56.10 g/hill, respectively. One-way analysis of variance indicated a significant difference in mean yield among the treatments ($F(2,87) = 60.25$, $p < 0.001$). Tukey's post hoc test further showed significant differences between all treatment pairs. Compared with the no-laser control, the scheduled laser treatment increased yield by an average of 35.47 g/hill, representing a 63.2% improvement. The measured yield per unit area was also higher in the scheduled laser treatment than in the AI-triggered laser and control treatments. The lower effectiveness of the AI-triggered laser may have resulted from the delay between bird detection and laser activation, as well as limitations in the laser scanning angle. Overall, scheduled laser operation effectively reduced bird damage and increased rice yield. When integrated with solar power and energy storage technologies, the system also shows potential for deployment in off-grid agricultural fields and for improving agricultural energy self-sufficiency.

Key Words: YOLOv11, Laser bird deterrence, Rice bird damage, Solar energy storage

INTRODUCTION

Bird damage is a major constraint on cereal production, particularly during grain filling and ripening. In rice fields, granivorous birds such as munias (Lonchura spp.) feed on developing grains from the milk stage to maturity, resulting in substantial yield losses. Conventional deterrents, including scarecrows, reflective materials, acoustic devices, and manual patrols, are often labor-intensive and may gradually lose effectiveness because birds become habituated to repeated stimuli.

Laser-based deterrence offers a nonlethal alternative for reducing bird activity without physical contact or chemical application. Previous studies have demonstrated that automated lasers can reduce bird presence and crop damage, although their effectiveness varies with bird species, ambient light, treatment distance, laser characteristics, and field conditions. Artificial intelligence and real-time object-detection models such as YOLO can further improve deterrent systems by activating the laser only when birds are detected. However, missed detections, processing delays, and limited camera or laser coverage may reduce field performance.

The lack of reliable electricity in remote agricultural fields also limits the continuous operation of cameras, computers, communication equipment, and laser devices. Integrating photovoltaic generation with battery storage may provide an autonomous energy supply for intelligent agricultural systems. Therefore, this study integrated a YOLOv11-based bird-detection model, laser deterrence, solar power, and energy storage to compare rice yields under AI-triggered laser, scheduled laser, and no-laser treatments and to evaluate the potential application of the system in off-grid agricultural fields.

MATERIALS AND METHODS

Experimental Site and Treatment Design

The field experiment was conducted in Pitou Township, Changhua County, Taiwan, with three treatment areas: AI-triggered laser (550 m²), scheduled laser (1,900 m²), and no-laser control (1,000 m²). Each laser treatment used an iChase L106 bird repeller and a Sony SNC-VM772R IP camera, while the control was monitored by camera only. The AI-triggered laser scanned for 2 min following bird detection, whereas the scheduled laser operated at predetermined times. The effects of the three treatments on rice yield were compared.

Bird-Detection Model

Images of wild birds were collected from the experimental field and manually annotated using LabelImg. A total of 500 annotated images were divided into training, validation, and test datasets at a ratio of 8:1:1. A YOLOv11 model was trained for 200 epochs using an input resolution of 640 × 640 pixels. Model performance was evaluated using a confusion matrix, precision, recall, F1-score, and mean average precision at an intersection-over-union threshold of 0.5 (mAP@0.5). The confusion matrix(fig.1) classified detection results as true positives (TP), false positives (FP), false negatives (FN), and true negatives (TN). Precision represented the proportion of predicted bird detections that were correct, whereas recall represented the proportion of actual birds successfully detected. The F1-score was calculated as the harmonic mean of precision and recall.

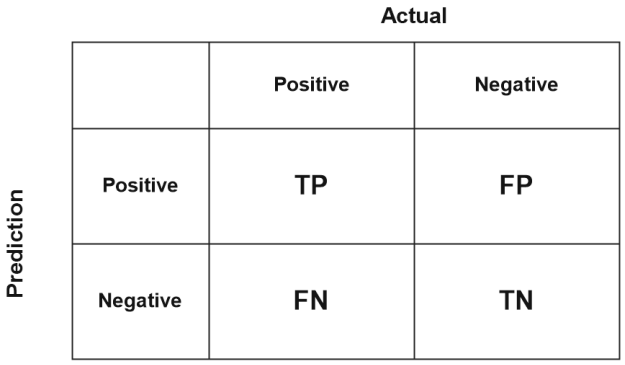

Fig.1 Confusion matrix

$$F1 - score = 2\frac{Precision \times Recall}{Precision + Recall} \quad (1)$$

$$Precision = \frac{TP}{TP + FP} \quad (2)$$

$$Recall = \frac{TP}{TP + FN} \quad (3)$$

Rice-Yield Sampling

Rice hills were selected as sampling units because they better represent overall plant productivity than individual tillers or panicles. Each treatment area was divided into front, middle, and rear sections, and ten hills were randomly collected from each section. This resulted in 30 samples per treatment and 90 samples in total. After sampling, grains were manually separated from the panicles, weighed, and recorded as g/hill. Total harvested yields were also measured to evaluate production per unit area. The recorded yields were 590, 2,140, and 1,000 kg for the AI-triggered laser, scheduled laser, and no-laser treatments, respectively.

Statistical Analysis

Mean yield differences among the three treatments were evaluated using one-way ANOVA, which compares between-group and within-group variation to determine whether at least one treatment mean differs significantly. The overall treatment effect was assessed using the F-statistic and its corresponding *p*-value. When the ANOVA result was significant, Tukey's HSD test was applied to identify significant differences between individual treatment pairs while controlling the family-wise error rate associated with multiple comparisons. Statistical significance was set at $p < 0.05$.

Energy-System Integration

The proposed system architecture incorporated photovoltaic generation and battery storage to support the camera, router, power-supply equipment, computing platform, and laser device in fields without grid electricity. The integration was evaluated as an off-grid application concept. Because detailed photovoltaic capacity, battery capacity, load profile, solar irradiation, and autonomy measurements were not included in the available experiment, the present study did not perform a quantitative energy-balance or battery-sizing analysis.

RESULTS & DISCUSSION

The YOLOv11 model achieved a precision of 0.900, recall of 0.629, F1-score of 0.740, and mAP@0.5 of 0.676. Mean rice yields were 68.40, 91.57, and 56.10 g/hill for the AI-triggered laser, scheduled laser, and no-laser treatments, respectively. Significant differences were observed among all treatments ($F(2,87) = 60.25$, $p < 0.001$). The scheduled laser increased yield by 63.2% compared with the control and was more effective than AI-triggered operation. Missed detections, activation delays, and limited laser coverage may have reduced the performance of the AI system. Solar power and battery storage also offer potential for off-grid operation, although further energy validation is required.

CONCLUSIONS

The scheduled laser treatment produced the highest rice yield, outperforming both the AI-triggered laser and no-laser treatments(Table 1). Although the YOLOv11 model provided reliable bird identification, missed detections and activation delays may have reduced the effectiveness of AI-triggered operation. Integrating the system with solar power and battery storage offers potential for off-grid agricultural applications, but further field testing and energy validation are required.

Table 1 Yield Trend Analysis.

Experimental methods	AI laser	Scheduled laser	Without laser
Actual rice yield(kg)	590	2140	1000
Area(m^2)	550	1900	1000
Per unit area(kg/m^2)	1.072	1.126	1

REFERENCES

Rodenburg, J., Demont, M., Sow, A., & Dieng, I. (2014). Bird, weed and interaction effects on yield of irrigated lowland rice. Crop Protection, 66, 46–52. https://doi.org/10.1016/j.cropro.2014.08.015

Micaelo, E. B., Lourenço, L. G. P. S., Gaspar, P. D., Caldeira, J. M. L. P., & Soares, V. N. G. J. (2023). Bird deterrent solutions for crop protection: Approaches, challenges, and opportunities. Agriculture, 13(4), 774. https://doi.org/10.3390/agriculture13040774

Blackwell, B. F., Bernhardt, G. E., & Dolbeer, R. A. (2002). Lasers as nonlethal avian repellents. The Journal of Wildlife Management, 66(1), 250–258. https://doi.org/10.2307/3802891

Brown, R. N., & Brown, D. H. (2021). Robotic laser scarecrows: A tool for controlling bird damage in sweet corn. Crop Protection, 146, 105652. https://doi.org/10.1016/j.cropro.2021.105652

Clausen, K. K., Marcussen, L. K., Knudsen, N., Balsby, T. J. S., & Madsen, J. (2019). Effectiveness of lasers to reduce goose grazing on agricultural grassland. Wildlife Biology, 2019(1), 1–8. https://doi.org/10.2981/wlb.00560

Manz, S. T., Sieving, K. E., Brown, R. N., Klug, P. E., & Kluever, B. M. (2024). Experimental assessment of laser scarecrows for reducing avian damage to sweet corn. Pest Management Science, 80(3), 1547–1556. https://doi.org/10.1002/ps.7888

Redmon, J., Divvala, S., Girshick, R., & Farhadi, A. (2016). You only look once: Unified, real-time object detection. In Proceedings of the IEEE Conference on Computer Vision and Pattern Recognition (pp. 779–788). https://doi.org/10.1109/CVPR.2016.91

SF-05

Proceedings of The 12th International Symposium on Machinery and Mechatronics for Agriculture and Biosystems Engineering (ISMAB 2026)
20-24 October 2026, Busan, Republic of Korea

AN EDGE-COMPUTING SYSTEM INTEGRATING ACOUSTIC RECOGNITION AND GAS SENSING FOR COW RUMINATION MONITORING

Chin-Cheng Wu*, Chung-Yen Chuang, Yi-Chich Chiu

Department of Biomechatronic Engineering, National Ilan University Taiwan
*Corresponding Author, Email: chincheng@niu.edu.tw

Abstract: Methane (CH_4) emissions from ruminant enteric fermentation constitute a major source of agricultural greenhouse gas emissions. Conventional measurement methods are often costly, labor-intensive, and restrictive to normal animal behavior. This study developed an ESP32-based wearable methane–acoustic monitoring system for dairy cows that integrates methane, acoustic, temperature, and humidity sensors. Mel-frequency cepstral coefficient (MFCC) features were extracted from acoustic signals and classified into feeding, rumination, and no-activity classes using a lightweight convolutional neural network (CNN) deployed on the ESP32. Field experiments demonstrated the simultaneous acquisition of methane concentration data and behavioral acoustic signals under natural farm conditions. The proposed system enables non-invasive, low-power, edge-based monitoring of individual methane emissions and supports precision livestock farming applications.
Key Words: Methane Monitoring, Wearable Device, Acoustic Recognition, Edge Computing

INTRODUCTION

Methane (CH_4) is a major greenhouse gas, and enteric fermentation in ruminants is a significant source of agricultural methane emissions. In cattle, methane is primarily emitted through eructation from the mouth and nostrils, contributing both to greenhouse gas emissions and to dietary energy loss. Therefore, monitoring methane emissions at the individual-animal level under practical farm conditions is important for precision livestock management.

Conventional methods, including respiration chambers, the sulfur hexafluoride (SF_6) tracer technique, and GreenFeed systems, provide reliable measurements. However, their suitability for long-term field monitoring is limited by restricted animal movement, invasive procedures, or reliance on voluntary visits to fixed measurement stations.

Wearable sensing technologies show potential for monitoring cattle behavior and detecting eructation through acoustic and vibration signals. However, most existing systems focus on a single monitoring function. Integrated wearable systems that employ acoustic-based behavior recognition to trigger methane sampling remain limited(Storm, 2012; Martinez-Rau, 2023; Deniz, 2017; Moncayo, 2026).

MATERIALS AND METHODS

The proposed wearable methane–acoustic monitoring system consisted of two modules:

an acoustic sensing module, and a methane sensing module (Fig. 1). The acoustic sensing module used an INMP441 microphone to acquire cattle acoustic signals and extract mel-frequency cepstral coefficients (MFCCs) in real time, while raw audio data were stored on a microSD card. The extracted MFCC features were transmitted via MQTT to the methane-sensing module, where an ESP32 performed convolutional neural network (CNN) inference.

The micro pump was activated to draw air from the mouth and nostril region into an SEN0565 sensor for methane concentration measurement. Temperature and relative humidity were measured simultaneously. During no-activity periods, the system remained in standby mode to reduce unnecessary pumping and power consumption. Measurement data and classification results were subsequently transmitted via MQTT to a Node-RED platform for real-time visualization and data storage. Fig. 2 illustrated the proposed edge-computing system configuration.

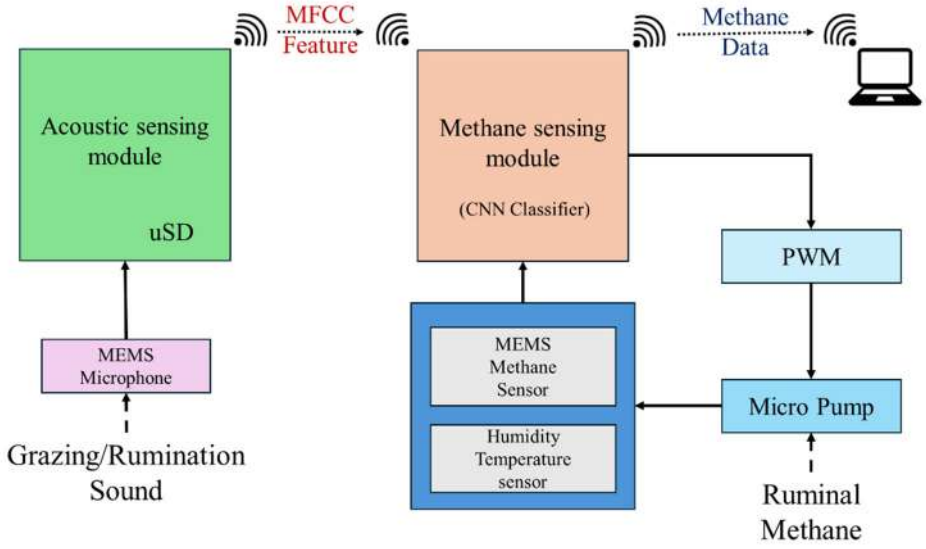

Fig. 1 System Architecture

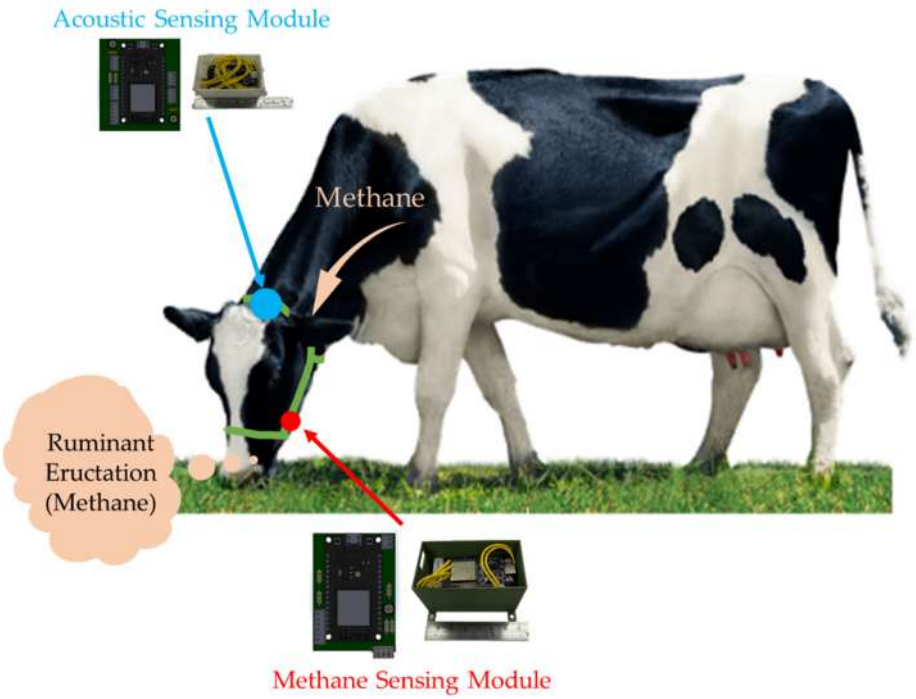

Fig. 2 System configuration

Lightweight Acoustic Recognition Algorithm

MFCCs were used as acoustic features for lightweight CNN-based classification of feeding, rumination, and no-activity behaviors on the ESP32. The trained model was converted to TensorFlow Lite and deployed on the ESP32 for edge inference. The classification results were used to trigger methane sampling.

MFCC features were extracted using a short-time Fourier transform (STFT), a Mel filter bank, and a discrete cosine transform (DCT). The fast Fourier transform (FFT) length and hop length were set to 1,024 and 512 samples, respectively. A total of 64 Mel filters and 32 MFCC coefficients were used, resulting in an input matrix of 32×32×1.

As shown in Fig. 3, the CNN architecture consisted of convolutional and max-pooling layers, followed by flattening, dense, dropout (rate = 0.3), and Softmax layers for three-class behavior classification.

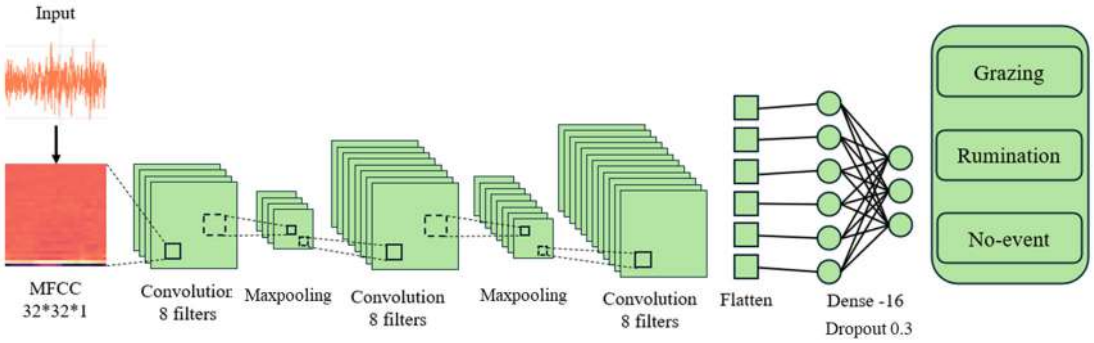

Fig. 3 Lightweight CNN Model

RESULTS & DISCUSSION

Methane Sensor Calibration

A calibration system (Fig. 4) was established to determine the relationship between the output voltage of the SEN0565 methane sensor and methane concentration. The calibration test was conducted over a concentration range of 0–2,000 ppm. Linear regression was used to evaluate the relationship between sensor output voltage and methane concentration, and the coefficient of determination (R^2) was calculated for the calibration trial.

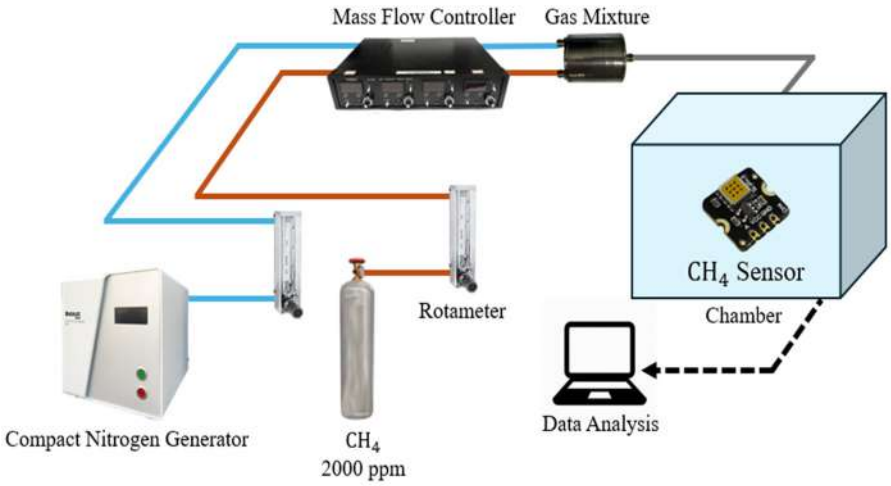

Fig. 4 Calibration experiment setup

The calibration performance of the SEN0565 methane sensor is shown in Fig. 5. The calibration curves showed coefficients of determination (R^2) greater than 0.98, indicating a strong relationship between sensor output voltage and methane concentration.

The results indicate that the sensor was suitable for detecting relative changes in methane concentration near the mouth and nostril region of dairy cows. However, because the wearable system measured local methane concentrations rather than whole-animal methane emissions, the measured values should not be interpreted directly as absolute methane production rates.

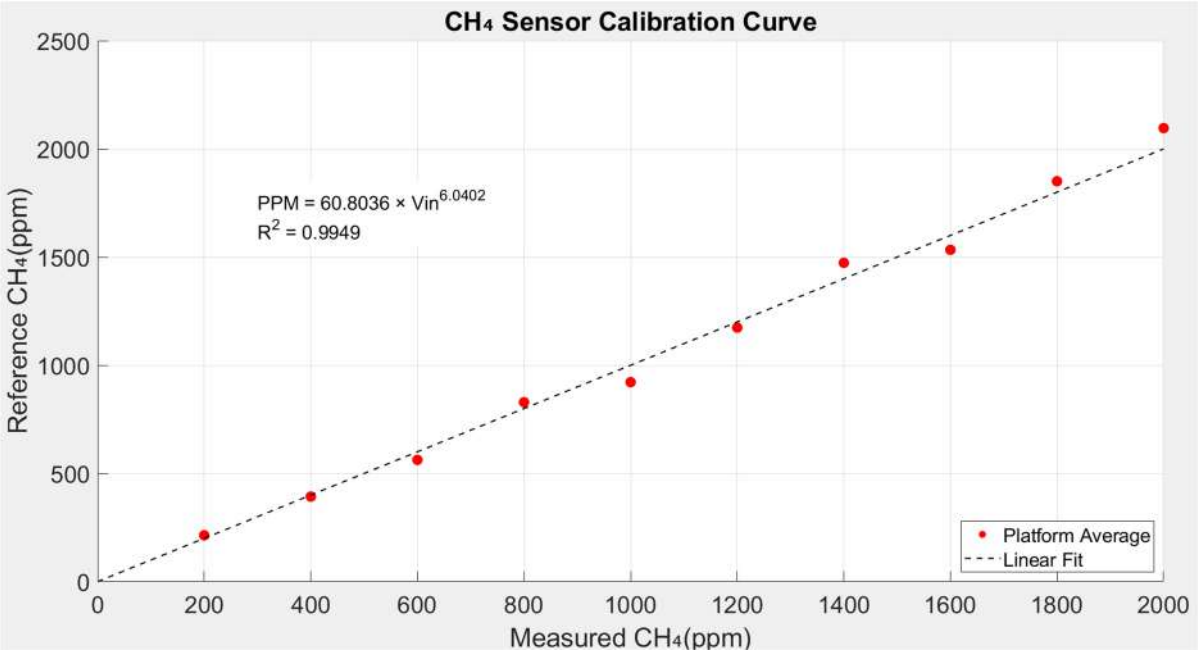

Fig. 5 Repeatability test of the methane sensor

Acoustic and Eructation Methane Signals

Field experiments demonstrated that the proposed system simultaneously recorded acoustic signals and local methane concentrations near the mouth and nostrils of dairy cows. As shown in Fig. 6, rumination exhibited relatively regular and continuous acoustic patterns, whereas feeding produced signals with larger and more irregular amplitude variations. The corresponding MFCC representations also showed distinct time-frequency characteristics for feeding and rumination, supporting their use as input features for behavior classification.

As shown in Fig. 7, methane concentration profiles differed between rumination and feeding periods. The methane concentrations recorded during feeding were generally higher and showed greater temporal variability than those recorded during rumination. This observation is consistent with previous findings that methane release patterns can vary with feeding activity, rumination, and eructation events (Crompton, 2011).

Because the system measured local methane concentration in parts per million (ppm), the recorded values may have been affected by head position, the timing of eructation, the distance between the sensor inlet and the emission source, and surrounding airflow conditions. Therefore, these measurements should be interpreted as localized methane signals rather than direct estimates of whole-animal methane emission rates. CNN-based classification of the recorded acoustic data identified rumination periods that were temporally aligned with the corresponding methane profiles, demonstrating the feasibility of acoustic-based control of methane sampling.

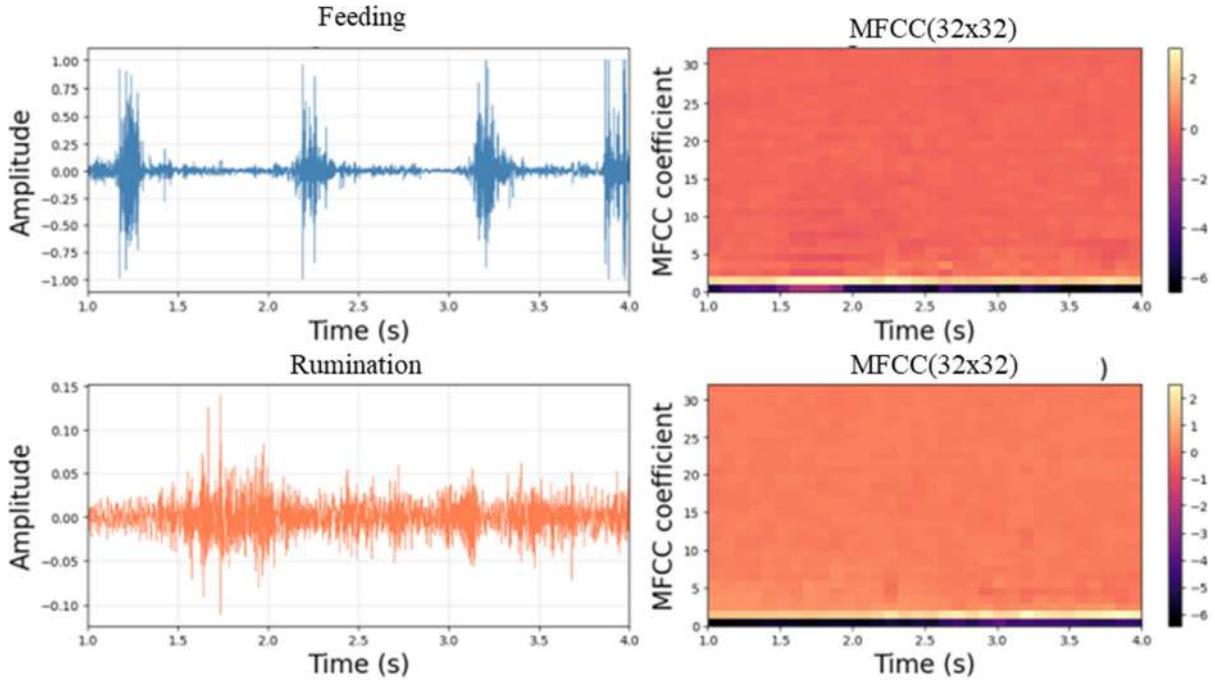

Fig. 6 Time-domain waveforms and time-aligned MFCC features for grazing and rumination acoustic activities.

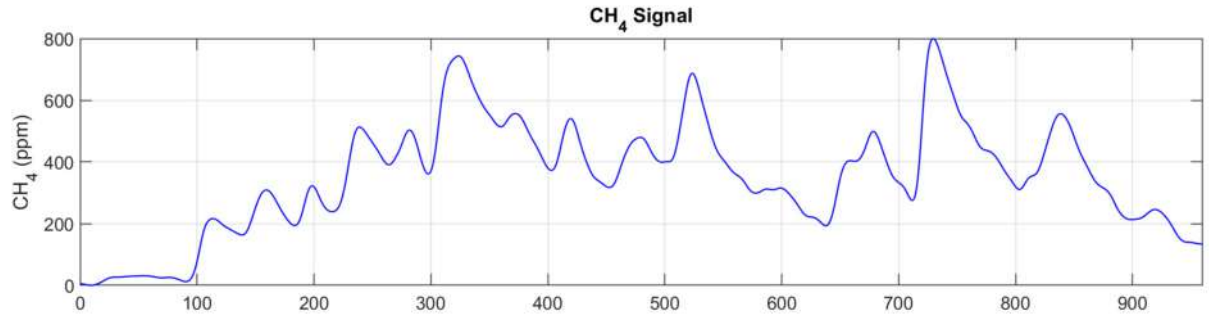

(a) Feeding

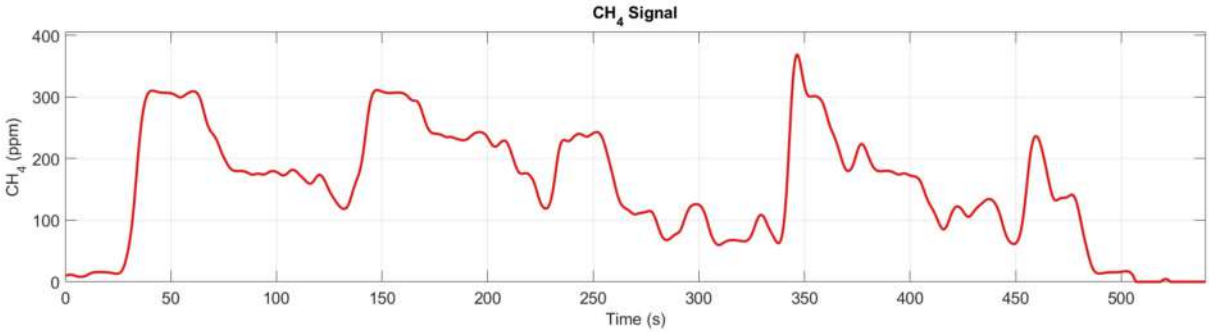

(b) Rumination

Fig. 7 Measurement results of methane concentration

CONCLUSIONS

This study developed an ESP32-based wearable acoustic–methane monitoring system that integrated an SEN0565 methane sensor, an INMP441 microphone, and temperature–humidity sensors for non-invasive monitoring of individual dairy cows. Sensor calibration demonstrated good repeatability, while mel-frequency cepstral coefficient (MFCC) features and a lightweight convolutional neural network (CNN) enabled on-device cattle behavior classification on the ESP32 platform.

Field experiments confirmed that the system simultaneously acquired acoustic signals and local methane concentration data near the mouth and nostrils of dairy cows under natural farm conditions. The results demonstrate the feasibility of integrating acoustic-based behavior recognition with localized methane monitoring to reduce unnecessary gas sampling and power consumption. Future work will involve experiments with additional animals, longer monitoring periods, and further evaluation of methane concentration patterns during feeding and rumination.

REFERENCES

[1] Storm, I.M.L.D., Hellwing, A.L.F., Nielsen, N.I., Madsen, J., Methods for measuring and estimating methane emission from ruminants, Animals, 2 (2012) 160–183. https://doi.org/10.3390/ani2020160.samvikresearch

[2] Martinez-Rau, L.S., Chelotti, J.O., Ferrero, M., et al., Daylong acoustic recordings of grazing and rumination activities in dairy cows, Scientific Data, 10 (2023) 359. https://doi.org/10.1038/s41597-023-02269-8.writers-camp

[3] Deniz, N.N., Chelotti, J.O., Galli, J.R., Planisich, A.M., Larripa, M.J., Rufiner, H.L., Giovanini, L.L., Embedded system for real-time monitoring of foraging behavior of grazing cattle using acoustic signals, Computers and Electronics in Agriculture, 138 (2017) 27–35. https://doi.org/10.1016/j.compag.2017.04.009.casrai

[4] Moncayo, J., Velasquez, M.L., Riveros, P.E., Hernandez, A.F., Gomez-Bautista, A., Riccio-Rengifo, C., Villegas, E.A., Mendez, D., Colorado, J.D., Jaramillo-Botero, A., Real-time eructation event prediction in livestock using head vibrations and machine learning in an IoT wearable device, Scientific Reports, 16 (2026) Article 1404.wordvice

[5] Crompton, L.A., Mills, J.A.N., Reynolds, C.K., France, J., Fluctuations in methane emission in response to feeding pattern in lactating dairy cows, Animal, 5 (2011) 551–558. https://doi.org/10.1017/S1751731110002058.

Smart Farm Systems and Renewable Energy 2 (SF-2)



SF-06

Proceedings of The 12th International Symposium on Machinery and Mechatronics for Agriculture and Biosystems Engineering (ISMAB 2026)
20-24 October 2026, Busan, Republic of Korea

DEVELOPMENT OF A VISION-BASED EARLY WARNING STRATEGY FOR FLOCK DISTRIBUTION IN BROILER HOUSES

Yu-Chi Liu, Ming-Yih Chang*

National Ilan University, Taiwan
*Corresponding Author--Email: mychang@niu.edu.tw

Abstract: In environmentally controlled broiler houses, abnormal flock distribution is often an early sign of improper environmental control, equipment malfunctions, or health issues. However, daily routine manual inspections provide only intermittent snapshots and may not detect such anomalies in time. In this study, an early warning strategy for abnormal flock distribution was developed using periodically captured images that were analyzed automatically. An in-house developed monitoring system with low-cost camera modules built on AIoT development boards was deployed at eight evenly distributed inspection points in a tunnel-ventilated broiler house. Top-view images were captured at 30-minute intervals and uploaded via Wi-Fi to a remote single-board computer, where they were stored and recorded in a database. Individual broilers in each image were recognized with a YOLO11 object detection model, and the detections were used to calculate two indices: flock density and the Clark–Evans nearest-neighbor index (R). An image was classified as abnormal when the density was below 11 or above 20 birds/m², or when the density was normal but R was below 0.90, indicating clustering. Since anomalies were usually temporary, the alarm was issued when an inspection point remained abnormal for 2 hours or when four or more inspection points were abnormal simultaneously. The experiment was conducted in the second half of a broiler grow-out cycle, from 18 to 36 days of age, and yielded 5,798 images. Of these, 13.04% were classified as abnormal: 11.49% with low density and 1.55% with high density. No clustering was observed. Twenty-nine alarms were issued, but excluded after manual review. Most alarms were attributed to the normal juvenile behavior during acclimatization of the new expanded environment. This system had successfully mapped the spatiotemporal changes of the flock distribution. After collecting more rearing data of broiler grow-out cycles in the future to refine the classification criteria, the early warning strategy may provide more precise information to the broiler keeper to perform more effective management.

Key Words: precision livestock farming, broiler, YOLO11, spatial distribution, early warning

INTRODUCTION

A commercial broiler farm often holds more than 100,000 birds, but on-site labor is limited, so it is difficult to keep track of the flock in every area of the house. Abnormal flock distribution is often an

early sign of uneven ventilation, interrupted water or feed supply, or even disease outbreaks. However, daily routine manual inspections cannot always detect the anomalies in time. Image-based monitoring of flock distribution has been demonstrated on some applications (Berckmans, 2014; Okinda et al., 2020). A previous study used only three cameras mounted high enough to monitor the floor of an entire broiler house and detected 95% of equipment malfunction events (Kashiha et al., 2013). However, the heights of broiler houses in Taiwan are relatively low, so each overhead camera could provide a restricted field of view and a large number of cameras is required to provide more shotspots to monitor the broiler flock.

The objectives of this study were to establish a low-cost vision-based broiler monitoring system in broiler houses, and to develop an early warning strategy for broiler abnormal distribution.

MATERIALS AND METHODS

2.1 Experimental Site and Image Acquisition

The experiment was conducted in a tunnel-ventilated broiler house with cooling pads, where eight inspection points were evenly distributed (Fig. 1). At each point, an AMB82-Mini AIoT development board with a camera lens was mounted 2.25 m above the floor and captured a top-view image every 30 minutes. The images were uploaded via Wi-Fi to a remote Raspberry Pi 4 single-board computer (SBC), then stored in a database.

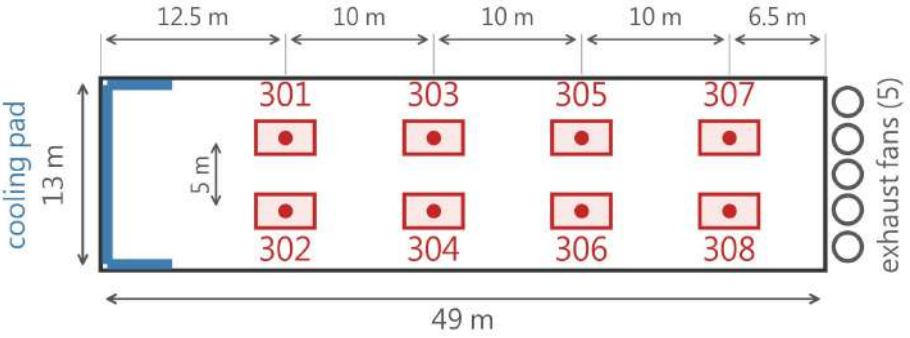

Fig.1 Schematic layout of eight inspection points in the experimental broiler house. The cooling pad is at the left end, and five exhaust fans are at the right end.

2.2 Image Processing and Detection

The images taken through the fisheye lens of the device were distorted near the edges, so distortion correction was applied first. A YOLO11n-seg instance segmentation model was then used to extract the contour of each bird. This model is constrained to process 640 × 640 pixel images only. Two hundred manual-labeled 640 × 640 pixel images extracted from previous production batches (ranging from 14 to 35 days of age) were selected as the training samples to develop the YOLO model. The developed model cannot process the original 1920 × 1080 monitoring image. Downscaling the original images would make the birds difficult to be recognized. Therefore, a 640 × 640 pixel sliding window with the stride of 512 pixels was assigned to scan the original image sequentially from left to

right and from top to bottom to extract the sub-images. The stride of 512 pixels ensured that birds lying on the edge of the previous window, which might not be correctly recognized, were fully covered by the next window. However, birds counted twice in the overlapping areas of two windows were merged by non-maximum suppression (NMS), and the centroid of each bird was then obtained.

2.3 Classification Indices and Thresholds

Two indices, flock density and flock spatial distribution pattern, were calculated from the number and positions of the birds detected in the monitoring images. The effective field of view of each image was 8.87 m² (3.97 × 2.23 m). At the actual stocking density of 15.1 birds/m², about 134 birds should appear in each image. The random variation of a count equals the square root of its expected value, $\sqrt{134} \approx 12$ birds, and the control limits were set at three times this value above and below the expected count (Montgomery, 2013). This gave a range of 99 to 168 birds, which corresponds to a density of 11 to 20 birds/m². The spatial distribution pattern was expressed by the Clark–Evans nearest-neighbor index R (Clark and Evans, 1954), which is the ratio of the observed mean distance from each bird to its nearest neighbor to the theoretical mean distance under a random distribution. The R value below 1 indicates clustering, and the value above 1 indicates a uniform distribution. When the numbers of birds detected in this batch were substituted into the associated Z test, clustering was significant at $R < 0.90$. The image was flagged as abnormal when its density was beyond the normal range, or when its density was normal but $R < 0.90$. The rules of the early warning prototype strategy were as follows: (1) an inspection point that remained abnormal for 1 hour was marked as a caution, and an alarm was triggered when the anomaly persisted for 2 hours; (2) an alarm was triggered immediately when the density stayed below 7 or above 23 birds/m² for 1 hour; and (3) when four or more inspection points were abnormal simultaneously, the situation was regarded as a facility-wide event and an alarm was triggered immediately.

RESULTS & DISCUSSION

Monitoring started on day 18 after chick placement, when all brooder guards had just been removed and the flock could move freely in the house. By the time the birds were marketed at 36 days of age, completing the grow-out cycle, 5,798 images had been obtained. Of these, 5,042 images (86.96%) had normal density, and their lowest R was only 0.94, so no clustering occurred. The remaining 756 images (13.04%) were flagged as abnormal, including 666 images (11.49%) with low density and 90 images (1.55%) with high density. Examples of the two types are shown in Fig. 2.



Fig.2 Examples of the two anomaly types: (a) low density at inspection point 303, 22 days of age, 3.5 birds/m², R = 1.16; (b) high density at inspection point 301, 22 days of age, 25.0 birds/m², R = 1.35.

Of all images flagged as abnormal, 71.4% appeared only briefly and did not continue into the next 30-minute interval, so they were regarded as normal movement of the birds. Under the warning rules above, 29 alarms were issued during the 19 days of monitoring: 23 in the early period (18 to 24 days of age) and 6 in the late period (32 to 36 days of age). The two periods had different causes. The 23 early alarms were concentrated at the rear of the house, and 3 of them were triggered by several inspection points being abnormal at the same time, all with higher density at the front and lower density at the rear. At that time, the flock had just been released from the space restriction of the brooder guards but still tended to stay in its former area and had not yet spread over the whole house. However, the density difference between the front and the rear decreased day by day and was no longer evident at 25 days of age, when the alarms stopped. The early alarms therefore reflected the flock spreading toward the rear rather than an actual anomaly. When the warning strategy is revised in the future, changes in bird age and on-site space management can be incorporated to eliminate such false alarms. The 6 late alarms were not concentrated in any particular area; instead, the measured density decreased throughout the house at the same time. By then, the birds had grown larger and were packed closely together in the images, making their contours difficult to separate. As a result, the detected density was low although the actual number of birds had not decreased. This issue requires further improvement of bird recognition in the late grow-out stage. The flock in this batch remained normal throughout the cycle. Although alarms were issued, each could be traced to a reasonable cause, showing that the strategy can reflect changes in flock status in a timely manner.

CONCLUSIONS

In this study, eight low-cost cameras were used for continuous image acquisition, flock density and the Clark–Evans nearest-neighbor index R were quantified at each inspection point, and a strategy for classifying and warning of abnormal distribution was established. In a field test during the second half of the grow-out cycle, 29 alarms were issued in 19 days, and each alarm could be traced to its cause, showing that the strategy reflects changes in flock status and directly indicates where they occur. Future work will adjust the classification thresholds for predictable changes during the grow-out cycle and continue to improve bird recognition in the late grow-out stage, so that the strategy can focus on anomalies that require intervention by farm managers.

REFERENCES

Berckmans, D. 2014. Precision livestock farming technologies for welfare management in intensive livestock systems. Rev. Sci. Tech. Off. Int. Epiz. 33(1): 189-196.

Clark, P. J., and F. C. Evans. 1954. Distance to nearest neighbor as a measure of spatial relationships in populations. Ecology 35(4): 445-453.

Kashiha, M. A., A. Pluk, C. Bahr, E. Vranken, and D. Berckmans. 2013. Development of an early warning system for a broiler house using computer vision. Biosyst. Eng. 116(1): 36-45.

Montgomery, D. C. 2013. Introduction to Statistical Quality Control. 7th ed. Hoboken, N.J.: John Wiley & Sons.

Okinda, C., I. Nyalala, T. Korohou, C. Okinda, J. Wang, T. Achieng, P. Wamalwa, T. Mang, and M. Shen. 2020. A review on computer vision systems in monitoring of poultry: A welfare perspective. Artif. Intell. Agric. 4: 184-208.

SF-07

Proceedings of The 12th International Symposium on Machinery and Mechatronics for Agriculture and Biosystems Engineering (ISMAB 2026)
20-24 October 2026, Busan, Republic of Korea

EFFECTS OF SEEDLING IMAGE GRADING ON MARKETABLE WEIGHT-BASED STAGGERED HARVESTING FOR PLANT FACTORY GROWN LETTUCE

Chen, I-I , Ming-Yih Chang *

National Ilan University, Taiwan
*Corresponding Author-- Email: mychang@niu.edu.tw

Abstract: Seedlings of lettuce in plant factories are usually transplanted directly onto grow-out raft boards without grading. Individual differences in growth often lead to uneven plant weight at harvest, making it difficult to determine the optimal harvest date. This study investigated the growth of different graded transplant seedlings, and the effects of grading on the harvest date and the energy use efficiency. Two major technologies were developed: image-based grading of transplant seedlings and real-time monitoring of plant weight. For transplant seedlings grading, the images of seedling on the nursery raft boards were analyzed by a deep learning model of the software YOLOv11n. All seedlings were detected their boundaries, calculated the leaf area individually, then sorted and categorized into four hierarchical grades based on the orders of leaf area size. The seedlings of each grade were transplanted on different grow-out raft boards. All grow-out raft boards were horizontally hung under load cells via a pulley system to measure the real-time weight of the raft board including lettuce, thereby estimating the average plant weight for each grade. When the average plant weight exceeded marketable target weight of 80 grams, the plants were harvested, and the lights over the grow-out raft board were turned off. The cultivation results showed that harvesting occurred on day 31, 32, 35, and 36, corresponding to their grade sequence, whereas ungraded lettuce was harvested on day 35. The Electricity Use Efficiencies in Lighting (EUE_L) during the grow-out stage (from day 21 to harvest), according to the grading sequence, were 4.2%, 3.25%, 2.76%, and 2.22%, respectively, compared to 2.81% for the ungraded group. Tukey's test showed that the EUE_L of Grade 1 was significantly superior to Grade 3, Grade 4, and the ungraded group. By utilizing the transplant seedling grading, it optimized energy-saving performance, staggered the harvest time to reduce excessive labor concentration. This study proposes a rationalized approach for smart production in plant factories.

Key Words: # YOLOv11n # Electricity Use Efficiency in Lighting # Staggered Harvesting

INTRODUCTION

The cost is always the main problem to be concerned with plant factories operations. Kozai et al. (2016) indicated that electricity and labor are the two main operational cost components, with electricity consumption accounting for 28% of total operational costs, primarily spent on lighting, and labor costs accounting for 26%. Enhancing energy use efficiency and reducing

labor burdens are critical challenges for achieving commercialization. Usually, the seedlings are transplanted without detailed size grading, and the lettuce is gathered in once-over harvest, not only reduces product consistency, complicates the packaging process, but also leads to high labor intensity in a short time frame and heavy burdens on labors. Proper seedling grading may maintain the product uniform and stagger the harvest burdens. However, the grading by human vision is labor-intensive and subjective. In recent years, numerous studies had explored plant growth monitoring technologies (Kim & van Iersel, 2022; Jin et al., 2023; Wang et al., 2023; Bakir & Gezer, 2025). The objectives of this study were to develop a computer-aided seedling grading approach to grade the seedling prior to the transplant, and to establish a real-time plant weight monitoring system during cultivation. Their effects on plant growth and energy use efficiency also be investigated.

MATERIALS AND METHODS

2.1 Image Recognition System for Leaf Area Calculation & Real-time Plant Weight Monitoring System

This study was conducted in a container-type plant factory with fully artificial lighting. Lettuce sprouts were cultivated on nursery raft boards accommodating 101 plants (cultivation density of 202 plugs/m²). On 21 days after sowing (DAS 21), images of the 101 seedlings were captured using a smartphone and imported into a YOLOv11n deep learning model to segment the edges of each seedling and calculate individual leaf areas. Based on the leaf area, the plants were sorted into four grades, with 22 plants each in sequence, and discarded the ranks beyond the 88th. (Fig. 1) The seedlings in the same grade were transplanted onto a 22-hole grow-out raft boards (dimensions of 50 cm × 110 cm, cultivation density of 44 plugs/m²). The plant factory container was equipped with two sets of four-tier cultivation racks, with each tier accommodating one raft board. Each board was hung beneath a load cell via a pulley mechanism to construct a continuous weight monitoring system, measuring the total weight of the lettuce on the board. The environmental data in the plant factory—including time, temperature, relative humidity, CO_2 concentration, single-tier cultivation weight, and overall equipment power consumption—were collected and recorded by a Raspberry Pi single-board computer served every 30 minutes.

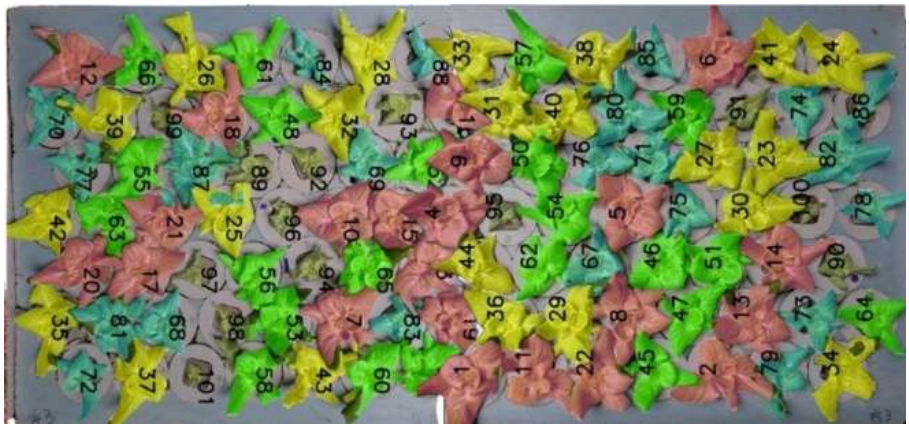

Fig.1 By leaf area grading, the lettuce seedlings were ranked into four grades, 22 seedlings in each grade: red for Grade 1, yellow for Grade 2, green for Grade 3, cyan for Grade 4, and gray for discarded seedlings.

2.2 Growth Environment & Energy Efficiency Assessment

The cultivation environmental conditions in this study were set as follows: a photoperiod of 16 hours light / 8 hours dark ; temperatures 27±1˚C day / 20±1˚C night ; relative humidity 70±5% day / 80±5% nigh. CO_2 concentration 1,200±100 ppm day / no supplement at night. The electrical conductivity (EC) of the nutrient solution 1.2±0.1mS/cm. The weight monitoring was conducted during the grow-out stage (DAS 21–harvest). Harvesting took place when the average plant weight reached 80 g and the shoot of each plant was individually weighed. While the harvest finished, the light was turned off. Four replicates were conducted in this study. The equation of electricity use efficiency, proposed by Kozai et al. (2016), was modified to focus on the use efficiency of lamp power consumption (EUE_L) during the grow-out stage Eq. (1):

$$EUE_L = \frac{fD}{E} \quad (1)$$

where:

f = chemical energy content of 20 MJ per kg dry weight
D = lettuce dry weight (5% of fresh weight, kg)
E= total lighting electricity consumption from DAS 21 to harvest date (J)

The specific growth rate (SGR) of lettuce was also calculated by Eq. (2):

$$W(t) = a \cdot e^{\,b \cdot t} \quad (2)$$

where:

W = Weight of lettuce at day t (g)
a = initial weight (g)
b = specific growth rate(g/day)
t = time (plant age, day)

RESULTS & DISCUSSION

To compare the harvest weights obtained by the on-line weighting system with the manual scale weighing, the weighing system exhibited an average error of 1.94%, and the paired t-test indicated no significant difference between these two ($p>0.05$), confirming the reliability of the system's measurements. Grade 1 seedlings, possessing the optimal initial state, reached the target harvest weight first on day 31. Subsequently, Grade 2 through Grade 4 reached the target on days 32, 35, and 36, respectively, whereas the ungraded group reached the target on day 35 (Fig. 2). This confirms that significant growth variations occur during the nursery stage, making pre-transplanting grading the key determinant of harvest scheduling. The SGR for Grades 1 and 2 was approximately 16.2–16.6 g/day; for Grades 3 and 4, the SGR was approximately 13.6–13.7 g/day; and for the ungraded group, the SGR was approximately 12.6 g/day. The staggered harvest scheduling and yield forecasting can be precisely managed by seedling grading.

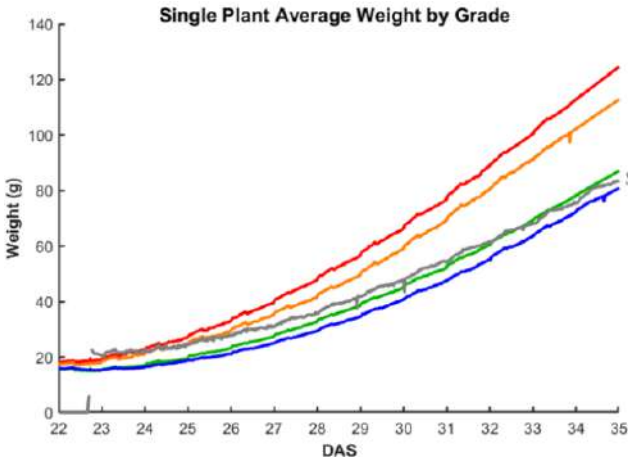

Fig.2 Average plant weight of lettuce by grade: red line for Grade 1(SGR=16.6 g/day), orange line for Grade 2(SGR=16.2 g/day), green line for Grade 3(SGR=13.6 g/day), and blue line for Grade 4(SGR=13.7g/day), grey line for ungraded (SGR=12.6 g/day).

Regarding the optimization of electricity use efficiency through staggered harvesting, EUE_L showed a significant decreasing trend according to the degree of grading (Grade 1 to Grade 4). Grade 1 achieved a mean EUE_L of 4.2%, followed by Grade 2 at 3.25%. Based on Tukey's comparison, there was no significant difference between the first two grades. Grade 1 was significantly superior to Grade 3 at 2.76%, Grade 4 at 2.22%, and ungraded at 2.81% (Fig. 2). All the four-grade lettuce was grown on the 4-tier grow rack with the staggered harvest, the lamp power consumption was 79.04 kWh, compared to 91.2 kWh under the same conditions for the ungraded control group. The graded cultivation reduced lamp electricity consumption by approximately 13.3%. This suggests that a dynamic control strategy—harvesting activates as soon as the average fresh weight of each grade reaches market size and immediately turns off the lighting—can effectively enhance electricity utilization efficiency.

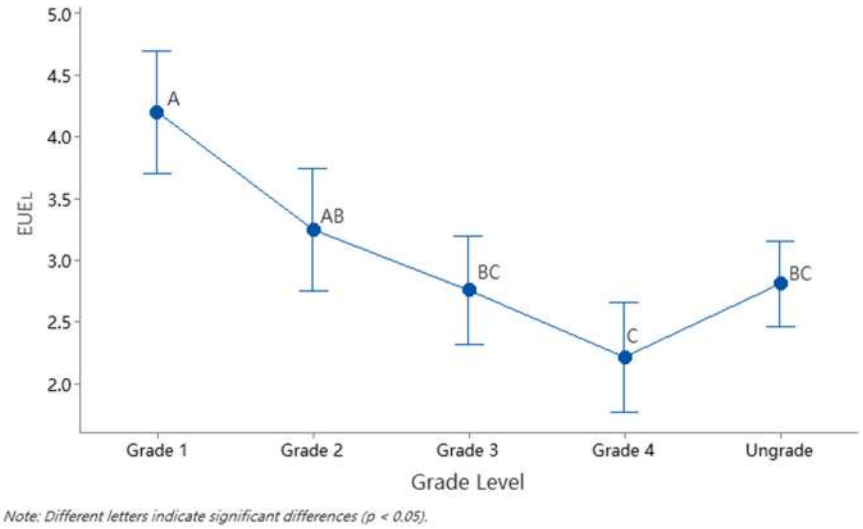

Fig.3 EUE_L of different grades

In addition, a quantitative evaluation of manual operation time revealed that the conventional method of non-graded, once-over harvesting tends to concentrate labor demand into a short time frame, increasing operational stress. Implementing the graded cultivation and staggered harvesting effectively distributes the dense harvest workload across sparse time frame.

Beyond providing more consistent product specifications that simplify packaging process, this approach effectively alleviates concentrated labor burdens, demonstrating practical benefits for commercial farm operations.

CONCLUSIONS

By implementing computer-aided seedling grading, this study not only optimizes energy use efficiency in plant factories, but also effectively staggering the harvest period and reducing concentrated labor burdens. This provides a valuable reference for rationalizing smart production management in plant factories.

REFERENCES

Chen, W.-T., Y.-H. F. Yeh, T.-Y. Liu, and T.-T. Lin. 2016. An automated and continuous plant weight measurement system for plant factory. Frontiers in Plant Science 7: 392.

Kim, C., and M. W. van Iersel. 2022. Morphological and physiological screening to predict lettuce biomass production in controlled environment agriculture. Remote Sensing 14(2): 316.

Jin, X., Jiao, H., Zhang, C., Li, M., Zhao, B., Liu, G., & Ji, J. (2023). Hydroponic lettuce defective leaves identification based on improved YOLOv5s. Frontiers in Plant Science, 14, 1242337.

Wang, Y., Wu, M., & Shen, Y. (2023). Identifying the growth status of hydroponic lettuce based on YOLO-EfficientNet. Plants, 12(1), 123.

Bakir, C., & Gezer, A. (2025). Real-Time Automatic Detection of Nutrient Deficiency in Lettuce Plants With New YOLOV12 model. Journal of Sensors, 2025, Article 5592225.

Kozai, T., G. Niu, and M. Takagaki. 2016. Plant factory: An indoor vertical farming system for efficient quality food production. Academic Press.

SF-08

Proceedings of The 12th International Symposium on Machinery and Mechatronics for Agriculture and Biosystems Engineering (ISMAB 2026)
20-24 October 2026, Busan, Republic of Korea

CWSI MAPPING USING POINT MEASUREMENT AND THERMAL IMAGING FOR CABBAGE FIELDS AND APPLE ORCHARDS

Md Mamunur Rashid[1], Jin Hongbin[1], Md Ashikur Rahman[1], Md Nasim Reza[1,2]
Se Yong Lee[3], Sun-Ok Chung[1,2*]

[1]Department of Smart Agricultural Systems, Graduate School, Chungnam National University, Daejeon 34134, Republic of Korea
[2]Department of Agricultural Machinery Engineering, Graduate School, Chungnam National University, Daejeon 34134, Republic of Korea
[3]FarmOS Co. Ltd., Anyang 14067, Republic of Korea
*Corresponding Author-- Voice: +82-42-821-6712, Email: sochung@cnu.ac.kr

Abstract: Efficient irrigation management requires spatially explicit information on crop water stress, particularly in heterogeneous upland fields and orchard systems where soil moisture, canopy structure, and canopy temperature vary within short distances. This study proposes a CWSI mapping approach using point-based and image-based measurements for cabbage fields and apple orchards. Canopy temperature was measured using infrared radiometric point sensors, fixed-position thermal cameras, and moving-platform thermal imaging systems. For cabbage fields, thermal images provided plot-level spatial information on canopy temperature variation under different irrigation and soil water content conditions. For apple orchards, tree-wise canopy temperature was extracted from fixed and moving thermal observations and calculated into relative CWSI values to identify spatial water-stress zones along tree rows. The results are expected to show that point measurements and thermal imaging can effectively capture spatial variation in crop water stress through CWSI mapping. In the apple orchard, the generated relative CWSI maps are expected to show clear tree-to-tree variability, with mean relative CWSI values ranging approximately from 0.17 to 0.86. Trees with CWSI values below 0.30 indicated as low-stress zones, values between 0.30 and 0.60 as moderate-stress zones, and values above 0.60 as high-stress zones. The high-CWSI areas are expected to correspond to warmer canopy regions detected by both fixed-position and moving-platform thermal imaging. Fixed-position imaging is expected to provide stable temporal monitoring at selected locations, while moving-platform imaging improved spatial coverage and identify stress differences across tree rows. In cabbage fields, CWSI separated relatively uniform well-irrigated areas from localized water-deficit zones, supporting field-level irrigation zoning. The agreement between image-derived canopy temperature and point-based infrared measurements showed reliable performance, with an estimated R^2 of 0.85–0.95 and RMSE of 0.8–1.5°C under stable acquisition conditions. The integration of point measurement and thermal imaging is expected to improve the reliability of CWSI-based water-stress diagnosis and provide a practical basis for site-specific irrigation scheduling in both cabbage fields and apple orchards.

Key Words: Crop Water Stress Index, CWSI Mapping, Thermal Imaging, Canopy Temperature, Point Measurement

INTRODUCTION

Water stress reduces transpiration through stomatal closure and raises leaf or canopy temperature relative to a well-watered surface. Canopy temperature therefore provides a direct plant-response signal that can complement soil water measurements. The crop water stress index (CWSI) normalizes this thermal response between lower and upper temperature limits, allowing measurements made under variable field conditions to be interpreted on a common scale (Jackson et al., 1981; Idso et al., 1981).

Infrared point sensors provide continuous measurements from defined canopy targets, but a limited field of view can miss tree-to-tree and within-plot variation. Thermal cameras resolve this variation spatially, although background pixels, canopy geometry, illumination, viewing angle, and changing weather can affect temperature estimates. Canopy masking and wet and dry reference temperatures are therefore important for producing interpretable stress indices (Jones et al., 2002; Maes and Steppe, 2012). Mobile thermal imaging can extend coverage along crop rows, while fixed cameras can repeatedly observe the same area. Compare their measurements with point infrared observations before using the mapped values for irrigation decisions.

This study aimed to develop and preliminarily evaluate a workflow that combines point infrared measurements with fixed-position and moving-platform thermal imaging to map relative CWSI in cabbage fields and apple orchards. The work focused on sensor placement, canopy-temperature extraction, cross-platform comparison, georeferenced mapping, and classifying low-, moderate-, and high-water-stress zones.

MATERIALS AND METHODS

Measurement Design

Thermal data were collected in cabbage fields at Chungnam National University and in an open-field apple orchard in Gangwon-do, Republic of Korea. The apple experiment divided 28 trees into four zones, A1 to A4, with two parallel tree lines. The field layout included fixed-position thermal camera, infrared thermometric sensors, and repeated observations from a ground-based moving thermal platform.

Table 1 Measurement geometry and analytical role of each sensing platform.

Measurement	Position	View	Role in analysis
Point infrared sensor	0.5-1.0 m from leaf or canopy ROI	0-30 degrees from canopy normal	Reference canopy-temperature trend
Moving thermal platform	1.0-1.5 m from outer canopy wall	10-30 degrees from canopy normal	Continuous coverage along tree rows
Fixed thermal camera	Approximately 3 m above canopy top	0-30 degrees from canopy normal	Repeated observation of a fixed ROI

Table 1 presents the sensor placements, field of view, and data-collection procedures, while Fig. 1 visualizes the data-collection applications for both cabbage and apple orchard fields.

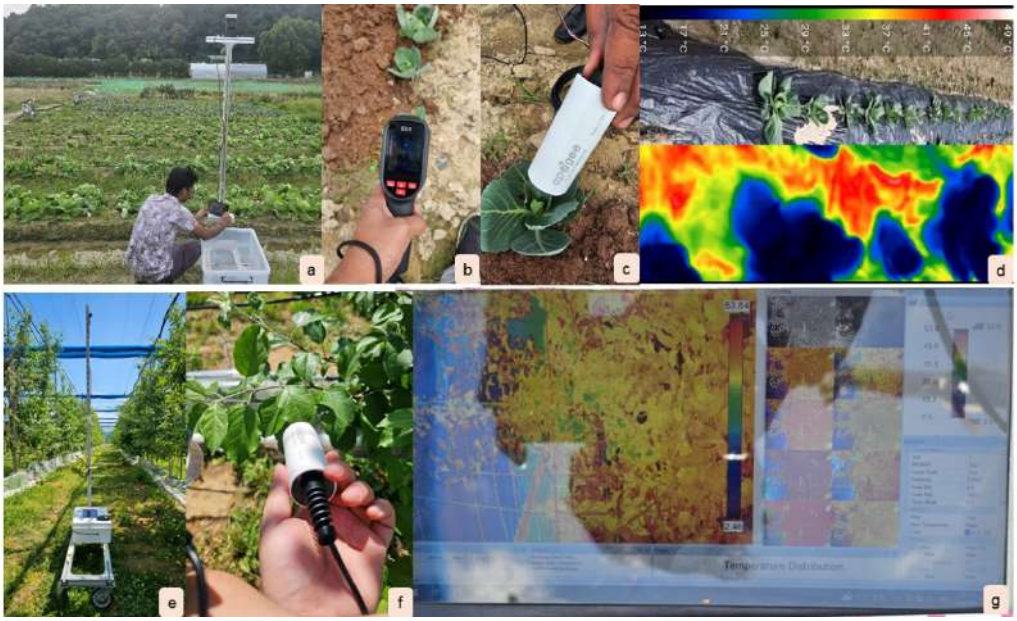

Fig.1 Thermal-imaging platforms used for canopy-temperature acquisition. From left to right, fixed-position (a), handheld (b), moving-platform (e), point measurements with IR sensor (f), data acquisition system (g), and visualization (d).

Thermal Image Processing

Each thermal frame was assigned to a crop region of interest (ROI). Non-canopy components were removed with a binary canopy mask, and the retained pixels were reconstructed as a canopy-only thermal frame. The canopy coverage ratio was recorded as a quality-control variable. Mean and median canopy temperature represented central tendency, while the 95th percentile described the warmer portion of the retained canopy distribution. A 15-frame rolling average was used to show the underlying temperature trend in mobile and fixed sequences without replacing the original observations.

Relative CWSI Calculation and Spatial Mapping

Relative CWSI was calculated from the canopy temperature and contemporaneous wet and dry reference temperatures. The normalized formulation is as follows, as in Equation (1).

$$CWSI = \frac{(T_c - T_a) - (T_c - T_a)_{ul}}{(T_c - T_a)_{ul} - (T_c - T_a)_{ll}} \quad (1)$$

where T_c is canopy temperature, T_a is air temperature, and $(T_c - T_a)_{ll}$ and $(T_c - T_a)_{ul}$ are the lower and upper limits of the canopy–air temperature difference, respectively. Subtracting the lower limit in the numerator sets the well-watered baseline to zero, while the difference between the upper and lower limits scales the index. Values were constrained to the interpretable range from 0 to 1 when small measurement deviations placed them outside that interval.

Sensor and image records were aligned with tree identifiers and spatial coordinates. Relative CWSI values were ordered along the two apple-tree lines and converted into continuous maps for fixed and moving observations. Values below 0.30 were designated low stress, values from 0.30 to 0.60 moderate stress, and values above 0.60 high stress. These classes were used as preliminary irrigation zones rather than crop-independent physiological thresholds.

Cross Platform Comparison

Point infrared measurements served as the reference trend for comparing fixed and moving thermal observations at the tree level. The preliminary comparison examined whether platforms reproduced the same spatial pattern, the magnitude and location of disagreement, and differences among zones. Final validation will use synchronized observations to calculate the coefficient of determination and root mean square error. These statistics were not calculated from the presentation plots alone.

RESULTS & DISCUSSION

Canopy Extraction and Temperature Stability

The masking workflow removed major background regions and retained spatially coherent canopy pixels in both moving and fixed thermal scenes. In the moving sequence, canopy coverage was commonly high but declined sharply when the platform view contained gaps or non-canopy objects. These declines coincided with more variable temperature descriptors. The rolling mean reduced isolated frame-to-frame excursions and preserved broader warming and cooling periods. The result supports canopy coverage as a necessary screening variable rather than treating every acquired frame as equally representative.

The 95th-percentile temperature remained above the mean and median because it represented the warmest retained canopy fraction. This metric may help locate water-stressed foliage, but it is also sensitive to sunlit leaves and residual warm background. Mean or median temperature is therefore more suitable for the primary cross-platform comparison, with the upper percentile retained as supporting information. This interpretation agrees with evidence that canopy illumination and pixel selection can substantially change thermal indices (Jones et al., 2002).

Tree Level Platform Comparison

All three sensing modes detected repeated temperature differences among the four orchard zones and individual trees. The fixed camera generally produced the warmest estimates and the largest tree-to-tree variation. The moving platform followed the spatial trend of the point infrared sensor more closely over many tree positions, although differences remained. The offset among platforms is consistent with their different viewing geometry, canopy area, proportions of sunlit and shaded leaves, and acquisition time. Thermal imagery can therefore improve spatial coverage, but platform-specific calibration and synchronized sampling remain necessary before treating the measurements as interchangeable.

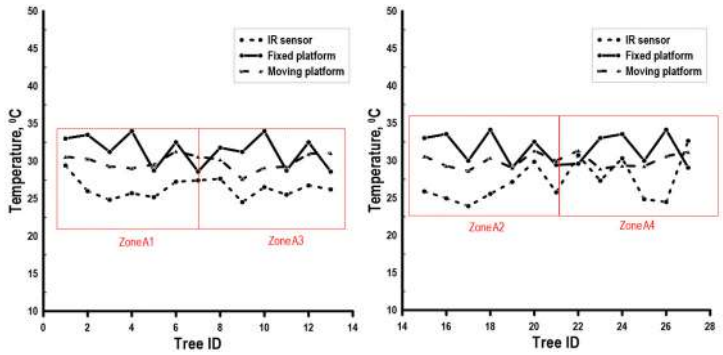

Fig. 3 Preliminary tree-level canopy-temperature comparison across zones A_1 to A_4. Point infrared measurements are shown with fixed-position and moving-platform thermal estimates.

Relative CWSI Mapping

The orchard maps resolved alternating low- and high-stress locations along the two tree lines. Mean relative CWSI values ranged from approximately 0.17 to 0.86 across the mapped trees. The fixed-camera map identified high relative CWSI near several repeated positions, including locally warm regions around positions 1, 2, 4, 10, 12, and 14, while cooler regions appeared near positions 5, 7, 11, and 13. The moving-platform map also separated stress zones, but its strongest warm and cool regions did not always coincide with the fixed map. This mismatch reinforces the need to compare only temporally aligned observations and to account for each platform's field of view.

In cabbage fields, the same workflow distinguished comparatively uniform cooler canopy areas under well-irrigated conditions from localized warmer regions associated with water deficit. The image-based maps added spatial context that a small number of point measurements could not provide. Similar high-resolution thermal mapping has been used to describe within-orchard variation in fruit-tree water status (Gonzalez-Dugo et al., 2013). For irrigation control, the present low, moderate, and high classes provide a practical zoning layer, but agronomic thresholds should be validated against soil water status and crop response before triggering automated irrigation.

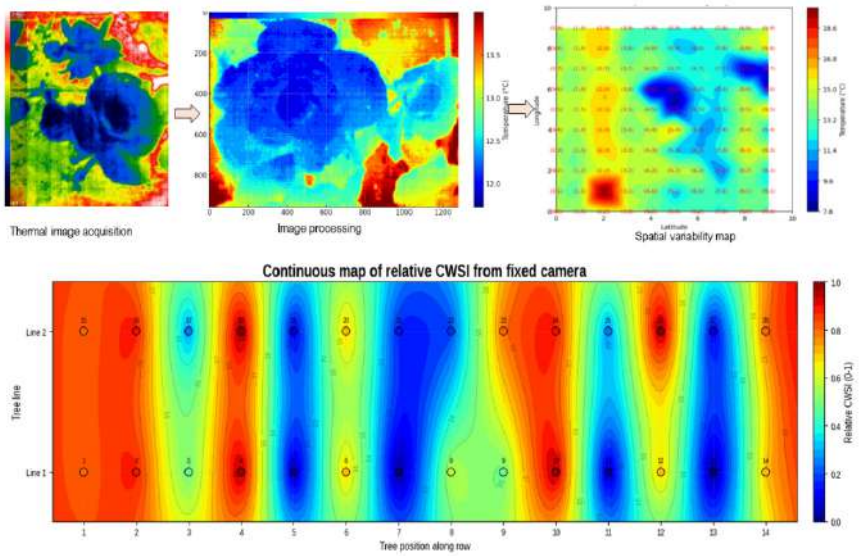

Fig. 4 Continuous relative CWSI maps from fixed-position and moving-platform thermal observations in the apple orchard. Circles indicate sampled tree positions along two rows.

Validation Requirements and Study Limitations

The current results establish the processing and mapping workflow, but the final accuracy estimates require synchronized point and image measurements under stable acquisition conditions. The expected validation range stated in the abstract, R^2 of 0.85-0.95 and RMSE of 0.8-1.5 °C, is a study target rather than a result calculated in this summary paper. Future analysis should also quantify uncertainty from reference temperatures, emissivity, solar illumination, wind, canopy coverage, camera angle, and time differences among measurements. Because surface temperature responds rapidly to weather, interpret thermal indices with contemporaneous environmental observations (Maes and Steppe, 2012).

CONCLUSIONS

A combined point and thermal-imaging workflow was developed for relative CWSI mapping in

cabbage fields and apple orchards. Canopy masking and coverage screening reduced contamination from non-crop pixels. Fixed cameras supplied repeated observations of selected areas, while the moving platform extended measurement coverage along apple-tree rows and generally followed the point-sensor trend more closely. Preliminary orchard maps showed substantial spatial variation, with relative CWSI values of approximately 0.17 to 0.86. The resulting low-, moderate-, and high-stress zones can support site-specific irrigation planning after calibration against synchronized point temperatures, soil water status, and crop response. The next stage should complete quantitative platform validation and test whether zone-based irrigation decisions remain repeatable across dates and weather conditions.

ACKNOWLEDGEMENTS

This work was supported by Korea Institute of Planning and Evaluation for Technology in Food, Agriculture and Forestry (IPET), through Industrialization of Open-Field Smart Agriculture Standard Model Program, funded by Ministry of Agriculture, Food and Rural Affairs (MAFRA) (Project No. RS-2025-02305238), Republic of Korea.

REFERENCES

Gonzalez-Dugo, V., P. J. Zarco-Tejada, E. Nicolas, P. A. Nortes, J. J. Alarcon, D. S. Intrigliolo, and E. Fereres. 2013. Using high resolution UAV thermal imagery to assess the variability in the water status of five fruit tree species within a commercial orchard. Precision Agric. 14: 660-678. https://doi.org/10.1007/s11119-013-9322-9.

Idso, S. B., R. D. Jackson, P. J. Pinter, Jr., R. J. Reginato, and J. L. Hatfield. 1981. Normalizing the stress-degree-day parameter for environmental variability. Agric. Meteorol. 24: 45-55. https://doi.org/10.1016/0002-1571(81)90032-7.

Jackson, R. D., S. B. Idso, R. J. Reginato, and P. J. Pinter, Jr. 1981. Canopy temperature as a crop water stress indicator. Water Resour. Res. 17(4): 1133-1138. https://doi.org/10.1029/WR017i004p01133.

Jones, H. G., M. Stoll, T. Santos, C. de Sousa, M. M. Chaves, and O. M. Grant. 2002. Use of infrared thermography for monitoring stomatal closure in the field: Application to grapevine. J. Exp. Bot. 53(378): 2249-2260. https://doi.org/10.1093/jxb/erf083.

Maes, W. H., and K. Steppe. 2012. Estimating evapotranspiration and drought stress with ground-based thermal remote sensing in agriculture: A review. J. Exp. Bot. 63(13): 4671-4712. https://doi.org/10.1093/jxb/ers165.

SF-09

Proceedings of The 12th International Symposium on Machinery and Mechatronics for Agriculture and Biosystems Engineering (ISMAB 2026)
20-24 October 2026, Busan, Republic of Korea

VARIABILITY CHARACTERIZATION OF AMBIENT ENVIRONMENTAL CONDITIONS FOR SMART GREENHOUSE NUTRIENT MANAGEMENT

Sakib Robin[1], Cholet Nyangoma Atulinda[2], Md Nasim Reza[1,2], Hyeunseok Choi[3], Sun-Ok Chung[1,2*]

[1]Department of Smart Agricultural Systems, Graduate School, Chungnam National University, Daejeon 34134, Republic of Korea
[2]Department of Agricultural Machinery Engineering, Graduate School, Chungnam National University, Daejeon 34134, Republic of Korea
[3]Korea Institute of Industrial Technology, Cheonan, 31056, Republic of Korea
*Corresponding Author--Voice: +82-42-821-6712, Email: sochung@cnu.ac.kr

Abstract: Ambient environmental conditions within greenhouses vary across different locations and over time, affecting crop growth, nutrient uptake, physiological responses, and production uniformity. Differences in air temperature, relative humidity, light intensity, and CO_2 concentration caused by solar radiation, ventilation, and air circulation create uneven growing conditions that influence crop nutrient requirements and reduce the efficiency of uniform greenhouse management. Therefore, this study characterized the variability of ambient environmental conditions in a smart greenhouse to provide a basis for precision nutrient management. A Wi-Fi-based wireless sensor monitoring system with 45 sensor nodes was installed in three vertical layers (lower canopy, middle, and upper), with each layer consisting of 15 sensor nodes arranged in a 5 × 3 grid. Air temperature, relative humidity, light intensity, and CO_2 concentration were continuously monitored at multiple locations to evaluate horizontal and vertical environmental variability. The collected data were analyzed using zone-wise comparisons, deviations from the greenhouse average, and spatial distribution maps to identify areas with different environmental conditions. The results showed clear differences across the greenhouse. Higher air temperatures and light intensities were observed in the upper regions, while the lower canopy maintained relatively higher humidity. CO_2 concentration also varied among different areas because of differences in ventilation and air circulation. Areas with poor airflow accumulated more heat, whereas shaded areas received lower light intensity because of reduced solar penetration. Based on these environmental differences, the greenhouse can be divided into management zones with different environmental characteristics and nutrient requirements. These findings demonstrate that sensor-based monitoring can effectively characterize ambient environmental conditions and provide useful information for smart greenhouse nutrient management through more precise nutrient supply and environmental control.

Key Words: Precision Agriculture, Smart Greenhouse, Spatial Variability, Environmental Condition, Sensor Node, Nutrient Supply

INTRODUCTION

Greenhouse production supports stable and year-round crop production by allowing greater control of environmental conditions. However, environmental conditions inside a greenhouse are not always uniform. Air temperature, relative humidity, light intensity, and CO_2 concentration can vary by location, height, and time of day. These conditions influence photosynthesis, respiration, transpiration, crop development, water use, and nutrient uptake. Temperature and relative humidity jointly determine vapor pressure deficit, which affects plant water movement and nutrient transport. (Yu et al., 2022) reported that high temperature and dry air reduced calcium absorption in tomato plants, whereas an appropriate vapor pressure deficit improved calcium absorption, water transport, and yield. Therefore, crops growing in different greenhouse zones may respond differently to the same nutrient supply.

Spatial variability inside greenhouses can result from greenhouse structure, covering materials, solar radiation, ventilation openings, air circulation, and shading. These factors can produce hotter upper zones, more humid lower zones, shaded areas, and locations with different CO_2 concentrations. (Ryu et al., 2014) observed spatial, vertical, and temporal differences in air temperature, relative humidity, photosynthetic photon flux density, and CO_2 concentration in Korean strawberry and tomato greenhouses. (Reza et al., 2023) also reported clear vertical and temporal variations in greenhouse environmental conditions during winter. Similarly, (Islam et al., 2025) identified spatial and temporal differences in temperature, humidity, CO_2 concentration, light intensity, and air movement during summer.

A sensor installed at only one location may not accurately represent the overall greenhouse condition. (Balendonck et al., 2014) used 100 wireless sensors in commercial greenhouses and found instantaneous spatial differences of up to ±5°C in air temperature and ±20% in relative humidity. Wireless sensor networks can collect environmental data from multiple locations, while spatial distribution maps can identify zones that differ from the greenhouse average. However, using multi-layer environmental variability data for zone-specific nutrient management remains limited. Understanding these differences is necessary to support precise environmental control and nutrient supply.

Therefore, this study characterized the horizontal, vertical, and temporal variability of air temperature, relative humidity, light intensity, and CO_2 concentration in a smart greenhouse to support precision nutrient management.

MATERIALS AND METHODS

EXPERIMENTAL DESIGN AND ENVIRONMENTAL VARIABILITY ANALYSIS

The study was conducted under greenhouse conditions to characterize the horizontal, vertical, and temporal variability of ambient environmental conditions. The greenhouse monitoring area was divided into three vertical layers: lower, middle, and upper. A total

of 45 wireless sensor nodes were installed, with 15 nodes arranged in a 5 × 3 grid within each layer. The sensor positions were selected to capture environmental differences along the greenhouse length, width, and height. Air temperature, relative humidity, light intensity expressed as photosynthetic photon flux density (PPFD), and CO_2 concentration were recorded at 2-min intervals. The collected measurements were transmitted via Wi-Fi to a central data-logging system and organized by sensor location, vertical layer, and collection time. Data were grouped into morning (08:00–12:00), daytime (12:00–19:00), and nighttime (19:00–08:00) periods to examine daily changes. We calculated node-wise and layer-wise means, minimums, maximums, ranges, and standard deviations for each environmental parameter. We also calculated each sensor measurement's deviation from the overall greenhouse average to identify locations with different environmental conditions. We generated two-dimensional spatial distribution maps for each vertical layer using Python-based interpolation of the 15 sensor measurements. We used the maps and statistical comparisons to identify hotter, drier, more humid, shaded, and poorly ventilated greenhouse zones.

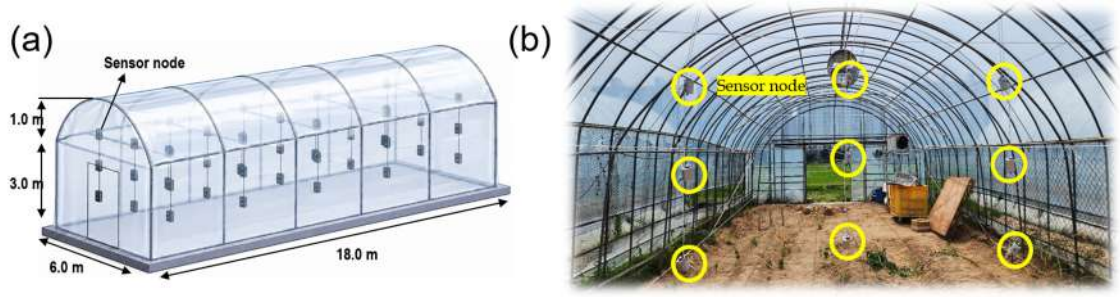

Fig.1 Experimental design and sensor node setup in CNU greenhouse: (a) sensor node setup plan in 3 layers, (b) sensor node setup in CNU greenhouse.

RESULTS & DISCUSSION

The analysis showed clear horizontal, vertical, and temporal differences in greenhouse environmental conditions. During the morning, mean air temperatures were 34.0, 35.5, and 37.1°C in the lower, middle, and upper layers, respectively. The corresponding daytime means increased to 37.3, 38.7, and 40.2°C, while nighttime means decreased to 27.5, 27.8, and 28.0°C. The upper layer reached a maximum mean temperature of 42.4°C, and the maximum temperature difference among the layers was 3.9°C. Relative humidity showed an opposite pattern to air temperature. Morning mean humidity was 69.8%, 66.5%, and 62.3% in the lower, middle, and upper layers, respectively, and decreased to 52.0%, 48.9%, and 45.0% during the daytime. Nighttime humidity increased to 86.0%, 85.0%, and 83.8%, respectively. Light intensity also increased with sensor height. Mean daytime PPFD values were 433, 550, and 671 μmol m^{-2} s^{-1} in the lower, middle, and upper layers, respectively. The upper layer reached a maximum mean PPFD of 1,156 μmol m^{-2} s^{-1}, while nighttime PPFD remained near zero. Mean daytime CO_2 concentrations ranged from 411 to 419 ppm and differed little among layers. At night, CO_2 concentrations increased to 493, 477, and 453 ppm in the lower, middle, and upper layers, respectively, with a maximum vertical difference of 55 ppm. The spatial maps

identified hotter and drier upper zones, more humid lower zones, shaded areas with lower PPFD, and areas with different CO_2 concentrations. These results indicate that a single sensor may not represent the entire greenhouse and show the potential of multi-location monitoring to support zone-specific environmental control and precision nutrient management.

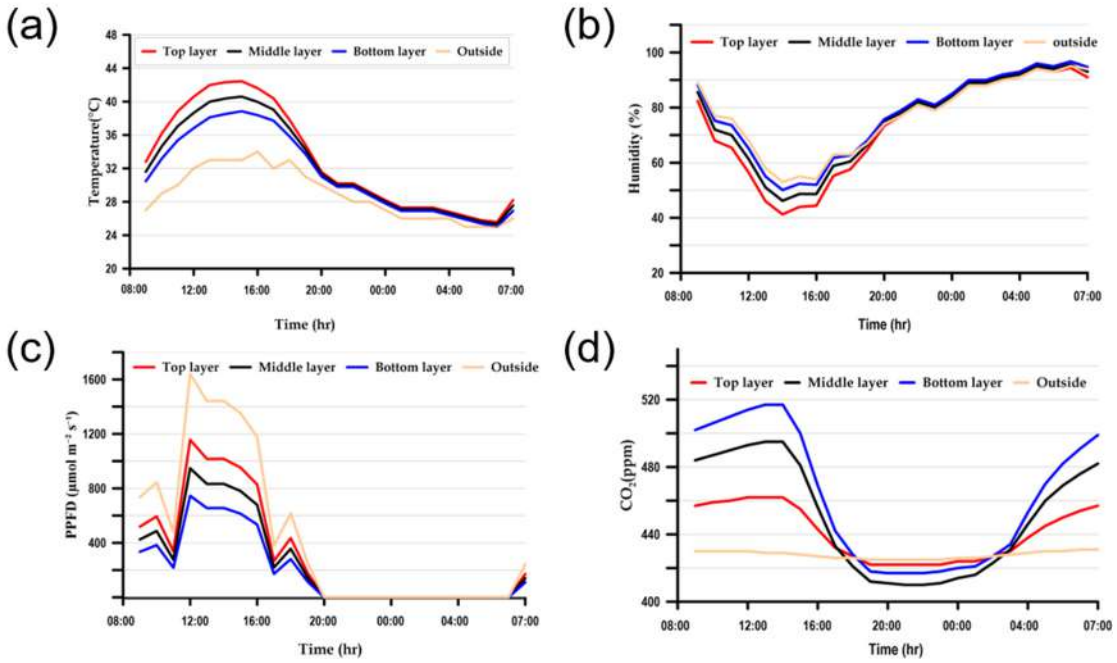

Fig.2 Temporal variations in (a) air temperature, (b) relative humidity, (c) PPFD, and (d) CO_2 concentration in the lower, middle, and upper greenhouse layers and outside.

CONCLUSIONS

The 45-node monitoring system successfully characterized the horizontal, vertical, and temporal variability of greenhouse environmental conditions. The upper layer showed higher daytime temperature and PPFD, while the lower layer maintained higher relative humidity. CO_2 concentration varied with time and location because of differences in ventilation and air circulation. The spatial maps identified areas with different environmental conditions, confirming that a single sensor cannot represent the entire greenhouse. These findings provide a basis for zone-specific environmental control and precision nutrient management. Future work will evaluate the system in larger crop-producing greenhouses and use long-term data to develop zone-specific nutrient supply strategies.

ACKNOWLEDGEMENTS

This work was supported by Korea Institute of Planning and Evaluation for Technology in Food, Agriculture and Forestry (IPET), through Smart Farm Multi-Ministry Package Innovation Technology Development Project Program, funded by Ministry of Agriculture, Food and Rural Affairs (MAFRA) (Project No. RS-2025-02310974), Republic of Korea.

REFERENCES

Balendonck, J., A. Sapounas, F. Kempkes, E. A. van Os, R. van der Schoor, B. A. J. van Tuijl, and L. C. P. Keizer. 2014. Using a wireless sensor network to determine climate heterogeneity of a greenhouse environment. Acta Horticulturae 1037: 539-546.

Islam, M. N., M. N. Reza, M. Z. Iqbal, K. H. Lee, M. K. Jang, and S. O. Chung. 2025. Spatial and temporal variability of environmental variables in Chinese solar greenhouses in the summer season. Horticulturae 11(4): 421.

Reza, M. N., M. N. Islam, M. Z. Iqbal, M. S. N. Kabir, M. Chowdhury, M. A. Gulandaz, M. Ali, M. K. Jang, and S. O. Chung. 2023. Spatial, temporal, and vertical variability of ambient environmental conditions in Chinese solar greenhouses during winter. Applied Sciences 13(17): 9835.

Ryu, M. J., D. K. Ryu, S. O. Chung, Y. K. Hur, S. O. Hur, S. J. Hong, J. H. Sung, and H. H. Kim. 2014. Spatial, vertical, and temporal variability of ambient environments in strawberry and tomato greenhouses in winter. Journal of Biosystems Engineering 39(1): 47-56.

Yu, X., M. Zhao, X. Wang, X. Jiao, X. Song, and J. Li. 2022. Reducing vapor pressure deficit improves calcium absorption by optimizing plant structure, stomatal morphology, and aquaporins in tomatoes. Environmental and Experimental Botany 195: 104786.

SF-10

Proceedings of The 12th International Symposium on Machinery and Mechatronics for Agriculture and Biosystems Engineering (ISMAB 2026)
20-24 October 2026, Busan, Republic of Korea

REAL-TIME SENSOR DATA QUALITY MONITORING AND FAULT DETECTION IN A VERTICAL FARM

Md Ashikur Rahman[1], Ezatullah Zakir[2], Md Mamunur Rashid[1], Su Young Lee[2], Md Nasim Reza[1,2], Sun-Ok Chung[1,2*]

[1]Department of Smart Agricultural Systems, Graduate School, Chungnam National University, Daejeon 34134, Republic of Korea
[2]Department of Agricultural Machinery Engineering, Graduate School, Chungnam National University, Daejeon 34134, Republic of Korea
*Corresponding Author-- Voice: +82-(0)42-821-6712, Email: sochung@cnu.ac.kr

Abstract: Reliable real-time environmental monitoring in vertical farms requires continuous data acquisition together with characterization of temporal and spatial variability. This study evaluated a local monitoring system using nine distributed sensor nodes measuring air temperature, relative humidity, CO_2 concentration, and photosynthetic photon flux density (PPFD) in a small-scale vertical farm. Measurements were acquired every 30 s and transmitted through Wi-Fi and MQTT to a Raspberry Pi 4B server, where Node-RED processed the records and InfluxDB provided time-series storage and visualization. Monitoring performance was evaluated using node-wise data continuity, temporal coefficient of variation, facility-operation response, and normalized spatial spread. Temperature and relative humidity showed low temporal variability, with coefficients of variation of 2.21% and 2.09%, respectively, whereas CO_2 and PPFD showed higher variability of 5.55% and 5.15%. CO_2 increased by 5.95% during the facility-active period, while PPFD changed by only -0.06%. PPFD exhibited the largest node-wise spatial spread at 14.11%. These results demonstrate that real-time environmental monitoring should consider both variable-specific temporal behavior and sensor location.

Key Words: Vertical farm, Sensor data quality, Fault detection, Real-time monitoring, Dashboard visualization.

INTRODUCTION

Vertical farming is a controlled-environment production system in which crops are cultivated in vertically stacked layers under regulated indoor conditions. Because crop growth depends strongly on artificial lighting, ventilation, temperature and humidity management, and CO_2 availability, continuous environmental monitoring is important for maintaining stable growing conditions and supporting reliable management decisions (Benke and Tomkins, 2017; Saad et al., 2021; Morella et al., 2023). However, environmental conditions in stacked cultivation systems can vary over both time and location, and a single sensor value or farm-wide average may not adequately represent conditions at different cultivation positions.

Recent smart-agriculture monitoring systems increasingly integrate wireless sensor nodes with lightweight communication protocols, local or cloud servers, time-series databases, and

visualization tools. MQTT, Node-RED, InfluxDB, and related open-source platforms have been applied to support continuous data acquisition, storage, and inspection in greenhouse and smart-farming environments (Dineva and Atanasova, 2022; Guijarro-Rubio et al., 2025). At the same time, sensor-data quality remains important because missing records, inconsistent measurements, and variable signal behavior can reduce the usefulness of real-time monitoring and subsequent analysis (Teh et al., 2020).

Therefore, real-time monitoring should evaluate not only whether measurements are successfully acquired, but also how environmental variables behave temporally and spatially across multiple sensor locations. In this study, a local monitoring system was implemented in a small-scale vertical farm using nine distributed environmental sensor nodes, a Raspberry Pi-based server, and InfluxDB time-series storage and visualization. The objective was to characterize node-wise data continuity, temporal variability, facility-operation response, and spatial heterogeneity of air temperature, relative humidity, CO_2 concentration, and photosynthetic photon flux density (PPFD). The analysis was designed to support variable-specific and node-specific interpretation of real-time environmental data rather than fault-classification performance.

MATERIALS AND METHODS

Experimental vertical farm and sensor monitoring system

The experiment was conducted in a small-scale indoor vertical farm at Chungnam National University, Daejeon, Republic of Korea. The facility contained nine cultivation beds, with one environmental sensor node installed in each bed. Each node measured air temperature, relative humidity, CO_2 concentration, and light intensity. Sensor readings were acquired at a fixed interval of 30 s, and each record contained a timestamp, node identifier, bed identifier, and the measured environmental variables.

The sensor nodes transmitted measurements through a local Wi-Fi network using the MQTT protocol. A Raspberry Pi 4B was used as the local monitoring server. The incoming MQTT messages were received by the broker, parsed using Node-RED, assigned node metadata, and stored in the InfluxDB time-series database. This architecture allowed the sensor nodes to perform lightweight acquisition and communication tasks while the local server handled data storage, inspection, and subsequent analysis.

Table 1. Experimental, sensor, and communication configuration.

Item	Configuration	Main specification / role
Monitoring duration	10 days	30 s sampling interval
Cultivation beds / nodes	9 / 9	One node per bed
Microcontroller	Arduino UNO R4 WiFi	Renesas RA4M1; ESP32-S3 Wi-Fi module
Temperature / RH	DHT22	-40 to 80 °C; 0 to 100% RH
CO_2	CM1106	0 to 5000 ppm; UART
Light	P5144-9	Light intensity to estimated PPFD

Wireless network	ipTIME N804R	2.4 GHz IEEE 802.11 b/g/n
MQTT	Mosquitto v2.1.2	port 1883; topic farm/sensor/data; QoS 0
Processing	Node-RED v4.1.10	JSON parsing and metadata assignment
Storage & Visualization	InfluxDB v2.9.1	organization: PA Lab; bucket: sensor_data

InfluxDB-based real-time data inspection

InfluxDB served as the local time-series storage platform and the primary interface for inspecting continuously acquired environmental measurements. The Data Explorer interface allowed querying stored records by node identifier, environmental variable, and time range. This enabled the operator to verify whether individual nodes were actively transmitting, whether timestamps were updating continuously, and whether historical data remained available for later analysis.

The InfluxDB interface also confirmed that the complete acquisition chain, from sensing and wireless transmission to server-side processing and storage, was functioning correctly. Time-series records stored in the database included timestamp, node ID, air temperature, relative humidity, CO_2 concentration, and estimated PPFD.



Figure 1. Real-time vertical farm monitoring system (a) experimental vertical farm and (b) InfluxDB Data Explorer interface on the Raspberry Pi local server.

Dataset preparation and monitoring-oriented analysis

Missing timestamps, invalid packets, physically invalid values, and reference-labeled abnormal intervals were excluded before environmental characterization, leaving 227,434 valid normal records. Because the LED system operated continuously, 09:00-18:00 was defined as the facility-active period and the remaining hours as the facility-inactive period.

Four normalized indicators were calculated. Missing-update burden was the number of missing timestamp positions divided by the 28,800 expected records per node. Temporal variability was expressed as coefficient of variation, CV = SD/mean × 100. Facility-operation response was calculated as (active mean - inactive mean)/inactive mean × 100. Spatial heterogeneity was calculated as (maximum node mean - minimum node mean)/overall mean × 100. These indices allowed direct comparison among variables with different units.

RESULTS & DISCUSSION

Real-time monitoring and node-wise continuity

The Raspberry Pi-based system successfully stored node-specific environmental records in InfluxDB, allowing direct verification of the complete sensing-to-storage pipeline. Missing timestamp positions were concentrated in a subset of nodes rather than being uniformly distributed. The largest missing-update burden occurred at node_03 (0.42%), followed by node_05 (0.21%), node_07 (0.17%), node_02 (0.12%), and node_08 (0.09%); the remaining nodes showed no missing timestamp positions. This indicates that network-wide completeness can remain high while individual nodes experience intermittent interruptions.

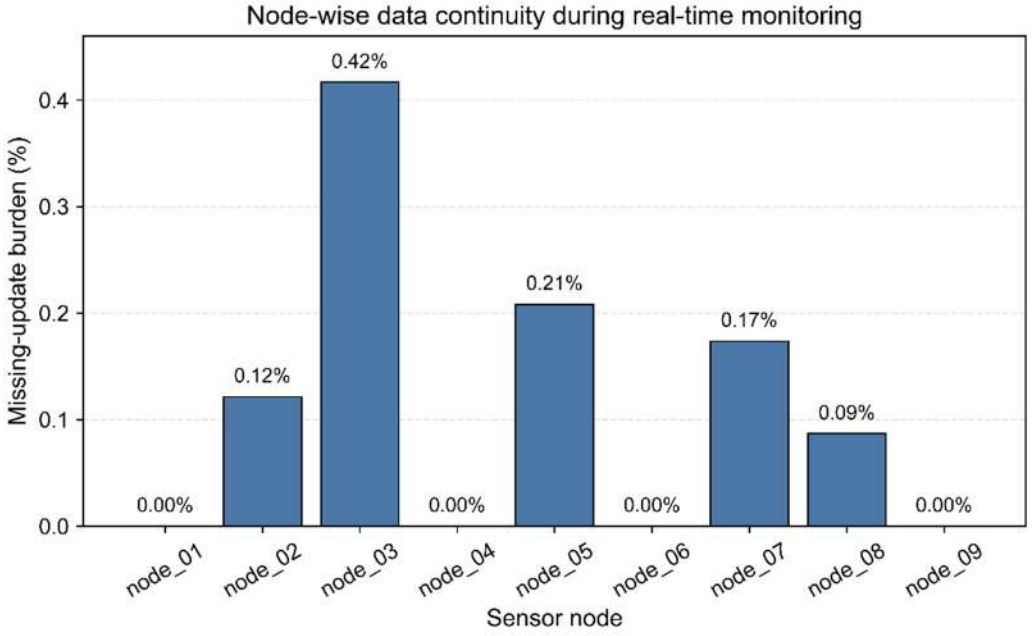

Figure 2. Node-wise missing-update burden during the 10-day monitoring period.

Temporal variability and facility-operation response

Temperature and relative humidity were comparatively stable, with temporal CV values of 2.21% and 2.09%, respectively. CO_2 and PPFD were more variable, with CV values of 5.55% and 5.15%. These differences show that a common variability criterion would not represent all environmental signals equally.

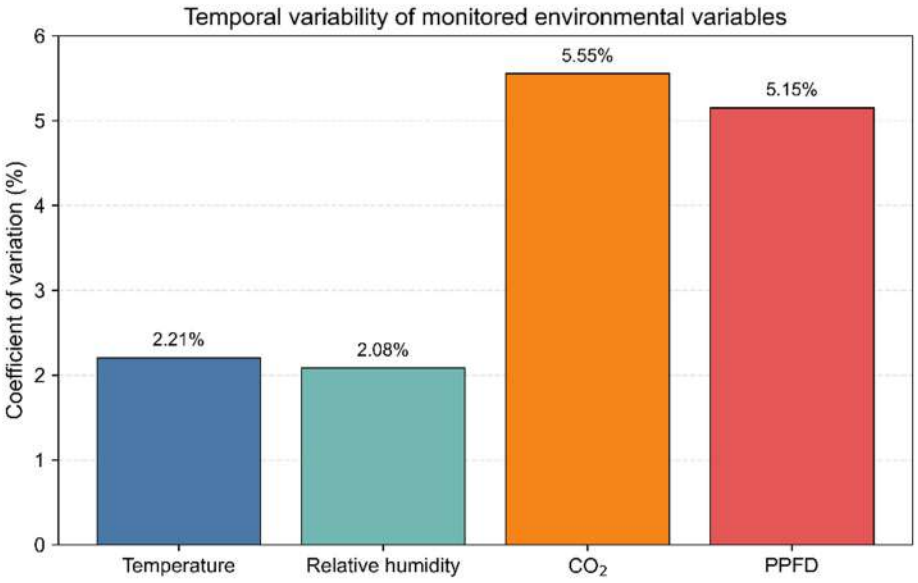

Figure 3. Relative temporal variability of the monitored environmental variables.

Routine facility activity affected the monitored variables differently. Temperature increased by only 0.30% and relative humidity decreased by 0.36%. CO_2 increased from 683.32 to 724.00 ppm, corresponding to a 5.95% increase. PPFD changed by only -0.06%, consistent with continuous LED operation. Thus, CO_2 interpretation should consider facility operating context more strongly than temperature, humidity, or PPFD.

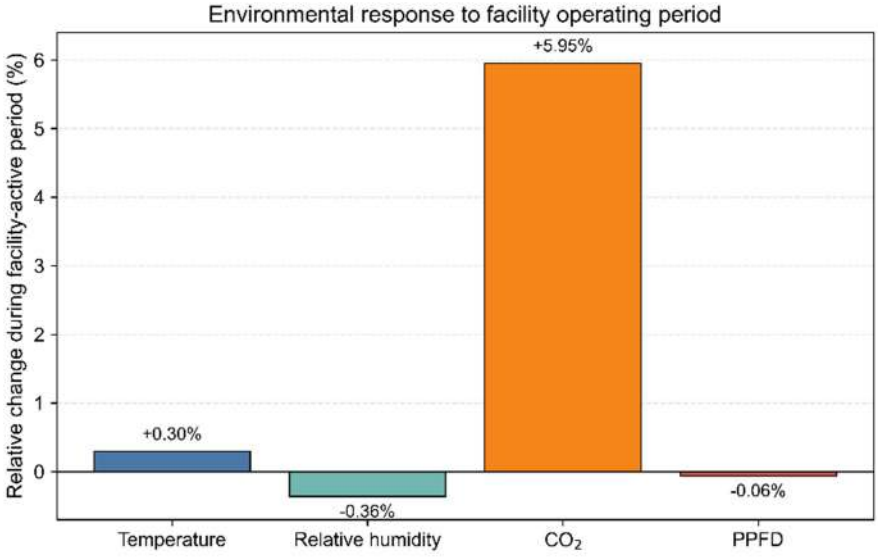

Figure 4. Relative changes in environmental variables during the facility-active period.

Node-wise spatial heterogeneity

Mean temperature among nodes ranged from 22.71 to 24.18 °C, relative humidity from 62.17 to 65.95% RH, CO_2 from 671.95 to 721.88 ppm, and PPFD from 235.82 to 271.87 μmol m^{-2} s^{-1}. The normalized spatial spread was 6.24% for temperature, 5.93% for relative humidity, 7.15% for CO_2, and 14.11% for PPFD. PPFD therefore showed the largest spatial heterogeneity, demonstrating that temporal stability did not imply spatial uniformity.

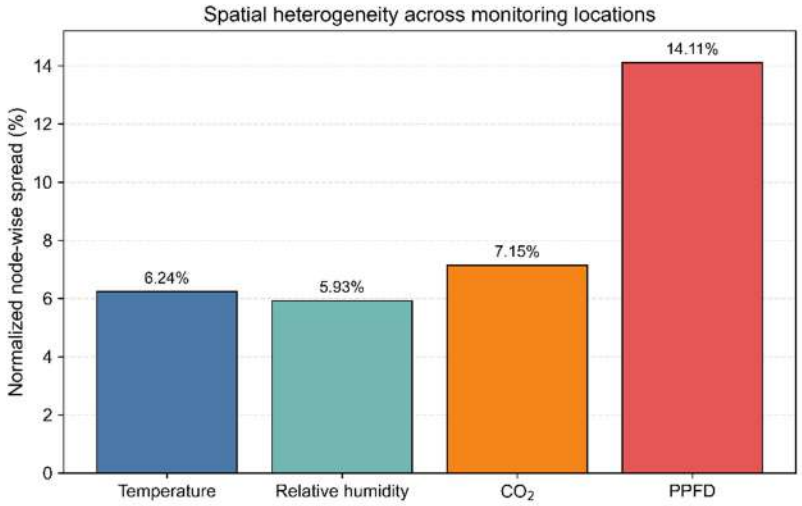

Figure 5. Normalized node-wise spatial spread across the nine monitoring locations.

Combined monitoring characteristics

The combined temporal-spatial map showed three distinct monitoring patterns. Temperature and relative humidity had low temporal and spatial variability. CO_2 had relatively high temporal variability but only moderate spatial spread, indicating stronger dependence on operating context. PPFD had the greatest spatial heterogeneity, making node location particularly important for light monitoring. These results support variable-specific and node-specific interpretation in real-time vertical farm monitoring.

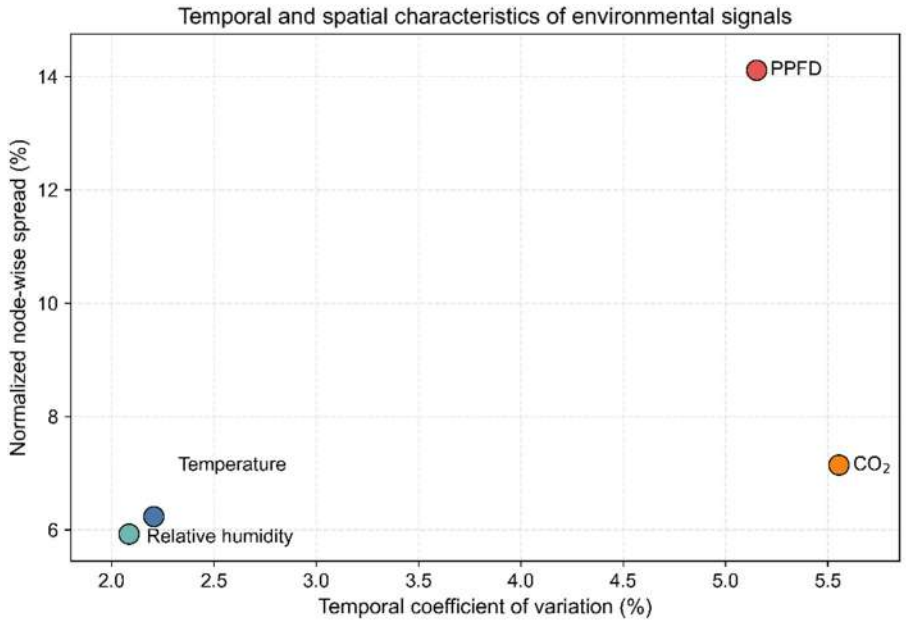

Figure 6. Relationship between temporal variability and node-wise spatial heterogeneity of the monitored environmental variables.

CONCLUSIONS

A Raspberry Pi and InfluxDB-based monitoring system successfully acquired and stored environmental measurements from nine sensor nodes in a small-scale vertical farm. Node-wise continuity analysis showed that data interruptions were limited but differed among monitoring locations. Temperature and relative humidity exhibited low temporal variability,

whereas CO_2 was more responsive to facility activity. PPFD remained temporally stable under continuous LED operation but showed the greatest node-wise spatial spread at 14.11%.
The results indicate that temporal stability does not necessarily represent spatial uniformity. Therefore, real-time vertical farm monitoring should preserve node identity and interpret environmental variables according to both temporal behavior and sensor location. The proposed monitoring approach provides a practical basis for node-specific environmental assessment and future data-driven management.

ACKNOWLEDGEMENTS

This work was supported by Korea Institute of Planning and Evaluation for Technology in Food, Agriculture and Forestry (IPET), through K-Vertical Farm Globalization Project, funded by the Ministry of Agriculture, Food and Rural Affairs (MAFRA) (Project No. RS-2025-02303373), Republic of Korea.

REFERENCES

Benke, K., and B. Tomkins. 2017. Future food-production systems: Vertical farming and controlled-environment agriculture. Sustainability 9: 1934.

Dineva, K., and T. Atanasova. 2022. Cloud data-driven intelligent monitoring system for interactive smart farming. Sensors 22: 6566

Guijarro-Rubio, O. E., D. Vinocunga-Pillajo, O. Del Real-Fleites, E. Guardado-Yordi, and A. Pérez-Martínez. 2025. Monitoring of environmental variables in greenhouse crops through an IoT wireless sensor network. DYNA.

Morella, P., M. P. Lambán, J. Royo, and J. C. Sánchez. 2023. Vertical farming monitoring: How does it work and how much does it cost? Sensors 23: 3502.

Saad, M. H. M., N. M. Hamdan, and M. R. Sarker. 2021. State of the art of urban smart vertical farming automation system. Electronics 10: 1422.

Teh, H. Y., A. W. Kempa-Liehr, and K. I.-K. Wang. 2020. Sensor data quality: A systematic review. Journal of Big Data 7: 11.

Post-harvest and Food Processing 1 (PH-1)



PH-01

Proceedings of The 12th International Symposium on Machinery and Mechatronics for Agriculture and Biosystems Engineering (ISMAB 2026)
20-24 October 2026, Busan, Republic of Korea

DEM SIMULATION OF APPLE MECHANICAL IMPACT RESPONSE

Jui-Chun Wang[1], Wei-Lun Hsu[1]*
[1] Department of Bio-industrial Mechatronics Engineering, National Chung Hsing University, Taichung, Taiwan
*Corresponding Author-- Voice: +886-4-2284-0377 ext. 401, Email: HWL@nchu.edu.tw

Abstract: Although the traditional Finite Element Method (FEM) provides valuable stress analysis insights, simulating soft biological tissues under large deformations often triggers severe mesh distortion and increases computational complexity. Therefore, this study aims to overcome the limitations of the traditional Finite Element Method (FEM) in simulating the impact of soft biological tissues, such as apples, where severe mesh distortion often leads to computational instability, making it difficult to capture large deformation and failure behaviors accurately. The primary objective is to construct a robust Discrete Element Method (DEM) model to accurately predict the mechanical responses and internal bruising mechanisms of apples during drop, compression, and impact tests. This research employs a bond-based DEM spherical model to simulate apple tissue, conducting explicit dynamic simulations. To investigate convergence and size effects, multiple models were established, including DEM models with uniform particle diameters progressively decreasing from 5 mm to 2 mm, alongside several FEM models. Microscopic parameters, such as particle size, were systematically analyzed in this study to investigate their effects on macroscopic mechanical behaviors. Model parameters, such as material properties and boundary condition settings, were derived from experimental data in previous literature and compared with a traditional FEM viscoelastic model. Simulation results show that DEM, through post-processing techniques, successfully verified stress conditions during dynamic contact and offered significant computational efficiency advantages, with FEM simulations requiring more than twice the computational time of DEM. Convergence tests indicate that force and displacement responses tend to stabilize when the particle size is reduced to 2 mm; it can be inferred that smaller particle sizes lead to higher model fidelity and more accurate numerical results. Compared to traditional FEM, the proposed DEM method not only drastically reduces computation time but also more authentically reproduces the microscopic failure mechanisms and internal stress transfer of fruit under impact. In the future, the development of multi-particle-size hybrid models can further enhance model fidelity and improve the accuracy of damage prediction, providing a highly reliable numerical analysis method for agricultural machinery design, post-harvest packaging, and harvest protection.

Key Words: Finite Element Method, Discrete Element Method, Size Convergence, Harvest protection

INTRODUCTION

Agricultural products (especially soft fruits like apples) are highly susceptible to mechanical damage during post-harvest handling, packaging operations (Scheffler et al., 2018; Liang et al., 2025), and transportation. Sudden impacts and collisions can cause internal bruising within the fruit, leading to severe economic losses and a decline in overall quality (Scheffler et al., 2018; Liang et al., 2025). Historically, numerical analyses of these impact events have heavily relied on the traditional Finite Element Method (FEM). Although FEM provides valuable insights for analyzing stress distribution, simulating the dynamic impact of soft biological tissues under large deformations often triggers severe mesh distortion and increases the complexity of computational simulations.

To overcome these limitations, the Discrete Element Method (DEM) has emerged as a highly promising alternative for evaluating mechanical damage in fresh produce (Scheffler et al., 2018). By modeling the fruit tissue as an assembly of discrete particles connected by cohesive bonds, DEM can inherently and more naturally handle material discontinuities, fracture propagation, and large deformations, while circumventing the mathematical complexities associated with mesh distortion (Liang et al., 2025). Furthermore, although the resolution and configuration of these particle assemblies critically influence both the accuracy of the physical representation and the computational time (Kafashan et al., 2021), comprehensive investigations into this aspect remain scarce in current literature. Therefore, the primary objective of this study is to construct and validate a robust DEM analysis framework to accurately predict the mechanical responses and damage mechanisms of agricultural products under various loading conditions, such as drop and compression. The apple was selected as the representative target due to the abundance of relevant literature. To address this research gap, this research specifically focuses on investigating the effect of particle size on convergence, as well as comparing the computational efficiency with traditional viscoelastic FEM models.

MATERIALS AND METHODS

Materials and Numerical Simulation Setup

The numerical simulations in this study employed the explicit dynamic solver LS-DYNA, utilizing LS-PrePost for all pre-processing and post-processing operations. To ensure the consistency of all physical quantities and computational boundaries, the entire system was strictly constructed using the mm-kg-s (length: millimeter, mass: kilogram, time: second) unit system. Furthermore, the simulation steps (time steps) were automatically determined and controlled by the solver based on the numerical stability criterion corresponding to the minimum particle or mesh size.

The apple tissue was modeled using a viscoelastic material model. Its shear relaxation behavior is primarily governed by parameters including the bulk modulus, short-time shear modulus (G0), long-time shear modulus (GI), and decay constant (BETA). These material parameters were calibrated based on drop, compression, and impact experimental data from the reference literature. Furthermore, to define the microscopic interactions between DEM particles, four parallel-bond parameters were introduced. The normal parallel-bond modulus and shear parallel-bond stiffness ratio govern the microscopic elastic stiffness and contact behavior between adjacent particles. Meanwhile, the parallel-bond maximum normal stress

and maximum shear stress define the ultimate thresholds for bond breakage. Because the primary focus of this study is to investigate elastic impact responses rather than macroscopic fracture behaviors, these two strength parameters are configured to provide infinite strength (set to 0), preventing any internal bond breakage during the simulation. Specifically, Material A was used for the drop test, while Material B was used for the compression and impact tests (see Table 1, Table 2).

Table 1

Apple Material A	(Scheffler et al., 2018)
Young's modulus(Pa)	2.52×10^6
Poisson's ratio	0.35
μ	0.34
Density(kg/m^3)	10^3
Bulk modulus(Pa)	2.8×10^6
G0(Pa)	9×10^5
GI(Pa)	2×10^5
BETA(1/s)	10
Normal Parallel-bond modulus	150
Shear Parallel-bond stiffness ratio	1
Parallel-bond maximum normal stress	0(infinite)
Parallel-bond maximum shear stress	0(infinite)

Table 2

Apple Material B	(Liang et al., 2025)
Young's modulus(Pa)	1.72×106
Poisson's ratio	0.35
μ	0.36
Density(kg/m^3)	103
Bulk modulus(Pa)	1.9×106
G0(Pa)	6×105
GI(Pa)	2×105
BETA(1/s)	10
Normal Parallel-bond modulus	80
Shear Parallel-bond stiffness ratio	1
Parallel-bond maximum normal stress	0(infinite)
Parallel-bond maximum shear stress	0(infinite)

DEM Framework and Particle Size Configuration

In the DEM approach, the apple model was constructed with a diameter of 8 cm and represented as an assembly of discrete spheres connected by breakable cohesive bonds to simulate internal particle interactions (Liang et al., 2025). To systematically investigate the effects of geometric resolution on mechanical responses and numerical convergence, this study established DEM models with varying particle resolutions. The uniform particle diameters in these models were progressively decreased from 5 mm to 2 mm (Fig.1 a–e), aiming to observe particle size effects during large deformation and dynamic contact simulations. Prior studies have reported that particle resolution significantly influences the accuracy of apple tissue modeling (Scheffler et al., 2018). By comparing the contact force histories and stress transfer behaviors across different particle resolutions, this study aims to determine the optimal

converged particle size that ensures computational accuracy while maintaining computational efficiency.

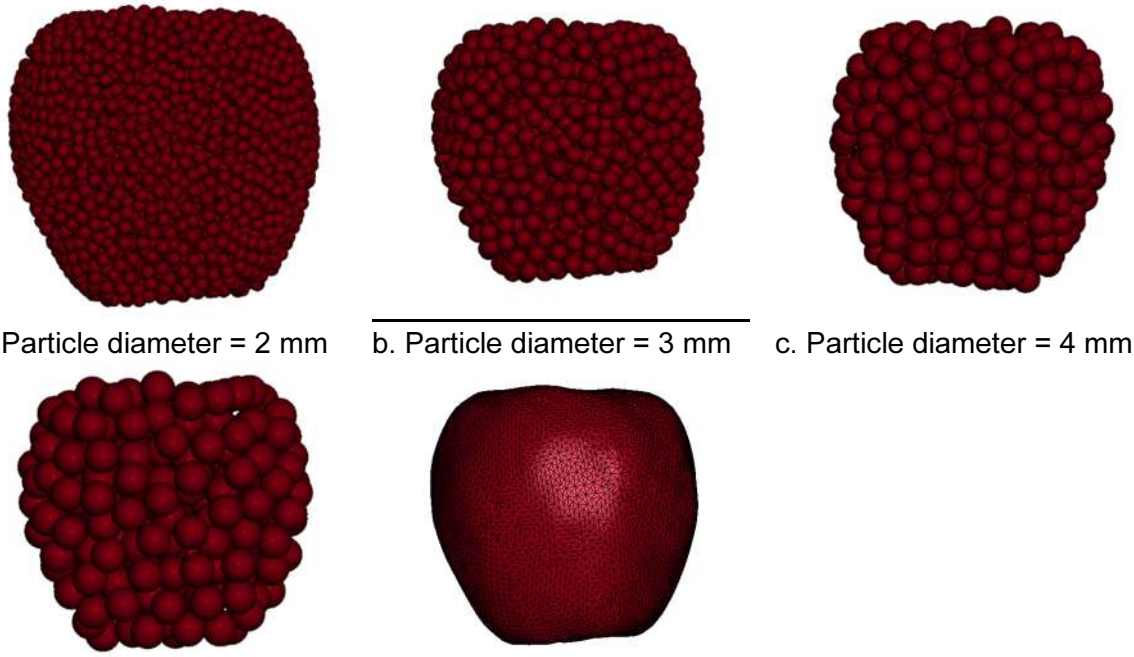

a. Particle diameter = 2 mm b. Particle diameter = 3 mm c. Particle diameter = 4 mm

d. Particle diameter = 5 mm e. Finite Element Model

Fig.1-DEM apple models with particle diameters from 2 mm to 5 mm, and the corresponding FEM model.

Boundary Conditions and Loading Scenarios

As discussed in the Introduction section, the apple was selected as the representative target due to the abundance of existing literature. In post-harvest processing, packaging operations, and transportation studies, drop, compression, and impact tests are widely conducted. To evaluate the performance of the FEM and DEM approaches for simulating agricultural products, these three tests were implemented and validated against published experimental results in the literature.

Drop Test (Fig.2): To simulate free-fall impact during post-harvest handling, the apple model was suspended above a horizontal rigid flat plate. The apple was freely dropped from heights of 10 cm, 20 cm, 40 cm, and 60 cm, respectively. Based on the prior parameter calibration, Material A was assigned to the apple tissue for this scenario. The simulation results were compared with experimental data from the literature (Scheffler et al., 2018).

Compression Test (Fig.3): To investigate the macroscopic force-displacement behavior under quasi-static compressive loading, the apple was positioned between two parallel rigid plates. The bottom plate was fully constrained in all degrees of freedom, while a constant downward displacement boundary condition was applied to the top plate. The top plate compressed the apple at a rate of 1 mm/min and stopped after reaching a displacement of 5 mm. Material B was assigned to the apple tissue in this test. The simulation results were compared with experimental data from the literature (Liang et al., 2025).

Impact Test (Fig.4): To simulate localized dynamic impact, the apple was placed against an L-shaped rigid plate, which provided basal and lateral support. A cylindrical impactor with a hemispherical head was positioned on the unrestrained side of the apple and driven to strike

the fruit surface at horizontal velocities of 0.81 m/s and 1.65 m/s. Consistent with the compression test, Material B was applied in this scenario. The simulation results were compared with experimental data from the literature (Liang et al., 2025).

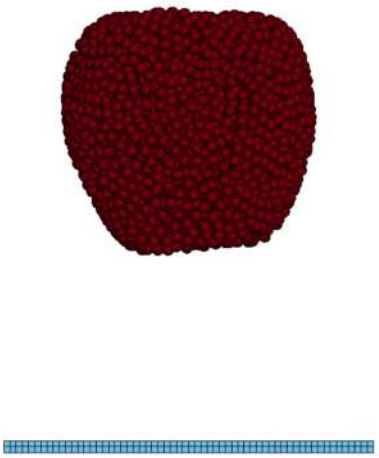

Fig.2-Drop test model

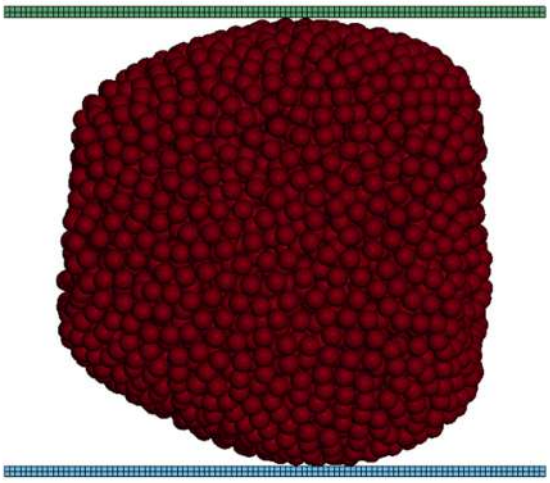

Fig.3-Compression test model

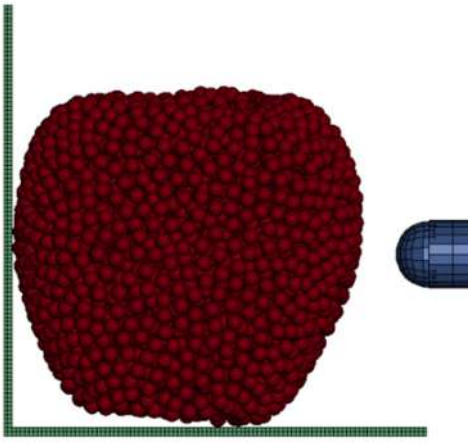

Fig.4-Impact test model

RESULTS & DISCUSSION

In this study, the mechanical behavior and dynamic response of apple tissue were systematically evaluated through three numerical testing scenarios: a drop test, a quasi-static compression test, and a high-velocity impact test. FEM and DEM models with varying particle resolutions (5 mm and 2 mm) were developed to assess their predictive accuracy against experimental reference data. The following sections present the detailed results, focusing on the influence of particle size effect, energy transmission, and structural convergence between the discrete and continuum modeling approaches.

Drop Test: The relationship between peak impact force and drop heights (10 cm, 20 cm, 40 cm, and 60 cm) is summarized in Fig.5. The reference data demonstrate a near-linear increase in peak impact force corresponding to the increase in potential energy. The FEM model slightly underestimated this peak force but accurately captured the overall trend. The DEM models

exhibited strong size-dependent behavior. The DEM 5 mm model recorded the lowest peak forces across all heights, indicating an overly compliant structural response. The DEM 2 mm model successfully converged with the FEM results, confirming that a sufficiently fine particle resolution allows the discrete element framework to match the dynamic force transmission capabilities of continuum models.

Compression test: The macroscopic force-displacement responses under quasi-static compression for the FEM, various DEM resolutions, and reference data are presented in Fig.6. The FEM model closely matched the reference experimental data throughout the 5 mm loading phase. A distinct size effect was observed across the DEM configurations: the model using 5 mm particles exhibited the softest mechanical response, significantly underestimating the compression force. As the particle diameter decreased from 5 mm to 2 mm, the macroscopic stiffness increased, and the force-displacement curve progressively converged toward the FEM baseline and reference data. The DEM 2 mm model demonstrated the highest fidelity, effectively replicating the continuum-level viscoelastic behavior of the apple tissue.

Impact test: The dynamic impact deformation-time histories at 0.81 m/s and 1.65 m/s are plotted in Fig.7 and Fig.8, respectively. In both velocity scenarios, the DEM models exhibited a clear convergence trend: decreasing the particle size from 5 mm to 2 mm progressively increased the peak deformation, making the DEM 2 mm response almost identical to the FEM prediction. However, an important unfavorable result must be noted: compared to the physical reference data, both the converged DEM 2 mm model and the traditional FEM model consistently underestimated the peak deformation. At an impact velocity of 1.65 m/s, the reference data recorded a peak deformation of approximately 10.2 mm, whereas the FEM and DEM 2 mm models peaked at only about 9.0 mm. This discrepancy indicates that while the current viscoelastic parameters and cohesive bond settings can capture macroscopic stiffness, they cannot fully replicate the localized, high-strain-rate cellular failure mechanisms. The underestimation is likely because macroscopic bonded particle models and FEM material cards struggle to simulate the local liquefaction of ruptured cells and the subsequent loss of turgor pressure during rapid dynamic loading. Furthermore, dimensional differences may also contribute to this error: the apple model used in this study has a diameter of 8 cm, whereas the experimental samples in the reference literature had a diameter of approximately 9 cm.

The DEM models demonstrated significant computational advantages. Specifically, while the traditional FEM viscoelastic model required [24 minutes] to complete the simulation, the highest-resolution DEM model (2 mm) only took [9 minutes], achieving a reduction in computation time of approximately 50%. These results confirm that a 2 mm particle diameter is the optimal convergence point, balancing high macroscopic accuracy with superior computational efficiency. Future development of multi-scale or hybrid DEM models will help address current limitations in predicting localized cellular damage.

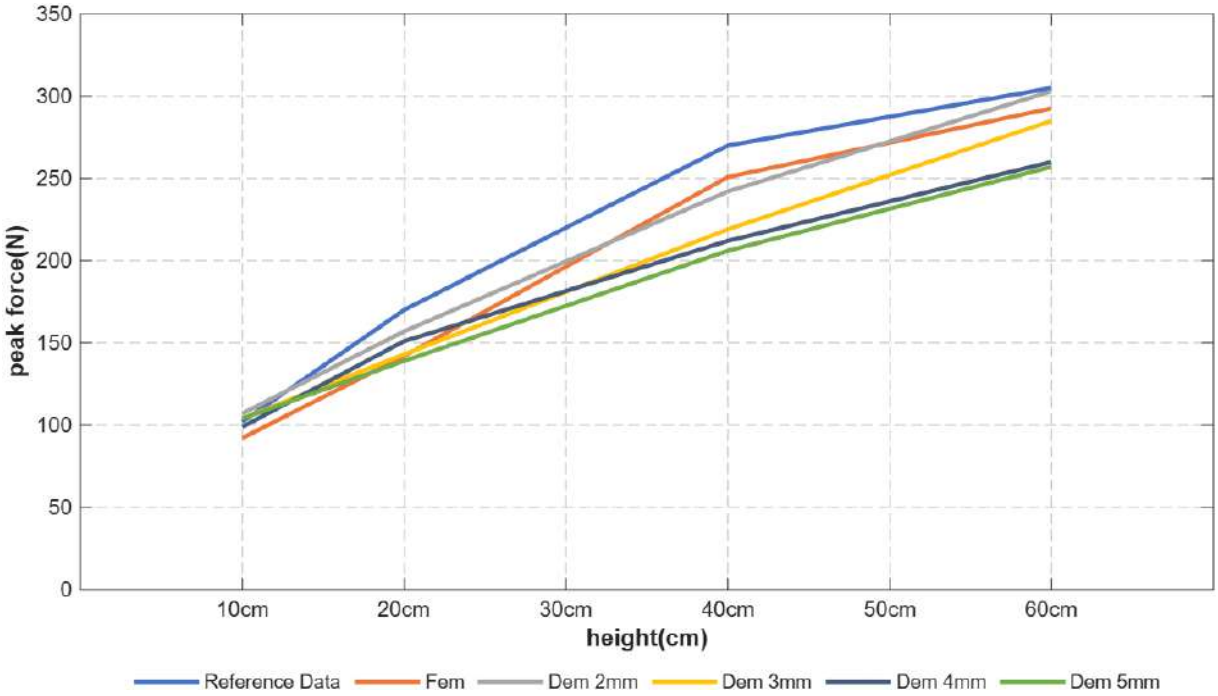

Fig.5- Peak impact force versus drop height for FEM and DEM models.

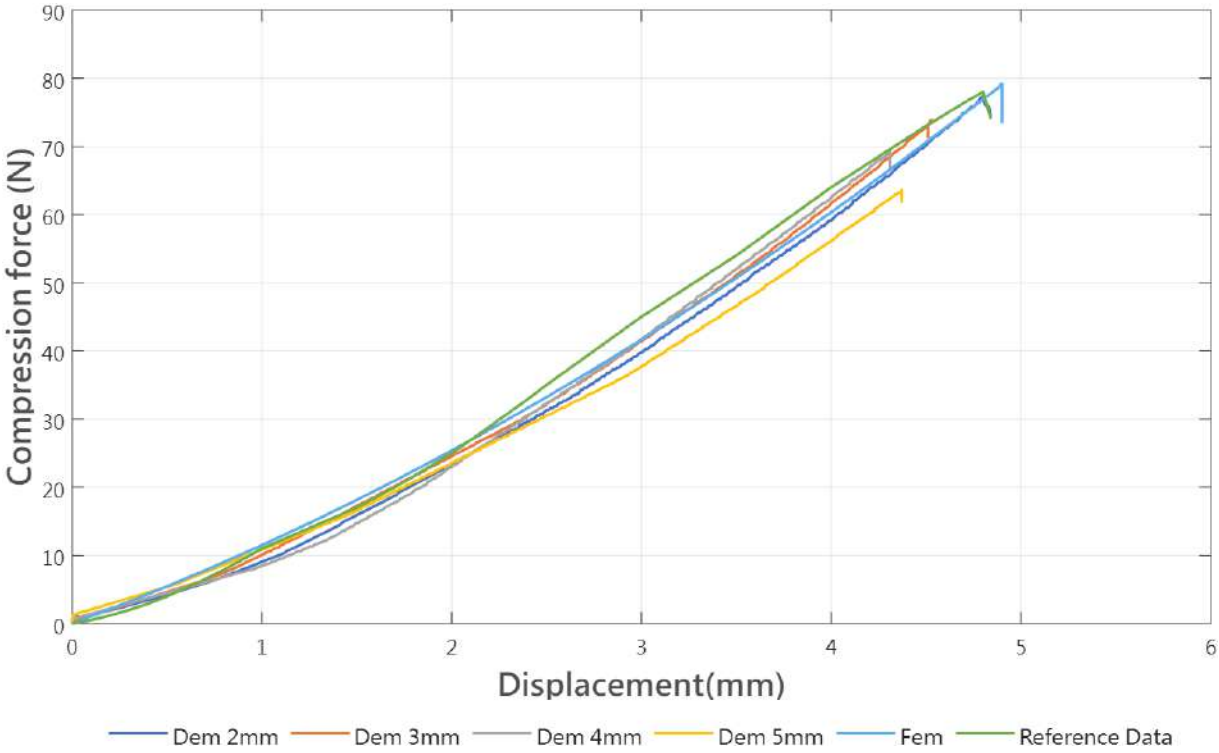

Fig.6- Force-displacement curves under quasi-static compression for FEM and DEM models.

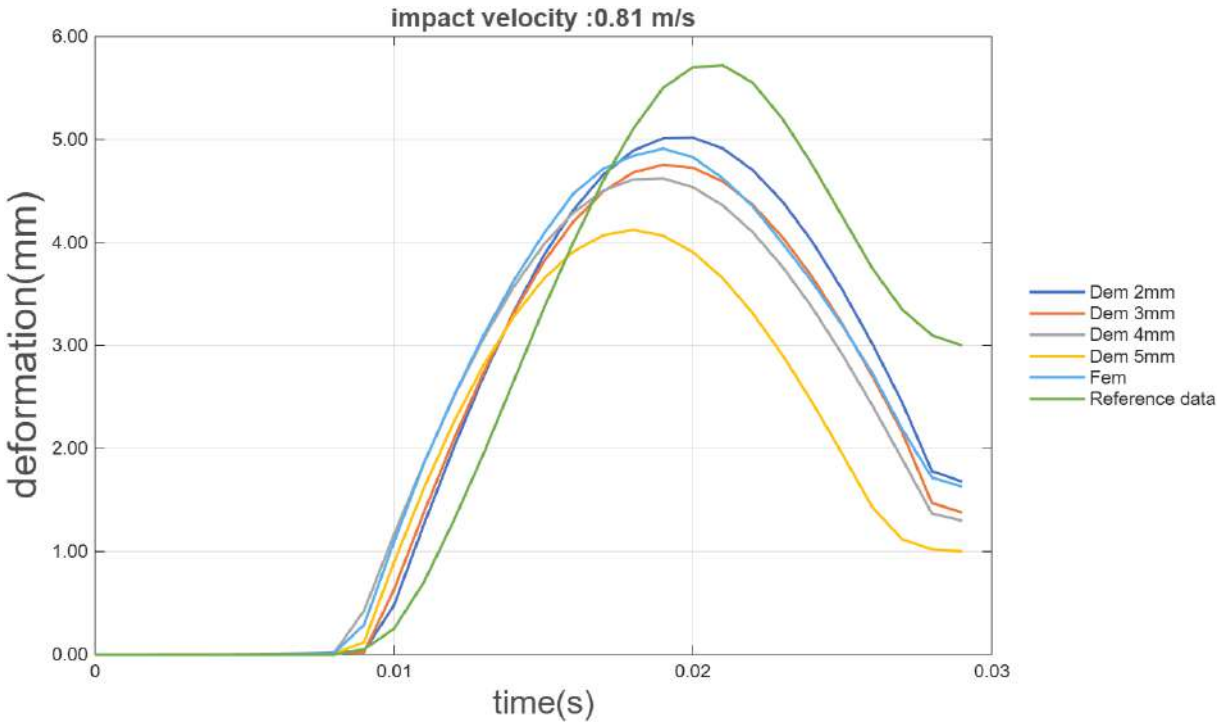

Fig.7- Comparison of deformation-time histories at an impact velocity of 0.81 m/s among reference data, FEM, and DEM models with varying particle resolutions.

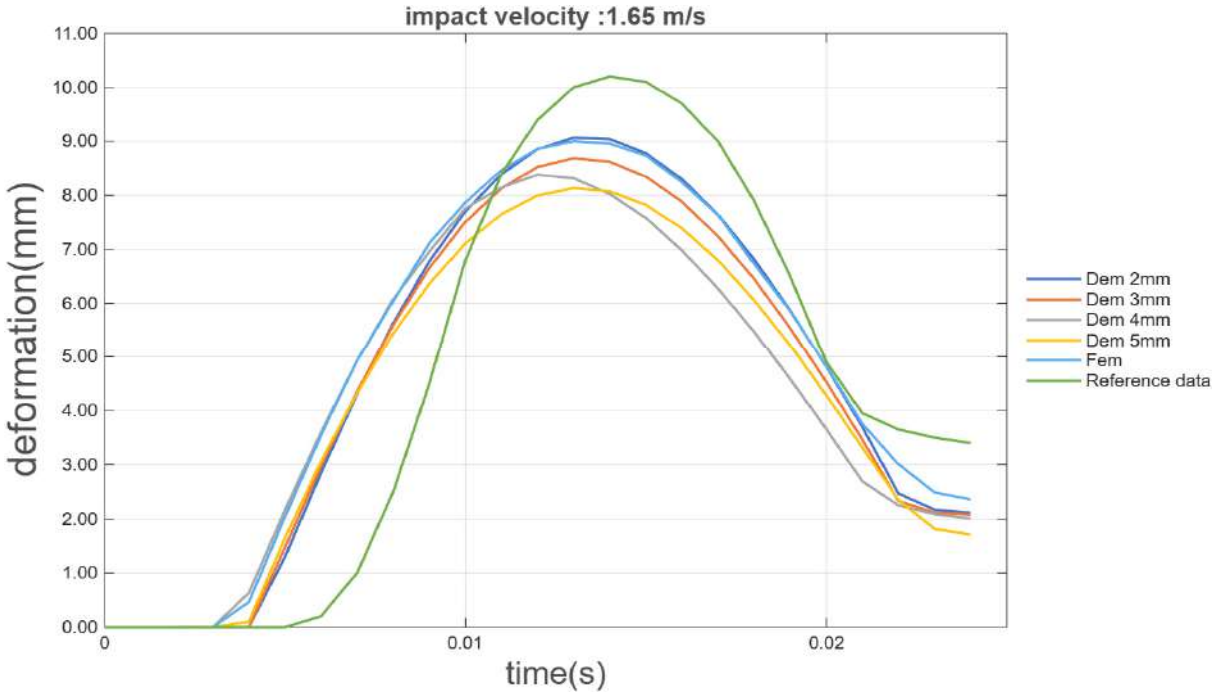

Fig.8- Comparison of deformation-time histories at an impact velocity of 1.65 m/s among reference data, FEM, and DEM models with varying particle resolutions.

CONCLUSIONS

This study applied a Discrete Element Method (DEM) approach to evaluate the mechanical responses of apples under various loading conditions. The investigation into particle size effects revealed that reducing the particle diameter to 2 mm enables the DEM model to accurately converge with FEM macroscopic predictions in quasi-static compression, free-fall drop tests, and dynamic impacts. Notably, the converged 2 mm DEM model achieved this high macroscopic fidelity while reducing computational time by more than 50% compared to the viscoelastic FEM approach.

However, limitations remain in capturing high-strain-rate localized cellular damage. Both DEM and FEM models underestimated peak deformations under high dynamic impacts, showing that relying solely on macroscopic material parameters is insufficient to accurately replicate microscopic mechanisms such as localized cellular liquefaction and turgor pressure loss following impact rupture. Future research can focus on developing more refined multi-scale or hybrid DEM models to enhance overall model fidelity. This advancement will help bridge the gap in microscopic damage prediction, ultimately providing a highly reliable numerical tool for optimizing agricultural machinery design and post-harvest packaging.

In the future, the development of multi-particle-size hybrid models can further enhance model fidelity and improve the accuracy of damage prediction, providing a highly reliable numerical analysis method for agricultural machinery design, post-harvest packaging, and harvest protection.

ACKNOWLEDGEMENTS

This work was supported by the National Science and Technology Council Grant No. MOST NSTC 114-2221-E-019-006-MY2.

REFERENCES

Kafashan, J., J. Wiacek, H. Ramon, and A. M. Mouazen. 2021. Modelling and simulation of fruit drop tests by discrete element method. *Biosystems Engineering* 212: 228-240.

Liang, Z., Z. Zhou, Y. Huang, and H. Yang. 2025. Assessing apple bruise susceptibility using the discrete element method. *Journal of Food Engineering* 394: 112517.

Scheffler, O. C., C. J. Coetzee, and U. L. Opara. 2018. A discrete element model (DEM) for predicting apple damage during handling. *Biosystems Engineering* 172: 29-48.

PH-02

Proceedings of The 12th International Symposium on Machinery and Mechatronics for Agriculture and Biosystems Engineering (ISMAB 2026)
20-24 October 2026, Busan, Republic of Korea

COLOR–UV IMAGE FUSION FOR NONDESTRUCTIVE PREDICTION OF EDAMAME WATER AND FRUCTOSE CONTENT

Takumi Murai[1], Gao Tianqi[2], Mayume Adachi[1], Yoshito Saito[2*]

[1]Graduate School of Science and Technology, Niigata University, 8050 Ikarashi 2-no-cho, Nishi-ku, Niigata 950-2181, Japan
[2]Faculty of Agriculture, Niigata University, 8050 Ikarashi 2-no-cho, Nishi-ku, Niigata 950-2181, Japan
*Corresponding Author-- Voice: +81-80-5491-1281, Email: ysaito@agr.niigata-u.ac.jp

Abstract: Nondestructive estimation of visitable soybean (edamame) quality traits can support postharvest grading, breeding evaluation, and processing decisions, but the value of combining visible color and ultraviolet (UV) images for physicochemical regression remains insufficiently quantified. This study evaluated paired Color RGB and UV RGB images for predicting edamame water content and fructose content. A dataset of 165 paired samples from two harvest years (2023, cultivar 'Yuagari Musume', n = 132; 2024, cultivar 'Sakanamame', n = 33) was used to compare Color-only, UV-only, and early Color+UV fusion inputs under an identical year-balanced 5-fold cross-validation design. Fusion images were represented as 6-channel tensors with Color RGB followed by UV RGB. ResNet-18 regression models were trained for independent water-content prediction, independent fructose-content prediction, and joint two-target prediction, yielding 45 formal training runs. For independent water-content prediction, Color+UV fusion achieved the lowest validation error, with MAE, RMSE, and R^2 of 1.47 ± 0.17 %, 1.88 ± 0.20 %, and 0.78 ± 0.03, respectively, corresponding to MAE reductions of 7.44% relative to Color RGB and 10.89% relative to UV RGB. For independent fructose-content prediction, fusion also produced the lowest mean MAE (0.15 ± 0.02 g/100 g DW), but the improvement was smaller (2.00% and 1.67% relative to Color RGB and UV RGB, respectively). Joint two-target training did not consistently improve either trait relative to independent single-target models. These results indicate that early Color-UV fusion is most beneficial for edamame water-content regression, while fructose-content prediction may benefit from additional spectral or biochemical information.

Key Words: Edamame; Ultraviolet imaging; Image fusion; Deep learning; Quality assessment.

INTRODUCTION

Edamame, the immature form of vegetable soybean (Glycine max L. Merr.), is valued for its fresh sensory profile, texture, sweetness, and nutritional composition. Water content and sugar-related compounds such as fructose change markedly with maturity and are widely used as indicators of harvest timing and eating quality (Sugimoto et al., 2010; Carneiro et al.,

2020; Wang et al., 2024). Because reference measurements for water and sugar content are destructive and labor-intensive, rapid and nondestructive estimation methods would be valuable for grading, storage monitoring, breeding trials, and process control.

Machine vision and spectral sensing offer nondestructive alternatives for quality evaluation, and deep learning has been applied widely to agricultural and food product assessment (Palumbo et al., 2023; Fakhlaei et al., 2024). Hyperspectral imaging can provide rich spectral information but is often expensive and complex (Barbedo, 2023); a lower-complexity alternative is to combine conventional color images with UV-excited fluorescence images, which may capture surface chemistry not fully expressed in visible appearance (Momin et al., 2023). Fusing RGB and hyperspectral information has recently improved vegetable soybean freshness classification (Bu et al., 2024). Using the same sample set, our group has separately reported a PLSR model based on color/fluorescence image features (Adachi et al., 2025) and a dual-input CNN with independent modality branches (Murai et al., 2026); however, pixel-level early fusion of Color and UV images for edamame water- and fructose-content regression has not yet been evaluated under a controlled cross-validation design.

The objective of this study was to evaluate early fusion of paired Color RGB and UV RGB images for nondestructive prediction of edamame water content and fructose content, by comparing Color-only, UV-only, and Color+UV fusion inputs, and independent versus joint two-target regression, under an identical year-balanced 5-fold cross-validation protocol using a ResNet-18 backbone.

MATERIALS AND METHODS

Plant material and reference measurements

Edamame pods were harvested in Niigata Prefecture, Japan. The dataset comprised 165 paired samples: 132 pods of cultivar 'Yuagari Musume' harvested from two fields between 19 July and 7 August 2023 (seven harvest dates spanning near-optimal maturity to slight pod yellowing), and 33 pods of cultivar 'Sakanamame' purchased from a local retail market in Niigata City, Japan on 26–27 September 2024 as an additional-year sample set (Table 1). For each sample, a paired Color RGB image, a UV-excited fluorescence image, water content, and fructose content were recorded.

Water content (%) was calculated as (wb − wd)/wb × 100, where wb and wd are the weights of

Table 1. Dataset composition and target distributions by year. Values are mean ± standard deviation.

Year	Samples	Water content (%)	Fructose content (g/100 g DW)
2023	132	72.08 ± 3.33	0.49 ± 0.33
2024	33	65.46 ± 1.50	0.39 ± 0.13
All	165	70.75 ± 4.04	0.47 ± 0.31

the vacuum-packed, boiled kernels before and after freeze-drying, respectively, measured with an electronic balance (GR-60, AS ONE). Fructose content (g/100 g DW) was quantified from kernel extracts using an ACQUITY UPLC system with an ACQUITY QDa mass detector (Waters); fructose was selected as the sugar-related target because it showed clear, consistent changes with harvest date in prior work on the same samples. Water content ranged from 63.03–77.90% (mean 70.75 ± 4.04%) and fructose content ranged from 0.03–1.85 g/100 g DW (mean 0.47 ± 0.31 g/100 g DW).

Image acquisition and Color–UV fusion input

Color images were captured under white LED illumination (LDL2-80X16SW2, CCS) with a polarizing filter to suppress specular reflection. UV-excited fluorescence images were captured under 365 nm UV LED illumination (LDL-71X12UV2-365-N, CCS) with a 390 nm cut-off UV-cut filter on the lens to exclude reflected UV light, so the recorded signal represents fluorescence emission rather than reflected UV. Both image types were acquired with a digital SLR camera (EOS Kiss X7, Canon; 70 mm macro lens, Sigma) at F5.6, ISO 800 (shutter speed 1/25 s for color, 1/5 s for fluorescence). Pod regions were segmented from the color image by Otsu thresholding with noise removal and hole filling; the resulting mask was applied to both images, which were cropped, zero-padded to a 1:1 aspect ratio, and resized to 512 × 512 pixels.

For the fusion experiments, the paired Color RGB and UV RGB arrays were concatenated along the channel dimension in the fixed order Color R, G, B, UV R, G, B, forming a 512 × 512 × 6 tensor (Figure 1). This early-fusion representation preserves spatial alignment at the input level and allows the convolutional backbone to learn joint filters across the visible and UV-excited fluorescence channels.

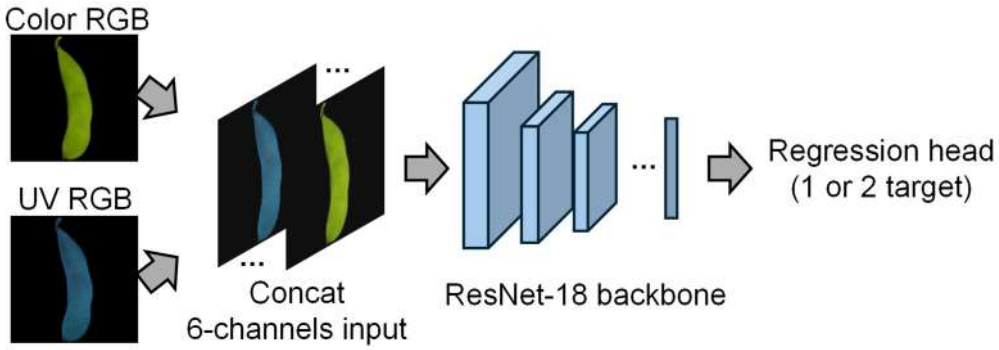

Figure 1. Early Color-UV fusion and ResNet-18 regression architecture. Paired Color RGB and UV-excited fluorescence (UV RGB) inputs are concatenated in the fixed channel order Color R, G, B, UV R, G, B to form a 512×512×6 fusion tensor, processed by a 6-channel-adapted ResNet-18 backbone with a linear regression head.

Cross-validation design and model training

A deterministic 5-fold cross-validation protocol with year-balanced folds was used for all comparisons, so that every validation fold contained samples from both 2023 and 2024 and all modality/task combinations shared identical fold assignments. The experimental matrix

comprised three input modalities (Color RGB, UV RGB, Color+UV fusion) and three prediction settings (water-only, fructose-only, joint water+fructose), yielding 45 formal training runs across five folds.

All models used a ResNet-18 backbone (He et al., 2016) initialized from ImageNet-pretrained weights. For the 6-channel fusion input, the first convolutional layer was adapted by repeating the pretrained 3-channel kernel and scaling it by the channel-count ratio; the classification head was replaced with a linear regression head (output dimension 1 for single-target models, 2 for joint models). Models were trained with AdamW (lr 1×10 ⁴, weight decay 0.05; Loshchilov and Hutter, 2019) for 300 epochs with cosine-annealing scheduling and an effective batch size of 32. Training used horizontal random flipping and mean-squared-error loss on train-fold standardized targets, and only the final-epoch checkpoint was retained. The implementation used MMPreTrain 1.2.0 (MMPreTrain Contributors, 2023) with project-local modules for the fusion backbone, heads, and metrics.

Evaluation metrics

Model performance was evaluated using mean absolute error (MAE), root mean squared error (RMSE), and coefficient of determination (R^2), computed after inverse transformation to the original target scale:

$$\mathrm{MAE} = \frac{1}{n}\sum_{i=1}^{n}|y_i - \hat{y}_i| \tag{1}$$

$$\mathrm{RMSE} = \sqrt{\frac{1}{n}\sum_{i=1}^{n}(\hat{y}_i - y_i)^2} \tag{2}$$

$$R^2 = 1 - \frac{\sum_{i=1}^{n}(y_i - \hat{y}_i)^2}{\sum_{i=1}^{n}(y_i - \bar{y})^2} \tag{3}$$

where yi and ŷi are the observed and predicted values, ȳ is the mean observed value, and n is the number of validation samples.

Results are reported as mean ± standard deviation across the five validation folds; no independent held-out test set was used in the formal experiment.

RESULTS & DISCUSSION

The dataset showed a clear year imbalance (80.0% of samples from 2023, 20.0% from 2024). The 2024 samples had lower mean water content (65.46 ± 1.50% vs. 72.08 ± 3.33% for 2023) and lower mean fructose content (0.39 ± 0.13 vs. 0.49 ± 0.33 g/100 g DW for 2023). The year-balanced 5-fold protocol preserved both years in every validation fold and reused identical fold assignments for all 45 runs, so paired modality comparisons were not confounded by differing fold composition.

For independent water-content prediction, Color+UV fusion achieved the best mean validation performance (Table 2): MAE 1.47 ± 0.17%, RMSE 1.88 ± 0.20%, and R^2 0.78 ± 0.03, versus

MAE 1.59 ± 0.20% for Color RGB and 1.65 ± 0.29% for UV RGB — reductions of 7.44% and 10.89%, respectively. For independent fructose-content prediction, fusion again had the lowest mean MAE (0.15 ± 0.02 g/100 g DW) and RMSE, but the improvement over Color RGB and UV RGB was only 2.00% and 1.67%, respectively — a much smaller fusion effect than for water content.

Table 2. Single-target regression performance. Values are mean ± standard deviation across five year-balanced validation folds.

Target	Modality	MAE	RMSE	R^2
Water content	Color RGB	1.59 ± 0.20 %	2.01 ± 0.29 %	0.75 ± 0.05
Water content	UV RGB	1.65 ± 0.29 %	2.08 ± 0.34 %	0.73 ± 0.06
Water content	Color+UV fusion	1.47 ± 0.17 %	1.88 ± 0.20 %	0.78 ± 0.03
Fructose content	Color RGB	0.15 ± 0.02	0.20 ± 0.04	0.54 ± 0.06
Fructose content	UV RGB	0.15 ± 0.01	0.20 ± 0.03	0.56 ± 0.06
Fructose content	Color+UV fusion	0.15 ± 0.02	0.19 ± 0.04	0.57 ± 0.11

In the joint water+fructose setting, fusion again gave the best water-content performance (MAE 1.51 ± 0.19%, an 11.12% reduction relative to Color RGB and 8.19% relative to UV RGB), and the lowest joint fructose-content MAE (0.15 ± 0.01 g/100 g DW), though the joint-model margins were minimal (≤0.86%). For both targets, the best result came from the independent fusion models rather than the joint models, indicating that the shared two-output representation did not provide a consistent advantage over target-specific regression heads.
The consistent improvement for water-content prediction is attributable to the input modality rather than experimental setup, since fold assignments, scaling, backbone, and schedule were held constant across modalities. Because the UV images are visible fluorescence images captured under 365 nm UV excitation rather than reflected-UV images, the complementary information likely reflects fluorescence-related surface responses in addition to the color, shape, and texture captured by the visible images.

Fructose-content prediction benefited less from fusion, consistent with fructose being an internal soluble-sugar trait that is not itself fluorescent and is only indirectly reflected in surface optical signals. A related dual-input CNN using the same dataset, with independent color and fluorescence branches fused at the feature level, achieved comparable accuracy (RMSE 0.20 g/100 g DW, R^2 0.54; Murai et al., 2026), and a PLSR baseline using handcrafted texture features achieved similar accuracy for both traits (Adachi et al., 2025). This suggests that branch-wise or feature-level fusion may extract fluorescence-related information at least as effectively as pixel-level concatenation for sugar-related traits.

This study has several limitations: the dataset was modest (n = 165) with an imbalanced year distribution; only early channel-level fusion was tested; and a single backbone (ResNet-18) was used. Future work should validate the approach on independent years and cultivars, and compare early fusion with branch-based fusion and multi-task formulations to improve fructose prediction.

CONCLUSIONS

This study compared Color RGB, UV RGB, and early Color+UV fusion for edamame water- and fructose-content regression under a year-balanced 5-fold cross-validation protocol. Across 45 formal runs, Color+UV fusion gave the best water-content performance in both independent and joint settings (independent fusion model: MAE 1.47 ± 0.17%, R^2 0.78 ± 0.03) and the lowest mean fructose-content MAE, though with a small margin. Joint two-target training did not consistently outperform independent single-target models. These findings support early Color-UV fusion as a promising, low-cost approach for edamame water-content estimation, while richer sensing or larger datasets may be needed for robust fructose-content prediction.

ACKNOWLEDGEMENTS

This work was supported by JSPS KAKENHI Grant Numbers JP25K22399 and JP25K02127, and by JSPS Research Fellowship for Young Scientists Grant Number 26KJ1244. The authors gratefully acknowledge this support.

REFERENCES

Adachi, M., T. Gao, T. Kaho, N. Otake, and Y. Saito. 2025. Estimation of maturity-related quality of edamame based on features of color and fluorescence images. Artificial Intelligence and Data Science 6(3): 912-924.

Barbedo, J. G. A. 2023. A review on the combination of deep learning techniques with proximal hyperspectral images in agriculture. Computers and Electronics in Agriculture 210: 107920.

Bu, Y., J. Hu, C. Chen, S. Bai, Z. Chen, T. Hu, G. Zhang, N. Liu, C. Cai, Y. Li, Q. Xuan, Y. Wang, Z. Su, Y. Xiang, and Y. Gong. 2024. ResNet incorporating the fusion data of RGB & hyperspectral images improves classification accuracy of vegetable soybean freshness. Scientific Reports 14: 2568.

Carneiro, R. C. V., S. E. Duncan, S. F. O'Keefe, Y. Yin, C. L. Neill, and B. Zhang. 2020. Sensory and consumer studies in plant breeding: A guidance for edamame development in the U.S. Frontiers in Sustainable Food Systems 4: 124.

Fakhlaei, R., A. Amani Babadi, C. Sun, N. Mat Ariffin, A. Khatib, J. Selamat, and X. Zou. 2024. Application, challenges and future prospects of recent nondestructive techniques based on the electromagnetic spectrum in food quality and safety. Food Chemistry 441: 138402.

He, K., X. Zhang, S. Ren, and J. Sun. 2016. Deep residual learning for image recognition. In Proc. IEEE Conf. Computer Vision and Pattern Recognition, 770-778.

Loshchilov, I., and F. Hutter. 2019. Decoupled weight decay regularization. In Int. Conf. Learning Representations.

MMPreTrain Contributors. 2023. OpenMMLab's pre-training toolbox and benchmark. Available at: https://github.com/open-mmlab/mmpretrain.

Momin, A., N. Kondo, D. F. Al Riza, Y. Ogawa, and D. Obenland. 2023. A methodological review of fluorescence imaging for quality assessment of agricultural products. Agriculture 13(7): 1433.

Murai, T., K. Itakura, M. Adachi, and Y. Saito. 2026. Estimation of maturity-related components in edamame pods using a dual-input CNN with color and fluorescence images. AI and Data Science J., in press.

Palumbo, M., M. Cefola, B. Pace, G. Attolico, and G. Colelli. 2023. Computer vision system based on conventional imaging for non-destructively evaluating quality attributes in fresh and packaged fruit and vegetables. Postharvest Biology and Technology 200: 112332.

Sugimoto, M., H. Goto, K. Otomo, M. Ito, H. Onuma, A. Suzuki, M. Sugawara, S. Abe, M. Tomita, and T. Soga. 2010. Metabolomic profiles and sensory attributes of edamame under various storage duration and temperature conditions. J. Agric. Food Chem. 58(14): 8418-8425.

Wang, P., D. Liu, D. Ni, S. Gao, Y. Hao, C. Xue, X. Chen, J. Zhao, H. Xing, and N. Guo. 2024. Genome-wide association study of sucrose content in vegetable soybean. BMC Plant Biology 24: 1264.

PH-03

Proceedings of The 12th International Symposium on Machinery and Mechatronics for Agriculture and Biosystems Engineering (ISMAB 2026)
20-24 October 2026, Busan, Republic of Korea

EFFECTS OF HYDROSTATIC PRESSURE TREATMENT ON THE FUNCTIONAL PROPERTIES OF BLACK GARLIC

Sayaka Nishi[1], Chandan Das[2], Takahisa Nishizu[3,4], Teppei Imaizumi[3,4*]

[1] Graduate School of Natural Science and Technology, Gifu University, 1-1 Yanagido, Gifu-city, Gifu, Japan
[2] Faculty of Chemical Engineering, Indian Institute of Technology Guwahati, Assam-781039, Guwahati, Assam, India
[3] Faculty of Applied Biological Sciences, Gifu University, 1-1 Yanagido, Gifu-city, Gifu, Japan
[4] Preemptive Food Research Center, Gifu University, 1-1 Yanagido, Gifu-city, Gifu, Japan
* Corresponding author: Tel: +81-58-293-2930; Email: Imaizumi.teppei.j6@f.gifu-u.ac.jp

Abstract: In recent years, various pretreatments have been investigated in food processing to improve subsequent processing efficiency and the functional properties of final products. However, few studies have investigated the application of hydrostatic pressure treatment to black garlic production. In this study, the effects of hydrostatic pressure pretreatment on the physicochemical properties and bioactive potential of black garlic were evaluated. Hydrostatic pressure treatment induced changes in the internal cellular structure of garlic, as indicated by electrical impedance measurements and scanning electron microscopy (SEM) observations. Black garlic produced following hydrostatic pressure treatment at 100 MPa showed enhanced browning and a slightly lower pH, as well as higher levels of total phenolic and flavonoid compounds and antioxidant activity. These results suggest that hydrostatic pressure treatment may enhance the release or extractability of bioactive compounds and accelerate browning during subsequent thermal processing. The results indicate that hydrostatic pressure treatment has potential for improving the production of black garlic.

Key Words: Black Garlic, Hydrostatic Pressure Treatment, Bioactive Compounds, Antioxidant Activity, Maillard Reaction

INTRODUCTION

Black garlic is produced from fresh garlic through a prolonged aging process, typically for about one month at high temperatures (approximately 70 °C) and high relative humidity (approximately 80 %) (Karishma et al., 2025). It is widely consumed in Asia due to its nutritional, biological, and potential health-promoting properties.

In recent years, various pretreatments have been investigated in food processing to improve subsequent processing efficiency and the functional properties of final products. Among these methods, hydrostatic pressure treatment is a non-thermal processing technique that can

induce changes in the structure and composition of endogenous food components, even at relatively moderate pressures such as 100 MPa (Navarro-Baez et al., 2022). However, few studies have examined the application of hydrostatic pressure treatment to black garlic production.
Therefore, the objective of this study was to evaluate the effects of hydrostatic pressure treatment on the physicochemical properties and bioactive potential of black garlic.

MATERIALS AND METHODS

Garlic cloves were peeled and vacuum-sealed in plastic bags. The samples were subjected to hydrostatic pressure treatment at 50 or 100 MPa for 2 days at approximately 40 °C. Following hydrostatic pressure treatment, the garlic samples were heated at 80 °C for 3 days and subsequently dried at 70 °C. Table 1 shows the appearance of the garlic under each condition. The dried samples were finely ground, and extracts were prepared by adding 10 volumes of 70% ethanol to the ground garlic. The mixture was thoroughly mixed and subjected to ultrasonication for 30 min, followed by filtration. The filtrate was centrifuged at 3,500 rpm for 1 h, and the resulting supernatant was collected for analysis.

For SEM observation, thinly sliced and freeze-dried garlic samples were coated with osmium and examined using a scanning electron microscope. Electrical impedance was measured by inserting two needle electrodes to a depth of 1 cm into each garlic clove. Color differences and browning intensity were measured according to the methods described by Li et al (2020) and Y. T. Chen et al (2020), respectively. pH was measured by using a pH meter. Total phenolic content and DPPH activity were measured according to the method described by Das et al (2018). Total flavonoid content was measured according to the method described by Bulut et al (2019). ABTS activity and FRAP assay were measured according to the methods described by Toledano Medina et al (2019) and Wang et al (2015), respectively.

Table.1 Appearance of garlic under each condition.

	Raw	50 MPa	100 MPa
Non-heat			
Heat			

RESULTS & DISCUSSION

Evaluation of color difference and browning intensity indicated that hydrostatic pressure treatment accelerated browning during subsequent thermal processing, suggesting its potential to improve processing efficiency in black garlic production. Electrical impedance measurements showed a tendency for the impedance arc to decrease following pressure treatment. In addition, SEM observations revealed small pores within the internal tissue of pressure-treated garlic. These structural changes suggest that hydrostatic pressure treatment disrupted the cellular structure and may have compromised cell membrane integrity.

Furthermore, black garlic produced following hydrostatic pressure treatment contained significantly higher levels of total phenolic and flavonoid compounds than the untreated control (Fig. 1). The DPPH, ABTS, and FRAP assays also demonstrated that black garlic prepared following hydrostatic pressure treatment exhibited high antioxidant activity. These effects may be associated with pressure-induced disruption of the cellular structure, which could enhance the release or extractability of bioactive compounds and facilitate subsequent Maillard reactions during thermal processing.

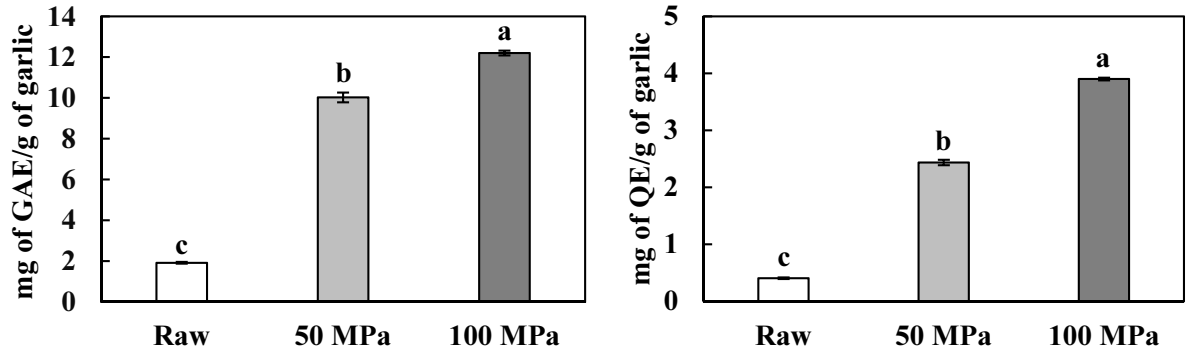

Fig.1 Bioactive compounds in garlic under each condition.
(Left: Total Phenolic Content (TPC), Right: Total Flavonoid Content (TFC))

CONCLUSIONS

Hydrostatic pressure treatment accelerated browning during subsequent thermal processing and enhanced the bioactive properties of black garlic. These findings suggest that hydrostatic pressure treatment has potential as an effective approach for improving the efficiency and functional properties of black garlic production.

REFERENCES

Bulut O, Akın D, Sönmez Ç, Öktem A, Yücel M and Öktem HA. 2019. Phenolic compounds, carotenoids, and antioxidant capacities of a thermo-tolerant Scenedesmus sp. (Chlorophyta) extracted with different solvents. Journal of Applied Phycology. 31: 1675–1683.

Chen, Y. T., Chen, Y. A., Lee, C. H., Wu, J. T., Cheng, K. C. and Hsieh, C. W. 2020. A strategy for promoting γ-glutamyltransferase activity and enzymatic synthesis of

S-allyl-(L)-cysteine in aged garlic via high hydrostatic pressure pretreatments. Food Chemistry, 316(February), 126347.
Das AB, Goud V V. and Das C. 2018. Extraction and characterization of phenolic content from purple and black rice (Oryza sativa L) bran and its antioxidant activity. Journal of Food Measurement and Characterization. 12: 332–345.
Karishma, P., Khar, A., Vasudev, S., Kumar, A. and Patel, R. 2025. Harnessing the antioxidant potential of black garlic: A study on bioactive compounds in 29 Indian garlic genotypes. Food Bioscience, 70(May), 107020.
Li, F., Cao, J., Liu, Q., Hu, X., Liao, X. and Zhang, Y. 2020. Acceleration of the Maillard reaction and achievement of product quality by high pressure pretreatment during black garlic processing. Food Chemistry, 318(February), 126517.
Medina MÁT, Pérez-Aparicio J, Moreno-Ortega A and Moreno-Rojas R. 2019. Influence of variety and storage time of fresh garlic on the physicochemical and antioxidant properties of black garlic. Foods. 8:.
Navarro-Baez, J. E., Martínez, L. M., Welti-Chanes, J., Buitimea-Cantúa, G. V. and Escobedo-Avellaneda, Z. 2022. High Hydrostatic Pressure to Increase the Biosynthesis and Extraction of Phenolic Compounds in Food: A Review. Molecules, 27(5).
Wang X, Liu R, Yang Y and Zhang M. 2015. Isolation, purification and identification of antioxidants in an aqueous aged garlic extract. Food Chemistry. 187: 37–43.

PH-04

Proceedings of The 12th International Symposium on Machinery and Mechatronics for Agriculture and Biosystems Engineering (ISMAB 2026)
20-24 October 2026, Busan, Republic of Korea

DEEP LEARNING-BASED ESTIMATION OF INTERNAL GARLIC CLOVE TRAITS FROM EXTERNAL BULB IMAGES

Jinho Son[1], Seoeun Lee[1], Daewook Kwon[1], Juhee Lee[1], Wonyeol Choi[1], Bumseok Park[1], Youngjune An[1], Hyunggyu Park[2], Yushin Ha[1,2*]

[1]Department of Bio-Industrial Mechanical Engineering, Kyungpook National University, Daegu 41566, Republic of Korea
[2]Upland-field Machinery Research Center, Kyungpook National University, Daegu 41566, Republic of Korea
*Corresponding Author-- Voice: +82-10-4520-2115, Email: yushin72@knu.ac.kr

Abstract: Garlic bulb quality is closely related to internal clove traits, such as clove number and arrangement. However, these traits are difficult to evaluate without cutting the bulb, which limits their use in rapid grading and large-scale postharvest inspection. This study explored the possibility of estimating hidden clove traits from external images of intact garlic bulbs.

A paired image dataset was prepared by capturing external views of garlic bulbs before cutting and internal cut-section views after cutting. The cut-section images were used to obtain reference information on clove number and internal structure. A supervised deep learning approach was then used to learn the relationship between the external appearance of intact bulbs and the internal traits observed after cutting. In the prediction stage, only external RGB images were used, allowing the process to remain non-destructive.

The results indicated that external bulb images contained useful visual cues related to internal clove characteristics. The model was able to estimate clove number with an error of approximately one clove and also provided approximate spatial information on the internal clove-bearing region. Differences in prediction performance were observed between garlic types, suggesting that internal structural complexity affects the difficulty of non-destructive prediction. Bulbs with simpler internal organization were generally easier to estimate, whereas bulbs with many closely arranged cloves were more challenging.

These findings suggest that external RGB imaging can be used as a practical tool for estimating hidden internal traits of garlic bulbs without destructive cutting. Although the approach does not directly reconstruct the complete internal structure, it provides useful information for postharvest quality evaluation, grading, breeding selection, and high-throughput phenotyping. The study highlights the potential of image-based non-destructive assessment as a supportive technology for garlic quality management.

Key Words: Garlic; clove count prediction; non-destructive; RGB image

PH-05

Proceedings of The 12th International Symposium on Machinery and Mechatronics for Agriculture and Biosystems Engineering (ISMAB 2026)
20-24 October 2026, Busan, Republic of Korea

VISION-BASED SWEET CORN MATURITY IDENTIFICATION FOR AUTOMATED POST-HARVEST GRADING

YI-SIANG WANG[1*] , PO-CHUN WANG[2], BING-YUAN HSIEH[3], Wu-Yang Sean [4]

[1]Department of Bio-Industrial Mechatronics Engineering, National Chung Hsing University, Taiwan
[2]Department of Bio-Industrial Mechatronics Engineering, National Chung Hsing University, Taiwan
[3]Department of Bio-Industrial Mechatronics Engineering, National Chung Hsing University, Taiwan
[4]Department of Bio-Industrial Mechatronics Engineering, National Chung Hsing University, Taiwan

*Corresponding Author-- Voice:+886-906830597, Email:yihsiang0425@gmail.com

Abstract: The post-harvest maturity of sweet corn critically determines its fresh-market quality. Conventional manual inspection is labor-intensive, time-consuming, and susceptible to operator fatigue and subjective judgment. This study proposes a computer vision-based maturity identification method using the YOLO11 object detection framework, establishing an inspection dark chamber, an annotated corn silk feature dataset, and performance evaluations. The image acquisition setup employs an RGB camera positioned under uniform vertical illumination within a non-reflective dark chamber. Based on distinctive morphological and chromatic transitions of corn silks—shifting from pale green during the immature stage to withered dark brown upon maturity—a binary object detection model was trained. Experimental results demonstrated that the model achieved a mean average precision (mAP@0.5) of 98.9% on an independent test set. This confirms the feasibility of identifying maturity via external silk characteristics, providing a robust engineering foundation for integration with continuous conveyor mechanisms and high-speed pneumatic sorting lines.

Key Words: Sweet corn, Maturity identification, YOLO11, Object detection, Corn silk features

INTRODUCTION

Sweet corn is a widely cultivated fresh-market crop, with its post-harvest maturity directly determining ear quality and market value. Immature ears exhibit underdeveloped kernels

and insufficient sugar accumulation, whereas overmature ears undergo starch conversion, leading to degraded flavor. During post-harvest grading, identifying mature ears for fresh markets while discarding immature ones is critical to maintaining grading standards.

The chromatic and morphological properties of apical corn silks serve as reliable external indicators of ear maturity. Silks in the immature stage remain turgid and exhibit a pale green or yellowish-green hue; upon reaching optimal harvest maturity, they desiccate into a curled, dark brown state. However, conventional visual inspection is prone to operator fatigue and fluctuating ambient lighting, rendering grading consistency difficult to sustain.

The long-term objective of this research is to develop an automated grading system integrating continuous conveyors with high-speed pneumatic sorting mechanisms. The current phase establishes a fundamental computer vision system to validate the feasibility of deep learning-based maturity classification via corn silk features. This paper details the construction of an inspection dark chamber, dataset annotation, and model performance using YOLO11, providing an engineering benchmark for subsequent mechatronic integration and field deployment.

MATERIALS AND METHODS

2.1 System Architecture for Sweet Corn Maturity Vision Identification

This study developed a post-harvest maturity identification pipeline for sweet corn, encompassing image acquisition, feature annotation, and deep learning model training and evaluation. The system utilizes an RGB camera positioned above an inspection dark chamber to capture sample imagery under controlled lighting conditions. Subsequently, a binary maturity annotation standard was established based on the desiccation degree and chromatic variations of apical corn silks. The YOLO11 object detection framework was implemented for model training and validation, evaluating both feature identification capabilities and bounding box localization accuracy on corn silk targets.

2.2 Image Acquisition Setup and Hardware Configuration

To eliminate ambient lighting fluctuations and maintain consistent image quality, a custom inspection dark chamber was constructed. Auxiliary LED lighting was integrated to deliver stable, uniform illumination, effectively suppressing ambient stray light and minimizing shadows across the ear surface, following post-harvest optical compartment designs established in previous sorting systems (Chakraborty et al., 2023; Sun et al., 2026).

Image acquisition was conducted using a manual-focus RGB USB camera (Spedal Full HD) mounted vertically 450 mm directly above the sample, ensuring complete coverage of the apical silks and external surface textures. Captured RGB images were stored in a workstation for offline preprocessing and annotation. The primary specifications and parameters of each system module are summarized in Table 1.

Table 1. Specifications of the experimental image acquisition setup and computing platform.

Equipment Module	Component / Model	Main Specifications and Parameters
Image Acquisition Sensor	Integrated Color USB Camera (Spedal Full HD)	Resolution: 1920 × 1080, RGB color format, manual focus
Inspection Dark Chamber and Light Source	Dark chamber equipped with auxiliary LED array	Top-down vertical illumination, working distance: 450 mm
Model Training Workstation	Deep Learning Computing Workstation	Intel Core Ultra 9 285K CPU, NVIDIA GeForce RTX 5090 GPU (32 GB VRAM), 64 GB RAM

2.3 Binary Maturity Definition and Dataset Annotation

A total of 500 fresh sweet corn ears were collected from local production fields. Based on agricultural marketing standards and expert visual inspection criteria, binary polygon annotations were implemented focusing on the apical corn silk characteristics:(1) Mature ears exhibit deep golden-brown to dark-brown corn silks, characterized by significant desiccation, dehydration, and shriveled curling at the tips, with underlying plump and well-developed kernels that meet fresh-market quality specifications; (2) Immature ears display tender pale green or yellowish-green silks that remain turgid and hydrated without signs of withering, with apical kernels remaining underdeveloped and lacking sufficient sugar accumulation.

To ensure objective model evaluation and prevent data leakage, the original 500 images were partitioned into training (400 images), validation (50 images), and independent test (50 images) sets at an 8:1:1 ratio. Offline data augmentation—comprising random rotation (±15°), horizontal flipping, and random brightness adjustments (±15%)—was applied exclusively to the training set, expanding it to 1,200 images to mitigate overfitting. The validation and test sets remained unaugmented to preserve evaluation integrity.

2.4 Deep Learning Model Training

This study implemented the YOLO11 object detection framework to construct the sweet corn maturity identification model. The training procedure was executed on the computing platform specified in Table 1, where pre-trained weights were loaded and fine-tuned using the aforementioned augmented dataset.

Regarding hyperparameter configurations, the input image resolution was standardized to 640 × 640 pixels, the batch size was set to 32, and the model was trained for 100 epochs. Model performance was evaluated using Precision, Recall, mAP@0.5, and the comprehensive metric mAP@0.5:0.95 as quantitative validation benchmarks.

RESULTS & DISCUSSION

3.1 Performance Evaluation of Binary Maturity Identification Model

The quantitative evaluation results of the proposed model on the independent test set (50 unaugmented images) are summarized in Table 2. Under an Intersection over Union (IoU) threshold of 0.5, the model achieved a mean average precision (mAP@0.5) of 98.9%, maintaining a robust mAP@0.5:0.95 of 83.2% across multiple strict thresholds. The overall Precision and Recall reached 98.0% and 95.0%, respectively. These metrics demonstrate that utilizing apical corn silk desiccation and chromatic morphology as external harvest maturity criteria provides superior discriminative capacity and engineering feasibility for post-harvest grading.

Table 2. Evaluation performance of the YOLO11 model on the independent test set for binary sweet corn maturity identification.

Evaluation Item	**Precision (%)**	**Recall (%)**	**mAP@0.5 (%)**
Corn silk features	98.0	95.0	98.9

3.2 Technical Challenges and Pathways Toward Real-Time Detection

Although the current model demonstrates superior identification performance (mAP@0.5 of 98.9%), the inference workflow currently relies on workstation-based offline batch processing and has not yet been integrated into a conveyor setup for real-time inspection. In a future continuous grading system operating at belt speeds exceeding 1.0 m/s, the end-to-end inference latency per image must be constrained within 50 ms to ensure

synchronized actuation of pneumatic or mechanical rejection mechanisms (Sun et al., 2026).

CONCLUSIONS AND FUTURE WORK

This study established a post-harvest sweet corn maturity identification method based on the YOLO11 object detection framework. Integrating an inspection dark chamber with uniform vertical illumination effectively suppressed ambient stray light. Utilizing apical corn silk desiccation and chromatic features as grading criteria, the model achieved an mAP@0.5 of 98.9%, a comprehensive mAP@0.5:0.95 of 83.2%, and Precision and Recall of 98.0% and 95.0%, respectively, on an unaugmented independent test set. These results validate the high engineering feasibility of applying computer vision to sweet corn maturity grading.

To address current limitations regarding offline computing and physical production line integration, future work will focus on two major milestones: (1) porting the trained model onto embedded edge computing platforms (such as the NVIDIA Jetson series) to minimize inference latency and achieve real-time continuous video processing, and (2) interfacing the vision system with conveyors, programmable logic controllers (PLC), and high-speed pneumatic rejection valves to establish a fully automated post-harvest sorting line.

REFERENCES

Chakraborty, S. K., A. Subeesh, K. Dubey, D. Jat, N. S. Chandel, R. Potdar, N. R. N. V. G. Rao, and D. Kumar. 2023. Development of an optimally designed real-time automatic citrus fruit grading-sorting machine leveraging computer vision-based adaptive deep learning model. *Eng. Appl. Artif. Intell.* 120: 105826.

Sun, H., C. Lv, F. Li, L. Zhou, K. Niu, S. Bai, Z. Zhu, and H. Jiang. 2026. A study on cherry tomato visual sorting method based on YOLOv10 with small object enhancement and edge deployment. *J. Food Compos. Anal.* 158: 109470.

PH-06

Proceedings of The 12th International Symposium on Machinery and Mechatronics for Agriculture and Biosystems Engineering (ISMAB 2026)
20-24 October 2026, Busan, Republic of Korea

INTERNAL STRUCTURAL ANALYSIS UNCOVERS MICROSCALE WATER MOLECULAR DIFFUSION IN POSTHARVEST SPINACH

Kohaku Kawase[1], Shinichiro Kuroki[2*]

[1]Graduate School of Agricultural Science, Kobe University, 1-1 Rokkodai, Nada-ku, Kobe 6578501 Japan
[2]Graduate School of Agricultural Science, Kyoto University, Kitashirakawa Oiwake-cho, Sakyo-ku, Kyoto, 6068502 Japan
*Corresponding Author-- Voice: +81-75-753-6170, Email: kuroki.shinichiro.4c@kyoto-u.ac.jp

Abstract: In postharvest fruits and vegetables, changes in water dynamics within the tissue precede deterioration. Capturing such internal changes is important for understanding the mechanisms underlying early-stage freshness deterioration. Water molecular diffusion provides a means of probing these hidden internal changes. In particular, leafy vegetables have thin-layered tissue containing extensive intercellular air spaces. Interpreting storage-induced changes in water diffusion in such tissue thus requires consideration of not only the physicochemical properties of water but also concomitant changes in tissue microstructure. In this study, X-ray computed tomography (CT), which enables high-resolution three-dimensional visualization of tissue microstructure, was combined with nuclear magnetic resonance (NMR) measurements of the water self-diffusion coefficient in stored spinach leaves. The objective was to interpret water molecular diffusion behavior in terms of changes in internal leaf microstructure.
Hydroponically grown spinach (*Spinacia oleracea* L., cv. Orai) was harvested eight weeks after sowing and stored in an incubator at 20 °C for up to 8 days. Five plants were sampled at each time point (storage days 0, 2, 4, 6, and 8), using different leaves from the same plant for the NMR and X-ray CT measurements. For the NMR measurements, leaf discs were excised using a cork borer (Φ 7 mm), avoiding major veins, and stacked in NMR test tubes. A pulsed NMR spectrometer (JNM-MU25A, JEOL) was used with a stimulated-echo sequence at a diffusion time (Δ) of 200 ms. The apparent self-diffusion coefficient, D_{200}, was calculated by fitting the signal attenuation curves to the Stejskal–Tanner equation using nonlinear least-squares regression. For X-ray CT measurements, approximately 0.4 × 0.7 cm mesophyll sections adjacent to the midrib were excised from the apical, middle, and basal regions of the leaf blade. The sections were held between plastic pieces in a microtube and imaged using a microfocus X-ray CT system (VOXIAbox, Voxel Works). The imaging conditions were a tube voltage of 80 kV, 1 × 1 binning, 64 accumulations, and a spatial resolution of 3.549 µm. In each reconstructed image, a central region of 700 × 300 voxels spanning the entire leaf thickness was defined as the region of interest. Porosity and the ratio of air-space surface area to air-space volume (specific surface area) were calculated using MATLAB R2026a.
The results showed that D_{200} and porosity decreased during storage, whereas specific surface area increased. These two structural changes suggest partial occupation of the intercellular air spaces and the formation of more complex interfacial structures, possibly associated with redistribution of water from intercellular compartments. Such microstructural changes likely contributed to the observed decrease in D_{200} by imposing greater constraints on water molecular diffusion. This study provides evidence linking microstructural changes in leaf tissue to reduced water mobility during the early stages of postharvest deterioration, offering new insights into the mechanisms underlying loss of freshness.

Key Words: NMR, X-ray CT, water dynamics, Self-diffusion coefficient, intercellular spaces

PH-07

Proceedings of The 12th International Symposium on Machinery and Mechatronics for Agriculture and Biosystems Engineering (ISMAB 2026)
20-24 October 2026, Busan, Republic of Korea

FROM CONTACT TO NEAR-CONTACTLESS ULTRASOUND: COUPLING EFFECTS ON APPLE FIRMNESS PREDICTION

Yudha Putra Arisandy[1,2], Chang-Hyup Lee[1,2], Jiwon Ryu[1,3], Sang-Yeon Kim[1,2], Dong-Heun Sung[1,2], Sun Seongmi[3], Ghiseok Kim[1,2,3*]

[1]Department of Biosystems Engineering, Seoul National University, Seoul, Republic of Korea
[2]Global Smart Farm Convergence Major, Seoul National University, Seoul, Republic of Korea
[3]Research Institute of Agriculture and Life Sciences, Seoul National University, Seoul, Republic of Korea
*Corresponding Author-- Voice: +82-2-880-4613, Email: ghiseok@snu.ac.kr

Abstract: Ultrasonic sensing has strong potential for nondestructive evaluation of fruit firmness during postharvest handling. However, its practical use can be affected by changes in acoustic coupling between the sensor and fruit surface. In particular, the contact force applied during measurement can alter the transmitted waveform and influence firmness estimation. This study investigates through-transmission ultrasound in apples under different coupling conditions, ranging from firm contact to near-contactless measurement. Ultrasonic responses were described using information from the time and frequency domains and were related to reference firmness through machine-learning methods. The results showed that coupling conditions influenced signal propagation, attenuation, and spectral behavior. Even so, useful firmness information remained available when the applied contact force was reduced. Combining temporal and spectral features also improved firmness prediction across different contact conditions. These findings show that ultrasonic firmness assessment does not always require strong mechanical contact with the fruit surface. The study also highlights the importance of sensor coupling in postharvest quality evaluation and supports the use of low-contact ultrasound for future automated grading.

Key Words: Through-transmission Ultrasound, Apple Firmness, Transducer–Fruit Coupling, Postharvest Quality, Machine Learning.

ACKNOWLEDGEMENTS

This work was carried out with the support of Cooperative Research Program for Agriculture Science and Technology Development (Project No. PJ01709503) Rural Development Administration, Republic of Korea.

Post-harvest and Food Processing 2 (PH-2)



PH-08

Proceedings of The 12th International Symposium on Machinery and Mechatronics for Agriculture and Biosystems Engineering (ISMAB 2026)
20-24 October 2026, Busan, Republic of Korea

FOREIGN OBJECT DETECTION IN POTATO CHUNKS USING RGB IMAGING AND DEEP LEARNING: PERFORMANCE AND LIMITATIONS

Trinh Thanh Duy[1], Minhyun Kim[12], Dong-Heun Sung[12], Seokha Hwang[12], Harin Jang[12], Ghiseok Kim[123*]

[1] Department of Biosystems Engineering, Seoul National University, Seoul, Republic of Korea
[2] Global Smart Farm Convergence Major, Seoul National University, Seoul, Korea
[3] Research Institute of Agriculture and Life Sciences, Seoul National University, Seoul, Korea
* Corresponding Author– Voice: +82-2-880-4603, Email: ghiseok@snu.ac.kr

Abstract: Foreign object contamination remains a challenge in food inspection, particularly when contaminants resemble the food material or conveyor belt. This study evaluated RGB imaging combined with deep learning for detecting foreign objects in potato chunks. A dataset of 1,800 images was divided into training, validation, and test sets of 1,200, 300, and 300 images, respectively. Foreign objects approximately 1.5 cm in size included stones, wood pieces, plant stems, screws, mealworms, polyethylene, polypropylene, and nylon strings. Different colors were incorporated to represent both visually contrasting contaminants and those resembling potatoes or the belt. The dataset included individual and mixed foreign-object categories, variable object quantities, and negative images containing potatoes only.

The model demonstrated high overall precision, recall, and mean average precision, supporting the potential of RGB-based detection for automated inspection under the investigated conditions. However, contaminants with colors similar to potatoes or the conveyor belt were more susceptible to missed detections and confusion with their surroundings. These findings indicate that limited visual contrast remains a constraint on detection reliability. Further experiments using X-ray imaging and hyperspectral imaging (HSI) cameras are needed to evaluate whether complementary structural and spectral information can improve the detection of visually ambiguous contaminants and enhance inspection reliability.

Key Words: Foreign object detection, RGB imaging, Deep learning, Potato chunks, Food inspection.

ACKNOWLEDGEMENTS

This work was supported by the Korea International Cooperation Agency (KOICA) under the title of “Project for Strengthening Agricultural Higher Education of VNUHCM (Vietnam National University-Ho Chi Minh City) in Vietnam” in 2021–2028 (No. 2021-00022).

This work was supported by Korea Institute of Planning and Evaluation for Technology in Food, Agriculture and Forestry (IPET) through High Value-added Food Technology Development Program, funded by Ministry of Agriculture, Food and Rural Affairs (MAFRA) (RS-2025-02215392).

PH-09

Proceedings of The 12th International Symposium on Machinery and Mechatronics for Agriculture and Biosystems Engineering (ISMAB 2026)
20-24 October 2026, Busan, Republic of Korea

SPECTRAL ANALYSIS OF POTATO SLICES AND FOREIGN MATERIALS USING SWIR HYPERSPECTRAL IMAGING

Harin Jang[1,2], Minhyun Kim[1,2], Seokha Hwang[1,2], Dong-Heun Sung[1,2], Trinh Thanh Duy[1], Ghiseok Kim[1,2,3*]

[1]Department of Biosystems Engineering, Seoul National University, Seoul 08826, Republic of Korea
[2]Global Smart Farm Convergence Major, Seoul National University, Seoul 08826, Republic of Korea
[3]Research Institute of Agriculture and Life Sciences, Seoul National University, Seoul 08826, Republic of Korea
*Corresponding Author -- Voice: +82-2-880-4603, Email: ghiseok@snu.ac.kr

Abstract: With the increasing automation of food manufacturing processes and the growing demand for advanced quality control, rapid and nondestructive detection of foreign materials has become increasingly important. Foreign materials encountered during food processing vary considerably in composition, shape, and thickness. Consequently, thin materials or those with appearances similar to food products may be difficult to distinguish using conventional imaging techniques. Hyperspectral imaging simultaneously provides spatial and continuous spectral information and can therefore be used to examine material-dependent differences in the physicochemical properties of food products and foreign materials.
In this study, short-wave infrared (SWIR) hyperspectral imaging was used to characterize the spectral properties of potato slices and representative foreign materials. Hyperspectral images were acquired over the wavelength range of 900–1700 nm for potato slices and foreign materials, including stone, wood, screws, mealworms, polyethylene (PE), polypropylene (PP), and nylon. To investigate the effect of placement conditions on spectral characteristics, the foreign materials were positioned either on the surfaces of potato slices or directly on a conveyor belt. The acquired images were converted into reflectance images using white and dark references, and mean reflectance spectra were extracted from selected regions of interest. Spectral preprocessing techniques, including smoothing, standard normal variate transformation, and spectral derivatives, were applied. Partial least squares discriminant analysis models were also developed to discriminate foreign materials from potato and conveyor-belt backgrounds. Models were constructed under different spectral preprocessing conditions, and their classification performance and optimal numbers of latent variables were assessed using cross-validation. This study presents an experimental and analytical framework for characterizing and discriminating foreign materials in food products using SWIR hyperspectral imaging and provides a methodological basis for nondestructive foreign-material inspection in food manufacturing processes.

Key Words: Potato, SWIR hyperspectral imaging, Foreign material detection, PLS-DA.

ACKNOWLEDGEMENTS

This work was supported by Korea Institute of Planning and Evaluation for Technology in Food, Agriculture and Forestry(IPET) through High Value-added Food Technology Development Program, funded by Ministry of Agriculture, Food and Rural Affairs(MAFRA)(RS-2025-02215392).

PH-10

Proceedings of The 12th International Symposium on Machinery and Mechatronics for Agriculture and Biosystems Engineering (ISMAB 2026)
20-24 October 2026, Busan, Republic of Korea

DEVELOPMENT OF A PORTABLE NEAR-INFRARED SPECTROSCOPY SYSTEM FOR MONITORING GOCHUJANG FERMENTATION

Dong Heun Sung[12], Jiwon Ryu[13], Kim Minhyun[12], Lee Jae-Eun[12], Trinh Thanh Duy[1], Ghiseok Kim[123*]

[1] Department of Biosystems Engineering, Seoul National University, Seoul, Republic of Korea
[2] Global Smart Farm Convergence Major, Seoul National University, Seoul, Korea
[3] Research Institute of Agriculture and Life Sciences, Seoul National University, Seoul, Korea
* Corresponding Author– Voice: +82-2-880-4603, Email: ghiseok@snu.ac.kr

Abstract: Gochujang is a traditional Korean fermented food that has attracted growing global interest as a high-value condiment. Its quality is largely determined by physicochemical changes induced by microbial metabolism during fermentation, making precise monitoring of quality indicators essential for consistent production. However, conventional analytical methods involve destructive and labor-intensive procedures, which are time-consuming and difficult to apply during production. Near-infrared (NIR) spectroscopy enables rapid and non-destructive measurement, but laboratory spectroscopic equipment generally requires a wired connection to a computer, limiting its use at production sites. In this study, a portable wireless NIR spectroscopy system was developed. Using the developed system, NIR spectra were acquired from gochujang samples collected at various stages of fermentation, and physicochemical reference values were measured using standard analytical methods. After applying various preprocessing techniques, machine learning models were developed to predict the physicochemical quality indicators. These results suggest the potential of the developed system as a practical tool for on-site, non-destructive quality monitoring in fermented food production.

Key Words: Gochujang Fermentation, Non-Destructive Monitoring, Near-Infrared Spectroscopy, Portable Spectrometer, Machine Learning

ACKNOWLEDGEMENTS

This work was supported by Korea Institute of Planning and Evaluation for Technology in Food, Agriculture and Forestry(IPET) through High Value-added Food Technology Development Program, funded by Ministry of Agriculture, Food and Rural Affairs (MAFRA)(RS-2024-00402850).

PH-11

Proceedings of The 12th International Symposium on Machinery and Mechatronics for Agriculture and Biosystems Engineering (ISMAB 2026)
20-24 October 2026, Busan, Republic of Korea

AUTOMATED QUALITY INSPECTION OF VANILLA BEANS USING COMPUTER VISION AND HYPERSPECTRAL IMAGING

Tzu-Yen Weng[1], Chih-Hsin Yeh[2], Yi-Hua Lin[2], Shih-Fang Chen[1*]

[1]Department of Biomechatronics Engineering, National Taiwan University
[2]Taoyuan District Agricultural Research and Extension Station, Ministry of Agriculture
*Corresponding Author--Voice: +886-2-3366-5354, Email: sfchen@ntu.edu.tw

Abstract: Vanilla's commercial value depends heavily on a labor-intensive post-harvest process, in which quality control at each stage critically determines final flavor and value. At present, both defect screening and moisture determination rely almost entirely on subjective human inspection, making it difficult to establish objective measurement standards. Moreover, the lack of a physically grounded moisture reference has hindered systematic evaluation of any automated alternative. This study developed an automated, objective quality determination framework integrating computer vision and hyperspectral imaging for two post-harvest stages: defect detection before cleaning (stage 1) and moisture content determination during drying (stage 2). In stage 1, a YOLOv11m-seg model was trained on 524 vanilla pod images, including 3,838 annotated pods across six categories for defect segmentation and classification; curvature and length thresholds were further determined via an iterative boundary-search procedure to distinguish curved and small pods. In stage 2, hyperspectral imaging data from 305 pods collected at multiple time points during a standardized oven-drying protocol were combined with Partial Least Squares Regression (PLSR) to predict moisture content, and wet-basis moisture content was then evaluated against two ground truths: subjective on-site human categorization and an objective 40-45% moisture threshold derived from oven-drying measurements, following the industry-accepted range for conditioning-ready vanilla. According to the results, the YOLOv11m-seg model with normal pods achieved F1-scores up to 0.98, with boundary refinement further raising curved and small pod F1-scores to 0.975 and 0.982. For stage 2, the PLSR model achieved a coefficient of determination (R^2) of 0.835 and root-mean-square error (RMSE) of 0.057; model predictions showed 0.84 classification agreement with the objective moisture threshold, compared with 0.61 agreement with subjective human categorization. The higher consistency with the objective reference indicated that the model captures physical moisture status more reliably than subjective human judgment, supporting the use of computer vision and hyperspectral imaging as objective alternatives to sensory inspection in vanilla post-harvest processing.

Key Words: Vanilla pods, deep learning, machine learning, hyperspectral Image

INTRODUCTION

Vanilla (*Vanilla planifolia*)'s commercial value depends on a labor-intensive post-harvest process, where quality control at each stage determines flavor and value. At present, both defect screening and moisture determination rely almost entirely on subjective visual and tactile inspection, which introduces substantial inter-operator variability and precludes

objective quality standards. Furthermore, the absence of a physically grounded moisture reference has made it difficult to systematically evaluate any automated alternative, as subjective labels cannot serve as reliable ground truth for validating model predictions. While computer vision and NIR spectroscopy have been applied separately for produce defect detection and moisture estimation (Widyaningrum et al., 2024), few studies have combined both approaches within a single framework for vanilla. This study addresses these gaps by (1) developing computer vision and hyperspectral imaging models for defect and moisture assessment across two critical post-harvest stages, and (2) establishing an objective, oven-drying-derived moisture reference against which both model predictions and existing subjective classifications can be jointly evaluated.

MATERIALS AND METHODS

Stage 1: Defect Detection Before Cleaning

A total of 524 vanilla green pod images were collected, comprising six categories (Fig. 1): 160 normal, 92 small, 90 curved, 62 insect, 51 scab, and 69 browning & cracking images, yielding 3,838 annotated pods in total. The dataset was divided into training, validation, and testing sets at a ratio of 7:2:1 at the image level to prevent pods from the same image from appearing in multiple subsets. A YOLOv11m-seg model was trained on this dataset to perform segmentation and classification across the six categories, evaluated using precision, recall, F1-score, and mAP50. Training was performed for 300 epochs with a batch size of 16 and an initial learning rate of 0.01, using AdamW and standard data augmentation (mosaic, fliplr, flipud, HSV jitter, translate, scale). No specific handling for class imbalance across categories was applied.

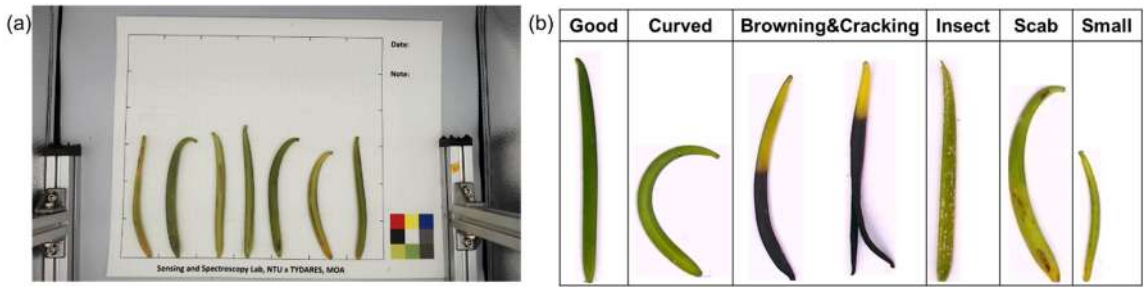

Fig.1 Vanilla pod imaging setup and category examples. (a) Hyperspectral image acquisition setup with a color calibration card; (b) Six categories of vanilla pods.

To further improve classification of curved and small pods, curvature and length were calculated for each segmented pod. The mask contour of each pod was extracted, followed by thinning to obtain its centerline, from which the length and curvature were then computed. Length was defined as the geodesic path length along the skeletonized centerline of the segmented pod, measured between its two farthest endpoints via distance transform, and curvature was calculated as a robust representative value of the local curvature along a third-order polynomial fit to the centerline, capturing the pod's sharpest bends while excluding extreme outliers. For each feature, an iterative boundary search was conducted on the training and validation sets to determine the optimal decision thresholds. The search started at the midpoint between two adjacent classes in the feature-value distribution and iteratively shifted outward with a step size of 0.1. At each candidate threshold, ground truth labels in the training set were reassigned, and the model was retrained and evaluated on the validation set

to identify the threshold with the highest F1-score. The optimal thresholds identified from the validation set were then fixed and applied to the held-out test set for the final performance evaluation reported in Table 1. These optimal thresholds were subsequently applied to screen out curved and small pods.

Stage 2: Moisture Content Prediction During Drying

Hyperspectral imaging was used to acquire spectral data from a total of 305 vanilla pods with three drying classifications. Hyperspectral image acquisition conditions are illustrated in Fig. 2. Two independent ground truths were established to evaluate the moisture classification framework. First, subjective on-site categorization was performed by experienced personnel. At the time of sample collection, all pods were classified into wet, medium, or dry categories based on visual appearance and tactile inspection. Second, objective moisture-based categorization was established using a scientifically defined moisture content threshold, determined as follows. All 305 pods were subjected to a standardized oven-drying protocol. Hyperspectral images were captured at multiple drying stages, and wet-basis moisture content (MC_{wb}) was determined gravimetrically at each stage following ISO 5565-2:1999. Since the subsequent conditioning stage involves further dehydration beyond drying, this study targeted an MC_{wb} of 40-45%, a range reported to remain acceptable for conditioning-ready vanilla pods (Havkin-Frenkel and Frenkel, 2006). Pods were accordingly categorized as wet (MC_{wb} > 45%), medium (40% ≤ MC_{wb} ≤ 45%), or dry (MC_{wb} < 40%). The comparison between these two ground truths enables evaluation of whether model predictions align more closely with objective physical measurement or with subjective human perception, thereby quantifying the added value of hyperspectral-based objective assessment over current sensory practice.

Spectral Preprocessing and Modeling

The dataset was randomly split into training and testing sets at an 8:2 ratio at the pod level, ensuring that spectra from the same pod at different drying stages were assigned to the same subsets. Three spectral preprocessing methods, Multiplicative Scatter Correction (MSC), Standard Normal Variate (SNV), and Savitzky–Golay (SG) smoothing (window size=11, polynomial order=2, derivative order=1), were compared, and PLSR with the optimal number of latent variables selected by 5-fold cross-validation on the training set predicted moisture content, evaluated by R^2 and RMSE. Predictions were then classified into wet, medium, and dry categories and evaluated against both ground truths described above using precision, recall, F1-scores, and overall accuracy. The experimental procedure is shown in Fig. 2.

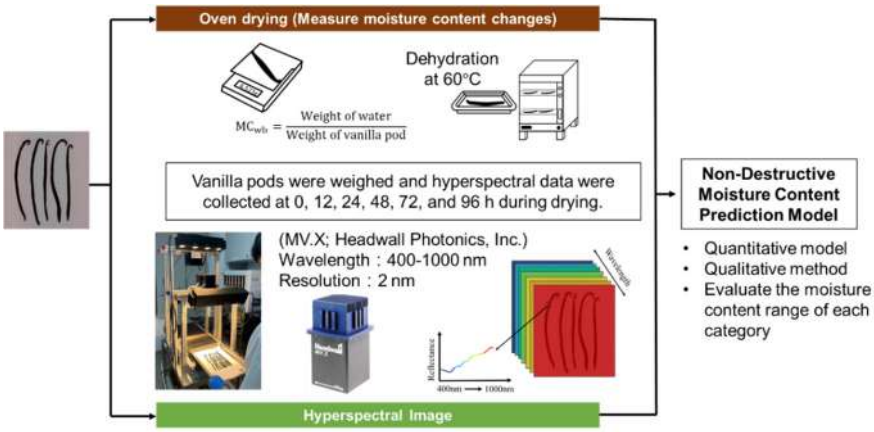

Fig.2 Workflow for non-destructive moisture content prediction method.

RESULTS & DISCUSSION

The YOLOv11m-seg model achieved stable performance across all six categories (Table 1), with the normal category, the primary category of interest, reaching the highest F1-score of 0.980. However, normal, curved, and small pods remain difficult to distinguish by length and curvature alone, motivating an objective boundary determination based on these two features. The optimal boundary ranges were 0.1016-0.1301 for curvature and 13.43-15.27 cm for length. Applying these boundaries improved the F1-scores of the normal, curved, and small categories as reported in Table 1, with curved and small pods showing more pronounced improvement.

Table 1 Model performance of six vanilla categories.

Category	Precision	Recall	F1-score (Before)	F1-score (After)
Browning & Cracking	0.952	0.971	0.962	0.962
Insect	0.987	0.962	0.974	0.974
Scab	0.933	0.933	0.933	0.933
Curved	0.970	0.941	0.955	**0.975**
Small	0.946	0.909	0.927	**0.982**
Normal	0.964	0.989	0.980	**0.982**

The PLSR model was evaluated using three spectral preprocessing methods after cross-validation. SNV achieved the best performance (R^2=0.835, RMSE=0.057), indicating potential for predicting moisture content from hyperspectral data. Although the model's predictive performance still needs improvement, the visualization of the continuous dehydration process in Fig. 3 still shows that moisture loss occurs preferentially from the head and tail ends of the vanilla pod. This pattern is consistent with industry experience, though further validation is needed to confirm this trend. Based on this result, the SNV-preprocessed PLSR predictions were subsequently used for classification analysis based on two types of ground truth, summarized in Table 2. Model predictions showed 0.84 classification agreement with the objective 40-45% moisture threshold derived from oven-drying measurements, but only 0.61 agreement with subjective on-site human categorization. This gap indicates that model predictions align more closely with the physical moisture status rather than replicating human perceptual habits. However, because the 40-45% interval defining the medium category is narrow, the medium category remained the weakest across both ground truths, and further improvement is still needed.

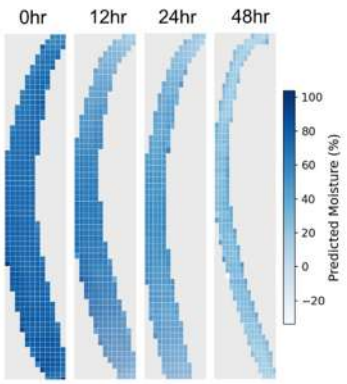

Fig.3 Continuous Moisture Prediction Visualization of Vanilla Pods.

Table 2 Classification results by two types of ground truth.

Criteria / Category	Subjective Classification (Human judgment)				Quantified Range (<40% / 40-45% / >45%)			
	Precision	Recall	F1-score	Acc.	Precision	Recall	F1-score	Acc.
Dry	0.76	0.44	0.56	0.61	0.84	0.76	0.80	0.84
Medium	0.52	0.21	0.30		0.32	0.44	0.37	
Wet	0.60	1.00	0.75		0.95	0.91	0.93	

CONCLUSIONS

This study developed a two-stage automated quality determination framework for vanilla post-harvest processing, covering defect detection and moisture assessment. In stage 1, the YOLOv11m-seg model achieved reliable classification across six categories, with length- and curvature-based threshold refinement raising curved, small, and normal pod F1-scores to 0.975, 0.982, and 0.982. In stage 2, PLSR with SNV preprocessing achieved R^2 of 0.835 and RMSE of 0.057; predictions showed higher agreement with the objective oven-drying-derived moisture threshold (0.84) than with subjective human categorization (0.61), indicating that the model captures physical moisture status more reliably than sensory judgment. Future work will focus on reducing prediction RMSE to improve medium-category discrimination and on exploring lower-cost spectral sensors for on-site deployment.

REFERENCES

Havkin-Frenkel, D., & Frenkel, C. (2006). Postharvest handling and storage of cured vanilla beans. *Stewart Postharvest Review*, *2*(4), 1-9.

Widyaningrum, W., Purwanto, Y. A., Widodo, S., Supijatno, S., & Iriani, E. S. (2024). Rapid assessment of vanilla (*Vanilla planifolia*) quality parameters using portable near-infrared spectroscopy combined with random forest. *Journal of Food Composition and Analysis*, *133*, 106346.

PH-12

Proceedings of The 12th International Symposium on Machinery and Mechatronics for Agriculture and Biosystems Engineering (ISMAB 2026)
20-24 October 2026, Busan, Republic of Korea

EXPLAINABLE DEEP LEARNING FOR ANALYSIS OF ONION STORAGE ENVIRONMENTAL DATA

Jaeeun Lee[1,2], Sang-Yeon Kim[2,3], Uik Lee[1,2], Ghiseok Kim[1,2,3*]

[1]Department of Biosystems Engineering, Seoul National University, Seoul 08826, Republic of Korea
[2]Convergence Major in Global Smart Farm, Seoul National University, Seoul 08826, Republic of Korea
[3]Research Institute of Agriculture and Life Sciences, Seoul National University, Seoul 08826, Republic of Korea
*Corresponding Author-- Email: ghiseok@snu.ac.kr

Abstract: Onion storage environments vary dynamically with temperature, relative humidity, carbon dioxide concentration, and product temperature. Understanding the temporal relationships among these variables is important for effective postharvest management, but conventional analytical approaches have limitations in representing complex time-dependent patterns and explaining the contribution of individual environmental variables. This study developed an explainable deep-learning framework for the integrated analysis of onion storage environmental data. Environmental and storage-related time-series data generated from completed onion storage experiments conducted under multiple storage conditions were used. The dataset included temperature, relative humidity, carbon dioxide concentration, vapor pressure deficit, product temperature, and derived environmental variables. After data preprocessing, time-series deep-learning models, including long short-term memory networks and Temporal Fusion Transformers, were developed together with conventional machine-learning models for comparison. Explainability methods were applied to quantify the relative importance of input variables and to examine how key environmental factors contributed to model outputs over time. The analysis was designed to characterize influential environmental conditions and temporal patterns relevant to onion storage management. This framework provides a basis for interpreting complex onion storage environmental data and supporting the development of data-driven postharvest management strategies.

Key Words: Onion storage, Explainable Artificial intelligence, Deep learning, Environmental monitoring, Time-series analysis

ACKNOWLEDGEMENTS

This work was supported by the Cooperative Research Program for Agriculture Science and Technology Development (Project Nos. RS-2022-RD010022 and RS-2022-RD010023), Rural Development Administration (RDA), Republic of Korea.

PH-13

Proceedings of The 12th International Symposium on Machinery and Mechatronics for Agriculture and Biosystems Engineering (ISMAB 2026)
20-24 October 2026, Busan, Republic of Korea

DEVELOPMENT AND OPERATIONAL PARAMETER OPTIMIZATION OF AN AUTOMATED SHELLING SYSTEM FOR DRIED LONGAN

Xin-Liang Lai [1*], Ching-Wei Cheng [1], Wu-Yang Sean [1], Ping-Kun Tsai [1]

[1] Dept. of Bio-industrial Mechatronics Engineering,
National Chung Hsing University, Taiwan

[1] Department of Bio-industrial Mechatronics Engineering, National Miao-Li Agricultural and Industrial Vocational High School, MiaoLi, 360, Taiwan, ROC

*Corresponding Author-- Voice: +886-90-508-6672, Email: thecold168@gmail.com

Abstract: This study developed an automated shelling system for dried longan and optimized its operational parameters, specifically focusing on dual-roller speeds and moisture conditioning pretreatment. The system utilized a dual-roller shelling mechanism (38 mm diameter, 3 mm gap) operating under differential rotation to induce combined normal compressive and tangential shear stresses for shell fracture. Experimental results indicated that increasing roller speed significantly enhanced cracking force; elevating motor speeds from 100 to 500 rpm led to a marked increase in shelling success, with peak shelling mechanics achieved at a differential speed ratio of 500:400 rpm (Motor A:Motor B). Moisture pretreatment effectively modulated shell toughness, where a post-spraying resting time of 6 min established an optimal balance between shell flexibility and stress crackability, yielding a global maximum shelling success rate of 96.7%. Conversely, insufficient resting (5 min) induced brittle shell fragmentation, whereas prolonged resting (7 min) resulted in shell over-softening, incomplete energy absorption, and increased pulp damage. Consequently, a 6-min resting time coupled with a 500:400 rpm speed combination was established as the optimal operational parameter set. These findings offer practical reference and theoretical foundations for the development of automated processing equipment for dried longan.
Key Words: Dried longan, Automated shelling, Dual-roller shear.

INTRODUCTION

Longan (Dimocarpus longan Lour.) is an evergreen fruit tree of the Sapindaceae family, widely cultivated in tropical and subtropical Asia. According to the 2024 Agricultural Statistics Yearbook, Taiwan's longan orchards encompass 10,296 hectares with an annual production of 49,346 metric tons, localized predominantly south of Taichung. Due to concentrated harvest windows and high metabolic rates, fresh longans are highly perishable (Hsieh, 2009). Thermal dehydration lowers moisture content and generates distinctive aromas, serving as a key strategy to extend shelf life and add commercial value.

Dried longan possesses documented therapeutic benefits; classical texts such as Bencao Gangmu and Shennong Bencao Jing record its splenetic and cardiovascular tonic properties (Cong et al., 2011; Zheng et al., 2015). Commercial offerings include intact shelled fruits and deshelled/pitted pulps. Driven by consumer convenience and industrial food manufacturing, demand for processed pulp has expanded, elevating shelling and pitting to critical unit operations.

Standard post-harvest processing comprises harvesting, grading, drying, and storage (Tseng, 1994). Dehydration converts the pericarp into a rigid shell, while the underlying pulp turns viscous and adheres to the inner wall, impeding shell removal. Shelling remains predominantly manual, requiring operators to crush shells and extract pulp individually. This practice is inherently labor-intensive and bottlenecked by agricultural workforce shortages. Furthermore, manual contact and shell fragment contamination compromise product hygiene. Consequently, implementing automated shelling and separation machinery is essential to enhance throughput, reduce labor reliance, and guarantee food safety.

MATERIALS AND METHODS

Test Materials and Pretreatment

Commercially dried in-shell longans were selected as test samples. Prior to testing, sample dimensions and moisture content were measured using a digital vernier caliper and a moisture analyzer, yielding an average geometric mean diameter (D_m) of 24.3 mm and an initial shell moisture content of 15.4% (wet basis). To minimize pulp damage and dust generation during mechanical shelling, samples were quantitative sprayed with 100 mL of water per 100 g of longans, followed by a designated resting time (t_r) for moisture conditioning to enhance shell toughness and softness.

System Architecture and Mechanism Design

The automated shelling system utilizes an integrated electromechanical control framework, comprising a feeding zone (1), a dual-roller shelling mechanism (2), an electronic control module (3), a shell-pulp separation mechanism (4), and a discharge zone (5) (Figure 1). The shelling unit consists of two 38 mm-diameter rollers driven by gearmotors for differential-speed rotation, with a roller gap set at 3 mm. The localized compressive and shear frictional forces generated by differential rotation fracture the shell without damaging the enclosed pulp.The operational workflow is depicted in Figure 2.

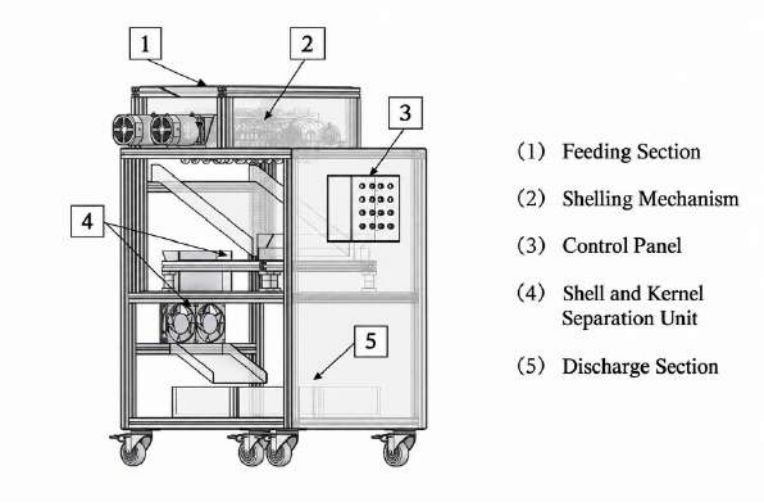

Fig.1 Schematic diagram of the automated dried longan shelling system.

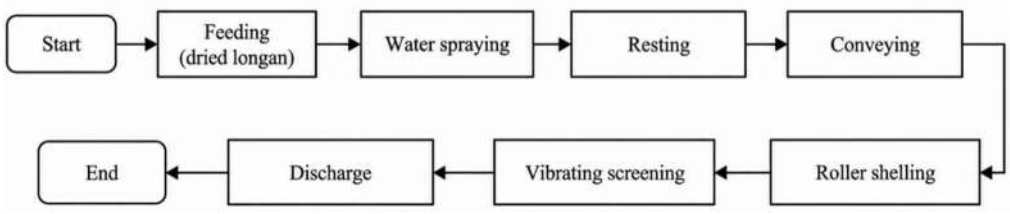

Figure 2. Process flowchart of the automated dried longan shelling operation.

Experimental Design and Operational Parameters

A two-stage optimization approach was implemented:

Stage 1 (Speed Optimization Test): Under fixed pretreatment conditions, 25 speed combinations of Motor A and Motor B were evaluated from 100 to 500 rpm (at 100 rpm intervals) to screen high-efficiency rotational speed ranges (N = 30 per trial).

Stage 2 (Conditioning Time Optimization): The four top-performing speed combinations from Stage 1 were selected to assess the impact of resting times (t_r = 5, 6, and 7 min) post-spraying on shelling performance (N = 30 per trial).

Performance Evaluation Metrics and Criteria

Shelling performance was quantitatively evaluated based on fruit integrity post-processing. The shelling success rate (S_r) was calculated using Equation (1):

$$S_r = \frac{N_s}{N_t} \times 100\% \qquad (1)$$

where N_s is the number of successfully shelled fruits, and N_t is the total number of tested samples.

Evaluation criteria for shelling outcomes are illustrated in Figure 3:

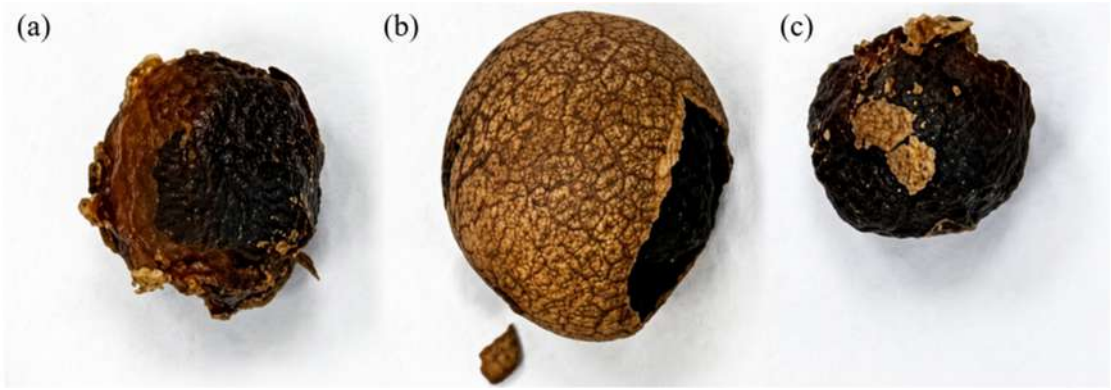

Figure 3. Evaluation criteria for dried longan shelling outcomes: (a) Successful shelling; (b) Unsuccessful shelling; (c) minor shell fragment adhesion.

Successful Shelling: Complete separation of pulp and shell (Figure 3a), or effective separation with only minor shell fragments adhering to the pulp surface (Figure 3c).

Unsuccessful Shelling: Incomplete shell removal or superficial shell cracking without separation (Figure 3b).

RESULTS & DISCUSSION

Effect of Dual-Roller Rotational Speed on Shelling Performance

The interactive effect of dual-roller speed combinations on the shelling success rate of dried longan is illustrated in Figure 4. The results indicate a significant upward trend in shelling success rate as the speeds of Motor A and Motor B were increased from 100 to 500 rpm.

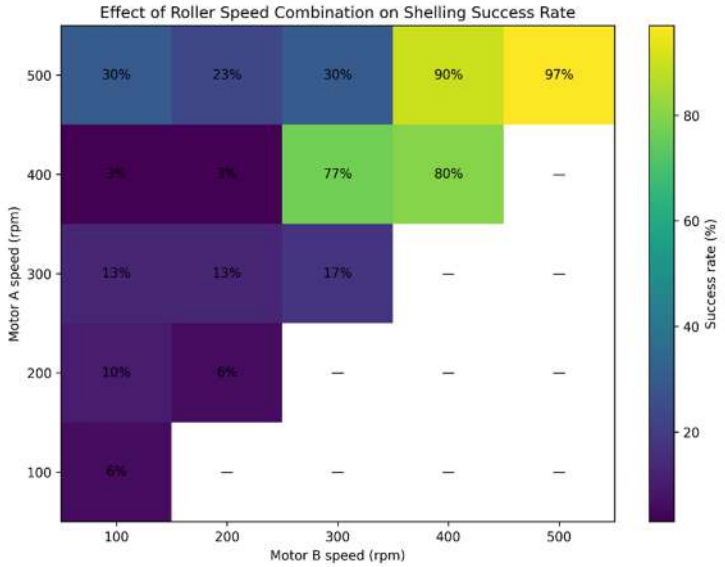

Figure 4. Heatmap of interactive effects of dual-roller speed combinations on dried longan shelling success rate.

Effect of Resting Conditioning Time on Shelling Performance

The interactive effects of post-spraying resting times and roller speed combinations on shelling performance are depicted in Figure 5. Moisture pretreatment altered shell toughness, directly influencing stress cracking behavior under mechanical shear.

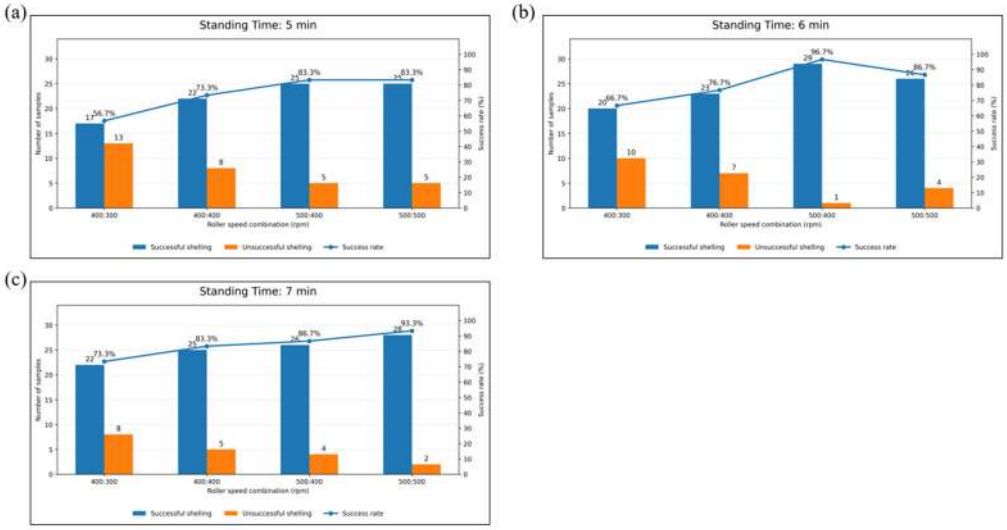

Figure 5. Interactive effects of post-spraying resting times and speed combinations on shelling performance: (a) 5 min resting; (b) 6 min resting; (c) 7 min resting.

CONCLUSIONS

This study evaluated the interactive effects of dual-roller speed combinations and post-spraying resting times on the shelling performance of dried longan. Increasing roller speeds enhanced shell fracture by integrating normal compressive and tangential shear stresses, with a differential speed set at 500:400 rpm (Motor A:Motor B) yielding optimal mechanical performance. Moisture conditioning played a crucial role in modulating shell toughness; a resting duration of 6 min established an ideal balance between shell flexibility and stress crackability, achieving a global maximum success rate of 96.7% under 500:400 rpm. Conversely, insufficient resting (5 min) caused shell fragmentation, whereas excessive resting (7 min) led to shell over-softening and subsequent pulp damage.

ACKNOWLEDGEMENTS

The authors would like to express their sincere gratitude to Binghong Farm for providing the dried longan samples for this study. Special thanks are also extended to all members of our laboratory for their valuable assistance and insightful suggestions during the mechanism development and experimental procedures.

REFERENCES

Cong, J. X., Chen, S. H., & Lu, G. Y. (2011). Modern pharmacological research progress on the efficacy of longan aril in invigorating the heart and spleen, nourishing blood, and calming the nerves. China Journal of Chinese Materia Medica, 36(20), 2908–2911 .

Hsieh, C.-C. (2009). Improvement of export storage and transportation techniques for longan (Research Project Report No. 98-AS-4.2.2-FD-ZA). Council of Agriculture, Executive Yuan, Taiwan .

Zeng, W. X. (1994). How to process dried longan. Fujian Agriculture, (8), 16 .

Zheng, X. Y., Zhang, L., & Liu, C. X. (2015). Research progress on chemical constituents and pharmacological effects of longan aril. Chinese Traditional and Herbal Drugs, 46(14), 2167–2173 .

Post-harvest and Food Processing 3 (PH-3)



PH-14

Proceedings of The 12th International Symposium on Machinery and Mechatronics for Agriculture and Biosystems Engineering (ISMAB 2026)
20-24 October 2026, Busan, Republic of Korea

TRANSFERABLE WEIGHT LOSS FORECASTING IN COLD-STORED ONIONS USING PHYSICS-CONSTRAINED DEEP LEARNING AND SHORT-TERM CALIBRATION

Sang-Yeon Kim[12], Jaeeun Lee[12], Uik Lee[1], Ghiseok Kim[123*]

[1]Department of Biosystems Engineering, Seoul National University, Seoul 08826, Republic of Korea
[2]Global Smart Farm Convergence Major, Seoul National University, Seoul 08826, Republic of Korea
[3]Research Institute of Agriculture and Life Sciences, Seoul National University, Seoul 08826, Republic of Korea
*Corresponding Author -- Voice: +82-2-880-4603, Email: ghiseok@snu.ac.kr

Abstract: Weight loss during commercial onion cold storage is not routinely monitored by direct weighing, making its progression difficult to assess. Although empirical regression models have been used to estimate storage losses, adapting forecasts to changing environmental histories and new storage lots remains a practical challenge. This study investigates whether combining physics-constrained deep learning with short-term calibration can improve the transfer of cumulative weight-loss forecasts across storage experiments. Models were evaluated using leave-one-experiment-out validation on three onion storage datasets collected in 2022 to 2025. The architectures included LSTM, GRU, CNN-LSTM, and a simplified temporal fusion transformer (TFT). The framework predicts weight-loss increments from environmental sensor histories and elapsed storage time and accumulates them into cumulative loss. A soft physical constraint encourages a positive linear relationship between predicted increments and a vapor-pressure-deficit-based rate signal within each training lot, allowing differences in scale and offset between lots. For a new lot, weight observations from an initial period are used to estimate a scale and offset correction, after which predictions require no further weight measurements. Models with and without physical constraints were compared under matched architectures, hyperparameters, and random seeds. Calibrated mechanistic models provided an additional reference. Preliminary matched comparisons after seven days of calibration showed a median paired improvement in post-calibration trajectory R^2 ($\Delta R^2 \approx +0.50$) for the physics-constrained TFT models over their equally calibrated unconstrained counterparts. The median paired difference was positive in all three held-out experiments, although absolute performance and calibration requirements varied among experiments. These findings suggest that physical constraints and initial weight measurements contribute complementary information for estimating otherwise unobserved weight loss during storage. Future integration with lot-level sensing and practical calibration procedures could make predicted weight loss an explicit criterion for storage and dispatch decisions.

Key Words: Postharvest management, Time-series forecasting, Physics-guided learning, Domain adaptation, Vapor pressure deficit

ACKNOWLEDGEMENTS

This work was supported by the Cooperative Research Program for Agriculture Science and Technology Development (Project Nos. RS-2022-RD010022 and RS-2022-RD010023), Rural Development Administration (RDA), Republic of Korea.

PH-15

Proceedings of The 12th International Symposium on Machinery and Mechatronics for Agriculture and Biosystems Engineering (ISMAB 2026)
20-24 October 2026, Busan, Republic of Korea

BENCHMARKING AND DEPLOYING REAL-TIME DEFECT SEGMENTATION MODELS ON A FRUIT SORTING LINE

Huynh Cao The Cuong[1], Seokha Hwang[12], Arisandy Yudha Putra[12], Ghiseok Kim[123]*

[1]Department of Biosystems Engineering, Seoul National University, Seoul, Korea
[2]Global Smart Farm Convergence Major, Seoul National University, Seoul, Korea
[3]Research Institute of Agriculture and Life Sciences, Seoul National University, Seoul, Korea
* Corresponding Author– Voice: +82-2-880-4603, Email: ghiseok@snu.ac.kr

Abstract: On-line fruit sorting requires a surface-defect segmentation model that is both accurate and fast enough to keep pace with a multi-camera conveyor that captures several images per fruit. This study reports the selection, adaptation, and large-scale deployment of such a model under real factory conditions. Three semantic segmentation architectures spanning the accuracy–speed trade-off were compared on both segmentation accuracy and inference latency: Mask2Former, representing high-accuracy mask-classification models; DDRNet, a purpose-built real-time architecture; and SegFormer, an efficient transformer that balances the two. SegFormer was selected for its balance of accuracy and real-time speed, which becomes decisive when multiple images per fruit must be processed within the line's time budget. The selected model was first trained on laboratory defect images, then fine-tuned with only about 200 annotated factory images, and finally deployed on a multi-camera conveyor where it processed several hundred thousand real fruit, producing a pixel-level defect ratio per fruit for a binary quality decision. We quantify the lab-to-line gap and the benefit of data-efficient fine-tuning by comparing the lab-only and fine-tuned models on a held-out, manually annotated factory test set. Using deployment timing logs, we confirm real-time feasibility: in steady state the model keeps pace with the acquisition rate, though with a narrow margin that motivates keeping the model lightweight. The results show that a suitable off-the-shelf architecture, adapted with modest annotation effort, can operate at line speed on large-scale real data. We discuss the limitations of exterior RGB grading and outline extensions toward standard-based multi-grade classification.

Key Words: fruit surface defect; semantic segmentation; real-time deployment; on-line sorting.

ACKNOWLEDGEMENTS

This work was supported by the Korea International Cooperation Agency (KOICA) under the title of “Project for Strengthening Agricultural Higher Education of VNUHCM (Vietnam National University-Ho Chi Minh City) in Vietnam” in 2021–2028 (No. 2021-00022).
This work was carried out with the support of Cooperative Research Program for Agriculture Science and Technology Development (Project No. PJ01709503) Rural Development Administration, Republic of Korea.

PH-16

Proceedings of The 12th International Symposium on Machinery and Mechatronics for Agriculture and Biosystems Engineering (ISMAB 2026)
20-24 October 2026, Busan, Republic of Korea

EFFECT OF $CACL_2$-ASSISTED VACUUM IMPREGNATION ON THE ELECTRICAL PROPERTIES OF CARROT TISSUE

Kumari Sapna[1], Takahisa Nishizu[2,3], Teppei Imaizumi[2,3*]

[1]Gifu University, United Graduate School of Agriculture Science, 1-1, Yanagido, Gifu-city, Gifu, Japan
[2]Gifu University, Faculty of Applied Biological Sciences, 1-1, Yanagido, Gifu-city, Gifu, Japan
[3] Gifu University, Preemptive Food Research Center,1-1, Yanagido, Gifu-city, Gifu, Japan
*Corresponding Author-- +81-58-293-2930, Email: Imaizumi.teppei.j6@f.gifu-u.ac.jp

Abstract: This study investigated the effect of $CaCl_2$-assisted vacuum impregnation on the electrical properties of carrot tissue. Carrot samples were vacuum impregnated at 400 hPa using 0–4% (w/v) $CaCl_2$. Firmness increased with $CaCl_2$ concentration, accompanied by a decrease in water-soluble pectin and an increase in chelator-soluble pectin. Electrical impedance spectroscopy was performed over a frequency range of 50 Hz to 5 MHz The Cole–Cole arc decreased with increasing $CaCl_2$ concentration. Extracellular resistance and intracellular resistance also generally decreased, whereas membrane-associated capacitance showed a non-linear response. These results indicate that the electrical response of $CaCl_2$-treated carrot tissue cannot be interpreted solely in terms of tissue structural changes and may also be influenced by changes in the ionic environment caused by $CaCl_2$ impregnation.

Key Words: Calcium chloride, Vacuum impregnation, Extracellular resistance, intracellular resistance, Cell Membrane capacitance.

INTRODUCTION

Electrical impedance spectroscopy (EIS) is a useful technique for evaluating changes in the internal condition of plant tissues during processing. The electrical response of plant tissue is influenced by the extracellular and intracellular regions as well as the cell membrane. Therefore, parameters such as extracellular resistance, intracellular resistance, and membrane-associated capacitance can provide information about changes occurring within the tissue (Ando & Imaizumi, 2021). EIS has also been applied to carrot tissue to evaluate changes associated with cell membrane condition and tissue structure during processing (Umehara et al., 2025).

However, changes in electrical impedance cannot always be explained only by cell membrane damage or structural changes. The electrical behaviour of plant tissue is also affected by the concentration and movement of ions within the tissue. Therefore, treatments that introduce ions into plant cells and intercellular spaces may directly influence the EIS response, making the interpretation of electrical properties more complex.

Calcium chloride ($CaCl_2$) treatment is commonly used in fruits and vegetables to improve firmness and maintain tissue structure. Ca^{2+} can interact with non-esterified carboxyl groups of pectin and strengthen the cell-wall network through calcium–pectin cross-linking (Cao et al., 2020). When $CaCl_2$ is introduced into the tissue, however, both Ca^{2+} and Cl^- may also change the ionic environment and electrical conductivity. Vacuum impregnation provides an effective way to introduce $CaCl_2$ solution into the internal spaces of plant tissue and therefore provides a useful model for studying these electrical changes.

Although EIS has been used to evaluate structural changes in plant tissues, the electrical response of tissue after $CaCl_2$-assisted vacuum impregnation is not fully understood. It is important to determine whether the observed electrical changes are related only to structural modification or are also influenced by the increased ionic content of the tissue. Therefore, this study aimed to investigate the effect of $CaCl_2$-assisted vacuum impregnation on the electrical properties of carrot tissue. Firmness and pectin characteristics were further examined to determine how the observed electrical changes relate to structural modifications within the carrot tissue.

MATERIALS AND METHODS

Fresh carrots were washed and cut into uniform cylindrical samples measuring 10 mm in diameter and 10 mm in height. Calcium chloride ($CaCl_2$) solutions ranging from 0 to 4% (w/v) were prepared. The carrot samples were immersed in the respective treatment solutions at a sample-to-solution ratio of 1:10 (w/v). Vacuum impregnation was carried out at 400 hPa for 8 min, followed by restoration to atmospheric pressure and an additional holding period of 10 min. After treatment, the samples were removed from the solutions and collected for further Electrical properties were evaluated using electrical impedance spectroscopy (EIS) over a frequency range of 50 Hz to 5 MHz using two needle electrodes. Cole–Cole plots and the parameters R_e, R_i, and C_m were used to assess changes in tissue electrical behavior. For pectin analysis, AIS was separated into WSP, CSP, and DASP fractions, and galacturonic acid was determined using the carbazole–sulfuric acid method. Degree of methylation were analyzed by FTIR using the bands around 1740 and 1630 cm^{-1}.

RESULTS & DISCUSSION

Vacuum impregnation with $CaCl_2$ increased carrot firmness, with the highest firmness observed at 4% $CaCl_2$. This improvement may be related to Ca^{2+} cross-linking with pectin carboxyl groups, which can strengthen the cell wall and reduce heat-induced softening. The degree of methylation remained statistically unchanged, showing only a slight decrease with increasing $CaCl_2$ concentration. Pectin fraction analysis showed a decreasing trend in WSP, an increase in CSP, and a decrease in DASP, suggesting redistribution and stronger association of pectin within the cell wall.

As shown in Fig. 1, the Cole–Cole arc decreased progressively with increasing $CaCl_2$ concentration, with the smallest arc observed at 4% $CaCl_2$. This decrease cannot be

interpreted solely as an indication of cell membrane damage because $CaCl_2$ impregnation also changes the ionic environment within the tissue, which may directly affect its electrical properties. As shown in Fig. 2, *R*e and *R*i generally decreased with increasing $CaCl_2$ concentration, whereas *C*m showed a non-linear response. These results indicate that $CaCl_2$ treatment affects EIS parameters differently and that changes in ionic composition should be considered when interpreting the electrical response of $CaCl_2$-treated plant tissue.

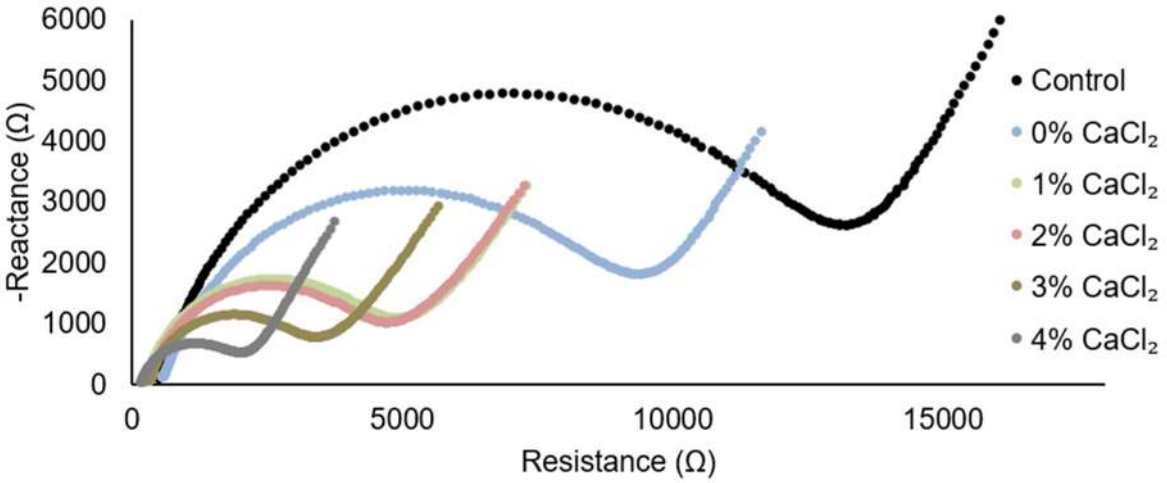

Fig. 1 Cole–Cole plots of carrot tissue treated with different $CaCl_2$ concentrations.

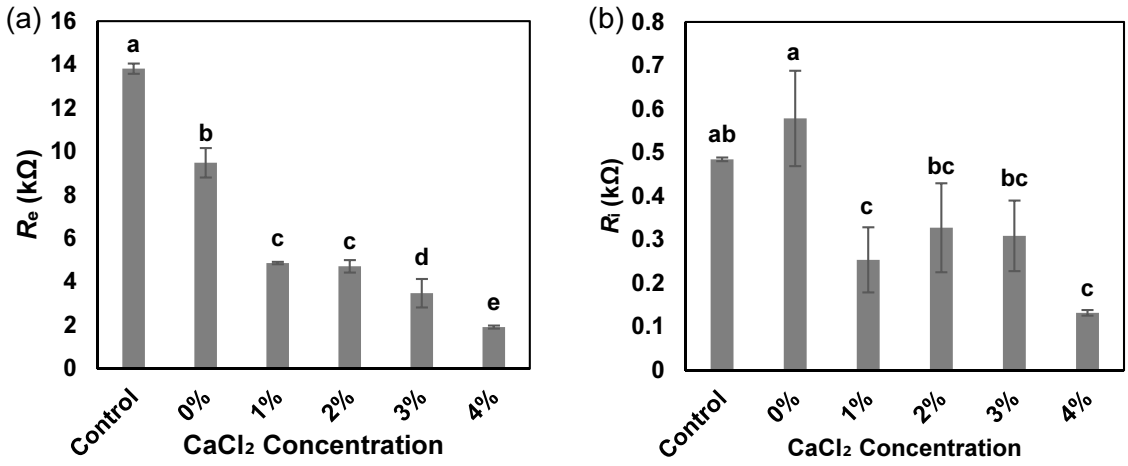

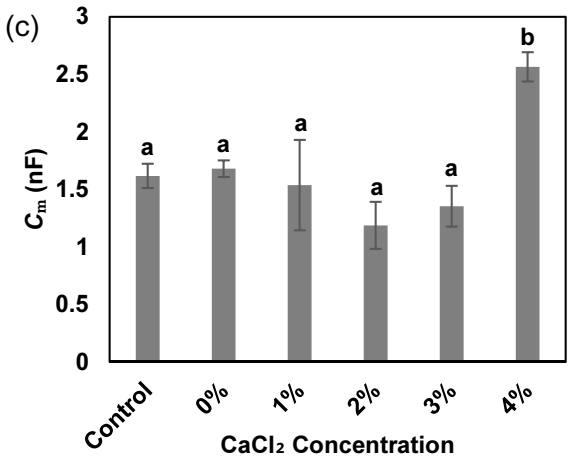

Fig. 2 Electrical impedance parameters, (a) extracellular resistance (R_e), (b) intracellular resistance (R_i), and (c) cell membrane capacitance (C_m) of carrot tissue treated with different concentrations of $CaCl_2$ using vacuum impregnation. Values are presented as mean and standard deviation (SD). Different lowercase letters indicate significant differences among treatments ($P < 0.05$, Tukey's test following one-way ANOVA).

CONCLUSIONS

This study provides a better understanding of the structural and electrical changes occurring in carrot tissue after $CaCl_2$-assisted vacuum impregnation. R_e and R_i generally decreased with increasing $CaCl_2$ concentration, while C_m showed a non-linear response. Changes in firmness and pectin characteristics also showed that $CaCl_2$ treatment affected the mechanical and cell-wall properties of the tissue. These findings suggest that the EIS response is influenced not only by structural changes but also by changes in the ionic environment caused by the introduction of Ca^{2+} and Cl^-. Thus, both tissue structure and ionic conductivity should be considered when interpreting the electrical properties of $CaCl_2$-treated plant tissues.

REFERENCES

Cao, L., Lu, W., Mata, A., Nishinari, K., and Fang, Y. 2020. Egg-box model-based gelation of alginate and pectin: A review. Carbohydrate polymers, *242*, 116389.

Ando, H., & Imaizumi, T. 2021. Changes in electrical properties and void distribution of mung bean sprouts during hot water heating. Food Science and Technology Research, *27*(2), 311-318.

Umehara, A., Oshima, T., Deshmukh, O. S., Nishizu, T., and Imaizumi, T. 2025. Detection of cell membrane disruption using electrical impedance spectroscopy and acceleration of cell wall modification in carrot processed under low temperature blanching. Journal of Food Engineering, *385*, 112270.

PH-17

Proceedings of The 12th International Symposium on Machinery and Mechatronics for Agriculture and Biosystems Engineering (ISMAB 2026)
20-24 October 2026, Busan, Republic of Korea

DEVELOPMENT OF AN ELECTRONIC NOSE FOR MONITORING GOCHUJANG FERMENTATION: GC–MS VOLATILE ANALYSIS AND SENSOR RESPONSE EVALUATION

Minhyun Kim[12], Jiwon Ryu[13], Dong-Heun Sung[12], Trinh Thanh Duy[12], Lee Uik[12], Ghiseok Kim[123*]

[1] Department of Biosystems Engineering, Seoul National University, Seoul, Republic of Korea
[2] Global Smart Farm Convergence Major, Seoul National University, Seoul, Korea
[3] Research Institute of Agriculture and Life Sciences, Seoul National University, Seoul, Korea
* Corresponding Author– Voice: +82-2-880-4603, Email: ghiseok@snu.ac.kr

Abstract: Gochujang fermentation involves dynamic physicochemical and volatile changes that influence its characteristic flavor and quality. This study evaluates the applicability of an electronic-nose system for monitoring these changes during gochujang fermentation and relates sensor responses to volatile compounds identified by solid-phase microextraction gas chromatography–mass spectrometry (SPME-GC-MS). Gochujang samples were collected at six fermentation stages: 0, 5, 10, 15, 20, and 25 days. At each stage, pH, amino nitrogen, salt content, and titratable acidity were measured to characterize physicochemical changes during fermentation. For sensor measurements, each sample and the sensor system were placed together in a sealed chamber and allowed to equilibrate before measurement. Gas responses were obtained using three sensor types: metal oxide semiconductor (MOS), photoionization detector (PID), and electrochemical sensors. The temporal variation in individual sensor signals and sensor-response patterns was evaluated across the fermentation period. Volatile compounds were analyzed using SPME-GC-MS to identify fermentation-related changes in aroma profiles. Relationships between physicochemical properties, sensor responses, and volatile compounds were further explored using multivariate statistical analysis. This integrated approach is expected to provide fundamental data for developing an electronic-nose-based system for rapid monitoring and quality evaluation of gochujang fermentation.

Key Words: Electronic nose; SPME-GC-MS; Gochujang Fermentation; Volatile compound; Gas Sensors

ACKNOWLEDGEMENTS (optional)

This work was supported by Korea Institute of Planning and Evaluation for Technology in Food, Agriculture and Forestry(IPET) through High Value-added Food Technology Development Program, funded by Ministry of Agriculture, Food and Rural Affairs(MAFRA)(RS-2024-00402850).

PH-18

Proceedings of The 12th International Symposium on Machinery and Mechatronics for Agriculture and Biosystems Engineering (ISMAB 2026)
20-24 October 2026, Busan, Republic of Korea

EARLY DETECTION OF FUTURE BROWNING SITES IN BASIL LEAVES USING HYPERSPECTRAL IMAGING

Ayumu Yamada[1], Shinichiro Kuroki[2*]

[1]Graduate School of Agricultural Science, Kobe University, 1-1 Rokkodai, Nada-ku, Kobe 6578501 Japan
[2]Graduate School of Agricultural Science, Kyoto University, Kitashirakawa Oiwake-cho, Sakyo-ku, Kyoto 6068502 Japan
*Corresponding Author-- Voice: +81-75-753-6170, Email: kuroki.shinichiro.4c@kyoto-u.ac.jp

Abstract: Basil leaves are highly susceptible to postharvest browning, which reduces their commercial value. Early and non-destructive detection of changes preceding visible browning could contribute to quality control and reduction of postharvest losses. This study aimed to detect early signs of browning using near-infrared (NIR) hyperspectral imaging and to evaluate its potential for identifying leaf regions at risk of subsequent browning.
Hydroponically cultivated sweet basil leaves were stored for 14 days at 4, 8, and 12 °C (three leaves per condition). RGB and hyperspectral images were acquired daily. RGB images were captured using a digital single-lens reflex camera, whereas hyperspectral images were acquired at 99 wavelengths between 1105–1672 nm. Polarizers were arranged in a crossed configuration to reduce specular reflection. To track the same leaf regions over time, all images were spatially aligned and standardized to 0.17 mm pixel^{-1}. Pixel-value variations due to imaging conditions were corrected using references captured alongside the samples: a color chart for RGB images and the reflectance of a silicone septum for hyperspectral images. We calculated the a* value of each pixel from the RGB images and normalized it to the value on day 0. We then extracted browning pixels using a threshold corresponding to visually detectable browning. For pixels browned by day 14, we traced their histories backward and defined the first day of continuous browning as the "browning onset day." We categorized the pixels according to browning onset day, whereas those remaining unbrowned by day 14 were assigned to the "non-browning group." Abraded regions and vein shadows were excluded from the analysis. This retrospective pixel tracking allowed pre-browning spectral changes to be examined at locations where browning subsequently developed. We mean-centered the reflectance spectra of all analyzed pixels and performed principal component analysis (PCA). Temporal changes in the second principal component (PC2) scores were then compared among groups.
Except for the group that browned within 1–5 days after harvest, browned groups' PC2 scores generally decreased during the first 2–3 days after harvest then increased several days prior to the browning onset day, whereas the non-browning group exhibited only minor fluctuations. Thus, the PC2 trajectory differed not only between browning and non-browning pixels but also according to browning timing. The PC2 loading showed a marked contribution around 1450 nm, a wavelength region strongly associated with water absorption, suggesting that pre-browning PC2 changes may reflect changes in tissue water status accompanying chilling injury. These results indicate that temporal changes in NIR spectral characteristics are associated with subsequent browning. Hyperspectral imaging may therefore provide a non-destructive means of identifying basil leaf regions at elevated risk of future browning before visible symptoms appear.

Key Words: chilling injury; near-infrared spectroscopy; pixel-wise analysis; spectral trajectory

PH-19

Proceedings of The 12th International Symposium on Machinery and Mechatronics for Agriculture and Biosystems Engineering (ISMAB 2026)
20-24 October 2026, Busan, Republic of Korea

DEEP SPECTRAL-SPATIAL LEARNING FOR APPLE BRUISE DETECTION AND INTERNAL DAMAGE ESTIMATION USING HYPERSPECTRAL IMAGING

Jiwon Ryu[1,2], Chang-Hyup Lee[1,3], Sang-Yeon Kim[1,2], Sungjay Kim[1,2], Minhyun Kim[1,3], Dong Heun Sung[1,3], Ghiseok Kim[1,2,3*]

[1] Department of Biosystems Engineering, Seoul National University, Seoul, Republic of Korea
[2] Research Institute of Agriculture and Life Sciences, Seoul National University, Seoul, Republic of Korea
[3] Integrated Major in Global Smart Farm, Seoul National University, Seoul, Republic of Korea
*Corresponding Author-- Voice: +82-2-880-4603, Email: ghiseok@snu.ac.kr

Abstract: Bruises are common postharvest defects of apples whose appearance varies with surface location, impact severity, and time after impact, complicating visual detection particularly during the early stages of bruising. To address this challenge, four three-dimensional (3D) U-Net variants of spectral-spatial encoders were compared for bruise detection from visible/near-infrared (Vis/NIR) hyperspectral images. Furthermore, features learned by the bruise detector were reused to classify impact level and estimate internal cross-sectional bruise area. Controlled bruises were induced at three impact levels and multiple surface locations on 87 Fuji apples. Hyperspectral images were acquired from six views over 18 days of storage, resulting in 870 image cubes with 1,676 annotated bruise instances. Bruise depth and internal cross-sectional area of browned tissue were measured by destructive sectioning. Among the four models, Hybrid 3D-2D U-Net achieved the highest test bounding box F1 score of 0.98 and a mask Dice score of 0.86. The model outperformed baseline detectors using inputs with three channels derived from principal component and band-ratio transformations, particularly for early, mild, and peripheral bruises, maintaining the F1 score above 0.98. Half-precision inference preserved both accuracy metrics at 87.63 frames per second. For the bruise severity estimation, models incorporating pretrained encoder features of bruise detection model achieved a test macro-averaged F1 score of 0.83 for impact level classification and a test Pearson r of 0.82 for internal cross-sectional bruise area estimation, outperforming the baseline models based on the mean reflectance spectrum. These results indicated that deep spectral-spatial learning supported robust bruise detection while extending hyperspectral assessment from bruise localization to estimation of internal damage severity.

Key Words: Apple, Bruise, Hyperspectral imaging, Nondestructive evaluation, Postharvest quality

ACKNOWLEDGEMENTS

This work was supported by Korea Institute of Planning and Evaluation for Technology in Food, Agriculture and Forestry (IPET) through High Value-added Food Technology Development Program, funded by Ministry of Agriculture, Food and Rural Affairs(MAFRA) (RS-2022-IP322054) and (2) the Unmanned Vehicle Core Technology Development Program of the Ministry of Science and ICT (MSIT) and the National Research Foundation of Republic of Korea (NRF) in 2026 (No. NRF-2023M3C1C1A01098410).

PH-20

Proceedings of The 12th International Symposium on Machinery and Mechatronics for Agriculture and Biosystems Engineering (ISMAB 2026)
20-24 October 2026, Busan, Republic of Korea

STARCH DIGESTIBILITY OF COOKED RICE WITH DIFFERENT POLISHING DEGREES

Yukiharu Ogawa[1*], Masatsugu Tamura[2]

[1]Graduate School of Horticulture, Chiba University, 648, Matsudo, Matsudo, 271-8510, Japan
[2]School of Agriculture, Utsunomiya University, 350, Mine-Machi, Utsunomiya, 321-8505, Japan
*Corresponding Author-- Voice: +81-47-308-8848, Email: ogwy@faculty.chiba-u.jp

Abstract: Rice (Oryza sativa L.) is one of the major carbohydrate sources, particularly in Asian countries. Brown rice is typically polished to remove the bran layer because the bran negatively affects the sensory qualities of cooked rice. It is also well known that cooked brown rice exhibits lower starch digestibility than polished rice. However, the bran layer contains various nutritional components, including proteins and lipids. Therefore, partially polished rice is sometimes produced to achieve a balance between nutritional value and sensory quality, although the starch digestibility of cooked partially polished rice has not been theoretically investigated. In this study, the starch digestibility of cooked rice with different polishing degrees was evaluated using a simulated in vitro gastrointestinal digestion method. Brown rice was polished to retain 99%, 97%, 95%, and 93% of its original weight, while rice polished to 90% of its original weight was used as a conventional polished-rice control. Each sample was cooked using a household rice cooker, and its starch digestibility was determined. The results showed that both the equilibrium starch hydrolysis percentage and the calculated hydrolysis rate of partially polished rice were comparable to those of conventional polished rice, whereas cooked brown rice exhibited significantly lower digestibility. Scanning electron microscopy of the cooked grain surface revealed that the bran layer was progressively removed with increasing polishing degree, resulting in gradual exposure of the endosperm. These exposed regions likely facilitated the penetration of digestive enzymes into the grain. Consequently, the starch digestibility of partially polished rice was nearly equivalent to that of conventional polished rice.

Key Words: Rice, Polishing, Bran layer, Starch digestibility, Kinetic constant

Post-harvest and Food Processing 4 (PH-4)



PH-21

Proceedings of The 12th International Symposium on Machinery and Mechatronics for Agriculture and Biosystems Engineering (ISMAB 2026) 20-24 October 2026, Busan, Republic of Korea

MILLIMATER-WAVE TRANSMISSION IMAGING FOR DETECTION OF FOREIGN MATERIAL IN POWDERED PARSLEY AND "AJINOMOTO"

Ayano Tamaoki[1], Kensuke Nakasuka[2], Tetsuhito Suzuki[2*]

[1]1577 Kurimamachiya-cho, Tsu, Faculty of Bioresources, Mie University, Japan
[2]1577 Kurimamachiya-cho, Tsu, Graduate School of Bioresources, Mie University, Japan
*Corresponding Author-- Voice: +81-59-231-9599, Email: t-suzuki@bio.mie-u.ac.jp

Abstract: Foreign material contamination is one of the problems in food manufacturing today, and it is particularly difficult to detect low-density foreign material in powdered foods. We have demonstrated that millimeter-wave irradiation of foreign material in parsley can detect foreign material from the concentric circles (diffraction pattern) that are generated around the material, even if it is smaller than the wavelength of the millimeter-wave. For this purpose, it is desirable that the detector be placed close to the object for imaging. In this study, a line inspection system combining a belt conveyor and a millimeter-wave linear camera was constructed, and foreign material inspection of plastic and rubber in parsley was demonstrated. Finally, the image features of background in some powdered foods such as parsley and "Ajinomoto" were compared to evaluate the potential for application in various powdered foods.

Cylindrical (size: 1, 2, 3 mm; material: plastic and rubber) foreign materials were fixed at equal intervals on the surface of a plastic belt with high millimeter-wave transmission. The belt was conveyed with a speed of 53 mm/s while feeding dried powdered parsley and Ajinomoto from a hopper at powder thicknesses of 4 and 6 mm. During the conveyance, millimeter waves with a frequency of 100 GHz (a wavelength of 3 mm) were vertically irradiated downward toward the belt, and transmission images were acquired by a linear camera placed just below the belt at 10 mm, with a line rate of 1000 Hz. The above image acquisition was repeated for a total of 70 images.

Circular patterns appeared in the transmission images at the position of the foreign material, and the larger oreign materials exhibited clearer circular diffraction patters. As a result of stacking parsley and Ajinomoto at powder thicknesses of 4 and 6 mm, Ajinomoto tended to have a coarser texture and higher density and to show rough background noise in the images than parsley, making it difficult to distinguish even foreign objects as small as 3 mm.

Key Words: Foreign material, Millimeter wave, Persley, Transmission imaging, Neural network analysis

INTRODUCTION

Foreign material contamination is one of the problems in food manufacturing today, and it is particularly difficult to detect low-density foreign material in powdered foods. Food production lines often equip a metal detector and/or X-ray imaging system to eliminate hard foreign objects

such as metals and stones(Morita,2003). However, organic objects with low density such as rubber and plastic are not detected because it is difficult to contrast them with food material. We have demonstrated that millimeter-wave irradiation of foreign material in parsley can detect foreign material from the concentric circles (diffraction pattern) that are generated around the material, even if it is smaller than the wavelength of the millimeter-wave(Yoshida,2019). For this purpose, it is desirable that the detector be placed close to the object for imaging. Additionally, in order to demonstrate the principle to actual food inspection, line inspection system with conveyer and sensing units is necessary. In this study, a line inspection system combining a belt conveyor and a millimeter-wave linear camera was constructed, and foreign material inspection of plastic and rubber in parsley and Ajinomoto was demonstrated. In addition, the effects of powder material and thickness on background noise were investigated.

MATERIALS AND METHODS

Cylindrical (size: 1, 2, 3 mm; material: plastic and rubber) foreign materials were fixed at equal intervals on the surface of a plastic belt with high millimeter-wave transmission. The belt was conveyed with a speed of 53 mm/s while feeding dried powdered parsley and Ajinomoto from a hopper at powder thicknesses of 4 and 6 mm. An IMPATT diode oscillator (TeraSense Inc., USA) was used as the millimeter-wave source, and a 256-element line sensor (TeraSense Inc., USA) was used for detection. During the conveyance, millimeter waves with a frequency of 100 GHz (a wavelength of 3 mm) were vertically irradiated downward toward the belt, and transmission images were acquired by a linear camera placed just below the belt at 10 mm, with a line rate of 1000 Hz(Nakasuka,2026).

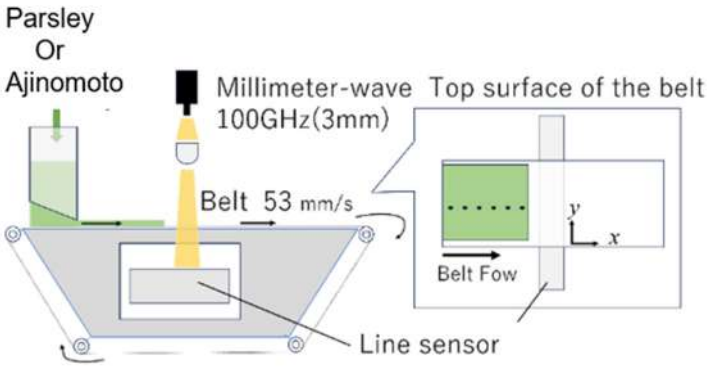

Fig.1 Schematic of the inspection system.

RESULT AND DISCUSSION

Background comparison

The background images of parsley and Ajinomoto were first compared visually. The image exhibited a stronger granular texture and greater background noise in the Ajinomoto than the parsley image as shown in Fig 2. However, quantitative analysis of the central region of the acquired images (15 pixels vertically × 30 pixels horizontally) showed only small differences in the image statistics. At a powder thickness of 4 mm, the mean pixel intensity and standard deviation were 123.9 and 19.6 for parsley, and 125.3 and 22.7 for Ajinomoto, respectively. At a powder thickness of 6 mm, these values were 123.3 and 22.0 for parsley, and 122.1 and 21.1 for Ajinomoto, respectively, as shown in Fig. 3. The change in mean intensity with powder thickness was larger for Ajinomoto than for parsley. In addition, the standard deviation increased with powder thickness for parsley, whereas it decreased for Ajinomoto. These results suggest that the effect of powder thickness on the image features depends on the powder

material. Furthermore, the mean intensity and standard deviation alone could not fully explain the visually observed differences between the two background images, suggesting that other image features may also contribute to these differences.

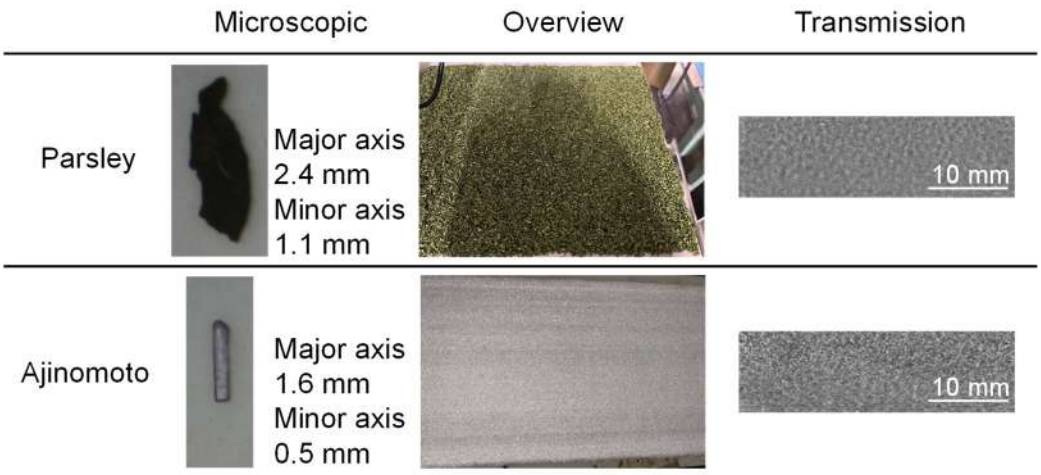

Fig.2 Appearance and transmission images obtained from parsley and Ajinomoto.

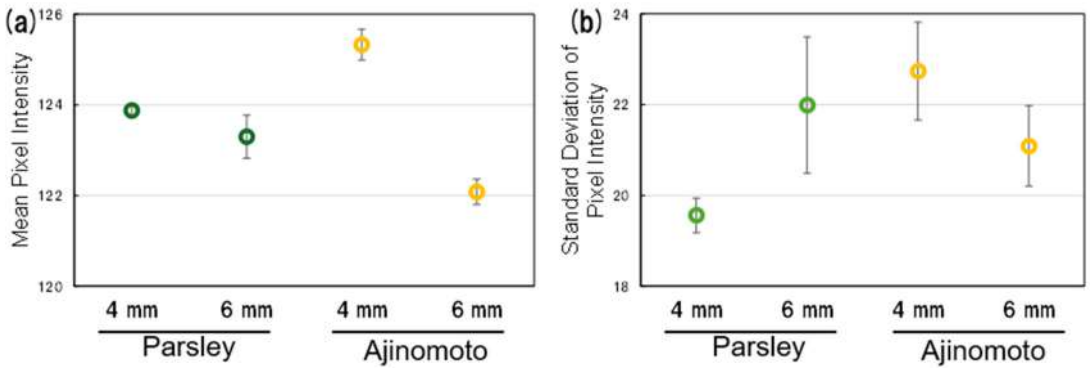

Fig.3 Comparison of image statistics between parsley and Ajinomoto
(a) mean pixel intensity and (b) standard deviation of pixel intensity.

Diffraction pattern of foreign objects

Circular diffraction patterns appeared at the locations of the foreign objects in the transmitted images, confirming the diffraction effect caused by the foreign particles. The diffraction patterns became more distinct as the particle size increased. When the foreign objects were covered with a 4 mm-thick layer of parsley, the diffraction patterns produced by the 1- and 2-mm foreign objects were obscured by the background texture and could not be visually distinguished. In contrast, the background texture of Ajinomoto appeared rougher than that of parsley, making it difficult to visually identify even the diffraction pattern of the 3-mm foreign object. For parsley, a deep learning–based pattern recognition method was investigated to detect diffraction patterns embedded in the complex background texture, demonstrating promising performance for practical foreign-object detection. A deep learning model will also be developed and evaluated for Ajinomoto images to investigate whether reliable foreign-object detection can be achieved under the more complex background texture.

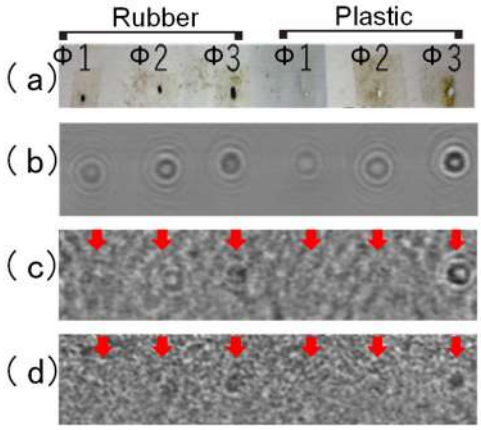

Fig.4 Transparent image obtained (a)appearance (b) without parsley, (c) with 4 mm-thick parsley layer and (d) with 4 mm-thick Ajinomoto layer.
(Red arrows indicate the positions of the foreign objects.)

CONCLUSIONS

A transmission imaging system using millimeter waves was constructed to detect low-density foreign objects such as rubber and plastic. A system equipped with a millimeter-wave light source, line sensor, and belt conveyor was constructed to capture images while moving the parsley and Ajinomoto to obtain real-time transmission images. When comparing the transparent images, Ajinomoto tended to have a coarser texture than parsley, making it difficult to distinguish even foreign objects as small as 3 mm. A neural network model was constructed to detect the circular diffraction patterns caused by the presence of foreign objects in transmitted images of parsley. Because the model demonstrated promising performance for practical foreign-object detection, the same approach is planned to be applied to Ajinomoto(Nakasuka,2026).

ACKNOWLEDGEMENTS

This work was supported by JSPS KAKENHI [Grant Number 24K01878 and 24K21900].

REFERENCES

Morita, K., Ogawa, Y., Thai, C.N., Tanaka, F. 2003. Soft X-Ray image analysis to detect foreign materials in foods. *Food Science and Technology Research*. 9(2):137-141.

Yoshida, R., Ogawa, Y., Kodama, Y., Nakajima, A., Suzuki, T., Kondo, N. 2019. Relationship between size of foreign objects in dried parsley and transmitted millimeter wave intensity distribution. *Journal of the Japanese Society of Agricultural Machinery and Food Engineers*. 81(3): 159–167.

K. Nakasuka, “Foreign Material Detection in Powdered Parsley Using Deep Learning of Millimeter-Wave Transmission Images,” Master’s thesis, Mie University, 2026.

PH-22

Proceedings of The 12th International Symposium on Machinery and Mechatronics for Agriculture and Biosystems Engineering (ISMAB 2026)
20-24 October 2026, Busan, Republic of Korea

WIRELESS SENSING SYSTEM WITH AN ONION MIMIC FOR AMBIENT TEMPERATURE, HUMIDITY, AND INTERNAL TEMPERATURE

Uik Lee[1], Jaeeun Lee[1,2], Sang-Yeon Kim[1,2], Ghiseok Kim[1,2,3*]

[1]Department of Biosystems Engineering, Seoul National University, Rep. Korea
[2]Integrated Major in Global Smart Farm, Seoul National University, Rep. Korea
[3]Research Institute of Agriculture and Life Sciences, Seoul National University, Rep. Korea
*Corresponding Author-- Ghiseok Kim, Email: ghiseok@snu.ac.kr

Abstract: Onion prices are highly volatile in South Korea. Because stored onions supply the market until the following spring, storage losses contribute to price fluctuations. According to a Rural Development Administration survey, unsuitable storage temperature and humidity shortened storage life by at least one month and increased decay losses to 15–25%, with particularly severe losses under continuous exposure to relative humidity of 90% or higher. Condensation on onion surfaces can leave moisture that promotes decay. Storage facilities generally monitor air temperature and humidity, allowing dew-point calculation but leaving onion temperature unknown. Onion temperature lags behind air temperature during door opening, defrosting, and gradual cooling after loading. Sensors inserted into real onions are unsuitable as long-term references because of respiration, water loss, and decay progressively alter the tissue. Condensation risk can be assessed by comparing the dew point with onion surface temperature. Adapting artificial-fruit approaches reported for apples and mangoes, a mimic with onion-like thermal properties placed among stored onions could provide a proxy for onion temperature through internal measurements. This study aims to develop a wireless sensing system that simultaneously monitors mimic internal temperature and ambient temperature and humidity using a mimic designed to mimic onion thermal behavior. The sensor node comprises a 30-mm-diameter board incorporating a single-chip module with integrated wireless communication, designed to fit within the mimic's upper section. Separate flexible sensor circuits position a core-temperature sensor at the center and a temperature–humidity sensor with a waterproof filter on the shell side. Nonvolatile memory was incorporated to retain measurements during communication outages. A capacitor-assisted power supply was designed to support peak transmission currents and enable extended operation from a single coin cell. The planned mimic comprises an onion-shaped shell designed for 3D printing and a gellan-gum hydrogel filling formulated, based on biological-tissue phantom recipes, to match onion thermal properties. Node performance and mimic thermal responses relative to real onions will be evaluated experimentally. The main board and both sensor circuits have been fabricated and assembled. Firmware has been developed for startup self-diagnostics, periodic measurement and transmission, and receiver-side error detection and decoding. Dew-point calculation, comparison with mimic temperature, data logging, and low-power standby remain to be implemented. Mimic fabrication and validation of the relationships between mimic temperature and actual onion internal and surface temperatures are also pending. The planned mimic

internal-temperature and condensation-risk information will serve as candidate inputs to an onion storage-loss prediction model in a related project. Modifying mimic geometry and filling composition could extend this approach to other stored agricultural products. The node could also support monitoring in distribution environments, such as transport vehicles, or accommodating other sensors using the same interface.

Key Words: Produce Mimic, Wireless Sensing System, Internal Temperature, Condensation, Onion Storage

ACKNOWLEDGEMENTS

This work was supported by the Cooperative Research Program for Agriculture Science and Technology Development (Project Nos. RS-2022-RD010022 and RS-2022-RD010023), Rural Development Administration (RDA), Republic of Korea.

PH-23

Proceedings of The 12th International Symposium on Machinery and Mechatronics for Agriculture and Biosystems Engineering (ISMAB 2026)
20-24 October 2026, Busan, Republic of Korea

NON-DESTRUCTIVE ESTIMATION OF THEANINE CONTENT IN FRESH SHADE-GROWN TEA LEAVES USING MULTI-EXCITATION FLUORESCENCE IMAGING

Mao Ito[1], Tsutomu Niwa[2], Tomoko Matsuda[3], Tetsuhito Suzuki[1*]

[1]1577 Kurimamachiya-cho, Tsu, Graduate School of Bioresources, Mie University, Japan
[2]992-2 Tsubakiyocho, Kameyama, Mie Prefecture Agricultural Research Institute, Japan
[3]13 Komeicho, Tsu, Crops and Horticulture Division, Agriculture, Forestry and Fisheries Department, Mie Prefecture, Japan
*Corresponding Author-- Voice: +81-59-231-9599, Email: t-suzuki@bio.mie-u.ac.jp

Abstract: Kabuse tea is a shaded green tea produced by covering tea plants before harvest. Theanine is an important quality indicator, and a simple, rapid, and non-destructive method for estimating its content is desirable. Previous studies have reported relationships between fluorescence image features and theanine content and differences in fluorescence characteristics among excitation wavelengths. These findings suggest that combining fluorescence information obtained under multiple excitation wavelengths may improve the estimation of theanine content. Therefore, this study aimed to evaluate whether integrating fluorescence image features acquired under ultraviolet, violet, and blue excitation wavelengths improves the accuracy of theanine estimation in fresh Kabuse tea leaves.

Fresh Kabuse tea leaves of the cultivar ‘Yabukita’ cultivated at the Mie Prefecture Agricultural Research Institute were used. Non-shaded, 85% shaded, and 98% shaded conditions were established, with shading periods of 15, 18, and 21 days before harvest. The first bud with three leaves was collected and numbered L1–L3 from the top. Color and fluorescence images were acquired under white LED illumination and 365, 420, and 465 nm excitation (UV-FL, V-FL, and B-FL, respectively) using a digital camera equipped with a 450 nm long-pass filter. Mean RGB intensities were calculated from leaf regions excluding veins and stems. Partial least squares regression (PLSR) was used to develop theanine estimation models using 75 samples. Five-fold cross-validation was performed to evaluate model performance, with theanine content measured by HPLC as the response variable and RGB features from L1–L3, together with leaf area, as explanatory variables.
The model using only UV-FL features achieved a coefficient of determination (R^2) of 0.49. Incorporating color, V-FL, and B-FL image features improved the prediction accuracy to $R^2 = 0.78$, suggesting that fluorescence information obtained under different excitation wavelengths provided complementary information for theanine estimation. To further improve the prediction accuracy, variation in developmental stage within the

same L1–L3 categories were considered. Therefore, the PLSR model was reconstructed by adding leaf area extracted from the images as an explanatory variable to reflect variation in developmental stage within the same leaf-position category. The addition of leaf area further improved the prediction accuracy, resulting in an R^2 of 0.81, an RMSE of 1.29, and an RPD of 2.30. VIP analysis identified the R and B features of UV-FL images, the R and G features of V-FL images, and leaf area as important explanatory variables, with VIP scores of 1 or higher across two or more leaf positions.

These results demonstrate that combining multi-wavelength fluorescence image features with growth-related information improves the estimation of theanine content in fresh Kabuse tea leaves and may contribute to a rapid and non-destructive method for evaluating Kabuse tea quality.

Key Words: fluorescence imaging, Kabuse tea, theanine, multiple excitation wavelengths, partial least squares regression

INTRODUCTION

Mie Prefecture is the largest producer of Kabuse tea in Japan, a type of shaded green tea cultivated by covering the tea plants for a certain period before harvest to enhance the umami-related amino acid theanine. Because theanine content is positively correlated with both tea quality and market value. Conventional methods for measuring theanine content include high-performance liquid chromatography (HPLC) and near-infrared spectroscopy. However, these are destructive testing methods, and due to their measurement time and cost, making rapid measurement of theanine content in production and distribution settings difficult. Therefore, there is a growing demand for a simple, rapid, and non-destructive method for estimating theanine content.

When fresh tea leaves are irradiated with ultraviolet light, they emit red fluorescence derived from chlorophyll and blue-green fluorescence associated with antioxidant compounds (Cerovic *et al.*, 1999). In a previous study, theanine estimation was investigated using tencha, the raw material for matcha, which is generally cultivated under longer shading periods than Kabuse tea. The study showed that an increase in red fluorescence associated with shading could be detected in ultraviolet-excited fluorescence images, and that theanine content could potentially be estimated using multivariate analysis based on image color features and the number of days of shading (Miyazaki, 2023). In addition, excitation-emission matrix (EEM) analysis revealed different fluorescence characteristics under 365 nm excitation and excitation wavelengths above 400 nm (Miyazaki, 2023). The result indicated that combining multiple excitation wavelengths may provide complementary information that cannot be obtained using a single excitation wavelength alone.

The cultivation methods and shading periods differ between tencha tea leaves examined in the previous study and Kabuse tea leaves examined in the present study. Tencha tea leaves are generally cultivated under relatively long-term shading using ‘tanagake’ covering, in which covering materials are placed over a frame above the tea plants (Kyoto Prefecture), whereas

Kabuse tea leaves are generally cultivated using ‘jikagake’ covering, in which covering materials are placed directly over the tea plants (Mori, 2015). Thus, the covering methods and cultivation conditions differ between the two types of tea. Therefore, the applicability of fluorescence imaging for estimating theanine content in fresh Kabuse tea leaves, particularly using multiple excitation wavelengths, needs to be further investigated. This study aimed to evaluate whether integrating fluorescence image features acquired under ultraviolet, violet, and blue excitation wavelengths improves the accuracy of theanine estimation in fresh Kabuse tea leaves.

MATERIALS AND METHODS

Fresh Kabuse tea leaves of the cultivar ‘Yabukita’ cultivated at the Mie Prefecture Agricultural Research Institute (Tsubakiyocho, Kameyama, Mie Prefecture) were used as experimental samples. To obtain samples with different theanine contents, three shading conditions (non-shaded, 85%, and 98% shading) were established, and each condition included three shading periods of 15, 18, and 21 days before harvest. The first bud with three leaves was collected from harvested tea shoots, and the leaves were numbered from the top as L1 to L3.

An imaging system consisting of a digital camera (Sony α7S III) equipped with a 450 nm long-pass filter was constructed (Fig. 1 (a)). Color images were acquired under white LED illumination, and fluorescence images were obtained under excitation wavelengths of 365, 420, and 465 nm, referred to as UV-FL, V-FL, and B-FL images, respectively. The exposure times for the color, UV-FL, V-FL, and B-FL images were 1/8 s, 13 s, 30 s, and 1 s, respectively. The ISO sensitivity was set to 400 for the color and B-FL images and to 1000 for the UV-FL and V-FL images. The aperture was fixed at F4.5 for all image acquisitions. Image analysis was performed using the mean R, G, and B pixel intensities of the leaf regions excluding the veins and stems (Fig. 1 (b)).

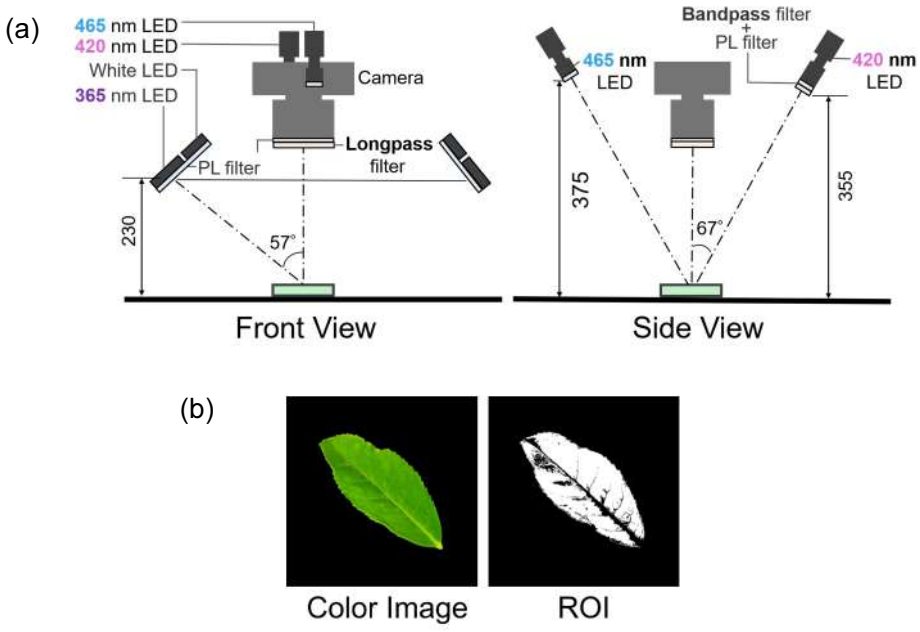

Fig.1 Image acquisition system and Region of Interest (ROI)

A theanine estimation model was developed using partial least squares regression (PLSR)

with 75 samples. The theanine content measured by HPLC was used as the response variable, while the RGB values (upper side) of L1–L3 extracted from color and multiple-excitation fluorescence images, together with leaf area, were used as explanatory variables. Five-fold cross-validation was performed to evaluate the model performance, and the optimal number of latent variables was determined based on RMSECV.

RESULTS & DISCUSSION

Representative images are shown in Fig. 2. The UV-FL images exhibited blue-green fluorescence, whereas the B-FL images showed a red fluorescence distribution different from that observed in the V-FL images, indicating that each excitation wavelength provided distinct fluorescence information.

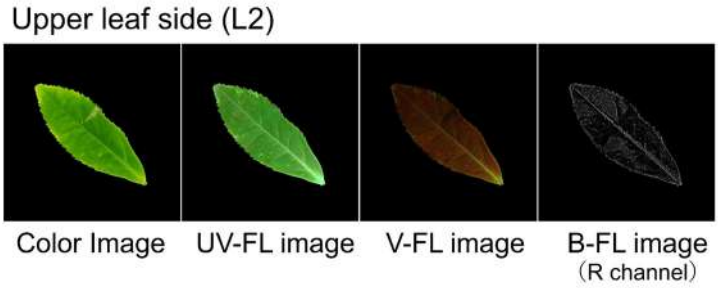

Fig.2 Color images and multi-excitation fluorescence images

PLSR was performed using the RGB values extracted from the color and fluorescence images. The prediction performance of the PLSR models using different feature sets is summarized in Table 1. When only the UV-FL image, which was reported to be effective in a previous study, was used, the coefficient of determination was $R^2 = 0.49$. Adding color image features improved R^2 to 0.57. Furthermore, incorporating V-FL and B-FL image features improved R^2 to 0.78, suggesting that fluorescence information obtained from multiple excitation wavelengths provided complementary information for theanine estimation. These results demonstrated that image-derived features alone could provide adequate prediction performance. To further improve the estimation accuracy, variation in developmental stage within the same leaf-position category was considered. Even within the same leaf position (L1–L3), leaves may differ in developmental stage, resulting in differences in leaf size. Therefore, the PLSR model was reconstructed by adding leaf area as an explanatory variable to reflect variation in developmental stage within the same leaf-position category and further improve the estimation accuracy.

Table 1 Prediction performance of PLSR models using different feature sets.

Features	R^2	RMSE	RPD
UV-FL	0.49	2.11	1.41
UV-FL + Color	0.57	1.93	1.54
UV-FL + Color + V-FL + B-FL	0.78	1.38	2.15

The addition of leaf area further improved the model performance, increasing R^2 from 0.78 to 0.81 and decreasing RMSE from 1.38 to 1.29 (Fig. 3) The resulting model achieved an RPD of 2.30, indicating a level of prediction accuracy suitable for quantitative prediction (Nicolai *et*

al., 2007). The prediction characteristics of the final model were further evaluated for each experimental group using the mean error and RMSE. The RMSE was larger in the shaded groups, which had medium to high theanine contents, than in the non-shaded group, indicating a tendency toward larger prediction errors under shaded conditions. Although the addition of leaf area improved the overall prediction accuracy, these results indicate that further improvement is needed to more accurately distinguish samples under different shading conditions.

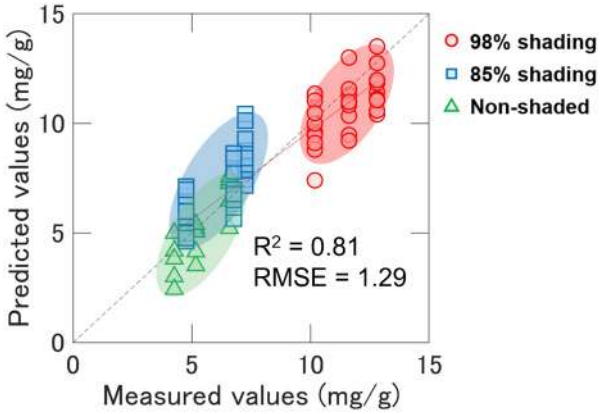

Fig.3 Relationship between measured and estimated theanine contents using the PLSR model with leaf area.

To identify the important explanatory variables in the theanine estimation model incorporating leaf area, variable importance in projection (VIP) scores were used to evaluate the contribution of each explanatory variable. As shown in Fig. 4, VIP scores of 1 or higher were observed for several image features and leaf areas across multiple leaf positions. In particular, the R and B features of UV-FL images, the R and G features of V-FL images, and leaf area showed high VIP scores in two or more of L1–L3. These results suggest that fluorescence features obtained under multiple excitation wavelengths, together with leaf area, were important explanatory variables for estimating theanine content.

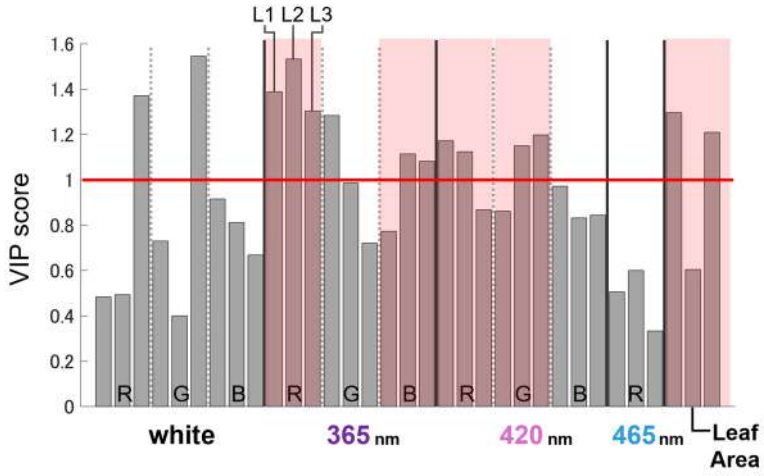

Fig.4 VIP scores of image features and leaf area in the PLSR model.

CONCLUSIONS

In this study, the feasibility of estimating theanine content in fresh Kabuse tea leaves using

fluorescence images acquired under multiple excitation wavelengths was investigated. The combination of color, V-FL, and B-FL image features improved the prediction accuracy compared with the model using only UV-FL features, suggesting that fluorescence information obtained from different excitation wavelengths provided complementary information for theanine estimation. The model incorporating multi-excitation image features achieved adequate prediction performance with an R^2 of 0.78. Furthermore, the addition of leaf area, as growth-related information obtained from fresh tea leaves, further improved the model performance, resulting in an R^2 of 0.81, an RMSE of 1.29, and an RPD of 2.30. These results suggest that combining multi-wavelength fluorescence image features with growth-related information may provide a promising approach for improving the non-destructive estimation of theanine content in fresh Kabuse tea leaves.

ACKNOWLEDGEMENTS

This work was supported by JSPS KAKENHI [Grant Number 24K21900] and Okasan-Kato Foundation.

REFERENCES

Cerovic, Z. G., G. Samson, F. Morales, N. Tremblay, and I. Moya. 1999. Ultraviolet-induced fluorescence for plant monitoring: Present state and prospects. Agronomie 19(7): 543-578. https://doi.org/10.1051/agro:19990701.

Kyoto Prefecture. n.d. Shade cultivation (covered tea cultivation). Kyoto Prefecture website. Accessed March 21, 2025. https://www.pref.kyoto.jp/chaken/mame_shade.html.

Miyazaki, M. 2023. Non-destructive Quantification of Leaf Maturity and Chemical Components of *Tencha* Fresh Leaves Using UV-induced Fluorescence. Master's thesis. Kyoto University, Kyoto, Japan.

Mori, N. 2015. Traditional tea “Ise-cha”: Aroma and taste. Journal of Japan Association on Odor Environment 46(2): 141–148. https://www.pref.kyoto.jp/chaken/mame_shade.html.

Nicolaï, B. M., K. Beullens, E. Bobelyn, A. Peirs, W. Saeys, K. I. Theron, and J. Lammertyn. 2007. Nondestructive measurement of fruit and vegetable quality by means of NIR spectroscopy: A review. Postharvest Biology and Technology 46(2): 99-118. https://doi.org/10.1016/j.postharvbio.2007.06.024.

PH-24

Proceedings of The 12th International Symposium on Machinery and Mechatronics for Agriculture and Biosystems Engineering (ISMAB 2026)
20-24 October 2026, Busan, Republic of Korea

NON-DESTRUCTIVE DETECTION OF INTERNAL FLESH ABNORMALITIES IN TILAPIA USING HYPERSPECTRAL IMAGING AND DEEP LEARNING

Pin-Wei Chen[1], Pi-Chung Wu[2], Kuo-Chi Liao[1], Shih-Fang Chen[1*]

[1]Department of Biomechatronics Engineering, National Taiwan University
[2]Fisheries Agency, Ministry of Agriculture
*Corresponding Author-- Voice: +886-2-3366-5354, Email: sfchen@ntu.edu.tw

Abstract: Tilapia production has declined continuously in recent years, while internal flesh abnormalities remain an important quality issue during production and processing. These abnormalities generally remain undetectable until the fish is sectioned, making quality inspection difficult and potentially causing production losses. To address this problem, this study applied hyperspectral imaging (HSI) combined with deep learning for the non-destructive detection of internal flesh abnormalities in tilapia. Two HSI systems covering different spectral ranges were evaluated, including visible-near-infrared HSI (VNIR HSI; 400–1000 nm) and near-infrared HSI (NIR HSI; 900–1700 nm). The study was divided into two phases. The first phase aimed to distinguish normal and abnormal fillets using only hyperspectral information acquired from the scaled external surface. Three one-dimensional convolutional neural network (1D-CNN) backbone architectures were compared. The 1D-CNN ResNet34 model achieved the best performance for both datasets, and fillet-level classification accuracies reached 0.92 for VNIR HSI and 0.98 for NIR HSI. The NIR HSI model showed the best abnormal fillet identification performance, with only one abnormal fillet misclassified in the testing set. In the second phase, visible lesion regions identified from the internal flesh images were mapped onto the external hyperspectral images to develop models for abnormality localization. The best pixel-level classification accuracies reached 0.66 and 0.69 for VNIR HSI and NIR HSI, respectively. Visualization of the prediction results showed that the predicted regions generally corresponded to the visible abnormalities on the internal flesh surface. These results demonstrate the potential of HSI for not only identifying abnormal tilapia fillets non-destructively but also providing spatial information for locating internal flesh abnormalities from the scaled external surface.

Key Words: Non-destructive assessment, Deep learning, Hyperspectral imaging, Aquaculture

INTRODUCTION

Tilapia plays an important role in Taiwan's aquaculture industry. However, internal flesh abnormalities can cause substantial losses during production and processing. One major challenge is that these abnormalities are generally not visible from the external surface and are often discovered only after the fish is sectioned. This makes it difficult to take preventive actions before processing and may also lead to conflicts between aquaculture farmers and fillet processors. Spectroscopic techniques can provide rapid and non-

destructive information related to the physical and chemical properties of biological materials. Moreover, hyperspectral imaging (HSI) simultaneously provides spectral and spatial information, allowing not only the identification of abnormal samples but also the spatial distribution of affected regions. Therefore, this study aims to develop non-destructive methods for detecting internal flesh abnormalities in tilapia using HSI combined with deep learning in two phases. Internal flesh abnormalities in this study refer to visible defects observed after sectioning, including mushy or deteriorated flesh, dark spots, and tail-region lesions (Fig 1), which are commonly associated with streptococcosis caused by *Streptococcus* spp. The goal of the first phase is to classify normal and abnormal samples while the second phase is to investigate whether internal abnormal regions could be located using only information obtained from the scaled external surface.



(a) (b) (c)

Fig.1 Demonstration of abnormal fillet from the internal side. (a) Normal fillet; (b)(c) fillets affected by streptococcosis.

MATERIALS AND METHODS

SAMPLE PREPARATION AND SPECTRAL DATA COLLECTION

Tilapia fillets were collected from multiple fishery cooperatives in Taiwan from 2024 to 2026. The flesh condition of each sample was evaluated by experienced fillet processors and classified as normal or abnormal. Before spectral measurement, the frozen vacuum-packed fillets were completely thawed. Hyperspectral images were acquired from both the scaled external surface and the internal flesh surface. Two hyperspectral cameras covering different spectral ranges were used (MVX and MVC NIR; Headwall Photonics, Inc., Bolton, MA, USA). The VNIR HSI camera covered a spectral range of 400-1000 nm with a spectral resolution of approximately 2 nm, while the NIR HSI camera covered 900-1700 nm with a spectral resolution of approximately 4 nm. The VNIR HSI dataset contained 357 fillets, including 156 normal and 201 abnormal samples, while the NIR HSI dataset contained 266 fillets, including 114 normal and 152 abnormal samples.

HSI PROCESSING AND MODEL DEVELOPMENT

The HSI analysis was divided into two phases. The first phase aimed to classify normal and abnormal fillets using hyperspectral images acquired only from the scaled external surface. The second phase was conducted to investigate whether internal abnormal

regions could be located using only hyperspectral information from the external surface. For the first phase, the fish region was first separated from the background. The external hyperspectral images were then divided into non-overlapping local windows. Windows containing at least 40% valid fish pixels were retained, while background regions were excluded. The spectra of the valid pixels within each retained window were averaged to generate one representative spectrum. Three one-dimensional convolutional neural network (1D-CNN) architectures, including VGG16, ResNet18, and ResNet34, were compared for classifying each window as normal or abnormal. The proportion of windows predicted as abnormal within each fillet was subsequently calculated, and a classification threshold was applied to determine the final fillet condition. For the second phase, visible lesion regions were manually annotated on the internal flesh images based on visual inspection. The annotated regions were labeled as Symptom, while the remaining fish regions were labeled as Without symptom. The resulting labels were then mapped onto the corresponding external hyperspectral images using Coherent Point Drift (CPD) (Myronenko & Song, 2010) for model development. Because the number of Without symptom pixels was substantially larger than that of Symptom pixels, random under-sampling was applied only to the Without symptom class in the training set to reduce class imbalance, while the validation and testing sets retained their original distributions. The same 1D-CNN architectures were subsequently applied for pixel-level classification to evaluate whether internal abnormal regions could be identified from the scaled external surface. Datasets were divided at the fillet level into training, validation, and testing sets at a ratio of 0.64:0.16:0.20. For the NIR HSI dataset, samples overlapping with the VNIR HSI testing set were retained in the testing set to provide a direct comparison between the two cameras.

RESULTS & DISCUSSION

For Phase 1, different window sizes and 1D-CNN backbones were evaluated for both HSI systems. The best performance for VNIR HSI was obtained using an 11 × 11-pixel window, while a 15 × 15-pixel window showed the best performance for NIR HSI. Among the three architectures, ResNet34 achieved the highest window-level classification accuracy for both datasets, reaching 0.75 for VNIR HSI and 0.80 for NIR HSI (Table 1). Using the ResNet34 predictions, the proportion of windows classified as abnormal within each fillet was further calculated. A threshold of 56% was applied to the VNIR HSI dataset, resulting in a fillet-level accuracy of 0.92, while a threshold of 38% achieved a fillet-level accuracy of 0.98 for the NIR HSI dataset. The NIR HSI dataset achieved the best performance for abnormal fillet identification, with only one abnormal fillet misclassified in the testing set (Fig. 2). For Phase 2, a similar performance trend was observed among the three backbones. ResNet34 again achieved the highest pixel-level classification accuracy, reaching 0.66 for VNIR HSI and 0.69 for NIR HSI, followed by ResNet18 and VGG16 (Table 2). Although the accuracies were moderate, visualization of the prediction results showed that the predicted lesion regions generally corresponded to the visible abnormal areas observed on the internal flesh surface (Fig 3). These results demonstrate that HSI can not only identify abnormal fillets from the scaled external surface, but also provide spatial information for estimating the location of internal flesh abnormalities.

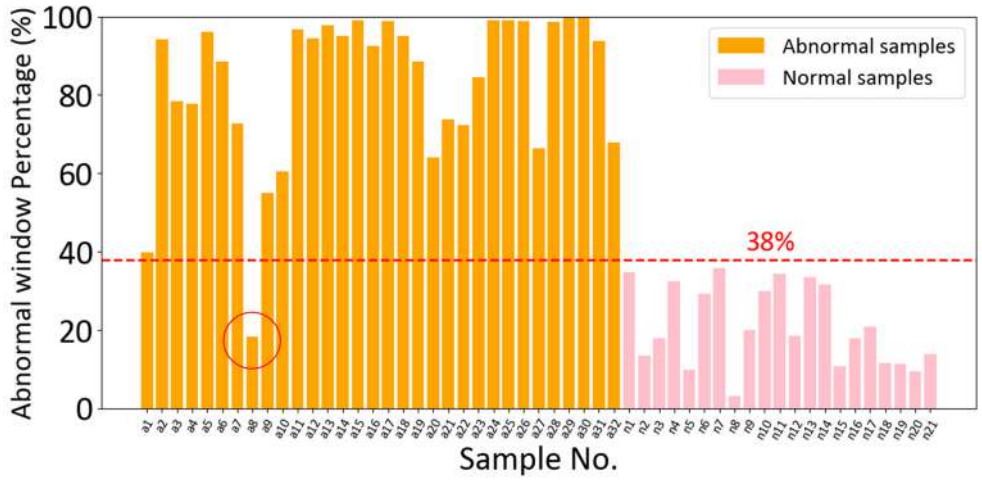

Fig.2 Distribution of abnormal window percentages predicted by the Phase 1 NIR HSI ResNet34 model, with the optimal fillet-level classification threshold (dashed line, 38%). Each bar represents one fillet.

Table 1 Classification accuracy of different 1D-CNN backbones in Phase 1.

Dataset \ Backbone	VGG16	ResNet18	ResNet34	Best model fillet-level accuracy
VNIR HSI	0.65	0.73	0.75	0.92
NIR HSI	0.69	0.75	0.80	0.98

Table 2 Classification accuracy of different 1D-CNN backbones in Phase 2.

Dataset \ Backbone	VGG16	ResNet18	ResNet34
VNIR HSI	0.60	0.64	0.66
NIR HSI	0.66	0.68	0.69

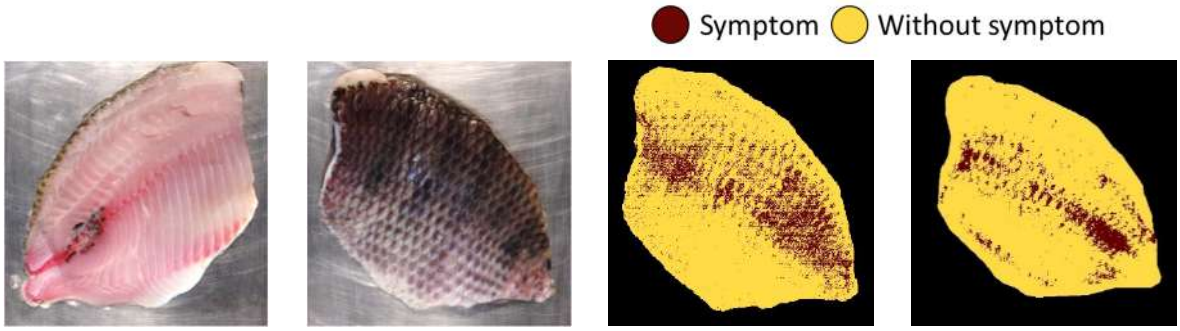

(a) (b) (c) (d)

Fig.3 Visualization of the phase 2 HSI 1D-CNN ResNet34 model.
(a) Inside image; (b) outside image; (c) VNIR HSI prediction; (d) NIR HSI prediction.

CONCLUSIONS

This study applied HSI combined with deep learning to develop a non-destructive method for detecting internal flesh abnormalities in tilapia from the scaled external surface.

Among the three 1D-CNN backbones, ResNet34 achieved the best performance for both VNIR HSI and NIR HSI. For Phase 1, the VNIR HSI and NIR HSI models achieved fillet-level classification accuracies of 0.92 and 0.98, respectively. For Phase 2, pixel-level classification accuracies reached 0.66 and 0.69, respectively, and the predicted regions generally corresponded to the visible abnormalities on the internal flesh surface. These results demonstrate that HSI has the potential not only to identify abnormal fillets non-destructively but also to provide spatial information for locating internal flesh abnormalities. Future work will focus on reducing CPD registration errors and exploring 2D- or 3D-CNN models to improve abnormality localization.

ACKNOWLEDGEMENTS

This research is supported by the Fisheries Agency, Ministry of Agriculture, Executive Yuan, Taiwan (115AS-6.3.1-F-04). The authors thank the participating fishery cooperatives and fillet processors for their support.

REFERENCES

Myronenko, A., & Song, X. 2010. Point set registration: Coherent point drift. *IEEE Transactions on Pattern Analysis and Machine Intelligence*, *32*(12), 2262-2275.

PH-25

Proceedings of The 12th International Symposium on Machinery and Mechatronics for Agriculture and Biosystems Engineering (ISMAB 2026)
20-24 October 2026, Busan, Republic of Korea

REAL-TIME MONITORING FOR ENDPOINT DETERMINATION IN COMMERCIAL-SCALE TWIN-SCREW FRUIT JUICE EXTRACTION

Dong-Hyeon Kim[1], Jae-Min Jung[2], Do-Hyeok Choi[2] and Wang-Hee Lee[1,2*]

[1]Department of Smart Agriculture Systems, Chungnam National University, Daejeon 34134, Republic of Korea
[2]Department of Smart Agriculture Systems Machinery Engineering, Chungnam National University, Daejeon 34134, Republic of Korea
*Corresponding Author-- Voice: +82-10-3550-4919, Email: wanghee@cnu.ac.kr

Abstract: Optimal conditions for juice extraction are commonly derived from laboratory-scale equipment, and these settings often fail to reproduce the same performance when transferred to commercial-scale operations. Process data acquired on commercial equipment under actual operating conditions are therefore required, yet continuous run-level data of this kind are rarely available. Hence, we aimed to determine when an individual extraction run can be terminated without a meaningful loss of juice recovery, using a real-time monitoring system installed on a commercial-scale twin-screw juice extractor. Apples and oranges, two fruits with contrasting tissue architecture, were processed in 20–kg batches under nine combinations of feeding and juicing screw speeds (3 × 3 factorial design; n = 18 runs), with seven process variables logged at 1 s intervals. Every time series was normalized to a 0-100% process progress scale, and the knee point of the cumulative juice curve was located at the point of maximum vertical distance between the normalized curve and the diagonal. Across runs that ranged from 1 min 18 s to 25 min 0 s, the knee point recovered a mean of 73.5% of the final juice within 49% of the processing time, corresponding to processing time savings of 24–76%. Apples reached the knee later than oranges (57% versus 41% of the processing time), which was consistent with the fibrous apple pomace being discharged more freely. The crossover point, at which the accumulated juice mass first exceeded the remaining input mass, occurred after 25–53% of the processing time at a juice recovery of 58–68% and required no curve fitting. The real-time yield stabilized within 1.6 (apples) and 0.8 (oranges) percentage points of its final value by 60% of the process progression. Based on the results, we concluded that continuous run-level monitoring converts the termination of juice extraction into a quantitative, in-process decision that can be implemented on existing monitoring hardware.

Key Words: Food processing, Juice yield, Knee-point detection, Postharvest management, Time-series data

ACKNOWLEDGEMENTS

This work was carried out with the support of "Cooperative Research Program for Agriculture Science and Technology Development (Project No. RS-2022-RD010012)" Rural Development Administration, Republic of Korea.

PH-26

Proceedings of The 12th International Symposium on Machinery and Mechatronics for Agriculture and Biosystems Engineering (ISMAB 2026)
20-24 October 2026, Busan, Republic of Korea

POST-HARVEST METABOLIC DYNAMICS IN LETTUCE AND THEIR ASSOCIATION WITH HYPERSPECTRAL RESPONSES

K.R.T. Amani Kahandawa[1,2], Yuzu Shiota[2], Shinichiro Kuroki[2*]

[1]Graduate School of Agricultural Science, Kobe University, 1-1 Rokkodai, Nada-ku, Kobe 6578501 Japan
[2]Graduate School of Agriculture, Kyoto University, Kitashirakawa Oiwake-cho, Sakyo-ku, Kyoto 6068502 Japan
*Corresponding Author-- Voice: +81-75-753-6170, Email: kuroki.shinichiro.4c@kyoto-u.ac.jp

Abstract: Postharvest quality changes in leafy vegetables are accompanied by complex metabolic changes during storage. GC-MS metabolomics provides compound-level information through destructive bulk measurements. Hyperspectral imaging (HSI), in contrast, provides nondestructive, spatially resolved spectral information, although the extent to which individual postharvest metabolites are reliably reflected in short-wave infrared (SWIR) spectra remains unclear. This study therefore aimed to identify GC-MS-detected metabolites predictable from SWIR-HSI and explore spatially resolved prediction within lettuce leaves.
Hydroponically grown lettuce (*Lactuca sativa* L.) was sampled at harvest and during storage at 10 and 20 °C (10 °C for 4, 8, and 12 d; 20 °C for 2, 4, and 6 d). Each leaf sample was first imaged by HSI (1100–1700 nm) and then frozen for GC-MS analysis, providing direct correspondence between spectral and metabolite data. GC-MS data were subjected to quality control, normalization, log10 transformation, and Pareto scaling. Partial least squares regression (PLSR) models were developed separately for 59 metabolites using mean reflectance spectra. Performance was evaluated by 50 repetitions of five-fold cross-validation across six spectral preprocessing methods, using either all 99 wavelengths or wavelengths selected by variable importance in projection (VIP > 1), with latent variables optimized by *RMSECV*. Metabolites with mean $R^2_{CV} \geq 0.50$ in at least one model were considered potential candidates. The three candidates with the highest mean R^2_{CV} after VIP-based wavelength selection were applied pixel-wise to generate exploratory prediction maps. Leaf-mean predictions were compared with GC-MS measurements using Pearson and Spearman correlations and by comparing storage-related trends.
Of the 59 metabolites screened, 14 achieved mean $R^2_{CV} \geq 0.50$ in at least one model. Citric acid, 2-aminopimelic acid, and succinic acid showed the three highest mean R^2_{CV} values after VIP-based wavelength selection (0.60–0.67). Leaf-mean predictions for citric acid and 2-aminopimelic acid showed strong linear and rank correlations with GC-MS measurements (Pearson r = 0.91; Spearman ρ = 0.89–0.91) and reproduced the major storage-related trends. Succinic acid showed weaker linear correlations (r = 0.34–0.52) but moderate rank correlations (ρ = 0.64–0.71). Pixel-wise prediction revealed heterogeneous within-leaf prediction patterns for these metabolites. Applying these models pixel-wise extended the leaf-level relationships into image space, providing spatially resolved information complementary to bulk GC-MS measurements. Local chemical validation, however, is required before these maps can be interpreted as true metabolite distributions.

Key Words: metabolomics, spatial mapping, lettuce, post-harvest quality

Precision Agriculture Machinery and Systems 5 (PA-5)



PA-25

Proceedings of The 12th International Symposium on Machinery and Mechatronics for Agriculture and Biosystems Engineering (ISMAB 2026)
20-24 October 2026, Busan, Republic of Korea

KEYPOINT-DRIVEN GEOMETIC POSE ESTIMATION FOR AUTONOMOUS SEEDBED LIFTING WITH NONHOLONOMIC MOBILE ROBOTS

Rattana Seng[1,3], Woo-Young Kim[2], Kyeong-Hwan Lee[1,2,3*]

[1]Department of Convergence Biosystems Engineering, Chonnam National University, Gwangju, Korea
[2]Agricultural Automation Research Center, Chonnam National University, Gwangju, Korea
[3]BK21 Interdisciplinary Program in IT-Bio Convergence System, Chonnam National University, Gwangju, Korea
*Corresponding Author-- Email: khlee@jnu.ac.kr

Abstract: Despite advances in agricultural automation, robust marker-free pose estimation for autonomous seedbed lifting remains an open problem in structured farming environments. Conventional solutions address this by attaching physical markers to seedbeds to enable pose estimation, at the cost of additional labor and preparation overhead. In this work, we propose a marker-less framework that instead estimates seedbed 3D pose directly from detected wheel keypoints, eliminating any dependency on pre-attached markers. The proposed system is deployed on a non-holonomic mobile robot and learning-based keypoint detector first localizes the seedbed's keypoints from RGB images; these keypoints are then fused with depth data to reconstruct the tray's three-dimensional geometry. The estimated pose subsequently serves as the basis for generating a feasible reference path that accounts for the robot's non-holonomic motion constraints, which is tracked using a Pure Pursuit controller that converts geometric pose data into smooth, responsive motion commands for accurate alignment beneath the target seedbed. Experimental results demonstrate that the proposed method achieves accurate and computationally efficient marker-less solution for autonomous seedbed transportation, demonstrating strong potential for practical deployment in real-world greenhouse environments.

Key Words: Marker-less pose estimation, keypoint detection, path generation, path tracking control.

ACKNOWLEDGEMENTS

This work was supported by Korea Institute of Planning and Evaluation for Technology in Food, Agriculture and Forestry (IPET), through K-Vertical Farm Globalization Project, funded by Ministry of Agriculture, Food and Rural Affairs (MAFRA) (Project No. RS-2025-02303373) and through K-Vertical Globalization Project, funded by Ministry of Agriculture, Food and Rural Affairs(MAFRA)(RS-2025-02283034).

PA-26

Proceedings of The 12th International Symposium on Machinery and Mechatronics for Agriculture and Biosystems Engineering (ISMAB 2026)
20-24 October 2026, Busan, Republic of Korea

PERSISTENT TARGET RE-IDENTIFICATION FOR HUMAN-FOLLOWING ROBOTS IN ORCHARD ENVIRONMENTS

Sanjay Tamang[1,3], Woo-Young Kim[2], Kyeong-Hwan Lee[1,2,3*]

[1]Department of Convergence Biosystems Engineering, Chonnam National University, Gwangju, Republic of Korea
[2]AI Agri-Tech Research Center, Chonnam National University, Gwangju, Republic of Korea
[3]BK21 Interdisciplinary Program in IT-Bio Convergence System, Chonnam National University, Gwangju, Republic of Korea
*Corresponding Author — Email: khlee@jnu.ac.kr

Abstract: Reliable target identification is essential for human-following agricultural robots operating in orchard environments. Conventional trackers may lose the designated person during occlusion, disappearance, identity switching, or interaction with visually similar workers. This study proposes an identity-aware human-following framework that combines person detection and multi-object tracking with an appearance-based identity memory. During registration, appearance embeddings, pose, and body-shape features are extracted from multiple target observations and stored as representative features using clustering. During tracking, candidate trajectories are evaluated using appearance similarity and complementary body-related cues. An adaptive recovery strategy prioritizes motion continuity during short interruptions and identity-memory matching after prolonged disappearance. The framework was evaluated under single-person, similar-person, and short- and long-term occlusion scenarios and compared with tracking and re-identification approaches. Results showed robust target preservation and reacquisition with reduced incorrect reassignment and real-time processing performance. The proposed framework therefore provides an effective balance between identity robustness and computational efficiency for human-following agricultural robots operating in dynamic orchard environments.

Key Words: Human-Following, Re-Identification, Identity Memory, Occlusion Recovery, Agricultural Robot

ACKNOWLEDGEMENTS

This work was supported by Korea Institute of Planning and Evaluation for Technology in Food, Agriculture and Forestry(IPET) through the Technology Commercialization Support Program, funded by Ministry of Agriculture, Food and Rural Affairs(MAFRA)(RS-2024-00395265) and was conducted with support of the Cooperative Research Program for Agricultural Science & Technology Development (Project No. RS-2025-04092968), National Institute of Horticultural and Herbal Science, Rural Development Administration, Republic of Korea.

PA-27

Proceedings of The 12th International Symposium on Machinery and Mechatronics for Agriculture and Biosystems Engineering (ISMAB 2026)
20-24 October 2026, Busan, Republic of Korea

EVALUATION OF SEED METERING AND IN-SOIL PLACEMENT CHARACTERISTICS OF A VACUUM TYPE POINT SEEDER USING SOYBEAN

Juhee Lee[1], Jinho Son[1], Wonyeol Choi[1], Bumseok Park[1], Hyunggyu Park[1,2], Yushin Ha[1,2*]

[1]Department of Bio Industrial Machinery Engineering, Kyungpook National University, Daegu 41566, Republic of Korea
[2]Upland Field Machinery Research Center, Republic of Korea
*Corresponding Author-- Voice: +82-10-4520-2115, Email: yushin72@knu.ac.kr

Abstract: In precision seeding, not only stable singulation of individual seeds but also accurate placement of discharged seeds at the intended positions is important. This study evaluated the seed singulation characteristics and final in-soil seed placement of a vacuum-type precision point seeding mechanism through laboratory tests using soybean seeds. Experiments were conducted using combinations of three suction-cell diameters, three forward speeds, and three nominal seed spacings while maintaining a constant vacuum pressure. Singulation performance was evaluated based on the number of seeds discharged per planting event using the quality of feed index (QFI), miss index (MISS), and multiple index (MULT). The suction-cell condition that provided the best singulation performance was selected for soil-bed tests at different forward speeds. Longitudinal seed spacing and lateral deviation from the theoretical planting centerline were analyzed using image processing. The singulation tests showed clear differences in performance among the suction-cell diameters. The largest suction-cell diameter produced a higher QFI and lower MISS than the smaller diameters. In contrast, changes in singulation performance associated with forward speed and nominal seed spacing were relatively small, while multiple-seeding events remained infrequent across the tested conditions. In the soil-bed tests, most seeds were placed within the target spacing range, although the dispersion of longitudinal seed spacing varied with forward speed. In addition, lateral deviation from the planting centerline tended to increase as forward speed increased. These results indicate that the performance of a vacuum-type precision point-seeding mechanism should be evaluated not only in terms of seed singulation at the metering stage but also by considering post-release seed delivery and final seed placement. The findings can provide a basis for further improvement of the suction, seed-guiding, and discharge components of precision point-seeding mechanisms.

Key Words: Vacuum seed metering, Precision seeding, Soybean, Seed singulation

PA-28

Proceedings of The 12th International Symposium on Machinery and Mechatronics for Agriculture and Biosystems Engineering (ISMAB 2026)
20-24 October 2026, Busan, Republic of Korea

RECONSTRUCTION-FREE SOIL PULVERISATION-RATIO ASSESSMENT FRAMEWORK: PIXEL-WISE PHYSICAL-SCALE RECOVERY FROM HETEROGENEOUS RGB-D

Zhewang Zhang[1,3], Kyeong-Hwan Lee[1,2,3*]

[1]Department of Convergence Biosystems Engineering, Chonnam National University, Gwangju, Korea
[2]AI Agri-Tech Research Center, Chonnam National University, Gwangju, Korea
[3]BK21 Interdisciplinary Program in IT-Bio Convergence System, Chonnam National University, Gwangju, Korea
*Corresponding Author-- Voice: +010-4014-4083, Email: khlee@jnu.ac.kr

Abstract: Vision-based soil pulverisation-ratio assessment provides an important basis for rapid evaluation of rotary-tillage quality and timely re-tillage decisions. However, existing vision-based methods cannot directly recover the true physical sizes of soil clods, while three-dimensional reconstruction is difficult to apply to real-time field assessment. Therefore, this study proposes a reconstruction-free heterogeneous RGB-D framework for recovering the physical scale of soil clods and enabling metric pulverisation-ratio assessment. The framework derives a pixel-wise physical-scale field from registered depth information and corrects its residual errors using sparse physical supervision. The corrected scale field is integrated with segmented clod regions to recover physical clod size and calculate the soil pulverisation ratio. Evaluation on 100 valid AprilTag reference regions showed that the scale MAPE decreased from 73.73% for the geometric prior to 4.88% after depth-conditioned correction. These results demonstrate the feasibility of recovering metric clod information without complete three-dimensional reconstruction, providing a basis for real-time visual assessment of soil pulverisation.

Key Words: Soil fragmentation, Heterogeneous RGB-D, Physical-scale recovery, Rotary tillage, Clod-size measurement

INTRODUCTION

Soil fragmentation after rotary tillage directly affects seedbed physical conditions and crop establishment, making quantitative assessment of post-tillage soil structure important for evaluating tillage quality. Conventional fragmentation assessment primarily relies on soil sampling, sieving, and particle-size analysis, which are labor-intensive and difficult to integrate into rapid field evaluation. Vision-based measurement provides a promising non-contact alternative because soil clods can be directly observed and quantified from post-tillage surface images, thereby providing information for evaluating rotary-tillage quality and supporting re-tillage decisions (Braunack and Dexter, 1989a,b; Varani et al., 2023; Huang et al., 2025).

However, reliable visual assessment of soil fragmentation requires the physical dimensions of individual clods rather than their apparent sizes in image pixels. Existing image-processing

methods can identify clod boundaries and extract image-based size information, while learning-based approaches have further improved clod recognition and aggregate-size classification (Bogrekci and Godwin, 2007b; Chimi-Chiadjeu et al., 2014; Alirezazadeh et al., 2021). Nevertheless, these measurements remain dependent on observation scale, and the physical area represented by each pixel varies with depth and image position under oblique field imaging. Depth sensing can provide metric geometric information, but previous RGB-D and point-cloud studies have mainly addressed scene-boundary measurement or controlled soil-shape analysis rather than direct recovery of spatially varying physical scale for field clod measurement (Ishii et al., 2023; Ji et al., 2024).

Multi-view photogrammetry can recover accurate metric soil geometry and has been applied to soil-surface and clod-size measurement, but it requires physical scaling references, image alignment, dense three-dimensional reconstruction, and subsequent geometric processing (Gilliot et al., 2017; Riegler-Nurscher et al., 2020; Herodowicz-Mleczak et al., 2022; Chen et al., 2024). This processing chain limits its suitability for rapid feedback during rotary-tillage operations. The key problem is therefore how to recover a spatially varying pixel-to-physical scale from field observations without reconstructing a complete three-dimensional soil surface. To address this problem, this study proposes a reconstruction-free physical-scale recovery framework using heterogeneous RGB-D observations, in which registered depth information provides a geometry-informed pixel-wise scale prior and sparse physical references supervise depth-conditioned residual correction. The present study focuses on evaluating the accuracy of the recovered physical-scale field, which provides the metric basis for subsequent physical clod-size decoding and visual pulverisation-ratio assessment.

MATERIALS AND METHODS

Overall framework

Figure 1 presents the proposed reconstruction-free framework for visual soil pulverisation assessment using heterogeneous RGB-D observations. Cross-modal registration first projects ZED2i depth onto the high-resolution ELP image plane to obtain aligned RGB, depth, and valid-depth data. Segmentation-guided instance indexing then provides pixel regions for individual soil clods, while the aligned depth is converted into a geometry-informed pixel-wise physical-scale prior and refined by a depth-conditioned residual correction model under sparse physical supervision. The corrected scale field is finally integrated within each clod mask to recover physical area and equivalent diameter, from which regional particle-size distribution and soil pulverisation ratio are derived.

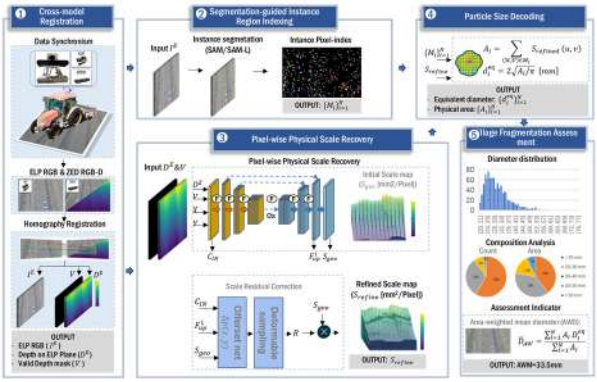

Fig. 1 Overall framework of the proposed reconstruction-free soil pulverisation assessment method based on heterogeneous RGB-D observations.

RESULTS & DISCUSSION

Evaluation of pixel-wise physical-scale recovery

Because the physical area represented by each image pixel varies with depth and image position under oblique field imaging, accurate scale recovery requires not only low numerical error but also a spatially consistent scale distribution across the image plane. Three representative field samples, Samples 176, 270, and 506, were therefore examined by jointly visualising the field observations, recovered three-dimensional physical-scale fields, and local AprilTag-based scale comparisons.

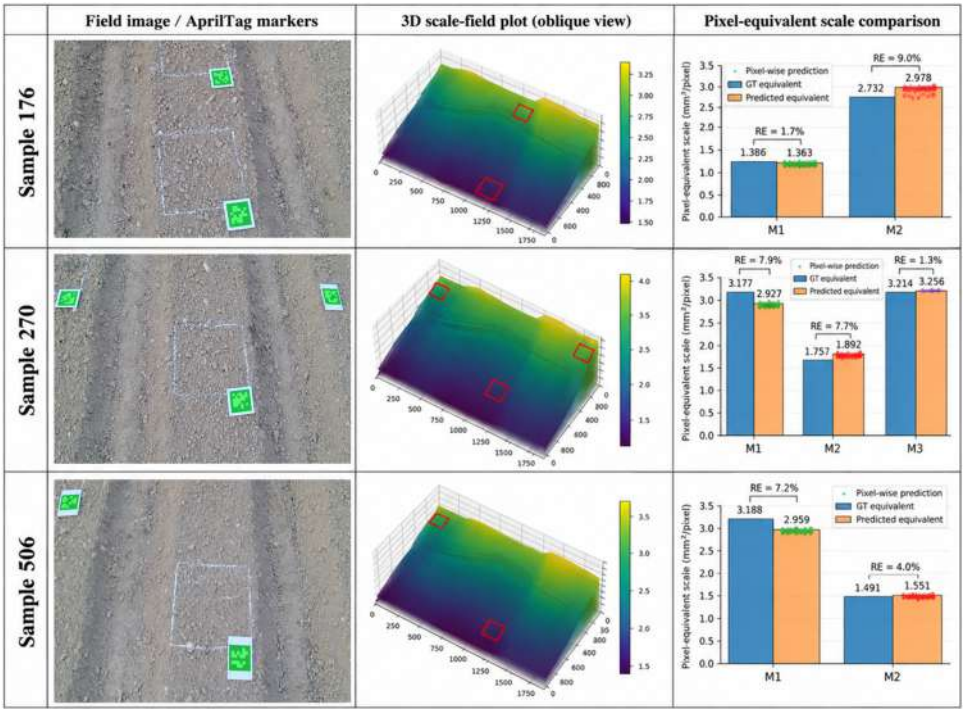

Fig. 2 Representative pixel-wise physical-scale recovery results for Samples 176, 270, and 506, showing field observations with AprilTag references, recovered three-dimensional scale fields, and local pixel-equivalent scale comparisons.

As shown in Fig. 2, the recovered physical-scale fields exhibited continuous spatial variation across the image plane rather than a uniform image-level conversion factor. The predicted scales at the AprilTag locations remained close to their corresponding physical references, with relative errors ranging from 1.3% to 9.0% across the displayed regions.

The continuous spatial gradients indicate that the recovered scale field responds to the perspective-dependent variation of pixel physical area, while the local agreement with the AprilTag references shows that this variation remains physically constrained. These representative results support the use of the recovered scale field as the metric basis for subsequent physical clod-size decoding.

While the representative samples demonstrate the spatial behaviour of the recovered scale field, reliable metric clod measurement also requires its accuracy to be verified over the full evaluation set. A total of 100 valid AprilTag reference regions from 81 field images were therefore used to compare the geometry-informed prior, global correction, and depth-conditioned correction under the same physical-reference conditions.

Table 1 Physical-scale recovery accuracy evaluated using 100 AprilTag reference regions.

Method	MAPE (%)	Median APE (%)	MAE (mm²)	RMSE (mm²)	Bias (%)
Geometry prior	73.73	74.97	18,875.5	19,194.9	+73.73
Global correction	6.05	4.46	1,548.7	2,003.9	−0.21
Depth-conditioned correction	**4.88**	**3.81**	**1,249.7**	**1,723.6**	**+0.20**

Note: MAE and RMSE are calculated from AprilTag physical-area estimates; 81 images contained 100 valid reference regions.

As shown in Table 1, the geometry-informed prior yielded a MAPE of 73.73%, which decreased to 6.05% after global correction and further to 4.88% after depth-conditioned correction. The final corrected scale achieved a median APE of 3.81%, an MAE of 1,249.7 mm², an RMSE of 1,723.6 mm², and a relative bias of 0.20%.

The large reduction obtained by global correction indicates that the geometry-informed prior contains a pronounced systematic scale residual, whereas the further improvement achieved by depth-conditioned correction suggests that the remaining error cannot be fully represented by a single global correction factor. The near-zero final bias further indicates that systematic over- or underestimation was largely removed, supporting the reliability of the corrected scale field for subsequent metric clod-size decoding and visual pulverisation-ratio assessment.

CONCLUSIONS

This study developed a reconstruction-free physical-scale recovery framework using heterogeneous RGB-D observations to support metric soil-fragmentation assessment under oblique field imaging. By combining a geometry-informed scale prior with sparse physical supervision and depth-conditioned residual correction, the proposed method reduced the scale MAPE from 73.73% to 4.88% across 100 valid AprilTag reference regions, with a median APE of 3.81% and a relative bias of 0.20%. These results demonstrate that spatially varying pixel-to-physical scale can be reliably recovered without complete three-dimensional reconstruction, providing the metric basis for subsequent physical clod-size decoding and visual pulverisation-ratio assessment. Future work will focus on validating clod-size estimation and plot-level pulverisation-ratio accuracy under broader field conditions.

ACKNOWLEDGEMENTS

This work was supported by Korea Institute of Planning and Evaluation for Technology in Food, Agriculture and Forestry(IPET) through Development of a smart agricultural utilization model in the field Project, funded by Ministry of Agriculture, Food and Rural Affairs(MAFRA)(No. RS-2025-02306132) and through the Agriculture, Food and Rural Affairs Convergence Technologies Program for Educating Creative Global Leader, funded by Ministry of Agriculture, Food and Rural Affairs(MAFRA)(714002-7).

REFERENCES

Alirezazadeh, P., F. Rahimi-Ajdadi, Y. Abbaspour-Gilandeh, N. Landwehr, and H. Tavakoli. 2021. Improved digital image-based assessment of soil aggregate size by applying convolutional neural networks. Computers and Electronics in Agriculture 191: 106499. https://doi.org/10.1016/j.compag.2021.106499.

Bogrekci, I., and R. J. Godwin. 2007. Development of an image-processing technique for soil tilth sensing. Biosystems Engineering 97: 323-331. https://doi.org/10.1016/j.biosystemseng.2007.03.025.

Braunack, M. V., and A. R. Dexter. 1989a. Soil aggregation in the seedbed: A review. I. Properties of aggregates and beds of aggregates. Soil and Tillage Research 14: 259-279. https://doi.org/10.1016/0167-1987(89)90013-5.

Braunack, M. V., and A. R. Dexter. 1989b. Soil aggregation in the seedbed: A review. II. Effect of aggregate sizes on plant growth. Soil and Tillage Research 14: 281-298. https://doi.org/10.1016/0167-1987(89)90014-7.

Chen, X., Y. Guo, J. Hu, G. Xu, W. Liu, G. Ma, Q. Ding, and R. He. 2024. Quantitative evaluation of post-tillage soil structure based on close-range photogrammetry. Agriculture 14: 2124. https://doi.org/10.3390/agriculture14122124.

Chimi-Chiadjeu, O., S. Le Hegarat-Mascle, E. Vannier, O. Taconet, and R. Dusseaux. 2014. Automatic clod detection and boundary estimation from digital elevation model images using different approaches. CATENA 118: 73-83. https://doi.org/10.1016/j.catena.2014.02.003.

Gilliot, J. M., E. Vaudour, and J. Michelin. 2017. Soil surface roughness measurement: A new fully automatic photogrammetric approach applied to agricultural bare fields. Computers and Electronics in Agriculture 134: 63-78. https://doi.org/10.1016/j.compag.2017.01.010.

Herodowicz-Mleczak, K., J. Piekarczyk, C. Kazmierowski, J. Nowosad, and M. Mleczak. 2022. Estimating soil surface roughness with models based on the information about tillage practices and soil parameters. Journal of Advances in Modeling Earth Systems 14: e2021MS002578. https://doi.org/10.1029/2021MS002578.

Huang, X., X. Wang, Y. Wang, Y. Shi, H. Lv, J. Zheng, and Y. Chen. 2025. Multi-objective optimization and experimental analysis of rotary tillage parameters for horticultural electric tractors. Computers and Electronics in Agriculture 231: 109962. https://doi.org/10.1016/j.compag.2025.109962.

Ishii, S., I. Suto, H. Tabe, K. Aono, M. Zhao, Y. Ueshige, K. Matsushita, T. Iritani, T. Hanamoto, M. Nakao, and K. Nagato. 2023. Construction of a soil clod recognition bench-scale experiment for discrete element method modeling of tilling phenomena. Journal of Terramechanics 109: 63-71. https://doi.org/10.1016/j.jterra.2023.06.004.

Ji, J., Z. Han, K. Zhao, Q. Li, and S. Du. 2024. Detection of the farmland plow areas using RGB-D images with an improved YOLOv5 model. International Journal of Agricultural and Biological Engineering 17: 156-165. https://doi.org/10.25165/j.ijabe.20241703.8810.

Riegler-Nurscher, P., G. Moitzi, J. Prankl, J. Huber, J. Karner, H. Wagentristl, and M. Vincze. 2020. Machine vision for soil roughness measurement and control of tillage machines during seedbed preparation. Soil and Tillage Research 196: 104351. https://doi.org/10.1016/j.still.2019.104351.

Varani, M., M. Mattetti, G. Molari, A. Biglia, and L. Comba. 2023. Correlation between power harrow energy demand and tilled soil aggregate dimensions. Biosystems Engineering 225: 54-68. https://doi.org/10.1016/j.biosystemseng.2022.11.008.

PA-29

Proceedings of The 12th International Symposium on Machinery and Mechatronics for Agriculture and Biosystems Engineering (ISMAB 2026)
20-24 October 2026, Busan, Republic of Korea

TRACKING ACCURACY EVALUATION OF AUTONOMOUS TRACTORS USING A HYBRID EKF–TRANSFORMER MODEL FOR REAR 3-POINT ESTIMATION

Md Rayhan Mahmud[1], Md Faruk Hossain[1] Ki-Dong Park[1], Ryu-Gap Lim[2]*

[1] Department of Smart Agriculture Engineering, Sunchon National University, Suncheon 57922, Republic of Korea
[2]Department of Convergence Biosystem Mechanical Engineering, Sunchon National University, Suncheon 57922, Republic of Korea
*Corresponding Author-- Voice: +82-61-750-3264, Email: limrg11@scnu.ac.kr

Abstract: To achieve reliable path-following performance for autonomous agricultural tractors, precise tracking evaluation is crucial. The Rear Three-Point (Rear 3-Point) is the reference point for driving accuracy evaluation as stipulated by ISO 12188 and the autonomous tractor evaluation requirements in Korea. However, sensor installation errors, vibration, and heading-induced bias can affect the direct measurement of the Rear 3-Point and thus the reliability of trajectory measurement. The effect of sensor installation conditions was first investigated in this study, and the results indicated that the coordinate standard deviation (STD) at the Rear 3-Point was 18.0 mm, while that at the cab was 0.6 mm. Therefore, the measurement reference was moved to the cab, and the trajectory of the Rear 3-Point was indirectly estimated using a hybrid Extended Kalman Filter (EKF) and Transformer model in this study. The EKF was used to estimate the position, yaw, and velocity of the tractor using a kinematic tractor model, while a scalar Kalman filter was first applied to stabilize the yaw signal and a Savitzky–Golay filter was used to attenuate minor vibrations. The stabilized heading and the fixed geometric relationship between the cab and Rear 3-Point were then utilized to determine the Rear 3-Point trajectory. These trajectories estimated by the EKF were then treated as labels to train an encoder-only Transformer model that learns the temporal relationship between cab motion and Rear 3-Point position. Field tests were conducted at the agricultural machinery test facility in Iksan using two autonomous agricultural tractors, MT5.73 and MT9.140, with a Leica TS13 Total Station used to measure the cab and Rear 3-Point trajectories. The estimation performance was evaluated using mean absolute error (MAE), root mean square error (RMSE), maximum error, standard deviation, and coefficient of determination (R^2). The RMSE for MT5.73 was 1.6 mm with a maximum error of 12.6 mm for the EKF, and 1.9 mm with a maximum error of 24.1 mm for the Transformer. The RMSE values for MT9.140 were 1.4 mm for both EKF and Transformer, while the maximum errors were 10.1 and 10.4 mm, respectively. Both methods achieved MAE values of less than or equal to 3.5 mm and were able to estimate the Rear 3-Point trajectory without IMU or steering sensor measurements, using only the cab coordinates. The results of this study demonstrate the feasibility of the indirect Rear 3-Point trajectory estimation method using a cab-based reference for reliable autonomous tractor tracking accuracy evaluation.

Key Words: Autonomous Agricultural Tractor, Tracking Accuracy, Rear Three-Point Hitch, Extended Kalman Filter, Transformer Model

ACKNOWLEDGEMENTS

This study was supported by the Korea Institute of Planning and Evaluation for Technology in Food, Agriculture and Forestry (IPET) through the Development Project for an Open-field Smart Agricultural Utilization Model, funded by the Ministry of Agriculture Food and Rural Affairs (MAFRA, RS-2025-02216783).

PA-30

Proceedings of The 12th International Symposium on Machinery and Mechatronics for Agriculture and Biosystems Engineering (ISMAB 2026)
20-24 October 2026, Busan, Republic of Korea

PREDICTION OF BARLEY SPIKE COUNT UNDER WATERLOGGING STRESS USING UAV-BASED MULTISPECTRAL IMAGERY

Do Hyun An[1], Ji An Kim[1], Hyo Jeong Lee[1], Ye Seong Kang[1*], Yeong Son Jo[1], Seung Ga Oh[2], Hui Su Bae[3], Woo Jin Im[3]

[1]Department of Smart Agro-industry, Gyeongsang National University, Jinju 52725, Republic of Korea
[2]Agri-Food Bio Convergence Institute, Gyeongsang National University, Jinju 52725, Republic of Korea
[3]National Institute of Crop Science, Rural Development Administration, Wanju 55365, Republic of Korea
*Corresponding Author-- Voice: +82-55-772-3222, Email: slow321@gnu.ac.kr

Abstract: Extreme precipitation patterns driven by climate change cause field waterlogging, severely limiting barley (*Hordeum vulgare* L.) yield due to reduced spike counts. This study aimed to evaluate the potential of unmanned aerial vehicle (UAV)-based multispectral imagery combined with machine learning models—Gaussian Process Regression (GPR) and Partial Least Squares Regression (PLSR)—to predict final spike counts and identify the optimal sensing timing and critical spectral indicators under soil moisture stress. Field experiments were conducted under three soil moisture treatments (optimal, waterlogged, and excessively waterlogged), and time-series UAV imagery was acquired across seven dates from March 23 to April 15. The GPR model generally exhibited superior and more stable prediction performance compared to PLSR. Both models achieved their highest prediction accuracy during the period between March 30 and April 1. On March 30, the GPR model achieved the peak performance on the validation dataset (R^2 = 0.7331, RMSE = 11.3164, RE = 11.7336%), while the PLSR model showed comparable results (R^2 = 0.7312, RMSE = 11.3558, RE = 11.7745%). High predictive accuracy was maintained on April 1 (R^2 = 0.7096 for GPR; R^2 = 0.7074 for PLSR) before declining in mid-April. Variable importance analysis using SHAP values and VIP scores revealed a temporal shift in dominant features, transitioning from RRI1 on March 30 to CCCI on April 1. These red-edge-based spectral indices effectively reflected chlorophyll degradation and tiller abortion during the panicle formation and booting stages. In conclusion, UAV-derived red-edge spectral metrics acquired during early reproductive stages are highly effective tools for early diagnosis of waterlogging damage and pre-harvest spike count estimation in barley.

Key Words: UAV, Multispectral imagery, Waterlogging stress, Spike count prediction, Gaussian process regression

INTRODUCTION

The exacerbation of extreme precipitation patterns due to climate change is increasing the frequency and intensity of waterlogging in agricultural fields, emerging as a major limiting factor for crop production (Ploschuk et al., 2018). Barley (*Hordeum vulgare* L.) is a cereal crop highly

vulnerable to waterlogging; hypoxic stress in the rhizosphere reduces chlorophyll content and photosynthetic capacity, inducing premature senescence (Castro et al., 2022). In particular, since the reduction in the number of spikes per plant is the primary cause of final yield loss when barley is subjected to waterlogging stress, early detection of waterlogging damage and subsequent yield prediction based on spike counts are essential.
Multispectral sensors mounted on unmanned aerial vehicles (UAVs) are increasingly being utilized in precision agriculture as a means for high-resolution, non-destructive spatio-temporal monitoring of crop growth status and stress responses (Zhang et al., 2025). Previous studies have reported time-series monitoring of key barley growth parameters, such as plant height and dry weight, using UAV image data (Na et al., 2017), as well as the derivation of vegetation index-based crop growth estimation models (Na et al., 2016). Furthermore, machine learning algorithms such as Partial Least Squares Regression (PLSR) and Gaussian Process Regression (GPR) are widely applied to accurately predict yield and key traits by analyzing the complex spectral reflectance characteristics of crops (Oehlschlager et al., 2018; Fei et al., 2021).

However, there is a lack of studies that compare the growth responses of barley under varying moisture stress levels (optimal, waterlogged, and excessively waterlogged) across multiple acquisition dates, while comprehensively predicting both mid-season and final spike counts. Therefore, this study aimed to predict the mid-season and final number of spikes in barley grown under different moisture conditions by utilizing vegetation indices and spectral characteristics extracted from UAV multispectral imagery combined with machine learning regression models (PLSR, GPR). Additionally, this study sought to identify the optimal UAV sensing timing and key spectral variables that achieve the highest prediction accuracy for yield components.

MATERIALS AND METHODS

Study Site and Experimental Design

This study was conducted in an experimental field located at the National Institute of Crop Science, Wanju-gun, Jeollabuk-do, Republic of Korea (35°50'35.19"N, 127°02'52.93"E). The target crop was barley (*Hordeum vulgare* L.), specifically analyzing the cultivar 'Keunalbori 1'. The total area of the experimental field was 20 m × 31.8 m. To evaluate crop growth responses under soil moisture stress, three treatment levels—optimal moisture, waterlogged, and excessively waterlogged conditions—were established in a split-plot arrangement with three replications. The area of each replicate plot was 2.5 m × 4.8 m. For the waterlogged and excessively waterlogged plots, irrigation was applied using a two-row, single-line drip hose configuration for 30 minutes each at 09:00, 13:00, and 17:00 daily from March 19 to April 3, 2026, thereby maintaining the soil volumetric water content (VWC) above 40%.

UAV Imaging and Image Processing, Field Surveys

Multispectral images were collected using an unmanned aerial vehicle (UAV; Matrice 300 RTK, DJI, China) equipped with a multispectral sensor (Altum-PT, MicaSense, USA). Flights were conducted at an altitude of 25 m, a flight speed of 1.5 m/s, and a 75% front and side overlap ratio, resulting in a ground sample distance (GSD) of 1.08 cm/pixel. To minimize the influence of fluctuating solar irradiance, image acquisition was performed between 10:00 and 14:00

across multiple dates: March 23, 25, 27, 30, April 1, 3, and 15. The acquired images were stitched and orthomosaics were generated using Pix4Dmapper (Pix4D SA, Switzerland), and pansharpening preprocessing was conducted using the open-source geographic information system software, QGIS. Subsequently, the calibrated images were converted into NDVI maps using ENVI Classic 5.6 (Exelis Visual Information Solutions, USA) according to Eq. (1), and a threshold was applied to remove the soil background.

$$NDVI = \frac{NIR-Red}{NIR+Red} \quad (1)$$

where:
NDVI = Normalized Difference Vegetation Index (-)
NIR = Reflectance in the near-infrared band (-)
Red = Reflectance in the red band (-)

To prevent data distortion caused by spectral mixing and mutual interference among moisture treatments, regions of interest (ROIs) were segmented and processed individually for the optimal, waterlogged, and excessively waterlogged plots, allowing for the independent extraction of barley canopy reflectance data for each treatment. For model calibration and validation, ground-based growth surveys were conducted on April 16, 20, 22, and 24 to measure the number of spikes at the mid-season growth stages. Final crop yield (final number of spikes) was evaluated after harvest and utilized as the dependent variable for the prediction models.

Statistical Analysis and Model Development

During data preprocessing, missing values were removed, and outliers were eliminated using the interquartile range (IQR) method. To address multicollinearity among the extracted spectral features, variance inflation factor (VIF) analysis was conducted, and only variables with a VIF of less than 10 were retained for analysis. To comprehensively predict the final number of spikes under varying moisture stress conditions and to identify the optimal prediction timing, independent modeling was performed for each sensing date by pooling the data from all moisture treatments. Partial least squares regression (PLSR) and Gaussian process regression (GPR) were selected as the predictive models. Leave-one-out cross-validation (LOOCV) was applied for model validation and performance evaluation, and hyperparameters were optimized to minimize the mean squared error (MSE) using grid search. For PLSR, the number of latent variables (n_components) was searched up to an upper limit determined by considering the number of features and the sample size. For GPR, a grid search was conducted on combinations of the RBF kernel's length scale (0.5, 1.0, 5.0) and the noise parameter (0.1, 1.0, 10.0). To compare the prediction performance of the final models, the coefficient of determination (R^2), root mean square error (RMSE), and relative error (RE) were utilized as evaluation metrics. Additionally, to identify key variables, Variable Importance in Projection (VIP) scores were calculated for the PLSR model, and SHapley Additive exPlanations (SHAP) analysis was performed for the GPR model.

RESULTS & DISCUSSION

Barley Spike Count Prediction Performance by Observation Time

The prediction results for the final spike counts of barley under varying moisture stress conditions indicated that both the Gaussian Process Regression (GPR) and Partial Least

Squares Regression (PLSR) models exhibited similar trends in performance variation across different sensing dates (Table 1 and 2). In terms of overall prediction accuracy, GPR demonstrated generally superior or more stable performance compared to PLSR. Among all sensing dates, both models achieved their highest prediction performance on March 30. Based on the validation dataset, the GPR model achieved an R^2 of 0.7331, RMSE of 11.3164, and RE of 11.7336%, while the PLSR model yielded an R^2 of 0.7312, RMSE of 11.3558, and RE of 11.7745%. Excellent predictive power was maintained for the data acquired on April 1, with the GPR model recording an R^2 of 0.7096, RMSE of 11.8035, and RE of 12.2387%, and the PLSR model recording an R^2 of 0.7074, RMSE of 11.8490, and RE of 12.2860% (Fig. 1). Conversely, performance gradually declined after April 3 (GPR R^2 = 0.6575), ultimately dropping to an R^2 of 0.5850 for GPR and 0.5941 for PLSR on April 15.

These results suggest that the period between March 30 and April 1 is the optimal sensing time, during which the physiological responses and differences in spike formation of barley induced by moisture stress are most distinctly reflected in the spectral reflectance characteristics.

Table 1. Comparison of prediction performance for final spike counts using Gaussian process regression (GPR)

		March 23	March 25	March 27	March 30	April 1	April 3	April 15
Calibration	R^2	0.7976	0.7613	0.6984	0.8050	0.7607	0.7167	0.6615
	RMSE	9.8538	10.7014	12.0304	9.6724	10.7159	11.6597	12.7437
	RE	10.2171	11.0959	12.4739	10.0290	11.1109	12.0896	13.2135
Validation	R^2	0.6351	0.6988	0.6442	0.7331	0.7096	0.6575	0.5850
	RMSE	13.2314	12.0213	13.065	11.3164	11.8035	12.8195	14.1107
	RE	13.7192	12.4644	13.5467	11.7336	12.2387	13.2921	14.6310

Table 2. Comparison of prediction performance for final spike counts using partial least squares regression (PLSR)

		March 23	March 25	March 27	March 30	April 1	April 3	April 15
Calibration	R^2	0.6560	0.7579	0.6947	0.7814	0.7601	0.7166	0.6601
	RMSE	12.8468	10.7777	12.1029	10.2413	10.727	11.6613	12.7700
	RE	13.3204	11.1751	12.5491	10.6188	11.1233	12.0912	13.2408
Validation	R^2	0.5481	0.6985	0.6496	0.7312	0.7074	0.6509	0.5941
	RMSE	14.7255	12.0271	12.9669	11.3558	11.849	12.9424	13.9558
	RE	15.2683	12.4705	13.4450	11.7745	12.286	13.4195	14.4703

Stress (MPa)

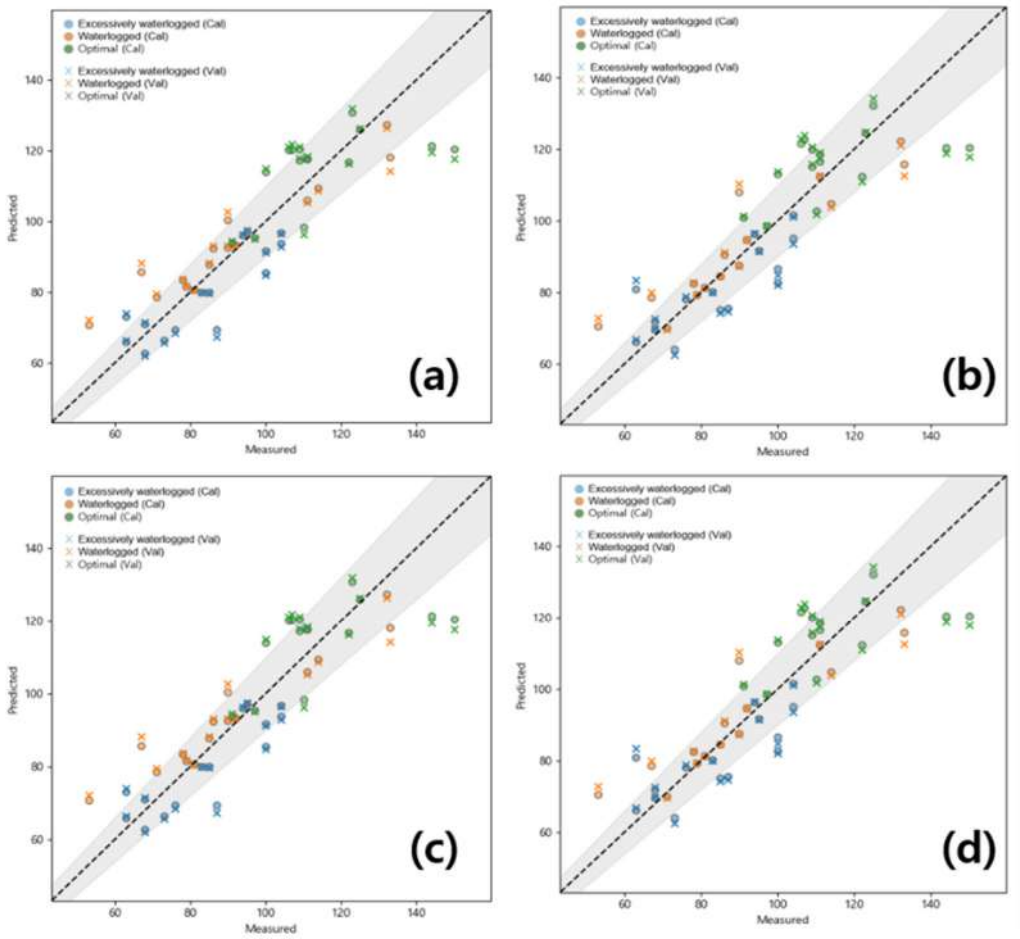

Fig.1 Linear relationship between predicted and measured final spike counts and performance of Gaussian process regression (GPR) and partial least squares regression (PLSR) models for predicting barley final spike counts (a: GPR on March 30; b: GPR on April 1; c: PLSR on March 30; d: PLSR on April 1).

Variable Importance Analysis for Prediction Models

To identify the key spectral variables that significantly contributed to the predictions, SHAP (SHapley Additive exPlanations) values for the GPR model and VIP (Variable Importance in Projection) scores for the PLSR model were analyzed using the data from March 30 and April 1, which showed the optimal prediction performance (Fig. 2). For March 30, which recorded the highest prediction performance, the SHAP analysis of the GPR model revealed that RRI1 exhibited an overwhelmingly high contribution, followed by RRI2, BRI, and GARI. Similarly, the VIP results of the PLSR model identified RRI1 as the most important variable, followed by BRI, RRI2, and GARI, confirming a highly similar variable importance pattern to that of the GPR model.

For the April 1 data, both models demonstrated a distinct shift in the key spectral variables for predicting spike counts. In the GPR model, CCCI emerged as the most influential variable, followed by CI, GLI, and BRI in order of importance. The PLSR model also identified CCCI as the most critical variable, with BRI, CI, and GLI following in contribution rank (Fig. 2).
The key variables extracted, RRI1 and CCCI, are spectral indices based on the red-edge band

that sensitively detect chlorophyll concentration and canopy vigor in crops (Fitzgerald et al., 2010). The period from late March to early April corresponds to the panicle formation and booting stages of barley, during which chlorophyll degradation caused by waterlogging directly leads to the degeneration of effective tillers and a subsequent reduction in the final spike count.

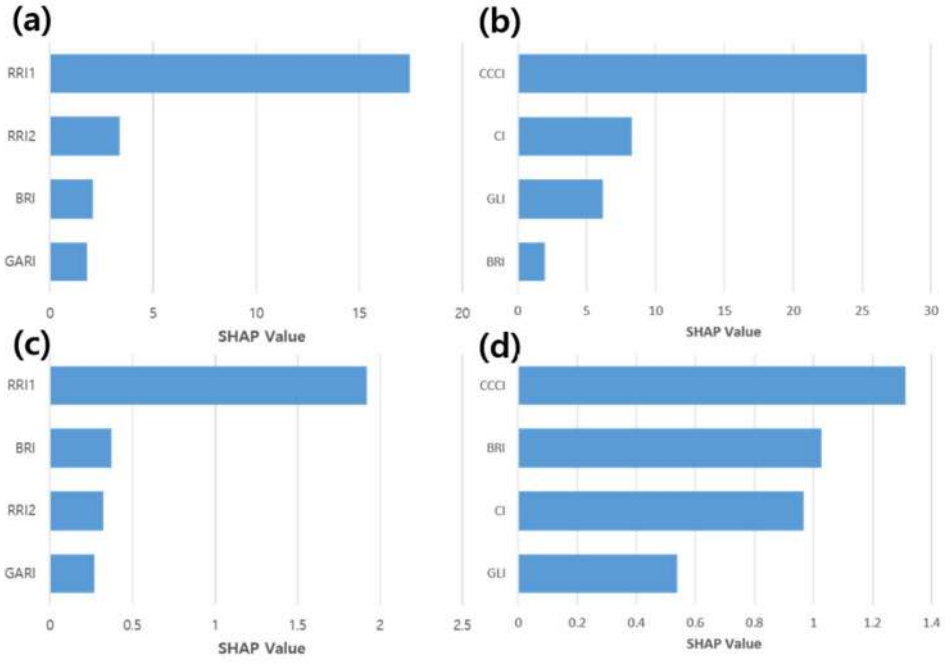

Fig.2 Shapley additive explanation (SHAP) values and variable importance in projection (VIP) scores for predicting final spike counts of barley: (a) SHAP values for GPR on March 30, (b) SHAP values for GPR on April 1, (c) VIP scores for PLSR on March 30, and (d) VIP scores for PLSR on April 1

CONCLUSIONS

This study demonstrated the potential of UAV-based multispectral imagery combined with machine learning models (GPR and PLSR) to predict final barley spike counts under varying waterlogging stress. GPR generally exhibited superior and more stable performance compared to PLSR. The optimal sensing window was identified as the period between March 30 and April 1, yielding the highest prediction accuracies. Specifically, on March 30, the GPR model achieved an R^2 of 0.7331, an RMSE of 11.3164, and an RE of 11.7336% on the validation dataset. High predictive power was also maintained on April 1 (GPR validation R^2 = 0.7096, RMSE = 11.8035, RE = 12.2387%). Variable importance analyses identified RRI1 and CCCI as the most critical spectral indices for predictions on March 30 and April 1, respectively. Because this optimal sensing window corresponds to the panicle formation and booting stages of barley, these red-edge-based indices effectively captured the physiological mechanism wherein waterlogging-induced chlorophyll degradation leads to tiller abortion and a subsequent reduction in spike counts. Ultimately, this study confirms that UAV-derived spectral indices during early reproductive stages are highly effective tools for the early diagnosis of waterlogging damage. Future studies should focus on multi-year validation across diverse cultivars to ensure model generalizability.

ACKNOWLEDGEMENTS

This work was carried out with the support of the “Development of image interpretation and quantification technology for weather stress damage in barley and red beans” project (Project No. RS-2026-25519310), National Institute of Crop Science, Rural Development Administration, Republic of Korea.

REFERENCES

Castro, J. de, R. D. Hill, C. Stasolla, and A. Badea. 2022. Waterlogging stress physiology in barley. Agronomy 12(4): 780.

Fei, S., M. A. Hassan, Z. He, Z. Chen, M. Shu, J. Wang, C. Li, and Y. Xiao. 2021. Assessment of ensemble learning to predict wheat grain yield based on UAV-multispectral reflectance. Remote Sensing 13(12): 2338.

Fitzgerald, G., D. Rodriguez, and G. O'Leary. 2010. Measuring and predicting canopy nitrogen nutrition in wheat using a spectral index—The canopy chlorophyll content index (CCCI). Field Crops Research 116(3): 318-324.

Na, S.-I., C.-W. Park, Y. Cheong, C.-S. Kang, I.-B. Choi, and K.-D. Lee. 2016. Selection of optimal vegetation indices for estimation of barley and wheat growth based on remote sensing - An application of unmanned aerial vehicle and field investigation data. Korean Journal of Remote Sensing 32(5): 483-497.

Na, S.-I., C. Park, K.-H. So, J. Park, and K. Lee. 2017. Mapping the spatial distribution of barley growth based on unmanned aerial vehicle. Available at: http://ieeexplore.ieee.org/document/8047029/.

Oehlschlager, J., U. Schmidhalter, and P. Noack. 2018. UAV-based hyperspectral sensing for yield prediction in winter barley. Available at: https://ieeexplore.ieee.org/document/8747260/.

Ploschuk, R. A., D. J. Miralles, T. D. Colmer, E. L. Ploschuk, and G. G. Striker. 2018. Waterlogging of winter crops at early and late stages: Impacts on leaf physiology, growth and yield. Frontiers in Plant Science 9: 1863.

Zhang, S., X. Wang, H. Lin, Y. Dong, and Z. Qiang. 2025. A review of the application of UAV multispectral remote sensing technology in precision agriculture. Smart Agricultural Technology 12: 101406.

Precision Agriculture Machinery and Systems 6 (PA-6)



PA-31

Proceedings of The 12th International Symposium on Machinery and Mechatronics for Agriculture and Biosystems Engineering (ISMAB 2026)
20-24 October 2026, Busan, Republic of Korea

NON-DESTRUCTIVE PREDICTION OF INTERNAL QUALITY IN ON-VINE MELONS USING HYPERSPECTRAL IMAGING AND MACHINE LEARNING

Gyumin Kim[12], Sungjay Kim[13], Xianghui Xin[12], Yeongjun Go[12], Jaeeun Lee[12], Donghyeon Seong[12], Ghiseok Kim[123*]

[1] Department of Biosystems Engineering, Seoul National University, Seoul, Republic of Korea
[2] Global Smart Farm Convergence Major, Seoul National University, Seoul, Korea
[3] Research Institute of Agriculture and Life Sciences, Seoul National University, Seoul, Korea
* Corresponding Author– Voice: +82-2-880-4603, Email: ghiseok@snu.ac.kr

Abstract: Melon, an annual vining fruit belonging to the family Cucurbitaceae, is one of the commercially most valuable fruit crops worldwide. At present, however, the harvest timing of melons is determined largely from external characteristics such as days after fruit set, rind color, and netting pattern, and therefore inevitably depends on the subjective judgment of the grower. In particular, soluble solids content (SSC) and firmness, the key indicators of melon quality, are difficult to measure non-destructively, which limits the accurate determination of the optimal harvest time and the assessment of fruit quality. In this study, a hyperspectral imaging system combining a mobile cart and a hyperspectral sensor was constructed inside a hydroponic melon greenhouse, and hyperspectral images of the fruits were acquired at successive growth stages. The actual SSC and firmness of the fruits were also measured destructively using a refractometer and a texture analyzer. Various preprocessing techniques were applied to the collected spectra, and non-destructive prediction models for SSC and firmness were subsequently developed using machine learning algorithms. The proposed approach is expected to contribute to the automated harvesting and sorting of melons, the establishment of quality management systems, and ultimately the advancement of smart farm technology.

Key Words: Melon, Hyperspectral imaging, Soluble solids content, Machine learning, Near-infrared

ACKNOWLEDGEMENTS

This work was supported by the Korea Institute of Planning and Evaluation for Technology in Food, Agriculture and Forestry (IPET) through the Smart Farm Innovation Technology Development Program, funded by the Ministry of Agriculture, Food and Rural Affairs (MAFRA), Republic of Korea (grant number RS-2025-02219360).

PA-32

Proceedings of The 12th International Symposium on Machinery and Mechatronics for Agriculture and Biosystems Engineering (ISMAB 2026)
20-24 October 2026, Busan, Republic of Korea

PRELIMINARY EVALUATION OF GLASS COATING EFFECTS ON HOPPER DISCHARGE AND FERTILIZER SPREADING DISTRIBUTION

Atsuru Fujimoto[1*]

[1]Department of Agro-environmental Science, Obihiro University of Agriculture and Veterinary Medicine, 2-11 Nishi, Inada, Obihiro, 080-8555, Japan
*Corresponding Author-- Voice: +81-155-49-5526, Email: fujimoto.a@obihiro.ac.jp

Abstract: Coatings for agricultural machinery should be evaluated for their effects on operating performance as well as surface protection. This study provided a preliminary evaluation of the effects of a glass coating on the inner hopper surface on fertilizer discharge and spreading distribution using discrete element method simulations and machine tests. Because friction coefficients of the coated surface could not be determined reliably, the simulations compared a painted steel hopper (baseline) with lower- and higher-friction hopper walls. With the baseline normalized to 100, the sum of the mean particle counts in the spreading measurement regions during 2–7 s after the start of shutter opening was 100.8 under low friction and 95.4 under high friction. The largest difference from the baseline in the proportion of particles at any position was 0.55 percentage points, and the spatial distributions nearly coincided. Machine tests using granular quicklime compared discharge over 10 s and transverse distribution across a 24 m width. Mean discharge decreased by approximately 3.0%, from 51.5 to 49.9 kg. Outdoor spreading distributions differed, but coating effects could not be separated from differences in wind and other test conditions. Within the simulated range, changing hopper-wall friction in either direction had little effect on the spatial particle distribution.

Key Words: glass coating, centrifugal fertilizer spreader, discrete element method, hopper discharge, granular fertilizer

INTRODUCTION

Glass and ceramic coatings can protect agricultural machinery surfaces by preserving appearance and limiting corrosion. When coatings are applied to surfaces in contact with materials such as fertilizer, their effects on operating performance through changes in friction should be quantified. Previous studies have reported that superhydrophobic coatings reduced clay adhesion to steel surfaces (Wan et al., 2025) and pesticide residue adhesion to spray tanks (Mu et al., 2025). In addition to these benefits, it is important to determine whether material delivery and spreading distribution are maintained after coating.

The effects of friction between fertilizer particles and the spreading disc and vanes on particle motion and spreading patterns have been investigated for centrifugal spreaders (Hofstee, 1995; Van Liedekerke et al., 2009). However, these studies did not establish the relationship between fertilizer delivery and friction changes caused by glass coating of the hopper interior.

Even at the same outlet setting, changes in hopper wall friction may alter material delivery to the disc. Precision fertilization also requires consideration of particle landing positions and spreading distribution, in addition to discharge quantity (Sharipov et al., 2021).

Outdoor spreading measurements can be affected by differences in conditions between test days. Numerical analysis allows particle behavior to be compared while maintaining friction conditions on surfaces other than the hopper interior. This study therefore examined the effects of lower and higher hopper wall friction, relative to a painted steel hopper, on discharge behavior and spreading distribution using a numerical spreader model. These results were compared with machine measurements of discharge and transverse spreading distribution before and after coating.

MATERIALS AND METHODS

Glass coating and test spreader

A glass coating similar to those used for automobiles was applied by G-MAX Inc. to the inner hopper surface of a twin-disc centrifugal fertilizer spreader (SULKY-BUREL, DPX series). Granular quicklime was used as the test material (Fig. 1). Travel speed was 7.5 km/h, PTO speed was 540 rpm, the outlet setting was 75, and the target application rate was 100 kg per 10 a (1,000 kg/ha). Tests were conducted in winter to limit changes in flowability associated with moisture absorption and caking.

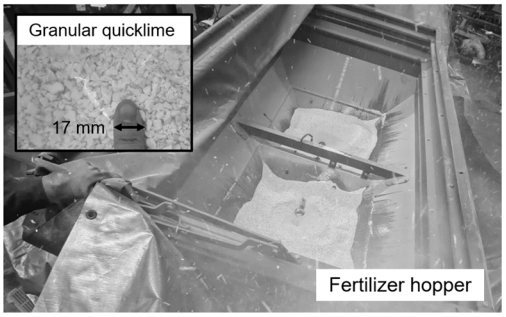

Fig. 1 Coated hopper interior and granular quicklime used in the tests.

Discrete element simulation

Simulations were performed using the discrete element method (DEM) in Granuleworks 8.2.0. A three-dimensional model representing the hopper, outlet, and spreading disc was constructed. An agitator was included to represent the machine mechanism and material motion within the hopper. Figure 2 shows the model and the probes used to evaluate hopper discharge and spreading distribution.

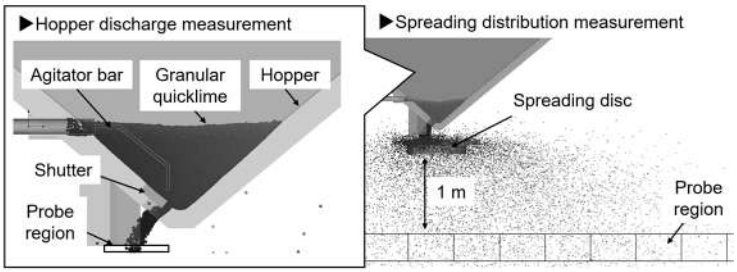

Fig. 2 Spatial arrangement of the 3D simulation model and measurement probes.

Three hopper-wall friction conditions were compared. The baseline represented the painted steel hopper before coating (Uncoated in Figs. 4 and 5), with particle–wall coefficients of static and kinetic friction of 0.46 and 0.37, respectively. The static friction coefficient was determined from the inclination angle at which fertilizer began to slide on a painted steel plate; the kinetic friction coefficient was not measured directly and was selected to approximate the sliding behavior observed on the plate. Because coefficients reproducing the sliding behavior on a coated plate could not be identified, friction on the hopper interior was shifted in both directions from the baseline: both coefficients were 0.20 in the low-friction condition, and the static and kinetic coefficients were 0.75 and 0.65 in the high-friction condition. Friction on all

other surfaces, including the spreading disc and agitator, and the particle–wall coefficient of restitution (0.22) were unchanged.

Particles were modeled as spheres with a diameter of 10 mm and a density of 1,700 kg/m³. Interparticle coefficients of static friction, kinetic friction, and restitution were 0.60, 0.48, and 0.20, respectively. The simulation duration was 20 s, the initial time step was 0.002 s, the number of DEM substeps was 200, and the output interval was 0.1 s. The spreading disc rotated at 800 rpm, and the agitator oscillated by ±20° at approximately 3 Hz. The shutter was opened by translation between 1 and 2 s after the start of the simulation.

Evaluation of simulated discharge and spreading distribution

A rectangular probe region measuring 0.40 × 0.40 × 0.02 m was placed below the hopper outlet in all three conditions. Discharged particles were counted at 0.1 s intervals with duplicate counting of individual particles disabled. Particles newly counted during each output interval were defined as discharged particles, and their running total as the cumulative number of discharged particles.

Twenty-one probe regions were used to measure the spreading distribution, and one additional probe region was used to measure hopper discharge. The spreading measurement regions were positioned 1.0 m below the spreading disc and arranged at 0.5 m intervals in the transverse direction. The spreading distribution was evaluated using particle counts within the 21 regions on the spreading side. Counts in each region were averaged over 50 output frames within 2–7 s after the start of shutter opening. To express the distribution from the single-sided model as distance from the spreader center, five regions on the opposite side of the center were reflected and added to regions at corresponding distances. The resulting position-dependent mean counts and their proportions of the total, referred to here as the spatial particle distribution, were compared. This distribution represents time-averaged occupancy of the measurement regions, rather than cumulative particle crossings or deposited mass.

Indoor fertilizer discharge tests

The spreader was operated indoors under identical settings before and after coating. Fertilizer discharged over 10 s was collected and weighed twice for each condition. The angle of repose was also measured to examine possible changes in bulk behavior with repeated use. Particle appearance was visually inspected for substantial changes in shape.

Transverse spreading distribution tests

Twenty-one collection trays were arranged across a working width of 24 m (Fig. 3). Fertilizer was spread while the tractor traveled at 7.5 km/h, and the mass collected in each tray was measured. Three tests were conducted for each condition. The transverse spreading pattern was obtained from the mean collected mass at each position. Wind conditions were obtained from the university meteorological station.

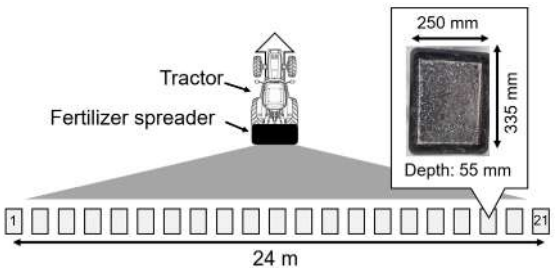

Fig. 3 Collection tray arrangement for measuring transverse spreading distribution.

RESULTS & DISCUSSION

Simulated hopper discharge

The time courses of discharged particle counts were broadly similar among the three conditions (Fig. 4). Counts increased rapidly after shutter opening and then declined toward zero. The initial peak was higher under low friction (308 particles per 0.1 s) than in the baseline (263) and under high friction (255), but the curves were close thereafter. The cumulative count reached half of its final value 0.1 s earlier under low friction and 0.3 s later under high friction than in the baseline. The final cumulative counts were 18,876 (baseline), 18,782 (low friction), and 19,069 (high friction), differing from the baseline by approximately 1.0% or less. Because almost all loaded particles were eventually discharged, the final count alone could not distinguish the conditions.

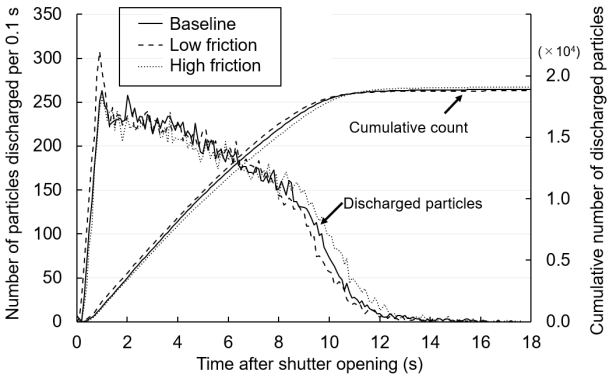

Fig. 4 Discharged and cumulative particle counts under three hopper-wall friction conditions.
(The left axis shows counts per 0.1 s interval, and the right axis shows their cumulative sum. Duplicate counting of individual particles was excluded. Time zero denotes the start of shutter opening.)

Simulated spreading distribution

The spatial particle distributions during 2–7 s after the start of shutter opening nearly coincided among the three conditions (Fig. 5). Mean counts summed across the spreading measurement regions were 1,123.90, 1,132.34, and 1,071.96 particles in the baseline, low-friction, and high-friction conditions, respectively (100.8 and 95.4 relative to a baseline of 100). The lower total under high friction corresponded to 4.1% fewer particles discharged from the hopper during the same period, indicating a smaller supply to the disc rather than a change in distribution shape. The largest difference from the baseline in the proportion of the total mean count at any position was 0.55 percentage points under low friction and 0.26 percentage points under high friction. The proportion in the region nearest the spreader center was 15.7%, 15.1%, and 15.5%, respectively, with no pronounced shift toward or away from the center.

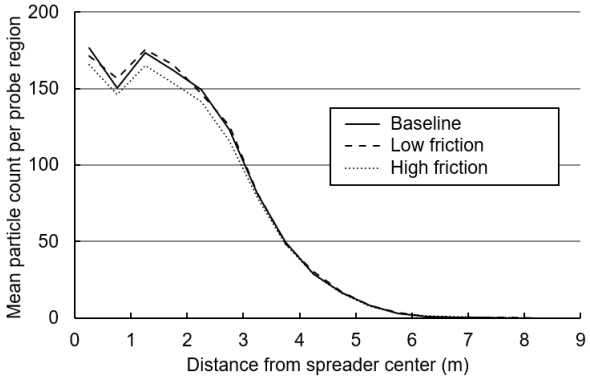

Fig.5 Spatial particle distributions under three hopper-wall friction conditions.
(Values are mean particle counts within each region over 50 output times during 2–7 s after the start of shutter opening. Regions on the opposite side were reflected about the spreader center and combined.)

Measured fertilizer discharge

Fertilizer masses discharged over 10 s were 51.1 and 51.8 kg before coating and 51.8 and 48.0 kg after coating (Fig. 6). The corresponding means were 51.5 and 49.9 kg. Thus, the mean after coating was approximately 3.0% lower, although the two coated measurements showed greater variation. Because each condition was tested only twice, these results were treated as a descriptive comparison.

The angle of repose ranged from 36.7° to 37.5° (Table 1), and no major changes in particle shape were observed visually. Under these test conditions and at a fixed outlet setting, glass coating of the hopper did not produce a marked increase in fertilizer discharge.

Measured transverse spreading patterns

Although total discharge did not increase in the indoor tests, the collected mass was higher after coating at several tray positions (Fig. 7). Mean wind speeds during the spreading tests were 1.2 m/s before coating and 1.0 m/s after coating; maximum gust speeds were 1.9 and 1.4 m/s, respectively. Because the tests were conducted on different days, coating effects could not be separated from differences in test conditions. Wind may have contributed, but its effect was not quantified.

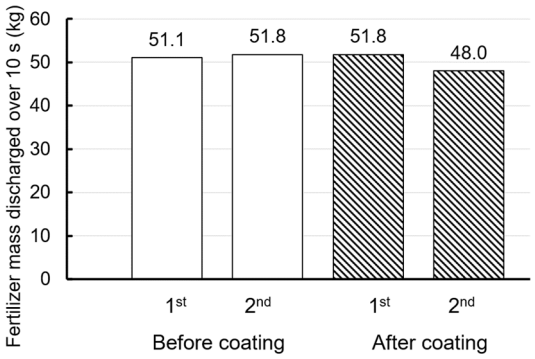

Fig. 6 Fertilizer mass discharged over 10 s before and after glass coating.

Table 1. Angle of repose of granular quicklime before and after glass coating.

Measurement	Before (°)	After (°)
1st	37.4	37.5
2nd	37.3	36.7

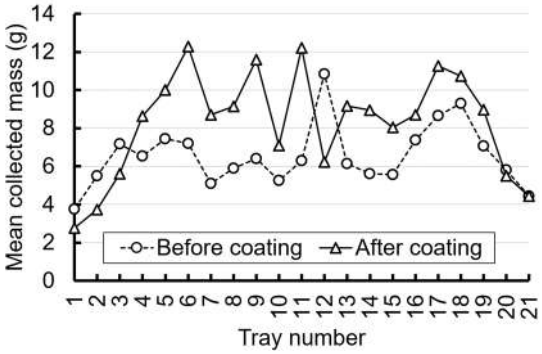

Fig. 7 Mean transverse spreading distributions before and after glass coating, based on three tests per condition.

Comparison of simulation and machine tests

The simulations showed little change in discharge behavior or spatial particle distribution when hopper-wall friction alone was reduced or increased from the baseline. These results suggest that the spatial particle distribution is relatively insensitive to hopper-wall friction under the simulated conditions.

Only one outlet setting and three hopper-wall friction conditions were examined, friction coefficients reproducing the coated surface were not identified, and the friction coefficients of the disc and vanes were unchanged in the simulation. The simulated values represent particle occupancy in probe regions, whereas the machine tests measured mass collected in trays; the two quantities cannot be compared directly. Discharge response at different outlet settings should also be examined if the coating is to be used on variable-rate spreaders.

CONCLUSIONS

1. When hopper-wall friction alone was lowered or raised from that of the painted steel baseline in the simulations, the spatial particle distribution was nearly unchanged; the largest difference from the baseline in the proportion at an individual position was 0.55 percentage points. The summed mean counts were 100.8 and 95.4 relative to a baseline of 100.
2. Mean fertilizer discharge over 10 s was 51.5 kg before coating and 49.9 kg after coating. With two measurements per condition, no consistent increase in discharge was observed after coating.

3. The coating effect on the outdoor transverse distribution could not be determined because the before- and after-coating tests were conducted under different conditions. Additional tests under comparable conditions are needed.

ACKNOWLEDGMENTS

The author gratefully acknowledges Kenji Masuda, President and Representative Director of G-MAX Inc., and the employees of G-MAX Inc. for providing technical expertise in agricultural machinery coatings and for applying the coating to the test spreader. This study was supported in part by the 2025 Regional Co-Creation Fund of the Center for Industry–University Collaboration, Obihiro University of Agriculture and Veterinary Medicine.

REFERENCES

Hofstee, J. W. 1995. Handling and spreading of fertilizers: Part 5, the spinning disc ty pe fertilizer spreader. Journal of Agricultural Engineering Research 62(3): 143–162. h ttps://doi.org/10.1006/jaer.1995.1073.

Mu, Y., M. Li, W. Li, Z. Fu, Y. Huang, Q. Yang, B. Feng, T. Chen, and J. Li. 2025. Design and fabrication of superhydrophobic micro-nano structures on the surface of spray tank for pesticide with robust mechanical-chemical properties. Colloids and Sur faces A: Physicochemical and Engineering Aspects 722: 137300. https://doi.org/10.10 16/j.colsurfa.2025.137300.

Sharipov, G. M., A. Heiß, S. L. Eshkabilov, H. W. Griepentrog, and D. S. Paraforos. 2 021. Variable rate application accuracy of a centrifugal disc spreader using ISO 117 83 communication data and granule motion modeling. Computers and Electronics in Agriculture 182: 106006. https://doi.org/10.1016/j.compag.2021.106006.

Van Liedekerke, P., E. Tijskens, and H. Ramon. 2009. Discrete element simulations of the influence of fertiliser physical properties on the spread pattern from spinning di sc spreaders. Biosystems Engineering 102(4): 392–405. https://doi.org/10.1016/j.biosy stemseng.2009.01.006.

Wan, Y., M. Sun, H. Peng, L. Ma, M. Liao, and H. Huang. 2025. A robust superhydro phobic coating fabricated by combination of laser texturing and electrostatic spraying for anti-soil adhesion. Applied Surface Science 703: 163355. https://doi.org/10.1016/j. apsusc.2025.163355.

PA-33

Proceedings of The 12th International Symposium on Machinery and Mechatronics for Agriculture and Biosystems Engineering (ISMAB 2026)
20-24 October 2026, Busan, Republic of Korea

COMPARISON OF MANUAL AND MECHANIZED TRANSPLANTING OF CABBAGE PRODUCTION IN GREENHOUSE CONDITIONS

Ezatullah Zakir[1], Md Nasim Reza[1,2], Cholet Nyangoma Atulinda[1], Sun-Ok Chung[1,2*]

[1]Department of Agricultural Machinery Engineering, Graduate School, Chungnam National University, Daejeon 34134, Republic of Korea
[2]Department of Smart Agricultural Systems, Graduate School, Chungnam National University, Daejeon 34134, Republic of Korea
*Corresponding Author-- Voice: +82-(0)42-821-6712, Email: sochung@cnu.ac.kr

Abstract: Cabbage is a major vegetable crop in Korea that requires timely and uniform transplanting for stable crop production and growth. Manual transplanting requires substantial labor and working time, whereas mechanical transplanting can improve operational efficiency. This study evaluated the performance of a single-row mechanical transplanter in comparison with manual transplanting under greenhouse conditions. One experimental greenhouse was divided into four plots. 35 days old cabbage seedlings were mechanically transplanted at target in-row spacings of 35, 40, and 45 cm in Plots 1–3, respectively, while Plot 4 was manually transplanted at 35 cm as the reference treatment. Transplanting performance was evaluated based on working time, labor requirement, missing plants, and spacing uniformity. RGB images were acquired after transplanting and during subsequent crop growth, and a YOLO11 model was applied to detect and count cabbage plants, identify missing planting positions, estimate in-row spacing, and assess canopy development. Mechanical transplanting reduced working time and labor requirements compared with manual transplanting. However, mechanical treatment showed a higher occurrence of missing plants, while greater variability in in-row spacing was observed in the manual treatment. The YOLO11 model effectively detected and counted cabbage plants and supported the identification of missing planting positions and spacing irregularities. At later growth stages, successfully established plants showed comparable canopy development between the mechanical and manual treatments. These results indicate that single-row mechanical transplanting can improve operational efficiency, while planting accuracy and stand uniformity remain important factors for improving transplanting performance and subsequent crop establishment.

Key Words: Precision agriculture, mechanical transplanting, greenhouse cabbage, YOLO11, planting uniformity.

INTRODUCTION

Cabbage is an important vegetable crop in Korea and has substantial economic and cultural value due to its extensive use in kimchi production. Stable cabbage production is therefore important for domestic consumption and the agricultural economy (Reza et al., 2025). However, Korean cabbage production faces challenges related to labor shortages, an aging agricultural

workforce, and rising labor costs (Reza et al., 2025; Ali et al., 2024). Transplanting is a critical operation in vegetable production because proper seedling placement affects crop establishment, growth, and final productivity. Manual transplanting requires considerable labor and working time, particularly during periods of high labor demand (Habineza et al., 2023). Delays in transplanting caused by limited labor availability may also reduce operational efficiency and affect crop establishment. These limitations have encouraged the use of mechanical transplanting systems. Vegetable transplanters can be classified according to their level of mechanization, including handheld, semi-automatic, and fully automatic systems (Habineza et al., 2023). Their performance is commonly evaluated using plant spacing, planting depth, transplanting efficiency, field capacity, seedling inclination, and mis-planting rate. Mechanical transplanting can improve field capacity and reduce labor requirements; however, transplanting quality depends on machine settings, seedling characteristics, planting distance, and cultivation conditions (Reza et al., 2025). Previous studies under Korean greenhouse conditions have demonstrated the potential of mechanical cabbage transplanting to improve operational efficiency compared with manual methods (Reza et al., 2025). However, mechanical operation may also result in missing plants, irregular spacing, or improper seedling placement. Therefore, machine performance should be evaluated not only in terms of working efficiency but also based on planting quality and subsequent crop development. Image-based monitoring provides an objective approach for evaluating transplanting quality after field operation. Deep-learning methods have been applied to detect and count cabbage seedlings and identify transplanting defects, supporting automated assessment of crop establishment (Wang et al., 2025). Therefore, this study evaluated a single-row mechanical cabbage transplanter in comparison with manual transplanting under greenhouse conditions by examining operational efficiency, planting uniformity, missing plants, and subsequent canopy development using RGB images and a YOLO11-based detection model.

MATERIALS AND METHODS

EXPERIMENTAL DESIGN AND PERFORMANCE EVALUATION

The study was conducted under greenhouse conditions to compare manual transplanting with a single-row mechanical cabbage transplanter. One greenhouse was divided into four experimental plots. Thirty-five-day-old cabbage seedlings were mechanically transplanted at target in-row spacings of 35, 40, and 45 cm in Plots 1–3, respectively, while Plot 4 was manually transplanted at 35 cm and used as the reference treatment. Transplanting performance was evaluated based on working time, labor requirement, missing-plant rate, and in-row spacing uniformity. Actual plant spacing was measured after transplanting to assess deviation from the target spacing and planting consistency. RGB images were acquired after transplanting and during subsequent crop development. A YOLO11 object-detection model was applied to detect and count cabbage plants, identify missing planting positions, and estimate plant spacing from the images. Model-derived plant counts were compared with manual observations, and canopy development was evaluated at later growth stages to compare crop establishment and growth between mechanical and manual transplanting treatments. The experimental greenhouse, mechanical and manual transplanting operations, and cabbage seedlings used for transplanting are shown in Fig. 1.

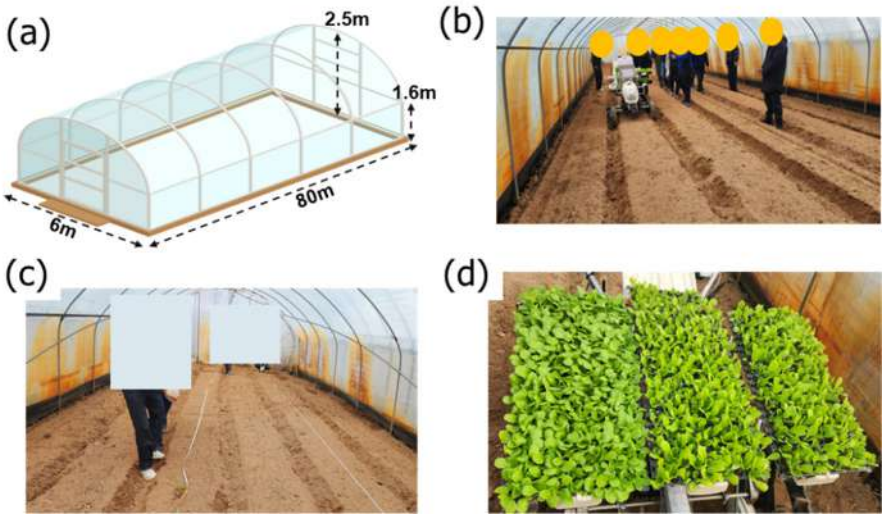

Fig.1 Experimental greenhouse and cabbage transplanting setup: (a) greenhouse dimensions, (b) mechanical transplanting operation, (c) manual transplanting operation, and (d) cabbage seedlings.

RESULTS & DISCUSSION

Mechanical transplanting improved operational efficiency compared with manual transplanting. Working time and labor requirement were reduced by approximately 65–70% and 60%, respectively. However, the mechanical treatments showed higher missing-plant rates than manual transplanting, indicating that further improvement in seedling feeding and placement accuracy was required. Mean spacing values remained close to the target settings of 35, 40, and 45 cm, although greater spacing variation was observed in manual transplanting than in the mechanical treatments. The transplanting performance of the mechanical and manual treatments, including missing-plant rate, actual in-row spacing, and spacing coefficient of variation, is summarized in Table 1. The YOLO11 model showed reliable detection and counting performance and was also used to identify missing planting positions and estimate in-row spacing from RGB images. The model also provided high counting accuracy, supporting objective evaluation of planting completeness and spacing uniformity. The detection performance of the YOLO11 model, including precision, recall, mAP@0.5, mAP@0.5:0.95, and counting accuracy, is presented in Fig. 2. YOLO11-based image analysis provided a consistent approach for evaluating plant counts, planting gaps, spacing distribution, and canopy development under greenhouse conditions. At later growth stages, canopy development of successfully established plants was comparatively similar between mechanical and manual treatments. This indicated that the main limitation of mechanical transplanting was related to initial planting accuracy, particularly missing plants and spacing uniformity, rather than subsequent crop growth.

Table 1 Comparison of transplanting performance between mechanical and manual cabbage transplanting methods

Parameter	Mechanical 35 cm	Mechanical 40 cm	Mechanical 45 cm	Manual 35 cm
Missing-plant rate (%)	7	8	9	2

Actual spacing (cm)	35 ± 1.5	40 ± 2	45 ± 2	35 ± 2.5
Spacing CV (%)	3	3	4	7

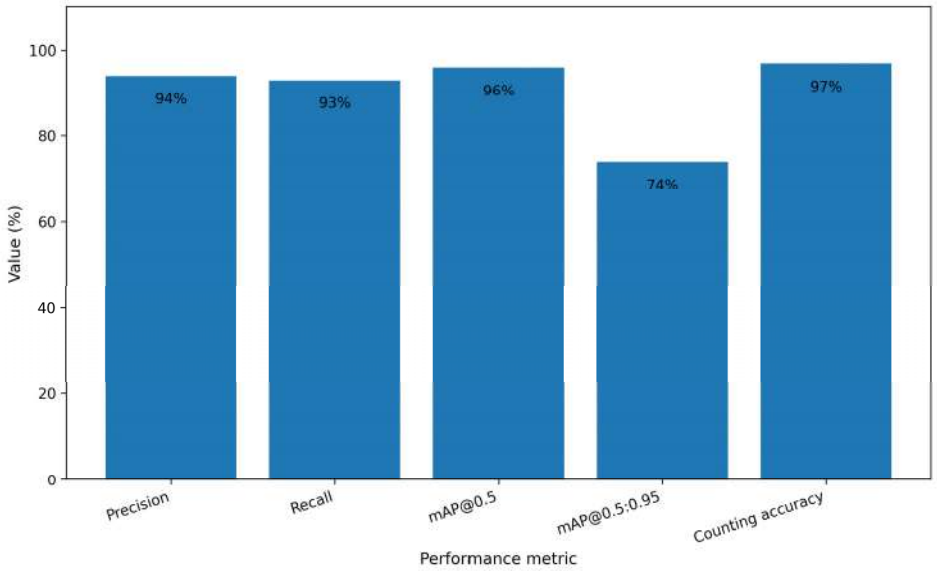

Fig. 2 Performance of the YOLO11 model for cabbage detection and transplanting quality evaluation.

CONCLUSIONS

Mechanical transplanting reduced labor dependence and improved operational efficiency under greenhouse conditions. The mechanical treatments maintained in-row spacing closer to the target values and showed lower spacing variability than manual transplanting. However, higher missing-plant rates were observed under mechanical transplanting, indicating that seedling feeding and deposition accuracy require further improvement. The YOLO11 model provided reliable plant detection and counting and was also used to identify missing planting positions, estimate in-row spacing, and evaluate canopy development from RGB images. At later growth stages, successfully established plants showed similar canopy development between mechanical and manual treatments. Overall, mechanical transplanting provided more uniform plant spacing, while improvement of planting completeness remains necessary for stable greenhouse cabbage production.

ACKNOWLEDGEMENTS

This work was supported by Korea Institute of Planning and Evaluation for Technology in Food, Agriculture, Forestry (IPET), through Machinery Mechanization Technology Development Program for Field Farming, funded by Ministry of Agriculture, Food and Rural Affairs (MAFRA) (Project No. RS-2023-00231026), Republic of Korea.

REFERENCES

Ali, M., M. A. Haque, M. A. Rahman, J. M. Moon, K. J. Kim, S. O. Chung, and H. I. Kim. 2024. Mechanization trends of cabbage harvesting practices: A review. *Precision Agriculture Science and Technology* 6(3): 218-237.

Chithra, G. 2025. Comparison of use of mechanical transplanters and manual transplanting for paddy cultivation in Thiruvananthapuram District. *Archives of Current Research International* 25(9): 681-688.

Habineza, E., M. Ali, M. N. Reza, J. K. Woo, S. O. Chung, and Y. Hou. 2023. Vegetable transplanters and kinematic analysis of major mechanisms: A review. *Korean Journal of Agricultural Science* 50(1): 113-129.

Reza, M. N., M. R. Karim, M. R. Ali, K. H. Lee, E. Bicamumakuba, K. Y. Lee, and S. O. Chung. 2025. Field evaluation of a transplanter and a collector under development for Korean spring cabbage production in greenhouses. *AgriEngineering* 7: 226.

Wang, Y., M. Liu, Y. Geng, J. Zhu, W. Chen, and C. Zhao. 2025. Research on cabbage transplanting status detection and operation quality evaluation in complex environments based on improved YOLOv10-TQ and DeepSort. *Frontiers in Plant Science* 16: 1726334.

PA-34

Proceedings of The 12th International Symposium on Machinery and Mechatronics for Agriculture and Biosystems Engineering (ISMAB 2026)
20-24 October 2026, Busan, Republic of Korea

BLOB SELECTION EVALUATION FOR VISION-BASED OUTDOOR ROBOT LOCALIZATION USING MOG2 SUBTRACTION

Nguyen Van Dieu[1], Tadashi Chosa[1]*

[1] Tokyo university of agriculture and technology
3-5-8 Saiwai-cho, Fuchu, Tokyo, 183-8509 Japan
*Corresponding Author-- Voice: +81-42-367-5721, Email: chosa@cc.tuat.ac.jp

Abstract: Vision-based positioning is an attractive approach for monitoring autonomous mobile robots in agricultural environments because it enables robot localization using a fixed camera without additional onboard sensors. However, outdoor conditions introduce challenges such as illumination changes, moving shadows, and vegetation sway, which often generate multiple foreground blobs during background subtraction. Consequently, accurate robot localization depends not only on detecting foreground regions but also on correctly identifying the blob corresponding to the robot. This study evaluated the effectiveness of several blob-selection methods for robot position recognition in a network-camera-based autonomous navigation system employing the MOG2 (Mixture of Gaussians 2) background-subtraction algorithm. A network camera installed at a height of 3.22 m with a depression angle of 38.56° monitored a 3 × 5 m robot operating area. Images were transmitted to a host computer via WiFi, where robot position was estimated and control commands were generated for a mobile robot. Robot trajectories were simultaneously recorded using a video camera and analyzed with motion analysis software to obtain reference positions. Four blob-selection methods were compared: (i) use of all detected blobs, (ii) removal of blobs smaller than 100 pixels, (iii) removal of blobs located more than 150 pixels from the previously recognized position, and (iv) clustering detected blobs using a Minimum Spanning Tree (MST) and selecting the cluster closest to the previous position estimate. Robot positions were calculated from the selected blobs and converted to ground coordinates through homography transformation. Approximately 24 min of operation produced 8,926 image frames. After excluding frames in which the robot was stationary or clearly misrecognized, 3,322 valid frames were analyzed. The results showed that using all detected blobs generated the largest deviation from the reference trajectory. All three blob-selection approaches improved localization performance. Mean positional errors were 0.336 m, 0.305 m, 0.334 m, and 0.334 m for methods (i), (ii), (iii), and (iv), respectively. Although the size-based filtering method achieved the smallest average error, the differences among the three selection methods were limited. Distance-based filtering and MST clustering produced nearly identical performance. Analysis of error distributions indicated that errors in the x-direction were centered around zero, whereas a systematic bias of approximately 0.28 m was observed in the y-direction. This bias was attributed to the oblique camera viewpoint, which caused both the top and side surfaces of the robot to be included in the detected moving region. After compensating for this systematic error, more than 65% of frames showed a positional deviation of less than 0.20 m from the reference trajectory. These results demonstrate that simple blob-filtering techniques can improve the robustness of MOG2-based outdoor robot

positioning, although further research is required to address severe blob misrecognition events and enhance reliability under varying outdoor conditions.

Key Words: vision-based positioning; autonomous mobile robot; MOG2 background subtraction; blob selection; agricultural robotics.

INTRODUCTION

Vision-based positioning provides a practical approach for monitoring mobile robots in agricultural environments, particularly when a fixed camera monitors a predefined work area (Bai et al., 2023; Wang et al., 2022). However, outdoor image sequences are often affected by illumination changes, shadows, vegetation movement, and other background variations (Rahmon et al., 2024; Zhang and Li, 2022). As a result, background subtraction may generate multiple foreground blobs in a single frame, not all of which correspond to the robot. Reliable position estimation therefore depends not only on detecting foreground regions but also on correctly identifying the blob associated with the robot.

In our previous network-camera-based robot supervision system, foreground regions were extracted using the MOG2 (Mixture of Gaussians 2) background-subtraction algorithm (Nguyen and Chosa, 2026). Although MOG2 is a classical method for moving-object detection, it has proven suitable for robot monitoring because of its low computational cost. In this study, the developed system was applied to outdoor autonomous navigation, and the validity of robot position recognition based on MOG2 was investigated. Under outdoor conditions, background subtraction frequently detects foreground blobs corresponding to objects other than the robot because of vegetation movement, illumination changes, and other environmental disturbances. Therefore, blob-selection methods were used to identify the blob corresponding to the robot, and the resulting positioning performance was evaluated.

MATERIALS AND METHODS

OVERVIEW OF THE EXPERIMENT

A network-camera-based robot supervision system developed by Nguyen and Chosa (2026) was used in this study. A network camera was installed at a height of 3.22 m with a depression angle of 38.56° to monitor and control an autonomous mobile robot (CuGo V3i, CuboRex Inc., Tokyo, Japan; 434 × 516 × 300 mm, L × W × H), preventing it from leaving a designated operating area. The camera captured images of the robot's workspace, consisting of a predefined 3 × 5 m area and its surroundings, and transmitted them to a host computer via Wi-Fi. The host computer estimated the robot's position from the captured images and sent control commands, including stop, reverse, and turning operations, to the robot via Wi-Fi. To obtain reference position data, the robot's motion was independently recorded using a video camera (LUMIX DC-FZ85, Panasonic Corporation, Osaka, Japan). The recorded video was analyzed with Kinovea (Version 2023.1.2, Kinovea Open Source Project), and the resulting trajectory was used as the ground-truth position reference (Fig. 1).

BLOB SELECTION AND ROBOT POSITIONING

Because MOG2 often detected multiple foreground blobs as robot candidates, four blob-selection methods were evaluated for robot position estimation:

i) using all detected blobs;

ii) removing blobs smaller than 100 pixels as noise;

iii) removing blobs located more than 150 pixels from the robot position estimated in the previous frame; and

iv) clustering the detected blobs using a minimum spanning tree (MST) and selecting the cluster closest to the robot position in the previous frame.

For each method, the robot position in the image was determined from the selected blobs, transformed into real-world coordinates using a homography transformation, and compared with the reference trajectory obtained from Kinovea analysis.

During approximately 24 min of operation, 8,926 image frames were saved on the host computer as control-history records. Frames in which the robot was stationary or clearly misrecognized were excluded from the analysis. Misrecognition was defined as a discrepancy of 680 mm or greater between the estimated robot position and the Kinovea-derived reference position, corresponding approximately to the robot's diagonal length. After filtering, 3,322 frames for which positions could be calculated using all four methods were retained for evaluation.

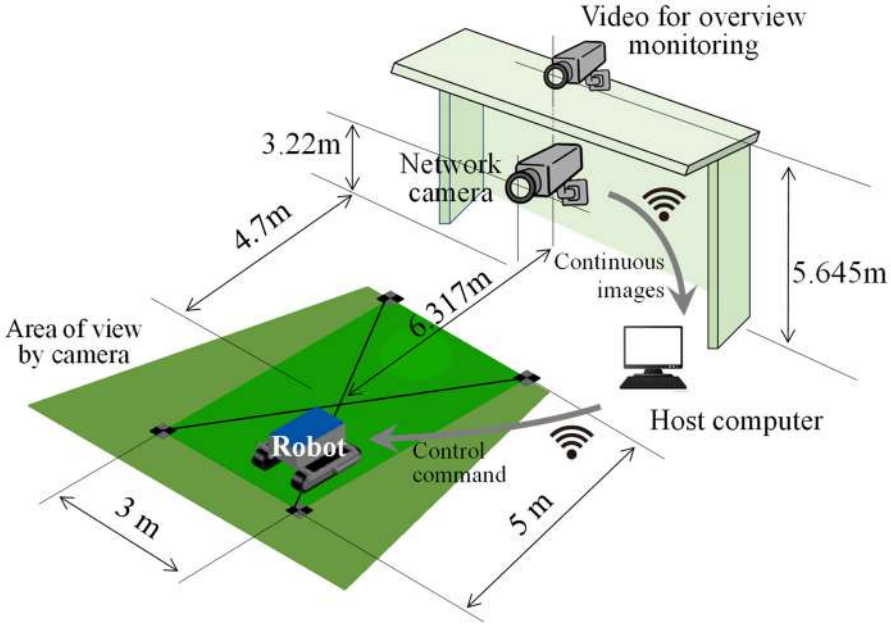

Fig.1 Overview of the experiment and placement of devices.

RESULTS & DISCUSSION

When all detected blobs were used, the positional error relative to the reference trajectory obtained from Kinovea was larger than that obtained with the other methods. In contrast, size-based filtering, distance-based filtering using the previous position estimate, and MST-based clustering all improved positioning accuracy. No difference was observed between the distance-based filtering and MST-based clustering methods (Table 1).

Table 1 Comparison of deviations from the ground truth for the four methods.

Classification	i) No removal	ii) Size-based removal	iii) Distance -based removal	iv) Minimum Spanning Tree
Numb. of data	3322	3322	3322	3322
Average (mm)	0.336	0.305	0.334	0.334
Standard dev.	0.082	0.150	0.079	0.079
Range	0.740	0.778	0.625	0.625

The error distribution for the size-based filtering method, which removed blobs smaller than 100 pixels and produced the smallest positional error, is shown in Fig. 2. The error distribution along the x-axis was centered near zero. In contrast, the y-axis errors exhibited a noticeable bias, indicating a systematic error of approximately 0.28 m. This bias is attributed to the oblique viewing angle of the network camera. Ideally, the robot position should correspond to the center of the robot's top surface. However, because the robot was observed from above at an oblique angle, both the top surface and portions of the side surfaces were detected as moving regions, causing a displacement between the detected blob center and the true robot position. Considering the robot height and the camera depression angle, the magnitude of the observed systematic error was consistent with the expected geometric offset. After compensating for this systematic error, more than 65% of the analyzed frames exhibited a positional difference of less than 0.2 m between the host-computer estimate and the reference position obtained from Kinovea (Fig. 3).

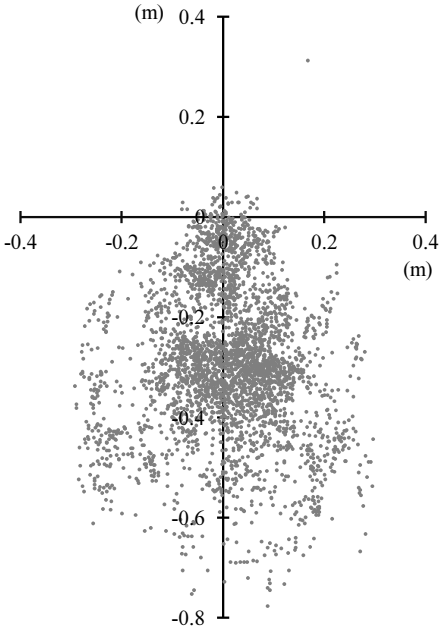

Fig. 2 Deviation from the standard (Results from size-based removal)

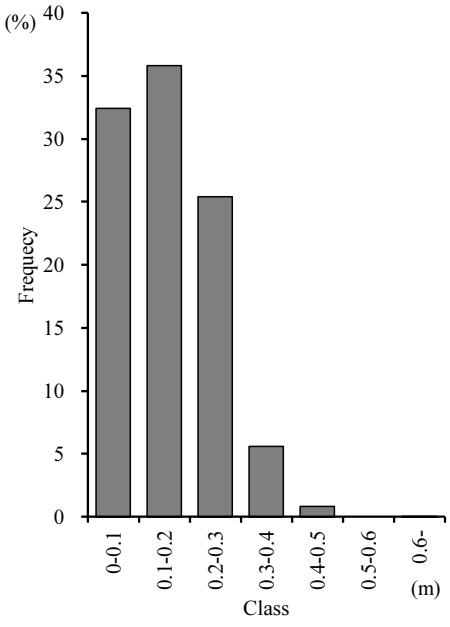

Fig. 3 Deviation from the standard after systematic error removal (Results from size-based removal)

CONCLUSIONS

This study investigated the accuracy of robot position recognition in a network-camera-based control system for a small mobile robot. Evaluation of blob-selection methods applied to foreground regions extracted by MOG2 revealed no substantial differences in positioning

accuracy among size-based filtering, distance-based filtering using the previous position estimate, and MST-based clustering. However, the analysis was limited to frames without blob misrecognition; therefore, further investigation is required to improve robustness against misrecognized blobs.

A systematic positional error was also observed, which was attributed to the oblique viewing angle of the network camera. Nevertheless, after compensating for this error, the positional difference from the reference trajectory was less than 0.2 m in more than 65% of the analyzed frames.

REFERENCES

Bai, Y., B. Zhang, N. Xu, J. Zhou, J. Shi, and Z. Diao. 2023. Vision-based navigation and guidance for agricultural autonomous vehicles and robots: A review. Computers and Electronics in Agriculture, 205, 107584. https://doi.org/10.1016/j.compag.2022.107584

Nguyen, V. D. and T. Chosa. 2026. Latency characterization in real-time robot supervision via network camera system. Engineering in Agriculture, Environment and Food, 19(1), 60–70. https://doi.org/10.37221/eaef.19.1_60

Mishra, G., and S. K. Mohanty. 2020. Efficient construction of an approximate similarity graph for minimum spanning tree based clustering. Applied Soft Computing, 97, 106676. https://doi.org/10.1016/j.asoc.2020.106676

Rahmon, G., K. Palaniappan, I. E. Toubal, F. Bunyak, R. Rao and G. Seetharaman. 2024. DeepFTSG: Multi-stream Asymmetric USE-Net Trellis Encoders with Shared Decoder Feature Fusion Architecture for Video Motion Segmentation. International Journal of Computer Vision, 132(3), 776–804. https://doi.org/10.1007/s11263-023-01910-x

Wang, T., B. Chen, Z. Zhang, H. Li, and M. Zhang. 2022. Applications of machine vision in agricultural robot navigation: A review. Computers and Electronics in Agriculture, 198, 107085. https://doi.org/10.1016/j.compag.2022.107085

Zhang, H., and H. Li. 2022. Interactive spatio-temporal feature learning network for video foreground detection. Complex & Intelligent Systems, 8(5), 4251–4263. https://doi.org/10.1007/s40747-022-00712-x

PA-35

Proceedings of The 12th International Symposium on Machinery and Mechatronics for Agriculture and Biosystems Engineering (ISMAB 2026)
20-24 October 2026, Busan, Republic of Korea

MEASUREMENT BIAS OF AN FDR SOIL MOISTURE SENSOR UNDER DRYING–REWETTING CONDITIONS

Minjoo Kim[1], Jaesung Park[1,2*], Seokyung Park[1]

[1]Department of Bio-Industrial Machinery Engineering, Pusan National University, Miryang 50463, Republic of Korea
[2] Department of Natural Resources Systems Engineering, Pusan National University, Yangsan 50612, Republic of Korea
[3]Life and Industry Convergence Research Institute, Pusan National University, Miryang 50463, Republic of Korea
*Corresponding Author -- Email: jaesung.park@pusan.ac.kr

Abstract: Frequency domain reflectometry (FDR) soil moisture sensors are widely used in smart farms and precision agriculture for continuous monitoring of soil water content. However, an FDR sensor measures only a small volume of soil around its prongs, whereas its calibration assumes that water is uniformly distributed. When evaporation or irrigation makes the soil water distribution non-uniform, the sensor reading may therefore differ from the actual water content of the soil. This study examined whether FDR sensor readings are overestimated or underestimated relative to the actual soil water content during drying and rewetting. Sandy loam was packed into a container placed on a load cell, which provided the reference water content of the whole soil, and an FDR sensor was installed in the soil. The soil was dried naturally, irrigated, and dried again, while the sensor and reference values were recorded continuously. The sensor reading did not follow the actual water content. During drying, the sensor overestimated the water content, by about 2 percentage points (%p) on average and up to about 3 %p. During irrigation, in contrast, the reference water content increased stepwise with each irrigation pulse, whereas the sensor reading hardly changed. As a result, the sensor underestimated the water content by more than 10 %p after irrigation, and it took more than a day for the reading to recover. The sensor reading was thus overestimated or underestimated depending on whether the soil was drying or being wetted. This bias is considered to result from the local measurement of the sensor combined with the non-uniform distribution of soil water, rather than from a sensor defect. FDR sensor readings should therefore be interpreted with care in irrigation management, particularly shortly after irrigation.

Key Words: Soil Moisture Sensor, FDR, Measurement Bias, Overestimation and Underestimation, Precision Agriculture

INTRODUCTION

Soil water content is essential information for crop management and irrigation decisions. Frequency domain reflectometry (FDR) soil moisture sensors are widely used in smart farms and precision agriculture because they are easy to install and can measure water content

continuously (Bittelli, 2011).

An FDR sensor measures the dielectric permittivity of the soil around its prongs and converts it into water content with a calibration equation such as that of Topp et al. (1980). The calibration assumes that water is uniformly distributed, but the sensor observes only a small volume of soil near the prongs (Robinson et al., 2008). In practice, evaporation and irrigation make the soil water distribution non-uniform, so the sensor reading may not represent the water content of the whole soil.

The objective of this study was to examine whether FDR sensor readings are overestimated or underestimated relative to the actual soil water content during drying and rewetting, using a load cell that continuously measures the water content of the whole soil as a reference.

MATERIALS AND METHODS

EXPERIMENTAL SETUP AND PROCEDURE

Figure 1 shows the experimental setup, and the experimental conditions are summarized in Table 1. Sandy loam was packed into an acrylic container placed on a load cell, and an FDR sensor (5TE, METER Group, USA) was inserted vertically into the soil. The soil was dried naturally for 480 h, irrigated by drip in three pulses of 500 mL (1.5 L in total), and then dried again. The load-cell mass and the sensor reading were recorded simultaneously at 10-min intervals for 729 h.

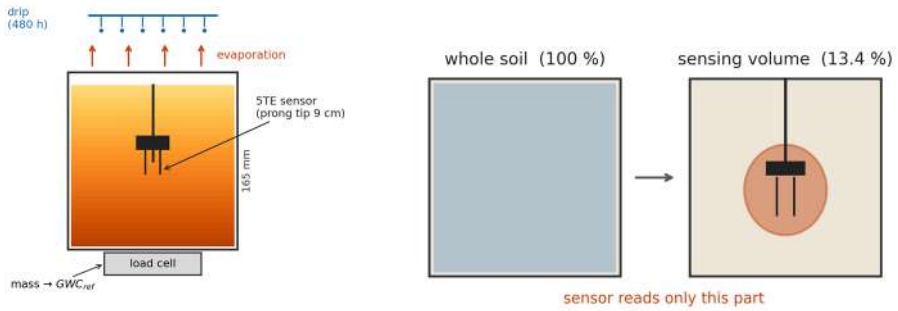

Fig. 1 (a) Schematic of the experimental setup and (b) sensing volume of the sensor relative to the whole soil volume.

Table 1 Experimental conditions.

Item	Description
Soil	Sandy loam (sand 69.4%, silt 29.1%, clay 1.5%)
Container	Acrylic, 180 × 180 × 200 mm; packing depth 165 mm; no drainage
Reference	Load cell under the container
Sensor	METER 5TE (FDR), prong tip at 9 cm depth
Procedure	Drying (0–480 h) → drip irrigation → re-drying (to 729 h)
Irrigation	3 pulses × 500 mL (10 min watering + 10 min rest), 1.5 L in total
Logging	10-min interval

WATER CONTENT CALCULATION

The sensor reading was converted into volumetric water content with Eq. (1). The reference water content of the whole soil was calculated from the load-cell mass with Eq. (2), and the two values were compared on a gravimetric basis using Eq. (3). The difference between them,

Eq. (4), was expressed in percentage points (%p); a positive value means overestimation and a negative value means underestimation by the sensor.

$$\theta_v = 4.3 \times 10^{-6}\varepsilon_a{}^3 - 5.5 \times 10^{-4}\varepsilon_a{}^2 + 2.92 \times 10^{-2}\varepsilon_a - 5.3 \times 10^{-2} \quad (1)$$

$$GWC_{\text{ref}} = \frac{M_t - M_c - M_s}{M_s} \times 100 \quad (2)$$

$$VWC = GWC \times \frac{\rho_d}{\rho_w} \quad (3)$$

$$\Delta = GWC_{\text{sensor}} - GWC_{\text{ref}} \quad (4)$$

where:

θ_v = Volumetric water content ($m^3\ m^{-3}$); ε_a = Apparent dielectric permittivity (-)
GWC, VWC = Gravimetric and volumetric water contents (%)
M_t, M_c, M_s = Total, container, and oven-dry soil masses (kg)
ρ_d, ρ_w = Dry bulk density of soil and density of water ($g\ cm^{-3}$)
Δ = Difference between sensor and reference values (%p)

RESULTS & DISCUSSION

SENSOR AND REFERENCE WATER CONTENT

Figure 2 shows the changes in the reference and sensor water contents. The sensor reading did not follow the reference value for most of the experiment. During drying, the sensor value remained above the reference value. After irrigation, the reference value increased immediately, whereas the sensor value rose only gradually and stayed below the reference for a while.

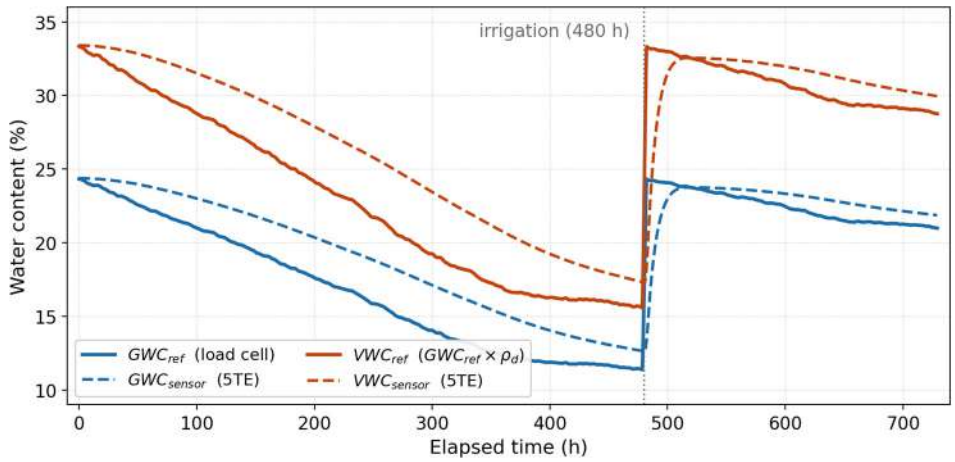

Fig. 2 Time series of reference (load cell, solid) and sensor (5TE, dashed) water contents; irrigation started at 480 h.

STEPWISE INCREASE DURING PULSE IRRIGATION

Figure 3 enlarges the irrigation period. The reference water content increased stepwise with each of the three 500 mL pulses, because the load cell detected the applied water immediately. In contrast, the sensor reading remained almost unchanged throughout the three pulses and could not distinguish them; it began to rise only gradually after irrigation had ended. The gap between the two values therefore widened with every pulse, and at the end of irrigation the sensor underestimated the water content by more than 10 %p. This indicates

that the applied water needed time to move down to the depth of the sensor.

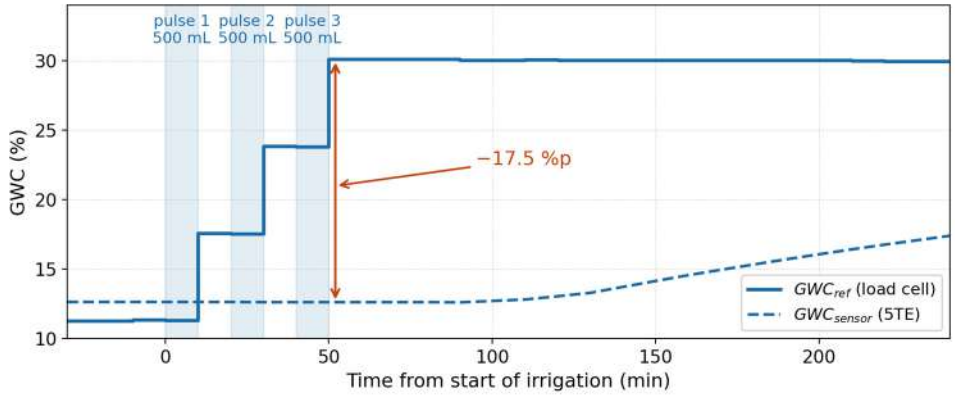

Fig. 3 Reference and sensor GWC during pulse irrigation. Shaded bands indicate the three 500 mL irrigation pulses.

OVERESTIMATION AND UNDERESTIMATION

Figure 4 shows the difference between the sensor and reference values. During drying, the sensor overestimated the water content by about 2 %p on average and by up to about 3 %p. Immediately after irrigation, the sensor underestimated the water content by more than 10 %p, and the underestimation disappeared only after more than a day. As the soil dried again, the sensor returned to slight overestimation. The direction of the measurement bias therefore depended on whether the soil was drying or being wetted.

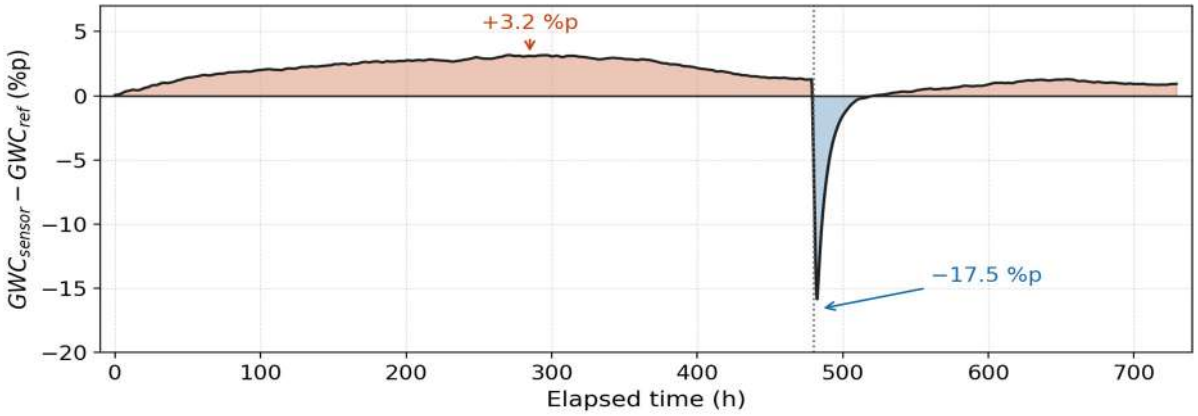

Fig. 4 Difference between sensor and reference GWC. Positive values denote overestimation and negative values denote underestimation by the sensor.

CAUSE OF THE MEASUREMENT BIAS

Because the soil dries from the surface, the soil around the sensor remains wetter than the soil as a whole during drying, which leads to overestimation. After irrigation, the load cell detects the added water at once, but the water takes time to reach the sensor, which leads to underestimation. The bias is therefore not a sensor defect but a result of measuring only a small part of a soil in which water is not uniformly distributed. Because the bias changes direction with soil conditions, a simple constant correction is not sufficient.

CONCLUSIONS

FDR soil moisture sensor readings were compared with the actual water content of the whole soil during drying and rewetting. The sensor overestimated the water content during drying

and underestimated it after irrigation, showing that sensor data can be biased in either direction depending on soil water conditions. FDR sensor readings should therefore be interpreted with care when used for irrigation decisions, particularly shortly after irrigation. Further studies will address correction methods that account for this bias.

ACKNOWLEDGEMENTS

This work was supported by the National Research Foundation of Korea(NRF) grant funded by the Korea government(MSIT) (RS-2026-25475333).
This research was supported by the ANCHOR program through the Busan Anchor Center, funded by the Ministry of Education (MOE) and Busan Metropolitan City, Republic of Korea.
(2026-RISE-02-004-2-4-6-1)

REFERENCES

Bittelli, M. 2011. Measuring soil water content: A review. *HortTechnology* 21(3): 293-300.

Robinson, D. A., C. S. Campbell, J. W. Hopmans, B. K. Hornbuckle, S. B. Jones, R. Knight, F. Ogden, J. Selker, and O. Wendroth. 2008. Soil moisture measurement for ecological and hydrological watershed-scale observatories: A review. *Vadose Zone J.* 7(1): 358-389.

Topp, G. C., J. L. Davis, and A. P. Annan. 1980. Electromagnetic determination of soil water content: Measurements in coaxial transmission lines. *Water Resources Res.* 16(3): 574-582.

Precision Agriculture Machinery and Systems 7 (PA-7)



PA-36

Proceedings of The 12th International Symposium on Machinery and Mechatronics for Agriculture and Biosystems Engineering (ISMAB 2026)
20-24 October 2026, Busan, Republic of Korea

DEVELOPMENT OF A GENERAL GUIDELINE FOR DATA-BASED INTEGRATED PEST MANAGEMENT UNDER ISO/TC 347

Seongmin Park[1], Soo Chung[1,2,3*]

[1] Research Institute of Agriculture and Life Sciences, Seoul National University, 1 Gwanak-ro, Gwanak-gu, Seoul 08826, Republic of Korea
[2]Department of Biosystems Engineering, College of Agriculture and Life Sciences, Seoul National University, 1 Gwanak-ro, Gwanak-gu, Seoul 08826, Republic of Korea
[3]Integrated Major in Global Smart Farm, Seoul National University, Seoul 08826, Republic of Korea
*Corresponding Author-- Voice: +82 2 8804606, Email: soochung@snu.ac.kr

Abstract: Data-based Integrated Pest Management (IPM) integrates multi-source field data with predictive models and increasingly automated control equipment. However, broader adoption remains constrained by the absence of an internationally agreed framework defining the essential functions of data-based IPM and the data and documentation it should produce. To address this gap, ISO/TC 347 established Ad Hoc Group 4 (AHG 4), Integrated Pest Management, to examine the need for an international deliverable and prepare a draft general guideline. This paper presents the group's organizational setting, working approach, and technical progress to date. The working draft has evolved from a descriptive document toward a more assessable requirement structure, with explanatory content transferred to an informative annex. The crop-protection process is organized as a nested-loop framework in which an annual management cycle encompasses recurring in-season activities of monitoring, decision-making, control, and evaluation. Rather than prescribing specific control outcomes, the draft focuses on documented decision-making processes, enabling application across diverse crops, regions, and production scales. Requirements for data and system capabilities further define the functional interface among monitoring devices, decision-support systems, and application equipment. Remaining technical issues and the further work required before progression toward a formal work item proposal are also discussed.

Key Words: Integrated pest management, International standardization, ISO/TC 347, Interoperability

PA-37

Proceedings of The 12th International Symposium on Machinery and Mechatronics for Agriculture and Biosystems Engineering (ISMAB 2026)
20-24 October 2026, Busan, Republic of Korea

STEM FOLLOWING AND CONTINUOUS CUTTING OF TOMATO LOWER LEAVES USING A FORCE CONTROLLED HEDGE TRIMMER-TYPE DE-LEAFING ROBOT

Masakazu Kashino[1*], Hideto Kurosaki[1], Tokihiro Fukatsu[1]

[1]Institute of Agricultural Machinery, NARO,
1-31-1, Kannondai, Tsukuba City, Ibaraki, Japan
*Corresponding Author-- Voice: +81-29-838-8966,
Email: kashino.masakazu229@naro.go.jp

Abstract: A tomato de-leafing robot equipped with a hedge trimmer as an end-effector was developed in this study. A position and orientation control method was also proposed to enable continuous lower-leaf cutting while allowing the hedge trimmer to follow the main stem by impedance control that uses the external forces acting on the hedge trimmer. Experiments conducted under practical cultivation conditions confirmed that the proposed method enabled the end-effector to follow the shape of the main stem without damaging it. The method also allowed the end-effector to move over protrusions and remaining petioles on the stem using a stuck recovery motion. In single-leaf cutting tests, the end-effector cut the lower-leaf petiole, moved over the remaining petiole, and re-established contact with the main stem, which required 5.6–6.3 s on average. The corresponding travel distance was 5.4–5.9 cm. These results clarified basic conditions related to the stability of continuous cutting. In two-leaf continuous cutting tests, the remaining petiole length on the stem side averaged 1.9 cm for the first lower leaf from the bottom and 2.9 cm for the second lower leaf, with greater variability observed for the second leaf. Overall, the findings indicate that the proposed method is effective for continuous cutting of tomato lower leaves; however, improvement of the stuck recovery motion is required to achieve stable and faster operation.

Key Words: Agricultural Robot, Robot arm, De-leafing, Force control, Tomato

INTRODUCTION

In labor-intensive large-scale greenhouse horticulture, the demand for robotic automation has been increasing. Although research and development on harvesting robots has been progressing toward maturity, there is a growing need to utilize manipulators for other greenhouse operations. Among these operations, lower-leaf removal requires a labor input comparable to that of harvesting; therefore, its automation is expected to substantially reduce labor requirements across the overall cultivation process. Previous studies on de-leafing robots have investigated methods such as cutting with scissor-type end-effectors (Zhou et al., 2022). However, under dense plant canopy conditions, such cutting strategies may encounter difficulties in identifying cutting points and positioning the end-effector appropriately. To address these limitations, we previously developed a tomato de-leafing robot equipped with a

hedge trimmer-type end effector as a method capable of cutting multiple leaves without requiring precise localization of each cutting point or a detailed approach motion (Kashino et al., 2026). Although this approach has advantages in terms of working speed, stable operation without damaging the main stem has remained an important issue. In our previous work, we proposed a basic cutting motion using force feedback and confirmed the feasibility of cutting a single lower leaf while allowing the hedge trimmer to follow the main-stem shape (Kashino et al., 2024). In this study, the force-control strategy of the hedge trimmer was extended to enable stable continuous cutting of multiple leaves. The strategy considered both main stem following and avoidance of being stuck on remaining petioles and protrusions. Furthermore, the resulting cutting motion was applied to continuous cutting of multiple lower leaves, and the cutting performance for individual leaves and the processing speed were quantitatively evaluated under conditions simulating practical cultivation.

MATERIALS AND METHODS

ROBOT SYSTEM AND POSITION AND ORIENTATION CONTROL OF THE HEDGE TRIMMER

The developed robot consisted of a six-axis manipulator (xArm6, UFACTORY) equipped at its tip with an arborist hedge trimmer (MUH267D, Makita) as the end-effector (Fig. 1). Lower leaves were cut when they met two reciprocating blades moving in opposite phases. A six-axis force–torque sensor (NAR055014R0A00, Leptrino) was mounted between the hedge trimmer and the manipulator to measure the force and moment acting on the end-effector during operation.

The position and posture of the hedge trimmer were controlled by impedance control, which adjusts end-effector motion according to the external force measured by the force–torque sensor. In this control scheme, virtual inertia and damping are assigned to the end-effector, and its position and posture are modified according to the difference between the target force and the measured force. This enables the hedge trimmer to maintain an appropriate contact force without applying excessive force to the tomato plant and to flexibly follow curvature and local irregularities of the main stem. In this study, translational motion was controlled using Eq. (1) in the translational directions, namely the direction perpendicular to the blade plane of the hedge trimmer (the direction shown in Fig. 1(b)) and the blade traveling direction.

$$M\,{}^{T}\ddot{\boldsymbol{x}} + D\,{}^{T}\dot{\boldsymbol{x}} = {}^{T}\boldsymbol{F}_{\mathrm{e}} - {}^{T}\boldsymbol{F}_{\mathrm{d}} \quad (1)$$

Here, the left superscript T indicates that each quantity is expressed in the tool coordinate system. $\boldsymbol{x} = [x_{\mathrm{tool}},\ y_{\mathrm{tool}}]^{\mathrm{T}}$ represents the correction amount of the end-effector position generated along the x and y axes of the tool coordinate system and does not represent the absolute position of the end-effector. M and D denote the virtual inertia and virtual damping, respectively. $\boldsymbol{F}_{\mathrm{e}}$ and $\boldsymbol{F}_{\mathrm{d}}$ are the external force and desired force. In addition, orientation control was applied to the rotational motion in the twisting direction of the blade, corresponding to the z-axis in Fig. 1(b), using Eq. (2).

$$I\ddot{\theta} + B\dot{\theta} + K(\theta - \theta_{\mathrm{ref}}) = T_{\mathrm{e}} \quad (2)$$

Here, θ denotes the rotational displacement relative to the horizontal plane, and θ_{ref} denotes the reference rotational displacement. I, B, and K represent the virtual rotational inertia, virtual rotational damping, and virtual rotational stiffness for one-axis rotation, respectively. The measured external moment is also included in the formulation. Since the hedge trimmer mainly contacted the main stem in this study, the force generated at the contact point was assumed to act perpendicular to the elongation direction of the main stem. To ensure that the force direction remained aligned with x_{tool}, that is, to keep the blade

traveling direction parallel to the elongation direction of the main stem, θ_{ref} was set as the rotational displacement of $\boldsymbol{F}_{\mathrm{e}}$ from the horizontal plane. A restoring torque was then generated according to the difference between the current and reference rotational displacements. In the experiment, the external moment was not used. During continuous cutting, the end effector must continue moving upward along the main stem even after cutting a lower leaf. At this stage, the guide plate may catch on a remaining petiole or protrusion, causing a large force in the y-direction. Therefore, based on threshold judgment of the y-direction force during operation, the system determined whether the hedge trimmer was stuck on a protrusion or remaining petiole. When catching was detected, the target rotational displacement was set to a value shifted by 0.5 rad from the current rotational displacement in the direction away from the main stem and this is hereafter referred to as the stuck recovery motion.

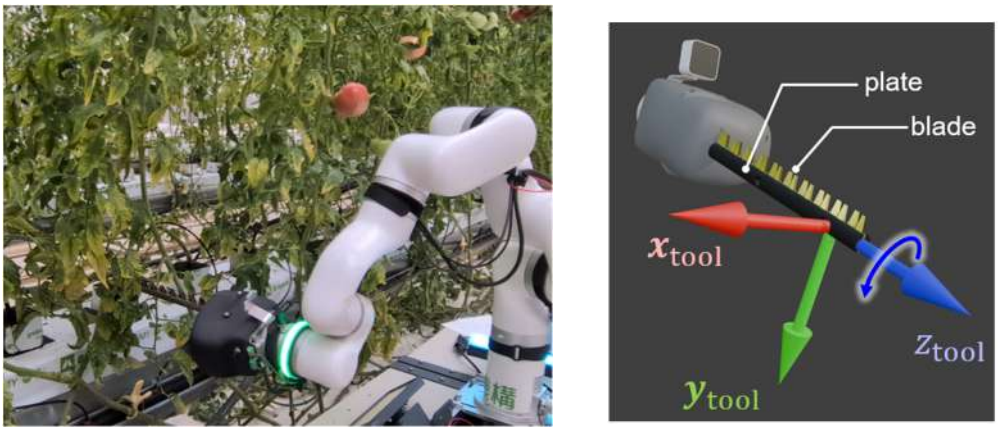

Fig.1 Appearance of the tomato de-leafing robot (a) and coordinate system of the hedge trimmer (b).

Experiment

To evaluate the continuous lower-leaf cutting performance of the robot system, cutting tests were conducted on tomato plants grown in a high-wire greenhouse. Cutting motions generated by the proposed control method were applied over ranges corresponding to one lower leaf and two lower leaves. The desired force was set to 1.5 N in the x-axis direction and 3.0 N in the y-axis direction, and the threshold of the y-direction force used to detect catching was set to 2.0 N. In the single-leaf cutting test, aluminum foil connected to ground was attached to the main stem, and the guide plate was connected to a pull-up digital input to detect contact between the main stem and the hedge trimmer. Using this setup, the time required for the end-effector to move over the petiole by the stuck recovery motion and re-establish contact with the main stem after cutting, as well as the corresponding travel distance along the main stem, was measured. In the two-leaf continuous cutting test, the remaining petiole length on the main stem after cutting was used as an index to compare cutting performance between the first and second lower leaves from the bottom. In all tests, lower leaves were selected such that the intersection angle between the hedge trimmer and the petiole, viewed from the vertical direction, was 30–90°.

RESULTS & DISCUSSION

Figure 2 shows the forces acting in the x and y-axis directions of the tool coordinate system during single-leaf cutting, together with the activation status of the stuck recovery motion, shown as 1 during operation, and the contact state with the main stem, also shown as 1 when

contact was detected. The impedance control based on the target forces enabled the hedge trimmer to move in the stem elongation direction while maintaining contact with the main stem. During lower-leaf cutting, at approximately 6.0–7.0 s in the figure, the stuck recovery motion allowed the end effector to move over the remaining petiole on the main stem after cutting (Fig. 3), while the blade continued to move upward stably without damaging the main stem. The observed sequence of the hedge trimmer motion was as follows: first, movement along the main stem while following its shape; second, cutting of the lower-leaf petiole by the blade; third, movement over the remaining petiole on the stem side; and fourth, re-contact with and renewed following of the main stem. When no stuck recovery motion was activated, movement along the unobstructed main stem occurred at approximately 5 cm/s. For the motions corresponding to the second through fourth steps, the average time from the start of cutting to re-contact with the main stem was 6.3 s when cutting leaves growing toward the inner side of the stem curvature and 5.6 s when cutting leaves growing toward the outer side. The corresponding travel distances along the main stem before re-contact were 5.9 cm and 5.4 cm, respectively. These results indicate that, after lower-leaf cutting, the hedge trimmer requires approximately 5–6 cm of travel along the main stem before it can recover stable following. Therefore, in continuous cutting of lower leaves, if the distance between adjacent lower leaves along the main stem is greater than this distance, the hedge trimmer is expected to cut the petiole near its base while maintaining contact with the main stem.

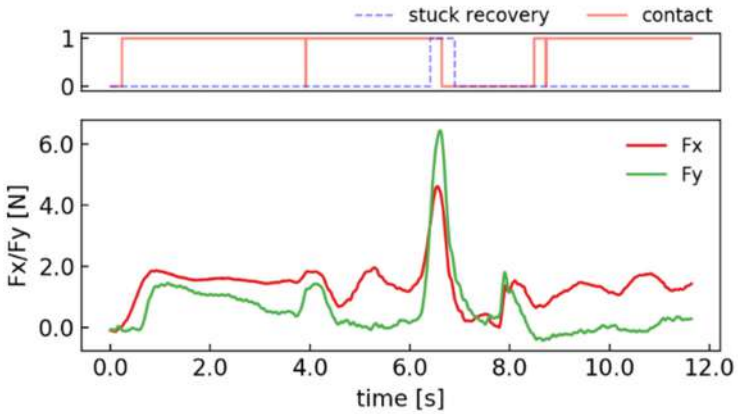

Fig. 2 Force acting on the hedge trimmer during the cutting motion (lower panel), stuck recovery motion status (shown as 1 during operation), and main stem contact state (shown as 1 when contact was detected) (upper panel).



Fig. 3 Remaining petiole of a lower leaf on the main stem after cutting.

Figure 4 shows the cutting performance for the first and second lower leaves from the bottom in each trial. The remaining petiole length was 1.9 cm on average with a standard deviation of 1.3 cm for the first lower leaf, and 2.9 cm on average with a standard deviation of 3.3 cm for the second lower leaf. These results confirmed that both the first and second lower leaves could be cut near the base of the petiole. However, the second lower leaf tended to leave a longer remaining petiole on the main-stem side and showed greater variability. One possible reason is that the second leaf was cut before the hedge trimmer had fully re-established contact with the main stem after cutting the first leaf. The time required for cutting two lower leaves ranged from 5 to 40 s for a travel distance of 15–35 cm. In many trials, considerable time was required for avoiding catching on the petiole, indicating that faster avoidance motion, for example by adjusting the rotational speed during the stuck recovery motion, is necessary to achieve a practical processing speed. In addition, the proposed method can cut a lower leaf only when the hedge trimmer intersects the petiole. Therefore, to efficiently process multiple lower leaves in a single motion, it will be necessary to visually estimate the elongation direction of petioles and determine an insertion direction of the hedge trimmer that can intersect multiple petioles.

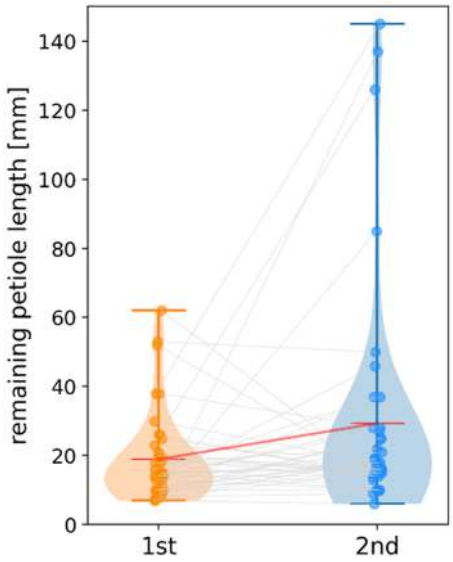

Fig. 4 Remaining petiole length on the main stem during continuous cutting (red lines indicate mean values).

CONCLUSIONS

In this study, we extended the force-control strategy of a previously developed hedge-trimmer-type tomato de-leafing robot to enable continuous cutting of multiple lower leaves and proposed a method for cutting lower leaves while allowing the end-effector to follow the main stem. Experiments under practical cultivation conditions confirmed that the combination of impedance control and stuck recovery motion enabled the robot to perform lower-leaf cutting without damaging the main stem. In the single-leaf cutting test, the time and travel distance required for re-contact with the main stem after cutting were used to clarify conditions necessary for stable cutting performance during continuous operation. In the two-leaf continuous cutting test, the remaining petiole length of the second leaf tended to be longer and more variable than that of the first leaf. These findings indicate that improvement of the re-contact motion after cutting will be important future tasks.

ACKNOWLEDGEMENTS

This work was supported in part by JSPS KAKENHI Grant Number 25K02135 and by a donation from Tokai Pickling Co., Ltd.

REFERENCES

Kashino, M., T. Fukatsu, N. Ota, T. Ota, and H. Kurosaki. 2024. Force control strategy for a tomato pruning task by a manipulator equipped with a hedge trimmer. 11th International Symposium on Machinery and Mechatronics for Agriculture and Biosystems Engineering (ISMAB 2024).

Kashino, M., H. Kurosaki, and T. Fukatsu. 2026. Development of a tomato de-leafing robot with a hedge trimmer-typed end-effector: Effect of hedge trimmer position and orientation on lower leaf removal performance. J. Japanese Soc. Agric. Machinery Food Eng. 88(3): 169–177.

Zhou, H., H. Wang, W. Au, H. Kang and C. Chen, 2022. Intelligent robots for fruit harvesting: Recent developments and future challenges. Precision Agriculture, 23, 1856-1907.

PA-38

Proceedings of The 12th International Symposium on Machinery and Mechatronics for Agriculture and Biosystems Engineering (ISMAB 2026)
20-24 October 2026, Busan, Republic of Korea

LiDAR-BASED HITCH CONTROL OF SOWING DEPTH FOR A GARLIC PLANTER UNDER LABORATORY CONDITIONS

Jumyeong Lee[1,2], Yong-Hyun Kim[1,2], Chankeun Lee[1,2] Seokhyun Ahn[1,2], Hak-Jin Kim[1,2*]

[1]Department of Biosystems Engineering, College of Agriculture and Life Sciences, Seoul National University, Seoul, 08826, Republic of Korea.
[2] Integrated Major in Global Smart Farm, College of Agriculture and Life Sciences, Seoul National University, Seoul, 08826, Republic of Korea.
*Corresponding Author-- Voice: +81-10-7771-4700, Email: kimhj69@snu.ac.kr

Abstract:

Consistent sowing depth is important for uniform garlic emergence. In ridge-based garlic cultivation, however, spatial variations in ridge height can continuously alter the relative position between the planter and the ridge surface, resulting in deviations from the target sowing depth. Previous depth-control approaches have generally generated control references directly from the measured soil. However, directly using the measured ridge profile as a position reference can introduce high-rate reference variations and frequent direction reversals that are incompatible with the finite velocity, acceleration, and reversal response of the hydraulic hitch, thereby degrading trajectory-tracking performance. Therefore, this study developed a preview-based sowing-depth control method that converts LiDAR-derived ridge geometry into a dynamically feasible hitch trajectory considering the response characteristics of the tractor hydraulic hitch. A 3D LiDAR mounted ahead of the planter was used to extract a continuous longitudinal profile of the ridge surface. Based on the geometric relationship between the sensed ridge surface and the planter, the ridge profile was converted into a raw hitch-position trajectory required to maintain the target sowing depth. The raw trajectory was then transformed into a dynamically feasible hitch trajectory by applying the motion constraints of the hydraulic hitch system, including allowable velocity, acceleration, and response delay. The generated trajectory was transmitted through CAN communication to the tractor electronic hitch regulation system, allowing the existing hydraulic three-point hitch to actively adjust the planter position. An indoor bench test reproducing spatial variations in ridge height was conducted to evaluate trajectory-tracking and sowing-depth control performance. The proposed approach provides a practical framework for reliable sowing depth control of garlic planters by linking preview ridge sensing with feasible hitch trajectory.

Key Words: Garlic sowing, Sowing depth, Hitch control, LiDAR, Feasible reference generation

Acknowledgement: This work was supported by the LS Mtron–SNU CALS Digital Agriculture Industry-Academia Collaboration Project (Grant No. 500-20231078).

PA-39

Proceedings of The 12th International Symposium on Machinery and Mechatronics for Agriculture and Biosystems Engineering (ISMAB 2026)
20-24 October 2026, Busan, Republic of Korea

SIMULATION STUDY OF REINFORCEMENT LEARNING-BASED STEERING CONTROL FOR AUTONOMOUS TRACTOR AT HEADLAND TURNS

Chankeun Lee[1,2], Hak-Jin Kim[1,2*], Yong-Hyun Kim[1,2], Jumyeong Lee[1,2], Seokhyun Ahn[1,2]

[1] Department of Biosystems Engineering, College of Agriculture and Life Sciences, Seoul National University, Seoul, 08826, Republic of Korea
[2] Integrated Major in Global Smart Farm, College of Agriculture and Life Sciences, Seoul National University, Seoul, 08826, Republic of Korea
*Corresponding Author-- Email: kimhj69@snu.ac.kr

Abstract: Path-tracking errors during headland turns can affect a tractor's position and heading when entering the next working row. Lateral slip on wet or sloping ground can contribute to these errors. Model-based slip compensation can improve tracking accuracy, but its performance depends on the accuracy of the vehicle model and slip estimates.
This study developed a reinforcement learning-based steering controller to reduce lateral and heading errors as the tractor enters the next working row after a headland turn. The controller was trained in simulation with ground friction and terrain slope varied individually and in combination. Comparative simulations were conducted in Isaac Sim using predefined headland turns connected to straight reference paths. Ground friction and terrain slope were varied at different locations along the turn to reproduce changes in slip conditions during the transition. The proposed controller was compared with nominal nonlinear model predictive control (NMPC) and NMPC with slip and terrain compensation under identical reference paths, speed profiles, sensor inputs, and steering constraints. Performance was evaluated using lateral and heading errors at the transition to the straight path, maximum and root mean square lateral tracking errors over the initial straight segment, and root mean square steering angle command rate. The proposed controller achieved lower lateral and heading errors at the transition to the straight path and lower lateral tracking errors along the subsequent straight segment than both NMPC controllers. Similar improvements were observed under friction and slope combinations not included in training. The RMS rate of change of the steering angle command was also lower than the values obtained with the two NMPC controllers. These results indicate that reinforcement learning-based steering control can improve tractor path tracking during headland turns under variable ground conditions and enhance robustness to changes in lateral slip

Key Words: Autonomous tractor, Headland turning, Path tracking, Lateral slip, Reinforcement learning

Acknowledgments: This work was supported by the Technology Innovation Program (00444634) funded by the Ministry of Trade, Industry & Energy (MOTIE, Korea).

PA-40

Proceedings of The 12th International Symposium on Machinery and Mechatronics for Agriculture and Biosystems Engineering (ISMAB 2026)
20-24 October 2026, Busan, Republic of Korea

EVALUATION OF AN ROI-BASED MODEL AND TWO-STAGE PIPELINE FOR TOMATO SURFACE DEFECT LOCALIZATION

Hojun Kwon [1], Chanseok Ryu [1]*, Changhyeok Park [1], Gangin Je [1], Hakchan Kim[1], Yeseong Kang [2], Dohyun An [2], Jian Kim [2]

[1] Department of Bio-System Engineering, Institute of Agriculture & Life Science, Gyeongsang National University, Jinju, 52828, Republic of Korea
[2] Department of Smart Agro-industry, Institute of Agriculture & Life Science, Gyeongsang National University, Jinju, 52725, Republic of Korea
*Corresponding Author-- Voice: +82-10-3204-4525, Email: ryucs@gnu.ac.kr

Abstract: Detecting the entire tomato can provide information on fruit location and condition but does not identify the specific locations of surface defects. This study extended whole-fruit detection to surface defect localization and evaluated a region-of-interest (ROI) approach motivated by observed missed small defects and false detections in the background. A total of 1,363 images were divided into 1,090 training, 136 validation, and 137 test images. Using YOLO26s, we compared a baseline trained to detect both tomato and defect classes in full images with an ROI model trained to detect only defects in crops generated from ground-truth tomato boxes. We also evaluated the complete pipeline, in which crops generated from boxes predicted by the tomato detector (Stage 1) were passed to the ROI defect detector (Stage 2). All three conditions were reevaluated using saved weights, the same test images, and the original defect ground truth under a common evaluation protocol. At a confidence floor of 0.001, defect mAP50 values for the baseline and ground-truth ROI model were 0.4636 and 0.4132, respectively, and mAP50–95 values were 0.1554 and 0.1456. Stage 1 achieved a tomato detection mAP50 of 0.9947. The complete pipeline, evaluated with a Stage 1 confidence threshold of 0.25, achieved defect mAP50 and mAP50–95 values of 0.3887 and 0.1388, respectively. No mAP improvement was observed with ground-truth ROIs, and the complete-pipeline evaluation established the performance of the two-stage system using predicted ROIs. However, because both the input region and training class configuration differed, the independent effect of ROI restriction could not be established. High tomato detection performance alone was insufficient to explain surface defect detection performance.

Key Words: tomato, surface defect, YOLO26s, region of interest, two-stage detection

INTRODUCTION

The external quality of tomatoes is an important criterion in postharvest sorting and marketability assessment. Surface defects such as cracks, wounds, discoloration, and decay provide indications of fruit quality. Limitations in the throughput and consistency of visual inspection have motivated research into image-based nondestructive inspection techniques (Cubero et al., 2011). Image-based automation has also been investigated

for tomato quality management (Mputu et al., 2024), and deep learning has been applied to agricultural image analysis to learn features such as color and shape directly from images (Kamilaris and Prenafeta-Boldú, 2018).

Object detection predicts both object classes and locations and can therefore be used to identify tomato fruits and localize surface defects. YOLO was proposed as a single-stage detection approach that makes these predictions using a single neural network (Redmon et al., 2016). Recent studies have applied YOLO models to tomato surface defect localization, with particular attention to capturing the features of small defects (Liang et al., 2025).

This study began with fruit-level detection, in which bounding boxes enclosed entire healthy and defective tomatoes. This approach identified fruit locations and conditions but did not indicate where defects occurred on the surface. Defect locations provide basic information for identifying abnormal regions and for future quality assessment based on defect size and distribution. Accordingly, the detection objective was extended from whole fruits to surface defect locations, and separate bounding boxes were assigned to tomato regions and defects.

Experiments on defect localization revealed missed small defects, duplicate predictions, and false detections in the background. These observations motivated a two-stage approach that first detects tomatoes and then searches for defects within the detected regions. Restricting the input to the vicinity of a tomato can reduce the surrounding background, but cropping also changes contextual information and the relative size of defects. Thus, background false detections motivated the ROI approach; they do not establish that the background caused poor performance or that cropping would improve performance.

The two-stage approach was examined through two evaluations. First, defects were detected in crops generated from ground-truth tomato boxes, and this ROI condition, which excluded tomato localization errors, was compared with the full-image baseline. Next, crops generated from boxes predicted by Stage 1 were passed to the same Stage 2 defect detector to evaluate the complete pipeline. By distinguishing tomato region detection, defect detection within ground-truth ROIs, and complete-pipeline detection using predicted ROIs, we sought to characterize the performance and limitations of each stage under the current dataset and model configurations.

MATERIALS AND METHODS

DATASET AND ANNOTATION

Images were obtained from the publicly available Tomato fruits dataset on Kaggle (nexuswho, n.d.). The original source of this public collection is the Tomato fruits dataset developed by Mputu et al. (2023), which contains RGB images collected for tomato quality classification. A total of 1,363 images were used in the final comparison. The data were randomly split at the image level into 1,090 training, 136 validation, and 137 test images, corresponding to an approximate 80:10:10 ratio. Test-set results were used for the final model comparison.

Tomato regions and surface defect locations were manually annotated using Roboflow. Defect types were combined into a single defect class rather than divided into subclasses, and separate bounding boxes were assigned to tomatoes and defects. When multiple defects were present on a single tomato, each defect was annotated with a separate

bounding box. Thus, the number of defect boxes does not necessarily equal the number of defective fruits. ROI data were generated from ground-truth tomato bounding boxes, with one crop per box. Table 1 presents the numbers of original images, tomato boxes, and crops in each data split.

DEFECT ANNOTATION PREPROCESSING AND GROUND-TRUTH ROI GENERATION

For the final comparison, defect annotations for which the product of normalized bounding-box width and height was less than 0.001 were removed, while tomato annotations were retained. This threshold represents bounding-box area relative to the image, rather than the physical area of a defect on the tomato surface. All subsequent comparisons evaluated the defects retained after preprocessing. Crops with no remaining defect annotations were retained with empty label files; they were not assumed to contain no actual defects.

Ground-truth ROIs were generated by adding a 5% margin on each side of the manually annotated tomato bounding box, based on its width and height. Crops were limited to the original image boundaries. A defect was assigned to a tomato if its center lay within the tomato box before the margin was added, and its coordinates were transformed into crop coordinates. Portions of defect boxes extending beyond crop boundaries were clipped to those boundaries. The generation records showed no unassigned or multiply assigned defects in any data split.

Table 1 Final data splits and ground-truth tomato ROI composition

Split	Original images	Tomato boxes	Defect labels	Crops without defect labels
Train	1,090	1,090	1,072	541
Validation	136	136	126	70
Test	137	137	137	69

MODEL CONFIGURATIONS AND EXPERIMENTAL DESIGN

The full-image baseline was a YOLO26s model trained to detect both tomato and defect classes in the preprocessed original images. Only its defect-class results were used in the final defect detection comparison. The ROI approach consisted of Stage 1 for locating tomato regions and Stage 2 for detecting defects within those regions. The two models were trained independently.

Stage 1 was trained with tomato as a single class after excluding defect annotations from the original labels. Stage 2 was trained with defect as a single class using the ground-truth ROI crops generated as described above. The original class indices were 0=defect and 1=tomato. For Stage 1, tomato was remapped to 0, whereas defect remained 0 for Stage 2. Crops without defect annotations were also included in Stage 2 training.

Stage 2 was evaluated under two input conditions. The first used ROIs generated from ground-truth boxes in the test images, thereby excluding Stage 1 localization errors. These results were compared with the full-image baseline. Because both the input regions and training classes differed between the models, this comparison assessed model configurations rather than isolating the effect of ROI restriction. The second condition evaluated the complete pipeline using ROIs generated from Stage 1 predictions as inputs to Stage 2. All three conditions—the full-image baseline, ground-

truth ROIs, and predicted ROIs—were reevaluated using saved best weights, without retraining.

COMMON EVALUATION PROTOCOL FOR THE THREE CONDITIONS

For the complete-pipeline evaluation, original test images were passed to Stage 1, and crops were generated from tomato predictions with confidence scores of at least 0.25. A 5% margin was added on each side of each predicted box, and crops were extracted at integer pixel coordinates within the image boundaries and passed to Stage 2. Ground-truth tomato boxes were not used to generate these crops. Stage 2 defect predictions were mapped back to original image coordinates by adding the crop origin.

Defect predictions from both ground-truth and predicted ROIs were mapped back to original image coordinates. When multiple ROIs were generated for an image, the restored predictions were pooled. The same final non-maximum suppression (NMS), with an IoU threshold of 0.7, was applied to all three conditions, including the full-image baseline. For the ROI conditions, the final defect score was the Stage 2 confidence score and was not multiplied by the Stage 1 score. All three conditions used identical input preprocessing, with an input size of 640 pixels, rect=False, and FP32 inference. The prediction-stage iou argument was set to 0.7 and max_det to 300. Final defect predictions after merging were also limited to 300 per image.

All three conditions used a common evaluation harness with 137 test images and 137 original defect ground-truth boxes. Unlike the annotation processing used to generate the crop dataset, reevaluation neither clipped defect ground-truth boxes to ROI boundaries nor excluded them based on ROI inclusion. The ground-truth ROI condition also used defect annotations from the original images rather than the training crop labels. Images without Stage 1 tomato predictions were included in the evaluation. To compare results on the same basis, all conditions were rescored in original image coordinates using identical ground truth, preprocessing, final NMS, and AP calculation functions.

MODELS AND TRAINING SETTINGS

YOLO26s initialized with pretrained weights was used in the final experiments (Ultralytics, n.d.). Training was performed on an NVIDIA T4 GPU in Google Colab. The environment for the original final experiments comprised Python 3.13.15, PyTorch 2.11.0+cu128, and Ultralytics 8.4.137. The additional complete-pipeline evaluation also used Ultralytics 8.4.137 and PyTorch 2.11.0+cu128.

According to the saved training records, the main settings for the full-image baseline and Stage 2 were an input size of 640 pixels, a batch size of 16, a maximum of 200 epochs, an early-stopping patience of 50, seed 42, and optimizer auto. The baseline's saved weights were reevaluated using the same final test split and confidence floors as the ground-truth ROI model.

PERFORMANCE EVALUATION

Performance was evaluated using precision (P), recall (R), mAP50, and mAP50–95. Precision is the proportion of predicted objects that are correctly detected, defined as P=TP/(TP+FP), and recall is the proportion of ground-truth objects that are correctly detected, defined as R=TP/(TP+FN). TP, FP, and FN denote correct detections, false detections, and missed detections, respectively, determined from class agreement and the IoU between predicted and ground-truth boxes. mAP50 is the mean of class-specific

AP values at an IoU of 0.50, while mAP50–95 averages mAP over IoU thresholds from 0.50 to 0.95 in increments of 0.05. Results were reported for the tomato class in Stage 1 and the defect class in defect detection.

The primary defect detection analysis used a confidence floor of 0.001, and results at 0.25 were also presented for continuity with earlier records. Improvement rates were not calculated from mAP values obtained at different confidence floors. P and R were the F1-based summary values reported by Ultralytics, distinct from values at a fixed operating point defined by the specified confidence floor. For all three conditions, the same Ultralytics box-matching and AP calculation functions were used to aggregate predictions across all test images. The IoU value of 0.7 used as an evaluation argument and for duplicate suppression was distinct from the AP matching IoU thresholds used to calculate mAP.

RESULTS AND DISCUSSION

FROM WHOLE-FRUIT DETECTION TO DEFECT LOCALIZATION

The initial fruit-level experiments detected entire tomatoes but did not identify surface defect locations. After defects were annotated separately, missed small defects, duplicate predictions, and false detections in the background were observed. Subsequent evaluation therefore focused explicitly on the defect class, and an approach that first located tomato regions and then detected defects was investigated. Because the initial experiments differed from the final defect detection experiments in data composition and evaluation targets, they are presented here as the motivation for extending the research objective rather than compared directly with the final test performance.

TOMATO REGION DETECTION PERFORMANCE OF STAGE 1

Stage 1 stopped early at epoch 165, with the best weights obtained at epoch 115. Test-set P, R, mAP50, and mAP50–95 were 0.9836, 0.9927, 0.9947, and 0.9924, respectively. Whole tomato regions were localized with high accuracy on the current test set. Defect localization performance was assessed separately in the following Stage 2 and complete-pipeline evaluations.

DEFECT DETECTION PERFORMANCE OF STAGE 2 WITH GROUND-TRUTH ROIS

Stage 2 stopped early at epoch 139, with the best weights obtained at epoch 89. Table 2 presents the defect detection performance of the full-image baseline and Stage 2 using ground-truth ROIs. At a confidence floor of 0.001, mAP50 and mAP50–95 were 0.4636 and 0.1554 for the baseline and 0.4132 and 0.1456 for Stage 2, respectively. Precision was lower with ground-truth ROIs, whereas recall was 0.4891, higher than the baseline value of 0.4599. At a confidence floor of 0.25, both mAP metrics for ground-truth ROIs were also lower than those of the baseline. With the current dataset, 5% margin, and training configuration, no mAP improvement was observed for the model using ground-truth ROIs.

Table 2 Test performance of the full-image baseline and Stage 2 with ground-truth ROIs

Confidence floor	Method	P	R	mAP50	mAP50–95
0.001	Full-image baseline	0.5720	0.4599	0.4636	0.1554
0.001	Ground-truth ROI	0.4507	0.4891	0.4132	0.1456
0.25	Full-image baseline	0.6747	0.4088	0.3042	0.1025
0.25	Ground-truth ROI	0.5579	0.3869	0.2708	0.0982

Because the ground-truth ROI evaluation did not use Stage 1 predictions, the difference from the baseline cannot be attributed to Stage 1 tomato localization errors. This indicates that providing accurate tomato locations alone did not guarantee improved mAP for the current Stage 2 configuration. Changes in context and defect scale caused by cropping, as well as the training class configuration, may have contributed. However, these factors were not tested independently, and no specific factor can be established as the cause.

EVALUATION OF THE COMPLETE STAGE 1–STAGE 2 PIPELINE

The complete pipeline using tomato boxes predicted by Stage 1 was evaluated on all 137 test images. At a Stage 1 confidence threshold of 0.25, every image had at least one tomato prediction, yielding 141 crops in total. These counts indicate prediction presence and crop numbers, not that every ground-truth tomato was correctly detected. Defect evaluation used the 137 defect ground-truth boxes in the original test images.

As shown in Table 3, at a Stage 2 confidence floor of 0.001, the complete pipeline achieved P, R, mAP50, and mAP50–95 values of 0.4395, 0.5182, 0.3887, and 0.1388, respectively. At a confidence floor of 0.25, the corresponding values were 0.4951, 0.3723, 0.2417, and 0.0917. These results represent overall defect detection performance when Stage 2, trained on ground-truth ROIs, was applied to ROIs predicted by Stage 1.

Table 3 Test performance of the complete Stage 1–Stage 2 pipeline using predicted ROIs

Confidence floor	Method	P	R	mAP50	mAP50–95
0.001	Predicted ROI pipeline	0.4395	0.5182	0.3887	0.1388
0.25	Predicted ROI pipeline	0.4951	0.3723	0.2417	0.0917

Under the common evaluation protocol, the complete pipeline had lower mAP50 and mAP50–95 than the ground-truth ROI condition at both confidence floors. At a confidence floor of 0.001, ground-truth ROIs achieved mAP50 and mAP50–95 values of 0.4132 and 0.1456, compared with 0.3887 and 0.1388 for predicted ROIs. However, recall with predicted ROIs was 0.5182, higher than 0.4891 with ground-truth ROIs, indicating that the metrics did not all change in the same direction. Because the two ROI conditions used the same Stage 2 weights and common evaluation protocol, this comparison represents the performance change when ground-truth boxes are replaced by predicted boxes for ROI generation. Nevertheless, both the number and locations of predicted ROIs differed, so the difference cannot be attributed solely to localization error. Despite the high fruit detection performance of Stage 1, surface defect localization remains a separate challenge requiring improvement.

LIMITATIONS

First, the full-image baseline was trained on both tomato and defect classes, whereas Stage 2 was trained only on defects in crops. The observed differences may therefore reflect both input regions and training class configurations. A control model trained only on defects in full images, with matched training and evaluation settings, is needed to examine the effect of input-region restriction more directly. The present results evaluate the current model configurations and neither establish nor refute the effectiveness of ROI approaches in general.

Second, the ROI margin was fixed at 5%, and neither the number of defect boxes clipped during training crop generation nor the changes in their areas were quantified. Different margins should be compared on the validation set, and performance should be analyzed by defect size and whether boxes were clipped. Although the evaluation criteria for ground-truth and predicted ROIs were unified, the effects of predicted ROI locations and counts on defect detection were not separately quantified.

Third, the source dataset includes multiple images of the same tomato (Mputu et al., 2023). This study used random image-level splitting, and whether the same fruit appeared in different splits was not verified. This limits interpretation of the current results, including the high Stage 1 performance, as evidence of generalization to new tomato fruits. Validation using fruit-level splits and data from other cultivars and imaging environments is needed.

Fourth, removing very small defect annotations restricted the evaluation scope. Empty-label crops indicate that no defect annotations remained after preprocessing. Thus, these results do not represent performance across all surface defect sizes. In addition, the complete pipeline was evaluated on test images from a single public data source; its performance and generalizability in practical sorting environments require separate validation.

CONCLUSIONS

This study extended fruit-level detection of entire tomatoes to surface defect localization and evaluated an ROI approach motivated by observed detection errors. Stage 1 located tomato regions, and Stage 2 was trained to detect defects in ground-truth ROIs. Ground-truth ROI evaluation and complete-pipeline evaluation using predicted ROIs were conducted separately. Although Stage 1 achieved high tomato detection performance, at a confidence floor of 0.001, Stage 2 with ground-truth ROIs achieved defect mAP50 and mAP50–95 values of 0.4132 and 0.1456, lower than the full-image baseline values of 0.4636 and 0.1554. No mAP improvement was observed for the ROI model configuration under the current conditions.

In the complete-pipeline evaluation, where ROIs predicted by Stage 1 were passed to Stage 2, defect mAP50 and mAP50–95 were 0.3887 and 0.1388, respectively, at a Stage 2 confidence floor of 0.001. Under the common evaluation protocol, both mAP metrics were lower for predicted ROIs than for ground-truth ROIs, and the three conditions could be compared directly. However, differences in input regions and training classes between the baseline and ROI models, together with the limitations of a single training run and split, preclude attributing performance differences solely to ROI restriction or tomato localization. Future work should include a full-image defect-only control, repeated training, and fruit-level data splitting to identify conditions that improve surface defect detection.

ACKNOWLEDGEMENTS

This work was supported by the Technology Innovation Program (RS-2022-KT218635, Development of smart farm management system and growth monitoring) funded by the Ministry of Trade, Industry and Resources (MOTIR, Korea).

REFERENCES

Cubero, S., N. Aleixos, E. Moltó, J. Gómez-Sanchís, and J. Blasco. 2011. Advances in Machine Vision Applications for Automatic Inspection and Quality Evaluation of Fruits and Vegetables. Food and Bioprocess Technology 4:487–504. https://doi.org/10.1007/s11947-010-0411-8

Kamilaris, A., and F. X. Prenafeta-Boldú. 2018. Deep learning in agriculture: A survey. Computers and Electronics in Agriculture 147:70-90.https://doi.org/10.1016/j.compag.2018.02.016

Liang, Z., T. Zhu, G. Teng, Y. Zhang, and Z. Gu. 2025. YOLO-RGDD: A Novel Method for the Online Detection of Tomato Surface Defects. Foods 14(14):2513. https://doi.org/10.3390/foods14142513

Mputu, H., A. Abdel-Mawgood, A. Shimada, and M. S. Sayed. 2023. Tomato fruits dataset for binary and multiclass classification. Mendeley Data, Version 1. https://doi.org/10.17632/x4s2jz55dx.1

Mputu, H. S., A. Abdel-Mawgood, A. Shimada, and M. S. Sayed. 2024. Tomato Quality Classification Based on Transfer Learning Feature Extraction and Machine Learning Algorithm Classifiers. IEEE Access 12:8283–8295. https://doi.org/10.1109/ACCESS.2024.3352745

nexuswho. n.d. Tomato fruits dataset. Kaggle. https://www.kaggle.com/datasets/nexuswho/tomatofruits

Redmon, J., S. Divvala, R. Girshick, and A. Farhadi. 2016. You Only Look Once: Unified, Real-Time Object Detection. Proceedings of the IEEE Conference on Computer Vision and Pattern Recognition, 779–788. https://doi.org/10.1109/CVPR.2016.91

Ultralytics. n.d. Ultralytics YOLO26. https://docs.ultralytics.com/models/yolo26/

PA-41

Proceedings of The 12th International Symposium on Machinery and Mechatronics for Agriculture and Biosystems Engineering (ISMAB 2026)
20-24 October 2026, Busan, Republic of Korea

MORPHOLOGY-INFORMED SPECTRAL–SPATIAL FUSION FOR LEAF WATER CONTENT ESTIMATION FROM HYPERSPECTRAL IMAGES

Chi-Won Choi [1, 2], Dae-Hyun Jung [1, 2*]

[1] Department of Smart Farm Science, Kyung Hee University, Yongin 17104, Republic of Korea
[2] Interdisciplinary Program in IT-Bio Convergence System, Kyung Hee University, Yongin 17104, Republic of Korea
*Corresponding Author-- Voice: +82-31-201-2657, Email: daehyun@khu.ac.kr

Abstract:
Climate change is increasing drought risk and constraining agricultural water availability. Efficient irrigation is essential for maintaining crop productivity. Accurate assessment of leaf water content (LWC) is therefore important for irrigation decisions because LWC is a key indicator of crop water status. Shortwave infrared (SWIR) hyperspectral imaging offers a nondestructive alternative to conventional destructive LWC measurements through its sensitivity to water absorption features. However, approaches relying solely on mean spectra do not explicitly incorporate leaf area or spatial heterogeneity in reflectance into predictions. This study developed a residual fusion model integrating spectral, area and spatial optical features to predict LWC in sweet basil (*Ocimum basilicum* L.). A total of 264 SWIR hyperspectral images (900–1700 nm) were acquired during three measurement sessions under progressive drought stress. LWC ranged from 62.50% to 93.15%. Machine learning models included support vector regression (SVR) and partial least squares regression (PLSR). Deep learning models included a multilayer perceptron (MLP), a one-dimensional convolutional neural network (1D-CNN), a Transformer and a hyperspectral image masked autoencoder (HSI-MAE). The baseline models used mean leaf spectra obtained under three preprocessing conditions: calibrated raw reflectance, Savitzky–Golay (SG) smoothing and standard normal variate (SNV) normalization. The proposed model used calibrated raw data to combine Kubelka–Munk (KM) spectral features at 64 preselected wavelengths, three area features derived from leaf pixel counts, and 42 spatial fast Fourier transform (FFT) features. The spatial features incorporated the normalized difference water index (NDWI) and proximity to vein candidates identified in the images. The MLP with SNV normalization achieved the highest mean R^2 of 0.8668 $\pm$ 0.0112 among the baseline model and preprocessing combinations. The proposed model achieved the best predictive performance compared with the six baseline models. It yielded an R^2 of 0.9223 $\pm$ 0.0014 with an RMSE of 1.8614 $\pm$ 0.0167 percentage points and an MAE of 1.4780 $\pm$ 0.0115 percentage points. These results demonstrate the potential of integrating spectral, area and spatial information from reflectance images for nondestructive LWC estimation and irrigation decision support in sweet basil.

Key Words: Precision Irrigation, Leaf water content, SWIR Hyperspectral Imaging, Kubelka-Munk transformation, Residual learning

ACKNOWLEDGEMENTS

This research was supported by a grant (23192MFDS106) from Ministry of Food and Drug Safety in 2026.

Precision Agriculture Machinery and Systems 8 (PA-8)



PA-42

Proceedings of The 12th International Symposium on Machinery and Mechatronics for Agriculture and Biosystems Engineering (ISMAB 2026)
20-24 October 2026, Busan, Republic of Korea

RAIL ENTRY TRAJECTORY ALGORITHM BASED ON FORWARD AND BACKWARD MOVEMENTS, CONSIDERING THE NAVIGATION SPACE OF A GREENHOUSE MOBILE ROBOT

Ji Won Choi[1,2], Soo Been Cho[1,2], Jung-sang Yoo[2], Seung-Hwan Yang[2*]

[1]Department of Biosystems Engineering, College of Agricultural and Life Sciences, Gyeongsang National University, 501, Jinju-daero, Jinju-si, Rep. of Korea
[2]Specialized Machinery and Robotics Group, Korea Institute of Industrial Technology, 119, Jipyeongseonsandan-3gil, Gimje-si, Rep. of Korea
*Corresponding Author-- Voice: +10-6728-3373, Email: yangsh@kitech.re.kr

Abstract: Greenhouse mobile robots require reliable rail-entry strategies that account for constrained maneuvering space and the position of the target rail when performing rail-based operations. These strategies are more important when using the four-wheel mobile robot platform with front-wheel steering, which was used in this study, than when using 2-wheel or mecanum-wheel ones. Depending on the relative position between the robot and the target rail, sufficient turning space may not be available for forward-only motion, requiring trajectory planning appropriate for different entry conditions. In this study, forward- and reverse-based trajectory algorithms were developed for a four-wheel mobile robot platform with front-wheel steering to enter greenhouse rails located at different positions, and a real-time position monitoring GUI was developed using Hall sensor and steering information. A forward-entry method was applied when sufficient turning space was available, otherwise a reverse-turning method was employed. The front-center point of the robot was defined as the coordinate origin, and its X–Y position, heading angle, and travel trajectory were estimated in real time based on the travel distance derived from Hall sensor measurements and the steering angle. The GUI displayed the position estimated from the actual robot motion, enabling evaluation of rail-entry performance and positional error relative to the target position. Based on these approaches, two alternative rail-entry strategies, forward and reverse entry, were proposed for selection according to the rail position and available maneuvering space. The developed real-time coordinate and trajectory monitoring system also enables quantitative evaluation of the travel behavior and final positional error for each entry strategy.

Key Words: Four-wheel type, Position estimation, Real-time localization, Odometry, Monitoring system

ACKNOWLEDGEMENTS

This research was supported by the Smart Farm Multi-Ministry Package Innovation Technology Development Project, funded by the Ministry of Agriculture, Food and Rural Affairs, the Ministry of Science and ICT, and the Rural Development Administration, and managed by the Korea Institute of Planning and Evaluation for Technology in Food, Agriculture and Forestry (IPET) and the Smart Farm R&D Agency (RS-2025-02219849).

PA-43

Proceedings of The 12th International Symposium on Machinery and Mechatronics for Agriculture and Biosystems Engineering (ISMAB 2026)
20-24 October 2026, Busan, Republic of Korea

DEVELOPMENT OF AN UNKNOWN OBJECT DETECTION ALGORITHM FOR ORCHARD ROBOTS USING A MONOCULAR RGB CAMERA

Seokhyun Ahn[1,2], Yong-Hyun Kim[1,2], Jumyeong Lee[1,2], Chankeun Lee[1,2], Hak-Jin Kim[1,2*]

[1]Department of Biosystems Engineering, College of Agriculture and Life Sciences, Seoul National University, Seoul 08826, Republic of Korea
[2]Integrated Major in Global Smart Farm, College of Agriculture and Life Sciences, Seoul National University, Seoul 08826, Republic of Korea
*Corresponding Author-- Hak-Jin Kim, Voice: +82-2-880-4614, Email: kimhj69@snu.ac.kr

Abstract: Reliable obstacle detection is essential for the safe operation of orchard robots, particularly under dense orchard canopies that can obstruct satellite signals and degrade positioning accuracy. However, conventional vision-based object detection models can recognize only the classes on which they were trained. Objects outside these classes may be interpreted as background and remain undetected, increasing the risk of collisions with unexpected obstacles. This study developed an unknown-object detection method for orchard robots using a monocular RGB camera. A YOLOX-s detector identified four known object classes, while an Object Localization Network (OLN) generated bounding-box proposals for all regions that are potentially considered objects. The outputs of the two models were compared to classify detected objects as known or unknown. An open-source dataset from NIA AI Hub was used for training and validation, with three of the seven annotated classes withheld to represent unknown objects. A test dataset was collected in a real-world orchard using orchard robot platform. On a validation dataset, the proposed method achieved 89.0% unknown-object recall while maintaining 98.8% recall for known objects. It processed images at 8.5 frames per second on a desktop GPU (NVIDIA GeForce RTX 3070 Ti). The method was evaluated qualitatively using a test dataset, which included unknown objects such as an umbrella, a doll, and a traffic cone. These results demonstrate that the proposed algorithm enables an orchard robot to detect unknown obstacles using only a monocular RGB camera. Future work will evaluate the method on an embedded controller mounted on an orchard robot.

Key Words: unknown object detection, orchard robot, monocular vision, class-agnostic proposal, obstacle detection

Acknowledgements: This work was supported by the Technology Innovation Program (00444634) funded by the Ministry of Trade, Industry & Energy (MOTIE, Korea). This study was conducted using open-source data for artificial intelligence learning (NIA AI HUB) provided by the National Information Society Agency.

PA-44

Proceedings of The 12th International Symposium on Machinery and Mechatronics for Agriculture and Biosystems Engineering (ISMAB 2026)
20-24 October 2026, Busan, Republic of Korea

DEEP REINFORCEMENT LEARNING-BASED ACTIVE SUSPENSION CONTROL FOR BODY LEVELING OF AN AGRICULTURAL MOBILE PLATFORM

Heonsoo Choi[1], Hyunggil Hong[1], Haeyong Yun[1], Yongjun Cho[1*]

[1]Korea Institute of Robotics and Technology Convergence, Republic of Korea
*Corresponding Author-- Voice: +82 10-4228-8776, Email: cyj@kiro.re.kr

Abstract: Recent advances in agricultural machinery have been driven by rapid progress in electrification and automation technologies, enabling not only improved energy efficiency but also more precise and flexible control. However, agricultural platforms must minimize unnecessary vibration transmitted to attached implements in order to maintain operational accuracy, and in some cases, conventional passive suspension systems are difficult to apply. Under such configurations, impacts and load variations caused by uneven terrain are directly transmitted to the actuators and vehicle body, creating a need for active mechanisms that can independently adjust the vertical position of each wheel according to terrain conditions.
This study proposes a deep reinforcement learning (DRL)-based active suspension control method for an agricultural 4WIS platform equipped with four independent lift actuators, with the objective of maintaining body attitude stability over irregular terrain. Unlike approaches that rely on external terrain perception using height maps or terrain scanners, the proposed method learns a control policy using only limited proprioceptive information obtained from an IMU and actuator encoders. Based on the body attitude and actuator states, the learned policy generates target positions for the individual lift actuators, and body posture is regulated through actuator tracking of these targets in response to terrain variations.
By reducing dependence on external terrain perception sensors and simplifying the observation space provided to the multilayer perceptron (MLP), the proposed framework aims to reduce the computational burden of the control system. Ultimately, this study demonstrates the feasibility of combining a minimal sensor configuration with DRL-based control as an active body-leveling framework for practical application to electrified agricultural platforms.

Key Words: Agricultural Robot, Active Suspension, Deep Reinforcement Learning, Proprioceptive Control, Four-Wheel Independent Steering (4WIS)

ACKNOWLEDGEMENTS

This work was supported by the Korea Institute of Planning and Evaluation for Technology in Food, Agriculture and Forestry (IPET) through the AX-based Intelligent Agricultural Infrastructure and Robot Technology Development Program (RS-2026-25522826) and the Agri-Food Export Enhancement Technology Development Program (00233150), funded by the Ministry of Agriculture, Food and Rural Affairs (MAFRA).

PA-45

Proceedings of The 12th International Symposium on Machinery and Mechatronics for Agriculture and Biosystems Engineering (ISMAB 2026)
20-24 October 2026, Busan, Republic of Korea

FEASIBILITY OF BURIED CROP DETECTION USING PROXIMAL GAMMA-RAY SPECTROSCOPY

Bum-Seok Park[1], Jin-Ho Son[1], Ju-Hee Lee[1], Won-Yeol Choi[1], Young-June An[1], Seo-Eun Lee[1], Dae-Wook Kwon[1], Hyung-Gyu Park[1,2], Yu-Shin Ha[1, 2*]

[1]Department of Bio Industrial Machinery Engineering, Kyungpook National University, Daegu 41566, Republic of Korea
[2]Upland Field Machinery Research Center, Republic of Korea[3]Affiliation and Address of the Third Author, Country
*Corresponding Author-- Voice: +82-10-4520-2115, Email: yushin72@knu.ac.kr

Abstract: Proximal gamma-ray spectroscopy is a non-contact technique that measures the energy distribution and spatial variability of gamma rays naturally emitted from soil and has been used to characterize the physical and chemical properties of soil. Because buried crops differ from the surrounding soil in density and water content, they may affect gamma-ray attenuation and scattering. Therefore, the potential application of proximal gamma-ray spectroscopy for belowground crop detection warrants investigation.

This study aims to analyze changes in gamma-ray signals associated with the presence of garlic and potato buried in soil using a SoilOptix proximal gamma-ray spectrometer. The experiment consists of three conditions: undisturbed soil, soil excavated and backfilled without a crop as a soil-disturbance treatment, and soil excavated and backfilled after crop burial. The crop-burial treatment is divided into garlic and potato treatments, and each treatment is independently replicated. Repeated scans are conducted before and after treatment while maintaining the same travel path, travel speed, and sensor height. Crop size, mass, volume, and actual burial location are recorded. Soil moisture and surface conditions are also examined, and soil analysis results from representative sampling points are linked to the gamma-ray measurements.

The collected data include total gamma-ray counts, counts within major energy windows, and raw gamma-ray spectra when available. Changes in gamma-ray signals before and after treatment and the variability among repeated measurements are analyzed. The undisturbed-soil and soil-disturbance treatments are compared to evaluate the effects of excavation and backfilling. The crop-burial and soil-disturbance treatments are then compared to assess signal differences associated with crop presence while controlling for the effects of soil disturbance. In addition, the spatial correspondence between gamma-ray signal anomalies and actual burial locations is evaluated to determine the feasibility of crop localization.

This study aims to provide a preliminary assessment of whether proximal gamma-ray spectroscopy can non-destructively detect the presence and location of buried crops and to identify its potential applications and limitations for belowground crop detection.

Key Words: Proximal soil sensing, Gamma-ray spectroscopy, Belowground crops, Non-destructive detection, Localization

PA-46

Proceedings of The 12th International Symposium on Machinery and Mechatronics for Agriculture and Biosystems Engineering (ISMAB 2026)
20-24 October 2026, Busan, Republic of Korea

DEVELOPMENT OF AN INDOOR–OUTDOOR AUTONOMOUS PATROL ROBOT FOR LIVESTOCK FACILITIES

Ayumu NAKASHIMA[1*], Yamato Sakurai[1*], Sutan Muhamad Sadam Awal[1*]
Dong Thanh PHAM[2*], Takashi OKAYASU[2*], Muneshi MITUOKA[2*]

[1]Graduate School of Bioresource and Bioenvironmental Sciences,Kyushu University,Japan
[2]Faculty of Agriculture, Kyushu University, Japan
*Corresponding Author-- Email: Nakashima.ayumu194@s.kyushu-u.ac.jp

Abstract: An autonomous mobile robot was developed to automate patrol travel and observation-data collection in livestock facilities. The tracked platform carries a 3D LiDAR, an inertial measurement unit (IMU), wheel odometry, an RTK-GNSS receiver, and an RGB camera. Mapping, localization, path planning, multi-point patrol, obstacle avoidance, point-triggered video capture, and record storage were integrated using ROS 2 Humble and Navigation2. Indoor localization can be selected from adaptive Monte Carlo localization (AMCL), expansion-resetting Monte Carlo localization (EMCL), and FAST-LIO2. Outdoors, RTK-GNSS position, wheel-derived forward velocity and yaw rate, and IMU yaw rate are fused using an extended Kalman filter. Tests were conducted in a university corridor along an approximately 51 m route comprising a home position and six observation points. All five AMCL patrols were completed (35/35 goals reached, 35/35 videos stored) in 368 ± 31 s over a 51.4 ± 1.2 m trajectory. Each of the three indoor localization methods reached 30/30 observation points; their motion times differed by no more than 3.2%, and lateral-deviation P95 values were below 10 cm. All seven obstacle-avoidance patrols were completed without observed contact or intervention. In an outdoor preliminary trial under an RTK-fixed solution, the robot autonomously reached one recorded goal, with an internally estimated residual of 0.21 m (within the 0.4 m tolerance) that was not verified against independent ground truth. A georeferencing function was also implemented to express the indoor map and GNSS coordinates in a common map frame, and a coordinate-triggered handoff at a designated gateway was designed. The study demonstrates an integrated basis for automating the travel, patrol, imaging, and storage stages of routine livestock-facility inspection. Validation in representative livestock environments and continuous indoor–outdoor trials remain necessary.

Key Words: livestock facility, patrol robot, autonomous patrol, precision livestock farming, RTK-GNSS

INTRODUCTION

Routine inspection of livestock facilities requires workers to repeatedly travel through buildings and visually check animals and their rearing environment. Because this task is repeated every day, automating travel along fixed routes and collecting observation data

would allow workers to concentrate on reviewing recorded information and making husbandry decisions. Autonomous robots have been used to acquire environmental information and images in poultry houses (Marin et al., 2024), and visual simultaneous localization and mapping (SLAM) that accounts for moving objects has been investigated for cowshed inspection robots (Du et al., 2025). A practical patrol robot, however, requires more than a localization algorithm: mapping, observation-point management, route following, obstacle avoidance, image capture, and record storage must operate as one workflow.

When an inspection route extends through outdoor passages or between buildings, a single localization method may not provide stable coverage of the entire route. LiDAR-map-based localization is effective where GNSS signals are blocked indoors, whereas RTK-GNSS provides absolute position information in open outdoor areas. Indoor–outdoor navigation using INS/GNSS/LiDAR switching has been reported (Li et al., 2020). For a repeatable operational patrol, the robot must additionally perform the handoff at a designated point along the route while preserving a common coordinate frame for Navigation2.

The objective of this study was therefore to develop a tracked robot that integrates indoor–outdoor localization, autonomous multi-point patrol, point-triggered video capture, and result management for automating the travel and data-collection stages of livestock-facility inspection. This paper presents the system configuration, indoor patrol results, a comparison of three indoor localization methods, obstacle-avoidance trials, a preliminary outdoor RTK-GNSS trial, and the design of a coordinate-triggered localization handoff.

MATERIALS AND METHODS

Robot and system configuration

The tracked robot uses an NVIDIA Jetson Orin Nano for onboard computation, a Livox MID-360 3D LiDAR for perception and mapping, an IMU for inertial data, a u-blox ZED-F9P RTK-GNSS receiver for outdoor positioning, and an RGB camera for observations (Fig. 1). Wheel odometry is calculated from the left and right tracks. ROS 2 Humble is the middleware, and Navigation2 performs path planning, following, goal checking, and recovery (Macenski et al., 2020). Table 1 lists the principal specifications and navigation parameters.

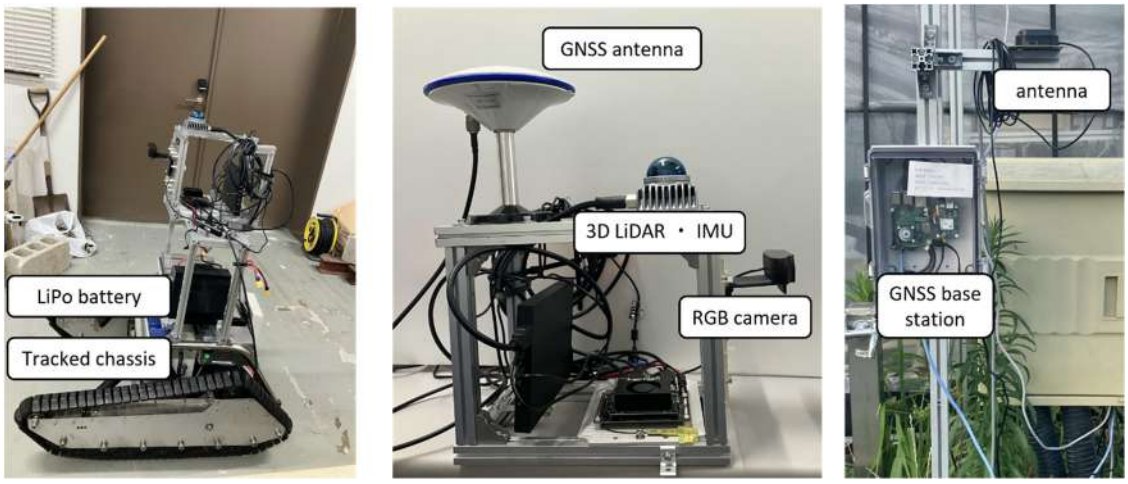

Fig. 1. Patrol robot and indoor–outdoor localization system.

Table 1. Principal robot specifications and navigation parameters.

Component	Model or setting	Function
Mobile platform	UNiBO-600 RC	Differential tracked chassis; 0.85 × 0.55 m; velocity commands via RS-232C
Onboard computer	Jetson Orin Nano	Ubuntu 22.04 and ROS 2 Humble; all processing on one onboard computer
3D LiDAR	Livox MID-360	3D point cloud and built-in IMU; mapping and localization input
RTK-GNSS	u-blox ZED-F9P	Onboard rover and custom Survey-In base station; direct NMEA parsing
Indoor goal tolerance	0.25 m, 14.3°	Navigation2 position and yaw tolerances
Outdoor goal tolerance	0.40 m	Navigation2 position tolerance for the preliminary outdoor trial

Mapping, localization, patrol, and common frame

A 3D point-cloud map was generated from the LiDAR and IMU using GLIM (Koide et al., 2024) and converted into a two-dimensional occupancy grid for Navigation2. Indoor localization can be selected from standard AMCL, expansion-resetting Monte Carlo localization (EMCL), which is designed to recover from erroneous convergence (Ueda et al., 2005), and FAST-LIO2, which uses a point-cloud map and LiDAR–IMU odometry (Xu et al., 2022). AMCL and EMCL receive a two-dimensional scan extracted horizontally from the MID-360 point cloud. The FAST-LIO2 configuration was extended to reject large pose corrections caused by erroneous iterative closest point convergence and to output localization-quality states.

A patrol route consists of a home position and multiple observation points. The patrol manager sequentially sends goals to Navigation2. After arrival at each point, the robot stops, records a video, and stores the patrol session, capture time, point identifier, and estimated position and orientation as metadata. A web interface is used to configure patrol conditions and, after capture, to search and replay videos, inspect metadata, and enter human interpretation results.

For outdoor operation, the extended Kalman filter in robot_localization (Moore and Stouch, 2016) fuses planar RTK-GNSS position, wheel-derived forward velocity and yaw rate, and IMU yaw rate. Absolute heading from a magnetometer or dual-antenna GNSS is not used. To represent indoor and outdoor positions in one coordinate system without rewriting the map file, a georeferencing function aligns the GNSS datum with the map, preserving existing observation points, patrol records, and image metadata.

Experimental procedure

Indoor trials were performed in a university corridor using an approximately 51 m route from home through six observation points and back to home, with seven stops in total. Five runs were performed with each of AMCL, EMCL, and FAST-LIO2. Patrol completion, goal arrival, elapsed time, estimated trajectory length, and stored videos were recorded. Goal arrival was determined by Navigation2. Trajectory repeatability was quantified as the 95th percentile (P95) of lateral deviations from a representative trajectory constructed separately for each

method. For motion-time comparison, capture and stationary intervals were removed, and movement was evaluated only until the first return to home.

Obstacle avoidance was evaluated in seven runs along a three-goal route. A solid obstacle approximately 1.5 m high was placed between Points 1 and 2 in five runs, a ladder was used in one run, and no obstacle was used in one run. Contact, manual intervention, and immobilization were assessed visually. In the outdoor preliminary trial, a position recorded under an RTK-fixed solution was used as a Navigation2 goal.

RESULTS & DISCUSSION

Indoor patrol and observation-data collection

All five AMCL runs returned from home via the six observation points and reached all 35 goals (Fig. 2). A video and associated metadata were generated at each of the 35 stops. The elapsed time was 368 ± 31 s (range: 337–418 s), and the estimated trajectory length was 51.4 ± 1.2 m, corresponding to a coefficient of variation of 2.3%. Immediately after capture, the residual between estimated and commanded goal pose averaged 0.25 m and 7.4° in yaw; these are within-system values, not errors against independent ground truth.

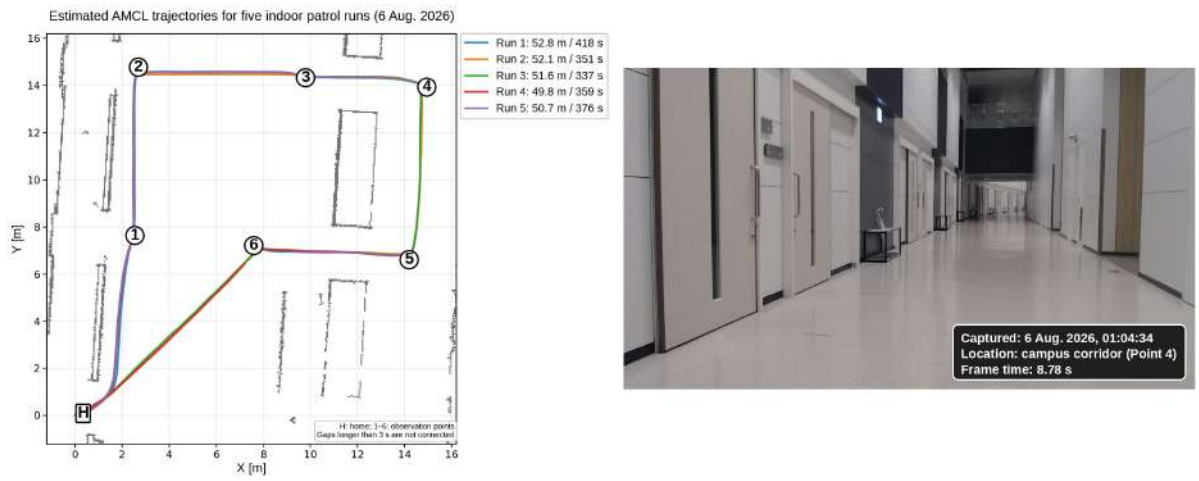

Fig. 2. Estimated trajectories of five AMCL indoor patrols and an example image stored at an observation point.

The video-management interface supported searching and replaying captured data, checking point, time, and estimated-pose metadata, and recording human interpretations. The dashboard summarized the AMCL trials as 5/5 completed patrols and 35/35 successful captures. The system therefore stored fixed-route travel and observation video collection as a single patrol unit. Animal identification and abnormal-behavior detection were not implemented, so the recorded video does not replace human interpretation.

Comparison of indoor localization methods

Table 2 compares the three localization methods. Each method achieved 30/30 arrivals at the six observation points, for 90/90 arrivals overall, and the physical robot returned to home in all

15 runs. For FAST-LIO2, however, Navigation2 accepted the final home goal in only 1/5 runs. In the other four runs, the minimum distance to home was 0.174–0.190 m, within the 0.25 m position tolerance, whereas the yaw difference was 28.9–103.6°, exceeding the 14.3° yaw tolerance. Thus, the formal failures arose from final-yaw convergence rather than failure to follow the route or physically return home.

After capture and stationary periods were removed, representative motion time to the first home return ranged from 210.6 to 217.3 s; the maximum difference was 3.2% relative to EMCL. Effective common-route distance ranged from 51.1 to 51.6 m. The longer total trajectory logged for FAST-LIO2 was mainly due to final-orientation correction after the first home return. Method-specific lateral-deviation P95 values were below 10 cm, with FAST-LIO2 having the smallest value. Only 24/35 FAST-LIO2, 27/35 AMCL, and 29/35 EMCL leg traces met the logging criteria; the methods therefore cannot be ranked conclusively from P95 alone.

Table 2. Comparison of indoor localization methods over five runs on the same route.

Metric	AMCL	EMCL	FAST-LIO2
Observation-point arrivals	30/30	30/30	30/30
Physical return to home	5/5	5/5	5/5
Navigation2 final-goal acceptance	5/5	5/5	1/5
Representative motion time to first home return (s)	215.1	210.6	217.3
Effective common-route distance (m)	51.6	51.1	51.4
Total logger-derived trajectory length (m)	51.4	51.1	54.7
Lateral-deviation P95 (cm)	9.9	5.8	4.9
Valid leg traces for repeatability analysis	27/35	29/35	24/35

Obstacle avoidance, outdoor trial, and indoor–outdoor extension

All seven obstacle-avoidance runs and all 21 goals were completed without observed contact, manual intervention, or immobilization. In the five runs with the approximately 1.5 m-high obstacle, maximum lateral deviation from the straight line between Points 1 and 2 was 0.52–0.58 m (mean: 0.55 m), compared with 0.17 m in the single no-obstacle run, showing a clear detour. The ladder run was also completed. Mean travel time and distance with the solid obstacle differed from the no-obstacle run by −1.7% and −0.3%, respectively. A single no-obstacle run precludes statistical inference about the cost of avoidance.

With the required antenna transform configured, the robot autonomously reached one recorded goal under an RTK-fixed solution. The internally estimated map-frame residual was 0.21 m, within the 0.40 m outdoor goal tolerance. This single feasibility trial did not measure error against independent ground truth; repeatability and the surveyed antenna mounting offset also remain unevaluated.

For patrols between facilities, indoor LiDAR-map and outdoor GNSS positions are expressed in the georeferenced common map frame, with a coordinate-triggered handoff at Gateway A on the indoor–outdoor boundary. On confirmed arrival and stopping within a prescribed radius, the final AMCL pose is passed once, through the common-map datum, as the initial condition of the GNSS-side extended Kalman filter, which then propagates yaw from wheel and IMU rates; GNSS quality gates the resumption of outdoor travel as a safety condition, not as the

handoff trigger. This function is implemented and the handoff sequence designed, but continuous operation has not yet been demonstrated; future trials will quantify handoff success, pose discontinuity, and route-completion accuracy.

CONCLUSIONS

A tracked mobile robot integrating mapping, selectable indoor localization, Navigation2 travel, waypoint patrol, obstacle avoidance, point-triggered video capture, RTK-GNSS localization, and record management was developed to automate patrol travel and observation-data collection. In a university corridor, AMCL completed 5/5 patrols, reached 35/35 goals, and stored 35/35 videos; all 7/7 obstacle-avoidance patrols were completed without observed contact or intervention. Outdoor RTK-GNSS navigation was feasible for one recorded goal, although absolute accuracy and repeatability remain unevaluated. A common indoor–outdoor map frame was implemented, and a coordinate-triggered handoff from the final AMCL pose to the GNSS-side extended Kalman filter at Gateway A was designed. Validation in livestock facilities, continuous indoor–outdoor operation with independently measured arrival error, and animal-safety and image-analysis functions (identification, abnormal-condition detection) remain necessary before the extent of inspection-task replacement can be quantified.

REFERENCES

Du, X., T. Li, X. Jin, X. Yu, X. Xie, and C. Zhang. 2025. GNV2-SLAM: Vision SLAM system for cowshed inspection robots. Frontiers in Robotics and AI 12:1648309. https://doi.org/10.3389/frobt.2025.1648309.

Koide, K., M. Yokozuka, S. Oishi, and A. Banno. 2024. GLIM: 3D range-inertial localization and mapping with GPU-accelerated scan matching factors. Robotics and Autonomous Systems 179:104750. https://doi.org/10.1016/j.robot.2024.104750.

Li, N., L. Guan, Y. Gao, S. Du, M. Wu, X. Guang, and X. Cong. 2020. Indoor and outdoor low-cost seamless integrated navigation system based on the integration of INS/GNSS/LIDAR system. Remote Sensing 12(19):3271. https://doi. org/10.3390/ rs12193271.

Macenski, S., F. Martín, R. White, and J. Ginés Clavero. 2020. The Marathon 2: A navigation system. In Proc. 2020 IEEE/RSJ Intl. Conf. on Intelligent Robots and Systems, 2718–2725. https://doi.org/10.1109/IROS45743.2020.9341207.

Marin, R. H., J. M. Caliva, and J. M. Kembro. 2024. Dynamics of changes in broiler spatial distribution induced by a robot with autonomous navigation along the growing cycle. Poultry Science 103(6):103710. https://doi.org/10.1016/j.psj.2024.103710.

Moore, T., and D. Stouch. 2016. A generalized extended Kalman filter implementation for the Robot Operating System. In Intelligent Autonomous Systems 13, 335–348. https://doi.org/10.1007/978-3-319-08338-4_25.

Ueda, R., T. Arai, K. Asanuma, K. Umeda, and H. Osumi. 2005. Recovery methods for fatal estimation errors on Monte Carlo localization. Journal of the Robotics Society of Japan 23(4):466–473. https://doi.org/10.7210/jrsj.23.466.

Xu, W., Y. Cai, D. He, J. Lin, and F. Zhang. 2022. FAST-LIO2: Fast direct LiDAR-inertial odometry. IEEE Transactions on Robotics 38(4):2053–2073. https://doi.org/ 10.1109/TRO.2022.3141876.

Precision Agriculture Machinery and Systems 9 (PA-9)



PA-47

Proceedings of The 12th International Symposium on Machinery and Mechatronics for Agriculture and Biosystems Engineering (ISMAB 2026)
20-24 October 2026, Busan, Republic of Korea

NATIONAL-SCALE PARCEL GEOMETRY AND FIDELITY EVALUATION OF ISOXML PRESCRIPTION MAPS FOR KOREAN FIELDS

Yi-Seo Min[1], Du-Han Kim[2], Wan-Soo Kim[1*]

[1]Department of Bio-Industrial Machinery Engineering, Kyungpook National University, Republic of Korea
[2]Daedong Co. Ltd., Republic of Korea
*Corresponding Author-- Voice: +82-10-8468-6602, Email: wansoo.kim@knu.ac.kr

Abstract: Variable-rate application (VRA) in precision agriculture depends on prescription maps that agricultural machinery can interpret and execute reliably. ISO 11783 (ISOBUS) standardizes this exchange through the ISOXML format, which defines three prescription-map structures—Grid Type 1, Grid Type 2, and Polygon treatment zones—each differing in data structure, spatial resolution, and prescription-value resolution. These structures were developed for large, grid-aligned fields, and their suitability for small and irregular parcels has not been evaluated. This study links a web-based ISO 11783-10 prescription-map generation system to a national-scale geometric characterization of Korean agricultural parcels. The system ingests Farm Map parcel boundaries and point-based soil or canopy data, applies interpolation and zoning, and outputs all three formats. Geometric indices were computed for all 11.2 million Farm Map polygons, and parcels were classified into six shape classes using statistically derived thresholds. Korean parcels are small (median 0.09 ha, width 23.5 m) but predominantly convex (median convexity 0.97); half of all parcels are below 0.1 ha, yet 62% of the farmland area lies in parcels above 0.2 ha. Unconsolidated parcels converge to a single convex-quadrilateral shape regardless of crop, whereas consolidated parcels carry the imprint of the 30 × 100 m standard plot, and orientation coherence exists only within consolidation districts. Twenty drone-surveyed parcels located at representative positions of the national distribution are used to quantify the prescription fidelity of the three formats against sub-metre drone-derived reference maps across grid cell sizes, using exogenous indices—misapplied area within the parcel, effective zone count under implement control resolution, fragmentation relative to working width, and file size—and to relate fidelity to parcel geometry and within-field variability. Preliminary results indicate that fidelity varies with parcel geometry even after accounting for variability, suggesting that national parcel-shape statistics may serve as an input to prescription-format selection under small-field conditions.

Key Words: ISO 11783; ISOXML; Prescription Map; Parcel Geometry; VRA

ACKNOWLEDGEMENTS

This work was supported by Korea Institute of Planning and Evaluation for Technology in Food, Agriculture, Forestry(IPET) through Open-field Smart Agriculture Utilization Model Development Program, funded by Ministry of Agriculture, Food and Rural Affairs(MAFRA)(RS-2025-02313171)

PA-48

Proceedings of The 12th International Symposium on Machinery and Mechatronics for Agriculture and Biosystems Engineering (ISMAB 2026)
20-24 October 2026, Busan, Republic of Korea

EFFECTS OF ANALYSIS REGION AND CANOPY HEIGHT ON LEAF AREA ESTIMATION IN PLANAR-CANOPY APPLE TREES

Je-Min Park[1], Yeong Hyeon Shin[1], Muhammad Amjad[1], Hyeon-Soo Kim[2], Woo-Jae Cho[1*]

[1]Department of Biosystems Engineering, College of Agriculture & Life Sciences, Gyeongsang National University, Jinju 52828, Republic of Korea
[2]Apple Research Institute, Gyeongsangnam-do Agricultural Research and Extension Services, Geochang 50124, Republic of Korea
*Corresponding Author-- Voice: +10-3363-7343, Email: woojae56@gnu.ac.kr

Abstract Recently, apple production is increasingly shifting from conventional open-center canopies to planar canopies. Planar canopies allow automated machines and robots to access the fruiting zone easily along consistent, repeatable trajectories. However, robotic-vision methods for estimating total leaf area in planar canopies remain challenging. One key challenge is that side-view imagery is captured as a continuous stream of frames. The area covered by each frame is determined by the camera's field of view and the travel speed, not by the canopy itself. As a result, a per-frame indicator mixes foliage from adjacent trees and from neighboring leaders with similar appearances. For individual-tree management, foliage observations obtained from the continuous image stream need to be associated with the corresponding tree to estimate its total leaf area. Foliage distribution, background conditions, and viewing angles vary across canopy heights. Consequently, image-based indicators from different height bands may differ in how well they explain total leaf area. Accordingly, both the lateral boundary and the vertical extent of the analysis region must be specified explicitly, using physical canopy coordinates rather than image coordinates. In this study, we examined how these two conditions influence side-view RGB-based indicators for planar-canopy apple trees. Continuous side-view images of apple trees were collected from three rows using a ground-based mobile robot. Leaf regions were segmented with the excess green minus excess red (ExGR) index using Otsu thresholding. Structure-from-Motion and Multi-View Stereo were employed to reconstruct the canopy in metric space, which enabled the analysis regions to be defined in physical coordinates. Leaf-occupancy indicators were then computed for individual trees and for five canopy-height bands. Reference total leaf area was determined for ten trees through complete leaf counts and sampled leaf-area measurements. Total leaf area was then estimated with a single proportional calibration coefficient using leave-one-tree-out cross-validation. Modifying the lateral definition of the analysis region changed the indicator for all trees, and the size of that change differed substantially across individuals. The average shift was largely absorbed by the calibration coefficient, but the remaining between-tree differences increased the cross-validated prediction error. Across the five height bands, the two mid-canopy bands at and just above camera height showed consistently stronger associations with total leaf area than did the lowest and uppermost bands. These findings show that the lateral boundary and the vertical range determine what portion of the canopy a side-view leaf-occupancy indicator actually represents. Limiting the analysis to the mid-canopy bands within a tree-specific lateral boundary offers a practical foundation for non-destructive, repeated

monitoring of leaf area for individual trees. The same approach of defining analysis regions in physical canopy coordinates can be extended to other per-tree robotic tasks, such as pruning, thinning, and yield assessment.

Key Words: Apple, Total leaf area, Structure-from-Motion, RGB imagery, Mobile robot

Acknowledgement: This study was supported by the project 'Development of an Integrated Automated Management Model for Gyeongnam-Adapted Planar Canopy Apple Orchards'(RS-2026-25548108) of the Rural Development Administration.

PA-49

Proceedings of The 12th International Symposium on Machinery and Mechatronics for Agriculture and Biosystems Engineering (ISMAB 2026)
20-24 October 2026, Busan, Republic of Korea

ISO 11783 PRESCRIPTION MAP GENERATION FROM WEED DISTRIBUTION AND VIRTUAL VERIFICATION FOR SPRAYING

Nayoung Kim[2], Changho Yun[3], Yeseong Kang[4], Deokheung Kim[5], Xiongzhe Han[1,2*]

[1]Department of Smart Systems Science, College of Agriculture and Life Sciences, Seoul National University, Seoul, Republic of Korea
[2]Research Institute of Agriculture and Life Sciences, College of Agriculture and Life Sciences, Seoul National University, Seoul, Republic of Korea
[3]Department of Agriculture Engineering, National Institute of Agricultural Sciences, Rural Development Administration, Jeonju, Republic of Korea
[4]Department of Smart Agro-Industry, College of Agriculture and Life sciences, Gyeongsang National University, Jinju, Republic of Korea
[5]GLINS Co., Ltd, Daejeon, Republic of Korea

*Corresponding Author-- Voice: +82-02-880-4559, Email: hanxiongzhe@snu.ac.kr

Abstract: This study proposed a methodology for generating variable rate prescription maps that reflect the spatial variability of weed density and coverage in garlic and onion fields, alongside a virtual communication execution verification framework based on the ISO 11783(ISOBUS) standard. To overcome the lack of field measured GPS weed distribution datasets, Kriging interpolation was applied to stochastically generate weed density and coverage maps capturing local variability. The generated target application rates were assigned to a 5-section control system of a 16m boom sprayer, engineered to perform site specific variable rate spraying independently per section. The prescription data was serialized into the ISO 11783-10 compliant TASKDATA structure, and the CAN message transmission process along virtual driving trajectories was quantitatively evaluated in an ISOsimulate environment. By deriving metrics such as agrochemical savings and application accuracy, this study simulation validated a precision variable rate decision making approach optimized for open field farming environments in Korea.

Key Words: ISO 11783, Prescription Map, Kriging Interpolation, Variable Rate Application, Virtual Verification

ACKNOWLEDGEMENTS

This work was supported by the Intelligent Agricultural Robot Core Infrastructure Technology Development Program (RS-2026-25531655) funded by the Rural Development Administration (RDA), Republic of Korea.

PA-50

Proceedings of The 12th International Symposium on Machinery and Mechatronics for Agriculture and Biosystems Engineering (ISMAB 2026)
20-24 October 2026, Busan, Republic of Korea

AN RGB-D VISION AND DIGITAL-TWIN FRAMEWORK FOR DUAL-ARM COOPERATIVE HARVESTING OF OCCLUDED STRAWBERRIES

Chen-En Lee, Chung-Liang Chang*

Biomechatronics Engineering Department,
National Pingtung University of Science and Technology
*Corresponding Author-- Voice: +886-8-7703202 ext. 7586,
Email: chungliang@mail.npust.edu.tw

Abstract: Occlusion by leaves is a major challenge for robotic strawberry harvesting because a fruit or its stem may not be fully visible or directly reachable by the picking arm. This study presents an occlusion-aware dual-arm harvesting framework in which one manipulator is responsible for fruit harvesting and the other manipulates obstructing leaves to expose the target. An RGB-D camera is used to detect strawberries and estimate their three-dimensional positions. The fruit center is determined from the RGB-D data, and the corresponding stem-cutting point is estimated using a predefined geometric offset. The harvesting arm is integrated with a ROS 2 digital-twin framework that combines the URDF kinematic model, real-time servo feedback, numerical inverse kinematics, and command execution on the physical manipulator. ArUco and ChArUco markers are used to register the virtual and physical workspaces, and a Gaussian radial basis function model is introduced to compensate for spatially varying end-effector positioning errors. When a strawberry is partially occluded, the second arm repositions the obstructing leaf to improve target visibility and provide sufficient access for harvesting. The harvesting arm then moves toward the estimated cutting point using collision-aware motion planning. Preliminary evaluation of the harvesting subsystem showed that ChArUco-based calibration and spatial error compensation reduced the mean end-effector positioning error from 39.97 mm to 19.35 mm, corresponding to a 51.6% reduction. The cross-validated prediction error of the compensation model also decreased from 21.31 mm to 7.24 mm. These results demonstrate the effectiveness of the proposed calibration and compensation method and establish the positioning accuracy required for subsequent dual-arm harvesting of partially occluded strawberries. Full-system experiments will further evaluate leaf-manipulation success, improvement in target visibility, harvesting success rate, and task completion time under different levels of occlusion.

Key Words: Strawberry harvesting, Dual-arm manipulation, RGB-D vision, Occlusion handling, Digital twin.

PA-51

Proceedings of The 12th International Symposium on Machinery and Mechatronics for Agriculture and Biosystems Engineering (ISMAB 2026)
20-24 October 2026, Busan, Republic of Korea

RICE HILL DETECTION AND INDIVIDUAL RICE GROWTH MAPPING USING UAV IMAGERY

Doan Le Cong[1,2], Gyujin Jang[1,3], Hak-Jin Kim[1,3,4*]

[1]Department of Biosystems Engineering, College of Agriculture and Life Sciences, Seoul National University, Seoul 08826, Republic of Korea
[2]Department of Information Technology, Faculty of Information Technology, An Giang University, Vietnam National University Ho Chi Minh City, Vietnam
[3]Integrated Major in Global Smart Farm, College of Agriculture and Life Sciences, Seoul National University, Seoul 08826, Republic of Korea
[4]Research Institute of Agriculture and Life Sciences, Seoul National University, Seoul 08826, Republic of Korea
*Corresponding author email: kimhj69@snu.ac.kr

Abstract: Monitoring each rice hill shows differences within a field that plot or field averages hide.. This requires each hill to be located first, which is feasible in transplanted fields. However, rice hill detection studies have mostly analysed a single acquisition date, whereas multi-temporal unmanned aerial vehicle (UAV) studies of rice height have been conducted at the plot level, so individual hills have rarely been tracked through the season. This study detects rice hills in multi-temporal UAV imagery with a deep learning detector and uses the detected hill positions to map the relative plant height of each hill over time. RGB imagery was collected in a machine-transplanted paddy field at the Suwon Farm of Seoul National University between 25 June and 30 August 2026 with a DJI Matrice 3D at a flying altitude of 33 m, giving a ground sampling distance of 0.95 cm. Six flights spaced 6 to 8 days apart and spanning 25 June to 30 July were selected for the present analysis. Each orthomosaic was reconstructed and divided into tiles for processing. A machine learning-based detector, pre-trained on paddy imagery and fine-tuned with manually corrected hills, was evaluated on spatially separated test blocks. Detected hill positions were fixed across dates, and the relative height of each hill was derived from the digital surface model (DSM) difference between each flight and the first flight, giving a height time series for every hill in the field. Preliminary results show that the workflow can locate individual hills on each flight date and produce a relative height map for each hill that can be followed over the study period. Quantitative evaluation of detection accuracy and height estimates is in progress. Extending the method from selected tiles to the whole field will require reducing processing time without loss of accuracy.

Key Words: rice hill detection, unmanned aerial vehicle, digital surface model, deep learning

ACKNOWLEDGEMENTS

This work was supported by the Korea International Cooperation Agency (KOICA) under the title of “Project for Strengthening Agricultural Higher Education of VNUHCM (Vietnam National University-Ho Chi Minh City) in Vietnam” between 2021 and 2028 (No. 2021-00022).

PA-52

Proceedings of The 12th International Symposium on Machinery and Mechatronics for Agriculture and Biosystems Engineering (ISMAB 2026)
20-24 October 2026, Busan, Republic of Korea

UAV-BASED ESTIMATION OF SOIL WATER CONTENT UNDER DIFFERENT SURFACE ROUGHNESS CONDITIONS USING RGB AND NIR IMAGERY

Jaehun Lee[1], Jaesung Park[1,2,3*], Minjoo Kim[1] , Seokyung Park[1] , Hyeonjun Hwang[1]

[1]Department of Bio-Industrial Machinery Engineering, Pusan National University, Miryang 50463, Korea
[2]Life and Industry Convergence Research Institute, Pusan National University, Miryang 50612, Korea
[3]Major in Natural Resources Systems Engineering, Pusan National University, Yangsan 50612, Korea

*Corresponding Author-- Voice: +82-10-4001-1225, Email: jaesung.park@pusan.ac.kr

Abstract: Soil surface roughness can alter image intensity through variations in illumination geometry and shadowing, complicating image-based estimation of soil water content. This study aimed to develop models for estimating gravimetric soil water content from RGB and near-infrared (NIR) imagery and to evaluate their applicability across surface roughness conditions for subsequent UAV-based field monitoring. Before field application, an indoor pilot experiment was conducted using nine trays containing a single soil, with three surface roughness levels and three replicates per level. The initial gravimetric water content was adjusted to a target of 20% and verified by measurement. Dry soil mass and the filling procedure were standardized across trays. Smooth surfaces were prepared by gently leveling the soil with a straightedge. Moderately and highly rough surfaces were produced using the same raking procedure at progressively greater working depths. Surface height variation was measured to characterize the roughness levels. During drying, RGB and NIR images were acquired using a stationary DJI Mavic 3M positioned vertically above the soil. External daylight was excluded, and artificial illumination providing usable visible and NIR signals was directed approximately 45° to the mean soil surface. Tray mass was measured close to each imaging event, and tray-averaged gravimetric water content was calculated using container mass and dry soil mass. Mean RGB and NIR image values were extracted from corresponding soil regions, excluding tray boundaries while retaining shadows generated by soil microrelief. Regression models using RGB alone and RGB combined with NIR were compared through cross-validation that kept all observations from each tray together. Performance was assessed using root mean square error, mean absolute error, bias, and the coefficient of determination. Models trained on smooth surfaces were additionally evaluated on unseen trays with different roughness levels within a common measured water-content range. The pilot analysis examined the contribution of NIR information and the error patterns associated with surface roughness and water content. Future field experiments will establish plots with different surface roughness levels and an initial target gravimetric water content of 20%. RGB and NIR images will be acquired repeatedly using a DJI Mavic 3M during drying, accompanied by soil sampling at locations corresponding to the image analysis regions. Independent field measurements will be used to evaluate model transferability and the effects of natural

illumination and flight altitude.

Key Words: Unmanned arial vehicle, Surface roughness, Soil water content, RGB imagery, Near-infrared imagery

ACKNOWLEDGEMENTS

This work was supported by the National Research Foundation of Korea(NRF) grant funded by the Korea government(MSIT) (RS-2025-23753014).

This research was supported by the ANCHOR program through the Busan Anchor Center, funded by the Ministry of Education (MOE) and Busan Metropolitan City, Republic of Korea. (2026-RISE-02-004-2-4-6-1)

AI and Information Processing 5 (AI-5)



AI-24

Proceedings of The 12th International Symposium on Machinery and Mechatronics for Agriculture and Biosystems Engineering (ISMAB 2026)
20-24 October 2026, Busan, Republic of Korea

CONTEXTUALIZING CNN ATTRIBUTION MAPS WITH IMAGE-DERIVED DESCRIPTORS IN MEDICINAL PLANT SEED CLASSIFICATION

Su-Min Chin[1,2], Yea-Jin Park[1,2], Dae-Hyun Jung[1,2*]

[1]Department of Smart Farm Science, Kyung Hee University, Yongin, Gyeonggi-do, Republic of Korea
[2]BK21 Interdisciplinary Program in IT-Bio Convergence System, Kyung Hee University, Yongin, Republic of Korea
*Corresponding Author: Email: daehyun@khu.ac.kr

Abstract: High classification accuracy in medicinal plant seed imaging does not clarify the visual properties associated with model responses. This study quantified spatial associations between convolutional neural network (CNN) attribution maps and predefined image-derived descriptors within the seed foreground. The dataset comprised 1,124 RGB images from five species, partitioned into 899 training and 225 held-out internal test images. Three CNNs achieved test accuracies of 99.56–100%. For ConvNeXt-Small, zero-baseline absolute Integrated Gradients (IG) showed the largest mean Spearman correlations with LAB L, Brightness, and fast Fourier transform low pass (0.4857, 0.4849, and 0.4804, respectively). These descriptors formed a highly redundant intensity and lightness cluster. Excluding the explicit input–baseline magnitude term reduced the associations by 46.30–49.20%, while positive associations remained. Baseline, signed IG, and Grad-CAM analyses further demonstrated variation across attribution representations. Separately, logistic regression using summary features from 29 descriptors achieved 97.78% test accuracy. The workflow provides quantitative visual context for CNN attribution patterns while distinguishing method-dependent spatial associations from descriptor-level class separability. The results do not establish causal feature use or biological diagnostic traits. Species–session confounding and the absence of external validation limit interpretation beyond the controlled imaging conditions.

Key Words: Medicinal plant seeds, CNN attribution, Integrated Gradients, Image-derived descriptors, Spatial association

INTRODUCTION

RGB imaging enables repeatable, nondestructive characterization of seed appearance, including shape measurements (Tanabata et al., 2012). Related medicinal plant taxa and potential substitutes can share overlapping visual properties. Alongside classification accuracy, seed image analysis requires evaluation of the visual properties spatially associated with prediction-related responses. IG and Grad-CAM locate attribution responses at different spatial levels (Sundararajan et al., 2017; Selvaraju et al., 2020), but high-response regions may coincide with multiple image properties. Predefined descriptors provide reproducible references for quantifying this overlap.

We quantified foreground-restricted attribution–descriptor associations, assessed dependence

on attribution representation, and separately evaluated class separability using descriptor summary statistics.

MATERIALS AND METHODS

Plant materials and image preparation

Seeds were obtained from the National Institute for Korean Medicine Development, with identities verified by nine qualified experts commissioned by the Ministry of Food and Drug Safety. The final dataset contained 1,124 images after exclusion of one multi-seed image: *Prunus armeniaca* (205), *P. sibirica* (223), *P. japonica* (228), *P. davidiana* (228), and *P. persica* (240). Each image represented a different physical seed, photographed once using a Samsung Galaxy S21 5G in a light chamber with a white background.

Foreground extraction used rembg without alpha matting. The largest contour guided orientation normalization and cropping; seeds were centered on a 512×512-pixel canvas, composited onto black, and resized to 224×224 pixels. Identical geometric transformations aligned images and masks. Manual orientation corrections affected 24 images before splitting; no color, texture, or contour edits were made. Blinding status was not documented.

Dataset partitioning and CNN training

A fixed stratified split (seed 42) assigned 899 images to training and 225 to held-out internal testing, with no physical seed shared across sets. Five-fold cross-validation was restricted to training data. During final training, a stratified 10% validation subset of the training set supported early stopping and checkpoint selection. Test images were excluded from training, selection, and tuning. ImageNet-pretrained ConvNeXt-Small, ResNet50, and EfficientNet-B0 were trained with AdamW, augmentation, and a maximum of 100 epochs. ConvNeXt-Small was the representative backbone for quantitative attribution analysis, rather than the highest-performing classifier.

Attribution and descriptor analyses

IG targeted the predicted-class logit using 100 Gauss–Legendre integration steps. The primary map summed absolute RGB-channel attributions from a black baseline defined before ImageNet normalization. Twenty-nine descriptors covered color/intensity, spatial frequency, texture, and edge/shape. Maps were aligned to 224×224 pixels and descriptor values normalized within each foreground. Spearman correlation was calculated per test image using foreground pixels only; means and 95% confidence intervals used 10,000 image-level bootstrap resamples.

Sensitivity analyses used Gaussian-blurred and training-mean baselines, path gradients excluding the explicit input–baseline magnitude term, signed IG, selected-layer Grad-CAM, progressive parameter randomization, and foreground-mask erosion. Descriptor redundancy was evaluated through pairwise foreground correlations and clustering. Separately, six statistics per descriptor—mean, standard deviation, median, 90th percentile, top-10% mean, and interquartile range—formed 174 summary features. Standardized logistic regression (C = 1) evaluated class separability. Top 3, 5, and 7 subsets were fixed from training-set out-of-fold (OOF) attribution rankings before testing; preprocessing estimators were fitted only on training data.

RESULTS & DISCUSSION

Classification performance and descriptor separability

All three CNNs achieved a mean cross-validation accuracy of 0.9989. Internal test performance was also high (Table 1), with one ConvNeXt-Small error among 225 images. These results establish a classification setting for attribution analysis under the study conditions; they do not demonstrate performance on independent acquisition settings.

Descriptor summaries retained class-discriminative information. Logistic regression using all 29 descriptors achieved 97.78% accuracy, compared with 80.44% for the redundant Top 3 intensity descriptors. Larger ranked subsets improved separability (Table 1). These tabular results evaluate information in descriptor summaries, not whether the CNN uses the same information.

Table 1 Classification performance on the held-out internal test set (n = 225).

Classifier and input representation	Accuracy (%)	Macro F1
ConvNeXt-Small · RGB images	99.56	0.9957
ResNet50 · RGB images	100.00	1.0000
EfficientNet-B0 · RGB images	100.00	1.0000
Logistic regression · all 29 descriptors	97.78	0.9785
Logistic regression · OOF Top 3	80.44	0.8045
Logistic regression · OOF Top 5	91.11	0.9127
Logistic regression · OOF Top 7	92.44	0.9256

Spatial associations and sensitivity to attribution representation

LAB L, Brightness, and FFT low pass had the largest zero-baseline absolute IG associations (Table 2; Fig. 1). Their pairwise mean correlations were 0.9321–0.9995, supporting a shared intensity and lightness cluster rather than three independent visual cues. Path-gradient analysis excluding the explicit input–baseline magnitude term reduced their mean associations by 46.30–49.20%, although positive associations remained (Table 2).

Table 2 Mean foreground Spearman correlations and sensitivity to the input–baseline magnitude term (225 images).

Descriptor	Absolute IG	95% CI for IG	Path gradient	Reduction (%)
LAB L	0.4857	0.4652–0.5062	0.2476	49.00
Brightness	0.4849	0.4643–0.5051	0.2464	49.20
FFT low pass	0.4804	0.4580–0.5029	0.2580	46.30

For absolute IG, Spearman correlations between the 29 descriptor rankings across black, Gaussian-blurred, and training-mean image baselines ranged from 0.6276 to 0.9000. Positive IG retained the leading intensity descriptors, whereas negative IG was most associated with LAB Chroma (0.0736). Grad-CAM was most associated with distance transform (0.6191). Complete parameter randomization reduced mean similarity to trained-model maps to 0.326 for absolute IG and 0.090 for path gradients. After two-pixel mask erosion, descriptor-ranking correlations with the original analysis were 0.872 and 0.980, respectively.

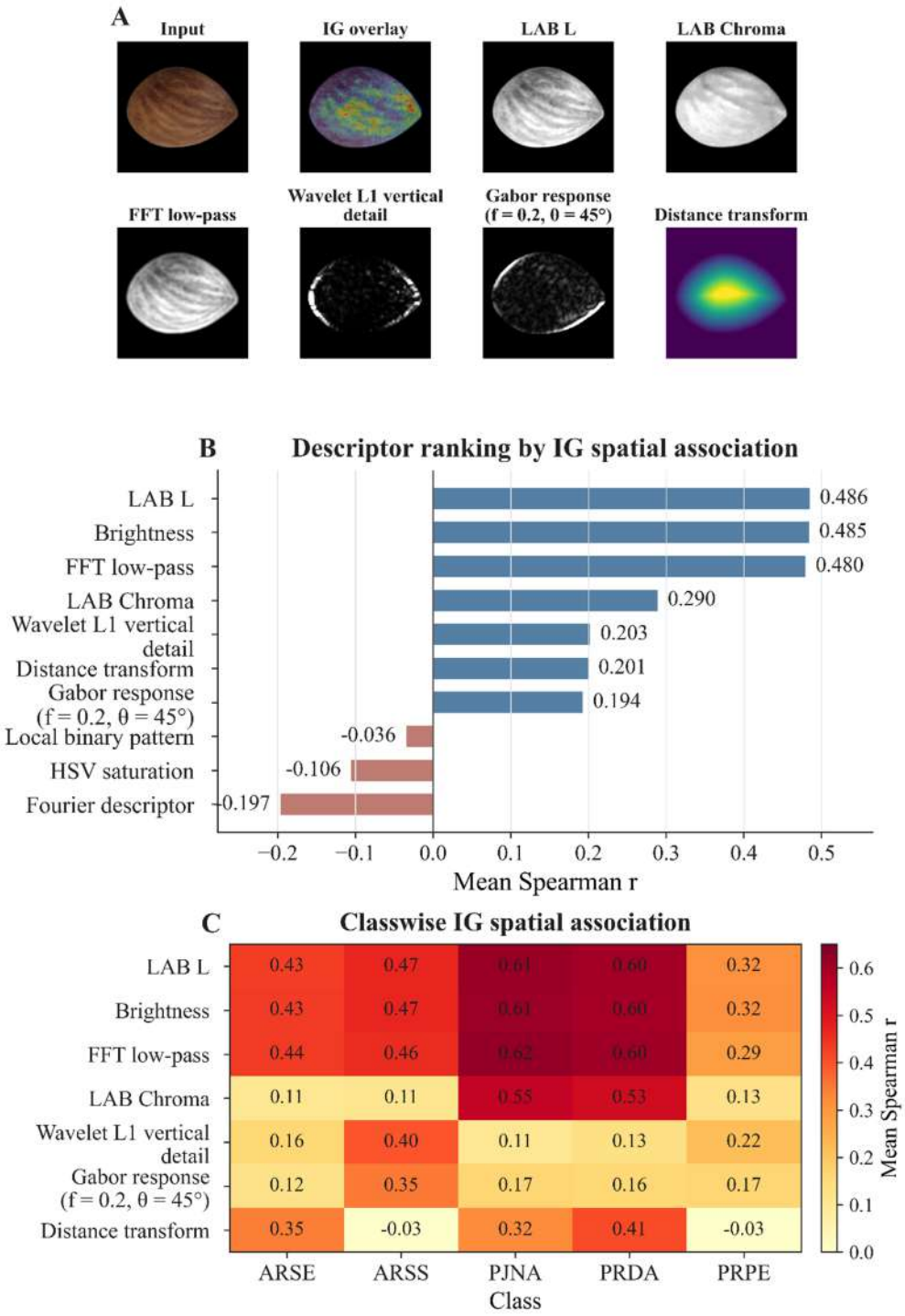

Fig. 1 Spatial context of ConvNeXt-Small zero-baseline absolute IG. (A) Representative input, IG overlay, and selected descriptor maps. (B) Mean foreground Spearman correlations across 225 held-out test images. (C) Classwise mean correlations. ARSE: *P. armeniaca*; ARSS: *P. sibirica*; PJNA: *P. japonica*; PRDA: *P. davidiana*; PRPE: *P. persica*. Descriptor maps were normalized per image within the foreground. Values summarize spatial co-distribution and do not establish causal or biological diagnostic traits.

Interpretation and limitations

The workflow distinguishes two analytical questions to contextualize CNN attribution patterns. Spatial association describes where attribution and descriptor responses co-occur within an

image. Descriptor classification describes whether aggregated visual information distinguishes dataset classes. Strong descriptor classification cannot validate a causal interpretation of spatial association. Correlated descriptors represent shared visual context; spatial correlation does not imply that perturbing a descriptor would change the prediction.

Baseline sensitivity and path-gradient comparisons show that much of the intensity association is related to attribution construction. Black-background compositing can introduce boundary contrast. Foreground restriction removes external background pixels from correlations but retains boundary-related structure inside the seed. Mask erosion retained leading intensity descriptors without establishing invariance to other preprocessing choices. Signed IG and selected-layer Grad-CAM provide different spatial representations and should not be treated as interchangeable explanations.

External generalization remains untested. Species were photographed in separate temporal blocks, and accession, lot, batch, and acquisition-session identifiers were unavailable. Consequently, species effects could not be separated from session effects despite distinct seeds in the train and test sets. Exposure, ISO, and digital zoom varied; exact camera distance and illumination color temperature were not recorded. Independent datasets spanning lighting, backgrounds, devices, and seed orientations are needed.

The descriptors are predefined image responses, not expert-defined diagnostic traits. Associations were summarized at the image level because pixels are spatially structured. Class-average maps were descriptive: orientation and centering did not provide scale or deformable registration. Summary features also discard detailed spatial arrangement. Authentication-oriented interpretation therefore requires independent biological, morphological, chemical, or genetic validation.

CONCLUSIONS

Foreground-restricted descriptor comparison quantified spatial associations between CNN attribution maps and image-derived visual references in medicinal seed classification. These associations depended on the input–baseline magnitude term and attribution representation and do not establish causal feature use. Descriptor summaries separately demonstrated class separability. Interpretation remains limited by acquisition confounding, method dependence, and the need for external validation.

ACKNOWLEDGEMENTS

This research was supported by a grant (23192MFDS106) from Ministry of Food and Drug Safety in 2026.

REFERENCES

Selvaraju, R. R., M. Cogswell, A. Das, R. Vedantam, D. Parikh, and D. Batra. 2020. Grad-CAM: Visual explanations from deep networks via gradient-based localization. International Journal of Computer Vision 128: 336–359.

Sundararajan, M., A. Taly, and Q. Yan. 2017. Axiomatic attribution for deep networks. Proceedings of Machine Learning Research 70: 3319–3328.

Tanabata, T., T. Shibaya, K. Hori, K. Ebana, and M. Yano. 2012. SmartGrain: High-throughput phenotyping software for measuring seed shape through image analysis. Plant Physiology 160: 1871–1880.

AI-25

Proceedings of The 12th International Symposium on Machinery and Mechatronics for Agriculture and Biosystems Engineering (ISMAB 2026)
20-24 October 2026, Busan, Republic of Korea

DEEP LEARNING-BASED WAVELENGTH SELECTION FOR MULTISPECTRAL SENSING OF FOREST FUEL MOISTURE CONTENT

Seung Woo Chun[1], Hong Gu Lee[1], Woo Hyeong Yu[1], Jeong Yong Shin[1], Jeong Woo Han[1], Woon Tak Han[1], Giyoung Kim[2], Sujung Ahn[3], Changyeun Mo[1,4*]

[1]Interdisciplinary Program in Smart Agriculture, Kangwon National University, Chuncheon 24341, Republic of Korea
[2]Agriculture and Life Sciences Research Institute, Kangwon National University, Chuncheon 24341, Republic of Korea
[3]Division of Forest Fire Research, National Institute of Forest Science, Seoul 02455, Republic of Korea
[4]Department of Biosystem Engineering, College of Agriculture and Life Sciences, Kangwon National University, Chuncheon 24341, Republic of Korea
*Corresponding Author-- Voice: +82-10-5147-5227, Email: cymoh100@kangwon.ac.kr

Abstract: Fuel moisture content (FMC) is a principal determinant of wildfire ignition probability, spread rate, and intensity. The conventional oven-drying method for measuring FMC is destructive, labor-intensive, and limited to point sampling, motivating non-contact optical alternatives. This study aimed to develop a rapid, non-destructive method for estimating forest litter FMC by combining visible-near-infrared (VNIR) and near-infrared (NIR) hyperspectral imaging with a one-dimensional convolutional neural network (1D-CNN), to identify a minimal wavelength subset suitable for a field-deployable multispectral sensor, and to evaluate generalization across tree species. Litter of four species (*Prunus sargentii*, *Quercus mongolica*, *Quercus variabilis*, *Pinus densiflora*) and a mixed sample were collected near Chuncheon, Korea, and dried under controlled conditions across three cycles, with reference FMC obtained by oven-drying. VNIR (400–1,000 nm) and NIR (895–1,720 nm) hyperspectral images were calibrated and reduced to representative spectra by region-of-interest extraction. Thirteen candidate wavelengths per band region were evaluated across five architectures, and the best-performing lightweight architecture was then used to exhaustively search the 1,716 possible six-band combinations. Among six-band combinations, a conifer-specialized configuration reached R^2 ≥ 0.98 (RMSEP 3–5%) in both VNIR and NIR. The recommended VNIR six-band combination (488.0, 550.2, 632.4, 692.5, 750.7, 937.1 nm) matched the top statistical combination in accuracy (R^2 = 0.99, RMSEP = 3.26%) while retaining a direct water-absorption wavelength, and is preferable to NIR on cost grounds. These results show that hyperspectral imaging with a lightweight 1D-CNN can estimate forest litter FMC accurately and non-destructively, reducing hundreds of hyperspectral bands to six filter-compatible wavelengths with negligible accuracy loss for a target species, providing a basis for a low-cost multispectral wildfire-fuel sensor.

Key Words: Forest fuel moisture content, Hyperspectral imaging, Wavelength selection, 1D convolutional neural network, Hardware-oriented band reduction

AI-26

Proceedings of The 12th International Symposium on Machinery and Mechatronics for Agriculture and Biosystems Engineering (ISMAB 2026)
20-24 October 2026, Busan, Republic of Korea

DEVELOPMENT OF A YOLO-SAM-BASED PIPELINE FOR STRAWBERRY LEAF EXTRACTION AND DISEASE SYMPTOM SYNTHESIS

Soo Been Cho[1,2], Ji Won Choi[1,2], Jung-sang Yoo[2], Jung Hyun Lee[3], Seung-Hwan Yang[2*]

[1]Department of Biosystems Engineering, College of Agricultural and Life Sciences, Gyeongsang National University, 501, Jinju-daero, Jinju-si, Rep. of Korea
[2]Specialized Machinery and Robotics Group, Korea Institute of Industrial Technology, 119, Jipyeongseonsandan-3gil, Gimje-si, Rep. of Korea
[3]Carbon & Light Materials Group, Korea Institute of Industrial Technology, 222, Palbok-ro Jeonju-si, Rep. of Korea
*Corresponding Author-- Voice: +10-6728-3373, Email: yangsh@kitech.re.kr

Abstract: Recently, deep learning technology becomes a main research method for recognizing plant diseases using images. For accurate disease recognition models, sufficient and balanced training data regarding disease is essential. However, it is difficult to obtain sufficient and balanced data for training disease recognition models because plant diseases occur only under specific periods and environmental conditions and the frequency of occurrence varies by disease class. In this study, a data augmentation pipeline that integrates leaf extraction with disease symptom synthesis was developed to supplement limited disease image datasets. As target plants, strawberry plants were used. Firstly, a YOLO-based object detection model was applied to RGB images of strawberry plants to detect leaf regions. Secondary, the detected bounding boxes were used as prompts for the Segment Anything Model (SAM) to segment individual leaf regions from several leaves in an image. Lastly, symptom regions were extracted from images of diseased leaves and synthesized onto the segmented regions of healthy leaves to generate synthetic diseased images. The developed pipeline implemented a continuous image-processing workflow from leaf detection and segmentation of the original RGB images to disease symptom synthesis, and the applicability of the generated synthetic images as training data for plant disease recognition was evaluated.

Key Words: Plant disease recognition, Synthetic data, Deep learning, Image segmentation, Training dataset

ACKNOWLEDGEMENTS

This research was supported by the Smart Farm Multi-Ministry Package Innovation Technology Development Project, funded by the Ministry of Agriculture, Food and Rural Affairs, the Ministry of Science and ICT, and the Rural Development Administration, and managed by the Korea Institute of Planning and Evaluation for Technology in Food, Agriculture and Forestry (IPET) and the Smart Farm R&D Agency (RS-2025-02307287).

AI-27

Proceedings of The 12th International Symposium on Machinery and Mechatronics for Agriculture and Biosystems Engineering (ISMAB 2026)
20-24 October 2026, Busan, Republic of Korea

REAL-TIME OPEN-VOCABULARY 3D OCCUPANCY PREDICTION FOR AUTONOMOUS AGRICULTURAL MACHINERY

Minwoo Kim[1,2], Sanghyeok Choi[1,2], Taehyun Jung[1,2], Gyeongmin Kang[1,2], Woosang Jeon[4], Taehyeong Kim[1,2,3,4]*

[1]Department of Biosystems Engineering, College of Agriculture and Life Sciences, Seoul National University, Seoul, 08826, Republic of Korea
[2]Integrated Major in Global Smart Farm, College of Agriculture and Life Sciences, Seoul National University, Seoul, 08826, Republic of Korea
[3]Research Institute of Agriculture and Life Sciences, Seoul National University, Seoul, 08826, Republic of Korea
[4]Artificial Intelligence Institute, Seoul National University, Seoul National University, Seoul, 08826, Republic of Korea
*Corresponding Author-- Voice: +82 02) 880-4596, Email: taehyeong.kim@snu.ac.kr

Abstract: For autonomous agricultural machinery operating in unstructured off-road environments, reliable perception requires real-time understanding of both 3D scene geometry and object semantics. Such environments contain uneven terrain, vegetation, machinery, and obstacles with ambiguous boundaries. 3D occupancy prediction represents free space, occupied regions, and their semantics in a voxel grid. However, dense semantic annotations are costly and fixed label sets limit recognition of unseen objects. We propose a real-time open-vocabulary 3D occupancy prediction framework based on camera–LiDAR fusion. The framework constructs 3D voxel representations and aligns them with semantic features from a vision foundation model. These voxel features are matched with text embeddings to enable prediction from arbitrary natural-language queries. The model is trained without manual voxel-wise semantic annotations and instead uses geometric occupancy supervision and voxel-wise visual feature targets. For evaluation, semantic pseudo ground truth is generated from Grounded SAM segmentation results and LiDAR point clouds. Experiments on the STONE off-road dataset used 2,988 training frames and 383 validation frames. The model achieved 85.10% geometric IoU and 29.67% mIoU over eight semantic classes, while running at 70.9 FPS on an NVIDIA RTX A6000 GPU. These results demonstrate the feasibility of real-time open-vocabulary 3D occupancy prediction for autonomous agricultural machinery without manual voxel-wise semantic annotations.

Key Words: 3D Occupancy Prediction, Open-Vocabulary Perception

ACKNOWLEDGEMENTS: This work was supported by the Technology Innovation Program funded by the Ministry of Trade, Industry and Energy (MOTIE, Korea) (RS-2025-25453780), the New Faculty Startup Fund and the Creative-Pioneering Researchers Program through Seoul National University, and the Agriculture and Food Convergence Technologies Program for Research Manpower Development (RS-2024-00398300) through the Korea Institute of Planning and Evaluation for Technology in Food, Agriculture and Forestry (IPET).

AI-28

Proceedings of The 12th International Symposium on Machinery and Mechatronics for Agriculture and Biosystems Engineering (ISMAB 2026)
20-24 October 2026, Busan, Republic of Korea

AUTOMATIC GENERATION OF THREE-DIMENSIONAL CUCUMBER CANOPY SCENES WITH HETEROGENEOUS LEAF SHAPES

Tatsuki Nishimura[1], Dong Thanh Pham[2], Muneshi Mitsuoka[2], Daisuke Yasutake[2,3], Takenori Ozaki[4], Seji Koga[4], Yasumaru Hirai[5], Takashi Okayasu[2,3*]

[1]Graduate School of Bioresource and Bioenvironmental Sciences, Kyushu University, 819-0395, Japan
[2]Faculty of Agriculture, Kyushu University, 819-0395, Japan
[3]Faculty of Agriculture and Marine Science, Kochi University, 783-0093, Japan
[4]Welzo Co., Ltd., 812-0013, Japan
[5]Faculty of Agriculture, Tottori University, 680-8553, Japan
*Corresponding Author-- Voice: +81-92-802-4632, Email: okayasu@bpes.kyushu-u.ac.jp

Abstract: Digital twins of greenhouses are expected to serve as virtual environments for developing and evaluating agricultural robots; however, a virtual canopy built by duplicating a single plant model lacks the plant-to-plant variation in shape that exists in real crops. This study aimed to develop a method that automatically generates three-dimensional (3D) cucumber canopy scenes in which leaf shape differs among individual plants. Leaf shape was quantified from scanned leaves by the centroid-to-boundary distance (CBD), and each leaf contour was generated by adding angularly smoothed random variation to a reference profile scaled by a function of the relative leaf position. The contours were converted into triangular meshes with leaf textures synthesized from real leaf images. The plant structure, including a stem axis length of 1.80 m and the attachment heights of 20 leaves, was derived from a point cloud of one cucumber plant. Thirty plants were arranged in NVIDIA Isaac Sim with the phyllotaxis randomized for each plant, and a canopy with heterogeneity at both the leaf and plant levels was generated automatically. The proposed method provides a basis for heterogeneous virtual canopies for evaluating agricultural robots and vision systems.

Key Words: Digital twin, Cucumber canopy, Leaf shape model

INTRODUCTION

Digital twins, in which virtual counterparts of physical objects are linked with data obtained from the real world, have been increasingly studied in agriculture (Pylianidis et al., 2021; Verdouw et al., 2021), including greenhouse horticulture (Ariesen-Verschuur et al., 2022). A virtual greenhouse is also expected to serve as an environment for developing and evaluating agricultural robots and machine vision systems.

For such an environment to be useful for evaluating robot perception, virtual plants should reproduce not only the geometry of a typical plant but also the variation among plants. In

cucumber canopies, for example, three-dimensional leaf shape patterns vary with the position of the leaf in the canopy (Schmidt and Kahlen, 2019). If a virtual canopy is built by duplicating a single plant model, this heterogeneity is lost, and the same local visual features may appear on different plants, which could cause a robot or camera system to confuse individual plants.

The objective of this study was to develop a method for automatically generating three-dimensional cucumber canopy scenes with heterogeneous leaf shapes based on a statistical leaf shape model derived from real leaf images.

MATERIALS AND METHODS

LEAF SHAPE MODEL

Leaves harvested in May 2025 from cucumber plants grown in a greenhouse at the Ito Campus of Kyushu University, Japan, were scanned with an image scanner. After the leaf orientation was aligned, the leaf region was extracted by thresholding in the HSV color space, binarization, and morphological processing, and its centroid and boundary were detected (Fig. 1).

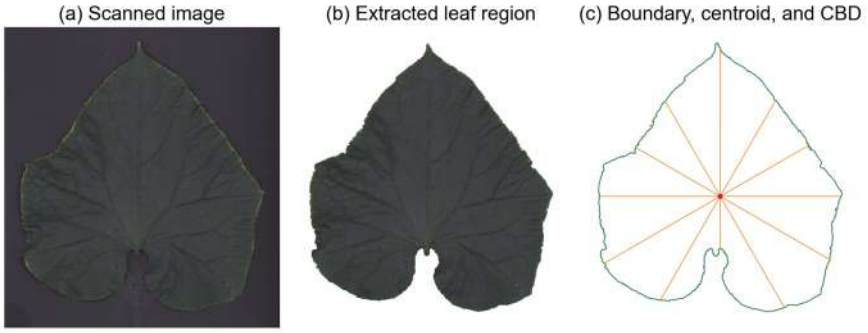

Fig. 1 Image processing of a scanned cucumber leaf: (a) scanned image, (b) leaf region extracted in the HSV color space, and (c) boundary (green), centroid (red), and examples of the CBD (orange).

For each leaf, the centroid-to-boundary distance (CBD) was calculated as a function of the angle θ around the centroid and normalized by that of the largest leaf, because leaves at different positions were similar in shape despite their different sizes. Using the relative leaf position lh (0 at the stem apex and 1 at the base), the leaf shape function $f(lh)$, which gives the leaf size relative to the largest leaf, and the function $\sigma(lh)$, which gives the standard deviation of the shape individual differences, were expressed as cubic functions.

The boundary of a reference leaf image, scaled to the measured maximum leaf length, was used as the reference profile $CBD_0(\theta)$ (Fig. 2a). Each leaf contour was obtained by multiplying $CBD_0(\theta)$ by the sum of $f(lh)$ and a weighted shape individual differences term consisting of angularly smoothed normal random numbers with the standard deviation $\sigma(lh)$; because the random numbers are resampled for every leaf, leaves at the same position have different contours.

3D LEAF AND PLANT MODEL

Each generated contour was converted into a triangular mesh on a lattice of concentric rings around the centroid. The leaf blades (front and back surfaces), petioles, and stem were created, and the leaves were placed automatically according to their attachment heights and azimuth angles. Leaf textures synthesized from multiple real leaf images were assigned so that the color and vein pattern differed among leaves and plants.

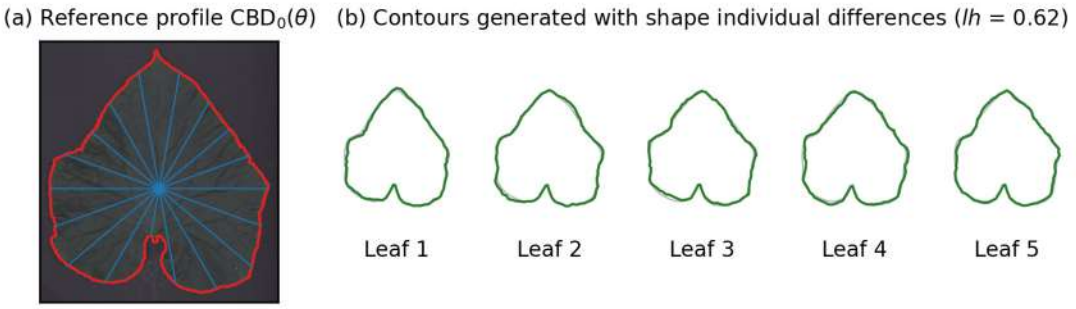

Fig. 2 Leaf shape model: (a) reference leaf with its boundary (red) and CBD (blue), and (b) five contours generated with shape variation at lh = 0.62 (green).

PLANT STRUCTURE FROM A POINT CLOUD

The plant structure was obtained from a point cloud of one cucumber plant (142,650 points) derived from Gaussian splatting. The stem base, stem apex, attachment point of each leaf, and maximum leaf length were measured manually using CloudCompare, and the height of each attachment point along the stem axis connecting the stem base and apex and its azimuth around the stem were calculated (Fig. 3a).

CANOPY SCENE GENERATION

The plant models were arranged in NVIDIA Isaac Sim 5.1.0 in three rows of ten plants with a plant spacing of 0.4 m and a row spacing of 1.2 m. The attachment heights and the number of leaves were common to all plants, and *lh* was assigned in order of height. The phyllotaxis was randomized for each plant (azimuth of the lowest leaf, direction of the spiral, and divergence angle with a mean of 137.5° and a standard deviation of 15°), and every leaf contour was generated independently.

RESULTS & DISCUSSION

From the point cloud, a stem axis length of 1.805 m and 20 leaves attached at heights from 0.081 to 1.722 m were obtained (Fig. 3a), and these values were shared by all plants. Leaves generated at the same relative leaf position kept the overall shape of CBD$_0$(θ) but differed in their local outlines (Fig. 2b). Combined with the randomized phyllotaxis, the generated canopy of 30 plants had heterogeneity at both the leaf and plant levels (Fig. 3b).

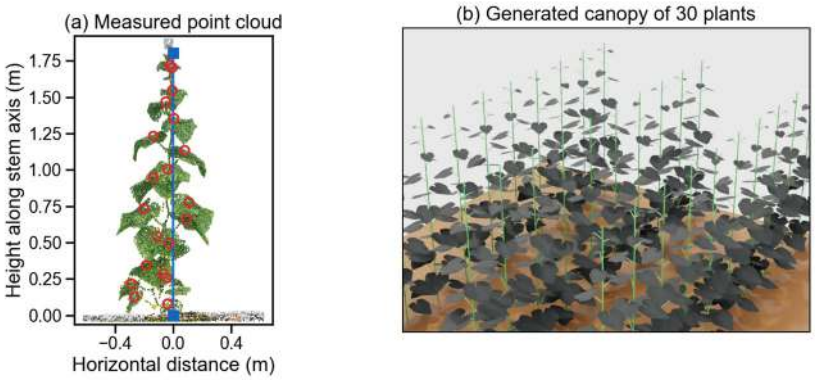

Fig. 3 (a) Measured point cloud with the stem axis (blue line), stem base and apex (blue squares), and leaf attachment points (red circles), and (b) generated canopy of 30 plants rendered with a single leaf texture.

The present model has limitations: leaf curvature and wilting are not represented, the attachment heights and the number of leaves were shared by all plants.

CONCLUSIONS

A method was developed for automatically generating 3D cucumber canopy scenes with heterogeneous leaf shapes by combining a leaf shape model based on real leaf images with the plant structure measured from a point cloud, and a canopy of 30 plants with heterogeneity at the leaf and plant levels was generated. Future work will compare the proposed canopy with a uniform canopy in feature matching and image recognition, and will incorporate mechanical deformation such as leaf curvature and wilting.

ACKNOWLEDGEMENTS

This study was conducted as part of a joint research project with Welzo Co., Ltd. and was supported by JSPS KAKENHI Grant Number 23K05477.

REFERENCES

Ariesen-Verschuur, N., C. Verdouw, and B. Tekinerdogan. 2022. Digital twins in greenhouse horticulture: A review. Comput. Electron. Agric. 199: 107183. https://doi.org/10.1016/j.compag.2022.107183

Pylianidis, C., S. Osinga, and I. N. Athanasiadis. 2021. Introducing digital twins to agriculture. Comput. Electron. Agric. 184: 105942. https://doi.org/10.1016/j.compag.2020.105942

Schmidt, D., and K. Kahlen. 2019. Positional variation rather than salt stress dominates changes in three-dimensional leaf shape patterns in cucumber canopies. In Silico Plants 1(1): diz011. https://doi.org/10.1093/insilicoplants/diz011

Verdouw, C., B. Tekinerdogan, A. Beulens, and S. Wolfert. 2021. Digital twins in smart farming. Agric. Syst. 189: 103046. https://doi.org/10.1016/j.agsy.2020.103046

AI-29

Proceedings of The 12th International Symposium on Machinery and Mechatronics for Agriculture and Biosystems Engineering (ISMAB 2026)
20-24 October 2026, Busan, Republic of Korea

RANKING-BASED LOSS FUNCTIONS FOR DEEP LEARNING PREDICTION OF POST-BLENDING COFFEE SENSORY ATTRIBUTES

Chih-Yun Tsai[1], Yu-Tang Chang[1], Shu-Ping Hung[2], Chia-Hung Peng[2], Chun-Ming Lu[2], Shih-Fang Chen[1]*

[1]Department of Biomechatronics Engineering, National Taiwan University, No. 1, Sec. 4, Roosevelt Rd., Taipei, Taiwan
[2]Information and Communications Research Laboratories, Industrial Technology Research Institute
No. 195, Sec. 4, Zhongxing Rd., Zhudong Township, Hsinchu County, Taiwan
*Corresponding Author-- Voice: +886-2-3366-5354, Email: sfchen@ntu.edu.tw

Abstract: Coffee blending is used to maintain consistency and achieve desired sensory profiles, but post-blending sensory attributes are not necessarily additive and blending ratios complicate formulation. In our previous study, a dual-input Transformer was developed to predict post-blending sensory attributes from pre-blend information of single origin components, including their NIR spectra and sensory attributes, together with blending ratios. Building on this model, the present study further considers the characteristics of sensory evaluation to improve prediction performance. Given that sensory reference values may retain variability even under standardized assessment by trained cuppers, relative differences among samples may be more informative than exact numerical agreement. Therefore, this study compared conventional mean squared error (MSE) loss for absolute sensory-value prediction with a ranking-based loss that additionally considers relative differences between samples. The dataset included 597 single origin coffees and 478 blended coffees, with seven cupping scores ranging from 6 to 10 and nine flavor intensities ranging from 0 to 5 as targets. The results showed that the ranking-based loss improved overall prediction performance for both cupping scores and flavor intensities on average. For cupping scores, average mean absolute error (MAE) decreased from 0.136 to 0.116 and average Kendall's tau increased from 0.154 to 0.161. For flavor intensities, average MAE decreased from 0.827 to 0.734 and Kendall's tau increased from 0.116 to 0.144. The more consistent improvement for flavor-intensity prediction suggests that the effectiveness of relative-order supervision may depend on target characteristics. Overall, ranking-based learning complemented conventional regression by preserving relative sensory differences while maintaining low numerical prediction error, providing more meaningful information for practical use.

Key Words: Deep learning, Near-infrared spectroscopy, Blend coffee, Coffee flavor, Ranking-based loss

INTRODUCTION

Coffee blending is commonly used to achieve desired sensory profiles, but post-blending sensory outcomes can be difficult to infer from the characteristics of component coffees and blending ratios. Our previous work demonstrated the potential of Transformer models for post-blending sensory prediction using pre-blend NIR spectra and blend composition (Tsai et al.,

2025). This study further considers sensory-target representation during training. Sensory scores may vary even under standardized evaluation by trained cuppers; thus, distinguishing stronger from weaker sensory attributes may be more meaningful than reproducing exact values alone. Conventional pointwise regression losses minimize prediction error without considering sample relationships. For squared-error regression, predictions tend toward the conditional mean, potentially reducing differences when reference values are closely distributed or uncertain. Ranking-based learning instead incorporates pairwise relationships (Burges et al., 2005). Therefore, MSE and ranking-based losses were compared under the same dual-input Transformer framework to evaluate whether relative sensory information improves prediction of seven cupping scores and nine flavor intensities.

MATERIALS AND METHODS

Coffee Samples and Sensory Labels

A total of 597 single origin coffee samples were used to prepare 478 blends at different ratios, including 87 two-coffee and 391 three-coffee blends. Sensory evaluations were conducted by professional cuppers to obtain prediction targets. These consisted of seven cupping quality scores—fragrance/aroma, flavor, aftertaste, acidity, body, balance, and overall—ranging from 6 to 10, and intensity scores for nine flavor groups—floral, fruity, sour/fermented, green/vegetable, other, roasted, spices, nutty/cocoa, and sweet—each ranging from 0 to 5.

NIR Spectra Collection

Near-infrared (NIR) spectra were collected following Chang et al. (2021) using an Antaris II spectrometer over 700–2500 nm at 2-nm resolution. Triplicate 900-dimensional spectra were obtained for each single-origin coffee. The 478 blended samples were split into training, validation, and testing sets at 0.64:0.16:0.20 at the blend-sample level.

Deep Learning Methods

A dual-input Transformer following Tsai et al. (2025) predicted post-blending sensory attributes from pre-blend information. Each blend was represented by component NIR spectra, pre-blend sensory attributes, and blending ratios. NIR and sensory inputs were processed by separate Transformer encoders (Vaswani et al., 2017). The encoded representations were combined according to the blending ratios and fused to form a representation of the blended coffee. Masking accommodated blends with different numbers of component coffees. The fused representation was mapped to seven cupping scores and nine flavor-intensity outputs.

Evaluation Metrics

Model performance was evaluated using mean absolute error (MAE) and Kendall's tau. MAE measured numerical deviation by averaging absolute differences between predicted and reference values, whereas Kendall's tau assessed relative ordering based on concordant and discordant sample pairs. Together, the two metrics evaluated both absolute sensory values and relative differences considered by the ranking-based loss.

Loss Functions

Two training objectives were compared using the same Transformer architecture and data split. The baseline used MSE loss, whereas the ranking-based model combined pointwise regression with pairwise ranking constraints. For each sensory attribute, sample pairs were formed within each training batch and included only when their absolute reference-value

difference exceeded a threshold, set to 0.25 for cupping scores and 0.05 for flavor intensities. The ranking direction was determined from the reference values, and a margin-based loss penalized incorrect ordering or insufficient separation between predictions:

$$\mathcal{L}_{\text{rank}} = \max(0, \text{m} - s_{ij}(\hat{y}_i - \hat{y}_j)) \quad (1)$$

where $\hat{y}_i$ and $\hat{y}_j$ represent the predicted values of samples i and j; s_{ij} indicates the reference ordering direction based on reference values; m is the ranking margin, set to 0.05 for cupping scores and 0.10 for flavor intensities. The final loss combined the regression and ranking terms:

$$\mathcal{L}_{total} = \lambda_{\text{MSE}}\mathcal{L}_{\text{MSE}} + \lambda_{\text{rank}}\mathcal{L}_{\text{rank}} \quad (2)$$

where λ_{rank} and λ_{MSE} control the contributions of the ranking and MSE terms, respectively. For both cupping-score and flavor-intensity prediction, λ_{MSE} was set to 1.0 and λ_{rank} to 1.5. These hyperparameters, including the pair-selection thresholds, ranking margins, and loss weights, were selected based on preliminary experiments on the validation set.

RESULTS & DISCUSSION

As shown in Table 1, the ranking-based loss reduced MAE across all seven cupping attributes, with the average decreasing from 0.136 to 0.116. In contrast, relative-order improvement was less consistent, with average Kendall's tau increasing only from 0.154 to 0.161 and several attributes showing lower values. Notably, Flavor showed the most pronounced decline, with Kendall's tau decreasing from 0.153 to 0.080. One possible explanation is that ranking supervision focuses on pairs with sufficiently large reference differences, while closely scored pairs receive no ranking constraint; ordering errors among these pairs may therefore reduce overall tau. Thus, ranking information improved numerical prediction consistently, but its effect on relative ordering varied across attributes.

Table 1 Comparison of loss functions for seven cupping-score predictions.

	MSE		Ranking-based	
	MAE	**tau**	**MAE**	**tau**
Fragrance/Aroma	0.142	0.110	0.118	0.166
Flavor	0.136	0.153	0.128	0.080
Aftertaste	0.136	0.181	0.124	0.145
Acidity	0.131	0.092	0.103	0.245
Body	0.126	0.254	0.092	0.231
Balance	0.135	0.199	0.124	0.154
Overall	0.145	0.092	0.125	0.107
Average	**0.136**	**0.154**	**0.116**	**0.161**

The effect of the ranking-based loss was more consistent for flavor-intensity prediction, as shown in Table 2. Average MAE decreased from 0.827 to 0.734, while Kendall's tau increased from 0.116 to 0.144. Eight of the nine flavor groups had lower MAE values, and seven had higher Kendall's tau values. Sour/fermented improved in both metrics, with MAE decreasing from 0.946 to 0.694 and Kendall's tau increasing from 0.283 to 0.322. In contrast, roasted showed a different pattern: MAE increased slightly from 1.016 to 1.051, whereas Kendall's tau increased from 0.018 to 0.125. This indicates that numerical prediction and relative ordering do not necessarily improve simultaneously, supporting the use of both metrics when evaluating ranking-based sensory prediction.

Table 2 Comparison of loss functions for nine flavor-intensity predictions.

	MSE		Ranking-based	
	MAE	tau	MAE	tau
Floral	1.222	0.046	1.118	0.116
Fruity	0.333	0.061	0.303	0.042
Sour/Fermented	0.946	0.283	0.694	0.322
Green/Vegetable	0.799	0.167	0.716	0.174
Other	1.095	0.228	1.028	0.237
Roasted	1.016	0.018	1.051	0.125
Spices	0.560	-0.008	0.364	0.021
Nutty/Cocoa	1.085	0.197	1.014	0.103
Sweet	0.386	0.049	0.322	0.159
Average	0.827	0.116	0.734	0.144

The different responses between cupping scores and flavor intensities may reflect target distributions. Flavor-intensity values were more broadly distributed, whereas cupping scores were concentrated within a narrower range. A broader distribution may provide more distinguishable pairs and a clearer ranking signal, while closely distributed values may yield fewer informative pairs and make relative ordering more sensitive to small prediction changes. This may explain the more consistent benefit of ranking-based learning for flavor-intensity prediction. Overall, the results suggest that ranking-based learning provides information beyond pointwise regression by explicitly considering relative relationships between samples.

CONCLUSIONS

This study examined whether relative sensory relationships in the training objective could improve post-blending sensory prediction. Compared with MSE loss, the ranking-based loss reduced prediction error for both cupping scores and flavor intensities, while relative-order improvement was more consistent for flavor-intensity prediction. This may reflect target distributions, with broader intensity variation providing more informative pairwise comparisons than concentrated cupping scores. These findings suggest that ranking information can complement regression, with benefits depending on sensory-target characteristics. Future work will investigate target-specific ranking strategies, including adaptive thresholds and margins, and assess robustness across sensory data and validation settings.

REFERENCES

Burges, C., Shaked, T., Renshaw, E., Lazier, A., Deeds, M., Hamilton, N., & Hullender, G. (2005). Learning to rank using gradient descent. *Proceedings of the 22nd International Conference on Machine Learning* (pp. 89-96).

Chang, Y. T., Hsueh, M. C., Hung, S. P., Lu, J. M., Peng, J. H., & Chen, S. F. (2021). Prediction of specialty coffee flavors based on near-infrared spectra using machine- and deep-learning methods. *Journal of the Science of Food and Agriculture*, *101*(11), 4705-4714.

Tsai, C. Y., Chang, Y. T., Hung, S. P., Lu, C. M., Chen, S. F., & Peng, C. H. (2025). Development of a deep learning-based recommendation system for coffee blending ratios optimization. In *2025 ASABE Annual International Meeting* (pp. 807–816). American Society of Agricultural and Biological Engineers.

Vaswani, A., Shazeer, N., Parmar, N., Uszkoreit, J., Jones, L., Gomez, A. N., Kaiser, L., & Polosukhin, I. (2017). Attention is all you need. *Advances in Neural Information Processing Systems*, *30*.

AI and Information Processing 6 (AI-6)



AI-30

Proceedings of The 12th International Symposium on Machinery and Mechatronics for Agriculture and Biosystems Engineering (ISMAB 2026)
20-24 October 2026, Busan, Republic of Korea

AI-BASED EARLY DETECTION OF VISUALLY SIMILAR TOMATO DISEASES AND DROUGHT: COMPARISON OF BIOIMPEDANCE SENSING AND RGB IMAGING

Yejin Kim[1,4], Daesik Son[3], Kyuseok Yang[1,4], Yulim Park[2,4], Dhayanti Makyorukty[2,4], Junseung Bae[1,4], Chanwoo Park[1,4], Soo Chung[1,3,4*]

[1] Department of Biosystems Engineering, Seoul National University, Republic of Korea
[2]Department of International Agricultural Technology, Seoul National University, Republic of Korea
[3]Research Institute of Agriculture and Life Sciences, Seoul National University, Seoul 08826, Republic of Korea
[4]Integrated Major in Global Smart Farm, College of Agriculture and Life Sciences, Seoul National University, Seoul, Republic of Korea

*Corresponding Author-- Voice: +82-880-4606, Email: soochung@snu.ac.kr

Abstract: Bacterial diseases and environmental stresses in tomato often produce visually similar symptoms, such as wilting and water-soaked lesions, while distinct visual symptoms may not appear during the early stage of stress development. These characteristics limit conventional image-based diagnosis for both early detection and discrimination of the underlying cause. In contrast, electrical responses may reflect internal physiological changes that are not visually apparent, providing a potential means to distinguish stresses with similar external symptoms and contributing to earlier diagnosis. The objective of this study was to compare the classification performance of BIS and RGB imaging at successive observation time points for early discrimination of drought and bacterial diseases in tomato.

At three weeks after sowing, tomato seedlings (*Solanum lycopersicum* L. cv. Daphnis) were assigned to five treatment groups: healthy control, drought stress, and three biotic stress treatments consisting of separate inoculations with *Xanthomonas euvesicatoria* (KACC 18723), *Pseudomonas syringae* (KACC 10459), and *Clavibacter michiganensis* subsp. *michiganensis* (KACC 16996). Tomato plants were monitored from 0 to 72 hours after treatment (HAT), with pathogen inoculation and drought treatment applied at 0 HAT. Bioimpedance spectra were acquired every 30 min over the range of 50 Hz to 1 MHz at 50 logarithmically spaced frequency points with a pair of wearable gold-film electrodes, while RGB images were captured every 24 h. For BIS analysis, multiple candidate base estimators were benchmarked, and the best-performing combination was integrated into an ensemble classifier. For image analysis, leaf regions were segmented using the Segment Anything Model (SAM), followed by DINO-based self-supervised representation learning with multiple convolutional neural network (CNN)- and transformer-based backbones. Model performance was evaluated at 6-h intervals for BIS data and at 24-h intervals for RGB image data after treatment.

The BIS-based model achieved over 85% classification accuracy at 6 HAT and gradually increased to approximately 97% at 72 HAT. In contrast, the image-based model showed a classification accuracy of only 43% at 6 HAT and reached a comparable accuracy of approximately 85% only at 72 HAT, when treatment-specific

visual symptoms became more distinguishable. Class-wise probability distributions and PCA projections showed a consistent pattern, with earlier separation among treatment groups in the BIS feature space.
Overall, two main findings were observed. First, BIS-based classification achieved a high level of discrimination approximately 66 HAT earlier than image-based classification under the tested conditions. Second, BIS also showed higher classification performance at 72 HAT, indicating its potential not only for early diagnosis but also for discriminating plant stresses with visually similar symptoms. The complementary physiological and visual information obtained from BIS and RGB imaging may further provide a basis for multimodal plant stress diagnosis.

Key Words: Bioimpedance spectroscopy, Plant stress diagnosis, Early detection, Machine learning

Acknowledgement
This work was supported by Korea Institute of Planning and Evaluation for Technology in Food, Agriculture and Forestry(IPET) and Korea Smart Farm R&D Foundation (KosFarm) through Smart Farm Innovation Technology Development Program, funded by Ministry of Agriculture, Food and Rural Affairs(MAFRA) and Ministry of Science and ICT(MSIT), Rural Development Administration(RDA) (RS-2025-02306378). This work was carried out with the support of "Cooperative Research Program for Agriculture Science and Technology Development (Project No. RS-2026-25506590)" Rural Development Administration, Republic of Korea. This research was supported by the BK21 FOUR, Global Smart Farm Educational Research Center, Seoul National University, Seoul, Korea.

AI-31

Proceedings of The 12th International Symposium on Machinery and Mechatronics for Agriculture and Biosystems Engineering (ISMAB 2026)
20-24 October 2026, Busan, Republic of Korea

IMPROVED KEYPOINT ESTIMATION USING A MULTI-TASK YOLO MODEL FOR WEED RECOGNITION IN GARLIC FIELDS

Sohyeon Kang[1], Junghwa Park[1], Seokyung Park[1], Minjoo Kim[1], Yeonsoo Kim[1,2,3] Jaesung Park[1,2,3*]

[1] Department of Bio-Industrial Machinery Engineering, Pusan National University, Miryang 50463, Re-public of Korea
[2] Life and Industry Convergence Research Institute, Pusan National University, Miryang 50463, Republic of Korea
[3] Department of Natural Resources Systems Engineering, Pusan National University, Yangsan 50612, Republic of Korea
*Corresponding Author-- Voice: +82-10-4001-1225, Email: jaesung.park@pusan.ac.kr

Abstract: For precision weeding, it is necessary not only to accurately recognize crops and weeds but also to precisely estimate target points that serve as references for weeding operations. In particular, weeding actions performed near the stem base of crops may cause crop damage; therefore, it is important to identify the region of interest corresponding to each plant instance while accurately estimating keypoint locations such as the stem base or growth point. In this study, a multi-task YOLO (You Only Look Once) model that simultaneously performs instance segmentation and pose estimation was developed to recognize crops and weeds in garlic fields and to estimate keypoint locations for crop avoidance or weed removal. The proposed model consists of a segmentation branch for delineating individual plant regions and a pose branch for predicting keypoints corresponding to the stem base or growth point. A feature fusion module was introduced between the two branches to utilize segmentation features for keypoint estimation. Through this module, spatial and morphological information encoded in the segmentation features was incorporated into the pose estimation process to improve keypoint localization accuracy. The proposed model aims to estimate the stem-base locations of garlic plants and weeding target points of weeds under garlic-field conditions characterized by narrow plant spacing and severe occlusion among plants, thereby providing positional information required for precise weeding while minimizing the risk of damage to garlic plants caused by weeding actuator operation.

Key Words: garlic field, weed recognition, YOLO, instance segmentation, pose estimation, multi-task learning, deep learning

ACKNOWLEDGEMENTS

This work was supported by the Korea Institute of Planning and Evaluation for Technology in Food, Agriculture, and Forestry(IPET) through the Open Field Smart Agriculture Technology Short-term Advancement Project, funded by the Ministry of Agriculture, Food, and Rural Af-fairs(MAFRA)(RS-2025-02313136).

AI-32

Proceedings of The 12th International Symposium on Machinery and Mechatronics for Agriculture and Biosystems Engineering (ISMAB 2026)
20-24 October 2026, Busan, Republic of Korea

DEVELOPMENT OF INTELLIGENT ROSE GROWTH MONITORING SYSTEM USING DEEP LEARNING AND BUD TRACKING

Yu-Shan Wang[1], Wei-Ling Chen[2], Hsing-Ying Chung[3], Shih-Fang Chen[1*]

[1]Department of Biomechatronics Engineering, National Taiwan University, Taiwan
[2] Floral Industry Innovation Center, Ministry of Agriculture, Taiwan
[3] Department of Plant Industry, National Pingtung University of Science and Technology, Taiwan
*Corresponding Author-- Voice: +886-2-3366-5354, Email: sfchen@ntu.edu.tw

Abstract: Accurate monitoring of rose growth stages is important for greenhouse cut-flower production, particularly for harvest planning and environmental management. However, growth monitoring in commercial greenhouses still relies mainly on manual observation, which is labor-intensive and difficult to maintain continuously. This study developed an automated rose monitoring system integrating rail-mounted image acquisition, deep learning-based growth stage recognition, and time-series bud tracking. A rail-mounted sensing platform equipped with Raspberry Pi camera modules was installed above rose beds to collect high-resolution top-view images under production conditions. The rose cultivar 'Laventine' was evaluated across four reproductive growth stages: visible bud formation (B1), bud enlargement (B2), petal exposure (B3), and harvest maturity (H). A YOLO26-based model was trained to detect rose buds and classify their growth stages, achieving an overall mAP50 of 0.862. Detection performance was satisfactory for B2, B3, and H, whereas B1 remained challenging because early buds were small and had limited contrast with the canopy background. To extend single-image recognition into temporal growth monitoring, a bud tracking procedure was developed using image alignment, centroid-based one-to-one association, long-term tracking memory, and growth-stage constraints. Time-series analysis showed average summer transition times of 5.13, 2.91, and 1.30 days for B1 to B2, B2 to B3, and B3 to H, respectively. These results demonstrate the feasibility of automated image-based monitoring for quantifying rose bud development and provide a scalable basis for harvest scheduling and precision greenhouse management.

Key Words: Rose phenotyping, Computer vision, Deep learning, Bud tracking, Precision horticulture

INTRODUCTION

Rose (*Rosa hybrida* Hort.) production in Taiwan faces challenges from labor shortages, rising costs, climate variability, and import competition. In commercial greenhouses, growth monitoring still depends mainly on manual observation, resulting in discontinuous records that are insufficient for linking environmental conditions with plant development and harvest readiness. Advances in IoT, computer vision, and deep learning provide opportunities for automated crop monitoring. This study developed a rail-mounted imaging framework for greenhouse roses, integrating RGB image acquisition, YOLO26-based bud growth stage

recognition, and time-series bud tracking. The system aims to quantify bud development, estimate growth-stage transitions, and provide a scalable basis for harvest scheduling and precision greenhouse management.

MATERIALS AND METHODS

SYSTEM DESIGN

Experiments were conducted at a commercially operated greenhouse in Nantou, Taiwan, using the rose cultivar 'Laventine'. A 28 m rail-mounted imaging system was installed approximately 2.8 m above the rose beds and stopped at predefined positions at approximately 2 m intervals (Fig. 1a). Each module was equipped with top-view and side-view Raspberry Pi camera modules for RGB image capture. Top-view images were captured at 4608 × 2592 pixels and used for growth stage recognition and time-series bud tracking.

GROWTH STAGE CLASSIFICATION MODEL

Rose bud stages were defined according to visually identifiable traits and practical greenhouse management requirements. Four reproductive growth stages were used: B1 (visible bud formation, initial emergence without enlargement), B2 (bud enlargement, rapid increase in bud size without opening), B3 (petal exposure, partial opening with visible pigmentation), and H (harvest maturity, fully expanded petals reaching marketable standards) (Fig. 1b).

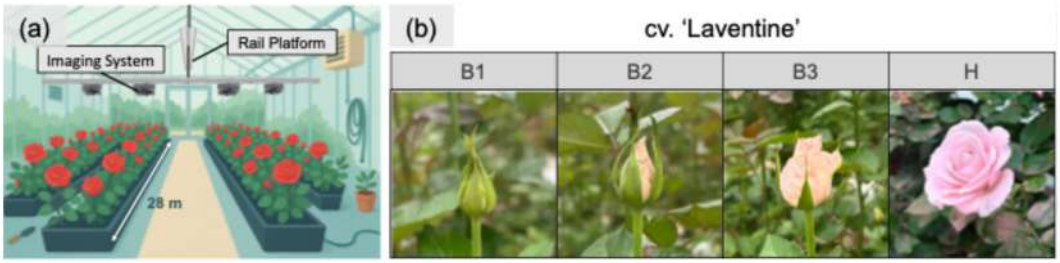

Fig. 1 (a) Rail-mounted imaging system deployment schematic,
(b) Growth stage classification of roses based on visible bud development (B1–H).

A YOLO26-m model was adopted for rose bud detection and growth stage classification. The dataset was split into training, validation, and testing subsets at a ratio of 7:1:2. Model training used 350 annotated images of 'Laventine', containing approximately 5,700 annotated buds. Performance was evaluated using precision, recall, and mAP50.

TIME-SERIES BUD TRACKING

To extend single-image detection into continuous growth monitoring, repeated images from fixed sampling points were processed chronologically. Buds detected by the trained detection model were aligned and associated across adjacent images using bounding-box-based translation correction and centroid-based greedy matching. A long-term tracking memory preserved each bud's ID, position, and stage history, allowing the same bud to retain a persistent ID across repeated images and enabling reconstruction of individual growth histories.

RESULTS & DISCUSSION

MODEL PERFORMANCE

The fine-tuned YOLO26-m model achieved overall mAP50 values of 0.862 (Table 1). Recognition was stable in B2, B3, and H stages, with mAP50 values above 0.93. B1 showed the lowest mAP50 of 0.631 because early buds were small, partially occluded, and low in contrast against the canopy background.

Table 1. Fine-tuned YOLO26-m performance across growth stages for 'Laventine'.

Class / Index	cv. 'Laventine'				
	B1	B2	B3	H	Total
Precision	0.656	0.860	0.881	0.802	0.800
Recall	0.696	0.909	0.884	0.933	0.856
mAP	0.631	0.944	0.932	0.942	0.862

BUD TRACKING AND GROWTH CYCLE ANALYSIS

Time-series tracking reconstructed individual bud histories and quantified temporal changes in growth stages, providing information beyond single-image recognition. Previous rose monitoring research (Shinoda et al., 2023) used moving overhead video with YOLOv5 and SORT to track roses and merge TrackIDs for stage-specific counting. In comparison, the present study uses fixed-position time-series images to maintain persistent bud IDs and reconstruct individual growth histories. After filtering unstable tracks, transition times were calculated for 2,241 buds from B1 to B2, 2,430 buds from B2 to B3, and 751 buds from B3 to H from May to June 2026. The average transition times were 5.13±1.58, 2.91±1.43, and 1.30±0.55 days, respectively. These results provide a basis for characterizing bud development and future analysis of environmental effects on growth.

CONCLUSIONS

This study developed an intelligent rose growth monitoring system integrating rail-mounted image acquisition, YOLO26-based growth stage recognition, and time-series bud tracking. The model achieved an overall mAP50 of 0.862 for 'Laventine', demonstrating the feasibility of automated rose bud detection under greenhouse conditions. Bud tracking provided temporal growth information, showing that 'Laventine' buds required approximately 5 days from B1 to B2, 3 days from B2 to B3, and 1 to 2 days from B3 to H in summer. Overall, the system provides a scalable foundation for harvest scheduling and precision greenhouse management. Future work will focus on improving early-bud detection and integrating environmental data to support growth and yield analysis.

ACKNOWLEDGEMENTS

The research was supported by the Ministry of Agriculture, Executive Yuan, Taiwan (Project No. 115AS-1.6.2-AS-15). Also thanks to Tzu-Ling Wang and Han-Sheng Chang for helping with the monitoring system set up.

REFERENCES

Jocher, G., Qiu, J., Liu, M., Lyu, S., Akyon, F. C., & Kalfaoglu, M. E. (2026). Ultralytics YOLO26: Unified real-time end-to-end vision models. *arXiv preprint arXiv:2606.03748.*

Shinoda, R., Motoki, K., Hara, K., Kataoka, H., Nakano, R., Nakazaki, T., & Noguchi, R. (2023). RoseTracker: A system for automated rose growth monitoring. *Smart Agricultural Technology, 5*, 100271. https://doi.org/10.1016/j.atech.2023.100271

AI-33

Proceedings of The 12th International Symposium on Machinery and Mechatronics for Agriculture and Biosystems Engineering (ISMAB 2026)
20-24 October 2026, Busan, Republic of Korea

EVALUATION OF STRATEGIES TO IMPROVE INTERANNUAL TRANSFERABILITY OF UAV-BASED MULTISPECTRAL PEPPER PLANT HEIGHT MODELS

Gangin Je[1], Chanseok Ryu[1*], Changhyeok Park[1], Hojun Kwon[1], Hakchan Kim[1], Yeseong Kang[2], Dohyun An[2], Jian Kim[2]

[1]Department of Bio-System Engineering, Institute of Agriculture & Life Science, Gyeongsang National University, Jinju, 52828, Republic of Korea
[2]Department of Smart Agro-industry, Institute of Agriculture & Life Science, Gyeongsang National University, Jinju, 52725, Republic of Korea
*Corresponding Author-- Voice: +82-10-3204-4525, Email: ryucs@gnu.ac.kr

Abstract: Pepper (Capsicum annuum L.) is an important vegetable crop in Korea, and efficient monitoring of plant growth is essential for crop management. Plant height is a useful growth indicator, but conventional measurements require repeated manual observations and considerable labor. UAV-based multispectral imagery provides a rapid and non-destructive alternative; however, models developed in a single growing season may lose accuracy when applied to other years because crop growth and environmental conditions vary among seasons. This study evaluated the interannual transferability of UAV-based pepper plant height models and examined strategies for improving cross-year prediction. Field experiments were conducted in Gimje-si, Republic of Korea, from 2023 to 2025. Seven vegetation indices were derived from UAV multispectral imagery, and ridge regression (RR), LASSO regression (LR), k-nearest neighbors regression (KNR), and random forest regression (RFR) were evaluated using 5-fold GroupKFold. RR was selected for 2023 and 2024, whereas LR was selected for 2025, with validation RMSE values of 5.817, 4.992, and 6.460 cm, respectively. However, cross-year RMSE increased to 15.08–69.78 cm, indicating limited interannual transferability. Growing degree days, cumulative solar radiation, and cumulative precipitation (CP) were individually added to the selected models. Their effects varied among source–target combinations, with the clearest improvement observed for the 2024-to-2023 RR model, where CP increased R^2 from −0.353 to 0.560 and reduced RMSE from 15.08 to 8.596 cm. As an additional exploratory analysis, all observations from 2023–2025 were integrated into a single dataset (n = 179). The integrated KNR model achieved validation R^2 = 0.688, RMSE = 8.791 cm, and MAPE = 6.833%, while providing a more continuous prediction distribution across a broader plant-height range. These results demonstrate the importance of evaluating UAV-based crop growth models using both within-year accuracy and cross-year transferability. Environmental information and multi-year data integration showed complementary potential for improving model robustness across variable growing conditions.

Key Words: UAV, multispectral imagery, plant height, cross-year transferability, multi-year integration

INTRODUCTION

Pepper (*Capsicum annuum* L.) is an important seasoning vegetable widely used in Korean cuisine and is one of the major vegetable crops in Korea in terms of cultivation area and production (RDA, 2020). Because pepper requires continuous management of crop growth and field conditions throughout the growing season, repeated assessment of crop growth can provide useful information for efficient crop management. Among various growth characteristics, plant height is a useful indicator for evaluating crop development and spatial variability within agricultural fields. However, conventional plant height measurements are generally performed manually and require considerable labor and time, particularly when repeated measurements are conducted over large areas. UAV-based remote sensing provides an alternative approach for rapid and non-destructive crop monitoring by acquiring high-resolution spatial and spectral information.

Multispectral imagery has been widely used for crop growth assessment because spectral reflectance and VIs can represent differences in canopy condition and crop development. UAV-based remote sensing also enables repeated observations at multiple growth stages and has been applied to non-destructive crop monitoring (Sun et al., 2023). However, relationships between spectral characteristics and crop growth may vary according to growth stage, environmental conditions, and field characteristics. Consequently, a model showing good performance within a single growing season may not maintain the same prediction accuracy when applied to another year. Evaluation of interannual transferability is therefore important for the practical application of UAV-based crop growth estimation models.

Cumulative environmental conditions may provide information that is not fully represented by spectral observations acquired on individual UAV flight dates. In particular, growing degree days, solar radiation, and precipitation may help characterize differences in crop development and growing conditions among years. Therefore, incorporating these variables with UAV-derived spectral information may improve the transferability of models developed in individual growing seasons.

The objectives of this study were to (1) select representative year-specific UAV multispectral-based pepper plant height models by considering both quantitative performance and observed–predicted distributions, (2) evaluate their transferability to other growing seasons, and (3) determine whether cumulative environmental variables could improve cross-year prediction.

MATERIALS AND METHODS

EXPERIMENTAL FIELDS AND PLANT HEIGHT MEASUREMENTS

Field experiments were conducted in pepper fields located in Yongji-myeon, Gimje-si, Jeonbuk State, Republic of Korea, during the 2023–2025 growing seasons. Different fields were used in each year. Pepper seedlings were transplanted on 2 May 2023, 2 May 2024, and 29 April 2025.

Thirty plants were originally planned for repeated monitoring during each survey period. In 2023, the number of monitored plants decreased to 15 in July because some of the originally monitored plants were affected by wilt disease. No plant-height survey was conducted in August, and 30 plants at a separate location were surveyed in September to supplement the dataset. These September plants were treated as independent samples. In 2025, the number of monitored plants was reduced to 11 from July onward because of reduced field-survey

personnel.
Because UAV image acquisition was constrained by weather and flight conditions, including precipitation, wind, and illumination conditions, imagery could not always be acquired on the same date as the field survey. Therefore, plant-height measurements were paired with the temporally closest UAV acquisition within each survey period.

Table 1 Field survey and UAV image acquisition schedule.

Year	Field survey date	Survey n	UAV acquisition date	Usable n
2023	27 June	30	28 June	25
	27 July	15	27 July	13
	25 September	30	25 September	24
2023 total		75		62
2024	25 June	30	19 June	27
	26 July	30	23 July	25
	9 August	30	14 August	21
2024 total		90		73
2025	20 June	30	19 June	26
	18 July	11	21 July	8
	12 August	11	14 August	10
2025 total		52		44

Survey n indicates the number of plants measured in the field before preprocessing. Usable n indicates observations retained after outlier processing.

UAV IMAGE ACQUISITION AND DATA PREPROCESSING

Multispectral imagery was acquired using a DJI Matrice 300 RTK UAV equipped with a MicaSense Altum-PT sensor. Flights were conducted at an altitude of 25 m and a flight speed of 4 m/s, with forward and side overlaps of 75%.
The acquired images were mosaicked using PIX4Dmapper (Pix4D S.A., Switzerland). The multispectral orthomosaics were processed by pansharpening and spatially registered in QGIS 3.28.11 (Quantum GIS, USA). Vegetation and nonvegetation areas were separated using the excess green (ExG) index in ENVI 5.3 (Exelis Visual Information Solutions Inc., USA), and reflectance values were extracted from plant-level regions of interest.

$$ExG = 2 \times Green - Blue - Red \quad (1)$$

For each acquisition date, outlier values in measured plant height and spectral reflectance were identified using the 1.5 × interquartile range (IQR) criterion and excluded from subsequent calculations. VIs were calculated from the retained reflectance values, and observations with complete plant-height and VI data were used for model development. After preprocessing, the annual datasets consisted of 62, 73, and 44 observations for 2023, 2024, and 2025, respectively.
Seven VIs were calculated from blue (B), green (G), red (R), red-edge (RE), and near-infrared (NIR) reflectance.

Table 2 Vegetation indices used in this study.

Vegetation index	Formula	Reference
GNDVI	(NIR − G) / (NIR + G)	Gitelson et al., 1996
NDRE	(NIR − RE) / (NIR + RE)	Barnes et al., 2000
NDVI	(NIR − R) / (NIR + R)	Rouse et al., 1974
BNDVI	(NIR − B) / (NIR + B)	Lee et al., 2021
VARI	(G − R) / (G + R − B)	Gitelson et al., 2002
NLI	(NIR^2 − R) / (NIR^2 + R)	Goel and Qin, 1994
SFDVI	(NIR + G) / (R + RE)	Martins et al., 2025

DEVELOPMENT AND SELECTION OF YEAR-SPECIFIC MODELS

Four regression algorithms were evaluated: ridge regression (RR), LASSO regression (LR), k-nearest neighbors regression (KNR), and random forest regression (RFR). Feature subsets and model hyperparameters were determined separately for each year. RR, KNR, and RFR used a forward–backward floating procedure for feature selection, whereas LR retained variables with non-zero coefficients after hyperparameter optimization.

Model evaluation was conducted using 5-fold GroupKFold, with repeated measurements from the same plant assigned to the same group. The September 2023 observations were assigned independent groups because they were obtained from a separate monitoring population.

Representative year-specific models were selected by considering calibration R^2, validation RMSE, calibration–validation consistency, and observed–predicted distributions. Validation performance and continuity of the predicted distribution were emphasized, whereas calibration performance was used as a diagnostic of model fit. Models showing pronounced horizontal clustering, in which predicted heights remained nearly constant across a range of measured heights, were deprioritized because such patterns indicated limited discrimination of individual plant-height variation.

Model performance was evaluated using R^2, RMSE, and MAPE.

CROSS-YEAR EVALUATION AND CUMULATIVE ENVIRONMENTAL VARIABLES

After a representative VI-only model was selected for each year, the model was fitted using the complete source-year dataset and directly applied to the other two years without additional feature selection or hyperparameter tuning.

Three cumulative environmental variables were evaluated: GDD with a base temperature of 10°C, CSR (MJ m^{-2}), and CP (mm). Each variable was accumulated from transplanting to the day before the corresponding UAV acquisition.

GDD, CSR, or CP was individually added to the selected VI configuration for each source year. The environmental variable was retained during model development, and model hyperparameters were re-optimized after its addition. Because plants observed on the same acquisition date shared the same cumulative environmental value, environmental-variable effects were evaluated using both quantitative performance metrics and observed–predicted distributions.

In addition, an exploratory multi-year analysis was conducted by pooling all retained observations from 2023 to 2025 (n = 179). RR, LR, KNR, and RFR were evaluated using the same 5-fold GroupKFold procedure. Because observations from all three years were included during model development, the integrated-model results were interpreted as internal validation rather than independent cross-year validation.

RESULTS & DISCUSSION

SELECTION OF YEAR-SPECIFIC VI-ONLY MODELS

The representative VI-only models differed among growing seasons. For 2023, RR using VARI and NLI was selected. Although KNR produced a lower validation RMSE, its observed–predicted distribution showed pronounced horizontal clustering, suggesting that predictions tended to concentrate around several height levels rather than continuously represent individual plant-height variation. Therefore, RR was considered more appropriate as the representative 2023 model. For 2024, RR using GNDVI, NDVI, BNDVI, VARI, NLI, and SFDVI was selected. For 2025, LR using NDRE, NDVI, BNDVI, VARI, NLI, and SFDVI was selected.

Table 3 Calibration and validation performance of the selected year-specific VI-only models.

Year	Model	R^2_C	RMSE_C (cm)	MAPE_C (%)	R^2_V	RMSE_V (cm)	MAPE_V (%)
2023	RR	0.835	5.258	4.066	0.781	5.817	4.563
2024	RR	0.510	4.678	4.354	0.401	4.992	4.821
2025	LR	0.861	5.734	4.454	0.778	6.460	4.885

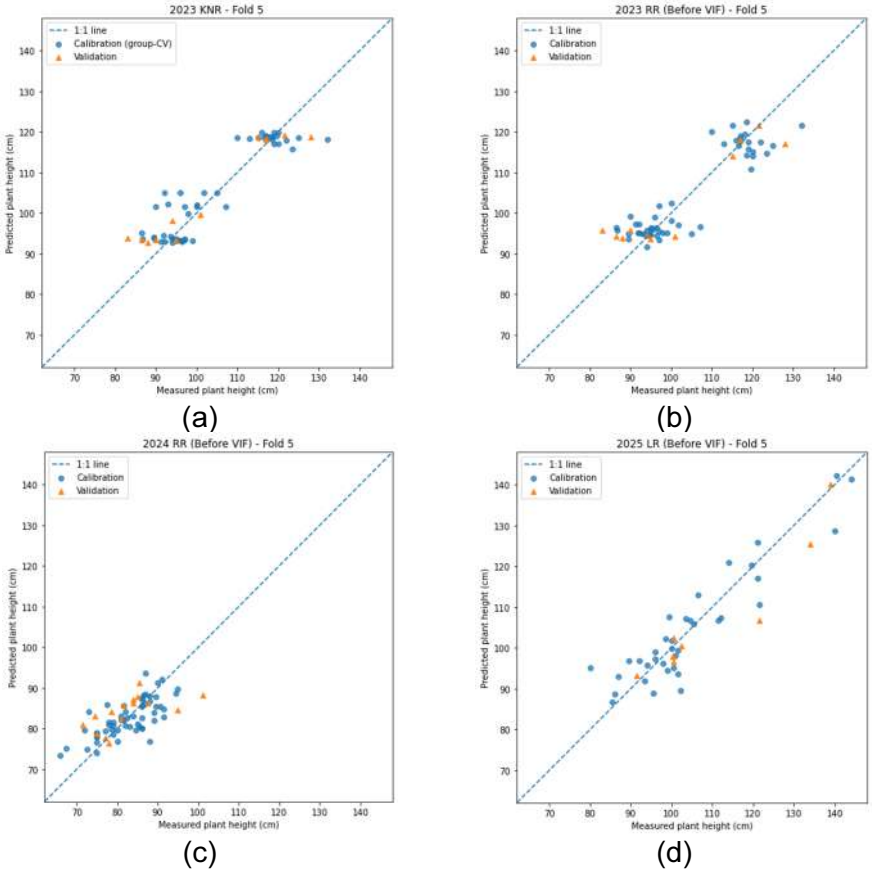

Fig.1 Observed–predicted distributions for representative validation folds: (a) 2023 KNR candidate with the lowest validation RMSE, (b) 2023 selected RR, (c) 2024 selected RR, and (d) 2025 selected LR.

The 2023 RR showed R^2_C = 0.835 and R^2_V = 0.781 with validation RMSE = 5.817 cm. The 2024 RR showed lower explanatory power (R^2_V = 0.401) but relatively low absolute error

(RMSE_V = 4.992 cm), whereas the 2025 LR model showed R^2_V = 0.778 and RMSE_V = 6.460 cm.

CROSS-YEAR TRANSFERABILITY OF YEAR-SPECIFIC MODELS

The selected year-specific models were subsequently applied directly to the other two years. Despite relatively low within-year validation errors, substantial reductions in prediction performance occurred in cross-year evaluation.

Table 4 Cross-year performance of the selected year-specific VI-only models.

Source year	Target year	Model	R^2	RMSE (cm)	MAPE (%)
2023	2024	RR	−19.45	30.29	34.94
	2025	RR	−0.121	16.40	13.46
2024	2023	RR	−0.353	15.08	13.00
	2025	RR	−0.623	19.73	12.02
2025	2023	LR	−2.634	24.72	17.60
	2024	LR	−107.6	69.78	54.37

The selected models showed negative R^2 values in all six cross-year combinations, with RMSE ranging from 15.08 to 69.78 cm.

The 2023 RR model showed particularly poor transfer to 2024, whereas its performance on 2025 was comparatively better. The 2024 RR model showed lower but still substantial errors for both target years. The largest deterioration occurred when the 2025 LR model was transferred to 2024.

These results indicate that good within-year calibration and validation performance did not guarantee interannual transferability. Differences in plant-height distributions, crop development, meteorological conditions, and field characteristics may have contributed to the source–target dependence. Moreover, because different experimental fields were used each year, meteorological effects cannot be completely separated from field-specific factors such as soil and management conditions.

EFFECTS OF CUMULATIVE ENVIRONMENTAL VARIABLES

Cumulative environmental variables were subsequently added to the selected year-specific models. Their effects varied among source–target combinations (Table 5).

Table 5 Best environmental-variable results for each cross-year application.

Source year	Target year	Best EV	R^2	RMSE (cm)	MAPE (%)
2023	2024	CP	−2.956	13.32	14.19
	2025	CSR	0.329	12.69	8.307
2024	2023	CP	0.560	8.596	7.252
	2025	CP	−0.417	18.44	10.94
2025	2023	CSR	−3.655	27.97	18.32
	2024	CP	−95.29	65.72	49.33

EV: environmental variable

Environmental variables reduced RMSE in five of the six cross-year combinations, although the magnitude and practical relevance of the improvement differed substantially.

The clearest improvement occurred for the 2024-to-2023 RR model. Addition of CP increased R^2 from −0.353 to 0.560 while reducing RMSE from 15.08 to 8.596 cm and MAPE from 13.00% to 7.252%. The observed–predicted distribution also moved closer to the 1:1 relationship, although some clustering remained.

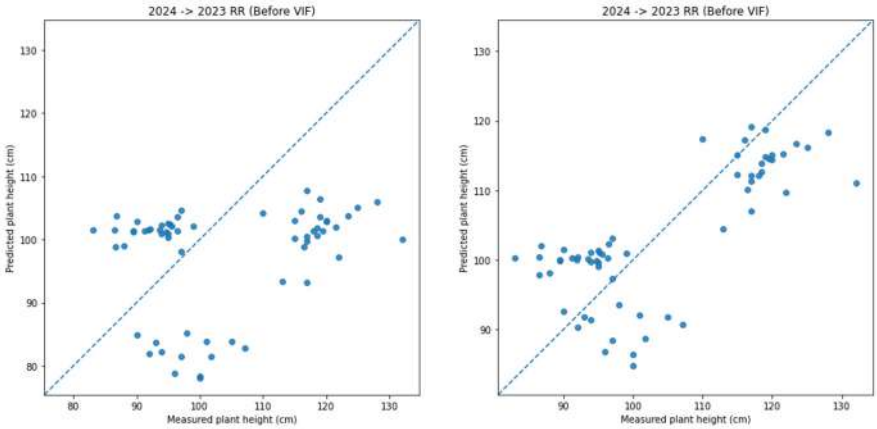

(a) (b)

Fig.2 Observed and predicted pepper plant heights for the 2024-to-2023 cross-year application of RR: (a) VI-only and (b) VI + CP.

For the 2023 models, CP and CSR substantially reduced RMSE when transferred to 2024 and 2025, respectively. However, some environment-augmented models showed stronger horizontal prediction clustering, indicating that improvement in aggregate metrics did not necessarily correspond to improved discrimination of individual plant-height variation. In contrast, none of the environmental variables improved the 2025-to-2023 LR model relative to VI-only, while the 2025-to-2024 improvements remained practically limited because prediction errors were still very large. Overall, the contribution of cumulative environmental variables was dependent on the source–target combination rather than universally beneficial.

EXPLORATORY MULTI-YEAR INTEGRATED ANALYSIS

Because the environmental-variable effects were inconsistent across source–target combinations, the additional exploratory multi-year analysis was examined as an alternative approach for representing a broader range of plant-height and growing conditions.
The integrated dataset consisted of 179 observations covering a plant-height range of 66–144 cm. Among the four algorithms, KNR provided the best balance between calibration and validation performance.

Table 6 Calibration and validation performance of the multi-year integrated models.

Model	R^2_C	RMSE_C (cm)	MAPE_C (%)	R^2_V	RMSE_V (cm)	MAPE_V (%)
RR	0.615	9.863	8.251	0.580	10.20	8.479
LR	0.637	9.579	8.117	0.565	10.28	8.648
KNR	0.660	9.260	7.097	0.688	8.791	6.833
RFR	0.943	3.787	2.780	0.597	9.913	7.368

The integrated KNR used GNDVI, BNDVI, VARI, NLI, and SFDVI and showed validation R^2 = 0.688, RMSE = 8.791 cm, and MAPE = 6.833%. In contrast, RFR showed substantially higher

calibration performance but a larger decrease during validation, indicating a greater calibration–validation gap.

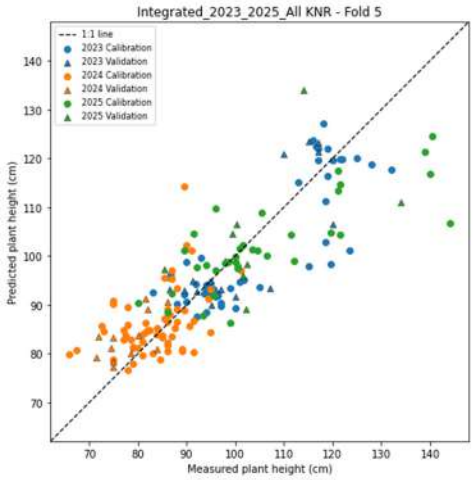

Fig.3 Observed–predicted distribution for Fold 5 of the integrated KNR model.

The integrated KNR predictions were distributed more continuously across the broader plant-height range than the pronounced horizontal bands observed in some year-specific and environment-augmented models. However, prediction-range compression and underestimation remained at greater plant heights, particularly above approximately 120 cm.
The integrated KNR also showed higher RMSE and MAPE than the selected year-specific models. Therefore, the integrated model should not be interpreted as more accurate than the year-specific models. Instead, the results indicate a trade-off between maximizing prediction accuracy under a specific growing season and representing a broader range of multi-year growth conditions within a single modeling framework.
Because all three years were included during development of the integrated model, its internal validation does not demonstrate improved external interannual generalization. Nevertheless, the broader and more continuous prediction distribution suggests that multi-year integration is a useful direction for reducing dependence on narrowly distributed year-specific training data. Independent leave-one-year-out or future-year validation is required to verify its actual interannual transferability.

CONCLUSIONS

This study evaluated the interannual transferability of UAV multispectral-based pepper plant height models using three growing seasons and examined complementary approaches for addressing performance degradation across years.
The selected year-specific models achieved relatively low within-year validation errors; however, their performance substantially deteriorated when transferred directly to other years. These findings demonstrate that within-year accuracy alone is insufficient for evaluating the practical applicability of UAV-based crop growth models and highlight the importance of examining external cross-year performance together with observed–predicted distributions.
Cumulative environmental information improved transferability under specific conditions. In particular, CP substantially improved the 2024-to-2023 RR model in both quantitative metrics and its observed–predicted relationship. However, the effects were source–target dependent, and some numerical improvements were accompanied by increased horizontal clustering.

The exploratory multi-year analysis further showed that integrating observations across growing seasons enabled a broader range of plant heights and growing conditions to be represented within a single model. The integrated KNR produced a relatively continuous prediction distribution and stable validation performance, although its prediction error was higher than that of the year-specific models and underestimation remained at greater plant heights.

Overall, this study provides a practical multi-year framework for evaluating UAV-based plant growth models beyond within-year accuracy and demonstrates the complementary potential of environmental information and multi-year data integration for improving model robustness. These findings provide a foundation for developing more transferable UAV-based crop monitoring systems. Additional multi-year and multi-site datasets, together with independent external validation, will be necessary to further improve and verify interannual generalizability.

ACKNOWLEDGEMENTS

This work was supported by the Technology Innovation Program (RS-2022-KT218635, Development of smart farm management system and growth monitoring) funded by the Ministry of Trade, Industry and Resources (MOTIR, Korea).

REFERENCES

Barnes, E. M., T. R. Clarke, S. E. Richards, P. D. Colaizzi, J. Haberland, M. Kostrzewski, P. Waller, C. Choi, E. Riley, T. Thompson, R. J. Lascano, H. Li, and M. S. Moran. 2000. Coincident detection of crop water stress, nitrogen status and canopy density using ground based multispectral data. In Proc. 5th International Conference on Precision Agriculture. Bloomington, Minn.

Gitelson, A. A., Y. J. Kaufman, and M. N. Merzlyak. 1996. Use of a green channel in remote sensing of global vegetation from EOS-MODIS. Remote Sens. Environ. 58(3): 289-298.

Gitelson, A. A., Y. J. Kaufman, R. Stark, and D. Rundquist. 2002. Novel algorithms for remote estimation of vegetation fraction. Remote Sens. Environ. 80(1): 76-87.

Goel, N. S., and W. Qin. 1994. Influences of canopy architecture on relationships between various vegetation indices and LAI and FPAR: A computer simulation. Remote Sens. Rev. 10(4): 309-347.

Lee, G., J. Hwang, and S. Cho. 2021. A novel index to detect vegetation in urban areas using UAV-based multispectral images. Appl. Sci. 11(8): 3472.

Martins, C. L., M. Pusch, W. A. C. Godoy, and L. R. do Amaral. 2025. Environmental covariates for sampling optimization and pest prediction in soybean crops. AgriEngineering 7(1): 21.

Rouse, J. W., R. H. Haas, J. A. Schell, and D. W. Deering. 1974. Monitoring vegetation systems in the Great Plains with ERTS. In Proc. 3rd Earth Resources Technology Satellite-1 Symposium, 309-317.

Rural Development Administration (RDA). 2020. Chili Peppers—Agricultural Technology Guide 115, Revised Edition. Jeonju, Republic of Korea: Rural Development Administration.

Sun, X., Z. Yang, P. Su, K. Wei, Z. Wang, C. Yang, C. Wang, M. Qin, L. Xiao, W. Yang, M. Zhang, X. Song, and M. Feng. 2023. Non-destructive monitoring of maize LAI by fusing UAV spectral and textural features. Front. Plant Sci. 14: 1158837.

AI-34

Proceedings of The 12th International Symposium on Machinery and Mechatronics for Agriculture and Biosystems Engineering (ISMAB 2026)
20-24 October 2026, Busan, Republic of Korea

INTEGRATED DEEP LEARNING SYSTEM FOR ORAL CANCER SCREENING, RISK STRATIFICATION, AND IMAGE QUALITY ASSURANCE

Jing-Han Jang[1], Cheng-Ying Chou[1],*, Shyh-Jye Chen[2], Jang-Jaer Lee[3], Ling-Ying Wei[3], Ting-Yi Chen[3]

[1] Department of Biomechatronics Engineering, National Taiwan University, Taipei 106, Taiwan
[2] National Taiwan University Hospital Yunlin Branch, Yunlin County 640, Taiwan
[3] Department of Dentistry, National Taiwan University Hospital, Taipei 100229, Taiwan
*Corresponding Author — Email: chenying@ntu.edu.tw

Abstract: Oral cancer continues to impose a substantial global burden of morbidity and mortality. Mobile image-based screening enables preliminary remote assessment using oral images. In addition to identifying lesions and their associated risks, all predefined oral sites must be captured correctly and completely to minimize the effects of incorrectly captured views, missing views, duplicate uploads, and insufficient fields of view on interpretation. This study developed an integrated deep learning system for oral cancer screening comprising oral-site recognition, field-of-view completeness assessment, lesion detection, and three-tier classification into low-, intermediate-, and high-risk categories. Clinical trial images from the Cancer Screening Center and the Department of Dentistry at National Taiwan University Hospital, as well as from Hualien Tzu Chi Hospital, were used for oral-site recognition and field-of-view completeness assessment. The oral-site recognition module achieved an accuracy of 99.45%, while the field-of-view completeness assessment achieved a Dice score of 0.968. The lesion detection and risk classification model was developed using a separate image dataset collected by the Department of Dentistry at National Taiwan University Hospital. At the box level, the model achieved an mAP@0.50:0.95 of 0.440, representing an absolute improvement of 5.07 percentage points over the best-performing single model. At the image level, the model achieved an overall accuracy of 86.46%, with a sensitivity of 97.42% for the high-risk category. When risk categories were disregarded, lesion detection achieved a sensitivity of 98.95% and a specificity of 96.46%. These results demonstrate that the system can verify oral-site coverage and field-of-view quality while simultaneously performing lesion localization and risk stratification, thereby supporting image quality control and preliminary referral decisions in mobile oral cancer screening.

Key Words: Oral Cancer, Deep Learning, Object Detection, Risk Stratification, Oral-Site Recognition

INTRODUCTION

Oral cancer remains a global health problem. Estimates for 2022 show marked geographic variation in cancers of the lip, oral cavity, and pharynx, with oral cavity cancer representing the

largest subsite group (Rumgay et al., 2026). Tobacco, alcohol, and areca-nut or betel-quid exposure account for a large proportion of preventable risk, and organized visual examination remains central to early detection in high-risk populations (Bouvard et al., 2022).

Mobile and remote screening can extend preliminary assessment beyond specialist clinics. Smartphone photographs can support remote review of oral lesions (Vinayagamoorthy et al., 2019). However, diagnostic performance alone does not ensure a reliable screening workflow. Each required oral site must be photographed, the submitted image must match the declared site, and the visible mucosal field must be sufficiently complete. An apparently negative image may otherwise reflect a missing view, an incorrect view, a duplicate upload, or inadequate exposure of the oral cavity rather than the absence of disease.

This study aimed to build and evaluate an integrated deep learning system that combines oral-site recognition, field-of-view completeness assessment, lesion localization, and three-tier risk stratification. The system was designed to provide image-quality checks at upload and to produce lesion-level and image-level outputs that can support preliminary referral decisions.

MATERIALS AND METHODS

System Overview

The workflow contains an acquisition-quality stage followed by lesion analysis (Fig. 1). The first stage verifies the submitted oral site, flags repeated or missing views within a screening session, and estimates the proportion of the image occupied by the visible oral cavity. Images that pass these checks proceed to lesion detection and image-level risk stratification. The system is intended for screening support and quality control rather than definitive diagnosis.

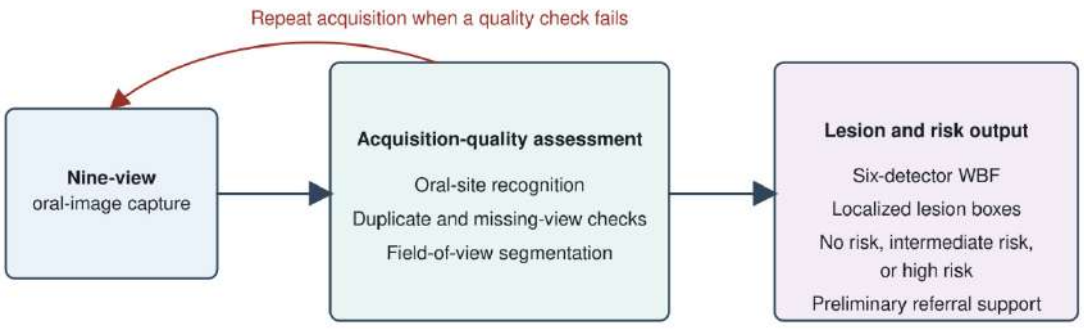

Fig. 1 Integrated workflow for acquisition-quality assessment, lesion localization, and risk stratification.

Data Sources and Task Definitions

Oral-site recognition and field-of-view assessment used clinical-trial images from the National Taiwan University Hospital Cancer Screening Center, the Department of Dentistry at National Taiwan University Hospital, and Hualien Tzu Chi Hospital. The nine views were upper gingiva, palate, right buccal mucosa, right lateral tongue, left lateral tongue, left buccal mucosa, floor of mouth, lower gingiva, and tongue. After quality review, the oral-site dataset contained 4,870

images and was divided by site into 3,414 training, 728 validation, and 728 test images. The segmentation dataset was prepared separately from the same source collections and included 191 held-out test images.

The lesion models used a separate collection from the Department of Dentistry at National Taiwan University Hospital. Green boxes indicated the no-risk category, yellow boxes indicated intermediate risk including precancerous lesions, and red boxes indicated high risk; images without annotated lesions were background. Representative annotations and predictions are shown in Fig. 2. The partitions contained 6,151 training images (6,673 boxes; 1,502 background images), 736 validation images (825 boxes), and 687 test images (869 boxes; 113 background images). Images were acquired with several devices.

For some portrait images, the annotation coordinates were transposed relative to the pixel arrays supplied to the detectors because the annotation and inference pipelines applied EXIF orientation differently. The boxes were transformed into the detector coordinate frame using the EXIF orientation tag, and four sets of duplicated boxes were removed before final evaluation.

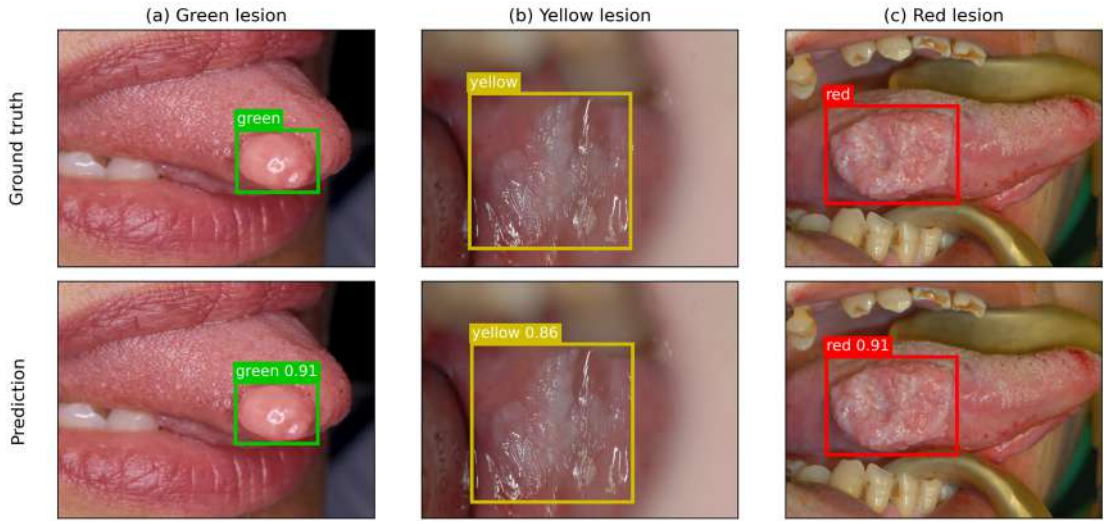

Fig. 2 Representative ground-truth annotations and WBF predictions for no-risk (green), intermediate-risk (yellow), and high-risk (red) findings.

Image Acquisition Quality Modules

Oral-site recognition

MobileNetV4, DINOv3, EfficientNetV2-S, and SwinV2 were compared under a common training pipeline. EfficientNetV2-S was selected for the final module (Tan and Le, 2021). It used 384 x 384 pixel inputs, AdamW optimization, cosine learning-rate scheduling, cross-entropy loss with 0.1 label smoothing, and early stopping. Augmentation included random resized cropping, color jitter, and rotation within 10 degrees. Horizontal flipping was disabled because laterality defines several classes.

At upload, class confidence and the highest-ranked predictions were compared with the user-

declared site. Feature-vector cosine similarity was calculated within each session to flag highly similar repeat uploads, while the session state recorded completed and missing sites.

Field-of-view completeness assessment

SAM 3 generated initial oral-cavity masks from the text prompt 'mouth' (Carion et al., 2025). The masks were visually reviewed and corrected before training. A MobileNetV3-Small encoder (Howard et al., 2019) and U-Net decoder (Ronneberger et al., 2015) formed a lightweight binary segmentation model trained with binary cross-entropy plus Dice loss. The predicted mask was used to calculate visible oral-cavity area as a percentage of all pixels. The prototype flagged images with less than 20% oral-cavity coverage for recapture.

Lesion Detection and Risk Stratification

Eight candidates were trained or screened: YOLOv7, YOLOv8-L, YOLO11-L, YOLOv12-L, YOLO26-L, Mamba-YOLO-B, DEIMv2-S, and DINO-4scale with a ResNet-50 backbone.

Six were retained and retrained for the final ensemble: YOLOv8-L, YOLO11-L, YOLOv12-L, YOLO26-L, DEIMv2-S, and DINO-4scale. The YOLO and DINO inputs were 800 pixels, while DEIMv2-S used 640 pixels. Vertical flipping was disabled because oral photographs have a fixed orientation. The detector families included an attention-centered YOLO architecture (Tian et al., 2025), a denoising DETR model (Zhang et al., 2023), and a real-time DETR pipeline using DINOv3 features (Huang et al., 2025).

Predictions were generated at a confidence threshold of 0.001. Proposals below 0.06 were removed, and the remaining predictions were combined independently by image and category using weighted boxes fusion (WBF) (Solovyev et al., 2021). Clustering thresholds were tuned for each risk category, and fused confidence reflected the number of contributing models. For image-level evaluation, the reference was the most severe annotated category and the prediction was the most severe category above 0.05, using the order high risk, intermediate risk, no risk, and background.

Evaluation Metrics

Oral-site recognition was evaluated using accuracy and macro-averaged F1 score. Segmentation was evaluated using intersection over union (IoU) and Dice score. Lesion localization used class-aware COCO metrics (Lin et al., 2014), including mAP@0.50:0.95, mAP at selected IoU thresholds, and average recall (AR). Image-level evaluation used accuracy, sensitivity, specificity, positive predictive value (PPV), and negative predictive value (NPV).

RESULTS & DISCUSSION

Oral-Site Recognition and Field-of-View Assessment

The oral-site classifier correctly classified 724 of 728 test images, yielding 99.45% accuracy and 99.46% macro-F1 (Fig. 3). Five of the nine classes reached 100% accuracy, and the lowest class accuracy was 98.73%. The field-of-view model achieved an IoU of 0.941 and a

Dice score of 0.968 on 191 test images; site-specific IoU ranged from 0.928 to 0.958. Representative segmentation outputs are shown in Fig. 4. These modules provide complementary checks for anatomical coverage and visible oral-cavity area before lesion analysis.

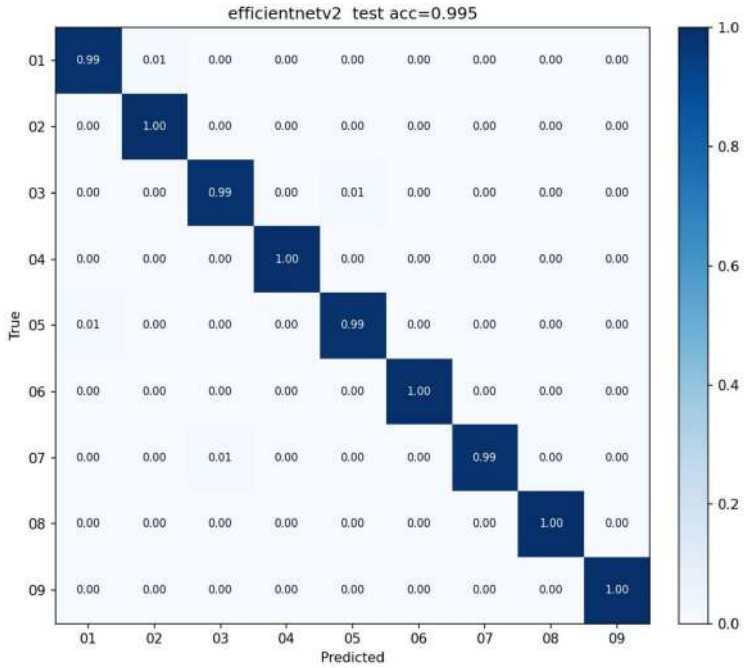

Fig. 3 Row-normalized confusion matrix for the final EfficientNetV2-S oral-site classifier. Codes 01-09 denote the nine predefined oral views.



Fig. 4 Representative oral-cavity segmentation outputs across the predefined oral views. Green overlays indicate the predicted visible oral-cavity regions.

Annotation Coordinate Frame Correction

Correcting the annotation coordinate frame produced the largest preprocessing gain observed in the lesion pipeline. In an intermediate ablation with fusion settings held fixed, no-risk mAP@0.50:0.95 increased from 0.375 to 0.440, while the high- and intermediate-risk values changed by less than 0.002. Overall mAP@0.50:0.95 increased from 0.380 to 0.401. This

finding shows that orientation conventions should be verified before localization errors are attributed to model architecture.

Box-Level Lesion Detection

The six-model WBF ensemble achieved a test mAP@0.50:0.95 of 0.4400, compared with 0.3893 for the best single model, YOLO26-L (Table 1). The absolute gain was 0.0507, or 5.07 percentage points. The ensemble reached mAP@0.50 of 0.6939 and mAP@0.75 of 0.4751. The high-risk and no-risk categories achieved mAP@0.50:0.95 values of 0.5265 and 0.5035, respectively, while intermediate-risk mAP was 0.2899. WBF did not maximize every recall measure: ensemble AR@100 was 0.6437, compared with 0.6701 for DEIMv2-S. Threshold selection therefore remains important when recall and review burden are balanced.

Table 1 Box-level performance on the test partition (687 images).

Method or category	mAP@0.50:0.95	mAP@0.50	mAP@0.75	AR@100
Best single (YOLO26-L)	0.3893	0.6453	0.3970	0.5179
Six-model WBF	**0.4400**	**0.6939**	**0.4751**	**0.6437**
WBF - no risk	0.5035	0.7491	0.5744	0.6489
WBF - high risk	0.5265	0.7988	0.5656	0.6945
WBF - intermediate	0.2899	0.5337	0.2855	0.5876

Image-Level Risk Stratification

Image-level accuracy was 86.46% across 687 test images (Table 2 and Fig. 5). High-risk sensitivity was 97.42%; specificity and PPV were 79.88% and 83.33%. Intermediate-risk sensitivity was lower at 48.76%, and 58 of 121 intermediate-risk images were classified as high risk. When the three lesion categories were collapsed into a single lesion-present class, sensitivity was 98.95%, specificity was 96.46%, PPV was 99.30%, and NPV was 94.78%. The system was therefore more reliable for detecting any lesion than for assigning the intermediate tier, and its output should be used for screening prioritization rather than histopathologic diagnosis.

Table 2 Image-level performance on the test partition (687 images).

Class	Images	Sensitivity	Specificity	PPV	NPV
No risk	104	82.69%	99.14%	94.51%	96.98%
High risk	349	97.42%	79.88%	83.33%	96.77%
Intermediate risk	121	48.76%	97.53%	80.82%	89.90%
Background	113	96.46%	98.95%	94.78%	99.30%
Overall (weighted)	**687**	**86.46%**	**89.04%**	**86.47%**	**96.01%**
Any lesion	**574**	**98.95%**	**96.46%**	**99.30%**	**94.78%**

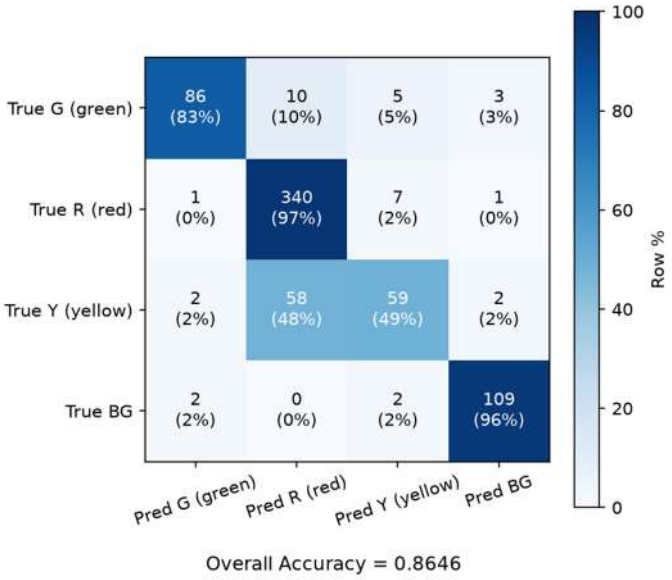

Fig. 5 Image-level confusion matrix for the six-model WBF ensemble. Cells show counts and row-normalized percentages.

Integrated Workflow and Study Limitations

The values reported here are internal development estimates. The oral-site data were divided at the image level, and patient-level independence across the image partitions has not been fully established for both collections. The risk model was also developed from a single-institution collection. Patient-grouped re-splitting and prospective external evaluation across institutions and devices are therefore required before clinical deployment.

The test set was also sensitive to sampling: random half-splits differed in mAP@0.50:0.95 by approximately 0.034. Across five prediction pools, the best validation scores were 0.466 to 0.468 with a standard deviation of 0.0004, limiting their ability to distinguish candidate systems. Detection was lower for images with a long side above 1,900 pixels (mAP@0.50 = 0.496) than for images below 800 pixels (0.734), and exploratory tiling did not improve performance.

CONCLUSIONS

The integrated system verified oral sites and field of view while localizing lesions and assigning screening risk. Oral-site accuracy was 99.45%, segmentation Dice was 0.968, WBF mAP@0.50:0.95 was 0.4400, and image-level accuracy was 86.46%. High-risk and any-lesion sensitivities were 97.42% and 98.95%. Future work should improve intermediate-risk discrimination and use patient-independent, multicenter prospective evaluation.

ACKNOWLEDGEMENTS

The authors gratefully acknowledge the National Taiwan University Hospital Cancer Screening Center and the Department of Dentistry for their support in image collection and annotation, as well as Hualien Tzu Chi Hospital for providing clinical images used in the image quality assurance modules.

REFERENCES

Bouvard, V., S. T. Nethan, D. Singh, et al. 2022. IARC perspective on oral cancer prevention. N. Engl. J. Med. 387(21): 1999-2005.

Carion, N., L. Gustafson, Y.-T. Hu, et al. 2025. SAM 3: Segment anything with concepts. arXiv:2511.16719.

Howard, A., M. Sandler, G. Chu, et al. 2019. Searching for MobileNetV3. In Proc. IEEE/CVF Intl. Conf. on Computer Vision, 1314-1324.

Huang, S., Y. Hou, L. Liu, X. Yu, and X. Shen. 2025. Real-time object detection meets DINOv3. arXiv:2509.20787.

Lin, T.-Y., M. Maire, S. Belongie, et al. 2014. Microsoft COCO: Common objects in context. In Computer Vision - ECCV 2014, 740-755. Cham, Switzerland: Springer.

Ronneberger, O., P. Fischer, and T. Brox. 2015. U-Net: Convolutional networks for biomedical image segmentation. In Medical Image Computing and Computer-Assisted Intervention, 234-241. Cham, Switzerland: Springer.

Rumgay, H., M. Colombet, A. Ramos da Cunha, et al. 2026. Global incidence of lip, oral cavity, and pharyngeal cancers by subsite in 2022. CA Cancer J. Clin. 76(1): 1-13.

Solovyev, R., W. Wang, and T. Gabruseva. 2021. Weighted boxes fusion: Ensembling boxes from different object detection models. Image Vis. Comput. 107: 104117.

Tan, M., and Q. V. Le. 2021. EfficientNetV2: Smaller models and faster training. In Proc. 38th Intl. Conf. on Machine Learning, 10096-10106. PMLR 139.

Tian, Y., Q. Ye, and D. Doermann. 2025. YOLOv12: Attention-centric real-time object detectors. In Advances in Neural Information Processing Systems 38.

Vinayagamoorthy, K., S. Acharya, M. Kumar, K. C. Pentapati, and S. Acharya. 2019. Efficacy of a remote screening model for oral potentially malignant disorders using a free messaging application: A diagnostic test for accuracy study. Aust. J. Rural Health 27(2): 170-176.

Zhang, H., F. Li, S. Liu, et al. 2023. DINO: DETR with improved denoising anchor boxes for end-to-end object detection. In Proc. Intl. Conf. on Learning Representations.

Field Machinery and Systems 3 (FM-3)



FM-14

Proceedings of The 12th International Symposium on Machinery and Mechatronics for Agriculture and Biosystems Engineering (ISMAB 2026)
20-24 October 2026, Busan, Republic of Korea

MULTIVARIATE MOBILITY ANALYSIS OF LUNAR ROVER WHEELS USING NUMERICAL METHOD UNDER LUNAR GRAVITY

Moo-Young Oh[1], Ju-Hyeon Ahn[1], Dan-A Kim[1], Se-Hee Park[1], Ji-Tae Kim[1,2*]

[1]Department of Convergence Biosystems Engineering, Chonnam National University, 77 Yongbong-ro, Buk-gu, Gwangju 61186, Republic of Korea
[2]Institute of Agricultural Science & Technology, Chonnam National University, 77 Yongbong-ro, Buk-gu, Gwangju 61186, Republic of Korea
*Corresponding Author-- Voice: +82-62-530-5188, Email: jtkim@jnu.ac.kr

Abstract: The mobility of a vehicle operating on deformable terrain is governed not only by system-level and wheel-level design variables but also by the interactions among them. Accurate prediction and evaluation of mobility therefore require that the combined effects of these variables be analyzed within a common design space. This study used discrete element simulation to analyze the combined effects of lunar rover wheel design variables — wheel radius, grouser height ratio, grouser spacing, and axle load per unit width — on mobility under lunar gravity. The design space was constructed using a four-factor Box–Behnken design comprising 27 conditions. Drawbar-pull load was applied to a wheel rotating at constant angular velocity so that slip developed from the relative motion between the wheel and the terrain, and the load was increased incrementally so that mobility could be evaluated as a function of slip. Of the 27 conditions, 19 satisfied the screening criterion applied at the self-propelled condition (slip $\leq$ 20%). For the retained conditions, slip, normalized dynamic sinkage, and power number increased with normalized drawbar-pull load, whereas tractive efficiency increased and then decreased. The effects of grouser height and spacing on power number were reversed between comparisons at equal drawbar load and at equal slip, while their effects on tractive efficiency were unchanged. These results indicate that the apparent effect of grouser geometry depends on the operating condition at which designs are compared, and support a staged wheel-design approach in which wheel size and loading are selected first and grouser geometry is then adjusted to manage the tractive efficiency–power number trade-off at the target operating condition.

Key Words: Lunar exploration rover, Discrete element method, Terramechanics, Box–Behnken design, Response surface methodology

INTRODUCTION

Lunar rover wheels generate thrust by compacting and shearing deformable lunar soil. Consequently, slip, sinkage, and traction performance are governed by wheel–soil interaction (Wong, 2010). These responses depend on wheel size, surface geometry, operating conditions, and environmental conditions (Ding et al., 2010; Skonieczny et al., 2012; Karpman et al., 2020). Because these factors interact, the effect of an individual design variable may change with the

wheel configuration and environment (Inotsume et al., 2019). Therefore, their coupled effects under lunar gravity should be evaluated separately for self-propelled and externally loaded conditions.

Kim et al. (2025) developed a discrete element method (DEM) model that represents the material behavior of Korea Lunar Simulant-1 (KLS-1; Ryu et al., 2018), together with a virtual single-wheel analysis procedure, and evaluated mobility responses for selected design variables.

The objectives of this study were to evaluate the combined effects of wheel radius, grouser-height ratio, grouser spacing, and load per unit width within a common design space and to determine whether the effects of grouser geometry on tractive efficiency (TE) and power number (PN) differ between comparisons at equal drawbar load and at equal slip.

MATERIALS AND METHODS

Experimental design and numerical analysis

A four-factor, three-level Box–Behnken design (BBD) comprising 27 conditions was constructed using wheel radius R, grouser-height ratio H, grouser spacing S, and load per unit width W/b (Box and Behnken, 1960). The grouser-height ratio was defined as $H = 100h/R$, where h is the grouser height and R is the wheel radius. Wheel width b was fixed at 0.16 m, and W/b was used as the loading variable (Table 1). All simulations were conducted under lunar gravity with a theoretical wheel rim speed $R\omega$ of 0.30 m/s. Mean responses were calculated over the 4–6 s quasi-steady interval at each drawbar-load step (Fig. 1).

Table 1 Factors and levels of the Box–Behnken design.

Factor	Symbol	−1	0	+1
Wheel radius (m)	*R*	0.10	0.13	0.16
Grouser-height ratio (%)	*H*	5	10	15
Grouser spacing (deg)	*S*	15	30	45
Load per unit width (N/m)	*W/b*	400	600	800

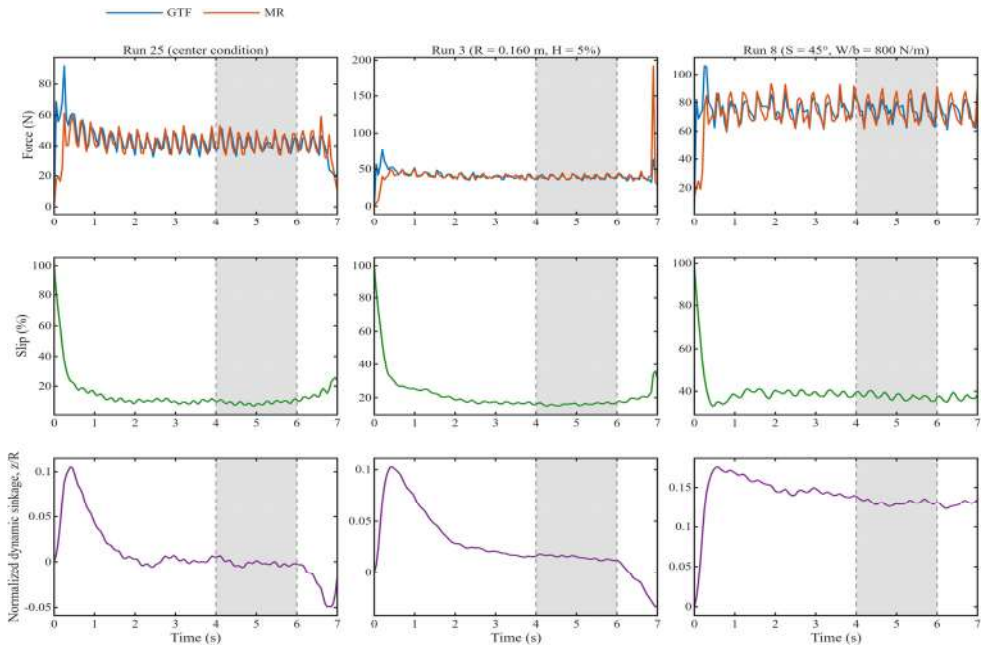

Fig.1 Time histories of GTF, MR, slip, and signed normalized dynamic sinkage for BBD Runs 25, 3, and 8. Shading indicates the 4–6 s quasi-steady averaging interval.

Screening criteria and response-surface modeling

Mobility performance was characterized using gross traction force (GTF), motion resistance (MR), drawbar pull (DP), slip (s), tractive efficiency (TE), and power number (PN), as defined in Eqs. (1)–(4).

$$GTF = T/R, \quad DP = GTF - MR \tag{1}$$

$$s = (1 - v/(\omega R)) \times 100 \tag{2}$$

$$TE = (DP/GTF)(100 - s) \tag{3}$$

$$PN = P/(Wv) = E/(Wd), \quad P = T\omega \tag{4}$$

where:

GTF = gross traction force (N)
T = wheel torque (N·m)
R = wheel radius (m)
DP = drawbar pull (N)
MR = motion resistance (N)
s = slip (%)
v = actual travel speed (m/s)
ω = wheel angular velocity (rad/s)
TE = tractive efficiency (%)
PN = power number (-)
P = wheel-shaft mechanical power (W)
W = vertical wheel load (N)
E = mechanical travel energy (J)
d = travel distance (m)
DP/W = normalized drawbar load (-)

At the self-propelled condition (DP/W = 0), designs with slip ≤ 20% were retained for subsequent traction-performance analysis. This threshold was used to exclude conditions with excessive speed loss and was not interpreted as an absolute immobility limit. Signed dynamic

sinkage z was defined relative to the wheel position at the onset of driving, with positive values denoting additional downward displacement and negative values denoting upward displacement relative to this reference position. Normalized sinkage z/R was used for comparisons among designs. For the retained designs, DP/W was varied from 0 to 0.25, and slip, z/R, TE, and PN were compared. This drawbar-load-controlled procedure differs from forced-slip testing, in which slip is prescribed (Liang et al., 2014). For the comparison at equal drawbar load, TE and PN were averaged over the common loading range DP/W = 0.05–0.25. For the comparison at equal slip, TE and PN at a common slip of 20% were estimated for each design whose observed slip range included 20%, using a piecewise cubic Hermite interpolating polynomial (PCHIP) without extrapolation. This comparison at equal slip follows earlier lunar-vehicle wheel evaluations that reported power number as a function of slip (Freitag et al., 1970).

A second-order response surface model (RSM) containing linear, pure quadratic, and two-factor interaction terms for the coded R, H, S, and W/b was fitted to each response (Montgomery, 2017). Reduced models were obtained by hierarchy-preserving backward elimination of statistically nonsignificant terms. The signs of the coded linear H and S coefficients were used to compare model tendencies more directly around the coded center point between the two operating-condition analyses. Because the models contained quadratic and interaction terms, these coefficients were not interpreted as global effects over the entire design space.

RESULTS & DISCUSSION

Self-propelled responses and screening outcomes

Of the 27 conditions, 19 satisfied the self-propelled slip criterion of 20%, whereas eight exceeded it. As shown in Fig. 2, most conditions that exceeded the criterion also exhibited relatively large positive dynamic sinkage, indicating substantial additional downward wheel displacement after the onset of driving. This pattern is consistent with inefficient conversion of wheel rotation into forward motion accompanied by greater vertical soil deformation.

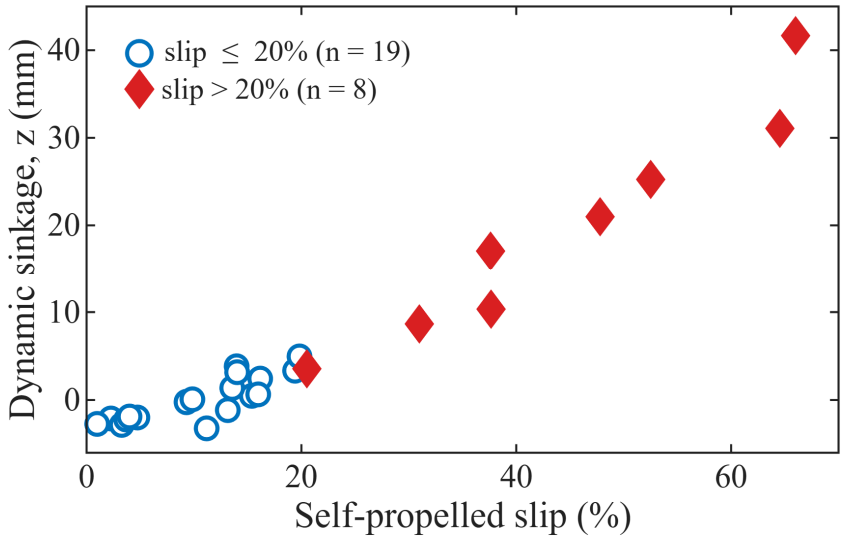

Fig.2 Self-propelled slip and signed dynamic sinkage for the 27 BBD conditions.

Across the 19 retained conditions, as DP/W increased from 0 to 0.25, the median values of slip, z/R, and PN increased from 11.20% to 70.65%, from −0.001 to 0.377, and from 0.475 to 2.565, respectively. Median TE increased to 14.13% at DP/W = 0.15 and then decreased to

9.43% at DP/W = 0.25. Thus, TE exhibited a peak response, whereas PN increased monotonically.

TE–PN responses at equal drawbar load and equal slip

At equal drawbar load, slip and travel speed differed among designs. At a common slip of 20%, the normalized speed loss was fixed, whereas the supported DP/W and required torque differed among designs. The signs of the coded linear H and S coefficients for TE were unchanged between the two comparisons, whereas those for PN were reversed (Table 2). The predicted H–S responses of PN under the two comparison conditions are shown in Fig. 3.

Table 2 Coded linear H and S coefficients under the two comparison conditions.

Response	*H* coefficient	*H* p-value	*S* coefficient	*S* p-value
Range-averaged TE	+0.541	<0.001	−0.317	<0.001
Range-averaged PN	−0.352	<0.001	+0.162	<0.001
TE at slip = 20%	+8.299	<0.001	−4.936	<0.001
PN at slip = 20%	+0.103	<0.001	−0.045	<0.001

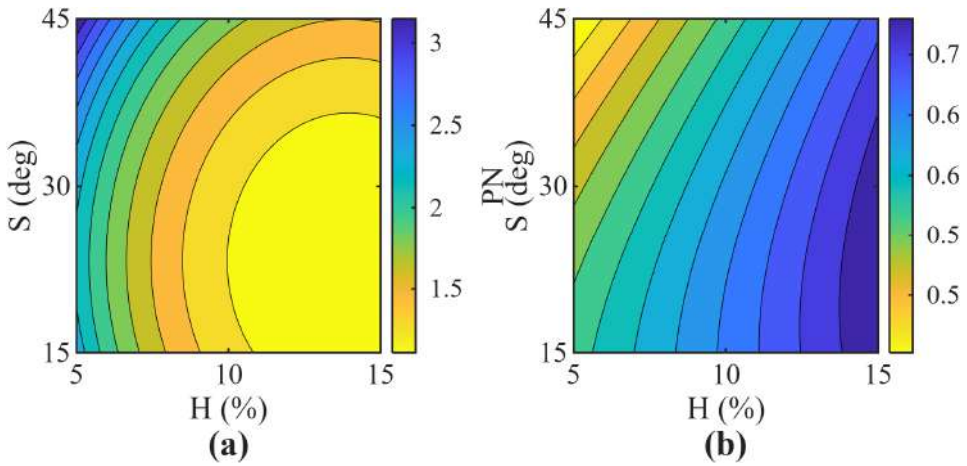

Fig.3 Predicted H–S response of PN at coded R = 0 and W/b = 0: (a) range-averaged PN over DP/W = 0.05–0.25 and (b) PN at slip = 20%.

At coded R = 0 and W/b = 0, the predicted response in Fig. 3(a) showed decreasing range-averaged PN with increasing H and increasing PN with increasing S; these trends reversed at equal slip in Fig. 3(b). Thus, taller grousers and narrower spacing were associated with lower speed loss and lower PN under a common traction demand. At the same slip, however, the same geometry was associated with greater supported drawbar load, higher required torque, and consequently higher PN. These results indicate that the predicted grouser-geometry trends depend on the operating condition used for comparison; therefore, TE and PN should be evaluated together.

CONCLUSIONS

Among the 27 coupled design conditions evaluated for KLS-1 under lunar gravity, 19 satisfied the self-propelled screening criterion. As normalized drawbar load DP/W increased, slip, z/R, and PN increased, whereas TE increased and then decreased. The reversal of the predicted PN trends associated with H and S between comparisons at equal drawbar load and at equal slip suggests a staged design approach in which wheel size and loading conditions are selected first, followed by adjustment of grouser geometry to manage the TE–PN trade-off at the target operating condition.

ACKNOWLEDGEMENTS

This work was supported by Chonnam National University (Grant No. 2024-1937-01).

REFERENCES

Box, G. E. P., and D. W. Behnken. 1960. Some new three level designs for the study of quantitative variables. Technometrics 2(4): 455-475.

Ding, L., H. Gao, Z. Deng, and J. Tao. 2010. Wheel slip-sinkage and its prediction model of lunar rover. J. Central South Univ. Tech. 17: 129-135.

Freitag, D. R., A. J. Green, and K. J. Melzer. 1970. Performance evaluation of wheels for lunar vehicles. Technical Report M-70-2. Vicksburg, Miss.: U.S. Army Engineer Waterways Experiment Station.

Inotsume, H., S. Moreland, K. Skonieczny, and D. Wettergreen. 2019. Parametric study and design guidelines for rigid wheels for planetary rovers. J. Terramech. 85: 39-57.

Karpman, E., J. Kovecses, D. Holz, and K. Skonieczny. 2020. Discrete element modelling for wheel-soil interaction and the analysis of the effect of gravity. J. Terramech. 91: 139-153.

Kim, J. T., T. K. Yeu, and Y. J. Park. 2025. Development of a numerical model for KLS-1 and mobility analyses based on the effects of design variables. Adv. Space Res. 75: 8357-8373.

Liang, Z., H. Gao, L. Ding, Z. Deng, and J. Qu. 2014. Analysis of driving efficiency for LRV wheels using forced-slip method. Adv. Space Res. 54: 2122-2130.

Montgomery, D. C. 2017. *Design and Analysis of Experiments*. 9th ed. Hoboken, N.J.: John Wiley & Sons.

Ryu, B. H., C. C. Wang, and I. Chang. 2018. Development and geotechnical engineering properties of KLS-1 lunar simulant. J. Aerospace Eng. 31: 04017083.

Skonieczny, K., S. J. Moreland, and D. S. Wettergreen. 2012. A grouser spacing equation for determining appropriate geometry of planetary rover wheels. In *Proc. IEEE/RSJ Intl. Conf. on Intelligent Robots and Systems*. Vilamoura, Portugal: IEEE.

Wong, J. Y. 2010. *Terramechanics and Off-Road Vehicle Engineering: Terrain Behaviour, Off-Road Vehicle Performance and Design*. 2nd ed. Oxford, U.K.: Butterworth-Heinemann.

FM-15

GUSWProceedings of The 12th International Symposium on Machinery and Mechatronics for Agriculture and Biosystems Engineering (ISMAB 2026)
20-24 October 2026, Busan, Republic of Korea

DEVELOPMENT OF AN EEPA-BASED DEM MODEL FOR PREDICTING CULTIVATOR-SWEEP FORCES UNDER DIFFERENT SOIL WATER CONTENTS

Dae-Wi Jeong[1], Min-Seung Kim[1], Se-O Choi[1], Shin-Young Noh[1], Ye-Na Lee[1], Yeon-Soo kim[1,2,3*], Jae-Sung Park[1,3], and Yong-Joo kim[4,5,6]

[1] Department of Bio-Industrial Machinery Engineering, Pusan National University, Miryang 50463, Republic of Korea
[2] Major of Natural Resources Systems Engineering, Pusan National University, Yangsan 50612, Republic of Korea
[3] Life and Industry Convergence Research Institute, Pusan National University, Miryang 50463, Republic of Korea
[4] Eco-Friendly Hydrogen and Electric Agricultural Machinery Research Institute, Chungnam National University, Daejeon 34134, Republic of Korea
[5] Department of Smart Agricultural Systems and Mechanical Engineering, Chungnam National University, Daejeon 34134, Republic of Korea
[6] Department of Smart Agriculture Systems, Chungnam National University, Daejeon 34134, Republic of Korea
*Corresponding Author--Voice: +8201-7748-6990, Email: yskim23@pusan.ac.kr

Abstract: Accurate prediction of soil–tool forces is important for evaluating the performance and loading characteristics of soil-engaging agricultural machinery. This study investigated the effects of soil water content and operating speed on cultivator-sweep forces and evaluated an Edinburgh Elasto-Plastic Adhesion (EEPA)-based discrete element method (DEM) model using independently established soil–steel interaction parameters. Soil-bin experiments were conducted using sandy loam soil at gravimetric water contents of 10, 15, 20, and 25% and horizontal operating speeds of 500, 750, and 1000 mm min^{-1}. Draft force (Fx) and vertical reaction force (Fy) were measured with four repetitions for each condition. The DEM model was evaluated at 1000 mm min^{-1} using moisture-dependent EEPA parameters previously established from cone-based soil–steel adhesion tests without recalibration using cultivator-sweep force measurements. Water content and operating speed significantly affected both Fx and Fy, whereas their interaction was not significant. The effect of water content was considerably greater than that of operating speed. Both force components followed the order 10% < 15% < 25% < 20%, with the highest resistance occurring at 20% water content. The DEM model reproduced the same water-content-dependent order for maximum Fx and Fy. The mean relative errors of the predicted maximum forces were 9.837% for Fx and 9.996% for Fy. These results indicate that moisture-dependent EEPA parameters established independently from cone-based soil–steel interaction retained predictive capability for maximum cultivator-sweep loading under the tested conditions.

Key Words: Discrete element method, EEPA, Soil–tool interaction, Cultivator sweep, Soil water content

INTRODUCTION

Reliable prediction of soil–tool interaction is important for the design and operation of agricultural soil-engaging machinery (Chen et al., 2013). During soil cutting, soil compression, shear failure, friction, adhesion, and displacement collectively generate resistance forces acting on the tool. These forces are commonly resolved into horizontal draft force and vertical reaction force. Draft force is directly related to traction and power requirements, whereas vertical reaction influences working-depth stability and structural loading.

The discrete element method (DEM) has been widely applied to simulate soil–tool interaction because it can represent particle rearrangement, soil accumulation, transient force development, and large soil deformation (Coetzee and Els, 2009; Chen et al., 2013; Aikins et al., 2021). However, the predictive capability of DEM strongly depends on the selected contact model and its parameterization. Many contact parameters cannot be measured directly and are therefore calibrated using macroscopic responses such as compression, penetration, shear, or soil–tool force. Consequently, a parameter set that reproduces one calibration response may not necessarily retain the same predictive capability under a different soil–tool configuration.

The Edinburgh Elasto-Plastic Adhesion (EEPA) contact model is suitable for representing cohesive and moisture-sensitive granular materials because it incorporates loading-history-dependent elastic–plastic deformation and adhesive contact behavior (Thakur et al., 2014). In the authors' preceding studies, moisture-dependent soil–steel adhesion and EEPA parameters for sandy loam soil were established using cone-based experiments (Jeong et al., 2025; Jeong et al., 2026). However, cone penetration and cultivator-sweep cutting involve different tool geometries, loading directions, and soil deformation mechanisms. Independent evaluation under sweep-cutting conditions is therefore necessary to determine whether the established parameter set can predict soil-engaging tool forces without direct fitting to the measured sweep force.

Water content and operating speed are also important factors governing soil–tool resistance. Changes in water content can modify soil consistency, inter-particle bonding, friction, plastic deformation, and soil–steel adhesion(Abbaspour-Gilandeh et al., 2018; Jeong et al., 2025), whereas operating speed can affect inertia, deformation rate, and development of the mobilized soil region.

Accordingly, the objective of this study was to investigate the effects of soil water content and operating speed on cultivator-sweep forces and to evaluate whether independently established moisture-dependent EEPA parameters could predict the maximum draft and vertical forces without recalibration using measured sweep-force data.

MATERIALS AND METHODS

Soil preparation and experimental conditions

Sandy loam soil collected from an upland agricultural field was used in this study. The soil consisted of 73.8% sand, 11.8% silt, and 14.4% clay. Its plastic and liquid limits were 9.282 and 25.723%, respectively. Four target gravimetric water contents of 10, 15, 20, and 25% were selected to represent soil conditions ranging from near the plastic limit to near the liquid limit.

The collected soil was oven-dried, crushed, and passed through a 2-mm sieve. The required amount of water was added to achieve each target water content, after which the soil was thoroughly mixed and allowed to equilibrate. The prepared soil was placed in the soil bin and compacted using the same filling, tamping, and leveling procedure for all experiments. The measured water contents were 9.91 ± 0.05, 14.89 ± 0.07, 20.04 ± 0.06, and 24.89 ± 0.13%, respectively.

Soil-bin cultivator-sweep experiment

Blade-cutting experiments were conducted using a custom-built soil-bin system consisting of an acrylic soil bin, an X–Y positioning stage, a two-axis force-measurement assembly, and a data-acquisition system. The internal dimensions of the soil bin were 285 × 140 mm, and the prepared soil-bed depth was 40 mm. The experimental setup is shown in Fig. 1(a).

The soil-engaging tool was an SS401 cultivator sweep with a width of 30 mm, thickness of 5 mm, rake angle of 30°, and sweep angle of 74°, as shown in Fig. 1(b). The working depth was fixed at 30 mm. Horizontal operating speeds of 500, 750, and 1000 mm min^{-1} were applied over a cutting distance of 100 mm.

Four independent repetitions were conducted for each combination of four water-content conditions (10, 15, 20, and 25%) and three operating speeds, resulting in a total of 48 experiments. Draft force (Fx) and vertical reaction force (Fy) were measured using a two-axis load cell, and the mean force over the horizontal cutting interval was used for statistical analysis.

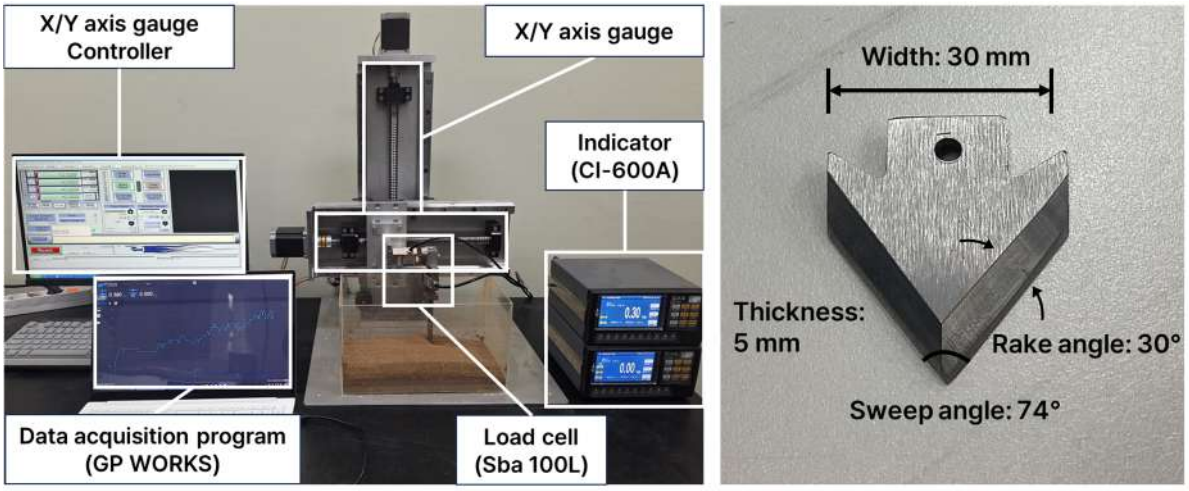

Fig.1 Soil-bin experimental apparatus and cultivator sweep geometry: (a) experimental setup for measuring draft and vertical forces, and (b) dimensions and angles of the SS401 cultivator sweep.

DEM simulation and model evaluation

An EEPA-based DEM model was developed to reproduce the soil–cultivator sweep interaction under the same geometric and operating conditions as the soil-bin experiment. The moisture-dependent DEM parameters were adopted from the authors' preceding cone-based calibration study and transferred to the present cultivator-sweep model without recalibration using the measured sweep-force data.

DEM simulations were conducted at 1000 mm min^{-1} for water contents of 10, 15, 20, and 25%. Experimental and simulated results were compared using the maximum draft force (Fx) and vertical reaction force (Fy). In addition, the particle-force distribution and soil accumulation around the cultivator sweep were examined qualitatively to visualize the development of soil–tool interaction during horizontal cutting. The relative error was calculated as:

$$RE = \frac{|F_p - F_e|}{F_e} \times 100 \quad (1)$$

Where:
$F_p = Predicted\ \ force\ \ (N)$
$F_e = Experimental\ \ force(N)$

RESULTS & DISCUSSION

Effects of water content and operating speed on cultivator-sweep forces

The measured draft force (F_x) and vertical reaction force (F_y) varied substantially with soil water content. When averaged across the three operating speeds, the mean F_x values were 1.431, 4.132, 6.670, and 4.842 N at water contents of 10, 15, 20, and 25%, respectively. The corresponding mean F_y values were 0.189, 1.290, 2.144, and 1.564 N. Thus, both force components followed the order 10% < 15% < 25% < 20%.

Operating speed also affected the measured forces, although its influence was smaller than that of water content. When averaged across the four water-content conditions, mean F_x increased from 4.115 N at 500 mm min⁻¹ to 4.487 N at 1000 mm min⁻¹, while mean F_y increased from 1.269 to 1.366 N.

Two-way ANOVA showed significant main effects of water content and operating speed on both F_x and F_y ($p<0.001p < 0.001$), whereas the water-content × operating-speed interaction was not significant ($p>0.05p > 0.05$). Water content showed substantially larger effect sizes than operating speed, with partial $\eta_p{}^2$ values of 0.989 and 0.991 for F_x and F_y, respectively. These results indicate that soil moisture state was the dominant factor governing cultivator-sweep resistance within the tested operating range.

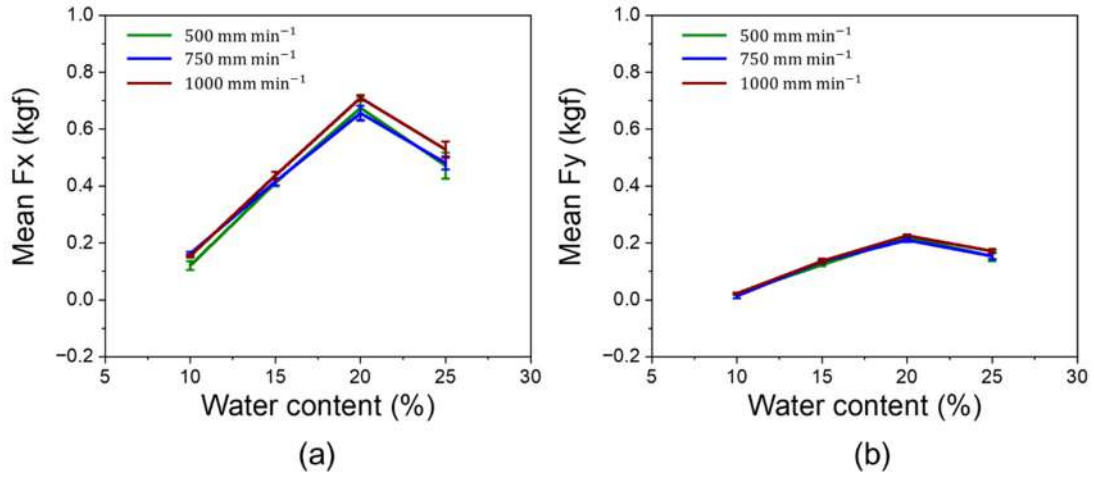

Fig.2 Effects of water content and operating speed on mean (a) draft force and (b) vertical reaction force. Values represent mean ± SD (n = 4).

The nonlinear response to water content was consistent with the moisture-dependent soil–steel adhesion reported in the authors' preceding studies (Jeong et al., 2025; Jeong et al., 2026). Soil–steel adhesive strength increased from 0.104 kPa at 10% water content to a maximum of 1.083 kPa at 20%, and subsequently decreased to 0.880 kPa at 25%. The highest cultivator-sweep resistance therefore coincided with the condition exhibiting the greatest measured soil–steel adhesion. However, the change in sweep resistance cannot be attributed

to adhesion alone because water content also affects inter-particle bonding, friction, and plastic deformation. The reduction in force at 25% water content, which approached the measured liquid limit of 25.723%, may additionally reflect increased plastic flow and lubrication under the wetter soil condition (Abbaspour-Gilandeh et al., 2018).

DEM prediction of maximum cultivator-sweep forces

The cone-based EEPA parameters were applied without recalibration using measured sweep-force data. At 1000 mm min^{-1}, the DEM reproduced the experimental maximum-force order of 10% < 15% < 25% < 20% for both Fx and Fy. Relative errors for maximum Fx ranged from 5.829 to 13.412%, while the MREs were 9.837% for Fx and 9.996% for Fy. The 20% water-content condition, which showed the highest experimental and simulated resistance, was selected for visualization.

Figure 3 shows the particle-force response at 20% water content. Elevated particle forces developed near the cutting edge and expanded into the mobilized soil during cutting. The spatial response was used qualitatively, whereas quantitative evaluation was based on measured Fx and Fy. These results indicate that the independently calibrated EEPA parameters retained predictive capability under cultivator-sweep cutting.

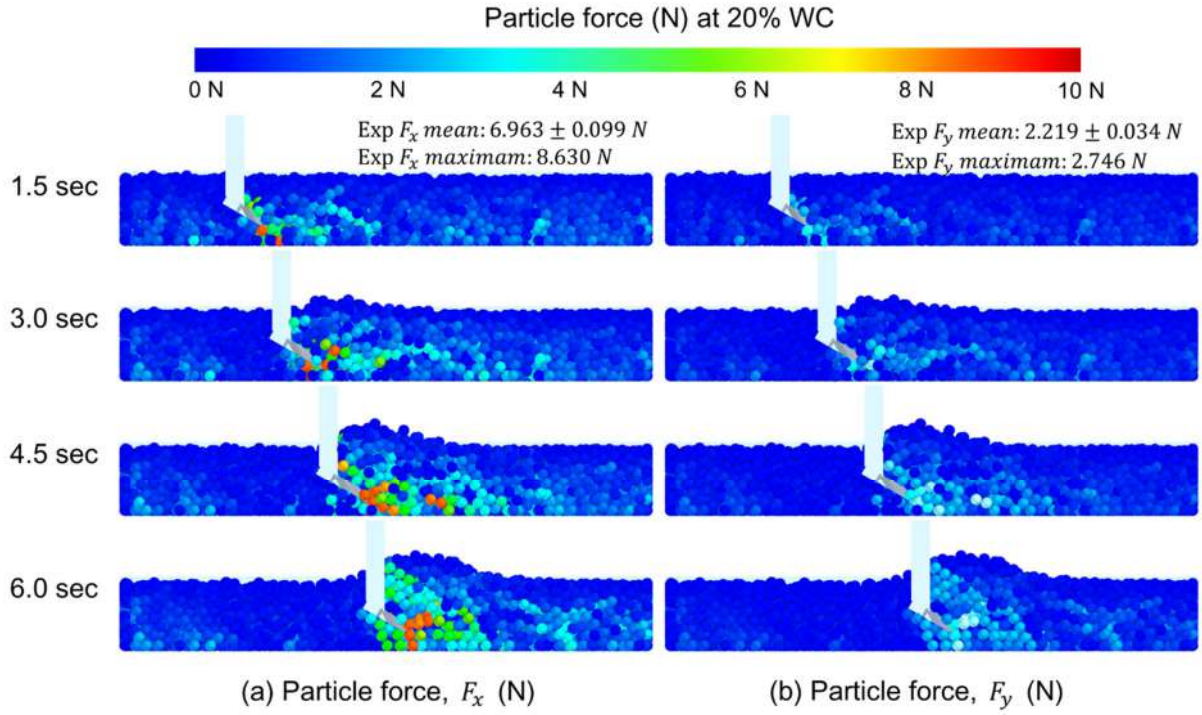

Fig.3 DEM-predicted soil–blade response at 20% water content.

CONCLUSIONS

The main conclusions are as follows:

1. Water content and operating speed significantly affected both draft and vertical forces, whereas their interaction was not significant. Water content had the substantially greater effect, and both force components followed the order 10% < 15% < 25% < 20%.
2. The highest soil–sweep resistance occurred at 20% water content, which also corresponded to the maximum independently measured soil–steel adhesive strength. Further increasing water content to 25% reduced both force components.

3. Without recalibration using cultivator-sweep force measurements, the cone-based EEPA model reproduced the complete water-content-dependent order of maximum force. The MREs were 9.837% for maximum draft force and 9.996% for maximum vertical reaction force, demonstrating the predictive capability of the transferred parameter set under the tested conditions.

These results provide a basis for applying independently calibrated moisture-dependent DEM models to predict tool loading and visualize soil–tool interaction in the virtual evaluation of soil-engaging agricultural machinery.

ACKNOWLEDGEMENTS (optional)

This work was supported by the Ministry of Agriculture, Food and Rural Affairs (MAFRA), through the Korea Institute of Planning and Evaluation for Technology in Food, Agriculture and Forestry (IPET), under the Offload Smart Agricultural Utilization Model Development Project (RS-2025-02313136).

REFERENCES

Abbaspour-Gilandeh, Y., F. Hasankhani-Ghavam, G. Shahgoli, V. R. Shrabian, and M. Abbaspour-Gilandeh. 2018. Investigation of the effect of soil moisture content, contact surface material and soil texture on soil friction and soil adhesion coefficients. *Acta Technologica Agriculturae* 21: 44-50.

Aikins, K. A., M. Ucgul, J. B. Barr, T. A. Jensen, D. L. Antille, and J. M. A. Desbiolles. 2021. Determination of discrete element model parameters for a cohesive soil and validation through narrow point opener performance analysis. *Soil and Tillage Research* 213: 105123.

Chen, Y., L. J. Munkholm, and T. Nyord. 2013. A discrete element model for soil-sweep interaction in three different soils. *Soil and Tillage Research* 126: 34-41.

Coetzee, C. J., and D. N. J. Els. 2009. Calibration of granular material parameters for DEM modelling and numerical verification by blade-granular material interaction. *Journal of Terramechanics* 46: 15-26.

Jeong, D.-W., B.-M. Bae, M.-S. Kim, S.-O. Choi, S.-Y. Noh, Y.-S. Kim, and Y.-J. Kim. 2025. Effect of soil texture and water content on the soil-material adhesion force. *Precision Agriculture Science Technology* 7: 103-113.

Jeong, D.-W., M.-S. Kim, S.-O. Choi, S.-Y. Noh, Y.-S. Kim, W.-S. Kim, S.-Y. Baek, and Y.-J. Kim. 2026. Effect analysis of soil texture and water content on soil adhesive force based on the discrete element method. *Scientific Reports*. https://doi.org/10.1038/s41598-026-46139-z

Thakur, S. C., J. P. Morrissey, J. Sun, J. F. Chen, and J. Y. Ooi. 2014. Micromechanical analysis of cohesive granular materials using the discrete element method with an adhesive elasto-plastic contact model. *Granular Matter* 16: 383-400.

FM-16

Proceedings of The 12th International Symposium on Machinery and Mechatronics for Agriculture and Biosystems Engineering (ISMAB 2026)
20-24 October 2026, Busan, Republic of Korea

TRACTOR OVERTURNING-PREVENTION CONTROL USING MACHINE LEARNING TO ESTIMATE THE CENTRE OF MASS

Hideo Tamashiro[1], Yuya Aoyagi[1*], Takeshi Shikanai[2], Masami Matsui[1], Shuto Ohara[1]

[1]Graduate School of Regional Development and Creativity, Utsunomiya University, Japan
[2] Faculty of Agriculture, University of the Ryukyus, Japan

*Corresponding Author-- Voice: +81-28-649-5513, Email: y_aoyagi@a.utsunomiya-u.ac.jp

Abstract: Tractor overturning accidents pose a serious safety risk, and countermeasures for such accidents are an urgent priority. Factors contributing to tractor overturning accidents include centre of mass (CoM) shifting caused by implement attachment or detachment and heavy object loading. Previous studies demonstrated that it is possible to accurately assess the risk of overturning by constructing a machine-learning model that estimates the vehicle's CoM from vibration data recorded while the tractor is in operation. Therefore, in this study, we utilised a machine-learning model to calculate the overturning angle based on the CoM position in real time. Furthermore, by incorporating a safety margin into the overturning angle, we calculated the breaking angle and developed a breaking control system that utilises the vehicle's pitching angle while in motion and the breaking angle. Additionally, we evaluated the control system based on the results obtained while travelling on terrain with a randomly varying slope angle. The control success rate of the developed control system under overturning conditions is likely to reach a maximum of approximately 45% when ascending a slope and 35% when descending. The control success rate under non-overturning conditions decreases as the safety margin increases. Furthermore, it was considered that, to improve the control success rate, it is necessary to select parameters appropriate to conditions such as the CoM position and travel speed.

Key Words: Machine learning, Simulation, Overturning Prevention, Centre of mass, Accident

INTRODUCTION

The fatalities per 100,000 agricultural workers is 7.9 in the United Kingdom (HSE, 2024), 18.6 in the United States (BLS, 2026a,b), and 14.8 in Japan (Ministry of Agriculture, Forestry and Fisheries, 2026), making this a crucial issue. Furthermore, the fatalities per 100,000 people in the domestic agricultural sector is three times that in the construction industry and approximately 13 times the average for all industries, representing an extremely high level. More than half of fatal agricultural accidents involve agricultural machinery. Rollover accidents involving ride-on tractors account for one quarter of the total number of accidents, making measures to address these incidents an urgent priority.

Regarding research on tractor roll-over and fall accidents, Aoyagi et al. (2016) recreated a sloping terrain where a backward overturning accident had actually occurred and conducted a four-degree-of-freedom behavioural simulation of a tractor travelling on sloped terrain. They also identified the phenomenon of front wheels losing contact with the ground at the accident site and demonstrated the need for appropriate terrain modification. Matsui et al. (2017) investigated the effect of varying the centre of mass (CoM) within the wheelbase during overturning, and identified an appropriate CoM for overturning accident prevention. However, owing to the implement attachment and detachment and the influence of loads, the CoM of a tractor's body shifts considerably, and tractors often travel between fields while in high risk of overturning. Therefore, it is important to monitor the CoM while the tractor is in motion and implement overturning-prevention controls based on this information.

Accordingly, Tamashiro et al. extracted features from vibration data recorded while a tractor was in motion, and constructed a machine-learning model using these features to estimate the vehicle's CoM. They demonstrated that the developed model can accurately assess the overturning risk. Therefore, in this study, we calculated the static overturning angle based on the CoM estimated in real time using the developed machine-learning model. Additionally, by incorporating a safety margin into the overturning angle, we calculated the breaking angle and developed a control system that utilises both the vehicle's pitching angle while travelling and the breaking angle. Furthermore, we examined the system's practicality based on control performance while driving over terrain with randomly varying gradient angles.

MATERIALS AND METHODS

VERIFICATION OF THE ESTIMATION ACCURACY OF MACHINE LEARNING MODELS AT MULTIPLE TRAVELING SPEEDS

In this study, training and test data for the machine-learning model were obtained from driving simulations. The simulation conditions were set with driving speeds ranging from 0.1–2.0 m/s (in 0.1 m/s increments), whilst the vehicle's CoM, slope angle, road surface roughness, and phase pattern were set following the literature (Tamashiro et al.). To minimise fluctuations in the travelling distance during the vibration acquisition period, its duration for the training and test data is presented in Table 1. Features were calculated from the vibration data for each condition, and the training and test datasets were constructed. For model construction, a bagging tree was used as the learning algorithm. For each speed, an uphill model was constructed using data in which the average pitching displacement was 0° or greater, and a downhill model was constructed using data in which the average pitching displacement was less than 0°. Furthermore, the accuracy and root mean square error (RMSE) were calculated for 40 models (20 uphill and 20 downhill) to verify the estimation accuracy.

Table 1 Vibration acquisition duration at each driving speed

Driving speed [m/s]	Vibration acquisition duration [s]
0.1	40.96
0.2, 0.3	20.48
0.4–0.7	10.24
0.8–1.5	5.12
1.6–2.0	2.56

OVERTURNING PREVENTION CONTROL USING A MACHINE-LEARNING MODEL

In the training model used for the control system, the slope angle in the simulation conditions was set to 0°–30° (in 2° increments), and training data were constructed for the CoM position, driving speed, road surface roughness, and phase pattern under the same conditions as for the uphill and downhill models. Furthermore, the training data were divided into ranges according to the travelling speed and mean pitching displacement (-20° or less, -20° to -10°, -10°–0°, 0°–10°, 10°–20°, and 20° or greater), and models were constructed for each range. A training model was used to estimate the CoM based on the driving speed and mean pitching displacement from the acquired vibration data. For each condition, features were calculated from the vibration data acquired 10 s after the start of the simulation at 1 s intervals to estimate the CoM. Furthermore, using the estimated CoM, the 40% trim mean was calculated at 60 s intervals. The static overturning angle was calculated from the CoM trimmed mean and the breaking angle was calculated by subtracting the safety margin (in 0.5° increments from 0.5°–3°) from the overturning angle. Fig. 1 shows a diagram of the control system. When the pitching angle exceeded the breaking angle, breaking control was performed using P control. In the control system, the target value was set to 0 m/s with K_p = 0.05–0.3 (in increments of 0.05). Control was performed using the product of deviation, K_p, and the ground reaction force as the braking force. Under overturning conditions, control was deemed successful if the vehicle halted; under non-overturning conditions, control was deemed successful if the breaking control was not activated. The success rates for each safety margin and K_p value were analysed.

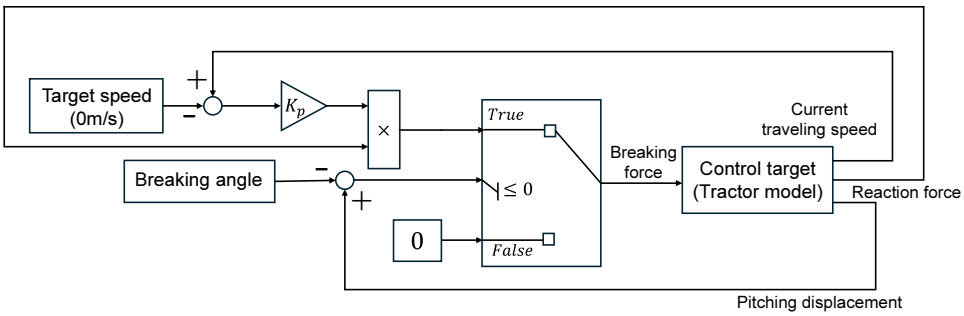

Fig.1 Diagram of the breaking control system.

SIMULATION CONDITIONS FOR OVERTURNING-PREVENTION CONTROL

The simulation conditions for control were set with the CoM positioned between 20% and 80% of the wheelbase from the rear axle (in 10% increments), and a travelling speed of 0.5–2.0 m/s (in 0.5 m/s increments). The test terrain was 400 m long, with the road surface roughness was set to ($P(f_0) = 0.5, 2, 8, 32, 128, 512$) and three types of phase patterns. An example of the test terrain is shown in Fig. 2. The terrain slope angle was 0°, 0°–5°, 5°–10°, 10°–15°, 15°–20°, 20°–25°, and 25°–30° for the 0–100-, 100–150-, 150–200-, 200–250-, 250–300-, 300–350-, and 350–400 m sections, respectively. Furthermore, within each distance range, three types of terrain were generated by varying the slope angle at random intervals of 8–12 m, and the vehicle was driven both ascending and descending.

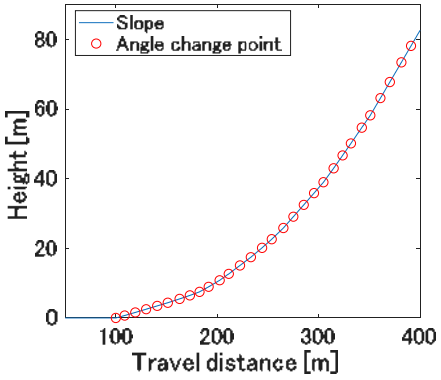

Fig.2 Example of the test terrain.

RESULTS & DISCUSSION

Figs. 3 and 4 show the accuracy rates and RMSE for the uphill and downhill models, respectively, at various speeds. The accuracy rate decreases as the travelling speed increases. The RMSE exhibited less variation in models with acquisition times of 5.12 and 2.56 s. This suggests that model accuracy is influenced by both the traveling speed and acquisition time.

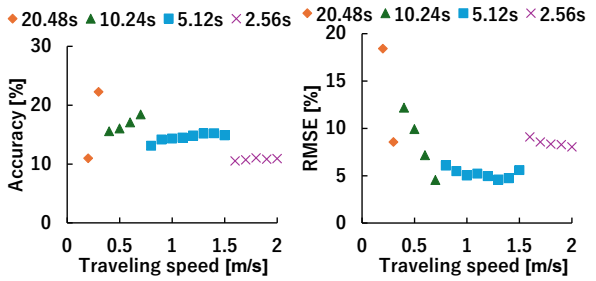

Fig.3 Accuracy and RMSE for the uphill model at various driving speeds.

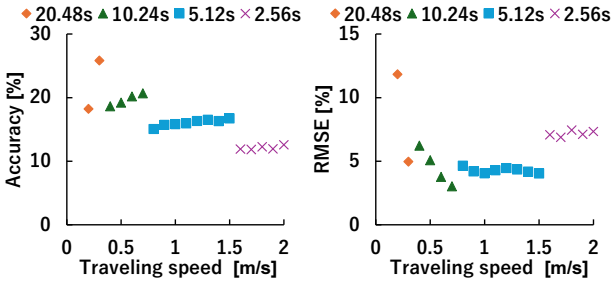

Fig.4 Accuracy and RMSE for the downhill model at various driving speeds.

Fig. 5 shows the vehicle's behaviour during uncontrolled and controlled operation. The stopping times differed for safety margins of 2° and 3°. This suggests the need for appropriate parameters for this condition.

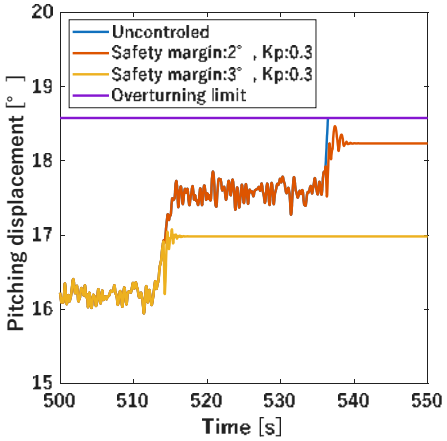

Fig.5 Pitching displacement for the controlled and uncontrolled conditions (CoM: 20%; traveling speed: 0.5 m/s; $P(f_0)$: 8; uphill).

Fig. 6 shows the control success rates for each safety margin and K_p value under overturning conditions. Under these conditions, the parameters yielding the highest control success rate while ascending were a safety margin of 3° and K_p = 0.1, resulting in a control success rate of approximately 45%. Furthermore, under overturning conditions while descending, the control success rate was higher for combinations with a large safety margin and small K_p value. The combination yielding the highest control success rate while descending was a safety margin of 3° and K_p = 0.05, resulting in a control success rate of approximately 35%. One factor cited for the lower control success rate during ascending travel compared with downhill travel was that the risk of forward overturning increased when a braking force was applied to the vehicle while travelling downhill.

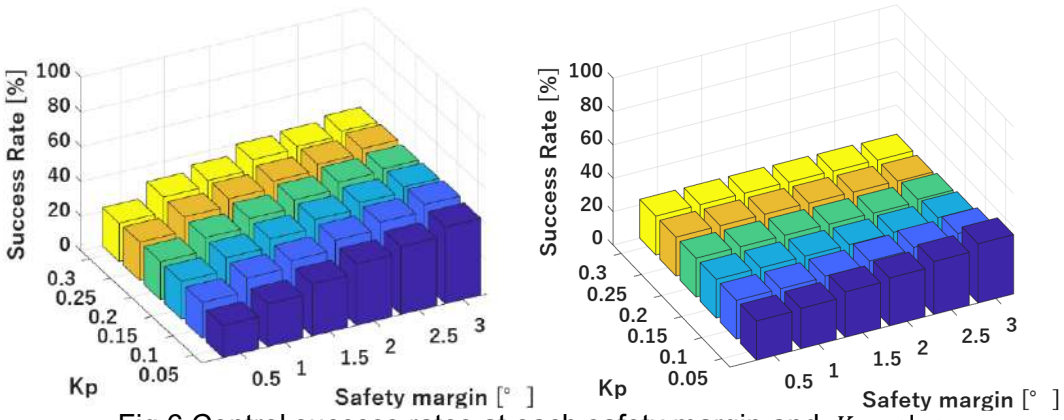

Fig.6 Control success rates at each safety margin and K_p value under overturning conditions (Left: uphill; Right: downhill).

Fig. 7 shows the control success rates for each safety margin under non-overturning conditions. In this case, the control success rate decreases as the safety margin increases. This suggests that, under non-overturning conditions, using a small safety margin can prevent control malfunctions. Additionally, it is necessary to select parameters appropriate for each condition, such as the CoM, to improve the control success rate.

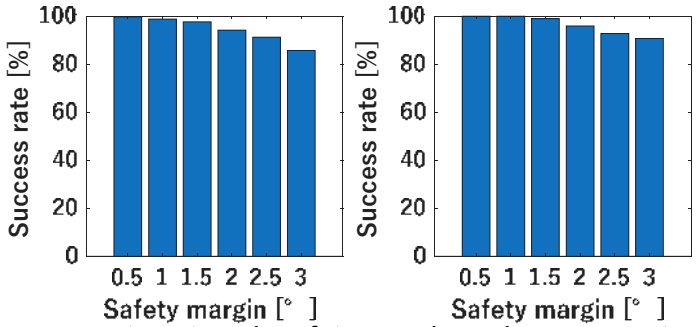

Fig.7 Control success rates at each safety margin under non-overturning conditions (Left: uphill; Right: downhill).

CONCLUSIONS

Fatal accidents in the agriculture sector are a major problem in Japan and internationally, with more than half of all fatal accidents involving agricultural machinery. Among such accidents, rollover and fall-from-height accidents involving ride-on tractors account for one quarter of all accidents, and measures are being taken to prevent these pressing issues. Owing to implement attachment and detachment and the influence of loads, a tractor's CoM varies

considerably, meaning that tractors travel between fields and other locations while in high risk of rollover. Consequently, it is crucial to monitor the CoM while the tractor is travelling and to implement overturning-prevention controls based on this information. Previous studies involved extracting features from vibration data recorded while the tractor was in motion and using a machine-learning model trained on these features to estimate the vehicle's CoM. The results demonstrated that the developed model could accurately assess the overturning risk. Therefore, in this study, we calculated the overturning angle based on the CoM estimated in real time using a machine-learning model. Furthermore, by incorporating a safety margin into the overturning angle, we calculated the breaking angle and developed a breaking control system utilising the vehicle's pitch displacement while in motion and the breaking angle. Additionally, we examined the system's practicality based on the control results obtained while driving on terrain with randomly varying slope angles.

The control success rate of the developed control system under overturning conditions was imminent, reaching a maximum of approximately 45% when ascending a slope and 35% when descending. The lower control success rate when descending was attributed to the increased risk of forward overturning when a braking force was applied to the vehicle while descending. Furthermore, the control success rate under non-overturning conditions decreased as the safety margin increased. This suggests that, under non-overturning conditions, using a small safety margin can prevent control malfunctions. Furthermore, it was considered necessary to select parameters appropriate for each condition, such as the CoM position, to improve the control success rate.

ACKNOWLEDGEMENTS

This work was partially supported by a Grant-in-Aid for Scientific Research (JP22H00388) and a Grant-in-Aid for Early-Career Scientists (JP22K14969 and JP25K18329).

REFERENCES

Aoyagi, Y., Matsui, M., Morio, D., Tamura, T., Uchikawa, T., Kimura, T., 2016. Study on tractor behavior based on accident topography. Journal of the Japanese Society of Agricultural Machinery and Food Engineers. 78: 529–535.

BLS. 2026a. Census of fatal occupational injuries, Table 3: Fatal occupational injuries for selected occupations, 2020-24. U.S. Bureau of Labor Statistics. Available at: www.bls.gov/news.release/cfoi.t03.htm. Accessed August 20, 2026.

BLS. 2026b. Occupational outlook handbook, agricultural workers. U.S. Bureau of Labor Statistics. Available at:www.bls.gov/ooh/farming-fishing-and-forestry/agricultural-workers.htm. Accessed August 20, 2026.

Tamashiro, H., Aoyagi, Y., Shikanai, T., Matsui, M., Ohara, S., Tractor centre of mass estimation using machine learning. Engineering in Agriculture, Environment and Food. (Under review).

HSE. 2024. Fatal injuries in agriculture, forestry and fishing in Great Britain 2022 / 23. UK: Health and Safety Executive (HSE). Available at: www.hse.gov.uk/agriculture/assets/docs/agriculture-fatal-injuries-2023.pdf. Accessed 9 September2026.

MAFF, 2026. Overview of fatal agricultural work accidents occurring in 2024. Japan: Available at: www.maff.go.jp/j/press/nousan/sizai/attach/pdf/250226-1.pdf. Accessed 9 September 2026.

Matsui, M., Aoyagi, Y., Morio, D., Tamura, T., Uchikawa, Y., Kimura, T., 2017. Study on tractor behavior based on accident topography ──swing mechanism modeling of front axle and influence of mass center position on anteroposterior fall ──. Journal of the Japanese Society of Agricultural Machinery and Food Engineers. 79: 59–65.

FM-17

Proceedings of The 12th International Symposium on Machinery and Mechatronics for Agriculture and Biosystems Engineering (ISMAB 2026)
20-24 October 2026, Busan, Republic of Korea

EVALUATION OF A NEW TWO-ROW CULTIVATION SYSTEM AND MECHANIZATION FOR SPRING POTATO PRODUCTION

Kilkyu Oh[1], Seungmin Lee[2], Ki Yong Lee[*]

[1]Department of Aircraft Mainterance, Chodang University, 380 Muan-ro, Muan-eup, Muan-gun, Jeonnam-Gwangju, Korea
[2]DAESIN AGRICULTURAL MACHINERY CO., LTD., 14-5 Sandan-gil, Bomun-myeon, Yecheon-gun, Gyeongsangbuk-do, Korea
*School of Electronic·Mechanical Engineering, Gyeongkuk National University, 1375 Gyeongdong-ro, Andong-si, Gyeongsangbuk-do, Korea-- Voice: +82-10-8766-8600, Email: kylee@gknu.ac.kr

Abstract: This study was conducted to evaluate a new two-row cultivation system for mechanized spring potato production. The effects of intra-row spacing on harvested weight, yield per unit area, and the proportion of marketable potatoes were investigated. The experiment consisted of a conventional two-row cultivation system and a new two-row cultivation system with intra-row spacings of 200, 250, and 300mm, with mechanical planting additionally evaluated at 300mm spacing. The new cultivation system showed improved harvest characteristics as intra-row spacing increased. Mechanized planting and harvesting reduced the time required for field operations, while mechanical digging resulted in lower digging damage than manual digging. These results indicate that the new 300mm two-row cultivation system and mechanized planting and harvesting can effectively improve the mechanization of spring potato production.

Key Words: Spring potato, Two-row cultivation, Intra-row spacing, Mechanization, Mechanized planting

INTRODUCTION

Potato is one of the major food crops in Korea, and spring potato is an important cropping type in domestic potato production. Various cultivation systems, including one-row cultivation on ridge beds and two-row cultivation on flat beds, are used for potato production, and the methods and operating conditions of planting and harvesting vary depending on the cultivation system. In particular, two-row cultivation can be suitable for mechanized operations using tractors and attached implements; therefore, it is necessary to establish a cultivation system suitable for mechanization.

To reduce labor requirements and improve work efficiency in potato production, mechanization needs to be expanded not only to harvesting but also to planting operations. However, when the cultivation system is modified to apply a tractor-mounted planter, changes in intra-row spacing, bed width, and furrow conditions may affect harvested weight and

marketability. Therefore, it is necessary to establish a new cultivation system suitable for mechanical planting and evaluate harvested weight, yield per unit area, and the proportion of marketable potatoes according to intra-row spacing, together with the effects of mechanized planting and harvesting.

This study established a new two-row cultivation system for application with a tractor-mounted planter and compared harvested weight, yield per unit area, and the proportion of marketable potatoes of spring potatoes according to intra-row spacing. In addition, the time required per unit area was compared between manual and mechanical planting under the new cultivation system, and the time required for cutting and digging was analyzed for manual and mechanical harvesting. Furthermore, digging damage was compared between manual and mechanical harvesting to evaluate the effects of mechanization in spring potato production considering harvest characteristics and work efficiency.

MATERIALS AND METHODS

Experimental Conditions and Cultivation Systems

In this study, conventional and new two-row cultivation systems were established to mechanize planting operations for spring potatoes, and harvest characteristics and work performance were compared according to intra-row spacing and planting method. The experimental conditions consisted of a conventional two-row cultivation system and a new two-row cultivation system with intra-row spacings(A) of 200, 250, and 300mm, together with mechanical planting at 300mm spacing under the new two-row cultivation system, resulting in five conditions in total.

The new cultivation system was developed by adjusting the bed width(B) and furrow width(C) of the conventional cultivation system considering the application of tractor-mounted implements. The conditions of each cultivation system are presented in Table 1. In particular, under the same 300mm intra-row spacing, differences in harvest characteristics and work performance between manual and mechanical planting were compared.

Table 1 Experimental cultivation systems and growing conditions.

Cultivation system		Planting method	(A) in-row spacing (mm)	(B) Bed width (mm)	(C) Furrow width (mm)	Experimental area (m²)
Conventional 2-row		Manual	300	800	500	3.90
New	200mm		200	900	550	2.90
	250mm		250			3.63
	300mm		300			4.35
Machine planting		Mechanical				

Planting was performed by forming beds followed by potato planting. Harvesting was conducted in the following order: vine cutting, removal of irrigation materials, removal of plastic mulch, digging, and collection. Vine cutting and digging were conducted using manual and mechanical harvesting methods, and working time and time required per unit area were compared. Harvest characteristics were compared mainly using the results of manual harvesting according to cultivation system and intra-row spacing, while mechanical planting was compared with manual planting under the same new 300mm cultivation condition.

Measurement and Analysis Methods

For harvest characteristics, the total number and total weight of harvested potatoes were measured, and yield per unit area was calculated based on the experimental plot area to

compare differences according to cultivation system and intra-row spacing. Harvested potatoes were classified into six grades according to individual weight, and the number and weight of potatoes in each grade were measured to analyze the weight distribution of potatoes according to intra-row spacing. Marketable potatoes were defined as potatoes weighing 50g or more, and the proportion of marketable potatoes was calculated based on the weight of marketable potatoes relative to the total harvested potato weight.

Work performance was evaluated for planting, vine cutting, and digging by measuring working area and working time. Working efficiency was calculated by dividing the working area by working time, and working time was converted to a 10-a basis and expressed as the time required per unit area. The time required per unit area for manual and mechanical planting and for manual and mechanical harvesting was compared to evaluate the mechanization effects of planting and harvesting operations.

Digging damage was measured to compare the digging damage rate between manual and mechanical harvesting. The digging damage rate was calculated as the proportion of damaged potatoes among all potatoes recovered after digging, and differences according to cultivation system and harvesting method were analyzed. Economic analysis was not conducted in this study; instead, the mechanization effects were evaluated based on harvested weight, yield per unit area, the proportion of marketable potatoes, time required per unit area, and digging damage rate.

RESULTS & DISCUSSION

Harvest Characteristics According to Cultivation System and Planting Method

Harvested weight and yield per unit area of potatoes harvested manually were investigated according to cultivation system and intra-row spacing, and the results of harvested weight are presented in Fig. 1. The new cultivation system showed an increasing trend in harvested weight as intra-row spacing increased. The new 300mm system showed 21.3% higher harvested weight than the conventional 300mm system.

Because the experimental plot areas differed among cultivation systems, yield per unit area was compared by considering the experimental area. The new cultivation system showed higher yield per unit area than the conventional cultivation system at intra-row spacings of 250mm or greater. Compared with the conventional 300mm system, the new 300mm system showed 8.8% higher yield per unit area.

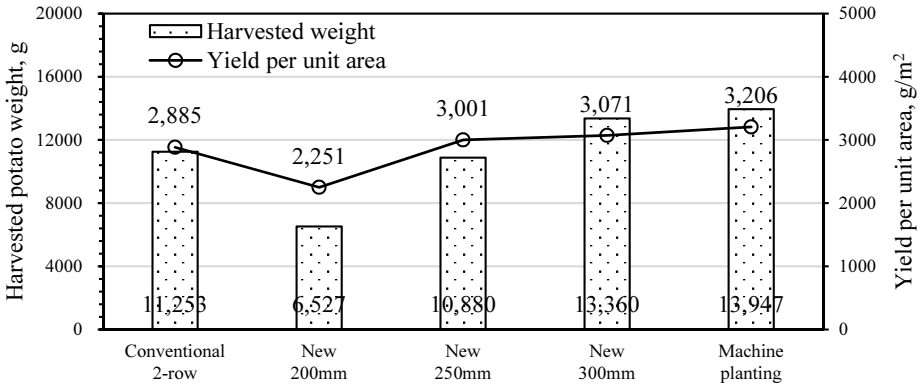

Fig.1 Comparison of harvested potato weight according to cultivation system and planting method.

Marketable potatoes were defined as potatoes weighing 50g or more, and the proportion of

marketable potatoes was calculated as the proportion of the weight of marketable potatoes relative to the total harvested potato weight. The results are presented in Fig. 2. The average proportion of marketable potatoes was 94.4%, and an increasing trend was observed as intra-row spacing increased. The new 300mm system showed a 2.1% higher proportion of marketable potatoes than the conventional 300mm system.

The weight distribution by grade shown in Fig. 3 also indicated an improvement in marketability with increasing intra-row spacing. Based on the total harvested potato weight, the proportions of grades 3, 4, 5, and 6 were 8.0, 38.5, 39.3, and 8.6%, respectively, with grade 5 accounting for the largest proportion. Compared with the conventional 300mm system, the new 300mm system showed 36.8% and 115.0% higher proportions of grade 5 and grade 6 potatoes, respectively.

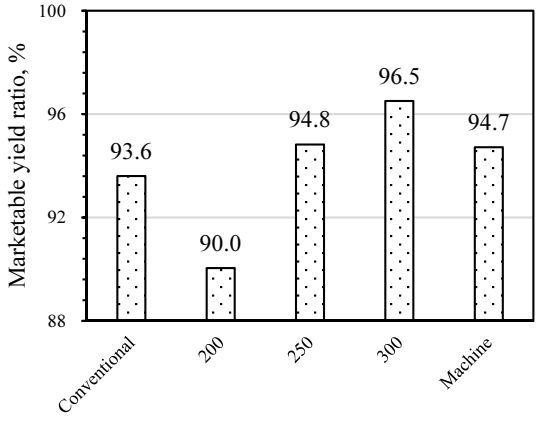

Fig. 2 Marketable potato yield ratio according to cultivation system.

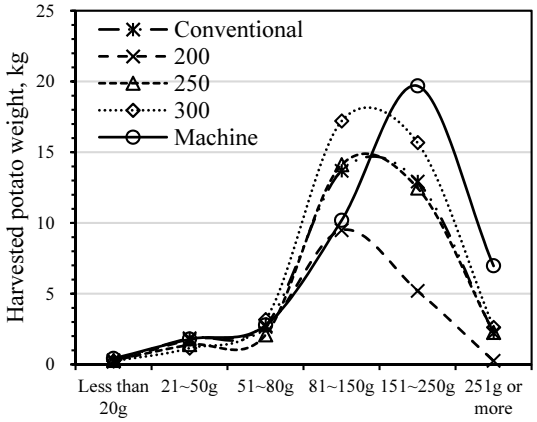

Fig. 3 Distribution of potato weight grades according to cultivation system and planting method.

Working Efficiency and Mechanization Effects at Major Operation Stages

To evaluate the effects of mechanization in potato production, working time(s), working area(m²), working speed(m/s), and working efficiency(h/10a) were investigated for planting, vine cutting, and digging operations. Working efficiency was expressed as the time required per unit area(10a), and differences according to operation stage and working method were compared.

For planting, working speed and working time were compared among the cultivation systems, and the results are presented in Fig. 4. In the new cultivation system, the time required per unit area decreased as intra-row spacing increased, from 2.66h/10a at 200mm to 1.78h/10a at 300mm. Under the same 300mm intra-row spacing, mechanical planting reduced the time required per unit area by 10.3% compared with manual planting. Similarly, a previous study reported working times of 1.0h/10a for machine planting, respectively[1]. The working speed of mechanical planting was 0.241m/s, which was similar to that of the conventional system at 0.247m/s.

For harvesting, working area, working time, and working efficiency for vine cutting and digging were compared between manual and mechanical harvesting, and the results are presented in Table 2. The working areas for manual and mechanical harvesting were 57.4m² and 1,478.6m², respectively, and substantial differences in working efficiency were observed depending on the harvesting method. Compared with manual harvesting, mechanical harvesting reduced the time required per unit area by 87.5% for vine cutting and 97.5% for digging, demonstrating a substantial reduction in working time through mechanization.

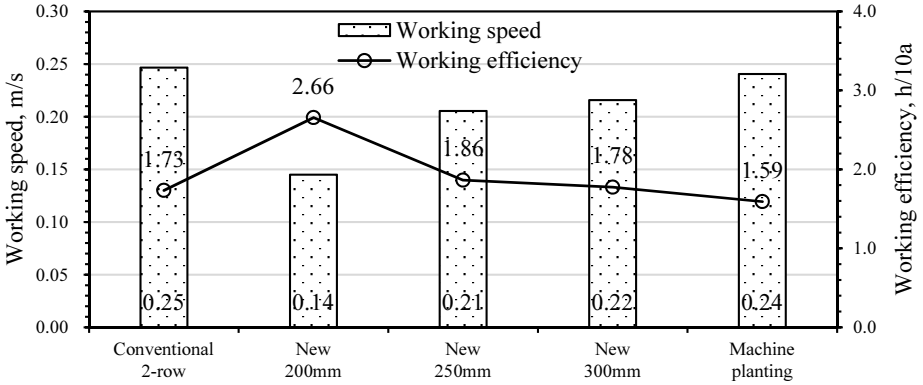

Fig. 4 Working speed and field capacity according to in-row spacing.

Table 2 Working performance of haulm cutting and potato digging according to harvesting method.

Category	Haulm cutting			Potato digging		
	Manual harvesting	Machine harvesting		Manual harvesting	Machine harvesting	
		Operation	Turning		Operation	Turning
Working time (s)	636	1,846	143	5,258	2,015	817
Field capacity (h/10a)	3.116	0.348	0.391	25.391	0.379	0.623

Digging Damage Rate According to Harvesting Method

Digging damage to potatoes was investigated, and the results are presented in Fig. 5. The average digging damage rates were 8.7% for manual harvesting and 4.5% for mechanical harvesting, indicating a lower damage rate with mechanical harvesting.

For manual harvesting, the digging damage rate tended to decrease as intra-row spacing increased in the new cultivation system. This result is considered to be related to the increased bed and furrow widths associated with increasing intra-row spacing, which may have reduced interference between the potatoes and digging tools during the digging operation.

For mechanical harvesting, the digging damage rate ranged from 3.28 to 5.29%, indicating relatively small differences according to cultivation system and intra-row spacing. The average digging damage rate in the present study was 4.5%. Previous studies reported damage rates of 4.7% for a gathering-type potato harvester[2].

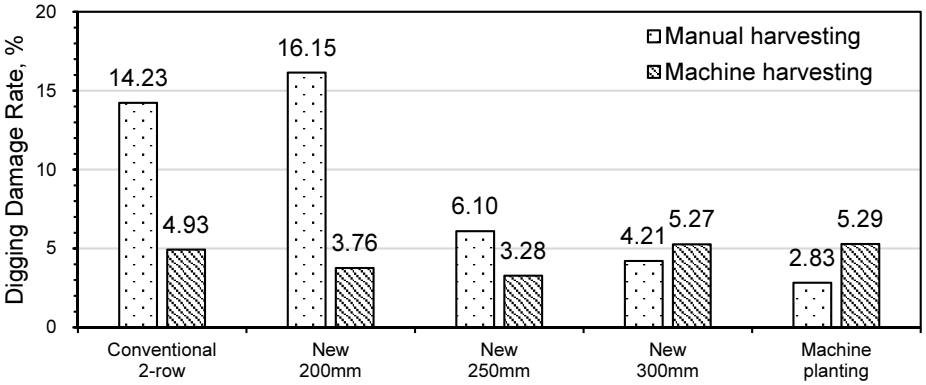

Fig. 5 Potato damage rate during the digging operation.

CONCLUSIONS

This study compared harvested weight, yield per unit area, and the proportion of marketable potatoes according to intra-row spacing in a new cultivation system and analyzed the time required per unit area and digging damage associated with mechanized planting and harvesting. The major results were as follows.

1. The new cultivation system showed an increasing trend in harvested weight and the proportion of marketable potatoes as intra-row spacing increased. Compared with the conventional 300mm system, the new 300mm system showed 21.3% higher harvested weight, 8.8% higher yield per unit area, and a 2.1% higher proportion of marketable potatoes.
2. In the new cultivation system, the time required per unit area for planting tended to decrease as intra-row spacing increased. Mechanical planting at 300mm spacing reduced the time required per unit area by 10.3% compared with manual planting.
3. Mechanization substantially reduced the time required per unit area for harvesting. Compared with manual harvesting, the time required for mechanical harvesting was approximately 1/8 and 1/41 for vine cutting and digging, respectively.
4. The average digging damage rate for mechanical harvesting was 4.2% lower than that for manual harvesting. In manual harvesting, the digging damage rate tended to decrease as intra-row spacing increased in the new cultivation system, whereas relatively small differences were observed among cultivation systems and intra-row spacings under mechanical harvesting.

Overall, the new 300mm cultivation system showed higher harvested weight, yield per unit area, and marketability than the conventional 300mm system. Mechanized planting and harvesting substantially reduced the time required for field operations, and mechanical digging also resulted in lower digging damage. Therefore, mechanized production using the new cultivation system was found to be effective for spring potato production.

ACKNOWLEDGEMENTS

This work was supported by Korea Institute of Planning and Evaluation for Technology in Food, Agriculture and Forestry(IPET) through Machinery Mechanization Technology Development Program for Field Farming Program, funded by Ministry of Agriculture, Food and Rural Affairs(MAFRA)(RS-2023-00235957).

REFERENCES

[1] Jang, M. K., J. H. Kim, and J. S. Nam. 2024. Economic analysis of manual and mechanical seeding for summer potatoes in highland of Gangwon-do. Journal of Agriculture & Life Science 58(6): 199-206.
[2] Lee, S.-H., T.-Y. Kang, Y. Choi, Y.-K. Kang, and Y.-H. Kim. 2020. Performance analysis of a gathering type potato harvester. Journal of Agriculture & Life Science 54(2): 94-100.

FM-18

Proceedings of The 12th International Symposium on Machinery and Mechatronics for Agriculture and Biosystems Engineering (ISMAB 2026)
20-24 October 2026, Busan, Republic of Korea

A CONTINUOUS MULTI-TARGET TOMATO HARVESTING STRATEGY WITH COARSE-TO-FINE PEDICEL-GUIDED MANIPULATION

Hao-Cheng Zuo[1], Bo-Jhih Chang[1] , Ping-Lang Yen[1*]

Department of Biomechatronics Engineering, National Taiwan University,
No. 1, Sec. 4, Roosevelt Road, Taipei 106, Taiwan, ROC.

*Corresponding Author-- Voice: +886 02-3366-5344, Email: plyen@ntu.edu.tw

Abstract: Automated tomato harvesting in greenhouses requires not only accurate localization of small, easily occluded pedicels but also reliable handling of multiple targets within the same field of view. This study proposes a continuous multi-target tomato harvesting strategy. The system first detects harvestable tomatoes, establishes a target set, and determines a bottom-to-top harvesting sequence according to the vertical positions of the fruits in the image. For each target, the robotic arm executes a point-to-point (P2P) coarse approach based on the target's three-dimensional position, followed by active viewpoint adjustment and laser-guided fine positioning to align the end-effector with the pedicel for cutting. After each target is either successfully harvested or skipped because valid pedicel information is unavailable, the system updates the target status and proceeds to the next target. In greenhouse experiments, 53 of 103 harvesting attempts were successful, yielding an overall harvesting success rate of 51.5% and an average harvesting time of approximately 27 s per fruit. In a continuous harvesting test, the system sequentially processed 11 tomato targets, 6 of which were successfully harvested. These results demonstrate the feasibility of integrating target sequencing, coarse approach, and fine pedicel manipulation for continuous multi-target tomato harvesting in greenhouse environments.

Key Words: Agricultural Robot, Tomato Harvesting, Target Sequencing, Pedicel Localization

INTRODUCTION

Existing robotic harvesting systems usually integrate visual perception, a robotic arm, and a dedicated end-effector to perform automated harvesting tasks (Droukas et al., 2023). For tomato harvesting, which requires cutting the pedicel, accurate localization of the cutting region and alignment of the end-effector are particularly important. Yoshida et al. (2020) used RGB-D point clouds to determine the cutting point on the main stem of the tomato truss; Ci et al. (2024) combined deep keypoint detection with point cloud information to estimate the three-dimensional pose of the peduncle nodes; Rong et al. (2026) accomplished tomato harvesting using coarse motion together with closed-loop visual correction.

In addition to the localization and fine manipulation of a single fruit, practical greenhouse harvesting must also deal with multiple targets within the same field of view or the same truss. The harvesting sequence may affect physical interference with neighboring fruits, branches, and leaves, thereby influencing the stability of continuous harvesting. Therefore, this study proposes a continuous multi-target tomato harvesting strategy, which first establishes a set of harvestable targets and plans a bottom-to-top harvesting sequence according to the vertical position of the fruits, and then combines a P2P coarse approach, active viewpoint adjustment, and laser-guided fine positioning to sequentially harvest multiple tomatoes.

MATERIALS AND METHODS

1. Robotic Tomato Harvesting System

This study focuses on the harvesting manipulation strategy of the robotic arm. The perception module provides the positions of the target tomato and its pedicel, while the robotic arm sequentially performs target approach, fine pedicel alignment, and pedicel cutting. The tomato harvesting system in this study consists of the following components: (1) a collaborative robotic arm, used to execute the harvesting motion; (2) an RGB-D camera, which detects the 3D position of the tomato during coarse positioning; (3) an RGB camera, which detects the pedicel position; (4) a laser rangefinder, which obtains the distances to the tomato and the pedicel when the arm has moved close to the tomato; and (5) an electric gripper, which performs the cutting action.

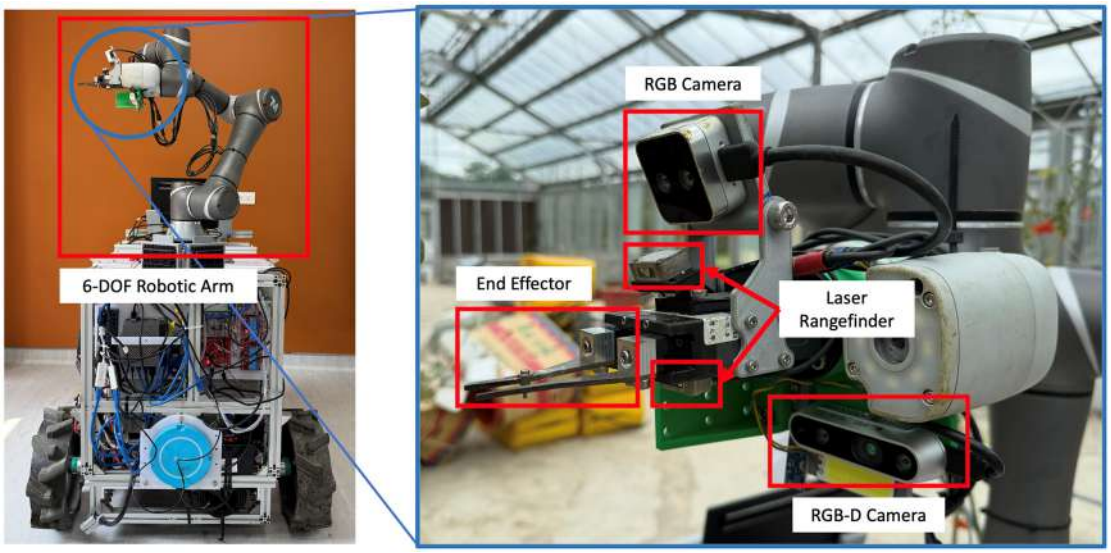

Fig 1. Hardware configuration of the robotic tomato harvesting module

2. Multi-Target Detection and Target Set Initialization

At the beginning of each continuous harvesting task, the RGB-D camera detects ripe tomatoes within the field of view and obtains the 2D image coordinates and 3D position of each target. To prevent the robotic arm from attempting to harvest unreachable targets, the system first excludes tomatoes beyond the specified harvesting distance according to the depth information, and further checks whether the 3D position of the target lies within the workspace of the robotic arm. Tomatoes satisfying these criteria form the initial target set.

$$\mathcal{T} = \{T_1, T_2, \dots, T_N\}$$

where each target T_i is defined as

$$T_i = (ID_i, u_i, v_i, x_i, y_i, z_i)$$

where ID_i is the identifier of the target tomato, (u_i, v_i) are the 2D center coordinates of the tomato in the RGB image, and (x_i, y_i, z_i) are the 3D coordinates of the target tomato. In the subsequent continuous harvesting process, the targets that have not yet been processed are selected from this target set for processing.

3. Harvesting Sequence Planning

When multiple harvestable tomatoes are present within the same field of view, a harvesting-sequence planning strategy is applied so that the system can directly switch to the next target after processing the current target. In the previous system, the targets were sorted according to the depth information obtained from the RGB-D camera, and the fruit closest to the camera was harvested first. However, in the greenhouse environment tested in this study, tomato trusses mainly hang vertically, and fruits in the

lower part of a truss are typically located farther outward. If upper fruits are harvested first, the robotic arm and end-effector may interfere with lower fruits or surrounding branches and leaves while entering the truss. Therefore, the vertical image coordinate is used for target sequencing, with harvesting proceeding from the lowest fruit upward.

$$T^* = arg \max_{T_i \in \mathcal{T}_{rem}} v_i$$

where $\mathcal{T}_{rem}$ denotes the set of targets that have not yet been processed. Since the image vertical coordinate v increases from top to bottom, the target with the largest v_i is assigned the highest harvesting priority. After each target is processed, that target is removed from the remaining target set, and the next target is selected according to the same rule, until all targets have been processed.

4. Continuous Coarse-to-Fine Harvesting Procedure

After the next harvesting target is determined, the system commands the robotic arm to move to a pre-harvest position in front of the tomato using point-to-point (P2P) motion. Because the primary approach motion uses the previously recorded 3D target coordinates, temporary instability in visual tracking does not interrupt the approach motion. After the robotic arm arrives at the pre-harvesting position, the system begins close-range pedicel detection; if valid pedicel information cannot be obtained, the current target is marked as unsuccessful, and the robotic arm returns to the predefined pose before proceeding to the next target.

When valid pedicel information is available, the system enters the coarse-to-fine pedicel-guided manipulation stage. The X- and Y-axes refer to the tool coordinate frame of the end-effector. First, the end-effector is rotated about the X-axis according to the pedicel orientation in the image to normalize its orientation. Then the observation viewpoint is adjusted about the Y-axis to increase the visible pedicel length in the image. After the active viewpoint adjustment is completed, the system uses the laser rangefinder to perform a lateral scan to search for the pedicel position, and moves the tool center point (TCP) to a position in front of the pedicel. The TCP is then adjusted vertically according to the laser measurements to align with the cutting point. After the final alignment is completed, the robotic arm moves forward along the harvesting direction and closes the electric gripper to cut the pedicel.

After the pedicel is cut, the robotic arm retracts while holding the tomato and places it in the collection basket. The system then updates the status of the current target and returns the robotic arm to the initial pose. If the current target cannot be harvested because valid pedicel information is unavailable, the target is marked as unsuccessful and removed from the remaining target set so that it is not retried during the same

harvesting task. The system then checks the remaining target set, $\mathcal{T}_{rem}$. If $|\mathcal{T}_{rem}| > 0$, the system selects the next harvesting target according to the aforementioned the next target is selected according to the bottom-to-top priority, and the P2P coarse approach and fine pedicel manipulation are repeated. If $|\mathcal{T}_{rem}| = 0$, the continuous harvesting task is terminated.

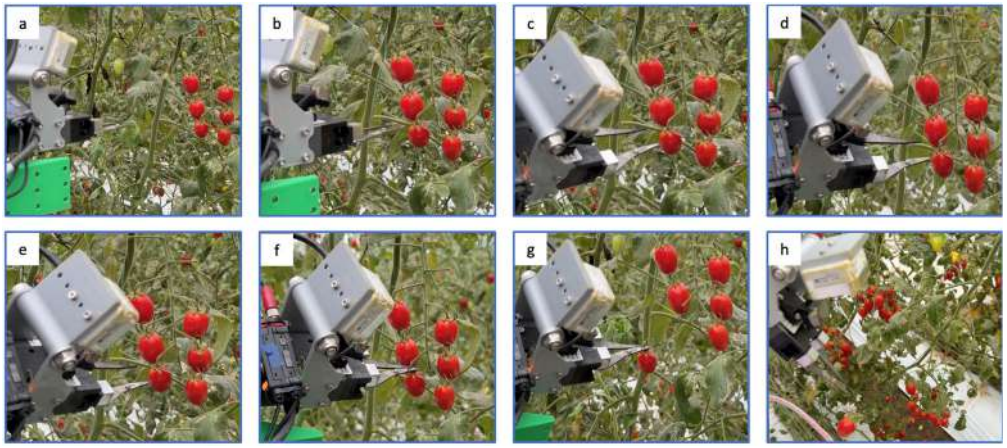

Fig 2. Operational sequence of the coarse-to-fine pedicel-guided manipulation procedure for a single tomato target.

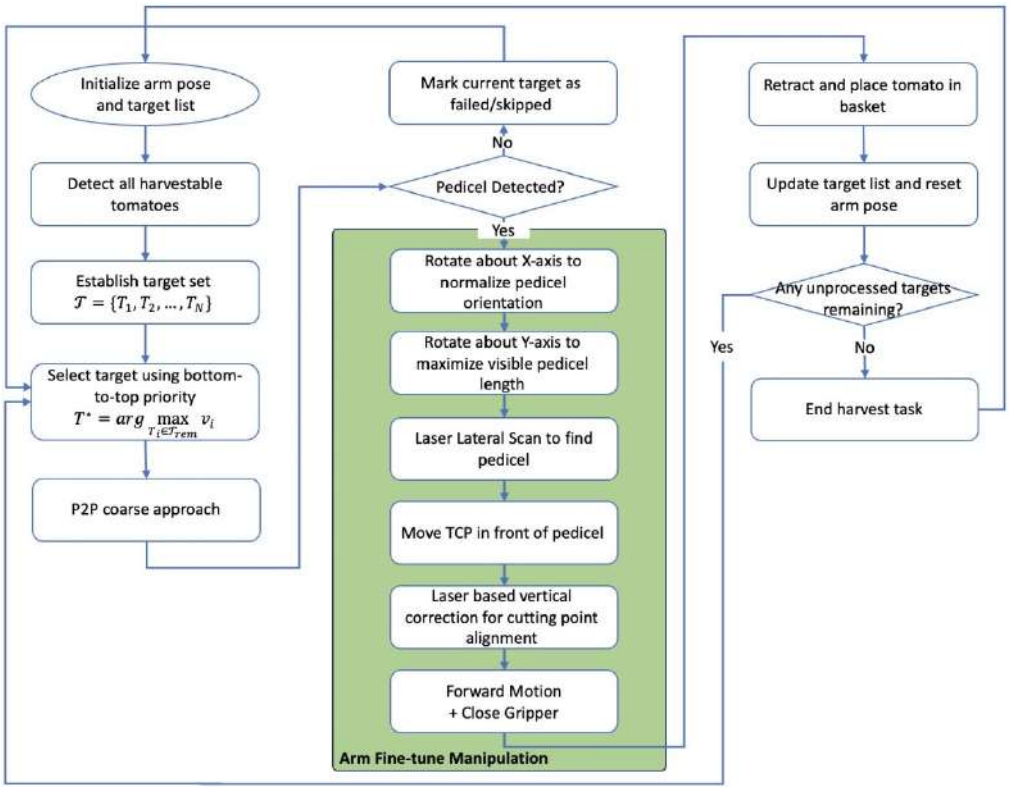

Fig 3. Flowchart of the proposed continuous multi-target tomato harvesting strategy with bottom-to-top target sequencing and coarse-to-fine pedicel-guided manipulation.

RESULTS & DISCUSSION

Tomato harvesting experiments were conducted under greenhouse conditions to evaluate the proposed continuous multi-target harvesting strategy and coarse-to-fine pedicel-guided manipulation procedure. The system sequentially performed three-dimensional tomato localization, P2P coarse approach, active viewpoint adjustment, laser scanning and fine alignment of the cutting point, and pedicel cutting and fruit placement. A total of 103 harvesting attempts were conducted, of which 53 resulted in successful harvests, corresponding to an overall harvesting success rate of 51.5% and an average harvesting time of about 27 s per fruit. The overall system performance is shown in Table 1.

To further validate the multi-target continuous harvesting capability, the system established a set of harvestable targets within the field of view at the beginning of the task, and selected the harvesting targets from bottom to top according to the vertical position of the fruits. In the continuous harvesting test, the initial target set contained 11 tomatoes, and the system was able to sequentially complete the operation procedure for all 11 targets, 6 of which were successfully harvested. This result shows that after completing each target, the system can update the target status and directly switch to the next target without restarting the overall harvesting task, verifying the feasibility of the proposed framework for multi-target continuous operation.

The distribution of failure cases is shown in Table 2. Among the 50 failure cases, 30 cases (60%) were due to the inability to obtain valid pedicel information, which is currently the main limitation; this was followed by physical interference involving the end-effector and the target fruit or neighboring vegetation, with 11 cases (22%). In addition, loss of pedicel information during the harvesting operation and incorrect pedicel association accounted for 14% and 4%, respectively. Although active viewpoint adjustment can improve pedicel visibility, when the pedicel is severely occluded by fruits or leaves, it may still be impossible to obtain valid information required for the subsequent laser-based fine alignment. On the other hand, the physical interference cases also indicate that there is still room for improvement in the motion trajectory of the end-effector when it enters a dense truss. Therefore, future work will focus on expanding the search range of valid observation postures and on improving the final approach and cutting motions, so as to further increase the harvesting success rate.

Overall, the results demonstrate that the system can perform a continuous multi-target harvesting workflow, including target initialization, target sequencing, coarse-to-fine manipulation, and transition to the next target. However, the overall harvesting success rate is still mainly limited by pedicel occlusion and close-range physical interference. In

addition to improving pedicel observation and fine positioning, future work will also compare different harvesting sequence strategies, such as nearest-first and bottom-to-top, in order to quantify the influence of target sequencing on the harvesting success rate, the physical interference rate, and the overall harvesting efficiency.

Performance Index	Result
Total harvesting attempts	103
Successful harvests	53
Failed harvests	50
Overall harvesting success rate	51.5%
Targets processed in continuous harvesting test	11
Successful harvests in continuous harvesting test	6
Average harvesting time	27 s/fruit

Table 1. Overall performance of the proposed tomato harvesting system.

Failure Mode	Cases	Share of failures (%)
Pedicel not visible	30	60%
Physical interference with fruits/plants	11	22%
Pedicel lost during harvesting	7	14%
Incorrect pedicel association	2	4%
Total	50	100%

Table 2. Failure analysis of the proposed tomato harvesting procedure.

CONCLUSIONS

This study proposes a continuous multi-target harvesting strategy for greenhouse tomatoes that integrates target-set establishment, bottom-to-top harvesting sequence planning, P2P coarse approach, active viewpoint adjustment, laser-guided fine alignment, and pedicel cutting. In greenhouse experiments, 53 of 103 harvesting attempts were successful, yielding an overall harvesting success rate of 51.5% and an average harvesting time of approximately 27 s per fruit. In the continuous harvesting test, the system sequentially processed 11 tomato targets, 6 of which were successfully harvested, demonstrating the feasibility of the proposed framework for continuous multi-target harvesting.

The main limitations of the current system are insufficient pedicel visibility and physical interference during close-range manipulation. Future work will focus on improving

pedicel observation and end-effector manipulation and on evaluating the effects of different harvesting sequences on harvesting success rate, physical interference, and overall harvesting efficiency.

ACKNOWLEDGEMENTS

The authors would like to thank the Taoyuan District Agricultural Research and Extension Station, Ministry of Agriculture, for providing the experimental site and support for the greenhouse tomato harvesting experiments.

REFERENCES

Ci, J., Wang, X., Rapado-Rincón, D., Burusa, A. K., & Kootstra, G. (2024). 3D pose estimation of tomato peduncle nodes using deep keypoint detection and point cloud. Biosystems Engineering, 243, 57–69.

Droukas, L., Doulgeri, Z., Tsakiridis, N. L., Triantafyllou, D., Kleitsiotis, I., Mariolis, I., Giakoumis, D., Tzovaras, D., Kateris, D., & Bochtis, D. (2023). A survey of robotic harvesting systems and enabling technologies. Journal of Intelligent & Robotic Systems, 107, Article 21.

Rong, J., Xiong, Z., Xue, C., Yuan, J., Zhang, C., Wang, P., Yuan, T., & Li, W. (2026). Field validation of vision-guided action policy generation for robotic tomato harvesting. Information Processing in Agriculture, in press.

Yoshida, T., Fukao, T., & Hasegawa, T. (2020). Cutting point detection using a robot with point clouds for tomato harvesting. Journal of Robotics and Mechatronics, 32(2), 437–444.

FM-19

Proceedings of The 12th International Symposium on Machinery and Mechatronics for Agriculture and Biosystems Engineering (ISMAB 2026)
20-24 October 2026, Busan, Republic of Korea

VIBRATION ANALYSIS OF A MECANUM WHEEL AGRICULTURAL TRANSPORT PLATFORM

Yeonsong Lee[1], Minkyo Kong[2], Sung-Bo Shim[1*]

[1]Department of Bio-Industrial Mechanical Engineering, Kyungpook National University, 80 Daehak-Ro, Buk-Gu, Daegu 41566, South Korea
[2]Kongsung Co., Ltd., 47 Hosan-Ro, Dalseo-Gu, Daegu 42711, South Korea
*Corresponding Author-- Voice: +82-10-2305-3276, Email: sbs80@knu.ac.kr

Abstract: Mecanum wheels allow a transport platform to change its direction of travel without reorienting the platform body. This capability may be useful in agricultural product processing centers and other facilities with limited maneuvering space. In such facilities, discrete obstacles on smooth floors can act as excitation sources, whereas vibration studies on agricultural machinery have commonly focused on random road excitation. Platform vibration can cause mechanical damage to transported agricultural products. This study investigated the vibration characteristics of a mecanum wheel agricultural transport platform and evaluated a seven-degree-of-freedom mathematical model for predicting the platform's vibration response.
Cleat tests were conducted on a smooth indoor floor using a 10-mm-high rectangular cleat under two wheel passage conditions and six loading conditions. Single-axis accelerometers on the wheel carriers measured vertical acceleration of each wheel, while a six-axis inertial measurement unit at the center of the platform body measured vertical acceleration, pitch angular velocity, and roll angular velocity. The measured time-domain responses were transformed into the frequency domain, where dominant vibration frequencies and the relationships among the vibration responses were analyzed across excitation and loading conditions. A seven-degree-of-freedom mathematical model of the platform was then established and validated against the experimental responses.

Key Words: Mecanum wheel, Agricultural transport platform, Cleat test, Loading condition, Vibration analysis

ACKNOWLEDGEMENTS

This research, undertaken at Kyungpook National University, was supported by the ANCHOR program through the Daegu ANCHOR Center, funded by the Ministry of Education (MOE) and the Daegu Metropolitan City, Republic of Korea.(2026-ANCHOR-03-001)

Field Machinery and Systems 4 (FM-4)



FM-20

Proceedings of The 12th International Symposium on Machinery and Mechatronics for Agriculture and Biosystems Engineering (ISMAB 2026)
20-24 October 2026, Busan, Republic of Korea

DEVELOPMENT OF A DEM-MBD CO-SIMULATION MODEL FOR PREDICTION PICKUP UNIT LOAD IN A 103KW-CLASS ROUND BALER

Min-Seung Kim[1], Dae-Wi Jeong[1], Se-O Choi[1], Shin-Young Noh[1], Ye-Na Lee[1], Yeon-Soo kim[1,2,3*], Yong-Joo kim[4,5,6]

[1] Department of Bio-Industrial Machinery Engineering, Pusan National University, Miryang 50463, Republic of Korea
[2] Major of Natural Resources Systems Engineering, Pusan National University, Yangsan 50612, Republic of Korea
[3] Life and Industry Convergence Research Institute, Pusan National University, Miryang 50463, Republic of Korea
[4] Eco-Friendly Hydrogen and Electric Agricultural Machinery Research Institute, Chungnam National University, Daejeon 34134, Republic of Korea
[5] Department of Smart Agricultural Systems and Mechanical Engineering, Chungnam National University, Daejeon 34134, Republic of Korea
[6] Department of Smart Agriculture Systems, Chungnam National University, Daejeon 34134, Republic of Korea
*Corresponding Author--Voice: +8201-7748-6990, Email: yskim23@pusan.ac.kr

Abstract: Round balers are subjected to continuously varying loads during crop pickup, transport, accumulation, and compression, which directly affect drivetrain performance, component durability, and energy consumption. However, repeated field load measurements are limited by crop availability and varying field conditions, while direct torque measurement at individual internal shafts is difficult because of complex drivetrain configurations. Therefore, a simulation-based approach capable of reproducing crop–machine interactions and estimating internal component loads is required.

This study investigated the operating loads of the pickup roller and pickup blade of a 103 kW-class round baler using field measurements and discrete element method–multibody dynamics (DEM–MBD) co-simulation. PTO torque and rotational speed were measured during field operation and converted to component-level reference values considering the actual drivetrain transmission ratios and mechanical efficiencies. To account for the structural characteristics of rice straw, the stems were classified into top, middle, node, and bottom sections. The measured mean tensile loads ranged from 83.44 to 110.08 N, while the mean shear loads ranged from 28.63 to 72.56 N. A bonded DEM model was calibrated using these mechanical properties, resulting in tensile-load errors of 0.05–0.65% and shear-load errors of 2.09–7.17%. The MBD model was calibrated under no-load conditions, resulting in torque errors of 0.06% for the pickup roller and 0.26% for the pickup blade.

The DEM–MBD co-simulation predicted a mean pickup-roller torque of 149.56 N·m, compared with a measurement-based converted torque of 143.97 N·m, corresponding to an error of 3.88%. For the pickup blade, the predicted and converted mean torques were 169.03 and 206.68 N·m, respectively, resulting in an error of 18.22%. These results indicate that the proposed approach can estimate the average operating loads of internal pickup components using externally measured PTO data without requiring direct torque measurement at individual shafts. The proposed framework can provide a practical basis for load analysis and drivetrain design of forage-processing machinery.

Key Words: DEM-MBD coupling simulation; Rice straw model; Round Baler; Torque prediction

FM-21

Proceedings of The 12th International Symposium on Machinery and Mechatronics for Agriculture and Biosystems Engineering (ISMAB 2026)
20-24 October 2026, Busan, Republic of Korea

EXPERIMENTAL AND THEORETICAL ANALYSIS OF SINGLE TIRE SOIL THRUST UNDER DIFFERENT NORMAL LOADS

Se-O Choi[1], Min-Seung Kim[1], Dae-Wi Jeong[1], Shin-Young Noh[1], Ye-Na Lee[1], Yeon-Soo Kim[1, 2*], Yong-Joo Kim[3, 4]

[1]Department of Bio-Industrial Machinery Engineering, Pusan National University, Miryang 50463, Republic of Korea
[2]Major of Natural Resources Systems Engineering, Pusan National University, Yangsan 50612, Republic of Korea
[3]Department of Smart Agricultural Systems and Mechanical Engineering, Chungnam National University, Daejeon 34134, Republic of Korea
[4]Department of Smart Agricultural Systems, Chungnam National University, Daejeon 34134, Republic of Korea

*Yeon-Soo Kim -- Voice: +82-10-7748-6990, Email: yskim23@pusan.ac.kr

Abstract: Accurate prediction of tire-soil interaction is important for evaluating the mobility and tractive performance of off-road vehicles and agricultural machinery. This study experimentally investigated the effect of normal load on the soil thrust of a single passenger car tire operating on dry sandy soil and evaluated the applicability of the Wong-Reece and Brixius terramechanics models. Soil-bin tests were conducted using a 205/60R16 radial tire under additional normal loads of 0, 10, 20, 30, and 40 kg. Soil thrust was calculated from the measured wheel torque and effective tire radius, and the measured time-series slip ratios were used as inputs for the theoretical calculations. The Wong-Reece model predicted soil thrust based on the tire-soil stress distribution and shear deformation relationship, whereas the radial ply Brixius formulation predicted gross traction using a mobility number-based empirical relationship. The measured mean soil thrust increased from 27.07 N at the 0 kg additional load condition to 47.19 N at the 40 kg additional load condition. The Wong-Reece model predicted 280.81-402.58 N, while the Brixius model predicted 454.79-592.41 N. Although both models reproduced the increasing trend of soil thrust with normal load, they substantially overestimated the measured values. The Wong-Reece predictions were approximately 8.5-10.4 times the experimental values, whereas the Brixius predictions were approximately 12.6-16.8 times greater. These results indicate that both models qualitatively captured the effect of normal load but showed limited quantitative applicability to the tested passenger car tire under the present dry sandy soil condition. Further refinement of model parameters and assumptions may therefore be required for accurate soil thrust prediction under these operating conditions.

Key Words: Soil-tire interaction, Soil thrust, Wong-Reece model, Brixius model, Normal load

INTRODUCTION

Off-road vehicles and agricultural machinery frequently operate on deformable terrain, where tire-soil interaction strongly affects traction, mobility, and energy efficiency. Variations in wheel load, slip ratio, soil strength, and sinkage alter the stress distribution within the tire-soil contact region and consequently influence the tractive force generated by the wheel. Therefore, reliable prediction of soil thrust under different loading conditions is important for evaluating and designing off-road mobility systems.

Soil-bin experiments provide direct measurements of tire performance under controlled soil conditions and are widely used to investigate tire-soil interaction (Zeng et al., 2022). However, experimental evaluation requires considerable time and resources when a wide range of operating and soil conditions is considered. Analytical, semi-empirical, and empirical terramechanics models have therefore been developed to estimate wheel performance using soil and tire parameters (Tiwari et al., 2010; Mason et al., 2018).

The Wong-Reece model describes tire-soil interaction based on the normal and shear stress distributions developed along the tire-soil contact region (Wong and Preston-Thomas, 1983; Lim and Le, 2021). The model considers soil pressure-sinkage characteristics and shear deformation behavior and has been widely used to estimate wheel thrust and torque on deformable terrain. In contrast, the Brixius model is based on an empirical mobility-number approach and predicts tire traction using cone index, tire geometry, wheel load, tire deflection, and slip ratio (Zoz and Grisso, 2003; Tiwari et al., 2010). Because the two models are based on different theoretical and empirical assumptions, their prediction characteristics may differ substantially depending on tire and soil conditions.

Most classical terramechanics models were developed primarily for agricultural or off-road tires and idealized wheel-soil conditions (Zoz and Grisso, 2003; Tiwari et al., 2010). Their direct applicability to passenger-car tires operating on loose sandy soil has not been sufficiently established. In particular, the effects of increasing normal load on the prediction accuracy of these models need to be evaluated using experimental data obtained under identical operating conditions.

Therefore, the objective of this study was to experimentally measure soil thrust of a single passenger car tire under different normal loads and to evaluate the applicability of the Wong-Reece and Brixius models by comparing their predictions with the measured results.

MATERIALS AND METHODS

Soil-bin Experiment

A soil-bin test system was used to measure the tractive performance of a single passenger-car tire on dry sandy soil. The test tire was a 205/60R16 radial tire with an effective radius of 0.3262 m and a width of 0.205 m. The total mass of the tire and drive assembly was 63.05 kg, and additional vertical loads of 0, 10, 20, 30, and 40 kg were applied during the tests. The tire was driven by an axle mounted motor, and the axle torque was recorded during wheel travel. Soil thrust was calculated from the measured axle torque and effective tire radius (Zeng et al., 2022). The slip ratio was determined from the theoretical travel distance based on tire rotation and the actual longitudinal travel distance. Time-series slip ratios measured under each load condition were used as inputs for the theoretical calculations.

$$H_{exp} = \frac{T_w}{r} \quad (1)$$

where:

H_{exp} = Experimental soil thrust (N)

T_{ω} = Wheel axle torque (N·m)

r = Tire radius (m)

Wong-Reece Model

The Wong-Reece model was used to analytically estimate the soil thrust generated by the tire. The model calculates the normal and shear stresses acting along the tire-soil contact region based on tire geometry, sinkage, slip ratio, and soil mechanical parameters. The normal stress distribution was determined using the pressure-sinkage relationship, while the shear stress was calculated using the Mohr-Coulomb shear strength relationship and shear deformation theory. In the present study, the tire radius and width were 0.3262 and 0.205 m, respectively. The soil cohesion and internal friction angle were 2.94 kPa and 18.8°, respectively. The shear deformation modulus was 0.000178 m. The Bekker pressure-sinkage parameters k_c, $k_{\emptyset}$, and n were 0.99 kN/m^{n+1}, 1528.43 kN/m^{n+2}, and 1.10. A sinkage of 0.042 m was applied for all normal load conditions. Experimentally measured time-series slip ratios were used in the calculation for each load condition.

$$j(\theta) = r\left[\left(\theta_f - \theta\right) - (1 - s)\left(sin\theta_f - sin\theta\right)\right] \quad (2)$$

where:

$j(\theta)$ = Shear displacement at angular position θ (m)

r = Tire radius (m)

θ_f = Tire entry angle (rad)

θ = Angular position within the tire-soil contacts region (rad)

s = Slip ratio

$$T_{WR} = br^2 \int_{\theta_r}^{\theta_f} [c + \sigma(\theta) tan\phi] \left[1 - \exp\left(-\frac{j(\theta)}{K}\right)\right] d\theta \quad (3)$$

where:

T_{WR} = Wheel torque predicted by the Wong-Reece model (N·m)

b = Tire width (m)

r = Tire radius (m)

c = Soil cohesion (Pa)

$\sigma(\theta)$ = Normal stress at angular position θ (Pa)

ϕ = Internal friction angle of soil (deg)

$j(\theta)$ = Shear displacement at angular position θ (m)

K = Shear deformation modulus (m)

$$H_{WR} = \frac{T_{WR}}{r} \quad (4)$$

where:

H_{WR} = Soil thrust predicted by the Wong-Reece model (N)

T_{WR} = Wheel torque predicted by the Wong-Reece model (N·m)

r = Tire radius (m)

Brixius Model

The radial ply Brixius formulation was used to predict tire traction using a mobility number (B_n) based empirical relationship. The mobility number was calculated from soil cone index, tire dimensions, wheel load, and tire deflection. The tire width and unloaded diameter were 0.205 and 0.6524 m, respectively, and tire deflection was assumed to be 0. The total vertical load

applied to the soil was calculated from the 63.05 kg base assembly mass plus the additional normal load. A representative cone index of 147.62 kPa, corresponding to the mean value within the upper 100 mm soil layer, was used to characterize soil strength. The gross traction ratio was calculated using the radial ply modification of the Brixius equation as a function of mobility number and measured slip ratio. The predicted gross traction force was obtained by multiplying the gross traction ratio by the corresponding vertical wheel load. The measured time-series slip ratios were applied under each normal load condition to maintain consistency with the experimental operating conditions.

$$B_n = \frac{CIbd}{W}\left(\frac{1+\frac{5\delta}{h}}{1+\frac{3b}{d}}\right) \quad (5)$$

where:

B_n = Mobility number
CI = Cone index of soil (Pa)
b = Tire width (m)
d = Tire diameter (m)
W = Vertical wheel load (N)
δ = Tire deflection (m)
h = Tire height (m)

$$GTR = 0.88(1 - e^{-0.1B_n})(1 - e^{-9.5s}) + 0.032 \quad (6)$$

where:

GTR = Gross traction ratio
B_n = Mobility number
s = Slip ratio

$$H_{Brixius} = GTR \times W \quad (7)$$

where:

$H_{Brixius}$ = Predicted gross traction force by the Brixius model (N)
GTR = Gross traction ratio
W = Vertical wheel load (N)

RESULTS & DISCUSSION

The experimentally measured soil thrust increased with increasing normal load, which is consistent with previous single wheel experiments reporting increasing traction force with wheel load on granular terrain (Zeng et al., 2022). The mean soil thrust increased from 27.07 N at the 0 kg additional load condition to 47.19 N at the 40 kg condition, corresponding to an approximately 1.74-fold increase. Both the Wong-Reece and radial ply Brixius models also predicted increasing soil thrust with normal load. The Wong-Reece predictions ranged from 280.81 to 402.58 N, whereas the Brixius predictions ranged from 454.79 to 592.41 N.

Table 1 Comparison of measured and predicted soil thrust under different normal loads.

Normal load kg	Experiment N	Wong-Reece N	Error %	Brixius N	Error %
0	27.07	280.81	937.2	454.79	1579.9
10	31.01	311.33	903.9	496.14	1499.8
20	33.14	341.91	931.6	531.14	1502.5
30	40.09	372.26	828.7	563.78	1306.5
40	47.19	402.58	753.0	592.41	1155.3

However, both models substantially overestimated the measured soil thrust over the entire load range. The Wong-Reece model predicted approximately 8.5-10.4 times the measured values, while the Brixius model predicted approximately 12.6-16.8 times the measurements. Despite the large discrepancies in absolute magnitude, both models reproduced the increasing tendency with normal load. When normalized to the 0 kg condition, the experimental soil thrust increased to 1.74 at 40 kg, whereas the Wong-Reece and Brixius predictions increased to approximately 1.43 and 1.30, respectively. These results indicate that both models qualitatively captured the effect of normal load but underestimated the relative load sensitivity and showed limited quantitative applicability to the tested passenger car tire and dry sandy soil condition.

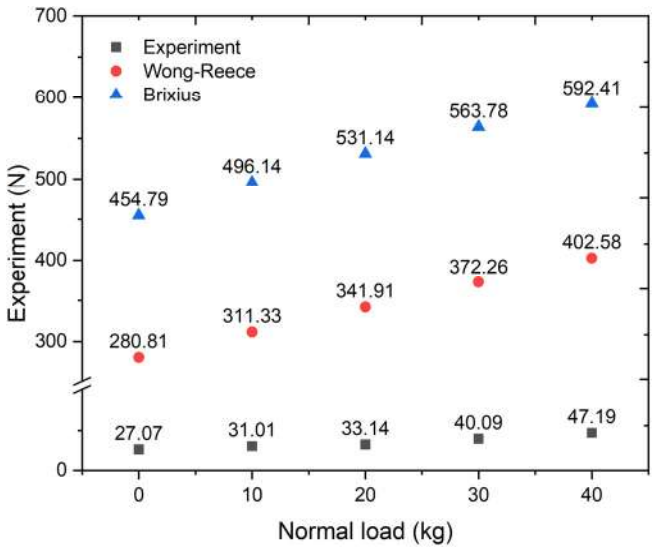

Fig.1 Comparison of measured and predicted soil thrust under different normal loads.

The large discrepancies may be associated with differences between the assumptions and calibration conditions of the classical models and the present passenger car tire and dry sandy soil conditions.

CONCLUSIONS

The soil-bin experiment showed that soil thrust increased with increasing normal load for the tested passenger car tire on dry sandy soil. Both the Wong-Reece and radial ply Brixius models reproduced the increasing trend of soil thrust with normal load; however, the absolute predictions were substantially higher than the measured values. The Wong-Reece model predicted approximately 8.5-10.4 times the measured soil thrust, whereas the Brixius model

predicted approximately 12.6-16.8 times the measured values.

Although both theoretical models qualitatively captured the effect of normal load, they underestimated the relative load sensitivity observed in the experiment and showed limited quantitative applicability under the present test conditions. These results suggest that further refinement of model parameters and assumptions, or the development of condition specific empirical or numerical approaches, may be required for accurate prediction of soil thrust passenger car tires operating on sandy terrain.

ACKNOWLEDGEMENTS

This work was supported by the Korea Institute of Planning and Evaluation for Technology in Food, Agriculture and Forestry (IPET) through the Agri-Food Export Enhancement Technology Development Program, funded by the Ministry of Agriculture, Food and Rural Affairs (MAFRA) (RS-2026-25527280).

REFERENCES

Lim, Y., and V. D. Le. 2021. Development of a new pressure-sinkage model for rover wheel-lunar soil interaction based on dimensional analysis and bevameter tests. *Journal of Astronomy and Space Sciences* 38(4): 237-250. https://doi.org/10.5140/JASS.2021.38.4.237.

Mason, G. L., J. M. Williams, F. Vahedifard, and J. D. Priddy. 2018. A unified equation for predicting traction for wheels on sand over a range of braked, towed, and powered operations. *Journal of Terramechanics* 79: 33-40. https://doi.org/10.1016/j.jterra.2018.05.005.

Tiwari, V. K., K. P. Pandey, and P. K. Pranav. 2010. A review on traction prediction equations. *Journal of Terramechanics* 47(3): 191-199. https://doi.org/10.1016/j.jterra.2009.10.002.

Wong, J. Y., and J. Preston-Thomas. 1983. On the characterization of the shear stress-displacement relationship of terrain. *Journal of Terramechanics* 19(4): 225-234.

Zeng, H., W. Xu, and M. Zang. 2022. Experimental investigation of tire traction performance on granular terrain. *Journal of Terramechanics* 104: 49-58. https://doi.org/10.1016/j.jterra.2022.09.002.

Zoz, F. M., and R. D. Grisso. 2003. Traction and tractor performance. ASAE Distinguished Lecture Series, Tractor Design No. 27. ASAE Publication No. 913C0403. St. Joseph, Mich.: American Society of Agricultural Engineers.

FM-22

Proceedings of The 12th International Symposium on Machinery and Mechatronics for Agriculture and Biosystems Engineering (ISMAB 2026)
20-24 October 2026, Busan, Republic of Korea

DEM-BASED PERFORMANCE EVALUATION OF A GARLIC CLOVE SORTER FOR MACHINE PLANTING

Won-Yeol Choi[1], Hyung-Gyu Park[1, 2], Jinho Son[1], Ju-Hee Lee[1], Bum-seok Park[1], Young-June An[1], Seo-Eun Lee[1], Dae-Wook Kwon[1], Yushin Ha[1, 2, *]

[1]Department of Bio-Industrial Machinery Engineering, Kyungpook National University, Daegu 41566, Republic of Korea
[2]Upland-Field Machinery Research Center, Kyungpook National University, Daegu 41566, Republic of Korea
*Corresponding Author-- Voice: +82-10-4520-2115, Email: yushin72@knu.ac.kr

Abstract: Garlic planting is a major operation in the garlic cultivation process because stable planting is essential for successful overwintering, crop management, and subsequent mechanized harvesting operations. Although the metering and planting units of a garlic planter can be precisely designed, planting performance may decrease when garlic cloves with various sizes and shapes are supplied to the hopper. Therefore, precise design and performance evaluation of a garlic clove sorter should precede the improvement of machine planting performance.
The objective of this study was to evaluate the size-based sorting performance of a garlic clove sorter using the DEM (Discrete Element Method). For this purpose, the external dimensions of garlic cloves from Daeseo, a major Nanji-type cultivar in Korea, were measured. Based on the normalized clove size distribution, garlic cloves were classified into four size grades, from Grade 1 to Grade 4. A three-dimensional particle model reflecting the shape characteristics of garlic cloves was then constructed, and the physical and contact properties required for DEM analysis were applied. A cylindrical sorter, which is commonly used in field operations, was modeled. The sorting performance was evaluated based on sorting accuracy, misclassification rate, and total sorting time.
The DEM simulation results showed a high sorting accuracy of more than 99%, and the total sorting time was 36 s. These results indicate that DEM-based analysis can be used to evaluate the sorting behavior and performance of a garlic clove sorter before physical fabrication or field application. In addition, precise garlic clove sorting can contribute to reducing the size variability of cloves supplied to a planter and provide basic data for improving single-clove metering stability through the future application of size-specific metering buckets.

Key Words: Garlic clove sorter, Discrete Element Method, Seed grading, Cylindrical sorter, Machine planting

ACKNOWLEDGEMENTS

This work was supported by Korea Institute of Planning and Evaluation for Technology in Food, Agriculture and Forestry (IPET) through the Machinery Mechanization Technology Development Program for Field Farming Program, funded by the Ministry of Agriculture, Food and Rural Affairs (MAFRA) (RS-2023-00236042)

FM-23

Proceedings of The 12th International Symposium on Machinery and Mechatronics for Agriculture and Biosystems Engineering (ISMAB 2026)
20-24 October 2026, Busan, Republic of Korea

HIERARCHICAL GREENHOUSE NAVIGATION USING POINT-LIO LOCALIZATION AND SEMANTIC AISLE FOLLOWING

Hao-Cheng Zuo[1], Bo-Jhih Chang[1] , Ping-Lang Yen[1*]

Department of Biomechatronics Engineering, National Taiwan University,
No. 1, Sec. 4, Roosevelt Road, Taipei 106, Taiwan, ROC.
*Corresponding Author-- Voice: +886 02-3366-5344, Email: plyen@ntu.edu.tw

Abstract: Autonomous greenhouse harvesting robots require reliable navigation both between crop rows and within narrow, unstructured aisles. This study presents a hierarchical global–local navigation framework for a tomato-harvesting robot. Point-LIO is used for 3D greenhouse mapping and global localization, while semantic local navigation is activated inside crop rows. SegFormer-B2 and camera–LiDAR fusion are used to identify the ground–vegetation boundary and generate an in-row navigation centerline. The framework also supports the registration of detected tomato positions in the global map for harvesting-oriented navigation. In greenhouse experiments, the semantic segmentation model achieved 67.2% mIoU, while the 22.5 m in-row navigation test achieved mean absolute lateral and heading errors of 0.026 m and 1.48°, respectively. The results demonstrate the feasibility of combining global localization with semantic local navigation for autonomous greenhouse harvesting applications.

Key Words: Agricultural Robotics, Greenhouse Navigation, Semantic Segmentation, Camera-LiDAR Fusion, Autonomous Harvesting

INTRODUCTION

Agricultural labor shortages have accelerated the development of robotic systems for labor-intensive agricultural operations [1]. Autonomous harvesting robots require not only crop detection and manipulation, but also reliable navigation between working areas and within narrow greenhouse crop rows. However, irregular vegetation and leaves extending into the aisle can interfere with conventional geometry-based navigation and lead to unstable crop-row boundary estimation.

This study proposes a hierarchical global–local navigation framework for an autonomous tomato-harvesting robot. Point-LIO [2] provides 3D mapping and global localization, while SegFormer-B2 [3] and camera–LiDAR fusion are used for semantic aisle following based on the ground–vegetation boundary. The framework is further designed to register tomato positions in the global map, providing a basis for navigation toward harvesting locations.

MATERIALS AND METHODS

1. Autonomous Harvesting Robot Platform

This study uses an autonomous tomato-harvesting robot as the experimental platform. The system consists of a differential-drive chassis, an RGB camera, a 3D LiDAR, an NVIDIA Jetson AGX Orin, and a robotic manipulator. High-level perception and navigation algorithms all run in the ROS 2 Humble environment.

The overall navigation system adopts a hierarchical architecture consisting of a global navigation layer and a semantic local navigation layer. Global navigation guides the robot toward a specified crop row or harvesting pose, while semantic local navigation is activated within the crop row to improve navigation stability in irregular vegetation environments.

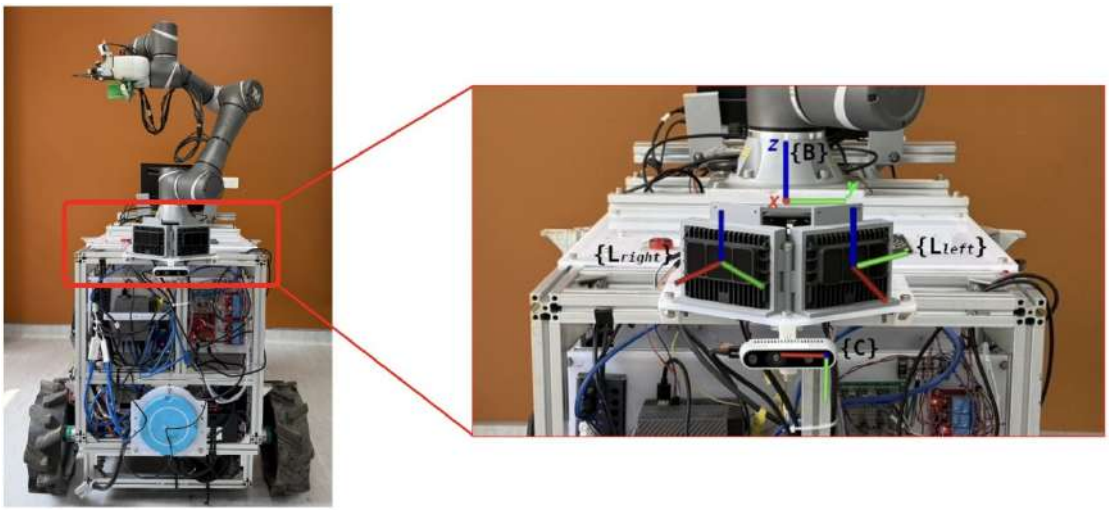

Figure 1. Autonomous greenhouse tomato-harvesting robot and onboard perception system.

2. Point-LIO Mapping and Localization

To obtain global spatial information of the greenhouse environment, a 3D LiDAR and an inertial measurement unit (IMU) are integrated using Point-LIO [2] to construct a 3D point-cloud map. Point-LIO fuses LiDAR and IMU measurements for real-time state

estimation and mapping. The resulting map serves as the global reference for subsequent localization and navigation. During navigation, the robot localizes itself within the pre-built map and continuously obtains its position and orientation in the global coordinate frame. The estimated pose is then used for global waypoint navigation and motion control.

3. Global Waypoint Navigation and Pose Control

The 3D point-cloud map generated by Point-LIO is used as the global reference for waypoint navigation. Based on the target crop row or harvesting pose, a sequence of global waypoints is manually specified in the global map to guide the robot toward the target region. The robot pose in the global coordinate frame is represented as

$$\mathbf{x}_r = [x_r,\ y_r,\ \phi_r]^T$$

and the target waypoint pose is defined as

$$\mathbf{x}_g = [x_r,\ y_r,\ \phi_r]^T$$

The position and heading errors are calculated as

$$e_x = x_g - x_r, e_y = y_g - y_r, e_\phi = \phi_g - \phi_r$$

These errors are used by the motion controller to generate the linear velocity v and angular velocity ω of the differential-drive platform. The robot continuously updates its pose based on Point-LIO localization and moves toward the current waypoint. After the waypoint is reached, the next waypoint is selected. Once the robot enters the target crop row, the system switches to semantic local navigation for stable aisle following.

4. Semantic Local Navigation

- Semantic Segmentation of the Greenhouse Environment

After the robot enters a greenhouse crop row, irregular leaves and stems may extend into the aisle, so path estimation based solely on geometric point clouds is easily disturbed by vegetation. Therefore, this study adopts a local navigation method based on semantic segmentation and camera–LiDAR fusion.

The RGB image is first fed into a SegFormer-B2 model [3] adapted to the greenhouse environment, which classifies the scene into traversable ground, vegetation, infrastructure, and dynamic obstacles.

The four categories are defined as follows:

1. Traversable Ground: areas that the vehicle can traverse, including soil and paved (concrete) aisles
2. Vegetation: tomato plants, leaves, stems, and other canopy vegetation
3. Infrastructure: greenhouse support posts and other fixed structures

4. Dynamic Obstacles: primarily personnel present in the work area

The purpose of this semantic classification is not to precisely identify different plant organs, but to establish an environmental representation sufficient to support vehicle navigation. For navigation, what matters most is determining which areas can be driven through safely and where the actual crop-row boundary lies.

- Camera–LiDAR Semantic Fusion

Semantic segmentation provides class information in the image domain but does not directly provide metric 3D information. Therefore, the segmentation results are fused with the LiDAR point cloud to obtain both semantic and spatial information. Let a 3D point in the LiDAR coordinate frame be denoted as:

$$p_L = [X, Y, Z, 1]^T$$

Using the camera intrinsic matrix $\boldsymbol{K}$and the rigid transformation from the LiDAR frame to the camera frame, the 3D point is projected onto the image plane according to the pinhole camera model:

$$s\mathbf{u} = \mathbf{K}\left[\mathbf{R}_L^C \middle| \mathbf{t}_L^C\right]\mathbf{p}_L$$

where,

$$\mathbf{u} = [u, v, 1]^T$$

represents the image coordinates, s is the scale factor, $\mathbf{K}$ is the camera intrinsic parameter matrix, and

$$\left[\mathbf{R}_L^C \middle| \mathbf{t}_L^C\right]$$

represents the rigid transformation from the LiDAR coordinate frame to the camera coordinate frame. Each LiDAR point projected onto a valid image pixel inherits the corresponding semantic label from the SegFormer output. The resulting semantic point cloud therefore contains both 3D geometric information and semantic class information, which is subsequently used for crop-row boundary extraction and local navigation.

- Ground–Vegetation Boundary Extraction

Instead of using the outer canopy geometry as the navigation boundary, only points classified as traversable ground and vegetation are retained. A dynamic sliding window moves along the direction of travel and identifies the lateral transition between the two semantic classes. The resulting transition points form the left and right crop-row boundaries, and their geometric midpoint is used to generate the local navigation centerline.

- Row-Switching

When the robot reaches the end of a crop row, the continuous ground–vegetation boundary gradually disappears, so the system needs to switch to the row-end

navigation mode. This study uses the vegetation information in the semantic point cloud to locate the crop-row endpoints, and applies DBSCAN [4] to cluster the candidate points to obtain the left and right crop-row corner points. Because the vehicle's rotation during the row-switching process may cause occlusion and measurement jitter, a Kalman filter [5] is further used to track the corner-point positions, in order to maintain a stable estimate of the row-end geometry.

Based on the tracked entry position of the target row, the system computes the lateral and heading errors, and then generates the linear and angular velocities required by the vehicle, allowing the robot to complete the row switch and enter the next crop row.

5. Harvesting-Oriented Navigation Workflow

To support harvesting tasks, detected tomato locations are integrated with the global navigation framework. The detected tomato positions are registered in the global map and subsequently used to determine corresponding harvesting poses for the mobile platform.

When performing a harvesting task, the system first uses global navigation to travel to the target crop row, then switches to semantic in-row navigation to approach the specified harvesting pose. Upon arrival, the vehicle stops so that the manipulator can carry out the subsequent harvesting operation. After the harvesting operation is completed, the system selects the next target and resumes navigation.

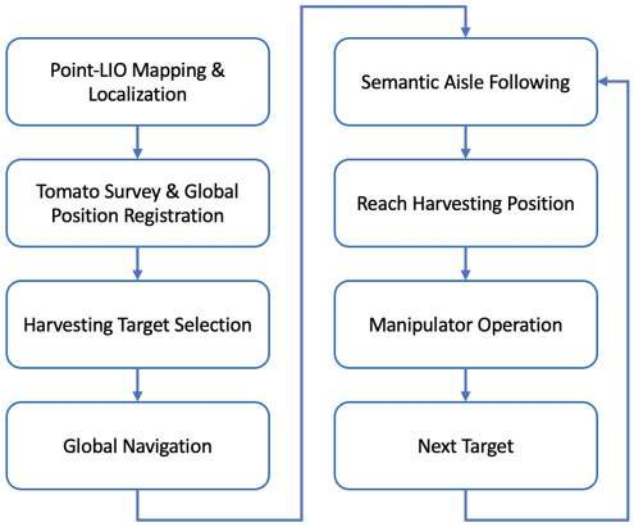

Figure 2. Hierarchical global–local navigation workflow for autonomous tomato harvesting.

RESULTS & DISCUSSION

1. Mapping and Localization

After using Point-LIO to build a 3D point cloud map of the greenhouse environment, the system can reconstruct the crop rows, aisles, and surrounding structures, and use this map as a reference for subsequent global localization and navigation. In actual tests, the robot was able to perform real-time localization within the pre-built map and continuously obtain its global position and orientation information.

These results indicate that Point-LIO mapping and localization provide the global spatial reference required for subsequent navigation. The estimated robot pose can be represented in the same map coordinate frame as the target harvesting poses, providing the basis for task-oriented navigation between different crop rows and working areas.

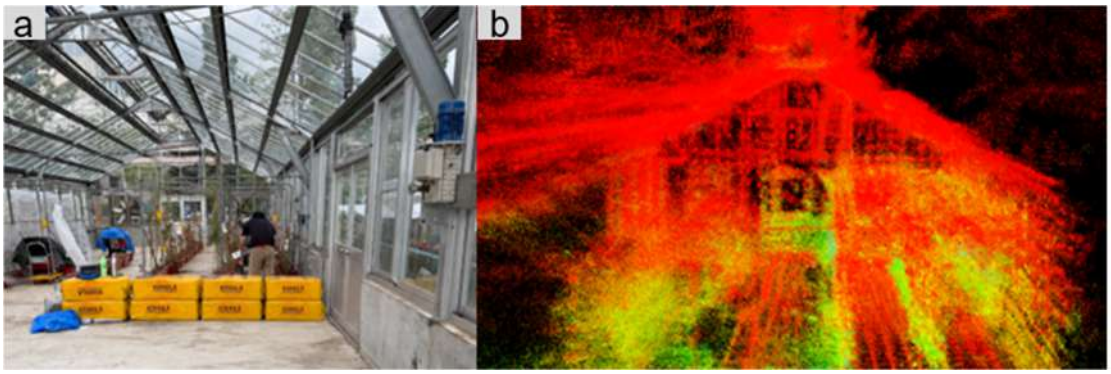

Figure 3. Point-LIO mapping in the greenhouse: (a) experimental environment and (b) reconstructed 3D point-cloud map.

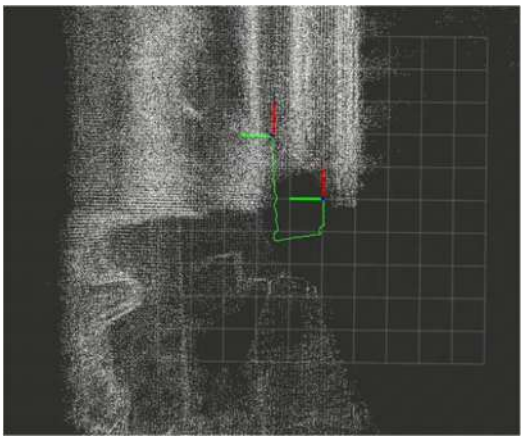

Figure 4. Robot localization in the pre-built map.

2. Semantic Aisle Navigation Performance

The semantic navigation method was validated in an actual greenhouse crop row. The SegFormer-B2 model, adapted to the greenhouse environment, achieved 67.2% mIoU

on the custom greenhouse dataset, showing that the model can effectively distinguish traversable ground from irregular vegetation.

In the 22.5 m autonomous crop-row navigation experiment, the system used a manually controlled center trajectory as the reference baseline. The results show that the mean absolute lateral error (MAE) was 0.026 m and the mean absolute heading error was 1.48˚, while the lateral RMS error was 0.0296 m.

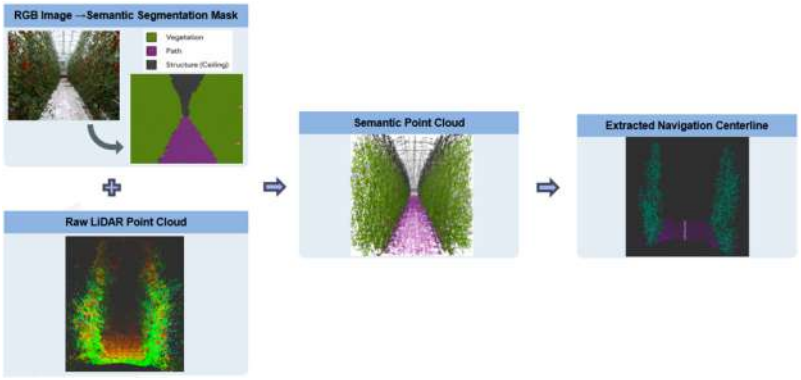

Figure 5. Semantic crop-row centerline extraction using camera–LiDAR fusion.

3. Integrated Navigation for Harvesting Applications

By combining Point-LIO global localization with semantic in-row navigation, the system forms a hierarchical navigation architecture. The global layer provides the robot's position and target-position information within the greenhouse map, while the local layer handles the highly irregular vegetation environment within the crop row. The two navigation approaches are therefore complementary: global navigation determines which work area the robot should travel to, while semantic navigation ensures that the robot can move stably along the aisle after entering a crop row.

Furthermore, tomato positions detected during the survey stage can be registered in the global map and used to determine corresponding harvesting poses. These harvesting poses can then serve as navigation targets for the mobile platform. The robot can first register tomato locations during a survey pass and subsequently revisit the corresponding harvesting regions using global navigation and semantic aisle following. This architecture extends the navigation system from simple aisle following into a mobility system oriented toward harvesting tasks.

However, the experimental validation in this study currently focuses mainly on Point-LIO mapping and localization and semantic crop-row navigation. The complete workflow of “patrolling, recording tomato positions, re-navigating to the harvesting point, and performing the harvest” has not yet undergone end-to-end quantitative testing. Therefore, the complete harvesting workflow is presented as a system-integration framework rather than a fully validated end-to-end harvesting pipeline.

CONCLUSIONS

This study proposes a hierarchical navigation architecture for autonomous greenhouse tomato-harvesting robots, combining Point-LIO mapping and localization, global waypoint navigation, and semantic-segmentation-based local crop-row navigation, and semantic-segmentation-based crop-row local navigation. Point-LIO provides the robot's global position and orientation within the greenhouse map, serving as the navigation basis for traveling to a specified crop row or harvesting area. After the robot enters a crop row, the system uses SegFormer-B2 and camera–LiDAR fusion to build a semantic point cloud, and extracts the navigation centerline from the ground–vegetation interface, reducing interference from irregular canopy geometry during in-row navigation. In actual greenhouse tests, the semantic segmentation model achieved 67.2% mIoU, and over a 22.5 m in-row navigation path, the mean absolute lateral and heading errors were 0.026 m and 1.48°, respectively.

This architecture further provides a basis for registering tomato positions in the global map and determining appropriate harvesting poses for subsequent navigation, extending the system from simple crop-row following to task-oriented autonomous harvesting navigation.

ACKNOWLEDGEMENTS

The authors would like to thank the Taoyuan District Agricultural Research and Extension Station, Ministry of Agriculture, and the private greenhouse farm in Houlong, Miaoli County, for providing experimental sites and support for the greenhouse tomato harvesting experiments.

REFERENCES

[1] V. Marinoudi, C. G. Sørensen, S. Pearson, and D. Bochtis, “Robotics and labour in agriculture. A context consideration,” Biosystems Engineering, vol. 184, pp. 111–121, 2019.

[2] D. He et al., “Point-LIO: Robust high-bandwidth light detection and ranging inertial odometry,” Advanced Intelligent Systems, vol. 5, no. 7, p. 2200459, 2023.

[3] E. Xie, W. Wang, Z. Yu, A. Anandkumar, J. M. Alvarez, and P. Luo, “SegFormer: Simple and Efficient Design for Semantic Segmentation with Transformers,” Advances in Neural Information Processing Systems, vol. 34, pp. 12077–12090, 2021.

[4] M. Ester, H.-P. Kriegel, J. Sander, and X. Xu, “A density-based algorithm for discovering clusters in large spatial databases with noise,” in Proc. 2nd Int. Conf. Knowledge Discovery and Data Mining, 1996, pp. 226–231.

[5] R. E. Kalman, “A New Approach to Linear Filtering and Prediction Problems,” Journal of Basic Engineering, vol. 82, no. 1, pp. 35–45, 1960.

FM-24

Proceedings of The 12th International Symposium on Machinery and Mechatronics for Agriculture and Biosystems Engineering (ISMAB 2026)
20-24 October 2026, Busan, Republic of Korea

FIELD RELIABILITY EVALUATION OF A SELF-BUILT IOT MONITORING DEVICE FOR APPLE COLD STORAGE

Joon-Mo Kangr[1], Hyuck-Joo Kim[1]

[1]Department of Smart Agricultural Engineering, Sunchon National University
*Corresponding Author-- Voice: +82-10-5743-7973, Email: agrihj@scnu.ac.kr

Abstract: Maintaining an apple cold store requires continuous, multi-parameter monitoring, because intermittent manual checks cannot track conditions between inspections. In this study, two self-built IoT monitoring devices—each combining a Raspberry Pi Zero 2 W controller with a DHT22 (temperature/humidity sensor), an SH-NDS-250 (CO_2 sensor), and a ZE03 (ethylene sensor)—were installed just inside the entrance of two commercial apple cold Stores (set-point temperature, 1°C) in Geochang, Gyeongnam Province. From 21 August 2025 to 21 April 2026, the two devices logged 850,303 and 958,585 field records, respectively. Data collection showed that all four measured variables (temperature, humidity, CO_2, and ethylene) had missing data in both cold Stores, but the pattern of missingness differed between them. In Store 1, all four variables dropped out simultaneously on two separate occasions because of an unstable power supply. In Store 2, temperature, humidity, and ethylene were recorded normally, but CO_2 readings stopped completely after 29 December 2025. Over the period of stable operation (1 November 2025–21 April 2026), the actual operating temperature was 0.49°C in Store 1, slightly below the 1°C set point, whereas Store 2 operated continuously at 2.54°C, 1.5°C above the set point. Over eight months of operation in two commercial cold Stores, the self-built apple cold-storage monitoring system developed in this study tracked four measured variables (temperature, humidity, CO_2, and ethylene) and identified two distinct failure modes.

Key Words: apple cold storage, IoT monitoring, sensor reliability, field deployment, fault diagnosis

INTRODUCTION (first level heading, bold, centered)

Prepare Maintaining a stable low-temperature environment during apple storage is central to cold-Store management, and continuously tracking temperature, relative humidity, CO_2 , and ethylene allows early detection of deviations from normal operation. Recent studies have applied IoT sensing to characterize apple cold-storage conditions and surface condensation (Sonawane et al., 2025) and to record environmental variability within commercial cold Stores using multi-point sensing (Jedermann et al., 2026). However, long-term field studies evaluating agricultural IoT devices in terms of data completeness and failure patterns over several months remain relatively scarce, and sensor faults are reportedly common in agricultural IoT systems, according to a review of the current status of sensor fault diagnosis in agricultural IoT (Zou et al., 2023).

This study evaluated the field reliability of a self-built IoT monitoring system deployed for eight months in two commercial apple cold Stores. Specifically, the main objectives were to measure

storage-environment monitoring indicators—temperature, relative humidity, CO_2 , and ethylene—over the long term, to quantify data completeness for each measured variable, and to characterize the failure modes responsible for missing data. In addition, the collected data were used to evaluate whether the measured values in each cold Store matched the respective set-point temperature, thereby confirming the practical applicability of the monitoring system.

MATERIALS AND METHODS

Apple Cold-Storage Environmental Monitoring System and Field Data

Two monitoring devices were self-built around a Raspberry Pi Zero 2 W (Fig. 1, Table 1). As shown in Table 1, each device comprised a temperature/humidity sensor (DHT22), a CO_2 sensor (SH-NDS-250), and an ethylene sensor (ZE03), and was powered by the cold Store's 220 V mains supply. One device was installed just inside the entrance of each of two commercial apple cold Stores (set-point temperature, 1°C) in the Geochang region of Gyeongnam Province. From 21 August 2025 to 21 April 2026, 850,303 and 958,585 field operation records were obtained from Store 1 and Store 2, respectively.

Each device used separate threads to read the temperature/humidity, ethylene, and CO_2 data independently of one another. The values read from each sensor were combined into a single record, transmitted to a central Flask server via MQTT, and simultaneously logged to a file on the device. The polling interval was set to 10 s, but the actual logging interval also included the time required for data processing and transmission. As a result, field data were logged at approximately 20-s intervals, and the median actual logging interval was 22 s in both cold Stores. This delay is commonly observed when a resource-constrained microcontroller processes multiple sensors sequentially, and similar IoT monitoring systems have been reported to show longer-than-intended actual intervals relative to the target transmission period (Rodriguez-Pabon et al., 2022).

Because the CO_2 sensor (SH-NDS-250) reads values via serial (UART) communication, it showed relatively frequent response delays and communication dropouts compared with the other sensors; accordingly, an automatic reconnection routine was applied only to this sensor, keeping the serial connection open at all times but closing and reopening the port after five consecutive non-responses or ten consecutive identical readings. All measured data (temperature, humidity, CO_2, and ethylene) were also uploaded to ThingSpeak, MathWorks' IoT cloud service. The central server stored the incoming data in a database, performed parallel file backups, and provided a real-time dashboard and an alert function for values outside preset ranges. Manufacturer-reported sensor accuracies are summarized in Table 1.

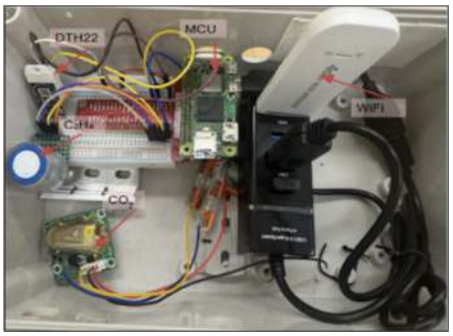

Fig.1 Self-built IoT monitoring device integrating the controller, wireless communication module, and environmental sensors.

Table 1 Configuration of the monitoring device and data.

Component	Specification	Manufacturer accuracy	Role / setting
Controller	Raspberry Pi Zero 2 W	—	Data acquisition and wireless transmission
Temperature/RH	DHT22	Temperature ±0.5°C, humidity ±2–5%	In-store air condition measurement
CO_2	SH-NDS-250	±(2% of full scale + 3% of reading), at 50°C	Gas concentration measurement
Ethylene	ZE03	Not disclosed	Gas concentration measurement
Field installation	Two devices, one per cold Store (2 sites)	—	Just inside entrance of each Store; set point 1°C
Analysis period	2025.08.21–2026.04.21	—	—

Assessment of Data Completeness and Reliability

The collected data were sorted chronologically based on Coordinated Universal Time (UTC), and duplicate records were removed. Records in which relative humidity fell outside the 0–100% range or CO_2 concentration was negative were regarded as sensor errors and excluded from the analysis.

To evaluate data completeness, the entire analysis period was divided into 10-min intervals. For each variable, an interval was classified as valid if it contained six or more error-free measurements, and completeness was defined as the proportion of valid intervals among all intervals. The timing of missing data for temperature, relative humidity, CO_2, and ethylene was also compared to infer the cause of data loss.

Missingness patterns were evaluated by comparing the timing of missing data for temperature, relative humidity, CO_2, and ethylene. Simultaneous interruption of records for all four variables was taken to indicate a device-wide problem, such as a power or communication failure, whereas a persistent anomaly confined to a single variable was taken to indicate a problem with that specific sensor or with its connection or data-processing pathway, warranting priority inspection. However, this comparison of missingness patterns was used only to distinguish whether a failure affected the entire device or was confined to a specific sensor, and was not used on its own to establish the exact physical cause, such as wiring damage or a communication fault.

To evaluate whether the in-store temperature was maintained near the 1°C set point, data from both cold Stores were used from 1 November 2025 to the end of the analysis period, excluding the initial stabilization period (21 August–31 October 2025). The mean and standard deviation were first calculated for temperature, relative humidity, CO_2, and ethylene in each cold Store. Because temperature was recorded at 20-s intervals and consecutive readings were therefore strongly autocorrelated, individual measurements were not used directly in the significance test; instead, daily mean temperatures were calculated and used as the unit of observation. A one-sample t-test was then performed for each cold Store to determine whether the mean temperature over the analysis period differed significantly from the 1°C set point. This

significance test was performed only for temperature, for which a set-point value exists; relative humidity, CO_2, and ethylene, which have no corresponding reference value, were reported only as descriptive statistics (mean and standard deviation).

RESULTS & DISCUSSION

Over the eight-month analysis period, Store 1 and Store 2 logged 850,303 and 958,585 records, respectively. The shaded interval in Fig. 2 represents the initial period, before stable operation was reached, during which apples were loaded and the temperature was brought down. Data completeness was evaluated as the proportion of 10-min intervals in which at least six valid measurements were obtained for each variable. In Store 1, completeness was 87.6% for all four variables (temperature, relative humidity, CO_2, and ethylene). In Store 2, temperature, relative humidity, and ethylene were 99.2% complete, whereas CO_2 completeness was only 52.9% (Table 2). Because all four variables were missing to the same extent in Store 1, this points to a device-wide problem, whereas in Store 2, where temperature, relative humidity, and ethylene remained stable but only CO_2 data were missing, the problem appears to be confined to the CO_2 sensor alone.

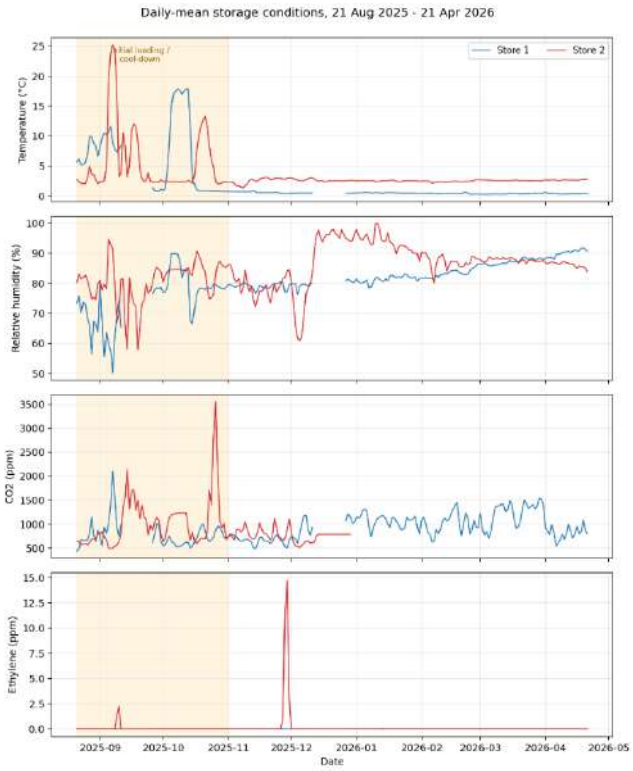

Fig. 2. Daily mean temperature, relative humidity, CO_2, and ethylene in Stores 1 and 2 throughout the analysis period.

In Store 1, temperature, humidity, CO_2, and ethylene data were entirely absent for roughly two weeks on two separate occasions, from 11 to 26 September 2025 and from 11 to 26 December 2025. These two interruptions account for essentially all of the missing data in Store 1 (12.4% of the analysis period). This was not attributable to the failure of a specific sensor but rather to an unstable power supply in the cold Store, which left the entire device offline during these periods. In Store 2, by contrast, temperature, humidity, and ethylene were recorded normally, but the CO_2 readings increasingly repeated the same value over time before stopping

completely after 29 December 2025. The device includes a function that automatically attempts to reconnect when the CO_2 sensor repeatedly fails to respond or returns the same value, but this did not restore normal operation. This failure was confirmed to result from a problem in the wiring connecting the sensor to the Raspberry Pi.

Table 2. Interval-based data completeness (%), 21 Aug 2025–21 Apr 2026.

Store	Temperature	Relative humidity	CO_2	Ethylene
1	87.6	87.6	87.6	87.6
2	99.2	99.2	52.9*	99.2

Excluding the initial stabilization period, from 1 November 2025 onward, the mean temperatures calculated from the raw recorded values were 0.49±0.33°C and 2.54±0.30°C in Stores 1 and 2, respectively, differing from the 1°C set point by −0.51°C and +1.54°C. Over the same period, relative humidity averaged 83.4±4.7% and 87.0±7.7%, and recorded CO_2 values averaged 966±283 ppm and 767±184 ppm, respectively (Table 3). A one-sample t-test comparing the daily mean temperature with the 1°C set point showed a statistically significant difference in both cold Stores ($p<0.001$). The 95% confidence intervals for the mean daily temperature were 0.47–0.51°C and 2.51–2.58°C, respectively. Because the overall variability of the data measured in both cold Stores was relatively small, the cooling equipment itself was judged to be operating stably. However, the fact that Store 2 was consistently maintained above the set point is a problem that intermittent manual inspection could easily overlook, and monitoring with the present system over an extended period is expected to allow such problems during apple storage to be detected and prevented at an early stage. As already reported in previous studies (Akdemir and Tagarakis, 2014; Jedermann et al., 2026), however, temperature and humidity can also vary by location within a cold Store, so future work should supplement this approach with measurements at multiple points within each Store.

Table 3. Mean ± standard deviation of each variable during the stable-operation period, 1 Nov 2025–21 Apr 2026.

Store	Temperature (°C)	humidity (%)	CO_2 (ppm)	Ethylene (ppm)
1	0.49 ± 0.33	83.4 ± 4.7	966 ± 283	0.00 ± 0.02†
2	2.54 ± 0.30	87.0 ± 7.7	767 ± 184*	0.18 ± 1.95‡

CONCLUSIONS

A self-built IoT system combining temperature, humidity, CO_2, and ethylene sensors with a Raspberry Pi Zero 2 W controller was installed in two commercial apple cold Stores and operated for eight months. During this period, the system logged more than 1.8 million records while maintaining continuous multi-parameter monitoring. Interval-based completeness exceeded 87% for all four variables in Store 1 and exceeded 99% for temperature, relative humidity, and ethylene in Store 2, but the CO_2 channel in Store 2 began returning a fixed value

and then stopped completely after 29 December 2025. The two instances of missing data had different causes: in Store 1, the entire device went offline twice because of an unstable power supply, whereas in Store 2 the failure was confined to the CO_2 sensor and its wiring. The study also confirmed that Store 2 had been operating 1.5°C above its set point, a problem that may be difficult to detect through periodic inspection alone.

These results confirm that long-term, continuous monitoring is feasible using the system developed in this study. Based on the problems identified in this study, a backup power supply for power outages, communication buffering, redundant gas-sensor wiring, or periodic self-diagnosis appear to be needed. In addition, because each device measured only a single point near the entrance, expanding monitoring to multiple locations within each cold Store and independently validating sensor accuracy against reference instruments are identified as necessary next steps.

ACKNOWLEDGEMENTS

This work was supported by the Rural Development Administration, Republic of Korea, through the Project for Developing Technology to Utilize Postharvest Management Data for Agricultural and Livestock Products (Project No. RS-2022-RD010023).

REFERENCES

Akdemir, S., and A. Tagarakis. 2014. Investigation of spatial variability of air temperature, humidity and velocity in cold stores by using management zone analysis. Tarım Bilimleri Dergisi-Journal of Agricultural Sciences 20: 175-186.

Jedermann, R., T. G. Hoffmann, D. A. Neuwald, F. Büchele, and P. V. Mahajan. 2026. Time-series dataset of air temperature, fruit surface temperature and humidity in commercial apple cold storage. Data in Brief 68: 113157.

Rodriguez-Pabon, C., G. Riva, C. Zerbini, J. Ruiz-Rosero, G. Ramirez-Gonzalez, and J. C. Corrales. 2022. An adaptive sampling period approach for management of IoT energy consumption: Case study approach. Sensors 22(4): 1472.

Sonawane, A. D., T. G. Hoffmann, R. Jedermann, M. Linke, and P. V. Mahajan. 2025. Investigating apple surface condensation and mass loss with IoT and predictive modelling. Postharvest Biology and Technology 225: 113520.

Zou, X., W. Liu, Z. Huo, S. Wang, Z. Chen, C. Xin, Y. Bai, Z. Liang, Y. Gong, Y. Qian, and L. Shu. 2023. Current status and prospects of research on sensor fault diagnosis of agricultural Internet of Things. Sensors 23(5): 2528.

Smart Farm Systems and Renewable Energy 3 (SF-3)



SF-11

Proceedings of The 12th International Symposium on Machinery and Mechatronics for Agriculture and Biosystems Engineering (ISMAB 2026)
20-24 October 2026, Busan, Republic of Korea

SENSOR PLACEMENT STRATEGY FOR ENVIRONMENTAL MONITORING IN VERTICAL FARMS BASED ON SPATIAL, VERTICAL, AND TEMPORAL VARIABILITY

Arnab Majumder[1], Md Razob Ali[1], Gusti Ayu Putri Mei Ulianti[1], Md Nasim Reza[1,2], Choa Mun Yun[3], Sun-Ok Chung[1,2*]

[1]Department of Agricultural Machinery Engineering, Graduate School, Chungnam National University, Daejeon 34134, Republic of Korea
[2]Department of Smart Agricultural Systems, Graduate School, Chungnam National University, Daejeon 34134, Republic of Korea
[3]SherpaSpace Inc., Daejeon 34028, Republic of Korea
*Corresponding Author - Voice: +82-(0)42-821-6712, Email: sochung@cnu.ac.kr

Abstract: Precise environmental monitoring is essential for maintaining uniform crop growth conditions in vertical farms. However, multilayer cultivation can generate spatial, vertical, and temporal variability in temperature, relative humidity, CO_2 concentration, and photosynthetic photon flux density (PPFD). Installing sensors at every cultivation layer and section may improve monitoring accuracy but increases system cost, installation complexity, and data-management requirements. The uniqueness of this study is a variability-based sensor-placement strategy that identifies representative nodes by evaluating spatial, vertical, and temporal data redundancy. The vertical farm consisted of 12 cultivation layers, with three beds per layer, resulting in 36 beds. One environmental sensor node was installed at the central canopy-level position of each bed, requiring 36 nodes. The 12 layers were grouped into six-layer pairs, and three supplementary nodes were installed for each pair to evaluate vertical and spatial variability, requiring 18 additional nodes. Thus, the initial monitoring system comprised 54 sensor nodes. Each node measured temperature, relative humidity, CO2 concentration, and PPFD. Data were collected continuously for one week. Spatial variability was assessed using heatmaps, descriptive statistics, and coefficients of variation, whereas temporal variability was evaluated using time-series patterns. Correlation and statistical analyses identified nodes exhibiting similar trends and insignificant differences. The results showed that edge nodes captured boundary effects, whereas central canopy-level nodes represented the crop-zone microclimate. Several nodes provided overlapping information, indicating that the sensor count could be reduced by approximately 40-60% without significantly decreasing monitoring accuracy. The proposed strategy supports cost-effective, scalable sensor deployment in commercial vertical farms.

Key Words: Environmental sensing, Microclimate variability, Sensor placement, Spatiotemporal monitoring, Vertical farm

INTRODUCTION

Vertical farms integrate multilayer cultivation, artificial lighting, hydroponic nutrient delivery, and environmental control to support year-round crop production within a compact footprint. By stacking cultivation beds, these systems can increase production per unit of land and reduce exposure to outdoor weather variability. Their performance, however, depends on maintaining suitable crop-zone conditions throughout the facility. Temperature, relative humidity, carbon dioxide (CO_2) concentration, and light intensity influence crop physiology and growth uniformity. Environmental monitoring must therefore describe the conditions experienced by the canopy rather than conditions at one convenient room-level position (Ahamed et al., 2023; Zakir et al., 2025).

Active environmental control does not guarantee spatial uniformity. Heat released by lighting can accumulate within individual cultivation layers, and restricted clearance between stacked beds can limit air mixing. Fans, air-conditioning outlets, return-air paths, structural frames, walls, and neighboring racks can create localized airflow patterns. Crop transpiration further modifies temperature and humidity around the canopy. These interacting factors can generate microclimates even when the facility-level controller indicates stable operation. A single sensor may consequently fail to represent boundary beds, poorly ventilated layers, or positions affected by lighting geometry. Airflow distribution and removal of lighting-generated heat remain important challenges in indoor vertical farming (Ahamed et al., 2023).

Environmental heterogeneity can be evaluated in spatial, vertical, and temporal dimensions. Spatial variability describes differences among racks, beds, and horizontal positions. Vertical variability describes differences among top, middle, and bottom cultivation layers, which may result from buoyancy, accumulated heat, and obstruction of airflow. Temporal variability reflects changes associated with lighting schedules and cyclic operation of ventilation, cooling, circulation, and nutrient-supply equipment. These dimensions should be evaluated together because two nodes with similar average values may respond differently during an operational transition. Controlled-environment studies have demonstrated measurable spatial, vertical, and temporal differences in temperature and humidity, confirming the need to verify representativeness before reducing measurement locations (Reza et al., 2023).

Wireless sensor networks can increase measurement coverage, but dense deployment raises hardware, calibration, communication, maintenance, and data-management requirements. Total monitoring cost includes not only the sensing elements but also installation, network infrastructure, database capacity, and long-term system management (Morella et al., 2023). Dense networks may also contain redundant nodes when neighboring positions record highly similar ranges and synchronized temporal patterns. An effective placement strategy should retain canopy and boundary positions that capture distinct behavior while removing positions that contribute little additional information. This requires variable-specific evaluation because temperature, humidity, CO_2, and light do not necessarily have the same spatial distribution.

A practical strategy is to use central canopy-level nodes for routine bed-level monitoring and supplementary nodes for evaluating layer and boundary effects. Descriptive statistics and coefficients of variation can quantify dispersion, heatmaps can show spatial structure, and synchronized time-series and correlation analyses can identify overlapping behavior. Therefore, this study evaluated spatial, vertical, and temporal variability in temperature, relative humidity, CO_2 concentration, and light intensity using a 54-node monitoring layout in a vertical farm. The objectives were to characterize rack- and layer-specific patterns, identify potentially redundant locations, and determine whether a reduced configuration could maintain representative environmental information while lowering monitoring cost and complexity.

MATERIALS AND METHODS

VERTICAL FARM AND MONITORING LAYOUT

The experiment was conducted in an indoor vertical farm at the Department of Agricultural Machinery Engineering, Chungnam National University, Daejeon, Republic of Korea. The monitoring area comprised four rack sections. Each section contained three vertical cultivation layers, and each layer contained three beds, resulting in 12 layers and 36 beds. Each bed measured approximately 0.90 m × 0.60 m. LED panels provided artificial lighting under a 16 h light and 8 h dark photoperiod. A circulating hydroponic system supplied nutrient solution through reservoir tanks, pumps, and solenoid valves.

One environmental sensor node was positioned at the central canopy-level location of each bed to characterize the local crop-zone environment. This arrangement required 36 bed-level nodes. Central placement was selected as the primary monitoring position because it was less directly affected by a single wall or structural boundary and could be aligned with the crop canopy. The central nodes were used as candidate representative positions, while supplementary nodes were used to examine whether vertical and boundary conditions were adequately represented.

SENSOR NODE AND CALIBRATION

Each wireless node integrated sensors for air temperature, relative humidity, CO_2 concentration, and light intensity. The node transmitted timestamped observations through a Wi-Fi router to a network server, where the records were stored in a database. The data structure included timestamp, rack section, cultivation layer, bed position, node identifier, temperature, relative humidity, CO_2 concentration, and light intensity. This standardized identification scheme allowed synchronized comparison among horizontal positions, vertical layers, and rack sections.

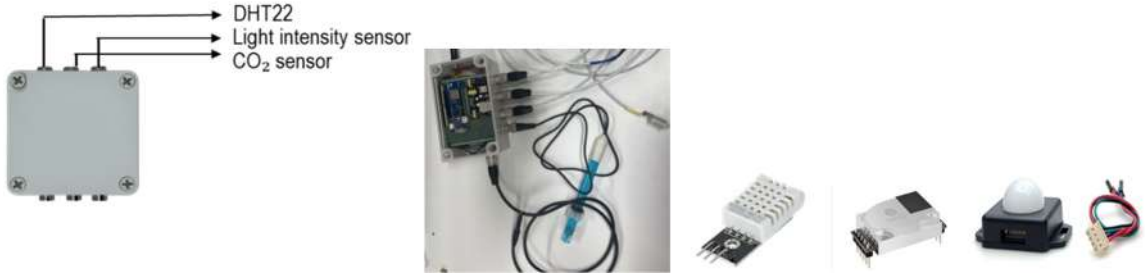

Fig.1 Sensor node (six pins), temperature and humidity, CO_2, light intensity sensor

Table 1. Calibration conditions and reference instruments or standards used for environmental sensor evaluation.

Parameter	Sensor model	Operating range	Working voltage	Accuracy	Max. sampling frequency	Resolution	Response time
Temperature / RH	DHT22	-40ºC to ± 80ºC, 0% to 100%	3.3 –6 V	RH ± 2%, temp. ±0.5 ºC	0.5 Hz	0.1 % RH, 0.1 ºC	2 s
CO_2 concentration	CM1106	0 – 5000 ppm	4.5 V – 5.5 V	± 50 ppm	1 Hz	1 ppm	±120 s
Light intensity (PPFD)	P5144-9	1-65,535 lx	3.3 V – 5 V	± 20%	8 Hz	1 lx	~0.5 ms

Before field deployment, the sensors were checked against reference instruments, including a thermo-hygrometer, CO_2 analyzer, and lux meter. Reference conditions were distributed across the operating range, and paired sensor and reference observations were recorded for five minutes at each condition. Linear regression in the form y = ax + b was used to estimate the calibration slope and offset. The calibration assessment considered the distribution of reference points, agreement with the regression line, and the magnitude of residual error. Nodes showing unstable output or unacceptable disagreement were corrected or excluded before installation.

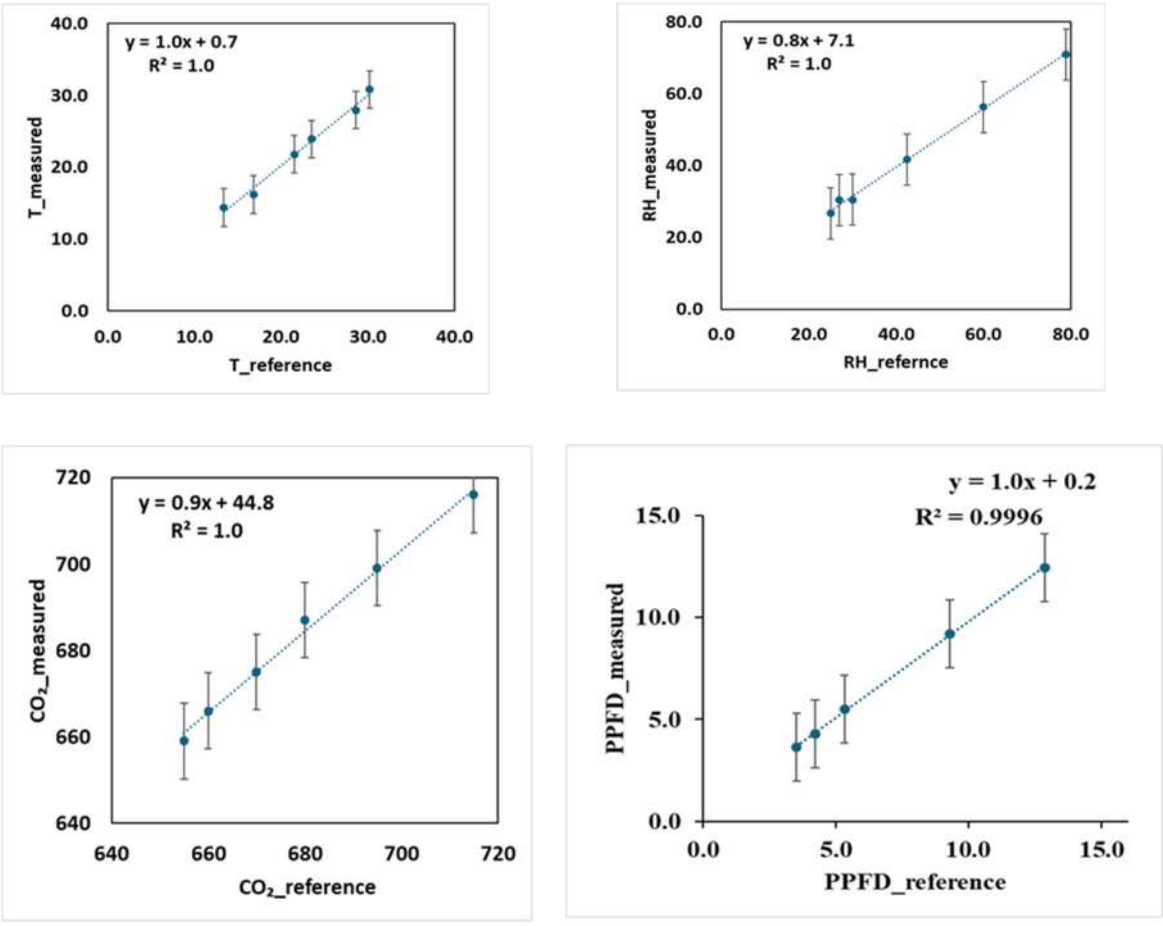

Fig.2 Calibration against reference instruments

Table 2. Calibration conditions and reference instruments or standards used for environmental sensor evaluation.

Variable	Reference instrument	Manufacturer/ model	Calibration range	No. of points	Duration/ point	Evaluation metrics
Temperature and humidity	Digital thermo-hygrometer	CAS / T023/ China	Temperature: 0–50°C; RH: 20–95%	Temperature: 5; RH: 5	10 min	MAE, RMSE, mean bias, and R^2
CO2	Portable NDIR CO_2 gas detector	Bosean / BH-90A-CO2 / Henan,China	0 – 1500 ppm	5	5 min	MAE, RMSE, mean bias, and R^2
Light intensity	Digital illuminance meter	JW Company, China / WT81	0–200,000 lx	5	5 min	MAE, RMSE, mean bias, and R^2

SUPPLEMENTARY LAYER-PAIR NODES

To assess variability that might not be represented by the central bed nodes, the 12 cultivation layers were grouped into six adjacent layer pairs. Three supplementary nodes were assigned to each pair and positioned to capture differences between the paired layers and nearby boundary conditions. This arrangement added 18 nodes, producing a complete network of 54 nodes. The combined design provided one permanent candidate node for every bed and targeted observations for testing vertical and boundary representativeness.

The supplementary layout was intended for sensor-reduction analysis rather than uniform permanent duplication. A supplementary node was considered necessary when it captured a persistent vertical gradient, a boundary-sensitive response, or a temporal pattern that differed from the corresponding central node. When supplementary and central nodes showed small differences and similar time-series behavior, the supplementary position was treated as a candidate for removal. The allocation and monitoring function of each node group are summarized in Table 1.

Table 2. Allocation of environmental sensor nodes in the 12-layer vertical farm.

Node group	Calculation	Number of nodes	Monitoring purpose
Central bed nodes	12 layers × 3 beds	36	Canopy-zone conditions in each bed
Layer-pair nodes	6 pairs × 3 nodes	18	Vertical and boundary variability
Complete system	36 + 18	54	Spatial, vertical, and temporal monitoring

DATA COLLECTION AND ANALYSIS

Environmental observations were collected continuously for seven days under normal vertical-farm operation. The monitoring period covered repeated light and dark cycles so that responses associated with the 16 h/8 h photoperiod could be evaluated. Before formal comparison, the system was allowed to stabilize, and incoming records were checked for

missing values, invalid readings, repeated timestamps, and communication interruptions. Measurements from all nodes were aligned by timestamp before spatial and temporal analyses. For each variable and node, the mean, standard deviation (SD), and coefficient of variation (CV) were calculated. The CV was calculated as the SD divided by the mean and expressed as a percentage. Rack-level statistics were used to compare overall environmental stability, while bed- and layer-level heatmaps were used to display horizontal and vertical gradients. Layer means were calculated separately for the top, middle, and bottom levels. The analysis retained node-level information and did not combine different rack sections into one facility-wide mean.

Temporal behavior was examined using synchronized time-series plots. Light and dark periods and recurring control responses were considered when interpreting node similarity. Pairwise correlation and statistical comparisons were used to identify positions with overlapping information or no meaningful difference from representative central locations. Sensor-reduction decisions considered preservation of temporal patterns, boundary-sensitive measurements, vertical gradients, and the stronger position dependence of light measurements. Potential reduction was expressed relative to the complete 54-node layout.

RESULTS & DISCUSSION

SPATIAL AND VERTICAL ENVIRONMENTAL VARIABILITY

The rack-level statistics indicated stable temperature but clear differences in the magnitude and variability of the other environmental variables. Mean temperature ranged from 23.1 to 23.6 °C among the four racks, with SD values of 0.19-0.22 °C and CV values of 0.80-0.93%. Mean relative humidity ranged from 61.5 to 67.4%. Its CV was lowest in Rack 3 (1.87%) and highest in Rack 2 (3.25%). Mean CO_2 concentration was approximately 825 ppm in Racks 1 and 3 but approximately 545-546 ppm in Racks 2 and 4. CO_2 CV values remained between 2.51 and 2.83%. Light intensity showed the greatest relative variability, with CV values of 3.60% in Racks 1 and 3 and 6.68% in Racks 2 and 4.

Rack	Statistics	Temperature (°C)	RH (%)	CO_2 (ppm)	Light(lx)
Rack1	Mean	23.1	67.3	825	1700
	SD	0.20	1.49	23.32	61.24
	CV (%)	0.88%	2.21%	2.83%	3.60%
Rack2	Mean	23.6	61.7	545.7	2050
	SD	0.21	2.01	14.25	136.93
	CV (%)	0.90%	3.25%	2.61%	6.68%
Rack3	Mean	23.3	67.4	825	1715
	SD	0.22	1.26	23.32	61.24
	CV (%)	0.93%	1.87%	2.83%	3.60%
Rack4	Mean	23.6	61.5	545	2055

SD	0.19	1.79	13.69	136.93
CV (%)	0.80%	2.90%	2.51%	6.68%

Spatial maps showed consistent horizontal and vertical structure within individual racks. In Rack 1, temperature increased from 22.90-23.00 °C at the top positions to 23.30-23.50 °C at the bottom positions. Relative humidity decreased from 68.5-69.3% at the top to 65.0-66.2% at the bottom. CO_2 concentration increased from 790-810 ppm to 840-860 ppm, while light intensity increased from 1600-1700 lux to 1700-1800 lux. Rack 3 showed a similar pattern, with temperature increasing from 23.1-23.2 °C at the top to 23.5-23.7 °C at the bottom and relative humidity decreasing from 68.4-69.2% to 65.6-66.4%.

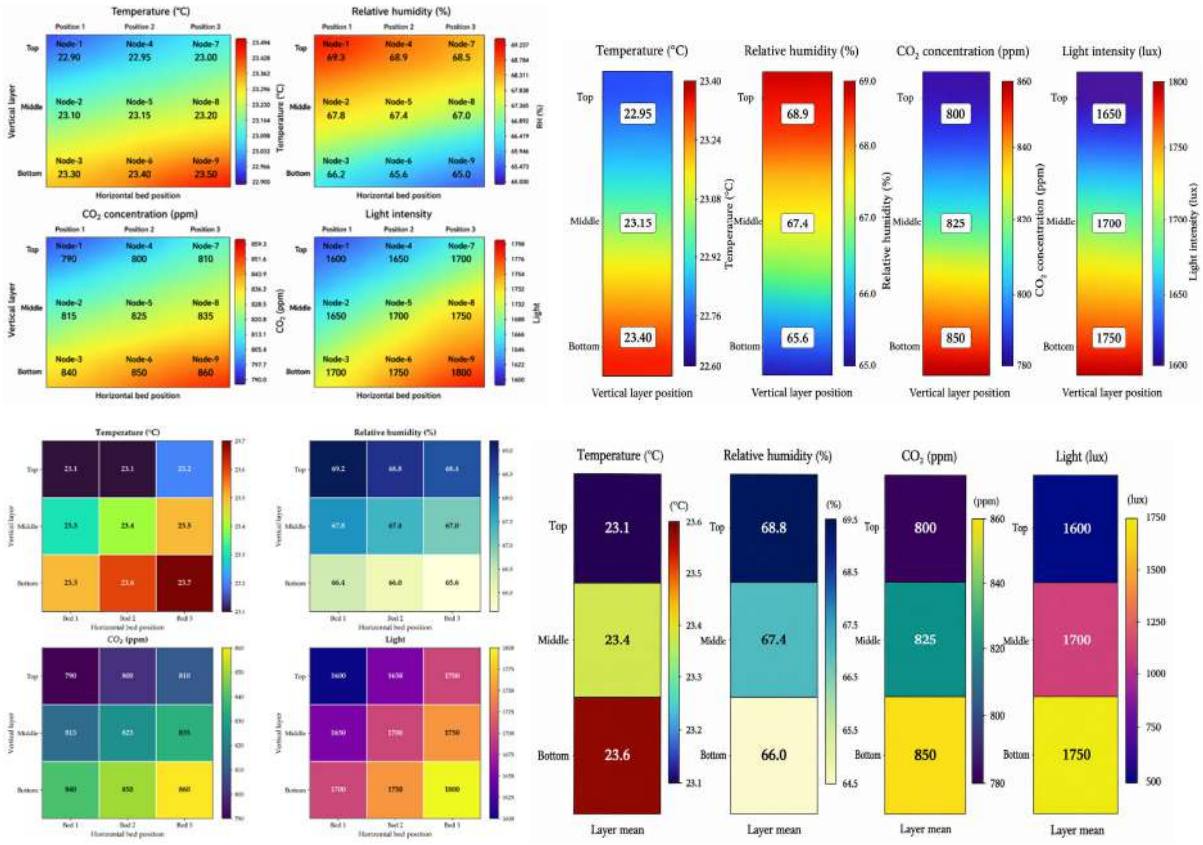

Fig.1 Spatial and vertical variability of rack-1 and rack-3

Racks 2 and 4 operated at lower relative humidity and CO_2 levels but showed comparable vertical directions. In Rack 2, temperature increased from 23.20-23.50 °C at the top to 23.70-23.90 °C at the bottom. Relative humidity decreased from 63.5-65.0% to 59.0-60.0%, CO_2 increased from 525-535 ppm to 560-565 ppm, and light intensity increased from 1850-1950 lux to 2150-2250 lux. Rack 4 showed temperature values of 23.4-23.5 °C at the top and 23.8-23.9 °C at the bottom. Relative humidity decreased from 63.0-64.0% to 59.0-60.0%, CO_2 increased from 525-535 ppm to 555-565 ppm, and light intensity increased from 1850-1950 lux to 2150-2250 lux.

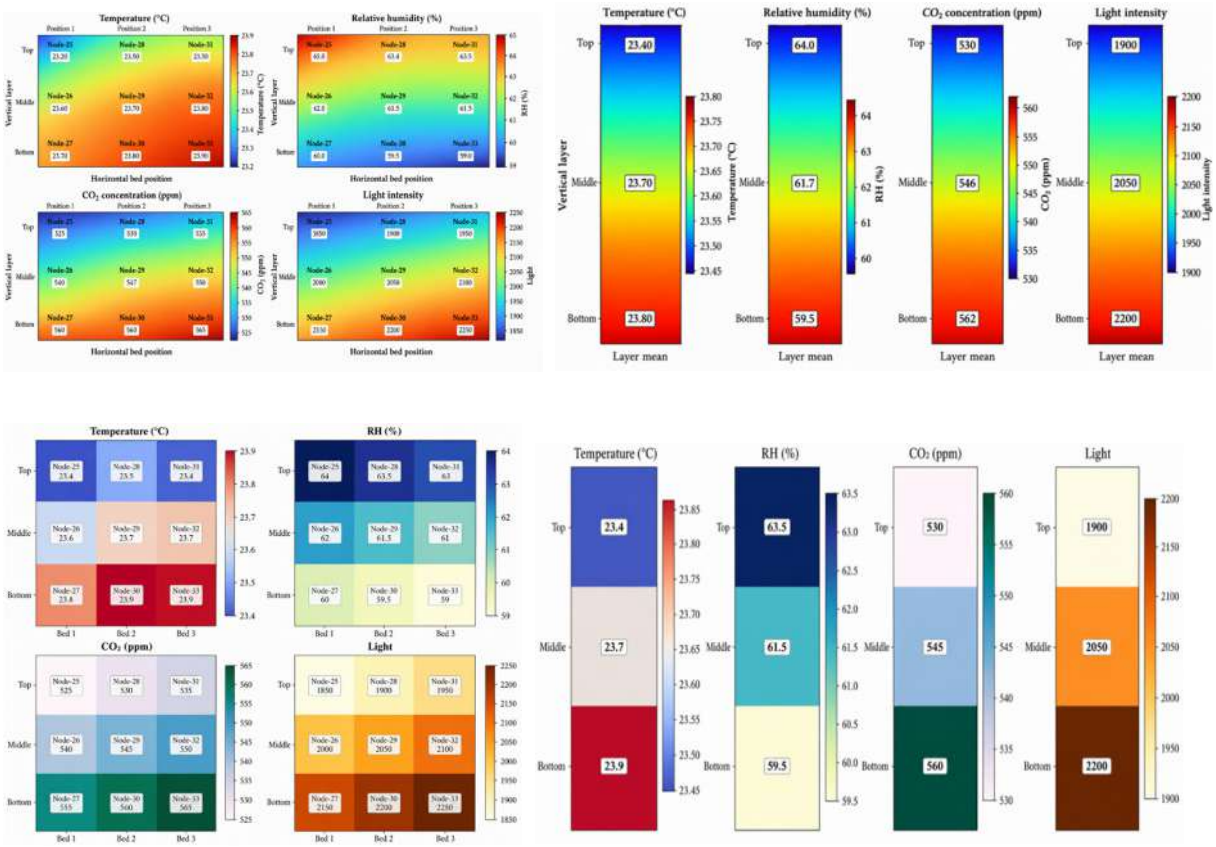

Fig.1 Spatial and vertical variability of rack-2 and rack-4

The repeated vertical direction across the four racks indicates that cultivation height influenced the measured environment despite active control. Temperature, CO_2 concentration, and light intensity generally increased toward the bottom layer, whereas relative humidity decreased. Horizontal differences within a layer were smaller than the top-to-bottom differences for most variables, although edge positions remained important for detecting boundary effects. These results support retaining selected layer-sensitive and boundary nodes rather than assuming that one cultivation level represents every level (Reza et al., 2023).

TEMPORAL SIMILARITY AND SENSOR REDUNDANCY

The synchronized records showed repeated temporal patterns associated with daily operation. Temperature varied within a comparatively narrow band, whereas relative humidity, CO_2 concentration, and light intensity displayed larger cyclic changes. Nodes within the same rack commonly followed similar timing, but their baselines remained separated according to layer and position. The parallel trajectories indicated that several neighboring locations responded to the same environmental-control events, while the vertical offsets confirmed that temporal similarity alone did not eliminate the need to preserve representative layer information.

Light measurements were strongly linked to the photoperiod and showed distinct transitions between illuminated and dark conditions. Their higher rack-level CV and larger vertical gradients confirmed that light sensing required a more conservative placement rule than temperature sensing. CO_2 records also showed cyclic behavior and clear rack-level differences, indicating that mixing and local supply or uptake conditions should be considered before nodes are removed. Accordingly, redundancy was interpreted using both correlation and magnitude

of difference. Nodes were treated as interchangeable only when they showed similar temporal patterns and sufficiently small spatial or vertical differences.

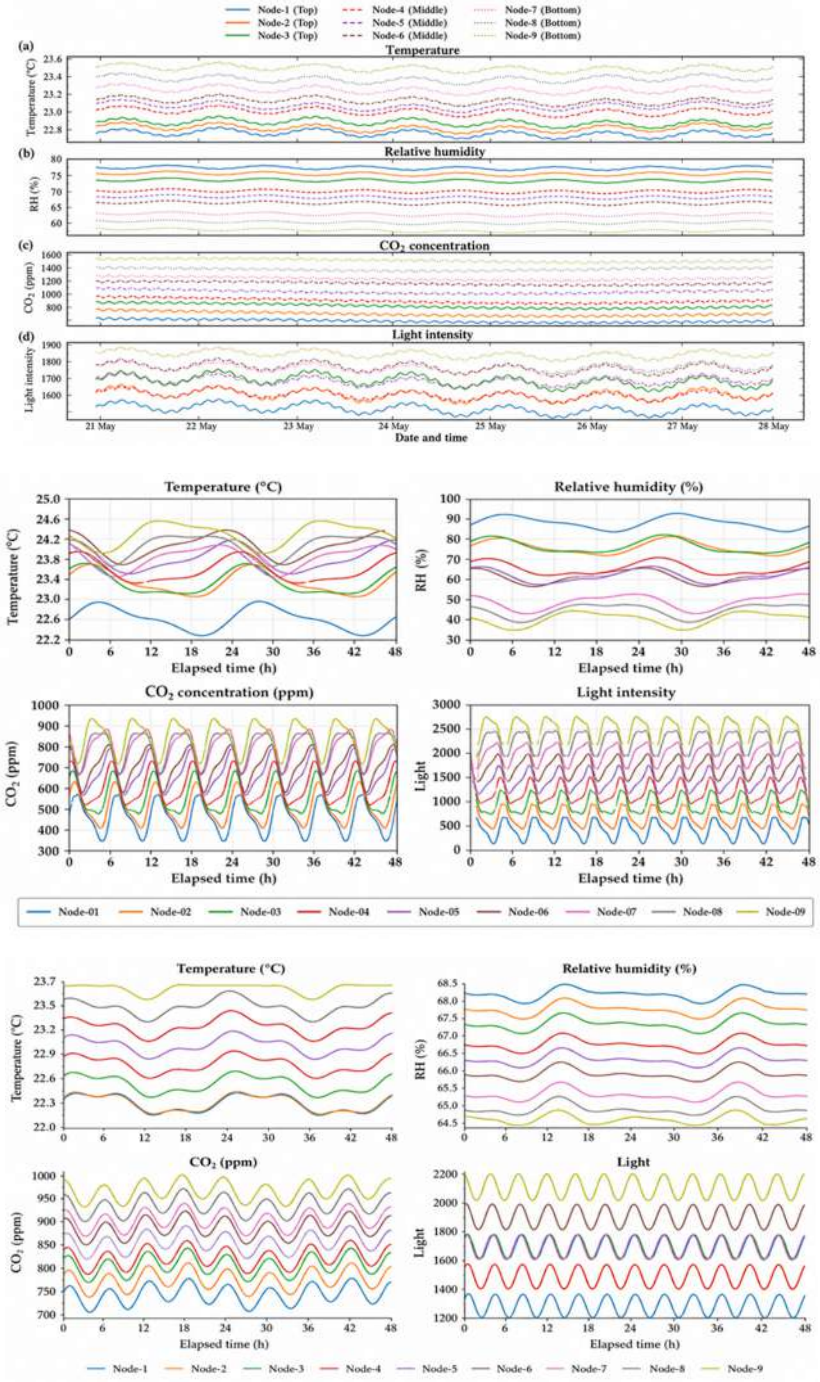

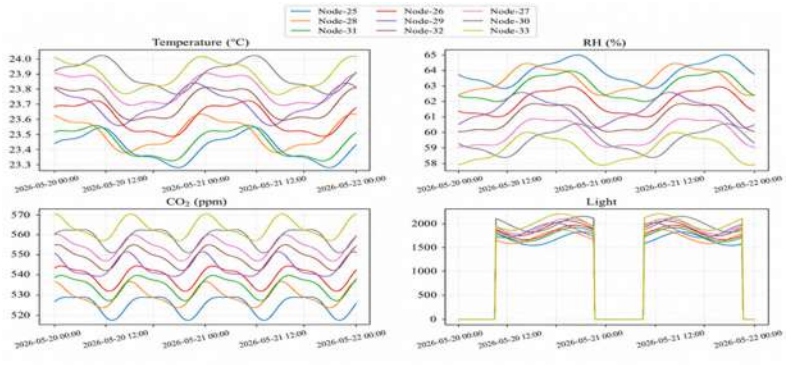

Fig.1 Temporal variability of rack-1, rack-2, rack-3, rack-4

The combined comparisons indicated that centrally positioned sensors could represent overall bed conditions when within-bed spatial differences were small. Selected supplementary nodes remained necessary for capturing layer gradients and boundary effects. Under this arrangement, approximately 40-60% of the sensor and monitoring cost could potentially be reduced while maintaining essential environmental information. This range represents a configuration-dependent estimate rather than a universal reduction rate. A conservative design should retain more nodes in racks with stronger gradients or higher light variability, and the selected network should be re-evaluated after changes in crop canopy, airflow, or lighting arrangement.

IMPLICATIONS FOR PRACTICAL DEPLOYMENT

A reduced network can lower hardware acquisition, calibration workload, wireless traffic, database volume, and maintenance requirements. These benefits are important because installed monitoring cost extends beyond sensor purchase and includes communication and system-management resources (Morella et al., 2023). The results support a central-bed-plus-selected-boundary strategy in which the 36 canopy-level nodes provide routine bed coverage and a smaller set of supplementary nodes preserves information on vertical and boundary behavior.

The findings should be interpreted within the tested facility and operating period. The analysis covered four racks and seven days of normal operation, and the observed gradients may change with crop growth stage, canopy density, fan settings, cooling load, or seasonal conditions. Sensor reduction should therefore follow a staged procedure: deploy a dense diagnostic network, quantify spatial and temporal representativeness, select essential nodes, and validate the reduced configuration under additional operating conditions. Longer experiments and within-bed comparison of center and corner positions are needed before the same configuration is generalized to commercial facilities.

CONCLUSIONS

The 54-node network characterized spatial, vertical, and temporal variability in temperature, relative humidity, CO_2 concentration, and light intensity across four vertical-farm racks. Temperature remained comparatively stable, with rack-level CV values below 1%, while relative humidity and CO_2 showed moderate variation. Light intensity had the highest relative

variability, reaching a CV of 6.68% in Racks 2 and 4. Across the racks, bottom layers were generally warmer and had higher CO_2 and light intensity, whereas relative humidity was lower than at the top layers. These repeated gradients demonstrated that measurements from one cultivation level should not automatically represent the full rack.

Central canopy-level nodes captured the dominant bed-level condition, while supplementary nodes identified boundary and layer-specific effects. The combined use of descriptive statistics, heatmaps, time-series comparison, correlation, and statistical testing provided a practical basis for distinguishing representative and redundant positions. The results indicated that a central-bed-plus-selected-boundary configuration could potentially reduce sensor and monitoring cost by approximately 40-60% without removing essential layer information. Light sensing requires more conservative placement because of its dependence on lamp geometry and shading. Future work should validate the reduced network over longer periods, different crop growth stages, altered airflow regimes, and commercial-scale facilities.

ACKNOWLEDGEMENTS

This work was supported by the Korea Institute of Planning and Evaluation for Technology in Food, Agriculture and Forestry (IPET) through K-vertical Globalization Project, funded by Ministry of Agriculture, Food and Rural Affairs (MAFRA) (RS-2025-02283034), Republic of Korea.

REFERENCES

Ahamed, M. S., M. Sultan, D. Monfet, M. S. Rahman, Y. Zhang, A. Zahid, M. Bilal, T. Ahsan, and Y. Achour. 2023. A critical review on efficient thermal environment controls in indoor vertical farming. Journal of Cleaner Production 425: 138923. https://doi.org/10.1016/j.jclepro.2023.138923.

Morella, P., M. P. Lamban, J. Royo, and J. C. Sanchez. 2023. Vertical farming monitoring: How does it work and how much does it cost? Sensors 23(7): 3502. https://doi.org/10.3390/s23073502.

Reza, M. N., M. N. Islam, M. Z. Iqbal, M. S. N. Kabir, M. Chowdhury, M. A. Gulandaz, M. Ali, M. K. Jang, and S. O. Chung. 2023. Spatial, temporal, and vertical variability of ambient environmental conditions in Chinese solar greenhouses during winter. Applied Sciences 13(17): 9835. https://doi.org/10.3390/app13179835.

Zakir, E., M. N. Reza, M. R. Karim, G. A. P. M. Ulianti, M. R. Ali, H. Jin, S. O. Chung, and M. S. N. Kabir. 2025. Remote management and variability assessment of environmental conditions for smart vertical farms: A review. Precision Agriculture Science and Technology 7(2): 114-133. https://doi.org/10.22765/pastj.20250010.APPENDIX (optional) or NOMENCLATURE (optional)

SF-12

Proceedings of The 12th International Symposium on Machinery and Mechatronics for Agriculture and Biosystems Engineering (ISMAB 2026)
20-24 October 2026, Busan, Republic of Korea

WATER STRESS VARIABILITY MAPPING BY GROWTH STAGE USING THERMAL VIDEO PROCESSING FOR CABBAGE GROWN IN GREENHOUSE

Md Nasim Reza[1,2], Ezatullah Zakir[2], Miao Miao Tu[2], Cholet Nyangoma Atulinda[2], Su Young Lee[2], Sun-Ok Chung[1,2*]

[1]Department of Smart Agricultural Systems, Graduate School, Chungnam National University, Daejeon, 34134, Republic of Korea
[2]Department of Agricultural Machinery Engineering, Graduate School, Chungnam National University, Daejeon 34134, Republic of Korea
*Corresponding Author-- Voice: +82-42-821-6712, Email: sochung@cnu.ac.kr

Abstract: Reliable identification of crop water stress is important for improving irrigation efficiency and maintaining uniform cabbage growth under greenhouse conditions. Thermal imaging can rapidly characterize canopy-temperature variability; however, conventional crop water stress index (CWSI) estimation generally requires radiometric images containing pixel-level temperature information. This study developed a video-derived, in situ-calibrated, spatiotemporal CWSI framework for estimating and mapping water-stress variability in greenhouse-grown cabbage using non-radiometric thermal videos. Videos were collected at 1, 30, 40, 60, and 90 days after transplanting (DAT). The workflow included frame-quality screening, video stabilization, thermal-palette normalization, growth-stage-adaptive canopy segmentation, plant tracking, and calibration using handheld leaf-temperature measurements. Greenhouse air temperature and relative humidity were used to calculate vapor pressure deficit, while light intensity was included to account for radiation variability. Because physical wet and dry references were unavailable, environmentally adjusted lower and upper thermal boundaries were estimated using quantile regression, and plant-level relative CWSI was calculated from normalized canopy-to-air temperature differences. Separately recorded GPS data were synchronized with selected video frames and refined using row identity, acquisition direction, plant sequence, and planting geometry to generate growth-stage-specific CWSI maps. The highest CWSI variability occurred at DAT 60, whereas DAT 40 showed the most uniform spatial distribution. Significant differences were observed among growth stages and cabbage rows, with distinct longitudinal gradients and several persistent high-CWSI zones, indicating possible irrigation, soil-water, or greenhouse microclimate effects. GPS-based georeferencing enabled visualization of localized stress patterns that were not evident from greenhouse-average values. Although the absence of raw radiometric data and physical wet and dry references limits interpretation as an absolute physiological CWSI, the proposed framework provides a practical approach for utilizing existing thermal videos. Future studies should validate the mapped stress zones using soil water content, stomatal conductance, leaf water potential, and yield measurements.

Key Words: Precision Agriculture, Cabbage, Crop Water Stress Index, Temperature, Greenhouse, Spatial Variability.

INTRODUCTION

Cabbage (*Brassica rapa* subsp. *pekinensis*) requires adequate water during establishment, rapid leaf expansion, and head development. Even in greenhouse production, spatial differences in emitter discharge, irrigation pressure, soil compaction, drainage, ventilation, and radiation can create nonuniform root-zone conditions. Greenhouse experiments with cabbage have shown that irrigation-system uniformity can influence the uniformity of crop growth and yield (Okasa et al., 2025), while stage-dependent water use and irrigation management strongly affect water-use efficiency (Zhou et al., 2020). Conventional measurements such as soil water content, leaf water potential, or stomatal conductance are valuable but are labor intensive and spatially sparse.

Thermal sensing provides a plant-based alternative because stomatal closure reduces transpirational cooling and usually increases canopy temperature relative to air temperature. The crop water stress index (CWSI) was developed to normalize the canopy-air temperature difference against lower and upper limits associated with high and low transpiration (Liu et al, 2026; Yadav et al., 2024). Infrared thermometry and thermal imaging have subsequently been used for irrigation scheduling and crop-water-status assessment (Pandya et al., 2023). CWSI mapping has also been demonstrated for spring Chinese cabbage using thermal infrared imagery, supporting the usefulness of spatial stress information for abnormal-growth assessment (Na et al., 2020). However, most methods assume access to radiometric images containing pixel-level temperature values. In the present dataset, only false-color Thermal Expert Q1 video was retained, with no raw radiometric matrix or camera metadata; therefore, a calibration model is required before quantitative temperature-based analysis.

Spatial interpretation also requires reliable georeferencing. During thermal-video collection, GPS positions were recorded separately while the thermal camera and GPS sensor moved along the center of each of four cabbage rows. The thermal and GPS streams must therefore be synchronized after acquisition before interpolation. IDW is suitable for producing a continuous surface from irregularly distributed measurements because nearby observations receive greater weights than distant observations. Accordingly, this study aimed to develop a video-derived, in situ-calibrated, spatiotemporal CWSI framework for estimating and mapping water-stress variability in greenhouse-grown cabbage using thermal data.

MATERIALS AND METHODS

STUDY AREA AND DATA ACQUISITION

The experiment was conducted in a cabbage greenhouse at Yesan, Republic of Korea. Cabbage plants were arranged in four parallel rows with row and plant spacings of 90 cm and 40 cm, respectively. Thermal observations were obtained at days after transplanting (DAT) 1, 30, 40, 60, and 90. A commercial thermal camera (model: TE Q1, Thermal Expert, Daejeon, Korea Republic) was mounted on a handheld platform and maintained approximately 1.2 m above the canopy while moving along the center of each row. Using a microconcroller automatic thermal video was captured and stored. GPS positions were recorded separately during the same passes, with the GPS sensor positioned close to the thermal camera. Greenhouse air temperature, relative humidity (RH), and light intensity were recorded, and handheld point-temperature measurements (model: E01, HIKMICRO, Hangzhou Microimage software Co., Ltd., Hangzhou, Zhejiang, China) was obtained from representative cabbage

leaves for thermal calibration. Table 1 shows the sensors specifications.

Table 1 Specifications of the thermal imaging and handheld thermometer.

Thermal Imaging Sensor	Handheld Infrared Thermometer
Model: TE – Q1	
Detector type: Mini-Bolometer	Model: HIKMICRO E01
Array format: 384 × 288 pixel	Array format: 160 × 120 pixel
Pixel pitch: 17 μm	Pixel pitch: 17 μm
Wavelength band: 8 ~ 14 μm	Wavelength band: 7.5 ~ 14 μm
Sensitivity: < 50mk @F/1, 300K; < 80mk	Sensitivity: < 40 mK (@ 25°C)
Frame rate: < 9 Hz	Frame rate: 25 Hz
FOV: 56.3º(H)×41.8º(V)-71.4º (diagonal)	FOV: 37.2º(H) × 50.0º(V)
Measurement range: 10°C ~ 150°C	Measurement range: -20ºC ~ 550ºC
	Accuracy: ± 0.2%

THERMAL INFORMATION EXTRACTION FROM VIDEO

Videos were decomposed into frames and screened to remove blurred and highly duplicated images. Because the video was non-radiometric, pixel colors were treated initially as relative thermal information rather than absolute temperature. Each video pixel was converted to the CIELAB color space and assigned to the closest color along the ordered thermal palette using a minimum color-distance criterion. CIELAB-based color-difference metrics are widely used to quantify perceptual differences between colors (Wang et al., 20223). In the present study, this principle was adapted to recover a one-dimensional relative thermal coordinate from the false-color thermal video. Each frame was converted from RGB to CIELAB color space, and the position of each canopy pixel along the ordered thermal palette was represented by a scalar thermal coordinate u. The closest palette position was obtained using Equation (1).

$$u_p = \arg\min_u \left\| Lab_p - Lab_{palette}(u) \right\|_2 \quad (1)$$

Matched handheld temperature measurements were then used to fit a monotonic calibration function, $T_c = f(u)$, where T_c is the reconstructed canopy temperature. Linear regression was tested first; monotonic spline or isotonic regression was used when the color-temperature relation was nonlinear. Calibration was evaluated using R^2 MAE, and RMSE. Cabbage canopy regions were segmented using thermal-palette intensity, local texture, spatial connectivity, expected row location, plant spacing, and temporal consistency across neighboring frames.

CWSI CALCULATION

Vapor pressure deficit (VPD) was calculated from greenhouse air temperature and RH, and the canopy-air temperature difference was calculated as $\Delta T = T_c - T_a$. The relative CWSI formulation followed the conventional CWSI normalization concept proposed by Jackson et al. [3], in which the canopy–air temperature difference is scaled between lower and upper thermal limits. Because physical wet and dry references were not available, environmentally adjusted lower (L_L) and upper (U_L) thermal limits were estimated from the 5th and 95th conditional quantiles of ΔT after accounting for VPD and light intensity. Lower and upper thermal boundaries were estimated using conditional quantile regression, following the regression-quantile framework. The resulting index was therefore interpreted as crop water stress index (CWSI) using Equation (2).

$$CWSI_i = \frac{\Delta T_i - L_{Li}}{UL_i - L_{Li}} \quad (2)$$

Values were bounded to 0-1 for visualization. Values approaching 0 indicated plants close to the cooler boundary of the measured population, whereas values approaching 1 indicated relatively warm plants under comparable greenhouse conditions.

GPS INTEGRATION, IDW MAPPING, AND VISUALIZATION

Thermal frames and GPS measurements were synchronized using acquisition time. Frame positions were obtained from the video start time, frame number, frame rate, and linear interpolation between consecutive GPS fixes. GPS trajectories were checked using row identity, acquisition direction, plant sequence, and planting geometry, and implausible positions were corrected or removed. Multiple frames from the same cabbage were aggregated into a single plant-level record containing row, coordinate, canopy temperature, and CWSI. The GPS coordinates were then transformed to a metric coordinate system, and CWSI was spatially interpolated using inverse distance weighting (IDW) according to Equation (3).

$$\hat{Z}_{(x_0)} = \frac{\sum_{i=1}^{n} w_i Z_{(x_i)}}{\sum_{i=1}^{n} w_i} \quad , \quad w_i = \frac{1}{d_i^p} \tag{3}$$

where, $Z_{(xi)}$ is plant-level CWSI, di is the distance from sample i to prediction location x_o, and p is the distance-decay exponent. An initial p = 2 was evaluated by leave-one-out cross-validation using MAE and RMSE. Separate maps were generated for DAT 1, 30, 40, 60, and 90.

RESULTS & DISCUSSION

GROWTH-STAGE VARIATION IN CWSI

CWSI varied clearly across the five cabbage growth stages (Figure 1). Mean CWSI increased from 0.36 at DAT 1 to 0.43 at DAT 30 and 0.47 at DAT 40, with progressively more localized high-stress zones. The highest stress occurred at DAT 60, with a mean CWSI of 0.62 and broad high-value regions concentrated mainly between 30 and 45 m; the maximum map-derived CWSI approached 0.90. At DAT 90, mean CWSI decreased to 0.48 and the extent of high-stress areas was reduced, although several central hotspots remained. Overall, thermal stress increased from DAT 1 to DAT 60 and declined thereafter. Stage-wise variability is summarized in Table 2.

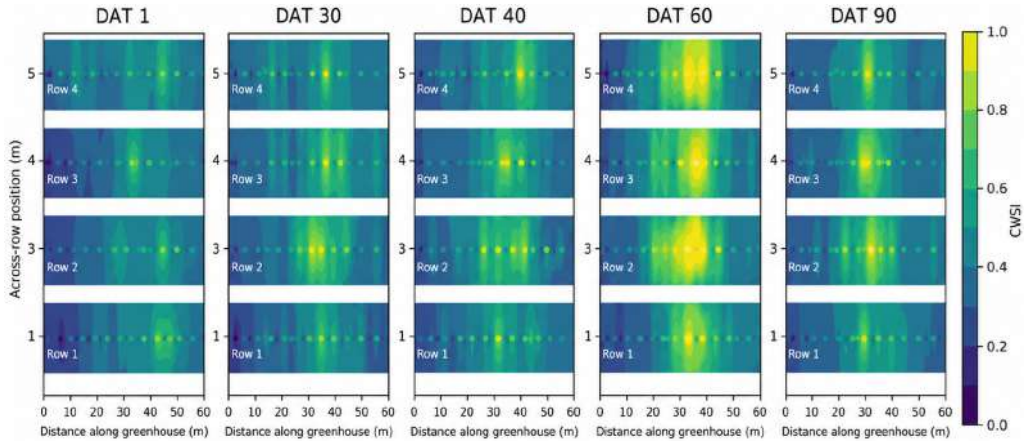

Fig. 1 Five-stage spatial distribution of CWSI across four cabbage rows at five growth stages.

Table 2 Stage-wise CWSI characteristics corresponding to the current five-stage growth map.

Growth stage	Mean CWSI	Approx. range	Spatial variability
DAT 1	0.36	0.18-0.60	Low-moderate
DAT 30	0.43	0.25-0.70	Moderate
DAT 40	0.47	0.25-0.80	Moderate-high
DAT 60	0.62	0.30-0.90	Highest
DAT 90	0.48	0.25-0.75	Moderate

ROW-WISE AND LONGITUDINAL SPATIAL VARIABILITY

The five-stage maps showed clear row-wise and longitudinal variation in CWSI. Localized high-CWSI areas were limited at DAT 1 but became more evident at DAT 30 and DAT 40, particularly in the central greenhouse sections. Rows 2 and 3 showed the most persistent hotspots, whereas Row 1 generally maintained lower CWSI values.

The strongest row-wise contrast occurred at DAT 60, when high-CWSI zones expanded across Rows 2–4, mainly between 30 and 45 m. Row 1 also showed increased stress, although over a smaller area. At DAT 90, both the magnitude and extent of high-CWSI zones decreased, but elevated values remained in the central portions of Rows 2 and 3. These persistent patterns indicate spatially nonuniform crop water status; however, the observed differences may also reflect irrigation distribution, soil conditions, greenhouse microclimate, or uncertainty associated with thermal calibration and GPS positioning.

Stage-Wise CWSI Trend

The stage averages followed the spatial pattern observed in Figure 1. Mean CWSI increased from 0.36 at DAT 1 to 0.43 at DAT 30 and 0.47 at DAT 40, before reaching the highest value of 0.62 at DAT 60 (Figure 2). The mean subsequently declined to 0.48 at DAT 90. The DAT 60 value was approximately 72% higher than the DAT 1 value, reflecting the substantially broader high-CWSI area visible in the corresponding map as shown in Figure 2.

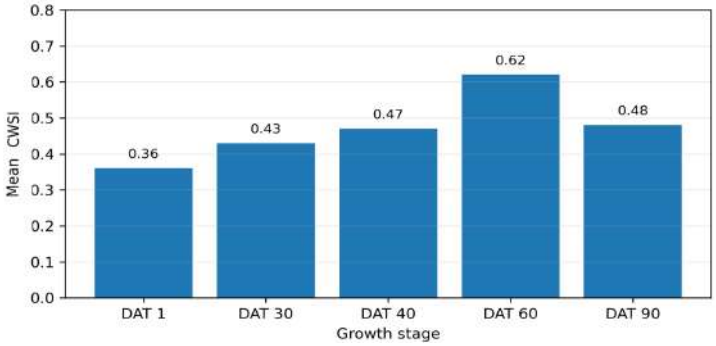

Fig. 2 CWSI values for the five cabbage growth stages, consistent with the spatial pattern.

GPS-BASED SPATIAL MAPPING AND PERSISTENT STRESS ZONES

Plant-level CWSI values were georeferenced using GPS data and interpolated with IDW to generate spatial stress maps. Persistent high-CWSI zones were concentrated mainly at 30–45 m in Rows 2 and 3, becoming most pronounced at DAT 60 and remaining evident at DAT 90. This pattern agrees with previous cabbage studies linking higher CWSI with water deficit and abnormal crop growth (Lee et al., 2019; Na et al., 2020). The results support GPS-

integrated CWSI mapping for identifying spatially nonuniform water-stress zones in greenhouse cabbage production.

CONCLUSIONS

This study developed a video-derived, in situ-calibrated framework for estimating and mapping crop water stress index in cabbage grown in greenhosue using non-radiometric thermal videos and GPS data. Thermal information was calibrated using handheld leaf-temperature measurements and normalized using greenhouse environmental conditions. The resulting CWSI values were integrated with GPS coordinates and mapped using IDW for five growth stages. The highest stress variability occurred at DAT 60, with persistent high CWSI zones mainly in Rows 2 and 3. The framework provides a practical approach for spatial water-stress assessment, although further validation is required to establish reliable irrigation thresholds.

ACKNOWLEDGEMENTS

This work was supported by Korea Institute of Planning and Evaluation for Technology in Food, Agriculture, Forestry (IPET), through Machinery Mechanization Technology Development Program for Field Farming, funded by Ministry of Agriculture, Food and Rural Affairs (MAFRA) (Project No. RS-2023-00231026), Republic of Korea.

REFERENCES

Lee, H. S., S. K. Kim, H. J. Lee, J. H. Lee, S. An, and S. G. Lee. 2019. Development of crop water stress index for Kimchi cabbage precision irrigation control. Hortic. Sci. Technol. 37: 490-498.

Liu, P., X. Shi, J. Yu, L. Wu, L. Jia, and M. Fan. 2026. Stage-specific construction of crop water stress index based on canopy–air temperature difference for potato water stress assessment in an arid region. Agric. Water Manag. 333: 110598.

Na, S.-I., H. Ahn, C.-W. Park, S.-Y. Hong, K.-H. So, and K.-D. Lee. 2020. Crop water stress index (CWSI) mapping for evaluation of abnormal growth of spring Chinese cabbage using drone-based thermal infrared image. Korean J. Remote Sens. 36(5): 667-677.

Okasha, A. M., E. T. Abdelkhaliq, and A. M. Zayton. 2025. Impact of irrigation water quality, frequency, and technique on cabbage yield, water productivity, and soil properties in clay soil. Egypt. J. Soil Sci. 65(2): 961-978.

Pandya, P., S. Parmar, D. Vadalia, and G. Prajapati. 2023. Thermal imaging and its application in irrigation water management. AgriTech Today 1: 40.

Wang, Z., K. Xu, Y. Yang, J. Dong, S. Gu, L. Xu, Y. Fang, and K. Ma. 2023. Measuring perceptual color differences of smartphone photographs. IEEE Trans. Pattern Anal. Mach. Intell. 45(8): 10114-10128.

Yadav, A., H. Upreti, and G. D. Singhal. 2024. Crop water stress index and its sensitivity to meteorological parameters and canopy temperature. Theor. Appl. Climatol. 155(4): 2903-2915.

SF-13

Proceedings of The 12th International Symposium on Machinery and Mechatronics for Agriculture and Biosystems Engineering (ISMAB 2026)
20-24 October 2026, Busan, Republic of Korea

USER-DEFINED MODEL COMPONENT DEVELOPMENT IN TRNSYS 18 FOR A DYNAMIC ENERGY SIMULATION: CASE STUDY OF A PCM-IN-CONTAINER

Qazeem Opeyemi Ogunlowo[1], Seung-hun Lee[1], Chan-min Kim[1], Hee-Woong Seok[1], Sun-hyoung Lee[1], Su-been Ahn[1], Han Kim[1], Jin-seo Choi[1], Yun-Jeong Lee[1], Yoon-Kyu Hur[2] , Jun-seop Mun[1], Hyeon-chae Kim[1], and Rack-woo Kim[2]*

[1] Research Institute of Agriculture and Life Sciences, Seoul National University, Seoul 08826, Republic of Korea
[2] Department of Biosystems Engineering, College of Agriculture and Life Sciences, Seoul National University, Seoul 08826, Republic of Korea
* Corresponding author--Voice: +82-2-880-4605, Email: rack88@snu.ac.kr

Abstract: Phase change materials (PCMs) can moderate indoor thermal conditions by storing daytime heat and releasing it when air temperature falls. This paper presents a user-defined TRNSYS 18 component (Type 207) for PCM contained in pipes or other containers that directly exchange heat with the zone air. The temperature-based component was linked to a greenhouse model and weather-data processor, then evaluated against scaled greenhouse experiments containing air, water, and Vaseline. For the water-filled model, simulated and measured air temperatures agreed closely (R^2 = 0.97, correlation coefficient = 0.99, RMSE = 2.01°C, and MAE = 1.33°C). The component also resolved the direction and rate of PCM energy storage, enabling separate analysis of charging and discharging periods from zone temperature. In a full-scale single-layer greenhouse case, water-filled structural pipes increased the simulated nighttime air temperature by up to 6.8°C at a filling-to-greenhouse-volume ratio of 4.99×10^{-4}. The component provides a practical route for dynamically assessing PCM containers in greenhouses and other zones where wall-based PCM models are unsuitable. Hysteresis is not represented and should be addressed in future extensions.

Key words: TRNSYS 18; user-defined component; phase change material; thermal energy storage; greenhouse; dynamic simulation.

ACKNOWLEDGEMENTS

"This work was partly supported by the Institute of Information & Communications Technology Planning & Evaluation(IITP)-ITRC(Information Technology Research Center) grant funded by the Korea government(MSIT)(IITP-2025-RS-2024-00438335) and National Research Foundation of Korea(NRF) grant funded by Korean government(MSIT)(RS-2024-00352168)"

SF-14

Proceedings of The 12th International Symposium on Machinery and Mechatronics for Agriculture and Biosystems Engineering (ISMAB 2026)
20-24 October 2026, Busan, Republic of Korea

ROBOTIC MULTI-VIEW RGB PHENOTYPING OF STRAWBERRY PETIOLE LENGTH WITHOUT DEPTH SENSING

Min-Woo Kim[1], Dae-Hyun Jung[1,2*]

[1] Department of Smart Farm Science, Kyung Hee University, Yongin, Gyeonggi-do, Republic of Korea; e-mail: alsdnwldns0513@khu.ac.kr
[2] BK21 Interdisciplinary Program in IT-Bio Convergence System, Kyung Hee University, Yongin, Republic of Korea
* Corresponding author, e-mail address: daehyun@khu.ac.kr

Abstract Petiole length is an important morphological indicator of strawberry (*Fragaria* × *ananassa*) growth, with elongation associated with low light and crowding. However, its measurement remains largely manual because endpoint occlusion and unreliable depth readings hinder image-based assessment. This study presents an RGB-based robotic framework for non-contact measurement of the straight-line distance between the petiole endpoints. The framework combines multi-view triangulation with uncertainty-aware viewpoint selection, choosing candidate views that minimize the predicted variance of the measured length. Candidate contributions are estimated by forward-projecting the current three-dimensional endpoint estimates without accessing the candidates' image observations or depth measurements. Validation against digital-caliper measurements yielded mean absolute errors (MAEs) of 4.07 mm in the development cohort and 2.65 mm in an independent greenhouse cohort acquired using a different robot arm. The proposed policy showed no consistent advantage over coverage-based or parallax-maximizing strategies in attaining the specified uncertainty threshold. Nevertheless, with five to seven views, its median predicted interval width was 8–21% narrower than that of the parallax-maximizing control in both cohorts (plant-level permutation $p < 0.05$). The predicted intervals were associated with absolute measurement error, although empirical calibration was required to address undercoverage. Visually assessed etiolated petioles were approximately 70% longer than normal petioles, illustrating an observational association with plant morphology. Automatic keypoint detection enabled length estimation with an overall MAE of 5.6 mm. These findings support RGB-based robotic petiole measurement as a potential tool for non-destructive strawberry phenotyping, while identifying limitations in translating reduced predicted uncertainty into improved measurement accuracy or acquisition efficiency.

Key Words: plant phenotyping; non-contact measurement; multi-view triangulation; viewpoint selection; strawberry; etiolation; greenhouse robotics

Acknowledgements
This research was supported by a grant (23192MFDS106) from Ministry of Food and Drug Safety in 2026.

SF-15

Proceedings of The 12th International Symposium on Machinery and Mechatronics for Agriculture and Biosystems Engineering (ISMAB 2026)
20-24 October 2026, Busan, Republic of Korea

3D RECONSTRUCTION OF GREENHOUSE CROPS: FROM SINGLE-CAMERA RGB-D MAPPING TO LIDAR–CAMERA INTEGRATION

Xianghui Xin[1,2], Sungjay Kim[1,3], Gyumin Kim[1,2], Yeongjun Go[1,2], Yudha Putra Arisandy[1,2], Seongmi Sun[3], Ghiseok Kim[1,2,3*]

[1]Department of Biosystems Engineering, Seoul National University, Seoul 08826, Republic of Korea
[2]Global Smart Farm Convergence Major, Seoul National University, Seoul 08826, Republic of Korea
[3]Research Institute of Agriculture and Life Sciences, Seoul National University, Seoul 08826, Republic of Korea
*Corresponding Author– Voice: +82-2-880-4603, Email: ghiseok@snu.ac.kr

Abstract: Repeated three-dimensional records of the same greenhouse plants would support growth monitoring and sample tracking in netted melon (*Cucumis melo* L. var. *reticulatus*), but a single depth camera cannot observe occluded surfaces, and a moving sensor accumulates pose error along a crop row. This study develops 3D reconstruction workflows for greenhouse melon rows, progressing from a single RGB-D camera toward a rail-guided LiDAR–camera cart, as the sensing layer of a time-versioned digital twin. In the first stage, a single Orbbec Femto Mega camera was used in three modes: handheld row scans reconstructed with RTAB-Map, handheld orbits around individual plants, and still color–depth captures of selected samples before harvest, followed by laboratory imaging of the harvested material; earlier cart-mounted scans used a rail-constrained motion model. In the second stage, a Livox Mid-360S LiDAR and two Femto Mega cameras were mounted on a rail cart, with measured rail travel and withheld check targets serving as physical references. Acquisition spanned three greenhouse sites over two growing seasons, producing several hundred RGB-D recordings of rows and individual plants and more than two hundred harvested melons, including one greenhouse revisited repeatedly with a fixed group of target plants. The single-camera baseline yields coherent row and plant reconstructions, with ghosting from leaf motion and drift along long rows as the main remaining limitations. For the cart, sensor-level quality checks and LiDAR-only rail-constrained reconstructions are in hand, and cross-sensor calibration and fused reconstruction are being evaluated against the single-camera baseline on matched scenes. Together with registration to stable greenhouse structure, these workflows form the acquisition layer of a digital twin in which each visit is preserved as a dated, metrically registered crop layer.

Key Words: greenhouse melon, RGB-D SLAM, LiDAR–camera fusion, 3D reconstruction, digital twin

ACKNOWLEDGEMENTS

This work was supported by the Program for Development of an AI-based Crop Monitoring and Diagnosis Platform (Project No. RS-2026-25516478), Rural Development Administration (RDA), Republic of Korea.

SF-16

Proceedings of The 12th International Symposium on Machinery and Mechatronics for Agriculture and Biosystems Engineering (ISMAB 2026)
20-24 October 2026, Busan, Republic of Korea

FEASIBILITY EVALUATION OF A LABORATORY-DEVELOPED EMBEDDED EC AND PH ANALYZER FOR HYDROPONIC NUTRIENT SOLUTIONS

Minki Kang[1], Hak-Jin Kim[2*], Yuna Kwon[1], Joonhwan Kim[4]

[1]Department of Biosystems Engineering, College of Agriculture and Life Sciences, Seoul National University, Seoul, 08826, Republic of Korea
[2]Integrated Major in Global Smart Farm, College of Agriculture and Life Sciences, Seoul National University, Seoul, 08826, Republic of Korea
[3]Libergon, Inc
*Corresponding Author-- Voice: +02-880-4614, Email: Kimhj69@snu.ac.kr

Abstract: Nutrient solution management in hydroponics is a key process that controls nutrient concentration and the overall nutrient solution environment based on electrical conductivity (EC) and pH. However, this is mostly carried out through manual measurement using handheld meters, which limits real-time management. Continuous pH and EC monitoring equipment is costly to apply in the field, so low-cost, field-usable measurement technology is needed. EC and H^+ ion-selective electrodes (ISEs) require different signal-processing conditions. In the EC channel, the gain, offset, and noise level of the circuit affect the reliability of the final EC estimate, while the H^+-ISE outputs a potential signal that requires a high-input-impedance circuit. In this study, an EC signal-processing circuit with an RC filter and an H^+-ISE measurement channel based on a high-input-impedance circuit were developed to verify the feasibility of applying a low-cost, field-usable system for simultaneous pH and EC measurement. A precision voltmeter (Agilent/HP 34401A) was used as the reference instrument to analyze the linearity and offset between the circuit output voltage and the raw voltage acquired by the Raspberry Pi in standard EC solutions. A pH measurement channel incorporating a high-input-impedance circuit for the H^+-ISE was integrated into the system, enabling automated two-point calibration with pH 4 and pH 7 standard solutions and subsequent nutrient solution measurement. Preliminary validation using unknown nutrient solution samples indicated that the EC and pH measurements from the developed system were consistent with those from a commercial reference meter, supporting the feasibility of the proposed low-cost monitoring approach

Key Words: Signal processing circuit, measurement accuracy, nutrient solution monitoring, Analog-to-digital converter.

Acknowledgement: This work was supported by SaeFarm Inc. under the project "Advancement of Soybean Leaf Area Index (LAI) Prediction Using Drone Aerial Imagery" (Grant No. 500-20260258).

Smart Farm Systems and Renewable Energy 4 (SF-4)



SF-17

Proceedings of The 12th International Symposium on Machinery and Mechatronics for Agriculture and Biosystems Engineering (ISMAB 2026)
20-24 October 2026, Busan, Republic of Korea

THERMAL PERFORMANCE OF A TRACKING LINEAR FRESNEL LENS SYSTEM WITH AN EVACUATED TUBE COLLECTOR

Seung-Hyeon Cheon[1], Byeong-Eun Moon[2]*

[1]Department of Smart Agricultural Engineering, Sunchon National University, Republic of Korea
[2]Department of Convergence Biosystems Engineering, Sunchon National University, Republic of Korea
*Corresponding Author-- Voice: +82-61-750-3263, Email: mbe25@scnu.ac.kr

Abstract A solar thermal system integrating a linear Fresnel lens, dual-axis solar tracking, an evacuated tube collector, and thermal storage was developed for agricultural facilities and evaluated through outdoor experiments and computational fluid dynamics analysis. A 2.24 m² PMMA lens concentrated sunlight, and water was heated in a helical copper coil inside the evacuated tube. Tests on August 24-26, 2026, at 1 L/min with 50 L of water showed daily mean outlet temperatures 4.2-5.2 °C above inlet temperatures. Collector efficiencies for selected 15-min intervals ranged from 18.9% to 38.8%, with daily interval means of 28.4-29.8%. The water temperature increased corresponding to 4.58-4.81 MJ of stored heat. System efficiencies estimated from stored heat relative to incident energy were 13.9-19.4%. Preliminary steady-state CFD analysis predicted water heating from 50.9 °C at the inlet to approximately 54.0 °C at the outlet and illustrated heat transfer through the internal air and copper coil. These results indicate potential for small-scale hot-water production and supplementary heating.

Key Words: Agricultural energy, Linear Fresnel lens, Evacuated tube collector, Helical copper tube, Computational fluid dynamics

INTRODUCTION

Solar thermal systems for protected horticulture require assessment of both collector heating and the thermal energy available for storage and supply (Kim et al., 2021). Integrating a linear Fresnel lens and an evacuated tube collector into an agricultural circulation and storage system requires consideration of tracking, heat collection, transport, and storage (Hussain et al., 2015).

This study developed a medium-scale concentrating solar thermal system with a linear Fresnel lens and dual-axis tracking. Collector inlet, outlet, and tank temperatures and thermal efficiencies were evaluated during outdoor operation. CFD analysis of the helical copper coil and internal air was also conducted to examine heat transfer and identify potential improvements.

MATERIALS AND METHODS

System Configuration

The system comprised concentrating, tracking and drive, collection, and circulation and storage components (Fig. 1). The PMMA linear Fresnel lens measured 1,600 × 1,400 × 5 mm, with an area of 2.24 m², a focal length of 1,000 mm, and a groove pitch of 0.6 mm. The collector was positioned along the focal line. Dual-axis tracking combined optical sensor voltage differences in the vertical and horizontal directions with recorded motor operating times. The drive unit, which combines a multistage reduction gearbox and a worm gear, has a final output speed of 0.3 rpm and was designed to maintain the tracking position by exploiting the worm gear's resistance to backdriving.

The collector comprised an evacuated tube (58 mm outer diameter, 2,000 mm length), a U-shaped reflector, and a helical copper coil (9.52 mm outer diameter, 1.0 mm wall thickness). The vacuum layer reduced external gas conduction and convection losses. Heat reached the coil through radiation and the internal air, then passed through the copper wall by conduction and into the water by convection. A pump, flow controller, and piping circulated water between the collector and a polyethylene tank with a maximum capacity of 200 L.

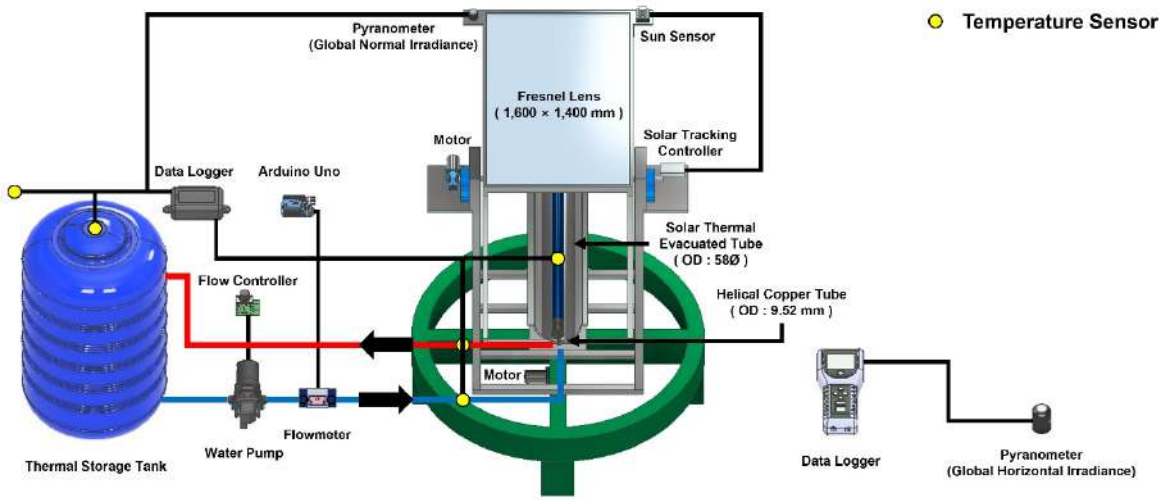

Fig. 1. Configuration of the solar thermal experimental system.

Experimental Conditions and Measurements

The experiments were conducted at the experimental farm of Sunchon National University (35.000116° N, 127.507244° E) from 10:00 to 17:00 on August 24-26, 2026. Flow was set to 1 L/min with 50 L of water. K-type thermocouples and PT100 sensors measured ambient, collector surface near the focus, inlet, outlet, and tank temperatures. A flow sensor and Arduino measured flow. Direct normal irradiance was estimated from global irradiance measured on normal and horizontal planes.

Performance Evaluation

Useful heat gain and collector efficiency were calculated using Eq. (1). Efficiency ranges and arithmetic means were determined from selected 15-min average intervals and distinguished from daily energy-weighted efficiencies.

$$Q_c = \dot{m} \cdot c_p \cdot (T_{out} - T_{in}), \qquad \eta_c = \frac{Q_c}{AI} \tag{1}$$

where:

$\dot{m}$ = Mass flow rate (kg/s)
c_p= Specific heat capacity (J/kg·K)
T_{in} = Collector inlet fluid temperature (℃)
T_{out} = Collector outlet fluid temperature (℃)
A = Concentrating area of a Linear Fresnel lens (m²)
I = Direct normal irradiance (W/m²)
Q_c = Solar energy input (W)
η_c = Collector efficiency (%)

Efficiency was fitted against the difference between mean fluid and ambient temperatures divided by irradiance using Eq. (2).

$$\eta_c = \eta_0 - a \cdot \frac{(T_m - T_a)}{I}, \qquad T_m = \frac{(T_{in} + T_{out})}{2} \tag{2}$$

where:

a = Heat loss coefficient (W/m²·K)
T_m = Mean fluid temperature in collector (℃)
T_a = Ambient temperature (℃)
T_{in} = Collector inlet fluid temperature (℃)
T_{out} = Collector outlet fluid temperature (℃)
I = Direct normal irradiance (W/m²)
η_c = = Direct normal irradiance (W/m²)
η_0 = Maximum collector efficiency (%)

Stored heat and system efficiency were calculated using Eq. (3) (Asrori and Susilo, 2022). Incident energy was approximated using daily mean irradiance and the elapsed time from the initial to maximum tank temperature.

$$Q_s = m \cdot c_p \cdot \frac{(T_f - T_i)}{\Delta t}, \qquad \eta_s = \frac{Q_s}{AI} \tag{3}$$

where:

m = Mass (kg)
c_p = Specific heat capacity (J/kg·K)
T_f = Maximum temperature (℃)
T_i = Initial temperature (℃)
t = Heating time (s)
A = Concentrating area of a Linear Fresnel lens (m²)
I = Direct normal irradiance (W/m²)
Q_s = Useful heat stored in tank (W)
η_s = System efficiency (%)

CFD Model and Boundary Conditions

A three-dimensional model included the evacuated tube, helical copper coil, water, and internal air. The internal air region was distinct from the vacuum insulation layer. The Poly-Hexcore mesh contained 5,515,039 cells, with minimum and mean orthogonal qualities of 0.24 and 0.93. A steady-state pressure-based solver employed the energy equation, SST k–ω turbulence model, and Discrete Ordinates radiation model.

The preliminary simulation specified an inlet temperature of 50.9 °C, a mass flow rate of 0.0333 kg/s, and an outlet gauge pressure of 0 Pa. Ambient and external radiation temperatures were 37.6 °C, and the external convection coefficient was 15 W/(m²·K). A heat

flux of 38,000 W/m² over 0.016 m² supplied 608 W. Internal metal/absorber and external glass emissivities were 0.1 and 0.9, respectively. Residuals and outlet temperature were monitored to assess convergence.

RESULTS & DISCUSSION

Time-Series Operational Characteristics

Time-series variations in solar irradiance and system temperatures were analyzed at a flow rate of 1 L/min on August 24–26, 2026. Daily mean irradiances were 596.7, 577.1, and 535.7 W/m², and mean ambient temperatures were 35.5, 38.2, and 38.0 °C, respectively. Collector surface temperatures exhibited sharp rises and falls in response to irradiance fluctuations, with daily means of 75.4, 78.7, and 77.6 °C. In contrast, inlet, outlet, and storage water temperatures varied more gradually. Daily mean outlet temperatures exceeded inlet temperatures by 4.2–5.2 °C, and maximum storage water temperatures reached 52.1, 61.4, and 58.5 °C, respectively (Fig. 2).

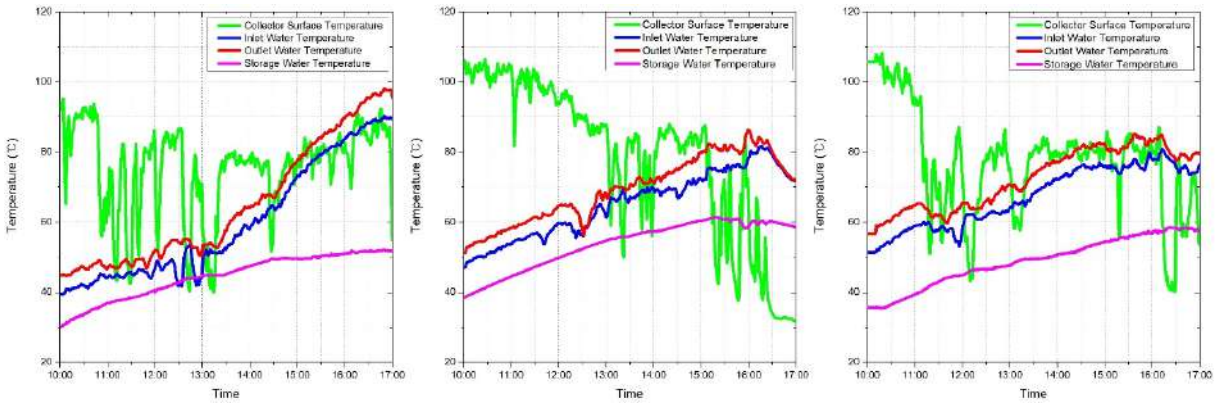

Fig. 2. Time-series variations in measured data over the three-day experiment.

Solar Tracking Operation and Thermal–Fluid Analysis

During automatic solar tracking, exponential regressions between solar irradiance and collector surface temperature yielded coefficients of determination of 0.2276, 0.5397, and 0.6696 on August 24–26, respectively. These relationships describe the collector's thermal response to irradiance variations during tracking. The differences among days were attributed to the combined effects of irradiance fluctuations, inlet water temperature, heat losses, and thermal inertia (Asrori and Susilo, 2022).

Outdoor Operation and Collector Performance

On all test days, the daily mean outlet water temperature exceeded the inlet temperature by 4.2–5.2 °C. The maximum instantaneous outlet temperature was 98.1 °C on August 24 (Table 1). Collector efficiencies for the selected intervals ranged from 18.9% to 38.8%, with daily interval means of 28.4–29.8%. Efficiency decreased as the difference between mean fluid and ambient temperatures increased relative to solar irradiance. Daily differences in the regression coefficients were attributed to the combined effects of irradiance variations, increasing inlet water temperature, and the collector's thermal response.

Table 1 Outdoor operating conditions and collector performance for selected 15-min intervals by date.

Classification	August 24th	August 25th	August 26th
Mean ambient temperature (°C)	35.5	38.2	38.0
Mean inlet temperature (°C)	59.9	65.2	67.2
Mean outlet temperature (°C)	64.9	69.4	72.4
Mean temperature rise (°C)	5.0	4.2	5.2
Interval efficiency range (%)	18.9-38.8	20.1-35.4	23.9-34.2
Mean interval efficiency (%)	28.4	29.8	29.0
Regression coefficient a (W/(m²·K))	1.56	2.96	2.03

Storage Performance and System Efficiency

The 50 L of water warmed by 21.9–23.0 °C and stored 4.58–4.81 MJ (1.27–1.34 kWh), with system efficiencies of 13.9–19.4% (Table 2). Despite lower mean irradiance, August 25 had a shorter time to maximum temperature and greater stored heat than August 24, yielding a higher ratio of stored heat to incident energy.

Table 2 Thermal storage performance with 50 L of water.

Classification	August 24th	August 25th	August 26th
Initial water temperature (°C)	30.2	38.5	35.5
Maximum water temperature (°C)	52.1	61.4	58.5
Temperature rise (°C)	21.9	22.9	23.0
Time to maximum temperature (s)	24,600	19,140	22,920
Stored thermal energy (MJ)	4.58	4.79	4.81
System efficiency (%)	13.9	19.4	17.5

Storage-based efficiencies were lower than mean selected-interval collector efficiencies. The former represent accumulated heat up to the maximum tank temperature, whereas the latter represent heat gained across the collector. Their difference reflects pipe and tank losses, thermal changes during operation, and the evaluation periods.

Preliminary CFD analysis predicted water heating from 50.9 °C to approximately 54.0 °C. Internal air temperatures ranged from approximately 37.7 to 115.0 °C, with a mean of 63.4 °C. Local hot regions and a gradual water temperature increase along the helical flow path illustrated heat transfer from the collector through the copper coil to the water (Fig. 3).



Fig. 3. Predicted water and internal air temperature distributions.

The simulated mass flow rate of 0.0333 kg/s corresponded to approximately 2.0 L/min, compared with 1 L/min in the outdoor tests. The approximately 3.1 °C temperature rise gave a heat gain of about 432 W, or 71% of the imposed 608 W. This ratio represents heat recovery

relative to the CFD heat input and differs from solar-based system efficiency. The effective efficiency of 0.28 used to calculate the equivalent heat flux served as an input coefficient reflecting collector characteristics. Further work will compare heat gain and pump power at different flow rates, considering coil heat transfer area and flow resistance.

CONCLUSIONS

This study integrated a linear Fresnel lens, dual-axis solar tracking, and an evacuated tube collector containing a helical copper coil with a circulation and thermal storage system. Thermal performance was evaluated through three days of outdoor experiments and preliminary CFD analysis. Time-series analysis showed that collector surface temperatures changed rapidly with irradiance fluctuations, whereas circulating and storage water temperatures varied more gradually. These observations illustrate differences in the thermal responses of the collector and water, together with the thermal storage characteristics.

At a flow rate of 1 L/min, daily mean collector inlet-to-outlet temperature rises were 4.2–5.2 °C, and daily mean collector efficiencies for the selected 15-min intervals were 28.4–29.8%. The 50 L of water warmed by 21.9–23.0 °C, storing 4.58–4.81 MJ of thermal energy, with estimated storage-based system efficiencies of 13.9–19.4%. These results demonstrate that evaluating stored thermal energy alongside collector temperature rise provides a comprehensive assessment of the system's thermal and storage performance.

Preliminary CFD analysis predicted water heating from 50.9 °C at the inlet to approximately 54.0 °C at the outlet and illustrated heat transfer from locally heated regions through the copper coil to the circulating water. The simulated flow rate was approximately 2 L/min, which differed from the experimental condition. Future work will use representative experimental data obtained at 1 L/min to conduct CFD simulations and validate the model by comparing numerical predictions with measurements. The validated model will then be used to analyze temperature distributions, heat gain rates, and pressure drops at different flow rates and identify suitable operating flow rates for improved collector performance.

ACKNOWLEDGEMENTS

This work was supported by the New and Renewable Energy Core Technology Development Program funded by the Ministry of Climate, Energy and Environment, Republic of Korea, in 2026 (RS-2026-25527755).

REFERENCES

Asrori, A., and S. H. Susilo. 2022. The development of Fresnel lens concentrators for solar water heaters: A case study in tropical climates. EUREKA: Physics and Engineering (3): 3-10.

Hussain, M. I., A. Ali, and G. H. Lee. 2015. Performance and economic analyses of linear and spot Fresnel lens solar collectors used for greenhouse heating in South Korea. Energy 90: 1522-1531.

Kim, M.-H., D. Kim, D.-W. Lee, and J. Heo. 2021. Applicability of a renewable energy convergence system based on seasonal thermal energy storage for greenhouse. Korean Journal of Air-Conditioning and Refrigeration Engineering 33(8): 395-403.

SF-18

Proceedings of The 12th International Symposium on Machinery and Mechatronics for Agriculture and Biosystems Engineering (ISMAB 2026)
20-24 October 2026, Busan, Republic of Korea

DEVELOPMENT OF A 3D CLINOSTAT PLATFORM FOR GROUND-BASED SIMULATED MICROGRAVITY RESEARCH IN AGRICULTURAL BIOSCIENCES

Uik Lee[1], Yeongjun Go[1,2], Jiwon Ryu[1,3], Ghiseok Kim[1,2,3*]

[1]Department of Biosystems Engineering, Seoul National University, Rep. Korea
[2]Integrated Major in Global Smart Farm, Seoul National University, Rep. Korea
[3]Research Institute of Agriculture and Life Sciences, Seoul National University, Rep. Korea
*Corresponding Author-- Ghiseok Kim, Email: ghiseok@snu.ac.kr

Abstract: Understanding how crops grow in space requires experiments under microgravity. However, even as spaceflight costs decline, the one-off nature of flight experiments makes it difficult to secure sufficient experimental time and replicate results despite substantial investments of time, effort, and money. Ground-based technologies that simulate microgravity and enable repeated experiments are therefore needed. A clinostat simulates microgravity by continuously reorienting a sample relative to gravity so that the time-averaged gravity vector approaches zero. Applying the same principle, biased rotational motion can produce a nonzero time-averaged vector, enabling the simulation of partial gravity, such as that on the Moon or Mars. This study aims to develop a three-dimensional (3D) clinostat platform that reproduces these time-averaged gravity conditions for rice experiments and verifies the achieved conditions through direct measurements. Based on an open-source design, the platform comprises nested inner and outer rotating frames, each driven by a servomotor through a timing belt. Rotation trajectories are generated using a previously reported method for target gravity levels of 0 g (microgravity), 0.17 g (Moon), and 0.38 g (Mars). Rather than inferring gravity conditions from motor commands, an inertial measurement unit (IMU) mounted on the inner frame independently measures the acceleration of the sample-bearing frame. The IMU is used exclusively for validation. A growth module was designed to support plant cultivation and observation during rotation. It secures a transparent vessel containing agar medium, LED lighting panels, and a camera with an onboard computer to the inner frame. Because the lighting and camera rotate with the sample, illumination and imaging maintain a consistent orientation relative to the sample. Slip rings transmit power only, while data are transmitted wirelessly. In July 2026, the clinostat was operated for 18 minutes under each condition with the previous sample frame installed. Unit acceleration vectors were recorded at 50 Hz. After excluding the first 8 seconds, during which the motors caught up with the commanded trajectory, the magnitudes of the time-averaged vectors were 0.013 g for microgravity, 0.170 g for lunar gravity, and 0.376 g for Martian gravity. All were within ±0.03 g of their respective targets. The motors and slip rings have been installed, and the lighting panels and camera have undergone bench testing. Before rice growth experiments, validation remains necessary for all three conditions with the growth module integrated, power delivery and imaging during rotation, and long-duration operation. Future development will also extend the platform to address other space environmental factors, including cryogenic temperatures, vacuum, ultraviolet radiation, plasma, and ionizing radiation.

Key Words: 3D Clinostat, Partial Gravity, Simulated Microgravity, Crop Growth, Space Agriculture

ACKNOWLEDGEMENTS

This work was supported by the commissioned research project “Establishment of a Crop Growth Evaluation System under Microgravity Conditions,” National Institute of Crop Science (NICS), Rural Development Administration (RDA), Republic of Korea.

SF-19

Proceedings of The 12th International Symposium on Machinery and Mechatronics for Agriculture and Biosystems Engineering (ISMAB 2026)
20-24 October 2026, Busan, Republic of Korea

OPTIMAL BASELINE DETERMINATION FOR STEREO VISION-BASED PLANT HEIGHT MEASUREMENT OF PEPPER SEEDLING TRAYS AT A FIXED CAMERA HEIGHT

Gunhui Park[1], Junghwa Park[1], Sohyeon Kang[1], Minjoo Kim[1], Jaesung Park[1,2,3*]

[1]Department of Bio-Industrial Machinery Engineering,
Pusan National University, Miryang 50463, Korea
[2]Major in Natural Resources Systems Engineering,
Pusan National University, Yangsan 50612, Korea
[3]Life and Industry Convergence Research Institute,
Pusan National University, Miryang 50463, Korea
*Corresponding Author-- Voice: +82-10-4001-1225, Email: jaesung.park@pusan.ac.kr

Abstract: Pepper (*Capsicum annuum* L.) accounted for the highest sales value and the third-highest production volume among vegetable seedlings produced by Korean nursery companies in 2024, making it an economically important target for automated growth monitoring. Seedling height (plant height) is a key indicator that nursery growers use to determine the optimal shipping time, and reliable, non-destructive measurement of this trait is therefore important for practical nursery management. Stereo vision offers a low-cost, non-contact means of estimating seedling height, but its depth resolution is inversely related to the camera baseline, while a larger baseline also increases the risk of stereo-matching failure caused by occlusion among overlapping canopy leaves. This trade-off has been reported for plants imaged within 1 m of the camera, but its optimal balance under a fixed, closer imaging distance and a densely planted seedling tray remains unclear. This study aimed to determine the baseline that best balances depth resolution and matching reliability for estimating pepper seedling height at a fixed 60 cm imaging height.

A stereo vision system was constructed using two Arducam OV5647 Camera Modules, each fitted with an identical 3.6 mm focal-length lens selected to keep the entire seedling tray (280 × 540 mm) within the field of view, and processed on a Raspberry Pi 5. Imaging height, lens, and the stereo matching algorithm (Semi-Global Block Matching, SGBM) were held constant, while the camera baseline was varied across four levels (35, 50, 65, and 80 mm). For each tray cell, the plant height was estimated from the highest valid disparity values within the segmented canopy region, and compared against manual caliper measurements to compute the root-mean-square error (RMSE), mean absolute error (MAE), and coefficient of determination (R^2). The measured accuracy at each baseline was further compared with the theoretically calculated depth resolution to identify the baseline at which matching failure begins to outweigh the theoretical gain in accuracy.

The results of this study are expected to identify the baseline that best balances depth accuracy and matching reliability for pepper seedling trays at a fixed 60 cm imaging height, providing practical guidance for implementing low-cost, non-destructive seedling height monitoring systems in commercial nursery operations.

Key Words: Stereo Vision, Baseline Optimization, Plant Height, Pepper Seedling, Occlusion

ACKNOWLEDGEMENTS

This research was supported by the ANCHOR Program through the ANCHOR Center, Gyeongsangnam-do, funded by the Ministry of Education (MOE) and the Gyeongsangnam-do Provincial Government, Republic of Korea (2026-RISE-16-20-0002), and by the Smart Farm Innovation Technology Development Program through the Korea Institute of Planning and Evaluation for Technology in Food, Agriculture and Forestry (IPET), funded by the Ministry of Agriculture, Food and Rural Affairs (MAFRA) (RS-2025-02306378).

Bio-processing Engineering 1 (BP-1)



BP-01

Proceedings of The 12th International Symposium on Machinery and Mechatronics for Agriculture and Biosystems Engineering (ISMAB 2026)
20-24 October 2026, Busan, Republic of Korea

HOLLOW FIBER MEMBRANE BASED VACUUM MEMBRANE DISTILLATION FOR AMMONIA NITROGEN REMOVAL

Megha Pramod[1a], Bo-Sheng Wu[1b], Wu-Yang Sean[1c]

[1a]Ph.D. Scholar, National Chung Hsing University, Taiwan
[1b]Master's Student, National Chung Hsing University, Taiwan
[1c]Associate Professor, National Chung Hsing University, Taiwan
*Corresponding Author-- Voice: +886 0978059003, Email: wysean@nchu.edu.tw

Abstract: The main sources of ammonia nitrogen (NH_3-N) wastewater discharge currently include livestock farming and agricultural activities, domestic sewage and various industrial wastewater. If discharged all the wastewater into the water bodies, it will cause serious environmental issues like eutrophication. The Taiwan Environmental Protection Agency issued a revised announcement of the Discharge Water Standards on July 21, 2021 based on Article 10 of the Water Pollution Control Act (Announcement No: Environmental Protection Agency Water No. 1101037394), tightening the standards for ammonia nitrogen emissions. This amendment specifies that from January 1,2025 for certain industrial categories and some specific restricted water areas, the maximum allowable concentration of ammonia nitrogen will be reduced from the original 40 mg/L to 20 mg/L. This study focuses on Vacuum membrane distillation (VMD) for treating high concentration ammonia-nitrogen wastewater. The research combines experimental comparison, single factor sensitivity analysis, optimization, comparison of PTFE and PP membrane and integration of Aspen Plus with PLC for offline working condition. Single-factor analysis reveals that temperature, vacuum pressure and feed concentration are key parameters affecting ammonia gas transport efficiency, requiring a balance between flux and sensitivity. Furthermore, Aspen Plus simulation coupled with a custom User Model was employed to evaluate the impact of feed conditions and to optimize the result. The optimization of this system provides 20% of ammonia nitrogen wastewater at the output side. The comparison of two membranes – Polytetrafluoroethylene and Polypropylene shows a result of highest ammonia and water flux for Polypropylene while the PTFE has highest separation factor and temperature polarization coefficient. This study also reveals that the concentration polarization effect for both the membranes are relatively same, which shows mass transfer limitations observed in this system are governed predominantly by thermal boundary layer than concentration boundary layer. The findings of this study provide practical insights for the future design and the integration of Aspen Plus system for offline judgement conditions.

Key Words: Ammonia recovery, Vacuum membrane distillation, Numerical simulation, Wastewater treatment, Aspen Plus simulation

INTRODUCTION

Effectively treating ammonia-nitrogen wastewater is a key issue in water pollution

management because discharging nitrogen-containing wastewater directly into natural water bodies can lead to water eutrophication and pollution (Capodaglio et al., 2015). Traditional ammonia-nitrogen removal methods such as denitrification, stripping and chemical precipitation are well-established methods, but they face problems like low efficiency, high energy consumption or complicating byproduct handling (Zhou et al., 2023). In comparison Membrane Distillation has become a hot research topic recently due to its low energy use, ease of operation and high selectivity.

Among these, hollow fiber membrane vacuum membrane distillation (VMD), shows great potential for treating high ammonia wastewater. VMD improves mass transfer driving force by reducing the vacuum pressure on the permeate side of the membrane, which effectively boosts permeate flux, ammonia recovery and wetting risks on the membrane (Gryta, 2012). Hollow fiber membranes, compared to traditional flat-sheet membranes, take up less space and provide a larger effective membrane area, making them especially suitable for resource recovery and zero-wastewater discharge systems (Ashoor et al., 2016). Vacuum Membrane distillation (VMD) has advantages such as low operating temperature, modular design, good resistance to fouling and the ability to effectively separate volatile ammonia, becoming a promising technology for ammonia nitrogen concentration and recovery applications (Abu-Zeid et al., 2015). The VMD system applies a vacuum on the cold side of the membrane distillation module to effectively reduce the vapor pressure difference across the membrane, making it easier for volatile solutes like ammonia to penetrate the hydrophobic membrane into the condensation side, thus improving separation efficiency (Abu-Zeid et al., 2015).

This research combines theoretical modeling and numerical simulation to deepens the understanding of complex transport phenomena in the membrane distillation process while also providing quantitative decision-making tools for the design and operation of industrial wastewater treatment systems, possessing significant academic value and engineering application significance. The research results will help improve the energy efficiency of high-concentration ammonia nitrogen wastewater treatment and lay the theoretical foundation for the subsequent system development and scaling experiments of the Industrial Technology Research Institute team.

The purpose of this study is to establish a purification system for ammonia water based on vacuum membrane distillation (VMD) simulation technology, wherein systematic analysis and optimization of its performance are conducted through numerical and process simulation methods. A numerical model of the VMD process was developed and its accuracy assessed through validation against a reference data (He et al., 2018). A sensitivity analysis conducted to identify the operating parameters with the greatest influence on system performance. The heat and mass transfer performance of polytetrafluoroethylene (PTFE) and polypropylene (PP) hollow fiber membrane was then compared under this framework. A system for the simulation was constructed in the Aspen Plus with a target of 20% of ammonia nitrogen at the output side and will integrate the system with Programmable Logic Controller (PLC) for the offline working condition in industry.

MATERIALS AND METHODS

VMD NUMERICAL SIMULATION SETUP

To investigate heat and mass transfer behavior in vacuum membrane distillation (VMD) using

hollow fiber membranes and its impact on ammonia nitrogen recovery, this study developed a one-dimensional steady state numerical simulation in MATLAB. The model discretizes the membrane module length from feed to membrane end using the control volume method, with a for-loop performing node-by-node calculations of local temperature, concentration and flux along the module.

The model first inputs the membrane parameters and experimental parameters before proceeding with subsequent calculations, aiming to obtain the results for ammonia flux and water flux. Due to the partial evaporation of the feed solution through membrane, there will be a loss of thermal energy, resulting in a temperature change at the feed inlet and outlet. A for loop is used to perform iterative calculations, with the loop set to tolerate a relative error of 10^{-4}. If the error exceeds 10^{-4}, the value from the previous iteration will be used to recalculate until the error is less than $10^{-4.}$

By assuming the inlet and outlet temperatures, the inlet flow rate and the parameters of hollow fiber membrane, the Prandtl number (Pr) and Reynold's number (Re) are calculated. The thermal convection coefficient of the inlet is estimated using heat transfer empirical formulas. Furthermore, the inlet membrane surface's partial vapor pressure is calculated based on the set of Henry's law and modified Antoine Equation. The newly obtained values will be subjected to error calculations against the initial assumed guesses at the start of the simulation. The relative error will be calculated by Eq. (1).

$$\text{Error} = \frac{|\text{initial guess} - \text{recalculated value}|}{\text{initial guess}} \quad (1)$$

VMD NUMERICAL MODEL VALIDATION AND ACCURACY ASSESSMENT

To verify the accuracy of the numerical model for vacuum membrane distillation established in this study, we used the experimental data presented by (He et al., 2018). Their research provided complete parameters and operating conditions for the membrane module, making it suitable as a reference for simulation comparison. The literature provides detailed membrane material properties (such as pore size, porosity, thickness and thermal conductivity), module geometric dimensions, operating conditions as well as corresponding experimental measurement results (including ammonia flux, water flux and ammonia nitrogen removal rate), ensuring reliability and completeness as a validation benchmark for the model.

This study simulates calculations based on the membrane materials and operational parameters provided in the literature, using a self-built MATLAB numerical model and compares the simulation result with experimental data from the literature. The results show that the simulated predictions and experimental results exhibit good consistency across various indicators, with the error of (≈±10%), indicating that this model has good reproducibility and predictive accuracy for the transport behavior of the VMD system. Table 1 represents the specifications of hollow fiber membrane from the reference.

In addition, through this verification step, further confirmation of the model will change the membrane parameters to use the 3M Liqui-Cel EXF Series 2.5*8 membrane contractor used by the Industrial Technology Research Institute team.

Table 1: Specifications of hollow fiber membrane for references

Parameters	Values	Units
Fiber inner diameter	200	μm
Fiber outer diameter	300	μm
Membrane pore size	80-90	nm
Membrane porosity	33	%
Module inner diameter	20	mm
Module outer diameter	22	mm
Number of fibers	500	-
Total module length	0.525	m
Effective hollow fiber length	0.375	m
Effective membrane area	0.12	m^2

SIMULATION PARAMETER SENSITIVITY ANALYSIS METHOD

In order to investigate the impact of membrane material parameters on the performance of a vacuum hollow fiber membrane distillation system, this study employs a single-factor sensitivity analysis method. Under fixed basic operating conditions, parameters are varied for different simulated operating conditions, and the trends of various factors on vapor flux and ammonia recovery efficiency are observed. The simulation operating parameters considered in the sensitivity analysis include: feed solution temperature, feed solution concentration, feed flow rate, feed solution pH value, and the vacuum pressure on the vacuum side, all of which are key properties affecting the thermal and mass transfer efficiency of the membrane. To ensure a more representative and scientifically based comparison, this study uses the membrane material parameters provided by (He et al., 2018) as shown in Table 2.

Table 2: Comparison of parameters of hollow fiber membranes in the references with 3M membrane.

Parameters	References/3M	PP	Units
Fiber inner diameter	200	200	μm
Fiber outer diameter	300	300	μm
Membrane pore size	80-90	30	nm
Membrane porosity	33	25	%
Module inner diameter	20	55.5	mm
Module outer diameter	22	-	mm
Number of fibers	500	10000	-
Total module length	0.525	-	m
Effective hollow fiber length	0.375	0.15	m
Effective membrane area	0.12	2.8274	m^2

In the simulation analysis, one simulation parameter is changed in each simulation while all other operational conditions remain unchanged based on the basic simulation settings. During the simulation process, the model will calculate and record the average vapor flux ($kg/m^2.h$), water vapor flux ($kg/m^2.h$), ammonia gas flux ($kg/m^2.h$) and ammonia membrane selectivity (%) under varying membrane parameters along with other performances.

ESTABLISHMENT OF SYSTEM SIMULATION MODEL

In order to further analyze the overall ammonia recovery efficiency of the vacuum hollow fiber membrane distillation system in the treatment of ammonia nitrogen wastewater, this study employs Aspen Plus V14 as the simulation platform to construct a system model applicable to

experimental operation conditions. The main purpose of this simulation is to optimize the output ammonia concentration to be 20%.

In the model establishment process, the feed side is set as a water phase mixture containing ammonia nitrogen, and the operating temperature range is set to 55-70℃ based on the aforementioned MATLAB numerical simulation condition. The overall system flow includes major units such as a feed preheater, membrane distillation unit, vacuum pump unit, condenser and ammonia gas recovery module with simulation parameters and connected based on actual operational needs and experimental scale (as shown in. Fig. 1). Table 3 is showing the description of module names used in Aspen Plus.

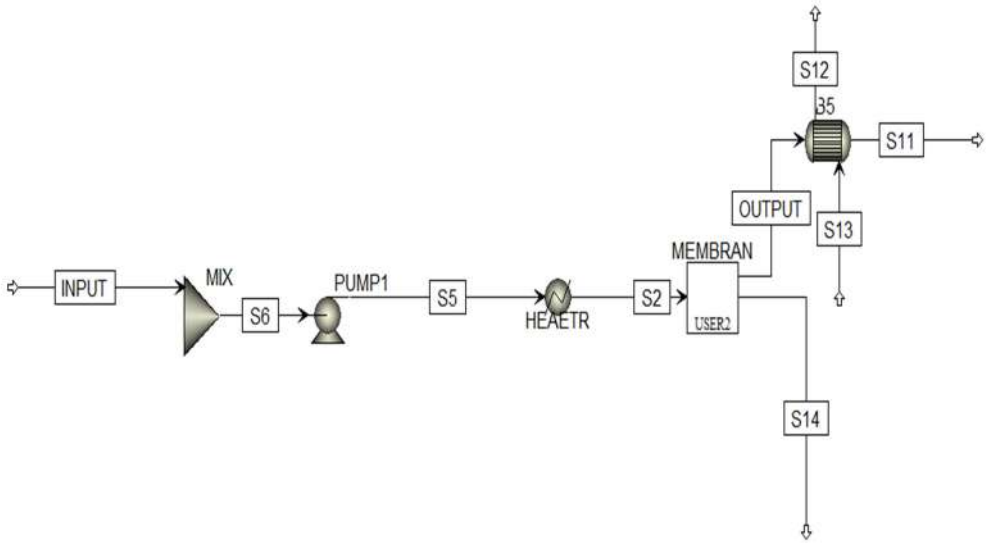

Fig. 1: Aspen Plus simulation setup

Table 3: Description of modules used in Aspen Plus

Unit operation module	Module Name	Select module type
Inlet	INPUT	Stream
Preheater	HEAT	Heater
Membrane distillation module	VMD	User Module
Condenser (B5)	CONDEN	Heat Exchanger

This study utilizes the User 2 module in Aspen Plus in conjunction with Excel to relay the properties and boundary conditions from various unit operations in Aspen Plus t the VMD model via Excel as an intermediary. MATLAB then executes the corresponding calculations and the results returned to Aspen Plus for subsequent thermal integration analysis and material balance processing.

OPTIMIZATION AND COMPARISON OF PTFE AND PP MEMBRANES

For obtaining the target ammonia of 20%, it is important to isolate the operating conditions. After completing the Aspen Plus system simulation setup, changing different parameters to get 20% ammonia. The optimization part is done manually by changing the basic settings. The feed temperature reduced to 45℃ from 55℃. Along with this, feed composition is also adjusted and establishing a localized baseline mole fraction at 0.08 for water and 0.02 for ammonia. Flow rate is setup to 7l/min from 5l/min. From Table 4, it is evident that the mole fraction of ammonia is achieved about 20%.

Table 4: Feed input and output variables in Aspen Plus

Parameters	FEED	OUTP UT
Temperature	45	60
Pressure	1	1
Flow rate	7	-
NH_3 Mole fraction	0.2	0.209302325581395
H_2O Mole fraction	0.8	0.790697674418605

Following the baseline parametric evaluation of polypropylene (PP), the study was extended to Polytetrafluoroethylene (PTFE) for comparative performance evaluation in VMD. We already discuss the parameters of hollow fiber membrane for polypropylene. The existing MATLAB simulation framework was modified by substituting PP's structural properties with those of PTFE. Ammonia flux, water flux, temperature polarization coefficient (TPC), Concentration Polarization coefficient (CPC) and separation factor were systematically analyzed as functions of feed temperature, with thermal and mass transport efficiencies evaluated using localized dimensionless coefficient. TPC is defined as the ratio of membrane surface temperature to bulk feed temperature; values approaching unity indicate minimal thermal boundary resistance, while values approaching zero signify high temperature polarization. CPC is defined as the ratio of feed water concentration to membrane surface concentration; a declining CPC toward zero denotes increasing concentration polarization, while values near unity reflect minimized mass transfer resistance. Membrane selectivity was evaluated via the separation factor (α), defined as the ratio of liquid permeating through the pores to the total liquid. A parameter critical for boundary layer analysis, particularly given ammonia's high volatility and rapid depletion at the feed-side membrane surface. Table 5 shows the comparison of PP and PTFE physical values provided by ITRI.

Table 5: Comparison of PP and PTFE parameters provided by ITRI

Parameters	Units	PP	PTFE
Fiber inner diameter	μm	200	1500
Fiber outer diameter	μm	300	2400
Membrane pore size	nm	30	200
Membrane porosity	%	25	60
Module inner diameter	mm	55.5	150
Module outer diameter	mm	-	-
Number of fibers	-	10000	2000
Total module length	m	-	0.98
Effective hollow fiber length	m	0.15	0.75
Effective membrane area	m^2	2.8274	3.6
Tortuosity	-	2.6	1.8

RESULTS AND DISCUSSION

VMD -NUMERICAL MODEL VERIFICATION

This section will first display comparison charts of simulated and experimental data, and further analyze the impact of various key parameters. In the figures, square markers represent experimental data from the literature, while the circular markers represent the results from the numerical simulation model established in this study.

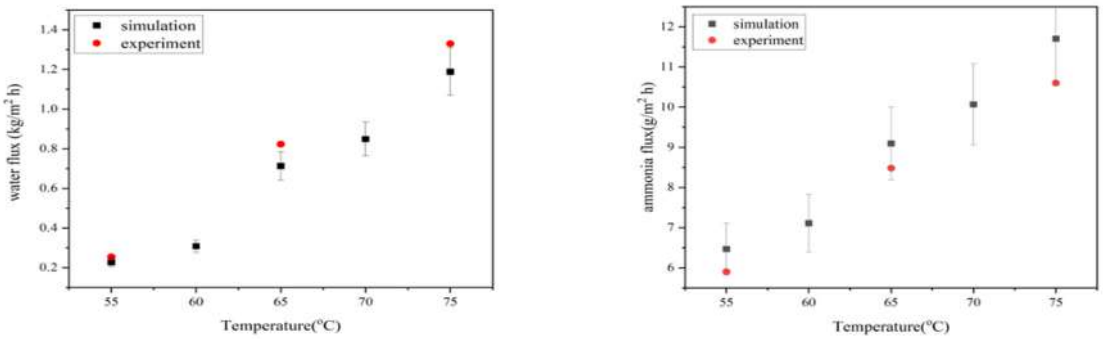

Fig. 2: Comparison of Ammonia flux and water flux with reference paper at different temperature.

Figure 2 shows the comparison of water flux and ammonia flux under different temperature with experimental data from the literature. As feed temperature increases, the vapor pressure and volatility of ammonia and water increases through the membrane. The ammonia flux and water flux will also increase through the membrane.

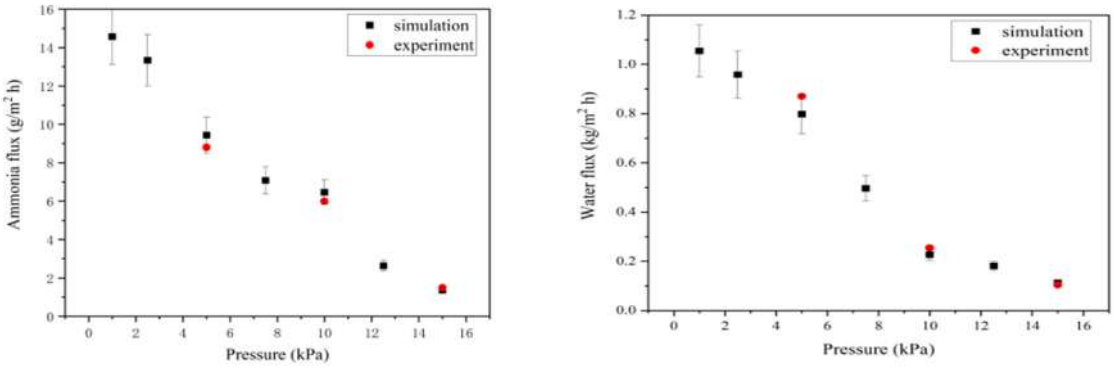

Fig. 3: Comparison of Ammonia flux and Water flux under different pressure with reference paper

Figure 3 shows the variation of ammonia flux and water flux at different pressures. As the vacuum pressure decreases, the difference in the driving force generated by ammonia gas on both sides of the membrane increases. This is because the decrease in vacuum pressure causes an increase in the vapor pressure on both sides of the membrane, significantly enhancing the transmission rate of ammonia gas through the membrane.

Figure 4 shows the variation of ammonia flux and water flux at different pH. The operating conditions were set with pH values ranging from 7.5 to 10. As pH increases, gaseous ammonia flux also increases. In case of pH, water flux is largely unaffected. In ammonia nitrogen solutions, ammonia primarily coexists in the forms of gaseous ammonia (NH_3) and ammonium ions (NH_4^+), with the ratio of the two being highly dependent on the pH value of the solution. According to the equilibrium relationship, the higher the pH value, the greater the proportion of gaseous ammonia, which helps to enhance the vapor pressure difference and mass transfer efficiency.

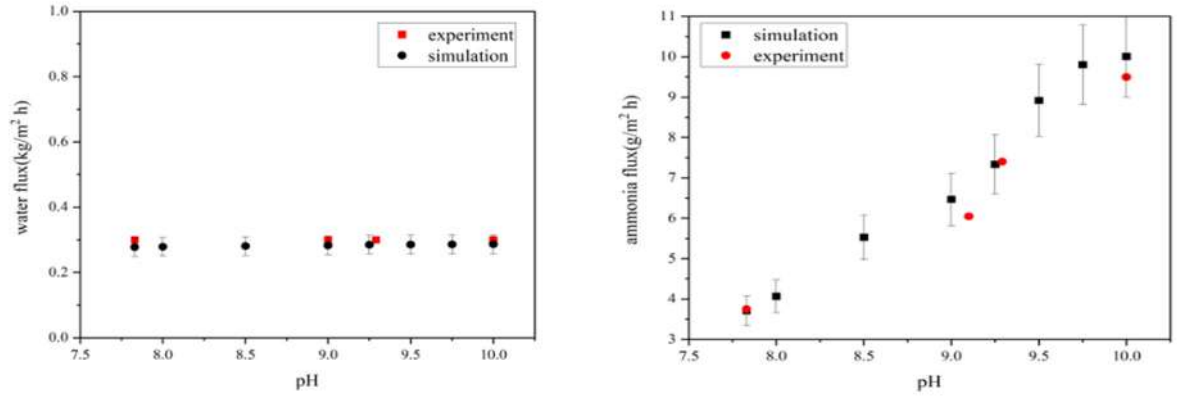

Fig. 4: Comparison of ammonia flux and water flux under different pH values in the reference

SENSITIVITY ANALYSIS RESULTS

Based on this research after setting new membrane conditions, a one factor sensitivity analysis was conducted to simulate and estimate the changes in system performance under different operating variables. This analysis effectively clarifies the impact of various operational conditions on ammonia gas flux and membrane ammonia selectivity (ammonia concentration on the vacuum side) and provides a basis for subsequent system optimization and experimental parameter adjustments. The calculation of membrane selectivity is as shown in Eq. (2)

$$\text{Selection rate} = \frac{\text{Ammonia flux}}{\text{Total flux}} \tag{2}$$

Through single-factor analysis, this will serve as an important basis for subsequent interaction analysis and system design optimization, enhancing the effectiveness and cost-effectiveness of the vacuum membrane distillation system in practical applications.

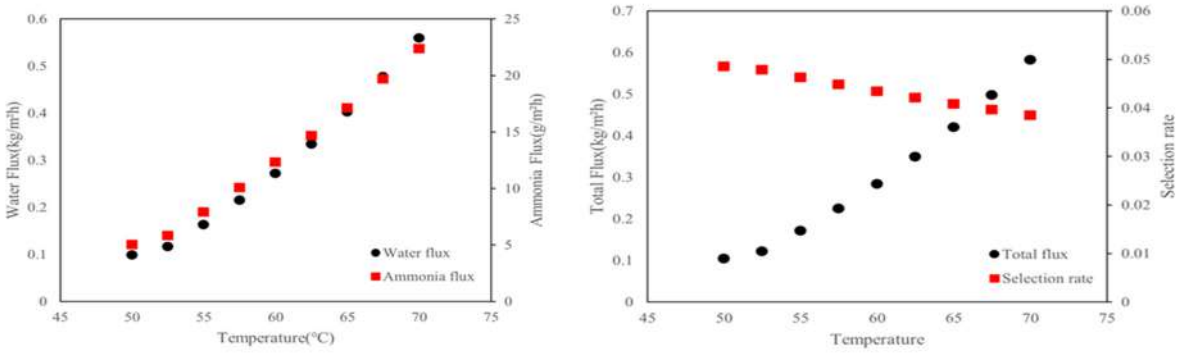

Fig. 5 & Fig. 6 : Comparison of water flux and ammonia flux and the comparison of total flux and selectivity with temperature respectively.

Figure 5 and Figure 6 indicates that as the feed temperature increases, both water flux and ammonia flux show an upward trend. This will increase the total flux throughout the membrane which results the substantial amount of water vapor at the permeate side and shows a downward trend for ammonia selectivity. This suggests that while the increase in temperature can effectively enhance the permeation rate of ammonia, it also significantly accelerates the evaporation and transport of water molecules, resulting in an increased proportion of water vapor in the overall flux, thereby diluting the concentration of ammonia in the permeate.

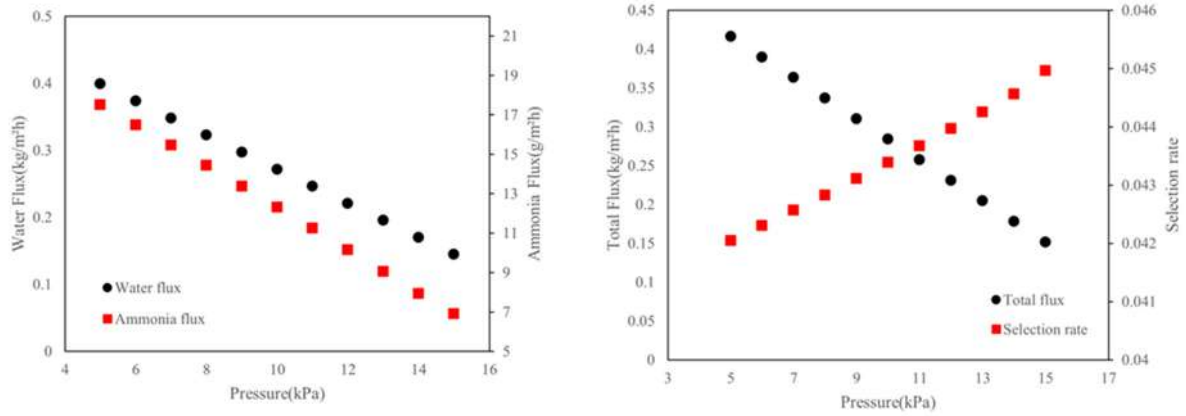

Fig. 7 & Fig. 8: Comparison of ammonia flux and water flux and comparison of total flux and selection rate with different pressure respectively.

Figure 7 and Figure 8 indicates that changes in vacuum pressure affects the ammonia gas flux and water flux. As vacuum pressure decreases, water flux and ammonia flux will increase and it is due to the vapor pressure difference across the membrane. This will result in the reduction of total flux and selectivity of the membrane will be higher. A stronger vacuum on the permeate side lowers the pressure there, which increases this pressure difference and pushes more gas molecules through the membrane. Since ammonia is more volatile and diffuses faster than water, its flux increases even more sharply under stronger vacuum conditions

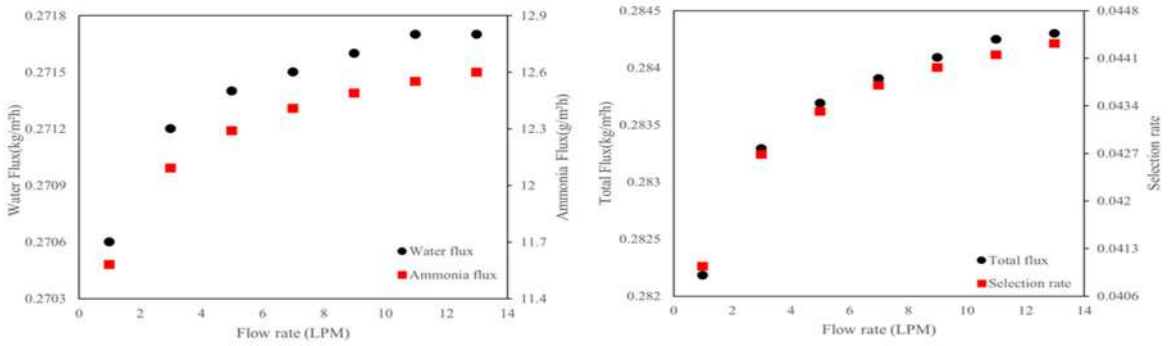

Fig. 9 and Fig. 10: Comparison of water flux and ammonia flux and comparison of total flow and selection rate with flow rate respectively.

Feed flow rate is another key parameter affecting VMD performance. Increasing the flow rate raises turbulence at the membrane surface, thinning the boundary layer and reducing concentration and temperature polarization. This helps maintain a stronger transmembrane driving force and improves mass transfer. Increasing flow rate from 1 to 9 LPM enhanced ammonia flux by 11.5–12.6 g/m²·h and ammonia selectivity by 0.041–0.0446 by weakening concentration and temperature polarization, though gains diminished at higher flow rates as the system approached a stable operating condition.

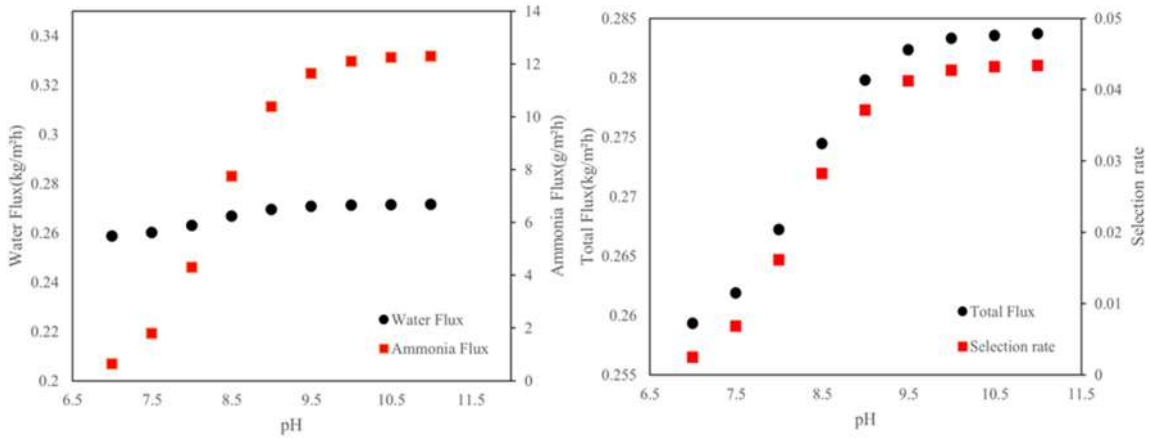

Fig.11 and Fig.12: Comparison of ammonia flux and water flux and comparison of total flux and selection rate at different pH value respectively.

Under different pH conditions, the effects on the water vapor and ammonia flux in the membrane distillation system show significant differences. Overall, the water flux is relatively minimally affected by changes in pH, mainly because the volatilization behavior of water vapor is not significantly influenced by pH. However, the ammonia flux is significantly affected by change in Ph. According to this chemical equilibrium, when the pH increases, the concentration in the solution decreases, and the reaction equilibrium shifts to the right, promoting the conversion of ionic ammonium to volatile gaseous ammonia, thereby effectively increasing the transmembrane transport flux of ammonia. According to the simulation results, within the pH range of approximately 7.5 to 10.5, the changes in ammonia flux are most pronounced, showing a rapid upward trend; however, when the pH exceeds 10.5, the volatilization ratio of ammonia approaches saturation, and the reaction equilibrium nears its limit, causing the increase in flux to slow down. This phenomenon shows that pH control is not only a key factor in regulating ammonia recovery efficiency, but is also closely related to the chemical stability and safety in actual operations.

COMPARISON RESULT OF PP AND PTFE

This section will discuss the comparison of ammonia flux, water flux, Separation factor, Temperature Polarization Coefficient (TPC) and Concentration Polarization coefficient with respect to temperature. The graph shown below is the result of showing ammonia flux with respect to temperature for the PP and PTFE membranes. The red line is showing the results of PP while the blue line shows the result of PTFE.

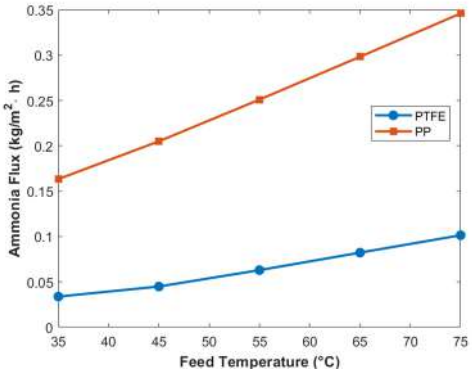

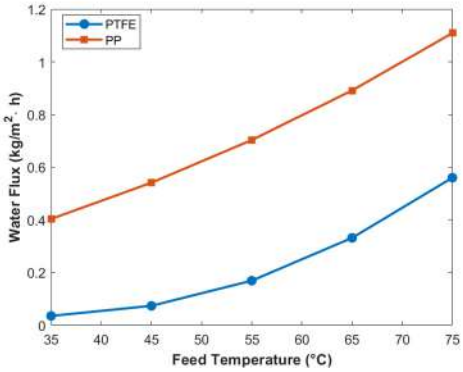

Fig.13 and Fig.14: Comparison of feed temperature with ammonia flux and water flux with temperature respectively.

Figure 13 and Figure 14 is showing a feed temperature with ammonia flux and water flux for PP and PTFE membrane. As feed temperature increases from 35℃ to 75℃, water flux and ammonia flux shows an upward trend for both the membranes. According to the Antoine equation and henry's law, increasing the feed temperature elevates both the vapor pressure and volatility of dissolved ammonia and water (Van Linden et al., 2022). Since the vacuum side pressure was held constant throughout the experiments, this rise in feed side vapor pressure directly widens the transmembrane vapor pressure difference which serves as the principal driving force in Vacuum Membrane Distillation (VMD).

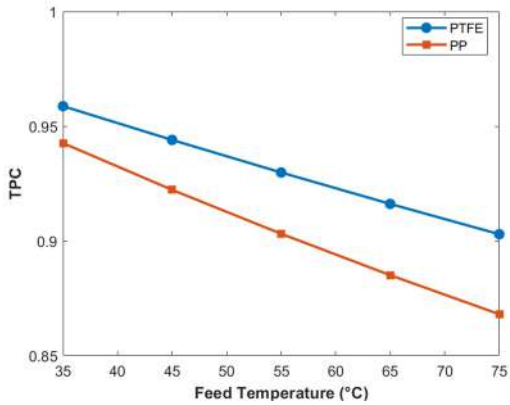

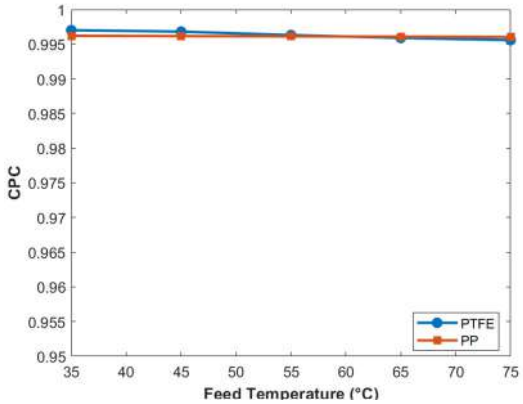

Fig.15 and Fig.16: Comparison of feed temperature with Temperature Polarization Coefficient (TPC) and Concentration Polarization Coefficient (CPC) respectively.

Figure 15 represents the variation of the temperature polarization coefficient (TPC) for PP and PTFE respectively. For both the membranes, TPC declined consistently with increasing feed temperature: the PP membrane (red) decreased from 0.94 to 0.86, while the PTFE membrane (blue) declined more moderately from 0.95 to 0.90 across the same temperature range. Notably, PTFE maintained consistently higher TPC values than PP across the entire temperature range, indicating superior thermal management to temperature polarization good. A TPC should be near to 1 and it indicates minimal thermal resistance (low temperature polarization). As the temperature rises, the vapor pressure of the volatile components increases exponentially, because the rate of vaporization increases faster than the rate at which heat can be replenished from the bulk liquid via convection or conduction (Suleman et al., 2021). This created a steep thermal gradient, and cause TPC to fall. It is evident that PTFE is more structurally superior to PP.

Figure 16 represents the variation of the concentration polarization coefficient (CPC) for PP and PTFE respectively. CPC value remained exceptionally stable and near unity across the entire temperature range, narrowly between 0.995 and 0.997 for both membrane types. A CPC approaching unity indicates that the ammonia concentration at the membrane surface closes to that of the bulk feed solution, shows negligible concentration polarization and efficient mass transfer of the solute from the bulk liquid to the membrane interface. The consistently high CPC values across both PP and PTFE membranes and their insensitivity to feed temperature, indicate that CPC do not constitute a limiting factor in this VMD system. This finding is very important because TPC result from the Figure 15, shows progressive decline with increasing temperature for both membranes. These results confirm that the mass transfer limitations observed in this system are governed predominantly by thermal boundary layer than concentration boundary layer.

CONCLUSIONS

This study focuses on numerical simulations and system integration analysis of the application of Vacuum Membrane Distillation (VMD) technology for the concentration treatment of high concentration ammonia nitrogen water bodies. This study first references the vacuum membrane distillation (VMD) model framework established by (He et al., 2018) for numerical simulations, and performs preliminary validation of the model using their publicly available data. The ammonia flux obtained from the simulations shows an average relative error of approximately 10% when compared to experimental data in the literature, indicating that this model possesses good accuracy and reference value. A single factor sensitivity analysis was conducted for operating temperature, vacuum pressure, flow rate, and pH value. Among these, the factor that has the best impact on increasing the total flux is the increase in vacuum pressure. A change in vacuum pressure from 5 kPa to 15 kPa results in an ammonia flux variation of 18-7 g/m2h. The change in ammonia selectivity is between 0.042 and 0.045. Therefore, appropriately reducing the permeate side pressure can effectively enhance ammonium flux while maintaining a relatively high ammonia selectivity, which has a crucial impact on system performance optimization. This study constructed a complete system simulation process using Aspen Plus, integrating a User Model (connecting numerical models via Excel) to achieve dynamic simulation and process integration. The simulation process includes feed preheating, VMD module, and condenser design. Through systematic parametric optimization of feed temperature, feed composition and volumetric flow rate, the system was capable of achieving a target permeate ammonia mole fraction of 20%. Comparative evaluation of PP and PTFE hollow fiber membranes revealed a flux performance and membrane transport quality. PP membranes are superior for higher ammonia and water flux while PTFE demonstrated good temperature polarization coefficient (TPC) and concentration polarization coefficient (CPC) analysis, with TPC identified as the dominant limiting factor over CPC. The research work is in the stage of integrating a system level simulation in to real world condition through Programmable Logic Controller (PLC).

ACKNOWLEDGEMENT

This work was supported by Industrial Technology Research Institute (ITRI), Taiwan.

REFERENCES

Abu-Zeid, M. A. E.-R., Y. Zhang, H. Dong, L. Zhang, H.-L. Chen, and L. Hou. 2015. A comprehensive review of vacuum membrane distillation technique. *Desalination* 356: 1–14. https://doi.org/10.1016/j.desal.2014.10.033

Ashoor, B. B., S. Mansour, A. Giwa, V. Dufour, and S. W. Hasan. 2016. Principles and applications of direct contact membrane distillation (DCMD): A comprehensive review. *Desalination* 398: 222–246. https://doi.org/10.1016/j.desal.2016.07.043

Capodaglio, A. G., P. Hlavínek, and M. Raboni. 2015. Physico-chemical technologies for nitrogen removal from wastewaters: a review. *Ambiente e Agua - An Interdisciplinary Journal of Applied Science* 10(3): 481–498. https://doi.org/10.4136/ambi-agua.1618

Gryta, M. 2012. Effectiveness of Water Desalination by Membrane Distillation Process. *Membranes* 2(3): 415–429. https://doi.org/10.3390/membranes2030415

He, Q., T. Tu, S. Yan, X. Yang, M. Duke, Y. Zhang, and S. Zhao. 2018. Relating water vapor transfer to ammonia recovery from biogas slurry by vacuum membrane distillation. *Separation and Purification Technology* 191: 182–191. https://doi.org/10.1016/j.seppur.2017.09.030

Suleman, M., M. Asif, and S. A. Jamal. 2021. Temperature and concentration polarization in membrane distillation: a technical review. *Desalination and Water Treatment* 229: 52–68. https://doi.org/10.5004/dwt.2021.27398

Van Linden, N., Y. Wang, E. Sudhölter, H. Spanjers, and J. B. Van Lier. 2022. Selectivity of vacuum ammonia stripping using porous gas-permeable and dense pervaporation membranes under various hydraulic conditions and feed water compositions. *Journal of Membrane Science* 642: 120005. https://doi.org/10.1016/j.memsci.2021.120005

Zhou, Y., Y. Zhu, J. Zhu, C. Li, and G. Chen. 2023. A Comprehensive Review on Wastewater Nitrogen Removal and Its Recovery Processes. *International Journal of Environmental Research and Public Health* 20(4): 3429. https://doi.org/10.3390/ijerph20043429

BP-02

Proceedings of The 12th International Symposium on Machinery and Mechatronics for Agriculture and Biosystems Engineering (ISMAB 2026)
20-24 October 2026, Busan, Republic of Korea

GRAVITY-ASSISTED TWO-STEP CRISPR-CAS12A SYSTEM FOR RAPID MOLECULAR DETECTION

Shauqi Abda'i Lubis[1], Jyh Jian Chen[2*]

[1]Department of Tropical Agriculture and International Coorporation, National Pingtung University of Science and Technology, 1, Shuefu Road, Neipu, Pingtung, 91201, Taiwan
[2]Department of Biomechatronics Engineering, National Pingtung University of Science and Technology, 1, Shuefu Road, Neipu, Pingtung, 91201, Taiwan
*Corresponding Author-- Voice: +886-92-876-6662, Email: chaucer@mail.npust.edu.tw

Abstract: In order to ensure food safety, rapid, accurate, and on-site pathogen detection methods are required. *Salmonella Typhimurium* is one of the bacterial pathogens frequently associated with food contamination and foodborne diseases. Laboratory-validated DNA-based detection methods generally require relatively long processing times and specialized equipment. Recombinase Polymerase Amplification (RPA) is an isothermal amplification method with potential for rapid detection because it can operate at a relatively low temperature of approximately 37 °C with an amplification time of around 20 minutes. Subsequently, the CRISPR-Cas12a system can be employed as a molecular detection method because the Cas12a protein can specifically recognize target DNA sequences guided by CRISPR RNA (crRNA). However, direct integration of RPA amplification and CRISPR-Cas12a detection within a single reaction chamber may encounter challenges related to reaction-condition compatibility, necessitating the separation of the amplification and detection steps. In this study, a microfluidic system consisting of two chambers was developed to integrate RPA amplification and CRISPR-Cas12a detection sequentially using gravity-driven flow. The first chamber was designed for RPA amplification at 37 °C, while the second chamber was used for the CRISPR-Cas12a reaction under separately controlled conditions. The transfer of the solution from the first chamber to the second chamber was passively driven by gravity, while a sealable air vent was incorporated to temporarily prevent fluid flow during the amplification process. Computational Fluid Dynamics (CFD) simulations were employed to analyze the thermal distribution and conditions within both chambers. The actual thermal conditions were experimentally validated using thermocouples to measure the liquid temperature and an infrared thermal camera to evaluate the temperature distribution on the system surface. Detection of *S. Typhimurium* was indicated by an increase in fluorescence from the FAM-based reporter, with an emission wavelength of approximately 520 nm and an excitation wavelength of 488 nm. The resulting fluorescence signal was subsequently measured using a spectroscopic sensor, enabling the development of a portable system with potential for on-site pathogen detection.

Key Words: CRISPR-Cas12a; Recombinase Polymerase Amplification; Gravity-Assisted System; Fluorescence Detection; *Salmonella Typhimurium.*

BP-03

Proceedings of The 12th International Symposium on Machinery and Mechatronics for Agriculture and Biosystems Engineering (ISMAB 2026)
20-24 October 2026, Busan, Republic of Korea

EFFECTS OF HIGH-VOLTAGE PULSE PRETREATMENT ON THE SURFACE AND STRUCTURAL CHARACTERISTICS OF RICE STRAW

Wu-Huan Hsu[1*], Tsung-Chun Lin[2], Yun-Sheng Lu[2]

[1]Agricultural Engineering Division, Taiwan Agricultural Research Institute, No.189, Zhongzheng Rd., Wufeng Dist., Taichung City 413008, Taiwan (R.O.C.)
[2]Plant Pathology Division, Taiwan Agricultural Research Institute, No.189, Zhongzheng Rd., Wufeng Dist., Taichung City 413008, Taiwan (R.O.C.)
*Corresponding Author-- Voice: +886-4-2331-7713, Email: swhh@tari.gov.tw

Abstract: The recalcitrance of lignocellulosic biomass, such as rice straw, presents a significant barrier to its efficient utilization as a substrate for mushroom cultivation. This study investigated the effects of high-voltage electrical pulse pretreatment on the surface morphology, chemical composition, and micro-crystalline structure of rice straw. Freshly harvested rice straw was treated with high-voltage discharge pulses at voltages ranging from 0 to 90 kV. Scanning electron microscopy (SEM) revealed that high-voltage pulses induced severe physical damage, generating micro-cracks, deep crevices, and increased porosity on the straw surface. Chemical composition analysis using the Van Soest method showed that the contents of cellulose (26.81%–27.08%), hemicellulose (34.22%–37.33%), and lignin (6.08%–6.80%) remained remarkably stable across all voltage treatments, indicating that, under the tested conditions, high-voltage pulse stimulation primarily altered physical structure rather than measurably degrading these lignocellulosic components. X-ray diffraction (XRD) analysis confirmed that the treated rice straw retained its native Cellulose I crystalline structure. However, the crystallinity index (CrI) calculated by Segal's method increased from 41.17% (Control) to 45.60% (Treated), accompanied by a 17.4% increase in the main 200 diffraction peak intensity and a slight shift toward a lower angle ($\Delta 2\theta = 0.34°$). These changes may reflect greater exposure of crystalline cellulose and altered lattice spacing following disruption of the surrounding matrix. The observed structural alterations may improve water uptake and enzyme accessibility for mushroom hyphae, but these functional effects require direct verification.

Key Words: Rice Straw, High-Voltage Pulse, Substrate Pretreatment, SEM Morphology, XRD Crystallinity

INTRODUCTION

In recent years, electric field-assisted processing technologies, such as pulsed electric fields (PEF) and moderate electric fields (MEF), have drawn substantial interest in biorefinery and food processing industries (Moens et al., 2020). By applying high-voltage pulses or alternating currents between electrodes, an increased transmembrane potential is induced across

biological cellular membranes, resulting in reversible or irreversible pore formation—a phenomenon known as electroporation (Moens et al., 2020). This effect significantly enhances electropermeability, accelerates mass transfer, and alters tissue rheological and mechanical properties (Liu et al., 2023). However, for agricultural by-products rich in cellulosic tissue, structural recalcitrance remains the primary obstacle to efficient recycling and bioconversion (Ravindran and Jaiswal, 2016; Szwarc and Głowacka, 2021).

Electrical pretreatments such as pulsed electric field (PEF) treatment can disrupt lignocellulosic plant tissues and increase surface damage and substrate accessibility. PEF treatment of rapeseed straw, for example, produced more severe plant-tissue surface damage than that observed in untreated material (Szwarc and Głowacka, 2021). More broadly, physical pretreatments can modify accessible surface area, porosity, and the relative accessibility of amorphous and crystalline cellulose regions (Ravindran and Jaiswal, 2016). Because PEF, moderate electric field (MEF), and high-voltage electrical discharge (HVED) differ in treatment configuration and energy-delivery mechanism, their effects should not be assumed to be identical.

In agricultural circular economies, rice straw serves as a suitable substrate for cultivating tropical and subtropical mushrooms, including the straw mushroom (Volvariella volvacea) (Thuc et al., 2020). Rice-straw mushroom is a protein-rich edible mushroom that can be cultivated on rice straw. Its first flush may occur approximately 14 days after incubation, whereas the total crop cycle is generally about 4–5 weeks under favorable conditions (Thuc et al., 2020). High-voltage pulse stimulation applied to colonized substrates or mushroom-growing logs has also been reported to promote fruiting-body formation in several cultivated mushroom species, although the response depends on species and voltage conditions (Takaki et al., 2014). Takaki et al. (2014) used output voltages of 50–130 kV with a 100 ns pulse width and reported that electrically stimulated substrates could produce fruit-body yields approximately 130%–180% of untreated controls in previous studies.

Proposed explanations for electrically stimulated fruiting include physical effects on hyphal structures and changes in fungal physiological activity, such as hydrophobin release and activation of certain enzymes, including laccase and protease; however, the detailed causal pathways remain incompletely resolved (Takaki et al., 2014; Mohd Jamil et al., 2018). Electrical spiking in fungi may also be associated with calcium waves, cytoplasmic flow, and the translocation of nutrients and metabolites, although this interpretation remains partly speculative (Gandia and Adamatzky, 2022).

The clear objective of this study is to evaluate the physical and chemical impacts of high-voltage electrical pulse pretreatment on rice straw substrates, specifically examining changes in surface morphology (SEM), lignocellulosic chemical composition (Van Soest method), and crystalline structure (XRD) to elucidate the structural modification mechanism.

MATERIALS AND METHODS

Application of electric pulse stimulation treatment

The experimental setup comprised a controller, low-voltage cables, a high-voltage pulse

generator, a sliding rail platform, and an adjustable scissor lift table (Fig. 1). The pulse generation system was manufactured by Yushin Electrical Technology (Japan) as described by Islam et al. (2013). The high-voltage generator was mounted on the sliding platform to control spatial discharge positions. Fresh rice straw was harvested from agricultural fields, cut into 5 cm segments, and arranged side-by-side on a grounded metal plate. The output voltage of the high-voltage generator was adjusted via the controller to supply impulse discharge voltages: 0 kV (Control), 30 kV, 60 kV, and 90 kV for the analysis of lignocellulosic chemical composition, and 0 kV (Control) and 90 kV for SEM observation.

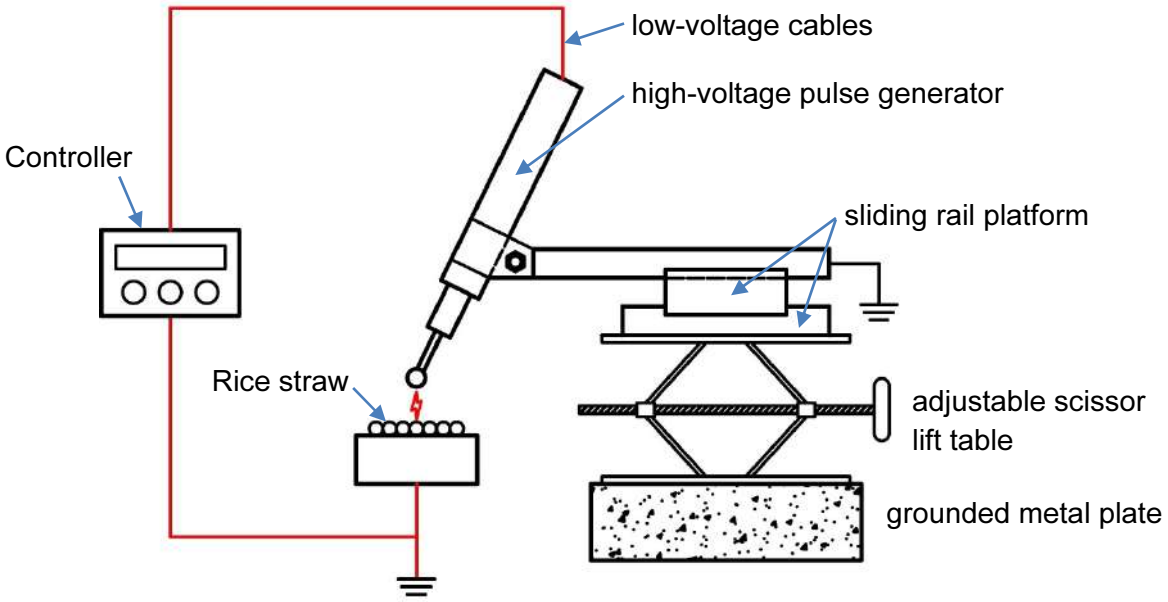

Fig.1 Experimental setup for pulse voltage stimulation on rice straw.

Surface and Structural Microscopic Observation

Scanning Electron Microscopy (SEM)

Surface microstructures of rice straw before and after discharge treatment were examined using a scanning electron microscope (JEOL, Model: JEOL/EO) operated at an accelerating voltage of 2.80 kV and a working distance of 42 mm.

X-Ray Diffraction (XRD) Analysis

XRD patterns were acquired using a Bruker D8 ADVANCE diffractometer (Cu-Kα radiation, $\lambda = 1.5406$ AA, operated at 40 kV and 40 mA). Dried straw samples were ground to pass through a 1.0 mm sieve. Scans were performed over a 2θ range of $2.00°$ to $40.00°$ with a step size of $0.02°$. The Crystallinity Index (CrI) was calculated using Segal's empirical method (Segal et al., 1959):

$$\text{CrI (\%)} = \frac{I_{200} - I_{\text{am}}}{I_{200}} \times 100\%$$

where I_{200} is the maximum intensity of the principal crystalline peak at $2\theta \approx 21.5°$--$22.0°$, and

I_{am} is the intensity of amorphous background scattering at $2\theta \approx 18.0°\text{-}18.5°$.

Lignocellulosic Chemical Composition Analysis

Chemical components (cellulose, hemicellulose, and lignin) were determined via sequential detergent extraction following the Van Soest et al. (1991) method. Dried ground samples (1.0 mm, $65°$C to constant weight) were analyzed in triplicate ($n = 3$), and results were expressed as percentage of dry matter (% DM).

RESULTS & DISCUSSION

Effect on Surface Morphology and Microstructure

Scanning electron micrographs (Fig. 2) illustrate marked structural transformation of rice straw under pulse discharge treatment. PEF-treated rapeseed straw has similarly shown more severe surface tissue damage than untreated material (Szwarc and Głowacka, 2021). However, direct comparison should be made cautiously because the treatment system, plant material, moisture condition, and electrical parameters differ from those used in the present study.

Similar Microstructural Features:

As shown in Figs. 2d–2f, the treated rice straw displayed distinct surface ruptures, deep crevices, torn edges, enlarged internal cavities, and interconnected pore-like structures. These observations demonstrate substantial physical disruption under the present treatment conditions. The increased surface irregularity and apparent porosity may improve water retention, aeration, and enzyme accessibility for fungal hyphae; however, these functional effects were not measured directly in this study and require further verification.

Differences Between Herbaceous and Woody Substrates:

Compared with the narrow longitudinal cracking previously observed in some woody mushroom-growing materials after electrical stimulation (Takaki et al., 2014), the rice straw examined here showed extensive delamination, peeling, cavity formation, and localized tearing. These differences may be related to the thin-walled, hollow structure of rice straw and its silica- and wax-containing epidermal surface. The specific contribution of thermal effects, mechanical stress, or electrical discharge to these features was not separately determined.

Effect on Cellulose, Hemicellulose, and Lignin Contents

Chemical composition analysis (Table 1) revealed that high-voltage pulse treatments (0 to 90 kV) did not significantly alter the absolute dry matter percentage of lignocellulosic components:

- **Cellulose:** Remained stable across all treatment groups (26.81%–27.08%), with differences within the observed standard deviations. Under the tested conditions, no measurable reduction in cellulose content was detected; this compositional result alone does not establish that no molecular-level modification occurred.
- **Hemicellulose:** Showed a minor increasing trend from 34.22% (30 kV) to 37.33% (90 kV), representing a 4.51% increase over Control (35.72%). This pattern may reflect variation in extraction or greater analytical accessibility after structural loosening, but the mechanism was not directly tested.
- **Lignin:** Displayed no monotonic degradation trend, remaining near 6.17% (Control),

6.08% (60 kV), and 6.11% (90 kV).

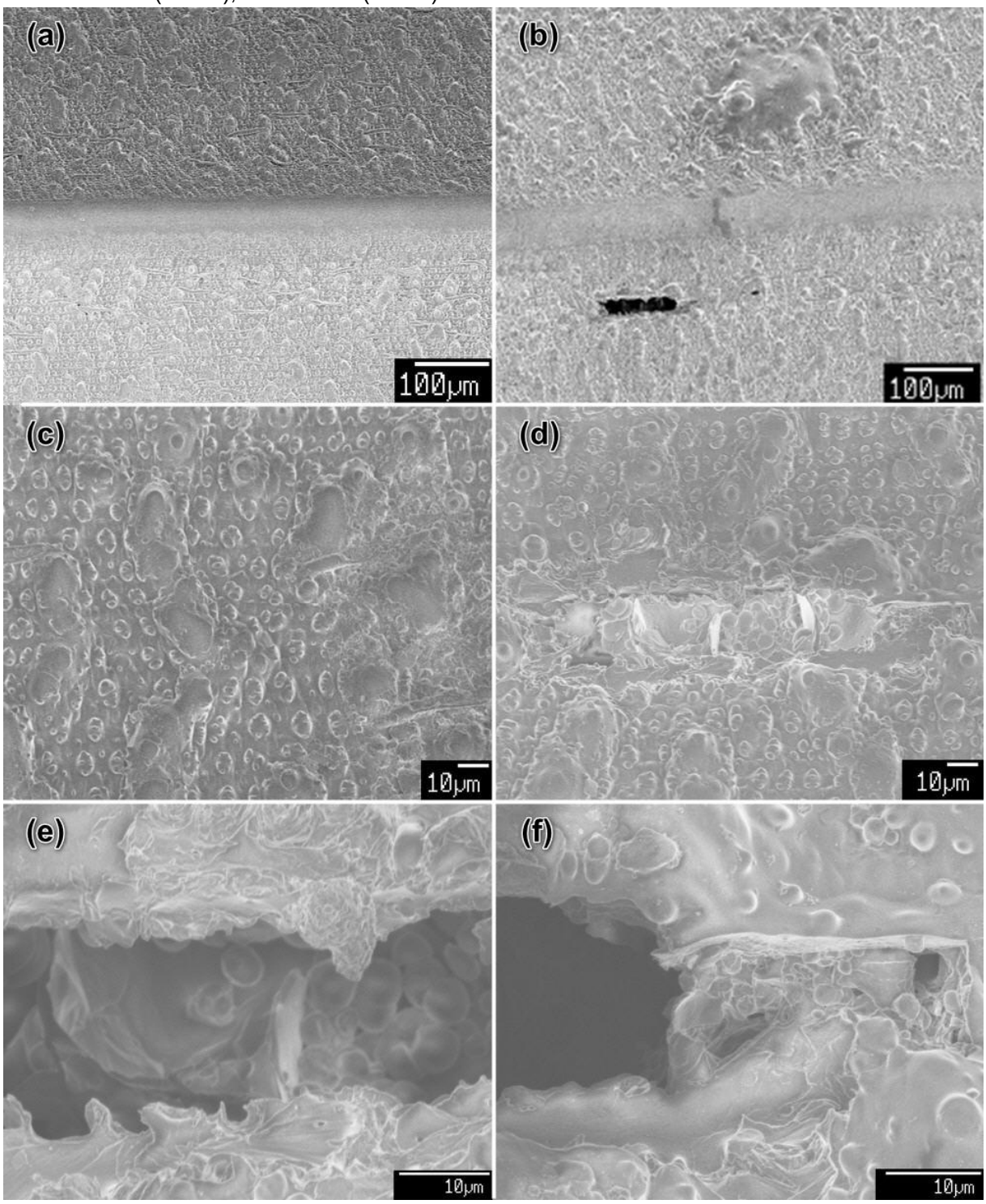

Fig. 2 Scanning electron micrographs of rice straw (a) before and (b), (c), (d), (e), (f) after high-voltage pulse treatments. White bar indicates 100µm in (a), (b) and 10 µm in (c), (d), (e) and (f).

Under the tested conditions, high-voltage pulse treatment did not produce a statistically detectable decrease in the measured cellulose, hemicellulose, or lignin fractions. Together with the SEM observations, these results suggest that the most evident treatment effect was physical restructuring rather than substantial compositional loss.

Table 1. Chemical composition of rice straw under different high-voltage pulse treatments (% DM).

Sample Voltage	Cellulose Content (% DM)	Hemicellulose Content (% DM)	Lignin Content (% DM)
0kV (Control)	26.81 ± 0.52	35.72 ± 2.34	6.17 ± 0.11
30kV	27.04 ± 0.97 (+0.86%)	34.22 ± 3.16 (-4.20%)	6.80 ± 0.73 (+10.21%)
60kV	27.02 ± 0.93 (+0.78%)	36.24 ± 2.39 (+1.46%)	6.08 ± 0.43 (-1.46%)
90kV	27.08 ± 0.39 (+1.01%)	37.33 ± 0.96 (+4.51%)	6.11 ± 0.65 (-0.97%)

Electric-field treatments have been reported to alter rheological properties, cell-wall characteristics, and the microstructure of plant tissues (Liu et al., 2023); however, that study did not directly demonstrate the absence of organic-carbon loss in lignocellulosic straw.

XRD Crystal Structure and Crystallinity Analysis

XRD patterns (Fig. 3) confirmed that both Control and Treated samples retained the Cellulose I crystalline allomorph, exhibiting characteristic peaks at $2\theta \approx 16.3°$--$16.6°$ (110 / $1\bar{1}0$ planes) and $2\theta \approx 21.6°$--$22.0°$ (200 plane). No transformation peak to Cellulose II ($2\theta \approx 20.0°$) was observed.

As detailed in Table 2, the Crystallinity Index (CrI) increased from 41.17% (Control) to 45.60% (Treated), with the primary 200 diffraction peak intensity (I200) rising by 17.4% (from 481.5 to 565.2 a.u.). This increase may indicate a greater relative exposure of crystalline microfibrils following alteration of surrounding amorphous regions. Because CrI calculated by Segal's empirical method is a relative index, the increase does not by itself demonstrate selective removal of hemicellulose or lignin. The 200 peak center shifted from 22.02° to 21.68° (Δ2θ = 0.34°), corresponding to an increase in calculated d-spacing. This shift is consistent with altered lattice spacing, but attributing it specifically to hydrogen-bond disruption requires additional structural evidence.

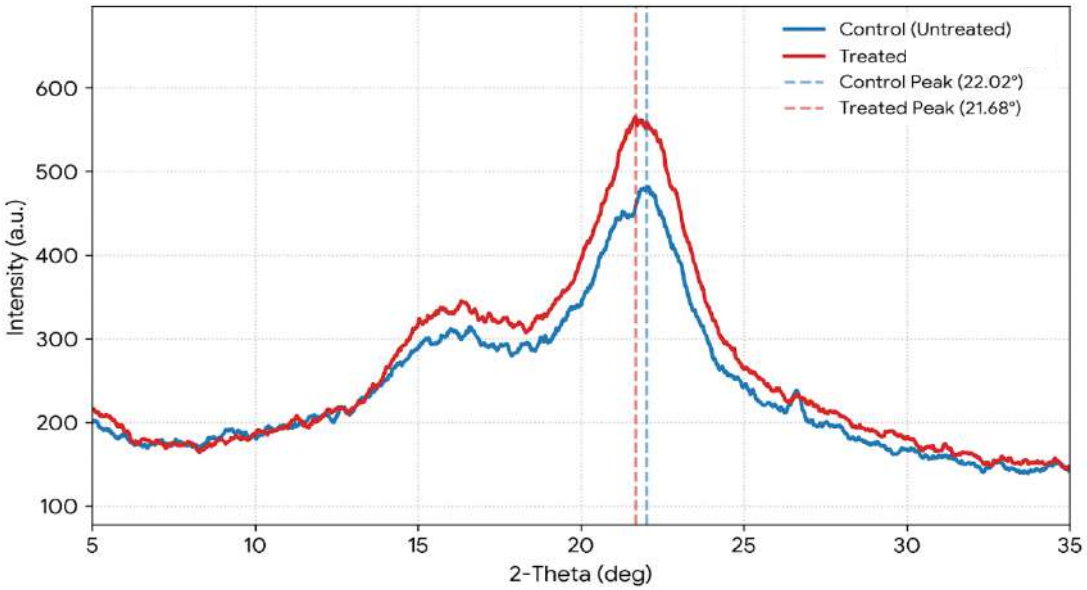

Fig. 3 XRD diffraction patterns of Control and Treated rice straw substrates.

Table 2. XRD diffraction parameters and Crystallinity Index (CrI) comparison.

Parameter / Crystallographic Feature	Control (Untreated)	Treated	Relative Change & Description
Principal Peak Position ($2\theta_{200}$)	22.02 °	21.68 °	Shifted left by $0.34°$ (d-spacing expansion)
Principal Peak Intensity (I_{200}, a.u.)	481.5	565.2	Increased by 17.4%
Secondary Peak Position ($2\theta_{110}$)	16.58 °	16.32 °	Shifted left by 0.26 °
Amorphous Intensity (I_{am}, a.u.)	283.3	307.5	Slight increase in background scattering
Crystallinity Index (CrI, %)	41.17%	45.60%	Absolute increase of 4.43%

CONCLUSIONS

1. High-voltage electrical pulse pretreatment substantially altered the observed surface morphology of rice straw, producing micro-cracks, deep cavities, and apparent cuticle delamination under the present treatment conditions.
2. No statistically detectable decreases in cellulose, hemicellulose, or lignin content were observed; therefore, the principal measured response was morphological rather than bulk compositional change.
3. XRD analysis showed an increase in Segal CrI from 41.17% to 45.60% and a shift of the 200 peak by Δ2θ = 0.34° without an apparent change from the native Cellulose I pattern. The peak shift suggests altered lattice spacing but does not, by itself, identify the underlying molecular mechanism.
4. High-voltage pulse pretreatment is a potentially useful physical approach for modifying rice-straw structure. Its effects on water uptake, enzyme accessibility, mushroom mycelial growth, and fruiting yield should be confirmed through direct functional experiments.

ACKNOWLEDGEMENTS

The authors express sincere gratitude to Prof. Shoji Ohga (Japan) for loaning the high-voltage pulse generator and controller used in this study during his collaboration with the Taiwan Agricultural Research Institute. Special thanks are also extended to the laboratory of Prof. Bi Yu, Department of Animal Science, National Chung Hsing University, for supporting the measurement and analysis of the lignocellulosic chemical composition of rice straw.

REFERENCES

Gandia, A., and A. Adamatzky. 2022. Electrical spiking of psilocybin fungi. *Communicative & Integrative Biology* 15(1):226–231.

Islam, F., A. T. M. F. Islam, and S. Ohga. 2013. Effect electric pulse application on the fruit body production of Tricholoma matsutake—in situ condition. *Korean Journal of Agricultural Science* 40(1):13–18.

Liu, J., W. Wang, H. Qu, X. Xiong, and X. Li. 2023. Effect of moderate electric field on rheological properties, cell wall components, and microstructure of apple tissue. *Journal of Food Engineering* 351:111516.

Moens, L. G., E. De Laet, J. Van Wambeke, A. M. Van Loey, and M. E. G. Hendrickx. 2020. Pulsed electric field and mild thermal processing affect the cooking behaviour of carrot tissues (Daucus carota) and the degree of methylesterification of carrot pectin. *Innovative Food Science & Emerging Technologies* 66:102483.

Mohd Jamil, N. A. B., C. Gomes, C. P. Kuen, Z. Kadir, and A. Gomes. 2018. Electrical stimulation for the growth of plants: With special attention to the effects of nearby lightning on mushrooms. *Asian Journal of Microbiology, Biotechnology and Environmental Sciences* 20:1332–1343.

Ravindran, R., and A. K. Jaiswal. 2016. A comprehensive review on pre-treatment strategy for lignocellulosic food industry waste: Challenges and opportunities. *Bioresource Technology* 199:92–102.

Segal, L., J. J. Creely, A. M. Martin, Jr., and C. M. Conrad. 1959. An empirical method for estimating the degree of crystallinity of native cellulose using the X-ray diffractometer. *Textile Research Journal* 29(10):786–794.

Szwarc, D., and K. Głowacka. 2021. Increasing the biogas potential of rapeseed straw using pulsed electric field pre-treatment. *Energies* 14(24):8307.

Takaki, K., K. Yoshida, T. Saito, T. Kusaka, R. Yamaguchi, K. Takahashi, and Y. Sakamoto. 2014. Effect of electrical stimulation on fruit body formation in cultivating mushrooms. *Microorganisms* 2(1):58–72.

Thuc, L. V., R. G. Corales, J. T. Sajor, et al. 2020. Rice-straw mushroom production. In M. Gummert, N. V. Hung, P. Chivenge, and B. Douthwaite (eds.), *Sustainable Rice Straw Management*, pp. 93–109. Springer.

Van Soest, P. J., J. B. Robertson, and B. A. Lewis. 1991. Methods for dietary fiber, neutral detergent fiber, and nonstarch polysaccharides in relation to animal nutrition. *Journal of Dairy Science* 74(10):3583–3597.

BP-04

Proceedings of The 12th International Symposium on Machinery and Mechatronics for Agriculture and Biosystems Engineering (ISMAB 2026)
20-24 October 2026, Busan, Republic of Korea

SELF-OXYGENATING SCAFFOLDS MODULATE HYPOXIC RESILIENCE AND EPIGENETICALLY GUIDE MUSCLE DEVELOPMENT

Woobin Choi[1,2 †], Yuseung Choi[1,2], Wooseok Jung[1], Kanghee Han[1], Daeun Jung[1], and Sangbae Park[1,2,3*]

[1] Department of Biosystems Engineering, Seoul National University, Republic of Korea
[2] Integrated Major in Global Smart Farm, Seoul National University, Republic of Korea
[3] Research Institute of Agriculture and Life Sciences, Seoul National University, Republic of Korea
*Corresponding Author-- Voice: +82-2-880-4601, Email: sb92park@snu.ac.kr

Abstract: Engineering volumetric whole-cut cultivated meat is fundamentally constrained by insufficient oxygen transport, particularly as increasing tissue thickness and cellular density elevate metabolic demand during myogenic differentiation. Most existing scaffolds depend on oxygen supplied from the surrounding culture environment and therefore cannot prevent the development of hypoxic regions that compromise cell survival, disrupt muscle maturation, and promote necrosis. To address this limitation, we developed an edible oxygen-generating scaffold composed of aligned electrospun gelatin nanofibers containing zein-encapsulated calcium peroxide nanoparticles. The hydrophobic zein coating moderates water penetration and calcium peroxide hydrolysis, thereby providing spatially confined oxygen release while limiting rapid peroxide decomposition and the associated accumulation of reactive oxygen species. Concurrently, the aligned fibrous architecture supplies anisotropic topographical cues that promote muscle-like cellular organization. Under experimentally induced hypoxia, cells cultured on the oxygen-generating scaffolds exhibited greater viability and attenuated HIF-1α activation relative to those cultured on non-oxygenating controls. Importantly, the controlled generation of reactive oxygen species remained below cytotoxic levels while supporting signaling associated with cellular and extracellular matrix remodeling. These findings suggest that regulated peroxide chemistry can contribute both oxygen supplementation and bioactive redox signaling during muscle tissue development. By combining controlled oxygen generation, modulation of the local redox environment, and structural guidance for myogenic organization in an entirely edible matrix, this scaffold provides a versatile strategy for producing thicker and more physiologically organized whole-cut cultivated meat.

Key Words: Self-oxygenating scaffold, cultivated meat, oxygenating nanoparticles, aligned nanofibers, hypoxic resilience

ACKNOWLEDGEMENTS (optional)

This work was supported by the Basic Science Research Program through the National Research Foundation of Korea (NRF) funded by the Ministry of Science and ICT (RS-2026-25504472), the Creative-Pioneering Researchers Program through Seoul National University (Project No. 0525-20250123)

BP-05

Proceedings of The 12th International Symposium on Machinery and Mechatronics for Agriculture and Biosystems Engineering (ISMAB 2026)
20-24 October 2026, Busan, Republic of Korea

REUSABLE AGAR HYDROGEL BEADS FOR CONTROLLED NUTRIENT DELIVERY IN HYDROPONIC SYSTEMS

Yeonseo Kim[1], Seyeong Heo[1], Hojin Wang[1], Sunho Park[1*]

[1]Department of Bio-Industrial Machinery Engineering, Pusan National University, Miryang, 50463, Republic of Korea

*Corresponding Author-- Voice: +82-010-5674-9330, Email: s.park@pusan.ac.kr

Abstract: Hydroponic cultivation enables controlled crop production but can be challenged by nutrient fluctuations, precipitation, and biofilm formation associated with conventional nutrient supplementation. In this study, agar hydrogel beads (AHBs) were developed as a reusable platform for controlled nutrient delivery in hydroponic systems. AHBs were fabricated via thermal emulsification and exhibited a uniform spherical morphology, high swelling capacity, and mechanical stability, enabling efficient nutrient absorption, retention, and sustained release. The use of AHBs helped maintain stable nutrient conditions while reducing biofilm formation in hydroponic reservoirs. In a hydroponic lettuce model, AHB application promoted leaf growth and nearly doubled chlorophyll content, accompanied by differential expression of genes associated with leaf development. Notably, the AHBs retained their structural and functional performance after repeated use. These findings demonstrate the potential of reusable agar hydrogel beads as a sustainable platform for controlled nutrient delivery and improved nutrient management in hydroponic systems.

Key Words: Agar hydrogel beads, Hydroponic cultivation, Sustainable nutrient management, Biofilm control, Reusability

BP-06

Proceedings of The 12th International Symposium on Machinery and Mechatronics for Agriculture and Biosystems Engineering (ISMAB 2026)
20-24 October 2026, Busan, Republic of Korea

ALGINATE–ZEIN CORE–SHELL MICROCAPSULES FOR SUSTAINED BACTERIA DELIVERY IN WILDFIRE-AFFECTED SOIL

Yeonseo Kim[1], Seyeong Heo[1], Hojin Wang[1], Sunho Park[1*]

[1]Department of Bio-Industrial Machinery Engineering, Pusan National University, Miryang, 50463, Republic of Korea

*Corresponding Author-- Voice: +82-010-5674-9330, Email: s.park@pusan.ac.kr

Abstract: Wildfires pose a significant threat to ecosystems by degrading soil properties and disrupting microbial communities essential for ecosystem recovery. However, the restoration of wildfire-affected soil remains challenging, highlighting the need for effective strategies to accelerate ecological recovery. Here, we developed a core–shell microcapsule consisting of a hydrophilic sodium alginate core and a hydrophobic zein shell for the encapsulation and sustained delivery of plant growth-promoting rhizobacteria (PGPR). The resulting alginate–zein microcapsules (AZMs) exhibited a porous shell structure that enabled sustained bacterial release while maintaining the viability of Bacillus subtilis for up to 60 days. Application of AZMs to wildfire-affected soil improved soil pH, dissolved organic carbon, and microbial enzymatic activities compared with untreated soil. Furthermore, AZM treatment upregulated genes associated with plant growth and nutrient transport in wheatgrass, indicating enhanced plant responses under fire-damaged conditions. Overall, this study demonstrates the potential of alginate–zein core–shell microcapsules as an eco-friendly and sustainable platform for PGPR delivery and microbial-assisted restoration of wildfire-affected soils.

Key Words: Wildfire, Core-Shell capsule, Plant growth-promoting rhizobacteria, Alginate–zein, Soil restoration

Bio-processing Engineering 2 (BP-2)



BP-07

Proceedings of The 12th International Symposium on Machinery and Mechatronics for Agriculture and Biosystems Engineering (ISMAB 2026)
20-24 October 2026, Busan, Republic of Korea

DEVELOPMENT AND VALIDATION OF A STRAWBERRY-SHAPED SENSOR FOR MEASURING FRUIT VIBRATION CHARACTERISTICS

Taiki Arao[1], Toyohiro Kato[1], Muneshi Mitsuoka[2], Masahiro Misumi[3], Takeshi Kuroyanagi[4], Takashi Okayasu[2*]

[1]Graduate School of Bioresource and Bioenvironmental Sciences, Kyushu University, 744 Motooka, Nishi-ku, Fukuoka 819-0395, Japan
[2]Faculty of Agriculture, Kyushu University, 744 Motooka, Nishi-ku, Fukuoka 819-0395, Japan
[3]Kyushu Okinawa Agricultural Research Center, NARO, 1823-1 Miicho, Kurume, Fukuoka 839-8503, Japan
[4]Western Region Agricultural Research Center, NARO, 1-3-1 Senyu-cho, Zentsuji, Kagawa 765-8508, Japan
*Corresponding Author-- Email: okayasu@bpes.kyushu-u.ac.jp

Abstract: Strawberry is a soft fruit that deforms easily under the external mechanical loads it receives, and the resulting bruises and abrasions markedly reduce its market value. Evaluating these loads requires the mechanical response of the fruit itself, but real fruit is destructible, varies between individuals and is difficult to instrument repeatably. Solving this problem requires detailed measurement and analysis of the dynamic behavior of the fruit itself, not just of its surroundings. Therefore, we developed a strawberry-shaped sensor reproducing the shape and mechanical properties of an actual strawberry. The sensor shell was made by a 3D-printed mold taken from a real strawberry, using oil-based clay blended with expanded polystyrene beads to match the mass of a real fruit, and a three-axis inertial measurement unit was embedded inside it. Ten pieces of strawberry fruit and the clay body of the sensor were compressed vertically by 3 mm to obtain the elastic modulus, and uniaxial excitation tests were then carried out at three excitation levels with the acceleration of the fruit, the sensor, the display carton and the vibration table acquired at 200 Hz. The mean elastic modulus of the fruit was 0.21 MPa, within the range reported for strawberries, and the initial slope of the stress-strain curve of the clay body was close to that of the real fruit. The power spectral density shapes of the fruit and of the sensor were similar, the overall root-mean-square acceleration agreed at approximately 5 m/s^2, and the transmissibility curves were similar at every excitation level, whereas the display carton behaved like the vibration table. The sensor therefore reproduces the static and dynamic behavior of real strawberry fruit and provides a repeatable, non-destructive means of measuring that behavior.

Key Words: Strawberry, Fruit-shaped sensor, Non-destructive measurement, Power spectral density, Vibration transmissibility

INTRODUCTION

Strawberry is a soft fruit, and it deforms easily under the external mechanical loads it receives. The vibration and impact imposed on the fruit cause bruises and abrasions on its surface and, in some cases, the destruction of the internal tissue, and the extent of the damage depends on the frequency and the direction of the load (Nakamura et al., 2007). Because such damage is often difficult to identify from external appearance, a method that quantitatively evaluates the mechanical load and the motion that the fruit itself receives is required.

The mechanical response of fruit has conventionally been characterized by attaching accelerometers to the container that holds the fruit or to the apparatus that excites it, which gives the mechanical input imposed on the fruit rather than the motion of the fruit itself. Simulated fruit containing an inertial measurement unit have therefore been used: an impact sensor embedded in an artificial lemon made of expanded polystyrene revealed where and why impacts occurred (Ikeda et al., 2010), and such impacts are known to accumulate in fresh produce as fatigue damage when they are repeated (Kitazawa, 2018). The data obtained in this way, however, reflect the behavior of the real fruit only as far as the simulated body resembles it: a body whose shape, mass distribution or elastic properties differ from those of the real fruit cannot be assumed to follow the motion of the fruit itself. Because the strawberry fruit is non-spherical and its flesh is soft and easily deformed, a fruit-shaped sensor must reproduce both the geometry and the mechanical properties of the real fruit, and its agreement with the real fruit has to be verified rather than assumed.

The objectives of this study were, first, to develop a strawberry-shaped sensor that simulates the shape and the mechanical properties of strawberry; second, to evaluate its elastic modulus by a loading test and to verify the validity of its mechanical properties by comparison with published values; and third, to compare the sensor and real strawberry fruit under uniaxial excitation in terms of the power spectral density (PSD), the overall root-mean-square acceleration (Grms) and the vibration transmissibility, in order to determine whether the sensor can be used as a substitute measuring body for real strawberry fruit.

MATERIALS AND METHODS

DEVELOPMENT OF THE STRAWBERRY-SHAPED SENSOR

A strawberry-shaped sensor was fabricated (Fig. 1) in a mold produced with a 3D printer from a three-dimensional shape model acquired from an actual strawberry fruit. The body was oil-based clay mixed with expanded polystyrene beads, adjusted so that its mass approached that of an actual strawberry fruit. To acquire the vibration and impact loads, an inertial sensor (WT9011DCL-BT50, WitMotion Shenzhen Co., Ltd., China) was embedded inside the body (Fig. 1). It acquires three-axis acceleration and angular velocity, and the data were recorded through Bluetooth communication.



Fig. 1 Strawberry-shaped sensor: (a) clay body in the 3D-printed mold; (b) embedded inertial sensor (WT9011DCL-BT50).

EVALUATION OF THE MECHANICAL PROPERTIES

Loading tests were carried out to determine how closely the mechanical properties of the clay body resemble those of an actual strawberry fruit. A universal testing machine (AUTOGRAPH AG-G, Shimadzu Corporation, Japan) and a measuring stand (ZTA-5N, Imada Co., Ltd., Japan) were used (Fig. 2). Ten strawberry fruits and the clay body of the sensor were compressed vertically by 3 mm under the same conditions and held for 10 s, and the load and the displacement were acquired. Stress-strain curves were produced from the load-displacement data, and the elastic modulus was calculated from the linear region at the beginning of loading.



Fig. 2 Loading test with the universal testing machine.

UNIAXIAL EXCITATION TEST AND VIBRATION EVALUATION INDICES

A uniaxial excitation test was carried out with a shaker (SA31, Shimadzu Rika Corporation, Japan) to compare the vibration of the strawberry fruit and of the sensor directly. Only the inner board of an inertial sensor of the same type was introduced into a strawberry fruit, and the fruit was placed alongside the strawberry-shaped sensor in the same display carton. Wireless nine-axis DSP motion sensors (SS-MS-SMA200G60, Sports Sensing Co., Ltd., Japan) were also installed on the vibration table and on the display carton, and acceleration was acquired at 200 Hz with all the sensors (Fig. 3).

Three excitation levels, referred to below as low, medium and high, were applied, and a stable interval of 20 s was extracted at each level for the analysis.

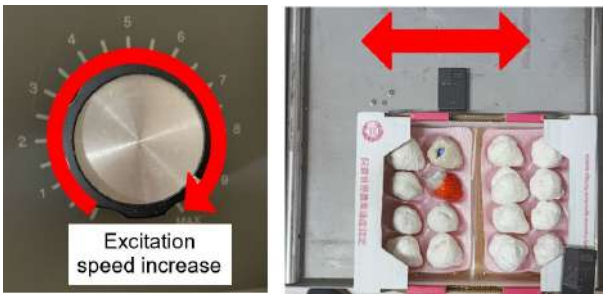

Fig. 3 Uniaxial excitation test (left: speed dial of the shaker; right: arrangement on the vibration table).

Following Takagi (2015) and Nakamura et al. (2019), the vibration intensity was evaluated with the overall root-mean-square acceleration Grms, which is calculated from the area of the PSD waveform by Equation (1).

$$G_{rms} = \sqrt{\sum_{1}^{n} A_k} \tag{1}$$

where:
G_{rms} = Overall root-mean-square acceleration (m/s^2)
A_k = Area of the *k*-th division of the PSD waveform divided into *n* parts ((m/s^2)^2)
n = Number of divisions of the PSD waveform (-)

The calculation used an analysis frame of 1 s, an overlap of 0 and a frequency range of 1 to 35 Hz and, as in Nakamura et al. (2019), the inflection point data with the least influence on Grms were deleted in order so that 15 or fewer inflection points remained. The PSD, the Grms and the transmissibility referred to the vibration table were then compared among the four objects.

RESULTS & DISCUSSION

MECHANICAL PROPERTIES OF THE STRAWBERRY-SHAPED SENSOR

Figure 4 shows the stress-strain relationships obtained at the beginning of loading. The curve of the clay body and that of the strawberry fruit agreed well. The mean elastic modulus of the ten strawberry fruit was 0.21 MPa, which is contained in the range of 0.141 to 0.279 MPa reported for strawberry fruit by An et al. (2023). The material design of the sensor therefore broadly reproduces the mechanical properties of the real fruit.

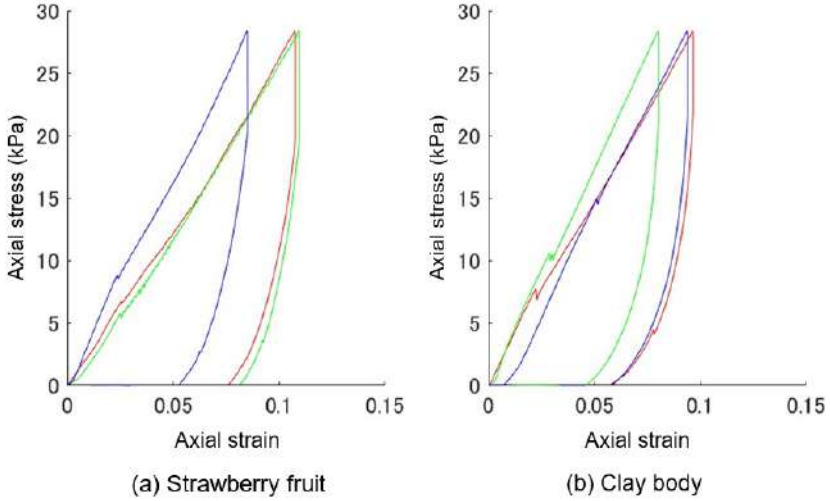

Fig. 4 Stress-strain relationships at the beginning of loading.

DYNAMIC RESPONSE OF THE SENSOR AND THE REAL FRUIT

Figure 5 shows the PSD of the strawberry fruit, the strawberry-shaped sensor, the display carton and the vibration table under the high excitation level. The PSD shapes of the strawberry fruit and of the strawberry-shaped sensor were similar, and an amplification tendency was confirmed near 15 to 25 Hz. Under the high excitation level, the Grms of both were of the order of about 5 m/s^2 and broadly agreed as a measure of the vibration intensity (Fig. 6). The transmissibility curves from the vibration table to the strawberry fruit and to the strawberry-shaped sensor also showed a similar tendency at all three excitation levels (Fig. 7). The display carton, in contrast, behaved like the vibration table in all three indices, which shows that the agreement is specific to the fruit and the sensor and is not simply an effect of the common input.

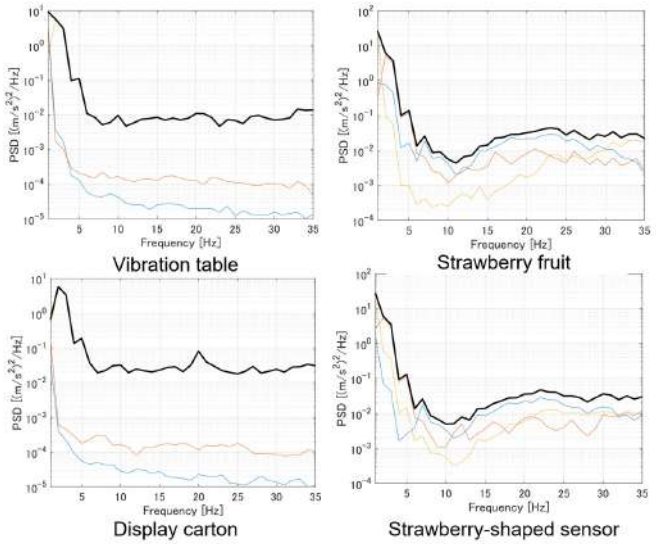

Fig. 5 PSD under the high excitation level.

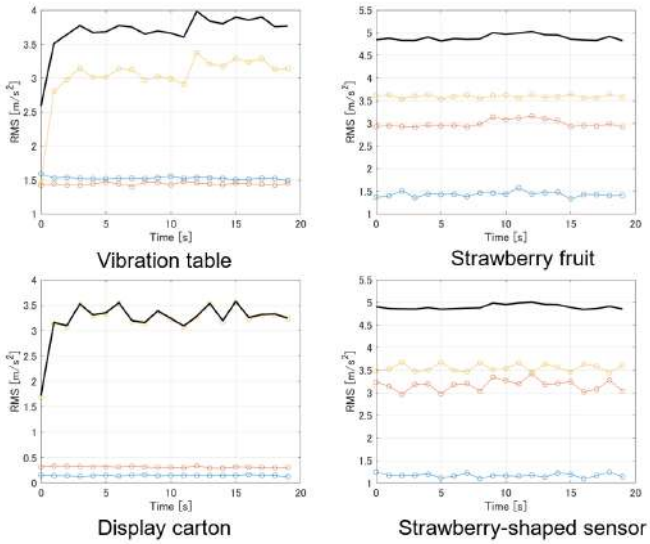

Fig. 6 Grms under the high excitation level (analysis frame 1 s).

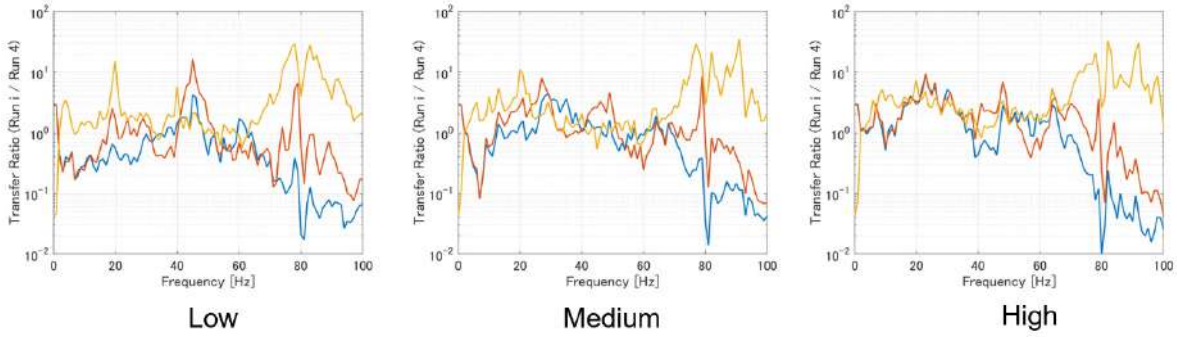

Fig. 7 Vibration transmissibility referred to the vibration table (blue: strawberry fruit; orange: strawberry-shaped sensor; yellow: display carton).

These results show that the strawberry-shaped sensor not only has a close elastic modulus but also simulates the behavior of the real fruit well in the PSD shape, the Grms scale and the transmission characteristics. Motion accompanied by rotation close to that of the strawberry fruit was also observed for the sensor during excitation; reproducing rotational behavior originating from the shape, and not only translational motion, is important when the fruit receives loads through friction against neighboring fruit and contact with the container that holds it.

CONCLUSIONS

A strawberry-shaped sensor made of oil-based clay mixed with expanded polystyrene beads was developed, and its agreement with real strawberry fruit was verified from both the static and the dynamic side. The elastic modulus fell within the range reported for strawberry fruit and the stress-strain relationships broadly agreed. Under uniaxial excitation, the fruit and the sensor showed similar PSD shapes, Grms values of the same order and similar transmissibility curves at every excitation level, while the display carton

followed the vibration table. The sensor therefore reproduces the average motion response of the fruit well.

It is concluded that the developed strawberry-shaped sensor is an effective substitute measuring body for evaluating the mechanical behavior of strawberry fruit non-destructively and with good repeatability, and a base technology for acquiring the response of soft fruit to the mechanical loads imposed on them.

ACKNOWLEDGEMENTS

A part of this study was carried out with the support of the project for the development and improvement of strategic smart agricultural technology, under the FY2022 supplementary budget and the FY2023 initial budget of Japan. The authors would like to express their gratitude for this support.

REFERENCES

An, X., Z. Li, G. Wegner, and M. Zude-Sasse. 2023. Effect of cell size distribution on mechanical properties of strawberry. Food Res. Int. 169: 2-11.

Ikeda, H., Y. Ishikawa, H. Kitazawa, F. Lu, S. Akasaka, and S. Shiota. 2010. Analysis of impacts received by lemon fruit from harvest to grading. Hort. Res. (Japan) 9(1): 107-112. (in Japanese)

Kitazawa, H. 2018. Evaluation of and countermeasures against the accumulated fatigue damage of fruits and vegetables caused by repeated impacts. J. Packaging Sci. Tech. Japan 27(1): 29-43. (in Japanese)

Nakamura, N., H. Umehara, H. Okadome, K. Nakano, S. Maezawa, and T. Shiina. 2007. Effects of vibration frequency and vibration direction on the damage of strawberry fruit. J. Soc. Agric. Structures Japan 38(2): 101-108. (in Japanese)

Nakamura, N., K. Sakamoto, T. Kaneda, M. Nagata, and T. Shiina. 2019. Evaluation of the vibration characteristics during domestic truck transportation in the export of strawberry fruit and implementation of three-dimensional random vibration tests. J. Soc. Agric. Structures Japan 50(3): 99-106. (in Japanese)

Takagi, M. 2015. A method for estimating the distribution environment from generally available indices and indexes. Packaging Tech. 53: 164-175. (in Japanese)

BP-08

Proceedings of The 12th International Symposium on Machinery and Mechatronics for Agriculture and Biosystems Engineering (ISMAB 2026)
20-24 October 2026, Busan, Republic of Korea

EFFECTS OF GELATIN NANOPARTICLES AND UREA, APPLIED INDIVIDUALLY OR IN COMBINATION, ON SEEDLING GROWTH OF ARABIDOPSIS THALIANA AND LETTUCE

Donggyu Du[123], Hyojin Moon[123], Shinyull Lee[123], Woochan Kim[123], Dream Kim[123], Jangho Kim[123*]

[1]Department of Convergence Biosystems Engineering, Chonnam National University, Gwangju 61186, Republic of Korea
[2]Department of Rural and Biosystems Engineering, Chonnam National University, Gwangju, 61186, Republic of Korea
[3]Interdisciplinary Program in IT-Bio Convergence System, Chonnam National University, Gwangju 61186, Republic of Korea
*Corresponding Author-- Voice: +82-62-530-5181, Email: rain2000@jnu.ar.kr

Abstract: The development of sustainable fertilization strategies that maintain crop productivity while reducing excessive dependence on chemical fertilizers has become increasingly important in modern agriculture. Gelatin nanoparticles (GNPs), biodegradable nanomaterials derived from gelatin, have recently attracted attention because of their potential to influence plant growth. This study evaluated the individual and combined effects of GNPs and urea on the seedling growth of Arabidopsis thaliana and lettuce (Lactuca sativa L.). GNPs were prepared using a two-step desolvation method, and seedlings were cultivated on Murashige and Skoog (MS) medium under four treatment conditions: MS, MS+GNPs, MS+Urea, and MS+GNPs+Urea. Plant growth was evaluated at 10 and 21 days by measuring primary root length, total fresh weight, leaf fresh weight, and, for lettuce, leaf area. GNP treatment alone generally resulted in higher mean values of primary root length and biomass-related parameters than the untreated MS control in both plant species, suggesting that GNPs themselves may influence seedling growth. When GNPs and urea were applied individually or in combination, treatments containing either GNPs or urea generally showed higher growth parameters than the MS control. The combined GNP+Urea treatment produced the highest mean values for several growth parameters in both Arabidopsis and lettuce, including primary root length and biomass-related traits. In lettuce, the combined treatment also resulted in the largest mean leaf area. However, the magnitude of the growth response varied depending on plant species, growth parameter, and cultivation period. These results suggest that GNPs can influence plant growth independently and that their combined application with urea may further modify plant growth responses. Therefore, GNPs may have potential as a biodegradable bio-based material for use in combination with conventional nitrogen fertilizer. Further studies are required to clarify the interaction between GNPs and urea and the physiological mechanisms underlying their effects on plant growth.

Key Words: Gelatin nanoparticles, Urea, Plant growth, Arabidopsis thaliana, Lactuca sativa

INTRODUCTION

With the introduction of nanotechnology into the agricultural field, various nanomaterials have been investigated for their potential applications in plant growth and crop production. Owing to their small particle size and large surface area, nanoparticles can increase contact with plant tissue surfaces, and some nanoparticles are known to influence plant growth and stress tolerance not only as carriers of nutrients but also through their intrinsic properties. However, for the practical application of nanomaterials in agriculture, it is necessary to specifically evaluate the effects of each material on plants. In particular, plant growth responses may vary depending not only on the type of nanomaterial but also on the plant species, treatment conditions, and growth stage. Therefore, comparative evaluation of plant responses under various conditions is essential for assessing the applicability of newly developed nanomaterials. Plant responses to nanomaterials cannot be fully understood based on a single experimental condition. First, because plant species differ in growth rate, root architecture, and nutrient requirements, the magnitude and pattern of responses to the same nanomaterial may vary among species. Second, when nanomaterials are applied together with conventional fertilizers, the observed effects may reflect both the intrinsic influence of the nanomaterial and the effects of fertilizer application. Distinguishing whether these two factors act independently or interact with each other can provide a clearer understanding of the role of each material. In addition, because plant growth progresses over time, it is also important to determine whether the effects of nanomaterials remain consistent between early and later growth stages. Therefore, the effects of newly developed nanomaterials on plants should be evaluated across different plant species, in combination with fertilizers, and at multiple growth stages.

Among various nanomaterials, biopolymer-based materials with high biodegradability and biocompatibility have received increasing attention for agricultural applications. Gelatin nanoparticles (GNPs) are biodegradable nanomaterials derived from gelatin, an animal-derived protein. Gelatin contains various functional groups, including amino and carboxyl groups, and the surface charge of gelatin molecules changes depending on the pH of the solution, which can strongly influence the desolvation process and the physicochemical properties of the resulting nanoparticles. Previous studies have shown that the matrix density of gelatin nanoparticles varies according to solution pH and desolvation conditions, resulting in differences in drug loading and protease-mediated release behavior. These findings indicate that the properties of GNPs can be modulated by fabrication conditions, particularly pH and surface charge. The two-step desolvation method, which is widely used for GNP fabrication, was developed to obtain relatively uniform nanoparticles by removing low-molecular-weight gelatin fractions during the first desolvation step, followed by redissolution of the high-molecular-weight fraction and subsequent second desolvation and crosslinking. Owing to their excellent biocompatibility and biodegradability, GNPs have long been investigated in the field of drug delivery, and their potential applications in plant systems have also recently been explored. Gelatin is a natural biopolymer rich in amino acids, and previous studies have reported that gelatin treatment can act as a biostimulant, promoting early root development and plant growth. In addition, GNPs have been reported to interact with plant root surfaces, facilitate nutrient uptake, and stimulate root growth even in the absence of additional fertilizer. These findings suggest that GNPs may not simply function as inert carriers but may also directly interact with plants and influence their growth.

When evaluating the effects of GNPs on plants, it is also reasonable to consider urea in combination with GNP treatment. Urea is the most widely used nitrogen fertilizer worldwide because of its high nitrogen content of approximately 46% and relatively low cost. However,

urea is rapidly hydrolyzed by urease in soil and converted into ammonium, during which substantial nitrogen can be lost through volatilization and leaching. It has been reported that only approximately 30–35% of applied urea is absorbed by crops. When GNPs and urea are applied together to plants, the intrinsic effects of GNPs on plant growth and the nitrogen-supplying effects of urea may occur simultaneously. By comparing the two materials individually and in combination, the independent effects of GNPs, the effects of urea alone, and the growth responses resulting from their combined application can be evaluated separately. Furthermore, two-way analysis of variance (ANOVA) can be used to distinguish the main effects of GNP and urea treatments as well as their interaction effects.

Therefore, in this study, the growth responses of *Arabidopsis thaliana* and lettuce (*Lactuca sativa* L.) to individual and combined applications of GNPs and urea were evaluated. *A. thaliana* is a model plant species belonging to the Brassicaceae family and is characterized by rapid growth and easily observable morphological changes, whereas lettuce is a leafy vegetable crop belonging to the Asteraceae family and differs from *Arabidopsis* in growth rate and morphological characteristics. Comparing these two species under the same treatment conditions enables evaluation of whether growth responses to GNPs and urea differ depending on plant species. Four treatment conditions were established: MS, MS+GNPs, MS+Urea, and MS+GNPs+Urea. Growth parameters, including primary root length, leaf area, and fresh weight, were measured at 10 and 21 days of cultivation to examine changes according to growth stage. Two-way ANOVA was used to distinguish the main effects and interaction effects of GNP and urea treatments, thereby evaluating the individual effects of GNPs and urea on plant growth and the responses resulting from their combined application.

MATERIALS AND METHODS

Preparation of Gelatin Nanoparticles

GNPs were prepared based on a two-step desolvation method. Gelatin type A was dissolved in deionized water at a concentration of 5% (w/v) and stirred thoroughly at 50°C to obtain a homogeneous gelatin solution. Acetone was then added to induce the first desolvation step. During this process, the relatively high-molecular-weight gelatin fraction was precipitated, while the supernatant containing the low-molecular-weight gelatin fraction was removed. The recovered high-molecular-weight gelatin fraction was subsequently redissolved in deionized water to a concentration of approximately 1% (w/v). The redissolved gelatin solution was adjusted to pH 3.0 using HCl and subjected to a second desolvation step by dropwise addition of acetone for approximately 1 h under stirring at 40°C and 600 rpm. During the second desolvation step, the gradual addition of acetone reduced the solubility of hydrated gelatin chains and promoted intermolecular aggregation, resulting in the formation of nanoparticles. The resulting GNP suspension was then stirred at 4°C for 1 h. To enhance the structural stability of the particles, 25% glutaraldehyde was added, and crosslinking was performed at 4°C for 12 h. After crosslinking, the GNPs were washed three times with 70% acetone and once with ultrapure water. The washed GNPs were then freeze-dried to remove moisture, and the resulting GNP powder was collected and stored for subsequent experiments (Fig. 1A).

Preparation of Basal Medium

Murashige and Skoog (MS) medium was used for the plant growth experiments. For each batch, the basal medium was prepared to a final volume of 700 mL. MS medium powder (1.54

g) and sucrose (21 g) were dissolved in approximately 600 mL of ultrapure water, and the final volume was adjusted to 700 mL with ultrapure water. The pH of the medium was adjusted to 5.6–5.8 using NaOH. The same procedure was repeated twice to prepare a total of 1,400 mL of MS basal medium. The prepared MS basal medium was sterilized by autoclaving at 121°C for 15–20 min using an autoclave (DH18CAT00210081; Daihan Scientific, Korea). After sterilization, the medium was allowed to cool before preparation of the treatment media.

Preparation of GNP and Urea Stock Solutions

The GNP stock solution was prepared by dispersing 0.052 g of GNP powder in 52 mL of ultrapure water to obtain a final concentration of 1 mg/mL. To minimize sedimentation and maintain a homogeneous dispersion, the suspension was continuously mixed before use and during preparation of the treatment media. The urea stock solution was prepared by dissolving 0.1 g of urea (CAS No. 57-13-6) in 25 mL of deionized water to obtain a final concentration of 4 mg/mL.

Preparation of GNP- and Urea-Containing Treatment Media

To compare plant growth responses to the individual and combined application of GNPs and urea, four treatment groups were established: MS, MS+GNPs, MS+Urea, and MS+GNPs+Urea. Each treatment medium was prepared by aliquoting the previously prepared and sterilized MS basal medium and adding the GNP stock solution, urea stock solution, or sterile ultrapure water according to the designated treatment condition. The first 700 mL batch of MS basal medium was used to prepare the MS+GNPs, MS, and MS+Urea treatment groups. For the MS+GNPs treatment, 145.6 mL of MS basal medium was supplemented with 1.12 g of Phyto agar and 14.4 mL of 1 mg/mL GNP stock solution, and the final volume was adjusted to 160 mL. The final GNP concentration was therefore 0.09 g/L. For the MS control, 182.0 mL of MS basal medium was supplemented with 1.40 g of Phyto agar and 18.0 mL of sterile deionized water to obtain a final volume of 200 mL. No GNPs or urea were added. For the MS+Urea treatment, 309.4 mL of MS basal medium was supplemented with 2.38 g of Phyto agar, 7.65 mL of 4 mg/mL urea stock solution, and 22.95 mL of sterile deionized water to obtain a final volume of 340 mL. The final urea concentration was therefore 0.09 g/L. The second 700 mL batch of MS basal medium was used to prepare the MS+GNPs, MS, and MS+GNPs+Urea treatment groups. The MS+GNPs and MS groups were prepared using the same procedures described above. For the MS+GNPs+Urea treatment, the final concentrations of GNPs and urea were adjusted to 0.09 g/L and 0.03 g/L, respectively, in a final volume of 340 mL. For this purpose, 30.6 mL of 1 mg/mL GNP stock solution and 2.55 mL of 4 mg/mL urea stock solution were used, and the remaining volume was adjusted with MS basal medium and sterile deionized water. After addition of the GNP and urea stock solutions, each treatment medium was thoroughly mixed to ensure uniform distribution of the components. In particular, media containing GNPs were continuously mixed until immediately before dispensing to minimize GNP sedimentation. Before solidification, the media were rapidly dispensed into square dishes or Magenta boxes. The dispensed media were allowed to solidify completely under aseptic conditions, sealed, stored at 4°C for approximately 24 h, and subsequently used for plant cultivation.

Plant Materials and Growth Conditions

Seeds of Arabidopsis thaliana Columbia-0 (Col-0, wild type; IS3731, Innovating Science, Aldon Corporation, Avon, NY, USA) and red leaf lettuce (Lactuca sativa L. 'Jeok Chi Ma'; ALE101, ASIA SEED Co., Ltd., Seoul, Republic of Korea) were used as plant materials. Seeds were surface-sterilized by treatment with 70% ethanol for 1 min, followed by sodium hypochlorite (NaOCl) solution for approximately 5 min, and then rinsed five to six times with sterile deionized water. To synchronize germination, Arabidopsis seeds were stratified under dark conditions at 4°C for 24 h before sowing on the medium. After stratification, the seeds were germinated and grown for 3 days. Seedlings with primary root lengths of approximately 5–8 mm and similar growth status were randomly selected. The selected seedlings were transferred to square dishes (Cat. No. 11125, 126.40 × 126.40 × 20.00 mm; SPL Life Sciences Co., Ltd., Republic of Korea) containing the respective treatment media. A total of 22 seedlings (n = 22) were used for each treatment group (Fig. 1C). Lettuce seeds were surface-sterilized and germinated using the same procedure. After germination, nine seedlings were placed in each Incu Tissue Culture Vessel (Cat. No. 310071, 72 × 72 × 100 mm; SPL Life Sciences Co., Ltd., Republic of Korea) containing the respective treatment medium. Three independent culture vessels were used for each treatment group and growth stage, resulting in a total of 27 seedlings (n = 27). Both Arabidopsis and lettuce were cultivated at 22–24°C, 70–80% relative humidity, and a light intensity of approximately 7,000 lux under a 12 h light/12 h dark photoperiod. Growth responses to the treatments were evaluated after 10 and 21 days of cultivation (Fig. 1C).

Growth Measurements

Primary root length, leaf area, total fresh weight, and leaf fresh weight were measured. Primary root length was defined as the distance from the root tip to the hypocotyl or the base of the shoot. Images were captured under identical conditions, calibrated using a scale reference, and analyzed using ImageJ. For lettuce, leaf area was determined by separating the leaves from the plants, arranging them without overlap, and capturing images. Leaf area was calculated using ImageJ after scale calibration, background removal, and threshold adjustment. Fresh weight was measured immediately after the plants were removed from the culture medium and residual medium and moisture on the root surface were removed using the same procedure for all samples. Total fresh weight of the whole plant was first measured, after which the leaves were separated and leaf fresh weight was measured independently.

For Arabidopsis, 22 seedlings per treatment group (n = 22) were analyzed. For lettuce, a total of 27 seedlings per treatment group and growth stage were analyzed, with nine seedlings grown in each of three independent culture vessels.

Statistical Analysis

All experimental data were expressed as mean ± standard deviation (SD). For experiments evaluating the individual and combined effects of GNPs and urea, two-way analysis of variance (ANOVA) was performed using the presence or absence of GNP treatment and urea treatment as independent factors. Tukey's multiple comparison test was used for post hoc comparisons among treatment groups. Statistical significance was set at $p < 0.05$.RESULTS & DISCUSSION State your major findings and results along with the discussion. Try to discuss your results by relating to previous findings by others as well as to the objectives and problems

mentioned in the INTRODUCTION section. Use figures and tables effectively along with sentences of statement. Do not omit mentioning important but rather unfavorable results. Any speculation or controversies should also be presented clearly and fairly. Avoid specific local references, inside comments, ambiguous terms and irony.

CONCLUSIONS

Plant Growth Responses to GNP Treatment Alone

Growth Response of *Arabidopsis thaliana*

To determine the effect of GNPs themselves on plant growth, *Arabidopsis thaliana* seedlings were cultivated on MS and MS+GNPs media, and growth responses were compared after 10 and 21 days of cultivation (Fig. 2). Visual comparison of the plants at day 21 showed that roots generally developed to a greater length in the GNP-treated group than in the MS control group (Fig. 2A) A similar tendency was observed in the quantitative growth parameters. Primary root length showed higher mean values in the MS+GNPs treatment than in the MS control at both 10 and 21 days, and primary root length increased in both groups as the cultivation period progressed (Fig. 2B). Total fresh weight was also higher in the GNP-treated group than in the control at both time points (Fig. 2C), and the same trend was observed for leaf fresh weight (Fig. 2D) These results indicate that the changes associated with GNP treatment were not limited to a specific plant organ, but were observed in both root elongation and shoot biomass accumulation. In particular, the finding that the MS+GNPs treatment showed higher growth parameters than the MS control even in the absence of an additional nitrogen source such as urea suggests that GNPs themselves may influence early plant growth. Park et al. (2024) reported that GNPs applied to plants can interact with root surfaces and influence root growth. Therefore, the changes in root length and fresh weight observed in the present study may also be related to interactions between GNPs and plant tissues. However, because nutrient uptake and physiological mechanisms following GNP treatment were not directly measured in this study, the mechanisms by which GNPs altered plant growth cannot be determined from the present results alone.

Growth Response of Lettuce

To determine whether the response to GNP treatment alone was also observed in another plant species, lettuce was cultivated under the same conditions (Fig. 3). Visual comparison of plants at day 21 showed that the overall plant size was greater in the MS+GNPs treatment than in the MS control (Fig. 3A). Morphological differences associated with the treatment were also observed in the separated roots and leaves (Fig. 3B, C).

Primary root length showed higher mean values in the GNP-treated group than in the control at both 10 and 21 days, with a more pronounced difference between the two groups at day 21 (Fig. 3D). The difference in total fresh weight between the two groups was relatively small at day 10, whereas at day 21 the GNP-treated group showed a higher value than the control (Fig. 3E). Leaf fresh weight was also higher in the GNP-treated group at day 21 (Fig. 3F), and leaf area was greater in the GNP-treated group than in the control (Fig. 3G).

These results suggest that GNP treatment may affect not only root elongation but also biomass accumulation and leaf development in lettuce. In particular, the more pronounced differences in several growth parameters at day 21 than at day 10 indicate that plant responses to GNP treatment may vary depending on growth stage. However, based on the current morphological parameters alone, it is difficult to determine whether these differences resulted from the

accumulation of GNP effects over time or from differences in plant responses associated with developmental stage.
Taken together, the results of GNP treatment alone in *Arabidopsis* and lettuce showed that both plant species tended to exhibit greater primary root length and fresh weight than their respective controls following GNP treatment. This suggests that growth responses to GNPs may not be limited to a particular plant species. However, because the magnitude of the changes differed according to plant species and growth stage, the effects of GNPs on plant growth should be evaluated using multiple growth parameters representing both root and shoot development rather than relying on a single parameter.

Plant Growth Responses to Individual and Combined Treatments with GNPs and Urea

After confirming that GNP treatment alone altered growth parameters in *Arabidopsis* and lettuce, plant growth responses were compared following treatment with GNPs and urea either individually or in combination. For this purpose, four treatment groups were established: MS, MS+GNPs, MS+Urea, and MS+GNPs+Urea. Growth parameters were measured after 10 and 21 days of cultivation. In this experiment, GNPs and urea were each applied at a concentration of 0.09 g/L, and the MS+GNPs+Urea treatment represented a combined treatment in which both materials were added to the same MS medium. Accordingly, the growth responses to the GNP+Urea treatment were evaluated as a combined application of the two materials and were not interpreted as evidence of urea loading into GNPs, a GNP-based delivery system, or a controlled-release fertilizer.

Growth Response of *Arabidopsis thaliana*

When *Arabidopsis* was cultivated under the four treatment conditions, differences in root growth among the treatment groups were visually observed at day 21 (Fig. 4A). Compared with the MS control, primary roots tended to be longer in the groups containing either GNPs or urea, and relatively longer roots were observed in the group receiving both GNPs and urea.
The quantitative results showed a similar trend. Primary root length had the lowest mean value in the MS control at both 10 and 21 days and increased in the GNP- and Urea-treated groups. The GNP+Urea combined treatment showed the highest mean value among the four treatment groups (Fig. 4B). A similar pattern among treatment groups was also observed at day 21.
For leaf fresh weight, higher values were observed in the GNP- and Urea-treated groups than in the control at both 10 and 21 days, with the highest mean value observed in the GNP+Urea combined treatment (Fig. 4C). Total fresh weight showed a similar pattern, with higher values in the treated groups than in the control and the highest value in the combined treatment (Fig. 4D).
These results indicate that GNPs and urea may each influence the early growth of *Arabidopsis*, and that combined application of the two materials may result in increased root growth and shoot biomass. However, the observation that the GNP+Urea group showed the highest mean values does not, by itself, demonstrate the existence of a synergistic effect between the two materials. Whether GNPs and urea independently influenced plant growth or whether an interaction occurred between the two treatments should be further evaluated using the interaction term in a two-way ANOVA.
In addition, because the control medium in this experiment was basal MS medium rather than a nitrogen-free medium, the growth responses to urea treatment should be interpreted as responses to additional urea supplied to the MS medium rather than as recovery from nitrogen deficiency. Therefore, the present results are best interpreted as a comparison of how supplemental urea and GNP treatment individually affected growth parameters in *Arabidopsis*.

Growth Response of Lettuce

The same four treatment conditions were applied to lettuce to compare the effects of individual and combined GNP and urea treatments (Fig. 5). Visual comparison of plants at day 21 showed a general increase in leaf growth in the GNP, Urea, and GNP+Urea treatment groups compared with the MS control, and relatively larger plants were observed in the combined treatment group (Fig. 5A). Comparison of the separated leaves also revealed differences in leaf size among the treatment groups (Fig. 5B), and differences in root morphology were observed between the control and treatment groups (Fig. 5C). Primary root length showed higher mean values in the individual GNP and Urea treatment groups than in the MS control at both 10 and 21 days, and the GNP+Urea combined treatment showed the highest value (Fig. 5D). Primary root length increased in all treatment groups with increasing cultivation period, and the combined treatment remained the highest at day 21. Differences among the four treatment groups were also observed for total fresh weight (Fig. 5E). At day 10, the GNP- and Urea-treated groups showed higher mean values than the control, while the GNP+Urea combined treatment showed the highest value. At day 21, total fresh weight was again highest in the combined treatment group, although the relative values of the GNP and Urea single-treatment groups varied depending on growth stage and the measured parameter. Leaf fresh weight also showed an increasing trend with treatment, and the highest mean value was observed in the combined treatment group at day 21 (Fig. 5F). Similarly, leaf area was greater in the GNP- and Urea-treated groups than in the MS control, with the largest mean value observed in the GNP+Urea combined treatment (Fig. 5G). These results indicate that the effects of GNPs and urea in lettuce may be expressed not only through root growth but also through leaf development and biomass accumulation. In particular, measurement of leaf area provided a more direct comparison of shoot growth in lettuce, and treatments containing either GNPs or urea tended to show greater leaf area than the control. Because urea can provide nitrogen required for plant growth, the increase in growth observed in the Urea-treated group may be related to the response to additional nitrogen supply. On the other hand, several growth parameters also increased following GNP treatment alone, indicating that the higher growth values observed in the combined treatment cannot be attributed solely to the effect of urea. However, in the present study, GNPs and urea were simply added together to the same medium, and urea loading into GNPs, release rate, nitrogen content in plant tissues, and nitrogen-use efficiency were not directly measured. Therefore, the increased growth observed in the GNP+Urea treatment cannot be interpreted as evidence of controlled urea release or improved delivery efficiency mediated by GNPs. Based on the current results, it remains necessary to determine whether the effects of the two treatments were simply additive or whether a true interaction existed between the two factors, which should be evaluated using the subsequent two-way ANOVA results.

Comparison of GNP and Urea Treatment Responses According to Plant Species and Growth Stage

Taken together, the results for *Arabidopsis* and lettuce revealed several common growth responses in the two plant species. First, under GNP treatment alone, both *Arabidopsis* and lettuce tended to show greater primary root length and fresh weight than the control. These findings suggest that, under the present experimental conditions, GNPs themselves may influence the growth of both plant species. Similarly, in experiments in which GNPs and urea were applied individually or together, both plant species generally showed higher growth parameters in the treatment groups than in the MS control. In particular, the GNP+Urea

combined treatment showed high mean values for primary root length, leaf fresh weight, and total fresh weight in *Arabidopsis*, as well as for primary root length, total fresh weight, leaf fresh weight, and leaf area in lettuce. However, the relative responses to the individual treatments were not consistent across all growth parameters. For some parameters, the GNP-treated group showed values similar to or higher than those of the Urea-treated group, whereas for other parameters, the Urea-treated group showed higher values. Therefore, the effects of GNPs and urea on plant growth should be evaluated by considering root elongation, leaf development, and biomass accumulation together rather than relying on a single growth parameter. Differences associated with growth stage were also observed. In some parameters, differences among treatment groups observed at day 10 were maintained or became more pronounced at day 21. In particular, differences in total fresh weight, leaf fresh weight, and leaf area among the lettuce treatment groups were more clearly observed at the later growth stage. These findings suggest that plant responses to GNPs and urea may vary depending on developmental stage. Because *Arabidopsis* and lettuce are different plant species with distinct growth rates and patterns of organ development, the magnitude of their responses to the treatments would not necessarily be expected to be identical. In this study, the two plant species were evaluated under the same treatment conditions to determine whether growth responses to GNPs and urea were restricted to a particular plant species or plant organ. Growth changes were observed in both species, although the magnitude of the responses differed depending on plant species, measured parameter, and growth stage. Overall, GNP treatment alone was associated with increases in several growth parameters in both *Arabidopsis* and lettuce, while the combined application of GNPs and urea resulted in high mean values for several growth parameters. These findings suggest that GNPs are biodegradable nanomaterials capable of influencing plant growth and that their combined application with urea may alter plant growth responses. However, the presence and mechanism of any interaction between the two materials cannot be determined from the current morphological growth parameters alone and should be further evaluated through statistical analysis and additional physiological studies.

ACKNOWLEDGEMENTS

This work was supported by a National Research Foundation of Korea (NRF) grant funded by the Korean government (MSIT) (RS-2024-00337706, RS-2025-02216206, RS-2020-NR049568, and RS-2022-NR067329). This work was also supported by the Korea Institute of Planning and Evaluation for Technology in Food, Agriculture and Forestry (IPET) through the Agriculture and Food Convergence Technologies Program for Research Manpower Development, funded by the Ministry of Agriculture, Food and Rural Affairs (MAFRA) (RS-2024-00397026). This work was supported by the Korea Institute of Planning and Evaluation for Technology in Food, Agriculture and Forestry (IPET) through the Companion Animal Intractable Disease Overcoming R&D Project, funded by the Ministry of Agriculture, Food and Rural Affairs (MAFRA) (RS-2026-25519399). This research was supported by the Commercialization Promotion Agency for R&D Outcomes (COMPA) funded by the Ministry of Science and ICT (MSIT) (RS-2025-25430866).

REFERENCES

Ahsan SM, Rao CM. 2017. The role of surface charge in the desolvation process of gelatin: Implications in nanoparticle synthesis and modulation of drug release. International Journal

of Nanomedicine 12:795-808.
Anderson AJ. 2018. The power of being small: Nanosized products for agriculture. Research in Plant Disease 24:99-112.
Coester CJ, Langer K, von Briesen H, Kreuter J. 2000. Gelatin nanoparticles by two step desolvation—A new preparation method, surface modifications and cell uptake. Journal of Microencapsulation 17:187-193.
Elzoghby AO. 2013. Gelatin-based nanoparticles as drug and gene delivery systems: Reviewing three decades of research. Journal of Controlled Release 172:1075-1091.
Murashige T, Skoog F. 1962. A revised medium for rapid growth and bio assays with tobacco tissue cultures. Physiologia Plantarum 15:473-497.
Park S, Safdar M, Kim W, Seol J, Kim D, Lee KH, Son HI, Kim J. 2024. Gelatin nanoparticles can improve pesticide delivery performance to plants. Small 20:2402899.
Schneider CA, Rasband WS, Eliceiri KW. 2012. NIH Image to ImageJ: 25 years of image analysis. Nature Methods 9:671-675.
Swify S, Mažeika R, Baltrusaitis J, Drapanauskaitė D, Barčauskaitė K. 2024. Review: Modified urea fertilizers and their effects on improving nitrogen use efficiency (NUE). Sustainability 16:188.
Wilson HT, Amirkhani M, Taylor AG. 2018. Evaluation of gelatin as a biostimulant seed treatment to improve plant performance. Frontiers in Plant Science 9:1006.
Zhao L, Lu L, Wang A, Zhang H, Huang M, Wu H, Xing B, Wang Z, Ji R. 2020. Nano-biotechnology in agriculture: Use of nanomaterials to promote plant growth and stress tolerance. Journal of Agricultural and Food Chemistry 68:1935-1947.

BP-09

Proceedings of The 12th International Symposium on Machinery and Mechatronics for Agriculture and Biosystems Engineering (ISMAB 2026)
20-24 October 2026, Busan, Republic of Korea

EXTRUSION-BASED 3D BIOPRINTING OF SOFT CARROT CALLUS USING AN ALGINATE–LAPONITE–METHYLCELLULOSE HYDROGEL AND QUANTIFICATION OF SECONDARY METABOLITES

Susmita Ghosh[1,2], Yeong-Jin Choi [4,5*], Hee-Gyeong Yi[1,2,3*]

[1] Department of Convergence Biosystems Engineering, College of Agriculture and Life Sciences (CALS), Chonnam National University (CNU), Gwangju, 61186, Republic of Korea
[2]Interdisciplinary Program in IT-Bio Convergence System, Chonnam National University
[3]Institute for Biomedical Science, Chonnam National University Hospital Hwasun, Hwasun, 58128, Republic of Korea
[4] Advanced Bio and Healthcare Materials Research Division, Korea Institute of Materials Science (KIMS) Changwon, 51508, Republic of Korea
[5] Advanced Materials Engineering, Korea National University of Science and Technology (UST), Daejeon, 34113, Republic of Korea
*Corresponding Author-- Dr. Yeong-Jin Choi, jinchoi@kims.re.kr and Prof. Hee-Gyeong Yi hgyi@chonnam.ac.kr

Abstract: Plant-based 3D bioprinting remains limited in its ability to regulate cell behavior and secondary metabolite production under well-defined structural conditions. In this study, we investigated the effect of scaffold geometry on plant cell function using an alginate–laponite–methylcellulose hydrogel system. An optimized formulation enabled stable extrusion and the fabrication of reproducible porous and non-porous constructs containing non-genetically modified carrot callus. Here, we establish a plant-focused extrusion bioprinting platform by defining the biofabrication window for this hydrogel system. Through systematic rheological characterization and printability analysis, a formulation composed of 3 wt.% alginate, 6 wt.% laponite, and 6 wt.% methylcellulose (3A6L6M) was identified as optimal for stable extrusion and cell encapsulation. Soft callus derived from hypocotyl tissue was generated using conventional tissue culture methods and used without genetic modification. Scaffold geometry influenced cell distribution, viability, and metabolic activity within the constructs. Porous scaffolds supported more uniform cell growth and exhibited significantly greater accumulation of carotenoid compounds than non-porous scaffolds. These differences can be attributed to improved nutrient diffusion and a more uniform spatial organization of cells within the porous structure. Overall, this study identifies scaffold geometry as an important parameter influencing plant cell metabolism and demonstrates a simple, non-genetic strategy for structure-guided plant biofabrication.

Key Words: *in vitro* culture, plant 3D bioprinting, scaffold geometry, biofabrication window, plant callus encapsulation, carotenoid compound

Poster

AI and Information Processing



AI-P01

Proceedings of The 12th International Symposium on Machinery and Mechatronics for Agriculture and Biosystems Engineering (ISMAB 2026)
20-24 October 2026, Busan, Republic of Korea

ESTIMATION OF RICE ABOVEGROUND WEIGHT FROM OVERHEAD 2D IMAGES

Byeonghan Lee[1*], Sangyeob Lee[1], Su-jin Jeong[1], Deok-Gyeong Seong[1]
Jeong-Ho Shin[1] and Gil-Seok Park[1]

[1]Gyeongsangnam-do Agricultural Research and Extension Services, Republic of Korea
*Corresponding Author-- Voice: +82-55-254-1194, Email: ys198@korea.kr

Abstract: This study examined the estimation of rice aboveground weight from overhead 2D images. A total of 1,952 RGB-NIR images were used to train U-Net and YOLOv11n-seg models, with ground-truth masks generated using NIR-based K-means clustering and manual correction. The segmented pixel counts showed quadratic relationships with aboveground fresh and dry weights, with R^2 values greater than 0.95. However, the RGB images showed inconsistent quality because exposure time and gain could not be maintained consistently under changing sunlight conditions. This variation in RGB image quality represents a limitation for the generalization of the segmentation models.

Key Words: Rice, Aboveground Weight, Image Segmentation

INTRODUCTION

Visual assessment of aboveground crop growth is useful for rapidly identifying genetic characteristics and crop conditions, but it has limitations in terms of reproducibility. Recently, image-based methods have been applied to estimate rice growth traits such as aboveground weight and leaf area index (Zheng et al., 2019; Yamaguchi et al., 2021). This study investigated whether rice aboveground weight could be estimated from overhead 2D images using deep learning-based segmentation.

MATERIALS AND METHODS

An RGB-NIR camera (GAL 5000-60ucNIR) was installed so that the distance from the ground to the lens was 2.5 m, and images of the rice canopy were captured. As growth progressed, the collected images were cropped to 512×512 pixels, and 1,952 images were selected.

For the segmentation masks, K-means clustering results from the NIR images were selected and then manually corrected so that only rice regions were included. The training and validation data were divided at a ratio of 8:2, and U-Net and YOLOv11n-seg were trained separately.

For the test data used to estimate aboveground weight, rice plants surrounding the target hill were removed immediately before imaging so that only one rice hill was included. The rice regions were segmented using the trained models, and the number of pixels in each binary mask was calculated. Fresh weight was measured immediately after imaging by harvesting.

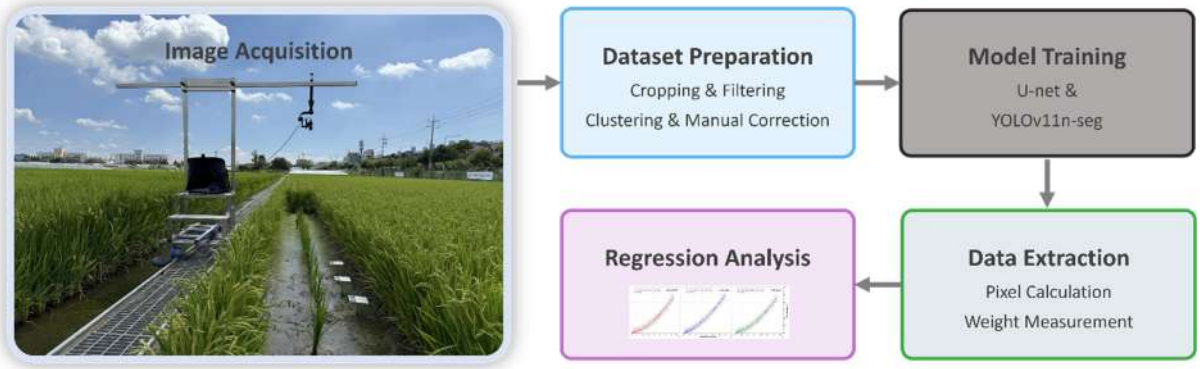

Fig.1 Overall flowchart of the study for estimating rice aboveground weight.

RESULTS & DISCUSSION

When the relationship between the number of pixels in the rice regions segmented by the U-Net and YOLO-based models and aboveground weight was expressed as a quadratic polynomial, the coefficient of determination (R^2) was greater than 0.95. However, clear differences were observed in the segmentation patterns of the two models. The U-Net-based model segmented dark regions inside the rice hill as background, whereas the YOLO-based model tended to segment them as rice.

These differences are presumed to be influenced by the method used to create the GT (Ground Truth). In this study, NIR-based K-means clustering results were accepted to a considerable extent as GT for regions with low visibility inside the rice hill, and visibility inside the hill was strongly affected by the progress of growth and image brightness conditions.

In addition, the RGB-NIR camera was sensitive to changes in sunlight, making it difficult to consistently set the exposure time and gain for each imaging time, and as a result, the RGB images did not always clearly represent the rice canopy as observed visually.

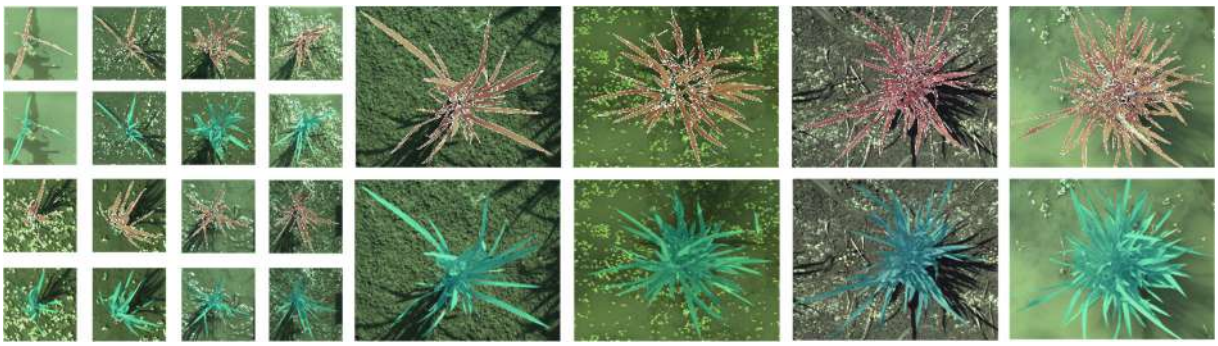

Fig.2 Visualization of rice segmentation results. The colored overlays indicate the rice regions predicted by the deep learning models (Green : YOLO based model)

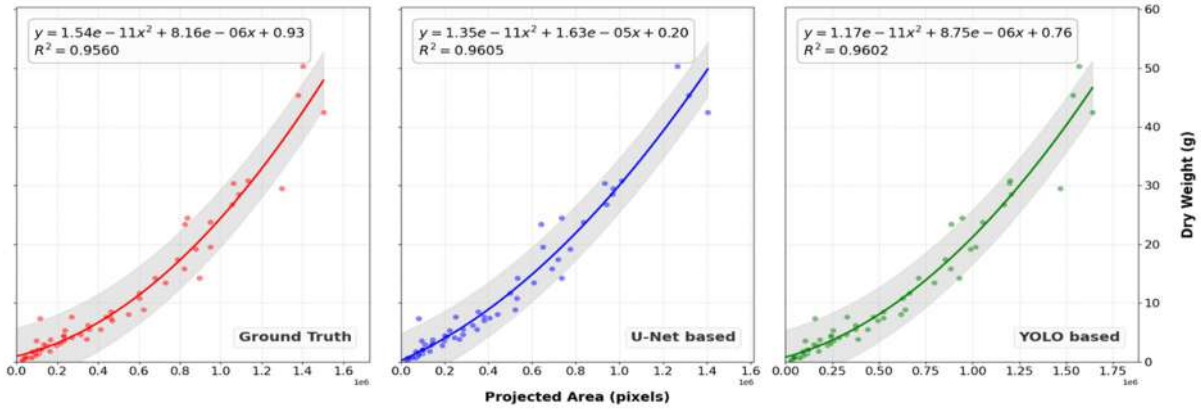

Fig.3 Regression analysis results between projected area and dry weight of rice

CONCLUSIONS

The dataset could be constructed rapidly using NIR-based K-means clustering, but the variation in RGB image quality represents a limitation to the generalization of the trained models. Future work will focus on improving segmentation performance for robotic applications rather than on estimating growth traits such as dry weight.

ACKNOWLEDGEMENTS

This work was supported by the project “Implementation of a Data Architecture for Regional-Scale Smart Agriculture” (Project No. LP0051822024).

REFERENCES

Yamaguchi, T., Y. Tanaka, Y. Imachi, M. Yamashita, and K. Katsura. 2021. Feasibility of combining deep learning and RGB images obtained by unmanned aerial vehicle for leaf area index estimation in rice. Remote Sens. 13(1): 84.

Zheng, H., T. Cheng, M. Zhou, D. Li, X. Yao, Y. Tian, W. Cao, and Y. Zhu. 2019. Improved estimation of rice aboveground biomass combining textural and spectral analysis of UAV imagery. Precision Agric. 20: 611-629.

AI-P02

Proceedings of The 12th International Symposium on Machinery and Mechatronics for Agriculture and Biosystems Engineering (ISMAB 2026)
20-24 October 2026, Busan, Republic of Korea

AN INTELLIGENT PASSION FRUIT DISEASE DIAGNOSIS SYSTEM USING ADVANCED YOLO ARCHITECTURES AND TRANSFER LEARNING

Chuan-Yi Chang[1], Chao-Wang Young[1]*

[1] Department of Biomechatronic Engineering, National Chiayi University, Chiayi, Taiwan
*Corresponding Author-- Email: youngcw@mail.ncyu.edu.tw

Abstract: The purpose of this study is to develop an automated detection system for passion fruit anthracnose and Pytophthora blight based on deep learning object detection technology. To address the issues of data scarcity and class imbalance in the original dataset (405 images of anthracnose and 144 images of phytophthora blight), data augmentation techniques including rotation, flipping, and brightness adjustments were implemented. This expanded the dataset to 1,620 anthracnose images and 655 phytophthora blight images (2,275 images in total), which were strictly split into a training set (1,820 images) and a validation set (455 images) at an 8:2 ratio.

Comparative experiments were conducted across eight model configurations using the YOLOv8 and YOLO11 architectures, evaluating two model scales under two initialization strategies: training from scratch versus using pretrained weights. The results indicate that across a standardized 150-epoch training scheme, utilizing pretrained weights significantly improves recall and mean average precision (mAP) without increasing training time.

Among all configurations, YOLOv8m (Pretrained) achieved the best performance, reaching an mAP50 of 90.62% and an mAP50-95 of 67.35%, demonstrating robust feature extraction and localization capabilities. While the newer YOLO11m exhibited comparable training efficiency (2 hours and 52 minutes), its mAP50 was slightly lower at 87.61%. For edge computing and real-time detection scenarios, YOLOv8n (Pretrained) achieved an mAP50 of 88.97%, serving as the optimal trade-off between lightweight efficiency and detection accuracy. This study provides a practical solution for precision disease management with high application value in field deployment and smart agriculture.

Key Words: Passion Fruit Disease, YOLO, Pretrained Weight, Object Detection.

INTRODUCTION

During field cultivation, passion fruit is highly susceptible to fungal and oomycete infections, particularly anthracnose and Phytophthora blight, which cause substantial yield losses. Traditional manual field inspections are labor-intensive, time-consuming, and subjective, making large-scale early warning difficult to achieve. With rapid advancements in deep learning, computer vision techniques have shown great potential in automated plant disease identification. However, the variable visual characteristics of lesions in complex field environments, subtle early symptoms, and limited field samples pose major challenges to detection accuracy and stability.

Recent studies have focused on lightweight YOLO architectures to enable real-time detection on embedded devices for passion fruit monitoring, while customized variants such as PHD-YOLO based on YOLOv11n have been developed to enhance detection accuracy under complex orchard conditions.

The objective of this study was to establish an automated passion fruit disease detection pipeline. By implementing data augmentation to overcome sample imbalance, this study systematically evaluates and compares the performance of YOLOv8 and YOLO11 across different model scales (nano and medium) and weight initialization strategies (scratch vs. pretrained) to determine the optimal configuration for field deployment.

MATERIALS AND METHODS

2.1 Dataset Construction and Augmentation

The overall workflow of the proposed passion fruit disease detection framework is illustrated in Fig. 1. The original collected dataset contained 405 images of anthracnose and 144 images of Phytophthora blight (549 images in total), exhibiting severe sample scarcity and class imbalance. Data augmentation techniques, including rotation, horizontal/vertical flipping, and brightness adjustments, were implemented to enhance model generalization and balance the class representation (As shown in Fig. 2). To strictly avoid data leakage, the original dataset was first partitioned into training and validation sets at an 8:2 ratio before applying image augmentation, ensuring that augmented variations of a specific image never appeared in the validation set. This process resulted in an augmented training set of 1,820 images (1,296 anthracnose, 524 Phytophthora blight) and a validation set of 455 images (324 anthracnose, 131 Phytophthora blight), totaling 2,275 images.

2.2 Experimental Design and Model Training

Experiments were conducted using two generations of object detection architectures: YOLOv8 and YOLO11. For each architecture, two model scales were tested under two initialization strategies: training from scratch and fine-tuning with pretrained weights, resulting in eight experimental groups. All models were trained for 150 epochs with an input resolution of 640 × 640 pixels. Evaluation metrics included Recall, mAP50, and mAP50-95.

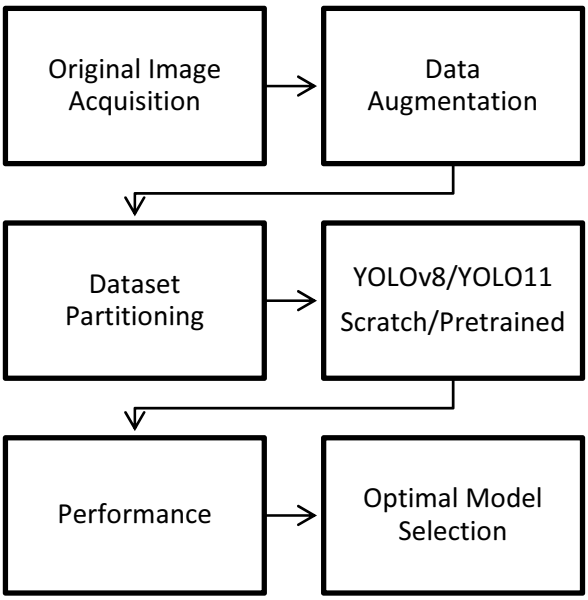

Fig. 1 Experimental flowchart.



Fig. 2 Representative symptom images and data augmentation examples for passion fruit anthracnose and Phytophthora blight.

RESULTS & DISCUSSION

3.1 Performance Comparison of Detection Models

The quantitative performance of the eight evaluated models is summarized in Table 1. Under identical training epochs, utilizing pretrained weights significantly accelerated feature convergence, leading to marked improvements in both recall and mAP without increasing training duration. Qualitative visual detection results confirmed that the optimal pretrained YOLOv8m model successfully localized both subtle, multi-instance lesions of anthracnose and broad symptomatic areas of Phytophthora blight under complex orchard illumination (As shown in Fig. 3). As shown in the training and validation metric trajectories (As shown in Fig. 4), the bounding box, classification, and distribution focal losses steadily decreased across 150

epochs, while the validation mAP50 rapidly stabilized above 90%. Among all configurations, pretrained YOLOv8m achieved the highest accuracy, reaching an mAP50 of 90.62% and an mAP50-95 of 67.35%.

Table 1 Performance comparison among different YOLO models.

Model Architecture	Size	Strategy	Training Time	Recall(%)	mAP50(%)	mAP50-95(%)
YOLOv8	n	Scratch	~2h40m	82.58	86.23	57.24
YOLOv8	n	Pretrained	~2h38m	85.3	88.97	63.3
YOLOv8	m	Scratch	~2h46m	84.13	89.41	63.98
YOLOv8	m	Pretrained	~2h44m	86.12	90.62	67.35
YOLO11	n	Scratch	~2h45m	80.31	84.98	57.10
YOLO11	n	Pretrained	~2h42m	83.1	86.6	60.1
YOLO11	m	Scratch	~2h51m	80.4	86.02	60.8
YOLO11	m	Pretrained	~2h52m	81.53	87.61	60.29



Fig. 3 Visual detection results of YOLOv8m (Pretrained) for anthracnose (left) and Phytophthora blight (right).

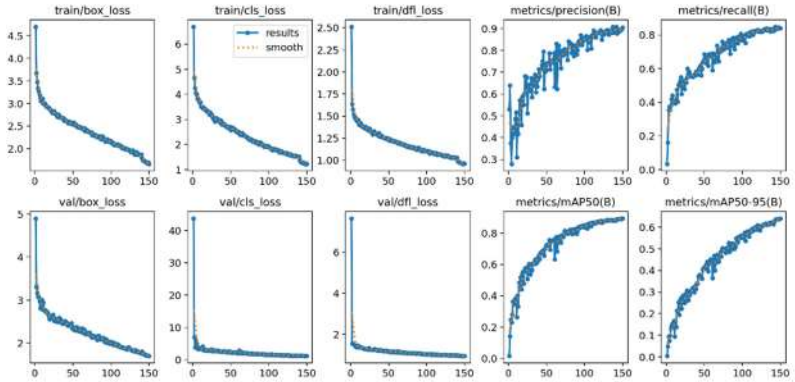

Fig. 4 Training loss and validation performance curves of YOLOv8m.

3.2 Deployment and Efficiency

Although the newer YOLO11m architecture exhibited comparable training efficiency (~2h52m), its mAP50 (87.61%) was slightly lower than that of YOLOv8m. This may be attributed to the attention mechanisms in YOLO11 requiring larger data distributions to optimize feature representation for subtle lesion characteristics. For practical edge-computing scenarios (such as handheld or UAV-mounted edge devices), pretrained YOLOv8n provided the most balanced performance, delivering 88.97% mAP50 with minimal computational overhead. These findings align with recent developments in embedded passion fruit monitoring, demonstrating that lightweight YOLO models combined with transfer learning provide an optimal trade-off between real-time inference speed and high diagnostic accuracy.

CONCLUSIONS

This study developed an automated detection system for passion fruit anthracnose and Phytophthora blight. Data augmentation effectively expanded the dataset to 2,275 images, and utilizing pretrained weights significantly enhanced detection performance across all architectures. Pretrained YOLOv8m delivered the highest overall accuracy (mAP50: 90.62%), while pretrained YOLOv8n offered an optimal lightweight solution for real-time field edge deployment. The findings demonstrate that architectural iteration alone does not guarantee superior detection performance; dataset size, symptom characteristics, and initialization strategies jointly determine field efficacy.

ACKNOWLEDGEMENTS

The authors would like to express their sincere gratitude to the Taiwan Agricultural Research Institute (TARI) for providing the passion fruit disease image datasets, which made the construction of a comprehensive dataset and subsequent deep learning model training and performance analysis possible.

REFERENCES

Ferentinos, K. P. 2018. Deep learning models for plant disease detection and diagnosis. *Comput. Electron. Agric.* 145: 311–318.

Luo, R., R. Zhao, X. Ding, S. Peng, and F. Cai. 2025. High-precision complex orchard passion fruit detection using the PHD-YOLO model improved from YOLOv11n. *Horticulturae* 11(7): 785.

Mohanty, S. P., D. P. Hughes, and M. Salathé. 2016. Using deep learning for image-based plant disease detection. *Front. Plant Sci.* 7: 1419.

Redmon, J., S. Divvala, R. Girshick, and A. Farhadi. 2016. You only look once: Unified, real-time object detection. In *Proc. IEEE Conf. Comput. Vis. Pattern Recognit. (CVPR)*, 779–788. Las Vegas, NV: IEEE.

Sun, Q., P. Li, C. He, Q. Song, J. Chen, X. Kong, and Z. Luo. 2024. A lightweight and high-precision passion fruit YOLO detection model for deployment in embedded devices. *Sensors* 24(15): 4942.

AI-P03

Proceedings of The 12th International Symposium on Machinery and Mechatronics for Agriculture and Biosystems Engineering (ISMAB 2026)
20-24 October 2026, Busan, Republic of Korea

A METHOD FOR GROUND ELEVATION MEASUREMENT USING MOVING BASE RTK AND TILT COMPENSATION FOR PADDY FIELD LEVELING

Shanon Yamaguchi[1], Tatsuro Taniyama[1], Kyosuke Nishizawa[1], Hiroshi Iwata[1*], Ken'ichi Yamaguchi[1], Yuki Ashihara[1]

[1]National Institute of Technology (KOSEN), Nara College,
22 Yata, Yamato-koriyama, Nara 639-1080, Japan
*Corresponding Author-- Voice: +81-734-55-6138, Email: iwata.info.nara-k.ac.jp

Abstract: Accurate land leveling -shirokaki- is an important process in paddy rice cultivation because uneven ground surfaces can cause nonuniform water depth after flooding and may adversely affect subsequent field operations and crop management. To support efficient land leveling, our research group has been developing a ground elevation measurement system using Moving Base Real-Time Kinematic (RTK) positioning, which can determine highly accurate relative coordinates between a base station and a rover. In our previous system, the measurement device had to be held vertically at each measurement point to obtain an accurate ground elevation. This requirement reduced measurement efficiency and could introduce errors when the operator was unable to maintain the device in a perfectly vertical orientation. To overcome this limitation, this study proposes an automatic tilt compensation method using a nine-axis inertial measurement unit (IMU). The pitch and roll angles measured by the IMU are used to estimate the inclination of the measurement device, and the vertical height from the positioning antenna to the ground is geometrically corrected according to the estimated orientation. This enables ground elevation to be measured without requiring the operator to keep the device vertical. A case study was conducted on a sloped area within our campus to evaluate the feasibility of the proposed method.

Key Words: RTK-GNSS, moving base RTK, Tilt Compensation, Rice Farming, IoT

INTRODUCTION

Japanese agriculture faces the dual challenges of a shrinking and aging workforce. One significant factor contributing to the shortage of new farmers is the high barrier to entry. As of 2023, the population of core agricultural workers had declined to less than half of its 2000 level (MAFF, 2024). This decline makes it increasingly important to reduce reliance on experience and intuition in agricultural operations. For example, essential tasks such as puddling (shirokaki)—which levels the soil surface to ensure uniform water depth and promote consistent crop growth—require considerable operator experience and intuition, presenting a steep learning curve for beginners (Fig. 1). To overcome this barrier, we have proposed a low-cost, high-precision ground elevation visualization system utilizing satellite positioning technology (Taniyama et al., 2026). The system can operate without an internet connection, measure relative elevation differences in real time, and visualize the ground surface in three

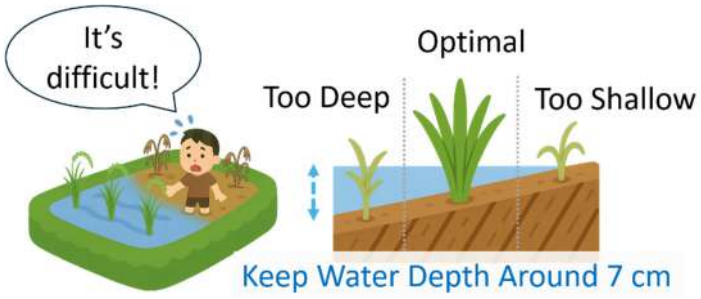

Fig. 1 Impact of Uneven Puddling on Rice Growth and Yield.

dimensions. By enabling new farmers to intuitively identify surface irregularities without relying on prior experience, the system supports more precise puddling.

RTK-GNSS has also been widely applied to agricultural vehicles for high-accuracy positioning and automated guidance, and several studies have combined RTK-GNSS with inertial sensors to improve vehicle navigation (Noguchi et al., 2001; Takai et al., 2014; Yang et al., 2016). However, these studies primarily focused on horizontal positioning and vehicle guidance and did not use Moving Base RTK to measure ground elevation. Our previous system utilizes Moving Base RTK to measure relative ground elevation in real time, but requires the measurement device to be held vertically at each measurement point. Therefore, the effect of device inclination on ground elevation measurement has not been addressed.

However, Our previous system requires the measurement device to be held vertically at each measurement point. When the device is tilted, the measured position of the antenna does not directly correspond to the vertical distance from the antenna to the ground, resulting in an error in the estimated ground elevation. Maintaining a vertical orientation at every measurement point is cumbersome and may reduce the efficiency of field measurements, particularly on uneven or sloped surfaces. Therefore, this study proposes an automatic tilt compensation method using a nine-axis inertial measurement unit (IMU). The proposed method estimates the pitch and roll angles of the measurement device and automatically corrects the ground elevation based on its orientation, enabling accurate measurements without requiring the operator to hold the measurement device vertically.

PROPOSED TILT COMPENSATION METHODS

The proposed system is based on the Moving Base RTK system developed by Taniyama et al. (2026), which enables highly accurate measurement of the relative position between a base station and a rover, with positioning errors of less than 1 cm in the horizontal (X and Y) directions and less than 2 cm in the vertical (Z) direction. In the conventional system, the rover is installed vertically on the ground, and the pitch and roll angles measured by the nine-axis IMU are confirmed to be zero. The elevation data are then recorded when the RTK positioning status is FIX. Under these conditions, the ground elevation can be obtained accurately from the relative position between the base station and the rover.

In the proposed system, the measurement device is assumed to be mounted on a tractor or similar agricultural vehicle to automatically survey the condition of a paddy field. Unlike the conventional measurement procedure, the vehicle may tilt when traveling over sloped or

uneven terrain. Therefore, the pitch and roll angles of the measurement device are not necessarily zero. To obtain the actual ground elevation under these conditions, the effect of the device inclination must be compensated for.

First, the ground elevation H_O is measured when the measurement device is in a horizontal orientation, where both the roll and pitch angles are zero. This value only needs to be measured once and remains constant as long as the mounting position of the measurement device is not changed.

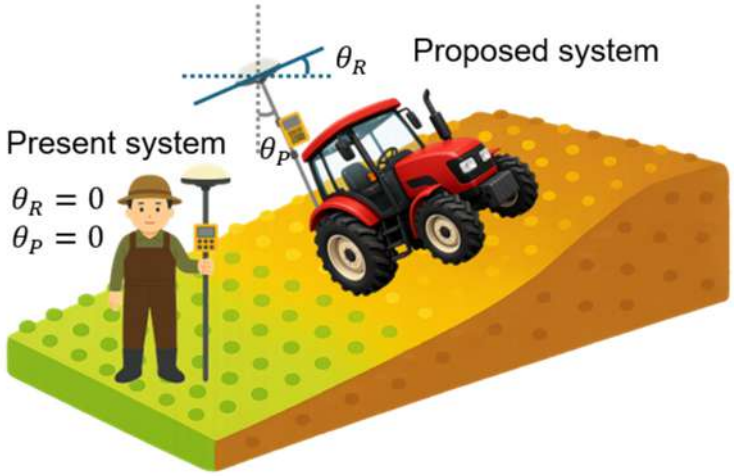

Fig. 2 Comparison of the Use Case of the Present and Proposed System

The Moving Base RTK system provides the relative elevation D of the rover with respect to the base station. When the measurement device is not tilted, the ground elevation H_T can therefore be calculated as $H_T = D + H_O$. When the device is tilted, the nine-axis IMU provides the roll angle θ_R and pitch angle θ_P. The vertical component of the distance between the RTK antenna and the ground is then obtained by applying the cosine of each tilt angle. Thus, the ground elevation can be calculated as

$$H_T = D + H_O \cos\theta_R \cos\theta_P \quad (1)$$

where:

H_T = The compensated ground elevation
D = The relative elevation between the base station and the rover
H_O = The original ground elevation
θ_P = The pitch angle
θ_R = The roll angle

This tilt compensation enables the proposed system to estimate ground elevation without requiring the measurement device to remain vertically oriented during field measurements.

EXPERIMENTAL RESULTS & DISCUSSION

The proposed tilt compensation method was evaluated through two experiments. In both experiments, the base station and rover were installed on a nearly level surface, and the antenna height from the ground was set to $H_O = 1.5\,\text{m}$. To simulate a tractor-mounted measurement system, the rover was mounted on a tripod fixed to a cart, allowing the rover to

be tilted at various angles.

First, an experiment was conducted to verify the validity of the proposed tilt compensation theory. The cart carrying the rover was gradually tilted from the horizontal position to approximately 80 degrees, and the ground elevation was measured at each tilt angle. Figure 3 shows the resulting three-dimensional elevation maps with tilt compensation (left) and without tilt compensation (right). In these 3D maps, the color gradient represents the measured elevation, where green indicates lower elevation and orange indicates higher elevation. The compensated map remained substantially flatter than the uncompensated map, indicating that the proposed method effectively reduced the influence of rover inclination.

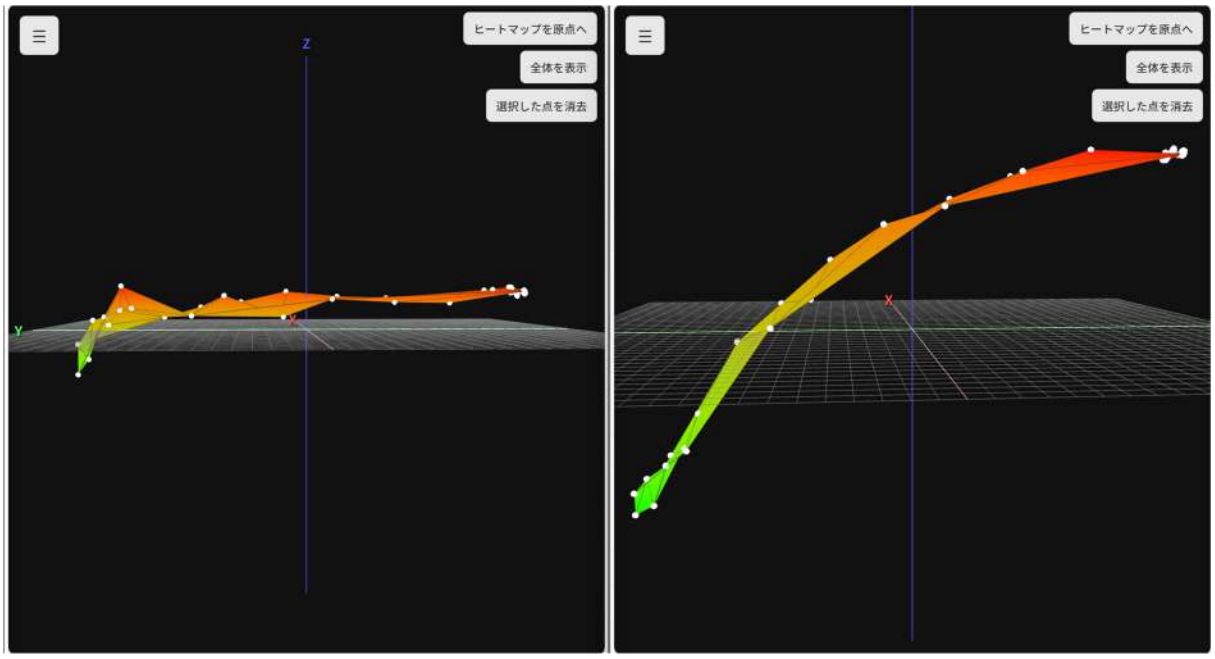

Fig. 3 The resulting three-dimensional elevation maps
with tilt compensation (left) and without tilt compensation (right)

Since the test surface was nearly level, the ideal measurement result was a flat surface. Without tilt compensation, however, the measurement error increased as the rover was tilted. In particular, when the cart was tilted to nearly 90 degrees, the maximum elevation error reached 0.257 m. This corresponds to the region where the uncompensated map shows a large decrease in elevation. Although this error is significant, such an extreme inclination is unlikely to occur in practical paddy field operations. When the tilt angle was limited to 45 degrees, the maximum error was reduced to 0.055 m, which was considered sufficiently accurate for practical ground elevation measurement. These results demonstrate that the proposed tilt compensation method correctly compensates for the effect of rover inclination and is applicable over a practical range of tilt angles.

Second, the proposed system was evaluated on an inclined test surface using the cart-mounted rover. Figure 4 shows the experimental setup. In Fig.4, the base station is positioned on the tripod on the left, and the rover is mounted on the cart on the right. The measurement was conducted by pushing the cart along the slope shown in the background of the photograph. Figure 5 shows the three-dimensional elevation maps obtained without tilt

compensation (left) and with tilt compensation (right). As explained in Fig. 3, green represents lower elevation and orange represents higher elevation. In Fig. 5, the right side (corresponding to the higher part of the slope in Fig. 4) is colored orange, and the left side (the lower part of the slope) is colored green, showing a clear elevation gradient. The system successfully measured the ground elevation while the rover was moving over the inclined surface, and the inclination of the ground was clearly represented in the resulting three-dimensional map. These results demonstrate that the proposed system can rapidly measure and visualize ground inclination without requiring the rover to be maintained in a vertical orientation.



Fig. 4 Experimental setup for ground elevation measurement on an inclined test surface.

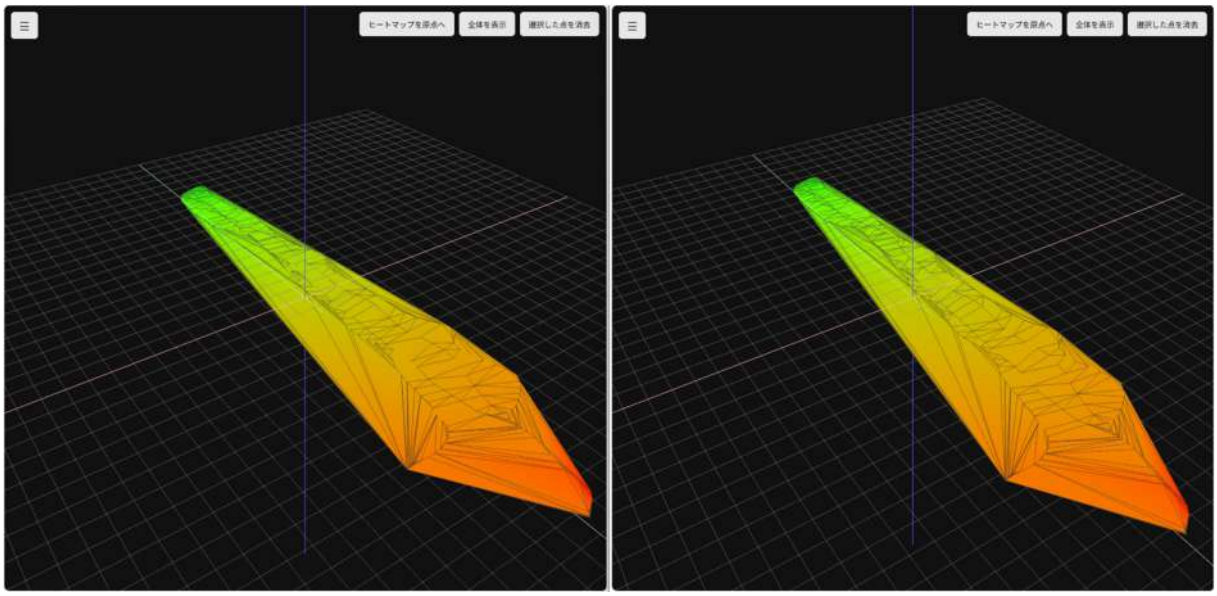

Fig. 5 Three-dimensional elevation maps of the inclined test surface: without tilt compensation (left) and with tilt compensation (right).

The two experiments confirm both the theoretical validity and practical feasibility of the proposed tilt compensation method. By eliminating the need to maintain a vertical measurement device, the proposed system can improve the usability of the Moving Base RTK-based ground elevation measurement system and facilitate its application to automated field surveying for paddy field leveling.

CONCLUSIONS

This study proposed an automatic tilt compensation method for a ground elevation measurement system using Moving Base RTK and a nine-axis IMU. The proposed method estimates the roll and pitch angles of the measurement device and compensates for the effect of device inclination on ground elevation measurements.

Experimental results using a cart-mounted rover demonstrated that the proposed method effectively reduced elevation errors caused by device inclination. The method achieved practical measurement accuracy over a range of tilt angles and enabled the system to measure and visualize ground inclination without requiring the measurement device to be held vertically. These results demonstrate the effectiveness of the proposed method in improving the usability of the Moving Base RTK-based ground elevation measurement system for paddy field leveling.

Future work will focus on field experiments in actual paddy fields by mounting the proposed system on a tractor. In addition to evaluating measurement accuracy under real operating conditions, feedback from farmers will be collected to assess the usability and practicality of the system. Based on this feedback, we aim to further improve the system and develop a practical and user-friendly tool for efficient paddy field leveling.

REFERENCES

MAFF. 2024. Overview of the Annual Report on Food, Agriculture and Rural Areas (FY2023). Tokyo, Japan: Ministry of Agriculture, Forestry and Fisheries. Available at: MAFF official PDF. Accessed 3 September 2026.

N. Noguchi, J. F. Reid, Q. Zhang, J. D. Will, and K. Ishii. 2001. Development of robot tractor based on RTK-GPS and gyroscope. ASAE Paper 01-1195. St. Joseph, Mich.: American Society of Agricultural Engineers. doi:10.13031/2013.7297.

R. Takai, L. Yang, and N. Noguchi. 2014. Development of a crawler-type robot tractor using RTK-GPS and IMU. Engineering in Agriculture, Environment and Food 7(4): 143–147. doi:10.1016/j.eaef.2014.08.004.

T. Taniyama, H. Kuwahata, K. Nishizawa, S. Yamaguchi, A. Shimaoka, H. Iwata, K. Yamaguchi, and Y. Ashihara. 2026. Contour Line Leveling for Beginners: An Affordable System for Visualizing Elevation Differences in Rice Fields. In Proc. of the 14th IIAE International Conference on Industrial Application Engineering 2026, pp. 27–34. Okayama, Japan: The Institute of Industrial Applications Engineers.

L. Yang, N. Noguchi, and R. Takai. 2016. Development and application of a wheel-type robot tractor. Engineering in Agriculture, Environment and Food 9(2): 131–140. doi:10.1016/j.eaef.2016.04.003.

AI-P04

Proceedings of The 12th International Symposium on Machinery and Mechatronics for Agriculture and Biosystems Engineering (ISMAB 2026)
20-24 October 2026, Busan, Republic of Korea

DECOUPLING SUBSTRATE AND SAMPLING DIRECTION IN NON-SPHERICAL COMPOUND EYES

You-Rong Zheng[1], Shang-Jui Fu[2], En-Cheng Yang[2], Cheng-Ying Chou[1*]

[1]Department of Biomechatronics Engineering, National Taiwan University, Taiwan
[2]Department of Entomology, National Taiwan University, Taiwan
*Corresponding Author-- Voice: +886-2-3366-9689, Email: chengying@ntu.edu.tw

Abstract: From an engineering perspective, a compound eye can be described by two separable layers: the substrate on which the facets are arranged and the sampling direction of each ommatidium, which acts as the eye's detector. The two layers are linked by the skew angle between each ommatidial optical axis and the local substrate normal, which in non-spherical eyes departs from zero and allows sampling density, expressed as the interommatidial angle ($\Delta\varphi$), to be redistributed without changing eye shape. The micro-CT algorithm ODA-3D can estimate this skew, but it detects ommatidia on a spherically unwrapped image and derives the substrate normal from neighboring ommatidial centers, so both layers become unreliable where the peripheral ommatidia of non-spherical eyes are strongly skewed. This study develops an algorithm that fits each ommatidium as a tube directly in the three-dimensional micro-CT volume, restricts detection to a stable signal band, and estimates the substrate normal from the local compound eye surface independently of neighboring ommatidia. Applied to a worker honeybee compound eye, the algorithm detected 3,589 ommatidia, approximately two-thirds of the reported total, with a median $\Delta\varphi$ of 2.18°, slightly above previous pseudopupil measurements of 1.6° to 2.1°, and the Kagome-like configuration of adjacent-pair midpoints indicated a regular hexagonal arrangement. Skew angle increased from the center toward the periphery, where detection failures remained due to lower signal contrast. Mapping substrate and sampling direction separately provides parameters for designing artificial compound eyes whose sampling distribution is not dictated by a spherical substrate.

Key Words: Compound Eye, Ommatidia, Skew Angle, Interommatidial Angle, Micro-CT

INTRODUCTION

The insect compound eye is composed of thousands of independent ommatidia, each equipped with its own corneal lens, crystalline cone, and rhabdom, receiving light signals from a specific angular space. This architecture reflects a trade-off between physical scale and survival demands. Whereas a single-lens system typically corrects spherical aberration by increasing lens thickness, adding lens layers, or extending focal length, such strategies are impractical for honeybees, whose body length is limited and whose flight requires strict weight control. The compound eye therefore decomposes the task of a single large aperture serving the entire visual field into a large number of independent small apertures, each responsible for

a small angular subspace, allowing each ommatidium to remain compact and lightweight without complex aberration-correction mechanisms.

The compound eye coordinates the specialization of its photoreceptors through two parameters: the interommatidial angle ($\Delta\varphi$) and angular sensitivity ($\Delta\rho$). $\Delta\varphi$ reflects the angular density with which ommatidial optical axes sample visual space, while $\Delta\rho$ reflects the range of light signals a single ommatidium can receive; together, these two parameters determine the information-acquisition efficiency of the visual system. This coordination strategy varies not only across species occupying different ecological niches, but also within a single species and even within a single individual, where resources are differentially allocated according to functional regionalization of the compound eye (Land, 1997). This body of evidence indicates that the compound eye has no single optimal design; rather, each eye represents a configuration adapted to the survival needs of a population or individual. Of these two parameters, $\Delta\varphi$ is determined directly by the geometry of the ommatidial axes and is therefore the focus of this study.

From an engineering standpoint, the geometry of a compound eye can be separated into two layers: the substrate, that is, the curved outer surface of the eye on which the facets are arranged, and the sampling direction of each ommatidium, which acts as an individual detector. In a spherical eye, the two layers are coupled, because every sampling direction coincides with the substrate normal, so eye shape alone determines $\Delta\varphi$ and the field of view. In non-spherical eyes, ommatidial axes need not be orthogonal to the substrate, so that horizontal and vertical $\Delta\varphi$ can vary independently (Stavenga, 1979; Land, 1997). The skew angle between an ommatidium's optical axis and the local substrate normal is therefore the parameter that links the two layers. For hardware design, this separation implies that the substrate can be kept to a simple, manufacturable curvature, while the sampling distribution is set by the magnitude and direction of skew assigned to each detector. Existing artificial compound eyes typically arrange detectors on a spherical substrate and orient each along the substrate normal, so that sampling density is fixed by substrate curvature. Extending such designs to non-spherical substrates by prescribing $\Delta\varphi$ between neighboring detectors alone requires a predefined lattice topology, and the resulting orientations become path-dependent when propagated across a curved, non-developable surface. Describing each ommatidium instead by its local substrate normal and skew avoids this dependence on neighbors, but requires that both quantities be measurable for every ommatidium.

However, existing methods for measuring $\Delta\varphi$ and $\Delta\rho$, such as the pseudopupil method (Seidl and Kaiser, 1981), intracellular recording (Rigosi et al., 2017), or the recently developed ODA-3D algorithm based on micro-computed tomography (micro-CT) image processing (Currea et al., 2023), have consistently served the biology and neuroscience communities; yet neither their measurement targets nor their precision meets the demands of artificial compound eye design, which requires the substrate and the sampling direction of every ommatidium to be recovered as separate quantities across the entire eye, including its periphery. ODA-3D moves in this direction by estimating an anatomical axis for each segmented crystalline cone and comparing it with an ideal axis, defined by the normals of planes formed by neighboring ommatidial centers (Currea et al., 2023). Both quantities, however, depend on the ommatidial lattice detected in a spherically unwrapped image, and in the honeybee, strongly skewed ommatidia in the lateral periphery of the eye were poorly segmented. ODA-3D also averages each axis over a neighborhood of ommatidia to reduce

noise, which the authors noted pulls axes near the eye margin toward the center. The horizontal $\Delta\varphi$ of the honeybee was consequently estimated at 0.82°, which the authors regarded as an underestimate relative to previous measurements (Currea et al., 2023). The region where substrate and sampling direction diverge most is therefore the region these measurements capture least reliably. In this study, we follow the concept of anatomical skewness in Currea et al. (2023) and define the skew angle at the point where the optical axis intersects the compound eye surface, but estimate the substrate normal from the local compound eye surface rather than from neighboring ommatidial centers, so that the substrate is characterized independently of whether the surrounding ommatidia are successfully detected.

The core value of this study lies in establishing an algorithm that recovers the substrate geometry and the sampling direction of each ommatidium as separate quantities directly from micro-CT images, without spherical projection. This approach is intended to support research in insect behavioral ecology and neuroscience while also serving as a bridge between the biological and engineering communities, translating nature's solution to task-dependent visual resource allocation into design inputs directly usable by engineers.

MATERIALS AND METHODS

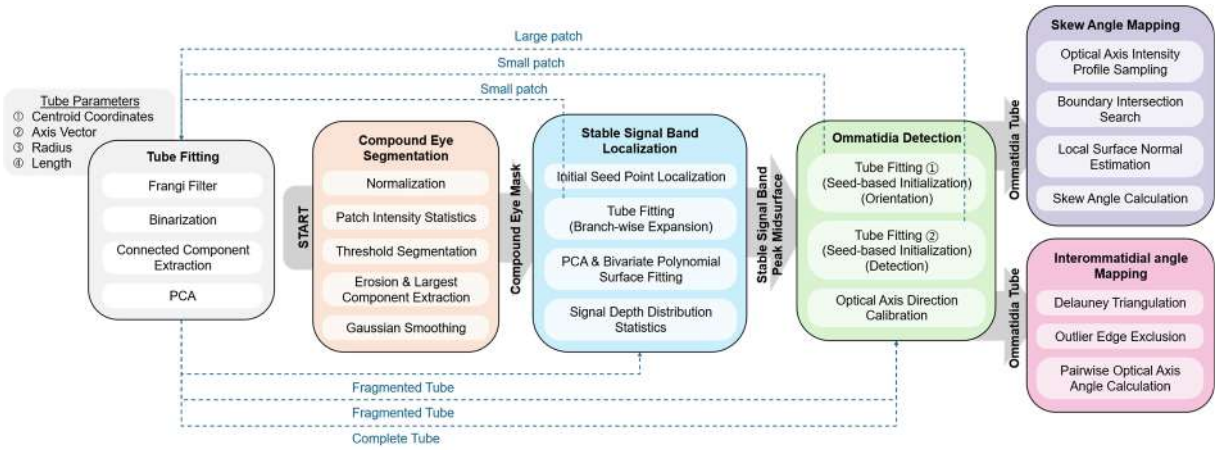

Fig. 1 Overview of the algorithm pipeline.

DATASET & IMAGE PREPROCESSING

The compound eye of a worker honeybee (*Apis mellifera*) was used as the study subject. The head sample was scanned using a Zeiss Xradia 515 Versa X-ray microscope, yielding a reconstructed volume with dimensions (X × Y × Z) of 1984 × 2032 × 1999 voxels and a spatial resolution of approximately 1.307 μm along all three axes.

Tissue outside the compound eye is first excluded from the image by the compound eye segmentation module to reduce the computational burden of the subsequent ommatidia detection. This module uses a threshold-based method. To simplify the voxel intensity distribution of the image, the normalized volume is divided into regularly arranged, non-overlapping patches, and the mean intensity within each patch is computed. A threshold is then determined based on the patch intensity histogram, with the segmentation result reviewed and adjusted accordingly, yielding an initial mask. Because this initial mask typically

encompasses a substantial amount of weakly connected noise, it is refined by retaining the largest connected component after an erosion operation, corresponding to a single compound eye of the honeybee, and further smoothed using Gaussian smoothing.

TUBE FITTING

The tube fitting module serves as the core of the proposed algorithm, used to detect and parameterize the tubular structures corresponding to ommatidia in the image. This module supports two implementation strategies, branch-wise expansion and seed-based initialization, with the choice between them determined by the source of the seed point and the patch size. The tube fitting module is always triggered by a single seed point, which is theoretically a voxel located on the optical axis of an ommatidium and serves to mark its location. A patch is constructed centered on the seed point, and a Frangi filter is applied to the patch to obtain a tubular response (Frangi et al., 1998), thereby enhancing tubular structures while suppressing non-tubular tissue and background noise.

Binarizing the tubular response yields multiple independent connected components within the patch, each corresponding to a candidate ommatidial signal. The connected component overlapping the seed point is retained, and principal component analysis (PCA) is performed on the coordinates of all voxels within this component. The direction of the first principal component is taken as the axis of the ommatidial tube, while within the plane spanned by the remaining two principal components, the mean radial distance of voxels from the axis is taken as the tube radius. Each tube reflects the structural signal of an ommatidium, and its axis is taken as an approximation of the ommatidial optical axis. A tube is then recorded by its centroid coordinates, axis vector, radius, and length.

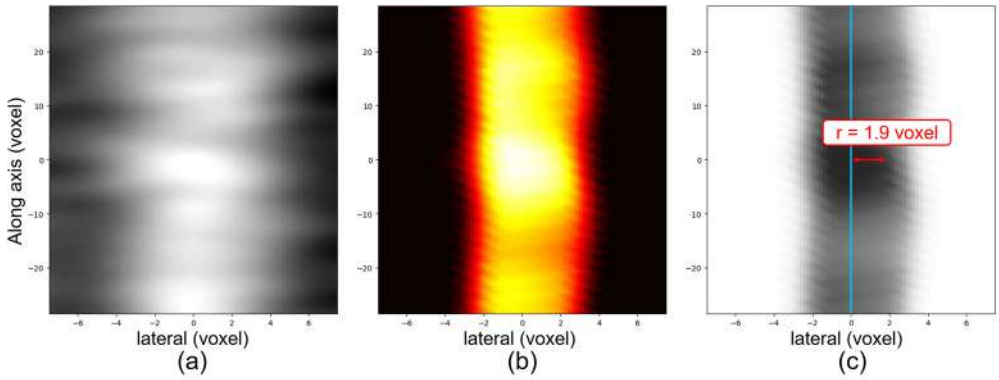

Fig. 2 Illustration of the tube fitting module. (a) Effect of applying the Frangi filter to a tubular structure in the raw image. (b) Effect of binarizing the tubular response obtained from the Frangi filter. (c) A tube fitted by PCA to the connected component obtained after binarization, with a diameter of approximately 4 voxels.

STABLE SIGNAL BAND LOCALIZATION

All ommatidia within the compound eye converge toward the side facing the brain, causing the boundaries between ommatidia to become increasingly indistinct in regions closer to the brain. To prevent such indistinct boundaries from interfering with subsequent ommatidia detection, the detection range must be restricted to image regions where the ommatidial signal remains stable. We observed that the signal is clearest around the center of each ommatidium, and

accordingly define the surface passing through the clearest signal region of every ommatidium as the midsurface of the compound eye. However, the compound eye mask is a continuously curved, closed shell, lacking the clearly decomposable, pairable offset surfaces characteristic of engineering thin-shell structures, and existing midsurface extraction methods cannot therefore be directly applied. A dedicated stable signal band localization module was developed to address this issue.

This module first applies a distance transform to the compound eye mask, and the voxel with the global maximum distance value closest to the compound eye mask centroid is selected as the starting point of the module. A patch is constructed centered on this point, and a three-dimensional fast Fourier transform (3D-FFT) is applied to identify the local ommatidial orientation and extract a cross-sectional slice perpendicular to it; a seed point located on this slice then triggers the tube fitting module to obtain the first tube. This tube is subsequently extended under the branch-wise expansion strategy: (1) the tube fitting module extends the initially fitted tube by constructing new patches at both ends along its axis, repeating fitting and merging within the current round until no further connected components overlapping the seed points are found; (2) at the end of each round, tubes whose length falls outside the interquartile range (IQR) of the tube length distribution are excluded, preventing low-quality detections from interfering with the seed points used to trigger the next round; (3) the seed points used to trigger each subsequent round of tube fitting are obtained from periodic signal peaks detected via two-dimensional FFT (2D-FFT) on the radial cross-sections of the tubes obtained in the previous round; (4) this branch-wise expansion of tube fitting continues until no new connected components overlapping the seed points are found.

Once the centroids of all tubes have been obtained, PCA is performed on their coordinates. The directions of the first two principal components define a reference plane, while the third principal component direction serves as the normal direction. All centroids are projected onto the reference plane to obtain 2D parametric coordinates, and a low-order bivariate polynomial surface is fitted using these coordinates as independent variables and the corresponding normal-direction offsets as the dependent variable, yielding the midsurface of the compound eye. To reduce the influence of outliers, iteratively reweighted least squares combined with Tukey's biweight function is employed to down-weight centroids with excessively large offsets during fitting (Beaton and Tukey, 1974).

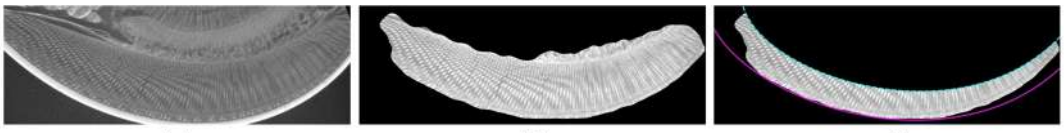

Fig. 3 Construction of the stable signal band. (a) Raw image. (b) Image after segmentation by the compound eye mask. (c) Image after further segmentation by the stable signal band.

To quantify the reliability of the ommatidial signal along the depth of the compound eye, the module samples a series of mutually parallel surfaces at successive depth offsets along the normal direction of the midsurface, and tabulates the distribution of seed point counts detected on each surface using a Laplacian of Gaussian (LoG) filter. The surface with the highest seed point count is taken as the center of the stable signal band, also referred to as the peak midsurface, and the band is defined as the range within one standard deviation of the seed point count distribution along the depth offset, on either side of this surface.

OMMATIDIA DETECTION

Once the stable signal band has been established, the ommatidia detection module measures the optical axis of each ommatidium in two steps. The tube fitting module is first triggered under the seed-based initialization strategy with a small patch, using a seed point obtained from the LoG filter applied to the peak midsurface, to estimate the tube's radius and axis. It is then triggered again with a larger patch aligned to this axis, sized according to the stable signal band and the tube radius so as to be slightly larger than the ommatidium, to obtain the final ommatidial tube.

Since the sign of the axis direction obtained from PCA carries no inherent meaning, each tube's axis is calibrated using the mask centroid as a reference: the dot product between the vector from the mask centroid to the tube centroid and the optical axis is computed, and the axis is reversed if this value is negative, ensuring all axes consistently point away from the mask centroid.

SKEW ANGLE MAPPING

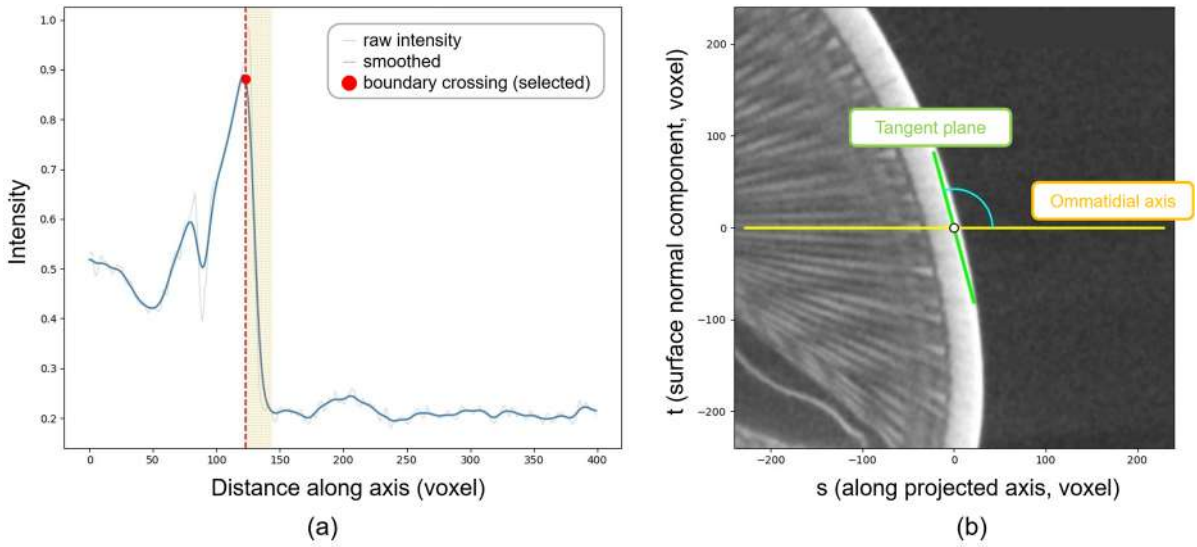

Fig. 4 Illustration of the skew angle calculation process. (a) One-dimensional voxel intensity profile sampled along the ommatidial optical axis. (b) The one-dimensional voxel intensity profile (yellow line) and the tangent plane at the intersection of the optical axis and the compound eye surface (green line), shown on the raw image.

The ommatidial skew angle is defined as the angle between the optical axis and the substrate normal at the point where the optical axis meets the compound eye surface. To compute the skew angle of each ommatidial tube, a one-dimensional voxel intensity profile $I(t)$ is sampled and smoothed along the optical axis, starting from the tube centroid and extending to a maximum distance T. For any candidate position t_i along this profile, three local statistics are defined:

$$I_{fg}(t_i) = median(I(t) : t \in [t_i - w_{fg}, t_i)) \quad (1)$$

$$I_{bg}(t_i) = median(I(t) : t \in [t_i, t_i + w_{bg})) \quad (2)$$

$$I_{tail}(t_i) = median(I(t) : t \in [t_i + w_{bg}, t_i + 3w_{bg})) \quad (3)$$

where:

I_{fg} = median intensity within the preceding w_{fg}-length interval, representing the reference intensity on the tissue side (a.u.)

I_{bg} = median intensity within the subsequent w_{bg}-length interval (a.u.)

I_{tail} = median intensity within the further subsequent $2w_{bg}$-length interval, used to confirm whether the low-intensity state persists (a.u.)

Candidate position t_i must simultaneously satisfy the following three conditions to be identified as a valid boundary intersection:

First, the local gradient must be negative:

$$I'(t_i) < 0 \tag{4}$$

Second, the intensity must decrease significantly:

$$I_{bg}(t_i) < (1 - m)I_{fg}(t_i) \tag{5}$$

where:

m = a preset relative decline threshold, $m \in (0, 1)$ (-)

Third, the low-intensity state must be sustained:

$$I_{tail}(t_i) \leq (1 + \varepsilon) \cdot I_{bg}(t_i) \tag{6}$$

where:

ε = a tolerance upper bound allowing I_{tail} to fluctuate slightly relative to I_{bg} without a significant subsequent increase, $\varepsilon > 0$ (-)

The final boundary intersection t^* is defined as the first position, when scanning t in ascending order, that simultaneously satisfies all three conditions above:

$$t^* = min\{t_i | I'(t_i) < 0 \wedge I_{bg}(t_i) < (1 - m)I_{fg}(t_i) \wedge I_{tail}(t_i) \leq (1 + \varepsilon)I_{bg}(t_i)\} \tag{7}$$

The corresponding 3D coordinates of the boundary intersection p^* are given by:

$$p^* = c + t^*\hat{a} \tag{8}$$

where:

c = tube centroid (voxel)

$\hat{a}$ = unit optical axis vector (-)

A patch is constructed centered on the resulting boundary intersection p^*, and the intensity statistics $I_{fg}(t^*)$ and $I_{bg}(t^*)$ obtained for the same ommatidium are used to define a threshold θ, taken as their midpoint, for binarization:

$$\theta = \frac{1}{2}[I_{fg}(t^*) + I_{bg}(t^*)] \tag{9}$$

The binarized image is then subjected to an erosion operation, and the difference between the original binarized result and the eroded result is taken to obtain a thin, shell-like set of surface voxels S, which approximately represents the geometric location of the compound eye surface within the patch. PCA is performed on the 3D coordinates of S, and the eigenvalues of the resulting covariance matrix are arranged in descending order as $\lambda_1 \geq \lambda_2 \geq \lambda_3$, with corresponding eigenvectors v_1, v_2 and v_3. The eigenvector v_3 corresponding to the smallest eigenvalue λ_3 is taken as the substrate normal $\hat{n}$ at that location, and its orientation is unified relative to the optical axis $\hat{a}$ such that both consistently point toward the exterior of the compound eye.

The skew angle is then computed as:

$$skew = arccos(|\hat{a} \cdot \hat{n}|) \quad (10)$$

Taking the absolute value of the dot product before applying the arccosine ensures that the resulting angle always falls within the range of 0° to 90°, unaffected by differences in the orientation convention of the two vectors.

INTEROMMATIDIAL ANGLE MAPPING

$\Delta\varphi$ is only meaningful between pairs of ommatidia that are genuinely adjacent in space, so an adjacency relationship between ommatidia must first be established. First, the centroids of all ommatidial tubes are projected onto the peak midsurface along the normal direction of its reference plane. Because the peak midsurface is parameterized over this reference plane, the 2D parametric coordinates of each ommatidium are given by:

$$(u_i, v_i) = \frac{(c_i - o)^T B}{s} \quad (11)$$

where:

c_i = centroid coordinate of the i-th ommatidium (voxel)
o = origin of the reference plane (voxel)
B = basis direction matrix of the reference plane (-)
s = scale normalization vector of the reference plane, applied element-wise (voxel)

Using this set of 2D coordinates as nodes, Delaunay triangulation is performed on all nodes, and the union of all edges in the resulting triangular mesh is taken as the initial adjacency set E_0.

If local gaps exist on the compound eye surface due to undetected ommatidia, Delaunay triangulation may produce non-physical long edges that span across such gaps and connect to distant nodes, causing the corresponding $\Delta\varphi$ to be spuriously inflated. To exclude such edges, the length of any edge (i, j) in E_0 is defined as the 3D Euclidean distance between the centroids of its two endpoints:

$$d_{ij} = \| c_i - c_j \| \quad (12)$$

where:

d_{ij} = 3D Euclidean distance between the centroids of ommatidia i and j (voxel)

Taking the median of all edge lengths as $\tilde{d}$, a reasonable upper bound is established based on the overall edge-length distribution: only edges with a length not exceeding a fixed multiple k_d of this median are retained, forming the final adjacency edge set E:

$$E = \{(i,j) \in E_0 | d_{ij} \leq k_d \tilde{d}\} \quad (13)$$

where:

$\tilde{d}$ = median of all edge lengths in E_0 (voxel)
k_d = fixed multiple defining the maximum allowable edge length (-)

For each pair of adjacent ommatidia (i, j) in the adjacency set E, their $\Delta\varphi$ is defined as the angle between the two optical axes:

$$\Delta\varphi_{ij} = arccos(\hat{a_i} \cdot \hat{a_j}) \quad (14)$$

where:

$\hat{a}_i$, $\hat{a}_j$ = unit optical axis vectors of the i-th and j-th ommatidia, respectively (-)

RESULTS & DISCUSSION

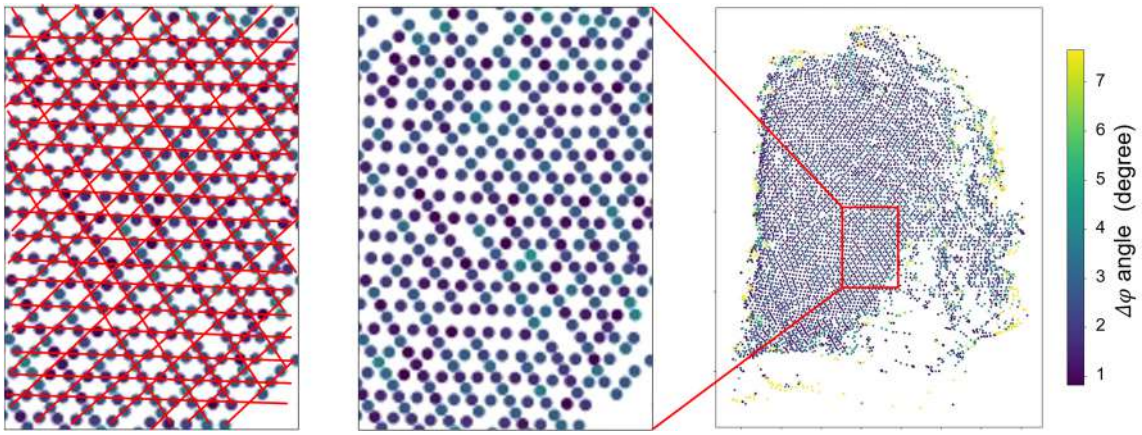

Fig. 5 Spatial distribution of $\Delta\varphi$ plotted at the midpoints of adjacent pairs.

A total of 3,589 ommatidia were detected in the compound eye sample, approximately two-thirds of the 5,375 ± 143 facets reported for worker honeybee eyes (Streinzer et al., 2013), yielding 7,384 adjacent pairs after Delaunay triangulation and edge-length filtering. The median of all $\Delta\varphi$ values was 2.18°, slightly above the range of 1.6° to 2.1° obtained by Seidl and Kaiser (1981) for worker honeybee compound eyes using the pseudopupil method. In the $\Delta\varphi$ distribution shown in Fig. 5, the midpoints of all adjacency edges form an array of corner-connected triangles enclosing hexagonal gaps, a configuration resembling the Kagome lattice. Because each adjacency edge connects the centers of two neighboring facets, its midpoint coincides with the midpoint of the hexagonal facet boundary they share, and the midpoints of the sides of a regular honeycomb lattice constitute a Kagome lattice (Syôzi, 1951). This configuration therefore indicates that the detected ommatidia follow the regular hexagonal facet arrangement of the compound eye, supporting the reliability of both the ommatidia detection and the adjacency relationships from which $\Delta\varphi$ was computed.

Furthermore, among the three extension directions constituting the Kagome-like configuration, the direction running from upper-left to lower-right in Fig. 5 exhibits an overall slightly higher $\Delta\varphi$ distribution than the other two directions. This directional discrepancy is consistent with the decomposition of compound eye sampling into horizontal and vertical $\Delta\varphi$ (Stavenga, 1979). Using ODA-3D on a honeybee eye, Currea et al. (2023) likewise found that horizontally oriented ommatidial pairs subtend larger angles than vertically oriented pairs, reflecting the oval shape of the honeybee eye. Quantifying $\Delta\varphi$ separately along each lattice direction, and relating these directions to the horizontal and vertical axes of the eye, will be addressed in future work.

Figure 6 shows the spatial distribution of ommatidial skew angles. Across the detected region, all three views consistently show that the skew angle gradually increases from generally low values in the central region toward the periphery, which is the region where ODA-3D, relying on a spherically unwrapped image, segmented strongly skewed ommatidia poorly (Currea et al., 2023). Because the proposed algorithm fits each ommatidium directly in the 3D volume, peripheral ommatidia that were detected retained this increasing skew rather than being distorted by projection. Nonetheless, high-angle outliers lacking spatial continuity remain along the eye margin, and detected ommatidia become sparse in the peripheral region visible toward the right of the eye in Fig. 6(b), which, together with the gaps in the $\Delta\varphi$ distribution in

Fig. 5, indicates that ommatidia in parts of the periphery could not be successfully detected. As examined below, these detection failures are attributable to regional variation in signal contrast rather than to the geometric distortion associated with spherical projection.

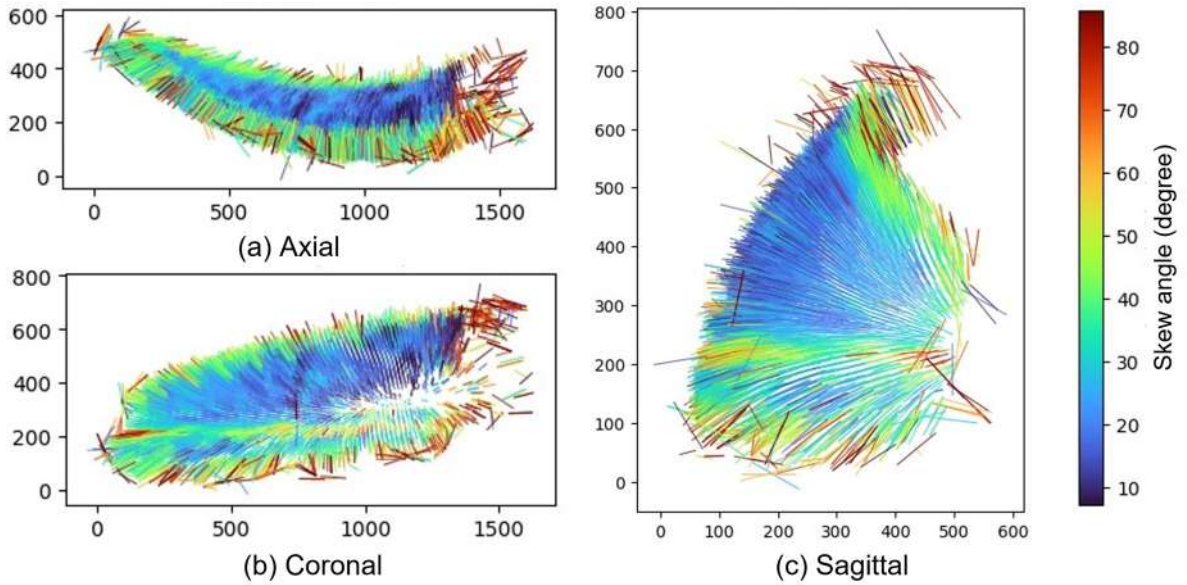

Fig. 6 3D visualization of the skew angle distribution.

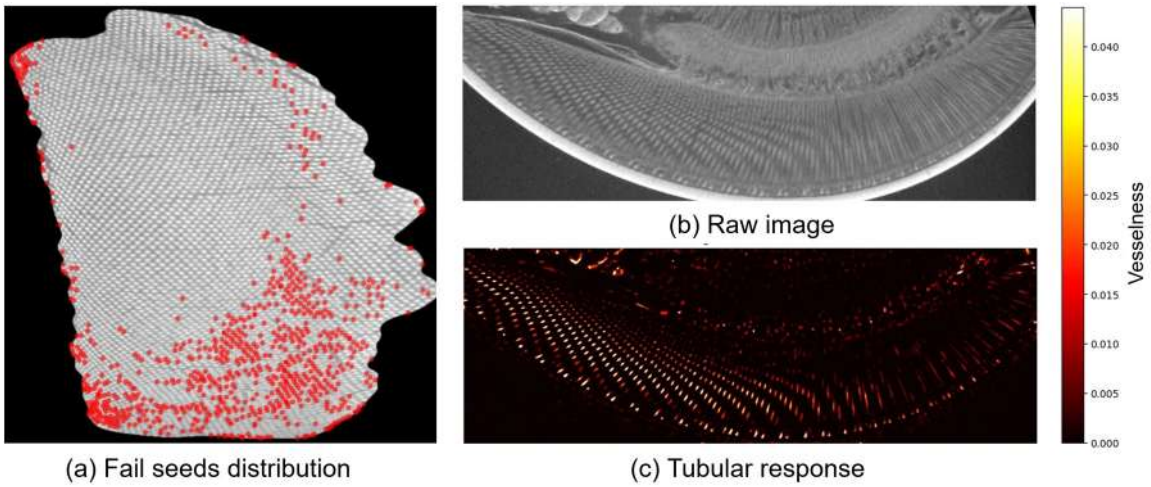

Fig. 7 Analysis of failure cases in ommatidial tube fitting. (a) Distribution of seed points for which tube fitting failed. (b) Raw slice image. (c) Tubular response obtained by applying the Frangi filter once to the region surrounding the raw slice.

Figure 7 examines cases in which a seed point exists but fails to produce a valid final ommatidial tube. Comparing Fig. 7(b) and Fig. 7(c) reveals that signal contrast varies across different regions of the compound eye. Because the Frangi filter response depends on local intensity statistics, ommatidia in low-contrast regions are less likely to survive binarization and subsequent tube fitting. This variation likely also contributes to the indentations observed along the edges of the compound eye mask (Fig. 3(b)), where the true eye morphology is not fully captured. Improving the robustness of both the compound eye segmentation module and the ommatidia detection module to variations in signal contrast is therefore an important direction for future refinement of this study.

The results support the per-ommatidium description motivated in the Introduction. Because the substrate normal and skew angle are measured locally, from a single ommatidium's optical axis and the surrounding compound eye surface, they remain available even where neighboring ommatidia are missed, as in the gaps observed in Figs. 5 and 6. Once the azimuthal direction of tilt is also resolved, these quantities would specify the sampling direction of each detector on a non-spherical substrate without propagating through a lattice of neighbors. Combined with local surface curvature, they may further link $\Delta\varphi$ to field of view and sensitivity, offering a path toward synthesizing non-spherical ommatidial arrays from target optical specifications and extending the geometric framework of Stavenga (1979) and Currea et al. (2023).

Finally, two further limitations should be noted. First, the skew angle computed here quantifies only the magnitude of deviation between the optical axis and the substrate normal; the azimuthal direction of this deviation, which is required to fully specify each ommatidium's sampling direction, remains to be incorporated. Second, a complete insect visual system typically relies on complementary interactions between the two compound eyes to support specific behaviors. As the present study analyzed only a single compound eye sample, the results cannot precisely orient the overall viewing direction of the visual system, nor can they yet be used to derive a set of optical parameters directly applicable to artificial compound eye design.

CONCLUSIONS

This study established an algorithm that recovers the substrate normal and sampling direction of individual ommatidia from micro-CT images without spherical projection, using the tube fitting module as its core component and the stable signal band localization module to restrict detection to regions of reliable signal. The algorithm detected 3,589 ommatidia, approximately two-thirds of the reported total, and reconstructed the skew angle and $\Delta\varphi$ distributions across the detected region of the compound eye, with skew angle increasing from the center toward the periphery.

The median $\Delta\varphi$ was 2.18°, slightly above the range obtained by Seidl and Kaiser (1981) using the pseudopupil method, and the Kagome-like configuration of adjacent-pair midpoints indicates that the detected ommatidia follow the regular hexagonal facet arrangement. By expressing each ommatidium through a locally measured substrate normal and skew angle, rather than through $\Delta\varphi$ propagated across a lattice of neighbors, this approach separates eye shape from sampling direction and provides design parameters for artificial compound eyes whose sampling distribution is not dictated by a spherical substrate.

Nonetheless, variation in signal contrast across different regions of the compound eye still caused some ommatidia to go undetected, and the present study analyzed only a single compound eye sample, limiting its ability to determine the overall viewing direction of the visual system or to derive a set of optical parameters directly applicable to artificial compound eye design. Future work will focus on improving the robustness of the compound eye segmentation and ommatidia detection modules to variations in signal contrast, resolving the azimuthal direction of skew in addition to its magnitude, quantifying $\Delta\varphi$ separately along each lattice direction to characterize horizontal and vertical sampling, extending the analysis to bilateral compound eye samples to establish overall viewing orientation, and relating the

skew angle to local surface curvature and $\Delta\varphi$ to jointly characterize field of view and sensitivity.

REFERENCES

Beaton, A. E., and J. W. Tukey. 1974. The fitting of power series, meaning polynomials, illustrated on band-spectroscopic data. *Technometrics* 16(2): 147-185.

Currea, J. P., Y. Sondhi, A. Y. Kawahara, and J. Theobald. 2023. Measuring compound eye optics with microscope and microCT images. *Communications Biology* 6(1): 246.

Frangi, A. F., W. J. Niessen, K. L. Vincken, and M. A. Viergever. 1998. Multiscale vessel enhancement filtering. In *International Conference on Medical Image Computing and Computer-Assisted Intervention*, 130-137. Berlin, Heidelberg: Springer Berlin Heidelberg.

Land, M. F. 1997. Visual acuity in insects. *Annual Review of Entomology* 42(1): 147-177.

Rigosi, E., S. D. Wiederman, and D. C. O'Carroll. 2017. Visual acuity of the honey bee retina and the limits for feature detection. *Scientific Reports* 7(1): 45972.

Seidl, R., and W. Kaiser. 1981. Visual field size, binocular domain and the ommatidial array of the compound eyes in worker honey bees. *Journal of Comparative Physiology* 143(1): 17-26.

Stavenga, D. G. 1979. Pseudopupils of compound eyes. In *Comparative Physiology and Evolution of Vision in Invertebrates: A: Invertebrate Photoreceptors*, 357-439. H. Autrum, ed. Berlin, Heidelberg: Springer Berlin Heidelberg.

Streinzer, M., A. Brockmann, N. Nagaraja, and J. Spaethe. 2013. Sex and caste-specific variation in compound eye morphology of five honeybee species. *PLoS ONE* 8(2): e57702.

Syôzi, I. 1951. Statistics of Kagomé lattice. *Progress of Theoretical Physics* 6(3): 306-308.

AI-P05

Proceedings of The 12th International Symposium on Machinery and Mechatronics for Agriculture and Biosystems Engineering (ISMAB 2026)
20-24 October 2026, Busan, Republic of Korea

EVALUATION OF eDNA ANALYSIS PIPELINES TO IDENTIFY FRESHWATER FISH SPECIES

Chao-You Sung[1], Zong-Yan Liu[2], Sheng-Kai Hsu[2], Jose A. Andres[3], Chien-Yu Chen[1*]

[1]Department of Biomechatronics Engineering, National Taiwan University, No. 1, Sec. 4, Roosevelt Road, Taipei 10617, Taiwan
[2]Institute for Genomic Diversity, Cornell University, Biotechnology Building, 526 Campus Road, Ithaca, NY 14853, USA
[3]IE School of Science and Technology, IE University, IE Tower, Paseo de la Castellana 259E, 28046 Madrid, Spain
*Corresponding Author-- Phone: +886-2-3366-5334, Email: chienyuchen@ntu.edu.tw

Abstract: Environmental DNA (eDNA) metabarcoding has become a powerful tool for aquatic biodiversity monitoring, yet the pipeline from raw sequencing reads to a final species list involves methodological decisions (primer trimming, denoising, and classifier choice) that strongly affect the outcome. Existing pipeline comparisons are largely constrained by the absence of an independent ground truth, and systematic evaluations for freshwater fish 12S rRNA data remain scarce. The objective of this study was to quantify the cost of three key pipeline decisions within a benchmarking framework grounded in independent ground truth. Two freshwater fish eDNA datasets sharing the MiFish-U primer set and the same ~170 bp hypervariable region of the 12S rRNA gene were analyzed: a Cornell dataset from New York State, USA (391 samples, Illumina NovaSeq, no ground truth) and Astorg 2025 (Illumina MiSeq, with an electrofishing ground truth of 19 species). Because both datasets share an identical marker and amplicon and differ only in sequencing platform and original pipeline, a single pipeline could be applied to both for a controlled comparison, allowing the ground-truth-free dataset to be validated indirectly. Precision, Recall, and F1 score were used to quantify the impact of (1) primer trimming strategy (fixed-length versus sequence-based), (2) the necessity of DADA2 denoising, evaluated against a no-denoising control, and (3) classifier choice among BLAST+, Kraken2, and QIIME2. Three findings emerged. First, the asymmetric MiFish-U primers leave residual primer sequence on the reverse reads under fixed-length trimming and generate numerous artifactual ASVs; sequence-based trimming reduced the ASV count from 21,169 to 5,902. Second, classifying reads without denoising inflated species counts through sequencing error, whereas DADA2 denoising consistently compressed Kraken2 species counts 59- to 160-fold across both datasets and raised the BLAST+ F1 from 0.356 to 0.667. Third, BLAST+ with alignment-length filtering achieved the highest observed F1 (0.667), similar to QIIME2 (0.647) and well above Kraken2 (0.326); under the short MiFish amplicon, MitoFish-derived reference database, and parameter settings tested here, Kraken2 produced more biogeographically implausible species assignments. Six strategies for raising Recall were additionally examined: database expansion and geographic priors were ineffective, and only DADA2 pseudo-pooling improved Recall while preserving Precision (F1 0.684). We therefore recommend sequence-based primer trimming, DADA2 denoising, and BLAST+ with alignment-length filtering as a defensible pipeline for MiFish eDNA studies, and conclude

that the Recall ceiling is set jointly by the precision trade-off inherent to denoising, the resolution limit of the marker gene, and the absence of eDNA signal, rather than by any single pipeline deficiency. These conclusions are conditional on the North American freshwater datasets and the single type of external ground truth tested here; generalization requires further datasets, ideally including mock communities of known composition.

Key Words: environmental DNA, metabarcoding, DADA2, MiFish, taxonomic classification

AI-P06

Proceedings of The 12th International Symposium on Machinery and Mechatronics for Agriculture and Biosystems Engineering (ISMAB 2026)
20-24 October 2026, Busan, Republic of Korea

PRELIMINARY STUDY ON IMPROVING THE COMPUTATIONAL EFFICIENCY OF A VIEWPOINT PROPOSAL SYSTEM FOR BUD DETECTION USING A REDUNDANT ROBOT ARM

Hiroyuki Terai[1,2*], Shinsuke Yasukawa[2]

[1]Department of Food and Agriculture Research, Local incorporated administrative agency Research Institute of Environment, Agriculture and Fisheries, Osaka Prefecture, Osaka, Japan
[2]Graduate School of Life Science and Systems Engineering, Kyushu Institute of Technology, Fukuoka, Japan
*Corresponding Author--, Email: TeraiH@knsk-osaka.jp

Abstract: To automate bud removal in greenhouse-grown eggplants, we investigated autonomous bud exploration using a robotic arm. In conventional surface-frontier-based viewpoint planning with a six-degree-of-freedom arm, verifying whether sampled viewpoints satisfy the arm's kinematic and motion constraints requires considerable computational time, particularly in environments with densely intermingled branches and leaves. Therefore, we conducted simulations to evaluate whether increasing arm redundancy to seven or eight degrees of freedom could reduce the computational time of validating sampled viewpoints. The results suggested that increased arm redundancy did not reduce this computational time and could instead increase the overall processing time. Future work should investigate alternative approaches based on the viewpoint-sampling characteristics identified in this study, such as suppressing, in real time, the sampling of viewpoints similar to those previously rejected.

Key Words: Next best view planning; Voxel based online exploration; Redundancy.

INTRODUCTION

Expanding the application of greenhouse robots to targets such as buds hidden by branches and leaves requires active exploration from multiple viewpoints. As the agricultural workforce continues to decline, greenhouse production requires the automation of diverse management tasks that have traditionally depended on manual labor [1]. Consequently, expanding the range of tasks that robots can perform has become increasingly important. This study focuses on bud removal in eggplants as one such task. In eggplants, branches and leaves tend to become densely intertwined, causing buds to be hidden behind them and resulting in missed detections when observations are made from a single position. To automate bud removal, a camera-mounted robotic arm must explore hidden buds by moving around the plant and observing it from various angles and record their three-dimensional positions on a map. Accordingly, this study focuses on viewpoint planning, which sequentially determines where the next observation should be made.

A major challenge in conventional surface-frontier-based viewpoint planning is the computational time required to reject infeasible viewpoints and propose alternatives, even when the viewpoints are potentially effective for observation. A surface frontier is a previously observed surface of an object adjacent to an unobserved region (Figure 1). By selecting viewpoints that can observe a large portion of this, the unobserved parts of the plant can be explored sequentially [3, 4]. However, even a viewpoint with high observation value may not be realizable by the robotic arm, and a collision-free path from the current position may not exist. Therefore, the arm configuration and the feasibility of the motion path must be checked for each candidate viewpoint, and infeasible candidates must be rejected. In environments with densely intermingled branches and leaves, this verification and resampling process is repeated extensively, increasing the computational time [4].

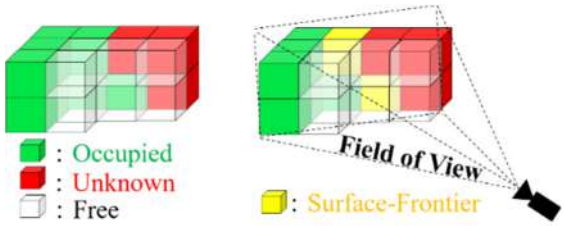

Fig.1 Voxel-based 3D map occupancy (3 states) and Concept of surface frontiers.

One possible way to reduce the rejection of viewpoint candidates is to increase the number of joints in the robotic arm. Increasing the number of joints provides more options for the arm configurations that can realize the same observation viewpoint, potentially enabling some candidates that would be rejected by a six-degree-of-freedom arm to be executed. On the other hand, increasing the number of joints makes the computation of arm poses and motion paths more complex. Therefore, in surface-frontier-based viewpoint planning, it is necessary to evaluate whether the reduction in rejected candidates achieved by increasing the degrees of freedom outweighs the additional computational load associated with pose computation and path generation.

This study compares six- to eight-degree-of-freedom robotic arms to determine the extent to which increased degrees of freedom can reduce the rejection of viewpoint candidates and improve the computational efficiency of viewpoint planning. The same viewpoint-planning procedure was applied to each arm in a simulation environment, and the time required to validate viewpoint candidates and the behavior during exploration were compared. In addition, rejected viewpoints were visualized to investigate the factors limiting the improvement achieved through arm redundancy. These results were then used to clarify the extent to which increasing arm degrees of freedom can improve performance and the remaining challenges on the viewpoint-proposal side.

MATERIALS AND METHODS

Overall Architecture of the Viewpoint Path Planning System

The viewpoint-planning system used in this study consists of three modules: Sensing, 3D Representation, and View Planning (Figure 2).

The Sensing module generates two types of images and outputs corresponding point clouds to separately record the target buds and the occupancy states of the plant and its surroundings for viewpoint planning at different resolutions. The first image is generated by applying instance

segmentation with YOLOv8-seg to buds located within 0.3 m of the camera in the captured RGB image, thereby generating point clouds of buds within a specified distance. The second image is generated by truncating distances beyond 0.5 m to record the structure and spatial occupancy up to a specified maximum distance.

The 3D Representation module uses two voxel maps based on truncated signed distance fields. Buds are maintained at high resolution, whereas the structures and surrounding space used for viewpoint planning are managed at low resolution. The two maps are updated differently. The Buds Map updates only the occupied regions corresponding to buds, whereas the Structure Map updates voxels along rays from the camera to either an object or the truncated maximum distance. Buds are counted from the clusters generated by Density-Based Spatial Clustering of Applications with Noise.

The View Planning module validates sampled viewpoints, generates feasible paths, and selects the next destination based on information gain and path length. Pose feasibility is evaluated using the Levenberg–Marquardt algorithm, while collision-free paths are verified with RRTConnect. Surface frontiers and multidirectional ray casting are used to calculate information gain and select the optimal viewing direction. Online-RRT*, proposed by Schmid et al. [2], then determines the path by balancing information gain and path length. After each observation, map and information gain are updated, and the tree is rewired when necessary.

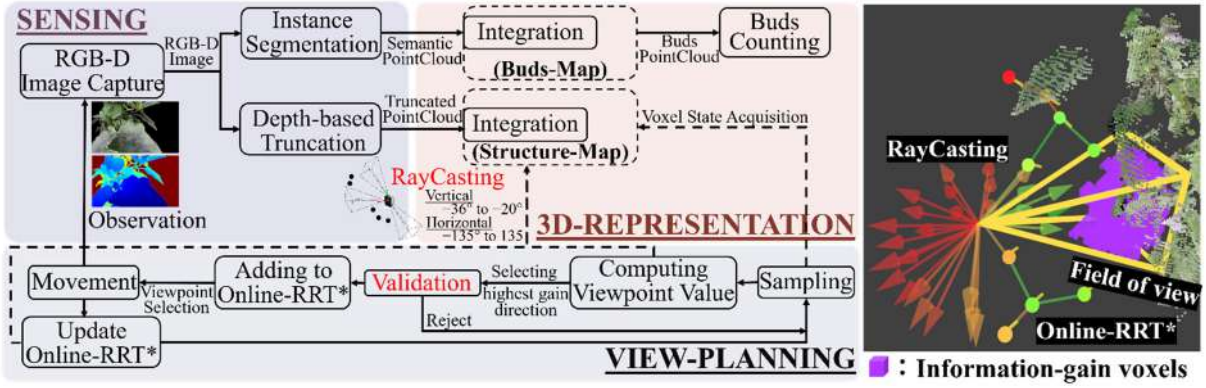

Fig.2 Processing Flow and Overview Diagram of Viewpoint Path Planning System

Surface Frontier-based Exploration Approach (Information Gain and Viewpoint Sampling Strategy)

The viewpoint-sampling strategy and information-gain calculation determine the camera position and orientation for detecting buds within the canopy. Following Menon et al. [5], viewpoints were sampled by randomly selecting free-space regions around surface frontiers within the field of view of each Online-RRT* node, provided that no occupied region was present within a diameter of 0.1 m. The surface-frontier concept proposed by Yamauchi et al. [3] was used to calculate information gain (Fig. 1). For each viewpoint, surface-frontier voxels were identified as Unknown voxels visible from the camera and having at least one Occupied voxel among their 26 neighboring voxels. The total number of these voxels was used as the viewpoint's information gain (Equation (1)). The field of view was defined by a ray-casting distance of 0.5 m, horizontal and vertical viewing angles of 28°, and a resolution of 10 × 10.

$$Gain_{View\ point} = \sum_{FoV} Gain_{\text{Surface Frontier}} \quad (1)$$

where:

$Gain_{\text{Surface Frontier}} \in \mathbb{R}_{>0}$ (-)

Experimental method

This experiment evaluated the extent to which increasing arm degrees of freedom can reduce rejected viewpoint candidates and the associated computation time in surface-frontier-based viewpoint planning.

Simulation environment

The simulation was conducted by placing a plant model in a game engine. A late-growth-stage eggplant model with a total length of 1.2 m was used [6], placed in Unreal Engine with collision surfaces defined. The exploration space was centered on the plant and measured 0.8 m in depth, 1.0 m in width, and 1.2 m in height (Figure 3). The simulation was executed on Ryzen 9 CPU and an RTX 4090 GPU. The GPU was used for rendering in UE4.

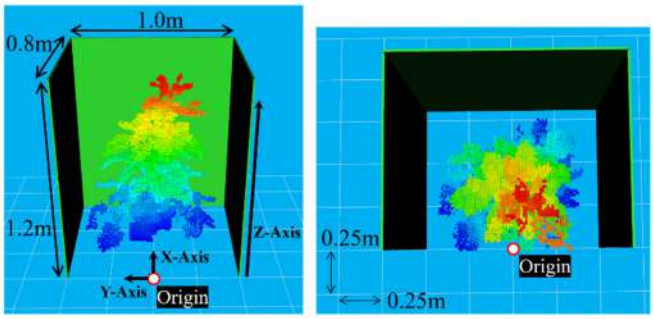

Fig.3 Exploration Space around the Plant Body
(Left: Front View; Right: Top View)

Robot arm configuration

The robot-arm configurations compared in this study comprised six-, seven-, and eight-degree-of-freedom arms (Figure 4). The movable range of the pedestal of each arm was set to -0.2-0.8 m along the X-axis, -0.6-0.6 m along the Y-axis, and 0-1.5 m along the Z-axis.

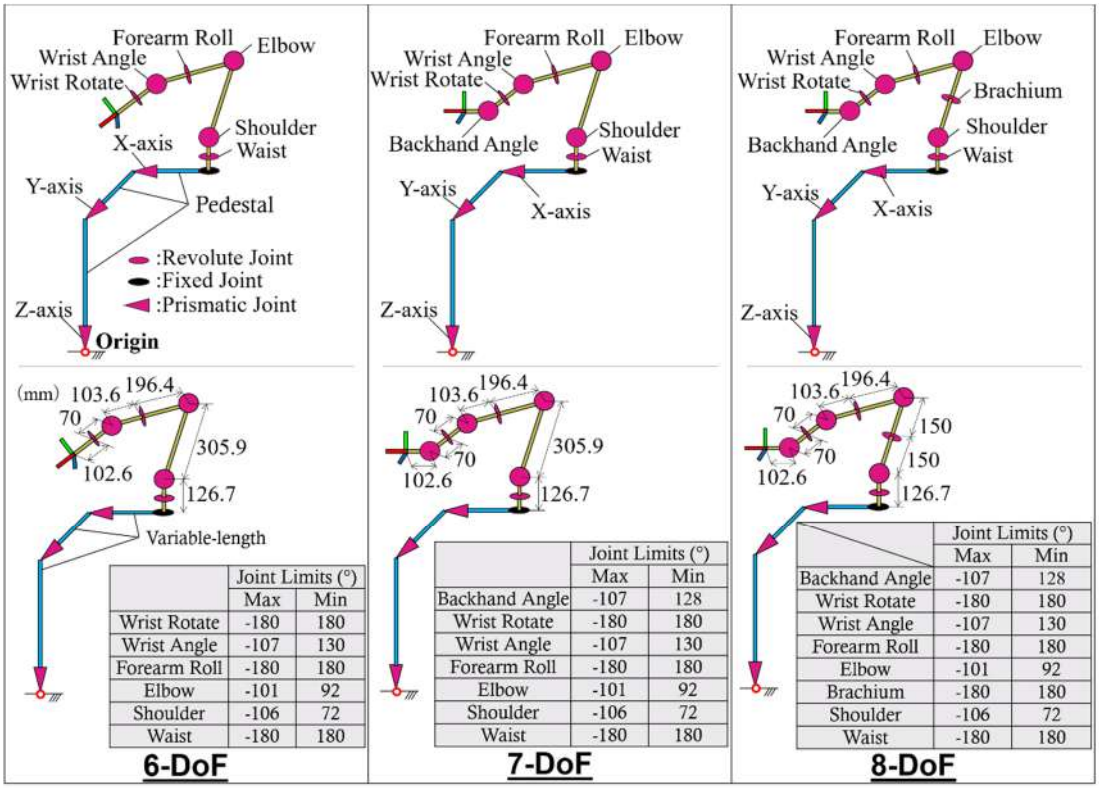

	Joint Limits (°)	
	Max	Min
Wrist Rotate	-180	180
Wrist Angle	-107	130
Forearm Roll	-180	180
Elbow	-101	92
Shoulder	-106	72
Waist	-180	180

	Joint Limits (°)	
	Max	Min
Backhand Angle	-107	128
Wrist Rotate	-180	180
Wrist Angle	-107	130
Forearm Roll	-180	180
Elbow	-101	92
Shoulder	-106	72
Waist	-180	180

	Joint Limits (°)	
	Max	Min
Backhand Angle	-107	128
Wrist Rotate	-180	180
Wrist Angle	-107	130
Forearm Roll	-180	180
Elbow	-101	92
Brachium	-180	180
Shoulder	-106	72
Waist	-180	180

Fig.4 Configuration of robot arm joints (Top) and length (Bottom).

Experimental method and Evaluation metrics

For a single eggplant plant, five independent trials were conducted for each arm configuration. At the beginning of each exploration, initial observations were obtained from eight viewpoints located in passage spaces where the arm did not contact the plant. The evaluation metrics were bud-detection precision and recall, the number of viewpoints used during exploration, total path length (the sum of the straight-line distances between consecutive viewpoints), collision rate, processing time per observation, and map-generation time.

RESULTS & DISCUSSION

The effect of increasing arm redundancy to reduce rejected viewpoint candidates was limited. As shown in Table 2, viewpoint validation required approximately 1.7–1.8 s for all arm configurations, and the number of rejected candidates remained approximately 17. Thus, no improvement was observed with increased arm redundancy. The validation process still required substantial computation time compared with voxel-map integration, which took approximately 0.5 s, and the total processing time per observation cycle (Table 2). Moreover, redundant arms tended to require longer movement times between viewpoints, increasing them by approximately 1–2 s (Table 2). As shown in Table 1, no differences in bud-detection accuracy were observed among all arm configurations.

The limited reduction in rejected candidates achieved by increasing arm redundancy was likely strongly influenced by the surface-frontier-based viewpoint-sampling strategy and information-gain design. Figure 5 shows the executed exploration path (red) and viewpoints rejected due to arm constraints (blue) of the eight-degree-of-freedom arm. Many viewpoints sampled based on surface frontiers were located deep inside the plant canopy, where the arm could not physically execute them. In addition, numerous viewpoints near the viewpoints used in the exploration path were rejected because of the viewing direction and other arm constraints.

Table 1 Bud exploration performance.

	Average					Standard deviation	
	Total view points	Total path length (m)	Collision rate (%)	Bud detection		Bud detection	
				Precision (%)	Recall (%)	Precision	Recall (%)
6-DoF	110	17.88	**0.5%**	89.2%	50.1%	4.7%	4.0%
7-DoF	110	17.98	**0.5%**	**91.1%**	**51.7%**	**4.1%**	3.9%
8-DoF	110	**17.87**	0.7%	**91.1%**	47.9%	5.1%	**1.5%**

Table 2 Processing time per observation cycle in View-Planning.

	Average							
	Viewpoint Sampling & Validation New-Viewpoint			Computing Viewpoint Value (s)	Adding to Online-RRT* (s)	Movement (s)	Update Online-RRT* (s)	Total (s)
	Total time (s)	Validation						
		Trial	Time (s)					
6-DoF	1.872	(17.4)	(1.789)	**0.018**	**0.077**	**2.348**	0.154	**4.469**
7-DoF	**1.814**	**(16.9)**	**(1.740)**	0.018	0.081	3.025	0.149	5.087
8-DoF	1.847	(17.3)	(1.773)	0.018	0.095	4.140	**0.148**	6.249

The objective of this study was to determine whether the reduction in candidate rejection achieved by increasing arm degrees of freedom would outweigh the additional computational load associated with pose calculation and path generation, and to clarify the extent of improvement achievable through increased arm degrees of freedom and the remaining challenges in viewpoint proposal.

In surface-frontier-based viewpoint planning, many viewpoints were sampled from viewing directions or regions that could not benefit from the increased pose and path options provided by arm redundancy. Rather, the expanded search space for joint-angle solutions may have increased the complexity of RRTConnect path generation, thereby prolonging movement time.

The results suggest that improving the computation time required for rejecting and resampling viewpoint candidates should be addressed through improvements to the viewpoint proposal strategy rather than through arm redundancy. As indicated by the circles in Fig. 5, several regions within the exploration space were observed where rejected viewpoints were concentrated. This suggests that computation time could be reduced by suppressing proposals from these regions during sampling, before the computationally expensive rejection and resampling process. In future work, suppressing similar sampling based on information about rejected viewpoints accumulated in real time will be important for accelerating the overall processing.

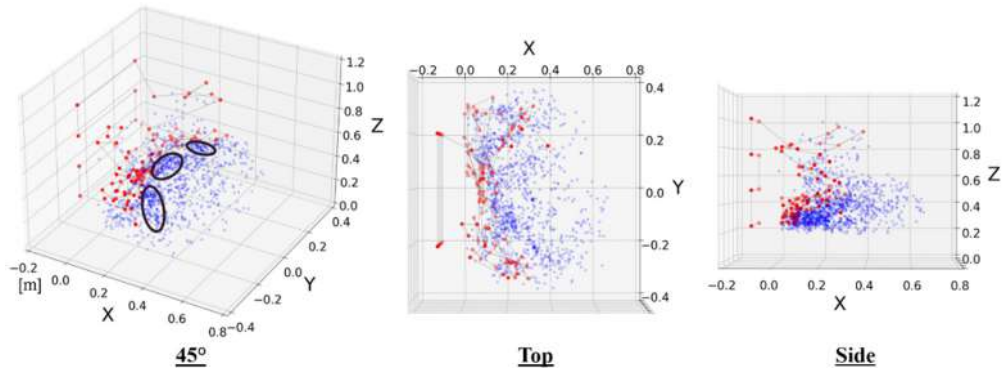

Fig.5 The exploration path (red) proposed by the surface frontier-based viewpoint planning algorithm and viewpoints (blue) rejected during sampling.

ACKNOWLEDGEMENTS

This work was supported by JSPS KAKENHI Grant Number JP 23K05482.

REFERENCES

[1] Ministry of Agriculture, Forestry and Fisheries. 2026. Situation surrounding Smart Agriculture. Available at: https://www.maff.go.jp/j/kanbo/smart/#h_3629484211717981 205741. Accessed 31 August 2026.

[2] Lukas Schmid, Michael Pantic, Raghav Khanna, Lionel Ott, Roland Siegwart, and Juan Nieto. An Efficient Sampling-based Method for Online Informative Path Planning in Unknown Environments. IEEE Robotics and Automation Letters, vol. 5, no. 2, pp. 1500-1507, April 2020.

[3] Yamauchi, B. A frontier-based approach for autonomous exploration. Proceedings of the IEEE International Symposium on Computational Intelligence in Robotics and Automation (CIRA), 1997, pp. 146-151, doi:10.1109/CIRA.1997.625325.

[4] Hiroyuki TERAI, Shinsuke YASUKAWA. An Efficient Viewpoint Planning Method with a Selective-Update Multi-Resolution Voxel Map -Toward Online Exploration of Plant Buds-. Robotics and Mechatronics Conference 2026 (ROBOMECH2026), July 2026.

[5] Rohit Menon; Tobias Zaenker; Nils Dengler; Maren Bennewitz. NBV-SC: Next Best View Planning Based on Shape Completion for Fruit Mapping and Reconstruction. 2023 IEEE/RSJ International Conference on Intelligent Robots and Systems (IROS).

[6] Hiroyuki TERAI, Shinsuke YASUKAWA. 3D Reconstruction of Plant Structures Covered by Leaves—Toward a Simulator to Assist Agricultural Automation—. JSME The 8th International Conference on Advanced Mechatronics (ICAM 2024).

AI-P07

Proceedings of The 12th International Symposium on Machinery and Mechatronics for Agriculture and Biosystems Engineering (ISMAB 2026)
20-24 October 2026, Busan, Republic of Korea

COMPARATIVE ANALYSIS OF INSTANCE SEGMENTATION MODELS FOR NET SEGMENTATION IN MELONS

Dong-Han Lee[1], Seongmin Lee[1], Jeong Gyun Kang[1], Jun-Woo Park[1]
Ho-seung Jang[1], Jayeong Paek[1*]

[1]Division of Agricultural Robot, Department of Agricultural Engineering,
National Institute of Agricultural Sciences, Jeonju, Republic of Korea
*Corresponding Author-- Voice: +82-63-238-4290, Email: jayeong0919@korea.kr

Abstract: Melon (*Cucumis melo* L.) quality grading is a critical process in the agricultural industry, as the density and uniformity of surface netting directly determine its premium market value. While manual visual inspection remains dominant in commercial sorting lines, it is highly subjective and labor-intensive. To establish an objective and automated grading system, this study systematically compared the performance of four state-of-the-art instance segmentation models (YOLO26-seg, Mask R-CNN, Cascade Mask R-CNN, and SOLOv2) specifically for segmenting the skin region of melons. A total of 120 images of 'Megaton' melons were collected under natural greenhouse lighting using an Intel RealSense D405 depth camera. To standardize the region of interest (ROI), 250×250 pixel square patches were automatically cropped from the center of YOLO11-detected melon bounding boxes, and the skin netting areas were annotated in polygon format using Roboflow. The dataset was partitioned into 100 images for training, 10 for validation, and 10 for testing.The experimental results demonstrated a distinct trade-off between segmentation accuracy and computational speed. Cascade Mask R-CNN achieved the highest spatial localization accuracy with a Mean Average Precision (mAP) of 0.9460 at mAP50 and 0.8480 at mAP75, which is considered to be due to its multi-stage detection head design, although it exhibited the lowest throughput at 12.55 Frames Per Second (FPS). Mask R-CNN demonstrated the second-best performance (mAP50: 0.9340, mAP75: 0.8210, 18.42 FPS), which is thought to be driven by its pixel-level RoIAlign alignment. SOLOv2 showed moderate precision (mAP50: 0.7700, mAP75: 0.4280, 18.04 FPS). Conversely, YOLO26-seg recorded the lowest accuracy (mAP50: 0.5080, mAP75: 0.2553) under limited-data constraints, but delivered outstanding real-time throughput at 52.85 FPS via its end-to-end NMS-free architecture.Based on these findings, Cascade Mask R-CNN and Mask R-CNN are judged to be highly suitable for high-precision, non-destructive quality inspection and netting density analysis systems. Meanwhile, YOLO26-seg is considered a viable candidate for high-speed real-time sorting lines, provided that its accuracy is augmented through future dataset expansion. These results are expected to contribute to the realization of fully automated and objective crop grading systems in smart farm environments.

Key Words: Melon, Instance segmentation, Deep learning

INTRODUCTION

Melon (*Cucumis melo* L.) is a highly valuable horticultural crop appreciated worldwide for its unique flavor, aroma, and premium commercial appeal. During the late developmental stages of melon, rapid internal expansion of the pulp exerts pressure on the outer rind, causing micro-cracks to form across the skin. These fissures subsequently heal with suberized cork tissue, eventually forming a complex and elevated network pattern known as netting (Akiba et al., 2022).

The physical characteristics of this netting—such as its density, thickness, uniformity, and overall coverage—serve as critical visual indicators of the fruit's internal quality, sweetness, and maturity, directly determining consumer preference and market grading standards in the agricultural sector (Yoon et al., 2023; Ho et al., 2023).

Precise evaluation of netting quality for sorting and grading is essential to increase agricultural income and standardize crop quality. Currently, however, net quality grading is predominantly reliant on manual visual inspection by experienced workers. This approach is not only time-consuming but also highly susceptible to errors caused by the subjectivity of evaluators and variations in ambient lighting, limiting the objectivity and consistency of the grading process. To overcome these limitations, research on automating net quality grading using computer vision technology is being actively pursued (Yoon et al., 2023).

Conventional approaches have typically relied on techniques such as color space conversion and thresholding to segment the netting from the background rind (Yoon et al., 2023). However, these traditional image processing algorithms are highly sensitive to variations in ambient lighting, shadows, and complex surface geometries, which can result in unstable segmentation and high error (Dias et al., 2018; Mavridou et al., 2019).

To overcome these limitations, deep learning-based computer vision technologies have been introduced to the field of agricultural quality inspection. Deep learning is a subfield of machine learning that utilizes multi-layered artificial neural networks to automatically learn high-level, abstract feature representations directly from raw pixel data, eliminating the need for manual feature extraction. In image segmentation tasks, these deep neural networks exhibit superior robustness against complex backgrounds, non-uniform illumination, and various noise sources, enabling precise and highly adaptive pixel-level segmentation of complex and irregular agricultural targets (Kamilaris et al., 2018).

Various deep learning architectures for instance segmentation offer distinct technical advantages. Mask R-CNN is a conceptually simple and flexible instance segmentation framework that extends Faster R-CNN by adding a branch for predicting segmentation masks in parallel with the existing classification and bounding box regression branches (He et al., 2017). Unlike traditional methods, this model introduces the RoIAlign layer, which eliminates the coarse spatial quantization errors of RoIPool by utilizing bilinear interpolation to preserve exact pixel-level spatial coordinates, thereby significantly improving mask prediction accuracy. Furthermore, it decouples mask prediction from class classification by generating binary masks for each class independently without class competition, relying on a separate classification branch for the final category assignment. Cascade Mask R-CNN is a multi-stage extension of the two-stage R-CNN framework designed to address the "paradox of high-quality detection,"

where detectors trained with high Intersection-over-Union (IoU) thresholds suffer from overfitting and inference-time quality mismatches (Cai and Vasconcelos, 2018). This model sequentially trains a series of detection heads with progressively increasing IoU thresholds. Here, bounding box regression acts as a resampling mechanism that adjusts the output distribution of the previous stage, progressively improving the quality of proposal boxes for the subsequent detector and mitigating overfitting. This multi-stage framework is extended to instance segmentation (Cascade Mask R-CNN) by integrating parallel mask heads into the cascade stages, enhancing mask segmentation performance by either placing a mask head at the final stage or adding mask branches at every stage. SOLOv2 is a direct, box-free, and anchor-free single-stage instance segmentation framework that inherits the SOLO principle of "segmenting objects by locations" (Wang et al., 2020). To maximize efficiency, it introduces a dynamic mask representation that decouples mask generation into mask kernel prediction (conditioned on grid cell locations) and unified mask feature learning, thereby yielding more precise boundary masks. Additionally, it proposes Matrix NMS, which replaces traditional sequential NMS with parallel matrix operations to perform mask non-maximum suppression in one shot, drastically reducing post-processing latency. Ultralytics YOLO26-seg is a unified real-time vision model built on the YOLO11 lineage, optimized for efficient deployment and real-time edge processing (Jocher et al., 2026). Architecturally, this model adopts a dual-head design comprising a default one-to-one head that ensures native, NMS-free end-to-end inference, and an optional one-to-many head that supports standard NMS decoding. It also completely removes Distribution Focal Loss (DFL) to streamline the regression head, thereby reducing parameters and expanding the regression range for large objects. For instance segmentation, it retains a lightweight prototype-coefficient formulation while incorporating a multi-scale proto module that integrates multi-scale pyramid features, along with a training-only auxiliary semantic segmentation loss to enhance mask quality.

Therefore, the objective of this study is to systematically compare the performance of YOLO26-seg, Mask R-CNN, Cascade Mask R-CNN, and SOLOv2 in segmenting the skin region of melons to establish an automated net quality evaluation system. To facilitate consistent feature extraction, a square region of interest (ROI) was cropped from the center of each melon image, and the skin area was labeled in a polygon format. A total of 120 labeled images were utilized, partitioned into 100 images for training, 10 for validation, and 10 for testing. This study systematically evaluates each model's segmentation accuracy and computational efficiency under limited-data constraints.

MATERIALS AND METHODS

Image Acquisition and Dataset Preparation

Melon (*Cucumis melo* L.) images were collected at the Goheung Smart Farm Innovation Valley in Jeollanam-do, South Korea, under natural greenhouse lighting conditions. Image acquisition was performed using a depth camera (RealSense D405, Intel, USA). To systematically extract a consistent region of interest (ROI) focusing on the melon skin netting, a two-step automated preprocessing pipeline was implemented. First, a dedicated melon fruit detection model trained on the YOLO11 architecture was deployed to predict the bounding boxes of individual melons. Second, a square ROI patch of size 250×250 pixels was cropped from the geometric center of each predicted bounding box. Within the cropped ROI, polygon annotation of the melon skin region was performed using the Roboflow platform. A total of 120 high-quality annotated images were prepared, which were divided into 100 images for training, 10 for validation, and

10 for testing.

Model Training and Experimental Setup

All four instance segmentation models (YOLO26-seg, Mask R-CNN, Cascade Mask R-CNN, and SOLOv2) were implemented and evaluated on a workstation running the Windows 10 operating system with Python (v3.10.20). YOLO26-seg was executed using the Ultralytics framework (v8.4.127), whereas Mask R-CNN, Cascade Mask R-CNN, and SOLOv2 were implemented using the MMDetection library (v3.3.0) supported by MMCV (v2.1.0) and MMEngine (v0.10.7). Model training and inference were accelerated via PyTorch (v2.1.2+cu118) and CUDA 11.8 on an NVIDIA GeForce RTX 3080 Laptop GPU. Supporting packages, including NumPy (v1.26.4) and OpenCV (v5.0.0), were utilized for high-dimensional image processing and array computations. To overcome the limitations of the small-scale dataset and prevent overfitting, transfer learning was utilized. For YOLO26-seg, the model was initialized with the pre-trained weights of the yolo26m-seg model. For Mask R-CNN, Cascade Mask R-CNN, and SOLOv2, the model backbones were initialized with ResNet-50 pre-trained weights, all of which were learned on the Microsoft Common Objects in Context (COCO) dataset. The training hyperparameters for each model were configured as follows: YOLO26-seg was trained for 1,000 epochs with a batch size of 16, utilizing the AdamW optimizer with an initial learning rate of 0.01. Mask R-CNN was trained for 12 epochs with a batch size of 2, utilizing the Stochastic Gradient Descent (SGD) optimizer with an initial learning rate of 0.02. Cascade Mask R-CNN was trained for 12 epochs with a batch size of 2, utilizing the SGD optimizer with an initial learning rate of 0.02. SOLOv2 was trained for 240 epochs with a batch size of 2, utilizing the SGD optimizer with an initial learning rate of 0.01.

RESULTS & DISCUSSION

Analysis of Computational Efficiency and Trade-offs

The quantitative evaluation of YOLO26-seg, Mask R-CNN, Cascade Mask R-CNN, and SOLOv2 was conducted using 120 cropped images (100 for training, 10 for validation, and 10 for testing) of melon skin regions. To systematically evaluate both segmentation accuracy and real-time feasibility, the Mean Average Precision at IoU thresholds of 0.50 (mAP50) and 0.75 (mAP75) was calculated alongside the inference speed in frames per second (FPS). The comprehensive performance metrics are summarized in Table 1.

Table 1 Performance comparision of instance segmentation models in melon skin regions

Model	mAP50	mAP75	FPS
YOLO26-seg	0.5080	0.2553	52.85
Mask R-CNN	0.9340	0.8210	18.42
Cascade Mask R-CNN	0.9460	0.8480	12.55
SOLOv2	0.7700	0.4280	18.04

Among the evaluated models, Cascade Mask R-CNN achieved the highest segmentation accuracy with an mAP50 of 0.9460 and an mAP75 of 0.8480. This superior performance is considered to be attributed to its multi-stage cascade architecture, which utilizes a sequence

of detection heads trained with progressively increasing IoU thresholds (Cai and Vasconcelos, 2018). The stage-by-stage resampling mechanism is judged to have successfully refined the complex and irregular boundaries of the melon netting, maintaining high localization quality even under strict overlap criteria (mAP75).

Mask R-CNN demonstrated the second-highest accuracy, yielding an mAP50 of 0.9340 and an mAP75 of 0.8210. The high spatial accuracy of Mask R-CNN is thought to be primarily driven by its RoIAlign layer, which uses bilinear interpolation to avoid coordinate quantization errors, thereby preserving precise pixel-to-pixel alignment between the input features and the predicted masks (He et al., 2017).

SOLOv2 exhibited moderate segmentation performance, achieving an mAP50 of 0.7700 and an mAP75 of 0.4280. While its location-based dynamic mask generation effectively localized larger structural patterns, it appears to have struggled to capture the ultra-fine, interlaced textures of the melon netting at stricter IoU thresholds, which is considered to have led to a substantial drop of 44.4% in mAP75 compared to mAP50 (Wang et al., 2020).

YOLO26-seg showed the lowest segmentation precision on this specific, limited-data dataset, with an mAP50 of 0.5080 and an mAP75 of 0.2553. Although YOLO26-seg employs an advanced dual-head design to optimize speed, the complete removal of Distribution Focal Loss (DFL) and the reduced regression capacity under highly restricted dataset sizes (100 training images) are considered to have limited its ability to converge on the highly complex, micro-scale features of the netting cork tissues (Jocher et al., 2026).

Analysis of Computational Efficiency and Trade-offs

In contrast to the accuracy trends, YOLO26-seg demonstrated outstanding computational efficiency, achieving an inference speed of 52.85 FPS, which is more than double the speed of any other evaluated model. This superior real-time capability is believed to be enabled by its native, end-to-end NMS-free inference architecture, which bypasses the post-processing bottlenecks typical of traditional anchor-based detectors (Jocher et al., 2026).

Mask R-CNN and SOLOv2 recorded comparable inference speeds of 18.42 FPS and 18.04 FPS, respectively. While SOLOv2 benefits from Matrix NMS to accelerate mask suppression via parallel matrix operations (Wang et al., 2020), its dynamic kernel convolution overhead is thought to have rendered its overall speed similar to that of the two-stage Mask R-CNN. Cascade Mask R-CNN recorded the lowest throughput at 12.55 FPS, which is considered to be a direct consequence of the sequential forward passes required through its multiple cascaded regression heads (Cai and Vasconcelos, 2018).

In conclusion, a clear trade-off between segmentation accuracy and inference speed appears to exist in the experimental results. For high-throughput industrial grading lines where real-time processing is paramount, YOLO26-seg is considered to serve as a viable option, provided that data augmentation or architectural scaling is applied to bolster accuracy. However, for applications requiring high-precision non-destructive netting density and uniformity analysis where localization accuracy is critical, Cascade Mask R-CNN and Mask R-CNN are judged to be the most suitable choices due to their superior pixel-level alignment and boundary definition.

CONCLUSIONS

This study systematically compared the performance of four state-of-the-art instance segmentation models—YOLO26-seg, Mask R-CNN, Cascade Mask R-CNN, and SOLOv2—specifically for segmenting the skin region of melons (*Cucumis melo* L.). The experimental results revealed a distinct trade-off between segmentation accuracy and computational efficiency. Cascade Mask R-CNN achieved the highest accuracy with an mAP50 of 0.9460 and an mAP75 of 0.8480, which is considered to be due to its multi-stage refinement process, though it exhibited the lowest throughput at 12.55 FPS. Conversely, YOLO26-seg demonstrated outstanding real-time feasibility at 52.85 FPS, despite displaying the lowest segmentation precision with an mAP50 of 0.5080 under the limited-data constraints of 120 images.

Consequently, for applications requiring high-precision, non-destructive quality analysis of netting density and uniformity, Cascade Mask R-CNN and Mask R-CNN are judged to be the most suitable choices. For high-throughput real-time sorting systems where execution speed is paramount, YOLO26-seg is considered to serve as a viable candidate, provided that further dataset expansion or augmentation is implemented to bolster accuracy. Future research is suggested to focus on deploying these models on edge-computing devices in practical smart farm sorting environments and correlating the segmented netting physical characteristics with actual fruit internal quality indices.

ACKNOWLEDGEMENTS

This study was supported by 2026 the R&D program(Project Number : RS-2025-02219360) between Rural Development Administration and Ministry of Agriculture, Food and Rural Affairs and Ministry of Science and ICT, Republic of Korea

REFERENCES

Akiba, Y., A. Ishibashi, M. Sato, and H. Shima. 2022. Empirical rule of fruit rind fragmentation in muskmelon netting. Journal of the Physical Society of Japan 91(10): 104801.

Cai, Z., and N. Vasconcelos. 2018. Cascade R-CNN: Delving into high quality object detection. In Proc. IEEE Conf. on Computer Vision and Pattern Recognition (CVPR), 6154-6162.

Dias, P. A., A. Tabb, and H. Medeiros. 2018. Apple flower detection using deep convolutional networks. Computers in Industry 99: 17-28. https://doi.org/10.1016/j.compind.2018.03.010

He, K., G. Gkioxari, P. Dollár, and R. Girshick. 2017. Mask R-CNN. In Proc. IEEE International Conference on Computer Vision (ICCV), 2961-2969.

Ho, T.-T., T. Hoang, K.-D. Tran, Y. Huang, and N. Q. K. Le. 2023. Non-destructive classification of melon sweetness levels using segmented rind properties based on semantic segmentation models. Journal of Food Measurement and Characterization 17(6): 5913-5928.

Jocher, G., J. Qiu, M. Liu, S. Lyu, F. C. Akyon, and M. E. Kalfaoglu. 2026. Ultralytics YOLO26: Unified real-time end-to-end vision models. arXiv preprint arXiv:2606.03748.

Kamilaris, A., and F. X. Prenafeta-Boldú. 2018. Deep learning in agriculture: A survey. Computers and Electronics in Agriculture 147: 70-90.

Mavridou, E., E. Vrochidou, G. A. Papakostas, T. Pachidis, and V. G. Kaburlasos. 2019. Machine vision systems in precision agriculture for crop farming. Journal of Imaging 5(12): 89.

Wang, X., R. Zhang, T. Kong, L. Li, and C. Shen. 2020. SOLOv2: Dynamic and fast instance segmentation. In Proc. Advances in Neural Information Processing Systems (NeurIPS 2020), 33: 17721-17732.

Yoon, S., M. Shin, J. H. Kim, J. W. Bang, H. J. Jeong, and T. I. Ahn. 2023. Analysis of the relationship between melon fruit growth and net quality using computer vision and fruit modeling. Journal of Bio-Environment Control 32(4): 456-465.

AI-P08

Proceedings of The 12th International Symposium on Machinery and Mechatronics for Agriculture and Biosystems Engineering (ISMAB 2026)
20-24 October 2026, Busan, Republic of Korea

IMPROVING ROBUSTNESS OF YOLO11-BASED MELON DETECTION USING OCCLUSION AND ILLUMINATION DATA AUGMENTATION

Seongho Lee[1], Donghan Lee[1], Jayeong Paek[1], Jeong Gyun Kang[1], Jun-Woo Park[1] Ho-seung Jang[1], Manjung Kim[1*]

[1]Department of Agricultural Engineering Division of Agricultural Robot, National Institute of Agricultural Sciences, Jeonju, Korea
*Corresponding Author-- Voice: +82-63-238-4059, Email: kmj0403@korea.kr

Abstract: Fruit detection in greenhouse environments can be affected by partial occlusion and illumination variation, which may reduce the reliability of vision-based crop monitoring systems. This study evaluated whether targeted data augmentation could improve the robustness of YOLO11-based melon detection under such challenging conditions. A total of 1,060 greenhouse RGB images were manually annotated for a single melon class and divided into training, validation, and test sets at a ratio of 7:2:1. A baseline YOLO11n model was trained using only the original training images, whereas an augmented model was trained using the same images together with artificially generated occlusion, brightness variation, and combined augmentation images. Different augmentation severity levels were used for training and evaluation to assess generalization to unseen conditions. Under the overall robustness test conditions, the augmented model improved mAP@0.5 from 0.6446 to 0.9839 and mAP@0.5:0.95 from 0.5661 to 0.8909. The improvement was particularly evident under occlusion. As the occlusion ratio increased from 40% to 85%, the baseline mAP@0.5 decreased from 0.5964 to 0.1799, whereas the augmented model maintained values of approximately 0.99 across all occlusion levels. Similar improvements were observed under combined occlusion and brightness conditions, while only small differences were found under brightness-only conditions. These results indicate that targeted data augmentation effectively improved YOLO11 robustness, particularly against fruit occlusion and combined visual disturbances. Further validation using naturally occurring occlusion and illumination variation in greenhouse environments is required to confirm the practical generalization of the proposed approach.

Key Words: Melon, Deep learning, Object detection, Greenhouse, Data augmentation

INTRODUCTION

Greenhouse crop production has increasingly adopted computer vision and deep learning technologies for automated crop monitoring, yield estimation, and robotic harvesting. These technologies enable repeated and non-contact acquisition of crop information and can reduce the labor required for conventional manual measurements. In particular, accurate fruit detection is an essential step for determining fruit location and quantity from RGB images. Afonso et al. (2020) demonstrated the applicability of deep learning for tomato fruit detection

and counting in greenhouse environments, while recent reviews have highlighted the growing use of deep-learning-based computer vision for crop monitoring, yield estimation, and other applications in smart greenhouses (Akbar et al., 2024).

Among deep-learning-based object detectors, the YOLO family has been widely adopted in agricultural vision applications because of its favorable balance between detection accuracy and inference speed. Recent studies have applied YOLO-based models to muskmelon detection under greenhouse conditions (Xu et al., 2024), and YOLO11-based models have also been investigated for fruit detection in complex greenhouse environments (Chen et al., 2025). These studies indicate that YOLO-based detectors have considerable potential for practical greenhouse crop monitoring.

However, high detection accuracy under favorable image conditions does not necessarily guarantee reliable performance in actual greenhouse environments. Fruits are frequently partially occluded by leaves, stems, or neighboring fruits, and their visual appearance can vary considerably according to illumination, shadow, viewing direction, and background conditions. In greenhouse muskmelon images, variations in lighting and fruit overlap have been reported as important factors affecting detection performance (Xu et al., 2024). Similarly, fruit detection datasets collected under high-light, low-light, backlight, shadow, leaf occlusion, and overlapping conditions have demonstrated the importance of environmental variability for robust fruit detection (He et al., 2025). Therefore, improving robustness to fruit occlusion and illumination variation is important for the practical application of object detection models in greenhouse environments.

Data augmentation is a widely used strategy for increasing the diversity of training data and improving model generalization without requiring a proportional increase in manually collected and annotated images. Conventional augmentation methods include geometric transformations, color modification, and brightness adjustment (Shorten and Khoshgoftaar, 2019). However, augmentation methods designed to reflect greenhouse-specific disturbances may be more effective for improving fruit detection robustness. Artificially introducing partial fruit occlusion and illumination variation into training images can expose the detector to environmental conditions that may be insufficiently represented in the original dataset. Furthermore, evaluating the trained model under disturbance levels different from those used during training can provide a more meaningful assessment of generalization to unseen conditions.

Therefore, the objective of this study was to evaluate the effect of occlusion- and brightness-based data augmentation on the detection performance and robustness of YOLO11 for melon detection in greenhouse RGB images. A baseline YOLO11 model was trained using the original training images, whereas an augmented YOLO11 model was trained using the same original images together with additional images generated using artificial fruit occlusion, brightness variation, and their combined transformations. To evaluate generalization, the models were tested under occlusion and illumination conditions with severity levels different from those used for training. Detection performance was evaluated using Precision, Recall, mean Average Precision at an intersection-over-union threshold of 0.5 (mAP@0.5), and mean Average Precision averaged over IoU thresholds from 0.5 to 0.95 (mAP@0.5:0.95). The performance of the baseline and augmented models was compared under identical test conditions to determine whether the proposed augmentation strategy improved robustness to fruit occlusion

and illumination variation.

MATERIALS AND METHODS

IMAGE DATASET

RGB images of melon fruits were acquired under greenhouse conditions and manually annotated for object detection. A total of 1,060 labeled images were used in this study, with melon fruit defined as a single object class. Each fruit was annotated using a bounding box, and the annotation information was stored in YOLO format. The dataset was divided into training, validation, and test sets at a ratio of 7:2:1.

The same original data split was maintained throughout all experiments to ensure a fair comparison between the baseline and augmented YOLO11 models. Images assigned to the training set were used only for model training and generation of augmented training images, whereas the validation and test datasets were generated exclusively from their respective original subsets. Thus, no image derived from the training set was included in either the validation or test dataset, thereby preventing data leakage among the three subsets.

The baseline YOLO11 model was trained using only the original training images, whereas the augmented YOLO11 model was trained using the same original images together with additionally generated occlusion, brightness, and combined augmentation images.

DATA AUGMENTATION

Artificial occlusion and brightness augmentation were applied to improve the robustness of melon detection under partial fruit obstruction and illumination variation. For occlusion augmentation, the location of each melon fruit was identified from its corresponding YOLO-format bounding-box annotation. Artificial occlusion was therefore applied specifically within the annotated fruit region rather than at arbitrary locations within the entire image.

Different augmentation levels were used for training and evaluation to examine the generalization ability of the YOLO11 model under conditions not directly observed during training. The validation and test datasets were generated using the same augmentation levels but from different original image subsets. The augmentation conditions applied to the training, validation, and test datasets are summarized in Table 1.

Table 1 Augmentation conditions applied to each dataset.

Dataset	Occlusion ratio (%)	Brightness factor
Training	30, 60, 80	0.25, 0.50, 1.8, 2.2
Validation	40, 70, 85	0.35, 0.65, 1.6, 2.0
Test	40, 70, 85	0.35, 0.65, 1.6, 2.0

The occluded area was defined relative to the melon bounding-box area, while the original bounding-box annotation was retained because the partially occluded fruit was regarded as the same target object. Brightness augmentation was performed by multiplying the RGB pixel intensities by predefined factors to simulate low- and high-illumination conditions. In addition

to occlusion-only and brightness-only augmentation, combined images containing both transformations were generated. All augmented images were added to the original training images rather than replacing them. Representative examples of the original and augmented images are shown in Fig. 1.

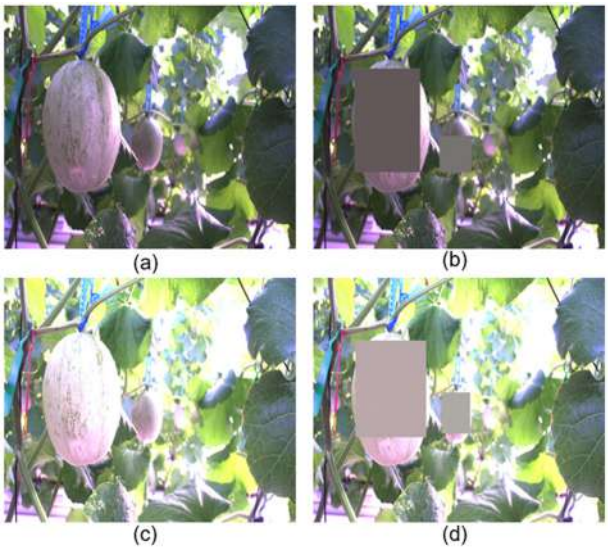

Fig.1 Examples of melon image augmentation: (a) original image; (b) 60% occlusion; (c) brightness factor of 1.80; and (d) combined 60% occlusion and brightness factor of 1.80.

OBJECT DETECTION MODEL TRAINING

A YOLO11n object detection model was used to evaluate the effect of the proposed data augmentation strategy. Pre-trained weights were used for model initialization, and transfer learning was performed for the single melon class.

Two YOLO11n models were trained under the same model configuration. The baseline model was trained using only the original training images, whereas the augmented model was trained using the same original images together with the generated occlusion, brightness, and combined augmentation images. Both models were trained for up to 100 epochs using an input image size of 640 × 640 pixels and a batch size of 16. Early stopping with a patience of 20 epochs was applied based on validation performance, and the model weights corresponding to the best validation performance were retained for final evaluation.

MODEL EVALUATION

The baseline and augmented YOLO11 models were evaluated using the same independent test dataset to ensure a direct comparison under identical conditions. The test dataset contained controlled occlusion and illumination variations with severity levels different from those used during training.

Detection performance was evaluated using Precision, Recall, mean Average Precision at an intersection-over-union threshold of 0.5 (mAP@0.5), and mean Average Precision averaged over IoU thresholds from 0.5 to 0.95 (mAP@0.5:0.95). In addition to overall detection performance, the models were evaluated separately according to occlusion level, brightness level, and combined augmentation conditions to determine how detection performance

changed with the severity of environmental disturbance.

Finally, the performance of the augmented YOLO11 model was compared with that of the baseline YOLO11 model under identical test conditions. The differences in Precision, Recall, mAP@0.5, and mAP@0.5:0.95 were used to quantify the improvement in robustness achieved by the proposed data augmentation strategy.

RESULTS & DISCUSSION

The overall detection performances of the baseline and augmented YOLO11 models are presented in Table 2. The augmented model showed substantially higher performance under the robustness test conditions. Compared with the baseline model, Precision increased from 0.7256 to 0.9570 and Recall from 0.6109 to 0.9412. In addition, mAP@0.5 increased from 0.6446 to 0.9839, while mAP@0.5:0.95 increased from 0.5661 to 0.8909. These corresponded to improvements of 0.2314, 0.3303, 0.3392, and 0.3248, respectively, indicating that the proposed augmentation strategy substantially improved the overall robustness of YOLO11 under the controlled disturbance conditions.

Table 2 Overall detection performance of the baseline and augmented YOLO11 models under robustness test conditions.

Model	Precision	Recall	mAP@0.5	mAP@0.5:0.95
YOLO11(Baseline)	0.7256	0.6109	0.6446	0.5661
YOLO11(Augmented)	0.9570	0.9412	0.9839	0.8909
Improvement	+0.2314	+0.3303	+0.3392	+0.3248

The effect of occlusion severity on detection performance is summarized in Table 3. The baseline YOLO11 model exhibited a pronounced reduction in performance as the occlusion ratio increased, with mAP@0.5 decreasing from 0.5964 at 40% occlusion to 0.1799 at 85% occlusion. In contrast, the augmented model maintained mAP@0.5 values of approximately 0.99 across all three occlusion levels. Consequently, the improvement achieved by augmentation became greater as the occlusion severity increased, reaching 0.8113 in mAP@0.5 at 85% occlusion. These results indicate that training with artificially occluded fruit images substantially reduced the performance degradation caused by partial fruit obstruction and improved the robustness of YOLO11 to unseen levels of occlusion.

Table 3 Detection performance under different occlusion conditions.

Occlusion ratio (%)	Baseline mAP@0.5	Augmented mAP@0.5	Improvement
40	0.5964	0.9896	+0.3932
70	0.3347	0.9910	+0.6562
85	0.1799	0.9913	+0.8113

In contrast to the occlusion results, relatively small differences between the baseline and augmented models were observed under brightness-only conditions (Table 4). Both models maintained high mAP@0.5 values across the evaluated brightness factors. At brightness factors of 0.35 and 0.65, the baseline model performed slightly better than the augmented model, whereas the augmented model showed modest improvements at brightness factors of 1.60 and 2.00. The largest improvement was observed at a brightness factor of 2.00, but the

difference in mAP@0.5 was only 0.0203. These results suggest that the baseline YOLO11 model already possessed considerable tolerance to the illumination variations evaluated in this study, and therefore the additional benefit of brightness augmentation was relatively limited compared with that of occlusion augmentation.

Table 4 Detection performance under different brightness conditions.

Brightness factor	Baseline mAP@0.5	Augmented mAP@0.5	Improvement
0.35	0.9824	0.9773	−0.0051
0.65	0.9821	0.9728	−0.0093
1.60	0.9639	0.9682	+0.0043
2.00	0.9329	0.9532	+0.0203

The benefit of augmentation was also evident when occlusion and brightness variation were simultaneously applied. As shown in Table 5, the baseline mAP@0.5 decreased from 0.6223 at 40% occlusion to 0.2707 at 85% occlusion under the combined conditions. In contrast, the augmented model maintained mAP@0.5 values above 0.985 across all combined occlusion levels. When all combined conditions were evaluated together, mAP@0.5 increased from 0.4261 for the baseline model to 0.9891 for the augmented model. These findings indicate that the proposed augmentation strategy was particularly effective in maintaining melon detection performance when fruit occlusion occurred alone or together with illumination variation.

Table 5 Detection performance under combined occlusion and brightness conditions.

Occlusion ratio (%)	Baseline mAP@0.5	Augmented mAP@0.5	Improvement
40	0.6223	0.9852	+0.3630
70	0.4044	0.9909	+0.5865
85	0.2707	0.9904	+0.7196

*In the combined augmentation condition, one brightness factor was randomly selected from 0.35, 0.65, 1.60, and 2.00 for each image.

However, the occlusion and illumination disturbances used in this study were artificially generated under controlled conditions. Therefore, the high performance of the augmented model, particularly under severe synthetic occlusion, should be interpreted as robustness to the augmentation conditions defined in this study rather than direct evidence of equivalent performance under naturally occurring leaf, stem, shadow, or fruit-overlap conditions. Further evaluation using greenhouse images containing naturally occurring occlusion and illumination variation is required to confirm the practical generalization of the proposed approach.

CONCLUSIONS

This study investigated the effect of occlusion- and illumination-based data augmentation on the robustness of YOLO11 for melon detection in greenhouse RGB images. The augmented YOLO11 model achieved substantially higher overall performance than the baseline model, with mAP@0.5 increasing from 0.6446 to 0.9839 and mAP@0.5:0.95 increasing from 0.5661 to 0.8909.

The improvement was primarily associated with enhanced robustness to fruit occlusion. The baseline model showed substantial performance degradation as the occlusion ratio increased, whereas the augmented model maintained consistently high detection performance even

under severe synthetic occlusion. Similar improvements were observed when occlusion and illumination variation were applied simultaneously. In contrast, both models exhibited relatively high and similar performance under brightness-only conditions, indicating a limited additional benefit from brightness augmentation within the evaluated range. Overall, the results demonstrate that targeted data augmentation can effectively improve YOLO11 robustness, particularly against fruit occlusion. Future studies should validate the proposed approach using naturally occurring occlusion and illumination variations in greenhouse environments.

ACKNOWLEDGEMENTS

This study was supported by 2026 the R&D program(Project Number : RS-2025-02219360) between Rural Development Administration and Ministry of Agriculture, Food and Rural Affairs and Ministry of Science and ICT, Republic of Korea.

REFERENCES

Afonso, M., H. Fonteijn, F. S. Fiorentin, D. Lensink, M. Mooij, N. Faber, G. Polder, and R. Wehrens. 2020. Tomato fruit detection and counting in greenhouses using deep learning. *Frontiers in Plant Science* 11: 571299.

Akbar, J. U. M., S. F. Kamarulzaman, A. J. M. Muzahid, M. A. Rahman, and M. Uddin. 2024. A comprehensive review on deep learning assisted computer vision techniques for smart greenhouse agriculture. *IEEE Access* 12: 4485-4522.

Chen, B. J., J. Y. Bu, J. L. Xia, M. X. Li, and W. H. Su. 2025. AFBF-YOLO: An improved YOLO11n algorithm for detecting bunch and maturity of cherry tomatoes in greenhouse environments. *Plants* 14(16): 2587.

He, H., O. M. Lawal, Y. Tan, and K. Cheng. 2025. An anchor-based YOLO fruit detector developed on YOLOv5. *PLOS ONE* 20(9): e0331012.

Shorten, C., and T. M. Khoshgoftaar. 2019. A survey on image data augmentation for deep learning. *Journal of Big Data* 6: 60.

Xu, D., R. Ren, H. Zhao, and S. Zhang. 2024. Intelligent detection of muskmelon ripeness in greenhouse environment based on YOLO-RFEW. *Agronomy* 14(6): 1091.

AI-P09

Proceedings of The 12th International Symposium on Machinery and Mechatronics for Agriculture and Biosystems Engineering (ISMAB 2026)
20-24 October 2026, Busan, Republic of Korea

DEVELOPMENT OF AN OPEN-SOURCE AUTOMATIC TRACKING SYSTEM FOR STYLET-BEARING NEMATODES UNDER A MICROSCOPE

Atsuru Fujimoto[1*], Taisuke Ekino[1]

[1]Department of Agro-environmental Science, Obihiro University of Agriculture and Veterinary Medicine, 2-11 Nishi, Inada, Obihiro, 080-8555, Japan
*Corresponding Author-- Voice: +81-155-49-5526, Email: fujimoto.a@obihiro.ac.jp

Abstract: Stylet-bearing nematodes are among the most economically damaging nematode groups in agriculture and forestry. Understanding how they use their stylet to detect host and non-host cues may support the development of new control strategies. Existing observation systems mainly track whole-body position, whereas tools for stylet-bearing nematodes have focused on static-image detection and counting. To our knowledge, no system has been specifically designed to automatically detect and follow the stylet of a stylet-bearing nematode. This study reports the ongoing development of an open-source, low-cost system that automatically detects and follows the nematode head under a compound microscope, reducing the labor required to observe head and stylet movement. The prototype combines a microscope-mounted USB camera, a motor-driven unit that automates the microscope's existing XY-stage control knobs, and a microcontroller receiving motion commands through an isolated USB-serial link. A Windows GUI application uses a keypoint-based deep learning model released under a permissive open-source license and commands the stage to keep the nematode in view. Preliminary trials confirmed that the integrated system could follow live nematodes under the microscope, although tracking performance has not yet been quantitatively evaluated. The model, fine-tuned at an input resolution of 384 px, achieved a best Keypoint AP50:95 of 0.374, with a detection rate of 32.1 Hz on the intended deployment GPU (RTX 4060 Ti). Evaluation with a synthetic video of known motion, with the stage held stationary, yielded a positional RMSE of 3.1 px (1.21 μm) and a stylet-orientation SD of 1.25°. The system will be released as open-source hardware and software to support behavioral observation in laboratories with modest equipment budgets.

Key Words: Stylet-bearing nematodes, Automatic Tracking, Deep Learning, Open-Source

INTRODUCTION

Stylet-bearing nematodes, including plant-parasitic cyst nematodes of the genera *Heterodera* and *Globodera*, are among the most economically damaging groups of plant pathogens worldwide (Jones et al., 2013), and stylet-bearing nematodes also damage forestry, as in the case of the pine wood nematode (*Bursaphelenchus xylophilus*), which causes pine wilt disease across Asia and Europe (Vicente et al., 2012). In Japan, cyst nematodes such as the soybean cyst nematode (*Heterodera glycines*; SCN) and the potato cyst nematodes (*Globodera rostochiensis* and *G. pallida*) are a major constraint on the large-scale, crop-rotation-based field agriculture of Hokkaido in Japan, and the same nematode groups also limit crop production in temperate agricultural regions worldwide.

These cyst nematodes locate a host root, penetrate it, and induce a specialized feeding site using a protrusible, hollow stylet through which effector proteins are secreted; the resulting host-finding, feeding, and avoidance behaviors are governed by a compact but functionally specialized nervous system, whose characteristic sensory neurons evolved in concert with the piercing apparatus, the stylet (Ekino and Shinya, 2025). Because this sensory and motor repertoire is itself a potential target for nematode control, understanding how stylet-bearing nematodes detect host and non-host cues and translate them into feeding or avoidance behavior is of direct practical relevance to developing new management strategies, in addition to its basic nematological interest (Han and Schroeder, 2025).

A variety of instruments have been developed to observe nematode behavior under a microscope. Commercial systems such as WormLab (MBF Bioscience) integrate specialized optics with tracking and analysis software, while open-source trackers developed mainly for *C. elegans* include Track-A-Worm (Wang and Wang, 2013), the Parallel Worm Tracker (Ramot et al., 2008), and Tierpsy Tracker (Javer et al., 2018). For stylet-bearing plant-parasitic nematodes specifically, research has instead concentrated on static-image detection and counting using convolutional object detectors such as YOLO variants, rather than real-time behavioral tracking (e.g., Pun et al., 2023).

Two gaps remain. Commercial tracking hardware is costly and vendor-specific, and therefore inaccessible to some laboratories. Closed-loop systems that identify the head and use a motorized stage to keep free-living nematodes such as *C. elegans* in view have been developed (Cronin et al., 2005); however, to our knowledge, no system specifically detects and follows the stylet of a stylet-bearing nematode.

Desktop 3D printing and low-cost printed-circuit-board fabrication now allow laboratories with modest resources to build custom optomechanical hardware. Accordingly, this study aims to develop an open-source, low-cost system, assembled from readily available components, that can be added onto an existing compound microscope with little to no modification to detect and follow the head of a stylet-bearing nematode, thereby reducing manual observation effort.

MATERIALS AND METHODS

System Overview

The system operates as follows, as shown in Fig. 1: a live video frame is acquired from the camera and the nematode head is localized by the detection model. A fixed deadzone is defined around the image center; when the detected head position moves outside this range,

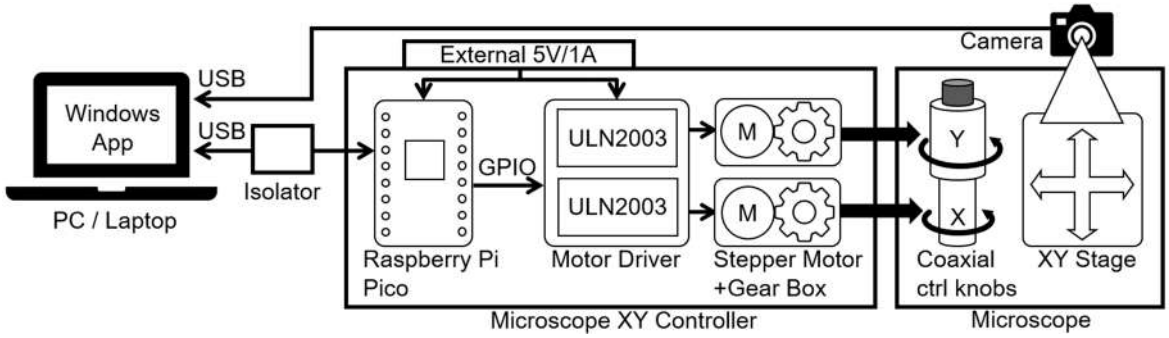

Fig. 1 System configuration diagram of the automatic nematode tracking system

the microcontroller commands the stepper motors to rotate the stage's X or Y control knob by a fixed, preset increment in the corresponding direction, which reduces the frequency of stage commands and the associated processing load. This response uses fixed-step, vision-based feedback control: stage displacement is not measured directly by an encoder. Instead, the head position detected in subsequent video frames provides feedback, and additional movement commands are issued as needed to return the specimen to the deadzone. All components are coordinated by a single Windows GUI application written in Python.

Hardware Configuration

Observations were made with a compound microscope (Olympus, CH-2 CHS) (Fig. 2) fitted with a fixed 0.5× relay lens and 4×, 10×, 40× and 100× objectives; the 40× objective was selected for tracking because it provides sufficient magnification to resolve the movement of the nematode head and stylet. Video was acquired with a HAYEAR HY-500B USB camera (native resolution 2592 × 1944) using the UVC interface via OpenCV; the resolution was set to its lowest selectable option (640 × 480) to increase processing speed. Rather than replacing the microscope's stage, the system automates its existing coaxial X/Y control knobs: two 28BYJ-48 stepper motors, each controlled through a ULN2003 driver board, are coupled to the knobs through a 20:60-tooth gear train (1:3 reduction). Motion commands were generated by a Raspberry Pi Pico running MicroPython and transmitted over USB serial. An ADuM3160 USB isolator was placed between the host PC and the Pico to protect the PC's USB port, and a separate external 5V/1A supply was used to secure stable power for the stepper motors.

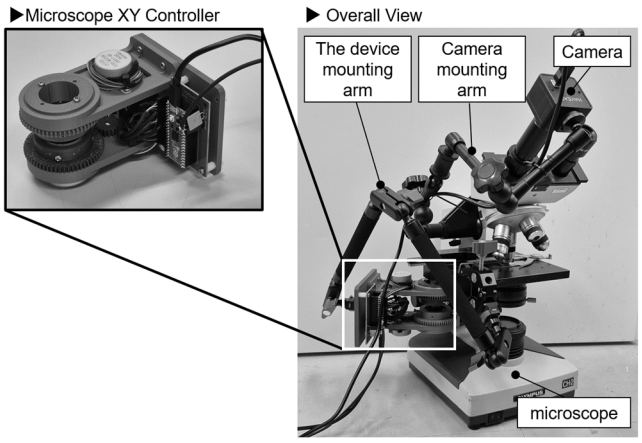

Fig. 2 Prototype of the automatic nematode tracking system mounted on a compound microscope

The total cost of the custom stage-knob actuation unit and controller—including 3D-printed parts (143 g PLA), stepper motors, motor drivers, bearings, arms, a USB isolator, a custom PCB, a Raspberry Pi Pico, and cabling—was approximately ¥17,200 (about $108 USD at the time of writing). All 3D-printed parts were fabricated in-house on the laboratory's own printer (Bambu Lab P1S) rather than through an external service.

Stage Calibration

The relationship between stepper-motor steps and physical stage displacement was calibrated under the 40x objective by jogging the stage a known number of steps and measuring the resulting displacement against a commercially available stage micrometer. The X- and Y-axes were calibrated to 160 and 230 steps/mm, respectively.. Backlash, measured directly via serial commands, was 38 steps on the X-axis and 21 steps on the Y-axis; this was compensated in firmware by always approaching a target position from a fixed direction. Because the gear train and stage housing are 3D-printed from PLA, these calibration values are expected to vary with the dimensional roughness of individual printed parts, and are therefore specific to this prototype rather than fixed constants of the design.

Nematode Detection Model

A dataset of microscope images of stylet-bearing nematode heads was collected and manually annotated with six keypoints per individual (Fig. 3). The detection model, RF-DETR Keypoint Preview, a preview-release keypoint-detection extension (Robinson, 2026) of the RF-DETR detection-transformer architecture (Robinson et al., 2025) released under the Apache License 2.0, was fine-tuned at an input resolution of 384 × 384 for one class (nematode head) with six keypoints per instance. Training used the AdamW optimizer with a learning rate of 1e-4 (1.5e-4 for the pretrained encoder), a batch size of 8 with gradient accumulation of 4, multi-scale and expanded-scale training with scale jitter, and exponential moving average (EMA) weight averaging; the learning-rate schedule dropped by a factor of 10 at epoch 100. Training was configured for up to 150 epochs with early stopping (patience of 20 epochs after an initial 5-epoch grace period, minimum improvement of 0.003) and stopped after 104 epochs (logged epochs 0-103).

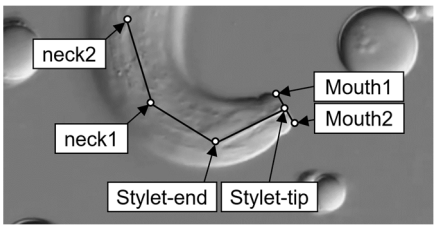

Fig. 3 Six annotated keypoints on the nematode head

Inference Benchmarking

Detection frame rate was benchmarked at batch size 1 on three GPUs: an RTX 4060 Ti (intended deployment GPU), a GTX 1660 Ti Max-Q (secondary/testing hardware), and an RTX 6000 Ada (training workstation).

GUI Application

The Tkinter-based GUI (Fig. 4) provides a live camera preview implemented with a Canvas widget to support mouse-drag region selection, overlay toggles for the detection crosshair, scale bar, and tracking range, and a scale-calibration workflow in which the user selects a known number of grid squares on a 0.1-mm-pitch stage micrometer slide to compute pixels-per-millimeter. All calibration values and operating settings are persisted to a configuration file to ensure reproducibility across sessions.

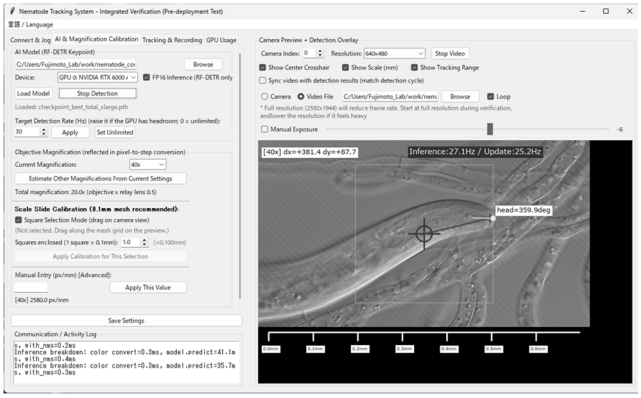

Fig. 4 Sample screen of the tracking verification application

RESULTS & DISCUSSION

Detection Model Performance

This system is at the prototype stage, built to prioritize getting the full detection-and-tracking pipeline working over optimizing performance. The deployed model (EMA checkpoint, epoch 91, confirmed from the checkpoint file's metadata) achieved a Keypoint AP50:95 of 0.374, the OKS (Object Keypoint Similarity)-based average precision metric for keypoint localization.

Inference Frame Rate

Detection frame rate at batch size 1 ranged from 7.1 Hz on the GTX 1660 Ti Max-Q to 43.8 Hz on the RTX 6000 Ada across the three evaluated GPUs. The intended deployment GPU (RTX

4060 Ti) reached 32.1 Hz, indicating headroom above the camera's frame rate rather than the actual control-loop rate, which is limited by the fixed-step, deadzone-triggered stage response described above.

Stage Calibration and Backlash

Stage calibration identified backlash of 38 steps (X-axis) and 21 steps (Y-axis), attributable to the roughness of the 3D-printed PLA gear train, as the dominant source of positioning error, larger than the underlying motor step resolution itself. Compensating for backlash in firmware was necessary to achieve adequate positioning repeatability. Adding a displacement sensor was considered but judged to add unwanted complexity; the current approach tolerates some error and will address it through hardware improvements such as higher-precision gearing.

Detection Positional Accuracy

Detection accuracy for position and stylet orientation was evaluated offline using a synthetic video generated to simulate motion within a static field of view: a still image of a nematode (including the stylet) was digitally translated, without rotation, along a 120-px-radius, 5-s-period circular path within a 640x480-px frame, so the true stylet orientation remained constant. The XY stage itself was not moved during this test; only the detection model's output (dx, dy, and estimated head angle) was compared against the known, pre-defined trajectory to compute position error (from the residual offset) and stylet-orientation error (from the variability of the estimated head angle). Table 1 summarizes the results. This test evaluates the AI detection model's accuracy in isolation, within a predetermined motion range, rather than the performance of the physical stage-control system, and represents a basic check rather than a full validation, since the constant-radius, constant-speed path does not include the abrupt direction changes, acceleration, or pauses characteristic of real nematode movement and feeding behavior.

Table 1. Detection positional and angular accuracy under the 40× objective lens (n = 41)

Metric	Value
Position error RMSE	3.1 px (1.21 μm)
Stylet-orientation error (SD)	1.25°

Tracking Performance and Remaining Issues

Preliminary trials with live nematode specimens confirmed that the system could follow a moving nematode and maintain its head within the microscope field of view. However, tracking performance has not yet been quantitatively evaluated in terms of tracking success rate, duration of continuous tracking, or the stability of head and stylet detection during feeding and turning behavior. These metrics will be evaluated in future real-specimen trials.

Future Development

The fixed-step, deadzone-triggered tracking strategy followed live nematodes and supported video recording of head and stylet movement. We plan to introduce adaptive step commands to improve tracking stability and responsiveness. Planned work includes using more metal gears and stage components to reduce positioning error caused by inaccuracies in 3D-printed PLA parts, and investigating methods to achieve reliable detection at around 10 Hz without an expensive GPU. We plan to evaluate a global-shutter camera to reduce rolling-shutter distortion. A project overview is available on our website (Fujimoto, 2026), through which the hardware design files and source code will be released under open-source licenses to support reproduction and development by other laboratories.

CONCLUSIONS

1. We developed an open-source, low-cost system that automatically detects and follows the head of a live nematode under a compound microscope, reducing the labor required to record head and stylet movement.
2. The deployed detection model (EMA checkpoint, epoch 91) reached a Keypoint AP50:95 of 0.374, with a detection frame rate of 32.1 Hz on the intended deployment GPU (RTX 4060 Ti); whether this translates into adequate real-time tracking performance has not yet been directly evaluated.
3. Future work will quantitatively evaluate tracking with live specimens, improve stage positioning and computational efficiency, and release the system as open-source hardware and software.

REFERENCES

Cronin, C. J., J. E. Mendel, S. Mukhtar, Y.-M. Kim, R. C. Stirbl, J. Bruck, and P. W. Sternberg. 2005. An automated system for measuring parameters of nematode sinusoidal movement. BMC Genetics 6: 5.

Ekino, T., and R. Shinya. 2025. Ultrastructural description of amphid neurons in the pine wood nematode indicates concurrent evolution of the stylet and specific neurons. Journal of Comparative Neurology 533(11): e70114.

Fujimoto, A. 2026. Open-Source Microorganism Tracking System. https://univ.obihiro.ac.jp/~fujimoto/Eng/nematode.html (accessed September 9, 2026).

Han, J., and N. E. Schroeder. 2025. Neuronal basis of host-finding and feeding in plant-parasitic nematodes. Annual Review of Phytopathology 63: 383-402.

Javer, A., M. Currie, C. W. Lee, et al. 2018. An open-source platform for analyzing an d sharing worm-behavior data. Nature Methods 15: 645-646. Software: https://github.com/Tierpsy/tierpsy-tracker

Jones, J. T., A. Haegeman, E. G. J. Danchin, H. S. Gaur, J. Helder, M. G. K. Jones, T. Kikuchi, R. Manzanilla-Lopez, J. E. Palomares-Rius, W. M. L. Wesemael, and R. N. Perry. 2013. Top 10 plant-parasitic nematodes in molecular plant pathology. Molecular Plant Pathology 14(9): 946-961.

MBF Bioscience. n.d. WormLab Imaging System. https://www.mbfbioscience.com/products/wormlab-imaging-system (accessed August 2026).

Pun, T. B., A. Neupane, and R. Koech. 2023. A deep learning-based decision support tool for plant-parasitic nematode management. Journal of Imaging 9(11): 240.

Ramot, D., B. E. Johnson, T. L. Berry Jr., L. Carnell, and M. B. Goodman. 2008. The Parallel Worm Tracker: A platform for measuring average speed and drug-induced paralysis in nematodes. PLoS ONE 3(5): e2208.

Robinson, I., P. Robicheaux, M. Popov, D. Ramanan, and N. Peri. 2025. RF-DETR: Neural architecture search for real-time detection transformers. arXiv preprint arXiv:2511.09554.

Robinson, I. 2026. Real-time keypoint detection with RF-DETR. Roboflow Blog. https://blog.roboflow.com/real-time-keypoint-detection-with-rf-detr/ (accessed August 2026).

Vicente, C., M. Espada, P. Vieira, and M. Mota. 2012. Pine wilt disease: a threat to European forestry. European Journal of Plant Pathology 133: 89-99.

Wang, S. J., and Z.-W. Wang. 2013. Track-A-Worm, an open-source system for quantitative assessment of *C. elegans* locomotory and bending behavior. PLoS ONE 8(7): e69653.

AI-P10

Proceedings of The 12th International Symposium on Machinery and Mechatronics for Agriculture and Biosystems Engineering (ISMAB 2026)
20-24 October 2026, Busan, Republic of Korea

ESTIMATING ANIMAL MOVEMENT PATHS USING MULTI-NODE INFRARED PYROELECTRIC SENSORS FOR WILDLIFE DAMAGE PREVENTION

Shota Sawada[1], Hiroshi Iwata[1*], Ken'ichi Yamaguchi[1]

[1]National Institute of Technology(KOSEN), Nara College, 22 Yata, Yamato-Koriyama, Nara 639-1080, Japan
*Corresponding Author-- Voice: +81-743-55-6138, Email: iwata@info.nara-k.ac.jp

Abstract: Wildlife damage to agricultural crops remains a significant challenge in Japan, compounded by an ongoing shortage of agricultural labour. Conventional countermeasures, including electric fencing and camera-based monitoring, are constrained by high implementation and maintenance costs. This study proposes a low-cost IoT system that employs a network of pyroelectric infrared sensors to estimate the movement paths and species of wildlife, thereby reducing the burden on farmers engaged in wildlife damage countermeasures. This paper specifically addresses the communication protocol linking the sensor nodes, given the transmission-time restrictions imposed by 920 MHz radio band regulations and the limited packet capacity of the wireless module (IM920s) employed. Each sensor node acquires 10-bit analogue data from three pyroelectric infrared sensors via an Arduino-based microcontroller; the data is compressed to 8 bits and packed into 32-Byte packets, enabling up to 10 data sets per transmission. An adaptive, threshold-based algorithm queues and transmits data only when a significant change in sensor value occurs or a fixed time interval elapses, substantially reducing the number of required transmissions while preserving essential behavioural information. Based on this design, the proposed scheme is expected to bring the transmission frequency within the regulatory limit of approximately three transmissions per second. A field experiment using four sensor nodes deployed around a 10 m × 10 m area, with a human subject as a preliminary proxy for wildlife, is planned to validate the feasibility of path estimation; the results will be presented at the symposium. This work is expected to contribute to the development of a practical, low-cost wildlife monitoring system.

Key Words: Wildlife damage, pyroelectric infrared sensor, IoT system, 920 MHz wireless communication

INTRODUCTION

The agricultural sector in Japan continues to face a range of structural challenges, among which the shortage of the labour force remains particularly acute. Compounding this issue is the persistent problem of crop damage caused by wildlife. According to recent statistics, the economic loss attributable to wildlife-induced crop damage in fiscal year 2024 amounted to approximately 18.8 billion yen(MAFF, 2025). Although this figure has exhibited a downward

trend since peaking in fiscal year 2012, the scale of the damage remains substantial and cannot be overlooked.

Conventional wildlife damage countermeasures have relied on inferring the responsible species from field evidence, such as feeding traces, followed by installing tailored physical barriers—electric fences or protective netting. However, identifying the responsible animal and maintaining such barriers often demand considerable labour, time, and cost, owing to factors including unanticipated intrusion routes and fence displacement or degradation. Camera-based monitoring offers an alternative, but remains constrained by high power consumption, recurring communication costs, and installation and maintenance burdens. These limitations underscore the need for an innovative, low-cost alternative capable of sustaining continuous monitoring with reduced labour, time, and cost.

Considering the above, this study proposes an IoT system that leverages pyroelectric infrared sensors to estimate both the movement paths and species of wildlife. The primary aim of this work is to reduce the burden placed on farmers engaged in wildlife damage countermeasures by enabling low-cost visualisation of animal behaviour together with real-time remote monitoring capability.

To this end, the present study evaluates the feasibility of the proposed system by acquiring and analyzing human behavioural data through a network of multiple pyroelectric infrared sensors, prior to its application to actual wildlife.

Our previous study conducted a preliminary investigation into a method for estimating the location and movement path of animals using pyroelectric infrared sensors. However, when practical deployment is considered, transmitting the complete time-series data obtained from many sensors proves difficult, owing to domestic radio regulations governing the use of the 920 MHz band and the limited transmission capacity of the IM920s wireless module employed in this system. Accordingly, this paper describes the design and implementation of a data compression method and transmission algorithm capable of transmitting sensor data without compromising the animal's behavioural characteristics, even within a constrained communication bandwidth(Sawada et al., 2026).

MATERIALS AND METHODS

Overview of Proposed System

The objective of this study is to achieve both low-cost visualisation of animal behaviour and a reduction in the burden placed on farmers engaged in wildlife damage countermeasures. To this end, this paper proposes an IoT system capable of autonomously detecting and notifying farmers of harmful animals entering farmland, as illustrated in Fig.1.

In the proposed system, pyroelectric infrared sensors are utilized to detect the intrusion of animals into the field. The detected values are uploaded via a gateway to an analysis server, where the animal's behaviour, species, and individual identity are analyzed. The results of this analysis are notified to the farmer's smartphone in real time, and the animal's movement path is displayed on a map. This enables farmers to remotely confirm the situation prior to visiting the site, thereby improving the efficiency of work preparation and reducing labour.

It should be noted that this paper focuses on the communication protocol and data compression algorithm components of this system and describes their design and implementation.

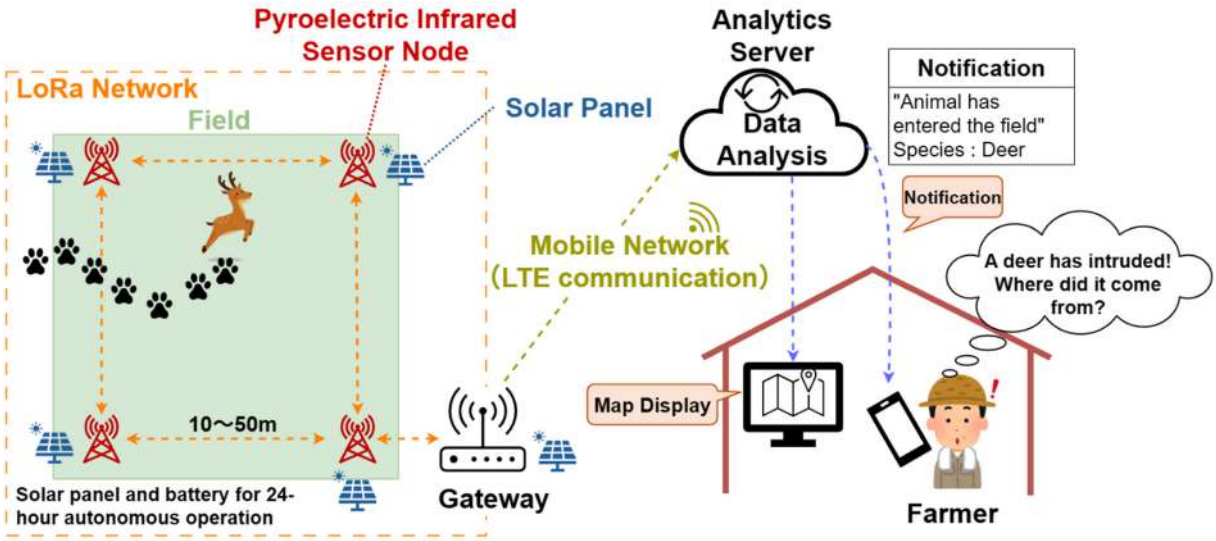

Fig. 1 Overview of the proposed wildlife damage countermeasure system

Hardware Configuration

The sensor node employed in this study comprises a pyroelectric infrared sensor, an Arduino, and the IM920s wireless communication module(Interplan, n.d.). The Arduino was implemented on a custom-designed board incorporating the ATmega328P, operated at 5 V and 16 MHz(Microchip Technology Inc., n.d.). The analogue voltage value detected by the pyroelectric infrared sensor is converted into a digital value by the Arduino's A/D conversion function, and the resulting value is then transmitted wirelessly via the IM920s (Fig.2).

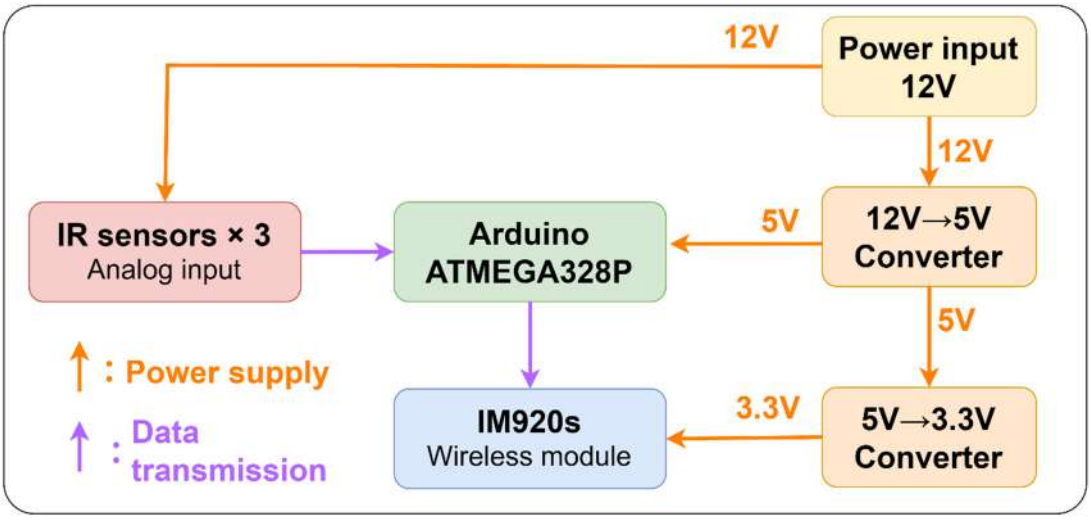

Fig. 2 Hardware configuration of the sensor node

Communication Constraints

The 920 MHz frequency band used by the IM920s is subject to Japanese radio law regulations, which restrict the cumulative transmission time to 360 seconds per hour(ARIB, 2023). According to the IM920s manual, under conditions of automatic route search, acknowledgement (ACK) enabled, and a 50% communication error rate, the guideline for the number of transmissions when sending 32-Byte data packets is approximately 11,000 times per hour, equivalent to approximately 3 transmissions per second.

Meanwhile, each sensor node comprises three pyroelectric infrared sensors, and a single A/D conversion via the Arduino's analogRead function requires approximately 100 μs(Microchip Technology Inc., 2018). Consequently, reading one set of data from the three sensors takes approximately 0.3 ms. Within the 350 ms transmission cycle assumed in this study, this reading process can be repeated approximately 100 times, resulting in the generation of a substantial volume of three-sensor data within each 350 ms intervals.

However, given the aforementioned transmission guideline of approximately three transmissions per second, sequentially transmitting all data generated within each 350 ms interval is not practical from the standpoint of transmission frequency. Accordingly, this study adopted an event-driven compression and transmission scheme, whereby data is transmitted only when a significant change in sensor value is detected, thereby reducing the number of required transmissions.

Data Compression

In this study, in order to capture the timing at which the pyroelectric infrared sensor exhibits a pronounced response, the lower 2 bits of the acquired 10-bit sensor value were discarded, compressing the value to 8 bits (1 Byte). As a result, data from three sensors is accommodated within 3 Bytes, allowing a single IM920s packet (32 Bytes) to store up to 10 data sets (30 Bytes). Furthermore, an adaptive transmission algorithm was implemented whereby data is added to a queue only when the difference from the previous value exceeds a predetermined threshold, and a packet is transmitted once either 10 data sets have accumulated in the queue or 300 ms have elapsed (Fig.3).

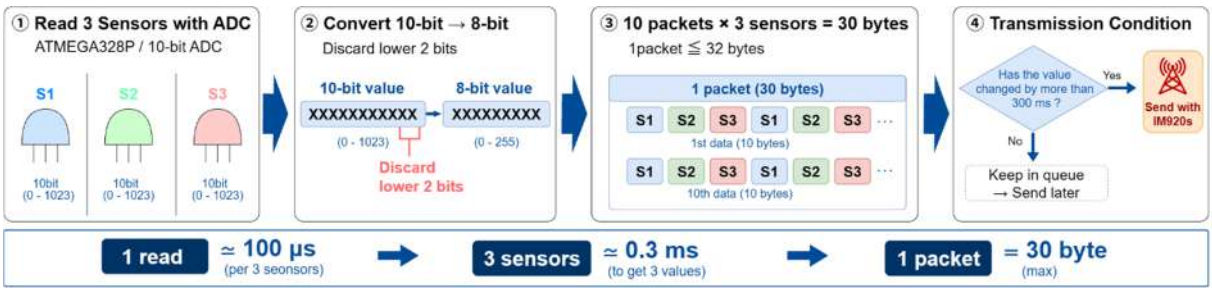

Fig. 3 Data compression and transmission algorithm

RESULTS & DISCUSSION

To verify the feasibility of the proposed method, a field experiment is planned for a 10 m × 10 m field. As shown on the left side of Fig.4, sensor nodes (Arduino No. A–No. D) are positioned

at the four corners of the field at 10 m intervals. Each sensor node is equipped with three pyroelectric infrared sensors (each with a detection angle of 144°), and the combination of three sensors was designed to secure 360° detection coverage. When a person passes through the field, the data detected by each sensor node will be collected and analyzed to verify whether the person's walking path can be estimated.

As shown on the right side of Fig.4, within each sensor node, the analogue values output by the three pyroelectric infrared sensors are acquired via the Arduino's A/D conversion and transmitted wirelessly via the IM920s. The transmitted data is designed to be forwarded to a higher-level network via an IM920s, a BeagleBone, and a 4GIM installed at the gateway. Each sensor node is designed to operate autonomously using a lead-acid battery, without requiring a commercial power supply.

In this experiment, the temporal variation in output data obtained from a total of 12 sensors across the four nodes will be analyzed, and, following application of the aforementioned data compression and transmission algorithm, it will be confirmed whether the person's movement path can be estimated. The specific experimental results and a discussion of path estimation accuracy will be presented in detail at the symposium.

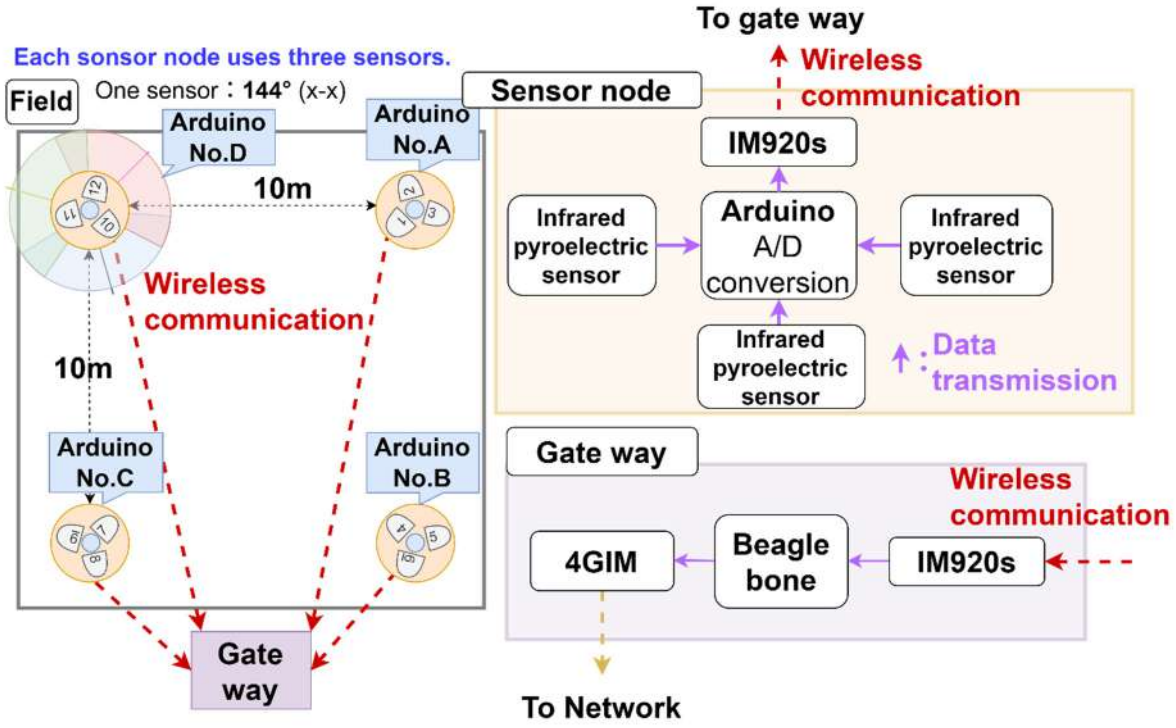

Fig. 4 Overview of the planned experiment

CONCLUSIONS

This study proposed a data compression method and an adaptive transmission algorithm for the efficient transmission of multi-point measurement data acquired using pyroelectric infrared sensors, under the communication constraints imposed on the IM920s within the 920 MHz band. By compressing 10-bit data to 8 bits and packing the resulting data into packets, transmission of 10 data sets (30 Bytes) per packet was made possible; furthermore, the

combination of threshold-based queuing and periodic transmission was designed to achieve efficient data transmission within the applicable regulatory constraints. Future work will involve quantitative verification experiments using the actual hardware, optimization of the threshold setting, and evaluation of communication stability in an actual field environment.

ACKNOWLEDGEMENTS

This work was supported by the Asahi Glass Foundation.

REFERENCES

ARIB. 2023. ARIB STD-T108: 920 MHz-Band Telemeter, Telecontrol and Data Transmission Radio Equipment. English translation. Ver. 1.5. Tokyo, Japan: Association of Radio Industries and Businesses (ARIB). Available at: https://www.arib.or.jp/english/html/overview/doc/5-STD-T108v1_5-E1.pdf. Accessed 10 September 2026.

Interplan. n.d. IM920s multi-hop 920 MHz radio module. Tokyo, Japan: Interplan Co., Ltd. Available at: https://www.interplan.co.jp/solution/wireless/im920s/im920s.php. Accessed 13 September 2026.

Microchip Technology Inc. n.d. ATmega328P. Chandler, Ariz.: Microchip Technology Inc. Available at: https://www.microchip.com/en-us/product/atmega328p. Accessed 14 September 2026.

Microchip Technology Inc. 2018. ATmega48A/PA/88A/PA/168A/PA/328/P Datasheet. Document No. DS40002061B. Chandler, Ariz.: Microchip Technology Inc. Chapter 23, "Analog-to-Digital Converter," Section 23.1 "Features." Available at: https://ww1.microchip.com/downloads/en/DeviceDoc/ATmega48A-PA-88A-PA-168A-PA-328-P-DS-DS40002061B.pdf. Accessed 10 September 2026.

Ministry of Agriculture, Forestry, and Fisheries. 2025. FY2022 Summary of the Annual Report on Food, Agriculture and Rural Areas in Japan. 257-261.

Sawada, S., H. Iwata, and K. Yamaguchi. 2026. Tracking Animal Movement Paths Using Multi-Node Infrared Pyroelectric Sensor Network for Low-Cost Wildlife Damage Prevention, Proceedings of the 14th IIAE International Conference on Industrial Application Engineering 2026, GS4-1, pp.197-203

AI-P11

Proceedings of The 12th International Symposium on Machinery and Mechatronics for Agriculture and Biosystems Engineering (ISMAB 2026)
20-24 October 2026, Busan, Republic of Korea

GENERALIZATION PERFORMANCE OF HYPERSPECTRAL IMAGING-BASED MODEL FOR MELON HARVEST-TIME PREDICTION

Seongmin Lee[1], Seongho Lee[1], Jeong Gyun Kang[1], Jun-Woo Park[1]
Ho-seung Jang[1], Jayeong Paek [1*]

[1]Division of Agricultural Robot, Department of Agricultural Engineering, National Institute of Agricultural Sciences, Jeonju, Republic of Korea
*Corresponding Author-- Voice: +82-63-238-4290, Email: jayeong0919@korea.kr

Abstract: This study aimed to evaluate the feasibility of Hyperspectral Imaging (HSI) for developing a non-destructive harvest-time prediction model for hydroponically grown melons. In particular, melons were categorized into three initial fruit size groups-small, medium, and large-and the generalization performance of the proposed method was evaluated across three fruit size groups. Hyperspectral data were acquired throughout the growing period, and three growth stages (early stage, intermediate stage, and harvest stage) were defined based on changes in the fruit shape index. Four spectral preprocessing methods (RAW, SNV, SG1, SNV+SG1) and five machine learning algorithms (PLS-DA, Logistic Regression, Random Forest, SVM, XGBoost) were applied and compared. Model performance was evaluated by comparing classification accuracy and F1-score, with particular focus on generalization across the different fruit size groups. The results indicated that the combination of SNV+SG1 preprocessing with the PLS-DA model achieved the highest performance, with both an accuracy and F1-score of 0.933. Furthermore, Variable Importance in Projection (VIP) analysis identified wavelengths near 540 nm, 780 nm, and 970 nm as the most effective spectral features for predicting harvest time. The optimal model also maintained a stable classification accuracy of over 90% for all initial fruit size groups, demonstrating that its prediction performance was robust to variation in fruit size. These results demonstrate that HSI can provide a reliable and non-destructive approach for model harvest-time prediction regardless of initial fruit size and support its potential application in automated harvest decision-making and robotic harvesting systems.

Key Words: Hyperspectral Imaging, Melon Harvest-time, Classification Prediction, Non-destructive, Machine learning

INTRODUCTION

Melons (*Cucumis melo* L.) are an important crop, and its economic value has been steadily rising because global demand is increasing. According to the Food and Agriculture Organization (FAO), global melon production is approximately 28.25 million tons a year, with a gross production value is estimated at approximately 14.9 billion USD (FAO, 2026).

However, the agricultural field urgently requires automation, due to a labor shortages and rising labor costs. To solve these challenges, researchers are actively studying automation technologies and robotic harvesting for greenhouse crops (Rajendran et.al., 2024).

Traditionally, melons have been harvested all at once. The harvest-time has been determined

based on the number of days after anthesis (DAA) and by destroying a small number of sampled fruits to test sugar levels. However, it is hard to guarantee that all melons reach the optimal harvest-time uniformly. This is because environmental conditions, such as temperature and sunlight, as well as differences among individual plants, can affect fruit growth and maturity. Therefore, new technologies that can predict the optimal harvest-time without damaging the fruit are needed for agricultural automation and robotic harvesting.

Recently, many studies have used Hyperspectral Imaging (HSI) to evaluate the internal quality of fruits non-destructively (Lu et al., 2020; Shah et al., 2025). Standard RGB cameras have limitations in assessing the internal quality of melons (Naqvi et al., 2025). In contrast, HSI uses visible and near-infrared(VIS-NIR) light and accurately measure internal qualities, such as chlorophyll breakdown and sugar accumulation (Chu et al., 2022).

Therefore, this study aimed to evaluate the potential of HSI to predict the harvest-time of melons grown in a hydroponic greenhouse. Specifically, a dataset was built that includes physical differences between individual melons, such as fruit size, in order to evaluate field applicability and generalization performance of the model. Five machine learning algorithms (PLS-DA, Logistic Regression, Random Forest, SVM, and XGBoost) were applied and their prediction performances were compared to find the best method.

MATERIALS AND METHODS

Experimental Material and Sampling

The ‘Megaton’ melon cultivar was used in this study. The melons were grown hydroponically in a greenhouse at the Goheung Smart Farm Innovation Valley (Fig. 1).

To evaluate the generalization performance of the model across different fruit sizes, the melons were divided into three groups based on fruit girth measured on November 3, 2025: small (10.9±1.8cm), medium (22.9±1.9cm), and large (26.6±1.2cm). Five melons were selected for each size group (Table 1)



Fig.1 Overview of the hydroponic greenhouse for melon cultivation

Table 1 Fruits size groups based on girth measurements at the initial growth stage

	Small Size	Medium Size	Large Size
Number of samples (n)	5	5	5
Horizontal girth (cm)	8.3±1.2	21.1±2.5	23.1±1.2
Vertical girth (cm)	10.9±1.8	22.9±1.9	26.6±1.2

Data Acquisition and Growth Stage Definition

Fig. 2 provides an overview of the overall workflow, from HSI acquisition to model performance evaluation, before the details of each step are described in the following section.

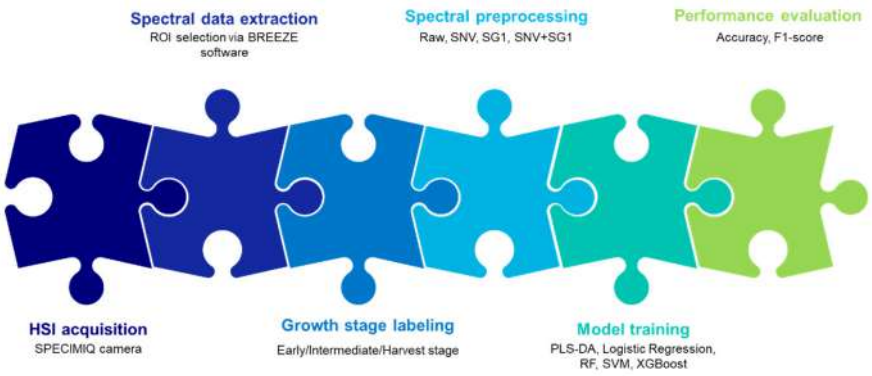

Fig.2 Steps used to build the harvest-time prediction model.

A SPECIM IQ camera was used for HSI. Imaging were taken once a week for a total of 8 times, from November 10 to December 30, 2025, with the same samples repeatedly imaged over time to construct a time-series dataset. The camera captured spectral data in the 400-1,000 nm wavelength range. Images were acquired at a working distance of approximately 60cm between the camera and the fruit.

Previous studies show that sugar levels increase after the plant's physical growth stops, showing a high correlation between fruit size expansion stopping and sucrose accumulation (Yan et al., 2026). Based on this, the fruit shape index (FSI) was analyzed. The growth was divided into three growth stages: early, intermediate, and harvest stage, to fit the goal of predicting harvest-time.

The FSI is originally defined as the ratio of straight-line length to diameter (Eq. (1)) (Périn et al., 2002):

$$FSI = \frac{l}{d} \tag{1}$$

where l and d are the straight-line length and diameter (cm), respectively. However, girth was measured with a tape measure instead of calipers in this study. Girth can be converted to the corresponding straight-line dimension using π, and this π cancels out when calculating the ratio (Neupane et al., 2023). Thus, FSI was calculated using Eq. (2):

$$FSI = \frac{L}{D} \tag{2}$$

where L and D are the vertical and horizontal girth (cm), respectively.

The FSI increased sharply at first and then stopped as the DAF increased (Fig. 3) Based on trend, the growth period was divided into three stages: early, intermediate, and harvest, to fit the goal of predicting harvest-time. Two imaging dates were selected from each of the three stages to prevent class imbalance, using the harvest stage - the stage with the least data (December 22 and 30) – as the reference. Accordingly, two dates were also selected from the early stage (November 10 and 17), and the intermediate stage (December 1 and 8), yielding 90 hyperspectral data in total (15 samples×6 imaging dates).

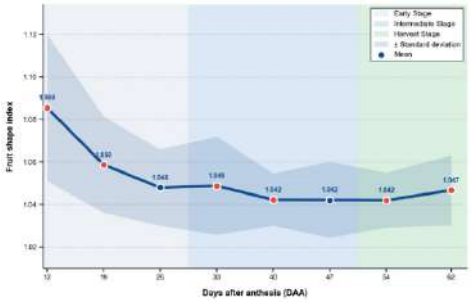

Fig. 3 Changes in FSI of melon fruit across days after anthesis (DAA).

Spectral Preprocessing

The BREEZE software was used to select the region of interest (ROI) in the hyperspectral images and to extract the spectral data. Python was used for the following preprocessing and prediction model analysis.

Before model training, the original raw spectral data (RAW) was preprocessed using SNV (standard Normal Variate), SG1 (Savitzky-Golay 1st derivative), and a combination of SNV and SG1 (SNV+SG1), resulting in four preprocessing conditions including RAW.

Prediction Model Development

A total of 90 hyperspectral data were used for model training and evaluation. These data were used to build harvest-time prediction models with PLS-DA, Logistic Regression, Random Forest, SVM, and XGBoost. Such a small dataset would lead to high variance under a conventional train-test split (Singh et al., 2021). Instead, Stratified Group K-fold cross-validation (5-fold, 5 repeats) was applied to the entire dataset. The data was grouped by sample to prevent data leakage, and the average performance across folds was reported as the final result (Broomé et al., 2023). Model performance was primarily compared using accuracy and F1-score, the latter defined as the harmonic mean of precision and recall (Powers, 2011), across all preprocessing model combinations; for the best-performing combination, precision and recall were additionally examined for each growth stage.

Wavelength Selection

The optimal number of latent variables (LVs, up to 10) for the PLS-DA model was determined via cross-validation to balance model complexity and predictive performance (Wold et al., 2001). Using this model, Variable Importance in Projection (VIP) scores were calculated to identify wavelengths with a VIP>1.0 as important predictors. Wavelengths near the spectral edges were excluded from interpretation due to lower sensor reliability in those regions.

RESULTS & DISCUSSION

Spectral Preprocessing Results

RAW, SNV, SG1, and SNV+SG1 were applied to the acquired spectral data. The results showed clear spectral differences between growth stages when using SG1 and SNV+SG1 (Fig. 4). This means that the 1st derivative effectively removed background noise and baseline variation while enhancing spectral feature associated with differences among growth stages (Rinnan et al., 2009). This finding was consistent with the prediction model performance results shown later (Table 2).

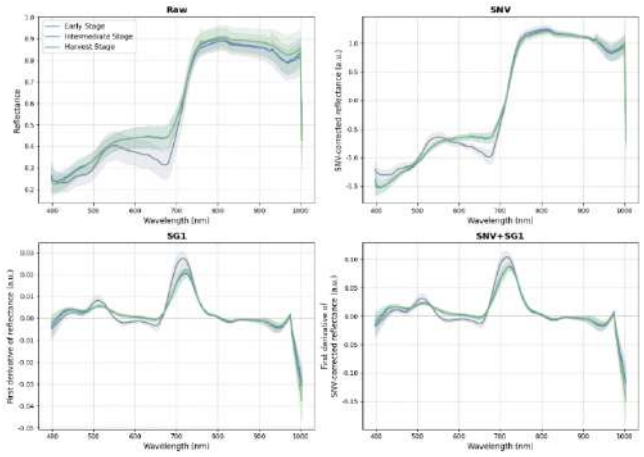

Fig. 4 Comparison of mean spectral reflectance profiles across preprocessing methods (Raw, SNV, SG1, SNV+SG1) by growth stage

Prediction Model Performance

Table 2 summarizes the classification performance of the five classification models under the four spectral processing methods. SNV+SG1+PLS-DA showed the best performance with an accuracy and F1-score of 0.933. This was followed by SG1+PLS-DA (0.920) and RAW+PLS-DA (0.909).

Table 2 Classification performance of preprocessing methods and machine models (5×5 fold Group Cross-Validation)

Rank	Preprocessing	Model	Accuracy	F1-score
1	SNV+SG1	PLS-DA	0.933±0.063	0.933±0.062
2	SG1	PLS-DA	0.920±0.075	0.920±0.075
3	RAW	PLS-DA	0.909±0.059	0.907±0.060
4	SNV+SG1	Random Forest	0.904±0.090	0.903±0.091
5	SG1	Random Forest	0.902±0.063	0.902±0.064
6	SNV+SG1	SVM	0.884±0.052	0.883±0.053
7	SNV+SG1	XGBoost	0.884±0.044	0.881±0.049
8	SG1	XGBoost	0.871±0.100	0.869±0.103
9	SG1	SVM	0.862±0.077	0.861±0.077
10	SNV	SVM	0.862±0.057	0.860±0.056

PLS-DA showed consistently high performance (0.862 to 0.933) regardless of the preprocessing methods. However, Logistic Regression showed the lowest performance across all methods (0.662 to 0.767). Random Forest, SVM, and XGBoost improved significantly when derivative preprocessing (SG1, SNV+SG1) was applied. This shows that PLS-based models are strong against multicollinearity. Therefore, they are better for hyperspectral data where wavelengths are highly connected (Wold et al., 2001).

Generalization Performance by Initial Fruit Size Group

The accuracy for each initial fruit size group (small, medium, large) was 97.3% for large size, 92.0% for small size, and 90.7% for medium size. The difference between groups was less than 6.6% (Table 3). This shows that the model keeps a stable performance despite differences in initial size. It suggests that the model has good generalization performance and can be applied to melons of various size.

Table 3 Classification accuracy of the SNV+SG1+PLS-DA model by initial fruit size group

Size	Accuracy
Small	92.0%
Medium	90.7%
Large	97.3%

Classification Performance by Growth Stage

The confusion matrix of the SNV+SG1+PLS-DA model showed recall of 95.33%, 93.33%, and 91.33% for the early, intermediate, and harvest stages, respectively (Fig.5). The largest error was harvest stage samples misclassified as intermediate (11 samples, 7.33%). Confusion also occurred between the early and harvest stage in both directions (7 and 2 samples), indicating that errors were not strictly confined to adjacent stages. Although their combined rate remained low (3.0%), this phenomenon may be attributed to variation in individual melon growth rates or specific spectral noise. Reflecting this trend, the F1-score decreased progressively from the early (0.957) to the intermediate (0.930) and harvest stages (0.913) (Table 4). It is considered that this is because the transition from the early stage to harvest-time is a gradual physical and biological process.

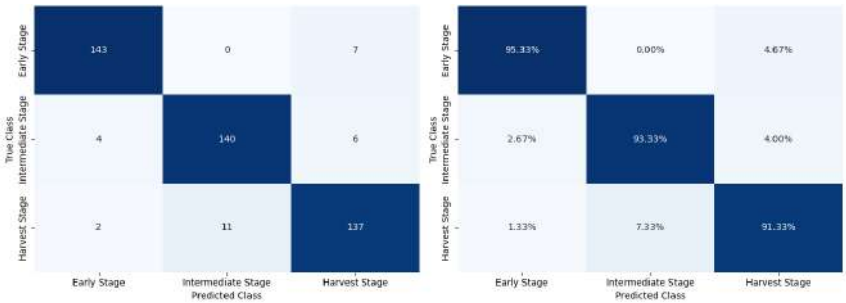

Fig. 5 Classification results of the SNV+SG1+PLS-DA model.

Table 4 Classification performance by class (SNV+SG1+PLS-DA)

Class	Precision	Recall	F1-score
Early Stage	0.960	0.953	0.957
Intermediate Stage	0.927	0.933	0.930
Harvest Stage	0.913	0.913	0.913

PLS-DA Score Plot Results

To visualize how the best performing PLS-DA model discriminated among growth stages in the reduced latent space, the score plot (LV1 vs LV2) was examined (Fig 6(A)).

In the PLS-DA score plot, samples from the early stage were clearly separated on the left side along the first latent variable (LV1). On the other hand, samples from the intermediate and harvest stages were distributed on the right side. Their group centers are distinct, but they overlap slightly. This means that as the harvest-time gets closer, internal changes slow down and the spectral patterns become similar. This explains why errors happened between neighboring growth stages in the earlier confusion matrix.

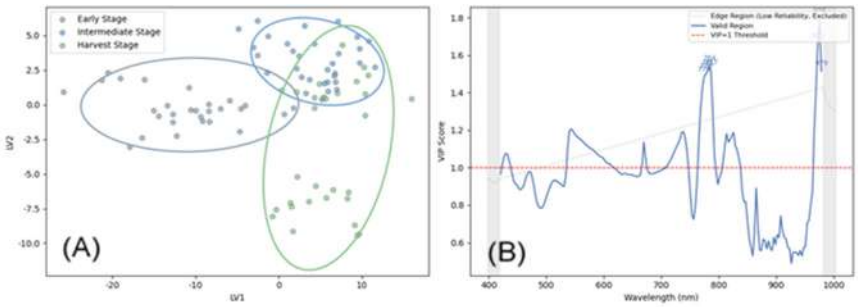

Fig. 6 (A) PLS-DA score plot (LV1 vs LV2) and (B) VIP Score by wavelength for the SNV+SG1+PLS-DA.

VIP-Based Wavelength Analysis

The most effective wavelengths were identified at approximately 542-548 nm in the visible light region and 771-786 nm and 969-978 nm in the near-infrared region (Fig. 6(B)). The visible region is associated with changes in fruit color, including chlorophyll degradation, while the near-infrared region is associated with spectral response related to internal constituents such as sugar accumulation and water content (Nicolaï et al., 2007). These results indicate that both visible and near-infrared spectral information contributed to the discrimination of melon growth stages and harvest-time prediction.

CONCLUSIONS

This study developed a HSI-based model to predict the harvest-time of melons. The results showed that combination of SNV+SG1 processing with the PLS-DA model achieved the best performance, with both the accuracy and F1-score reaching 0.933. The wavelengths near 540 nm, 780 nm, 970 nm were confirmed as effective for predicting the harvest-time. When the model was evaluated across different initial fruit size groups, it showed a stable classification accuracy of over 90% for all groups. These results demonstrate the robust generalization performance of the proposed model across variations in initial fruit size. Overall, the findings confirm the feasibility of using HSI for non-destructive melon harvest-time prediction and suggest its potential application to automated harvest decision-making and robotic harvesting systems.

ACKNOWLEDGEMENTS

This study was supported by 2026 R&D program (Project Number: RS-2025-02219360) between Rural Development Administration and Ministry of Agriculture, Food and Rural Affairs and Ministry of Science and ICT, Republic of Korea.

REFERENCES

FAO. 2025. FAOSTAT: Crops and livestock products. Rome, Italy: Food and Agriculture Organization of the United Nations. Available at: https://www.fao.org/faostat/en/#data/QCL. Accessed 4 September 2026.

Lu, Y., W. Saeys, M. Kim, Y. Peng, and R. Lu. 2020. Hyperspectral imaging technology for quality and safety evaluation of horticultural products: A review. *Trends in Food Science & Technology* 99: 63-73.

Naqvi, L.H., B. Balasubramaniam, J. Li, L. Liu, and B. Li. 2025. Four-dimensional hyperspectral imaging for fruit and vegetable grading. *Agriculture* 15(15): 1702.

Neupane, C., M. Pereira, A. Koirala, and K. B. Walsh. 2023. Fruit sizing in orchard: A review from caliper to machine vision with deep learning. *Sensors* 23(8): 3868.

Nicolaï, B. M., K. Beullens, E. Bobelyn, A. Peirs, W. Saeys, K. I. Theron, and J. Lammertyn. 2007. Nondestructive measurement of fruit and vegetable quality by means of NIR spectroscopy: A review. Postharvest Biology and Technology 46(2):99-118.

Périn, C., L. S. Hagen, N. Giovinazzo, D. Besombes, C. Dogimont, and M. Pitrat. 2002. Genetic control of fruit shape acts prior to anthesis in melon (Cucumis melo L.). *Molecular Genetics and Genomics* 266(6): 933-941.

Powers, D. M. W. 2011. Evaluation: From precision, recall and F-measure to ROC, informedness, markedness and correlation. *Journal of Machine Learning Technologies* 2(1): 37-63.

Rajendran, V., B. Debnath, S. Mghames, W. Mandil, S. Parsa, S. Parsons, and A. Ghalamzan-E. 2024. Towards autonomous selective harvesting: A review of robot perception, robot design, motion planning and control. *Journal of Field Robotic* 41(7):2247-2279.

Rinnan, Å., F. van den Berg, and S. B. Engelsen. 2009. Review of the most common pre-processing techniques for near-infrared spectra. *TrAC Trends in Analytical Chemistry* 28(10): 1201-1222.

Shah, I. H., W. Jinhui, X. Ding, X. Li, A. Rehman, M. A. Manzoor, Y. Zhang, Q. Niu, P. Li, and L. Chang. 2025. A non-destructive approach: Estimation of melon fruit quality attributes and nutrients using hyperspectral imaging coupled with machine learning. *Smart Agricultural Technology* 10: 100811.

Singh, V., M. Pencina, A. J. Einstein, J. X. Liang, D. S. Berman, and P. Slomka. 2021. Impact of train/test sample regimen on performance estimate stability of machine learning in cardiovascular imaging. *Scientific Reports* 11: 14490.

Wold, S., M. Sjöström, and L. Eriksson. 2001. PLS-regression: A basic tool of chemometrics. *Chemometrics and Intelligent Laboratory Systems* 58(2): 109-130.

Yan, B.F., M. Zhao, C. Y. Zhang, and L.L. Shi. 2026. Allocation of essential minerals within the fruit of melon: Vascular supply shifts and constraints on tissue accumulation during development. *Scientia Horticulturae* 363:114911.

AI-P12

Proceedings of The 12th International Symposium on Machinery and Mechatronics for Agriculture and Biosystems Engineering (ISMAB 2026)
20-24 October 2026, Busan, Republic of Korea

LESION DETECTION AND DISEASE STAGE CLASSIFICATION IN STRAWBERRY AND TOMATO USING DEEP LEARNING

Tae-Hwi Lee[1,2], Yu-Jin Jeon[1,2], Dae-Hyun Jung[1,2*]

[1]Department of Smart Farm Science, Kyung Hee University, Yongin 17104, Republic of Korea
[2]BK21 Interdisciplinary Program in IT-Bio Convergence System, Kyung Hee University, Yongin 17104, Republic of Korea
*Corresponding Author-- Voice: +82-31-201-2657, Email: daehyun@khu.ac.kr

Abstract: Timely crop disease management requires lesion localization and assessment of symptom progression. This study evaluated a modular deep-learning framework for six diseases and physiological disorders in strawberry and tomato: strawberry gray mold, powdery mildew, and tip burn, and tomato gray mold, leaf mold, and bacterial canker. A total of 21,654 lesion bounding boxes were used with a group-safe data split. YOLO11m localized lesions and identified target classes, and disease-specific EfficientNet-B2 models classified cropped lesion regions into S2 (early stage) or S3 (outbreak). Grad-CAM++ provided qualitative visualizations of regions associated with stage predictions. YOLO11m achieved a validation mAP@0.50 of 85.99%. Among lesions detected as the correct target class with an intersection over union of at least 0.50, the mean conditional stage accuracy across the six classes was 88.06%. Tomato bacterial canker had only 4.8% detection coverage, limiting interpretation of its stage-classification accuracy. Activation maps frequently overlapped visible symptoms but sometimes extended into surrounding tissue. These findings demonstrate the potential of a modular detection–classification framework and emphasize the need to interpret stage accuracy alongside detection coverage.

Key Words: Crop Disease Detection, Disease Stage Classification, Grad-CAM++, Explainable AI

INTRODUCTION

Image-based deep learning supports automated crop disease diagnosis through classification, object detection, and segmentation (Das et al., 2025). In tomato leaf disease detection, variations in lesion scale and complex backgrounds remain important challenges (Yan and Li, 2025). Disease management also requires information about symptom progression beyond the presence and location of a disease.

Recent studies have addressed disease severity assessment by distinguishing subtle visual differences and learning lesion-focused representations to reduce background interference (Li and Li, 2025; Yu et al., 2025). These approaches motivate examining lesion detection and

subsequent stage classification as separate components, so that limitations at each step can be identified.

The objective of this study was to evaluate YOLO11m lesion detection and EfficientNet-B2 classification into S2 (early stage) and S3 (outbreak) for six diseases and physiological disorders in strawberry and tomato, and to qualitatively examine prediction-associated regions using Grad-CAM++.

MATERIALS AND METHODS

Dataset Construction and Group-Safe Split

A total of 21,654 lesion bounding boxes were used for six diseases and physiological disorders: strawberry gray mold, powdery mildew, and tip burn, and tomato gray mold, leaf mold, and bacterial canker. To prevent data leakage, a group-safe split was applied so that images originating from the same acquisition group were assigned exclusively to the training, validation, or test set. Acquisition date or image sequence information was used to define the groups. For tomato bacterial canker, group assignments were further adjusted at the group level to ensure that both S2 and S3 samples were represented in the training, validation, and test sets. The image split and total number of lesion bounding boxes are summarized in Table 1.

Table 1. Image split and total number of lesion bounding boxes.

Split	Number of images
Train	11,251
Validation	2,312
Test	2,708
Total lesion bounding boxes	21,654

Note: Tomato bacterial canker test support comprised 4 S2 and 17 S3 lesions.

Label Refinement and Disease Stage Definition

Existing bounding box annotations were reviewed according to disease-specific symptoms and image acquisition conditions. Annotations that were visually indistinguishable from healthy tissue or did not contain clear symptoms were excluded, and observable symptomatic regions were retained for stage classification. Disease progression was standardized into S2 (early stage) and S3 (outbreak), with disease-specific visual criteria applied to distinguish the two stages. S1 was not included because the stage classifier was designed to distinguish S2 and S3 within already detected lesion regions.

Modular Disease Detection and Stage Classification Framework

A YOLO11m detector initialized with pretrained weights was trained to localize lesions and identify one of the six target classes. Training used an input size of 768 pixels, a batch size of 8, a maximum of 50 epochs, a random seed of 42, and an early-stopping patience of 15. The lesion regions detected by YOLO11m were cropped with 10% contextual padding around each bounding box. The crops were converted to RGB, resized to 260 × 260 pixels, and normalized using ImageNet statistics. Horizontal flipping, color jittering, and rotations of ±8° were applied to the training data, whereas no augmentation was applied to the validation and test data.

The disease class predicted by YOLO11m was used to select the corresponding EfficientNet-B2 model for S2/S3 classification. Each model was trained to distinguish S2 from S3 using cross-entropy loss, and the checkpoint with the highest validation macro-F1 score was selected as the final stage-classification model. The modular detection and stage-classification framework is illustrated in Fig. 1.



Fig. 1 Overview of the proposed disease detection and stage classification framework. (a) YOLO11m detects lesions and identifies disease classes. Detected regions are cropped with 10% contextual padding and routed to disease-specific EfficientNet-B2 models for classification into S2 (early stage) or S3 (outbreak). (b) Architecture of the EfficientNet-B2 stage classifier and post hoc Grad-CAM++ interpretation. (c) Representative images of the six target classes.

Grad-CAM++ Analysis

Grad-CAM++ activation maps were generated post hoc for the trained EfficientNet-B2 stage classifiers and overlaid on lesion images. The correspondence between highly activated regions and visible symptoms was examined qualitatively.

Performance Evaluation

Each annotated lesion was matched to the YOLO11m prediction with the highest intersection over union (IoU) among predictions of the same target class. A match required IoU ≥ 0.50. Matched lesions were evaluated using the corresponding EfficientNet-B2 stage classifier.

Detection coverage was the proportion of annotated lesions that met the matching criteria. Conditional stage accuracy was the proportion of matched lesions correctly classified as S2 or S3. Detector misses, incorrect target-class predictions, and predictions with IoU < 0.50 were excluded from this accuracy metric.

RESULTS & DISCUSSION

Disease Detection and Stage Classification

YOLO11m achieved a validation precision of 89.73%, recall of 78.38%, mAP@0.50 of 85.99%, and mAP@0.50:0.95 of 72.25%. Figure 2 shows the training loss and validation performance across epochs.

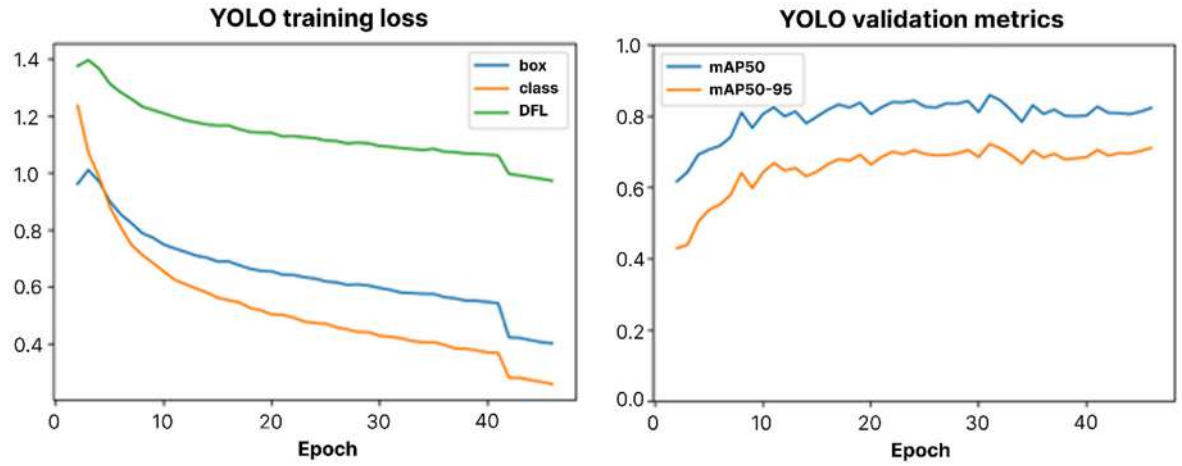

Fig. 2. Training loss and validation performance of YOLO11m. The left panel shows bounding box regression loss (box), classification loss (class), and distribution focal loss (DFL). The right panel shows validation mAP@0.50 and mAP@0.50:0.95 across training epochs.

Using the matching criteria defined above, the mean conditional stage accuracy across the six target classes was 88.06%. This value describes stage classification following successful lesion detection and target-class identification; it is not the end-to-end accuracy across all annotated lesions. Table 2 summarizes detection coverage and conditional stage accuracy for each target class.

Table 2. Detection coverage and conditional stage accuracy for six target classes.

Disease	Detection coverage (%)	Conditional stage accuracy (%)
Strawberry gray mold	96.9	86.5
Strawberry powdery mildew	99.0	89.8
Strawberry tip burn	97.1	94.7
Tomato gray mold	100.0	82.0
Tomato leaf mold	100.0	75.3
Tomato bacterial canker	4.8	100.0

The three strawberry targets achieved detection coverage of 96.9–99.0% and conditional stage accuracy of 86.5–94.7%. Tip burn had the highest conditional stage accuracy among these targets, followed by powdery mildew and gray mold.

Tomato gray mold and leaf mold both achieved 100.0% detection coverage, but their conditional stage accuracies were 82.0% and 75.3%, respectively. Their principal limitation therefore occurred during stage discrimination after successful detection. Subtle differences in symptom progression may contribute to this difficulty, consistent with the challenges addressed in recent severity-assessment research (Li and Li, 2025). Tomato bacterial canker had only 4.8% detection coverage: one of 21 annotated lesions met the matching criteria. Its 100.0% conditional stage accuracy was therefore based on a single lesion and cannot support a reliable assessment of stage-classification performance. These contrasting patterns show

why detection coverage and conditional stage accuracy must be considered together when evaluating a sequential detection–classification pipeline.

Grad-CAM++ Visualization

Ten cases per target class were examined, yielding 60 Grad-CAM++ visualizations. Representative examples are shown in Fig. 3. Highly activated regions frequently overlapped visible discoloration, powdery symptoms, browning, or necrosis, but sometimes extended into surrounding tissue. Yu et al. (2025) also used Grad-CAM to examine attention in disease severity assessment. The present Grad-CAM++ maps provide qualitative evidence of prediction-associated regions, but do not by themselves establish the biological validity or reliability of the predictions.

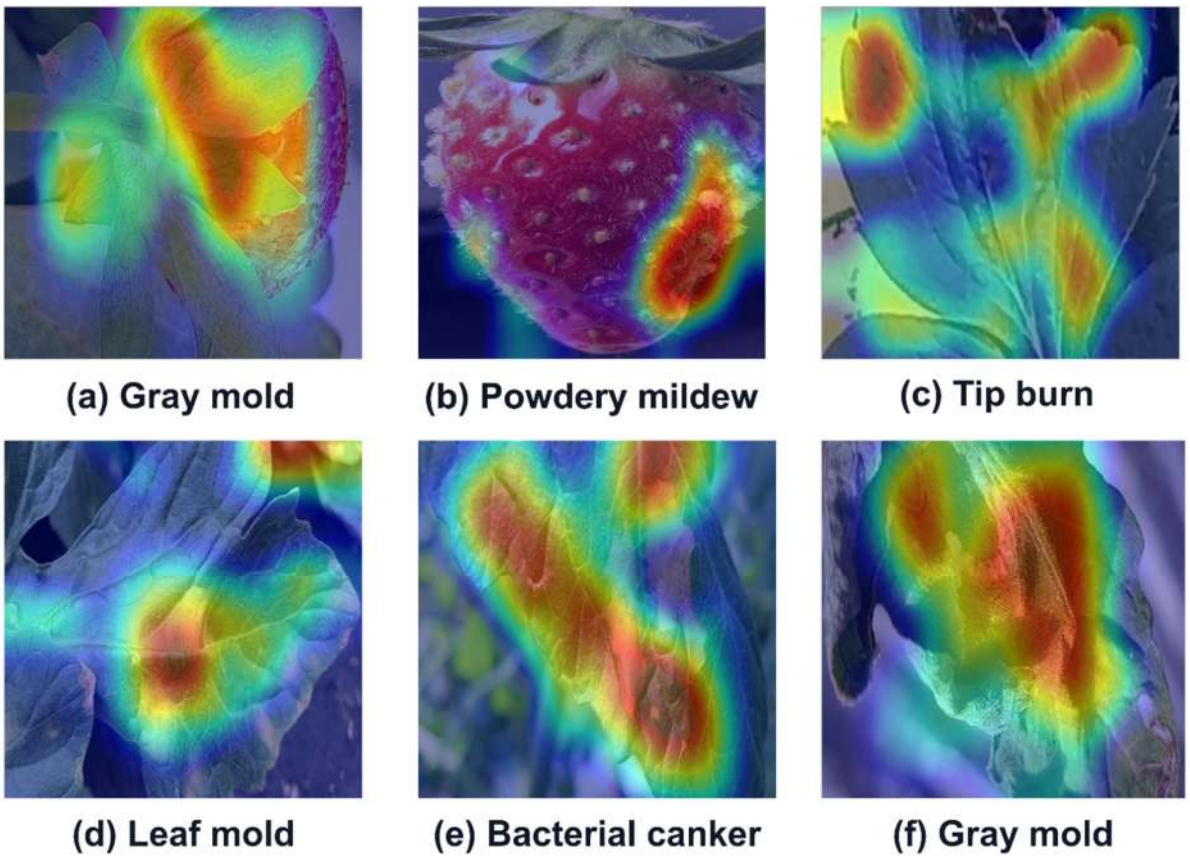

Fig. 3. Representative Grad-CAM++ visualizations for the six target classes: (a) strawberry gray mold, (b) strawberry powdery mildew, (c) strawberry tip burn, (d) tomato leaf mold, (e) tomato bacterial canker, and (f) tomato gray mold. Warmer colors indicate image regions with relatively greater contribution to the EfficientNet-B2 S2/S3 stage-classification prediction; interpretation is qualitative.

CONCLUSIONS

The YOLO11m–EfficientNet-B2 framework combined lesion detection with S2/S3 stage classification for six strawberry and tomato target classes. Validation detection mAP@0.50 was 85.99%, and mean conditional stage accuracy was 88.06%. Performance limitations differed by target class: tomato gray mold and leaf mold were limited mainly by stage discrimination, whereas bacterial canker was limited by low detection coverage. Grad-CAM++ provided

qualitative insight into prediction-associated regions. Reliable interpretation of this modular framework requires reporting detection coverage alongside stage accuracy. Additional data are needed to evaluate poorly detected classes.

REFERENCES

Das, A., F. Pathan, J. R. Jim, M. M. Kabir, and M. F. Mridha. 2025. Deep learning-based classification, detection, and segmentation of tomato leaf diseases: A state-of-the-art review. Artificial Intelligence in Agriculture 15(2): 192-220. https://doi.org/10.1016/j.aiia.2025.02.006.

Li, X., and S. Li. 2025. KDI-Transformer: A method for identifying kiwifruit leaf disease severity in complex environments. Computers and Electronics in Agriculture 237: 110745. https://doi.org/10.1016/j.compag.2025.110745.

Yan, C., and H. Li. 2025. CSPNet: A feature interaction network for tomato leaf disease detection in complex scenarios. Computers and Electronics in Agriculture 238: 110823. https://doi.org/10.1016/j.compag.2025.110823.

Yu, Y., X. Wu, P. Yu, Q. Wan, Y. Dan, Y. Xiao, and Q. Wang. 2025. Location-guided lesions representation learning via image generation for assessing plant leaf diseases severity. Plant Phenomics 7(2): 100058. https://doi.org/10.1016/j.plaphe.2025.100058.

AI-P13

Proceedings of The 12th International Symposium on Machinery and Mechatronics for Agriculture and Biosystems Engineering (ISMAB 2026)
20-24 October 2026, Busan, Republic of Korea

WHY THE BEST MODEL CHANGES: IMAGE-BASED FRESH-WEIGHT ESTIMATION OF LETTUCE UNDER TRAINING–DEPLOYMENT SHIFTS

Ki-Su Park[1], Woo-Joo Choi[1], Myongkyoon Yang[2, 3*]

[1]Department of AI in Agriculture, Graduate School of AI Convergence, Jeonbuk National University, Jeonju 54896, Republic of Korea
[2]Department of Bioindustrial Machinery Engineering, Jeonbuk National University, Jeonju 54896, Republic of Korea
[3]Institute of Agricultural Machinery & ICT Convergence, Jeonbuk National University, Jeonju 54896, Republic of Korea
*Corresponding Author: yangmk@jbnu.ac.kr

Abstract: AI-based agricultural prediction models may perform differently across training and deployment conditions. A model that performs best within the training distribution may not retain the same advantage under an unseen cultivation cycle or beyond the training range. This study compared lettuce fresh-weight estimation models with varying flexibility and structural constraints under in-distribution, distribution-shift, and extrapolation conditions. The dataset comprised 869 top-view images of 266 butterhead lettuce plants (cv. 'Fairy') from three cultivation cycles, with fresh weights of 0.02–69 g. Morphological phenotypes and raw-pixel vectors were evaluated using linear, tree-based, and MLP models, original images using a ResNet18 CNN, and projected area using an allometric model. Evaluation included plant-level random splits, an unseen cultivation cycle, out-of-range prediction, and growth-stage extrapolation. Within the training distribution, the CNN achieved the lowest MAPE of 12%, while morphological phenotype inputs outperformed raw-pixel vectors. Under the unseen-cycle evaluation, model rankings changed, with the allometric model achieving 23% MAPE versus 29% for the CNN. Beyond the training range, tree-based models and the CNN showed increased errors, whereas the allometric model remained more stable. For late-stage prediction from early-stage data, the allometric model achieved 29% MAPE versus 37–46% for more flexible models. The ranking shift reflected differences in extrapolation behavior: more flexible models exploited complex relationships within the training data, but these relationships became less reliable beyond the observed range, whereas the relatively constrained form of the allometric model was associated with a more consistent response under extrapolation. Thus, in-distribution performance alone may not identify the best model under distribution shift or extrapolation.

Key Words: fresh weight estimation, model selection, extrapolation, distribution shift

ACKNOWLEDGEMENTS

This work was supported by the National Research Foundation of Korea (NRF) grant funded by MSIT (2022R1C1C2005959), and by IPET and KosFarm through the Smart Farm Innovation Technology Development Program (MAFRA, MSIT, RDA, RS-2025-02315611).

AI-P14

Proceedings of The 12th International Symposium on Machinery and Mechatronics for Agriculture and Biosystems Engineering (ISMAB 2026)
20-24 October 2026, Busan, Republic of Korea

DATA-DRIVEN IDENTIFICATION OF THI THRESHOLDS FOR PRODUCTIVITY AND EGG GRADE DISTRIBUTION IN LAYING HENS

Leecheon Kim[1], Darae Kang[2*]

[1]Department of Animal Science, Jeonbuk National University, Republic of Korea
[2]Department of Animal Biotechnology, Jeonbuk National University, Republic of Korea
*Corresponding Author- Voice: +82-63-270-2610, Email: drkang@jbnu.ac.kr

Abstract: Heat stress is a major constraint on the productivity of commercial laying hens, and the temperature-humidity index (THI) is widely used to quantify the combined thermal load imposed by temperature and relative humidity. Reported THI thresholds vary considerably across studies, however, and are often derived from a single population or a short observation period, leaving it unclear whether different production traits diverge at the same or at distinct thermal loads. In this study, we used large-scale, multi-farm longitudinal records to identify data-driven THI breakpoints for laying rate, egg weight, and low-grade egg ratio, and to determine whether cumulative heat exposure exerts effects beyond same-day THI. Daily records were compiled from four commercial laying hen farms in South Korea (2018-2026); a set of 26 batches meeting data-completeness criteria was used for the breakpoint and heat-load analyses. Each outcome was first adjusted for hen age and batch fixed effects, and the resulting residuals were regressed against THI using segmented (breakpoint) regression. A cumulative heat-load index, defined as the rolling mean of THI in excess of each trait's breakpoint over 3-, 5-, 7-, and 14-day windows, was then regressed against each outcome. Laying rate exhibited a breakpoint at THI 62.0, increasing slightly with THI up to this point ($\beta = 0.167$, $p = 0.001$) before declining sharply above it ($\beta = -0.312$, $p<0.001$). Low-grade egg ratio remained unchanged below THI 80. ($p = 0.956$) but increased sharply above it ($\beta = 0.0088$, $p <0.001$). Egg weight declined gradually across nearly the entire THI range ($\beta = -0.061$, $p < 0.001$) and leveled off only above THI 80.5 ($\beta = 0.382$, $p = 0.059$, marginal). The cumulative heat-load index was significantly associated with laying rate and low-grade egg ratio at every window length, with the effect strengthening as the window lengthened from 3 to 14 days, but it was not significantly associated with egg weight at any window length. These results indicate that laying rate is the most broadly heat-sensitive trait, responding to both concurrent and cumulative thermal load from a comparatively low THI, whereas low-grade egg ratio responds only once heat load becomes severe and sustained, and egg weight follows a distinct, largely THI-independent declining trend. Compared with literature-based THI zone boundaries (comfort/alert at THI 70; alert/danger at THI 75.5; danger/emergency at THI 81), the laying-rate breakpoint identified here falls below the published comfort threshold, suggesting that commercial multi-farm flocks may begin losing productivity earlier than existing zone classifications imply. These findings provide a practical, data-driven basis for establishing trait-specific environmental control criteria in smart layer house management.

Key Words: Temperature-humidity index; laying hen; breakpoint regression; cumulative heat load; smart farm environmental control

INTRODUCTION

Rising ambient temperature and humidity are recognized as major environmental stressors affecting the productivity of commercial laying hens (Kim et al., 2024). The temperature-humidity index (THI), which combines temperature and relative humidity into a single index, is widely used to quantify heat stress in livestock production, and published THI zone classifications (comfort, alert, danger, and emergency) are commonly applied as reference boundaries (Zulovich and DeShazer, 1990; Kim et al., 2021). However, such classifications are often derived from a limited number of populations or short observation periods, and it remains unclear whether laying rate, egg weight, and egg-grade distribution deviate from normal patterns at the same thermal load or whether some traits respond earlier than others.

Farm-level longitudinal data are inherently confounded by hen age and batch-to-batch variation, both of which can obscure or distort the true relationship between environmental stress and productivity unless explicitly controlled. Therefore, adjusting for age and batch effect before estimating THI breakpoints allows thermal responses to be evaluated independently of major non-environmental sources of production variation.

The objective of this study was to identify data-driven THI breakpoints for laying rate, egg weight, and low-grade egg ratio using age- and batch-adjusted residuals from multi-farm longitudinal records, to determine whether cumulative heat-load exposure affects these traits beyond same-day THI, and to compare the resulting breakpoints with published THI zone boundaries.

MATERIALS AND METHODS

DATASET AND ANALYSIS WORKFLOW

The analysis proceeded from raw daily housing, environmental, and production records through THI calculation, batch x age adjustment (residuals versus batch-age expected values), breakpoint regression (threshold THI estimation), and cumulative heat-load index analysis (3-, 5-, 7-, 14-day rolling mean), to assessment of threshold persistence.
Daily production and environmental records were obtained from four commercial laying hen farms in South Korea, comprising 18 houses over approximately 8 years (2018-2026). THI was calculated from indoor temperature and relative humidity using the NRC formula (°F-based). For the breakpoint and cumulative heat-load analyses, 26 batches meeting additional data-completeness criteria were selected, yielding 10,602-10,724 daily observations depending on the outcome variable. Low-grade egg ratio was defined as the sum of weak-shelled and broken/soiled eggs, excluding undersized-but-normal eggs.

STATISTICAL ANALYSIS

Each outcome (laying rate, egg weight, low-grade egg ratio) was regressed on hen age (cubic polynomial) and batch fixed effects, and the residuals from this model were used in all subsequent analyses to remove age-related and batch-level confounding. This step was necessary because laying rate rises sharply from 20 weeks, peaks near 90% around 25-35 weeks, and gradually declines with age thereafter, with substantial variation across houses;

without removing this age pattern, it would be confounded with any THI-related effect.

Age- and batch-adjusted residuals were then modeled as a function of THI using segmented (breakpoint) regression to estimate the THI value at which each trait's slope changes. A cumulative heat-load index, defined as the rolling mean (3, 5, 7, and 14 days) of daily THI in excess of each trait's estimated breakpoint, was regressed on the corresponding outcome to test for delayed or accumulated effects beyond same-day THI. Because the three traits had different breakpoints, a separate heat-load index was computed for each outcome using its own estimated threshold.

RESULTS & DISCUSSION

The dataset covered a wide THI range (39.6-87.4; Fig. 1), with the bulk of observations concentrated between THI 55 and 75.

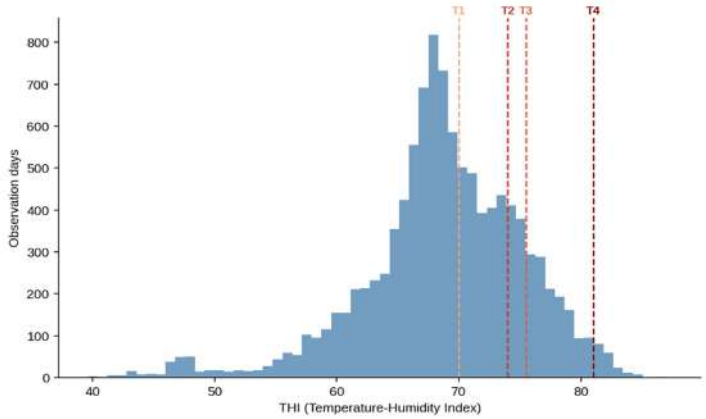

Fig.1. Distribution of daily THI values, with reference THI zone boundaries from the literature (T1: comfort/alert, 70; T2: laying rate breakpoint reported for Thai native hens, 74; T3: alert/danger, 75.5; T4: danger/emergency, 81)(Loengbudnark et al., 2023; Kim et al., 2024)

Segmented regression on the age- and batch-adjusted residuals identified three distinct breakpoints (Table 1, Fig. 2). Laying rate rose slightly with THI up to 62.0 (β = +0.167, p = 0.001) before declining sharply above it (β = -0.312, p<0.001). Egg weight declined steadily across nearly the full THI range (β = -0.061, p<0.001) and only leveled off above THI 80.5, above which the slope became positive but was only marginally significant (β = +0.382, p = 0.059). In contrast, the low-grade egg ratio remained relatively stable below THI 80.0 but increased sharply above this breakpoint (β = +0.0088, p<0.001).

Table 1. Segmented (breakpoint) regression results for age- and batch-adjusted residuals.

Residual	Breakpoint (THI)	Slope below	Slope above
Laying rate (%p)	62.0	+0.167**	-0.312***
Egg weight (g)	80.5	-0.061***	+0.382†
Low-grade egg ratio	80.0	0.000 (n.s.)	+0.0088***

** p<0.01, *** p<0.001, †marginal (p=0.059), n.s: not significant

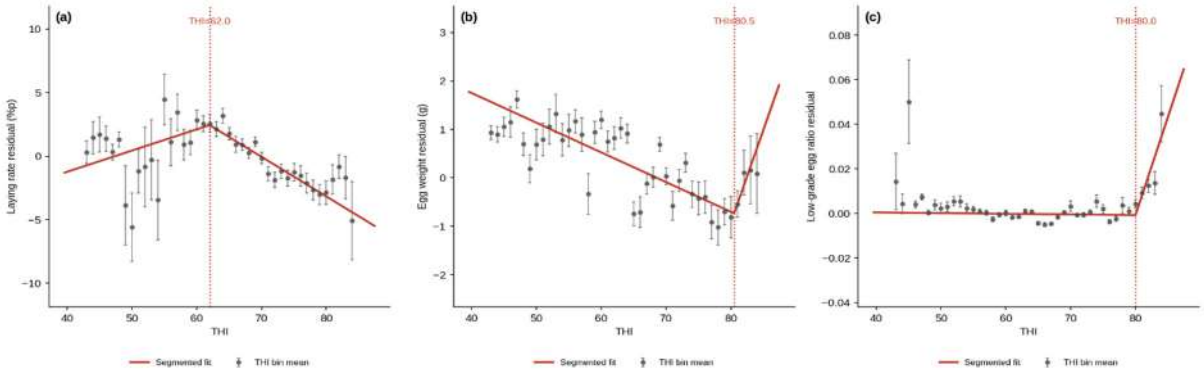

Fig.2. Segmented regression fits for (a) laying rate, (b) egg weight, and (c) low-grade egg ratio residuals as a function of THI. Points are THI-bin means ± SEM; dashed lines mark the estimated breakpoints.

Contrary to our initial expectation that egg quality traits would respond only at extreme heat load, laying rate showed the lowest breakpoint (THI 62.0) of the three traits. This value was substantially below both the conventional comfort-to-alert boundary of THI 70 proposed for laying hens (Fig. 1) and the THI 74 threshold previously reported for the onset of declining egg production in Thai native hen (Loengbudnark et al., 2023; Kim et al., 2024). This indicates that, in this commercial condition, laying rate began to depart from its age-adjusted expected trajectory at a substantially low thermal load than existing literature-based zone classifications would suggest. However, the breakpoint identified here should be interpreted as an empirical production-response breakpoint rather than a universal physiological threshold for heat stress, particularly because thermal responses can vary with genotype, age, and production conditions (Mignon-Grasteau et al., 2015).

Low-grade egg ratio and egg weight, by contrast, showed breakpoints (80.0 and 80.5) close to the published danger/emergency boundary (THI 76-81), indicating that egg quality metrics only diverge under more severe heat load (Kim et al., 2021). Thus, the separation between the laying-rate breakpoint and those of the egg-related traits supports a trait-specific hierarchy of thermal sensitivity rather than a single THI threshold applicable to all production traits.

The cumulative heat-load analysis (Table 2) reinforced this pattern. The heat-load index was significantly associated with laying rate and low-grade egg ratio at every window length (3-14 days), with the standardized effect strengthening as the window lengthened – consistent with a cumulative or delayed component to heat stress on these two traits. Egg weight, however, showed no significant association with cumulative heat load at any window, suggesting that its gradual decline across the THI range reflects a mechanism distinct from accumulated thermal exposure. Previous cyclic heat-stress studies have similarly shown persistent reductions in feed intake and egg production during prolonged exposure, demonstrating that the duration of heat exposure contributes to production losses in addition to heat intensity (Barrett et al. 2019).

Table 2. Standardized regression coefficients for the cumulative heat-load index by rolling window.

Residual	3d window	7d window	14d window	Pattern
Laying rate	-0.117***	-0.123***	-0.131***	Strengthens with window
Egg weight	+0.005	+0.007	+0.004	No significant effect
Low-grade egg ratio	+0.113***	+0.129***	+0.145***	Strengthens with window

*** p<0.001.

Taken together, these results suggest that laying rate – not egg quality – is the earliest and most broadly heat-sensitive production trait in this dataset, responding to both concurrent and cumulative thermal load from a comparatively low THI. Low-grade egg ratio functions as a later-stage indicator that only reflects heat stress once exposure becomes severe and sustained, while egg weight follows a largely independent declining trend that is not explained by cumulative heat load. This pattern differs from the assumption, common in single-trait heat-stress studies, that all production traits share a common thermal threshold.

CONCLUSIONS

Using age- and batch-adjusted residuals from a multi-farm and multi-year commercial dataset, this study identified trait-specific THI breakpoints for laying rate (62.0), low-grade egg ratio (80.0), and egg weight (80.5, marginal). Laying rate was the most heat-sensitive trait, responding to both same-day and cumulative thermal load from a THI well below published comfort-zone boundaries, while low-grade egg ratio responded only under severe, sustained heat load and egg weight followed a distinct, largely THI-independent decline. These trait-specific, data-driven thresholds provide a practical basis for prioritizing laying-rate monitoring as an early trigger for environmental control interventions in smart layer house management, with low-grade egg ratio serving as a secondary indicator of severe heat stress. Future work will extend this threshold-identification framework to additional production and environmental variables within the same longitudinal dataset.

ACKNOWLEDGEMENTS

This work was supported by Korea Institute of Planning and Evaluation of Technology in Food, Agriculture and Forestry (IPET) and Korea Smart Farm R&D Foundation (KosFarm) through Smart Farm Innovation Technology Development Program, funded by Ministry of Agriculture, Food and Rural Affairs (MAFRA) and Ministry of Science and ICT (MSIT), Rural Development Administration (RDA)(RS-2025-02314059).

REFERENCES

Barrett, N. W., K. Rowland, C. J. Schmidt, S. J. Lamont, M. F. Rothschild, C. M. Ashwell, and M. E. Persia. 2019. Effects of acute and chronic heat stress on the performance, egg quality, body temperature, and blood gas parameters of laying hens. Poultry Sci. 98(12): 6684-6692.

Kim, D. H., Y. K. Lee, S. H. Kim, and K. W. Lee. 2021. The impact of temperature and humidity

on the performance and physiology of laying hens. Animals 11(1): 56.
Kim, H. R., C. Ryu, S. D. Lee, J. H. Cho, and H. Kang. 2024. Effects of heat stress on the laying performance, egg quality, and physiological response of laying hens. Animals 14(7): 1076.
Loengbudnark, W., V. Chankitisakul, and W. Boonkum. 2023. The genetic impact of heat stress on the egg production of Thai native chickens (Pradu Hang dum). PLoS ONE 18(2): e0281328.
Mignon-Grasteau, S., U. Moreri, A. Narcy, X. Rousseau, T. B. Rodenburg, M. Tixier-Boichard, and T. Zerjal. 2015. Robustness to chronic heat stress in laying hens: A meta-analysis. Poultry Sci. 94(4): 586-600.
Zulovich, J. M., and J. A. DeShazer. 1990. Estimating egg production declines at high environmental temperatures and humidities. ASAE Paper No. 90-4021. St. Joseph, Mich.: American Society of Agricultural Engineers.

AI-P15

Proceedings of The 12th International Symposium on Machinery and Mechatronics for Agriculture and Biosystems Engineering (ISMAB 2026)
20-24 October 2026, Busan, Republic of Korea

DEEP LEARNING-BASED MODEL FOR OPTIMAL HARVEST STAGE IDENTIFICATION AND SIZE GRADING OF SHIITAKE MUSHROOM

Che-Wei Liu[1,*], Chien-Ying Lee[1], Syuan-You Lin[2], Chi-Wei Liu[3], and Yao-Chuan Tsai[1]

[1]Dept. of Bio-Industrial Mechatronics Engineering, National Chung Hsing University, Taichung, Taiwan
[2]Dept. of Horticulture, National Chung Hsing University, Taichung, Taiwan
[3]Senmu Farm, Taichung, Taiwan
*Corresponding Author-- Voice: +886968935626, Email: ben935626@gmail.com

Abstract: Shiitake mushroom (*Lentinula edodes*) is an economically important crop in Taiwan and is rich in various nutritional components. However, harvesting is still predominantly performed manually, resulting in considerable labor and time costs. Determining whether mushrooms have reached the optimal harvest stage relies heavily on visual assessment of pileus opening and white characteristics along the pileus margin, making the decision subjective and highly dependent on individual experience. To address this issue, this study proposes a deep learning-based model for optimal harvest stage identification of shiitake mushrooms and analyzes the relationship between environmental conditions and mushroom size. First, top-view images were collected using fisheye network cameras and transmitted to a storage server, followed by image preprocessing and the development of an optimal harvest timing identification model using YOLOv11 (You Only Look Once – Version 11). The model automatically determines whether mushrooms have reached the harvestable stage. Environmental data were further integrated to investigate the relationship between environmental conditions and mushroom size and to identify environmental conditions favorable for producing larger mushrooms. The results showed that the proposed model achieved a precision of 73.5% and a recall of 94.7% in identifying harvestable mushrooms. The developed system can reduce labor requirements, provide real-time and consistent harvest decision-making, and support growers in optimizing cultivation management strategies to increase the proportion of large-sized shiitake mushrooms. This study provides a foundation for future intelligent production management and automated harvesting systems.

Key Words: Shiitake mushroom, Optimal harvest stage identification, Deep learning

INTRODUCTION

Shiitake mushroom (*Lentinula edodes*) is rich in protein, minerals, and various vitamins, including vitamins B, C, and D, and possesses considerable nutritional and functional value. Among cultivated mushroom species, shiitake is one of the most widely consumed and cultivated mushrooms worldwide due to its distinctive texture, flavor, nutritional value, and medicinal properties (Li C., 2022). Environmental factors have a significant influence on the

formation and development of shiitake fruiting bodies. Light intensity, temperature, humidity, and carbon dioxide concentration are important factors affecting mushroom growth and determining the appropriate harvest time (Sakamoto Y., 2018). Shiitake mushroom harvesting still relies heavily on manual inspection, with the optimal harvest stage determined by visual characteristics such as pileus opening and white features along the pileus margin. This approach is highly dependent on growers' experience and may result in inconsistent harvest timing and reduced product value when harvesting is delayed.

Therefore, this study proposes a deep learning-based image recognition method to automatically identify whether shiitake mushrooms have reached the optimal harvest stage, reducing labor requirements and improving harvesting consistency. In addition, the size of harvestable mushrooms is analyzed in conjunction with environmental data, including temperature, humidity, and carbon dioxide concentration, to investigate the relationship between cultivation conditions and mushroom size. The results provide a reference for cultivation management and environmental control and establish a foundation for future intelligent production management and automated harvesting systems.

MATERIALS AND METHODS

IMAGE UNDISTORTION AND CROPPING

First, chessboard images captured from different angles were collected for camera calibration. The OpenCV Fisheye Camera Model was used to estimate the camera intrinsic parameters and lens distortion coefficients, which were then applied to image correction. After calibration, YOLOv11 was used to detect and crop the four central mushroom baskets, thereby reducing the influence of non-target objects and distortion near the image edges.

DEVELOPMENT OF THE SHIITAKE MUSHROOM OPTIMAL HARVEST STAGE IDENTIFICATION MODEL

Based on the presence or absence of white characteristics along the pileus margin, the mushrooms were annotated into two classes: "harvestable" and "non-harvestable," as shown in Figure 1. Manual annotation was performed using Roboflow. The images were then divided into three datasets for model training: Dataset 1 consisted of the original images, Dataset 2 consisted of images subjected to CLAHE image preprocessing, and Dataset 3 consisted of CLAHE-preprocessed images combined with data augmentation. YOLOv11 was used for model training with an image size of 1280 × 1280 pixels, and the best-performing weights were selected for optimal harvest stage detection of shiitake mushrooms.

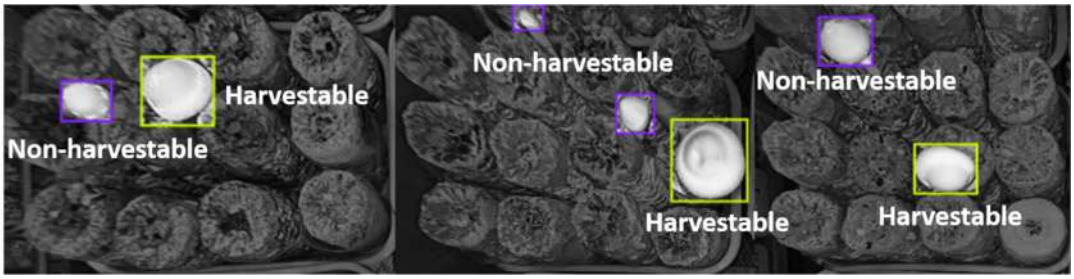

Fig.1 Annotation status of the shiitake mushroom optimal harvest stage identification model

DEVELOPMENT OF THE SHIITAKE MUSHROOM SIZE GRADING MODEL

This study used the harvestable shiitake mushrooms detected by the optimal harvest stage identification model as the target objects. The bounding box information generated by the model was used to estimate the actual diameter of each mushroom, based on which size grading was performed. Subsequently, the internal environmental conditions of the cultivation room, as shown in Figure 2, were analyzed to determine the conditions associated with the highest proportion of large-sized mushrooms.

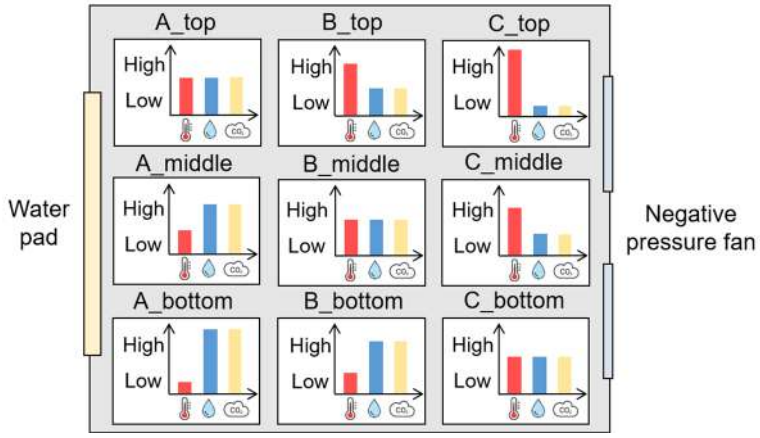

Fig.2 Internal environmental conditions of the cultivation room

RESULTS & DISCUSSION

THE SHIITAKE MUSHROOM OPTIMAL HARVEST STAGE IDENTIFICATION MODEL

Dataset 1 consisted of the original images and achieved a precision of 64.4% and a recall of 94.7%. Dataset 2 consisted of images subjected to CLAHE preprocessing and achieved a precision of 69.7% and a recall of 92.1%. Dataset 3 consisted of CLAHE-preprocessed images combined with data augmentation and achieved a precision of 73.5% and a recall of 94.7%. Comparison of the training performance among the three datasets showed that Dataset 3, which combined CLAHE preprocessing with data augmentation, achieved the best overall performance. The best training results are presented in Table 1.

Table 1 The best training results

	CLAHE-preprocessed images combined with data augmentation		
	Harvestable	Non- Harvestable	Average
Precision	0.735	0.746	0.741
Recall	0.947	0.663	0.805
mAP50	0.908	0.819	0.864
mAP50-95	0.779	0.592	0.686

THE SHIITAKE MUSHROOM SIZE GRADING MODEL

The daily numbers of harvestable shiitake mushrooms in each size category across different zones of the cultivation room are shown in Figure 3. The bottom layer of Zone B had the highest yield of large-sized mushrooms. This result may be attributed to the relatively balanced

microenvironmental conditions in this location, which contributed to its superior production of large-sized mushrooms.

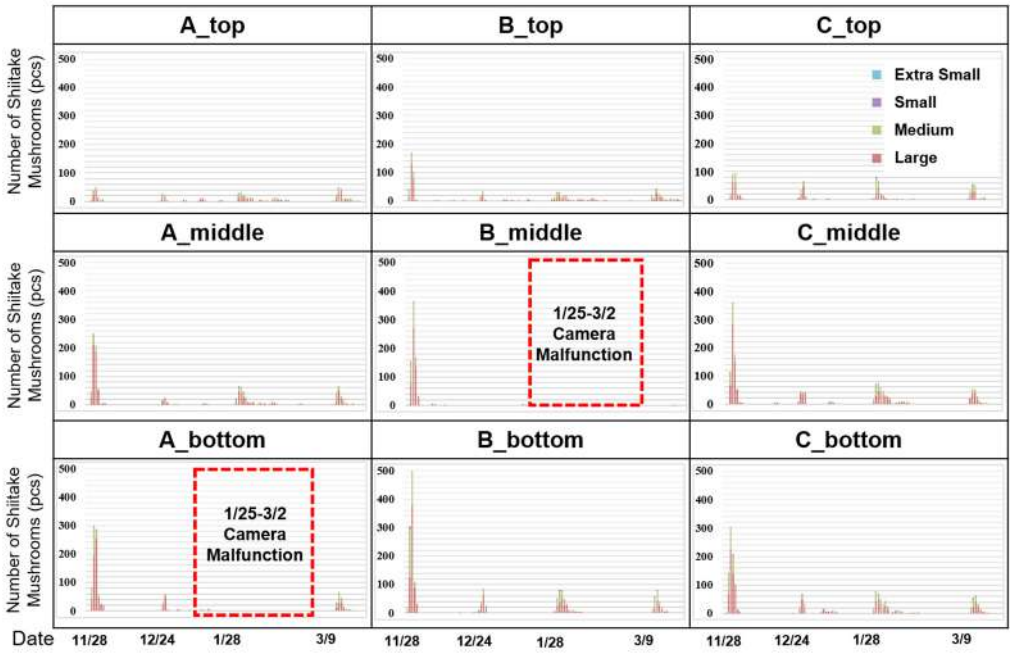

Fig.3 The daily numbers of harvestable shiitake mushrooms in each size category across different zones of the cultivation room

CONCLUSIONS

The optimal harvest stage identification model developed in this study achieved a precision of 73.5% and a recall of 94.7%, demonstrating its effectiveness in reducing the occurrence of underdeveloped mushrooms. By integrating mushroom size and environmental data, the results showed that the bottom layer of Zone B produced the highest yield of large-sized mushrooms. This finding suggests that this area provides relatively balanced conditions in terms of temperature, humidity, carbon dioxide concentration, and airflow, which are favorable for continued fruiting body development and the production of larger shiitake mushrooms.

REFERENCES

Li, C., and S. Xu. 2022. Edible mushroom industry in China: Current state and perspectives. *Applied Microbiology and Biotechnology* 106(11): 3949-3955.

Sakamoto, Y. 2018. Influences of environmental factors on fruiting body induction, development and maturation in mushroom-forming fungi. *Fungal Biology Reviews* 32(4): 236-248.

AI-P16

Proceedings of The 12th International Symposium on Machinery and Mechatronics for Agriculture and Biosystems Engineering (ISMAB 2026)
20-24 October 2026, Busan, Republic of Korea

COMPARING REAL-TIME INFERENCE PERFORMENCE AND ENERGY EFFICIENCY OF EDGE DEVICES FOR WEED DETECTION

Jae-Min Lee[1], Seung-Jin Jeong[2], Ryu-Gap Lim[1]*

[1]Department of Convergence Biosystem Mechanical Engineering, Sunchon National University, Sunchon, Korea

[2]Department of Smart Agricultural Engineering, Sunchon National University, Sunchon, Korea

*Corresponding Author-- Voice: +82-61-750-3264, Email: limrg11@scnu.ac.kr

Abstract: Edge-based image processing is needed for open-field precision weed control systems to detect weeds in real-time and to rapidly control devices according to the detection results to treat weeds and save time. The edge devices deployed on agricultural robots must run inference with low computation resources and power consumption, which requires both computation performance and resource utilization to be considered for edge devices to be deployed on agricultural robots. In this study focus on evaluation of comparison real-time inference performance, computational resource utilization and power consumption of the NVIDIA Jetson Orin Nano, Jetson Orin NX, and Jetson AGX Orin using the same weed detection model. The weed detection was performed using the YOLOv12n that showed excellent detection accuracy in previous studies. A total of 42,000 images of 14 weed species were created by taking a random sample of 3,000 images per class from an AI Hub dataset that was publicly available. The data set was split into training, validation and testing sets at a ratio of 70:15:15. The YOLOv12n model was trained on an NVIDIA GPU with the default Ultralytics training pipeline, and the weights and test data were the same for all three devices. The model was optimized with FP16 precision on each device with TensorRT. Real-time processing performance was measured in terms of frames per second (FPS), inference latency and total latency (including preprocessing and postprocessing) time. Power consumption during inference and utilization of computational resources (GPU utilization, GPU memory usage) were also measured to evaluate the utilization of computational resources during model execution. Using the measured processing speed and power consumption, the performance per Watt (FPS/W) and the energy consumption per frame were computed and compared for inference performance and energy efficiency of the three devices. This study quantitatively evaluated a weed detection model and quantified the results of the impact of various computational resources on real-time processing performance and energy efficiency of edge devices. It was intended to serve as a foundation for the selection of edge devices to meet the needs of agricultural mobile robots and selective weed control systems.

Keywords: YOLOv12n, weed detection, Jetson Orin, edge computing, TensorRT,

ACKNOWLEDGEMENTS

This work was carried out with the support of “Research Program for Agriculture Science and Technology Development (Project No. RS-2026-25521438)” Rural Development Administration, Republic of Korea.

AI-P17

Proceedings of The 12th International Symposium on Machinery and Mechatronics for Agriculture and Biosystems Engineering (ISMAB 2026)
20-24 October 2026, Busan, Republic of Korea

COMPARISON OF ENSEMBLE METHODS FOR GREENHOUSE TOMATO YIELD PREDICTION USING HETEROGENEOUS CROP MODELS

Woo Hyeok Jeong[1], Seung A Kim[2], Meoung Hun Lee[3*]

[1,2,3*]Sunchon National University, 255 Jungang-ro, Suncheon 57922, Republic of Korea
*Corresponding Author—Meoung Hun Lee Voice: +82-10-3777-5544,
Email: leemh777@scnu.ac.kr

Abstract: This study compared four ensemble methods for integrating heterogeneous crop-model predictions of greenhouse tomato yield. A statistical surrogate dataset containing a reference yield and three model predictions was generated for 300 cases. Simple averaging, median aggregation, inverse-RMSE weighting, and linear stacking were evaluated under normal, biased, and outlier conditions using 30 repeated 60:20:20 training-validation-test splits. Under the normal condition, linear stacking achieved R^2 = 0.957, RMSE = 0.420 kg m^{-2}, and MAE = 0.331 kg m^{-2}, reducing RMSE by 39.3% relative to the best individual model. It also produced the lowest RMSE under biased and outlier conditions (0.454 and 0.458 kg m^{-2}). Method differences were significant under all conditions ($p < 0.001$). Linear stacking was the most effective method when calibration data represented the relevant error structure.

Key Words: Greenhouse Tomato, Yield Prediction, Crop Growth Model, Ensemble Method, Linear Stacking

INTRODUCTION

Greenhouse tomato yield is influenced by environmental and management conditions. TOMGRO, TOMSIM, SIMPLE, and DSSAT-based models are used for yield prediction, but structural and sensitivity differences can produce divergent results (Jones et al., 1991; Fink et al., 2023). Multi-model ensembles may reduce this uncertainty, although performance depends on the combination method (Wallach et al., 2018; Yin et al., 2025). This study compared four ensemble methods under normal, biased, and outlier conditions.

MATERIALS AND METHODS

Reference yields for 300 cases were sampled from a normal distribution (mean 13.0, SD 2.0 kg m^{-2}) and truncated to 7.0-19.0 kg m^{-2}. Model A had bias -0.30 kg m^{-2} and error SD 0.75 kg m^{-2}; Model B had bias +0.40 kg m^{-2} and error SD 0.60 kg m^{-2}; and Model C had no bias and error SD 1.05 kg m^{-2}. A shared error (SD 0.25 kg m^{-2}) represented uncertainty in common inputs.

Original predictions defined the normal condition. The biased condition added 1.0 kg m^{-2} to

Model B; the outlier condition added ±2.0-3.0 kg m^{-2} to Model C for 30 cases (10%). The ensembles were simple averaging, median aggregation, validation-error inverse-RMSE weighting, and linear-regression stacking (Wolpert, 1992). For each condition, 60:20:20 training-validation-test splits were repeated 30 times. R^2, RMSE, and MAE were calculated. Differences were tested using Friedman and Holm-corrected Wilcoxon tests.

RESULTS & DISCUSSION

Reference yield averaged 13.16 ± 2.05 kg m^{-2} (8.08-18.92 kg m^{-2}). Normal-condition RMSE was 0.795, 0.692, and 1.090 kg m^{-2} for Models A, B, and C. All ensembles outperformed Model B, the best individual model. Linear stacking achieved RMSE 0.420 kg m^{-2} and R^2 0.957, reducing RMSE by 39.3%.

In biased and outlier conditions, linear stacking retained the lowest RMSE (0.454 and 0.458 kg m^{-2}), followed by inverse-RMSE weighting (0.531 and 0.490 kg m^{-2}; Table 1). Linear stacking was significantly better than every alternative (Holm-adjusted $p < 0.001$), as its coefficients adjusted for model-specific bias and inter-model relationships. However, it was recalibrated for each condition using additive linear-error data; its advantage therefore applies when calibration data represent the error and may not extend to unseen or nonlinear errors.

Table 1. Mean RMSE values of individual models and ensemble methods under different prediction conditions (kg m^{-2})

Method	Normal	Biased	Outlier
Model A	0.795	0.836	0.804
Model B	0.692	1.492	0.724
Model C	1.090	1.130	1.342
Simple average	0.475	0.584	0.558
Median	0.533	0.735	0.592
Inverse-RMSE weighting	0.443	0.531	0.490
Linear stacking	**0.420**	**0.454**	**0.458**

CONCLUSIONS

Linear stacking produced the lowest RMSE in all conditions by accounting for model-specific bias and inter-model relationships. It is therefore promising when representative calibration data are available, but validation with actual greenhouse tomato data and independent error conditions is required.

ACKNOWLEDGEMENTS

This work was carried out with the support of “Research Program for Agriculture Science and Technology Development (Project No. RS-2026-25516985)” Rural Development Administration, Republic of Korea.

REFERENCES

Fink, M., A. Daniels, C. Qian, V. M. Velásquez, S. Salotra, and D. Wollherr. 2023. Comparison of dynamic tomato growth models for optimal control in greenhouses. In Proc. 2023 IEEE Int. Conf. on Agrosystem Eng., Tech. and Applications, 28-33. doi:10.1109/AGRETA57740.2023.10262422.

Jones, J. W., E. Dayan, L. H. Allen, H. van Keulen, and H. Challa. 1991. A dynamic tomato growth and yield model (TOMGRO). Trans. ASAE 34(2): 663-672. doi:10.13031/2013.31715.

Wallach, D., P. Martre, B. Liu, et al. 2018. Multimodel ensembles improve predictions of crop-environment-management interactions. Global Change Biol. 24(11): 5072-5083. doi:10.1111/gcb.14411.

Wolpert, D. H. 1992. Stacked generalization. Neural Networks 5(2): 241-259.

Yin, X., G. Leng, J. Qiu, et al. 2025. Crop model ensemble averaging: A large but underappreciated uncertainty source for global crop yield projections under climate change. Earth's Future 13(6): e2024EF005900. doi:10.1029/2024EF005900.

AI-P18

Proceedings of The 12th International Symposium on Machinery and Mechatronics for Agriculture and Biosystems Engineering (ISMAB 2026)
20-24 October 2026, Busan, Republic of Korea

A STUDY ON THE FEASIBILITY OF A STAND-ALONE SAP-FLOW SENSOR FOR PRECISION IRRIGATION

Muhammad Amjad[1], Yeong-Hyeon Shin[1], Je-Min Park[2], Jin Woo Nam[3], Mi Young Lim[4], Ji Woong Bang[4], Myeongsuk Kim[4], Junyoung Park[5], Soo Chung[6], Woo-Jae Cho[12]*

[1] Department of Biosystems Engineering, College of Agriculture & Life Sciences, Gyeongsang National University, Jinju, Republic of Korea
[2] Department of Bio-Industrial Machinery Engineering, College of Agriculture & Life Sciences, Gyeongsang National University, Jinju, Republic of Korea
[3] Gyeongnam Agricultural Research and Extension Services, Jinju 52733, Republic of Korea
[4] Rural Development Administration of South Korea - National Institute of Horticultural and Herbal Science
[5] Department of Biosystems Engineering, Seoul National University, Seoul, Republic of Korea
[6] Integrated Major in Global Smart Farm, Seoul National University, Seoul, 08826, Republic of Korea
*Corresponding Author-- Voice: +82-55-772-1892, Email: woojae56@gnu.ac.kr

Abstract: Precision irrigation in greenhouse crop production increasingly relies on multiple environmental and physiological sensors, which raises system cost and complexity and limits adoption in commercial greenhouses. Sap flow sensing offers a plant-based alternative that directly reflects the internal water status of the crop, but its use for irrigation decision-making has mainly been explored in combination with other sensors rather than as a stand-alone monitoring approach. The objective of this study was to evaluate whether a single sap-flow sensor, without auxiliary environmental or soil sensors, could provide sufficient information to determine the irrigation status of greenhouse paprika (Capsicum annuum), as a step toward a simplified, single-sensor irrigation control system. Continuous measurements of sap flow, irrigation input, and drainage output were collected from commercially grown paprika plants and synchronized at 1-minute resolution. The sap flow time series was preprocessed and segmented into individual irrigation cycles, each classified by drainage ratio into Deficit (<15%), Optimal (15–25%), or Excessive (>25%) irrigation. Five features mean flow, maximum flow, cumulative flow, peak count, and flow slope were derived from the single sap-flow signal for each cycle, and their separability across irrigation categories was tested using the Kruskal-Wallis H-test and one-way ANOVA. Cumulative sap flow was the only feature to approach statistical separability by Kruskal-Wallis ($p = 0.031$), though the corresponding ANOVA result did not reach significance ($p = 0.055$). Mean, maximum, and cumulative flow were strongly inter-correlated, while peak count and slope carried largely independent information. These results indicate that a single sap-flow sensor can provide meaningful, though currently limited, information for irrigation status determination, with cumulative flow as the most promising indicator. This supports the feasibility of a simplified irrigation control strategy based on a single sap-flow sensor and defines the analytical basis for the validation study required before real-time deployment.

Key Words: Precision irrigation; Water-use efficiency; Sap-flow; Greenhouse cultivation; Irrigation scheduling

INTRODUCTION

Irrigation scheduling has a direct effect on water-use efficiency and yield in greenhouse crops, where the growing medium provides limited buffering and a poorly timed irrigation event can shift a plant from optimal hydration to stress within hours (Dannehl et al., 2015). Commercial greenhouses commonly rely on timer-based, solar radiation-based, or substrate moisture-based control, but each depends on a proxy for plant water use rather than on plant water transport itself, and existing precision irrigation strategies typically combine several sensor types to reach acceptable performance, which raises sensing cost and system complexity and limits adoption in commercial settings (Palumbo et al., 2021). Sap flow sensing measures xylem water flux directly and has been proposed as a physiological alternative for irrigation scheduling (Navarro et al., 2022). but existing sap-flow-based strategies still combine it with auxiliary environmental sensors rather than using it as a stand-alone input.
The objective of this study was to evaluate whether sap-flow-derived features alone, without environmental parameters, can distinguish among these three irrigation categories, and to identify which single sap-flow feature carries the strongest and most independent discriminatory value as a candidate for a simplified, single-parameter irrigation control strategy.

MATERIALS AND METHODS

Experimental Site and Data Collection

The study was conducted in a commercial-type greenhouse at the National Institute of Horticultural and Herbal Science (NIHHS), Haman-gun, Republic of Korea, where paprika was grown. Sap-flow sensors were installed on three plants per substrate, and continuous sap-flow measurements were logged at one-minute intervals from stem-mounted sensors over a 30-day period, from April 11 to May 10, 2026, synchronized with irrigation and drainage volume records from the facility's automated fertigation control system. The site has a fully equipped greenhouse with standard control over temperature, humidity, CO_2 concentration, and solar radiation, conditions typical of commercial greenhouse horticulture in South Korea.

Irrigation Cycle Detection and Drainage Ratio Classification

Reliable automated identification of individual irrigation cycles from the continuous mass-balance signal was a prerequisite for all subsequent feature extraction and classification. Each irrigation cycle, defined as the period from the onset of water delivery to the completion of post-irrigation drainage, served as the basic analytical unit of this study. Because the raw load-cell signal contains noise from mechanical vibration and transient disturbances during manual handling, a statistically robust thresholding strategy was needed to distinguish genuine irrigation events from background fluctuations. Cycle boundaries were identified from the irrigation and drainage mass-flow signal using an interquartile range (IQR)-based thresholding method, in which the detection threshold was set at the third quartile (Q3) of the signal plus 1.5 times the interquartile range This rank-based threshold resists the positive outliers common in load-cell and flow-meter data, since such outliers inflate the mean but have little effect on quartile estimates. For each detected cycle, the drainage ratio was calculated as

$$\text{Drainage ratio}_{\text{Cycle}} = \frac{\text{Drainage amount}_{\text{Cycle}}}{\text{Irrigation amount}_{\text{Cycle}}} \times 100$$

and used to classify the cycle as Deficit (<15%), Optimal (15–25%), or Excessive (>25%) irrigation.

Irrigation Cycle Detection and Drainage Ratio Classification

Five descriptive features were extracted from the one-minute sap-flow series within each detected cycle. Mean flow (mm min^{-1}) is the average rate over the cycle. Maximum flow (mm min^{-1}) is the peak instantaneous rate, sensitive to the post-irrigation recovery pulse. Cumulative flow (mm) is the summed flow over the cycle duration, indexing total water uptake per event. Peak number is the number of local maxima in the smoothed signal, detected with a prominence-based peak-finding algorithm, and reflects the regularity of transpiration pulses. Slope (mm min^{-1} per unit time) is the linear-regression trend of flow across the cycle, reflecting the rate of post-irrigation hydraulic recovery.

Statistical Analysis

Two complementary tests were applied to each sap-flow feature. the Kruskal-Wallis H-test and one-way ANOVA, to identify those carrying meaningful information for distinguishing the three irrigation states. Kruskal-Wallis served as the primary non-parametric test, since the small per-class sample sizes and non-normal feature distributions expected under field conditions violated ANOVA's normality assumption; ANOVA was run in parallel as a parametric reference. A feature was classified as strongly discriminative only if it was significant ($p < 0.05$) in both tests. Pearson and Spearman correlation analyses were also performed across the five sap-flow features to assess redundancy: high correlation in both metrics indicated overlapping information, while low correlation confirmed that a feature captured an independent aspect of the plant hydraulic response. Only features that were statistically significant and weakly correlated with one another were retained as candidates for the single-parameter irrigation control strategy. All data processing, statistical analysis, and feature extraction were implemented in Python using NumPy, SciPy, and pandas.

RESULTS & DISCUSSION

Irrigation events were detected from the continuous mass-flow signal using an IQR-based threshold, and each same-day pair of consecutive events was treated as one irrigation cycle, with a day's final event closing the preceding cycle rather than starting a new one.

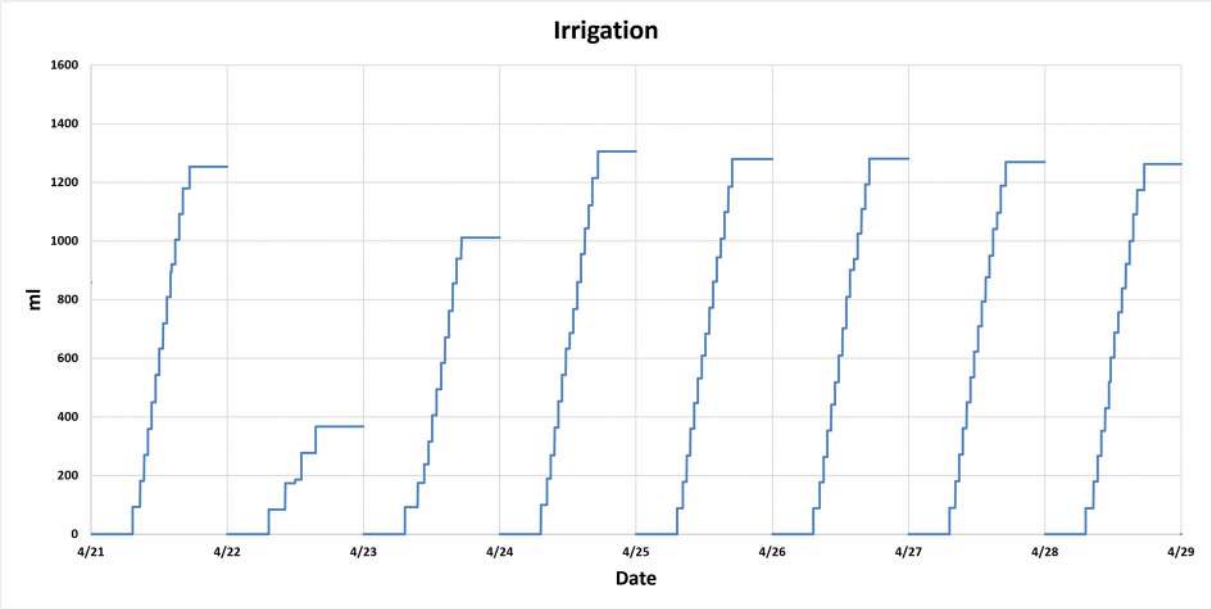

Figure 1 . Cumulative irrigation volume (ml) over a representative period, illustrating the daily staircase pattern used for IQR-based detection of irrigation events. Each step corresponds to a single detected event, and the signal resets to zero at the start of each day.

Among the five extracted sap-flow features, only slope showed statistically significant discrimination across the three irrigation states by the Kruskal–Wallis test.

Table 1. Kruskal-Wallis, ANOVA results for the five sap-flow features across the Irrigation cycles.

Feature	Kruskal H	Kruskal p	ANOVA F	ANOVA p	Result
Mean	5.31	0.07	3.28	0.038	Weak
Max	2.97	0.22	0.74	0.47	Weak
Accumulation	6.93	0.031	2.93	0.054	Strong
Peak Number	0.42	0.80	0.21	0.80	Weak
Slope	0.15	0.92	0.45	0.63	Weak

Among the five sap-flow features, cumulative flow was the only one to approach statistical separability across the three irrigation categories by the Kruskal-Wallis test. The corresponding ANOVA result for cumulative flow did not reach significance ($p = 0.055$). Mean flow showed the reverse pattern: significant by ANOVA ($p = 0.039$) but not by Kruskal-Wallis ($p = 0.070$); since a feature was treated as strongly discriminative only when both tests agreed, this disagreement left mean flow classified, alongside maximum flow, peak number, and slope, as a weak discriminator. The divergence between the two tests for mean flow illustrates why the non-parametric test was retained as the primary criterion. The underlying feature distributions were non-normal enough that the parametric result alone would have been misleading.

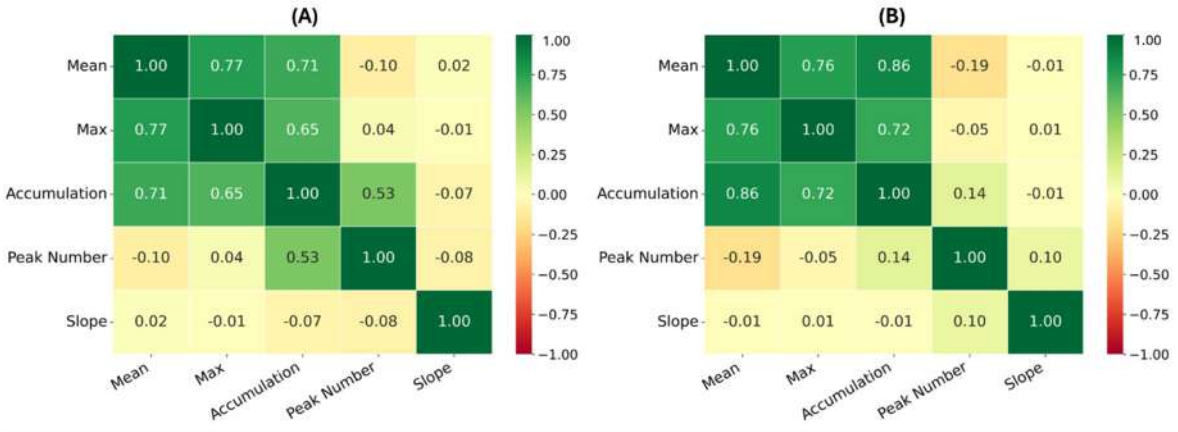

Figure 2. Pearson (A) and Spearman (B) correlation coefficients among the five sap-flow features (mean, maximum, cumulative flow, peak number, and slope), showing strong inter-correlation among mean, maximum, and cumulative flow, and near-zero correlation of slope with all other features.

Correlation analysis (Fig. 2) showed that mean, maximum, and cumulative flow were strongly inter-correlated (Pearson r = 0.65–0.77; Spearman r = 0.72–0.86), consistent with all three being derived from the same underlying flow magnitude. Peak number correlated moderately with cumulative flow (Pearson r = 0.53) but only weakly with mean and maximum flow, while slope was essentially uncorrelated with every other feature ($|r| \leq 0.11$ in both metrics), indicating that slope and peak number carry information largely independent of the flow-magnitude features. Taken together, these results indicate that sap flow alone offers limited but non-trivial discriminatory value for irrigation classification. Cumulative flow was the only feature to approach separability and remains the most defensible candidate for a single-parameter control rule.

To evaluate cumulative sap flow as a practical single-parameter control rule, each cycle's cumulative flow value was standardized to a z-score, and threshold cutoffs were derived from the median z-score within each irrigation category if $z \leq -0.442$ was classified as Optimal Irrigation, $-0.442 < z \leq -0.292$ as Excessive Irrigation, and $z > -0.292$ as Deficit Irrigation. Applying this rule across all 338 cycles yielded an overall classification accuracy of 46.2% (156 of 338 correctly classified; Fig. 3), exceeding the 33% expected under random three-class assignment but well short of a level suitable for autonomous control. Per-class recall was uneven: Deficit Irrigation, the majority class, was correctly identified in 54.3% of cases (119/219) and Optimal Irrigation in 56.3% of cases (27/48), while Excessive Irrigation was correctly identified in only 14.1% of cases (10/71), with most Excessive cycles instead misclassified as Optimal or Deficit. This pattern is consistent with the correlation and significance results above: because cumulative flow overlaps substantially between adjacent categories, a single fixed threshold cannot cleanly separate three overlapping distributions, particularly for the Excessive class, whose values sit between the other two rather than at a distinct extreme.

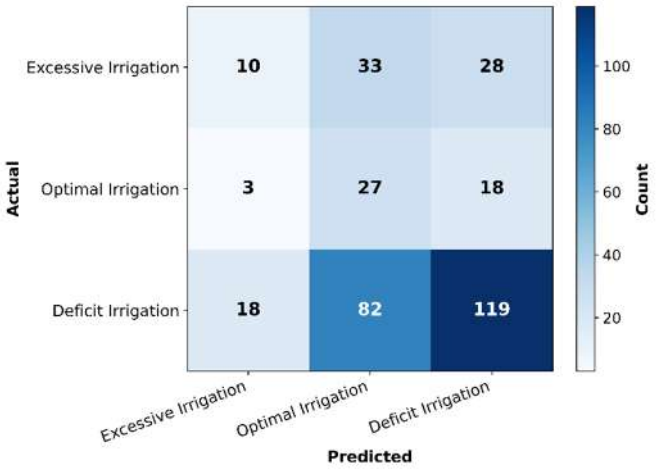

Figure 3. Confusion matrix of the z-score-based classification of irrigation categories using cumulative sap flow, showing counts of actual versus predicted irrigation status (overall accuracy = 46.2%).

Conclusions

This study evaluated whether sap flow alone could distinguish Deficit, Optimal, and Excessive irrigation in greenhouse paprika, and found that cumulative flow was the only feature to approach statistical separability, with the Deficit-versus-Optimal comparison showing the strongest, though not significant, pairwise trend, while mean flow, maximum flow, peak number, and slope showed no consistent discriminatory value a z-score threshold rule based on cumulative flow reached 46.2% accuracy, exceeding chance but still limited, particularly for the Excessive category, reflecting overlap between adjacent irrigation states. These findings establish cumulative sap flow as the basis for a simplified, single-parameter irrigation control strategy and define the analytical framework for the subsequent validation setup, including a more balanced sample across irrigation categories and refinement of the classification rule, required prior to real-time deployment.

ACKNOWLEDGEMENTS

This work was supported by the project “Establishment of a New Agricultural Climate Change Response System” (RS-2024-00400787) funded by the Rural Development Administration of Korea.

REFERENCES

Dannehl, D., Suhl, J., Ulrichs, C., & Schmidt, U. (2015). Evaluation of substitutes for rock wool as growing substrate for hydroponic tomato production. *J. Appl. Bot. Food Qual*, *88*(6877), 10.5073.

Navarro, A., Scotto di Covella, F., Cacini, S., Sodini, M., Traversari, S., Venezia, A., & Massa, D. (2022). Testing sap-flow sensors to predict irrigation of soilless tomato fertigated with saline water. XXXI International Horticultural Congress (IHC2022): International Symposium on Innovative Technologies and Production 1377,

Palumbo, M., D’Imperio, M., Tucci, V., Cefola, M., Pace, B., Santamaria, P., Parente, A., & Montesano, F. F. (2021). Sensor-based irrigation reduces water consumption without compromising yield and postharvest quality of soilless green bean. *Agronomy*, *11*(12), 2485.

AI-P19

Proceedings of The 12th International Symposium on Machinery and Mechatronics for Agriculture and Biosystems Engineering (ISMAB 2026)
20-24 October 2026, Busan, Republic of Korea

CANDIDATE-LEVEL RESCORING DETERMINES DETECTION PERFORMANCE UNDER SCARCE LESION ANNOTATION

Peng-Yuan Wu[1], Shyh-Jye Chen[2], Cheng-Ying Chou[1*]

[1]Department of Biomechatronics Engineering, National Taiwan University, Taipei, Taiwan
[2]Department of Medical Imaging, National Taiwan University Hospital, Taipei, Taiwan
*Corresponding Author-- Voice: +886-2-3366-9689, Email: chengying@ntu.edu.tw

Abstract: Pelvic computed tomography (CT) is often acquired for reasons unrelated to the prostate, which makes it a candidate for opportunistic prostate cancer screening, but lesion annotations for CT are lacking. The intended route is to learn lesion detection on magnetic resonance imaging (MRI) and transfer it to CT with pseudo-labels. This study examined, on biparametric MRI, whether the choice of semi-supervised scheme or the way case-level decisions are read out matters more when annotations are scarce. Using a patient-level split of the public PI-CAI dataset (1198 training, 140 validation and 138 test cases), a two-stage detector was built: an nnU-Net produces a lesion probability map, and a gradient-boosted classifier, trained once and then frozen, rescores candidate lesions using 149 features. Four published semi-supervised methods, each from a different family of deep semi-supervised learning, and a detector-filtered pseudo-labeling scheme were trained under a 67% annotation budget and compared with the PI-CAI score, the mean of case-level area under the receiver operating characteristic curve and lesion-level average precision. Rescoring raised the fully supervised baseline from 0.362 to 0.625, with a case-level AUROC gain of 0.228 (95% confidence interval 0.105 to 0.350), and increased the PI-CAI score of every configuration. Scored from the probability map alone, the five semi-supervised schemes spanned 0.213 to 0.579; after rescoring they spanned 0.611 to 0.681, and their ranking changed. Case-level precision-recall analysis on the 36 positive and 102 negative test cases showed the same convergence, and voxel-level Dice did not track detection. Candidate-level rescoring, rather than the semi-supervised scheme, governed case-level detection, so comparisons of such schemes should fix and report the readout.

Key Words: Prostate cancer, Lesion detection, Semi-supervised learning, False-positive reduction, Magnetic resonance imaging

INTRODUCTION

Pelvic computed tomography is acquired routinely, and much of it is ordered for vascular, abdominal or oncological indications unrelated to the prostate. A prostate lesion visible on such a scan lies outside the scope of the requested examination. An automated detector could flag these cases, but training one requires voxel-level lesion annotations, which would have to be drawn slice by slice by specialist radiologists. This work therefore

learns lesion detection on biparametric magnetic resonance imaging (bpMRI), where a large annotated public dataset exists, as the first step toward transferring it to unannotated CT through pseudo-labels.
Detection on bpMRI is itself difficult. Clinically significant lesions occupy a small fraction of the image, and their signal overlaps with benign prostatic hyperplasia, so false positives are common. nnU-Net is the standard segmentation baseline (Isensee et al., 2021). Decoupled false-positive reduction adds a second classifier on top of the segmentation output (Saha et al., 2021); later work argued that this stage should see the context around each candidate (Magoulianitis et al., 2025); and the PI-CAI study established a common benchmark (Saha et al., 2024).

Semi-supervised learning is the usual response to scarce annotation, and a survey of deep semi-supervised learning groups such methods into generative, consistency regularization, graph-based, pseudo-labeling and hybrid families (Yang et al., 2023). Pseudo-labeling methods turn predictions into training targets, guided by radiology reports (Bosma et al., 2023) or by competition among networks (Wu et al., 2023). Consistency methods train a student to agree with a slowly updated teacher (Tarvainen and Valpola, 2017), optionally only where the teacher is certain (Yu et al., 2019). Generative methods can enlarge minority structures (Gu et al., 2024), and graph-based methods exploit relations among features (Wang et al., 2025). Comparisons of such schemes usually change several components at once and report voxel-level Dice, which does not measure whether a case is flagged.

The objectives of this study were (1) to build a two-stage detector whose candidate classifier is trained once and frozen, so that it can serve both as a case-level readout and as a pseudo-label filter; (2) to compare semi-supervised methods from four families with a shared backbone, preprocessing and evaluation; and (3) to determine whether the choice of scheme or the choice of readout has the larger effect on case-level detection.

MATERIALS AND METHODS

Dataset and Protocol

Biparametric MRI (T2-weighted, apparent diffusion coefficient [ADC] and high b-value images) from the public PI-CAI dataset (Saha et al., 2024) was split at the patient level into 1198 training, 140 validation and 138 test cases. The test set contained 36 positive cases with 38 lesions and 102 negative cases. Lesions occupy less than 0.1% of image voxels, and 72% of training cases contain no lesion. The annotation budget is the fraction of lesion-positive training cases that keep their voxel-level annotations; the remaining positive cases were used as unlabeled data. All configurations shared one nnU-Net plan (patch 16 × 320 × 320 voxels, spacing 3.0 × 0.5 × 0.5 mm, batch size 2) and were evaluated on a single fold with the final checkpoint, without ensembling.

Two-Stage Detector

Stage 1 is the nnU-Net, which outputs a voxel-wise lesion probability map. Candidate lesions are connected components of that map above 0.10 with at least 20 voxels, a low threshold chosen so that Stage 1 favors recall. For each candidate, Stage 2 computes 149 features: size,

the mean and maximum Stage-1 probability, the fractions of the candidate in the peripheral and transition zones, and 72 radiomic features each from the ADC image in the candidate core and in a dilated neighborhood restricted to the prostate. A gradient-boosted decision tree classifier rescores each candidate. It was trained once on out-of-fold candidates from the training set, frozen, and applied unchanged to every configuration (Fig. 1).

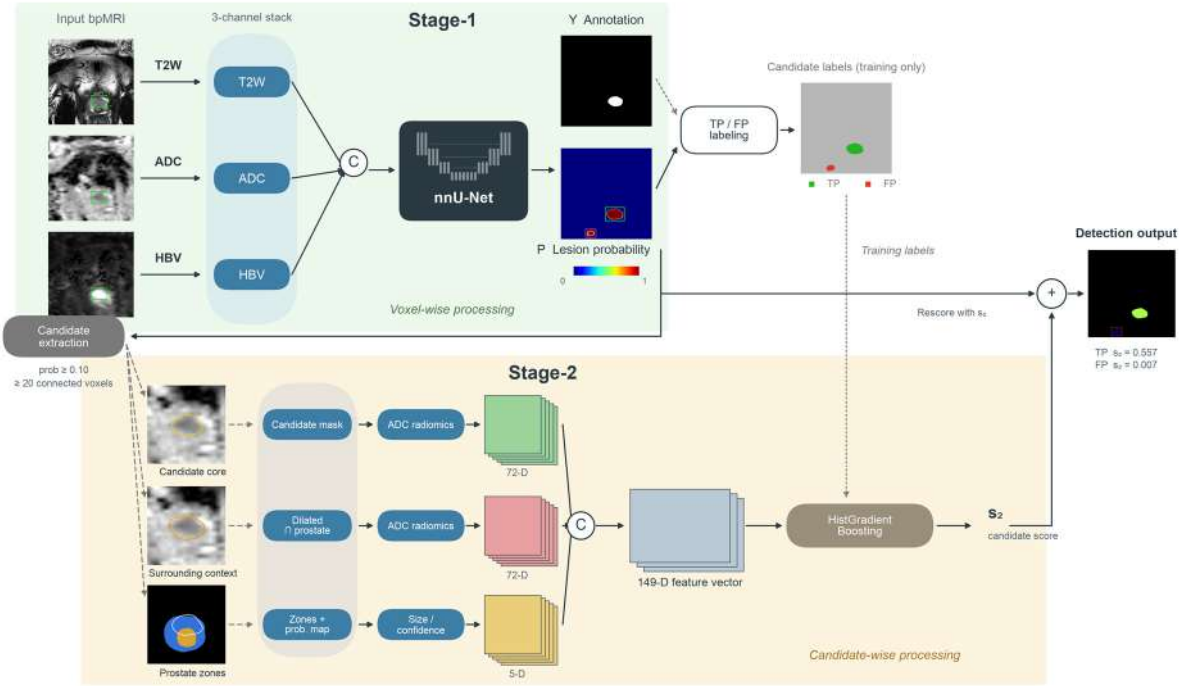

Fig. 1 Two-stage detection pipeline. Stage 1 (nnU-Net) maps the T2-weighted, ADC and high b-value (HBV) images to a lesion probability map P. Candidates are described by 72 ADC radiomic features from the candidate core, 72 from its surroundings within the prostate and five size, zone and confidence features, and a gradient-boosted classifier assigns each candidate the score s . Dotted lines mark signals used only to train this classifier. Only the training scheme of Stage 1 differs between configurations.

Semi-Supervised Schemes

All schemes were implemented inside the nnU-Net training loop with the shared plan and evaluation; where an original method required an architectural change, the closest equivalent that fits the shared plan was used. One published method was taken from each of four of the five families in the taxonomy of Yang et al. (2023), shown in Fig. 2; no hybrid method is included because the re-implemented hybrid method collapsed during training. Detector-filtered pseudo-labeling predicts lesions on unlabeled cases, scores the candidates with the frozen Stage-2 classifier and keeps only candidates scoring at least 0.5 as pseudo-labels; 74 unlabeled cases contributed pseudo-labels. From the pseudo-labeling family, ComWin (Wu et al., 2023) forms pseudo-labels by comparing the confidence maps of co-trained networks. From consistency regularization, UA-MT (Yu et al., 2019) makes a student agree with an exponential-moving-average teacher (Tarvainen and Valpola, 2017) on low-uncertainty voxels, with uncertainty estimated from eight passes with Gaussian input noise instead of Monte Carlo dropout and the consistency weight ramped up to 0.1. From the generative family, STAC (Gu et al., 2024) enlarges lesions by warping images and labels along a signed distance function

computed in millimeters; it was built on the same teacher-student framework and applied with a probability of 0.5. From the graph-based family, GraphCL (Wang et al., 2025) adds copy-paste mixing and graph-based feature clustering at the encoder bottleneck. All models used the nnU-Net optimizer and polynomial learning-rate schedule for 1000 epochs from an initial rate of 0.01, except detector-filtered pseudo-labeling, which was trained for 400 epochs from 0.001. This deviation is marked in Table 1 and examined below.

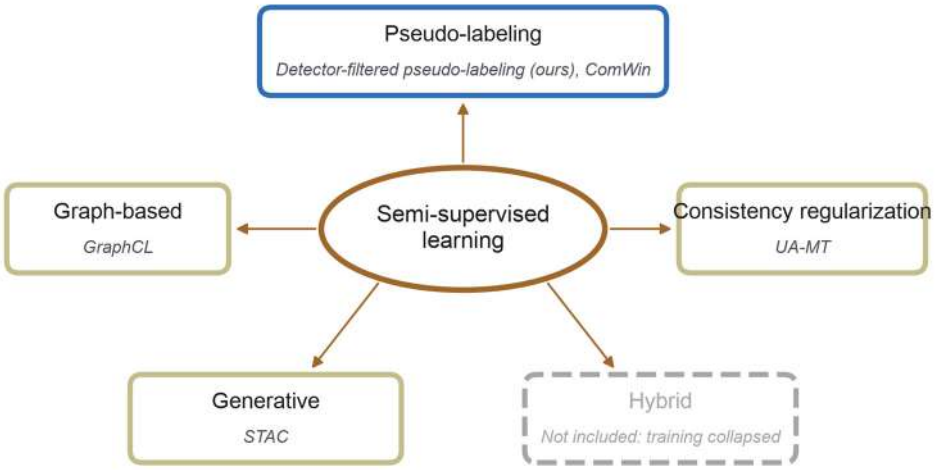

Fig. 2 Families of deep semi-supervised learning (Yang et al., 2023) and the methods compared in this study. The hybrid family is not represented because the re-implemented hybrid method collapsed in every training attempt.

Evaluation

Detection was evaluated with the PI-CAI protocol (Saha et al., 2024). A predicted lesion is a hit when its intersection over union with a reference lesion is at least 0.10, and the case-level score is the maximum lesion score in the case. Two readouts were compared on the same candidates: the Stage-1 readout scores a candidate by its maximum Stage-1 probability, and the two-stage readout by the Stage-2 classifier. Case-level discrimination, measured by the area under the receiver operating characteristic (ROC) curve, and lesion-level average precision are combined into the PI-CAI score in Eq. (1). Because the test set is imbalanced, case-level precision-recall curves were also analyzed, and voxel-level Dice was computed on the positive test cases. Uncertainty was estimated from 2000 bootstrap resamples of the test cases, stratified by case label and paired between the two readouts.

$$\text{PI-CAI score} = \frac{\text{AUROC+AP}}{2} \quad (1)$$

where:

AUROC = area under the case-level ROC curve (-)
AP = average precision of lesion-level detection (-)

RESULTS & DISCUSSION

Primary Benchmark and Gain from Rescoring

Table 1 compares all configurations on the test set. Adding Stage 2 increased the PI-CAI score

of every configuration, by 0.032 to 0.441. For the fully supervised baseline, the score rose from 0.362 to 0.625 and case-level AUROC from 0.520, close to chance, to 0.748; the paired bootstrap 95% confidence interval of this AUROC gain was 0.105 to 0.350. The AUROC gain excluded zero for six of the seven configurations; the exception was detector-filtered pseudo-labeling (−0.001, −0.077 to 0.074), whose smaller PI-CAI gain came from lesion-level average precision. The gain follows from the case-level decision rule. Under the Stage-1 readout, the case score is the most confident candidate, so a single confident false positive misclassifies a negative case. Stage 2 replaces that score with a judgment based on size, zone and ADC appearance: in the example of Fig. 1, a true and a false positive with Stage-1 probabilities of 0.999 and 0.975 received Stage-2 scores of 0.557 and 0.007.

Table 1 Detection and segmentation performance on the 138-case test set. The supervised models used 100% or 67% of the lesion annotations, and all semi-supervised schemes used 67%. Gain is the two-stage minus the Stage-1 PI-CAI score. †Trained for 400 epochs from an initial learning rate of 0.001; all other configurations for 1000 epochs from 0.01.

Configuration	Dice	Stage 1	Two-stage			Gain
		PI-CAI	AUROC	AP	PI-CAI	
Supervised (100%)	0.699	0.362	0.748	0.503	0.625	+0.263
Supervised (67%)	0.760	0.489	0.751	0.522	0.636	+0.147
Pseudo-labeling (ours)†	0.711	0.579	0.729	0.492	0.611	+0.032
UA-MT	0.703	0.433	0.762	0.529	0.645	+0.212
STAC	0.705	0.444	0.784	0.579	0.681	+0.237
ComWin	0.655	0.213	0.776	0.532	0.654	+0.441
GraphCL	0.685	0.392	0.773	0.533	0.653	+0.261

Convergence Across Semi-Supervised Schemes

Figure 3 shows that the effect was not specific to one configuration. Under the Stage-1 readout the five semi-supervised schemes spanned 0.213 to 0.579; after rescoring they spanned 0.611 to 0.681, so the range shrank from 0.366 to 0.071. The ranking was not preserved: detector-filtered pseudo-labeling moved from first to last, and ComWin from last to second among the seven configurations. ComWin is the edge case that explains the reversal. Every negative test case contained at least one of its detections above a probability of 0.5, which pushed its Stage-1 AUROC below chance to 0.336, although its lesion-level sensitivity at that threshold, 0.92, was within the 0.89—0.95 range of the other configurations. Its low Stage-1 score thus reflected miscalibrated confidence on negative cases rather than missed lesions, and after rescoring its AUROC reached 0.776. A Stage-1 comparison therefore largely measures how each scheme calibrates confidence on negative cases.

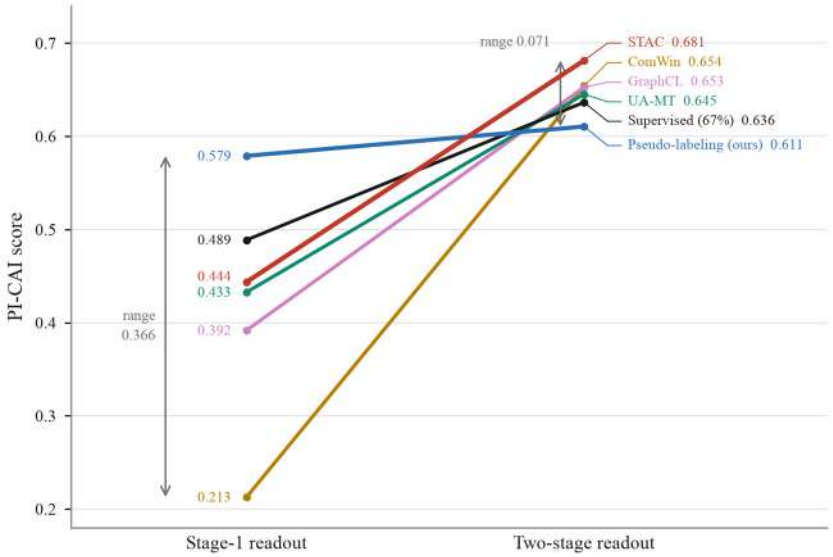

Fig. 3 PI-CAI score under the Stage-1 readout and after Stage-2 rescoring. The range across the five semi-supervised schemes shrinks from 0.366 to 0.071, and their order changes.

Case-Level Decisions Under Class Imbalance

With 36 positive and 102 negative test cases, a classifier without skill has a precision of 0.26, so the case-level decision was also examined with precision-recall curves (Fig. 4). Under the Stage-1 readout, the case-level average precision of the five schemes ranged from 0.19 to 0.50, and several curves stayed near the no-skill level. After rescoring it ranged from 0.55 to 0.63, and the best precision attainable at a recall of at least 0.8 increased for every scheme, from 0.263 to 0.372 before rescoring to 0.341 to 0.475 after. Voxel-level Dice did not follow these case-level decisions. The supervised model at 67% had the highest Dice (0.760) but ranked fifth of seven after rescoring, and across the seven configurations the Spearman correlation between Dice and two-stage PI-CAI score was −0.43. Dice rewards boundary agreement on positive cases, whereas screening depends on ranking negative cases below positive ones, so choosing a model by Dice would not have chosen the best detector.

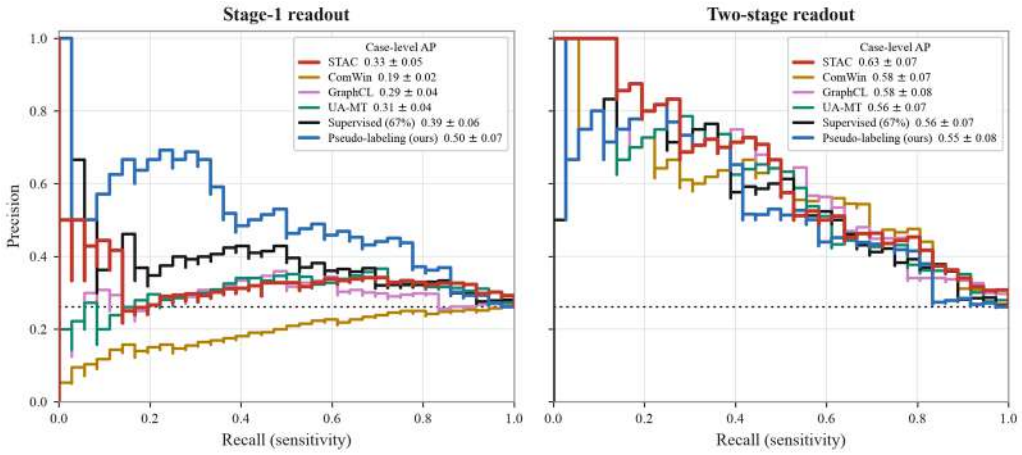

Fig. 4 Case-level precision-recall curves under the Stage-1 readout (left) and after rescoring (right). The dotted line marks the prevalence of positive cases (0.26); legend values are average precision with bootstrap standard deviation.

Confounders, Training Collapse and Variability

Two confounders affect the comparison of schemes. Detector-filtered pseudo-labeling was trained for 400 epochs from an initial learning rate of 0.001 (Table 1), so its Stage-1 lead should not be credited to its pseudo-labels alone: in an additional run, lowering the initial learning rate of the fully supervised model from 0.01 to 0.001 raised its Stage-1 PI-CAI score from 0.362 to 0.616 but its two-stage score only from 0.625 to 0.661. Training settings thus move the Stage-1 readout far more than the rescored one. In addition, pseudo-labeling gained the least from rescoring (+0.032), plausibly because its pseudo-labels had already been screened by the same frozen classifier.

Training under this class imbalance was fragile. STAC applied at every iteration, as in the original work, reached a patch-level validation Dice of 0.57 at epoch 508, then declined and stayed near zero from about epoch 750, finally predicting no lesions. With lesions below 0.1% of voxels, a consistency loss averaged over all voxels is nearly minimized when teacher and student both predict background, and lesion enlargement likely made the teacher's targets less reliable; applying STAC to half of the training samples avoided the collapse. The re-implemented hybrid method collapsed to background in both training attempts, including one in which the unsupervised weight was ramped up from near zero, so the hybrid family is not represented. For UA-MT, the uncertainty mask retained 99.9% to 100% of voxels from epoch 37 onward, so it behaved almost like a plain mean teacher; the dominant errors here are confident false positives, which an uncertainty filter does not remove.

The differences among rescored schemes are small relative to test-set variability. Bootstrap standard deviations were about 0.07 for case-level average precision and 0.045 to 0.055 for AUROC, so the ordering among the top schemes, with STAC first, should be regarded as provisional. All results come from one data split with 138 test cases and a single training run per configuration.

CONCLUSIONS

Semi-supervised methods from four families and a detector-filtered pseudo-labeling scheme were compared for prostate lesion detection on bpMRI, with a frozen candidate classifier as a fixed second stage. Rescoring increased the PI-CAI score of every configuration, compressed the differences between schemes from 0.366 to 0.071 in PI-CAI score and changed their ranking, and case-level precision-recall analysis showed the same convergence. On this task the readout had a larger effect on case-level detection than the choice of scheme, and Dice was not a reliable proxy for detection among the compared configurations. Comparisons of semi-supervised schemes should therefore fix and report both the readout and the training schedule. The candidate classifier is the component intended to filter pseudo-labels when the model is transferred to unannotated pelvic CT, the next stage of this work.

REFERENCES

Bosma, J. S., A. Saha, M. Hosseinzadeh, I. Slootweg, M. de Rooij, and H. Huisman. 2023. Semisupervised learning with report-guided pseudo labels for deep learning-based prostate cancer detection using biparametric MRI. Radiol. Artif. Intell. 5(5): e230031. https://doi.org/10.1148/ryai.230031

Gu, Y., Y. Liu, Z. Sun, J. Zhu, Y. Xu, and L. Najman. 2024. Shape transformation driven by active contour for class-imbalanced semi-supervised medical image segmentation. In Proc. 2024 IEEE Int. Conf. Bioinformatics and Biomedicine (BIBM), 1966-1973. Piscataway, N.J.: IEEE. https://doi.org/10.1109/BIBM62325.2024.10822225

Isensee, F., P. F. Jaeger, S. A. A. Kohl, J. Petersen, and K. H. Maier-Hein. 2021. nnU-Net: A self-configuring method for deep learning-based biomedical image segmentation. Nat. Methods 18(2): 203-211. https://doi.org/10.1038/s41592-020-01008-z

Magoulianitis, V., J. Yang, C. A. Alexander, and C.-C. J. Kuo. 2025. RadHop-Net: A lightweight radiomics-to-error regression for false positive reduction in MRI prostate cancer detection. In Proc. 2025 IEEE Int. Symp. Biomedical Imaging (ISBI), 1-5. Piscataway, N.J.: IEEE. https://doi.org/10.1109/ISBI60581.2025.10980816

Saha, A., M. Hosseinzadeh, and H. Huisman. 2021. End-to-end prostate cancer detection in bpMRI via 3D CNNs: Effects of attention mechanisms, clinical priori and decoupled false positive reduction. Med. Image Anal. 73: 102155. https://doi.org/10.1016/j.media.2021.102155

Saha, A., J. S. Bosma, J. J. Twilt, B. van Ginneken, A. Bjartell, A. R. Padhani, . . . H. Huisman. 2024. Artificial intelligence and radiologists in prostate cancer detection on MRI (PI-CAI): An international, paired, non-inferiority, confirmatory study. Lancet Oncol. 25(7): 879-887. https://doi.org/10.1016/S1470-2045(24)00220-1

Tarvainen, A., and H. Valpola. 2017. Mean teachers are better role models: Weight-averaged consistency targets improve semi-supervised deep learning results. In Advances in Neural Information Processing Systems 30 (NIPS 2017), 1195-1204. Red Hook, N.Y.: Curran Associates.

Wang, M., H. Su, J. Li, C. Li, N. Yin, L. Shen, and J. Guo. 2025. GraphCL: Graph-based clustering for semi-supervised medical image segmentation. In Proc. 42nd Int. Conf. Machine Learning, 64367-64376. PMLR 267. https://proceedings.mlr.press/v267/wang25cq.html

Wu, H., X. Li, Y. Lin, and K.-T. Cheng. 2023. Compete to win: Enhancing pseudo labels for barely-supervised medical image segmentation. IEEE Trans. Med. Imaging 42(11): 3244-3255. https://doi.org/10.1109/TMI.2023.3279110

Yang, X., Z. Song, I. King, and Z. Xu. 2023. A survey on deep semi-supervised learning. IEEE Trans. Knowl. Data Eng. 35(9): 8934-8954. https://doi.org/10.1109/TKDE.2022.3220219

Yu, L., S. Wang, X. Li, C.-W. Fu, and P.-A. Heng. 2019. Uncertainty-aware self-ensembling model for semi-supervised 3D left atrium segmentation. In Proc. Medical Image Computing and Computer Assisted Intervention (MICCAI 2019), 605-613. Cham, Switzerland: Springer. https://doi.org/10.1007/978-3-030-32245-8_67

AI-P20

Proceedings of The 12th International Symposium on Machinery and Mechatronics for Agriculture and Biosystems Engineering (ISMAB 2026)
20-24 October 2026, Busan, Republic of Korea

INTERPRETABLE HERBAL MEDICINE IMAGE CLASSIFICATION USING A CONCEPT BOTTLENECK MODEL

JIN-SEOK OH[1,2], Dae-Hyun Jung[1,2*]

1Department of Smart Farm Science, Kyung Hee University, Yongin 17104, Republic of Korea
2BK21 Interdisciplinary Program in IT-Bio Convergence System, Kyung Hee University, Yongin 17104, Republic of Korea
*Corresponding Author-- Voice: +82-31-201-2657, Email: daehyun@khu.ac.kr

Abstract: Deep learning–based image classification can support herbal medicine identification, but the visual features underlying model predictions are often difficult to interpret. Herbal medicine identification requires not only high classification accuracy but also understandable prediction rationales whose validity can be examined. This study therefore introduced a Concept Bottleneck Model (CBM) as a complementary approach to interpreting predictive visual features at the concept level, using ResNet-50 as a performance benchmark.

Models were developed to classify six herbal medicine categories: Bokbunja (Rubus coreanus Miq.), Sangsimja (Morus alba L.), Hwadong Bokbunja (Rubus chingii Hu), Sancho (Zanthoxylum schinifolium Siebold & Zucc.), Chopinamu (Zanthoxylum piperitum (L.) DC.), and Hwacho (Zanthoxylum bungeanum Maxim.). The CBM used CLIP to calculate cosine similarities between images and textual concept descriptions, which were then passed to a linear classifier. Starting with 100 concepts, evaluation scores were calculated using four weighting combinations of CLIP-based class separability (S), classifier importance (W), and semantic validity assessed through visual evaluation (M). Only concepts included in the removal candidate sets of all four combinations were progressively eliminated. Concept configurations were compared primarily using validation loss. The final CBM comprised 81 concepts and achieved a test accuracy of 94.53%, whereas ResNet-50 achieved 98.51% accuracy using the same data split.

Analysis of class-specific weights and image-level concept scores revealed that concepts describing “wrinkled and shriveled texture” and “distinct lenticels (small bumps) on bark” contributed to classification scores for Hwadong Bokbunja. For Sancho, contributing concepts included “curled or rolled up bark” and “steamed and sun-dried black appearance” To extend interpretation beyond textual descriptions, concepts were also presented visually by indicating the corresponding regions in the images.

This study demonstrates that explicit concepts can support the examination of prediction rationales in herbal medicine image classification through textual and visual

representations. This complementary approach facilitates understanding of classification results and assessment of the plausibility of their supporting features. By making prediction rationales available for inspection, the approach has the potential to support trust in herbal medicine classification and help users understand and apply classification decisions.

Key Words: Herbal Medicine Identification, Concept Bottleneck Model, Explainable AI, CLIP, Image Classification

ACKNOWLEDGEMENTS

This research was supported by a grant (23192MFDS106) from Ministry of Food and Drug Safety in 2026.

AI-P21

Proceedings of The 12th International Symposium on Machinery and Mechatronics for Agriculture and Biosystems Engineering (ISMAB 2026)
20-24 October 2026, Busan, Republic of Korea

FORECASTING AFTERNOON GREENHOUSE SOLAR RADIATION WITH GK2A CLOUD OPTICAL THICKNESS AND DAY-AHEAD WEATHER FORECASTS

Hyein Lee[1], SuYeon Lee[1], JooEun Lee[1], JoonYong Kim[2*]

[1]Data Engineering Team, FarmOS Inc., Anyang-si, Gyeonggi-do 14067, Republic of Korea
[2]Research Institute of Agriculture and Life Sciences, Seoul National University, Seoul 08826, Republic of Korea
[*]Corresponding Author-- Voice: +82-2-880-4612, Email: tombraid@snu.ac.kr

Abstract: Insufficient daily solar radiation is one of the major factors depressing the growth and yield of greenhouse crops. Surface solar radiation comprises a deterministic component determined by solar geometry and a stochastic component dominated by cloud transmittance. The former follows a predictable seasonal cycle, whereas the latter varies from day to day; days on which the daily radiation integral falls below the crop requirement can therefore occur in any season. Supplementary lighting is required to compensate for such deficits, and its operating schedule and target dose must be determined by mid-morning of the day. Day-ahead short-term weather forecasts alone, however, can hardly account for the variation in same-day solar radiation driven by the actual development and movement of clouds. In this study, a model was developed that predicts the clear-sky index by combining the short-term forecast of the Korea Meteorological Administration with the same-day morning cloud optical thickness (COT) from the Geostationary Korea Multi-Purpose Satellite-2A (GK2A), and converts the prediction into afternoon cumulative solar radiation. Satellite data were summarized into 33 directional and radial variables extracted from spatial windows of 50–200 km radius around the target site, rather than from a single pixel, to capture clouds approaching the site. To isolate the contribution of the same-day satellite observation, a forecast-only model of identical structure but excluding the satellite variables was used as the reference, and the two models were compared using 317 days of data spanning a full year from a site in Jinju, Gyeongsangnam-do, Korea, with day-wise five-fold cross-validation. For predictions updated at 09:00, the mean absolute error of the afternoon cumulative solar radiation decreased from 2.05 to 1.38 MJ/m² (33%), and the coefficient of determination improved from 0.685 to 0.852, with the improvement extending across the observed range, including the low-radiation days on which supplementary lighting is required. Obtained within the morning, this prediction provides the information basis for determining the operating time and target light dose of supplementary lighting, and thus serves as the prediction component of a decision-support module for smart greenhouses.

Key Words: smart greenhouse, supplementary lighting, solar radiation forecasting, cloud optical thickness, decision support

INTRODUCTION

In greenhouse production, insufficient solar radiation is a major factor limiting photosynthesis and yield, and supplementary lighting is required on days when the daily radiation integral falls below the crop requirement (Hao et al., 2018; Kaiser et al., 2019). The daily radiation integral is determined jointly by astronomical factors such as day length and solar elevation and by meteorological factors such as cloud-induced attenuation; days of low solar radiation can therefore occur in any season. Because supplementary lighting accounts for a large share of the electricity consumed in greenhouse operation (van Iersel and Gianino, 2017), the absence of a basis for deciding when and how much to operate it leads simultaneously to growth losses from under-operation and energy waste from over-operation. If the decision on whether to operate the lighting and on the target light amount could be made according to the afternoon solar radiation conditions of the day, both losses could be reduced at once; this, however, requires information for predicting the afternoon solar radiation during the morning.

Information currently available to greenhouse operators mostly consists of short-term forecasts issued on the previous day. Although such forecasts reflect synoptic-scale changes in pressure systems, they can hardly incorporate the variation in same-day solar radiation caused by the actual development and movement of clouds (Diagne et al., 2013; Theocharides et al., 2020). Actual solar radiation varies widely even under the same sky-condition forecast, so models driven only by forecasts exhibit systematic errors, particularly on cloudy days. We hypothesize that this limitation stems mainly from the limited information content of the input data rather than from the model structure: whether an individual day becomes radiation-deficient is governed largely by the cloud conditions of the day, which are not fully captured by the day-ahead forecast, and same-day cloud observations are therefore required.

Geostationary meteorological satellites are a data source capable of providing such same-day information. The Geostationary Korea Multi-Purpose Satellite-2A (GK2A) observes the Korean Peninsula at a spatial resolution of 2 km and provides cloud optical thickness products (Lee et al., 2023). The single-pixel value at the target site, however, is vulnerable to missing data and local noise, and above all cannot contain information on clouds that have not yet arrived. Given that weather systems over the Korean Peninsula generally move from west to east, the cloud distribution west of the site can function as a leading indicator of the cloud amount to arrive later, which provides the rationale for treating satellite data not as a point value but as a spatial distribution.

The objective of this study is to develop a model that predicts afternoon cumulative solar radiation by combining the day-ahead short-term forecast of the Korea Meteorological Administration with the same-day morning GK2A cloud optical thickness as spatial-window-based variables, and to quantify the contribution of the same-day satellite observation to prediction accuracy through comparison with a model of identical structure excluding the satellite variables. The forecast update time was set to 09:00, when the operating plan of supplementary lighting is established during the morning.

MATERIALS AND METHODS

Study site and data

The study was conducted at a site in Pyeonggae-dong, Jinju, Gyeongsangnam-do, Korea. Among the data acquired from July 3, 2025 to August 5, 2026, 317 days on which the forecast, satellite, and ground measurements were all available were used in the analysis. Ground-measured solar radiation served as the reference for both training and evaluation. Twenty-four variables, including sky condition, precipitation type and amount, air temperature, relative humidity, and wind speed, were constructed from the day-ahead short-term forecast of the Korea Meteorological Administration, to which GK2A cloud optical thickness images acquired at one-hour intervals from 06:00 to 09:00 on the day of prediction were combined.

Satellite spatial variables

Because the use of a single pixel alone is vulnerable to missing data and local noise, the satellite data were summarized into 33 variables within spatial windows centered on the target site. For radii of 50, 100, and 200 km, the COT mean, maximum, and cloud cover fraction, the east-west and north-south gradients, and the central pixel value were computed, together with the morning mean and the value immediately preceding the reference time of each variable, and the morning change in the east-west gradient. The directional variables were included because the cloud distribution west of the site functions as a leading indicator of the cloud amount to arrive later.

Prediction model and validation

The prediction targets were the hourly solar radiation from 12:00 to sunset on the day. To remove the scale variations associated with season and time of day, the clear-sky index, defined as the measured solar radiation divided by the clear-sky reference irradiance, was adopted as the learning target. The clear-sky reference irradiance was calculated by applying a site-specific quantile correction to the Haurwitz model (Haurwitz, 1945), and the predicted clear-sky index was multiplied by the reference irradiance to convert it into the hourly solar radiation and the afternoon cumulative solar radiation. At inference, only the information obtainable before 09:00 on the day was used, so that the operating conditions of actual use were replicated. LightGBM (learning rate 0.05, num_leaves 31, 400 rounds) was employed as the regression model, and the predictions from five random seeds were averaged.

Validation was performed with day-wise five-fold cross-validation. All hours of the same date were assigned to the same fold because the solar radiation at adjacent hours within a day is strongly correlated; with an hour-wise split, the information of the same day would appear in both training and validation, and the performance would be overestimated. The reported metrics were aggregated over the out-of-fold predictions for the entire period. The reference for comparison was a forecast-only model in which only the satellite variables were removed while the input composition, learning target, hyperparameters, and validation split were kept identical. Because the two models differ only in the composition of the input data, the difference in performance can be interpreted as the amount of information additionally provided by the same-day satellite observation. Performance was evaluated in terms of the mean absolute error (MAE), the root mean square error (RMSE), and the coefficient of determination (R^2).

RESULTS & DISCUSSION

Overall prediction performance

The contribution of the same-day satellite observation was isolated by comparing two models that share the learning target, hyperparameters, and day-wise cross-validation split, and differ only in whether the morning GK2A COT variables are included. For afternoon cumulative solar radiation, the forecast-only model produced an MAE of 2.05 MJ/m², an RMSE of 2.89 MJ/m², and an R^2 of 0.685 (Table 1). Adding the same-day morning satellite COT variables reduced the MAE to 1.38 MJ/m² and the RMSE to 1.98 MJ/m², decreases of 33% and 31%, respectively, and raised the R^2 to 0.852. Because the two models differ only in input composition, this gain is attributable mainly to the information content of the same-day observation. An MAE of 1.38 MJ/m² at the 09:00 update suggests that the afternoon solar resource can be estimated with accuracy that may support determining the operating schedule and the target light dose of supplementary lighting on the same morning.

Table 1 Prediction performance for afternoon cumulative solar radiation (317 days, out-of-fold, updated at 09:00).

Model	MAE (MJ/m²)	RMSE (MJ/m²)	R^2
Day-ahead forecast only	2.05	2.89	0.685
Day-ahead forecast + same-day morning satellite COT	1.38	1.98	0.852

Error behavior across the solar radiation range

Because prediction accuracy under conditions of low solar radiation is of particular importance for supplementary lighting decisions, the error structure over the observed range of solar radiation was examined using the observed-versus-predicted scatter plots in Fig. 1. The forecast-only model exhibited a systematic regression-to-the-mean pattern: overprediction on days with low observed solar radiation and underprediction on days with high observed solar radiation, with the points widely scattered around the 1:1 line. This is the error structure expected when the input carries little information on the actual development and movement of the day's clouds (Diagne et al., 2013; Kumar et al., 2020). With the morning satellite variables, the points converged to the 1:1 line over the entire range, and the scatter in the segment with low solar radiation (below 10 MJ/m²) decreased markedly. The improvement therefore extended across the range, including the low-radiation segment in which supplementary lighting decisions are made.

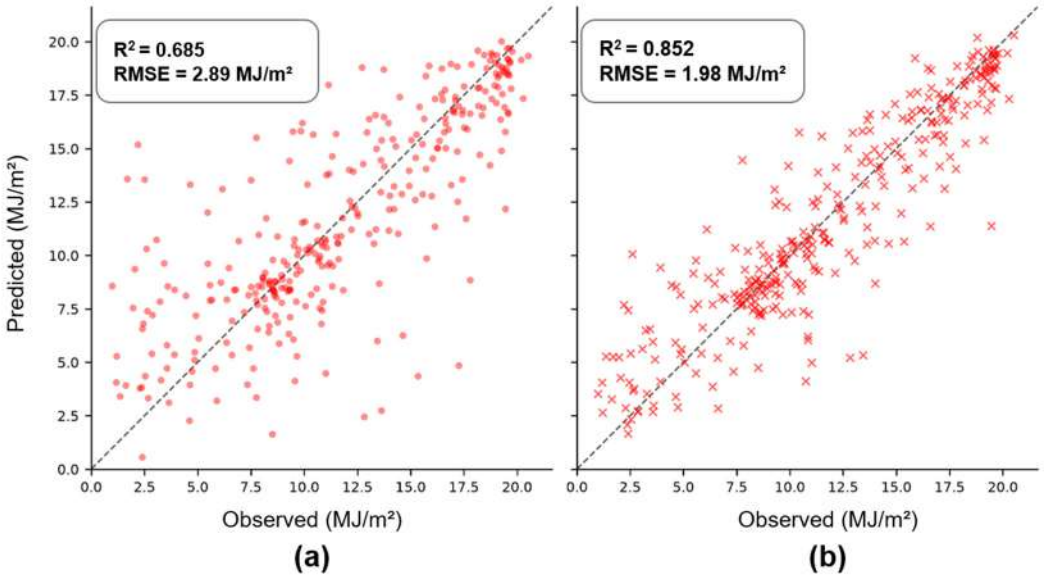

Fig. 1. Observed vs. predicted afternoon cumulative solar radiation; dashed line: 1:1 line (a: day-ahead forecast only; b: forecast + same-day morning satellite COT). Axis values are in MJ/m².

Limitations and outlook

The present result is based on 317 days of data at a single site, so generalization to other regions and terrain conditions requires separate validation. Because the analysis period spans the entire year, the prediction performance should also be examined separately by season. Whether the improvement in prediction accuracy translates into reduced lighting energy consumption and a measurable crop response remains to be demonstrated at the greenhouse scale.

CONCLUSIONS

In this study, a model was developed for predicting afternoon solar radiation for supplementary lighting decisions in greenhouses by combining the day-ahead short-term forecast with the same-day morning cloud optical thickness of the Geostationary Korea Multi-Purpose Satellite-2A (GK2A) as spatial-window-based variables. Compared with a model of identical structure excluding the satellite variables, the MAE of the afternoon cumulative solar radiation decreased from 2.05 to 1.38 MJ/m² (a 33% reduction), and the coefficient of determination improved from 0.685 to 0.852, with the improvement extending across the observed range, including the low-solar-radiation days on which supplementary lighting is required. Because this accuracy is achieved using only the data acquired by 09:00, the model provides, within the morning, a prediction component for determining the operating time and target light dose of supplementary lighting. Future research should include validation of generalization performance through extension to multiple sites, the establishment of criteria for converting the predicted solar radiation into decisions on lighting operation, and quantitative evaluation of the actual reduction in lighting energy consumption and of the crop growth response.

ACKNOWLEDGEMENTS

This work was carried out with the support of "Research Program for Agriculture Science and Technology Development (RS-2025-02303401)" Rural Development Administration, Republic of Korea.

REFERENCES

Diagne, M., M. David, P. Lauret, J. Boland, and N. Schmutz. 2013. Review of solar irradiance forecasting methods and a proposition for small-scale insular grids. Renew. Sustain. Energy Rev. 27: 65-76.

Hao, X., X. Guo, J. Lanoue, Y. Zhang, R. Cao, J. Zheng, C. Little, D. Leonardos, S. Kholsa, B. Grodzinski, and M. Yelton. 2018. A review on smart application of supplemental lighting in greenhouse fruiting vegetable production. Acta Hortic. 1227: 499-506.

Haurwitz, B. 1945. Insolation in relation to cloudiness and cloud density. J. Meteorol. 2(3): 154-166.

Kaiser, E., T. Ouzounis, H. Giday, R. Schipper, E. Heuvelink, and L. F. M. Marcelis. 2019. Adding blue to red supplemental light increases biomass and yield of greenhouse-grown tomatoes, but only to an optimum. Front. Plant Sci. 9: 2002.

Kumar, D. S., G. M. Yagli, M. Kashyap, and D. Srinivasan. 2020. Solar irradiance resource and forecasting: A comprehensive review. IET Renew. Power Gener. 14(10): 1641-1656.

Lee, D. K., C. K. Kim, S. S. Yum, H.-G. Kim, and Y.-H. Kang. 2023. Comparison of cloud optical thickness of GK-2A and HIMAWARI satellites by using UV-A irradiance in Daejeon. J. Korean Sol. Energy Soc. 43(3): 87-98.

Theocharides, S., G. Makrides, A. Livera, M. Theristis, P. Kaimakis, and G. E. Georghiou. 2020. Day-ahead photovoltaic power production forecasting methodology based on machine learning and statistical post-processing. Appl. Energy 268: 115023.

van Iersel, M. W., and D. Gianino. 2017. An adaptive control approach for light-emitting diode lights can reduce the energy costs of supplemental lighting in greenhouses. HortScience 52(1): 72-77.

AI-P22

Proceedings of The 12th International Symposium on Machinery and Mechatronics for Agriculture and Biosystems Engineering (ISMAB 2026)
20-24 October 2026, Busan, Republic of Korea

ZERO-SHOT OPEN-VOCABULARY DETECTION WITH TRANSFER LEARNING FOR BLOSSOM-END ROT IDENTIFICATION IN A COMMERCIAL TOMATO GREENHOUSE

Hyein Lee[1], Young-Kyun Jang[2], JoonYong Kim[3*]

[1]Data Engineering Team, FarmOS Inc., Anyang-si, Gyeonggi-do 14067, Republic of Korea
[2]GreenCS Co., Ltd., 7, Ecosandan 4-ro, Damyang-eup, Damyang-gun, Jeonnam-Gwangju Integrated Special City, Republic of Korea
[3]Research Institute of Agriculture and Life Sciences, Seoul National University, Seoul 08826, Republic of Korea
*Corresponding Author-- Voice: +82-2-880-4612, Email: tombraid@snu.ac.kr

Abstract: Comprehensive acquisition and integrated use of growth, environmental, and image data remain uncommon in commercial smart farms, although required for growth-oriented environmental control. As a preliminary step, this study developed an image-based pipeline for identifying blossom-end rot, a physiological disorder of tomato fruit. Data were collected in a commercial tomato greenhouse in Goheung, Jeollanam-do, Republic of Korea, using a mobile camera that traversed the crop row and captured images at nine predefined grid positions; a total of 4,181 time-series images were acquired from 11 April to 24 July 2026.

The pipeline consists of two stages. In the detection stage, Meta's Segment Anything Model 3 (SAM 3) detected tomato fruits in a zero-shot, open-vocabulary manner using only a text prompt, eliminating the need for bounding-box annotation. Detected regions were cropped and passed to the classification stage, where an EfficientNetV2-S model classified each fruit as healthy or affected by blossom-end rot. Training combined target-greenhouse crops with a publicly available tomato image dataset, and augmentation including blur and compression degradation accommodated the limited resolution of the crops. On a test set of 140 crops collected in the target greenhouse and held out from training, an accuracy of 92.1% was achieved, with a recall of 0.857 for blossom-end rot and 0.986 for healthy fruit. The results indicate that fruit crops obtained without bounding-box annotation can be classified for blossom-end rot; detection performance was not quantified in this study. Future work will improve the recall for the affected class and extend the approach to a multimodal model combining image and environmental data toward growth-oriented environmental control.

Key Words: greenhouse, open-vocabulary detection, crop monitoring, tomato, blossom-end rot

INTRODUCTION

Environmental control systems that regulate air temperature, relative humidity, carbon dioxide concentration, and irrigation have been increasingly adopted in protected horticulture. In most commercial facilities, however, control decisions are based solely on environmental set points, and the actual state of the crop is not incorporated into the control loop. Implementing growth-oriented environmental control, in which control targets are adjusted according to the observed state of the crop, requires that growth, environmental, and image data be acquired together and linked within a single framework. Such comprehensive acquisition remains rare in the field, and datasets in which greenhouse imagery is paired with concurrently recorded environmental data are correspondingly scarce.

Among the crop states observable from imagery, physiological disorders of fruit are of considerable practical interest because they directly determine marketable yield. Blossom-end rot is a representative physiological disorder in which a sunken necrotic lesion develops at the blossom end of the tomato fruit. It is not caused by a pathogen but is associated with localized calcium deficiency in the developing fruit, which is in turn mediated by water stress, high transpiration demand, and rapid fruit enlargement (Ho & White, 2005; Taylor & Locascio, 2004). Because its occurrence is governed by environmental conditions, blossom-end rot is a suitable target for linking image-based observation to environmental control.

Deep learning methods for fruit detection in greenhouses have advanced considerably, yet they ordinarily require a large number of manually drawn bounding boxes. This requirement incurs a particularly high cost for tomato canopies, in which dozens of fruits at different maturity stages appear within a single frame under partial occlusion. Open-vocabulary detection provides an alternative that removes this requirement altogether. Following the Segment Anything Model, which generated class-agnostic masks from geometric prompts, and its successor, which extended the approach to video through streaming memory, Segment Anything Model 3 (SAM 3) introduced promptable concept segmentation, in which a short noun phrase retrieves all instances of the corresponding concept (Carion et al., 2026). Comparable approaches oriented toward real-time processing have also been proposed (Cheng et al., 2024). Whereas such models enable objects of a general category to be localized without task-specific annotation, fine-grained distinctions such as the symptoms of a physiological disorder are not reliably expressed by text prompts, and it is therefore reasonable to delegate them to a separate classifier.

The conditions under which greenhouse imagery is acquired also warrant consideration. Studies of fruit detection and disorder recognition are frequently conducted in research facilities, or on imagery captured after the canopy has been prepared so that fruits are clearly exposed. Imagery from a commercially operated farm differs fundamentally from these conditions. The canopy is managed according to the grower's work schedule rather than for the convenience of imaging, so that leaves are not removed to expose the fruit; as a result, a substantial proportion of fruits are observed partially occluded by leaves, under uneven illumination, or at oblique angles. Moreover, because there is no benefit in leaving an affected fruit on the truss, the grower removes it within a few days of symptom appearance, so that affected fruits do not accumulate in the canopy. The class imbalance in imagery acquired from an operating farm is therefore not an artifact arising from dataset construction but a direct reflection of ordinary cultivation management. A method intended for application in commercial facilities should accordingly be developed on imagery acquired under these conditions rather than on curated imagery; the present study therefore treats occlusion as a given property of the target domain and draws all test crops from the operating greenhouse.

The objective of this study was to establish, as a preliminary step toward a growth-oriented environmental control system, the methodological feasibility of identifying blossom-end rot in tomato fruit from imagery acquired in a commercially operated greenhouse without bounding-box annotation. Specifically, this study aimed to detect tomato fruits in unprepared canopy imagery acquired by a mobile camera through zero-shot open-vocabulary detection using the text prompts "tomato", "unripe tomato", and "ripening tomato"; to classify the detected fruits as healthy or affected by blossom-end rot using a transfer-learned convolutional neural network; and to demonstrate that the two stages can be chained without bounding-box annotation under the occlusion conditions encountered in the target facility's image stream.

MATERIALS AND METHODS

Image acquisition

Images were acquired in a commercially operated tomato greenhouse in Goheung, Jeollanam-do, Republic of Korea. The cultivar under production was 'Dafnis'. A mobile camera system was used in order to acquire imagery of the crop from multiple viewpoints; the camera traversed the crop row along the horizontal axis and was positioned at three heights along the vertical axis, capturing images at nine predefined grid positions. Imaging was performed four times daily at each position, at 06:00, 10:00, 14:00, and 16:00, at a native resolution of 3,840 × 2,160 pixels. A total of 4,181 images were acquired between 11 April and 24 July 2026. Compared with imaging from a single fixed viewpoint, this scheme secures broader canopy coverage but entails variation in object size across positions, with the median shorter side of the detected fruit regions ranging from approximately 65 to 94 pixels depending on the grid position.

The greenhouse remained under commercial production throughout the acquisition period, and no manipulation of the canopy was performed for the purpose of imaging.

Environmental data, including air temperature, relative humidity, and solar radiation, were logged at one-minute intervals in the same greenhouse. These data were not used in the present study and are being accumulated for the multimodal extension described in the Conclusions.

Detection and classification pipeline

The proposed pipeline consists of two stages, text-prompted detection followed by crop-wise classification, and its overall configuration is presented in Fig. 1. Detection was performed using the promptable concept segmentation capability of SAM 3. Tomato objects were detected by supplying the text prompts to the model, and no bounding-box annotation, fine-tuning, or exemplar box was provided, so that the detection stage operated in a fully zero-shot, open-vocabulary manner. In post-processing, candidate boxes generated by the multiple prompts were merged with non-maximum suppression using an intersection-over-union threshold of 0.7, so that each fruit was represented by a single box. Inference was performed at an input resolution of 1,008 pixels, matching the resolution at which the perception encoder of SAM 3 was trained, with a confidence threshold of 0.6 and half-precision weights. The predicted masks were not used; only the corresponding axis-aligned bounding boxes were retained. Each box was expanded by 8% of its width and height so as to include the fruit boundary, clipped to the image extent, and cropped. Regions whose shorter side was below 60 pixels were excluded, since enlarging them to the classifier input resolution leaves

insufficient textural information for discrimination. The detection results were stored as text in normalized centre-coordinate, width, and height format, one file per image, so that the two stages could be executed independently.

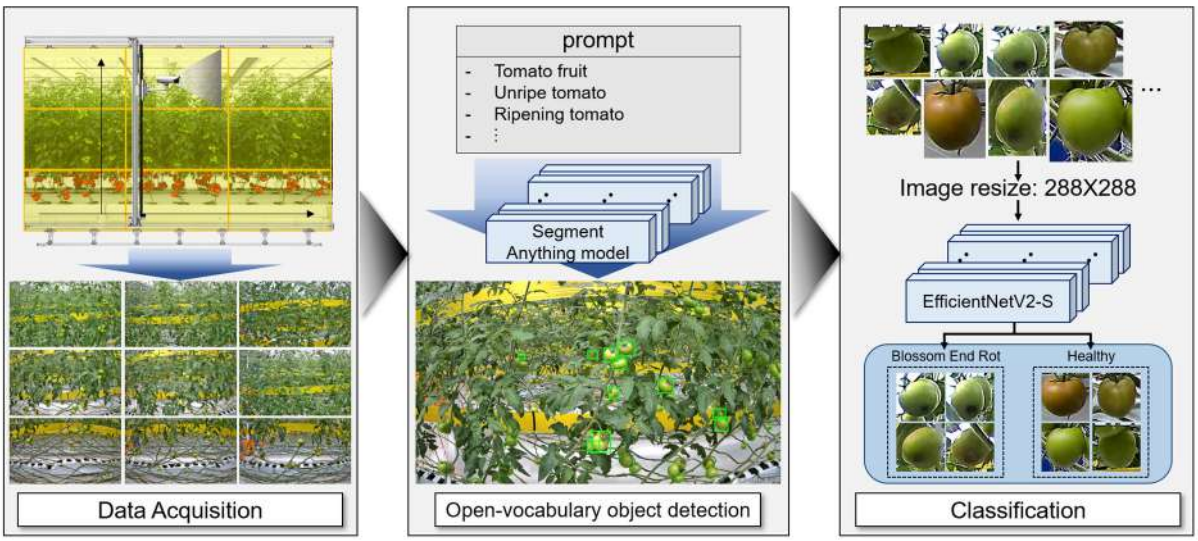

Fig. 1 Overview of the proposed two-stage pipeline. Tomato fruits are detected in a zero-shot, open-vocabulary manner using a text prompt, cropped with a fixed margin, and classified as healthy or affected by blossom-end rot.

For classification, an EfficientNetV2-S network (Tan & Le, 2021) initialized with ImageNet-pretrained weights was transfer-learned for binary classification of healthy fruit and fruit affected by blossom-end rot. The classification dataset was constructed by combining crops obtained from the target greenhouse with a publicly available tomato image dataset. The dataset was divided at the image level, so that no image used for training or validation contributed crops to the test set. The test subset consisted of 140 crops collected exclusively in the target greenhouse, comprising 70 healthy fruits and 70 fruits affected by blossom-end rot, and was used in neither training nor validation. The test crops were produced automatically by the detection stage described above, including the filter that excluded regions smaller than 60 pixels, and were then reviewed manually so that the true labels could be assigned. Each crop was labelled by the study authors as affected when a lesion was visible at the blossom end. The 70 healthy crops were extracted by first setting aside a separate set of images of the tomato plants in the target greenhouse and then cropping the tomato fruits from those held-out images. The balanced composition was chosen to evaluate the scarce affected class reliably under the limited number of affected fruits available in the field, and the reported performance is based exclusively on these held-out crops.

Because crops extracted from canopy-scale imagery are smaller and less sharp than the close-up images contained in the public dataset, the augmentation was designed to reduce this gap. Training images were resized with the aspect ratio preserved, padded to a square, and randomly cropped at scales of 0.7 to 1.0 to an input size of 288 × 288 pixels. Horizontal and vertical flips, rotation within ±15°, color jitter, Gaussian blur, and JPEG compression degradation at quality factors of 40 to 95 were applied stochastically, followed by channel-wise normalization and random erasing. At evaluation, only resizing and center cropping to 300 × 300 pixels were applied, without augmentation.
Training was carried out for 40 epochs with a batch size of 32. The AdamW optimizer was used

with a one-cycle schedule at a peak learning rate of 3×10^{-4}, a weight decay of 1×10^{-4}, and a dropout rate of 0.3, and the loss function was cross-entropy with label smoothing of 0.05 and inverse-frequency class weighting. Mixed-precision arithmetic was used throughout, and the checkpoint achieving the highest validation accuracy was used for evaluation. At inference, detection was executed once per image and the resulting crops were classified in batches of 64, so that the number of GPU calls remained small even for frames containing many fruits. All experiments were conducted on a workstation equipped with an NVIDIA RTX PRO 4500 Blackwell GPU with 32 GB of memory, using PyTorch 2.14 with CUDA 13.0.

RESULTS & DISCUSSION

On the test set of 140 crops collected in the target greenhouse and held out from training and validation, the transfer-learned EfficientNetV2-S achieved an overall accuracy of 92.1% (129 of 140 crops; Table 1).

Table 1 Classification performance on the test set of 140 crops collected in the target greenhouse.

	precision	recall	f1-score	support
Blossom-end rot	0.984	0.857	0.916	70
Healthy	0.873	0.986	0.926	70

Recall for blossom-end rot was 0.857, indicating that 10 of the 70 affected crops were assigned to the healthy class, whereas only 1 of the 70 healthy crops was classified as affected, giving a precision of 0.984 for the affected class. This precision holds at the 50% prevalence of the test set; with the same sensitivity and specificity, it would fall to about 0.87 at a prevalence of 10% and 0.76 at 5%. The errors are thus concentrated in missed detections rather than in false alarms. For a monitoring application this direction is the less favorable of the two, since an unreported affected fruit removes the opportunity for intervention altogether, whereas a false alarm can be resolved by inspection. Examination of the misclassified crops indicated that most of the ten missed affected fruits showed an early-stage lesion that was small and pale relative to the surrounding shading at the blossom end, a confusion that is aggravated by the limited resolution of crops extracted from canopy-scale imagery.

CONCLUSIONS

This study demonstrated the feasibility of classifying blossom-end rot in tomato fruit crops obtained from imagery acquired in a commercially operated greenhouse. By detecting tomato fruits in a zero-shot, open-vocabulary manner using SAM 3 with multiple text prompts, the bounding-box annotation ordinarily required to train a detection model was dispensed with, and the detected crops were classified by a transfer-learned EfficientNetV2-S, yielding an accuracy of 92.1% on 140 crops collected in the target greenhouse, with a recall of 0.857 for the affected class and 0.986 for healthy fruit. Both stages operated on canopy imagery for which no preparation had been carried out for the purpose of photography. Because the test set was balanced, the reported precision does not represent field precision at the lower prevalence expected in production, and detection performance was not quantified in this study. Future work is planned along two directions. A small annotated subset will be constructed for

evaluation purposes so that detection performance can be quantified; and the approach will be extended to a multimodal model that combines the environmental data recorded concurrently in the same greenhouse with the imagery, thereby elucidating the relationship between the occurrence of blossom-end rot and antecedent environmental conditions and completing the loop toward growth-oriented environmental control.

ACKNOWLEDGEMENTS

This work was supported by Korea Institute of Planning and Evaluation for Technology in Food, Agriculture and Forestry(IPET) and Korea Smart Farm R&D Foundation(KosFarm) through Smart Farm Innovation Technology Development Program, funded by Ministry of Agriculture, Food and Rural Affairs(MAFRA) and Ministry of Science and ICT(MSIT), Rural Development Administration(RDA) (RS-2025-02305220).

REFERENCES

Carion, N., Gustafson, L., Hu, Y.-T., Debnath, S., Hu, R., Suris Coll-Vinent, D., Ryali, C., Alwala, K. V., Khedr, H., & Huang, A. (2026). Sam 3: Segment anything with concepts. *International Conference on Learning Representations*, *2026*, 138846–138923.

Cheng, T., Song, L., Ge, Y., Liu, W., Wang, X., & Shan, Y. (2024). Yolo-world: Real-time open-vocabulary object detection. *2024 IEEE/CVF Conference on Computer Vision and Pattern Recognition (CVPR)*, 16901–16911.

Ho, L. C., & White, P. J. (2005). A cellular hypothesis for the induction of blossom-end rot in tomato fruit. *Annals of Botany*, *95*(4), 571–581.

Tan, M., & Le, Q. (2021). Efficientnetv2: Smaller models and faster training. *International Conference on Machine Learning*, 10096–10106.

Taylor, M. D., & Locascio, S. J. (2004). Blossom-end rot: a calcium deficiency. *Journal of Plant Nutrition*, *27*(1), 123–139.

AI-P23

Proceedings of The 12th International Symposium on Machinery and Mechatronics for Agriculture and Biosystems Engineering (ISMAB 2026)
20-24 October 2026, Busan, Republic of Korea

DEVELOPMENT OF AN ALGORITHM FOR PEPPER FRUIT AND FLOWER DETECTION AND COUNTING USING TWO-SIDED OBLIQUE UAV IMAGERY

Hyeonjun Lee[1], Taeyoung Woo[1], Dohyeon Jeong[1], Junyeong Kim[1], Dong-Wook Kim[1*]

[1]Department of Smart Farm Engineering, Kongju National University, Yesan, Korea
*Corresponding Author: Voice: +82-10-7478-8033, Email: dwk8033@kongju.ac.kr

Abstract: Pepper fruit and flower counts provide useful information for monitoring crop development and estimating potential yield. However, conventional unmanned aerial vehicle (UAV) surveys using nadir image acquisition and orthomosaic generation primarily capture the upper canopy, limiting the visibility of fruits and flowers obscured by foliage along the sides of crop rows. In this study, an algorithm was developed to detect and count pepper fruits and flowers using two-sided oblique UAV imagery. A field experiment was conducted with 200 pepper plants representing four cultivars in Wanju, Korea. RGB images were automatically acquired using a DJI Mavic 3 at an altitude of 6 m with a gimbal pitch angle of −40° (40° below the horizontal) from both sides of the crop rows. Image acquisition was conducted on June 26, July 10, July 21, July 27, August 11, and August 24, 2026, covering early to late growth stages. Reference counts were obtained by manually counting fruits and flowers on each plant in the field. YOLO11 was fine-tuned to detect three object classes—pepper plants, pepper fruits, and flowers—and SAM 2.1 Hiera-L was used to delineate individual plant regions using detected plant bounding boxes as prompts. To evaluate the validity of two-sided counting, fruit and flower detections were grouped by plant with the aid of these regions, and the combined counts from both viewing directions were compared with the corresponding field-measured counts. The automated two-sided counts showed strong correlations with field-measured fruit and flower counts across the sampled growth stages. These results suggest that low-altitude, two-sided oblique UAV imagery combined with object detection and plant segmentation has potential for estimating pepper fruit and flower counts at the individual-plant level from early to late growth stages.

Key Words: Pepper, Two-sided oblique UAV imagery, Object detection, Instance segmentation, Crop monitoring

Acknowledgements: This research was supported by the Rural Development Administration research project (Project No.: RS-2025-02214915).

AI-P24

Proceedings of The 12th International Symposium on Machinery and Mechatronics for Agriculture and Biosystems Engineering (ISMAB 2026)
20-24 October 2026, Busan, Republic of Korea

DEVELOPMENT OF A DEEP LEARNING-BASED METHOD FOR DETECTING SOYBEAN PLANTING GROUPS AND COUNTING PLANTS FROM UAV IMAGERY

Taeyoung Woo[1], Hyeonjun Lee[1], Junyeong Kim[1], Dohyeon Jeong[1], Dong-Wook Kim[1*]

[1]Department of Smart Farm Engineering, Kongju National University, Yesan, Republic of Korea

*Corresponding Author-- Voice: +82-10-7478-8033, Email: dwk8033@kongju.ac.kr

Abstract: Mechanical soybean sowing using rotary-disc seed meters can cause nonuniform seedling counts across planting groups, requiring early identification of underpopulated and overcrowded groups. This study developed and evaluated a two-stage deep-learning-based method for detecting planting groups and estimating plant counts from UAV orthomosaic imagery. The field in Gimje, Republic of Korea, contained 800 predefined groups in eight designated rows. Colored foam-board markers were placed at 10-group intervals, and plants in each group were manually counted to provide reference data. RGB images were acquired at an altitude of 6 m above ground level with a minimum overlap of 80% and photogrammetrically processed into an orthomosaic. Ground control points supported geometric correction, while a reflectance panel placed during image acquisition supported radiometric calibration. The corrected orthomosaic was the sole image source for annotation and model development; field observations supplied the reference counts. Each group was annotated with a polygonal region of interest encompassing the plants and the soil between them. Group-centered image patches were divided into training, validation, and test subsets. YOLOv8-seg was first used to detect and segment planting-group regions. The resulting polygonal masks were used to extract image patches for a Vision Transformer-based regression model that estimated the plant count in each group. Detection and segmentation performance was evaluated using precision, recall, mAP@0.5, F1 score, and polygon-level intersection over union (IoU). Counting performance was assessed using the mean absolute error (MAE), root mean square error (RMSE), and the proportion of groups whose predicted count matched the field reference. Groups with fewer than two plants were classified as replanting candidates, whereas groups with more than three plants were classified as thinning candidates. The method integrates planting-group detection, plant-count estimation, and management classification for future evaluation under additional field conditions.

Key Words: Soybean, UAV imagery, Early stand assessment, Planting-group detection, Decision support

Acknowledgements: This research was supported by the Rural Development Administration research project (Project No.: RS-2025-02214915).

AI-P25

Proceedings of The 12th International Symposium on Machinery and Mechatronics for Agriculture and Biosystems Engineering (ISMAB 2026)
20-24 October 2026, Busan, Republic of Korea

INDIVIDUAL-PLANT SPAD ESTIMATION IN FIELD-GROWN PEPPER USING UAV-DERIVED SPECTRAL, TEXTURAL, AND STRUCTURAL INFORMATION

Dohyeon Jeong[1], Hyeonjun Lee[1], Junyeong Kim[1], Taeyoung Woo[1], Dong-Wook Kim[1*]

[1]Department of Smart Farm Engineering, Kongju National University, Yesan, Republic of Korea

*Corresponding Author -- Voice: +82-10-7478-8033, Email: dwk8033@kongju.ac.kr

Abstract: Soil Plant Analysis Development (SPAD) values are widely used as non-destructive indicators of leaf chlorophyll status for crop growth monitoring. This study developed and evaluated plant-level SPAD prediction models for field-grown pepper using spectral, textural, and structural information derived from unmanned aerial vehicle (UAV) imagery. A total of 200 pepper plants from four cultivars (50 plants per cultivar) were surveyed on six dates between 26 June and 25 August 2026 at the National Institute of Horticultural and Herbal Science in Wanju, Republic of Korea. SPAD values were measured using a SPAD-502Plus meter, with measurements from five leaves averaged for each plant. UAV-based RGB and multispectral imagery were acquired over the experimental field. Ground control points (GCPs) were used to improve geometric accuracy during orthomosaic generation, and a reflectance calibration panel was used for radiometric correction of the multispectral imagery. Vegetation masks were generated from NDVI images using Otsu thresholding and noise removal, and the vegetation component nearest to each plant center was assigned to the corresponding plant. Twenty-five vegetation indices were calculated, and their mean, median, and standard deviation were extracted at the plant level. Gray-level co-occurrence matrix (GLCM)-based texture features, including contrast, homogeneity, energy, and correlation, were extracted from the segmented canopy regions. Canopy width was automatically extracted from RGB imagery as a structural feature. It was calculated as the distance between canopy boundaries along a transect passing through the plant center and perpendicular to the local crop-row direction. The extracted features were matched with ground-measured SPAD values. Partial least squares regression (PLSR), support vector regression (SVR), and random forest regression (RFR) were used as feature-based prediction models. A convolutional neural network (CNN) regression model was also evaluated using five-band multispectral image patches to automatically learn spectral and spatial features. Model performance was evaluated using leave-one-date-out cross-validation, in which each survey date was held out once for testing while the remaining dates were used for model development. Performance was assessed using the coefficient of determination (R^2), root mean squared error (RMSE), and mean absolute error (MAE). The feature-based and CNN models were compared to evaluate their suitability for non-destructive plant-level SPAD estimation in field-grown pepper.

Key Words: Pepper, SPAD, UAV multispectral imagery, Vegetation indices, Image texture, Canopy width

Acknowledgements: This research was supported by the Rural Development Administration research project (Project No.: RS-2025-02214915).

AI-P26

Proceedings of The 12th International Symposium on Machinery and Mechatronics for Agriculture and Biosystems Engineering (ISMAB 2026)
20-24 October 2026, Busan, Republic of Korea

REGRESSION-BASED PREDICTION OF HUMAN AFFECTIVE CHANGES FROM INSECT SOUND MEL-SPECTROGRAMS

Junyeong Kim[1], Su Ji Jang[2], Hyeonjun Lee[1], Dohyeon Jeong[1], Taeyoung Woo[1], Dong-Wook Kim[1*]

[1]Department of Smart Farm Engineering, Kongju National University, Yesan, Korea
[2]Jeonbuk State Agricultural Research & Extension Services, 413 Seodong-ro, Iksan-si, Jeonbuk State 54591, Republic of Korea
*Corresponding Author: Voice: +82-10-7478-8033, Email: dwk8033@kongju.ac.kr

Abstract: Sound-producing insects represent valuable bioacoustic resources with potential applications in digital healing and sound-based affect regulation. This study investigates the relationship between Mel-spectrogram patterns of cricket and katydid sounds and listeners' self-reported affective changes. A dataset comprising 47 insect sound recordings, representing 19 cricket and 28 katydid taxa, was prepared, and each recording was converted into a Mel-spectrogram to represent its spectral and temporal patterns. A complete blinded listening assessment was designed in which approximately 50 participants evaluate the entire set of 47 sound stimuli. The identity of each insect is concealed, and the sound stimuli are presented in an individually randomized order. Based on Russell's circumplex model of affect, the affective change induced by each sound stimulus is assessed along the valence dimension, ranging from unpleasant to pleasant, and the arousal dimension, ranging from calm to activated. Each dimension is evaluated using a four-point scale coded as −2, −1, +1, and +2, and the resulting valence and arousal ratings are combined to form a single coordinate in the two-dimensional affective space. The participant responses are aggregated for each insect sound and assigned to the corresponding Mel-spectrogram as two-dimensional target labels. Acoustic representations are extracted directly from the Mel-spectrograms using a pretrained convolutional neural network encoder, and multi-output support vector regression is subsequently applied to estimate the valence–arousal coordinates. Predictive performance is evaluated using leave-one-out cross-validation (LOOCV), with one sound stimulus held out in each iteration. The proposed approach provides a framework for predicting human affective changes from insect sound Mel-spectrograms and may support the selection of bioacoustic resources suitable for digital healing and affect-responsive sound content.

Key Words: Russell's Circumplex Model, Bioacoustics, Insect Sound, Mel-Spectrogram, Valence–Arousal

Acknowledgements: This research was supported by the Rural Development Administration and Jeollabuk-do, Republic of Korea (Project No. RS-2026-25550121)

AI-P27

Proceedings of The 12th International Symposium on Machinery and Mechatronics for Agriculture and Biosystems Engineering (ISMAB 2026)
20-24 October 2026, Busan, Republic of Korea

EFFECTS OF MARKER-HEIGHT VARIATION ON TRACTOR–IMPLEMENT RELATIVE POSE IN SIMULATED EXTERNAL AERIAL MEASUREMENT

Jaewoo Kim[1], Eun-Kuk Kim[2], Tae-Ho Han[2], Hyunggun Kim[1*]

[1]Department of Biomechatronic Engineering, Sungkyunkwan University, Republic of Korea
[2]Agricultural Machinery Test Team, Korea Agriculture Technology Promotion Agency, Republic of Korea
*Corresponding Author: Hyunggun Kim, Email: hkim.bme@skku.edu

Abstract: Marker-height variation was evaluated for tractor–implement relative pose measurement from an external unmanned aerial vehicle (UAV). Body poses were estimated separately from static simulated images. Four upward-facing markers retained their size, horizontal footprint, and mean height. Three layouts were considered: a coplanar reference configuration (P0) and two noncoplanar configurations with alternating vertical offsets of ±0.075 m (N1) and ±0.150 m (N2). Evaluation was performed on 270 images comprising 90 matched blocks collected across 45–65 m altitudes and 0° and 20° viewing angles from nadir. N1 and N2 showed lower mean and median translation, rotation, and virtual-point errors, including against post hoc strengthened P0 (hybrid). Mean rotation errors were 0.551° for N1 and 0.352° for N2, compared with 2.903° for strengthened P0. Point errors were higher than those of P0 in 28 blocks for N1 and 23 blocks for N2. These findings demonstrate that noncoplanar marker arrangements improved aggregate pose-estimation accuracy, while the magnitude and consistency of these gains depended on viewing geometry and solver selection. Validation under field conditions remains necessary.

Key Words: Aerial measurement, Marker height, Relative pose, Simulation, Tractor–implement.

INTRODUCTION

An external unmanned aerial vehicle (UAV) provides a common view of the tractor and implement, requiring marker layouts to be evaluated in terms of the resulting combined relative pose estimate. Kalaitzakis et al. (2021) investigated two-marker bundles bent convexly by 90°, while García-Ruiz et al. (2023) mounted custom markers on polyhedral faces. Unlike these tilted-face targets, the present study adopts a more controlled comparison, introducing geometric variation exclusively through marker height while retaining face directions, count, size, horizontal footprint and mean height.

This study aimed to determine how height variation alone affects relative translation and rotation and whether these effects persist under a strengthened planar baseline. The primary contribution of the study therefore lies in a controlled, matched empirical comparison rather than in the development of a new solver or relative-transformation method.

MATERIALS AND METHODS

Static cuboid models representing the tractor and implement were each equipped with four upward-facing AprilTag 36h11 markers (Olson, 2011). Marker side length was 0.5 m at the black border, center spacing was 1.4 × 0.9 m, and the markers were positioned at a mean height of 0.2 m above the body surface. An identical marker configuration was used for both bodies, with P0 offsets set to zero and alternating N1 and N2 offsets of ±0.075 m and ±0.150 m with respect to P0, respectively (Fig. 1). Relative translation between the tractor and implement was held constant at (−3.8, 0, 0.5) m, while only the implement orientation was varied, without modeling hitch kinematics. Rendering and pose estimation used the same camera calibration for 3840 × 2160 images, while lighting and material properties were held constant across all conditions.

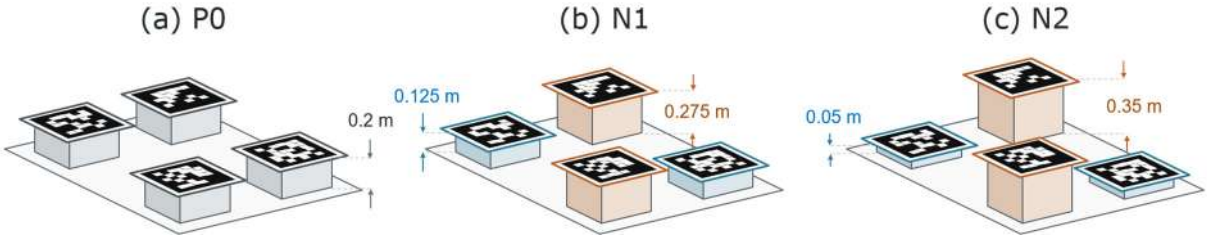

Fig. 1. Height-only layouts with unchanged marker face orientations. Orange and blue indicate high- and low-positioned markers, respectively. Square supports are schematic and were not evaluated as mounting hardware.

Table 1 summarizes 90 matched blocks distributed across three layouts, for a total of 270 unique images. The predefined XY offsets were not considered independent random replicates. Standard deviations (SD) were calculated using a denominator of 90, and quantiles were obtained by linear interpolation.

Body poses were estimated from pooled tag corners using sequential quadratic programming perspective-n-point (SQPnP; Terzakis and Lourakis, 2020). Post hoc P0 checks reprocessed the 90 images and stored corners uaing infinitesimal plane-based pose estimation (IPPE; Collins and Bartoli, 2014) or a hybrid SQPnP/IPPE implementation, with Levenberg–Marquardt refinement applied in both cases. Valid candidates were required to have positive depth, detections from ≥2 tags per body, and a reprojection root-mean-square error (RMSE) ≤3 pixels; the candidate with the minimum-error pose was then selected without ground truth. Primary results were retained unchanged, and relative poses were calculated using Eq. (1).

$$\hat{T}_{TI} = \hat{T}_{CT}^{-1}\hat{T}_{CI}. \quad (1)$$

Here, T_{AB} maps coordinates from B to A; hats denote estimates, and C, T, I refer to the camera, tractor, and implement. Peripheral field markers were excluded from body-pose estimation and from the computation in Eq. (1).

Table 1. Simulation conditions.

Varied condition	Levels
UAV altitude	45, 55, 65 m
Angle from nadir	0°, 20°
Relative implement orientation	Neutral; yaw −15°, +15°; pitch +8°; roll +8°
Fixed XY look-at offsets	(0, 0), (+0.25, −0.25), (−0.25, +0.25) m

Errors were quantified by translation distance, geodesic rotation angle, and distance between the estimated and true positions of a virtual point at (−1.2, 0, 0.5) m in the implement frame, with the origin located at the lower center. The virtual point was neither rendered nor detected and does not correspond to a physical hitch or validated tool tip. Its positional discrepancy therefore integrates the effects of both translation and rotation errors.

RESULTS & DISCUSSION

All 270 relative estimates were successfully obtained, including two N1 images containing three rather than four implement tags. N1 and N2 showed lower means and medians across all three error measures compared with the primary and hybrid P0 configurations (Table 2; Fig. 2).

Table 2. Relative errors (mean ± SD; 90 cases per analysis; *post hoc).

Analysis	Translation (m)	Rotation (°)	Point (m)
P0: primary	0.218 ± 0.413	4.302 ± 7.309	0.224 ± 0.481
N1: primary	0.073 ± 0.055	0.551 ± 0.332	0.071 ± 0.054
N2: primary	0.062 ± 0.042	0.352 ± 0.197	0.061 ± 0.041
P0: IPPE*	0.146 ± 0.100	2.904 ± 3.221	0.142 ± 0.097
P0: hybrid*	0.146 ± 0.100	2.903 ± 3.220	0.142 ± 0.097

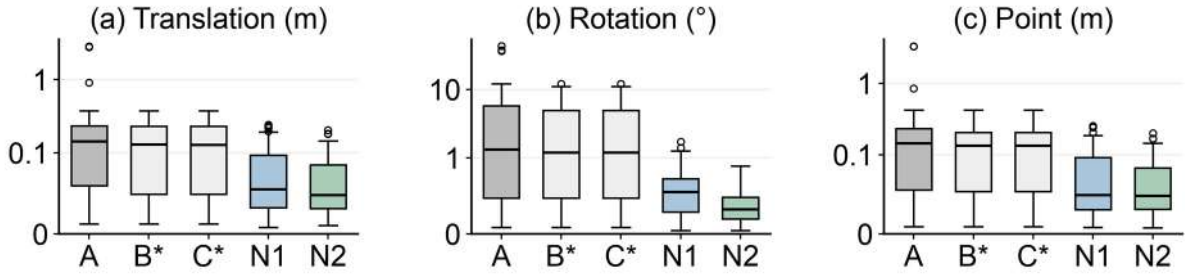

Fig. 2. Relative errors. A: primary P0, B: IPPE P0, C: hybrid P0; N1: primary N2: primary. Boxes indicate the interquartile range (IQR; Q1–Q3), with horizontal lines denoting the medians. Whiskers extend to the most extreme values within 1.5 × IQR, and circles represent all outliers. Symlog thresholds were 0.1 m, 1°, 0.1 m; 90 cases/group. *Post hoc P0 reuse; 270 unique images.

Strengthening P0 reduced the maximum point error from 3.321 to 0.425 m, indicating that the original extreme errors were not an inevitable consequence of planar geometry. However, N1 and N2 exhibited larger point errors than hybrid P0 in 28 of 90 and 23 of 90 blocks, respectively. These data indicate that the improvements were neither universal nor attributable solely to rotational effects.

In contrast to previous studies based on tilted target configurations, this study examined height variation alone. The resulting measured effects therefore encompass the combined contributions of rendering, marker detection, and pose estimation. Several factors relevant to real-world deployment, including mounting feasibility, calibration mismatch, dynamic motion, field performance, hitching, world-frame path estimation, and control performance, were beyond the scope of the present validation.

CONCLUSIONS

Marker-height variation was investigated for tractor–implement relative pose measurement using an external UAV. Noncoplanar marker configurations improved aggregate pose-estimation accuracy, while the magnitude and consistency of these gains depended on viewing geometry and solver selection. These findings suggest that marker elevation can improve estimation performance, although its effectiveness is contingent on the geometric and algorithmic conditions.

ACKNOWLEDGEMENTS

This research was supported by the Rural Development Administration of Korea (RS-2026-25548199).

REFERENCES

Collins, T., and A. Bartoli. 2014. Infinitesimal plane-based pose estimation. Int. J. Comput. Vis. 109(3): 252–286.

García-Ruiz, P., F. J. Romero-Ramirez, R. Muñoz-Salinas, M. J. Marín-Jiménez, and R. Medina-Carnicer. 2023. Fiducial objects: Custom design and evaluation. Sensors. 23(24): 9649.

Kalaitzakis, M., B. Cain, S. Carroll, A. Ambrosi, C. Whitehead, and N. Vitzilaios. 2021. Fiducial markers for pose estimation: Overview, applications and experimental comparison of the ARTag, AprilTag, ArUco and STag markers. J. Intell. Robot. Syst. 101(4): 71.

Olson, E. 2011. AprilTag: A robust and flexible visual fiducial system. In Proc. IEEE Int. Conf. Robotics Automation, 3400–3407. A. Bicchi, ed. Piscataway, NJ: IEEE.

Terzakis, G., and M. Lourakis. 2020. A consistently fast and globally optimal solution to the perspective-n-point problem. In Computer vision – ECCV 2020, 478–494. Vedaldi, A., H. Bischof, T. Brox, and J. M. Frahm, eds. Cham, Switzerland: Springer International Publishing.

AI-P28

Proceedings of The 12th International Symposium on Machinery and Mechatronics for Agriculture and Biosystems Engineering (ISMAB 2026)
20-24 October 2026, Busan, Republic of Korea

DEVELOPMENT OF POULTRY VOCAL MONITIORING SYSTEM FOR CHICKEN RESPIRATORY DISEASE DETECTION

Li-Yun Huang, Jun-Qian Zhu, and Yao-Chuan Tsai

Department of Bio-Industrial Mechatronics Engineering, National Chung Hsing University, Taiwan
*Corresponding Author-- Voice: +886-965-453-841, Email: andyhuang.twmail@gmail.com

Abstract: With the demand of chicken meat and eggs increased year by year, poultry breeding has become more and more important in livestock industry. During the breeding, threats such as illness or heat stress would affect poultry health and impact the production. Experienced farmers typically assess breeding poultry health by observing poultries' appearance, vocalization and appetite. However, these observations require considerable effort to the farmers. Besides, the daily observing process could frequently disrupt the regular lives of poultry. There have been many studies on the animal signals for assessing the health conditions. The sound is an important index for assessing the poultry health conditions. Poultry vocalization shows high correlation with their health and environment. The objective of this study is to develop a vocal monitoring system to observe unusual poultry vocal behavior caused by infectious respiratory diseases in a commercial poultry house. The monitoring device, which consists of a microphone and an embedded system, was installed in poultry houses to record audio on an hourly basis. The recorded audio files were processed by algorithms to eliminate background noise and detect different kinds of poultry vocalizations, including healthy sounds, sick sounds, and non-poultry sounds. The daily variations in the quantity of these vocalizations were analyzed to assess poultry vocal behaviors. Our results indicate that poultry vocal behavior changes significantly in response to different health conditions. This study provides a warning value for assessing chicken health. By comparing long-term monitoring results with farmers' subjective records of chicken health, the results show that the warning value is highly correlated with farmers' assessments of poultry illness. The developed system could monitor poultry automatically and non-disruptively, aiming to reduce manual labor and assist farmers in assessing poultry health conditions.

Keywords: Poultry breeding, Audio processing, Automatic monitoring system, Chicken respiratory disease, Chicken disease detection

AI-P29

Proceedings of The 12th International Symposium on Machinery and Mechatronics for Agriculture and Biosystems Engineering (ISMAB 2026)
20-24 October 2026, Busan, Republic of Korea

INVESTIGATION OF PLANT STEM CELL REGENERATION USING DEEP LEARNING-BASED IMAGE PROCESSING

Kai-lun Liu[1*], Han Tang[2], Yao-Chuan Tsai[1]

[1] Department of Bio-industrial Mechatronics Engineering, National Chung Hsing University, Taiwan

[2] Graduate Institute of Biochemistry, National Chung Hsing University, Taiwan

*Corresponding Author-- Voice: +886-0902-390-892, Email: s112040025@smail.nchu.edu.tw

Abstract:

Investigating plant cell reprogramming and regeneration responses provides essential microscopic parameters for optimizing stress-resilient crops. Although *Physcomitrium patens* is widely utilized as a model species, conventional analytical methods remain highly labor-intensive, lack standardization and objectivity, and are prone to human oversight and misclassification. To eliminate manpower bottlenecks and ensure data quality, this study establishes an automated standard by developing an image recognition system specifically targeting cell "division" and "outgrowth"—phenomena induced when wounded cells re-enter the cell cycle—thereby achieving high-throughput, automated analysis.

We evaluated and compared various image processing workflows and deep learning models, ultimately employing a YOLO11m-seg image segmentation model integrated with Slicing Aided Hyper Inference (SAHI) and Contrast Limited Adaptive Histogram Equalization (CLAHE). This combination significantly enhances boundary detection accuracy for tiny, densely packed plant cells. Furthermore, a human-AI collaborative platform was developed using PyQt5. The system integrates automated AI recognition, rapid manual correction/counting, and spreadsheet export capabilities, drastically streamlining the cell quantification process. Featuring built-in data annotation and transfer learning functions, the software supports client-side model retraining and expansion. Overall, this intelligent system effectively evaluates and boosts counting efficiency while substantially reducing human counting errors and omissions.

Key Words: *Physcomitrium patens*, Cell Reprogramming, Human-AI Collaboration, Deep Learning

INTRODUCTION

Investigating plant cell reprogramming and regeneration helps optimize the development of stress-resilient crops. *Physcomitrium patens* is widely used as a model species in related research, as it undergoes cell division and outgrowth upon injury—phenomena that require quantifying both cell types to evaluate regeneration. However, current experiments rely heavily

on manual counting, which is labor-intensive, time-consuming, and lacks objective standards. To address these limitations, this study aims to develop a deep learning-based intelligent image processing system for automated cell counting and establish a human-AI collaborative platform, thereby alleviating labor burdens, significantly boosting efficiency, and ensuring the precision of research data.

MATERIALS AND METHODS

This study utilizes the model organism *Physcomitrium patens* to capture microscopic images of regenerating cells following physical damage, focusing on observing cell division and outgrowth dynamics.

In terms of image processing and AI model analysis, various combinations of image enhancement and detection techniques were evaluated. To improve the identification rate of small cells, Slicing Aided Hyper Inference (SAHI) was incorporated alongside Contrast Limited Adaptive Histogram Equalization (CLAHE) to enhance fine image details. These preprocessing techniques were evaluated across deep learning models, including CST-YOLOv7 and YOLO11m. To overcome the limitations of traditional bounding boxes—where mutual occlusion in dense cell clusters impairs accurate interpretation, the optimized final framework adopts the instance segmentation model YOLO11m-seg to achieve precise cell contour extraction.

Regarding system development, a human-in-the-loop interactive platform was constructed using the PyQt5 framework. This application integrates AI automated detection, manual correction tools (enabling users to add or delete counts), and spreadsheet export functionalities. Crucially, the system features a built-in transfer learning mechanism that allows the model to continuously update its weights based on recent manual annotations by the user, thereby establishing a standardized, low-labor automated cell counting workflow.

RESULTS & DISCUSSION

In this study, during the cell division and regeneration process of *Physcomitrium patens* following physical damage, the primary imaging challenges to overcome were extremely small and dense objects and insufficient background contrast. Experimental results demonstrated that applying Contrast Limited Adaptive Histogram Equalization (CLAHE) (Pizer et al., 1987) effectively redistributed pixel values, significantly improving the contrast between plant cells and the background and markedly accentuating cell edge features. Furthermore, to address feature loss typically caused by directly feeding high-resolution images into the model, this study integrated Slicing Aided Hyper Inference (SAHI)(Akyon et al., 2022). The results confirmed that dividing original high-resolution images into overlapping patches for inference—coupled with CLAHE preprocessing—substantially reduced missed detections within dense cell clusters and significantly boosted the recall rate for small objects.

Regarding model architecture performance, this study evaluated and compared CST-YOLOv7 and YOLO11m under various image processing scenarios, as summarized in Table 1. Experimental data indicated that while YOLO11m exhibited acceptable performance in basic object detection, YOLO11m-seg achieved precise geometry segmentation of cell contours required for complex morphological analysis. Considering inference speed, accuracy, and segmentation granularity, YOLO11m-seg combined with SAHI and CLAHE was ultimately

confirmed as the optimal framework, demonstrating the highest accuracy and robustness when handling complex backgrounds and overlapping cells. The model training results for cell division detection are summarized in Table 1.

Table 1 Model Training Results (Cell Division)

Model selection	Precision	Recall	F1-score
CST-YOLOv7	0.81	0.48	0.60
YOLO11m	0.76	0.54	0.63
YOLO11m-seg	0.73	0.58	0.65

Beyond algorithmic advancements, this study successfully developed a PyQt5-based desktop application (Fig. 1), effectively translating academic research into a practical tool. Results demonstrate that implementing this software enables AI to automate counting and segmentation tasks. To address misclassifications caused by image noise, the built-in rapid manual correction tools allow users to perform seamless fine-tuning. Crucially, the system integrates report export capabilities with a transfer learning mechanism. This allows every manual user correction to be fed back to the model as new training data, enabling its weights to automatically update and evolve. This human-in-the-loop, closed-loop system not only significantly reduces labor costs but also delivers a high-throughput, continuously optimizable intelligent solution for fundamental research on plant stem cell regeneration.

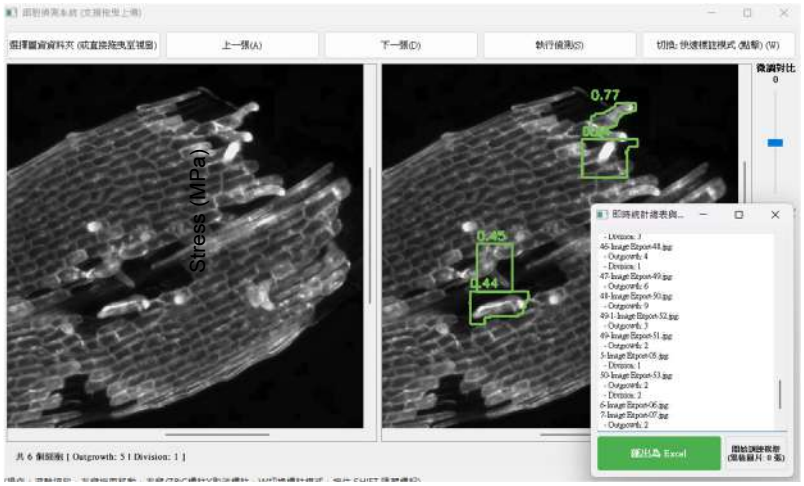

Fig.1 Application in actual use.

CONCLUSIONS

By integrating YOLO11m-seg, SAHI, and CLAHE technologies, this study successfully achieves precise and automated image analysis for plant cell regeneration. Furthermore, a dedicated software platform featuring transfer learning was developed to enable seamless AI–human collaboration, effectively resolving the time-consuming challenges of manual counting and providing an efficient, intelligent solution for plant biology research.

REFERENCES

Pizer, S. M., et al. 1987. Adaptive histogram equalization and its variations. *Computer Vision, Graphics, and Image Processing* 39(3): 355-368.

Akyon, F. C., S. O. Altinuc, and A. Temizel. 2022. Slicing aided hyper inference and fine-tuning for small object detection. In *Proc. IEEE International Conference on Image Processing (ICIP)*, 966-970.

AI-P30

Proceedings of The 12th International Symposium on Machinery and Mechatronics for Agriculture and Biosystems Engineering (ISMAB 2026)
20-24 October 2026, Busan, Republic of Korea

LLM AGENT-BASED CITRUS DISEASE AND PEST DIAGNOSIS USING FIELD IMAGING AND MICROFLUIDIC PCR

Yin-Hao Lai[1], I-Huai Lu[1], Li Chang[2], Ming-Chung Chiu[3], Ting-Hsuan Hung[2], Shiuh-Feng Shiao[3], Joe-Air Jiang[1*]

[1] Department of Biomechatronics Engineering, National Taiwan University, Taipei, Taiwan
[2] Department of Plant Pathology and Microbiology, National Taiwan University, Taipei, Taiwan
[3] Department of Entomology, National Taiwan University, Taipei, Taiwan
*Corresponding Author-- Voice: +886-2-3366-5341, Email: jajiang@ntu.edu.tw

Abstract: Citrus production is continuously threatened by diverse diseases and insect pests with complex and overlapping symptoms, making reliable diagnosis based solely on field observations challenging. This study developed an LLM-agent-based framework integrating field imaging, artificial intelligence, expert knowledge, and microfluidic polymerase chain reaction (PCR) for citrus disease and pest diagnosis. The LLM agent serves as the central reasoning and coordination layer to integrate symptom descriptions, image-based predictions, similar diagnostic cases, and citrus-specific expert knowledge. A ConvNeXt-Tiny model was incorporated for image classification, while case retrieval provided additional reference evidence for diagnostic reasoning. When molecular confirmation is required, the system links the preliminary assessment to a modular microfluidic PCR platform and subsequently incorporates molecular results into the final diagnosis. Preliminary evaluations demonstrated strong image classification performance and showed that different diagnostic evidence sources provide complementary information, particularly under uncertain or cross-domain conditions. The proposed framework demonstrates the potential of LLM agents to bridge rapid field screening and molecular verification for explainable and evidence-based citrus health management.

Key Words: Citrus disease and pest diagnosis, LLM agent, Microfluidic PCR, Computer vision, Precision agriculture.

INTRODUCTION

Citrus is one of the most widely cultivated fruit crops worldwide; however, its production is continuously threatened by a wide range of diseases and insect pests. Common threats include Huanglongbing (HLB), citrus canker, citrus tristeza virus (CTV), Asian citrus psyllid (*Diaphorina citri*), citrus leafminer, and citrus aphids. These diseases and pests can cause diverse symptoms on leaves, shoots, and fruits, including chlorosis, mottling, lesions, deformation, defoliation, and growth decline (Ghosh et al., 2022; Naqvi et al., 2022). In practical orchard environments, symptom expression may vary with infection stage, environmental

conditions, and plant physiological status, while different diseases and pests may produce similar or overlapping visual characteristics. Consequently, diagnosis based solely on field symptoms and visual observations can be difficult, particularly during early or atypical stages of infection. Integrating rapid field observations with more specific diagnostic evidence is therefore important for improving the reliability of citrus disease and pest identification.

Recent advances in generative artificial intelligence and large language models (LLMs) have demonstrated considerable potential for agricultural knowledge services, disease diagnosis, and decision support. Multimodal LLMs can interpret field images and textual descriptions, while retrieval-augmented generation enables domain-specific knowledge and expert experience to be incorporated into model reasoning. Furthermore, the emerging LLM-agent paradigm extends conventional question-answering systems by allowing LLMs to coordinate multiple tools, data sources, and diagnostic procedures. Nevertheless, most existing agricultural applications primarily rely on visual observations or textual knowledge, with limited integration of field diagnosis, molecular verification, and expert knowledge within a unified reasoning framework (Liu et al., 2024; Singh et al., 2024).

Therefore, this study develops an LLM-agent-based citrus disease and pest diagnostic system that integrates real-time field symptom observations, expert diagnostic cases and knowledge, and PCR results obtained using a modular microfluidic testing platform. By combining phenotypic evidence with molecular confirmation, the proposed framework aims to provide more reliable, explainable, and evidence-based diagnosis for intelligent citrus health management.

MATERIALS AND METHODS

An LLM-agent-based platform was developed to integrate field observation, artificial intelligence, expert knowledge, and molecular detection for citrus disease and pest diagnosis. The LLM agent serves as the central reasoning and coordination layer, connecting user inputs with image analysis, knowledge retrieval, and molecular verification. The system was implemented using separate computing resources for edge operation and LLM-based inference, as shown in **Fig. 1**, enabling integrated field diagnosis and on-site testing.



Fig.1 Computing platforms used for LLM inference and edge deployment.

LLM Agent-Based Multi-Evidence Diagnosis

Field diagnosis integrates user-provided symptom descriptions and citrus leaf images with multiple AI-based and knowledge-based resources. Image analysis includes visual symptom extraction, image classification, and retrieval of similar diagnostic cases. A ConvNeXt-Tiny model was employed as one of the image-based diagnostic components, as shown in **Fig. 2**.

Expert diagnostic cases and citrus-specific knowledge were additionally incorporated to provide domain evidence. Rather than directly adopting the output of an individual model, the LLM agent integrates these heterogeneous sources to evaluate their consistency and uncertainty. The resulting assessment provides a primary diagnosis, possible differential diagnoses, supporting evidence, and recommendations for further molecular confirmation when necessary.

LLM-Guided Microfluidic PCR Verification and Diagnostic Integration

When further confirmation is required, the LLM agent links the preliminary assessment to a modular microfluidic PCR platform for molecular verification. Appropriate testing procedures are retrieved from predefined PCR protocols, while physical execution remains separated from LLM-based reasoning to maintain operational reliability. The microfluidic platform integrates sample transport, thermal control, nucleic acid amplification, and fluorescence detection for on-site pathogen testing. After molecular detection, the PCR result is returned as additional diagnostic evidence. The LLM agent then jointly interprets molecular findings with field symptoms, image-based predictions, retrieved cases, and expert knowledge to generate an integrated final assessment based on both phenotypic and molecular evidence.

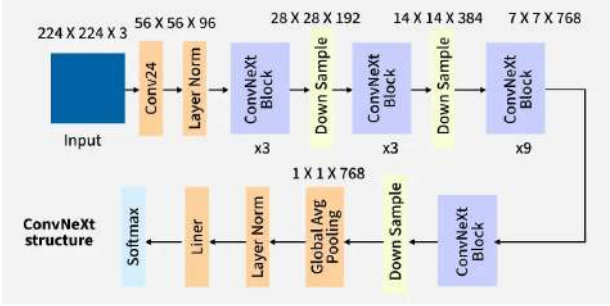

Fig.2 ConvNeXt-Tiny architecture for citrus disease and pest image classification.

RESULTS & DISCUSSION

The proposed system was evaluated at both individual-module and integrated-diagnosis levels to investigate the feasibility of combining image-based analysis, knowledge retrieval, LLM reasoning, and molecular verification for citrus disease and pest diagnosis. First, the image classification model was evaluated using internal validation data to examine its ability to distinguish common citrus diseases and pests. The trained model achieved high classification performance under the internal data distribution, demonstrating that visual characteristics such as lesion patterns, discoloration, and leaf texture can provide effective diagnostic information. However, additional external images collected under different backgrounds and imaging conditions were used to examine cross-domain robustness, since high internal accuracy may not directly represent diagnostic performance under practical field conditions.

The contribution of different diagnostic evidence sources was further investigated through ablation experiments. Comparisons were conducted among image classification, similar-case retrieval, direct LLM interpretation, and combinations of multiple evidence sources. The results indicated that image classifiers provided strong discrimination for known target classes, whereas LLM-based reasoning offered additional advantages in integrating visible symptoms, expressing diagnostic uncertainty, and identifying cases that did not clearly belong to

predefined categories. Similar-case retrieval was also evaluated using both internal and external images. Although retrieval performance decreased under domain shifts, incorporating a small number of external reference cases substantially improved retrieval performance without requiring complete model retraining, indicating its potential as an incrementally expandable diagnostic memory.

Finally, the complete LLM-agent framework will be evaluated using field cases requiring different levels of diagnostic evidence. The agent will integrate symptom observations, image predictions, retrieved cases, expert knowledge, and, when required, molecular testing results to generate the final assessment. Particular attention will be given to cases involving conflicting or insufficient evidence, where molecular confirmation can provide an independent diagnostic source beyond visual symptoms. Overall, the preliminary results suggest that individual AI components have different strengths, while their coordinated use through an LLM agent provides a promising approach for combining rapid field screening with evidence-based diagnostic reasoning. This framework will be further validated using diverse field samples and PCR-confirmed cases to assess its practical applicability for citrus health management.

CONCLUSIONS

This study developed an LLM-agent-based framework for citrus disease and pest diagnosis by integrating field symptom observation, image-based analysis, expert knowledge, and microfluidic PCR verification. The proposed approach enables the LLM agent to coordinate heterogeneous diagnostic evidence and provide interpretable assessments rather than relying on a single prediction source. Preliminary evaluations demonstrated the complementary strengths of image classification, case retrieval, and LLM-based evidence integration for field diagnosis. Molecular testing further provides an independent source of evidence for cases requiring pathogen confirmation. Future work will focus on expanding expert-validated cases, incorporating additional disease-specific PCR protocols, and conducting large-scale field validation to improve the robustness and practical applicability of the system.

ACKNOWLEDGEMENTS

This research was supported by the National Science and Technology Council (NSTC), Taiwan, under Grant Nos. NSTC 114-2321-B-002-038, NSTC 113-2313-B-002-039-MY3, and NSTC 114-2640-B-002-002.

REFERENCES

Ghosh, D., S. Kokane, B. K. Savita, P. Kumar, A. K. Sharma, A. Ozcan, et al. 2022. Huanglongbing pandemic: Current challenges and emerging management strategies. *Plants* 12(1): 160.

Liu, X., Z. Liu, H. Hu, Z. Chen, K. Wang, K. Wang, and S. Lian. 2024. A multimodal benchmark dataset and model for crop disease diagnosis. In *Proc. European Conference on Computer Vision*, 157-170. Cham, Switzerland: Springer Nature Switzerland.

Naqvi, S. A. H., J. Wang, M. T. Malik, U. U. D. Umar, A. Hasnain, M. A. Sohail, et al. 2022. Citrus canker—Distribution, taxonomy, epidemiology, disease cycle, pathogen biology, detection, and management: A critical review and future research agenda. *Agronomy* 12(5): 1075.

Singh, N., J. Wang'ombe, N. Okanga, T. Zelenska, J. Repishti, Mishra, and A. Nambi. 2024. Farmer.Chat: Scaling AI-powered agricultural services for smallholder farmers. *arXiv preprint arXiv:2409.08916*.

AI-P31

Proceedings of The 12th International Symposium on Machinery and Mechatronics for Agriculture and Biosystems Engineering (ISMAB 2026)
20-24 October 2026, Busan, Republic of Korea

COMPUTER VISION FOR BAT DETECTION AND TRACKING IN INFRARED-ILLUMINATED CAVE VIDEOS

Yu-Wei Chang*, Chen-Wei Liang

Department of Biomechatronic Engineering, National Ilan University, Yilan, Taiwan

*Corresponding author: viccyc2003@gmail.com

Abstract: Fixed cameras can record bat activity over extended periods, but manual review and annotation of accumulated video remain time-consuming. This study developed a traditional computer vision workflow for bat detection and tracking in infrared-illuminated videos from Jiugong Tunnel, Kinmen. Background modeling and multiscale morphology extracted moving candidates brighter or darker than their surroundings. Adaptive water-region masking, fragmented-box consolidation, insect-oriented filtering, and historical ghost suppression were combined with Kalman prediction, Hungarian assignment, and short-term track recovery. Evaluation used 29 selected clips that had not been used for parameter adjustment. Manual review identified 189 bat appearance events, of which 152 were successfully matched to confirmed system outputs, yielding an event-level recall of 80.4%. The human-reconciled system count was 158 events, including six false or duplicate events, yielding an event-level precision of 96.2%. Mean absolute counting error was 1.48 events per clip. Qualitative review identified briefly visible targets, activity near the water-region boundary, and closely spaced flight as important failure scenarios. These results support the feasibility of the workflow for candidate-event screening and assisted review of the evaluated videos. Its candidate regions and track information can also support manually verified dataset construction for future deep learning studies. The findings describe selected event clips rather than continuous, unattended monitoring performance.

Key Words: Bat monitoring, Computer vision, Infrared imaging, Multi-object tracking, Event counting

INTRODUCTION

Bat activity and roost use provide information relevant to ecological monitoring and conservation (Jones et al., 2009). At coastal underground roosts, limited access, insufficient visible light, and tidal water constrain field observations. Fixed cameras retain records for repeated inspection, but fast flight and overlapping targets make manual event counting difficult. Computer vision has previously supported bat tracking in thermal imagery (Betke et al., 2007); the present study instead analyzes reflected infrared light from an actively illuminated camera.

Deep learning learns hierarchical image representations (LeCun et al., 2015), but site-specific model development requires suitable data and validation. We developed a rule-based workflow for a fixed camera, combining background differences with temporal evidence and scene-specific interference handling. The objectives were to evaluate bat appearance-event correspondence and counting error, identify failure scenarios, and provide candidate regions and track information for subsequent human review and dataset construction.

MATERIALS AND METHODS

Study Site and Video Data

Videos were acquired in the first tunnel of Jiugong Tunnel, Kinmen. The granite tunnel contains water connected to the sea, with tidally varying levels. Access and camera installation were restricted to the pedestrian walkway (Fig. 1). The camera was operated at a fixed viewpoint with infrared illumination; its view was naturally tilted by installation constraints. Nighttime walkway lighting was switched off. An uncalibrated smartphone illuminance application gave approximate walkway readings of 0.06–0.12 lx. These readings describe visible-light conditions only, not infrared irradiance or the exposure conditions of individual clips.



Figure 1. Image acquisition and study environment: (a) surveillance view; (b) tunnel and walkway; (c) camera installation procedure. Panels are ordered from left to right.

The monitoring system supplied more than 100 selected event clips at 1920 × 1080 pixels and approximately 20 fps. Scenes included water reflections, insects, brightness changes, and simultaneous bright and dark targets. Detection operated at the input resolution; water-region estimation used a reduced-resolution image and returned a full-size mask. Development clips informed rules and parameters. Evaluation was performed offline on a researcher-side computer, without integration into the live stream.

Processing Overview

Figure 2 summarizes the functional workflow. Track history informs interference filtering and temporal confirmation; human event matching is a separate evaluation step.

Video input and preprocessing
↓
Bright and dark candidate extraction
↓
Interference filtering ← Track history
↓
Temporal confirmation and tracking
↓
Human-assisted event evaluation (outside automatic processing)

Figure 2. Functional overview. Temporal processing feeds track history back to interference filtering; the final step requires human review.

Candidate Extraction and Temporal Tracking

Frames were converted to grayscale. Background differences, thresholding, and contour analysis extracted candidate locations and bounding boxes, following the background-subtraction principle (Piccardi, 2004). Bright and dark labels refer to contrast against the background, not body color or species. Dark candidates combined motion differences and multiscale black-hat morphology; small bright candidates received top-hat checks (Haralick et al., 1987). Large bright candidates retained a broader body region to accommodate wing motion.

Unmatched candidates accumulated area, brightness, displacement, and temporal correspondence evidence. Eligible bright candidates followed a shorter confirmation path, subject to additional conditions. Kalman prediction (Kalman, 1960) and Hungarian assignment (Kuhn, 1955) associated candidates with tracks using predicted and last-measured positions, overlap, area, direction, and appearance. Temporarily lost tracks could recover their IDs within time and distance limits. IDs represent short-term associations, not biological identities.

Table 1. Selected extraction parameters and development rationale.

Parameter	Value	Rationale
Dark difference / black-hat thresholds	13 / 13	Retain weak dark candidates; later checks reject noise.
Black-hat kernel sizes	11 × 11 and 15 × 15 pixels	Empirical compromise between target detail and fine clutter.
Small-bright top-hat kernel / threshold	9 × 9 pixels / 14	Local bright-feature check in the small-candidate branch.
General minimum contour area	35 pixels²	Small bats often occupied about 40 pixels²; observed noise was often below 30.
Large bright candidate boundary	1000 pixels²	Route large, briefly visible candidates to additional size-specific rules.

Values were selected from development observations, not exhaustive optimization. Alternative black-hat scales gave no clear practical improvement. Area thresholds are branch-specific, not biological criteria; intensity thresholds act on image responses, not illuminance. Evaluation parameters remained fixed.

Environmental Interference and Ghost Suppression

A water-region mask was estimated from local background brightness and variation, then stabilized morphologically and temporally. Nearby candidates required stronger displacement, direction, and continuity evidence. Insect-oriented checks combined speed, solidity, bounding-box occupancy, and area variation. Bright main-body boxes absorbed smaller internal fragments; proximity and overlap checks suppressed duplicate candidates. Historical positions and flight direction defined ghost-check regions, with selective background updating. Current bright candidates and matched targets were protected, although closely spaced real bats could still be suppressed.

Human Reference Events and Evaluation

Source records and frame comparisons were used to exclude development overlap. Ambiguous bat–insect cases were recorded separately. The final evaluation comprised 29 selected clips, processed with the unchanged Lesson34_8 program and parameters. Clips were not random samples of the complete monitoring period, and some shared an original recording source.

A bat appearance event was continuous flight, including brief disappearance when continuity remained clear. Re-entry or uncertain continuity initiated a new event; distinguishable simultaneous bats were counted separately. Only confirmed green-box outputs were matched to reference events by timing, position, and trajectory. Repeated confirmations of one event contributed one match plus extra counts. New appearances that reused an ID were counted separately after review and flagged as association errors. Counts are therefore human-reconciled, not unique-ID totals.

For N clips, counting error was calculated as:

$$MAE = \frac{1}{N}\sum_{i=1}^{N}|S_i - H_i| \quad (1)$$

H_i and S_i are manual and human-reconciled counts for clip i. MAE does not normalize for duration or event count. Recall was M/H and precision was M/S, where M denotes successful matches and H and S total reference and system events. These are event-level measures, not bat–insect classification accuracy. Wilson 95% reference intervals (Wilson, 1927) assume independent events and do not adjust for source clustering or clip-selection bias.

RESULTS & DISCUSSION

Event Correspondence and Counting Performance

Table 2. Event-level evaluation on the selected clips.

Measure	Result
Evaluation clips	29
Manual bat appearance events	189
Human-reconciled system events	158
Successful event matches	152
Unconfirmed or not independently counted	37
False or duplicate extra events	6
Counting MAE	1.48 events/clip
Event-level recall (95% reference interval)	80.4% (74.2–85.5%)
Event-level precision (95% reference interval)	96.2% (92.0–98.2%)

Absolute per-clip differences summed to 43 events, exceeding the net undercount of 31. Aggregate totals therefore hide opposing errors; Table 2 also reports event-level correspondence.

Representative Outputs and Failure Scenarios

Figure 3 illustrates confirmed targets and challenging candidates. Panels (a) and (b) show single- and multiple-target outputs. They document these frames, rather than independently establishing long-term identity continuity.

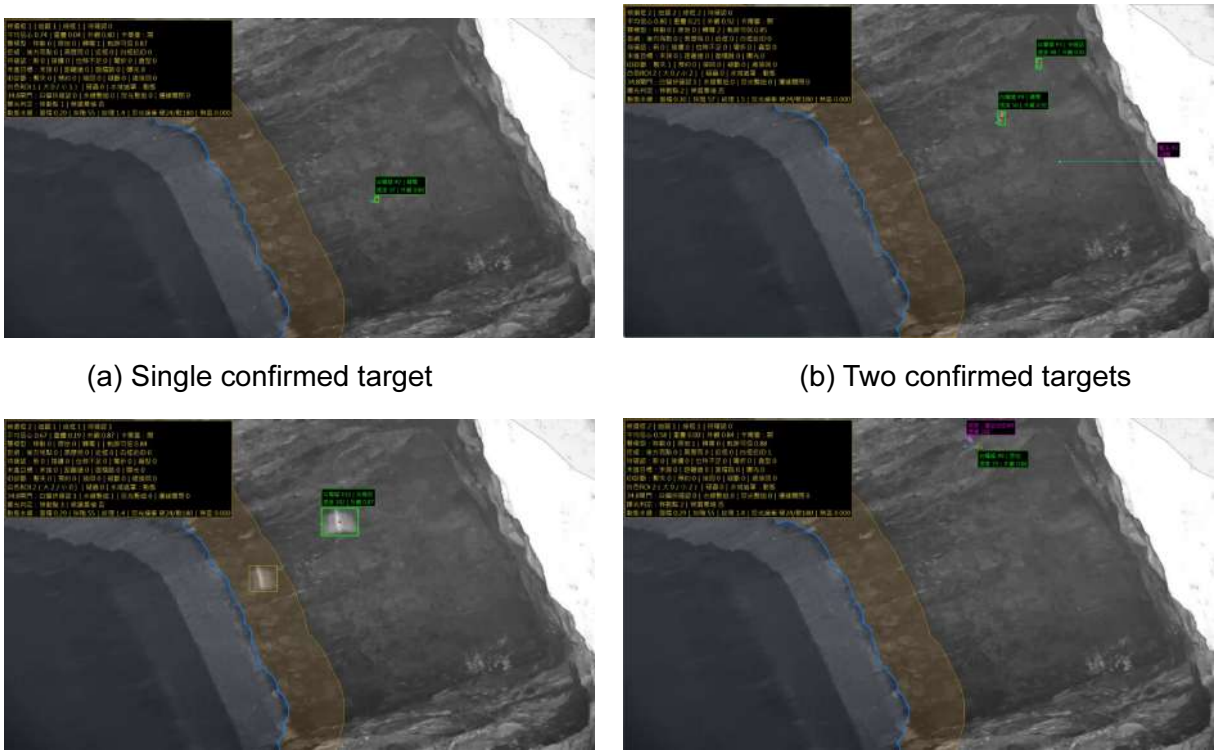

(a) Single confirmed target

(b) Two confirmed targets

(c) Tentative candidate near water

(d) Nearby candidate rejected

Figure 3. Representative outputs. Green boxes indicate confirmed targets; the yellow box in (c) remains tentative. The purple label in (b) denotes a lost track, not an additional current detection. In (d), a candidate identified as a bat during manual video review was rejected near an existing bright track. Original diagnostic overlays are retained.

Manual review identified briefly visible small bright targets as a recurring failure scenario: candidates could leave before sufficient confirmation evidence accumulated. Water-region activity also produced missed events. For example, cam1_evt2910 contained nine reference events and seven matches, with the remaining observations noted near water. Figure 3(c) illustrates an unconfirmed candidate in this guard region; a single frame cannot establish the cause of an entire missed event.

Close flight challenged candidate separation and track association. In cam1_evt3188, six reference events yielded three system events, including an unconfirmed target and failures to count nearby bats separately. The rejection label in Fig. 3(d) specifically indicates proximity to an existing bright ID; it should not be interpreted as definitive evidence of a ghost. Two reviewed appearances in cam1_evt2895 and cam1_evt2906 reused previous IDs despite confirmation. These were counted by event after human review, illustrating that successful detection does not ensure correct identity association.

Extra counts included fragments, ghosts, and re-established tracks, not solely insects. These observations identify priorities for controlled testing.

Scope and Implications

The selected clips support preliminary feasibility for candidate screening in the observed setting. They do not estimate all-day performance or total activity. Manual references lacked inter-observer agreement assessment, and the study did not measure frame-level localization, processing speed, or annotation time savings. Clips with more events do not necessarily contain more simultaneous bats. Continuous recordings and explicit overlap labels are needed to study crowding effects. No direct performance comparison with thermal tracking or deep learning is claimed.

CONCLUSIONS

The workflow matched 152 of 189 bat appearance events in 29 selected infrared-illuminated clips. Event-level recall was 80.4%, precision was 96.2%, and counting MAE was 1.48 events per clip. These findings support its use as a candidate-screening and human-review aid in the evaluated environment. Brief appearances, water-region activity, and closely spaced flight remain priorities for improvement. Candidate regions and tracks can support manually verified datasets, provided missed and difficult examples are also included. Future work will evaluate continuous footage, source-grouped uncertainty, runtime, and review effort, and compare learning-based approaches under the same test protocol.

REFERENCES

Betke, M., D. E. Hirsh, A. Bagchi, N. I. Hristov, N. C. Makris, and T. H. Kunz. 2007. Tracking large variable numbers of objects in clutter. In Proc. IEEE Conf. Computer Vision and Pattern Recognition, 1–8. IEEE. doi:10.1109/CVPR.2007.382994.

Haralick, R. M., S. R. Sternberg, and X. Zhuang. 1987. Image analysis using mathematical morphology. IEEE Trans. Pattern Anal. Mach. Intell. PAMI-9(4): 532–550. doi:10.1109/TPAMI.1987.4767941.

Jones, G., D. S. Jacobs, T. H. Kunz, M. R. Willig, and P. A. Racey. 2009. Carpe noctem: The importance of bats as bioindicators. Endangered Species Res. 8: 93–115. doi:10.3354/esr00182.

Kalman, R. E. 1960. A new approach to linear filtering and prediction problems. J. Basic Eng. 82(1): 35–45. doi:10.1115/1.3662552.

Kuhn, H. W. 1955. The Hungarian method for the assignment problem. Naval Res. Logistics Quarterly 2(1–2): 83–97. doi:10.1002/nav.3800020109.

LeCun, Y., Y. Bengio, and G. Hinton. 2015. Deep learning. Nature 521: 436–444. doi:10.1038/nature14539.

Piccardi, M. 2004. Background subtraction techniques: A review. In Proc. IEEE Int. Conf. Systems, Man and Cybernetics, Vol. 4, 3099–3104. IEEE. doi:10.1109/ICSMC.2004.1400815.

Wilson, E. B. 1927. Probable inference, the law of succession, and statistical inference. J. American Stat. Assoc. 22(158): 209–212. doi:10.1080/01621459.1927.10502953.

AI-P32

Proceedings of The 12th International Symposium on Machinery and Mechatronics for Agriculture and Biosystems Engineering (ISMAB 2026)
20-24 October 2026, Busan, Republic of Korea

ANGULAR-MARGIN LEARNING FOR SPARSE-ENROLMENT CATTLE FACE RE-IDENTIFICATION: WITHIN-BREED REPLICATION AND BIDIRECTIONAL CROSS-DATASET EVALUATION

Jongho Park[1], Youngjun Na[2], Imjoung Choi[1], Sumin Seo[1], Joungho Lee[1], Youngjun Choi[3*], Jung Eek Son[1,4*]

[1]Korea Smart Farm R&D Foundation, Sejong 30121, Republic of Korea
[2]Animal Data Laboratory, Antller Inc., Seoul 05029, Republic of Korea
[3]School of Animal Life Convergence Science, Hankyong National University, Anseong 17579, Republic of Korea
[4]Department of Agriculture, Forestry and Bioresources, Seoul National University, Seoul 08826, Republic of Korea

*Corresponding Author:
Younjun Choi -- Voice: +82-031-670-5093, Email: cyj2114@hknu.ac.kr
Jung Eek Son-- Voice: +82-044-559-5601, Email: sjeenv@kosfarm.re.kr

Abstract: Camera-based cattle identification should register animals from few photographs without retraining the feature extractor. This study tested whether ArcFace angular-margin loss becomes more valuable as the enrolment gallery shrinks, whether this relationship repeats across breeds, and whether its advantage transfers between datasets. Six feature extraction networks were trained with cross-entropy (CE) or CE+ArcFace. Data comprised 3,260 face images from 333 Hanwoo cattle and 2,878 images from 289 Holstein cattle. A closed-set reference protocol varied images used jointly for training and gallery construction. In the primary identity-disjoint protocol, the networks learned from one set of identities and identified unseen identities from galleries of two, three, or four images while the representation remained fixed. Bidirectional cross-dataset evaluation applied each breed's checkpoints to unseen identities of the other. Within Hanwoo, DINOv2-ViT-B/14 with CE+ArcFace achieved 96.92 ± 0.29% Rank-1 accuracy with two gallery images. The mean ArcFace advantage increased from 7.90 percentage points with four images to 10.05 with two, and all six networks showed a significantly larger ArcFace advantage with two than with four gallery images. Within Holstein, the same configuration achieved 92.54 ± 1.80% with two images. ArcFace improved all 18 network-by-gallery comparisons, but the mean increase in its advantage from four to two images was smaller and not significant for individual networks after correction. ArcFace improved all 36 cross-dataset comparisons, but the four-to-two change depended on transfer direction and network. Across both breeds, the improvement was associated with a larger genuine-to-nearest-impostor decision margin rather than tighter gallery centroids. Thus, ArcFace's absolute retrieval benefit transferred across the evaluated cattle datasets, whereas the extent to which it buffered sparse enrolment was representation- and domain-dependent.

Key Words: Cattle face re-identification, ArcFace, Few-shot enrolment, Domain shift, Metric learning

AI-P33

Proceedings of The 12th International Symposium on Machinery and Mechatronics for Agriculture and Biosystems Engineering (ISMAB 2026)
20-24 October 2026, Busan, Republic of Korea

COMPARATIVE EVALUATION OF MACHINE LEARNING ALGORITHMS FOR PREDICTING WEEKLY YIELD OF HYDROPONIC CUCUMBER IN A SMART FARM

JongWon Park[1], kyeonghee Choi[1], Kyongeun Jeon[1], Heekyoung Lee[1],

Soosang Hahm[1], TaeHwan Kang[2*]

[1]Smart Agriculture Research Division, Chungcheongnam-do Agricultural Research and Extension Services, Yesan, Republic of Korea

[2*]Department of Smart Farm Engineering, Kongju National University, Yesan, Republic of Korea

*Corresponding Author — Email: lamokth@kongju.ac.kr

Abstract: This study evaluated four machine learning (ML) algorithms — Ridge regression, Random Forest (RF), Gradient Boosting Machine (GBM), and XGBoost — alongside two process-based crop models (DSSAT and AquaCrop) for weekly yield prediction of hydroponically grown cucumber in a smart greenhouse. Environmental sensor data collected at 10-minute intervals from September to December 2025 were aggregated into daily features and transformed into 37 derived variables, generating 18 weekly prediction samples from two greenhouse zones across nine harvest weeks (weeks 7–15 post-transplanting). Process-based models were calibrated using observed crop-growth variables and evaluated against the full observed weekly yield dataset. Machine-learning models were evaluated using 18-fold leave-one-out cross-validation (LOOCV) applied to individual weekly samples, with Min–Max scaling performed within each training fold. DSSAT achieved high accuracy for node count (R^2=0.913) and plant height (R^2=0.985), but substantially underestimated fruit yield (R^2=−0.14, RMSE=1.265 fruit/m²/week), indicating limitations of the radiation-use efficiency (RUE)-based assimilate partitioning approach. AquaCrop showed the highest R^2 among all evaluated models (R^2=0.841, RMSE=0.472, NRMSE=15.7%, cumulative yield error 2.70%), with canopy cover reaching a maximum of 88% by GDD 330–430°C·day post-transplanting. Among the ML algorithms, XGBoost achieved the lowest RMSE (0.449 fruit/m²/week) and an R^2 of 0.825 (NRMSE=14.9%). Feature importance analysis showed that the 10-day and 7-day DLI moving averages accounted for 33.8% and 27.9% of the total feature importance, respectively, suggesting that recent cumulative light conditions were strongly associated with weekly yield variation.

Keywords: Smart farm, Hydroponic cucumber, Machine learning, XGBoost, Yield prediction

INTRODUCTION

Cucumber (Cucumis sativus L.) is an important protected-horticulture crop in Chungcheongnam Province, Republic of Korea. The adoption of smart farm technology — which integrates sensor-based environmental monitoring with data-driven management — offers a pathway to stable, high-quality production through hydroponic cultivation. However, effective smart-farm management requires reliable approaches for translating continuously monitored environmental conditions into timely yield forecasts.

Process-based models such as DSSAT and AquaCrop simulate crop growth using mechanistic representations of crop development and environmental processes, and have been widely applied in field-crop contexts. Their applicability to intensive hydroponic production systems, where crop management and harvest practices differ from those of field crops, requires further evaluation. Data-driven machine learning approaches, by contrast, learn directly from observational data and can capture complex, non-linear relationships between environmental variables and yield without explicit mechanistic assumptions.

The objective of this study was to compare DSSAT, AquaCrop, and four machine-learning algorithms for weekly yield prediction of hydroponically grown cucumber and to identify environmental features associated with yield variation.

MATERIALS AND METHODS

Experimental Setup

The experiment was conducted at the Smart Greenhouse Facility of the Chungcheongnam-do Agricultural Research and Extension Services, Yesan, Republic of Korea. Cucumber (cv. Dadagi Goodmorning) was grown hydroponically using Korean Standard nutrient solution from 3 September to 17 December 2025 (15 weeks; 105 days). Environmental data (temperature, humidity, solar radiation, CO_2 , EC, pH) were recorded at 10-minute intervals by a compound environmental controller. After quality screening (removal of records with sensor malfunctions and missing values), approximately 11,000 valid records per zone were retained, representing approximately 73% of the scheduled 10-minute observations over the 105-day growing period. The target variable was weekly marketable fruit yield (fruit/m²/week).

Feature Engineering

Raw sensor data were screened for extreme values using the 5th and 95th percentiles, and missing observations were filled by linear interpolation. Ten daily environmental and crop-growth-related features were derived: mean air temperature (ADT), daytime temperature (T_day), night-time temperature (T_night), day–night temperature difference (DIF), daily light integral (DLI), daytime vapour pressure deficit (VPD_day), reference evapotranspiration (ET , Penman–Monteith), growing degree days (GDD, base 10°C), photosynthetic-light-to-temperature ratio (PTR = DLI/ADT), and CO_2 concentration.

To account for a potential time lag between recent environmental conditions and subsequent fruit harvest, three categories of lag features were added: (1) trailing

moving averages at 7, 10, and 14 days for DLI, temperature, and VPD; (2) 7-day and 14-day lag variables; and (3) cumulative GDD and DLI from transplanting, plus high-temperature (>30°C) and high-VPD (>1.5 kPa) stress-day counts. The final feature matrix comprised 37 features and 18 weekly prediction samples, derived from two greenhouse zones across nine harvest weeks (weeks 7–15 post-transplanting). Min–Max scaling was applied separately within each LOOCV training fold and then applied to the corresponding validation sample to prevent data leakage.

NRMSE Definition

Normalised RMSE (NRMSE) was calculated as NRMSE (%) = (RMSE / $\bar{y}$) × 100, where $\bar{y}$ is the mean of the observed weekly yield values.

Model Development and Evaluation

Process-based models: DSSAT was parameterised using the Beta temperature response function and PAR-interception-based dry-matter production equation, with key parameters calibrated against observed vegetative-growth variables only (node count and plant height; PHINT: 14.2°C·day/node; RUE: 2.8 g DM/MJ; GDD_flower: 310°C·day; LAI_max: 3.82 m²/m²); weekly fruit yield was not used for parameter calibration and was reserved for independent model evaluation. AquaCrop was configured using the canopy-cover development model and water-productivity approach (WP*: 18.9 g/m²/mm; Kcb: 0.951; HI: 0.183), with parameters calibrated against observed canopy and biomass variables; weekly marketable fruit yield was reserved for model evaluation.

Process-based models (DSSAT and AquaCrop) were not evaluated using cross-validation; instead, their predictions across all 18 weekly samples were compared with the corresponding observed yield values. Machine-learning models: Ridge regression, Random Forest, Gradient Boosting Machine, and XGBoost were each trained and evaluated using 18-fold leave-one-out cross-validation (LOOCV), with one of the 18 weekly samples held out as the validation set in each fold. The two samples from the same harvest week were treated as independent observations and could appear in separate folds. Model performance was assessed using the coefficient of determination (R^2), root mean square error (RMSE), mean absolute error (MAE), and normalised RMSE (NRMSE) as defined above. Mean absolute error (MAE) was included as an additional scale-dependent accuracy metric (Willmott and Matsuura, 2005).

RESULTS & DISCUSSION

Process-Based Model Performance

DSSAT reproduced observed vegetative growth relatively well, with R^2 values of 0.913 for node count (RMSE=4.91 nodes) and 0.985 for plant height (RMSE=25.3 cm). However, it substantially underestimated fruit yield (R^2=−0.14, RMSE=1.265 fruit/m²/week), predicting a cumulative yield of 19.1 fruit/m² against the observed 27.0 fruit/m² (approximately 30% underestimation). This underestimation may be related to limitations in representing fruit set, fruit development duration, and fruit abscission within the current model configuration; additional parameters would be required to improve yield prediction performance.

AquaCrop showed higher predictive agreement with the observed weekly yield.

Canopy cover developed rapidly during weeks 3–4 post-transplanting (GDD 330–430°C·day), reaching a maximum of 88%, before declining after GDD_sen = 753°C·day. The model achieved R^2=0.841, RMSE=0.472 fruit/m²/week, NRMSE= 15.7%, and a cumulative yield error of 2.70%, making it the model with the highest R^2 among all evaluated models in this study.

Table 1. Comparative model performance metrics.

Model	R^2	RMSE	MAE	NRMSE (%)	Note
DSSAT	−0.14	1.265	—	—	Yield underestimation
AquaCrop	**0.841†**	0.472	—	**15.7†**	Highest R^2
Ridge	0.776	0.508	0.393	16.9	Linear
Random Forest	0.648	0.637	0.489	21.2	Ensemble
GBM	0.811	0.467	0.362	15.5	Boosting
XGBoost	0.825	**0.449‡**	0.336	**14.9‡**	**Lowest RMSE & NRMSE**

† Highest R^2 among all evaluated models. ‡ Lowest RMSE and lowest NRMSE (14.9%) among all evaluated models, based on $\bar{y}$ = 3.006 fruit/m²/week (pooled observed mean, n = 18).

Machine Learning Algorithm Comparison

Among the four ML algorithms, XGBoost achieved the lowest RMSE (0.449 fruit/m²/week) and the lowest NRMSE (14.9%), with an R^2 of 0.825, followed closely by GBM (R^2=0.811, RMSE=0.467, NRMSE=15.5%). Ridge regression (R^2=0.776) also performed reasonably well despite its linearity. Random Forest showed the lowest predictive performance among the ML models (R^2=0.648, NRMSE=21.2%). Given the small sample size (n=18), the observed performance differences should be interpreted cautiously, and the specific causes of lower performance require further validation with larger datasets.

Feature importance analysis showed that the 10-day DLI moving average (33.8%) and 7-day DLI moving average (27.9%) accounted for 61.7% of the total feature importance, suggesting that recent cumulative light conditions were strongly associated with weekly yield variation over the observed growing period. This pattern is biologically plausible because fruit yield at harvest may reflect environmental conditions experienced during preceding developmental stages, as environmental conditions during the period preceding harvest are expected to influence ongoing fruit development, given that the interval from anthesis to commercial harvest in cucumber varies with cultivar and growing conditions.

Compared with AquaCrop, XGBoost showed a lower RMSE (0.449 vs. 0.472 fruit/m²/week), a lower NRMSE (14.9% vs. 15.7%), but a slightly lower R^2 (0.825 vs. 0.841). Thus, XGBoost achieved lower prediction errors in absolute and relative terms, while AquaCrop showed stronger agreement in terms of R^2. The physical interpretability of AquaCrop makes it valuable for scenario analysis and agronomic insight, whereas XGBoost may offer practical advantages for operational yield forecasting in data-rich smart-farm environments.

CONCLUSIONS

This study compared two process-based crop models and four machine-learning algorithms for weekly yield prediction of hydroponically grown cucumber under smart-greenhouse conditions. The following conclusions were drawn:

(1) DSSAT reproduced vegetative growth (node count R^2=0.913; plant height R^2=0.985) but substantially underestimated fruit yield (R^2=−0.14). The RUE-based assimilate partitioning approach did not adequately capture cucumber fruit yield dynamics, and additional parameters representing fruit set, development duration, and abscission would be required.

(2) AquaCrop showed strong agreement with observed yield (R^2=0.841, NRMSE=15.7%, cumulative error 2.70%), indicating that the transpiration-driven biomass configuration used in this study provided useful weekly yield estimates under the tested hydroponic conditions, and showed the highest R^2 among all evaluated models.

(3) XGBoost achieved the lowest RMSE (0.449 fruit/m²/week) and the lowest NRMSE (14.9%) among all evaluated models, with an R^2 of 0.825. AquaCrop showed the highest R^2 (0.841) but slightly higher RMSE and NRMSE. DLI-related moving-average features were among the most influential predictors, suggesting that recent cumulative light conditions were associated with weekly yield variation in the observed crop cycle.

Given the small number of samples (n=18) and the leave-one-out design in which zone samples from the same harvest week could appear in separate folds, predictive performance may be optimistic relative to a strictly time-based holdout. These results should be considered preliminary and validated using additional growing seasons. Future work will incorporate root-zone EC treatment, evaluate week-grouped cross-validation strategies, and extend the dataset to improve generalizability.

ACKNOWLEDGEMENTS

This research was supported by the Smart Farm Multi-Ministry Package Innovation Technology Development Program (RS-2025-02307287), funded by the Ministry of Agriculture, Food and Rural Affairs, the Ministry of Science and ICT, and the Rural Development Administration of the Republic of Korea.

REFERENCES

Chen, T., and C. Guestrin. 2016. XGBoost: A scalable tree boosting system. In Proc. 22nd ACM SIGKDD International Conference on Knowledge Discovery and Data Mining, 785–794. New York, NY: ACM. https://doi.org/10.1145/2939672.2939785.

Jones, J. W., G. Hoogenboom, C. H. Porter, K. J. Boote, W. D. Batchelor, L. A. Hunt, P. W. Wilkens, U. Singh, A. J. Gijsman, and J. T. Ritchie. 2003. The DSSAT cropping system model. Eur. J. Agron. 18(3–4): 235–265. https://doi.org/10.1016/S1161-0301(02)00107-7.

Raes, D., P. Steduto, T. C. Hsiao, and E. Fereres. 2009. AquaCrop—The FAO crop model to simulate yield response to water: II. Main algorithms and software description. Agron. J. 101(3): 438–447. https://doi.org/10.2134/agronj2008.0140s.

Vanthoor, B. H., P. H. de Visser, C. Stanghellini, and E. J. van Henten. 2011. A methodology for model-based greenhouse design: Part 2, description and validation of a tomato yield model. Biosyst. Eng. 110(4): 378–395. https://doi.org/10.1016/j.biosystemseng.2011.08.005.

Willmott, C. J., and K. Matsuura. 2005. Advantages of the mean absolute error (MAE) over the root mean square error (RMSE) in assessing average model performance. Clim. Res. 30(1): 79–82. https://doi.org/10.3354/cr030079.

AI-P34

Proceedings of The 12th International Symposium on Machinery and Mechatronics for Agriculture and Biosystems Engineering (ISMAB 2026)
20-24 October 2026, Busan, Republic of Korea

BUILDING A MULTIMODAL HYPERSPECTRAL IMAGE DATASET FOR CHARACTERIZING PHYSIOLOGICAL DISORDERS IN SMART FARM-GROWN TOMATOES

JongWon Park[1], kyeonghee Choi[1], Kyongeun Jeon[1], Heekyoung Lee[1],

Soosang Hahm[1], TaeHwan Kang[2*]

[1]Smart Agriculture Research Division, Chungcheongnam-do Agricultural Research and Extension Services, Yesan, Republic of Korea

[2*]Department of Smart Farm Engineering, Kongju National University, Yesan, Republic of Korea

*Corresponding Author — Email: lamokth@kongju.ac.kr

Abstract: Accurate, non-destructive identification of physiological disorders in greenhouse tomato is essential for quality management and productivity in smart farm environments. This study developed a multimodal imaging dataset to support future deep-learning-based classification of three tomato physiological disorders: blossom-end rot (BER), poor coloring (PC), and deformed fruit (DF). Each disorder was experimentally induced in hydroponically grown tomato plants (cherry cv. TY Saetbyeol; round cv. Defnis; transplanted 30 September 2025) by manipulating the nutrient solution composition based on the Dutch PBG standard: calcium supply was eliminated and KNO_3 doubled for BER; all potassium supply was removed for PC; and a combination of triple KNO_3 with boron deficiency was applied for DF. Visible-to-near-infrared (vNIR) hyperspectral images (400–1,000 nm; 204 bands; 512 × 512 pixels spatial resolution) were acquired weekly using a Specim IQ camera alongside colour-chart-calibrated RGB images. Principal component analysis (PCA) of the extracted leaf spectra revealed different spectral distribution patterns among treatment groups, with clearer separation for PC and BER than for DF: PC formed an independent cluster extending along both PC1 and PC2 axes; BER exhibited reduced NIR reflectance in the 800–950 nm range; and DF showed no distinctive spectral signature, remaining diffusely distributed near the PCA centroid. The dataset currently comprises 360 RGB images (1.55 GB) and 32 vNIR hyperspectral cubes (approximately 9.7 GB in total), with data collection ongoing. These preliminary findings demonstrate the potential of vNIR imaging for characterizing tomato physiological disorders and provide a foundation for subsequent classification-model development.

Keywords: Smart farm, Tomato, Hyperspectral imaging, Physiological disorder, Principal component analysis

INTRODUCTION

Tomato (Solanum lycopersicum L.) is an economically important protected-horticulture crop worldwide. In smart farm environments, early and accurate detection of physiological disorders — blossom-end rot, poor coloring, and deformed fruit — is critical because visual inspection is labour-intensive, subjective, and incapable of detecting sub-visual stress before symptoms become commercially damaging.

Visible-to-near-infrared (vNIR) hyperspectral imaging captures per-pixel reflectance spectra across hundreds of narrow bands, enabling the characterisation of biochemical and structural changes in plant tissue. However, the application of hyperspectral imaging to smart-farm-grown tomato physiological disorders remains underexplored.

To our knowledge, we did not identify a publicly available labelled dataset specifically targeting these three physiological disorders in smart-farm-grown tomato under controlled hydroponic conditions. The objective of this study was to (1) experimentally induce three tomato physiological disorders under controlled hydroponic conditions, (2) acquire paired RGB and vNIR hyperspectral images at weekly intervals, (3) characterise the spectral distribution patterns of each disorder group via PCA, and (4) construct a structured and labelled multimodal dataset for subsequent deep-learning model development.

MATERIALS AND METHODS

Plant Material and Growing Conditions

Tomato seedlings (cherry cv. TY Saetbyeol and round cv. Defnis) were transplanted on 30 September 2025 into a smart greenhouse at the Chungcheongnam-do Agricultural Research and Extension Services (CARES), Yesan. Nutrient solution was supplied manually at 200 mL per irrigation event, with 5–10 irrigation events per plant per day depending on solar radiation. Environmental parameters (temperature, humidity, solar radiation) were continuously monitored by a compound controller.

Disorder Induction Protocol

Four treatment groups were established using a Dutch PBG-based nutrient solution as the reference formulation. Treatment-specific modifications to the A and B stock solutions were applied to induce target disorders (Table 1). EC levels were maintained at 2.5 dS/m (control), 4.0 dS/m (BER), 3.0 dS/m (PC), and 3.0 dS/m (DF). Growth measurements (plant height, stem diameter, leaf length, leaf width) were recorded weekly.

Table 1. Nutrient solution treatment design for disorder induction.

Treatment	Key Modification	EC (dS/m)	Target Disorder
Control	Standard Dutch PBG-based nutrient solution	2.5	None
BER	Ca^{2+} supply eliminated; NO_3^--N supplied as KNO_3 only (2× KNO_3)	4.0	Blossom-end rot
PC	All K^+ supply removed (K_2SO_4 = 0, KNO_3 = 0)	3.0	Poor coloring
DF	KNO_3 tripled (3×) + boron supply eliminated (H_3BO_3 = 0)	3.0	Deformed fruit

Hyperspectral Image Acquisition and Processing

Hyperspectral images were acquired weekly using a Specim IQ push-broom camera (Specim Spectral Cameras Ltd., Oulu, Finland) covering 400–1,000 nm across 204 spectral bands at a spatial resolution of 512 × 512 pixels. Each raw hyperspectral cube was approximately 310 MB. A calibrated colour reference chart was included in each scene as a reference for image preprocessing and colour consistency. RGB images were simultaneously captured using a mobile phone camera for visual reference. Spectral reflectance was extracted from region-of-interest (ROI) areas on representative leaves using ENVI software, and per-treatment spectral profiles were assembled for PCA.

RESULTS & DISCUSSION

Plant Growth Response

Plant height increased progressively across all treatment groups from transplanting through the final measurement on 24 November 2025. The BER treatment produced the tallest plants (137.0 cm at week 8), followed by DF (131.4 cm), control (128.5 cm), and PC (122.9 cm). Stem diameter was similar across treatments (13–18 mm). Treatment effects on stem diameter were evaluated using one-way analysis of variance (ANOVA), and no statistically significant differences were observed among groups ($p > 0.05$), suggesting that the treatments did not produce a consistent, large reduction in overall vegetative growth. Leaf width in the DF treatment showed a more pronounced declining trend over time compared to other groups.

Spectral Characterisation by PCA

PCA of the extracted vNIR reflectance spectra (PC1: 87.7% of variance; PC2: 7.6%) revealed different spectral distribution patterns for each treatment group:

Poor coloring (PC): Formed the most clearly separated cluster, extending broadly along both PC1 and PC2 axes. This spectral separation may be associated with changes in pigment-related optical properties under potassium-deficient conditions, which altered reflectance across the visible wavelength range (400–700 nm). Chlorophyll and carotenoid contents were not directly measured in the present study.

Blossom-end rot (BER): Formed a relatively compact cluster, distinguished primarily by reduced NIR reflectance in the 800–950 nm region compared to other treatment groups. The present study extracted spectra from leaf ROIs; the observed NIR reflectance reduction in leaves may reflect changes in tissue water status or cell turgor associated with the high-EC, calcium-deficient treatment condition, although this relationship was not directly verified through physiological measurements.

Deformed fruit (DF): Remained diffusely distributed near the PCA centroid without forming a distinct cluster, suggesting that the induced DF conditions did not produce a consistent, treatment-specific leaf spectral signature. The diffuse distribution suggests that leaf spectral variation alone may be insufficient to differentiate this treatment group, and that spatial or texture-based features may provide additional discriminatory information.

Dataset Construction Status

As of December 2025, the dataset comprised 360 RGB images (1.55 GB; approximately 4.3 MB per image) and 32 vNIR hyperspectral cubes with a total size of approximately 9.7 GB. All images were acquired at weekly intervals across four treatment groups. Data acquisition is ongoing through the completion of the growing season. The data pipeline follows five sequential steps: (1) field acquisition with colour reference chart; (2) spectral extraction using ENVI; (3) per-treatment labelling; (4) PCA and spectral characterisation; (5) assembly into deep-learning training datasets.

CONCLUSIONS

This study developed a labelled multimodal (RGB and vNIR hyperspectral) imaging dataset for three experimentally induced physiological disorders in smart-farm-grown tomato. Key findings are:

(1) Three major disorders — BER, PC, and DF — were successfully induced under controlled hydroponic conditions by targeted nutrient solution modification, with disorder-related symptoms confirmed by visual observation over the growing period.

(2) PCA of vNIR spectra (PC1: 87.7%; PC2: 7.6%) indicated that PC showed the clearest spectral separation, while BER was characterised by reduced reflectance in the 800–950 nm region. DF did not form a distinct spectral cluster in the present analysis, suggesting that additional spatial or structural features may be needed for its differentiation.

(3) The dataset, currently comprising 360 RGB and 32 vNIR hyperspectral images, provides a preliminary foundation for developing deep-learning-based physiological disorder classification models under smart-greenhouse conditions. However, the dataset remains limited in size and classification performance has not yet been independently evaluated.

Future work will expand the dataset to increase the number of hyperspectral images per disorder class, incorporate quantitative physiological measurements to support spectral interpretation, and develop and validate classification models using independent samples and growing periods.

ACKNOWLEDGEMENTS

This research was supported by the Smart Farm Multi-Ministry Package Innovation Technology Development Program (RS-2025-02307287), funded by the Ministry of Agriculture, Food and Rural Affairs, the Ministry of Science and ICT, and the Rural Development Administration of the Republic of Korea.

REFERENCES

Behmann, J., A.-K. Mahlein, T. Rumpf, C. Römer, and L. Plümer. 2015. A review of advanced machine learning methods for the detection of biotic stress in precision crop protection. Precis. Agric. 16(3): 239–260. https://doi.org/10.1007/s11119-014-9372-7.

Mahlein, A.-K., E.-C. Oerke, U. Steiner, and H.-W. Dehne. 2012. Recent advances in sensing plant diseases for precision crop protection. Eur. J. Plant Pathol. 133(1): 197–209. https://doi.org/10.1007/s10658-011-9878-z.

Sun, D.-W. 2010. Hyperspectral Imaging for Food Quality Analysis and Control. San Diego, CA: Academic Press/Elsevier. https://doi.org/10.1016/C2009-0-18234-0.

Wold, S., M. Sjöström, and L. Eriksson. 2001. PLS-regression: a basic tool of chemometrics. Chemom. Intell. Lab. Syst. 58(2): 109–130. https://doi.org/10.1016/S0169-7439(01)00155-1.

Nagasubramanian, K., S. Jones, A. Singh, S. Sarkar, A. Singh, and B. Ganapathy subramanian. 2019. Plant disease identification using explainable 3D deep learning on hyperspectral images. Plant Methods 15: 98. https://doi.org/10.1186/s13007-019-0479-8.

Keresztes, J. C., D. Goodarzi, and W. Saeys. 2016. Real-time hyperspectral image analysis to estimate the leaf health status using machine learning. Comput. Electron. Agric. 124: 174–184. https://doi.org/10.1016/j.compag.2016.04.004.

AI-P35

Proceedings of The 12th International Symposium on Machinery and Mechatronics for Agriculture and Biosystems Engineering (ISMAB 2026)
20-24 October 2026, Busan, Republic of Korea

FLOW MATCHING ENABLES HIGH-RESOLUTION TREE SKELETONIZATION FROM OCCLUDED POINT CLOUDS

Dayeon Yang[1,2], Chanyoung Ju[2,3], Pyojin Kim[1]**

[1]Gwangju Institute of Science and Technology, Republic of Korea
[2]Korea Institute of Industrial Technology, Republic of Korea
[3]University of Science and Technology, Republic of Korea
*Corresponding Author-- Voice: +82-62-600-6450, Email: cyju@kitech.re.kr

Abstract: Recovering tree branch topology from 3D point clouds is essential for orchard automation, but self-occlusion often results in incomplete observations. Diffusion-based methods can infer missing structures by generating skeleton nodes from observed point clouds; however, increasing node density to represent fine branches can introduce off-centerline nodes and reduce precision. We address this limitation by replacing stochastic diffusion with deterministic Flow Matching for stable high-resolution generation. The proposed method generates approximately 17,000 skeleton nodes per tree and uses trajectory-based directional consistency for topology reconstruction. On a public apple orchard benchmark, the proposed method achieves an F1-score of 47.24 at high node resolution, compared with 37.46 for the diffusion-based baseline under the same settings. Qualitative results also show improved alignment with branch centerlines and better reconstruction of fine-scale structures.

Key Words: Tree skeletonization, Flow matching, 3D point cloud, Branch topology, Orchard automation

INTRODUCTION

Real-world orchard environments contain complex arrangements of trunks, branches, leaves, and fine twigs, making it challenging to accurately reconstruct tree branching structures from 3D sensor observations. Although humans can readily infer the underlying branching structure even when trunks and major branches are partially occluded by leaves and fine twigs, recovering such partially observed structures remains challenging for computer vision systems. In particular, tree topology provides important information for growth monitoring, structural analysis, yield and canopy estimation, as well as robotic applications such as automated pruning, thinning, and harvesting (He et al., 2018; You et al., 2022). Our ultimate target is pear trees, which typically exhibit complex branching structures and dense canopies, making it particularly difficult to infer their underlying topology from partial sensor observations (Costes et al., 2006; Li et al., 2025).

Tree skeletonization aims to recover the centerlines and connectivity of branches from 3D

point clouds. Previous studies have primarily estimated the medial structure by predicting offsets from surface points or directly reconstructing 3D skeleton nodes (Tagliasacchi et al., 2009; Livny et al., 2010; Cao et al., 2010; Du et al., 2019). However, severe self-occlusion caused by leaves and fine branches often results in sparse and incomplete observations of the woody structure, making it difficult to reliably reconstruct missing branch segments and their connectivity. To address this limitation, recent studies have explored generative approaches that learn structural characteristics and branching patterns to infer unobserved parts of tree structures.

In particular, diffusion-based generative models have recently been applied to tree skeletonization, generating skeleton nodes and branch directions conditioned on 3D point clouds and subsequently recovering the tree topology (Marks et al., 2025). Denoising Diffusion Probabilistic Model (DDPM) learns data distributions through a progressive noise addition and denoising process (Ho et al., 2020). However, a limited number of generated nodes may fail to adequately represent fine branches, while simply increasing the node count degrades reconstruction precision, as more nodes are placed away from the actual branch centerlines. Moreover, as higher-resolution generation requires stronger conditioning to recover more detailed structures, stochastic sampling can make it difficult to maintain consistent node positions throughout the generation process. Therefore, a new generative approach is needed to effectively incorporate conditional information from partially observed point clouds while maintaining stable generation of fine-scale structures at high resolution.

To address this issue, we propose replacing the conventional stochastic diffusion process with a deterministic generation process based on Flow Matching, enabling the reconstruction of high-resolution tree skeletons from partially observed orchard point clouds (Lipman et al., 2023). Flow Matching generates samples by integrating a learned velocity field along an ordinary differential equation (ODE), providing deterministic generation trajectories. Therefore, this study aims to develop a deterministic Flow Matching-based approach for high-resolution tree skeletonization and to evaluate its effectiveness in reconstructing fine-scale branch structures and topology from partially observed point clouds. We evaluate the proposed method using an existing public dataset, while additionally constructing a self-collected orchard dataset for future evaluation under diverse orchard conditions.

METHODS

Dataset and Evaluation

This study uses the public apple tree 3D skeletonization benchmark for initial evaluation of the proposed method (Marks et al., 2025). Although pear trees are the ultimate target of this study, our own pear orchard dataset is currently being constructed to cover various seasonal and growth conditions. Therefore, the publicly available dataset acquired from a real apple orchard was used to initially evaluate the skeleton reconstruction performance under leafy conditions. The dataset contains 280 apple trees scanned 10 times over one year during the growing season using a terrestrial laser scanner (TLS), providing 3D point clouds acquired at different stages with varying amounts of foliage. The original training, validation, and test splits defined by the dataset were used without modification.

The reference skeletons were generated from the final scan acquired after the leaves had

fallen. Under leaf-off conditions, branch surfaces are more directly observable and self-occlusion is minimized, allowing the overall woody branch structure to be captured. AdTree was applied to the segmented trees to extract their hierarchical branch structures from the trunk to higher-order branches (Du et al., 2019). AdTree is a geometry-based method that reconstructs branch centerlines and connectivity using a minimum spanning tree. The tree instance segmentation obtained from the final scan was then propagated to the point clouds acquired at other dates through nearest-neighbor search.

The predicted and reference skeletons were uniformly sampled along the branches, and Precision, Recall, and F1-score were used to evaluate the skeleton reconstruction performance.

Proposed Method

We use DiffTS, the diffusion-based tree skeletonization method proposed by Marks et al. (2025), as the baseline. In DiffTS, each skeleton node is represented as a six-dimensional state consisting of its 3D position and branch direction. While DiffTS generates skeleton nodes through the stochastic denoising process of DDPM, we replace this process with deterministic Flow Matching by integrating the learned velocity field through an ODE.

$$x^{(t-\Delta t)} = x^{(t)} - \sigma_{max}\Delta t\hat{\epsilon}(x^{(t)}, t, \mathrm{C}) \quad (1)$$

where:
$x^{(t)}$= Node state at time t
$\triangle t$= Integration time step
σ_{max}= Maximum noise scale
$\hat{\epsilon}$= Classifier-free guidance prediction
C= Input point cloud

Since Eq. (1) contains no stochastic term, the same initial state always produces the same trajectory.

To reconstruct fine-scale branches, the number of nodes was increased to approximately 17,000. Under this condition, strong classifier-free guidance is required to suppress node dispersion, but in a stochastic sampler, the noise re-injected at each step interacts with the amplified guidance, making the trajectory unstable. In a preliminary experiment at an intermediate node resolution, the precision of the stochastic sampler dropped to 22.10 at a guidance weight of five, whereas deterministic generation maintained 38.72 under the same condition. Deterministic generation structurally avoids this issue.

We further utilize the node-wise directional information obtained from the deterministic trajectory to quantify the consistency of the generation process as a confidence measure.

$$k_i = \frac{1}{T}\sum_{t=1}^{T}\left\langle \frac{\hat{\epsilon}_i^{(t)}}{\left\|\hat{\epsilon}_i^{(t)}\right\|}, \frac{\bar{\epsilon}_i}{\|\bar{\epsilon}_i\|}\right\rangle \quad (2)$$

where:
k_i= Trajectory confidence of node i
T= Number of integration steps
$\hat{\epsilon}_i^{(t)}$= Predicted velocity direction of node i at time t

$\bar{\epsilon}_i$= Mean predicted velocity direction of node i over the trajectory

The resulting confidence is incorporated into the MST edge cost to prioritize connections between nodes with higher directional consistency. Therefore, the proposed method combines stable high-resolution node generation through Flow Matching with trajectory-aware topology reconstruction to recover fine-scale branch structures and their connectivity.

RESULTS & DISCUSSION

Table 1 Skeleton reconstruction performance on the apple tree test set (%). DiffTS (baseline) follows the reported settings, while DiffTS (tuned) applies the same post-processing optimization used in our method. Best performance with respect to a particular metric is **bold** and the second best is underlined.

Approach	Precision [%] ↑	Recall [%] ↑	F1-score [%] ↑
AdTree	14.99	**54.96**	22.92
Smart-Tree	21.86	26.93	23.98
TreeQSM	17.87	48.90	25.72
DiffTS (baseline, vox 0.06)	41.68	39.05	38.62
DiffTS (tuned, vox 0.06)	42.65	47.38	44.05
DiffTS (tuned, vox 0.025)	30.64	52.70	37.46
Ours (vox 0.06)	43.50	44.35	44.12
Ours (vox 0.025)	**48.31**	47.97	**47.24**

Table 1 compares the proposed method with existing approaches. The vox column denotes the voxel size used for node generation, which determines the number of generated skeleton nodes and applies only to diffusion-based methods. For geometry-based methods, the number of nodes is determined internally by each algorithm. A smaller voxel size produces denser node spacing, allowing finer branches with smaller diameters to be represented. This is advantageous for applications requiring fine-grained structural information, such as identifying pruning points.

Among the geometry-based methods, AdTree achieves the highest recall of 54.96 but has a precision of only 14.99, indicating an overestimation of the actual branch structure due to the large number of generated nodes. TreeQSM shows a similar trend, with a recall of 48.90 and a precision of 17.87. The proposed method achieves an F1-score of 47.24, representing an improvement of 8.62 over the reported F1-score of DiffTS (38.62). It also achieves the highest precision of 48.31 while maintaining a recall of 47.97, thereby reducing the trade-off between precision and recall.

However, part of this improvement is attributable to the post-processing settings rather than the generation process itself. When the same post-processing settings are applied to the baseline, the F1-score of DiffTS at the same voxel size increases from 38.62 to 44.05, primarily due to an increase in recall from 39.05 to 47.38. Therefore, to isolate the effect of

the generation process, the two diffusion-based methods were compared using the same sampling steps and post-processing parameters.

At a voxel size of 0.06, the two methods achieve similar F1-scores of 44.05 and 44.12. However, when the voxel size is reduced to 0.025, increasing the number of generated nodes by approximately 5.7 times, their behaviors diverge. The F1-score of DiffTS decreases to 37.46, whereas that of the proposed method increases to 47.24. Both methods show improved recall, indicating that the higher resolution enables more branches to be captured. However, the precision of DiffTS drops sharply from 42.65 to 30.64, resulting in an overall performance degradation, as the denser node set places more nodes away from the actual branch centerlines. In contrast, the proposed method maintains a precision of 48.31 at the same resolution, demonstrating that the benefit of increased node resolution can be effectively realized through deterministic generation.

Figure 1 shows the reconstruction results for the same tree using the two methods. The proposed method provides broader coverage of the ground-truth structure, including upper shoots and lateral branches, whereas DiffTS concentrates nodes around the main trunk and misses more lateral branches. In the enlarged regions, DiffTS produces nodes widely distributed away from the branch axis, while the proposed method places nodes more closely along the branch centerlines. This observation is consistent with the precision difference shown in Table 1. However, both methods fail to reconstruct some branches that are not observed in the input point cloud, indicating that the absence of observational information limits the recoverable structure.

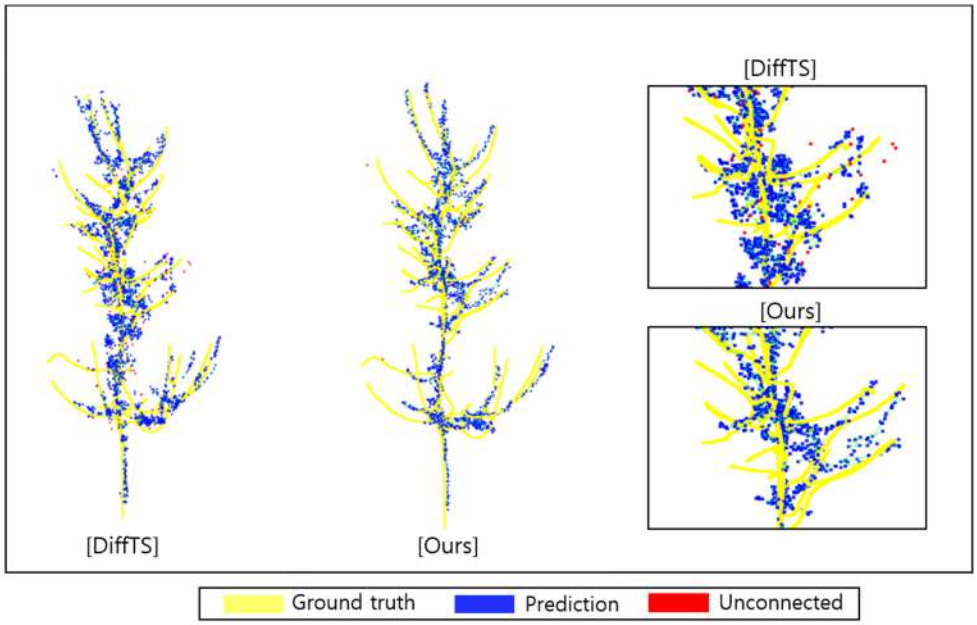

Fig.1 Qualitative comparison on a test tree. Yellow: ground-truth skeleton, blue: predicted nodes, red: nodes that remained unconnected after spanning-tree construction. Right: magnified views of the same region. DiffTS places nodes away from the branch axis, while the proposed method aligns them along the centerline.

CONCLUSIONS

This study confirmed that the performance of diffusion-based tree skeletonization is

constrained by the resolution of the generated nodes, and that simply increasing the number of nodes can degrade performance by introducing nodes that deviate from branch centerlines. To address this issue, we replaced the stochastic sampler with Flow Matching-based deterministic generation, enabling stable generation of approximately 17,000 nodes and improving the F1-score from 38.62 to 47.24. However, both methods failed to reconstruct branches that were not observed in the input point cloud, indicating a limitation caused by insufficient conditional information. Future work will investigate approaches to enhance conditional information and further validate the proposed method using the self-collected pear tree dataset.

ACKNOWLEDGEMENTS

This work was supported by the Korea Institute of Planning and Evaluation for Technology in Food, Agriculture and Forestry (IPET) through the High Value-added Food Technology Development Program, funded by the Ministry of Agriculture, Food and Rural Affairs (MAFRA) (No. 1545027880), and by the Korea Institute of Industrial Technology (KITECH) internal project (JK260002, Development of All-Diamond CMOS Technology based on a Smart Lab).

REFERENCES

Cao, J., A. Tagliasacchi, M. Olson, H. Zhang, and Z. Su. 2010. Point cloud skeletons via Laplacian based contraction. Proc. IEEE Shape Modeling International: 187-197.

Costes, E., P. É. Lauri, and J. L. Regnard. 2006. Analyzing fruit tree architecture: Implications for tree management and fruit production. In Horticultural Reviews, 32: 1-61. J. Janick, ed. Hoboken, N.J.: John Wiley & Sons.

Du, S., R. Lindenbergh, H. Ledoux, J. Stoter, and L. Nan. 2019. AdTree: Accurate, detailed, and automatic modelling of laser-scanned trees. Remote Sensing 11(18): 2074.

He, L., and J. Schupp. 2018. Sensing and automation in pruning of apple trees: A review. Agronomy 8(10): 211.

Ho, J., A. Jain, and P. Abbeel. 2020. Denoising diffusion probabilistic models. Advances in Neural Information Processing Systems 33: 6840-6851.

Li, J., H. Sun, G. Wu, H. Xu, S. Tao, W. Guo, K. Qi, H. Yin, S. Zhang, S. Ninomiya, and Y. Mu. 2025. Structural parameter determination and pruning pattern analysis of pear tree shoots for dormant pruning. Plant Phenomics 7(4): 100136.

Lipman, Y., R. T. Q. Chen, H. Ben-Hamu, M. Nickel, and M. Le. 2023. Flow matching for generative modeling. International Conference on Learning Representations.

Livny, Y., F. Yan, M. Olson, B. Chen, H. Zhang, and J. El-Sana. 2010. Automatic reconstruction of tree skeletal structures from point clouds. ACM Transactions on Graphics 29(6): 151:1-151:8.

Marks, E. A., L. Nunes, F. Magistri, M. Sodano, R. Marcuzzi, L. Zimmermann, J. Behley, and C. Stachniss. 2025. Tree skeletonization from 3D point clouds by denoising diffusion. Proceedings of the IEEE/CVF International Conference on Computer Vision: 27607-27617.

Tagliasacchi, A., H. Zhang, and D. Cohen-Or. 2009. Curve skeleton extraction from incomplete point cloud. ACM Transactions on Graphics 28(3): 71:1-71:9.

You, A., C. Grimm, A. Silwal, and J. R. Davidson. 2022. Semantics-guided skeletonization of upright fruiting offshoot trees for robotic pruning. Computers and Electronics in Agriculture 192: 106622.

Bio-processing Engineering



BP-P01

Proceedings of The 12th International Symposium on Machinery and Mechatronics for Agriculture and Biosystems Engineering (ISMAB 2026)
20-24 October 2026, Busan, Republic of Korea

GROWTH AND MORPHOLOGICAL RESPONSES OF *PYTHIUM ULTIMUM* UNDER SIMULATED MICROGRAVITY

Hyeon Tae Kim[1*], Jeong-In Choi[2], Si-joong Lee[2]

[1]Department of Biosystems Engineering, Institute of Smart Space Agriculture, Gyeongsang National University, Jinju, 52828, Republic of Korea
[2]Department of Smart Farm, Institute of Smart Space Agriculture, Gyeongsang National University, Jinju, 52828, Republic of Korea

*Corresponding Author-- Voice: +82-55-772-1896, Email: bioani@gnu.ac.kr

Abstract: Long-duration space exploration requires sustainable crop-production systems; however, closed-loop hydroponic environments may also increase the risk of waterborne plant pathogens. This study investigated the effects of repeated free-fall-based reduced-gravity exposure on the growth, hyperspectral characteristics, and hyphal morphology of *Pythium ultimum*. A laboratory-scale drop tower with an effective drop distance of 1.215 m provided approximately 0.5 s of free fall per cycle and about 112.3 min of cumulative exposure per day. *P. ultimum* was cultured under 1G and repeated free-fall conditions and evaluated using RGB imaging, hyperspectral imaging (450–950 nm), and scanning electron microscopy (SEM). Colony expansion was delayed under repeated free fall, with 1G colonies reaching full coverage on Day 5 and repeated free-fall colonies on Day 6. Hyperspectral analysis showed significant culture-day effects across all spectral regions, while treatment effects were mainly observed above 500 nm. PLS-DA clearly discriminated the two treatments after exposure, and wavelengths in the 900–950 nm region contributed strongly to classification during the late culture stage. SEM analysis showed a lower mean hyphal width under repeated free fall (2.68 μm) than under 1G (3.07 μm), together with greater morphological variability. These results indicate that repeated short-duration free-fall exposure may delay colony development and alter the optical and morphological characteristics of *P. ultimum*, providing baseline information for pathogen-risk assessment in closed crop-production systems for space environments.

Key Words: *Pythium ultimum*, Repeated free fall, Simulated microgravity, Hyperspectral imaging, Scanning electron microscopy

BP-P02

Proceedings of The 12th International Symposium on Machinery and Mechatronics for Agriculture and Biosystems Engineering (ISMAB 2026)
20-24 October 2026, Busan, Republic of Korea

A REPLACEABLE COMPOSITE DIELECTRIC FILM FOR LOW-COST PCB-BASED DIGITAL MICROFLUIDICS

Hung Pin Pan[1], Yen-Wen Lu[1*]

[1]Department of Biomechatronics Engineering, National Taiwan University, No. 1, Sec. 4, Roosevelt Rd., Da'an Dist., Taipei City 10617, Taiwan
*Corresponding Author-- Voice: +886-2-3366-5346, Email: yenwenlu@ntu.edu.tw

Abstract: Digital microfluidics (DMF) based on electrowetting-on-dielectric (EWOD) enables programmable droplet manipulation for biomedical applications. However, biofouling of droplet-contacting surfaces can limit device reusability, while replacing the entire device increases operating costs. Printed circuit boards (PCBs) are attractive substrates for EWOD devices because of their low manufacturing cost and compatibility with vertical electrical routing. However, surface irregularities from standard PCB fabrication can compromise dielectric uniformity and reliable droplet actuation. In this study, a PCB-based DMF platform incorporating a replaceable composite dielectric film is proposed. The film integrates dielectric, adhesion, and hydrophobic functions and is conformally attached to the PCB through vacuum-assisted lamination, allowing the droplet-contacting surface to be peeled off and replaced after use. Electrowetting characterization showed a decrease in apparent contact angle from 110.7° at 0 V to 69.7° at 200 V at 1 kHz, and stable transport of a 2.2 μL droplet was achieved at 157 V. Basic DMF operations, including droplet generation, splitting, transport, and mixing, were also demonstrated. These results demonstrate the feasibility of a replaceable surface architecture for improving the practicality and reusability of low-cost PCB-based DMF platforms.

Key Words: Digital microfluidics, electrowetting-on-dielectric, printed circuit board, replaceable dielectric film

INTRODUCTION

Digital microfluidics (DMF) enables the programmable manipulation of discrete droplets with volumes ranging from the nanoliter to microliter scale. Among the various actuation mechanisms used in DMF, electrowetting-on-dielectric (EWOD) has been widely adopted because individual droplets can be transported, generated, split, merged, and mixed by electrically controlling their apparent contact angles. This capability enables flexible and reconfigurable liquid handling without the pumps, valves, and tubing typically required in conventional channel-based microfluidic systems (Pollack et al., 2002). As a result, EWOD-based DMF has been increasingly investigated for applications in biochemical and biomedical analysis, including nucleic acid analysis, immunoassays, protein analysis, and cell-based assays (Xu et al., 2023).

Conventional EWOD devices are commonly fabricated using microfabrication processes to

define electrode arrays and subsequently form dielectric and hydrophobic layers. Although these processes provide well-controlled device structures, their fabrication cost and complexity can limit the development of large-area or disposable DMF devices. Printed circuit board (PCB) technology provides an attractive alternative because electrode patterns, multilayer electrical routing, and vertical interconnections can be fabricated using mature and relatively low-cost manufacturing processes. Gong and Kim (2008) demonstrated a two-dimensional EWOD electrode array using multilayer PCB technology, showing the potential of PCBs for independently addressable and reconfigurable DMF systems. More recently, PCB-based platforms have been further developed toward large-scale and automated droplet manipulation (Xing et al., 2021). However, the surface topography of as-fabricated PCBs and the resulting requirements for dielectric and hydrophobic coatings remain important challenges. Additional post-processing is generally required to provide a sufficiently smooth and electrically reliable droplet-actuation surface, which increases fabrication complexity and reduces some of the cost advantages of PCB-based devices (Kim and Gong, 2010).

The droplet-contacting surface is particularly important for DMF devices intended for biological applications, such as nucleic acid extraction from whole blood (Hung et al., 2017), as nonspecific adsorption of biomolecules can cause biofouling, droplet pinning, sample loss, and cross-contamination (Freire, 2016; Abdul Latip et al., 2017). Replaceable functional films provide an alternative to permanently deposited dielectric and hydrophobic coatings by allowing the liquid-contacting surface to be renewed independently of the electrode substrate. Previous studies have demonstrated this concept using a free-standing double-layer membrane on PCB-based DMF devices (Xing et al., 2021) and a polymer–ion-gel–fluoropolymer composite film capable of low-voltage EWOD actuation (Cao et al., 2023). These studies demonstrate the feasibility of replaceable film architectures for PCB-based DMF devices. However, further simplification of film composition and attachment using commercially available materials may improve fabrication accessibility and facilitate integration with conventional PCB substrates. Accordingly, a simple replaceable film capable of conforming to the non-planar PCB surface would be advantageous for low-cost PCB-DMF systems.

Therefore, the objective of this study was to develop and characterize a PCB-based DMF device incorporating a simple replaceable composite dielectric film. The proposed film consists of a commercial polyimide (PI) film with a polydimethylsiloxane (PDMS) adhesion layer on the PCB-facing side and a Teflon hydrophobic layer on the droplet-facing side. The PDMS layer promotes conformal attachment between the film and the PCB electrode surface while maintaining a peelable interface for film replacement. The electrowetting response of the composite film was characterized by contact-angle measurements, and droplet transport performance was evaluated as a function of applied voltage. Fundamental DMF operations, including droplet generation, splitting, transport, and mixing, were further demonstrated to evaluate the feasibility of the proposed replaceable-film approach.

MATERIALS AND METHODS

Device Architecture and Materials

The PCB-DMF device developed in this study consists of three main components, as illustrated in Fig.1(a): an ITO-glass top plate, a replaceable dielectric film, and a PCB bottom plate containing the electrode array. The ITO-coated glass was coated with Teflon to provide a

hydrophobic top surface. The replaceable film consisted of a 12.5 μm-thick polyimide (PI) substrate, an approximately 5 μm PDMS adhesion layer on the PCB-facing side, and an approximately 200 nm Teflon hydrophobic layer on the droplet-facing side, as shown in Fig. 1(b). The bottom plate was fabricated using a double-sided copper PCB on an FR-4 substrate. Electrical signals were routed vertically through the PCB so that each electrode could be addressed from the reverse side, thereby simplifying the electrode layout. A 200 μm gap was maintained between the top plate and the replaceable dielectric film.

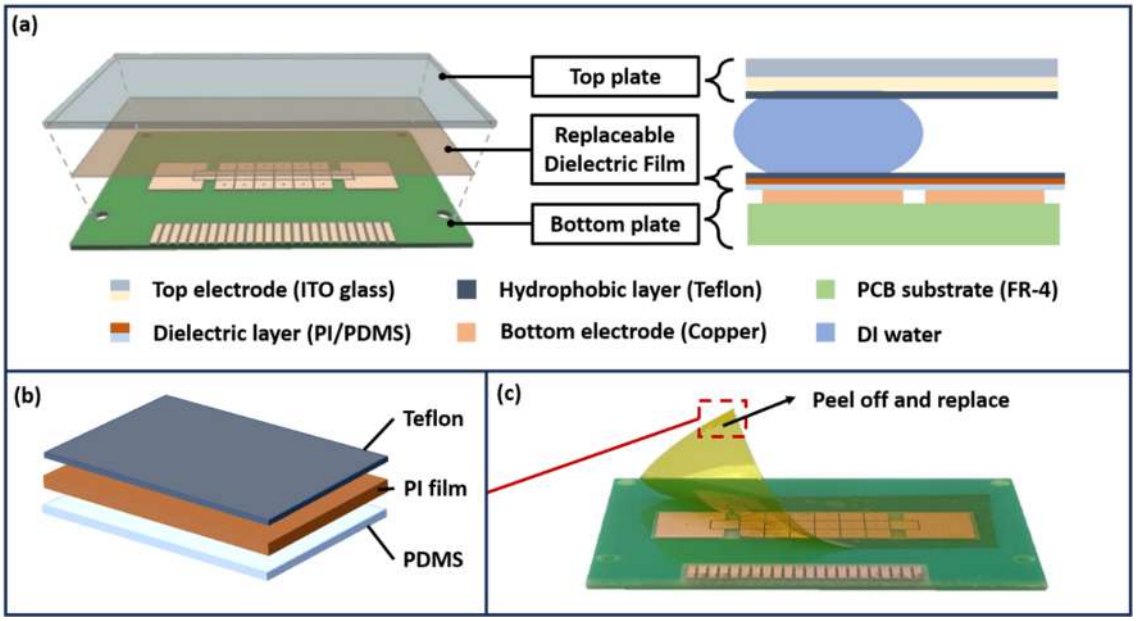

Fig.1 Schematic illustration of the PCB-DMF device: (a) device architecture, (b) structure of the replaceable dielectric film, and (c) peel-and-replace concept allowing the underlying PCB electrode substrate to be retained.

Design and Fabrication of the PCB-DMF Substrate

The bottom electrode substrate was fabricated using a rigid FR-4 PCB because of its low cost, mechanical rigidity, and compatibility with standard PCB manufacturing processes. The electrode array consisted of 3 × 3 mm copper electrodes separated by 150 μm gaps. Electrical routing was placed on the reverse side of the PCB and connected to the top electrodes through plated vias.

Preparation of the Replaceable Dielectric Film

To provide a smooth and replaceable droplet-contacting surface, the PI film was coated with a PDMS adhesion layer on the lower side and a Teflon hydrophobic layer on the upper side as shown in Fig.1(b). The PDMS base and curing agent were mixed at a 10:1 mass ratio, diluted with toluene at a 1:1 mass ratio, coated onto the PCB-facing side, and cured at 130 °C for 20 min. After the film was flipped over, the Teflon solution was spin-coated onto the droplet-facing side at 3000 rpm for 30 s and baked at 180 °C for 20 min. After fabrication, the composite film was laminated onto the PCB electrode array and subjected to vacuum for 3 min to promote conformal attachment and minimize trapped air at the film–PCB interface. After each experiment, the film could be peeled off and replaced while the PCB electrode substrate was retained for subsequent use.

Experimental Setup and Characterization

An electrical actuation and imaging system, shown in Fig.2, was developed to apply a controlled voltage between the top and bottom electrodes. The actuation and imaging configuration followed that used in our previous DMF studies (Cheng et al., 2023; Yang et al., 2023). A function generator produced a 1 kHz square-wave signal, which was amplified by a high-voltage amplifier with an output range of 0–200 V. The amplified signal was delivered to a custom relay board containing 15 relays, which routed the actuation voltage to selected electrodes through a PCB connector. The relay board was controlled using a DAQ module connected to a computer, allowing each electrode to be independently switched through a Python-based user interface. An oscilloscope was connected to the relay board to monitor the applied waveform. Droplet motion was recorded using a digital microscope. An in-house OpenCV-based image-processing routine was used to segment the droplet by HSV thresholding and track its centroid frame by frame. The resulting trajectory was used to calculate droplet displacement and transport velocity with a spatial calibration of 0.059 mm/pixel.

Contact Angle Measurement

Apparent contact angles were measured using a 10 μL DI-water droplet at applied voltages of 0, 60, 150, and 200 V at 1 kHz. Side-view images of the droplet were recorded using a High-speed camera, and the apparent contact angle was determined using ImageJ.

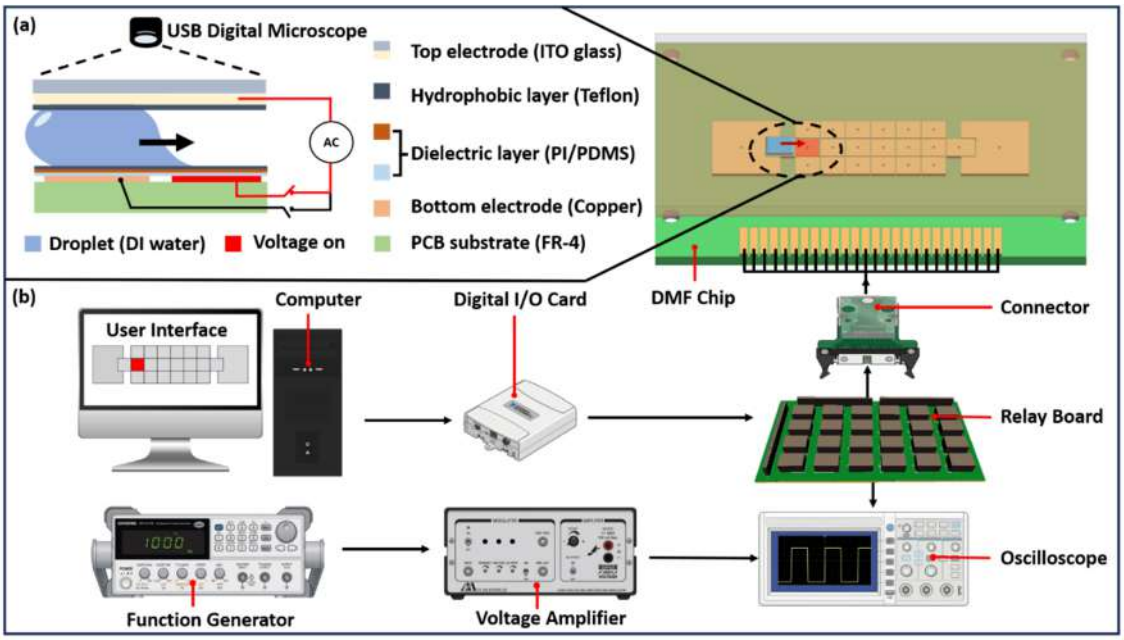

Fig.2 Experimental setup for DMF actuation.

RESULTS & DISCUSSION

Electrowetting Contact Angle Characterization

The electrowetting response of the replaceable dielectric film is summarized in Table 1. At an

actuation frequency of 1 kHz, the apparent contact angle decreased monotonically from 110.7° at 0 V to 69.7° at 200 V, corresponding to a total contact-angle change of approximately 41°. The initial contact angle above 110° indicates that the Teflon-coated surface retained sufficient hydrophobicity after film fabrication and vacuum-assisted lamination. The progressive decrease in contact angle with increasing voltage confirms that the applied electric field can effectively modulate the droplet–surface interfacial condition through the PI/PDMS/Teflon composite stack. Therefore, the replaceable film functions not only as a physical covering layer for the PCB surface but also as an effective dielectric and hydrophobic interface for EWOD actuation. This voltage-dependent contact-angle response is consistent with the subsequent droplet-transport experiments.

Table 1 Apparent contact angle of the replaceable dielectric film at different applied voltages at 1 kHz.

Applied voltage (V)	0	60	150	200
Contact angle (°)	110.7	98.4	88.1	69.7

PCB-DMF Performance

Basic droplet-manipulation operations using the PCB-DMF device are demonstrated in Fig.3, including droplet generation, splitting, transport, and mixing. These operations rely on coordinated electrowetting actuation of adjacent electrodes to control droplet motion and deformation. Successful droplet transport indicates that the laminated composite film provides a sufficiently continuous actuation surface for droplets to move between adjacent electrodes. Furthermore, these results suggest that the proposed platform could support more complex droplet-manipulation sequences in future applications.

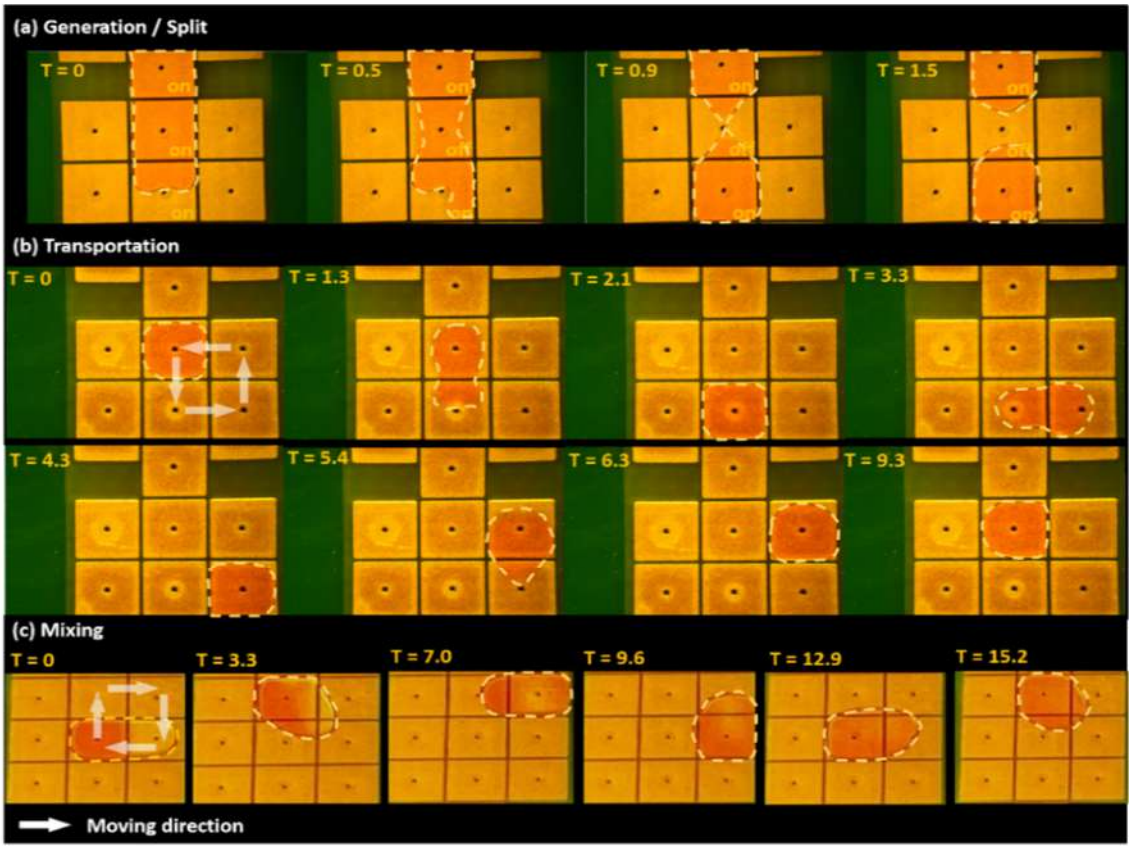

Fig.3 Demonstration of basic droplet manipulation on the PCB-DMF device: (a) droplet generation and splitting using the common three-electrode method. All three electrodes are turned on at T = 0 to elongate the liquid; the middle electrode is then turned off at T = 0.5, necking develops at T = 0.9, and the liquid is separated into two sub-droplets at T = 1.5. (b) Electrodes along a circular path are turned on one by one, transporting a single droplet around the loop and demonstrating the ability to move a droplet along a prescribed path. (c) Two merged droplets are circulated along the same path to demonstrate droplet mixing. Time stamps are given in seconds; arrows indicate the direction of droplet motion.

Droplet Transport Velocity

For quantitative characterization of droplet transport, a 2.2 μL DI-water droplet was actuated at 1 kHz while the applied voltage was increased stepwise from 100 to 200 V. The resulting transport velocities are shown in Fig.4. Stable droplet transport was first observed at 157 V, corresponding to a transport velocity of approximately 0.9 mm/s. The transport velocity increased sharply above approximately 160 V, reaching approximately 7.8 mm/s at 170 V and continuing to increase at higher applied voltages.

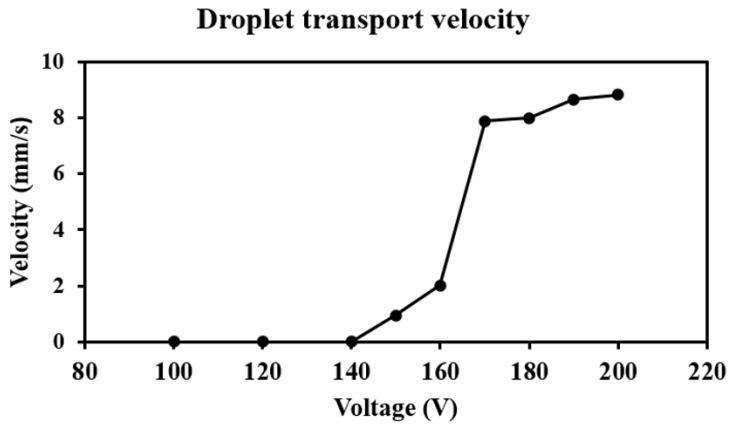

Fig.4 Droplet transport velocity as a function of applied voltage.

Threshold-like behavior suggests that a minimum electrowetting force is required to overcome interfacial resistance and contact-line pinning on the device surface. At lower voltages, contact-angle modulation is insufficient to sustain droplet motion. Once this threshold is exceeded, stronger electrowetting increases the net driving force, leading to a rapid rise in transport velocity. The relatively high actuation threshold may partly be attributed to the thick composite dielectric stack, which reduces capacitance per unit area and therefore requires a higher voltage to generate sufficient electrowetting force. A similar trade-off was observed in our previous DMF work, in which the dielectric layer was thickened to maintain reliability with electrolyte-containing reagents at the cost of a higher actuation voltage (Yang et al., 2023).

Increasing transport velocity at higher voltages is consistent with the contact-angle measurements, where greater voltage-induced modulation was observed as voltage increased. This agreement between static contact-angle response and dynamic droplet transport supports the effectiveness of the composite film as an EWOD actuation interface. Future optimization of film thickness may help lower actuation voltage while preserving dielectric integrity and conformal attachment to the PCB surface.

CONCLUSIONS

A PCB-based DMF device incorporating a replaceable PI/PDMS/Teflon composite film was developed in this study. The film functions as the droplet-contacting dielectric and hydrophobic layers on the reusable PCB substrate for DMF devices. At an actuation frequency of 1 kHz, the apparent contact angle decreased from 110.7° at 0 V to 69.7° at 200 V. Stable transport of a 2.2 μL droplet was first observed at 157 V, and fundamental DMF operations, including droplet generation, splitting, transport, and mixing, were successfully demonstrated. These results support the feasibility of renewing the droplet-contacting surface through film replacement while retaining the underlying PCB electrode substrate. Future work will focus on film-to-film reproducibility, repeated replacement cycles, dielectric reliability, and performance with biological samples.

ACKNOWLEDGEMENTS

The authors gratefully acknowledge the financial support from the National Science and Technology Council, Taiwan (NSTC 114-2221-E-002-077-MY3; NSTC 115-2640-B-002-001).

REFERENCES

Abdul Latip, E. N., L. Coudron, M. B. McDonnell, I. D. Johnston, D. K. McCluskey, R. Day, and M. C. Tracey. 2017. Protein droplet actuation on superhydrophobic surfaces: A new approach toward anti-biofouling electrowetting systems. RSC Adv. 7(78): 49633-49648.

Cao, J., X. Zeng, S. Shen, H. Feng, X. Qin, M. Jin, Z. Liu, and L. Shui. 2023. Replaceable dielectric film for low-voltage and high-performance electrowetting-based digital microfluidics. Langmuir 39(29): 10189-10198.

Cheng, Y.-H., T.-J. Yang, and Y.-W. Lu. 2023. Simultaneous multiple-droplet generation with meniscus filling on digital microfluidics chip. Sens. Actuators B Chem. 390: 133989.

Freire, S. L. S. 2016. Perspectives on digital microfluidics. Sens. Actuators A Phys. 250: 15-28.

Gong, J., and C.-J. Kim. 2008. Direct-referencing two-dimensional-array digital microfluidics using multilayer printed circuit board. J. Microelectromech. Syst. 17(2): 257-264.

Hung, P.-Y., P.-S. Jiang, E.-F. Lee, S.-K. Fan, and Y.-W. Lu. 2017. Genomic DNA extraction from whole blood using a digital microfluidic (DMF) platform with magnetic beads. Microsyst. Technol. 23(2): 313-320.

Kim, C.-J., and J. Gong. 2010. EWOD droplet microfluidic devices using printed circuit board fabrication. In *Micro/Nano Technology Systems for Biomedical Applications: Microfluidics, Optics, and Surface Chemistry*, 232-265. C.-M. Ho, ed. Oxford, UK: Oxford University Press.

Pollack, M. G., A. D. Shenderov, and R. B. Fair. 2002. Electrowetting-based actuation of droplets for integrated microfluidics. Lab Chip 2(2): 96-101.

Xing, Y., Y. Liu, R. Chen, Y. Li, C. Zhang, Y. Jiang, Y. Lu, B. Lin, P. Chen, R. Tian, X. Liu, and X. Cheng. 2021. A robust and scalable active-matrix driven digital microfluidic platform based on printed-circuit board technology. Lab Chip 21: 1886-1896.

Xu, X., L. Cai, S. Liang, Q. Zhang, S. Lin, M. Li, Q. Yang, C. Li, Z. Han, and C. Yang. 2023. Digital microfluidics for biological analysis and applications. Lab Chip 23: 1169-1191.

Yang, T.-J., Z.-H. Lin, and Y.-W. Lu. 2023. Self-powered digital microfluidics driven by rotational triboelectric nanogenerator. Nano Energy 110: 108376.

BP-P03

Proceedings of The 12th International Symposium on Machinery and Mechatronics for Agriculture and Biosystems Engineering (ISMAB 2026)
20-24 October 2026, Busan, Republic of Korea

친환경 초임계 CO_2 공정 기반 세모가사리 고부가 기능성 원료 개발

ECO-FRIENDLY SUPERCRITICAL CO_2 EXTRACTION FOR VALUE-ADDED FUNCTIONAL INGREDIENTS FROM AHNFELTIOPSIS FLABELLIFORMIS

이요셉 [1], 최재혁 [1], 박성완 [2], 선우훈 [1,2*]
Yo Seph Lee[1], Jae Hyeok Choi[1], Sung Wan Park[2], Hoon Seonwoo[1,2*]

[1] 국립순천대학교 스마트농업공학과
[2] 국립순천대학교 스마트농업전공
[1]Department of Smart Agricultural Engineering, Sunchon National University, Sunchon, Republic of Korea
[2]Smart Agriculture Major, Sunchon National University, Suncheon, 57922, Republic of Korea
*Corresponding Author-- Email: uhun906@scnu.ac.kr

Abstract: Ahnfeltiopsis flabelliformis, a red marine algae in which funoran, polyphenols, and flavonoids are rich, is a highly promising resource for functional foods, pharma ceutical, and cosmetic applications. Unfortunately, conventional hot-water and organic solvent extraction methods suffer from thermal degradation, oxidative decomposition, and residual solvent contamination, confirming the limitation of the production of high-quality functional ingredients. In this study, we developed an eco-friendly super critical CO_2 extraction process to efficiently recover bioactive compounds from A. flabelliformis and comprehensively compared its performance with conventional methods. Pretreated algal biomass first underwent supercritical CO_2 extraction at 40–55°C and 300 bar to remove lipophilic compounds, followed by extraction of the residual biomass using distilled water without or with ethanol as a co-solvent to recover funoran and water-soluble compounds. Major bioactive compounds including floridoside and shinorine and structural and thermal stability were analyzed by several equipments and, as a result, the suitablity of heavy metal analysis and safety evaluations of treated samples were confirmed compared to those of functional raw materials. In conclusion, the supercritical CO_2 process was proved to preserve better bioactive compounds and to yield solvent-free, non-toxic ingredients. Integrating supercritical and aqueous extraction would establish an efficient and scalable biorefinery platform recovering multiple valuable fractions from a single marine biomass source, providing a foundation for value-added utilization of marine bioresources and sustainable, eco-friendly functional material industries, particularly within the biotechnology sector.

Key Words: Sargassum confusum, Supercritical CO2 extraction, Fucoxanthin, Marine biotechnology, Biorefinery

ACKNOWLEDGEMENTS

This paper was supported by Sunchon National University Glocal University Project Fund in 2025.

BP-P04

Proceedings of The 12th International Symposium on Machinery and Mechatronics for Agriculture and Biosystems Engineering (ISMAB 2026)
20-24 October 2026, Busan, Republic of Korea

SUSTAINABLE HIGH-THROUGHPUT 3D FOOD PRINTING VIA UPCYCLED SESAME MEAL ISOLATED PROTEIN INKS FOR PLANT BASED MEAT ANALOGUES

Yuseung Choi[1,2], Hyun-Su Choi[1], Hyunjin Lee[3], Woobin Choi[1], Kanghee Han[1], Sungchul Shin[3,4,5], Yong-Ro Kim[1,2,3], and Sangbae Park[1,2,3*]

[1]Department of Biosystems Engineering, Seoul National University, Seoul, Korea
[2]Integrated Major in Global Smart Farm, Seoul National University, Seoul, Korea
[3]Department of Agriculture, Forestry, and Bioresources, Seoul National University, Seoul, Korea
[4]Research Institute of Agriculture and Life Sciences, Seoul National University, Seoul, Korea
[5]Department of Biomaterials Engineering, Seoul National University, Seoul, Korea
*Corresponding Author-- Email: sb92park@snu.ac.kr

Abstract: The exponential growth of global population and environmental degradation have exposed the limitations of conventional agriculture, driving growing interest in sustainable food systems, wherein 3D printing of meat analogues has emerged as a promising solution. However, soy protein isolate (SPI), the most widely used protein source for printable inks, can be formulated only up to approximately 15% protein content, limiting the nutritional density and structural quality of printed meat analogues. Meanwhile, sesame meal, a protein-rich byproduct of sesame oil pressing, remains underutilized as low-value feed or fertilizer. Here, we extracted protein from sesame meal and formulated it into a high-concentration ink for high-speed 3D food printing. The sesame protein ink was printed flawlessly at 30% protein content, twice the printable limit of SPI-based inks. Furthermore, its superior elasticity compared with SPI facilitated the formation of aligned fibrous structures along the programmed printing paths. These results demonstrate the upcycling of an agricultural byproduct into a high-value food material and suggest a scalable strategy for high-speed manufacturing of high-quality fibrous meat analogues.

Key Words: Sesame meal isolated protein, Up cycling, High-concentration protein ink, High-throughput 3D printing, Fibrous texture, Plant-based meat analogue

ACKNOWLEDGEMENTS

This work was supported by the Basic Science Research Program through the National Research Foundation of Korea (NRF) funded by the Ministry of Science and ICT (RS-2026-25504472). and supported by the Creative-Pioneering Researchers Program through Seoul National University (Project No. 0525-20250123)

BP-P05

Proceedings of The 12th International Symposium on Machinery and Mechatronics for Agriculture and Biosystems Engineering (ISMAB 2026)
20-24 October 2026, Busan, Republic of Korea

EFFECT OF UREA LOADING METHOD AND DRYING CONDITION ON ALGINATE-BASED SLOW-RELEASEING FERTILIZER BEADS

Jaehyeok Choi[1], Yoseph Lee [1], Sungwan Park [2], Jae Woon Lim[3], Hoon Seonwoo[3]*

[1]Department of Smart Agriculture Engineering, Sunchon National University, 255 Jungang-ro, Suncheon 57922, Republic of Korea
[2]Department of Smart Agriculture major, Sunchon National University, 255 Jungang-ro, Suncheon 57922, Republic of Korea
[3]Department of Convergent Biosystems Enginerring, Sunchon National University, 255 Jungang-ro, Suncheon 57922, Republic of Korea
*Corresponding Author-- Voice: +82-10-8715-2536, Email: uhun906@scnu.ac.kr

Abstract: Petroleum-based polymer-coated controlled-releaseing fertilizers leave non-degradable coating shells in soil as microplastics. On the other hand, sodium alginate is suggested as a biodegradable alternative because it is derived from renewable seaweed and is naturally degraded in soil. However, urea diffused from alginate beads too rapidly, and many of efforts made to slow this diffusion have caused new environmental problems of their own. This study aims to develop an eco-friendly method to evaluate whether cellulose nanofiber (CNF) and carboxymethyl cellulose (CMC) reinforce the internal structure of the beads so that the initial burst release of freeze-dried beads can be suppressed, and to determine how urea loading method and drying condition govern pore structure and nitrogen release. In a preliminary experiment, alginate beads containing humic acid, poly(vinyl alcohol) and citric acid were formed by ionotropic gelation, and urea was loaded by immersion in a near-saturated urea solution. Release in deionized water was measured at 420 nm using p-dimethylaminobenzaldehyde. The post-loaded beads released in the bead essentially all of the loaded urea within 72 h, indicating that the absorbed urea resided in the bead surface rather than in the bead core. Then urea was incorporated directly into the precursor solution and also added to the gelation bath to suppress diffusive loss. Because urea can be condensed to phytotoxic biuret near 133 °C, freeze drying was replaced thermal curing, and it will be assessed whether CNF/CMC reinforcement can reduce the pores generated by freeze drying and thereby suppress urea release. As a result the beads with reinforcement were evaluated to decrease the pore size, nitrogen release, biuret content, soil burial degradation against a commercial polymer-coated fertilizer. The results are expected to provide a processing route for biodegradable slow-release fertilizers that sustain nitrogen use efficiency without leaving microplastic residues in soil.

Key Words: Slow-release fertilizer, Sodium alginate, Cellulose nanofiber, Freeze drying, Urea releas

ACKNOWLEDGEMENT

This paper was supported by Sunchon National University Glocal University Project Fund in 2026
This work was supported by the National Research Foundation of Korea(NRF) grant funded by the Korea government(MSIT)(RS-2025-16069666)

BP-P06

Proceedings of The 12th International Symposium on Machinery and Mechatronics for Agriculture and Biosystems Engineering (ISMAB 2026)
20-24 October 2026, Busan, Republic of Korea

EFFECTS OF STARCH RETROGRADATION ON REHYDRATABLE, EDIBLE SCAFFOLD FOR CULTURED MEAT

Yeonggeol Hong[1], Agatha Harta Muliani[1], Kyoung-Je Jang[1,2*]

[1]Department of Bio-Systems Engineering, Institute of Smart Farm, Gyeongsang National University, Jinju 52828, Republic of Korea
[2]Department of Bio-industrial Machinery Engineering, Gyeongsang National University, Jinju 52828, Republic of Korea
*Corresponding Author-- Voice: +82-10-9775-9784, Email: kj_jang@gnu.ac.kr

Abstract: Starch offers a promising scaffold component because of its food relevance and ability to form physically associated networks through gelatinization and retrogradation. However, how retrogradation influences the performance of dried and subsequently rehydrated starch scaffolds remains insufficiently understood. This ongoing study examines the relationships among retrogradation, crystalline organization, mechanical stability, and cellular responses in mung bean starch scaffolds intended for cultivated meat production. Scaffolds are prepared by gelatinizing aqueous mung bean starch formulations, applying defined pre-drying aging periods, drying the resulting gels at 35°C, and rehydrating the films before evaluation. Starch concentration and aging duration are compared under controlled processing conditions, with film thickness recorded to account for geometric differences. X-ray diffraction is used to characterize crystalline organization and relative crystallinity, while scanning electron microscopy examines surface and cross-sectional morphology with explicit consideration of sample-preparation effects. Tensile testing and geometry-appropriate compression testing assess mechanical behavior before and/or after defined periods of exposure to culture medium. These measurements are designed to distinguish initial scaffold properties from changes associated with hydration and prolonged incubation. C2C12 myoblast culture is used to evaluate attachment, spreading, and subsequent growth on selected scaffolds. Planned model cargo-release measurements will assess whether retrogradation and surface functionalization alter early and subsequent release kinetics. Rather than assuming that higher crystallinity necessarily improves scaffold performance, the study tests whether an appropriate balance between crystalline reinforcement and hydration-dependent flexibility supports stable cell culture. The integrated experimental framework is intended to identify processing–structure–function relationships that guide the development of rehydratable scaffolds based on edible ingredients for cultivated meat.

Key Words: Cultured meat, Edible scaffolds, Strach retrogradation, Myoblast attachment, Hydrogel

ACKNOWLEDGEMENTS

This work was carried out with the support of “Research Program for Agriculture Science and Technology Development (Project No.RS-2026-25519136)” Rural Development Administration, Republic of Korea and by the National Research Foundation of Korea (NRF) grant funded by the Korea government (MSIT) (RS-2025-02216206).

BP-P07

Proceedings of The 12th International Symposium on Machinery and Mechatronics for Agriculture and Biosystems Engineering (ISMAB 2026)
20-24 October 2026, Busan, Republic of Korea

MITIGATING EXPERIMENTAL DATA LIMITATIONS IN MICROBIAL CELL FACTORY RESEARCH VIA PHYSICS-INFORMED MACHINE LEARNING

WooKyung Lee[1], Dohyeok Choi[1], KwangYoung Park[2], Hee Taek Kim[2], Wang-Hee Lee[1,3]*

[1] Department of Smart Agriculture Systems Machinery Engineering, Chungnam National University, Daejeon 34134, Korea
[2] Department of Food Science and Technology, Chungnam National University, Daejeon 34134, Korea
[3] Department of Smart Agriculture Systems, Chungnam National University, Daejeon 34134, Korea
*Corresponding Author--Email: wanghee@cnu.ac.kr

Abstract: Microbial cell factories are a core platform for producing amino acids and other bio-based materials, but quantifying their intracellular metabolic state remains a bottleneck for bioprocess design and monitoring. ^{13}C-metabolic flux analysis (^{13}C-MFA), the reference method, requires costly isotope-labeling experiments, so high-quality flux data are inherently scarce and conventional data-hungry machine learning (ML) is difficult to apply. This study aimed to mitigate this data-scarcity problem by embedding a physical law, steady-state mass balance, into ML models that predict intracellular fluxes from extracellular measurements. A central carbon metabolism network of *Corynebacterium glutamicum* (58 metabolites, 87 reactions) was constructed at the resolution of ^{13}C-MFA data. Two physics-informed models were developed: a physics-informed neural network (PINN), which penalizes the mass-balance residual in its loss function, and a null-space-parameterized multilayer perceptron (NSP-MLP), which confines its output to the null space of the stoichiometric matrix so that mass balance is satisfied by construction and only three coefficients must be learned. Both models were trained on 45 literature-derived ^{13}C-MFA datasets (wild-type, lysine-, glutamate-, protein- and valine-producing strains), with 29 exchange fluxes lumped into 11 inputs to limit overfitting, and were evaluated by nested leave-one-out cross-validation. A quadratic-programming step enforced flux feasibility. Against experimentally measured fluxes, PINN and NSP-MLP reduced the mean root mean square error (RMSE) by approximately 31% and 26% relative to flux balance analysis (FBA), the best conventional method, and outperformed parsimonious FBA and enzyme-constrained FBA by a wider margin (statistically significant, $p < 0.05$). PINN ranked within the top two methods in 86.7% of datasets. RMSE was 21–48% lower than that of FBA in four of five strain groups, whereas FBA remained competitive for a valine-producing group of only two datasets, showing that exchange fluxes alone can under-determine intracellular states. These results show that physical constraints can be built into ML models trained on limited experimental data to obtain accurate and physically consistent flux estimates. Because the inputs are extracellular measurements, the approach offers a basis for bioprocess monitoring, bottleneck identification and scenario-based strain design in smart biomanufacturing.

Key Words: Physics-informed machine learning, Metabolic flux, Data scarcity, Bioprocess monitoring, *Corynebacterium glutamicum*

ACKNOWLEDGEMENTS

This research was supported by the National Research Foundation of Korea (NRF) grant funded by the Korea government (MSIT) (RS-2025-24535664).

BP-P08

Proceedings of The 12th International Symposium on Machinery and Mechatronics for Agriculture and Biosystems Engineering (ISMAB 2026)
20-24 October 2026, Busan, Republic of Korea

PHOTOSYNTHETIC SELF-OXYGENATING CULTURED MEAT VIA COAXIAL BIOPRINTING OF CHLORELLA-MUSCLE CELL BIOINK

Kanghee Han[1], Yuseung Choi[1,2], Daeun Jung[1], Woobin Choi[1,2], Woo Seok Jung[1], Sangbae Park[1,2,3,*]

[1]Department of Biosystems Engineering, Seoul National University, Seoul, Korea
[2]Integrated Major in Global Smart Farm, Seoul National University, Seoul, Korea
[3]Research Institute for Agriculture and Life Sciences, Seoul National University, Seoul, Korea
*Corresponding author Sangbae Park Voice: +82-02-880-4601, Email: sb92park@snu.ac.kr

Abstract: With the growing global demand for sustainable food resources, cultivated meat has attracted considerable attention as a promising approach to meeting the increasing demand for animal protein. However, a major limitation of cultivated meat is the inability to fabricate tissues beyond a critical thickness because of hypoxia-induced necrosis. Chlorella generates oxygen through photosynthesis and has therefore been widely incorporated into biomaterials designed to alleviate central hypoxia. In this study, we developed a 3D-printed Chlorella–muscle cell composite tissue using a coaxial nozzle to continuous oxygen supply Chlorella-laden outer bioink layer encapsulated a C2C12-laden core bioink. To build a system that can synchronize consumption and production of O2 in Chlorella-muscle cell composite tissue, we measured dissolved oxygen (DO) in each ink. We employed rheological characterization and printability assessment to evaluate compatibility of the bioinks for printing. Cell viability in Chlorella bioink was analyzed by performing LIVE/DEAD and chlorophyll measurement. Cell viability, proliferation, differentiation in C2C12 bioink were measured by LIVE/DEAD, PCR, and WST-1. Finally, we observed outstanding potential of tissue formation and myogenic differentiation in our products. Collectively, the chlorella-muscle cell construct is expected to contribute to increasing the thickness of cultured meat.

Key Words: Photosynthetic, Self-oxygenating, Chlorella, Coaxial bioprinting, Cultivated Meat

ACKNOWLEDGEMENT

This research was supported by the Tech Incubator Program for Startup(TIPS), funded by the Ministry of SMEs and Startups(MSS), Republic of Korea (RS-2024-00553930) and Basic Science Research Program through the National Research Foundation of Korea (NRF) funded by the Ministry of Education (RS-2025-24092970)).

Field Machinery and Systems



FM-P01

Proceedings of The 12th International Symposium on Machinery and Mechatronics for Agriculture and Biosystems Engineering (ISMAB 2026)
20-24 October 2026, Busan, Republic of Korea

FABRICATION AND FACTORIAL TESTING OF A PULLING TEST RIG FOR A SELF-PROPELLED RADISH HARVESTER

Seok-Jun Hong[1], Il-Su Choi[1*], Young-Hwa Kim[1], Jea-Keun Woo[1], Chun-Gu Lee[1], Kyu-Ho Lee[1], Yun-Jeong Yang[1], Si-Yun Kim[1], Myeong-Hee Lee[1], Kyung-Sik Choi[1]

[1]Field Farming Mechanization Division, National Institute of Agricultural Sciences, Rural Development Administration, Jeonju, 54875, Republic of Korea
*Corresponding Author-- Voice: +82-63-238-4186, Email: cis1981@korea.kr

Abstract: Radish is a major field crop cultivated in the Republic of Korea. Its cultivation area decreased from 21,030 ha in 2014 to 18,497 ha in 2024, while production declined from 1,296,970 to 1,035,645 tons over the same period. Although the overall mechanization rate of radish farming is 61.2%, the harvesting mechanization rate remains only 5.7%. Harvesting requires 15.0 h/10a, accounting for approximately 30.3% of the total labor input of 49.5 h/10a. Therefore, a high-performance radish harvester is needed to reduce harvesting labor and address the decline and aging of the rural workforce. This study fabricated a pulling test rig and conducted factorial experiments to determine appropriate operating conditions for the pulling unit of a self-propelled radish harvester. The test rig consisted of a foliage-guiding unit, a pulling and conveying unit, a supporting frame, and a hydraulic drive system. The foliage-guiding unit raised lodged foliage and guided it between the pulling belts, which gripped the foliage, extracted the radishes from the soil, and conveyed them rearward. The rig was installed in a circular soil bin with the pulling angle fixed at 30°. Nine operating conditions were established by combining three travel speeds (0.20, 0.25, and 0.30 m/s) with three pulling-belt speeds (0.40, 0.50, and 0.60 m/s), and each condition was tested in triplicate. Radishes of the 'Cheonghwang' cultivar were used. Pulling and conveying performance was evaluated based on the percentages of completely extracted and successfully conveyed radishes, respectively. The pulling rate tended to increase with increasing pulling-belt speed at all travel speeds. The highest pulling rate of 93.33% was obtained at a travel speed of 0.25 m/s combined with pulling-belt speeds of 0.50 and 0.60 m/s, with corresponding conveying rates of 92.50% and 96.67%, respectively. Considering both performance indicators, the best operating condition was a travel speed of 0.25 m/s and a pulling-belt speed of 0.60 m/s, corresponding to a belt-to-travel speed ratio of 2.4. These results can provide fundamental information for determining appropriate operating speeds for the pulling unit of a self-propelled radish harvester.

Key Words: radish harvester, pulling test rig, pulling rate, conveying rate, speed ratio

FM-P02

Proceedings of The 12th International Symposium on Machinery and Mechatronics for Agriculture and Biosystems Engineering (ISMAB 2026)
20-24 October 2026, Busan, Republic of Korea

COMPARATIVE EVALUATION OF THE TORSIONAL PERFORMANCE OF STEEL WIRE CLAMPS AND STEEL PLATE CLAMPS FOR GALVANIZED STEEL TUBE CONNECTIONS IN GREENHOUSE STRUCTURES

Cheng-Chang Lien[1], Yu-Min Wang[2*], Zong-Xian Xie[3], Jun-Han Mei[4]

[1]Department of Biomechatronic Engineering, National Chiayi University, Chiayi, Taiwan

*Corresponding Author--Tel:+886-5-2717972. Email: 1140275@mail.ncyu.edu.tw

Abstract: Greenhouses are essential facilities for improving crop growing conditions, quality, and yield.However, greenhouse structures are vulnerable to extreme weather events, particularly the strong winds and intense short-duration rainfall associated with typhoons. This study compared the torsional performance of steel wire clamps and steel plate clamps, which are commonly used to connect steel pipes in simple greenhouse structures in Taiwan and Japan, respectively. Hot-dip galvanized steel pipes with outside diameters of 42.1 mm and 26.8 mm were used as the vertical and horizontal members and were connected using 3.8-mm diameter steel wire clamps or steel plate clamps. Loads were applied with a universal testing machine in horizontal right-rotation and left-rotation directions at test speeds of 5, 10, 20, 30, and 60 mm/min. Force-displacement data were recorded, converted to torque-radian curves, and used to calculate rotational stiffness. At all test speeds, the torque of each specimen increased to a peak and then decreased. The peak torque of the steel plate clamps ranged from 78 to 90 N·m in right rotation and from 72 to 87 N·m in left rotation. The right-rotation curves were more concentrated, indicating more consistent torsional performance, which was inferred to be related to the engagement direction of the clamp. The peak torque of the steel wire clamps ranged from 17 to 20 N·m in right rotation and from 22 to 25 N·m in left rotation; the better left-rotation performance was attributed to differences between the long and short arms of the clamps. The rotational stiffness of the steel plate clamps was approximately 283.34 N·m/rad, which was 5.8 times that of the steel wire clamps (49.06 N·m/rad). Steel plate clamps showed greater performance and lower variability in right rotation, whereas steel wire clamps performed better and more consistently in left rotation.Overall, steel plate clamps exhibited superior torsional resistance, indicating their potential to enhance the torsional performance of pipe connections in simple greenhouse structures. These findings provide useful information for greenhouse structural design and connector selection.

Key Words: Greenhouse structures, Hot-dip galvanized steel pipe, Steel wire clamps, Steel plate clamp, Rotational stiffness.

FM-P03

Proceedings of The 12th International Symposium on Machinery and Mechatronics for Agriculture and Biosystems Engineering (ISMAB 2026)
20-24 October 2026, Busan, Republic of Korea

EFFECTS OF SHORT-TERM NATURAL AGING ON THE MECHANICAL PROPERTIES OF GREENHOUSE PLASTIC FILMS

Cheng-Chang Lien[1], Po-Yu Zeng[1*], Zong-Xian Xie[1], Jun-Han Mei[1]

[1]Department of Biomechatronic Engineering, National Chiayi University, Chiayi, Taiwan
* Corresponding Author--Tel: +886-5-2717972. Email: 1140274@mail.ncyu.edu.tw

Abstract: Plastic films used in agricultural facilities in Taiwan must possess adequate tensile strength and resistance to aging in order to maintain structural functionality and a suitable crop-growing environment. In this study, four commercially available polyolefin (PO) films from different brands, each with a thickness of 0.15 mm, were selected and designated as PO-A, PO-B, PO-C, and PO-D. The effects of natural aging duration on the mechanical properties of greenhouse roof films were investigated. The four films were installed on the roofs of self-constructed small-scale greenhouses and subjected to natural outdoor exposure. Samples were collected after 1, 2, and 3 months of aging for tensile testing and were compared with their initial values to characterize changes in mechanical properties during natural aging. The results showed that the mechanical properties of the films exhibited different degrees of fluctuation and deterioration with increasing natural aging duration. After 3 months of aging, the average tensile strength of PO-D decreased from an initial value of 31.36 MPa to 27.77 MPa, while its maximum elongation decreased from 1064.51% to 1025.82%. The relatively small overall changes indicated superior mechanical stability. Although PO-C exhibited the highest initial tensile strength (31.40 MPa), its tensile strength decreased to 22.19 MPa after 3 months of aging, and its maximum elongation decreased from 1032.53% to 706.53%, indicating more pronounced deterioration in mechanical properties. Overall, prolonged natural exposure to solar radiation, temperature, and other environmental factors progressively altered the mechanical properties of the films. Among the four materials, PO-D exhibited comparatively better mechanical stability during the 3-month natural aging period. These findings provide an empirical basis and reference for evaluating the early-stage changes and long-term aging behavior of greenhouse plastic film materials.

Key Words: agricultural facilities, greenhouse plastic film, natural aging, mechanical properties

INTRODUCTION

Greenhouse plastic films play an important role in modern agricultural facilities by providing light transmission, thermal insulation, and regulation of the internal microclimate, thereby creating relatively stable growing conditions for crops. During actual service, however, plastic films are exposed to outdoor environments for extended periods and are continuously subjected to solar radiation, ultraviolet radiation, high temperatures, moisture, wind, rain, oxidation, and other environmental factors. These conditions may induce polymer-chain scission, cross-linking, or other structural changes, resulting in progressive deterioration of mechanical properties and ultimately affecting durability and service life. Because greenhouse covering films are directly exposed to natural environments and continuously experience solar radiation, temperature fluctuations, wind, and rain, their resistance to aging is a major factor governing the performance of greenhouse covering materials. Previous studies have frequently employed artificial accelerated aging, such as elevated-temperature or ultraviolet exposure, to shorten testing periods and evaluate aging behavior. Nevertheless, actual outdoor environments simultaneously involve solar radiation, temperature, humidity, precipitation, and other factors, whose combined effects may produce degradation behavior different from that observed under a single artificial aging condition. Therefore, this study selected four commonly available commercial PO films, designated PO-A, PO-B, PO-C, and PO-D, and installed them on the roofs of self-constructed small-scale greenhouses for natural outdoor exposure. Tensile tests were conducted after 1, 2, and 3 months of exposure to compare changes in tensile strength and maximum elongation under different natural aging durations. The objective was to evaluate the short-term mechanical stability of different PO films under natural exposure conditions and to provide a reference for selecting greenhouse roof covering materials and for subsequent durability studies.

MATERIALS AND METHODS

Four commercially available polyolefin (PO) films, each with a thickness of 0.15 mm, were selected and designated as PO-A, PO-B, PO-C, and PO-D. All four materials are commonly used as greenhouse covering films in agricultural facilities. The films were installed on the roofs of self-constructed small-scale greenhouses and subjected to natural outdoor exposure for 3 months. Samples were collected after 1, 2, and 3 months of aging to evaluate the effects of solar radiation, temperature and humidity, wind, and precipitation on film mechanical properties. After sampling, tensile tests were conducted in accordance with ASTM D882. Specimens measured 20 mm × 150 mm, the crosshead speed was 500 mm/min, and each treatment included 10 specimens (n = 10). Force-displacement curves were recorded and converted to stress-strain curves. Tensile strength (MPa) and maximum elongation (%) were analyzed and compared with those of the unexposed initial samples. Experimental data are expressed as mean ± standard deviation. Statistical significance was evaluated using one-way analysis of variance (one-way ANOVA) followed by Tukey's multiple-comparison test, with the significance

level set at α = 0.05. Different lowercase letters indicate significant differences among aging durations for the same film, whereas different uppercase letters indicate significant differences among films at the same aging duration.

RESULTS & DISCUSSION

Figure 3 presents the stress-strain curves of the four PO films after 0–3 months of natural aging. The curves show that natural outdoor exposure induced different degrees of change in the stress-strain behavior of the films. As aging duration increased, the maximum stress and strain at break of some films gradually decreased, indicating that exposure to the natural environment affected both film strength and ductility. In addition, the magnitude of change differed among the PO films, suggesting material-dependent resistance to natural aging. The maximum tensile strength and maximum elongation of each film are quantitatively compared in the following sections.

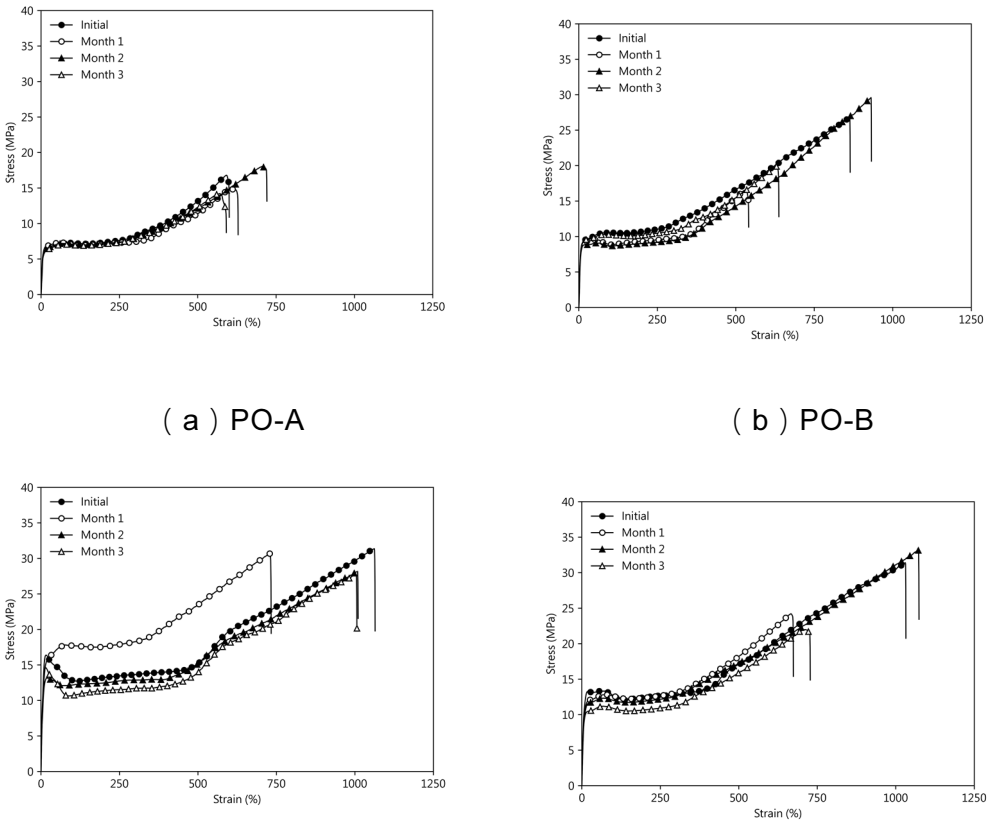

(a) PO-A (b) PO-B

(c) PO-C (d) PO-D

Figure 3. Stress-strain curves of four PO films after 0–3 months of natural aging: (a) PO-A, (b) PO-B, (c) PO-C, and (d) PO-D.

The tensile strength of the four PO films changed to different extents with increasing natural aging duration. The initial tensile strengths were 17.54 MPa for PO-A, 26.80 MPa

for PO-B, 31.40 MPa for PO-C, and 31.36 MPa for PO-D, with PO-C and PO-D exhibiting the highest initial values. As natural exposure progressed, the tensile strength of each film showed varying degrees of fluctuation and decline. After 3 months of aging, PO-D retained a tensile strength of 27.77 MPa, indicating comparatively good strength retention after short-term natural aging. According to the significance analysis in Table 1, the films responded differently to aging duration. For PO-A, some significant differences were observed among aging durations: the initial value did not differ significantly from that after 2 months, whereas the tensile strength after 3 months was significantly lower than the initial value, indicating a certain degree of short-term fluctuation and decline. For PO-B and PO-C, significant differences were observed among all four aging durations. In both films, tensile strength decreased after the first month, recovered during the second month, and declined again during the third month, demonstrating pronounced short-term fluctuations during natural aging. For PO-D, no significant difference was found between the initial value and the value after 1 month, whereas the tensile strengths after 2 and 3 months were significantly lower than the initial and 1-month values. No significant difference was observed between 2 and 3 months, indicating that PO-D maintained relatively stable mechanical strength during the early exposure period, followed by a decline that subsequently tended to stabilize. At each aging duration, the four PO films also exhibited different significance groupings, indicating inherent differences in tensile strength among film types. Overall, both natural aging duration and film type affected the tensile strength of PO films, and substantial differences were observed in the ability of the materials to retain mechanical performance.

Table 1. Tensile strength of four PO films after natural aging

Film type	Tensile strength (MPa)			
	Initial	1 month	2 months	3 months
PO-A	17.54 ± 0.86^{aC}	15.55 ± 0.90^{dD}	16.14 ± 1.86^{adB}	14.08 ± 0.79^{cD}
PO-B	26.80 ± 0.41^{bB}	17.18 ± 1.42^{dC}	30.68 ± 1.12^{aB}	19.87 ± 0.46^{cC}
PO-C	31.40 ± 3.63^{aA}	25.21 ± 1.50^{cB}	33.83 ± 1.03^{bA}	22.19 ± 0.56^{dB}
PO-D	31.36 ± 1.01^{aA}	32.44 ± 1.38^{aA}	27.98 ± 1.61^{bC}	27.77 ± 1.30^{bA}

Note: Values are presented as mean ± standard deviation (n = 10). Different lowercase letters within the same row indicate significant differences among aging durations for the same film; different uppercase letters within the same column indicate significant differences among films at the same aging duration. Statistical analysis was performed using one-way ANOVA followed by Tukey's multiple-comparison test, with significance set at $p < 0.05$.

Maximum elongation reflects the ductility of film materials under tensile loading. The results showed that the maximum elongation of the PO films followed different trends as natural aging duration increased, indicating differences in their sensitivity to environmental exposure. According to the significance analysis in Table 2, the maximum elongation of PO-A did not differ significantly among the initial, 1-month, and 2-month conditions, whereas a significant decrease was observed after 3 months. This indicates that the ductility of PO-A remained relatively stable during the early stage of short-term exposure. For PO-B and PO-C, significant differences were observed among aging

durations. In both films, maximum elongation decreased markedly after the first month, recovered during the second month, and decreased again during the third month, indicating that their ductility was more strongly affected by short-term natural aging. The maximum elongation of PO-D also varied with aging duration, showing a pronounced decrease after 1 month and recovery after 2 months. After 3 months, however, PO-D still maintained a relatively high maximum elongation, indicating comparatively better retention of ductility. In addition, differences in uppercase-letter groupings among films at the same aging duration indicate significant differences in elongation capacity among the PO films. Overall, maximum elongation did not exhibit a simple linear decline with aging duration but instead showed varying degrees of fluctuation, reflecting the differing effects of film type and natural exposure duration on film ductility.

Table 2. Maximum elongation of four PO films at different natural aging durations

Film type	Maximum elongation (%)			
	Initial	1 month	2 months	3 months
PO-A	614.35 ± 13.25^{aD}	628.78 ± 20.28^{aC}	627.15 ± 51.31^{aC}	579.13 ± 18.01^{bD}
PO-B	851.60 ± 33.15^{bC}	554.17 ± 23.26^{dD}	986.51 ± 54.26^{aB}	630.62 ± 8.64^{cC}
PO-C	1032.53 ± 137.99^{bB}	678.77 ± 36.17^{cB}	1099.00 ± 71.15^{aA}	706.53 ± 39.01^{cB}
PO-D	1064.51 ± 55.62^{aA}	715.46 ± 37.37^{cA}	1105.79 ± 66.26^{aA}	1025.82 ± 48.03^{bA}

Note: Values are presented as mean ± standard deviation (n = 10). Different lowercase letters within the same row indicate significant differences among aging durations for the same film; different uppercase letters within the same column indicate significant differences among films at the same aging duration. Statistical analysis was performed using one-way ANOVA followed by Tukey's multiple-comparison test, with significance set at $p < 0.05$.

CONCLUSIONS

Taken together, the tensile strength and maximum elongation results demonstrate that the four PO films underwent different degrees of change in mechanical properties under the same natural exposure conditions, indicating differences in their ability to retain performance during natural aging. With increasing aging duration, the mechanical properties of the films did not follow a simple linear decline but instead exhibited varying degrees of fluctuation and deterioration. For PO-D, the maximum tensile strength decreased from an initial value of 31.36 MPa to 27.77 MPa after 3 months of aging, while maximum elongation decreased from 1064.51% to 1025.82%. These comparatively small overall changes indicate better mechanical stability during the study period. In contrast, although PO-C exhibited relatively high initial tensile strength and maximum elongation, both properties decreased substantially after 3 months of aging, indicating that initial mechanical properties alone do not fully represent the ability of a film to retain performance after natural aging. Therefore, the selection of greenhouse roof covering films should consider not only their initial mechanical properties but also their ability to retain mechanical performance under actual outdoor conditions. Because the natural exposure period in this study was limited to 3 months, the present results primarily reflect

short-term aging trends. Future studies should extend the exposure duration and incorporate environmental factors such as solar radiation, temperature, and humidity to further establish a basis for evaluating the durability of greenhouse films.

REFERENCES

1. Graziano, A., Jaffer, S., & Sain, M. (2019). Review on modification strategies of polyethylene/polypropylene immiscible thermoplastic polymer blends. Journal of Elastomers & Plastics, 51(4), 291–336.
2. Al-Helal, I., Picuno, P., Alsadon, A. A., Ibrahim, A., Shady, M., & Abdel-Ghany, A. M. (2022). Effect of shape, orientation and aging of plastic greenhouse covers on the degradation rate of optical properties in arid climates. Applied Sciences, 12(5), 2709.
3. Mourad, A. H. I. (2010). Thermo-mechanical characteristics of thermally aged polyethylene/polypropylene blends. Materials & Design, 31(2), 918–929.

FM-P04

Proceedings of The 12th International Symposium on Machinery and Mechatronics for Agriculture and Biosystems Engineering (ISMAB 2026)
20-24 October 2026, Busan, Republic of Korea

DEVELOPMENT OF VIRTUAL UPLAND FIELD ENVIRONMENTS WITH SPATIALLY VARYING FRICTION FOR TRACTOR DRIVING SIMULATION

Eun-Chae Roh[1], Kyung-Do Kwon[1], Chang-Ho Yun[1], Chang-Ju Yang[1]*

[1]Division of Agricultural Robot, Department of Agricultural Engineering, National Institute of Agricultural Sciences, Rural Development Administration, 310 Nongsaengmyeong-ro, Deokjin-gu, Jeonju 54875, Republic of Korea
*Corresponding Author-- Voice: +82-63-238-4097, Email: nobel1st@korea.kr

Abstract: Tractor driving simulation under spatially varying field conditions requires virtual environments that represent both terrain geometry and friction at individual wheel contact points. This study developed a virtual upland field in NVIDIA Isaac Sim as a foundation for simulating a tractor equipped with a ridging implement and quantitatively evaluated four-wheel contact conditions. A 100 m × 40 m field contained 32 ridges, each 0.275 m high. Ridge spacing was set to 1.25 m because a 2.50 m -wide implement forms two ridges simultaneously; this spacing defined the minimum transverse spatial unit for distinguishing ground influences on the left and right wheels. A separate 2.15 m × 2.50 m grid was defined using the tractor wheelbase and implement working width. A synthetic friction coefficient field spanning 0.30~0.70 was generated with a longer spatial correlation length along the ridges than across them. To assign one friction coefficient per ground patch, the range was divided into eight equal intervals of width 0.05, with interval midpoints of 0.325~0.675 assigned as material coefficients. Eight levels were selected through a preliminary comparison of 2~32 levels, with 30 repetitions per condition: recovery of the transverse correlation length improved up to eight levels, whereas further refinement changed it by no more than 0.01 m. Friction coefficients were sampled at four wheel contact points along a back-and-forth working path. After discretization, the longitudinal-to-transverse correlation-length ratio decreased from the prescribed value of 6.40 to 5.82 ± 0.32, while directional dependence was retained. At a track width of 1.51 m, the mean left–right friction coefficient difference was 0.1193 ± 0.0075, and the mean range across all four wheels was 0.1512 ± 0.0074. The proportion of the path along which at least one contact point encountered the lowest three material levels increased from 58.3% for two contact points to 64.8% for four. These results demonstrate the importance of considering all four wheel contact points when assessing friction differences and exposure to low-friction regions. The analysis was limited to contact conditions derived from synthetic friction fields; actual heading deviations caused by implement loads and tire-soil interactions were not validated. Coupling the environment with tractor-implement dynamics and calibrating it against field measurements will support future evaluation of heading deviations and steering control for path recovery on heterogeneous ground.

Key Words: open-field environments, virtual maps, driving simulation, ground friction, Isaac Sim

INTRODUCTION

Ground conditions, including soil moisture, affect tractor traction, slip, and tractive efficiency (Kim et al., 2021). Jeon et al. (2023) developed a model for predicting the traction power and driving torque of a tracked upland multipurpose platform and validated it using measured data. Kang et al. (2025) simulated the driving torque and slip ratio of a wheeled agricultural robot platform at different slope angles and travel speeds under a constant friction coefficient.

These studies focused on drivetrain performance and slope-dependent driving characteristics; differences in contact conditions arising from spatially varying friction within a field were not their primary focus. Analyzing driving behavior under spatially varying ground conditions therefore requires virtual representations of both field geometry and ground properties at individual wheel contact locations.

This study aimed to establish a basic virtual environment for driving simulation of a tractor equipped with a ridging implement. Specifically, a virtual upland field incorporating ridge geometry and spatially varying friction coefficients was developed in NVIDIA Isaac Sim, and friction coefficient differences among four wheel contact points along a working path were quantified.

MATERIALS AND METHODS

The virtual field measured 100 m long and 40 m wide and contained 32 ridges spaced 1.25 m apart. Ridge spacing was determined from an operating configuration in which a 2.50 m -wide implement forms two ridges in a single pass. Half the working width, or 1.25 m, was therefore adopted as the minimum transverse spatial unit for distinguishing ground influences on the left and right wheels. Ridge height was set to 0.275 m, based on the 25~30 cm range presented in the Rural Development Administration's drainage management guidance (RDA, 2026). Separately, the field was divided into 2.15 m × 2.50 m grid cells based on the tractor wheelbase and implement working width.

Agricultural soil properties can exhibit spatial anisotropy associated with planting-row orientation and management practices (Oliveira et al., 2022). To represent this spatial characteristic in the virtual ground, a synthetic friction coefficient field was generated under the modeling assumption that the correlation length was longer along the ridges than across them. Friction coefficients ranged from 0.30 to 0.70.

In the ground-patch configuration used in this study, the physics engine assigned one friction coefficient to each patch. The continuous friction field was therefore discretized for assignment to patch-specific surface materials. The range of 0.30~0.70 was divided into eight equal intervals of width 0.05, and the interval midpoints(0.325, 0.375, 0.425, 0.475, 0.525, 0.575, 0.625, and 0.675) were assigned as the friction coefficients of the corresponding material levels. The number of levels was selected through a preliminary comparison covering 2~32 levels, with 30 repetitions per condition. Recovery of the transverse spatial correlation length improved up to eight levels, whereas changes beyond eight levels remained within 0.01 m. Eight levels were thus adopted because further refinement provided negligible improvement (Fig. 1). The arbitrarily generated friction coefficient values in Fig. 1(d) illustrate how values are classified into material-level intervals. These values are classification examples; the physics

engine used the interval midpoint assigned to each level.

A back-and-forth working path with a working width of 2.50 m was then defined. The four wheel contact locations along the path were calculated using the tractor wheelbase and track width. Friction coefficients were sampled at each contact point to compare friction conditions among the wheels.

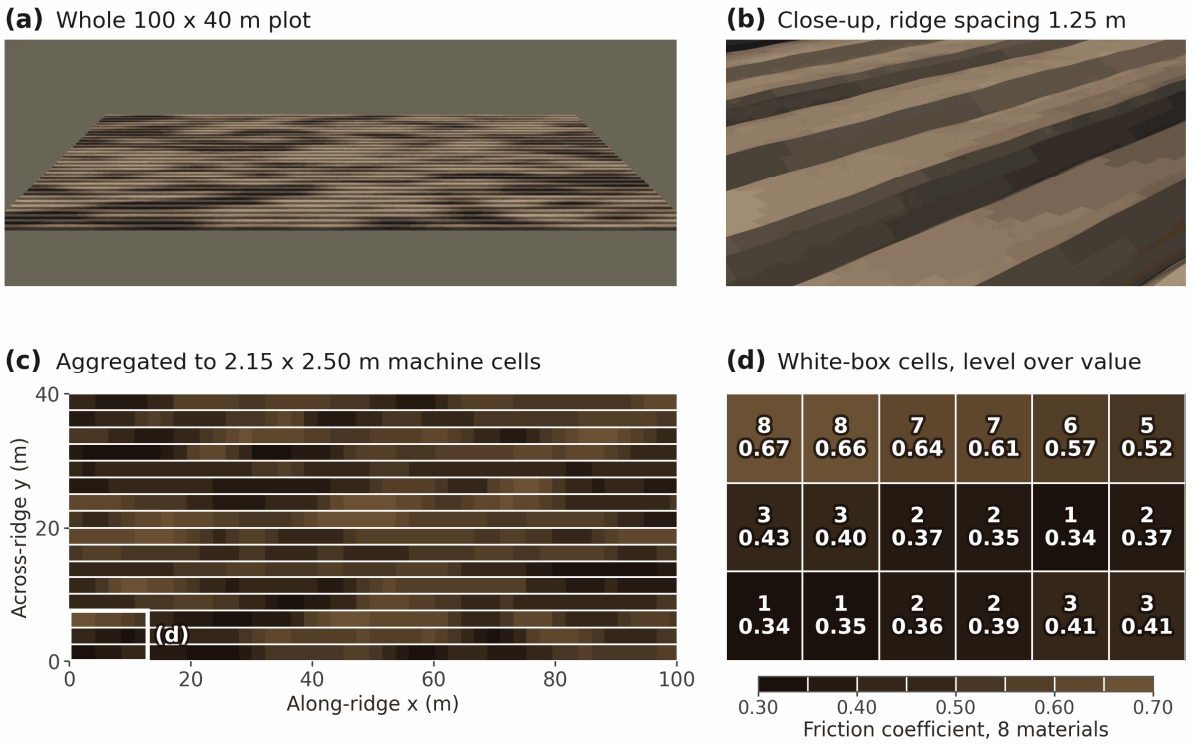

Fig.1 Virtual upland field incorporating ridge geometry and spatially varying friction coefficients.
(a) Overview of the 100 m × 40 m field rendered in NVIDIA Isaac Sim;
(b) enlarged view showing eight color-coded surface material levels and 1.25 m ridge spacing; (c) friction coefficient distribution aggregated over 2.15 m × 2.50 m grid cells; and (d) illustrative mapping between arbitrarily generated friction coefficient values (bottom) and their corresponding material levels (top). The values in (d) illustrate interval classification and are distinct from the interval midpoints applied in the physics engine.

RESULTS & DISCUSSION

Figure 1 shows the geometry and friction coefficient distribution of the virtual field. After discretization into eight surface material levels, the longitudinal-to-transverse spatial correlation-length ratio was 5.82 ± 0.32. Although lower than the prescribed value of 6.40, this ratio indicates that greater spatial continuity along the ridges was retained after discretization. At a track width of 1.51 m, the mean left–right friction coefficient difference along the working path was 0.1193 ± 0.0075 (Fig. 2a). The mean difference between the maximum and minimum friction coefficients across all four wheels was 0.1512 ± 0.0074. The proportion of the path along which at least one contact point encountered a low-friction region, defined as the lowest three material levels, increased from 58.3% when two contact points were considered to 64.8% when all four were considered (Fig. 2b). These results indicate that an assessment based only

on left and right contact points may underestimate both the range of friction coefficients encountered by the four wheels and exposure to low-friction regions.

Tractor and implement loads during rotary tillage have been reported to vary with tillage conditions and gear selection (Kim et al., 2023). Future evaluations of driving behavior during field operations should therefore consider implement loads together with wheel–ground contact conditions.

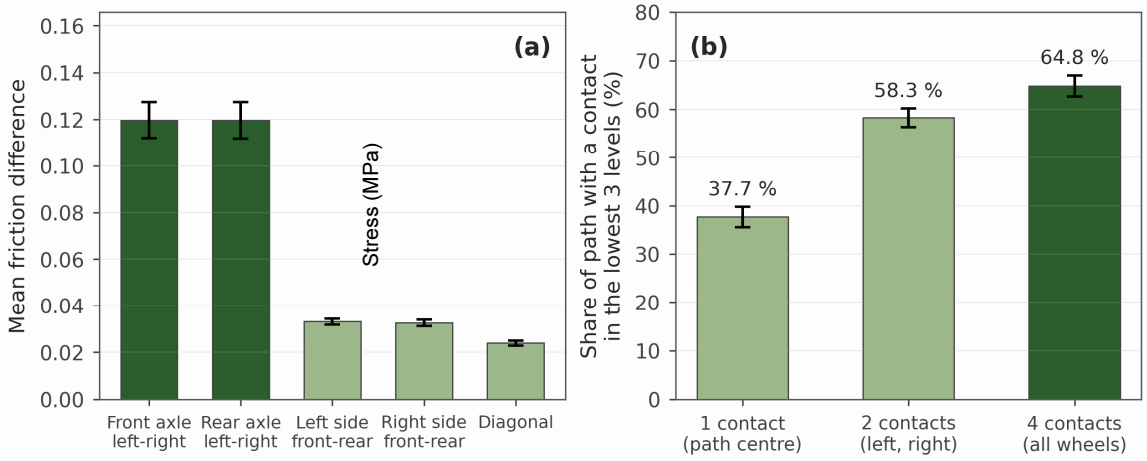

Fig.2 Comparison of friction conditions at wheel contact points for a track width of 1.51 m.
(a) Mean friction coefficient differences among contact points;
(b) proportion of the path along which at least one contact point encounters the lowest three material levels. Error bars indicate standard deviations.

CONCLUSIONS

This study presented a method for constructing a virtual upland field that combines ridge geometry with spatially varying ground friction and quantitatively analyzed conditions in which a tractor's four wheels encounter different friction coefficients. The results demonstrate the need to consider all four wheel contact points when evaluating friction differences and exposure to low-friction regions. However, the analysis used synthetic friction fields and did not validate actual heading deviations caused by implement loads or tire–soil interactions. Future work will couple the virtual field with tractor and implement dynamics models and calibrate it against field measurements to evaluate heading deviations and steering control for path recovery on heterogeneous ground.

ACKNOWLEDGEMENTS

This work was carried out with the support of "Cooperative Research Program for Agriculture Science and Technology Development (Project No. RS-2026-25530203)" Rural Development Administration, Republic of Korea.

REFERENCES

Jeon, H. H., S. M. Baek, S. Y. Baek, Y. S. Hong, T. J. Kim, Y. Choi, Y. K. Kim, S. H. Lee, and Y. J. Kim. 2023. Development and validation of simulation model for traction power and driving torque prediction of upland multipurpose platform (in Korean, with English abstract). J. Drive and Control 20(1): 16-26. https://doi.org/10.7839/ksfc.2023.20.1.016

Kang, H. J., M. J. Park, C. W. Yang, M. J. Park, J. D. Park, H. H. Jeon, M. H. Lee, S. M. Baek, S. Y. Baek, J. Y. Choi, and Y. J. Kim. 2025. Development of a simulation model for evaluating the driving performance of a multipurpose agricultural field robot platform (in Korean, with English abstract). J. Drive and Control 22(4): 171-179. https://doi.org/10.7839/ksfc.2025.22.4.171

Kim, W. S., Y. J. Kim, S. U. Park, and Y. S. Kim. 2021. Influence of soil moisture content on the traction performance of a 78-kW agricultural tractor during plow tillage. Soil Tillage Res. 207: 104851. https://doi.org/10.1016/j.still.2020.104851

Kim, Y. S., B. M. Bae, W. S. Kim, Y. J. Kim, S. D. Lee, and T. J. Kim. 2023. Working load analysis of a 42 kW class agricultural tractor according to tillage type and gear selection during rotary tillage operation. Agriculture 13(8): 1556. https://doi.org/10.3390/agriculture13081556

Oliveira, A. L. G., J. P. de Lima, T. L. Brasco, and L. R. do Amaral. 2022. The importance of modeling the effects of trend and anisotropy on soil fertility maps. Comput. Electron. Agric. 196: 106877. https://doi.org/10.1016/j.compag.2022.106877

RDA. 2026. Drainage management techniques for upland crops grown in paddy fields (video, in Korean; title translated). Rural Development Administration. Available at: https://www.nongsaro.go.kr/portal/ps/psb/psby/vodPlay.ps?mvpNo=3774&menuId=PS65512. Accessed 15 September 2026.

FM-P05

Proceedings of The 12th International Symposium on Machinery and Mechatronics for Agriculture and Biosystems Engineering (ISMAB 2026)
20-24 October 2026, Busan, Republic of Korea

A SURVEY-BASED ANALYSIS ON HEAT-ILLNESS PREVENTION COMPLIANCE AMONG FLORICULTURE FARMERS

Joon-Hyung Park[2], Moon-Kyeong Jang[1,2], Chan-Young Lee[1,2], Ju-Seok Nam[1,2*]

[1]Interdisciplinary Program in Smart Agriculture, Kangwon National University, Chuncheon 24341, Republic of Korea
[2]Department of Biosystems Engineering, Kangwon National University, Chuncheon 24341, Republic of Korea
*Corresponding Author-- Voice: +82-33-250-6497, Email: njsg1218@kangwon.ac.kr

Abstract: Rising heatwave frequency and intensity in the Republic of Korea have sharply increased heat-illness cases at agricultural worksites. Prior studies on heat-illness prevention among farmers mostly focused on a single crop type, overlooking combined facility/open-field work, and rarely examined actual field compliance with work-stage-specific guidelines. This study used the Rural Development Administration (RDA) checklist (14 items) to assess heat-illness prevention compliance among floriculture farmers in Gimpo-si, comparing rates by work stage, sex, and cultivation type. Overall compliance was 84.7%. In-work monitoring showed the lowest compliance (76.7%), reflecting a tendency to prioritize efficiency. Female farmers showed lower compliance than males in protective equipment use (–19.8 percentage points) and in-work rest (–12.1 percentage points), indicating a need for female-tailored equipment, education, and relief from the dual burden of farm and household labor. Facility-only farms outperformed combined-cultivation farms in symptom checks and rest adjustment (by 40 and 20 percentage points), likely due to larger work areas and more frequent movement. Conversely, combined-cultivation farms showed 20 percentage points higher compliance in equipment use and water intake, reflecting direct exposure to heat risk in open-field work. These results suggest compliance is shaped by a complex interplay of cultivation type, sex, work practices, and labor burden, offering baseline data for future prevention education and support measures.

Key Words: Compliance rate, Facility cultivation environment, Floricultural farmers, Heat-related illness, Preventive guidelines

ACKNOWLEDGEMENTS

This work was supported by the Korea Institute of Planning and Evaluation for Technology in Food, Agriculture and Forestry (IPET), funded by the Ministry of Agriculture, Food and Rural Affairs (MAFRA), through the Field Farming Mechanization Promotion Technology Development Program (RS-2023-00235957).

FM-P06

Proceedings of The 12th International Symposium on Machinery and Mechatronics for Agriculture and Biosystems Engineering (ISMAB 2026)
20-24 October 2026, Busan, Republic of Korea

DEVELOPMENT AND PERFORMANCE EVALUATION OF AN ELECTRIC AGRICULTURAL TRANSPORTER

Cheng-Chang Lien*, Min-Jie Li, Zong-Xian Xie, Jun-Han Mei

Department of Biomechatronic Engineering, National Chiayi University, Chiayi, Taiwan
*Corresponding Author– Voice: +886-5-271-7972, Email: lanjc@ncyu.edu.tw

Abstract: The intensifying impacts of climate change driven by global warming have placed growing pressure on agricultural production. As sustainable development, carbon emission reduction, and the promotion of smart agriculture continue to gain importance, agricultural transport equipment traditionally powered by internal combustion engines is increasingly facing pressure to transition toward low-carbon alternatives. This study converted an existing diesel-powered agricultural transport vehicle into an electric vehicle and evaluated its performance. Testing was conducted in accordance with the current Performance Testing Methods and Provisional Standards for Agricultural Transport Vehicles (TS11), covering vehicle specifications, speed, driving range, gradeability, and current measurement. The vehicle retained the chassis of the original diesel vehicle, while the powertrain was replaced with a 6 kW electric motor powered by two 36 V lithium iron phosphate ($LiFePO_4$) batteries connected in series, with a total capacity of 120 Ah. Test results showed that, in low gear, the vehicle's maximum speed under no-load and full-load (500 kg) conditions was 19.9 km/h and 16.5 km/h, respectively, both meeting the required standard (≤ 20 km/h); the minimum turning radius was 5.26 m. Gradeability testing showed that the vehicle could climb a slope with a geometric angle of 15° under a full load of 300 kg, could remain parked on the slope without sliding back, and could resume climbing after the power was switched off and restarted. Continuous-operation testing showed a driving range of 41.94 km (approximately 3.29 h of operation) under no load and 26.65 km (approximately 2.06 h of operation) under full load. Based on Taiwan's electricity carbon-emission coefficient, and for the same driving distance, the electric vehicle was estimated to reduce CO_2 emissions by approximately 55.1% compared with a conventional diesel transport vehicle. The electric agricultural transport vehicle developed in this study met all current performance standards, demonstrating its feasibility for promotion and mass production, and can serve as a reference for domestic farmers selecting electrified agricultural transport equipment.

Key Words: Agricultural machinery electrification, Electric transport vehicle, Performance testing

INTRODUCTION

In recent years, global climate change and rising environmental awareness have driven international efforts to promote carbon neutrality and net-zero emission policies (IEA, 2023). As a result, agricultural transport equipment traditionally powered by diesel engines has faced increasing pressure to transition toward low-carbon alternatives. To achieve the goal of decarbonizing agricultural machinery, this study converted an existing diesel-powered agricultural transport vehicle into an electric vehicle. Performance testing was conducted in accordance with the Performance Testing Methods and Provisional Standards for Agricultural Transport Vehicles (TS11) issued by the Taiwan Agricultural Research Institute (TARI, 2025), Ministry of Agriculture, evaluating speed, driving range, gradeability and slope-holding ability, and operating electrical parameters, while also assessing the carbon reduction benefit of the vehicle.

The objective of this study was to develop and evaluate an electric agricultural transport vehicle converted from a diesel-powered platform, to verify its compliance with the TS11 performance standard through a series of field tests, and to quantify the carbon reduction benefit achieved relative to a conventional diesel-powered transport vehicle over an equivalent driving distance.

MATERIALS AND METHODS

The electric agricultural transport vehicle was developed in collaboration with Shun Nong Industrial Co., Ltd. The vehicle has a total weight of 1,080 kg and body dimensions of 341 cm (length) × 141 cm (width) × 142 cm (height), and retains the chassis and frame design of the original diesel vehicle. The diesel engine was replaced with a brushless DC (BLDC) motor (rated power 6 kW, rated speed 3,600 rpm) manufactured by Shuoyang Motor Co., Ltd., powered by two 36 V–120 Ah lithium iron phosphate ($LiFePO_4$) batteries connected in series to supply DC 72 V, together with an AC 220 V/6 A charger requiring 6–8 hours for a full charge. Power is transmitted through a belt drive to the clutch, and then through the transmission and drive shaft to the front and rear differentials to drive the wheels, as shown in Fig. 1. Performance tests were conducted under both no-load and loaded conditions in accordance with the TS11 standard: level-ground tests used a standard 500 kg tractor ballast weight, while slope tests used 302.4 kg of bottled-water ballast for the gradeability and slope-parking tests, as shown in Fig. 2.

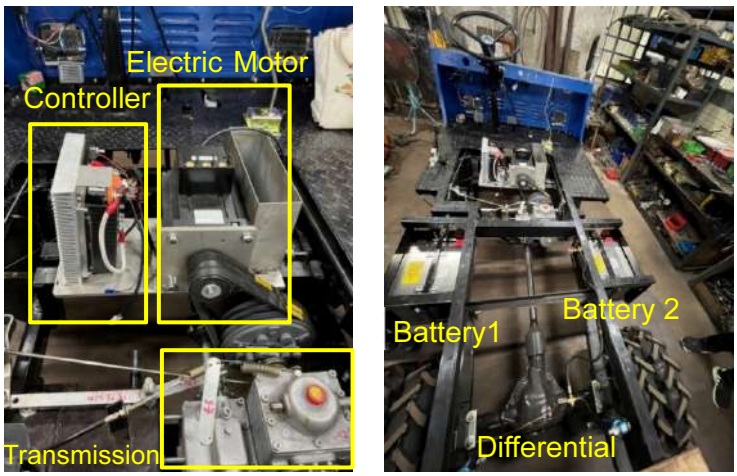

Fig. 1 Electric motor power unit and drivetrain of the electric agricultural transport vehicle



Fig. 2 Ballast weights used for the loaded performance tests of the electric agricultural transport vehicle

RESULTS & DISCUSSION

Minimum Turning Radius

The minimum turning radius of the vehicle was measured using a water-drip trace method. The steering wheel was turned to its full-lock position, and water was dripped from behind the outer front tire during two full revolutions to trace the turning path; three trials were conducted for each of the left and right turns. The minimum turning radius was calculated as half of the maximum diameter of the water-drip trace, as measured with a tape measure, as shown in Fig. 3. The average minimum turning radii of the electric agricultural transport vehicle were 5.26 m for left turns and 5.30 m for right turns.



Fig. 3 Water-drip trace method used to measure the turning path and minimum turning radius of the electric agricultural transport vehicle

Maximum Speed Test

Under both no-load and 500 kg loaded conditions, the vehicle was driven at full throttle in each gear to determine its maximum speed. A stopwatch was used to time the vehicle over a 10 m section of road, and the speed for each gear was calculated from the recorded time, as shown in Table 1. The results show that in low gear 3, the maximum speeds under no-load and 500 kg loaded conditions were 19.94 km/h and 16.50 km/h, respectively; in reverse gear (R), the difference in maximum speed between the two conditions was small, at 5.92 km/h and 5.72 km/h, respectively.

Table 1 Comparison of maximum speed by gear in low range (L) for the electric agricultural transport vehicle

State	Gear 1 (km/h)	Gear 2 (km/h)	Gear 3 (km/h)	Gear R (km/h)
No load	5.98±0.06*	12.22±0.08	19.94±0.20	5.92±0.10
Loaded	5.15±0.05	12.07±0.07	16.50±0.21	5.72±0.07

* Mean ± standard deviation, n = 3 trials.

Continuous-Operation Test and Carbon Reduction Evaluation

A GPS data logger was used to record the battery driving range of the vehicle during continuous operation in low gear 3; the results are shown in Table 2. Under no-load conditions, the driving time was approximately 3 h 17 min 26 s, with a total driving distance of 41.94 km; under a 500 kg load, the driving time was approximately 2 h 3 min 37 s, with a total driving distance of 26.65 km. Regarding carbon reduction benefits, Lin *et al.* (2023) estimated the diesel consumption of an agricultural transport vehicle at approximately 0.06 L/km; using the diesel carbon-footprint coefficient of 3.562 kgCO_2e/L announced by Taiwan's Ministry of Environment, the diesel vehicle would emit approximately 8.98 kg CO_2 over the same driving distance. The battery pack of the electric vehicle (72 V–120 Ah) has a total energy capacity of approximately 8.64 kWh; using Taiwan's 2025 electricity carbon-emission coefficient of 0.467 kgCO_2e/kWh, the electric vehicle emits approximately 4.03 kg CO_2 for the same distance – a reduction of approximately 4.95 kg CO_2 compared with the diesel vehicle, corresponding to a carbon reduction benefit of approximately 55.1%. These results indicate that electrification provides a substantial contribution to the low-carbon transition of agricultural transport equipment.

Table 2 Battery driving range of the electric agricultural transport vehicle during continuous operation

State	Driving Time (h:m:s)	Distance Traveled (km)	Average Speed (km/h)
No load	3:17:26	41.94	12.7
Loaded (500 kg)	2:03:37	26.65	13.3

Slope Climbing and Parking Test

Under a 300 kg load, the vehicle was braked while traveling both uphill and downhill; the parking brake was then engaged and the power switched off for ten minutes to observe whether the vehicle would remain stationary on the slope. The parking-brake test was conducted on a slope with an inclination of 16° (the standard requires at least 15°), and the results met the test standard, as shown in Fig. 4. The vehicle was able to complete the climb under a 300 kg load in all trials; after braking on the slope and switching off the power for ten minutes, no backward sliding was observed, and the vehicle was able to resume climbing smoothly after the power was restored, meeting the requirements of the TS11 standard.



Fig. 4 Field test setup for the slope braking and parking test of the electric agricultural transport vehicle

Electrical Parameter Measurement During Operation

Under no-load conditions, in low gears 1 through 3, current versus time was recorded under four throttle operating modes (full, mid, mid-low, and low throttle); the results are shown in Fig. 5 through Fig. 7. In every gear, a distinct current peak occurred during the initial acceleration phase under full throttle, and this peak increased with gear number, as shown in Table 3, indicating that the drive motor demands a higher instantaneous torque output when the accelerator is fully depressed.

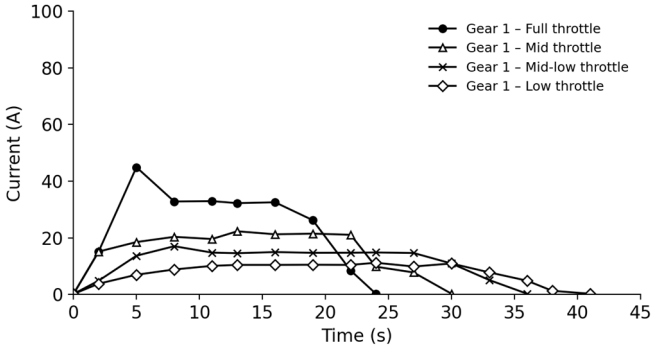

Fig. 5 Current variation over time while operating in low gear 1

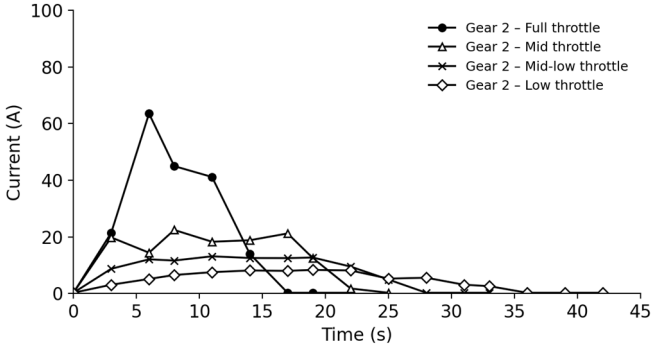

Fig. 6 Current variation over time while operating in low gear 2

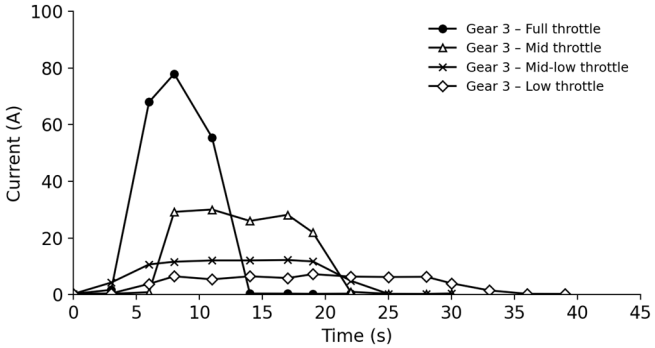

Fig. 7 Current variation over time while operating in low gear 3

Table 3 Comparison of current and voltage across gears and throttle modes under no-load conditions

State	Peak Current (A)	Voltage (V)	Vehicle Speed (km/h)	Average Current (A)
Gear 1, full throttle	44.93	79.13±0.38 ^{c**}	6.29	32.6
Gear 1, mid throttle	—*	79.16±0.19 ^{bc}	4.43	21.7
Gear 1, mid-low throttle	—	79.24±0.15 ^{b}	3.17	14.8
Gear 1, low throttle	—	79.50±0.13 ^{a}	2.40	10.7
Gear 2, full throttle	63.53	79.11±0.52 ^{c}	12.21	43.1
Gear 2, mid throttle	—*	79.32±0.22 ^{b}	6.47	19.5
Gear 2, mid-low throttle	—	79.40±0.13 ^{b}	4.19	12.6
Gear 2, low throttle	—	79.54±0.13 ^{a}	2.82	8.19
Gear 3, full throttle	77.93	78.93±0.72 ^{c}	18.15	55.5
Gear 3, mid throttle	—*	79.24±0.30 ^{b}	9.98	28.1
Gear 3, mid-low throttle	—	79.39±0.14 ^{ab}	4.87	12.2
Gear 3, low throttle	—	79.52±0.09 ^{a}	2.38	6.5

* No distinct current peak observed.

** Mean ± standard error; different lowercase superscript letters within the same gear indicate a significant difference in voltage among throttle modes ($P < 0.05$), Fisher's LSD test.

CONCLUSIONS

The electric agricultural transport vehicle developed in this study met the TS11 standard across all performance tests, including speed, driving range, gradeability, and slope parking. In low gear 3, the vehicle's speed under no-load and 500 kg loaded conditions was 19.94 km/h and 16.50 km/h, respectively, and its driving range was 41.94 km and 26.65 km, respectively, with a carbon reduction benefit of approximately 55.1%. Overall, the vehicle combines reliable performance with environmental sustainability benefits and demonstrates strong potential for promotion and mass production, providing a reference for domestic farmers selecting electrified agricultural transport equipment.

REFERENCES

IEA. 2023. CO2 Emissions in 2022. Available at https://iea.blob.core.windows.net/assets/3c8fa115-35c4-4474-b237-1b00424c8844/CO2Emissionsin2022.pdf

Lin, C.-C., H.-W. Chiu, and F.-P. Shih. 2023. A preliminary study on the carbon-reduction capability of electric agricultural machinery: The case of an agricultural transport vehicle. Technical Service 34(4): 23-27.

TARI. 2025. Performance testing of agricultural machinery (Agricultural transport vehicles). Department of Agricultural Engineering, Taiwan Agricultural Research Institute, Ministry of Agriculture. Accessed 12 August 2025. Available at https://www.tari.gov.tw/sub/content/index.asp?Parser=1,30,416,386,404

FM-P07

Proceedings of The 12th International Symposium on Machinery and Mechatronics for Agriculture and Biosystems Engineering (ISMAB 2026)
20-24 October 2026, Busan, Republic of Korea

DEVELOPMENT OF A SMART SPRINKLER WITH VARIABLE WATER FLOW DEPENDING ON THE WATER SUPPLY LOCATION(1) (WATER VOLUME CONTROL USING AN ELECTRONIC VALVE)

Jin Hyun Kim[1] · Seol Ha Kim[2] · Jeong Hun Kim[3] · Won Hyeong Lee[3] · Seok Hyun Seo[4] · Dong Seok Kim[5] · Sang Hun Lee[5]*

[1]Department of Precision Mechanical Engineering, Kyungpook National University, Sangju, 37224, Republic of Korea
[2]Department of Precision Mechanical Engineering, Kyungpook National University, Sangju, 37224, Republic of Korea
[3]Department of Precision Mechanical Engineering, Kyungpook National University, Sangju, 37224, Republic of Korea
[4]Sinsung Engineering, Dongmyeong-myeon, Chilgok-gun, Gyeongsangbuk-do, 39858, Republic of Korea
[5]Department of Upland Crop Science, National Institute of Crop Science, RDA, Miryang, 50424, Republic of Korea
[5*]Department of Upland Crop Science, National Institute of Crop Science, RDA, Miryang, 50424, Republic of Korea
*Corresponding author: Sang Hun Lee (Tel) +82-55-350-1256 (E-mail) sangusa@korea.kr

Abstract

Sprinklers, with a small number of nozzles, rotate 360° in the air while supplying water, thereby reducing installation costs relatively. On the other hand, the area where water use overlaps increases, resulting in at least 9.1% water loss. This study aimed to develop a smart sprinkler capable of supplying water in a square shape, instead of the previously circular sprinkler. To supply in a square shape, the water volume and spray distance must vary according to the rotational position of the sprinkler. Therefore, this study identified the injection characteristics of sprinklers according to rotational position recognition, rotational speed, the time required for right- and left-turns, and pipe length

Ket Words: Smart sprinkler, Sprinkler, Rotation angle, Spray distance

INTRODUCTION

A sprinkler is an irrigation device that can achieve maximum effect in the control of field crops by using minimal piping. Generally, drip irrigation is applied through drip devices (drip irrigation) or microtubes depending on the crop layout, so the cost of drip irrigation and the resulting waste increase significantly. In contrast, sprinklers rotate 360° with a small sprinkler head and supply water from the air, so the installation cost of irrigation is relatively low, whereas they have the drawback of spraying water in a circular pattern. At this time, the overlapping water is wasted with an excess of water of at least 9.1%. Therefore, in this study, in order to develop a smart sprinkler that can save water, we aim to 1) convert the 360° rotation method into a 180° rotation method, and 2) develop it so that it sprays from outside the field into the interior. This method must be followed by adjusting the water supply pressure according to the sprinkler's rotational position. In other words, it was carried out to develop a new sprinkler capable of controlling the water flow distance and volume according to the shape of the field.

MATERIAL AND METHODS

1. Recognition of the sprinkler's rotation angle

<Fig. 1> shows a scene where an encoder is attached to the sprinkler to recognize its rotational position, measuring it together with the water spray distance. The sprinkler's rotation position was installed on the upper shaft, where the sprinkler's central axis and body are connected together. The sprinkler was designed to rotate freely between the lower and upper parts. <Fig. 2> is the piping diagram of the sprinkle device, and <Table 1> indicates the specifications of the pump and motor.



(A) (B)

Fig. 1 Sprinkler equipped with an encoder for rotation detection(A) and experiment scene(B)



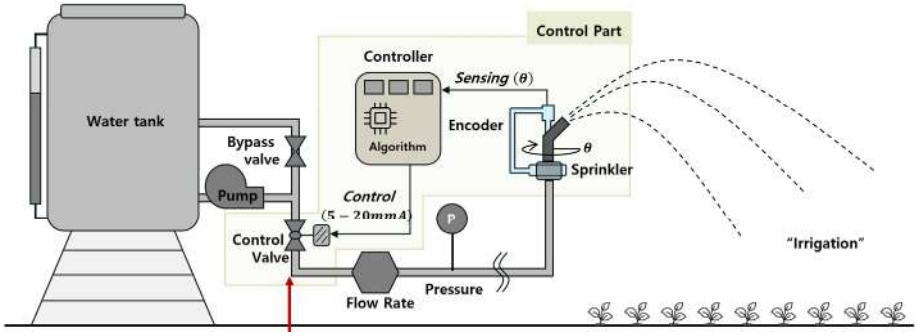

(A) (B)

Fig. 2 Rotational position recognition(A) and flow control device(B)

Table 1. Pump and motor specifications of water supply system

Classifica--tion	Inlet and outlet diameters	Rated voltage, three phases	Rated current	Outlet amount	Compression height	Motor output
Pump	32 mm	220/380V	9.2/5.4A	200 L/min	52 m	2.2 kW
Classifica -tion	Motor output	Rated voltage	Rated current	Efficiency	rpm	allowable Temp.
Motor	2.2 kW	220/380V	8/5.0A	85.5%	3,500	-15~40℃

2. A water spray distance control device through electronic valve control

To control the water spray distance using electronic valve control, an electronic valve was installed in the piping as shown in <Fig. 3>. The electronic valve (KE02, VLLMAN, China) is a butterfly valve (electrically actuated) that can be used in water, air, gas, oil, and chemical fluids, and its specifications are as shown in <Table 2>

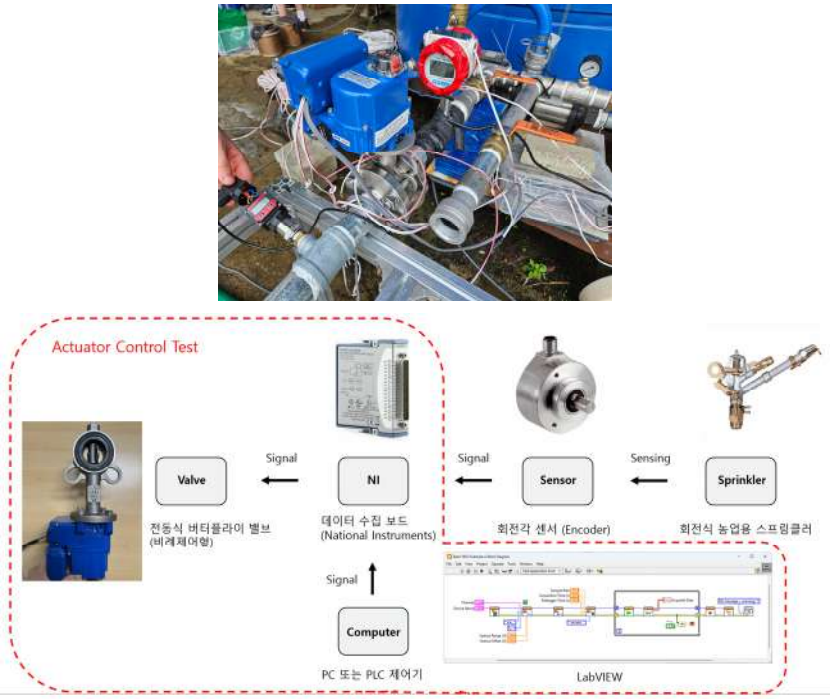

(A) (B)

Fig. 3 Electronic Valve(A) and Rotation Position Recognition System(B)

Table 2. Specifications of the electronic valve

Classification	Characteristcs
Valve size	40A(1 1/2“)~300A(12”)
Actuator model	KE Series
Operating media	AC 24V, 110V, 220V, 380V, 440V
Ambient Temp.	-20~60℃
Rotating angle	90℃±5°
Body Rating	10 kg/㎠
Actuator option	Color selest/proportional control (4~20mA)

RESULTS AND DISCUSSION

1. The water spray forms of conventional sprinklers and smart sprinklers

In this study, we aimed to improve the conventional use of sprinklers by introducing a new watering method. Conventional sprinklers, which operate by rotating 360°, have a major drawback: a large amount of overlapping water (9.1%) occurs, resulting in significant water waste <Fig. 4, A>. Therefore, it was proposed to develop a method, as shown in <Fig. 4, B>, to control the amount of water by adjusting the sprinkler’s rotation angle. In other words, since the field area is rectangular, the water supply should also be provided in a rectangular shape, and for this purpose, the amount of water and the water distance should

increase or decrease depending on the rotational position of the sprinkler. When supplying water using this method, labor can be greatly reduced if the sprinkler is not installed on the field each time, but rather the piping is fixed to the outer edge of the field.

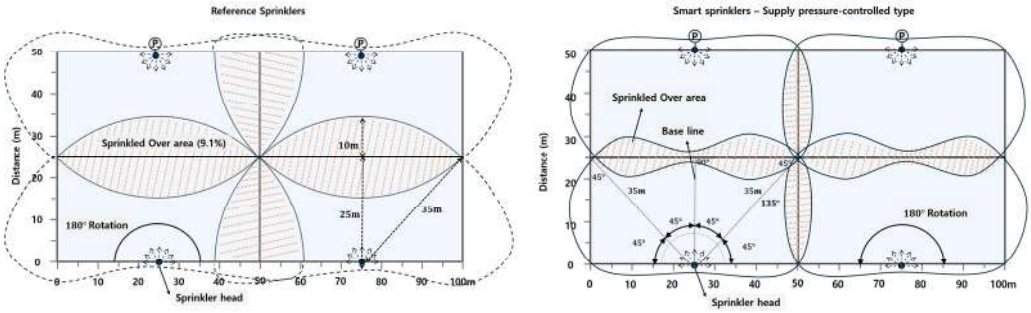

(A) (B)

Fig. 4 The spray forms of conventional sprinkler(A) and smart sprinkler(B)

2. Design of a sprinkler for increasing spray distance

It was developed mainly for large-scale use in sprinklers currently marketed in our country. In addition, the problems arising were improved by comparing the design of excellent overseas products. It is most advantageous for sprinklers to spray water both far and evenly. To supply water over long distances, there should be as few parts inside the sprinkler as possible that cause pressure disturbances, and the obstruction to the flow of water should be reduced. Also, the higher the injection pressure, the more naturally advantageous it is. Therefore, by analyzing the problems of the existing sprinkler, a new design was developed as shown in <Table 3>. As a result of designing it in a way that enlarges the internal dimensions of the sprinkler to improve the flow of the fluid, the discharge distance increased by 5－6 m.

Table 3. Expansion of the sprinkler's inner diameter(19 mm → 25 mm)

Current product	Design dimension(inner diameter 19 mm)	
	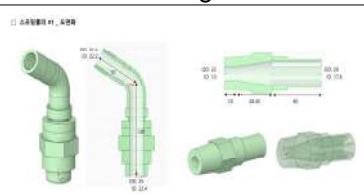	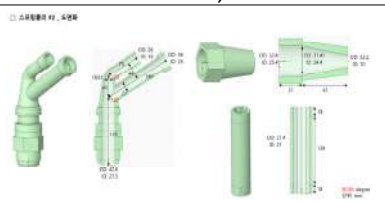
Developed product	Design dimension(inner diameter 25 mm)	
	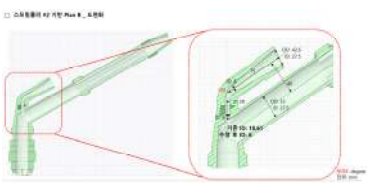	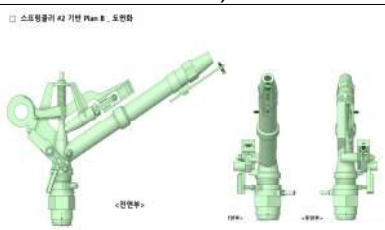

3. Water delivery time to pipe length

Because sprinklers are designed to spray from the outside into the interior of the field, in agricultural practice the distance between where the sprinkler is located and the water reservoir can be as great as 25 meters. Therefore, data on the length of the piping and data on the time difference according to the forward and reverse rotation of the sprinkler are also required. <Fig. 5>, forward rotation means rotating clockwise, and reverse rotation means rotating counterclockwise. First, the left and right turn angles were based on 46°, and the supply pressures were applied at 2, 3, and 4 bar. In right turn, it took 22－27 seconds, whereas in the left turn it took 5－8 seconds. In other words, right turn takes about four times longer than left turn, providing a temporal margin to control spray pressure. And in terms of the effect on the length of the piping, the longer the length, the more 2－3 seconds were required for the rotation time. This is the data required to account for 2－3 seconds when controlling the pump's discharge pressure by considering the length of the piping. The sprinkler rotates when the water from the upper nozzle of the two nozzles hits the impact plate, imparting rotational force. And it also simultaneously serves to supply water at a short distance. Conversely, in reverse rotation, the sprinkler itself physically rotates due to its own rotational spring, so the time is greatly shortened, making it unsuitable for control.

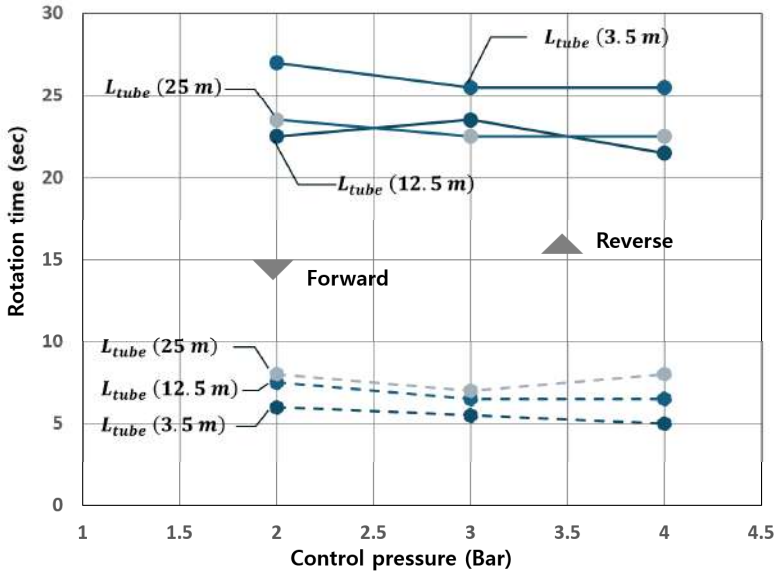

Fig. 5 Required time according to the rotation direction by spray pipe length

4. Changes in pressure according to the opening and closing of the electronic valve

The development of the smart sprinkler aimed to change the spray distance according to the rotation angle, so it sought to alter the pressure and flow rate by opening the electronic valve. However, when the supply pressure was varied

to 2, 3, and 4 bar, the pressure changes according to the opening ratio of the electronic valve were almost nonexistent, as shown in <Fig. 6>. When opening or closing the electronic valve more than 50%, only a slight drop in pressure occurred. The reason the electronic valve could not induce changes in flow or pressure was that, when the pressure supplied by the pump was high, no other cause could be found except for the slight flow disturbance it caused. Therefore, it was fundamentally impossible to control the flow and pressure by opening and closing an electronic valve and thereby change the injection distance.

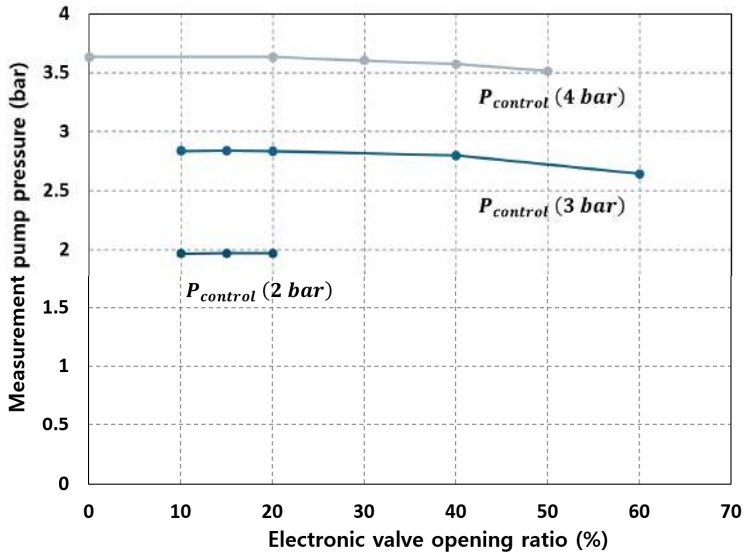

Fig. 6 Pressure change due to opening of an electronic valve

5. Pressure changes between the pump and the sprinkler according to the length of piping

In actual agricultural fields, the location of the water source and pump changes from the location of the sprinkler. Also, if the length of the piping is long, the loss in supply pressure will follow. To develop a smart sprinkler, the pressure loss caused by piping distance must be compensated. <Fig. 7> indicates the change in pressure with respect to the length of the piping. Overall, when the supply pressure was not large, the pressure loss also increased. When the pipe length was 3.5 m, the pressure decreased by 0.15 bar at 2 bar, but decreased by 0.25 bar at 3.7 bar. There was no significant difference when the pipe length was 12.5 m and 25 m. The pressure reduction ratio was less than 10% at 3.5 m, and pressure differences of 10－17% occurred at 12.5 m and 25.0 m. Therefore, considering cases where the piping length is long and where the supply pressure changes, it is necessary for the control program to compensate for the decreasing pressure. <Fig. 8> shows the change in flow rate with respect to the length of the piping. In the figure, the flow rate increases at an almost

constant rate according to the supply pressure, but there was little change with respect to the length of the piping.

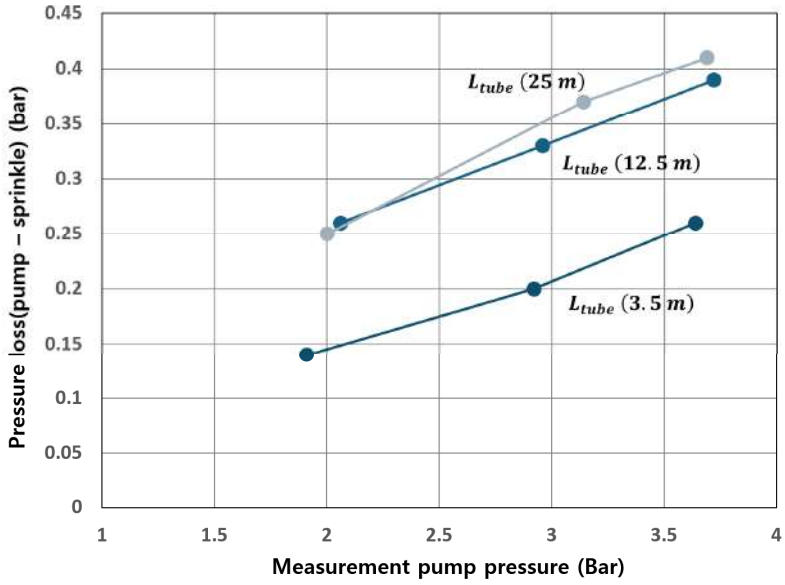

Fig. 7 Pressure loss according to spray pipe length

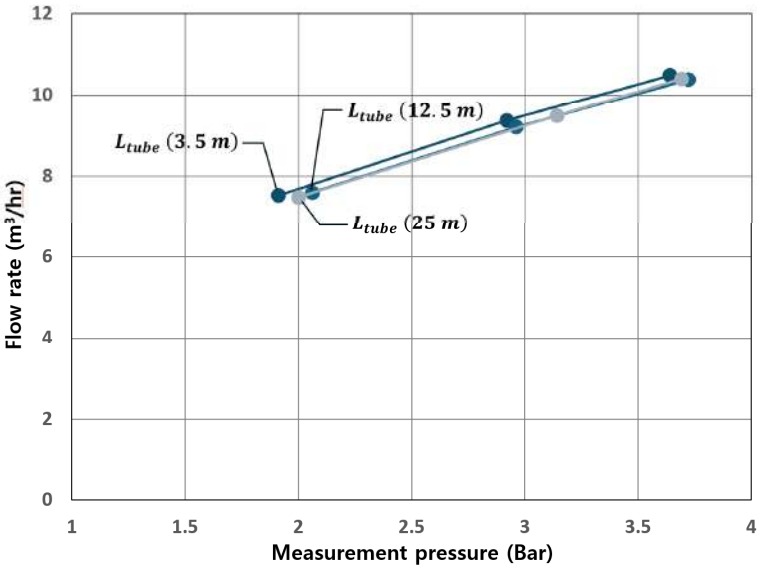

Fig. 8 Change in flow rate according to spray pipe length

CONCLUSION

Sprinklers, with a small number of nozzles, rotate 360° in the air while supplying water, thereby reducing installation costs relatively. On the other hand, the area where water use overlaps increases, resulting in at least 9.1% water loss. This study aimed to develop a smart sprinkler capable of supplying water in

a square shape, instead of the previously circular sprinkler. To supply in a square shape, the water volume and spray distance must vary according to the rotational position of the sprinkler. Therefore, this study identified the injection characteristics of sprinklers according to rotational position recognition, rotational speed, the time required for right- and left-turns, and pipe length, and the main results are as follows.

1) To increase the spray distance, the internal diameter of the sprinkler was enlarged from 19 mm to 25 mm, resulting in an increase of about 5－6 m in the spray distance.

2) The time for water to reach the pipeline length was somewhat affected by the length.

3) In the case of varying pipe lengths of 3.5 m, 12.5 m, and 25 m, the longer the length, the more the sprinkler's rotation time increased by 2 to 3 seconds

4) Under a turning condition of 46°, the left and right turns were completed within 22－27 seconds for right turns and within 5－8 seconds for left turns, allowing the supply pressure and flow rate to be controlled only during right turns.

5) Since there was no pressure change due to opening or closing the electronic valve, it was determined that it could not be applied to controlling the sprinkler's spray distance.

6) In terms of pressure changes between the pump and the sprinkler according to pipe length, a difference of 0－17% was observed with length.

ACKNOWLEDGEMENTS

This study was conducted with support from the Rural Development Administration's agenda projector project, "Development of Technologies for Reducing Damage from Agricultural Weather-Related Disasters (Research and Development Project No. RS-2025-02303472)"

REFERENCES

Han KH, Jang YS, Cho HR, Choi JY, Jeong SO and Kim HJ. 2013. A Study on the Development of Irrigation System in Facilities Plantation Plantation using IT. Research Report. National Academy of Agricultural Sciences. Rural Development Administration.

FAO. 1992. Small-scale pumped irrigation: energy and cost-FAO. Food and agricultural organization of the united nations. Rome. Italy.

Kim JH, Kim YJ, Kim SH, Choi RJ, Eum DH and Kim TW. 2024. Development of Spray Collision Dripper with Combined Function of Drip Irrigation and Spray Hose. Journal of Agriculture & Life Science 59(1) pp.99-114.

National Data Agency(NDA). 2025. https://mods.go.kr/unifSearch/search.es. (2025.12.19).

Yanmar. 2025. http;//www.yanmar.com/media/news/2021/02/28053741/irrigation_agri_202510.pdf. (2026. 4. 20).

Yousui HG. 2024. Design Criteria for Land Improvement Project Planning (Agricultural Water of Field Crops). Japanese Ministry of Agriculture, Forestry and Fisheries. 19-24.

Filipe Gama J.V. and Hong SG. 2020. Assessment of Irrigation Efficiency and Water Distribution by the Different Pressures and Nozzles Angle of the Sprinkler Irrigation System. Proceeding of the KSAE 2020 autumn conference. 63.

FM-P08

Proceedings of The 12th International Symposium on Machinery and Mechatronics for Agriculture and Biosystems Engineering (ISMAB 2026)
20-24 October 2026, Busan, Republic of Korea

DEVELOPMENT OF A SMART SPRINKLER WITH VARIABLE WATER FLOW DEPENDING ON THE WATER SUPPLY LOCATION(2) (WATER VOLUME CONTROL USING AN INVERTER)

Jin Hyun Kim[1] · Seol Ha Kim[2] · Jeong Hun Kim[3] · Won Hyeong Lee[3] · Seok Hyun Seo[4] · Dong Seok Kim[5] · Sang Hun Lee[5]*

[1]Department of Precision Mechanical Engineering, Kyungpook National University, Sangju, 37224, Republic of Korea
[2]Department of Precision Mechanical Engineering, Kyungpook National University, Sangju, 37224, Republic of Korea
[3]Department of Precision Mechanical Engineering, Kyungpook National University, Sangju, 37224, Republic of Korea
[4]Sinsung Engineering, Dongmyeong-myeon, Chilgok-gun, Gyeongsangbuk-do, 39858, Republic of Korea
[5]Department of Upland Crop Science, National Institute of Crop Science, RDA, Miryang, 50424, Republic of Korea
[5*]Department of Upland Crop Science, National Institute of Crop Science, RDA, Miryang, 50424, Republic of Korea
*Corresponding author: Sang Hun Lee (Tel) +82-55-350-1256 (E-mail) sangusa@korea.kr

Abstract

The smart sprinkler aims to spray optimally onto a quadrilateral field by adapting to changes in supply pressure and flow. At this time, the sprinkler must appropriately adjust the supply flow rate and spray distance according to the rotational position by controlling the motor's rotational power; the most suitable device used here was a motor RPM control method utilizing pulse variation.

Key Words : Smart sprinkler, Sprinkler, Inverter, Flow rate.

INTRODUCTION

The conventional sprinkler rotates 360°, whereas the new smart sprinkler is designed to rotate 180°, spraying water inward from outside the square farmland. To spray in a square shape, the distance over which the water is sprayed must vary depending on the rotational position (angle), and the flow rate must change simultaneously. Therefore, it is possible only if the sprinkler can recognize the rotation angle, regulate supply pressure, control flow rate, manage forward and reverse rotation times, and control spray distance. An electronic valve was used to control the supply pressure and flow, but the pressure and flow were not properly controlled. It was determined that controlling flow and pressure by using a valve in the middle of a pipeline through which fluid flows was difficult. It was thought that changes in supply pressure and flow could fundamentally be controlled by changes in the motor's rotational speed, that is, by changes in output. The motor speed control operates normally at a pulse of 380 VAC and 60 Hz. At this time, a method for controlling the motor's rpm through pulse variation was considered. The suitable electronic device for this is an inverter, and the changes in flow and supply pressure through the inverter were judged to be suitable for developing a smart sprinkler.

MATERIAL AND METHODS

1. Improvement of sprinklers for increasing spray distance

The most important aspects in the development of smart sprinklers are: 1) uniformity of flow rate, 2) expansion of spray distance, and 3) control of spray volume and spray distance according to the rotation angle. It was constructed as shown in <Fig. 1> to increase the sprinkler's spray distance.

S2 splinkle	S2 splinkle (length increase)	S2 splinkle (Internal diameter enlargement)	New S2 splinkle
			

Fig. 1 Design modifications for increasing the spray distance of the S2 sprinkler

2. Manufacture of a vane for increasing spray distance

To increase the sprinkler's spray distance, a vane was designed and inserted inside the spray pipe. Vain applied three methods to increase the pressure of the fluid inside the branch pipe: gradually narrowing the cross-section and installing a collar <Fig. 2>.

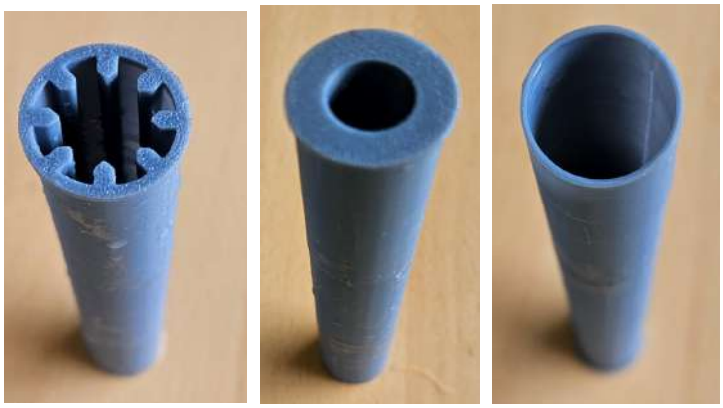

(A) Vain 1 (B) Vain 2 (C) Vain 3

Fig. 2 A vane made inside the nozzle to increase the ejection distance

3. Flow and pressure control using inverters

The electronic valve used to control the spray distance proved ineffective, so the motor output was controlled to vary the sprinkler's spray distance. Since the motor output control uses a 60 Hz pulse, an inverter (AC continuously variable drive) was applied to vary the pulse. The inverter specifications are the same as in <Table 1>, and the experimental setup is the same as in <Fig. 3>.

Table 1. Inverter(AC continuously variable drive) specification

Model	Output	Input volt, 2~3 Phase	Input volt, 3~4 Phase	Keypad	UL Type
LSLV-G100	0.4~4.0kW	200~240V	380~480V	E-LED	O-UL Open Type

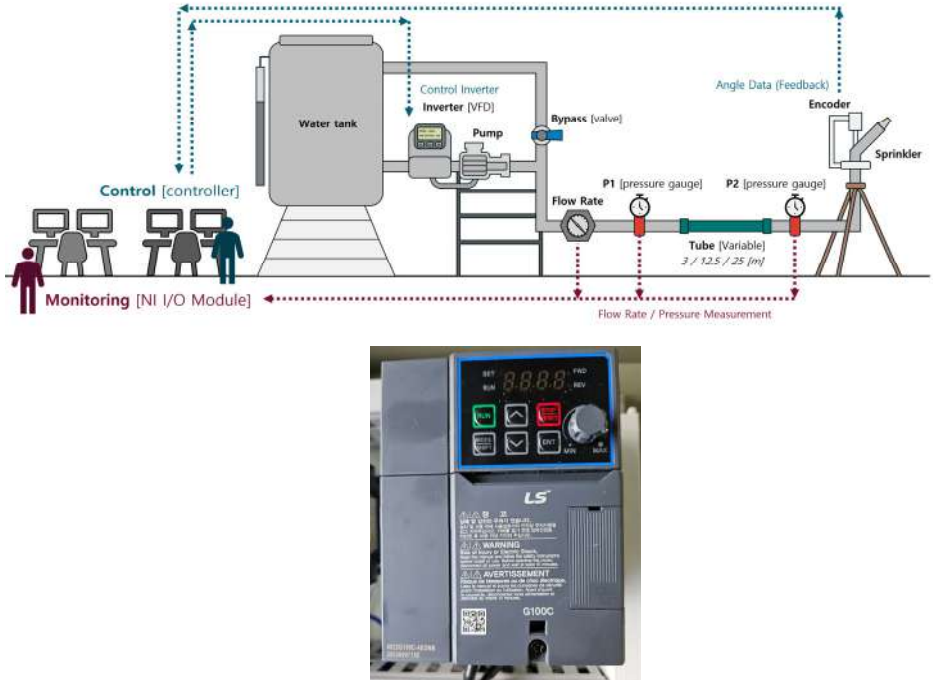

Fig. 3 Flow and pressure control using inverters

4. Position detection sensor that recognizes right and left rotation

The sprinkler can spray while rotating 360°, but it has a structure that allows it to spray while rotating left and right within a limited angle. The device for adjusting the rotation angle is designed and manufactured with a structure in which a protrusion attached to the sprinkler body rotates left and right between the angle adjustment bars. To develop a smart sprinkler, the origin must be remembered when rotating. Therefore, it was designed so that if the system always reaches the origin after each first cycle, it sends a home position signal to the controller. <Fig. 4> is a photo of the proximity sensor used as the origin signal attached, and <Table 2> indicates the specifications.

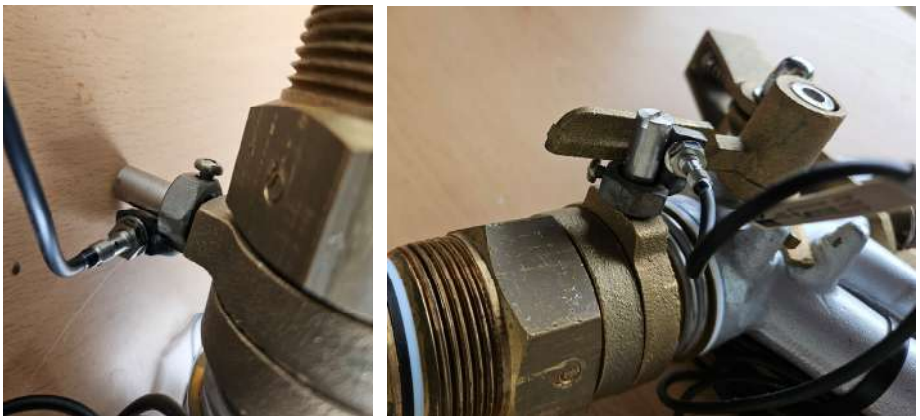

Fig. 4 Proximity(Position) sensor for recognizing forward and reverse rotation

Table 2. Proximity(Position) sensor specification

Model	Operating Temp.	Volt range	Current range	Sensing distance	Sensor diameter
E2E-S05S12-WC-C1	-25~70℃	10~30Vdc	100mA	3~6mm	3mm

■ Omron coperation, China

RESULTS AND DISCUSSION

1. The effect of spray distance through improvements in the sprinkler

To increase the spray distance of the sprinkler, the nozzle diameters of all devices designed and manufactured were made uniform at 10 mm. Also, the nozzle inclination angle was set to 25° for (A) and (B), and to 30° for (C) and (D). At this time, the supply pressure was applied at 4 bar throughout. The maximum spray distances were found to be (A) 25 m, (B) 26 m, (C) 29 m, and (D) 32 m. The spray distance increased by about 6 m compared to the beginning due to the effect of a reduced pressure drop in the fluid, which resulted from significantly increasing the internal diameter of the sprinkler from 19

mm to 25 mm. Another factor appears to be that increasing the nozzle's inclination angle to 30° seems to extend the falling distance <Table 3>. When the sprinkler's spray distance increases, it has the effect of expanding the area that can be supplied.

Table 3. Spray distance due to changes in sprinkler design

Classification	S2 splinkle (A)	S2 splinkle (length increase, B)	S2 splinkle (Internal diameter enlargement, C)	New S2 splinkle (D)
N0zzle angle	25°	25°	30°	30°
Maximum spray distance, m	25	26	29	32

2. The effect of vane on increasing spray distance

To increase the spray distance of the sprinkler(C), a vane was installed inside the spray pipe, and the experimental results are shown in <Fig. 5>. The supply pressure was 2, 3, and 4 bar, and with the Vain installed, the maximum reach could not reach 30 m. Overall, the spray distance was uniformly high in Vain 3 and lowest in Vain 2. In the case of Vain1, it was found to be high only at 4 bar, which was considered an error arising from the experimental conditions. The vane installed inside to increase the jet distance instead resulted in a reduction in internal pressure, leading to the conclusion that it was ineffective.

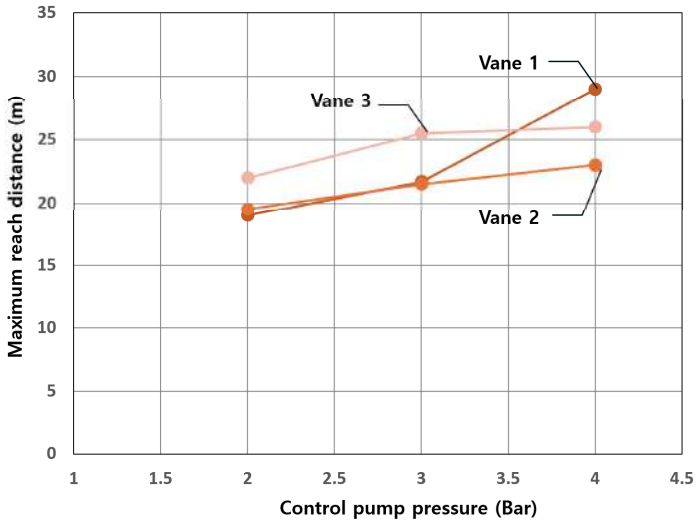

Fig. 5 Maximum spray distance according to the shape of the vain

3. Supply pressure and maximum spray distance for pipe length

The results of measuring the spray distance with respect to changes in the piping length of the sprinkler (C) are shown in <Fig. 6>. Measurements of the spray distance at pipe lengths of 3.5 m, 12.5 m, and 25 m showed no significant change. It was found that the distance increased with higher pressure, but the

effect of pipe length on the spray distance was minimal. At this time, the effect of the wind was measured to be not very large, at 0.2 m/s. However, it was determined that further experiments would be needed in the future regarding the spray distance relative to the length of the piping.

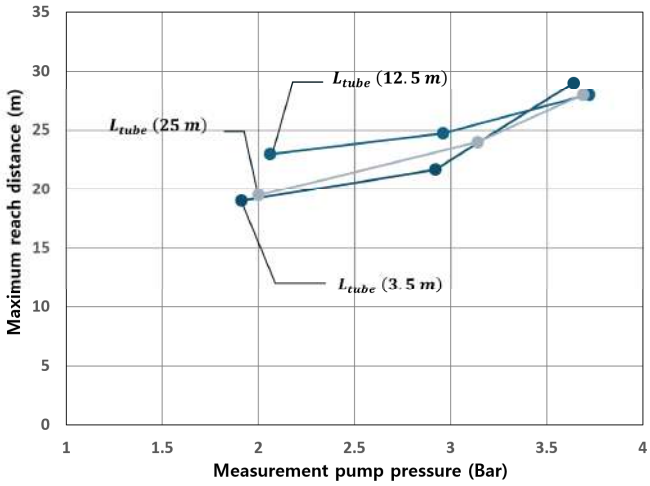

Fig. 6 Maximum spray distance by supply pressure according to pipe length

4. Changes in frequency and motor speed according to inverter settings

The inverter's frequency setting was adjusted in 0 to 10 steps. At this time, the change in frequency according to the unit is as shown in <Fig. 7>. As shown in the figure, the current applied to a motor with AC 380 V is 60 Hz. The inverter showed a linear proportionality from 4 soeed to 10 speed at 30 Hz and 60 Hz. However, it was judged that it would have no effect at 4 speed or below, so the experiment was conducted at 7 speed or above. The motor's rotational speed was found to be 3,500 rpm at 10 speeds and 1,750 rpm at 4 speeds

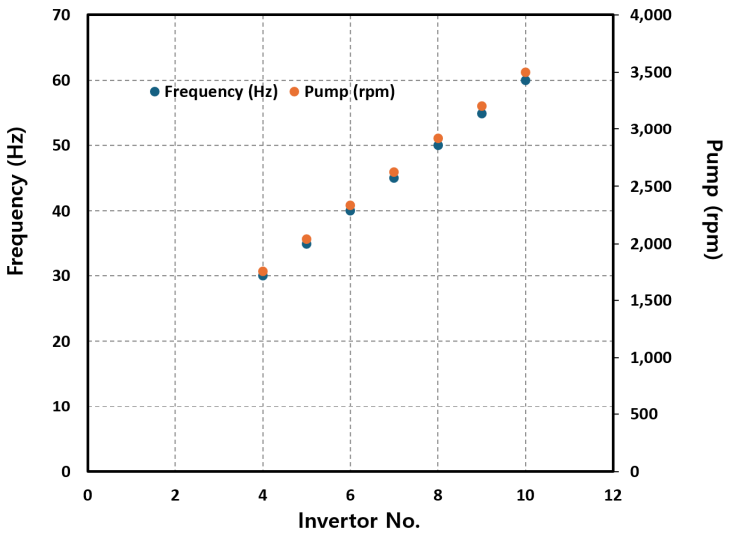

Fig. 7 Changes in frequency and motor speed according to inverter settings

5. The difference in inlet and outlet pressure according to the inverter settings

The difference in the sprinkler inlet pressure and outlet pressure according to the inverter frequency setting is as shown in <Fig. 8>. The difference between inlet pressure and outlet pressure refers to the pressure that is actually present at the outlet when setting the supply pressure, so the pressure loss affects the spray path. Therefore, it is considered desirable to program it with the set pressure in mind, as the pressure decreases accordingly. Also, when the number of inverter stages is low that is, when the motor's rotational rpm is low the pressure difference becomes pronounced. Therefore, the flow rate is also supplied sparingly. When sprayed with a sprinkler onto a quadrilateral farmland, this results in a reduction in distance over short distances while also decreasing the flow rate. Conversely, it means that in the case of a long distance, the flow rate increases and the spray path length also increases.

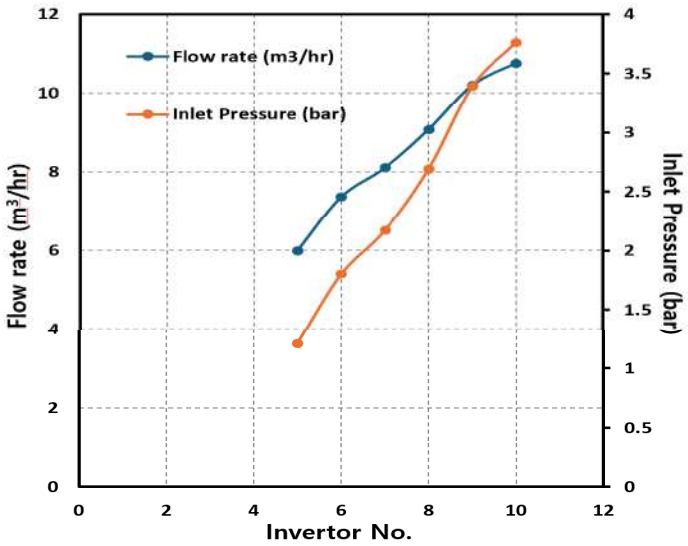

Fig. 8. The difference in inlet and outlet pressure according to inverter settings

6. Changes in flow rate according to changes in supply pressure

When the inlet pressure was set to 2, 3, and 4 bar, the change in flow rate appeared as Y = 1.8456X + 3.9598, as shown in <Fig. 9>. In a sprinkler, the spray distance corresponding to pressure is proportional to the flow rate. Despite differences in the set conditions, the results were an average of 7.55 Ton/h at 2 bar, 9.2-9.4 Ton/h at 3 bar, and 10.4 Ton/h at 4 bar. In <Fig. 8>, depending on the inverter settings, the flow rate changes, which in turn also changes the spray distance and simultaneously increases the supply pressure. Therefore, as a condition for developing a smart sprinkler, it was judged desirable to limit the number of inverter stages to a maximum of 10 in order to control the motor's maximum speed of 3,500 rpm. In addition, it was found that the spray distance and flow rate could be adjusted by controlling the number of inverter stages.

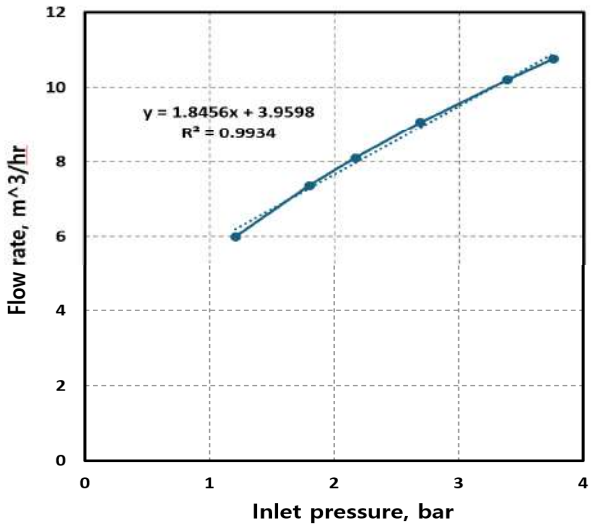

Fig. 9 Change in flow rate according to changes in supply pressure

7. The relationship among pipe length, flow rate, and maximum spray distance according to supply pressure

The correlation between pipe length, flow rate, and maximum spray distance through inverter control is <Fig. 10>. Several characteristics emerged as control conditions for optimizing sprinkler application on a quadrilateral shaped farmland. In other words, the effect on the length of the piping was minimal, and the flow rate according to the supply pressure remained very constant. In addition, flow rate was directly related to spray distance, and supply pressure changed the flow rate. Ultimately, inverters have become capable of controlling both flow and supply pressure through the motor's rotational speed. In the next installment, we plan to propose an algorithm for optimizing row spacing in a quadrilateral-shaped farmland by utilizing their correlation relationships.

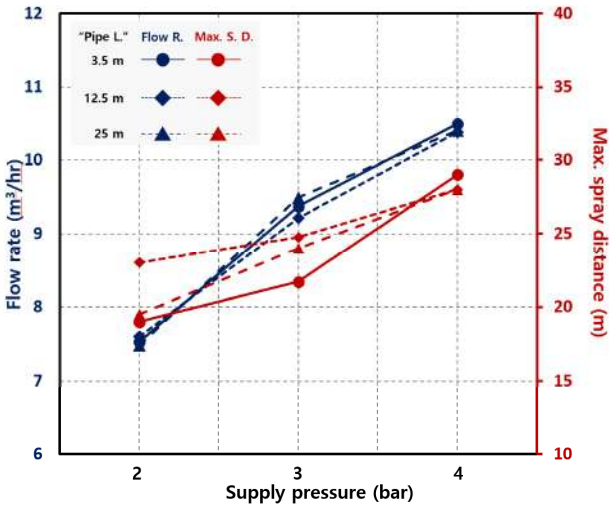

<Fig. 10> The Relationship Between Pipe Length, Flow Rate, and Maximum Spray Distance According to Supply Pressure

CONCLUSION

The smart sprinkler aims to spray optimally onto a quadrilateral field by adapting to changes in supply pressure and flow. At this time, the sprinkler must appropriately adjust the supply flow rate and spray distance according to the rotational position by controlling the motor's rotational power; the most suitable device used here was a motor RPM control method utilizing pulse variation. The main results of the study are as follows.

1. In improving the spray distance, the maximum spray distance increased to 32 m by enlarging the internal diameter of the sprinkler to 25 mm.
2. The Vain, developed to increase the spray distance, showed no effect.
3. The maximum spray distances measured at pipe lengths of 3.5 m, 12.5 m, and 25 m did not show significant differences.
4. The changes in frequency and motor speed according to the inverter settings were controlled proportionally and well, and it was judged to be suitable for the use of the four-sided farmland.
5. In the difference between inlet pressure and outlet pressure according to inverter settings, it is more pronounced when the number of inverter stages is low, that is, when the motor's rotational rpm is low, and at the same time the flow rate is supplied less.
6. The change in flow rate according to changes in supply pressure was found to be, despite differences in the set conditions, an average of 7.55 Ton/h at 2 bar, 9.2-9.4 Ton/h at 3 bar, and an average of 10.4 Ton/h at 4 bar.
7. In the relationship among pipe length, flow rate, and maximum jet distance according to supply pressure, the effect on pipe length was small, and the flow rate according to supply pressure was very constant.

ACKNOWLEDGEMENTS

This study was conducted with support from the Rural Development Administration's agenda projector project, "Development of Technologies for Reducing Damage from Agricultural Weather-Related Disasters (Research and Development Project No. RS-2025-02303472)"

REFERENCES

Han KH, Jang YS, Cho HR, Choi JY, Jeong SO and Kim HJ. 2013. A Study on the Development of Irrigation System in Facilities Plantation Plantation using IT. Research Report. National Academy of Agricultural Sciences. Rural Development Administration.

FAO. 1992. Small-scale pumped irrigation: energy and cost-FAO. Food and agricultural organization of the united nations. Rome. Italy.

Kim JH, Kim YJ, Kim SH, Choi RJ, Eum DH and Kim TW. 2024. Development of Spray Collision Dripper with Combined Function of Drip Irrigation and Spray Hose. Journal of Agriculture & Life Science 59(1) pp.99-114.

National Data Agency(NDA). 2025. https://mods.go.kr/unifSearch/search.es. (2025.12.19).

Yanmar. 2025. http;//www.yanmar.com/media/news/2021/02/28053741/irrigation_agri_202510.pdf. (2026. 4. 20).

Yousui HG. 2024. Design Criteria for Land Improvement Project Planning (Agricultural Water of Field Crops). Japanese Ministry of Agriculture, Forestry and Fisheries. 19-24.

Filipe Gama J.V. and Hong SG. 2020. Assessment of Irrigation Efficiency and Water Distribution by the Different Pressures and Nozzles Angle of the Sprinkler Irrigation System. Proceeding of the KSAE 2020 autumn conference. 63.

FM-P09

Proceedings of The 12th International Symposium on Machinery and Mechatronics for Agriculture and Biosystems Engineering (ISMAB 2026)
20-24 October 2026, Busan, Republic of Korea

PRELIMINARY FIELD EVALUATION OF A MODEL PREDICTIVE CONTROL SYSTEM FOR ROTARY TILLAGE BASED ON SOIL PULVERIZATION RATIO

Hirotaka Tsuchikawa[1*], Shintaro Noda[1], Keita Kurashiki[1], Hidefumi Saito[1], Yuka Nakano[1]

[1]National Agriculture and Food Research Organization (NARO), Tsukuba, Japan
*Corresponding Author: Hirotaka Tsuchikawa, Email: tsuchikawa.hirotaka234@naro.go.jp

Abstract: In autonomous rotary tillage, the operation needs to be adjusted according to soil conditions in real time. Rotary tillage is a nonlinear multiple-input multiple-output process in which travel speed and PTO speed jointly affect soil pulverization, while machine operation is subject to actuator and operating constraints. This study designed and implemented a nonlinear model predictive control (MPC) system for real-time rotary tillage. The controller optimized travel-speed and PTO-speed commands while explicitly considering their allowable ranges and rates of change. The optimization was performed online every 0.1 s over a 4.0 s horizon. Field experiments compared five 70 m runs under constant-speed operation with five runs under MPC operation. The experimental results confirmed that the controller functioned as designed, keeping travel speed and PTO speed within their specified ranges. The variance among the five run mean pulverization ratios decreased from 13.2%^{2} under constant-speed operation to 9.89%^{2} under MPC operation. However, additional replicated experiments are required to determine whether this tendency represents a reproducible control effect.

Key Words: Robot tractor, Rotary tillage, Automation, Soil pulverization ratio, Model predictive control

INTRODUCTION

Autonomous tractors can execute planned paths and machine commands, but rotary tillage quality still varies with soil conditions. Autonomous operation therefore requires a control system that observes the resulting soil condition and adjusts machine operation during tillage. The soil pulverization ratio is an indicator of tillage quality. It is defined as the proportion of soil clods with a maximum diameter of 2 cm or less within a unit volume. Reducing its variability is important for achieving uniform seedbed conditions and improving the consistency of subsequent crop growth.

Travel speed and PTO speed are two principal variables influencing the soil pulverization ratio and are therefore available for regulating the tillage process. These variables jointly affect tillage performance and exhibit different dynamic responses. Rotary tillage control is

therefore a nonlinear multiple-input multiple-output problem. Practical control must also satisfy bounds on machine inputs and limits on how rapidly those inputs can change. MPC is well suited to this problem. It can explicitly handle nonlinear dynamics, multiple manipulated variables, and operational constraints within a single control framework.

The objective of this study was to design and implement a constrained nonlinear MPC system for real-time rotary tillage and to conduct an initial field evaluation of its feasibility.

MATERIALS AND METHODS

The developed control system was based on the previously reported sensor-driven tractor control architecture (Tsuchikawa et al., 2026), as shown in Figure 1. The system consisted of a soil pulverization ratio sensor, a sensor computer, a control computer, and interfaces for commanding tractor travel speed and PTO speed. As shown in Figure 2, the soil pulverization ratio sensor was mounted behind the rotary tiller and consisted of a camera, an RTK-GNSS module, a sensor mount, and a height-adjustment mechanism. Images acquired during tillage were processed by the sensor computer using the previously developed soil pulverization ratio estimation method (Noda et al., 2025), and the estimated value was transmitted to the control computer. The nonlinear MPC formulation used three physical states: tractor travel speed, PTO speed, and soil pulverization ratio. The manipulated variables were the commanded travel speed and commanded PTO speed. First-order actuator models represented the travel-speed and PTO-speed responses, and experimentally identified input dead times were included in the control model.

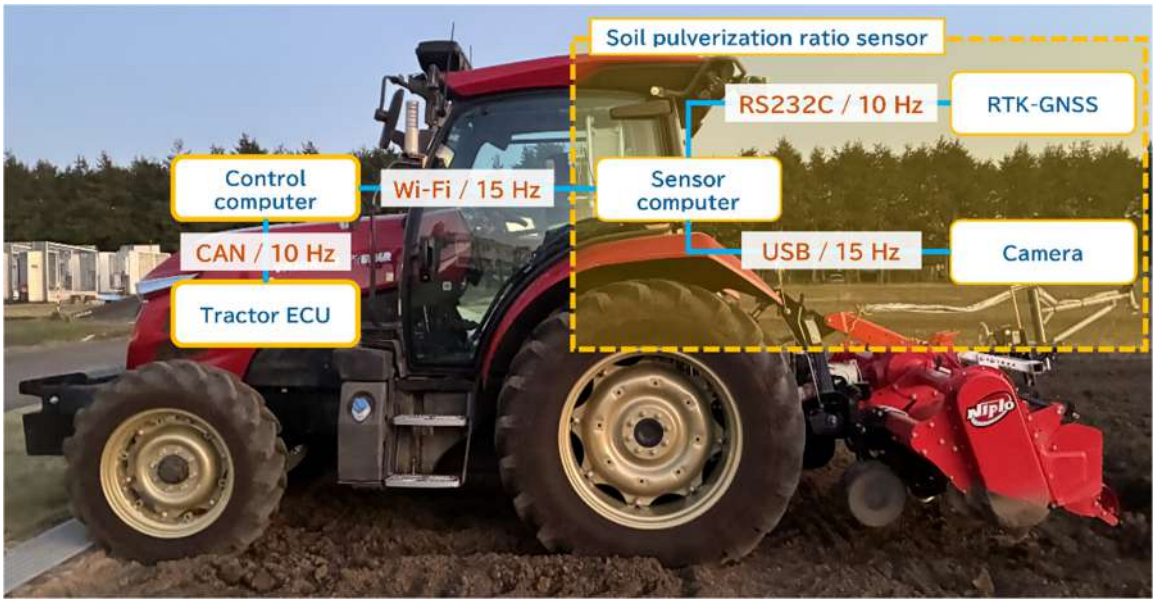

Fig.1 Architecture of the developed sensor-driven tractor control system (reproduced from Tsuchikawa et al., 2026). The system consists of a soil pulverization ratio sensor, a controller, a tractor and an implement.

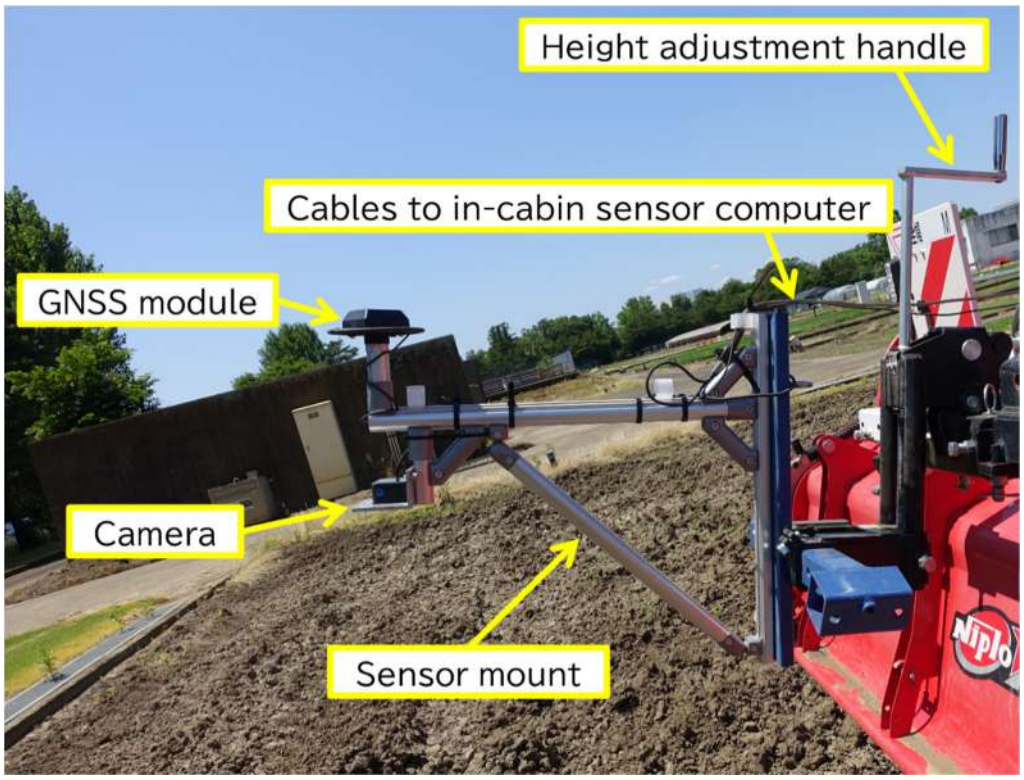

Fig.2 Soil pulverization ratio sensor mounted on the implement (reproduced from Tsuchikawa et al., 2026). The sensor consists of a camera, a GNSS module, a sensor mount, a height adjustment handle, and cables connected to the in-cabin sensor computer.

The nonlinear MPC was formulated as the following constrained optimal-control problem. The stage and terminal costs were defined as follows:

$$L(\boldsymbol{x},\boldsymbol{u}) = \frac{1}{2}\left(\boldsymbol{x}-\boldsymbol{x}_{ref}\right)^{T} Q\left(\boldsymbol{x}-\boldsymbol{x}_{ref}\right) + \frac{1}{2}\left(\boldsymbol{u}-\boldsymbol{u}_{ref}\right)^{T} R\left(\boldsymbol{u}-\boldsymbol{u}_{ref}\right) \quad (1)$$

$$\phi(\boldsymbol{x}) = \frac{1}{2}\left(\boldsymbol{x}-\boldsymbol{x}_{ref}\right)^{T} Q_f\left(\boldsymbol{x}-\boldsymbol{x}_{ref}\right) \quad (2)$$

The resulting optimization problem was:

$$\underset{\boldsymbol{x}_{k_s},\cdots,\boldsymbol{x}_{k_s+K},\ \boldsymbol{u}_{k_s},\cdots,\boldsymbol{u}_{k_s+K-1}}{\text{minimize}} \ \phi\left(\boldsymbol{x}_{k_s+K}\right) + \sum_{k=k_s}^{k_s+K-1} L(\boldsymbol{x}_k, \boldsymbol{u}_k)$$

$$\text{subject to}_{\,k_s\le k\le k_s+K} \begin{cases} \boldsymbol{x}_{k_s} = \overline{\boldsymbol{x}}_{\text{init}} \\ \boldsymbol{x}_{k+1} = F(\boldsymbol{x}_k,\boldsymbol{u}_k) \\ \overline{\boldsymbol{x}}_{\text{lb}} \le \boldsymbol{x}_k \le \overline{\boldsymbol{x}}_{\text{ub}} \\ \overline{\boldsymbol{u}}_{\text{lb}} \le \boldsymbol{u}_k \le \overline{\boldsymbol{u}}_{\text{ub}} \end{cases} \quad (3)$$

where:

$\boldsymbol{x}$ = 3 × 1 state vector consisting of travel speed, PTO speed, and soil pulverization ratio

$\boldsymbol{x}_k$ = state vector at step k

$\boldsymbol{x}_{ref}$ = reference vector of $\boldsymbol{x}$

$\boldsymbol{u}$ = 2 × 1 control-input vector consisting of travel-speed and PTO-speed commands

$\boldsymbol{u}_k$ = control-input vector at step k

$\boldsymbol{u}_{ref}$ = reference vector of $\boldsymbol{u}$

Q = weighting matrix for the state variables

R = weighting matrix for the control inputs
Q_f = weighting matrix for the terminal cost
k_s = current time step
K = prediction horizon
$\overline{\boldsymbol{x}}_{\text{init}}$ = current state
$F(\boldsymbol{x}_k, \boldsymbol{u}_k)$ = nonlinear state transition function
$\overline{\boldsymbol{x}}_{\text{lb}}$ = lower bound on the state vector
$\overline{\boldsymbol{x}}_{\text{ub}}$ = upper bound on the state vector
$\overline{\boldsymbol{u}}_{\text{lb}}$ = lower bound on the control inputs
$\overline{\boldsymbol{u}}_{\text{ub}}$ = upper bound on the control inputs

The nonlinear optimization problem was implemented in CasADi and solved using IPOPT every 0.1 s over 40 steps, corresponding to a 4.0-s horizon. The controller explicitly considered the allowable ranges of the travel-speed and PTO-speed commands and their maximum changes per control cycle. The first optimized travel-speed and PTO-speed commands were applied to the tractor, after which the optimization was repeated using the latest measurements.

Field experiments compared constant-speed operation with MPC operation. Five 70-m runs were conducted for each treatment, and each 70-m run was treated as one independent experimental unit. In the constant-speed treatment, travel speed was fixed at 0.556 m/s and PTO speed was fixed at 540 rpm. In the MPC treatment, the target soil pulverization ratio was set to 68.5%, based on the mean obtained under constant-speed operation. Travel speed was constrained to 0.278-0.833 m/s, and PTO speed was constrained to 432-545 rpm. The measured travel speed and PTO speed were recorded to confirm that the tractor followed the optimized commands. The mean soil pulverization ratio was calculated for each run, and the five run means were used to summarize treatment performance.

RESULTS & DISCUSSION

As shown in Figure 3, the measured travel speed and PTO speed closely followed their respective command values and remained within the prescribed operating ranges. Changes in the control inputs were observed in response to deviations of the soil pulverization ratio from the target value, indicating that the controller adjusted machine operation according to the measured soil condition.

As summarized in Table 1, the mean soil pulverization ratio was 68.6% under constant-speed operation and 70.8% under MPC operation. The variance among the five run means was 13.2%² and 9.89%², respectively. The available data were insufficient to establish a reproducible control effect. Nevertheless, the MPC treatment showed a numerically lower variance than the constant-speed treatment. This result suggests the potential for reducing soil pulverization variability.

A limitation of this initial evaluation was the small number of independent runs. Only five independent runs were available for each treatment. Consequently, it was difficult to determine whether the observed difference resulted from the controller or from random

variation. Additional replicated field experiments are therefore required. Such experiments are needed to determine whether the observed tendency can be reproduced.

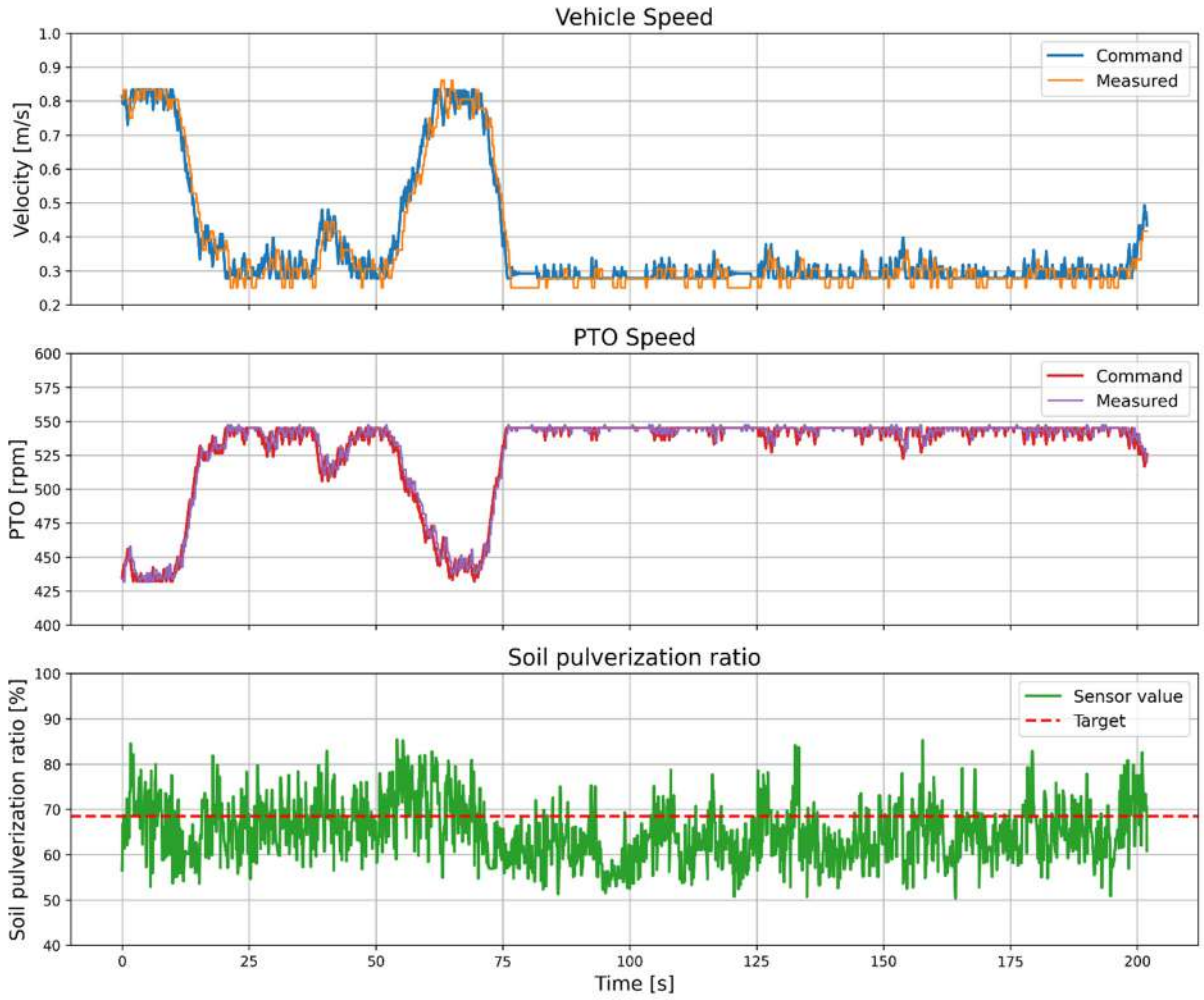

Fig. 3 Time histories of the commanded and measured travel speed, the commanded and measured PTO speed, and the measured soil pulverization ratio during an MPC-controlled field run. The dashed red line indicates the target soil pulverization ratio of 68.5%.

Table 1 Mean soil pulverization ratio and variance among the five run means under constant-speed and MPC operations.

Classification	Constant speed	MPC
Mean (%)	68.6	70.8
Variance (%^{2})	13.2	9.89

CONCLUSIONS

A nonlinear multiple-input multiple-output MPC system was designed and implemented for rotary tillage. Field tests confirmed that the travel-speed and PTO-speed commands could be varied within the specified ranges and that the measured values responded to these

commands. Although the present comparison did not clearly demonstrate an improvement in soil pulverization under MPC operation, the variance among the five run mean pulverization ratios was numerically lower under MPC operation than under constant-speed operation, suggesting a potential reduction in between-run variability. The principal contribution of this initial study is the design and field implementation of the control system. Additional field experiments are required to determine whether the observed tendency represents a reproducible control effect.

REFERENCES

Tsuchikawa, H., S. Noda, H. Saito, K. Kurashiki, and W. Iijima. 2026. Development and evaluation of an interoperable sensor-driven tractor control system for rotary tillage. Smart Agricultural Technology 14: 102286

Noda, S., H. Saito, K. Kusa, K. Tateishi, W. Iijima, and J. Nakagawa. 2025. Real-time estimation of soil pulverization ratio after tillage using a camera mounted on agricultural machinery. Smart Agricultural Technology 13: 101687.

FM-P10

Proceedings of The 12th International Symposium on Machinery and Mechatronics for Agriculture and Biosystems Engineering (ISMAB 2026)
20-24 October 2026, Busan, Republic of Korea

KINEMATIC ACCELERATION FOR BONDED-PARTICLE DISCRETE ELEMENT SIMULATION OF ROTARY CORE DRILLING

Joon-Seo Kim[1], Sang-Wook Park[1], Seung-Yeon Lee[1], Tae-Kyeong Yeu[2], Ji-Tae Kim[1,3*]

[1]Department of Convergence Biosystems Engineering, Chonnam National University, 77 Yongbong-ro, Buk-gu, Gwangju 61186, Republic of Korea
[2]Ocean and Maritime Digital Technology Research Division, Korea Research Institute of Ships and Ocean Engineering (KRISO), 32 Yuseong-daero 1312beon-gil, Yuseong-gu, Daejeon 34103, Republic of Korea
[3]Institute of Agricultural Science & Technology, Chonnam National University, 77 Yongbong-ro, Buk-gu, Gwangju 61186, Republic of Korea
*Corresponding Author-- Voice: +82-62-530-5188, Email: jtkim@jnu.ac.kr

Abstract: Rock fragmentation and core formation in rotary core drilling are governed by the mechanical interaction between the core bit and the rock, and the analysis of this interaction is essential for the design and performance evaluation of core drilling systems. The bonded-particle discrete element method (DEM), which reproduces rock breakage through the failure of inter-particle bonds, is well suited to such analyses. However, DEM requires a small-time step to ensure numerical stability, and simulating drilling at actual operating rates therefore entails an excessive computational cost. To overcome this limitation, this study proposes a kinematic acceleration method that reduces the computational cost of bonded-particle DEM analysis of rotary core drilling. The engineering properties of the target rock were reproduced using a bonded-particle DEM model, and the operating mechanism of the core drill was implemented using a dynamics solver. The angular velocity and the penetration rate prescribed at the bit were then increased by a common acceleration factor, so that the penetration per revolution, and hence the kinematics of the drilling process, remained unchanged while the simulated drilling time decreased in inverse proportion to the factor. The accelerated model was verified against the actual operating condition by comparing the mechanical specific energy and the bond breakage generated during penetration at identical penetration depths, and both conditions yielded similar mechanical responses. The proposed method provides a practical means of reducing the computation time of bonded-particle DEM analyses, and is expected to be applicable to sensitivity analyses of the design parameters of rotary core drilling.

Key Words: Rotary core drilling, Discrete element method, Bonded-particle model, Accelerated simulation, Computational cost

INTRODUCTION

Rotary core drilling removes an annular region through the rotation and axial penetration of a hollow bit, leaving a cylindrical rock core. The process involves local cracking and

fragmentation at the bit–rock interface, followed by fragment separation. Rock-cutting analyses must therefore account for both fracture and the motion of detached material (Rojek et al., 2011). Although the finite element method is effective for evaluating stress and deformation, its continuum formulation has limitations in representing these discontinuous processes. The bonded-particle discrete element method (DEM) represents rock failure through interparticle bond breakage and provides an approach for analyzing bit–rock interactions (Potyondy and Cundall, 2004).

DEM has been used to investigate drilling loads, fragmentation, and core integrity (Wang et al., 2025). However, the small time steps required for stable explicit integration make simulations at actual drilling rates computationally demanding, limiting repeated calibration and comparisons across operating conditions. Increasing the operating rates offers a means of shortening simulated physical time, but the resulting effects on contact and failure behavior must be considered. Penetration-rate effects reported for granular materials also motivate careful assessment of rate scaling, although their implications for bonded-rock drilling require separate investigation (Cerfontaine et al., 2021).

This study develops a bonded-particle DEM model of rotary core drilling and introduces accelerated operating conditions based on proportional scaling of angular velocity and penetration rate. It establishes the associated kinematic relationships and evaluates mechanical response, fragmentation behavior, and computational efficiency at common penetration depths. This paper presents the model construction, the kinematic basis of the scaling, and the outcome of the depth-aligned comparison; the quantitative response deviations and the measured speedup across scaling factors are reported separately.

MATERIALS AND METHODS

BONDED-PARTICLE MODEL OF CORE DRILLING

The rock specimen consists of spherical particles with a size distribution and interparticle bonds. The model represents equivalent macroscopic stiffness, strength, and brittle failure behavior without explicitly reproducing the rock microstructure. Tensile and shear failure of interparticle bonds gives rise to cracks and detached fragments (Potyondy and Cundall, 2004). Because bit deformation and damage are assumed negligible relative to rock deformation and fracture, the core bit is modeled as a rigid body to reduce computational cost. The model is implemented in Ansys Rocky, Release 2026 R1 (ANSYS, Inc., 2026).

Target macroscopic properties are selected with reference to tests on seafloor massive sulfide (SMS) simulants reported by Zhang et al. (2024). Particle and bond parameters are calibrated through numerical material tests to reproduce the target stiffness, strength, and brittle failure characteristics (Potyondy and Cundall, 2004).

In actual drilling, weight on bit (WOB) provides the axial load, and penetration is governed by bit–rock interaction. In the present model, the target penetration rate is prescribed together with bit rotation, so WOB is not applied independently. The resulting axial reaction force is treated as the mechanical response corresponding to WOB. The model reproduces annular fragmentation around the crown, particle detachment, and formation of a cylindrical core inside the bit. Fig. 1 shows the physical drilling concept and DEM simulation; the downward arrow in

panel (a) represents WOB during actual drilling.

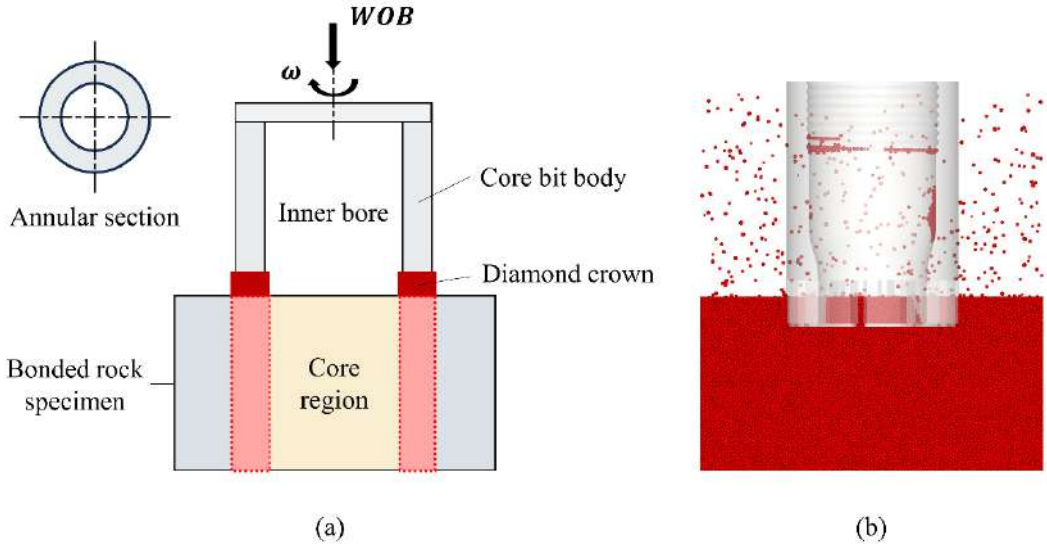

Fig. 1 Rotary core drilling: (a) schematic configuration and (b) DEM simulation.

ACCELERATED OPERATING CONDITIONS

The reference condition is defined by angular velocity ω_0 and axial penetration rate v_0. The accelerated condition multiplies both rates by a common factor λ, while retaining the model geometry, material properties, and target penetration depth H. For constant prescribed rates over the drilling interval, the operating rates and simulated physical times satisfy Eq. (1).

$$\omega_\lambda = \lambda\omega_0,\ v_\lambda = \lambda v_0,\ t_\lambda = \frac{t_0}{\lambda},\ \lambda > 1 \tag{1}$$

where:

λ = Scaling factor (-)

ω_0, ω_λ = Reference and accelerated angular velocities (rad s^{-1})

v_0, v_λ = Reference and accelerated penetration rates (m s^{-1})

t_0, t_λ = Reference and accelerated physical times (s)

With angular velocity expressed in rad s^{-1}, penetration per revolution, p, satisfies Eq. (2).

$$p_\lambda = \frac{2\pi v_\lambda}{\omega_\lambda} = \frac{2\pi\lambda v_0}{\lambda\omega_0} = \frac{2\pi v_0}{\omega_0} = p_0 \tag{2}$$

where:

p_0, p_λ = Reference and accelerated penetrations per revolution (m rev^{-1})

Geometric similarity changes model dimensions while retaining their proportions. By contrast, the present method leaves the geometry unchanged and scales only the operating rates, so penetration per revolution and the resulting cutting path remain unchanged. Table 1 summarizes the two conditions in terms of operating rates, penetration per revolution, total bit revolutions, and simulated physical time.

Table 1 Kinematic comparison of reference and accelerated conditions.

Parameter	Reference	Accelerated
Model configuration	Identical	Identical
Operating rates (ω, v)	ω_0, v_0	$\lambda\omega_0, \lambda v_0$
Penetration per revolution (p)	p_0	p_0
Target penetration depth	H	H
Total bit revolutions	H/p_0	H/p_0
Simulated physical time	H/v_0	$H/\lambda v_0$

The ratio of angular velocity to penetration rate governs the prescribed rotation–penetration path; keeping this ratio constant provides kinematic consistency between the two conditions. Mechanical and fragmentation behavior must still be evaluated separately because particle inertia, contact evolution, and bond failure can vary with operating rate. The accelerated physical time in Eq. (1) describes only the nominal reduction in simulated duration. Actual computational savings are therefore quantified from measured wall-clock time.

RESPONSE AND COMPUTATIONAL EFFICIENCY ASSESSMENT

Both conditions use identical particle arrangements, bond states, contact parameters, and boundary conditions so that differences in the initial state do not affect the comparison. Because acceleration changes the simulated time associated with each drilling stage, outputs are aligned by bit penetration depth or normalized penetration depth. Axial reaction force F_z and bit torque T characterize the mechanical response. Mechanical specific energy (MSE), introduced by Teale (1965), expresses the axial and rotational work per unit excavated volume and is calculated using Eq. (3).

$$MSE = \frac{F_z}{A_b} + \frac{T\omega}{A_b v}, \; A_b = \frac{\pi}{4}(D_o^2 - D_i^2) \tag{3}$$

where:

MSE = Mechanical specific energy (J m^{-3} or Pa)
F_z = Axial reaction force (N)
T = Bit torque (N m)
A_b = Annular excavation area (m^2)
D_o, D_i = Bit outer and inner diameters (m)
ω = Angular velocity (rad s^{-1})
v = Penetration rate (m s^{-1})

In Eq. (3), the first and second terms represent the axial and rotational specific-energy components, respectively.

The assessment considers mean levels, fluctuations, and depth-dependent trends in axial reaction force, torque, and MSE over a common interval excluding initial-contact transients. Fragmentation is characterized by cumulative bond breakage and its spatial distribution, whereas core integrity is evaluated from residual-core continuity, internal bond damage, and overall geometry.

Equivalence is judged from the consistency of these measures over the selected penetration interval rather than from point-by-point agreement between instantaneous signals. Relative deviations and changes in failure patterns are examined across scaling factors.

Computational speedup S_c is defined by Eq. (4) to distinguish actual wall-clock savings from the reduction in simulated physical time.

$$S_c = \frac{t_{wall,0}}{t_{wall,\lambda}} \tag{4}$$

where:

S_c = Computational speedup (-)

$t_{wall,0}, t_{wall,\lambda}$ = Reference and accelerated wall-clock times (s)

Wall-clock time is measured using the same hardware, solver settings, particle count, parallel-computing resources, and output intervals. Mechanical and fragmentation consistency is considered together with computational speedup to identify an acceleration range that reduces computation time without substantially changing the principal core-drilling responses.

RESULTS & DISCUSSION

The simulation in Fig. 1(b) captures localized fragmentation and particle detachment around the bit crown while retaining a central, core-shaped particle column.

Equations (1) and (2) show that proportional rate scaling leaves penetration per revolution unchanged. At a prescribed depth, both conditions require the same number of bit revolutions and accumulate an equal rotation angle, whereas simulated physical time is reduced to 1/λ of the reference value (Table 1). These relationships establish kinematic consistency along the drilling path.

Evaluation over a common penetration interval shows that axial reaction force, bit torque, and MSE are maintained under the accelerated condition, as are the bond-breakage pattern and residual-core geometry. The measured wall-clock time decreases, although the realized speedup does not follow the nominal scaling factor because numerical stability, contact dynamics, and fracture evolution also govern computational cost. The upper bound of the applicable scaling factor is therefore set by the rate sensitivity of the mechanical and fracture behavior rather than by the kinematic relationships alone, although the corresponding numerical values are reported separately.

CONCLUSIONS

The bonded-particle DEM model represents the principal fragmentation and core-formation processes of rotary core drilling. Scaling angular velocity and penetration rate by a common factor retains penetration per revolution, the drilling path, and the number of bit revolutions at a common target depth while reducing simulated physical time.

Depth-aligned measures show comparable mechanical, energetic, and fracture-related behavior in the two conditions, together with stable residual-core geometry. The measured wall-clock time decreases accordingly. These outcomes support proportional rate scaling as a practical means of improving the efficiency of bonded-particle DEM while retaining the principal features of core drilling.

ACKNOWLEDGEMENTS

This research was supported by the Korea Institute of Marine Science & Technology Promotion (KIMST), funded by the Ministry of Oceans and Fisheries, Republic of Korea (RS-2026-25527073).

REFERENCES

ANSYS, Inc. 2026. *Ansys Rocky*. Release 2026 R1. Canonsburg, Pa.: ANSYS, Inc.

Cerfontaine, B., M. O. Ciantia, M. J. Brown, and Y. U. Sharif. 2021. DEM study of particle scale and penetration rate on the installation mechanisms of screw piles in sand. Comput. Geotech. 139: 104380.

Potyondy, D. O., and P. A. Cundall. 2004. A bonded-particle model for rock. Int. J. Rock Mech. Min. Sci. 41(8): 1329–1364.

Rojek, J., E. Oñate, C. Labra, and H. Kargl. 2011. Discrete element simulation of rock cutting. Int. J. Rock Mech. Min. Sci. 48(6): 996–1010.

Teale, R. 1965. The concept of specific energy in rock drilling. Int. J. Rock Mech. Min. Sci. Geomech. Abstr. 2(1): 57–73.

Wang, X., Y. Wu, Z. Gao, H. Hao, L. Zhou, J. Li, and M. Gao. 2025. Performance evaluation and selection of the core drill bits for lunar rock. Geomech. Geophys. Geo-Energy Geo-Resour. 11: 61. https://doi.org/10.1007/s40948-025-00976-w

Zhang, B., H. Lu, J. Yang, L. Deng, and P. Sun. 2024. Experimental study on the proportioning and mechanical properties of simulated materials of deep-sea seafloor massive sulfide. Ocean Eng. 295: 116955.

FM-P11

Proceedings of The 12th International Symposium on Machinery and Mechatronics for Agriculture and Biosystems Engineering (ISMAB 2026)
20-24 October 2026, Busan, Republic of Korea

EFFECT OF UNDERCARRIAGE CONFIGURATION ON THE MOBILITY OF DEEP-SEA TRACKED VEHICLES OVER HYDROTHERMAL VENT-FIELD TERRAIN

Moo-Young Oh[1], Ju-Hyeon An[1], Dan-A Kim[1], Se-Hee Park[1], Tae-Kyeong Yeu[2], Ji-Tae Kim[1,3*]

[1] Department of Convergence Biosystem Engineering, Chonnam National University, 77 Yongbong-ro, Buk-gu, Gwangju, Republic of Korea
[2]Ocean and Maritime Digital Technology Research Division, Korea Research Institute of Ships and Ocean Engineering (KRISO), 32 Yuseong-daero 1312beon-gil, Yuseong-gu, Daejeon 34103, Republic of Korea
[3]Institute of Agricultural Science & Technology, Chonnam National University, 77 Yongbong-ro, Buk-gu, Gwangju 61186, Republic of Korea
*Corresponding Author-- Voice: +82-62-530-5188, Email: jtkim@jnu.ac.kr

Abstract: Seafloor massive sulfide (SMS) deposits and ferromanganese crusts are gaining importance as potential mineral resources, increasing the need for mobile systems that can efficiently survey and sample seabed resources. The hydrothermal vent fields along the Central Indian Ridge, the target area of this study, comprise steep slopes and sediment-covered bedrock, so the tracked undercarriage of an exploration vehicle must be designed for such terrain, although the subsea environment makes design and evaluation by at-sea trials impractical. Multibody dynamics (MBD) models of five tracked vehicles differing in the number of tracks, the ground contact length, and the undercarriage configuration were therefore developed and evaluated in terms of required driving force, driving characteristics, and terrain adaptability. The terrain was idealized as rigid bedrock and represented by flat, inclined, and sinusoidal undulating surfaces, with the track–terrain contact described by a Coulomb friction model. The five vehicles behaved similarly on flat terrain, whereas their dynamic responses differed clearly on inclined and undulating terrain. The four-track vehicles showed improved terrain-following capability as the ground contact length of each track decreased, and the contact load distribution and load transfer varied with the configuration and arrangement of the bottom rollers. These results indicate that design should account not only for the total ground contact area but also for the contact length of each track and for the load sharing produced by the roller arrangement.

Key Words: Seabed exploration, Tracked vehicle, Multibody dynamics, Driving torque, Terrain adaptability

ACKNOWLEDGEMENTS

This research was supported by Korea Institute of Marine Science & Technology Promotion (KIMST) funded by the Ministry of Oceans and Fisheries, Korea (RS-2026-25527073).

FM-P12

Proceedings of The 12th International Symposium on Machinery and Mechatronics for Agriculture and Biosystems Engineering (ISMAB 2026)
20-24 October 2026, Busan, Republic of Korea

GROWTH CHARACTERISTICS OF LEAFY VEGETABLE SEEDLINGS FOR ESTABLISHING SUITABLE SIZE CRITERIA FOR MECHANICAL TRANSPLANTING

Inseok Hwang[1], Changseop Shin[1*], Donggyu Kim[1], Dohyun Ahn[1]

[1]Department of Biosystems Engineering, Chungbuk National University, South Korea
*Corresponding Author-- Voice: +82-43-261-2584, Email: shinchang7@cbnu.ac.kr

Abstract: This study investigated seedling height and width across sowing dates in Chinese cabbage, cabbage, and broccoli to provide baseline data for identifying suitable seedling sizes associated with low missing-plant rates during mechanical transplanting. Seeds were sown at 2-day intervals and raised in 128-cell plug trays. Eight trays per crop, representing seedlings aged 16–30 days after sowing, were evaluated. Seedlings were raised in a nursery under the same growing conditions as commercial seedlings produced for sale to farmers. Each tray was divided into four sections, with seven seedlings assessed per section, yielding 672 growth measurement records for analysis. Seedling height was defined as the vertical distance from the growing-medium surface to the highest point of the plant in its natural position, and seedling width as the maximum horizontal spread viewed from above. Across sowing dates, tray mean height ranged from 5.21 to 7.98 cm for Chinese cabbage, 3.58 to 7.73 cm for cabbage, and 4.15 to 9.32 cm for broccoli. The corresponding ranges of tray mean width were 9.68–14.10, 5.01–9.77, and 4.69–9.68 cm, respectively. Chinese cabbage had greater mean seedling width than the other two crops at every sowing date, whereas the ranking of crops by seedling height varied with sowing date. These findings indicate that crop-specific differences in both seedling height and width should be considered when establishing size criteria for mechanical transplanting. The results provide baseline data for selecting seedling size classes for subsequent transplanting trials. Future work will involve raising each crop at staggered sowing dates and assessing seedling size at different seedling ages alongside missing-plant rates during mechanical transplanting to identify suitable seedling sizes associated with low missing-plant rates.

Key Words: Leafy vegetable, Mechanical transplanting, Seedling age, Seedling size

Acknowledgements: This research was supported by the Regional Innovation System & Education (RISE) program through the (Chungbuk Regional Innovation System & Education Center), funded by the Ministry of Education (MOE) and the (Chungcheongbuk-do), Republic of Korea. (2026-RISE-11-014-01). This work was carried out with the support of "Cooperative Research Program for Agriculture Science & Technology Development (RS-2026-25486657)" Rural Development Administration, Republic of Korea.

FM-P13

Proceedings of The 12th International Symposium on Machinery and Mechatronics for Agriculture and Biosystems Engineering (ISMAB 2026)
20-24 October 2026, Busan, Republic of Korea

DEM SOIL PARAMETER CALIBRATION USING ANGLE OF REPOSE AND CONE PENETRATION TEST

Donggyu Kim[1], Sebin Jeong[1], Changseop Shin[1]*

[1]Department of Biosystems Engineering, Chungbuk National University, Cheongju, Republic of Korea
*Corresponding Author—Voice: +82-43-261-2584, Email: shinchang7@cbnu.ac.kr

Abstract: In recent agricultural applications, increasing attention has been paid to the accuracy of analyses of soil–agricultural machinery interactions. To improve analytical accuracy, a DEM soil model capable of appropriately reproducing the physical behavior of actual soil is required. This study aimed to calibrate the major contact parameters of an EDEM soil model based on laboratory soil tests and to evaluate the reproducibility of the model through an independent validation test. Soil samples were adjusted to a moisture content of 5%, and the soil particle system in EDEM was constructed based on the measured bulk density. A static angle of repose test and a UTM-based cone penetration test were conducted for parameter calibration. In the cone penetration test, a cone was mounted on a Universal Testing Machine (UTM), and penetration resistance was measured as a function of penetration depth. The results of the cone penetration test, together with those of the static angle of repose test, were used as calibration targets for the DEM model. Subsequently, a design of experiments approach was applied using Design-Expert. Major contact parameters were screened using a Plackett–Burman design, their ranges were narrowed, and a Box–Behnken design was then employed to determine the optimal parameter combination that minimized the differences between the experimental and simulation results. The optimized model produced a static angle of repose of 29.91°, which was close to the experimentally measured value of 29.61°. The simulated cone penetration behavior reproduced the overall trend observed in the experiment, with an RMSE of 7.84 kPa. In addition, an independent dynamic angle of repose test, which was not used in the calibration process, was conducted for further validation. The experimental and simulated values were 47.70° and 46.91°, respectively, showing close agreement. The DEM soil model developed in this study was able to reproduce different soil behaviors and is expected to serve as a fundamental model for future analyses of interactions between agricultural machinery components and soil, as well as for coupled simulations.

Key Words: Discrete Element Method, Soil-Machine Interaction, Parameter Calibration, Cone Penetration Test

Acknowledgements: This work was carried out with the support of "Cooperative Research Program for Agriculture Science & Technology Development (RS-2025-02216071)" Rural Development Administration, Republic of Korea.

FM-P14

Proceedings of The 12th International Symposium on Machinery and Mechatronics for Agriculture and Biosystems Engineering (ISMAB 2026)
20-24 October 2026, Busan, Republic of Korea

ENGINE SAFETY CONTROL MODULE FOR BACKPACK BRUSH CUTTERS USING PPE WEAR AND TILT SIGNALS

Young-Tae Yun* Jeong-Min Lee Seok-Cheol Yu Jae-Seung Noh

Department of Agricultural Engineering, National Institute of Agricultural Sciences, Jeonju, Republic of Korea
*Corresponding Author—Voice: +63-238-4143, Email: yyt1990@korea.kr

Abstract: Backpack brush cutters are operated with high-speed rotating blades while being carried on the operator's back. Therefore, an automatic safety control system is required to prevent engine operation when personal protective equipment (PPE) is not properly worn and to rapidly stop the engine in emergency situations such as operator falls. This study aimed to develop an engine safety control module that detects both PPE wear status and brush cutter tilt and automatically interrupts the ignition system when missing PPE or a fall is detected.

The system consisted of PPE-mounted transmitter modules and a receiver/engine control module installed on the brush cutter. Touch sensors (TS01S) were attached to a face shield, left and right anti-vibration gloves, and left and right knee guards. A 1:5 wireless communication system was designed using an nRF24LE-series circuit integrating a microcontroller unit (MCU) and 2.4 GHz radio frequency (RF) communication, allowing five PPE wear signals to be transmitted to a single receiver. The receiver independently monitored the wear status of the five PPE items. Engine operation was maintained only when all PPE items were properly detected. If one or more PPE items were not detected, a mechanical relay grounded the ignition coil circuit to stop the engine. A gyroscope sensor was also integrated into the engine control module. When an abnormal tilt associated with an operator fall was maintained for a specified period, the same engine shutdown circuit was activated. To improve field applicability, the MCU and RF circuits were integrated into a single one-board PCB with an embedded PCB pattern antenna. In addition, the external power switch was replaced with a reed-switch-based contactless power control system, and a low-power standby function was applied.

As a result, the transmitter module was miniaturized to approximately 30 mm × 12 mm, and PPE wear status and operator fall conditions could be integrated into a single engine shutdown circuit. Further tests will evaluate engine shutdown response time during PPE donning and doffing and engine stop time at different tilt angles to optimize the control thresholds and operational reliability. The developed module is expected to provide a basis for advanced safety control and future commercialization of backpack brush cutters.

Key Words: Backpack brush cutter, Engine safety control, PPE wear detection

Acknowledgement: This work was supported by the Rural Development Administration (RDA), Republic of Korea (No. PJ01780802).

FM-P15

Proceedings of The 12th International Symposium on Machinery and Mechatronics for Agriculture and Biosystems Engineering (ISMAB 2026)
20-24 October 2026, Busan, Republic of Korea

ANALYSIS OF ISO 18497 SAFETY REQUIREMENTS FOR OPEN-FIELD AGRICULTURAL ENVIRONMENTS IN THE REPUBLIC OF KOREA

Seung-hun Lee[1], Qazeem Opeyemi Ogunlowo[1], Chan-min Kim[1], Hee-Woong Seok[1], Sun-hyoung Lee[1], Su-been Ahn[1], Han Kim[1], Jin-seo Choi[1], Yun-Jeong Lee[1], Yoon-Kyu Hur[2] , Jun-seop Mun[1], Hyeon-chae Kim[1], and Rack-woo Kim[2]*

[1] Research Institute of Agriculture and Life Sciences, Seoul National University, Seoul 08826, Republic of Korea
[2] Department of Biosystems Engineering, College of Agriculture and Life Sciences, Seoul National University, Seoul 08826, Republic of Korea
* Corresponding author--Voice: +82-2-880-4605, Email: rack88@snu.ac.kr

Abstract: As autonomous agricultural machinery is increasingly deployed, appropriate safety requirements are needed for operator protection, obstacle response, and the prevention of unintended excursions from operating zones. This study analyzed the principal requirements of ISO 18497 and identified considerations for applying the standard to open-field agricultural environments in the Republic of Korea.

ISO 18497-1 through ISO 18497-4 and relevant standards, safety guidelines, technical reports, and academic literature were reviewed. The analysis focused on operating modes, operator presence, obstacle protection systems, autonomous operating zones, risk-reduction functions, and verification methods. These requirements were examined in relation to small and irregularly shaped fields, paddy levees, irrigation canals, farm roads, sloped terrain, and environments shared by agricultural machinery and people.

The analysis indicated that obstacle detection and stopping conditions, autonomous operating zone boundaries, prevention of boundary excursions, and verification of safety functions are key considerations. More specific application criteria and test scenarios are required to reflect the field configurations and operating conditions of the Republic of Korea. The findings can support the adoption of ISO 18497 as Korean Standards and the development of safety testing and validation criteria for autonomous agricultural machinery.
Key words: autonomous agricultural machinery, ISO 18497, obstacle protection system, autonomous operating zone, safety standard

ACKNOWLEDGEMENTS

"This work was carried out with the support of "Cooperative Research Program for Agriculture Science & Technology Development (Project No. RS-2026-25547672)" Rural Development Administration, Republic of Korea. "

FM-P16

Proceedings of The 12th International Symposium on Machinery and Mechatronics for Agriculture and Biosystems Engineering (ISMAB 2026)
20-24 October 2026, Busan, Republic of Korea

DESIGN AND PRELIMINARY EVALUATION OF A MULTI-CHANNEL PNEUMATIC STRIKER FOR GARLIC HARVESTER DISCHARGE

Kyu-Ho Lee[1], Chun-Gu Lee[1*], Il-Su Choi[1], Seok-Jun Hong[1], Yeong-Hwa Kim[1], Jea-Keun Woo[1], Yun-Jeong Yang[1]

[1]Field Farming Mechanization Division, National Institute of Agricultural Sciences, Rural Development Administration, Jeonju, Korea

*Corresponding Author-- Voice: +82-63-238-4229, Email: cglee0507@korea.kr

Abstract: A multichannel pneumatic striker was designed to support selective foreign-matter removal and reduce sorting labor at a garlic-harvester conveyor discharge. This study presents its mechanical design, a kinematic assessment of target arrival conditions, and separately documented contact observations using controller-commanded channel actuation. The final design specifies 12 independently actuated single-acting pneumatic cylinders, 12 solenoid valves, and 25 × 100 mm plastic fingers, with a nominal cylinder stroke of 30 mm and an approximately 45° upward swing. Individual channel actuation provides a mechanism for spatially selective target contact. A gravity-only point-mass model was evaluated at assumed release speeds of 0.8, 1.0, and 1.2 m/s and an initial direction of +5°. At a 0.40 m drop, calculated flight times were 292.8–296.4 ms, while horizontal displacements ranged from 0.233 to 0.354 m. Thus, similar flight times corresponded to different arrival positions, emphasizing the need to coordinate striker placement with actuation scheduling. Preliminary bench tests demonstrated target contact in 20/20 finger-center trials and 10/10 trials at one internal boundary with one adjacent finger actuated. These observations indicate contact reachability at the placements; equivalence between the tested configuration and the final design requires confirmation. Further tests will investigate lateral target placements and spatial overlap conditions between adjacent channels. The design and calculated arrival conditions provide a physical basis for subsequent vision-guided synchronization, with removal effectiveness and garlic protection as distinct outcomes for further evaluation.

Key Words: Garlic harvesting, Pneumatic striker, Multichannel actuation, Trajectory analysis, Target contact

INTRODUCTION

A locally actuated striker at a garlic-harvester conveyor discharge is intended to contact selected foreign-material targets. Its evaluation should distinguish target contact from downstream removal and effects on nearby garlic bulbs. Garlic-harvester evaluations have likewise reported soil separation and bulb damage as distinct outcomes (Borkar et al., 2018). Wang et al. (2022) linked potato discharge trajectories to rod-ejector size and position. Here, the assembly design, mechanism views and physical finger detail are examined alongside

conditional trajectory calculations and separately contact observations.
The objectives were to describe the multichannel striker mechanism, calculate scenario-based arrival conditions, and summarize controller-commanded contact observations for subsequent placement and synchronization studies.

MATERIALS AND METHODS

Mechanical configuration

Figure 1 combines the assembly drawing (a), prototype photograph (b), drawing-defined advance and return positions (c, d), and a close-up of the striker finger (e). It relates the mechanism design to the physical finger structure.

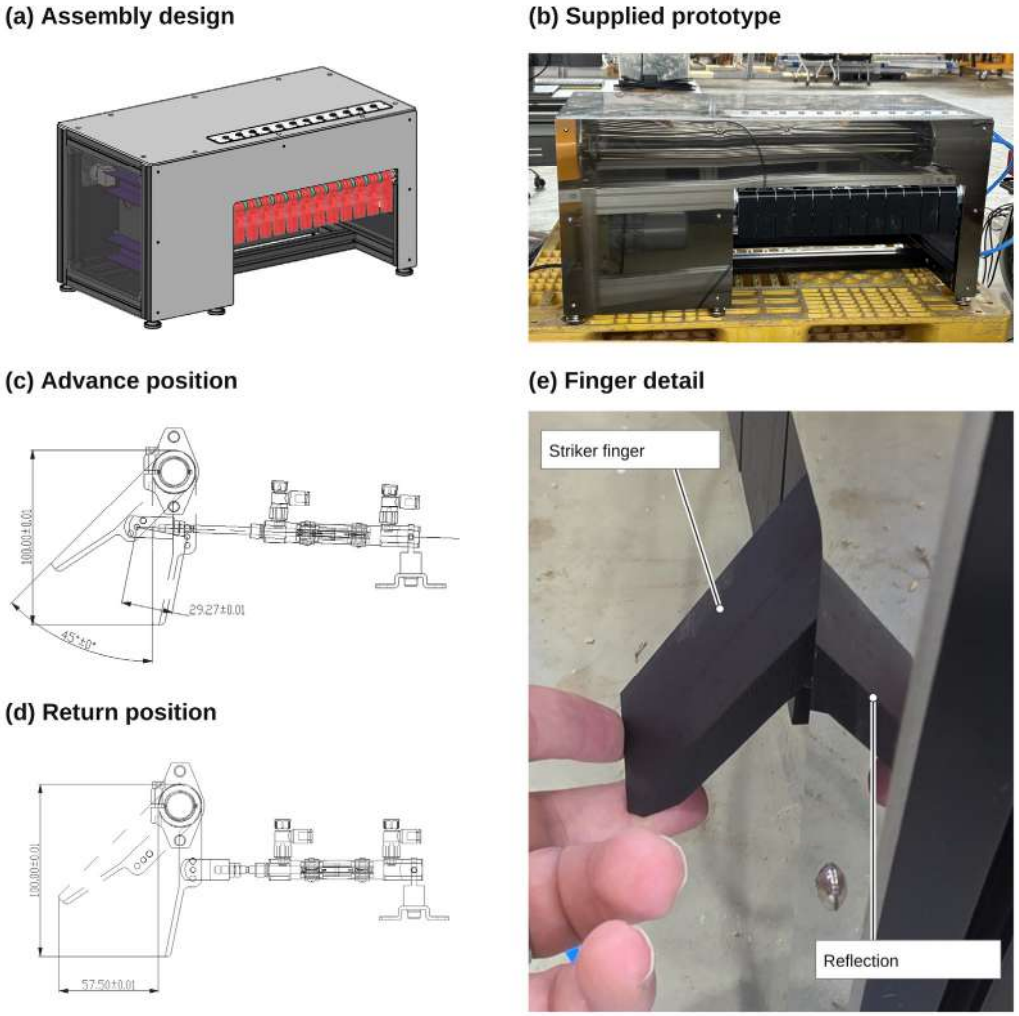

Fig. 1. Multichannel striker configuration: (a) assembly drawing; (b) supplied prototype; (c) advance and (d) return positions from the fabrication drawing; and (e) close-up photograph of a striker finger. Drawing annotations are displayed in grayscale. Reflected features are identified in (e). Panel scales differ.

Kinematic assessment

A gravity-only point-mass model was evaluated at assumed object release speeds of 0.8, 1.0 and 1.2 m/s and an initial direction of +5°, based on target operational specifications. The

release point is the origin, x is forward and y is upward. The trajectories are described by Eqs. (1) and (2) (Moebs et al., 2016).

$$x(t) = v_0 \cos(\theta_0)\ t \quad (1)$$

$$y(t) = v_0 \sin(\theta_0)\ t - \frac{gt^2}{2} \quad (2)$$

where:
x and y = distances (m)
t = time after release (s)
v_0 = assumed release speed (m/s)
θ_0 = the direction above $+x$
g = 9.81 m/s^2

$$b = v_0 \sin(\theta_0); \quad t_h = \frac{b + \sqrt{b^2 + 2gh}}{g}; \quad x_h = v_0 \cos(\theta_0)\ t_h \quad (3)$$

where:
$h = -y$ (m)
t_h = arrival time (s)
x_h = displacement (m)

The designated target interception zone was set to x = 0.15-0.25 m and h = 0.20-0.40 m, interpreted relative to the same release origin. They are a design scenario rather than a measured swept volume. Air resistance, target rotation, transverse motion and the finger trajectory are outside this pre-impact calculation.

Controller-commanded bench-test conditions

Bench tests used controller-commanded actuation of selected channels. The discharge conveyor was operated at an input speed of 85 rpm. Ten nominal 60 mm and ten nominal 80 mm targets were prepared, with respective mean masses of 147.3 and 231.7 g. These preparation counts are separate from the trial totals. Evaluated target positions included a finger center and one internal boundary, where one adjacent finger was actuated. The endpoint was target contact.

RESULTS & DISCUSSION

Calculated arrival conditions

The mechanism positions in Fig. 1 describe the intended finger motion, whereas Fig. 2 shows the calculated target paths before contact. Table 1 lists representative arrivals at two drop heights under the +5° scenario. At a 0.40 m drop, calculated flight times ranged from 292.8 to 296.4 ms and horizontal displacement from 0.233 to 0.354 m. The approximately 0.121 m spread in arrival position despite similar flight times highlights the need to consider placement and actuation scheduling together.

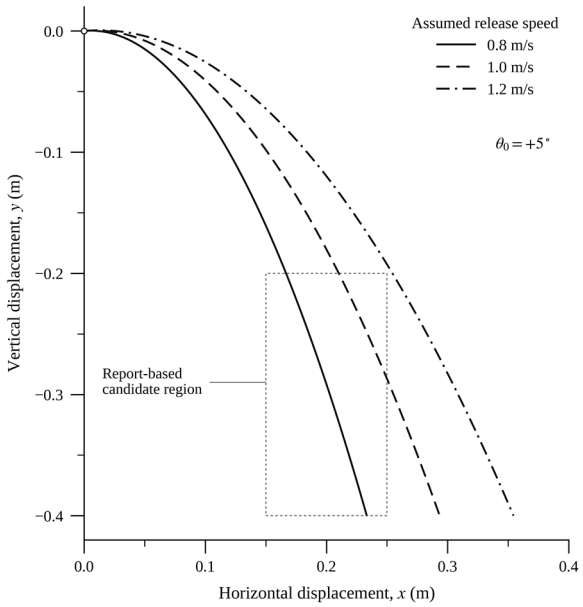

Fig. 2. Calculated pre-impact trajectories for three assumed release speeds and an initial direction of +5°. The unfilled rectangle denotes report-based candidate coordinates under a common-origin assumption; it is not a validated interception region.

These calculations provide scenario-based coordinates for placement studies, rather than a prediction of contact with the moving finger. Approximately 0.30 s denotes flight duration from release to the specified drop height, not an established sensing-to-actuation delay budget.

Table 1. Representative model calculations for an initial direction of +5°.

Assumed speed (m/s)	Drop (m)	Arrival time (ms)	Horizontal position (m)
0.8	0.20	209.2	0.167
1.0	0.20	211.0	0.210
1.2	0.20	212.9	0.254
0.8	0.40	292.8	0.233
1.0	0.40	294.6	0.293
1.2	0.40	296.4	0.354

Target-contact observations

Target contact was successfully achieved in 20/20 trials and 10/10 trials at one internal boundary (Table 2). These observations support reachability at the placements. Conditional exact intervals were calculated separately under an independent-trial assumption.

Table 2. Target-contact experimental results with controller-commanded actuation.

Placement	Contact / trials	Conditional 95%
Finger center	20 / 20	83.2-100
One internal boundary	10 / 10	69.2-100

The photographs in Fig. 1 document the prototype and finger structure; contact counts are reported separately in Table 2 While initial bench tests demonstrated contact reachability, subsequent work will further characterize in-field sorting dynamics under diverse crop sizes and continuous feed conditions. Contact observations and calculated trajectories therefore provide distinct evidence; downstream removal, non-target retention and garlic damage remain separate evaluation endpoints.

CONCLUSIONS

The assembly and mechanism drawings, together with photographs of the prototype and striker finger, describe the multichannel striking mechanism for garlic-harvester discharge. The conditional time–position analysis supports placement studies, while controller-commanded contact observations support reachability at the placements. Further tests will examine lateral target placements and spatial overlap between adjacent channels to characterize contact coverage and channel-specific performance. Subsequent vision-guided synchronization studies will evaluate downstream removal and garlic protection as distinct outcomes.

ACKNOWLEDGEMENTS

This work was supported by the Cooperative Research Program for Agriculture Science and Technology Development (Project No. PJ01768101) funded by the Rural Development Administration, Republic of Korea.

REFERENCES

Borkar, N. T., P. K. Sahoo, and P. M. Barik. 2018. Design and development of tractor operated garlic harvester with oscillating soil separator. Journal of Agricultural Engineering (India) 55(2): 13–20. doi:10.52151/jae2018552.1650.

Moebs, W., S. J. Ling, and J. Sanny. 2016. University Physics Volume 1. Section 4.3, Projectile Motion. OpenStax. https://openstax.org/books/university-physics-volume-1/pages/4-3-projectile-motion. Accessed 9 September 2026.

Wang, S., J. Geng, X. Rao, and H. Xu. 2022. Simulation and experimental study of potato conveyor trajectory for optimization design of belt-fed potato sorter. Journal of the ASABE 65(2): 379–392. doi:10.13031/ja.14724.

FM-P17

Proceedings of The 12th International Symposium on Machinery and Mechatronics for Agriculture and Biosystems Engineering (ISMAB 2026)
20-24 October 2026, Busan, Republic of Korea

CHARACTERIZATION OF THE DASHING BEHAVIOUR OF A WALKING TRACTOR CONSIDERING OPERATOR RESPONSE

Shuto Ohara[1], Yuya Aoyagi[1*], Takeshi Shikanai[2], Masami Matsui[1], Hideo Tamashiro[1]

[1]Graduate School of Regional Development and Creativity, Utsunomiya University, Japan
[2] Faculty of Agriculture, University of the Ryukyus, Japan
*Corresponding Author-- Voice: +81-28-649-5513, Email: y_aoyagi@a.utsunomiya-u.ac.jp

Abstract: Walking tractors are regarded as posing a serious accident risk: reversing in confined spaces or dashing (sudden forward acceleration) of the machine can lead to serious accidents such as being caught in machinery or entanglement in rotating parts. In this study, a four-degree-of-freedom behaviour simulator was developed for walking tractors considering operator response. By running tillage-travel simulations under various road surface irregularity and friction coefficient combinations, we examined operator influence on dashing behaviour during tillage travel. When the operator response was not considered, the results showed that at friction coefficients of 0.5 or lower the braking resistance was smaller than the tillage resistance, producing dashing regardless of road surface irregularities. At friction coefficients of 0.6 or higher, the walking tractor could travel at a speed close to the set speed; however, as the road surface became rougher, dashing occurred owing to surface irregularities. When the operator response was considered, at friction coefficients of 0.6 or higher, machine pitching induced by a force acting opposite to the travel direction lifted the drive wheels off the ground, reducing the braking resistance and exacerbating dashing.

Key Words: Walking tractor, Operator response, Tillage-travel simulation, Dashing.

INTRODUCTION

The widespread adoption and advancement of agricultural machinery has improved the efficiency of farm work and reduced its physical burden on humans. Concurrently, fatal accidents involving agricultural machinery have become a serious problem. Fatalities per 100,000 agricultural workers reached 14.8 in Japan (MAFF, 2026), 7.9 in the United Kingdom (HSE, 2023), and 18.6 in the United States (BLS, 2026a, b). Internationally, a study conducted in Thailand reported that walking tractors were the leading cause of agricultural-machinery-related injuries (Maiyapakdee et al., 2026). The risk of accidents is regarded as a serious concern in regions such as Southeast and South Asia, where walking tractors are widely used. In Japan, the number of fatal accidents during agricultural work remains high at approximately 280 per year (average for 2015–2024). Furthermore, most of these fatal accidents result from machinery operation: approximately 22 fatal accidents per year involve walking tractors (average for 2015–2024). Walking tractors are used on small-scale farmlands in mountainous and hilly areas and inside greenhouses, where reversing in confined spaces or dashing of the machine can lead to serious accidents such as being caught in machinery or entanglement in rotating parts.

Previous studies have analysed the vibration characteristics and safety of walking tractors using a two-degree-of-freedom behaviour model (Inoue et al., 1994) and have measured the human body load when the operator is trapped between a loop-type handle and an object behind the machine (Umeno et al., 2024). However, these studies have not yet characterised the dangerous dynamic behaviours involved in walking tractor operation. Characterising these dangerous dynamic behaviours through mechanical analysis and formulating effective countermeasures would be beneficial for agricultural work safety.

The dashing behaviour of a walking tractor during tillage occurs when the force applied by the operator to the handlebar acts in addition to the tillage resistance and the braking resistance of the drive wheels. However, few studies have analysed the behaviour of walking tractors during tillage while considering operator response. Therefore, in this study, a four-degree-of-freedom behaviour simulator was developed for walking tractors considering operator response. In formulating the operator model, we introduced not only physical characteristics but also cognitive and decision-making abilities and reaction time as input variables for the model. Additionally, tillage-travel simulations were conducted under various road surface irregularity and friction coefficient combinations, and the operator's influence on dashing behaviour was examined.

MATERIALS AND METHODS

DYNAMIC MODEL OF A WALKING TRACTOR

Fig. 1 shows the behaviour models from the side and rear views during tillage operation for a walking tractor. We formulated the equations of motion for four degrees of freedom: vertical, pitching, rolling, and horizontal direction. The equations of motion are given in Eqs. (1)–(4), and the drive-wheel and rotary-unit reaction force calculation formulas are given in Eq. (5). Based on these equations of motion, we developed an original program using MATLAB/Simulink.

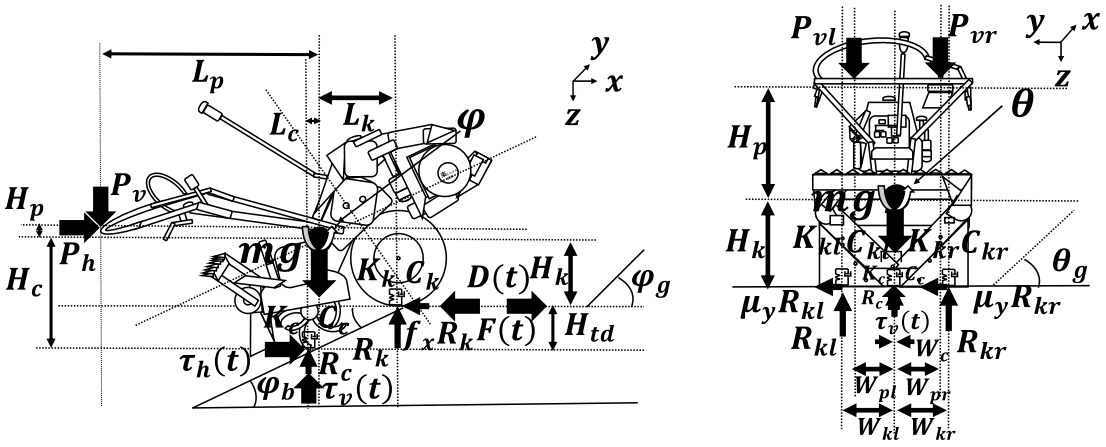

Fig.1 Behavior models during tillage travel (side (left) and rear (right) views).

The tillage resistance reaction forces and angles of action for the downcut and upcut blades were generated using lognormal and normal random numbers, respectively. Assuming a tillage depth of 0.16 m, Table 1 provides the maximum, mean, and standard deviation of each blade type (Kawamura et al., 1980). Based on the rotary structure of the test machine, the number

of blades in action for each type was determined based on tillage depth. The logarithmic standard deviation and mean were calculated from the values listed in Table 1 using Eqs. (6) and (7), respectively, and the tillage resistance reaction forces and angles of action are given by Eqs. (8) and (9), respectively. The tillage resistance reaction forces acting in the vertical and horizontal directions are given by Eqs. (10) and (11), respectively. Finally, the braking resistance and driving force are given by Eqs. (12) and (13), respectively.

$$m\ddot{Z} = mg - (R_{kr} + R_{kl} + R_c)\cos\theta_g \cos\varphi_g + f_x(R_{kr} + R_{kl})\sin\varphi_g + \mu_y(R_{kr} + R_{kl})\sin\theta_g \\ -\tau_v(t)\cos\theta_g \cos\varphi_g - \tau_h(t)\sin\varphi_g + F(t)\sin\varphi_g + P_{vr} + P_{vl} - D(t)\sin\varphi_g \quad (1)$$

$$m\ddot{X} = -(R_{kr} + R_{kl} + R_c)\cos\theta_g \sin\varphi_g - f_x(R_{kr} + R_{kl})\cos\varphi_g \\ -\tau_v(t)\cos\theta_g \sin\varphi_g - F(t)\cos\varphi_g - F_{\tau h}(t)\cos\varphi_g + \tau_h(t)\cos\varphi_g + P_{hr} + P_{hl} \quad (2)$$

$$I_y\ddot{\varphi} = (R_{kr} + R_{kl})L_k - f_x(R_{kr} + R_{kl})H_k - \big(R_c + \tau_v(t)\big)L_c + \tau_h(t)H_c \\ +\big(D(t) - F(t)\big)H_k + (P_{vr} + P_{vl})L_p - (P_{hr} + P_{hl})H_p \quad (3)$$

$$I_x\ddot{\theta} = (R_{kr} - R_{kl})W_k - \mu_y(R_{kr} + R_{kl})H_k - P_{vr}W_{pr} + P_{vl}W_{pl} + \big(R_c + \tau_v(t)\big)W_c \quad (4)$$

$$R = (Z + \varphi L + \theta W)K + \big(\dot{Z} + \dot{\varphi}L + \dot{\theta}W\big)C \quad (5)$$

$$\sigma_{ln} = \left(6 - \sqrt{36 - 8ln(\tau_{max}/\tau_{mean})}\right)/2 \quad (6)$$

$$\mu_{ln} = ln(\tau_{mean}) - (\sigma_{ln})^2/2 \quad (7)$$

$$\tau(t) = e^{(\mu_{ln} + \sigma_{ln}\varepsilon_\tau)} \quad (\varepsilon_\tau \text{ is a normal random variable with mean 0 and variance 1}) \quad (8)$$

$$\alpha(t) = \alpha_{mean} + \alpha_{sd}\varepsilon_\alpha \quad (\varepsilon_\alpha \text{ is a normal random variable with mean 0 and variance 1}) \quad (9)$$

$$\tau_v(t) = \tau(t)\sin\alpha(t) \quad (10)$$

$$\tau_h(t) = \tau(t)\cos\alpha(t) \quad (11)$$

$$F(t) = |\tau_h|, \ if(|\tau_h| < |\mu_x(R_{kr} + R_{kl})|, \ \tau_h > 0) and \big(\dot{X} = V_{set}\big) \\ = |\mu_x(R_{kr} + R_{kl})|, \quad if\big(\dot{X} > V_{set}\big) \quad (12)$$

$$D(t) = |\tau_h|, \ if(|\tau_h| < |\mu_x(R_{kr} + R_{kl})|, \ \tau_h < 0) and \big(\dot{X} = V_{set}\big) \\ = |\mu_x(R_{kr} + R_{kl})|, \quad if\big(\dot{X} < V_{set}\big) \quad (13)$$

Table 1 Tillage resistance reaction force $\tau(t)$ and angle of action $\alpha(t)$ for each blade type.

		downcut blade		upcut blade	
Item		$\boldsymbol{\tau}$[N]	$\boldsymbol{\alpha}$[°]	$\boldsymbol{\tau}$[N]	$\boldsymbol{\alpha}$[°]
maximum:	$(\tau_{max}, \alpha_{max})$	**240**	**50**	**290**	**220**
mean:	$(\tau_{mean}, \alpha_{mean})$	**80**	**40**	**60**	**210**
standard deviation:	(τ_{sd}, α_{sd})	**50**	**4**	**80**	**2**

DYNAMIC MODEL OF THE OPERATOR (TRAVEL POSTURE DURING TILLAGE)

Referring to the anthropometric database (AIST, 2001), the linear regression equations of body

segment dimensions against stature based on anthropometric data for each percentile are given by Eqs. (14)–(18). In this study, a 50th-percentile young male was assumed with a stature of $H_{ym} = 1.71$ m. The basic travel posture is defined as an operating posture that imposes a relatively low physical load on the operator, in which the upper arm is in contact with the trunk and the forearm angle relative to the upper arm falls within 45°–90° (Sicat et al., 1999). The handle height corresponding to the basic posture was determined for each body parameter and selected within the four-step adjustment range of the test machine. The angle formed between the forearm and upper arm is given by Eq. (19). The angle formed between the upper arm and trunk axis when the machine moves away from the operator and the arm becomes fully extended is given by Eq. (20). The distance travelled by the handle axis from the basic posture to the point of full arm extension is defined as the limit distance and is given by Eq. (21).

As human behaviour involves a stronger derivative action and almost no integral action in situations in which control is difficult (Hayashi, 1977), the operator's tracking of the machine was modelled using proportional-derivative (PD) control. For PD control, $K_P = 9200$ and $K_D = 3900$ were set. The reference value was defined as the fore-aft distance between the operator and machine, and the output was defined as the operator's walking force. The operator's cognitive, decision-making, and motor abilities were represented by applying a moving average to the control reference value. The operator's response delay was represented by adding a time delay to the moving-averaged reference value. The equation of motion for the operator's fore-aft tracking movement is given by Eq. (22), while the walking force is given by Eq. (23). Based on these equations, a state in which the relative distance between the operator and the machine exceeds the limit distance was defined as "dashing"—indicating that the operator can no longer keep up with the machine—and the forces acting on the handlebar in the direction opposite to the operator's direction of travel (P_{hr} and P_{hl}) were added accordingly.

$$L_{se} = 0.25H_{ym} - 0.09 \tag{14}$$

$$L_{eh} = 0.25H_{ym} - 0.09 \tag{15}$$

$$L_{eg} = 0.70H_{ym} - 0.16 \tag{16}$$

$$L_{sh} = L_{se} + L_{eh} \tag{17}$$

$$L_{sg} = L_{se} + L_{eg} \tag{18}$$

$$\theta_e = \cos^{-1}\left(\frac{L_{eg} - H_{hdl}}{L_{eh}}\right) \tag{19}$$

$$\theta_s = \cos^{-1}\left(\frac{L_{sg} - H_{hdl}}{L_{sh}}\right) \tag{20}$$

$$L_{sf} = L_{sh}\sin\theta_s - L_{eh}\sin\theta_e \tag{21}$$

$$m_h\ddot{x}_h = F_w \tag{22}$$

$$F_w = \left\{K_P\left(\bar{x}_d(t) - x_h(t)\right) + K_D\left(\dot{\bar{x}}_d(t) - \dot{x}_h(t)\right)\right\} \tag{23}$$

TILLAGE-TRAVEL SIMULATION CONDITIONS

We compared the behaviour of the walking tractor model with and without operator response considered. The travel speed was set to 0.88 m/s. The force applied to the handlebar was 82.8 N vertically downward (the resultant of P_{vr} and P_{vl}) in both models (Umeno et al., 2021), and in the model considering operator response, 100 N was additionally applied horizontally, opposite to the direction of travel (the resultant of P_{hr} and P_{hl}), when dashing occurred. Based on previous studies, the operator model parameters were set to a moving-average window of 1 s and a time delay of 0.3 s (Hashimoto et al., 1970; Uno et al., 1999). Road surfaces were generated using a road-surface generation algorithm (Watanabe et al., 2017); based on the road-surface evaluation reference lines (ISO, 1995), five road surfaces with different degrees of roughness ($P(f_0) = 2 - 8192$) were generated. The friction coefficient between the drive wheels and the road surface varied between 0.1 and 1.0 in increments of 0.1. For each road surface and friction coefficient combination, 30 tillage-travel simulations were conducted. When dashing occurred (i.e., when the relative distance between the operator and machine exceeded the limit distance), the behaviour was evaluated over 5 s following the onset of dashing, and the influence of operator response on dashing behaviour was examined.

RESULTS & DISCUSSION

Figs. 2 and 3 show the occurrence of dashing for each road surface roughness and friction coefficient combination for the models without and with operator response, respectively. In the figures, × indicates conditions under which dashing occurred and continued for 5 s, indicates conditions under which dashing did not occur, and indicates conditions under which dashing occurred but subsided within 5 s. As shown in Fig. 2, at friction coefficients of 0.5 or lower, the braking resistance was smaller than the tillage resistance, and dashing occurred regardless of road surface irregularity. At friction coefficients of 0.6 or higher, the braking resistance was larger than the tillage resistance, and the machine could travel at approximately the set speed. However, as the road surface became rougher, dashing occurred owing to the effect of surface irregularity. As shown in Fig. 3, at friction coefficients of 0.6 or higher, considering the force acting opposite to the travel direction worsened the occurrence of dashing.

Figs. 4 and 5 show the travel speed, set speed, and horizontal component of acceleration at a friction coefficient of 0.6 for the model without and with operator response, respectively, and Figs. 6 and 7 show the left and right drive-wheel reaction forces, horizontal component of the tillage resistance, and pitching angle. As shown in Figs. 4 and 5, after dashing occurred at 46.34 s, the negative acceleration became dominant in the case without operator response, and the speed decreased to the set speed at 47.22 s. Conversely, in the case considering operator response, positive acceleration became dominant, and the speed reached approximately 1.4 m/s at 47.22 s. Comparing Figs. 6 and 7 reveals that in both cases the tillage resistance remained within a certain range (mean of approximately 210 N) during the 46.34–47.22-s interval, and that the braking resistance averaged approximately 240 N in the case without operator response. In the case considering operator response, machine pitching caused by the force acting on the handlebar opposite to the travel direction lifted the drive wheels off the ground, and the braking resistance decreased to a mean of approximately 80 N. When the force acting opposite to the travel direction was added as a resisting force, the mean value was approximately 180 N.

These results show that, regarding the influence of the operator on dashing behaviour, the operator's inability to keep up with the machine produces a force on the handlebar acting opposite to the travel direction, which causes the machine to pitch and lifts the drive wheels off the ground, thereby worsening the occurrence of dashing.

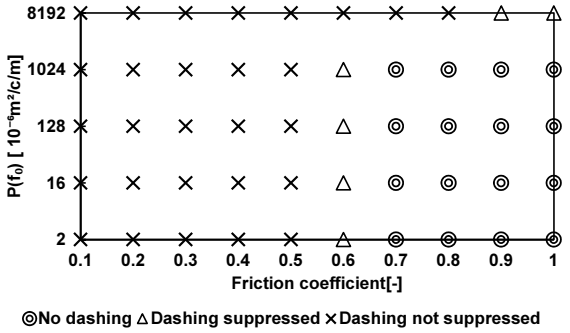

Fig. 2 Occurrence of dashing for each road surface roughness and friction coefficient combination in the model without operator response.

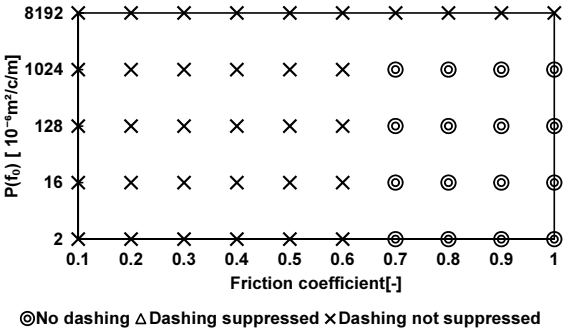

Fig. 3 Occurrence of dashing for each road surface roughness and friction coefficient combination in the model with operator response.

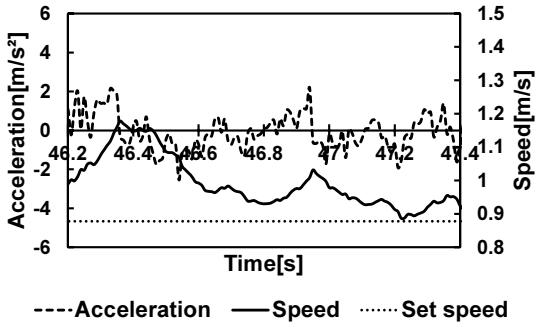

Fig. 4 Travel speed and acceleration in the model without operator response.

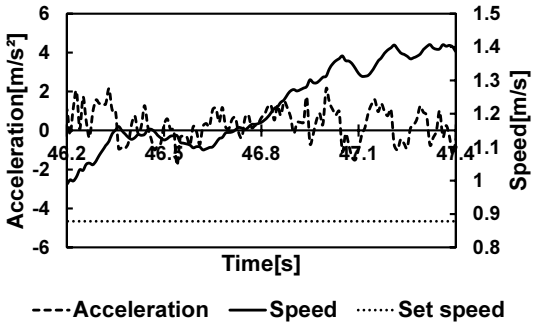

Fig. 5 Travel speed and acceleration in the model with operator response.

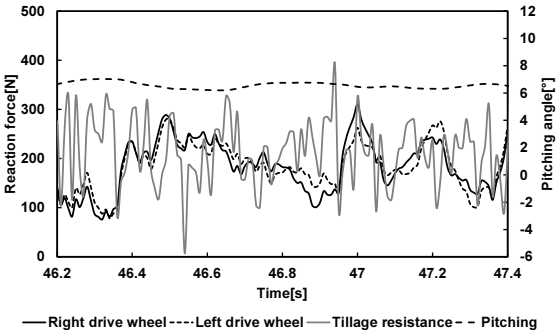

Fig. 6 Reaction forces and pitching angle in the model without operator response.

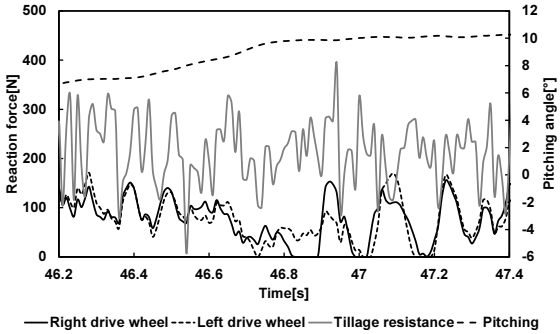

Fig. 7 Reaction forces and pitching angle in the model with operator response.

CONCLUSIONS

Walking tractors are regarded as posing a serious accident risk: reversing in confined spaces or dashing of the machine can lead to serious accidents such as being caught in machinery or entanglement in rotating parts. In this study, a four-degree-of-freedom behaviour simulator was developed for walking tractors considering operator response, and tillage-travel simulations were conducted under various road surface irregularity and friction coefficient combinations to examine the influence of the operator on dashing behaviour. When operator response was not considered, at friction coefficients of 0.5 or lower, the braking resistance was smaller than the tillage resistance, and dashing occurred regardless of the road surface irregularity. At friction coefficients of 0.6 or higher, the machine could travel at approximately the set speed; however, as the road surface became rougher, dashing occurred owing to the effect of surface irregularity. When operator response was considered, at friction coefficients of 0.6 or higher, machine pitching caused by the force acting opposite to the travel direction lifted the drive wheels off the ground, reducing the braking resistance, and thereby worsening the occurrence of dashing. In future work, it will be important to establish safe operating methods for each combination of conditions and provide guidance on how to respond to emergencies.

ACKNOWLEDGEMENTS

This work was supported by a Utsunomiya University Grant for the Advancement of Early-Career Faculty and a Utsunomiya University Graduate School of Regional Development and Creativity Research Encouragement Grant for Graduate Students.

REFERENCES

AIST. 2001. AIST anthropometric database 1991-92. National Institute of Advanced Industrial Science and Technology. Available at: https://www.airc.aist.go.jp/dhrt/91-92/. Accessed September 7, 2026.

BLS. 2026a. Census of fatal occupational injuries, Table 3: Fatal occupational injuries for selected occupations, 2020-24. U.S. Bureau of Labor Statistics. Available at: https://www.bls.gov/news.release/cfoi.t03.htm. Accessed August 20, 2026.

BLS. 2026b. Occupational outlook handbook, agricultural workers. U.S. Bureau of Labor Statistics. Available at: https://www.bls.gov/ooh/farming-fishing-and-forestry/agricultural-workers.htm. Accessed August 20, 2026.

Hashimoto, H., and H. Akashi. 1970. Limit of human controller in man-machine systems. Jpn. J. Ergon. 6(6): 259-266.

Hayashi, Y. 1977. Man's control behavior. IATSS Rev. 3(4): 223-230.

HSE. 2023. Fatal injuries in agriculture, forestry and fishing in Great Britain, 1 April 2022 to 31 March 2023. Health and Safety Executive. Available at: https://www.hse.gov.uk/agriculture/assets/docs/agriculture-fatal-injuries-2023.pdf. Accessed September 7, 2026.

Inoue, E., O. Kawatate, and J.-S. Choi. 1994. Study on the dynamic stability of a walking tractor (2): Dynamic characteristics and their analysis. Sci. Bull. Fac. Agric. Kyushu Univ. 48(3/4):

219-230.

ISO. 1995. ISO 8608: Mechanical vibration — Road surface profiles — Reporting of measured data. Geneva, Switzerland: International Organization for Standardization.

Kawamura, N., and S. Shibusawa. 1980. Studies of deeper rotary tillage (I): Model test of tilling with two blades. J. Jpn. Soc. Agric. Mach. 42(2): 211-219.

MAFF. 2026. Promotion policy for farm work safety measures in 2026. Ministry of Agriculture, Forestry and Fisheries. Available at: https://www.maff.go.jp/j/seisan/sien/sizai/s_kikaika/anzen/attach/pdf/zennkoku-38.pdf. Accessed September 7, 2026.

Maiyapakdee, C., S. Norkaew, N. Homkham, T. Baubhom, K. Ivanovitch, and T. Kaewdok. 2026. Occupational prevalence with agricultural machinery related injuries among rice farmers in Bang Rakam district, Phitsanulok Province, Thailand. Clin. Epidemiol. Glob. Health 37: 102285.

Sicat, J. C. V., M. Mitarai, and M. Nagata. 1999. Ergonomic design of a walking tractor handle. J. Jpn. Soc. Agric. Mach. 61(2): 53-59.

Umeno, S., M. Tomita, M. Tanaka, I. Harada, M. Matsumoto, and Y. Kikuchi. 2021. Measurement of loads on the handle of a walking tractor: loads generated during tilling and entrapment. J. Jpn. Soc. Agric. Mach. Food Eng. 83(2): 125-126.

Umeno, S., M. Tomita, M. Tanaka, Y. Kikuchi, and M. Matsui. 2024. Measurement of mechanical action during entrapment by a walking tractor: elucidation of the entrapment mechanism assuming an operator restrained by a loop-type handle. J. Jpn. Soc. Agric. Mach. Food Eng. 86(4): 221-230.

Uno, H., and K. Hiramatsu. 1999. Relationship between time margin and driver's steering avoidance in an emergent situation. Jpn. J. Ergon. 35(4): 219-227.

Watanabe, M., and K. Sakai. 2017. Road surface generation algorithm for a tractor driving simulator. J. Jpn. Soc. Agric. Mach. Food Eng. 79(2): 149-157.

NOMENCLATURE

	Nomenclature	Unit
m	Mass of Walking Tractor	kg
g	Gravitational Acceleration	m/s^2
τ_v	Vertical Component of Tilling Resistance Force	N
τ_h	Horizontal Component of Tilling Resistance Force	N
F	Braking Resistance	N
D	Driving Force	N
R_k	Reaction Force of Wheel	N
R_c	Reaction Force of Rotary	N
P_v	Vertical Component of Force Acting on Handle	N
P_h	Horizontal Component of Force Acting on Handle	N
f_x	Horizontal Rolling Resistance of Driving Wheel	N
f_y	Lateral Rolling Resistance of Driving Wheel	N
Z	Vertical Displacement	m
X	Forward Displacement	m
φ	Pitching Angle	rad
θ	Rolling Angle	rad
φ_g	Pitching Angle due to Terrain Slope	rad
θ_g	Rolling Angle due to Terrain Slope	rad
φ_b	Pitching Angle due to Tilling Depth	rad
μ_x	Horizontal Friction Coefficient of Driving Wheel	$-$
μ_y	Lateral Friction Coefficient of Driving Wheel	$-$
L_k	Horizontal Distance from Centre of Gravity to Driving Wheel Axle	m
W_k	Lateral Distance from Centre of Gravity to Driving Wheel Axle	m
H_k	Vertical Distance from Centre of Gravity to Driving Wheel Axle	m
L_c	Horizontal Distance from Centre of Gravity to Point of Action of Resultant Rotary Tilling Resistance	m
W_c	Lateral Distance from Centre of Gravity to Point of Action of Resultant Rotary Tilling Resistance	m
H_c	Vertical Distance from Centre of Gravity to Point of Action of Resultant Rotary Tilling Resistance	m
L_p	Horizontal Distance from Centre of Gravity to Point of Action on Handle	m
W_p	Lateral Distance from Centre of Gravity to Point of Action on Handle	m
H_p	Vertical Distance from Centre of Gravity to Point of Action on Handle	m
H_{td}	Tilling Depth	m
σ_{ln}	Logarithmic Standard Deviation	$-$
μ_{ln}	Logarithmic Mean	$-$
V_{set}	Set Speed	m/s
L_{se}	Length from Shoulder to Elbow	m
L_{eh}	Length from Elbow to Handle Grip Axis	m
L_{eg}	Height from Elbow to Ground	m
L_{sh}	Length from Shoulder to Handle Grip Axis	m
L_{sg}	Height from Shoulder to Ground	m

FM-P18

Proceedings of The 12th International Symposium on Machinery and Mechatronics for Agriculture and Biosystems Engineering (ISMAB 2026)
20-24 October 2026, Busan, Republic of Korea

A STUDY ON THE PREDICTION OF DRAFT AND VERTICAL FORCES DURING MOULDBOARD PLOUGHING USING MACHINE LEARNING

Shin-Young Noh[1], Dae-Wi Jeong[1], Min-Seung Kim[1], Se-O Choi[1], Ye-Na Lee[1], Yeon-Soo Kim[1,2,3]*, Jae-Sung Park[1,3], Yong-Joo Kim[4,5,6], Sang-Dae Lee[7], Jeong-Gil Kim[7], Seung-Je Cho[7]

[1]A Department of Bio-Industrial Machinery Engineering, Pusan National University, Miryang 50463, Republic of Korea
[2]A Major of Natural Resources Systems Engineering, Pusan National University, Yangsan 50612, Republic of Korea
[3]Life and Industry Convergence Research Institute, Pusan National University, Miryang 50463, Republic of Korea
[4]Eco-Friendly Hydrogen and Electric Agricultural Machinery Research Institute, Chungnam National University, Daejeon 34134, Republic of Korea
[5]Department of Smart Agricultural Systems and Mechanical Engineering, Chungnam National University, Daejeon 34134, Republic of Korea
[6]Department of Smart Agriculture Systems, Chungnam National University, Daejeon 34134, Republic of Korea
[7]Specialized Machinery and Robotics Group, Korea Institute of Industrial Technology, Gimje 54325, Korea
*Corresponding Author-- Voice: +82-10-7748-6990, Email: yskim23@pusan.ac.kr

Abstract: Draft and vertical forces are important for evaluating tractor load characteristics and tillage performance. During mouldboard ploughing, these forces change continuously due to the interaction between the soil and the implement. Previous machine-learning studies have mainly focused on predicting draft force using tractor operating data. However, studies predicting both draft and vertical forces during mouldboard ploughing are limited. In this study, field experiments were conducted in Dangjin, Chungcheongnam-do, Korea, using a 42 kW-class tractor (TX58, TYM, Korea) equipped with a six-row mouldboard plough (WJSP-6S, Woongjin, Korea). The tractor was operated at the M3 gear stage (7.18 km/h). During the field test, tractor load and performance data were measured using a load measurement system. Tillage depth, travel speed, engine speed, engine torque, front and rear wheel torque, and main hydraulic pressure were used as input variables to predict draft and vertical forces. A multilayer perceptron-based artificial neural network (MLP-ANN) was used to develop a prediction model based on the measured field data. The performance of the developed model was evaluated by comparing the predicted and measured draft and vertical forces using R^2 and RMSE. The developed model is expected to provide a useful method for estimating draft and vertical forces and evaluating tractor–implement performance during tillage operations.

Key Words: Agricultural tractor, Machine learning, Artificial Neural Network, Tillage force, Mouldboard plough

ACKNOWLEDGEMENTS

This work was supported by the Ministry of Agriculture, Food and Rural Affairs (MAFRA), through the Korea Institute of Planning and Evaluation for Technology in Food, Agriculture and Forestry (IPET), under the Offload Smart Agricultural Utilization Model Development Project (RS-2025-02313136).

FM-P19

Proceedings of The 12th International Symposium on Machinery and Mechatronics for Agriculture and Biosystems Engineering (ISMAB 2026)
20-24 October 2026, Busan, Republic of Korea

FATIGUE BEHAVIOR ANALYSIS AND LIFE ASSESSMENT OF A SCALED HOLLOW CYLINDICAL RUBBER FENDER UNDER FULLY COMPRESSIVE LOADING

Yung-Chuan Chiou[1*], Po-Yu Weng[2], Bo- Jyun Lin[3]

[123] Department of Biomechatronic Engineering, National Chiayi University, No. 300 Syuefu, Chiayi City 600355, Taiwan

*Corresponding Author-- Voice: +008-271-7667, Email: solas@mail.ncyu.edu.tw)

Abstract: In this study, a scaled hollow cylindrical rubber fender with a height of 100 mm was investigated. Fully compressive cyclic fatigue tests were conducted under five different compression ranges to characterize the cyclic response of the scaled rubber fender at different compression levels. Based on the experimental results, fatigue-life curves were established using the strain range and stress range as fatigue-damage parameters to predict the fatigue life of the hollow cylindrical rubber fender. Furthermore, based on the observed cyclic responses during the fully compressive tests, energy-based damage parameters were proposed to improve the prediction of the fatigue life of the scaled rubber fender under fully compressive cyclic displacement loading.

Key Words: Rubber fender; fatigue life; fully compressive cyclic loading.

INTRODUCTION

Marine fenders are cushioning devices installed in harbors, as shown in Fig. 1. They absorb the impact energy generated during vessel berthing through deformation while reducing the reaction force, thereby protecting wharves and quay walls and minimizing the risk of structural damage. With the advancement of globalization, maritime transportation has become a vital link connecting national economies. Consequently, the number of vessels engaged in maritime trade and their sailing frequency have gradually increased, resulting in increasingly intensive harbor operations. In other words, rubber fenders installed at port terminals are repeatedly subjected to vessel impact loads throughout their service life. Such cyclic loading may cause progressive damage accumulation within the rubber, eventually leading to crack initiation and deterioration of fender performance. Therefore, evaluating the fatigue damage of rubber fenders under repeated loading is essential for ensuring port safety and developing appropriate maintenance strategies. From this perspective, the present study focuses on hollow cylindrical rubber fenders, which are widely used in port facilities. Systematic fatigue tests were conducted to investigate their



Fig.1: rubber fender installed in harbors

cyclic mechanical response and subsequently evaluate their fatigue life.

MATERIALS AND METHODS

The H2000 hollow cylindrical rubber fender (Height=2000mm) manufactured by Chih Cheng Rubber Factory Co., Ltd., Taiwan, was adopted as the prototype, and geometrically scaled specimens at a scale ratio of 1:20 were fabricated for performance and fatigue testing. In accordance with the PIANC guidelines [1], the performance test consisted of a preliminary compression procedure involving three repeated compression cycles, followed by the main compression test. All compression tests were conducted at a constant displacement rate of 0.1 mm/s up to a maximum compression displacement of 65 mm. Full-compression cyclic fatigue tests were conducted on the experimental fenders under five prescribed strain-range conditions using stroke control in this study. Five compression displacement ranges—50, 45, 38, 30, and 25 mm—were investigated under fully compressive cyclic loading with a sinusoidal waveform. Each test was terminated when the cyclic load range decreased by 20% from its initial value.

RESULTS & DISCUSSION

Figure 2 presents the experimental stress–strain curves of the rubber fender specimens. The dashed lines represent the individual experimental curves, whereas the solid line represents the mean curve. The close agreement among the individual curves demonstrates the high repeatability of the experimental results. Therefore, the mean curve was used as the basis for the subsequent analyses. All curves exhibited a characteristic “initial increase–subsequent decrease–final increase” trend, confirming that the tested fender was a buckling-type rubber fender. Figures 3–7 show the final deformation configurations of the rubber fenders subjected to cyclic compression displacement ranges of 25, 30, 38, 45, and 50 mm, respectively. Each fatigue test was terminated when the cyclic load amplitude decreased by 20% from its initial value. As shown in Figs. 3(a)–(e), all specimens exhibited buckling-dominated fatigue failure.

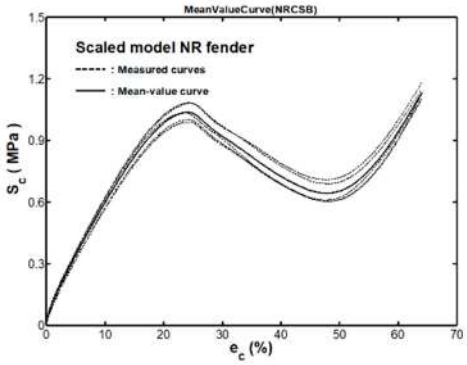

Fig.2: Comparison were made between the measured S_c-e_c curves (dash-lines) and the mean S_c-e_c curves (solid-line) obtain from individual tested scaled rubber fender.

(a) **(b)** **(c)**





Fig.3 Failure configuration of the scaled rubber fender under cyclic compression displacement range of (a) 25 mm, (b) 30mm, (c) 38mm，(d)45mm and (e) 50mm.

The specimen subjected to the 50 mm displacement range exhibited a second-mode buckling failure, as shown in Fig. 3(e), whereas the other specimens exhibited first-mode buckling failure.In this study, three physical indices—the cyclic stress-range index, cyclic energy-absorption index, and cyclic stored-energy index—were selected to characterize the evolution of the cyclic behavior of the experimental fenders. These indices are defined in Fig. 4(a), while their relationships with the number of loading cycles are presented in Figs. 4(b)–4(d), respectively.

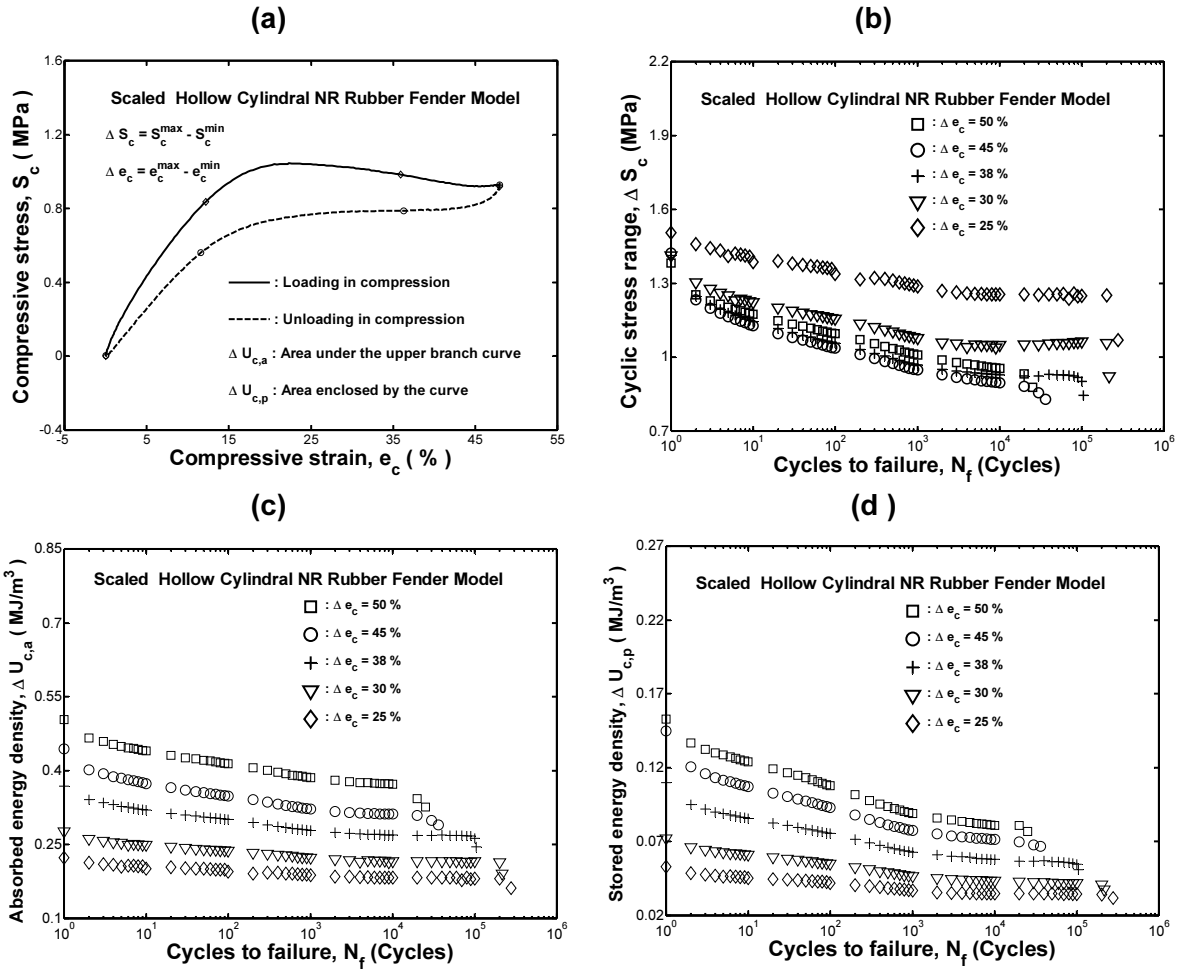

Figure 4. Definitions and fatigue-cycle-dependent variations of the cyclic performance indices: (a) definition of the cyclic indices; (b) cyclic stress range; (c) cyclic absorbed energy density;

and (d) cyclic stored energy density as functions of the number of cycles to failure.

As shown in Fig. 4(b), under each prescribed strain-range condition, the corresponding stress range, ΔS, gradually decreased with increasing number of loading cycles until pronounced fatigue cracks developed and the specified test-termination criterion was reached. In addition, as the prescribed strain range increased, the cyclic stress-response curves generally shifted downward along the stress axis. However, the cyclic stress-response curve corresponding to a strain range of 50% was located between those obtained at strain ranges of 38% and 45%. This distribution indicates that the variation in stress range, ΔS, when used as a fatigue-damage parameter, cannot clearly reflect the effect of the prescribed strain range on the fatigue life of the experimental fenders. The cyclic curves established using the cyclic energy-absorption index and cyclic stored-energy index are presented in Figs. 4(c) and 4(d), respectively. Examination of both energy index–cycle number (*N*) curves clearly shows that, under each prescribed strain-range condition, the two cyclic energy indices gradually decreased with increasing number of loading cycles. Moreover, a larger strain range generally resulted in higher values of both cyclic energy indices. The distributions of these energy-based cyclic curves are consistent with the trend that a larger prescribed strain range leads to a shorter fatigue life. These observations demonstrate that energy-based indices can serve as effective fatigue-damage parameters for characterizing the consumption of fatigue life in the experimental fenders subjected to cyclic compression at different displacement ranges.

To establish the fatigue-life curve, the experimental data were first analyzed using linear regression on a log–log scale, with the controlled strain range ($\Delta\varepsilon_c$) plotted on the vertical axis and the number of cycles to failure (NfN_f) on the horizontal axis. Accordingly, a fatigue-life relationship using the controlled strain range as the fatigue-damage parameter was established as follows:

$$\Delta e_c\,(\text{mm/mm}) = 8.0339 \times (N_f)^{-0.2735} \qquad (1)$$

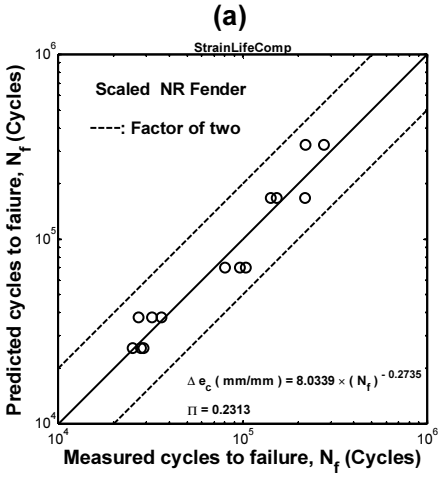

Fig 5(a): comparison of predicted values to observed values using the Δe_c damage parameter.

A comparison between the fatigue lives predicted using Eq. (1) and the experimentally measured results is presented in Fig. 5(a). The solid diagonal line represents perfect agreement between the predicted and measured fatigue lives, whereas the upper and lower dashed lines indicate predicted lives equal to twice and one-half of the measured lives, respectively, thereby defining the factor-of-two bounds. A data point located above the diagonal line indicates that the predicted fatigue life is greater than the measured value, representing a non-conservative prediction. Conversely, a data point below the diagonal line indicates that the predicted fatigue life is lower than the measured value, representing a conservative prediction. As shown by the data distribution in Fig. 5(a), the fatigue-life predictions obtained using the controlled strain range as the fatigue-damage parameter are distributed on both sides of the perfect-agreement line, and all data points fall within the factor-of-two bounds. These results demonstrate that Eq. (1) provides satisfactory predictions of the fatigue life of the scaled NR fender.

Furthermore, based on the variations in the cycle-dependent indices shown in Figs. 4(c) and 4(d), the corresponding index values at half the fatigue life ($N_f/2$) were selected as fatigue damage parameters. The experimental data were then transformed into logarithmic form and subjected to linear regression analysis on log–log coordinates to establish the relationships between the cycle-dependent damage parameters, $\Delta U_{c,a}$ and $\Delta U_{c,p}$, and the fatigue life, N_f. The resulting regression equations are presented in Figs. 5(b) and 5(c), respectively. The comparisons between the predicted and measured fatigue lives exhibit trends similar to that

observed in Fig. 5(a). All data points are distributed on either side of the line of perfect agreement and fall within the factor-of-two error bounds. These results demonstrate that the fatigue-life relationships established using $\Delta U_{c,a}$ and $\Delta U_{c,p}$ as damage parameters can reasonably predict the fatigue life of the tested rubber fenders.

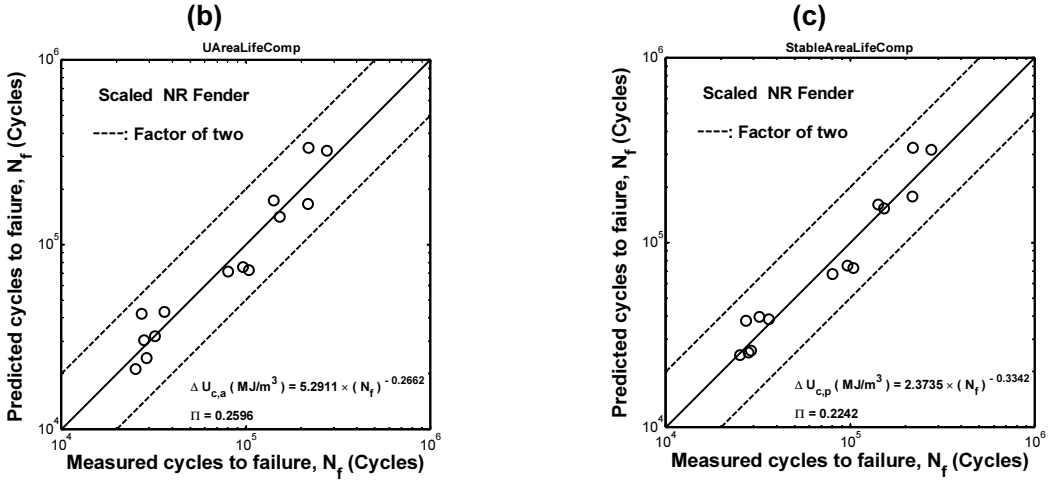

Fig 5: comparison of predicted values to observed values using the (b) $\Delta U_{c,a}$ and (c) the $\Delta U_{c,p}$ damage parameters.

However, a qualitative examination of the data distributions in Figs. 5(a)–5(c) can only confirm that the established fatigue-life relationships provide satisfactory predictive capability. It cannot further determine which of the three fatigue damage parameters, Δe_c, $\Delta U_{c,a}$ and $\Delta U_{c,p}$, provides the highest fatigue-life prediction accuracy. Therefore, the prediction accuracy index, Π, defined in Eq. (2), was employed to quantify the overall deviation of the data points in Figs. 5(a)–5(c) from the line of perfect agreement. This index was subsequently used as the basis for comparing the fatigue-life prediction accuracy of the three damage parameters.

$$\Pi = \sqrt{\sum_{i=1}^{n=14}(\Delta_i - 1)^2/n} \qquad (2)$$

where Δ_i represents the ratio of the predicted fatigue life to the measured fatigue life for the ith data point, and n is the total number of data points in each figure.

According to Eq. (2), a lower value of Π indicates that the overall data distribution is closer to the line of perfect agreement and, consequently, that the fatigue-life prediction is more accurate. A comparison of the Π\Pi values presented in Figs. 5(a)–5(c) shows that $\Delta U_{c,p}$ yields the lowest Π value. Therefore, the fatigue-life relationship based on $\Delta U_{c,p}$ provides higher prediction accuracy than those based on Δe_c and $\Delta U_{c,a}$.

CONCLUSIONS

1. The hardness measurements of 20 NR rubber fender specimens yielded an average Shore A hardness of 59.81 with a standard deviation of 0.85, indicating good manufacturing quality and high consistency among the specimens.
2. The compressive stress–strain curves of the hollow cylindrical NR fenders exhibited an S-shaped response, indicating that the tested fenders were buckling-type fenders.
3. The fatigue life gradually decreased with increasing compressive displacement range, demonstrating a clear fatigue degradation trend.
4. Three fatigue-life prediction relationships were established in this study. Among them, the relationship based on plastic strain energy provided the highest fatigue-life prediction accuracy.

REFERENCES

1. PIANC, 2002, Guidelines for the Design of Fender Systems: 2002, Report of Working Group 33 of the Maritime Navigation Commission, International Navigation Association, Brussels, Belgium.
2. Shen, M. Y., Chiou, Y. C., Tan, C. M., Wu, C. C., and Chen, W. J., 2020, “Effect of Wall Thickness on Stress-Strain Response and Buckling Behavior of Hollow-Cylinder Rubber Fenders,” Materials, Vol. 13, No. 5, Article 1170.
3. SHIBATA INDUSTRIAL Co., Ltd., Company Website, image source.
4 . Woo, C. S., Kim, W. D., and Kwon, J. D., 2008, “A Study on the Material Properties and Fatigue Life Prediction of Natural Rubber Component,” Materials Science and Engineering: A, Vols. 483–484, pp. 376–381.
5. Wu, C. C., and Chiou, Y. C., 2019, “Stress-Strain Response of Cylindrical Rubber Fender under Monotonic and Cyclic Compression,” Materials, Vol. 12, No. 2, Article 282.

FM-P20

Proceedings of The 12th International Symposium on Machinery and Mechatronics for Agriculture and Biosystems Engineering (ISMAB 2026)
20-24 October 2026, Busan, Republic of Korea

COMPARATIVE ANALYSIS OF SWEET POTATO ESTABLISHMENT RATES IN CONVERTED PADDY AND UPLAND FIELDS FOR THE DEVELOPMENT OF A STANDARD CULTIVATION MODEL

Jinho Won[1], Sun-Bin Min[1], Jeongju Chae[1], Yongjin Cho[1, 2, 3], Dae Cheol Kim[1, 2, 3 *]

[1] *Department of Agricultural Machinery Engineering, Jeonbuk National University, Korea*
[2] *Department of Bioindustrial Machinery Engineering, Jeonbuk National University, Korea*
[3] *Institute of Agricultural Machinery ICT Convergence, Jeonbuk National University, Korea*
**Corresponding Author-- Voice: +82-63-270-2613, Email: dckim12@jbnu.ac.kr*

Abstract: This study compared the establishment rates of sweet potato slips in a converted paddy field and an upland field to provide baseline data for developing a standard cultivation model. Two cultivars, 'Hopungmi' and 'Beniharuka,' were transplanted, and establishment rates were evaluated at 8, 15, and 21 days after transplanting. In the converted paddy field, 'Hopungmi' showed slightly higher establishment rates than 'Beniharuka,' while both cultivars maintained rates above 90% throughout the observation period. In the upland field, 'Hopungmi' also showed higher establishment rates; however, the overall rates were lower than those observed in the converted paddy field. Because field type was confounded with location, transplanting date, environmental conditions, and potentially operator-related factors, the observed differences cannot be attributed solely to field type. Nevertheless, the results confirm that sweet potato slips can establish successfully in converted paddy fields and provide preliminary data for developing field-specific standard cultivation models. Further replicated experiments that control environmental and operational factors and include yield and economic assessments are required.

Key Words: *sweet potato, converted paddy field, upland field, standard cultivation model, establishment rate*

INTRODUCTION

Sweet potato is one of the major upland crops cultivated in the Republic of Korea. It is relatively tolerant of pests and diseases and can be grown under marginal soil conditions (Won et al., 2024). In addition, its yield per unit area exceeds that of several staple crops, including wheat and maize, making it an attractive crop for farmers (Park et al., 2021; Lee et al., 2022; Lee et al., 2023; Won et al., 2024). Sweet potato is also popular among consumers because it contains minerals, dietary fiber, beta-carotene, and other functional components (Won et al., 2024). It is consumed fresh, roasted, and as an ingredient in processed products, including pet snacks.

Meanwhile, the Republic of Korea has experienced a structural oversupply of rice as rice consumption has declined. In response, the government has implemented policies that reduce rice-planted area and encourage the production of alternative food and forage crops in paddy fields. Consequently, sweet potato cultivation in converted paddy fields has emerged and is gradually increasing. Although sweet

potato is still primarily cultivated in upland fields, few studies have directly compared its establishment, productivity, and economic performance between converted paddy and upland fields. Therefore, this study compared the establishment rates of two sweet potato cultivars in a converted paddy field and an upland field to generate baseline data for the development of a standard cultivation model.

MATERIALS AND METHODS

1. Experimental Sites

Two experimental sites were established in Iksan and Gimje, Jeonbuk State, Republic of Korea, to compare the establishment rates of sweet potato slips under different field conditions. The converted paddy field was located at the Jeonbuk State Agricultural Research and Extension Services in Iksan. The upland field was established in cooperation with a local farmer in Gimje (Fig. 1). Because the two field types were located at different sites, site-specific environmental and management factors were considered when interpreting the results.



Fig. 1. Experimental sites: (A) converted paddy field in Iksan and (B) upland field in Gimje.

2. Sweet Potato Cultivars and Transplanting

Two sweet potato cultivars, ‘Hopungmi’ and ‘Beniharuka,’ were manually transplanted using the conventional method. Transplanting was conducted on May 11 in Iksan and May 16 in Gimje.
Establishment was assessed three times, at 8, 15, and 21 days after transplanting. The total number of transplanted slips and the numbers of established and non-established slips were counted in each ridge. A slip was classified as established when visual inspection indicated that it remained viable and capable of continued growth. A slip with desiccated aboveground tissue and no apparent potential for continued growth was classified as non-established (Fig. 2).

The establishment rate was calculated using Eq. (1):

$$ER\ (\%) = (N_e / N_t) \times 100 \qquad \text{Equation (1)}$$

where ER is the establishment rate, N_e is the number of successfully established plants, and N_t is the total number of transplanted plants.

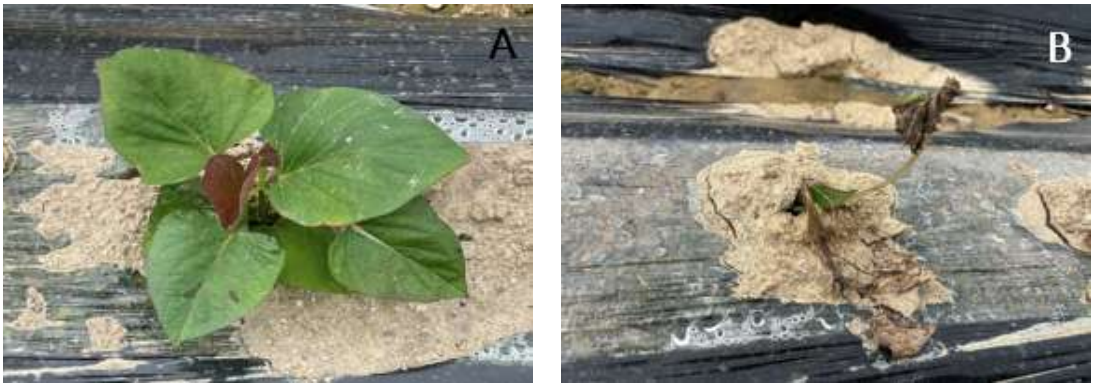

Fig. 2. Examples of sweet potato slips after transplanting: (A) established slip and (B) non-established slip.

RESULTS & DISCUSSION

Figure 3A shows the establishment rates of the two cultivars in the converted paddy field in Iksan. At 8, 15, and 21 days after transplanting, the establishment rates of 'Hopungmi' were 97.8%, 97.5%, and 95.9%, respectively, whereas those of 'Beniharuka' were 96.1%, 93.5%, and 90.9%, respectively. Although 'Hopungmi' consistently showed slightly higher values than 'Beniharuka,' both cultivars maintained establishment rates above 90% throughout the observation period. These results indicate that both cultivars established successfully under the conditions of the converted paddy field used in this study and suggest the potential suitability of sweet potato as an alternative crop in converted paddy fields.

Figure 3B shows the establishment rates in the upland field in Gimje. The establishment rates of 'Hopungmi' were 97.8%, 93.1%, and 89.5% at 8, 15, and 21 days after transplanting, respectively. The corresponding rates of 'Beniharuka' were 91.0%, 80.4%, and 80.6%. Thus, 'Hopungmi' showed higher establishment rates than 'Beniharuka' at all observation times, and both cultivars generally showed lower rates in the upland field than in the converted paddy field.

However, the differences between the two fields should be interpreted cautiously. Field type was not independently replicated and was confounded with location, transplanting date, weather conditions, soil moisture, transplanting depth and angle, and operator skill. Therefore, the observed differences cannot be attributed exclusively to field type. Additional replicated trials under controlled or well-documented conditions are needed to quantify the effects of field type and cultivar and to identify management practices that reduce establishment losses.

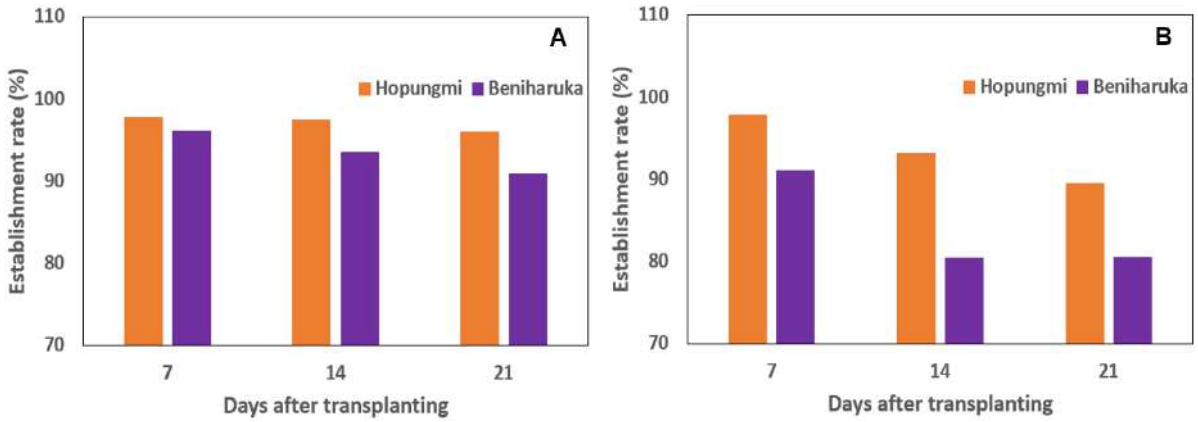

Fig. 3. Establishment rates of two sweet potato cultivars in (A) the converted paddy field and (B) the upland field.

CONCLUSIONS

This study compared the establishment rates of two sweet potato cultivars grown in a converted paddy field in Iksan and an upland field in Gimje as a preliminary step toward developing a standard cultivation model. ‘Hopungmi’ and ‘Beniharuka’ were manually transplanted, and establishment rates were measured at 8, 15, and 21 days after transplanting. In the converted paddy field, both cultivars maintained establishment rates above 90%, with ‘Hopungmi’ showing slightly higher rates than ‘Beniharuka.’ In the upland field, ‘Hopungmi’ also showed higher establishment rates, whereas the rates of both cultivars were generally lower than those measured in the converted paddy field.

The results demonstrate that sweet potato slips can establish successfully in a converted paddy field under the conditions examined. However, because field type, location, transplanting date, and other cultivation factors were not separated experimentally, further replicated studies are required before a general field-type effect can be established. Future work will assess yield, harvest performance, cultivation conditions, and economic feasibility to support the development of field-specific standard cultivation models.

ACKNOWLEDGEMENTS (optional)

This work was supported by the Korea Institute of Planning and Evaluation for Technology in Food, Agriculture and Forestry (Project No. RS-2023-00236201).

REFERENCES

1. Lee, G. T., S. Y. Lee, H. M. Cho, Y. J. Jo, Y. J. Jung, M. N. Chung, J. S. Lee, and H. S. Jeong. 2023. Quality characteristics of dried purple sweet potato with heat treatment and enzymatic saccharification. Journal of the Korean Society of Food Science and Nutrition 52: 947–952.
2. Lee, H. W., S. Y. Lee, Y. J. Jung, Y. J. Jo, M. N. Chung, J. S. Lee, and H. S. Jeong. 2022. Quality characteristics of yang-gaeng prepared with the addition of colored sweet potato powder. Journal of the Korean Society of Food Science and Nutrition 51: 1238–1243.
3. Park, M. K., H. U. Lee, Y. Hwang, Y. S. Cho, and H. W. Jang. 2021. Effect of quality characteristics of various cultivars of sweet potato on puree viscosity. Journal of the Korean Society of Food Science and Nutrition 50: 1375–1384.
4. Won, J. H., D. C. Kim, J. Y. Han, O. R. Park, and Y. J. Cho. 2024. Evaluation of a prototype double-conveyor sweet potato harvester for low-damage rate. Journal of Agricultural, Life and Environmental Sciences 36(4): 522–533.

FM-P21

"Proceedings of the 12th International Symposium on Machinery and Mechatronics for Agriculture and Biosystems Engineering (ISMAB 2026) 20-24 October 2026, Busan, Republic of Korea"

MAPPING SOIL HARDNESS USING UNMANNED PLOUGHING WORKING DATA

Adeer Maluk Jacob Ajak[1] , Atsuru Fujimoto[2]

[1]Graduate School of Animal and Veterinary Science and Agriculture,Obihiro University of Agriculture and Veterinary Medicine,2-11 Nishi, Inada ,Obihiro 080-8555,Japan.
[2]Department of Agro-environmental Science, Obihiro University of Agriculture and Veterinary Medicine,1-11 Nishi, Inada ,Obihiro ,080-8555,Japan.
*Corresponding Author–Voice:+81-155-49-5526,Email: fujimoto@obihiro.ac.jp

Abstract: Autonomous tractors generate operating data that may support soil assessment in addition to machine control. This study examined the relationship between engine power during autonomous ploughing and soil cone index(CI), and evaluated a procedure for integrating tractor operating data with point-based soil measurements. Field trials were conducted in deliberately compacted and loosened strips. Soil penetration resistance was measured using a cone penetrometer ,and CI values at a depth of 20 cm served as the reference soil measurements. Autonomous ploughing was performed using a reversible plough at target working depth of 20 cm and a target forward and a forward speed of 6.4 km/h. Engine speed and torque were logged via the Controller Area Network(CAN) while position data were obtained using real-time kinematic Global Navigation Satellite System (RTK_GNSS) receiver. Engine Power was calculated from engine speed and torque, and the resulting dataset was synchronized by timestamp and spatially matched with CI sampling locations to construct a regression model. This data integration aims to develop a high-resolution field-scale mapping approach by using robotic tractor operating data as a substitute for soil resistance, thereby overcoming the spatial limitations of the conventional point-based sampling. However, the ability of engine power to precisely predict CI was not fully established under the tested conditions. Uneven compaction ,large soil clods ,and variation in actual ploughing depth may have contributed to variability in engine power demand. This study demonstrates a procedure for integrating tractor operating data with soil measurements, but further validation is needed before it can support reliable field-scale CI estimation. Future work should account for actual working depth and other operating and soil conditions that influence engine power and penetration resistance.

Key Words: Robotic Tractor, CAN-bus, RTK-GNSS, Engine Power and Soil Cone Index.

FM-P22

Proceedings of The 12th International Symposium on Machinery and Mechatronics for Agriculture and Biosystems Engineering (ISMAB 2026)
20-24 October 2026, Busan, Republic of Korea

ANALYSIS OF SPRAY CHARACTERISTICS OF A SPEED SPRAYER ACCORDING TO NOZZLE TYPE AND AIRFLOW RATE

Yun-Jeong Yang[1], Il-Su Choi[1], Young-Hwa Kim[1], Jea-Keun Woo[1], Seok-Jun Hong[1], Hyun-Ho Noh[2], Chun-Gu Lee[1*]

[1]Field Farming Mechanization Division, National Institute of Agricultural Science
[2]Residual Chemical Assessment Division, National Institute of Agricultural Science
*Corresponding Author-- Voice: +82-63-238-4229, Email: llccgg@korea.kr

Abstract: The implementation of the Positive List System (PLS) has increased the need for safe spraying technologies that reduce spray drift to surrounding fields during pesticide application. In particular, speed sprayers commonly used in orchards apply pesticides by using airflow to transport spray droplets into the tree canopy; therefore, the deposition and movement characteristics of droplets may vary depending on nozzle type and airflow conditions. Accordingly, this study aimed to analyze the spray characteristics of an SS by comparing the proportion of spray droplets collected at different locations according to nozzle type and airflow rate for drift reduction. Three nozzle types were selected: a ceramic nozzle originally installed on the speed sprayer, an AITX nozzle with drift-reduction characteristics, and a TXR nozzle commonly used in commercial orchards. The experiment was conducted on a lawn at the Department of Agricultural Engineering using a tower-type speed sprayer, which was operated at a travel speed of 2 km/h. The airflow rate was set as two levels corresponding to fan rotational speeds of 2,200 and 2,600 rpm, considering the operating conditions of the speed sprayer. The test area consisted of five measurement rows arranged at 4 m intervals along the travel direction of the speed sprayer. In each measurement row, water-sensitive paper holders were placed at lateral distances of 2, 4, 8, and 12 m on both sides of the speed sprayer centerline. Water-sensitive papers were installed on each holder at heights of 0.25, 1, and 2 m above the ground, resulting in a total of 120 water-sensitive papers for each test condition. After each test, droplet deposition characteristics were analyzed using an image analysis program for water-sensitive papers. The droplet deposition characteristics at different locations according to nozzle type and airflow rate analyzed in this study can provide basic data for establishing speed sprayer operating conditions considering pesticide spray drift reduction.

Key Words: Airflow rate, Drift reduction, Nozzle, Speed sprayer

FM-P23

Proceedings of The 12th International Symposium on Machinery and Mechatronics for Agriculture and Biosystems Engineering (ISMAB 2026)
20-24 October 2026, Busan, Republic of Korea

EFFECT OF GARLIC CLOVE PLANTING ANGLE ON GROWTH AND YIELD UNDER MECHANICAL PLANTING

Hye-Min Oh[1]*, Woo-Young Cho[1], Young-Jun You[1], Hye-Jeong Jeong[1], Yu-Shin Ha[2,3], Mun-Jung Lee[1]

[1]Organic Agriculture Research Institute, Gyeongbuk Agricultural Research & Extension Service, Uiseong 37339, Korea
[2]Department of Smart Bio-industrial Machinery Engineering, Kyungpook National University, Daegu 41566, Korea
[3]Upland Field Machinery Development Center, Kyungpook National University, Daegu 39061, Korea

*Corresponding Author-- Voice: +82-054-832-9669, Email: ohme5020@korea.kr

Abstract: The need for garlic mechanization has increased due to labor shortages and an aging rural population. Mechanical planting can reduce labor and production costs, but garlic cloves may be planted at various angles during the planting process. This study investigated the distribution of planting angles during mechanical planting using a tractor-mounted garlic planter and evaluated growth, bulb size distribution, and yield according to planting angle. The experiment was conducted at the Organic Agriculture Research Institute, Gyeongsangbuk-do Agricultural Research and Extension Services, Uiseong, Republic of Korea. Garlic cloves were planted at 0°, 45°, 90°, 135°, and 180°, and planting angle, number of cloves per planting hole, bulb size distribution, and yield were measured. During mechanical planting, 33.4% of cloves were planted at 0–45° and 60.0% at 45–90°, indicating that 93.4% were planted at angles of 90° or less. Yields at 0°, 45°, and 90° were 1,070, 1,036, and 1,032 kg·10a^{-1}, respectively, whereas yields at 135° and 180° decreased to 799 and 837 kg·10a^{-1}, respectively. Some growth characteristics also tended to decrease at angles above 90°. These results indicate that planting angles from 0° to 90° had little effect on yield, whereas angles above 90° reduced yield. The findings provide basic information for improving the accuracy and stability of mechanical garlic planting.

Key Words: garlic; mechanical planting; planting angle; growth; yield

FM-P24

Proceedings of The 12th International Symposium on Machinery and Mechatronics for Agriculture and Biosystems Engineering (ISMAB 2026)
20-24 October 2026, Busan, Republic of Korea

DESIGN AND DEVELOPMENT OF AN ELECTRIC PLATFORM-BASED INTELLIGENT GARLIC SCAPE REMOVAL SYSTEM

Tae Wook Kang[1]. Chang Shoo Kim[2]. Seung Heon Cho[3]. Jungsil Kim[4].

[1]Jeonnam-Gwangju Special Metropolitan City Agricultural Research & Services Smart Agriculture Center
[2]EUNIL Co, Ltd. Technology Research Institute,
[3]MOBILUS, Inc. Saseong-ro 75beon-gil, #102-3006, Gwangmyeong-si, Gyeonggi-do South Korea
[4]Department of Smart Bio-Industrial Mechanical Engineering, Kyungpook National University
*Corresponding Author-- Voice: +82-10-4503-7925, Email: kang4330@korea.kr

Abstract: Domestic rural areas are facing severe labor shortages due to an aging population, leading to increased efforts to mechanize upland farming. Garlic scape removal is an important field task that must be completed within a relatively short period, resulting in a high labor demand. However, despite the ongoing mechanization of upland farming, the automation of garlic scape removal is still at an early stage of development. Currently available machines generally rely on manual height adjustment, making real-time adaptation to variations in plant height difficult during operation. Furthermore, they can cause severe damage to garlic leaves while cutting the scapes. Such leaf damage may reduce photosynthetic capacity and nutrient accumulation during the critical bulb-bulking stage, while also decreasing the operational efficiency of cutting machine.

In alignment with current trends in agricultural robotics and smart farming technologies, this study aims to develop a walking-type smart electric garlic scape remover designed to reduce manual labor and improve operational efficiency. Considering the domestic agricultural environment, which is characterized by small-scale, multi-crop farming and uneven field conditions, the proposed system was designed with a modular structure consisting of an 'electric platform' for off-road navigation and an independent 'garlic scape cutting unit.' To implement an effective cutting mechanism while minimizing the mechanical load, the growth height of garlic scapes was collected from actual garlic fields and used as fundamental design for determining the cutting configuration and operation range.

As a result, an electric platform prototype capable of stable operation under uneven field conditions was successfully developed. Furthermore, a lightweight cutting unit

was designed based on the collected garlic scape height data to optimize its dimensions and operating range while minimizing the mechanical load on the electric platform. The integration of the developed electric platform prototype with the currently designed lightweight cutting unit is expected to reduce the intensive labor required for garlic scape removals and improve the efficiency of field operations. farmers. Additionally, it can be widely applied to other agricultural tasks involving horizontal-cutting, collecting, and processing, thereby contributing to the broader mechanization of upland farming operations. Ultimately, this study is expected to provide a practical foundation for enhancing the global competitiveness of compact, intelligent electric agricultural machinery and for exploring new market opportunities in this emerging field.

Key Words: Garlic Scape, Electric Platform, Lightweight Cutter, Agricultural Robot, Prototype.

ACKNOWLEDGEMENTS

This research was supported by the Jeonnam-Gwangju Integrated Special City Agricultural Research and Extension Services (Project number: LP005779032026)

FM-P25

Proceedings of The 12th International Symposium on Machinery and Mechatronics for Agriculture and Biosystems Engineering (ISMAB 2026)
20-24 October 2026, Busan, Republic of Korea

THEORETICAL STRESS ANALYSIS OF A 55-KW SELF-PROPELLED SWEET POTATO HARVESTER

Sakib Robin[1], Md Nasim Reza[1,2], Ezatullah Zakir[2], Karma Osama Sayed Ismaail[2], Jong Won Lee[3], Il-Su Choi[4], Sun-Ok Chung[1,2*]

[1]Department of Smart Agricultural Systems, Graduate School, Chungnam National University, Daejeon 34134, Republic of Korea
[2]Department of Agricultural Machinery Engineering, Graduate School, Chungnam National University, Daejeon 34134, Republic of Korea
[3]Research & Development Departement, Dooroo Machinery & Trading Co., Asan 31420, Republic of Korea
[4]Field Farming Mechanization Division, National Institute of Agricultural Sciences, Rural Development Administration, Jeonju 54875, Republic of Korea
*Corresponding Author-- Voice: +82-(0)42-821-6712, Email: sochung@cnu.ac.kr

Abstract: The main components of a self-propelled sweet potato harvester are subjected to torque, bending, vibration, and soil resistance during operation. This study evaluated the structural response of key components of a 55-kW self-propelled sweet potato harvester using theoretical load determination and static finite element analysis (FEA) in SolidWorks Simulation. The components analyzed were the crawler drive sprocket, conveyor drive shaft, conveyor supporting frame, and vibrating digging unit. Representative loads were determined from machine operating conditions and literature-based soil parameters. The crawler sprocket showed a maximum von Mises stress of 30.17 MPa and a minimum factor of safety (FOS) of 17.57 under an equivalent load of 6.33 kN. For the conveyor drive shaft, theoretical and FEA stresses were compared under no-load, crop-load, and full crop-soil-load conditions. The conveyor supporting frame showed a maximum stress of 89.33 MPa, maximum displacement of 1.222 mm, and minimum FOS of 2.74. The digging unit showed the highest stress of 687.8 MPa and the lowest FOS of 1.60 under a 7.784 kN soil-resistance load. All analyzed components remained below their adopted yield strengths under the static loading conditions investigated. These results can be used to identify critical components and improve the structural design of the sweet potato harvester.

Key Words: Sweet Potato Harvester, Crawler Drive System, Finite Element Analysis, SolidWorks Simulation, Structural Safety.

INTRODUCTION

Sweet potato harvesting combines digging, lifting, conveying, soil separation, and crop collection in a single field operation. In a self-propelled harvester, these operations transfer traction, torque, crop-soil weight, and soil resistance through the driving, conveying, supporting, and digging structures. Structural evaluation of these load-carrying components is therefore required to identify critical regions before field operation.

Finite element analysis (FEA) is widely used to evaluate stress concentration and deformation of agricultural machinery components under defined loading conditions. Theoretical calculations are also useful for establishing physically meaningful FEA loads and for checking numerical results. Islam et al. (2021) combined theoretical stress analysis and FEA for an agricultural transmission mechanism. Similarly, analytical stress calculations have been compared with SolidWorks simulation results to examine the agreement between theoretical and numerical stress predictions (Zarzoor et al., 2018).

Therefore, this study aimed to evaluate the structural stress and safety of selected key components of a 55-kW self-propelled sweet potato harvester using theoretical analysis and SolidWorks finite element simulation. The crawler drive sprocket, conveyor drive shaft, conveyor supporting frame, and vibrating digging unit were analyzed based on maximum von Mises stress and factor of safety.

MATERIALS AND METHODS

Self-propelled sweet potato harvester

The self-propelled sweet potato harvester analyzed in this study was developed to perform digging, lifting, conveying, soil separation, and crop collection in a single field operation. The machine had overall dimensions of approximately 5.3 × 2.25 × 2.2 m (length × width × height), an empty mass of approximately 3,300 kg, and a rated engine power of 55 kW. A crawler-type driving system was used to provide mobility and traction during harvesting.

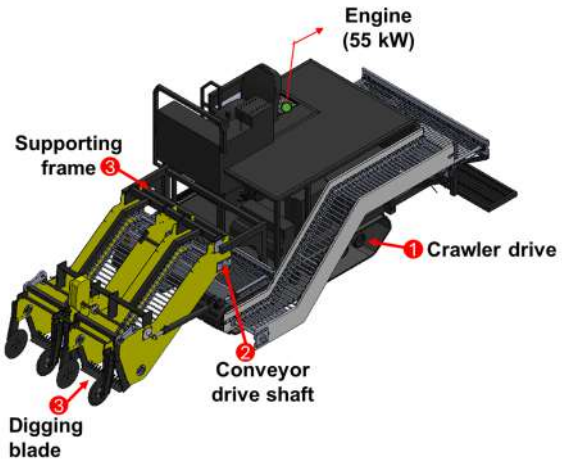

Fig.1 Three-dimensional model of the 55-kW self-propelled sweet potato harvester.

The major working components consisted of the crawler driving unit, disc coulters, vibrating digging unit, lifting mechanisms, primary conveyor, transfer conveyor, secondary conveyor, and collection conveyor. For the structural analysis, four representative components were selected based on their function and expected loading characteristics: (1) crawler drive sprocket, (2) conveyor drive shaft, (3) conveyor supporting frame, and (4) vibrating digging unit. Furthermore, the crawler drive sprocket was evaluated under transmitted torque and sprocket reaction, while the conveyor shaft was analyzed under drive torque and associated shaft loading. The conveyor frame was evaluated under supporting loads generated by the conveyor and transported material, whereas the vibrating digging unit was analyzed considering digging resistance and vibration-related loading. The structural responses were

evaluated using maximum von Mises stress, deformation, and factor of safety, with additional theoretical stress analysis performed for the conveyor drive shaft.

Structural analysis procedure

Three-dimensional CAD models of the selected components were prepared and analyzed using SolidWorks Simulation 2025 SP5.0 (Dassault Systemes, France). Material properties were assigned according to the component material, followed by fixture definition, theoretical load application, and curvature-based mesh generation. Local mesh refinement was applied around selected load-transfer and high-gradient regions where required. Linear static analyses were performed to determine von Mises stress, resultant displacement, equivalent strain, and factor of safety. The same general sequence of geometry definition, meshing, boundary-condition application, loading, and stress evaluation has been used in previous FEA studies of agricultural machinery components (Islam et al., 2021). The analysis workflow is shown in Fig. 2.

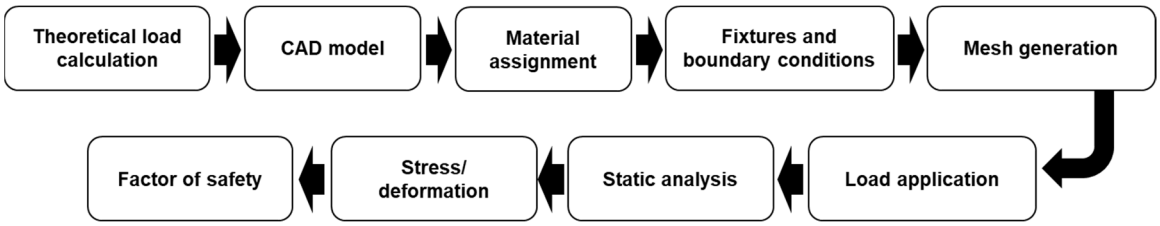

Fig.2 Structural analysis procedure for the selected harvester components.

Theoretical load and stress analysis

Theoretical analysis was conducted to determine the representative loads for the selected components before finite element analysis. The crawler sprocket was evaluated using equivalent crawler resistance, the conveyor drive shaft using transmitted torque, the supporting frame using the crop-soil load, and the vibrating digging unit using equivalent soil resistance. For the crawler system, the maximum design condition considered a loaded machine mass of 4,200 kg, rolling-resistance coefficient of 0.05, and a 15° slope. The total crawler resistance was calculated from rolling and grade resistance and was divided equally between the two tracks using Eqs. (1).

$$R_t = C_{rr} W\cos(\theta) + W\sin(\theta) \quad (1)$$

Where R_t was total crawler resistance (N), C_{rr} was the rolling-resistance coefficient (-), W was machine weight (N), and θ was slope angle. The calculated total resistance was 12.65 kN, giving an equivalent load of 6.33 kN per drive sprocket.

For the conveyor drive shaft, torsional shear stress and equivalent von Mises stress were calculated using Eqs. (2) and (3).

$$\tau = \frac{16T}{\pi d^3} \quad (2)$$

$$\sigma_{vM} = \sqrt{3}\tau \quad (3)$$

Where τ was torsional shear stress (MPa), d was shaft diameter (mm), and σ_{vM} was equivalent von Mises stress (MPa). The shaft was evaluated under no-load, crop-load, and full crop-soil-load torques of 111.2, 250.2, and 278.0 Nm, respectively. The corresponding theoretical stresses were 22.78, 51.25, and 56.94 MPa.

For the conveyor supporting frame, the full-load condition was represented by the combined weight of the conveyor-related components and transported crop-soil material. An equivalent moving mass of 200 kg was considered, and the corresponding structural load was calculated using Eqs. (4).

$$W_f = mg \quad (4)$$

where W_f was the applied frame load (N), m was the equivalent supported mass (kg), and g was gravitational accelerate

on (9.81 m/s²)

For the vibrating digging unit, the representative soil-resistance load was estimated using a simplified specific soil-resistance relationship, calculated using Eqs. (5).

$$F_d = kBd \quad (5)$$

where F_d was the digging resistance (N), k was the specific soil resistance (Pa), B was the effective digging width (m), and d was the digging depth (m). A specific soil resistance of 70 kPa was adopted to represent a relatively high-resistance soil condition based on the range reported by Varga et al. (2013). The effective digging width measured from the CAD model was 0.556 m, while a digging depth of 0.20 m was selected based on sweet potato digging conditions (Akhir et al., 2014). Therefore, the equivalent digging resistance was calculated as 7,784 N (7.784 kN).

Finite element model and loading conditions

Finite element analysis was performed using SolidWorks Simulation for the crawler drive sprocket, conveyor drive shaft, conveyor supporting frame, and vibrating digging unit. The three-dimensional CAD models were assigned the corresponding material properties. The loading conditions obtained from the theoretical analysis were then applied to the relevant load-transfer regions. Static structural analysis was conducted to determine the maximum von Mises stress, resultant deformation, and factor of safety. The analysis sequence followed material-property definition, boundary-condition setting, load application, static stress analysis, and structural-safety evaluation.

Table 1 Finite element model and loading conditions of the selected components.

Component	Material	Applied load
Crawler drive sprocket	AISI 1045 / S45C	6.33 kN on loaded tooth flank
Conveyor drive shaft	S45C	111.2, 250.2, and 278.0 Nm torque
Conveyor supporting frame	SS400	1.962 kN
Vibrating digging blade	HARDOX 400	7.784 kN

The factor of safety for each component was calculated using Eqs. (6).

$$SF = \frac{\sigma_y}{\sigma_{vM,\max}} \tag{6}$$

Where SF was the factor of safety (-), σ_y was material yield strength (MPa), and the $\sigma_{vM,\max}$ was maximum von Mises stress obtained from FEA (MPa).

For the conveyor drive shaft, the finite element stress was additionally compared with the theoretical stress calculation.

RESULTS & DISCUSSION

Crawler drive sprocket

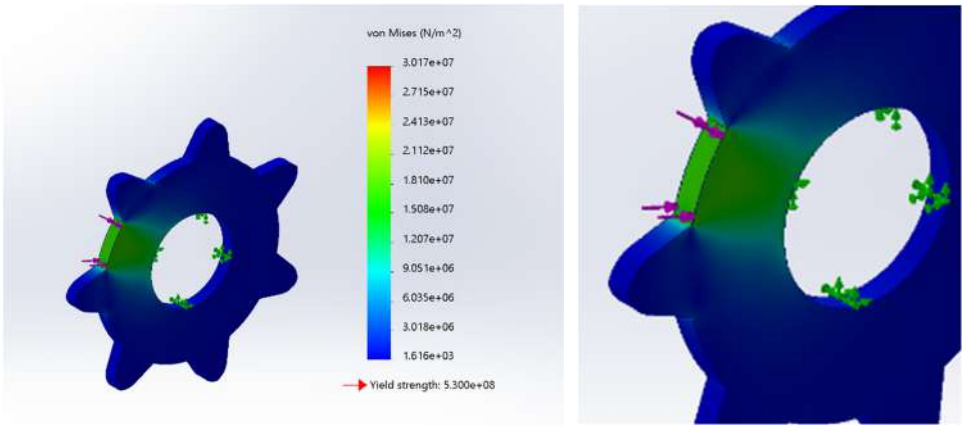

Fig.3 Von Mises stress distribution of the crawler drive sprocket.

Figure 3 shows the von Mises stress distribution of the crawler drive sprocket under the applied load of 6.33 kN. The maximum stress was found to be 30.17 MPa near the loaded tooth and the adjacent load-transfer region. The maximum displacement was 0.00316 mm. The minimum factor of safety was 17.57. Therefore, the stress developed in the sprocket was lower than the yield strength under the considered loading condition.

Conveyor drive shaft and supporting frame

The stress of the conveyor drive shaft increased with applied torque. The maximum FEA stresses were 22.97, 52.81, and 58.32 MPa for the no-load, crop-load, and full crop-soil-load conditions, respectively. The corresponding theoretical stresses were 22.78, 51.25, and 56.94 MPa. The FEA results were therefore in good agreement with the theoretical calculations.

Table 2 Comparison of theoretical and FEA stresses of the conveyor drive shaft.

Condition	Torque (Nm)	Theoretical stress (MPa)	FEA stress (MPa)	Difference (%)
No-load	111.2	22.78	22.97	0.81
Crop-load	250.2	51.25	52.81	3.04
Full crop-soil load	278.0	56.94	58.32	2.42

For the conveyor supporting frame, the maximum von Mises stress was found to be 89.33 MPa under the applied load of 1.962 kN. The maximum displacement was 1.222 mm and occurred around the middle part of the loaded frame. The minimum factor of safety was 2.74. Therefore, the stress developed in the supporting frame remained below the yield strength of SS400 under the considered full-load condition.

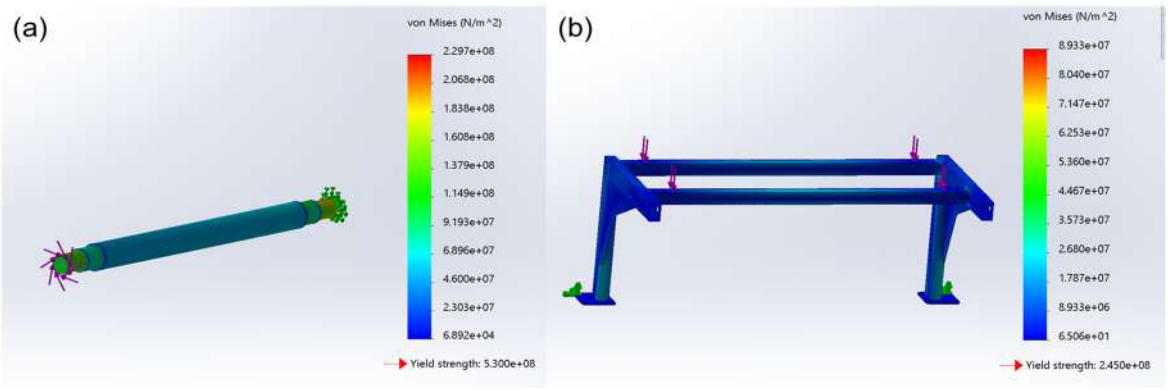

Fig.4 Structural analysis of the conveyor system: (a) von Mises stress distribution of the conveyor drive shaft and (b) von Mises stress distribution of the conveyor supporting frame.

Vibrating digging unit

Figure 5 shows the structural response of the vibrating digging unit under a digging resistance of 7.784 kN. The maximum von Mises stress was 687.8 MPa, and the maximum displacement was 3.143 mm. The minimum factor of safety was 1.60, which was the lowest among the components analyzed.

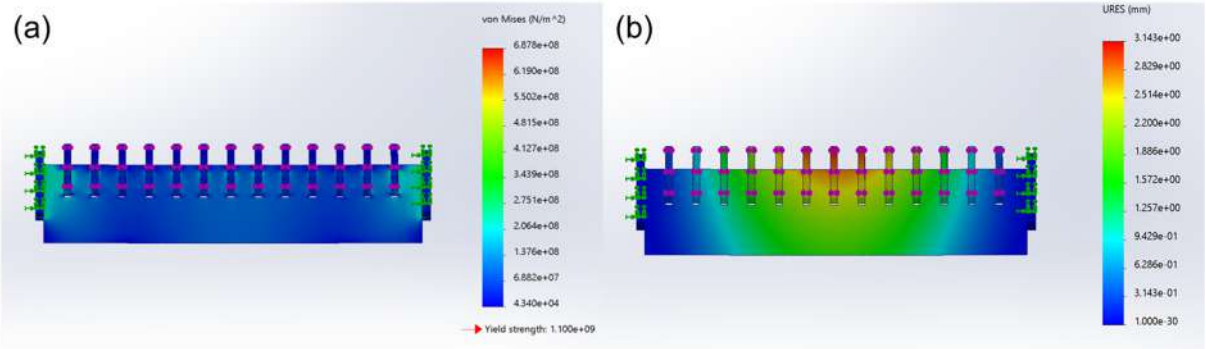

Fig.5 Structural analysis of the vibrating digging unit: (a) von Mises stress distribution and (b) resultant displacement.

The structural analysis results of all selected components are summarized in Table 3. The maximum stress, displacement, and minimum factor of safety were compared to identifying the component with the highest structural load response.

Table 3 Structural analysis results of the selected components.

Component	Applied load	Max. stress (MPa)	Min. FOS
Crawler drive sprocket	6.33 kN	30.17	17.57
Conveyor drive shaft	207.5 Nm	69.50	7.63
Conveyor frame	1.962 kN	89.33	2.74
Vibrating digging unit	7.784 kN	687.80	1.60

The digging unit showed the highest maximum stress and the lowest factor of safety among the analyzed components, whereas the crawler drive sprocket showed the largest static safety margin. Nevertheless, all analyzed components remained below their respective adopted yield strengths under the applied static loading conditions.

CONCLUSIONS

This study evaluated the structural response of the crawler drive sprocket, conveyor drive shaft, conveyor supporting frame, and vibrating digging unit of a 55-kW self-propelled sweet potato harvester using theoretical load calculations and static FEA. The crawler sprocket and conveyor supporting frame showed maximum stresses of 30.17 and 89.33 MPa, respectively. The theoretical and FEA stresses of the conveyor shaft showed good agreement under the three loading conditions. The vibrating digging unit showed the highest maximum stress of 687.8 MPa and the lowest factor of safety of 1.60 under a soil-resistance load of 7.784 kN. All analyzed components remained below their adopted yield strengths under the static loading conditions investigated. Future work should validate the theoretical loads through field measurements and evaluate dynamic and fatigue loading during actual harvesting.

ACKNOWLEDGEMENTS (optional)

This work was carried out with the support of "Development of Field-customised Multipurpose Field Agricultural Machinery (Project No. RS-2025-02243151)", Rural Development Administration, Republic of Korea.

REFERENCES

Akhir, Md. H., D. Ahmad, I. Rukunudin, S. Sulaiman, and A. Yahya. 2014. Design and development of a sweet potato digging device. Pertanika Journal of Science & Technology 22(1): 43-53

Islam, M. N., M. Z. Iqbal, M. Chowdhury, M. Ali, K. Shafik, M. S. N. Kabir, D.-H. Lee, and S.-O. Chung. 2021. Stress and fatigue analysis of picking device gears for a 2.6 kW automatic pepper transplanter. Applied Sciences 11(5): 2241.

Varga, F., M. Mojzis, and R. Abrahám. 2013. Soil resistance and its impact on tillage depth. Acta Technologica Agriculturae 16(1): 26-30.

Zarzoor, A. K., N. Almuramady, and E. S. Hussein. 2018. Stress analysis for spur gears using Solid Works simulation. International Journal of Mechanical Engineering and Technology 9(11): 927-936.

FM-P26

Proceedings of The 12th International Symposium on Machinery and Mechatronics for Agriculture and Biosystems Engineering (ISMAB 2026)
20-24 October 2026, Busan, Republic of Korea

DESIGN OF A FULL-BOOM SHIELD AND SPRAY RECOVERY SYSTEM FOR DRIFT REDUCTION

Chun-Gu Lee[1], Ilsu Choi[1], Younghwa Kim[1], Jea-keun Woo[1]
Kyu-ho Lee[1], Siyun Kim[1], Seokjoon Hong[1], Jeekeun Lee[2], Dong Hyeon Kang[3]

[1]Dept. of Agricultural Engineering, Rural Development Administration, Jeonju, 54875, Korea
[2]Dept. of Mechanical System Eng., Jeonbuk National University, Jeonju, 54896, Korea
[3]Dept. of liberal arts, Korea Nat'l University of Agriculture and Fisheries, Jeonju, 54874, Korea
*Corresponding Author-- Voice: +82-10-4706-2549, Email: llccgg@korea.kr

Abstract: Spray drift during pesticide application can reduce application efficiency and cause off-target contamination of adjacent crops and the surrounding environment. Although boom sprayers generally produce relatively less drift than some other pesticide application methods, additional drift-reduction technologies are still required because drift can occur depending on wind conditions and spraying parameters. In this study, an experimental boom-sprayer apparatus was designed to investigate spray drift and to support the development of an integrated drift-reduction system. Based on physical shielding concepts reported in previous studies, a full-boom shield system was designed to reduce the influence of crosswind on the spray cloud. The shield consists of transparent panels and flexible skirt sections to maintain visibility of the spray pattern while limiting lateral airflow into the spray zone and allowing flexible contact with irregular crop surfaces. In addition, a spray recovery system was designed to collect droplets transported laterally and deposited on the inner surfaces of the shield. Captured liquid is guided toward a lower collection section for recovery and potential recirculation. The resulting experimental system integrates shielding and liquid recovery functions into a single platform, enabling separate evaluation of off-target drift, shield deposition, recovered liquid volume, and target deposition. Future experiments will compare shielded and unshielded conditions under different wind speeds and spraying parameters to quantify drift-reduction and spray-recovery performance. The proposed system is expected to provide a basis for the development of an integrated technology that reduces off-target spray movement while recovering a portion of spray liquid that would otherwise be lost during pesticide application.

Key Words: Boom sprayer, Spray drift, Full-boom shield, Spray recovery, Drift reduction

ACKNOWLEDGEMENTS

This work was carried out with the support of "Cooperative Research Program for Agriculture Science and Technology Development (Project No. RS-2026-25466964)" Rural Development Administration, Republic of Korea.

Post-harvest and Food Processing



PH-P01

Proceedings of The 12th International Symposium on Machinery and Mechatronics for Agriculture and Biosystems Engineering (ISMAB 2026)
20-24 October 2026, Busan, Republic of Korea

EFFECTS OF PRE-FREEZING ON POLYPHENOL CONTENT AND DPPH RADICAL SCAVENGING ACTIVITY IN MICROWAVE-VACUUM DRIED APPLE

Akari Saito[1], Takahiro Orikasa[2*], Shoji Koide[2], Yasumasa Ando[3]

[1]Graduate school of Arts and Sciences, Iwate University, 3-18-8 Ueda, Morioka, Iwate 020-8550, Japan
[2]Faculty of Agriculture, Iwate University, 3-18-8 Ueda, Morioka, Iwate 020-8550, Japan
[3]Institute of Food Research, NARO, 2-1-12 Kannondai, Tsukuba, Ibaraki, 305-8642, Japan
*Corresponding Author-- Voice: +81-19-621-6179, Email: orikasa@iwate-u.ac.jp

Abstract: Microwave-vacuum drying (MVD) is an efficient method for producing dried fruits; however, it often causes sample deformation. Although pre-freezing followed by thawing has been used to suppress deformation, its impact on antioxidant activity remains unclear. This study investigated the effects of pre-freezing and thawing on the antioxidant properties of apples during MVD. Apple pieces were subjected to three treatments: frozen and thawed before drying (FTD), frozen and dried without thawing (FD), and dried without freezing or thawing (D). In FTD samples, total color difference increased, accompanied by marked decreases in the retentions of polyphenols and DPPH radical scavenging activity. This quality decline was attributed to cell membrane damage from freezing, which disrupted cellular localization between polyphenol oxidase and substrates, alongside drip loss and enhanced chemical reactions during ambient thawing. In contrast, no significant difference was observed between the FD and D , likely because immediate freezing after shaping followed by reduced pressure drying minimized oxygen exposure. These results demonstrate that while freezing and thawing operations degrade antioxidant quality, drying apples in a frozen state without a thawing step successfully preserves their antioxidant activity.

Key Words: Microwave-vacuum drying, Pre-freezing, Apples, Antioxidant activity

INTRODUCTION

In recent years, efforts have been made to develop processed fruit products that leverage functional properties and regional characteristics. Apples are a major agricultural product of Iwate Prefecture and are considered effective in preventing lifestyle-related diseases due to their high antioxidant content. Microwave-vacuum drying (MVD) is a method used in the production of dried fruit, a type of processed fruit product. MVD is utilized in the production of dried fruits, a common type of processed fruit product. Although MVD can efficiently remove internal moisture and maintain high product quality within a short drying time, it may cause significant deformation of the sample. Furthermore, a method involving freezing and thawing the samples prior to drying (pre-freezing) has been reported as a means to suppress such deformation, but natural thawing at room temperature and atmospheric pressure may lead to

a significant decline in quality. Pre-freezing without a thawing step could potentially eliminate this drawback. However, previous studies have not examined the changes in antioxidant activity, and there are few reports on the effect of pre-freezing on antioxidant properties. Therefore, in this study, we investigated the effect of pre-freezing and thawing on antioxidant activity during the MVD of apples.

MATERIALS AND METHODS

Commercially available apples (Fuji) were cored into cylinders (6 cm in diameter and 1 cm thickness), cut crosswise, and shaped into fan-shaped pieces weighing approximately 23 ± 0.6 g. Samples were kept for 3 days in a freezer at -40 ℃ and thawed for 3 hours in an incubator at 25 ℃, followed by MVD (FTD), those frozen and dried without thawing (FD), those dried without freezing or thawing (D), and those frozen and thawed without drying (FT).

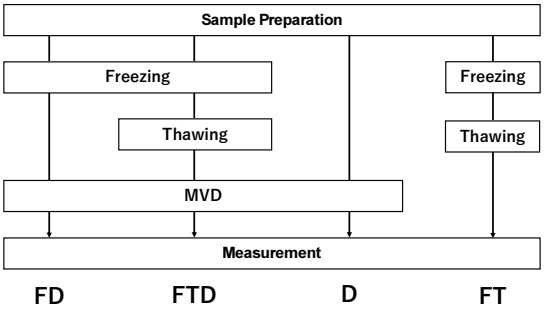

Fig.1 Experimental Groups

For drying, a plastic tray was placed in the desiccator of a microwave reactor, and four samples were arranged on it. The internal pressure was maintained at 3 kPa throughout the drying process. The samples were irradiated with microwaves at an output power of 200 W (4.7 W/g-fresh weight) with 5-s irradiation/5-s pause cycles. The drying time was 100 min for the D and 80 min for the FD and FTD.

The total color difference was measured with a chroma meter before and after the drying treatment. Polyphenol content was measured using the Folin–Ciocalteu method. The DPPH radical scavenging activity was measured with a slight modification of the method described by Oki.

RESULTS & DISCUSSION

In FTD samples that were frozen and then thawed, an increase in total color difference (Figure 2), along with decreases in polyphenol retention (Figure 3) and DPPH radical scavenging activity retention (Figure 4), were observed. This was attributed to the disruption of cellular localization between polyphenol oxidase and polyphenols caused by freezing-induced membrane damage, as well as drip loss and enhanced chemical reactions during prolonged thawing at room temperature and atmospheric pressure. On the other hand, the lack of significant difference between the FD and D is thought to be because freezing was performed immediately after shaping, and subsequent drying under reduced pressure minimized oxygen exposure, which plays a major role in the loss of antioxidant activity.

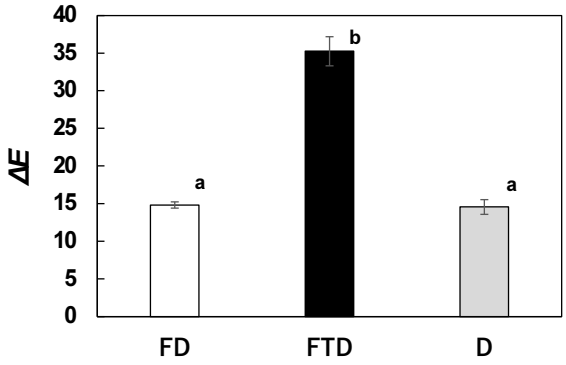

Fig.2 Total color difference

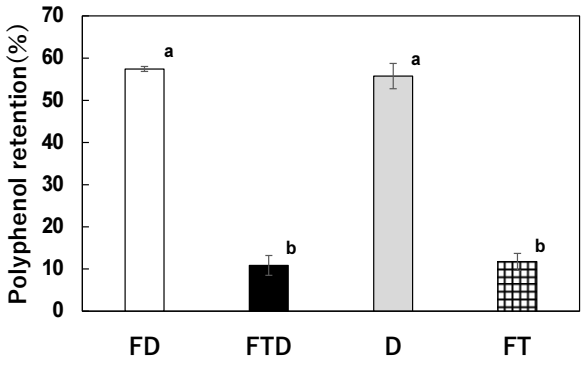

Fig.3 Polyphenol retention

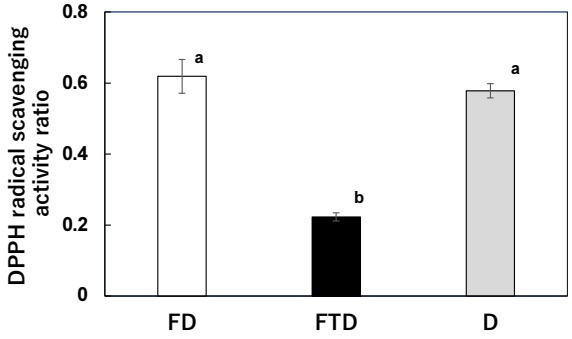

Fig.4 DPPH radical scavenging activity ratio

The error bars mean S.E. (n=3).
Different lower case letters represent significant differences (P<0.05) by Tukey-Kramer test.

CONCLUSIONS

The results of this study confirmed that freezing and thawing operations, which were previously considered beneficial for physical properties, cause a decline in quality in terms of antioxidant activity. However, the results suggest that antioxidant activity could be significantly improved by drying the product while still frozen, without undergoing a thawing process.

ACKNOWLEDGEMENTS

This work was supported by JSPS KAKENHI, Grant Number JP23K23736(Grant-in-Aid for Scientific Research(B))

REFERENCES

Ando, Y., and Nei, D. 2024. Effects of different pre-freezing methods and pressure levels on the pore structure and mechanical properties of microwave-vacuum-dried apple. Journal of Food Engineering. 369: 111944.

Noguchi, S. 2009. Chapter 2: Chemistry of Food Freezing, in New Edition Food Freezing Technology, 19–32. Suzuki, T. ed.

Oki, T. 2008. Chapter II: Functional Assessment Experimental Methods, 1. Functional Evaluation Using Chemical and Enzymatic Reactions, 1) Antioxidant Activity Evaluation Method, (1) DPPH Radical Scavenging Activity Evaluation Method, in Manual for Assessment of Food Functionality (II). The Japanese Society for Food Science and Technology, 71–78.

PH-P02

Proceedings of The 12th International Symposium on Machinery and Mechatronics for Agriculture and Biosystems Engineering (ISMAB 2026)
20-24 October 2026, Busan, Republic of Korea

ROOM-TEMPERATURE ETHYLENE GAS SENSOR BASED ON GRAPHENE OXIDE AND ZINC OXIDE

Kuan-Ju Chen*, Yao-Chuan Tsai

Department of Bio-industrial Mechatronics Engineering, National Chung Hsing University, Taichung, Taiwan
* Corresponding Author--Voice:+886-937250770, Email:lulu021500@gmail.com

Abstract: Ethylene is a crucial plant hormone governing fruit ripening and senescence, making its real-time monitoring vital for extending shelf life and reducing food waste. Although conventional analytical instruments offer high accuracy, they are bulky, expensive, and unsuitable for on-site continuous monitoring. This study presents a non-heated, room-temperature ethylene gas sensor based on graphene oxide (GO) and zinc oxide (ZnO) nanocomposites. The device employs copper interdigital electrodes, onto which suspensions of GO as well as GO/ZnO nanocomposites were deposited via drop-casting. The gas-sensing characteristics of 1.38 g GO, 1 g GO, and 1.38 g GO/ZnO nanocomposite films were systematically compared. Ethylene gas concentrations ranging from 20 to 100 ppm were prepared using the partial pressure method in a sealed chamber to evaluate the resistance response at room temperature. Experimental results demonstrate that the sensitivity of the GO thin film increased significantly by 45.62%. This enhanced performance can be attributed to the smaller cross-sectional area and lower electrical conductivity of the thinner film, which allows gas molecule adsorption to exert a more prominent modulation effect on the conductive channels. Furthermore, incorporating n-type ZnO nanostructures into the p-type GO matrix created p-n heterojunctions and depletion layers at the interface, resulting in an increased baseline resistance. Compared to pure GO films of equivalent thickness, the GO/ZnO composite sensor exhibited a sensitivity increase of approximately 12.4% along with a markedly faster desorption rate. This improvement indicates that ZnO provides abundant catalytic active sites and lowers the reaction activation energy. Regarding repeatability, the 1 g GO film demonstrated excellent stability with minimal baseline drift, whereas the GO/ZnO composite film displayed superior desorption and recovery kinetics. Overall, this research demonstrates the feasibility of GO/ZnO heterostructures for highly sensitive and rapid ethylene detection under non-heated, room-temperature conditions, showing immense potential for future applications in smart agriculture and cold-chain monitoring of fresh produce.
Key Words: Ethylene gas sensor, Graphene oxide, Zinc oxide, Room temperature, Heterojunction

INTRODUCTION

Climacteric fruits, such as bananas, apples, and mangoes, continue to ripen after harvest. The key mechanism driving this process is autocatalytic ethylene production, which triggers the fruit ripening cascade. After harvest, excessive ethylene accumulation accelerates decay, leading to significant economic losses and food waste. According to the Food and Agriculture

Organization (FAO) of the United Nations, approximately 22% of fruits produced globally are lost due to inadequate post-harvest management before reaching consumers. Previous ethylene sensing technologies primarily fall into three categories: (1) optical methods, such as a multi-channel optical spectrometer based on non-dispersive infrared (NDIR) technology proposed in 2009, which introduced additional channels to eliminate cross-interference from refrigerant leaks and ethanol [1]; (2) electrochemical methods, such as an electrochemical ethylene sensor reported in 2012 that utilized a thin layer of ionic liquid as an electrolyte to replace strong acids [2]; and (3) metal oxide semiconductor (MOS) methods, such as a sensor developed in 2020 featuring a Cr_2O_3 catalytic layer to efficiently oxidize and filter interfering gases into harmless or low-reactivity products before they reach the underlying sensing layer [3]. However, these three approaches suffer from high costs, susceptibility to temperature and humidity variations, and the requirement for high operating temperatures, respectively. Therefore, the objective of this study is to develop a cost-effective, lightweight, and easy-to-operate ethylene sensor capable of operating at room temperature.

MATERIALS AND METHODS

In this experiment, aqueous graphene oxide (GO) solution and zinc oxide (ZnO) powder were selected as the main sensing materials. A hybrid solution of GO and ZnO was prepared with mass percentages of 36.70 wt% for GO and 3.45 wt% for ZnO. By decorating ZnO nanoparticles onto the surface of the GO thin film, the room-temperature sensing performance of the device toward ethylene gas was enhanced. Polyimide (PI) was utilized as the sensor substrate, featuring copper interdigitated electrodes with both line width and spacing set to 0.5 mm. Three types of test specimens were fabricated via the drop-casting method: (A) 1.38 g GO, (B) 1 g GO, and (C) 1.38 g GO/ZnO. Six common gas sensor performance parameters were evaluated and analyzed: response, sensitivity, repeatability, response time, stability, and selectivity.

RESULTS & DISCUSSION

Scanning electron microscopy (SEM) images reveal that pristine GO exhibits a typical stacked flake-like structure, whereas ZnO particles are observed adhering to the surface of GO nanosheets in the GO/ZnO composite.Regarding the effect of GO film thickness, under the same ethylene concentration, the sensitivity of 1g GO was enhanced by 45.62% compared to that of 1.38g GO. This phenomenon can be explained by the electrode resistance formula: as the number of GO thin-film layers decreases, the proportion of resistivity change induced by gas adsorption increases, thereby enhancing device sensitivity.

Regarding the effect of ZnO composite modification, incorporating ZnO nanostructures in the 1.38g GO/ZnO sample increased sensitivity by approximately 12.4% relative to pristine 1.38g GO. Under a high initial resistance state, the narrowing of the depletion region at the p-n junction leads to a more pronounced rate of resistance change, thereby boosting the sensing response. However, the stability of 1.38g GO/ZnO decreased, mainly because SEM observations indicate non-uniform coverage of ZnO on GO, with p-n junction characteristics appearing only in localized regions. The response and desorption times of 1.38g GO/ZnO were shortened to 130 s and 135 s, respectively, confirming that ZnO modification effectively accelerates the adsorption and desorption rates of gas molecules.All three sets of devices exhibited a decaying trend in response values during a 10-day continuous test (Fig. 1), showing a gradual decline from Days 1–5 and a significant degradation phase from Days 6–7. After 10

days, the total attenuation rates were 40.5% for 1.38g GO, 34.8% for 1g GO, and 37.1% for 1.38g GO/ZnO.Selectivity testing against absolute ethanol, isopropanol, and acetone (Fig. 2) revealed negative responses toward absolute ethanol and isopropanol, alongside an extremely low response toward acetone. The sensor displayed a strong positive response exclusively toward ethylene gas, demonstrating high selectivity and the ability to effectively distinguish ethylene from interfering alcohol and ketone gases.

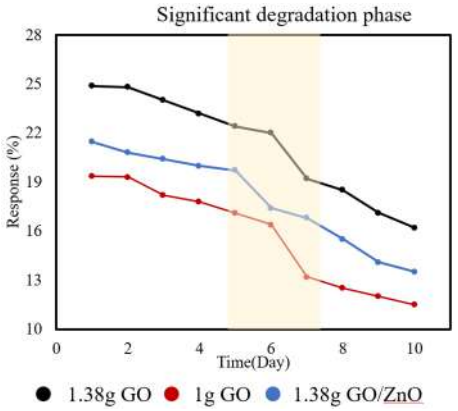

Fig. 1 Long-term stability test.

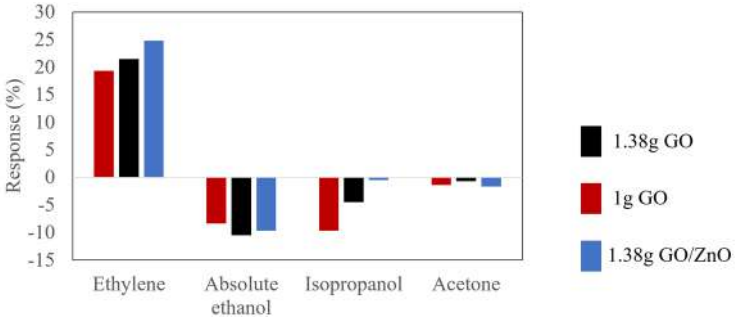

Fig. 2 Selectivity.

CONCLUSIONS

This study successfully developed a room-temperature ethylene gas sensor based on GO and ZnO nanocomposites. The GO/ZnO nanocomposite exhibits high sensitivity, good linear response, and excellent repeatability toward ethylene gas at room temperature, providing a clear hardware structural design reference for future miniaturized, low-power, room-temperature sensing devices applied in real-time fruit ripeness monitoring.

ACKNOWLEDGEMENTS

Special thanks to Prof. Tsai for his technical assistance in experiments and insightful guidance on drafting this manuscript.

REFERENCES

Fonollosa, J., Halford, B., Fonseca, L., Santander, J., Udina, S., Moreno, M., Hildenbrand, J., Wöllenstein, J., & Marco, S. (2009). Ethylene optical spectrometer for apple ripening monitoring in controlled atmosphere store-houses. *Sensors and Actuators B: Chemical*, *136*(2), 546–554.

Zevenbergen, M. A. G., Wouters, D., Dam, Van A. T., Brongersma, S. H., & Crego-Calama, M. (2011). Electrochemical Sensing of Ethylene Employing a Thin Ionic-Liquid Layer. Analytical Chemistry, 83(16), 6300–6307.

Jeong, S. Y., Moon, Y. K., Kim, T. H., Park, S. W., Kim, K. B., Kang, Y. C., & Lee, J. H. (2020). A New Strategy for Detecting Plant Hormone Ethylene Using Oxide Semiconductor Chemiresistors: Exceptional Gas Selectivity and Response Tailored by Nanoscale Cr_2O_3 Catalytic Overlayer. *Advanced Science*, *7*(7).

PH-P03

Proceedings of The 12th International Symposium on Machinery and Mechatronics for Agriculture and Biosystems Engineering (ISMAB 2026)
20-24 October 2026, Busan, Republic of Korea

EFFECTS OF MICROWAVE-VACUUM DRYING PROCESSING ON THE PHYSICAL PROPERTIES OF BANANA CHIPS

Jan Jeng Huang[1], Jia Fang Li[1]*
[1]Department of Food Science , National Chiayi University, Chiayi Taiwan
*Corresponding Author—Tel: +886-5-2717612. Email: hjj@mail.ncyu.edu.tw

Abstract: This experiment used bananas as raw material to making banana chips by microwave-vacuum drying. The production of banana chips involved a two-stage process with progressively increasing microwave power (5000W, 8000W). The response surface methodology was employed, three-variable and three-level design were the sodium bicarbonate concentration (0–1.0%), banana slice thickness (5–11 mm), and drying time (5000W/40–50 mins, 8000W/10–20 mins) as factors to determine the physical properties and sensory evaluation of each product group. The results showed that, based on the crispness, color, and sensory characteristics of product's, the optimal process conditions were: sodium bicarbonate concentration of 0.5%, sample thickness of 0.8 cm, and drying time of 5,000 W for 45 min and 8,000 W for 12 mins. Compared to commercially available dried banana chips, there are moisture content less than 10%, especially freeze drying (moisture content 5%), this cause of brittleness, and this banana chips product utilizes an optimal microwave- vacuum drying process to achieve the same brightness (L* value) as vacuum-fried products and the crispness as similar the freeze-dried products, but the texture characteristics better than freeze-dried banana chips, and the product was oil-free composition. The main reason was using the microwave- vacuum dried banana chips have uniform and larger pores, while freeze-dried banana chips have smaller and finer pores, and the using vacuum frying banana chips which contains more than 10~15% oil. Overall, microwave-vacuum drying technology can produce the products with a golden-yellow appearance and a crispy texture, resulting in fat-free and healthy products.

Key Words: Microwave-vacuum drying, Banana chips, Response surface methodology,

PH-P04

Proceedings of The 12th International Symposium on Machinery and Mechatronics for Agriculture and Biosystems Engineering (ISMAB 2026)
20-24 October 2026, Busan, Republic of Korea

DEVELOPMENT OF AN IMPELLER FOR BROWN RICE MACHINE SPECIFICALLY FOR MEDIUM GRAIN RICE

Seok-Jin Lee[1], Sun-young Lee[1] Jong-seung Cho[1], Ji-Ae Lee[1], Kyung-Soo Kim[2], Sung-Ha Hong[3], Hwang-Gye Lee[4], Jin-Hyun Kim[4], Tae-Wook Kim[4*]

[1]Leehwa Industry Co.
[2]Leehwa Rocom Co.
[3]Special Researcher Institute of Agri-Biotechnology Convergence
[4]Department of Precision Mechanical Engineering, College of Science and Technology, Kyungpook National University
[4]Corresponding author. Tel.: +82-54-350-1278, E-mail address: kimtw@knu.ac.kr

Abstract

In a country where rice is the staple food, the growing preference for brown rice is because brown rice contains rice bran and germ attached to it, making it rich in protein, fat, and fiber, and low in carbohydrates. It is also known to be rich in dietary fiber, helping to relieve constipation and obesity, purify the blood, and thereby prevent circulatory diseases and enhance natural healing power, thereby helping to prevent cancer and various adult diseases. In this study, wear tests were conducted on three materials TPU, PE, and urethane to improve a metal plate impeller with a urethane impeller. The results were presented in the order of PE > TPU > urethane. Therefore, we conducted a performance test experiment using urethane, which has the highest overall wear resistance, as the material for the impeller.

Key Words : Brown rice machine, Impeller, Rice milling, Urethane impeller

INTRODUCTION

87.4% of the world's rice production is produced in the Asia region. The major rice-producing countries are known to be India (1st), China (2nd), Indonesia (3rd), Thailand (5th), and the Philippines (8th). Unlike Korea, these countries have either japonica or long grain rice as their staple food. In order to export our country' short grain milling machine, it must be improved so that it can mill medium-grain or long grain rice. In the case of a single grain, the ratio of rice

length to diameter is 1.72-2.99; in the case of a medium grain, it is 3.72-4.23; and in the case of a long grain, it is much larger, at 5.38. Of course, the types of rice cultivated may vary by country. As such, if the rice length are long, they break more easily, producing many broken pieces and causing efficiency to drop sharply. Therefore, to mill a medium-sized grain, the structure and method of the machine must be changed. When rice is milled, the first thing that must be removed is the husk, called the bran, and the machine used at this time is a brown rice huller. A rice huller is a machine that removes the husk from dried rice by rubbing it against a rotating impeller. In this study, a metal-made impeller was developed into a urethane impeller and applied, and its performance was evaluated.

MATERIAL AND METHODS

1. Principles of rice milling

There are methods of drying the rice and then immediately milling it, or milling it using a brown rice mill. Recently, as interest in health has increased, the demand for brown rice has grown, leading to increased demand for rice milling machines combined with brown rice milling machines. <Fig. 1> refers to a general milling machine that produces only white rice and a combined milling machine that can produce both white rice and brown rice. The method of removing the outer husk of rice can occur through friction between the husks of different rice plants and impact, but it can also break. To remove the husk from rice, it is important to dry the rice so that its moisture content is within the range of 15-18%. Brown rice, which has a glutinous rice hull, is also more beneficial to health in terms of its components, but its sugar content is particularly much lower at 55-72% compared to white rice's 77.5-88%. However, the best part is that it tastes good and is easy to digest, but its vitamin B1 content is 0.1 mg/100g, which is significantly less than brown rice's 0.54 mg/100g.



Fig. 1 The difference between a conventional milling machine and a milling machine for both brown rice and white rice

2. Brawn rice milling machines and impellers

A rice huller is designed to rotate the dried rice fed into the hopper with an impeller, thereby inducing friction to remove the husk. The most important part here is the impeller. <Fig. 2> indicates the structure of the brawn rice milling machines. The most important part of the Brawn rice milling machines is <Fig. 3>. As shown in the illustration, the impeller with a metal plate attached weighs 2,208 grams and has the drawbacks of a short service life and high torque requirements during rotation. In contrast, the urethane impeller weighs 1,017 grams, which is half the weight of the metal plate impeller. In addition, it also has the advantage of increasing yield by more than 10%.

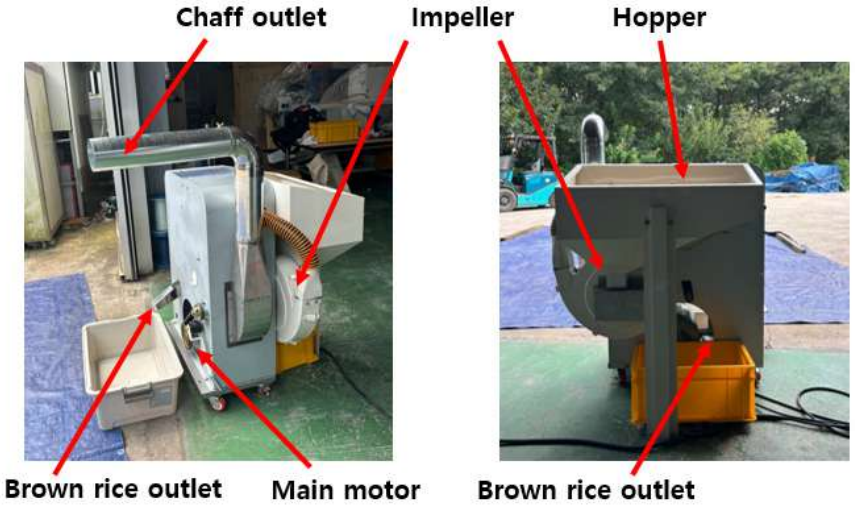

Fig. 2 Name of main part of brown rice machine

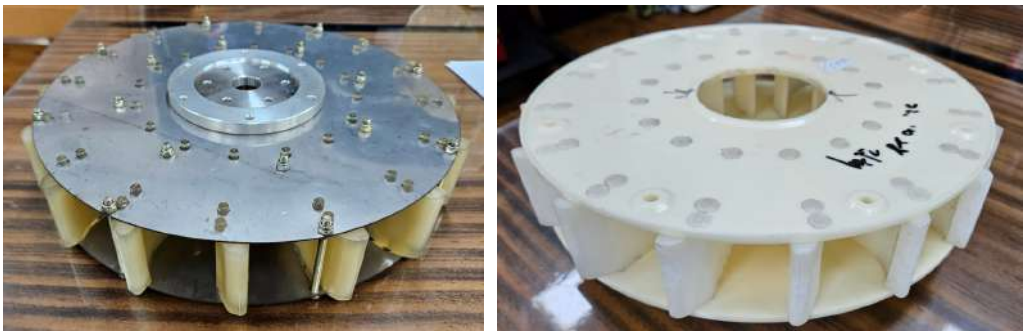

(A) (B)

Fig. 3 Metal plate impeller (A) and urethane impeller (B)

3. Impeller material

The material used to develop a plastic impeller is <Fig. 4>. (A) indicates thermoplastic polyurethane (TPU), (B) indicates PE (polyethylene), and (C) indicates general urethane. Evaluations of friction and service life for these three types of materials are very important because they determine the performance of the brown rice and the replacement cycle of parts. And the impeller blade,

positioned between the side plates rather than on the side plates of the impeller, has a higher frictional specific weight. The wear, friction coefficient, and strength tests for the three materials were conducted at the Institute of Precision Mechanical and Chemical Systems Convergence, College of Science and Technology, Kyungpook National University.

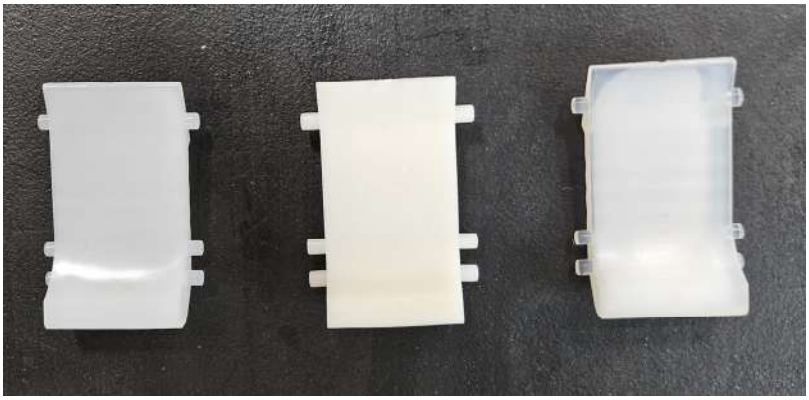

(A) (B) (C)

Fig. 4 Thermoplastic Polyurethane, TPU (A), PE (B), Urethane (C) of blade material for a mold-made impeller fin

4. Impeller friction coefficient tester

To measure the friction coefficient of TPU, PE (polyurethane), and urethane impellers, the device is <Fig. 5>, ASTM G133-95 (USA) was used. <Table 1> shows the specifications of a friction coefficient tester.

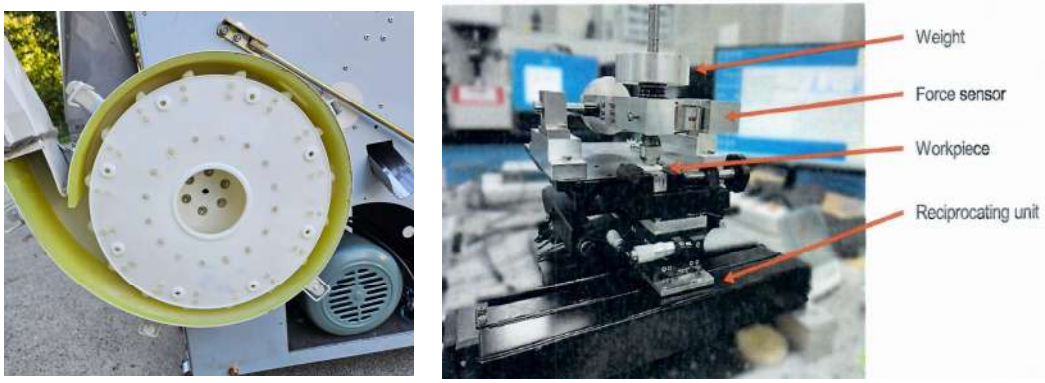

(A) Impeller for brown rice (B) Device of friction measurement

Fig. 5 Impeller for brown rice (A) and Device of friction measurement (B)(ASTM G133-95 linear reciprocating ball-on-flat sliding wear)

Table 1. Specification of ASTM G133-95

Parameter	Value
Tribometer	Reciprocating type
Cycle/Duration	500/250s
Normal load	1.96 N
Frequency/Speed	2 Hz/12 mm/s
Stroke	3 mm
Temperature	20~23℃
Humidity	20~25%
Counter surface	Zr(Φ3 mm)

RESULTS AND DISCUSSION

w

1. Characteristics of white rice and brown rice

In Central Asian countries such as China, Thailand, Vietnam, the Philippines, and India, household rice mills for 200-300 kg/h are highly preferred. One reason for this is also that agriculture still accounts for a large proportion. In addition, the conditions for milling through large RPCs, as in our country, are not yet mature, and above all, the cost of logistics transportation is also a major obstacle. Table 2 shows the nutrients and characteristics of white rice and brown rice. White rice has less protein and more calories than brown rice. Brown rice has bran and germ attached, so it is rich in protein, fat, and fiber, low in carbohydrates, and abundant in dietary fiber. It is known to relieve constipation and obesity, purify the blood, and thereby help prevent circulatory diseases and enhance natural healing, thereby helping to prevent cancer and various adult diseases.

Table 2. Nutrients and Characteristics of White Rice and Brown Rice

Classification	nutrient	Characteristic
White rice 	Moisture 14.1%, protein 6.5%, fat 0.4%, carbohydrates 77.5－88.0%, fiber 0.4%, ash 0.5% Calories 340 kcal/100g	Benefit: tastes good and digests well Weakness: Vitamin B1 0.1 mg/100 g, Biliary colic, diabetes
Brown rice 	Moisture 15.5%, protein 7.4%, fat 3.0%, carbohydrates 55.0－71.8%, fiber 1.0%, ash 1.3% Calories 340 kcal/100g	Benefit: Vitamin B1 0.54mg/100g. Rich in nutrients Weakness: The taste is inferior to white rice, Ineffective digestion and absorption

2. Characteristics of metal impellers and urethane impellers

A brown rice husker is required to function in peeling off only the husk from rice with minimal impact and friction. Therefore, if the impeller itself is heavy or the load is large during rotation, rice breakage occurs, and ultimately a large amount of broken grains are produced. In addition, assembly and production costs are also a practical problem. Therefore, an impeller that is fundamentally lightweight and has appropriate friction is advantageous, and the material of the impeller blades is also very important. Above all, the biggest problem appears to be that bolts are used to join the metal plates, causing impact to the rice and damaging the brown rice. In addition, the metal impeller weighs 2,208 grams, making it about twice as heavy as the urethane impeller. If it is twice as heavy, the motor's rotational torque must also be twice as high, and the power required will also be doubled. In addition, the metal impeller has 48 protrusions per side, so there are 96 in total. This protrusion causes an impact on the brown rice, breaking it and causing it to crumble.

Table. 3. Characteristics of metal impellers and urethane impellers

Classification	Benefit	Weakness
Metal impeller 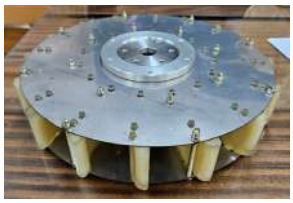	1) Price: 130,000 KRW (Assembly and production costs are three times higher ↑)	1) Weight: 2,208 gram 2) Lifespan: 5－8 tons per unit 3) Brown rice yield: 85－87% 4) Processing time: 1－2 pieces/hour 5) Manual Assembly Method 6) Material: plastic + stainless steel
Urethane impeller 	1) Weight: 1,017 gram 2) Lifespan: 24 Ton per unit 3) Brown rice yield: 95% ↑ 4) Processing time: 10 pieces/hour 5) Heat-pressing method (processability) 6) Material: plastic resin	1) Price: 350,000 KRW (Assembly production cost 60－70% ↓)

3. Measurement of strength, durability, and wear resistance according to the material of impeller blades

The side panels of the brown rice impeller were made identically of ABS material, which is most widely used in developed countries. The impeller blades were manufactured in three types: TPU, PE, and urethane, and wear tests were

conducted by mounting them on a test machine. The impeller wing experiment involved regularly alternating bonding three materials to a single impeller. And 300 kg of rice was subjected to an experiment in which it was divided into six repetitions of 50 kg each. The test results showed differences in the degree of wear among the materials of the impeller blades: TPU, PE, and urethane. In tests of the three types of materials, the order was PE > TPU > urethane. This showed a different result than the wear condition seen with the naked eye. Generally, when the coefficient of friction is low, wear also decreases, so the wear rate tends to decrease as well. However, it may appear differently in the brown rice experiment. Because the abrasion test involves sliding against each other with a constant force and speed, PE performed best. However, in a cosmetic milling impeller, the rice has the force of collision, that is, the impact load, so it may appear differently. Also, when the rough husk of rice impacts the impeller blades, it may not necessarily produce results such as those of a wear test. Overall, urethane, which has the highest wear resistance, was used as the material.

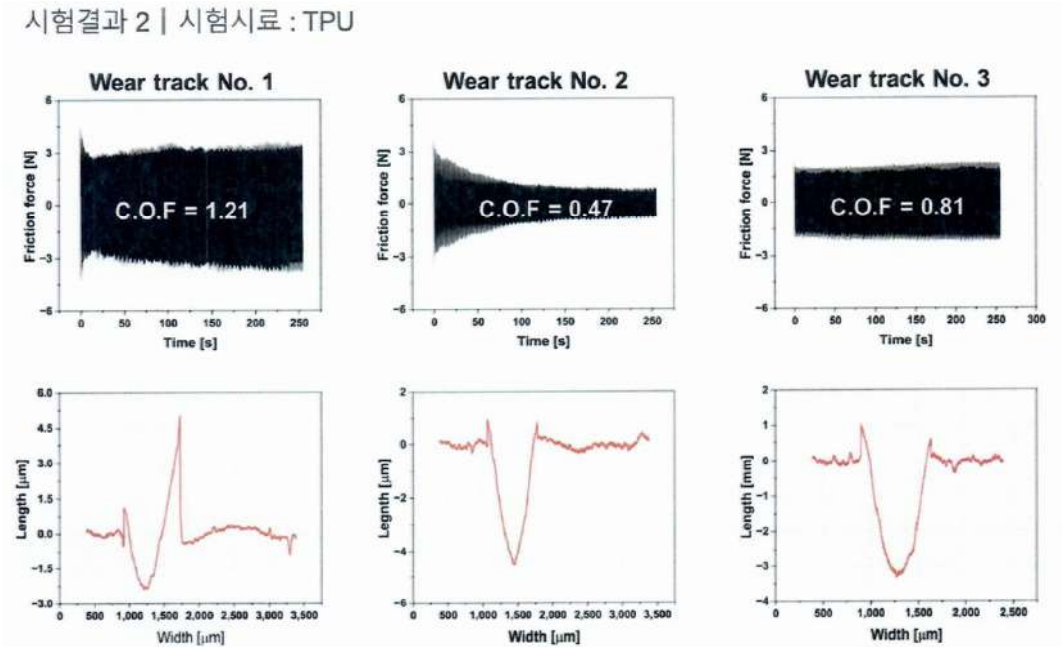

Fig. 5 Results of the wear resistance test of thermoplastic polyurethane (TPU) material

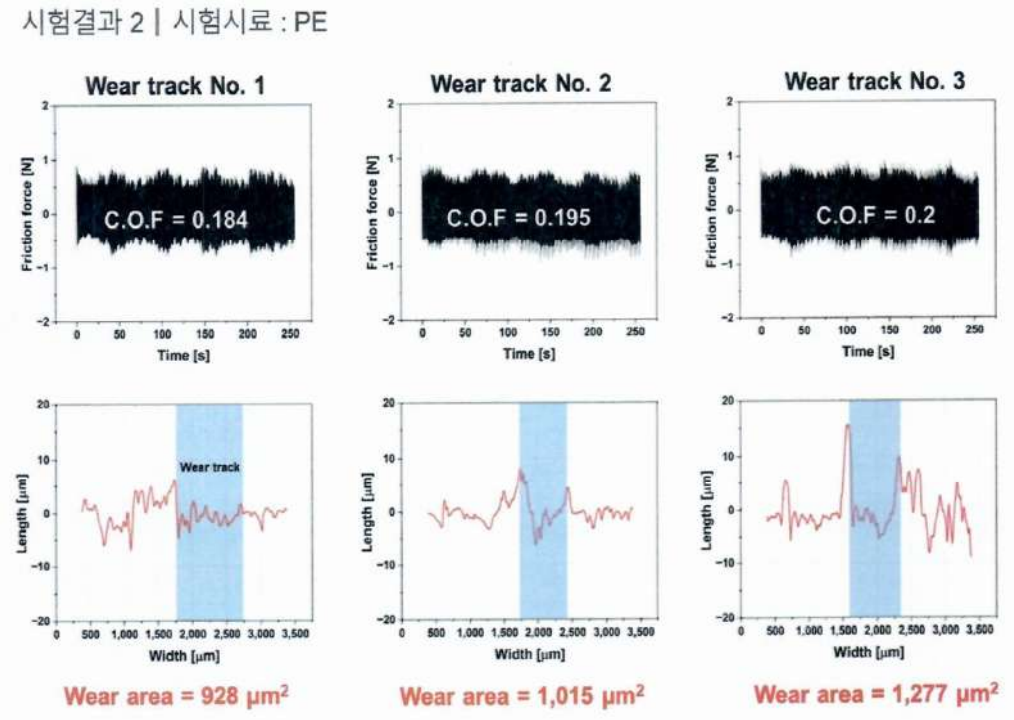

Fig. 6 Wear resistant test results of PE material

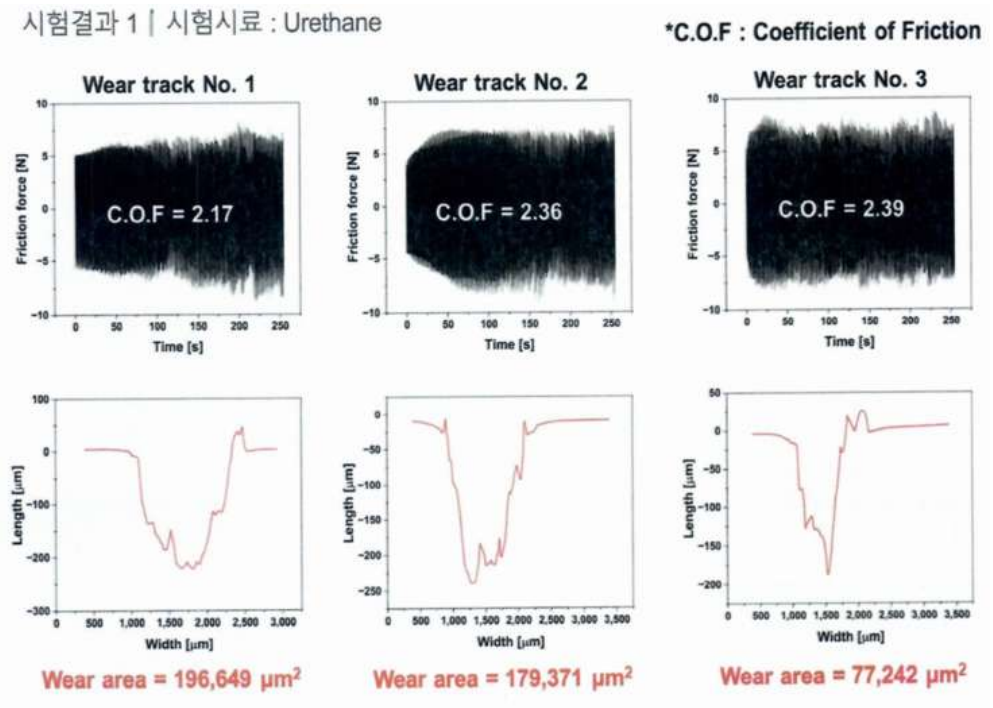

Fig. 7 Results of the wear resistance test of urethane material

Table 4. Wear resistance and amount of wear of TPU, PE, and Urethane

Workpiece	C.O.F. (Avg.)	Wear area(Avg.)
Urethane	2.3	151,087 ㎛²
PE	0.19	1,073 ㎛²
TPU	0.83	1,604 ㎛²

4. Performance evaluation of a milling machine

Using a urethane impeller, the brown rice test was performed twice, as in <Table 5>: four preliminary runs and two main runs. In the preliminary test, rice husks were not discharged, and the amount of brown rice discharged was less than 80%. However, in this experiment, as the impeller rotation was reduced from 2800 rpm to 2660 rpm, the impact on the rice decreased, and the number of broken grains also decreased. In addition, by increasing the capacity by enlarging the impeller inner diameter from 90 mm to 100 mm and thereby increasing the amount of brown rice discharged, it was possible to discharge more than 500 kg/h of brown rice. In addition, to further increase the brown rice output, it was also necessary to adjust the motor capacity from 1 ps to 1.5 ps. Under the conditions of this experiment 1 and 2, it is possible to select the inverter settings, but it was judged that setting it to 6 was more appropriate than setting it to the maximum of 7. At this time, setting the supply level to 5 was evaluated as the best. Finally, the brown rice yield after removing the bran was measured as follows: with 10 kg of input, 8.14 kg of brown rice was removed, and 1.6 kg of rice husks were removed (total 8.14 + 1.6 = 9.74 kg), resulting in a brown rice yield of 97.4%.

Table 5. Performance testing of brown rice using urethane impellers (preliminary test + main test)

	Input Rice (kg)	Inverter (rpm)	Supply livel	Motor pulely (rpm)	Main pulley (rpm)	Main (rpm)	Power consumption	Time (sec)	BR output (kg)	RH optput (kg)	P output (kg)	BRO/h (kg/h)
1 (PT)	10	7 2800	4 (half open)	Ø126 1750	Ø66 3200	3340		113	7.62	X	X	240
2 (PT)	10	7 2800	6 (max open)	Ø126 1750	Ø66 3200	3340	1.61A 2.46A	71	7.92	X	X	399.3
3 (PT)	10	7 2800	6 (max open)	Ø126 1750	Ø66 3200	3340	1.51A 3.4A	37	8.0	X	X	763.1
4 (PT)	10	7 2800	4 (max open)	Ø126 1750	Ø66 3200	3340	1.53A 2.60A	60	7.98	X	X	478.8
1 (MT)	10	7 2800	5 (max open)	Ø126 1750	Ø66 3200	3340	1.47A 2.71A	55	8.08	1.60	0.22	526.9
2 (MT)	10	6.6 2660	5 (max open)	Ø126 1750	Ø66 3200	3340	1.40A 2.51A	57	8.14	1.60	0.24	514.1

※ PT: preliminary test, MT: main test), BR: Brown rice, RH: Rice husks, P:Peel, BRO/h: Brown rice output/h



(A) (B) (C) (D)

Fig. 8 Changes in rice due to processing for medium grain, (A) Paddy, (B) Brown rice, (C) Rice, (D) Broken rice

CONCLUSION

In a country where rice is the staple food, the growing preference for brown rice is because brown rice contains rice bran and germ attached to it, making it rich in protein, fat, and fiber, and low in carbohydrates. It is also known to be rich in dietary fiber, helping to relieve constipation and obesity, purify the blood, and thereby prevent circulatory diseases and enhance natural healing power, thereby helping to prevent cancer and various adult diseases. In this study, wear tests were conducted on three materials TPU, PE, and urethane to improve a metal plate impeller with a urethane impeller. The results were presented in the order of PE > TPU > urethane. Therefore, we conducted a performance test experiment using urethane, which has the highest overall wear resistance, as the material for the impeller. By reducing the impeller rotation from 2800 rpm to 2660 rpm, the impact on the rice decreased, and the broken rice also decreased. In addition, by increasing the capacity by enlarging the impeller inner diameter from 90 mm to 100 mm and thereby increasing the amount of brown rice discharged, it was possible to discharge more than 500 kg/h of brown rice. Finally, the brown rice yield after removing the bran was measured as follows: with 10 kg of input, 8.14 kg of brown rice was removed, and 1.6 kg of rice husks were removed (total 8.14 + 1.6 = 9.74 kg), resulting in a brown rice yield of 97.4%

ACKNOWLEDGEMENTS

This research was conducted with support from the Ministry of Agriculture, Food and Rural Affairs' Technology Commercialization Support Project in 2024, under the project titled "Development for the Commercialization of a Set-Type Rice Mill for Domestic and Export Strategy" (Project No. RS-2024-00401064).

REFERENCES

[1] ITC Reade map. 2021. Code 8437 Machines for Cleaning, Sorting or Grading Seed, Grain or Dried Leguminous Vegetables; Machinery used in the Milling Industry or for the Working of Cereals or Dried Leguminous Vegetables (excluding farm-type machinery, heat treatment equipment, centrifugal dryers and air filters).

[2] Son, C. M., 2012, Development of Integrated Small-Size Grinding Machine for Long Grain Rice, Thesis of Doctor's Degree.

[3] Park, K. K., Ha, Y. S., Son, C. M., Hong, D. H., Nam, S. H., Kim, K. S., Lee, S. J., Lee, S. Y., 2011, Development of an Integrated Compact Rice Mill for Strategic Export, Report on Agriculture Technology Development Project of Ministry of Agriculture, Fisheries and Food Research, Publication registration number: 11-1541000 -001217-01.

[4] Lee, S. J., Ha, Y. S., 2014, Analysis of Structural Factor and Performance of Farmhouse Rice Milling Machines, Current Research od Agiculture and Life Science, 32:2 91-97, http://dx.doi.org/10.14518/crals.2014.32.2.012.

[5] KIPRIS, 20230210, Search of Key words, http://kpat.kipris.or.kr/kpat/searchLogina.do?next=MainSearch).

[6] ISO, 2023, Rice Milling-Symbols and Equivalent Terms and Cereals and Pulses-Specification and Test Methods Part 1: Rice. htts://www.evs.ee/et/iso-3971-1977.

[7] AMTEC was created in response to the need for an official testing agency for agricultural machinery to guide stakeholders in determining suitability of agricultural machinery under Philippine conditions. AMTEC was established in 1977 through a Memorandum of Agreement (MOA) between the Department of Agriculture (DA) and University of the Philippines at Los Baños (UPLB). AMTEC is administered by UPLB through the College of Engineering and Agro-Industrial Technology(CEAT).

PH-P05

Proceedings of The 12th International Symposium on Machinery and Mechatronics for Agriculture and Biosystems Engineering (ISMAB 2026)
20-24 October 2026, Busan, Republic of Korea

ESTIMATION OF ADDED SORBITOL CONCENTRATION IN CARROT USING RAMAN SPECTROSCOPY

Shiori Furukawa[1], Takahisa Nishizu[2,3], Teppei Imaizumi[2,3*]

[1] Graduate School of Natural Science and Technology, Gifu University, 1-1, Yanagido, Gifu-city, Gifu, 501-1193, Japan
[2] Faculty of Applied Biological Sciences, Gifu University, 1-1, Yanagido, Gifu-city, Gifu, 501-1193, Japan
[3] Preemptive Food Research Center, Gifu University, 1-1 Yanagido, Gifu-city, Gifu, 501-1193, Japan
*Corresponding Author-- Voice: +81-58-293-2930, Email: imaizumi.teppei.j6@f.gifu-u.ac.jp

Abstract: Raman spectroscopy provides distinct characteristic peaks that are associated with the molecular structures of substances. These spectral features can provide information about the chemical components of a sample, which may be useful for concentration estimation in food materials. This study investigated the estimation of sorbitol concentration in carrots using Raman spectroscopy. Carrot–sorbitol samples with sorbitol concentrations ranging from 0 to 100 g/L were prepared and analyzed by Raman spectroscopy. The carrot–sorbitol samples exhibited spectral features associated with both carrot and sorbitol, and sorbitol-related features were observed in some regions. OPLS-DA using the 0 and 100 g/L samples was performed to examine spectral differences caused by sorbitol addition. Four wavenumbers were selected based on their contributions to the spectral differences and their relationships with sorbitol concentration. A multiple linear regression model using four selected spectral variables achieved an R^2 above 0.8, substantially improving the estimation accuracy compared with the single-peak model. These results suggest that Raman spectroscopy can provide spectral information useful for estimating sorbitol concentration in carrot by combining multiple spectral variables.

Key Words: Raman spectroscopy, Carrot, Sorbitol, Concentration estimation

INTRODUCTION

Raman spectroscopy provides distinct characteristic peaks that reflect the molecular structures of substances. These peaks provide spectral information related to the chemical structures of the components in a sample. Although food is a composite matrix, utilizing such structure-related spectral information may enable concentration estimation while providing a basis for interpreting the spectral variables used in the estimation. In particular, vegetables often exhibit considerable variation in chemical composition among individual samples, making such chemically interpretable information potentially useful for concentration estimation in food materials.

Furukawa et al. (2026) reported a strong linear relationship between glycerol concentration and Raman peak intensity ratio in carrots treated by vacuum impregnation, suggesting the potential of Raman spectroscopy for estimating the concentration of an additive introduced into food tissues. However, the applicability of this approach to other substances has not been fully investigated.

In this study, the potential of Raman spectroscopy for estimating additive concentration in food was investigated by estimating sorbitol concentration in carrots.

MATERIALS AND METHODS

Sample preparation

A carrot extract solution was prepared by grinding carrots. The carrot extract solution and sorbitol solution were mixed in a ratio of 8:2 to prepare samples with sorbitol concentrations of 0, 10, 20, 40, 60, 80, and 100 g/L. Samples with sorbitol concentrations of 30, 50, 70, and 90 g/L were additionally prepared for model validation.

Raman spectroscopy

A 9-μL aliquot of each sample was mixed with 1 μL of dimethyl sulfoxide (DMSO) as an internal standard, followed by Raman spectroscopic measurement. Raman spectra were acquired over the range of 200–3000 cm^{-1} using a laser power of 50 mW, an exposure time of 1 s, and 64 accumulations. Each sample was measured six times. The obtained spectra were normalized using the intensity of the DMSO reference peak at 307 cm^{-1}.

Spectral analysis and concentration estimation

OPLS-DA was performed using the 0 and 100 g/L samples to identify spectral variables contributing to the spectral differences associated with sorbitol addition. For the wavenumbers identified by OPLS-DA, correlations between peak intensity and additive concentration were evaluated across the 0-100 g/L concentration range, and four wavenumbers were selected for concentration estimation. A multiple linear regression model was constructed using the peak intensities at the four selected wavenumbers as predictor variables and additive concentration as the response variable. The estimated and actual concentrations were then compared using the 30, 50, 70, and 90 g/L samples. The performance of the model was also compared with that of a single-peak model.

RESULTS & DISCUSSION

Figure 1 shows the Raman spectra of carrot, sorbitol, and carrot–sorbitol samples. The carrot–sorbitol samples exhibited spectral features associated with both carrot and sorbitol, with sorbitol-related features observed in several regions. These spectral features were further analyzed using OPLS-DA to examine differences associated with sorbitol addition (Fig. 2). The resulting score plot showed a clear separation between the two concentration groups, indicating differences in the spectral profiles associated with sorbitol addition.

A multiple linear regression model was then constructed using four selected spectral variables. This model achieved an R^2 value greater than 0.8, substantially improving the estimation accuracy compared with the single-peak model. These results suggest that combining multiple spectral variables can improve the estimation of sorbitol concentration in carrot.

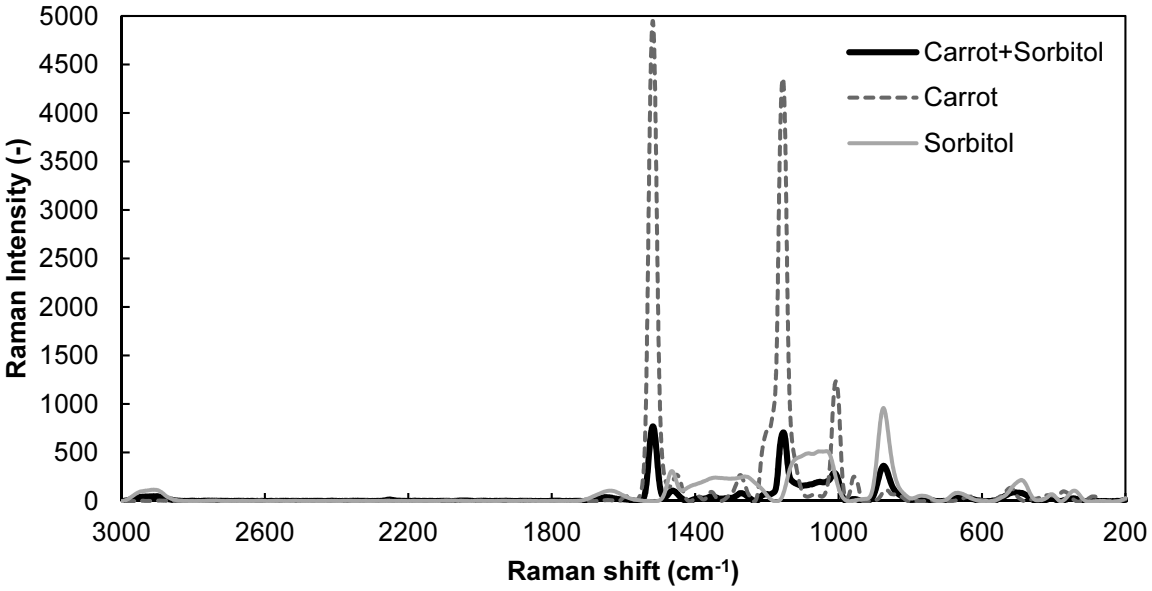

Fig. 1. Raman spectra of carrot, sorbitol, and carrot–sorbitol samples.

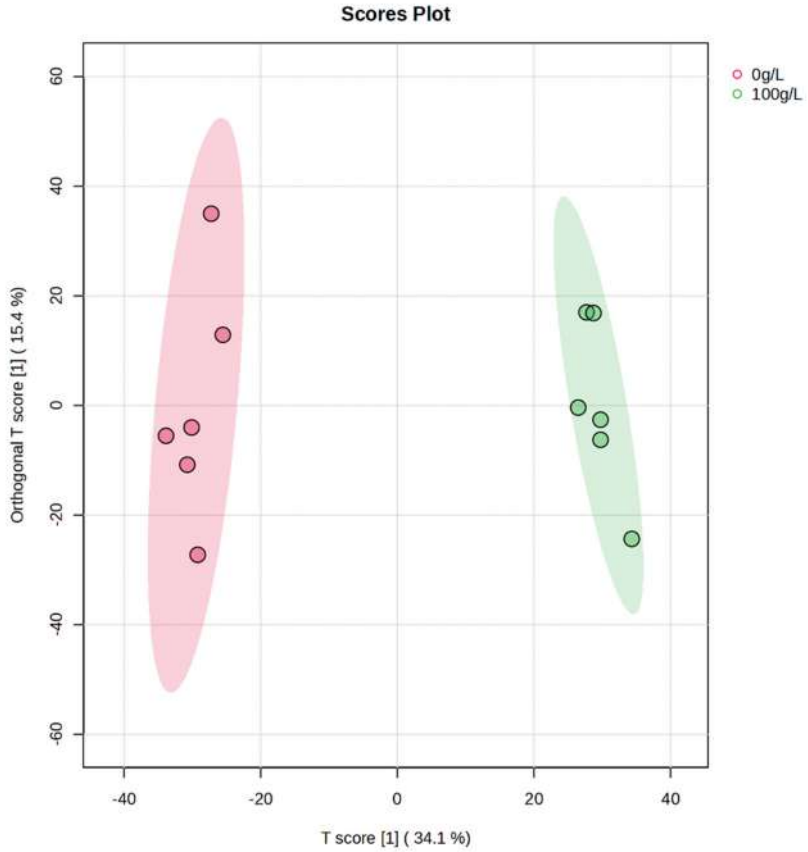

Fig. 2. OPLS-DA score plot of carrot–sorbitol samples with sorbitol concentrations of 0 and 100 g/L.

CONCLUSIONS

This study showed the potential of Raman spectroscopy for estimating sorbitol concentration using multiple spectral variables, even when the spectra of carrot and sorbitol overlap. The method will be further applied to sorbitol-impregnated carrots and other food–additive combinations.

REFERENCES

Furukawa, S., A. Ichinobe, T. Nishizu, and T. Imaizumi. 2026. Effects of Vacuum Impregnation–Induced Glycerin Penetration on Drip Suppression in Frozen Carrots and Its Evaluation Using Raman Spectroscopy. Transactions of the Japan Society of Refrigerating and Air Conditioning Engineers 43(2).

PH-P06

Proceedings of The 12th International Symposium on Machinery and Mechatronics for Agriculture and Biosystems Engineering (ISMAB 2026)
20-24 October 2026, Busan, Republic of Korea

EFFECT OF SUB-ZERO TEMPERATURE STORAGE ON PHYSICOCHEMICAL PROPERTIES AND MICROBIOLOGICAL QUALITY OF FRESH-CUT YELLOW BELL PEPPERS

Shuri Takahashi[1], Takahiro Orikasa[2], Shoji Koide[2*]

[1]Graduate School of Arts and Sciences, Iwate University, 3-18-8 Ueda, Morioka, Iwate 020-8550, Japan
[2]Faculty of Agriculture, Iwate University, 3-18-8 Ueda, Morioka, Iwate 020-8550, Japan
*Corresponding Author-- Voice: +81-19-621-6182, Email: shojides@iwate-u.ac.jp

Abstract: Fresh-cut yellow paprika samples were subjected to sub-zero temperature storage at −2 °C for 10 days, and physicochemical properties and microbiological quality were evaluated. There were no significant differences in weight loss, color difference, sugar content, L-ascorbic acid content and malondialdehyde content among the sample stored at 5 °C for 5 days (T5-D5), 5 °C for 10 days (T5-D10), −2 °C for 5 days (T2-D5), and −2 °C for 10 days (T2-D10). Regarding microbiological quality, no significant differences were observed in the number of aerobic bacteria, *Pseudomonas* spp., and mold and yeast among T5-D5, T5-D10, T2-D5 and T2-D10. However, the number of aerobic bacteria, *Pseudomonas* spp., and yeast in the sample stored at −2 °C for 10 days decreased by approximately 2 Log_{10} CFU/g compared the sample stored at 5 °C for 10 days. Sub-zero temperature storage at −2 °C could be stored without freezing for 10 days with keeping not only physicochemical properties but also suppresses the growth rate of bacteria and mold and yeast.

Key Words: yellow pepper, fresh-cut yellow bell pepper, sub-zero temperature

INTRODUCTION

Low-temperature storage suppresses respiration and water evaporation in fresh vegetables, and prevents the consumption of ingredients and microbial growth. Thus, Low-temperature storage is basic method for maintaining freshness and quality. Recently, sub-zero temperature storage has been known as an effective technology for retarding both quality loss and microbial growth in fresh-cut vegetables (Liu et al., 2020). In this study, we conducted experiments on the sub-zero temperature storage at −2 °C of yellow bell peppers (*Capsicum annuum* L.). Here, we will evaluate the effects of sub-zero temperature storage at −2 °C on physicochemical properties and microbiological quality of fresh-cut yellow bell peppers.

MATERIALS AND METHODS

Yellow bell peppers (*Capsicum annuum* L.) were purchased at a commercial market in Morioka in Japan. The yellow bell peppers were cut into 20 g wedges with a knife, and calyx and

placenta were removed. These yellow bell pepper samples were individually placed into an OPP film. These samples packages were placed in a polypropylene containers and stored in the incubator for 5 days at 5 °C (hereinafter referred to as T5-D5), for 10 days at 5 °C (T5-D10), for 5 days at −2 °C (T2-D5), or for 10 days at −2 °C (T2-D10). In this study, weight loss, color difference, sugar content, L-ascorbic acid content (L-AsA), hardness, malondialdehyde content (MDA), electrical conductivity, electrical impedance, and microbiological quality were evaluated. For comparison, fresh samples (F) and samples frozen at −80 °C followed by thawing (DS) were also prepared for the measurements. Electrical conductivity was measured according to the method of Fan et al. (2005), and electrolyte leakage was calculated according to the following equation:

$$\text{Electrolyte leakage } (\%) = C_{30}/C_T \times 100 \quad \cdots \quad (1)$$

where C_{30} is the electrical conductivity after 30 min of shaking ($\mu S/cm$) and C_T is the electrical conductivity after autoclaving ($\mu S/cm$), respectively.

RESULTS & DISCUSSION

Results showed that no significant differences were observed in weight loss, color difference L-ascorbic acid content and MDA content among T5-D5, T5-D10, T2-D5 and T2-D10. Electrical impedance analysis showed that these samples showed obvious circular arcs. This indicated that the cell membrane had been intact during storage. Electrolyte leakage of T5-D5 (6.58 ± 0.68 %) was significantly lower than that of F (9.27 ± 0.65 %), and no increase in electrolyte leakage was observed among all storage conditions. Thus, our results imply that the cell membrane structure was maintained and the produce could be stored without chilling injury. There were no significant differences in the number of aerobic bacteria, *Pseudomonas* spp., and mold and yeast among T5-D5, T5-D10, T2-D5 and T2-D10 (Fig.1, Fig.2). However, the number of aerobic bacteria, *Pseudomonas* spp., and yeast in T2-D10 tended to be decreased by approximately 2 Log_{10} CFU/g in that of T5-D10. Therefore, sub-zero temperature storage at −2 °C is a promising preservation technology that maintains physicochemical properties while effectively retarding the growth of bacteria and mold and yeast.

Table.1 Quality of fresh-cut yellow bell pepper during storage.
Data shown are the mean (n=3) ± SD

	Weight loss [%]	ΔE [-]	Sugar content [Bx%]	L-AsA content [mg/100g]	Hardness [N]	MDA content [mM/g FW]	Electrolyte leakage [%]
F	-	-	4.2±0.31 ^{a}	69.67±4.76 ^{a}	18.35±1.05 ^{a}	5.29±1.79 ^{a}	9.27±0.65 ^{a}
T5-D5	0.27±0.01 ^{a}	2.71±0.88 ^{a}	4.2±0.24 ^{a}	71.53±18.19 ^{a}	14.05±1.17 ^{b}	7.14±0.74 ^{a}	6.58±0.68 ^{b}
T2-D5	0.33±0.09 ^{a}	2.06±0.38 ^{a}	4.1±0.37 ^{a}	63.13±10.10 ^{a}	17.03±1.85 ^{ab}	6.97±0.92 ^{a}	9.00±1.03 ^{ab}
T5-D10	0.36±0.09 ^{a}	2.92±0.67 ^{a}	4.0±0.37 ^{a}	68.53±11.08 ^{a}	16.64±1.11 ^{ab}	7.05±0.74 ^{a}	7.99±2.64 ^{ab}
T2-D10	0.25±0.04 ^{a}	3.01±0.69 ^{a}	4.1±0.57 ^{a}	79.73±8.42 ^{a}	17.07±2.37 ^{ab}	6.88±0.74 ^{a}	8.50±1.04 ^{ab}

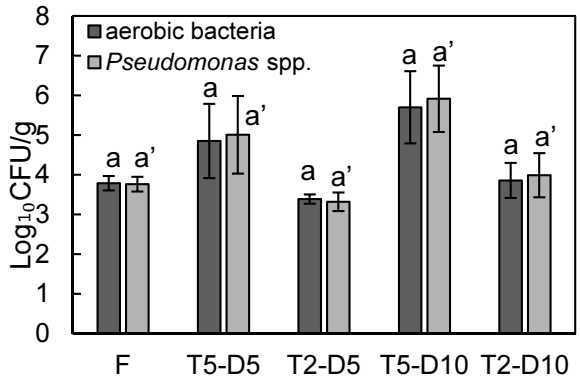

Fig.1 Changes in aerobic bacteria and *Pseudomonas* spp. counts during storage
Data shown are the mean (n=3) ± SD

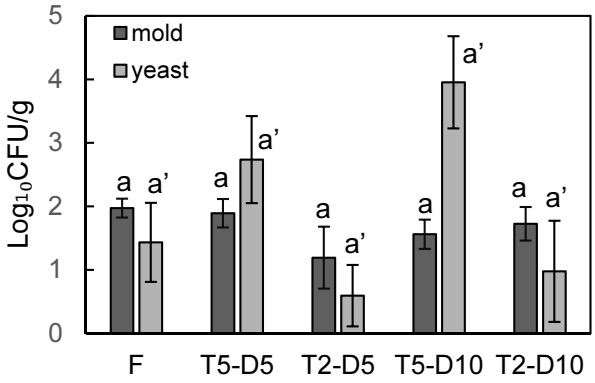

Fig.2 Changes in mold and yeast counts during storage
Data shown are the mean (n=3) ± SD

CONCLUSIONS

In this study, the effect of sub-zero temperature storage of fresh-cut yellow bell peppers on the physicochemical properties and microbiological quality were evaluated. Physicochemical property measurements showed that no significant differences were observed among each conditions in weight loss, color difference, sugar content, L-ascorbic acid content (L-AsA) and malondialdehyde content. Regarding microbiological quality, no significant differences were observed in aerobic bacteria, *Pseudomonas* spp., and mold and yeast among among T5-D5, T5-D10, T2-D5 and T2-D10. However, the counts of aerobic bacteria, *Pseudomonas* spp., and yeast in the sample stored at −2 °C for 10 days decreased by approximately 2 Log_{10} CFU/g compared the sample stored at 5 °C for 10 days. Sub-zero temperature storage at −2 °C could be stored without freezing for 10 days with keeping not only physicochemical properties but also suppresses the growth rate of bacteria and mold and yeast.

REFERENCES

Fan, X., Sokorai, K. J. B., 2005. Assessment of radiation sensitivity of fresh-cut vegetables using electrolyte leakage measurement. Postharvest Biology and Technology, 36, 191–197.

Liu, D. K., Xu, C. C., Guo, C. X., Zhang, X, X., 2020. Sub-zero temperature preservation of fruits and vegetables: A review. Journal of Food Engineering, 275, 109881.

PH-P07

Proceedings of The 12th International Symposium on Machinery and Mechatronics for Agriculture and Biosystems Engineering (ISMAB 2026)
20-24 October 2026, Busan, Republic of Korea

INFLUENCE OF BOTTLE-DERIVED SIGNALS ON RAMAN SPECTROSCOPIC AUTHENTICATION OF JAPANESE WHISKY

Masato Yoshisako[1], Mihir Kumar Purkait[2], Takahisa Nishizu[3,4], Teppei Imaizumi[3,4*]

[1]Graduate School of Natural Science and Technology, Gifu University, 1-1, Yanagido, Gifu-city, Gifu, 501-1193, Japan
[2]Department of Chemical Engineering, Indian Institute of Technology Guwahati, Assam 781039, India
[3]Faculty of Applied Biological Sciences, Gifu University, 1-1, Yanagido, Gifu-city, Gifu, 501-1193, Japan
[4]Preemptive Food Research Center, Gifu University, 1-1 Yanagido, Gifu-city, Gifu, 501-1193, Japan
*Corresponding Author-- Voice: +81-58-293-2930, Email: imaizumi.teppei.j6@f.gifu-u.ac.jp

Abstract: The increasing demand for whisky has raised concerns regarding counterfeiting, highlighting the need for reliable and non-destructive certification methods. This study evaluated the applicability of Raman spectroscopy to Japanese whisky certification and investigated the influence of bottle-derived spectral information. Four whisky samples were measured in brand-specific bottles, a unified bottle, and by direct measurement. Raman spectra in the 200-1200 cm^{-1} region were analyzed using principal component analysis (PCA). PCA using brand-specific bottles clearly separated WJ1 from the other samples, whereas this separation disappeared when using a unified bottle or direct measurement. Furthermore, a similarity comparison between direct measurements and measurements taken through brand-specific containers yielded a coefficient of determination of 0.8, clearly demonstrating that the optical properties of the bottles influence the Raman spectrum. These results suggest that spectral information from both the whisky and brand-specific bottle contributed to the distinction, demonstrating the potential of Raman spectroscopy for non-destructive certification using unopened bottles.

Key Words: Japanese whisky, Certification, Raman spectroscopy, Non-destructive analysis

INTRODUCTION

In recent years, rising global demand has led to a shortage of whisky supply, exacerbating price increases and counterfeiting problems. Therefore, establishing robust certification methods to maintain market credibility has become an urgent issue.

Conventionally used GC-MS analysis has primarily focused on Scotch and Bourbon whisky, with limited research on Japanese whisky. Furthermore, this method involves destructive testing requiring opening of the bottle, which can damage the product's commercial value. In

contrast, Raman spectroscopy is non-destructive, requires no pretreatment, is less affected by water, and provides characteristic spectral features associated with molecular structures. This characteristic may enable not only statistical distinction among samples but also chemical interpretation of the spectral variables responsible for the distinction. Such interpretability is particularly important for authentication because spectral variations unrelated to the intrinsic chemical composition of the product may otherwise contribute to sample discrimination.

Even in whisky, whose main components are water and alcohol, Raman spectroscopy can comprehensively detect diverse molecular vibrations, including trace components derived from the barrel, allowing for identification based on brand-specific spectral characteristics.

Therefore, this study focuses on Raman spectroscopy, which allows for non-destructive measurement of unopened bottles, aiming to evaluate its effectiveness in the certification of Japanese whisky and to clarify the impact of container-derived signals on certification accuracy.

MATERIALS AND METHODS

Four whisky samples-one Bourbon (WB), one Scotch (WS), and two Japanese whiskies (WJ1 and WJ2)-were analyzed using a compact Raman spectrometer (PR-1W, JASCO). The samples were contained in their original commercial packages: a polyethylene terephthalate bottle for WB, a clear glass bottle for WS and WJ2, and an amber glass bottle for WJ1.

Spectra were acquired under three measurement conditions: "in brand-specific bottle", "in common bottle", and "direct measurement (after unsealing)". The acquisition parameters were set to a laser power of 50 mW, an exposure time of 1 s, 64 accumulations, and a spectral range of 200-3000 cm^{-1}.

In a preliminary experiment, difference spectra were calculated by subtracting both the container signals and the spectrum of a 40 % (v/v) aqueous ethanol solution. This revealed whisky-specific peaks in the 200–1200 cm^{-1} region (fingerprint region). Consequently, spectral data within this range were extracted for subsequent similarity evaluation and principal component analysis (PCA).

RESULTS & DISCUSSION

As shown in Fig 1, PCA using bottles of each brand clearly separated WJ1 from other brands, while some overlap was observed between WS and WJ2. Examination of the wavenumbers contributing to the separation revealed that the principal component loadings of PC1 were high (0.9 or higher) across almost the entire wavenumber range, making it difficult to identify specific chemical structures. On the other hand, in PC2, signals thought to originate from silicon dioxide, esters, and aromatic rings were observed in the wavenumber range where the loadings exceeded 0.7. This suggests that spectral features originating from both the container and the whisky may contribute to the separation of PC2.

Furthermore, as shown in Fig 2, when similarity evaluation was performed based on WJ1, and the cosine similarity was plotted on the x-axis and the correlation coefficient on the y-axis, a clear tendency for the same brand to be concentrated in the upper right corner was observed.

This suggests that Raman spectral similarity can be used to evaluate genuine products using both indicators. To investigate the factors influencing the separation in PCA using bottles of each brand, PCA was performed using a unified bottle and direct measurement. The results showed that WJ1 overlapped with other groups under both conditions, and the clear separation observed in the bottles of each brand was not achieved. This suggests that, in the separation of whiskies by bottle type, information from the container, not just the whisky itself, may significantly contribute.

Therefore, the coefficient of determination (R^2) of the Raman spectra from direct measurements and measurements using each container was compared. The results showed that while R^2 was approximately 0.98 for many samples in direct measurements and measurements using the brand-specific container, WJ1 showed a low value of 0.80. On the other hand, in measurements using the unified container, R^2 was 0.95 or higher, including for WJ1. This suggests that the spectral change due to the brand-specific container was significant for WJ1, potentially contributing to its separation by PCA. Furthermore, since the WJ1 container was more strongly colored compared to other brands, this suggests that not only the material but also optical properties such as color may be involved in the container's influence.

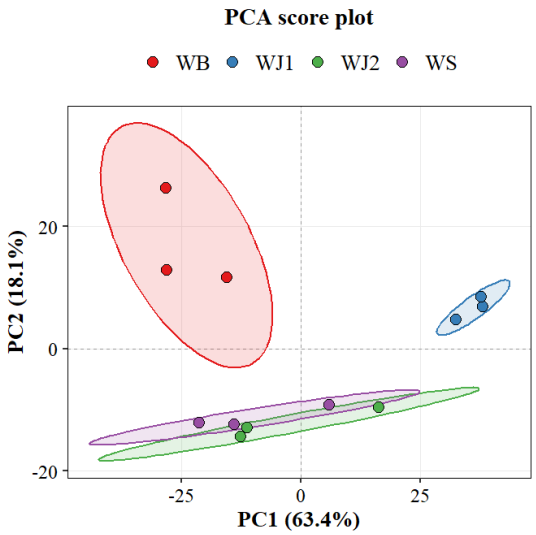

Fig 1. PCA score plot based on Raman spectra of whiskies obtained from brand-specific bottles.

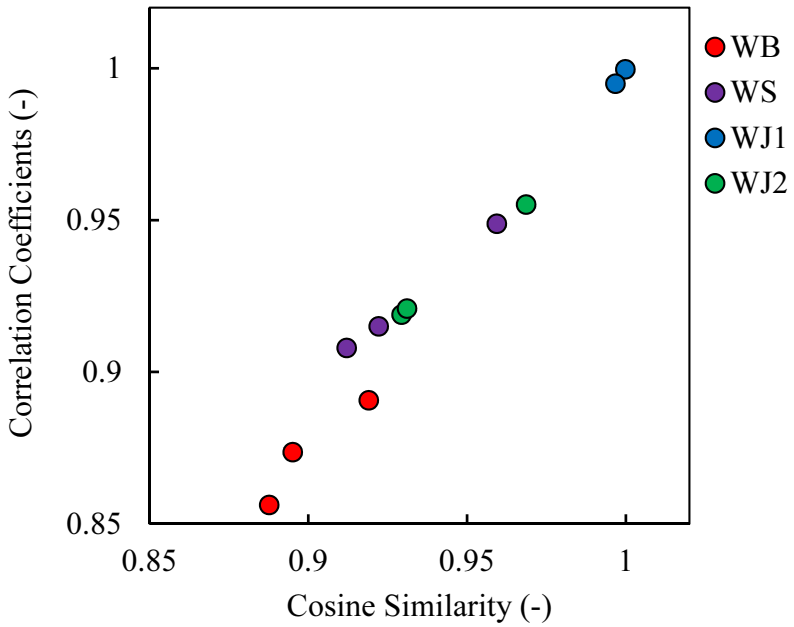

Fig 2. Similarity evaluation map centered on WJ1 based on cosine similarity and correlation coefficient.

CONCLUSIONS

Raman spectroscopy enabled non-destructive distinction of Japanese whisky based on brand-specific spectral characteristics, including information derived from the bottle. However, PCA results indicated that container-derived signals, particularly those affected by the material and optical properties of the bottle, can influence the classification results. These findings demonstrate the potential of Raman spectroscopy for the certification of Japanese whisky using unopened bottles, while highlighting the importance of accounting for container-derived signals to improve certification accuracy.

REFERENCES

Yun, J., S. Kang, J. H. Jeong, J. E. Lee, and T. W. Kim. 2026. Impact of data scaling strategies on volatile marker selection in GC-MS-based classification of single malt, blended, and American bourbon whiskies. *J. Food Compos. Anal.* 156: 109302.

PH-P08

Proceedings of The 12th International Symposium on Machinery and Mechatronics for Agriculture and Biosystems Engineering (ISMAB 2026)
20-24 October 2026, Busan, Republic of Korea

ANTIOXIDANT PROPERTIES OF COFFEE SUBSTITUTES MADE FROM GERMINATED LEGUMES AND CEREALS

Reina Tanaka[1], Takahisa Nishizu[2,3], Nijolė Vaitkevičienė [4], Teppei Imaizumi[2,3*]

[1]Graduate School of Natural Science and Technology, Gifu University, 1-1, Yanagido, Gifu-city, Gifu, 501-1193, Japan
[2]Faculty of Applied Biological Sciences, Gifu University, 1-1, Yanagido, Gifu-city, Gifu, 501-1193, Japan
[3]Preemptive Food Research Center, Gifu University, 1-1 Yanagido, Gifu-city, Gifu, 501-1193, Japan
[4]Faculty of Agronomy , Agriculture Academy ,Vitautas Magnus University, Studentų g. 11, LT-53361 Akademija, Kaunas District, Lithuania

Abstract: Climate change has affected coffee production, increasing interest in coffee substitutes prepared from cereals and legumes. This study aimed to characterize the antioxidant properties of coffee substitutes prepared from germinated plant materials and evaluate the effects of germination and roasting on these properties. Six plant materials, including three legumes (lentil, mung bean, and chickpea) and three cereals (brown rice, barley, and buckwheat), were germinated and roasted at 220°C for 40 min. Antioxidant capacity was evaluated using DPPH and ABTS radical-scavenging assays, and 12 phenolic compounds were quantified using HPLC. In addition, the effects of germination and roasting were evaluated in lentil and buckwheat by comparing untreated and germinated-and-roasted samples. The total phenolic content (TPC) was also determined using the Folin–Ciocalteu method. In lentil, DPPH and ABTS radical-scavenging activities significantly increased after germination and roasting, accompanied by a significant increase in TPC. In buckwheat, no significant change in antioxidant capacity was observed, while TPC significantly decreased. Among the six coffee substitutes, buckwheat exhibited the highest antioxidant capacity in both assays, whereas lentil showed the highest total concentration of the 12 phenolic compounds quantified by HPLC. These results demonstrate that the effects of germination and roasting, as well as the antioxidant and phenolic characteristics of coffee substitutes, vary depending on the plant material.

Key Words: Coffee substitutes; Germination; Roasting; Antioxidant capacity; Phenolic compounds

INTRODUCTION

Climate change associated with global warming has affected coffee production, raising concerns about its future supply (Bunn et al., 2015). Consequently, coffee substitutes produced by roasting cereals and legumes have attracted increasing attention (Tahmouzi et al., 2024). In addition to their sensory qualities, coffee substitutes may provide added value through bioactive compounds derived from their raw materials. Germination activates seed metabolism and can alter the contents and compositions of bioactive compounds, including phenolic compounds (Park et al., 2024). Thus, germinated cereals and legumes may represent promising materials for the development of coffee substitutes with distinctive functional properties. However, limited information is available on how antioxidant properties and phenolic compound profiles differ among coffee substitutes produced from different germinated plant materials.-The objective of this study was to characterize the antioxidant properties and phenolic compounds of coffee substitutes prepared from different germinated cereals and legumes, as well as the effects of germination and roasting on these properties.

MATERIALS AND METHODS

SAMPLE PREPARATION

Three legumes (lentil, mung bean, and chickpea) and three cereals (brown rice, barley, and buckwheat) were used. The seeds were germinated by soaking in mineral water under static conditions. After germination, they were roasted at 220°C for 40 min and ground to prepare coffee substitute samples.

ANTIOXIDANT PROPERTIES

Each sample was extracted with 80% ethanol, and its antioxidant capacity was evaluated using DPPH and ABTS radical-scavenging assays. For both assays, the reaction was conducted in the dark for 16 min. Absorbance was measured at 517 nm for the DPPH assay and 734 nm for the ABTS assay using a UV–Vis spectrophotometer.

PHENOLIC COMPOUNDS

Twelve phenolic compounds (rosmarinic acid, ferulic acid, rutin, caffeic acid, epicatechin, catechin, gallic acid, protocatechuic acid, chlorogenic acid, o-coumaric acid, p-coumaric acid, and m-coumaric acid) were quantified using high-performance liquid chromatography (HPLC) with a UV detector at 280 nm and a NUCLEODUR Sphinx RP column (150 × 4.6 mm, 5 µm). Acetonitrile and 1% acetic acid were used as the mobile phases under gradient elution.

STATISTICAL ANALYSIS

Data were analyzed using analysis of variance (ANOVA), followed by Tukey–Kramer's HSD test using R version 4.5.0. Differences were considered statistically significant at $p < 0.05$.

RESULTS & DISCUSSION

CHANGES IN ANTIOXIDANT PROPERTIES OF LENTIL AND BUCKWHEAT FROM UNTREATED TO GERMINATED AND ROASTED SAMPLES

The effects of germination and roasting on antioxidant properties differed between lentil and buckwheat. The GR/U ratios of DPPH and ABTS radical-scavenging activities were 2.57 and 4.23 in lentil, respectively, compared with 1.22 and 0.90 in buckwheat. In lentil, both DPPH and ABTS radical-scavenging activities significantly increased after germination and roasting. In buckwheat, DPPH radical-scavenging activity tended to increase, whereas ABTS radical-scavenging activity tended to decrease; however, neither change was statistically significant (Fig. 1A, B). The GR/U ratio of total phenolic content (TPC) was 4.64 in lentil and 0.84 in buckwheat. TPC significantly increased in lentil after germination and roasting, whereas it significantly decreased in buckwheat (Fig. 1C).

In lentils, an increase in TPC corresponded with an increase in antioxidant capacity. Germination has been reported to increase phenolic content in lentils through the activation of enzymes involved in phenolic biosynthesis (Park et al., 2024), which may have contributed to the enhanced antioxidant capacity. In contrast, despite the significant decrease in TPC in buckwheat, no significant change in antioxidant capacity was observed. Overall, these results demonstrate that the effects of germination and roasting on antioxidant properties vary depending on the plant material.

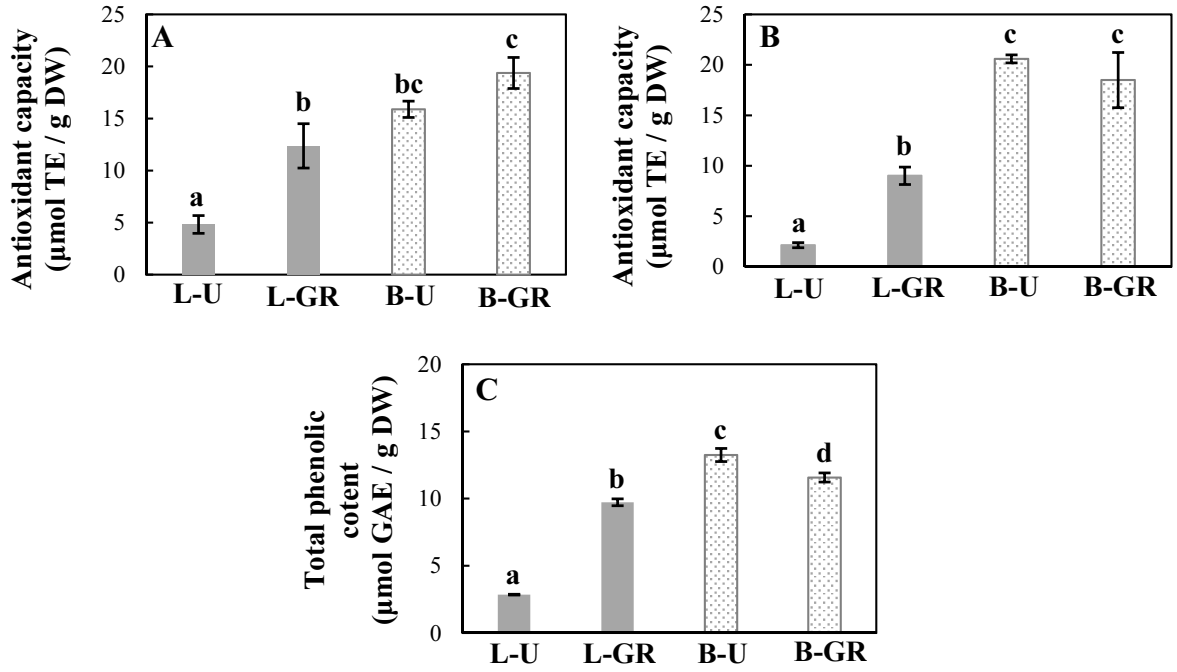

Fig.1. Effects of germination and roasting on the antioxidant capacity and total phenolic content of lentil and buckwheat. (A) DPPH radical-scavenging activity, (B) ABTS radical-scavenging activity, and (C) total phenolic content (TPC). L-U, untreated lentils; L-GR, germinated and roasted lentils; B-U, untreated buckwheat; B-GR, germinated and roasted buckwheat. Values are expressed as mean ± SE (n = 5). Different lowercase letters indicate significant differences between the treatments within each plant material ($p < 0.05$).

ANTIOXIDANT PROPERTIES AND PHENOLIC PROFILES OF COFFEE SUBSTITUTES FROM SIX PLANT MATERIALS

To further investigate differences among plant materials, the antioxidant properties and phenolic compound profiles of coffee substitutes prepared from six different plant materials were compared. Buckwheat exhibited the highest values in both DPPH and ABTS radical-scavenging assays (Fig. 2A). The high antioxidant capacity of buckwheat may be partly attributed to the antioxidant compounds formed through the Maillard reaction during roasting. Reducing sugar levels in buckwheat have been reported to increase during germination (Shreeja et al., 2021), which may promote the Maillard reaction during subsequent roasting. In contrast, the total concentration of the 12 phenolic compounds quantified by HPLC was significantly higher in lentil than in the other plant materials (Fig. 2B). Lentil contained relatively high levels of flavonoids, including rutin, catechin, and epicatechin, which may have contributed to its high concentration of quantified phenolic compounds. Previous studies have also reported that flavonoids are a major class of phenolic compounds in lentil (Xia et al., 2023). The finding that buckwheat exhibited the highest antioxidant capacity, whereas lentil had the highest total concentration of quantified phenolic compounds, suggests that antioxidant capacity may be influenced not only by the total amount of phenolic compounds but also by their composition and other antioxidant compounds formed during processing.

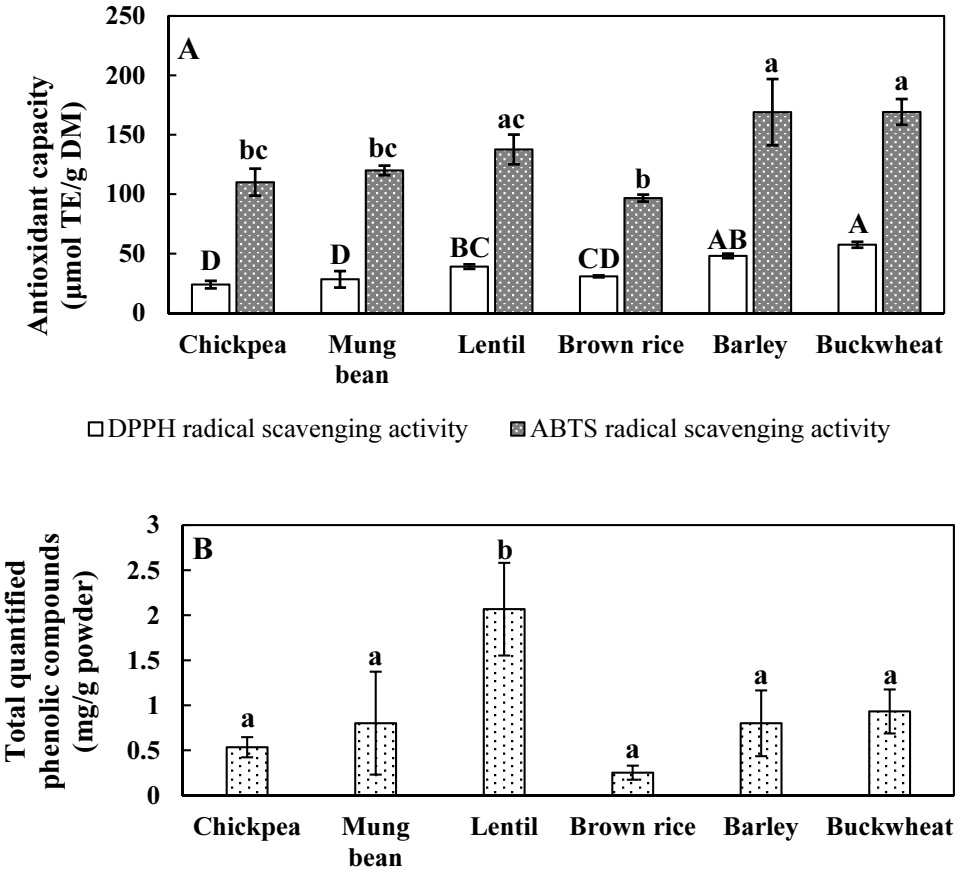

Fig.2 Antioxidant capacity and phenolic compound levels of coffee substitutes prepared from six plant materials. (A) DPPH and ABTS radical scavenging activities, and (B) total

concentration of the 12 phenolic compounds quantified by HPLC. Values are expressed as mean ± SE (n = 5). Different lowercase letters indicate significant differences among samples (Tukey–Kramer HSD test, $p < 0.05$).

CONCLUSIONS

In this study, the effects of germination and roasting on antioxidant properties were evaluated in lentil and buckwheat, followed by a comparison of coffee substitutes prepared from six different plant materials. In lentil, the antioxidant capacity and total phenolic content (TPC) increased after germination and roasting, whereas in buckwheat, no significant change in antioxidant capacity was observed, and TPC decreased. Among the six coffee substitutes, buckwheat exhibited the highest antioxidant capacity, whereas lentil showed the highest total concentration of the 12 phenolic compounds quantified by HPLC. These results demonstrate that the effects of germination and roasting, as well as the antioxidant and phenolic characteristics of coffee substitutes, vary depending on the plant material.

REFERENCES

Bunn, C., P. Läderach, J. G. Pérez Jimenez, C. Montagnon, and T. Schilling. 2015. Multiclass classification of agro-ecological zones for Arabica coffee: An improved understanding of the impacts of climate change. *PLOS ONE* 10(10), 1-14

Park, Y. R., S.-J. Kwon, J. H. Kim, S. Duan, and S. H. Eom. 2024. Light-induced antioxidant phenolic changes among the sprouts of lentil cultivar. *Antioxidants* 13(4), 1-13

Shreeja, K., S. S. Devi, W. J. Suneetha, and B. N. Prabhakar. 2021. Effect of germination on nutritional composition of common buckwheat (*Fagopyrum esculentum* Moench). International Research Journal of Pure and Applied Chemistry: 1–7

Tahmouzi, S., S. S. Nasab, B. Alizadeh-Salmani, L. Zare, N. Mollakhalili-Meybodi, and A. Nematollahi. 2024. Coffee substitutes: A review of the technology, aracteristics, application, and future perspective. *Comprehensive Reviews in Food Science and Food Safety* 23(6), 8-14

Xia, M., M. Li, T. S. P. De Souza, C. Barrow, F. R. Dunshea, and H. A. R. Suleria. 2023. LC-ESI-QTOF-MS2 characterization of phenolic compounds in different lentil (*Lens culinaris* M.) samples and their antioxidant capacity. Frontiers in Bioscience-Landmark 28(3): 1-14

PH-P09

Proceedings of The 12th International Symposium on Machinery and Mechatronics for Agriculture and Biosystems Engineering (ISMAB 2026)
20-24 October 2026, Busan, Republic of Korea

METABOLITE PROFILES AT HARVEST AS POTENTIAL INDICATORS OF POSTHARVEST SHELF LIFE IN BROCCOLI SPROUTS UNDER DIFFERENT CULTIVATION TEMPERATURES

Ayana Kawabata[1], Kohei Nakano[2*]

[1] Graduate School of Natural Science and Technology, Gifu University, Japan
[2] The United Graduate School of Agricultural Science, Gifu University, Japan
*Corresponding Author-- Email: nakano.kohei.i7@f.gifu-u.ac.jp

Abstract: Preharvest environmental conditions can strongly influence postharvest quality, yet the metabolic basis linking cultivation temperature to subsequent shelf life remains poorly understood. This study investigated whether differences in cultivation temperature alter the metabolic status of broccoli sprouts at harvest and whether these changes are associated with postharvest quality deterioration. Broccoli sprouts were cultivated at 15℃ and 25℃, and subsequently stored under identical conditions at 10℃. Changes in color characteristics during storage were evaluated using a colorimeter, while metabolite profiles immediately after harvest were comprehensively analyzed by GC-MS/MS combined with multivariate analyses, including partial least squares discriminant analysis (PLS-DA).

Sprouts cultivated at 25℃ showed an earlier decrease in chroma than those cultivated at 15℃, indicating more rapid postharvest quality deterioration. Clear differences in metabolite composition were already evident at harvest. Aspartic acid and 4-aminobutyric acid (GABA) accumulated at higher levels in sprouts cultivated in 25℃, whereas sugars including xylose and sucrose were more abundant in those cultivated at 15℃. These differences in metabolite profiles at harvest were associated with subsequent differences in shelf life.

The results demonstrated that the cultivation temperature leaves a measurable metabolic signature that is closely related to postharvest deterioration. In particular, the metabolic shifts observed under the higher cultivation temperature was associated with reduced shelf-life potential. These findings suggest that metabolite profiles at harvest may provide useful indicators of the postharvest quality potential of fresh produce and highlight the importance of preharvest temperature management for extending shelf life.

Key Words: Broccoli sprout, Shelf-life, Metabolomics, Cultivation Temperature, Postharvest quality

INTRODUCTION

To prevent postharvest quality deterioration of fresh produce, optimization of storage conditions during distribution, particularly, low-temperature management, is widely practiced (Mercier et al., 2017). However, shelf life is determined not only by postharvest storage

conditions but also by pre-harvest environment in which crops are grown. As emphasized in horticultural science, the postharvest quality and shelf-life potential of fresh horticultural crops are largely established during pre-harvest growth, because postharvest technologies can maintain quality but cannot improve the quality established at harvest (Hewett, 2006).

Plants adjust their metabolism in response to environmental conditions during growth, and cultivation temperature can therefore influence their metabolic status at harvest. Such differences in metabolite composition may subsequently affect stress tolerance, senescence, and postharvest deterioration. Nevertheless, the relationships among cultivation temperature, metabolic status at harvest, and subsequent shelf-life performance remain poorly understood. Recently, comparative metabolomics studies have demonstrated that temperature conditions can markedly alter metabolite profiles and metabolic pathways in Brassicaceae crops (Amjadi et al., 2024), suggesting that metabolomic profiling may provide a useful approach for elucidating how preharvest thermal conditions influence postharvest quality.

This study aimed to determine how cultivation temperature affects the metabolic status of fresh produce at harvest and its subsequent shelf-life potential. Broccoli sprouts were used as a model crop because of their short cultivation period and were cultivated at either 15°C or 25°C. After harvest, sprouts from both cultivation temperature were stored at 10°C under the same storage condition, and changes in color characteristics were monitored over time using a colorimeter. In addition, comprehensive metabolite profiling by GC-MS/MS was conducted immediately after harvest to identify cultivation-temperature-dependent metabolic differences and to examine their association with subsequent shelf-life performance.

MATERIALS AND METHODS

Plant material and storage test

Broccoli sprout seeds (Calabrese variety) were cultivated in an incubator under two temperature conditions of 15°C and 25°C. After harvest, the sprouts were sealed in containers to maintain high humidity, and stored at 10°C. Samples were collected on days 0, 3, 6, and 9 of storage. The collected samples were freeze-dried and pulverized, and the chroma (C* value) of the powdered samples was measured using a colorimeter. Changes in chroma during storage were used as an index of quality deterioration (Koukounaras et al., 2009).

Metabolite extraction and analysis

To compare the metabolite profiles at harvest, comprehensive metabolite profiling was conducted. Broccoli sprouts sampled on day 0 were freeze-dried and pulverized, after which polar metabolites were extracted using the Bligh and Dyer method. After adding ribitol as an internal standard, the extract were subjected to a two-step derivatization consisting of methoxmation with methoxyamine hydrochloride followed by trimethylsilylation with MSTFA to enhance the volatility and stability of polar metabolites (Frolova et al., 2026). The derivatized samples were then analyzed by GC-MS/MS (GCMS-TQ8040NX, Shimadzu Corporation) in multiple reaction monitoring (MRM) mode, monitoring 475 transitions. The acquired data were corrected for analytical drift using quality control-based robust LOESS signal correction (QC-RLSC) and normalized to sample weight. Partial Least Squares Discriminant Analysis (PLS-DA) were performed using MetaboAnalyst.

RESULTS & DISCUSSION

The chroma of the powder samples tended to decrease with increasing storage duration in both the 15°C and 25°C cultivation groups (Fig, 1). In particular, the 25°C cultivation group showed a more rapid decrease in chroma than the 15°C cultivation group. This difference indicates that cultivation temperature affected postharvest color retention during storage.

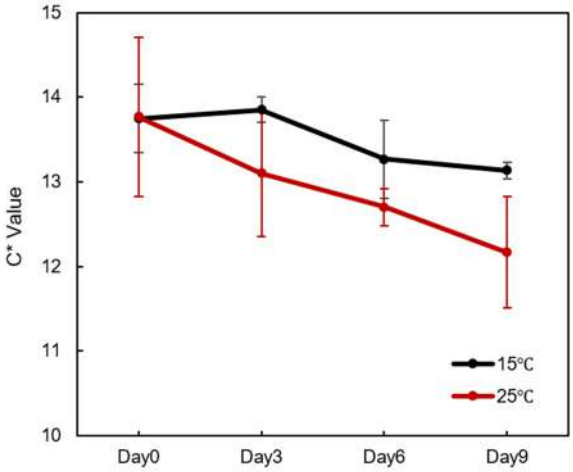

Fig. 1 Changes in chroma (C*) of freeze-dried broccoli sprout powder during storage.

In the PLS-DA score plot of the metabolite profiles (Fig. 2), samples from the 15°C and 25°C cultivation groups formed distinct clusters along component 1, indicating differences in the metabolite profiles at harvest between the two cultivation temperatures..

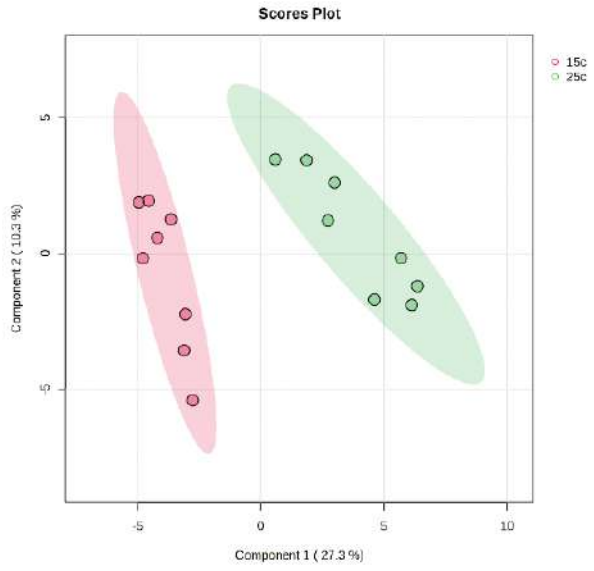

Fig. 2 PLS-DA score plot of metabolite profiles of broccoli sprouts cultivated at 15°C and 25°C.

Hierarchical clustering (Fig. 3) and VIP scores (Fig. 4) identified metabolites that contributed to the differences between the two cultivation-temperature groups. In the 25°C cultivation group, higher level of amino acids such as aspartic acid and other metabolites, including 4-aminobutyric acid (GABA), 3-aminopropanoic acid, and 5-oxoproline, were observed

compared with the 15°C cultivation group. Several of these metabolites have been associated with plant responses to environmental stress, including osmotic adjustment and reactive oxygen species scavenging, suggesting that the metabolic state of sprouts cultivated at 25°C may may reflect a greater stress response than that of sprouts cultivated at 15°C (Li et al., 2016). The higher levels of GABA and aspartic acid observed at 25°C are also consistent with metabolic responses previously reported in plants exposed to elevated temperatures (Raza, 2022).

On the other hand, the 15°C cultivation group showed higher levels of sugars such as xylose and sucrose at harvest. Xylose is associated with cell-wall polysaccharides, whereas sucrose serves as an important carbon and energy source. The higher abundance of these sugars at harvest may indicate differences in carbon metabolism and reserve status between the two cultivation temperatures and may be associated with the greater postharvest quality retention observed in the 15°C cultivation group (Ghorbanzadeh et al., 2023). Conversely, the lower abundance of these sugars in sprouts cultivated at 25°C may reflect altered carbohydrate metabolism under the higher cultivation temperature, as elevated temperatures trigger rapid shifts in carbohydrate metabolism where soluble sugars are actively consumed or remobilized during stress responses (Xalxo et al., 2020).

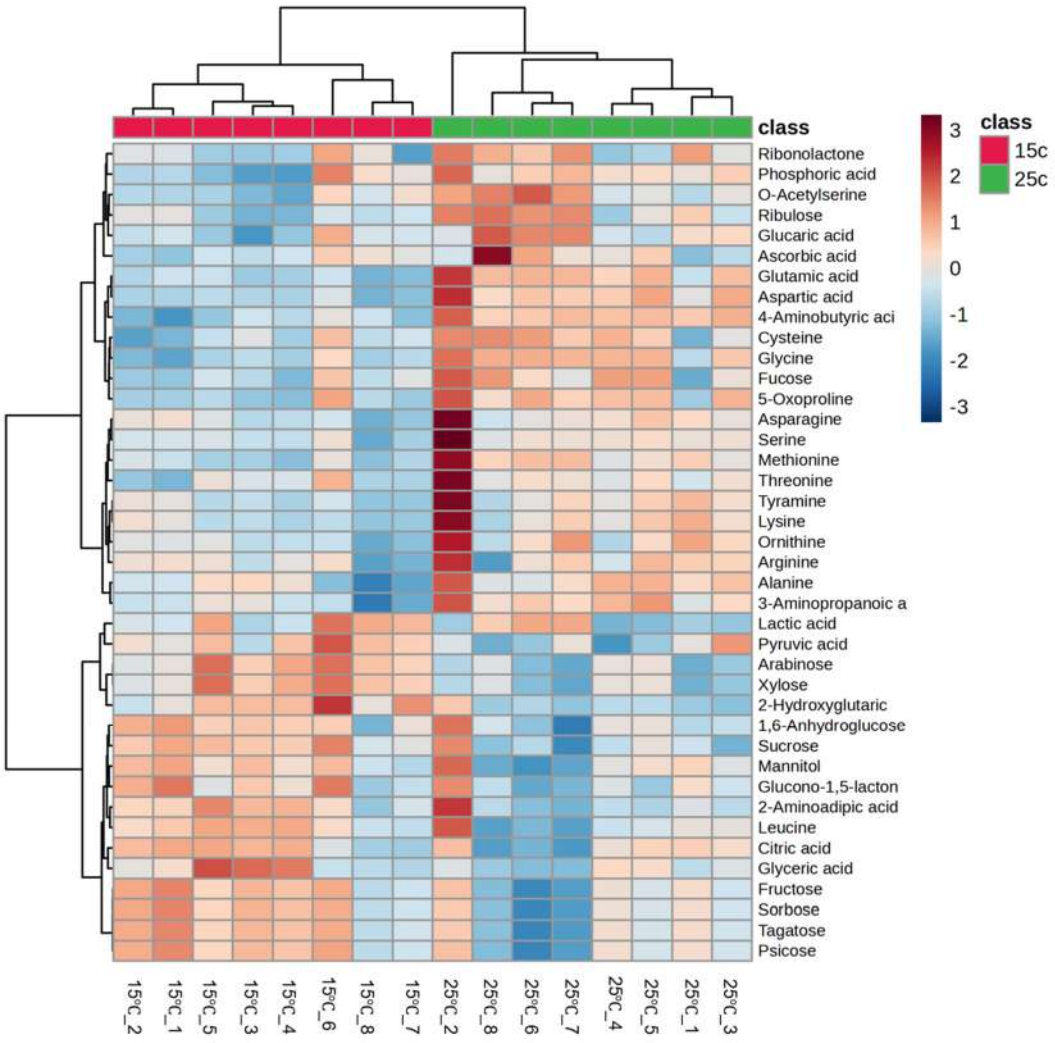

Fig. 3 Hierarchical clustering of metabolites identified as important by PLS-DA.

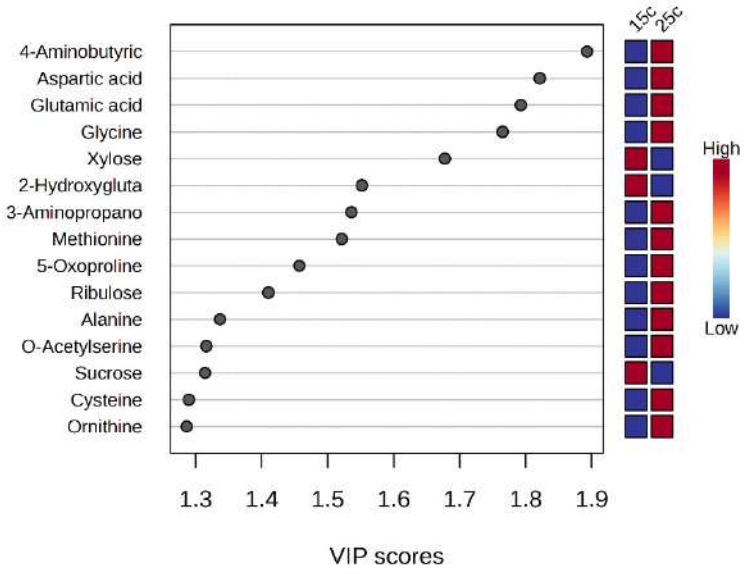

Fig. 4 Variable importance in projection (VIP) scores of metabolites identified by PLS-DA.

CONCLUSIONS

In this study, comprehensive metabolite profiling was performed at harvest in broccoli sprouts cultivated at 15°C and 25°C. The results demonstrated that sprouts cultivated at 25°C showed higher levels of metabolites associated with stress responses, including GABA and aspartic acid, and exhibited more rapid postharvest color deterioration than those cultivated at 15°C. In contrast, sprouts cultivated at 15°C showed higher levels of sugars such as xylose and sucrose at harvest, which were associated with better postharvest quality retention.

These findings demonstrate that cultivation temperature influences the metabolic status of broccoli sprouts at harvest and that these metabolic differences are associated with subsequent shelf-life performance. The identification of metabolites associated with shelf-life potential may also provide a basis for developing sensing technologies capable of evaluating the physiological status and predicting the postharvest quality of fresh produce at harvest. In future studies, linking such metabolic markers with nondestructive optical or spectral sensing techniques may enable rapid estimation of shelf-life potential without destructive chemical analysis. The effects of other preharvest environmental stresses should also be examined to determine whether common metabolite markers can be identified for predicting shelf-life potential. These findings provide fundamental insights into the link between preharvest environmental conditions, metabolic status at harvest, and postharvest quality of fresh produce.

REFERENCES

Amjadi, Z., H. Hamzehzarghani, V. M. Rodriguez, Y.-J. Huang, and F. Farahbakhsh. 2024. Studying temperature's impact on Brassica napus resistance to key regulatory mechanisms using comparative metabolomics. Scientific Reports 14: 19865.

Frolova, N., A. Orlova, V. Popova, T. Bilova, and A. Frolov. 2026. Gas chromatography-mass spectrometry (GC-MS) in the plant metabolomics toolbox: Sample preparation and instrumental analysis. Biomolecules 16(1): 16.

Ghorbanzadeh, Z., R. Hamid, F. Jacob, M. Zeina Abedini, G. H. Salekdeh, and M. R. Ghaffari. 2023. Comparative metabolomics of root-tips reveals distinct metabolic pathways conferring drought tolerance in contrasting genotypes of rice. BMC Genomics 24: 152.

Hewett, E. W. 2006. An overview of preharvest factors influencing postharvest quality of horticultural products. International Journal of Postharvest Technology and Innovation 1(1): 4–15.

Koukounaras, A., A. S. Siomos, and E. Sfakiotakis. 2009. Impact of heat treatment on ethylene production and yellowing of modified atmosphere packaged rocket leaves. Postharvest Biology and Technology 54: 172-176.

Li, Z., J. Yu, Y. Peng, and B. Huang. 2016. Metabolic pathways regulated by γ-aminobutyric acid (GABA) contributing to heat tolerance in creeping bent grass (Agrostis stolonifera). Scientific Reports 6: 30338.

Mercier, S., S. Villeneuve, M. Mondor, and I. Uysal. 2017. Time–Temperature Management Along the Food Cold Chain: A Review of Recent Developments. Comprehensive Reviews in Food Science and Food Safety 16(4): 647–667.

Raza, A. 2022. Metabolomics: a systems biology approach for enhancing heat stress tolerance in plants. Plant Cell Reports 41(3): 741–763.

Xalxo, R., B. Yadu, J. Chandra, V. Chandrakar, and S. Keshavkant. 2020. Alteration in carbohydrate metabolism modulates thermotolerance of plant under heat stress. In Heat Stress Tolerance in Plants: Physiological, Molecular and Genetic Perspectives, 77–114. S. H. Wani and V. Kumar, eds. John Wiley & Sons Ltd.

PH-P10

Proceedings of The 12th International Symposium on Machinery and Mechatronics for Agriculture and Biosystems Engineering (ISMAB 2026)
20-24 October 2026, Busan, Republic of Korea

DEVELOPMENT AND COMPARATIVE EVALUATION OF SEGMENTATION MODELS FOR SURFACE DEFECT DETECTION IN MULTIPLE FRUIT TYPES

Seokha Hwang[12], Harin Jang[12], Kim Minhyun[12], Huynh Cao The Cuong[1], Donghyeon Seong[12], Ghiseok Kim[123*]

[1] Department of Biosystems Engineering, Seoul National University, Seoul, Republic of Korea
[2] Global Smart Farm Convergence Major, Seoul National University, Seoul, Korea
[3] Research Institute of Agriculture and Life Sciences, Seoul National University, Seoul, Korea
* Corresponding Author– Voice: +82-2-880-4603, Email: ghiseok@snu.ac.kr

Abstract: Surface defects are an important factor in assessing the external quality of fruit, and accurate detection of defective regions is essential for image-based quality inspection. This study aimed to acquire surface defect image data from multiple fruit types, including apples, Korean melons, and persimmons, and identify a suitable segmentation model through comparative performance evaluation. Surface defect regions in the acquired images were annotated to construct a dataset for model training. Using the constructed dataset, multiple segmentation models were developed and trained to delineate defective regions on fruit surfaces. Their defect segmentation performance was compared, and the best-performing model among those evaluated was selected. The resulting dataset and comparative findings provide a basis for selecting segmentation models for fruit surface defect detection and may support the further development of image-based fruit quality inspection systems.

Key Words: Fruit surface defects, Defect detection, Image segmentation, Dataset construction, Model comparison

ACKNOWLEDGEMENTS

This work was carried out with the support of Cooperative Research Program for Agriculture Science and Technology Development (Project No. PJ01709503) Rural Development Administration, Republic of Korea.

PH-P11

Proceedings of The 12th International Symposium on Machinery and Mechatronics for Agriculture and Biosystems Engineering (ISMAB 2026)
20-24 October 2026, Busan, Republic of Korea

EFFECTS OF HIGH-PRESSURE PRETREATMENT ON CHEMICAL COMPOSITION OF ARABICA COFFEE BEANS

Nisa Vinka Nurul Hayati[1], Manami Yamada[2], Teppei Imaizumi[2*], Takahisa Nishizu[2]

[1]Graduate School of Natural Science and Technology, Gifu University, Tokai National Higher Education and Research System, 1-1 Yanagido, Gifu, 501-1193, Japan
[2]Faculty of Applied Biological Sciences, Gifu University, Tokai National Higher Education and Research System, 1-1 Yanagido, Gifu, 501-1193, Japan
*Corresponding Author-- Email: imaizumi.teppei.j6@f.gifu-u.ac.jp

Abstract: High-pressure processing (HPP) was investigated as a pretreatment to modify the chemical composition and aroma profile of Arabica coffee beans. Green coffee beans were subjected to HPP treatment at 100 MPa and 40 °C for 24 hours, followed by drying at 50 °C for 5 hours. Chlorogenic acid (CGA), caffeine, and free amino acids (FAA) were analyzed in the green coffee beans, while volatile compounds were analyzed after roasting using GC/MS-MS. The results showed that HPP significantly increased the measured CGA, caffeine, and total FAA, with significant increases in several individual amino acids. After roasting, exploratory PCA showed separation between control and HPP-treated coffee subsamples, with higher semi-quantitative value of several roasting-related volatile compounds in HPP-treated samples. Overall, HPP pretreatment modified both the chemical composition of green coffee beans and the volatile compounds formed during roasting, indicating its potential as a processing technology for modulating coffee aroma characteristics.

Key Words: high-pressure processing; coffee pretreatment; chlorogenic acid; free amino acids; volatile compounds.

INTRODUCTION

The global coffee market is increasing annually, with estimated increases of 5.8% and 2.2% in production and consumption, respectively (ICO, 2023). During roasting, compounds naturally present in green coffee beans undergo complex chemical reactions that generate volatile compounds that contribute to coffee aroma through thermal reactions such as the Maillard and Strecker reactions, lipid oxidation, and phenolic degradation. Amino acids, sugars, lipids, and phenolic compounds, such as chlorogenic acids (CGAs), are important aroma precursors because they contribute to volatile compound formation (Cao et al., 2023). In addition, postharvest processing can alter the composition of green coffee beans before roasting, thereby affecting the aroma profile of the final roasted coffee (Pereira et al., 2019).

High-pressure processing (HPP) is a technology that applies pressure at ambient or low temperatures to enhance quality through fluids, such as water. Previous studies showed that HPP may modify chemical compositions of coffee beans, including amino acids and lipids (Chen et al., 2018; Li et al., 2024). These changes may alter the availability or transformation of aroma precursors during coffee roasting and may also influence non-volatile compounds such as CGAs and caffeine. Thus, HPP pretreatment has the potential to modify both. The chemical characteristics and aroma formation of coffee beans. However, the effects of HPP pretreatment on the chemical composition of coffee beans, particularly CGAs, caffeine, and amino acids, remain insufficiently understood.

Therefore, this study aimed to investigate the effects of high-pressure pretreatment on the chemical composition of Arabica coffee beans. Chlorogenic acids, caffeine, and amino acids were analyzed using high-performance liquid chromatography (HPLC). Volatile compounds in the roasted beans were also evaluated preliminary using gas chromatography-mass spectrometry (GC-MS).

MATERIALS AND METHODS

HYDROSTATIC PRESSURE PRETREATMENT

Mandheling Lintong Arabica green coffee beans (Grade 1) were vacuum-packed with water and subjected to high-pressure processing at 100 MPa and 40 °C for 24 hours. The pre-treated coffee beans were dried at 50 °C for 5 hours with a forced-convection oven (DKM300, Yamato, Japan). Untreated green coffee beans were used as control.

CHEMICAL COMPOSITION ANALYSIS

Green coffee beans were ground and extracted with 60% methanol for chlorogenic acid and caffeine analysis, and with 0.1 mmol/L HCl for free amino acid (FAA) analysis. CGA and caffeine were quantified using HPLC-UV, while FAA were analyzed by HPLC with fluorescence detection after pre-column derivatization. Quantification was performed using external calibration curves prepared from the corresponding standards.

VOLATILE COMPOUNDS ANALYSIS

Control and HPP-treated beans were roasted under the same conditions (roasting level 5, 15 min), cooled, and ground. Volatile compounds were extracted using HS-SPME with 2-octanol as internal standard and analyzed using GC-MS/MS. Volatile compounds were identified using the SMART Aroma Database and compared based on semi-quantitative values relative to the internal standard.

STATISTICAL ANALYSIS

Chemical composition data were compared using an independent samples t-test, with statistical significance of $p < 0.05$. Exploratory principal component analysis (PCA) of the semi-quantitative volatile data was performed using MetaboAnalyst 6.0. Data are expressed as mean ± standard deviation.

RESULTS & DISCUSSION

CHEMICAL COMPOSITION

Figure 1 displays the CGA and caffeine content of control and HPP green coffee beans. HPP treatments significantly increased the measured CGA and caffeine contents in green coffee beans. This increase may be associated with improved extractability caused by pressure-induced changes in cellular structure.

Figure 2 shows the total and individual FAA contents of control and HPP green coffee beans. HPP treatments significantly increased the total FAA and several individual FAA, such as Gln, His, Gly, Arg, Trp, and Leu. The increase may be associated with pressure-induced changes in cellular structure and endogenous enzyme activity.

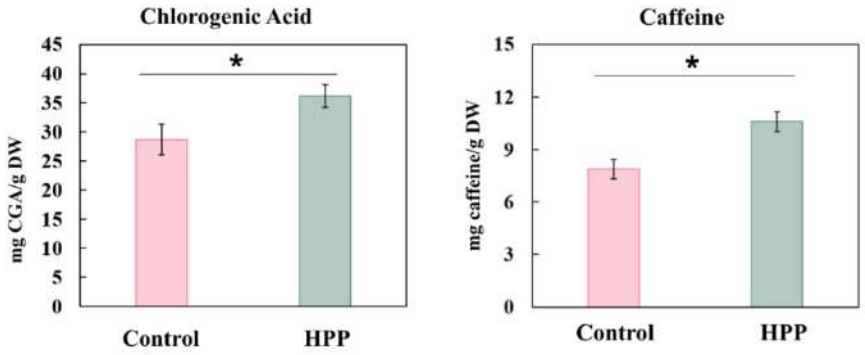

Figure 1. CGA and caffeine in green coffee beans (mean ± SD, n = 3; t-test, $p < 0.05$).

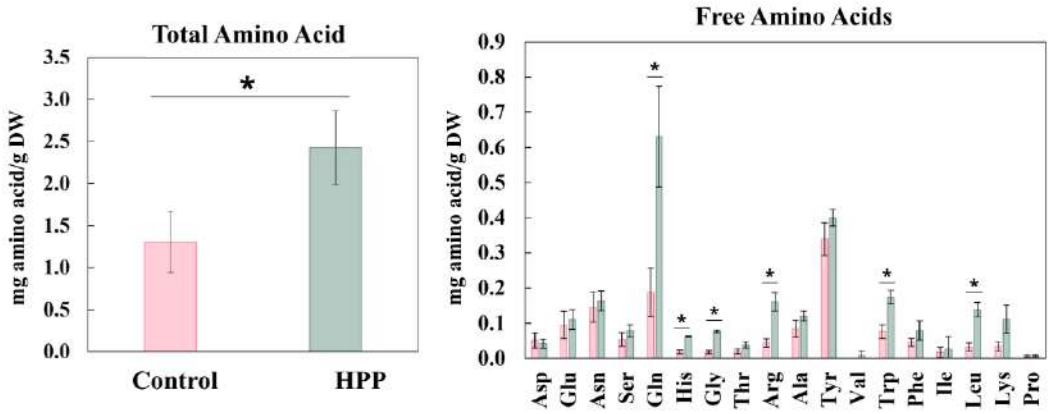

Figure 2. Total and free amino acids in green coffee beans (mean ± SD, n = 3; t-test, $p < 0.05$)

VOLATILE AROMA COMPOUNDS

Exploratory PCA score plot of volatile compounds showed separation between control and HPP-treated roasted coffee. The HPP-treated samples showed higher mean semi -quantitative values of several roasting-related volatile compounds. These differences may be associated with HPP-induced changes in aroma precursor composition, including the increased FAA content observed in green coffee beans.

CONCLUSIONS

HPP pretreatment significantly increased the measured contents of chlorogenic acid, caffeine, and free amino acids in green coffee beans. The increases in chlorogenic acid and caffeine may be associated with improved extractability resulting from pressure-induced structural changes, while changes in free amino acids may involve structural and enzymatic effects of HPP.

Volatile compound analysis also indicated differences between control and HPP-treated coffee after roasting, with several roasting-related compounds showing higher semi-quantitative values in HPP-treated samples. These results suggest that HPP pretreatment may modify the composition of aroma precursors in green coffee beans and consequently influence volatile compound formation during roasting. Further studies using independent experimental batches are needed to confirm the effects on volatile compounds and clarify their relationship with coffee flavor.

REFERENCES

Cao, X., Wu, H., Viejo, C. G., Dunshea, F. R., & Suleria, H. A. R. (2023). Effects of postharvest processing on aroma formation in roasted coffee – a review. In *International Journal of Food Science and Technology*, 58(3), 1007–1027. https://doi.org/10.1111/ijfs.16261

Chen, B. Y., Huang, H. W., Cheng, M. C., & Wang, C. Y. (2018). Influence of high-pressure processing on the generation of γ-aminobutyric acid and microbiological safety in coffee beans. *Journal of the Science of Food and Agriculture*, *98*(15), 5625–5631. https://doi.org/10.1002/jsfa.9106

International Coffee Organization. (2023). Coffee Report and Outlook. https://www.ico.org

Li, Z., Gao, Z., Niu, Z., Yan, J., Hu, Y., Cao, C., Ye, J., Liu, T., Liu, X., & Tian, H. (2024). Effects of ultra-high pressure processing on microstructure, water distribution and lipidomics variances of Arabica coffee beans. *LWT*, *209*, 116784. https://doi.org/10.1016/J.LWT.2024.116784

Pereira, G. V., de Carvalho Neto, D. P., Magalhães Júnior, A. I., Vásquez, Z. S., Medeiros, A. B. P., Vandenberghe, L. P. S., & Soccol, C. R. (2019). Exploring the impacts of postharvest processing on the aroma formation of coffee beans – A review. *Food Chemistry*, *272*, 441–452. https://doi.org/10.1016/J.FOODCHEM.2018.08.061

PH-P12

Proceedings of The 12th International Symposium on Machinery and Mechatronics for Agriculture and Biosystems Engineering (ISMAB 2026)
20-24 October 2026, Busan, Republic of Korea

FUNDAMENTAL STUDY ON NON-DESTRUCTIVE DETECTION FOR CRYSTALLIZED SYMPTOMS OF TARO WITH X-RAY IMAGE

Noriko Takahashi[1*], Keiji Konagaya[2], Takumi Tachibana[3], Kazunori Ninomiya[4], Yuri Shimamoto[4], Nina Alissa Favergeat[4], Ziwei Zheng[4], Naoshi Kondo[5]

[1] Graduate School of Agriculture, Ehime University, Japan
[2] Faculty of Collaborative Regional Innovation, Ehime University, Japan
[3] Ehime Research Institute of Agriculture, Forestry and Fisheries, Japan
[4] Shibuya Seiki Co. Ltd., Japan
[5] Graduate School of Agriculture, Kyoto University, Japan
*Corresponding Author-- Voice: +81-89-946-9761, Email: takahashi.noriko.mm@ehime-u.ac.jp

Abstract: The relationship between relative density and gray scale value of X-ray image taro was investigated for non-destructive detection of crystalized in this study. The obtained X-ray image was processed and calculated the gray scale value. A negative correlation was found between gray scale and relative density for R = 0.84. Our results suggested that crystalized taro would be detected the difference in relative density using X-ray imaging non-destructively.

Key Words: Crystalized taro, Non-destructive detection, Relative density, Water content, X-ray image

INTRODUCTION

The annual yield of taro in Ehime prefecture is increasing and 8,270 ton and 4th in Japan according to the Ministry of Agriculture, Forestry, and Fisheries (MAFF) of Japan (MAFF, 2025). The crystalized symptoms of taro (crystalized taro) was occurred due to the inhibition of assimilate translocation and the crystalized taro has unfavorable texture for customer, therefore, it is essential to detect the crystalized taro non-destructively. As non-destructive measurements, X-ray imaging technique has been widely used to detect the quality of food (Ogawa et al., 2005; Kotwaliwale et al., 2014). The objective of this research is to investigate the relationship between relative density and gray scale value of X-ray image for non-destructive detection of crystalized taro.

MATERIALS AND METHODS

Taro (*Colocasia esculenta* (L.) Schott) of the cultivar “Ehime-Noushi V2 gou” were harvested in November 2025. Normal taro was grown with conventional method, whereas crystalized taro was treated with cutting taro leaf stalk in August 2025. Taro samples were peeled to remove the skin and cut perpendicularly to the direction of fiber at equal intervals of 10 mm (Fig. 1).

The sample number was 336 for normal taro and 579 for crystalized taro, respectively. Water content was calculated the fresh weight and dry weight after drying using the dry oven (DMR620TP, Advantec Toyo Kaisha, LTD) adjusted at 60 ºC for 7 days, as follow Eq. (1):

$$WC = \frac{FW - DW}{FW} \times 100 \quad (1)$$

where:

WC = Water content (%)
FW= Fresh weight (g)
DW = Dry weight (g)

The X-ray image was obtained with line sensor camera (C14300-05UL, Hamamatsu Photonics K. K.) and X-ray generator (TRIX30, Torek Co., Ltd.). Table 1 shows the experimental condition for X-ray image acquisition. The obtained X-ray image was processed and calculated the gray scale value using Open CV package in Python (ver.3.8.8). Relative density was calculated with fresh weight and number of pixels of taro area in X-ray image, as follow Eq. (2):

$$RD = \frac{FW}{NP} \quad (2)$$

where:

RD = Relative density (-)
NP = Number of pixels of taro area

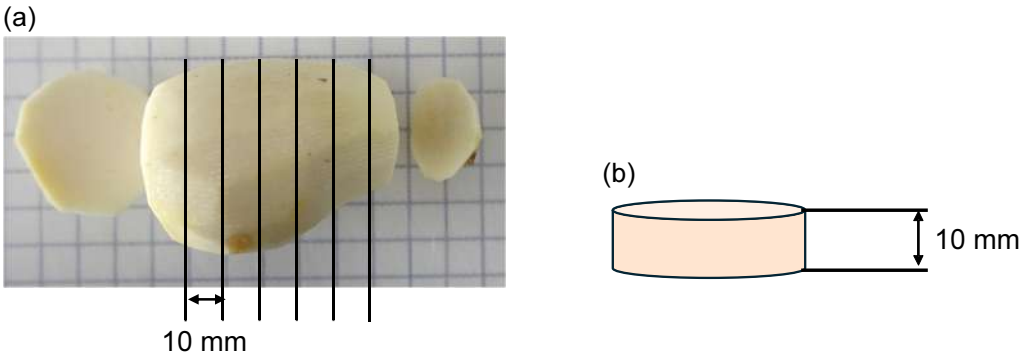

Fig.1 Sample preparation of cutting taro (a) and sample image for X-ray image acquisition (b).

Table 1 Experimental condition for X-ray image acquisition.

Tube voltage (kV)	40
Tube current(mA)	40
Slit width (mm)	15
Captured image area (mm)	256
Image resolution (mm/pixel)	0.4
Image size (pixel)	640 × 2000

RESULTS & DISCUSSION

Water content, relative density, and gray scale value of normal and crystalized taro are shown in Figure 2. Water content of crystalized taro was larger than that of normal taro (Fig.2(a)).

Uritant and Takeuchi (1990) found that the larger water content and smaller starch content in the crystalized taro compared with normal taro. These results suggested that starch in crystalized taro might be replaced to water due to the inhibition of assimilate translocation. Relative density of crystalized taro was significantly smaller than that of normal taro (Fig.2(b)), whereas gray scale value of crystalized taro was significantly larger than that of normal taro (Fig.2(c)). Tanaka (2009) reported the linear relationship between the gray scale value in X-ray image and moisture content (R^2 = 0.93). These findings suggested that large gray scale value in X-ray image might represent the increase water content in crystalized taro due to the reduction of density. A negative correlation was found between gray scale value in X-ray image and relative density for R = 0.84 (Fig.3).

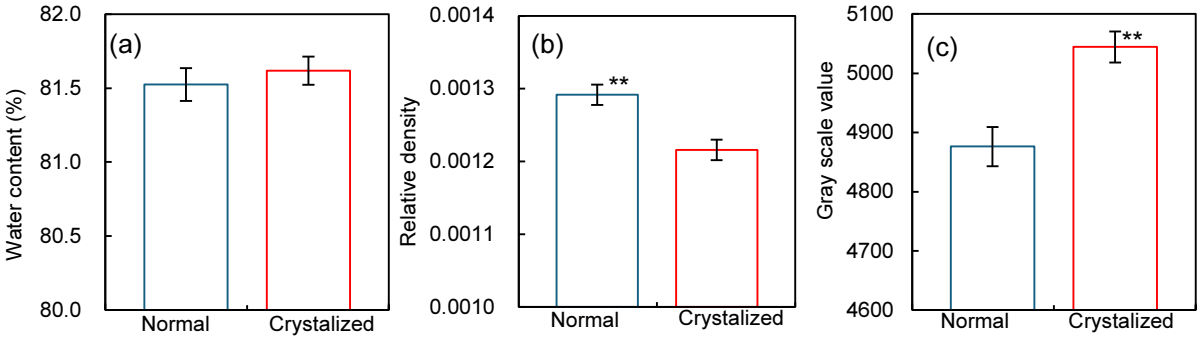

Fig.2 Water content (a), relative density (b), and gray scale value (c) of normal and crystalized taro（** : $p < 0.01$, Normal : n = 336, Crystalized: n = 579）.

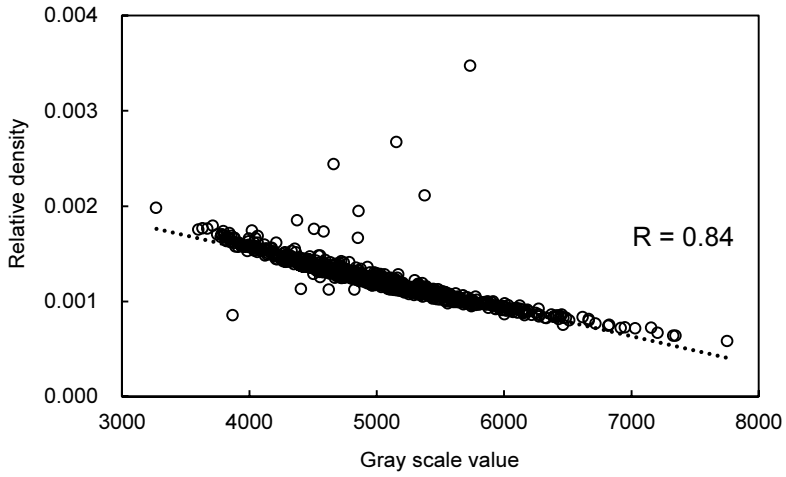

Fig.3 Scatter plot of gray scale value in X-ray image versus relative density of taro.

CONCLUSIONS

The relationship between relative density and gray scale value of X-ray image was investigated for non-destructive detection of crystalized taro in this study. The crystalized taro was higher water content and lower relative density compared with the normal taro. The gray scale value of X-ray images consisted with the high gray scale value as resulting high water content and low density in crystalized taro. Our result suggested that crystalized taro would be detected

the difference in water content and relative density and these parameters could be measured using X-ray imaging non-destructively. The classification model of crystalized taro will be developed for non-destructive detection in the future study.

REFERENCES

Kotwaliwale, N., K. Singh, K., A. Kalne, S. Narayan Jha, N. Seth, and A. Kar. 2014. X-ray imaging methods for internal quality evaluation of agricultural produce. J. Food Sci. Technol. 51: 1-15.

MAFF (Ministry of Agriculture, Forestry, and Fisheries). 2025. Report of statistical survey on vegetable production. Japan: MAFF. (In Japanese). https://www.maff.go.jp/j/tokei/kouhyou/sakumotu/sakkyou_yasai/index.html.

Ogawa, Y., N. Kondo, and S. Shibusawa. 2005. Internal quality evaluation of fruit with X-ray CT. J.SHITA, 17(2): 75-83.

Tanka, T., S. Avramidis, and S. Shida. 2009. Evaluation of moisture content distribution in wood by soft X-ray imaging. J. Wood Sci. 55: 69-73.

Uritant, I., and W. Takeuchi. 1990. Food-scientific investigations on so-called crystalline taro occurring in the child-corm of an early-maturing *Colocasia antiquorum* named cv.Ishikawa-wase. Nippon Shikuhin Kyogyo Gakkaishi, 37(4): 306-310.

PH-P13

Proceedings of The 12th International Symposium on Machinery and Mechatronics for Agriculture and Biosystems Engineering (ISMAB 2026)
20-24 October 2026, Busan, Republic of Korea

EFFECTS OF FRUIT CANOPY POSITION IN THE TREE ON WATER LOSS AND CUTICLE STRUCTURE OF 'KAWACHI BANKAN' FRUIT DURING STORAGE

Tomoka Ida[1], Keiji Konagaya[2], Nanako Saito[2], Noriko Takahashi[1*]

[1]Graduate School of Agriculture, Ehime University, Ehime 790-8566, Japan
[2]Faculty of Collaborative Regional Innovation, Ehime University, Ehime 790-8577, Japan
*Corresponding Author-- Voice: +81-89-946-9761, Email: takahashi.noriko.mm@ehime-u.ac.jp

Abstract: Kawachi Bankan is expected to increase for exporting to Europe. In this study, the effects of fruit canopy position in the tree on water loss and cuticle structure of 'Kawachi Bankan' fruit were investigated during storage. The water loss, thickness of cuticle of fruits from outer and inner fruits of canopy were measured during storage. Our results showed that the fruit water loss of inner fruit was significantly greater than that of outer fruits during storage. There was no significant difference in the cuticle thickness between outer canopy and inner canopy. The cuticle structure of the outer canopy fruits with light microscope observation was uniformly band-shaped, whereas in the inner canopy was found the invaginated part at the cell of the epidermis under the cuticle.

Key Words: Citrus, Cuticle, Inner canopy, Outer canopy, Water loss

INTRODUCTION

Ehime Prefecture has the highest citrus production volume in Japan. Kawachi Bankan is one of the citrus fruits produced in Ehime Prefecture. It is expected to increase for exporting to Europe as "Japanese grapefruits". The fruit quality and cuticle structure have been found to be affected with fruit position in the tree canopy and correlated with the light transmission on the tree (Serna-Escolano et al., 2024). Furthermore, the cuticle has been reported that the ability to absorb UV-B radiation (González Moreno et al., 2022). Since the role of the cuticle of fruits is to control the water loss, the low permeability of the cuticle of the fruits makes it possible to control water loss during storage. In this study, the effects of fruit canopy position in the tree on water loss and cuticle structure of 'Kawachi Bankan' fruit were investigated during storage.

MATERIALS AND METHODS

Kawachi Bankan (*Citrus kawachinensis*) trees were grown at Ainan Town, Minamiuwa

District, Ehime Prefecture in Japan. Fruits were harvested from the two canopy positions, i) from outer canopy in the tree (n = 5), ii) from inner canopy of the tree (n = 5). Fruits with no physiological water damage from chill injury were selected for the experiment. At the harvesting, the vertical and transverse diameters were measured with caliper. Harvested fruits were stored at 20 ◦C from May 20th to June 25th in 2025 for 36 days. The fresh weight was measured at days 0, 16, 36 of storage. Fruit water loss during storage was calculated from the fresh weight at storage 0 day and the weight during storage with Eq. (1).

$$Fruit\ \ water\ \ loss = \frac{W_0 - W_i}{W_0} \times 100 \quad (1)$$

where:

W_0 = Fresh weight at storage 0 day (g)

W_i = Fresh weight at storage *i* day (g)

After storage, the cuticle structure was observed with light microscope. First, 3×3 mm sections of fruits rind were cut from the equator of fruits. These sections were embedded in a frozen tissue embedding medium (OCT compound) and frozen for 18 hours at −30 ◦C. Second, the frozen sections were cut into 7 um slices with a microtome. Then, the slices fixed onto slide glasses, and immersed in a staining solution (Oil red O) for 30 minutes. Finally, the sections were washed with 50 % isopropanol, rinsed with distilled water, and the stained red cuticle structure was observed with light microscope.

For measuring the thickness of cuticle of the fruits after storage, the cuticle was isolated as following the method from Huelin and Gallop (1951). The reaction solution contains of 0.4 g/L oxalic acid and 1.8 g/L ammonium oxalate was used for isolating cuticle from the fruit rind. The isolated cuticle was washed with distilled water and dried for 10 minutes at 40 ◦C using dry oven. The cuticle thickness was measured at 20 points per sample using a double-sphere micrometer (BMD-25MX, Mitsutoyo Corporation) with an accuracy of ±1 um.

RESULTS & DISCUSSION

Table 1 shows the results of the fruit quality of Kawachi Bankan from the outer and inner fruits in the canopy at the harvesting. There were no significant differences in vertical diameter, transverse diameter, and fruit weight between the outer and inner fruits. The fruit water loss of inner fruit was significantly greater than that of outer fruits (Fig. 1). The cuticle thickness of the outer fruit was tended to have a thicker cuticle compared with that of the inner fruits (Fig. 2).

Table1 Fruit quality of Kawachi Bankan from the outer and inner fruits in the canopy at the harvesting.

Fruits position	Vertical diameter (mm)	Transverse diameter (mm)	Fresh weight (g)
Outer canopy	95.61	94.24	346.34
Inner canopy	89.12	93.28	339.10
	NS	NS	NS

NS：No significant differences (*n* = 5)

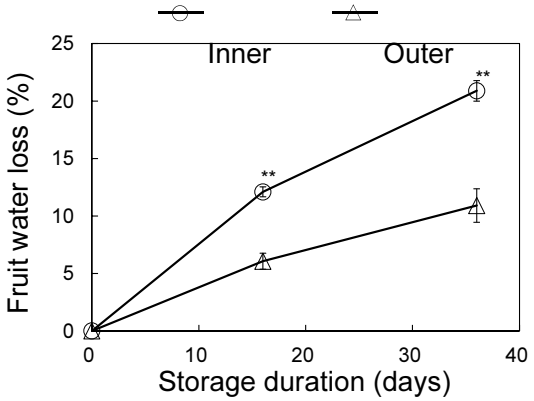

Fig.1 Fruit waster loss of outer and inner fruit during storage at 20 ◦C for 36 days (**: $p < 0.01$, $n = 5$).

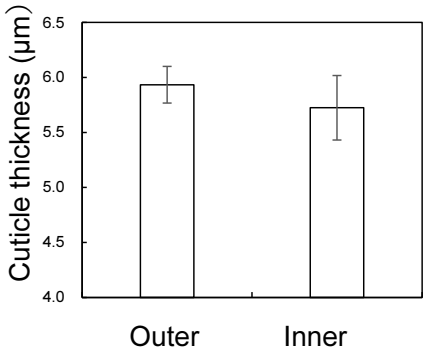

Fig.2 The thickness of the cuticle after storage on the outer and inner fruit after 36 days storage ($n = 5$).

The results of the microscopic observation of the cuticle are shown in Fig,3. The cuticle structure of the outer fruits was uniformly band-shaped (Fig.3(a)), whereas in the inner fruits was found the invaginated part at the cell of the epidermis under the cuticle (Fig3(b)).

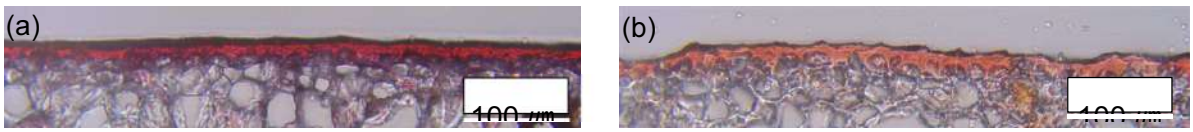

Fig.3 Light micrograph of the rind cross section stained with Oil red O showing the cuticle structure of (a) outer (b) inner after 36 days storage.

CONCLUSIONS

In this study, the effects of fruit canopy position in the tree on water loss and cuticle structure of ‘Kawachi Bankan’ fruit were investigated during storage. The significant difference in fruit water loss between outer and inner fruits was observed. during storage 36 days at 20 ◦C. Although there was no significant difference in cuticle thickness between outer and inner fruits after 36 days storage, the cuticle structure of the outer canopy fruits with light microscope observation was uniformly band-shaped, whereas in the inner canopy was found the invaginated part at the cell of the epidermis under the cuticle. Our results suggested that the cuticle microstructure would differ between the outer and inner fruits in the tree.

REFERENCES

Edwards D. 1993. Cell and tissues in in the vegetative sporophytes of early land plants. New Phytol. 125: 225-247.

González Moreno A., A. de Cózar, P. Prieto et al. 2022. Radiationless mechanism of UV deactivation by cuticle phenolics in plants. Nat. Commun. 13: 1786.

Huelin F. E., and R. A. Gallop. 1951. Studies in the natural coating of apples, 1. Preparation and properties of fractions. Aust. J. Biol. Sci., 4(4): 526-532.

Serna-Escolano V., M. J. Giménez, M. Sarrano, D. Valero, M. E. García-Pastor, A. Dobón-Suarez, M. Gutiérrez-Pozzo, M. Giménez-Berenguer, and P. J. Zapata. 2024. Fruit position on tree canopy affects fruit quality traits in ‘Sanguinelli’ blood oranges. Horticulture. 10: 949.

PH-P14

Proceedings of The 12th International Symposium on Machinery and Mechatronics for Agriculture and Biosystems Engineering (ISMAB 2026)
20-24 October 2026, Busan, Republic of Korea

DEVELOPMENT OF A DEEP LEARNING MODEL FOR AUTOMATIC FIVE-GRADE QUALITY CLASSIFICATION OF PEELED GARLIC USING MULTI-VIEW IMAGES

Hyeon-Chae Yu[1], Saet-Byeol Park[1], Ji-Hee Han[1], Seong Min Kim[2*]

[1]Department of Agricultural Engineering, National Institute of Agricultural Sciences, Rural Development Administration, Jeonju-si, 54875, Korea
[2]Department of Agricultural Machinery Engineering, Jeonbuk National University, Jeonju-si, 54896, Korea
*Corresponding Author -- Voice: +82-63-270-2617, Email: smkim@jbnu.ac.kr

Abstract: Peeled garlic accounts for a large share of domestic garlic consumption, yet its size and quality grading still relies on manual visual inspection, which suffers from subjectivity, inconsistency, and high labor cost. This study aimed to develop and evaluate a model that automatically classifies peeled garlic into five grades — three size grades (large, medium, small) and two quality grades (defective, reject) — using multi-view images and a convolutional neural network (CNN). Three cameras captured each garlic clove simultaneously from three viewpoints. Each view was treated as an individual training sample, and the object-level grade was determined by a separate rule. The dataset was split at the object level so that the three views of the same clove never appeared across the training, validation, and test sets, preventing information leakage (15,458 training, 3,309 validation, and 3,311 test images). EfficientNet-B3 was used as the backbone, initialized with ImageNet pre-trained weights and fine-tuned over all layers. A class-weighted cross-entropy loss was applied to compensate for class imbalance (normal to reject ratio of approximately 4.4 to 1). On the fixed test set of 3,311 images, the model achieved an accuracy of 0.8949, a macro F1 of 0.8647, and a balanced accuracy of 0.8664. The rate at which defective or reject cloves were misclassified as normal was only 1.0% (32 of 617), indicating a low risk of shipping defective product as normal. The main confusions occurred between the large and medium size grades and between the defective and reject grades; because each pair is routed to the same category of outlet, their effect on actual sorting was minor. These results demonstrate that a multi-view, CNN-based classifier is applicable to real-time automatic sorting of peeled garlic.

Key Words: peeled garlic, image classification, deep learning, EfficientNet, quality grading

INTRODUCTION

Garlic is a major seasoning vegetable with high domestic consumption, and distribution in the peeled form, after washing and peeling, continues to grow. Peeled garlic is graded into large, medium, and small by size, while cloves with defects such as

browning, blackening, or physical damage, or those that are decayed, must be removed. Grading is therefore directly linked to product value.

At present, peeled garlic processing and sorting depend largely on the eyes and hands of workers. Manual sorting is difficult to keep consistent because criteria vary between workers, its accuracy declines with fatigue during long operations, and it carries a heavy labor cost together with difficulty in securing workers. To reduce this burden, semi-automatic machinery for garlic cutting, shelling, and peeling has been developed (Guardia et al., 2023), and these limitations increase the need for automation of the grading step as well.

Image-based approaches have drawn attention as an alternative. Convolutional neural networks (CNNs) have shown strong performance in judging the size, shape, color, and defects of agricultural products from images alone, and have been applied to garlic processing, for example to the post-harvest removal of garlic cloves (Lee et al., 2025). Non-destructive imaging has also been studied for peeled garlic, including hyperspectral imaging for origin authentication (Yang et al., 2025) and multi-view imaging for three-dimensional phenotyping of garlic bulbs (Zhan et al., 2026). Because a CNN learns the visual features needed for discrimination from data without requiring hand-crafted features, it is well suited to a target such as peeled garlic with diverse defect types.

The objective of this study is to develop a model that classifies peeled garlic into five grades — three size grades and two quality grades — using multi-view images and a CNN, and to quantitatively evaluate its performance and misclassification characteristics on a fixed test set.

MATERIALS AND METHODS

Multi-view Image Acquisition

To capture each garlic clove simultaneously from three directions, three cameras were used. The three cameras were arranged to view the same point on the conveyor from different angles, and the three images were acquired at the same instant as a clove passed the imaging position. The resolution of each image was 720 × 576. The three-view images represent different observations of a single clove and provide complementary information for size and defect judgment.

Dataset

The classification targets were five grades in total: three size grades (normal_large, normal_medium, normal_small) and two quality grades (defective, reject). Normal grades were divided by size, and the defective and reject grades were distinguished by the degree of damage or decay. Each of the three camera views was treated as an individual training sample, and the final grade of a clove was determined by a separate decision rule that combined the predictions of its three views.

The data were split into training, validation, and test sets at the object (clove) level. That is, the three views of the same clove were not allowed to appear in different splits, preventing the information leakage that would arise if the same object were used for both training and evaluation. The final split comprised 15,458 training, 3,309 validation, and 3,311 test images. The dataset was imbalanced between normal and defective grades, with a ratio of normal (sum of large, medium, and small) to reject-side classes of approximately 4.4 to 1, which was compensated during training.

Preprocessing

Each original image (720 × 576) was converted to 224 × 224 by aspect-ratio-preserving letterbox resizing: the longer side was fitted to 224 pixels and the remaining area was padded with black, without cropping, so that the object shape was neither distorted nor partially lost. The images were then normalized with the ImageNet mean and standard deviation. For training augmentation, only horizontal flipping was applied. Color augmentation was not used because many defects, such as browning, blackening, and greening, are color-based signals, and color distortion could damage the cues that the model needs to learn.

Model and Training

EfficientNet-B3 was used as the classification model. EfficientNet is a CNN family characterized by compound scaling, which balances the depth, width, and input resolution of the network with a single coefficient (Tan and Le, 2019); B3, of intermediate size, offered a suitable balance of accuracy and computation for this task with a fixed camera rig and 224 × 224 input. The model has about 10.7 million parameters and 26 MBConv blocks, each containing channel attention (squeeze-and-excitation), and requires 2.22 GFLOPs per image.

The network was initialized with ImageNet-1k pre-trained weights and fine-tuned over all layers on the present dataset. The loss function was a class-weighted (inverse-frequency) cross-entropy to compensate for class imbalance. The optimizer was Adam with a fixed learning rate of 1×10^{-3} (no scheduler), a batch size of 32, and up to 100 epochs with early stopping (patience 7). The random seed was fixed at 42 for reproducibility. The checkpoint with the lowest validation loss was selected as the final model (epoch 16), and the test set was scored only once with this checkpoint.

Evaluation

Performance was computed on the fixed test set of 3,311 images. The metrics were overall accuracy, macro F1 (the simple mean of per-class F1), balanced accuracy (the mean of per-class recall), and the precision, recall, and F1 of each of the five grades together with the 5 × 5 confusion matrix. Two practical safety metrics were also computed: the rate at which actual defective or reject cloves were classified as normal (risk of shipping defective product as normal), and the rate at which actual normal cloves were classified as defective or reject (yield loss).

RESULTS & DISCUSSION

Overall Classification Performance

On the test set of 3,311 images, the overall accuracy was 0.8949 (2,963 correct), the macro F1 was 0.8647, and the balanced accuracy was 0.8664 (Table 1). Per-class performance is shown in Table 2. normal_small was highest at an F1 of 0.9685, and defective was lowest at an F1 of 0.7810. The relatively low performance of the defective grade is attributed to the diversity of defect types and the visual similarity of some defective cloves to the reject grade.

Table 1 Overall classification performance on the test set (3,311 images).

Metric	Value
Accuracy	0.8949
Macro F1	0.8647
Balanced accuracy	0.8664
Defect/reject → normal misclassification rate	0.0519
Normal → defect/reject misclassification rate	0.0167

Table 2 Per-grade classification performance.

Grade	Precision	Recall	F1	Support
normal_large	0.8538	0.8632	0.8585	636
normal_medium	0.8760	0.8420	0.8587	747
normal_small	0.9652	0.9718	0.9685	1,311
defective	0.7760	0.7862	0.7810	304
reject	0.8447	0.8690	0.8567	313

Misclassification Characteristics

As shown in the confusion matrix (Table 3), the main misclassifications were of two kinds. The first was confusion between normal_large and normal_medium (56 and 67 cloves, respectively), occurring for cloves near the size boundary. The second was confusion between defective and reject (44 and 30 cloves, respectively), occurring for cloves with similar degrees of damage. Both are routed to the same category of outlet — large and medium both go to normal outlets, and defective and reject both go to reject outlets — so their effect on actual sorting is small.

The most important error in practice is the case in which a defective or reject clove is classified as normal, so that defective product is shipped as normal. This rate was only 1.0% (32 of the 617 defective and reject cloves), confirming that the risky misclassification is at a low level. Conversely, the yield loss from normal cloves being classified as defective or reject was 1.67% (45 of 2,694 normal cloves).

Table 3 Confusion matrix (rows: actual grade, columns: predicted grade; values are counts).

Actual \ Pred.	n_large	n_med	n_small	defect	reject
normal_large	549	56	1	28	2
normal_medium	67	629	41	7	3
normal_small	2	30	1274	4	1
defective	17	1	3	239	44
reject	8	2	1	30	272

Discussion

The overall accuracy of 0.895 and the risky misclassification rate of 1.0% show that a multi-view, CNN-based classifier can be applied practically to real-time sorting of peeled garlic.

The high performance of normal_small in particular (F1 0.9685) indicates that identification of small normal product is stable. The relatively low defective performance stems from the diversity of defect types and could be improved by reinforcing defect-location information or by expanding the data.

CONCLUSIONS

This study developed and evaluated a model that classifies peeled garlic into five size and quality grades using multi-view images and EfficientNet-B3. On an object-level test set of 3,311 images, the model achieved an accuracy of 0.8949 and a macro F1 of 0.8647, and the risky misclassification rate of defective product as normal was low at 1.0%. The main misclassifications were confusion at the size boundary and between the defective and reject grades; because these are routed to the same category of outlet, their effect on actual sorting was small.

Future work will include the use of defect-location information to improve defect discrimination, a binary classification scheme that allows the sorting stringency to be adjusted on site, and field validation on an actual sorting machine.

ACKNOWLEDGEMENTS

This work was carried out with the support of the Research Program for Agricultural Science & Technology Development (Project No. PJ01762104), National Institute of Agricultural Sciences, Rural Development Administration, Republic of Korea.

REFERENCES

Guardia, L. A. L., J. M. H. Caballero, H. D. C. Acosta, S. A. C. Quijano, and R. D. L. C. Casaño. 2023. Design of a semi-automatic machine to improve garlic processing for the optimization of procedures (cutting, shelling and peeling) in agricultural areas. In 2023 IEEE 14th Annual Ubiquitous Computing, Electronics & Mobile Communication Conference (UEMCON), 788-792. IEEE.

Lee, C. H., S. Y. Kim, E. Kim, S. Kim, S. J. Hong, and G. Kim. 2025. Convolutional neural network-integrated image processing method for the post-harvest removal process of garlic clove (Allium sativum). Applied Eng. in Agric. 41(4): 441-451.

Tan, M., and Q. V. Le. 2019. EfficientNet: Rethinking model scaling for convolutional neural networks. In Proc. 36th Int. Conf. Machine Learning (ICML), 6105-6114.

Yang, R., W. Wei, and Y. Feng. 2025. Hyperspectral imaging for non-destructive origin authentication of peeled garlic products. Food Bioscience 107298.

Zhan, Y., S. Yang, M. Lu, M. Shao, L. Wang, R. Fan, and Y. Li. 2026. Non-destructive three-dimensional phenotyping of garlic bulbs based on multi-view imaging. Horticulturae 12(7): 887.

PH-P15

Proceedings of The 12th International Symposium on Machinery and Mechatronics for Agriculture and Biosystems Engineering (ISMAB 2026)
20-24 October 2026, Busan, Republic of Korea

CLASSIFICATION AND SEGMENTATION OF EXTERNAL DEFECTS IN ORIENTAL MELON USING RGB IMAGIN AND DEEP LEARNING

Saet-Byeol Park[1], Hyeon-Chae Yu[1*], Ji-Hee Han[1]

[1]Department of Agricultural Engineering, National Institute of Agricultural Sciences, Rural Development Administration, Jeonju-si, 54875, Korea

*Corresponding Author – Voice: +82-63-238-4118, Email: hyeonchae1@korea.kr

Abstract: External quality inspection of oriental melon (*Cucumis melo* var. *makuwa*) at agricultural produce processing centers (APCs) still relies largely on visual assessment by operators, which limits grading consistency and processing efficiency. This study developed an RGB image-based deep learning pipeline for four-class external defect classification (normal, browning, abnormal coloration, and deformity) and segmentation of browning regions. A total of 8,791 surface images acquired with a single RGB camera were split by imaging session into training, validation, and test sets at a ratio of approximately 70:15:15. A ResNet18 classifier trained on background-masked images achieved an accuracy of 97.5% and a macro F1-score of 0.971 on the test set. For browning segmentation, YOLO11n-seg and U-Net were compared on the same segmentation test set; YOLO11n-seg achieved an mIoU of 0.835 and a Dice coefficient of 0.870, outperforming U-Net (mIoU 0.692; Dice 0.730). Background masking improved ResNet18 accuracy by 0.30 percentage points and increased U-Net mIoU from 0.692 to 0.728, but had little effect on YOLO11n-seg. On an RTX 3080 GPU, the total processing time for the classifier and both segmentation models was approximately 49.3 ms per image (about 20.3 FPS). Class-date confounding was identified for some abnormal coloration and deformity samples, indicating that the reported accuracy may overestimate generalization performance under diverse field conditions. These results demonstrate the potential of RGB imaging and deep learning for automated external quality assessment and real-time sorting of oriental melon.

Key Words: Oriental melon, External quality inspection, Deep learning, Image classification, Segmentation

INTRODUCTION

Oriental melon is one of the major greenhouse fruit vegetables produced and consumed in Korea, and fruit appearance strongly influences commercial grade and market value. Surface browning, abnormal coloration, and deformity are major external defects that reduce marketability. At agricultural produce processing centers (APCs), these external quality attributes are typically assessed visually by experienced operators during sorting.

Visual sorting results can vary with the experience and skill of the operator, and consistency may decline as fatigue accumulates over long working hours. In addition, sorting lines that handle large volumes of produce continuously require automation that can evaluate quality rapidly while maintaining a uniform standard. Image-based quality assessment therefore offers an effective way to assist or automate conventional visual sorting.

Deep learning-based computer vision has been widely applied to quality grading, external defect classification, and defect region detection for agricultural products (Chuquimarca et al., 2024). Machine vision-based quality assessment has also been introduced into actual sorting processes for real-time detection and grading (Xu and Lu, 2024). Image classification using convolutional neural networks (CNNs) determines a quality category from the features of the whole fruit, whereas segmentation models estimate not only the presence of a defect but also its location and area at the pixel level.

Among the external defects of oriental melon, browning often occurs locally on the fruit surface; therefore, image-level classification alone cannot quantify the location and distribution of the defect. The melon surface also contains white longitudinal grooves, shading, and natural color variation, which limits the use of simple color thresholds to delineate browning regions. Combining classification and segmentation is therefore useful for assessing the quality class while localizing the defect region.

The objectives of this study were to (1) classify oriental melon surface images into four external quality classes, (2) segment browning regions using two different architectures, and (3) analyze the effect of background masking on classification and segmentation performance. Model processing time was also measured, and limitations associated with the training data composition and imaging conditions were examined in relation to application in an actual sorting system.

MATERIALS AND METHODS

Image Acquisition and Dataset

Surface images for external quality assessment of oriental melon were acquired using a single RGB camera installed above a roller conveyor. As each fruit rolled along the conveyor, ten images were captured per fruit, covering different parts of the surface. The collected images were divided into four classes: normal, browning, abnormal coloration, and deformity.

The normal class was defined as fruit with no observable external defects such as browning, abnormal coloration, or deformity. The browning class was defined as fruit with a discolored surface region that was clearly darker than the surrounding tissue and extended over a discernible area; faint shading or light stains along the white longitudinal grooves were regarded as normal surface variation. Abnormal coloration was defined as an atypical overall surface color or hue, whereas deformity was defined by abnormal shape, size, proportion, or symmetry.

The dataset consisted of 8,791 images. To prevent similar consecutive images from being included in both the training and test sets, the data were split by imaging session rather than by individual image into training, validation, and test sets at approximately 70:15:15. The random seed was fixed at 42 to ensure reproducibility of the split. The class distribution is shown in Table 1.

Table 1 Class distribution of the classification dataset.

Class	Train	Val	Test	Total
Normal	3,037	643	666	4,346
Browning	1,075	220	231	1,526
Abnormal coloration	688	142	149	979
Deformity	1,360	290	290	1,940
Total	**6,160**	**1,295**	**1,336**	**8,791**

Classification Model

An ImageNet-pretrained ResNet18 was used as the classification model, with the final output layer modified to four classes: normal, browning, abnormal coloration, and deformity (He et al., 2016). A weighted cross-entropy loss was applied to compensate for class imbalance. Bounding-box cropping was not applied, so that the shape and proportion information required for deformity classification was retained. Excessive color augmentation was also avoided, because color is an important feature of the browning and abnormal coloration classes.

Background Masking

Background masking, which retains only the melon region, was applied as preprocessing to reduce the influence of background and illumination conditions on classification. Models were trained separately on the original and the masked images, and their classification and segmentation performance was compared.

Browning Segmentation

Browning regions were annotated as polygons using LabelMe and then converted to binary masks. Two architectures with different prediction schemes were compared. YOLO11n-seg is a lightweight instance segmentation model that detects individual browning regions and generates polygonal masks (Jocher et al., 2023). In contrast, U-Net was trained without pretrained weights and performs dense pixel-wise prediction (Ronneberger et al., 2015).

Segmentation training used 5,872 images from the normal and browning classes, with polygon annotations provided for the browning regions.

Evaluation Protocol

All models used the same data split. Hyperparameters and segmentation thresholds were determined on the validation set and then applied once to the test set. Classification performance was evaluated using accuracy, precision, recall, F1-score, and macro F1-score, and segmentation performance using mIoU and the Dice coefficient. Processing speed was measured per image on an NVIDIA RTX 3080 GPU.

RESULTS & DISCUSSION

Classification Performance

The background-masked ResNet18 classifier achieved an overall test accuracy of 97.5% and a macro F1-score of 0.971. Class-wise results are shown in Table 2. All four classes exceeded an F1-score of 0.94, indicating generally high classification performance. The browning class showed the lowest recall (0.944), meaning that some browned fruits were assigned to other classes. In practical sorting, misclassifying defective fruit as normal directly affects quality control; therefore, recall for the defect classes should be considered together with overall accuracy.

Table 2 Class-wise classification performance of the background-masked ResNet18 model (test set).

Class	Samples	Precision	Recall	F1	Accuracy (%)
Normal	666	0.978	0.981	0.980	98.1
Browning	231	0.945	0.944	0.944	97.2
Abnormal coloration	149	0.973	0.966	0.970	96.4
Deformity	290	0.983	0.986	0.985	98.6
Overall / Macro	**1,336**	**0.970**	**0.969**	**0.971**	**97.5**

Effect of Background Masking

ResNet18 classification accuracy increased from 97.16% on the original images to 97.46% on the masked images, an improvement of 0.30 percentage points. The mIoU of YOLO11n-seg was almost unchanged, at 0.835 for the original images and 0.833 for the masked images. In contrast, the mIoU of U-Net improved from 0.692 to 0.728, showing that the effect of background masking depended on the model architecture (Table 3). The current GUI uses the ResNet18 trained on masked images together with the YOLO11n-seg and U-Net models trained on the original images.

Table 3 Effect of background masking on test-set performance.

Model	Original	Masked	Difference
Classification (accuracy, %)	97.16	97.46	+0.30
YOLO11n-seg (mIoU)	0.835	0.833	-0.002
U-Net (mIoU)	0.692	0.728	+0.036

Segmentation: YOLO11n-seg versus U-Net

Table 4 compares the two segmentation models. For browning segmentation, YOLO11n-seg achieved an mIoU of 0.835 and a Dice coefficient of 0.870, whereas U-Net achieved 0.692 and 0.730, respectively. The masks predicted by YOLO11n-seg therefore showed greater spatial agreement with the ground-truth masks.

Table 4 Browning segmentation performance on the test set.

Model	mIoU	Dice	Processing time (ms)
YOLO11n-seg	0.835	0.870	22.5
U-Net (no pretrained weights)	0.692	0.730	15.2

Processing Speed

On an RTX 3080 GPU, the processing time per image was 11.6 ms for ResNet18, 22.5 ms for YOLO11n-seg, and 15.2 ms for U-Net (Table 5). The total processing time of the GUI pipeline running all three models was approximately 49.3 ms, corresponding to about 20.3 FPS. This value represents the processing performance of the models for a single image and should be distinguished from the fruit throughput of an actual sorting system.

Table 5 Processing speed per image on an NVIDIA RTX 3080 GPU.

Stage	Processing time (ms)	Processing speed (FPS)
Classification (ResNet18)	11.6	86.1
Segmentation (YOLO11n-seg)	22.5	44.4
Segmentation (U-Net)	15.2	65.9
Complete pipeline (all three models)	**49.3**	**20.3**

Limitations

The main limitation of this study is class-date confounding, in which some abnormal coloration and deformity samples were strongly associated with specific imaging dates. Splitting the data by imaging session prevented similar consecutive images from being included in both the training and test sets; however, the models may still have learned date-specific illumination, saturation, and color characteristics together with the actual external defects. Performance degradation was also observed in field images acquired under imaging conditions not represented in the training data. Therefore, the reported classification performance should be interpreted as specific to the conditions represented in the current dataset.

Future work should use additional data in which each quality class is evenly represented across multiple imaging dates and illumination conditions, and generalization performance should be verified using independent field data. The criteria for browning assessment should also be refined, and fruit-level classification accuracy and ejection performance should be evaluated on an actual sorting line.

CONCLUSIONS

This study established an RGB image-based deep learning pipeline for four-class external defect classification and segmentation of browning regions in oriental melon. Using 8,791 images, the background-masked ResNet18 achieved a test-set accuracy of 97.5% and a macro F1-score of 0.971. For browning segmentation, YOLO11n-seg achieved an mIoU of 0.835 and a Dice coefficient of 0.870, outperforming U-Net (mIoU 0.692; Dice 0.730). Background masking improved the performance of ResNet18 and U-Net but had no clear effect on YOLO11n-seg. On an RTX 3080 GPU, the classifier and both segmentation models required approximately 49.3 ms per image. Because class-date confounding was identified, the generalization of the models, together with fruit-level classification accuracy and ejection performance, should be verified further using independent data acquired under diverse imaging conditions and on an actual sorting line. These results support the feasibility of RGB image-based automated external quality assessment for oriental melon and provide baseline information for the development of smart APC sorting systems.

ACKNOWLEDGEMENTS

This work was carried out with the support of the Research Program for Agricultural Science & Technology Development (Project No. RS-2022-RD010265), Rural Development Administration, Republic of Korea.

REFERENCES

Chuquimarca, L. E., B. X. Vintimilla, and S. A. Velastin. 2024. A review of external quality inspection for fruit grading using CNN models. Artif. Intell. Agric. 14: 1-20. https://doi.org/10.1016/j.aiia.2024.10.002

He, K., X. Zhang, S. Ren, and J. Sun. 2016. Deep residual learning for image recognition. In Proc. IEEE Conf. Computer Vision and Pattern Recognition (CVPR), 770-778. Las Vegas, Nev.: IEEE. https://doi.org/10.1109/CVPR.2016.90

Jocher, G., A. Chaurasia, and J. Qiu. 2023. Ultralytics YOLO. Ver. 8.0.0. Available at: https://github.com/ultralytics/ultralytics. Accessed 15 September 2026. https://github.com/ultralytics/ultralytics

Ronneberger, O., P. Fischer, and T. Brox. 2015. U-Net: Convolutional networks for biomedical image segmentation. In Medical Image Computing and Computer-Assisted Intervention - MICCAI 2015, 234-241. Cham, Switzerland: Springer. https://doi.org/10.1007/978-3-319-24574-4_28

Xu, J., and Y. Lu. 2024. Prototyping and evaluation of a novel machine vision system for real-time, automated quality grading of sweetpotatoes. Comput. Electron. Agric. 219: 108826. https://doi.org/10.1016/j.compag.2024.108826

PH-P16

Proceedings of the 12th International Symposium on Machinery and Mechatronics for Agriculture and Biosystems Engineering (ISMAB 2026)
20-24 October 2026, Busan, Republic of Korea

IMPACT ON ELECTRICAL AND PHYSICOCHEMICAL PROPERTIES OF Ag/TiO_2 NANOCOMPOSITE-ASSISTED VACUUM-IMPREGNATED CARROT

Sourav Kumar Singha[1,2], Takahisa Nishizu[1,2] Teppei Imaizumi[1,2*]

[1]Faculty of Applied Biological Sciences, Gifu University, 1-1 Yanagido, Gifu, 501-1193, Japan
[2]Preemptive Food Research Center, Gifu University, 1-1 Yanagido, Gifu City, Gifu, 501-1193, Japan
*Corresponding Author- Voice: +81-0905-877-8185, Email: imaizumi.teppei.j6@f.gifu-u.ac.jp

Abstract: Vacuum impregnation (VI) facilitates the introduction of external solutions into plant tissues and may therefore provide an approach for investigating the effects of photocatalytically generated reactive species on internal tissue. This study evaluated the effects of Ag/TiO_2-assisted photocatalytic treatment combined with VI on the structural and physicochemical properties of carrot tissue. Two VI conditions were applied: a 10-min vacuum period followed by a 10-min relaxation period (10/10 min) and a 30-min vacuum period followed by a 30-min relaxation period (30/30 min). UV-C irradiation was applied during the relaxation period. The prepared Ag/TiO_2 nanoparticles (NPs) had a crystallite size of 16.4 nm and exhibited photocatalytic activity, as demonstrated by methyl orange degradation under UV irradiation. Carotenoid content was 23.04% and 26.62% higher in Ag/TiO_2-treated carrots than in the corresponding VI controls under the 10/10- and 30/30-min conditions, respectively. Total phenolic content increased after the 10/10-min treatment but decreased after the 30/30-min treatment compared with untreated carrots. The 10/10-min Ag/TiO_2 treatment also resulted in significantly higher firmness after heating. Changes in electrical impedance parameters and the degree of methylesterification of pectin further indicated that the treatment affected cell wall-related properties. These results demonstrate that Ag/TiO_2-assisted photocatalytic treatment combined with VI can modify the structural and physicochemical properties of carrot tissue, with the effects depending on treatment duration.

Key Words: Vacuum Impregnation, Ag/TiO_2 nanocomposite, Photocatalytic activity, Carrot, Nutrient release.

INTRODUCTION

Different treatments such as ultrasound, cold plasma, and ozone have been applied to enhance the nutritional, structural, and physicochemical characteristics of food products through the generation of reactive species (Fernandes & Rodrigues, 2021; Premjit et al., 2022; Soria & Villamiel, 2010). Photocatalysts such as Ag/TiO_2 and ZnO nanoparticles (NPs) can similarly generate reactive species upon light irradiation (Bhatkhande et al., 2002). Santoscoy-Berber et al. (2021) reported that treatment of carrots with Ag NP solutions (0–40 mg/L) for 3 min enhanced antioxidant properties and phenolic content, with the greatest effects observed at 20 mg/L. Similarly, X. Guo et al. (2024) reported that soaking litchi in a 100 mg/L ZnO NP

suspension for 2 min significantly increased total anthocyanin content, TPC, and DPPH radical scavenging activity. These findings suggest that NP treatment can induce oxidative stress in postharvest produce and thereby modify its phytochemical properties. Although it is well established that NP can induce oxidative stress in plants, this stress can have either positively or negatively effects on phytochemical accumulation and other quality attributes of fresh produce, depending on its intensity and duration (Duarte Sierra et al., 2020). However, previous studies on photocatalytic NPs have focused mainly on phytochemical properties, with limited attention to their effects on tissue structure.

Reactive species generated by other treatments have also been shown to affect structural properties of plant tissues. For example, plasma-activated water (PAW), which contains various reactive species, has been reported to delay blueberry softening and reduce the activities of cell wall pectin-degrading enzymes (Cheng et al., 2023). Furthermore, after plasma treatment, the degree of esterification of pectin was also decreased significantly (Z. Guo et al., 2024). These findings suggest that reactive species may affect not only phytochemical properties but also cell wall-related structural properties. However, conventional immersion treatments primarily expose the tissue surface to photocatalysts and reactive species, making it difficult to evaluate their effects within the tissue. Vacuum impregnation (VI) can facilitate the introduction of an external solution into plant tissues and therefore provides a means of investigating the effects of photocatalytic treatment on internal tissue. Combining VI with photocatalysis may thus provide an approach to expose internal plant tissues to photocatalytically generated reactive species. However, to the best of our knowledge, no study has investigated the incorporation of photocatalysts into a VI solution or their effects on the quality and structural properties of fresh produce.

Therefore, the objective of this study was to evaluate the effects of Ag/TiO_2-assisted photocatalytic treatment combined with VI on carrot tissue. Carrot was selected as the model food because it is relatively low in porosity and thus provides a suitable model for evaluating the effects of VI-assisted treatment on internal tissue (Radziejewska-Kubzdela et al., 2023). The effects of the treatment on selected quality parameters, including electrical properties, firmness, degree of methylesterification (DM), carotenoid content, and TPC, were evaluated.

MATERIALS AND METHODS

PREPARATION OF TiO_2 AND Ag/TiO_2 NP

Initially, TiO_2 NP was prepared from titanium isopropoxide (TTIP). Briefly, 20 mL of TTIP was dissolved into 140 mL of 2-propanol (99%, Merck), followed by the dropwise addition of 5 mL of deionized water under continuous stirring to initiate hydrolysis and condensation. The resulting sol was aged for 24 h and then dried for 4 h at 110 ºC. Subsequently, the dried material was calcined at 500 ºC for 2 h to obtain TiO_2 NP powder.

For the preparation of Ag/TiO_2 NP, 10 g of the prepared TiO_2 NP powder was dispersed in, 55.6 mL of 0.05 M $AgNO_3$ solution under continuous stirring for 24 h to achieve the desired Ag loading. The mixture was then dried at 110 ºC for 24 h and calcined for 12 h at 500 ºC to promote the deposition of Ag onto the TiO_2 surface, producing Ag/TiO_2 NP (Singha et al., 2023). Finally, the resulting powder was ground using a ball mill to obtain a more uniform particle size.

PREPARATION VI CARROT SAMPLES

For VI, carrots were cut into cylindrical pieces with a diameter of 20 mm and a thickness of 10 mm using a cork borer. The carrot samples were completely immersed in 1% Ag/TiO_2 suspension prepared in water at a sample-to-solution ratio of 1:4 (w/v) in a beaker. The beaker was then placed in a desiccator where the pressure was rapidly reduced to 100 hPa and maintained for 10 or 30 min, according to the treatment condition, with or without Ag/TiO_2 NP. Subsequently, during the relaxation period, the pressure was rapidly restored to atmospheric pressure and maintained for an additional 10 or 30 min. During the relaxation period, the submerged samples were exposed to UV-C light (Seven beauty UV-C clean system KD-01, 253.7nm). The distance between the UV source and surface of the solution was 70mm. Finally, both treated and untreated samples were collected for further analyses.

CHARACTERIZATION OF TiO_2 AND Ag/TiO_2 NP

Initially, the crystal structure and phase composition of the prepared TiO_2 and Ag/TiO_2 NPs were characterized using an X-ray diffractometer (XRD; SmartLab, Rigaku). The crystallite grain size was calculated from the XRD pattern using the Scherrer equation (Singha et al., 2023). To evaluate the photocatalytic performance of the prepared Ag/TiO_2 NP, the degradation of methyl orange (MO) was investigated. Briefly, 50 mL of 70 ppm MO solution containing 1% Ag/ TiO_2 NP was exposed to UV light for 60 min. Prior to UV irradiation, the suspension was stirred in the dark to establish adsorption–desorption equilibrium between the MO and Ag/TiO_2 NP. Subsequently, the absorbance data were taken using UV-vis spectrophotometer at every 10 min following the method described by Singha et al. (2023).

ANALYSIS OF SELECTED QUALITY PARAMETERS OF CARROT SAMPLES

Electrical impedance analysis was performed to evaluate the electrical properties of VI carrot samples using an LCR meter (3532–50, HIOKI). Two stainless needle electrodes connected to the meter were inserted into the sample to a depth of meter 9 mm from the surface. To evaluate the effect of the treatment on the resistance of carrot tissue to softening during heating, firmness was measured according to Umehara et al. (2025) with slight modifications. All samples were heated in a water bath at 95 °C for 10 min and then subjected to a compression test using a texture analyzer (TA.XT Plus, Stable Micro Systems) equipped with a 5-mm cylindrical probe. The samples were compressed to 40% strain at a rate of 1 mm s^{-1}, and the peak force (N) was defined as firmness. The degree of DM of pectin was determined from cell wall materials extracted from carrot samples using an FT-IR spectrometer (FT/IR-4700, JASCO), according to Umehara et al. (2025). DM was calculated from the absorption bands at 1600 and 1740 cm^{-1}. TPC was determined using the Folin–Ciocalteu method. Briefly, 5 g of sample was homogenized with 30 mL of 80% methanol for 2 min at 8,000 rpm and centrifuged at 15,000 rpm for 10 min at 4 °C. The supernatant was reacted with Folin–Ciocalteu reagent and Na_2CO_3 for 1 h at room temperature, and the absorbance was measured using a UV–Vis spectrophotometer (V-730BIO, JASCO) with gallic acid as the standard. Carotenoid content was determined according to Md Saleh et al. (2022). 1 g of sample was homogenized with 15 mL of hexane (60:40, v/v) for 2 min at 8,000 rpm and incubated in the dark at 4 °C for 1 h. The extract was adjusted to 25 mL with the extraction solvent, and the absorbance was measured at 450 nm using the UV–Vis spectrophotometer.

RESULTS & DISCUSSION

According to Scherrer equation, the prepared Ag/TiO_2 NP showed a lower crystallinity where the crystalline size of Ag/TiO_2 NP was 16.4 nm. The incorporation of Ag into TiO_2 NP increased the crystallinity, which contributed to enhance photocatalytic activity of Ag/TiO_2 NP. Under UV illumination, the prepared Ag/TiO_2 NP degraded 15.32% of the methyl orange dye within 60 min.

Fig. 1 shows the equivalent circuit parameters of each sample obtained from the impedance measurements. The intercellular resistance (*Ri*) significantly increased in Ag/TiO_2-100-30 but decreased in W-100-30. However, there was no significant difference in cell membrane capacitance (C_m) of all samples. These two electrical properties indicates that there may be a limited impact in cell membrane. The extracellular resistance R_e significantly decreased in Ag/TiO_2-100-10 whereas W-100-10 showed no significant difference. The unchanged (R_e) in W-100-10 may indicate that the pores in the carrot tissue were compressed during the vacuum period but recovered their original structure during the relaxation period. In contrast, the presence of Ag/TiO_2 in the VI solution may have modified the cell wall materials, limiting their ability to return to their original structure during the relaxation period and consequently reducing tissue porosity. Imaizumi et al. (2017) showed the similar findings, in which extracellular resistance decreased in respect with decreasing porosity of sweet potato. Ag/TiO_2-100-10 exhibited a significant increase in firmness compared with C which supports the observed changes in the electrical properties. DM of pectin also decreased after treatment, with Ag/TiO_2-100-30 exhibiting the lowest DM.

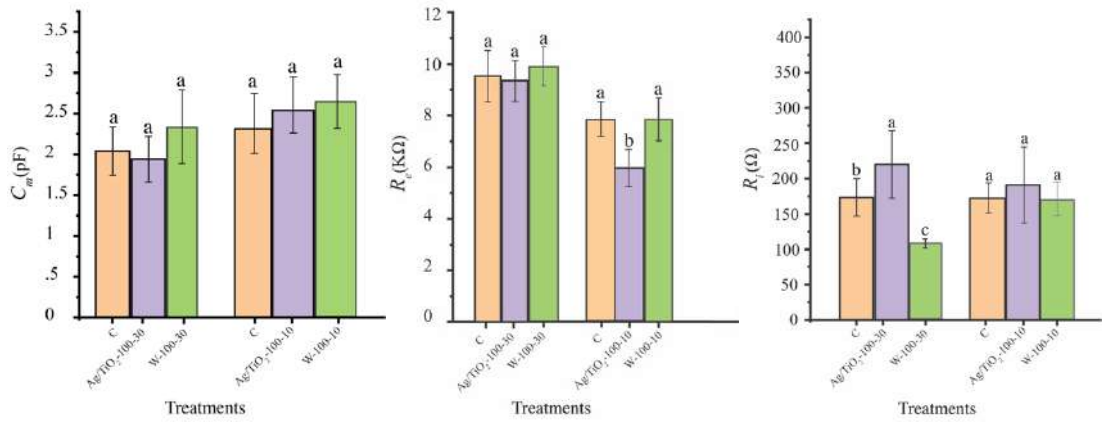

Fig. 1 Electrical impedance parameters of carrot samples. C_m: cell membrane capacitance, R_e: extracellular resistance, R_i: intracellular resistance. Alphabets represent significant differences, Mean±SD, $p < 0.05$.

However, prolonged exposure to Ag/TiO_2 NP may have contributed to the lower TPC observed in Ag/TiO_2-100-30 compared with the untreated fresh carrots (C), whereas Ag/TiO_2-100-10 showed significant increase of TPC. Furthermore, greater carotenoid content retention was observed following the incorporation of Ag/TiO_2 NP into the VI solution. Carotenoid content decreased after VI compared with C. According to Radziejewska-Kubzdela et al. (2023), the decrease in carotenoids during VI may be attributed to tissue loosening, which can increase the susceptibility of carotenoids to oxidation. However, carotenoid content increased by 23.04% in Ag/TiO_2-100-10 compared with C-100-10, while a 26.62% increase was observed in Ag/TiO_2-100-30 compared with C-100-30 (Fig. 2). Overall, these results suggest that the incorporating Ag/TiO_2 NP into the VI solution can significantly enhance the selected qualities of carrots.

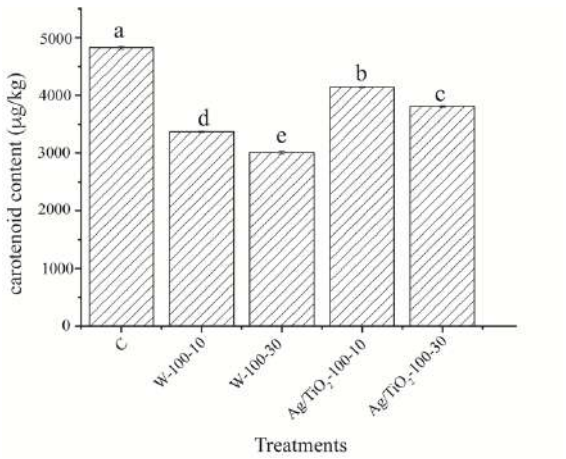

Fig. 2 Effect of Ag/TiO_2 NP treatments carotenoid content in raw and vacuum impregnated carrot slices. Alphabets represent significant differences, Mean±SD, $p < 0.05$.

CONCLUSIONS

The application of Ag/TiO_2 NP and its photocatalytic properties during vacuum impregnation resulted in modification to the structural properties and enhancement of the physicochemical properties of carrot. The findings also demonstrated that this treatment effectively mitigated the quality deterioration associated with conventional vacuum impregnation treatment. In the present study, the vacuum and UV-assisted relaxation times were fixed at 10 and 30 min to represent relatively lower and higher exposure levels, respectively, allowing the effects of treatment duration to be compared under controlled conditions. Further investigation using a broader range of treatment durations is warranted to identify the optimum processing time and to better understand the response of carrot tissue to Ag/TiO_2 NP-assisted vacuum impregnation.

REFERENCES

Bhatkhande, D. S., Pangarkar, V. G., & Beenackers, A. A. C. M. (2002). Photocatalytic degradation for environmental applications – a review. *Journal of Chemical Technology & Biotechnology*, *77*(1), 102–116. https://doi.org/10.1002/jctb.532

Cheng, J.-H., He, L., Sun, D.-W., Pan, Y., & Ma, J. (2023). Inhibition of cell wall pectin metabolism by plasma activated water (PAW) to maintain firmness and quality of postharvest blueberry. *Plant Physiology and Biochemistry*, *201*, 107803. https://doi.org/10.1016/j.plaphy.2023.107803

Duarte-Sierra, A., Tiznado-Hernández, M. E., Jha, D. K., Janmeja, N., & Arul, J. (2020). Abiotic stress hormesis: An approach to maintain quality, extend storability, and enhance phytochemicals on fresh produce during postharvest. *Comprehensive Reviews in Food Science and Food Safety*, *19*(6), 3659–3682. https://doi.org/10.1111/1541-4337.12628

Fernandes, F. A. N., & Rodrigues, S. (2021). Cold Plasma Processing on Fruits and Fruit Juices: A Review on the Effects of Plasma on Nutritional Quality. *Processes*, *9*(12), 2098. https://doi.org/10.3390/pr9122098

Guo, X., Li, Q., Luo, T., Xu, D., Zhu, D., Li, J., Han, D., & Wu, Z. (2024). Zinc Oxide Nanoparticles Treatment Maintains the Postharvest Quality of Litchi Fruit by Inducing Antioxidant Capacity. *Foods*, *13*(21), 3357. https://doi.org/10.3390/foods13213357

Guo, Z., Wu, S., Zheng, H., Lin, J., Lei, H., & Yu, Q. (2024). Effects of dielectric barrier discharge plasma modification on structure, physicochemical and functional properties of watermelon peel pectin. *Food Hydrocolloids*, *147*, 109350. https://doi.org/10.1016/j.foodhyd.2023.109350

Imaizumi, T., Tanaka, F., Sato, Y., Yoshida, Y., & Uchino, T. (2017). Evaluation of electrical and other physical properties of heated sweet potato. *Journal of Food Process Engineering*, *40*(3), e12490. https://doi.org/10.1111/jfpe.12490

Md Saleh, R., Kulig, B., Arefi, A., Hensel, O., & Sturm, B. (2022). Prediction of total carotenoids, color, and moisture content of carrot slices during hot air drying using non-invasive hyperspectral imaging technique. *Journal of Food Processing and Preservation*, *46*(9). https://doi.org/10.1111/jfpp.16460

Premjit, Y., Sruthi, N. U., Pandiselvam, R., & Kothakota, A. (2022). Aqueous ozone: Chemistry, physiochemical properties, microbial inactivation, factors influencing antimicrobial effectiveness, and application in food. *Comprehensive Reviews in Food Science and Food Safety*, *21*(2), 1054–1085. https://doi.org/10.1111/1541-4337.12886

Radziejewska-Kubzdela, E., Szadzińska, J., Biegańska-Marecik, R., Spiżewski, T., & Mierzwa, D. (2023). Effect of ultrasound on mass transfer during vacuum impregnation and selected quality parameters of products: A case study of carrots. *Ultrasonics Sonochemistry*, *99*, 106592. https://doi.org/10.1016/j.ultsonch.2023.106592

Santoscoy-Berber, L. S., Antunes-Ricardo, M., Gallegos-Granados, M. Z., García-Ramos, J. C., Pestryakov, A., Toledano-Magaña, Y., Bogdanchikova, N., & Chavez-Santoscoy, R. A. (2021). Treatment with Argovit® Silver Nanoparticles Induces Differentiated Postharvest Biosynthesis of Compounds with Pharmaceutical Interest in Carrot (Daucus carota L.). *Nanomaterials*, *11*(11), 3148. https://doi.org/10.3390/nano11113148

Singha, S. K., Hoque, S. M., Das, H., & Alim, M. A. (2023). Evaluation of chitosan-Ag/TiO2 nanocomposite for the enhancement of shelf life of chili and banana fruits. *Heliyon*, *9*(11), e21752. https://doi.org/10.1016/j.heliyon.2023.e21752

Soria, A. C., & Villamiel, M. (2010). Effect of ultrasound on the technological properties and bioactivity of food: A review. *Trends in Food Science & Technology*, *21*(7), 323–331. https://doi.org/10.1016/j.tifs.2010.04.003

Umehara, A., Oshima, T., Deshmukh, O. S., Nishizu, T., & Imaizumi, T. (2025). Detection of cell membrane disruption using electrical impedance spectroscopy and acceleration of cell wall modification in carrot processed under low temperature blanching. *Journal of Food Engineering*, *385*, 112270. https://doi.org/10.1016/j.jfoodeng.2024.112270

PH-P17

Proceedings of The 12th International Symposium on Machinery and Mechatronics for Agriculture and Biosystems Engineering (ISMAB 2026)
20-24 October 2026, Busan, Republic of Korea

STUDY ON KEY FACTORS BY MOISTURE CONTENT TO IMPROVE CLEANING EFFICIENCY OF DOMESTIC WHEAT

Eun-Jin Kwak[1], Dong-Gwan Shin[2], Hoon Kim[2] , Jae-Woong Han[1*]

[1]Department of SmartFarm Engineering, Kongju National University, Yesan, Republic of Korea
[2]Smart Manufacturing Research Group, Korea Food Research Institute, Wanju , Republic of Korea
*Corresponding Author-- Voice: +82 10-2005-5899 Email: hanwoong@kongju.ac.kr

Abstract: A specific gravity separator performs separation using a combination of the number and dimensions of deck riffles, deck vibration amplitude, and airflow rate, all of which must be adjusted depending on the physical properties of the grain being processed. In practice, most separators available in South Korea are designed exclusively for rice, which limits their applicability to other grains. Furthermore, the wheat-cleaning process still relies heavily on sieving and aspiration, resulting in low cleaning efficiency. Therefore, developing a specific gravity separator suitable for domestic wheat first requires characterization of the moisture-dependent physical and aerodynamic properties of domestic wheat, which provide fundamental data for separator design. Accordingly, this study aimed to identify and predict the moisture-dependent physical and aerodynamic properties of four major domestic wheat cultivars—Kumgang, Saekumgang, Baekjjung, and Jogyeong—as fundamental data for the development of a separator utilizing specific gravity and terminal velocity. Four or five moisture content levels were established for each cultivar, and specific gravity and terminal velocity were measured in triplicate at each moisture content level. Established empirical models were applied for prediction, while a new model was developed for terminal velocity and validated based on the coefficient of determination ($R2$). Results indicated that, as moisture content decreased, specific gravity increased while terminal velocity decreased across all four cultivars. The minimum and maximum specific gravity values were 1.27 and 1.38, respectively, while the minimum and maximum terminal velocity values were 4.06 and 8.08 m/s, respectively. Based on the cultivar-specific physical and aerodynamic property data, significant differences in specific gravity and terminal velocity were identified, indicating their potential for use as separation criteria to distinguish foreign materials from sound kernels. Therefore, the findings of this study are expected to provide fundamental data for the future development of a dedicated specific gravity separator for domestic wheat.

Key Words: Domestic wheat, Model equation, Specific gravity, Terminal velocity, Sorting

ACKNOWLEDGEMENTS

This research was funded by the R&D program for Rural Development Administration (RDA), Republic of Korea (Project No. RS-2025-02263107)

PH-P18

Proceedings of The 12th International Symposium on Machinery and Mechatronics for Agriculture and Biosystems Engineering (ISMAB 2026)
20-24 October 2026, Busan, Republic of Korea

ANALYSIS OF DRYING CHARACTERISTICS OF A CIRCULATING CROSS-FLOW GRAIN DRYER FOR DOMESTIC WHEAT USING SIMULATION

Woo-Jin Choi[1], Dong-Gwan Shin[2], Hoon Kim[2] , Jae-Woong Han[1*]

[1]Department of SmartFarm Engineering, Kongju National University, Yesan, Republic of Korea
[2]Smart Manufacturing Research Group, Korea Food Research Institute, wanju, Republic of Korea
*Corresponding Author-- Voice: +82 10-2005-5899, Email: hanwoong@kongju.ac.kr

Abstract: Improving the post-harvest drying process is essential for the stable supply and quality of domestic wheat. However, circulating cross-flow grain dryers, designed for rice, are also used to dry wheat, causing reduced drying rate, prolonged drying time, increased energy consumption, and quality deterioration. Resolving these issues requires repeated drying experiments, but the harvest period of domestic wheat is limited to late May–mid June, and the fuel and grain costs involved make it difficult to test a wide range of conditions. While operating conditions can be adjusted during operation, structural design factors are difficult to modify once manufactured and require careful design-stage evaluation. Previous studies, however, focused only on operating conditions, leaving structural specifications unchanged from existing rice dryers without validation. Therefore, this study used a circulating cross-flow dryer simulation model for domestic wheat to examine the importance of structural design factors for wheat-dedicated dryer design. With optimal operating conditions fixed for four commercial dryer capacities (30, 12, 8.5, and 6.5 tons), grain column thickness was varied from 0.10 to 0.40 m at 0.02 m intervals, and drying time, drying rate, energy consumption, and germination decreasing rate were analyzed. Drying time and energy consumption increased both when layers were too thin, due to insufficient heat exchange, and too thick, due to increased airflow resistance, yielding an optimal thickness range for each capacity. In the 8.5- and 6.5-ton dryers, with lower airflow rates, performance declined continuously without recovery beyond this range, while the germination decreasing rate decreased markedly with increasing thickness. The grain column thickness used in commercial dryers (0.23 m for 30- and 12-ton, 0.13 m for 8.5- and 6.5-ton) fell within this optimal range, confirming the existing specifications are appropriate; these findings can serve as a design factor for domestic wheat dryers.

Key Words: Drying time, Drying rate, Germination rate, Total energy consumption, Airflow rate

ACKNOWLEDGEMENTS

This research was funded by the R&D program for Rural Development Administration (RDA), Republic of Korea (Project No. RS-2025-02263107)

PH-P19

Proceedings of The 12th International Symposium on Machinery and Mechatronics for Agriculture and Biosystems Engineering (ISMAB 2026)
20-24 October 2026, Busan, Republic of Korea

DEVELOPMENT OF AN OPERATION SCHEDULING PROGRAM FOR DOMESTIC WHEAT DRYING AND STORAGE FACILITIES

Jun-Yeong Kim[1], Dong-Gwan Shin[2], Hoon Kim[2], Jae-Woong Han[1]*

[1]Department of SmartFarm Engineering, Kongju National University, Yesan, Republic of Korea
[2]Smart Manufacturing Research Group, Korea Food Korea Food Research Institute,wanju, Republic of Korea

*Corresponding Author-- Voice: +82-10-2005-2899, Email: Hanwoong@kongju.ac.kr

Abstract: A drying and storage facility is designed for the processing and handling of harvested grain. When the harvest period coincides across a large number of farms, drying operations are frequently delayed, and grain subjected to prolonged exposure under high-moisture conditions undergoes quality deterioration. To address this limitation, a previous study proposed a grain dryer operation scheduling method whereby drying simulation results are derived from grain and dryer information, and harvest timing is determined according to dryer operation. The method comprises three stages: an input data acquisition stage, in which grain and dryer information are entered; an execution stage, in which the drying simulation is performed; and a scheduling stage, in which harvest timing is determined from the simulation output. In the present study, a program was developed to establish the operation schedule of a domestic wheat drying and storage facility. The program accepts as input the specifications and operating parameters of a recirculating cross-flow dryer, ambient air conditions, and the regional wheat yield, from which the drying time required to attain the target moisture content and the daily processing capacity are computed, and the drying sequence and schedule are generated. Because drying time is governed by operating parameters such as drying air temperature and airflow rate as well as by ambient temperature and humidity, daily processing capacity varies with the applied settings even for an identical dryer; the schedule is therefore recalculated whenever input conditions are modified. The developed program enables determination of an appropriate drying schedule through comparison of regional wheat yield with the processing capacity of the facility, thereby mitigating losses from drying delays and contributing to enhanced quality of domestic wheat.

Key Words: Domestic wheat, Drying and storage facility, Drying simulation, Operation scheduling, Recirculating cross-flow dryer.

ACKNOWLEDGEMENTS (optional)

This research was funded by the R&D program for Rural Development Administration (RDA), Republic of Korea (Project No. RS-2025-02263107)

PH-P20

Proceedings of The 12th International Symposium on Machinery and Mechatronics for Agriculture and Biosystems Engineering (ISMAB 2026)
20-24 October 2026, Busan, Republic of Korea

DEVELOPMENT OF EMBEDDED DYNAMIC QR SCANNER AND IOT SENSOR NODES FOR AGRICULTURAL PRODUCT TRACEABILITY

Sung-Min Han[1], Hyo-Eun Lee[1], Su-Hyeon Lim[2], Dong-Soo Ryu[3], Seong-Min Kim[1,3*]

[1]Department of Agricultural Engineering, Graduate School, Jeonbuk National University, Jeonju 54896, Republic of Korea
[2]National Institute of Horticultural and Herbal Science, Rural Development Administration, Wanju 55365, Republic of Korea
[3]Research Center for Agricultural Machinery and ICT Convergence, Jeonbuk National University, Jeonju 54896, Republic of Korea
* Corresponding Author -- Voice: +82-63-270-2617, Email: smkim@jbnu.ac.kr

Abstract: Maintaining quality and ensuring traceability throughout the fresh agricultural produce supply chain face severe challenges due to information fragmentation and the high deployment cost of dedicated sensing infrastructure. Conventional static Quick Response (QR) codes cannot reflect dynamic state changes during distribution, while active RFID systems require cost-prohibitive dedicated reader infrastructure. To address these problems, this study designed and implemented a low-cost embedded hardware system comprising a handheld Dynamic QR (DQR) scanner terminal and a Fruit Digital Twin (FDT) IoT sensor node. The handheld DQR scanner integrates a microcontroller, a 2D optical barcode scan engine, a status display, an acoustic indicator, and a rechargeable battery within an ergonomic pistol-grip housing. The embedded firmware implements a non-volatile local FIFO buffering queue utilizing onboard flash memory, ensuring continuity without data loss even during temporary network disconnections in agricultural distribution facilities. The FDT sensor node, mimicking the physical characteristics of commercial apples, incorporates a multi-modal sensing module—including temperature, humidity, 3-axis shock and acceleration, illuminance, and positioning sensors—along with ultra-low-power power control circuitry and a high-capacity battery to continuously monitor distribution microenvironments and dynamic impacts. Performance evaluation results confirmed the rapid decoding responsiveness of the scanner, lossless local caching, and cloud synchronization performance during communication outages, and demonstrated long-term maintenance-free operation through ultra-low-power control of the FDT node. The developed embedded hardware system possesses high practical application value as an economical and highly reliable edge terminal infrastructure capable of collecting field microenvironments and dynamic handling states without data loss even in harsh agricultural distribution environments.

Key Words: Dynamic QR , Hardware Architecture, Fruit Digital Twin, Edge Computing, Agricultural Product Traceability

INTRODUCTION

Fresh agricultural produce continues biological metabolism even after harvest; thus, rapid quality degradation occurs upon exposure to temperature, humidity, vibration, and impact during distribution, resulting in annual postharvest losses of 10% to 30%

(Defraeye et al., 2019; Sun, 2013). Conventional RFID technology designed to prevent this has limitations in dissemination to small- and medium-sized agricultural products processing centers (APCs) due to the high cost of dedicated reader infrastructure, and static QR codes cannot dynamically reflect postharvest sorting and storage history after printing (Alfian et al., 2020).

To overcome these limitations, Dynamic QR (DQR) and Fruit Digital Twin (FDT) technologies linked in real time with cloud databases are drawing attention as alternatives (Grieves and Vickers, 2017; Defraeye et al., 2021; Pylianidis et al., 2021; Verdouw et al., 2021; Cho et al., 2023). However, existing studies are biased toward software algorithms and continuous communication environments, failing to sufficiently reflect the actual demands for dedicated terminals for workers and rural logistics sites where communication blind spots are frequent. Therefore, the objective of this study is to develop low-cost, high-reliability embedded hardware and edge-to-cloud infrastructure for fresh agricultural product traceability, with the specific research objectives as follows

Design and fabrication of a handheld DQR scanner terminal: Development of a dedicated terminal integrating an ESP32-S3 MCU, a 2D CMOS optical barcode engine, a status display OLED, audiovisual feedback devices, and LittleFS-based non-volatile local buffering queue firmware to prevent data loss during communication disconnection into an ergonomic 3D-printed housing (15° inclined pistol grip) for the convenience of operators in agricultural products processing centers (APCs) and logistics sites.

Design and fabrication of a Fruit Digital Twin (FDT) sensor node: Development of a standalone IoT sensor node integrating multi-modal sensors (temperature/humidity, 3-axis shock/acceleration, illuminance for box opening detection, GPS), ultra-low-power circuitry (AP2112 LDO, MOSFET load switch) to maximize battery life, and adaptive Sleep-Wake power control firmware inside a spherical 3D-printed enclosure that mimics the physical dimensions and heat capacity of actual fruit during distribution.

Verification of design and fabrication: Evaluation of optical decoding performance according to distance, angle, and illumination environmental conditions; verification of LittleFS offline caching integrity and cloud atomic synchronization speed under wireless communication disconnection and network recovery environments; and verification of field application reliability through quantitative measurement of current consumption and battery operating lifespan for each system operation mode.

MATERIALS AND METHODS

OVERALL SYSTEM ARCHITECTURE

The end-to-end architecture of the proposed dynamic fresh agricultural produce traceability system consists of four tiers, as illustrated in Fig. 1: 1) Field Device Tier, 2) Edge Measurement Tier, 3) Network Pipeline Tier, and 4) Cloud Database Tier. Among these, this paper focuses on hardware infrastructure implementation and experimental validation, specifically detailing the development of the Field Device Tier and the Edge Measurement Tier. The Field Device Tier comprises individual packaging cartons and high-durability Dynamic QR (DQR) labels (Denso Wave, 2026) affixed to their surfaces, serving as physical and

logical identification reference entities. The Edge Measurement Tier represents the core hardware development focus of this study, consisting of a handheld DQR scanner terminal that reads DQR codes at logistics checkpoints and binds spatiotemporal metadata, and a Fruit Digital Twin (FDT) sensor node deployed inside cartons to measure temperature, humidity, shock, ambient light, and GPS location data in real time.

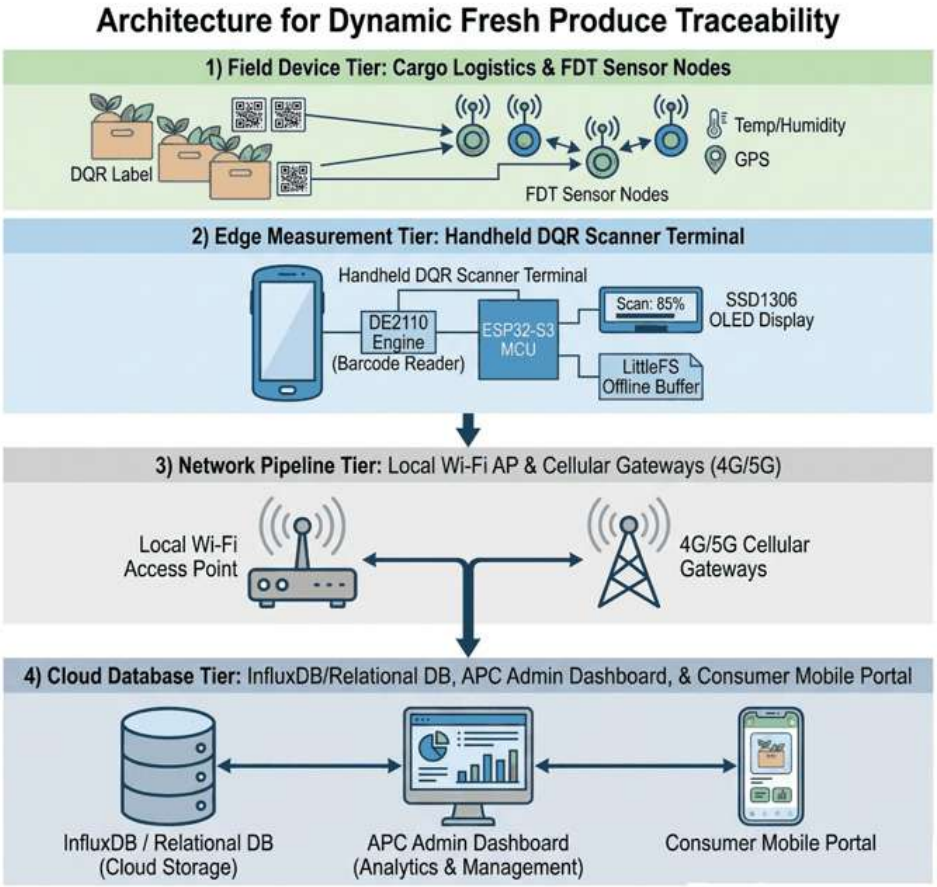

Fig. 1. End-to-end multi-tier hardware, network, and cloud database architecture for dynamic agricultural produce traceability.

HANDHELD DQR SCANNER TERMINAL DESIGN

The handheld DQR scanner terminal is architected around an ESP32-S3-WROOM-1 main microcontroller (240 MHz dual-core, 8 MB Flash), integrated with a GM77 2D CMOS barcode module (640×480 resolution, UART interface), a 0.96-inch SSD1306 OLED display (I2C), a 90 dB active buzzer and dual LEDs (green/red) for status indication, and a pistol-grip microswitch trigger. The power management subsystem incorporates an 18650 Li-ion battery (2,600 mAh), a TP4056 charging and protection circuit, an MT3608 5 V step-up boost converter, and an AMS1117-3.3 LDO regulator, establishing stable 3.3 V and 5.0 V multi-level power buses.

FRUIT DIGITAL TWIN (FDT) SENSOR NODE DESIGN

The Fruit Digital Twin (FDT) sensor node was fabricated on a custom 50 mm × 50 mm carrier PCB, integrating a Beetle ESP32-C6 main microcontroller with an SHT45 temperature /

humidity sensor (accuracy: ±0.1°C, ±1.5% RH), an MPU6050 3-axis accelerometer (±16g range, 2.5g shock interrupt), a BH1750 ambient light sensor (carton breach detection), and an ATGM336H/NEO-6M GPS module. To maximize the operational lifespan of the 5,000 mAh Li-ion battery, an AP2112-3.3 ultra-low quiescent current (1.5 μA) LDO regulator and a MOSFET load-switch power gating circuit were implemented to govern a three-state power state machine: 1) Active Mode (continuous sensing and 2-s interval MQTT transmission), 2) Periodic Sleep-Wake Mode (tickless deep sleep for 58 s followed by 2 s of sensing and transmission within a 60-s cycle), and 3) Eco Mode (MOSFET power gating of sensors/GPS, local buffering of temperature and humidity at 5-min intervals, and batch Wi-Fi transmission every 15 min). In addition, an Anomaly Alert mechanism was implemented using external interrupts to immediately wake the node from sleep and report events upon carton opening (sudden surge in ambient illuminance) or drop impacts exceeding 2.5g.

HARDWARE DESIGN AND FABRICATION VERIFICATION METHODS

Optical Decoding Performance and Success Rate Evaluation Method

The optical scan decoding performance was evaluated under simulated dynamic operating environments of agricultural product distribution centers APC across varying label dimensions (15×15 to 40×40 mm), scanning distances (50 to 400 mm), angles of incidence (0 to 45°), and ambient illumination levels (50 to 10,000 lx). The scan response latency was automatically and precisely measured via firmware using the internal high-resolution hardware timer of the ESP32-S3, calculated as the time elapsed from the external interrupt triggered by the microswitch trigger actuation to the completion of the UART data frame receive interrupt handling upon code decoding by the GM77 engine. Each experimental condition was evaluated with 50 repeated trials to determine the valid decoding success rate (%) and the mean decoding latency (Mean ± SD, ms).

LittleFS Offline Buffering and Network Recovery Synchronization Verification Method

LittleFS (Little File System) is a lightweight, power-fail-resilient file system designed for microcontrollers that safeguards against data corruption during abrupt power loss and optimizes flash wear-leveling. Under nominal Wi-Fi connectivity, the scanner directly transmits scan events to the cloud server via REST HTTP POST requests; upon network disconnections, it sequentially buffers transaction records within a dedicated 4 MB LittleFS partition on the ESP32-S3. For validation, the local flash write latency (ms/record) was evaluated across 200 consecutive scan events without data loss while Wi-Fi was blocked. Furthermore, upon network restoration, the reconnection detection latency and synchronization throughput (records/s) were measured as the terminal identified connectivity and executed atomic batch commits to the server database in groups of 10 records.

Power Consumption and Battery Endurance Verification Method

The operational lifespans of the handheld DQR scanner terminal (ESP32-S3, 2,600 mAh battery) and the FDT sensor node (ESP32-C6, 5,000 mAh battery) were evaluated through power consumption modeling based on the electrical ratings from component datasheets and duty cycle proportions across operational modes. The scanner was evaluated under Standby Mode, Continuous Scanning Mode, and Typical Scanning Mode (10 scans per minute). The

FDT node was evaluated under Active Monitoring Mode (2-s interval MQTT transmission), Periodic Sleep-Wake Mode (58-s deep sleep and 2-s active operation within a 60-s cycle), and Ultra-Low-Power Eco Mode (MOSFET power-gated 5-min sleep and 15-min batch transmission). The weighted average current consumption (mA) and power dissipation (mW) were computed from the operating current draw and duty cycles of active components, and the continuous operational endurance in hours (h) and days (days) was projected relative to nominal battery capacities.

RESULTS AND DISCUSSION

HANDHELD DQR SCANNER TERMINAL FABRICATION RESULTS

The electrical circuit block configuration and hardware interconnection netlist of the handheld DQR scanner terminal were constructed as shown in Fig. 2, integrating the ESP32-S3 microcontroller, GM77 2D barcode engine, SSD1306 OLED display, buzzer, and multi-rail power management subsystem. Based on this electrical schematic architecture, the mechanical design and physical prototype assembly were successfully completed (Fig. 3). The housing enclosure was designed using OpenSCAD with an ergonomic pistol-grip structure featuring a 15° forward inclination angle, and was fabricated via FDM 3D printing using industrial-grade PETG filament (0.2 mm layer height, 35% infill). By applying an ergonomic lightweight design, wrist fatigue of operators during prolonged handheld field tasks was minimized. Physical durability was ensured by incorporating a microswitch trigger rated for 100,000 cycles and an acrylic protective lens window. Furthermore, visual and auditory feedback provided by the rear 0.96-inch SSD1306 OLED display, a 90 dB buzzer, and dual LEDs enables operators to intuitively verify decoding results even in noisy or dimly lit environments within agricultural processing centers.

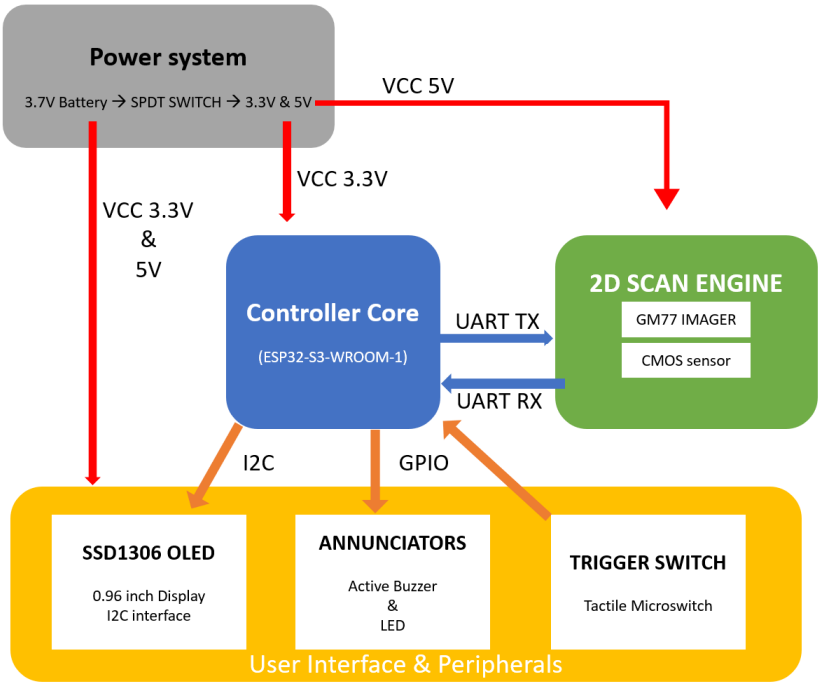

Fig. 2. Schematic block diagram and electrical netlist interconnections of the handheld DQR scanner terminal.

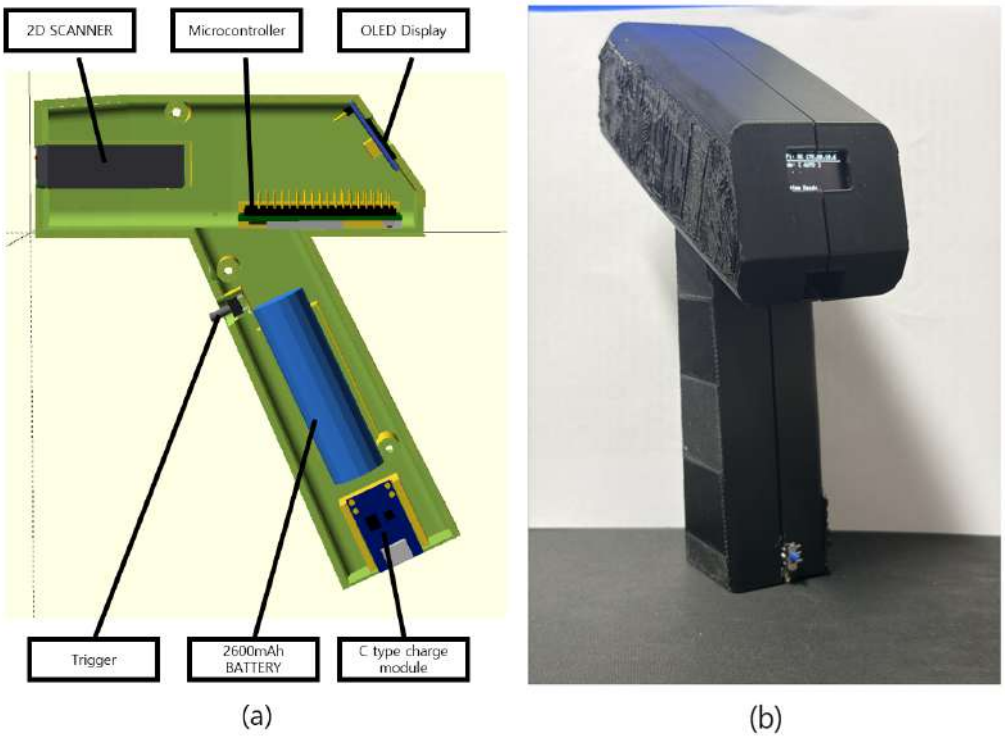

Fig. 3. Mechanical design and physical prototype of the handheld DQR scanner terminal: (a) 3D CAD model illustrating the upper enclosure assembly and optical scan engine aperture, and (b) fabricated physical prototype showcasing the rear OLED display and ergonomic pistol grip.

FRUIT DIGITAL TWIN (FDT) SENSOR NODE FABRICATION RESULTS

The schematic circuit block diagram and electrical netlist interconnections of the FDT sensor node were designed as depicted in Fig. 4, establishing hardware interface circuitry between the ESP32-C6 microcontroller, SHT45 temperature/humidity sensor, MPU6050 3-axis accelerometer, BH1750 ambient light sensor, and GPS module on a custom 50 mm × 50 mm double-sided carrier PCB. Based on this circuit infrastructure, a biomimetic enclosure-integrated prototype mimicking the physical form factor of commercial produce (apples) was designed and fabricated (Fig. 5). The primary hardware-integrated prototype was successfully fabricated, and node refinement is currently underway for field deployment validation. In the prototype stage, normal communication addressing and electrical interface operations of the SHT45 (0x44), MPU6050 (0x68), and BH1750 (0x23) sensors were confirmed via I2C bus scanner utility verification.

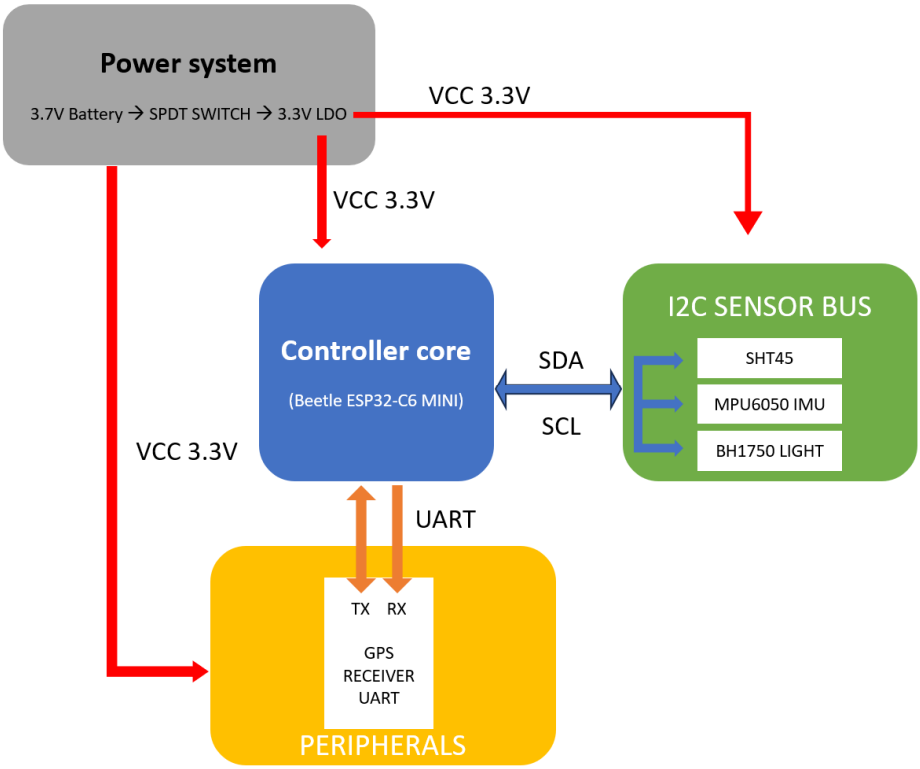

Fig. 4. Schematic circuit block diagram and electrical netlist interconnections of the Fruit Digital Twin (FDT) sensor node.

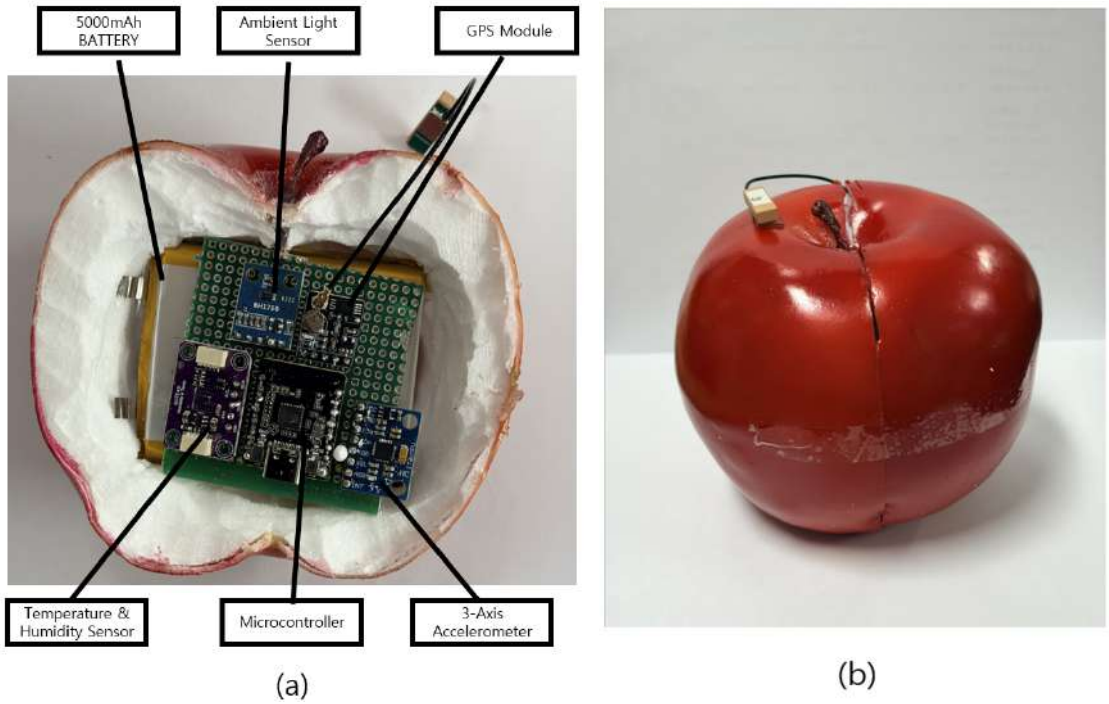

Fig. 5. Physical prototype and 3D cross-sectional assembly of the biomimetic Fruit Digital Twin (FDT) sensor node: (a) 3D cross-sectional mechanical design model showing the spatial arrangement of the internal double-layer carrier PCB, multi-modal sensor suite, and rechargeable Li-ion battery inside the biomimetic apple (FDT), and (b) fabricated physical prototype of the biomimetic apple (FDT) casing equipped with an external patch antenna module.

Furthermore, the MPU6050 accelerometer embedded in the FDT sensor node established a foundation for precisely monitoring physical shocks and vibrations exerted on fruits during transit based on 3-axis dynamic acceleration and impact signals.

HARDWARE VERIFICATION AND OPERATIONAL RELIABILITY

Optical Decoding Speed and Success Rate Evaluation

The decoding performance of the GM77 2D CMOS optical barcode engine embedded in the developed handheld DQR scanner terminal was quantitatively evaluated under various physical parameter conditions (scanning distance, angle of incidence, and ambient illumination) simulating actual agricultural logistics environments (Table 1).

Table 1. Quantitative evaluation of DQR decoding speed and success rate under operational variants.

Operational Scenario	Parameter Condition	Trials	Success Rate (%)	Mean Decoding Latency (ms)
Label Physical Size	15 mm × 15 mm	50	94.0	168 ± 16
Label Physical Size	20 mm × 20 mm	50	98.0	131 ± 13
Label Physical Size	30 mm × 30 mm (Optimal)	50	100.0	115 ± 8
Label Physical Size	40 mm × 40 mm	50	100.0	107 ± 6
Scanning Distance	50 mm	50	100.0	142 ± 12
Scanning Distance	200 mm (Optimal)	50	100.0	118 ± 8
Scanning Distance	400 mm	50	98.0	186 ± 18
Scanning Angle (Tilt)	0° (Normal)	50	100.0	118 ± 8
Scanning Angle (Tilt)	30° Off-axis	50	100.0	134 ± 14
Scanning Angle (Tilt)	45° Off-axis	50	96.0	212 ± 24
Ambient Illumination	50 lx (Dim Storage)	50	100.0	126 ± 10
Ambient Illumination	580 lx (Indoor Office)	50	100.0	118 ± 8
Ambient Illumination	10,000 lx (Outdoor Sunlight)	50	94.0	238 ± 32

As summarized in Table 1, the scanner terminal achieved a rapid mean decoding latency of 118 ± 8 ms and a 100% decoding success rate under standard logistics conditions (30 × 30 mm label, 200 mm distance, and 580 lx indoor illumination). Moreover, it consistently maintained a high recognition success rate above 94.0% and a stable response time below

238 ms across a broad range of dynamic operational parameters, including label dimensions (15 to 40 mm), scanning distances (50 to 400 mm), angles of incidence (0 to 45°), and illumination environments (50 to 10,000 lx), thereby demonstrating its suitability for deployment in agricultural product distribution facilities.

LittleFS Offline Buffering and Network Recovery Synchronization Verification

In the Wi-Fi disconnection test, all 200 consecutive scan records were successfully buffered to LittleFS without a single data omission (mean write latency: 14.2 ms/record). Upon network restoration, the terminal detected connectivity within 1.8 s and completed full database synchronization in 4.62 s (throughput: 43.3 records/s).

Power Consumption and Battery Endurance Verification

The current consumption, power dissipation, and projected battery endurance of the handheld DQR scanner terminal and the FDT sensor node across operational modes were calculated based on the specifications of major components and the operational duty cycle ratios (Table 2).

Table 2. Electrical current draw and estimated battery endurance across operational modes.

Operational Mode	Active Subsystems	Voltage (V)	Current (mA)	Power (mW)	Battery (mAh)	Estimated Endurance
Scanner Standby	ESP32-S3 (Wi-Fi), OLED ON	3.7	48.5	179.5	2,600	53.6 h
Scanner Continuous Scan	ESP32-S3, GM77 Imager, OLED	3.7	218.0	806.6	2,600	11.9 h
Scanner Field Operation	10 scans/min (Intermittent)	3.7	82.4	304.9	2,600	31.6 h
FDT Active Mode	ESP32-C6, All Sensors, MQTT (2 s)	3.7	94.2	348.5	5,000	53.1 h
FDT Sleep-Wake Mode	60 s Cycle (58 s Sleep, 2 s Active)	3.7	12.8 (Avg)	47.4	5,000	390.6 h (16.2 days)
FDT Eco Mode	5 min Sleep, 15 min Wi-Fi Batch	3.7	1.94 (Avg)	7.18	5,000	2,577.3 h (107.4 days)

The handheld DQR scanner terminal was evaluated across Standby, Continuous Scanning, and Typical Scanning modes according to field working conditions. In Standby Mode, the barcode engine is powered down while maintaining Wi-Fi connectivity and the OLED display, drawing 48.5 mA and providing an operational standby of up to 53.6 hours. Conversely, Continuous Scanning Mode, where the barcode engine and illumination LEDs remain perpetually enabled, exhibited the highest consumption of 218.0 mA, lasting 11.9 hours. Typical Scanning Mode, simulating practical packing center operations with intermittent scanning at 10 scans per minute, yielded an average current draw of 82.4 mA by combining instantaneous scanning current with standby current. Consequently, the scanner equipped

with a 2,600 mAh battery operates for approximately 31.6 hours without recharging, confirming reliable field deployment for approximately four consecutive 8-hour work shifts.

The FDT sensor node was engineered to optimize power consumption in accordance with produce distribution duration and monitoring objectives. Active Mode, which keeps the microcontroller and all sensors continuously powered while transmitting data every 2 s, draws 94.2 mA and operates for approximately 53.1 hours. Periodic Sleep-Wake Mode, intended for typical distribution transit, maintains ultra-low-power deep sleep for 58 s out of every 60 s and wakes for only 2 s to perform sensing and transmission; this drastically reduces the average current draw to 12.8 mA, achieving an endurance of 16.2 days. Furthermore, Ultra-Low-Power Eco Mode for long-distance transport completely gates power to auxiliary sensors via MOSFET switches, records temperature and humidity locally at 5-minute intervals, and performs batch Wi-Fi transmission every 15 minutes, minimizing the average current draw to 1.94 mA. This demonstrates that continuous monitoring for up to 107.4 days (approximately 3.5 months) is achievable with a 5,000 mAh battery, confirming its practical viability across the entire fresh produce supply chain lifecycle.

CONCLUSIONS

In this study, an embedded hardware and edge-to-cloud infrastructure was successfully designed, fabricated, and experimentally verified for dynamic traceability and ambient distribution monitoring across fresh agricultural produce supply chains. The primary achievements and contributions of this study are summarized as follows:

First, the handheld DQR scanner terminal was implemented by integrating an ESP32-S3 microcontroller, a 2D CMOS barcode engine, an OLED display, and a 2,600 mAh battery within an ergonomic 15° forward-tilt pistol-grip housing. In addition, LittleFS-based non-volatile local FIFO caching firmware was embedded to guarantee 100% data continuity during network outages.

Second, the Fruit Digital Twin (FDT) sensor node was engineered within a spherical enclosure biomimicking the form factor of commercial apples, integrating temperature/humidity, 3-axis acceleration/shock, ambient light, and GPS sensors along with a 5,000 mAh battery, coupled with adaptive sleep-wake and eco-mode firmware driven by ultra-low-power management circuitry.

Finally, comprehensive hardware verification and field viability assessments demonstrated an optical decoding latency of 118 ± 8 ms with a 94.0% to 100% success rate, lossless caching of 200 scan events during network disconnections, and high-speed database synchronization within 4.62 s (throughput: 43.3 records/s). Furthermore, battery endurance modeling projected continuous operations of 31.6 hours (~4 consecutive shifts) for the scanner terminal, 16.2 days for the FDT node in periodic sleep-wake mode, and 107.4 days in ultra-low-power eco mode, validating its practical feasibility across the entire cold chain lifecycle.

The proposed embedded hardware system overcomes the economic and functional constraints of conventional expensive active RFID infrastructures and static barcode systems. By synergistically combining low-cost commercial off-the-shelf (COTS) components, 3D-printed biomimetic enclosures, and non-volatile local caching firmware, this study

establishes an edge data acquisition architecture optimized for agricultural distribution facilities. In particular, it substantially enhances the reliability of fresh produce traceability by guaranteeing lossless data continuity even in wireless blind zones frequently encountered in cold storage warehouses and packing centers.

Future research will focus on finalizing the component assembly of the FDT carrier PCB prototype and conducting comprehensive field trials along actual refrigerated freight vehicles and Agricultural Product Processing Center (APC) logistics routes. By coupling environmental temperature, humidity, and vibration telemetry collected during long-term transit with produce quality prediction and respiration metabolic kinetics models, the system will be further evolved into a next-generation smart agri-food cold chain monitoring platform featuring seamless synchronization between physical hardware and cloud digital twins.

ACKNOWLEDGEMENTS

This work was supported by the Research Program for Agricultural Science & Technology Development (Project No. RS-2022-RD010347), National Institute of Horticultural and Herbal Science, Rural Development Administration, Republic of Korea, and the "Contract Quota Support Program" of the Korea Industrial Technology Association (KOITA) funded by the Ministry of Science and ICT (MSIT).

REFERENCES

Alfian G., M. Syafrudin, U. Farooq, M. Ma'arif, M. Syaekhoni, N. Fitriyani, J. Lee, and J. Rhee. 2020. Improving the efficiency of an RFID-based traceability system for perishable food by utilizing IoT sensors and a machine learning model. Food Control 110: 107016.

Cho J., C. Kim, K. J. Lim, J. Kim, B. Ji, and J. Yeon. 2023. Web-based agricultural infrastructure digital twin system integrated with GIS and BIM concepts. Computers and Electronics in Agriculture 215: 108441.

Defraeye T., G. Tagliavini, W. Wu, K. Prawiranto, S. Schudel, M. A. Kerisima, P. Verboven, and A. Bühlmann. 2019. Digital twins probe into food cooling and biochemical quality changes for reducing losses in refrigerated supply chains. Resources, Conservation and Recycling 149: 778–794.

Defraeye T., C. Shrivastava, T. Berry, W. Wu, D. Onwude, S. Schudel, and P. Verboven. 2021. Digital twins are coming: Will we need them in supply chains of fresh horticultural produce? Trends in Food Science & Technology 109: 245–258.

Denso Wave. 2026. QR Code Technology and Specifications. Available at: www.denso-wave.com.

Grieves M., and J. Vickers. 2017. Digital Twin: Mitigating Unpredictable, Undesirable Emergent Behavior in Complex Systems. In Transdisciplinary Perspectives on System Complexity, 85–113. Springer.

Pylianidis C., S. Osinga, and I. N. Athanasiadis. 2021. Introducing digital twins to agriculture. Computers and Electronics in Agriculture 184: 105942.

Sun G. 2013. Research on the Fresh Agricultural Product Supply Chain Coordination with Supply Disruptions. Discrete Dynamics in Nature and Society 2013: 416790.

Verdouw C., B. Tekinerdogan, A. Beulens, and S. Wolfert. 2021. Digital twins in smart farming. Agricultural Systems 189: 103046.

PH-P21

Proceedings of The 12th International Symposium on Machinery and Mechatronics for Agriculture and Biosystems Engineering (ISMAB 2026)
20-24 October 2026, Busan, Republic of Korea

EFFECTS OF POST-HARVEST DRYING DELAY ON QUALITY CHANGES IN DOMESTIC WHEAT

Soo-In Kim[1], Dong-Gwan Shin[2], Hoon Kim[2] , Jae-Woong Han[1*]

[1]Department of SmartFarm Engineering, Kongju National University, Yesan, Republic of Korea
[2]Smart Manufacturing Research Group, Korea Food Research Institute, wanju, Republic of Korea
*Corresponding Author-- Voice: +82 10-2005-5899 Email: hanwoong@kongju.ac.kr

Abstract: Domestic wheat cultivation area and production have increased with the expansion of the double-cropping system; however, climate-related shifts in harvest timing cause the sowing period of the succeeding crop to overlap with wheat harvest, leading to concentrated grain intake and consequent drying delays due to limited processing capacity at drying and storage facilities. During such delays, wheat retained in ton bags with residual field heat and high moisture undergoes rapid respiration and microbial activity, elevating internal temperature and humidity and thereby inducing quality deterioration, including reduced germination rate and increased fatty acid value. Accordingly, this study aims to analyze the effects of drying delay under varying drying-facility operating conditions on wheat quality and to establish a field-applicable allowable limit for drying delay duration. Using the cultivar Kumgang, 1,000 kg of wheat was stored for 10 days in June 2026 at the experimental laboratory of Kongju National University, with samples periodically collected to monitor internal temperature and humidity and to analyze changes in moisture content, germination rate, and fatty acid value of the raw grain. Internal temperature and humidity increased continuously during the delay period, with the bag center exhibiting higher temperatures than the periphery due to restricted heat dissipation, whereas moisture content remained largely unchanged owing to the sealed condition of the ton bag. Germination rate declined progressively with increasing delay duration, falling below the 95% standard early in the delay period, while fatty acid value increased continuously, eventually exceeding the 20 mg KOH/100 g threshold, and the allowable drying delay period was determined based on the duration over which both criteria remained within standard. These findings empirically characterize the pattern of quality deterioration in domestic wheat resulting from post-harvest drying delay and are expected to inform the establishment of harvest and drying schedules aligned with regional drying-facility capacity.

Key Words: Domestic wheat, Drying delay, Safe storage period, Germination rate, Fatty acid value

ACKNOWLEDGEMENTS

This research was funded by the R&D program for Rural Development Administration (RDA), Republic of Korea (Project No. RS-2025-02263107)

PH-P22

Proceedings of The 12th International Symposium on Machinery and Mechatronics for Agriculture and Biosystems Engineering (ISMAB 2026)
20-24 October 2026, Busan, Republic of Korea

DEEP LEARNING-BASED JUICE EXTRACTION RATE PREDICTION AND SPEED OPTIMIZATION FOR A TWIN-SCREW JUICER USING SENSOR TIME-SERIES DATA

Jae-Min Jung[1], Dong-Hyeon Kim[2*], Tae-Hyeon Kim[2], and Wang-Hee Lee[1,2*]

[1]Department of Smart Agriculture Systems Machinery Engineering, Chungnam National University, Daejeon 34134, Korea
[2]Department of Smart Agriculture Systems, Chungnam National University, Daejeon 34134, Republic of Korea
*Corresponding Author-- Voice: +82-42-821-6720, Email: wanghee@cnu.ac.kr

Abstract: Conventional juicers operate at fixed mechanical settings, limiting their ability to accommodate changes in extraction conditions. This study developed a deep learning framework to predict juice extraction rates and support real-time recommendations for the operating speeds of a twin-screw juicer. Weight sensor time-series data were collected for carrot, pear, orange, and apple under 48 combinations of extraction and input speeds. A five-stage preprocessing procedure addressed sensor noise, material replenishment, and extraction completion, yielding 113 continuous segments from 32,706 observations. These segments were combined using synthetic transitions derived from measured machine startup profiles to generate over 2.1 million observations. A long short-term memory (LSTM) model with a material embedding layer used 20-second input sequences to predict extraction rates over the subsequent 5 seconds. Under fixed-speed conditions, the coefficients of determination (R^2) were 0.958, 0.986, 0.965, and 0.993 for carrot, pear, orange, and apple, respectively. The corresponding values under synthetic speed-transition conditions were 0.951, 0.967, 0.987, and 0.994. Mean residuals were close to zero, although mild underprediction at higher extraction rates was observed for carrot and pear. These results indicate the potential of the framework to support dynamic speed optimization. Validation using experimentally measured speed transitions is required to assess its performance under actual changes in operating speed.

Key Words: Twin-screw juicer, Long short-term memory, Time-series prediction, Data augmentation, Speed optimization.

INTRODUCTION

The growing demand for health-conscious food products has increased interest in fresh juice as a means of nutrient delivery (Agarwal et al., 2019; Benton and Young, 2019). Variations in raw material characteristics require adaptable juice extraction conditions, but conventional twin-screw juicers operate at fixed speeds, limiting real-time process optimization. Electronic nose and tongue systems have been investigated for juice quality assessment (Lee et al., 2019; Osmólska et al., 2023), while optimal extraction speeds for pear and carrot have been examined to improve juicer performance (Kim et al., 2025). These applications address

product quality and operating conditions, respectively; however, translating continuous sensor feedback into dynamic speed recommendations remains a challenge.

Real-time sensing provides immediate information on process conditions and supports smart manufacturing applications such as fault detection, condition monitoring, and yield estimation (Amna et al., 2023; Yu et al., 2025). In juice extraction, continuous weight measurements can capture changes in juice output and provide a basis for predicting extraction rates. Deep learning, particularly recurrent architectures designed to capture temporal dependencies, has shown promise in agricultural process modeling (Han et al., 2023). Applying these approaches to juicer operation requires preprocessing to address sensor noise and material replenishment, together with training data that represent speed transitions. A model capable of predicting extraction responses under these conditions could support adaptive operating decisions.

This study aimed to develop a predictive framework to support real-time recommendations for the operating speeds of a twin-screw juicer. The specific objectives were to develop preprocessing and data augmentation procedures informed by the extraction process, train an LSTM model with a material embedding layer to predict juice extraction rates under fixed-speed and synthetic speed-transition conditions, and evaluate predictive performance for carrot, pear, orange, and apple.

MATERIALS AND METHODS

Physics-Informed Preprocessing

A five-step preprocessing pipeline was applied sequentially to each batch:

1. Negative weight and juice measurements attributed to sensor noise were set to zero.
2. Measurements recorded before the first nonzero juice measurement were excluded from the analysis.
3. For carrot and pear, material replenishment during extraction was identified by a rate of increase in weight exceeding 2.0 kg/s. These events and the 10 observations immediately preceding and following each event were marked for exclusion.
4. Abrupt increases in the juice extraction rate exceeding 1.0 kg/s immediately after a zero reading were identified as sensor errors.
5. Extraction completion was identified when both the rolling standard deviation of the juice extraction rate, calculated over 10 consecutive observations, fell below 0.003 kg/s and the measured weight was below 2.0 kg. These criteria were applied only to the second half of each batch.

Following preprocessing, 27,504 observations (84.1% of the original dataset) were retained across the four materials.

Identification of Continuous Segments

Material replenishment during carrot and pear extraction introduced discontinuities into the time series. Sliding windows spanning these discontinuities could produce artificial spikes in the calculated juice extraction rate. Each batch was therefore divided into continuous segments at replenishment events, and the 10 observations immediately before and after each event were excluded. Segments containing fewer than 30 observations were discarded. This procedure yielded 113 segments: 20 for carrot, 75 for pear, 9 for orange, and 9 for apple.

Data Augmentation

The original dataset contained measurements collected only under fixed-speed conditions. To represent responses to changes in operating speed, synthetic sequences were generated using an augmentation procedure informed by measured machine startup profiles. Each sequence combined three segments obtained under different speed conditions, with two synthetic transition intervals of 25 time-steps each. The juice extraction rate within each transition interval was calculated as follows:

$$q(t) = q_a + (q_\beta - q_a)s(t) \qquad (1)$$

where $q(t)$ is the synthetic juice extraction rate at time step t; q_a is the mean extraction rate over the final 10 observations of the preceding segment; q_β is the stable extraction rate at the target speed; and $s(t)$ is the normalized cumulative startup profile for that speed.

This procedure approximated the gradual response of the machine during a speed transition. A total of 2,652 unique sequences were generated, comprising 2,122 training sequences and 530 test sequences and approximately 2.1 million observations. Training and test sequences were assigned during data generation, and the designated test sequences were excluded from model training.

Feature Engineering and Model Architecture

All scaling parameters were estimated from the entire preprocessed dataset before it was divided into training, validation, and test sets. Consequently, information about the distributions of the validation and test data was incorporated into preprocessing. This constitutes a potential source of bias in the performance estimates, and its magnitude has not been quantified.

The model represented the four materials using an eight-dimensional embedding and included two stacked LSTM layers with 128 and 64 units. A dropout layer with a rate of 0.3 followed each LSTM layer. The subsequent fully connected layer contained 32 units with rectified linear unit activation, and a five-unit output layer with sigmoid activation predicted normalized juice extraction rates over the next 5 seconds. The model was trained using mean squared error loss and the Adam optimizer with an initial learning rate of 1×10^{-3} and a batch size of 256. Training was stopped after seven consecutive epochs without improvement in validation loss. The learning rate was reduced by half after four consecutive epochs without improvement.

Dataset Split and Evaluation

The data were organized into training, validation, and two test sets (Table 1). Original segments were partitioned at the batch level, whereas augmented sequences were assigned to the training set or Test B during generation. Augmented training and test sequences were generated from a shared pool of 113 original segments and startup profiles. Thus, Test B evaluated predictive performance on newly assembled speed-transition sequences constructed from shared source data, rather than on independent segments or previously unobserved startup dynamics.

Table 1. Composition of the training, validation, and test datasets.

Set	Windows	Windows
Train	77 original segments + 2,122 augmented sequences	1,657,885
Validation	18 original segments (unseen batches)	3,690
Test A	18 original segments (fixed-speed, unseen)	2,632
Test B	530 augmented sequences (speed-transition, unseen)	403,044

Sliding windows comprised 20 input time steps and five prediction time steps, with a stride of one-time step. Windows were generated separately within each segment to avoid spanning segment boundaries. Predictive performance was evaluated using the coefficient of determination (R^2), root mean square error (RMSE), and mean absolute error (MAE).

RESULTS & DISCUSSION

Model Training

The lowest validation losses were obtained between epochs 47 and 50. Training and validation losses followed similar trajectories from approximately epoch 15 onward, with little divergence. These patterns suggest limited overfitting with the selected dropout rate of 0.3 and early stopping criterion.

Fixed-Speed Evaluation (Test A)

The model achieved R^2 values above 0.95 for all four materials in fixed-speed batches excluded from training (Table 2, Figure 1). Apple had the highest R^2 (0.993), followed by pear (0.986), orange (0.965), and carrot (0.958). For apple, the model predicted extraction rates close to zero after 150 time steps, capturing the decline in juice output near the end of extraction.

Table 2. Predictive performance for Test A using fixed-speed batches excluded from training.

Material	Test Batch (ES, IS)	R^2	RMSE (kg/s)	MAE (kg/s)
Carrot (C)	Batch 5 (7, 3)	0.958	0.0021	0.0016
Pear (P)	Batches 8, 17, 24, 25	0.986	0.0068	0.0051
Orange (O)	Batch 7 (2, 8)	0.965	0.0058	0.0037
Apple (A)	Batch 4 (25)	0.993	0.0048	0.0038

Speed-Transition Evaluation (Test B)

Under synthetic speed-transition conditions, R^2 values were 0.951, 0.967, 0.987, and 0.994 for carrot, pear, orange, and apple, respectively. Values for orange and apple exceeded those obtained under fixed-speed conditions (Table 3, Figure 1). Predictions followed changes in extraction rate within the synthetic transition intervals. However, these intervals were

generated from startup profiles associated with the target speeds, and similar response patterns may have been represented in the training data. Test B therefore assesses performance on held-out synthetic sequences and does not establish predictive accuracy for experimentally observed speed transitions.

Table 3. Predictive performance for Test B using synthetic speed-transition sequences excluded from training.

Material	Number of sequences	R^2	RMSE (kg/s)	MAE (kg/s)
Carrot (C)	100	0.951	0.0028	0.0020
Pear (P)	200	0.967	0.0087	0.0057
Orange (O)	115	0.987	0.0059	0.0035
Apple (A)	115	0.994	0.0055	0.0040

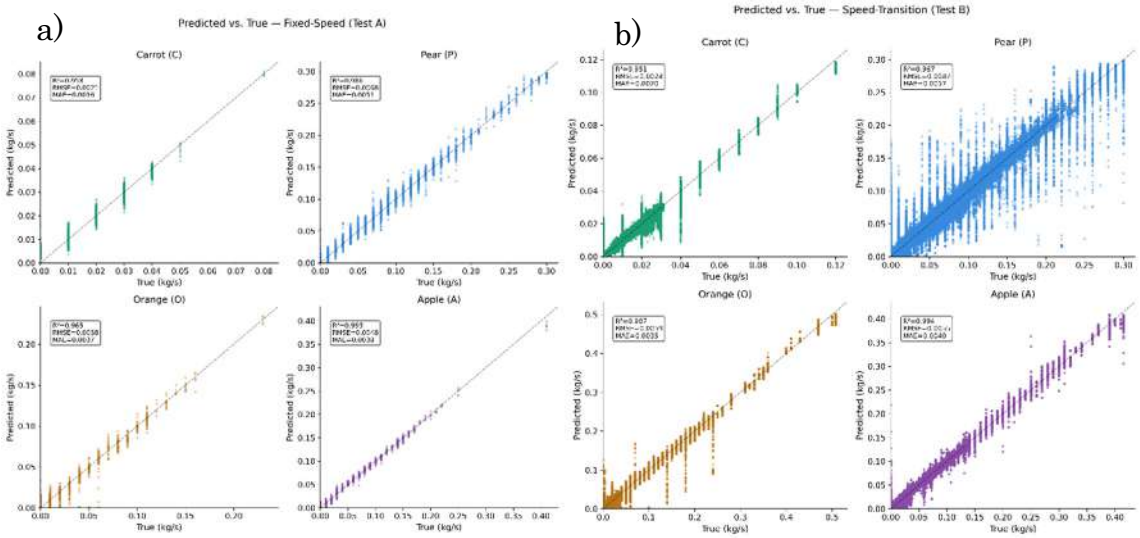

Fig. 1. Predicted versus reference juice extraction rates (kg/s) for (a) Test A, comprising fixed-speed batches excluded from training, and (b) Test B, comprising synthetic speed-transition sequences excluded from training. Results are shown for the four materials. The dashed line denotes the 1:1 relationship.

Residual Analysis

Breusch–Pagan tests indicated heteroscedasticity for all four materials, with greater residual variability at higher extraction rates. Mean residuals were close to zero in all groups, with an overall mean of −0.000153. Nevertheless, statistically significant relationships between residuals and predicted values were observed for pear and carrot, indicating mild underprediction at higher extraction rates. These results suggest that errors depend on the operating conditions, despite the small overall mean residual, and warrant further assessment before practical application.

CONCLUSIONS

This study developed a deep learning framework for predicting juice extraction rates in a twin-screw juicer. Preprocessing addressed sensor noise, material replenishment, and

extraction completion, while data augmentation combined continuous segments with synthetic speed transitions derived from measured startup profiles. An LSTM model with a material embedding layer achieved R^2 values above 0.95 for all four materials under both fixed-speed and synthetic speed-transition conditions. These findings support further investigation of the framework for real-time operating speed recommendations. Future work should evaluate experimentally measured speed transitions, extend the prediction horizon beyond 5 seconds, and examine models tailored to materials with limited training data.

ACKNOWLEDGEMENTS

This work was carried out with the support of "Cooperative Research Program for Agriculture Science and Technology Development (Project No. RS-2022-RD010012)" Rural Development Administration, Republic of Korea.

REFERENCES

Agarwal, S., V. L. Fulgoni III, and D. Welland. 2019. Intake of 100% fruit juice is associated with improved diet quality of adults: NHANES 2013–2016 analysis. Nutrients 11(10): 2513.

Amna, M. W., M. W. Akram, G. Q. Li, M. Z. Akram, M. Faheem, M. M. Omar, and M. G. Hassan. 2023. Machine vision-based automatic fruit quality detection and grading. Frontiers of Agricultural Science and Engineering 12(2): 274–287.

Benton, D., and H. A. Young. 2019. Role of fruit juice in achieving the 5-a-day recommendation for fruit and vegetable intake. Nutrition Reviews 77(11): 829–843.

Han, S. H., H. Mutahira, and H. S. Jang. 2023. Prediction of sensor data in a greenhouse for cultivation of paprika plants using a stacking ensemble for smart farms. Applied Sciences 13(18): 10464.

Kim, T. H., J. M. Jung, and W. H. Lee. 2025. Development and optimization of a real-time monitoring system of small-scale multi-purpose juice extractor. Foods 14(2): 227.

Lee, S. M., H. J. Park, H. S. Kim, J. Y. Kim, S. H. Lee, J. S. Jang, and M. H. Lee. 2019. Quality characterization by various juice extraction method and changes in physiological activities by in vitro digestion of Angelica keiskei, Brassica oleracea, and Oenanthe javanica vegetable juices. Journal of the Korean Society of Food Science and Nutrition 48(7): 718-727

Osmólska, E., M. Stoma, and A. Starek-Wójcicka. 2023. Juice quality evaluation with multisensor systems — a review. Sensors 23(10): 4824.

Yu, K., M. Zhong, W. Zhu, A. Rashid, R. Han, M. S. Virk, and X. Ren. 2025. Advances in computer vision and spectroscopy techniques for non-destructive quality assessment of citrus fruits: A comprehensive review. Foods 14(3): 386.

Precision Agriculture Machinery and Systems



PA-P01

Proceedings of The 12th International Symposium on Machinery and Mechatronics for Agriculture and Biosystems Engineering (ISMAB 2026)
20-24 October 2026, Busan, Republic of Korea

A STEREO VISION AND 3D POINT CLOUD-BASED BREEDING ASSISTIVE SYSTEM FOR SWEET POTATO SHOOT PHENOTYPING

Ting-Han Lin[1*], Shang-Yu Hsieh[1], Chin-Ying Yang[2], Shu-Yun Chen[2], Chung-Feng Kao[2], Po-Hsien Lu[3], Tsai-Wen Yang[4], Yao-Chuan Tsai[1]

[1]Dept. of Bio-Industrial Mechatronics Engineering, National Chung Hsing University, Taichung, Taiwan
[2]Dept. of Agronomy, National Chung Hsing University, Taichung, Taiwan
[3]Chiayi Agricultural Experiment Branch, Agricultural Research Institute, Taiwan
[4]Taoyuan District Agricultural Research and Extension Station, Ministry of Agriculture, Taiwan
*Corresponding Author-- Email: hanklin0306@gmail.com

Abstract: Sweet potato (*Ipomoea batatas*) breeding typically takes eight to over ten years, during which trait measurement and line screening require substantial labor and time. The Chiayi Agricultural Experiment Station of the Taiwan Agricultural Research Institute preserves the largest sweet potato germplasm repository in Taiwan, housing over 1,400 accessions. Conventional breeding relies heavily on manual assessment of aboveground phenotypic traits, such as plant height, fractional green canopy cover, and leaf dimensions. However, these manual evaluations are susceptible to subjective bias and measurement errors, undermining assessment consistency and efficiency. Moreover, under extreme rainfall caused by climate change, sweet potatoes under waterlogging stress readily exhibit physiological symptoms such as leaf chlorosis and reduced leaf area. Consequently, the accurate quantification of shoot morphology and growth status has become a critical assistive technology for evaluating stress-tolerant cultivars. In this study, an automated quantitative phenotyping system for sweet potato shoots was developed by integrating a mobile platform, stereo vision, and deep learning. On the hardware side, a mobile cart equipped with an isolated light-shielding enclosure and a depth camera was constructed, effectively mitigating variations in ambient field lighting. A pinhole camera back-projection model was employed to reconstruct 3D point clouds of individual sweet potato plants. Furthermore, a YOLO11s-seg instance segmentation model was integrated to delineate individual leaf boundaries, enabling the automated extraction of morphological traits including plant height, green canopy coverage, and individual leaf geometric dimensions. Experimental results demonstrated that the 3D point cloud reconstruction required only 5 seconds of computation time, and the YOLO11s-seg model achieved a mean average precision (mAP50) of 0.87 for leaf segmentation. The system accurately captured leaf structural characteristics and visualized differences in plant growth under varying stress conditions. Demonstrating strong potential for digital, standardized, and automated evaluation, this system—with further expansion of training datasets and algorithmic pipelines—serves as a reliable tool for sweet potato shoot phenotyping and stress-tolerance breeding.

Key Words: Sweet potato, High-throughput phenotyping, 3D point cloud, Instance segmentation, Waterlogging stress.

INTRODUCTION

With global warming leading to increasingly frequent extreme weather events—such as droughts, torrential rainfall, and extreme temperature fluctuations-cultivation and manage ment face immense challenges. In response to these climatic pressures, breeding novel and resilient crop varieties has become an urgent priority. Sweet potato (*Ipomoea batatas*) is one of Taiwan's essential coarse grain crops, with a total annual yield reaching 198,500 metric tons in 2023. Although Yunlin County represents the largest cultivation area in Taiwan, increasing extreme precipitation has led to a gradual decline in sweet potato yields. Consequently, breeders are actively working to develop flood-tolerant varieties.

However, conventional breeding workflows are labor-intensive and time-consuming, typically spanning over 8 to 10 years through hybridization, trial cultivation, phenotypic screening, preservation, and subsequent on-farm validation before a variety is finalized. The Chiayi Agricultural Experiment Station serves as the primary germplasm repository for sweet potatoes in Taiwan, conserving over 1,400 accessions with extensive breeding expertise. Throughout the breeding cycle, conducting field evaluations to assess the aboveground vegetative vigor of experimental lines demands substantial manual labor and time.

To address this bottleneck, this study aims to develop a sweet potato aboveground pheno typic trait breeding assistive system. By facilitating field-based phenotypic surveys, this system significantly reduces labor costs and time requirements, thereby enhancing breeding throughput and establishing a foundation for digital phenotyping methodologies.

MATERIALS AND METHODS

Depth Camera Sensing and 3D Stereo Vision Geometric Measurement

In this study, a binocular stereo depth camera was employed as the primary sensor for acquiring phenotypic imagery of sweet potato canopies. The camera system integrates left and right infrared sensors, an infrared projector, and an RGB color sensor, with a fixed stereo baseline (B) of 50 mm. The device captures RGB images at a resolution of 1920 × 1080 pixels and depth images at 1280 × 720 pixels, with a minimum detection range of 0.1 m. To mitigate motion blur and tilt artifacts induced by vehicle movement across field terrain, the integrated Inertial Measurement Unit (IMU) utilizes a tri-axial accelerometer to monitor gravity alignment for horizontal leveling and a tri-axial gyroscope to track rotational angular velocities.

Spatial depth estimation is derived from the triangular similarity principle in binocular stereoscopy. The horizontal disparity (d) is determined by the coordinate displacement between the left and right image planes The spatial depth Z is calculated as follows:

$$Z = \frac{f \times B}{d} \tag{1}$$

where f denotes the focal length of the camera, B represents the baseline distance between the stereo sensors, and d is the calculated disparity.

Following spatial registration between the depth and RGB image coordinates, the actual physical width *W* of the target instance is determined using the segmented pixel mask width *w* and its corresponding average aligned depth Z:

$$W = \frac{w \times Z}{f} \tag{2}$$

where W is the actual physical width of the instance, w is the segmented pixel mask width, Z represents the average aligned depth, and f is the focal length along the x-axis.

Extraction of Sweet Potato Shoot Phenotypic Parameters

To quantitatively assess the growth vigor and morphological development of sweet potato canopies, three primary aboveground phenotypic traits—leaf dimensions, plant height, and canopy green cover ratio—were extracted by integrating stereoscopic vision geometry with instance segmentation algorithms. As shown in Fig. 1 (a) and (b), leaf dimensions were evaluated by measuring leaf length from the petiole junction to the leaf apex and leaf width across the widest lamina lobes. Furthermore, plant height was determined as the vertical distance from the cultivation ridge baseline to the uppermost growing apex of the canopy shown in Fig. 1 (c), which was calculated from the aligned depth map as the spatial depth difference between the highest point of the canopy mask and the ground reference surface.

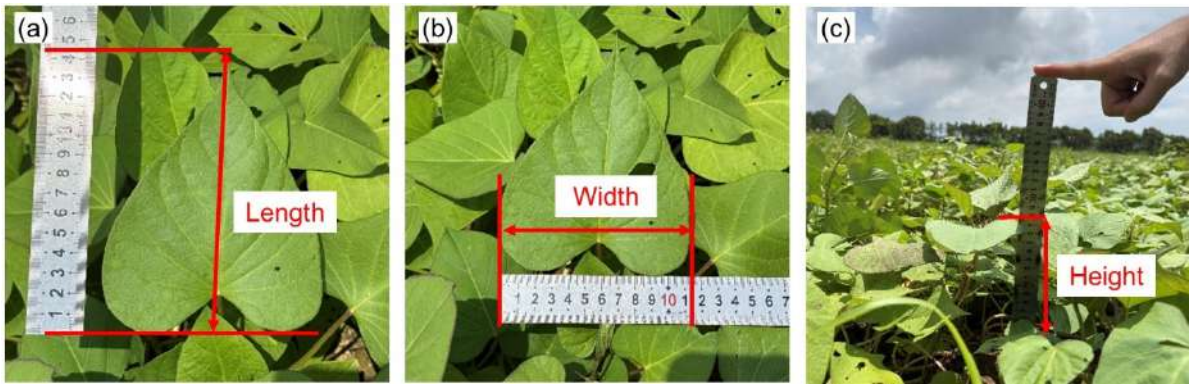

Fig. 1 Manual ground-truth measurement criteria for aboveground sweet potato phenotypic traits: (a) leaf length, (b) leaf width, and (c) plant height.

Dataset Preparation and Leaf Mask Labeling

To construct the training dataset for the instance segmentation model, polygon mask annotations were conducted using the Roboflow platform. The annotation protocol categorized leaves into two distinct classes based on morphological completeness: fully visible leaves with distinct, unoccluded boundaries were defined as complete leaves (Complete leaf, annotated with purple polygon contours), whereas leaves subject to overlapping occlusion, curling, or partial edge truncation were designated as partial leaves (Partial leaf, annotated with red polygon contours). This precise polygon annotation strategy enables the deep learning network to effectively delineate overlapping leaf boundaries and ensures that subsequent phenotypic dimensional extractions are strictly performed on structurally intact leaves.



Fig. 2 Sweet potato leaf polygon mask annotation protocol (purple contours: complete leaves; red contours: partial/occluded leaves).

Visualization of Leaf Boundary Delineation and Size Estimation

The visualization of leaf instance segmentation and dimensional estimation is shown in Fig. 3 The system precisely delineates the boundary contours of individual complete leaves (indicated by green polygons) and automatically determines the principal axes corresponding to leaf length (red lines) and leaf width (blue lines) based on morphological features. By integrating spatial depth registration, the system accurately estimates the physical dimensions of each targeted leaf in real-time (displaying the instance ID, length L, and width W in millimeters), successfully demonstrating robust phenotypic trait extraction even amidst complex canopy backgrounds and leaf overlaps.

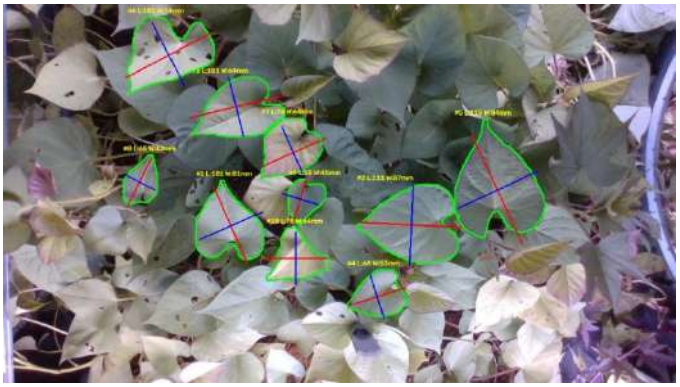

Fig. 3 Leaf instance segmentation and automated dimension extraction (green: boundary; red: length; blue: width).

Field Experimental Sites and Crop Management

To evaluate the reliability and robustness of the developed phenotyping system across diverse agro-ecological conditions, field experiments were conducted at two distinct research facilities in Taiwan: the Chiayi Agricultural Experiment Station of the Taiwan Agricultural Research Institute (TARI) and the Taoyuan District Agricultural Research and Extension Station (TYDARES) of the Ministry of Agriculture. At the Chiayi station, the experimental field comprised 20 rows organized into two subplots (10 rows per plot), with 25 plants per row spaced 1 m apart, evaluating approximately 182 sweet potato breeding lines transplanted on April 21 during the spring–summer cropping season. At the Taoyuan station, the trial consisted of 24 rows across two subplots (12 rows per plot), accommodating 20 plants per

row at an identical 1 m intra-row spacing, encompassing approximately 182 breeding lines transplanted on April 23 for the same cropping season. Standardized raised-ridge cultivation and sufficient plant-to-plant spacing were maintained across both experimental sites to facilitate unrestricted canopy development and ensure accurate, non-destructive individual-plant image acquisition via the ground-based stereoscopic vision platform.

RESULTS & DISCUSSION

In this study, the YOLOv11s-seg model was used for instance segmentation of sweet potato leaves. The annotated image dataset was categorized into complete and occluded/partial leaves and split into a training set of 175 images, a validation set of 22 images, and a test set of 21 images. The input resolution was set to 640×640 pixels, and the model was trained for 300 epochs. Recognition performance is shown in Fig. 4 and Table 1. Across all classes, precision, recall, and mAP50 reached 0.63, 0.74, and 0.68, respectively. The model performed best on the primary measurement target—complete leaves—achieving a precision of 0.78, a recall of 0.87, and mAP50 and mAP50-95 values of 0.87 and 0.74, respectively. In contrast, due to mutual overlap and occlusion among leaves, the mAP50 for occluded/partial leaves was 0.49.

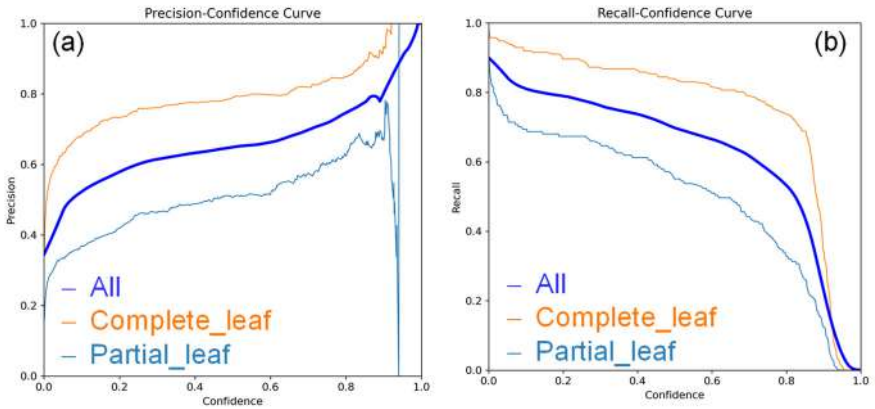

Fig.4 Model training and evaluation results (a) precision curve; (b) recall curve.

Table 1 Evaluation results of sweet potato leaf instance segmentation using YOLOv11s-seg.

	Precision	Recall	mAP50	mAP50-95
All	0.63	0.74	0.68	0.68
Partial_leaf	0.49	0.61	0.49	0.33
Complete_leaf	0.78	0.87	0.87	0.74

To validate the geometric measurement accuracy of the proposed system, the four largest leaves detected per plant were selected as benchmarks and compared with manual physical measurements for leaf length and width. By integrating depth images with 3D point cloud information, the system conducted spatial geometric estimation with an overall computation time of approximately 5 seconds. The comparison of leaf dimensions is illustrated in Fig. 5. Across the evaluated plant samples, the variation trends in leaf length and width extracted by the automated system showed high consistency with manual ground truth values, demonstrating that the system can effectively capture the leaf development patterns and morphological scale trends of the plant population.

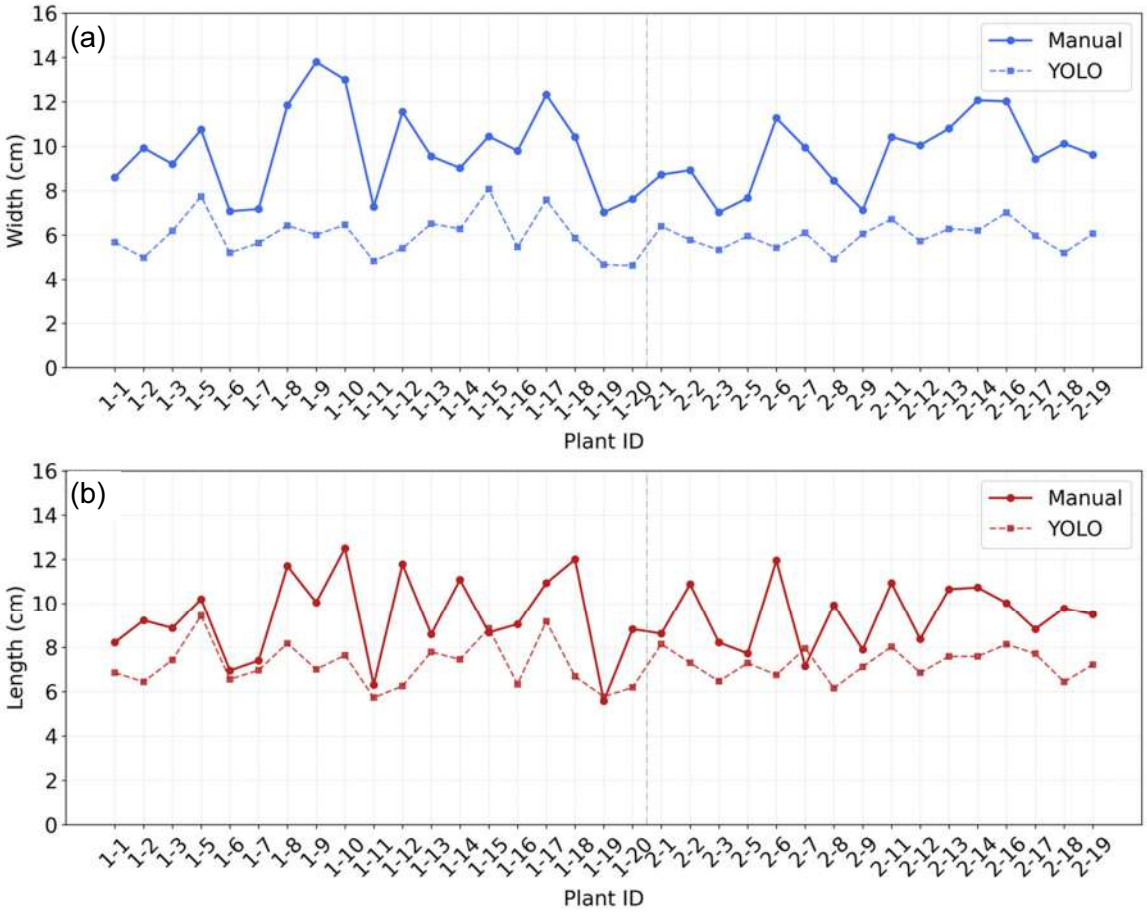

Fig. 5 Comparison of leaf dimensions between manual measurements and model-based automated estimations: (a) Leaf width; (b) Leaf length.

CONCLUSIONS

This study has successfully extracted shoot phenotypic trait data for sweet potato, including plant height, leaf length, and leaf width. The experimental results reveal that although discrepancies exist between the system-detected absolute leaf dimensions and manual measurements, the overall morphological variation trends are highly consistent with manual field surveys. Consequently, the generated 3D point cloud serves not only as a reliable tool for geometric estimation but also as a valuable digital reference for breeders during subsequent visual phenotypic evaluations.

REFERENCES

Jiang, Y., Li, C., Paterson, A. H., Sun, S., Xu, R., & Robertson, J. (2018). Quantitative analysis of cotton canopy size in field conditions using a consumer-grade RGB-D camera. Frontiers in Plant Science, 8, 2233.

Qiu, R., Zhang, M., & He, Y. (2022). Field estimation of maize plant height at jointing stage using an RGB-D camera. *The crop journal*, *10*(5), 1274-1283.

Yu, S., Liu, X., Tan, Q., Wang, Z., & Zhang, B. (2024). Sensors, systems and algorithms of 3D reconstruction for smart agriculture and precision farming: A review. *Computers and Electronics in Agriculture*, *224*, 109229.

PA-P02

Proceedings of The 12th International Symposium on Machinery and Mechatronics for Agriculture and Biosystems Engineering (ISMAB 2026)
20-24 October 2026, Busan, Republic of Korea

COMMUNICATION AND DRIVE INTEGRATION OF GANTRY-TYPE ROBOT

Zhen-Fan Lin [1], Chao-Wang Young [1*]

[1] Department of Biomechatronic Engineering, National Chiayi University, Taiwan
*Corresponding Author-- Voice: +886-5-271-7679, Email: *youngcw@mail.ncyu.edu.tw*

Abstract: In response to the ongoing transformation of Taiwan's agricultural sector and the gradual shortage of agricultural labor, smart agriculture has emerged as an important approach to improving production efficiency. Orchids, as one of Taiwan's representative export flowers, hold a significant position in the international market. However, their growth is highly sensitive to changes in water availability, light intensity, and environmental conditions, making precise cultivation and management essential. Traditional manual methods for repositioning plants and performing routine plant management are labor-intensive and make it difficult to adjust management strategies in real time.

This Study is based on an existing gantry-type smart robot and focuses on the integration of its communication architecture and drive control system for application in orchid greenhouse cultivation. The system integrates image recognition, an XYZ robotic arm, Controller Area Network (CAN) communication, and a dual-battery power architecture. A depth camera is used to identify whether individual plants require repositioning and whether they show signs of disease. The recognition results are transmitted from the NVIDIA Orin to a Raspberry Pi via the CAN Bus.

The communication protocol primarily adopts the Controller Area Network (CAN) Bus. Since the Raspberry Pi does not have a built-in CAN interface, an MCP2515 CAN controller is employed as an interface between the Raspberry Pi and the CAN Bus. Multiple communication nodes are established within the system. The Orin is responsible for transmitting forward and backward movement commands, while the Permanent Magnet Synchronous Motor (PMSM) motor controller continuously reports parameters such as motor speed (RPM), controller temperature, and voltage. The Raspberry Pi serves as the master receiving node, collecting signals from the other nodes and executing the corresponding forward or backward movements. This Study implements remote control through a WebSocket-based web interface, battery power monitoring, and a CAN Bus communication architecture. By integrating the Raspberry Pi, PMSM motor controller, Battery Management System (BMS), and Orin into a multi-node communication network, a stable and integrated communication system is established for smart orchid greenhouse applications.

Key Words: CAN Bus, Raspberry Pi, Gantry Robot.

INTRODUCTION

Smart agriculture has emerged as an important approach to improving agricultural production efficiency. Orchids are highly sensitive to environmental conditions, and their cultivation requires careful management to maintain optimal growth. Traditional manual management is labor-intensive and time-consuming, making it difficult to achieve both high operational efficiency and precise cultivation management.

In conventional orchid pot sorting operations, workers primarily rely on manual inspection to evaluate the growth conditions of individual orchid plants. The process also involves manually correcting the orientation of orchid pots and screening for diseased plants. These operations require considerable labor and may result in inconsistent handling efficiency.

To address these challenges, this study focuses on the development of an automated mobile platform for orchid gantry robot (As shown in Fig.1). The system is developed through a collaborative effort between National Chiayi University and National Sun Yat-sen University. In this collaboration, National Chiayi University focuses on the control and operation of the wheel hub motors for the mobile platform, while the other components of the system are developed by the collaborating team.



Fig. 1 The gantry robot in actual orchid garden.

The objective of this study is to develop and evaluate the wheel hub motor control system and its operation on the automated platform, with the goal of improving the efficiency and stability of orchid pot handling operations.

MATERIALS AND METHODS

2.1 Experimental Equipment

This study is based on an existing intelligent robotic platform with mechanical improvements, building upon the results of previous research. The system uses a Raspberry Pi as the main control platform. At the hardware level, an MCP2515 CAN controller is connected to the Raspberry Pi through the Serial Peripheral Interface (SPI) and interfaces with the PMSM motor controllers provided by the manufacturer. Table 1 presents the basic design specifications and parameters of the PMSM motors provided by the manufacturer.

Table 1 Basic Parameters of the PMSM Motor.

Parameters	Values
Supply voltage (V)	48
Rated Power (kW)	500
Motor Weight (Kg)	15
Rated Speed (rpm)	130
Vehicle Speed (km/h)	7
Efficiency	82%
Pole pairs	10
CAN baud rate (Kbps)	500

The robotic platform adopts a four-wheel configuration, consisting of two front drive wheels and two rear support wheels, as shown in Fig. 2.

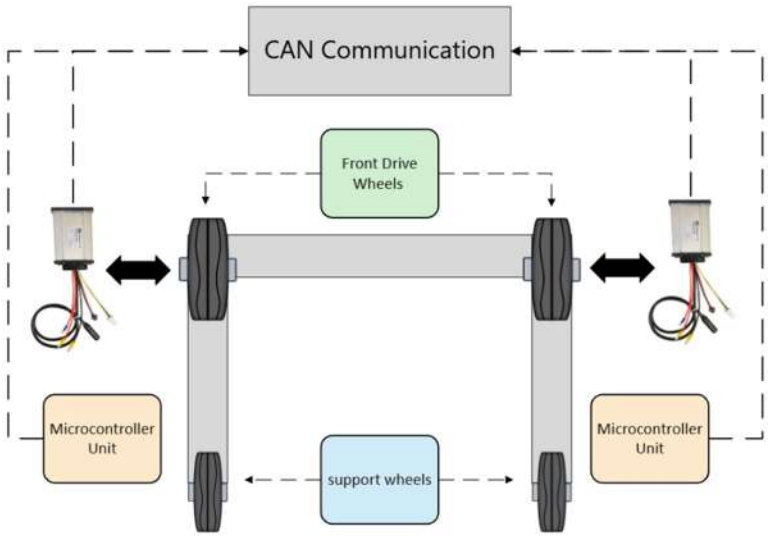

Fig. 2 Design of a vehicle with a PMSM motor system.

The power system uses a Cymmetrik-provided lithium iron phosphate ($LiFePO_4$) battery pack as the primary power source. The battery pack incorporates a battery management system (BMS) with CAN communication capability, which transmits battery status information to the Raspberry Pi. A WZ5012L step-down converter is then used to convert the 48 V DC input voltage to the voltage levels required by the individual devices. The specifications of the battery pack are summarized in Table 2.

Table 2 Detailed Specifications of Cymmetrik's $LiFePO_4$ Battery.

Parameters	Values
Cells Structure	15S2P
Battery Weight (kg)	12
Nominal Capacity (Ah)	30
Nominal Voltage (V)	48
Standard Discharge Current (A)	60
Communication Protocol	CAN

2.2 Experimental Methods

The Raspberry Pi transmits control commands to the motor controllers using the CANopen communication protocol to implement robot motion functions, including forward and backward movement. Meanwhile, the Raspberry Pi receives status information from the motor controllers, including motor speed (RPM) and controller temperature.

The system uses systemd to configure the control program to start automatically at system boot. After startup, the program automatically establishes a web-based service, allowing users to control the robot through a web interface and monitor the motor speed (RPM), controller temperature, and battery level in real time.

In this study, the robot's moving speed is configured at three levels: low speed (0x64), medium speed (0xFA), and high speed (0x190), providing different speed options for various operational requirements.

RESULTS & DISCUSSION

3.1 Speed Performance

Under the three speed settings, the vehicle speed and the RPM feedback from the motor controller exhibited an approximately linear relationship, as shown in Table 3. This relationship can serve as a basis for speed control in future applications.

Table 3 Standard Speed Performance and Motor RPM.

Speed Command	Vehicle Speed	RPM
0x64	1.47 km/h	60~70
0xFA	3.5 km/h	160~170
0x190	5.24 km/h	260–270

3.2 Battery Consumption

The battery consumption data collected during the orchid greenhouse tests are shown in Table 4. The arm-side battery had a lower consumption rate in the fourth test because the robot remained idle for most of the test period.

Table 4 Battery Consumption Rates during Greenhouse Tests.

Trial	Arm-side Battery	Motor-side Battery
Trial 1	3.10 %/h	1.70 %/h
Trial 2	3.33 %/h	1.11 %/h
Trial 3	3.33 %/h	1.48 %/h
Trial 4	1.47 %/h	1.18 %/h

CONCLUSIONS

In previous studies, a fixed value (0xFF) was used for motor driving. However, greenhouse tests showed that the low-speed mode provided more time for image processing. Therefore, operating the motor at a lower speed resulted in more stable overall system operation and was

found to be a more suitable control method.

For power management, the battery consumption data obtained from the experiments can be used to estimate the system operating time under different operating conditions, providing a reference for future system planning and applications.

Since the wheel hub motors used in this study do not have encoders, motor position feedback is not available, limiting the ability to perform high-precision position control. If precise positioning or closed-loop control is required in future applications, motors with encoder feedback could be adopted to improve position control performance and accuracy.

ACKNOWLEDGEMENTS

This study was supported by the Ministry of Agriculture of Taiwan (115AS-1.6.2-AS-02). And thank Star Orchids, STARS CO., LTD., and Cymmetrik Enterprise CO. LTD. for providing the experimental materials and support that contributed to the successful completion of this study.

REFERENCES

CiA 301 4.2.0. 2011. CANopen application layer and communication profile.

International Organization for Standardization. 2026. ISO 11898-2:2026 Road vehicles-Controller area network (CAN)-Part 2: High-speed physical medium attachment (PMA) sublayer. Geneva, Switzerland: ISO.

Microchip Technology Inc. 2015. AN228: A CAN Physical Layer Discussion.

Monk, S. 2022. Raspberry pi cookbook. O'Reilly Media, Inc.

Wei, Y. J., 2025. Research on communication and driving system of the gantry autonomous watering trunk. Thesis. Taiwan Chiayi.: National Chiayi University, Department of Biome chatronic Engineering.

PA-P03

Proceedings of The 12th International Symposium on Machinery and Mechatronics for Agriculture and Biosystems Engineering (ISMAB 2026)
20-24 October 2026, Busan, Republic of Korea

BASED ON DEEP LEARNING AND IMAGE PROCESSING AN AUTOMATED FIELD-BASED PHENOTYPIC TRAIT MEASUREMENT AND BREEDING SUPPORT SYSTEM FOR SWEET POTATOES

Shang-Yu Hsieh [1*], Ting-Han Lin[1], Chin-Ying Yang[2], Po-Hsien Lu[3], Yao-Chuan Tsai[1]

[1]Dept. of Bio-Industrial Mechatronics Engineering, National Chung Hsing University, Taichung, Taiwan
[2]Dept. of Agronomy, National Chung Hsing University, Taichung, Taiwan
[3]Chiayi Agricultural Experiment Branch, Agricultural Research Institute, Taiwan
*Corresponding Author-- Email: shsunlu@gmail.com

Abstract: Driven by extreme climate change and an estimated 70% increase in global food demand by 2050, incorporating artificial intelligence into agriculture is vital for industry transformation. Although sweet potato is a key staple crop in Taiwan with an annual yield of 198,500 metric tons in 2023, phenotypic evaluations still rely on labor-intensive, subjective manual inspections. This practice causes observer fatigue and lacks quantitative accuracy, creating a major bottleneck in breeding efficiency. To resolve these challenges, this study developed an automated field-based phenotypic measurement system combining image processing and deep learning. A custom carrier, refined across four generations to navigate rugged terrain and soft soil, features 27.5-inch large-diameter wheels for ridge tracking stability, an acrylic support structure, and an independent shadowing mechanism that standardizes lighting. While an ArUco marker system was initially deployed for pixel-to-metric transformations, frequent marker occlusion by soil and vines prompted an upgrade to an Intel RealSense D435i depth camera. Integrating an inertial measurement unit (IMU) to eliminate tilt errors, this infrared stereo vision setup enables markerless 3D spatial quantification across key cultivars (Tainung No. 57, 66, 73, and hybrid lines). To resolve over-segmentation and count inflation caused by class imbalance, a targeted balancing strategy was applied before training a YOLOv11 instance segmentation model. The model achieved a precision of 0.961, a recall of 0.972, and an end-to-end inference time of about 3 seconds per image for tuberous root shape classification. For dimensional quantification, prediction errors for root length and width were constrained within 1 cm. Superimposed histograms and kernel density estimation (KDE) curves closely coincided with manual ground truth, validating the faithful reconstruction of actual field trait distributions. Compared to traditional manual inspection (1.33 plants/min), the system achieves a throughput of 8.54 plants/min—a 543% gain that reduces field labor demand by about 84%. Planned for deployment across primary, intermediate, and advanced breeding trials, this platform provides structured phenotypic datasets to empower data-driven selections and accelerate breeding cycles.

Key Words: YOLOv11, Deep Learning, Phenotypic Trait, Instance Segmentation, High-Throughput.

INTRODUCTION

With global food demand projected to surge by 70% by 2050 and the global sweet potato market expanding toward USD 23.9 billion by 2032, developing resilient, high-yield cultivars is essential for food security. In Taiwan, vital cultivars such as Tainung No. 57, 66, and 73 anchor domestic staple production. However, sweet potato breeding faces a critical operational bottleneck during post-harvest phenotypic evaluation. Conventional workflows require breeders to manually retrieve, align, and visually inspect tuberous roots directly along field ridges. This manual practice is labor-intensive, time-consuming, and highly prone to subjective observer bias and physical fatigue, restricting high-throughput screening across expansive hybrid populations.

To overcome these challenges, this study developed an automated field phenotypic measurement system combining robotics, computer vision, and deep learning. The system features a custom agricultural carrier equipped with large-diameter wheels and an independent shadowing mechanism to stabilize ridge navigation while eliminating ambient lighting interference. To resolve marker occlusion issues caused by clinging soil and vines, an Intel RealSense D435i depth camera paired with an inertial measurement unit was incorporated for dynamic tilt compensation, enabling robust markerless 3D spatial quantification. Furthermore, an optimized YOLOv11 instance segmentation model with class-balancing strategies was implemented to accurately classify root shapes and extract geometric traits. By rigorously validating dimensional precision, statistical distribution fidelity, and field throughput against manual ground truth, this automated framework establishes an objective, high-throughput pipeline that generates structured digital datasets to accelerate sweet potato breeding cycles.

Phenotyping Measurement Technique Based on Depth Sensors and Pose Compensation

MATERIALS AND METHODS

To further improve the automation level of field measurements and eliminate the operational constraints associated with physical markers, this study implemented an Intel RealSense D435i depth camera, transitioning the measurement mechanism from 2D scale calibration to 3D spatial sensing, as illustrated in Fig.1. Integrating infrared stereo vision technology, the camera acquires disparity information between the target object and the camera via dual infrared sensors, deriving depth data based on the triangulation principle.

where Z represents the object depth, f is the lens focal length, B denotes the baseline distance of the camera, and d is the disparity between the left and right images. Furthermore, with w denoting the mask pixel width extracted by the YOLO model and Z representing the aligned center depth, pixel alignment with the RGB image enables the system to accurately determine the actual depth value at the center point of the sweet potato storage root. Consequently, the target of directly computing physical dimensions without physical reference scales is achieved.

To address the vibrations and vehicle tilting caused while traversing the furrows, the system performs dynamic pose compensation using the built-in Inertial Measurement Unit (IMU) of the D435i. By detecting the gravity vector via the accelerometer, the system senses the camera's tilt angle relative to the ground in real time and compensates for image coordinates using a rotation matrix.

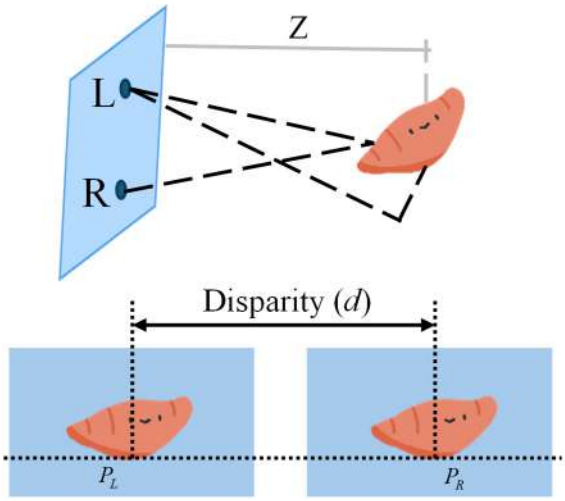

Fig. 1 Schematic diagram of stereo vision disparity and depth measurement principle.

Classification Standards for Sweet Potato Storage Root Shapes

The classification criteria for sweet potato storage root shapes in this study refer to the morphological definitions established by the International Union for the Protection of New Varieties of Plants (UPOV) and the five categories conventionally utilized by the Agriculture and Food Agency in Taiwan: long-fusiform, short-fusiform, round, cylindrical, and irregular.

However, subsequent discussions with professional breeders revealed that long-fusiform, short-fusiform, and cylindrical roots exhibit pronounced geometric similarities, all characterized by symmetric longitudinal elongation. Even under manual visual inspection, distinguishing subtle differences in aspect ratios remains challenging, which can introduce classification ambiguities and degrade model accuracy during deep learning training. To mitigate model confusion arising from overly subtle intra-class variations, these three morphologically similar categories were consolidated and uniformly labeled as "fusiform" shown in Fig. 2.

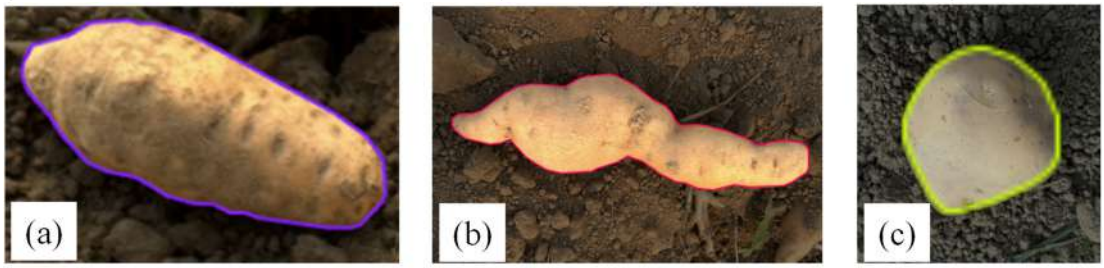

Fig. 2 Classification Standards for Sweet Potato Storage Root Shapes: (a) fusiform, (b) irregular, and (c) round.

RESULTS & DISCUSSION

Initially, a baseline dataset comprising 800 images was deployed with single-class bounding-box annotation to validate in-situ detection feasibility. The model yielded an mAP@0.5 of 0.990, verifying its robustness against complex agro-ecological backgrounds.

To facilitate automated grading, the target classes were extended to fusiform, round, and irregular geometries. However, naturally skewed harvest yields introduced severe class imbalance, with irregular roots comprising merely 558 instances. This discrepancy induced backpropagation gradient bias, degrading the mAP@0.5 to 0.870 and provoking substantial instance over-segmentation.

To mitigate this limitation, a dataset-balancing protocol was executed across 1,716 training frames, bolstering irregular instances to 2,056 via targeted data augmentation. Consequently, the optimized YOLOv11-s architecture achieved a Precision of 0.921 and an mAP@0.5 of 0.935 shown in Table 1, demonstrating effective suppression of background false-positives and sustained boundary continuity across morphologically complex roots.

Table 1 Model training

Model	Datasets	Precision	Recall	mAP@ 0.5	mAP@ 0.5:0.95
YOLOv11-s	Fusiform 2369 Round 237 Irregular 393	0.873	0.708	0.793	0.743
	Fusiform 2336 Round 474 Irregular 786	0.881	0.708	0.785	0.741
	Fusiform 1541 Round 1943 Irregular 558	0.846	0.863	0.87	0.821
	Fusiform 1706 Round 1623 Irregular 2056	0.921	0.905	0.935	0.918

To evaluate the system's feasibility for high-throughput breeding selection, population phenotypic profiles were evaluated using histograms overlaid with Kernel Density Estimation (KDE) distributions shown in Fig. 3. By filtering stochastic individual noise, KDE effectively models the natural continuous probability density of phenotypic traits. As depicted the predicted KDE curves showed substantial alignment with ground-truth measurements across both length and width dimensions. The congruence in modal peaks and variance dispersion across distinct trials demonstrates robust batch-to-batch repeatability, accurately capturing central tendencies while retaining critical extreme morphological phenotypes.

(a)

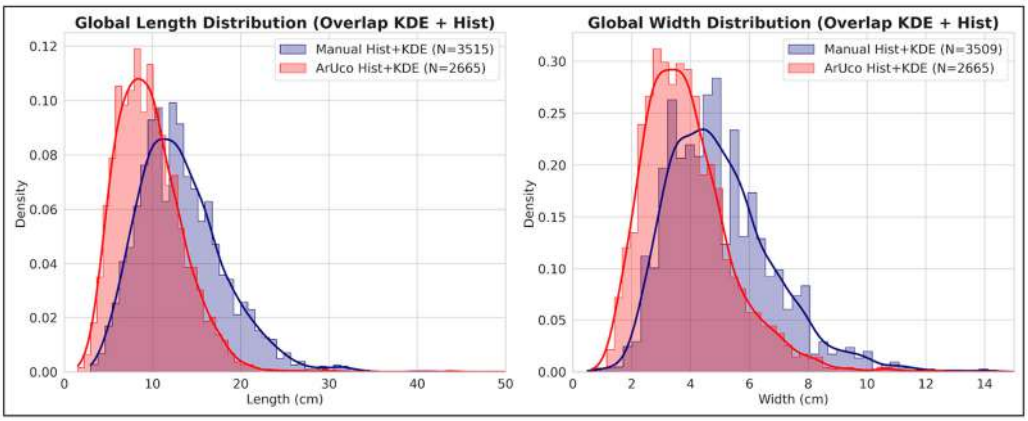

(b)

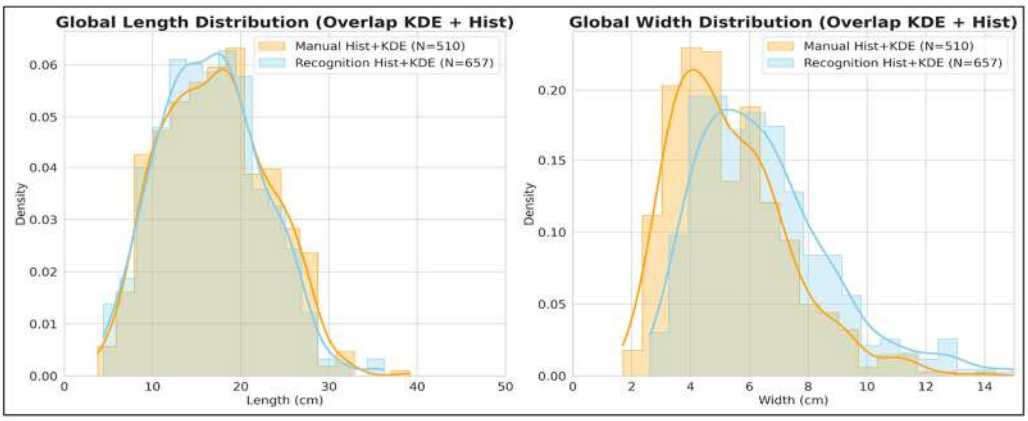

Fig. 3 Histogram Overlaid with Kernel Density Estimation (KDE) Curve: (a) First experiment; (b) Second experiment.

To accurately quantify sweet potato physical traits, an automated system was developed and benchmarked against manual measurements. The initial setup utilized a monocular webcam with planar ArUco markers; however, the absence of depth perception and the height offset between markers and roots induced perspective distortions, causing substantial discrepancies between predicted (13.26 cm) and manual (9.66 cm) lengths shown in Table 2.

Table 2 Comparison of Model Predictions and Manual Measurements Using ArUco Markers

	Model Prediction	Manual Measurement
Length	13.26±5.98	9.66±4.74
Width	5.04±2.36	3.87±1.88

To resolve this limitation, the hardware was upgraded to an Intel RealSense D435i depth camera, computing the center depth via RGB-D streams for dynamic scale conversion. Across two field trials evaluated with histograms and Kernel Density Estimation (KDE), the first trial yielded length and width errors of 0.11 cm and 0.85 cm shown in Table 3, respectively, while the second trial exhibited errors of 0.28 cm and 0.93 cm. These results demonstrate that the 3D depth-sensing system consistently constrains dimensional errors within 1 cm, ensuring high fidelity and field robustness shown in Table 4.

Table 3 Comparison of Depth Camera Model Predictions and Manual Measurements in Trial 1

	Model Prediction	Manual Measurement
Length	12.68±4.61	12.79±4.76
Width	5.63±1.63	4.78±1.7

Table 4 Comparison of Depth Camera Model Predictions and Manual Measurements in Trial 2

	Model Prediction	Manual Measurement
Length	17.07±5.81	17.35±5.98
Width	6.47±2.42	5.54±2.06

CONCLUSIONS

This study presents an automated sweet potato field phenotyping system integrating deep learning, stereo vision, and embedded computing. A mobile cart with 27.5-inch wheels and an illuminated shading chamber was developed to navigate uneven furrows under stable optical conditions. To address natural harvest class imbalance, a dataset-balancing protocol enhanced the YOLOv11 instance segmentation network, achieving a Precision of 0.921 and an mAP@0.5 of 0.935. An Intel RealSense D435i depth sensor with IMU dynamic pose compensation constrained measurement error within 1 cm, with KDE profiles closely matching ground-truth distributions. Deployed on an NVIDIA Jetson Orin Nano, the system achieved a throughput of 8.54 plants/min (a 543% increase over manual methods) and saved 75% labor, offering robust support for high-throughput digital breeding.

REFERENCES

R. Girshick, "Fast R-Cnn", Proceedings of the IEEE international conference on computer vision, pp. 1440-1448, 2015.

K. He, X. Zhang, S. Ren and J. Sun, "Deep Residual Learning for Image Recognition", Proceedings of the IEEE conference on computer vision and pattern recognition, pp. 770-778, 2016.

J. Redmon, S. Divvala, R. Girshick and A. Farhadi, "You Only Look Once: Unified, Real-Time Object Detection", Proceedings of the IEEE conference on computer vision and pattern recognition, pp. 779-788, 2016.

J. Canny, "A Computational Approach to Edge Detection", IEEE Transactions on Pattern Analysis and Machine Intelligence, no. 6, pp. 679-698, 2009, doi. 10.1109/TPAMI.1986.4767851.

S. Liu, L. Qi, H. Qin, J. Shi and J. Jia, "Path Aggregation Network for Instance Segmentation", Proceedings of the IEEE conference on computer vision and pattern recognition, pp. 8759-8768, 2018.

M. Minervini, H. Scharr and S. A. Tsaftaris, "Image Analysis: The New Bottleneck in Plant Phenotyping [Applications Corner]", IEEE Signal Processing Magazine, vol. 32, no. 4, pp. 126-131, 2015, doi. 10.1109/MSP.2015.2405111.

T.-Y. Lin, P. Goyal, R. Girshick, K. He and P. Dollár, "Focal Loss for Dense Object Detection", Proceedings of the IEEE international conference on computer vision, pp. 2980-2988, 2017.

PA-P04

Proceedings of The 12th International Symposium on Machinery and Mechatronics for Agriculture and Biosystems Engineering (ISMAB 2026)
20-24 October 2026, Busan, Republic of Korea

DEEP LEARNING-BASED LOW-ACTIVITY STANDING ABNORMALITY DETECTION AND EAR-TAG TRACKING IN DAIRY COWS

Yu-Lun Tseng*, Yao-Chuan Tsai

Dept. of Bio-Industrial Mechatronics Engineering, National Chung Hsing University, Taichung, Taiwan
*Corresponding Author-- Voice: +886987920042, Email: darren050126@gmail.com

Abstract: Labor shortages and an aging workforce have increased the demand for automated monitoring systems in dairy farming. Traditional manual inspection is labor-intensive and makes long-term monitoring of cow behavior and individual animals difficult. This study developed a deep learning-based low-activity standing abnormality detection and ear-tag tracking system using a controllable Pan-Tilt-Zoom (PTZ) camera. The camera patrolled 18 predefined monitoring positions, while YOLOv11n was used to classify dairy cow postures as standing or lying. For standing cows in the stall area, activity between consecutive patrols was evaluated using bounding-box center-point displacement and Intersection over Union (IoU). Cows that continuously remained standing and satisfied the low-activity thresholds were identified as suspected abnormal individuals. The PTZ camera was subsequently adjusted in pan, tilt, and optical zoom to capture the head and ear tag for individual identification. The posture detection model achieved Precision and Recall values of 0.902 and 0.913, respectively, whereas the ear-tag detection model achieved 0.971 and 0.998. The optimal thresholds for center-point displacement and IoU were 27 pixels and 0.67, with Balanced Accuracy values of 92.3% and 96.2%, respectively. The optical zoom experiment showed that 12× magnification provided the highest average ear-tag digit recognition accuracy of 63%. These results demonstrate the feasibility of the proposed system for automatically detecting low-activity standing cows and identifying individual animals, providing a potential approach for early warning and smart dairy farm management.

Key Words: Dairy cow, Low-activity standing, Deep learning, PTZ camera, Ear-tag recognition

INTRODUCTION

Labor shortages and an aging workforce have become important challenges in dairy farming. Traditional manual inspection of cow behavior and health conditions requires considerable labor and makes continuous monitoring difficult. Behavioral changes are closely associated with the health status of dairy cows. (Eriksson et al. 2021) reported that prolonged standing behavior may be associated with hoof lesions and other health problems. In addition, (Mattachini et al. 2011) demonstrated that intermittent observations at fixed time intervals can effectively represent the standing and lying behavior of dairy cows.

The objective of this study was to develop an automated early-warning system integrating a controllable PTZ camera and deep learning. Cow posture was identified from patrol images, while center-point displacement and IoU between consecutive patrols were used to identify cows exhibiting persistent standing with low activity. Ear-tag tracking and digit recognition were subsequently performed to obtain individual identification information.

MATERIALS AND METHODS

SYSTEM WORKFLOW

The overall workflow of the proposed system is shown in Fig. 1. A controllable PTZ camera was used to patrol predefined monitoring positions in the stall area, and YOLOv11n models were developed for posture and ear-tag detection. The posture model classified cows into stand and lay classes and provided bounding-box information for subsequent low-activity analysis. When a standing cow satisfied the low-activity criteria, the ear-tag tracking procedure was activated. The ear-tag model detected head and ear_tag classes to guide the camera toward the cow's head and ear tag. The captured ear-tag image was segmented into individual digits, and a convolutional neural network (CNN) classified digits from 0 to 9 to obtain the identification number of the detected cow.

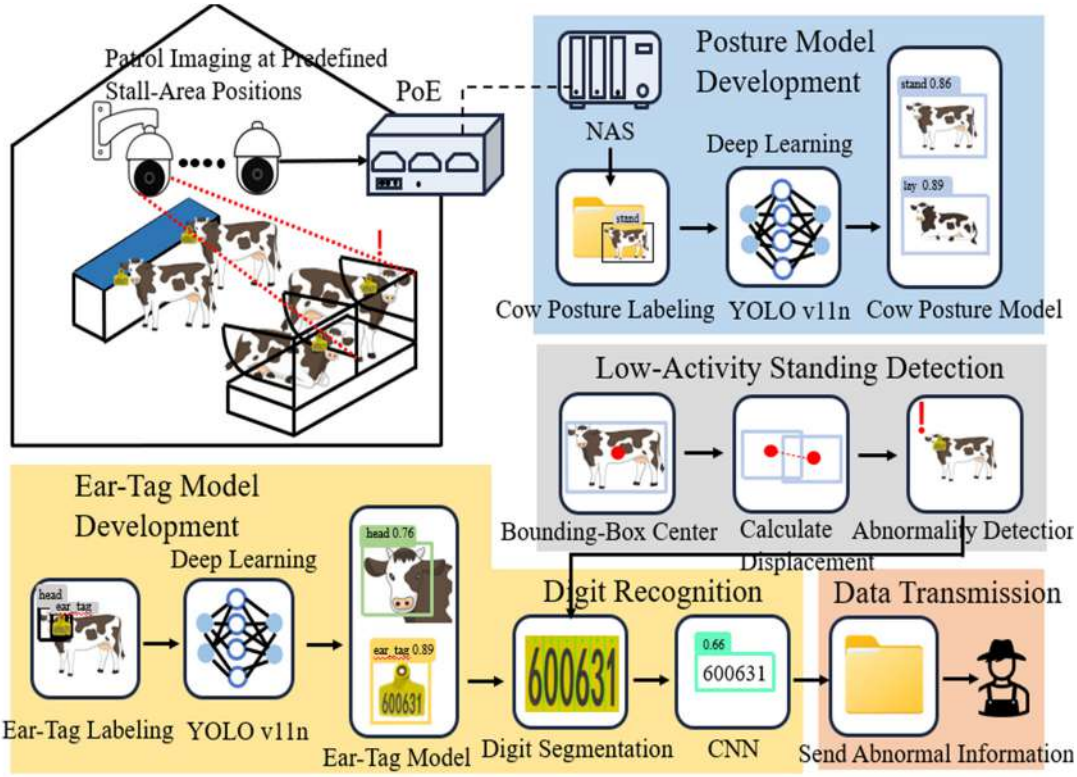

Fig.1 Overall workflow of the proposed system.

LOW-ACTIVITY DETECTION

Cow activity was evaluated using consecutive patrol images acquired at the same monitoring position, as shown in Figs.2(a) and (b) Two methods, center-point displacement and intersection over union (IoU), were used for low-activity detection. Center-point displacement

was calculated from the center coordinates of the bounding boxes between two consecutive patrols, where a smaller displacement indicated lower activity. IoU was calculated from the overlap between consecutive bounding boxes, where a higher IoU indicated a smaller change in position. A cow was classified as exhibiting low-activity standing when it continuously remained standing and its activity measurements satisfied the predefined thresholds.

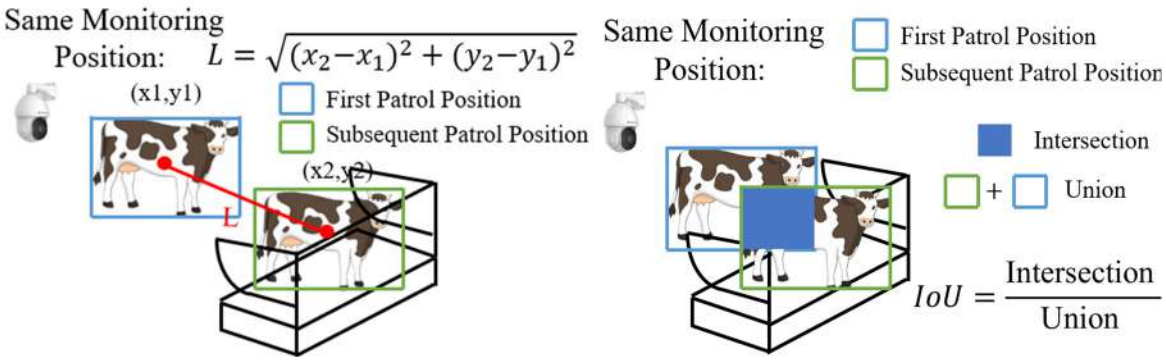

Fig. 2(a) Center-point displacement method and (b) IoU-based overlap method.

RESULTS & DISCUSSION

MODEL PERFORMANCE

The posture detection model achieved Precision, Recall, and mAP50 values of 0.902, 0.913, and 0.949, respectively. The ear-tag detection model achieved values of 0.971, 0.998, and 0.993, respectively. For the digit classification model, the Precision, Recall, and F1-score for the segmented single-digit images from 0 to 9 were all 1.00, indicating good classification performance.

LOW-ACTIVITY DETECTION THRESHOLDS

As shown in Fig. 4, the optimal thresholds for center-point displacement and IoU were 27 pixels and 0.67, respectively. Low-activity samples generally exhibited smaller center-point displacement and higher IoU values than moving samples, indicating that both methods could distinguish low-activity cows from moving cows.

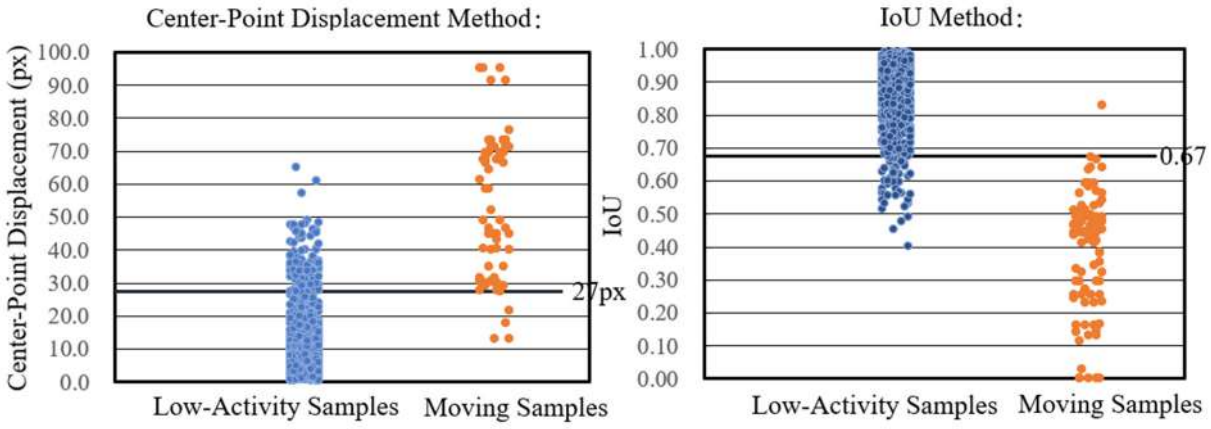

Fig. 4 Thresholds for low-activity detection using center-point displacement and IoU.

OPTICAL ZOOM MAGNIFICATION

The effect of optical zoom magnification on ear-tag digit recognition is shown in Fig. 5. The highest average recognition accuracy was obtained at 12× magnification, reaching 63%. When the magnification was increased to 30×, the accuracy decreased to 14%, mainly due to reduced image brightness and unstable focusing. Therefore, 12× optical zoom was considered more suitable for ear-tag image acquisition under the tested conditions.

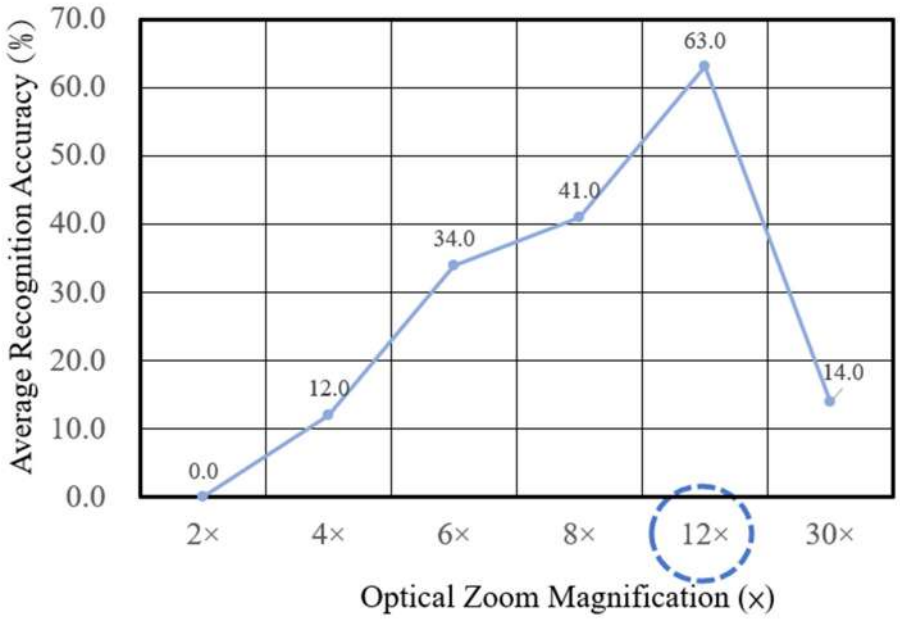

Fig. 5 Average ear-tag digit recognition accuracy at different optical zoom magnifications.

CONCLUSIONS

This study developed a deep learning-based low-activity standing early-warning system for dairy cows using a controllable PTZ camera. The system integrated posture detection, center-point displacement and IoU analysis, ear-tag tracking, and digit recognition to automatically identify low-activity standing cows and obtain individual identification information. The results demonstrate the feasibility of the proposed system as a non-contact monitoring approach for automated dairy cow health management.

REFERENCES

Eriksson, H. K., R. R. Daros, M. A. G. von Keyserlingk, and D. M. Weary. 2021. Standing behavior and sole horn lesions: A prospective observational longitudinal study. *Journal of Dairy Science* 104(10): 11018-11034.

Mattachini, G., E. Riva, and G. Provolo. 2011. The lying and standing activity indices of dairy cows in free-stall housing. *Applied Animal Behaviour Science* 129(1): 18-27.

PA-P05

Proceedings of The 12th International Symposium on Machinery and Mechatronics for Agriculture and Biosystems Engineering (ISMAB 2026)
20-24 October 2026, Busan, Republic of Korea

CONSTRUCTION AND TASK-LEVEL VALIDATION OF A VIRTUAL PLATFORM FOR A SPONGE-SEEDLING TRANSPLANTING ROBOT UNDER VARIABLE TRAY POSES

Tianle Shen[1,3], Phanith Chea[1,3], Dong-Hoo Shin[1], Young-Min Kim[1], Lim-Du Hee[1], Woo-Young Kim[2], Kyeong-Hwan Lee[1,2,3*]

[1]Department of Convergence Biosystems Engineering, Chonnam National University, Gwangju, Korea
[2]AI Agri-Tech Research Center, Chonnam National University, Gwangju, Korea
[3]BK21 Interdisciplinary Program in IT-Bio Convergence System, Chonnam National University, Gwangju, Korea
*Corresponding Author — Email: khlee@jnu.ac.kr

Abstract: Densely arranged sponge seedling blocks may remain locally connected before transplanting. Direct extraction can disturb adjacent blocks, while narrow gaps require the blades to align with block boundaries and enter in the correct directions. Fixed insertion poses and transfer trajectories cannot be reused directly when either tray is translated or rotated. This study therefore addresses the automatic generation of reachable and geometrically correct tasks that satisfy safety constraints for separation, grasping, transfer, and placement under varying tray poses. We developed a ROS 2-based virtual platform integrating a UR10e manipulator, an eye-in-hand stereo camera, and a two-blade parallel gripper. Tray-local coordinates define block boundaries and destination holes and support generation of a 21-step task with reachability and clearance checks. The platform completed three rounds, each covering nine destination holes. All 1,000 randomized dual-tray scenes within the prescribed domain passed complete task-feasibility checks, and grid scanning identified the feasible workspace of each tray. The platform can therefore update valid transplanting tasks as tray poses vary, supporting task-flow verification and workstation-layout screening before physical deployment.

Key Words: Sponge seedling transplanting, Agricultural robot, Virtual platform, Parameterized task planning, Workspace analysis

ACKNOWLEDGEMENTS

This work was supported by Korea Institute of Planning and Evaluation for Technology in Food, Agriculture and Forestry (IPET), through K-Vertical Farm Globalization Project, funded by Ministry of Agriculture, Food and Rural Affairs (MAFRA) (Project No. RS-2025-02303373) and Korea Institute of Planning and Evaluation for Technology in Food, Agriculture and Forestry(IPET) through the Advanced Agricultural Machinery Industrialization Technology Development Program, funded by Ministry of Agriculture, Food and Rural Affairs(MAFRA)(32003003).

PA-P06

Proceedings of The 12th International Symposium on Machinery and Mechatronics for Agriculture and Biosystems Engineering (ISMAB 2026)
20-24 October 2026, Busan, Republic of Korea

EFFECTS OF FIELD SIZE AND SHAPE ON THE OPERATIONAL FEASIBILITY AND COVERAGE PERFORMANCE OF AUTONOMOUS AGRICULTURAL MACHINERY

Yong-Hyun Kim[1,2], Jumyeong Lee[1,2], Chankeun Lee[1,2], Seokhyun Ahn[1,2], Hak-Jin Kim[1,2*]

[1]Department of Biosystems Engineering, College of Agriculture and Life Sciences, Seoul National University, Seoul 08826, Republic of Korea
[2]Integrated Major in Global Smart Farm, College of Agriculture and Life Sciences, Seoul National University, Seoul 08826, Republic of Korea
*Corresponding Author-- Hak-Jin Kim, Voice: +82-2-880-4614, Email: kimhj69@snu.ac.kr

Abstract: In South Korea, land consolidation has historically been implemented to enlarge and reshape agricultural fields and improve farm roads and irrigation infrastructure, thereby facilitating efficient machinery operation. Previous studies have reported improvements in field efficiency and reductions in labor and production costs following land consolidation. However, these benefits have primarily been evaluated in the context of conventional mechanization. As agricultural machinery advances toward higher levels of automation and autonomy and machine–implement systems become larger, it remains unclear whether existing actual field plots can spatially accommodate autonomous field operations and how field geometry affects coverage performance. This study investigated the effects of field size and shape on the operational feasibility and geometric coverage quality of autonomous field operations using large-scale agricultural spatial data in South Korea. The Korean Farm Map, an open spatial dataset, was used to characterize the nationwide distribution of field size and geometry for paddy and upland fields. Two contrasting case-study groups representing consolidated paddy fields and fragmented upland fields were selected for detailed coverage-path analysis. Coverage layouts were generated under two machine–implement configurations with different spatial requirements. Operational feasibility was assessed based on whether sufficient headland and interior working areas could be generated within each field. For feasible fields, coverage rate and overlap ratio were calculated as indicators of theoretical geometric coverage quality. Nationwide analysis showed clear differences in field size and geometry between paddy and upland fields and between consolidated and non-consolidated farmland. In the case studies, coverage-layout feasibility generally increased with field size and decreased with the larger machine–implement configuration. Feasibility was substantially higher in consolidated paddy fields than in fragmented upland fields. Field shape also influenced coverage performance among feasible fields, with irregular geometries generally resulting in less favorable coverage characteristics. These results demonstrate that field size and shape are important spatial factors affecting the applicability and performance of autonomous agricultural machinery.

Key Words: Autonomous agricultural machinery, Field geometry, Coverage path

Acknowledgements: This work was supported by the Technology Innovation Program (00444634) funded by the Ministry of Trade, Industry & Energy (MOTIE, Korea).

PA-P07

Proceedings of The 12th International Symposium on Machinery and Mechatronics for Agriculture and Biosystems Engineering (ISMAB 2026)
20-24 October 2026, Busan, Republic of Korea

INTERFERENCE-GUIDED BRANCH MANIPULATION FOR DUAL-ARM ROBOTIC PRUNING

Chao Teng[1,3], Woo-Young Kim[2], Kyeong-Hwan Lee[1,2,3*]

[1]Department of Convergence Biosystems Engineering, Chonnam National University, Gwangju, Korea
[2]AI Agri-Tech Research Center, Chonnam National University, Gwangju, Korea
[3]BK21 Interdisciplinary Program in IT-Bio Convergence System, Chonnam National University, Gwangju, Korea
*Corresponding Author-- Voice: +010-4014-4083, Email: khlee@jnu.ac.kr

Abstract: Dense surrounding branches can obstruct pruning tool access to target branches. This study proposes an interference-guided branch manipulation method for dual-arm robotic pruning. Multiple pruning poses are generated around the target branch, and the swept space of the full end effector is used to identify whether a pose is blocked and determine where and how much the obstructing branch must be displaced. The resulting manipulation state is used to update the branch configuration and recover geometrically feasible pruning access. Evaluation on 30 branch configurations with 360 candidate pruning poses showed that 84.5% of initially blocked candidates became feasible after branch manipulation, increasing the overall geometric feasibility rate to 91.1%. The key contribution is to convert pruning tool interference from a collision checking result into a branch manipulation state.

Key Words: Dual-arm Robot, Robotic Pruning, Branch Manipulation, Swept-space Analysis.

ACKNOWLEDGEMENTS

This work was supported by Korea Institute of Planning and Evaluation for Technology in Food, Agriculture and Forestry(IPET) through the Agriculture and Food Convergence Technologies Program for Research Manpower development, funded by Ministry of Agriculture, Food and Rural Affairs(MAFRA)(RS-2024-00397026) and was conducted with support of the Cooperative Research Program for Agricultural Science & Technology Development (Project No. RS-2025-04092968), National Institute of Horticultural and Herbal Science, Rural Development Administration, Republic of Korea.

PA-P08

Proceedings of The 12th International Symposium on Machinery and Mechatronics for Agriculture and Biosystems Engineering (ISMAB 2026)
20-24 October 2026, Busan, Republic of Korea

RGB-BASED 3D RECONSTRUCTION AND PHENOTYPING WORKFLOW FOR TOMATO PLANTS

Yi Chen[1,3], Kyeong-Hwan Lee[1,2,3*]

[1]Department of Convergence Biosystems Engineering, Chonnam National University, Gwangju, Korea
[2]AI Agri-Tech Research Center, Chonnam National University, Gwangju, Korea
[3]BK21 Interdisciplinary Program in IT-Bio Convergence System, Chonnam National University, Gwangju, Korea
*Corresponding Author-- Voice: +82-62-530-0622, Email: khlee@jnu.ac.kr

Abstract: 3D plant phenotyping provides detailed structural information for non-destructive crop growth monitoring and phenotypic analysis, but reliable acquisition and processing of plant 3D data remain challenging. This study aims to establish a multi-view RGB-based 3D phenotyping platform for tomato plants and to evaluate the feasibility of the complete workflow from image acquisition to subsequent phenotypic analysis. A phenotyping platform consisting of an RGB camera, a rotating platform, and a control unit was developed for multi-view image acquisition. Tomato plants were reconstructed into 3D point clouds using a structure-from-motion and multi-view stereo (SfM-MVS) workflow. Existing open-source methods were further tested for point-cloud processing, leaf extraction, surface reconstruction, and surface flattening. The developed platform successfully acquired multi-view images and generated 3D tomato plant models. The reconstructed point clouds could be further processed for organ-level analysis, demonstrating the feasibility of connecting image acquisition, 3D reconstruction, and downstream phenotyping procedures. The established platform and processing workflow provide a technical foundation for 3D tomato phenotyping. Future work will focus on improving organ segmentation and quantitative phenotype extraction algorithms, validating measurements against ground-truth data, and extending the system toward longitudinal 3D/4D plant growth analysis.

Key Words: Tomato phenotyping, 3D reconstruction, Point cloud, Multi-view imaging, Plant phenotyping

ACKNOWLEDGEMENTS

This work was was conducted with support of the Cooperative Research Program for Agricultural Science & Technology Development (Project No. RS-2025-04092968), National Institute of Horticultural and Herbal Science, Rural Development Administration, Republic of Korea and Korea Institute of Planning and Evaluation for Technology in Food, Agriculture and Forestry(IPET) through the Open Field Smart Agriculture Technology Short-term Advancement Program, funded by Ministry of Agriculture, Food and Rural Affairs(MAFRA)(32203703).

PA-P09

Proceedings of The 12th International Symposium on Machinery and Mechatronics for Agriculture and Biosystems Engineering (ISMAB 2026)
20-24 October 2026, Busan, Republic of Korea

SIMULATION OF PESTCIDE TRANSPORT IN A SOYBEAN-GROWING FIELD: A CASE STUDY OF DINOTEFURAN

Uk Heo, Jongsoon Kim*

Department of Bio-industrial Machinery Engineering, Pusan National University, Miryang, Gyeongnam 50463, Republic of Korea
*Corresponding Author-- Voice: +82-55-350-5426, Email: jongsoon-kim@pusan.ac.kr

Abstract: Bean bug (*Riptortus pedestris*) is major pest in soybean production, causing substantial reduction in both yield and seed quality. Dinotefuran is an effective insecticide for controlling bean bugs; however, its residues in soil can adversely affect crop growth and the surrounding environment. Therefore, understanding the transport and persistence of dinotefuran in soil under actual soybean-growing condition is essential for its safe and effective use. This study simulated the depth-resolved transport and persistence of dinotefuran over four consecutive years in a soybean field in Miryang, Republic of Korea. The coupled SWAP-PEARL model was applied from 2022 to 2025 using a 2 m soil profile with a free-drainage lower boundary. Dinotefuran was applied to the soybean canopy three times each summer at 20 g/ha in 2022, 2023, 2024, whereas no application was made in 2025 to evaluate its residual persistence and dissipation. Dinotefuran concentrations in the upper 0.2 m increased sharply within several days after each application and subsequently declined, while downward transport resulted in its gradual accumulation in the subsoil. Consequently, approximately 1 μg L^{-1} remained at a depth of 1 m before the beginning of each subsequent growing season. The solute front advanced downward at approximately 5 mm/day, reaching a depth of 1 m within six months and 2 m within one year. Peak concentration occurred approximately 10 days after application near the soil surface but were delayed by nearly two months at a depth of 1 m. These results indicate that dinotefuran may persist beyond a single growing season and migrate below the soybean root zone. The findings provide invaluable information when applying dinotefuran for sustainable soybean production.

Key Words: Dinotefuran, Soil residue, Solute transport, PEARL, Soybean

PA-P10

Proceedings of The 12th International Symposium on Machinery and Mechatronics for Agriculture and Biosystems Engineering (ISMAB 2026)
20-24 October 2026, Busan, Republic of Korea

BIAS-AUGMENTED IEKF-BASED GNSS/INS INTEGRATION ALGORITHM FOR AUTONOMOUS AGRICULTURAL TRACTORS

Choongmin Lee[1], Wonhee Lee[2], Kwanjin Kim[3*]

[1,2] Hanwha Aerospace, LS Business Division, Navigation Bussiness Center, Navigation Business Team, 86, Cheonggyecheon-ro, Jung-gu, Seoul, South Korea
[3*]Hanwha Aerospace, LS Business Division, Navigation Bussiness Center, 86, Cheonggyecheon-ro, Jung-gu, Seoul, South Korea
*Corresponding Author-- Voice: +82-10-7455-4690, Email: kwanjin1.kim@hanwha.com

Abstract: To ensure continuity of the navigation solution in GNSS-shadowed environments or during temporary signal outages, GNSS/INS integration is widely employed, typically using a loosely coupled algorithm based on an extended Kalman filter(EKF). A conventional error-state EKF locally linearizes the nonlinear inertial navigation dynamics and measurement models around the current state estimate. When attitude errors increase because of sensor errors or when aggressive rotational motion amplifies linearization errors, the propagated covariance may no longer accurately represent the actual error distribution. Consequently, the consistency of state correlations and the Kalman gain may deteriorate, potentially resulting in large navigation errors even after correction using GNSS measurements. In contrast, an invariant extended Kalman filter(IEKF), in which the estimated and true states are represented on the $SE_2(3)$ Lie group and their discrepancy is defined as an invariant error, reduces the dependence of the error dynamics on the estimated trajectory. This enables more consistent linearization and covariance propagation under large initial errors and highly nonlinear motion. This paper proposes a loosely coupled navigation algorithm based on a bias-augmented IEKF. Position, velocity, and attitude errors are corrected on the Lie group, while gyroscope and accelerometer biases are incorporated as additive state variables. The proposed algorithm first performs a GNSS position update, followed by a velocity-constraint update based on the non-holonomic constraint(NHC) and a zero-velocity update during stationary condition, thereby suppressing the accumulation of velocity errors and the divergence of position errors. During the GNSS position and NHC updates, corrections to the yaw angle and the z-axis gyroscope bias are disabled to prevent erroneous estimates of these states. To compensate for the resulting lack of yaw observability, a conditional heading update based on the GNSS course-over-ground(COG) is applied during driving segments in which the COG is sufficiently aligned with the vehicle yaw angle. The condition is analyzed and measurement noise level is adaptively changed based on three filtering logic. Vehicle test results demonstrate that the corrected navigation solution successfully tracks the GNSS reference information in terms of position and velocity.

Key Words: INS, GNSS, EKF, IEKF, NHC

PA-P11

Proceedings of The 12th International Symposium on Machinery and Mechatronics for Agriculture and Biosystems Engineering (ISMAB 2026)
20-24 October 2026, Busan, Republic of Korea

DEVELOPMENT OF A MACHINE LEARNING MODEL FOR PREDICTING SOIL MOISTURE IN CROP FIELDS USING WEATHER AND IRRIGATION DATA

Gyeong-Tae Kim[1], Hyung-Min Kim[1], Jun-Ha Choi[1], Hwang Gyu Lee[2], Tae-Wook Kim[2], Jin-Hyun Kim[2], Dong Suk Kim[3], Sang-Hun Lee[3], Suk-Ju Hong[1]*

[1]Department of Smart Bio-industrial Mechanical Engineering, Kyungpook National University, Daegu 41566, Republic of Korea
[2]Department of Precision Mechanical Engineering, Kyungpook National University, Sangju 37224, Republic of Korea
[3]Smart Agricultural Technology Research Division, National Institute of Crop and Food Sciences, RDA, Miryang 50424, Republic of Korea
*Corresponding Author-- Voice: +82-10-5108-1589, Email: hsj5596@knu.ac.kr

Abstract: Reliable estimates of soil moisture can support irrigation scheduling when continuous field measurements are unavailable. Beyond agriculture, soil moisture plays an important role in hydrological processes, ecosystem functioning, and land–atmosphere interactions. Its broad relevance has motivated numerous studies on soil moisture prediction using meteorological data. However, comparatively few studies have explicitly incorporated irrigation inputs into predictive models for managed agricultural fields, where water supply depends on both rainfall and irrigation. This study investigated the use of machine learning to predict soil moisture in soybean fields from weather and irrigation data. Field observations were obtained between June and October 2025 from an experiment comprising five irrigation treatments. Weather and irrigation data served as model inputs, while measured soil moisture provided the reference values for model training and evaluation. Predictive performance was assessed using the coefficient of determination (R^2) and root mean square error (RMSE). The study addresses the growing need for practical water management tools in upland agriculture, where drought threatens production and the cost of sensor deployment constrains spatial coverage. The proposed approach could complement field monitoring by providing soil moisture estimates where direct measurements are limited, thereby supporting more informed irrigation decisions and the wider adoption of precision water management.

Key Words: Soil Moisture, Machine Learning, Irrigation, Regression, Water Management

PA-P12

Proceedings of The 12th International Symposium on Machinery and Mechatronics for Agriculture and Biosystems Engineering (ISMAB 2026)
20-24 October 2026, Busan, Republic of Korea

A REVIEW ON METAL BINDER JETTING PROCESSES APPLYING ACTIVE POWDER FEEDING-RECOATING MODULES

DoHyun Ahn[1], YeJin Park[2], PilHo Lee[3], ChangSeop Shin[4]

[1]Department of Biosystems Engineering, Chungbuk National University, South Korea
[2]Department of 3D Printing, Korea Institute of Machinery and Materials
*Corresponding Author-- Voice: +82-43-261-2584, Email: shinchang7@cbnu.ac.kr

Abstract: Metal components used in agricultural machinery and precision farming systems require high productivity and reliable manufacturing processes to produce complex and functional parts. Metal binder jetting (MBJ) has attracted attention as a high-productivity additive manufacturing technology with potential for producing metal components with complex geometries. However, the formation of non-uniform powder layers when using highly cohesive fine powders remains a major limitation that can degrade the quality and dimensional accuracy of final parts. This review investigates the effects of an integrated ribbon feeder module on the spreading uniformity of cohesive fine powders in the MBJ process. Previous studies on powder spreading mechanisms, recoating conditions, and active powder supply systems were reviewed and compared. In particular, the effects of recoating speed and feeder rotation speed were analyzed by quantitatively evaluating the defect area observed on spread powder layers and comparing the relative changes under different operating conditions. The reviewed results indicate that a single-direction screw feeder can mitigate powder agglomeration and reduce coating defects by continuously supplying powder to the recoating region. The quantitative analysis showed that the most significant reduction in defect area was achieved under conditions of low recoating speed and high feeder rotation speed, indicating that the balance between powder supply and recoater motion plays an important role in determining layer uniformity. Future research is needed to apply an active powder feeding system to the production of metal parts for agricultural machinery.

Key Words: Metal Binder Jetting, Powder Feeding-Recoating Module, Ribbon Feeder, Powder Layer Uniformity, Active Powder Feeding

Acknowledgements: This work was carried out with the support of "Cooperative Research Program for Agriculture Science & Technology Development (RS-2025-02216071)" Rural Development Administration, Republic of Korea.

PA-P13

Proceedings of The 12th International Symposium on Machinery and Mechatronics for Agriculture and Biosystems Engineering (ISMAB 2026)
20-24 October 2026, Busan, Republic of Korea

THEORETICAL POWER REQUIREMENT OF A SPRAYER MODULE FOR A MULTIPURPOSE ELECTRIC PEPPER CULTIVATION PLATFORM

Md Nasim Reza[1,2], Hongbin Jin[1], Miao Miao Tu[2], Md Mamunur Rashid[1], Sujeong Jeong[2], Jong-Su Lee[3], Sun-Ok Chung[1,2*]

[1]Department of Smart Agricultural Systems, Graduate School, Chungnam National University, Daejeon, 34134, Republic of Korea
[2]Department of Agricultural Machinery Engineering, Graduate School, Chungnam National University, Daejeon 34134, Republic of Korea
[3]Daesin Agricultural Machinery Engineering, Co., Ltd., Yecheon 36815, Republic of Korea
*Corresponding Author-- Voice: +82-42-821-6712, Email: sochung@cnu.ac.kr

Abstract: A sprayer module for a multipurpose electric agricultural platform requires coordinated sizing of the nozzle arrangement, liquid flow, operating pressure, and motor power. This study established a theoretical design procedure for a tunnel-type sprayer intended for chili pepper cultivation. Agronomic requirements for major diseases and insect pests were first organized to define the upper application rate. The hydraulic system was then sized from a target spray volume of 2,000 L ha^{-1}, a 3.6 m effective working width, and travel speeds of 1.0–3.0 km h^{-1}. The proposed arrangement used four spray columns, three twin-outlet nozzle bodies per column, and 24 outlet ports directed toward eight crop faces. Total flow was calculated from application rate, speed, and working width, while nozzle flow was obtained by distributing the total demand across the nozzle bodies and outlets. Pump input power was calculated for pressures of 0.50–1.50 MPa using a hydraulic efficiency of 0.70, followed by a 20% design factor. At the nominal speed of 2.0 km h^{-1}, the required total flow was 24 L min^{-1}, corresponding to 2.0 L min^{-1} per twin-outlet body and 1.0 L min^{-1} per outlet. Calculated pump power increased linearly from 0.29 to 0.86 kW across the pressure range, and the design power increased from 0.34 to 1.03 kW. At 1.0 MPa, the module required 0.57 kW, or 0.69 kW after application of the design factor. The analysis provides traceable hydraulic and electrical design values for integrating the sprayer module with the battery, controller, and motor architecture of the electric platform.

Key Words: Precision Agriculture, Electric Agricultural Platform, Hydraulic Power, Pepper, Pump Sizing Spray Flow Rate

INTRODUCTION (first level heading, bold, centered)

Chili pepper (*Capsicum annuum* L.) production requires repeated crop-protection operations because foliage, flowers, and fruit remain exposed to diseases and insect pests over an extended growing period. Anthracnose, Phytophthora blight, bacterial leaf spot, viral diseases, tobacco budworm, beet armyworm, and aphids create different treatment schedules and

coverage requirements. Conventional hand-held or backpack spraying places the operator close to the spray cloud and produces variable walking speed, nozzle distance, and deposition. A robot developed for chili production demonstrated the direct connection between autonomous mobility and localized liquid delivery, while also identifying worker exposure and inconsistent coating as central limitations of manual practice (Mashori et al., 2023). Similar mobile systems have combined autonomous navigation, plant recognition, and electronically controlled spraying to separate the operator from the treated zone (Baltazar et al., 2021; Wang et al., 2022).

Recent spraying studies have advanced from basic mechanization toward target-responsive application. Robotic sprayers now integrate perception, autonomous navigation, and electronic spray control (Baltazar et al., 2021; Wang et al., 2022; Nasir et al., 2023). In these systems, the spraying module represents a defined electrical load because application rate, working width, travel speed, operating pressure, and pump efficiency collectively determine hydraulic and electrical power requirements.

This relationship is important for multipurpose electric platforms because propulsion, sensing, control, and implement motors share the battery supply. Oversizing the sprayer drive increases mass, cost, and energy consumption, whereas undersizing reduces flow and pressure stability. The nozzle arrangement must also correspond to crop geometry to ensure adequate liquid distribution across the canopy. Compact robotic sprayers and variable-rate systems commonly use electronic control of pressure or flow according to operating conditions (Kassim et al., 2020; Jiao et al., 2025).

Previous studies have primarily addressed navigation, target recognition, variable-rate control, and spray performance, while the translation of agronomic application requirements into pump and motor power remains less clearly defined. Therefore, the objective of this study was to calculate theoretical power requirement of a sprayer module for a multipurpose electric pepper-cultivation platform.

MATERIALS AND METHODS

PLATFORM AND SPRAYER ARCHITECTURE

The analyzed machine consisted of a tracked electric platform carrying a battery-storage system, a main controller, traction motors, and interchangeable cultivation modules. The sprayer formed one implement branch of this architecture and used a dedicated electric motor to drive the liquid pump. The tunnel configuration incorporated four vertical spray columns. Each column carried three twin-outlet nozzle bodies; therefore, the module contained 12 nozzle bodies and 24 outlet ports. The columns enclosed the crop rows and directed spray toward eight canopy faces. The effective width covered three row-spacing intervals, giving a working width of 3.6 m.

PLATFORM AND SPRAYER ARCHITECTURE

The design sequence began with the pepper growth stage and associated disease or pest. The treatment requirement defined the spray volume and effective area. Vehicle speed and effective width then determined total liquid flow. The selected nozzle arrangement divided this demand among the nozzle bodies and outlet ports. Finally, operating pressure and pump efficiency defined the electrical input required by the pump motor.

The source agronomic schedule included application volumes of 1500–2000 L per ha for anthracnose, at least 1500–2000 L per ha for Phytophthora blight, and 2000 L per ha for bacterial leaf spot. Tobacco budworm treatment used 1000–1500 L per ha, whereas aphids and beet armyworm used 1500–2000 L per 1ha. The upper common rate, 2000 L per ha, was selected as the design case.

Table 1 Hydraulic and geometric design parameters.

Parameter	Symbol	Value
Target application rate	A	2,000 L ha^{-1}
Working width	B	3.6 m
Nominal travel speed	v	2.0 km h^{-1}
Spray columns	-	4
Twin-outlet bodies	N_n	12
Outlet ports	N_o	24
Pump efficiency	η	0.70
Design factor	f	1.20

THEORETICAL CALCULATIONS AND ANALYSIS

For a nozzle located at distance H from the crop and having spray angle θ, the geometric spray width W was calculated using Equation (1).

$$W = 2H\tan\left(\frac{\theta}{2}\right) \quad (1)$$

Total module flow Q was derived directly from application rate A, travel speed v, and effective width B using Equation. (2).

$$Q = \frac{AvB}{600} \quad (2)$$

The flow assigned to one twin-outlet body q_n and one outlet q_o followed Equaitons (3) and (4).

$$q_n = Q/N_n \quad (3)$$

$$q_o = \frac{Q}{N_o} \quad (4)$$

where, N_n = 12 and N_o = 24. The pressure–flow response of a fixed nozzle followed the square-root relationship shown in Equation (5).

$$Q_2 = Q_1\sqrt{\frac{p^2}{p^1}} \quad (5)$$

Pump input power P was calculated using Equation (6).

$$P = \frac{pQ}{600\eta}, \quad P_e = 1.20P \quad (6)$$

where, p is pressure in bar, Q is flow in L min^{-1}, and η is overall pump efficiency. A 20% design factor produced the selected power P_e. The analysis used η = 0.70, v = 1.0–3.0 km h^{-1}, Q = 24 L min^{-1} for the pressure comparison, and p = 5–15 bar (0.50–1.50 MPa).

RESULTS & DISCUSSION

FLOW REQUIREMENT AND NOZZLE DISCHARGE

At the 2.0 km h^{-1} nominal operating speed, the product of 2,000 L ha^{-1}, 2.0 km h^{-1}, and 3.6 m produced a total requirement of 24 L min^{-1}. Division across 12 twin-outlet bodies gave 2.0 L min^{-1} per body, and division across 24 outlets gave 1.0 L min^{-1} per outlet. These values

preserve equal delivery across the four columns when each column carries the same number of nozzle bodies.

Flow demand varied in direct proportion to travel speed because application rate and working width remained fixed. Increasing speed from 1.0 to 3.0 km h^{-1} increased total flow from 12 to 36 L min^{-1}. The associated twin-outlet demand increased from 1.0 to 3.0 L min^{-1}, and individual outlet demand increased from 0.50 to 1.50 L min^{-1}. The nominal 2.0 km h^{-1} case occupied the midpoint of the evaluated range and established the 24 L min^{-1} pump flow criterion.

Table 2 Flow requirement as a function of platform speed.

Speed (km h^{-1})	Total flow (L min^{-1})	Per twin outlet (L min^{-1})	Per outlet (L min^{-1})
1.0	12	1.0	0.50
1.5	18	1.5	0.75
2.0	24	2.0	1.00
2.5	30	2.5	1.25
3.0	36	3.0	1.50

PUMP POWER REQUIREMENT

For a constant flow of 24 L min^{-1} and 70% efficiency, pump input power increased linearly with operating pressure. The calculated values were 0.29, 0.43, 0.57, 0.71, and 0.86 kW at 0.50, 0.75, 1.00, 1.25, and 1.50 MPa, respectively. Application of the 20% design factor increased these values to 0.34, 0.51, 0.69, 0.86, and 1.03 kW. At the 1.0 MPa reference point, the hydraulic output was 0.40 kW, the corresponding pump input was 0.57 kW, and the design value was 0.69 kW. The difference between hydraulic output and input represents the conversion loss embedded in the 0.70 efficiency term.

The pressure analysis also defines the electrical integration boundary of the sprayer module. Operation at 0.50–1.00 MPa places the factored load below 0.70 kW, whereas operation at 1.25–1.50 MPa increases the load to 0.86–1.03 kW. Thus, pressure selection produces a larger change in module power than redistribution of a fixed total flow among nozzles. Nozzle count controls discharge per point, but it does not change total pump flow when application rate, width, and speed remain constant.

Table 3 Pump power at a constant flow of 24 L min^{-1}.

Pressure (MPa)	Calculated power (kW)	Power with 20% factor (kW)
0.50	0.29	0.34
0.75	0.43	0.51
1.00	0.57	0.69
1.25	0.71	0.86
1.50	0.86	1.03

HYDRAULIC AND ELECTRICAL INTEGRATION

For a fixed nozzle orifice, flow varies with the square root of pressure; therefore, doubling the pressure increases flow by $\sqrt{2}$ rather than twofold. Maintaining the application rate across 1.0–3.0 km h^{-1} requires a 3:1 flow range, which would require a 9:1 pressure range if the nozzle orifice remained unchanged. Accordingly, the controller must coordinate travel speed, flow rate,

and operating pressure. At the nominal design point of 2.0 km h^{-1}, 1.0 MPa, and 2,000 L ha^{-1}, the 24 outlets require a total flow of 24 L min^{-1} and a factored pump power of 0.69 kW.

CONCLUSIONS

A theoretical hydraulic-power model was established for a tunnel-type sprayer mounted on a multipurpose electric pepper-cultivation platform. The design used a 3.6 m working width, a target application rate of 2,000 L ha^{-1}, four spray columns, 12 twin outlet nozzle bodies, and 24 outlet ports. At 2.0 km h^{-1}, total flow was 24 L min^{-1}, equal to 2.0 L min^{-1} per twin outlet body and 1.0 L min^{-1} per outlet. Across 0.50–1.50 MPa, calculated pump power ranged from 0.29 to 0.86 kW and the corresponding values with a 20% design factor ranged from 0.34 to 1.03 kW. The nominal 1.0 MPa operating point required 0.57 kW pump input and 0.69 kW design power. The resulting design point links crop protection application requirements directly to nozzle discharge, pump capacity, and the electric load of the modular platform.

ACKNOWLEDGEMENTS

This work was supported by Korea Institute of Planning and Evaluation for Technology in Food, Agriculture and Forestry (IPET), through the Promotion of Mass Technology Commercialization Program, funded by Ministry of Agriculture, Food and Rural Affairs (MAFRA) (Project No. RS-2025-02217679), Republic of Korea

REFERENCES

Mashori, N. A., W. N. S. E. Wan Jusoh, A. F. Abd Aziz, et al. 2023. Development of pesticide sprayer robot prototype for chilli farm application. Int. J. Integr. Eng. 15: 217–226.

Baltazar, A. R., F. N. dos Santos, A. P. Moreira, A. Valente, and J. B. Cunha. 2021. Smarter robotic sprayer system for precision agriculture. Electronics 10: 2061.

Wang, S., J. Song, P. Qi, C. Yuan, H. Wu, L. Zhang, W. Liu, Y. Liu, and X. He. 2022. Design and development of orchard autonomous navigation spray system. Front. Plant Sci. 13: 960686.

Nasir, F. E., M. Tufail, M. Haris, J. Iqbal, S. Khan, and M. T. Khan. 2023. Precision agricultural robotic sprayer with real-time tobacco recognition and spraying system based on deep learning. PLOS ONE 18: e0283801.

Kassim, A. M., M. F. N. M. Termezai, A. K. R. A. Jaya, A. H. Azahar, S. Sivarao, F. A. Jaafar, and M. S. M. Aras. 2020. Design and development of autonomous pesticide sprayer robot for fertigation farm. Int. J. Adv. Comput. Sci. Appl. 11: 545–551.

Jiao, Y., S. Zhang, Y. Jin, L. Cui, C. Chang, S. Ding, Z. Sun, X. Xue, and Q. Zhou. 2025. Research progress on intelligent variable-rate spray technology for precision agriculture. Agronomy 15: 1431.

PA-P14

Proceedings of The 12th International Symposium on Machinery and Mechatronics for Agriculture and Biosystems Engineering (ISMAB 2026)
20-24 October 2026, Busan, Republic of Korea

SELF-CALIBRATING VIDEO MEASUREMENT OF CORRIDOR CROWDING AND ITS ASSOCIATION WITH DAIRY COW LAMENESS SCORING

Jia-Ming Zhou[1], Wen-Lin Chu[1,2*], Hsin-I Chiang[3]

[1]Department of Bio-Industrial Mechatronics Engineering, National Chung Hsing University, Taichung 402202, Taiwan
[2]Agricultural Automation Center, National Chung Hsing University, Taichung 402202, Taiwan
[3]Department of Animal Science, National Chung Hsing University, Taichung 402202, Taiwan
*Corresponding Author-- Voice: +886-4-2284-0377 ext. 509, Email: wlchu@nchu.edu.tw

Abstract: In a single-file corridor only the longitudinal gap matters, and in pixels that gap neither transfers between cameras nor stays constant across one frame. This study builds a self-calibrating video measurement of corridor crowding, validates it in its own right, and quantifies how that exposure relates to expert lameness scoring. Because a straight corridor projects as a projective map of its arc length, the pixels spanning one body length are a two-parameter function of image column; fitting it to the population median box width needs no calibration target, and integrating its reciprocal gives spacing in body lengths, on which the corridor crowding index is the traversal mean of a bounded proximity kernel. On 113 raceway videos of Holstein cows (327 traversals), rectification removed the dependence of apparent body length on image position (Spearman 0.39 to -0.03), the index survived 20 % detection loss and 10 % box inflation with rank correlation above 0.996, and systematic bias moved it about 6 times as far as random noise at the same level. On 169 traversals with three independent expert scores of 91 cows, a higher index was associated with lower odds of a lame consensus label (odds ratio 0.38 per interquartile range, 95 % CI 0.19 to 0.76), where the overlap fraction it replaces gave 0.66 (0.42 to 1.03). Crowding thus becomes a recorded condition of each observation rather than an unmeasured difference between them, and lameness-scoring datasets should carry it beside the score.

Key Words: corridor crowding, projective rectification, instance segmentation, measurement validation, lameness scoring

INTRODUCTION

How closely animals are packed decides what a camera, and a human scorer, can see of any one. Crowding degrades camera-based monitoring on dairy farms (Toulemonde et al., 2026); motivation alone shifts gait with no change in health (Mokhtarnazif et al., 2020); and scorers report walking speed entering their judgement (Linardopoulou et al., 2026). Space allowance in square metres (Thompson et al., 2020) presumes room to move, and group spacing is nearest-neighbour distance (Chopra et al., 2024) or box proximity, whose definition changes

the conclusions (Orsini et al., 2025). In a raceway one animal wide, area per animal is uninformative and that distance collapses onto the longitudinal gap, in pixels neither transferable nor constant.

The two objectives are to establish a dimensionless measurement of corridor crowding, validated in its own right, and to quantify how the resulting exposure relates to expert lameness scoring, whose label is assumed to depend only on the animal. That assumption is weak. Reported prevalence varies widely with how scoring was done (Wessels et al., 2025), ten observers reached a Fleiss kappa of 0.28 (Wilson et al., 2026), and inconsistent annotation propagates into models trained on it (Sylolypavan et al., 2023).

MATERIALS AND METHODS

Data acquisition and traversal extraction

Side-view videos (4106 × 1758 px, 30 fps) were recorded at Yuanlin Farm, a commercial Holstein herd in Houli, Taichung, Taiwan, as cows left the milking parlour through a fenced single-file raceway. A YOLO11m-seg model trained on crops of this raceway (single class, mask mAP50-95 0.839) ran with ByteTrack at 640 px, animals behind the fence excluded by track median box height and image row. A traversal is a track crossing the frame, matched to the score sheet by entry order. 113 of the 117 recorded videos gave 327 traversals, median duration 10.5 s, identity from the parlour radio-frequency identification tag. Traversals were scored on a three-point lameness scale, the consensus being the majority of three scorers, with 2 or 3 counting as lame; an early block carries duplicated score columns, leaving 172 traversals with three independent scores, of which 169 reached a majority and enter the criterion analysis over 91 cows.

Projective scale field and arc-length rectification

A straight corridor is a straight line in the world, so the map from corridor arc length to image column is projective, $x(t) = (\alpha t + \beta)/(\gamma t + \delta)$, whose coefficients $\alpha, \beta, \gamma, \delta$ are fixed by the camera pose and matter only through their ratios. Differentiating it gives the pixels spanning one unit of world length at column x, as shown in Eq. (1).

$$s(x) = \frac{dx}{dt} \propto \left(x_v - x\right)^2 \tag{1}$$

where:

$s(x)$ = pixels spanning one unit of world length at a given image column (px/BL)

x = image column (px)

t = corridor arc length (BL)

x_v = vanishing point of the corridor axis (px)

The square root of the scale is affine in image column, $\sqrt{s(x)} = a + bx$, so the field has two free parameters and extrapolates under a geometric constraint, not a smoothing assumption. Each animal holds a fixed length while it crosses, so where the mix of body sizes does not change with image column the detector's population median box width estimates the scale up to a constant that cancels once distances are in body lengths (BL). Only a box wholly inside the frame has a measurable apparent length, and near the edge only a short box fits, so the two parameters come from count-weighted least squares over equal-width column bins, excluding those whose centre lies within half a reference body length, the 95th percentile of box width, plus the edge margin. Arc length then follows in closed form, with $u(0) = 0$ at the left edge, as $u(x) = 1/(ab) - 1/[b(a + bx)]$.

Corridor crowding index

Each detection maps to an interval on the rectified axis, and for the scored animal and any other in the same frame the signed separation d_{ij} is the larger of the two end-to-end differences, positive being a clear gap in body lengths and negative meaning the projections overlap. A single camera cannot resolve overlap into depth, so the kernel scores it as contact, an upper bound on proximity. The per-frame nearest-neighbour distance $d(t)$ is the minimum over all other animals, and the index is the traversal mean of a bounded kernel on that gap, as shown in Eq. (2). Frames with no other animal detected contribute zero, and the mean runs over frames in which the scored animal was detected.

$$\mathrm{CCI} = \frac{1}{T}\sum_{t=1}^{T} \exp\left(-\frac{\max(d(t),0)}{L}\right) \tag{2}$$

where:

CCI = corridor crowding index of the traversal (-)

T = frames of the traversal in which the scored animal was detected (-)

$d(t)$ = nearest-neighbour gap of the scored animal in one frame (BL)

L = kernel length scale, fixed a priori at 1 BL

The index lies between 0 and 1, reaches 1 at contact and falls to 0.05 at three body lengths, combining how close with how long. Three cue families are kept apart because their causal standing differs. Proximity is set by the neighbours, the animal's own speed by the animal, and the release interval by the handler. Speed enters only as a covariate, since a lame cow slows with no neighbour involved (Frondelius et al., 2022).

Validation design

Six checks were specified in advance, and V1 tests whether rectification removes the dependence of apparent body length on image position. V2 degrades the detector with box-edge noise (1 to 5 % of box width), lost detections (5 to 20 %), a stricter confidence floor, and inflation of every box (3 to 10 %), the last being the one that moves every box the same way. V3 refits the field on random halves of the videos and on each session, then applies one session's field to the other. V4 compares the index against annotations written during scoring, V5 tests its separability from the animal's own progression, and V6 how its association with the consensus label compares with the overlap fraction it replaces, the share of frames with overlapping projections, which needs no scale field.

RESULTS & DISCUSSION

Scale field and rectification

The fit reached a coefficient of determination of 0.82 and put the vanishing point 47×10^{3} px outside the frame, so the camera is nearly perpendicular to the corridor (Fig. 1a). The scale still varies by 18 % across the frame, 883 to 1045 px per body length, so one global scale misstates every gap that spans it; the corridor spans 4.27 body lengths (Fig. 1b). Over 107943 untruncated detections the rank correlation between body length and image column fell from 0.39 to -0.03, and the binned median profile halved its spread, 0.113 to 0.062 BL (Fig. 1c). The coefficient of variation fell only from 0.095 to 0.089 and should not fall further. Rectification removes the position-dependent component, not genuine variation in body size and head carriage.

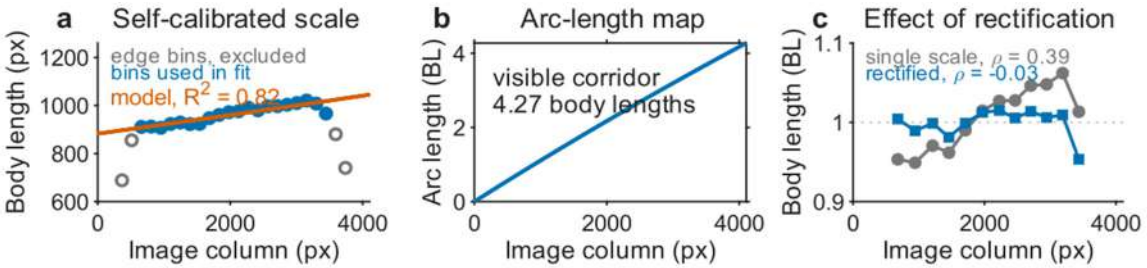

Fig. 1 Self-calibration. (a) Median box width per equal-width column bin, fitted on the 20 untruncated bins; (b) arc length in body lengths (BL); (c) body length against image position.

Across all 327 traversals the index had a median of 0.58 and an interquartile range of 0.61, with 54 % showing projected overlap in at least one frame and a median gap of 0.17 BL. Animals either walk alone or file out nose to tail, and Fig. 2 shows one of each.

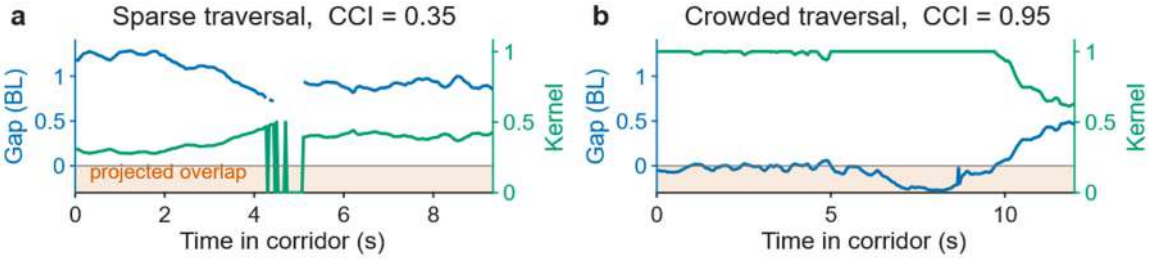

Fig. 2 Measurement on two traversals. Left axis, nearest-neighbour distance; right axis, the proximity kernel the index averages. Shading marks projected overlap, scored as contact.

Robustness and calibration stability

The index barely moved under random box-edge error but is not indifferent to detection loss or systematic error (Fig. 3). Edge noise at 5 % of box width changed it by 0.0034 on average, zero-mean error averaging out over the frames; a fifth of detections discarded changed it by 0.081 and a confidence floor of 0.7 by 0.014. Inflating every box by 5 %, the error a segmentation model makes consistently, changed it by 0.019, about 6 times random noise at the same level. Rank order survived all of it (Spearman above 0.991).

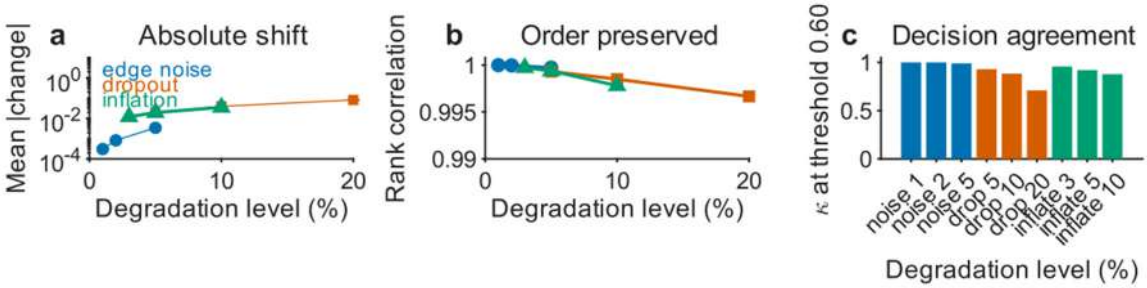

Fig. 3 Index under detector degradation, all 327 traversals. (a) Mean absolute change, log scale; (b) rank correlation with the unperturbed index; (c) decision agreement at 0.60, an operating point fixed in advance. 10 repeats for the random sweeps, bars in (a) their standard deviation; inflation is deterministic, confidence floor not plotted.

Over 12 random half-splits of the videos the index changed by 0.0003, and a field fitted on one recording session and applied to the other, shot months apart, changed it by 0.0010 with identical binary decisions. That transfer is within one camera and one corridor, and the model fitted the earlier session less well (0.52 against 0.85), which is the limit of the claim.

Construct and criterion validity

The index is strongly rank-aligned with co-presence (Spearman 0.93 against linear density)

but weakly related to the scored animal's own speed (-0.17, and -0.14 partialling out density), while the overlap fraction gave -0.23 on the same traversals. Detection confidence fell with the index (-0.36), so the two are not independent. The 4 traversals annotated as clumped, held up or pushed sat at the 76th percentile against the 17th for the 3 annotated as running, short of significance at this sample size (rank-sum P = 0.057) and supporting a direction rather than a rate.

On the 169 traversals with three independent scores the share labelled lame fell monotonically across quartiles of the index, 0.76 to 0.50 (Fig. 4a). Per interquartile range the odds were 0.38 (95 % CI 0.19 to 0.76, P = 0.007), cow-clustered with recording day as a fixed effect, and 0.35 (95 % CI 0.17 to 0.73, P = 0.006) with the animal's own rectified speed added. The same model on the overlap fraction gave 0.66 (95 % CI 0.42 to 1.03, P = 0.066), with an unclustered Akaike information criterion higher by 5.7 (Fig. 4b). The design is observational, and one mechanism needs no scorer. A lame cow walks slowly and, released with a group, may fall behind into open corridor, lowering her index for reasons unrelated to how she is judged. Adding her own speed left the odds at 0.35, but speed is not position in the group, so whether crowding biases the scorer, reflects the gait, or both, is not identified.

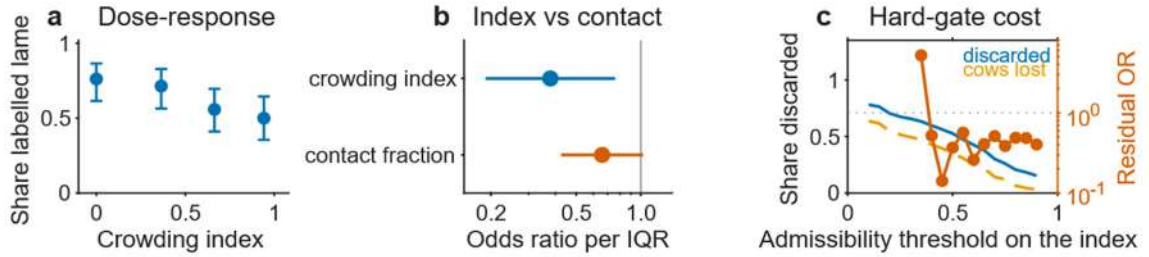

Fig. 4 Criterion validity, 169 traversals of 91 cows. (a) Share labelled lame by quartile of the index (n = 42 to 43), Wilson intervals; (b) odds ratio per interquartile range, cow-clustered, 95 % intervals; (c) hard-gate cost; thresholds keeping fewer than 60 traversals are omitted, their residual odds ratios reaching 10^6 under quasi-separation.

Implications and limitations

The obvious use of an exposure measure is a hard gate; the sweep prices it (Fig. 4c). A threshold of 0.60 discards 43 % of the labelled traversals and leaves 23 of 91 cows with nothing usable, for a residual odds ratio among those kept of 0.26 (P = 0.095); 0.80 discards 21 % and leaves 0.49 (P = 0.146). The loosest gate swept, 0.90, costs 15 % of traversals and 3 cows and leaves 0.40 (P = 0.032), the one threshold whose residual association is significant. Cheap gates leave the association standing and severe ones leave estimates too imprecise to judge, so the index belongs in the analysis as a covariate and in the dataset record as a reported condition, not a pipeline filter. Longer observed release intervals went with lower exposure (Spearman -0.43), the share above the threshold falling from 61 % of the 214 traversals with a predecessor in view to 46 % among the 83 released at least 5 s later, though those intervals were observed, not assigned.

The scale field assumes a straight corridor and a fixed camera; a curved raceway or a moving camera would need two-dimensional rectification. Depth is not observed, so overlap is scored as contact and the index is an upper bound wherever Fig. 2 is shaded; a neighbour outside the frame goes undetected. Body length comes from apparent box length, so head carriage leaves a residual. Transfer was tested within one installation, the convergent sample is seven annotations, and the criterion analysis is observational, from one farm and three scorers, with no independent measure of true lameness.

CONCLUSIONS

Corridor crowding in a single-file raceway can be measured from ordinary side-view video in body lengths without a calibration target, and on this farm higher crowding went with lower odds of a lame consensus label. Treating the corridor as one-dimensional reduces rectification to a two-parameter projective scale field fitted from the detector's own boxes, so no other instrument is needed. The index kept its rank order under every degradation tested; what moved it was lost detections and systematic box inflation, not zero-mean box noise, so an implementation must control detector recall and bias. Gating on crowding discards 15 % to 43 % of the traversals without demonstrably removing that association, and whether it reflects the scorer or a slow animal falling behind the group is not settled here, so the measurement, not the filter, is the useful object. A lameness-scoring dataset thus gains a crowding value that means the same thing in every frame and at every camera distance, carried beside the score as an auditable condition.

ACKNOWLEDGEMENTS

The authors thank Yuanlin Farm for access to the herd and raceway, the field staff, and the three scorers. This research was supported (in part) by NSTC 113-2634-F-005-002- project Smart Sustainable New Agriculture Research Center (SMARTer). The authors appreciate the funding organizations for their financial support.

REFERENCES

Chopra, K., H. R. Hodges, Z. E. Barker, J. A. Vázquez Diosdado, J. R. Amory, T. C. Cameron, D. P. Croft, N. J. Bell, A. Thurman, D. Bartlett, and E. A. Codling. 2024. Bunching behavior in housed dairy cows at higher ambient temperatures. J. Dairy Sci. 107(4): 2406-2425. doi:10.3168/jds.2023-23931.

Frondelius, L., S. Van Weyenberg, H. Lindeberg, A. Van Nuffel, J. Maselyne, and M. Pastell. 2022. Spatial behaviour of dairy cows is affected by lameness. Appl. Anim. Behav. Sci. 256: 105763. doi:10.1016/j.applanim.2022.105763.

Linardopoulou, K., L. Viora, G. King, J. Le Kernec, and N. N. Jonsson. 2026. How reliable is visual lameness scoring? Assessing human label variability for use in automated detection systems. J. Dairy Res. 93(2): 258-264. doi:10.1017/s0022029926102180.

Mokhtarnazif, S., A. M. C. Smid, D. M. Weary, A. Mohamadnia, and M. A. G. von Keyserlingk. 2020. Short communication: Motivation to walk affects gait attributes. J. Dairy Sci. 103(10): 9481-9487. doi:10.3168/jds.2019-18060.

Orsini, C. A. E. M., B. Hegedűs, L. E. van der Zande, I. Reimert, P. Bijma, and J. E. Bolhuis. 2025. Impact of proximity definitions and sampling rates on social networks in pigs based on tracking using computer vision. Sci. Rep. 15(1). doi:10.1038/s41598-025-93830-8.

Sylolypavan, A., D. Sleeman, H. Wu, and M. Sim. 2023. The impact of inconsistent human annotations on AI driven clinical decision making. npj Digit. Med. 6(1). doi:10.1038/s41746-023-00773-3.

Thompson, J. S., J. N. Huxley, C. D. Hudson, J. Kaler, J. Gibbons, and M. J. Green. 2020. Field survey to evaluate space allowances for dairy cows in Great Britain. J. Dairy Sci. 103(4): 3745-3759. doi:10.3168/jds.2019-17004.

Toulemonde, A. C., A. Madouasse, Y. Le Cozler, and R. Guatteo. 2026. Assessing the reliability of camera-based identification, activity monitoring, and location in housing systems on dairy farms. JDS Commun. 7(3): 371-377. doi:10.3168/jdsc.2025-0886.

Wessels, W., E. A. M. Bokkers, I. J. M. de Boer, E. Meijer, T. B. Rodenburg, M. Hostens, and G. Koop. 2025. A systematic review and meta-analysis of lameness scoring methods and the prevalence of lameness of dairy cows in northwest Europe. J. Dairy Sci. 108(9): 10037-10059. doi:10.3168/jds.2025-26585.

Wilson, J. P., V. Thorup, and N. J. Bell. 2026. Interobserver agreement when using a four-point mobility scoring system to score dairy cattle from video footage. Vet. Rec. 199(3). doi:10.1002/vetr.70801.

PA-P15

Proceedings of The 12th International Symposium on Machinery and Mechatronics for Agriculture and Biosystems Engineering (ISMAB 2026)
20-24 October 2026, Busan, Republic of Korea

A PLANT GROWTH MONITORING SYSTEM BASED ON A PORTABLE LASER-INDUCED GRAPHENE SENSOR

I-Yin Chang[1*] and Yao-Chuan Tsai [1]

[1]Department of Bio-Industry Mechatronics Engineering, National Chung Hsing University, Taiwan
*Corresponding Author-- Voice: +886 971730836, Email: yiyin2546@gmail.com

Abstract: The scope and principal objectives of this study focus on addressing the critical agricultural challenge of abnormal stem thinning and elongation phenomena in tomato plants by developing an innovative biaxial flexible growth monitoring sensor. This sensor integrates laser-induced graphene (LIG) with polydimethylsiloxane (PDMS) to achieve high compliance and sensitivity. Regarding the methods utilized, a horizontal-vertical orthogonal scanning technique was systematically designed and implemented to construct the LIG sensing network, and the fabrication parameters were systematically optimized. Specifically applying a laser power of 2.75 W, a scanning speed of 10 mm/s, and a line spacing of 0.075 mm, it achieved an outstanding transfer-molding yield of 99.71%. Summarizing the experimental results, the sensor successfully isolated transverse stem expansion interference from longitudinal growth signals, exhibited a broad maximum sensing range of up to 24% with exceptional sensitivity (yielding a gauge factor as high as 6536.2), and maintained remarkably stable, repeatable resistance output waveforms across 100 dynamic tensile fatigue cycles. Consequently, it effectively captured real-time stem micro-elongation and established continuous deformation curves capable of accurately differentiating normal plant development from stress-induced elongation states. The principal conclusions derived from this work indicate that the established real-time plant physiological monitoring mechanism serves as a highly reliable and precise foundation for evaluating crop robustness, providing early warnings for plant elongation in smart agriculture, and offering broad scalability for future precision management in protected crop cultivation.

Key Words: Flexible sensor, Tomato plant elongation, Growth dynamics monitoring, Smart agriculture, Plant deformation measurement

INTRODUCTION

In recent years, technology has been gradually introduced into the agricultural industry, combining with precision agriculture for protected cultivation. Maintaining an ideal microclimate and growing environment is crucial for crop yield. Among various issues, tomato plants are prone to elongation when subjected to insufficient light, accompanied by abnormal stem thinning, excessive internode length, and tissue brittleness, which severely impact disease resistance and yield.

Traditionally, plant monitoring has largely relied on manual visual inspection or destructive measurements, making it difficult to perform long-term continuous tracking. To address this,

this study designed a biaxial flexible growth monitoring sensor attached to tomato stems to synchronously measure changes in stem length without interfering with natural growth.
To address this issue, the main objective of this study is to establish a real-time measurement and analysis mechanism for plant elongation, assisting in the automated adjustment of cultivation environmental parameters, reducing the impact of elongation on crops, and providing a forward-looking reference for smart agriculture.

MATERIALS AND METHODS

Fabrication of the Flexible Strain Sensor

This experiment aims to fabricate a flexible strain sensor attachable to plant stems, utilizing laser-induced graphene (LIG) as electrodes and polydimethylsiloxane (PDMS) as a flexible stretchable substrate, thereby combining electrical conductivity with mechanical flexibility. The fabrication process flow is illustrated in Fig. 1. First, a commercial laser engraver was used to induce photothermal conversion on a 125-μm-thick polyimide (PI) film, preparing porous laser-induced graphene via a cross-interleaved laser processing method for both longitudinal and transverse directions. Next, after mixing the PDMS prepolymer and curing agent, a 1-mm PTFE mold was utilized to control the substrate thickness during casting, followed by transfer-printing the LIG onto the PDMS substrate. Finally, copper wires were connected to both ends using silver paste to complete the encapsulation.

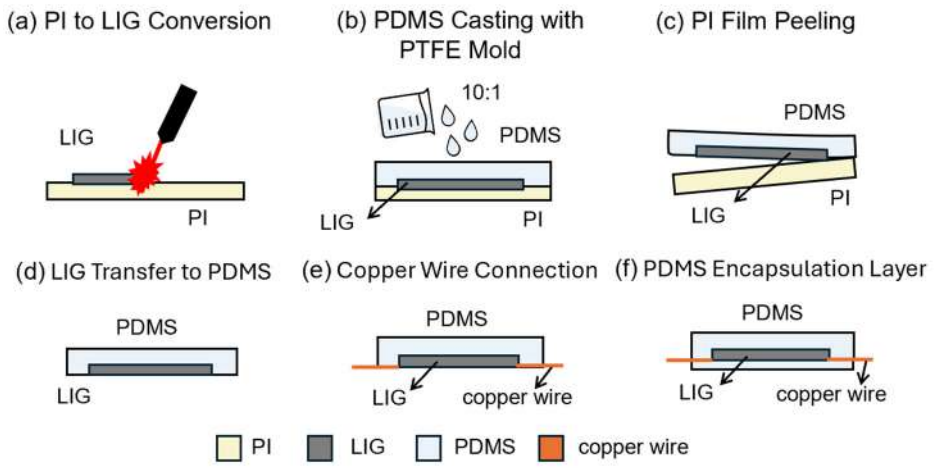

Fig.1 Fabrication flow of the flexible LIG

Sensor Performance Evaluation

Real-time growth variations in plant stem length and diameter were analyzed. Sensitivity, expressed as the gauge factor (GF), is a critical indicator for evaluating the performance of strain sensors. A higher value indicates that the sensor is more sensitive to minor changes, allowing significant resistance variations to be induced by extremely small strains. In the experiment, the collected relative resistance change data were plotted on a graph, with the horizontal axis representing the degree of stretching and the vertical axis representing the relative resistance change. By performing linear fitting to calculate the slope of the plot, the GF value of the sensor was obtained as expressed in Eq. (1).

$$\mathrm{GF} = \frac{\Delta R/R_0}{\Delta L/L_0} \quad (1)$$

where:
ΔR= change in resistance after deformation (Ω)
R_0= initial resistance (Ω)
ΔL= change in length (mm)
L_0= initial length (mm)

RESULTS & DISCUSSION

Optimization of Laser Fabrication Parameters

To ensure that the sensor exhibits excellent electrical conductivity and transfer-molding quality, this study systematically optimized three major laser parameters: "power, speed, and line spacing." The primary reason is that an excessively high areal energy density—determined by power and speed—can easily cause substrate ablation and embrittlement, while an excessively low-density results in incomplete carbonization; additionally, excessive line spacing prevents the tracks from overlapping, leading to a break in electrical conductivity. As shown in Table 1, a continuous conductive network can be effectively constructed, and the highest transfer-molding yield achieved, when using a laser power of 2.75 W, a scanning speed of 10 mm/s, and a scanning line spacing of 0.075 mm.

Table 1 Comparison of transferred area ratio under different laser parameters of power, speed, and line spacing

Speed: 10 mm/s, Spacing: 0.05 mm						
Power	2 W	2.25 W	2.5 W	2.75 W	3 W	3.25 W
transferred area ratio	89.02%	87.62%	88.88%	91.53%	89.19%	88.13%

Power: 2.75 W, Speed: 10 mm/s						
Spacing	0.05	0.075	0.01	0.125	0.15	0.175
transferred area ratio	95.74%	99.71%	96.82%	96.92%	81.11%	82.69%

Power: 2.75 W, Spacing: 0.05 mm				
Spacing	7.5mm/s	10mm/s	12.5mm/s	15mm/s
transferred area ratio	95.74%	99.71%	96.82%	96.92%

Dynamic Tensile Performance and Sensitivity Analysis

To evaluate the regularity of laser energy density on the sensing range and sensitivity of the device, dynamic tensile tests were conducted under different laser powers in this experiment. As shown in Fig. 2, the relative resistance change of the sensor under longitudinal stretching was significantly higher than that under transverse stretching, which prevents the lateral expansion of the plant stem from interfering with the longitudinal elongation signal. Among them, 2.00 W achieved a maximum sensing range of up to 24%, and exhibited extremely high sensitivity and a step-like response in the high-strain region.

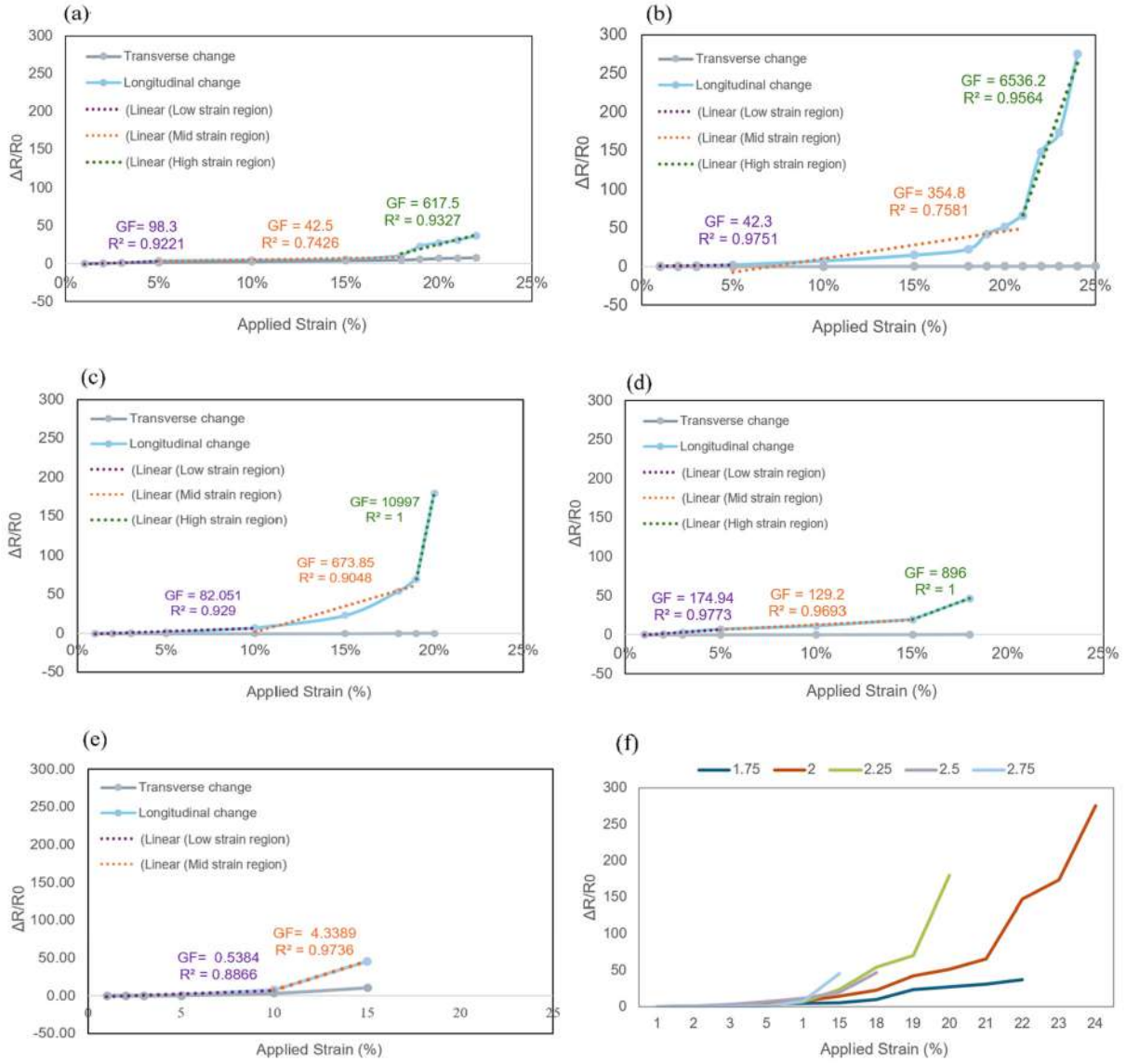

Fig.2 Comparison of the sensor's dynamic tensile response and segmented sensitivity under different laser powers: (a) 1.75 W; (b) 2.00 W; (c) 2.25 W; (d) 2.50 W; (e) 2.75 W; (f) Comprehensive comparison of the vertical-axis strain responses.

While the parameter set of 2.75 W, 0.075 mm, and 10 mm/s achieves the highest transferred area ratio (99.71%) ensuring structural integrity during transfer molding, the 2.00 W condition exhibits superior sensing performance. This discrepancy arises because lower laser power preserves a more porous and flexible microstructure that is prone to favorable resistance changes under strain, whereas higher energy density tends to form a more densely structured carbon layer with reduced electromechanical responsiveness.

Cyclic Stability and Dynamic Durability Performance

This paper systematically investigates the electromechanical performance of the LIG/PDMS-based strain sensor fabricated with a laser power of 2.00 W. First, the sensor was fixed on a tensile testing device to evaluate its resistance response characteristics under varying strain amplitudes. As shown in Fig. 3, when step-wise tensile strains of 10%, 15% and 20% were

applied, the relative resistance variation rate of the sensor reached approximately 500%, 2000%, and 6000%, respectively, demonstrating a clear step-wise strain response and excellent sensitivity. Furthermore, through dynamic cyclic tensile testing, the sensor exhibited regular, symmetrical, and peak-consistent resistance waveforms during continuous deformation, proving its favorable dynamic response speed and repeatability. A long-term durability test of 100 cycles was further conducted. The results indicate that although a slight adaptation adjustment occurred after the initial cycles, the sensor subsequently maintained a highly stable resistance output range without significant performance degradation or structural failure. This reveals that the sensor possesses outstanding anti-fatigue properties and long-term stability, holding great potential for applications in high-intensity and repetitive deformation scenarios such as precision agriculture or plant growth monitoring.

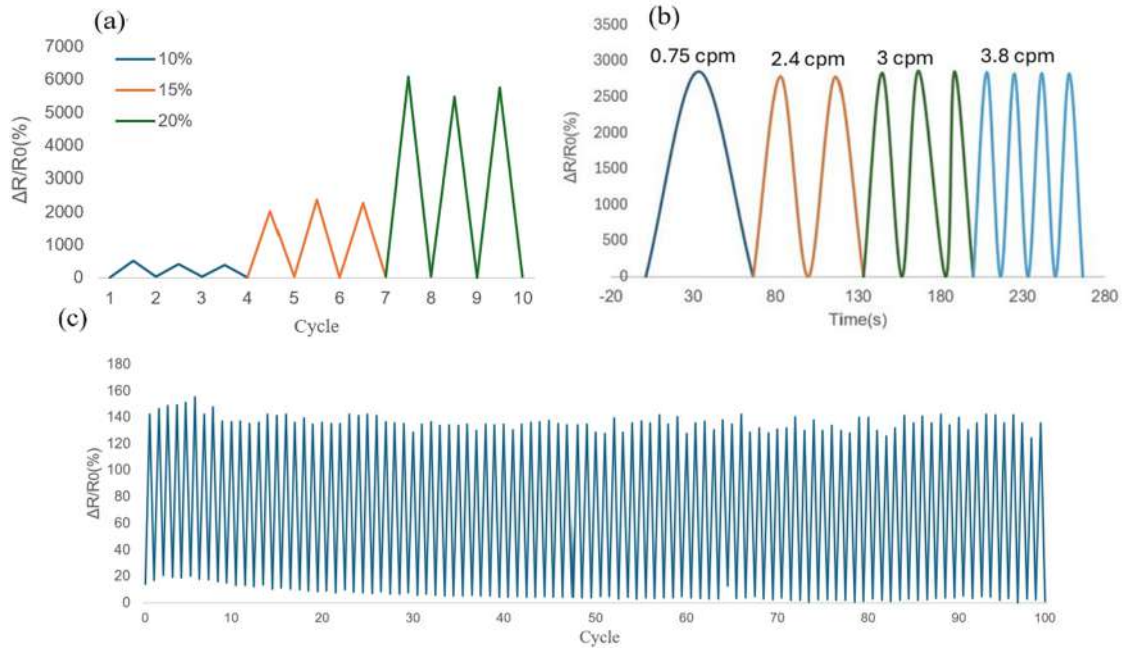

Fig. 3 Performance of the flexible wearable LIG/PDMS-based strain sensor: (a) Step-wise strain response of the sensor under varying strain amplitudes; (b) Dynamic cyclic response of the sensor under continuous stretching and releasing at various loading frequencies; (c) Cyclic stability and durability test of the sensor over 100 continuous loading-unloading cycles.

CONCLUSIONS

This study proposes and investigates a biaxial flexible growth monitoring sensor based on LIG and PDMS. By systematically optimizing the laser parameters, a highly continuous and stable conductive network was established, achieving a high transfer-molding yield of up to 99.71%. Furthermore, the sensor's orthogonal intersecting structure exhibits significant anisotropy and high sensitivity, effectively isolating bidirectional deformation interference. Future work will focus on integrating advanced machine learning algorithms for multi-signal decoupling and expanding the sensor's capability to simultaneously track environmental factors such as temperature and humidity.

REFERENCES

Han, F., M. Li, H. Ye, and G. Zhang. 2021. Materials, electrical performance, mechanisms, applications, and manufacturing approaches for flexible strain sensors. *Nanomaterials* 11(5): 1220.

Jedynak, P., K. F. Trzebuniak, M. Chowaniec, P. Zgłobicki, A. K. Banas, and B. Mysliwa-Kurdziel. 2022. Dynamics of etiolation monitored by seedling morphology, carotenoid composition, antioxidant level, and photoactivity of protochlorophyllide. *Arabidopsis thaliana* 12: 772727.

Lin, J., Z. Pen, Y. Liu, F. Ruiz-Zepeda, R. Y., E. L.G. Samuel, M. J. Yacaman, B. I. Yakobson, and J. M. Tour. 2014. Laser-induced porous graphene films from commercial polymers. *Nature Communications* 5(1): 5714.

Liu, L., C. Cai, Z. Qian, P. Li, and F. Zhu. 2024. Application of laser-induced graphene flexible sensor in monitoring large deformation of reinforced concrete structure. *Sensors* 24: 7444.

Lo Presti, D., J. Di Tocco, S. Cimini, S. Cinti, C. Massaroni, R. D'Amato, M. A. Caponero, L. De Gara, and E. Schena. 2023. Plant growth monitoring: design, fabrication, and feasibility assessment of wearable sensors based on fiber bragg gratings. *Sensors* 23(1): 361.

PA-P16

Proceedings of The 12th International Symposium on Machinery and Mechatronics for Agriculture and Biosystems Engineering (ISMAB 2026)
20-24 October 2026, Busan, Republic of Korea

MOISTURE GRADING OF SPHAGNUM MOSS MEDIA USING MULTI-SOURCE FEATURE FUSION AND NEAR-INFRARED IMAGING

Xue-Ru Huang[1], Wei-Ling Chen[2], Hsi-Chun Hung[2], Wen-Lin Chu[1*]

[1]Dept. of Bio-Industrial Mechatronics Engineering, National Chung Hsing University, Taichung, Taiwan
[2]Floral Industry Innovation Center, Ministry of Agriculture, Taiwan
*Corresponding Author-- Voice: +886-4-2284-0377, Email: wlchu@nchu.edu.tw

Abstract: Conventional moisture assessment of *Sphagnum* moss media in *Phalaenopsis* orchid cultivation relies on subjective manual palpation or intrusive probes that risk root injury and pathogen transmission. Optical sensing offers a non-destructive alternative, yet non-uniform moss dehydration induces severe volume scattering that confounds single-feature assessments. This study developed a non-contact binary moisture grading system using near-infrared (NIR) imaging and a Support Vector Machine (SVM) with a 30% volumetric water content (VWC) classification threshold. Three complementary optical features—Mean reflectance, Standard Deviation (Std), and the 92nd percentile (PR92)—were extracted from flat-field corrected images. Cost-sensitive weighting was introduced to address natural class imbalance (1:3.23). Evaluated on an independent test set (103 samples) via stratified sampling, the weighted RBF-SVM achieved an overall accuracy of 83.5%, with balanced dry and wet sensitivities of 0.83 and 0.84, and a weighted F1-score of 0.84. Multi-feature fusion and asymmetric penalty weighting effectively overcome dehydration heterogeneity and minimize false-negative dry predictions, providing a robust quantitative basis for automated greenhouse irrigation.

Key Words: Sphagnum moss substrate, Near-infrared imaging, Non-destructive sensing, Moisture classification, Cost-sensitive SVM

INTRODUCTION

Phalaenopsis orchids are economically vital export floral crops in Taiwan, where substrate moisture directly governs root physiology, disease incidence, and blooming quality. Commercial cultivation primarily employs *Sphagnum* moss for its superior water retention and aeration. However, conventional moisture assessment relies on subjective manual touch or intrusive probes that risk root injury and pathogen cross-contamination. Developing a non-

contact, non-destructive, and quantitative moisture evaluation system is therefore essential for automated greenhouse management.

Near-infrared (NIR) imaging exploits water absorption bands (O–H bonds), where higher moisture reduces surface reflectance (Beć et al., 2020; Lu et al., 2020). However, the dehydration of *Sphagnum* moss is intrinsically heterogeneous. As moisture evaporates, air replaces water in hyaline cells, and the resulting refractive index disparity triggers pronounced volume scattering (Sini-Selina et al., 2023). This spatial heterogeneity produces local reflectance fluctuations that degrade single-point or mean-reflectance predictions, especially within the moisture transition zone (25%–35% VWC).

To overcome media heterogeneity, combining multi-dimensional statistical features with machine learning offers a robust solution (Sharma et al., 2020; Yu et al., 2023). This study developed a non-contact binary moisture grading system for *Sphagnum* moss based on NIR imaging. The objectives were to: (1) establish a standardized imaging protocol to characterize *Sphagnum* reflectance across moisture regimes; (2) extract Mean, Standard Deviation (Std), and 92nd percentile (PR92) features from flat-field corrected images, identifying the optimal percentile via sensitivity analysis; and (3) construct a cost-sensitive class-weighted SVM model at a 30% VWC threshold to resolve class imbalance and ensure reliable moisture classification for greenhouse automation.

MATERIALS AND METHODS

Experimental *Phalaenopsis* orchids (*Phalaenopsis* Sogo Yukidian 'V3') were cultivated in 2.8-inch soft plastic pots with *Sphagnum* moss at the Floral Industry Innovation Center, Ministry of Agriculture, Yunlin, Taiwan. To establish a broad moisture spectrum from saturation to desiccation, three irrigation intervals (5, 10, and 15 days) were implemented across 7 sampling sessions over 7 months. Each session sampled 30 plants per treatment (90 images per session). After eliminating edge artifacts and outliers, 512 validated sample records were obtained.

The image acquisition system was enclosed in a matte-black dark box to eliminate ambient light. An NIR camera (ISUZU OPTICS 4.0 MP color & RAW-RGB IR USB 3.0) was mounted vertically at a 50 cm working distance perpendicular to the medium surface. Symmetrical 45° illumination was provided by a 120 W halogen source via dual-head gooseneck optical fibers to minimize surface shadows. Ground-truth volumetric water content (VWC) was recorded using a Delta-T moisture sensor. Based on commercial irrigation standards, a 30% VWC threshold was established, partitioning the 512 records into dry (VWC ≤ 30%, 121 samples) and wet (VWC > 30%, 391 samples) classes.

To eliminate spatial illumination non-uniformity and sensor dark current, a dark-field image (I_D , lights extinguished and lens capped) and a standard white reference panel image (I_W) were acquired prior to sample scanning. Relative reflectance (R) was computed via flat-field correction as defined in Eq. (1):

$$\mathrm{R} = \frac{I_S - I_D}{I_W - I_D} \tag{1}$$

Where:

R = Relative reflectance of the target pixel (-)
I_S = Raw gray-level intensity of the sample pixel (-)
I_D = Dark current intensity of the camera sensor (-)
I_W = Raw gray-level intensity of the standard white calibration panel (-)

From each calibrated image, a region of interest (ROI) centered on the *Sphagnum* moss surface was delineated to extract three statistical features: (1) Mean reflectance, representing overall optical absorption; (2) Standard Deviation (Std), capturing spatial variation from uneven drying; and (3) 92nd percentile (PR92), capturing volume scattering from dehydrated hyaline cells while rejecting extreme specular noise.

The dataset exhibited natural class imbalance (121 dry vs. 391 wet samples, ratio ~ 1:3.23). Stratified sampling with a fixed random seed (random_state = 42) at an 8:2 ratio was applied to allocate 409 training and 103 independent testing samples while preserving class distributions. Features were standardized via Z-score scaling fitted solely on training data. An RBF-kernel SVM was employed for nonlinear classification. To counter minority-class misclassification, asymmetric cost-sensitive weighting was incorporated into the SVM objective function, penalizing dry margin errors ($w_{dry} : w_{wet} = 3.5 : 1$). Performance was evaluated on the test set using confusion matrices, accuracy, recall, precision, and weighted F1-score.

RESULTS & DISCUSSION

Physical Correlation between Medium Moisture and NIR Features

A significant negative linear correlation was observed between moss VWC and mean NIR reflectance (Fig. 1). Linear regression yielded r = -0.742 (R^2 = 0.551, slope = -0.00415, intercept = 0.486). As moisture increases, intensified light absorption by O–H bonds diminishes reflectance. Conversely, progressive dehydration allows air to enter hyaline cells, producing refractive index mismatches that trigger volume scattering and elevate NIR reflectance.

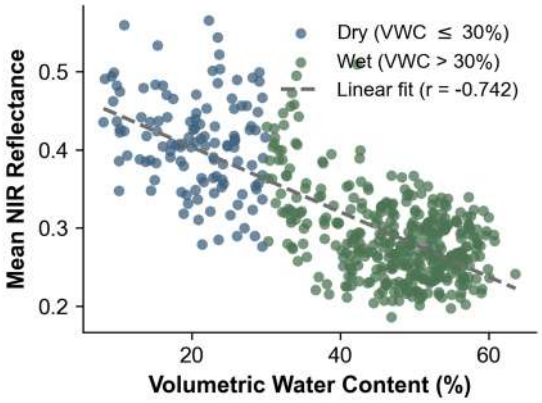

Fig. 1 Linear regression scatter plot between volumetric water content (VWC) and mean NIR reflectance of Sphagnum moss.

Mean, Std, and PR92 features were compared between moisture classes (Fig. 2). Mean (dry: 0.409 ± 0.089; wet: 0.286 ± 0.061) and PR92 (dry: 0.536 ± 0.103; wet: 0.354 ± 0.071) exhibited distinct class separation (Fig. 2a, c). Standard deviation (Fig. 2b) was substantially higher in dry moss (0.078 ± 0.021) than in wet moss (0.047 ± 0.015), confirming marked spatial variance during dehydration. While individual features overlap within the 25%–35% VWC transition zone, fusing Mean, Std, and PR92 provides complementary descriptors for robust classification.

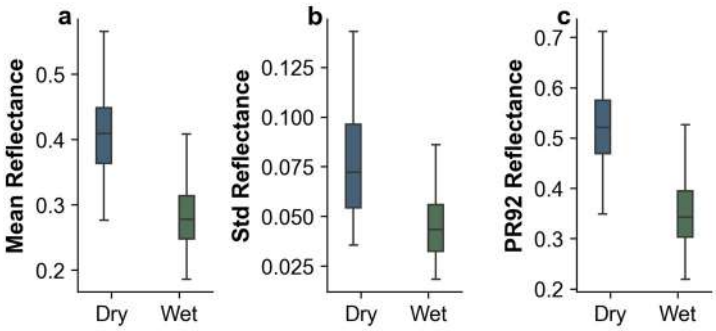

Fig. 2 Boxplots of optical features across dry and wet Sphagnum moss media: (a) Mean reflectance, (b) Standard deviation, and (c) 92nd percentile reflectance.

Percentile Feature Selection and Sensitivity Analysis

Feature sensitivity was examined across percentiles PR50 to PR99 (Fig. 3). Correlation with VWC increased monotonically from |r| = 0.722 at PR50 to 0.756 at PR99 (Fig. 3a). Concurrently, 5-fold cross-validation SVM accuracy remained stable (~87%) across PR85 to PR95, peaking at PR92 (accuracy = 87.12%, r = -0.752, Fig. 3b). While percentiles above PR95 showed slightly higher correlations, they are susceptible to sensor saturation and specular noise. Hence, PR92 was chosen as the optimal high-reflectance feature.

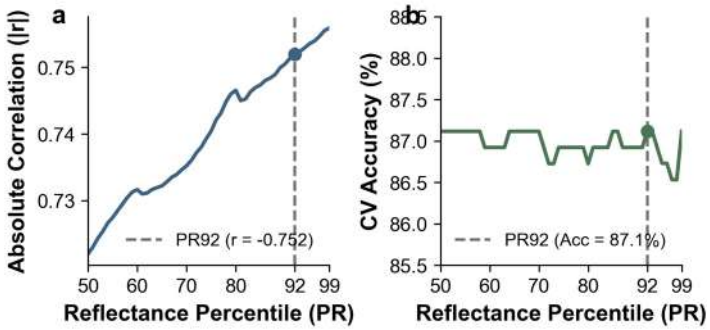

Fig. 3 Sensitivity analysis across reflectance percentiles (PR50 to PR99): (a) correlation with VWC, (b) SVM cross-validation accuracy.

Support Vector Machine Performance and Class Weighting

The classification performance of the RBF-SVM model on the independent test set (103 samples) is summarized in Table 1 and Fig. 4. The model achieved an overall accuracy of 83.5% (86/103) and a weighted average F1-score of 0.84. Balanced sensitivities (recall) of 0.83 (20/24) for dry samples and 0.84 (66/79) for wet samples were achieved, along with precisions of 0.61 for dry and 0.94 for wet classes, respectively.

Table 1. Classification performance of the weighted SVM model on the independent test set.

Class	Precision	Recall	F1 - score
Dry	0.61	0.83	0.7
Wet	0.94	0.84	0.89
Weighted Avg	0.86	0.84	0.84

Balanced detection stems directly from asymmetric class weighting. In commercial greenhouses, failing to detect dry plants risks severe root desiccation and yield loss. In sensitivity testing across penalty ratios (Fig. 5,where $w_{wet} = 1$ was fixed and w_{dry} was varied from 1 to 5), the symmetric unweighted model ($w_{dry} : w_{wet} = 1:1$) exhibited marked majority-class bias with an unacceptably low dry recall of 73.6% (wet recall 91.6%, accuracy 87.3%).

Elevating the relative dry penalty to $w_{dry} : w_{wet} = 3.5:1$ shifted the decision boundary to prioritize minority errors, significantly boosting dry recall to 88.5% (wet recall 86.5%) with negligible change in overall accuracy (86.9%), proving the efficacy of asymmetric cost-sensitive regularization.

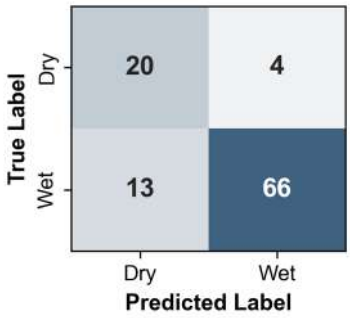

Fig. 4 Confusion matrix of the weighted SVM model on the independent test set (103 samples).

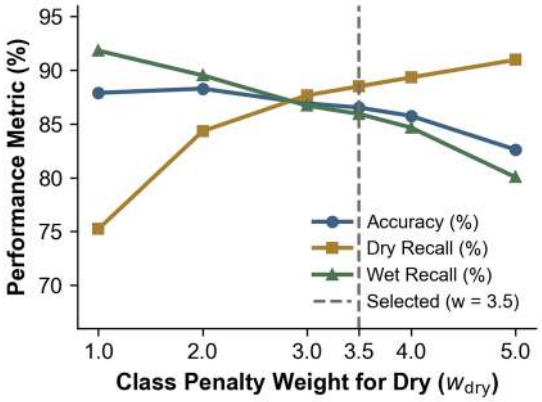

Fig. 5 Classification performance across varying asymmetric class penalty weight ratios on dry samples ($w_{dry} : w_{wet} = 1:1$ to $w_{dry} : w_{wet} = 5:1$,with $w_{wet} = 1$ fixed.

Objective Function Convergence

The numerical convergence of the SVM objective function during optimization is presented in Fig. 6. Both the symmetric unweighted ($w_{dry} : w_{wet} = 1:1$) and asymmetric cost-weighted ($w_{dry} : w_{wet} = 3.5:1$) models converged stably within 30–40 iterations. The weighted model converged to a higher loss asymptote because the 3.5 penalty scaling applied specifically to dry margin errors increases the objective loss on minority-class violations, reflecting intentional cost re-weighting rather than solver instability.

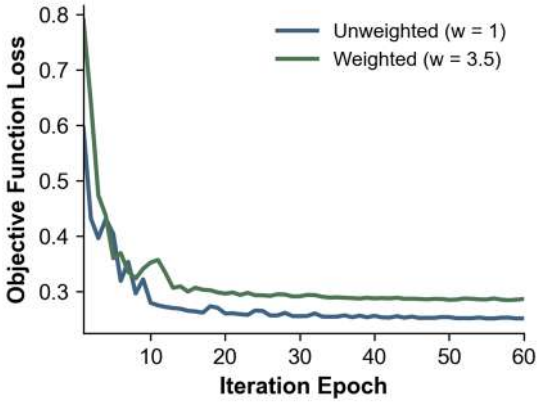

Fig. 6 Convergence of SVM objective function loss across optimization iterations for unweighted $w_{dry} : w_{wet} = 1:1$) and weighted ($w_{dry} : w_{wet} = 3.5:1$) models.

CONCLUSIONS

This study established a non-contact binary moisture classification system for *Sphagnum* moss media in *Phalaenopsis* cultivation using NIR imaging and SVM. By fusing Mean, Std, and PR92 features with cost-sensitive weighting, the RBF-SVM model achieved 83.5% overall accuracy on an independent test set, with balanced dry and wet recalls of 0.83 and 0.84, and a weighted F1-score of 0.84. Multi-feature fusion resolves estimation errors caused by dehydration heterogeneity, while asymmetric weighting mitigates false-negative dry errors, providing a reliable quantitative foundation for automated greenhouse irrigation.

ACKNOWLEDGEMENTS

This research was supported by the National Science and Technology Council of Taiwan under grant number 115-2813-C-005-137-B, entitled 'Establishment of a Non-Contact Multispectral Imaging Prediction Model for Medium Surface Moisture Content in *Phalaenopsis* Vegetative Stage.

REFERENCES

Beć, K. B., Grabska, J., & Huck, C. W. (2020). Near-Infrared Spectroscopy in Bio-Applications. *Molecules*, *25*(12), 2948.

Lu, B., Dao, P. D., Liu, J., He, Y., & Shang, J. (2020). Recent Advances of Hyperspectral Imaging Technology and Applications in Agriculture. *Remote Sensing*, *12*(16), 2659.

Sharma, A., Jain, A., Gupta, P., & Chowdary, V. (2020). Machine Learning Applications for Precision Agriculture: A Comprehensive Review. *IEEE Access*, *9*, 4843-4873. https://doi.org/10.1109/ACCESS.2020.3048415

Sini-Selina, S., Juola, J., Burdun, I., Vasander, H., & Rautiainen, M. (2023). Intra- and interspecific variation in spectral properties of dominant Sphagnum moss species in boreal peatlands. *Ecology and Evolution*, *13*(6). https://doi.org/https://doi.org/10.1002/ece3.10197

Yu, H., Hu, Y., Qi, L., Zhang, K., Jiang, J., Li, H., Zhang, X., & Zhang, Z. (2023). Hyperspectral Detection of Moisture Content in Rice Straw Nutrient Bowl Trays Based on PSO-SVR.*Sustainability*, *15*(11), 8703.

PA-P17

Proceedings of The 12th International Symposium on Machinery and Mechatronics for Agriculture and Biosystems Engineering (ISMAB 2026)
20-24 October 2026, Busan, Republic of Korea

AUTOMATED PIPELINE FOR CONSTRUCTING AND BENCHMARKING A TOP-VIEW DAIRY COW IMAGE DATASET USING RFID INTEGRATION

Yu-Min Lee[1], Wen-Lin Chu[1,2*], Chien-Kai Wang[3]

[1]Department of Bio-Industrial Mechatronics Engineering, National Chung Hsing University, Taichung 402202, Taiwan
[2]Agricultural Automation Center, National Chung Hsing University, Taichung 402202, Taiwan
[3]Department of Animal Science, National Chung Hsing University, Taichung 402202, Taiwan
*Corresponding Author-- Voice: +886-4-2284-0377 ext. 509, Email: wlchu@nchu.edu.tw

Abstract: To overcome the massive costs of building farm-specific annotated datasets for computer vision-based individual dairy cow identification, this study developed an automated dataset construction pipeline centered on a sorting gate radio frequency identification (RFID) system. The system automatically captured and archived gate-crossing images by cow identification number, utilizing top-view cameras at the entrance and exit combined with a YOLO11n-based virtual fence. After quality sampling of the frames, the Segment Anything Model 3 (SAM 3) generated pre-annotated back masks, which were subsequently refined via manual correction. Visual manual inspection of 1,382 images from 22 individual cows confirmed that no identity misassignments were observed. The median intersection over union (IoU) of the SAM 3 target cow masks reached 0.977, with manual intervention (in 97.8% of the frames) primarily concentrated on clearing masks of other cows in the background. Under a strictly mutually exclusive individual data split, the mask mean average precision (mAP@50–95) of YOLO11n/s/m-seg on four unseen individuals ranged from 0.829 to 0.850 (with a single-frame latency of 16.9 ms to 23.4 ms). Empirical results demonstrated that the sorting-gate RFID system completely eliminated the need for manual identity annotation, although the mask boundaries still required manual geometric fine-tuning. Furthermore, the marginal performance gaps among the models were smaller than the individual variance across evaluation subsets, indicating that in a realistic open-set environment, the evaluation scale critically affects the ability to discriminate among models.

Key Words: Holstein dairy cows, radio frequency identification, automated dataset construction, mutually exclusive individual split

INTRODUCTION

The dorsal coat patterns of Holstein dairy cows exhibit lifelong stability and individual-specific biological features, making non-contact computer vision-based individual re-identification (Re-ID) a highly promising approach to overcome the limitations of hardware sensors (Guarnido-Lopez et al., 2025; Menezes et al., 2025). However, severe domain shift across different farms causes mean average precision (mAP) and Rank-1 accuracy to decrease from 95.3% and 98.2% to 8.0% and 13.7%, respectively, compelling individual facilities to construct their own

identity-annotated datasets (Dubourvieux et al., 2023). To overcome the practical bottlenecks of time-consuming and error-prone manual frame-by-frame annotation, this study developed an automated top-view image dataset construction pipeline centered on sorting gate radio frequency identification (RFID) crossing records, thereby eliminating the need for manual identity annotation at the hardware level.

To evaluate the real-world feasibility of this pipeline, this study focused on two primary objectives. First, to verify of automated RFID identity assignments and quantifying the manual fine-tuning burden required for masks pre-annotated by the Segment Anything Model 3 (SAM 3). Second, to apply artificially inflated performance caused by the spatiotemporal autocorrelation of consecutive frames, this study strictly applied a mutually exclusive individual data split to reflect the practical scenario of herd replacement(Andrew et al., 2021; Freitas et al., 2026). Under this rigorous splitting strategy, the mask quality and inference latency of three scaled YOLO11 instance segmentation models were evaluated on unseen individuals, establishing a standardized benchmark for the low-cost construction of open-set feature libraries across farms.

MATERIALS AND METHODS

Experimental Site and Image Acquisition

Top-view images (2880 × 1620 px, 30 fps) were collected at the National Chung Hsing University livestock experimental farm in Taichung, Taiwan. Two Synology BC500 cameras were mounted **five meters high** above the alleyway floor at the entrance and the exit of the automated sorting gate and recorded continuously to a network video recorder (NVR). During the image preprocessing stage, the system retrieved video streams from the corresponding cameras within a specified time window. When the object detector confirmed that a cow's bounding box entered a predefined virtual boundary, the event clip was automatically extracted and archived by cow identification number (Fig. 1a)

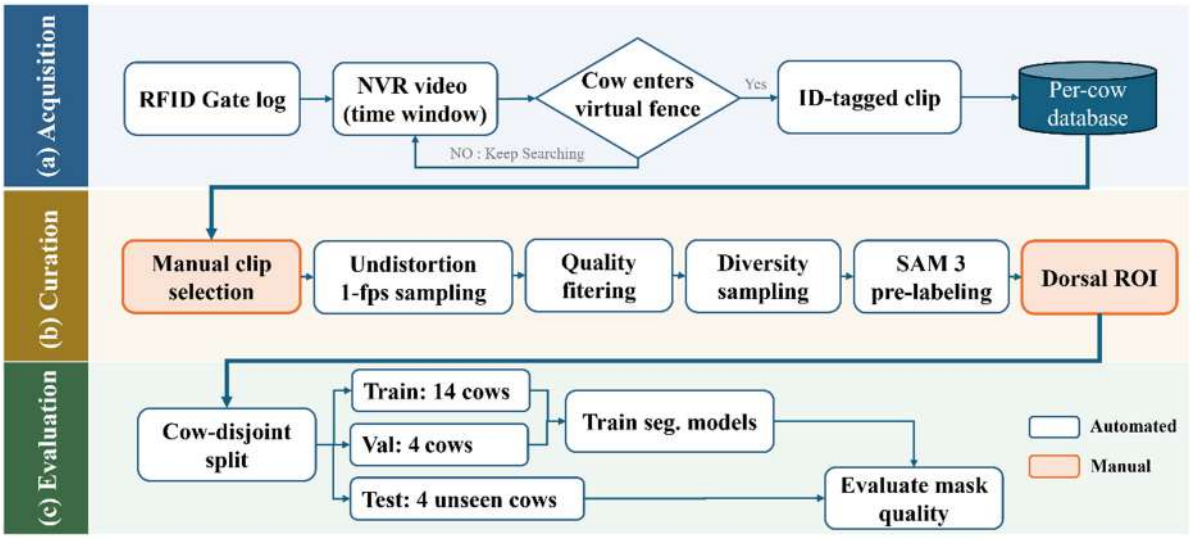

Fig. 1 Dataset construction and evaluation pipeline. (a) RFID crossing records define the image retrieval time window; once the object detector confirms the cow has entered the virtual boundary, the event clip is extracted and archived by cow identification number. (b) Following manual clip selection, frames undergo distortion correction, quality filtering, and diversity sampling. The Segment Anything Model 3 (SAM 3) then generates pre-annotated masks, followed by manual mask refinement and identity verification. (c) The dataset is split by individual, ensuring that cows in the test set remain entirely unseen during model training. Orange boxes indicate steps requiring manual intervention.

Virtual Fence-Based Image Extraction

The object detector trained on the top-view images was YOLO11n, fine-tuned from COCO pre-trained weights. A total of 398 top-view images were randomly split into a training set of 318 images and a validation set of 80 images (an 8:2 ratio). The model was trained with an input resolution of 640 × 640 px, a batch size of 16, and a learning rate of 0.002 for 150 epochs. Data augmentation techniques included rotation, translation, scaling, flipping, and mosaic. The deployed weights achieved a precision of 0.975, a recall of 0.974, and a mean average precision (mAP@50) of 0.985 on the validation set.

The virtual fence determination is based on the intersection over area (IoA), which represents the proportion of the cow bounding box area that falls within the virtual fence polygon, as shown in Eq. (1).

$$IoA(B,R) = \frac{|B \cap R|}{|B|} \tag{1}$$

where:

$|B \cap R|$ = intersection area of the bounding box and ROI (px²)

$|B|$ = area of the cow bounding box (px²)

By utilizing only the bounding box area as the denominator, this ratio represents the proportion of the cow bounding box located within the region of interest (ROI), independent of the total fence area. If intersection over union (IoU) were applied instead, the metric would be disproportionately diluted when the fence area is significantly larger than the bounding box. When this ratio exceeds 0.15 for any detected bounding box, the system classifies the cow as entering the fence and triggers video recording. The resulting video segment comprises a 10s pre-trigger buffer and 10s of post-trigger footage.

Frame Filtering and Mask Annotation

After correcting for lens distortion using a checkerboard calibration, the captured video segments are sampled at 1 fps. To ensure image quality, the system sequentially filters out frames that are excessively dark (grayscale standard deviation < 15), blurry (Laplacian variance < 100), feature disproportionately small target cows (< 5% of the frame area), or exhibit low detection confidence (< 0.3). This process ultimately yielded 9,405 key frames across 799 video segments. For this phase, 1,382 images (from 283 segments) representing 22 individual cows were selected for instance segmentation annotation. The annotation pipeline initially utilizes SAM 3 to automatically generate pre-annotated masks of the back contours and heads. Subsequently, manual refinement is performed to adjust mask boundaries and verify individual identities frame-by-frame against the sorting gate RFID records. To maintain the stringency of single-target recognition, any non-target cows appearing in the frame are classified as background.

Mutually Exclusive Individual Split

To prevent artificially inflated model performance caused by high spatiotemporal autocorrelation among adjacent consecutive frames, this dataset was partitioned strictly by individual cows. Accounting for the distributional differences in image counts per individual (10 to 118 images), a greedy allocation strategy was applied to distribute 22 cows into a training set (14 cows, 961 images), a validation set (4 cows, 205 images), and a test set (4 cows, 216 images) targeting a 70:15:15 ratio, as shown in Table 1. The individual cows and video segments are mutually exclusive across the three subsets, establishing the test set as genuinely unseen targets to objectively evaluate the model's feature generalization capability under an open-set scenario.

Table 1 Dataset partitioning details for the mutually exclusive individual split.

Subset	Number of cows	Number of segments	Number of images	Proportion (%)
Training set	14	189	961	69.5
Validation set	4	50	205	14.8
Test set	4	44	216	15.6
Total	22	283	1,382	100.0

Segmentation Model Training and Evaluation

A single-class instance segmentation model was trained using the Ultralytics framework, evaluating three YOLO11 scales (n, s, and m-seg). The models were fine-tuned from COCO pretrained weights with an input resolution of 640×640 and a batch size of 16. Training employed the AdamW optimizer and mixed-precision training, incorporating standard geometric and color jitter augmentations with mosaic stitching (excluding rotation).

Performance was evaluated on the test set (comprising unseen individuals) using mask mean average precision at thresholds of 50 (mAP@50), 75 (mAP@75), and 50 to 95 (mAP@50-95). Inference performance was benchmarked on a single NVIDIA TITAN V GPU (12 GB, FP32). To reflect pure inference efficiency, we measured the median forward pass latency with a batch size of 1 for single-image evaluation, and the average throughput (FPS) on the test set with a batch size of 16, both excluding pre- and post-processing times.

RESULTS & DISCUSSION

Validation of Automated Data Pipeline

Through manual verification of all 1,382 images, no identity misclassifications were found, eliminating the need for manual corrections of RFID-assigned identity labels. Regarding the segmentation masks, 97.8% of the 1,356 images pre-annotated by SAM 3 required manual post-processing. Specifically, SAM 3 generated an average of 4.0 instances per image, with 84.5% of the images requiring the removal of extraneous cows and 70.5% requiring boundary refinements for the target cow. The median intersection over union (IoU) between the SAM 3 initial pre-annotations and the finalized manual masks was 0.977, with 95.1% achieving an IoU above 0.90. Consequently, while this pipeline successfully automates individual identity labeling, mask generation still necessitates manual intervention. The ground truth used for subsequent segmentation evaluation comprised these finalized manual masks rather than the raw SAM 3 pre-annotations.

Segmentation Performance on Unseen Individuals

Under the strict mutually exclusive individual split where test set cows were completely unseen by the model, all three model scales achieved an overall mask mAP@50-95 exceeding 0.82, confirming that the automatically generated masks possess excellent geometric consistency and generalization capability to effectively capture the back features of unfamiliar cows. In terms of model scaling, the larger YOLO11m-seg demonstrated superior feature representation, achieving an mAP@50-95 of 0.850 (and an mAP@75 of 0.923). It more precisely fitted the dorsal curvatures and complex coat-color boundaries of the cows while maintaining an inference speed of 166.6 FPS. Although the ultra-lightweight YOLO11n-seg experienced a slight drop in overall mAP@50-95 to 0.829 due to limited model capacity, it achieved the highest coarse localization score (mAP@50 of 0.952) alongside an inference throughput of 736.6 FPS. Meanwhile, YOLO11s-seg struck a practical balance between precision (mAP@50-95 of 0.835) and speed (394.8 FPS) as shown in Table 2. Overall, these

results validate the feasibility of employing lightweight instance segmentation models to balance contour quality with edge-device real-time processing.

Table 2 Performance of the three YOLO11 instance segmentation models on the test set.

Model	Parameters (M)	Computational Complexity (GFLOPs)	mAP@50–95	Latency (ms)	Throughput (FPS)
YOLO11n-seg	2.84	9.57	0.829	**16.93**	**736.6**
YOLO11s-seg	10.07	32.78	0.835	18.30	394.8
YOLO11m-seg	22.34	112.89	**0.850**	23.35	166.6

Limitations and Future Work

Deploying this automated pipeline across other commercial dairy farms still entails prerequisite conditions regarding system integration and field adaptation. First, the pipeline heavily relies on millisecond-level synchronization between the sorting gate RFID signals and the NVR video timestamps; if a target facility lacks open communication interfaces or utilizes traditional channels without RFID readers, the automated identity-association mechanism becomes constrained. Second, the virtual fence trigger threshold (IoA) is closely bound to passage dimensions and camera mounting heights, necessitating initial geometric calibration upon cross-site deployment. Furthermore, 97.8% of the SAM 3 pre-annotated masks in this study still required manual removal of accompanying background cows, indicating that the degree of crowding and pushing within the passageway directly impacts data curation costs. Future research will focus on introducing target-cow locking algorithms empowered by geometric constraints and spatial prompting to eliminate the manual cleaning burden under multi-cow crowding. Establishing a rapid cross-site calibration protocol will also enable the annotation-free pipeline to be seamlessly transferred across heterogeneous farms, laying a standardized feature foundation for subsequent end-to-end individual re-identification.

CONCLUSIONS

This study developed an automated dataset construction pipeline for top-view dairy cow imagery using sorting-gate RFID records to trigger image capture, eliminating the need for manual identity labeling. Through manual verification of the 1,382 annotated images across 22 individuals, no identity misclassifications were identified. While SAM 3 pre-annotation necessitated manual intervention in nearly all instances (97.8%), this was predominantly for removing background cows from the masks, whereas the median intersection over union (IoU) between the target cow pre-annotations and finalized masks reached 0.977; thus, mask curation still requires manual oversight. Under a mutually exclusive individual split evaluation across four unseen test cows, the YOLO11n/s/m-seg models achieved mask mAP@50–95 scores ranging from 0.829 to 0.850, with single-image inference latencies between 16.93 ms and 23.35 ms. However, performance variations among models were smaller than the variance between the two four-cow evaluation subsets, indicating that model selection must be validated upon expanding the evaluation scale. Future work includes scaling the annotations to the entire herd, employing multiple random seeds for repeated splits to estimate variance, conducting stratified evaluations based on coat-color patterns, and training a dorsal pattern-based individual identification model utilizing this dataset and partitioning protocol.

ACKNOWLEDGEMENTS

This research was financially supported by the National Science and Technology Council (NSTC), Taiwan, under grant no. NSTC115-2313-B-005-012. We are also grateful to the

Livestock Trial Farm of National Chung Hsing University, Taichung, Taiwan, for their full support in coordinating site access and facilitating the installation of the camera monitoring system.

REFERENCES

Andrew, W., Gao, J., Mullan, S., Campbell, N., Dowsey, A. W., & Burghardt, T. (2021). Visual identification of individual Holstein-Friesian cattle via deep metric learning. *COMPUTERS AND ELECTRONICS IN AGRICULTURE*, *185*, Article 106133. https://doi.org/10.1016/j.compag.2021.106133

Dubourvieux, F., Lapouge, G., Loesch, A., Luvison, B., & Audigier, R. (2023). Cumulative unsupervised multi-domain adaptation for Holstein cattle re-identification. *Artificial Intelligence in Agriculture*, *10*, 46-60. https://doi.org/10.1016/j.aiia.2023.10.002

Freitas, L. A., Dorea, J. R. R., Weigel, K. A., & Rosa, G. J. M. (2026). Individual identification of dairy cows with occluded camera views using open-set contrastive learning model. *JOURNAL OF DAIRY SCIENCE*, *109*(9), 9489-9500. https://doi.org/10.3168/jds.2025-28109

Guarnido-Lopez, P., Pi, Y., Tao, J., Mendes, E. D. M., & Tedeschi, L. O. (2025). Computer vision algorithms to help decision-making in cattle production. *ANIMAL FRONTIERS*, *14*(6), 11-22. https://doi.org/10.1093/af/vfae028

Menezes, G. L., Alves, A. A. C., Negreiro, A., Ferreira, R. E. P., Higaki, S., Casella, E., Rosa, G. J. M., & Dorea, J. R. R. (2025). Color-independent cattle identification using keypoint detection and Siamese neural networks in closed- and open-set scenarios. *JOURNAL OF DAIRY SCIENCE*, *108*(9), 9662-9680. https://doi.org/10.3168/jds.2024-26069

PA-P18

Proceedings of The 12th International Symposium on Machinery and Mechatronics for Agriculture and Biosystems Engineering (ISMAB 2026)
20-24 October 2026, Busan, Republic of Korea

RELATING MACRONUTRIENT RATIOS IN THE TISSUE CULTURE MEDIUM TO PHALAENOPSIS GROWTH

Yi-Wei Lin[1], Wen-Lin Chu[1]*, Chan-Yi Lin[1]

[1]Department of Bio-Industrial Mechatronics Engineering, National Chung Hsing University, Taichung 402202, Taiwan
*Corresponding Author-- Voice: +886-4-2284-0377 ext. 509, Email: wlchu@nchu.edu.tw

Abstract: This study used quarter-strength Murashige and Skoog medium (1/4 MS) as the basal formulation to examine how the ratios of N, K, P, Ca, and Mg affect the growth of *Phalaenopsis* plantlets in vitro. Each of the five factors was assigned five levels, from +0% to +40% above its 1/4 MS concentration, and 25 treatment combinations were arranged according to an $L_{25}(5^6)$ Taguchi orthogonal array with ten plantlets per treatment. Bud count, fresh weight, leaf area, plant height, and canopy width were measured over the first subculture cycle. The responses were analyzed by the nominal-the-best signal-to-noise (S/N) ratio combined with an entropy-weighted grey relational analysis. The optimal formulation indicated by the response table was N +0%, K +30%, P +40%, Ca +30%, and Mg +10%, with phosphorus exerting the largest influence (Delta = 0.0814). The best measured combination, L14 (N +20%, K +30%, P +0%, Ca +30%, Mg +10%), gave plant height and fresh weight increments 38.1% and 46.4% above those of the unamended 1/4 MS control, indicating that adjusting macronutrient ratios can improve the growth performance of *Phalaenopsis* plantlets in vitro. Because the present data cover only the first subculture cycle, the acclimation response of the plantlets may have masked part of the treatment effect; subculture will therefore be continued, and analysis of variance will be applied in future work to test the statistical significance of each factor.

Key Words: *Phalaenopsis*, tissue culture, macronutrients, Taguchi method, grey relational analysis.

INTRODUCTION

Phalaenopsis spp. is an important potted flower crop whose commercial planting material is produced almost entirely by tissue culture, and the success of in vitro culture depends largely on the composition and ratios of the inorganic nutrients in the medium (Mahdavi et al., 2025). Macronutrients (N, P, K, Ca, Mg, and S) account for the greater part of the total inorganic salts in the medium and therefore govern cell division, organ differentiation, and regeneration efficiency in vitro. Nitrogen (N) is a constituent of proteins and chlorophyll, and the ratio of its nitrate (NO_3^-) and ammonium (NH_4^+) forms affects nitrogen assimilation and the pH of the medium, which in turn alters the availability of other ions (Bosman et al., 2024; Zhang et al., 2022). Phosphorus (P) is a constituent of nucleic acids, membrane phospholipids, and adenosine triphosphate (ATP), and energy metabolism becomes limited when it is deficient (Davis et al., 2022). Potassium (K) is involved in osmotic regulation; calcium (Ca) is a constituent of the cell wall and membrane and moves poorly in closed vessels because transpiration is suppressed; and

magnesium (Mg) is the central ion of chlorophyll. These three cations compete with one another during root uptake, so an excess of any one of them can induce an antagonistic deficiency (Dölger et al., 2025), which makes their ratios more critical than their absolute concentrations. The ionic strength of Murashige and Skoog (MS) medium is relatively high and readily imposes stress on orchids, which are adapted to nutrient-poor habitats, so half-strength MS (1/2 MS) is commonly used instead (Tinoammini et al., 2024); proportional dilution, however, reduces all elements simultaneously and cannot change their relative ratios.

Because a basal formulation can only be enriched by adding compounds and the concentration of an individual element cannot be reduced, 1/4 MS was selected as the basal medium in this study so that all five elements retained room for upward adjustment. On this basis, the objectives of this study were to design media with different N, P, K, Ca, and Mg ratios, to quantify their effects on the growth performance of *Phalaenopsis* plantlets in vitro, to analyze the relationship between each macronutrient and the growth indicators, and to establish macronutrient ratio guidelines for *Phalaenopsis* that can serve as a reference for improving the formulations used in commercial micropropagation.

MATERIALS AND METHODS

Culture Conditions and Experimental Design

The white-flowered cultivar *Phalaenopsis* Sogo Yukidian 'V3' was used as the plant material. The basal medium was 1/4 MS supplemented with 3 mg·L^{-1} 6-benzyladenine (BA), 18 g L^{-1} sucrose, and 7.5 g L^{-1} agar, and the pH was adjusted to approximately 5.3 before autoclaving. Temperature, relative humidity, and light intensity were kept identical for all culture vessels, and the analysis covered the first growth cycle, from the day of transplanting to day 60. Using the concentration of each macronutrient in 1/4 MS as the baseline, nitrogen (N), potassium (K), phosphorus (P), calcium (Ca), and magnesium (Mg) were defined as five control factors, each at five levels of +0%, +10%, +20%, +30%, and +40%, designated as levels 1 to 5; the supplements were supplied as NH_4NO_3, K_2SO_4, NaH_2PO_4, $CaCl_2{\cdot}2H_2O$, and $MgSO_4{\cdot}7H_2O$, respectively. Because a full factorial design of five factors at five levels would require 5^5 = 3125 treatments, which is impractical, 25 formulations were arranged using an $L_{25}(5^6)$ Taguchi orthogonal array, with five vessels per treatment and two plantlets per vessel, giving 250 plantlets in total. Every treatment was a one-directional increment applied to the same 1/4 MS baseline, so that both the ratios among the elements and their absolute concentrations changed simultaneously; L1, which received no supplement, was the standard 1/4 MS and served as the within-experiment control. The individual plantlet was the unit of analysis, so vessel-level pseudo-replication could not be separated.

Measurement of Growth Indicators

The responses of the orthogonal array were, in order, bud count, fresh weight, leaf area, plant height, and canopy width. Bud count was recorded by manual counting and fresh weight with an electronic balance, whereas the remaining three were obtained from image data. An industrial camera with a resolution of 3648 × 3648 pixels (model A3B00CU000) fitted with a 12 mm fixed-focus lens (model CR-C1220-10M) was used, illuminated by an LED source with a color temperature of 6500 K at a working distance of 250 mm. One side-view image and one top-view image were captured for each plantlet.

In the image processing workflow, a 1024 × 1024 pixel region of interest was first cropped by coordinates, and an initial mask was generated by Segment Anything Model 2 and then imported into Label Studio for inspection and correction. The dataset comprised 1069 images, which were split into training, validation, and test sets in a ratio of 70%,

15%, and 15% and combined with on-the-fly data augmentation. U-Net was adopted as the semantic segmentation architecture, and leaf area, plant height, and canopy width were then derived from a 15 mm square scale reference.

Signal-to-Noise Ratio of the Nominal-the-Best Quality Characteristic

The growth increment of the individual plantlet was taken as the object of analysis. Because the foremost requirement of micropropagation is that the plantlets must not vary while still being replicated in large numbers under stable conditions, the nominal-the-best quality characteristic was adopted. In addition, the bud count increment was zero for every plantlet in L11, L15, L21, and L24, so the S/N ratio was undefined for those treatments; a penalty value equal to ten times the lowest S/N ratio of that response was substituted.

Entropy-Weighted Grey Relational Analysis

The nominal-the-best S/N ratios of the five responses across the 25 runs formed the decision matrix. The matrix was first normalized by the larger-the-better criterion using Eq. (1), and the objective weight of each response was then obtained by the entropy weight method using Eq. (2), in which $0 \cdot \ln 0 = 0$ was defined when the information entropy was computed. Taking the ideal value of 1 as the reference sequence, the grey relational coefficients were calculated using Eq. (3) and were then combined into a weighted grey relational grade (GRG) as given in Eq. (4).

$$X_{\text{norm}} = \frac{X - X_{\min}}{X_{\max} - X_{\min}} \in [0,1] \tag{1}$$

$$e_j = -\frac{1}{\ln m}\sum_{i=1}^{m} p_{ij} \ln p_{ij}, \quad \omega_j = \frac{1 - e_j}{\sum_{j=1}^{n}\left(1 - e_j\right)} \tag{2}$$

$$\gamma_{ij} = \frac{\Delta_{\min} + \zeta \cdot \Delta_{\max}}{\Delta_{ij} + \zeta \cdot \Delta_{\max}} \tag{3}$$

$$\text{GRG}_i = \sum_{j=1}^{n} \omega_j \cdot \gamma_{ij} \tag{4}$$

where:

X = nominal-the-best signal-to-noise ratio of a response (dB)
p_{ij} = proportion of the normalized value of run i to the sum of response j (-)
e_j = information entropy of response j (-)
ω_j = entropy weight of response j (-)
m = number of experimental runs, m = 25 (-)
n = number of responses, n = 5 (-)
Δ_{ij} = absolute difference between the normalized value and the ideal value of the reference sequence (-)
ζ = distinguishing coefficient, ζ = 0.5 (-)
γ_{ij} = grey relational coefficient (-)

RESULTS & DISCUSSION

Nominal-the-Best Signal-to-Noise Ratios and Optimal Levels of Each Quality Characteristic

The optimal level combination was not consistent across the five characteristics; the response table of the nominal-the-best S/N ratios is given in Table 1. In terms of rank, phosphorus had the largest Delta for plant height at 4.02 dB, nitrogen had the largest

Delta for both leaf area and canopy width at 3.22 and 3.46 dB, respectively, and magnesium had the largest Delta for fresh weight at 5.15 dB. Except for plant height, the optimal nitrogen level of the remaining four characteristics fell at level 1 or 2, indicating that raising the nitrogen concentration above the 1/4 MS baseline did not make the plantlets grow better or more uniformly. Although the Delta values for bud count reached 36 to 40 dB, this was mainly a consequence of the penalty values assigned to the four treatments in which the increment was zero.

Table 1 Response table of the nominal-the-best signal-to-noise ratios of each quality characteristic. Delta is the range of the level-average signal-to-noise ratios of a factor.

Response	Factor	Level 1	Level 2	Level 3	Level 4	Level 5	Optimal level	Delta	Rank
Plant height	N	4.10	4.32	6.25	5.94	4.73	Level 3	2.15	4
	K	5.14	3.69	4.23	6.41	5.87	Level 4	2.73	2
	P	**4.39**	**4.98**	**3.28**	**5.37**	**7.30**	**Level 5**	**4.02**	**1**
	Ca	5.28	5.37	4.51	6.07	4.10	Level 4	1.97	5
	Mg	5.22	6.43	4.12	4.60	4.96	Level 2	2.31	3
Leaf area	**N**	**7.89**	**6.06**	**4.84**	**4.67**	**6.71**	**Level 1**	**3.22**	**1**
	K	6.94	5.51	5.36	6.72	5.63	Level 1	1.58	4
	P	7.95	5.75	4.82	5.84	5.82	Level 1	3.13	2
	Ca	6.06	6.17	5.75	5.87	6.33	Level 5	0.57	5
	Mg	7.22	6.68	4.20	6.05	6.03	Level 1	3.01	3
Canopy width	**N**	**7.89**	**8.26**	**6.64**	**4.80**	**5.13**	**Level 2**	**3.46**	**1**
	K	7.20	6.45	5.74	7.50	5.83	Level 4	1.75	4
	P	6.31	7.28	6.86	5.66	6.62	Level 2	1.62	5
	Ca	6.46	7.83	5.58	6.17	6.67	Level 2	2.25	3
	Mg	7.01	6.54	5.02	6.66	7.49	Level 5	2.46	2
Fresh weight	N	8.21	7.47	7.04	5.47	7.92	Level 1	2.74	3
	K	7.91	7.17	7.70	6.04	7.30	Level 1	1.87	5
	P	6.88	10.88	6.20	6.20	5.95	Level 2	4.93	2
	Ca	6.11	5.87	8.21	7.40	8.51	Level 5	2.64	4
	Mg	**4.77**	**7.74**	**7.01**	**9.92**	**6.68**	**Level 4**	**5.15**	**1**
Bud count	N	−5.52	−6.46	−44.16	−8.37	−43.92	Level 1	38.64	4
	K	**−44.79**	**−8.11**	**−5.11**	**−24.08**	**−26.34**	**Level 3**	**39.67**	**1**
	P	−7.78	−24.97	−8.25	−44.40	−23.03	Level 1	36.62	5
	Ca	−7.36	−25.92	−44.59	−5.71	−24.85	Level 4	38.88	2
	Mg	−45.62	−7.49	−6.81	−25.00	−23.51	Level 3	38.81	3

Entropy-Weighted Grey Relational Grade and Optimal Formulation

The objective weights obtained by the entropy weight method were, in descending order, fresh weight (0.2571), plant height (0.2307), leaf area (0.1987), bud count (0.1978), and canopy width (0.1157). The five highest grey relational grades were L14 (0.6578), L5 (0.6449), L10 (0.6373), L23 (0.6345), and L9 (0.6265), and the lowest was L24 (0.4589); L14 corresponds to N +20%, K +30%, P +0%, Ca +30%, and Mg +10%. The grey relational grade was then treated as a single response to construct the response table in

Table 2. The optimal level combination was N +0%, K +30%, P +40%, Ca +30%, and Mg +10%, and the factors ranked by Delta were phosphorus (0.0814), nitrogen (0.0646), magnesium (0.0638), potassium (0.0521), and calcium (0.0461).

Table 2 Response table of the grey relational grade.

Factor	Level 1	Level 2	Level 3	Level 4	Level 5	Optimal level	Delta	Rank
N	0.5951	0.5763	0.5430	0.5391	0.5305	Level 1	0.0646	2
K	0.5600	0.5303	0.5523	0.5824	0.5591	Level 4	0.0521	4
P	**0.5832**	**0.5860**	**0.5179**	**0.5078**	**0.5892**	**Level 5**	**0.0814**	**1**
Ca	0.5745	0.5565	0.5304	0.5764	0.5463	Level 4	0.0461	5
Mg	0.5358	0.5921	0.5283	0.5765	0.5513	Level 2	0.0638	3

The optimal phosphorus level indicated by the response table was level 5, which is the opposite of the level in the best measured run, L14. The main effect of phosphorus in Table 2 is U-shaped: the mean grey relational grades at levels 1, 2, and 5 differ by only 0.0060, whereas the mean standard deviation among the five formulations within a single level reaches 0.046, which is far larger than that difference, so the three levels are not substantively distinguishable. Furthermore, the level averages in the response table are marginal effects of a factor over the various combinations of the other four factors, whereas L14 is the measured value of one specific combination and therefore also contains the interactions that the additive model does not account for. The discrepancy between the two must still be verified by a confirmation experiment.

Physiological Significance and Practical Implications of the Macronutrients

Nitrogen was optimal at +0% and tended toward the low levels in four of the five characteristics, consistent with the epiphytic, nutrient-poor habitat of *Phalaenopsis*. Nitrogen was supplemented as NH_4NO_3, so raising its concentration also raised the ammonium proportion; ammonium uptake releases H^+ and lowers medium pH (Bosman et al., 2024), aggravating ionic stress. Phosphorus was optimal at +40% and had the largest Delta. At 9.67 $mg \cdot L^{-1}$ it is the most dilute of the five elements in 1/4 MS, and as a constituent of ATP, nucleic acids, and membrane phospholipids it most likely limits actively dividing tissue (Davis et al., 2022). Magnesium was optimal at +10%; it competes with potassium and calcium during root uptake, where an excess of any one may induce antagonistic deficiency (Dölger et al., 2025). Potassium and calcium were optimal at +30% but had the smallest Delta values, so their increments mattered little. Overall, the standard 1/4 MS medium (L1) ranked only sixth at 0.6236, whereas the plant height and fresh weight increments of L14 exceeded those of L1 by 38.1% and 46.4%, indicating that macronutrient ratios matter more than absolute concentrations.

Acclimation Effect in the First Subculture Cycle and Future Work

Because these data cover only the first subculture cycle after transfer to the adjusted formulations, several results deviated from expectation: the optimal levels of the five characteristics were inconsistent, and the Delta values spanned only 0.046 to 0.081. The plantlets were presumably still acclimating to the new ionic and osmotic conditions within the 60-day period, so that treatment effects were partly masked by individual variation and the data do not yet reflect the true effects of the macronutrient ratios. Subculture will therefore be continued at two-month intervals, and the second and third growth cycles will be analyzed by the same procedure once the plantlets are fully acclimated. As acclimation ends, within-treatment variation should decrease while between-treatment effects emerge, raising the discriminating power of the S/N ratio and the grey relational

grade and stabilizing the optimal level of each factor. Analysis of variance will then test the statistical significance and contribution of each macronutrient, and a confirmation experiment will be conducted on the resulting optimal formulation.

CONCLUSIONS

Using a 1/4 MS baseline, this study evaluated the combined effect of five macronutrient ratios on *Phalaenopsis* plantlets in vitro by means of an $L_{25}(5^6)$ orthogonal array and an entropy-weighted grey relational analysis. The optimal levels of the individual characteristics were inconsistent, so no single characteristic is sufficient to determine the formulation. After the multiple responses were integrated, phosphorus exerted the largest influence and calcium the smallest, indicating that phosphorus is the element most likely to become limiting in a dilute formulation, whereas nitrogen should not be raised further above the 1/4 MS level. The optimal formulation derived from the additive model and the best measured run, L14, were opposite for nitrogen and phosphorus, which reflects the confounding of interactions with main effects in the $L_{25}(5^6)$ design; the result of the factor-by-factor optimization therefore still requires verification by a confirmation experiment.

REFERENCES

Bosman, R. C., van Rooyen, I. L., Brancken, J., Brink, H. G., & Nicol, W. (2024). Simultaneous pH and EC control in hydroponics through real-time manipulation of the ammonium-to-nitrate ratio in the nutrient solution. *SCIENTIA HORTICULTURAE*, *332*, Article 113185. https://doi.org/10.1016/j.scienta.2024.113185

Davis, B., Lim, W. H., Lambers, H., Dixon, K. W., & Read, D. J. (2022). Inorganic phosphorus nutrition in green-leaved terrestrial orchid seedlings. *ANNALS OF BOTANY*, *129*(6), 669-678. https://doi.org/10.1093/aob/mcac030

Dölger, J. L., Sagervanshi, A., Pitann, B., & Mühling, K. H. (2025). The magnesium-specific uptake and translocation transporters ZmMGT10 and MGR6 are upregulated not only by magnesium deficiency but also by high potassium concentrations in maize. *PLANT PHYSIOLOGY AND BIOCHEMISTRY*, *224*, Article 109977. https://doi.org/10.1016/j.plaphy.2025.109977

Mahdavi, Z., Daylami, S. D., Vakilian, K. A., & Vahdati, K. (2025). Machine learning-based macronutrients optimization enhances nitrogen uptake and growth in Phalaenopsis plantlets. *PLANT CELL TISSUE AND ORGAN CULTURE*, *162*(2), Article 46. https://doi.org/10.1007/s11240-025-03166-4

Tinoammini, N., Aazhivaendhan, G., & Kumar, T. S. (2024). Invitro germination and optimization of basal media for protocorm-like bodies proliferation in Dienia ophrydis (J. Koenig) Seidenf. *RHIZOSPHERE*, *29*, Article 100854. https://doi.org/10.1016/j.rhisph.2024.100854

Zhang, K. Y., Wu, Y. Y., Su, Y., & Li, H. T. (2022). Implication of quantifying nitrate utilization and CO2 assimilation of Brassica napus plantlets in vitro under variable ammonium/nitrate ratios. *BMC PLANT BIOLOGY*, *22*(1), Article 392. https://doi.org/10.1186/s12870-022-03782-8

PA-P19

Proceedings of The 12th International Symposium on Machinery and Mechatronics for Agriculture and Biosystems Engineering (ISMAB 2026)
20-24 October 2026, Busan, Republic of Korea

NON-DESTRUCTIVE PREDICTION OF SUBSTRATE MOISTURE CONTENT IN *PHALAENOPSIS* ORCHIDS USING HYPERSPECTRAL IMAGING

Wei-Chun Lin[1], Wen-Lin Chu[1*], Wei-Ling Chen[2], Hsi-Chun Hung[2]

[1]Department of Bio-Industrial Mechatronics Engineering, National Chung Hsing University, Taichung, Taiwan
[2]Floral Industry Innovation Center, Ministry of Agriculture, Taiwan
*Corresponding Author-- Voice: +886-4-2284-0377 ext. 509, Email: wlchu@nchu.edu.tw

Abstract: *Phalaenopsis* is one of Taiwan's most important export flowers, and the management of substrate moisture content during cultivation directly affects plant growth and subsequent flowering quality. At present, the substrate moisture content of sphagnum substrate is mainly evaluated based on growers' empirical judgment or insertion-type sensors. However, empirical judgment is easily affected by subjective experience, while insertion-based measurement may cause root damage and increase the risk of disease transmission. Therefore, this study developed a non-contact prediction method for estimating the substrate moisture content of sphagnum substrate in Phalaenopsis by integrating near-infrared hyperspectral imaging with machine learning. The experimental materials were 2.8-inch potted seedlings of Phalaenopsis Sogo Yukidian 'V3'. Different substrate moisture conditions were established using three irrigation-frequency treatments, namely watering once every 5, 10, and 15 days. After flat-field correction, the hyperspectral image data were cropped to retain the stable spectral range from 946.1 to 1672.6 nm. The corrected spectral data were then preprocessed using Savitzky-Golay smoothing (SG), standard normal variate transformation (SNV), and SG-SNV, respectively, to develop GPR models. The results showed that the model using SG preprocessing achieved the best performance, with a prediction set coefficient of determination of (R_P^2) of 0.816 and an RMSEP of 5.242%. These results demonstrate that near-infrared hyperspectral imaging can be used for the non-contact prediction of substrate moisture content in sphagnum substrate of *Phalaenopsis*, and can serve as a basis for subsequent key-wavelength selection and the development of low-cost multispectral detection devices.

Key Words: *Phalaenopsis*, sphagnum substrate, substrate moisture content, hyper spectral imaging, machine learning

INTRODUCTION

Phalaenopsis is a high-value floricultural crop with strong export competitiveness in Taiwan, and its production highly depends on environmentally controlled greenhouses. During the transition from the vegetative growth stage to the flower-forcing stage, substrate moisture directly affects flowering quality, including spike length, total flower number, and double-spike rate. However, current irrigation management mainly relies on growers' subjective experience

and lacks real-time and objective scientific evidence. At present, the substrate moisture content (SMC) of sphagnum substrate in commercial production is mainly evaluated using probe-type sensors, such as the Delta-T W.E.T. Sensor Kit, or through visual inspection and manual assessment. However, because 2.8-inch pots have limited space and dense root systems, probe insertion is time-consuming and labor-intensive, and may damage roots and increase the risk of cross-infection. In contrast, empirical judgment is easily affected by the fact that surface evaporation occurs faster than internal moisture loss, resulting in substantial errors and making precise irrigation management difficult to achieve. Near-infrared spectroscopy mainly reflects the vibrational absorption of chemical bonds such as C-O, O-H, and C-H, among which the O-H bond is highly associated with water content. Lu et al. (2020) reported that water exhibits distinct absorption peaks at 965, 1190, and 1450 nm, confirming that near-infrared spectroscopy can effectively capture changes in moisture content. To overcome plant damage caused by invasive measurement and the limitations of subjective assessment, this study focused on the sphagnum substrate of 2.8-inch potted *Phalaenopsis*. Near-infrared hyperspectral images were acquired using an internally scanning hyperspectral imaging system with a spectral range of 906–1759 nm and were subjected to flat-field correction. The measurements obtained from the Delta-T W.E.T. Sensor Kit were used as the ground-truth reference for substrate moisture content, and a non-contact machine learning regression model was developed for SMC prediction.

MATERIALS AND METHODS

Plant Material and Experimental Design

The *Phalaenopsis* plants used in this experiment were cultivated in a standard environmentally controlled greenhouse at the Gukeng Experimental Station in Yunlin, Taiwan. The experimental materials were 2.8-inch potted seedlings of *Phalaenopsis* Sogo Yukidian ‘V3’, with sphagnum moss as the cultivation substrate. To establish a dataset covering different substrate moisture conditions, ranging from high to low moisture content, three irrigation-frequency treatments were designed: watering once every 5, 10, and 15 days. This design was used to obtain substrate data under different moisture conditions and to avoid collecting samples with similar moisture contents in each sampling session. The experiment lasted approximately seven months, during which seven data collection sessions were conducted. Each session included the three irrigation treatments, with 30 plants for each treatment. Therefore, 90 hyperspectral image datasets of *Phalaenopsis* substrate were obtained in each session. A total of 630 hyperspectral image datasets were collected throughout the experiment. After excluding questionable hyperspectral data, 543 valid datasets were retained for analysis.

Data Acquisition and Standard Operating Procedure

The hyperspectral image data in this study were acquired using an IONC-NIR1 near-infrared (NIR) hyperspectral camera (Isuzu Optics, Taiwan). As shown in Fig.1, the imaging system consisted of one NIR hyperspectral camera with a spectral range of 906 to 1759 nm, four halogen lamps with a spectral range of 450 to 2000 nm, and a copy-stand fixture. Hyperspectral data were collected using Spectral Image-NIR software (Isuzu Optics, Taiwan), while the substrate moisture content data were acquired using a Delta-T WET Sensor Kit (Fig.2).



Fig.1 Actual photograph of the NIR hyperspectral camera.



Fig.2 Delta-T WET Sensor Kit.

Before acquiring the hyperspectral image data, the halogen light sources were warmed up for 30 min to ensure stable operation of the imaging system. During the warm-up period, the camera focus and the distance between the camera and the substrate surface were adjusted to approximately 0.30 m. The scanning speed and exposure time of the internally scanning hyperspectral camera were set to 1.86 mm/s and 0.8 ms, respectively. After the warm-up was completed, the white reference, dark current, and sample images were acquired sequentially. Because the acquired hyperspectral image data may be affected by the illumination angle of the light sources, flat-field correction was performed before analysis to obtain relative reflectance (Lee et al., 2026). The relative reflectance was calculated using Eq. (1).

$$R = \frac{I_S - I_D}{I_W - I_D} \times R_W \quad (1)$$

where:

R = relative reflectance at each wavelength (%)

I_S = raw reflected intensity of the sample at each wavelength (-)

I_D = dark current intensity with lights off (-)

I_W = 99% white reference image (-)

R_W = reflectance of the white reference panel, equal to 99% (%)

Spectral Extraction

In the top-view hyperspectral images of cultivated *Phalaenopsis*, the substrate surface was often directly occluded by plant leaves or affected by shadow interference, and exposed roots were commonly present on the substrate surface. Therefore, data labeling was performed by manually selecting regions of interest (ROI). For each hyperspectral image of *Phalaenopsis*, ROIs were selected through visual inspection while avoiding areas covered by leaves, shadows, exposed roots, and the edges of plastic pots. Each ROI was set to 20 × 20 px.

Effective Spectral Range

Due to signal attenuation at both ends of the spectral range caused by the hyperspectral camera and light source intensity, the white reference spectrum gradually approached the dark current during flat-field correction. Consequently, the denominator term in the flat-field correction equation, ($I_W - I_D$) approached zero, resulting in unstable relative reflectance calculations. The first 24 and the last 51 high-noise bands were removed, and the most stable spectral region from 946 to 1672 nm, consisting of 437 bands, was retained for subsequent analysis.

Spectral Preprocessing

During the acquisition of hyperspectral image data, the spectra may be affected by instrumental noise, baseline drift, and spectral scattering caused by irregular sample surfaces. Therefore, spectral preprocessing can be used to reduce hyperspectral camera noise and light scattering effects, as well as to eliminate the influence of baseline drift. Savitzky-Golay (SG) smoothing can improve the signal-to-noise ratio by reducing noise while preserving the main spectral features (Abriha et al., 2026). According to Cui et al. (2025), standard normal variate (SNV) transformation can reduce the influence of light scattering. In this study, SG, SNV, and SG followed by SNV were applied to preprocess the original hyperspectral data, and their model performances were compared.

Model Training and Evaluation Metrics

Gaussian process regression (GPR) is a machine learning regression algorithm that establishes the relationship between input features and output responses through a Gaussian process. It uses known data to predict unknown samples and is therefore suitable for problems with limited data or nonlinear characteristics. GPR uses a kernel function to calculate the similarity between different data points and to model their relationships, thereby enabling model training and prediction (Alkhattabi et al., 2026). Different kernel functions represent different assumptions about the data, and their selection directly affects the generalization ability of the model. In particular, the choice of kernel function determines the assumed smoothness of the data. In this study, a GPR model was developed using the rational quadratic kernel. The 543 datasets were randomly divided into training and test sets at a ratio of 4:1, including 434 datasets for training and 109 datasets for testing. The coefficient of determination (R^2) and root-mean-square error (RMSE) are commonly used evaluation metrics for assessing model performance. A good model should have a higher R^2 and a lower RMSE. These metrics were calculated using Eq. (2) and Eq. (3), respectively.

$$R^2 = 1 - \frac{\sum_{i=1}^{n}(y_i - \hat{y}_i)^2}{\sum_{i=1}^{n}(y_i - \bar{y})^2} \tag{2}$$

$$\mathrm{RMSE} = \sqrt{\frac{1}{n}\sum_{i=1}^{n}(y_i - \hat{y}_i)^2} \tag{3}$$

where:

y_i = measured SMC of the i-th sample (%)

$\hat{y}_i$ = predicted SMC of the i-th sample (%)

$\bar{y}$ = mean measured SMC (%)

n = total number of samples used for evaluation (-)

Hyperspectral image data were mainly collected using Spectral Image-NIR software (Isuzu Optics, Taiwan). Data preprocessing, data labeling, and model training were all performed on a personal computer using MATLAB R2025b.

RESULTS & DISCUSSION

In this study, SG, SNV, and SG-SNV preprocessing methods were applied to the hyperspectral image data, and the resulting hyperspectral curves are shown in Fig.3. The results indicate that SG preprocessing effectively reduced noise and produced smoother spectral curves. SNV preprocessing reduced the influence of light scattering, resulting in more consistent spectral

curves for the same material. The SG-SNV preprocessing method combined the advantages of both approaches by producing smoother curves and reducing noise associated with the equipment and background illumination.

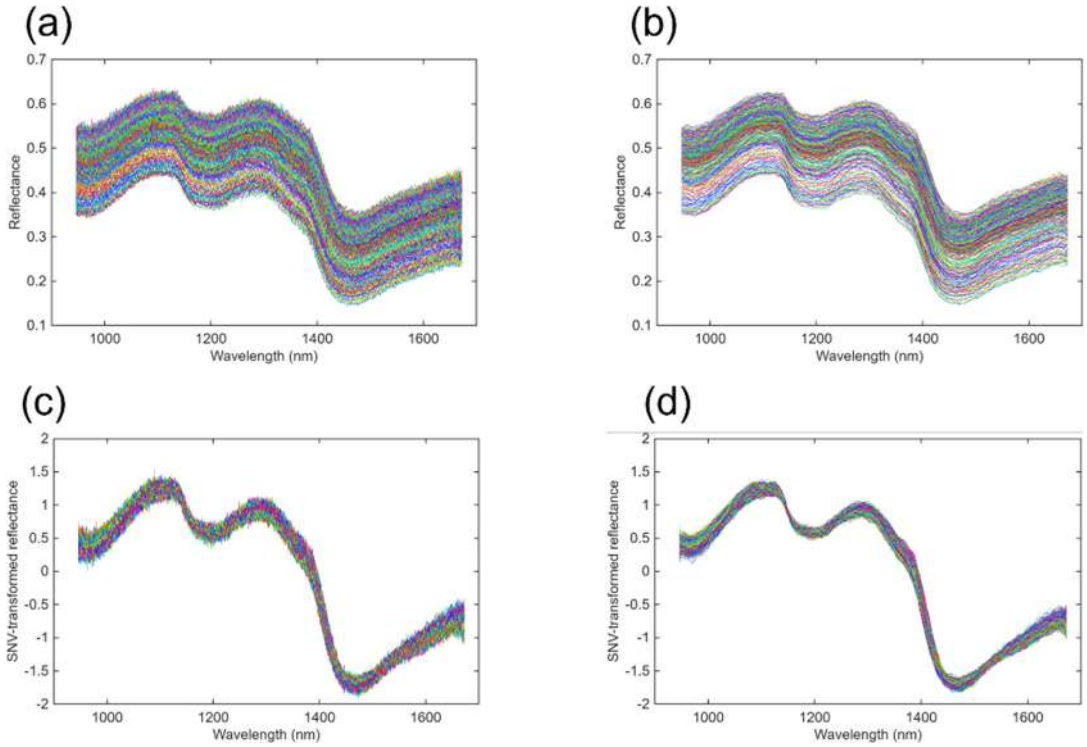

Fig.3 Relative reflectance curves after hyperspectral preprocessing. (a) RAW data; (b) SG; (c) SNV; (d) SG-SNV.

Although spectral preprocessing improved the signal-to-noise ratio of the hyperspectral data, the improvement in model performance was not significant. Prediction models were developed using hyperspectral data processed with different preprocessing methods, and the model results are shown in Table 1. Based on the evaluation metrics, the model using SG preprocessing achieved the best performance, with an R_P^2 and RMSEP of 0.816 and 5.242%, respectively. In contrast, the model using SNV preprocessing performed worse than that using the RAW data, with an R_P^2 and RMSEP of 0.802 and 5.432%, respectively. These results indicate that preprocessing does not necessarily improve model performance compared with models trained using RAW data.

Table 1 Training results of the GPR models using RAW data and different preprocessing methods.

Preprocessing	Cross-validation set		Prediction set	
	R_{CV}^2	RMSECV (%)	R_P^2	RMSEP (%)
RAW	0.826	5.203	0.804	5.406
SG	0.824	5.232	0.816	5.242
SNV	0.806	5.496	0.802	5.432
SG-SNV	0.801	5.554	0.813	5.282

CONCLUSIONS

This study developed a non-contact prediction model for the substrate moisture content (SMC)

of sphagnum substrate in *Phalaenopsis* by integrating near-infrared hyperspectral imaging with machine learning. Different irrigation-frequency treatments were applied to obtain data covering various substrate moisture conditions, and the SMC measured using a Delta-T W.E.T. Sensor Kit was used for model training and validation. After flat-field correction, effective spectral range cropping, and different preprocessing methods, the hyperspectral data were used to predict SMC using a GPR model. The results showed that SG preprocessing reduced hyperspectral noise and produced smoother spectral curves, while SNV preprocessing reduced the influence of light scattering. However, the model results after preprocessing were not always superior to those obtained using RAW data. Among the tested methods, the GPR model combined with SG preprocessing achieved the best prediction performance, with a tprediction set R_P^2 of 0.816 and an RMSEP of 5.242%. This indicates that the method can effectively establish the relationship between near-infrared spectral features and the SMC of sphagnum substrate. On the other hand, although SNV and SG-SNV improved the consistency of the spectral curves, their prediction results did not outperform those of SG, indicating that spectral preprocessing methods should be selected according to the characteristics of the data. This study confirms the feasibility of applying near-infrared hyperspectral imaging to the non-contact detection of SMC in sphagnum substrate of *Phalaenopsis*, which can reduce root damage and the time-consuming operation associated with conventional probe-type sensors. Future work may further focus on key-wavelength selection to reduce data dimensionality and equipment cost, and on the development of multispectral imaging systems or real-time detection devices.

ACKNOWLEDGEMENTS

This study was financially supported by the Ministry of Agriculture through the project "Development of AI-Based Non-Destructive Prediction and Environmental Control Decision-Making Technologies for Water and Nutrient Status in *Phalaenopsis* (Project No. 115 農科-1.6.2-創-02). The authors gratefully acknowledge this support.

REFERENCES

Abriha, D., Diószegi, G., Kovács, L., Burai, P., & Szabó, S. (2026). Context-dependent performance of Savitzky-Golay smoothing in hyperspectral Forest species classification: A Bayesian hierarchical assessment. *Ecological Informatics*, *97*, 103914. https://doi.org/10.1016/j.ecoinf.2026.103914

Alkhattabi, L., Waqas, S., Imran, M., Almarshoud, M. A., Aljehani, A., & Hanbazazah, A. (2026). Process modeling of total nitrogen removal in rotating biological contactor through artificial neural networks and Gaussian process regression. *Cleaner Waste Systems*, *15*, 100544. https://doi.org/10.1016/j.clwas.2026.100544

Cui, Y., Lv, Z., Fan, Y., Song, Y., Wu, Y., Zhao, X., Diao, C., Zhao, C., Xu, Z., & Wang, W. (2025). Spatial-spectral joint preprocessing for hyperspectral image analysis using 3D-ResNet: Application to coal ash content estimation. *Measurement*, *246*, 116535. https://doi.org/10.1016/j.measurement.2024.116535

Lee, D.-H., Yoon, S., & Lim, H.-H. (2026). Prediction of bentonite water content using visible and near-infrared spectroscopy combined with partial least squares regression. *Nuclear Engineering and Technology*, *58*(2), 103926. https://doi.org/10.1016/j.net.2025.103926

Lu, B., Wang, X., Liu, N., He, K., Wu, K., Li, H., & Tang, X. (2020). Feasibility of NIR spectroscopy detection of moisture content in coco-peat substrate based on the optimization characteristic variables. *Spectrochimica Acta Part A: Molecular and Biomolecular Spectroscopy*, *239*, 118455. https://doi.org/10.1016/j.saa.2020.118455

PA-P20

Proceedings of The 12th International Symposium on Machinery and Mechatronics for Agriculture and Biosystems Engineering (ISMAB 2026)
20-24 October 2026, Busan, Republic of Korea

DISTANCE-ADAPTIVE DEPTH CAMERA–LIDAR FUSION FOR PROXIMITY WARNING ON AGRICULTURAL MACHINERY

Seung-Yong Seo[1], Jin-Yeong Lee[2], Jae-Min Lee[2], Ryu-Gap Lim[2*]

[1]Department of Smart Agriculture Engineering, Sunchon National University, Suncheon 57922, Republic of Korea
[2]Department of Convergence Biosystems Machinery Engineering, Sunchon National University, Suncheon 57922, Republic of Korea
*Corresponding Author — Voice: +82-61-750-3264, Email: limrg11@scnu.ac.kr

Abstract: Operators of agricultural machinery cannot see much of the area immediately around the vehicle, and a useful proximity warning depends on knowing how far away a detected object actually is. Neither sensor commonly used for this purpose gives that distance reliably across the full working range: stereo depth error grows with the square of distance, whereas LiDAR ranging error stays essentially constant. We built the fusion rule directly on that contrast. Modelling both errors and solving for the point where they are equal yields a crossover distance of 3.87 m, and the inverse-variance weights follow from the models themselves rather than from parameter fitting. Objects are detected with YOLO11m, trained on 155,061 labelled instances across five agricultural classes, and the complete pipeline runs on a single edge computing platform carried on the tractor. We evaluated the system in an open field against RTK-GNSS reference distances, collecting 2,604 synchronized samples while the tractor approached a person and a stationary tractor from both the front and the rear at 3, 5 and 7 km/h. Fusion brought the RMSE of distance estimation down to 0.205 m, 33.2% below the depth camera alone, with gains of 20.5–38.3% across the 3–12 m band where a warning matters most. Beyond 12 m the benefit fell away, because valid LiDAR points landed inside the detected bounding box in only 61.7% of frames. That coverage is governed by target width and by the vertical angular resolution of the LiDAR, so the two jointly limit what fusion can achieve — a relationship that can guide sensor selection for other agricultural and livestock platforms.

Key Words: sensor fusion; inverse-variance weighting; depth camera; LiDAR; distance estimation; agricultural machinery safety; RTK-GNSS; object detection

ACKNOWLEDGEMENTS

This work was supported by Korea Institute of Planning and Evaluation for Technology in Food, Agriculture and Forestry (IPET) through [Program Name], funded by Ministry of Agriculture, Food and Rural Affairs (MAFRA) (RS-2026-25522826).

PA-P21

Proceedings of The 12th International Symposium on Machinery and Mechatronics for Agriculture and Biosystems Engineering (ISMAB 2026)
20-24 October 2026, Busan, Republic of Korea

END-SENSING SYSTEM FOR IRRIGATION MONITORING IN BUILDING-INTEGRATED VERTICAL FARMS

Joo won Jeong[1], Meong Hun Lee[2*]

[1]Sunchon National University, 255 Jungang-ro, Suncheon-si, Jeollanam-do 57922, Republic of Korea
[2]Sunchon National University, 255 Jungang-ro, Suncheon-si, Jeollanam-do 57922, Republic of Korea
*Corresponding Author-- Voice: +82-3777-5544, Email: leemh777@gmail.com

Abstract: High-rise building-integrated vertical farms require reliable water and nutrient-solution delivery to cultivation zones located at different levels. Elevation, branch length, local resistance, valve operation, and partial blockage can cause delayed or interrupted supply. This study proposes an end-sensing-based irrigation monitoring architecture for such systems. A central tank and pump supply multiple cultivation zones through a main riser and branch lines, and an end-sensing device is installed at each branch terminal. The controller monitors response occurrence and response time after irrigation starts and interprets each branch as normal, restricted, or abnormal using a zone-specific reference. A drainage-return path is also considered so that sensing water can be recovered by the recirculating system. The proposed approach provides a simple zone-level monitoring method without installing a sensor at every outlet and can serve as a basic mechatronic element for irrigation management in building-integrated vertical farms.

Key Words: Vertical Farm, Building-Integrated Agriculture, Irrigation Monitoring, End-Sensing, Nutrient Solution Supply

INTRODUCTION

Vertical farms use vertically stacked cultivation layers and commonly employ hydroponic irrigation methods to deliver water and nutrients (Vatistas et al., 2022). Building integration can further connect farm operation with building water, nutrient, and energy flows (Blom et al., 2023). In high-rise configurations, however, cultivation zones can be distributed across different elevations and branch lines, creating zone-dependent hydraulic conditions.

Narrow irrigation passages can also be affected by physical, chemical, or biological clogging, and partial blockage can reduce discharge uniformity (Nakayama and Bucks, 1991; Capra and Scicolone, 1998). A simple method that confirms whether nutrient solution reaches the end of each branch can therefore provide a useful line-level indication. The objective of this study is to propose an end-sensing-based irrigation monitoring architecture for high-rise building-integrated vertical farms and to define its basic diagnostic logic and evaluation framework.

MATERIALS AND METHODS

System Configuration

The proposed system consists of a nutrient-solution tank, pump, main supply riser, cultivation-zone branch lines, terminal end-sensing devices, and a monitoring controller. When nutrient solution reaches a branch terminal, the sensor transmits a response to the controller. A drainage-return path can reconnect the sensing point to the recirculation line so that nutrient solution is recovered after detection.

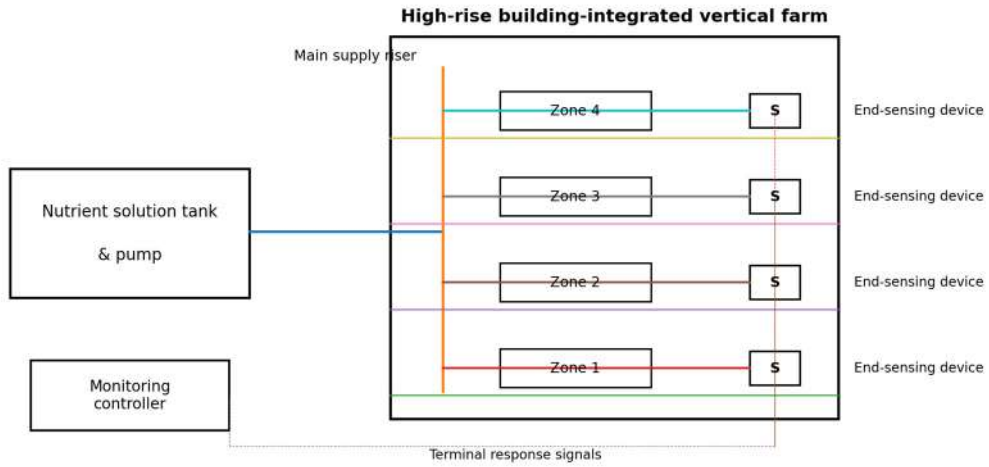

Fig.1 Conceptual configuration of end-sensing-based irrigation monitoring for a high-rise building-integrated vertical farm.

Terminal-Response Diagnostic Logic

The controller compares the irrigation start time with the terminal response from each branch. A response within the zone-specific reference range indicates normal supply, a delayed response indicates a branch requiring inspection, and no response within the allowable period indicates a possible blockage or supply fault. Because static head and line resistance differ among building levels, the reference range should be calibrated separately for each cultivation zone.

Table 1 Diagnostic interpretation based on the terminal response.

Branch condition	Terminal response	Diagnostic interpretation
Normal	Response occurs within reference time	Normal supply
Restricted	Delayed response	Branch inspection recommended
Abnormal	No response within allowable period	Possible blockage/ supply fault

Evaluation Framework

A short-form evaluation can compare normal supply, restricted flow, and interrupted-supply conditions while maintaining fixed pump, valve, and pressure-control settings. The primary variables are response occurrence, response time, and repeatability. Reference ranges

should be established separately for each cultivation zone because elevation and branch geometry affect hydraulic response.

RESULTS & DISCUSSION

The proposed architecture converts the irrigation condition of each cultivation-zone branch into a terminal response that can be monitored by a central controller. This allows a multi-level vertical farm to be screened by cultivation zone rather than by individual outlet. A delayed or missing response can trigger inspection of the relevant branch before more detailed maintenance is performed.

Interpretation must account for high-rise hydraulic effects. Elevation, pressure regulation, branch length, and simultaneous valve operation can change response time even when no clogging is present, so zone-specific baselines are necessary. The end-sensing signal also cannot localize the exact fault. For practical deployment, it can be combined with pump pressure, branch flow rate, electrical conductivity, or valve-status information. Connection of the sensing path to a return line may reduce nutrient-solution loss in recirculating systems. Future experiments should quantify response thresholds, detection accuracy, and long-term reliability at different building levels.

CONCLUSIONS

An end-sensing-based irrigation monitoring architecture was proposed for high-rise building-integrated vertical farms. Terminal response occurrence and delay are used as simple indicators of branch condition, enabling zone-level screening with a relatively simple sensor structure. Because hydraulic response varies with elevation and branch geometry, zone-specific calibration is required. Future work will validate the method under controlled flow restrictions, elevation differences, and repeated irrigation cycles.

ACKNOWLEDGEMENTS

This work was supported by Korea Institute of Planning and Evaluation for Technology in Food, Agriculture and Forestry (IPET) through the K-Vertical Farm Globalization Project, funded by the Ministry of Agriculture, Food and Rural Affairs (MAFRA) (RS-2025-02305776).

REFERENCES

Blom, T., A. Jenkins, and A. van den Dobbelsteen. 2023. Synergetic integration of vertical farms and buildings: reducing the use of energy, water, and nutrients. Frontiers in Sustainable Food Systems 7: 1227672.

Capra, A., and B. Scicolone. 1998. Water quality and distribution uniformity in drip/trickle irrigation systems. Journal of Agricultural Engineering Research 70(4): 355-365.

Nakayama, F. S., and D. A. Bucks. 1991. Water quality in drip/trickle irrigation: A review. Irrigation Science 12(4): 187-192.

Vatistas, C., D. D. Avgoustaki, and T. Bartzanas. 2022. A systematic literature review on controlled-environment agriculture: How vertical farms and greenhouses can influence the sustainability and footprint of urban microclimate with local food production. Atmosphere 13(8): 1258.

PA-P22

Proceedings of The 12th International Symposium on Machinery and Mechatronics for Agriculture and Biosystems Engineering (ISMAB 2026)
20-24 October 2026, Busan, Republic of Korea

PHYSICAL AI-BASED ARCHITECTURE FOR AUTONOMOUS AGRICULTURAL ROBOT OPERATIONS

Kiwoong Song[1], MyeongHun Lee[2*]

[1]Sunchon National University, 255 Jungang-ro, Suncheon-si, Jeollanam-do 57922, Republic of Korea
[2]Sunchon National University, 255 Jungang-ro, Suncheon-si, Jeollanam-do 57922, Republic of Korea
*Corresponding Author-- Voice: +82-3777-5544, Email: leemh777@gmail.com

Abstract: Agricultural robots must operate under variable crop shapes, occlusion, illumination, and complex plant structures. Conventional task-specific robotic systems often separate perception, planning, and control, which can limit adaptation to changing environments. This paper proposes a conceptual Physical AI-based architecture for autonomous agricultural operations. The architecture integrates multimodal perception, semantic understanding, task reasoning, action generation, robot control, and closed-loop feedback. Selective greenhouse harvesting is presented as a representative application. Vision-language-action (VLA) models are considered as a potential interface between semantic understanding and physical robot actions. The proposed framework provides a basis for future implementation and experimental validation of autonomous agricultural robots.

Key Words: Agricultural robot, Physical AI, Vision-language-action model, Autonomous harvesting, Embodied AI

INTRODUCTION

Agricultural robots have been developed for harvesting, monitoring, spraying, and other labor-intensive operations. However, autonomous agricultural manipulation remains difficult because crop appearance, position, accessibility, and surrounding obstacles continuously vary. Selective harvesting robots must therefore combine perception, manipulation, and motion control under uncertain conditions (Arad et al., 2020; Kootstra et al., 2021).

Recent vision-language-action (VLA) models provide a new approach for connecting visual perception and task instructions directly with robot actions. RT-2 demonstrated that visual-language representations can be transferred to robotic control, while OpenVLA provides an open framework for adapting VLA models to robotic tasks (Zitkovich et al., 2023; Kim et al., 2025).

The objective of this study is to propose a Physical AI-based architecture that connects perception, reasoning, action, and physical feedback for autonomous agricultural robot operations.

MATERIALS AND METHODS

The proposed architecture consists of five functional stages: multimodal perception, semantic understanding, task reasoning, action generation, and execution with feedback.

RGB-D cameras and robot-state information are first used to perceive crops and surrounding objects. The observations are converted into semantic information such as crop identity, ripeness, position, accessibility, and obstacles. A reasoning module then interprets the agricultural task and determines an appropriate sequence of actions.

For selective harvesting, for example, the system may identify a ripe and reachable fruit, plan an approach path, generate a grasping or cutting action, and execute the operation through a robotic manipulator. VLA models can provide a connection between semantic task information and robot action generation. Low-level motion control and safety constraints remain separated from high-level AI reasoning to ensure reliable physical execution.

After each action, new sensory observations are returned to the perception module, forming a closed-loop process.

The proposed architecture was organized as a conceptual closed-loop framework for autonomous agricultural robot operation. Selective harvesting was used as a representative application to define the interaction among perception, reasoning, action generation, and robot control.

Proposed Physical AI Architecture

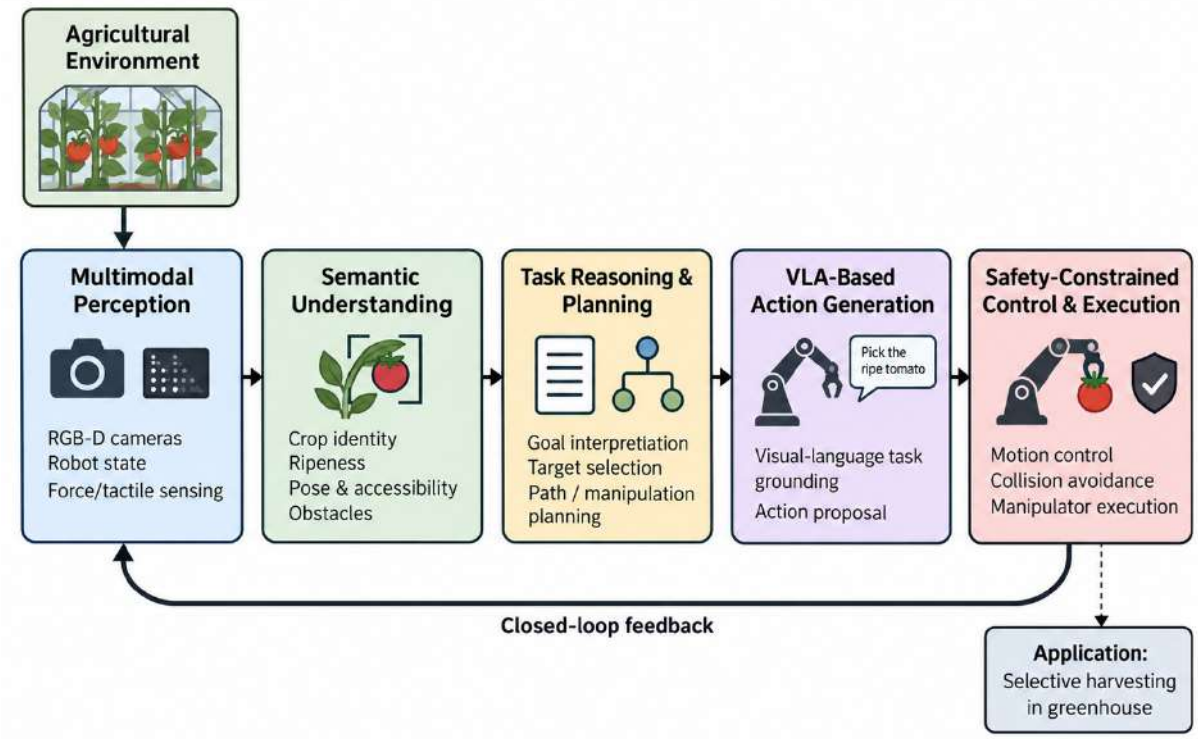

Fig.1 Conceptual Physical AI-based architecture for autonomous agricultural robot operations.

RESULTS & DISCUSSION

The proposed architecture extends conventional agricultural robot pipelines by introducing semantic reasoning between perception and physical action. Instead of processing only geometric target positions, the robot can conceptually consider task-relevant information such as ripeness, accessibility, and surrounding obstacles.

VLA models may further enable high-level task instructions to be connected with robot actions. However, agricultural environments require strict consideration of collision avoidance, crop damage, response time, and reliability. Therefore, Physical AI reasoning should complement rather than replace conventional robot control and safety mechanisms.

The architecture presented in this paper is conceptual and has not yet been experimentally validated. Future evaluation should consider harvesting success rate, crop damage, operation time, and robustness under changing greenhouse conditions.

CONCLUSIONS

A compact Physical AI-based architecture for autonomous agricultural robots was proposed. The framework connects multimodal perception, semantic understanding, task reasoning, VLA-based action generation, robot control, and closed-loop feedback. Selective harvesting was used as a representative application. Future work will implement the proposed framework and validate its performance in real greenhouse environments.

ACKNOWLEDGEMENTS

This work was supported by Korea Institute of Planning and Evaluation for Technology in Food, Agriculture and Forestry(IPET) and Korea Smart Farm R&D Foundation(KosFarm) through Smart Farm Innovation Technology Development Program, funded by Ministry of Agriculture, Food and Rural Affairs(MAFRA) and Ministry of Science and ICT(MSIT), Rural Development Administration(RDA)(RS-2024-00399033)

REFERENCES

Arad, B., J. Balendonck, R. Barth, O. Ben-Shahar, Y. Edan, T. Hellström, et al. 2020. Development of a sweet pepper harvesting robot. J. Field Robotics 37(6): 1027-1039. https://doi.org/10.1002/rob.21937.

Kim, M. J., K. Pertsch, S. Karamcheti, T. Xiao, A. Balakrishna, S. Nair, et al. 2025. OpenVLA: An open-source vision-language-action model. Proc. 8th Conf. Robot Learning, PMLR 270: 2679-2713.

Kootstra, G., X. Wang, P. M. Blok, J. Hemming, and E. J. van Henten. 2021. Selective harvesting robotics: Current research, trends, and future directions. Current Robotics Reports 2: 95-104. https://doi.org/10.1007/s43154-020-00034-1.

Zitkovich, B., T. Yu, S. Xu, P. Xu, T. Xiao, F. Xia, et al. 2023. RT-2: Vision-language-action models transfer web knowledge to robotic control. Proc. 7th Conf. Robot Learning, PMLR 229: 2165-2183.

PA-P23

Proceedings of The 12th International Symposium on Machinery and Mechatronics for Agriculture and Biosystems Engineering (ISMAB 2026)
20-24 October 2026, Busan, Republic of Korea

A DATA ACQUISITION STABILITY EVALUATION FRAMEWORK FOR MULTISENSING DEVICES IN SMART PIG BARNS

Hyun Jun Kim[1], Ik Tae Choi[2], Lee Meoung Hun[3*]

[1,2,3*]Sunchon National University, 255 Jungang-ro, Suncheon 57922, Republic of Korea
*Corresponding Author—Meoung Hun Lee Voice: +82-10-3777-5544,
Email: leemh777@scnu.ac.kr

Abstract: This study presents a framework for evaluating multisensing data acquisition before deployment in smart pig barns. Deterministic synthetic logs were used to examine missing records, duplication, delay, and channel absence. The framework distinguishes records that miss an arrival deadline from records unobserved at an evaluation cutoff, and assesses channel completeness separately. Representative cases show that received record counts alone can conceal different acquisition conditions. The contribution is a reproducible check of evaluation rules; physical device reliability and field performance remain untested.

Key Words: Smart pig barn, Multisensing, Data acquisition, Data completeness, Synthetic logs

INTRODUCTION

Environmental monitoring in smart pig barns requires timely data from multiple sensor channels. A received record count alone does not establish whether scheduled records arrived on time or included all required channels.

This study aims to define and check acquisition metrics using controlled synthetic scenarios before field deployment.

MATERIALS AND METHODS

A virtual acquisition schedule contained 17,280 records at 5-s intervals over 24 simulated hours. Four binary presence flags represented temperature, relative humidity, carbon dioxide, and ammonia channels; no environmental values were generated. A common ideal clock was assumed. Each record used a device ID, restart ID, and sequence number as its unique key. The arrival deadline was 2 s after the scheduled time, and the observation cutoff W was 120 s after the nominal acquisition period. Both boundaries were inclusive.

Fault injection covered omission, duplication, delay, and channel absence, with dispersed, mixed, and burst placements affecting 1.25%, 5%, or 10% of scheduled records. Combined faults, block-length sensitivity, restart identity, and boundary cases supplemented the design. The 79 deterministic scenario runs were checked against expected counts; they were not independent field trials.

The received-row ratio R, unique-record completeness C, and on-time completeness P were expressed as percentages of scheduled records. R included duplicate rows; C and P counted each record once. G_T and G_W were the longest runs of deadline-missed and cutoff-unobserved slots, respectively, multiplied by 5 s. They describe scheduled-slot spans, not measured communication outages or permanent loss. Channel completeness was evaluated at both boundaries by taking the union of presence flags across eligible copies of the same record. The minimum across channels summarized the least complete stream, with individual channel results retained.

RESULTS & DISCUSSION

All 79 runs matched the specified expected values. Table 1 compares cases with 864 affected slots (5%). Dispersed omissions were isolated, whereas burst cases affected consecutive slots. The delayed records arrived 60.1 s after their scheduled times.

Table 1. Representative results from deterministic synthetic logs.

Scenario	C (%)	P (%)	G_T (s)	G_W (s)
Dispersed omission	95	95	5	5
Burst omission	95	95	4,320	4,320
Burst delay	100	95	4,320	0

C: unique-record completeness; P: on-time completeness. G_T and G_W are defined in Materials and Methods.

Dispersed and burst omissions had identical completeness but different continuity spans. Burst omission and burst delay shared the same G_T, while G_W distinguished records unobserved at W from those recovered within the observation window. This separation prevents a deadline violation from being interpreted automatically as lasting data loss.

When omissions and duplicate copies co-occurred, R was 100% although C was 95%. When a late copy supplied an absent channel, P remained 100%, but minimum channel completeness was 95% at the deadline and 100% at W. Different fault histories also produced identical aggregate metrics, so these metrics describe acquisition states without uniquely identifying their causes.

CONCLUSIONS

Joint reporting of completeness, timeliness, continuity, and channel availability provides a clearer basis for reviewing acquisition logs than received counts alone. The synthetic checks support consistent metric interpretation before installation; they do not establish sensor accuracy, hardware durability, or field reliability. Future work will apply the framework to available pig-barn testbed logs under project RS-2024-00399033 and adjust timing criteria to operational requirements.

ACKNOWLEDGEMENTS

This work was supported by the Korea Institute of Planning and Evaluation for Technology in Food, Agriculture and Forestry (IPET) and the Korea Smart Farm R&D Foundation (KosFarm) through the Smart Farm Innovation Technology Development Program, funded by the Ministry of Agriculture, Food and Rural Affairs (MAFRA), the Ministry of Science and ICT (MSIT), and the Rural Development Administration (RDA) (Grant No. RS-2024-00399033).

PA-P24

Proceedings of The 12th International Symposium on Machinery and Mechatronics for Agriculture and Biosystems Engineering (ISMAB 2026)
20-24 October 2026, Busan, Republic of Korea

DEVELOPMENT OF A VISION-GUIDED ROBOTIC ARM FOR AUTOMATED TOMATO POLLINATION

Li-Yun Wen*, Yi-Rou Hung, Wei-Lun Hsu, and Yao-Chuan Tsai

Department of Bio-Industrial Mechatronics Engineering, National Chung Hsing University, Taichung, Taiwan
*Corresponding Author-- Email: ariel777.wen@gmail.com

Abstract: Tomato pollination directly affects fruit set and fruit quality, yet greenhouse pollination still relies heavily on manual experience. This study developed an automated tomato pollination system integrating image recognition, flowering-stage determination, pollination strategies, and robotic arm control. A YOLOv8-based inflorescence detection model was trained using 1,212 images with 2,745 annotations. The YOLOv8s model achieved Precision, Recall, and F1-score values of 0.81, 0.79, and 0.79, respectively, while the flowering-stage classification model achieved 0.91, 0.93, and 0.92. Four pollination treatments were evaluated. Hormone treatment achieved the highest success rate (52.59%), followed by vibration (48.47%), and both showed decreasing success rates with increasing temperature. A robotic system integrating an Intel RealSense D405, Jetson Orin Nano, and a six-degree-of-freedom robotic arm was also developed to perform autonomous scanning, inflorescence detection, three-dimensional localization, and target approach.

Key Words: Tomato, Flowering-Stage Determination, Automated Pollination, Pollination Success Rate, YOLOv8

INTRODUCTION

Tomato pollination directly affects fruit set and fruit quality. However, flowering-stage determination and pollination operations in greenhouses largely rely on manual experience, increasing labor requirements and reducing operational consistency. Image recognition has been applied to tomato flower classification for robotic operations (Hiraguri et al., 2023), while pollination methods and environmental conditions can also affect fruit set (Dingley et al., 2022).

Therefore, integrating visual recognition with automated pollination operations is necessary to reduce dependence on manual decision-making. The objective of this study was to integrate YOLOv8-based inflorescence detection, flowering-stage determination, pollination treatments, depth sensing, and robotic arm control to develop an automated tomato pollination system.

MATERIALS AND METHODS

A total of 1,212 tomato images with 2,745 annotated inflorescences were used to train a YOLOv8s detection model. The dataset was divided into training, validation, and test sets at

an 8:1:1 ratio, with an input size of 832 × 832 pixels and 150 training epochs. Detected inflorescences were further classified as pollinatable or non-pollinatable using 288 images divided at an 8:2 ratio, forming a two-stage recognition framework for pollination-stage determination. Precision, Recall, and F1-score were used to evaluate model performance.

Pollination experiments were conducted using 48 tomato plants under four treatments: no artificial intervention, air blowing, vibration, and hormone treatment, with 12 plants per treatment. Treatments were performed daily at 10:00 a.m., and pollination success rate was calculated based on subsequent fruit set. The relationship between mean indoor temperature and pollination success rate was also analyzed.

The robotic system integrated an Intel RealSense D405 depth camera, Jetson Orin Nano, and a six-degree-of-freedom robotic arm. The arm autonomously scanned tomato plants according to predefined scanning positions and performed inflorescence detection and flowering-stage determination. When a pollinatable inflorescence was detected, depth information was used to obtain its three-dimensional coordinates and guide the robotic arm to approach the target.

RESULTS & DISCUSSION

The Precision, Recall, and F1-score of the inflorescence detection model were 0.81, 0.79, and 0.79, respectively, whereas those of the flowering-stage classification model were 0.91, 0.93, and 0.92, respectively, as shown in Table 1. The flowering-stage classification model achieved an F1-score of 0.92, indicating that the two-stage recognition process could effectively determine whether a target inflorescence was at a suitable pollination stage. The higher performance of the flowering-stage classification model suggests that the two-stage recognition framework is suitable for identifying pollinatable and non-pollinatable inflorescences, providing reliable information for subsequent target localization and robotic arm operation.

Table 1. Performance of the inflorescence detection and flowering-stage classification models

Model	Precision	Recall	F1-score
Inflorescence detection	0.81	0.79	0.79
Flowering-stage classification	0.91	0.93	0.92

The success rates of the four pollination treatments are shown in Fig. 1(a). Hormone treatment achieved the highest pollination success rate of 52.59%, followed by vibration treatment at 48.47%. Both treatments showed better performance than air blowing and no artificial intervention. The relationship between mean indoor temperature and pollination success rate was further analyzed, as shown in Fig. 1(b). The success rates of both hormone and vibration treatments showed decreasing trends with increasing temperature, indicating that environmental temperature, in addition to the pollination method, may affect tomato pollination performance. These results suggest that selecting an appropriate pollination method is important for improving fruit set. In addition, temperature should be considered when determining suitable pollination conditions in greenhouse cultivation.

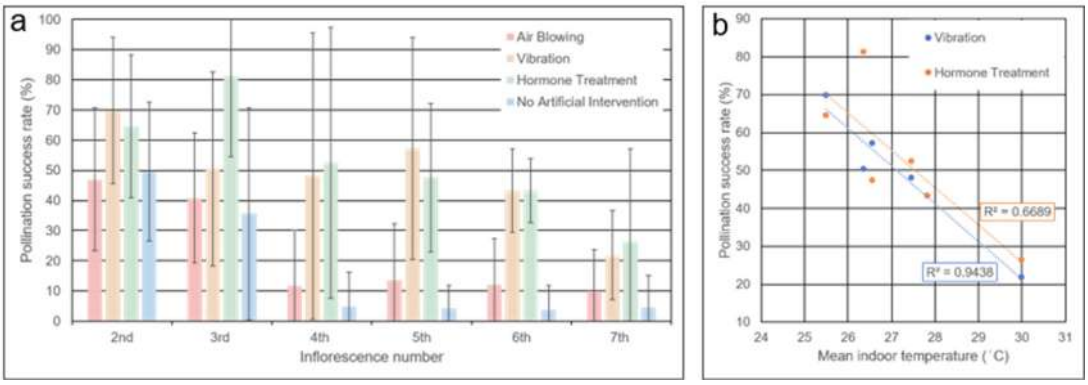

Fig. 1. (a) Pollination success rates under different pollination treatments; (b) relationship between temperature and pollination success rate.

As shown in Fig. 2, the system autonomously scanned tomato plants, detected inflorescences, and identified pollinatable targets through flowering-stage classification. Their 3D coordinates were obtained from depth data, allowing the robotic arm to approach the detected targets. These results demonstrate the feasibility of integrating image recognition, 3D localization, and robotic arm control for automated tomato pollination.



Fig. 2. (a) Tomato inflorescence detection; (b) target identification and three-dimensional localization; (c) robotic arm approach test.

CONCLUSIONS

This study developed tomato inflorescence detection and flowering-stage determination models, with the classification model achieving an F1-score of 0.92. Hormone and vibration treatments showed higher pollination success rates, while increasing temperature was associated with lower success rates. The integrated robotic system successfully performed autonomous scanning, inflorescence detection, three-dimensional localization, and target approach, demonstrating the feasibility of automated tomato pollination. Future work will integrate a pollination end-effector to complete the automated process.

REFERENCES

Dingley, A., S. Anwar, P. Kristiansen, N. W. M. Warwick, C. H. Wang, B. M. Sindel, and C. I. Cazzonelli. 2022. Precision pollination strategies for advancing horticultural tomato crop production. *Agronomy* 12(2): 518.

Hiraguri, T., T. Kimura, K. Endo, T. Ohya, T. Takanashi, and H. Shimizu. 2023. Shape classification technology of pollinated tomato flowers for robotic implementation. *Scientific Reports* 13: 2159.

PA-P25

Proceedings of The 12th International Symposium on Machinery and Mechatronics for Agriculture and Biosystems Engineering (ISMAB 2026)
20-24 October 2026, Busan, Republic of Korea

DEEP LEARNING-BASED TOMATO AXILLARY SHOOT RECOGNITION WITH ROBOTIC ARM POSITIONING

Yi-Rou Hung[1]*, Li-Yun Wen[1], Syuan-You Lin[2], Yao-Chuan Tsai[1]

[1]Department of Bio-Industrial Mechatronics Engineering, National Chung Hsing University, Taichung, Taiwan
[2]Department of Horticulture, National Chung Hsing University, Taichung, Taiwan
*Corresponding Author-- Email: s112040071@mail.nchu.edu.tw

Abstract: Tomato (*Solanum lycopersicum*) is an important horticultural crop worldwide, and appropriate pruning and axillary shoot management can improve yield stability and fruit quality. However, axillary shoot removal is still largely performed manually and is affected by labor shortages and greenhouse working conditions, creating a practical need for automated axillary shoot recognition and localization. Accurate recognition remains challenging because tomato axillary shoots are small, resemble the main stem and petiole in appearance, and are frequently occluded by leaves in complex greenhouse scenes. In this study, an image dataset of beefsteak tomato plants was established and YOLO-based deep-learning models were evaluated using different recognition strategies. To improve reliability, a two-stage "detect-then-classify" workflow was developed: an object-detection model first localized leaf-axil regions, and cropped regions were then classified according to axillary shoot presence. The classification accuracy reached 90%, and the overall recognition performance was superior to direct axillary shoot detection. The vision results were further integrated with RGB-D three-dimensional localization and robotic-arm control to complete a workflow from image recognition and target determination to robotic-arm positioning. The results provide a basis for integrating an end-effector cutting mechanism and developing an automated tomato pruning system.

Key Words: Tomato, Axillary Shoot Recognition, Deep Learning, YOLO, Automated Pruning

INTRODUCTION

Tomato is an important horticultural crop that requires continuous pruning during protected cultivation because axillary shoots emerging from leaf axils can develop into new branches that compete with the main stem for light, space, and nutrients, resulting in a dense canopy with reduced ventilation, light interception, and fruit production. Appropriate pruning and axillary shoot control can improve plant growth, yield, and fruit quality (Ara et al., 2007; Maboko et al., 2011) and may also reduce disease risk under humid canopy conditions (Ally et al., 2023). However, axillary shoot removal must be performed repeatedly throughout the growing period and remains highly dependent on manual labor. In recent years, deep learning has been increasingly applied to the recognition of tomato fruits, flowers, and plant structures, and Giang et al. (2022) demonstrated the use of RGB-D images and semantic segmentation for tomato axillary shoot detection. Nevertheless, reliable axillary shoot recognition remains challenging because axillary shoots are relatively small, visually similar

to the main stem and petioles, and frequently occluded by surrounding foliage. Therefore, this study aimed to compare different recognition strategies for tomato axillary shoot identification, evaluate a two-stage workflow consisting of leaf-axil detection followed by axillary shoot classification, and integrate RGB-D-based three-dimensional localization with robotic-arm control toward the development of an automated tomato pruning system.

MATERIALS AND METHODS

The plant material was the 'Lock' beefsteak tomato cultivar, and images were collected from greenhouses at National Chung Hsing University and in Beigang under different growth stages, illumination conditions, viewing angles, and foliage occlusion. YOLO-based models were trained using three recognition strategies: Model I simultaneously detected the main stem, petiole, and axillary shoot; Model II detected only axillary shoots; and Model III first detected leaf axils and then classified the cropped regions according to axillary shoot presence or absence. For robotic positioning, the center pixel coordinates (u, v) of each detected leaf axil were combined with the RGB-D depth value z and transformed into camera coordinates using intrinsic parameters. Hand-eye calibration was subsequently applied to convert the coordinates into the robotic-arm base coordinate system, which was used to guide the robotic arm toward the target leaf axil (Fig. 1).

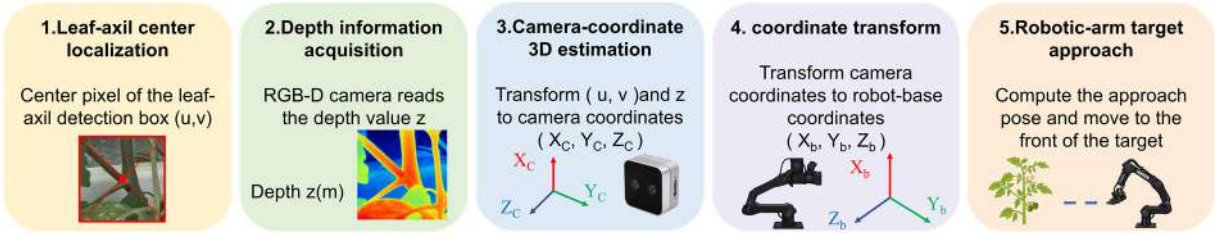

Fig. 1 Workflow for three-dimensional leaf-axil localization and robotic-arm target approach.

RESULTS & DISCUSSION

COMPARISON OF RECOGNITION STRATEGIES

Clear differences in recognition performance were observed among the three strategies. Recognition Model I provided relatively complete plant-structure information, but the visual similarity among the main stem, petiole, and axillary shoot increased class confusion, particularly when axillary shoots were small or partially occluded. Although Recognition Model II reduced label complexity, its performance remained limited because small axillary shoots occupied only a small portion of the image and were easily affected by foliage occlusion and complex greenhouse backgrounds.

Recognition Model III showed the most stable performance. Rather than relying solely on the visual appearance of small axillary shoots, this strategy used the leaf axil as a structural cue to restrict the recognition region. Because leaf axils have relatively consistent positional and geometric features, background interference and organ ambiguity were reduced. These results indicate that incorporating plant morphological characteristics can improve recognition reliability under complex greenhouse conditions.

Under the same YOLOv8 architecture, the annotation target and recognition strategy clearly affected model performance. Recognition Model I achieved a precision of 0.55 and mAP of 0.39, whereas Recognition Model II achieved a precision of 0.39 and mAP of 0.28. For Recognition Model III, the leaf-axil detection stage achieved a precision of 0.75 and mAP of 0.63, while the classification accuracy reached 90%. The major performance metrics are summarized in Fig. 2.

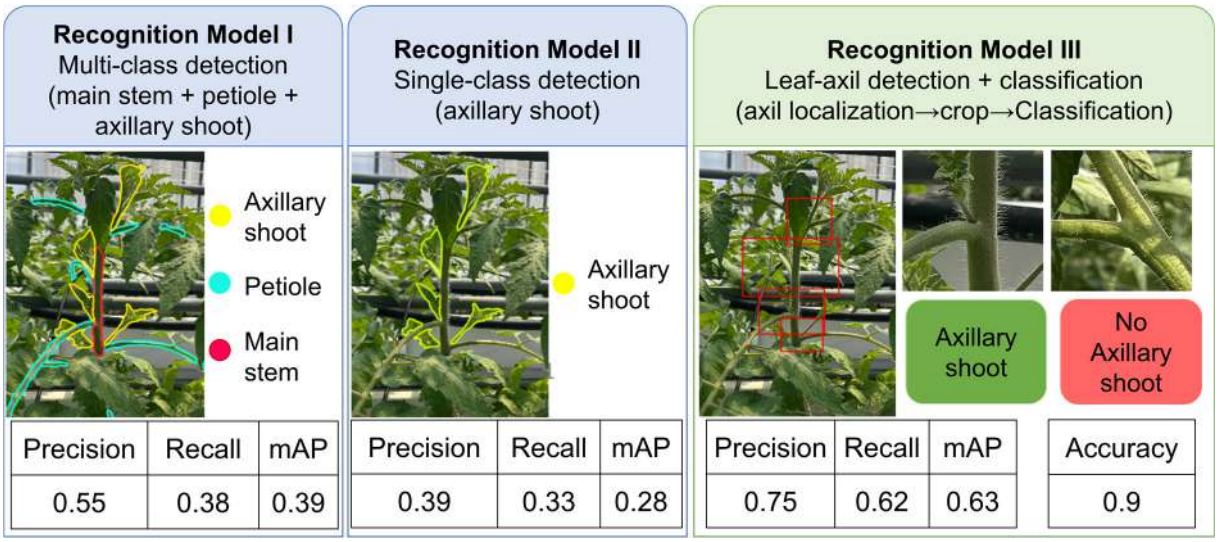

Fig. 2 Comparison of the major performance metrics of the three recognition strategies.

INTEGRATION OF RECOGNITION AND ROBOTIC POSITIONING

Beyond recognition performance, the detected targets were converted into spatial information for robotic operation. RGB-D depth information was used to obtain the three-dimensional position of each detected leaf axil, and the transformed coordinates were subsequently applied to robotic-arm approach control, linking image-based recognition with physical target positioning. Although the current system focuses on target recognition and robotic positioning rather than actual axillary shoot removal, it provides a practical basis for future integration of a safe cutting region and an end-effector cutting mechanism to complete automated pruning.

CONCLUSIONS

This study established an axillary shoot recognition and localization workflow for greenhouse tomatoes. Compared with direct axillary shoot detection, the “leaf-axil detection + axillary shoot classification” strategy was better able to address small-target size, occlusion, and complex-background problems and could be further integrated with RGB-D three-dimensional localization and robotic-arm control. Future work will focus on expanding data collection under diverse environmental conditions, improving the stability of leaf-axil detection, and establishing a safe cutting zone and end-effector cutting mechanism to complete automated tomato axillary shoot removal.

REFERENCES

Ally, N. M., H. Neetoo, V. M. Ranghoo-Sanmukhiya, and T. A. Coutinho. 2023. Greenhouse-grown tomatoes: Microbial diseases and their control methods: A review. Int. J. Phytopathol. 12(1): 99-127.

Ara, N., M. K. Bashar, S. Begum, and S. S. Kakon. 2007. Effect of spacing and stem pruning on the growth and yield of tomato. Int. J. Sustain. Crop Prod. 2(3): 35-39.

Giang, T. T. H., T. Q. Khai, D.-Y. Im, and Y.-J. Ryoo. 2022. Fast detection of tomato sucker using semantic segmentation neural networks based on RGB-D images. Sensors 22(14): 5140.

Maboko, M. M., C. P. Du Plooy, and S. Chiloane. 2011. Effect of plant population, fruit and stem pruning on yield and quality of hydroponically grown tomato. Afr. J. Agric. Res. 6(22): 5144-5148.

PA-P26

Proceedings of The 12th International Symposium on Machinery and Mechatronics for Agriculture and Biosystems Engineering (ISMAB 2026)
20-24 October 2026, Busan, Republic of Korea

DEVELOPMENT OF A DISCRETE ELEMENT MODEL FOR DEHISCED KOREAN GINSENG SEEDS

Jin-Woo Park[1], Ju-Hyun Kim[2], Seung-Gwi Kwon[3], Wan-Soo Kim[1*]

[1]Department of Bio-Industrial Machinery Engineering, Kyungpook National University, Daegu, 41566, Rep. Korea
[2]Punggi Ginseng Research Institute, Yeongju, 36052, Rep. Korea
[3]BULLS Co., Ltd., Seongju, 40053, Rep. Korea
*Corresponding Author-- Voice: +82-53-950-5794, Email: wansoo.kim@knu.ac.kr

Abstract: Ginseng seeds are approximately six times more expensive than seeds of other upland crops, making precision sowing important for minimising seed loss. Ginseng sowing still relies on labour-intensive manual work or mechanical seeders prone to missed seeding and multiple-seed pickup, so vacuum seed-metering systems are being considered. However, dehisced ginseng seeds vary considerably in size and shape and have a high moisture content, so their metering behaviour needs quantitative analysis. Discrete element method (DEM) and coupled computational fluid dynamics (CFD)–DEM simulations have been applied to seed behaviour, but improving their accuracy requires a seed model that reflects the shape and properties of the actual seeds. This study aimed to develop a DEM model of dehisced Korean ginseng (*Panax ginseng*) seeds representing the size and shape variation of the population. Three-axis dimensions and dehiscence status were measured for 300 seeds, 100 from each of the 4–5, 5–6, and 6–7 mm sieve-size groups. Density, moisture content, and friction and restitution coefficients against SUS304, the seed-metering plate material, were also measured as DEM inputs. For representative geometries, seeds with length-to-width (L/W) ratios near the population mean were first selected to minimise planar-shape variation. The length-to-thickness (L/T) ratio, which characterises thickness variation, was then divided into three intervals by quartiles, and the seed closest to each interval median was selected as the thin, intermediate, or thick representative and reconstructed in three dimensions. Each geometry was converted into a multi-sphere particle in EDEM (Altair Engineering Inc., Troy, MI, USA) and scaled to the measured size distribution to form a seed population model. Models with different sphere numbers were compared by volumetric deviation and computational time to balance accuracy and efficiency. The model will be evaluated by comparing simulated and measured angles of repose for each size group. This model is expected to serve as a basis for coupled CFD–DEM simulations of airflow and seed behaviour in a vacuum seed-metering device for predicting metering performance.

Key Words: Discrete element method, Ginseng seed, Multi-sphere model, Vacuum seed-metering device, Angle of repose

ACKNOWLEDGEMENTS

This work was carried out with the support of “Cooperative Research Program for Agriculture Science and Technology Development (Project No. RS-2026-25466540)” Rural Development Administration, Republic of Korea.

PA-P27

Proceedings of The 12th International Symposium on Machinery and Mechatronics for Agriculture and Biosystems Engineering (ISMAB 2026)
20-24 October 2026, Busan, Republic of Korea

REQUIRED POWER OF AN AIR-DRILL SEEDER BY MUTIBODY DYNAMICS SIMULATION

Kang Uk Lee[1], Choong Ho Lee[1]*

[1]A[1]Dept. of Indusrial Engineering, Jeonju University, Jeonju, Korea

*Corresponding Author: Choong Ho Lee(leech@jj.ac.kr)

Abstract: Air drill seeder is a tractor-mounted implement designed for simultaneous seeding and fertilization. It consists of a rotavator and a press roller, utilizing vacuum pressure via flexible hoses to perform seeding and fertilizing during tillage. Power supplied from the tractor is delivered to the rotavator gearbox, transferred through a universal joint to the side gear, and finally transmitted as torque to the rotary shaft connected by a flange coupling to rotate the blades. In this study, operational stability was evaluated by analyzing the drive torque values of the left and right rotary shafts on flat and inclined terrain using RecurDyn which is a multi-body dynamics (MBD) software. The inclined terrain was modeled at a 25% slope in accordance with the agricultural machinery test standards of the agricultural mechanization promotion in Korea. For a standard dry field size of 991 m^2 (300 pyeong), the inclination was set to 7.5 degrees, the dynamic contact friction coefficient to 0.2, the rotary shaft speed to 94 rpm, the simulation steps to 300, and the simulation duration to 10 seconds. The MBD analysis showed that the maximum torque values on flat ground were 5.5 kW on the left and 4.1 kW on the right, whereas on the slope, they were 6.6 kW on the left and 8.5 kW on the right. The simulation results confirmed no risk of slippage or rollover during climbing performance testing. Based on these analysis results, future work will involve conducting a fatigue analysis using the average torque.

Key Words: Air Drill Seeder, Rotor Shaft, Driving Torque, MBD, Recurdyn

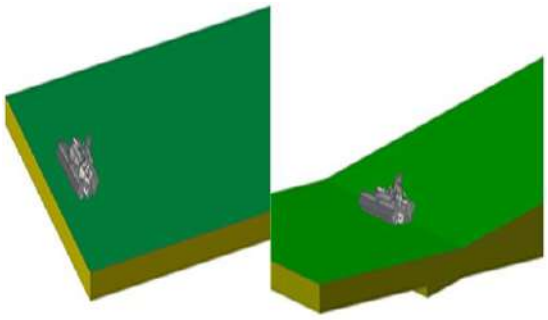

Fig. 1 Virtual modeling of ground

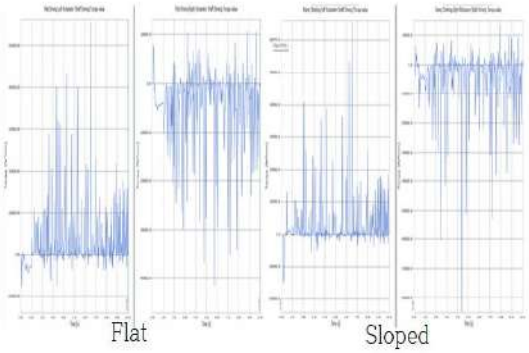

Fig. 2 Required power on flat and sloped surfaces

ACKNOWLEDGEMENTS

This work was supported by the technology commercialization support program (2026) through the Korea Institute of Planning and Evaluation for Technology in Food, Agriculture and Forestry (IPET), funded by the Ministry of Agriculture, Food and Rural Affairs (MAFRA), and the regional specialized industry talent development program of Jeonbuk TP(2026).

PA-P28

Proceedings of The 12th International Symposium on Machinery and Mechatronics for Agriculture and Biosystems Engineering (ISMAB 2026)
20-24 October 2026, Busan, Republic of Korea

ANALYSIS OF SEED DISCHARGE CHARACTERISTICS ACCORDING TO THE CHANGES IN THE GEOMETRY OF AN AIR SEEDER SEED DELIVERY TUBE

Dae Seong Lee[1], Choong Ho Lee[1]*

[1]Dept. of Indusrial Engineering, Jeonju University, Jeonju, Korea

*Corresponding Author : Choong Ho Lee(leech@jj.ac.kr)

Abstract: This study was conducted a particle-based analysis using the Moving Particle Semi-implicit (MPS) method in Particleworks to investigate the effects of seed delivery pipe geometry on the movement and discharge characteristics of seed particles in an air drill seed supply system. The seed delivery pipe was simplified, and three analysis models were developed. Model 1 was designed as a basic model with a straight pipe. Model 2 was constructed by adding a 90° bend to Model 1 to change the direction of seed particle movement. Model 3 was developed based on Model 2 by reducing the outlet cross-sectional area and extending the pipe length to investigate the effects of changes in the outlet geometry and seed delivery path. Seed particles were generated under identical conditions for all models, and their movement through the delivery pipe was analyzed. A measurement region was established at the lowest outlet of each model to calculate the time-dependent volumetric flow rate. The results were compared among the three models, confirming that changes in pipe curvature, outlet cross-sectional area, and pipe length affected the discharge flow characteristics of the seed particles. These results provide a basis for understanding seed discharge characteristics according to the geometry of air drill seed delivery pipes using the MPS method and for evaluating structural improvements and optimal design conditions for stable air seed delivery.

Key Words: UAir Drill Seeder, Volumetric Flow Rate, Particleworks, MPS, Seed Delivery Tube



Fig.1 model 1

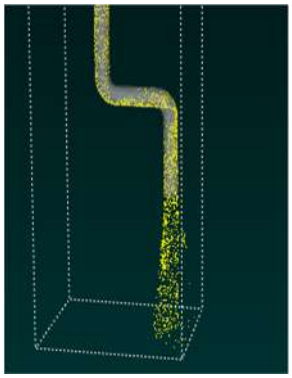

Fig.2 model 2

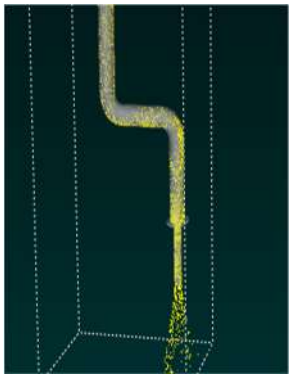

Fig.3 model 3

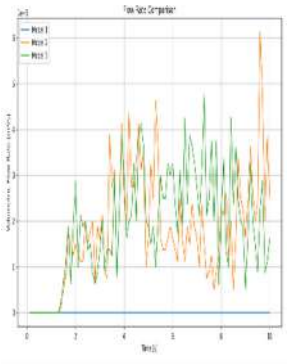

Fig.4 Grape

ACKNOWLEDGEMENTS

This work was supported by the ministry of agriculture, food and rural affairs and the ministry of trade, Industry and energy, with funding from the Jeonbuk State, through the Korea Institute of planning and evaluation for technology in food, agriculture and forestry (IPET) under the “2026 technology commercialization support program” and the “2026 regional specialized industry human resources development program,” as well as the “2026 Regional Innovation cluster development (Non-R&D) human resources development program ‘Intelligent Machinery Lab.’”

PA-P29

Proceedings of The 12th International Symposium on Machinery and Mechatronics for Agriculture and Biosystems Engineering (ISMAB 2026)
20-24 October 2026, Busan, Republic of Korea

STITCH-BASED STRAIN SENSOR FOR REAL-TIME MONITORING OF STEM CIRCUMFERENCE VARIATION

Jongho Baek[1,2], Junyoung Park[1,2], Soo Chung[1,2,3*]

[1] Department of Biosystems Engineering, Seoul National University, Seoul, Korea
[2] Integrated Major in Global Smart Farm, Seoul National University, Seoul, Korea
[3] Research Institute of Agriculture and Life Sciences, Seoul National University, Seoul, Korea
*Corresponding Author-- Voice: +82-880-4606, Email: soochung@snu.ac.kr

Abstract: Variations in stem circumference reflect changes in stem growth, water uptake, and transpiration. Real-time monitoring of these variations supports growth rate estimation, water status assessment, and decisions on irrigation scheduling and correction of sap flow measurements affected by stem dimensional changes. However, conventional stem diameter variation sensors are often costly, difficult to install, and require complex fabrication procedures, limiting their large-scale field application.

This study developed a simple, plant-wearable, stitch-based strain sensor. The sensor was fabricated by sewing silver-coated conductive thread onto an elastic self-adhesive bandage. The stitch-based strain sensor exhibited measurable changes in electrical resistance in response to cyclic stretching and release. Using the resistance changes obtained from repeated stretch-release tests, each sensor was individually calibrated to establish the relationship between sensor deformation and resistance change. Eight calibrated sensors were attached to the stems of eight tomato plants, and resistance-related signals associated with variations in stem circumference were acquired by a Raspberry Pi Pico. The data were recorded by a Raspberry Pi at 1-s intervals and averaged into 1-min values for analysis. Greenhouse environmental data and signals from a temperature-compensation sensor were collected simultaneously to correct the measured resistance for temperature effects. Stem circumference variation estimated from the sensor data was validated against vernier caliper measurements and additionally tracked using images acquired with a Raspberry Pi Camera. Sensor resistance changes exhibited a strong positive correlation with corresponding stem circumference measurements obtained using a vernier caliper.

The developed sensor enabled real-time monitoring of diurnal variations and growth trends in stem circumference. The simple construction using readily available materials may facilitate sensor fabrication for multi-plant monitoring. This continuous, non-destructive monitoring of stem circumference may reduce the labor associated with repeated manual measurements and support plant status monitoring. These results suggest the applicability of the sensor for precise monitoring of plant growth, precision irrigation, water status assessment, and sap flow correction in smart farming systems.

Keywords: Stem circumference, Wearable strain sensor, Plant growth monitoring, Real-time monitoring

ACKNOWLEDGEMENTS

This work was carried out with the support of "Cooperative Research Program for Agriculture Science and Technology Development (Project No. 2024-00400787)" Rural Development Administration, Republic of Korea; the BK21 FOUR, Global Smart Farm Educational Research Center, Seoul National University, Seoul, Republic of Korea; and the Korea Institute of Planning and Evaluation for Technology in Food, Agriculture and Forestry(IPET) and Korea Smart Farm R&D Foundation(KosFarm) through Smart Farm Innovation Technology Development Program, funded by Ministry of Agriculture, Food and Rural Affairs(MAFRA) and Ministry of Science and ICT(MSIT), Rural Development Administration(RDA) (RS-2025-02306378).

PA-P30

Proceedings of The 12th International Symposium on Machinery and Mechatronics for Agriculture and Biosystems Engineering (ISMAB 2026)
20-24 October 2026, Busan, Republic of Korea

UAV RGB IMAGE-BASED ANALYSIS OF CROP ROWS AND MISSING PLANTS IN PADDY-FIELD SOYBEAN FOR PRECISION WEEDING

In Seop Jang[1], June-Young Han[1], Sun-Bin Min[1], Dae-Cheol Kim[2,3], Yongjin Cho[2,3*]

[1] Department of Agricultural Machinery Engineering, Jeonbuk National University, Korea
[2] Department of Bioindustrial Machinery Engineering, Jeonbuk National University, Korea
[3] Institute of Agricultural Machinery&ICT Convergence, Jeonbuk National University, Korea
**Corresponding Author-- Voice: +82-63-270-2615, Email: choyj@jbnu.ac.kr*

Abstract: Weeding is an essential agricultural operation for ensuring stable crop growth and productivity, but it requires considerable labor input. Consequently, there is a growing need for mechanized and automated weeding systems. In particular, image-based selective weeding technologies have been investigated to minimize crop damage and reduce unnecessary herbicide application. The implementation of precision weeding requires spatial information on crop rows and plant distribution to establish crop-protection zones and determine appropriate weeding paths. This study analyzed crop rows and missing plants in paddy-field soybean using unmanned aerial vehicle (UAV) RGB imagery to generate baseline spatial information for crop-protection zone setting and precision-weeding operations.

The study was conducted in a paddy field cultivated with soybean in Gimje, Jeonbuk State, Republic of Korea. Ten ridges were selected for analysis. Soybeans were sown on June 19, 2026, at a target within-row spacing of 40 cm. UAV RGB images were acquired on July 3, approximately two weeks after sowing, when most plants had emerged. A DJI Matrice 4E equipped with an RGB camera was operated at a flight altitude of 20 m and a flight speed of 5 m/s using distance-interval image capture. The front and side overlaps were both set to 75%. The acquired images were processed using Pix4Dfields to generate an orthomosaic. Image processing and spatial analyses were then performed to extract crop rows, estimate within-row plant spacing, and identify potential locations of missing plants.

A total of 4,460 soybean plant locations were detected. The representative within-row spacing was approximately 39.2 cm, which was comparable to the target spacing of 40 cm. The estimated missing-plant rate was approximately 0.22%. Spatial information on the detected crop rows and missing-plant locations was also compiled to characterize crop arrangement and the distribution of plant gaps within the field.

The results demonstrate that UAV RGB imagery can provide baseline spatial information for precision weeding during the early growth stage of paddy-field soybean. The resulting crop-row and missing-plant maps could support the establishment of crop-protection zones around soybean rows and the development of operational plans for robotic weeding. Further studies should evaluate detection accuracy using field reference data and verify the applicability of the proposed approach across different crop growth stages, weed densities, and imaging conditions.

Key Words: crop-row detection; missing-plant detection; paddy-field soybean; precision weeding; UAV RGB imagery

ACKNOWLEDGEMENTS

This work was supported by the Korea Institute of Planning and Evaluation for Technology in Food, Agriculture and Forestry (IPET) (Grant No. [RS-2023-00236201]). This work was supported by the Korea Planning & Evaluation Institute of Industrial Technology (KEIT) (Grant No. [RS-2025-25460711]).

PA-P31

Proceedings of The 12th International Symposium on Machinery and Mechatronics for Agriculture and Biosystems Engineering (ISMAB 2026)
20-24 October 2026, Busan, Republic of Korea

SPATIAL ESTIMATION OF PADDY SOIL PROPERTIES BY INTEGRATING MULTI-TEMPORAL UAV SPECTRAL FEATURES AND BLOCK KRIGING

June-Young Han[1], In-Seop Jang[1], Jeongju Chae[1], Seong-Won Lim[1], Dae-Cheol Kim[1,2,3], Yongjin Cho[1,2,3*]

[1] Department of Agricultural Machinery Engineering, Jeonbuk National University, Korea
[2] Department of Bioindustrial Machinery Engineering, Jeonbuk National University, Korea
[3] Institute of Agricultural Machinery&ICT Convergence, Jeonbuk National University, Korea
**Corresponding Author-- Voice: +82-63-270-2615, Email: choyj@jbnu.ac.kr*

Abstract: The chemical and physical properties of paddy soils provide essential information for nutrient management and variable-rate fertilizer application. However, high-density field sampling requires substantial time and cost. This study evaluated the spatial estimation of soil properties by integrating multi-temporal unmanned aerial vehicle (UAV) multispectral features with block kriging. A total of 120 composite soil samples were collected from four paddy fields, with 30 sampling zones established in each field and five subsamples combined within each zone. The samples were analyzed for pH, soil organic matter (SOM), total nitrogen (TN), SiO_2, sand, silt, clay, electrical conductivity (EC), cation exchange capacity (CEC), exchangeable Ca, Mg, and K, total organic carbon (TOC), and available phosphorus (P_2O_5).

Five reflectance bands and 12 spectral indices were derived from UAV multispectral imagery acquired before transplanting (when the soil surface was exposed; C1) and during four crop growth stages (C2–C5). The 1-m-resolution UAV features were spatially aggregated by averaging them within each composite-soil sampling zone.

The multi-temporal UAV model used 85 candidate features derived from C1–C5. Feature selection and model tuning were performed exclusively within the training data of each outer validation fold. For spatial validation, each field was divided into five contiguous blocks along the y-axis. In each fold, six sampling zones were withheld for validation, while the remaining 24 zones were used for model training. Ordinary block kriging with an exponential semi-variogram was used as the geostatistical benchmark. The 1-m kriging predictions within each withheld sampling zone were averaged to generate predictions at the same spatial support as the observed composite soil samples. The final ensemble model used weights ranging from 0 to 1, estimated solely from cross-fitted predictions generated within the outer training data for the UAV and block-kriging models.

Across 56 field–property combinations representing 14 soil properties in four fields, the mean pooled out-of-fold R^2 values were 0.126 for the multi-temporal UAV model, 0.195 for block kriging, and 0.238 for the ensemble model. The ensemble model outperformed block kriging in 31 of the 56 combinations. Relatively high predictive performance was obtained for TOC (R^2 = 0.576), SOM (0.564), pH (0.562), exchangeable Ca (0.528), TN (0.489), available P_2O_5 (0.392), and exchangeable Mg (0.386). In contrast, EC (−0.280), silt (−0.180), and clay (−0.146) showed negative R^2 values, indicating limited evidence of reliable predictive performance. Nitrogen fertilizer rate (NF) was evaluated as an auxiliary variable; however, field f4 was excluded from the R^2 calculation because its uniform fertilizer prescription produced no variance.

Integrating sampling-zone-averaged UAV spectral features with block kriging improved the spatial estimation of selected soil properties. However, the ensemble model did not consistently outperform the individual models across all soil properties and fields. Further studies incorporating additional sampling zones, independent-year datasets, soil moisture, topographic variables, and management histories are needed to evaluate the external generalizability of the proposed approach.

Key Words: UAV multispectral imagery; paddy soil properties; multi-temporal data integration; block kriging; nested spatial cross-validation

ACKNOWLEDGEMENTS

This work was supported by the Korea Institute of Planning and Evaluation for Technology in Food, Agriculture and Forestry (IPET) (Grant No. [RS-2023-00236201]).
This work was supported by the Korea Planning & Evaluation Institute of Industrial Technology (KEIT) (Grant No. [RS-2025-25460711]).

PA-P32

Proceedings of The 12th International Symposium on Machinery and Mechatronics for Agriculture and Biosystems Engineering (ISMAB 2026)
20-24 October 2026, Busan, Republic of Korea

EVALUATION OF SATELLITE IMAGERY FOR PREDICTING ELECTRICAL CONDUCTIVITY IN PADDY SOILS

Sun-Bin Min[1], In Seop Jang[1], JeongJu Chae[1], Dae-Cheol Kim[1,2,3], Yongjin Cho[1,2,3*]

[1] Department of Agricultural Machinery Engineering, Jeonbuk National University, Korea
[2] Department of Bioindustrial Machinery Engineering, Jeonbuk National University, Korea
[3] Institute of Agricultural Machinery&ICT Convergence, Jeonbuk National University, Korea
**Corresponding Author-- Voice: +82-63-270-2615, Email: choyj@jbnu.ac.kr*

Abstract: Conventional soil sampling and laboratory analysis for characterizing the spatial variability of paddy soil properties require considerable time and cost. Therefore, efficient estimation methods using satellite-derived spectral information need to be investigated. This study evaluated the potential of multi-source satellite imagery for predicting soil electrical conductivity (EC) at the sampling-zone level in paddy fields.

A total of 48 soil samples were collected from two paddy fields located in Jeonbuk State, Republic of Korea. To minimize temporal discrepancies between satellite observations and ground measurements, Sentinel-2 and PlanetScope images acquired closest to the soil-sampling date were selected. The Sentinel-2 multispectral instrument covers the visible, near-infrared, and shortwave-infrared regions from approximately 443 to 2,190 nm. Of its 13 spectral bands, 10 surface-reflectance bands (B2–B8, B8A, B11, and B12), covering approximately 490–2,190 nm, were used in this study. PlanetScope SuperDove imagery comprises eight bands covering the visible to near-infrared regions from approximately 431 to 885 nm. Band reflectance values and spectral indices derived from the two satellite datasets were spatially aggregated for each soil-sampling zone and used as candidate predictors of soil EC.

Random forest models were developed and compared under three input conditions: Sentinel-2 data alone, PlanetScope data alone, and a combination of the two satellite datasets. Feature processing, hyperparameter optimization, and model evaluation were performed within a nested five-fold cross-validation framework to reduce information leakage and provide a more reliable assessment of predictive performance.

The highest EC prediction performance was obtained by combining Sentinel-2 and PlanetScope imagery. The combined model achieved a coefficient of determination (R^2) of 0.653 and a root mean square error (RMSE) of 0.101 dS m^{-1} in the nested cross-validation. In an additional stability assessment using 10 repetitions of five-fold cross-validation, the optimized model achieved a mean R^2 of 0.661 ± 0.018, indicating relatively low variation in predictive performance across different data partitions. The improved performance of the combined model suggests that the high spatial resolution of PlanetScope imagery and the broader spectral coverage of Sentinel-2, including the shortwave-infrared region, provided complementary information for estimating within-field EC variability.

These results demonstrate the potential of combining Sentinel-2 and PlanetScope spectral data to estimate spatial variability in EC within the paddy fields examined. The proposed approach could support preliminary soil-variability mapping and the

delineation of management zones for site-specific soil and fertilizer management. However, because the model was developed using only 48 samples collected from two fields and was not evaluated in independent fields, the results do not yet demonstrate spatial generalizability. Further studies should incorporate soil data collected across diverse fields and over multiple years, and apply field-independent spatial validation to evaluate model robustness and transferability

Key Words: multi-source satellite imagery; paddy soil; PlanetScope; satellite remote sensing; Sentinel-2; soil electrical conductivity;

ACKNOWLEDGEMENTS

This work was supported by the Korea Institute of Planning and Evaluation for Technology in Food, Agriculture and Forestry (IPET) (Grant No. [RS-2025-02306132])
This work was supported by the Korea Institute of Planning and Evaluation for Technology in Food, Agriculture and Forestry (IPET) (Grant No. [RS-2023-00236201])

PA-P33

Proceedings of The 12th International Symposium on Machinery and Mechatronics for Agriculture and Biosystems Engineering (ISMAB 2026)
20-24 October 2026, Busan, Republic of Korea

DEVELOPMENT OF A SPATIAL OVERLAY FRAMEWORK FOR UAV-DERIVED NDVI AND PADDY SOIL PROPERTY MAPS

Seong-won Lim[1], Jin-ho Won[2], June-Young Han[2], Dae-Cheol Kim[2,3,4], Yong-jin Cho[1,2,3,4*]

[1]Department of AI in Agriculture, Jeonbuk National University, Korea
[2]Department of Agricultural Machinery Engineering, Jeonbuk National University, Korea
[3]Department of Bioindustrial Machinery Engineering, Jeonbuk National University, Korea
[4]Institute of Agricultural Machinery&ICT Convergence, Jeonbuk National University, Korea
**Corresponding Author-- Voice: +82-63-270-2615, Email: choyj@jbnu.ac.kr*

Abstract: Soil conditions and crop growth generally exhibit substantial spatial variability within agricultural fields. Analyses based on zone-level mean values may not adequately represent localized variations within a field. This study established a pixel-based spatial analysis framework to investigate the relationships between paddy soil properties and rice growth using soil property maps and the normalized difference vegetation index (NDVI) derived from unmanned aerial vehicle (UAV) multispectral imagery.

The study was conducted using data collected in 2024 from a paddy field located in Gongju, Chungcheongnam-do, Republic of Korea. UAV multispectral imagery was acquired to generate an NDVI map that represents the spatial variability in rice growth. Soil samples were analyzed for pH, electrical conductivity (EC), organic matter (OM), available phosphorus (P_2O_5), available silicate (SiO_2), total nitrogen (TN), exchangeable potassium (Ex-K), and cation exchange capacity (CEC). The spatial distributions of these soil properties were estimated using kriging interpolation in Surfer and represented as continuous soil property maps.

The soil property maps and UAV-derived NDVI map were transformed to a common coordinate reference system, spatial extent, and pixel resolution. Because the soil properties and NDVI had different units and value ranges, the datasets were normalized to a common scale before comparison. Soil management-need values were determined by considering the agronomic direction and the appropriate range of each soil property. Pixel-based spatial overlay analysis was then conducted separately for each soil property to investigate its spatial relationship with NDVI.

The overlaid pixels were classified into four spatial relationship types: (1) low management need and favorable rice growth, (2) high management need and poor rice growth, (3) low management need but poor rice growth, and (4) high management need but favorable rice growth. The spatial distributions and area proportions of these four types were compared to evaluate the degree of spatial agreement between soil management needs and rice growth conditions.

The proposed framework distinguished areas where unfavorable soil conditions coincided with reduced rice growth from areas showing contrasting soil and crop-growth patterns. It also enabled comparison of the spatial relationships between individual soil properties and NDVI at the pixel level. The results provide baseline information to

delineate priority management zones and develop site-specific soil and crop management strategies. Further studies will quantify the spatial agreement between each soil property and NDVI and evaluate the applicability of the proposed framework across different fields and growing seasons.

Key Words: *Kriging, normalized difference vegetation index, paddy soil properties, pixel-based spatial overlay, rice growth variability, UAV multispectral imagery*

ACKNOWLEDGEMENTS

This work was supported by the Korea Institute of Planning and Evaluation for Technology in Food, Agriculture and Forestry (IPET) (Grant No. RS-2023-00236201).This work was supported by the Korea Institute of Planning and Evaluation for Technology in Food, Agriculture and Forestry (IPET) (Grant No. RS-2025-02306132).

PA-P34

Proceedings of The 12th International Symposium on Machinery and Mechatronics for Agriculture and Biosystems Engineering (ISMAB 2026)
20-24 October 2026, Busan, Republic of Korea

FIELD-SPECIFIC RELATIONSHIPS OF PROXIMAL SOIL SENSOR MEASUREMENTS WITH ORGANIC MATTER AND TOTAL NITROGEN IN PADDY SOILS

JeongJu Chae[1], Jinho Won[1], Seongwon Lim[1], Dae-Cheol Kim[1,2,3], Yongjin Cho[1,2,3*]

[1] Department of Agricultural Machinery Engineering, Jeonbuk National University, Korea
[2] Department of Bioindustrial Machinery Engineering, Jeonbuk National University, Korea
[3] Institute of Agricultural Machinery&ICT Convergence, Jeonbuk National University, Korea
**Corresponding Author-- Voice: +82-63-270-2615, Email: choyj@jbnu.ac.kr*

Abstract: Accurate information on the spatial variability of soil properties is essential for site-specific soil and nutrient management. However, conventional soil sampling and laboratory analysis require considerable time and cost, limiting their application to high-density field surveys. Proximal soil sensing offers a rapid alternative for collecting spatially continuous soil information. This study evaluated field-specific relationships between proximal soil sensor measurements and soil organic matter (SOM) and total nitrogen (TN) contents in paddy fields.

The study was conducted in two paddy fields, designated F1 and F2, located in Iksan, Jeonbuk State, Republic of Korea. Each field was divided into 24 sampling zones, resulting in a total of 48 zones. Field measurements were collected using a Veris MSP3 mobile proximal soil-sensing platform. Optical sensor responses in the red and near-infrared (NIR) regions and shallow and deep apparent electrical conductivity (EC_a) measurements were recorded together with geographic coordinates.

For each sampling zone, soil collected from five locations along the sensor travel line was combined to prepare one composite sample. The SOM and TN contents of the samples were subsequently determined through laboratory analysis. Sensor measurements were assigned to their corresponding soil-sampling zones using geographic coordinates and spatially aggregated to calculate representative values for each zone. Pearson and Spearman correlation analyses were conducted separately for F1 and F2 and for the pooled dataset to compare field-specific and overall relationships of the sensor variables with SOM and TN.

Preliminary analysis showed that the relationships of the optical sensor responses with SOM and TN differed between the two fields. In F1, the red and NIR sensor responses tended to decrease as SOM and TN increased, whereas relatively weak opposite trends were observed in F2. The shallow and deep ECa measurements tended to increase with SOM and TN in the pooled dataset, while the corresponding relationships within each field were less evident. These results suggest that relationships observed in pooled multi-field data may be influenced by differences in soil conditions between fields and may not directly represent spatial relationships within individual fields.

The findings indicate that field-specific soil conditions and spatial variability should be considered when applying proximal soil sensors to the assessment of SOM and TN. This study provides baseline information for characterizing the spatial variability of paddy soil properties and for developing field-scale soil-property estimation models based on proximal sensing. Further studies incorporating additional fields and explanatory variables, including soil moisture and texture, are needed to identify the factors

responsible for field-dependent sensor responses and to evaluate model transferability across fields.

Key Words: *proximal soil sensing; soil organic matter; total nitrogen; apparent electrical conductivity; field-specific relationship; spatial variability*

ACKNOWLEDGEMENTS

This work was supported by the Korea Institute of Planning and Evaluation for Technology in Food, Agriculture and Forestry (Project No. RS-2025-02306132).
This work was supported by the Korea Institute of Planning and Evaluation for Technology in Food, Agriculture and Forestry (Project No. RS-2023-00236201).

PA-P35

Proceedings of The 12th International Symposium on Machinery and Mechatronics for Agriculture and Biosystems Engineering (ISMAB 2026)
20-24 October 2026, Busan, Republic of Korea

GENETIC ALGORITHM-BASED FEATURE EXTRACTION FROM VISIBLE TRANSMISSION SPECTRA AND IMAGES FOR CHICKEN EMBRYO SEX PREDICTION

Akito Arimura[1], Hitomi Shibagaki[1], Tetsuhito Suzuki[1]*

[1] 1577 Kurimamachiya-cho, Tsu, Graduate School of Bioresources, Mie University, Japan
*Corresponding Author-- Voice: +81-59-231-9599, Email: t-suzuki@bio.mie-u.ac.jp

Abstract: The routine culling of roughly 7 billion day-old male chicks annually presents a critical animal welfare challenge, urgently necessitating a non-destructive *in ovo* sex classification method. While previous studies have attempted classification using spectroscopy and image analysis, they have faced the challenge of not sufficiently narrowing down the effective wavelengths and features. Isolating these useful features while maintaining classification accuracy is essential for developing a practical and simple measurement system in the future. Therefore, the objective of this study is to introduce a multi-objective genetic algorithm as a novel approach to fuse the distinct characteristics of imaging (reflecting structural changes) and spectroscopy (reflecting compositional changes). By doing so, this study aims to complement missing information, improve classification accuracy, and specify the optimal features, ultimately leading to the development of a simplified classification system. The introduced algorithm is highly suitable for this research, as it offers the distinct advantage of simultaneously minimizing classification errors and the number of extracted features. In the experiment, transmission spectra and images were acquired using 200 fertilized eggs at the onset of incubation (Day 0) and every 24 hours thereafter. After optimizing the models, the highest classification accuracy of 78.3% was achieved by fusing Day 2 image data with Day 5–7 spectral data, while significantly reducing the number of features. Furthermore, a same-day fusion model using Day 2 images and spectra demonstrated an accuracy of 76.0%, proving the effectiveness of early classification on Day 2 of incubation. The features isolated and the fusion method established in this study provide a strong foundation for developing a low-cost measurement device applicable to commercial incubators, thereby making a profound contribution to eliminating the routine culling of male chicks.

Key Words: chicken egg, sex identification, spectroscopy, transmitted imaging, animal welfare

INTRODUCTION

While the global demand for poultry products continues to expand, the industry faces a critical animal welfare challenge. In the egg-laying industry, male chicks are routinely culled immediately post-hatch because they cannot lay eggs, resulting in the elimination of

approximately 7 billion chicks annually worldwide. Consequently, there is an urgent demand for an *in ovo* (pre-hatch) sex classification method. Existing commercial techniques require perforating the eggshell to extract allantoic fluid; however, such invasive methods carry a high risk of contamination and have not been widely adopted.

Previous studies have explored non-destructive sex classification methods using visible transmission spectroscopy. Significant differences in light transmittance between male and female embryos were confirmed during the early stages of incubation, specifically at wavelengths associated with light absorption by blood. This suggests a sex-based difference in the rate of embryonic development, including blood production (Rahman et al., 2020). Furthermore, focusing on transmission imaging, studies have indicated that sex differences manifest in the area categorized by brightness levels during early incubation (Chihara, 2022). Because the brightness area reflects the degree of yolk expansion occurring in the initial stages of embryonic growth, the brightness distribution is expected to serve as a promising evaluation metric for sex determination (Shibagaki, 2025). By conducting an integrated analysis of the distinct characteristics obtained from both spectroscopy and imaging, there is potential for synergistic improvements in classification accuracy. Spectroscopy provides compositional information corresponding to specific wavelengths, whereas imaging captures structural and spatial information within the egg. Therefore, the objective of this study is to establish a highly accurate, non-destructive *in ovo* sex classification technology during the early stages of incubation through a multi-modal analysis that fuses these complementary data sources.

MATERIALS AND METHODS

EXPERIMENTAL SETUP

A schematic overview of the experimental setup is illustrated in Fig. 1. All measurements were conducted inside a darkroom. Light from a Xenon lamp (MAX-350, Asahi Spectra Co., Ltd.) was guided through a quartz optical fiber and irradiated upwards from the bottom of the sample egg. The spectral characteristics of the transmitted light were measured using a detection fiber and a spectrometer (PMA-12 C14880-1, Hamamatsu Photonics K.K.) positioned directly on the irradiation axis. For image acquisition, the sample egg was placed horizontally and illuminated from bottom side. A color camera (WRAYCAM VEX-120, WRAYMER Inc.) was positioned such that its central lens axis was inclined at a 30-degree angle relative to the irradiation axis. To enhance the visual contrast of the embryo and blood vessels, a bandpass filter with a center wavelength (CWL) of 550 nm was inserted into the light source.

EXPERIMENTAL PROCEDURE

Two hundred fertilized white eggs (Julia Lite, Nippon Layer K.K.) were incubated at 37.8°C for 21 days using a commercial incubator. The eggs were temporarily removed from the incubator at the onset of incubation (Day 0) and every 24 hours thereafter to acquire transmission spectra and images. Sex identification was definitively established by feather sexing two days post-hatch.

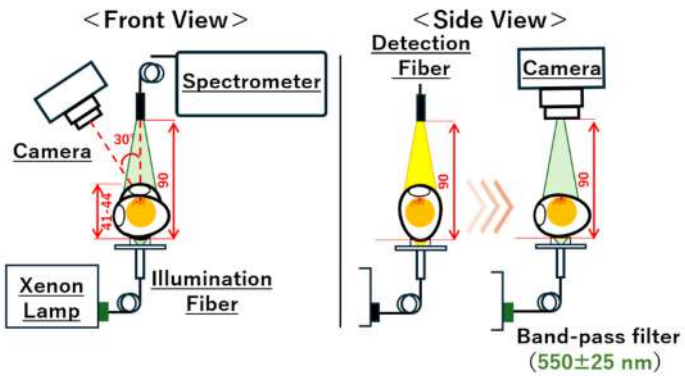

Fig. 1 Schematic overview of the experimental setup.

DATA ANALYSIS

For the transmission spectra (450–940 nm), a Savitzky-Golay (SG) smoothing filter was applied. For the images, after removing the background and normalizing by the total egg area, the brightness histograms were fitted with a Lorentzian function assuming three distinct regions, from which peak height ($\boldsymbol{A_{(n)}}$), center ($\boldsymbol{\mu_{(n)}}$), and variance ($\boldsymbol{\sigma_{(n)}}$) were extracted to quantify the size and density of the internal regions. To evaluate initial variable effectiveness, Welch's *t*-test was employed. For spectra, *p*-values of all two-wavelength transmittance ratios were computed to identify discriminative bands. Similarly, extracted image features were statistically evaluated. Partial Least Squares Discriminant Analysis (PLS-DA) was conducted to evaluate classification accuracy. To overcome overfitting in conventional data fusion, a multi-objective genetic algorithm, specifically the Non-dominated Sorting Genetic Algorithm II (NSGA-II), was introduced. This multi-objective optimization simultaneously minimized the PLS-DA classification error (via 10-fold cross-validation) and the number of selected features, thereby eliminating noise and maximizing model interpretability.

RESULTS & DISCUSSION

STATISTICAL EVALUATION VIA WELCH'S *T*-TEST

For the spectral data, significant differences were confirmed in the near-infrared region (720–850 nm) on Days 5 to 7 of incubation based on the transmittance ratio of two-wavelength combinations (Fig. 2). Since near-infrared light can penetrate relatively deep into biological tissues, this likely reflects the manifestation of some sex differences in tissue growth and development. Conversely, in the analysis of the Day 2 image data, although relatively low p-values were observed for the ratios of peak widths ($\boldsymbol{\sigma_{(2)}/\sigma_{(1)}}$ and $\boldsymbol{\sigma_{(3)}/\sigma_{(1)}}$), none of the extracted brightness histogram features were identified as statistically significant ($p < 0.05$) (Fig. 3). This result suggests that sex differences in early spatial structures, such as the localized development of the initial vascular network and the physical expansion of the embryo, are too subtle to be clearly discriminated using any single image variable independently.

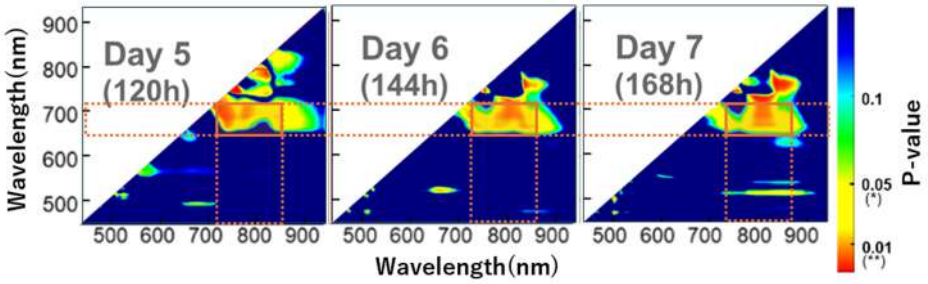

Fig. 2 Results of Welch's *t*-test for the transmittance ratio of two-wavelength combinations in spectral data (Day 5–7).

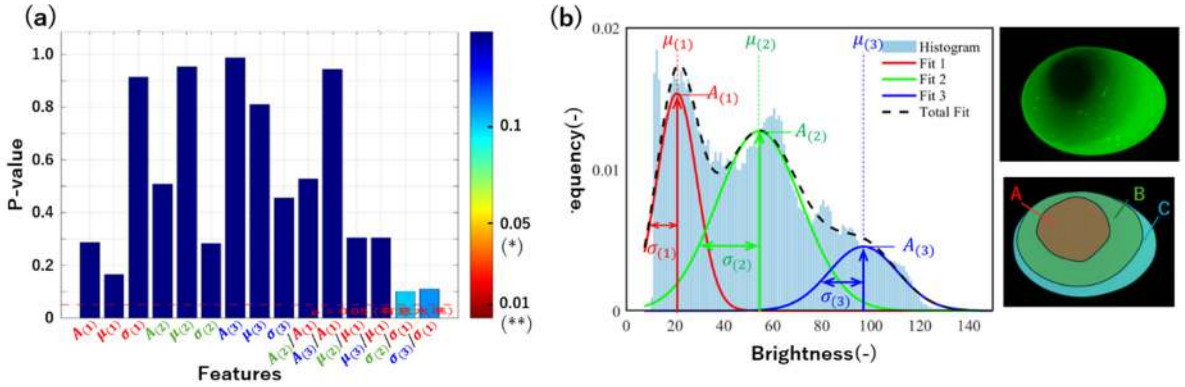

Fig. 3 Extraction and evaluation of Day 2 image features.
(a) Results of Welch's *t*-test. (b) Brightness histogram and schematic of the extracted features.

CLASSIFICATION ACCURACY OF PLS-DA

To evaluate the classification performance, we conducted PLS-DA, with the accuracies summarized in Table 1. For the spectral data, utilizing the cumulative data (720–850 nm) from Days 5 to 7—which were deemed effective by the *t*-test—significantly improved the classification accuracy to 76.6%(Ref.2) compared to using single-day data (Ref.1). Conversely, the model based solely on Day 2 image features yielded a low accuracy of 61.7%(Ref.3). Combining all Day 2 image features with the same-day spectral data (450–940 nm) increased the accuracy to 66.3%(Ref.4). Based on the *t*-test results, we attempted manual feature selection by isolating variables that exhibited relatively low *p*-values, but the accuracy remained unchanged.

Given the superior predictive capability of the spectral data, we explored a data fusion strategy by augmenting the Day 5–7 NIR spectral baseline with Day 2 image features. However, whether integrating all image features or creating manual subsets, the accuracy plateaued at 74.9% (Ref.7), failing to surpass the spectral-only baseline (76.6%). This limitation arises because simple univariate evaluations (*t*-tests) cannot adequately account for the complex variable interactions and informational redundancy inherent in high-dimensional fused data. Consequently, a more sophisticated optimization approach that comprehensively evaluates feature combinations became essential.

Table 1 Classification accuracies of individual modalities and various fusion models.

Ref.	Features		Accuracy	
	Spectrum	Image	Day 2	Day 5-7
1	All	-	62.3 %	65–68 %
2	NIR:720-850/700 nm (Day 5-7 cumulative)	-	-	76.6 %
3	-	All	61.7 %	-
4	All	All	66.3 %	-
5	All	$\boldsymbol{\sigma_{(2)}/\sigma_{(1)}}$, $\boldsymbol{\sigma_{(3)}/\sigma_{(1)}}$	66.3 %	-
6	Selected by NSGA-II	Selected by NSGA-II	76.0 %	-
7	NIR:720-850/700 nm (Day 5-7 cumulative)	All	74.9 %	
8	NIR:720-850/700 nm (Day 5-7 cumulative)	Selected by NSGA-II	78.3 %	

GENETIC ALGORITHM-BASED MULTI-OBJECTIVE FEATURE SELECTION

Table 1 presents the classification accuracies when applying NSGA-II to two datasets: a same-day fusion dataset combining Day 2 image features with Day 2 spectral data, and a time-lagged fusion dataset combining Day 2 image features with cumulative Day 5–7 NIR spectral data (Ref.6, 8). The specific wavelengths and image features selected by this optimization for the same-day fusion model are illustrated in Fig. 4(a) and (b), respectively. Interestingly, when optimizing the time-lagged fusion model (Day 5–7 spectrum + Day 2 image), NSGA-II consistently selected the exact same two image features: $\boldsymbol{\mu_{(3)}}$ and $\boldsymbol{\sigma_{(2)}/\sigma_{(1)}}$.

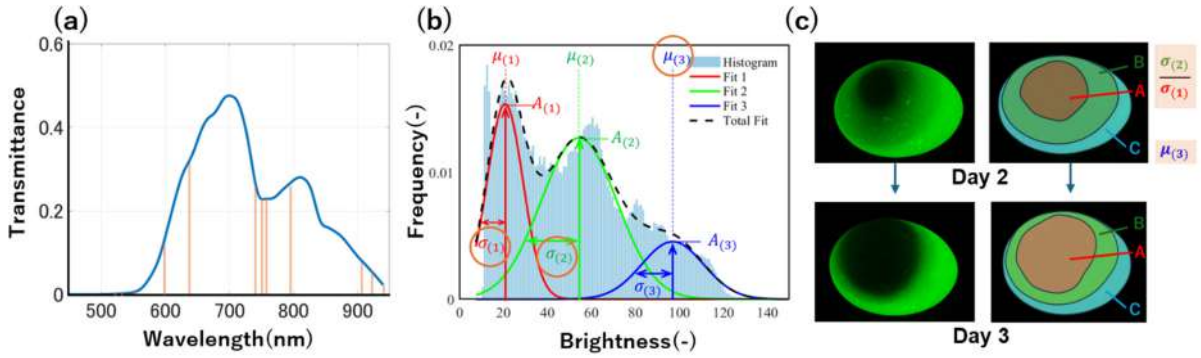

Fig. 4 Selected Features by NSGA-II: (a) wavelengths (orange line) and (b) image features. (c) Transmission images showing the disappearance of the intermediate brightness region from Day 2 to Day 3.

$\boldsymbol{\mu_{(3)}}$, which represents the center position of the brightest transmitted light region, likely functions as a robust baseline reference to compensate for individual variations, such as eggshell thickness and overall egg transparency. On the other hand, $\boldsymbol{\sigma_{(2)}/\sigma_{(1)}}$ represents the ratio of variances between the intermediate ($\boldsymbol{\sigma_{(2)}}$) and darkest ($\boldsymbol{\sigma_{(1)}}$) brightness regions. Since the darkest region ($\boldsymbol{\sigma_{(1)}}$) corresponds to the embryo body and initial vascular formation, taking its ratio with the intermediate brightness region effectively quantifies the spatial complexity of

how the vascular network expands outward.

Observing the transmission images on Day 3 of incubation (Fig. 4(c)), the intermediate brightness region tends to disappear, shifting away from the three-stage brightness distribution. Consequently, any differences in the growth rate will cause this variance ratio ($\boldsymbol{\sigma_{(2)}/\sigma_{(1)}}$) to fluctuate sensitively among individuals on Day 2. Given that the growth rates of the embryo and vascular network are known to differ between sexes (Rahman et al., 2020), the consistent selection of these features by the algorithm provides strong evidence that it successfully captured these biological sex differences in developmental speed through spatial information.

CONCLUSIONS

This study aimed to improve the accuracy of *in ovo* sex classification by fusing spectral and imaging modalities. By integrating Day 2 image features with the highly predictive Day 5–7 near-infrared spectral data, we achieved the highest overall classification accuracy of 78.3%. Furthermore, the same-day fusion on Day 2 demonstrated an accuracy of 76.0%, showing the exceptional utility of combining brightness histogram indicators with specific spectral absorption bands. A pivotal outcome of this optimization approach was identifying Day 2 as a highly effective embryonic age for early measurement and clarifying the essential modalities required at this stage.

Driven by these insights, future research will focus on developing a simple, low-cost measurement device capable of *in situ* data acquisition directly within commercial incubators. By targeting this early developmental stage and implementing only the precisely selected wavelengths and critical image features, a highly efficient and practical measurement system can be constructed. Ultimately, the implementation of this high-precision sex classification system will not only enhance productivity and operational efficiency in the poultry industry but also eliminate the routine culling of day-old male chicks, thereby making a profound contribution to animal welfare.

ACKNOWLEDGEMENTS

This work was supported by JSPS KAKENHI [Grant Number 24K01878].

REFERENCES

Chihara, M. 2022. Sex prediction of early stage incubated chicken eggs using visible transmittance imaging and spectroscopic analysis. Graduation Thesis. Kyoto University.

Rahman, A., et al. 2020. Nondestructive sex-specific monitoring of early embryonic development rate in white layer chicken eggs using visible light transmission. Briti. Poult. Sci. 61(2): 209-216.

Shibagaki, H. 2025. Relationship between Luminance Histograms of Transmitted Images of Incubating Chicken Eggs and Embryo Sex. Graduation Thesis. Mie University.

PA-P36

Proceedings of The 12th International Symposium on Machinery and Mechatronics for Agriculture and Biosystems Engineering (ISMAB 2026)
20-24 October 2026, Busan, Republic of Korea

MULTI-VIEW CHICKEN FLOCK UNIFORMITY ESTIMATION COMBINING PERSPECTIVE TRANSFORMATION AND IMAGE ANALYSIS

Ting-Shao Chen[1*], Ming-Kun Hsieh[2], Kuang-Fu Chang[3], Yao-Chuan Tsai[1]

[1]Department of Biomechatronics Engineering, National Chung Hsing University
[2]Graduate Institute of Microbiology and Public Health, National Chung Hsing University
[3] iCHASE CO., LTD.
*Corresponding Author-- Voice: +886-98-894-3378, Email: danielasd902@gmail.com

Abstract: Traditional poultry houses mostly rely on temperature and humidity sensors for environmental monitoring, yet it is difficult for them to fully cover microclimate variations across large-scale areas. As the most intuitive biological indicator, the spatial distribution uniformity of chickens can directly reflect the flock's perception of the environment, allowing breeders to grasp the actual comfort level within the facility. However, current image monitoring systems are constrained by hardware structures, and cameras often need to be mounted at an angle, resulting in perspective distortion in the images. To solve this problem, this study developed a low-cost, high-accuracy "Single-View Poultry House Uniformity Estimation System." The system first applies perspective transformation technology to correct the tilted images into top-down views, establishing a unified calculation baseline. In the image analysis stage, considering that tilted viewing angles cause severe overlapping and occlusion among the birds, traditional individual recognition methods are difficult to apply. Therefore, this study introduces image binarization technology to accurately separate the main bodies of the chickens from the background, thereby objectively quantifying the pixel ratio and distribution density of broilers in the corrected images. Furthermore, the system conducts dynamic analysis by comparing images taken before and after a period of time, effectively monitoring the flock's clustering or scattering trends in response to environmental changes. This project is expected to verify the feasibility of monitoring local hotspots in poultry houses using a single camera, establish a cost-effective non-contact monitoring model, and implement smart agriculture applications.

Key Words: Smart Agriculture, Perspective Transformation, Image Binarization, Spatial Distribution Uniformity

INTRODUCTION

Traditional manual inspection of broilers is not only time-consuming and prone to causing stress to the flock, but it is also difficult to achieve objective round-the-clock recording. To address this, this study introduces image processing technology to develop a non-contact automated monitoring system. By real-time analyzing the flock's spatial distribution, density changes, and behavioral dynamics, it accurately identifies hot zones in the poultry house, aiming to provide a scientific decision-making basis for breeding management and health early warning.

MATERIALS AND METHODS

Image Acquisition and Pre-processing Calibration

Figure 1 illustrates the equipment configuration and camera perspective. To correct spatial distortion from tilted cameras, we apply Perspective Transformation to calibrate and divide continuous field images into independent grids (Figure 2). This establishes a unified calculation baseline. During pre-processing, the system classifies images into normal, severe overexposure, or nighttime infrared modes based on color saturation and average brightness. To preserve vital lighting features, local overexposure is evaluated directly on the original perspective-warped grid rather than a cropped frame.

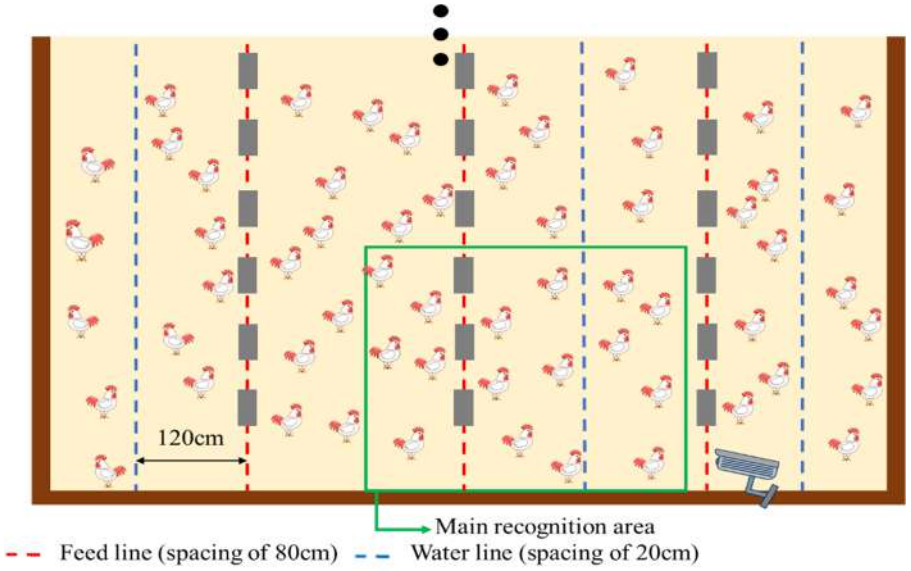

Figure 1. Field equipment configuration diagram

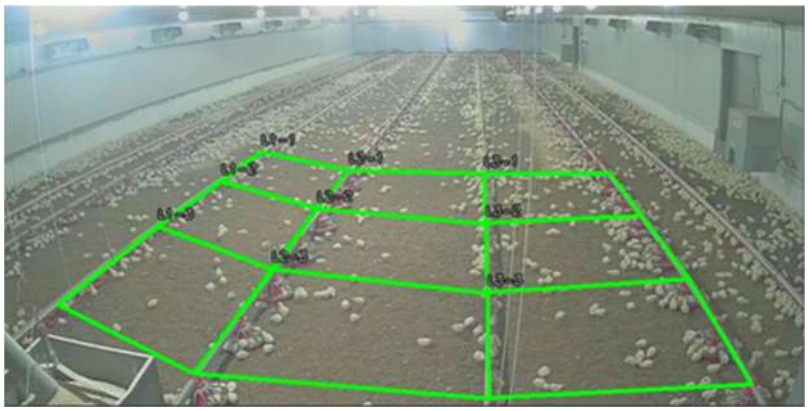

Figure 2. Actual camera view and physical perspective grid division

Spatial Feature Extraction and Temporal Dynamic Tracking

For spatial feature extraction of the broilers, the system utilizes Otsu's thresholding algorithm combined with morphological operations, such as erosion and dilation, to eliminate background noise. For the more challenging nighttime infrared images, image enhancement and blurring techniques are further incorporated to successfully calculate and quantify the area proportion of chickens within each grid. In addition to analyzing the static distribution in single images, this system introduces a temporal dynamic comparison mechanism. As shown in Figure 3, by continuously capturing frames at short time intervals (e.g., from 22:00 to 22:15), the system effectively tracks the aggregation and dispersion of broilers in local areas (indicated by the red circles in Figure 3). By comparing the changes in the pixel proportions of chickens across time-series images, the system calculates the temporal variation rate of the spatial distribution, thereby accurately capturing short-term clustering displacement and restless behaviors within the broiler house.



Figure 3. Tracking of local dynamic changes in the broiler flock across continuous time intervals.

RESULTS & DISCUSSION

To quantify the spatial distribution and dynamic characteristics of the flock, the perspective-corrected image is divided into N grids, where $O_{i,t}$ represents the chicken pixel ratio (occupancy) of the i-th grid at time t. The mean occupancy μ_t across all grids at time t is calculated as Equation (1):

$$\mu_t = \frac{1}{N}\sum_{i=1}^{N} O_{i,t} \tag{1}$$

Next, the Spatial Distribution Standard Deviation S_t is used to evaluate the static uniformity of the flock's distribution at that moment, as shown in Equation (2):

$$S_t = \sqrt{\frac{1}{N-1}\sum_{i=1}^{N}\left(O_{i,t} - \mu_t\right)^2} \tag{2}$$

To track the dynamic activity of the flock, this system further calculates the sum of the absolute differences in pixel proportions for each grid between consecutive time points, defined as the

Temporal Activity Rate $\boldsymbol{A_t}$, given by Equation (3):

$$A_t = \sum_{i=1}^{N} \left| O_{i,t} - O_{i,t-1} \right|, t = 1,2,\cdots \quad (3)$$

Based on these quantitative metrics, the flock's status throughout the day can be presented by static distribution uniformity and dynamic activity characteristics. Observing the static distribution, the spatial distribution standard deviation ($\boldsymbol{S_t}$) mostly remains stable and fluctuates slightly within a low range of 5 to 15 throughout the day, indicating that the flock's distribution in the monitored area is relatively uniform, without long-term extreme clustering or crowding occurring (Figure 4). In terms of dynamic activity, the spatial distribution time-varying rate ($\boldsymbol{A_t}$) maintains a stable baseline below 50 during most time periods, but at specific times of the day, significant peaks exceeding 150, or even as high as 250 and above, appear (Figure 5). The two data sets jointly present the characteristic of "stable standard deviation but sudden instantaneous increase in time-varying rate," indicating that while the flock's overall spatial occupancy rate remains uniform, large-scale positional shifts or active movements occur at specific moments. Inferred from the time points when the data occurs, these brief surges in activity are mainly directly related to flock dynamics caused by routine events within the farm.

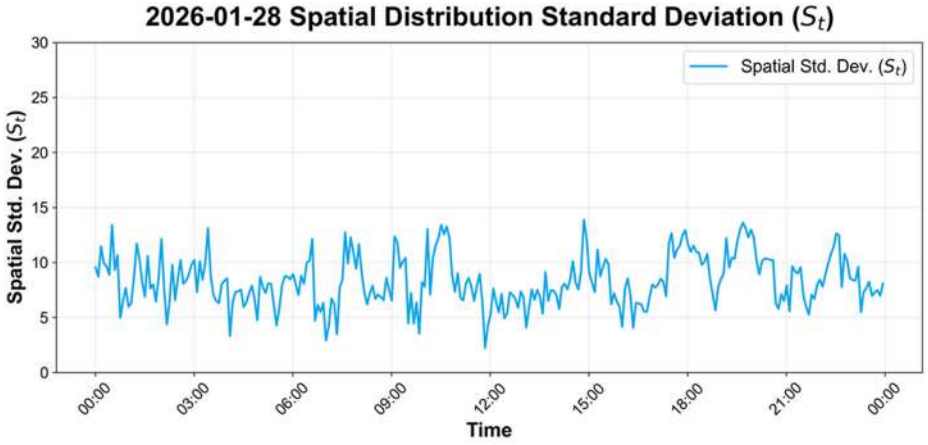

Figure 4. Chicken spatial standard deviation

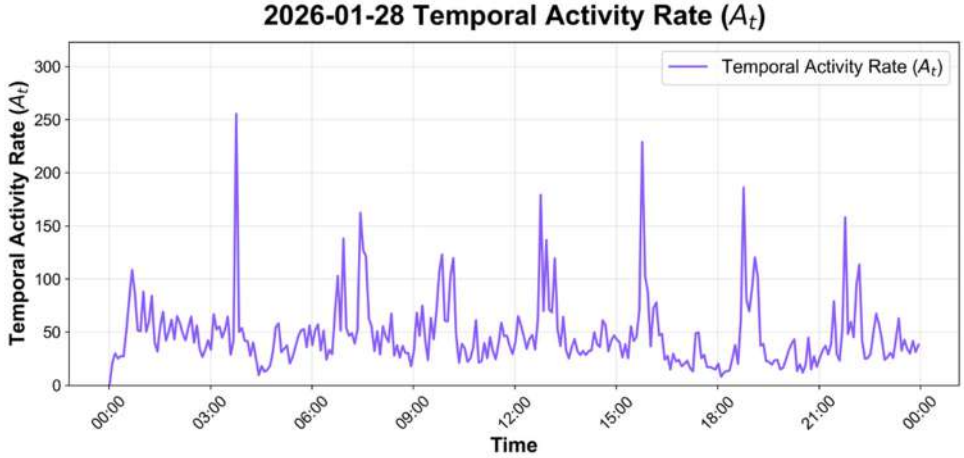

Figure 5. Chicken spatial distribution time-varying rate

CONCLUSIONS

The poultry house uniformity estimation system developed in this study, combining perspective transformation and image binarization technology, effectively overcomes viewing angle and lighting interference. Experiments have confirmed that through the spatial distribution standard deviation (S_t) and time-varying rate (A_t), the flock's static distribution and dynamic activity characteristics can be accurately quantified. This system verifies the feasibility of low-cost image monitoring and can be combined with environmental data in the future to assist automated breeding and abnormality early warning.

REFERENCES

1. Kashiha, M., Pluk, A., Bahr, C., Vranken, E., & Berckmans, D. (2013). Development of an early warning system for a broiler house using computer vision. Biosystems Engineering, 116, 36–45.
2. Guo, Y., Chai, L., Aggrey, S. E., Oladeinde, A., Johnson, J., & Zock, G. (2020). A machine vision-based method for monitoring broiler chicken floor distribution. Sensors, 20, 3179.

PA-P37

Proceedings of The 12th International Symposium on Machinery and Mechatronics for Agriculture and Biosystems Engineering (ISMAB 2026)
20-24 October 2026, Busan, Republic of Korea

WORK PATH OPTIMIZATION ALGORITHM FOR AUTONOMOUS BOOM SPRAYING IN RIDGE CULTIVATION ENVIRONMENTS

Deok-Keun Kim[1], Ji Won Choi[2,3], Soo Been Cho[2,3], Jung-sang Yoo[3], Seung-Hwan Yang[3*]

[1]Interdisciplinary Program for Agriculture & Life science, Chonnam Nat'l Univ., 33, Yongbong-ro, Jeonnam-Gwangju, Republic of Korea
[2]Department of Biosystems Engineering, College of Agricultural and Life Sciences, Gyeongsang Nat'l Univ., 501, Jinju-daero, Jinju-si, Republic of Korea
[3]Specialized Machinery and Robotics Group, Korea Institute of Industrial Technology, 119, Jipyeongseonsandan-3gil, Gimje-si, Rep. of Korea
*Corresponding Author-- Voice: +10-6728-3373, Email: yangsh@kitech.re.kr

Abstract: With the advancement of agricultural mechanization, research on autonomous agricultural operations, including tillage, seedbed preparation, and crop spraying, has been continuously conducted. While autonomous spraying equipment has been commercialized in countries where flat-field cultivation is common, research on autonomous spraying for ridge cultivation, which is common in Korea, remains limited. Therefore, this study aimed to develop an optimal spraying path and an algorithm for minimizing overlapping spray areas for autonomous boom spraying under ridge cultivation conditions. The proposed algorithm was developed based on the specifications of the boom sprayer and tractor, including boom width, nozzle spray width and spacing, the distance between the outermost nozzle and the tractor rear axle, and tractor track width, as well as ridge width and spacing. The algorithm was developed to spray the appropriate amounts of pesticide per unit area. For each case, travel paths were generated, overlapping spray areas were calculated, and the number of nozzles to be deactivated was determined. The proposed algorithm was compared with a conventional spraying method to evaluate the reduction in spraying paths and travel distance. When the expansion condition was satisfied, the number of ridges covered in a single operation increased by two, resulting in a path reduction of approximately 18–22% for 7–9 ridges per operation. Since U-turns accounted for approximately 51–62% of the total travel distance, the reduction in U-turns contributed significantly to an overall travel-distance reduction of approximately 10–20%. The results indicate that the proposed algorithm can optimize spraying paths and reduce overlapping spraying, spraying paths, and travel distance under ridge cultivation conditions. The algorithm may be applied to practical implementation of autonomous boom sprayers for the ridge cultivation environments of Korea.

Key Words: Autonomous operation, Agricultural operation, Boom sprayer, Agricultural robot, Electrification

ACKNOWLEDGEMENTS

This work was supported by the Industrial Fundamental Technology Development Program (20018486, Development and demonstration of various working machine modules applicable to upland agriculture for full processes) funded by the Ministry of Trade, Industry & Energy (MOTIE, Republic of Korea).

PA-P38

Proceedings of The 12th International Symposium on Machinery and Mechatronics for Agriculture and Biosystems Engineering (ISMAB 2026)
20-24 October 2026, Busan, Republic of Korea

DESIGN AND ADSORPTION CHARACTERISTIC ANALYSIS OF A SEED FEEDING DEVICE FOR NON-DESTRUCTIVE FOREST SEED SORTING

Hwang-Gyu Lee[1], Chung-Kwan Lee[2], Chan-Eun Kim[3], Tae-Wook Kim[3*]

[1]School of Advanced Science and Technology Convergence Major in Precision Mechanical Engineering, Kyungpook National University, Sangju, 37224, Korea.
[2]Real Tech, Room 436, Daegu Convergence R&D Center, 62, Seongseogongdan-ro 11-gil, Dalseo-gu, Daegu 42713, Korea.
[3]Department of Precision Mechanical Engineering, Kyungpook National University, Sangju, 37224, Korea.
*Corresponding Author-- Voice: +82-10-3805-8222, Email: kimtw@knu.ac.kr

Abstract: Forest seeds vary considerably in size, shape, and internal soundness depending on the tree species and collection environment, making a stable individual-seed supply technology essential for applying a nondestructive sorting system. This study designed an individual-seed supply device for a nondestructive forest-seed sorting system based on a hyperspectral camera and determined the optimal suction pressure for pine seeds. The supply device was configured to individually pick up seeds using a vacuum manifold and needle-shaped suction needles. It was designed to move between the pickup and delivery positions through the reciprocating motion of linear guides on both sides and a central air cylinder. Pine seeds with an average size of 5.2 × 2.9 mm and an average weight of 12.4 mg per seed were used in the experiment. Suction needles with an inner diameter of 0.91 mm, approximately 30% of the minor diameter of the seeds, were applied. The vacuum pressure was adjusted stepwise using a low-vacuum regulator, ranging from −1.0 to −3.0 kPa in five increments of 0.5 kPa, and the success of single-seed pickup was evaluated. The results showed that a vacuum pressure of −1.0 kPa was suitable for individually picking up pine seeds.

Key Words: Forest seeds, Seed sorter, Non-destructive sorting, Near-infrared spectroscopy, Seed supply device.

INTRODUCTION

Forest seeds vary considerably in size, shape, and internal soundness depending on the tree species and collection environment, making it difficult to accurately identify high-quality seeds based solely on their external appearance. Because seed quality directly affects germination rate and seedling production, it is important to sort high-quality seeds before sowing.

Conventional agricultural seed-sorting systems continuously process large quantities of seeds and primarily classify them based on color information, making them difficult to apply to forest seeds, which exhibit substantial variation in individual characteristics. Therefore, it is

necessary to develop a nondestructive sorting technology that can supply forest seeds individually and reliably, assess their internal condition, and prevent damage to the seeds.

This study designed an individual-seed supply device for application in a hyperspectral-camera-based nondestructive forest-seed sorting system. The device was configured to arrange the seeds in a matrix with uniform spacing and supply them to the inspection unit, enabling the spectral characteristics of each forest seed to be measured reliably. The supply device consisted of an air cylinder and a two-axis linear guide system, and a vacuum manifold with needle-shaped suction needles was employed to individually pick up and transfer multiple seeds.

In addition, the seed supply device was designed, and the suction characteristics of seeds from different tree species were analyzed to determine the optimal suction-pressure conditions for stable seed pickup.

MATERIALS AND METHODS

Experimental Seeds

Pine seeds were used for the adsorption characteristic analysis. The seeds had an average major diameter of 5.2 mm, a minor diameter of 2.9 mm, and an average weight of 12.4 mg per seed.

Design of the Seed Supply Device

The seed supply device was designed to individually adsorb multiple forest seeds and supply them at regular intervals. The adsorption unit consisted of a vacuum manifold equipped with syringe-needle-type adsorption needles arranged in a single row. The transfer unit consisted of linear guides positioned on both sides of the device and a centrally located air cylinder. The manifold was designed to move between the adsorption position and the supply position according to the reciprocating motion of the air cylinder. After the seeds were adsorbed under negative pressure and transferred to the supply position, the adsorption was released by applying positive pressure, and the manifold returned to its initial position to repeat the supply process. Fig 1. shows the three-dimensional design of the seed supply device.

Figure 1 3D Design of the Seed Feeding Device

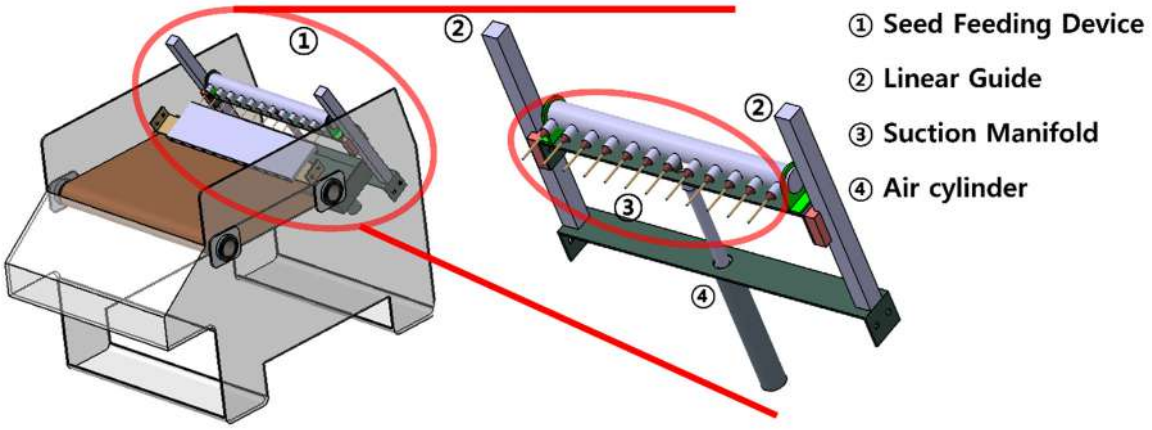

Fig 1. 3D Design of the Seed Feeding Device.

Continuous supply of individual seeds requires an appropriate vacuum pressure that can effectively adsorb the seeds. If the vacuum pressure is too low, insufficient adsorption may occur, whereas an excessively high pressure may cause multiple seeds to be adsorbed simultaneously. Therefore, analyzing the vacuum pressure at which single-seed adsorption is possible is important for ensuring supply accuracy.

Experimental Apparatus for Adsorption Characteristics

The experimental apparatus for analyzing adsorption characteristics consisted of a Venturi ejector, supply regulator, low-vacuum regulator, pressure sensor, and adsorption manifold. Compressed air was supplied to the Venturi ejector through the supply regulator to generate a vacuum. The generated vacuum pressure was then adjusted to the low pressure required for the experiment using the low-vacuum regulator. After the adjusted vacuum pressure was confirmed with the pressure sensor, it was supplied to the adsorption manifold and syringe-needle-type adsorption needles to conduct the seed adsorption experiments.

Experimental and Analytical Methods

Figure 2 Experimental Setup for Forest Seed Suction Feeding

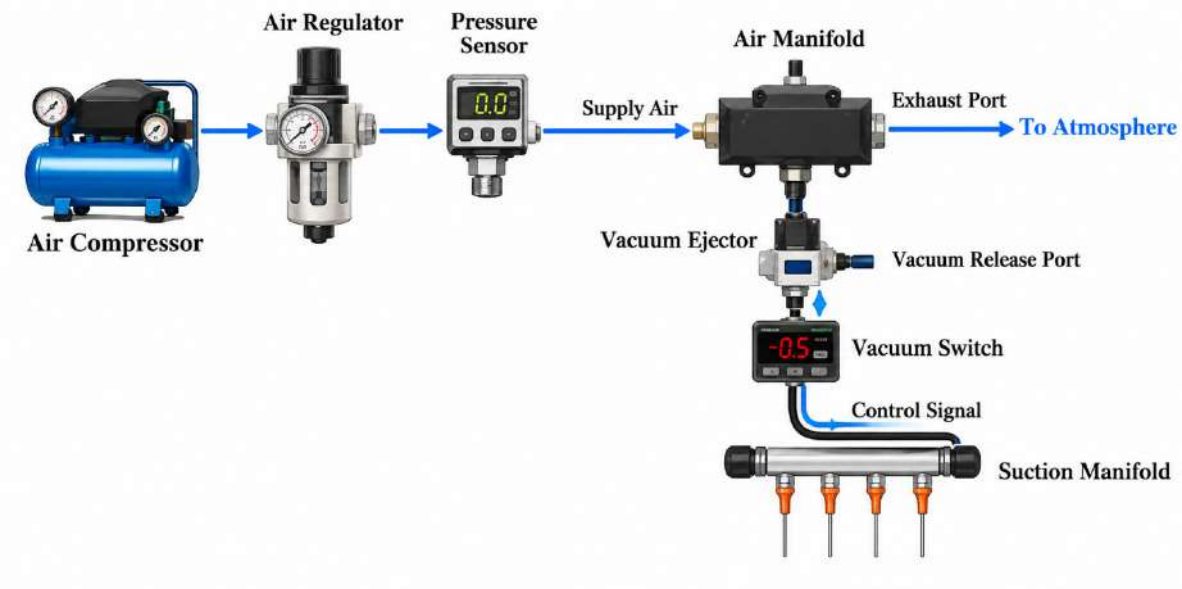

Fig 2. Experimental Setup for Forest Seed Suction Feeding.

Pine seeds measuring 5.2 × 2.9 mm and weighing 12.4 mg were used in the experiment. The inner diameter of the adsorption needles was set to approximately 0.91 mm, or 30% of the minor diameter of the seeds, to prevent multiple seeds from being adsorbed simultaneously.

To analyze adsorption performance under different pressure conditions, five pressure levels were established from −3.0 kPa to −1.0 kPa at intervals of 0.5 kPa. Single-seed adsorption performance at each pressure level was evaluated through 100 repeated trials. Fig 2. shows the configuration of the forest seed adsorption and supply experimental apparatus.

RESULTS & DISCUSSION

At a vacuum pressure of −1.0 kPa, all four adsorption needles achieved single-seed adsorption in 89 of the 100 repeated trials. In the remaining 11 trials, a seed failed to be adsorbed by one of the needles. In contrast, at vacuum pressures of −1.5 kPa or higher in magnitude, multiple seeds were adsorbed by some of the needles. Therefore, within the pressure range examined in this study, approximately −1.0 kPa was considered an appropriate vacuum pressure condition for single-seed adsorption of pine seeds. **Figure 3** shows the pine seed adsorption experiment.

Figure 3 Pine Seed Suction Experiment



Fig 3. Pine Seed Suction Experiment.

CONCLUSIONS

This study designed a seed supply device for application in a hyperspectral-camera-based non-destructive forest seed sorting system and analyzed the optimal adsorption pressure for pine seeds. When syringe-needle-type adsorption needles with an inner diameter of approximately 0.91 mm, corresponding to 30% of the minor diameter of the seeds, were applied, a vacuum pressure of −1.0 kPa was identified as suitable for single-seed adsorption. These results confirmed that pine seeds could be stably adsorbed individually even under low vacuum pressure. In future studies, adsorption conditions according to various tree species and needle diameters will be further analyzed to establish stable supply conditions for forest seed sorting systems.

ACKNOWLEDGEMENTS

This research was supported by the 2026 Seed Utilization Efficiency Technology Development Program of the Korea Forestry Promotion Institute (Project Title: Development of high-efficiency processing technology for forest seeds, Project Number: 2400000396).

REFERENCES

Feng, L., S. Zhu, F. Liu, Y. He, and Y. Bao. 2019. Hyperspectral imaging for seed quality and safety inspection: A review. Plant Methods 15: 1-25. Available at: https://doi.org/10.1186/s13007-019-0476-y.

Kaliniewicz, Z., and P. Tylek. 2019. Aspects of the process of sorting European black pine seeds. Forests 10(11): 966. Available at: https://doi.org/10.3390/f10110966.

Novikova, T., C. B. da Silva, P. Tylek, S. Evdokimova, and A. Novikov. 2022. How can the engineering parameters of the NIR grader affect the efficiency of seed grading? Agriculture 12(12): 2125. Available at: https://doi.org/10.3390/agriculture12122125.

Rahman, A., and B.-K. Cho. 2016. Assessment of seed quality using non-destructive measurement techniques: A review. Seed Sci. Res. 26(4): 285-305. Available at: https://doi.org/10.1017/S0960258516000234.

Tigabu, M. 2003. Characterization of forest tree seed quality with near infrared spectroscopy and multivariate analysis. PhD diss. Umeå, Sweden: Swedish University of Agricultural Sciences. Available at: https://pub.epsilon.slu.se/262/.

Xia, Y., Y. Xu, J. Li, C. Zhang, and S. Fan. 2019. Recent advances in emerging techniques for non-destructive detection of seed viability: A review. Artificial Intell. in Agric. 1: 3-17. Available at: https://doi.org/10.1016/j.aiia.2019.05.001.

Yasmin, J., M. R. Ahmed, C. Wakholi, S. Lohumi, and P. Mukasa. 2022. Near-infrared hyperspectral imaging for online measurement of the viability detection of naturally aged watermelon seeds. Front. Plant Sci. 13: 986754. Available at: https://doi.org/10.3389/fpls.2022.986754.

PA-P39

Proceedings of The 12th International Symposium on Machinery and Mechatronics for Agriculture and Biosystems Engineering (ISMAB 2026)
20-24 October 2026, Busan, Republic of Korea

DISCUSSION OF STRUCTURAL SAFETY OF AN AUTONOMOUS AGRICULTURAL MOBILITY VEHICLE

Sang Min Lee[1], Kang Uk Lee[1], Jung Min Bae[1], Dae Seong Lee[1], Choong Ho Lee[1]*

[1]Dept. of Indusrial Engineering, Jeonju University, Jeonju, Korea

*Corresponding Author: Choong Ho Lee(leech@jj.ac.kr)

Abstract: PIn this study, modal analysis and static structural analysis were performed using ANSYS based on the finite element method to identify structurally vulnerable areas and evaluate the structural stability of an autonomous agricultural vehicle. First, modal analysis was conducted on the entire vehicle model to examine the deformation modes at each natural frequency. The frame and connection areas exhibiting relatively large deformations were then identified as structurally vulnerable regions. Subsequently, static structural analysis was performed on a simplified vehicle model with unnecessary components removed to investigate the equivalent stress and deformation under applied loads. The analysis results showed a maximum equivalent stress of 68 MPa and a maximum total deformation of 0.10478 mm, with relatively high stress concentrations observed around the frame connections. Based on the yield strength of SS400, which is 245 MPa, the safety factor was calculated to be approximately 3.60. In addition, structural analyses of the track rail and support shaft were conducted based on the vulnerable areas and load transfer paths identified through modal analysis. This study identified the structurally vulnerable areas of the autonomous agricultural vehicle. In future work, multibody dynamics analysis will be conducted to simulate potential structural issues under actual operating conditions by considering the torque acting on the support components during vehicle operation and the dynamic behavior of the vehicle.

Key Words: Modal Analysis, Structural Analysis, Track Rail, Finite Element Analysis (FEA)

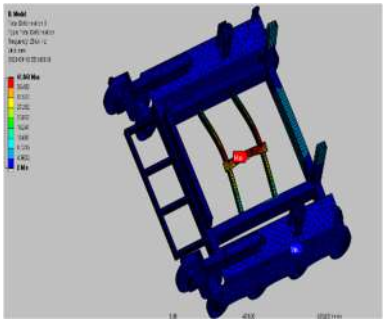

Fig. 1 Modal Analysis

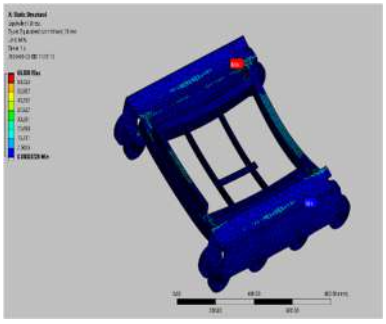

Fig. 2 Structural Analysis

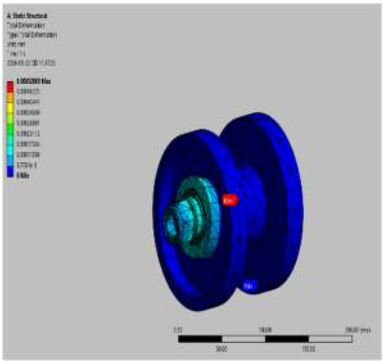

Fig. 3 Structural Analysis of Wheel Axis

ACKNOWLEDGEMENTS

This project (outcome) was conducted with the support of the Regional Innovation System & Education (RISE) Center in Jeonbuk, funded by the Ministry of Education and Jeonbuk State in 2026, as part of the Regional Innovation System & Education (RISE) program (2026-RISE-13-JJU).

PA-P40

Proceedings of The 12th International Symposium on Machinery and Mechatronics for Agriculture and Biosystems Engineering (ISMAB 2026)
20-24 October 2026, Busan, Republic of Korea

DEVELOPMENT AND DEMONSTRATION OF A MODULAR SMART FARM ROBOT FOR WHOLE-CYCLE STRAWBERRY CULTIVATION

Lae-Kyoung Lee[1*], Su-Yong An[1]

[1]Electronics and Telecommunications Research Institute, Daegu, Korea
**Corresponding Author-- Voice: +82-10-3861-7777, Email: laeklee@etri.re.kr

Abstract: Most greenhouse robots are designed for a single agricultural task and, owing to the characteristics of the crop, can be operated only for limited purposes and periods, which considerably constrains their field adoption and service optimization. To address these limitations, this study proposes an autonomous modular smart farm robot system that supports the entire strawberry cultivation cycle. By applying digital twin-based Sim2Real technology to model diverse greenhouse environmental conditions, crop growth states and the robot system itself, the proposed approach enhances real-world robot operation and control and enables simulation of various agricultural services, thereby supporting effective service improvement in the real greenhouse.

Key Words: Strawberry greenhouse, Modular robot, Autonomous navigation, Digital twin, Isaac Sim

INTRODUCTION

Strawberry cultivation generally requires multiple agricultural operations to be performed both sequentially and in parallel, yet most greenhouse robots are designed for a single task, such as harvesting (Xiong et al., 2020) or growth monitoring (Park et al., 2025; Sánchez-Molina et al., 2024). Such single-task robots have low utilisation and high introduction costs, and multipurpose platforms have therefore been proposed as an alternative (Sánchez-Molina et al., 2024). Modular robots such as Thorvald II reconfigure the mobile platform itself (Grimstad and From, 2017), whereas systems that exchange task modules on a common base to support the entire strawberry cultivation cycle remain rare. Moreover, each task module can only be tested at the corresponding cultivation and growth stage, which severely constrains field demonstration and scenario validation. Although digital twins have recently been applied to address this issue, existing studies have been limited to single tasks (Mirbod et al., 2025; Singh et al., 2025).
The objectives of this study were to: (1) propose the architecture of an autonomous smart farm robot platform that provides practical agricultural services in strawberry greenhouses by exchanging modules suited to each stage of the cultivation cycle (spraying, harvesting, crop management and transport); (2) implement autonomous spraying in a real strawberry greenhouse to advance in-greenhouse robot control and optimise service operation; and (3) verify the stability and efficiency of robot operation in a digital twin greenhouse built in NVIDIA Isaac Sim.

DEVELOPMENT AND FIELD DEMONSTRATION OF A MODULAR SMART FARM ROBOT SYSTEM

ROBOT PLATFORM AND TASK MODULES

The smart farm robot proposed in this study to support the entire strawberry cultivation cycle is an expandable robot system consisting of a base robot platform and interchangeable task modules (Fig. 1). The base platform is wheel-driven and uses hybrid wheels that allow it to travel on both flat floors and rail sections. The task modules, including spraying, harvesting, transport and crop management modules, are connected to the base platform through a standardised interface and can be exchanged according to the user's work schedule. The base platform is equipped with wired and wireless communication (Wi-Fi, CAN and RS-232), an RGB-D camera (RealSense D455, Intel Corp., USA) and front and rear 2D LiDAR sensors. Using these components, it performs autonomous navigation functions, including SLAM, localization, path planning and obstacle avoidance. In conjunction with the robot–sensor–IoT integrated control system, it also controls the attached task module and monitors its status. This enables agricultural services to be operated with a single robot or with multiple robots.

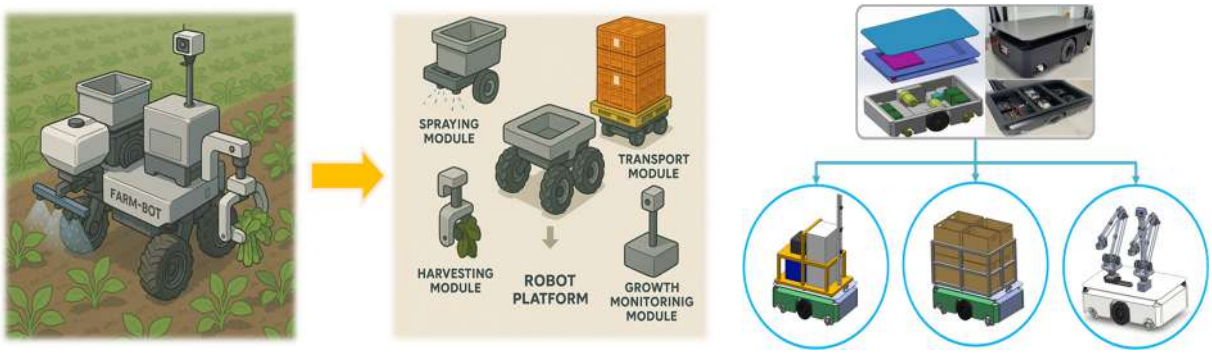

Fig.1 Expandable smart farm robot: base platform and spraying, harvesting and transport modules.

FIELD DEMONSTRATION IN A REAL GREENHOUSE AND DIGITAL TWIN-BASED SIMULATION

To evaluate the performance and field applicability of the proposed modular smart farm robot system, validation and comparison experiments were conducted in both a real strawberry greenhouse and a digital twin greenhouse (Fig. 2). The digital twin greenhouse was constructed by digitizing the crops and facilities of the real greenhouse using images and 3D LiDAR data. In the real greenhouse, autonomous spraying along planned paths and manual spraying by the user were performed in parallel under the same conditions as conventional strawberry spraying and then compared. The results showed that the proposed robot system achieved a level of usability and field applicability satisfactory to the user. In addition, driving simulations in the NVIDIA Isaac Sim-based digital twin greenhouse confirmed that sensor inputs and driving performance consistent with those in the real environment were reproduced.

CONCLUSIONS

In this study, an autonomous modular smart farm robot system that supports the entire strawberry cultivation cycle was proposed. A comparative usability evaluation of autonomous



(a)



(b)

Fig.2 (a) Real greenhouse and (b) digital twin in Isaac Sim, with robot trajectories in both environments.

and manual spraying in a real greenhouse confirmed the field applicability of the proposed system. In addition, the digital twin greenhouse reproduced task and driving characteristics consistent with those in the real environment. This result provides a basis for future verification of crop growth simulation and collaboration among multiple agricultural robots in a virtual environment.

ACKNOWLEDGEMENTS

This work was supported by Electronics and Telecommunications Research Institute (ETRI) grant funded by the Korean government. [26ZD1170, Advancement and Commercialization of Daegu-Gyeongbuk Regional Strategic Industries (Robots, Mobility, AI, Medical, etc.) & 26AD1530, Establishment of a Regionally-Integrated Academic-Research Innovation Convergence Platform]

REFERENCES

Grimstad, L., and P. J. From. 2017. The Thorvald II agricultural robotic system. Robotics 6(4): 24. https://doi.org/10.3390/robotics6040024

Mirbod, O., D. Choi, and J. K. Schueller. 2025. From simulation to field validation: A digital twin-driven sim2real transfer approach for strawberry fruit detection and sizing. AgriEngineering 7(3): 81. https://doi.org/10.3390/agriengineering7030081

Park, H., N. Shin, S. Kum, S. K. Kim, Y. Kim, S. Choi, D. Y. Won, and H. K. Suh. 2025. Development and evaluation of automated monitoring systems for multi-stage strawberry growth detection using advanced deep learning models. J. Biosyst. Eng. https://doi.org/10.1007/s42853-025-00282-z

Sánchez-Molina, J. A., F. Rodríguez, J. C. Moreno, J. Sánchez-Hermosilla, and A. Giménez. 2024. Robotics in greenhouses. Scoping review. Comput. Electron. Agric. 219: 108750. https://doi.org/10.1016/j.compag.2024.108750

Singh, R., L. Seneviratne, and I. Hussain. 2025. A deep learning-based approach to

strawberry grasping using a telescopic-link differential drive mobile robot in ROS-Gazebo for greenhouse digital twin environments. IEEE Access 13: 361-381. https://doi.org/10.1109/ACCESS.2024.3520233

Xiong, Y., Y. Ge, L. Grimstad, and P. J. From. 2020. An autonomous strawberry-harvesting robot: Design, development, integration, and field evaluation. J. Field Robot. 37(2): 202-224. https://doi.org/10.1002/rob.21889https://doi.org/10.1109/ACCESS.2024.3520233

PA-P41

Proceedings of The 12th International Symposium on Machinery and Mechatronics for Agriculture and Biosystems Engineering (ISMAB 2026)
20-24 October 2026, Busan, Republic of Korea

PREDICTION OF SOYBEAN PLANT HEIGHT AND STEM DIAMETER USING UAV MULTISPECTRAL IMAGERY AND GROWTH RESPONSES TO SMART CULTIVATION TREATMENTS

ChangHyeok Park[1], ChanSeok Ryu[1*], GangIn Je[1], HoJun Kwon[1], Gang-Jin Lee[2]

[1] Department of Bio-System Engineering, Institute of Agriculture & Life Science, GyeongSang National University, Jinju-si 52828, Korea
[2] Institute of Agriculture & Life Science, GyeongSang National University, Jinju-si 52828, Korea
*Corresponding Author-- Voice: +82-55-772-1897, Email: ryucs@gnu.ac.kr

Abstract: This study compared the plant height and stem diameter of soybean under smart cultivation treatments combining subsurface drip irrigation, subsurface drainage and unmanned aerial vehicle (UAV, drone) spraying with those of a non-irrigated control, and developed regression models to estimate both traits from vegetation indices derived from UAV multispectral imagery. An experimental field (66.5 m × 13.3 m) in Miryang, Gyeongsangnam-do, Korea was divided into five zones assigned to ABD (irrigation/drainage + boom-sprayer weed control + drone pest control), ADD (irrigation/drainage + drone weed and pest control) and WWW (non-irrigated control), and soybean plant height, stem diameter and multispectral reflectance were surveyed in August and September of 2022 and 2023. Plant height and stem diameter were compared among treatments with independent-samples t-tests, and forward-selection multiple linear regression (MLR) and four tree-based models were built from 39 vegetation indices on the data pooled across years and months (plant height, n = 150; stem diameter, n = 200) and evaluated by plant-grouped cross-validation. In 2023, plant height was greater in ADD (65.4 cm) and ABD (61.6 cm) than in WWW (58.3 cm) ($p < 0.05$), whereas no increase in plant height was observed in the irrigated/drained treatments in 2022, and stem diameter did not differ among treatments in either year. Rainfall from July to the August survey date was 767.5 mm in 2023, about 3.5 times that of 2022 (222.0 mm), suggesting that subsurface drainage reduced excess root-zone moisture and sustained stem elongation in the wet year of 2023. Among the regression models, Random Forest showed the highest performance for plant height (R^2v 0.925, RMSEv 6.29 cm, MAPEv 6.08%), and MLR was the best for stem diameter (R^2v 0.465, RMSEv 1.76 mm, MAPEv 15.40%). UAV multispectral vegetation indices can therefore be used for non-destructive estimation of soybean plant height, and combining them with weather data is expected to improve the accuracy of treatment-level growth diagnosis.

Keywords: Soybean, UAV multispectral imagery, Vegetation index, Plant height, Stem diameter, Subsurface drainage

INTRODUCTION

Soybean has its greatest water requirement during the reproductive stage, when pods set and seeds fill, and water deficit during this period limits growth and yield (Desclaux et al., 2000). Subsurface drip irrigation and subsurface drainage are technologies for keeping root-zone moisture stable, and UAV-based spraying reduces labor and soil compaction by farm machinery. Because weather conditions differ from year to year, the effect of a smart cultivation system combining these technologies needs to be verified through multi-year field trials.

Plant height and stem diameter are basic traits that represent the growth status and lodging resistance of soybean. UAV multispectral imagery can survey a large field in a short time and has been studied as a means of replacing such field surveys (Maimaitijiang et al., 2020). In addition to NDVI (Rouse et al., 1974), various vegetation indices such as VARI (Gitelson et al., 2002), TCARI (Haboudane et al., 2002), CVI (Vincini et al., 2008), ARI (Gitelson et al., 2001) and NGRDI (Tucker, 1979) are used as growth indicators. In agricultural datasets with small sample sizes, machine learning models with many variables tend to overfit, and performance is overestimated when variable selection is not separated from the validation data (Varma and Simon, 2006). Linear and tree-based models therefore need to be compared under the same cross-validation conditions. The objectives of this study were (1) to compare soybean plant height, stem diameter and vegetation indices of treatments applying subsurface drip irrigation, subsurface drainage and UAV spraying with those of a control in a two-year (2022–2023) field trial, and (2) to develop and compare multiple linear regression and tree-based models that predict plant height and stem diameter from UAV multispectral vegetation indices pooled across years and months.

MATERIALS AND METHODS

Experimental Field and Treatments

The experiment was conducted on soybean (Glycine max (L.) Merr. cv. Seonpung) in an experimental field of the Department of Southern Area Crop Science, National Institute of Crop Science, in Miryang, Gyeongsangnam-do, Korea. In 2022 and 2023, the same experimental field (66.5 m × 13.3 m) was divided into five 13.3-m-wide zones, and three treatments were assigned (Fig. 1, Table 1). ABD and ADD shared subsurface drip irrigation, subsurface drainage, mechanized sowing, combine harvesting, digital traps, drone pest control and an integrated control program, and differed only in weed control method: boom sprayer (ABD) or drone (ADD). The control (WWW) was not irrigated, and weeds and pests were controlled manually.

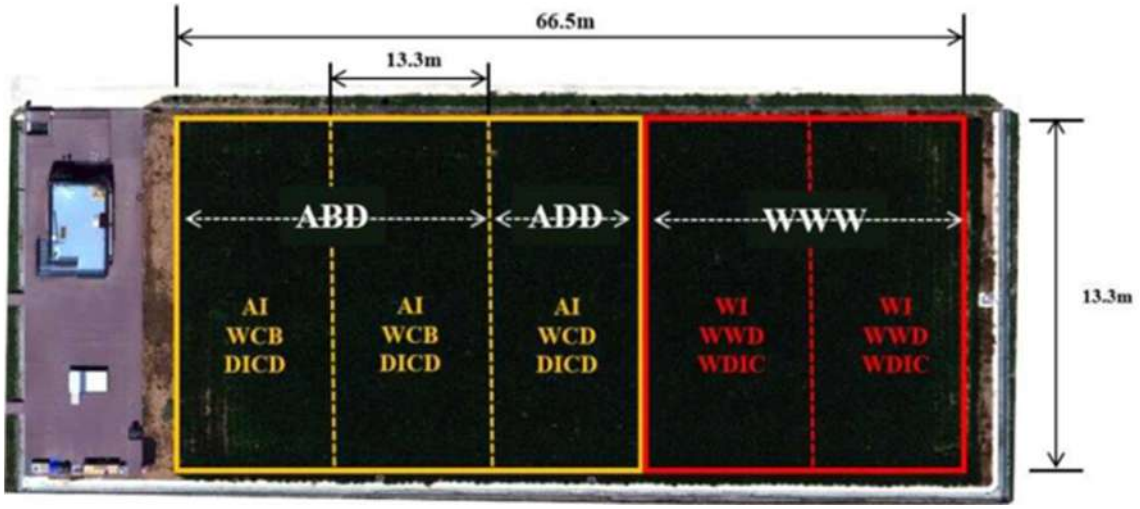

Fig. 1 Field layout and technologies applied to each treatment.

Table 1 Treatment configuration

Treatment	Irrigation · drainage	Weed control	Pest control
ABD	Subsurface drip + subsurface drainage	Boom sprayer	Drone
ADD	Subsurface drip + subsurface drainage	Drone	Drone
WWW	Non-irrigated	Manual	Manual

Growth Survey

Plant height (cm) and stem diameter (mm) were measured on 10 plants per zone (20 plants for ABD, 10 for ADD and 20 for WWW; 50 plants per year) in 2022 (22 August and 21 September) and 2023 (22 August and 20 September). In 2022, different plants were surveyed in August and September (50 plants per survey date), and plant height was not measured in September. In 2023, the same 50 plants were measured repeatedly in August and September to calculate growth in plant height and stem diameter between August and September. Accordingly, plant height was analyzed for three survey dates (n = 150; 50 in 2022 and 100 in 2023), and stem diameter for four survey dates (n = 200; 100 per year).

UAV Imagery and Vegetation Indices

Spectral data were acquired on each growth survey date using a UAV (DJI Matrice 300 RTK) equipped with a multispectral sensor (MicaSense Altum-PT). Images were taken at an altitude of 25 m with 75% overlap and a flight speed of 4 m/s, giving a ground sampling distance (GSD) of 1.07 cm/pixel at 25 m. Blue, Green, Red, Red-edge (RE) and NIR reflectance of each plant was extracted from the UAV multispectral imagery, and 39 vegetation indices were calculated. The eight vegetation indices used in the final regression models are listed in Table 2.

Table 2 Vegetation indices used in the regression models

Index	Formula	Reference
BRI	(1/Green − 1/RE) / NIR	–
VARI	(Green − Red) / (Green + Red − Blue)	Gitelson et al. (2002)
TCARI	3[(RE − Red) − 0.2(RE − Green)(RE / Red)]	Haboudane et al. (2002)
CVI	NIR × Red / Green²	Vincini et al. (2008)
DVI	NIR − Red	Tucker (1979)
ARI	1/Green − 1/RE	Gitelson et al. (2001)
NGRDI	(Green − Red) / (Green + Red)	Tucker (1979)
GRVI	NIR / Green	Tucker (1979)

Statistical Analysis

Outliers in the five bands, plant height and stem diameter were removed using the 1.5 × IQR rule. Plant height, stem diameter and the eight vegetation indices were then compared among treatments (ABD–ADD, ABD–WWW, ADD–WWW), together with monthly changes, using independent-samples t-tests for each survey date. Analyses were performed in Python (scikit-learn, SciPy).

Regression Models and Validation

Plant height (n = 150) and stem diameter (n = 200) were used as target variables with data pooled across years (2022, 2023) and months (August, September). Multiple linear regression (MLR) was built by forward selection: starting from a model with no variables, the variable that most increased the 5-fold cross-validated R^2 within the training data was added one at a time, and selection stopped when R^2 no longer increased or five variables had been selected. As tree-based models, Decision Tree (depth 3), Random Forest (300 trees; Breiman, 2001), Extra Trees (300 trees; Geurts et al., 2006) and Gradient Boosting (200 iterations, depth 2; Friedman, 2001) were compared, and the model with the highest R^2v for each trait

was compared with MLR. Validation used group 5-fold cross-validation, grouped by year and plant number and repeated five times, so that data from the same plant were never split between training and validation; MLR variable selection was performed independently within each training fold of the outer cross-validation. Calibration performance (R^2c, RMSEc, MAPEc) was calculated from predictions of a model fitted to all data on the same data, and validation performance (R^2v, RMSEv, MAPEv) from predictions for plants excluded from training.

RESULTS & DISCUSSION

Plant Height and Stem Diameter by Treatment

Table 3 shows the t-test results for plant height and stem diameter by treatment. In the data pooled across years and months, plant height and stem diameter did not differ among treatments ($p > 0.1$; Table 3). Plant height differed greatly between years, ranging from 105 to 109 cm in 2022 and from 58 to 65 cm in 2023, which is attributed to the influence of weather. By year, plant height in 2022 (August) was lower in ABD (105.4 cm) than in ADD and WWW (109.3 cm each) ($p \leq 0.035$), because zone 1 of ABD (101.5 cm) was shorter than zone 2 (109.2 cm). In 2023, plant height was greater in ADD (65.4 cm) and ABD (61.6 cm) than in WWW (58.3 cm) ($p < 0.001$ and $p = 0.033$, respectively). Stem diameter did not differ among treatments in either year ($p > 0.1$). In 2022, plant height was not measured in September, and September stem diameter did not differ between ABD (9.6 mm) and WWW (9.9 mm) ($p = 0.668$). Rainfall from July to the August survey date was 767.5 mm in 2023, about 3.5 times that of 2022 (222.0 mm), and Typhoon Khanun brought 369.5 mm over two days on 9–10 August 2023. Because ABD and ADD were equipped with subsurface drainage in addition to subsurface drip irrigation, subsurface drainage is considered to have reduced excess root-zone moisture and sustained stem elongation in the wet year of 2023. In 2022, when July–August rainfall was low, no increase in plant height was observed among treatments, and the heavy rainfall from Typhoon Hinnamnor in early September (322.0 mm over two days) was short-lived and appears not to have affected differences in stem diameter among treatments.

Table 3 Plant height and stem diameter (mean ± standard deviation) by treatment for the pooled data and for each year, with independent-samples t-test p-values.

Trait	ABD	ADD	WWW	ABD–ADD	ABD–WWW	ADD–WWW
2022–2023						
Plant height (cm)	76.2 ± 22.0	80.0 ± 21.8	75.3 ± 24.7	0.432	0.841	0.377
Stem diameter (mm)	9.2 ± 2.6	9.9 ± 2.2	9.2 ± 2.4	0.128	0.962	0.115
2022						
Plant height (cm)	105.4 ± 4.9	109.3 ± 3.9	109.3 ± 3.5	0.035*	0.005**	0.986
Stem diameter (mm)	10.7 ± 2.4	11.5 ± 1.5	10.7 ± 2.2	0.135 (W)	0.962	0.154
2023						
Plant height (cm)	61.6 ± 7.9	65.4 ± 6.6	58.3 ± 5.3	0.068	0.033* (W)	<0.001***
Stem diameter (mm)	7.7 ± 1.7	8.4 ± 1.5	7.8 ± 1.4	0.127	0.857	0.122

(W) Welch's t-test; * $p < 0.05$, ** $p < 0.01$, *** $p < 0.001$.

Regression Models for Plant Height and Stem Diameter Pooled Across Years and Months

Table 4 and Fig. 2 present the regression results and scatter plots of each model. For plant height, MLR forward selection (BRI, VARI, TCARI, CVI, DVI) yielded R^2v 0.924, RMSEv 6.32 cm and MAPEv 6.87%, and Random Forest yielded R^2v 0.925, RMSEv 6.29 cm and MAPEv 6.08%, showing similar performance (Table 4, Fig. 2). For stem diameter, MLR (CVI, NGRDI, TCARI, GRVI) achieved R^2v 0.465, RMSEv 1.76 mm and MAPEv 15.40%, outperforming Random Forest (R^2v 0.425, MAPEv 15.74%), the best of the tree-based models.

Table 4 Performance of plant height and stem diameter regression models

Trait · model	Vegetation indices	R^2c	RMSEc	MAPEc	R^2v	RMSEv	MAPEv
Plant height (cm, n = 150)							
MLR (forward selection)	BRI, VARI, TCARI, CVI, DVI	0.936	5.78	6.06	0.924	6.32	6.87
Random Forest	CVI, ARI, BRI	0.980	3.25	3.19	**0.925**	6.29	6.08
Stem diameter (mm, n = 200)							
MLR (forward selection)	CVI, NGRDI, TCARI, GRVI	0.513	1.68	14.80	**0.465**	1.76	15.40
Random Forest	CVI, BRI, VARI	0.828	1.00	8.34	0.425	1.82	15.74

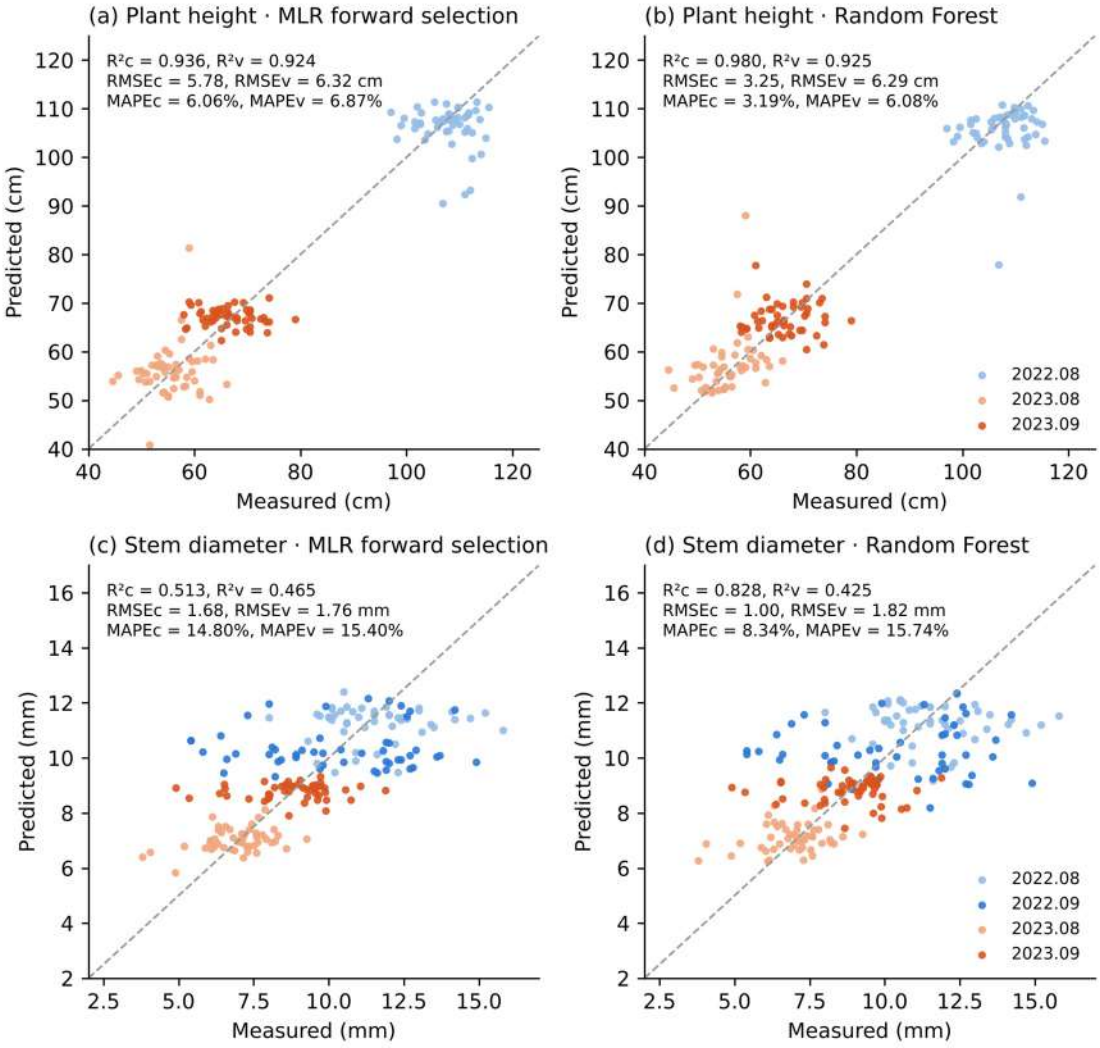

Fig. 2 Measured values versus cross-validated predictions of the models: (a) plant height MLR, (b) plant height Random Forest, (c) stem diameter MLR, (d) stem diameter Random Forest.

The final MLR equation for plant height was Plant height = 165.27 + 0.729·BRI − 217.9·VARI − 102.5·TCARI − 4.97·CVI + 59.0·DVI, and all coefficients were significant ($p < 0.01$). VARI and TCARI were selected in 72% and 68% of the 25 training folds, respectively, making them the most stable variables. The final MLR equation for stem diameter was Stem diameter = 18.77 − 0.948·CVI − 26.36·NGRDI − 10.77·TCARI + 0.431·GRVI, in which NGRDI and TCARI were significant ($p \leq 0.002$). Stem diameter had a lower R^2v and a larger MAPEv (15%) than plant height, indicating that stem thickness is difficult to estimate from spectral information captured above the canopy. For both traits, Random Forest had higher R^2c than MLR but lower R^2v, indicating a tendency to overfit the training data. CVI, BRI, VARI and ARI were commonly identified as important variables in both MLR and the tree-based models, indicating that chlorophyll- and pigment-related indices contributed mainly to plant height estimation.

CONCLUSIONS

This study compared the plant height and stem diameter of soybean in 2022–2023 under smart cultivation treatments applying subsurface drip irrigation, subsurface drainage and UAV spraying with those of a non-irrigated control, and developed regression models to estimate both traits from UAV multispectral vegetation indices. Among the regression models built on data pooled across years and months, Random Forest showed the highest performance for plant height (R^2v 0.925, RMSEv 6.29 cm, MAPEv 6.08%), and multiple linear regression (MLR) for stem diameter (R^2v 0.465, RMSEv 1.76 mm, MAPEv 15.40%). In the treatment comparison, plant height of the irrigated and drained treatments (ABD, ADD) was greater than that of the control in 2023, when July–August rainfall was high, but did not differ in 2022, when rainfall was low, indicating that the effect of subsurface drainage in alleviating excess soil moisture varied with annual rainfall conditions. Although the vegetation-index-based models estimated plant height with high accuracy, they did not capture the differences in plant height among treatments in September after canopy closure. UAV multispectral imagery can therefore be used for non-destructive estimation of soybean plant height, and accumulating data from various regions and combining them with weather data is expected to improve the accuracy of growth diagnosis.

ACKNOWLEDGEMENTS

This work was supported by Korea Institute of Planning and Evaluation for Technology in Food, Agriculture and Forestry(IPET) through AX-based Intelligent Collaborative Farm Work Industrialization Technology Development Program, funded by Ministry of Agriculture, Food and Rural Affairs(MAFRA)(RS-2026-25528721).

REFERENCES

Breiman, L. 2001. Random forests. *Machine Learning* 45(1): 5-32.

Desclaux, D., T. T. Huynh, and P. Roumet. 2000. Identification of soybean plant characteristics that indicate the timing of drought stress. *Crop Sci.* 40(3): 716-722.

Friedman, J. H. 2001. Greedy function approximation: A gradient boosting machine. *Ann. Statist.* 29(5): 1189-1232.

Geurts, P., D. Ernst, and L. Wehenkel. 2006. Extremely randomized trees. *Machine Learning* 63(1): 3-42.

Gitelson, A. A., M. N. Merzlyak, and O. B. Chivkunova. 2001. Optical properties and nondestructive estimation of anthocyanin content in plant leaves. *Photochem. Photobiol.* 74(1): 38-45.

Gitelson, A. A., Y. J. Kaufman, R. Stark, and D. Rundquist. 2002. Novel algorithms for remote estimation of vegetation fraction. *Remote Sens. Environ.* 80(1): 76-87.

Haboudane, D., J. R. Miller, N. Tremblay, P. J. Zarco-Tejada, and L. Dextraze. 2002. Integrated narrow-band vegetation indices for prediction of crop chlorophyll content for application to precision agriculture. *Remote Sens. Environ.* 81(2-3): 416-426.

Hurlbert, S. H. 1984. Pseudoreplication and the design of ecological field experiments. *Ecol. Monogr.* 54(2): 187-211.

Maimaitijiang, M., V. Sagan, P. Sidike, S. Hartling, F. Esposito, and F. B. Fritschi. 2020. Soybean yield prediction from UAV using multimodal data fusion and deep learning. *Remote Sens. Environ.* 237: 111599.

Mutanga, O., and A. K. Skidmore. 2004. Narrow band vegetation indices overcome the saturation problem in biomass estimation. *Int. J. Remote Sens.* 25(19): 3999-4014.

Rouse, J. W., R. H. Haas, J. A. Schell, and D. W. Deering. 1974. Monitoring vegetation systems in the Great Plains with ERTS. In *Proc. 3rd Earth Resources Technology Satellite-1 Symposium*, NASA SP-351, 309-317. Washington, D.C.: NASA.

Tucker, C. J. 1979. Red and photographic infrared linear combinations for monitoring vegetation. *Remote Sens. Environ.* 8(2): 127-150.

Varma, S., and R. Simon. 2006. Bias in error estimation when using cross-validation for model selection. *BMC Bioinformatics* 7: 91.

Vincini, M., E. Frazzi, and P. D'Alessio. 2008. A broad-band leaf chlorophyll vegetation index at the canopy scale. *Precision Agric.* 9(5): 303-319.

Smart Farm Systems and Renewable Energy



SF-P01

Proceedings of The 12th International Symposium on Machinery and Mechatronics for Agriculture and Biosystems Engineering (ISMAB 2026)
20-24 October 2026, Busan, Republic of Korea

DEVELOPMENT OF A MULTIMODAL AI-BASED POULTRY HEALTH MONITORING SYSTEM INTEGRATING EDGE COMPUTING AND TRANSFER LEARNING FOR LAYING HEN PRODUCTION

Fu-Kai Chang[1*], Tsui-Lan Chou[3], Ming-Kun Hsieh[2] , and Yao-Chuan Tsai[1]

[1]Dept. of Bio-Industrial Mechatronic Engineering, National Chung Hsing University, Taichung, Taiwan
[2]Graduate Institute of Microbiology and Public Health, National Chung Hsing University, Taichung, Taiwan
[3]Chang-wang Farm, Hsinchu, Taiwan
*Corresponding Author—Email:fukaiz384@gmail.com

Abstract:
As the laying hen industry moves toward smart and welfare-friendly farming, real-time flock health monitoring has become increasingly important. Reducing the labor required for manual inspection is also a key goal in precision livestock farming. This study proposes a multimodal artificial intelligence health monitoring system for cage-free laying hens. The system integrates edge computing, transfer learning, image recognition, environmental sensing, acoustic analysis, and farm management records. A Jetson Orin Nano was used as the edge computing platform. A PTZ network camera periodically patrolled the poultry house and captured images of the flock. Transfer learning was used to adapt an existing eye abnormality detection model developed for native chickens to the laying hen environment.Field validation was conducted at a laying hen farm in Hsinchu County, Taiwan. Multimodal data were collected, including eye images, environmental factors, body weight, egg production, mortality, and farm management records. The original native-chicken model showed limited performance when directly applied to laying hen images. After transfer learning, the recognition performance improved. The dataset was further refined and balanced so that normal and abnormal samples each accounted for 50% of the data. Data augmentation included rotation, flipping, brightness adjustment, and contrast adjustment. The input image size was increased to 1280 pixels. The optimized model achieved precision values of 0.738 and 0.787 for the normal and abnormal classes, respectively. The corresponding recall values were 0.748 and 0.701. These results show that transfer learning, data augmentation, class balancing, and higher image resolution can improve eye abnormality detection in laying hens.The on-site cameras were also connected to the Jetson Orin Nano through an API. This allowed the trained model to perform edge inference directly at the farm. The system can identify normal and abnormal eyes in real time and generate preliminary annotation results. These outputs can then be transmitted to a smart monitoring platform for manual review and dataset correction. This workflow can reduce the workload of routine inspection and image annotation. Overall, the proposed framework integrates visual, acoustic, environmental, and production management information. It provides a basis for future health assessment and early disease warning in laying hens. Future work will incorporate comb recognition, acoustic recognition, and additional multimodal data to build a more comprehensive intelligent poultry health monitoring and disease early warning system.

Key Words: Edge Computing, Deep Learning, Chicken Eyes, Poultry Health

INTRODUCTION

Traditional cage-free poultry farming relies heavily on manual inspection and farmers' experience. Frequent movement between poultry houses may increase the risk of pathogen transmission, while subjective health assessments are difficult to standardize and pass on. Moreover, by the time visible signs of disease are detected, infection may have already spread within the flock for several days, highlighting the need for a real-time and objective early-warning system.

MATERIALS AND METHODS

2.1 Chicken data set

The image dataset was collected using a hen eye and comb recognition system consisting of a PTZ network camera and a Jetson Orin Nano. The camera was configured with 49 predefined monitoring points and different zoom levels to avoid obstacles such as feeding lines, nest boxes, and feed bins. Image collection was conducted five times per day at 06:00, 09:00, 12:00, 15:00, and 17:00. During each patrol, one image was captured at each monitoring point to collect data on eye and comb abnormalities in laying hens, and the image size is 3840×2160 pixels.

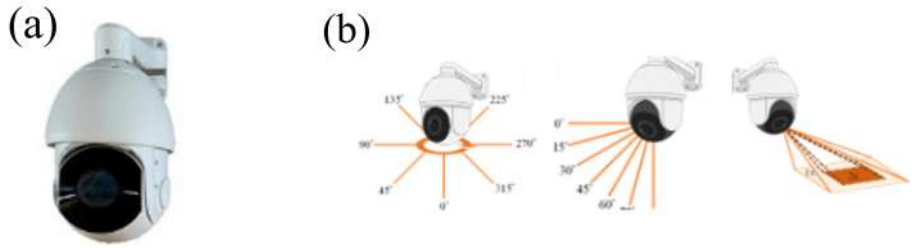

Figure 1. (a) Global-King camera. (b) Panning angles, Tilting angles, Zoom levels.

2.2 Establishment of chicken eye abnormality detection

An eye abnormality detection model had previously been developed using image data collected from native chickens. However, the laying hens in the current farm are Lohmann layers, whose eye and periocular features differ slightly from those of native chickens. Therefore, after collecting images from the target farm, transfer learning was applied to adapt the existing native chicken model and develop a model specifically for laying hens. The on-site cameras are connected via API to a Jetson Orin Nano edge computing platform, where the trained model performs local inference to identify normal and abnormal eyes. The system automatically generates preliminary annotation files, which are subsequently reviewed and corrected manually, thereby improving the efficiency of dataset annotation and model development.



Figure 2. (a) Raw image data. (b) Eyelid swelling images

RESULTS & DISCUSSION

3.1 Chicken eye detection model identification results

This study used YOLOv7 to develop a chicken eye abnormality recognition model. After dataset correction and class balancing, a total of 825 images were used for training, 84 images for validation, and 86 images for testing. The training set contained 1,318 normal and 1,194 abnormal eye instances, the validation set contained 136 normal and 121 abnormal instances, and the test set contained 139 normal and 121 abnormal instances. Data augmentation, including ±15° rotation, flipping, brightness adjustment, and contrast adjustment, was applied during model training, and the input image size was set to 1280 pixels. Select the confidence level value as 0.5, test set Precision as 0.787, and Recall as 0.701 shown in Table 1.

Table 1 Test set detection result table.

Classification	Precision	Recall
Normal	0.738	0.748
Abnormal	0.787	0.701

CONCLUSIONS

This study established a laying hen eye abnormality recognition system through transfer learning, achieving an abnormal-eye recognition accuracy of approximately 0.78. Data augmentation, class balancing, and increased image resolution further improved the recognition performance. During July, laying hens were frequently exposed to high-temperature and high-humidity conditions, which may have reduced feed intake, increased production stress, and contributed to a higher number of abnormal deaths. These findings suggest that laying hen health and mortality may be influenced by multiple factors, including heat stress, nutritional status, and farm management. Therefore, integrating visual, environmental, acoustic, and production-related information has the potential to provide a more comprehensive assessment of flock health. In the future, acoustic features, comb recognition, additional egg production records, and longer-term data will be incorporated to further improve the multimodal health monitoring framework and enhance its capability for early health-risk warning in laying hens.

ACKNOWLEDGEMENTS

Thanks to Mrs. Chou Tsui-Lan from Xinpu, Hsinchu, Taiwan Livestock Farm. Provide an experimental or commercial site for this research and assist in system installation and troubleshooting. Experiments conducted to facilitate this study.

REFERENCES

Adejola, Y. A., T. Z. Sibanda, I. Ruhnke, J. Boshoff, S. Pokhrel, and M. Welch. 2025. Forecasting egg production performance and fluctuations in commercial free-range poultry systems using a random forest model. *Smart Agricultural Technology* 12: 101380.

Chen, Y. C., J. H. Huang, H. Y. Hu, Y. C. Chen, M. W. Wu, M. K. Hsieh, and Y. C. Tsai. 2026. A deep-learning-based early warning system for abnormal eye conditions in chickens. *Poultry Science* 105(6): 106735.

Pajić, M., S. Knežević, B. Djurdjević, V. Polaček, D. Todorović, T. Petrović, and S. Lazić. 2022. Diagnosis of infectious laryngotracheitis outbreaks on layer hen and broiler breeder farms in Vojvodina, Serbia. *Animals* 12(24): 3551.

Italiya, J., A. A. Ahmed, A. A. A. Abdel-Wareth, and J. Lohakare. 2025. An AI-based system for monitoring laying hen behavior using computer vision for small-scale poultry farms. *Agriculture* 15(18): 1963.

Yin, H., C. Liu, Y. Gao, W. Fan, B. Xiao, L. Cao, S. G. Hassan, and S. Liu. 2021. A novel method to predict laying rate based on multiple environment variables. *IEEE* Access 9: 115488-115496.

SF-P02

Proceedings of The 12th International Symposium on Machinery and Mechatronics for Agriculture and Biosystems Engineering (ISMAB 2026)
20-24 October 2026, Busan, Republic of Korea

A TWO-STAGE DEEP LEARNING-BASED MULTI-TYPE ABNORMAL COMB RECOGNITION SYSTEM

Yun-I Chu[1]*, Yu-Jen Shih[1], Fu-Kai Chang[1], Ming-Kun Hsieh[2] and Yao-Chuan Tsai[1]

[1] Department of Bio-Industrial Mechatronics Engineering, National Chung Hsing University, Taichung, Taiwan
[2] Graduate Institute of Microbiology and Public Health, National Chung Hsing University, Taichung, Taiwan
*Corresponding Author-- Voice: +886-965-413-931, Email: chloechu970720@gmail.com

Abstract: With the rapid development of smart agriculture, environmental sensing and image-based monitoring technologies have been increasingly applied to poultry production. However, current poultry house monitoring systems mainly focus on environmental parameters such as temperature, humidity, and gas concentrations, while flock health assessment still relies largely on manual inspection, which is labor-intensive and subjective. Changes in comb color and morphology may reflect the health status of chickens, suggesting the potential of comb characteristics as non-invasive health indicators. In this study, a controllable camera system was installed in a commercial red-feather native chicken farm to collect images and develop a multi-type abnormal comb recognition system. A single five-class model was initially used to classify normal combs, cyanosis, pallor, inversion, and scab. However, because multiple abnormalities may occur simultaneously on the same comb, class confusion was observed. Therefore, a two-stage deep learning framework was developed, in which combs were first localized and subsequently analyzed using four independent binary classification models for cyanosis, pallor, inversion, and scab. Experimental results showed that the mean F1-score of the four abnormality types improved from approximately 0.46 to 0.69 compared with the single five-class model. In addition, the system automatically calculates and uploads daily abnormal comb ratios, providing quantitative information for flock health monitoring and early warning management. These results demonstrate the potential of the proposed system for automated and non-invasive poultry health monitoring in commercial production environments.
Key Words: Comb, Abnormality Detection, Image Recognition, Deep Learning

INTRODUCTION

Taiwanese native chickens have a relatively long production cycle, high activity level, and substantial individual variation, which make flock health management challenging. At present, flock health assessment still depends largely on manual inspection, making continuous monitoring difficult. Because comb color and morphology can change with the health condition of chickens, comb appearance has potential as a non-invasive health monitoring indicator (Bakar et al., 2023; Wei et al., 2024). Two-stage deep learning approaches have also been applied to poultry health monitoring by combining object localization with

subsequent abnormality detection (Zaman et al., 2025). Considering that cyanosis, pallor, inversion, and scab may occur simultaneously on the same comb, a recognition method capable of preserving multiple abnormal characteristics is required.

The objective of this study was to develop a two-stage deep learning system for multi-type abnormal comb recognition. The proposed system first localizes chicken combs and then applies four binary classification models to identify individual abnormality types. The outputs are integrated to support flock health monitoring in a commercial red-feather native chicken production environment.

MATERIALS AND METHODS

Research framework

A controllable camera was installed in a commercial red-feather native chicken farm to collect chicken images, with comb appearance used as the target for recognition. As shown in Fig. 1, the system adopts a two-stage deep learning framework. The first stage performs comb localization. In the second stage, the localized comb images are separately analyzed for cyanosis, pallor, inversion, and scab. The outputs of the individual models are then integrated as information for flock health monitoring.

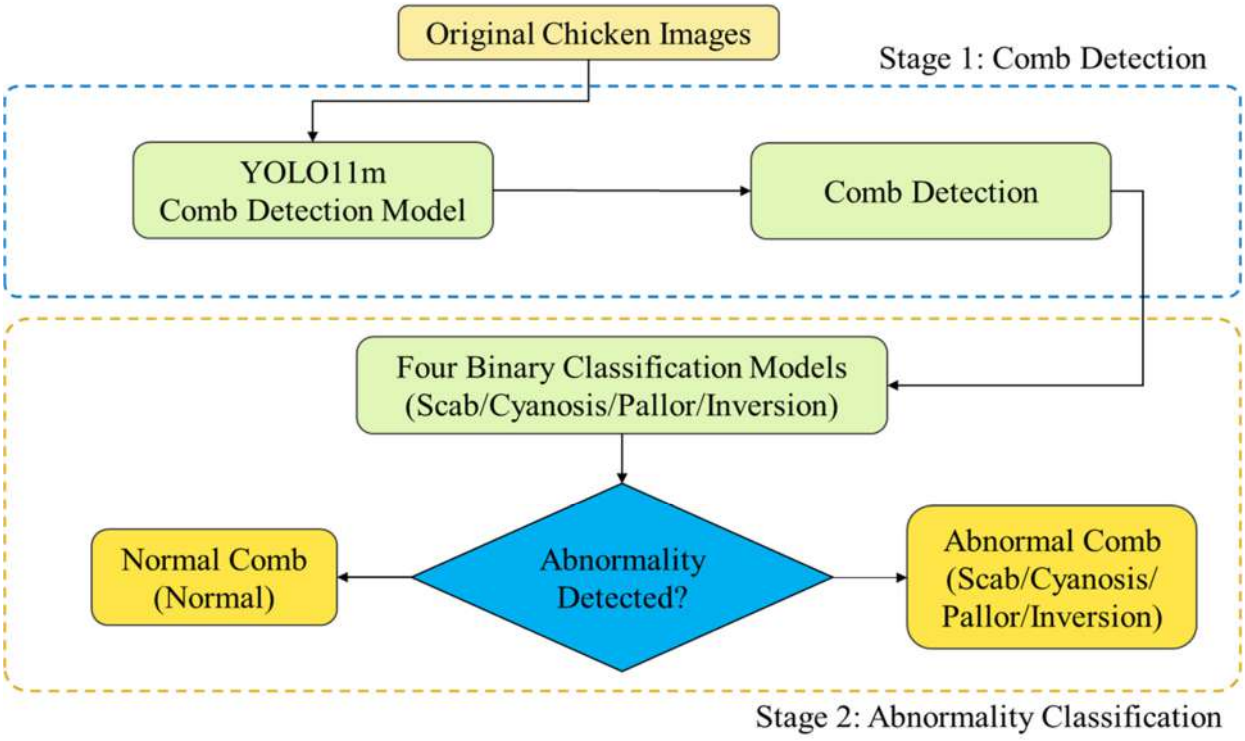

Fig. 1 Two-stage workflow for comb localization and abnormality recognition.

Model development

A single five-class model was first established to identify normal combs, cyanosis, pallor, inversion, and scab. Because a single comb may simultaneously exhibit multiple abnormal characteristics, each comb could be assigned only one class in the five-class dataset. Labels were therefore assigned according to the priority order of cyanosis, pallor, inversion, and scab.

The model used YOLO11m with an input image size of 1088 × 1088 pixels, a batch size of 8, and 300 training epochs. The dataset contained 973 training images, 122 validation images, and 122 test images.

To reduce class confusion in multi-class recognition, a two-stage deep learning model was further established. In the first stage, YOLO11m was used for comb localization using 973 training images, 122 validation images, and 122 test images. In the second stage, four binary classification models were separately developed for normal/cyanosis, normal/pallor, normal/inversion, and normal/scab. Because abnormal combs occur less frequently under commercial poultry-house conditions, the number of abnormal images available for model development was limited; therefore, each binary dataset was constructed from the samples actually collected. The training, validation, and test sets contained 555, 69, and 70 images for normal/cyanosis; 233, 29, and 29 images for normal/pallor; 376, 46, and 48 images for normal/inversion; and 233, 29, and 29 images for normal/scab, respectively.

Model performance evaluation

Model performance was evaluated using confusion matrices. Precision, Recall, and F1-score were calculated to compare the performance of the comb localization model and the abnormality recognition models.

RESULTS & DISCUSSION

The first-stage comb localization model achieved Precision, Recall, and F1-score values of 0.723, 0.845, and 0.779, respectively. The Recall of 84.5% indicates that the model was able to detect most chicken combs. Table 1 compares the single five-class model with the four binary classification models. Overall, the binary models outperformed the single five-class model, reducing class confusion while retaining information on multiple abnormalities that may occur on the same comb.

Table 1 Comparison of recognition performance between the single five-class model and four binary classification models.

Class	Single five-class model			Four binary classification models		
	Precision	Recall	F1-score	Precision	Recall	F1-score
Cyanosis	0.500	0.375	0.429	0.753	0.550	0.636
Pallor	0.308	0.444	0.364	0.727	0.615	0.666
Inversion	0.571	0.372	0.451	0.859	0.619	0.720
Scab	0.556	0.676	0.610	0.783	0.700	0.739

When the proposed models were applied to images from the 202602 commercial red-feather native chicken flock, changes in the ratios of different comb abnormalities showed trends similar to several on-farm health and management events (Fig. 2). The pallor ratio increased during periods when coccidiosis and bloody feces were observed. The cyanosis ratio increased during the period when respiratory-related medication was administered. In the later production stage, the scab ratio increased as fighting and pecking became more frequent. These observations suggest that changes in comb abnormalities may have potential as non-invasive indicators for flock health and management monitoring.

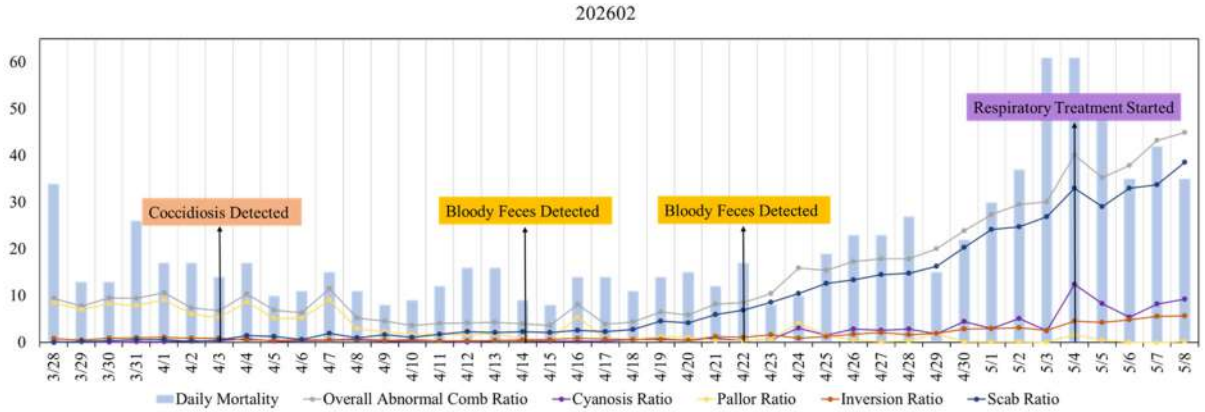

Fig. 2 Changes in comb abnormality ratios and on-farm health and management events.

CONCLUSIONS

This study developed a two-stage deep learning system for multi-type abnormal comb recognition using comb localization followed by four binary classification models. The two-stage framework reduced class confusion and improved recognition performance compared with a single five-class model. In addition, changes in abnormal comb ratios showed trends similar to selected on-farm health events, indicating the potential of comb abnormalities as non-invasive indicators for flock health monitoring.

REFERENCES

Bakar, M. A. A. A., P. J. Ker, S. G. H. Tang, M. Z. Baharuddin, H. J. Lee, and A. R. Omar. 2023. Translating conventional wisdom on chicken comb color into automated monitoring of disease-infected chicken using chromaticity-based machine learning models. *Frontiers in Veterinary Science* 10:1174700. https://doi.org/10.3389/fvets.2023.1174700.

Wei, T. Y., T.-H. Lin, and Y. C. Tsai. 2024. Comb color analysis of broilers through the video surveillance system of a poultry house. *Brazilian Journal of Poultry Science* 26(1):eRBCA-2023-1891. https://doi.org/10.1590/1806-9061-2023-1891.

Zaman, M. R., M. A. H. Bappy, M. M. Hossain, and M. S. Hossain. 2025. Data-efficient deep learning framework for real-time Avian Pox identification in broiler chickens using two-stage approach. *Smart Agricultural Technology* 12:101246. https://doi.org/10.1016/j.atech.2025.101246.

SF-P03

Proceedings of The 12th International Symposium on Machinery and Mechatronics for Agriculture and Biosystems Engineering (ISMAB 2026)
20-24 October 2026, Busan, Republic of Korea

PERFORMANCE AND FIELD APPLICABILITY OF A SIMPLIFIED DRINKING-WATER TEMPERATURE CONTROL SYSTEM FOR BROILER HOUSES

La-Hoon Cho[1], JinKyung Kwon[2], Chung-Geon Lee[1], Jae Kyung Jang[1], Sung-Wook Yun[1], Jong-Pil Moon[1],Seong-Heon Kim[1]*

[1]Smart Farm Development Division, National Institute of Agricultural Sciences, Rural Development Administration, 166, Nongsaengmyeong-ro, Iseo-myeon, Wanju-gun, Jeonbuk-do 55365, Republic of Korea
[2]Agricultural Robot Division, National Institute of Agricultural Sciences, Rural Development Administration, 166, Nongsaengmyeong-ro, Iseo-myeon, Wanju-gun, Jeonbuk-do 55365, Republic of Korea
*Corresponding Author-- Voice: +82-63-238-4083, Email: shk0606@korea.kr

Abstract: Heat stress can reduce feed intake and body weight gain in broilers and increase mortality. Supplying cooled drinking water is one practical approach to reducing heat load. Previous studies developed integrated systems that combined poultry-house heating and cooling with temperature-controlled drinking water. However, these systems required large storage tanks and additional air-conditioning components, increasing system scale and operational complexity.
In this study, a simplified drinking-water heating and cooling system was developed for commercial broiler houses with approximately 20,000 birds. A water-level-controlled module for preparing medicated or supplemented drinking water was also incorporated. The developed unit can provide both cooled and heated drinking water. Because the present study was conducted during summer, only cooling performance was evaluated. Source water at approximately 20°C was tested at heat-exchange tank setpoints of 10.0, 12.5, and 15.0°C. The supply flow was set at 6.6–7.0 L/min. Gravimetric measurements during applicable test runs indicated an actual flow of approximately 6.3 kg/min. Continuous operation was evaluated for 9 h from 09:00 to 18:00.
The mean coefficient of performance (COP) ranged from 1.96 to 2.60, and the system completed the planned 9-h operation under all test conditions. For field validation in Iksan, Republic of Korea, 21,000 broilers were placed in both a cooled-water house and a comparison house. Cumulative mortality was 744 and 1,108 birds, respectively. Body weight one day before shipment was 1,750 g in the cooled-water house and 1,670 g in the comparison house. Farmer interviews also indicated that water-level-controlled filling could reduce repeated tank-level checks during preparation of medicated or supplemented drinking water. These results demonstrate the technical feasibility of simplifying the previous integrated concept while retaining drinking-water cooling capability under commercial-house-relevant operating conditions.

Key Words: Broiler, Drinking water temperature, Heat stress, Heat pump, Water management

INTRODUCTION

Heat stress is a major environmental constraint on broiler production. Exposure to high ambient temperatures can reduce feed intake and body weight gain while increasing feed conversion ratio and mortality (Liu et al., 2020).

Drinking water plays an important role in broiler thermoregulation and production performance. Water demand increases as environmental temperature rises, particularly when birds rely on respiratory evaporation to dissipate heat. Adequate drinking-water supply is therefore important during periods of high temperature (Tabler et al., 2022).

Cooled drinking water can also contribute to heat-stress management. Beker and Teeter (1994) reported that feed intake and body weight gain improved as drinking-water temperature decreased from 43.3 to 10°C under heat-stress conditions. The increase in body temperature during heat exposure was also lower in birds receiving 10°C water. More recently, Kaya and Dereli Fidan (2023) evaluated drinking-water temperature as a management factor for broilers exposed to high ambient temperature.

In the Republic of Korea, heat-pump-based systems have been developed to combine poultry-house air conditioning with temperature-controlled drinking water. Paek et al. (2016) designed an integrated system that included an air-to-water heat pump, thermal storage, and a drinking-water tank. The authors also identified the need for further optimization according to poultry-house size and flock scale. A subsequent field study reported favorable broiler responses during summer operation of an air-conditioning and drinking-water supply system (Paek et al., 2017).

The previous approach combined whole-house environmental conditioning with drinking-water temperature management. Consequently, large storage tanks and air-conditioning components were required. Although this configuration enables integrated environmental control, it increases the scale and number of components required for farm deployment. A simpler system focused on drinking-water temperature control may therefore be more suitable when temperature-controlled water is the primary objective.

Broiler farms also use drinking water to administer vaccines, medications, vitamins, and other supplements. Preparation requires a predetermined quantity of water before a product is added at its prescribed dilution ratio. In conventional farm practice, growers may repeatedly check tank markings or water levels while filling. Automating water-volume adjustment and assisting the mixing process could reduce these repetitive tasks without requiring an automatic chemical-dosing system.

The objectives of this study were to simplify a previously developed integrated concept for broiler drinking-water temperature management, evaluate cooling performance under a commercial-house-relevant water-flow condition, and assess field applicability on a commercial broiler farm. The practical utility of a water-level-controlled preparation module was also evaluated qualitatively through farmer interviews.

MATERIALS AND METHODS

Development of the drinking-water temperature control system

The developed system focused on temperature control of water supplied directly to broiler drinking lines. Unlike the previous integrated system, whole-house air-conditioning components were excluded. The present configuration therefore included only the components required to heat or cool drinking water and supply it to an individual poultry house.

The unit was designed for both cooling and heating operation. However, the experimental period occurred during summer. Therefore, only cooling performance was evaluated in the present study. Heating performance will be evaluated under cold-season operating conditions. A water-level-controlled preparation module was incorporated to assist with medicated or supplemented drinking-water preparation. The module was not designed to automatically meter or inject medications.

The preparation sequence began by setting the required water volume. A water-level sensor controlled filling until the target level was reached. The grower then manually added the selected medication, vitamin, or other supplement according to the prescribed dilution ratio. After product addition, the solution was mixed using the installed mixing or recirculation device and subsequently supplied to the drinking lines.

Medication type, dilution ratio, storage requirements, and allowable use period after preparation vary among products. Therefore, the system did not include multiple chemical reservoirs or automatic product-metering devices. Instead, the design focused on simplifying water-volume adjustment and mixing while maintaining a compact system configuration.

Cooling performance test

Cooling performance tests were conducted from July 28 to August 25, 2026. Source-water temperature was approximately 20°C. Heat-exchange tank setpoints were 10.0, 12.5, and 15.0°C.

The test temperature range was selected with reference to previous studies and practical poultry-water management information. Beker and Teeter (1994) evaluated cooled water at 10°C and also reported a body-temperature response after administration of 12.8°C water under heat stress. Practical poultry-management guidance identifies approximately 10–15°C as a comfortable drinking-water temperature range for mature birds (University of Kentucky, n.d.). Therefore, 10 and 15°C were selected as the lower and upper conditions, and 12.5°C was used as an intermediate setpoint.

The water-flow condition was selected with reference to reported commercial broiler-house demand. Czarick et al. (2020) estimated an average drinking-water flow of approximately 1.4 gal/min, equivalent to 5.3 L/min, for 20,000 broilers at 50 days of age consuming approximately 1,700 gal/day over a 20-h lighting period. Tabler et al. (2022) reported that a typical 500-ft broiler house requires approximately 2 gal/min, or 7.6 L/min, to meet basic drinking-water demand. The same source emphasized the importance of meeting peak demand when large birds are raised during hot weather.

These values were used as engineering references for selecting a commercial-house-relevant

operating condition rather than as a biological definition of optimum flow. The supply flow was set at 6.6–7.0 L/min. Actual flow was checked gravimetrically by weighing water discharged during a fixed time interval. Measurements made after implementation of the gravimetric procedure averaged approximately 6.3 kg/min.

The system was operated from 09:00 to 18:00 to evaluate 9 h of continuous operation during the daytime period of elevated outdoor temperature. Accumulated water flow, cooling energy, and electrical energy consumption were recorded at 1-h intervals. Cooling COP was calculated as accumulated cooling energy divided by electrical energy consumption over the same operating period.

Each test period consisted of three daily runs. The 12.5°C condition was evaluated during two separate three-day periods. Two daily records contained isolated missing or discontinuous cumulative meter readings. These values were reconciled using adjacent sequential readings before calculation of daily energy use.

Table 1 Operating conditions for the cooling performance test

Parameter	Test condition
Source-water temperature	Approximately 20°C
Heat-exchange tank setpoint	10.0, 12.5, and 15.0°C
Set supply flow	6.6–7.0 L/min
Gravimetrically verified flow	Approximately 6.3 kg/min
Daily operation	09:00–18:00 (9h)
Replication	Three daily runs per test period
Measurements	Water flow, cooling energy, electrical energy
Performance index	COP

Field experiment

Field validation was conducted on a commercial broiler farm in Iksan, Republic of Korea. On July 23, 2026, 21,000 broilers were placed in the cooled-water house and 21,000 in the comparison house.

The two houses had comparable facility configurations and were managed under the same farm management protocol. Temperature-controlled drinking water was the primary experimental difference between the houses.

The drinking-water setpoint in the cooled-water house was adjusted stepwise during the growing period. The initial setting was 18°C and was subsequently reduced to 17, 15, 14, and 13°C. Farm records were collected for water-meter readings, mortality, body weight.

Mortality was accumulated from placement through the day before shipment. Farm-recorded body weight was used to describe growth. The final comparison used the value recorded on August 23, one day before shipment.

The field trial consisted of one cooled-water house and one comparison house on a single commercial farm. The data were therefore treated as a technical house-to-house comparison.

Inferential statistical testing was not applied because independent house-level replication was not available.

Qualitative evaluation of the water preparation module

The field relevance of the preparation module was assessed qualitatively through interviews with broiler growers. Interview topics included conventional medication-water preparation, frequency of tank-level checks, methods used to determine water volume, expected changes in work procedures, and additional improvement needs.

RESULTS & DISCUSSION

Cooling performance

Table 2 summarizes cooling performance for the four test periods. Mean COP ranged from 1.96 to 2.60, and all daily tests completed the planned 9-h operating period.

Table 2 Representative cooling performance for each test period

Test condition	Runs (n)	Cooling energy (kWh)	Electrical energy (kWh)	COP
10.0°C	3	30.4	14.0	2.16
12.5°C (period 1)	3	28.5	14.6	1.96
15.0°C	3	23.9	9.9	2.43
12.5°C (period 2)	3	35.0	13.5	2.60

※cooling energy, electrical energy, and COP are mean values of the three daily runs within each test period.

COP did not vary monotonically with heat-exchange tank setpoint. In particular, the two 12.5°C test periods produced different mean values. This indicates that nominal tank setpoint alone did not explain the observed variation in energy performance. Differences among test dates and system operating conditions may also have contributed. Accordingly, COP was not interpreted as a direct function of setpoint.

The primary engineering objective was to determine whether the simplified system could sustain cooling operation under a water-flow condition relevant to a commercial broiler house. The selected flow condition was comparable in magnitude to reported commercial broiler-house water demand (Czarick et al., 2020; Tabler et al., 2022). The system completed the planned daytime operation under all temperature conditions.

Previous work combined drinking-water temperature control with whole-house air conditioning (Paek et al., 2016). In contrast, the present configuration excluded whole-house air-conditioning components and focused on the drinking-water function. Continuous operation under the tested conditions indicates that the core water-temperature-control function was retained after simplification.

Field performance

As summarized in Table 3, cumulative mortality was lower in the cooled-water house. The mortality count was approximately 32.9% lower than that of the comparison house. Recorded body weight one day before shipment was 80 g, or approximately 4.79%, greater in the cooled-water house.

Table 3 Major observations from commercial-farm field validation

Parameter	Cooled-water house	Comparison house	Difference
Initial placement (birds)	21,000	21,000	—
Cumulative mortality (birds)	744	1,108	−364
Mortality rate (%)	3.54	5.28	−1.73
Body weight one day before shipment (g)	1,750	1,670	+80

Lower cumulative mortality and a greater pre-shipment body weight were observed in the cooled-water house. The direction of these observations is consistent with previous studies in which cooled drinking water was associated with favorable broiler responses under high-temperature conditions (Beker and Teeter, 1994; Paek et al., 2017).

However, the present field validation used one cooled-water house and one comparison house on a single farm. House-level replication was not available. The production differences should therefore be interpreted as field observations associated with the two management conditions rather than as isolated causal effects of drinking-water temperature. Additional replicated field trials are required before a production benefit can be generalized.

Field applicability of the water preparation module

Farmer interviews indicated that water volume for medication or supplement preparation was commonly determined by visually checking tank-level markings. During filling, growers sometimes needed to return repeatedly to the tank to determine whether the desired level had been reached. Some interviewees reported checking tank level approximately five to seven times per day.

The level-controlled filling function could reduce the need for repeated manual water-volume adjustment while retaining grower control over product selection and dosage. Because medications and supplements differ in dilution ratios and handling requirements, the simplified design avoided additional storage and automatic chemical-metering hardware. Interview responses suggested that level-controlled filling could reduce repeated tank checks and simplify preparation work. However, work time and worker travel were not measured quantitatively. Future evaluations should measure preparation time, number of tank checks, and worker movement to quantify any labor-saving benefit.

CONCLUSIONS

A simplified drinking-water temperature control system was developed by excluding whole-house air-conditioning components from the previous integrated concept. The unit was designed for both cooling and heating, although only cooling performance was evaluated during the summer study period. Under the selected commercial-house-relevant flow condition, the system completed 9 h of continuous daytime operation, with mean COP values ranging from 1.96 to 2.60.

Commercial-farm validation showed mortality rates of 3.54% and 5.28% and pre-shipment body weights of 1,750 and 1,670 g in the cooled-water and comparison houses, respectively. Because the trial included only one house per condition, these differences should be

interpreted as field observations rather than independently replicated treatment effects.

The water-level-controlled preparation module also showed potential to simplify medication-water preparation without automatic chemical dosing. Future work should evaluate winter heating performance, repeat field validation across multiple houses and production cycles, and quantify the labor requirements associated with medication-water preparation.

ACKNOWLEDGEMENTS

This work was supported by the “Cooperative Research Program for Agricultural Science and Technology Development” (Project No. PJ01779903), Rural Development Administration, Republic of Korea, and the 2026 RDA Fellowship Program of the National Institute of Agricultural Sciences, Rural Development Administration, Republic of Korea.

REFERENCES

Beker, A., and R. G. Teeter. 1994. Drinking water temperature and potassium chloride supplementation effects on broiler body temperature and performance during heat stress. J. Applied Poultry Res. 3(1): 87-92. https://doi.org/10.1093/japr/3.1.87.

Czarick, M., C. Mou, and B. D. Fairchild. 2020. Drinker line flow rates. Poultry Housing Tips 32(5). Athens, Ga.: University of Georgia, College of Agricultural and Environmental Sciences.

Kaya, M., and E. Dereli Fidan. 2023. The effect of drinking water temperature and stocking density on broiler performance, meat quality and some behavioral traits at high ambient temperature. J. Hellenic Veterinary Medical Soc. 74(1): 5315-5324. https://doi.org/10.12681/jhvms.29349.

Liu, L., M. Ren, K. Ren, Y. Jin, and M. Yan. 2020. Heat stress impacts on broiler performance: A systematic review and meta-analysis. Poultry Sci. 99(11): 6205-6211. https://doi.org/10.1016/j.psj.2020.08.019.

Paek, Y., G. C. Kang, J. P. Moon, T. S. Lee, and J. K. Kwon. 2016. Optimum design of environmental improvement system for poultry buildings by air conditioning and drinking water using heat pump. Journal of the Korean Society of Mechanical and Aviation Technology 18(1): 141-147. https://doi.org/10.17958/ksmt.18.1.201602.141.

Paek, Y., S. W. Kang, J. K. Jang, and Y. H. Kim. 2017. Development of air-conditioning and drinking water supply system using air-water heat pump. In Proc. Korean Society for Agricultural Machinery Spring Conference, 22(1): 118.

Tabler, T., J. Wells, and W. Zhai. 2022. Water-related factors in broiler production. Publication 2742. Mississippi State, Miss.: Mississippi State University Extension Service.

University of Kentucky. n.d. Chapter 12: Water temperature. Lexington, Ky.: University of Kentucky, Department of Animal and Food Sciences. Accessed 7 September 2026.

SF-P04

Proceedings of The 12th International Symposium on Machinery and Mechatronics for Agriculture and Biosystems Engineering (ISMAB 2026)
20-24 October 2026, Busan, Republic of Korea

CFD-BASED AIRFLOW ANALYSIS AND OPTIMIZATION OF HVAC AND DUST COLLECTION SYSTEMS IN BROILER HOUSES

Sun-hyoung Lee[2], Rack-woo Kim[1*], Su-been Ahn[2], Seung-hun Lee[2], Chan-min Kim[2], Hee-woong Seok[2], han Kim[2], Yun-jeong Lee[2], Yoon-kyu Hur[1], Hyeon-Chae Kim[2]

[1] Department of Biosystems Engineering, College of Agriculture and Life Sciences, Seoul National University, Seoul 08826, Republic of Korea
[2] Research Institute of Agriculture and Life Sciences, Seoul National University, Seoul 08826, Republic of Korea

*Corresponding Author-- Rack-woo Kim Voice: +82-10-5448-7067, Email: rack88@snu.ac.kr

Abstract: The Korean broiler industry faces increasing challenges due to rising feed and energy costs, and poor indoor air quality. Particulate matter and NH_3 accumulation adversely affects the working environment and animal welfare, while inefficient environmental control increases energy consumption. This study aimed to analyze airflow in a mechanically ventilated broiler house using computational fluid dynamics (CFD) and establish a basis for optimizing dust collection and heating and cooling.
A commercial broiler farm in Namwon, Jeonbuk State, Republic of Korea, with a capacity of approximately 60,000 birds, was selected. CFD geometry was developed based on the actual facility, and field experiments were conducted at air inlet opening ratios of 33%, 67%, and 100% with different numbers of operating exhaust fans. Airflow rate and static pressure were analyzed using the orifice equation and fan performance characteristics to determine inlet discharge coefficients and derive an on-site fan performance curve.
The results showed that airflow characteristics varied with inlet opening ratios and exhaust fan operation. Inlet discharge characteristics and an on-site fan performance curve were obtained as facility-specific boundary conditions for CFD simulations. The developed CFD framework will be used to evaluate airflow distribution and optimize dust collector and heating and cooling system placement, contributing to improved indoor air quality and energy efficiency in broiler houses.

Key Words: Broiler house, Computational fluid dynamics (CFD), Dust collector, Heating and cooling system, Energy efficiency

ACKNOWLEDGEMENTS

“This work was supported by Korea Institute of Planning and Evaluation for Technology in Food, Agriculture and Forestry(IPET) and Korea Smart Farm R&D Foundation(KosFarm) through Smart Farm Innovation Technology Development Program, funded by Ministry of Agriculture, Food and Rural Affairs(MAFRA) and Ministry of Science and ICT(MSIT), Rural Development Administration(RDA)(RS-2025-02216818)”

SF-P05

Proceedings of The 12th International Symposium on Machinery and Mechatronics for Agriculture and Biosystems Engineering (ISMAB 2026)
20-24 October 2026, Busan, Republic of Korea

PREDICTION OF METHANE EMISSIONS IN SWINE HOUSING BY MACHINE LEARNING APPLIED TO CONTINUOUS SENSOR DATA

Su-Been Ahn[2], Rack-Woo Kim[1*], Hang-Ju Cho[1], Yoo-Kyoung Seo[1], Da-Yeon Song [1]

[1] Department of Biosystems Engineering, College of Agriculture and Life Sciences, Seoul National University, Seoul 08826, Republic of Korea
[2] Research Institute of Agriculture and Life Sciences, Seoul National University, Seoul 08826, Republic of Korea

*Corresponding Author-- Rack-woo Kim Voice: +82-10-5448-7067, Email: rack88@snu.ac.kr

Abstract: Methane is recognised as a principal air pollutant emitted from swine housing facilities, yet its temporal variability and the factors governing its emission remain inadequately quantified under commercial production conditions. The present study characterised CH_4 concentrations by means of continuous sensor-based monitoring and identified the most influential environmental and management variables through the application of machine-learning models. Data integrity was ensured by outlier detection employing a Hampel filter, whilst missing observations were addressed through a hybrid imputation procedure. Three predictive models—Random Forest, LightGBM, and histogram-based gradient boosting (HistGB)—were subsequently developed and comparatively evaluated, of which HistGB afforded the best predictive performance (R^2 = 0.83) together with the lowest RMSE. Model interpretation indicated that feed intake, slurry pH, and temperature constituted the principal determinants of CH_4 emission, whereas ventilation rate and relative humidity predominantly explained the observed variability in ammonia (NH_3). These findings demonstrate that rigorous preprocessing combined with gradient-boosting approaches enables reliable characterisation of gas concentration dynamics and prioritisation of controllable determinants, thereby supporting improved gas mitigation and management strategies in intensive pig production systems.

Key Words: Smart Farming, AI, Precision livestock farming to address new global challenges Manure management, from the barn to the field Smart barns, controlled-environment livestock facilities

ACKNOWLEDGEMENTS

“This work was supported by Korea Institute of Planning and Evaluation for Technology in Food, Agriculture and Forestry(IPET) and Korea Smart Farm R&D Foundation(KosFarm) through Smart Farm Innovation Technology Development Program, funded by Ministry of Agriculture, Food and Rural Affairs(MAFRA) and Ministry of Science and ICT(MSIT), Rural Development Administration(RDA)(RS-2024-00399033)”

SF-P06

Proceedings of The 12th International Symposium on Machinery and Mechatronics for Agriculture and Biosystems Engineering (ISMAB 2026)
20-24 October 2026, Busan, Republic of Korea

INTERNATIONAL STANDARDIZATION TRENDS FOR DATA INTEROPERABILITY IN AGRICULTURAL ELECTRONICS AND DATA-DRIVEN AGRIFOOD SYSTEMS

Hyuk Ki[1*], Hyunseok Lee[1], Sanghyuk Lee[1], Jihyeong Kim[1]

[1]Korea Agriculture Technology Promotion Agency, Iksan, Republic of Korea
*Corresponding Author-- Voice: +82-10-8564-8597, Email: hyukkki@koat.or.kr

Abstract: The digital transformation of agriculture has increased the generation and exchange of data among agricultural machinery, sensors, and farm management systems. As these systems become increasingly connected, interoperability has become an important issue for the effective utilization of agricultural data across production, operation, and management processes. International standardization therefore plays an important role in enabling consistent communication, interpretation, and exchange of data among heterogeneous agricultural systems.
This study examines international standardization activities related to agricultural machinery and data-driven smart farming, focusing on ISO/TC 23/SC 19, Agricultural electronics, and ISO/TC 347, Data-driven agrifood systems. The scopes, major standards, and standardization activities of the two committees were reviewed and compared from the perspective of data interoperability. ISO/TC 23/SC 19 mainly addresses electronic systems, communication, control, and data exchange associated with agricultural machinery. Its major standards include the ISO 11783 series, which provides a standardized framework for communication and data exchange between tractors, implements, electronic control units, and farm management systems. In comparison, ISO/TC 347 addresses broader data interoperability across agrifood systems, including semantic interoperability, data models, terminology, and data exchange among heterogeneous agricultural systems.
The review indicates that the two standardization areas address different but complementary levels of agricultural data interoperability. Standards developed within ISO/TC 23/SC 19 provide a technical basis for machinery-level communication and operational data exchange, while activities within ISO/TC 347 support broader system-level interoperability by promoting consistent interpretation and reuse of agricultural data. This relationship suggests that effective smart farming environments require not only standardized communication between machines and devices, but also common approaches for structuring and understanding data across systems.
These findings indicate that considering both agricultural machinery communication standards and broader agrifood data standards can contribute to more consistent and scalable data exchange. Coordinated standardization approaches across these areas will be important for supporting interoperable smart farming systems and improving the utilization of agricultural data.

Key Words: ISO/TC 23/SC 19, ISO/TC 347, Agricultural machinery, Smart farming, Data interoperability

SF-P07

Proceedings of The 12th International Symposium on Machinery and Mechatronics for Agriculture and Biosystems Engineering (ISMAB 2026)
20-24 October 2026, Busan, Republic of Korea

IMPACT OF INITIAL MOISTURE ON FUEL QUALITY AND ENERGY RECOVERY DURING TORREFACTION

Sunyong Park*

Department of Biosystems Engineering, Kangwon National University, Hyoja 2 Dong 192-1, Chuncheon-si, Republic of Korea
*Corresponding Author-- Email: psy0712@kangwon.ac.kr

Abstract: Initial moisture can affect both the energy demand and reaction behaviour of woody-biomass torrefaction. Quercus mongolica was torrefied at 260 °C for 30 min under nitrogen with initial moisture contents of 0, 15, 25, and 35% (wet basis). Product yields, solid fuel properties, and representative liquid and gas compositions were evaluated. Solid yield decreased from 83.74 to 59.18% as moisture increased, while liquid yield increased from 9.80 to 36.31%. The dry condition gave the strongest carbon enrichment and the highest energy recovery. However, solid HHV at 15 and 25% moisture was not significantly different, indicating that moderate initial moisture can retain comparable fuel-energy density without complete predrying. Liquid products became richer in furans and syringyl-type phenolics, whereas the gas phase was dominated by CO_2. Overall, 15-25% initial moisture provided the most practical compromise between fuel performance and drying burden.

Key Words: Initial moisture content, hardwood biomass, torrefaction, energy yield, product distribution

INTRODUCTION

Torrefaction is a mild thermochemical treatment, generally conducted at 200-300 °C, that improves biomass fuel quality through partial devolatilisation, deoxygenation, and carbon enrichment. Most experimental studies use oven-dried feedstock for repeatability, although industrial wood chips normally contain substantial moisture and complete predrying requires additional energy. Water may also influence heat transfer, dehydration, decarboxylation, hydrolysis, and condensable-product formation; therefore, initial moisture should be treated as a process variable rather than only as a preprocessing burden (Bach and Skreiberg, 2016; Chen et al., 2021).

This study examined how initial moisture content affects product distribution, solid-fuel quality, and energy recovery during torrefaction of Quercus mongolica. The main objective was to identify whether a moderate moisture range could retain useful fuel properties while reducing the need for deep drying.

MATERIALS AND METHODS

Mongolian oak chips were sieved to 10-25 mm, oven-dried, and reconditioned with distilled water to 15, 25, and 35% moisture on a wet basis; the dry material was used as the 0% condition. Samples were equilibrated for more than 12 h and verified by oven drying. Approximately 400 g was treated in a 5 L tubular reactor at 260 °C for 30 min under continuous nitrogen flow of 1 L/min. Condensable vapours were recovered at -10 °C and non-condensable gas was collected separately.

Mass yield (MY) was calculated from torrefied and initial sample mass. Elemental composition, proximate composition, higher heating value (HHV), and combustion-related indices were determined for the solid products. Energy yield (EY) was calculated as EY = (HHV_T/HHV_R) × MY, where R and T denote raw and torrefied biomass. Liquid and gas products were analysed chromatographically, and HHV differences among moisture conditions were statistically compared using Duncan's multiple range test.

RESULTS & DISCUSSION

Initial moisture strongly changed the distribution of products (Table 1). Solid yield declined continuously from 83.74% at 0% moisture to 59.18% at 35%, while liquid yield increased from 9.80 to 36.31%. Gas yield varied much less, remaining near 4.5-6.5%. The response indicates that increasing moisture mainly shifted biomass-derived material toward condensable products rather than permanent gas formation.

Table 1 Product distribution at different initial moisture contents.

Initial moisture (%)	Solid yield (%)	Liquid yield (%)	Gas yield (%)
0	83.74	9.80	6.46
15	76.84	17.55	5.61
25	69.07	26.43	4.50*
35	59.18	36.31	4.51*

**Calculated by difference from reported solid and liquid yields; minor discrepancies may arise from rounding.*

The dry condition produced the greatest solid-fuel upgrading. Carbon reached 57.14% and oxygen decreased to 36.58%, whereas the moisture-conditioned samples contained 49.66-50.91% C and 42.54-43.74% O. Volatile matter increased and fixed carbon decreased as initial moisture increased, showing that water moderated extensive devolatilisation and carbon concentration. Raw biomass HHV was 19.25 MJ/kg, and torrefaction increased HHV to 20.62-21.27 MJ/kg. The dry condition gave the highest value and an energy yield of 92.56%, but the 15 and 25% conditions were not significantly different in HHV. Thus, the main energetic penalty of moderate moisture arose from reduced solid retention rather than a large decrease in fuel-energy density.

Moisture also altered the by-products. Furfural increased from 13.97% of identified oxygenated liquid compounds under dry conditions to 44.15, 34.27, and 45.09% at 15, 25, and 35% moisture, respectively, while syringyl-type phenolics were prominent at high moisture. The non-condensable gas contained 88.19-92.11% CO2; CO decreased from 11.65% at 0% moisture to 7.38% at 35%, and gas HHV declined accordingly. These results show a shift from carbon-enrichment-oriented solid production toward greater condensable formation as initial water increased.

CONCLUSIONS

Initial moisture was a governing parameter in *Quercus mongolica* torrefaction. Oven-dry feedstock maximised carbon enrichment, HHV, solid retention, and energy recovery, whereas increasing moisture promoted condensable-product formation and reduced solid yield. Nevertheless, 15-25% moisture maintained similar solid HHV and therefore represents a practical operating window when the energy cost of complete predrying is considered. A 35% moisture level caused a clear deterioration in solid-fuel and energy-recovery performance.

REFERENCES

Bach, Q. V., and O. Skreiberg. 2016. Upgrading biomass fuels via wet torrefaction: A review and comparison with dry torrefaction. Renewable and Sustainable Energy Reviews 54: 665-677.

Chen, D., A. Gao, Z. Ma, D. Fei, Y. Chang, and C. Shen. 2018. In-depth study of rice husk torrefaction: Characterization of solid, liquid and gaseous products, oxygen migration and energy yield. Bioresource Technology 253: 148-153.

Chen, W. H., B. J. Lin, Y. Y. Lin, Y. S. Chu, A. T. Ubando, P. L. Show, H. C. Ong, et al. 2021. Progress in biomass torrefaction: Principles, applications and challenges. Progress in Energy and Combustion Science 82: 100887.

Park, S., S. J. Kim, K. C. Oh, S. Y. Kim, H. E. Kim, and D. H. Kim. 2025. Predictive modelling of lignocellulosic biomass fuel changes during torrefaction via mass reduction. Journal of the Energy Institute 118: 101910.

SF-P08

Proceedings of The 12th International Symposium on Machinery and Mechatronics for Agriculture and Biosystems Engineering (ISMAB 2026)
20-24 October 2026, Busan, Republic of Korea

DEVELOPMENT OF A TRACKED GREENHOUSE MOBILE MAPPING SYSTEM USING 3D LIDAR AND 2D SLAM

Ping-Chun Chen*, Fu-Kai Chang, Li-Yun Wen, Wu-Yang Shih, and Yao-Chuan Tsai

Department of Bio-Industrial Mechatronics Engineering, National Chung Hsing University
*Corresponding Author-- Voice: +886908057588, Email: justinchen0808@gmail.com

Abstract: With the rapid advancement of smart agriculture technologies, autonomous mobile vehicles have been increasingly applied to greenhouse transportation, inspection, and automated operations to reduce labor requirements and improve operational efficiency. However, autonomous navigation in greenhouse environments remains challenging due to narrow aisles, numerous obstacles, and limited or obstructed Global Navigation Satellite System (GNSS) signals. In this study, a tracked greenhouse transport vehicle was employed as the mobile platform to develop a mobile robotic system integrating three-dimensional (3D) LiDAR with two-dimensional (2D) simultaneous localization and mapping (SLAM).

The proposed system integrates 3D LiDAR sensing with a 2D SLAM architecture for environmental perception, mapping, pose estimation, and vehicle control. The 3D point cloud data acquired by the LiDAR are processed through height filtering and horizontal projection and then converted into 2D LaserScan data for Hector SLAM. This approach enables the system to utilize the environmental sensing capability of 3D LiDAR while maintaining the computational efficiency of 2D SLAM on the Jetson Nano platform. The system also integrates an Arduino-based chassis controller to enable forward, backward, and turning motions of the tracked vehicle.

Experimental evaluation included Hector SLAM parameter tuning and vehicle-based mapping tests. The results showed that a translational update threshold of 0.05 m and an angular update threshold of 0.02 rad provided relatively stable mapping performance on the current computing platform. During mobile mapping experiments, normal vibration generated by the tracked vehicle did not cause significant map distortion or obvious instability in pose estimation. The developed platform integrates environmental sensing, point cloud processing, localization and mapping, and chassis control, providing a basis for subsequent autonomous navigation development. Future work will focus on integrating the ROS Navigation framework, visual recognition, robotic manipulators, and autonomous task decision-making functions for greenhouse inspection, automated transportation, and other smart agricultural applications.

Key Words: ROS, 3D LiDAR, Hector SLAM, mobile mapping, greenhouse robot

INTRODUCTION

Smart agriculture has increasingly incorporated autonomous mobile vehicles to reduce labor requirements in agricultural operations. Compared with outdoor farmlands, greenhouse environments are characterized by narrow aisles, dense obstacles, and limited Global Navigation Satellite System (GNSS) signal availability, which pose challenges to autonomous localization and navigation. In recent years, LiDAR and simultaneous localization and mapping (SLAM) technologies have been widely applied to localization, mapping, and autonomous navigation of agricultural and greenhouse mobile robots [1–3]. Among these approaches, Hector SLAM performs scan matching and map construction using laser scan data [4].

Therefore, this study employs a tracked greenhouse transport vehicle as the mobile platform and integrates a 3D LiDAR sensor, Jetson Nano, Robot Operating System (ROS), Hector SLAM, and an Arduino-based chassis control system. The acquired 3D point cloud data are converted into 2D LaserScan data for localization and mapping. Hector SLAM parameter tuning and vehicle-based mapping experiments are conducted in an actual greenhouse environment to evaluate mapping performance and motion stability, providing a basis for subsequent autonomous navigation development.

MATERIALS AND METHODS

2.1 Overall System Architecture

In this study, a tracked greenhouse transport vehicle was used as the mobile platform. As shown in Fig. 1, the system mainly consists of an LS-C16 3D LiDAR sensor, a Jetson Nano, an Arduino microcontroller, motor drivers, and left and right DC motors. The Jetson Nano operates in a Robot Operating System (ROS) environment and is responsible for LiDAR data acquisition, point cloud processing, and Hector SLAM computation.

For chassis control, the Arduino serves as the main controller and receives keyboard control commands from the ROS system. The motor drivers regulate the rotational speed and direction of the motors on both sides, enabling the tracked vehicle to perform forward motion, backward motion, and turning maneuvers. The developed architecture integrates environmental sensing, SLAM computation, and chassis control, providing the hardware and software foundation for subsequent mapping, localization, and autonomous navigation development. The prototype of the developed tracked mobile vehicle is shown in Fig. 2.

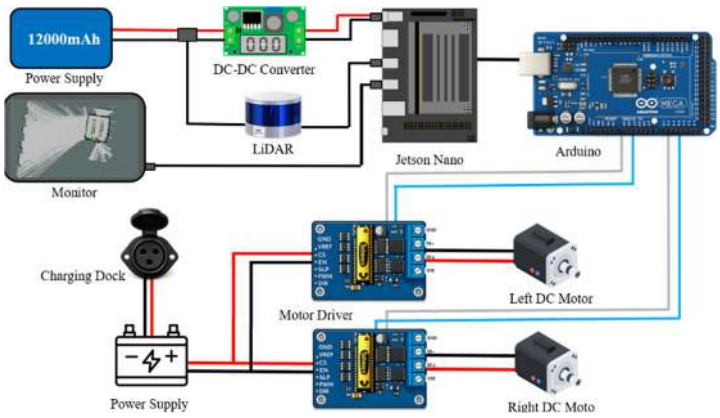

Fig. 1. System architecture of the tracked greenhouse mobile vehicle.



Fig. 2. Prototype of the tracked mobile vehicle.

The experimental evaluation was divided into two parts: SLAM parameter tuning and vehicle-based mapping tests. In the first part, different translational and angular update thresholds were compared to evaluate their effects on map quality and computational performance. In the second part, the LiDAR sensor was mounted on the tracked vehicle to investigate whether vibration generated during vehicle motion caused significant map distortion or instability in pose estimation.

2.2 Point Cloud Processing and SLAM

The 3D point cloud acquired by the LS-C16 LiDAR was processed using the ROS pointcloud_to_laserscan node. Height filtering and horizontal projection were applied to extract point cloud data within a specified vertical range, and the nearest point within each angular interval was retained. The processed point cloud was then converted into 2D LaserScan data and provided as input to Hector SLAM [4]. Hector SLAM estimates the vehicle pose through scan matching and constructs a 2D occupancy grid map of the surrounding environment.

3.1 Hector SLAM Parameter Tuning Results

As shown in Fig. 3, reducing the translational update threshold from 0.40 m to 0.05 m resulted in more continuous map updates and improved mapping consistency. For the angular update threshold, as shown in Fig. 4, a threshold of 0.10 rad resulted in a relatively low update frequency during turning. Reducing the threshold to 0.01 rad increased the update frequency but also imposed a higher computational load on the Jetson Nano. Considering both mapping stability and computational performance, a translational update threshold of 0.05 m and an angular update threshold of 0.02 rad were selected for subsequent vehicle-based mapping experiments.

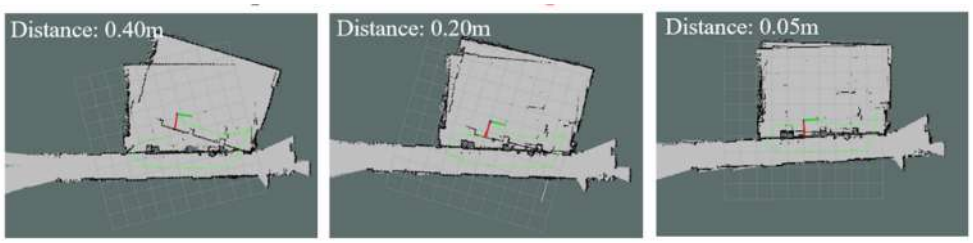

Fig. 3. Effect of translational update threshold on map quality.

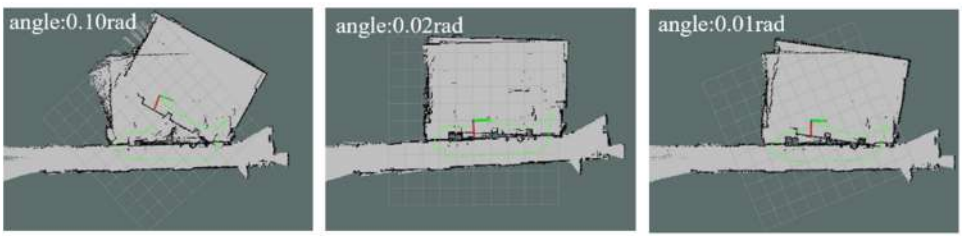

Fig. 4. Effect of angular update threshold on map quality.

3.2 Vehicle-Based Mapping Results

After the LiDAR sensor was mounted on the tracked vehicle, environmental maps could be

continuously generated while the vehicle moved through greenhouse aisles. During the experiments, no significant map distortion or obvious instability in pose estimation caused by normal vehicle vibration was observed. These results indicate that the current LiDAR mounting configuration and point cloud processing procedure are capable of supporting mobile mapping on the tracked platform. However, the current evaluation is primarily based on qualitative observations of map consistency. In future work, external measurement references will be introduced to quantitatively evaluate mapping and localization errors.

CONCLUSIONS

In this study, a tracked greenhouse transport vehicle was used as the mobile platform, and 3D point cloud data acquired by the LS-C16 LiDAR were converted into 2D LaserScan data using the ROS pointcloud_to_laserscan node for Hector SLAM. The parameter evaluation showed that a translational update threshold of 0.05 m and an angular update threshold of 0.02 rad provided relatively stable mapping performance while maintaining an acceptable computational load on the Jetson Nano. During vehicle-based mapping experiments, normal vibration generated by the tracked vehicle did not result in significant map distortion or obvious instability in pose estimation.

The developed system currently integrates environmental sensing, point cloud processing, localization and mapping, and chassis control, thereby establishing a mobile robotic platform for subsequent autonomous navigation development. Future work will integrate the ROS Navigation framework and quantitatively evaluate system performance using navigation success rate, goal-reaching error, navigation time, path length, and obstacle avoidance success rate. Visual recognition, robotic manipulators, and autonomous task decision-making functions will also be incorporated to further develop the platform for greenhouse transportation, inspection, and other smart agricultural applications.

ACKNOWLEDGEMENTS

This section should be placed at the end of the paper before the REFERENCES section. This section includes acknowledgments of financial, institutional and personal support. These are optional.

REFERENCES

K. Liu, J. Yu, Z. Huang, L. Liu, and Y. Shi, “Autonomous navigation system for greenhouse tomato picking robots based on laser SLAM,” *Alexandria Engineering Journal*, vol. 100, pp. 208–219, 2024.

S. Jiang, S. Wang, Z. Yi, M. Zhang, and X. Lv, “Autonomous navigation system of greenhouse mobile robot based on 3D LiDAR and 2D LiDAR SLAM,” *Frontiers in Plant Science*, vol. 13, Art. no. 815218, 2022.

F. B. P. Malavazi, R. Guyonneau, J.-B. Fasquel, S. Lagrange, and F. Mercier, “LiDAR-only based navigation algorithm for an autonomous agricultural robot,” *Computers and Electronics in Agriculture*, vol. 154, pp. 71–79, 2018.

S. Kohlbrecher, O. von Stryk, J. Meyer, and U. Klingauf, “A flexible and scalable SLAM system with full 3D motion estimation,” in *Proc. 2011 IEEE Int. Symp. Safety, Security, and Rescue Robotics (SSRR)*, pp. 155–160, 2011.

SF-P09

Proceedings of The 12th International Symposium on Machinery and Mechatronics for Agriculture and Biosystems Engineering (ISMAB 2026)
20-24 October 2026, Busan, Republic of Korea

RESISTIVE AMMONIA SENSOR BASED ON POLYPYRROLE, ZINC OXIDE, AND REDUCED GRAPHENE OXIDE COMPOSITES

Chih-Chieh Liu* and **Yao-Chuan Tsai**

Department of Bio-Industrial Mechatronics Engineering, National Chung Hsing University, Taiwan
Voice: +886 936057325, Email: nelson20050325@gmail.com

Abstract: Ammonia is a common hazardous gas in livestock farms, greenhouses, and industrial environments. Long-term exposure may adversely affect human health, crop growth, and animal health; therefore, the development of a room-temperature, low-power, and selective ammonia sensor is important. In this study, polypyrrole (PPy), zinc oxide (ZnO), and reduced graphene oxide (rGO) were used to prepare a composite material, which was drop-coated onto the surface of an interdigitated electrode to fabricate a resistive ammonia sensor. PPy provides protonation and deprotonation reactions, ZnO enhances gas adsorption and heterojunction effects, and rGO serves as an electron transport pathway. The results showed that PPy/ZnO/rGO exhibited a response of approximately 17.3% to 50 ppm ammonia at 25 °C, with response and recovery times of approximately 240 s and 330 s, respectively. Over the range of 6–120 ppm, the response increased with ammonia concentration, with a coefficient of determination of 0.97. Three repeated tests at an ammonia concentration of 50 ppm yielded a relative standard deviation of 0.92%. In the selectivity test at 100 ppm, the response to ammonia was approximately 20.78%, which was substantially higher than those to acetone, ethanol, and isopropanol. The PPy/ZnO material was also evaluated for comparison, showing an average response of approximately 42.72% at 50 ppm ammonia. After the incorporation of rGO, a conductive transport network was formed, resulting in a lower response magnitude but substantially shorter response and recovery times. This study demonstrates that PPy/ZnO/rGO enables room-temperature detection with good linearity, repeatability, and selectivity, and can be applied to low-power agricultural environmental monitoring.

Key Words: ammonia sensor, polypyrrole, zinc oxide, reduced graphene oxide, interdigitated electrode

INTRODUCTION

Ammonia (NH) is an irritating and toxic volatile gas commonly found in livestock production, greenhouse cultivation, and industrial processes. Exposure to high NH concentrations may adversely affect human health and crop growth; therefore, ammonia concentration monitoring is important. Although conventional metal-oxide semiconductor sensors offer high sensitivity, they generally require operating temperatures of approximately 200–400 °C, increasing power consumption and system complexity. Polypyrrole (PPy) can react with NH at room temperature (Joulazadeh and Navarchian, 2015). Zinc oxide (ZnO) can provide gas adsorption sites and form a p–n heterojunction, whereas reduced graphene oxide (rGO) possesses good electrical conductivity and can improve charge transport.

Therefore, this study developed a room-temperature resistive ammonia sensor based on PPy/ZnO/rGO and evaluated its concentration response, repeatability, and selectivity.

MATERIALS AND METHODS

Polypyrrole (PPy), zinc oxide (ZnO), and reduced graphene oxide (rGO) were used as the sensing materials. The protonation/deprotonation characteristics of PPy toward NH , the surface reactivity and p–n heterojunction of ZnO, and the electrical conductivity of rGO were utilized to develop a room-temperature ammonia sensor.

The PPy/ZnO/rGO composite was prepared by chemical oxidative polymerization. ZnO or ZnO/rGO was added to a 0.6 M FeCl ·6H O aqueous solution and allowed to stand for 30 min, followed by the addition of pyrrole monomer and stirring for 3 h. The reaction product was collected by vacuum filtration, washed with distilled water and ethanol, and dried at 60 °C. The resulting material was then dispersed to form a suspension, coated onto the surface of an interdigitated electrode, and characterized by scanning electron microscopy (SEM) to observe its surface morphology.

Gas-sensing experiments were conducted at room temperature using resistance variation as the sensing signal. Tests included ammonia concentrations ranging from 6 to 120 ppm, a repeatability test at 50 ppm, and selectivity tests using 100 ppm ammonia, acetone, ethanol, and isopropanol.

RESULTS & DISCUSSION

The SEM images in Fig. 1 show that the sensing film covered the copper electrode and interdigitated region. At magnifications of 1,000× and 5,000×, the composite surface structure formed by the PPy matrix, ZnO particles, and rGO sheets could be identified, indicating that the composite material was successfully deposited on the sensing electrode.

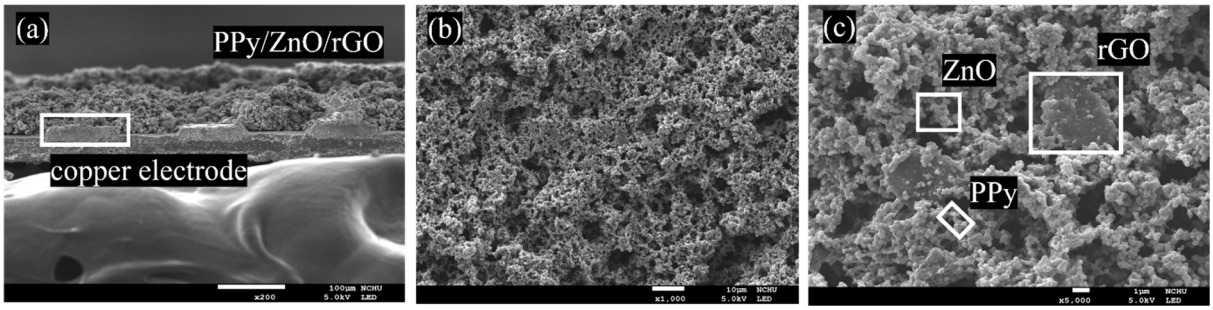

Fig. 1. SEM images of the PPy/ZnO/rGO composite: (a) cross-section view, (b) surface morphology at 1,000× magnification, and (c) surface morphology at 5,000× magnification.

As shown in Fig. 2, the PPy/ZnO/rGO sensor exhibited distinct and reversible resistance changes at different NH concentrations, indicating good gas adsorption and desorption capability. As the NH concentration increased from low to high, the sensing response gradually increased, and a good linear relationship was observed between concentration and response (R^2 = 0.9675), demonstrating its potential for quantitative concentration analysis. In the repeatability test, the resistance-change trends and amplitudes were similar among repeated measurements, confirming good reproducibility and stability. In addition, the gas selectivity test showed that the response to NH was substantially higher than those to acetone, ethanol, and isopropanol, confirming the good selectivity of the PPy/ZnO/rGO composite toward ammonia and its potential for room-temperature ammonia monitoring.

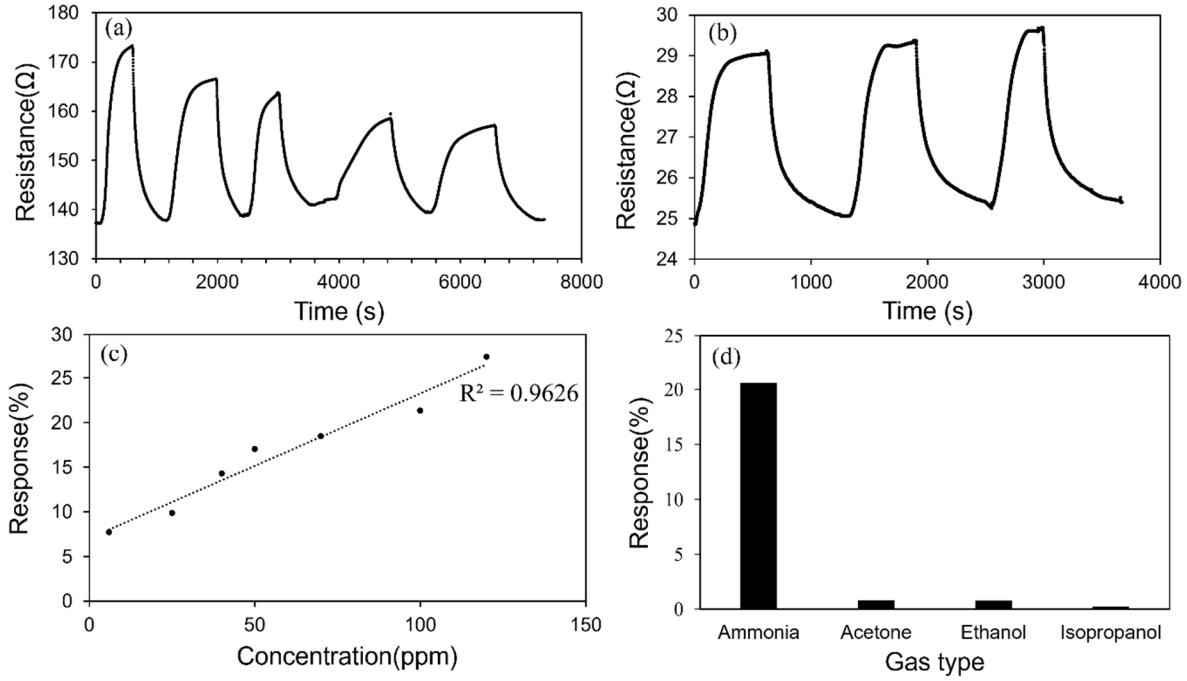

Fig. 2 Sensing performance of the PPy/ZnO/rGO sensor: (a) response at different ammonia concentrations (b) repeatability (c) concentration-response relationship (d) gas selectivity test.

CONCLUSIONS

In this study, a PPy/ZnO/rGO composite was successfully prepared and integrated with an interdigitated electrode to establish a room-temperature ammonia sensor. The experimental results showed that the sensing response increased with NH concentration and exhibited good linearity and repeatability. The selectivity test showed that the response to NH was substantially higher than those to acetone, ethanol, and isopropanol. SEM observations also showed that the material had a rough and porous structure, which is favorable for gas adsorption and diffusion. Overall, the results demonstrate that this composite has potential for room-temperature, low-power, and selective ammonia sensing and may be applied to agricultural environmental monitoring and industrial safety monitoring.

REFERENCES

Joulazadeh, M., and A. H. Navarchian. 2015. Ammonia detection of one-dimensional nano-structured polypyrrole/metal oxide nanocomposites sensors. Synthetic Metals 210: 404–411.

Tai, H., Z. Yuan, W. Zheng, Z. Ye, C. Liu, and X. Du. 2016. ZnO nanoparticles/reduced graphene oxide bilayer thin films for improved NH_3-sensing performances at room temperature. Nanoscale Research Letters 11: 130.

Sun, J., X. Shu, Y. Tian, Z. Tong, S. Bai, R. Luo, D. Li, and C. C. Liu. 2017. Facile preparation of polypyrrole-reduced graphene oxide hybrid for enhancing NH_3 sensing at room temperature. Sensors and Actuators B: Chemical 241: 658–664.

Qin, Y., B. Zhang, and Z. Zhang. 2019. Combination of PPy with three-dimensional rGO to construct bioinspired nanocomposite for NH_3-sensing enhancement. Organic Electronics 70: 240–245.

SF-P10

Proceedings of The 12th International Symposium on Machinery and Mechatronics for Agriculture and Biosystems Engineering (ISMAB 2026)
20-24 October 2026, Busan, Republic of Korea

RELATIONSHIP BETWEEN MUSHROOM FRUITING INITIATION RATE AND ENVIRONMENTAL FACTORS USING IMAGE RECOGNITION AND DATA ANALYSIS

Chien-Ying Lee[1*], Yu-Jen Shih[1], Wu-Yang Sean[1], Chi-Wei Liu[2], Yao-Chuan Tsai[1]

[1] Dept. of Bio-Industrial Mechatronics Engineering, National Chung Hsing University, Taiwan
[2]Senmu Farm, Xinshe District, Taichung, Taiwan
*Corresponding Author: Email: mcjh60417@gmail.com

Abstract: Fruiting initiation in mushroom cultivation is strongly affected by environmental conditions, yet field assessment and environmental regulation still rely largely on manual inspection and grower experience. This study developed an integrated workflow combining image recognition, environmental sensing, spatial interpolation, machine learning, and explainable artificial intelligence (XAI) to analyze the relationship between shiitake fruiting initiation rate and environmental factors. Experiments were conducted at Senmu Farm in Xinshe District, Taichung, Taiwan. Fisheye cameras and environmental sensors were used to collect cultivation images and temperature and relative humidity data. After fisheye-image correction and cropping, a YOLO model was used to detect shiitake mushrooms and substrate bags for automated calculation of fruiting initiation rate. Environmental conditions at camera locations were estimated using inverse distance weighting (IDW) with actuator-delay correction. After data augmentation, the detection model achieved Precision, Recall, and mAP50-95 values of 0.973, 0.968, and 0.842, respectively. Among the evaluated machine-learning models, Random Forest achieved the best predictive performance, with an RMSE of 0.167 and an R^2 of 0.64. XAI analysis identified the three-day average temperature as the most influential feature, followed by the difference between the three-day average temperature and the current-day temperature. These results indicate that fruiting initiation is associated not only with accumulated temperature conditions over preceding days but also with subsequent decreases in temperature. The proposed workflow provides a quantitative basis for subsequent cultivation-environment regulation and improvement of fruiting efficiency.

Key Words: image recognition, smart agriculture, machine learning, data analysis

INTRODUCTION

In recent years, extreme weather events have become increasingly frequent, and environmental factors such as temperature, relative humidity, and light intensity have substantial effects on mushroom fruiting initiation and growth. Although environmental sensing and control systems are increasingly being introduced into mushroom cultivation, fruiting assessment and environmental regulation still largely depend on manual observation and cultivation experience. Automated image analysis and data-driven modeling can provide more objective information for cultivation management; YOLO-based detection and counting have also been evaluated in complex agricultural environments,while explainable machine-learning methods can improve interpretation of agricultural dat.

Therefore, the objective of this study was to integrate image-based fruiting assessment, environmental sensing, spatial interpolation, machine learning, and XAI to quantify the relationship between shiitake fruiting initiation rate and environmental factors, with the aim of identifying environmental variables that can support improved cultivation management and fruiting efficiency.

MATERIALS AND METHODS

This study was conducted at Senmu Farm in Xinshe District, Taichung, Taiwan. Environmental sensors and fisheye cameras were installed in a multi-tier cultivation facility, as shown in Fig. 1, to synchronously collect temperature, relative humidity, and shiitake images. After fisheye-image correction, YOLO was used to detect shiitake mushrooms and substrate bags and to calculate the fruiting initiation rate. Inverse distance weighting (IDW) spatial interpolation was then applied to estimate temperature and relative humidity at each camera location, together with actuator-delay correction. Finally, machine-learning models and XAI were used to analyze the relationship between environmental factors and shiitake fruiting initiation rate

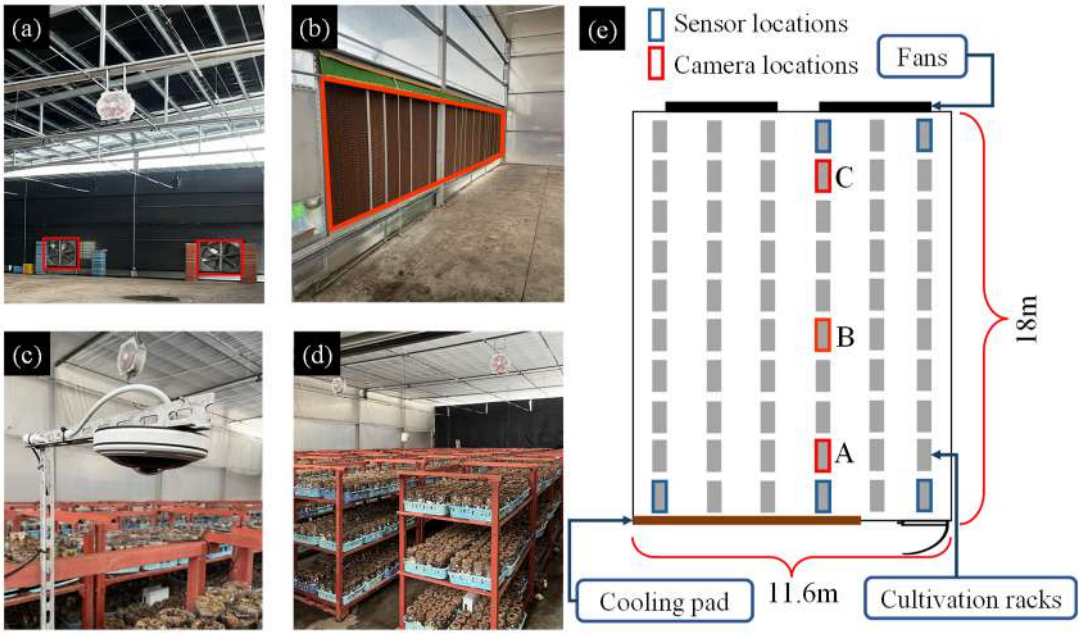

Fig. 1 Experimental site layout: (a) negative-pressure fans; (b) cooling pad; (c) fisheye camera; (d) multi-tier cultivation racks; (e) top view of equipment layout.

RESULTS & DISCUSSION

After image correction and data augmentation, the YOLO model achieved overall precision and recall values of 0.973 and 0.968, respectively, while mAP50-95 reached 0.842. These results indicate that the model can reliably detect shiitake mushrooms and substrate bags for automated calculation of fruiting initiation rate. Environmental information for each cultivation location was established using IDW spatial interpolation and actuator-delay correction and was then aligned with the fruiting data. As shown in Fig. 2, Random Forest achieved the best predictive performance among the evaluated machine-learning models, with an RMSE of 0.167 and an R^2 of 0.64, indicating a nonlinear relationship between environmental factors and fruiting initiation rate.

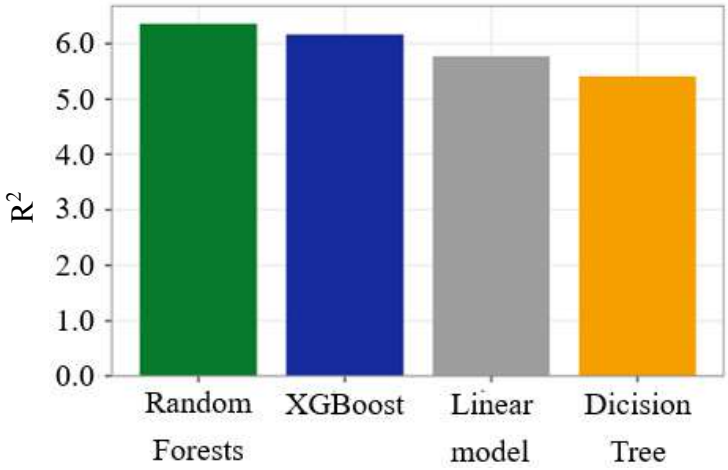

Fig. 2 Comparison of predictive performance among machine-learning models.

As shown in Fig. 3, the XAI analysis indicated that the three-day average temperature was the most influential feature, followed by the temperature decrease, defined as the difference between the three-day average and current-day temperatures. This suggests that shiitake fruiting initiation is associated with both preceding temperature conditions and a subsequent temperature decrease. The XAI results provide an interpretable basis for examining environmental effects beyond predictive performance alone, consistent with explainable methods in agricultural data analysis.

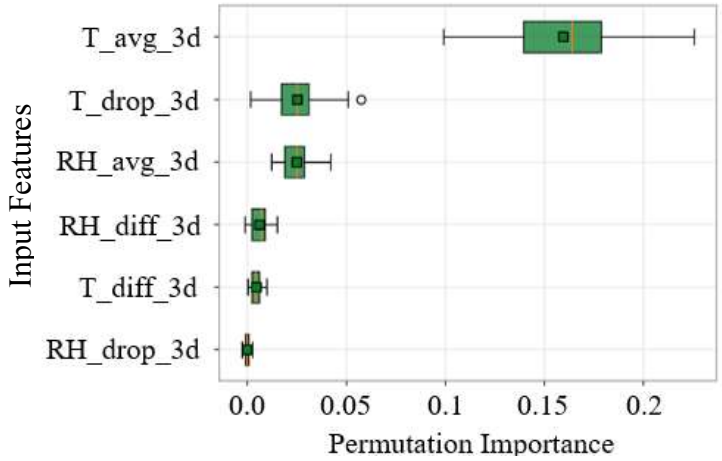

Fig. 3 Permutation importance of environmental features in the Random Forest model.

CONCLUSIONS

This study integrated image recognition, environmental sensing, machine learning, and XAI to establish an analytical workflow for mushroom fruiting initiation rate and environmental factors. Random Forest achieved the best predictive performance among the tested models, and the three-day average temperature and the degree of temperature decrease were identified as important factors affecting fruiting initiation. These findings provide a quantitative reference for subsequent cultivation-environment regulation and for improving the fruiting efficiency of substrate bags.

REFERENCES

Ryo, M. 2022. Explainable artificial intelligence and interpretable machine learning for agricultural data analysis. *Artificial Intelligence in Agriculture* 6:257-265.

Sapkota, R., Z. Meng, M. Churuvija, X. Du, Z. Ma, and M. Karkee. 2025. Comprehensive performance evaluation of YOLOv12, YOLO11, YOLOv10, YOLOv9 and YOLOv8 on detecting and counting fruitlet in complex orchard environments. arXiv preprint arXiv:2407.12040.

SF-P11

Proceedings of The 12th International Symposium on Machinery and Mechatronics for Agriculture and Biosystems Engineering (ISMAB 2026)
20-24 October 2026, Busan, Republic of Korea

COMPARATIVE LIFE CYCLE ASSESSMENT OF SMART AND CONVENTIONAL SEEDLING NURSERY SYSTEMS

Kyungjae Song [1], Changseop Shin[1*]

[1]Department of Biosystems Engineering, Chungbuk National University, South Korea
*Corresponding Author-- Voice: +82-43-261-2584, Email: shinchang7@cbnu.ac.kr

Abstract: LCA (Life Cycle Assessment) can be used to quantitatively evaluate the environmental impacts associated with resource and material inputs in agricultural production processes. Smart seedling nursery systems can improve cultivation efficiency through sensor-based monitoring, remote irrigation, and environmental control; however, they require additional equipment and electricity use. This study aimed to compare the environmental impacts of smart and conventional greenhouse nursery systems for Chinese cabbage, cabbage, and broccoli by conducting a Life Cycle Assessment based on an established Life Cycle Inventory (LCI). The system boundary was defined from sowing to immediately before transplanting. Inputs of electricity, irrigation water, growing media, seeds, agricultural materials, and equipment were investigated, while the material composition, weight, transportation distance, and service life of reusable equipment were also considered. Chinese cabbage was cultivated for 22 days, whereas cabbage and broccoli were cultivated for 27 days. The conventional nursery system was irrigated daily with 700 mL of water per tray, whereas the smart nursery system was irrigated with 520 mL per tray at 2-day intervals, resulting in a 62.9% reduction in irrigation water use. Management time was reduced by 74.9% in the smart nursery system compared with the conventional nursery system, reflecting differences in irrigation, monitoring, shading, and fertilization-related management tasks. These results indicate that the smart nursery system can improve management efficiency and reduce irrigation water use, while additional electricity and equipment inputs should be considered when evaluating its overall environmental performance. SimaPro, a software tool for Life Cycle Assessment, was used to analyze the environmental impacts of the smart and conventional nursery systems based on the established LCI. In future work, the experiment will be conducted in triplicate to improve the reliability of the results.

Key Words: Smart nursery, Conventional greenhouse nursery, Life Cycle Inventory, Life Cycle Assessment.

ACKNOWLEDGEMENTS

This work was carried out with the support of "Cooperative Research Program for Agriculture Science &Technology Development (RS-2026-25466112)" Rural Development Administration, Republic of Korea.

SF-P12

Proceedings of The 12th International Symposium on Machinery and Mechatronics for Agriculture and Biosystems Engineering (ISMAB 2026)
20-24 October 2026, Busan, Republic of Korea

ELECTRODE STATUS DIAGNOSIS FOR REAL-TIME IN-SITU MONITORING OF HYDROPONIC NUTRIENT SOLUTIONS USING ION-SELECTIVE ELECTRODES

Yuna Kwon[1], Hak-Jin Kim[2*], Minki Kang[1], Joonhwan Kim[3]

[1]Department of Biosystems Engineering, College of Agriculture and Life Sciences, Seoul National University, Seoul, 08826, Republic of Korea
[2]Integrated Major in Global Smart Farm, College of Agriculture and Life Sciences, Seoul National University, Seoul, 08826, Republic of Korea
[3]Libergon, Inc
*Corresponding Author-- Voice: +02-880-4614, Email: Kimhj69@snu.ac.kr

Abstract: Hydroponic nutrient-solution management commonly relies on electrical conductivity (EC), which cannot directly identify ion-specific concentration changes or ionic imbalance. Ion-selective electrodes (ISEs) enable real-time ion monitoring; however, long-term field operation may compromise measurement reliability through baseline drift, sensitivity loss, and signal instability. Previous work quantified signal abnormalities using a self-diagnostic index, but a single score is limited in identifying faulty channels and supporting maintenance decisions. This study proposes a statistical condition-diagnosis framework for a remote multichannel ISE system. A 12-channel system comprising three ISEs each for nitrate (NO_3^-), potassium (K^+), sodium (Na^+), and calcium (Ca^{2+}) was used. In each measurement cycle, low-standard, high-standard, and sample solutions were introduced sequentially, and five electromotive-force measurements were acquired per channel. Electrode condition was assessed from baseline drift, changes in standard-response separation, within-cycle variability, and deviation from the median response of replicate electrodes. Temporal changes were evaluated using statistical control limits, and multivariate anomaly detection was used to assess combined abnormality patterns. Persistent abnormalities confined to an individual channel were distinguished from common-mode abnormalities across multiple channels. Channels were classified as valid, requiring inspection or recalibration, or requiring replacement. Diagnostic results were remotely provided to support maintenance decisions, and only validated channels were used for concentration estimation. The framework will be evaluated in a non-recirculating hydroponic system.

Key Words: ion-selective electrode; hydroponic nutrient solution; multichannel monitoring; statistical condition diagnosis; electrode redundancy

ACKNOWLEDGEMENTS: This work was supported by the LS Mtron–SNU CALS Digital Agriculture Industry-Academia Collaboration Project (Grant No. 500-20231078).

SF-P13

Proceedings of The 12th International Symposium on Machinery and Mechatronics for Agriculture and Biosystems Engineering (ISMAB 2026)
20-24 October 2026, Busan, Republic of Korea

COOLING PERFORMANCE AND AI-BASED PREDICTION OF GREENHOUSE ACTUATOR CONTROL SIGNALS AND VALIDATION

Min Hwan Yu[1], Kyeong Sik Kang[2], Seon Yeop Kim[2], Dae Hyun Kim[1, 2*]

[1]Department of Biosystems Engineering, Kangwon National University, Chuncheon, Republic of Korea
[2]Department of Interdisciplinary Program in Smart Agriculture, Kangwon National University, ChunCheon, Republic of Korea
*Corresponding Author-- Voice: +82-10-5095-0516, Email: daekim@kangwon.ac.kr

Abstract: Maintaining a stable greenhouse environment requires appropriate control in response to changing external weather conditions, particularly as rising temperatures and summer heatwaves increase the need for effective cooling and environmental control. This study evaluated environmental control characteristics under high-temperature conditions and the cooling effect of an air-fog system, while developing AI models to predict control signals for major greenhouse actuators using data obtained from an expert-defined rule-based control system. Experiments were conducted in two identical Venlo-type double-layer plastic greenhouses, with indoor and outdoor environmental data and actuator operation data collected at 1-min intervals. The two greenhouses were initially operated under the same control strategy, followed by a crossover fogging test in which the fog-on and fog-off treatments were switched between the greenhouses. The results demonstrated a cooling effect under high outdoor temperatures, while the internal temperature and humidity were maintained within the intended control ranges. The crossover test confirmed that the cooling response was consistent between the two greenhouses. Based on the accumulated cooling-control data, AI models were constructed to predict the operating states of the fog system and major environmental control actuators. Candidate algorithms were trained and evaluated for each actuator, and the best-performing algorithms were selected as the final prediction models. The results demonstrate the cooling performance of the air-fog system under high-temperature conditions and the feasibility of using data from an expert-defined rule-based control system to develop AI-based actuator-state prediction models.

Key Words: Greenhouse cooling, Artificial intelligence, Environmental control, Expert-defined rule-based control, Imitation learning

ACKNOWLEDGEMENTS

This work was supported by the Korea Institute of Planning and Evaluation for Technology in Food, Agriculture and Forestry (IPET) through the Smart Farm Multi-Ministry Package Innovation Technology Development Program, funded by the Ministry of Agriculture, Food and Rural Affairs (MAFRA) (grant number RS-2025-02221279).

SF-P14

Proceedings of The 12th International Symposium on Machinery and Mechatronics for Agriculture and Biosystems Engineering (ISMAB 2026)
20-24 October 2026, Busan, Republic of Korea

ENVIRONMENTAL AND ENERGY ANALYSIS OF A MINI-GREENHOUSE USING LED PWM AND CFD

Ga Eun Kim[1], Soo min Lim[1], Kyeong Sik Kang[2], Seon Yeop Kim[2], DaeHyun Kim[1,2]*

[1]Department of Biosystems Engineering, Kangwon National University, Chuncheon, Republic of Korea
[2]Department of Interdisciplinary Program in Smart Agriculture, Kangwon National University, Chuncheon, Republic of Korea
*Corresponding Author — Voice: +82-10-5095-0516, Email: daekim@kangwon.ac.kr

Abstract: This study aimed to analyze the internal temperature distribution of a greenhouse under different LED PWM output levels and ventilation fan operating conditions, and to identify operating conditions capable of maintaining a stable thermal environment. LED systems generate heat while providing the required light environment, and in small-scale greenhouses with limited internal space, changes in LED output and ventilation conditions may cause localized temperature increases and spatial temperature variations. Such localized heating and non-uniform thermal conditions can affect system stability and the maintenance of a consistent internal environment during long-term operation. Therefore, it is necessary to quantitatively evaluate the temperature distribution under different LED output and ventilation conditions. The LED PWM output levels were set at 60%, 80%, and 100%, and temperatures were measured at multiple locations inside the greenhouse under each condition to evaluate spatial temperature variation. In addition, changes in the internal temperature distribution were compared according to whether the ventilation fan was operated, in order to assess the effect of fan operation on temperature uniformity and the mitigation of excessive temperature rise. Computational fluid dynamics (CFD) analysis was also conducted by incorporating the actual geometry of the greenhouse, LED configuration, and ventilation conditions. The spatial distributions of internal temperature and airflow were analyzed under different PWM output levels and ventilation fan operating conditions, and the reliability of the CFD results was evaluated by comparison with measured temperature data. Through these analyses, the thermal response of the greenhouse to LED PWM output levels and ventilation fan operating conditions was quantitatively assessed, and operating conditions capable of reducing spatial temperature variation and localized temperature rise were examined. This study is significant in that it integrates experimental measurements with CFD analysis to evaluate the thermal stability of a greenhouse and to provide operating guidelines for maintaining a stable internal environment while reducing the risk of overheating during long-term system operation.

Key Words: Greenhouse, PWM control, Thermal stability, Operational safety, Computational fluid dynamics

ACKNOWLEDGEMENTS

This work was supported by the Korea Institute of Planning and Evaluation for Technology in Food, Agriculture and Forestry (IPET) through the Smart Farm Innovation Technology Development Program, funded by the Ministry of Agriculture, Food and Rural Affairs (MAFRA) (grant number RS-2025-02221279); and by the Basic Science Research Program through the National Research Foundation of Korea (NRF), funded by the Ministry of Education (grant number RS-2021-NR060130). The funding sources had no role in the study design, data collection, analysis and interpretation, manuscript preparation, or the decision to submit the article for publication

SF-P15

Proceedings of The 12th International Symposium on Machinery and Mechatronics for Agriculture and Biosystems Engineering (ISMAB 2026)
20-24 October 2026, Busan, Republic of Korea

FUEL PROPERTY EVALUATION AND MACHINE LEARNING PREDICTION FOR CATALYTIC TORREFACTION OF *QUERCUS VARIABILIS*

Chae Young Jang[1], Su Jeong Lee[1], Kyeong Sik Kang[2], Seon Yeop Kim[2], Sunyong Park[1], Dae Hyun Kim[1,2*]

[1]Department of Biosystems Engineering, Kangwon National University, Chuncheon, Republic of Korea
[2]Department of Interdisciplinary Program in Smart Agriculture, Kangwon National University, Chuncheon, Republic of Korea
*Corresponding Author-- Voice: +82-10-5095-0516, Email: daekim@kangwon.ac.kr

Abstract: Torrefaction can improve the fuel properties of biomass; however, mass and energy recovery characteristics may vary depending on process severity and catalyst application conditions. This study compared the torrefaction characteristics of *Quercus variabilis* treated with K CO , Na CO , and CaO and constructed machine learning models to predict mass yield and gross heating value based on experimental data. Torrefaction experiments were conducted at 230, 270, and 310 °C for 20, 40, and 60 min, with catalyst loadings of 1, 3, and 5 wt%. After torrefaction, mass yield, elemental and proximate compositions, GHV, and energy yield were analyzed. Process conditions, elemental analysis results, and proximate analysis results were used as input variables, and the predictive performance of MLR, SVR, RF, GBM, XGBoost, and CatBoost was compared. As process severity increased, mass yield decreased, while carbon content, fixed carbon content, and GHV increased, with the magnitude of these changes differing among catalysts. K CO - and Na CO -treated samples showed pronounced carbon and fixed carbon enrichment and improvement in GHV, whereas CaO-treated samples maintained relatively higher mass yield. Machine learning models based on elemental and proximate analysis generally showed better predictive performance than process-condition-based models, and similar trends were observed in the independent validation. Based on the overall predictive performance, GBM, CatBoost, and RF were selected as the final prediction algorithms.

Key Words: Catalytic torrefaction, *Quercus variabilis*, Mass yield, Gross heating value, Machine learning

INTRODUCTION

Fossil fuel consumption has contributed to increasing carbon emissions and climate change, thereby increasing the need for sustainable alternative energy sources (Rial, 2024; Friedlingstein et al., 2025). Biomass has consequently attracted attention as a renewable alternative energy source (McKendry, 2002). However, raw biomass has limitations in storage and handling because of its high moisture content, low energy density, and hygroscopicity, requiring pretreatment to improve its fuel properties (Chen et al., 2021). Torrefaction is a thermal pretreatment process in which biomass is heated at approximately 200–300 °C under oxygen-free or oxygen-limited conditions. This process removes moisture and some volatile compounds while increasing carbon content and energy density, thereby improving the properties of biomass as a solid fuel (Chen et al., 2021). However, torrefaction requires additional energy to reach and maintain the target temperature, and mass yield may decrease with increasing temperature and residence time due to thermal decomposition and the release of volatile compounds (Chen et al., 2021). Catalysts can therefore be applied to promote torrefaction reactions, although their effects may vary depending on catalyst type and loading (Safar et al., 2019; Richa et al., 2022). In addition, torrefaction characteristics are influenced by multiple factors, including temperature, residence time, and catalyst conditions, making machine learning a useful approach for predicting their complex relationships based on experimental data (Manatura et al., 2023).

Therefore, this study aimed to compare and analyze the torrefaction characteristics of *Quercus variabilis* treated with K CO , Na CO , and CaO and to construct and evaluate machine learning models for predicting mass yield and GHV based on the experimental data obtained.

MATERIALS AND METHODS

Materials and Experimental Design

Domestic hardwood forest biomass, *Quercus variabilis*, was sieved to a particle size of ≤2 mm and dried at 105 °C for 24 h before use. K CO and Na CO (≥99.0%, Daejung Chemicals & Metals Co., Ltd., Republic of Korea), and CaO (≥97.0%, Daejung Chemicals & Metals Co., Ltd., Republic of Korea) were used as catalysts. Torrefaction experiments were conducted at 230, 270, and 310 °C with residence times of 20, 40, and 60 min. Catalyst type and catalyst loadings of 1, 3, and 5 wt% were used as experimental factors. Rather than applying all possible combinations, the experimental conditions were systematically selected by considering the levels of each factor.

Torrefaction and Fuel Property Analysis

Torrefaction experiments were conducted using a torrefaction furnace (N7/H/B410, Nabertherm GmbH, Germany). To limit reactions with oxygen, 70 g of each sample was placed in a sealed stainless-steel container. Each condition was tested in triplicate, and the sample mass was measured after approximately 30 min of cooling following torrefaction. Mass yield was calculated using Eq. (1) to correct for the contribution of catalyst mass to the measured yield.

$$MY[\%] = \frac{M_{Torrefied} - M_{Catalyst}}{M_{Initial} - M_{Catalyst}} \times 100 \quad (1)$$

where:
MY = Mass yield (%)
$M_{Initial}$ = Initial mass of sample before torrefaction (g)
$M_{Catalyst}$ = Mass of catalyst added (g)
$M_{Torrefied}$ = Mass of sample after torrefaction (g)

Elemental composition (C, H, N, and S) was analyzed using a CHNS analyzer (EA3000 Series, EuroVector, Italy). Oxygen content (O) was calculated using Eq. (2).

$$O[\%] = 100 - (C + H + N + S) \quad (2)$$

where:
O = Oxygen content (%)
C = Carbon content (%)
H = Hydrogen content (%)
N = Nitrogen content (%)
S = Sulfur content (%)

Proximate analysis was performed using a thermogravimetric analyzer (prepASH 340, Precisa, Switzerland) in accordance with ASTM D7582 to determine moisture, ash, and volatile matter contents (ASTM International, 2024). Fixed carbon content was calculated using Eq. (3).

$$FC[\%] = 100 - (MC + VM + Ash) \quad (3)$$

where:
FC = Fixed carbon content (%)

MC = Moisture content (%)
VM = Volatile matter content (%)
Ash = Ash content (%)

Gross heating value (GHV) was measured using a bomb calorimeter (6400, Parr Instrument Company, USA).

Energy yield was calculated using Eq. (4).

$$EY[\%] = \frac{GHV_{Torrefied}}{GHV_{Raw}} \times MY \quad (4)$$

where:
EY = Energy yield (%)
$GHV_{Torrefied}$ = Gross heating value after torrefaction (MJ/kg)
GHV_{Raw} = Gross heating value before torrefaction (MJ/kg)
MY = Mass yield (%)

Construction and Performance Evaluation of Machine Learning Models

Machine learning models were constructed to predict mass yield and GHV in the torrefaction process using process conditions, elemental analysis results, and proximate analysis results as input variables. Six algorithms, including Multiple Linear Regression (MLR), Support Vector Regression (SVR), Random Forest (RF), Gradient Boosting Machine (GBM), XGBoost, and CatBoost, were compared, and hyperparameters were optimized through internal validation. Model predictive performance was evaluated using the coefficient of determination (R^2), root mean square error (RMSE), and mean absolute error (MAE), which were calculated according to Eqs. (5)–(7), respectively.

$$R^2 = 1 - \frac{\sum_{i=1}^{n}(y_i - \widehat{y_i})^2}{\sum_{i=1}^{n}(y_i - \bar{y})^2} \quad (5)$$

$$RMSE = \sqrt{\frac{1}{n}\sum_{i=1}^{n}(y_i - \hat{y}_i)^2} \quad (6)$$

$$\text{MAE} = \frac{1}{n}\sum_{i=1}^{n}|yi - \hat{y}i| \quad (7)$$

where:

y_i = Observed value

$\hat{y}i$ = Predicted value

$\bar{y}$ = Mean of observed values

n = Number of observations

Leave-One-Out Cross-Validation (LOOCV) was applied to assess the generalization performance of the models given the limited dataset. Experimental data that were not used for modelconstruction were used as an independent validation dataset to evaluate the final predictive performance.

RESULTS & DISCUSSION

Mass Yield

Mass yield generally decreased as process severity increased, and the extent of this change differed depending on catalyst type. In particular, K CO - and Na CO -treated samples showed relatively greater mass loss under high-temperature and long-residence-time conditions, whereas CaO-treated samples maintained relatively higher mass yield. Changes in mass yield also varied depending on catalyst type and process conditions, including temperature and residence time. In particular, the increased mass loss observed for K CO - treated samples at high temperatures was consistent with trends reported in previous torrefaction studies of woody biomass (Richa et al., 2023).

Elemental Analysis

As torrefaction severity increased, carbon content generally increased, while hydrogen and oxygen contents decreased, and the degree of carbon enrichment varied depending on catalyst type. K CO - and Na CO -treated samples showed relatively greater carbon enrichment at high temperatures, whereas compositional changes in CaO-treated samples were comparatively moderate. In addition, H/C and O/C ratios decreased with increasing process severity, and the extent of these changes varied with catalyst type and process conditions, indicating differences in carbonization behavior.

Proximate Analysis

Proximate analysis showed that K CO - and Na CO -treated samples exhibited relatively greater decreases in volatile matter and increases in fixed carbon under high-temperature

conditions, whereas these changes were more moderate in CaO-treated samples. This trend was consistent with the catalyst-dependent carbon enrichment observed in the elemental analysis, indicating that the extent of compositional changes in the solid fuel varied with catalyst type. In addition, ash content tended to increase depending on catalyst application conditions, suggesting that changes in the inorganic fraction of the final solid product should also be considered when evaluating catalyst effects.

Gross Heating Value and Energy Yield

GHV generally increased with increasing process severity, although the extent of improvement varied depending on catalyst type. K CO - and Na CO -treated samples showed relatively higher GHV under high-temperature conditions, which was considered to be associated with carbon and fixed carbon enrichment. In contrast, CaO-treated samples showed comparatively moderate changes in GHV. Changes in GHV were influenced by catalyst type, catalyst loading, and process conditions. Energy yield reflected the balance between improved GHV and reduced mass yield. While K CO - and Na CO -treated samples showed more pronounced improvements in GHV, CaO-treated samples maintained relatively higher mass yield. Therefore, catalyst effects should be evaluated by considering both fuel quality improvement and energy recovery characteristics.

Machine Learning-Based Prediction Performance for Mass Yield and GHV

For both mass yield and GHV prediction, models based on elemental and proximate analysis generally showed better predictive performance than models based on process conditions, and similar trends were observed in the independent validation. In particular, elemental-analysis-based models showed high predictive performance for GHV. Based on the overall performance across input variables and prediction targets, GBM, CatBoost, and RF were selected as the final prediction algorithms.

CONCLUSIONS

This study compared the torrefaction characteristics of *Quercus variabilis* treated with K CO , Na CO , and CaO and constructed machine learning models to predict mass yield and GHV based on experimental data. K CO - and Na CO -treated samples showed pronounced carbon and fixed carbon enrichment and improvements in GHV, whereas CaO-treated samples maintained relatively higher mass yield, demonstrating distinct catalyst-dependent characteristics. In the machine learning analysis, models based on elemental and proximate analysis generally showed high predictive performance. Based on the overall predictive performance and independent

validation results, GBM, CatBoost, and RF were selected as the final prediction algorithms.

ACKNOWLEDGEMENTS

This work was supported by the Korea Institute of Planning and Evaluation for Technology in Food, Agriculture and Forestry (IPET) through the Smart Farm Multi-Ministry Package Innovation Technology Development Program, funded by the Ministry of Agriculture, Food and Rural Affairs (MAFRA) (grant number RS-2025-02221279).

REFERENCES

ASTM International. 2024. ASTM D7582-24: Standard test methods for proximate analysis of coal and coke by macro thermogravimetric analysis. West Conshohocken, PA.: ASTM International.

Chen, W. H., B. J. Lin, Y. Y. Lin, Y. S. Chu, A. T. Ubando, P. L. Show, H. C. Ong, J. S. Chang, S. H. Ho, A. B. Culaba, A. Petrissans, and M. Petrissans. 2021. Progress in biomass torrefaction: Principles, applications and challenges. Progress in Energy and Combustion Science 82: 100887.

Friedlingstein, P., et al. 2025. Global Carbon Budget 2024. Earth System Science Data 17(3): 965-1039.

Manatura, K., B. Chalermsinsuwan, N. Kaewtrakulchai, E. E. Kwon, and W. H. Chen. 2023. Machine learning and statistical analysis for biomass torrefaction: A review. Bioresource Technology 369: 128504.

McKendry, P. 2002. Energy production from biomass (Part 1): Overview of biomass. Bioresource Technology 83(1): 37-46.

Rial, R. C. 2024. Biofuels versus climate change: Exploring potentials and challenges in the energy transition. Renewable and Sustainable Energy Reviews 196: 114369.

Richa, L., B. Colin, A. Petrissans, R. L. Quirino, W. H. Chen, and M. Petrissans. 2022. Potassium carbonate as a catalyst for wood torrefaction. Energy Proceedings 27.

Richa, L., B. Colin, A. Petrissans, C. Wallace, J. Wolfgram, R. L. Quirino, W. H. Chen, and M. Petrissans. 2023. Potassium carbonate impregnation and torrefaction of wood block for thermal properties improvement: Prediction of torrefaction performance using artificial neural network. Applied Energy 351: 121894.

Safar, M., B. J. Lin, W. H. Chen, D. Langauer, J. S. Chang, H. Raclavska, A. Petrissans, P. Rousset, and M. Petrissans. 2019. Catalytic effects of potassium on biomass pyrolysis, combustion and torrefaction. Applied Energy 235: 346-355.

SF-P16

Proceedings of The 12th International Symposium on Machinery and Mechatronics for Agriculture and Biosystems Engineering (ISMAB 2026)
20-24 October 2026, Busan, Republic of Korea

ANALYSIS OF NUTRIENT UPTAKE PATTERNS IN FOGPONICS-CULTIVATED SEED POTATOES ACROSS GROWTH STAGES

Yeong Hyeon Shin[1], Je-Min Park[1], Muhammad Amjad[1], Uk-Hyeon Yeo[2*], Woo-Jae Cho[1*]

[1]Department of Biosystems Engineering, College of Agriculture & Life Sciences, Gyeongsang National University, Jinju 52828, Republic of Korea
[2]Department of Agricultural Engineering, Gyeongsang National University, Jinju 52828,
*Corresponding Author-- Voice: +10-3363-7343, Email: woojae56@gnu.ac.kr

Abstract: Fogponics is a soilless cultivation method in which nutrient solution is delivered to the root zone as micron-sized fog droplets. Fogponics delivers nutrient solution to the root zone as mocron-sized droplets, minimizing the amount of water and nutrients required within the root environment. However, unlike substrate-based systems, where the growing substrate retains water and nutrients between irrigation, fogponics has limited buffering capacity between fog cycles. As a result, changes in the nutrient solution can be more immedietly reflected in the nutrient supply to the roots. This characteristic is particularly important for crops such as potato, which have different nutrient requirements throughout their growth cycle. Potato have different nutrient requirements at different stages of growth, with changes occurring during vegetative growth, tuber initiation, and tuber bulking. However, information on stage-specific ion uptake in fogponics-grown potatoes remains limited. In this study, seed potatoes were grown in a fogponics system managed using EC-based nutrient replenishment. Nutrient solution replenishment was conducted based on water level and EC measurements when the solution level decreased to below a set level. Nutrient solution samples obtained before and after each replenishment were analyzed by an external laboratory for individual ion concentrations. Ion uptake at each growth stage was estimated based on the replenishment volume and changes in ion concentration. This study investigated changes in individual ion uptake across the growth stages of seed potatoes grown in a fogponics system. Based on the observed ion uptake patterns, this study aims to propose a stage-specific nutrient management model.

Key Words: Fogponics, Seed Potato, Growth Stage, Nutrient Uptake Pattern

Acknowledgement: This work was supported by the Korea Institute of Planning and Evaluation for Technology in Food, Agriculture and Forestry (IPET) through the Export Activation Program for Strategic Items(RS-2025-02313370).

SF-P17

Proceedings of The 12th International Symposium on Machinery and Mechatronics for Agriculture and Biosystems Engineering (ISMAB 2026)
20-24 October 2026, Busan, Republic of Korea

VERIFYING A DRAFT STANDARD BEFORE ENACTMENT: IMPLEMENTATION AND MEASUREMENT OF SMART GREENHOUSE NODE DISCOVERY

Dae-Hyun Jung[1], Inchan Choi[2], JoonYong Kim[3*]

[1]Department of Smart Farm Science, Kyung Hee University, Yongin-si, Gyeonggi-do 17104, Republic of Korea
[2]Division of Smart Farm Development, Department of Agricultural Engineering, National Institute of Agricultural Sciences, 310, Nongsaengmyeong-ro, Deokjin-gu, Jeonju-si, Jeollabuk-do 54875, Republic of Korea
[3]Research Institute of Agriculture and Life Sciences, Seoul National University, Seoul 08826, Republic of Korea
[*]Corresponding Author-- Voice: +82-2-880-4612, Email: tombraid@snu.ac.kr

Abstract: Korean Industrial Standards for smart greenhouses define Modbus data exchange over serial lines and TCP. A controller that reaches a node can read its information area, but reaching it is the problem: TCP needs an IP address and service port, a DHCP-assigned address may change, and without discovery the controller is configured by hand. This work addresses that gap in a draft extension to KS B 7958 and asks which defects each kind of verification exposes before enactment. The new part specifies discovery with mDNS and DNS-SD; advertisements supply connection information, and the node registers remain the reference for checking it. We applied four verification channels to the draft: document review, a reference implementation, automated tests, and behavioral measurement. The implementation extended an existing library for this standard series and delegated the protocols to python-zeroconf and pymodbus, and a separate measurement harness shares no code with it. Testing used node appliances and a virtual node for controlled address changes. The channels produced six items. The principal one is a requirement gap between the new part and the standards it builds on: this design needs a node serial number that exists, persists and is unique, but the published standards leave it optional, so a controller cannot tell a returning node from a new one. In virtual-node trials a node without a serial advertised two identities when only its service port changed, and two nodes sharing a serial advertised one. We proposed those properties as a requirement for revising the standards. One item is a candidate clarification of the draft, two were issues in our own library, and a test partly confirmed the optionality clause. Measurement added a defect in our own implementation: after an address change, a running node kept advertising the old address and was not rediscovered, although the draft requires immediate re-announcement. For an advertising appliance, browser startup through register verification took a median of 0.12 s over fifteen preliminary rounds (0.07–0.22 s), excluding boot and approval time. Discovery removed three manually entered parameters per node; registration approval remained. Implementation and measurement found issues that the preceding document review had not reported, although we did not test whether another channel could have produced them. The case supports implementing and measuring a draft while its text can still change, with performance claims limited to the tested conditions.

Key Words: smart greenhouse, service discovery, standardization, reference implementation, pre-enactment verification

INTRODUCTION

A smart greenhouse is assembled from equipment made by different manufacturers. The integrated controller must read sensors and drive actuators it did not ship with, and Korean Industrial Standards for smart greenhouses exist to make that possible (Korean Agency for Technology and Standards [KATS], 2022, 2024). They define a common data model over Modbus on a serial line and TCP: what a node is, how its measurements and commands are laid out, and how a controller addresses them.

A controller that can reach a node reads its information area (KATS, 2022) to identify the equipment specification and register layout. That describes capabilities; a stable identity for recognizing the same node later is separate.

The initial connection requires an address. On a serial bus, installers configure a slave identifier at the node. TCP requires an IP address and a service port, a DHCP-assigned address may change, and DHCP does not assign the Modbus port. Without discovery or another address- management mechanism, the controller needs manual entry of connection information and updates whenever it changes. If an old address is reassigned, a controller that does not verify node identity may read valid data from the wrong equipment. Each exchange can be correct on its own while identity is not continuous, and conformance testing checks the exchanges (Modbus Organization, 2009).

Earlier work analyzed a communication standard and built an open-source implementation against it (Kim et al., 2018), and conformance test systems have been built to support standardization (Zhao et al., 2012). Both were applied to published standards; here the implementation ran alongside the drafting.

The aim of this work was to verify one draft part *before* enactment, and to record what each way of examining it turns up. Four channels were applied to the same text: document review, a reference implementation, automated tests, and behavioral measurement. The object under test was how a controller discovers TCP nodes without manual configuration.

MATERIALS AND METHODS

From an observed gap to a new part

The omission was first recorded as a formal requirement entry against the published TCP standard, in an analysis repository that separates extracts of published standards, contradictions between them, and gaps where every standard is silent. Node discovery was a gap of the third kind.

The specification written against that requirement closes the gap in the standard, not in a product. The central choice was to define no new protocol. Multicast DNS and DNS-based service discovery (Cheshire and Krochmal, 2013a, 2013b) are already standardized and widely implemented, and delegating name probing, conflict resolution and cache expiry to them keeps the agricultural standard to what is specific to agriculture: what a greenhouse node must say about itself.

The design rule that governs the whole specification is that **an advertisement is a hint and the register bank is the authority**. The advertisement carries only what a controller needs to reach a node and select its equipment specification. Everything it acts on afterwards is read from the registers and checked against the advertisement, and where the two disagree the registers win.

The draft was submitted to the working group as a candidate new part of the series now under revision; numbering and text remain provisional. The text implemented here is the part as it

stood after a series-wide consistency round in August 2026. Document review of the series is recorded as twelve numbered issues; those reaching this part concern terminology, part names and cross-references, and none addresses the behavior it specifies.

Reference implementation and automated tests

In parallel we implemented that part in an existing implementation of this standard series: a Python library with a virtual-node simulator that already covers its published parts. The discovery package is seven modules of about 1,500 lines and has passed through five revisions. It delegates what the draft delegates: mDNS and DNS-SD to python-zeroconf, carried as an optional dependency, and Modbus to pymodbus. Three choices supported evaluation of the draft, without assuming every implementation difficulty came from the text:

1. **Only what the draft specifies was implemented.** Reimplementing the delegated protocols would have moved the difficulty away from the text under test. 2. **The specification-facing layer was kept free of transport dependencies**, so what a node says about itself can be tested without a network. 3. **The optionality clause was honored literally.** The draft requires that discovery be optional and that a node's Modbus service work without it, so the implementation treats the discovery library as an optional dependency and a test runs with that import blocked.

Sixty-two automated tests in three suites checked the implemented behavior against selected requirements: advertisement field encoding, the browse-resolve-verify path, and behavior with the optional dependency blocked.

Measurement on appliances and a virtual node

Discovery was measured on a node appliance on a shared laboratory network. The harness was written from the draft separately, calling python-zeroconf and pymodbus directly, and shares no application code with the implementation under test. It is therefore a second reading of the same requirements; because both rest on the same two third-party libraries, it does not validate those.

For M1 the appliance was already advertising and remained running between rounds, and each round created a fresh Zeroconf instance. Timing began before browser startup, including socket preparation, and ended at register verification after resolution and connection, excluding node boot and user approval. The fifteen rounds describe controller-side discovery of an available node, not discovery after power-on.

M2 comprised two separate, single-run experiments: a controlled address change on a continuously running virtual node, observed for 300 s, and an appliance reboot with an address change, where contact was restored after 133 s dominated by boot time. Neither is a protocol latency.

Measurement was aimed at behavior rather than scale, and split into four angles (Table 1), each directed at a different way the specified behavior could fail in operation.

Table 1. The four measurement angles, and what each one settles.

ID	Measured	Purpose
M1	Time from browse start until a node is **usable** — resolved, connected, and its advertisement checked against its registers	Browser-start-to-verification latency, excluding boot and user approval
M2	Recovery after address change: separate live virtual-node and rebooted-appliance trials	The condition that made manual configuration fragile

M3	Unicast fallback time over a /24, at several probe concurrencies	Is the fallback clause practical, and how wide is the policy it leaves open
M4	Manually entered configuration parameters per node at initial installation	The benefit, in the installer's units

RESULTS & DISCUSSION

What each channel exposed

The reference implementation and its tests exercised the discovery requirements, and the tested path could be implemented using mDNS and DNS-SD — feasibility for that path, not conformance in general. Implementation, testing and measurement produced six items (Table 2). What each one means depends on attribution: one is a requirement gap between the new part and the standards it builds on, one a candidate clarification of the draft, two were issues in our own library, one partly confirms a clause, and one is a non-conformance of our own implementation.

Table 2. What the channels produced, and how each item is classified. Item 1 is a gap between parts, not an error inside one; items 3, 4 and 6 are in our own implementation.

#	Item	Class (first seen in)	Disposition
1	This discovery design needs a node serial number that exists, persists across restarts and address changes, and is unique; the published standards leave it optional	Cross-standard requirement gap (implementation)	Proposed as a requirement covering those three properties
2	The draft does not state how an advertised name binds to the address published under it; nodes sharing one host name published over each other's addresses	Candidate clarification (downstream integration)	Resolved using the unique per-node instance name the draft already defines; whether the binding needs its own clause is open
3	Our client API entered discovery at one fixed unit identifier, so serial-line buses using others returned an empty list	Implementation issue, not this draft (implementation)	Fixed in the library; the draft fixes the identifier for TCP nodes, and TCP behavior was correct throughout
4	A serial-line server accepted advertisement configuration and reported the exclusion only at information level	Implementation diagnostics (implementation)	Raised to a warning; the draft already scopes discovery to TCP and the exclusion itself worked from the first release
5	With the discovery dependency blocked, advertisement construction still succeeded and the discovery call raised the specified error	Partial confirmation of the optionality clause (automated test)	Kept as a regression test; whether a node then serves Modbus is not covered
6	A running virtual node did not re-announce after an address change, serving at the new address while advertising the old one	Non-conformance of our implementation (measurement)	Three clauses require immediate re-announcement on address change; which layer failed was not separated

Item 1 is the consequential one. The discovery procedure establishes trust in a node on first sight and refuses to transfer that trust to a different host later. That mechanism needs the node serial number held in the node information area to exist, to persist across restarts and address changes, and to be unique among nodes. The published standards leave the field optional, so a conforming node need not provide the identity this design needs. Two of those properties were tested on virtual nodes. Where a node carries no serial our implementation derives one from its network position, so two instances of one definition, separated only by service port, advertised different identities, while an instance carrying a serial kept its own. Two instances sharing a serial were given two names by the delegated conflict rule but one identity. The move changed a port, not an address. Optionality is coherent while nodes are reached at addresses installers typed, and discovery removes that premise. The gap is between parts rather than inside one, which is why review of either text alone did not expose it. We proposed the three properties as a requirement for revising the sibling standard.

Attribution is easy to skip. Items 3 and 4 arose while implementing the draft but do not count against it: the draft fixes the entry identifier for TCP nodes and states the transport it applies to, and both repairs were ours. Item 2 concerns a binding the delegated standard already defines, and the repair used a name the draft itself specifies. Counting every difficulty met while implementing a draft as a defect in it would overstate what implementation shows.

Discovery behavior

For an already advertising appliance, browser startup through register verification took a median of 0.12 s over fifteen preliminary rounds (0.07–0.22 s), passing in all fifteen; two appliances using the same preset were distinguished by hardware-derived serial values.

In the controlled virtual-node trial the process remained running and its serial was fixed while the interface address changed, and the controller did not rediscover it within the observation window. Nine samples from 5 s to 213 s after the change showed the new address responding to Modbus while the advertisement still named the removed address. In the separate appliance trial with reboot, contact was restored and the appliance recognized as the same node, which does not establish that reboot was necessary.

With 254 candidate addresses, TCP port 502 and a 1 s connection timeout, the unicast fallback over a /24 took 4.1 s at probe concurrency 64 and 233.8 s at concurrency 1. These whole-subnet times are not comparable to the single-node M1 latency, and only the fallback path was timed.

In the tested setup, discovery removed manual entry of three per-node configuration parameters: IP address, service port, and equipment specification. The unit identifier is not counted: the standard fixes it for TCP nodes. The count excludes network provisioning and the explicit registration approval that remained required, so zero parameters does not mean zero human involvement. The separate reboot trial restored contact without address re-entry, but recovery during continuous operation was not demonstrated.

Limitations

The measurements come from one or two appliances on a shared laboratory network we did not control, and the controlled address-change run used a virtual node on a single host. Scale remains unmeasured, as does behavior across switched and wireless segments. Each address-change result is a single run, and the M1 measurements are preliminary: appliance model and software- version details remain incomplete in the run manifest.

The harness reads the draft separately, but the node implementation is our own, so the count

is not a lower bound on what another implementation would find. We recorded where each item first appeared and did not test whether another channel could have produced it, so nothing here establishes that the channels are independent.

Finding 6 is a defect in our implementation rather than an omission in the draft: three clauses require immediate re-announcement when a node's address changes, and the delegated protocol requires the same (Cheshire and Krochmal, 2013a). What we did not separate is the layer. The delegated library keeps the address records it registered at startup and does not watch the interface, so whether our code or that choice is at fault remains open, and no node built on another mDNS implementation was tested.

CONCLUSIONS

A draft extension to KS B 7958 specifies node discovery using mDNS and DNS-SD, with node registers as the reference for verifying advertised information. The tested path removed manual entry of connection and equipment parameters; registration approval remained.

In this case, implementation and behavioral measurement surfaced issues that the preceding document review had not reported, and that review had reported issues of a different kind — titles, terms and cross-references. One item is a requirement gap between parts: this design needs a serial number that exists, persists and is unique, which the published standards leave optional. We proposed that as a requirement. One is a defect that measurement found in our own implementation: a running node did not re-announce after an address change, which three clauses of the draft require. Two further items were also ours, and what implementing a draft raises must be attributed before it counts against the text. These results do not establish complete conformance, general discovery performance, or independence between the channels.

ACKNOWLEDGEMENTS

This work was carried out with the support of "Cooperative Research Program for Agriculture Science and Technology Development (Project No. RS-2026-25505860)" Rural Development Administration, Republic of Korea.

REFERENCES

Cheshire, S., and M. Krochmal. 2013a. Multicast DNS. RFC 6762. Fremont, Cal.: Internet Engineering Task Force.

Cheshire, S., and M. Krochmal. 2013b. DNS-based service discovery. RFC 6763. Fremont, Cal.: Internet Engineering Task Force.

KATS. 2022. KS X 3267:2022 RS485 MODBUS interface between sensor/actuator node and greenhouse controller in smart greenhouse. Seoul, Korea: Korean Standards Association.

KATS. 2024. KS B 7958:2024 Smart greenhouse — Modbus interface based on transmission control protocol (TCP) between nodes and greenhouse integrated controller. Seoul, Korea: Korean Standards Association.

Kim, J. Y., S. Kim, and J. Lee. 2018. Comparative analysis of TTAK.KO-06.0288-Part3 and development of an open-source communication library for greenhouse control system. J. Biosyst. Eng. 43(1): 72-80.

Modbus Organization. 2009. Modbus TCP conformance test specification, ver. 3.0. Hopkinton, Mass.: Modbus Organization.

Zhao, Z., W. Huangfu, L. Sun, Z. Shi, and W. Gan. 2012. An open conformance test system towards the standardization of wireless sensor networks. Int. J. Distrib. Sens. Netw. 8(12): 931869.

SF-P18

Proceedings of The 12th International Symposium on Machinery and Mechatronics for Agriculture and Biosystems Engineering (ISMAB 2026)
20-24 October 2026, Busan, Republic of Korea

ADMITTING INSTALLED EQUIPMENT TO AN OPEN-FIELD STANDARD UNDER DEVELOPMENT: WHAT THE GATEWAY BOUNDARY COSTS

Hyein Lee[1], Jae-Seok Seo[2], JoonYong Kim[3*]

[1]Data Engineering Team, FarmOS Inc., Anyang-si, Gyeonggi-do 14067, Republic of Korea
[2]R&D Center, UBN Corporation, Room 501, DNEX, 160, Alphacity 1-ro, Suseong-gu, Daegu 42250, Republic of Korea
[3]Research Institute of Agriculture and Life Sciences, Seoul National University, Seoul 08826, Republic of Korea
[*]Corresponding Author-- Voice: +82-2-880-4612, Email: tombraid@snu.ac.kr

Abstract: A Korean Industrial Standard for data communication of stationary equipment in open-field agriculture is being drafted. Its spread depends less on its text than on the installed base: field equipment uses links defined by its maker, and few growers will replace working hardware. The draft therefore places a conversion gateway at its lower boundary. This work asks whether that boundary carries traffic, whether equipment built for an existing protocol can be admitted without replacement, and what that costs. No published document says what open-field equipment speaks, so we targeted a class: equipment reporting over a register-oriented serial line with a fixed layout. An enacted Korean greenhouse standard of that class served as the equipment side; it stands for the installed base, not for greenhouses. We implemented the whole lower boundary of the draft, not a mapping table: observation, commands, status, stored configuration, and queries for past data. It ran against emulated nodes over a real serial line, a network link, and a real broker. The boundary carries traffic, and upward translation is not what costs: reading a full node over the serial line took 769 ms, converting it 25 µs. All 400 commands to 16 actuators were answered within the time the draft allows, the slowest at 1211 ms, 40 % of the limit. At 32 ms per slot, a fixed answer time would be used up by about 93 slots on one line, or 62 at the driver's default buffer setting; this is arithmetic from one rig, not a demonstrated capacity. Because this gateway polls and answers in one loop, its slowest answers run a polling pass long. The draft names neither the line nor the scheduling policy, nor what instant an observation time means, which moves by a whole pass. In the tested configuration, emulated nodes implementing this standardized register-based protocol were admitted through the gateway. The cost lies not in the vocabulary but in the duties the draft gives the gateway. It sets a fixed answer time without saying on what line it holds, and a retention window without bounding the reply: the largest reply sent held 13 min; beyond that, the publish exceeded our client's 10 kB ceiling and the session dropped. Building the gateway during drafting produced 50 items, 35 of them points the draft does not settle.

Key Words: open-field agriculture, standardization, gateway, interoperability, reference implementation

INTRODUCTION

Open-field agriculture in Korea uses stationary equipment such as weather masts, soil probes, water meters, and irrigation controllers to report to farm management systems. No enacted Korean Industrial Standard describes how that equipment should carry its data, and one is now being drafted. The question is not whether the text can be enacted, but whether equipment already working in the field will come to speak it.

That is decided by the installed base. Equipment already working in the field reports over whatever protocols its manufacturers chose, and a grower with a working weather station will not replace it because a new standard exists. A standard that can be met only by new hardware is unlikely to spread. The draft therefore places a conversion gateway at its lower boundary: it governs the segment between the gateway and the farm management system and deliberately leaves the segment between the gateway and the equipment unregulated, so that whatever is already installed can be brought in behind a translator, not replaced.

That design choice moves the risk rather than removing it. If the obligations the draft places on the gateway cannot be met over the lines the installed equipment uses, the boundary is one on paper only. Whether two vocabularies line up can be settled by reading the two texts. Whether a gateway answers in time over the line the equipment uses cannot, and that is the question this work takes up.

Implementations and conformance test systems have been built against communication standards for this domain before (Zhao et al., 2012; Kim et al., 2018), but against standards already published, where finding a defect yields an erratum. Here the implementation ran alongside the drafting, while the text could still be changed.

The purpose of this study was to determine whether equipment built for an existing protocol can be admitted to the draft standard through a gateway without being replaced, to measure what that admission costs, and to return to the drafting process, before enactment, what only a running implementation could expose.

MATERIALS AND METHODS

The equipment side: a class, not a product

No single published document describes what open-field equipment speaks. Vendor protocols are numerous, partly undocumented, and cannot be cited, so a study built on one could not be checked by anyone else. What can be stated is the class: a stationary node reporting over a register-oriented serial line (Modbus Organization, 2006), with a register layout fixed in advance and a read that costs time in proportion to what is read. A finding that follows from those properties follows for the class.

We therefore used an enacted standard of that class as the equipment side: the Korean Industrial Standard for serial Modbus between sensor and actuator nodes and a greenhouse integrated controller (Korean Agency for Technology and Standards [KATS], 2022a). It was chosen for evidentiary rather than agronomic reasons: it is enacted, so every claim made against it traces to a published document, and it comes with machine-readable specification assets and emulators, so the exercise is reproducible without proprietary material. Its units and value ranges are delegated to a sibling standard (KATS, 2022b), and its equipment type and unit tables to another (KATS, 2022c).

It stands here for the class, not for greenhouses, and no claim is made that greenhouse equipment is deployed in open fields.

What was implemented

A crosswalk between the two observation vocabularies had to exist before anything could be published, and we built one by comparing the enacted texts. It is a prerequisite, not a result: which codes each side defines is settled by reading the documents. What follows is confined to what running the gateway showed.

The gateway was built from the draft, and it implements the lower boundary as a whole rather than a vocabulary crosswalk: observation reporting, command downlink to actuators, status transmission, the retained configuration declaration, the historical data query, and the notice left behind when the gateway dies. Each is an obligation the draft places on the gateway, and each can fail whether or not the vocabulary maps. The crosswalk is one part of the work; the obligations are the larger part, and where most of what follows was found.

Two rules shaped it. Where the draft specifies nothing, the implementation does not quietly decide: the feature defaults to off, the log says it is unregulated, and any value we were forced to choose is recorded with its reasoning. Where a rule exists but is unimplemented, it fails loudly, because a misread register emerges as a plausible number nobody questions.

It was written in a language different from the existing tooling for the equipment side, so the two would not inherit a single reading of the specification format, and the places where those readings disagreed were themselves reportable: one defect in the existing tooling was found and fixed, and seven places where the format admits two readings were returned to the repository that holds it. It reuses 17 published equipment specification files and 46 equipment type codes. Every measurement report carries the revision of each document it implements, the transport, and the settings the draft leaves open, because numbers without those conditions are not evidence.

Test configuration and measurement

One gateway served two emulated nodes at once: one on a physical RS-485 line at 9600 baud, 8 data bits, no parity, 1 stop bit, and a second over TCP. The gateway host was a laptop (Intel Core 7 240H, 32 GB, Ubuntu 26.04); its effect on the results is small, since the only processor-bound stage, translation, is four orders of magnitude below the serial read. The gateway polls its nodes and answers requests in a single loop; a preemptive mode exists but was off, and this rig cannot show its effect because only one node is slow. The broker ran on a separate machine, so the publishing path included a real network. For the command measurements the serial node was reconfigured to present actuators. Table 1 lists what was measured and what each measurement answers.

Table 1. Measurements and the question each answers.

ID	Measured	Question
M1	Time from the end of the equipment read until the message is handed to the client library	What does translation itself cost
M2	Time to complete one polling pass, per node and per equipment slot	What does the line beneath the gateway cost
M3	Time from a command arriving to its acceptance, with and without a write to the equipment	Can the gateway meet the draft's response obligation
M4	Message size by kind	Is the payload carriable on field links
M5	Unattended endurance: lost observations, reconnections, resident memory	Does it hold without an operator

M1 and M2 were separated only after a 33 h run showed one instrument spanning both, reporting the serial line as translation cost; the M1 values come from a later run with the instrument corrected. M3 alternates commands that reach the equipment with commands the gateway answers alone, so acceptance can be compared with and without a write.

RESULTS & DISCUSSION

The boundary carries traffic, and the gateway is not what it costs

Table 2 sets the cost of translation against the cost of reaching the equipment. Translation averaged 25 us over 138 observations from both nodes, while the 69 passes over the serial node took 769 ms each. Each node published one observation message per minute and all of them were timed, so 69 passes on each of two nodes give 138 observations, each carrying all 24 slots of its node.

Table 2. Cost of one observation, 24 equipment slots, 68 min, adapter buffer timer at 1 ms.

Stage	n	Minimum	Mean	Maximum
Translation, up to the client library	138	13 us	25 us	44 us
Serial line read, 24 slots	69	761 ms	769 ms	779 ms

The downward path tells the same story about where time goes. Table 3 reports 400 commands issued to 16 actuators with the two kinds alternating: those that found the actuator in another state were accepted and wrote to the equipment, and those that found it already in the requested state were refused by the gateway without a write. Every answer of either kind arrived inside the response obligation the draft places on the gateway, and the slowest of the 400 used 40 % of the prescribed limit (value withheld until public comment).

Table 3. Command path (16 actuators, command kinds alternating, n = 400, adapter buffer timer at its default).

Answer	Minimum	Median	Maximum
Accepted, wrote to the equipment	44.4 ms	53.0 ms	982 ms
Refused without a write	43.9 ms	47.1 ms	1211 ms

The two medians differ by 5.9 ms, which bounds the write loosely rather than measuring it: the draft's model returns acceptance before the operation completes, so the answer does not wait for the write. The tails say more than the medians. The longer one belongs to the group that never touched the equipment, and both are about a polling pass long. This run kept the adapter's default buffer timer, where the same 24 slots take about 1150 ms rather than the 769 ms of Table 2. It is the gateway's own loop, not the equipment write, that decides how late an answer can be.

Observation messages ran from 470 to 570 B for 24 slots and 723 to 745 B for 30, the configuration declaration 2081 B, and status messages 89 B. The declaration is the largest single message and the one that has to be carried whole. No field link was in the rig, so these sizes are for comparison against a link budget, not a claim about any particular link. A separate 33.4 h unattended run published 8009 messages, of which 4004 were observations, and settled its resident memory after 17 h. Its own counters recorded no lost observation and no reconnection; the published stream was not compared against a receiver, so the claim is that the gateway never detected a loss.

Translation on the upward observation path therefore costs almost nothing in processing time. The downward path was not measured the same way. The draft has the gateway answer before the write completes, so the times in Table 3 bound the whole acceptance path rather than isolating translation inside it, and no claim is made here about what downward conversion costs. What decides whether the gateway keeps the promises the draft makes on its behalf lies elsewhere, and the text names none of it. Per equipment slot the serial line costs 32.0 ms,

so the prescribed limit divided by that cost is about 93 slots on one line if slot reads were all that consumed it. That figure is a calculation from a per-slot cost under one rig and one scheduling policy, not a capacity we demonstrated. It moves with both. The same line gave 48 ms per slot until we lowered the default buffer timer of the USB serial adapter, which changes the arithmetic from 62 slots to 93; and because this gateway polls and answers in one loop, a request that arrives early in a pass waits for the pass. A driver setting and a scheduling choice, neither of them named in any clause, move what a conformant gateway can carry.

What the draft leaves open

The implementation produced 50 items for the drafting process. Thirty-five hold whatever equipment sits below the gateway, because they concern what the draft does not say rather than what the equipment cannot do. Table 4 gives the eight that a measurement settles, without clause references, since the draft is not in public comment.

Table 4. Eight points the draft leaves unspecified, and what each one costs.

What the draft does not say	What the rig showed	If left
The line a response deadline assumes	93 slots per line, 62 on the driver default	Conformance turns on an unnamed setting
A size bound on a reply carrying retained data	The last reply to leave held 13 min; the window it may be asked for is counted in hours	No answer is sent and the session drops with it
What instant an observation time refers to	A read pass takes 769 ms	Start or end of the read differ by a pass
Whether a status trigger is per gateway or per node	We implemented one reading and had to change it	Traffic differs by node count; two honest readings
Where the shortest status interval is measured from	From the previous send it becomes 119.9 s	The stated bound is not the one implemented
The keep-alive behind a liveness notice	A killed process shows 0.0 s; a cut line 18.2 s after a 10 s keep-alive and 38.1 s after 30 s	Time to see a dead gateway is unset
What the notice a dying gateway leaves means	It fires on every reconnection	A reconnection reads as a stop
Whether a retained declaration must be restored	Our gateway refilled it 1 s after the broker returned, on its own initiative	Absent cannot be told from forgotten

One row needs its conditions stated. The draft bounds how long data must be retained but not how large a reply may be, so asking for the whole window is conformant. At 752 B per record the largest reply that left carried 13 records; the whole window would be 1440 records at 1.08 MB. Such a reply meets our client library's 10 kB default packet ceiling first, and fails worse than a refusal: the gateway records that it answered, the publish never leaves, the session drops, and no result code reaches the requester. The ceiling is ours and would differ elsewhere; the draft's part is that no bound is stated at all, so one query can take down the session that the liveness notice then reports as a stop.

The other fifteen divide differently: four are places where the draft asks for something this class of equipment cannot supply, which is a property of the boundary rather than a defect in the text, and eleven fall outside the draft, among them five for the published specification assets and three defects of our own. The first round is in the drafting record, and the second has been submitted to the standards development body. Whether the text changes is that body's

decision; what this work claims is that the evidence was produced while the text was still open.

Limitations

The equipment side is a stand-in, and a different legacy protocol would put different demands on the gateway. The nodes were emulated rather than vendor firmware, although the serial line, network, and broker were real, so what is shown is that this protocol can be carried over a real line, not that a particular installed device joins without replacement. Only one node was on the RS-485 line, so contention there is known by calculation. Translation time ends when the message is handed to the client library, and observations go at a quality of service with no acknowledgement (OASIS, 2019), so no later instant is observable. Interoperability against an independent implementation remains to be done.

CONCLUSIONS

Emulated nodes implementing this standardized register-based protocol were admitted to the draft open-field standard through the gateway in the tested configuration. The boundary carried traffic both ways, and the gateway is not what makes admission expensive: translation averaged 25 us against 769 ms on the serial line, an actuator command was answered a median 5.9 ms later than one the gateway refused without a write, and it ran 33.4 h unattended without recording a loss.

What a gateway can promise is bounded by the line beneath it and by how the gateway schedules its own work, and both bounds belong in the text. An obligation stated as a fixed time is not implementable until the conditions under which it holds are stated with it. Here the arithmetic moved by half on a serial driver default, and under that same default the latest answers were as long as a polling pass, because polling and answering shared one loop. Neither the line configuration nor the scheduling policy appears in any clause.

Building the implementation during drafting produced 50 items, 35 of them points the draft does not settle, and they were raised while the text was still open. Defects of this kind are cheaper to settle then than after enactment.

ACKNOWLEDGEMENTS

This work was supported by the Korea Institute of Planning and Evaluation for Technology in Food, Agriculture and Forestry (IPET) through the Open-Field Smart Agriculture Application Model Development Program, funded by the Ministry of Agriculture, Food and Rural Affairs (MAFRA) (Project No. RS-2025-02307027).

REFERENCES

KATS. 2022a. KS X 3267:2022 RS485 MODBUS interface between sensor/actuator node and greenhouse controller in smart greenhouse. Seoul, Korea: Korean Standards Association.

KATS. 2022b. KS X 3269:2022 Smart greenhouse sensor metadata. Seoul, Korea: Korean Standards Association.

KATS. 2022c. KS X 3286:2022 RS485/MODBUS-based smart greenhouse node/device registration procedures and description specification. Seoul, Korea: Korean Standards Association.

Kim, J. Y., S. Kim, and J. Lee. 2018. Comparative analysis of TTAK.KO-06.0288-Part3 and development of an open-source communication library for greenhouse control system. J. Biosyst. Eng. 43(1): 72-80.

Modbus Organization. 2006. Modbus over serial line specification and implementation guide, ver. 1.02. Hopkinton, Mass.: Modbus Organization.

OASIS. 2019. MQTT version 5.0. OASIS standard. Burlington, Mass.: OASIS.

Zhao, Z., W. Huangfu, L. Sun, Z. Shi, and W. Gan. 2012. An open conformance test system towards the standardization of wireless sensor networks. Int. J. Distrib. Sens. Netw. 8(12): 931869.

SF-P19

Proceedings of The 12th International Symposium on Machinery and Mechatronics for Agriculture and Biosystems Engineering (ISMAB 2026)
20-24 October 2026, Busan, Republic of Korea

THREE-DIMENSIONAL SHAPE AND VOLUME ANALYSIS OF A PIG MODEL USING MULTI-VIEW DEPTH IMAGES

Seung Hyeon Cheon[1], Byeong Eun Moon[1]*

[1]Department of Convergence Biosystems Engineering, Sunchon National University, Suncheon 57922, Republic of Korea

*Corresponding Author-- Voice: +82-61-750-3263, Email: mbe25@scnu.ac.kr

Abstract: This study evaluated three-dimensional (3D) shape reconstruction and volume measurement of a pig model using multi-view depth images. Three RGB-Depth cameras (RealSense D455f) were arranged at Top-90°, Side-45°, and Side-0° views. RGB extrinsic calibration was performed with a ChArUco board, and the resulting transformations were converted to the depth coordinate systems using the factory RGB-to-depth calibration of each camera. Registration performance was evaluated from 26 ChArUco depth-image sets. Dimensional accuracy was then verified with rectangular and cylindrical reference objects, followed by voxel-based reconstruction of a pig model from 10 repeated measurements. The overall RMSE of the three registered point clouds relative to a common plane was 7.70±1.97 mm. For the reference objects, MAPE ranged from 0.14 to 2.37% and RMSE from 1.13 to 4.85 mm. The pig model was reconstructed using 3-mm voxels, and its mean volume was 14.761±0.054 L with a coefficient of variation (CV) of 0.365%. Relative error against a 3D-scanner reference volume of 15.176 L was -2.73%. CVs of trunk volume, length, mean width, and mean cross-sectional area were 0.330-0.451%. The results show that multi-view depth imaging can provide repeatable quantitative measurements of 3D shape and volume under controlled pig-model conditions and can serve as a technical basis for future non-contact body-shape and body-weight assessment of live pigs.

Key Words: Body measurement, Depth camera, Pig model, Precision livestock farming, 3D point clouds

INTRODUCTION

Monitoring body weight and body conformation is essential for growth assessment, feeding management, and shipment decisions in pig production. Conventional weighing scales and manual body measurements require animal handling and labor, while movement during measurement reduces repeatability. Consequently, vision-based non-contact methods have been investigated to obtain body dimensions and estimate live weight. RGB-Depth cameras are particularly useful because depth information enables direct representation of the animal surface as a 3D point cloud. Previous studies have measured body length, height, width, heart girth, and cross-sectional features from pig point clouds and have used these descriptors for weight estimation (Li et al., 2022).

A single overhead view, however, cannot directly observe hidden side surfaces, and pig posture and location can alter the visible geometry and cause missing depth data. Multi-view systems can reduce occlusion by integrating point clouds from several cameras. Kwon and Mun (2022) reconstructed pig surface meshes from multiple depth cameras, and Kwon et al. (2023) derived morphometric variables from reconstructed 3D models for weight estimation. For such systems, reliable inter-camera calibration, depth-coordinate registration, dimensional accuracy, and repeatability must be established before application to freely moving animals.

The objective of this study was therefore to quantify the measurement performance of a three-camera multi-view depth system under controlled conditions using a pig model. Specifically, we evaluated (1) RGB extrinsic calibration and depth-coordinate registration, (2) dimensional accuracy using reference objects, (3) voxel-based 3D reconstruction and volume accuracy of the pig model, and (4) repeatability of trunk morphometric indices.

MATERIALS AND METHODS

IMAGE ACQUISITION SYSTEM

A pig model representing an approximately 20-30 kg piglet (length 0.66 m, height 0.41 m, width 0.22 m) was measured using three RealSense D455f RGB-Depth cameras. Cameras were fixed to an aluminum-profile frame and arranged as Top-90°, Side-45°, and Side-0° views so that the dorsal and lateral surfaces were covered simultaneously. RGB and depth images were acquired at 1280×720 pixels and 15 fps. Raw Z16 depth images were stored without interpolation or alignment to the RGB coordinate system. A software synchronization procedure used global timestamps of depth frames; only camera triplets with a maximum timestamp difference of 50 ms or less were accepted. Ten synchronized image sets were acquired with the model position and posture fixed.

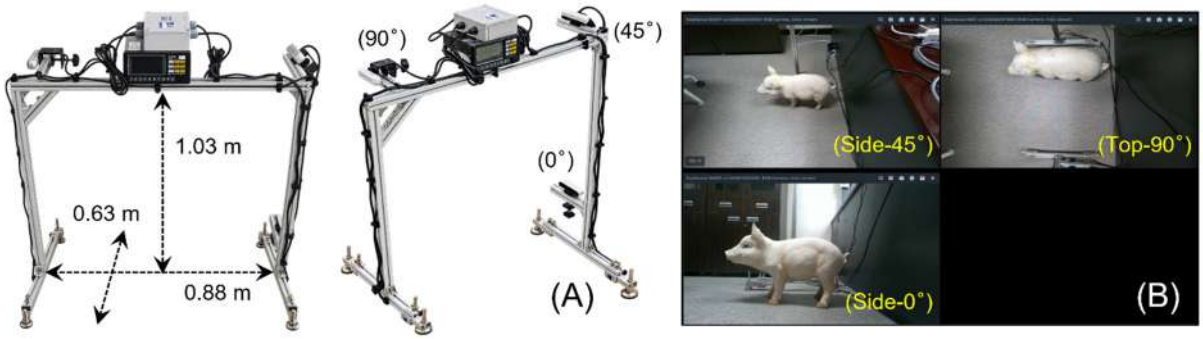

Fig. 1 Configuration of the multi-view RGB-Depth image acquisition system: (A) experimental setup, (B) RGB images from the three camera views.

CALIBRATION, REGISTRATION, AND ACCURACY VALIDATION

RGB extrinsic calibration was conducted with a 6×8 ChArUco board (30-mm square size and 22-mm marker size). Images were collected while varying board position, distance, roll, pitch, and yaw. For each adjacent camera pair (Top-90°/Side-45° and Side-45°/Side-0°), 15 poses were used for calibration and 5 independent poses for validation. Stereo calibration was performed with fixed RGB intrinsics. The inter-camera RGB transformations were combined with the factory RGB-to-depth transformations of each camera to obtain depth-coordinate

transformations, and the Top-90° depth coordinate system was used as the common reference. Registration was evaluated using 26 synchronized depth-image sets of the ChArUco board by calculating plane angle difference, plane position difference, point-to-plane RMSE, and RMSE to a common plane fitted to all three point clouds. No ICP or post-registration correction was applied.

Dimensional accuracy was assessed with a rectangular box (reference dimensions 380×285×195 mm) and a cylindrical duct assembly (length 605 mm; evaluated diameters 200 and 250 mm). Twenty-two box poses with different positions and horizontal rotations and ten repeated duct measurements were analyzed. Principal component analysis and plane fitting were used for box dimensions, while cross-sectional circle fitting was used for duct diameters. Mean error, MAE, RMSE, and MAPE were calculated against reference dimensions.

3D RECONSTRUCTION AND MORPHOMETRIC ANALYSIS

For each pig-model image set, raw depth images were converted to point clouds and transformed to the Top-90° coordinate system. The floor plane was removed, the model region was segmented, and the principal body axis was determined. The 3D space was discretized into 3-mm voxels. A voxel was retained when it was consistent with the pig-model masks and measured depth surfaces from the cameras; additional surface-near voxels were included to compensate for missing depth and registration uncertainty. Because the cameras mainly observed the top and one side, the reconstructed visible side was mirrored about the estimated sagittal plane to complete the opposite side. Volume was calculated from the occupied voxel count. A reference volume of 15.176 L obtained previously by 3D scanning of the same pig model (Lee, 2017) was used only for final accuracy evaluation. The trunk region was extracted from changes in horizontal and longitudinal cross-sectional area, and trunk volume, length, mean width, and mean cross-sectional area (CSA) were calculated for all 10 sets. Repeatability was expressed as CV.

RESULTS & DISCUSSION

CALIBRATION AND DEPTH-COORDINATE REGISTRATION

RGB stereo calibration produced reprojection RMS values of 0.520 pixels for Top-90°/Side-45° and 0.616 pixels for Side-45°/Side-0°. Independent validation yielded symmetric epipolar RMSE values of 0.319±0.065 and 0.461±0.129 pixels, respectively. After conversion to the depth coordinate systems, mean plane-angle differences among camera pairs were 0.53-0.73°, whereas plane-position differences varied more substantially. Top-90°/Side-0° showed a small position difference of 1.90±1.41 mm, while pairs involving Side-45° showed 14.30±3.18 and 15.33±2.71 mm. The overall RMSE of all three point clouds relative to a common plane was 7.70±1.97 mm (range 5.22-12.32 mm). The Side-45° view contributed the largest common-plane error (11.64±4.70 mm). These errors were larger than values reported for multi-camera systems that subsequently applied ICP refinement (Kwon and Mun, 2022; Kwon et al., 2023), but the present system intentionally evaluated the direct calibration chain without ICP or post-correction.

DIMENSIONAL ACCURACY OF REFERENCE OBJECTS

Despite the inter-camera registration error, dimensional measurements were substantially more accurate than the worst pairwise plane offsets. For the box, MAPE was 0.41% for length,

0.83% for width, and 2.37% for height; the corresponding RMSE values were 1.81, 2.72, and 4.85 mm. The height was consistently overestimated by 4.61 mm on average. For the duct, length MAPE was 0.14% and RMSE was 1.13 mm. Diameter MAPE values were 1.82% at 200 mm and 1.37% at 250 mm, with RMSE values of 3.83 and 3.64 mm. The low standard deviations in repeated duct measurements (0.77-1.34 mm) indicate stable measurement under fixed conditions. The different signs of box-height and duct-diameter errors suggest that residual error depends on object geometry, surface orientation, and the point-cloud feature used for measurement rather than on a single uniform coordinate offset.

PIG-MODEL RECONSTRUCTION, VOLUME, AND MORPHOMETRICS

All 10 image sets produced complete reconstructed shapes containing the trunk, head, legs, and tail. Measured total volume ranged from 14.690 to 14.844 L, with a mean of 14.761±0.054 L and a CV of 0.365%. Compared with the 15.176-L 3D-scanner reference, mean volume error was -0.414 L and relative error was -2.73%; all repeated measurements underestimated the reference. The bias is likely associated with residual depth-registration error, discretization at the 3-mm voxel boundary, missing depth around complex regions such as the head and legs, and the symmetry-based completion of the unobserved side. Nevertheless, the small CV indicates that these effects were highly repeatable in the fixed-pose experiment.

Trunk metrics showed similarly high repeatability. Mean trunk volume was 8.720±0.038 L (CV 0.440%), trunk length was 341.10±1.45 mm (0.425%), mean width was 160.99±0.53 mm (0.330%), and mean CSA was 25,563.7±115.2 mm² (0.451%). At normalized trunk positions of 25%, 50%, and 75%, the 50% position had the largest width, vertical extent, and CSA. Position-specific CVs ranged from 0.293 to 1.611% for width, from 0.519 to 0.580% for vertical extent, and from 0.488 to 0.618% for CSA. These results support the use of reconstructed 3D geometry for extracting local and global morphometric descriptors, consistent with previous multi-view pig reconstruction studies (Kwon and Mun, 2022; Kwon et al., 2023). However, the present evaluation used a rigid symmetric model; actual pigs exhibit posture changes, abdominal deformation, asymmetric body surfaces, hair/skin reflectance effects, and continuous movement. Field validation must therefore address pose selection, motion synchronization, occlusion, and robustness of segmentation before the same metrics are used for automatic live-weight estimation.

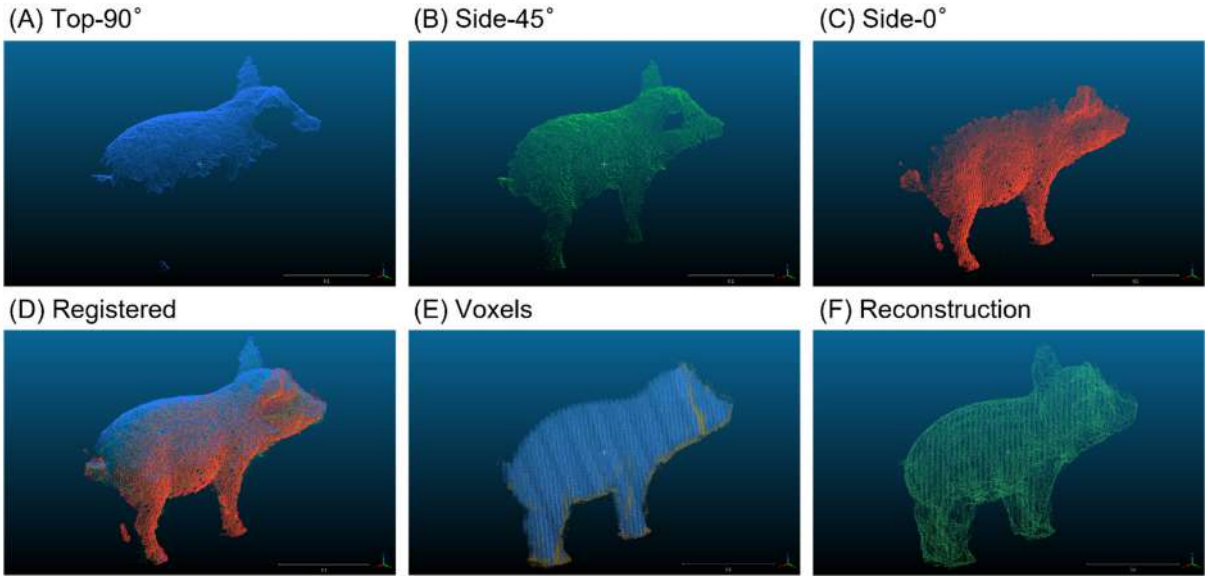

Fig. 2 Voxel-based 3D reconstruction of the pig model from multi-view point clouds.

Table 1 Summary of measurement accuracy and repeatability of the multi-view RGB-Depth system.

Evaluation	Metric	Result
Depth registration	Overall common-plane RMSE	7.70±1.97 mm
Box measurement	MAPE	0.41-2.37%
Duct measurement	MAPE	0.14-1.82%
Pig-model volume	Mean±SD	14.761±0.054 L
Pig-model volume	Relative error	-2.73%
Pig-model volume	CV	0.365%
Trunk morphometrics	CV	0.330-0.451%

CONCLUSIONS

A three-camera multi-view RGB-Depth system was evaluated for 3D measurement of a pig model. Direct depth-coordinate registration without ICP produced an overall common-plane RMSE of 7.70±1.97 mm, while reference-object measurements achieved MAPE values of 0.14-2.37%. Voxel-based reconstruction yielded a mean pig-model volume of 14.761±0.054 L, corresponding to -2.73% error against a 3D-scanner reference and 0.365% repeatability CV. Trunk morphometric CVs were 0.330-0.451%. The system therefore provided repeatable 3D shape and volume measurements under controlled conditions. Future work will focus on live pigs under farm conditions, with particular attention to motion, posture variability, occlusion, automated segmentation, and the use of 3D morphometrics for non-contact weight estimation.

ACKNOWLEDGEMENTS

This work was supported by a Research promotion program of Sunchon National University (SCNU).

REFERENCES

Kwon, K., and D. Mun. 2022. Iterative offset-based method for reconstructing a mesh model from the point cloud of a pig. Computers and Electronics in Agriculture 198: 106996.

Kwon, K., A. Park, H. Lee, and D. Mun. 2023. Deep learning-based weight estimation using a fast-reconstructed mesh model from the point cloud of a pig. Computers and Electronics in Agriculture 210: 107903.

Lee, M. H. 2017. Estimation pig's volume by using laser scanner and CCD camera. M.S. thesis. Jinju, Republic of Korea: Gyeongsang National University.

Li, G., X. Liu, Y. Ma, B. Wang, L. Zheng, and M. Wang. 2022. Body size measurement and live body weight estimation for pigs based on back surface point clouds. Biosystems Engineering 218: 10-22.

Special Session

Proceedings of The 12th International Symposium on Machinery and Mechatronics for Agriculture and Biosystems Engineering (ISMAB 2026)
20-24 October 2026, Busan, Republic of Korea

CHARACTERISTICS OF TACTILE SENSORS IN GRASPING OPERATIONS FOR FRUIT AND VEGETABLES USING FIVE-FINGERED ROBOT HAND

Ji Won Choi[1,2], Soo Been Cho[1,2], Jung-sang Yoo[2], Seung-Hwan Yang[2*]

[1]Department of Biosystems Engineering, College of Agricultural and Life Sciences, Gyeongsang National University, 501, Jinju-daero, Jinju-si, Gyeongsangnam-do, Republic of Korea
[2]Specialized Machinery and Robotics Group, Korea Institute of Industrial Technology, 119, Jipyeongseonsandan-3gil, Gimje-si, Rep. of Korea
*Corresponding Author-- Voice: +10-6728-3373, Email: yangsh@kitech.re.kr

Abstract: Interests in utilizing humanoid robots for agricultural tasks are increasing while humanoid robots are about to apply for manufacturing and logistics industries. The humanoid robots are expected to be utilized for harvesting and sorting tasks in the agricultural sector. In particular, the humanoid robots having five-fingered hands may work diverse and precise tasks as much as human. In this study, various types of fruit and vegetables such as apples, bananas and cherry tomatoes were grasped using a five-fingered robot hand, and then the operational characteristics of the hand were investigated. The five-fingered robot hand was mounted on a manipulator and controlled using a teleoperation grove. When a human hand wearing the grove grasps an object, the robot hand simultaneously grasps the same another object. Through these experiments, which fingers should be used and how tactile pressure of each finger is introduced were investigated. The fingers used and their pressures are influenced by the shape and hardness of the object. Furthermore, although the five-fingered robot hand is similar with a human hand, its operating degrees of freedom are limited compared with the human hand so that the hand motion for grasping has to be adjusted for the robot hand. The robot hand used in this study has 11 joints and 32 to 60 tactile sensor points on the fingertips and palm. Consequently, specific methods to grasp apples, bananas and cherry tomatoes were proposed and the characteristics of tactile sensors were measured.

Key Words: Agricultural robot, Humanoid, End-effector, Pressure sensor, Teleoperation

ACKNOWLEDGEMENTS

This study was supported by the Korea Institute of Industrial Technology (KITECH) under the project "Development of Physical AI and Core Technologies for Autonomous Humanoid Tasks" (No. UR260076).

Proceedings of The 12th International Symposium on Machinery and Mechatronics for Agriculture and Biosystems Engineering (ISMAB 2026)
20-24 October 2026, Busan, Republic of Korea

PERCEPTION AND AUTONOMY IN AGRICULTURAL ROBOTICS: CROP PERCEPTION, SLAM, AND MULTI-ROBOT CONTROL

Chanyoung Ju[1,2,*]

[1]Korea Institute of Industrial Technology (KITECH), Republic of Korea
[2]University of Science and Technology (UST), Republic of Korea
*Corresponding Author-- Voice: +82-62-600-6450, Email: cyju@kitech.rer.kr

Abstract: Agricultural robots must operate in environments that are unstructured, repetitive, dynamic, and only partially observable. Reliable autonomy therefore depends not on a single algorithm but on the coordinated design of perception, localization, planning, and control. This study presents selected research on perception and autonomy in agricultural robotics, with emphasis on crop perception, SLAM-based navigation, and multi-robot control, and discusses a practical pathway toward vision-language-action (VLA)-enabled operations.

The crop-perception studies address two task-oriented problems. First, AI-based recognition of crop diseases and pests is connected to target localization and autonomous precision spraying. Second, segmentation and skeleton extraction are used to estimate topological crop structures, including stems, branches, endpoints, and candidate cutting points, for robotic pinching and pruning. The navigation studies investigate multimodal SLAM and autonomous driving in smart farms and agricultural products processing centers (APCs), where narrow passages, repetitive crop rows, appearance changes, dynamic obstacles, and wheel slip challenge robust state estimation. The multi-robot studies combine supervisory control with reinforcement learning. In this architecture, the supervisor constrains unsafe or infeasible state transitions, while reinforcement learning improves task allocation and operational performance within the admissible behavior space.

A cross-domain analysis of these studies yields three observations. First, crop perception should be assessed not only by recognition accuracy but also by task relevance, geometric consistency, and topological correctness. Second, agricultural SLAM should represent semantic and task states in addition to robot poses and geometric maps. Third, multi-robot learning requires explicit coordination and safety mechanisms to prevent collisions, deadlocks, and invalid task sequences. Based on these observations, the paper outlines a hierarchical VLA extension in which natural-language instructions are grounded in perceived crop and environment states, decomposed into task and skill sequences, and executed through verified navigation and control modules rather than direct end-to-end actuation. This synthesis provides a system-level perspective on connecting crop-level perception, environment-level navigation, and fleet-level coordination.

Key Words: Agricultural robotics, Perception, Autonomy, SLAM, Multi-robot control

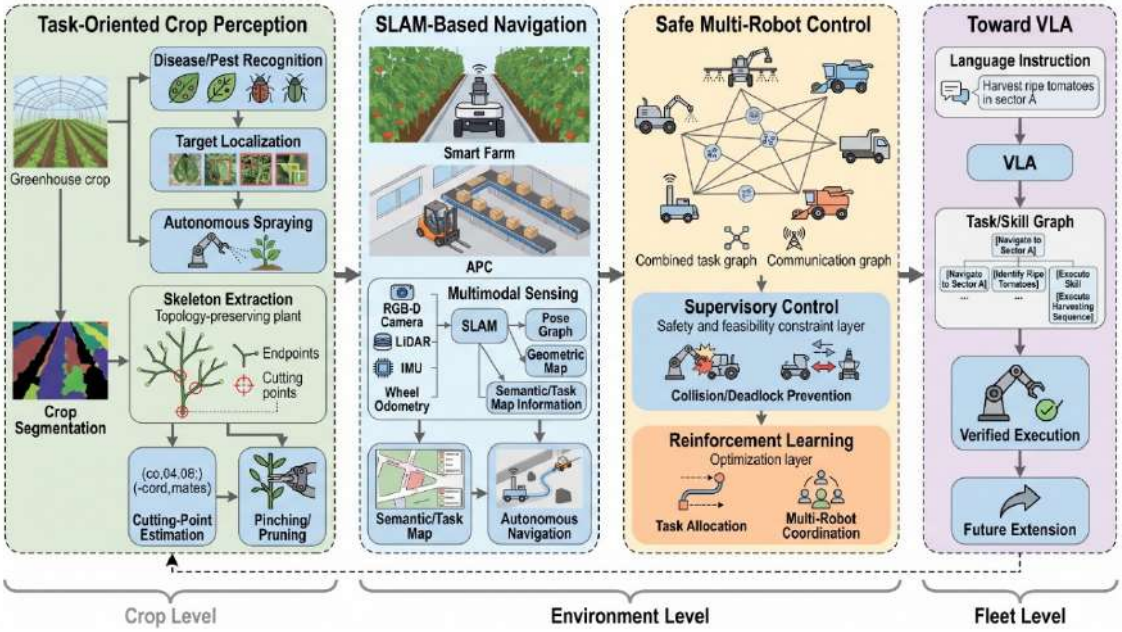

Fig.1 Research scope linking task-oriented perception, SLAM-based autonomous navigation, safe multi-robot control, and a hierarchical extension toward VLA-enabled agricultural operations.

ACKNOWLEDGEMENTS

This work was supported in part by Korea Institute of Planning and Evaluation for Technology in Food, Agriculture and Forestry(IPET) and Korea Smart Farm R&D Foundation(KosFarm) through Smart Farm Innovation Technology Development Program, funded by Ministry of Agriculture, Food and Rural Affairs(MAFRA) and Ministry of Science and ICT(MSIT), Rural Development Administration(RDA)(RS-2025-02307287), and in part by Ministry of Economy and Finance (MOEF) under the Institutional Strategic Development (ISD) Program administered by the Korea Institute of Industrial Technology (KITECH) (Project No. JK260002).

Proceedings of The 12th International Symposium on Machinery and Mechatronics for Agriculture and Biosystems Engineering (ISMAB 2026)
20-24 October 2026, Busan, Republic of Korea

DEVELOPMENT OF AN IMITATION LEARNING ALGORITHM FOR STRAWBERRY HARVESTING IN IRREGULAR ENVIRONMENTS

Byung-Kil Han[1], Taeyong Choi[1*], Jongcheon Park[1]

[1]Advanced Robotics Research Center, Research Institute of AI Robotics, Korea Institute of Machinery and Materials, South Korea
*Corresponding Author-- Email: taeyongc@kimm.re.kr

Abstract: Vertical farms have attracted increasing attention as a solution to global agricultural challenges, including soil and water pollution, labor shortages, shrinking arable land, and production instability caused by climate change. By artificially controlling light, temperature, humidity, and nutrient supply in an enclosed space, they enable stable crop production independent of seasonal conditions, and their uniform, structured cultivation environment makes them particularly well suited to robotic automation. Recently, Physical AI approaches that combine camera-based perception, robotic manipulation, and Vision-Language-Action (VLA) models have been applied to agricultural tasks such as harvesting high-value crops like strawberries. However, most existing VLA-based methods assume relatively structured scenes in which the manipulated objects are clearly distinguishable from their surroundings. In vertical farms, by contrast, multiple visually similar fruits are densely arranged and the target object is frequently occluded by leaves, stems, or neighboring fruits. Under such conditions, an RGB-centric End-to-End VLA policy that does not explicitly utilize the spatial position of the target and its relationship to surrounding objects may confuse targets or determine an inaccurate approach direction and position, degrading grasping and harvesting performance. In this paper, we propose a target-object information-augmented VLA model for autonomous strawberry harvesting using a bimanual robot in vertical farm environments. The proposed method augments the conventional VLA inputs with explicit target-object information obtained from a perception module. Objects in the wrist-camera image are detected using an open-vocabulary detector driven by text prompts, and among the detected candidates whose bounding-box centers fall within a predefined region of interest, the one closest in depth is selected as the harvesting target. Its 3D position, estimated from the bounding box and depth map, is concatenated with the robot state, while a segmentation mask generated by the Segment Anything Model is blended with the RGB image to emphasize the visual region of the target. These augmented inputs are fed to a VLA policy enabling it to exploit both the spatial and visual information of the object to be manipulated. The proposed pipeline was implemented on a Robotis AI Worker FFW-SG2 bimanual robot and evaluated in a three-tier strawberry harvesting environment inspired by vertical farms, where the task comprises target recognition, approach, grasping, detachment, transport, and placement into a storage bin.

Key Words: Bimanual robot, Imitation learning, Strawberry harvesting, Agricultural robot

ACKNOWLEDGEMENTS

This research was supported by the Technology Innovation Program (2410011794, “Agriculture dual-arm robot autonomy technology based on force posture composite learning”) funded by the Ministry of Trade, Industry and Energy, Korea Government.

Proceedings of The 12th International Symposium on Machinery and Mechatronics for Agriculture and Biosystems Engineering (ISMAB 2026)
20-24 October 2026, Busan, Republic of Korea

DEVELOPMENT OF A ROBOTIC TOOL FOR STEMLESS STRAWBERRY HARVESTING

Taeyong Choi[1*], Byung-Kil Han[1], Jongcheon Park[1]

[1]Advanced Robotics Research Center, Research Institute of AI Robotics, Korea Institute of Machinery and Materials, South Korea
*Corresponding Author-- Email: taeyongc@kimm.re.kr

Abstract: This study develops a robotic end-effector for strawberry harvesting in greenhouses. Fruit detachment is a fast, coupled pull-and-twist motion, and reproducing it with a multi-motor wrist under feedback control makes the device heavy, slow and costly to maintain. The proposed device instead performs the detachment mechanically using a two-degree-of-freedom (2-DOF) mechanism. The first mechanism bends the stem and calyx by pulling the bottom of the strawberry, diverging from typical human motion. The second mechanism stores elastic energy using a spring and, upon release, executes a rapid rotational motion mimicking a human wrist to pluck the fruit in a single action. Soft pads on the fingers protect the fruit surface, and no pneumatic supply or compressor is required, so the unit stays light and compact enough for mobile platforms and narrow greenhouse aisles. The required snap speed and trajectory were specified from measured human harvesting motion rather than assumed. Harvesting videos (1920x1080, 30 fps) were processed with a SAM2.1 video predictor that segments the fruit and the hand simultaneously; a three-state estimator (direct observation, grasp-reference prediction under a hand-fixed rigid-body assumption, and optical-flow propagation) recovered the fruit trajectory and pose even while the hand fully enclosed the fruit, and the recovered motion was decomposed into a circular-arc rotation plus a linear translation of the rotation center. The observed motion characteristics were then used to set the snap stroke, the rotation range, and the target speed of the mechanism. A prototype built to this specification was fabricated and bench-tested on strawberries: it reproduced the prescribed trajectory repeatably and detached fruit from the peduncle without visible damage. Specifying a passive, motion-guided mechanism from measured human motion is thus a practical route to fast and simple harvesting tools.
Key Words: Harvesting end-effector, Strawberry harvesting, Motion-based design, Agricultural robot

ACKNOWLEDGEMENTS

This research was supported by the Technology Innovation Program (2410011794, “Agriculture dual-arm robot autonomy technology based on force posture composite learning”) funded by the Ministry of Trade, Industry and Energy, Korea Government.

Proceedings of The 12th International Symposium on Machinery and Mechatronics for Agriculture and Biosystems Engineering (ISMAB 2026)
20-24 October 2026, Busan, Republic of Korea

APPLICATION AND PERFORMANCE EVALUATION OF OFFSET DRIVING PATHS FOR ORCHARD WEEDING ROBOTS

Jaewan Koo[1], Kyon-Mo Yang[1], and Kap-Ho Seo[1*]

[1]Regional R&D Division, Korea Institute of Robotics & Technology Convergence, Pohang, 37553, Korea
*Corresponding Author-- Email: neoworld@kiro.re.kr

Abstract: This study evaluated the application of offset driving paths for orchard weeding robots to expand the effective working area. The reference path was divided into straight and curved sections, and offset paths were generated only for straight sections while the original path was maintained in curved sections. The offset distance was determined based on the physical working width and required overlap of the weeding implement. In the field experiment, a working width of 0.6 m and an overlap of 0.2 m were used, resulting in an offset interval of 0.4 m. Driving tests were conducted using an agricultural mobile robot in an actual orchard. The generated paths maintained consistent lateral spacing in straight sections and provided continuous driving through curved sections. The mean tracking error in straight sections was approximately 4 cm. The results demonstrate that offset driving paths can effectively extend the working coverage of orchard weeding robots using a single reference path.

Key Words: Agricultural robot, Orchard, Weeding, Offset path, Path tracking.

INTRODUCTION

Agricultural robots have been increasingly investigated to reduce labor requirements and improve the efficiency of repetitive field operations such as weeding. For practical field operation, agricultural robots require not only reliable localization and path tracking but also path-planning methods that consider the characteristics of the working environment and agricultural task (Slaughter et al., 2008; Bechar and Vigneault, 2016). In agricultural operations, the driving path should also provide efficient coverage of the target working area rather than simply connecting navigation points (Oksanen and Visala, 2009).

For orchard weeding, the working width and overlap of the weeding implement should be considered together with the robot driving path. Jeon et al. (2023) developed a path generation and control system for unmanned orchard weeding using parameters such as the weeding width, number of operations, and robot width, and evaluated its driving performance in an apple orchard. More recently, Oh et al. (2026) developed an autonomous navigation framework for an orchard weeding robot, including automatic path generation considering robot width and overlap, and validated its path-tracking performance under field conditions. These studies demonstrate the importance of working-width-based path generation for effective orchard weeding operations.

However, applying a uniform lateral offset to an entire reference path may also modify the geometry of curved and turning sections. Therefore, applying offset paths only to straight working sections while maintaining the original reference path in curved sections can provide a practical approach for orchard operations.

The objective of this study was to apply offset driving paths selectively to straight working sections for orchard weeding and to evaluate the generated paths and path-tracking performance using an agricultural mobile robot under actual orchard conditions.

MATERIALS AND METHODS

Offset Path Generation for Orchard Weeding

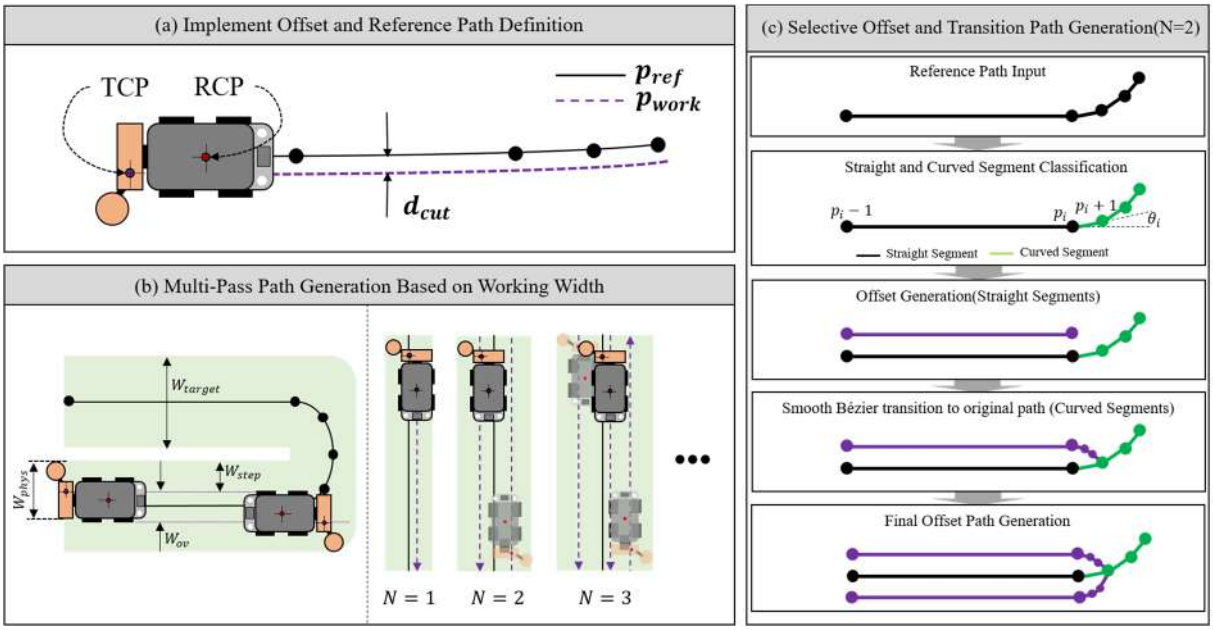

Fig. 1 Concept of offset path generation for orchard weeding: (a) implement offset and reference path definition, (b) multi-pass path generation based on working width, and (c) selective offset and transition path generation.

In this study, offset driving paths were generated from a single reference path to extend the working coverage of an orchard weeding robot. As shown in Fig. 1(a), the offset direction was defined based on the reference path of the robot and the mounting position of the weeding implement. The path interval, W_{step}, was determined considering the physical working width of the implement and the required overlap between adjacent passes.

Multiple working paths were generated according to the target working area and the required number of passes, N, as illustrated in Fig. 1(b). In the experiment, the physical working width and overlap were set to 0.6 m and 0.2 m, respectively, resulting in a path interval of 0.4 m. Multiple driving paths were then generated based on the reference path.

The orchard path was divided into straight working sections and curved or turning sections. As shown in Fig. 1(c), the calculated offset was applied only to the straight sections, while the original reference path was maintained in the curved sections. Transition paths were generated

between the offset straight paths and the original curved path to provide continuous path connections. This approach extends the working coverage in straight sections while avoiding excessive deformation of curved paths.

RESULTS & DISCUSSION

Figure 2 shows the offset driving paths generated from the reference path (RDDF) according to the number of working passes, N. The target spacing between adjacent working paths, W_{step}, was set to 0.4 m. For N = 2, two working paths were generated with lateral offsets of approximately 0.2 m on both sides of the reference path, resulting in a spacing of 0.4 m between the two paths.

For N = 3, the original reference path was maintained as the center path, while two additional paths were generated with lateral offsets of 0.4 m on both sides. The specified offset distance was consistently maintained in the straight sections, while the offset paths were connected to the original path in curved and turning sections. These results demonstrate that multiple weeding paths can be generated from a single reference path according to the required number of passes and working width.

The mean lateral tracking error in the straight working sections was approximately 0.04 m, indicating that the generated offset paths could be reliably followed under orchard conditions.

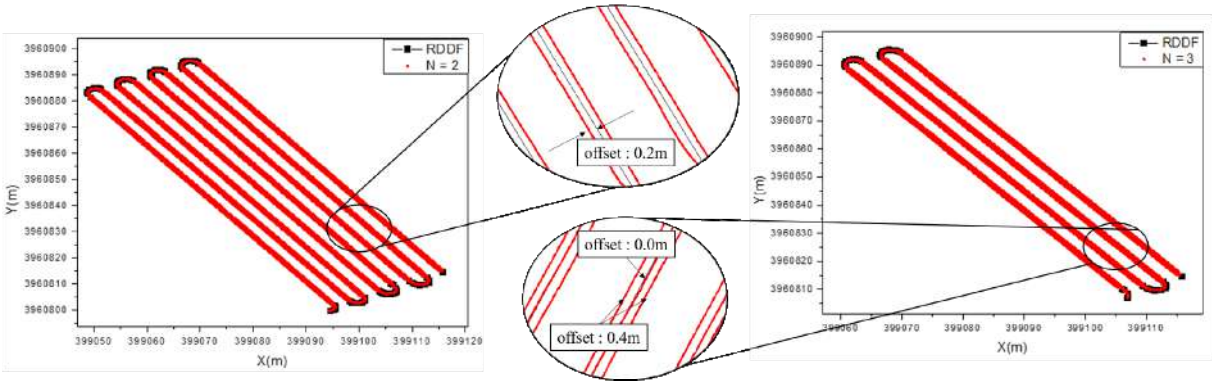

Fig. 2. Comparison of the reference path (RDDF) and generated offset paths for N=2 and N=3

CONCLUSIONS

This study generated and evaluated offset driving paths for an agricultural robot performing orchard weeding operations. The spacing between working paths was determined based on the working width and overlap of the weeding implement, and multiple paths were generated from a single reference path for N=2 and N=3 working conditions. The specified offsets were applied to straight working sections, while the original reference path was maintained in curved and turning sections to minimize unnecessary path deformation. The results confirmed that continuous working paths could be generated while maintaining the required spacing between adjacent passes. The proposed approach can improve the utilization of a single reference path and extend the working coverage of orchard weeding robots under different operating conditions.

ACKNOWLEDGEMENTS

This research was supported in part by the Korea Evaluation Institute of Industrial Technology (20018401), Republic of Korea.

REFERENCES

Bechar, A., and C. Vigneault. 2016. Agricultural robots for field operations: Concepts and components. Biosystems Engineering 149: 94-111. https://doi.org/10.1016/j.biosystemseng.2016.06.014.

Jeon, J. T., H. S. Jang, C. J. Yang, K. D. Kwon, Y. K. Hong, and G. H. Kim. 2023. Development of the path generation and control system for unmanned weeding robot in apple orchards. Journal of Drive and Control 20(4): 27-34.

Oh, S., H. Y. Jeon, J. Seo, K. H. Choi, and K. S. Kim. 2026. Field-validated navigation framework for orchard weeding robots using multimodal sensor fusion. International Journal of Control, Automation, and Systems 24(7): 1721-1738. https://doi.org/10.1007/s12555-026-00103-9.

Oksanen, T., and A. Visala. 2009. Coverage path planning algorithms for agricultural field machines. Journal of Field Robotics 26(8): 651-668. https://doi.org/10.1002/rob.20300.

Slaughter, D. C., D. K. Giles, and D. Downey. 2008. Autonomous robotic weed control systems: A review. Computers and Electronics in Agriculture 61(1): 63-78. https://doi.org/10.1016/j.compag.2007.05.008.

Proceedings of The 12th International Symposium on Machinery and Mechatronics for Agriculture and Biosystems Engineering (ISMAB 2026)
20-24 October 2026, Busan, Republic of Korea

METHOD FOR HETEROGENEOUS SENSOR DATA FUSION AND CROP 3D DATA GENERATION FOR AI ROBOT DEMONSTRATION IN FACILITY AGRICULTURE

Donghoon Kim[1], Yeonho Jo[1], Kwangjin Lim[1], Kangin Choi[1], Byoungjun Kim[1], Sunghwan Jeong[1*]

[1]Jeonbuk Regional Branch, Korea Electronics Technology Institute (KETI), Jeonju 54853, Republic of Korea
*Corresponding Author-- Voice: +82-63-219-0056, Email: shjeong@keti.re.kr

Abstract: Spatially aligned visual and three-dimensional (3D) crop data are required to support the validation of AI robots through crop growth assessment in controlled-environment agriculture. This study designed a framework for generating fused 3D crop data by integrating camera–LiDAR calibration, LiDAR–LiDAR calibration, and panoramic image generation to address differences in sensor coordinate systems and observation coverage.
Camera–LiDAR calibration was performed by estimating inter-sensor rotation and translation from geometric relationships derived from checkerboard detection. The estimated extrinsic parameters and camera intrinsic parameters were used to project 3D points onto images, establishing correspondences between image pixels and point clouds within overlapping fields of view. LiDAR–LiDAR calibration was performed using point-cloud feature extraction and iterative closest point (ICP) registration, enabling local point clouds from individual LiDAR sensors to be merged within a common reference coordinate system.
The fusion framework was designed to combine overlapping images into a panorama and associate it with the merged point cloud by applying image-to-panorama coordinate transformations to the image coordinates of projected 3D points. This mapping enables image color information and selected crop regions to be linked to the corresponding observed 3D points.
After both calibration procedures were completed, the sensors were deployed in an operational greenhouse to collect images and point clouds, establishing an experimental basis for merging local 3D data and performing projection-based sensor fusion. Future work will evaluate registration and reprojection accuracy and validate the integrated data for crop region extraction and the analysis of spatial crop growth characteristics.

Key Words: Controlled-environment agriculture, Heterogeneous sensor fusion, Sensor calibration, Panoramic imaging, 3D crop data.

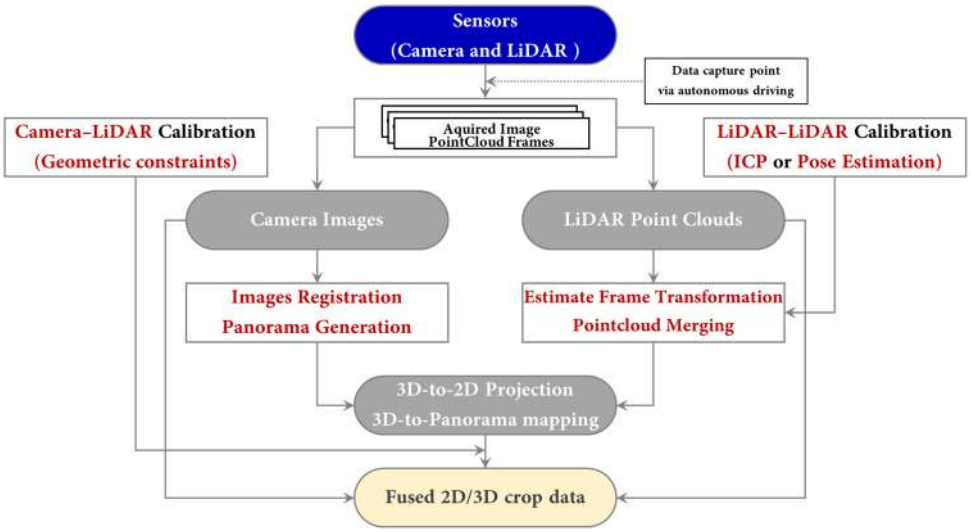

Fig.1 Flowchart of 3D crop data fusion using LiDAR and cameras.

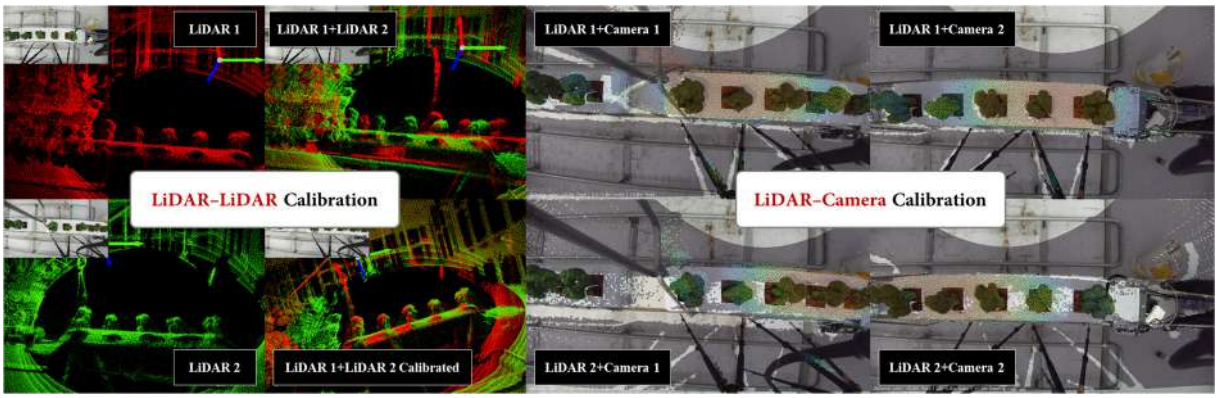

Fig.2 Verification of LiDAR and camera calibration results for data collected in the greenhouse

ACKNOWLEDGEMENTS

This work was supported by the Technology Innovation Program(or Industrial Strategic Technology Development Program)(RS-2026-25553719, Project for Establishing a Demonstration Infrastructure for AI Robots in Facility Agriculture) funded By the Ministry of Trade, Industry and Resources(MOTIR, Korea).

KAMICO
한국농기계공업협동조합



2026 KIEMSTA
Korea International Exhibition of Machinery, Equipment, Science and Technology for Agriculture

대한민국국제농기계자재박람회

2026.11.4(수) ~ 7(토)

exco (대구광역시)

주최·주관 농림축산식품부 대구광역시 KAMICO 한국농기계공업협동조합 농민신문사

홈페이지 www.ekiemsta.com | 문의 041-411-2133~7

daedong

AI to the Field

대동 AI 트랙터 HX

AI 농업의 시대를 열다

HX 1400 AI | HX 1200 AI



1588-2172

AI트랙터가 인건비는 낮추고 생산성은 높여 농사의 전 과정을 혁신합니다

앱 하나로 농사 짓다

앱으로 여러 대를 동시에 원격 관제 및 작업 관리가 가능합니다.

국내 최초 비전 기반

스마트 루프에 장착된 6개의 카메라가 사람처럼 보면서 작업합니다.

쓸 수록 성능이 좋아지다

데이터를 스스로 학습하고 알아서 업그레이드하며 매일 진화합니다.

농사의 결과를 바꾸다

감 대신 데이터로 판단해 지비용 고수익을 실현하고 정밀농업까지 가능합니다.

DJI 농업용 드론, 이제 대동 대리점에서 만나보세요

LS Tractor

시간을 이기는 트랙터

MT9



더 강력하게

우수한 연비의 143마력
FPT 엔진

더 안락하게

듀얼 클러치 미션,
캐빈 서스펜션

더 쉽고, 더 빠르게

전자식 로더 조이스틱,
로드센싱, 수평/경심 제어

더 여유롭게

2.1cm 초정밀
자율작업

센트럴A/S센터 (063) 722-3366 | 남부A/S센터 (061) 820-8001 | 동부A/S센터 (054) 434-4873 | 뉴홀랜드서비스 (061) 335-1119
경기영업소 (031) 8011-2100 | 강원영업소 (033) 812-2370 | 충북영업소 (043) 716-1133 | 충남영업소 (042) 825-3090 | 경남영업소 (055) 800-821


TYM
75
YEARS
SMART
미래
PREMIUM
경쟁력과 가치
HERITAGE
75년의 역사
www.tym.world

혁신제품 NEP 경북스타기업 국가품질경영대상

Bulls 주|불스

스마트 미래농업!
불스와 함께!

BGP-540
마늘·양파 수집기



BG-1580BC
콩 파종기(피복)



BG-2400CA
콩 파종기(무피복, 액액살포)



BGF-3(G)
정밀 시비기



BG-1200A
마늘·양파 휴립복토기



BG-1200GSC
마늘줄기 절단기



BG-1300SC
양파줄기 절단기



BG-1400HO
양파 수확기



BG-1300HC
마늘 수확기



BG-150-7SGP
마늘 파종기(무피복)



Bulls 주|불스
www.bulls.co.kr

본사 및 상주공장 경북 상주군 용암면 [illegible] 1272 (용청리)
T. 054.954.2810 F. 054.954.2720



농업회사 법인 엔에프지(주) & 주식회사 정진 에프피시

☞ 회사 소개

- 플라즈마 기술을 활용한 식품제조 가공 방법과 대규모 제조 공정을 보유하고 있고, 대형 유통업체의 직접 납품 코드를 보유하고 있기 때문에 농산물 재배부터 가공 및 판매유통을 하는 농산물 전문 생산 판매 기업 입니다.





☞ 인증 현황

HACCP 인증 | 이노비즈인증 | ISO 45001 | ISO 9001 | ISO 14001 | 녹색친환경 사용인증 | 플라즈마 기술 특허

☞ 대표 제품

[조각 과일]



[샐러드]



[스테비아 가공]



ALPHAON

주식회사 알파온

www.alphaon.kr

지능형 자율주행 모빌리티 & 3D 비전 카메라 솔루션

자율주행 무인 AGV/ AMR



3D 비전 카메라



모빌리티 원격제어 솔루션



(주) HMC

농축산 작업기 전문제작 기업 (주)HMC가 여러분과 함께하겠습니다



다목적 땅속작물 수확기

고구마, 감자, 땅콩, 생강, 마늘, 양파, 야콘, 속세, 토란 등 땅속작물 수확

★ 트랙타용 · 승용관리기용 땅속작물 수확기 ★

★ 유압목토기 ★



★ 농산물절단기 / 마늘종기파쇄기 ★

★ 마늘파종기 / 퇴토기 ★



★ 고구마, 감자 수확후 흙털기기 및 줄수정 겸용 작업 ★

★ 정량기용 · 관리기용 땅속작물 수확기 ★



★ 다목적 땅속작물 수확기의 특징 - 2중 진동날 ★

2중 진동날 방식으로 마늘, 양파, 땅콩 등 비닐이 있는 상태로 수확 작업을 하여도 수확기 앞 부분에 흙이 쌓이거나 비닐을 덜고 가는 현상이 없으며 뿌리의 흙 털림이 월등 합니다.

농가의 획기적인 노동력 절감! 땅속작물 수확의 신기원! 대신에이씨엠이 농가의 일손이 되어 드립니다.

[주]대신에이씨엠

www.dae-shin.net

정부 보조 및 융자 사업 상담 환영

전화.054-652-3907

팩스.054-652-3908

The 12th International Symposium on

Machinery and Mechatronics for Agricultural and Biosystems Engineering

ISMAB2026

